
Proceedings of the First International Symposium on

**RECENT ADVANCES IN QUANTITATIVE
REMOTE SENSING**

Auditori de Torrent, Spain
16-20 September 2002

Editor

José A. Sobrino
Global Change Unit
Universitat de València, Spain

Published by
Publicacions de la Universitat de València.
C/del Batxiller, 1-1
46010 València
publicacions@uv.es

RECENT ADVANCES IN QUANTITATIVE REMOTE SENSING

Edited by
José A. Sobrino
Universitat de València, Spain

Typesetting: M. Gómez, J. C. Jimenez, G. Sòria, M. Romaguera and J. El Kharraz.

Copyright © 2002 by the Authors

All rights reserved. This book or parts thereof, may not be reproduced in any form or by any means, electronic or mechanical, including photocopying, recording or any information storage and retrieval system now known or to be invented, without written permission from the authors.

Financial support for production of this book was given by the Generalitat Valenciana (Consellería de Innovación y Competitividad and Consellería de Medio Ambiente).

ISBN: 84-370-5515-6
Depósito legal: V-4325-2002
Printed in Spain by Guada Impresores S. L.

Preface

The first International Symposium on Recent Advances in Quantitative Remote Sensing, was held in Torrent, Spain from September 16 to 20, 2002. It was sponsored and organized by the University of Valencia (UVEG), Global Change Unit (GCU), Spain. Other sponsors include:

- City Council of Torrent (Spain);
- National Aeronautics and Space Administration (NASA);
- European Space Agency (ESA);
- European Commission (EU)
- Consellería de Medio Ambiente de la Generalitat Valenciana (Spain);
- Consellería de Innovación y Competitividad de la Generalitat Valenciana (Spain);
- Ministerio de Ciencia y Tecnología (Spain).

This Symposium addressed the scientific advances in quantitative remote sensing in connection with real applications. Its main goal was to assess the state of the art of both theory and applications in the analysis of remote sensing data, as well as to provide a forum for researcher in this subject area to exchange views and report their latest results. In this proceeding 133 of the 183 contributions presented in both plenary and poster sessions are arranged according to the scientific topics selected. For each topic the first papers are those presented in plenary sessions. The poster papers are ranked in the same order as the final programme.

To conclude, I would particularly like to thank the participants who have contributed to constructive discussions and the members of the International Scientific Committee, who greatly contributed to select the papers presented at the Symposium providing an attractive scientific programme. The symposium took place in Torrent in excellent conditions thanks to the UVEG, City Council of Torrent, NASA, ESA, EU, Consellerías de Medio Ambiente and Innovación de la Generalitat Valenciana for their material and financial support. The success is also due to the efforts made by the Organizing Committee: by the chairperson Pilar Gómez, and by the members Mónica Gómez, Jauad El Kharraz, Juan Carlos Jiménez, Guillem Sòria, Juan Cuenca and also by the collaboration of Mireia Romaguera and Malena Zaragoza. Many thanks to all of them.

José A. Sobrino
Symposium Chairperson
Global Change Unit,
Universitat de València

Valencia, November 2002

International Scientific Committee:

Chairperson:

J. A. SOBRINO

UNIVERSITY OF VALENCIA, SPAIN

Members

G. ASRAR

NASA, WASHINGTON, D.C., USA

G. CHEHBOUNI

IRD, CESBIO, TOULOUSE, FRANCE

A. P. CRACKNELL

UNIVERSITY OF DUNDEE, UK

A. GILLESPIE

UNIVERSITY OF WASHINGTON, USA

G. GUTMAN

NASA, WASHINGTON, D.C., USA

A. HUETE

UNIVERSITY OF ARIZONA, USA

M. LEROY

MEDIAS-FRANCE, CNES, TOULOUSE, FRANCE

X. LI

UNIVERSITY OF BOSTON, USA

Z.-L. LI

LSIIT, CNRS, STRASBOURG, FRANCE

J. LIU

IGSNRR, BEIJING, CHINA

J. MORENO

UNIVERSITY OF VALENCIA, SPAIN

F. NERRY

LSIIT, CNRS, STRASBOURG, FRANCE

A. OLIOSO

INRA, AVIGNON, FRANCE

F. PRATA

CSIRO, AUSTRALIA

S. QUEGAN

UNIVERSITY OF SHEFFIELD, UK

M. RAST

ESA/ESTEC, THE NETHERLANDS

A. ROYER

UNIVERSITY OF SHERBROOKE, CANADA

J. SHI

ICISS, UCSB, USA

Z. SU

ALTERRA, WAGENINGEN, THE NETHERLANDS

M. VERSTRAETE

JRC, ITALY

Z. WAN

ICISS, UCSB, USA

J. P. WIGNERON

INRA, BORDEAUX, FRANCE

Organizing Committee:

Chairperson:

P. GÓMEZ

SYMPOSIUM, TORRENT, SPAIN

Members:

M. GÓMEZ

UNIVERSITY OF VALENCIA, SPAIN

J. EL KHARRAZ

UNIVERSITY OF VALENCIA, SPAIN

J. C. JIMÉNEZ

UNIVERSITY OF VALENCIA, SPAIN

G. SÒRIA

UNIVERSITY OF VALENCIA, SPAIN

J. CUENCA

UNIVERSITY OF VALENCIA, SPAIN

J. A. SOBRINO

UNIVERSITY OF VALENCIA, SPAIN

CONTENTS

Preface

iii

NASA Earth Science Enterprise. A New Window on the World: International Partnerships and the Progress of NASA's Earth Observing System G. Asrar	1
---	----------

1. ESPECTRO SOLAR/ SOLAR SPECTRUM

Sesión Oral / Oral session

Accumulation of spectral BRDF knowledge for quantitative remote sensing of land surfaces	7
---	----------

X. Li, J. Wang , F. Gao, A. Strahler and L. Su

Improved modelling of multiple scattering in leaf canopies: the model SAIL++ W. Verhoef	11
---	-----------

Inter-sensor calibration of vegetation indices for monitoring and continuity studies of ecosystem variability	21
--	-----------

A. Huete, H. Yoshioka, T. Miura, H. J. Kim and X. Gao

Simulation of reflectance spectra in boreal coniferous forest	31
--	-----------

T. Nilson and A. Kuusk

Estimation of vegetation water content with MODIS data and radiative transfer simulation	39
---	-----------

P. J. Zarco-Tejada and S. L. Ustin

Leaf pigment retrievals from DAISEX data for crops at Barrax: effects of sun-angle and view angle on inversion results	45
---	-----------

J. R. Miller, J. Moreno, P. J. Zarco-Tejada, L. Alonso and D. Haboudane

Sesión Poster / Poster session

Use of Dempster-Shafer evidence theory for multi-scale data fusion	52
---	-----------

S. Le Hégarat-Masclé, D. Richard and C. Ottlé

Estimating the accuracy of vegetation variables retrieved from multiangular data	56
---	-----------

N. Widen

Potential of hyperspectral indices for estimating crop residue cover	61
---	-----------

M. Chevrier, A. Bannari, J.-C. Deguise, H. McNairn and K. Staenz

Mapping soil properties using remote sensing and geostatistics	69
---	-----------

F. López-Granados, S. Atenciano, M. Jurado-Expósito, A. García-Ferrer, M. Sánchez de la Orden, J. M. Peña-Barragán and L. García-Torres

Estimation of plant water content of agricultural canopies using hyperspectral remote sensing	77
--	-----------

C. M. Champagne, K. Staenz , A. Bannari, H. P. White, J. C. Deguise and H. McNairn

Hyperspectral monitoring of physiological parameters of wheat during a vegetation period using AVIS data N. Oppelt and W. Mauser	85
Upper Paraguay river water level prediction using precipitation and NDVI W. T. Liu, F. M. Ayres, A. T. Salles and C. Padovani	93
A new approach to characterize aerosols from their optical depth spectral values. Simulated case study J. L. Gómez-Amo, M. P. Utrillas, V. Estellés, R. Pedrós and J. A. Martínez-Lozano	100
Measured hot spot directional signatures of agricultural crops during DAISEX'99 using POLDER data F. Camacho-de Coca, M. Leroy, J. P. Gastellu-Etchegorry and F.J. García-Haro	108
Retrieval of water quality parameters of perialpine lakes in Austria by means of hyperspectral ROSIS data D. Floricioiu, E.Rott, C. Riedl and H. Rott	116
Use of a forest reflectance model for empirical estimation of Norway spruce characteristics from hyperspectral remote sensing imagery M. Schlerf and C. Atzberger	121
Object-based retrieval of structural and biochemical canopy characteristics using SAIL+PROSPECT canopy reflectance model: A numerical experiment C. Atzberger	129
Remote sensing of Saharan aerosol over land and sea K. Ourtirane and A. Faid	139
Impact of Saharan aerosol on solar radiation in the Tamanrasset area A. Faid and K. Ourtirane	146
Sequential BRDF inversion for mapping snow cover using a multi-scale analytical canopy reflectance model R. A. Fernandes and S. G. Leblanc	152
Determining the contribution of shaded elements of a canopy to remotely sensed hyperspectral signatures H. P. White, L. Sun, K. Staenz, R. Fernandes and C. M. Champagne	159
Mapping vineyard soil surface features by very high spatial resolution remote sensing T. Wassenaar, J. M. Robbez-Masson, F. Baret and P. Andrieux	167
Monitoring of wheat crop evapotranspiration and irrigation in arid conditions using phenology derived from optical satellite data B. Duchemin, P. Maisongrande, F. Frappart, M. Magnac, G. Chehbouni, G. Dedieu and B. Mougnot	177
CLAMP : A model of leaf clumping in canopies N. Rochdi, F. Baret, B. Combal and M. Chelle	184
Assessing recent algorithms devoted to albedo estimation using the airborne ReSeDa/ POLDER database F. Jacob and A. Olivos	191

Influence of spatial heterogeneity and scaling on leaf area index estimates from remote sensing data	199
S. Garrigues, D. Allard, M. Weiss, F. Baret, S. Marni and H. Jeanjean	
The 3-D scene computer simulation of the field crop canopy	207
M. Wu, Q. Zhu, L. Su, J. Wang, Y. Xiang, T. Shihao and P. Wang	
Validating LAI using hyperspectral imagery over agricultural canopies	210
A. Pacheco, A. Bannari, K. Staenz, H. McNairn and J. C. Deguise	
Potential of Getis statistics to characterize the radiometric spatial uniformity and temporal stability of test sites used for the calibration of Earth observation sensors	216
A. Bannari, K. Omari, P. M. Teillet and G. Fedosejevs	
Fusion of different spatial and spectral resolution images: development, application and comparison of new methods based on wavelets	228
M. González-Audicana, X. Otazu, O. Fors, R. García and J. Nuñez	
Comparison between the different curvatura models of terrain for determining the degree of soil humidity	238
M. J. Porres-de-la-Haza and J. E. Pardo-Pascual	
VEGETATION/SPOT4 data for use in meteorological models: surface albedo product and land cover mapping	246
L. Franchistéguy, J. L. Campeaux, S. Garrigues, R. Lacaze and J. L. Roujean	
Land surface albedo retrieval via kernel-based BRDF modeling: statistical inversion method, models comparison, and an optimal design scheme for the angular sampling	252
O. Pokrovsky and J. L. Roujean	
Radiación solar en las islas Baleares mediante imágenes de satélite	261
H. Flores-Tovar, J. M. Baldasano, N. Vera and P. Nadal	
Using NOAA-AVHRR and SPOT-VGT data to estimate surface parameters: application to a mesoscale meteorological model	268
N. Pineda, O. Jorba, J. Jorge and J. M. Baldasano	
Factor analysis of Landsat-TM for vegetation cover quantification in a dehesa ecosystem	277
M.P. González-Dugo, P. Fernández-Rebollo, J. V. Giráldez-Cervera and J. E. Guerrero-Ginel	
Advances in the use of DEMs for improved quantitative analysis of multiscale remote sensing data	282
J. C. García and J. Moreno	
Análisis de corredores ecológicos a nivel comarcal, mediante clasificación supervisada de la imagen de satélite LANDSAT-TM. Caso particular de la sierra de Ancares	287
M. L. Gil, A. González and I. Cañas	
Instalation, setup and preliminary results of a CIMEL CE318-2 in Burjassot, Spain	295
V. Estellés, J. L. Gómez-Amo, A. Segarra, M. P. Utrillas and J. A. Martínez-Lozano	

Quantitative analysis of cropland's BRDF anisotropy using airborne POLDER data	303
F. Camacho-de Coca, F. J. García-Haro and M. A. Gilabert	

Distinguishing cover crops and bare soils in olive groves using remote sensing	309
J.M. Peña-Barragán, F. López-Granados, S. Atenciano, M. Jurado-Expósito, J. L. González-Andújar, M. Sánchez-de la Orden, A. García-Ferrer and L. García-Torres	

2. SINERGIA/ SYNERGY

Sesión Oral / Oral session

On estimation of turbulent heat fluxes and evaporation with radiometric measurements: past, present and future	319
Z. B. Su	

Assimilation of remote sensing data into crop simulation models and SVAT models	329
A. Olioso, Y. Inoue, J. Demarty, J. P. Wigneron, I. Braud, S. Ortega-Farias, P. Lecharpentier, C. Ottlé, J. C. Calvet and N. Brisson	

Active vegetation fluorosensing: present state and prospects	339
I. Moya, A. Ounis, Z. G. Cerovic and Y. Goulas	

Land cover classification at a regional scale in Iberia: separability in a multi-temporal and multi-spectral data set of satellite images	348
A. Lobo, P. Legendre, J. L. González-Rebollar, J. Carreras and J. M. Ninot	

Remote sensing monitoring of desertification, phenology and droughts	354
A. Karnieli and G. Dall'Olmo	

The EuroSTARSS airborne campaign over land surfaces (SMOS mission): First results	363
K. Saleh, J. P. Wigneron, E. López Baeza, J. C. Calvet, T. Pellarin, M. Berger and L. Simmonds	

Sesión Poster / Poster session

Mapping paleoflooded areas on evaporative playa deposits over sandy sediments (Tablas de Daimiel, Spain) using hyperspectral DAIS 7915 and ROSIS spectrometer data	371
A. Riaza, R. Mediavilla, E. Garcia-Meléndez, M. Suarez, A. Hausold, U. Beisl and H. Van Der Werff	

Soil-vegetation indices developed from spectral signatures recorded by various satellites	380
K. Dabrowska-Zielinska, W. Kowalik, M. Gruszczynska, A. Hoscilo and K. Stankiewicz	

Estimating foliar chlorophyll concentration at leaf and canopy level using a model-empirical synthesized method	388
C. Yan, Q. Liu, Z. Niu and C. Wang	

Flux estimation with the MESONH model over the Alpillés	397
D. Courault, P. Lacarrère, F. Jacob, A. Olioso, P. Clastre, P. Lecharpentier, O. Marloie and L. Prévot	

Spectral characteristics and feature selection of hyperspectral remote sensing data	403
X. G. Jiang, L. Tang, C. Wang and C. Wang	

Brazilian soybean yield prediction using satellites stress indices W. T. Liu, A. L. Souza and F. Kogan	409
Parameterization of land surface heat fluxes over inhomogeneous landscape of Tibetan Plateau and arid area by combining satellite remote sensing with field observations Y. M. Ma, Z. B. Su, M. Menenti, Z. L. Li, O. Tsukamoto, H. Ishikawa and T. Koike	416
Multi-sensor flood crisis management and case-based database over the Moselle river (France) J. B. Henry, N. Tholey and P. De Fraipont	426
D.A.R.T.: a 3-D model for simulating satellite images and surface radiation budget E. Martin, J. P. Gastellu-Etchegorry, F. Gascon, P. Gentine and A. Belot	431
Development and application of SiSPAT-RS SVAT model at field scale during the Alpilles-ReSeDA experiment: multiobjective calibration in a context of remote sensing data assimilation J. Demarty, C. Ottlé, I. Braud, A. Oliso and J. P. Frangi	442
Mapping surface sensible heat flux from thermal infrared and reflectances data using various models over the Alpilles test site A. Oliso, C. Hasager, F. Jacob, T. Wassenaar, A. Chehbouni , O. Marloie, P. Lecharpentier and D. Courault	450
Estimation of evapotranspiration on heterogeneous pixels T. Wassenaar, A. Oliso, C. Hasager, F. Jacob and A. Chehbouni	458
Land cover, surface temperature and leaf area index maps from satellites used for the aggregation of momentum and temperature roughnesses C. B. Hasager, N. O. Jensen and A. Oliso	466
Comparison of two surface energy balance models using ASTER data F. Jacob, A. French, T. Schmugge, K. Ogawa and B. Kustas	474
Using LANDSAT-TM imagery to detect landslides impacts on montane forests of NW Argentina L. Paolini, J. A. Sobrino and J. C. Jiménez-Muñoz	482
Semi-supervised method for crop classification using hyperspectral remote sensing images L. Gómez-Chova, J. Calpe, E. Soria, G. Camps-Valls, J. D. Martín and J. Moreno	488
The VALENCIA ANCHOR STATION: A reference Cal/Val area for low-resolution remote sensing data and products E. López-Baeza, C. Antolín-Tomás, A. Bodas-Salcedo, J. F. Gimeno-Ferrer, K. Saleh-Contell, F. Ferrer, N. Castell-Balaguer, C. Doménech-García, M. A. Sánchez-Alandí and A. Velázquez-Blázquez	496
Information content of HyMap hyperspectral imagery C. Bacour, F. Baret and S. Jacquemoud	503
Passive vegetation fluorosensing using atmospheric oxygen absorption bands S. Evain, A. Ounis, F. Baret, Y. Goulas, J. Louis, Z. G. Cerovic and I. Moya	509

Evaluation of texture analysis techniques to characterize vegetation L. A. Ruiz, A. Fdez-Sarría and J. Recio	514
Remote sensing monitoring crop growth A. Calera, J. González-Piqueras and J. Meliá	522
Study of the land use changes effects on the evapotranspiration in central Spain using remote sensing techniques S. Lanjeri, D. Segarra, A. Calera and J. Meliá	530
Satellite remote sensing of drought conditions and vegetation monitoring in Spain during the period 1987-2001 F. González-Alonso, A. Calle, J. L. Casanova, A. Romo and J. M. Cuevas	537
Mejora en los métodos de registro de imágenes SPOT en función de las características del terreno F. J. Martín, C. Pinilla and F. J. Ariza	541
Comparación de matrices de confusión celda a celda mediante Bootstrapping F. J. Ariza, C. Pinilla and J. L. García	550
A simple method to calculate reference evapotranspiration: application to the Azul Basin, Buenos Aires, Argentina R. Rivas, V. Caselles and E. Valor	557
Wavelet transform as a tool to detect land degradation from remotely sensed data J. F. Gimeno-Ferrer, M. A. Gilabert and J. Meliá	560
Retrieval of biophysical parameters from DAIS data J. C. Jiménez-Muñoz, M. Gómez, J. A. Sobrino, G. Soria, J. El Kharraz and J. Labed-Nachbrand	566
 3. INFRARROJO TÉRMICO/ THERMAL INFRARED Sesión Oral / Oral session	
Quality assessment and validation of the MODIS global land-surface temperature Z. Wan, Y. Zhang, Q. Zhang and Z.-L. Li	575
Quantitative estimates of emissivity using ASTER data T. Schmugge, F. Jacob, A. French and K. Ogawa	585
Relativity of isothermal definition and its scaling effects in quantitative thermal infrared remote sensing R.H. Zhang, Z.-L. Li, X. Tang, X. Sun, H.B. Su, C. Zhu and Z. Zhu	590
 Sesión Poster / Poster session	
Retrieval of plant and soil temperature by AMTIS data W. Fan, Y. Zhang and X. Xu	600
The component temperature of mixed pixel retrieved by multi-angle combined multi-time thermal infrared remotely sensed data X. Xu, W. Fan and Y. Zhang	605

Integrating VNIR and TIR information in inversion of land surface component Temperature	609
Q. Liu, L. Chen, Q. Xiao, Q. H. Liu and G. L. Tian	
Development and application of time process information of radiometric temperature for soil and vegetation to invert surface fluxes	616
R. H. Zhang, X. Sun, Z.-L. Li, Z. Zhu, H.B. Su and X.Z. Tang	
Definition of component effective emissivity for heterogeneous and non-isothermal surfaces and its Monte Carlo calculation	624
L.-F. Chen, Z.-L. Li, Q.-H. Liu, S. Chen, Y. Tang and B. Zhong	
Derivation of land surface temperatures from MODIS data using general split-window technique	631
C. O. Mito, G. Laneve, and M. M. Castronuovo	
The urban heat island effect in the SAO PAULO metropolitan region by AVHRR and the influence in the human health	639
A. L. Farias de Souza and O. Massambani	
The use of HIRLAM climate predictions and AVHRR data for the calculation of evapotranspiration rates in Denmark	646
E. Boegh, H. Soegaard, J. H. Christensen, C. B. Hasager, N. O. Jensen, N. W. Nielsen and M. S. Rasmussen	
Atmospheric correction of IR satellite data using neural networks	651
F.-M. Götsche and F.-S. Olesen	
Comparison of Meteosat-7 and (A)ATSR data over land: A sensitivity analysis	656
E. J. Noyes, J. J. Remedios, D. T. Llewellyn-Jones and M. C. Edwards	
Using MODIS land surface temperature and normalized difference vegetation index products for monitoring drought in the southern Great Plains, USA	664
P.-X. Wang, Z. Wan and X.-W. Li	
Change analysis of land surface temperature in China using NOAA-AVHRR data	672
C. Y. Wang, H. Yan and Z. Niu	
Experimental system for the study of the directional thermal emission of natural surfaces	679
Z.-L. Li, R. H. Zhang, X. Sun, H. B. Su, X. Z. Tang, Z. Zhu and J. A. Sobrino	
Sensitivity of TIR directional emittance to soil water content and LAI in the soil-vegetation-atmosphere system	686
L. Jia, M. Menenti and Z.-L. Li	
Retrieval of thermo-optical properties of materials using field (3-5 μm) & (8-14 μm) infrared imaging combined with a multi-temporal regression method	692
F. Nerry, M.-P. Stoll and A. Malaplate	
Estimating land surface temperature in South America from NOAA-AVHRR images and reanalysis data	698
L. Morales, J. C. Parra and J. A. Sobrino	
Sea surface temperature assessment during the wind and salinity experiment (WISE)	707
V. Caselles, R. Niclòs, E. Rubio, C. Coll, A. Camps and J. Font	

4. MICROONDAS/ MICROWAVES

Sesión Oral / Oral session

- Recent progress in estimating snow properties using multi-parameter SAR** 713
J. Shi
- Estimation of soil moisture and surface roughness using two radar configurations** 724
M. Zribi, M. Dechambre and N. Baghdadi
- Model based forest height estimation for forest biomass estimation** 731
K. P. Papathanassiou, I. Hajnsek, T. Mette and S. R. Cloude
- Monitoring land surface soil moisture from L-band microwave radiometry: Retrievals from multi-angular observations** 741
J. P. Wigneron, Y. Kerr, J. C. Calvet, T. Pellarin, M. Pardé and S. Schmidl Søbjaerg
- An improved estimation technique for rainfall over land surfaces using active and passive microwave satellite data** 751
J. Schulz and P. Bauer
- Sea surface salinity and wind speed retrieved from a Tower-based L-Band radiometer in the NW mediterranean** 761
C. Gabarró, J. Font, A. Camps and M. Vall-Ilosera

Sesión Poster / Poster session

- Quantitative comparison of IEM calculations with L-band SAR measurements in agricultural areas** 770
J. Shi, M. Herold and C. C. Schmullius
- Offshore wind resources quantified from satellite SAR: methodology and technical Aspects** 778
C. B. Hasager, B. Furevik, S. C. Pryor and R. J. Barthelmie
- Seasonal changes of polarimetric parameters from crops-a comparison of different decomposition approaches at L-band** 783
T. Riedel and C. C. Schmullius
- Effects of environmental factors on multi-frequency and full-polarization backscatter signatures over paddy field** 793
Y. Inoue, T. Kurosu, H. Maeno, T. Kozu and S. Uratsuka
- Regional mapping of sahelian herbaceous production from a combined use of ERS scatterometer data and a water balance model with an evolution strategies algorithm** 802
L. Jarlan, P. Mazzega, E. Mougin, B. Duchemin, Y. Tracol, P. L. Frison, M. Schoenauer and P. Hiernaux
- Merging of airborne laser altimeter data and RADARSAT data to develop a digital elevation model** 810
N. Baghdadi, B. Bourguine, S. Cavelier, J.-P. Chilès, C. King, P. Daniels, J. Perrin and C. Truffert
- The retrieval of aerodynamic surface roughness from SAR remote sensing image** 818
C. Zhu, R. H. Zhang, J. Wang, Q. Xu and G. Jin

On-board medium resolution SAR processing for fast image generation A. Vidal-Pantaleoni and M. Ferrando	823
Comparison of different speckle reduction techniques in SAR images using wavelet Transform A. Vidal-Pantaleoni and D. Martí	831
Characterizing the vegetation microwave parameters dependence on view angle and polarization (SMOS mission) M. Pardé, J. P. Wigneron, A. Chanzy and P. Ferrazzoli	839
Land surface monitoring using a combination of active and passive microwave and optical satellite sensors L.N. Guijarro, V. Lakshmi, Y. H. Kerr and G. Chehbouni	847
 5. PROYECTOS RECIENTES Y MISIONES DE OBSERVACIÓN DE LA TIERRA /RECENT PROJECTS AND EARTH OBSERVATION MISSIONS Sesión Oral / Oral session	
Monitoring global climate change: the Advanced Along Track Scanning Radiometer (AATSR) M. C. Edwards, D. Llewellyn-Jones and D. Smith	857
Simulation of SPECTRA like scenes using coupled leaf, canopy and atmospheric radiative transfer models H. Bach and W. Verhoef	863
Preparados para el lanzamiento del MSG-1 E. Oriol-Pibernat	871
 Sesión Poster / Poster session	
Estudio del fenómeno migratorio de la mariposa Monarca con ayuda de imágenes SPOT M.-L. España-Boquera, F. Baret and J.-F. Hanocq	874
VEGETATION/SPOT. An operational mission for the Earth monitoring. Presentation of new standard products P. Maisongrande, B. Duchemin and G. Dedieu	880
Preliminary pigment retrieval results from a sparse-canopy poplar plantation in northern Italy using hyperspectral data C. Panigada, J. R. Miller, M. Meroni, T. Noland, M. Boschetti, R. Colombo, C.M. Marino and M. Packalen	885
Effects of chlorophyll concentration on green LAI prediction in crop canopies: Modelling and assessment D. Haboudane, J. R. Miller, E. Pattey, P. J. Zarco-Tejada and I. Strachan	891
LAI retrieval from multi-angle and hyperspectral observations in an intensively-managed poplar plantation M. Meroni, R. Colombo, M. Boschetti, C. Panigada, M. Rossini, P. A. Brivio and J. R. Miller	900

Radiometric saturation of LANDSAT-7 ETM+ data over the Negev desert (Israel): Problems and solutions	904
A. Karnieli, E. Ben-Dor, B. Yunden and R. Lugasi	
The potential of the TERRA-ASTER sensor to retrieve radiative properties over semi-arid regions	913
F. Jacob, T. Schmugge, K. Ogawa, A. French and J. Ritchie	
Assimilation of high temporal frequency SPOT data to describe canopy functioning- the case of wheat crops in the ADAM experiment in Romania	921
C. Lauvernet, F. X. Le Dimet, F. Baret, H. Deboissezon, J.C. Favard, R. Vintila, C. Lázár and A. Badea	
Localización de construcciones rurales en la imagen de satélite IKONOS y gestión de las mismas mediante un sistema de información geográfica	927
M. L. Gil, A. González and I. Cañas	
Land cover change monitoring in the mediterranean basin using NOAA-PATHFINDER time series (1981-2001): WATERMED project	935
J. A. Sobrino, J. El Kharraz, M. Romaguera, M. Gómez, J. C. Jiménez-Muñoz and G. Sòria	
Water vapour retrieval from MODIS data	941
J. El Kharraz, J. A. Sobrino, M. Gómez, J. C. Jiménez-Muñoz and G. Sòria	
Angular variation of thermal infrared emissivity for some natural surfaces from laboratory and field measurements	946
J. A. Sobrino, J. Cuenca and G. Sòria	
Surface temperature retrieval from AATSR data: multichannel and multiangle Algorithms	952
G. Sòria, J. A. Sobrino, J. Cuenca, A. J. Prata, J. C. Jiménez-Muñoz, M. Gómez and J. El-Kharraz	
Study of the radiance to flux inversion within the framework of the EARTHCARE Mission	956
A. Bodas-Salcedo, J. F. Gimeno-Ferrer, E. López-Baeza and J. P. V. Poiars-Baptista	
Retrieval of biophysical parameters using directional spectral mixture analysis	963
F.J. García-Haro, F. Camacho-de Coca and J. Meliá	
Directional effects on observations of Land Surface Temperature with AVHRR over Africa	971
A. C. Pinheiro, J. L. Privette, R. Mahoney and C. J. Tucker	
AUTHOR INDEX	979
FIGURES IN COLOUR	987

Proceedings of the First International Symposium on

**RECENT ADVANCES IN QUANTITATIVE
REMOTE SENSING**

Auditori de Torrent, Spain
16-20 September 2002

Editor

José A. Sobrino

Global Change Unit
Universitat de València, Spain

Published by
Publicacions de la Universitat de València.
C/del Batxiller, 1-1
46010 València
publicacions@uv.es

RECENT ADVANCES IN QUANTITATIVE REMOTE SENSING

Edited by
José A. Sobrino
Universitat de València, Spain

Typesetting: M. Gómez, J. C. Jimenez, G. Sòria, M. Romaguera and J. El Kharraz.

Copyright © 2002 by the Authors

All rights reserved. This book or parts thereof, may not be reproduced in any form or by any means, electronic or mechanical, including photocopying, recording or any information storage and retrieval system now known or to be invented, without written permission from the authors.

Financial support for production of this book was given by the Generalitat Valenciana (Consellería de Innovación y Competitividad and Consellería de Medio Ambiente).

ISBN: 84-370-5515-6

Depósito legal: V-

Printed in Spain by Guada Impresores S. L.

Preface

The first International Symposium on Recent Advances in Quantitative Remote Sensing, was held in Torrent, Spain from September 16 to 20, 2002. It was sponsored and organized by the University of Valencia (UVEG), Global Change Unit (GCU), Spain. Other sponsors include:

- City Council of Torrent (Spain);
- National Aeronautics and Space Administration (NASA);
- European Space Agency (ESA);
- European Commission (EU)
- Consellería de Medio Ambiente de la Generalitat Valenciana (Spain);
- Consellería de Innovación y Competitividad de la Generalitat Valenciana (Spain);
- Ministerio de Ciencia y Tecnología (Spain).

This Symposium addressed the scientific advances in quantitative remote sensing in connection with real applications. Its main goal was to assess the state of the art of both theory and applications in the analysis of remote sensing data, as well as to provide a forum for researcher in this subject area to exchange views and report their latest results. In this proceeding 133 of the 183 contributions presented in both plenary and poster sessions are arranged according to the scientific topics selected. For each topic the first papers are those presented in plenary sessions. The poster papers are ranked in the same order as the final programme.

To conclude, I would particularly like to thank the participants who have contributed to constructive discussions and the members of the International Scientific Committee, who greatly contributed to select the papers presented at the Symposium providing an attractive scientific programme. The symposium took place in Torrent in excellent conditions thanks to the UVEG, City Council of Torrent, NASA, ESA, EU, Consellerías de Medio Ambiente and Innovación de la Generalitat Valenciana for their material and financial support. The success is also due to the efforts made by the Organizing Committee: by the chairperson Pilar Gómez, and by the members Mónica Gómez, Jauad El Kharraz, Juan Carlos Jiménez, Guillem Sòria, Juan Cuenca and also by the collaboration of Mireia Romaguera and Malena Zaragoza. Many thanks to all of them.

José A. Sobrino
Symposium Chairperson
Global Change Unit,
Universitat de València

Valencia, November 2002

International Scientific Committee:

Chairperson:

J. A. SOBRINO

UNIVERSITY OF VALENCIA, SPAIN

Members

G. ASRAR

NASA, WASHINGTON, D.C., USA

G. CHEHBOUNI

IRD, CESBIO, TOULOUSE, FRANCE

A. P. CRACKNELL

UNIVERSITY OF DUNDEE, UK

A. GILLESPIE

UNIVERSITY OF WASHINGTON, USA

G. GUTMAN

NASA, WASHINGTON, D. C., USA

A. HUETE

UNIVERSITY OF ARIZONA, USA

M. LEROY

MEDIAS-FRANCE, CNES, TOULOUSE, FRANCE

X. LI

UNIVERSITY OF BOSTON, USA

Z.-L. LI

LSIIT, CNRS, STRASBOURG, FRANCE

J. LIU

IGSNRR, BEIJING, CHINA

J. MORENO

UNIVERSITY OF VALENCIA, SPAIN

F. NERRY

LSIIT, CNRS, STRASBOURG, FRANCE

A. OLIOSO

INRA, AVIGNON, FRANCE

F. PRATA

CSIRO, AUSTRALIA

S. QUEGAN

UNIVERSITY OF SHEFFIELD, UK

M. RAST

ESA/ESTEC, THE NETHERLANDS

A. ROYER

UNIVERSITY OF SHERBROOKE, CANADA

J. SHI

ICESS, UCSB, USA

Z. SU

ALTERRA, WAGENINGEN, THE NETHERLANDS

M. VERSTRAETE

JRC, ITALY

Z. WAN

ICESS, UCSB, USA

J. P. WIGNERON

INRA, BORDEAUX, FRANCE

Organizing Committee:

Chairperson:

P. GÓMEZ

SYMPOSIUM, TORRENT, SPAIN

Members:

M. GÓMEZ

UNIVERSITY OF VALENCIA, SPAIN

J. EL KHARRAZ

UNIVERSITY OF VALENCIA, SPAIN

J. C. JIMÉNEZ

UNIVERSITY OF VALENCIA, SPAIN

G. SÒRIA

UNIVERSITY OF VALENCIA, SPAIN

J. CUENCA

UNIVERSITY OF VALENCIA, SPAIN

J. A. SOBRINO

UNIVERSITY OF VALENCIA, SPAIN

CONTENTS

Preface

iii

NASA Earth Science Enterprise. A New Window on the World: International Partnerships and the Progress of NASA's Earth Observing System G. Asrar	1
---	----------

1. ESPECTRO SOLAR/ SOLAR SPECTRUM **Sesión Oral / Oral session**

Accumulation of spectral BRDF knowledge for quantitative remote sensing of land surfaces X. Li, J. Wang , F. Gao, A. Strahler and L. Su	7
---	----------

Improved modelling of multiple scattering in leaf canopies: the model SAIL++ W. Verhoef	11
---	-----------

Inter-sensor calibration of vegetation indices for monitoring and continuity studies of ecosystem variability A. Huete, H. Yoshioka, T. Miura, H. J. Kim and X. Gao	21
---	-----------

Simulation of reflectance spectra in boreal coniferous forest T. Nilson and A. Kuusk	31
--	-----------

Estimation of vegetation water content with MODIS data and radiative transfer simulation P. J. Zarco-Tejada and S. L. Ustin	39
---	-----------

Leaf pigment retrievals from DAISEX data for crops at Barrax: effects of sun-angle and view angle on inversion results J. R. Miller, J. Moreno, P. J. Zarco-Tejada, L. Alonso and D. Haboudane	45
--	-----------

Sesión Poster / Poster session

Use of Dempster-Shafer evidence theory for multi-scale data fusion S. Le Hégarat-Masclé, D. Richard and C. Ottlé	52
--	-----------

Estimating the accuracy of vegetation variables retrieved from multiangular data N. Widen	56
---	-----------

Potential of hyperspectral indices for estimating crop residue cover M. Chevrier, A. Bannari, J.-C. Deguise, H. McNairn and K. Staenz	61
---	-----------

Mapping soil properties using remote sensing and geostatistics F. López-Granados, S. Atenciano, M. Jurado-Expósito, A. García-Ferrer, M. Sánchez de la Orden, J. M. Peña-Barragán and L. García-Torres	69
---	-----------

Estimation of plant water content of agricultural canopies using hyperspectral remote sensing C. M. Champagne, K. Staenz , A. Bannari, H. P. White, J. C. Deguise and H. McNairn	77
--	-----------

Hyperspectral monitoring of physiological parameters of wheat during a vegetation period using AVIS data N. Oppelt and W. Mauser	85
--	-----------

Upper Paraguay river water level prediction using precipitation and NDVI W. T. Liu, F. M. Ayres, A. T. Salles and C. Padovani	93
A new approach to characterize aerosols from their optical depth spectral values. Simulated case study J. L. Gómez-Amo, M. P. Utrillas, V. Estellés, R. Pedrós and J. A. Martínez-Lozano	100
Measured hot spot directional signatures of agricultural crops during DAISEX'99 using POLDER data F. Camacho-de Coca, M. Leroy, J. P. Gastellu-Etchegorry and F.J. García-Haro	108
Retrieval of water quality parameters of perialpine lakes in Austria by means of hyperspectral ROSIS data D. Floricioiu, E.Rott, C. Riedl and H. Rott	116
Use of a forest reflectance model for empirical estimation of Norway spruce characteristics from hyperspectral remote sensing imagery M. Schlerf and C. Atzberger	121
Object-based retrieval of structural and biochemical canopy characteristics using SAIL+PROSPECT canopy reflectance model: A numerical experiment C. Atzberger	129
Remote sensing of Saharan aerosol over land and sea K. Ourtirane and A. Faid	139
Impact of Saharan aerosol on solar radiation in the Tamanrasset area A. Faid and K. Ourtirane	146
Sequential BRDF inversion for mapping snow cover using a multi-scale analytical canopy reflectance model R. A. Fernandes and S. G. Leblanc	152
Determining the contribution of shaded elements of a canopy to remotely sensed hyperspectral signatures H. P. White, L. Sun, K. Staenz, R. Fernandes and C. M. Champagne	159
Mapping vineyard soil surface features by very high spatial resolution remote sensing T. Wassenaar, J. M. Robbez-Masson, F. Baret and P. Andrieux	167
Monitoring of wheat crop evapotranspiration and irrigation in arid conditions using phenology derived from optical satellite data B. Duchemin, P. Maisongrande, F. Frappart, M. Magnac, G. Chehbouni, G. Dedieu and B.Mougenot	177
CLAMP : A model of leaf clumping in canopies N. Rochdi, F. Baret, B. Combal and M. Chelle	184
Assessing recent algorithms devoted to albedo estimation using the airborne ReSeDa/ POLDER database F. Jacob and A. Oliosio	191
Influence of spatial heterogeneity and scaling on leaf area index estimates from remote sensing data S. Garrigues, D. Allard, M. Weiss, F. Baret, S. Marni and H. Jeanjean	199
The 3-D scene computer simulation of the field crop canopy M. Wu, Q. Zhu, L. Su, J. Wang, Y. Xiang, T. Shihao and P. Wang	207

Validating LAI using hyperspectral imagery over agricultural canopies A. Pacheco, A. Bannari, K. Staenz, H. McNairn and J. C. Deguise	210
Potential of Getis statistics to characterize the radiometric spatial uniformity and temporal stability of test sites used for the calibration of Earth observation sensors A. Bannari, K. Omari, P. M. Teillet and G. Fedosejevs	216
Fusion of different spatial and spectral resolution images: development, application and comparison of new methods based on wavelets M. González-Audicana, X. Otazu, O. Fors, R. García and J. Nuñez	228
Comparison between the different curvatura models of terrain for determining the degree of soil humidity M. J. Porres-de-la-Haza and J. E. Pardo-Pascual	238
VEGETATION/SPOT4 data for use in meteorological models: surface albedo product and land cover mapping L. Franchistéguy, J. L. Campeaux, S. Garrigues, R. Lacaze and J. L. Roujean	246
Land surface albedo retrieval via kernel-based BRDF modeling: statistical inversion method, models comparison, and an optimal design scheme for the angular sampling O. Pokrovsky and J. L. Roujean	252
Radiación solar en las islas Baleares mediante imágenes de satélite H. Flores-Tovar, J. M. Baldasano, N. Vera and P. Nadal	261
Using NOAA-AVHRR and SPOT-VGT data to estimate surface parameters: application to a mesoscale meteorological model N. Pineda, O. Jorba, J. Jorge and J. M. Baldasano	268
Factor analysis of Landsat-TM for vegetation cover quantification in a dehesa ecosystem M. P. González-Dugo, P. Fernández-Rebollo, J. V. Giráldez-Cervera and J. E. Guerrero-Ginel	277
Advances in the use of DEMs for improved quantitative analysis of multiscale remote sensing data J. C. García and J. Moreno	282
Análisis de corredores ecológicos a nivel comarcal, mediante clasificación supervisada de la imagen de satélite LANDSAT-TM. Caso particular de la sierra de Ancares M. L. Gil, A. González and I. Cañas	287
Installation, setup and preliminary results of a CIMEL CE318-2 in Burjassot, Spain V. Estellés, J. L. Gómez-Amo, A. Segarra, M. P. Utrillas and J. A. Martínez-Lozano	295
Quantitative analysis of cropland's BRDF anisotropy using airborne POLDER data F. Camacho-de Coca, F. J. García-Haro and M. A. Gilabert	303
Distinguishing cover crops and bare soils in olive groves using remote sensing J. M. Peña-Barragán, F. López-Granados, S. Atenciano, M. Jurado-Expósito, J. L. González-Andújar, M. Sánchez-de la Orden, A. García-Ferrer and L. García-Torres	309

2. SINERGIA/ SYNERGY

Sesión Oral / Oral session

On estimation of turbulent heat fluxes and evaporation with radiometric measurements: past, present and future	319
Z. B. Su	

Assimilation of remote sensing data into crop simulation models and SVAT models	329
A. Oliso, Y. Inoue, J. Demarty, J. P. Wigneron, I. Braud, S. Ortega-Farias, P. Lecharpentier, C. Ottlé, J. C. Calvet and N. Brisson	

Active vegetation fluorosensing: present state and prospects	339
I. Moya, A. Ounis, Z. G. Cerovic and Y. Goulas	

Land cover classification at a regional scale in Iberia: separability in a multi-temporal and multi-spectral data set of satellite images	348
A. Lobo, P. Legendre, J. L. González-Rebollar, J. Carreras and J. M. Ninot	

Remote sensing monitoring of desertification, phenology and droughts	354
A. Karnieli and G. Dall’Olmo	

The EuroSTARSS airborne campaign over land surfaces (SMOS mission): First results	363
K. Saleh, J. P. Wigneron, E. López Baeza, J. C. Calvet, T. Pellarin, M. Berger and L. Simmonds	

Sesión Poster / Poster session

Mapping paleoflooded areas on evaporative playa deposits over sandy sediments (Tablas de Daimiel, Spain) using hyperspectral DAIS 7915 and ROSIS spectrometer data	371
A. Riaza, R. Mediavilla, E. Garcia-Meléndez, M. Suarez, A. Hausold, U. Beisl and H. Van Der Werff	

Soil-vegetation indices developed from spectral signatures recorded by various satellites	380
K. Dabrowska-Zielinska, W. Kowalik, M. Gruszczynska, A. Hoscilo and K. Stankiewicz	

Estimating foliar chlorophyll concentration at leaf and canopy level using a model-empirical synthesized method	388
C. Yan, Q. Liu, Z. Niu and C. Wang	

Flux estimation with the MESONH model over the Alpilles	397
D. Courault, P. Lacarrère, F. Jacob, A. Oliso, P. Clastre, P. Lecharpentier, O. Marloie and L. Prévot	

Spectral characteristics and feature selection of hyperspectral remote sensing data	403
X. G. Jiang, L. Tang, C. Wang and C. Wang	

Brazilian soybean yield prediction using satellites stress indices	409
W. T. Liu, A. L. Souza and F. Kogan	

Parameterization of land surface heat fluxes over inhomogeneous landscape of Tibetan Plateau and arid area by combining satellite remote sensing with field observations	416
Y. M. Ma, Z. B. Su, M. Menenti, Z. L. Li, O. Tsukamoto, H. Ishikawa and T. Koike	

Multi-sensor flood crisis management and case-based database over the Moselle river (France)	426
J. B. Henry, N. Tholey and P. De Fraipont	
D.A.R.T.: a 3-D model for simulating satellite images and surface radiation budget	431
E. Martin, J. P. Gastellu-Etchegorry, F. Gascon, P. Gentine and A. Belot	
Development and application of SiSPAT-RS SVAT model at field scale during the Alpilles-ReSeDA experiment: multiobjective calibration in a context of remote sensing data assimilation	442
J. Demarty, C. Ottlé, I. Braud, A. Oliso and J. P. Frangi	
Mapping surface sensible heat flux from thermal infrared and reflectances data using various models over the Alpilles test site	450
A. Oliso, C. Hasager, F. Jacob, T. Wassenaar, A. Chehbouni, O. Marloie, P. Lecharpentier and D. Courault	
Estimation of evapotranspiration on heterogeneous pixels	458
T. Wassenaar, A. Oliso, C. Hasager, F. Jacob and A. Chehbouni	
Land cover, surface temperature and leaf area index maps from satellites used for the aggregation of momentum and temperature roughnesses	466
C. B. Hasager, N. O. Jensen and A. Oliso	
Comparison of two surface energy balance models using ASTER data	474
F. Jacob, A. French, T. Schmugge, K. Ogawa and B. Kustas	
Using LANDSAT-TM imagery to detect landslides impacts on montane forests of NW Argentina	482
L. Paolini, J. A. Sobrino and J. C. Jiménez-Muñoz	
Semi-supervised method for crop classification using hyperspectral remote sensing images	488
L. Gómez-Chova, J. Calpe, E. Soria, G. Camps-Valls, J. D. Martín and J. Moreno	
The VALENCIA ANCHOR STATION: A reference Cal/Val area for low-resolution remote sensing data and products	496
E. López-Baeza, C. Antolín-Tomás, A. Bodas-Salcedo, J. F. Gimeno-Ferrer, K. Saleh-Contell, F. Ferrer, N. Castell-Balaguer, C. Doménech-García, M. A. Sánchez-Alandí and A. Velázquez-Blázquez	
Information content of HyMap hyperspectral imagery	503
C. Bacour, F. Baret and S. Jacquemoud	
Passive vegetation fluorosensing using atmospheric oxygen absorption bands	509
S. Evain, A. Ounis, F. Baret, Y. Goulas, J. Louis, Z. G. Cerovic and I. Moya	
Evaluation of texture analysis techniques to characterize vegetation	514
L. A. Ruiz, A. Fdez-Sarría and J. Recio	
Remote sensing monitoring crop growth	522
A. Calera, J. González-Piqueras and J. Meliá	
Study of the land use changes effects on the evapotranspiration in central Spain using remote sensing techniques	530
S. Lanjeri, D. Segarra, A. Calera and J. Meliá	

Satellite remote sensing of drought conditions and vegetation monitoring in Spain during the period 1987-2001	537
F. González-Alonso, A. Calle, J. L. Casanova, A. Romo and J. M. Cuevas	
Mejora en los métodos de registro de imágenes SPOT en función de las características del terreno	541
F. J. Martín, C. Pinilla and F. J. Ariza	
Comparación de matrices de confusión celda a celda mediante Bootstrapping	550
F. J. Ariza, C. Pinilla and J. L. García	
A simple method to calculate reference evapotranspiration: application to the Azul Basin, Buenos Aires, Argentina	557
R. Rivas, V. Caselles and E. Valor	
Wavelet transform as a tool to detect land degradation from remotely sensed data	560
J. F. Gimeno-Ferrer, M. A. Gilabert and J. Meliá	
Retrieval of biophysical parameters from DAIS data	566
J. C. Jiménez-Muñoz, M. Gómez, J. A. Sobrino, G. Sòria, J. El Kharraz and J. Labed-Nachbrand	
 3. INFRARROJO TÉRMICO/ THERMAL INFRARED	
Sesión Oral / Oral session	
Quality assessment and validation of the MODIS global land-surface temperature	575
Z. Wan, Y. Zhang, Q. Zhang and Z.-L. Li	
Quantitative estimates of emissivity using ASTER data	585
T. Schmugge, F. Jacob, A. French and K. Ogawa	
Relativity of isothermal definition and its scaling effects in quantitative thermal infrared remote sensing	590
R.H. Zhang, Z.-L. Li, X. Tang, X. Sun, H.B. Su, C. Zhu and Z. Zhu	
 Sesión Poster / Poster session	
Retrieval of plant and soil temperature by AMTIS data	600
W. Fan, Y. Zhang and X. Xu	
The component temperature of mixed pixel retrieved by multi-angle combined multi-time thermal infrared remotely sensed data	605
X. Xu, W. Fan and Y. Zhang	
Integrating VNIR and TIR information in inversion of land surface component Temperature	609
Q. Liu, L. Chen, Q. Xiao, Q. H. Liu and G. L. Tian	
Development and application of time process information of radiometric temperature for soil and vegetation to invert surface fluxes	616
R. H. Zhang, X. Sun, Z.-L. Li, Z. Zhu, H.B. Su and X.Z. Tang	
Definition of component effective emissivity for heterogeneous and non-isothermal surfaces and its Monte Carlo calculation	624
L.-F. Chen, Z.-L. Li, Q.-H. Liu, S. Chen, Y. Tang and B. Zhong	

Derivation of land surface temperatures from MODIS data using general split-window technique	631
C. O. Mito, G. Laneve, and M. M. Castronuovo	
The urban heat island effect in the SAO PAULO metropolitan region by AVHRR and the influence in the human health	639
A. L. Farias de Souza and O. Massambani	
The use of HIRLAM climate predictions and AVHRR data for the calculation of evapotranspiration rates in Denmark	646
E. Boegh, H. Soegaard, J. H. Christensen, C. B. Hasager, N. O. Jensen, N. W. Nielsen and M. S. Rasmussen	
Atmospheric correction of IR satellite data using neural networks	651
F.-M Götsche and F.-S. Olesen	
Comparison of Meteosat-7 and (A)ATSR data over land: A sensitivity analysis	656
E. J. Noyes, J. J. Remedios, D. T. Llewellyn-Jones and M. C. Edwards	
Using MODIS land surface temperature and normalized difference vegetation index products for monitoring drought in the southern Great Plains, USA	664
P.-X. Wang, Z. Wan and X.-W. Li	
Change analysis of land surface temperature in China using NOAA-AVHRR data	672
C. Y. Wang, H. Yan and Z. Niu	
Experimental system for the study of the directional thermal emission of natural surfaces	679
Z.-L. Li, R. H. Zhang, X. Sun, H. B. Su, X. Z. Tang, Z. Zhu and J. A. Sobrino	
Sensitivity of TIR directional emittance to soil water content and LAI in the soil-vegetation-atmosphere system	686
L. Jia, M. Menenti and Z.-L. Li	
Retrieval of thermo-optical properties of materials using field (3-5 μm) & (8-14 μm) infrared imaging combined with a multi-temporal regression method	692
F. Nerry, M.-P. Stoll and A. Malaplate	
Estimating land surface temperature in South America from NOAA-AVHRR images and reanalysis data	698
L. Morales, J. C. Parra and J. A. Sobrino	
Sea surface temperature assessment during the wind and salinity experiment (WISE)	707
V. Caselles, R. Niclòs, E. Rubio, C. Coll, A. Camps and J. Font	

4. MICROONDAS/ MICROWAVES

Sesión Oral / Oral session

Recent progress in estimating snow properties using multi-parameter SAR	713
J. Shi	
Estimation of soil moisture and surface roughness using two radar configurations	724
M. Zribi, M. Dechambre and N. Baghdadi	
Model based forest height estimation for forest biomass estimation	731
K. P. Papathanassiou, I. Hajnsek, T. Mette and S. R. Cloude	

Monitoring land surface soil moisture from L-band microwave radiometry: Retrievals from multi-angular observations	741
J. P. Wigneron, Y. Kerr, J. C. Calvet, T. Pellarin, M. Pardé and S. Schmidl Søbjaerg	
An improved estimation technique for rainfall over land surfaces using active and passive microwave satellite data	751
J. Schulz and P. Bauer	
Sea surface salinity and wind speed retrieved from a Tower-based L-Band radiometer in the NW mediterranean	761
C. Gabarró, J. Font, A. Camps and M. Vall-Ilosera	
Sesión Poster / Poster session	
Quantitative comparison of IEM calculations with L-band SAR measurements in agricultural areas	770
J. Shi, M. Herold and C. C. Schmullius	
Offshore wind resources quantified from satellite SAR: methodology and technical Aspects	778
C. B. Hasager, B. Furevik, S. C. Pryor and R. J. Barthelmie.	
Seasonal changes of polarimetric parameters from crops-a comparison of different decomposition approaches at L-band	783
T. Riedel and C. C. Schmullius	
Effects of environmental factors on multi-frequency and full-polarization backscatter signatures over paddy field	793
Y. Inoue, T. Kurosu, H. Maeno, T. Kozu and S. Uratsuka	
Regional mapping of sahelian herbaceous production from a combined use of ERS scatterometer data and a water balance model with an evolution strategies algorithm	802
L. Jarlan, P. Mazzega, E. Mougin, B. Duchemin, Y. Tracol, P. L. Frison, M. Schoenauer and P. Hiernaux	
Merging of airborne laser altimeter data and RADARSAT data to develop a digital elevation model	810
N. Baghdadi, B. Bourguine, S. Cavelier, J.-P. Chilès, C. King, P. Daniels, J. Perrin and C. Truffert	
The retrieval of aerodynamic surface roughness from SAR remote sensing image	818
C. Zhu, R. H. Zhang, J. Wang, Q. Xu and G. Jin	
On-board medium resolution SAR processing for fast image generation	823
A. Vidal-Pantaleoni and M. Ferrando	
Comparison of different speckle reduction techniques in SAR images using wavelet Transform	831
A. Vidal-Pantaleoni and D. Martí	
Characterizing the vegetation microwave parameters dependence on view angle and polarization (SMOS mission)	839
M. Pardé, J. P. Wigneron, A. Chanzy and P. Ferrazzoli	
Land surface monitoring using a combination of active and passive microwave and optical satellite sensors	847
L.N. Guijarro, V. Lakshmi, Y. H. Kerr and G. Chehbouni	

5. PROYECTOS RECIENTES Y MISIONES DE OBSERVACIÓN DE LA TIERRA /RECENT PROJECTS AND EARTH OBSERVATION MISSIONS

Sesión Oral / *Oral session*

Monitoring global climate change: the Advanced Along Track Scanning Radiometer (AATSR) 857

M. C. Edwards, D. Llewellyn-Jones and D. Smith

Simulation of SPECTRA like scenes using coupled leaf, canopy and atmospheric radiative transfer models 863

H. Bach and W. Verhoef

Preparados para el lanzamiento del MSG-1 871

E. Oriol-Pibernat

Sesión Poster / *Poster session*

Estudio del fenómeno migratorio de la mariposa Monarca con ayuda de imágenes SPOT 874

M.-L. España-Boquera, F. Baret and J.-F. Hanocq

VEGETATION/SPOT. An operational mission for the Earth monitoring. Presentation of new standard products 880

P. Maisongrande, B. Duchemin and G. Dedieu

Preliminary pigment retrieval results from a sparse-canopy poplar plantation in northern Italy using hyperspectral data 885

C. Panigada, J. R. Miller, M. Meroni, T. Noland, M. Boschetti, R. Colombo, C.M. Marino and M. Packalen

Effects of chlorophyll concentration on green LAI prediction in crop canopies: Modelling and assessment 891

D. Haboudane, J. R. Miller, E. Pattey, P. J. Zarco-Tejada and I. Strachan

LAI retrieval from multi-angle and hyperspectral observations in an intensively-managed poplar plantation 900

M. Meroni, R. Colombo, M. Boschetti, C. Panigada, M. Rossini, P. A. Brivio and J. R. Miller

Radiometric saturation of LANDSAT-7 ETM+ data over the Negev desert (Israel): Problems and solutions 904

A. Karnieli, E. Ben-Dor, B. Yunden and R. Lugasi

The potential of the TERRA-ASTER sensor to retrieve radiative properties over semi-arid regions 913

F. Jacob, T. Schmugge, K. Ogawa, A. French and J. Ritchie

Assimilation of high temporal frequency SPOT data to describe canopy functioning-the case of wheat crops in the ADAM experiment in Romania 921

C. Lauvernet, F. X. Le Dimet, F. Baret, H. Deboissezon, J.C. Favard, R. Vintila, C. Lázár and A. Badea

Localización de construcciones rurales en la imagen de satélite IKONOS y gestión de las mismas mediante un sistema de información geográfica 927

M. L. Gil, A. González and I. Cañas

Land cover change monitoring in the mediterranean basin using NOAA-PATHFINDER time series (1981-2001): WATERMED project	935
J. A. Sobrino, J. El Kharraz, M. Romaguera, M. Gómez, J. C. Jiménez-Muñoz and G. Sòria	
Water vapour retrieval from MODIS data	941
J. El Kharraz, J. A. Sobrino, M. Gómez, J. C. Jiménez-Muñoz and G. Sòria	
Angular variation of thermal infrared emissivity for some natural surfaces from laboratory and field measurements	946
J. A. Sobrino, J. Cuenca and G. Sòria	
Surface temperature retrieval from AATSR data: multichannel and multiangle Algorithms	952
G. Sòria, J. A. Sobrino, J. Cuenca, A. J. Prata, J. C. Jiménez-Muñoz, M. Gómez and J. El-Kharraz	
Study of the radiance to flux inversion within the framework of the EARTHCARE Mission	956
A. Bodas-Salcedo, J. F. Gimeno-Ferrer, E. López-Baeza and J. P. V. Poiars-Baptista	
Retrieval of biophysical parameters using directional spectral mixture analysis	963
F.J. García-Haro, F. Camacho-de Coca and J. Meliá	
Directional effects on observations of Land Surface Temperature with AVHRR over Africa	971
A. C. Pinheiro, J. L. Privette, R. Mahoney and C. J. Tucker	
AUTHOR INDEX	979
FIGURES IN COLOUR	987

NASA Earth Science Enterprise A New Frontier International Partners in the Progress of NASA's Earth Observing System

Ghassem R. Asrar
Associate Administrator for Earth Science
U.S. National Aeronautics and Space Administration

The National Aeronautics and Space Administration (NASA) Earth Science Enterprise (ESE) is dedicated to understanding the total Earth system and the effects of natural and human-induced changes on the global environment. The vantage point of space provides us with an exciting and unique opportunity to obtain information about our planet's land, atmosphere, ice, oceans, and biota that cannot be obtained in any other way.

The Programs of NASA's Earth Science Enterprise study the interactions among these components to advance the new discipline of Earth System Science, with a near-term emphasis on global climate change.

International cooperation is essential for addressing the compelling questions we must now address to advance the study of our home planet. Earth Science is inherently international in its scope and function - global scientific questions require global collaboration to find answers. Decision makers worldwide require an objective scientific knowledge base to plan their actions and the credibility of data and information depends on international participation in the scientific process.

Progress:

Unprecedented Accomplishments in Earth Observing

NASA ESE has progressed significantly since the early development of satellite remote sensing in the 1960's. Combined with the birth and evolution of the Earth System Science concept in the last decade, NASA's Earth observing satellites have achieved unprecedented accomplishments, providing the first holistic view of the major interactions among the Earth's atmosphere, oceans, and continents.

Constantly improving remote-sensing systems have significantly broadened the parameters and coverage of observations, providing increased capability to observe, document, and understand natural and human-induced changes to the Earth System. NASA has launched sixteen satellites in the last decade and is planning to develop and launch seven more over the next five years alone.

Since its inception in 1958, NASA has sought mutually beneficial cooperation with other nations and groups of nations in the peaceful application of its activities. The calibration and validation of space-based observation requires regional experts and in situ data from around the world. Individual nations or regions cannot afford the comprehensive systems required to explore and understand the Earth System.

Recognizing the critical importance of international collaboration to its mission, NASA ESE currently has over 300 cooperative agreements with over 60 nations in every region of the world. Below are a few that highlight the recent progress in Earth Observations Systems.

- Jointly developed by NASA and the French Space Agency (CNES), the TOPography EXperiment-Poseidon (TOPEX/Poseidon), launched in 1992, has become the longest running Earth-orbiting radar satellite in history. TOPEX/Poseidon provides global observations of unprecedented accuracy that are used to map sea surface topography, track and provide early warning of El Nino/La Nina events, and explore long-term changes such as the Pacific Decadal Oscillation. Jason, the follow-on collaboration between NASA and CNES launched in 2001, continues and improves this critical data set, providing scientists a unique, revolutionary view of our oceans.

- The twin satellites of the Gravity Recovery And Climate Experiment (GRACE), a joint partnership between NASA and the German Aerospace Center (DLR) launched in March 2002, will map the Earth's gravity field and its variations with a precision never before accomplished. Data from GRACE will allow improved determination of ocean circulation; improve understanding of atmospheric-ocean heat exchange; yield crucial information about the distribution and movement of mass within the solid Earth and its fluid surroundings; create a better profile of Earth's atmospheric temperature; and support a number of important studies on global climate change.
- NASA's Earth Observing System Aqua satellite carries a suite of new instruments developed by NASA, the National Space Development Agency of Japan (NASDA), and the Brazilian Space Agency (AEB). Launched in May 2002, Aqua observations are already exceeding the expectations of the world meteorological community. The on-board sensors measure atmospheric temperature and moisture content, clouds, precipitation, soil moisture, terrestrial snow and sea ice, and sea surface temperature. This set of precise measurements will improve weather predictions by increasing the understanding of the Earth's climate and its variations.
- Spacecraft constellations are the new paradigm in increasing satellite data output. Many small spacecraft flying in formation can gather concurrent science data, lower total mission risk, and increase science return. Enhanced formation flying technology also increases flexibility and minimizes ground support equipment requirements. The Argentine Commission on Space Activities (CONAE) is a partner in NASA's pioneering endeavor in formation flying. The AM Constellation consists of four satellites: NASA's New Millennium Program Earth Observing-1 (EO-1), Landsat-7, and Terra satellites, and CONAE's Satelite de Aplicaciones Cientificas C (SAC-C).

Promise:

Exciting Opportunities for S&T Applications

We are increasingly aware that sound scientific understanding is required to better serve the needs of society. NASA's progressing capabilities present exciting opportunities to answer high-priority science questions with profound national and international economic and policy relevance. Moving beyond the scientific and technological benefits of Earth Observing System, NASA is finding broad applications to the challenges faced by economic and policy decision-makers and those who manage the world's natural resources. Below are just a few examples of how NASA's satellites observations are contributing to countless applications of social benefit.

• Water Management:

Worldwide, growing populations and economic activity stress water resources for drinking, irrigation, and fishing and recreation. Many areas face critical pollution problems or shortages. The Tropical Rainfall Measurement Mission (TRMM) is providing insight into the complex atmospheric processes that influence rainfall patterns. The Global Precipitation Measurement (GPM) Constellation will be implemented as a multi-national partnership and will transition critical measurements begun by TRMM to an operational system with global coverage.

• Disaster Preparedness – Wildfires:

The Moderate Resolution Imaging Spectroradiometer (MODIS) Land Rapid Response System is able to provide true color and false color composite Terra MODIS images within 2-6 hours of the satellite overpass. Daily imagery of fire extent is being provided to a number of users, both domestically and internationally, allowing managers on the ground to directly obtain and utilize this information. When the fires are over, data from MODIS and other Earth Observing System instruments are used to map the burned areas and plan rehabilitation.

• Air Quality:

The Aerosol Robotic Network (AERONET) is an optical, ground-based aerosol monitoring spectral radiometer network that provides globally distributed near-real-time observations of aerosols that can be used for many applications,

including monitoring air quality and tracking pollution trends. NASA's AERONET cooperation expands to many countries, including Argentina, Australia, Bolivia, Botswana, Canada, Chile, European Union, France, India, Japan, Mexico, Moldova, Mongolia, Morocco, Mozambique, Poland, Portugal, Russia, South Africa, Suriname, Sweden, Turkey, the United Kingdom, and Zambia.

- Resource Management:

Environmental Assessment: NASA is cooperating with researchers in Central America, creating regional maps to assist in understanding environmental conditions of the Mesoamerican Biological Corridor, a regional collection of protected areas established by the governments of Central America. By exchanging data and providing training on remote sensing techniques, NASA is preparing Central America to be self sufficient in preserving and managing its precious natural resources.

Vision:

Geospatial Information for Decision-Makers

A critical part of NASA's vision and mission are to "improve life here...to understand and protect our home planet." In order to realize this, NASA ESE is dedicated to improving future Earth Observing Systems through advanced technology application. As envisioned, these future systems will provide a broad range of geospatial information to decision-makers in a timely and affordable manner on a routine basis. This vision depends on our continued commitment to advances in science, technology, and international cooperation. We, at NASA, are pleased to work with Space Agencies and scientists from around the world in exploring our home planet. We invite you to learn more about NASA's Earth Science Enterprise through our Web site at <http://www.earth.nasa.gov>.

1. ESPECTRO SOLAR / SOLAR SPECTRUM

Accumulation of spectral BRDF knowledge for quantitative remote sensing of land surfaces

Xiaowen LI [1, 2], Jindi WANG [1], Feng GAO [2], Alan STRAHLER [2], Lihong SU [1]
[1] *Research Center for Remote Sensing and Department of Geography, Beijing Key Laboratory for Remote Sensing of Environment and Digital Cities, Beijing Normal University, Beijing 100875, PR China. Tel.: 86-10-62209966; Fax: 86-10-62209977; Email: lix@crsa.bu.edu*
[2] *Department of Geography and Center for Remote Sensing, Boston University, Boston, MA 02215, U.S.A.*

ABSTRACT -Quantitative remote sensing aims at the accurate retrievals of land surface parameters from remotely sensed data. An effective approach using a priori knowledge in remote sensing inversion has been explored in our previous studies. There are two major obstacles in using this approach. One is the accumulation of a priori knowledge. The other is the structure to make use of the knowledge base in remote sensing. In this paper, we present our newly funded project to build a spectral knowledge base for typical objects of land surfaces. The knowledge base consists of four layers: 1) the spectral feature database of typical materials of land surface; 2) the spectral Bidirectional Reflectance Distribution Function (BRDF) database for some typical land covers, associated with their structure information; 3) the landscape patterns at different spatial scales and associated plant growth models of typical vegetation covers; and 4) the user interface layer, supported by geographical information management system with data sharing mechanism. Layers 1 and 2 are connected through widely available validated physical remote sensing models. These built-in models then form a model base. Layers 2 and 3 are connected by simple linear mixture models. Layer 4 provides a linkage between system and users which makes our spectral knowledge base of land surfaces an easier tool for users in quantitative remote sensing applications.

1 INTRODUCTION

Remote sensing has become one of the important technologies for acquiring spatial and temporal information of the land surface. Remotely sensed data are extensively used in many scientific research fields, which require high accurate information retrieval. Quantitative remote sensing aims to the accurate retrieval on land surface biophysical parameters from remotely sensed data. For many years, it has been expected to achieve this by means of the spectral measurements indoor or in fields. For this reason, many kinds of spectral databases of different materials and land covers have been established (Wharton, 1987; Grove, et al., 1992). However, these databases are hard to use in remote sensing applications, such as in land cover classification. One of the major reasons is that measurement conditions in laboratory are quite different from conditions while remote sensing images are actually acquired (Li, 1989). These conditions include land surface structure, measurement geometries, spatial scales and temporal season when images are acquired.

The multi-angular remotely sensed data carries extra information, which may serve as an important complementation for spectral features. The bi-directional reflectance models can be used to retrieve land surface parameters, such as the vegetation leaf

area index (LAI) and albedo. For instance, in the MODIS BRDF/Albedo production, the global albedo of land surface is retrieved through a semi-empirical BRDF model. Studies show that a successful model inversion requires enough accurate multiangular measurements. In the cases when the information content from the remotely sensed data is not satisfied, a prior knowledge is required in order to get better estimation (Li et al., 1998; Gao et al., 2002). Another possible application of spectral database is the conversion from narrow band albedo to broadband albedo. Broadband albedo is linear weighted by narrow band albedo in the MODIS BRDF/Albedo production using the fixed narrow band to broad band conversion coefficients. However, for an accurate conversion, the fixed coefficient is hard to satisfy all land surface types. For example, the coefficients for vegetation may quite different as for snow and ice. The spectral database can provide such kind of information and thus improve the results. Because land surface is often inhomogeneous and most land surface parameters are changing with time, the spectral database should include those temporal changing information, i.e., not only the spectral data but also environmental variables related with the spectral measurements. Therefore, the spectral and relative parameters database are needed for getting more accurate estimation of land surface parameters.

In this paper, we present our work sketch on how to build such a spectral BRDF knowledge base and the main problems to make it a good tool for remote sensing applications. The architectures and functions of the knowledge base are also discussed below.

2 SPECTRAL KNOWLEDGE BASE

The spectral knowledge base will be built for typical land surface types. The six main typical objects are vegetation, soil, mineral and rock, ice and snow, water body and build-up targets. The spectral knowledge base consists of four parts, namely, the spectral measurement database, the spectral image database, the remote sensing model base and the prior knowledge database.

The spectral measurement database contains spectral data of the typical objects and the related environmental variables measured in laboratories or in fields. The space-borne, airborne remotely sensed data are the major sources of the spectral image base. Both of them are the data components of the spectral knowledge base.

The remote sensing model base contains physically based models, which are used in spectrum simulation and prediction to enhance the function of the stored spectral data, such as to predict the spectrum of an object when it is not included in the database but required by remote sensing application users. The prior knowledge base is an important support to make the models being available in spectral prediction, such as in spectral data analysis, objects recognizing and in land surface parameters estimation.

The fourth part is a remote sensing experimental platform of the spectral knowledge base, which serves as a user interface on remote sensing application and scientific research as well.

In order to build such a powerful spectral knowledge base, the research works will be divided in several steps. First, we will collect the existed measured spectral data of different typical objects of land surface and establish a basic experimental database. The spectral data will be analyzed based on whether and how the data can be stored in the database. The measured data will be divided into several classes according to the data's quality and integrity, and will be described clearly for referencing. In the meanwhile, we will make up the model base and use the available data to test function of the models. Methods will be developed on combining the model and measured data to do the spectral prediction. Then the technical standard for spectra and the related environmental variables measurement will be made clearly, by referring some famous international synthetic remote sensing experiments and considering the problems in current measurement methods. After that we will do some necessary field measurements to have typical spectrum of objects. The knowledge base

will be built by collecting the land cover and land use map, the regional distribution of vegetation coverage and soil classification, the distribution of mineral and rock resources, the DEM database, and the crop growth and development data, and the technical characteristics of current on-board remote sensing instruments, etc. The research work on the knowledge base application will be developed at the same time.

3 SPECTRAL DATA IN THREE MEASURING SCALES

The research on spectral features of objects are the significant foundation in remote sensing applications. The land cover and land use classification and image interpretation are usually based on the spectrum recognizing method. Many kinds of spectrum matching technique are developed recently. However, sometimes users cannot get the expected accuracy for classification and recognition. One of the problems is that the spectral data of objects measured in different scales are not comparable. It is rarely to setup the correct relation between the spectrum of objects measured indoor or in fields and the spectral image data acquired through remote sensing observations. So that the scale effect has to be considered in this regarding.

Actually, considering the requirements of applications, the spectral measurement data can be classified into three types, the spectrum of materials, the spectrum of endmembers and the spectrum of remote sensing pixels. The typical spectrum of material is usually measured in laboratories or in fields under the standard measurement conditions. The measuring samples need to be selected as the typical ones, and should also be described in details. This kind of spectral data can be taken as the relative stable and certain data to be used as model parameters. For example, we measure the VIS/NIR spectrum of leaves and soils in crop fields, the spectrum of mineral samples in laboratories. The so-called spectrum of endmember in this paper is the spectrum of components of a pixel (pixels), it is a basic parameter in general remote sensing model. For example, in scene integrated geometric optical BRDF model on canopy reflectance, the sunlit crown, sunlit background, shaded crown and shaded background are endmembers of the modeled forest pixel. Their spectra are the main parameters of the model, which may different from the spectrum of leaves and soils. The spectrum of pixel comes from remote sensing observations, which is what the users care mostly. Our spectral knowledge base will distinguish the three kinds of spectrum clearly, which will be make the user have a clear concept when make use of them, especially in the development of spectrum matching technology when user want to have the pixel's classification by means of the spectral database. This

approach need more research works to understand and describe their spectrum features and the relationship between them. It is also a scaling-up problem.

4 INTERPOLATION AND EXTENSION OF SPECTRAL DATA BY USING BRDF MODELS

As the applied standard spectral database, spectrum of most of typical objects of land surface should be stored in the spectral knowledge base. But the changing of the objects are infinite, we actually can not include the all cases for even one given object. Such as for winter wheat, we almost can't have the all spectrum for its whole growing seasons, and for different places. Considering its application, sometimes users may require the winter wheat's spectrum for a given date at a specific place, which may not be stored in the database. In such case, the spectral knowledge base should be able to figure out of the suitable spectrum and its uncertainty for user. We are going to achieve this by spectrum prediction or spectrum simulation based on our prior knowledge and model bases.

The spectrum prediction is by means of the physically based remote sensing model and applicable empirical model on object, such as a crop simulation model, as well as the knowledge base. When a user makes the requirement on the spectrum of a given

object, the system should provide it from the already stored related spectrum and other knowledge.

For example, our database stored some standard spectrum of winter wheat at its different growing seasons, the user requires the spectrum at a given season in order to learn the growing state from his remote sensing image. The spectrum from the exist known spectrum and relative structural parameters of several growing seasons will be calculated with spectral prediction modular, the crop simulation model will provide the information about the growing tend, the knowledge base will provide the information about phenological and regional characteristics, the spectral database will provide the spectrum of material and components and the typical relative winter wheat's structural parameters. In this way, the modular can be able to interpolate and extend the spectrum in temporal and spatial scales, and to predict the spectrum at a given FOV, a given sunlight under the observation and atmospheric conditions. The uncertainty of the estimation will be also given with the prediction. Some of them will be supported by model metadata.

The spectral simulation and modelling modular will be with two main functions to meet the requirements of remote sensing application users, spectral reference data and reference parameter of land surface.

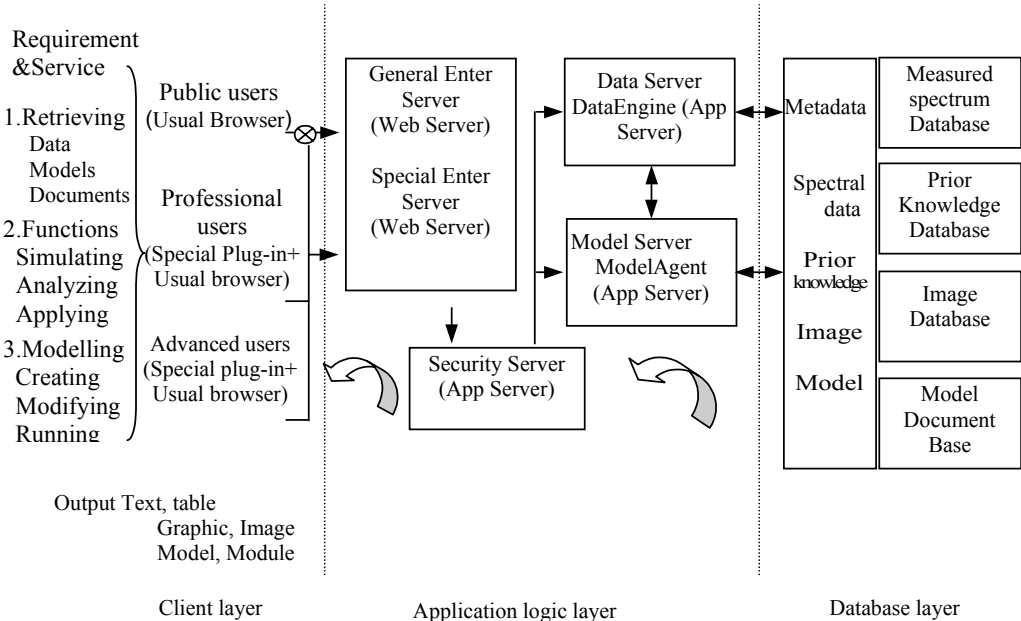


Figure 1. Architecture of the spectral knowledge base

When a user gives their studied on an object of land surface and its spatial characteristics, the type of vegetation, leave area index, the atmospheric condition and the terrain, the spectral knowledge base will provide spectral data of the object for user to refer. When user gives the time and position of the remote sensed object, and the vegetation coverage, the spectral knowledge base will provide the available algorithm and the estimation on structural parameters of the object.

5 ARCHITECTURE OF SPECTRAL DATABASE AND ITS DISTRIBUTION

Three-tier architecture is adopted to develop the spectral knowledge base (figure 1), client layer, function layer and database layer. The client layer is the interface of the knowledge base, users can retrieve data and run models under this interface. The functions layer provides computing methods by which its functions are implemented. The DataEngine and ModelAgent are designed to extract data in the databases and call models in the model base. The database layer maintains the spectral database, the image base, the land surface prior database, and model base based on the metadata stored and managed by the metadata database. The users will be classified into three types: public users, professional users and advanced users. The security also is a key consideration in the system design of the spectral knowledge base. The spectral knowledge base is designed to be distributed through internet.

6 DISCUSSION

The goal of establishment of the spectral knowledge base is to meet the requirement of the quantitative remote sensing applications. Scientists have developed many state-of-the-art models which can be used to retrieve key parameters of land surface. Unfortunately, they are not general available. On the other side, the scientists worked in remote sensing data applications often complain on the accuracy of the data. The spectral knowledge base discussed in this paper is trying to make a connection between them, and severing as the scientific data platform for modelers and the referential spectral data for application users. In this proposed spectral BRDF knowledge base, we will provide the integrated data sets which combined spectral data and relative environment variables. It is also possible to estimate the land surface spectrum feature using the knowledge base and embedded model simulation.

ACKNOWLEDGEMENTS

This research is supported by the China Special Funds for Major State Basic Research Project (G20000779), the High-Technology Research Development Project (2001AA135030) and the China Natural Science Foundation's project (40171068).

REFERENCES

- Gao, F., Jin, Y., Li, X., Schaaf, C. B., and Strahler, A. H., 2002, Bidirectional NDVI and atmospherically resistant BRDF inversion for vegetation canopy. *IEEE Trans. Geoscience and Remote Sensing*, **40**: 1269-1278.
- Grove, C. L., Hook, S. J., and Paylor, E. D., 1992, Laboratory reflectance spectra for 160 materials 0.4-2.5 micrometers, JPL Publications 92-2, Jet Propulsion Laboratory, Pasadena, CA.
- Li, X., 1989, Bidirectional reflectance and angular signature of objects (in Chinese). *China Remote Sensing of Environment*, **4**: 67-72.
- Li, X., Wang, J., Hu, B., and Strahler, A. H., 1998, On utilization of prior knowledge in inversion of remote sensing models. *Science in China (Series D)*, **41**: 580-586.
- Wharton, S. W., 1987, A spectral-knowledge-based approach for urban land-cover discrimination. *IEEE Trans. Geoscience Remote Sensing*, **25**, 272-282.

Improved modelling of multiple scattering in leaf canopies: the model SAIL++

Wout Verhoef

National Aerospace Laboratory NLR

P.O. Box 153, 8300 AD Emmeloord, The Netherlands

Tel. +31-527-248253, Fax +31-527-248210

e-mail address: verhoef@nlr.nl

ABSTRACT – *The model SAIL++ has been developed for an improved modelling of multiple scattering in leaf canopies in the solar spectral region. This has been accomplished by the application of $N+2$ stream radiative transfer theory to homogeneous vegetation canopies with random leaf azimuth orientation. For the single scattering contribution, modelling of the hot spot effect is incorporated according to the theory of A. Kuusk. The results indicate that, compared to the SAIL model, the more refined modelling of multiple scattering in SAIL++ is significant especially in the near infrared, for high LAI and more erectophile leaf angle distributions. Although reflectance differences of the order of 3% in the near infrared are not dramatic, retrieval of LAI by means of model inversion using simpler models might lead to systematic overestimations for dense canopies. Simulations with the new model also indicate that the absolute contribution of multiple scattering to the anisotropy in the BRDF remains modest, which in retrospect appears to justify the approximations applied in the SAIL model. In the software development of the new model much attention has been paid to numerical stability and efficient execution of the code. Therefore the use of the new model is recommended, also because in principle it allows a better framework for modelling the interaction with a non-Lambertian soil or a non-uniform incident sky radiance distribution.*

1 INTRODUCTION

One important aspect in canopy reflectance modelling that plays an important role especially in the near infrared part of the spectrum is the contribution due to multiple scattering inside the leaf canopy. In other parts of the spectrum the absorption of radiation by the leaves in a canopy is mostly considerable, and in that case singly scattered radiation will form the dominant contribution to the canopy reflectance, because each next scattering event will generate a contribution that is only a fraction of its predecessor. However, in the near infrared usually less than ten percent of the radiation incident on a leaf is absorbed, and therefore in this spectral region multiple scattering may generate the dominant contribution.

The effect of multiple scattering is difficult to model by means of exact numerical methods and therefore one always has to rely on approximations, either by purely numerical approaches such as ray-tracing, or by discretisations in the angular and spatial domains. In most multiple scattering radiative transfer methods one assumes a one-dimensional medium, implying that variations in the horizontal plane other than stochastic ones are not considered. By the way, this does not mean that typical 3D-effects, such as the shadowing of sunlight and the bidirectional scattering of light by leaves with arbitrary orientation in 3D

space, could not be accounted for in such models. The 1D character refers only to the macroscopic properties, which are supposed to remain constant in the horizontal plane.

For atmospheric optics several semi-analytical methods have been developed such as the discrete ordinates method (DISORD). Here the angular domain is often discretised by means of expansion of the scattering phase functions of aerosols and Rayleigh scattering in spherical harmonics functions (Stamnes, 1988). However, in many applications of this method one assumes that the scattering medium is isotropic, meaning that the interception and scattering properties of radiation are independent of the incidence direction. This condition of isotropy is fulfilled for media consisting of spherical particles or non-spherical particles with random orientation. Leaf canopies in general do not fulfil this condition. In leaf canopies the interception of radiation depends on the leaf angle distribution and the incidence direction. The scattering phase function depends on the leaf angle distribution and the directions of incidence as well as scattering, even if one assumes that the leaves themselves are Lambertian reflectors and transmitters. In the SAIL model (Verhoef, 1984 & 1985) multiple scattering is treated by a very crude angular discretisation: the angular domain

is divided into the upward and the downward hemisphere and one assumes that after more than one scattering event the flux is semi-isotropic, i.e. the multiply scattered radiance is assumed to be constant in each hemisphere. For horizontal Lambertian leaves and a Lambertian soil this representation would be exact, but in any other case it would only be an approximation. Although in SAIL all scattering and extinction coefficients fulfil the law of energy conservation, which implies that there can be no "numerical" losses of radiant energy, there will be the effect that in the top-of-canopy reflectance the multiple scattering contribution shows less anisotropy than it would have in an exact model. The solution discussed in this paper is the N+2 stream method (Verhoef, 1998), which is a generalisation of the method applied in the SAIL model. The SAIL model can be considered as being based on a four-stream method, in which two streams are the diffuse upward and downward semi-isotropic fluxes discussed above, and the other two streams are specular incident solar flux and radiance in the observer's direction. In the N+2 stream method both hemispheres are divided into $N/2$ angular segments, and in each segment one assumes that the radiance is constant. With this refinement in the description of the multiply scattered internal radiation field one can expect more accurate results of bidirectional canopy reflectance calculations, especially in the near infrared. This can be important, since at high LAI only the near infrared reflectance is still sensitive to changes of LAI, and therefore, for a reliable retrieval of high LAI values from near infrared reflectances by model inversion techniques, the model used has to be as accurate as possible.

In this paper the N+2 stream method is briefly described. The resulting new model is called SAIL++ and several aspects of its development are discussed, as well some first numerical results, compared to those from other models.

2 N+2 STREAM THEORY

The N+2 stream method for modelling of radiative transfer in non-isotropic media has been described in Verhoef (1998). In the EU-project CROMA (Crop Reflectance Operational Models in Agriculture) this method has been implemented for homogeneous vegetation canopies in order to improve the modelling of the multiple scattering contribution. In this method an equal-weight tessellation of each hemisphere is applied in order to define the angular segments. With this tessellation each segment contributes equally to the total irradiance on a horizontal plane if the radiance over the whole hemisphere is constant. This can be accomplished by choosing equal intervals in the azimuth angle and equal intervals in the cosine

squared of the zenith angle. In the SAIL++ model 12 azimuth sectors of 30 degrees wide and 3 intervals of the zenith angle per hemisphere are used, giving a total number of diffuse streams $N = 72$. This tessellation, together with the numbering of azimuth sectors and zenith zones, is illustrated in Fig. 1.

Note that the sun is supposed to be positioned at the centre of azimuth sector 1. Since for the supposedly randomly oriented leaf azimuth distribution the scattering is symmetric with respect to the principal plane, only 7 azimuth sectors need to be distinguished for a complete description of the diffuse radiation field.

**N-stream tessellation of hemisphere for $N = 72$
(36 segments of equal weight per hemisphere)**

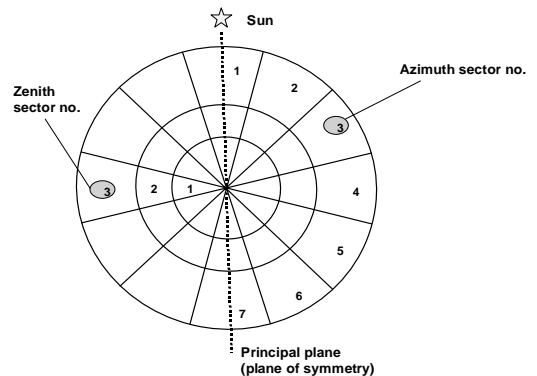


Fig. 1 Applied equal weight tessellation illustrated for the upper hemisphere

In the N+2 stream method three stages can be identified. In the first stage all extinction and scattering coefficients are computed from the optical and structural properties of the medium and the given observational constellation (sun-object-sensor geometry). This phase is still independent of the total optical thickness of the medium (LAI in the case of a leaf canopy). In the second stage the radiative transfer equation is solved for a given optical thickness or LAI. The solution consists of the reflectance and transmittance factors of the layer for all combinations of incident and scattered flux types (specular and diffuse).

After the above two stages one more step is necessary, namely addition of the soil background. In this last stage the optical properties of the canopy layer are combined with the soil's reflectance properties.

Mathematically, there is much similarity between the N+2 stream method and the discrete ordinates method. In the N+2 stream method one uses angular segments to represent scattered diffuse fluxes, whereas discrete ordinates are carefully selected "key" directions that represent the directional scattering. In the former case the arrangement of segments (tessellation)

is derived from the requirement of equal weights in the contribution to the total irradiance on a horizontal plane. In the DISORD method the choice of directions is usually found from the Gaussian division points, which are optimum for efficient integration over the angular domain. However, both methods lead to similar systems of linear differential equations, and in both cases the solution can be obtained in several ways. Important numerical approaches are adding/doubling (De Haan, 1987) and SOSA, successive orders of scattering approximation (Myneni *et al.*, 1987). In both cases the spatial dimension (vertical) is discretised into thin slabs. An analytical approach is eigenvector decomposition. In this case the spatial dimension remains continuous and the solution is expressed in linear combinations of exponential functions. The latter approach has been applied for the solution of the N+2 stream system of differential equations, which is given by

$$\frac{d}{Ldx} \begin{pmatrix} E_s \\ \mathbf{E}^- \\ \mathbf{E}^+ \\ E_o \end{pmatrix} = \begin{pmatrix} k & & & \\ -s & \mathbf{A} & -\mathbf{B} & \\ s & \mathbf{B} & -\mathbf{A} & \\ w & \mathbf{v}^T & \mathbf{v}^T & -K \end{pmatrix} \begin{pmatrix} E_s \\ \mathbf{E}^- \\ \mathbf{E}^+ \\ E_o \end{pmatrix} \quad (1)$$

Here L represents the total LAI of the layer and x is the so-called relative optical height co-ordinate, which by convention runs from -1 at the bottom to 0 at the canopy top. An infinitesimal increment of LAI in vertical direction is written as $dL = Ldx$. The bracketed vectors contain all N+2 "streams" or fluxes, consisting of the direct solar downward flux, the diffuse downward flux vector, the diffuse upward flux vector and the upward radiance in the observer's direction. The supermatrix contains all extinction and scattering coefficients, and these consist of scalars (printed normal), subvectors (printed bold) and submatrices (capitals printed bold). Vacant places are supposed to indicate zeros. This matrix-vector representation is a direct generalisation of the corresponding four-stream case to N+2 streams.

The method of solution applied to this system of linear differential equations is based on eigenvector decomposition, which implies that it is fast and does not require iteration. However, in general this method can give rise to numerical instability under particular circumstances (Verhoef, 1998) and if not properly taken care of, this may lead to unexpected results. Some other particular points in the applied method of solution are summarised below.

- The contributions due to singly scattered solar radiation and multiply scattered flux are separated. The single scattering contribution is calculated in the same way as in the SAILH model (Verhoef, 1998), so as to accommodate the hot spot effect associated with the finite leaf size. The

treatment of this effect is based on the theory of Kuusk (1985).

- In the contribution due to multiple scattering a turbid medium approach is followed, assuming infinitesimally sized flat leaves.
- An azimuthal DCT (discrete cosine transform) is applied in order to separate azimuthal dependencies from zenith angle dependencies. This is similar to what usually is done in the DISORD method. By this transformation one realises a considerable reduction in required storage space and computation time.
- All potential numerical instabilities due to (near) singularities are automatically intercepted by expressing the general solution in a small number of specially constructed functions, instead of just a linear combination of exponential functions.

The result of the second stage can be illustrated by means of the following matrix-vector equation:

$$\begin{pmatrix} E_s(b) \\ \mathbf{E}^-(b) \\ \mathbf{E}^+(t) \\ E_o(t) \end{pmatrix} = \begin{pmatrix} \tau_{ss} & & & \\ \boldsymbol{\tau}_{sd} & \mathbf{T}_{dd} & \mathbf{R}_{dd} & \\ \boldsymbol{\rho}_{sd} & \mathbf{R}_{dd} & \mathbf{T}_{dd} & \\ \rho_{so} & \boldsymbol{\rho}_{do}^T & \boldsymbol{\tau}_{do}^T & \tau_{oo} \end{pmatrix} \begin{pmatrix} E_s(t) \\ \mathbf{E}^-(t) \\ \mathbf{E}^+(b) \\ E_o(b) \end{pmatrix} \quad (2)$$

This equation describes the relation between all incident fluxes at the top (t) and the bottom (b) of the canopy layer on one hand (right-hand side vector) and the resulting reflected and transmitted fluxes on the other (left-hand side vector). The (super)matrix is called the layer scattering matrix, as it comprises the result of internal extinction and scattering for the entire canopy layer. Due to the reciprocity relations between incident and scattered radiation the diffuse reflectance and matrices are symmetric.

In the N+2 stream method the reflectance of a soil surface at the bottom of the canopy can be described by the equation

$$\begin{pmatrix} \mathbf{E}^+(b) \\ E_o(b) \end{pmatrix} = \begin{pmatrix} \mathbf{r}_s & \mathbf{R}_s \\ \mathbf{r}_s & \mathbf{r}_s^T \end{pmatrix} \begin{pmatrix} E_s(b) \\ \mathbf{E}^-(b) \end{pmatrix} \quad (3)$$

in which the reflectance quantities (matrix, vectors and scalar) describe the non-Lambertian reflection properties of the surface. Combining equations (2) and (3) above it is possible to derive the upward fluxes at the top of the canopy as a function of the incident downward fluxes. This is called the adding method, which can also be used to combine different canopy layers in a vertical stack. For the model SAIL++ however, which is described in the next section, only one homo-

geneous canopy resting on a Lambertian soil has been considered.

3 THE MODEL SAIL++

3.1 Extinction and scattering coefficients

The extinction and scattering coefficients in the SAIL++ model are based on the assumption of a random leaf azimuth distribution and all coefficients of Eq. (1) can be derived from the interception function G and the volume scattering phase function Γ . In turn, both of these more fundamental functions can be expressed in the leaf inclination distribution function (LIDF), single leaf reflectance ρ and transmittance τ , and sun-object-sensor geometry.

All extinction and scattering coefficients of the model can be defined in a generic way by means of the following equations:

$$\kappa_{\text{gen}} = \overline{G(\mu)} \frac{2\Delta\mu}{\Delta\mu^2}$$

$$\sigma_{\text{gen}} = \frac{2\pi}{N} \overline{\Gamma(\mu_i, \mu_o, \Delta\varphi)} \frac{2\Delta\mu_i}{\Delta\mu_i^2} \frac{2\Delta\mu_o}{\Delta\mu_o^2}$$

in which

$\mu_i = \cos \theta_i$, where θ_i is the incidence zenith angle
 $\mu_o = \cos \theta_o$, where θ_o is the observer's zenith angle
 $\Delta\varphi$ = the relative azimuth difference

The quantities κ_{gen} and σ_{gen} are generically defined extinction and scattering coefficients, respectively, and they apply to specular as well as diffuse fluxes within angular segments. For the latter case, each overbar indicates averaging over an angular segment in 2 dimensions (zenith angle and azimuth), so for diffuse-diffuse scattering coefficients one has to determine an average of the volume scattering function over 4 dimensions, as in this case segments of incident radiation as well as segments of scattered radiation are involved. In the above expressions the case of specular radiation from the sun or in the observer's direction is accommodated by means of the limit

$$\lim_{\Delta\mu \rightarrow 0} \left[\frac{2\Delta\mu}{\Delta\mu^2} \right] = \frac{1}{\mu}$$

As an example, the bidirectional area scattering coefficient w is given by

$$w = \frac{2\pi\Gamma(\mu_s, \mu_o, \psi)}{N\mu_s\mu_o}$$

Here $\mu_s = \cos \theta_s$ and ψ is the relative azimuth sun-observer. For all other scattering coefficients numerical integration is required to calculate angular averages over segments. For this, each segment is subdivided into 12 equal intervals of μ (the cosine of the zenith angle) and 12 equal intervals of the azimuth angle φ .

The division by N in the definition of the scattering coefficients is necessary in order to maintain the reciprocity relations with respect to incident and scattered fluxes in Eq. (1). It also expresses the fact that with a finer angular division each segment contributes less to the total scattered flux. Finally, also for a division in two hemispheres ($N = 2$), such as the one of the SAIL model, the same definition of scattering coefficients can be applied.

In order to maintain a high computational speed, the angular integrals over each output segment of the geometric parts of the volume scattering phase function have been determined for a large number of incidence directions once and for all for each leaf inclination angle and the results have been stored in a 7-dimensional double-precision array. The dimensions of this data structure are the following:

1. Incidence zenith zone (1-3)
2. Within-zone angular index (1-13)
3. Scattering zenith zone (1-6)
4. Azimuth sector index (1-7)
5. Within-sector angular index (1-13)
6. Leaf inclination angle index (1-13)
7. Scattering mechanism (1-2)

The array contains the diffuse scattering coefficients to the 42 segments (6 zenith zones and 7 azimuth sectors) for 36 incidence zenith angles and 12 incidence azimuth positions relative to the sectors for the hypothetical cases $\rho = 1$ and $\tau = 1$ (7th dimension). This is sufficient for accurate interpolation and integration towards diffuse-diffuse scattering coefficients for any combination of ρ and τ .

Computation of the array takes only a couple of minutes, but nevertheless for operational use this is too long if it has to be done for each call of the model. In the SAIL++ model the array is read in from disk only on the first call and next it is used in two ways. First, interpolation is applied to compute specular-diffuse or diffuse-directional scattering coefficients. Second, numerical integration is applied to compute all diffuse-diffuse scattering coefficients. However, this operation also needs to be done only once during the first call.

By means of the 7-dimensional array one can compute all extinction and scattering coefficients from sun-object-sensor geometry, leaf optical characteristics and the leaf angle distribution parameters, without any need to perform angular integrations over segments.

During the generation of the array, fundamental physical relationships, such as the reciprocity relations and the law of energy conservation, are used as checks to maintain a high numerical precision. This guarantees that the matrices of diffuse scattering coefficients are always exactly symmetrical and that the angular distribution of scattered radiation is such that its sum over all directions always equals the totally intercepted radiation times the single leaf albedo, the sum of leaf reflectance and leaf transmittance.

3.2 Leaf inclination distribution

The fixed set of leaf inclinations used in the model SAIL++ is identical to the one applied in the previous models SAIL and SAILH, namely the series of angles 5, 15, 25, 35, 45, 55, 65, 75, 81, 83, 85, 87, 89 degrees. This is sufficient to characterise most leaf angle distributions and their effect on extinction and scattering for any direction. The finer division in the interval 80-90 degrees is applied because of the high sensitivity of the directional extinction and scattering functions to this specific part of the leaf angle distribution when the zenith angle is close to zero.

The LIDF is parameterised by means of two parameters, a and b (Verhoef, 1998). Both can vary between -1 and 1 , under the constraint that the sum of their absolute values always be less than or equal to unity. The parametrisation of the LIDF is related to the sum of two sine functions with amplitudes equal to a and $b/2$. This sum function is given by

$$y = a \sin x + \frac{1}{2}b \sin 2x$$

where x is in the range $0 - \pi$. By means of a simple transformation of the co-ordinates this function is changed into a relation between the leaf inclination angle θ_ℓ and the cumulative frequency of occurrence

$F(\theta_\ell)$. This transformation is given by

$$F(\theta_\ell) = (x + y) / \pi$$

$$\theta_\ell = (x - y) / 2$$

After this, parameter a controls the average leaf inclination angle (ALA) within a range of 8.52 ($a = 1$) and 81.48 degrees ($a = -1$). Parameter b characterises the "bimodality" of the distribution, in the sense that for high values of this parameter there is a high frequency of both horizontal and vertical leaves, whereas for low

values the same average leaf angle is realised by means of more intermediate inclinations. In this way one can generate good prototypes of extremophile and plagiophile leaf angle distributions. The combination $a = 0$, $b = 0$ gives the uniform leaf inclination distribution, in which case each leaf slope has the same probability of occurrence. From given parameters a and b , the leaf inclination angle average (when expressed in radians) and its variance can be found from the analytical expressions

$$\bar{\theta}_\ell = \frac{\pi}{4} - \frac{2}{\pi}a$$

$$\sigma^2(\theta_\ell) = \frac{\pi^2}{48} - \left(\frac{4}{\pi^2} - \frac{1}{4}\right)a^2 + \frac{b}{4}\left(1 + \frac{b}{4}\right)$$

From these equations it follows that the mean leaf inclination angle is linearly related to parameter a . The variance of the leaf inclination distribution depends quadratically on both parameters and increases with the bimodality parameter b , as could be expected. Extreme standard deviations are 7.7 and 41.2 degrees, which occur for $b = -1$ and $b = 1$, respectively, with $a = 0$. This illustrates that by means of the (a, b) parametrisation one can realise a large range of possible leaf angle distributions.

3.3 Solution of the radiative transfer equation

In the N+2 stream method, radiative transfer in a canopy layer is represented by means of the system of linear differential equations as given by Eq. (1). Such a system of differential equations can be solved in several ways. Numerical methods such as adding and doubling divide the medium into thin slabs of finite optical thickness and are based on the replacement of the system of differential equations by a system of finite difference equations. These methods require a number of iteration steps and therefore are not very fast. An analytical solution can be obtained by means of eigenvector analysis. In this method the diffuse flux vector is linearly transformed in such a way that the scattering matrix becomes diagonal, so that a solution is obtained that can be expressed as a linear combination of exponential functions.

In the particular solution of the N+2 stream system implemented in SAIL++ several techniques have been applied in order to reduce storage space requirements and computational efforts, and to ensure numerical stability. These can be summarised as follows:

- By means of an azimuthal DCT (discrete cosine transform) the zenithal dependence of light scattering is separated from the azimuthal dependence. By this transformation the dimension of the matrices **A** and **B** describing diffuse scattering

can be reduced from 36×36 to seven times 3×3. The seven independent systems so obtained correspond to the seven angular frequencies in the azimuth domain. This step, which is appropriate only for azimuthally isotropic media, is often applied in the DISORD (discrete ordinates) method for atmospheric scattering (Stamnes *et al.*, 1988), but for leaf canopies with random leaf azimuth orientation it can be applied as well.

- In the analytical solution all potential numerical singularities are intercepted by means of specially constructed combinations of exponential functions. The most essential of these functions are given by

$$S(x) = \begin{cases} \frac{e^{\lambda Lx} - e^{-\lambda L(1+x)}}{\lambda} & ; (\lambda > 0) \\ L(1+2x) & ; (\lambda = 0) \end{cases}$$

$$J(k, x) = \begin{cases} \frac{e^{\lambda Lx} - e^{kLx}}{k - \lambda} & ; (k \neq \lambda) \\ -Lx e^{kLx} & ; (k = \lambda) \end{cases}$$

$$J(K, x) = \begin{cases} \frac{e^{\lambda Lx} - e^{KLx}}{K - \lambda} & ; (K \neq \lambda) \\ -Lx e^{KLx} & ; (K = \lambda) \end{cases}$$

In these functions x is the relative optical height, λ is one of the eigenvalues of the diffuse scattering system, and k and K are the extinction coefficients in the directions of the sun and the observer, respectively. If the exponentials in the above functions would have been kept separated in the formulation of the analytical solution, the singularities (the second conditions mentioned) could lead to attempts of computing differences between vary large numbers, giving inaccurate or even unpredictable results. With the set of functions above, these problems are easily intercepted by means of a simple test on the absolute value of the denominator. In Stamnes *et al.* (1988) and Nakajima & King (1992) the J -functions are not applied, and therefore their respective atmospheric models might still be prone to the mentioned singularities.

- The eigenvalues are defined by the equation

$$(A + B)(A - B)Y = Y\Lambda^2$$

where Y is the matrix of eigenvectors, and Λ^2 the diagonal matrix of squared eigenvalues. For $N = 72$ one obtains 3 absolute eigenvalues for each of the 7 azimuthal frequencies, so 21 eigenvalues in total. The singularity $\lambda = 0$ occurs for the zero azimuthal frequency in the case of conservative

scattering. This singularity changes the character of the S -function from a hyperbolic sine into a purely linear function in x and L . Nakajima and King (1992) also define hyperbolic sine and cosine basis functions in order to intercept numerical problems due to high optical thicknesses and conservative scattering

- The solution is written in terms of elements of a layer scattering matrix such as represented by Eq. (2). Each element automatically fulfils the reciprocity relations, as the analytical solution has been formulated as an entirely symmetric function of sun-object-sensor geometry.
- As explained already in the previous section, pre-computed tabular data stored in a 7-dimensional array are used to overcome the necessity of angular integration of scattering coefficients over segments
- A modular structure of the code has been designed so as to avoid unnecessary repetition of calculations. This is illustrated by means of Fig. 2, which shows the division of the code into 14 modules, and indicates which modules are invoked on a detected change of one or more of the input parameters shown in the left column. For instance, a change of canopy LAI will only result in execution of modules 11-14, as other modules are independent of the value of LAI. In Fig. 2 "leaf" refers to the optical properties of the leaves, viz. reflectance, transmittance or both, and "view" refers to viewing zenith angle or relative azimuth, or both.

Parameter change	Modules executed													
	1	2	3	4	5	6	7	8	9	10	11	12	13	14
LIDF	1				1	1	1	1	1	1	1	1	1	1
sun		1			1	1	1			1			1	1
view			1	1						1			1	1
leaf					1	1	1	1	1	1	1	1	1	1
LAI											1	1	1	1
hot spot parameter														1

Fig. 2 Modular structure of the SAIL++ subroutine

The final solution of the radiative transfer equation is expressed by the quantities of the layer scattering matrix of Eq. (2). Of these quantities, the bidirectional reflectance factor is split in two terms by

$$\rho_{so} = \rho_{so}^s + \rho_{so}^d$$

in which the first term represents the contribution due to singly scattered sunlight and the second the contribution due to multiple scattering. One additional output, which is related to the hot spot effect, is the bidirectional gap fraction for the complete canopy layer,

τ_{ssoo} . The single scattering contribution and the bidirectional gap fraction are computed using the hot spot effect theory of Kuusk, 1985.

3.4 Addition of the soil's contribution

In order to incorporate the contribution from the soil, the adding algorithm is used. By this algorithm the reflectance properties of the top of the canopy for a black soil are transformed into the same quantities for the non-black soil with given soil reflectance properties. The result is given by the following four equations, in which the terms with an asterisk indicate the result after adding the soil:

$$\begin{aligned} \mathbf{R}_{dd}^* &= \mathbf{R}_{dd} + \mathbf{T}_{dd}(\mathbf{I} - \mathbf{R}_s \mathbf{R}_{dd})^{-1} \mathbf{R}_s \mathbf{T}_{dd} \\ \mathbf{r}_{sd}^* &= \rho_{sd} + \mathbf{T}_{dd}(\mathbf{I} - \mathbf{R}_s \mathbf{R}_{dd})^{-1} (\mathbf{r}_s \tau_{ss} + \mathbf{R}_s \tau_{sd}) \\ \mathbf{r}_{do}^{*\top} &= \rho_{do}^\top + (\tau_{do}^\top \mathbf{R}_s + \tau_{oo} \mathbf{r}_s^\top)(\mathbf{I} - \mathbf{R}_{dd} \mathbf{R}_s)^{-1} \mathbf{T}_{dd} \\ \mathbf{r}_{so}^* &= \rho_{so}^s + \tau_{ssoo} \mathbf{r}_s + \rho_{so}^d \\ &\quad + \tau_{do}^\top (\mathbf{I} - \mathbf{R}_s \mathbf{R}_{dd})^{-1} (\mathbf{r}_s \tau_{ss} + \mathbf{R}_s \tau_{sd}) \\ &\quad + \tau_{oo} \mathbf{r}_s^\top (\mathbf{I} - \mathbf{R}_{dd} \mathbf{R}_s)^{-1} (\tau_{sd} + \mathbf{R}_{dd} \mathbf{r}_s \tau_{ss}) \end{aligned}$$

In the last equation, which describes the bidirectional reflectance of the ensemble canopy-soil, the first two terms on the right form the single scattering contribution. The remaining three terms are due to multiple scattering of solar incident flux.

In SAIL++ it is assumed that the soil is a Lambertian reflector, and in this case the above equations can be computed in a simplified way for two reasons

- The azimuthal DCT applied to a Lambertian soil gives only a non-zero result for the zero azimuthal frequency, which means that for all higher frequencies the soil's reflectance effectively equals zero
- In the implementation of the above equations it is no longer necessary to execute the mentioned matrix inversions, as in the case of a Lambertian soil reflectance all elements of \mathbf{R}_s become equal (this is a consequence of the equal-weight tessellation) and the repeated reflections at the canopy-soil interface can directly be expressed by a single matrix that is a simple function of the canopy's diffuse reflectance matrix \mathbf{R}_{dd} and the soil's reflectance factor.

3.5 User aspects

The model SAIL++ has been implemented at NLR in Fortran on a PC. It consists of some 25 subroutines and the total amount of code is substantially larger than the one of its predecessor models. All matrix

manipulation routines are included in order to eliminate any possible dependency on commercial software packages. Thanks to the modular structure of the SAIL++ subroutine, the execution speed remains sufficiently high for applications at hyperspectral resolution and for model inversion purposes. The required input parameters for a single model run are

L	LAI, leaf area index
a	LIDF parameter a
b	LIDF parameter b
q	Hot spot size parameter
ρ	Single leaf reflectance
τ	Single leaf transmittance
r_s	Soil's reflectance factor
θ_s	Solar zenith angle
θ_o	Observer's zenith angle
ψ	Relative azimuth angle

The output consists of the elements of the layer scattering matrix defined by Eq. (2), plus a number of quantities of the canopy-soil ensemble, viz.

- bidirectional reflectance total, and separated into single and multiple scattering contributions
- hemispherical reflectance
- canopy layer total transmittance
- canopy layer absorbance

The latter quantities can be important for energy balance modelling problems and *e.g.* calculation of fraction APAR in visible wavelengths.

4 RESULTS

The functioning of the new model SAIL++ has been investigated by checking its internal consistency and by comparing its outputs to those of other models. The internal consistency can be investigated by means of the following tests:

- Is the sum of all scattering coefficients equal to the associated extinction coefficient of the incident radiation, multiplied by the sum of single reflectance and transmittance, and does this hold for any incidence angle and type of incident flux (specular, diffuse)?
- Do all scattering coefficients fulfil the reciprocity relations?

Both properties have been investigated by extensive numerical experiments and debugging. This has resulted into incorporation of routines for normalisation and symmetrisation, so as to reach a very high degree of conformity to the above requirements.

Comparisons with the much simpler predecessor model SAILH should indicate what the effect of the refinement in the description of the diffuse flux field is on the bidirectional canopy reflectance, as both models differ only with regard to this aspect. For the near infrared, Fig. 3 shows the result of such a comparison for a moderately planophile canopy ($a = 0.5$; $b = -0.5$), an LAI of 4 and a solar zenith angle of 45 degrees. It shows the bidirectional reflectance profile in

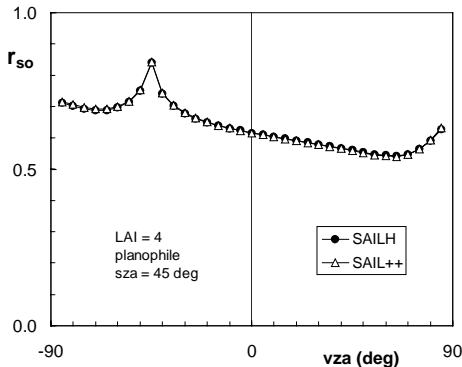


Fig. 3 Comparison SAILH vs. SAIL++ for planophile LIDF

the principal plane for both models, with the hot spot peak on the left. In this case the difference in output between both models is very small. For a moderately erectophile leaf angle distribution ($a = -0.5$; $b = -0.5$) one obtains the result as displayed in Fig. 4. Here the results for SAIL++ are 2 to 4 % higher in absolute reflectance than for SAILH. Both results are for a black soil, so that only the canopy contributes to the output.

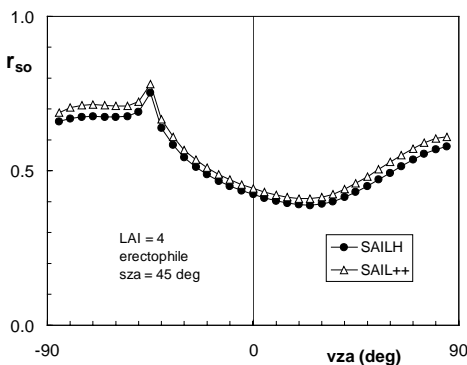


Fig. 4 Comparison SAILH vs. SAIL++ for erectophile LIDF

Fig. 5 shows a more detailed comparison between the models. Here both improvements from SAIL to SAIL++ (hot spot effect and multiple scattering) are illustrated. The curve with black triangle symbols

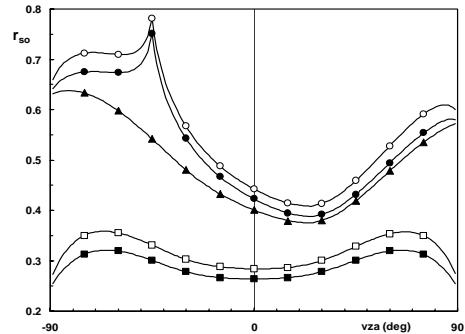


Fig. 5 Model comparison of total bidirectional reflectance for SAIL (triangles), SAILH (black circles) and SAIL++ (white circles). Squares indicate multiple scattering contributions for SAILH (black) and SAIL++ (white)

shows the total bidirectional reflectance obtained from SAIL (i.e. SAILH without the hot spot effect). The circles give the result for SAILH (black) and SAIL++ (white), with both showing a pronounced hot spot peak on the left side of the principal plane. By the way, from this it also appears that the hot spot effect is not limited to the actual hot spot region. The multiple scattering contribution of both SAIL and SAILH is illustrated by the curve with black squares. In these models the multiple scattering contribution depends only on the viewing zenith angle, so the curve is symmetric about the nadir point in the middle. In SAIL++ (white squares) this contribution can have an azimuthal dependence, but it appears that the shape of the profile nevertheless remains almost symmetric in the principal plane, which suggests a very weak azimuth dependence. There is a difference in level however. The multiple scattering contribution in SAIL++ is 2 to 4% higher than in SAILH. Multiple scattering contributes about 30% to the total bidirectional reflectance, which means that in the near infrared roughly one half of the total signal can be attributed to this component.

Fig. 6 illustrates a model comparison result for SAIL++ (white) with Parcinopy (black), a ray tracing model (Chelle, 1997). From these results, which have been obtained for a spherical leaf angle distribution, it appears that the multiple scattering contribution (squares) is very much alike for both models. The single scattering contributions (triangles) however are rather different in two aspects. First, the hot spot effect is hardly expressed in the Parcinopy result, and second, there appears to be a systematic difference in the

forward scattering section of the principal plane. For SAIL++ the minimum is much closer to nadir. The reason for this discrepancy between both models is as yet unknown.

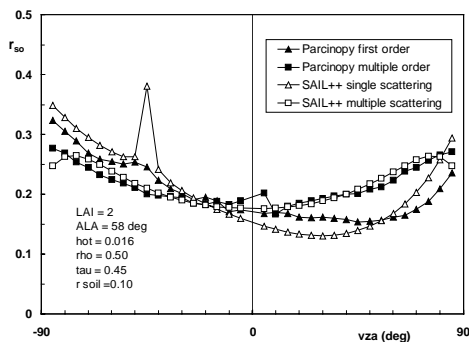


Fig. 6 Single (triangles) and multiple scattering (squares) contributions for Parcinopy (black) and SAIL++ (white)

This section is concluded with an analysis of bidirectional reflectance profiles obtained from SAILH and SAIL++ for different soil reflectance levels. The results are presented in Fig. 7. This gives an opportunity to check whether the higher multiple scattering contribution to the reflectance found for SAIL++ and a black soil also occurs for SAIL++ with a white soil (100% soil reflectance). From Fig. 7 this appears not

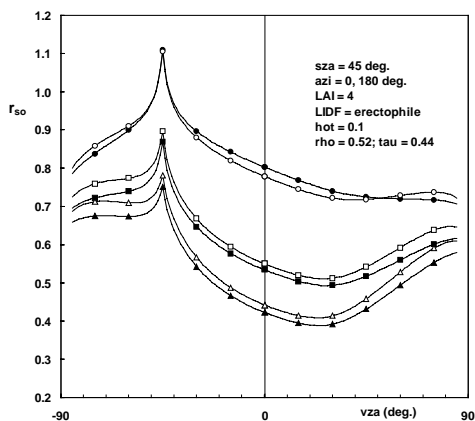


Fig. 7 BRDF profiles from SAILH (black symbols) and SAIL++ (white symbols) for different soil reflectance levels of 0.0 (triangle), 0.5 (square) and 1.0 (circle)

to be the case. For a white soil the situation has reversed for the viewing angles around nadir. In this case SAILH produces the highest reflectance. One may conclude that for SAILH the sensitivity to the

soil's reflectance is somewhat higher than for SAIL++, which can be explained by a somewhat higher diffuse transmittance of SAILH. The law of energy conservation demands that this must be compensated by a lower diffuse reflectance of SAILH compared to SAILH, and this is exactly what is observed with the canopy reflectance for a black soil background. The bidirectional reflectance profiles of both models for a white soil are different, but on practically the same level. This indicates that the more accurate modelling of multiple scattering possible with SAIL++ alters the division of scattered radiation over reflection and transmission, but the sum of both remains approximately the same.

In the RAMI numerical experiment (Pinty *et al.*, 2001) a version of SAIL called ProSAIL (like SAILH, this model also includes the hot spot effect and it was coupled to the leaf model PROSPECT) was compared to several other 1D and 3D canopy reflectance models. Unfortunately, due to a wrong specification of input parameters in half of the cases, no definite conclusions on this comparison could be drawn yet.

5 CONCLUSIONS

The N+2 stream method of radiative transfer theory has been applied to leaf canopy reflectance modelling, which has resulted in the new SAIL++ model. Differences with the simpler model SAILH are only significant in the NIR, for high LAI and erectophile leaf angle distribution. Multiple scattering in SAIL++ differs from SAILH in level rather than anisotropy. The differences between both models are only modest, and in retrospect this appears to justify the simplifications introduced for the multiple scattering calculations applied in SAILH.

Due to its modular structure, SAIL++ is only moderately slower in execution time than SAILH. In SAIL++ several precautions have been taken to ensure numerical stability and it has a higher accuracy than SAILH, so use of this improved model is recommended. The modular structure of the software of SAIL++ avoids any unnecessary repetition of calculations and therefore this model is still suitable for calculation of reflectance spectra at hyperspectral resolution and for application in optimisation loops such as often used during model inversion.

ACKNOWLEDGEMENT

The work presented in this paper has partly been performed under contract of the European Union in the 5th Framework project CROMA (Crop Reflectance Operational Models for Agriculture) which was coordinated by Hervé Poilvé of Astrium SAS in Toulouse, France. Frédéric Baret and Bruno Combail of

INRA, Avignon, France, are acknowledged for providing results of comparison calculations with the Parcinyopy model.

REFERENCES

- Chelle, M., 1997, Développement d'un modèle de radiosité mixte pour simuler la distribution du rayonnement dans les couverts végétaux, Thèse Université de Rennes I
- De Haan, J.F., 1987, Effects of aerosols on the brightness and polarization of cloudless planetary atmospheres, Ph.D. Thesis, Free University, Amsterdam
- Kuusk, A., 1985, The hot spot effect of a uniform vegetative cover, *Sov. J. Rem. Sens.* 3: 645-658
- Myneni, R.B., Asrar, G. and Kanemasu, E.T., 1987, Light scattering in plant canopies: the method of successive orders of scattering approximations (SOSA), *Agr. Forest Meteor.* 39:1-12
- Nakajima, T. and King, M.D., 1992, Asymptotic theory for optically thick layers: application to the discrete ordinates method, *Applied Optics* 31 (36):7669-7683
- Pinty, B., Gobron, N., Widlowski, J.-L., Gerstl, S.A.W., Verstraete, M.M., Antunes, M., Bacour, C., Gascon, F., Gastellu, J.-P., Goel, N.S., Jacquemoud, S., North, P., Qin, W. and Thompson, R., 2001, Radiation transfer model intercomparison (RAMI) exercise, *Journal of Geophysical Research*, Vol. 106, No. D11, pp. 11937-11956
- Stamnes, K., Tsay, S.-C., Wiscombe, W. and Jayaweera, K., 1988, Numerically stable algorithm for discrete-ordinate-method radiative transfer in multiple scattering and emitting layered media, *Applied Optics* 27(12):2505-2509
- Verhoef, W., 1984, Light scattering by leaf layers with application to canopy reflectance modeling: the SAIL model, *Remote Sens. Environ.*, Vol. 16, pp. 125-141
- Verhoef, W., 1985, Earth observation modeling based on layer scattering matrices, *Remote Sens. Environ.*, Vol.17, pp. 165-178
- Verhoef, W., 1998, Theory of radiative transfer models applied in optical remote sensing of vegetation canopies, Ph.D. Thesis, Wageningen Agricultural University, 310 p.

Inter-Sensor Calibration of Vegetation Indices for Monitoring and Continuity Studies of Ecosystem Variability

Alfredo Huete¹, Hiroki Yoshioka², Tomoaki Miura¹, Ho Jin Kim¹, Xiang Gao¹

¹Department Soil, Water and Environmental Science

University of Arizona, Tucson, Arizona U.S.A. ahuete@ag.arizona.edu

²Department of Applied Information Science and Technology

Aichi Prefectural University, Japan

ABSTRACT - Numerous satellite sensor systems useful in terrestrial Earth observation and monitoring have recently been launched and their derived products are increasingly being used in regional and global vegetation studies. The use of these multi-resolution sensors offer much opportunity for vegetation studies aimed at understanding the terrestrial carbon cycle, climate change, and land cover conversions. Spectral vegetation indices are one example of widely-used satellite-based products for mapping temporal and spatial variations in surface biophysical parameters. Vegetation index products from SeaWiFS, VEGETATION, MODIS, Landsat, and other sensors are now widely available for monitoring both seasonal and long-term ecosystem dynamics. However, data continuity and compatibility problems among the various satellite products due to differences in sensor characteristics as well as algorithms must first be addressed. In this paper we analyze the broadband reflectance and VI relationships among the various sensors with the use of airborne and spaceborne hyperspectral data sets. We focus on the spectral issues (filter response function, bandwidth, center wavelength) influencing the vegetation index products and the issues involved in their synergistic use, translation, data continuity, and scaling. Our results indicate that inter-sensor VI relationships were neither linear nor unique and varied with land cover and surface composition. Thus, prior knowledge of ecosystem parameters, such as leaf area index and soil brightness are needed for exact translation.

1 INTRODUCTION

Numerous satellite sensor systems useful in terrestrial Earth observation and monitoring have recently been launched and satellite-derived products from these fine and moderate resolution sensors are increasingly being used in regional and global vegetation studies. Moderate resolution sensors have coarse pixel sizes (100 m to 1000 m) but frequent revisit periods (1 – 4 days) and their observations are useful for change detection, monitoring of ecosystem seasonality, inter-annual variations for climate change studies, land cover change studies, and input to net primary and net ecosystem production (NPP, NEP) models. Fine resolution sensors are capable of capturing more detailed vegetation dynamics related to land conversion and ecosystem management with pixel sizes typically ranging from 30 m to <1 m (Landsat, Ikonos, Quickbird).

The use of multi-resolution satellite data observations can help advance our understanding and analysis of the terrestrial carbon cycle and aid in mapping ecosystem variability including land cover conversions. Multi-sensor data may be exploited by combining fine- with moderate resolution sensors for scaling studies (e.g. ASTER

and MODIS) and seasonality studies (e.g. Landsat ETM+ with MODIS).

A common feature of these satellite sensor systems is their inclusion of red and near-infrared (NIR) spectral bands for vegetation studies. These two bands exhibit sensitivity to chlorophyll concentrations and leaf structure and quantity. They are typically ratioed or linearly combined to create vegetation indices (VI's) to more accurately map spatial and temporal variations in the Earth's vegetative cover. There is currently a 20+ year, time series data record of normalized difference vegetation index (NDVI) values from the NOAA-AVHRR series of satellite sensors which could be extended with the newer satellite data products (Los, 1993; Roderick et al., 1996). The Landsat series of sensors have also produced an archived data set that can be processed into useful information for global change studies. Vegetation index products from the AVHRR, SeaWiFS, VEGETATION, MODIS, Landsat, and other sensors are now being used to monitor both seasonal and long-term land cover changes. Consequently, there is great interest in maintaining data continuity and compatibility across the sensor-specific data sets (Gitelson and Kaufman, 1998).

Compatibility problems among the satellite data products exist due to differences in sensor

characteristics and the algorithms used to process the data. The spectral characteristics of the red and NIR bands vary greatly among sensors in their filter response functions, bandwidths, and center wavelength (Fig. 1,2). There are also radiometry (signal to noise), spatial (point spread function and pixel size), and temporal (revisit times) differences as well.

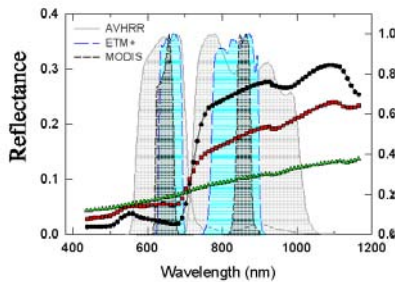


Figure 1. MODIS, Landsat ETM+, and NOAA-AVHRR normalized bandpass filters superimposed onto three hyperspectral reflectance signatures (Miura et al., 2002).

In Fig. 1, the normalized red and NIR spectral response functions of the AVHRR, ETM+, and MODIS bands are shown over three typical spectral reflectance signatures of soil, medium- and dense vegetation. The MODIS bands are very narrow in comparison with the coarse AVHRR bands, while the ETM+ bands are intermediate in width. The red and NIR band centers, as well as bandwidths are shown for 14 moderate and fine resolution sensors in Fig. 2. There appears to be an inverse trend of red bandwidth vs. center wavelength (Fig. 2a). The sensor contrasts, or distance, between the center NIR and red wavelengths are as short as 150 nm (ASTER) to as far apart as 300 nm (Landsat MSS).

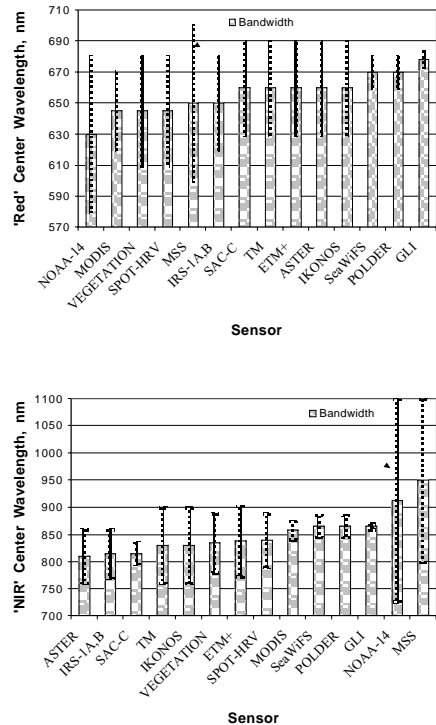


Figure 2. Variations in red (top) and NIR (bottom) wavelength centers and bandwidths for a variety of satellite sensors ranked in order of increasing wavelength center.

The goal of VI continuity is to normalize the spectral, temporal, spatial, and radiometric differences among sensors for the purposes of (1) extension of stable time series data sets for monitoring ecosystem change; and (2) for scaling studies from fine resolution to moderate resolution satellite data sets (Teillet et al., 1997; Gao et al., 2002). We consider VI continuity to be attained when the VI values computed from the reflectance data produced by the different sensors become the same for the same target under identical conditions (Yoshioka et al., 2002). The issue of data product continuity is particularly relevant to the inter-relationships between the AVHRR time series record (1981-) with MODIS (2000 -) and other moderate resolution sensors; the extension of AVHRR and MODIS data records to the NPOESS Preparatory Project (NPP); and the synergistic use of fine (Landsat, ASTER) and moderate (MODIS, SeaWiFS, AVHRR, GLI, VEGETATION) resolution sensors.

In this study we focus on the spectral characteristics of multiple sensors and their influence on the derived VI values. The objectives

of this study are to investigate the continuity and compatibility of VI's among sensors with different bandpasses and to investigate target sensitivities and dependencies of the translation coefficients among sensors. The goal of such a study is to determine the feasibility of development of a theoretical basis and quantitative methodology for the sensor-dependent relationships of reflectances and VI's.

2 METHODS AND APPROACH

2.1 Approach

There are several ways to approach the problem of multi-sensor data continuity and provide inter-sensor translation coefficients:

- (1) Use 'real' satellite sensor observations from multiple instruments. The advantages are that this is the real data from which we wish to establish translation and encompasses all sources of uncertainty, including filter degradation and calibration drift. With this approach, one can also encompass a global set of land cover and seasonal surface conditions for the sensor comparisons. The main disadvantages include the time intervals between different sensor 'looks' to the same target with possible variations resulting from sun angle and atmosphere differences. One must also be precise in co-registration of the two sensor data sets with uncertainties resulting from geolocation error.
- (2) One can utilize a finer resolution sensor data set to simulate the responses of a coarser resolution sensor data set. Thus, we can utilize hyperspectral and fine spatial resolution Hyperion data to simulate a MODIS, SeaWiFS, AVHRR, and GLI pixel. The advantage is that only a single atmosphere is involved and there are no spatial registration errors. The disadvantage is that the data is synthetic and the spectral response functions and modulation transfer function (MTF) need to be approximated.
- (3) One can also utilize low level airborne and field-based field radiometry, such as Analytical Spectral Devices (ASD) data. This has the advantage of eliminating the sensor-dependent atmosphere effects enabling one to focus on inter-sensor comparisons related to the ecosystem targets of interest. This is useful from a spectral standpoint but has less utility in studying the spatial pixel size inter-dependencies between sensors.
- (4) Finally, one can mathematically derive inter-relationships among sensors through models, including leaf biochemical models, soil models, canopy radiative transfer models, and atmosphere radiative transfer models (Jacquemoud et al., 1996; Verhoef, 1984; Vermote et al., 1997). This has the advantage of complete control of surface, atmosphere, and sensor effects. The main limitation concerns the extent to which modeled data depicts actual sensor-target results, particularly over heterogeneous surfaces.

2.2 Data

In this study we primarily utilized spaceborne EO-1 Hyperion hyperspectral data, airborne AVIRIS hyperspectral data, and light aircraft-based hyperspectral ASD data sets to investigate inter-sensor compatibility and continuity. We also include some real, observed data from MODIS and AVHRR, as well as from MODIS and Landsat ETM+ as examples. The hyperspectral imager, Hyperion, is part of the Earth Orbiter 1 (EO-1), launched in November 2000 as part of NASA's New Millennium program which focused on new, more cost effective technologies for Earth observation. The Hyperion hyperspectral imager is a pushbroom sensor providing 220, 10 nm bands covering the spectrum from 400 to 2500 nm. Hyperion data were acquired for a variety of biomes, including the Harvard Forest broadleaf deciduous forest (Lat./Lon: 42.538 degrees, -72.171 degrees, elevation = 200m) the Maricopa Agriculture Center in Arizona (Lat./Lon: 33.07 degrees, -111.97 degrees; elevation = 400m), and the Mandalgobi semiarid grassland site in Mongolia (Lat./Lon: 45.995 degrees, 106.327 degrees; elevation = 1400m). All three sites are primary core validation sites (http://modis-land.gsfc.nasa.gov/val/coresite_gen.asp) for the Earth Observing System (EOS). The Hyperion data were first convolved to the sensor bandpasses of interest followed by an atmosphere correction with '6S' using a standard atmosphere model.

Low-level Airborne Visible/ Infrared Imaging Spectrometer (AVIRIS) flights were conducted in the semiarid Monte Desert of Central Argentina on February 15, 2001 at the Ñacuñán Biosphere Reserve (34°02'S; 67°54'W; elevation = 540m). The AVIRIS imaging spectrometer operates in the 400 to 2450 nm region collecting 224 spectral bands with a nominal 10 nm spectral response function. AVIRIS flew at an altitude of 4 km yielding 4 m pixels. The vegetation communities in this area consists of mesquite

forests (algarrobal), creosotebush- dominated communities (jarillal), degraded sand-dune areas with mixed creosotebush and mesquite (medanal), and severely degraded areas with sparse creosotebush (peladal). The AVIRIS sensor was flown at 2 km AGL, yielding 4 m pixels. The AVIRIS data was corrected for atmosphere and converted to surface reflectances with the aid of an atmosphere correction program, ATREM, constrained with co-registered surface ASD measurements, used as calibration ground control points.

We also collected light-aircraft (ultralight) measurements with a full-range ASD spectroradiometer at the Araguaia National Park (ANP) (S 10°5', W 50°3') in Brazil, July 25-26, 2001. The area represents a tropical forest-savanna transitional zone with various land cover types, including both undisturbed savanna and forest as well as converted pastures. The ultralight flew "below the atmosphere" at 150 m AGL at a speed of 30 m per second collecting a single spectrum every ~1 second over a ground spatial resolution of 13m by 30m. The data were acquired between 10:30 – noon and calibrated to ground reflectances by taking a ratio to the readings made over a Spectralon white reference panel before and after the flight.

All hyperspectral data were spectrally convolved to the multi-sensor bandpasses, from which the NDVI and enhanced vegetation index (EVI) were computed:

$$NDVI = (\rho_{NIR} - \rho_{red}) / (\rho_{NIR} + \rho_{red}), \quad (1)$$

$$EVI = G (\rho_{NIR} - \rho_{red}) / (L + \rho_{NIR} + C_1 \rho_{red} - C_2 \rho_{blue}) \quad (2)$$

where ρ_{NIR} , ρ_{red} and ρ_{blue} are the NIR, red, and blue reflectances; L is a soil correction factor, C_1 and C_2 are the atmosphere resistance terms, and G is a gain factor. The coefficients from the MODIS EVI product were used, $G=2.5$, $L=1$, and C_1 and C_2 as 6 and 7.5, respectively (Huete et al., 2002).

2.3 Statistical Analyses

Comparisons among the multi-sensor data sets were made using various statistical 'goodness-of-fit' measures. The 'mean deviation' (MD) was used to measure systematic deviation, e.g., if the data from a sensor is systematically higher than that of another sensor,

$$MD = \frac{\sum_{i=1}^k m_i - d_i}{k} \quad (3)$$

3 RESULTS

3.1 Airborne ASD data over Cerrado & Forest, Brazil

A sample of the spectral reflectance signatures derived from the light aircraft, ASD data over the various land cover conditions encountered at the Araguaia site is depicted in Fig. 3. The equivalent MODIS bandpass simulated NDVI and EVI values for these signatures are provided as well.

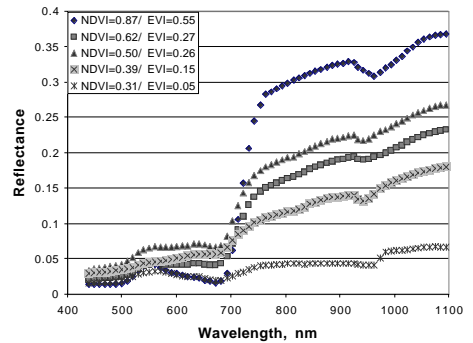


Figure 3. Sample hyperspectral reflectance signatures from the low altitude airborne ASD data over the Araguaia, Brazil site.

Using MODIS as a reference, the convolved, moderate resolution, multi-sensor NDVI values for over 1,000 spectra from one overflight are shown in Fig. 4. As would be expected, the NDVI values are fairly well correlated among the various sensors and overall, NDVI values were within 5% of the MODIS NDVI values, on average. For continuity purposes, however, one can note the discrepancies from the 1:1 line and the need for sensor-specific translation equations. The AVHRR derived NDVI resulted in the highest values (mean deviations of ~+0.012) with the MMRS sensor from SACC-C producing the lowest NDVI values (mean deviations of -0.029), relative to the

MODIS sensor. Deviations were much larger at the lower half of NDVI values (<0.6) than at the higher values with more vegetation present. Deviations were most serious at intermediate NDVI values (0.2 – 0.6) where, relative to MODIS, NDVI values were as much as 20% lower (MMRS) and 10% higher (AVHRR).

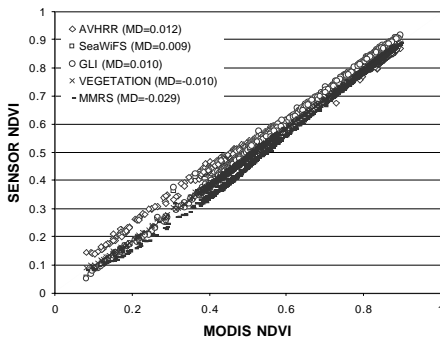


Figure 4. Intercomparison of ASD-convolved MODIS NDVI with other ASD-convolved moderate resolution sensors.

A more extreme example of VI discontinuity occurs when intercomparisons among the Landsat derived NDVI values are made (Fig. 5). Mean deviations between the Thematic Mapper (ETM+, TM) bands and the Multispectral Scanner (MSS) bands were as high as 0.086 when MSS band 6 (700 – 800 nm) is used for VI computation. This is nearly 10% of the normal NDVI range. In this case, only the extreme low and high NDVI values were close to the 1:1 line between MSS and TM. Maximum differences among the sensor VI's occurred at NDVI ~ 0.35 in which the MSS (band 6) NDVI was ~20% lower and the MSS (band7) NDVI was ~30% higher compared with ETM+.

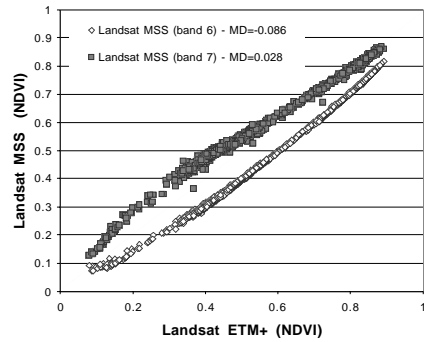


Figure 5. Intercomparison of ASD-convolved Landsat ETM+ NDVI with the Landsat MSS derived NDVI.

3.2 AVIRIS data over the Monte Desert, Argentina

Sample spectral reflectance signatures from the AVIRIS image acquired at the Nacuñán Biosphere Reserve are shown in Fig. 6 for the major vegetation communities. Visually, one can see that 'red' reflectances tend to be higher over the MODIS bandpass interval compared with that of the AVHRR. It is more difficult to compare the NIR reflectances due to spectral overlap of the AVHRR- NIR band onto the 'red edge' (Fig. 6). A crossplot of the resulting NDVI values at this semiarid site is shown in Fig. 7. Each sensor has a separate relationship with the MODIS NDVI with slopes close to 1, but significantly varying offsets.

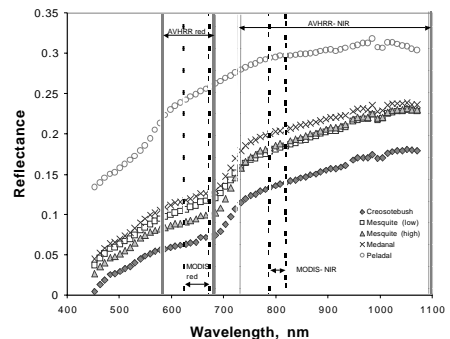


Figure 6. Sample AVIRIS spectral reflectance signatures for the different vegetation communities at the Nacuñán Biosphere Reserve, Argentina. MODIS and AVHRR bandwidths are superimposed.

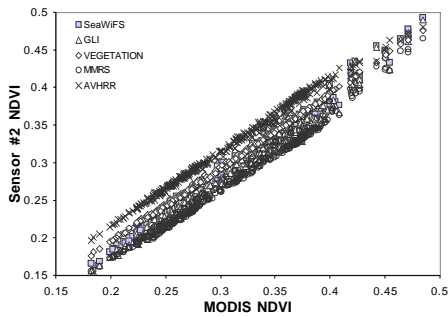


Figure 7. AVIRIS-convolved MODIS NDVI comparisons with a series of AVIRIS-convolved moderate resolution sensors.

A plot of the NDVI deviations (Fig. 8) reveal that the AVHRR is approximately +0.02 NDVI units higher than MODIS and the MMRS sensor is -0.04 units lower than the MODIS NDVI. The deviations are greatest at around a MODIS NDVI ~ 0.35. For this dataset, sensor-induced deviations are much greater than vegetation-type induced deviations within a specific sensor. The EVI relationships show similar relationships but with less deviations and a slightly negative slope to the AVHRR – MODIS relationship, indicating that AVHRR – MODIS differences decrease with increasing amounts of vegetation. Maximum deviations occurred at around MODIS EVI values of 0.15.

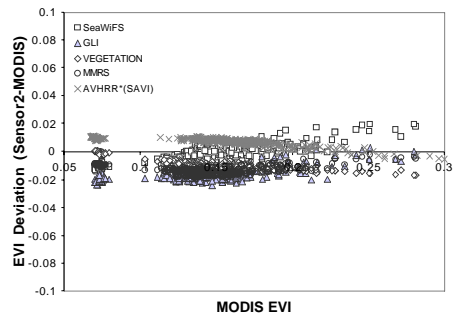
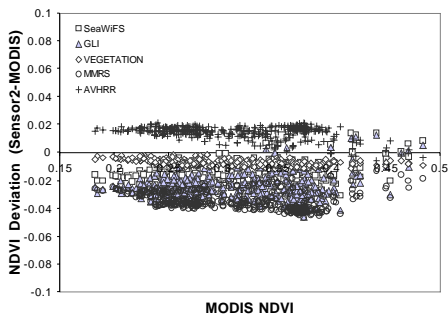


Figure 8. Deviations of AVIRIS-convolved NDVI (top) and EVI values (bottom) from moderate resolution sensor bandpasses relative to the AVIRIS-convolved MODIS NDVI and EVI.

3.3 Hyperion data at multiple sites

The results of NDVI inter-sensor comparisons from the spaceborne Hyperion data at three separate sites are shown in Fig. 9. The three Hyperion image data sets represent three atmospheres that introduce a new source of uncertainty to our inter-sensor comparisons such that between site differences may be the result of land cover type influences or atmosphere influences on the different spectral bandpasses. Bandpass differences result in different atmospheres which strongly affect the NDVI. Although standard atmosphere correction techniques were applied, one cannot be sure of a complete and accurate correction, especially when a uniform atmosphere across an image is assumed. Nevertheless, the Hyperion data is collected immediately after a Landsat ETM+ overpass and minutes before the MODIS nadir overpass and thus represents a realistic comparison test of sensor-dependent NDVI's across space and time.

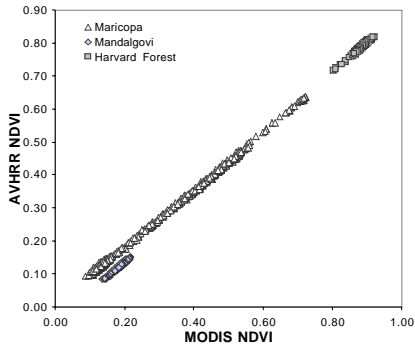


Figure 9. Hyperion-convolved AVHRR NDVI vs. the MODIS NDVI for three sites.

A MODIS NDVI value of 0.20 resulted in a fairly similar AVHRR value over the Maricopa site, but a significantly lower AVHRR value at the Mongolia site. The deviation observed with the Mongolia data could be a real land cover influence on VI inter-relationships or it could also be an atmosphere correction artifact.

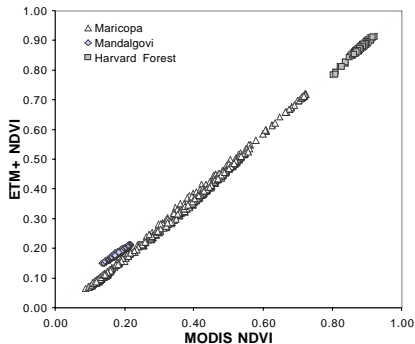


Figure 10. Hyperion-convolved AVHRR NDVI vs. the MODIS NDVI for three sites.

The relationships observed in Figs. 10 and 11 are not linear, but curvilinear relationships. The disparity among the 3 sites is more evident in the EVI cross-sensor comparisons (Fig. 11). The EVI relationships resemble those from the NDVI except for the Harvard Forest site. All the deviations appear more accentuated in the EVI plots. Miura et al. (2002) did document a curvilinear relationship and land cover induced change in the VI relationships.

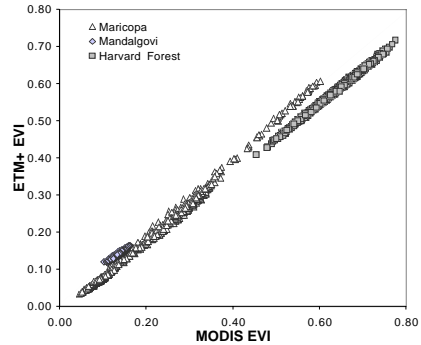


Figure 11. Hyperion convolved ETM+ vs. MODIS EVI for three sites.

3.4 Comparisons with real sensor data

In Fig. 12, we plot actual Landsat ETM+ data collected at nearly the same time as MODIS data at the Jornada Experimental Range in New Mexico, an EOS core validation site. Both data sets are at nadir view and the 30 m ETM+ data have been aggregated to the 500 m MODIS pixel size, but without accounting for the point spread function (Gao et al., 2002). The resulting reflectance and VI relationships were fairly close to the 1:1 line and the average RMSE values are equivalent to the mean deviation values we derived from the AVIRIS and Hyperion bandpass simulations. However, it is very difficult to assess the cause of the deviations between the two sensors as co-registration errors and uncertainties in the atmosphere correction may also affect the relationship seen in Fig. 12, in addition to the different bandpasses. Atmosphere correction on the MODIS data was accomplished with climatology while that for the ETM+ was based on '6S' and sun photometer measurements of optical depth.

The MODIS and AVHRR composite data show even more discrepancies between sensor NDVI's, most of which are independent of target based spectral bandpass influences (Fig. 13). The NOAA-14, 2000 data over the Seville core validation site in New Mexico show the overwhelming influence of atmosphere water vapor content on the NDVI values. The AVHRR NIR bandpass is very sensitive to water vapor while the narrow MODIS NIR bandpass completely avoids water vapor influences. The water vapor effect is stronger in the more humid

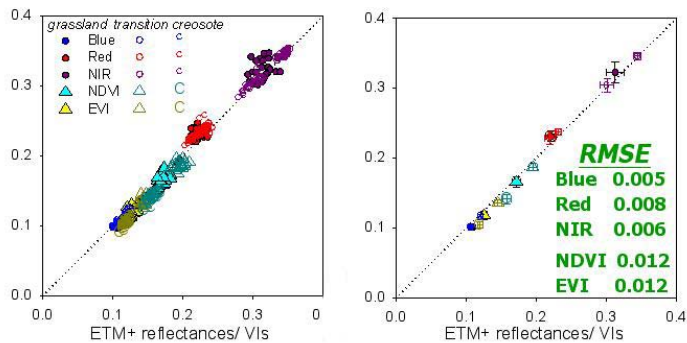


Figure 12. Actual MODIS nadir-view reflectance and VI data plotted against corresponding Landsat ETM+ data at the Jornada Experimental Range, New Mexico.

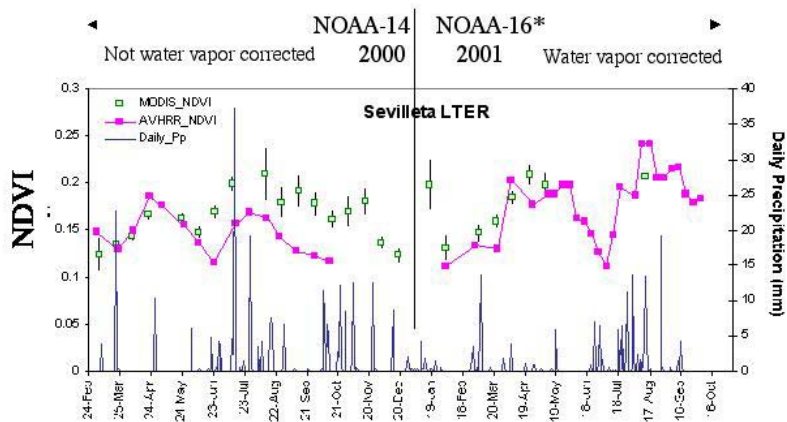


Figure 13. Actual MODIS and AVHRR composited NDVI data for the years 2000 (NOAA-14) and 2001 (NOAA-16).

growing season and nearly disappears in the dry winter season. The NOAA-16, 2001 data shows MODIS and AVHRR based NDVI's to track each other fairly well. The 2001 AVHRR NDVI data is corrected for water vapor and thus becomes more similar to the MODIS data. The composited data from both sensors show very large fluctuations due to clouds, residual atmosphere variations, and sun angle/ view angle variations. These affect the resulting NDVI values to a much greater extent than spectral bandpass differences, by an order of magnitude (Fig. 13).

4 CONCLUSION

In shifting from an older sensor to a newer one, one can take advantage of 'state of the art' technology advancements (e.g. better sensor materials) and improved scientific knowledge (e.g. better spectral band configurations), however, there is the dilemma of maintaining data continuity across a time series data record while allowing for new and improved algorithms and data processing.

In this study we were able to utilize hyperspectral data sets from space and aircraft to investigate multi-sensor inter-relationships among vegetation index values. We found that inter-sensor VI relationships were neither linear nor unique and varied with land cover type and surface composition. Thus, prior knowledge of ecosystem parameters, such as leaf area index and soil brightness are needed for exact translation.

Numerical modelling and effective use of leaf, soil, canopy, and atmosphere radiant transfer models offer the possibility of developing such target specific VI translation coefficients. The extent to which an exact translation is needed, however, depends on the application and purpose to which the VI is being applied. Exact solutions may be desirable for climate change studies but not required in land conversion and management studies. One must also consider the other sources of uncertainty that influence the accuracy of the VI products, such as atmosphere and cloud contamination and BRDF-related influences. These external factors influence the VI values by an order of magnitude greater than spectral bandpass differences.

The Hyperion is particularly valuable in that it is part of the Constellation series with Landsat ETM+, Terra, and SACC-C. This, within minutes

and under similar atmosphere and sun angle conditions, all of the Constellations series of sensors view the same Earth's surface at nadir view.

We also noted that there are many potential synergies between sensors, such as in combining broad with narrowband responses in the 'red' region. The narrower 'red' channel may be more chlorophyll sensitive, but the coarser 'red' band may not saturate as easily in high biomass ecosystems.

Acknowledgement

This work was supported by a NASA EO-1 grant NCC5-478 and NASA MODIS contract NAS5-31364.

5 REFERENCES

- Elvidge, C.D., and Chen, Z., 1995, Comparison of broad-band and narrow-band red and near-infrared vegetation indices, *Remote Sensing of Environment*, **54**, 38-48.
- Gao, X., Huete, A.R., and Didan, K., 2002, Radiometric and biophysical validation of MODIS vegetation indices at La Jornada Experimental Range, *Remote Sens. Environ.* (in press).
- Gitelson, A.A., and Kaufman, Y.J., 1998, MODIS NDVI optimization to fit the AVHRR data series-spectral considerations, *Remote Sensing of Environment*, **66**, 343-350.
- Huete, A., Didan, K., Miura, T., and Rodriguez, E., 2002, Overview of the Radiometric and Biophysical Performance of the MODIS Vegetation Indices. *Remote Sensing of Environment (special issue, in press)*.
- Jacquemoud, S., Ustin, S.L., Verdebout, J., Schmuck, G., Andreoli, G., and Hosgood, B., 1996, Estimating leaf biochemistry using the PROSPECT leaf optical properties model, *Remote Sensing of Environment*, **56**, 194-202.
- Los, S., 1993, Calibration adjustment of the NOAA AVHRR normalized difference vegetation

index without recourse to component Channel 1 and 2 data, *International. Journal of Remote Sensing*, **14**, 1907-1917.

Miura, T., Huete, A. R., Yoshioka, H., and Kim, H.J., 2002, An application of airborne hyperspectral and EO-1 Hyperion data for inter-sensor calibration of vegetation indices for regional-scale monitoring, *Proceedings of the IGARSS 2002 – 24th Canadian Symposium on Remote Sensing, Toronto, Canada, June 24-28*.

Roderick, M., Smith, R., and Lodwick, G., 1996, Calibrating long-term AVHRR-derived NDVI imagery, *Remote Sensing of Environment*, **58**, 1-12.

Teillet, P., Staenz, K., Williams, D.J., 1997, Effect of spectral, spatial, and radiometric characteristics on remote sensing vegetation

indices of forested regions, *Remote Sensing of Environment*, **61**, 139-148.

Verhoef, W., 1984, Light scattering by leaf layers with application to canopy reflectance modeling: the SAIL model, *Remote Sensing of Environment*, **16**, 125-141.

Vermote, E.F., Tanré, D., Deuzé, J.L., Herman, M., and Morcrette, J.J., 1997, Second simulation of the satellite signal in the solar spectrum, 6S: An overview, *IEEE Transactions Geoscience and Remote Sensing*, **35**, 675-686.

Yoshioka, H., Miura, T., Yamamoto, H., and Huete, A., 2002, A technique of inter-sensor VI translations using EO-1 Hyperion data to minimize systematic differences in spectral band-pass filters, *Proceedings of the IGARSS 2002 – 24th Canadian Symposium on Remote Sensing, Toronto, Canada, June 24-28*.

Simulation of reflectance spectra in boreal coniferous forest

Tiit Nilson, Andres Kuusk.

Tartu Observatory, 61602 Tõravere, Tartumaa, Estonia

nilson@aai.ee, andres@aai.ee

ABSTRACT - The latest version of forest reflectance model by Kuusk and Nilson (2000) was applied in the spectral mode (400-2500 nm) to test its performance on a few coniferous forests in Sweden by comparing with the helicopter-borne reflectance spectra over the forests measured by Syrén and Alm (1996) by means of GER-2600 spectrometer. When the model was run in the direct mode, as inputs for the model, forest inventory data and the results of ground-based measurements of ground vegetation reflectance spectra, plant canopy analyzer and of canopy transmission measurements were used. The model relies on leaf optical models like PROSPECT2 by Jacquemoud et al. (1996) and needs as additional inputs the concentrations of several leaf biochemical constituents (chlorophyll, water, protein (or nitrogen), lignin and cellulose) and structural characteristics (LWA, g/cm², and effective number of cell layers). The values of biochemical constituents from the LOPEX and ACCP databases were used in the simulations. The resulting simulated reflectance spectra systematically overestimated reflectance in the middle and partly in the near infrared region. This fact does not allow to effectively invert the measured spectra for the leaf biochemical constituents showing absorption features in the middle infrared. Indeed, when the model was inverted, using 50 reflectance factor values all over the spectrum, the retrieved values of chlorophyll concentration were more or less reasonable, however, the estimates of other biochemical constituents occurred at their maximum allowed values.

As possible reasons for the systematical deviations in the middle infrared the following are pointed out: performance problems of the applied leaf optical model(s) for conifer needles, spectra measurement errors, ignoring by the reflectance model the shoot-level clustering effects for the scattering phase function.

1 INTRODUCTION

During recent years much attention has been paid to the use of multispectral and high-spectral resolution reflectance data over different types of vegetation. In vegetation remote sensing, high-spectral resolution remote sensing is mainly oriented towards the estimation of biochemical constituents in leaves, although so far the spectroscopic methods seem to provide acceptable results on dried and ground leaf samples in the laboratory, only. In the report, the possibilities to estimate the concentrations of biochemical constituents in tree leaves from the measured stand reflectance spectra via inversion of the reflectance model are discussed. The analysis is done by a case study.

2 MATERIALS AND METHODS

2.1 Reflectance model

The latest version of the forest reflectance model by Kuusk and Nilson (2000) was used in the spectral mode. The model enables one to calculate the reflectance spectrum of a forest in the spectral region from 400 to 2500 nm with a step of 5 nm (or 1 nm, depending on the leaf optical model used). Different

leaf optical properties models have been incorporated into the forest reflectance model, each of them requiring a specific set of input data. With the leaf optical model PROSPECT2 by Jacquemoud et al. (1996), the concentrations of several leaf biochemical constituents (chlorophyll, water, protein (or nitrogen), lignin and cellulose) and structural characteristics (specific leaf weight, LWA, g/cm², and the effective number of cell layers) are used to form the input to the model. We have changed the original PROSPECT2 biochemical parameter units from g/cm² into concentrations (expressed as percentage of dry matter) in order to better solve the inverse problem. With our formulation we can determine the LWA (total amount of dry matter per unit leaf area or roughly leaf thickness), and the concentrations of different constituents via inversion either separately or all together. This way we can easily avoid retrieving abnormally high contents of any of the biochemical. Alternatively to PROSPECT2, other leaf optical models, such as PROSPECT3 (Fourty et al., 1996) or LIBERTY (Dawson et al., 1998) with the respective input data can be used in the role of the leaf optical model within the forest reflectance model.

Other input data needed to run the forest reflectance model include the stand inventory data

(tree height, crown length and diameter, trunk breast-height diameter, stem number), leaf and branch area indices, a tree distribution pattern and a shoot-level clumping parameter, and the set of parameters for the ground vegetation.

2.2 Ground-based site data

Two coniferous stands located in the suburb region of Stockholm, Sweden were chosen for a more detailed analysis: a 65-year-old pure Norway spruce (*Picea abies*) stand and a 33-year-old pure Scots pine (*Pinus sylvestris*) stand. The stands were surveyed by a Swedish National Forest Inventory (NFI) team in 1997. The following parameters were derived from the measured data (Table 1) and used as inputs for the forest reflectance model: stand density (trees/m²), basal-area-weighted average tree height (m), crown length (m) and breast-height diameter (cm). Additional information about the structural stand parameters was obtained from the measurements of canopy closure and angular distribution of gap fraction by means of a canopy analyzer CI-100. Leaf and branch area indices were estimated by inverting the measured angular distributions of the gap fraction data by means of Nilson's (1999) algorithm.

Table 1.

Used in the simulation values for the stand structural parameters of the studied 65-year-old spruce and 33-year-old pine stands

Parameter	Spruce	Pine
Stem number, trees/m ²	0.0742	0.2597
Tree height, m	24.6	11.4
Crown length, m	16.8	7.9
Crown radius, m	1.95	1.10
Breast-height diameter, DBH, cm	25.5	13.5
Leaf area index, LAI, m ² /m ²	6.40	3.73
Branch area index, BAI, m ² /m ²	0.77	0.67
Tree distribution pattern parameter, C	1.67	1.86
Canopy closure	0.751	0.852
Shoot-level clumping index, κ	0.6	0.56
Specific (one-sided) leaf area, SLA, m ² /kg	6.6	6.0
BAI/LAI	0.12	0.18

2.3 Spectral reflectance data

Reflectance spectra of the stands have been measured by means of GER-2600 spectrometer from a helicopter by Syrén and Alm in August 1997 (unpublished, personal communication). A series of ground-based measurements of reflectance spectra of ground vegetation below these stands was carried out by the

same GER-2600 instrument in July 2001 (Lang et al., 2002).

2.4 Biochemical data

Tree needle and ground vegetation leaf biochemical data, needed to run the PROSPECT or other leaf optical models, were not measured. Instead, data from existing in the literature databases LOPEX (Leaf Optical Properties EXperiment) (Hosgood et al., 1995) and ACCP (Accelerated Canopy Chemistry Program) (Aber and Martin, 1999) were used to form the 'expert' estimates for the contents of lignin+cellulose, protein and water and their uncertainties (see Table 3). For chlorophyll concentrations in needles, data from Linder (1980) were used.

2.5 Inversion algorithm

The forest reflectance model as well as the incorporated ground vegetation reflectance model were run in the inverse mode, too, mainly to estimate the contents of leaf or needle biochemical constituents. When inverting the measured ground vegetation or forest canopy spectra, the following merit function was minimized

$$F = \sum_{i=1}^n \frac{[R_{\lambda_i}^{simul} - R_{\lambda_i}^{meas}]^2}{\varepsilon_{\lambda_i}^2} + \sum_{j=1}^m \left(\frac{x_j - x_{ej}}{\Delta x_j} \right)^2 \rightarrow \min \quad (1)$$

where

$R_{\lambda_i}^{simul}$ and $R_{\lambda_i}^{meas}$ are the reflectance factors at the wavelength λ_i ($i = 1, 2, \dots, n$) simulated and measured, respectively;

x_j are the model input parameters to be determined via inversion ($j = 1, 2, \dots, m$);

ε_{λ_i} are the uncertainties of the measured reflectance factors;

x_{ej} are the expert estimates and

Δx_j are the preset uncertainties of the parameter x_j .

The parameters x_j are supposed to vary within the preset (biophysical) limits, $x_j \in [x_{jmin}, x_{jmax}]$. If in the course of search a parameter falls outside these limits, a 'penalty' is added to the merit function.

By choosing the set of wavelengths λ_i we have a possibility to put emphasis on one or several regions of the spectrum. In this study, altogether 50 wavelengths ($n = 50$) were chosen in the merit function (Eq. 1). These wavelengths were located more or less uniformly over the spectrum (see Figs. 1 and 2). However, the informative wavelengths for

estimating the biochemical composition of leaves as indicated by several authors (Curran et al., 2001, Dawson et al., 1999, etc.) were preferred. The estimates of uncertainties of the biochemical parameters were obtained from the LOPEX database (Hosgood et al., 1995).

In this study, in the role of the uncertainties ε_i , the standard deviations of different helicopter-borne sample reflectance spectra over the same forest stand were used. For the estimation of ground vegetation parameters, the uncertainties ε_i corresponded to the standard deviation of reflectance among different measured plots of ground vegetation in the same stand.

3 RESULTS AND DISCUSSION

3.1 Ground vegetation reflectance spectrum and its inversion

The measured reflectance spectra of ground vegetation for the two stands under study are presented on Figs. 1 and 2. In addition, the simulated by the ground vegetation reflectance submodel reflectance spectra are presented, while the simulation was carried out with the ground vegetation parameters determined via inversion of the measured spectra (Table 2).

The following parameters were left free for the inversion: green LAI of the ground vegetation, leaf relative size (SL), contents of chlorophyll (C_{AB}), protein (C_P), lignin+cellulose (C_C) and water (C_W) in leaves, and the coefficients at the Price vectors (Price, 1990) (S_1 , S_2 , S_3 , S_4) for the description of the underlying soil and litter. The rest set of the parameters was kept fixed at guessed values. The spherical orientation of leaves was assumed. This inversion could be evaluated as successful, since the inverted values for such important parameters as the LAI, chlorophyll content, and of coefficient at the first Price vector, seem to be realistic (Table 2). We can observe an acceptable coincidence between the average measured reflectance spectra and the simulated reflectance spectra with the input parameters obtained via inversion. The most problematic spectral region seems to be the water absorption band at 1900 nm, where for ground vegetation spectra in both stands, the simulated spectra are biased with respect to the measured ones. In the near infrared (NIR) region of the spectrum, especially from 1000 to 1200 nm, the measured spectra exceed those simulated. In spite of acceptable agreement, a problematic issue is that several retrieved values of biochemical parameters occurred at the preset upper limits. Among these values, the concentrations of lignin+cellulose and

protein should be pointed out. This may refer to problems in the evaluation of absorption in the middle infrared part of the spectrum by the PROSPECT2 leaf optical model. For the ground vegetation under the spruce stand, another inversion was carried out for the spectrum calculated as the average spectrum reduced by one-standard deviation (for comments see the text below).

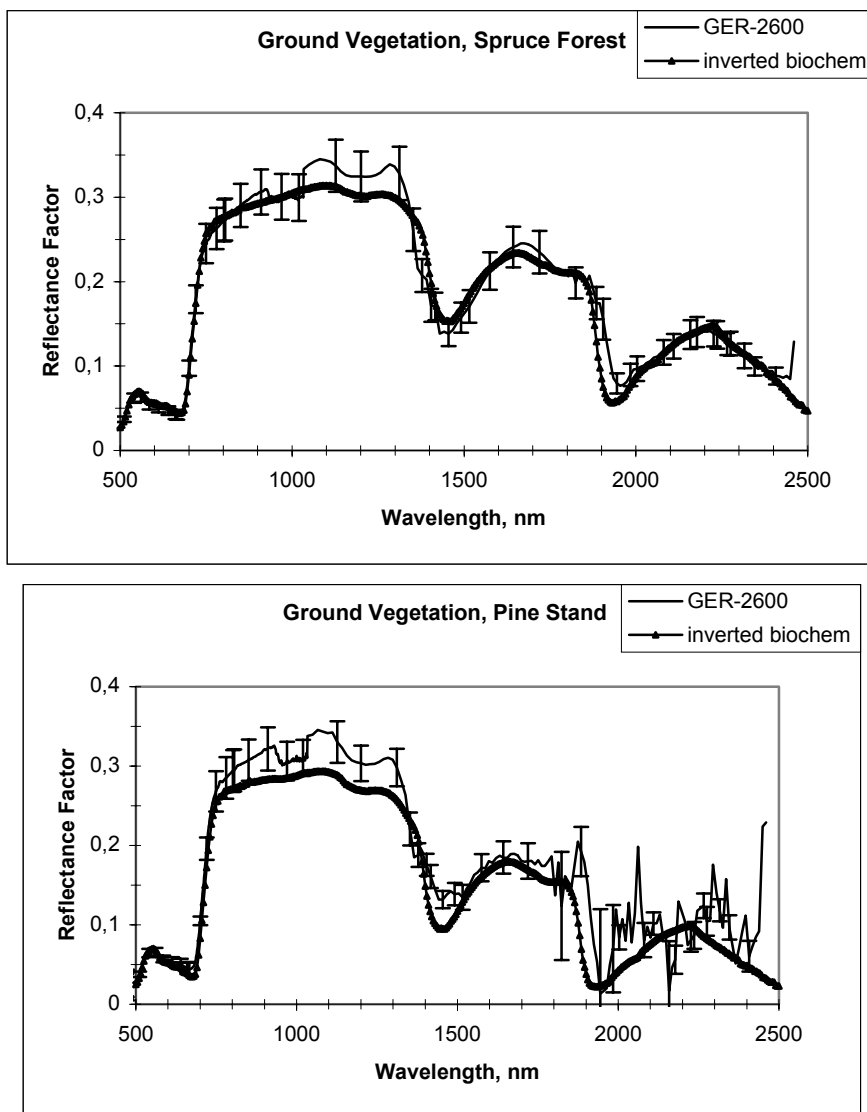
Table 2. The set of ground vegetation parameters for the 65-year-old spruce and 33-year-old pine stands as determined via inversion of the measured ground vegetation reflectance spectra (Figs. 1 and 2)

Parameter	Spruce, avg	Spruce, avg-stdev	Pine, avg
LAI, m ² /m ²	1.12	1.23	1.93
SL	0.4*	0.4*	0.4*
C_{AB} , mg/g	7.72	6.94	7.18
C_C , % of dry mass	45*	45*	45*
C_P , % of dry mass	22*	22*	22*
C_W , % of dry mass	80	95	163
S_1	0.209	0.098	0.141
S_2	-0.069	-0.062	-0.100*
S_3	-0.040	-0.050*	-0.048
S_4	-0.040*	-0.037	-0.040*

* preset limit value in the inversion

3.2 Coniferous forest reflectance spectra and their inversion

First, the forest reflectance model was run in the direct mode and the reflectance spectra for both stands were calculated. The set of structural parameters of the tree canopy was that of presented in Table 1, while for the ground vegetation the parameters obtained from the inversion of the measured ground vegetation spectra (Table 2) were used. Three sets of biochemical parameters of tree needles were used in the simulation: the expert (average) values, the expert values minus uncertainty (simultaneously for all biochemical parameters) and the expert values plus uncertainty (Table 3). The latter two sets of parameters were used to study the sensitivity of the reflectance spectra with respect to changes in the concentrations of these biochemical constituents. On Figs. 3 and 4, these three simulated spectra are compared with the helicopter-borne measured spectra.



Figs. 1 and 2. The ground vegetation reflectance spectrum in the 65-year-old spruce (upper figure) stand and 33-year-old pine (lower) stand, respectively, as obtained from the ground-based measurements by means of a GER-2600 spectrometer, the error bars showing the standard error of reflectance at the wavelengths used in the inversion. In addition, the simulated reflectance spectrum ('inverted biochem') is given in which the inverted values of the biochemical parameters have been used.

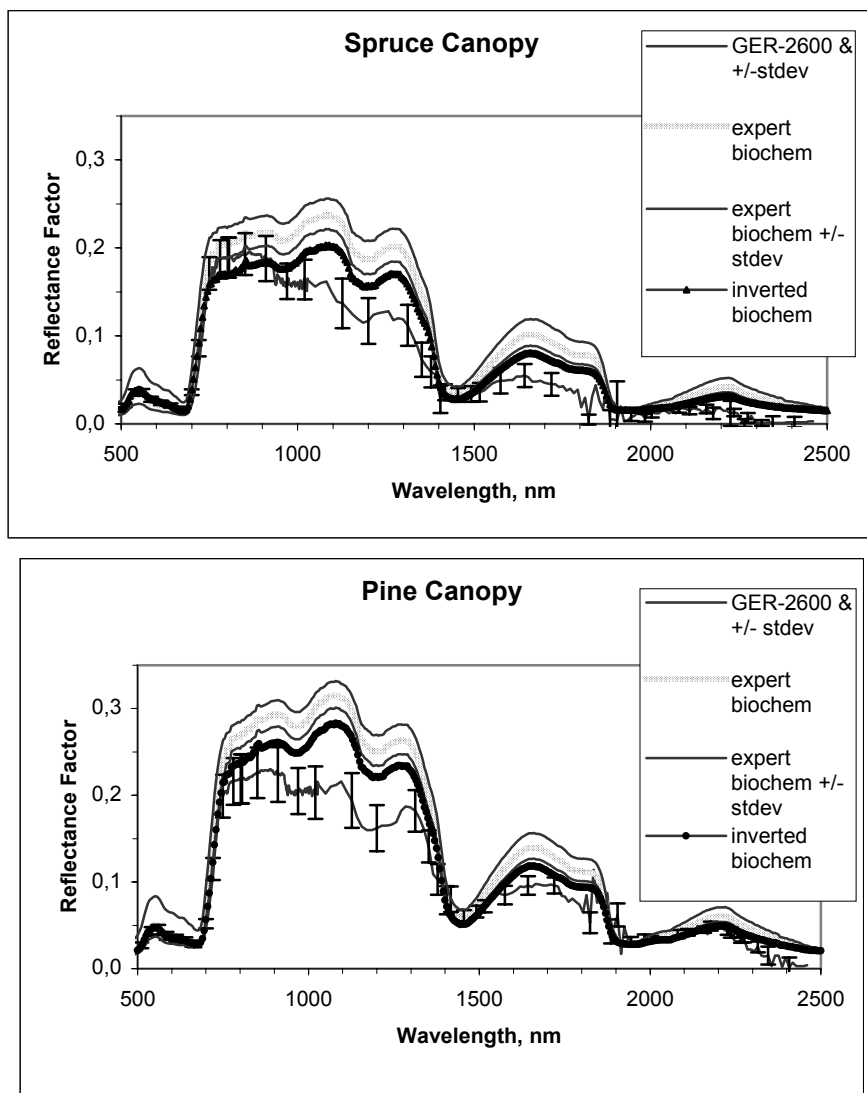


Fig. 3 and 4. A comparison of the measured by GER-2600 reflectance spectra with the simulated spectra for the spruce (upper figure) and pine (lower) stands under consideration. The error bars show the standard deviation of the measured reflectance factors at the wavelengths used in the inversion. In the simulated spectra, the expert values for the needle biochemical components are used together with the estimated one-standard-deviation effects of these constituents. In addition, the simulated spectra with the biochemical component values obtained via inversion are given.

Table 3. Used in the simulations ‘expert’ values of biochemical parameters of spruce and pine needles, their uncertainties, preset lower and upper limits in the inversion and the inverted values for pine and spruce.

Parameter	Spruce				Pine	
	Ave rage	Uncert ainty	Preset limits	Invert ed	Ave rage	Inver ted
Chlorophyll, mg/g of Dry mass	3.5	2	1, 15	4.53	3.5	6.17
Protein, % of dry mass	8	3	3, 20	20*	7	20*
Lignin+ Cellulose, % of dry mass	43	10	20, 55	55*	45	55*
Water, % of dry mass	150	30	50, 200	200*	150	200*

* preset upper limit value in the inversion

We see that the simulated spectra, especially when the inverted values of needle biochemical parameters are used, agree well with the measured spectra in the visible part of the spectrum. In the middle infrared (MIR), however, the simulated reflectances, despite of rather good qualitative agreement, are systematically higher than those in the measured spectra.

3.3 Discussion

Some scaling issues seem to be rather typical when the remotely sensed signals are compared with the simulations or inverted by means of reflectance models. With our present data, the most difficult problems appeared in the MIR region of the spectrum, in which the simulations clearly overestimated reflectance. So, to obtain reasonable results from the inversion, the model should simulate lower reflectance in the MIR region.

Which means do we have to get darker model-simulated forests in the NIR and MIR regions?

- Adding more absorbing substance (lignin, cellulose, protein, water) either by increasing the respective concentrations in leaves (needles), increasing the leaf thickness (LWA) or increasing the total amount of leaves (needles). However, as simulated by the PROSPECT2 leaf optical model, the sensitivity of stand reflectance on the concentration of lignin, cellulose and protein is far less than is needed to get a quantitative coincidence between the simulated and measured reflectances in the middle infrared on Figs. 3 and 4. The conclusion was confirmed by our simulations, when the

concentrations of all biochemical compounds increased by one standard deviation (see the uncertainties in Table 3) and decreased, respectively, were applied. When the LWA was also estimated via inversion, the resulting LAI was abnormally high. So, to get better fit between the simulated and measured reflectances in the middle infrared, extremely high LAI values are needed.

- The real background is darker than the simulated ground vegetation because of under-representation of rough-surface plots in the ground vegetation measurements. An example of one-standard-deviation reduction of ground vegetation reflectance was tested (see ‘avg-stdev’ data for the spruce stand in Table 2), but its effect on stand reflectance was insufficient to explain the differences between the simulated and measured spectra in the MIR region. This is because the studied stands have rather closed canopies.
- To introduce more shadows in the canopy by considering several tree size classes. As a rule, the more uneven is the size distribution of trees, the more shadows appear in the canopy and the darker is the forest. The inventory measurements carried out indicated that at least three different size classes could be separated in the pine forest. When we repeated our reflectance spectra simulation using the expert values of biochemical parameters, with three size classes of trees, the resulting spectrum was reduced all over the spectrum at approximately from 3 to 5 per cent, which is clearly insufficient to achieve the desired agreement.
- To decrease the parameter N (effective number of cell layers) in the PROSPECT model. This parameter controls the leaf reflectance/transmittance ratio, the larger N the larger this ratio. By changing N value from 3 to 2, considerable reduction of stand reflectance occurred in the visible and MIR regions (from 12 to 20 per cent). In the NIR region, because of considerable contribution of multiple scattering, the change was considerably less (from 3 to 4 per cent). For spruce, the respective effect was still larger in the visible and middle infrared ranging from 16 to 27 per cent (and from 2 to 3 per cent in the near infrared). However, in our simulation we have already used the value $N=1.7$, which could even be too low for conifer needles.

We see that all the discussed means do not result in an acceptable agreement between the measured and simulated spectra in the MIR region. In some cases we

have to use unrealistic parameter values to reach the agreement.

Which could be the reasons for systematic deviations between the measured from helicopter and simulated reflectance spectra, especially in the middle infrared part of the spectrum? Possible explanations for the problem are:

- The PROSPECT leaf optical model underestimates absorption in the MIR part of the spectrum at least for conifer needles. (A similar tendency seems to exist for the deciduous forests as well).
- The forest reflectance model used systematically overestimates reflectance because of ignoring the shoot (and perhaps branch) structure effects on shoot (branch) phase function. In the present forest reflectance model, the shoot-level clumping and its effect on the radiation attenuation has been considered. However, as shown in (Smolander and Stenberg, 2002), the clumping of needles in shoots has its effect on shoot albedo and phase function, too. A cluster of needles (shoot) is darker than the equivalent collection of non-overlapping needles. In the present version of the model, this effect is neglected, and it seems that just the scattering phase function of coniferous shoots could be the major reason for the overestimation. The effect should be seen in all regions of the spectrum and be absolutely largest in the NIR region. An introduction of this effect into the model means that the simulated reflectances in the visible part of the spectrum would decrease, too. This will result in lower retrieved chlorophyll concentrations in tree needles, than those obtained through inversion here (Table 3). Indeed, many authors have reported considerably lower chlorophyll concentrations in conifer needles.
- There could be systematic errors in the measurements by the GER-2600 spectrometer, especially in the helicopter measurements, such as caused by problems with the synchronous determination of irradiance spectrum at the top of canopy during the measurement of radiance spectra. Especially problematic seems to be the spectral region beyond 1000 nm covered by the MIR sensor of the spectrometer.

It is obvious that a considerable part of success in applying such inversion methods is determined by the ability of the incorporated leaf (needle) optical model to reproduce the quantitative relations between leaf optical properties and concentrations of the

biochemical compounds. The PROSPECT leaf optical model has been derived for planar leaves, and thus its application to needles can cause problems. We made a comparison of needle reflectance and transmittance spectra simulated by PROSPECT and LIBERTY models with the same values for the comparable structural and biochemical parameters effective just in the middle infrared part of the spectrum. The values of input parameters for jack pine needles from (Dawson et al. 1998) were used and the concentrations of biochemical parameters were recalculated into the PROSPECT2 model input parameters, too. It appeared that LIBERTY predicted lower reflectance and lower transmittance compared with PROSPECT2 model. Especially this effect was notable in the MIR part of the spectrum. It is not trivial to understand which physical mechanism can explain the additional absorption simulated by LIBERTY, since the absorption spectra of 'dry matter' (biochemical components) used in these two models were essentially the same. However, there seemed to be problems in LIBERTY with scaling of different components when the total for all biochemical constituents absorption coefficient was calculated. In addition, the LIBERTY model contains a factor 'baseline absorption' which controls the absorption in the near infrared region of the spectrum, too. It remains somewhat unclear, how the baseline absorption should be determined in practical applications. Nevertheless, there is a hope that when using LIBERTY leaf optical model instead of PROSPECT, the simulated pine and spruce crown reflectances would be considerably lower, and the respective stand reflectances closer to the spectra measured by the GER-2600 spectrometer.

An alternative approach to estimate the biochemical needle parameters could be based on a similar analysis of derivative spectra, i.e. we can define a merit function to be minimized similar to Eq. 1, in which instead of reflectance factors their spectral derivatives are used. By taking derivatives, additive errors are excluded, however, multiplicative sources of errors have their effect on the derivative spectra, too.

3.4 Conclusions

With the particular data set and reflectance model, even if the procedures of regularization in the inversion algorithm were applied, and a 'mathematically' correct solution of the inverse problem was obtained, the inversion of measured reflectance spectra for the biochemical constituents of needles did not have much sense. The main result of the inversion was that all the biochemical components having absorption in the MIR region should be at their maximum allowed level. Although the retrieved values of needle chlorophyll content appear to be higher than

typically reported in many literature sources for other conifers, and no direct tests were made to validate the numbers obtained, the estimation of chlorophyll from the measured stand spectra seemed to be more reliable.

At the present level of knowledge, it is extremely difficult to solve the inverse problem of estimating the needle biochemical concentrations from the remotely sensed stand-level reflectance factor spectra. In addition to the scaling issues and model validity problems in some spectral regions, data for a considerable set of model input parameter values not to be estimated through inversion should be known. This may be a problematic issue in many practical cases. For a better further success, new effective leaf, needle and shoot optical models are needed.

For these reasons, so far the methods that rely on determination of the relative absorption features or are less sensitive to scaling problems, like the band-depth analysis following the continuum removal (Kokaly and Clark, 1999) should be preferred. It is well possible that the main role of canopy reflectance models could be transforming these relative features from a leaf to canopy level.

3.5 Acknowledgments

The authors thank Per Syrén (Metria, Kiruna, Sweden) and Göran Alm (Department of Geography, Stockholm University) for providing the helicopter-borne spectra over the forests under study. The ground-based spectrometer measurements in the stands studied were made by Mait Lang and Tõnu Lükk. The work has been supported by the Swedish RESE (Remote Sensing for the Environment) Program and Estonian Science Foundation grant no 4696.

3.6 References

- Aber, J. D., and Martin, M., 1999, ACCP Leaf Chemistry Data. Available online [<http://www-eosdis.ornl.gov>] from the ORNL Distributed Active Archive Center, Oak Ridge National Laboratory, Oak Ridge, TN, USA.
- Curran, P. J., Dungan, J. L., and Peterson, D. L., 2001, Estimating the foliar biochemical concentration of leaves with reflectance spectrometry. Testing the Kokaly and Clark methodologies. *Remote Sensing of Environment*, **76**, 349-359.
- Dawson, T. P., Curran, P. J., and Plummer, S. E., 1998, LIBERTY: modeling the effects of leaf biochemical concentration on reflectance spectra. *Remote Sensing of Environment*, **65**, 50-60.
- Dawson, T. P., Curran, P. J., North, P. R. J., and Plummer, S. E., 1999, The propagation of foliar biochemical absorption features in forest canopy reflectance: A theoretical analysis. *Remote Sensing of Environment*, **67**, 147-159.
- Fourty, Th., Baret, F., Jacquemoud, S., Schmuck, G., and Verdebout, J., 1996, Leaf optical properties with explicit description of its biochemical composition: direct and inverse problems. *Remote Sensing of Environment*, **56**, 104-117.
- Hosgood, B., Jacquemoud, S., Andreoli, G., Verdebout, J., Pedrini, G., and Schmuck, G., 1995, Leaf Optical Properties EXperiment (LOPEX), Report EUR-16095-EN, European Commission, Joint Research Centre, Institute for Remote Sensing Applications, Ispra, Italy, 15 pp.
- Jacquemoud, S., Ustin, S. L., Verdebout, J., Schmuck, G., Andreoli, G., and Hosgood, B., 1996, Estimating leaf biochemistry using the PROSPECT leaf optical properties model. *Remote Sensing of Environment*, **56**, 194-202.
- Kokaly, R. F., and Clark, R. H., 1999, Spectroscopic determination of leaf biochemistry using band-depth analysis of absorption features and stepwise multiple linear regression. *Remote Sensing of Environment*, **67**, 267-287.
- Kuusk, A., and Nilson, T., 2000, A directional multispectral forest reflectance model. *Remote Sensing of Environment*, **72**, 244-252.
- Lang, M., Kuusk, A., Nilson, T., Lükk, T., Pehk, M., Alm, G., 2002, Reflectance spectra of ground vegetation in sub-boreal forests. *International Journal of Remote Sensing*, (forthcoming). Data available online [<http://www.aai.ee/bgf/ger2600/>]
- Linder, S., 1980, Chlorophyll as an indicator of Nitrogen status of coniferous seedlings. *New Zealand Journal of Forestry Science*, **10**, 166-175.
- Nilson, T., 1999, Inversion of gap frequency data in forest stands. *Agricultural and Forest Meteorology* **98-99**, 437-448.
- Price, J. C., 1990, On the information content of the soil reflectance spectra. *Remote Sensing of Environment*, **33**, 113-121.
- Smolander, S., and Stenberg, P., 2002, Small scale clumping in conifers changes the relationship between LAI and canopy spectral albedo. *Journal of Geophysical Research*, (forthcoming).

Estimation of Vegetation Water Content from MODIS Data and Radiative Transfer Simulation

Pablo J. Zarco-Tejada and Susan L. Ustin

Center for Spatial Technologies and Remote Sensing (CSTARS)

Department of Land, Air and Water Resources (LAWR)

Veihmeyer Hall

University of California, Davis

Davis, CA 95616, USA

pzarco@cstars.ucdavis.edu, slustin@ucdavis.edu

ABSTRACT- Radiative-transfer physically-based studies have previously demonstrated the relationship between leaf water content and leaf-level reflectance in the near-infrared spectral region. The successful scaling up of such methods to the canopy level requires modeling the effect of canopy structure and viewing geometry on reflectance bands and optical indices used for estimation of water content, such as NDWI and SRWI. This study conducts a radiative transfer simulation, linking leaf and canopy models, to study the effects of leaf structure, dry matter content, leaf area index, and the viewing geometry, on the estimation of leaf equivalent water thickness from canopy-level reflectance. The applicability of radiative transfer model inversion methods to MODIS is studied, investigating its spectral capability for water content estimation. A field sampling campaign was undertaken for analysis of leaf water content from leaf samples in 10 study sites of chaparral vegetation in California, USA, between March and June 2000. MODIS reflectance data were processed from the same period for equivalent water thickness estimation by model inversion linking the PROSPECT leaf model and SAILH canopy reflectance model. MODIS reflectance and viewing geometry values obtained from MOD09A1 product, and LAI from MOD15A2 were used as inputs in the model inversion for estimation of leaf equivalent water thickness, dry matter, and leaf structure. Results showed good correlation between the time series of MODIS-estimated equivalent water thickness and ground measured leaf fuel moisture content ($r^2=0.7$), showing that radiative transfer methods can be used for global monitoring of vegetation water content with MODIS.

1 INTRODUCTION

Quantitative estimation of leaf biochemical and canopy biophysical variables is a key element in vegetation monitoring, a major goal in terrestrial ecology, and a long-term research objective given the complexity of the vegetation canopies and phenomena (Verstraete *et al.*, 1994). Accurate estimates of leaf pigments, nitrogen, dry matter, water content, and leaf area index (LAI) from remote sensing can assist in determining vegetation physiological status (Peñuelas *et al.*, 1994), the study of the species and seasonal dependence (e.g. Belanger *et al.*, 1995), and may serve as bioindicators of vegetation stress (e.g. Luther and Carroll, 1999; Zarco-Tejada *et al.*, 2001). The remote determination of one of these biochemical constituents, vegetation water content, has important implications in forestry (Gao and Goetz, 1995), it is essential for drought assessment in natural vegetation, and it is a major driver in predicting the susceptibility to fire (Chandler *et al.*, 1983; Pyne *et al.*, 1996; Ustin *et al.*, 1998).

Several studies demonstrate the existing link between leaf-level reflectance in the 400-2500 nm spectral region and water in the leaf through optical indices and radiative transfer modeling (Gausman *et al.*, 1970; Jacquemoud and Baret, 1990; Ceccato *et al.*, 2001). The primary and secondary effects of water content on leaf reflectance were studied by Carter (1991) showing that sensitivity of leaf reflectance to water content was greatest in spectral bands centered at 1450, 1940, and 2500 nm, with indirect or secondary effects found at 400 nm, in the red edge at 700 nm. The broad use of leaf radiative transfer models such as PROSPECT (Jacquemoud and Baret, 1990) enable the simulation of the leaf optical properties as a function of structural and biochemical constituents such as chlorophyll a+b (Ca+b), dry matter (Cm), and leaf equivalent water thickness (Cw).

Several research efforts focus on the application of leaf-level indices calculated from water-absorption bands, statistical relationships between leaf reflectance and leaf water content, and scaling-up methods to canopy level through radiative transfer simulation. The

Normalized Difference Water Index (NDWI) calculated as $(R_{860}-R_{1240})/(R_{860}+R_{1240})$ was suggested by Gao (1996) in a theoretical study, demonstrating its potential applicability for canopy-level water content estimation due to the liquid water absorption band centered at 1240 nm enhanced by canopy scattering. Nevertheless, Zarco-Tejada and Ustin (2001) showed in a simulation study the dependency of NDWI and the Simple Ratio Water Index (SRWI, R_{858}/R_{1240}) on leaf-level variables such as leaf structure and dry matter content, and most importantly, on canopy LAI.

These partially successful results obtained when estimating vegetation water content demonstrate the need for modeling efforts to account for leaf and canopy variables and the viewing geometry. The work presented here investigates the applicability of radiative transfer techniques to MODIS reflectance data for vegetation water content estimation. A simulation study with synthetic spectra and MODIS-equivalent spectra is presented, investigating the spectral capabilities of MODIS for estimating leaf equivalent water thickness by inversion of a linked leaf-canopy model. Further, a seasonal field study was undertaken for leaf sampling and analysis of leaf fuel moisture content from 10 study sites, measuring fresh and dry weight of leaf samples. Time-series of MODIS reflectance spectra from the study sites during the period of the field experiment were used for model inversion to estimate equivalent water thickness by radiative transfer simulation.

2 MODEL SIMULATION AT THE LEAF AND CANOPY LEVELS WITH WATER INDICES

MODIS bands centered at 858 and 1240 nm, with 35 and 20 nm bandwidth respectively, are used to build the Normalized Difference Water Index (NDWI, $[(R_{860}-R_{1240})/(R_{860}+R_{1240})]$ (Gao, 1996), and the Simple Ratio Water Index (SRWI, R_{860}/R_{1240}) (Zarco-Tejada and Ustin, 2001) for vegetation water content estimation. The location of MODIS bands R1240 on the edge of the liquid water absorption (Figure 1), and R858 used for normalization and insensitive to water content changes (Gao, 1996) make these indices potentially suitable for global monitoring of vegetation water content from MODIS. The effects of atmospheric water vapor and aerosol scattering on R858 and R1240 MODIS bands were demonstrated by Gao (1996) to cause small perturbations on these reflectance bands for remote estimation of water content.

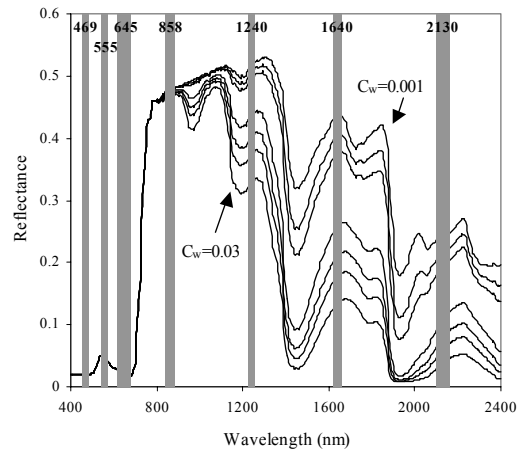


Figure 1. Modeling canopy-level reflectance using PROSPECT-SAILH models for different values of leaf water thickness ($C_w=0.001$ to $C_w=0.03$ cm) showing location of MODIS bands. PROSPECT parameters used were $N=1.5$, $C_m=0.019$ g/cm², and for SAILH $LAI=5$, $plagiophile$ $LADF$, $ts=35^\circ$, $tv=0^\circ$, $ps=0^\circ$.

The SRWI water index was studied through radiative transfer simulation to account for effects due to water content C_w , leaf dry matter C_m , and leaf internal structure N using the PROSPECT leaf model, for a range of values of C_w (in cm) and C_m (in g/cm²) between 0.001 and 0.03, and N between 0.5 and 2.5. The primary variables affecting SRWI at the leaf level are C_w and N , with little effect of the C_m constituent on this optical index. The leaf internal structure has a major effect on SRWI at low values (N between 0.5 and 1) with less effect as N increases, but suggesting that both N and C_m leaf variables need to be taken into account for accurate estimates of C_w from SRWI.

At the canopy level, the water index SRWI was simulated to account for canopy structural characteristics such as LAI and the viewing geometry described by sun angle (ts), view angle (tv), and relative azimuth angle (ps). The simulation study illustrates the large effect of LAI on SRWI index calculated from canopy-level simulated reflectance and variable C_w (Figure 2). The simulation shows that SRWI is highly sensitive to the canopy structural parameter LAI, obtaining a 40% variation when SRWI is modeled with $C_w=0.03$ cm and LAI changes from 2 to 10, demonstrating the large dependency of water-related optical indices on LAI. For high LAI values, SRWI is still sensitive to changes in leaf water, with index saturation starting after $LAI > 10$.

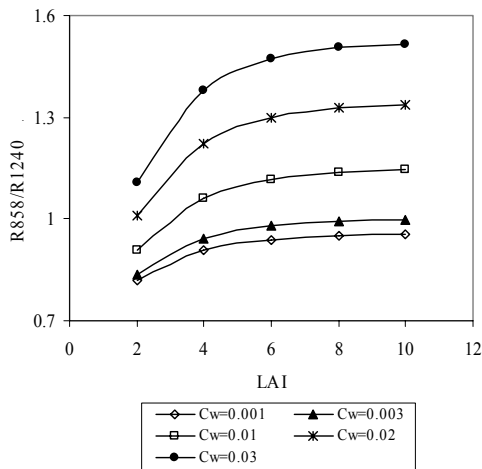


Figure 2. Modeling the effects of SRWI optical index at the canopy level as a function of LAI, and a range of equivalent water thickness values ranging from $C_w=0.001$ cm to $C_w=0.03$ cm. PROSPECT-SAILH were used for the simulation of leaf and canopy reflectance with other input parameters $C_m=0.019$ g/cm², $N=1.5$, $Ca+b=50$ µg/cm², plagiophile LADE, and viewing geometry $ts=30^\circ$, $tv=0^\circ$, and $ps=0^\circ$.

The effects of soil reflectance on the SRWI index and on the absolute reflectance were studied with 3 soil spectra of extreme reflectance values in the 400-2500 nm range used as input in the PROSPECT – SAILH linked model. Simulation results obtained for low C_w values ($C_w=0.001$) to high equivalent water thickness ($C_w=0.03$) and for a LAI range of 1 to 10 show as expected that soil effects on the SRWI optical index are greater at LAI values less than 2. When LAI values are greater than 4, no background effects are found on SRWI for any C_w range, with no effects on the absolute reflectance. These results suggest that the effects of soil on canopy reflectance need to be considered when estimating C_w with low LAI, but showing that the primary drivers of SRWI variation are LAI and C_w , with less than 10% variation in SRWI for extreme soil values with low LAI.

These simulation results show that optical indices proposed for water content estimation at canopy level need appropriate modeling methods to account for leaf and canopy-level variables. The effects of leaf internal structure, leaf constituents $Ca+b$, C_m and C_w on canopy reflectance, soil reflectance effects, and canopy structural characteristics with high effects on the indices, such as LAI, prevent the direct application of SRWI and NDWI on reflectance imagery for accurate mapping of water content.

3 ESTIMATION OF C_w BY MODEL INVERSION FROM MODIS-EQUIVALENT SYNTHETIC SPECTRA

A simulation study was conducted to study the spectral capability of MODIS for retrieving C_w using radiative transfer model inversion methods. Leaf reflectance and transmittance spectra were simulated in the 400-2500 nm spectral range at the MODIS bands using the sensor spectral bandwidth and relative spectral response. One hundred spectra were generated using the PROSPECT model with random leaf parameters within the following ranges: N (0.5-2.5), $Ca+b$ (20-80 µg/cm²), C_w (0.001-0.03 cm) and C_m (0.001-0.03 g/cm²). The same method was used to generate another set of 100 canopy-level synthetic spectra by the linked PROSPECT – SAILH models, using the same random input leaf parameters, and random canopy structural variable LAI (1-10) and viewing geometry parameters ts (10° - 60°), tv (10° - 60°), and ps (0° - 180°). The leaf angle distribution function was set to plagiophile, and soil reflectance set to a nominal field-measured spectrum. The hotspot effect incorporated in SAILH (Kuusk, 1985) takes into account the leaf size and the associated shadowing effects on the bidirectional reflectance, calculating the hotspot parameter as the ratio of the leaf size to the canopy height (s/l).

The sets of 100 leaf and 100 canopy-level synthetic spectra were used as inputs for the model inversion to estimate the leaf parameters that generated the original spectra, and the retrieval capabilities of C_w assessed under different assumptions. In this method of inverting a canopy reflectance model coupled with a leaf model (Jacquemoud, 1993; Jacquemoud *et al.* 2000; Kuusk, 1998; Demarez and Gastellu-Etcheberry, 2000; Zarco-Tejada *et al.*, 2001) the leaf radiative transfer simulation uses leaf biochemical constituents as inputs to model leaf reflectance and transmittance that are in turn used as input for the canopy reflectance model.

Results at the leaf level, therefore using only the PROSPECT model and four variables subject to inversion (N , $Ca+b$, C_w , and C_m) show that C_w can be estimated using the full spectrum (as previously demonstrated by Jacquemoud *et al.*, 1996) and using the seven MODIS bands ($r^2=0.9$ in all cases) even when all four leaf variables are subject to inversion. These simulation results demonstrate that MODIS bands are placed in spectral regions capable of determining C_w when four leaf variables N , $Ca+b$, C_w , and C_m are unknown. When pigment content is set to a fixed value ($Ca+b=33$ µg/cm² in this case), therefore guessing only N , C_w , and C_m , the determination coefficient obtained is $r^2=0.93$ when

estimating Cw from MODIS bands, and $r^2=0.99$ from the full spectrum. Moreover, when the optical indices SRWI and NDWI are used as merit functions, with no other spectral information than R858 and R1240 nm reflectance bands in the function built for error calculation, results also demonstrate that Cw can be properly estimated when all four leaf variables are subject to inversion ($r^2=0.97$).

At the canopy level study with synthetic spectra, the four leaf variables N, Ca+b, Cw, and Cm were subject to inversion along with additional variables such as LAI, and viewing geometry ts, tv, and ps. When Cw is the only variable subject to estimation, determination coefficients are $r^2=0.99$ in all four cases (from full spectrum, MODIS bands, SRWI, and NDWI). MODIS spectra are capable of estimating Cw when the three leaf parameters N, Cw, and Cm are subject to inversion, Ca+b is set to a fixed value, and LAI and viewing geometry are known ($r^2=0.84$ for full spectrum, and $r^2=0.8$ for MODIS-equivalent spectra). When the 4 leaf variables N, Ca+b, Cw, and Cm and the canopy LAI are inverted, determination coefficients for the full spectra is $r^2=0.87$, and $r^2=0.67$ for MODIS-equivalent spectra, demonstrating that inverting five variables at the same time with seven MODIS bands obtains worse results than when using the full spectrum. When Ca+b is set to a fixed value and N, Cw, Cm, and LAI are estimated, results are $r^2=0.69$ from the full spectrum, and $r^2=0.53$ from the MODIS equivalent spectra. These results demonstrate that MODIS equivalent spectra can be used to estimate Cw from canopy-level reflectance, obtaining $r^2=0.99$ if all other variables are known (N, Ca+b, Cm, LAI), $r^2=0.8$ if N, Cm, and Cw are inverted, Ca+b is fixed and LAI is known, $r^2=0.67$ if N, Ca+b, Cw, Cm, and LAI are estimated, and $r^2=0.53$ if N, Cw, Cm and LAI are estimated, with Ca+b fixed. The use of SRWI and NDWI indices as only components of the merit function fails at canopy level if more than 3 variables are subject to inversion, but obtaining $r^2=0.69$ if N, Cw, and Cm are estimated, Ca+b is fixed, and LAI is known. Results of this simulation study with synthetic MODIS-equivalent spectra demonstrate the theoretical capability of MODIS to estimate Cw by model inversion.

4 APPLICATION OF MODEL INVERSION METHODS TO MODIS DATA FOR WATER CONTENT ESTIMATION

A field sampling campaign was conducted for analysis of leaf fuel moisture content, measuring fresh and dry weight from leaf samples collected in 10 study sites of chaparral vegetation in California (USA) between March and June, 2000. Data collection was conducted as part of research work to study spatially explicit models of fire spread through chaparral fuels (Morais,

2001). MODIS reflectance data were obtained from the same period of field data acquisition for Cw estimation by model inversion linking the PROSPECT leaf model with the SAILH canopy reflectance model. Chaparral species sampled were *Adenostoma fasciculatum*, *Adenostoma sparsifolium*, *Artemisia californica*, *Ceanothus megacarpus*, *Salvia leucophylla*, and *Salvia mellifera* located within the area -118.913° long, 34.1523° lat and -118.5619° long, 34.0496° lat in California, USA (Figure 3).

MODIS surface reflectance product MOD09A1 (500m spatial resolution) and leaf area index (LAI) product MOD15A2 (1 km spatial resolution) were used for Cw estimation during the period June to September 2000. These MODIS reflectance images are 8-day composites of the surface spectral reflectance for each band at 469 nm (20 nm bandwidth), 555 nm (20 nm), 645 nm (50 nm), 858.5 nm (35 nm), 1240 nm (20 nm), 1640 nm (24 nm), and 2130 nm (50 nm). LAI (from MOD15A2 product), and reflectance, viewing geometry parameters sun angle (ts), view angle (tv) and relative azimuth angle (ps) (from MOD09A1 product) were extracted for every pixel in the composited reflectance image. The range of variation for the viewing geometry of all MODIS reflectance spectra used in this study was 11° to 38° for ts, 10° to 61° for tv, and -24° to 138° for ps.

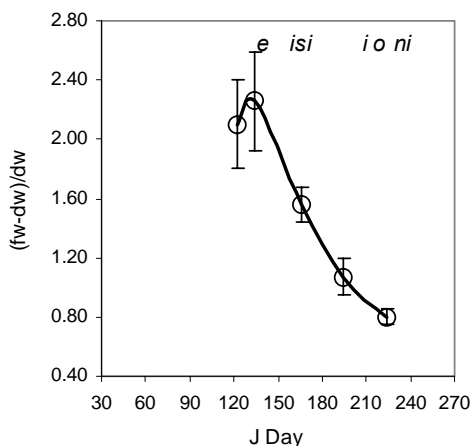


Figure 3. Leaf Fuel Moisture content (LFM) calculated as $(fw-dw)/dw$ at one site for March-September 2000, showing the variation of leaf water content over time.

The time series of MODIS reflectance were used for inversion in the linked leaf - canopy reflectance model as described in the previous sections. The

iterative optimization technique consisted of building the merit function with the SRWI optical index, as well as using all MODIS reflectance bands, with viewing geometry (ts, tv, and ps) and LAI from the MODIS products. Variables subject to inversion were the leaf structural parameter N , leaf dry matter C_m , and leaf equivalent water thickness C_w , with variables set to constant values in the inversion procedure $Ca+b=33 \mu\text{g}/\text{cm}^2$, plagiophile LADF, and soil spectral reflectance measured in the field. Estimation of leaf C_w by iterative optimization was compared with ground measured water content from each study site using the MODIS data coinciding with dates used for leaf sampling. Results obtained comparing the estimated C_w by inversion with the field-measured leaf fuel moisture content (Figure 4) demonstrated the capability of MODIS reflectance data to track changes of water content in vegetation. C_w estimated using SRWI index as merit function achieved $r^2=0.54$, obtaining better results $r^2=0.7$ when all MODIS bands are used in the model inversion, consistent with the simulation study performed in previous sections. These results suggest that seasonal estimates of leaf water content can be conducted by radiative transfer modeling from MODIS reflectance bands using inversion techniques.

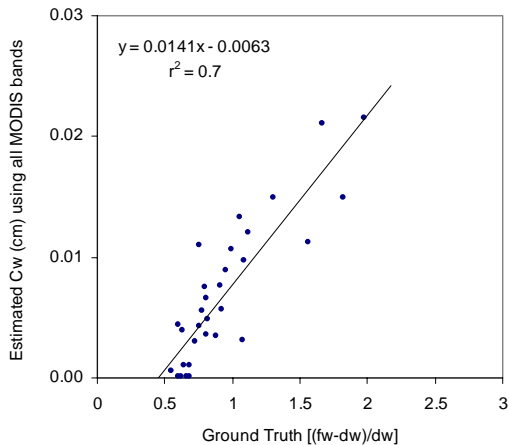


Figure 4. Relationship achieved between ground truth LFM [(fw-dw)/dw] measured in all study sites and C_w estimated by model inversion from MODIS reflectance using all reflectance bands for the period June-September 2000.

5 CONCLUSIONS

Simulation methods and results from the modeling and field studies described demonstrate that leaf water content can be globally monitored with MODIS data. Optical indices previously suggested in the literature as potential indicators of vegetation water content, such as SRWI and NDWI, were used in a simulation study with linked leaf-canopy models. Leaf and canopy-level variables such as leaf structure, dry matter content, soil reflectance, LAI, and the viewing geometry were studied through model simulation to account for their effects on the optical indices built from R858 and R1240 MODIS bands. Modeling analysis demonstrates that SRWI and NDWI are highly sensitive to LAI. For high LAI values the SRWI index is still sensitive to changes in leaf equivalent water thickness, with saturation starting at LAI greater than 10. These results are consistent with previous studies that indicate the need for modeling methods to account for leaf and canopy-level effects on the optical indices, especially LAI, therefore preventing the application of such indices directly on the imagery for estimation of C_w . Synthetic spectra were generated in two simulation studies at leaf and canopy levels using continuous reflectance and MODIS-equivalent spectra to study the capability of MODIS bands to successfully retrieve C_w by inversion. Inversion methods both at the leaf and canopy levels demonstrated that C_w could be successfully estimated by the MODIS bands when leaf variables N , C_w , and C_m are subject to inversion.

Model inversion methods proposed here for C_w estimation were confirmed using MODIS reflectance and ground data of leaf fuel moisture content collected between March and September 2000 from 10 study sites of chaparral vegetation in California (USA). MODIS reflectance, viewing geometry ts, tv, ps, and LAI were used as inputs for the model inversion. Successful results were found when comparing MODIS-estimated C_w with ground truth leaf fuel moisture (fw-dw)/dw from the study sites, obtaining $r^2=0.7$ when all MODIS bands are used for model inversion. This simulation and field study results suggest that a linked leaf-canopy radiative transfer approach can be used for global monitoring leaf water content from MODIS data and inversion methods.

6 ACKNOWLEDGMENTS

This work was supported by NASA contract NAG5-9360. The authors gratefully acknowledge M. Morais and D. Roberts (University of California, Santa Barbara) and C. Lee (California State University, Long Beach) for their contribution with leaf data.

7 REFERENCES

- Belanger, M. J., Miller, J. R., and Boyer, M. G., 1995, Comparative relationships between some red edge parameters and seasonal leaf chlorophyll concentrations, *Canadian J. of Rem. Sens.*, 21:16-21.
- Carter, G.A., 1991, Primary and secondary effects of water content of the spectral reflectance of leaves, *Am. J. Bot.* 78:916-924.
- Ceccato, P., Flasse, S., Tarantola, S., Jacquemoud, S., Gregoire, J.M., 2001, Detecting vegetation leaf water content using reflectance in the optical domain, *Remote Sensing of Environment*, 77:22-33.
- Chandler, C., Cheney, P., Thomas, P., Traub, L., and Williams, D., 1983, *Fire in Forestry*, Vol. I. Forest Fire Behaviour Effects. Wiley, New York.
- Demarez, V., and Gastellu-Etchegorry, J.P., 2000, A Modeling Approach for Studying Forest Chlorophyll Content, *Rem. Sensing of Environment*, 71:226-238.
- Gao, B.-C., and Goetz, A.F.H., 1995, Retrieval of equivalent water thickness and information related to biochemical components of vegetation canopies from AVIRIS data, *Remote Sensing of Environment*, 52:155-162.
- Gao, B.-C., 1996, NDWI - A normalized difference water index for remote sensing of vegetation liquid water from space, *Remote Sensing of Environment*, 58:257-266.
- Gausman, H.W., Allen, W.A., Cardenas, R. and Richarson, A.J., 1970, Relation of light reflectance to histological and physical evaluations of cotton leaf maturity, *Appl. Optic.* 9:545-552.
- Jacquemoud, S. and Baret, F., 1990, Prospect: A model of leaf optical properties spectra, *Remote Sensing of Environment*, 34:75-91.
- Jacquemoud, S., 1993, Inversion of the PROSPECT+SAIL canopy reflectance model from AVIRIS equivalent spectra: theoretical study, *Remote Sensing of Environment*, 44:281-292.
- Jacquemoud, S., Ustin, S. L., Verdebout, J., Schmuck, G., Andreoli, G. and Hosgood, B., 1996, Estimating leaf biochemistry using the PROSPECT leaf optical properties model, *Remote Sensing of Environment*, 56:194-202.
- Jacquemoud, S., Bacour, C., Poilve, H., and Frangi, J.P., 2000, Comparison of four radiative transfer models to simulate plant canopies reflectance—Direct and inverse mode, *Remote Sensing of Environment*, 74:471-481.
- Kuusk, A., 1998, Monitoring of vegetation parameters on large areas by the inversion of a canopy reflectance model, *International Journal of Remote Sensing*, 19:2893-2905.
- Luther, J. E., and Carroll, A. L., 1999, Development of an index of Balsam Fir vigor by foliar spectral reflectance, *Remote Sensing of Environment*, 69:241-252.
- Morais, M., 2001, Comparing Spatially Explicit Models of Fire Spread through Chaparral Fuels: A New Model Based Upon the Rothermel Fire Spread Equation. MA Thesis. University of California, Santa Barbara.
- Peñuelas, J., Gamon, J.A., Fredeen, A.L., Merino, J., and Field, C.B., 1994, Reflectance indices associated with physiological changes in nitrogen- and water-limited sunflower leaves, *Remote Sensing of Environ.* 48:135-146.
- Pyne, S.J., Andrews, P.L., and Laven, R.D., 1996, *Introduction to Wildland Fire*, 2nd Ed., John Wiley and Sons, Inc., New York.
- Ustin, S.L., Roberts, D.A., Pinzon, J., Jacquemoud, S., Gardner, M., Scheer, G., Castañeda, C.M., and Palacios-Orueta, A., 1998, Estimating canopy water content of chaparral shrubs using optical methods, *Remote Sensing of Environment* 65:280-291.
- Verstraete, M. M., Pinty, B., and Myneni, R., 1994, Understanding the biosphere from space: strategies to exploit remote sensing data, In *Proc. 6th Int. Symp. Physical Measurements and Signatures in Remote Sensing*, Val d'Isère, France, 17-21 January, CNES, Paris, pp. 993-1004.
- Zarco-Tejada, P. J., Miller, J. R., Noland, T. L., Mohammed, G. H., and Sampson, P. H., 2001, Scaling-up and model inversion methods with narrow-band optical indices for chlorophyll content estimation in closed forest canopies with hyperspectral data, *IEEE Transactions on Geosciences and Remote Sensing*, 39(7), 1491-1507.
- Zarco-Tejada, P.J. and Ustin, S.L., 2001, Modeling Canopy Water content for Carbon estimates from MODIS data at Land EOS Validation sites, *International Geoscience and Remote Sensing Symposium*, 2001, IGARSS '01, Vol.1, pp. 342- 344.

Leaf pigment retrievals from DAISEX data for crops at BARRAX: Effects of sun-angle and view-angle on inversion results

John R. Miller^{1,2}, Jose Moreno³, Pablo J. Zarco-Tejada⁴, Luis Alonso³ and Driss Haboudane²

1) Department of Physics and Astronomy, York University, 4700 Keele St., Toronto, Ontario, M3J 1P3, Canada jrmiller@yorku.ca

2) Centre for Research in Earth and Space Science (CRESS), Petrie Science Building, York University, 4700 Keele St., Toronto - Ontario M3J 1P3, Canada, driss@terra.phys.yorku.ca

3) Department of Thermodynamics, Faculty of Physics, University of Valencia, Dr. Moliner 50, 46100 Burjassot, Valencia, Spain

4) Grupo de Optica Atmosférica (GOA-UVA), Escuela Técnica Superior de Ingenierías Agrarias, Campus de La Yutera, Universidad de Valladolid, Avda. de Madrid, 44, Palencia, 34004 Spain, pzarco@iaf.uva.es

ABSTRACT—The use of combined leaf and canopy models to retrieve biophysical crop variables are increasingly thought to provide an effective means of providing quantitative input needed to determine stress condition and improve crop yield predictions based on physiological condition. Nevertheless, the sensitivity of such retrieval results to changes in view and sun angle are needed if efficient single-view optical image data are to attain operational agriculture use. Although some studies have been carried out using synthetic model data, similar studies using real data have been very limited due to the unavailability of such data sets. In this research the focus is on the retrieval of leaf pigment (chlorophyll *a+b*). Some recent studies have demonstrated model-based retrievals of leaf chlorophyll with RMSEs $< 5 \mu\text{g}/\text{cm}^2$ by comparison with field sampling and subsequent laboratory chemical analysis. The research reported here uses the extensive DAISEX data set acquired at Barrax, Spain in 1999 and 2000. Airborne data collection strategies provided DAIS, ROSIS and HyMap hyperspectral data in which various field study plots have been observed under widely varying view angles and also at significantly different solar zenith angle. Nearly simultaneously, a comprehensive field data set was acquired on specific crop plots which provided measurements of the following relevant crop variables among others: LAI, percent vegetation cover, leaf chlorophyll content, biomass, leaf and canopy water content, and soil reflectance. We use a combined modeling and indices-based approach, which predicts the leaf chlorophyll content while minimizing LAI influence and underlying soil effects. The sensitivity of leaf chlorophyll predictions with changes in view and sun angle are reported and analyzed through modeling studies for a range of plots in the DAISEX data set.

1 INTRODUCTION AND BACKGROUND

Recent research activities have focused on understanding the relationships between vegetation optical properties and photosynthetic pigment concentrations within green leaf tissues, namely: chlorophyll *a*, chlorophyll *b*, and carotenoids. Various approaches are being developed to estimate the chlorophyll content both at the leaf and canopy scales. Generally, these use some combination of empirical and semi-empirical methods and canopy model inversions (Gitelson et al., 1996; Blackburn, 1999; Datt, 1999; Daughtry et al., 2000; Demarez and Gastellu-Etchegorry, 2000; Zarco-Tejada et al., 2001). Amongst these investigations, there are studies of

optical indices for chlorophyll estimation, which focus on evaluating the reflectance in individual narrow bands, band reflectance ratios and combinations, and the characteristics of derivative spectra. Attention is paid to identify different combinations of spectral bands to minimize variations arising from other confounding factors and to maximize sensitivity to chlorophyll content. Their concept and formalism are based on the relationships existing between chlorophyll concentrations and some specific narrow spectral bands. The spectral regions that are identified as the most suitable to chlorophyll effects study are those around 680 nm, corresponding to absorption peak of chlorophyll *a*, and 550 nm matching with the minimum chlorophyll absorption in the visible domain. Some recent studies (Haboudane et al., 2002) have demonstrated model-based retrievals of leaf

chlorophyll a+b (denoted Chl a+b, below) using airborne imaging spectrometers data over agriculture crops with RMSEs <5 mg/cm² by comparison with field sampling and subsequent laboratory chemical analysis. For the research results reported in this paper we have used the Haboudane et al. (2002) approach for pigment retrieval on the extensive DAISEX data set acquired at Barrax, Spain in 1999 and 2000. Airborne data collection strategies provided DAIS, ROSIS and HyMap hyperspectral data in which various field study plots have been observed under varying view angles and also at significantly different solar zenith angles. This has allowed preliminary conclusions on the effect of sun/view angles on leaf pigment retrievals.

2 LEAF CHLOROPHYLL a+b CONTENT RETRIEVAL APPROACH

The approach adopted for retrieval of leaf chlorophyll a+b content in this study, appropriate to agricultural crops throughout the growing season was that of as Haboudane et al. (2002), reviewed briefly below. To develop this methodology forward simulations at a 5 nm spectral interval were conducted with the turbid medium SAILH canopy model (Verhoef, 1984; Kuusk, 1985) coupled to the PROSPECT leaf model (Jacquemoud and Baret, 1990) for LAI values (0.1 to 8), 12 leaf chlorophyll content (5 to 60 µg/cm²), and three sun zenith angles (27, 33, 45 degrees). These simulations used PROSPECT input parameters Cw, Cp, and Cc assigned nominal values of 0.001 cm, 0.0012 g/cm², and 0.002 g/cm², respectively, and the scattering parameter N= 1.4 for corn based on their leaf optical measurements. For the SAIL model a spherical leaf angle distribution was chosen. In summary, it was reported that leaf pigment retrieval (Chl a+b) can be achieved through relating the combined optical index TCARI/OSAVI to leaf pigment using simulations with the PROSPECT-SAILH leaf canopy model, as follows:

$$TCARI = 3 * [(R700 - R670) - 0.2 * (R700 - R550) * (R700 / R670)] \quad [1]$$

$$OSAVI = (1 + 0.16) * (R800 - R670) / (R800 + R670 + 0.16) \quad [2]$$

with the prediction relationship:

$$Chl\ a+b\ (\mu g/cm^2) = -30.194 \ln(TCARI/OSAVI) - 18.363 \quad [3]$$

The combined index TCARI/OSAVI achieved high sensitivity to the whole range of leaf total chlorophyll, yet minimizing sensitivity to changes in crop LAI, for the range of solar zenith angle 27 to 45 degrees, and nadir viewing. The evaluation of this algorithm based on field leaf sampling and laboratory pigment analysis in corn at Canadian sites [with Chl a+b ranging from 20 to 52 µg/cm² in plots with a large range in nitrogen treatment] and airborne CASI image data [for view/solar zenith angle ranges (0→17)/(22→35)] showed a correlation between algorithm predictions and field data with $r^2 = 0.80$ and RMSE = 4.3 µg/cm². These algorithms have been subsequently extensively evaluated with CASI hyperspectral data over corn, wheat, and soybean crops at 3 periods during the growing season with similar results.

Accordingly, Equations [1] to [3] were considered to provide a suitable basis for a preliminary assessment of the effects of solar/view geometry changes on the retrieval values of leaf Chl a+b. The DAISEX dataset for Hymap and ROSIS sensors were processed using these algorithms to derive estimates of Chl a+b; results of this analysis and comparison to field data are reported below.

3 APPLICATION TO DAISEX

For the purposes of the inter-comparison and evaluation of biophysical variable retrieval algorithms a database has been generated at the University of Valencia, Spain, to encompass the airborne hyperspectral data processed to above-canopy spectral reflectance (i.e. bi-directional reflectance factor (BRF)), spatially-sampled averages over a 3 pixel x 3 pixel window and the corresponding, nearly-simultaneous field data. The objective of this database was to facilitate ingestion of input files containing all the information needed for variable retrievals, assessment of dependence on sun/view geometry, specific sensor, as well as assessment against field data. See Muller and Hausold (2001) and the DAISEX web site: <http://io.uv.es/projects/daisex> for details on the flights, sensors, and ground data methods for data collection at Barrax, Spain in 1998, 1999 and 2000.

Prior to proceeding with the analysis approach proposed above, two important questions arise to guide us in the selection of data to be processed, and in the context in which results are to be interpreted. The issues are: (i) pigment content retrieval algorithm sensitivity to spectral position and bandwidth of the sensor systems which have generated the DAISEX data image set (DAIS, Hymap, and ROSIS in this case

(Muller et al., 2001)), and (ii) pigment content retrieval algorithm sensitivity to the range in sun-view geometry of the DAISEX data set.

With respect to the first issue we emphasize that the algorithm proposed (Haboudane et al. 2002) is derived using model simulations at 5 nm spectral sampling, and narrow bandwidths. The Chl a+b prediction Equation [3] is premised on measurements at spectral positions 550, 670, 700, and 800 nm. Haboudane *et al.* (2002) describe that additional calculations using nearby wavelengths differing from the nominal by up to 5 nm revealed quick degradation of the LAI-insensitivity performance of the TCARI/OSAVI index. Accordingly, based on the reported FWHM bandwidths in the visible-NIR spectral range of 25 nm, 16 nm, and 7.5 nm for DAIS, HYMAP and ROSIS, respectively, only data from the latter two sensors were considered suitable for this investigation. In fact, although HYMAP data will be subject to some errors that warrant additional investigation for this algorithm its inclusion was considered necessary to provide the range of solar zenith angles and view angles required for this study. In addition, individual HYMAP and ROSIS spectra were re-sampled to the specific wavelengths of the algorithm to allow its correct application.

With respect to the second issue of the pigment retrieval sensitivity to sun/view geometry changes, PROSPECT-SAILH simulations which performed to examine view-solar angle effects on Chl a+b Retrievals for the model parameters (Chl a+b = 40; N=1.5; Cw=0.01; Cm=0.01; hotspot = 0.1; LAI=2; LADF = spherical) for a range of view-sun angles in the solar plane (Figure 1). Results of the sensitivity analysis demonstrate that large variations of TCARI/OSAVI are found at view angles larger than 40°, with very small effects on the index when the view angle is near nadir (Figure 1, top). The effects of the view and sun angle on the estimated Chl a+b through the prediction relationship [Eq. 3] are within the RMSE of accuracy at view angle range of 0-30°, with less than 5 µg/cm² error (Figure 1, bottom). These results indicate the robustness of the prediction relationship based on the TCARI/OSAVI index, with small perturbations due to the viewing geometry and therefore suitable for *scaling up* for a different range of sun angle and view angle conditions.

4 ANALYSIS OF DAISEX 1999, 2000 DATA

The results of analysis is first reported as averages and standard deviation on a sampling transect by transect

basis. Tables 1 and 2 show results on this basis for 2000 and 1999, respectively. The important comparison is between columns 5 and 6 which represent algorithm-derived and field-measured total chlorophyll content averaged over the number of

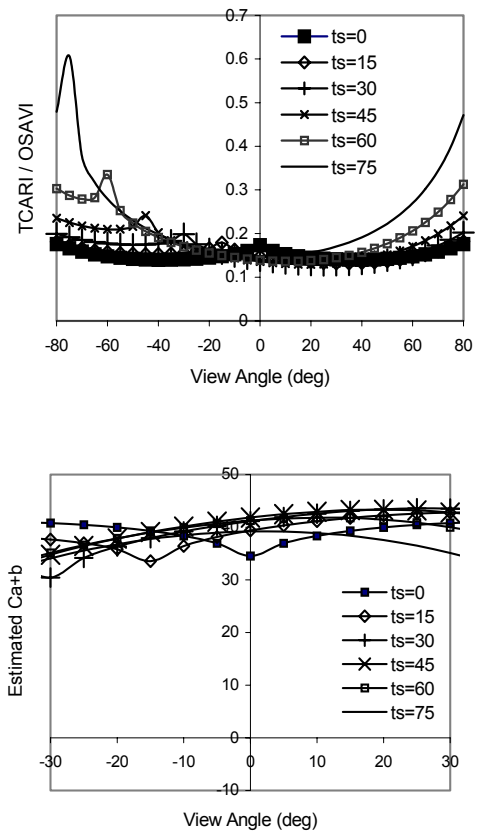


Figure 1. Expected Retrieval Errors for Chl a+b using predictive relationships based on TCARI/OSAVI & *scaling-up* approach Chl a+b > 5 µg/cm² RMSE in hotspot and VZA > 20. Thus observable systematic changes in pigment retrieval results are indicated for the range of view-sun angles in DAISEX data, nevertheless, with expected errors < 10 µg/cm².

sampling points in each transect, followed by the standard deviation (SD) for each transect. Details about the field vegetation sampling at Barrax are described in Garcia et al. (2001) and Moreno et al. (2001). In general, field data exhibit a much higher SD than the airborne data for each specific transect. Further, field averages often differ significantly from retrieved pigment averages.

Table 1: Crop Biophysical Field Data and Model Estimated Chl a+b for Selected Crops/Fields: DAISEX-2000.
[Barrax Site 2000 data collection: bar1 and bar2 are parallel flight lines, flown perpendicular to the solar plane; dataset “h00bar1” designates Hymap sensor (h), 2000 (00), flight line 1(bar1)]

Crop	Field ID	Sampling Points in transect	Plant Height in m.	% Cover (SD)	Estimated Chl_a+b (SD) in $\mu\text{g}/\text{cm}^2$	Field Chl_a+b (SD) in $\mu\text{g}/\text{cm}^2$	Date	Airborne DataSet ID
Alfalfa	V29	1-15	0.5	94.8 (3.1)	26.9 (0.9)	13.0 (3.3)	29-June-00	h00bar1
		1-15	0.5	94.8 (3.1)	33.2 (1.2)	13.0 (3.3)	29-June-00	h00bar2
		1-15	0.5	94.8 (3.1)	41.9 (2.5)	13.0 (3.3)	29-June-00	r00bar2
Corn	V1	1-10	0.9	60.2 (11.7)	39.9 (2.1)	35.9 (8.5)	29-June-00	h00bar1
		1-10	0.9	60.2 (11.7)	46.8 (1.9)	35.9 (8.5)	29-June-00	h00bar2
		1-10	0.9	60.2 (11.7)	49.2 (2.4)	35.9 (8.5)	29-June-00	r00bar1
Corn	V14b	1-5	0.9	83.2 (2.9)	43.5 (1.6)	38.9 (15.4)	29-June-00	h00bar1
		1-5	0.9	83.2 (2.9)	47.3 (0.8)	38.9 (15.4)	29-June-00	h00bar2
		1-5	0.9	83.2 (2.9)	54.4 (1.8)	38.9 (15.4)	29-June-00	r00bar1
S. Beet	V20	1-4	--	67.8 (8.3)	13.8 (0.7)	17.0 (7.6)	29-June-00	h00bar1
		1-4	--	67.8 (8.3)	22.4 (1.1)	17.0 (7.6)	29-June-00	h00bar2

Table 2: Crop Biophysical Field Data and Model Estimated Chl a+b for Selected Crops/Fields: DAISEX-1999.
[Barrax Site 1999 data collection: bar1 (north-south) flight line; bar2 (east-west); dataset “h99bar1_12” designates Hymap sensor (h), 1999 (99), bar1 (north-south line), and nominally 12:00 local time (12)]

Crop	Field ID	Sampling Points in transect	Plant Height in m.	% Cover (SD)	Estimated Chl_a+b (SD) in $\mu\text{g}/\text{cm}^2$	Field Chl_a+b (SD) in $\mu\text{g}/\text{cm}^2$	Date	Data Set
Alfalfa	V16	1-6	0.6	--	36.2 (0.6)	26.8 (6.7)	3-June-99	h99bar1_12
		T1-T15	0.6	--	44.8 (1.2)	15.7 (5.8)	4-June-99	h99bar1_15
		M1-M15 MC1-MC8	0.6	--	32.9 (1.3)	27.0 (13.4)	4-June-99	h99bar1_9
		1-6	0.6	--	26.0 (3.9)	26.8 (6.7)	3-June-99	h99bar2_12
		T1-T15	0.6	--	41.4 (1.4)	15.7 (5.8)	4-June-99	h99bar2_15
		M1-M15 MC1-MC8	0.6	--	38.7 (1.6)	27.0 (13.4)	4-June-99	h99bar2_9
Barley	V20	1-12	0.6	68	--	7.2 (2.3)	3-June-99	h99bar1_12
		1-12	0.6	68	--	7.2 (2.3)	3-June-99	h99bar2_12
Corn	SV3	B1-B6 A7-A15 C1-C5	0.2	--	--	54.6 (44.0)	4-June-99	h99bar1_9
		B1-B6 A7-A15 C1-C5	0.2	--	--	54.6 (44.0)	4-June-99	h99bar2_9
S. Beet	SV6	1-7	0.1	--	35.3 (3.3)	42.2 (18.2)	3-June-99	h99bar1_12
		B6-B15 C16-C20	0.1	--	42.0 (2.6)	33.9 (21.8)	4-June-99	h99bar1_12
		A1-A5 B6-B16 B16-C20	0.1	--	37.0 (1.8)	24.5 (20.4)	4-June-99	h99bar1_15
		1-7	0.1	--	29.5 (3.4)	42.2 (18.2)	3-June-99	h99bar1_9
		B6-B15 C16-C20	0.1	--	39.4 (2.7)	33.9 (21.8)	4-June-99	h99bar2_12
		A1-A5 B6-B16 B16-C20	0.1	--	38.8 (1.6)	24.5 (20.4)	4-June-99	h99bar2_15

The results of some detailed investigations are shown below in Figures 2 -5. To begin, we illustrate the potential of the DAISEX data set in Figures 2 and 3. In Figure 2 the results for 2000

from Hymap and ROSIS for a single transect for corn, (Field V-1). Although retrievals are similar, systematic differences between the two views (bar

1 versus bar 2) are noted, and can be considered

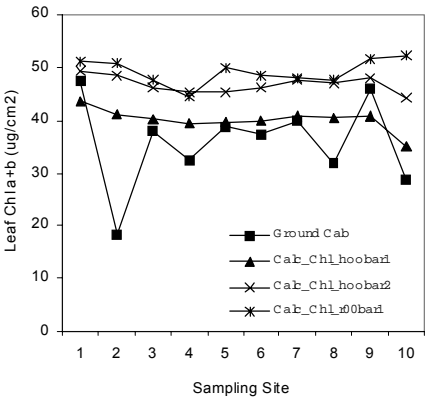


Figure 2. Comparison between field data for corn field V1 and variable retrieval estimates by sensor (Hymap – h; ROSIS – r) and different sensor view (Bar 1 vs Bar 2) for 2000.

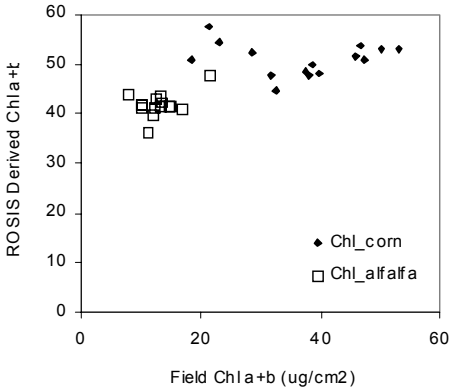


Figure 3. Assessment of ROSIS Chl a+b retrieval results for 2000 for two different crops, alfalfa and corn.

likely a result of view geometry differences.

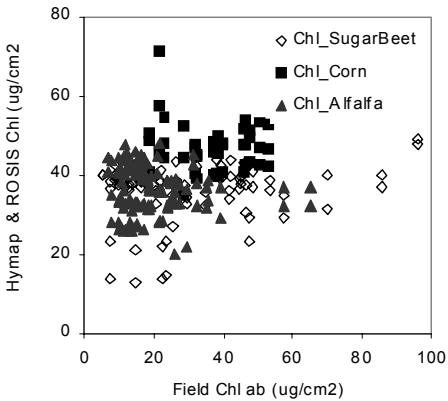


Figure 4. DAISEX 99 and 00 Chl a+b retrieval results from Hymap and ROSIS, for all observations, showing a correlation $R^2 = 0.04$.

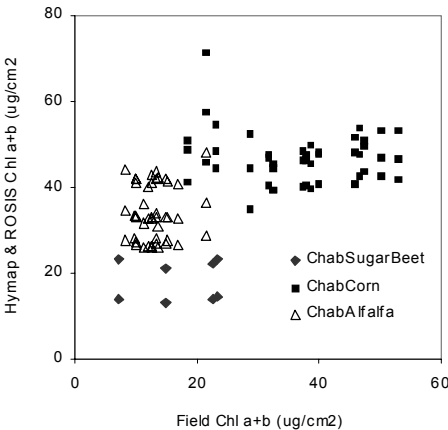


Figure 5. Chl a+b retrieval results for HYMAP and ROSIS using only 2000 data, which shows a correlation improving to $R^2 = 0.30$.

In Figure 3 the retrieved results are compared to field-measured Chl a+b for all relevant ROSIS data. This figure illustrates a general observation from this analysis; the observed range of Chl a+b in the field data was significantly larger than in the retrieved results.

Next we show the global analysis results: that is, the comparison between retrieval results from all Hymap and ROSIS data compared with field data.

In Figure 4 we show this comparison for all sampling points for DAISEX 1999 and 2000, whereas in Figure 5 we show only results from the 2000 DAISEX campaign. Clearly, the correlation between retrieved and field Chl a+b data improves from $R^2 = 0.04$ to $R^2 = 0.30$ when only 2000 data is used. There are many possible explanations for the results above: model estimate sensitivity to view/solar variations, different spatial scales between field and airborne averaging, data quality in field sampling, etc. Issues related to spatial sampling and variability has received considerable attention within the DAISEX community and questions about the consistency of field data quality has also been raised (personal communication). These issues will require further attention as to their interpretation and significance, beyond the scope of this study at this time.

Nevertheless, if an adequate assessment of algorithm performance in terms of absolute accuracy is not easily obtained from this data set for Chl a+b, it is still possible to address issue of the sensitivity of estimates of crop variables to view/solar direction changes or to different sensors for identical sampling lines. This is the objective of the subsequent analysis.

The retrieved results are compared for pairs of flights, bar 1 and bar 2, each pair occurring with minimal change in solar zenith angle (SZA) between them but with differences in view zenith angle (VZA) for any specific field sampling site observed. All sampling sites and crops for which a pair of airborne measurements were available were used in this analysis. A summary of the results of this study of sensitivity of the retrieval results on the view-sun geometry is depicted in Figure 6, in which Chl a+b estimated from one sun-view geometry configuration are plotted against those from another sun-view geometry. For 1999 different sun-view geometries can be compared for image acquisition nominally at times 9:00, 12:00 and 15:00 whereas for 2000 only one sun-view geometry condition was available.

Some systematic dependencies on sun-view geometry are seen in Figure 6. In general such differences appear to be less than $10 \mu\text{g}/\text{cm}^2$, in agreement with the model simulations on expected sensitivity (Figure 1). However, the 1999 Barrax data acquired near 12:00 show much higher discrepancies suggesting the need for a canopy model which properly accounts for sunlit soil contributions.

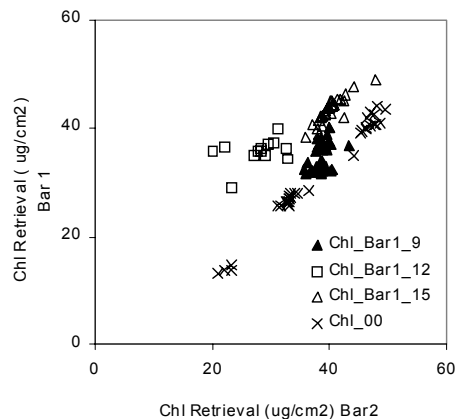


Figure 6. Retrieval sensitivity to view-sun geometry effects – all crops 1999 & 2000: same sites, different views.

5 CONCLUSIONS

Optimized index and scaling up with PROSPECT-SAILH with parameters appropriate to a particular sun-view geometry was previously seen to provide an approach to mapping canopy Chl a+b with RMSEs $< 5 \mu\text{g}/\text{cm}^2$ using a Canadian data set (Haboudane et al. 2002). For DAISEX '99 and '00 data from Hymap & ROSIS differences between field data and retrievals far exceeded expected errors. However, sun-view angle differences in retrievals observed in DAISEX data provide the basis for further analysis into the angle-sensitivity of retrieval approaches on a relative basis only (due to unexplained discrepancies with field data).

These results suggest some systematic effects exist which need study and explanation: differences between ROSIS and Hymap when sampling the same transect, or differences between Hymap estimates as a function of view/azimuth angles. In this study the magnitude of these systematic differences and the specific pairs of flights showing largest anomalies have been identified.

One disadvantage of the scaling-up approach used in this preliminary analysis is the dependence of the prediction algorithm on the specific

wavelengths or on bandwidth used in the modeling. Therefore a more generic inversion methodology is

deemed to offer the flexibility needed to continue this study.

6 REFERENCES

- Blackburn, G. A. (1999), Relationships between spectral reflectance and pigment concentrations in stacks of deciduous broadleaves. *Remote Sens. Environ.* 70: 224-237.
- Datt, B. (1999), A new reflectance index for remote sensing of chlorophyll content in higher plants: tests using Eucalyptus leaves. *J. Plant Physiol.* 154: 30-36.
- Daughtry, C. S. T., Walthall, C. L., Kim, M.S., Brown de Colstoun, E., and McMurtrey III, J. E. (2000), Estimating corn leaf chlorophyll concentration from leaf and canopy reflectance. *Remote Sens. Environ.* 74: 229-239.
- Demarez, V., and Gastellu-Etchegorry, J. P. (2000), A modeling approach for studying forest chlorophyll content. *Remote Sens. Environ.* 1: 226-238.
- Garcia, J. C., C. Cinat, F. Montero, A. Brasa, L. Alonso, M. C. Gonzalez, J. R. Ruiz, C. Martinez, A. Palacios, and J. Moreno (2001), Vegetation and soil measurements at Barrax. *Proc. DAISEX Final Results Workshop*, ESA SP-499, pp.79-87, held ESTEC, Netherlands 15-16 March 2001.
- Gitelson, A. A., Merzyak, M. N., and Lichtenthaler, H. K. (1996), Detection of red edge position and chlorophyll content by reflectance measurements near 700 nm. *J. Plant Physiol.* 148: 501-508.
- Haboudane, D., Miller, J. R., Tremblay, N., Zarco-Tejada, P. J., and Dextraze, L. (2002). Integrated narrow-band vegetation indices for prediction of crop chlorophyll content for application to precision agriculture, *Remote Sens. Environ.* 81:416-426.
- Jacquemoud, S., and Baret, F. (1990), Prospect: A model for leaf optical properties spectra. *Remote Sens. Environ.* 34: 75-91.
- Kuusk, A. (1985), The hot spot effect on a uniform vegetative cover. *Sov. J. Remote Sens.* 3: 645-658.
- Moreno, J., L. Alonso, M. C. Gonzalez, J. C. Garcia, C. Cunat, F. Montero, A. Brasa, O. Botella, R. J. Zomer, and S. L. Ustin (2001), Vegetation properties from imaging data acquired at Barrax in 1998, 1999 and 2000. *Proc. DAISEX Final Results Workshop*, ESA SP-499, pp.197-207, held at ESTEC, Netherlands 15-16 March 2001.
- Muller, A. and Hausold, A. (2001), The airborne imaging spectrometer data acquisition programme in 1998, 1999 and 2000. *Proc. DAISEX Final Results Workshop*, ESA SP-499, pp. 7-11, held at ESTEC, Netherlands 15-16 March 2001.
- Muller, A., Gege, P., and Cocks, T. (2001), The airborne imaging spectrometers used in DAISEX. *Proc. DAISEX Final Results Workshop*, ESA SP-499, pp. 3-6, held at ESTEC, Netherlands 15-16 March 2001.
- Verhoef, W. (1984), Light scattering by leaf layers with application to canopy reflectance modeling: The SAIL model. *Remote Sens. Environ.* 16: 125-141.
- Zarco-Tejada, P. J., Miller, J. R., Noland, T. L., Mohammed, G. H., and Sampson, P. H. (2001), Scaling-up and model inversion methods with narrow-band optical indices for chlorophyll content estimation in closed forest canopies with hyperspectral data. *IEEE Trans. on Geoscience and Remote Sens.* 39: 1491-1507.

S. Le Hégarat-Masclé, D. Richard, C. Ottlé
 CETP/CNRS, 10-12 av. de l'Europe, 78140 Vélizy, France.
 sylvie.masclé@cetp.ipsl.fr

ABSTRACT- *In the remote sensing domain, the combination of multi-scale satellite data appears as a new challenge. It should provide significant improvements in Earth monitoring by use of the complementary of the data presenting either high spatial resolution or high time repetitiveness. Here, we propose an algorithm based on the Dempster-Shafer evidence theory, which allows the modeling of the mixed feature of the low spatial resolution pixels, and the modeling of the class confusion when time information is not sufficient, by consideration of compound hypotheses such as unions of classes. It has been applied on SPOT/HRV image and NOAA/AVHRR series, and the results have clearly shown the improvement brought by the proposed data fusion.*

1. INTRODUCTION

Nowadays, the number of operational remote sensing satellite is considerable. They operate in different wavelength domains, and at different spatial and temporal resolutions. The information acquired is very rich and complementary. The interest of the combination of the different kinds of information appeared soon (e.g. Lee *et al.*, 1987). Considerable works have been performed in this direction using data corresponding to different wavelength domains (e.g. Schistad Solberg *et al.*, 1994).

However, only few works focused on the combination of data acquired at different spatial and temporal resolutions, whereas, for many applications, both multi-temporal and fine spatial resolution (which are generally incompatible for a same global Earth sensor) information are useful.

Most of the works led in the field of multi-scale data fusion deal with the enhancement of (generally multi-spectral) lower resolution imagery by introducing (mono-spectral) high resolution data (e.g. Chavez *et al.*, 1991; Price, 1999). Some others works (e.g. Kong and Vidal-Madjar, 1988) are closer to our purpose: the data fusion of high time repetitiveness images, such as NOAA/AVHRR ones, and high spatial resolution images, such as SPOT/HRV ones. However, the obtained results rather stress the difficulty of such a combination.

In this paper, we propose a solution to overcome this problem using the mathematical framework of the Dempster-Shafer (DS) evidence theory (Shafer, 1976). This theory, which allows the representation of both imprecision and uncertainty, has already shown its suitability for remote sensing data fusion problems (Lee *et al.*, 1987; Le Hégarat-Masclé *et al.*, 1997; Le Hégarat-Masclé *et al.*, 1998; Le Hégarat-Masclé *et al.*, 2000).

In section II, this paper will deal with the way DS theory can be used for multi-scale data fusion. The application to NOAA/AVHRR and SPOT/HRV data is presented in section III. Section IV gathers our conclusions.

1.1 Dempster-Shafer theory basis and application

One major advantage of Dempster-Shafer theory is that it can deal with any union of classes. This allows to represent "mixed" pixels, which can occur in the two main cases (we denote C_k , $k \in [1, c]$, the researched singleton classes which are distinguishable from multi-source data):

- In the coarse spatial resolution image, each time several structures corresponding to different classes are included in a same (mixed) pixel, this latter should be rather classified (in mono-source low spatial resolution classification) in the union of the involved classes;
- In high spatial resolution image, if some classes C_k cannot be distinguished (e.g. because of the lack of the temporal information), they should be gathered in a same ("mixed") class of the mono-source high spatial resolution classification.

We denote A_i , $i \in [1, c_1]$, and B_j , $j \in [1, c_2]$, the mono-source classes corresponding respectively to the high spatial resolution image and to the low one, and \mathbf{m}_1 and \mathbf{m}_2 their respective mass functions. Then, we distinguish four main cases of singleton class C_k :

- C_k is distinguishable both on the high resolution image (it corresponds to class A_i) and on the low resolution image (B_j class). C_k writes $A_i \cap B_j$, and its data fusion mass is

$$\mathbf{m}(C_k) = \frac{\mathbf{m}_1(A_i) \times \mathbf{m}_2(B_j)}{1 - K};$$

- C_k is distinguishable on the high resolution image (class A_i), but it is mixed with other classes in the low spatial resolution image (it corresponds to small structures of smaller size than the low

resolution pixel), appearing in several low resolution classes ($B_{j1}, B_{j2}, \dots, B_{jn}$), which represent different combinations of C_k with other classes. C_k writes $A_i \cap (B_{j1} \cup B_{j2} \cup \dots \cup B_{jn})$, and $m(C_k)$ is

$$\frac{m_1(A_i) \times [m_2(B_{j1}) + m_2(B_{j2}) + \dots + m_2(B_{jn})]}{1 - K};$$

- C_k is distinguishable on the low resolution image (class B_i) but it is mixed with other class(es) in the high resolution image (it corresponds to a class which cannot be distinguished without multi-temporal information). If it is present in the ($A_{j1}, A_{j2}, \dots, A_{jn}$) high resolution (mixed) classes, C_k writes $(A_{j1} \cup A_{j2} \cup \dots \cup A_{jn}) \cap B_i$, and $m(C_k) =$

$$\frac{[m_1(A_{j1}) + m_1(A_{j2}) + \dots + m_1(A_{jn})] \times m_2(B_i)}{1 - K}.$$

- C_k belongs to some mixed classes both in the high spatial resolution image, and in the low one, but the singletons with which it is mixed are different in the two cases. Thus, it can be distinguished from multi-source information as $A_i \cap B_j$, and

$$m(C_k) = \frac{m_1(A_i) \times m_2(B_j)}{1 - K}.$$

The data fusion algorithm is thus the following.

First, distinguishable classes from each mono-source data set separately are estimated either from mono-source classification result analysis or from *a priori* knowledge. From the two class sets $\{A_i, 1 \leq i \leq c_1\}$ and $\{B_j, 1 \leq j \leq c_2\}$, the set of singleton classes of data fusion is derived and written in terms of union or intersection of the mono-source classes A_i and B_j . Then, the mono-source mass functions are derived such that the sum of the masses over 2^Θ is equal to 1. Like in (Le Hégarat-Masclé *et al.*, 2000), when different singletons are indistinguishable from mono-source information, the mass is affected to their union rather than to the singletons themselves. We have also the possibility to not consider the mono-source information (i.e. not classify the pixel from mono-source information) by assigning a non null mass to \emptyset . This allows to take into account the possibility of some classification errors, corresponding to mono-source information to much noisy or erroneous to be exploitable (in a success way).

After mono-source mass combination according to the Dempster's rule, we obtain the "radiometric" data fusion mass function. It is then combined with a "spatial" data fusion mass function (Le Hégarat-Masclé *et al.*, 1998). This "regularization" step is iterative. The advantage of using the Dempster's rule to introduce spatial information is that the weight of the spatial information in the final decision is automatically fitted to the level of radiometric ignorance.

The last step of the algorithm consists in checking that the information of the low resolution image has not been mis-interpreted. In the case of mixed pixels, the observed resulting signal may be the same or close to the signal corresponding to another class B_j .

2. APPLICATION TO ACTUAL MULTI-SCALE DATA

2.1 Data

This algorithm has been tested on data acquired over the Alpilles region (Rhône river basin, France). The considered high (20 m) spatial resolution data is a SPOT/HRV XS image, acquired on August 30, 1997 (cf. Fig.1-a). The considered low (1 km) spatial resolution data set is constituted by the 9 clear (no cloud) NOAA/AVHRR images available in 1997 (cf. Fig.1-b). Only the two first AVHRR channels (1 Visible, and 1 NIR) have been considered.

Eleven land cover types have to be identified (see Table 1). The sole use of the SPOT/HRV data does not enable us to distinguish some of them. In particular, the sclerophyllous vegetation and the two kinds of forests are mixed in a same class A_1 , the pasture and the arable lands are also gathered in a same class A_2 , the rice fields and the orchards both belongs to A_3 ; the other land cover types (vineyards, agricultural fields, urban areas and water) correspond to classes A_4 to A_7 . In the case of the NOAA/AVHRR multitemporal series, we assume that all the different land cover types can be distinguished thanks to the high temporal resolution. However, some objects may be too small to correspond to an entire image pixel. This is the case of the Rhône river. Figure 2 shows the result of (a) SPOT/HRV multispectral classification, and (b) NOAA/AVHRR multispectral (visible and PIR channels) and multitemporal classification. The respective identification rates are given in Table I. In the case of the SPOT/HRV image, the Rhône river is well identified, but there are many ambiguities between vegetation types, and the urban class is broadly over estimated. In the case of the NOAA/AVHRR image, some vegetation types, such as rice fields, or the urban areas, can now be distinguished, but the coarse resolution prevents the discrimination of small objects.

2.2 Results of data fusion

Table 1 gives the supervised definition of the SPOT-AVHRR fusion singletons from the mono-source classes. The sclerophyllous vegetation and the coniferous forest have been gathered because we did not succeed in separating them.

Figure 3 shows the data fusion results. Comparing the data fusion results with the mono-source classifications, we note the improvement: SPOT/HRV resolution image has introduced details and fine structure such as the river, or the more precise edges

of the different class areas (of course, when high resolution image is not able to distinguish two or more classes, the low resolution pixel shape is still visible), and high temporal resolution image series allows to distinguish most of the researched land cover types. However, in the North part of the site, the orchard class still overlaps the crop class, due both to the fine

imbrication of these two classes, and to the poor performance of SPOT/HVR to distinguish the crop class from other classes such as the urban one. Comparing the identification rates obtained by mono-source classification and data fusion, on Table I, confirms in a quantitative way, the previous qualitative comments.

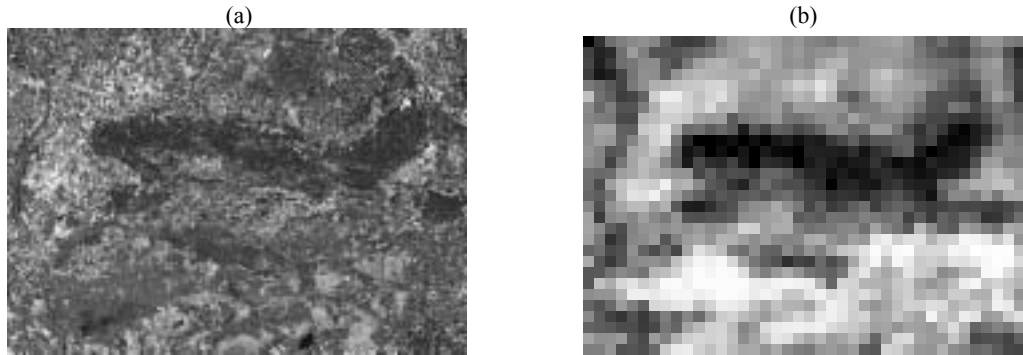


Fig.1. Colored composition of (a) SPOT/HRV spectral bands, (b) NOAA/AVHRR NIR band respectively acquired on March 10, April 10, and September 9.

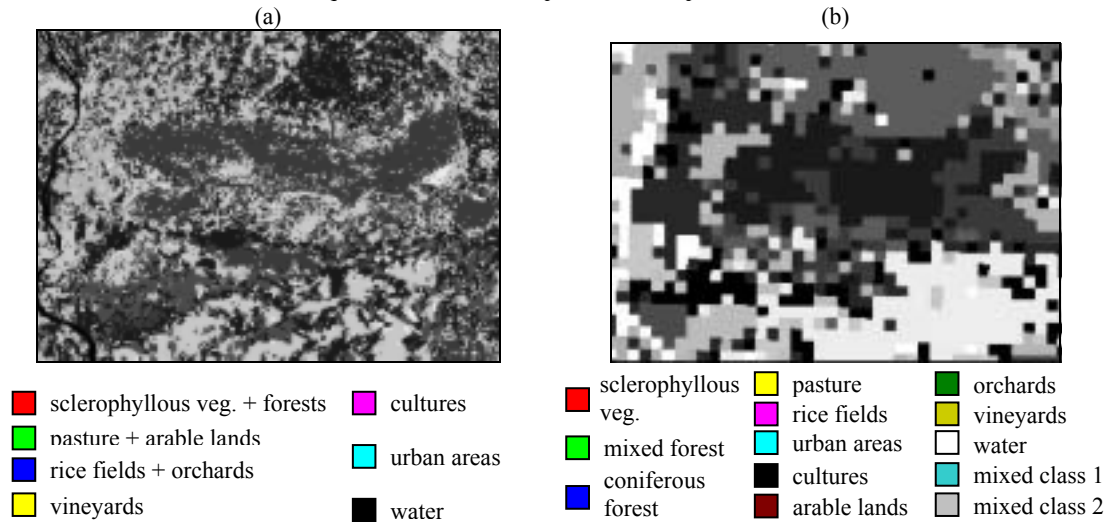


Fig.2. Results of mono-source classifications: (a) SPOT/HRV, and (b) NOAA/AVHRR

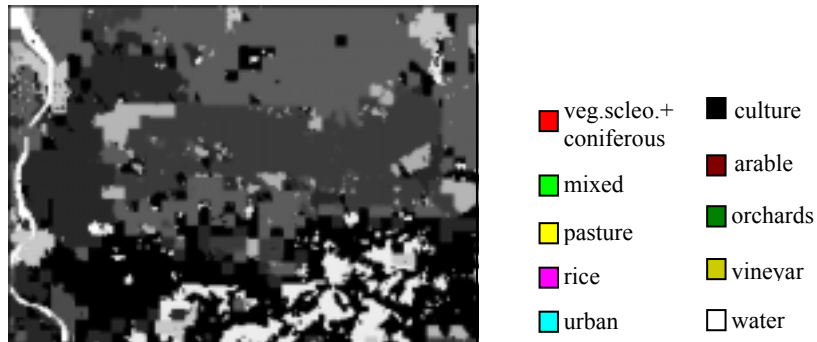


Fig.3. Results of SPOT-AVHRR data fusion

Table 1.- Identification rates (in %) of the different land cover types, and supervised definition of the singletons considered in the spot-avhrr data fusion.

LAND COVER	IDENTIFICATION RATES (%)			DATA FUSION SINGLETON DEFINITION
	SPOT/ HRV	NOAA/ AVHRR	DATA FUSION	
sclerophyllous vegetation	43.7	59.9		
coniferous forest	17.2	32.7	89.9	$A_1 \cap (B_1 \cup B_3)$
mixed forest	17.9	58.8	72.3	$A_1 \cap B_2$
pasture land	26.9	55.9	86.6	$A_6 \cap B_4$
rice fields	5.8	89.4	89.0	$A_3 \cap B_5$
urban areas	10.9	56.4	54.4	$A_6 \cap B_6$
culture fields	43.8	67.8	77.3	$[\Theta^{(1)} \cap (B_7 \cup B_{13})] \cup [(A_3 \cup A_5) \cap B_4]$
arable land	48.5	81.9	81.8	$(A_2 \cup \Theta^{(1)}) \cap B_8$
orchards	31.1	76.1	67.8	$[(A_3 \cup \Theta^{(1)}) \cap B_9] \cup (A_3 \cap B_{10})$
vineyards	37.4	27.4	84.5	$A_4 \cap (B_{10} \cup B_3)$
water	86.5	29.0	92.5	$A_7 \cap B_{11}$

3. CONCLUSION

In this paper, we have presented a method based on the Dempster-Shafer evidence theory for combining multi-scale data. Results obtained on satellite data (NOAA/AVHRR series and SPOT/HRV image) clearly demonstrate the improvement brought by such a combination, compared to mono-source data use.

4. REFERENCES

- Lee T., Richards J. A., and Swain P. H., 1987, "Probabilistic and evidential approaches for multisource data analysis", *IEEE TGARS*, **25**(3):283-293.
- Schistad Solberg A. H., Jain A. K., and Taxt T., 1994, "Multisource classification of remotely sensed data: fusion of Landsat TM and SAR images", *IEEE TGARS*, **32**(4):768-778.
- Chavez P.S., Sides S.C., and Anderson J.A., 1991, "Comparison of three different methods to merge multiresolution and multispectral data: Landsat TM and SPOT Panchromatic", *Photogram. Eng. and Rem. Sens.*, **57**(3):265-303.
- Price J.C., 1999, "Combining multispectral data of differing spatial resolution", *IEEE TGARS*, **37**(3):1199-1203.
- Kong X.N., and Vidal-Madjar D., 1988, "Effet de la résolution spatiale sur les propriétés statistiques des images satellites : une étude de cas", *IJRS*, **9**(8):1315-1328.
- Shafer G., 1976, *A Mathematical Theory of Evidence*, Princeton, NJ: Princeton University Press.
- Le Hégarat-Masclé S., Bloch I., and Vidal-Madjar D., 1997, "Application of Dempster-Shafer evidence theory to unsupervised classification in multisource remote sensing", *IEEE TGARS*, **35**(4):1018-1031.
- Le Hégarat-Masclé S., Bloch I., and Vidal-Madjar D., 1998, "Introduction of neighborhood information in evidence theory and application to data fusion between radar and optical images with partial cloud cover", *Pattern Recognition*, **31**(11):1811-1823.
- Le Hégarat-Masclé S., Quesney A., Vidal-Madjar D., Taconet O., Normand M., and Loumagne C., 2000, "Land cover discrimination from multitemporal ERS images and multispectral LANDSAT images: a study case in an agricultural area in France", *IJRS*, **21**(3):435-456.

ESTIMATING THE ACCURACY OF VEGETATION VARIABLES RETRIEVED FROM MULTIANGULAR DATA

N. Widen,
Finnish Geodetic Institute
Nina.widen@fgi.fi

ABSTRACT *New missions and technically advanced sensors are being developed by scientists to monitor our planet from space at different scales and resolutions. Characterizing the terrestrial biomes on a global scale is a key issue in understanding climate change and the evolution of the Earth-atmosphere system. New advanced models on radiation in plant canopies and more heterogeneous biomes are used to interpret top of atmosphere data and extract information on the Earth's surface. This paper presents an investigation on extraction of canopy and leaf level variables from multidirectional monochromatic remotely sensed data. The purpose is to evaluate the performance of a model in a controlled environment, using artificial input data. Some encouraging results are derived, indicating that both canopy and leaf level variables can be derived with a reasonable accuracy within the constraints of the experiment. Scaling issues, including temporal, spectral and spatial resolution, and surface heterogeneity are not addressed in this experiment.*

1 INTRODUCTION

BRDF has been an important scientific topic in the remote sensing branch for over two decades. The effect was first studied by astronomers in connection with planetary science and backscattering from planetary surfaces. Related phenomena are also encountered in atmospheric sciences and climatology, concerning scattering of light in the earth's atmosphere. The consequences of BRDF in remote sensing are twofold; i) anisotropic effects have to be accounted for in analysis and interpretation of images acquired from space, and ii) BRDF can be exploited to extract information on the terrestrial ecosystem both on a local and a global scale. The latest developments in radiation transfer modeling science, along with the new generation of spaceborne platforms and sensors have been particularly beneficial for the understanding of climatic and ecological processes.

2 OVERVIEW OF IMAGE INTERPRETATION METHODS

2.1 Interpretation using NDVI

The most basic methods to interpret and extract information from multispectral images are based on analysing the spectral signature of individual pixels in the image through different types of band ratios and vegetation indices. Vegetation indices are sensor specific, and merging of data from different sensors and platforms is not straightforward. The problem arises from different bandwidths and spectral

sensitivities of different sensors, as well as issues related to atmospheric scattering and absorption, varying solar angles, and issues of scale. Scaling issues addresses problems related to spatial resolution (e.g. pixel size) of sensors, such as increases in sub-pixel heterogeneity with decreasing spatial resolution. In this context, surface heterogeneity arises both from textural effects, such as fractional coverage and spatial clumping of leaves and branches, as well as the presence of multiple types of vegetation.

Certain optimization procedures can be designed to extract the same vegetation variable from data delivered by different sources in such a way that no discrepancies exist between sensors, as outlined in Gobron et. Al, 2000. Their approach is to derive sensor-specific vegetation indices which are insensitive to atmospheric effects, viewing geometry, bandwidth, and spectral response of the sensor, and which generate equivalent values of the requested vegetation variable. The objective is to facilitate vegetation related studies on a global scale, including monitoring of plant productivity and photosynthetic activity, which are important indicators of the status of the terrestrial ecosystem.

Construction and analysis of time series which span nearly two decades of global NDVI data gathered by the AVHRR instrument have been used to detect statistically significant long term trends related to climate change and global greening (Zhou et. al., 2001). The paper proposes that the successively larger increases in growing season NDVI in Eurasia, and length of active growing period of plants during the analyzed period of time are responses to a simultaneously occurring persistent rising of land

surface temperature, and the subsequent increase of growing season duration defined by average surface temperature.

NDVI based retrieval methods for leaf area index (LAI) and fraction of absorbed photosynthetically active radiation (FAPAR) exploit the empirical correlation between NDVI and LAI/FPAR. Empirical methods are both site- and sensor-specific, but computationally inexpensive. FAPAR is commonly used as a substitute for chlorophyll abundance in vegetation.

2.2 Imaging spectroscopy and BRDF

In the early years of space science, the potential of the directional signature of surface reflectance as a source of information on surface structure was poorly known and exploited. The research on BRDF during the past two centuries, and development of new space platforms and sensors specifically to exploit directional effects have created opportunities to retrieve more exact and detailed variables related to vegetation structure and optical properties. Radiation transfer algorithms provide more generic and flexible interpretation tools for extraction of both leaf and canopy level variables. Issues of bandwidth and viewing geometry, as well as surface heterogeneity can easily be addressed with the more advanced tools.

The wavelength dependence of BRDF reflects spectral heterogeneity of a biome. The problem is best understood over incompletely covering or sparse shrubs and grasslands, and croplands where varying fractions of bare soil are visible within the field-of-view in different viewing directions. A larger fraction of the incoming radiation is able to penetrate to the bottom of the canopy in vertical viewing directions, which makes the vegetation appear darker in the strongly scattering infrared region, and brighter near the chlorophyll absorptions bands in the red spectral range. Gap fraction as seen by the sensor tends to decrease at slant viewing angles, which gives an impression of a more homogeneous surface. The largest rate of change of reflectance with viewing angle occurs in the infrared spectral range. Spectral BRDF analysis of multiple samples within the same biome or land-use class is a potential tool for detecting and quantifying surface heterogeneity experimentally.

2.3 On the role of scaling issues

Scaling issues in the context of land surface monitoring are related to spectral and spatial resolution of different sensors. The ongoing product development in space technology and increasing use

of data fusion have created new demands for better understanding of the relation between vegetation variables retrieved from remotely sensed data, and scale.

In the spectral sense, the problem is characterized by sensor bandwidth and spectral heterogeneity of land surfaces. Spectral heterogeneity denotes the presence of multiple cover types within the same pixel, and is an important concept for calibration of vegetation indices and information derived thereof. A first approximation to deal with spectrally heterogeneous pixels is linear combination of homogeneous spectra. This approach, which is justified for monodirectional data, is completely suppressing canopy architecture, and the directional signature of reflectance. Decontamination of vegetation indices relies on knowledge of the number and species of subpixel cover types, which is usually unavailable. Use of multidirectional data will generally provide a better constrained problem, with additional information on canopy architecture given by the angular signature available. Current operational or pre-operational algorithms to extract vegetation variables from spaceborne data rely on look-up-tables (LUT) for solving the inverse problem. To account for scaling in this context, different look-up-tables can be generated for various types of biomes, characterized by the level of heterogeneity.

The incorporation of scaling algorithms directly in radiation transfer models is so far an almost unexploited subject.

3 ESTIMATING THE ACCURACY OF RETRIEVED VARIABLES

3.1 Description of the experiment

This experiment has been designed to explore the retrieval of quantitative information on terrestrial vegetation using multidirectional remote sensing data in a single spectral band. It is generally known that the information content of monodirectional data is insufficient to provide in-depth information about terrestrial vegetation. Multispectral monodirectional data can be used to identify different types of terrestrial biomes (bare soil, vegetation, snow and ice, etc.) and estimate vegetation variables using empirical relationships. The requirements on data analysis methods are dictated by the information level of output variables. Issues of scale (pixel size) and spatial heterogeneity are ignored in this experiment.

The input data of the experiment is generated using a discrete ordinates radiative transfer model with soil background. Variables characterizing the canopy are leaf area index, leaf hemispherical transmittance and leaf hemispherical reflectance. Additional

characteristics are horizontal and vertical leaf angle distributions (planar leaves or vertical leaves) to describe canopy architecture. A soil background characterized by single scattering albedo of soil particles is incorporated in the program to better account for sparse canopies. The solar zenith angle is set to 40° and fraction of direct solar radiation 0.9.

Experimental data is always contaminated by systematic or random measuring errors or background noise caused by technical or environmental factors. The synthetic input data has been modified by adding random noise drawn from a probability distribution to create a meaningful experiment. A Lorentz function is suitable for an experiment which involves multidirectional measurements. The function is defined as

$$p(y)dy = \frac{1}{\pi} dy / (1+y^2) \quad (1)$$

and its inverse indefinite integral is the tangent function. Random deviates drawn from the Lorentz distribution can easily be generated with the transformation method as outlined by Press et. al. The function is scaled to describe an error of approximately δ in such a way that the generated random deviates are in the range $[-\delta, +\delta]$, with outliers outside the range (Figure 1). The corresponding gaussian distribution with $3\sigma = \delta$ is also plotted. In this experiment the upper limit of measuring error δ for each measuring geometry is set to 20% of the generated BRDF value.

A repeated experiment with approximately 1000 samples each in red and green spectral ranges is carried out to investigate the uniqueness of the solution and estimate the accuracy of output canopy variables. The nature of required output information and computational cost dictates the choice of spectral bands for retrieval of vegetation variables. The bulk of information on canopy and leaf optical properties lies in the visible and near infrared range. Major absorption bands by pigments (Chlorophyll and Carotenoids) are centered in the blue (450 nm) and red (670 nm), with low absorption in the green (550 nm) and near the red edge (transition between red and near infrared). Leaf water absorption bands are mainly in the infrared range (1450 nm and 1950 nm). Weakly scattering high absorption bands are computationally inexpensive compared with the strongly scattering near infrared plateau, and in certain contexts more useful for inversion problems.

3.2 Results

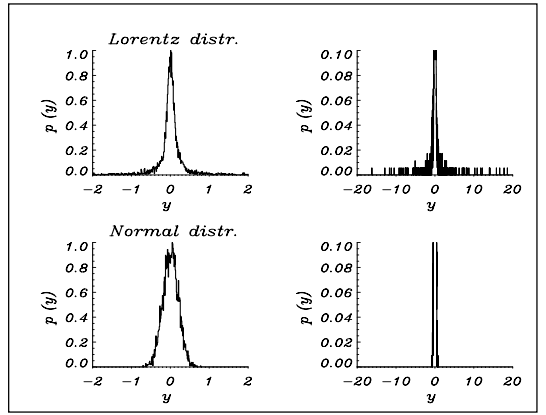


Figure 1 Random deviates drawn from two different probability distributions.

Normalized distributions of estimated variables are plotted in Figures 2-3. The abscissa y is defined as output-true value, in other words the difference between estimated variable and its true value, and $p(y)$ is a frequency normalized to the central maximum. The distribution of estimated LAI is centered at the true value ($=3$), and the width of the central maximum is less than 0.5 units. The frequency of outliers is low, and the number of saturated results ($LAI > 6$), which are left out from the figure, is negligible. Leaf absorptance and soil distributions are also centered at their true values. Model variables leaf reflectance and leaf transmittance are replaced with leaf absorptance for convenience, to save space. The benefits of the weakly scattering red spectral band for vegetation studies are evident. The same experiment with a lower number of samples using the near infrared spectral band yielded less accurate output and significantly higher computing time. Somewhat unexpectedly, the soil variable is the most stable quantity within this experiment. True values of the variables are: soil albedo 0.20 (550 nm), and 0.26 (670 nm); leaf absorptance 0.70 (550 nm), and 0.86 (670 nm).

The positions of centers of distributions are of particular interest, in view of the uniqueness of the solution. Interdependences between two or more variables can be detected through displacements of the central maxima, as well as the existence of secondary maxima. A certain complementarity between canopy and background variables, could be expected, in that the model to some degree can compensate variations in leaf variables by changing the soil albedo. In view of this experiment, the leaf and canopy variables appear to be largely independent.

The number of outliers indicates the sensitivity of the model to a certain variable. Leaf and soil variable

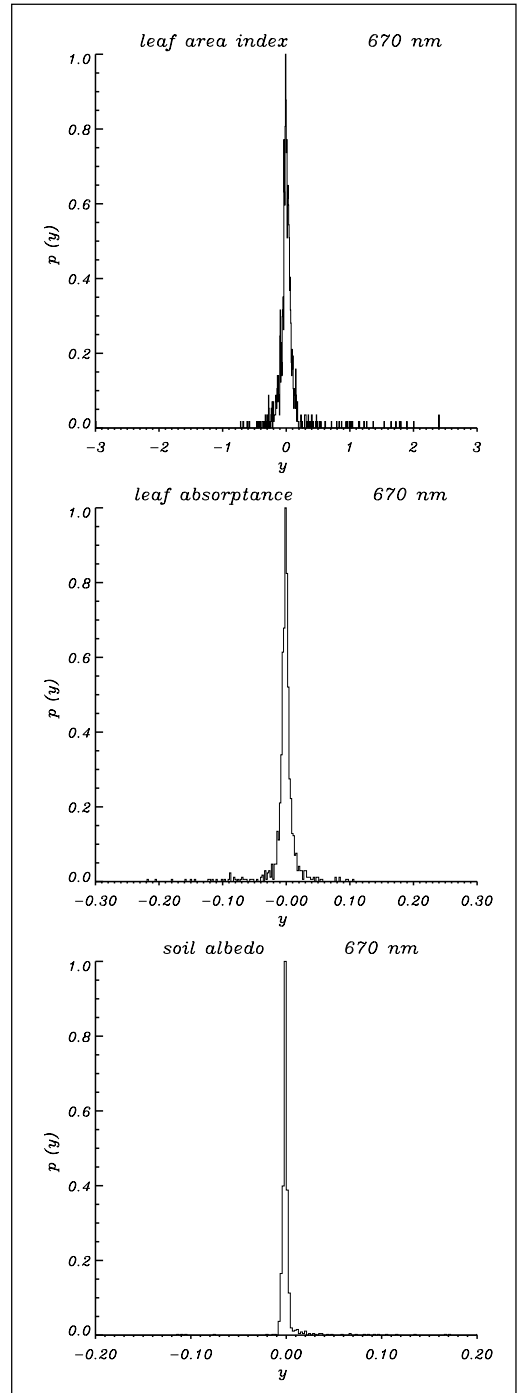
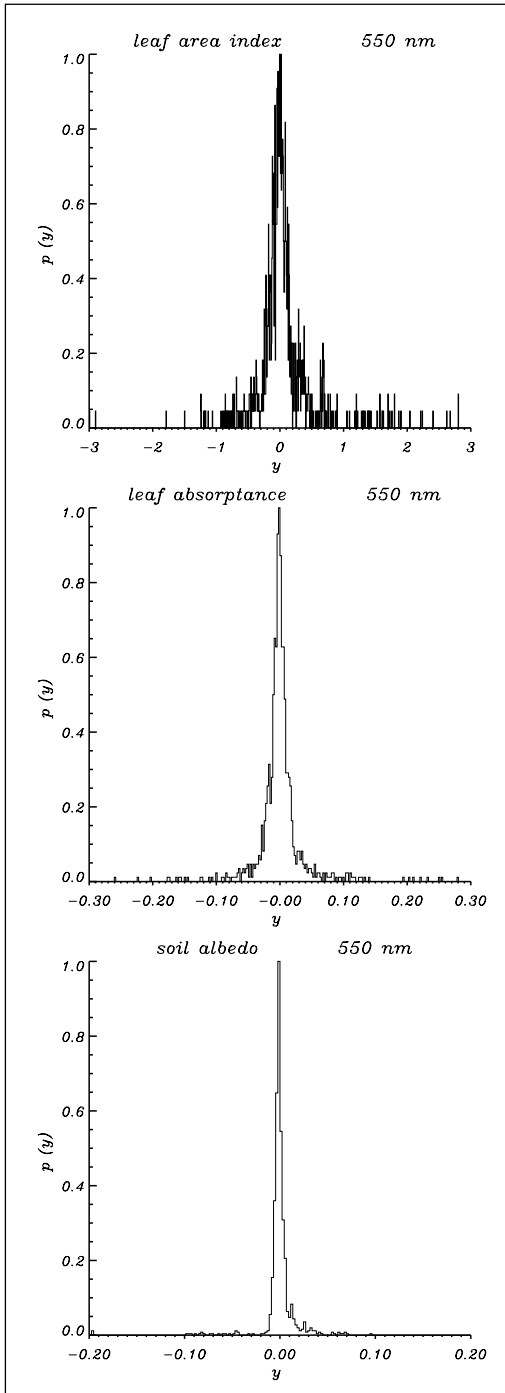


Figure 2(left) and 3 (right) Estimated vegetation and soil attributes in two experiments. The abscissa y is defined as difference between estimation and true value, $p(y)$ is a normalized frequency.

distributions include a very low frequency of outliers, indicating that these variables are less sensitive to noise level and other variations in input data. Leaf area index is the most noise-sensitive variable.

The conclusions of the study are: (1) The model is able to correctly retrieve the required variables in this rather idealized experiment (2) No complementarity between variables has been detected in this exercise (3) The inversion is stable despite a comparatively high noise level in the input data.

4 SUMMARY

The objective of this experiment was to evaluate the retrieval of canopy variables from BRDF data in single spectral bands using a radiative transfer model. The main focus is on testing the model itself; its power to provide a unique solution to this inverse problem. An idealized experiment has been designed with synthetic input data including a controlled amount of random noise. The choice of artificial data ensures that the true value of each involved quantity is known, and all different aspects of the experiment can be controlled. The distribution of noise has been chosen to describe the nature of multiangular measurements as closely as possible.

Despite a high noise level of 20%, the quality of retrieved canopy and leaf variables is good. The distributions of estimated variables are centered on the true values, the central maxima are narrow, and no secondary maxima exist. The soil variable proved to be the most accurate in this experiment.

It has been proposed, that in certain circumstances an ambiguity between background and vegetation variables is possible, in that a radiation transfer model can compensate variations in canopy variables by changing soil brightness. This means that variables are not truly independent, and the solution to the inverse problem is not unique. No complementarity between variables can, however, be detected in this study.

The use of radiation transfer models to retrieve physically measurable variables from remotely sensed data hinges on the potential of the model to accurately reproduce the characteristic spectral BRDF signature of a chosen biome as a function of a relatively small number of variables. Verification against experimental top-of-canopy data in each individual biome ensures that the model can correctly describe the interaction of the radiation field with the earth's surface. The validation of forest biome models is still incomplete, and remains as a subject for future research.

5 REFERENCES

- Gobron, N., Pinty, B., Verstraete, M., Martonchik, J., Knyazikhin, Y., and Diner, D., 2000, Potential of multiangular spectral measurements to characterize land surfaces: Conceptual approach and exploratory application. *Journal of Geophysical Research*, **Vol. 105 D13**.
- Gobron, N., Pinty, B., Verstraete, M., Widlowski, J-L., 2000, Advanced vegetation indices optimized for upcoming sensors: Design, performance and applications. *IEEE Transactions on Geoscience and Remote Sensing*, **Vol. 38 No. 6**.
- Zhou, L., Tucker, C., Kaufmann, R., Slayback, D., Shabanov, N., and Myneni, R., 2001. Variations in northern vegetation activity inferred from satellite data of vegetation index during 1981 to 1999. *Journal of Geophysical Research*, **Vol. 106 D17**.
- Press, W., Flannery, B., Teukolsky, S., and Vetterling, W. Numerical Recipes: The art of scientific computing (Cambridge University Press).

M.Chevrier¹, A. Bannari¹, J.-C. Deguise², H. McNairn², and K. Staenz^{1,2}

¹ Remote Sensing and Geomatics of Environment Laboratory, Department of Geography, University of Ottawa, Ottawa (Ontario) K1N 6N5, Phone. (613) 562-5800 (Ext. 1042), Fax (613) 562-5145;

² Canada Centre for Remote Sensing, Natural Resources Canada, 588 Booth Street, Ottawa (Ontario), K1A 0Y7

Email: m.chevrier@moncanoe.com

ABSTRACT – This study focuses on the potential of indices for estimation of crop residue cover in an agricultural environment. Several indices were compared (BI, CAI, NDI, SACRI, MSACRI and CRIM) in order to identify the ones that are more suitable for estimation of fraction of corn residue cover. For this purpose, ground-based reflectance measurements, collected with a GER3700 spectroradiometer and resampled to the Probe-1 spectral band characteristics were used in this investigation together with hyperspectral Probe-1 data. The results indicate that for the ground-based reflectance the best residue indices for the estimation of crop residue cover are the CRIM and MSACRI-1 with a standard error of estimate of 20.2 % and 22.7 % respectively. For the Probe-1 data, the results demonstrated that the MSACRI-1 was much more representative of the ground reference information and outperformed the other indices.

1. INTRODUCTION

Conservation of crop residue after harvesting is an effective anti-erosion measure (Freebairn and Worcker, 1986). With as little as 15 % corn residue cover, erosion can be reduced by 75 % (Ketcheson and Stonehouse, 1983). As for the environmental aspect, crop residue improves soil structure, increases organic matter content in the soil, has positive influences on water infiltration, evaporation and on soil temperature (Aase and Tanaka, 1991) it can also play an important role on fixing CO₂ to the soil (Rice, 2002). Furthermore, data on residue cover percentages are useful for input into soil erosion models such as the Universal Soil Loss Equation (Wischmeier and Smith, 1978). Several techniques for identifying and mapping crop residue exist, such as the visual estimate method, line-transect method, point intercept method, meter stick method, spiked wheel method and photographic method (Chevrier *et al.*, 2002). However, these methods are time consuming, not suitable for large area coverage and very costly to operate on large areas (Daughtry *et al.*, 1996). One challenge of remote sensing, as a potential alternative to detect crop residue and to monitor agricultural fields in Canada, is to differentiate residue from bare soil, especially when residue has been weathered. Over the years, scientists have developed several vegetation indices for quantitative evaluation of vegetation cover (Bannari *et al.*, 1995). Due to the absence of chlorophyll in senescent vegetation and in crop residue, these indices are not suited for estimation of crop residue cover (Cyr *et al.*, 1995). Scientists had to find new spectral ranges

that are more adequate for crop residue. They developed new indices that are suited for quantitative evaluation of crop residue cover. Furthermore, the development of residue indices is difficult because they must be independent of optical properties of bare soil, colour and brightness (Bannari *et al.*, 1999). Six major crop residue indices are found in the literature. These are the Brightness Index (BI) (Major *et al.*, 1990), Cellulose Absorption Index (CAI) (Daughtry *et al.*, 1997), Normalized Difference Index (NDI) (McNairn and Protz, 1993), Soil Adjusted Corn Residue Index (SACRI) (Biard *et al.*, 1995), Modified Soil Adjusted Corn Residue Index (MSACRI) (Bannari *et al.*, 2000), and Crop Residue Index Multiband (CRIM) (Biard and Baret, 1997). Due to the large number of crop residue indices, it is imperative to know which indices provide the optimal estimation of crop residue cover. For that purpose, two different objectives were pursued:

- Selection of appropriate spectral range and, subsequently, the best crop residue index for optimal estimation of crop residue cover using GER3700 ground-based spectroradiometer measurements resampled to the Probe-1 hyperspectral bands; and
- Estimation of crop residue cover from airborne hyperspectral Probe-1 data using the different crop residue indices.

The results in this study were limited to corn residue, for detail results on other types of residues (wheat, weed, soybean and sunflower) refer to Chevrier (2002).

2. DATA USED

2.1 Study Site

The data were acquired at the IHARF (Indian Head Agricultural Research Foundation) farm, which is located about three kilometres east of Indian Head, Saskatchewan (Canada) (50°32'15"N, 103°40'10" W). Complementary sets of spectroradiometric measurements were also acquired at the Agriculture Canada Experimental farm in Lennoxville, Québec (Canada) (45°22'15"N, 71°51'35" W).

2.2 Ground Measurements

A series of reflectance measurements were collected between 400 nm to 2500 nm with the GER3700 spectroradiometer. The reflectance of corn residue was measured with varying percentages of residue cover. Additional information was collected, including height, orientation and colour of the residue, surface soil moisture, and presence or absence of green vegetation. A series of spectroradiometric measurements were acquired for thirty soil samples, representing different soil moisture levels, soil roughness, and soil colours. The field-of-view of the GER3700 was 10° and the distance between the target and the instrument was 1.85 m, which gives a diameter of 32.37 cm on the target. Digital photos of crop residue were also taken to calculate the percentage cover of residue. The percent cover was calculated using an unsupervised Isodata classification algorithm.

2.3 Hyperspectral Image Data

The Probe-1 hyperspectral sensor is an airborne sensor with 128 spectral bands covering the visible near-infrared (VNIR) and short wave infrared (SWIR) from 400 nm to 2500 nm. The spectral resolution varies between 11 nm and 22 nm. The aircraft was flown at a 2500 m altitude above sea level resulting in a spatial resolution of 5 m. The Probe-1 data were radiometrically calibrated to remove calibration errors (Secker *et al.*, 2001) and atmospherically corrected to achieve surface reflectance (Staenz and Williams, 1997). Note that to preserve radiometric integrity of each pixel in the image, no geometric correction of the Probe-1 data was carried out.

2.4 Description of the Crop Residue Indices

Major *et al.* (1990) developed the BI (equation 1), which uses the first four bands of Landsat TM. It has been proven that the BI is dependent of the optical properties of bare soil (Bannari *et al.*, 1999). Daughtry *et al.* (1997) based their study on the absorption of cellulose between 1975 nm and 2225 nm for the distinction of residue and bare soil and came up with the CAI (equation 2). Although studies have shown

that the CAI is independent of the optical properties of bare soil, it has also been demonstrated that it is only suited for small amounts of crop residue cover (Bannari *et al.*, 1999). McNairn and Protz (1993) reported the sensitivity of the near infrared and created the NDI (equation 3), which is based on the same concept as the NDVI but where red and near infrared (NIR) bands are substituted with NIR and SWIR bands. The NDI is affected by the optical properties of bare soil. However, this index gives good results when using bands ETM-7 (2100nm – 2350 nm) and ETM-5 (1550 nm – 1750 nm) (Bannari *et al.*, 1999). In order to minimize the effect of the optical properties of bare soil of the NDI, Biard *et al.* (1995) proposed the SACRI (equation 4), which integrates the soil line concept. The principles of this index are inspired from the transformation of the SAVI (Soil Adjusted Vegetation Index) in TSAVI (Transformed Soil Adjusted Vegetation Index). The SACRI is less sensitive to the optical properties of bare soil than the NDI, but works best with small amounts of crop residue cover (Bannari *et al.*, 1999). Another crop residue index was developed by the modification of the SACRI into MSACRI (Bannari *et al.*, 2000). This index uses two specific SWIR spectral bands, ETM-5 and ETM-7 (equation 5). The interest in using these two spectral bands is because this region of the spectrum is recognised as being favourable to identify various types of rocks, soils, dry vegetation as well as green vegetation. This index gives good results and is independent of the optical properties of bare soil (Bannari *et al.*, 2000). Biard and Baret (1997) then developed the CRIM (equation 6), which uses a linear unmixing model to extract the fraction corresponding to crop residue from the soil-residue complex. Contrary to other indices, where specific regions of the spectrum are used, the CRIM may be applied to any set of spectral bands to discriminate residues from bare soils. The results obtained with the CRIM are a direct estimate of residue cover fraction in the range of 0 to 1. Research has demonstrated that the CRIM is not very sensitive to variations in soil optical properties due to changes in moisture and roughness levels (Biard and Baret, 1997). The equations of these indices are as follows:

$$BI = \rho_{TM1} + \rho_{TM2} + \rho_{TM3} + \rho_{TM4}, \quad (1)$$

$$CAI = [0.5 * (\rho_x + \rho_y) - \rho_z], \quad (2)$$

$$NDI = (\rho_{TM4} - \rho_{TM5}) / (\rho_{TM4} + \rho_{TM5}), \quad (3)$$

$$SACRI = \frac{\alpha (\rho_{TM4} - \alpha \rho_{TM5} - \beta)}{(\alpha \rho_{TM4} + \rho_{TM5} - \alpha \beta)} \quad (4)$$

$$MSCARI = C^{ste} \frac{[a (\rho_{ETM5} - a \rho_{ETM7} - b)]}{-(a \rho_{ETM5} + \rho_{ETM7} - ab)} \quad (5)$$

$$CRIM = \frac{\tan(\delta)}{\tan(\zeta)} = \frac{\cos(\delta)}{\cos(\zeta)} * \sqrt{\frac{1 - \cos^2(\delta)}{1 - \cos^2(\zeta)}}, \quad (6)$$

where:

ρ_{TM1} is the reflectance measured in TM1;

ρ_{TM2} is the reflectance measured in TM2;

ρ_{TM3} is the reflectance measured in TM3;

ρ_{TM4} is the reflectance measured in TM4;

ρ_{TM5} is the reflectance measured in TM5;

ρ_{ETM5} is the reflectance measured in ETM5;

ρ_{ETM7} is the reflectance measured in ETM7;

ρ_x is the reflectance measured between 1975 and 2025 nm;

ρ_y is the reflectance measured between 2175 and 2225 nm;

ρ_z is the reflectance measured between 2075 and 2125 nm;

α is the slope of the soil line (TM4/TM5);

β is the ordinate at the origin of the soil line (TM4/TM5);

C^{ste} is a multiplicative constant of 5;

a is the slope of the soil line (ETM5/ETM7);

b is the intercept of the soil line (ETM5/ETM7);

δ is the angle between a point (M) and soil line; and ζ is the angle between the soil line and residue line.

Instead of using TM1 through TM5, ETM5 and ETM7 for the calculation of the different indices, the reflectance measurements of the GER3700, resampled to the Probe-1 hyperspectral bands, were used. The resampled Probe-1 bands that were closest to the centre wavelength of each TM bands were selected. Therefore, instead of using TM1, TM2, TM3, TM4, TM5, ETM5 and ETM7, bands 5, 10, 17, 27, 104, 84 and 110 of the Probe-1 hyperspectral sensor were used. Furthermore, the most successful bands to discriminate crop residues from bare soil of the Probe-1 hyperspectral sensor were also identified and used to derive the NDI, SACRI and MSACRI indices. These bands are centred at 943 nm (Probe-1 band 36) and 2303 nm (115). The selection of these two bands is based on the analysis of the first derivative of corn and bare soil, and the separability of the ground-based spectroradiometric data as well as with the Probe-1 sensor (Chevrier *et al.*, 2002).

3. RESULTS AND DISCUSSIONS

3.1 Ground Data

Regarding the sensitivity of the BI to corn residue, the values range from 25.05 % to 80.95 %. This index tends to overestimate the rate of coverage when the residue cover is less than 60 %. However, this index underestimates the rate of coverage when the residue

cover exceeds 70 %. The standard error of estimate was used as an accuracy measure for the performance of different indices this measure is 19.92 % for the BI. Figure 1 provides the results of the BI for corn residue, and shows that the points are mostly well distributed. Indeed, as residue coverage increases the BI also tends to increase. When the rate of coverage exceeds 75 %, it is shown that there is a saturation problem.

The CAI appears less accurate than the BI, because it gives negative values. For example, many CAI values are negative and range from -104.0 % to 84.5%. From Figure 2, presenting this index for corn residue, several conclusions can be drawn. The CAI generally underestimates the rate of residue coverage. One exception is the data point with 73.71 % actual coverage versus an estimated value of 76.5 %. The standard error of estimate of the CAI is 67.97%. The index values increase as residue increases. Contrary to Bannari *et al.* (1999), the study shows that it performs better when the residue coverage is greater than 50 %.

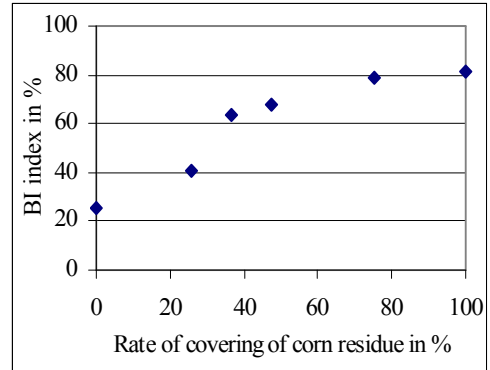


Fig. 1: BI of a soil covered by corn residue obtained with the GER3700 resampled to the Probe-1 hyperspectral bands.

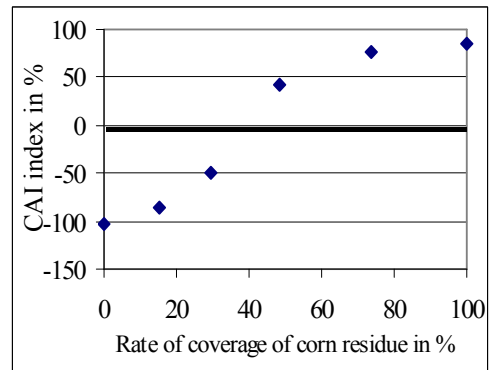


Fig. 2: CAI of a soil covered by corn residue obtained with the GER3700 resampled to the Probe-1 hyperspectral bands.

In conclusion, this index performs poorly to lower coverage rates of corn residue, but does provide better results when the Coverage rates are over 50%.

Two sources of data will be presented for the NDI. NDI-1 is the traditional index, where the reflectance measurements of the GER3700 were convolved to bands 27 (827.6 nm) and 104 (2109.7 nm) of the Probe-1 sensor. NDI-2 is the modified index, which uses the most successful bands of the Probe-1 hyperspectral sensor to discriminate crop residues from bare soil, which are bands 36 (943 nm) and 115 (2303 nm). From Figure 3 several observations can be made. First of all, it is evident that the traditional index (NDI-1) is less effective than the modified index (NDI-2). For example, many of NDI-1 values are negative and only range from -9.35 % to 2.72 %. On the other hand, the NDI-2 values are closer to the measured residue coverages and range from 8.83 % to 32.11 %. However, both indices tend to underestimate the percentage of corn residue. The standard error of the estimate is 57.89% for NDI-1 and 35.23 % for NDI-2. Furthermore, when the rate of coverage exceeds 75% there is a saturation problem with NDI-2. In fact, the NDI-2 value slightly decreases when the rate of coverage is in the range from 75 % to 100 %. The traditional index NDI-1 was not able to properly estimate the amount of residue (Bannari *et al.*, 1999). It is also obvious that the NDI-1 values are all close to 0 %. In conclusion, it appears that the NDI-2 is a better estimate, especially when the residue coverage rate is below 35 %.

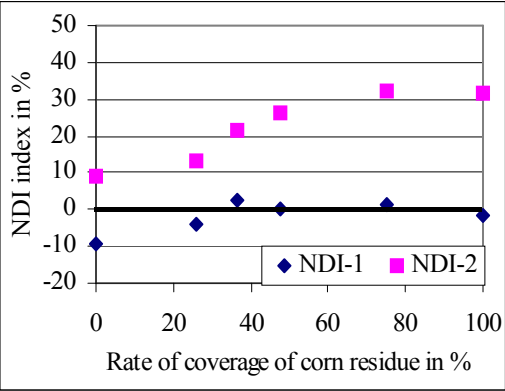


Fig. 3: NDI of a soil covered by corn residue obtained with the GER3700 resampled to the Probe-1 hyperspectral bands.

Two different SACRI indices were calculated. SACRI-1 is again the traditional index where reflectance measurements of the GER3700 were convolved to bands 27 (827.6 nm) and 104 (2109.7 nm) of the Probe-1 sensor. SACRI-2 is a modified index, which uses bands 36 (943 nm) and 115 (2303

nm) of Probe-1. The soil line must be considered for the calculation of the SACRI. Figure 4 shows the SACRI values for corn. It illustrates that the traditional index, SACRI-1, is less effective than the modified index, SACRI-2. Negative values are generated with the SACRI-1 and the range of values is small, between -1.31 % and 6.23 %. In comparison, the estimates retrieved with SACRI-2 are higher (8.01 % to 41.92%) and more representative of the actual residue coverage. The standard error of the estimate is 54.57 % for SACRI-1 and 28.59 % for SACRI-2. Both indices underestimate the percentage of corn residue. Furthermore, the estimates of corn residue from the SACRI-2 index are more accurate at coverages lower than 45 %. This index provides poor estimates for residue coverages above 60 % and a saturation problem arises when the rate exceeds 75%.

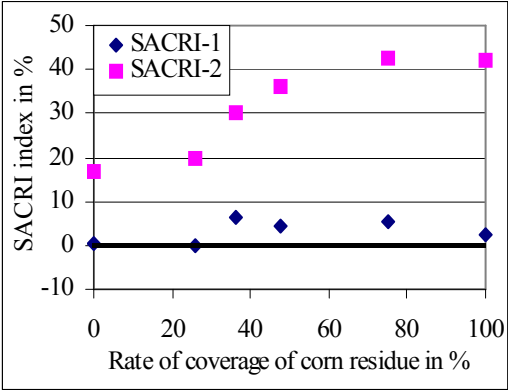


Fig. 4 : SACRI of a soil covered by corn residue obtained with the GER3700 resampled to the Probe-1 hyperspectral bands.

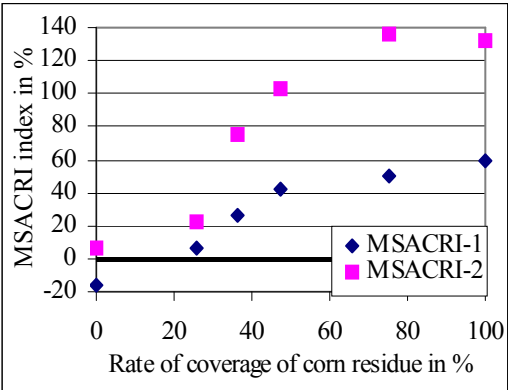


Fig. 5: MSACRI of a soil covered by corn residue obtained with the GER3700 resampled into Probe-1 hyperspectral bands.

Two variations of MSACRI were tested. The traditional index (MSACRI-1) where reflectance measurements of the GER3700 were convolved to bands 84 (1655.8 nm) and 110 (2216.5 nm) of the Probe-1 sensor, whereas the modified index (MSACRI-2) uses the Probe-1 bands 36 (943 nm) and 115 (2303 nm). As with SACRI, the soil line must be considered. Figure 5 shows the MSACRI values for corn and demonstrates that the traditional index (MSACRI-1) is more effective than the modified index (MSACRI-2) for the estimation of corn residue. The estimated values from MSACRI-1 range between 3.9 % to 73.24 % with a standard error of estimate of 22.69 %. In comparison, the values from MSACRI-2 range from 1.21 % to 133.34 % with an error of 39.82%. It is interesting to observe that MSACRI-1 always underestimates the residue coverage, whereas MSACRI-2 overestimates the coverage. As illustrated in Figure 5, with MSACRI-2 there is a saturation problem when the rate of coverage exceeds 75 %.

The values of the CRIM index range between 18.98% to 94.82 %. This index always overestimates the coverage for corn except when residue coverage is 100 %. In this case, the estimated value is 94.82 %. The standard error of the estimate is 20.20 %. As illustrated in Figure 6, the residue estimates increase when the measured residue coverage increases. CRIM appears to work better when the rate of coverage is lower than 25 %. The average errors are larger when the rate exceeds 25 %. It appears that there is a saturation problem when the rate exceeds 75 %.

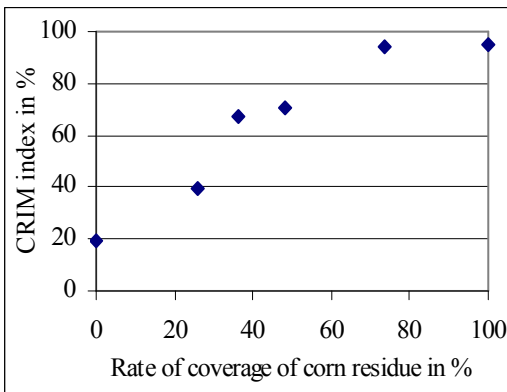


Fig. 6 : *CRIM of soil covered by corn residue obtained with the GER3700 resampled to the Probe-1 hyperspectral bands.*

The performances of indices are listed according to their standard error of estimate. The index with the smallest standard error is BI (19.99 %), followed by CRIM (20.20 %), MSACRI-1 (22.69 %), SACRI-2 (28.59 %), NDI-2 (35.23 %), MSACRI-2 (39.82 %),

SACRI-1 (54.57 %), NDI-1 (57.89 %) and CAI (67.97 %). Surprisingly, the BI had a smaller standard error of estimate than the CRIM, SACRI and MSACRI, which take into account the soil line in their calculation. The soils at the IHARF farm were dark (low reflectance) which obviously benefited the BI. The results would not have been the same if the soils were brighter. In fact, due to the BI equation, the estimation of corn residue would have been much higher and the standard error of estimate would have increased. Therefore, the CRIM and MSACRI-1 were the better indices to estimate the rate of corn residue cover using GER3700 ground-based spectroradiometer measurements convolved to the Probe-1 hyperspectral bands.

3.2 Image Data

The results based on the image data were focused on four specific sites of the IHARF farm (Figure 7). Sites 1 and 2 were patches of pure bare soil and pure residue, respectively. Site 3 had a residue cover of 71.32 %, a bare soil cover of 9.12 % and a vegetation cover of 19.56%. Whereas site 4 had a residue cover of 44.62 %, a bare soil cover of 25.26%, and a vegetation cover of 30.12 %. Figures 8 and 9 represent the residue maps derived from the empirical indices BI, CAI, NDI-1 and NDI-2, and semi empirical indices SACRI-1, SACRI-2, MSACRI-1 and MSACRI-2. The different values of the indices were grouped into seven classes (Class 1 = 0-0.15; Class 2 = 0.15-0.30; Class 3 = 0.30-0.45; Class 4 = 0.45-0.60; Class 5 = 0.60-0.75; Class 6 = 0.75-0.90; Class 7 = 0.90-1.00).

With regard to the BI, shown in Figure 8 (A), several conclusions can be drawn. Site 2 (100% residue cover) was estimated perfectly with a value between 90 and 100 %. As for site 1 (0% residue cover), the BI estimated the amount of residue to be between 15 and 30 %. For site 3 (71.32 % residue cover; 9.12 % bare soil cover; and 19.56 % vegetation cover), the BI underestimated the amount of residue by 30 to 60 %. In addition, absolutely no pixels representing soil were shown. For site 4 (44.62 % residue cover; 25.26% bare soil cover; and 30.12 % vegetation cover), the BI provided a good estimate for the amount of residue (30 to 60 %), but once again the results showed no bare soil. Therefore, the results obtained with the BI were not very accurate in estimating the amount of residue on the IHARF farm. When the rate of coverage is between 40 and 75 %, the BI underestimated the rate of coverage.

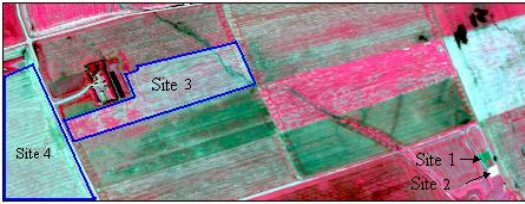


Figure 7: Probe-1 image of the IHARF farm in Saskatchewan, Canada.

The results retrieved with CAI are shown in Figure 8 (B). As with the BI, the CAI correctly estimated the amount of residue from site 2 with values between 90 and 100%. Site 1 (0 % residue cover) again had a good estimate with 15 to 30 % residue cover. The amount of residue from site 3 was overestimated. Almost all pixels from site 3 indicate estimates between 60 and 75 %. Again no pixels representing bare soil were shown. For site 4, the CAI greatly overestimated the amount of residue. Again most of the pixels were estimated to be between 60 and 75% while the actual rate of coverage was 44.62 % and no bare soil was shown even if the portion of bare soil was 25.26 %. The results show that the CAI does not estimate accurately the amount of residue on the IHARF farm. When the rate of coverage is higher than 40 % and lower than 75 %, the CAI tends to overestimate the rate of coverage.

The NDI-1 and NDI-2 values of the IHARF farm are shown in Figures 8 (C) and 8 (D). For both indices, site 2 (100 % residue cover) was again perfectly estimated with values between 90 and 100%. With regard to site 1 (0 % residue cover), the NDI-1 and NDI-2 estimated the amount of residue to be between 15 and 30 %. When observing the results of these two indices on site 3, several conclusions can be drawn. They both estimated the residue amount to be between 30 and 60 % as well as being between 90 to 100 %, but no bare soil was shown. The large majority of pixels of NDI-2 overestimated the rate of coverage of residue. In fact, they have been classified as being between 90 and 100 %. For NDI-1, one third of the pixels correspond to 30 to 45 % residue cover; one third to 45 to 60 % residue cover and one third to 90 to 100% residue cover. As for site 4, NDI-1 greatly overestimated the amount of residue cover. Most of the pixels were classified as having a residue cover of 90 to 100 %. About one tenth of the pixels were classified as residue cover of 15 to 30 %, which obviously represents bare soil. The NDI-2 index was a little better than NDI-1 in estimating the amount of residue. The majority of pixels were classified as residue cover of 45 to 60 %. However, one third of the pixels were classified as 90 to 100% residue cover and one tenth between 15 and 30 %, which again represents the bare soil. The results obtained with both

the NDI-1 and NDI-2 are not very encouraging, as they do not accurately estimate the amount of residues. When the rate of coverage is between 40 and 75 %, both indices overestimate the rate of coverage.

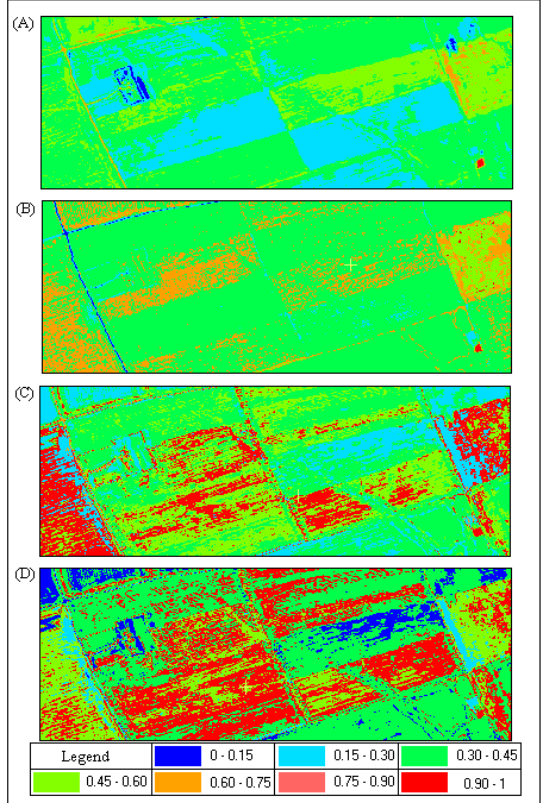


Figure 8: BI (A), CAI (B), NDI-1 (C), and NDI-2 indices extracted from fields of the IHARF farm.

The SACRI-1 and SACRI-2 are shown in Figures 9 (A) and 9 (B). With regard to site 2 (100% residue cover) both indices perfectly estimated the residue cover between 90 and 100 %. For site 1 (0 % residue cover), the SACRI-1 and SACRI-2 estimated the amount of residue to be between 15 and 30 %, while for site 3, both indices underestimated the rate of coverage. The large majority of the pixels were classified as residue cover of 30 to 60 % No bare soil was shown for either indices. With regard to site 4, SACRI-1 did estimates the amount of residue to be between 30 and 60 %, but only a few pixels were classified as bare soil. On the other hand, SACRI-2 accurately estimated the amount of residue from site 4. In fact, half of the pixels were classified as 30 to 45% residue cover, with the remaining pixels having a 15 to 30 % residue cover (bare soil). In conclusion, both indices underestimated the amount of residue on site 3, but SACRI-2 was very accurate in classifying site 4.

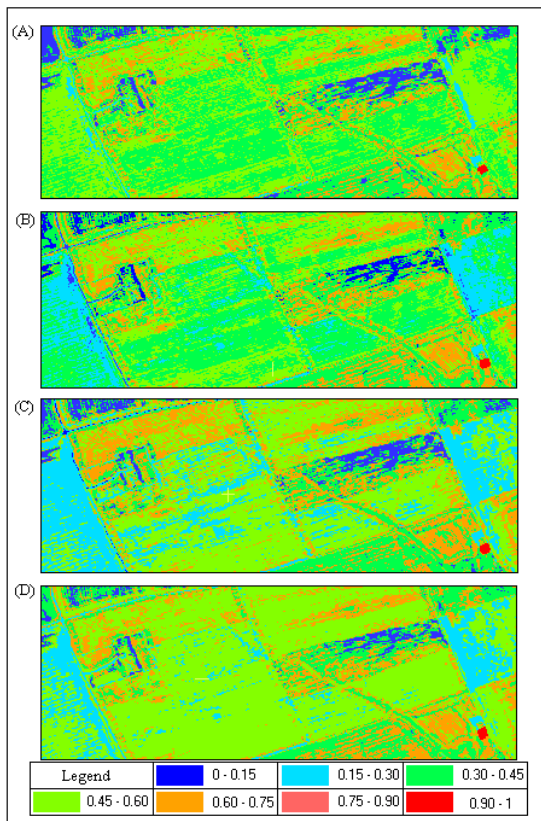


Figure 9 : SACRI-1 (A), SACRI-2 (B), MSACRI-1 (C), and MSACRI-2 (D) indices extracted from filed of the IHARF farm.

With regard to the MSACRI-1 and MSACRI-2, shown in Figures 9 (C) and 9 (D), respectively, several conclusions can be made. Both indices correctly estimated the amount of residue on site 2 (100 % residue cover). In fact, these two indices estimated the amount of residue to be between 90 and 100 %. For site 1 (0 % residue cover), the MSACRI-1 and MSACRI-2 estimated the amount of residue to be between 15 and 30 % while the real rate of coverage of bare soil was 100 %. With respect to site 3, MSACRI-1 accurately estimated the amount of residue. In fact, the large majority of the pixels were classified as residue cover of 45 to 75 % while some pixels were assigned to 15 to 30% residue cover, which represents bare soil (9.12 %). MSACRI-2 was not as accurate as MSACRI-1. The vast majority of the pixels were classified as residue cover of 45 to 60 %. For site 4 (44.62 % residue cover; 25.26 % bare soil cover; and 30.12 % vegetation cover), six tenth of MSACRI-1 pixels were classified as having a residue cover of 15 to 30% and four tenth were classified to be between 45 and 60 %. The results of MSACRI-2 were similar. Half of the pixels were estimated to have a

residue cover between 15 and 30 % while the other half were between 45 and 60 %. Accordingly, the results obtained with the MSACRI-1 over the IHARF farm were accurate for the estimation of the amount of residue. The estimation of crop residue cover of the different sites is shown on Table 1a, 1b, 1c and 1d.

Table 1a: Estimation of crop residue cover of site 1

Site 1 (0 % residue cover)	Estimation
BI	15 – 30 %
CAI	15 – 30 %
NDI-1	15 – 30 %
NDI-2	15 – 30 %
SACRI-1	15 – 30 %
SACRI-2	15 – 30 %
MSACRI-1	15 – 30 %
MSACRI-2	15 – 30 %

Table 1b: Estimation of crop residue cover of site 2

Site 2 (100 % residue cover)	Estimation
BI	90 – 100 %
CAI	90 – 100 %
NDI-1	90 – 100 %
NDI-2	90 – 100 %
SACRI-1	90 – 100 %
SACRI-2	90 – 100 %
MSACRI-1	90 – 100 %
MSACRI-2	90 – 100 %

Table 1c: Estimation of crop residue cover of site 3

Site 1 (71.32 % residue cover)	Estimation
BI	30 – 60 %
CAI	60 – 75 %
NDI-1	30 – 60 % and 90 – 100 %
NDI-2	90 – 100 % and 30 – 60 %
SACRI-1	30 – 60 %
SACRI-2	30 – 60 %
MSACRI-1	45 – 75 %
MSACRI-2	45 – 60 %

Table 1d: Estimation of crop residue cover of site 4

Site 1 (44.62 % residue cover)	Estimation
BI	30 – 60 %
CAI	60 – 75 %
NDI-1	90 – 100 %
NDI-2	45 – 60 %
SACRI-1	30 – 60 %
SACRI-2	30 – 45 %
MSACRI-1	45 – 60 %
MSACRI-2	45 – 60 %

4. CONCLUSIONS

This study tested the performance of nine different crop residue indices on agricultural fields in Saskatchewan, Canada. These indices are the BI, CAI, NDI-1, NDI-2, SACRI-1, SACRI-2, MSACRI-1, MSACRI-2, and CRIM. Firstly, the accuracy of these indices was examined using ground reflectance measurements obtained with the GER3700 convolved to the Probe-1 hyperspectral bands for corn residues at various rates of coverage. The results indicated that the CRIM and the MSACRI-1 are better indices to estimate the residue cover, because they both take into account the soil line. Next, all the indices were applied to Probe-1 hyperspectral image data acquired over several agricultural fields. The MSACRI-1 estimates of residue cover were much more representative and outperformed the other indices.

ACKNOWLEDGMENT

The authors would like to thank NSERC for financial support and CCRS for making the hyperspectral Probe-1 image data available as well as for its financial support. They would also like to thank Khalid Omari, Nancy Lemay and Karl Van Kessel of the University of Ottawa for technical support.

REFERENCES

- Aase, J.K., and Tanaka, D.L., 1991, Reflectance from four wheat residue cover densities as influenced by three soil backgrounds. *Agronomy Journal*, Vol. 83, pp. 753-757.
- Bannari, A., Morin, D. and Bonn, F., 1995, A Review of Vegetation Indices. *Remote Sensing Reviews*, Vol. 13, pp. 95-120.
- Bannari, A., Haboudane, D. and Bonn, F., 1999, Potentiel des mesures multispectrales pour la distinction entre les résidus de cultures et les sols nus sous-jacents. Forth International Airborne Remote Sensing Conference and Exhibition/ 21st Canadian Symposium on Remote Sensing, Ottawa, Ontario, Canada, 21-24 June 1999.
- Bannari, A., Haboudane, D., and Bonn, F., 2000, Intérêt du moyen infrarouge pour la cartographie des résidus de cultures. *Journal canadien de télédétection*, Vol. 26, No. 5, pp. 384-393.
- Biard, F., Bannari, A., and Bonn, F., 1995, SACRI (Soil Adjusted Corn Residue Index): un indice utilisant le proche et le moyen infrarouge pour la détection de résidus de cultures de maïs. 17ème Symposium Canadien sur la Télédétection, Saskatoon (Saskatchewan), Canada, pp. 413-419.
- Biard, F., and Baret, F., 1997, Crop Residue Estimation Using Multiband Reflectance. *Remote Sensing Environment*, Vol. 59, pp. 530-536.
- Chevrier, M., Bannari, A., Deguises, J.-C., McNairn, H., and Staenz, 2002, Hyperspectral Narrow-Wavebands for Discriminating Crop Residue from Bare Soil. *IEEE International Geoscience and Remote Sensing Symposium (IGARSS'02) /24th Canadian Symposium on Remote Sensing*, Toronto, Ontario, Canada, 24-28 June 2002.
- Chevrier, M., 2002, Potentiel de la télédétection hyperspectrale pour la cartographie des résidus de cultures. Thèse de maîtrise, Université d'Ottawa, Ottawa, Ontario, Canada, en rédaction.
- Cyr, L., Bonn, F., and Pesant, A., 1995, Vegetation indices derived from remote sensing for estimation of soil protection against water erosion. *Ecological Modelling*, Vol. 79, No. 3, pp., 277-285.
- Daughtry, C.S.T., McMurtrey, J.E., Chapelle, E.W., Hunter, W.J., and Steiner, J.L., 1996, Measuring Crop Residue Cover Using Remote Sensing Techniques. *Theoretical and Applied Climatology*, Vol. 54, pp. 17-26.
- Daughtry, C.S.T., Nagler, P.L., McMurtrey, J.E., and Lindwall, C.L., 1997, Measuring Crop Residue Cover by Shortwave Infrared Reflectance. *Agronomy, Abstracts*, p. 27.
- Freebairn, D.M. et Wockner, G.H. (1986) A Study of Soil Erosion on Vertisols of the Eastern Darling Downs, Queensland 1: Effects of Surface Conditions on Soil Movement Within Sontour Bay Catchments. *Australian Journal of Soil Science*, vol. 24, pp. 135-158.
- Ketcheson, J.W., and Stonehouse, D.P., 1983, Conservation tillage in Ontario. *Journal of Soils and Water Conservation*, Vol. 38, pp. 253-254.
- Major, D.J., Larney, F.L., and Lindwall, C.W., 1990, Spectral reflectance characteristics of wheat residue. *Proceedings of International Geoscience and Remote Sensing Symposium*, Vol. 1, pp. 603-607.
- McNairn, H., and Protz, R., 1993, Mapping Corn Residue Cover on Agricultural Fields in Oxford County, Ontario, Using Thematic Mapper. *Canadian Journal of Remote Sensing*, Vol. 19, No. 2, pp. 152-159.
- Rice, C.W., 2002, Storing Carbon in Soil : Why and How ? *Geotimes*, January 2002, pp. 1-5.
- Secker, J., Staenz, K., Gauthier, R.P., and Budkewitsch, P., 2001, Vicarious Calibration of Hyperspectral Sensors in Operational Environments. *Remote Sensing of Environment*, Vol. 76, pp 81-92.
- Staenz, K., and Williams, D.J., 1997, Retrieval of Surface Reflectance from Hyperspectral Data Using a Look-Up Table Approach. *Canadian Journal of Remote Sensing*, Vol. 23, No. 4, pp. 354-368.
- Wischmeier, W.H. and Smith, D.D., 1978, Predicting rainfall erosion losses - a guide to conservation planning, S.S. Department of Agriculture, *Agriculture Handbook*, No. 537, 58 pp.

Mapping soil properties using remote sensing and geostatistics

López-Granados F.*, Atenciano S.*, Jurado-Expósito M.*, García-Ferrer A.**,
Sánchez de la Orden M.***, Peña-Barragán J.M.* and García-Torres L.*

* *Weed Science Dept., Intitute for Sustainable Agriculture/CSIC, Apdo. 4084, 14080 - Córdoba (Spain)*

** *Remote Sensing Dept., ETSIAM. University of Córdoba, Avda. Menéndez Pidal s/n, 14004 - Córdoba (Spain)*

E-mails: cs9logrf@uco.es; satenciano@cap.junta-andalucia.es; cs9disaj@uco.es; irlgapoa@uco.es;
ig1saorm@uco.es; pa2pebaj@uco.es; ml1gatol@uco.es.

ABSTRACT- *Farmers consider fields as a whole. Fertilizers, herbicides and other crop inputs have been applied without taking into account spatial variations in field characteristics which results in over and/or under-application areas. Under-treated zones do not reach optimum levels whereas over-treated ones could show high risk of pollution. Nowadays, precision farming or the agriculture based in site-specific management provides a methodology for optimizing inputs and reducing environmental contamination. Spatial distribution of soil properties can be obtained by geostatistics using kriging from an "in situ" and expensive sampling strategy, or by remote sensing. Soil reflectance is a property which derives from inherent spectral behaviour of each soil component. We compared various prediction methods for mapping of soil properties using two combinations of secondary information. Prediction methods used were statistical (linear correlation) and geostatistical plus statistical analyses (ordinary kriging and kriging with local mean). The secondary information used were bare soil colour aerial photograph and soil attributes (pH, organic matter and potassium). The best prediction method for mapping organic matter was kriging with local mean in combination with the reflectance in the blue band.*

1 INTRODUCTION

Traditionally farm managers consider fields as a whole. Fertilisers, chemicals and other crops inputs have been applied without taking into account spatial variations in field characteristics. Cause of that, treatments result in over-application and under-application areas. Under-treated zones do not reach optimum levels of exploitation whereas in over-treated ones there may be high risk of pollution of the environment.

Nowadays, site-specific management systems provide a method in which cost reduction, optimisation of crop yield and environmental protection are included. Precision farming consists in applying just where is necessary and just with the adequate amount of product. This kind of agricultural management involves both, knowing spatial distribution of field deficiencies and patch-spraying technologies. Since sprayers capable of varying agrochemicals rates do exist, researchers must supply correct ways for mapping biotical and abiotical factors as nutrient levels or soil texture that have high and direct influence in crop yields.

Spatial distribution of any field property can be obtained by different techniques such as simple inverse distance calculations (Breghe *et al.*, 1992), autocorrelation (Dieleman and Mortensen, 1999) or

kriging (López-Granados *et al.*, 2002), but all of them require grid sampling which involves time consuming and high cost. So, these approaches are not very feasible on a large scale due to their high cost in money and time. Cause of that, prediction methods that use secondary information to extend sparse and expensive soil measurements have been developed: simple linear regression (Moore *et al.*, 1993), regression trees (Mckenzie and Ryan, 1997) and geostatistical methods such as co-kriging (Odeh *et al.*, 1995) or kriging with external drift (Goovaerts, 1998).

When secondary information is available (aerial photograph, satellite image, crop yield data, soil sampling, elevation data, etc.), it should be used to model soil attributes because, even though they are poorly correlated, there are hybrid methods (statistical and geostatistical) that using this information may perform better than ordinary kriging itself (Bishop and McBratney, 2001).

One of the most interesting source of secondary information is remote sensing if a relationship between soil properties and reflectance could be achieved.

Soil reflectance is a property which derives from inherent spectral behaviour of each soil component (mineral, organic and fluid matters). Several studies have evaluated the usefulness of land surface spectral variation in developing predictive models for mapping the soil. Thus, organic-matter, moisture, mineral

oxides, texture and surface conditions have all demonstrated influences on soil reflectance (Stoner and Baumgardner, 1981). However, one difficulty exists in deriving soil information from remotely sensed data due to the complex nature of those relationships.

Baumgardner *et al.* (1970) found that organic-matter content could be predicted from light reflectance with a linear or curvilinear relation in the visual and infrared range. Otherwise, Fernandez *et al.* (1988), Henderson *et al.* (1992) and Schulze *et al.* (1993), observed that this relationship is poor if soil samples were collected from large geographic areas or different landscape, probably due to different types of parent material.

Varvel *et al.* (1999), using aerial photography, found correlations of brightness values from the blue, green and NIR bands with both organic-matter and Bray-1 P contents. These correlations, although statistically significant, were considered low. Odeh and McBratney (2000), and Bishop and McBratney (2001) demonstrated that AVHRR data (from NOAA), bare soil LANDSAT TM imagery and bare soil colour photograph have been useful for the creation of field extent soil property maps (i.e. clay content and soil apparent electrical conductivity) using different prediction models (statistical and geostatistical techniques).

Our aim is to use remote sensing, in this case aerial photograph of bare soil, to delineate soil property maps based on the soil sampling and using different prediction methods. Three different methods were applied: simple linear regression, ordinary kriging plus regression and kriging with local mean. In those cases colour aerial imagery is used as secondary information source.

The objectives of this paper were:

- a) To use the simple linear regression method for mapping spatial distribution of soil properties by establishing the relationships between reflectance values, from colour aerial photography, and soil attributes from grid sampling.
- b) To apply a mixed method for mapping soil characteristics involving ordinary kriging plus linear regression between kriging estimates and reflectance values from a colour image.
- c) To map spatial distribution of soil attributes using kriging with local mean in which the local mean are reflectance values obtained from a colour aerial photograph.
- d) To compare the three previously described approaches for soil prediction.

2 MATERIALS AND METHODS

2.1. Secondary information data set

2.1.1. Soil sampling

The study site was a 27-ha field located in Arahál-Seville ($x=269.657$; $y=4.131.142$). Typical andalusian wheat-sunflower rotation is being followed under conventional tillage.

A selected area of 2.5 ha was sampled within the field using a grid of 20 m by 35 m resulting 96 sampled points. Soil samples were collected to a depth of 0-15 cm in early November 1998 before wheat sowing. Each sample consisted in 500 g of soil picked with a little spade. Points were georeferenced using a submeter accuracy differential global positioning system (DGPS) *Trimble Pathfinder Pro-XRS* equipped with a *TDC-1* unit. Samples from every grid point were analysed to determine pH, texture (percentage of sand, lime and clay), organic-matter (%), phosphorus (ppm) and potassium (meq) obtaining seven soil variables with 96 values everyone.

2.1.2. Aerial photography

Colour aerial photographs of bare soil were taken in October 1998 before wheat sowing. A *Wild RC-10* camera with filter, lens *AF/15 UAG* and a focal distance of 153.26 mm was used. The film was *Agfa Aviphot Color H-100 PE-1*. The flight altitude was 1525 m so the average scale was 1:10.000.

Photographs were digitized with a HP-Scanjet 4C scanner using a resolution of 800 points per inch resulting a pixel size of 35.6 μ m. Field images were introduced into the geographic information system *Ilwis* (*International Institute for Aerospace Survey and Earth Sciences, Enschede, The Netherlands*, ILWIS, 1997). Images were georeferenced into Universal Transverse Mercator projection using tiepoints which coordinates were measured with the DGPS described above. Images were then rectified and blue, green and red bands were separated.

It was selected for this research one image in which the whole studied area appeared centered. Figure 1 shows the colour aerial image of the studied field and the 96 soil sampled points.

2.2. Prediction methods

2.2.1. Simple linear regression

Every sampled soil point was located in the image and their corresponding reflectance values in blue, green and red were extracted. It was checked that all variables (soil properties and reflectance levels in visual range) were normally distributed. Pearson linear correlations were established between soil variables and reflectance values in blue, green and red, accepting a confidence level of 95% ($p=0.05$).

Regression equations were calculated for those soil variables that showed higher significant correlations with reflectance levels. Using these equations spatial distribution maps were constructed.

2.2.2. Ordinary kriging plus regression

In order to provide an improved prediction map, the seven soil variables were kriged using the ordinary kriging method (an univariate interpolation method based on a weighting scheme widely used in soil science (Webster and Oliver, 2001). Previously, the corresponding semivariogram models were validated (Deutsch and Journel, 1998).

Kriging estimates were located in the photograph (as their coordinates were known) and their reflectance values in blue, green and red bands were extracted. It was checked that all new variables (kriging estimates of soil properties and reflectance levels) were normally distributed. Pearson linear correlations were established between soil attributes and reflectance, accepting a confidence level of 95% ($p=0.05$).

For those variables showing significant correlations, linear regression equations were calculated. By using those equations, spatial distribution maps of soil properties were done.

2.2.3. Kriging with local mean

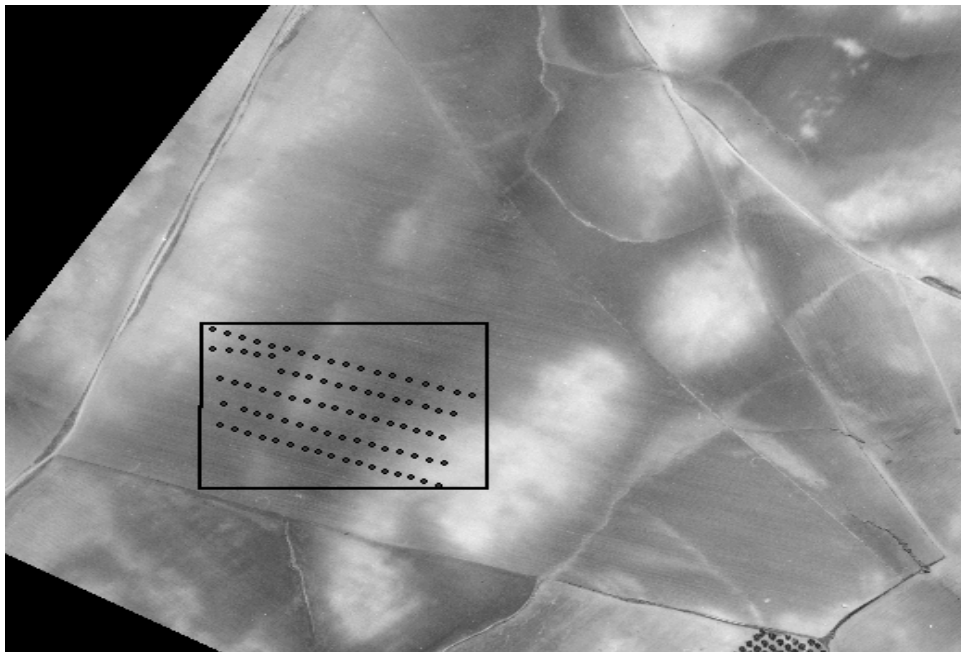
This method is an interpolation method that incorporates secondary information into the kriging system. It uses the secondary information to characterize the spatial trend of the primary (target) variable and performs simple kriging on the residuals (Goovaerts, 1997). In the case of a secondary continuous attribute, the local mean can be a regression (linear or not) of the secondary attribute value.

Thus, the seven original soil variables were fitted to a linear function of the reflectance values in blue, red and green. At each sampling point, the residual value is computed by subtracting the trend estimate (linear function) from the primary datum. Then, the semivariogram of the residuals was computed and modeled, and simple kriging on the residuals. The final estimate of every soil property is obtained by adding the trend estimate to the simple kriged estimate of the residuals (Goovaerts, 1997; Deutsch and Journel, 1998).

2.3. Comparison between the different methods

Various validation indices can be used as a measure of prediction quality, the most common of which is the mean square error. The comparative performance of

Figure 1. “El Caracol” field (Arahal-Seville). Studied area and soil points sampled.



the prediction models was gauged by using MSE of the ordinary kriging as the standard, as this does not take into account the reflectance values (Bishop and McBratney, 2001).

It was selected a point set with known values according to the three approaches analysed. For each point and each variable mean square error was calculated as an overall indication of the precision quality. Larger values of MSE indicate lower accuracy than smaller values (Odeh and McBratney, 2000).

3. RESULTS AND DISCUSSION

Table 1. Pearson linear correlations between soil properties and reflectance values for the 96 sampled points.

	Sand	Clay	Lime	Organic matter	pH	Phosphorus	Potassium
Blue	-0.3063	0.2393	0.2125	0.4380	-0.2563	0.1688 ns	-0.3333
Green	-0.2551	0.2123	0.1495 ns	0.3067	-0.2428	0.1313 ns	-0.2707
Red	-0.2107	0.1747 ns	0.1241 ns	0.2456	-0.2438	0.1175 ns	-0.2187

Table 2. Regression equations of soil variables showing a higher correlation with reflectance.

Regression equations	
Organic matter = 1.00872 + 0.00343 * Blue	R ² =0.1919
PH = 7.89749 – 0.00198 * Blue	R ² =0.0657
Potassium = 2.57118 – 0.00764 * Blue	R ² =0.1111

3.2. Ordinary Kriging plus regression

Pearson linear correlations between soil kriged estimates and reflectance variables appear in Table 3. Sand, clay, lime, organic-matter, pH and potassium were significantly correlated with visible range reflectance and the corresponding regression equations are shown in Table 4. Phosphorus was the soil property that presented the lowest correlation coefficients. By using those relationships, maps of organic matter, pH and potassium were constructed

3.1. Simple linear regression

Table 1 shows the Pearson linear correlations between soil and reflectance variables. Organic-matter, pH and potassium shown a higher significant correlation with reflectance in the blue band, although it was very low. Regression equations are presented in Table 2. In all cases the blue band was used for fitting the regression equations because its correlation coefficients were higher.

and are shown in Figure 2. In all cases correlation coefficients were higher and predictions of soil properties were improved (Table 3) in comparison with those shown in Table 1 and Table 2. So, ordinary kriging is an useful method for increasing the number of available “sampled” points without added costs.

In this study, a sparse soil sampling was spatially extended and prediction maps based on the regression equations were improved.

High organic-matter content areas coincide with low pH zones probably due to organic acids presence.

Table 3. Pearson linear correlations between ordinary kriging estimates of soil variables and reflectance values.

	Sand	Clay	Lime	Organic matter	pH	Phosphorus	Potassium
Blue	-0.3262	0.3207	0.4247	0.6034	-0.5550	0.0376	-0.6843
Green	-0.2905	0.2874	0.3133	0.4971	-0.6308	0.1157	-0.6091
Red	-0.2516	0.2603	0.2143	0.4210	-0.6479	0.1668	-0.5226

Table 4. Regression equations for those soil variables showing significant correlations according to Table 3.

Regression equations	
Sand = $47.3892 - 0.15222 * \text{Blue}$	$R^2 = 0.1064$
Clay = $20.0546 + 0.06309 * \text{Blue}$	$R^2 = 0.1028$
Lime = $37.1618 + 0.03609 * \text{Blue}$	$R^2 = 0.1804$
Organic-matter = $1.01479 + 0.00326 * \text{Blue}$	$R^2 = 0.3641$
pH = $7.77922 - 0.000564 * \text{Red}$	$R^2 = 0.4198$
Potassium = $2.35749 - 0.0049 * \text{Blue}$	$R^2 = 0.4682$

3.3. Kriging with local mean

Regression equations presented in Table 1 were used for determining local means in sampled soil points. Figure 3 shows the kriging with local mean results for organic-matter, pH and potassium. There is some similarity in the pattern of organic-matter, pH and potassium as produced by the ordinary kriging plus regression (Figure 2). However, ordinary kriging plus regression over-smoothed the spatial variability of organic matter, pH and potassium. Comparatively, the kriging with local mean reflects more the local variation than the ordinary kriging plus regression.

3.4. Comparison between the different prediction methods

Mean square errors for the three approaches appear in Table 5. According to that information simple linear regression method resulted the poorest prediction because it produced the highest MSE in comparison to the other methods. That was due to the low correlations between soil attributes and reflectance values.

For the other two methods the results were less conclusive. While kriging with local mean was the best method for organic-matter, ordinary kriging plus regression was better for pH and potassium. Lower correlation coefficients between pH-reflectance and potassium-reflectance (Table 1) in comparison to organic-matter-reflectance could be the explanation because the local means were calculated using the regression equations and for this soil attribute the

fitting was better. Bishop and McBratney (2001) found that when kriging of the residuals were incorporated to the different prediction models studied, the RMSE (root-mean-square error) was lower. They indicated that kriging with external drift, which is an interpolation method very similar to kriging with local mean, was the best prediction method for mapping soil properties. However, in our study kriging of the residuals was carried out in kriging with local mean and MSE was not lower for pH and potassium.

This study has demonstrated that a few soil observed sites combined with aerial photograph and statistical and gestatistical techniques are adequate for mapping soil properties.

It could be concluded that:

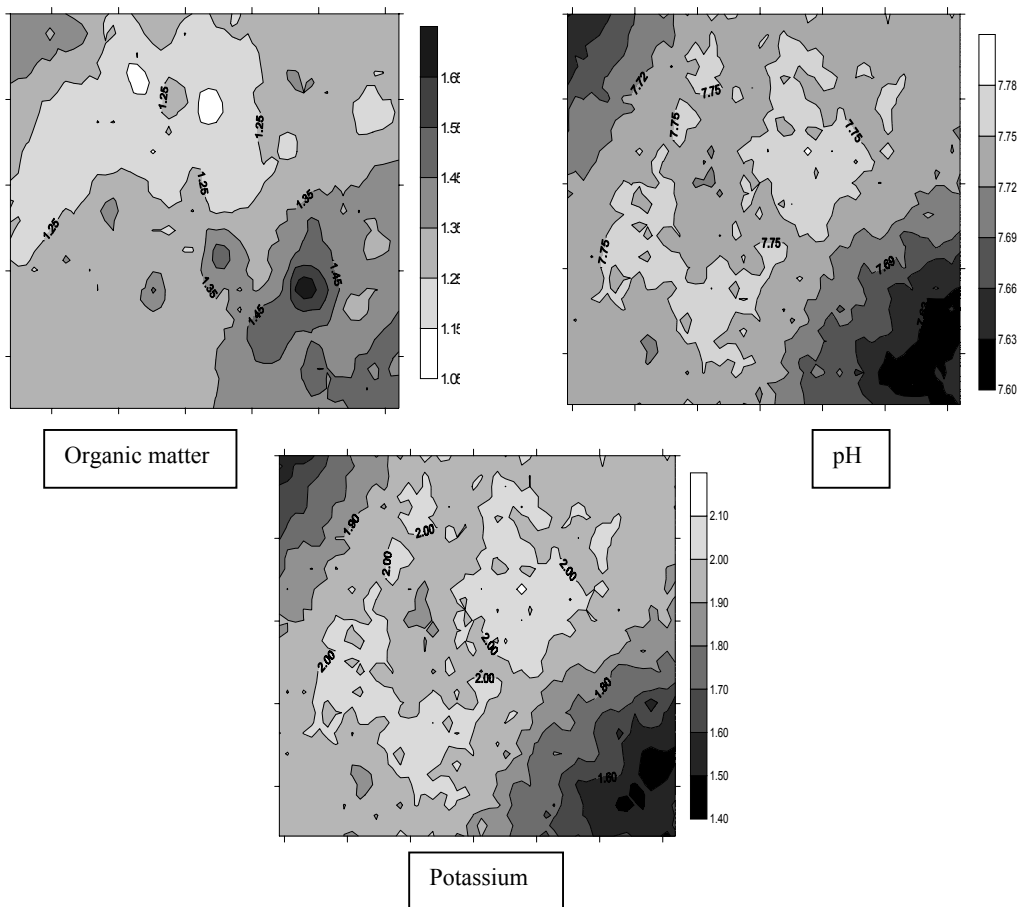
- The linear regression method performed very poorly in predicting the soil property studied.
- For those variables presenting high correlation with reflectance, kriging with local mean results adequate. Besides, using this method the variance of the kriging residuals is known so it is a robust approach.
- For variables with low correlations with reflectance the ordinary kriging plus regression is a simpler method that permits to obtain a global idea of the spatial distribution of soil properties.

Research is in progress involving more prediction methods to compare their accuracy in mapping soil properties.

Table 5. Mean square errors for the three compared methods when estimating organic-matter, pH and potassium levels.

Prediction Method	Organic-matter	PH	Potassium
Regression	0.006516875	0.001137054	0.012664483
Ordinary kriging plus regression	0.006432134	0.000651655	0.009453339
Kriging with local mean	0.001871207	0.000889906	0.01060378

Figure 3. Isoline maps of organic-matter, pH and potassium as predicted by kriging with local mean.



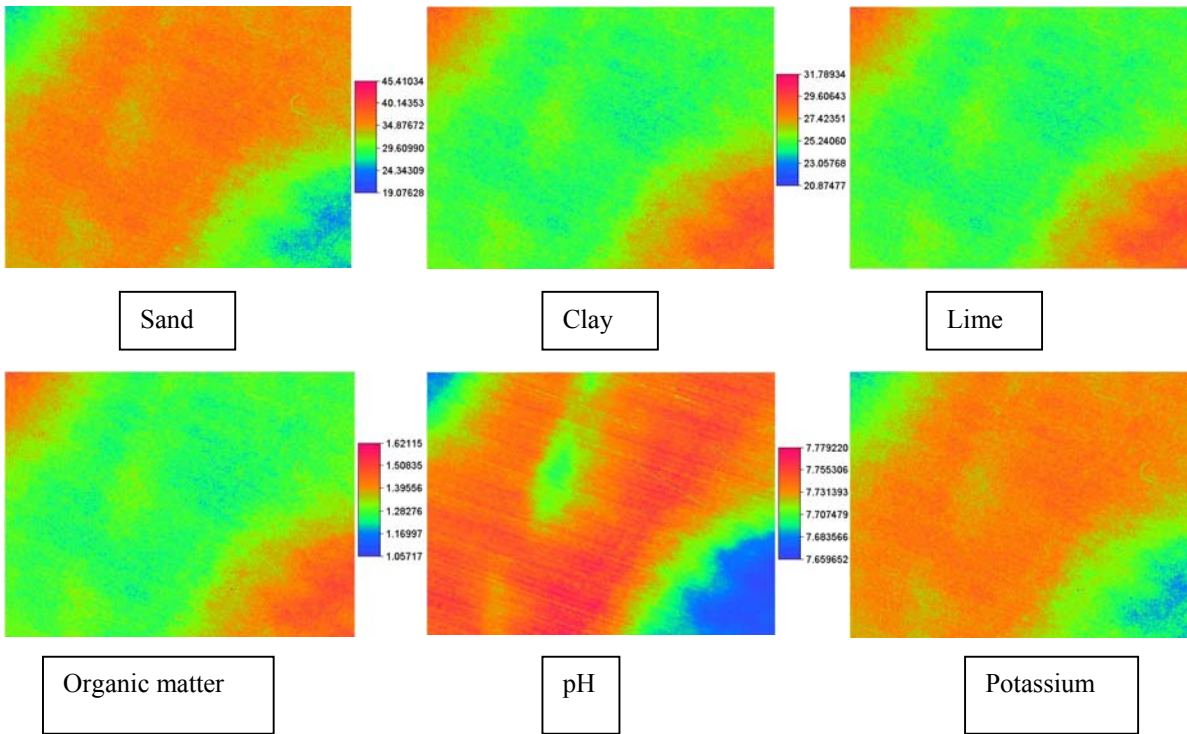
4. ACKNOWLEDGEMENTS

This research was financed by the Spanish Commission of Science and Technology, project: AGF 99-0878.

5. REFERENCES

- Baumgardner, M.F., Kristof, S.J., Johannsen, C.J., and Zachary, A., 1970, Effects of organic matter on the multispectral properties of soils. *Indiana Academy Science*, **79**, 413-422.
- Bishop, T.F.A., and McBratney, A.B., 2001, A comparison of prediction methods for the creation of field-extent soil property maps. *Geoderma*, **103**, 149-160.
- Bregt, A.K., Gesing, H.J., and Alkasuma, M., 1992, mapping the conditional probability of soil variables. *Geoderma*, **53**, 15-29.
- Deutsch, C.V., and Journel, A.G., 1998, GSLib. Geostatistical software library and user's guide, 2nd. Edition. Oxford University Press, New York.
- Dieleman, J.A., and Mortensen, D.A., 1999, Characterizing the spatial pattern of *Abutilon theophrasti* seedling patches. *Weed Research*, **42**, 648-657.
- Fernández, R.N., Schulze, D.G., Coffin, D.L., and Van Scoyoc, G.E., 1988, Color, organic matter, and pesticide adsorption relationships in a soil landscape. *Soil Science Society of America Journal*, **52**, 1023-1026.
- Goovaerts, P., 1997, Local estimation: Accounting for a single attribute. In *Geostatistics for Natural Resources Evaluation*. Oxford University Press, pp. 125-181.
- Goovaerts, P., 1998, Geostatistical tools for characterizing the spatial variability of microbiological and physico-chemical soil properties. *Biology and Fertility of Soils*, **27**, 315-334.
- Henderson, T.L., Baumgardner, M.F., Franzmeier, D.P., Stott, D.E., and Coster, D.C., 1992, High dimensional reflectance analysis of soil organic matter. *Soil Science Society of America Journal*, **56**, 865-872.
- ILWIS Development, ITC, 1997, ILWIS 2.1. for windows Reference Guide (Enschede: The International Institute for Aerospace Survey and Earth Sciences (ITC).
- López-Granados, F., Jurado-Expósito, M., Atenciano, S., García-Ferrer, A., Sánchez de la Orden, M., and García-Torres, L., 2002, Spatial variability of agricultural soil parameters in southern Spain. *Plant and Soil*, in press.
- McKenzie, N.J., and Ryan, P.J., 1997, Spatial prediction of soil properties using environmental correlation. *Geoderma*, **89**, 67-94.
- Moore, I.D., Gessler, P.E., Nielsen, G.A., and Peterson, G.A., 1993, Soil attribute prediction using terrain analysis. *Soil Science Society of America Journal*, **57**, 443-452.
- Odeh, I.O.A., McBratney, A.B., and Chittleborough, D.J., 1995, Further results on prediction of soil properties from terrain attributes: heterotopic cokriging and regression-kriging. *Geoderma*, **67**, 215-225.
- Odeh, I.O.A., and McBratney A.B., 2000, Using AVHRR images for spatial prediction of clay content in the lower Naomi Valley of eastern Australia. *Geoderma*, **97**, 237-254.
- Schulze, D.G., Nagel, J.L., Van Scoyoc, G.E., Henderson, T.L., Baumgardner, M.F., and Stott D.E., 1993, Significance of organic matter in determining soil colors. In *Soil Color*, edited by J.M. Bigham and E.J. Ciolkosz (SSSA Spec. Publ. 31. SSSA, Madison, WI), pp. 71-90.
- Stoner, E.R., and Baumgardner, M.F., 1981, Characteristic variations in reflectance of surface soils. *Soil Science Society of America Journal*, **45**, 1161-1165.
- Varvel, G.E., Schlemmer, M.R., and Schepers, J.S., 1999, Relationship between spectral data from an aerial image and soil organic matter and phosphorus levels. *Precision Agriculture*, **1**, 291-300.
- Webster, R., and Oliver, M., 2001, Local estimation or prediction: kriging. In *Geostatistics for Environmental Scientists*. John Wiley and Sons, Ltd (England), pp. 149-191.

Figure 2. Sand, clay, lime, organic-matter, pH and potassium maps obtained when applying the ordinary kriging plus regression.



Estimation of plant water content from a multispectral and a hyperspectral sensor

Catherine M. Champagne^{a*}, Karl Staenz^b, Abdou. Bannari^c, H. Peter White^b, Jean-Claude Deguise^b and Heather McNairn^b

^aMIR Télédétection inc, 110 rue de la Barre (226), Longueuil, QC, Canada, J4K 1A3

^bCanada Centre for Remote Sensing, Natural Resources Canada, 588 Booth St., Ottawa, ON, Canada
K1A 0Y7

^cRemote Sensing and Geomatics of Environment Laboratory, Department of Geography, University of Ottawa, P.O. Box 450, Stn. A, Ottawa (Canada), K1N 6N5
catherine.champagne@ccrs.nrcan.gc.ca

ABSTRACT Hyperspectral models developed to estimate plant water content have had limited application under field conditions and have not been rigorously validated. A physical model using a spectrum matching technique was applied to hyperspectral data to directly calculate the canopy equivalent water thickness (EWT) using a look-up table approach. The objective of this study was to test the validity of this algorithm using plant water content information collected under field conditions, and to relate this to the needs of precision agriculture. Image data were acquired over two experimental test sites in Canada, near Clinton, Ontario and Indian Head, Saskatchewan, using the Probe-1 airborne hyperspectral sensor. Plant biomass samples were collected simultaneously from plots spanning fourteen fields of various crop types (wheat, canola, corn, beans and peas). The model was validated against EWT estimated from biomass samples. The model predicts EWT in the range found with all crop types pooled together, a root mean squared error (RMSE) of 26.8 % of the average. The model was sensitive to within-crop variability for broad leaf crops such as peas, corn, and beans (RMSE = 24.4%, 12.0, 21.8%, respectively). The RMSE for canola was relatively high (39.9%) as a result of a poor prediction at low water contents. The model proved a poor predictor of EWT in wheat (RMSE = 69.9%). EWT is related to plant biomass and leaf area index (LAI).

1 INTRODUCTION

The analysis of plant spectra measured from hyperspectral sensors using advanced models holds the potential to estimate plant physiological properties over relatively large areas. Reflectance in the near and short-wave infrared (NIR and SWIR, respectively) is influenced by the amount of liquid water in the target, expressed as a series of absorption features at 970, 1180, 1450, 1940 and 2500 nm. At the canopy scale, NIR bands have proven more sensitive to variation in plant water content due to the stronger reflectance signal.

The water index (WI), based on the relative depth of the 970 nm absorption feature, has been correlated with ground measures of plant water content at both leaf and canopy scales (Peñuelas *et al.*, 1993; Gamon *et al.*, 1999). The index has been found to be a good indicator of plant water stress (measured as relative water content) under extreme drought conditions where leaf area is not highly variable (Peñuelas *et al.*, 1997). The WI is more strongly related to plant water content, which is a function of canopy biomass, than water stress, which is related to the physiological state of water in the plant (Gamon *et al.*, 1999).

An increased understanding of the interaction of light within a plant canopy has led to more complex models to estimate plant water content. Reflectance in the NIR and SWIR are related to the overlapping absorption of atmospheric water vapour at 940 and 1130 nm and vegetation liquid water at 970 and 1180 nm. The absorption peak of liquid water is offset to longer wavelengths, corresponding to the larger intermolecular forces of water in this phase (Green *et al.*, 1991). The transmission of radiation in these overlapping absorption bands is directly related to the total amount of water in each phase in a given pixel. Using a radiative transfer model, a curve fitting procedure was developed to estimate column atmospheric water vapour, and separate this amount from the liquid water (measured as equivalent water thickness, EWT) in the target vegetation, based on the offset in the absorption minima (Gao and Goetz, 1990).

The EWT is defined as the hypothetical thickness of a sheet of liquid water in the target (Allen *et al.*, 1969) and is related to the path length of light radiation in the canopy. Curve-fitting models have been applied using AVIRIS data over vegetated landscapes (Gao and Goetz, 1994; Roberts *et al.*,

1998; Ustin *et al.*, 1998) but have had limited application and validation over agricultural landscapes. The objective of this study is to validate this model using a version modified by Staenz *et al.* (1997) over an agricultural landscape and determine the sensitivity of this measure to within-field variation in plant water content.

2 MATERIALS AND METHODS

Airborne hyperspectral data and ground validation measures were collected over two agricultural sites in Canada representing a range of crop types and site characteristics. Field campaigns were conducted during the growing seasons near Clinton, Ontario (43°N, 81°W) in 1999 and Indian Head, Saskatchewan (50°N, 104°W) in 2000.

At the Clinton site, six test fields were chosen for ground validation measures, ranging in size from 19 to 36 hectares. Three were seeded with corn (*Zea mays* L.) and three with white beans (*Phaseolus vulgaris* L.). No nitrogen or seeding treatments were delineated within the fields.

For the Indian Head site, fields were located on a precision test farm of the Indian Head Agricultural Research Foundation. Eight 12-hectare fields were chosen for ground measurements, four seeded with wheat (*Triticum aestivum* L.), two seeded with canola (*Brassica napus* L.), and two with peas (*Lathyrus aphaca* L.). Each field was divided into four sections of approximately 3 hectares each to delimit treatments. Variable rate fertilizer applications were made in canola and wheat fields; variable rate seeding treatments were made in pea fields. Patches of bare soil, double seeded and crop residue were established in an adjacent field (approximately 20 m by 20 m in dimension).

2.1 Image Acquisition and Processing

Image data were acquired using the airborne Probe-1 hyperspectral sensor (Earth Search Sciences Inc., 2001). The Probe-1 is a "whiskbroom style" instrument that collects data in the cross-track direction by mechanical scanning and in the along-track direction by movement of the airborne platform. This sensor collects upwelling radiance in 128 spectral bands in the visible, NIR and SWIR between 440 nm and 2500 nm. The bandwidth is between 11 and 18 nm at full width half maximum (FWHM). Probe-1 is mounted on a three-axis gyrostabilizer to minimize geometric distortion from the aircraft movement. The flying altitude was 2500 m (above ground level) for a swath width of 3 km and a spatial resolution of 5 m at nadir.

Image processing was carried out using the Imaging Spectrometer Data Analysis System

(ISDAS), a software package, developed at the Canada Centre for Remote Sensing, for processing and analysing hyperspectral data (Staenz *et al.*, 1998). A vicarious calibration of the sensor was required to correct for errors in the calibration coefficients supplied with the data (Secker *et al.*, 2001). A radiometric re-calibration of the sensor radiance was made using ground spectra obtained simultaneous to aircraft data acquisition over a pseudo-invariant site (bare soil in Clinton and a section of pavement in Indian Head), using a portable spectroradiometer (GER Corporation, 1990).

2.2 Calculation of Image EWT

Image data were used to calculate canopy equivalent water thickness using a spectral curve fitting procedure described by Staenz *et al.* (1997) and implemented in the ISDAS atmospheric correction module. The model calculates canopy EWT by modelling reflectance as a linear function adjusted for water absorption in the near infrared. An initial set of modelled surface reflectances was selected over the 940 nm atmospheric water absorption region and adjusted for liquid water transmittance. The adjusted surface reflectance was converted to at-sensor radiance using look-up table parameters derived using the MODTRAN 4 radiative transfer code (Berk *et al.*, 1999). The predicted at-sensor radiance was compared to the measured radiance using a non-linear least-squares fitting technique (Press, 1992). The model retrieves both the atmospheric water vapour content and the canopy liquid water on a pixel-by-pixel-basis.

2.3 Ground Data Collection

Measurements of plant biomass used to calculate plant water content were made on the day of image acquisition for each study site. Approximately eight to thirteen sampling sites were selected per field. Sampling sites were selected to reflect within-field variability, based on elevation and soil maps, for a total of 154 locations. Each sampling site was georeferenced. At each sampling site, three replicates were taken within 2-3 m of the center of the site location to reflect local variation in plant biomass. At each replicate, all of the above-ground crop biomass was harvested within a 0.5 m by 0.5 m area. Samples were weighed and dried to obtain fresh and dry mass.

Plant EWT was calculated as (Jacquemoud and Baret, 1990):

$$EWT_{Biomass} = \frac{(FM - DM)}{LA}, \quad (1)$$

where LA is the leaf area and FM and DM are the fresh and dry masses, respectively. The LA for this

study was not measured directly, but was estimated from plant dry matter as:

$$LA = DM \times SLA, \quad (2)$$

where SLA is the specific leaf area. The SLA is defined as the area of leaf per unit of dry leaf matter and is a crop-specific parameter that quantifies the internal structure of plant leaves, and is more or less constant for non-senescent leaves. For this experiment, indicative values were used from a table established by Keulen (1986).

The mass of water calculated was made on pooled samples of aboveground biomass, with no distinction made between stem and leaf water content. In general, leaves dominate the scattering of radiation within agricultural canopies (Knippling, 1970). The stem water content, however, is a significant portion of the total canopy biomass, particularly in the early stages of growth. For this reason, the values of biomass EWT were corrected for the stem-to-leaf ratio, to compensate for the effect of stem water content on these measures. The dry matter partitioning for agricultural crops is more strongly related to crop type than to individual growing conditions (Heemst, 1986). For this study, measured and modelled dry matter partition as a function of crop growth stage were estimated from studies on wheat (Schulze, 1982), corn (Heemst, 1986), soybean (Penning de Vries *et al.*, 1989), canola (Hocking *et al.*, 1997) and pea (Baigorri *et al.*, 1999). Values for white bean were taken from soybean data due to the morphological similarities between these crops. Leaf proportions were estimated based on growth stage (days after sowing) and a correction factor (based on the mass) was applied to the total value of EWT.

2.4 Image Registration

Ground sampling sites were located in the Probe-1 image using an image-to-image registration with high-resolution georeferenced images (1 m IKONOS panchromatic for Indian Head sites and 1 m

orthophotos for Clinton sites). The georeferenced image was warped to fit the Probe data using a 2nd order polynomial. Due to the high root mean squared error (average RMSE = 2.6 pixels) of the image registration, image data were averaged from 3 by 3-pixel window surrounding the georeferenced location.

2.5 Model Validation

To validate the model, the coefficient of determination and the root mean squared error (RMSE) were calculated. The RMSE and the standard deviation are given as a percentage of the average values. For this research, the observed values were those from the plant sampling (EWT_{Biomass}) and the predicted values were from the image (EWT_{Image}).

3 RESULTS

3.1 Model Validation

Model fit statistics were calculated for EWT_{Biomass} values calculated both with and without stem water content for all crops combined (Table 1). The intercept for both cases is positive, indicating that the model is overestimating the amount of water in the canopy. This overestimation is reduced by 0.01 cm when the proportion of water attributable to stems is removed from the calculation of EWT_{Biomass} . The RMSE was much lower when biomass measures included the leaf water content only (26.8% versus 58.4%). This suggests that the model is more sensitive to leaf water content than the water content of the whole plant. This is advantageous for agricultural applications, where leaf water content responds more distinctly to drought conditions than the water content of the stem and leaves combined (Champagne *et al.*, 2001).

There is a larger scatter in the data at values of EWT less than 0.15 cm. This is largely a result of the large scatter in the data for wheat fields, which will be discussed in section 3.3.

Table 1. Fit statistics for observed EWT and image-derived EWT (where $EWT_{Biomass}$ and EWT_{Image} are the equivalent water thicknesses calculated from biomass samples and image data models; E_{Image} and $E_{Biomass}$ are the standard deviations as a percentage of the mean values; a and b are the slope and intercept of the least squares regression line; RMSE is the root mean squared error given as a percentage of the average value; D is the index of agreement; and R^2 the coefficient of determination, indicated in bold at significance level $p < 0.001$), given for the linear best fit line and a linear model fit through the bare soil point.

Case		$EWT_{Biomass}$ (cm)	EWT_{Image} (cm)	$E_{Biomass}$ (%)	E_{Image} (%)	a	b	RMSE (%)	R^2	R^2 (including bare soil point)
All Fields Combined	Stem + Leaves	0.191	0.142	55.4	40.8	0.8	0.06	58.4	0.76	
	Leaves Only	0.121	0.142	55.0	40.8	0.8	0.05	26.8	0.76	
Grouped by Crop Type (Leaves Only)	Bean	0.098	0.101	7.5	19.9	-0.1	0.13	21.8	0.01	0.11
	Corn	0.241	0.240	11.4	6.4	0.2	0.22	12.0	0.00	0.66
	Canola	0.101	0.131	57.0	38.2	0.9	0.06	39.6	0.76	0.76
	Pea	0.127	0.154	25.1	21.1	0.9	0.04	24.4	0.74	0.81
	Wheat	0.073	0.111	28.5	27.2	0.1	0.10	69.9	0.01	0.01

3.2 Background and geometric effects on modelled EWT

Image-derived measures such as EWT may be sensitive to variability that is related to differences in soil brightness or other background elements like crop residues. The early development phase of the crops and the minimum tillage used at both study sites resulted in a significant presence of crop residues and soil in the sensor field-of-view. Average EWT_{Image} values for patches of pure soil, and residue were examined. The bare soil patch had an EWT_{Image} value of 0.050 cm and the residue patch had a value of 0.007 cm. These values fall within the error bounds of the model, suggesting that soil and residue moisture did not contribute significantly to extracted EWT_{Image} .

The effects of view angle and illumination geometry on image-derived vegetation indices are significant (White *et al.*, 2001). For this study, image data were not normalized for directional effects, with most images acquired at approximately the same local sun time. Variations in view angle within a single image were not found to significantly influence the results. Future work will focus on the correction of errors due to variation in view/illumination geometry, since they have been found to cause some variation in estimated plant water content (White *et al.*, 2002).

3.3 Modelling crop and field variability

The dynamics of EWT as a measure of plant water content are further illustrated by examining the relationship between modelled and measured EWT on a species by species basis. Overall, the corn crop showed the highest EWT, with a decreasing EWT for peas, canola, wheat and beans (average EWT_{Image} = 0.240, 0.154, 0.131, 0.111, 0.010 cm, respectively). This follows the pattern of dry matter and water content distribution among the crop types (Fig. 1), confirming other studies that have found canopy estimates of plant water content largely driven by

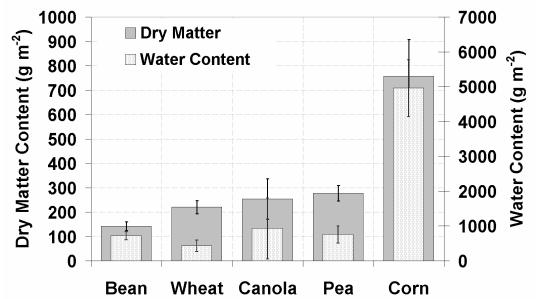


Fig. 1. Dry matter and water content values for each crop type.

biomass distribution (Gamon *et al*, 1999).

A strong linear relationship was found for peas and canola, with R^2 values of 0.74 (significance level, $p = 0.001$) and 0.76 ($p = 0.001$), respectively (Table 1). The scatter plot of predicted and observed EWT shows that corn and bean crops were (with one exception) clumped within a limited range of EWT (Fig. 2), whereas the range of EWT for canola and peas was comparatively wider (57.0 % and 25.1 % variability, respectively). As a result of this limited dynamic range in corn and beans, R^2 values for these crops are low and not statistically significant. When R^2 values are recalculated using a bare soil point (with and EWT_{Image} value of 0.05cm and a $EWT_{Biomass}$ value of 0.0 cm, the relationship becomes stronger for corn ($R^2 = 0.66$). The relationship does not improve for beans substantially due to the very small range in $EWT_{Biomass}$ (7.5 %) compared to EWT_{Image} (19.9 %) for that crop. The linear fitting results for wheat were low despite a comparatively wider dynamic range of EWT in the data ($R^2 = 0.01$; $R^2 = 0.05$ including the bare soil point).

The RMSE for corn, bean, canola and pea crops was 12.0, 21.8, 39.6, and 24.4 % of the measured

value, respectively. The higher RMSE for canola is largely a result of a poorer model fit. The predicted values are consistently higher than the measured values in this range of water values. This suggests that the ratio of stems to leaves for crops at this growth stage was not estimated correctly, or that the water content measured by the sensor includes a combination of both leaves and stems. Overall, the model is providing a good estimation of EWT for these crops.

The relationship between measured and modelled EWT for wheat showed the highest RMSE and the largest scatter in the data (Table 1, Fig. 1). The wheat crop showed significant variability within the four fields studied, with percentage variability of 28.5 % for $EWT_{Biomass}$ and 27.2 % for EWT_{Image} . The overall average water content was the lowest for the five crop types, with $EWT_{Biomass}$ of 0.073 cm. The RMSE was the highest for the five crops at 69.9%. The large scatter in the data suggests that the different radiation scattering regimes within the canopy for broadleaf and grass species influences the depth of water absorption features. It is possible that the erectophile nature of wheat leaves measured at a

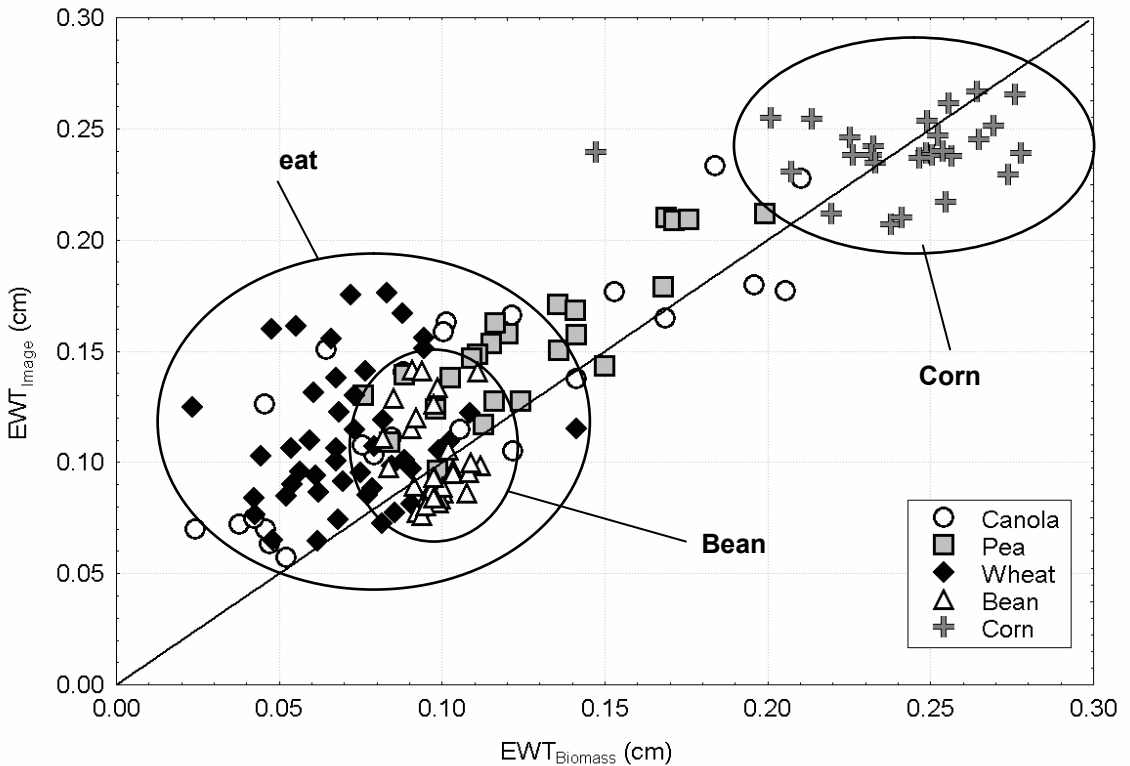


Fig. 2. Relationship between EWT_{Image} and $EWT_{Biomass}$. Circled values represent clusters of data discussed in section 3.3.

canopy scale produces an optical path length that includes a highly variable proportion of leaves and stems, and that the EWT_{Image} values are not consistently representative of leaf or stem water content. Future work will establish the proportion of leaves and stems in the field-of-view of the sensor and will establish a mixing ratio to improve the understanding of plant parameters measured from airborne and satellite platforms.

3.4 Application of EWT to vegetation studies

The biological meaning of EWT must be understood in order for it to be an effective tool in vegetation studies. The canopy value of EWT used is related exponentially to the gravimetric water content of the plant (GWC_F), given as a percentage of the fresh mass (Fig.3). The relationship is slightly variable for each plant type, resulting from variability in specific leaf area and variation in the relationship between fresh and dry mass. The relationship is weak for EWT_{Image} ($R^2 = 0.24$) due to the large scatter in the EWT_{Image} values for beans. When beans are excluded from the model, the relationship improves ($R^2 = 0.64$).

EWT is primarily driven by changes in actual water content, which is, in turn, driven by changes in biomass. The EWT is related to NDVI ($R^2 = 0.77$), which is largely a measure of canopy structure and related to the total biomass through the leaf area index (LAI). This indicates that most of the variability in EWT is related to variation in canopy structure; primarily, increases in canopy height and LAI. The relationship between LAI and EWT is inherent: the EWT is a measure of the optical thickness of water in a stack of leaves; therefore increases in the quantity of leaves increases both the LAI and the EWT. Water thickness has been suggested to be a stronger indicator of canopy structure and LAI than indices, such as

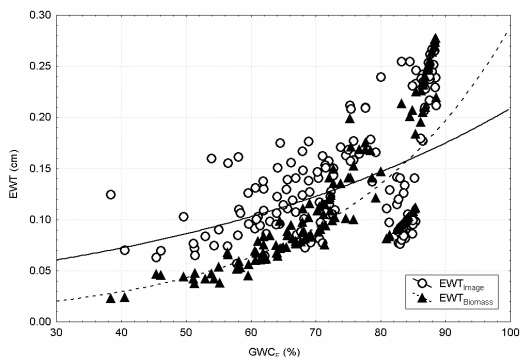


Fig. 3. Relationship between gravimetric water content (GWC_F) and EWT calculated from biomass and image data. Lines indicate a best-fit exponential model for $EWT_{Biomass}$ ($R^2 = 0.85$) and EWT_{Image} ($R^2 = 0.24$).

NDVI, which tend to saturate at LAI values greater than 3.0 (Roberts et al., 1998). The intercorrelation between physiological manifestations of water stress (such as stomatal closure) and variation in structural manifestations of water stress (such as variations in leaf water content) cannot be totally isolated from one another (Hsaio and Bradford, 1983). Optical measures of plant water content, in an agricultural context, can instead form part of an integrated approach to crop management (Strachan et al., 2001).

4 CONCLUSIONS

A spectrum-matching technique for the prediction of canopy water was validated over an agricultural landscape. Overall, the model provides a significant relationship with canopy equivalent water thickness (EWT) when all crop types are pooled together, with an RMSE of 26.8%. The model is more sensitive to leaf water content than plant water content, and future validation work should isolate these values in the biomass measurements.

A breakdown of the estimation of EWT for individual crops revealed that the sensitivity of the model to variations in EWT. The model was sensitive to the high variability pea crops (24.4%) and provided a good prediction of EWT in canola at higher water content (RMSE = 39.9%). The low level of variability in corn and bean crops prevented a statistically significant result from being found, but the low RMSE suggests that the model accurately estimated EWT for these crops (RMSE = 12.0 and 21.8% for corn and beans, respectively). The application of this model to agricultural field management would require a greater understanding of the causes of variation in EWT and the link to crop production. The poor results for wheat (RMSE = 69.9%) suggest that the source of scattering of radiation from these canopies is a variable combination of leaves and stems. The influence of stems in grass species reflectance should be examined further.

The relationship of EWT to LAI ($R^2 = 0.67$) makes it a useful tool to use in conjunction with other remote sensing measures for an integrated system of crop management.

Future work will be done to examine measures of EWT in relation to precision agriculture. A follow-up study was made in 2002 at Indian Head to examine seasonal variation in optical remote sensing products such as EWT. Two wheat fields were studied during three field campaigns over the growing season. Leaf-level spectral measurements were made at each sampling site, coincident with biomass sampling. Hyperion hyperspectral satellite imagery was acquired over the site to examine potential to scale-up the estimation of water content to space-borne platforms.

ACKNOWLEDGEMENTS

This research was carried out as part of a master's thesis project at the University of Ottawa and the authors wish to thank them for financial support through the Natural Sciences and Engineering Research Council (NSERC). The authors gratefully acknowledge all participants in the Clinton and Indian Head field campaigns.

REFERENCES

- Allen, W.A., H.W. Gausman, A.J. Richardson, and J.R. Thomas, 1969, Interaction of isotropic light with a compact leaf, *Journal of the Optical Society of America*, **58**(8), 1023-1028.
- Baigorri, H., M.C. Antolín, and M. Sánchez-Díaz, 1999. Reproductive response of two morphologically different pea cultivars to drought, *European Journal of Agronomy*, **10**, 119-128.
- Berk, A., G.P. Anderson, P.K. Acharya, J.H. Chetwynd, L.S. Bernstein, E.P. Shettle, M.W. Matthew, and S.M. Adler-Golden, 1999, *MODTRAN 4 User's Manual*, Air Force Research Laboratory, Hanscom AFB, Maryland, U.S.A.
- Champagne, C., E. Pattey, A. Bannari, and I.B. Strachan, 2001, Mapping crop water status: issues of scale in the detection of crop water stress using hyperspectral indices, Proceedings of the 8th International Symposium on Physical Measurements and Signatures in Remote Sensing, Aussois, France, pp.79-84.
- Earth Search Sciences Inc., 2001, About Probe-1, Kalispell, MT., www.earthsearch.com/technology.
- Gamon, J.A., H.-L. Qiu, D.A. Roberts, S.L. Ustin, D.A. Fuentes, A. Rahman, D. Sims, and C. Stylinski, 1999, Water expressions from hyperspectral reflectance: implications for ecosystem flux modeling. Proceedings of the Eighth Annual Airborne Visible/Infrared Imaging Spectrometer (AVIRIS) Workshop, Pasadena, CA, JPL Publication, cd-rom.
- Gao, B.-C., and A.F.H. Goetz, 1990, Column atmospheric water vapor and vegetation liquid water retrieval from Airborne Imaging Spectrometer data, *Journal of Geophysical Research*, **95**, 3549-3564.
- Gao, B.-C., and A.F.H. Goetz, 1994, Extraction of dry leaf spectral features from reflectance spectra of green vegetation, *Remote Sensing of Environment*, **47**, 369-374.
- Geophysical and Environmental Research Corporation, 1990, GER 3700 *Spectroradiometer User's Manual*, v.2.1, 55 pages.
- Green, R.O., J.E. Conel, J.S. Margolis, C.J. Brugge, and G.L. Hoover, 1991, An inversion algorithm for the retrieval of atmospheric and leaf water absorption from AVIRIS radiance with compensation for atmospheric scattering, Proceedings of the Third Annual Airborne Visible/Infrared Imaging Spectrometer (AVIRIS) Workshop, Pasadena, California, JPL Publication 91-28, pp.51-61.
- Heemst, H.D.J. van., 1986, Crop phenology and dry matter distribution, in *Modelling of Agricultural Production*, H. van Keulen and J. Wolf (eds), pp. 26-38.
- Hocking, P.J., P.J. Randall, and D. DeMarco, 1997, The response of dryland canola to nitrogen fertilizer: partitioning and mobilization of dry matter and nitrogen, and nitrogen effects on yield components, *Field Crops Research*, **54**, 201-220.
- Hsiao, T. C., and K. J. Bradford. 1983, Physiological consequences of cellular water deficits, Chapter 6A. *Limitations to Efficient Water Use in Crop Production*, edited by H. M. Taylor, W.R. Jordan, and T. R. Sinclair (eds.), American Society of Agronomy, Madison, WI. pp. 227-265.
- Jacquemoud, S., and Baret F, 1990, PROSPECT: a model of leaf optical properties spectra, *Remote Sensing of Environment*, **34**, 75-91.
- Keulen, H. van., 1986, Plant data, in *Modelling of Agricultural Production*, edited by H. van Keulen and J. Wolf, pp. 235-247.
- Knipling, E.B., 1970. Physical and physiological basis for the reflectance of visible and near infrared radiation from vegetation, *Remote Sensing of Environment*, **1**, 155-159.

- Penning de Vries, F.W.T., D.M. Jansen, H.F.M. ten Berge, and A. Bakema, 1989, *Simulation of Ecophysiological Processes in Several Annual Crops*, Purdoc: Wageningen, 332 pages.
- Peñuelas, J., I. Filella, C. Biel, L. Serrano, and R. Savé, 1993, The reflectance at the 950-970 region as an indicator of plant water status, *International Journal of Remote Sensing*, **14**(10), 1887-1905.
- Peñuelas, J., J. Piñol, R. Ogaya, and I. Filella, 1997, Estimation of plant water concentration by the reflectance water index WI (R900/R970), *International Journal of Remote Sensing*, **18**(13), 2869-2875.
- Press, W.H., S.A. Teulkosky, W.T. Vetterling, and B.P. Flannery, 1992, *Numerical Recipes in C*, Cambridge University Press, Cambridge, England, 994 pages.
- Roberts, D.A., K. Brown, R. Green, S. Ustin, and T. Hinckley, 1998, Investigating the relationship between liquid water and leaf area in clonal populus, Summaries of the Seventh JPL Earth Science Workshop held in Pasadena, CA, cd-rom
- Schulze, E.-D. 1982. Plant Life Forms and Their Carbon, Water and Nutrient Relations, in *Physiological Plant Ecology II*, edited by O.L. Lange, P.S. Nobel, C.B. Osmond and H. Ziegler, pp. 615-667.
- Secker, J., K. Staenz, R.P. Gauthier, and P. Budkewitsch, 2001; Vicarious calibration of airborne hyperspectral sensors in operational environments, *Remote Sensing of Environment*, **76**, 81-92.
- Staenz, K., and T. Szeredi, R.J. Brown, H. McNairn, and R. Van Acker, 1997, Hyperspectral information extraction techniques applied to agricultural data for detection of within field variations, in Proceedings of the International Symposium, Geomatics in the Era of RADARSAT (GER'97) held in Ottawa, Canada, cd-rom.
- Staenz, K., T. Szeredi, and J. Schwarz, 1998. ISDAS-A system for processing/analyzing hyperspectral data, *Canadian Journal of Remote Sensing*, **42**(2), 99-113.
- Strahan, I.B., E. Pattey, J. Boisvert, and J. Daoust, 2001, Impact of nitrogen and environmental conditions on corn as detected by hyperspectral reflectance, *Remote Sensing of Environment*, **80**, 213-224.
- Ustin, S.L. and D.A. Roberts, J. Pinzón, S. Jacquemoud, M. Gardner, G. Scheer, C.M. Castañeda and A. Palacios-Orueta, 1998, Estimating canopy water content of chaparral shrubs using optical methods, *Remote Sensing of Environment*, **65**, 280-291.
- White, H.P., J.R. Miller, and J.M. Chen, Four-scale linear model for anisotropic reflectance (FLAIR) for plant canopies. I: Model description and partial validation. *IEEE Transactions on Geoscience and Remote Sensing*, **39**(5), 1072-1083.
- White H. P. , Sun L. , Champagne C. , Staenz K. , Leblanc S. G., 2002, BRDF Normalization of Hyperspectral Image Data, IGARSS 2002, held at Toronto, Canada, June 24-28 , 2002.

Hyperspectral Monitoring of Physiological Parameters of Wheat during a Vegetation Period Using AVIS Data

N. Oppelt, W. Mauser

Department for Earth and Environmental Sciences

Ludwig-Maximilians-University Munich, Luisenstr. 37/III

80333 Munich, Germany

n.oppelt@iggf.geo.uni-muenchen.de, w.mauser@iggf.geo.uni-muenchen.de

ABSTRACT - *Information on the quantity and spatial distribution of canopy physiological and biochemical components is of importance for the study of nutrient cycles, productivity, vegetation stress and, more recently, in driving ecosystem models. In this context, remote sensing can play a unique and essential role because of its ability to acquire synoptic information at different time and space scales. This paper presents parts of a two-year field and laboratory study with the new airborne hyperspectral sensor, the Airborne Visible near Infrared Imaging Spectrometer (AVIS) over a test site in the Bavarian Alpine foothills, Germany (48° 6' N, 11° 17' E). The 80 band AVIS was developed at the Department for Earth and Environmental Sciences of the University of Munich and records the 550-980 nm spectral range. Using this system, 18 hyperspectral data sets were collected between April and September of 1999 and 2000. Weekly measurements of several plant parameters (height, biomass, chlorophyll content, nitrogen content) were carried out during these time periods on three (1999) and six (2000) fields of winter wheat, whereby two different cultivars were investigated in 2000.*

After system correction and calibration, the hyperspectral data was atmospherically corrected and reflection calibrated. Finally, the plant canopy and bare soil patches were separated by unmixing the spectra. The vegetation end members represent the biochemical and structural entities of the plants, which can be analysed for their chemical compounds. The statistical analysis was carried out using the Chlorophyll Absorption Integral (CAI). Both the chlorophyll and nitrogen content of the leaves showed good correlations with the CAI on field mean basis. These results as well as two-dimensional information on these parameters will be presented to provide information about the spatial heterogeneity within a field.

1 INTRODUCTION

In the context of a growing interest in remote sensing for vegetation applications (Verstraete et al., 1996; Brisco et al., 1998), this study investigated the possibilities of hyperspectral imaging for the extraction of information relevant to agriculture as well as vegetation or hydrological modelling.

Biochemical components of vegetation canopies such as chlorophyll and nitrogen are among essential parameters that control physiological processes (Hopkins, 1995). Therefore, in this experiment the chlorophyll and nitrogen content of wheat were focused.

Nitrogen (N) is often considered to be the most important limiting factor, after water deficiency, for biomass production in natural ecosystems. In arable land N fertilisation can provide a sufficient N supply for plants to achieve the potential yield. To ensure an optimum yield the application of N is often higher than the minimum required for the maximum crop growth.

At the present time, farmers must take into account the environmental consequences of their practices, especially the leaching of N into the ground water leading to its endangering.

Chlorophyll is the key parameter for photosynthesis; therefore the chlorophyll content of plant leaves is an indicator both for the photosynthetic capacity of a plant or a canopy and for eventually existing stress or disease (Blackburn, 1998).

Chlorophyll determines the reflectance of plant leaves by its characteristic absorption features in the visible domain (VIS). Nitrogen itself does not absorb or reflect in the wavelength domain recorded by AVIS, but former studies showed that nitrogen could be determined spectroscopically using visible bands (Thomas & Oerther, 1972; Tsay et al., 1982; Yoder & Daley, 1989). These results rely on the close relationship between nitrogen and chlorophyll (Gates et al., 1965; Gausman, 1977; Yoder & Pettigrew-Cosby, 1995).

Two problems occurred using that approach: Firstly, plants tend to "luxury" N consumption, which

is bound to storage proteins, amino acids or free nitrate in the plants (Hopkins, 1995; Lemaire, 1997). This leads to a reduced chlorophyll-nitrogen correlation at high N availability (Johnson & Billow, 1996). Secondly, most of the existing indices or ratios used for the derivation of leaf chlorophyll become saturated at high chlorophyll contents (Filela & Penuelas, 1994; Blackburn, 1998). The Chlorophyll absorption integral (*CAI*) seems to be not affected by saturation as much as indices or ratios (Oppelt, 2002). Therefore, this approach is focused.

The objective of this study was to (1) determine the correlation between chlorophyll and nitrogen in wheat leaves; (2) investigate whether the chlorophyll and nitrogen contents of winter wheat could be derived on a mean field basis using the *CAI* and (3) whether the spatial variability within a field could be determined from reflectance spectra.

2 INSTRUMENTATION AND METHODOLOGY

2.1 The Airborne Visible / near Infrared imaging Spectrometer AVIS

The imaging spectrometer AVIS was built to overcome the difficulties of the highly cost-intensive use of existing airborne imaging spectrometers such as AVIRIS, ROSIS or HYMAP, especially for multitemporal applications. AVIS was designed as a cost-effective tool for environmental monitoring and enables the deployment of a hyperspectral sensor for both scientific research and educational purposes (Oppelt, 2002).

AVIS is based on a direct sight spectrograph (SPECIM V9) coupled to a standard Black & White CCD camera (HAMAMATSU C5999). The signal received by the CCD is read out and sent via a frame grabber to a PC, where the data are stored on the hard disc together with additional data of a Geographical Positioning System (GPS) connected to the system. The GPS provides data including date, time, geographical position and altitude.

The system operates with 240 bands in the 550-1050nm wavelength region. The original spectral sampling interval is 2nm, but with a spectral resolution of 6nm the data are oversampled by the factor three. The last six bands of the resulting 80-band data set cannot be used because the lens limits the spectral range at 1000nm. The Signal to Noise Ratio (SNR) of the system decreases rapidly towards the near infrared (NIR), especially above 800nm. At wavelengths above 950nm the signal cannot be accurately separated from the noise, hence these wavelengths are not used for analysis. Lens settings were changed in 2000 leading to different SNRs for the years 1999 (45dB) and 2000 (47dB). The spatial resolution across track is 300 pixels with a spatial sampling rate of 390 pixels. The

field of view (FOV) of the system is 1.19rad. The resulting instantaneous field of view (IFOV) can be rated at 3.10mrad across track and 2.98mrad along track. The spatial resolution on ground depends on the altitude and, in this study, varies from about 2m flown at 600m above ground to 10m at 3000m.

The radiometric, spectral and geometric properties of AVIS are summarised in Fig. 1.

Parameter	Description
Spectral range	550-1000nm
Spectral resolution	6nm
Spectral sampling / resampling	2nm / 6nm
Radiometric sampling	10bit
Number of bands used	74
SNR	45dB (1999), 47dB (2000)
Spatial resolution	300 pixels per image line
Spatial sampling	390 pixels per image line
FOV	1.19rad
IFOV across track	3.1mrad
IFOV along track	2.98mrad

Fig. 1: AVIS specifications

AVIS can be installed in a chassis that fits onto a standard aircraft camera mount. During flight the camera is cooled by a Peltier element to provide a steady camera temperature and to avoid noise due to a high dark current. The resulting camera temperature is stored with the GPS data in a header for each image.

2.2 Test area

The test area is located about 25km southwest of Munich in the Bavarian Alpine foothills, Germany (48°6' N, 11° 17' S). This area is embedded between the Ammersee in the east and the Starnberger See in the west. The municipalities Gilching and Andechs limit the test area at the northern and southern edge respectively. The variation in ground elevation is less than 120m and the predominant soil types are cambisols.

Two weather stations of the Bavarian network of agro-meteorological stations enable access to local weather monitoring. Station No. 72 (Gut Hüll), which is located at the northeastern edge of the test site, and station No. 80 (Rothenfeld) at the southern edge provide meteorological data such as precipitation, soil and air temperature, total radiation and air humidity.

Within this test area, three and six fields of winter wheat were investigated in 1999 and 2000

respectively. In 1999 the variety “Bussard” was focused, while the varieties “Bussard” and “Capo” were monitored in 2000. Similar sowing dates ensured a parallel development of the plants during a growing period, which guaranteed a homogeneous data basis for analysis.

2.3 Ground data

Weekly measurements of several plant parameters (plant height, phenology, biomass, chlorophyll and nitrogen content of the leaves) were carried out from April to September 1999 and from April to August 2000 respectively (see also Fig. 3). For each test field, plant samples that showed an average developmental state were taken at three sampling points, which were located along a field diagonal. The measurement periods covered the development from the beginning of stem elongation till ripening. The phenological stages were determined according to the EUCARPIA scale (EC) (Zadoks et al., 1974).

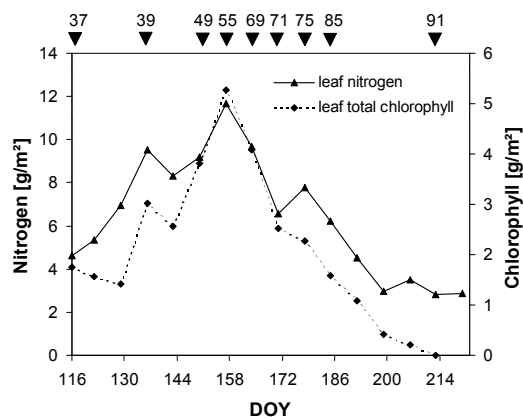


Fig. 2: Development of mean field chlorophyll and nitrogen content of wheat leaves (variety Bussard) measured in 2000 (DOY = Day Of Year; ▼ = EC stages)

The chlorophyll analysis was performed on sun leaves with a photometer using the method described by Porra et al. (1989). The nitrogen content was analysed in a CHN-O Rapid according to the CHN elemental analysis method. Chlorophyll and nitrogen content was derived as content per area [g/m²]. The development of both parameters is presented in Fig. 2 as an example for the variety Bussard.

2.4 Remotely sensed data

During the measurement periods, twelve and nine data sets were gathered in 1999 and 2000 respectively using a Dornier Do-27 aircraft. The campaign

calendar, including the dates for ground and AVIS measurements, is given Fig. 3.

During the two years of monitoring, bad conditions with cloudy and rainy weather during certain periods prevented AVIS measurements. Especially in June and August 1999 as well as in April and July 2000, the weather led to gaps between measurement sets.

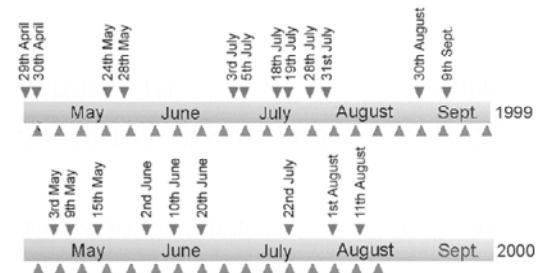


Fig. 3: Campaign calendar for 1999 and 2000

The AVIS data had to pass several preprocessing steps before they could be used for parameter derivation. First the data had to be system corrected, including dark current and flat field correction as well as wavelength calibration. Then the data were atmospherically corrected and reflection calibrated using PULREF (Bach, 1995) which is based on the radiative transfer model Lowtran-7 (Kneizys et al., 1988). Field spectrometer data of a concrete target (hangar of the German aerospace center, which is located in the test area) were used for the external calibration to reflectances. In addition, a field spectrometer (GER SIRIS) was used to validate the airborne measurements. Finally, the data were geometrically corrected using the GPS data. The preprocessing results are roughly geo-referenced image stripes providing reflectance spectra for each pixel.

2.5 The Chlorophyll Absorption Integral CAI

The CAI derives the chlorophyll content by measuring the area between a straight line connecting two points of the red edge and the curve of the red edge itself. Therefore, it is an approach on the basis of a spectral envelope measurement. The end points can be chosen interactively. For this study they were set at 600nm and 735nm. Thus, the CAI is defined as shown in equation 1 (Oppelt & Mauser, 2001):

$$CAI = \int_{R_{600}}^{R_{735}} R(EQ) \quad (1)$$

where

R_{735} = reflectance at 735nm [%],

R_{600} = reflectance at 600nm [%],

$R(EQ)$ = envelope quotient.

The envelope quotient is calculated according to equation 2:

$$R(EQ) = \frac{Rs_i}{Re_i} \quad (2)$$

where

Rs_i = reflectance of the vegetation spectrum at band i [%],

Re_i = reflectance of the envelope at band i [%].

The end points were chosen in such a way that the chlorophyll absorption feature could be monitored as well as the reflectance level in the NIR. Changes in the reflectance of the plants due to their developmental stage, chlorophyll status or stress, which influence the absorption depth and width as well as the position of the red edge, can be measured using this approach. The development of the *CAI*, which was derived from AVIS measurements in 1999, is shown in **Fig. 4** as an example for the same test field as presented in **Fig. 2**.

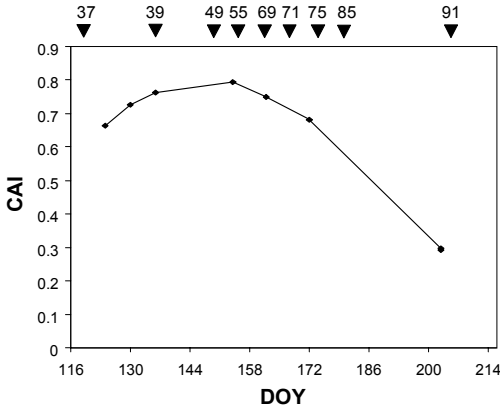


Fig. 4: Development of the *CAI* as derived from AVIS measurements of the test field presented in **Fig. 2**

Oppelt (2002) found in a comparative study between the *CAI* and several other ratios or indices, that the saturation of the ratios is presumably due to a flattening of the chlorophyll absorption around 680nm, which for wheat canopies occurs at chlorophyll contents above 1g/m². These observations are in accordance to Filela & Penuelas (1994), which assumed a saturation of the chlorophyll absorption effect for well-fertilized pepper and bean canopies. The other indices and ratios are directly affected by the flattening, while the *CAI* is not affected because a flattening of the chlorophyll absorption at 680nm leads to an increase of the chlorophyll reflection peak at 550nm. Saturation of the *CAI* occurs when the position of the red edge shifts towards shorter wavelengths.

3 RESULTS

A precondition for the analysis was that the chlorophyll and nitrogen data sets are normally distributed. To check for normal distribution the level of significance p as well as the Kolmogorov-Smirnov-test were computed. The level of significance was set to 5% ($p < 0.05$). The confidence interval of the coefficient of correlation was calculated as an additional test for significance using the Fisher transformation.

Linear correlation equations were used for analysis. The results could not be improved when polynomial or exponential regression equations were used. Sometimes higher coefficients of correlations could be derived, but the results became ambiguous for low and high parameter values.

3.1 Correlation between chlorophyll and nitrogen in wheat leaves

The sample size for this analysis included 127 measurements each of nitrogen and chlorophyll, which were carried out during the ground truth campaigns in 1999 and 2000.

Fig. 5 provides the correlation results of this analysis: When all varieties were analysed together, significantly high correlations could be observed for the chlorophyll a, b and total chlorophyll content and the nitrogen content of the leaves. The next step was the separation of the sample size into vegetative growth, which is mainly characterized by the accumulation of biomass, and generative growth, where fruits are formed and developed. The separation date was set to EC 40 (booting), where the inflorescence is formed. From this state, nitrogen is increasingly dislocated from leaves and stems into the growing fruits. For agricultural applications the vegetative growth is mainly of importance, because during that phase fertilisation can influence the yield. The separation shows that no significant correlation could be derived for the vegetative growth phase, while significantly high correlations could be observed for the generative growing period.

The results for the vegetative growth improve greatly, when the varieties were analysed individually. Then, high coefficients of correlation could be derived between chlorophyll a and nitrogen for the whole growing period as well as for the vegetative or generative growth. However, the degree of correlation is significantly higher when the phenological states (before/after EC 40) are investigated separately. The total chlorophyll content is also significantly highly correlated with the nitrogen content.

	All stages	Before EC 40	After EC 40
All varieties	N	N	N
Chl.a	0.91	0.67	0.94
Chl.b	0.88	n.s.	0.95
Ch.a+b	0.91	0.59	0.95
Bussard			
Chl.a	0.87	0.94	0.93
Chl.b	0.81	n.s.	0.95
Ch.a+b	0.87	0.95	0.94
Capo			
Chl.a	0.83	0.95	0.94
Chl.b	0.62	n.s.	0.95
Ch.a+b	0.79	0.89	0.94

Fig. 5: Coefficients of correlation r between chlorophyll and nitrogen content [g/m^2] of wheat leaves (correlations that describe at least 2/3 of the variance are highlighted; n.s. = not significant)

The correlations with nitrogen and chlorophyll b are very heterogeneous: when the varieties were analysed together, high coefficients of correlation could be found when the phenological states are not separated as well as during vegetative growth, while no significant relation could be derived for the generative phase. When analyzing the varieties individually, significantly high correlations could only be observed after booting. The low correlation between chlorophyll b and nitrogen for the Capo variety also reduced the relationship between total chlorophyll and nitrogen content.

These results show that a strong correlation between the chlorophyll and nitrogen content of wheat leaves, which is the basis for the derivation of the nitrogen content via the chlorophyll absorption features in the VIS, cannot be supposed implicitly. When the nitrogen content has to be derived as an input parameter for modeling approaches, where normally the varieties grown are not known but the species are, high correlations can be supposed for the whole vegetation period.

For precision farming applications, where the nitrogen status of the wheat plants is a very important variable for the amount of fertilisation, especially during the vegetative growth, the variety grown has to be considered. This is due to different chlorophyll levels of the varieties, which are congenital (Wollring, 1995). Furthermore, it seems to be more promising for the derivation of the nitrogen content when the chlorophyll a content is investigated.

These results are in good accordance with Peltonen et al. (1995) and Wollring (1995) who found a close relationship between the nitrogen content and chlorophyll meter readings during stem elongation (EC30—39) of winter wheat.

3.2 Derivation of chlorophyll and nitrogen content on a mean field basis using the *CAI*

The results of the derivation are presented in Fig. 6. The *CAI* was able to predict the chlorophyll and N contents for the whole vegetation period as well as for the generative growth phase, but failed during vegetative growth. When the parameters were derived for the varieties individually, the correlation patterns differ much for the two varieties.

	All stages	Before EC 40	After EC 40
All varieties			
N [g/m^2]	0.87	0.33	0.83
Chl. a [g/m^2]	0.92	0.63	0.90
Chl. b [g/m^2]	0.85	0.42	0.90
Chl. a+b [g/m^2]	0.91	0.61	0.91
Bussard			
N [g/m^2]	0.82	n.s.	0.68
Chl. a [g/m^2]	0.85	0.77	0.88
Chl. b [g/m^2]	0.77	0.65	0.87
Chl. a+b [g/m^2]	0.84	0.77	0.88
Capo			
N [g/m^2]	0.73	0.68	0.79
Chl. a [g/m^2]	0.73	0.88	0.82
Chl. b [g/m^2]	0.62	0.50	0.83
Chl. a+b [g/m^2]	0.72	0.82	0.83

Fig. 6: Coefficients of correlation r using linear equations for wheat (correlations that describe at least 2/3 of the variance are highlighted)

For the Bussard variety, significantly high correlations could be derived after booting as well as for the whole growing period. In contrast, high coefficients of correlation were observed for both the vegetative and generative growth, but low correlations were found for the whole vegetation period.

The nitrogen content could be deduced from the *CAI* when the varieties were analysed together and when the chlorophyll content could be derived as well. When the cultivars were investigated separately, the nitrogen content could only be derived for Bussard when all phenological stages were analysed together. The degree of correlation between the *CAI* and the nitrogen content of the Capo variety was reasonably high, but could not explain 2/3 of the variances.

The reason for this behaviour was found in the different chlorophyll and nitrogen levels of the cultivars: Fig. 7 and Fig. 8 point out the problem that the *CAI* becomes saturated at high chlorophyll and nitrogen contents respectively. The results could be improved when chlorophyll and nitrogen contents per area above 2.5g/m^2 and 8g/m^2 respectively were removed from the data samples.

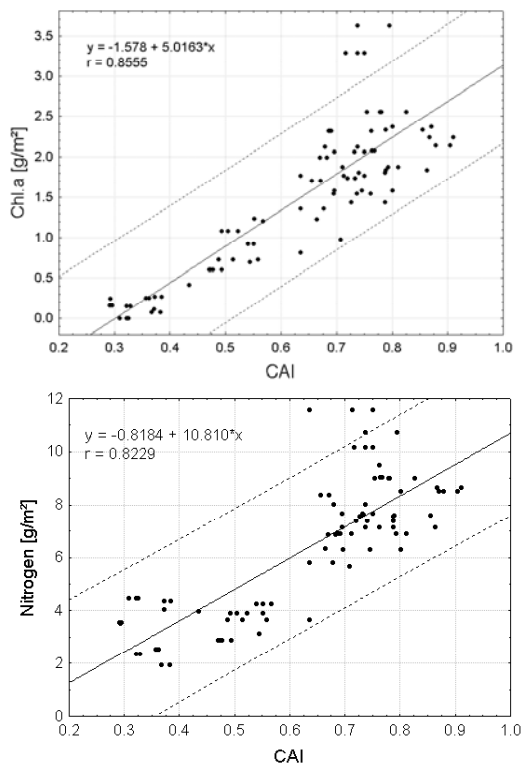


Fig. 7: Linear correlation between *CAI* and chlorophyll a content per area (top) and nitrogen content per area (bottom) for the variety Bussard

The Bussard variety is characterized by high chlorophyll values during the vegetative growing period, leading to poor results for the derivation of this parameter using the *CAI*. The Capo leaves do not contain as much chlorophyll as the Bussard's do, therefore the *CAI* was able to predict their chlorophyll content. In contrast, the nitrogen level of the Capo variety is much higher compared to Bussard, thus much of the nitrogen values are above the saturation limit of the *CAI*.

Hence, the following conclusion can be derived: The *CAI* is a useful approach for deriving the chlorophyll content of wheat if the saturation limit for these parameters is not exceeded. Within its scope, N can be derived using the *CAI* if firstly it is significantly highly correlated with the chlorophyll content, i.e. if a significantly highly correlation between the chlorophyll and nitrogen content exists, and secondly, if the nitrogen values do not exceed the saturation level. This interaction leads to the

correlation patterns of the whole sample size as well as of the two varieties investigated.

3.3 Spatial variability of chlorophyll and nitrogen within a field

As shown in the previous section, the *CAI* can be used to estimate the chlorophyll and nitrogen contents accurately for low and medium contents for the Bussard variety. This enables the identification of areas with different pigment contents within a field.

Fig. 8 shows the spatial variability of the chlorophyll a and nitrogen content in a Bussard field. The AVIS measurement was made on May 3rd 2000 (DOY 124) during stem elongation. The chlorophyll and nitrogen contents, which were on this date measured on the ground, lay between 1.01 and 1.50g/m² chlorophyll a as well as 4.08 and 6.48g/m² nitrogen respectively. Therefore, the saturation levels are not exceeded. The derivation of the parameter contents was conducted using the equations given in **Fig. 7**. This field was chosen because a yield map is available, which provides the spatial distribution of the yield, which is highly correlated with the nitrogen status of the plants amongst other parameters such as soil characteristics or precipitation (Osman et al., 1977; Schellberg, 1990).

Fig. 8 shows the inner field variability of the nitrogen content as measured on the ground. These nitrogen values are in good accordance with the calculated *CAI* nitrogen values, when the saturation level, which can be set to approx. 8g/m², is not exceeded. When comparing the yield map and the spatial nitrogen pattern measured with AVIS on May 3rd the accordance is quite good: the rough division of the northern part of the field, which shows high nitrogen contents, and the lower right edge, where a lower N level was calculated. The areas with high N levels show higher yield than the areas with low N content. In contrast, the northern outside margin of the *CAI* image, which shows very high nitrogen contents, cannot be verified in the yield map as well as the southwestern edge of the field, which shows a low N level. When comparing the *CAI*-N with the yield map, it has to be considered, that two more N fertilizations were given after May 3rd, i.e. on May 9th (DOY 109) and June 6th (DOY 155), which also influence the yield. Furthermore, the soil as well as the precipitation has a great impact on the yield, which was not taken into consideration here.

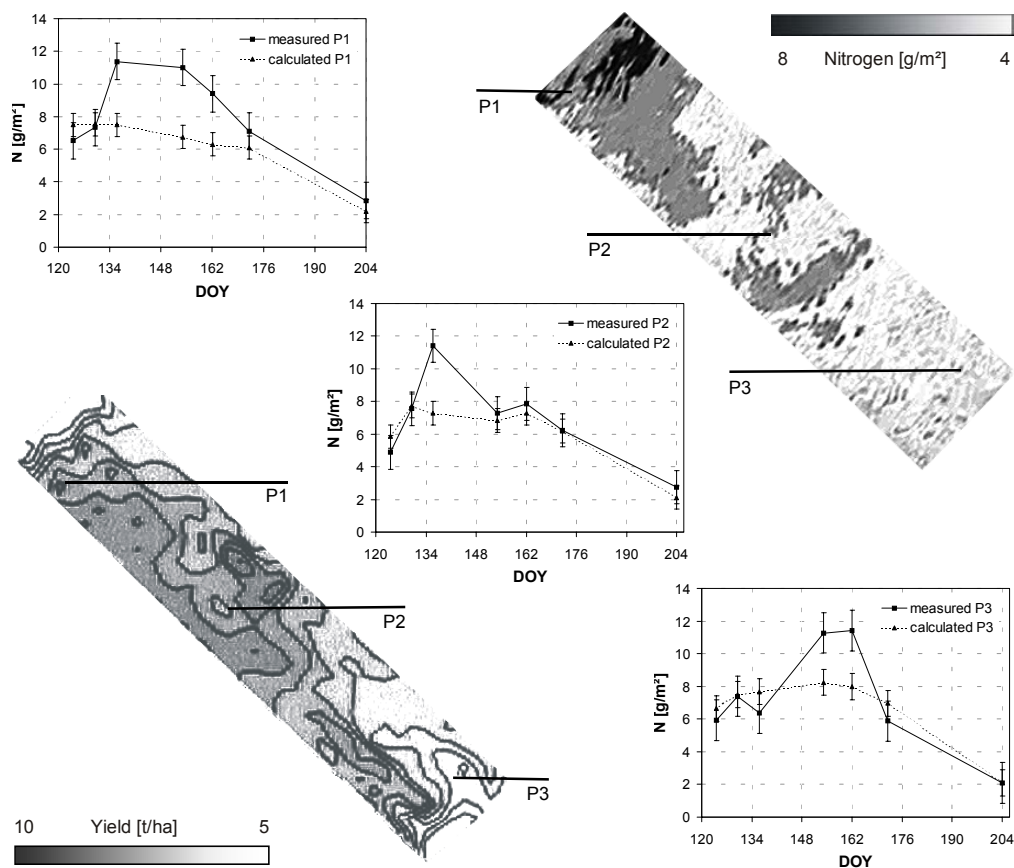


Fig. 8: Development of nitrogen per area derived from ground and AVIS measurements (graphs) in 2000, nitrogen derived from AVIS measurements made on May 3rd 2000 (DOY 124) and yield measurement of 2000 of a wheat field (variety Bussard) (equation used for the derivation of N is given in Fig. 7)

4 CONCLUSION

The *CAI* turned out to be a good predictor for the chlorophyll content of the wheat canopies investigated, but the different chlorophyll levels of the varieties has to be taken into account. Saturation occurs at chlorophyll contents above 2.5g/m². Therefore the derivation of chlorophyll using the *CAI* is more efficient for varieties that are characterized by low chlorophyll levels.

The nitrogen content could be derived if (1) a significantly high correlation exists between leaf chlorophyll content and leaf N, (2) the *CAI* shows significantly high correlations with the chlorophyll content (below the saturation level of 2.5g/m²) and (3) if the nitrogen content of the wheat canopy does not exceed the N saturation level (8g/m²).

For modeling approaches, where normally only the species is known, the *CAI* can be used for the deduction of the photosynthetic capacity of the canopy

throughout the vegetation period. For precision farming applications, where chlorophyll and N are needed especially during the vegetative growth, the congenital levels of chlorophyll and N level must be taken into consideration.

ACKNOWLEDGEMENTS

We wish to thank the German research association (DFG) for partly sponsoring the development of AVIS and the ground campaign within the group project "Coupling of Hydrological and Biological Processes on Landscape Level".

REFERENCES

Bach, H., 1995, Die Bestimmung hydrologischer und landwirtschaftlicher Oberflächenparameter aus hyperspektralen Fernerkundungsdaten. In

- Münchner Geographische Abhandlungen, Reihe B, Band 21.
- Blackburn, G.A., 1998, Quantifying chlorophylls and carotenoids at leaf and canopy scales: an evaluation of some hyperspectral approaches. In *Rem. Sens. Environm.*, Vol. 66, pp. 273-285.
- Brisco, B., Brown, R.J., Hirose, T., McNairn, H., Staenz, K., 1998, Precision agriculture and the role of remote sensing: a review. In *Can. J. of Rem. Sens.*, Vol. 24 (3), pp. 315-327.
- Datt, B., 1998, Remote sensing of chlorophyll a, chlorophyll b, chlorophyll a+b and total carotenoid content in eucalyptus leaves. In *Rem. Sens. Environm.*, Vol. 66, pp. 111-121.
- Filela, I., Penuelas, J., 1994, The red edge position and shape as indicators of plant chlorophyll content, biomass and hydric status. In *Int. J. Rem. Sens.*, Vol. 15 (7), pp.1459-1470.
- Gates, D.M., Keegan, H.J., Schleter, J.C., Weidner, V.R., 1965, Spectral properties of plants. In *Applied Optics*, Vol. 4 (1), pp.11-20.
- Gausman, H.W., 1977, Reflectance of leaf components. In *Rem. Sens. Environm.*, Vol. 6, pp. 1-9.
- Hopkins, W.G., 1995, Introduction to plant physiology. (John Wiley & Sons, New York).
- Kneizys, F.X., Anderson, G.P., Shettle, E.P., Gallery, W.O., Abreu, L.W., Selby, J.E., Chetwynd, J.H., Clough, S.A., 1988, LOWTRAN-7. Air Force Geophysics Laboratory, Environmental Research Papers No. 1010, Hanscom, Massachusetts.
- Oppelt, N. & Mauser, W., 2001, The chlorophyll content of maize (zea mays) derived with the airborne imaging spectrometer AVIS", Proceeding of the 8th Int. Symposium "Physical Measurements & Signatures in Remote Sensing", 8-12 January, Aussois, France, pp. 407-412.
- Oppelt, N., 2002, Monitoring plant chlorophyll and nitrogen status using the airborne imaging spectrometer AVIS. PhD thesis, Ludwig-Maximilians-University Munich.
- Osman, A.M., Goodman, P.J., Cooper, J.P., 1977, The effects of nitrogen, phosphorus and potassium on rates of growth and photosynthesis of wheat. In *Photosynthetica*, Vol. 11, pp. 66-75.
- Peltonen, J., Virtanen, A., Haggren, E., 1995, Using a chlorophyll meter to optimise nitrogen fertiliser application for intensely-managed small grain cereals. In *J. of Agron. & Crops*, Vol. 74, pp. 309-318.
- Porra, R.J., Thompson, W.A., Kriedman, P.E., 1989, Determination of accurate extinction coefficients and simultaneous equations for assaying chlorophyll a and b extract with four different solvents: verification of the concentration of chlorophyll standards by atomic absorption spectroscopy, In *Biochemical Biophysical Acta*, Vol. 975, pp. 384-394.
- Schellberg, J., 1990, Die spektrale Reflexion von Weizen – ein Beitrag zur Zustandsbeschreibung landwirtschaftlicher Kulturpflanzenbestände durch Fernerkundung. PhD thesis, Hohe Landwirtschaftliche Fakultät der Friedrich-Wilhelms-Universität zu Bonn.
- Thomas, J.R. & Oerther, G.F., 1972, Estimating nitrogen content of sweet pepper leaves by reflectance measurements. In *Agron. J.*, Vol.64, pp.11-13.
- Tsay, M.L., Gjierstad, G.H., Glover, R., 1982, Tree leaf reflectance: a promising technique to rapidly determine nitrogen and chlorophyll concentration. In *Can. J. For. Res.*, Vol. 12, pp. 788-792.
- Verstraete, M.M., Pinty, B., Myneni, R.B., 1996, Potential and limitations of information extraction on the terrestrial biosphere from satellite remote sensing. In *Rem. Sens. Environm.*, Vol. 58, pp.201-214.
- Wollring, J., 1995, Der Chlorophyllgehalt als Maßstab zur Ermittlung der 2. und 3. N-Gabe bei Winterweizen. Institut für Pflanzenernährung und Umweltforschung Hannighof, Hydro Agri Deutschland, unpublished.
- Yoder, B.J. & Daley, L.S., 1989, Development of a visible spectroscopic method for determining chlorophyll a and b in vivo in leaf samples. In *Spectroscopy*, Vol. 5, pp. 44-50.
- Yoder, B.J. & Pettigrew-Cosby, R.E., 1995, Predicting nitrogen and chlorophyll content and concentrations from reflectance spectra (400-2500nm) at leaf and canopy scales. In *Rem. Sens. Environm.*, Vol. 53, pp.199-211.
- Zadoks, J.C., Chang, T.T., Konzak, C.F., 1974, A decimal code for the growth stages of cereals, In *Weed Research*, Vol. 14, pp. 415-421.

Upper Paraguay River Water Level Prediction Using Precipitation and NDVI

William T. Liu¹, Fábio M. Ayres¹, Ayr T. Salles¹ and Carlos Padovani²
Universidade Católica Dom Bosco, Campo Grande, 79117-900-MS, Brazil;

²*EMBRAPA/Pantanal, Corumbá, 79320-900-MS, Brazil.*

will@ucdb.br, guara@cpap.embrapa.br

ABSTRACT *In this study, a combined use of Precipitation (PCP) and monthly maximum value composite Normalized Difference Vegetation Index (NDVI) data is proposed to predict monthly River Water Level (RWL) at Ladário station, which monitors the Upper Paraguay River Basin (UPRB) flood conditions. Averaged monthly PCP data were obtained from six rainfall stations and averaged NDVI data were obtained from a rectangular area covering these rainfall stations. The data of June 1981 to February 1993 were used for model construction while the data of November 1994 to September, 2000 were used for model validation. The results showed that the model had R^2 of 0.757 and RMSE of 0.424. An averaged absolute error of 16.85% was obtained from the model validation, using RWL data period of April 1995 to September 2000. It has demonstrated that the potential of using PCP and NDVI to predict river water level.*

1. INTRODUCTION

The UPRB has a catchment's area of 484,970 km², which is located at the central part of South America, covering parts of western Brazil (372,501 km²), Eastern Bolivia (80,843 km²) and northeastern Paraguay (31,626 km²). Figure 1 shows the basin boundary. The annual rainfall ranges from 1100 mm to 1900 mm with a distinct wet dry season. Most part of the basin is very flat which forms the world largest continental wetland called Pantanal. The Pantanal wetland covers an area of 138,000 km². The Pantanal holds one of the most diversified human patrimony, housing innumerable floras and faunas. The region suffers frequent floods during rainy season and frequent drought during dry season. The combination of improper land management on sandy soils in the upper basin causes serious erosion and acceleration of sediment load in the flood plain for the past thirty years. Besides the gradual loss of farmlands, unpredicted floods often result serious cattle loss. On the other hand, due to recent increase of river transportation, riverbanks erosion in low water level period becomes more seriously each year. Although some work has been done to predict floods occurrence using probability analysis and real time RWL data (Galdino and Clarke, 1997). It is improper to predict RWL using PCP data only since the RWL reflects the result of fast surface runoff water and slow subsurface water flow of a whole basin. A summer intensive rainfall can easily reach 300 mm in wet season. During dry season, no rainfall can last for as long as 2 to 3 months. But minimum RWL never reaches zero in a large catchment's basin area. Recent advances in satellite data application have shown that NDVI infers

quite well vegetation greenness conditions which indicates ample soil moisture status but shows up with a certain time lag after a certain rainfall event (Liu et al., 1994; Liu and Kogan, 1996; Liu and Juarez, 2001). Some green surfaces inferred by NDVI always exist as long as the river does not dry out in a certain river basin. It means that a NDVI annual cycle is similar to a RWL annual cycle although NDVI does saturate while the surface greenness reaches its maximum. PCP may relate well with a high RWL in wet season while as NDVI may relate well with a low RWL in dry season. Therefore the purpose of this study is to develop a river water level forecast model using both rainfall and NDVI for flood management and for erosion as well as river transportation traffic control.

2. METHODS

2.1 Location and Data Used

RWL data recorded at the Ladário hydrological station (Latitude: 19° 05'S; Longitude: 57° 30'W) for the period of January of 1981 to December of 2000 provided by the Brazilian Marine Corp at Corumbá, Mato Grosso do Sul State were used in this study. For the same period, monthly PCP data of six rainfall stations, including Arenópolis (14.51°S, 56.1°W), Quebo (14.65°S, 56.11°W), Porto Estrela (15.31°S, 56.23°W), Ponte Cabaçal (15.47°S, 57.9°W), N. S. Livramento (15.77°S, 56.35°W) and Barão de Melgaco (16.19°S, 55.95°W), provided by the Brazilian National Electrical Energy Agency (Agencia Nacional de Energia Elétrica, ANEEL) were used. The locations of RWL and PCP measurement stations were

shown in the Figure 1. Averaged values of six station rainfall data were used to represent the rainfall amount received in the upper part of the UPRB. RWL represents the river water level of the drainage area indicated by the area above the dash line (Fig. 1).

NOAA AVHRR GAC NDVI monthly maximum value composite data with a resolution of 8 km by 8 km for the period of August 1981 to September 2000 (except 1994), provided by the GSFC/NASA were used in this study. A rectangular area located at 14.2°-16.3° and 55.5° - 58.0°W were taken as a window to obtain area averaged monthly NDVI data.

2.2 Model Construction and Validation

Correlations of RWL to PCP and RWL to NDVI were carried out to investigate the time lag of RWL in responding to PCP and NDVI in order to select candidate independent variables for model construction. A stepwise multiple linear regression technique was applied to construct the model. The data of June 1981 to February 1993 were used for model construction while the data of November 1994 to September, 2000 were used for model validation.

3. RESULTS AND DISCUSSIONS

3.1 RWL Response to PCP and NDVI

Inter annual and seasonal hydrological variability during the studied period were analyzed by comparing the time series plots of RWL, PCP and NDVI for 4 extreme RWL cases, including highest RWL year in rainy season; lowest RWL year in dry season, highest RWL in dry season and lowest RWL in rainy season. Figures 2 to 5 presented the time series plots of RWL, PCP and NDVI for these four cases. The results showed that in wet season the highest RWL with 6.57 m occurred in April of 1988 and the lowest RWL m occurred in July of 1986 with 4.2 m. Also showed that in dry season the highest RWL with 3.30 m occurred in December of 1992 and the lowest RWL with 1.19 m occurred in November of 1999.

Minimum monthly RWL (mostly in November and December) occurred after the beginning of wet season, while the maximum monthly RWL (mostly in July) occurred in the peak of dry season. In general, both minimum and maximum RWL occurred 5 to 6 months after PCP and 2 to 4 months after NDVI reached their minimum and maximum. But it is interesting to note that in high rainfall years, the highest RWL reached its maximum in April which was two to three months earlier than in normal years (June-July). It means that in high rainfall years, a high intensity rainfall in wet season cause high surface runoff water, which result the anticipation of RWL reaching its maximum. On the other hand, in all the years studied, the lowest

RWL occurred between November and December with little variation.

It is also important to notice that NDVI reached a value of 0.60 mostly in November and remained above this value for a period as long as 8 to 9 months (November to June or July). It means that vegetation surface reaches its maximum greenness right after the beginning of the wet season. Further increase of rainfall amount in the following months does not increase NDVI. NDVI maintains its maximum 2 to 3 months after the end of the wet season. It indicates that in a flat basin, higher soil moisture generally maintains for a longer period of time. One has to notice that a free water surface absorbs both visible and near infrared bands such as NOAA band 1 and 2 that result a close zero or negative NDVI value. Therefore, in the wet season, NDVI saturates at a low value of around or lower than 0.6, since a larger flood area will reduce the basin averaged NDVI value. This fact limits the application of NDVI to predict high RWL in wet season. On the other hand, the peak PCP period lasts only two to three months, which occurs mostly between December to March. Therefore, in wet season, PCP infers better high RWL. Nevertheless, rainfall amount in dry season (mostly occurred in June to August) is close to zero, which fails to infer low RWL. Therefore both PCP and NDVI were considered for model construction since we could not find good model either by using NDVI or PCP along.

3.2 RWL Model

Table 1 shows the correlations of RWL to PCP and RWL to NDVI with a time lag of RWL from zero to the month with a highest correlation coefficient (r). The results showed that a highest r-value of 0.75 were obtained for RWL in responding to PCP after 5 months and a highest r-value of 0.63 was obtained for RWL in responding to NDVI after 3 months.

By examining the correlation coefficients presented in the Table 1, six parameters, including PCP1, PCP2, SPCP12, NDVI3, NDVI4 and SNDVI34 were used as independent variables and RWL6 as dependent variable for model construction. Number 1, 2, 3, 4 and 6 represent month 1, 2, 3, 4 and 6 respectively. For example, taking PCP1 as PCP of June, RWL6 is RWL of November. SPCP12 represents sum of PCP1 and PCP2 while SNDVI34 presents sum of NDVI3 and NDVI4. By applying the Stepwise Multiple Linear Regression technique, the model was obtained and presented by the following equation:

$$RWL6 = 1.40172 + 1.9374NDVI3 - 0.32325NDVI4 + 0.0009527PCP1 + 0.00491SPCP12$$

The model had a R^2 value of 0.757 with a RMSE of 0.424. The averaged absolute error of 16.80% was period of November 1981 to February 1993. It was observed that the model simulated mostly quite well the occurrences and magnitudes of maximum and minimum RWL. But failed to simulate the occurrence of peak RWL in 3 years including: 1982, 1985 and 1988. The peak RWL were all occurred in April instead of the simulated in July. From looking into the RWL data, it was observed that all these 3 years had maximum RWL over 6 meters. It may indicate that the model still fails to simulate a high rainfall year in wet season. A larger volume of surface runoff water caused by intensive summer rainstorm may contribute significantly to anticipate the RWL to reach its peak value 1 to 3 months before normal rainfall years. The model also failed to simulate peak RWL in years of 1984, 1989 and 1993. Instead of rising to a peak RWL occurred in July, the simulated RWL had a dip and then rose again in the following month. A lower NDVI caused by a larger flood area may contribute to this error. Therefore further study on the rainfall behaviors should be made in order to detect the anticipation of peak RWL in high rainfall years and correct the abnormal dip of RWL caused by low NDVI in the peak of rainy season.

obtained for the simulated RWL. Figure 6 showed the comparison of observed and simulated RWL for the

3.3 Model Validation

Figure 7 shows the results of model validation by comparing observed and predicted RWL for the period of April 1995 to September 2000. The averaged absolute error was 16.85%, which was quite stable since this value was very close to the simulated RWL (16.80%). The predicted RWL showed that there were 37 cases out of 66 months had absolute error within 10% and 10 cases had absolute error over 30%. In general, the model predicted quite well the RWL at Ladário Station. But in the a particular low RWL occurred in 1999, the model overestimated RWL with errors over 30%. From checking the rainfall of this year, it was observed that there were almost no rainfall from May to August and lower rainfall amount in September (40 mm) and October (80 mm). It demonstrated that the model failed to predict extreme events those were not included in the model construction. This in fact is a weak point of statistical regression method. Considering the complexity of water inter flow between sub basins in this very flat river basin, the RWL prediction model presented here works reasonable well. This simple approach may provide us a useful tool to predict RWL and hence to prevent floods damage in high RWL period as well as to control river transportation traffic in order to prevent riverbank erosion during low RWL period.

Table 1 – Correlation Coefficients (r) of PCP x RWL; NDVI x RWL and PCP x NDVI with 1 month time lag for each step of correlation.

Time Lag (month)	Correlation Coefficient (r)		
	PCP x RWL	NDVI x RWL	PCP x NDVI
0	-0.5604	0.0846	0.2948
1	-0.2264	0.3849	0.5570
2	0.1661	0.6005	0.6484
3	0.5312	0.6507	0.5762
4	0.7545	0.5377	-
5	0.6458	-	-

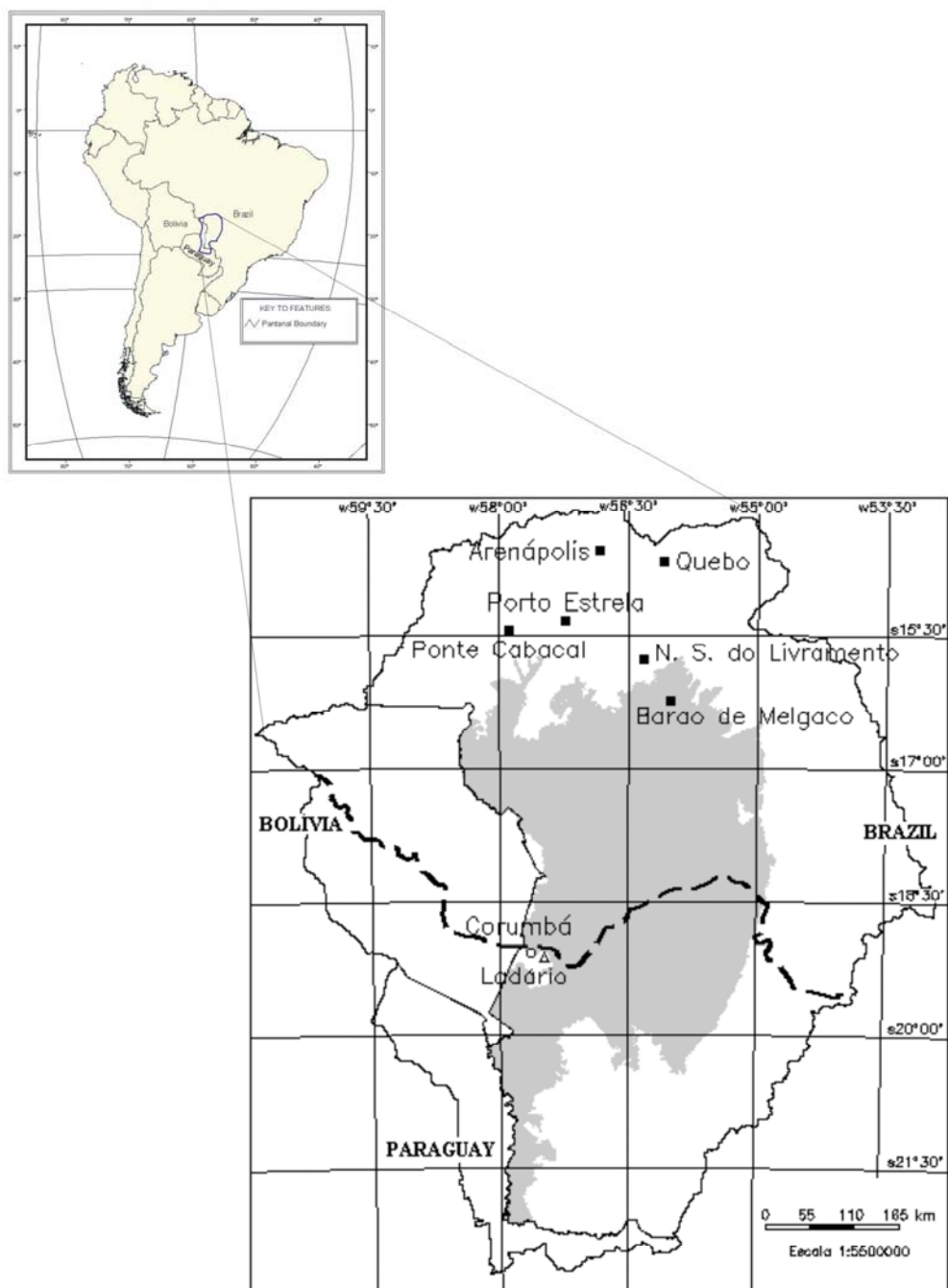
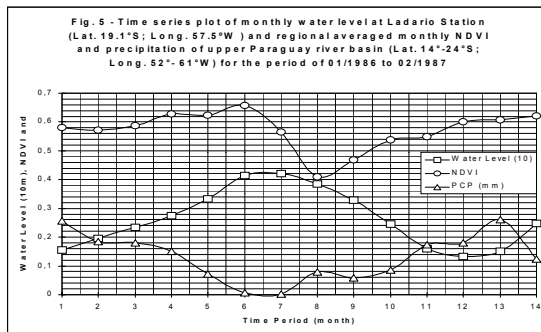
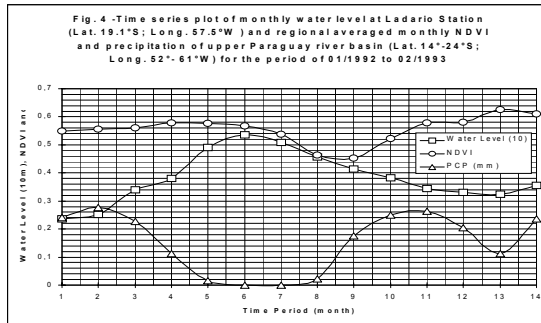
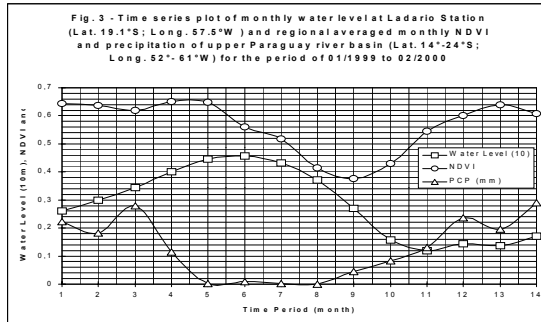
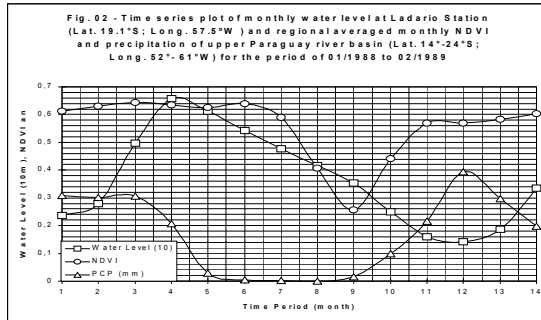
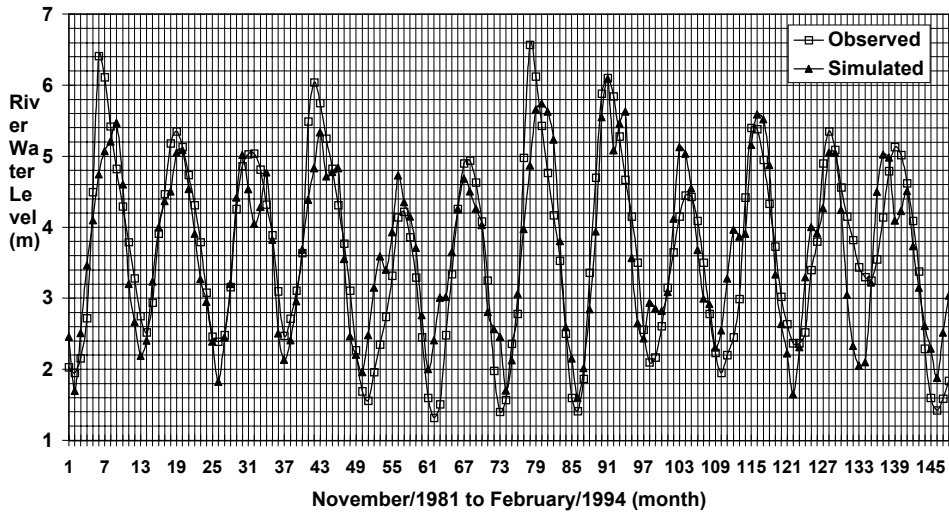


Figure 1. Locations of the upper Paraguay basin river water level (RWL) at the Ladário hydrological station (Latitude: $19^{\circ} 05' S$; Longitude: $57^{\circ} 30' W$) and six rainfall stations, including Arenópolis ($14.51^{\circ} S$, $56.1^{\circ} W$), Quebo ($14.65^{\circ} S$, $56.11^{\circ} W$), Porto Estrela ($15.31^{\circ} S$, $56.23^{\circ} W$), Ponte Cabacal ($15.47^{\circ} S$, $57.9^{\circ} W$), N. S. Livramento ($15.77^{\circ} S$, $56.35^{\circ} W$) and Barão de Melgaco ($16.19^{\circ} S$, $55.95^{\circ} W$). The RWL data collects the drainage water of the upper sub basin area separated by the dash line.



Figures 2, 3, 4 & 5. the time series plots of RWL, PCP and NDVI for 4 extreme RWL cases, including highest RWL year in rainy season; lowest RWL year in dry season, highest RWL in dry season and lowest RWL in rainy season.

Fig. 6 - Comparison of observed and simulated river water level for the period of November, 1981 to February, 1994 at Ladário Station (19.1°S;57.5W), MS, Brazil



4. CONCLUSION AND SUGGESTIONS

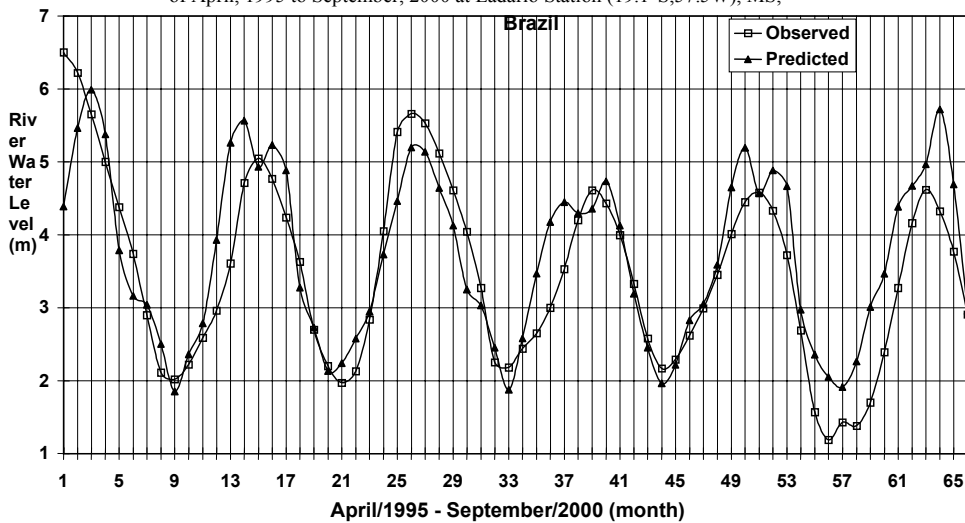
This study has demonstrated that the potential use of PCP and NDVI to predict river water level in a rather flat river basin such as the Upper Paraguay River Basin. It is suggested that several sub basins models should be constructed to evaluate the consistency of the method as well as to improve the prediction accuracy. Also the incorporation of NDVI data into hydrological simulation model may provide better spatial quantification of soil moisture availability that in turns may improve basin water balance estimation. Further research work should be carried out to improve basin Digital Elevation Model (DEM), to find out the compound effect of NDVI and PCP on RWL and to investigate the advance of floods between sub basins through hydrological simulation approach.

ACKNOWLEDGMENTS

This paper is part to research under taken in association with the Ducks Unlimited Pantanal-GIS Pilot Project financed by the US Forest Service International Program. The authors wish to thank the Distributed Active Archive Center (Code 902.2) at the Goddard Space Flight Center, Greenbelt, MD, 20771,

for producing the data in their present form and distributing them. The original data products were produced under the NOAA/NASA Pathfinder program, by a processing team headed by Ms. Mary James of the Goddard Global Change Data Center; and the science algorithms were established by the AVHRR Land Science Working Group, chaired by Dr. John Townshend of the University of Maryland. Goddard's contributions to these activities were sponsored by NASA's Mission to Planet Earth program.

Fig. 7 Comparison of observed and predicted river water level for the period of April, 1995 to September, 2000 at Ladário Station (19.1°S;57.5W), MS,



5. REFERENCES

- Liu W.T.H., O. Massambani and C. Nobre, 1994. Satellite Vegetation response to drought in Brazil. *Int. Journal Climatology*, 14:343-354.
- Liu W.T.H. and F. Kogan, 1996. Monitoring regional drought using vegetation condition index. *Int. Journal of Remote Sensing*, 17:2761-2782
- Liu W.T. and R. N. Juarez, 2001. ENSO drought Prediction of Northeast Brazil Using NDVI. *International Journal of Remote Sensing*, V22 (17): 3483-3501
- R. N. Juárez and W.T. Liu, 2001. "NDVI FFT analysis of spatial climatic variation in northeast Brazil". *International Journal of Climatology*, V21 (14): 1803-1820.
- Sergio Galdino and Robin T. Clarke, 1997. Probabilidade de ocorrência de cheia no Rio Paraguai, em Ladário. MS – Pantanal. 1997. *Circulação Técnica* N° 23, EMBRAPA-CPAP, Corumbá, MS. 58p.

A new approach to characterize aerosols from their optical depth spectral values. Simulated case study

José L. Gómez-Amo, Maria P. Utrillas, Víctor Estellés, Roberto Pedrós and José A. Martínez-Lozano

Grupo de Radiación Solar, Universitat de Valencia, Valencia, Spain
jmartine@uv.es

ABSTRACT In this work, we try to develop a new method to determine the spectral contribution to the aerosol optical thickness due to each type of aerosols. In order to separate these contributions it is necessary to have the spectral aerosol optical thickness and aerosol size distribution. We use this distribution function to identify the different types of aerosols so it is possible to reconstruct the aerosol optical thickness taking into account the contribution of each type of aerosols. The validation of this method will be carried out by verifying that the spectral aerosol optical thickness corresponds to the addition of the optical thickness obtained for each type of aerosols which are identified.

1 INTRODUCTION

For the new generation of satellites (King et al., 1999; Diner et al., 1999) aerosol models which link aerosol properties to readily satellite-measured variable are desirable (Remer and Kaufman, 1998). Generally, the algorithms employed for such purpose use a model which can simulate the characteristics of the aerosols. Nevertheless it is difficult to identify what kind of aerosols is present at a certain moment in a particular place, since usually there are different kinds of aerosols at the same time. Therefore is necessary an accurate information about the radiative and optic properties of the atmospheric aerosols along with their space-time distribution (Schwartz and Andreae, 1996; Penner et al., 2001). In addition it is required the development of algorithms that relate such properties to parameters easily measured from satellite (JGR, 1997).

Aerosol optical depth (from now on AOD) is the single most comprehensive variable to remotely assess the aerosol burden in the atmosphere from ground based instruments, which are the simplest, most accurate and easy to maintain monitoring system (Holben et al., 2001). The AOD is used to characterize aerosols and, e.g., to make atmospheric corrections to satellite remotely sensed data. In this sense, currently the AERONET network (Holben et al., 1998) fills the gap left after previous measurement networks whose results had been widely questioned (Dutton et al., 1994; WMO, 1994) were ended.

Therefore it seems reasonable that the measurements of AOD are the starting point to obtain the characteristics of the atmospheric aerosols, usually

a mixture of different types above the measurement site. The usual procedure consist in parameterisation of the experimental values of AOD that not necessarily describe the nature of the aerosols. The most widely used procedure is based on the Angstrom formulation (Angstrom 1929). Such methodology relates the AOD with the wavelength using only two parameters, known as the turbidity coefficient (β) and the wavelength exponent (α).

$$\tau_a = \beta \lambda^{-\alpha} \quad (1)$$

Several attempts to apply the a coefficient in Remote Sensing can be found in the literature of the last twenty years. Lately there is a increasing interest in the question due to the work of O'Neill et al. (2001, 2002). They have developed a new approach, using the Shifrin formulation (1995), based on geometric interpretation of the AOD versus the wavelength.

In the present work we propose an alternative approach, based on the Mie theory using inversion methods and the aerosol microphysical properties to determine the spectral contribution to the aerosol optical thickness due to each type of aerosols. The validation of this method will be carried out by verifying that the spectral aerosol optical thickness corresponds to the addition of the optical thickness obtained for each type of aerosols which are identified.

This approach is currently under development and a further validation using experimental values of AOD is required. Therefore this work describes the

first stage of the approach and some preliminary results corresponding to simulations with different models of aerosols are shown.

2 METHODOLOGY

We aim to establish a method to know the different types and proportion of aerosols present simultaneously in a atmospheric column above a certain place. The inputs will be the AOD experimental values for several wavelengths. In principle we will limit the analysis to the visible spectrum (400-670 nm) and later will be applied to UV (until 300 nm) and NIR (until 1100 nm), which constitutes the spectral range of the spectroradiometers available in our group: Licor 1800 and Optronics 754 (Martínez-Lozano et al., 2002).

In a first stage the experimental measurements will correspond to the direct solar irradiance extinction. For a greater accuracy, particularly the inversion algorithms, we will use measurements of sky radiance in the principal and almucantar plane carried out with a CIMEL (Estellés et al. 2002) sunphotometer and the Optronics spectroradiometer mounting a telescope.

The final objective of this work is to establish a relationship between the experimental optical thickness and those corresponding to the different types of present aerosols. As a first step we will find out whether the current inversion methods allow us to reconstruct for every wavelength, λ_j , the relationship

$$\tau(\lambda_j) = \sum \tau_i(\lambda_j) \quad (2)$$

with τ_i the AOD of each type of aerosols that contributes to the total AOD (τ).

If we assume that both the set of values of $\tau(\lambda_j)$ and each particular set $\tau_i(\lambda_j)$ are continual functions, not necessarily of the Angstrom type, the final objective of this paper can be expressed as to establish functional relationships between the parameters defining $\tau(\lambda_j)$ y $\tau_i(\lambda_j)$. The starting point is that: a) the expression (14) is satisfied for every wavelength; b) according to the spectral characteristics of our instruments, at least 300 relationship in the form of (14) are available.

In this work we present the results corresponding to the first stage of the work, which is the inspection of the feasibility of the reconstruction of (14) for experimental values for AOD. We have performed simulation for combination for aerosols with known characteristics, previously to the application to measured data. Such combinations have been obtained from the software package OPAC (Optical Properties of Aerosol and Clouds) (Hess et al., 1998).

The main difference between our methodology and the geometrical approximation of O'Neill et al. (2001), apart from the mathematical algorithms used, is that we aim to determine the types of aerosols whereas O'Neill et al. focus on determining the aerosols in the fine and coarse mode of the bimodal distribution – not taking into account their origin. The method introduced here has an additional difficulty as it has a physical basis instead of a geometric one. It assumes that a concrete type of aerosol can contribute (with different relative weight) to both modes of the bimodal distribution.

We have to point out that this a preliminary work, still far away from establishing univocally the functional relationships for the optical depths if they exist. Therefore the authors would appreciate any suggestion on this question.

Regarding to the objectives of the present work, we have applied the following methodology:

1) Determination of the aerosol size distribution

From the spectral values of the total AOD, $\tau(\lambda_j)$, the size distribution, $n_c(r)$, for the aerosols in an atmospheric column is determined. As the amount of measurements of solar irradiance extinction is much higher than the measurements of the sky radiance we have applied the King inversion algorithm (King et al., 1978; King, 1982) to obtain the size distribution. For further studies it is scheduled to use sky radiance measurements which require more complex algorithms such as those developed by Nakajima et al. et al. (1983, 1996) and Dubovik y King (2000).

2) Identification of the aerosol components

The identification of the different aerosol components in the atmosphere is based on the size distribution. The starting point are the parameters that fit the sum of lognormal functions, in the form of (9), that constitute the size distribution. These fitting parameters are (r_{Mi} , N_i y σ_i) and we compare them to the aerosol databases (D'Almeida et al., 1991; Hess et al., 1998) to identify component. This method considers the modal radius but in further studies could consider some type of combination between the tabulated components to reconstruct the modes of the size distribution more accurately. In this combination the effective radius might be more useful. Once the components that reconstruct the size distribution are obtained, the refractive index for each mode could be obtained and subsequently the extinction efficiency factor for each one.

3) Calculation of the optical thickness

The optical thickness of each type of aerosols identified in the previous section is obtained by direct integration of the Mie expression:

$$k_{\text{at}}(i) = \int_{r_s}^{r_b} \pi r^2 Q_{\text{ci}}(n, r, \lambda) n_{\text{ci}}(r) dr \quad (3)$$

This integration can be done in different ways: a) by using the whole size distribution function, so that the total optical thickness, $\tau(\lambda_j)$, is obtained; b) by integration each mode separately, which allows us to determine the contribution of each mode to the total optical depth $\Sigma \tau_i(\lambda_j)$. In principle both optical thickness does not necessarily coincide as the integration procedure is different.

4) Validation of the method

This method is validated by comparing the optical depth obtained with experimental measurements of extinction with the sum of each single component. In addition we can perform a simultaneous validation of the inversion method used for the size.

3. RESULTS

As a first step to validate the method, in the previous section we have used simulations in order to control all the variables of the system. These variables include the physical parameters that characterise the aerosols (size, refractive index, etc.) and the total optical thickness result of the combination of several components of aerosols. We will refer to the combination as type of aerosols (maritime, continental, desert, arctic, etc.).

We have used these simulation to determine the total AOD using the physical parameters of the aerosols as an input (direct method) as well as to reconstruct the characteristics of the different types of aerosols using the total AOD (inverse method).

We present here the results obtained for two types of aerosols in OPAC database (Hess et al., 1998): continental polluted and desert aerosols. The size distribution has been obtained using r_{Mi} , N_i y σ_i , where i refers to each component of these two aerosol types. In OPAC database it also appears the values of the maximum (r_{max}) and minimum (r_{min}) radius which avoids hypothesis on the integration limits.

3.1 Direct method: determination of the spectral AOD

a) Continental polluted aerosol

This type of aerosols is characteristic of urban areas highly polluted by human activity. According to OPAC software (Hess et al., 1998) the aerosols are an external mixture of three components: a) water soluble (hereafter waso50 as the relative humidity selected for the simulations is 50%); b) insoluble aerosol (from now on inso); c) soot. The contribution and the physical characteristics of each component to the mixture appear in the table I.

Table I. Continental polluted aerosol. Physical characteristics

	N_i (cm^{-3})	r_{Mi} (μm)	σ_i	r_{min} (μm)	r_{max} (μm)	Number mixing ratios (n_i)
Waso	15700	0.0262	2.24	0.006	25	0.685
Inso	0.6	0.471	2.51	0.005	20	0.298
Soot	34300	0.0118	2.00	0.005	20	0.044
Total	50000					

In order to determine the size distribution in an atmospheric column we have to define previously the aerosol vertical profile. In our case we have introduced the simplifivative hypothesis that the aerosols are homogeneously distributed in the boundary layer at two kilometres above the ground level. Applying this hypothesis to the values in table I and assuming lognormal monomodal size distributions for each component we obtain figure 1. In this figure, we also have included the curve result of the addition of the three components. It can be seen that the resulting size distribution is bimodal and that the fine mode is more important than the coarse one.

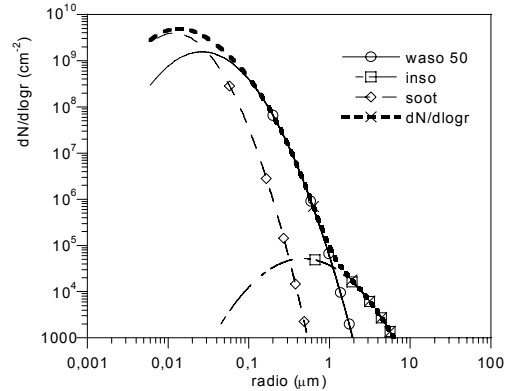


Figure.1. Continental polluted aerosol size distribution

From the curves in figure I, we have obtained the AOD values by integrating the equation (15). This integration has been done in the two different ways mentioned in the previous section so we obtain $\tau(\lambda_j)$ y

$\Sigma\tau_i(\lambda_j)$. We have used the wavelengths 350, 400, 500, 550, 610 and 670 nm.

The Mie extinction efficiency factor, $Q_e(n,r,\lambda)$, depends on the radius, the wavelength and the refractive index. If we calculate the optical thickness for a single component, its refractive index is known for the spectral range that we consider. This is not the case when the integration is performed for the total size distribution. In our case we have derived the refractive index from the combination of the refractive indexes of each component weighted with its number mixing ratio.

$$n = \sum_i^N n_i v_i \quad , \quad m = \sum_i^N m_i v_i \quad (4)$$

The table II and the figure 2 show that the water soluble component is the main contribution to AOD, with an average value of 80%, although it is

wavelength dependent. The contributions of the other two components are about 16% for soot and 4% for insoluble.

b) Desert aerosol

This type of aerosols is used to characterise aerosols in the deserts all over the world, without taking into account the local properties. The aerosols are mineral particles of different sizes distributed in three modes, nucleation (minm), accumulation(miam) and coarse (micm). In small proportion there are water soluble aerosols (waso). The physical properties of each component and its contribution to the mixture are shown in table III (Hess et al., 1998).

Table II. Continental polluted AOD

λ (λ)	τ	τ_{waso}	τ_{ivso}	τ_{soot}	$\Sigma\tau_i$	τ_{OPAC}	MAD% ($\Sigma\tau_i$)	MAD% (τ)
350	0.5705	0.3531	0.0098	0.0843	0.4472	0.4115	8.0	38.6
400	0.4965	0.3048	0.0099	0.0599	0.3746	0.3556	5.1	39.6
450	0.4558	0.2640	0.0100	0.0510	0.3250	0.3930	4.8	45.1
500	0.4370	0.2250	0.0100	0.0440	0.2790	0.2704	3.1	61.6
550	0.4100	0.2006	0.0102	0.0438	0.2546	0.2376	6.7	72.5
610	0.3556	0.1721	0.0103	0.0334	0.2158	0.2058	4.7	72.8
670	0.3438	0.1634	0.0103	0.0315	0.2052	0.1780	0.6	93.1

where n_i and m_i are the real and imaginary part of the refractive index respectively, N is the number of components and v_i is the number mixing ratio of each component.

Finally, the table II and the figure 2 show the optical thickness obtained using the two integration methods described above. It also appear the theoretical OPAC values for this type of aerosols and the deviations with respect to them, in terms of relative MAD (Mean Absolute Deviation).

The most outstanding conclusion that we can draw is that the AOD obtained by adding each component, $\Sigma\tau_i$ differs more than 30% from the results when integrating directly the size distribution sum of the total sum τ . If we compare both results with the OPAC AOD, τ_{OPAC} , we find that the difference with $\Sigma\tau_i$ are 4-8% and practically constant over the wavelength range. However the differences between τ and τ_{OPAC} are more than a 40% with a strong dependence with increasing wavelength.

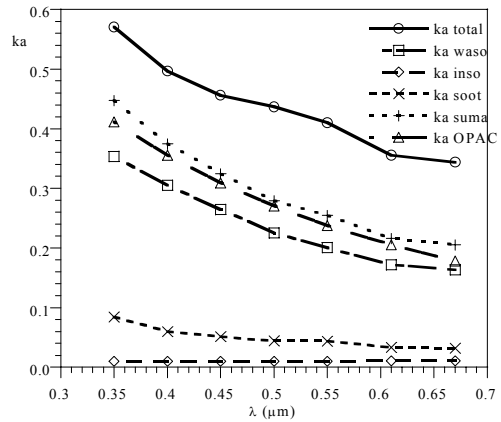
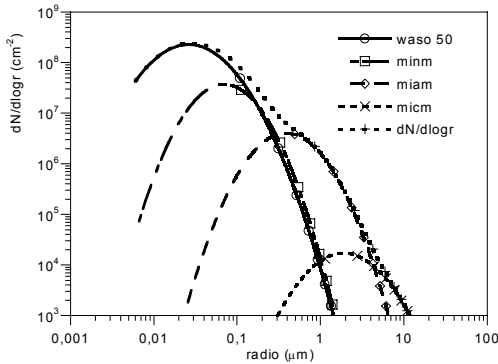
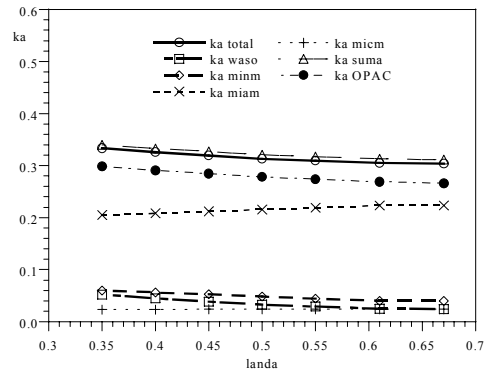


Figure 2. Continental polluted AOD

The size distributions for each component appear in figure 3, using the properties in table III and assuming again a boundary layer of 2 km. It can be seen that the curve for the mixture is bimodal and the difference between the height of the modes is lower than the previous case. Following the same procedure that we used before, the table IV and the figure 4 show the optical thickness obtained.

Table III. Desert aerosol. Physical characteristics

	N_i (cm^{-3})	r_{Mi} (μm)	σ_i	r_{\min} (μm)	r_{\max} (μm)	Number mixing ratios (n_i)
Minm	269.5	0.07	1.95	0.005	20	0.018
Miam	30.5	0.39	2.00	0.005	20	0.033
Micm	0.142	1.90	2.15	0.005	60	0.747
Waso	2000	0.0262	2.24	0.006	25	0.202
Total	2300					

**Figure 3.** Desert aerosol size distribution**Figure 4.** Desert aerosol AOD

c) Angstrom coefficients

The AOD values for the two previous cases have been fitted to Angstrom-like expressions and the α value has been obtained from the logarithmic linear fitting of (1). The aim of these fittings is to establish relationships between the α values for each AOD. The ideal situation would be to relate α for $\Sigma\tau_i$ with α for each τ_i . In the other hand, as our experimental data (Martínez-Lozano et al., 2001) exhibit a change in the AOD slope around 550 nm, the fittings have been performed in three ranges, 350-670 nm, 350-550 nm and 550-670 nm.

Table IV. Desert aerosol AOD

λ (nm)	τ	τ_{waso}	τ_{minm}	τ_{miam}	τ_{micm}	$\Sigma\tau_i$	τ_{OPAC}	MAD% ($\Sigma\tau_i$)	MAD% (τ)
350	0.34887	0.0518	0.0596	0.2050	0.0236	0.3400	0.2989	13.7	11.5
400	0.34181	0.0447	0.0560	0.2085	0.0237	0.3330	0.2911	14.4	11.8
450	0.33536	0.0387	0.0523	0.2121	0.0238	0.3269	0.2844	14.9	12.3
500	0.32950	0.0330	0.0483	0.2156	0.0239	0.3208	0.2784	15.2	12.3
550	0.32453	0.0294	0.0445	0.2191	0.0240	0.3127	0.2735	14.3	13.2
610	0.31949	0.0252	0.0401	0.2232	0.0242	0.3127	0.2683	16.5	13.5
670	0.31946	0.0240	0.0401	0.2232	0.0242	0.3114	0.2659	17.1	14.2

As the table IV shows, for this type of aerosols the values of $\Sigma\tau_i$ and τ are very similar, with differences lower than 3% for the spectral range that we use. In this case both values are higher than τ_{OPAC} . The average values of the relative MAD are 11-14% in the case of $\Sigma\tau_i$ and 13-17 % in the case of τ . The values are almost independent of the wavelength, though the higher values are for higher wavelengths.

The table IV shows that for this type of aerosols the main contribution to AOD is due to mineral particles in the accumulation mode, with a 67%. The nucleation and coarse modes contribute with a 15% and 7%, respectively, and water soluble particles with a 10%.

The results are in table V (continental polluted aerosols) and table VI (desert aerosols). Except for the continental polluted aerosol, the values of α used in $\Sigma\tau_i$ and τ are similar for the three ranges considered.

Table V. Continental polluted aerosols. Angstrom power exponent

	α (350-670nm)	error	α (350-550nm)	error	α (550-670nm)	error
Total	0.77	0.04	0.73	0.07	0.9	0.3
Waso	1.25	0.03	1.25	0.04	1.1	0.3
Inso	-0.081	0.009	-0.080	0.016	-0.05	0.03
Soot	1.56	0.15	1.6	0.2	1.8	0.6
Suma	1.34	0.04	1.27	0.03	1.81	0.15
OPAC	1.25	0.03	1.20	0.03	1.45	0.04

Table VI. Desert aerosols. Angstrom power exponent

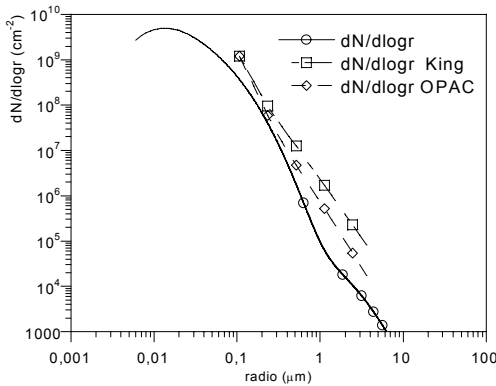
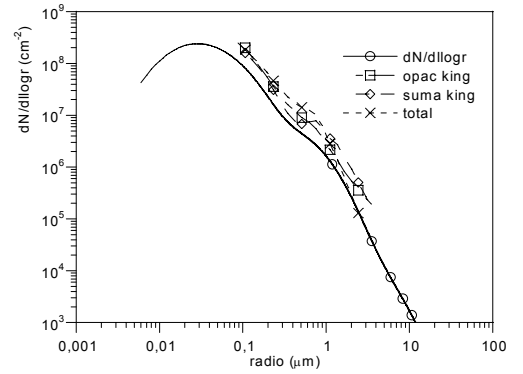
	α (350-670nm)	error	α (350-550nm)	error	α (550-670nm)	error
Total	0.146	0.009	0.1606	0.0016	0.08	0.04
Waso	1.25	0.03	1.25	0.04	1.08	0.26
Minm	0.67	0.04	0.63	0.04	0.5	0.3
Miam	-0.142	0.008	-0.148	0.004	-0.09	0.05
Micm	-0.037	0.002	-0.038	0.002	-0.029	0.015
Suma	0.142	0.008	0.157	0.004	0.09	0.03
OPAC	0.184	0.006	0.197	0.012	0.143	0.011

3.2 Inverse method: size distributions retrieved from spectral AOD

Using the values of optical depth sum, total and OPAC, obtained in previous cases the size distribution function has been reconstructed by inversion using the King method. With this reconstruction we can assess the validity of the King algorithm to retrieve the size distribution as well as to compare the reconstructed optical thickness with the input values.

Some of the size distributions obtained applying the King method are show in the figures 5 and 6. We have to point out that the limitations of King method will make difficult the appropriate reconstruction of the modes with a modal radius higher than $1\mu\text{m}$. The different distributions have been reconstructed and fitted, and the results are in tables VII and VIII.

In this case we have taken the last iteration because it had a value closer to the experimental one. In the continental polluted case the differences between the first and last iteration are lower and the first iteration is the one that gets closer to the real value. The results are

**Figure 5.** Aerosol size distribution obtained from King inversion algorithm. Continental polluted aerosols type.**Figure 6.** Aerosol size distribution obtained from King inversion algorithm. Desert aerosols type.

From the optical thickness reconstructed using the King algorithm, the Angstrom parameters have been recalculated, in order to compare them with the results of the direct method (tables VIII and IX). In this case the fitting have only been performed in the range $[350, 670]$ nm. The reason is that the King algorithm uses the Angstrom expression to recalculate the optical thickness and the retrieved parameter will not change in another spectral range.

Table VII. Continental polluted aerosols and Desert aerosol fits.

	Continental Polluted			Desert		
$R < 0.5$	N_i ($\square\text{m}^{-3}$)	r_{Mi} (μm)	σ_i	N_i ($\square\text{m}^{-3}$)	r_{Mi} (μm)	σ_i
Total	$3.0 \cdot 10^{10}$	0.013	2.2	$1.2 \cdot 10^9$	0.012	3.3
Suma	$3.3 \cdot 10^{10}$	0.014	2.2	$1.0 \cdot 10^9$	0.014	2.6
Opac	$4.7 \cdot 10^{10}$	0.014	2.1	$2.8 \cdot 10^9$	0.009	3.2
$R > 0.5$						
Total	$1.2 \cdot 10^8$	0.07	2.6	$6.8 \cdot 10^6$	0.52	3.0
Suma	$2.6 \cdot 10^7$	0.16	1.7	$4.3 \cdot 10^6$	0.63	3.4
Opac	$3.8 \cdot 10^7$	0.09	2.4	$9.4 \cdot 10^6$	0.30	3.2

Table VIII. Continental polluted aerosols. Angstrom power exponent

	α King	error	α	error	RMS (%)	R correl.
Total	0.76	0.06	0.7498	0.0018	2.7	0.99 0.99
Waso	1.25	0.03	1.106	0.003	4.5	0.99 0.99
Inso	-0.028	0.009	-0.028	0.009	0.004	0.82 0.82
Soot	1.56	0.15	1.432	0.010	6.0	0.97 0.99
Suma	1.34	0.04	1.34	0.03	1.9	0.99 0.99
OPAC	1.25	0.03	1.25	0.03	0.11	0.99 0.99

The values of RMS asses how well the King algorithm can reconstruct the optical thickness. The values α King are obtained fitting to the Angstrom expression the reconstructed optical thickness using the King method. The unlabeled α values were obtained previously by the direct method. In general, both

values coincide except when the discrepancies RMS are slightly higher (in bold font)

Table IX. Desert aerosols. Angstrom power exponent

	α King	error	α	error	RMS (%)	R	correl.
Total	0.146	0.009	0.146	0.008	0.25	0.99	0.99
Waso	1.25	0.04	1.243	0.006	2.4	0.99	0.99
Minm	0.67	0.04	0.670	0.012	1.9	0.99	0.99
Miam	-0.141	0.008	-0.142	0.008	0.06	0.99	0.99
micm	-0.042	0.003	-0.041	0.004	0.11	0.99	0.97
suma	0.147	0.014	0.147	0.011	0.31	0.98	0.99
OPAC	0.186	0.006	0.186	0.006	0.24	0.99	0.99

4 CONCLUSIONS

It is difficult to find clear conclusions about this work because it has been only a first step in the development of this new method. In spite of that it has been possible to determine the contribution of each aerosol component to the whole mixture of aerosols. Furthermore we think that the addition of the optical thickness of each component is the best way to determine the total aerosol optical depth because no assumptions about the extinction efficiency factor are necessary.

At this moment we are already working on the improvement of this technique and its validation using experimental data.

ACKNOWLEDGEMENTS

During this work J.L. Gómez Amo was funded by a research grant from the University of Valencia.

5 REFERENCES

- Angstrom, A., 1929, On the atmospheric transmission of sun radiation and on the dust in the air. *Geografis. Annal.*, 11, 156-166.
- D'Almeida, G.A., Koepke P., and Shettle, E.P., Atmospheric aerosols. Global climatology and radiative characteristics, 561 pp., A. Deepak Publishing, Hampton, Virginia, 1991.
- Dubovik, O., and King, M.D., 2000, A flexible inversion algorithm for retrieval of aerosol optical properties from sun and sky radiance measurements, *J. Geophys. Res.*, 105, 20673-20696.
- Dutton, E. G., Patrick, R., Ryan S. and DeLuisi, J. J. "Features and effects of aerosol optical depth observed at Mauna Loa, Hawaii: 1982-1992", *J. Geophys. Res.*, 99, 8295-8306, 1994.
- Estellés, V., Utrillas, M.P., Gómez-Amo, J.L., Pedrós R., and Martínez-Lozano, J.A., 2002, Aerosol characteristics over a mediterranean coastal site from a CIMEL 318-2 sunphotometer measurements. preliminary results. *I. J. Rem. Sen.* (submitted).
- Hess, M., Koepke, P. and Schult, I., 1998, Optical properties of aerosol and clouds: the software package OPAC, *Bull. Am. Meteor. Soc.*, 79, 831-844.
- Holben B.N., T.F. Eck, I. Slutsker, D. Tanré, J.P. Buis, A. Setzer, E. Vermote, J.A. Reagan, Y.J. Kaufman, T. Nakajima, F. Lavenue, I. Jankowiak, A. Smirnov, 1998, AERONET-A Federated instrument network and data archive for aerosol characterization, *Rem. Sensing Environ.*, 66, 1-16.
- Holben, B.N. et al. (23 authors), , 2001, An emerging ground-based aerosol climatology: Aerosol optical depth from AERONET, *J. Geophys. Res.*, 106, 12067-12097.
- JGR (Special issue), 1997. Passive remote sensing of the tropospheric aerosol and atmospheric corrections of the aerosol effect *J. Geophys. Res.*, 102.
- King M. D., Byrne, D.M., Herman, B. M. and Reagan, J. A., 1978, Aerosol size distribution obtained by inversion of spectral optical depth measurements, *J. Atmos. Sci.*, 35, 2154-67.
- King M.D., 1982, Sensitivity of constrained linear inversions to the selection of Lagrange multiplier, *J. Atmos. Sci.*, 39, 1356-69.
- King, M.D., Kaufman, Y.J., Tanré, D. and T. Nakajima, T., 1999, Remote sensing of tropospheric aerosols from space: past, present, and future, *Bull. Am. Meteor. Soc.*, 80, 2229-2259.
- Martínez-Lozano J. A., Utrillas, M.P., Pedrós,, Tena, F., Díaz, J.P., Expósito, F.J., Lorente, J., de Cabo, X, Cachorro, V., Vergaz R., and Carreño, V., 2002, Intercomparison of spectroradiometers for global and direct solar irradiance in the visible range, *J. Atmos. Ocean Tech.*, in press.
- Nakajima, T., Tanaka M. and Yamakuchi, T., 1983: Retrieval of the optical properties of aerosols from aureole extinction data, *App. Opt.*, 22, 2951-2959.
- Nakajima, T., Tonna, G., Rao, R., Boi, P. Kaufman, Y. and Holben, B., 1996: Use of sky brightness

- measurements from remote sensing of particulate polydispersions, *App. Opt.*, 35, 2675-2686.
- O'Neill, N.T., Eck, T.F., Holben, B.N., Smirnov, A., Dubovik, O. and Royer, A., 2001, Bimodal size distribution influences on the variation of Angstrom derivatives in spectral and optical depth space, *J. Geophys. Res.*, 106, 9787-9806.
- O'Neill, N.T., Eck, T.F., Holben, B.N., Smirnov, A., Royer, A. and Li, Z., 2002, Optical properties of boreal forest fire smoke derived from sun photometry, *J. Geophys. Res.*, 107, 1029/2001JD000877.
- Remer, L. A. and Kaufman, Y. J. Dynamic aerosol model: Urban/industrial aerosol, *J. Geophys. Res.*, 103, 13859-13871, 1998.
- Penner, J.E., Reaith, L., Murphy, D., Nganga, J. and Pitari, G., 2001, The aerosols, their direct and indirect effects, in *Climate Change: The Scientific Basis*, edited by J. Houghton, Y. Ding, D.J. Griggs, M. Noguer, P.J. van der Linden, X. Dai, K. Maskell and C.A. Johnson, pp. 289-348, Cambridge Univ. Press, New York.
- Schwartz, S.E. and Andreae, M.O., 1966, Uncertainty in climate change caused by aerosols, *Science*, 272, 1121-1122.
- Shifrin, K.S., 1995, Simple relationships for the Angstrom parameter of disperse systems, *App. Opt.*, 34, 4480-4485
- WMO, Report on the measurements of atmospheric turbidity in BAPMoN, GAW Report No. 94, 1994.

Measured Hot Spot Directional Signatures of Agricultural Crops during DAISEX'99 using POLDER data

F. Camacho-de Coca¹, M. Leroy², J.P. Gastellu-Etchegorry² and F.J. García-Haro¹

¹*Department of Thermodynamics, University of Valencia.*

C/Dr. Moliner, 50. 46100 Burjassot. Valencia, Spain.

²*CESBIO, UMR CNES-CNRS-UPS*

18,av. e. belin, 31055. Toulouse, France.

fernando.camacho@uv.es, marc.leroy@medias.cnes.fr

ABSTRACT- *In this paper, we have investigated several hot spot directional signatures of different agricultural crops measured with the POLDER instrument during the DAISEX'99 campaign. This instrument provides us with a directional resolution of about 0.3° in phase angle and a spatial resolution of 20 m. The hot spot signature is retrieved with the assumption of spatial homogeneity of the target. The spectral dependence of the hot spot has been investigated in four channels (443, 550, 670 and 800 nm). The hot spot directional signature has been fitted to a function of the phase angle as predicted by the radiative transfer theory within the leaf canopies. The retrieved parameters (half width and amplitude) show different findings. The half width values have ranged between 1 and 2 degrees, being quite independent of the canopy cover type. The amplitude values have shown results according with the expected reflectance of the scatters. The estimated leaf reflectance values at noon were typically 0.4 in the near infrared region for all vegetated unit. The spectral leaf reflectance is consistent and shows the potential of the hot spot measurements to retrieve the leaf biochemical content.*

1 INTRODUCTION

When the angle between the sun and view directions (phase angle, ξ) tends to zero the reflected radiance of a surface rises sharply up to its maximum value, exactly at zero phase angle. Seelinger interpreted correctly this effect observing Saturn's rings (Seelinger 1887). In optical remote sensing, this effect is known as the hot spot and it constitutes a fine BRDF signature of the Earth's surfaces. It was initially observed in aerial photography as a bright area around the shadow of the plane. From the first moment, the hot spot was recognized as possible structural identifier of the vegetation canopies (Gerstl and Simmer 1986).

From Seelinger up to now, the shadow-hiding mechanism (Hapke et al. 1996, Hapke 1993) has been the physical process accepted to explain the hot spot effect. This mechanism takes place when the size of scatters is large compared with the wavelength and, thus, well-defined shadows appear. These shadows are visible at large phase angle but close to zero phase angle they are hiding by the objects (leaves, soil particles) that cast them. Hence, close to the backscattering the reflectance is manifestly enhanced. In addition, when the size of scatters is lower or approximately equal to the wavelength, the shadow-hiding mechanism cannot describe properly the hot spot effect. A different mechanism known as coherent-backscatter or weak photon localization has been then identified as responsible of the hot spot. The coherent-backscatter explains the hot spot as a constructive

interference phenomenon (Barabanenkov et al. 1991). The half width of the coherent-backscatter peak increases linearly with the wavelength, whereas in the shadow-hiding theory the half width of the hot spot is expected to be independent of wavelength. Furthermore, single scattering does not contribute to coherent-backscattering, which depends on multiply scattered light, whereas the shadow-hiding is important only for once scattered radiation.

Many hot spot models, mostly accounted for by the shading mechanism, have been developed in order to incorporate the hot spot to the leaf canopy BRDF models. A review of hot spot modeling can be found in Qin and Goel (1995). These models point out the interest in the hot spot measurements from remote sensing applications. Since the half width of the hot spot is proportional to the photon mean free path, it should be dependent of structural parameters such as leaf area index (LAI), leaf dimension (D) or canopy height (H). Therefore, the hot spot could have utility as a land cover classifier. Moreover, the amplitude of the hot spot gives access to the reflectance of the foliage elements or soil grains (Bréon et al. 2002).

The possibility to obtain the hot spot directional signature from remote sensing platforms has been demonstrated in the literature (Bréon et al. 1997). The first hot spot data set of major biomes from space have already been produced using the POLarization and Directionality of Earth Reflectance (POLDER) instrument onboard the ADvanced Earth Observing System (ADEOS) (Bréon et al. 2002). The analysis of this data set shows a lower variability in the hot spot

half widths than the expected from the theoretical approaches (Qin and Goel, 1995), whereas the amplitude of the hot spot presents proportional values to the leaf reflectance.

The measurement and analysis of the hot spot effect was one of the priorities during the Digital Airborne Spectrometer Experiment (DAISEX) campaigns of the ESA (ESA 2001). In the 1999 campaign, the POLDER and the Hyperspectral MAPping (HyMAP) instruments recorded satisfactorily the hot spot directional signatures of different agricultural crops. In this paper, we present the results of the hot spot directional signatures measured using POLDER imagery. Our main objective is to analyze the potential and limits of the hot spot signature to retrieve canopy biophysical information.

2. EXPERIMENT DESCRIPTION

2.1. Test Site

The experiment site is a 3 km by 3 km area centered at 39° 3' N, 2° 5' W, which is located 28 km from Albacete (Spain), close to the Barrax town. This area was selected by ESA for the DAISEX campaigns during 1998, 1999 and 2000 (ESA 2001). The POLDER instrument flew in the 1999 campaign. A supervised classification of the area was made based on field information. During that summer, the dominant cultivation in the area was approximately 53% dry land (29% barley, 24% fallow) and 42% irrigated land (15% corn, 11% alfalfa, 8% wheat; 2% legumes, 2% sugar beet, and 4% others) with a 5% of unclassified data.

2.2 Airborne POLDER data

In the DAISEX campaign, the spectral filters of the POLDER instrument were centered at 443, 500, 550, 590, 670, 700, 720, 800, and 864 nm wavelength. The POLDER field-of-view (FOV) was along track and cross track of $\pm 43^\circ$ and $\pm 51^\circ$ respectively. This resulted in a ground FOV of $7.4 \times 5.6 \text{ km}^2$ for the typical flight altitude of 3000 m. At this flight altitude the spatial resolution was 20 m (Leroy et al. 2001).

Four flights with the ARAT plane carrying POLDER and LEANDRE instruments were performed in the 1999 campaign. They correspond to 3rd June at noon (from 11:29 to 12:31 UT), 4th June in the morning (from 07:16 to 08:15 UT) and in the afternoon (from 13:57 to 15:01 UT), and 5th June in the morning (from 06:57 to 08:02 UT). In each flight

the POLDER instrument records around 140 spectral images, which constitutes a POLDER sequence. One image is acquired within 3 seconds, and the acquisition is repeated every 10 seconds, with an overlap between consecutive images. Thus, in a sequence, every pixel is observed with different viewing directions, typically between 30-60 covering a wide range of the directional space. The POLDER reflectance images were calibrated, geo-coded and corrected for atmospheric effects as it is specified in Leroy et al (2001).

3. METHODOLOGY

The methodology followed is that of Bréon et al (2002), which is mainly based on an original measurement principle to retrieve hot spot at a fine spatial resolution from POLDER imagery. This methodology is briefly described below.

3.1. Measurement principle

In a sequence of POLDER images, the viewing geometry for a pixel given changes between 5-10° degrees in consecutive snapshots covering the full directional range. This is a suitable directional resolution to reconstruct the BRDF of the surfaces. However, for a proper description of the reflectance enhancement at the backscattering, a finer directional resolution is needed and, consequently, a new measurement principle should be considered. This measurement principle is based on the assumption of spatial homogeneity of the target. If this assumption is verified then the variability in the measured radiance with the viewing angle may be considered as a directional signature. Thereby, a spatial heterogeneity correction should be done in order to reduce spurious contribution to the reflectance variability with the viewing geometry. Once we identify a hot spot belonging to a homogeneous area, we measure the reflectance corresponding to a region centered in the hot spot pixel. The size of this region will be determined by the spatial resolution and the typical size of the samples. In this work, the maximum size of the hot spot region is 7×7 pixels (approximately $140 \times 140 \text{ m}^2$). In this area, the phase angle changes typically 0.3° per pixel. Thanks to the multi-angular POLDER data, we can use different snapshots in order to increase the directional coverage. This method was satisfactorily tested over an Australian site and later applied on a global scale using POLDER data (Bréon et al. 2002).

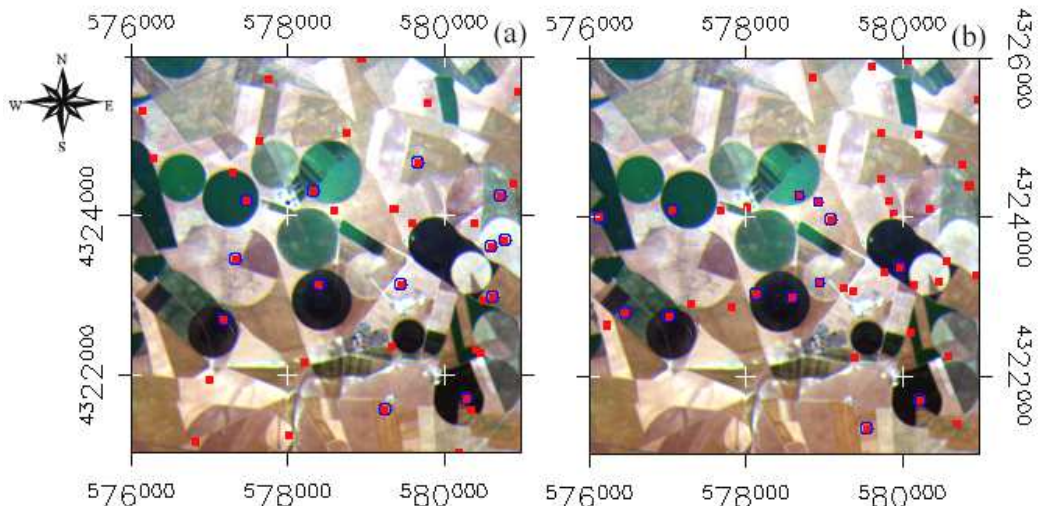


Figure 1. Location of the hot spots (band 5) in the study area: a) Noon, b) Afternoon.

3.2. Data processing

We have only processed the POLDER atmospherically corrected data acquired at noon and in the afternoon. In the other two flights, the POLDER FOV is lower than the sun zenith angle and, thereby, the hot spot condition is not satisfied by any pixel in the image. In order to undertake a spectral analysis of the hot spot we have selected four bands: 443 nm, 550 nm, 670 nm and 800 nm. The blue band serves to identify an aerosol contribution to the backscattering peak. First, we have identified for each image the pixel satisfying the hot spot condition, locating 79 hot spots from 205 useful snapshots. Figure 1 shows the exact location of the hot spots in band 5 (670 nm). Afterwards, only 27 hot spots belonging to homogeneous fields and far enough from the crop boundary were identified (blue circles in the figure 1). In fact, the hot spot location moves around 250 m from the first to the last band, which is roughly a half of the field length. It hampers the spectral analysis of the hot spot because some spectral channels will be missing. For the final selection of the spectral hot spots, we have obtained the nadir reflectance in a 7x7 pixels window centered at backscattering. A threshold

of 10% in the variability coefficient (mean value/standard deviation) was found to give satisfactory results to filter out heterogeneous samples. Finally, 24 hot spot were selected (12 at noon + 12 in the afternoon) but the four spectral channels have been only considered in 12 cases (7+5) (see table 1).

For increasing the directional coverage of the hot spot directional signature, we have made use of additional images of the corresponding POLDER sequence. In order to minimize the fluctuations induced by the apparent solar movement, we have used only those sequences where the change in the sun zenith angle is lower than 0.5° at noon and lower than 1.5° in the afternoon. A simple spatial heterogeneity correction has been made using patches of data far away from the backscattering. The deviation from the mean reflectance was considered as a bias that was subsequently subtracted from the hot spot directional signature.

The hot spots belong to different agricultural cover types, from bare soil to the densest alfalfa crop. Then, the next step was the classification of the located hot spots (see table 1). The number of hot spots (HS) is expressed as the sum of the two flights.

Table 1. Structural parameters and number of hot spots (Noon + Afternoon) of the different selected samples.

Samples	Acronym	HS	Height (m)	LAI	FVC* (%)
Corn	C	3+1	0,12-0,2	0,26±0,11	25
Wheat	W	3+5	0,7-0,85	-	95
Barley	B	3+3	0,55-0,65	3,2±0,4	90
Alfalfa	A	1+1	0,6-0,7	2,5±0,5	100
Alfalfa cut	Ac	0+1	-	-	75
Legumes	L	0+1	-	-	100
No classified	N.C.	1+0	-	-	-
Soil	S	1+0	-	-	0

The available field data show similarities in height and LAI for the developed alfalfa, wheat and barley crops. The fraction of vegetation coverage (FVC) was derived from HyMAP imagery using a variable and multiple endmember spectral mixture analysis (VMESMA) procedure (García-Haro et al. 2002).

3.3. Theoretical approach

The theoretical approach followed to retrieve biophysical information from the hot spot signature is that of Bréon et al (2002). This model assumes geometrical-optical principles to derive the overlap function, S , based on the model of Jupp and Strahler (1991). They define this function as the ratio between the illuminated shadow and the view shadow to the nadir projection area. They used then the Boolean set theory for developing a more general algorithm of the hot spot in continuous canopies with horizontal distributed leaves. Bréon et al (2002) assume randomly distributed leaves (uniform angular distribution). In this case, the mean projection of the leaf surfaces along a particular direction defined by θ is constant, $1/2$. The hot spot is explained as a correlation between the downward and upward transmissions. Hence, at a level z , the apparent position of the leaves is correlated regarding the inward and outward radiance paths. Consequently, the leaf area density considered is not $u_L(t)\delta t$ but rather $u_L(t)[1-S(d/D)/2]\delta t$, where u_L is the leaf area density at a level t , D is the typical leaf dimension, d is the decorrelation length and S is the overlap function. In the case of uniform oriented leaves, the decorrelation length is related to the phase angle (ξ) rather than to the more common $\Delta(\theta_s, \theta_v, \phi)$ function. The decorrelation length is then written as (see formal demonstration in Bréon et al 2002):

$$d = \frac{2(z-t)}{\mu_s + \mu_v} \cdot \xi \quad (1)$$

where $\mu_{s,v} = \cos\theta_{s,v}$

The expression for the upward and downward transmission is then used to derive the single scattering reflectance R_s for thick canopies with a negligible soil contribution. The radiative transfer modeling indicates that the reflectance can be fitted accurately using the following expression.

$$R = \frac{\Delta R_{HS}}{1 + \xi / \xi_0} + b\xi + c \quad (2)$$

ΔR_{HS} is the amplitude of the hot spot, which is given by the difference of the modeled reflectance when consider the hot spot effect ($S=1$) and without consider it ($S=0$).

$$\Delta R_{HS} = \frac{1}{2} R_s \Big|_{\xi=0} = \frac{\rho_{leaf}}{3\mu_s} \quad (3)$$

where ρ_{leaf} is the leaf reflectance.

And ξ_0 is the half width at half maximum:

$$\xi_0 = \frac{LD}{6.4H} \quad (4)$$

Hence, we can fit the measured data to the function expressed in equation 1 to derive the amplitude and the half width of the hot spot. The half width is related to the ratio between LAI, leaf size and height of the cover, whilst the amplitude is related to the leaf reflectance.

4. RESULTS AND DISCUSSION

Figure 2 shows a selection of the hot spot directional signatures obtained from the POLDER sequence. A window of 7×7 pixels ($140 \times 140 \text{ m}^2$) was used for every patch view, each one corresponding to a different image. The data is plotted as a function of the signed phase angle. This takes a positive value if the corrected view angle ($\theta_v \cos\phi$) is larger than the solar zenith angle and vice versa. We can observe that from approximately -40° to -10° the reflectance increase linearly. This trend is associated to the macro-structure of the sample and, thus, can be connected to the surface scattering process. Beyond -40° the linear trend fails and the reflectance increase because of the so-called gap effect, mostly for vertical oriented canopies in presence of the multiple scattered radiation (e.g. figure 2g and 2h). Close to the backscattering the reflectance increases sharply since the phase angle tends to zero due to the hot spot effect. This trend is now associated to a different physical mechanism linked to the volume scattering process, *i.e.* the joint probabilities of transmission of penetrating and reflected radiation within the canopy. Thereby, the term of hot spot should be reserved only to this fine resolution peak. Figure 2 shows also the theoretical hotspot signature as predicted by equation 2. We can observe a good fit of the function in the interval from -40° to 5° phase angle. Results have also shown that this function provides a lower RMS error than the more common exponential function (Kuusk, 1985). Moreover, for the fitting approach considered, it gives narrower and more realistic half widths, especially in the afternoon flight where the directional signature presents a lower number of data. These results are in agreement with the fact that the exponential function overestimates the hot spot width with relation to other approaches (Qin and Goel, 1995), mainly because the exponential function does not vanish even when there is not overlap. In figure 2 we can see that the hot spot effect appears independently of the canopy cover type. The hot spot directional signatures show a similar behavior for the soil, the class with lowest cover (corn), and the senescent barley. The optical properties of these classes change linearly with the wavelength. In contrast, the samples with a high amount of photosynthetically active vegetation, such as the wheat

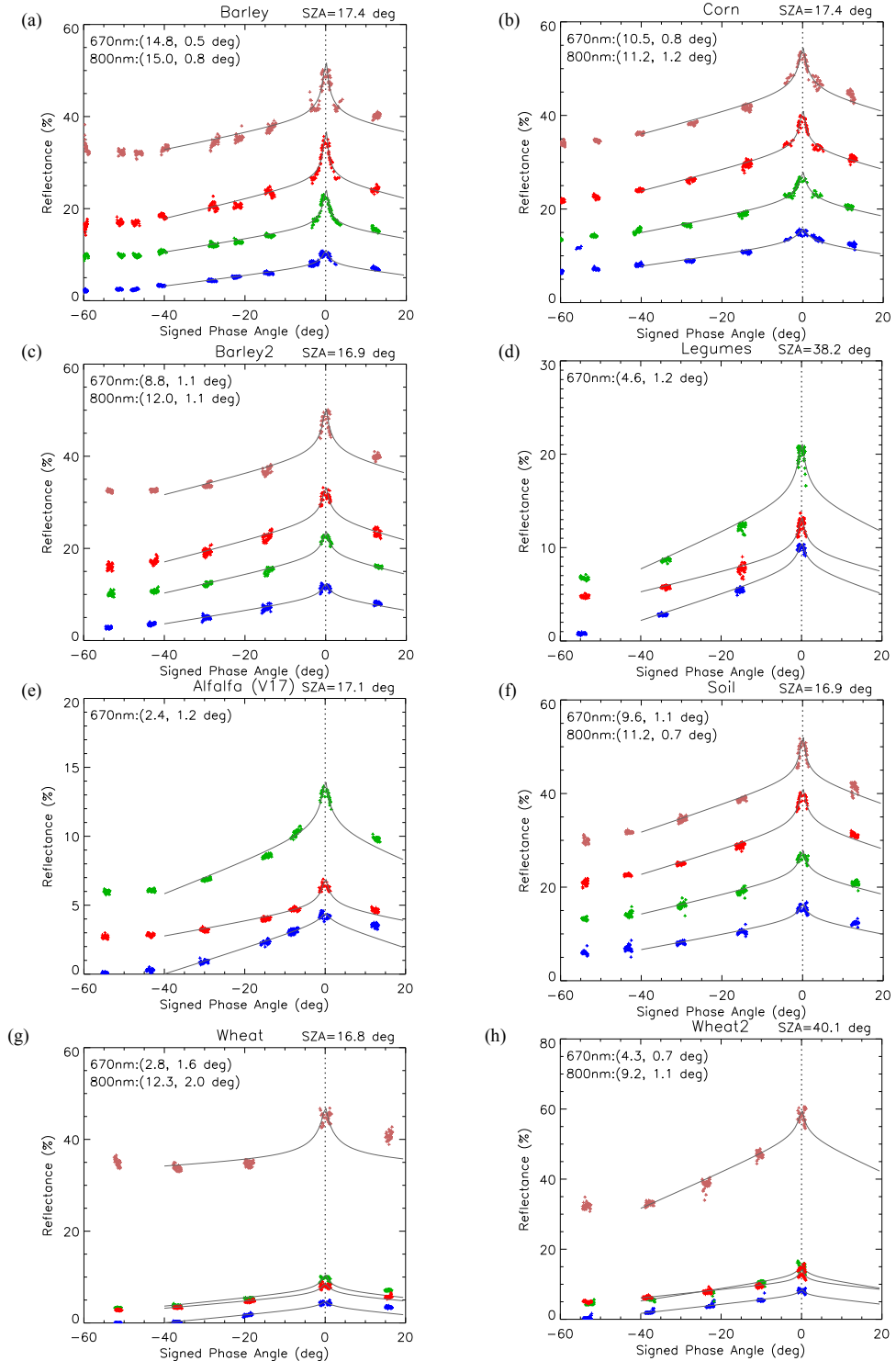


Figure 2. Hot Spot directional signatures as a function of the signed phase angle (negative when $\theta, \cos\phi < \theta_s$) measured under different sun zenith angle (SZA). The line shows the fit of the data using the function of equation 2. On the top left side is written the amplitude and the half width at 670 and 800 nm.

cover, present greater differences between the visible and NIR signatures. On the top left side of the graphs, we have showed the retrieved values for the amplitude and the half width at 670 nm and 800 nm. The barley cover is shown twice (figures 2a and 2c). In figure 2a, the hot spot peak has been characterized using two images whilst in figure 2c only one image has been used. The use of two patches close to the backscattering results in a more accurate representation of the hot spot effect and, consequently, retrieved parameters offer a higher confidence. The differences are quite important in both amplitude and half width. This is no surprising because the higher the sampling in the hot spot domain, the better the likely accuracy of retrieved parameters. For the wheat sample the two graphs corresponds to the two different flights. In this case, the number of patches considered in the fit is also different. The results show also large differences in both amplitude, affected by the sun position, and half width. In this case, we should note a higher spatial variability that results in a worse fit around the hot spot.

For improving the stability of the solutions, the fit was made in a two-step process. First, the linear part was fitted to the data existing between -10° and -40° to derive the linear coefficients b and c . Then the equation was fit between a phase angle limit of -20° and $+5^\circ$ to derive the amplitude and the half width. The root mean square (RMS) error was calculated to evaluate the fit quality around the hot spot ($\pm 5^\circ$). In addition, the amplitude to RMS ratio has been used to evaluate the signal-to-noise ratio of the measured hot spot signatures. The values of the relative RMS are typically 2-4% in the noon flight and 4-7% in the afternoon. It shows the best quality of the hot spot fit in the noon flight images. For spectral channels, the blue band shows the worst fit in relative terms, whereas the near infrared band shows the lowest values. The signal-to noise ratio was higher at 550 nm, with typical values of 14 at noon and 10 in the afternoon, whereas the worst ratio values (<10) were found at 443. In general, the signal-to-noise ratio shows slightly higher values at 670 nm than at 800 nm

nm. Neither RMS nor signal-to-noise ratio present significant differences regarding the canopy cover type.

To assess the stability of retrieved parameters, a sensitivity analysis has been conducted by combining 3 different window sizes (25, 36, 49 pixels) with 3 different phase angle limits $L=\{-15^\circ, -20^\circ, -25^\circ\}$. This analysis provides us with the confidence interval of the estimates. In general, the retrieved amplitude increases and the half width decreases slightly with the window size, i.e. at increasing the number of points depicting the hot spot. Concerning the phase angle limits considered in this assessment, the retrieved parameters are quite insensitive showing differences on the order of 0.1 in both amplitude and half width.

Figure 3 shows the estimated hot spot half widths, which mostly range between 1° and 2° . The samples have been ordered from low to high vegetation coverage; a different number with the same label indicates different parcel, whilst C and C' (W and W') refers to the same parcel. We can observe the lack of a regular tendency with the canopy cover type, including bare soil and densest vegetated surfaces such as alfalfa or wheat. The results indicate that at this spatial and directional resolution the half width presents a lower variability than that predicted by the above model. This finding has been previously reported in Bréon et al (2002) over the major IGBP land cover types. Therefore, it seems to be quite difficult to interpret the hot spot half width in terms of structural parameters of the canopy cover. In fact, the hot spot formation should be a quite complex problem since vegetation canopies present a detailed architecture with different elements such as leaves, buds and also spikes in developed cereal crops, with a particular level of aggregation (clumping) and interstices through which light can penetrate (Roujean 2000). However, most of the hot spot modeling has been accounted for by using the leaf or the crown as the basic unit to compute the mutual shadowing, which is a strong simplification (Qin and Goel 1995). In addition, the distribution of the data points in the hot spot region seems to be insufficient for

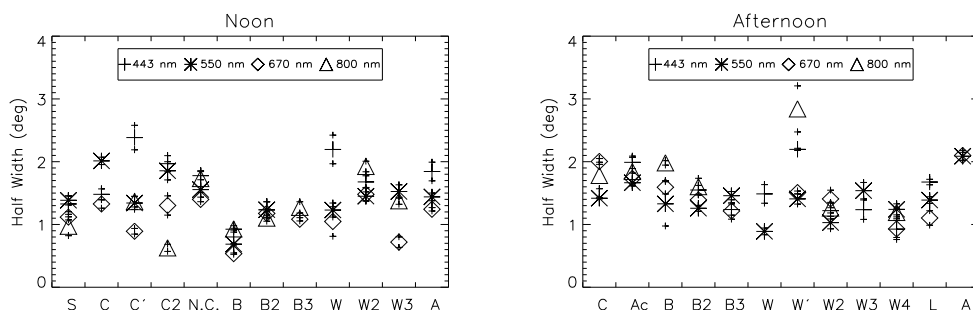


Figure 3. Retrieved hot spot half width in the noon and in the afternoon flights (acronyms appears in table 1).

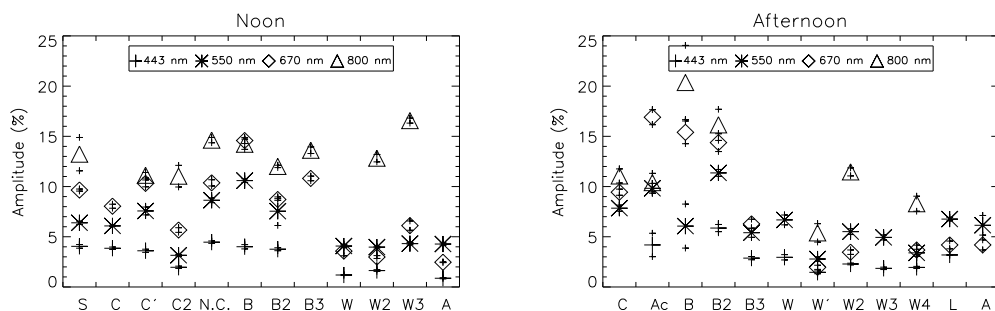


Figure 4. Retrieved hot spot amplitude in the noon and in the afternoon flights (acronyms appears in table 1).

determining accurately the amplitude and half width of the hot spot peak. We have more confidence in the results with a better sampling.

Concerning the spectral channels, the blue band shows roughly higher values than the other bands. If we reject this channel because of its worst fit, we obtain that in dense vegetated surfaces the spectral variability of the half width within its confidence interval is typically about 0.4° , without observing any regular spectral tendency. The spectral variability is not expected from the shading theory and it could be associated to the inversion procedure rather than to a physical process. The soil and corn samples show spectral differences up to 1° . In these cases, the hot spot half width decreases with the wavelength as opposed to the trend predicted by the coherent backscatter mechanism (Hapke, 1993). Although both mechanisms can occur in the same medium, it is expected that one dominates the formation of the hot spot. In addition, at longer wavelengths (>700 nm), the increasing multiple scattered radiance may favor the coherent mechanism (Hapke et al. 1996). Further investigations are required to explain this spectral dependence and determine if the coherent backscattering contribute to the enhancement of reflectance at backscatter, especially in the NIR

region.

Figure 4 shows the retrieved amplitude. Unlike the half width, the amplitude presents a regular pattern regarding the canopy cover type. The spectral variability is also consistent with the expected reflectance of leaves and soil particles. Photosynthetically active vegetated samples (alfalfa, wheat, legumes) show higher amplitude in the green channel than in the blue and red ones, showing the highest values for the NIR. In contrast, non-photosynthetically active samples (soil and barley) show wavelength scaled amplitude according to the optical properties of the dry leaves. The derived amplitude is higher in the afternoon flight than at noon, in agreement with the theoretical formulation considered above (eq. 3). The variability within the classes is slightly higher than it could be expected from the nadir reflectance values. This could be partly associated to the errors introduced in the inversion procedure. Finally, the lowest amplitude values at 443 nm indicate the low aerosol contribution to the hot spot (Breón et al. 2002).

Finally, the leaf reflectance of the samples was estimated using the equation 3. This equation is valid for thick canopies, i.e. when the soil contribution is negligible. Therefore, the soil and corn ($\sim 25\%$ cover)

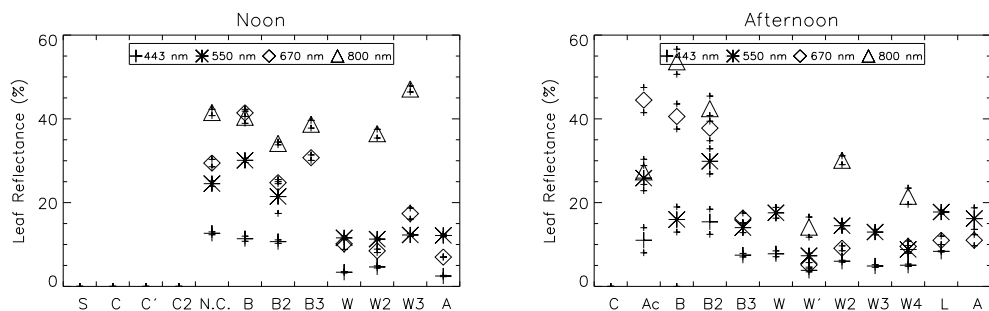


Figure 5. Leaf reflectance estimation in the noon and afternoon flights.

targets have been not considered. Results can be observed in figure 5. In general, the results are satisfactory when using the more confident data (noon flight). The estimated spectral leaf reflectance shows coherent results. For example, barley presents increasing reflectance values with the wavelength as expected from its senescent stage, whereas green vegetated samples show high values at 550 nm than at 670 nm. In the noon flight, we can observe certain variability in samples corresponding to a same canopy type, e.g. samples B and B2, because of the differences in amplitude previously reported (see figure 2a and 2c). The afternoon flights present worse results mainly associated to the directional under-sampling. This result in an underestimation of NIR reflectance for the wheat samples.

5. CONCLUSION

In this paper, we have analyzed the hot spot directional signatures of different vegetation covers derived from POLDER airborne data acquired during DAISEX'99 campaign. The retrieval of the hot spot directional signatures relies on the assumption of spatial homogeneity of the target. The data points of the hot spot signature have been fitted to a function of the phase angle (eq 3). The amplitude and the half-width of the measured hot spot have been retrieved using the method proposed by Br  on et al. 2002.

The half width ranged between 1  -2   independently of the canopy cover type. This reveals the difficulty to infer structural information of the canopies from the half width. Some samples (soil, corn, barley) have shown an unexpected spectral dependence of the hot spot half width. Further investigations should be desirable to explain this result.

The retrieved values of the amplitude of hot spot and the leaf reflectance are consistent with the expectations, providing thus information linked with the phenological status of the canopy.

Nevertheless, the retrieved parameters are quite sensitive to the distribution of data points along the hot spot geometry. In fact, the hot spot domain is roughly 5 degrees in phase angle. Consequently, and because the noise in the data, a poor sampling of this domain will translate into biased estimates of the hot spot parameters. In this way, the amplitude seems to be underestimated and the half-width overestimated when the hot spot peak is undersampled. Complementary measures of the hot spot from HyMAP data taken during this campaign will be used to analyze both the influence of the sampling in the hot spot domain and the spectral dependence in the half-width.

ACKNOWLEDGEMENTS

This work has been partially supported by the 'Scientific Analysis of the ESA Airborne Multi-Annual Imaging Spectrometer Campaign DAISEX' project. Special thanks are due to Dr. F.M. Br  on for his contribution to this work.

REFERENCES

- Barabanenkov, Y.N., Y.A. Kravtsov, V.D. Ozrin and A.I. Saichev, 1991, Enhanced backscattering in optics, In *Progress in Optics*, vol. 29 (E. Wolf, Ed.), Elsevier, New York, pp. 65-197.
- Br  on, F.M., F. Maignan, M. Leroy and I. Grant, 2002, Analysis of the hot spot directional signatures measured from space, *Journal of Geophysical Research*, 107, D16, 10.1029-10.1044
- Br  on, F.M., V. Vanderbilt, M. Leroy, P. Bicheron, C.L. Walthall and J.E. Kalshoven, 1997, Evidence of hot spot directional signatures from airborne POLDER measurements, *IEEE Transactions on Geoscience and Remote Sensing*, 35, 2, 479-484.
- ESA, 2001, Proceedings of the DAISEX final results workshop, ESA SP-499, ESA Publication Division, ESTEC, The Netherlands, July 2001 (277 pp).
- Garc  a-Haro, F.J., Sommer, S. and Kemper, T. (2002), Variable multiple endmember spectral mixture analysis (VMESMA): a high performance computing and environment analysis tool, *Remote Sensing of Environment*, in revision.
- Hapke, B., D. Dimucci, R. Nelson and W. Smythe, 1996, The cause of the hot spot in vegetation canopies and soils: shadow-hiding versus coherent backscatter. *Remote Sensing of Environment*, 58, 63-68.
- Hapke, B., 1993, Topics in remote sensing 3: Theory of Reflectance and Emittance Spectroscopy, Cambridge University Press. 455 pp.
- Jupp, D.L.B. and A.H. Strahler, 1991, A hotspot model for leaf canopies, *Remote Sensing of Environment*, 38, 193-210.
- Kuusk, A., 1985, The hot spot effect of a uniform vegetative cover, *Soviet Journal of Remote Sensing*, 3, 645-658.
- Leroy, M, O. Hatecoeur, F. Ponchaut, L. Alonso-Chorda, and J. Moreno, 2001, The airborne POLDER data in the DAISEX'99 campaign, ESA SP-499, ESA Publication Division, ESTEC, The Netherlands, July 2001, 13-22.
- Qin, W. and N.S. Goel, 1995, An evaluation hotspot models for vegetation canopies, *Remote Sensing Reviews*, 13, 121-159.
- Roujean, J.L., 2000, A parametric hot spot model for optical remote sensing application, *Remote Sensing of Environment*, 71: 197-206.
- Seeliger, H., 1887, Zur theorie der Beleuchtung der grossen planeten insbesondere des Saturn, *Abhandl. Bayer. Akad. Wiss. Math-Naturw. Kl. II* 16: 405-516.

Retrieval of Water Quality parameters of Perialpine lakes in Austria by means of Hyperspectral Rosis data

D. Floricioiu, E. Rott¹, C. Riedl and H. Rott.

Institute of Meteorology and Geophysics University of Innsbruck, ¹Institute for Botany, University of Innsbruck, Innsbruck, Austria
dana.floricioiu@uibk.ac.at

ABSTRACT - The applicability of the ROSIS hyperspectral spectrometer data to map water quality parameters of perialpine lakes is investigated. As test sites four deep lakes in the Salzkammergut region of Austria located at an altitude of about 500 m a.s.l. were selected. The lakes are oligo- to mesotrophic with typical chlorophyll-*a* concentration below 10 $\mu\text{g l}^{-1}$ throughout the year. On 5 July 2001 four swaths were acquired by the hyperspectral ROSIS-03 Sensor onboard of a Dornier 228 aircraft. Intensive field activities were carried out parallel to the overflight. Radiometric measurements and water samples taken from several points were analysed. For atmospheric correction of the level-1 ROSIS data the 6S radiative transfer code was used. The aerosol properties like optical depth and size distribution are derived from sun photometric measurements. Radiosonde data from the synop network were used as input for the atmospheric model. Spectral signatures measured in situ and derived from the ROSIS data are compared. The available data set was used to develop algorithms for retrieval of water quality parameters. In a first approach empirical algorithms based on ratios between spectral bands were tested. The atmospherically corrected ROSIS reflectance was resampled to ENVISAT MERIS spectral bands 2 to 7 (442 to 665 nm) to study the possibilities of this sensor for water quality applications. The most promising combinations of spectral bands for the retrieval of chlorophyll – *a* concentration correspond to MERIS band ratios 3/6, 3/7, 4/5 and 4/6.

1. INTRODUCTION

An airborne campaign with the Reflective Optics System Imaging Spectrometer (ROSIS) was carried out on 5 July 2001 on lakes in the region Salzkammergut (13°22'E, 47°50'N) in Austria (Fig. 1a). The aim of the campaign was to develop methods for radiometric correction of spectrometer data and to develop algorithms for water quality monitoring in perialpine environment. The selected lakes for the campaign are Mondsee (14.3 km²), Wallersee (6.4 km²), Irrsee (3.5 km²) and Wolfgangsee (13 km²) located at altitudes between 480 and 553 m a.s.l. The lakes are oligo- to mesotrophic with typical chlorophyll-*a* concentration below 10 $\mu\text{g l}^{-1}$ throughout the year. Field measurements were carried out parallel to the ROSIS overflights with the sun photometer and the portable spectroradiometer. Water samples were collected at locations along the flight line.

2. TEST SITES AND DATA SETS

2.1 The test sites

The average depth of the selected lakes in the Salzkammergut region ranges from 9 (Wallersee) to 37 m (Mondsee) and the maximum depth from 24 to

68 m, respectively. Mean and maximum depth of Irrsee are 15 and 37 m, respectively. The lakes were selected to represent the actual trophic gradient of the larger perialpine areas of Austria which covers oligotrophic to mesotrophic situations. The thermic lake types are actually at the transition between typical temperate dimictic situations (with a permanent winter ice- and snowcover) and warm monomictic situation (when no wintercover is formed). The biological parameters influencing the optical conditions are showing pronounced seasonal variations which can vary in relation to different year to year climatic conditions. Maximum phytoplankton densities and chlorophylls are normally related to the spring and autumn mixing periods, whereas during summer the quantities are reduced. In spite of these variations primary productivity remains at a high level during summer and affects the biogenically induced decalcification processes influencing the optical conditions in the lakes.

2.2 The airborne data set

The ROSIS sensor has a CCD array imaging simultaneously 512 samples across the flight direction and 115 spectral bands in the range 416 – 872 nm with a spectral sampling of 4 nm. The FOV is $\pm 8^\circ$, the IFOV is 0.56 mrad and the radiometric encoding 14

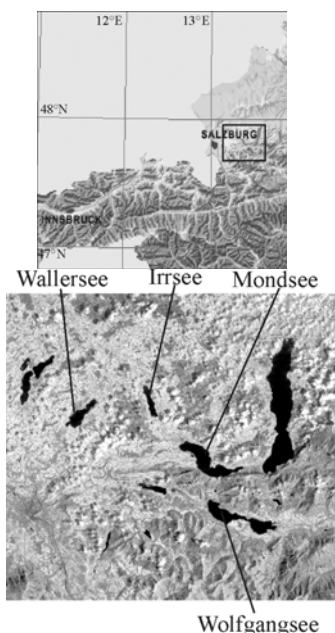


Fig. 1 (a) The location of the test site in the area Salzammergut in Austria. (b) Landsat 5 TM scene from 9 Aug. 1989 showing the selected lakes.

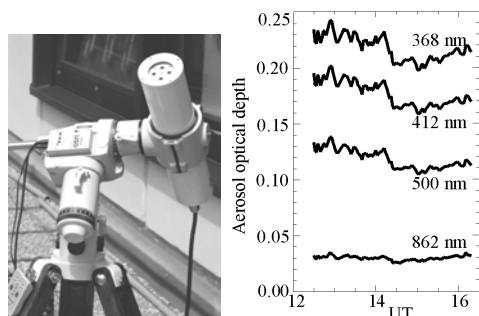


Fig 2: The PFR instrument and AOD measurements on 5 July 2001

bits. For a detailed description of the actual version of the sensor ROSIS-03 see (Gege et al, 1998).

Four swaths were acquired over the lakes on 5 July 2001. The acquisitions started at 10:33 UTC until 11:11 UTC. The flight altitude was about 5000 m a.s.l. which corresponds to a swath width of 1.4 km and a pixel size of 2.7 m.

3. FIELD MEASUREMENTS

The field work, carried out parallel to the ROSIS overflights, consisted of radiometric measurements and acquisition of water samples. In addition meteorological data (air temperature, pressure, wind)

and radiosonde data from stations in and close to the test site were collected.

3.1 Radiometric measurements

Measurements of atmospheric transmittance of solar radiation were carried out near Mondsee on 5 July 2001 with the Precision Filter Radiometer (PFR) (Roth & Wehrli, 1999) shown in figure 2. The instrument operates in 4 channels: 368, 412, 500 and 862 nm. Every second minute the PFR starts a measuring cycle. The aerosol optical depth and information about the aerosol size distribution were derived from these measurements with the SPM Toolbox software package (Ingold, 1998) and used as input for the atmospheric correction model.

On the lakes surface reflectance spectra were collected along transects parallel to the flight line with a portable FieldSpec UV/VNIR HandHeld spectroradiometer. The instrument operates between 325 and 1075 nm with 512 spectral channels and a view angle of 25°. Measured spectra for each lake are shown in figure 3.

3.2 Limnology data

Limnological data are available from the same location as the spectroradiometer measurements. The water samples were collected at two depths: 0.75 and 2.0 m. The available data include measurements of the Secchi depth, Chlorophyll-*a*, TSS (total suspended solids) and the organic portion of it (OSS) and attenuation at 440 nm. Chlorophyll was measured according to ISO/TC 147 (1988) hot ethanol extraction. TSS were measured by filtration of 1 or 2 l of lakewater through precombusted glasfibre filters after drying to constant weight at 80°C. OSS from

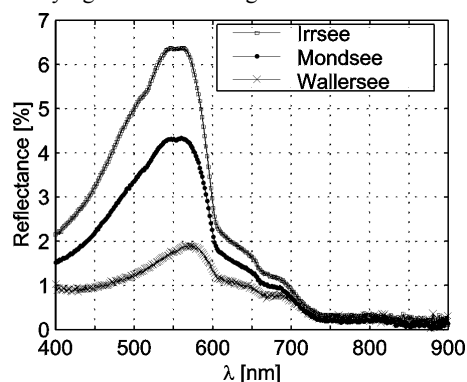


Fig 3: Reflectance above the water surface measured with the Field Spec spectroradiometer.

TSS are based on weight loss by ignition to 450°C. Background attenuation at 440 nm was measured for unfiltered and filtered (0.2mm poresize) lakewater

using 50 mm cuvettes in a double beam spectrophotometer against filtered deionized water.

The properties derived from the water samples at 0.75 m are summarized in Table 1. The chlorophyll concentrations are low (less than $5 \mu\text{g l}^{-1}$ with the highest concentrations in Wallersee but small maximum horizontal variations in all 3 lakes ranking between 20 and 30 % of the average. The Secchi depth shows no variability in the small Irrsee but highest maximum variability with almost 50 % of the mean in Wallersee. The interpretation of the variations between and within the lakes is difficult since the approaches to identify optical interacting particles (the measurements of TSS, OSS) and substances (measurement of background attenuation) are not sensitive enough.

Table 1. Limnological Data of Irrsee, Mondsee and Wallersee measured on 5 Juli 2001. z_{sd} - Secchi Disk depth, Chl-*a*, TSS, OSS - concentration of chlorophyll-*a*, total and organic sediments, respectively. The samples were collected at 0.75 m depth.

Sampl. point	Chl- <i>a</i> [$\mu\text{g l}^{-1}$]	z_{sd} [m]	TSS [mg l^{-1}]	OSS [mg l^{-1}]	Attenuation 440 nm Filtered
Irrs1	1.80	2.4	3.40	1.40	n.a.
Irrs2	1.73	2.4	3.30	1.40	n.a.
Irrs3	1.42	2.4	3.00	1.40	n.a.
Mond1	2.23	3.0	2.65	1.00	0.007
Mond2	1.95	2.3	n.a.	n.a.	0.010
Mond3	1.68	3.3	n.a.	n.a.	0.008
Mond4	1.68	2.9	1.70	0.55	0.005
Mond5	1.81	3.2	2.75	0.40	0.007
Wall1	4.33	4.2	2.15	1.05	0.007
Wall2	5.17	2.4	2.40	1.30	0.008
Wall3	4.19	3.4	2.80	1.60	0.010
Wall4	4.75	3.4	2.80	1.80	0.007
Wall5	4.19	5.3	1.85	0.60	0.010

4. ATMOSPHERIC CORRECTION

Our atmospheric correction procedure is based on the 6S software (Vermote et al, 1997), release 6.2. A mean aerosol optical depth at 550 nm of 0.1056 was derived from the PFR measurements on 5 July and used in 6S. For the aerosol model the Junge distribution was chosen with the Junge parameter of 3.0. Compared to the standard continental aerosols model for the Junge distribution the diffuse irradiance and transmissivity

due to scattering particles are higher. The lower 17 km of the atmosphere were described by air temperature, pressure and absolute humidity profiles derived from the radiosonde data at the station München acquired at 12:00 UTC. The station München is situated 80 km away from the Salzkammergut region at an altitude of 484 m a.s.l. Since an ozone vertical profile was not available for this date, ozone values from the standard mid latitude summer model were used. Anyhow in the spectral range of ROSIS and the flight altitude of 5 km the ozone concentration does not influence the atmospheric correction results. The radiosonde data describe the humidity profile of the atmosphere at the time of the overflight, leading to better radiative transfer results in the water vapour absorption bands.

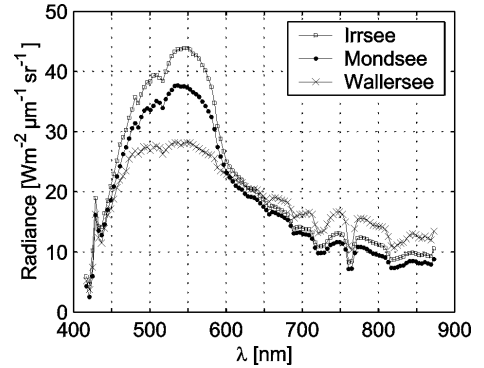


Fig. 4: ROSIS measured radiance of the three lakes.

4.1 The model

For each spectral band, b , the water surface reflectance was derived from the ROSIS radiance, $L(b)$ by

$$\rho(b) = \frac{\pi(L(b) - L_p(b, z))}{E(b, z)T_u(b, z)} \quad (1)$$

where $L_p(b)$ is the path radiance, $E(b, z)$ the total solar irradiance reaching the surface, $T_u(b, z)$ is the upward transmission coefficient through the atmosphere at the altitude z a.s.l. These 3 quantities were determined with 6S under the atmospheric conditions described above. The total solar irradiance is the sum of direct, diffuse and environment irradiance. For the calculation of environment irradiance the spectral reflectance of lake water implemented in 6S was replaced by *in situ* spectroradiometer measurements.

In figure 4 ROSIS radiance spectra of each lake at one measurement point are shown. The ROSIS spectral bands below 450 nm are noisy and were not taken into

account for further study. The lowest radiance is observed on Wallersee because of its brown water. This colour is due to the algal bloom of the *Ceratium* algae (Czernin-Chudenitz, 1986). The radiance peaks are located at 544 or 548 nm for Irrsee, 532 to 544 nm for Mondsee and 532 or 536 nm for Wallersee.

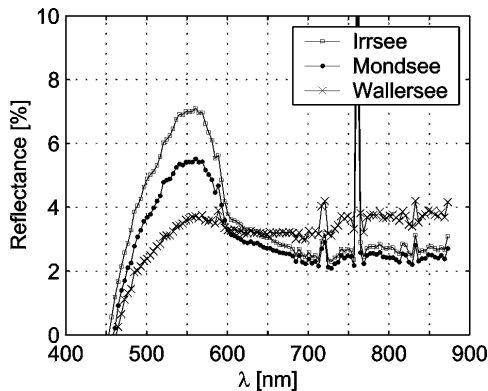


Fig. 5: ROSIS Reflectance of the three lakes calculated with the radiative transfer model.

The reflectance spectra derived after atmospheric correction of ROSIS data are shown in Fig. 5. The spectral bands centered at 720 nm and 760 nm are overcorrected by 6S. Especially at 760 nm, where a narrow O_2 absorption band exists, the wavelength dependence of the transmission coefficient could not be correctly modelled with the 2.5 nm resolution of 6S. At wavelengths up to 500 nm the low ROSIS reflectance may be due to an overestimation of path radiance. Around 550 nm the green peak reflectance dominates whereas above 600 nm the ROSIS reflectance is too high. Possible source of atmospheric correction errors in this region are the underestimation of path radiance, the sun glitter effect and the uncertainties in the phase function and size distribution of aerosols.

5. RETRIEVAL OF WATER QUALITY PARAMETERS

As an initial attempt to determine relationships between spectral reflectance and water quality parameters we applied statistical techniques. One of the objectives is to study the possible applications of the Medium Resolution Imaging Spectrometer (MERIS) of the European ENVISAT satellite for water quality monitoring.

The FieldSpec measured spectra above the water surface and the atmospherically corrected ROSIS reflectance were resampled to MERIS VIS spectral bands 2 to 7 (442 to 665 nm, with 10 nm bandwidth). Correlations between reflectance ratios corresponding to two MERIS bands and $Chl-a$

concentrations measured on the three lakes were calculated. Because MERIS Band 2 was generated from the noisy ROSIS bands below 450 nm, the ratios using MERIS band 2 reflectance could not be tested. A maximum correlation coefficient of -0.92 was obtained for the reflectance ratio between the 490 and 620 nm spectral bands corresponding to MERIS bands 3 and 6 (Fig. 6). The relationship between $Chl-a$ concentration in $\mu g \cdot l^{-1}$ and the reflectance ratio derived from ROSIS data was expressed as:

$$\begin{aligned} \rho(490nm) / \rho(620nm) = & \quad (2) \\ -0.1918 \cdot Chla + 1.4457 \end{aligned}$$

High correlations were also obtained between the reflectance ratios 490nm/665nm, and 510nm/620nm corresponding to MERIS spectral bands 3/7 and 4/6, respectively.

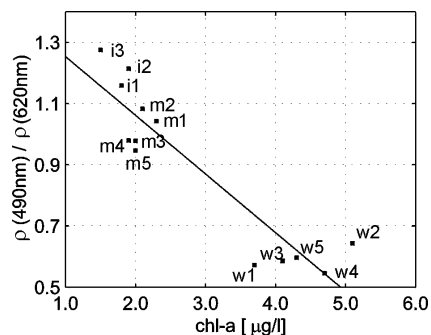


Fig. 6: Regression between $Chl-a$ concentration and reflectance ratio between spectral bands corresponding to MERIS bands 3 and 6. The squares represent measurement points at Irrsee (i), Mondsee (m) and Wallersee (w). The correlation between measurements and reflectance ratio is -0.92.

The correlations of the reflectance ratios with the other water quality parameters were weak. For the Secchi disk depth the best correlation is 0.66 with MERIS band ratios 3/6, 4/5 and 4/6. For TSS maximum correlation of 0.32 was observed for ratios with MERIS band 5. The concentration of yellow substance correlates with $Chl-a$ therefore the same spectral combinations can be used to retrieve this variable.

These results partially confirm the conclusions of Kallio et al (2001) who investigated series of reflectance ratios for limnological algorithms on Finnish lakes.

6. SUMMARY AND CONCLUSION

ROSIIS hyperspectral data acquired over 4 meso- to oligotrophic lakes in Austria were analysed. The atmospheric correction was carried out with the 6S radiative transfer model. By replacing the standard functions with the measured aerosol optical depth, Junge distribution, radiosonde profiles for temperature, pressure and humidity, and reflectance spectra measured above the water surface the radiative transfer results are considerably improved. Problems in the correction occurred for some narrow absorption bands because of the limited spectral resolution of the model and due to underestimation of path radiance, the sun glitter effect and the uncertainties in the phase function and size distribution of aerosols.

The possibilities to use ENVISAT MERIS for water quality applications on perialpine lakes were investigated. Correlations between the concentrations of optically active substances and ROSIS reflectance ratios (resampled to MERIS spectral bands) were calculated. The most promising combinations of spectral bands for the retrieval of Chl-*a* concentration correspond to MERIS band ratios 3/6, 3/7, 4/5 and 4/6. For z_{sd} , TSS, OSS and yellow substance the correlations are weak.

ACKNOWLEDGEMENTS

This work was supported by the Austrian Ministry of Education, Science and Culture (BMB:WK). We thank M. Dokulil and J. Wanzenböck from the Institute for Limnology at Mondsee and A. Jagsch at Bundesanstalt für Wassergüte Scharfling for supporting the field campaign on the lakes.

REFERENCES

- Czernin-Chudenitz, 1986, Die Entwicklung der Phytoplanktons, Raumbezogene Forschung und Planung im Land Salzburg 2, Ed. P. Jäger, 507 p.
- Gege, P., D. Beran, W. Mooshuber, J. Schulz, H. van der Piepen, 1998, System analysis and performance of the new version of the imaging spectrometer ROSIS, 1st EARSel Workshop on Imaging Spectroscopy, Eds. M. Schaepman, D. Schläpfer, K. Itten, 29 - 35.
- Ingold, T., 1998, SPM-Toolbox Documentation, Research Report, Institute for Applied Physics, Univ. of Bern.
- ISO 10260 1992, Water quality. Measurements of biochemical parameters. Spectrophotometric determination of chlorophyll *a*, Internat. Standardiz. Organisation, Geneva.
- Kallio, K., T. Kutser, T. Hannonen, S. Koponen, J. Pulliainen, J. Vepsäläinen and T. Pyhälähti, 2001, Retrieval of water quality from airborne imaging spectrometry of various lake types in different seasons, *The Science of The Total Environment*, **268**, Issues 1-3, 59-77.
- Roth, H and C. Wehrli, 1999, PFR-Precision Filter Radiometer Documentation version 2., prepared at PMOD/WRC Davos.
- Vermote, E., Tanré, D., Deuzé, J.L., Herman, M., & Morcrette J.J., 1997, Second Simulation of the Satellite Signal in the Solar Spectrum, 6S: An Overview, IEEE TGRS, 35 (3), 675 – 686.

M. Schlerf, C. Atzberger

Remote Sensing Department, University of Trier

Geozentrum, D-54286 Trier, Germany

schlerf@uni-trier.de, atzberge@uni-trier.de

ABSTRACT - *A forest reflectance model (INFORM) was used in the direct mode to simulate bi-directional canopy reflectance spectra from which regression equations between canopy variables and various spectral indices have been developed. INFORM ('Invertible Forest Reflectance Model') calculates forest bi-directional spectral reflectance from 400 to 2500 nm as a function of structural and biochemical forest characteristics, such as stem density, leaf area index, crown coverage as well as leaf chlorophyll and water content. The simulation was driven by randomly chosen parameter combinations, covering the typical range of values that apply to Norway spruce (Picea abies). Empirical relationships between spectral indices derived from the synthetic reflection spectra and corresponding canopy characteristics were developed through regression analysis. We systematically analyzed reflectance ratios, normalized differences, inflection wavelengths and also first-order derivatives. The empirical models were applied to geometrically and atmospherically corrected remote sensing imagery (HyMap) and field-sampled reference data of 29 reference plots covered by Norway spruce at Idarwald test site, Germany. Foliar samples were obtained according to standardized procedures shortly after the aircraft overpass and subjected to routine biochemical analysis for chlorophyll (a+b) and water content. Structural canopy parameters were obtained during field campaigns in 1999 and 2000. Developed regression equations were applied to the HyMap spectra and estimated canopy parameters were compared to those obtained through ground sampling. The obtained results seem to be promising.*

1 INTRODUCTION

Knowledge about forest structural and chemical variables is vital to both scientific research and forest resource management. Forest inventories routinely collect data on stem density to assess timber volume. Models estimating fluxes of matter and energy, such as Forest-BGC (Running & Coughlan, 1988; Running et al., 1994), have been developed to determine the role that forests have in the fixing of atmospheric carbon. The application of those models depend on the availability of reliable spatial data on biophysical and chemical vegetation characteristics.

Estimates of structural and chemical canopy variables by traditional field sampling methods are time-consuming and difficult to realize for regional to global scales. Remote sensing in contrast, using airborne or spaceborne spectrometers, has the potential for estimating these attributes even at large scales.

One way to derive a certain canopy variable from remotely sensed reflectance data is to find an empirical relation between the canopy reflectance and the variable measured in the field. This predictive relationship can then be used to estimate the variable for the entire image. However, forest canopy reflectance is controlled by many internal factors such as LAI, stem density, cover, understorey LAI and also

external factors such as illumination and viewing geometry. If those factors fluctuate a relationship between the desired variable and the spectral response can possibly not be found due to disturbing effects. Consequently, statistical regression models can hardly be applied to conditions other than those found during calibration.

In this context, canopy reflectance models constitute a unique and powerful alternative because they allow to fully control all structural and chemical canopy variables and also the external parameters. Models describing radiative transfer through leaves and vegetation canopies (see review by Goel, 1988) increase the understanding of plant reflectance. A reflectance model (leaf and/or canopy scale) relates the spectral information via a complex mathematical function to leaf and canopy variables. Estimation of these variables can be achieved through inversion of a reflectance model (inverse mode). However, a given reflectance signal may be generated by more than one set of parameter combinations because several variables affect canopy reflectance in the same way and a unique solution can then not be determined (ill-posed problem) (Combal & Baret, 2001). As an alternative to a computationally intensive model inversion, a physical-based model can also be employed in the direct mode to find predictive

relationships between the canopy input variables and the calculated reflectance. This approach has recently found wide application: In a theoretical study, Broge & Leblanc (2001) compared broadband and hyperspectral VIs for the estimation of LAI and canopy chlorophyll density. Equations predictive of forest chemistry (cellulose, lignin and proteins) were assessed by Gastellu-Etchegorry & Bruniquel-Pinel (2001) using a 3-dimensional reflectance model. However, most of the studies did not attempt to validate the theoretically derived prediction equations on measured data.

2 OBJECTIVES

The objectives of this study are to (i) investigate how modelled HyMap reflectance data can be used for estimating structural and chemical forest variables and (ii) to examine the applicability of derived predictive equations on real data.

The study consists of three stages: (1) simulation of visible to mid-infrared bi-directional spectral reflectance of forest canopies with variable structure and chemistry using a canopy reflectance model; (2) determination of predictive relationships between spectral indices and canopy properties with linear regression; (3) application of the predictive equations to remotely sensed image data and comparison of predicted with field-measured values of canopy variables.

3 DATA AND FIELD AREA

The area of study (49°40'N, 7°10'E) is located in the Idarwald forest in south-western Germany on the north-western slope of the Hunsrück mountain ridge. The dominant forest species are Norway spruce (*Picea abies*), beech (*Fagus sylvatica*), oak (*Quercus petraea*) and Douglas fir (*Pseudotsuga menziesii*). Active forestry practices in this area include selective cutting, plantation establishment and thinning.

Hyperspectral image data were acquired in July 1999 using the HyMap sensor built by Integrated Spectronics, Australia. HyMap records data in 128 contiguous spectral bands covering the spectral range of 0.4–2.5 μm with a spectral resolution of 10–20 nm. The spatial resolution was set to 5 m with a full scene covering 4 km x 10 km.

Radiometric corrections of the HyMap data were performed at the Remote Sensing Department, University of Trier following an approach by Hill et al. (1995). The processing steps involved atmospheric correction and sensor calibration. The first step converted digital numbers to at-sensor-radiances. In the second step, the effects of the atmosphere were removed including errors due to pixel orientation. A

number of HyMap channels (14) were omitted from further analysis for the reason of high noise in these wavebands. The dataset was geocoded using parametric image processing software PARGE (Schläpfer et al., 1998).

Field data was collected during campaigns in 1999 and 2000. A number of structural variables were measured in 29 forest stands; additionally foliar samples were collected for chemical analysis in 10 of the stands. The canopy variables were obtained from quadratic plots of 30 m length. Structural parameters include stem density, cover (canopy closure) and LAI. Stem density was obtained by counting the number of trees in a plot. Canopy closure was visually estimated; in addition, vertical, sky looking photographs were taken of the crown canopy in order to estimate canopy closure. LAI was estimated from measurements using a Li-Cor LAI-2000 instrument. Measured values, although they represent rather the effective canopy area index instead of the effective leaf area index due to the non-random distribution of leaves were not corrected. Foliar samples were obtained according to standardized procedures from the upper part of the crown of three randomly selected trees within each plot shortly after the aircraft overpass. Foliage from the sampled branches were removed separately by age class and randomly selected subsamples were subjected to routine biochemical analysis for chlorophyll a and b (Lichtenthaler, 1987) and water content.

The forest reflectance model INFORM (Atzberger, 2000) is essentially a combination of SAIL (Verhoef, 1984), PROSPECT (Jacquemoud & Baret, 1990) and FLIM (Rosema et al., 1992). It describes the spectral bi-directional reflectance of the forest canopy as the probability of the sensor to observe a crown or the ground, respectively. Crown transmission, crown reflectance and understory reflectance are basically calculated by the SAIL and PROSPECT models. Calculation of crown transmission has been modified by a correction term accounting for woody canopy components. Leaf spectral reflectance and transmittance are calculated through the PROSPECT model.

3 METHODS

3.1 Computation of reflectance spectra

Canopy reflectance spectra were computed with the INFOR model (Atzberger, 2000) using the range of parameter values given in Table 1. The reflectance spectra were computed in the 114 wavebands of the HyMap sensor excluding those channels previously identified as 'bad bands'.

Table 1: Input variables for computation of canopy spectra

Variable	Abbrev.	Range	Unit
Leaf area index	LAI	1-8	m ² m ⁻²
Canopy closure	CO	0.2-0.8	-
Stem density	D	200-1000	ha ⁻¹
Chlorophyll a+b concentration	CABL	10-100	µg cm ⁻²
Water content	CWL	0.01-0.05	cm

The simulation of the reflectance spectra was driven by randomly generated parameter values within the aforementioned ranges. A total of 20.000 spectra were simulated to take into account parameter combinations that typically occur in Norway spruce forests. The frequency distribution of the variables show the following patterns: The variables D, CABL and CWL are equally distributed; CO is derived from the crown radius (equally distributed) and is skewed to the right as a result of squaring. Canopy LAI is the product of tree LAI (equally distributed) and CO and thus is skewed to the left. Two more variables, canopy CAB (CABC) and canopy CW (CWC) are derived as the product of LAI and leaf CAB (CABL) and leaf CW (CWL), respectively.

3.2 Calculation of VIs

Traditional vegetation indices (VIs) are based on discrete bands, usually located in Red and NIR wavelengths. They are generally divided into ratio indices and orthogonal indices. Ratio indices are calculated independently of soil reflectance properties, whereas orthogonal indices include parameters referring to the soil line. Hyperspectral VIs, such as the red edge inflection point (REIP), typically require a contiguous coverage of the spectral range by narrow bands.

The ratio vegetation index (RVI) and the normalized difference vegetation index (NDVI) are based on the reflectance in the Red and NIR part of the spectrum:

$$RVI = \frac{\rho_{NIR}}{\rho_{Red}} \quad (1)$$

$$NDVI = \frac{\rho_{NIR} - \rho_{Red}}{\rho_{NIR} + \rho_{Red}} \quad (2)$$

Generally, these indices tend to minimize the effects of illumination conditions while enhancing the contrast

between vegetation and soil (Baret & Guyot, 1991). In the present study, RVI and NDVI were not only calculated for Red and NIR wavebands, but for all possible $n \times n - 1$ two-band combinations ($n=114$).

The abrupt increase in reflectance at the transition from Red to NIR wavelengths, defined by the point of maximum slope, is generally referred to as the “red edge” (Horler et al. 1983). The wavelength position of the red edge, named red edge inflection point (REIP), occurs between 680 and 740 nm. The REIP depends on the amount of chlorophyll seen by the sensor (Dawson & Curran 1998). The chlorophyll amount present in a vegetation canopy is characterised by the chlorophyll concentration of the leaves and the LAI. An increase in chlorophyll moves the REIP to longer wavelengths and vice versa. REIP was computed by two different techniques: the Inverted Gaussian model (IGM) introduced by Bonham-Carter (1988) and the Lagrangian interpolation (LGI), proposed by Dawson & Curran (1998).

The IGM method fits a Gaussian normal function to the reflectance at the red edge and the estimated REIP is then the midpoint on the ascending part of the modelled curve:

$$R_{est}(\lambda) = R_s - (R_s - R_0) \cdot e^{-\frac{(\lambda - \lambda_0)^2}{2\sigma^2}} \quad (3)$$

where R_s is the reflectance maximum (“shoulder” reflectance), usually at approximately 780-800 nm; R_0 is the reflectance minimum, usually at about 670-690 nm; λ_0 is the wavelength of the reflectance minimum; σ is the Gaussian shape parameter with unit nm. The red edge inflection point is then derived from $REP_{IGM} = \lambda_0 + \sigma$. The function is fitted through the measured reflectance data points $R_{mes}(\lambda)$ by adjusting iteratively the values of R_s , R_0 , λ_0 and σ in such a way that the root mean square error (RMSE) is minimized. The LGI technique is applied to the approximate first-derivative of the reflectance spectrum. A second order polynomial is fitted directly to three bands of the first-order derivative spectrum.

Besides VIs, also approximate first-order derivatives were calculated according to

$$D(\lambda_j) = \frac{R(\lambda_{j+1}) - R(\lambda_{j-1})}{\lambda_{j+1} - \lambda_{j-1}} \quad (4)$$

where $D_{mes}(\lambda_j)$ is the measured first-derivative transformation at the midpoint with wavelength j between the wavebands $j-1$ and $j+1$; $R(\lambda_{j-1})$ and $R(\lambda_{j+1})$ are the reflectances at the bands $j-1$ and $j+1$, respectively. Derivatives were shown to be less sensitive to soil background variations but are subject to sensor noise (Demetriades-Shah et al. 1990).

3.3 Establishment of predictive relationships

A phenomena generally observed is the saturation of a spectral index with increasing value of a canopy variable (Guyot et al., 1992). For instance, NDVI starts to saturate with increasing LAI above a critical LAI value of 3, resulting in an exponential relationship. To overcome this problem of non-linearity, we decided to work with the natural logarithm of the variables. Coefficients of determination (r^2) between the spectral indices and the logarithm of the canopy variables were calculated. The correlations for CO and D were performed using the entire dataset (nobs=20.000); by doing so the other variables were allowed to have maximum variability. In the case of CABC and CABL, the range of CWL was limited to 0.02-0.04 cm and for CWC and CWL, the range of CABL was limited to 0.35-0.55 $\mu\text{g cm}^{-2}$, reducing the number of observations to 10.000. For LAI both range limits (CABL and CWL) were applied, leaving 5.000 data points for the analysis. Two-dimensional correlation matrices were computed for the ratios and normalized differences, correlation spectra for the first-order derivatives and absolute reflectance. Single values of r^2 resulted in the case of the REIP.

Optimal wavelengths were selected according to three conditions: (1) r^2 between VI and variable is high (2) root mean square error between actual and

predicted value is minimal (3) the wavelength or the wavelength region can be attributed to the investigated variable.

Regressions between the spectral indices of optimal wavelengths and the variables were computed and predictive equations established.

3.4 Application to image data

Predictive relationships were applied to the HyMap imagery. Image pixels not representing spruce forest had been masked out using a mask derived from an unsupervised image classification. Image pixels centred around the forest plots were extracted and the mean value was calculated. Predicted with field-measured values of canopy variables were compared.

4 RESULTS AND DISCUSSION

The canopy reflectances simulated with the forest canopy reflectance model were compared with the reflectances observed by the HyMap sensor. The shapes of the modelled and observed reflectance curves and also the absolute levels of reflectance generally correspond well. However, between 1020 and 1200 nm features atypical from known vegetation spectra occur; those wavebands were excluded from further analysis.

Table 2: Coefficients of determination (r^2) between VIs and canopy variables derived from simulated reflectance spectra (++: $r^2 > 0.9$, +: $0.7 \leq r^2 < 0.9$, o: $0.5 \leq r^2 < 0.7$, -: $0.3 \leq r^2 < 0.5$, , —: $r^2 < 0.3$). Symbols behind a slash (/) indicate that a relationship also exists between measured HyMap reflectance spectra and field-measured canopy variables. Bold symbols indicate that an agreement exists for exact wavelength positions. LAI=Leaf area index, CO=Canopy closure (cover), D=Stem density, CABC=Canopy chlorophyll content, CABL=Leaf chlorophyll concentration, CWC=Canopy water content, CWL=Leaf water content

Category	VI	LAI	CO	D	CABC	CABL	CWC	CWL
Ratio vegetation indices	NIR/NIR	o/o	o	o/o	—	—	o	—
	Green/NIR	o	+	+	o	—	—	—
	Red/NIR	—	o	o	—	—	—	—
	RE/NIR	o	+/o	+	+/o	+	—	—
	MIR/NIR	—	o	o	—	—	o	—
	Red/MIR	—/o	—/—	o/o	—	—	—	o/o
First-order derivatives	NIR'	o	+	+	—	—	o	—
	RE'	—	+	+	o	—	—	—
	Red'	—	—	—	—	o	—	—
	MIR'	—	o	o	—	—	o	o
Reflectances	NIR	—	+	+	—	—	—	—
	Green	—	—	—	o	o	—	—
Red edge inflection points	REIP _{IGM}	—/o	o	o	+	o	—	—
	REIP _{LGI}	—/o	o	—	o	—	—	—

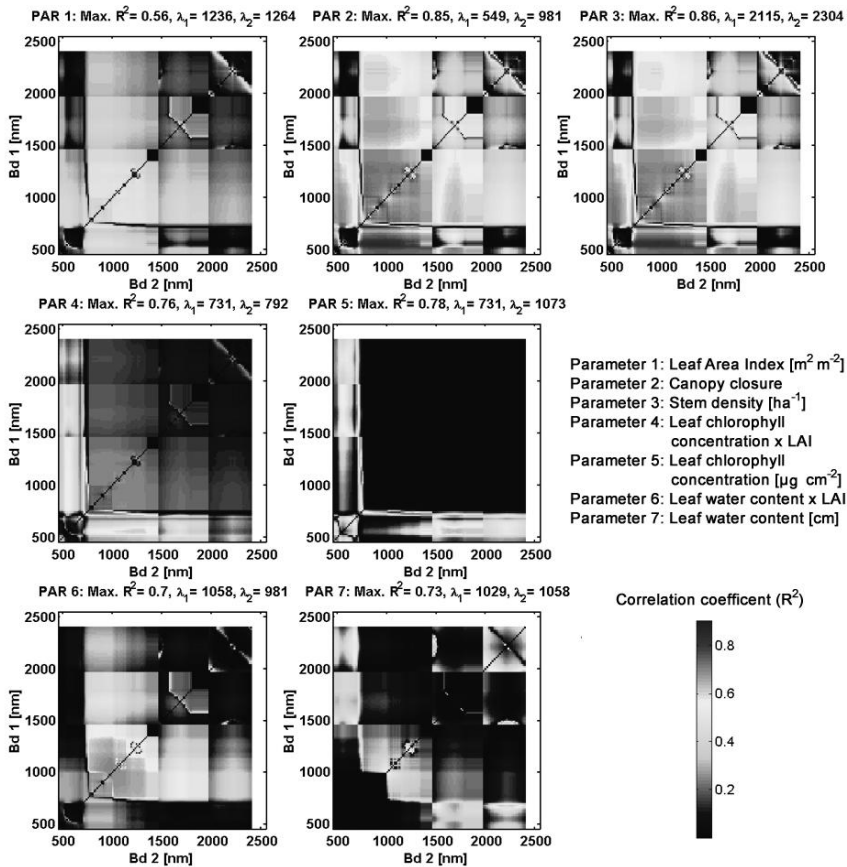


Figure 1: Two-dimensional correlation matrices. Each matrix consists of 114×114 elements. Each element is the result of a correlation analysis of up to 20,000 data points (see text for details).

Table 2 summarizes the results obtained from the correlation matrices using RVIs (Figure 1) and the correlation spectra (Figure 2). The correlation matrices achieved with NDVIs essentially show the same patterns; hence they are not discussed separately. LAI shows moderately high r^2 in the NIR wavelength region and in the Red Edge (RE/NIR); CO and D are well correlated with ratios in the Green and Red Edge, first derivative reflectance in the NIR and RE, absolute reflectance in the NIR and also show moderate r^2 with the REIP. CABC and CABL are well correlated with the RE/NIR ratio and perform moderately with absolute reflectance in the Green. REIP performs better with CABC than with CABL. CWC and CWL correlate best with ratios where MIR is involved and with the first-order derivative in the MIR region. These results illustrate in most of the cases well known absorption properties of the canopy variables. The green reflection peak, the red absorption feature and the position of the red edge inflection point are strongly determined by the canopy chlorophyll content;

however, Red/NIR does not correlate with CABC or CABL. The wavelengths region located at and between the water absorption peaks in the mid-infrared wavebands are determined by the canopy water content. The amount of leaves influences the reflection characteristics in the NIR. CO and D control the reflectance properties in both the VIS and NIR regions.

Optimal wavelengths according to the aforementioned criteria were found for all seven variables. The corresponding relationships are plotted in Figure 3. High coefficients of determination and low rmse values were derived for CO, D and CABL. Relatively low r^2 and a relatively high value of rmse was obtained for LAI. CWC and CWL performed moderately well. From these results it can be concluded that the modelled HyMap reflectance data can be used for the estimation of structural and chemical forest characteristics. However, the transfer of the predictive relations to the measured HyMap data was difficult. As can be seen from Table 3, only

for LAI and D predictive equations could be successfully applied to the measured HyMap data and validated by the field-measured variables. For CO, CABC and CWL similar wavelengths positions but not exactly the ones proposed by the theoretical study were found. For the moment it is not clear what reasons cause these deviations. More detailed analyses are underway.

In Figure 4 predicted against ground-measured LAI is plotted. LAI was estimated using the predictive

equation proposed by the modelling results. Figure 5 shows the predicted LAI at the Idarwald test site.

5 CONCLUSION

The main conclusions of this study are:

The forest canopy reflectance model was able to simulate the general shape and the absolute levels of reflectance of observed reflectance spectra, but differences were found for some wavelengths.

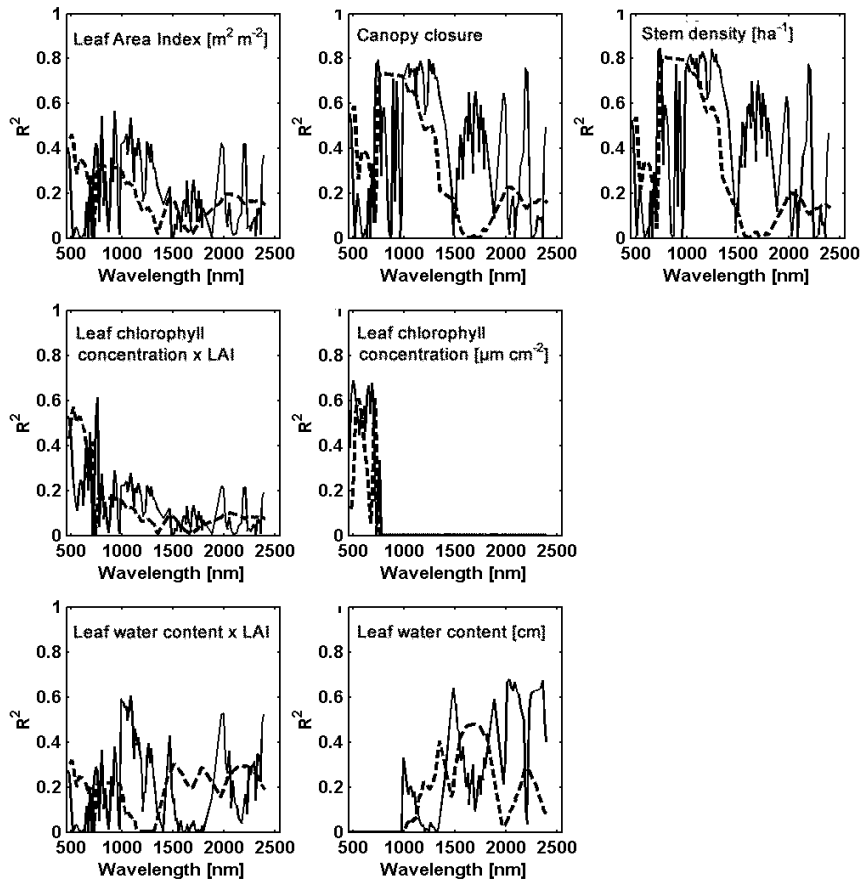


Figure 2: Correlation spectra. Broken thick line: Reflectance; Straight thin line: First-order derivative of reflectance.

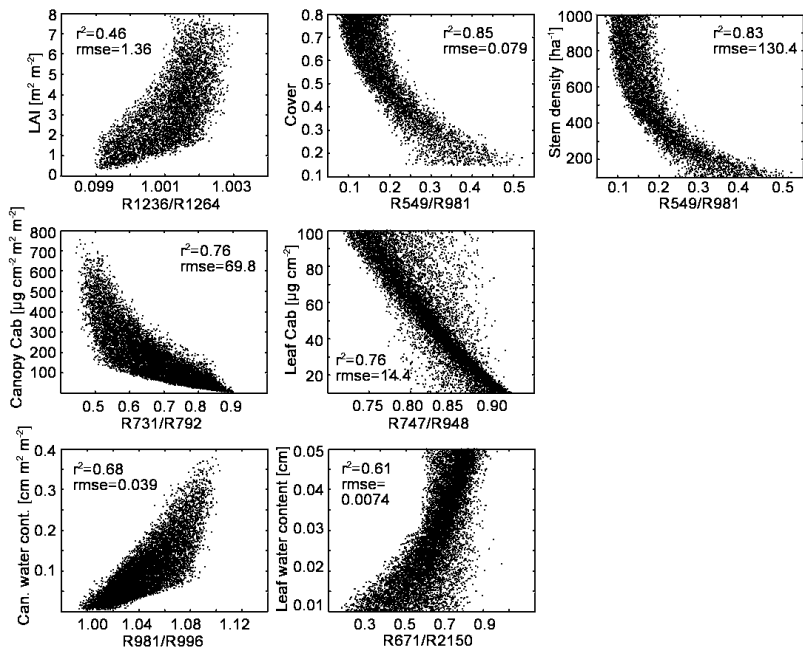


Figure 3: Plots of canopy variables against ratio vegetation indices from synthetic data. The wavelengths positions represent the best result obtained. Correlation and regression analysis was performed on the variables after the logarithm had been taken.

Correlations between randomly generated input variables and vegetation indices derived from modelled reflectances are relatively high for most of the variables and predictive equations can be derived.

Transfer of predictive relationships to real data is difficult. Although there is a correspondence in the wavelength regions for most of the variables, exact wavelengths positions where relationships exists between VIs and canopy variables for both simulated spectra and measured HyMap spectra exist only for LAI and stem density.

Some useful relationships were found, but the general validity of the relationships is limited due to the low sampling size in this study.

6 ACKNOWLEDGEMENTS

This research was financially supported by the German Research Community (DFG). The authors are grateful to Dr. Joachim Hill for the radiometric and geometric correction of the HyMap data. We thank Dr. Willy Werner who carried out the chemical analysis of the foliage samples and Samuel Bärish for his assistance with the field and laboratory work.

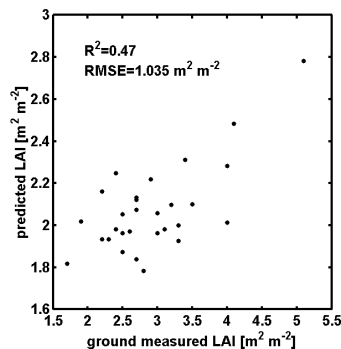


Figure 4: Predicted against ground measured LAI. **Table 3:** Wavelengths positions where relationships exists between VIs and canopy variables for both simulated spectra and measured HyMap spectra

Variable	VI INFORM	VI HyMap	Agreement
LAI	$\rho 885/\rho 1221$	$\rho 890/\rho 1225$	yes
CO	$\rho 702/\rho 885$	$\rho 735/\rho 1200$	no
D	$\rho 1207/\rho 1279$	$\rho 1210/\rho 1285$	yes
CABC	$\rho 731/\rho 792$	$\rho 750/\rho 950$	no
CWL	$\rho 671/\rho 2150$	$\rho 600/\rho 1680$	no



Figure 5: Predicted LAI at the Idarwald test site derived from HyMap data overlaid by forest stand borders. Dark pixels correspond to low and bright pixels to high LAI values, respectively. Black pixels represent non-coniferous stands.

7 REFERENCES

- Atzberger, C. (2000): Development of an invertible forest reflectance model: The INFOR-model. In: Buchroithner (Ed.): *A decade of trans-european remote sensing cooperation*. Proceedings of the 20th EARSel Symposium, 14-16 June 2000, Dresden. Balkema Publishers, Lisse: 39-44.
- Baret, F. & Guyot, G. (1991): Potential and limits of vegetation indices for LAI and APAR assessment. *Remote Sensing of Environment*, 35: 161-173.
- Bonham-Carter, G. F. (1988): Numerical procedures and computer program for fitting an inverted Gaussian model to vegetation reflectance data. *Computers & Geosciences*, 14: 339-356.
- Broge, N. H. & Leblanc, E. (2000): Comparing prediction power and stability of broadband and hyperspectral vegetation indices for estimation of green leaf area index and canopy chlorophyll density. *Remote Sensing of Environment*, 76: 156-172.
- Combal, B. & Baret, F. (2001): Estimation of chlorophyll content from remote sensing observations in the solar domain. In: Leroy (Ed.): *Physical measurements and signatures in remote sensing*, Aussois, France: 461-471.
- Dawson, T. P.; Curran, P. J. (1998): A new technique for interpolating the reflectance red edge position. *International Journal of Remote Sensing*, 19: 2133-2139.
- Demetriades-Shah, T. H.; Steven, M. D.; Clark, J. A. (1990): High resolution derivative spectra in remote sensing. *Remote Sensing of Environment*, 33: 55-64.
- Gastellu-Etchegorry, J. P. & Bruniquel-Pinel, V. (2001): A model approach to assess the robustness of spectrometric predictive equations for canopy chemistry. *Remote Sensing of Environment*, 76: 1-15.
- Goel, N. S. (1988): Models of vegetation canopy reflectance and their use in estimation of biophysical parameters from reflectance data. *Remote Sensing Reviews*, 4: 1-212.
- Guyot, G.; Baret, F.; Jacquemoud, S. (1992): Imaging spectroscopy for vegetation studies. In: Toselli & Bodechtel (Eds.): *Imaging spectroscopy: Fundamentals and prospective applications*. ECSC, EEC, EAEC, Brussels, Luxembourg.
- Hill, J.; Mehl, W.; Radeloff, V. (1995): Improved forest mapping by combining corrections of atmospheric and topographic effects. In: J. Askne (Ed.): *Sensors and environmental applications of remote sensing*, Proc. 14th EARSel Symposium, Göteborg, Sweden, 6-8 June 1994. A.A. Balkema: Rotterdam, Brookfield: 143-151.
- Horler, D. N.; Dockray, M.; Barber, J. (1983): The red edge of plant leaf reflectance. *International Journal of Remote Sensing*, 4: 273-288.
- Jacquemoud, F.; Baret, F. (1990): PROSPECT: A model of leaf optical properties spectra. *Remote Sensing of Environment*, 34: 75-91.
- Lichtenthaler (1987): Chlorophylls and carotenoids, the pigment of the photosynthetic biomembranes. *Methods in Enzymology*, 148: 350-382.
- Rosema, A.; Verhoef, W.; Noorbergen, H. (1992): A new forest light interaction model in support of forest monitoring. *Remote Sensing of Environment*, 42: 23-41.
- Running, S. W. (1994): Testing Forest-BGC ecosystem process simulations across a climatic gradient in Oregon. *Ecological Applications*, 4: 238-247.
- Running, S. W.; Coughlan, J. C. (1988): A general model for forest ecosystem processes for regional applications. I. Hydrologic balance, canopy gas exchanges and primary production processes. *Ecological Modeling*, 42: 125-154.
- Schläpfer D.; Schaepman M. E.; Itten K. I. (1998): PARGE: Parametric Geocoding Based on GCP-Calibrated Auxiliary Data. *SPIE Int. Symp. on Opt. Sc, Eng. and Instr.*, San Diego: 334-344.
- Verhoef, W. (1984): Light scattering by leaf layers with application to canopy reflectance modeling: The SAIL model. *Remote Sensing of Environment*, 16:125-141.

Object-based retrieval of structural and biochemical canopy characteristics using SAIL+PROSPECT canopy reflectance model: A numerical experiment

Clement Atzberger

Remote Sensing Department, University of Trier, Behringstrasse, D-54286 Trier, Germany
atzberger@feut.de

ABSTRACT - Spatial maps of structural and biochemical canopy characteristics are required in precision agriculture and other related fields. Cost-effective, timely and repetitive, these variables can be delivered only by means of remote sensing. Although much progress has been achieved in the last two decades concerning the (physically based) modeling of spectral canopy reflectances, the “ill-posed” nature of the model inversion remains problematic – that means, different parameter combinations of physically based reflectance models may yield almost identical bi-directional reflectance spectra. Therefore, in the inverse mode, it is not always assured that an unique solution exists. With this paper we demonstrate how to regularize the inversion of a well known canopy reflectance model (SAIL+PROSPECT), using simultaneously pixel and object signatures in a neural network approach. Such object signatures are available when images are segmented, respectively, when field boundaries have been digitized prior to analysis. The improved retrieval of canopy variables compared to the standard pixel-based inversion is demonstrated on synthetic spectra of 100.000 image objects (representing agricultural fields). The concurrent use of pixel and objec signatures allows the retrieval of LAI, leaf chlorophyll and leaf water content with accuracies (PRMSE) of 5 to 8 % for large parameter ranges. Coefficients of determination (R^2) were in the range 0.85 (leaf chlorophyll content) to 0.94 (leaf water content).

1 INTRODUCTION

In precision agriculture, maps of canopy characteristics like LAI, leaf chlorophyll content (Cab), and equivalent leaf water thickness (Cw) can be used to spatially adapt management practices, with potentially positive benefits for both the farmer and the environment (Schueller, 1992; Auerhammer, 1999).

The cost effective, timely and repetitive mapping of these biophysical variables is feasible only with remote sensing techniques (Moran et al., 1997; Baret et al., 2000). However, the estimation of vegetation characteristics is far from being trivial, since many (canopy and external) factors influence canopy reflectance (e.g. Baret, 1991; Guyot, 1990). This yields highly variable statistical models (Curran, 1994) and led to the development of physically based canopy reflectance models (reviews in Goel, 1988; Myneni et al., 1989). They model the radiative transfer inside the canopy and simulate a unique spectral signature for a given parameterization. However, the reverse is not true (e.g. Combal & Baret, 2001). For a given spectral signature it is not always sure that a sole parameter set can be retrieved, because different parameterizations may yield almost identical signatures. For example, it has been shown for agricultural crops, that the spectral signature of a sparse canopy with planophile leaf orientation resembles very much one of a dense, erectophile canopy (Baret & Guyot, 1991; Baret & Jacquemoud, 1994).

Different strategies may be used to overcome this so-called “ill-posed problem” (Combal et al., 2001). One possibility to handle this problem is to increase the number of spectral bands, or to use the multi-directional measurement capacity of sensors like MISR and others. However, since vegetation generally lack diagnostic absorption features, even hyperspectral data are not always sufficient to retrieve the desired canopy variables (Verstraete et al., 1996; Baret & Fourty, 1997; Fourty & Baret, 1997). The use of multi-directional measurements seems promizing (e.g. Barnsley et al., 1997; Qi et al., 1995), but such imagery will not always be available and their use adds additional difficulties to the (radiometric) preprocessing (Strahler et al., 2000).

Combal et al. (2001) proposed and demonstrated how to use *a priori* knowledge to regularize the inversion process in a look-up-table (LUT) based approach. Their algorithm accounts in a first step only for the radiometric information. All the inputs where the error between measured spectra and the spectra stored in the LUT is lower than the measurement uncertainty are kept as acceptable solutions with regard to the radiometric information. In the second step, from the selected LUT entries, only the entry that is closest to the prior information is considered as the best estimate of the canopy variables. Therefore, this algorithm concurrently exploits the radiometric and prior information. Of course, this will be feasible only if such information is available.

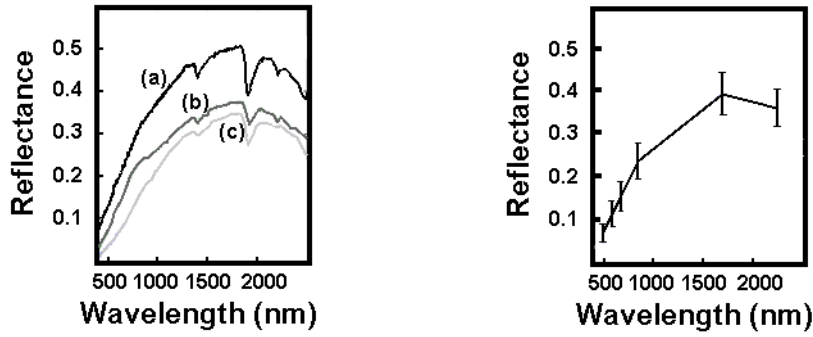


Figure 1. Reference “end-member” soil reflectance spectra from the ASTER spectral library (JPL, 1999) (left) and simulated soil reflectances (mean and standard deviation) in Landsat TM channels (right). The end-member soils are: (a) very dark grayish brown loam, (b) brown sandy loam, and (c) black loam. For simulation of soil reflectance in Landsat TM channels a spectral mixing approach has been followed, which allows the original end-member spectra to be scaled to simulate moisture and roughness induced brightness changes. For details refer to the text.

Multitemporal datasets offer the possibility to observe the radiometric evolution of a crop during the growing season. If a (mechanistic) crop growth model is coupled with a canopy reflectance model (CRM) one is able to reparameterize the CRM by minimizing the residues between observed and modeled multitemporal reflectance patterns (Délécolle et al., 1992). This yields more consistent estimates of the canopy variables and avoids the inversion of the canopy reflectance model (e.g. Atzberger et al., 2001).

Another way to use multi-temporal datasets has been presented by Koetz (2001) in the framework of the CROMA project (CROMA, 2000). Here, canopy variables are estimated first from each single image

alone. The temporal evolution of the retrieved canopy variables is then fitted by an empirical model. The fitted values are afterwards used as *a priori* information in the inversion process. This procedure is repeated until a stabilization of the results is obtained.

With this study, we present a new methodology which uses intra- and interchannel statistical features of spatially continuous image objects to regularize the inversion process. Such statistical features are, for example, available when the objects of interest are agricultural fields rather than single pixels. Objects may be easily determined either through image segmentation techniques (Baatz & Schäpe, 2000), or from digitized/vectorized field boundaries.

Table 1. Applied inputs to generate the biophysical parameter distributions of the image objects (each with 25 pixels) (left) and resulting parameter distribution of the validation data set (nobs=30.000) (right). The approach to generate randomly biophysical parameter distributions of image objects is $VAR = VAR_{min} + rand_{uniform}(25,1) * VAR_{range}$ with VAR being the variables of the canopy reflectance model (i.e. LAI, ALA, Cab, Cw, Cm, N and s). The two random variables (uniform distribution) VAR_{min} and VAR_{range} may take any value between the lower and upper bounds indicated for each biophysical variable. $rand_{uniform}(25,1)$ is a random generator ($\in \{0,1\}$) for the 25 pixels of each image object (uniform distribution) for all variables except LAI, Cab and Cw. For these variables, the random generator is replaced by the so-called beta distribution ($\in \{0,1\}$) with two parameters: a and b . The distributions of two parameters are generated randomly (uniform distribution) so that $0.5 \leq (a,b) \leq 4.0$

Inputs to generate parameter distributions of image objects			Statistics of the resulting parameter distributions (validation data set)			
VAR	VAR_{min}	VAR_{range}	min	max	$mean$	$s.d.$
LAI	$\in \{0,3\}$	$\in \{1,6\}$	0.01	8.63	3.25	1.52
Cab	$\in \{20,80\}$	$\in \{10,40\}$	20.1	118.6	62.4	19.2
Cw	$\in \{0.004,0.034\}$	$\in \{0.005,0.025\}$	0.004	0.058	0.027	0.010
ALA	$\in \{20,70\}$	$\in \{2,10\}$	20.1	79.5	48.0	14.7
Cm	$\in \{0.002,0.018\}$	$\in \{0.001,0.002\}$	0.002	0.020	0.011	0.005
N	$\in \{1,2.8\}$	$\in \{0.1,0.2\}$	1.01	2.98	1.98	0.52
s	$\in \{0.01,0.09\}$	$\in \{0.01,0.01\}$	0.020	0.100	0.060	0.023

Since agricultural fields are mono-crops with similar phenological development, assumptions can be made for example about the intra-field variability of the average leaf angle (ALA) which yields different object signatures for planophile and erectophile canopies. We will show on synthesized data corresponding to the reflective channels of Landsat TM, that the object-based modeling and inversion approach is useful in regularizing the inversion process and helps to get more reliable estimates of LAI, leaf chlorophyll (Cab) and leaf water content (Cw).

2 METHODS

2.1 General outline

Standard backpropagation neural networks have been trained with synthesized object and pixel signatures to allow the simultaneous estimation of three important canopy variables from spectral data in Landsat TM reflective channels (i.e. LAI, Cab and Cw). For this purpose, we first created a large database using a crop reflectance model (CRM) consisting of three well established sub-models (cf. §2.2). The dataset consists of 2.5 Mio reflectance spectra in Landsat TM channels (≈ 100.000 image objects \times 25 pixels) and the corresponding model parameters. From the 25 reflectance spectra of each image object, the so-called object signatures have been calculated:

- mean and standard deviations of spectral channels
- R^2 between spectral channels
- regression coefficients (slope and intercept) between spectral channels.

These object signatures have then been assigned to one randomly chosen pixel of the object and the remaining 24 pixels were discarded. Thus, in total, 100.000 data points were available characterized by their original pixel signature (i.e. the spectra reflectance in the 6 TM channels), the corresponding parameter set, and their object signature.

To ensure a meaningful interpretation of the results the original dataset has been divided into a training dataset (70.000 data points) and a validation dataset (30.000 data points). Validation is therefore performed on completely independent data and statistics to be shown will always refer to this dataset. To compare the performance of the new approach to the traditional approach, neural networks have also been trained without the so-called object signatures – all other conditions being the same. This is the standard (i.e. pixel-based) approach to which the new methodology will be compared.

2.2 The reflectance models

To simulate above canopy reflectance spectra, we used the leaf optical properties model PROSPECT

(Jacquemoud & Baret, 1990) and the canopy reflectance model SAIL (Verhoef, 1984). Both are well known and validated reflectance models. For more detailed descriptions see also Jacquemoud & Baret (1990), Jacquemoud et al. (1995; 2000) and Fourty et al. (1996).

Leaf Optical Properties: the PROSPECT Model

The PROSPECT leaf optical properties model provides leaf reflectance (ρ_l) and transmittance spectra (τ_l) for input in the SAIL model as a function of only four variables: (i) leaf chlorophyll content (Cab), (ii) leaf water content (Cw), (iii) leaf dry matter content (Cm), and (iv) a leaf structure index (N). For the applied parameterizations, see §2.3.

Soil Reflectance

The soil optical properties (ρ_{soil}) of agricultural crops can be quite variable – both inside and between fields. To approximate as much as possible soil reflectance variability observed in reality, we used a spectral mixing approach with three quite different “end-member” soils from the ASTER spectral library (JPL, 1999) (Fig. 1a): (a) a very dark grayish brown loam, (b) a brown sandy loam, and (c) a black loam.

In a first step, we randomly generated relative abundances of the three soil types so that, for a given image object, they sum up to 100 %. Each pixel of an image object has then split up into 100 subpixels, to which we assigned randomly one of the three soil types (with corresponding soil reflectances) in a way that their summed surfaces corresponded to their relative abundances. The reflectance of a given pixel is then simply the mean of the corresponding 100 sub-pixel reflectances.

To simulate moisture and roughness induced changes in soil brightness we afterwards multiplied the resulting pixel reflectances with a soil brightness factor (α_{soil}) randomly drawn from a normal distribution with mean 1 and s.d. of 0.1. This scaling factor is assumed to be constant inside a given image object. Resulting mean and standard deviations of soil reflectances in Landsat TM channels are shown in Fig. 1b to illustrate the resulting variability in ρ_{soil} . Note that the approach to simulate soil reflectance resulted not only in offsets of the mean reflectance spectra indicated in Fig. 1b. For example, R^2 between TM-2 and TM-7 soil reflectance was only 0.76.

Canopy Reflectance: the SAIL model

Above canopy reflectance (ρ) was simulated by the four-stream radiative transfer model SAIL fed by the previously described soil (ρ_{soil}) and leaf optical properties (ρ_l , τ_l). The SAIL model has been chosen because it requires only few other input parameters (i.e. LAI, ALA, s , θ_z , θ_v and $skyl$). It assumes the canopy to be a homogeneous semiinfinite medium with Lambertian leaves described by their reflectance

and transmittance spectra (pl, tl). Canopy structure is described by the leaf area index (LAI) and an ellipsoidal leaf inclination distribution with random azimuth orientation characterized by the average leaf angle (ALA). The original SAIL model was modified by Kuusk (1991) to take into account the hot-spot feature, using the ratio (s) between leaf size and canopy height.

2.3 Model parameterization

A total number of 2.5 Mio above canopy reflectance spectra have been simulated using the above described reflectance models (100.000 image objects with 25 pixels each). To minimize computer processing time we simulated only reflectances for the central wavelengths of each TM reflective channel - therefore specific sensor models have not been used. For all simulations, we assumed nadir observation ($\theta_v=0^\circ$) and set the solar zenith angle (θ_z) to 40° . The proportion of diffuse irradiance (skyl) is wavelength dependent and varies both in space and time (Iqbal, 1983; Zibordi & Voss, 1989). However, it has been demonstrated, that skyl has only a very small influence on canopy reflectance (Clevers & Verhoef, 1991). Therefore, we fixed this parameter to 0.1 for all wavelengths and simulations. We further assumed that atmospheric effects had been completely removed prior to the analysis.

To approximate as much as possible reality, we assigned a set of parameter distributions to each object from which the parameterizations of the individual pixels were derived (here 25). The parameter distributions were randomly drawn according to Table 1, with no crop-specific ranges and/or parameter intercorrelations. This ensures a wide applicability of the trained networks to different crops and/or phenologies. When more information on typical intra-field parameter distributions will be available, this will be incorporated into the approach.

average leaf angle (ALA)

The average leaf angle of a canopy is crop-specific and depends also on its phenological state. Nevertheless, for a given image and agricultural field (i.e. image object), we assumed that its intra-field variability should be quite low (less than 10°), since agricultural fields are usually mono-crops with more or less similar phenological development. Therefore, we restricted intra-field variability between 2° and 10° while maintaining the whole inter-field variability between 20° and 80° (Table 1).

leaf area index, leaf chlorophyll content and equivalent leaf water thickness (LAI, Cab and Cw)

Parameter distributions of these three important variables have to cover wide ranges and variabilities and may show different degrees of skewness etc. We therefore decided to simulate these distributions using scaled and offset beta distributions. This ensures a

great variability of parameter distributions inside and between image objects.

For each of the three biophysical variables, the two independent coefficients of the beta distribution (a and b) were randomly drawn between 0.5 and 4. The resulting 25 values $\alpha=\{0\ 1\}$ have than scaled and offset by random values (Table 1).

N, Cm and s

The remaining SAIL+PROSPECT parameter N, Cm and s have only small influences on canopy reflectance (Jacquemoud, 1993; Jacquemoud et al., 1995; 2000; Fourty et al., 1996). Therefore, for each image object and parameter, we simply assigned a (random) intra-field variability and minimum value (Table 1). From these distributions, the parameter of the individual (25) pixels of a given image object have been extracted.

2.4 Calculation of object signatures

From the 25 simulated reflectance spectra of each image object, the so-called object signature has been calculated and assigned to one randomly chosen "pixel" of the object. Note that only this selected pixel has been further considered when estimating LAI, Cab and Cw.

We calculated for each spectral channel (i) the mean, and (ii) standard deviation (s.d.) of the spectral reflectances, (iii) the intercorrelation (R^2) between spectral channels, and the corresponding (iv) slope, and (v) intercept of the linear relation, respectively. This resulted in an object signature with 57 variables which has been concatenated to the original pixel signature (6 values). No attempts have been made so far to select the most appropriate object signatures.

2.5 Neural networking

For the purpose of this study we decided to use standard backpropagation neural networks with three layers: input, hidden and output layer. Provided there are enough neurons in the hidden layer these networks are known to be good function approximators (Kimes et al., 1998). Moreover, once training of the network weights is completed, appliance of the neural nets to multispectral (satellite) data is very fast.

After some initial tests, we decided to use neural nets with 15 neurons in the hidden layer (log-sigmoid transfer functions), and 3 neurons in the output layer (linear transfer functions). 70.000 out of 100.000 data points with known LAI, Cab and Cw (i.e. the so-called training dataset) have been used to train the network. Prior to training all input and output variables have been normalised.

After training, the neural nets have been used to estimate the three variables of interest from the validation dataset (30.000 independent data points).

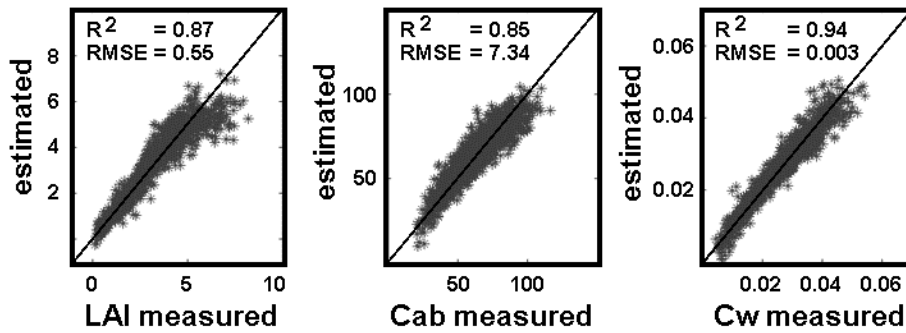


Figure 2. Measured versus estimated biophysical canopy variables using the developed object-based inversion approach with concurrent use of pixel and object signatures in Landsat TM channels (validation data set). Only 3.000 out of 30.000 data points are shown. Units of LAI, leaf chlorophyll and leaf water content are m^2/m^2 , $\mu\text{g}/\text{cm}^2$ and cm , respectively.

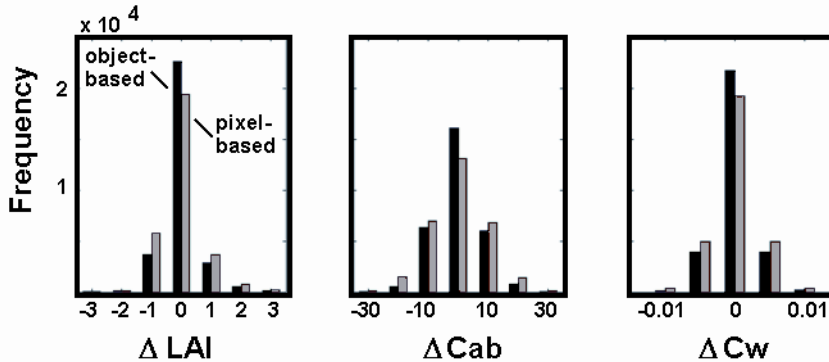


Figure 3. Deviations between measured and estimated biophysical canopy variables using canopy reflectance spectra in Landsat TM channels for the new object-based approach (black columns) and the standard (i.e. pixel-based) approach (grey columns) (validation data set; nobs=30.000).

Spectral reflectances have been recalculated from these estimates using SAIL+PROSPECT to assess the correspondance between original spectra and “estimated” spectra. Due to the iterative nature of the neural network training, the results depend on the initial values randomly assigned to the network weights. We therefore repeated training for both approaches 10 times. However, differences between resulting network outputs were found to be negligible (e.g. less than 2 % variability in RMSE between “measured” and estimated variables). We will therefore show in §3 only results of 1 randomly chosen neural net out of 10. Results of the remaining 9 neural nets were absolutely comparable.

2.6 Validation and statistics

The main interest has been to compare the overall performance of the new object-based approach to the

results obtained with the standard (i.e. pixel-based) approach. For this purpose, we calculated for each of the three variables of interest (LAI, Cab and Cw) six statistics between “measured” parameter values and their corresponding estimates: RMSE, PRMSE, T value, R^2 , and slope and intercept of the linear relation, respectively. Note that for this purpose only the completely independent validation dataset has been used (n=30.000). The T value is similar to the R^2 value, except that it measures the scattering about the 1:1 line. The T values was included because it allows a direct evaluation of the equality between variables (Fourty & Baret, 1997).

Beside the overall performance, we also analyzed the errors (RMSE) in the estimated variables for restricted parameter ranges. This allows us to detect interdependences between variables and to indentify conditions with conspicuous behavior.

3.1 Overall performance

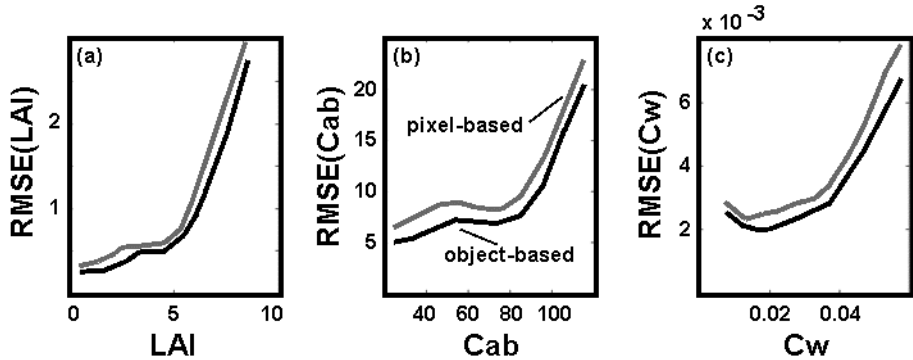


Figure 4. Root mean square error (RMSE) of the estimated biophysical canopy variables as a function of their measured values for the new object-based inversion approach (black lines) and the standard (i.e. pixel-based) inversion of canopy spectra (grey lines) in Landsat TM channels (validation data set; nobs=30.000). Measurements of LAI, Cab and Cw have been regrouped into 9, 10 and 11 equidistant parameter spaces, respectively. Units of LAI, leaf chlorophyll and leaf water content are m^2/m^2 , $\mu g/cm^2$ and cm, respectively.

PRMSE of the variables were in the order of 5 to 8 %, with slopes and intercepts approaching the 1:1 line (Table 2). Amongst the three variables, equivalent leaf water thickness showed somewhat smaller errors (PRMSE) than LAI and leaf chlorophyll content.

Compared to the standard (pixel-based) approach, the proposed methodology allowed for all canopy variables more reliable results (Table 2). The frequency histograms of the deviations between estimated and “true” parameter values reveal for the object-based approach always better centered histograms with less mis-estimated values (Fig. 3). The fact that both approaches have been compared on exactly the same data with identical network structures proves that the object signatures are useful in regularizing the inverse problem, without the necessity to use *a priori* knowledge.

Moreover, our results demonstrate the power of the employed neural nets in this pattern recognition and function approximation problem.

3.2 Leaf area index (LAI)

The use of object signatures proved useful in estimating the LAI. The overall RMSE dropped from 0.66 (pixel-based) to 0.55 (object-based), which corresponds to a PRMSE of 6.3 % (Table 2). As expected, errors in the estimated LAIs increased with canopy coverage due to saturation effects (Fig. 4a) (e.g. Gobron et al., 1997). Compared to the pixel-based approach, the object-based method always showed smaller errors (Fig. 4a).

Errors were found to increase with decreasing ALA (Fig. 5a). Using an analytical canopy reflectance model, Gobron et al. (1997) demonstrated that planophile canopies tend to more efficiently shade the

Table 2. Statistics describing the accuracy in the retrieved biophysical vegetation parameters for the new object-based inversion approach (left) compared to the standard (i.e. pixel-based) inversion (right) of canopy reflectance spectra in Landsat TM channels (validation data set; nobs=30.000). The T value is similar to the R^2 value, except that it measures the deviation from the 1:1 line. Δ mean is the difference between measured and estimated means of the variables. Units of LAI, leaf chlorophyll and leaf water content are m^2/m^2 , $\mu g/cm^2$ and cm, respectively.

	Object-based			Pixel-based		
	LAI	Cab	Cw	LAI	Cab	Cw
R^2	0.87	0.85	0.94	0.81	0.78	0.91
Slope	0.869	0.854	0.937	0.812	0.780	0.909
Intercept	0.43	9.09	0.002	0.62	13.77	0.002
RMSE	0.55	7.34	0.0026	0.66	9.04	0.0030
PRMSE (%)	6.3	7.4	4.8	7.6	9.2	5.7

T value	0.87	0.85	0.94	0.81	0.78	0.91
Δ mean	0.004	-0.008	0.000	0.012	0.024	0.000

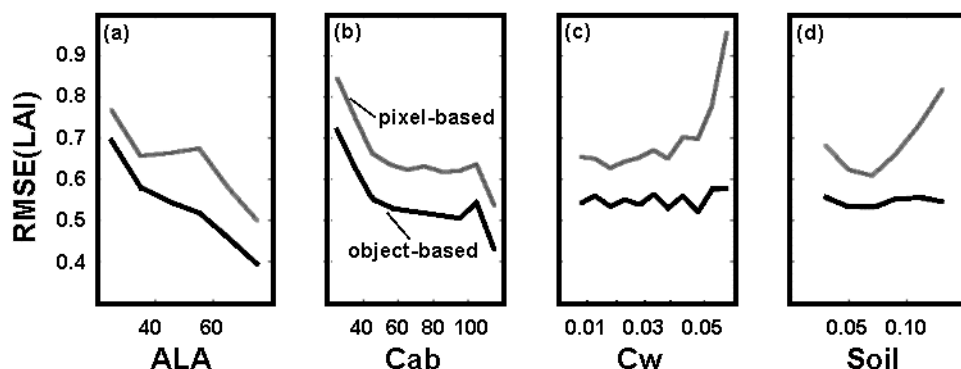


Figure 5. Root mean square error (RMSE) of estimated LAI as a function of (a) average leaf angle, (b) leaf chlorophyll content, (c) leaf water content, and (d) soil brightness in TM channel 1 for the new object-based inversion approach (black lines) and the standard (i.e. pixel-based) inversion (grey lines) of canopy reflectance spectra in Landsat TM channels (validation data set; nobs=30.000). Measurements of ALA and soil brightness have been regrouped both into 6 equidistant parameter spaces. For regroupment of Cab and Cw see Fig. 4. Units of LAI, leaf chlorophyll and leaf water content are m^2/m^2 , $\mu\text{g}/\text{cm}^2$ and cm, respectively.

soil. Therefore, they more quickly reach the radiative semi-infinite condition, were the downward radiance field within the canopy becomes independent of further increases in LAI.

The retrievability of LAI shows also a small dependence on leaf chlorophyll content (Fig. 5b). Since leaf transmittance is inversely related to Cab, the (perturbing) effect of the underlying soil decreases with increasing leaf chlorophyll content. This may explain the pattern shown in Fig. 5b. However, the same dependence has not been observed for the equivalent leaf water thickness (Cw) (Fig. 5c). Here, the errors in the estimated LAIs are found to be independent from this leaf variable. Apparently, the network weights of the object-based approach do not rely very strongly on Landsat-TM channels influenced

by Cw. This has not been the case for the standard pixel-based approach, where LAI retrievability was strongly influenced by both variables: Cab and Cw (Fig. 5b and 5c).

Compared to the pixel-based approach, it is also interesting to note that the influence of soil brightness on LAI retrievability completely disappeared (Fig. 5d). Apparently, the use of object signatures is an effective way to cancel out variations of soil brightness and composition. Not surprisingly, the influence of the hot spot parameter was very low (not shown). This parameter influences canopy reflectance the most strongly in the hot spot direction, not investigated here. Only for very dense canopies ($\text{LAI} > 6$) we found a (positive) relation between the hot spot parameter and the LAI retrievability (not shown).

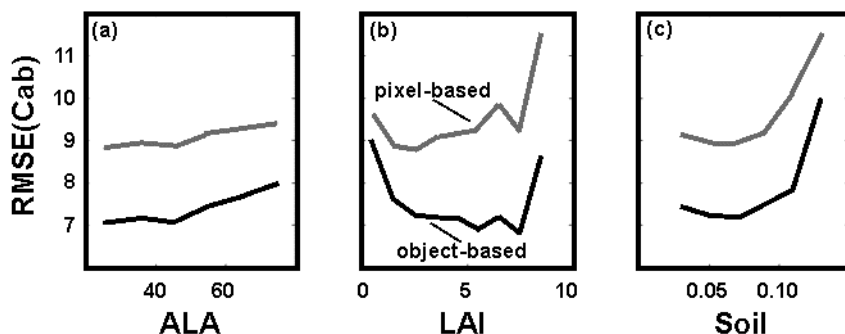


Figure 6. Root mean square error (RMSE) of estimated leaf chlorophyll content as a function of (a) average leaf angle, (b) LAI, and (c) soil brightness in TM channel 1 for the new object-based inversion approach (black lines) and the standard (i.e. pixel-based) inversion (grey lines) of canopy reflectance spectra in Landsat TM channels

(validation data set; nobs=30.000). Concerning the equidistant regroupment of parameter spaces see Fig. 4 and 5. Units of LAI, leaf chlorophyll and leaf water content are m^2/m^2 , $\mu\text{g}/\text{cm}^2$ and cm, respectively.

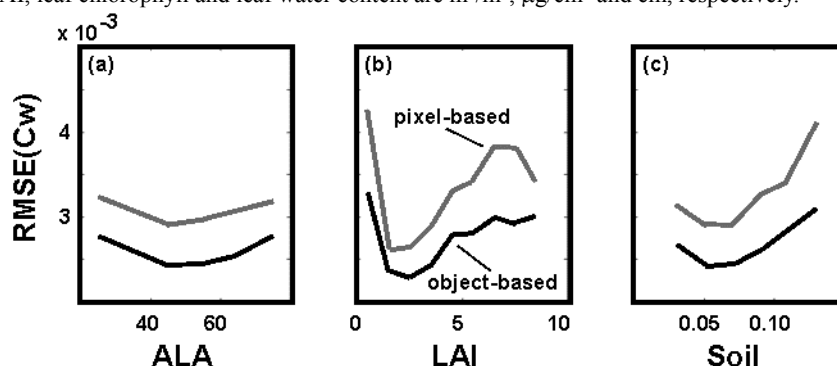


Figure 7. Same as Fig. 6 except that RMSE are for leaf water content.

3.3 Leaf biochemical composition (Cab and Cw)

Although the object signatures proved useful for all canopy variables, they were especially helpful in predicting the leaf chlorophyll content - a variable generally known to be predictable only with difficulties (Combal et al., 2001) (Table 2).

Like LAI, retrievability of Cab and Cw decreased towards higher values due to saturation effects (Fig. 4b and 4c). Also, as expected, the retrievability of leaf biochemicals depended on canopy coverage (Fig. 6b and 7b). However, it is interesting to note that the object-based approach diminished the influence of the actual LAI on the estimation accuracy of Cab and Cw compared to the standard pixel-based approach.

The general pattern is that both, very low ($\text{LAI} \leq 2$) and very high densities ($\text{LAI} \geq 8$) increased the errors in the two leaf biochemical variables. For open canopies, soil variability has a very strong influence on canopy signature, and thus explains the increasing errors. However, for very dense canopies, the investigations of Baret and Jacquemoud (1994) predict an increasing estimation accuracy. It is not clear, why our results were in contradiction to their simulations.

The influence of the actual soil brightness on the retrievability of Cab and Cw was less strong but still noticeable (Fig. 6c and 7c). Especially very bright soils increased the estimation errors, but also the darkest soils. This demonstrates that spectral channels with leaves brighter and darker than the underlying soil were implied in the estimation of leaf biochemical variables. Otherwise, one should have expected a monotonous trend, not found in our data.

Theoretical analysis of Baret & Jacquemoud (1994) showed that retrievability of leaf biochemicals should be a little bit better for planophile than for erectophile canopies. This trend is only found for the leaf chlorophyll content (Fig. 6a), but not for the leaf water content (Fig. 7a). Finally, the hot spot parameter

had no influence on Cab and Cw retrievability (not shown).

4 CONCLUSIONS

Standard inversion procedures of physically based reflectance models use generally only the radiometric information of the pixel under consideration to estimate the (biophysical) variables of interest. Our research demonstrates that - at least for agricultural crops with intra-field variabilities of the average leaf angle less than 10° - inter- and intra-channel statistical features of the corresponding image objects are useful in regularizing the inversion process and help to get more reliable results.

When pixel and object signatures are used concurrently, the employed neural net with 15 neurons in the hidden layer allows the retrieval of LAI, leaf chlorophyll and leaf water content with accuracies (PRMSE) of 5 to 8 % for large parameter ranges of 0-9 m^2/m^2 (LAI), 20-120 $\mu\text{g}/\text{cm}^2$ (Cab) and 0.004-0.06 cm (Cw), respectively. Moreover, first tests reveal that the new object-based approach is much less sensible to instrument noise than the standard pixel-based inversion (not shown).

Of course, the results are valid only for the conditions and implicit assumptions of our study and depend particularly on the validity and correctness of the employed SAIL and PROSPECT reflectance models. The logical next step will be to test the approach on real data.

ACKNOWLEDGEMENT

The critical review of the manuscript by Martin Schlerf is greatly acknowledged. The author thanks Frédéric Baret and Stéphane Jacquemoud for providing the MATLAB codes of SAIL and PROSPECT models. The financial support from the German Research Foundation (DFG) during the SFB 522

(1999-2002) has been appreciated. Hopefully, DFG will continue to support the completion of this study, which is already yet acknowledged.

REFERENCES

- Atzberger, C., Guérif, M. & Delécolle, R. (2001): The use of GRAMI crop growth model and SPOT data for biomass estimations in winter wheat.- in: Leroy (Ed.): Physical measurements and signatures in remote sensing, Aussois, France, 705-711
- Auerhammer, H. (1992): Precision farming for the site-specific fertilisation.- in: Zeitschrift für Agrarinformatik, 3: 58-66
- Baatz, M. & Schäpe, A. (2000): Multiresolution segmentation- an optimization approach for high quality multi-scale image segmentation.- in: Strobel et al. (Eds.): Angewandte Geographische Informationsverarbeitung, Salzburg, 12-23
- Baret, F. (1991): Vegetation canopy reflectance: Factors of variation and application for agriculture.- in: Hunt (Ed.): Physical Measurements and Signatures in Remote Sensing, Courchevel, France, 145-167
- Baret, F. & Guyot, G. (1991): Potentials and limits of vegetation indices for LAI and APAR assessment.- in: Remote Sensing of Environment, 35: 161-173
- Baret, F. & Jacquemoud, S. (1994): Modeling canopy spectral properties to retrieve biophysical and biochemical characteristics.- in: Hill & Miegier (Eds.): Imaging Spectrometry - A Tool for Environmental Observations. ECSC, EEC, EAEC, Brussels und Luxemburg, 145-167
- Baret, F. & Fourty, T. (1997): The limits of a robust estimation of canopy biochemistry.- in: Guyot & Phulpin (Eds.): Physical measurements and signatures in remote sensing, 413-420
- Baret, F., Weiss, M., Troufleau, D. Prévot, L. & Combal, B. (2000): Maximum information exploitation for canopy characterisation by remote sensing.- in: Aspects of Applied Biology 60 - Remote sensing in agriculture, 71-82
- Barnsley, M.J., Allison, D.A. & Lewis, P. (1997): On the information content of multiple view angle (MVA) images.- in: International Journal of Remote Sensing, 18(9): 1937-1960
- Clevers, J.G.P.W. & Verhoef, W. (1991): Modellig and synergetic use of optical and microwave remote sensing. Report 2: LAI estimation from canopy reflectance and WdVI: a sensitivity analysis with the SAIL model.- BCRS Report 90-39, 70p.
- Combal, B. & Baret, F. (2001): Estimation of chlorophyll content from remote sensing observations in the solar domain.- in: Leroy (Ed.): Physical measurements and signatures in remote sensing, Aussois, France, 461-471
- Combal, B., Baret, F., Poilvé, H. & Polverin, U. (2001): Using multispectral reflectance to retrieve LAI and chlorophyll content of Maize and Soybean.- in: Leroy (Ed.): Physical measurements and signatures in remote sensing, Aussois, France, 499-504
- CROMA (2000): Crop reflectance operational models for agriculture. Description of work.- Energy, Environment and Sustainable Development work programme, EF5/PhD/0035.00
- Delécolle, R., Maas, S.J.; Guérif, M. & Baret, F. (1992): Remote sensing and crop production models: present trends.- in: ISPRS Journal of Photogrammetry and Remote Sensing, 47: 145-161
- Fourty, T., Baret, F., Jacquemoud, S., Schmuck, G. & Verdebout, J. (1996): Leaf optical properties with explicit description of its biochemical composition: Direct and inverse problems.- in: Remote Sensing of Environment, 56: 104-117
- Fourty, T. & Baret, F. (1997): Vegetation water and dry matter contents estimated from Top-of-the-Atmosphere reflectance data: A simulation study.- in: Remote Sensing of Environment, 61: 34-45
- Gobron, N., Pinty, B., Verstraete, M. M. (1997): Theoretical limits to the estimation of the leaf area index on the basis of visible and near-infrared remote sensing data.- in: IEEE Trans. Geoscience and Remote Sensing, 35(6): 1438-1445
- Goel, N.S. (1988): Models of vegetation canopy reflectance, their use in estimation of biophysical parameters from reflectance data.- in: Remote Sensing Reviews, 4: 1-212
- Guyot, G. (1990): Optical properties of vegetation canopies.- in: Steven & Clark (Eds.): Applications of remote sensing in agriculture, London, Butterworth, 19-43
- Iqbal, M. (1983): An introduction to solar radiation.- Academic Press, 334 p.
- Jacquemoud, S. & Baret, F. (1990): PROSPECT: A model of leaf optical properties spectra.- in: Remote Sensing of Environment, 34: 75-91
- Jacquemoud, S. (1993): Inversion of the PROSPECT+SAIL canopy reflectance model from AVIRIS equivalent spectra: Theoretical study.- in: Remote Sensing of Environment, 44: 281-292
- Jacquemoud, S., Baret, F., Andrieu, B., Danson, M. & Jaggard, K. (1995): Extraction of vegetation bio-

- physical parameters by inversion of the PROSPECT+SAIL Models on Sugar Beet canopy reflectance data. Application to TM and AVIRIS sensors.- in: *Remote Sensing of Environment*, 52: 163-172
- Jacquemoud, S., Bacour, C., Poilvé, H. & Frangi, J.-P. (2000): Comparison of four radiative transfer models to simulate plant canopies reflectance: Direct and inverse mode.- in: *Remote Sensing of Environment*, 74: 471-481
- Jet Propulsion Laboratory (1999): Reproduced from the ASTER spectral library through the courtesy of the Jet Propulsion Laboratory, California Institute of Technology, Pasadena, California. Copyright © 1999, California Institute of Technology
- Kimes, D.S.; Nelson, R.F.; Manry, M.T.; Fung, A.K. (1998): Attributes of neural networks for extracting continuous vegetation variables from optical and radar measurements.- in: *International Journal of Remote Sensing*, 19(14): 2639-2663
- Kötz, B. (2001): Use of coupled evolution and radiative transfer models to derive biophysical canopy characteristics from multispectral/ temporal remote sensing data.- unpublished Master Thesis, University of Trier, Germany
- Kuusk, A. (1991): The hot spot effect in plant canopy reflectance.- in: Myneni & Ross (Eds.): *Photon-Vegetation-Interactions: Applications in Optical Remote Sensing and Plant Ecology*, Springer Verlag, 139-159
- Moran, S. M., Inoue, Y. & Barnes, E.M. (1997): Opportunities and limitations for image-based remote sensing in precision crop management.- in: *Remote Sensing of Environment*, 61: 319-346
- Myneni, R.B., Ross, J. & Asrar, G. (1989): A review on the theory of photon transport in leaf canopies.- in: *Agricultural Forest Meteorology*, 45: 1-153
- Qi, J., Cabot, F., Moran, M.S. & Dedieu, G. (1995): Biophysical parameter estimations using multi-directional spectral measurements.- in: *Remote Sensing of Environment*, 54: 71-83
- Schueller, J.K. (1992): A review and integrating analysis of spatially-variable control of crop production.- in: *Fertilizer Research*, 33: 1-34
- Strahler, A. Barnsley, M.J., Borel, C.C., Gerstl, S.A.W., Diner, D.J., Prata, A.J. & Walthall, C.L. (2000): Multiangle remote sensing: past, present and future.- in: *Remote Sensing Reviews*, 18: 83-102
- Verhoef, W. (1984): Light scattering by leaf layers with application to canopy reflectance modeling: The SAIL model.- in: *Remote Sensing of Environment*, 16: 125-141
- Verstraete, M., Pinty, B., Myneni, R. B. (1996): Potential and limitations of information extraction on the terrestrial biosphere from satellite remote sensing.- in: *Remote Sensing of Environment*, 58: 201-214
- Zibordi, G. & Voss, K. J. (1989): Geometrical and spectral distribution of sky radiance: Comparison between simulations and field measurements.- in: *Remote Sensing of Environment*, 27: 343-358

K. Ourtirane, A. Faïd

Laboratoire de Génie de l'Environnement

Université de Béjaïa (Algeria)

E-mail : kourtirane@yahoo.fr

ABSTRACT- *The Sahara exports every year thousands tons of dust over the Tropical Atlantic and Mediterranean sea. In order to follow the trajectories of these particles, it is necessary to detect them using remote sensing. We consider digital data from both visible (Vis: 0.4 - 1.1 μm) and thermal infrared (IR: 10.5 – 12.5 μm) channels of the operational meteorological satellite Meteosat. The Meteosat data were available in the B2 format of ISCCP products and in full resolution. We consider also the measurements of aerosol concentration near the ground in order to compare the satellite signal to amount of aerosols in the Tamanrasset area (south Algeria). The image processing was made using mainly the functions of MATLAB: histogram equalization, filtering and outline extraction. We use successively the filters of Gauss and differentiation. The images obtained after processing show clearly the presence of Saharan aerosols in the atmosphere and its movement toward west and north Sahara. Moreover, we remark that the differential filter is suitable to provide a quantitative estimate of the atmospheric dust content. The statistical relation between aerosol concentration and satellite infrared signal in the Tamanrasset area is significant.*

1 INTRODUCTION

The Sahara is an important source of aerosol particles (Husar et al., 1997). It exports every year thousands tons of dust across the Mediterranean sea (Dulac et al., 1992; Kubilay et al., 2000), the Atlantic (Prospero and Nees, 1987; Li et al., 1996) and towards Europe (Reiff et al., 1986; Smirnov et al., 1998).

Mineral dust transported from Sahara has a considerable impact on the ecosystems. It influences the earth radiative balance (Tanré et al., 1988). On one side, by reflecting the solar energy into the space, aerosol has a cooling effect on the earth-atmosphere system (Cautenet et al., 1992). To some extent, such cooling effect can cut off the warming effect on the trace gas like carbon dioxide. On the other side, by acting as cloud concentration nuclei, Saharan aerosol plays an important role to initiate the cloud formation process (Levin et al., 1996). The aerosol affects also the PH of precipitations (Loye-Pilot et al., 1986), stimulates the surface marine productivity by providing nutrients (Bergametti et al., 1992) and deposition on the sea bottom makes important contributions to the clay mineral content of marine sediments (Guerzoni et al., 1997).

The remote sensing techniques can be used to detect Saharan dust clouds and satellite data have been used to detect movements and source areas of Saharan dust plums (Legrand et al., 1985 and 1988; Coudé-Gaussen, 1987; Bergametti, 1989). Furthermore, it was shown that aerosol optical depths may be derived from visible or infrared satellite data (Moulin et al., 1997 and 2001; Tanré et al., 1997; Kaufman et al., 2000; Legrand et al., 2001). In the visible range, over oceans, dust was detected easily because of low values

of oceanic surface albedo (Dulac et al., 1992). Satellite remote sensing of dust can also be conducted using thermal infrared (Tanré and Legrand, 1991, Ackerman, 1997; Wald et al., 1998).

In this paper, we focus on the use of Meteosat data and the techniques of image processing to detect and follow the Saharan dust plums.

2 THE DATA BASE

2.1 Satellite data

Digital data from both visible (Vis: 0.4 - 1.1 μm) and thermal infrared (IR: 10.5 – 12.5 μm) channels of the operational meteorological satellite Meteosat were obtained from the European Space Operation Center (ESOC), Darmstadt, Germany. Data were coded over 8 bits, so that numerical values were integers between 0 and 255. The Meteosat data were available in the B2 format of ISCCP products (noted B2) and in full resolution (noted FR). For the B2 format, the ground resolution is about (30x30) km^2 in the two bands. For FR format, the resolution is (2.5x2.5) km^2 in the visible channel and (5x5) km^2 in the thermal infrared channel.

The ISCCP images in the format B2 were sampling every 3 hours (2h30mn, 5h30mn, 8h30mn, 11h30mn, 14h30mn,...). We use the B2 images recorded at 14h30mn in the period April-June 1989, in the area situated between the latitudes 20°N and 50°N, and the longitudes 20°W and 20°E. Each image was represented by a matrix of 91 lines and 112 columns.

The FR images were obtained every 30 minutes (00h, 00h30mn,...). We use the FR images recorded in June 2000 at 12 h. We choose the area situated

between the latitudes 12,57°N-37.39°N and the longitudes 12°W-12°E.

2.2 Aerosol data

Airborne particles were sampled at the site of Assekrem (23°16' N , 05°38' E). The site was situated at an altitude of 2710 m on the plateau of the Hoggar (Sahara). This location is typical of the southern Sahara. The absence of industrial activity and the vehicular traffic in this area eliminate the possible sources of anthropogenic pollutants.

The particle size distribution represents the number of particles per unit volume and granulometric class; it was measured by the Laser Particle Counter Model 237. The particle counter uses a laser diode light source and collection optics for particle detection. Particles scatter light from the laser diode beam in the direction of the collection optics. The collection optics focuses the light on a photodiode that converts the bursts of light into electrical pulses. The pulse height is a measure of particle size. During each measurement, the apparatus was brought outside in order to sample ambient air entering through a driven diaphragm pump with low flow rate. The captor was ordered with six particle size channels: >0.3 µm, >0.5 µm, >0.7 µm, >1 µm, >2 µm and >5 µm. The data were recorded three times in day: 09 h, 12 h and 15 h.

3 IMAGE PROCESSING

To detect easily the dust plum, it is necessary to use the image processing techniques. The steps of processing are: the histogram equalization, the filtering and the outline extraction. We use successively the filters of Gauss and differentiation.

3.1 Histogram equalization

Histogram equalization is a technique used to enhance contrast in all parts of the image. This technique employs a monotonic, non-linear mapping which re-assigns the intensity values of pixels in the input image such that the output image contains a uniform distribution of intensities (i.e. a flat histogram).

3.2 Filtering

a.) Gaussian filter

Noise is reduced by convoluting the image with a Gaussian filter. One of the principle justification for using the Gaussian as the smoothing filter is due to its frequency response. The Gaussian distribution used

has the form:
$$G(x,y) = \frac{1}{2\pi\sigma^2} \exp\left(-\frac{x^2+y^2}{2\sigma^2}\right)$$

Where σ represents the standard deviation of the distribution.

b.) Differential filter

This filter transforms a satellite signal $x(i,j,k)$ to a new signal $\Delta x = x_m(i,j) - x(i,j,k)$ obtained by subtracting the original signal from the maximal signal $x_m(i,j)$. The symbols (i,j) represent the position of a pixel and k indicates the image number.

The corrected satellite data is compared to data which would be obtained from a clear and dust-free atmosphere. During daytime, dust and clouds are associated to a decrease of a satellite response. So, the clear and dust-free response is empirically approximated by selecting the maximum response, pixel by pixel, from a time-series of Meteosat images (Legrand et al., 1985). The length of the series is 7 days, a compromise conciliating the conflicting goals of a good elimination of clouds and dust and a weak bias due to seasonal effects. This obtained composite which approximates a completely clear and dust-free image, is called a reference image (RI). Then, the atmospheric elements, clouds and dust, are separated from the surface by subtracting the original image from the RI, which results in difference images (DI)

3.3 The outline extraction

We use the function ‘‘contourf’’ of MATLAB. We display a contour plot of the data in an intensity image and label the levels of the contours.

4 RESULTS AND DISCUSSIONS

To comprehensive the different steps of image processing, we begin with the comparison of the original image and the image obtained after histogram equalization (figures 1 to 4). We remark that the image obtained after histogram equalization is more improved. In the figure 5, we show the influence of Gaussian filter in the improvement of the image. In the figures 6 to 8, we show respectively the outline of original, reference and differential image. In this last image, we can easily detect Saharan aerosol, it corresponds to the values of the signal exceeding the numerous value 60. To follow the movement of Saharan during its transport, we use the difference image of six consecutive days. In the figure 9, we show the six consecutive images (chronological time-series of six days). We remark that the aerosol moved towards west and north. Indeed, in the last day (jour 6), the most part of aerosol was situated in the north-west.

To confirm the influence of Saharan aerosol on the satellite signal, we compare them statistically. We found a correlation equal to -0.64 between aerosol particles and infrared satellite signal. This explains and confirms that the presence of Saharan aerosols in the atmosphere diminishes the satellite signal.

We can explain these results as follows. The presence of Saharan aerosols in the atmosphere reduces the solar flux incident to the surface. Hence, the temperature of the ground surface and the related

thermal infrared emission of the latter will drop. This effect is obviously maximum during the middle of the day, when the thermal impact of the solar radiation is at its peak.

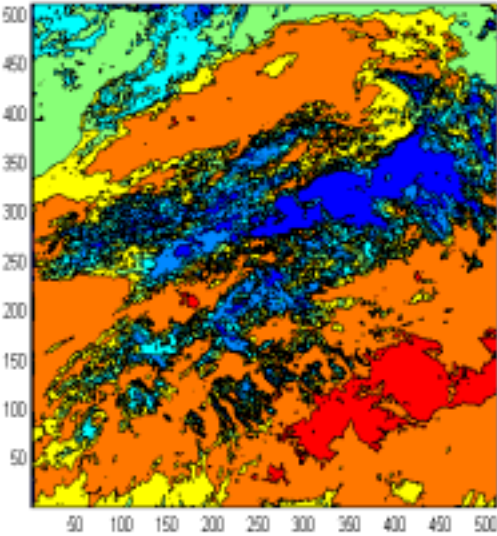


Figure 1: Original image

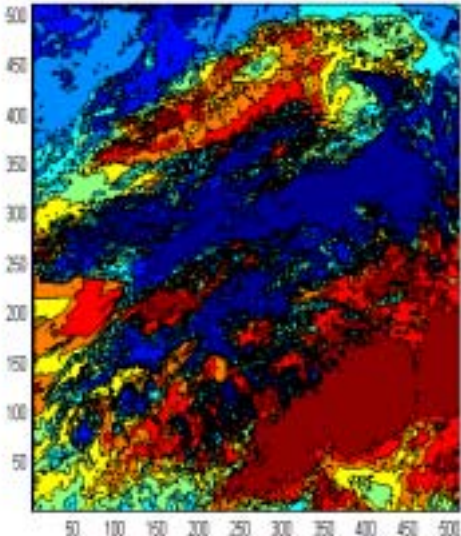


Figure 2: Image obtained after histogram equalization

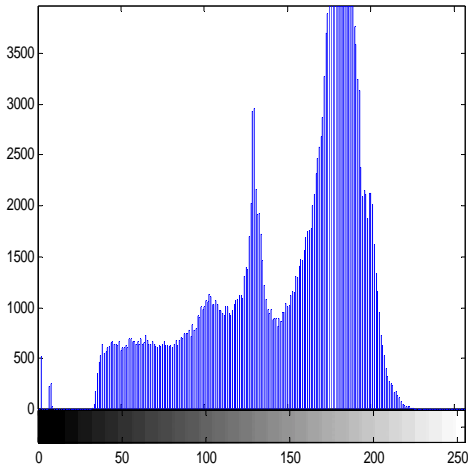


Figure 3: Histogram of original image

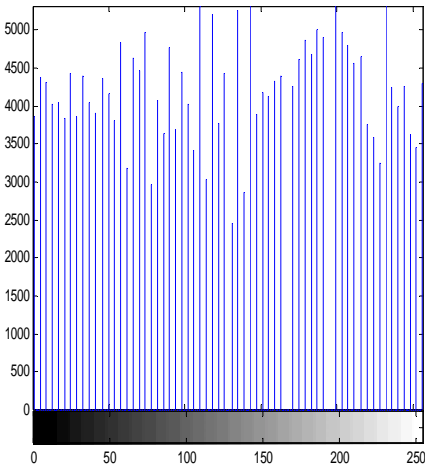


Figure 4: Histogram of the image after equalization

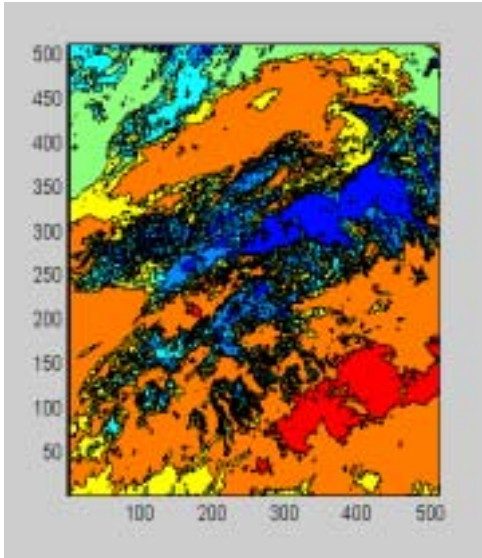


Figure 5: Image obtained after Gaussian filtering

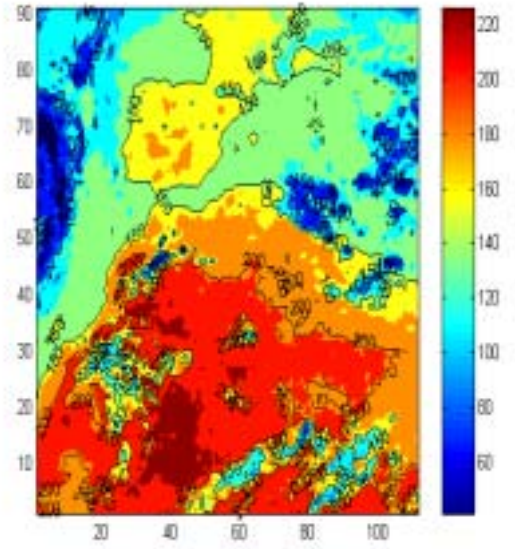


Figure 6: Outline of original image

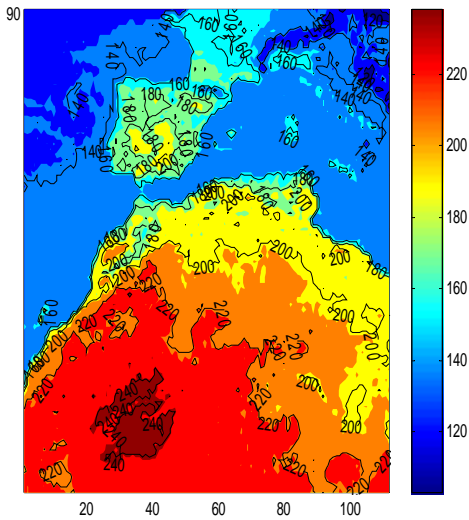


Figure 7: Outline of reference image

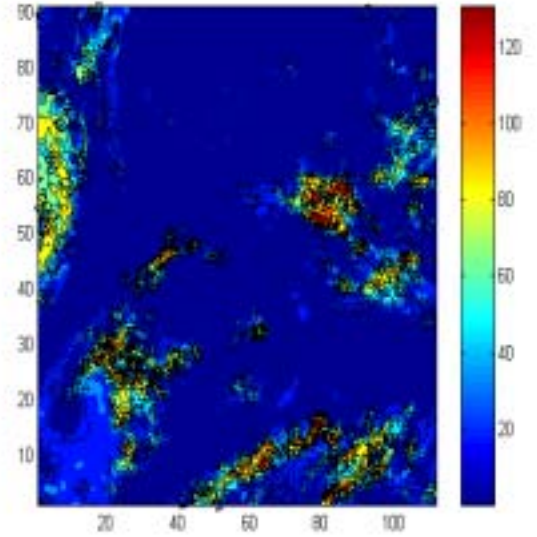


Figure 8: Outline of image obtained after Differential filtering

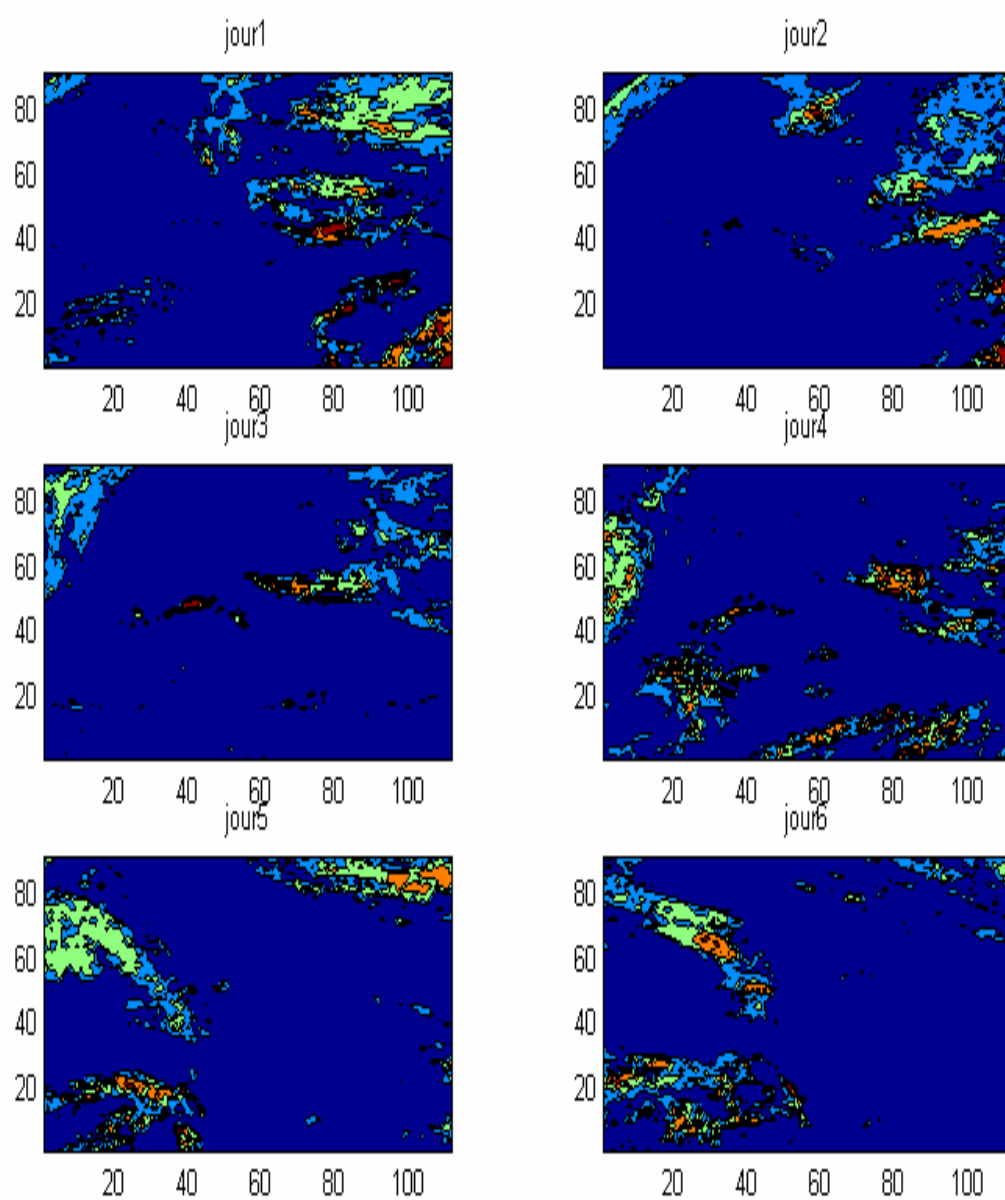


Figure 9 : Aerosol movement followed from the first day (jour 1) to the sixth day (jour 6)

5 CONCLUSION

The methods used in image processing as histogram equalization and Gaussian filter give an improved image. The signal obtained with the differential filter is proportional to the amount of Saharan aerosol. It appears to be tightly correlated according to linear regression between the signal and aerosol concentration.

Over the ocean, the contrast in the visible is sufficient to map the dust areas. In the band 10.5-12.5 μm and over land, the interpretation is especially good after using the differential filter. There was insufficient contrast in the infrared measurements between clear and dust covered ocean to delineate the dust boundaries. The 5.5-7.1 μm channel was useful to separate Saharan aerosol and cirrus free areas over seas.

REFERENCES

- Ackerman, S.A., 1997, Remote sensing aerosols using infrared observations, *J. Geophys. Res.*, 102, pp. 17,069-17,079.
- Bergametti, G., Gomes, L., Remoudaki, E., Desbois, M., Martin, D., and Buat-Ménard, P., 1989, Present transport and deposition patterns of African dusts to the northwestern Mediterranean, in *Paleoclimatology and Paleometeorology: Modern and Past Patterns of Global Atmospheric Transport*, edited by M. Leinen and M. Sarnthein, Kluwer Academic, Boston, Mass., pp. 227-252.
- Bergametti, G., Remoudaki, E., Losno, R., Steiner, E., and Chatenet, B., 1992, Source, transport and deposition of atmospheric phosphorus over the northwestern Mediterranean, *J. Atm. Chemistry*, 14, pp. 501-513.
- Cautenet, G., Legrand, M., Cautenet, S., Bonnel, B., and Brogniez, G., 1992, Thermal impact of Saharan dust over land. Part I: Simulation, *J. Appl. Meteor.*, 31, pp. 166-180.
- Coudé-Gaussen, G., Rognon, P., Bergametti, G., Gomes, L., Straus, B., Gros, J.M., and Le Coustumer, M.N., 1987, Saharan dust on Fuerte Ventura Island (Canaries): Chemical and mineralogical characteristics, air mass trajectories and probable sources, *J. Geophys. Res.*, 92, pp. 9753-9771.
- Dulac, F., Tanré, D., Bergametti, G., Buat-Menard, P., Desbois, M., and Sutton, D., 1992, Assessment of the African airborne dust mass over the western Mediterranean sea using meteosat data, *J. Geophys. Res.*, 97, pp. 2489-2506.
- Guerzoni, S., Molinaroli, E., and Chester, R., 1997, Saharan dust inputs to the western Mediterranean Sea: depositional patterns, geochemistry and sedimentological implications, *Deep-sea Research II* 44, pp. 631-654.
- Husar, R.B., Prospero, J.M., and Stowe, L.L., 1997, Characterization of tropospheric aerosols over the oceans with the NOAA advanced very high resolution radiometer optical thickness operational product, *J. Geophys. Res.*, 102, pp. 16,889-16,909.
- Kaufman, Y.J., Karnieli, A., and Tanré, D., 2000, Detection of dust over deserts using satellite data in the solar wavelengths, *IEEE Trans. Geosci. Remote Sensing*, 38, pp. 525-531.
- Kubilay, N., Nickovic, S., Moulin, C., and Dulac, F., 2000, An illustration of the transport and deposition of mineral dust onto the eastern Mediterranean, *Atm. Env.*, pp. 34, pp. 1293-1303.
- Legrand, M., Bertrand, J.J., and Desbois, M., 1985, Dust clouds over West Africa: a characterization by satellite data, *Ann. Geophys.*, 3, pp. 777-784.
- Legrand, M., Desbois, M., and Vovor, K., 1988, Satellite detection of Saharan dust: optimised imaging during nighttime, *J. Clim.*, 1, pp. 256-264.
- Legrand, M., Plana-Fattori, A., and N'doumé, C., 2001, Satellite detection of dust using the IR imagery of Meteosat. 1. Infrared difference dust index, *J. Geophys. Res.*, 106, D16, pp. 18,251-18,274.
- Levin, Z., Ganor, E., and Gladstein, V., 1996, The effect of desert particles coated with sulfate on rain formation in the eastern Mediterranean, *J. Appl. Meteor.*, 35, pp. 1511-1523.
- Li, X., Maring, H., Savoie, D., Voss, K., and Prospero, J.M., 1996, Dominance of mineral dust in aerosol light-scattering in the North Atlantic trade winds, *Nature*, 380, pp. 416-419.
- Loye-Pilot, M.D., Martin, J.M., and Morelli, K., 1986, Saharan dust: influence on the rain acidity

- and significance for atmospheric input to Mediterranean, *Nature*, 321, pp. 427-428.
- Moulin, C., Guillard, F., Dulac, F., and Lambert, C.E., 1997, Long-term daily monitoring of Saharan dust load over ocean using Meteosat ISCCP B2 data : 1. Methodology and preliminary results for 1983-1994 in the Mediterranean, *J. Geophys. Res.*, 102, pp. 16,947-16,958.
- Moulin, C., , Gordon, H.R., Chomko, , R.M., Banzon, V.F., and Evans, R.H., 2001, Atmospheric correction imagery through thick layers of Saharan dust, *Geophys. Res. Lett.*, 28, pp. 5-8.
- Prospero, J.M., and Nees, R.T., 1987, Deposition rate of particulate and dissolved aluminium derived from Saharan dust in precipitation at Miami, FL, *J. Geophys. Res.*, 92, pp. 14723-14731.
- Reiff, J., Forbes, G.S., Spieksma, F.T.M., and Reynders, J.J., 1986, African dust reaching northwestern Europe: a case study to verify trajectory calculations, *J. Climate Appl. Meteor.*, 25, pp. 1543-1567.
- Smirnov, A., Holben, B.N., Slutsker, I., Welton, E.J., and Formenti, P., 1998, Optical properties of Saharan dust during ACE2, *J. Geophys. Res.*, 103, D21, pp. 28,079-28,092.
- Tanré, D., Devaux, C., Herman, M., and Santer, R., 1988, Radiative properties of desert aerosols by optical ground-based measurements at solar wavelengths, *J. Geophys. Res.*, 93, D11, pp. 14,223-14,231.
- Tanré, D., and Légrans, M., 1991, On the satellite retrieval of Sahara dust optical thickness from blurring effects in thematic mapper data, *J. Geophys. Res.*, 96, pp. 5221-5227.
- Tanré, D., Kaufman, Y.J., Herman, M., and Mattoo, S., 1997, Remote sensing of aerosol properties over oceans using MODIS/EOS spectral radiances, *J. Geophys. Res.*, 102, pp. 16,971-16,988.
- Wald, A., Kaufman, Y.J., Tanré, D., and Gao, B.C., 1998, Daytime and nighttime detection of mineral dust over desert using the thermal IR, *J. Geophys. Res.*, 103, 32,307-32,313.

Impact of Saharan aerosol on solar radiation in the Tamanrasset area

A.Faid, K. Ourtirane

Laboratoire de Génie de l'Environnement

Université de Béjaia (Algeria)

E-mail : kourtirane@yahoo.fr

ABSTRACT- We use three types of data which were measured at Tamanrasset (22.78 °N, 5.5 °E) and Assekrem (23.26 °N, 5.64 °E): solar radiation, aerosol and atmospheric visibility. The solar radiation is represented by the monochromatic radiation, at $\lambda = 0.50 \mu\text{m}$, the direct solar radiation in the spectrum bands 0.28-0.53 μm , 0.53-0.63 μm , 0.63-0.69 μm and 0.69-4 μm and the scattered radiation. The aerosol factors are expressed by the mass concentration and the particle number. We consider three short periods (November 1996 - February 1997, May - July 1997 and October - December 1997) and a long period (November 1998- October 1999). From the data of solar radiation, we calculate the atmospheric turbidity using Volz, Kasten and Angström models. We compare then turbidities, solar radiation, aerosol factors and visibility using correlation and regression analysis. We remark that the turbidities are related significantly with the mineral aerosol concentration and the visibility. For example, in the period may - July 1997, the relationship between the Kasten turbidity T_1 and the aerosol concentration C gives : $R(T_1, C) = 0.88$, $F = 682,5$, $t_1 = 65.4$, $t_2 = 26.12$, for a number of observations equal to 207. All the results show that the Saharan aerosol has a real impact on the solar radiation extinction. Furthermore, we remark that the particle number with intermediate sizes (0.7 – 1 μm) is related significantly with turbidity and scattered radiation. This result can be explained by the Mie scattering of the solar radiation.

1. INTRODUCTION

Atmospheric aerosol plays an important role in radiative processes. The balance between aerosol absorption and scattering (Fraser and Kaufman, 1985) determines its ability to counteract greenhouse warming and to affect atmospheric heating rates (Carlson and Benjamin, 1980; Alpert et al., 1998). As aerosol particles interact with solar and terrestrial radiation, they perturb the radiative budget (Liou et al., 1978; Coakley, 1983).

The Sahara is a major source of dust aerosols (Prospero, 1990). This aerosol has an important climatic impact (Tegen and Lacis, 1996; Moulin et al., 1997). The optical depth of Saharan aerosol was determined by Tanré et al. (1988a and 1988b) and Haywood et al. (2001).

The focus of this paper is to estimate the extinction of solar radiation in the presence of saharan aerosol. Two measuring sites are considered : Tamanrasset and Assekrem. The two sites are selected by the W.M.O. in the cadre of Global Atmospheric Wash (GAW) program. The choice of these sites was motivated by the fact that the anthropogenic constituents in the Hoggar area is negligible. Indeed, the sites of Tamanrasset and Assekrem are far than industrial areas. Furthermore, the Tamanrasset region is an important source of Saharan aerosol and its soil is very susceptible to wind erosion. Indeed, it was showed that the absence of nonerodible elements is very

favourable for the dust production. To our knowledge, the Tamanrasset soil is naked.

Three types of data are used: solar radiation, visibility and aerosol. Firstly, we describe the data measurements. Then, we present the formulas used to compute the Volz and Kasten turbidities. In last, we search the eventual relationships between the Saharan aerosol and the solar radiation extinction using the statistical methods.

2. EXPERIMENTAL PROGRAM

A large-scale aerosol and solar radiation program is carried out as a part of the Global Atmospheric Wash program (GAW). One of the principal objectives was to assess the impacts of desert dust storms on long-range aerosol transport and the increases in atmospheric turbidity over the region.

The measurement stations of Tamanrasset (1377 m) and Assekrem (2710 m) are about 70 km apart. Assekrem has the advantage of being at a higher elevation. In all measurements, the meteorological parameters were considered.

2.1 Solar radiation measurements

Two parameters of solar radiation were measured: the monochromatic and the direct solar radiation. The monochromatic radiation was measured with a sunphotometer at the green channel ($\lambda=0.50 \mu\text{m}$). The direct radiation was measured with a pyrheliometer in the following spectrum bands: 0.28 - 4 μm , 0,53 - 4 μm , 0,63 - 4 μm and 0,695 - 4 μm .

The measures of the monochromatic radiation were made three times in day: 09 h, 12 h and 15 h, from January 1996 to December 1997. The measures of the direct radiation were made at 10 h, 12 h and 14 h. The measures were not made when the sun was obscured by clouds and dust of exceptional intensity.

2.2 Aerosol measurements

Two types of measures were carried out in Tamanrasset and Assekrem : the number of particles per granulometric class and the massic concentration of aerosol. The number of particles was measured with a Laser Particle Counter. The counter is ordered with six particles size channels: $>0.3 \mu\text{m}$, $>0.5 \mu\text{m}$, $>0.7 \mu\text{m}$, $>1 \mu\text{m}$, $>2 \mu\text{m}$, $>5 \mu\text{m}$. The data are recorded three times in day: 09 h, 12 h and 15 h. From November 1996 to February 1997, the measures were made at Tamanrasset. But, after March 1997, the equipment was removed to Assekrem. In Assekrem, we use only the data of May-July 1997 and October-December 1997.

The aerosol concentration is obtained by sampling the atmospheric air with a debit of 3 l/mn through a tube into an instrument which contains a precision balance and a filter. The equipment was installed at Assekrem. The measures were begun on October 1997. In this work, we use only the data of October to December 1997.

3. DATA PROCESSING

3.1 Volz turbidity

Computations of Volz turbidity are made according to the usual Bouguer-Lambert-Beer law expressing the measured intensity at wavelength λ :

$$I_{\lambda} = I_{0\lambda} \exp \left[-m \left(\frac{P}{P_0} \tau_{\lambda}^R + \tau_{\lambda}^{OZ} + \tau_{\lambda}^a \right) \right]$$

where:

I_0 = extraterrestrial intensity which depends of the day j of the year as:

$$I_0 = 1367 \left[1 + 0,034 \cdot \cos[0,01746(0,986j - 2)] \right]$$

τ_{λ}^R = Rayleigh scattering coefficient for air molecules at the wavelength λ ,

τ_{λ}^{OZ} = absorption coefficient for ozone at λ ,

τ_{λ}^a = extinction coefficient for aerosol at λ , it is the Volz turbidity,

P = station pressure,

P_0 = standard pressure at sea level = 1013,2 hPa,

m = optical air mass.

The parameter m can be calculated using the following expression (De Brichambaut and Vauge, 1982):

$$m = \frac{1 - 0,1z}{\sin(h) + 0,15(h + 3,885)^{-1,253}}$$

Where z is the station altitude in kilometers and h the solar height. The height h is given by the expression:

$$\sin(h) = \sin(\theta) \sin(\delta) + \cos(\theta) \cos(\delta) \cos(\omega)$$

where:

θ = station latitude,

δ = solar declination : $\sin(\delta) = 0,4 \cdot \sin(0,986j - 80)$,

ω = solar horair angle , it is expressed as :

$$\omega = \left(TU + \frac{\varphi}{15} + \frac{\Delta t}{60} - 12 \right) \frac{\pi}{12} \text{ in radians}$$

where:

φ = station longitude,

$$\Delta t = [2(0,986j + 100)] - 7,7 \sin(0,986j - 2)$$

TU= universal time.

τ_{λ}^R and τ_{λ}^{OZ} are calculated using respectively the following expressions (Orgeret, 1985):

$$\tau_{\lambda}^R = 8,79 \cdot 10^{-3} \lambda^{-4}$$

$$T_0 = \exp(-m \cdot \tau_{\lambda}^{OZ}) = 1 - a - b$$

with

$$a = \frac{0,002118 \cdot X}{1 + 0,0042 \cdot X + 0,00000323 \cdot X^2};$$

$$b = \frac{0,1082 \cdot X}{1 + 13,86 \cdot X} + \frac{0,00658 \cdot X}{1 + (10,36 \cdot X)^2}$$

and $X=3,5m$

3.2 Linke turbidity

The Linke turbidity T_1 is calculated using the Kasten formula:

$$I = I_0 \exp \left[-\frac{m T_1}{0,9m + 9,4} \right]$$

where:

I = direct solar radiation in the spectrum band 0,28 - 4 μm ,

I_0 and m are defined precendently,

T_1 = Linke turbidity.

3.3 Angström turbidity

It is determined from the measures of a direct solar radiation in the large spectrum band not affected by the water vapor absorption ($0,28 < \lambda < 0,63 \mu\text{m}$). Taking into account the attenuation by molecular scattering and ozone absorption, and the hypothesis that the aerosol scattering is proportional to $\lambda^{-\alpha}$, we have to solve the following equation:

$$I_s(\lambda) = I_{0s}(\lambda) \exp \left[-m \left(\frac{p}{p_0} \tau_{\lambda}^R + \tau_{\lambda}^{oz} + \beta \lambda^{-\alpha} \right) \right]$$

$I_s(\lambda)$: Direct solar spectral intensity,

$I_{0s}(\lambda)$: extraterrestrial solar spectral irradiance, which depends of the day j of the year (as calculated precedently) and the spectrum band,

β : Angstrom turbidity coefficient.

α : Wavelength exponent, which is equal to 1,3 for aerosol.

The other parameters are defined precedently.

We calculate β in two spectrum bands : 0,28 - 0,53 μm and 0,53 - 0,63 μm .

4 STATISTICAL COMPARISON OF SOLAR AND AEROSOL DATA

Before entering upon the relationships between the Saharan aerosol and the solar radiation extinction, we begin by the estimation of the maximum, minimum and average values of the data in each period. Table 1 offers a general view of the computed data of aerosol, visibility and turbidities. For the three periods, we determine the maximum, minimum and average values of :

- the particle number per granulometric class,
- the Volz, Linke and Angstrom turbidities,
- the visibility.

Table 1 : Maximum, minimum and average values of the aerosol and solar radiation parameters

		Nov. 96 - Feb. 97			May - July 97			October - Dec 97		
		Max.	Min.	Mean	Max.	Min.	Mean	Max.	Min.	Mean
Aerosol ($\mu\text{g}/\text{m}^3$)		-----	-----	-----	-----	-----	-----	307.8	02.7	75.10
Aerosol Number	> 0.3 μm	306503	5365	43354	166370	5845	58021	82896	280	18754
	> 0.5 μm	211655	1206	13274	126223	1335	27612	53783	20	7863
	> 0,7 μm	151393	687	8879	101234	810	18891	43856	19	5695
	> 1 μm	112067	466	6534	80694	552	13635	34957	18	4297
	>2 μm	30386	143	1987	23817	111	3268	10403	01	1215
	> 5 μm	3935	29	319	1935	09	241	798	00	105
Volz turbidity		1.508	0.383	0.482	2.03	0.53	0.922	1.2	0.36	0.546
Linke turbidity		12.53	2.0	2.75	19.06	2.92	6.36	9.0	2.08	3.44
Angs. Turbidity β_1 in 0.28-0.53 μm		0.452	0.0001	0.032	0.515	0.00	0.135	0.20	0.00	0.049
Angs. Turbidity β_2 in 0.53-0.63 μm		1.580	0.090	0.261	1.174	0.16	0.505	0.58	0.20	0.305
Visibility (in km)		55	03	47	55	0.30	28.6	70	04	44.5

Because of the later installation of the aerosol captor (October 1997), the massic concentration parameter is used only in the period October-December 1997. We

illustrate the average values of particle number for each period in the figure 1.

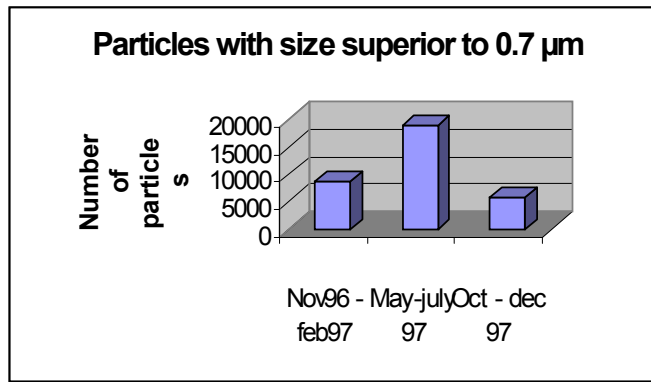


Figure 1: Average values of particle number for each period

We remark that the aerosol number in Tamanrasset is more important than the amount of Assekrem. This difference can be explained by the two following facts :

1°) The aerosol number decreases with the height (Durand and Druilhet, 1983);

2°) Tamanrasset station is more proximate than the aerosol sources.

Furthermore, we remark that the three turbidities are more important in the period May-July 1997. This difference can be related to the seasonal variation of the emission with maximum in summer and minimum in winter (Jaenicke, 1979).

In order to search an eventual relationship between the Saharan aerosol and the solar radiation extinction, represented by Volz, Linke and Angström turbidities, we use the correlation and regression methods. The significance of the models is tested by an evaluation of the correlation, Fisher and Student coefficients. The lack of data , for solar radiation, is caused by obscuration of the sun by clouds. Therefore, the chronological time-series of the observed variables (x_i , y_i) are not chronological.

The correlation coefficients between aerosols and turbidities are given in the table 2.

Table 2 : Correlation coefficients between turbidities and aerosol parameters

	Nov 96 - February 97			May - July 97			October-December 97		
	T_1	τ_{λ}^a	β_1	T_1	τ_{λ}^a	β_1	T_1	τ_{λ}^a	β_1
Aerosol $> 0.3 \mu\text{m}$	0.82	0.70	0.74	0.64	0.60	0.61	0.82	0.80	0.54
	0.88	0.84	0.81	0.73	0.67	0.70	0.85	0.82	0.64
number $> 0.5 \mu\text{m}$	0.88	0.83	0.82	0.75	0.67	0.72	0.85	0.82	0.64
$> 0.7 \mu\text{m}$	0.88	0.83	0.81	0.75	0.67	0.73	0.85	0.81	0.64
$> 1 \mu\text{m}$	0.85	0.79	0.79	0.76	0.66	0.75	0.86	0.81	0.66
$> 2 \mu\text{m}$	0.73	0.69	0.69	0.65	0.51	0.66	0.85	0.80	0.65
$> 5 \mu\text{m}$									
Aerosol amount	----	----	---	----	---	---	0.76	---	---
Visibility	---	-	---	---	- 0.75	---	--	- 0.83	---
		0.69							

Table 3 : The number of observations for each correlation

	Nov 96 - February 97			May - July 97			October - December 97		
	T_1	τ_{λ}^a	β_1, β_2	T_1	τ_{λ}^a	β_1, β_2	T_1	τ_{λ}^a	β_1, β_2
Particle number	209	269	209	167	263	167	209	230	209
Massic concentration	-----	-----	-----	-----	-----	-----	132	-----	-----
Visibility	-----	269	-----	-----	263	-----	-----	230	-----

From the tables 2 and 3, we can see that all the correlations are significant. We observe narrow relationships between aerosol parameters and solar radiation extinction factors. The increase of the turbidities is related to the increases of aerosol number and massic concentration, and the decrease of the visibility. The important correlations are obtained with the Linke turbidity and in the period November 96 - February 97. There could be a few reasons of this relationship:

- the pyrliometer is perhaps more preferment than the sunphotometer

- In the period November 96 - February 97, the aerosol number and the solar radiation intensities were measured at the same site: Tamanrasset.

Furthermore, we remark that the Angstrom turbidity, calculated in the spectrum band 0,28 - 0,53 μm , is well correlated with the Saharan aerosol number.

The regression equations, between aerosol parameters (massic concentration C and particle number N) and turbidities (β and T_1), and the significant tests of correlation (R), Student (t_1 and t_2) and Fisher (F) are given in the table 4.

Table 4: Regression equations aerosol parameters - turbidities and significant tests

Period	Equation	R	F	t_1	t_2
Nov 96 - Feb 97	$\tau_{\lambda}^a = 0.427 + 4.19.10^{-6}.N_{0.5}$	0.839	631.8	104.6	25.1
May - July 97	$\tau_{\lambda}^a = \text{EXP}(0.32 - 1.54.Vis)$	- 0.774	389.5	12.9	- 19.7
Oct 97 - Dec 97	$\tau_{\lambda}^a = 1.13 - 1.31.10^{-5}.Vis$	- 0.832	510.3	42.4	- 22.6
Oct 97 - Dec 97	$\tau_{\lambda}^a = 0.43 + 1.41.10^{-5}.N_{0.5}$	0.817	457.8	50.6	21.4
Nov 96 - Feb 97	$T_1 = 2.31 + 5.10^{-5}.N_{0.7}$	0.880	708.8	66.2	26.6
Oct 97 - Dec 97	$T_1 = 2.27 + 3.6.10^{-5}.N_{0.5}$	0.884	741.1	65.3	27.2
Oct 97 - Dec 97	$T_1 = 2.61 + 0.0134.C$	0.760	175.8	24.7	13.3

We show in the figure 2 the linear regression between the number of particles, with size superior to 0.5 μm , and the parameter turbidity of Kasten (T_1).

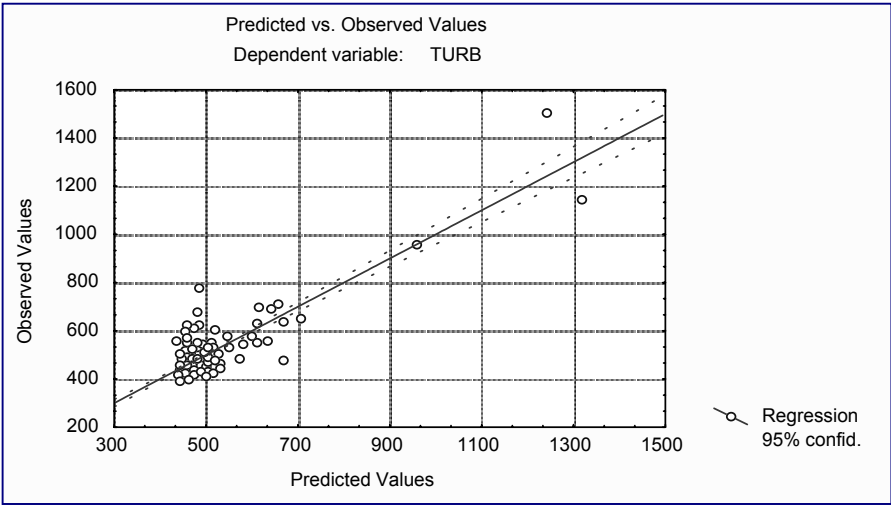


Figure 2: Curve regression between Kasten turbidity and aerosol number

CONCLUSION

We remark that the particle number with intermediate sizes ($N_{0.5}$ and $N_{0.7}$) is related significantly with the

two turbidities (β and T_1). This result can be explained by the Mie scattered of the solar radiation. The massic concentration C is although proportional to the Linke turbidity. Almost relationships are linear. However, in the period May - July, the relationship between the

Voltz turbidity and the horizontal visibility is exponential. In this period, the dust frequency is more important and all the significant relationships (we are not written all the significant regression equations) obey to the multiplicative or exponential models.

REFERENCES

- Alpert, P., Kaufman, Y., Shay El, Y., Tanré, D., da Silva, A., Schubert, S., and Joseph, Y.H., 1998, Quantification of dust-forced heating of the lower troposphere, *Nature*, 395, pp. 367-370.
- Carlson, T.N., and Benjamin, S.G., 1980, Radiative heating rates of Saharan dust, *J. Atmos. Sci.*, 37, pp. 193-213.
- Coakley, J.A., Cess, R.D., and Yurevich, F.B., 1983, The effect of tropospheric aerosol on the earth's radiation budget: a parametrization for climate models, *J. Atmos. Sci.*, 40, pp. 116—138.
- De Brichambaut, C.P., and Vauge, C., 1982, Le gisement solaire, *Ed. Lavoisier TEC&DOC*.
- Durand, P., and A. Druilhet, Contribution à l'étude de la structure turbulente de la couche limite convective sahélienne en présence de brume sèche, *La Météorologie*, 29, pp. 213-226, 1983.
- Fraser, R.S., and Kaufman, Y.J., 1985, The relative importance of aerosol scattering and absorption in remote sensing, *IEEE J. Geosc. Rem. Sens.*, GE-23, pp. 525-633.
- Haywood, J.M., Francis, P.N., Geoogdzhayev, I., Mishchenko, M., and Frey, R., 2001, Comparison of Saharan dust aerosol optical depths retrieved using aircraft mounted pyranometers and 2-channel AVHRR algorithms, *Geophys. Res. Lett.*, 28, pp. 2393-2396.
- Jaenicke, R., 1979, Monitoring and critical review of the estimated source strength of mineral dust from the Sahara, in *Saharan Dust : Mobilisation, Transport, Deposition*, edited by C. Morales, , *SCOPE Rep. 14*, John Wiley, New York, pp. 233 - 242.
- Liou, K.N., Freeman, K.P., and Sasamori, T., 1978, Cloud and aerosols effects on the solar heating rate of the atmosphere, *Tellus*, 30, pp. 62-70.
- Moulin, C., Guillard, F., Dulac, F., Lambert, C.E., Chazette, P., Jankowiak, I., Chatenet, B., and Lavenu, F., 1997, Long-term daily monitoring of Saharan dust load over ocean using Meteosat ISCCP B2 data : 2. Accuracy of the method and validation using sun photometer measurements, *J. Geophys. Res.*, 102, pp. 16,959-16,969.
- Orgeret, M., Les piles solaires, 1985, *Ed. Masson*, pp. 1-24.
- Prospero, J.M., 1990, Mineral-aerosol transport to the North Atlantic Ocean Pacific: the impact of Africa and Asian sources in the long-range atmospheric transport of natural and contaminant substances, *Ed. A.H. Knap and Norwell (Kluwer Acad.)*, pp. 59-86.
- Tanré, D., Devaux, C., Herman, M., and Santer, R., 1988a, Radiative properties of desert aerosols by optical ground-based measurements at solar wavelengths, *J. Geophys. Res.*, 93, D11, pp. 14,223-14,231.
- Tanré, D., Deschamps, P.Y., Devaux, C., and Herman, M., 1988b, Estimation of Saharan aerosol optical thickness from blurring effects in thematic mapper data, *J. Geophys. Res.*, 93, D12, pp. 15,955-15,964.
- Tegen, I., and Lacis, A.A., 1996, Modeling of particle size distribution and its influence on the radiative properties of mineral dust aerosol, *J. Geophys. Res.*, 101, 19237-19244.

Sequential BRDF inversion for mapping snow cover using a multi-scale analytical canopy reflectance model

Richard A. Fernandes and Sylvain G. Leblanc

Natural Resources Canada, Earth Sciences Sector, Canada Centre for Remote Sensing

Richard.Fernandes@ccrs.nrcan.gc.ca Sylvain.LebLANC@ccrs.nrcan.gc.ca

ABSTRACT - Our goal was to assess the use of time series of directional reflectance data acquired from instruments on daily polar orbiting sensors for mapping transitions between snow on and snow off conditions within northern ecosystems. We developed a new multi-scale analytical canopy (MAC) BRDF model to describe the relative contributions of single and multiply scattered photons to top-of-canopy radiance as a function of both acquisition geometry and target characteristics. MAC includes a multi-scale theory to describe the effect of clumping upon the BRDF and an extension of the gap-size distribution theory of Norman and Miller from one to two dimensions. MAC was tested using both airborne POLDER measurements and below canopy gap fraction data from BOREAS conifer sites. SPOT-VEGETATION daily time series of surface reflectance were acquired over BOREAS targets. Screening for residual atmospheric effects was performed using an iterative form of LOESS regression. The MAC model was unable to provide precise fits to time series observations at a pixel due in part to poor angular sampling within the time series data and residual atmospheric effects. However, the LOESS smoothed time series tends to reduce variability due to view zenith in a manner that could potentially allow for robust snow cover detection. Further investigation using additional daily data from sensors sampling closer to the principal plane is required to assess the full capability of the MAC model for sequential BRDF inversion.

1 INTRODUCTION

Current and planned polar-orbiting satellites with infrared and visible band sensors offer better than daily repeat coverage. This data could potentially provide sufficient temporal and spatial sampling to produce useful large area maps of changing surface characteristics such as snow cover. Changing acquisition geometry and atmospheric effects must be considered when monitoring transitions between snow and snow-free conditions. Semi-empirical models have been applied to normalise for view geometry effects but typically do not allow for an explicit accounting of understorey contributions to top-of-canopy reflectance. We present a Multi-scale Analytical Canopy (MAC) BRDF model, based in part on 4-Scale (Chen and Leblanc, 2001), to relate understorey reflectance to the BRDF. Secondly, we describe a method using iterative LOESS fitting (Cleveland and Develin, 1989) to reduce atmospheric contamination in daily reflectance time series. The ability of MAC to describe snow-off BRDF observations is assessed using airborne POLDER data (Leroy and Breon, 1996) and SPOT Vegetation (VGT, Anonymous, 2002) data over BOREAS sites. We determine the potential for using alternatively the fitted MAC model or statistical approaches for tracking changes in snow cover using daily VGT data with varying acquisition geometry.

2 MULTI-SCALE ANALYTICAL CANOPY (MAC) REFLECTANCE MODEL

2.1 Vertical Decomposition of Radiant Exitance

The BRDF for irradiance I_s along angle Ω_i is:

$$R_I(\Omega_i, \Omega_v) = \frac{\left[I_{Fvi}(\Omega_i, \Omega_v) + I_{Fvz}(\Omega_i, \Omega_v) \right] + \left[I_{Gvi}(\Omega_i, \Omega_v) + I_{Gvz}(\Omega_i, \Omega_v) \right]}{I_s(\Omega_i)} \quad (1)$$

Where the terms $I_s(\Omega_i, \Omega_v)$ correspond to mean, over the canopy upper boundary, component radiances from specified canopy surfaces in the view direction Ω_v . The subscripts F and G denote foliage and ground respectively and the prefixes v,i and z denote viewed, illuminated and shaded respectively. Mean sunlit and shaded viewed foliage and surface radiances are decomposed into the contributions of respective fractional areas from each plane Z over the canopy height H:

$$I_{F_{vi}}(\Omega_i, \Omega_v) = \int_{0^+}^H F_{vi}(z) [I_S(z, \Omega_i, \Omega_v) + I_D(z, \Omega_i, \Omega_v)] dz \quad (2)$$

$$I_{F_{vz}}(\Omega_i, \Omega_v) = \int_{0^+}^H [F_v(z) - F_{vi}(z)] I_D(z, \Omega_i, \Omega_v) dz \quad (3)$$

$$I_{G_{vi}}(\Omega_i, \Omega_v) = F_{vi}(0) [I_S(0, \Omega_i, \Omega_v) + I_D(0, \Omega_i, \Omega_v)] \quad (4)$$

$$I_{G_{vz}}(\Omega_i, \Omega_v) = [1 - F_{vi}(0)] I_D(0, \Omega_i, \Omega_v) \quad (5)$$

Where $F_v(z)$ is the fraction of Z containing viewed surfaces and $F_{vi}(z)$ is the fraction of Z containing surfaces both viewed and illuminated. I_D corresponds to upwelling diffuse radiance of canopy elements in the view direction estimated by applying a turbid media radiative transfer model (Sellers 1986) using the canopy effective LAI and a modified single scattering albedo (Smolander, S. personal communication) to account for within shoot scattering.

The fraction of a plane, Z , at height z occupied by sunlit foliage is given by:

$$F_{vi}(z) = F_v(z) F_i(z) [1 - f_{HS}] + [F_v(z) F_i(z)]^{0.5} f_{HS} \quad (6)$$

The terms $F_i(z)$, $F_v(z)$, f_{HS} corresponding to the fraction of Z containing viewed and illuminated foliage alternatively and gaps contributing to the hotspot effect respectively are given by:

$$F_v(z) = \frac{\partial p(z, 0, \Omega_v, \Omega_v)}{\partial z} \quad (7)$$

$$F_i(z) = \frac{\partial p(z, 0, \Omega_i, \Omega_i)}{\partial z} \quad (8)$$

$$f_{HS} = \frac{p(z, \lambda_z, \Omega_i, \Omega_v)}{p(z, 0, \Omega_i, \Omega_v)} \quad (9)$$

Here $p(z, \lambda, \Omega_1, \Omega_2)$ is the probability of a gap of size λ or larger on Z given shadows cast by canopy elements above Z in both direction Ω_1 and Ω_2 .

2.2 Multi-Scale Estimation of the Bi-Directional Gap Size Distribution $p(z, \lambda, \Omega_i, \Omega_v)$

The canopy is decomposed into a set of nested elements such that the elements at scale $k-1$ are always found within an element at scale k . Each scale consists of equal elements sharing the same stationary process specifying their position and orientation within an element at the next coarser scale. The union of the projection of an opaque version of an element at scale k on Z in direction Ω_i and Ω_v is given by:

$$X_k(z, \Omega_i, \Omega_v) = S_k(z, \Omega_i) + S_k(z, \Omega_v) - O_k(z, \Omega_i, \Omega_v) \quad (10)$$

Where $S_k(z, \Omega)$ is the region of a shadow cast in direction Ω on the plane Z and $O_k(z, \Omega_i, \Omega_v)$ is the overlap region of the shadows cast in direction Ω_i and Ω_v . Extending the result of Miller and Norman (1971) from one to two dimensions, the area on Z where a line $L(\lambda, \Omega_\lambda)$ of length λ oriented along the ray Ω_λ connecting the same point of the element on both projections overlaps with X_k is given by:

$$A_k(\lambda, z, \Omega_i, \Omega_v) = \overline{Mes}[L(\lambda, \Omega_\lambda) * X_k(z, \Omega_i, \Omega_v)] \quad (11)$$

The operator \overline{Mes} is the expected value of the measure operator corresponding to the area in Z where its argument is positive.

Following Nilson (1999), the probability of a gap on Z within the projected shadow area of an element of scale $k+1$ (e.g. the entire stand) containing a number of elements at scale k (e.g. patches of trees) positioned according to a binomial process with density ρ_k is given by:

$$P_{k+1}(\lambda, z, \Omega_i, \Omega_v) = \exp \left[\frac{-\Phi_k(\lambda, z, \Omega_i, \Omega_v) \times \rho_{ki}(\lambda, z, \Omega_i, \Omega_v)}{A_k(\lambda, z, \Omega_i, \Omega_v)} \right] \quad (12)$$

where

$$\Phi_k(\lambda, z, \Omega_i, \Omega_v) = \frac{-\ln[1 - (1 - P_k)] \mp GI_k(\lambda, z, \Omega_i, \Omega_v)}{1 \mp GI_k(\lambda, z, \Omega_i, \Omega_v)} \quad (13)$$

and

$$GI_k(\lambda, z, \Omega_i, \Omega_v) = 1 \mp \rho_k \sigma_k \quad (14)$$

where a minus sign corresponds to a positive binomial distribution and a positive sign for a negative binomial distribution and GI is the Fisher's grouping index. The extent of clumping is determined using σ_k corresponding to the "living area" of an element at scale k .

2.3 Implementation for Forest Canopies

Targets are decomposed into the following scales: patches, crowns or trunks, within crown elements.

Branches and foliage are not described as separate statistical processes as they are often spatially correlated (Kucharik et al., 1998). For simplicity, we use a single effective $G(0)$ function and clumping factor for within crown elements. Additionally, a shoot geometric shadow function (Chen and Leblanc, 2000) is applied instead of resolving shadowing within a shoot using a binomial process so Eq. (6) gives:

$$F_{vi}(z) = \Gamma_s(\xi) \left\{ \begin{aligned} &F_v(z)F_i(z)[1 - f_{HS}] \\ &+ [F_v(z)F_i(z)]^{0.5} f_{HS} \end{aligned} \right\} \quad (15)$$

Both trunks and crown shadows are treated as independent statistical processes as in (Kuusk and Nilson, 2000) using a cylinder-on-cone shape profile suitable for the Boreal stands considered in this study. Patches are described as cylindrical volumes extending to the canopy height H .

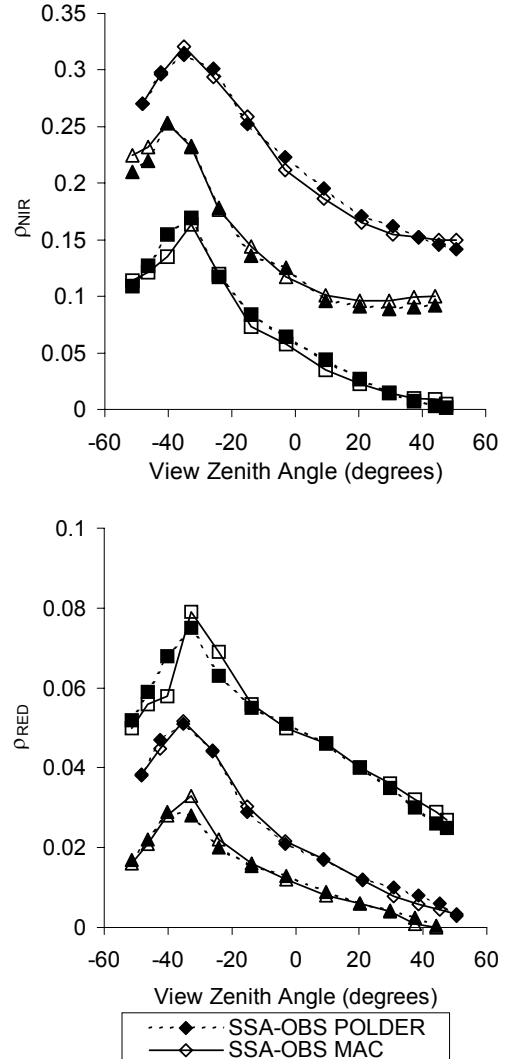
Equation (11) is written in terms of regions and requires explicit specification of both the location and shape of cast shadows to be exactly computed. Since both the individual projected shadows and the overlap area of these shadows can be non-convex we resort to a simplifying set of assumptions to allow an analytical solution. We assume the individual projected shadows are convex shapes for which relatively simple solutions can be found for their overlap area with $L(\lambda, \Omega_\lambda)$. The overlap region of a single shadow is then approximated by an ellipse with the same area as the actual shadow. The eccentricity of the ellipse is specified using a principal axis corresponding to the shadow dimensions parallel and perpendicular to the direction of projection. The ellipse dilated to match the area of the actual shadow. The overlap area of the two ellipses is estimated using Li and Strahler (1986).

2.4 MAC Model Validation

The MAC model was validated using the BOREAS POLDER data and canopy structural parameters for Boreal conifer stands cited in Leblanc et al. (1999). Element reflectance values and parameters governing patch scale clumping were selected to provide the best match to the observed BRDF while falling within the range of published values. This fitting was performed given the relatively large variability in element reflectance both within and between BOREAS sites. Agreement between observed and modelled BRDF's is good as indicated in Figure 1 for the principal plane for three BOREAS conifer sites. Root mean square errors are similar to those reported for the 5-Scale model. Comparisons of modelled versus measured

below canopy gap fraction (Chen and Cihlar, 1996) shown in Figure 2 suggest that the fitted reflectance and clumping parameters did not compromise the physical validity of the model.

Figure 1: Comparison of airborne POLDER observations over three conifer stands within the BOREAS study area with forward model estimates from MAC. The observations correspond to approximately 250m square footprints centred on each stand. Forward model fits were produced by using in-situ structural parameters and varying leaf and surface reflectance and element clumping to minimize the root mean square error to observations.



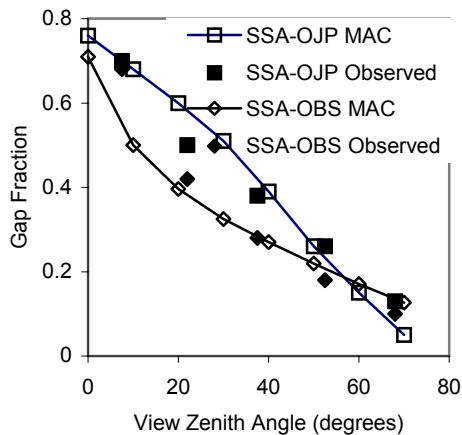


Figure 2. Comparison of observed below canopy gap fraction based on LICOR LAI-2000 measurements with estimates produced by the MAC model corresponding to fits shown in Figure 1. In-situ observations are averages of gap fraction over zenithal rings while MAC estimates are derived in 1 degree increments. Deviations near nadir are expected given the inability of the in-situ sensor to be positioned directly under a tree trunk.

3 SPOT4-VEGETATION CLOUD SCREENING

VGT S1 daily surface reflectance imagery were provided under the VEGA2000 programme. This product was atmospherically corrected using SMAC with constant atmospheric parameters at a given location. Cloud and snow screening had been already applied and was reported using a Status Mask (Lissens et al., 2000). Figure 3 provides sample band B02 (RED) time series over the SSA-OBS mature black spruce site and the nearby Prince Albert airport classified according to the status mask. The mask gives reasonable results for snow vs no-snow for the airport but clearly fails in identifying both snow conditions for the SSA-OBS and in labelling winter cloudy conditions as Indeterminate No Snow rather than Indeterminate Snow. The serious error in labelling conifer stands as snow free in winter was also common over much of the Canadian boreal zone.

Cloud screening of VGT data is challenging in the winter due to the lack of a thermal channel. We make use of two empirical trends to screen for clouds both in winter and summer: cloudy pixels tend to have higher visible (B02) reflectance than either vegetated surfaces or snow covered forests (Viterbo and Betts, 1999) and higher short-wave infrared reflectance that snow

covered surfaces (Rosenthal and Dozier, 1996). The combination of these two trends suggest that cloudy conditions can be screened by considering anomalies from the typical temporal variability in reflectance in both visible and SWIR bands. LOESS smoothing was applied to the time series of SWIR reflectance in an iterative manner to identify a lower bounding curve. The range of uncertainty around the curve was specified based on land cover dependent fits of BRDF using the semi-empirical NTAM model (Latifovic et. al., 2002) together with the known VGT observation geometry. Observations outside this range were removed from analysis. The remaining observations were then subject to a second LOESS smoothing based on red reflectance. LOESS smoothed curves are shown in Figure 3 for two of the study sites.

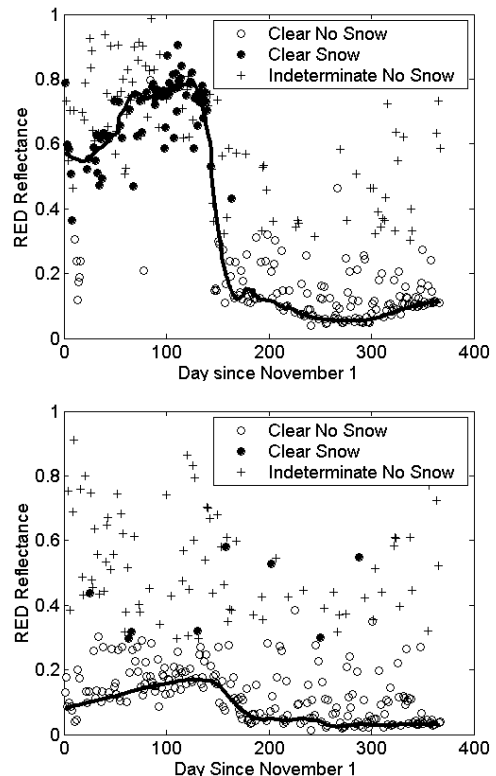


Figure 3: RED at surface reflectance from VGT S1 data over a grass field at the Prince Albert airport (upper) and SSA-OBS site (lower). Data area classified using the VGT status mask into clear and indeterminate cloud conditions and snow versus no-snow surface conditions. Clear errors in snow cover classification based on the VGT status mask are seen for winter periods for the SSA-OBS site. The iterative LOESS smoothed estimate is also shown.

4 SEQUENTIAL BRDF INVERSION

Our study was restricted to cases where the only free parameters assumed unknown compared to the forward model validation were the patch density and understorey reflectance. This approach may be a substantial simplification of the number of varying canopy parameters within a land cover category. We were unable to produce accurate (e.g. relative root mean square error less than 50%) fits of observed directional reflectance between day-of-year 250-350 over the three study sites using the MAC model. However, as it typical over most of Canada, the majority of VGT observations corresponded to relative azimuth angles at least 30 degrees away from the principle plane. The dynamic range of the BRDF shape was therefore substantially reduced in comparison to the principal plane measurements shown in Figure 1.

The restricted range of angles at a given VGT pixel implies that BRDF variability should not be a major issue with snow cover detection provided the detection threshold is determined on a per-pixel basis. Additionally, assuming the LOESS smoothing is robust to cloud contamination, the smoothed time series will represent the expected value of the BRDF signal over the full range of view zenith and relative azimuth angles. Hence, the only angular effect in the smoothed time series should be related to solar zenith angle and vegetation phenology.

We tested this hypothesis with the LOESS smoothed SWIR reflectance over the three conifer targets after he date with minimum solar zenith angle.

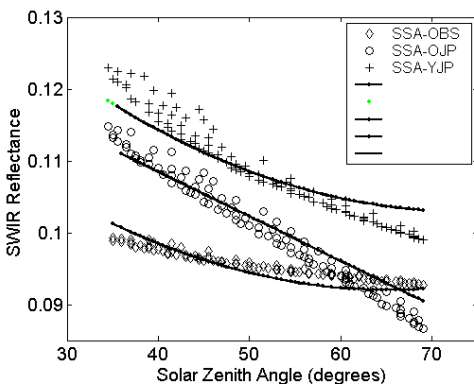


Figure 4: Observed and MAC model relationship between LOESS smoothed SWIR reflectance and solar zenith angle for conifer targets. The strong

relationships confirms that view angle variability has been reduced due to the LOESS smoothing.

The use of conifer targets minimizes phenological variability as overstorey LAI varies by less than 5% from mid to late growing season (Chen, 1996). As shown in Figure 4, a strong, almost linear, relationship was observed at all three conifer sites between smoothed SWIR reflectance and solar zenith angle. To further test the cause and effect hypothesis we compared MAC model estimates of reflectance (averaged over a uniform distribution of view zenith angles and relative azimuth angles found in the VGT data at each site) at each solar zenith angle. Again, the model was applied by fixing the structural parameters to those found from the POLDER forward modelling exercise. The fits shown represent the lowest root mean square error as a function of varying understorey and canopy element SWIR reflectance. Figure 5 shows the estimated normalised difference snow index (NDSI) based on the loess smoothed reflectances. The snow cover fraction based on extreme values of the index are more realistic than the VGT status mask.

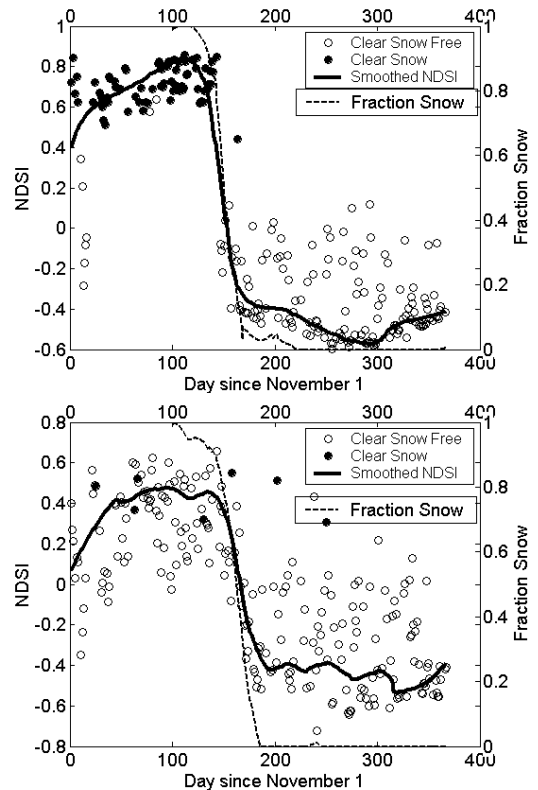


Figure 5: Normalised difference snow index time series from VGT daily data over the Prince Albert

airport (upper) and SSA-OBS (lower) together with loess smoothed curves and estimates snow fraction.

5 DISCUSSIONS AND CONCLUSIONS

The MAC model represents both simplifications and improvements over the 4-Scale model on which it was based. It abandons the use of Neyman grouping and, in the interest of simplicity, does not explicitly resolve multiple scattering. However, it was able to fit the POLDER conifer sites with similar performance as 4-Scale. MAC was also able to match observed below canopy gap fraction measurements to a reasonable degree after considering that the model was fit for 1km sites but the measurements were over 300m transects within the sites. We are currently testing the accuracy to which MAC represents the entire gap size distribution as measured using the TRAC instrument and airborne LIDAR over these sites

Screening for atmospheric contamination is essential before fitting any BRDF model to angular measurements. The current VGT cloud masking contained a large number of indeterminate pixels that had to be screened. In addition, the variability of the cloud free pixels were also much larger than found in the BOREAS POLDER data. There is also a concern with commission errors as there were very few clear snow pixels labelled for conifer sites such as the SSA-OBS. Iterative LOESS smoothing was able to find reasonable estimates of cloud free pixels although there may be differences in performance elsewhere in cases where either too many consecutive cloudy observations are present or the NTAM based uncertainty intervals for the curve-fit are not representative. More testing is required in this regard and additional BRDF measurements from sensors such as POLDER may help to further define the envelope of plausible cloud free observations.

The MAC model was unable to provide fits that explained a substantial portion of variance in cloud free VGT single pixel data. There are two reasons for this difference in performance between the fits to airborne POLDER data versus VGT data. Primarily, the VGT data was off the principal plane and therefore spanned a far smaller range of variation over the BRDF surface than the principal plane POLDER data. Secondly, the VGT data was likely noisier given its use of fixed atmospheric corrections and potentially varying spatial footprint. Clearly, additional angular sampling, preferably close to the principal plane is required before either forward or inverse fitting of BRDF models can be considered..

Although the original idea of using a BRDF model fitted using snow off data did not work it appears that

the LOESS smoothing may drastically reduce the need to consider BRDF effects when mapping transitions in surface conditions using VGT data over small ranges of solar zenith angle. Our empirical and model based analysis using SWIR time series suggests that only a SZA effect remains, out of other acquisition geometry effects, after LOESS smoothing. We hypothesize that the use of the an NDSI derived from LOESS smoothed reflectance may act to reduce the snow cover mapping problem to a predominantly linear mixture problem with endmembers defined by the index just prior and after the dominant decrease in the index.

Future work will focus on testing this assumption using in-situ and fine resolution image based snow cover measurements for validation. The impact of varying snow and overstorey reflectance during melt, and the spatial covariation of overstorey and snow patches may need to be incorporated into a mixture model approach. In addition, iterative LOESS smoothing requires a minimum span of observations (in our case 3 days) that may limit the performance of this approach in near-real time applications. More work is required to determine snow cover mapping performance during real time acquisition. Finally, we were unable to demonstrate the usefulness of MAC for interpreting inversion of time series data due to the limited range of acquisition angles and noise in the data set. BRDF assimilation may still have a role in refining snow cover estimates in cases where sufficient cloud free angular sampling is available.

Acknowledgements: We would like to acknowledge the VEGA2000 program and Dr. Leroy and Dr. Breon for providing reflectance data. In addition, Rasim Latifovic, Robert Fraser and Josef Cihlar provided assistance. We would also like to thank Dr. John Norman for discussions regarding MAC. Finally, we credit Dr. Jing Chen for the idea to use the gap size distribution to determine the "hotspot effect".

6 REFERENCES

- Anonymous, 2002, VEGETATION user guide, <http://www.spotimage.fr/data/images/vege/VEGETAT/home.htm> (web document).
- Chen, J.M., 1996, Optically-based methods for measuring seasonal variation of leaf area index in boreal conifer stands. *Agriculture and Forest Meteorology*, 80, 135-163.
- Chen, J.M. and Cihlar, J., 1996, Retrieving leaf area index of boreal conifer forests using Landsat TM images. *Remote Sensing of Environment*, 55-153-162.

- Chen, J.M. and Leblanc, S.G., 2001, Multiple-scattering scheme useful for geometric optical modelling. *IEEE Trans. Geoscience and Remote Sensing*, 39, 1061-1071.
- Cleveland, W.S., and S.J. Devlin, locally-weighted regression: an approach to regression analysis by local fitting. *Journal of American Statistical Association*, 83, 596-610.
- Kucharik, C.J., Norman, J.M. and Gower, S.T., 1998, Measurements of branch area and adjusting leaf area index indirect measurements. *Agriculture and Forest Meteorology*, 91,69-88.
- Kuusk, A. and Nilson, T., 2000, A directional multispectral forest reflectance model. *Remote Sensing of Environment*, 72, 244-252.
- Latifovic, R., Cihlar, J. and Chen, J.M., 2002, A comparison of BRDF models for the normalization of satellite optical data to a standard sun-target –sensor geometry. *IEEE Trans. Geoscience and Remote Sensing* accepted.
- Leblanc, S.G., Bicheron, P., Chen, J.M., Leroy, M. and Cihlar, J., 1999, Investigation of Directional Reflectance in Boreal Forests with an Improved Four-Scale Model and Airborne POLDER Data. *IEEE Trans. Geoscience and Remote Sensing*, 37, 1396-1413.
- Leroy, M. and Breon, F.M., 1996, Surface reflectance angular signatures from airborne POLDER data. *Remote Sensing of Environment*, 38, 193-210.
- Li, X. and Strahler, A., 1986, Geometrical-optical bi-directional reflectance modeling of a conifer forest canopy. *IEEE Trans. Geoscience and Remote Sensing*, 24,906-919.
- Lissens, G., Kempeneers, P. and Fierens, F., 2000, Developmment of cloud, snow and cloud shadow mask for VEGETATION imagery, Vegetation 2000 Symposium Proceedings, available at <http://vegetation.cnes.fr> (web site).
- Miller, E.E. and Norman, J.M., 1971, A sunflect theory for plant canopies, I. Lengths of sunlit segments along a transect. *Agronomy Journal*, 63, 735-738.
- Nilson, T., 1999, Inversion of gap-frequency data in forest stands. *Agriculture and Forest Meteorology*, 98-99,449-462.
- Rosenthal, W. and Dozier, J., 1996, Automated mapping of montane snow cover at subpixel resolution from the Landsat Thematic Mapper. *Water Resources Research*, 32, 115-130.
- Sellers, P. J. 1986. Canopy reflectance, photosynthesis and transpiration. *International Journal of Remote Sensing*, 6:1335-1372.
- Viterbo, P. and Betts, A.K., 1999, The impact on ECMWF forecats of changes to the albedo of the boreal forest in the presence of snow. *Journal of Geophysical Research*, D22, 27803-28710.

Determining the Contribution of Shaded Elements of a Canopy to Remotely Sensed Hyperspectral Signatures

H. Peter White¹, Lixin Sun², Karl Staenz¹, Richard Fernandes¹, Catherine M. Champagne³

¹ Canada Centre for Remote Sensing – Natural Resources Canada, Ottawa, ON, Canada, K1A 0Y7

² Dendron Resources Surveys Inc., Ottawa, ON, Canada, K1Z 5L9

³ MIR Télédétection Inc., Québec, PQ, Canada, J4K 1A3

Email: PWhite@NRCan.GC.Ca

ABSTRACT - Hyperspectral imagery has the potential to become a useful tool for monitoring and extracting biophysical properties of vegetated areas. Exploitation of this potential relies on the ability to relate at-canopy spectral reflectance to biophysical characteristics of vegetation and derive both sunlit and shaded component proportions and spectral profiles. Increased application of hyperspectral imagery to these areas is expected with the advent of space borne hyperspectral sensors (such as EO-1 Hyperion and CHRIS-PROBA). Such imagery of vegetated scenes is influenced however by the well known bidirectional reflectance distribution (BRDF) effect.

One method of determining the contribution of shaded overstorey vegetation and background to observed spectral reflectance is to determine, by model inversion, the proportion of shaded surfaces viewed by the sensor, and the relative intensity of the radiative flux incident on these surfaces. This can be achieved by modelling the overall reflectance as composed of mean sunlit and shaded reflectance components, combined with an analytical description of the shaded radiant flux. Assuming a land cover type with consistent mean foliage and background reflectance, inversion of a semi-empirical model can be used to determine BRDF coefficients, which can then be applied to normalize the imagery to a specific view/sun geometry. If the modelled spectral coefficients directly relate to canopy properties, then BRDF normalization can also provide information to help directly relate the canopy architectural and biophysical properties to the remotely sensed signal. One such model, FLAIR, has been successfully used to investigate canopy characteristics from airborne and satellite spectral imagery.

1 INTRODUCTION

With the addition of hyperspectral sensors to the variety of spaceborne remote sensing instruments presently orbiting the Earth, an extra dimension of detail has become more accessible to remote sensing scientists. While hyperspectral sensors have existed for many years, they have remained part of airborne and near-surface investigative efforts until recently, with the launch of EO-1 Hyperion and CHRIS-PROBA missions. Future planned launches of ARIES and NEMO demonstrates the interest of the scientific and environmental communities in utilizing hyperspectral imagery of land surfaces on a more continual bases.

One common application of spaceborne remote sensing imagery is to relate the remotely sensed broadband signals to biophysical properties of vegetative surfaces (for example see [Badhwar et al., 1996; Abuelgasim et al., 1998; Bicheron and Leroy, 1999; and Chen et al., 2002]). While this has been a

successful approach for many applications, these studies have been faced with the challenge of accounting for the anisotropic characteristics of vegetative surface reflectance, the bidirectional reflectance distribution function or *BRDF*, where the observed reflectance is influenced by both the view angle of the sensor and the location of the sun (solar angle) [for example, see Goel, 1988, White et al., 2001].

Unlike broadband studies which relate biophysical properties to reflectance magnitude, hyperspectral data has the potential to relate high resolution spectral features to their associated canopy properties. Previous studies have already noted how increased spectral information can improve the ability to relate multi-angular data to canopy properties [Abuelgasim et al. 1996; Peddle et al, 1999; Broge and Leblanc, 2000; White et al, 2001]. Indeed, investigations relating spectral features directly to canopy biophysical and architectural properties have already demonstrated significant potential [Zarco et al., 1999; Champagne et al., 2001]. But like broadband

reflectance, these spectral features are also influenced by the canopy *BRDF* phenomena.

The FLAIR Model (Four-Scale Linear Model for AnIsotropic Reflectance) was initially designed to model these angular influences on canopy reflectance (the bidirectional reflectance factor, or *BRF*) [White et al., 2001; 2002]. Based on a physical description of canopy structure (as detailed by the Four-Scale Model of Chen and Leblanc [1997]), the FLAIR model is also designed for inversion of multi-angular *BRF* to provide quantitative information about the observed canopy. Thus the influences of shade and multiple scattering on the observed reflectance is used in part to relate biophysical characteristics to canopy *BRF*. Indeed, the importance of determining the shaded spectral properties has been noted in several studies [for example, see Hall et al, 1995; Peddle et al., 1999; Beaudet et al., 2002; Sabol Jr. et al., 2002]

The influences of foliage and background multiple scattering changes as a function of wavelength. For example, scattering is minimal in the red spectral region, but significant in much of the near infrared. Thus shaded contributions to the observed *BRF* are spectrally dependant, providing important information towards the determination of foliage density (i.e., effective *LAI*). By including wavelength dependant scattering properties to FLAIR inversion, an additional constraint is applied. Plus, by using the dynamic range of scattering regimes available with hyperspectral bidirectional reflectance (*BRF_λ*), biophysical characteristics of a canopy have the potential of being determined without the need for significant multi-angular acquisitions.

Multi-scattering influences on the *BRF_λ* are here modelled by determining the downwelling irradiance on shaded components of a canopy using the two-stream radiative transfer described by Sellers [1985; 1987]. FLAIR inversion of several spectral bands simultaneously now has additional constraints on the magnitude of the contribution of shaded surfaces to the observed *BRF_λ*. This FLAIR inversion procedure is presently being implemented with the Imaging Spectrometer Data Analysis System (ISDAS) processing software [Staenz et al., 1998] developed at the Canada Centre for Remote Sensing – Natural Resources Canada, and an agricultural test site is being used as a validation site for this procedure.

2 FLAIR INVERSION

2.1 The FLAIR Model – A Brief Review

FLAIR expresses the canopy bidirectional spectral reflectance factor (*BRF_λ*) as the weighted sum of four scene component mean spectral reflectance factors (shaded overstorey – *R_{ztλ}*, shaded background – *R_{zgλ}*,

sunlit overstorey – *R_{tlλ}*, sunlit background – *R_{gλ}*), expressed as:

$$BRF_{\lambda} = R_{zt\lambda} k_{zt} + R_{zg\lambda} k_{zg} + R_{tl\lambda} k_t + R_{g\lambda} k_g \quad (1)$$

Spectral reflectance factors are defined as the ratio of nadir reflected radiance from a scene component to the nadir reflected radiance from a 100% Lambertian panel located at the top-of-canopy directly above the target. The four kernels (*k_x*) define the viewed scene component proportions, functions of the effective leaf area index (*eLAI*) [Chen et al., 1991] and the view/sun geometry (*k_x* ≡ *k_x*(*eLAI*; *θ_v*, *φ_v*, *θ_i*, *φ_i*)). For more information on the FLAIR model see White et al. [2001; 2002].

Shaded reflectance factors are now constrained using a two-stream radiative transfer algorithm to derive the downwelling irradiance intensity at the shaded surface relative to the top-of-canopy. Multi-scattering ratios are defined for both the overstorey and background as *R_{zt}*/*R_t* and *R_{zg}*/*R_g* respectively.

2.2 Modified Simplex Method for FLAIR Inversion

When limited to one spectral band, variations in observed reflectance from multiple view/sun angle image acquisitions demonstrates the influence of architecture on canopy *BRF*. When multiple spectral bands are inverted concurrently, the spectral scattering characteristics of the canopy components also become relevant. This limits the range of potential canopy architectural influences which can result in the observed *BRF_λ*.

With hyperspectral imagery, consisting of over 150 spectral bands, it becomes computationally expensive and redundant to invert all bands. Instead, inversion uses spectral bands (~10) which do not correlate within the spatial region of interest (ROI). When the purpose is to examine a specific spectral feature, inversion begins using uncorrelated bands over the whole hyperspectral range of the sensor, then is repeated for bands related to the spectral feature using the previous resulting reflectance factors and *eLAI* as additional constraints.

Inversion of FLAIR is performed using a modified simplex method (for a full description of the simplex method, see Vetterling et al. [1990]), where spectral reflectance factor constraints are defined using the observed *BRF_λ*, kernels determined for a given *eLAI* and view/sun geometry. The process continues iteratively over values of *eLAI* until a minimum constraint volume is reached.

The modified simplex method is applied by defining a *4b* dimensional space defined by the four reflectance factors coefficients for each spectral band, *b*. Primary constraints are defined for each dimension based on the allowed range of each reflectance factor

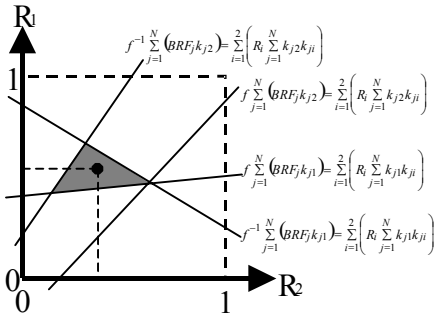


Figure 1 : Example modified simplex inversion of a two kernel, two reflectance system. Secondary constraints are indicated by their equations. As f decreases, so does the minimal constraint volume, represented by the grey area. The black dot indicates the reflectance values reported by the inversion procedure for this case.

($0 \leq R_x \leq 1$ to start, can be adjusted based on user input or model examination of data as will be outlined.).

Secondary constraints are then defined for each band based on the view/sun angular orientation (per pixel) and observed BRF_λ . For each spectral band (from N image acquisitions), four secondary constraints are determined. A discrepancy factor, f , is applied to the secondary constraints to provide upper and lower limits to the quality of the inversion, which doubles the number of secondary constraints (see figure 1). These secondary constraints define hyperplanes in the $4b$ dimensional component reflectance space. When f is large, the hyperplanes will not define a closed bound volume within the boundaries of the primary constraints. On the other hand, when f is small, then no individual volume will be bound by all hyperplanes.

An inversion iteration is complete when a value of f is found (if it exists) where all hyperplanes act as boundaries to the minimum constraint volume. As the procedure iterates over values of $eLAI$ the minimum constraint volume will decrease (f approaches unity) as the value of $eLAI$ approaches values reasonable for the canopy. In this way, FLAIR inversion provides discrepancy factors, f , as a function of $eLAI$. The resulting values of $eLAI$ and component reflectance factors for the minimum value of f are selected as the most probable values for the canopy. If BRF_λ values are chosen from a spatial region, then the inversion results will represent average values for that region.

Additional information on the inversion process can be obtained from White et al. [2001; 2002].

2.3 Simplified Modified Simplex Method Example

As an example to the inversion procedure, consider a hypothetical surface with two component constituents describable by two kernels (k_1, k_2) with two distinct reflectance factors (R_1, R_2) and no shadowing. Let there be N image acquisitions taken in one spectral band. In this case, the modified simplex inversion procedure would be defined in two reflectance dimensions, with four secondary constraints. For each $eLAI$ iteration, the modified simplex method results in the smallest discrepancy factor, f , where the constraint volume remains bounded by all secondary constraints, as shown in figure 1.

As $eLAI$ approaches a value reasonable for this hypothetical canopy, f approaches a minimum value (and the minimal constraint volume approaches zero). Inversion is complete when a global minimum of f is determined, and the reflectance factors which fall within that volume are reported.

3 MULTI-SCATTERING RATIO

With a focus on improving the extraction of shaded contributions to the observed spectral reflectance while simultaneously determining the radiant flux levels in this shaded canopy proportion, FLAIR inversion was further constrained with a two-stream radiative transfer model. The multi-scattering ratio is defined by the relative intensity of downwelling irradiance within a canopy on surfaces where the direct solar beam is not incident (i.e., shaded surfaces). Diffuse and direct radiative flux incident at the top-of-canopy will scatter throughout the canopy as multiple reflectance events from plant and background surfaces occur. To derive the relative magnitude of the downwelling diffuse irradiance incident on the shaded canopy components, the two-stream radiative transfer model detailed by Sellers [Sellers, 1985; 1987] is incorporated into the FLAIR inversion algorithm.

FLAIR inversion is performed, and the resulting mean sunlit spectral reflectance factors and mean $eLAI$ are used to determine the mean shaded spectral reflectance factors via the two-stream model. If FLAIR derived shaded reflectance factors are outside a pre-set range when compared to the two-stream model derived values, then the primary constraints assigned to the sunlit reflectance factors are modified and inversion is repeated. If FLAIR inversion results in an extremely bright sunlit surface and dark shaded surface (relative to the two-stream model) then the sunlit reflectance factors are constrained to lower values. Alternatively, if the derived sunlit reflectance factors are low, with bright shaded areas then the

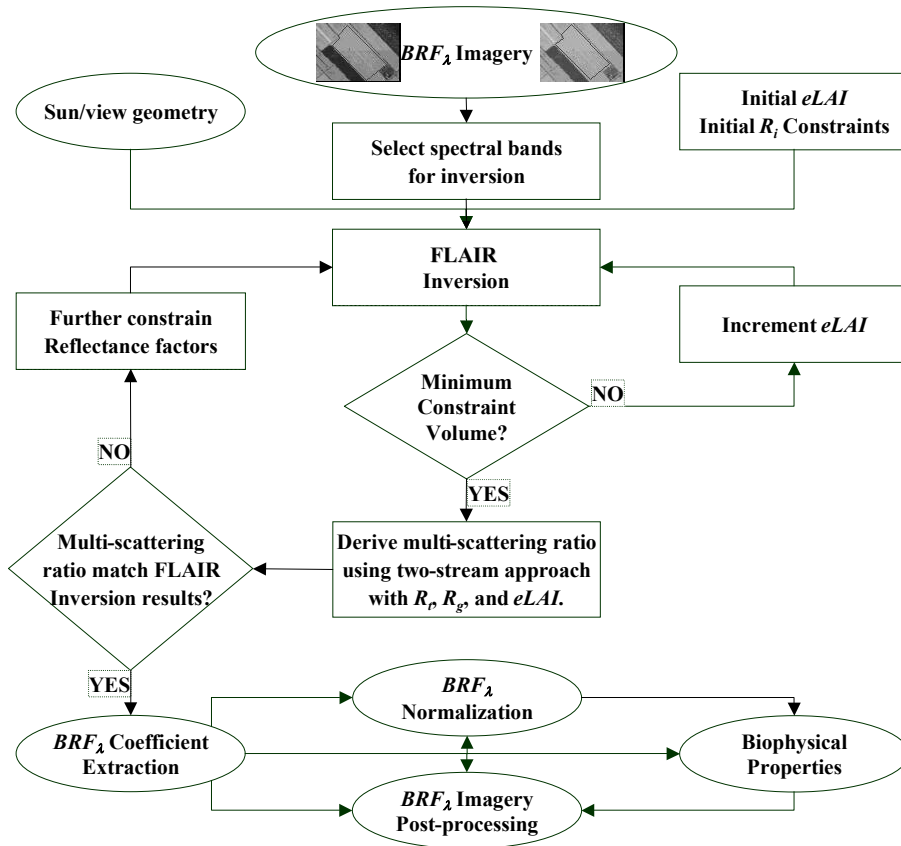


Figure 2: Processing sequence for FLAIR inversion of multi-angular hyperspectral imagery as will be implemented as a procedure in ISDAS (Imaging Spectrometer Data Analysis System developed at Natural Resources Canada – Canada Centre for Remote Sensing).

lower constraint to the sunlit reflectance factors is raised. Thus a physical constraint is given to the contribution of shaded components to observed canopy BRF_{λ} .

The two-stream radiative transfer model presented by Sellers [1985; 1987] follows from the work of Dickinson [1983], where the upward and downward diffuse irradiance within a canopy is modelled for a random foliage distribution with isotropically reflecting leaf elements. Both diffuse sky and direct sun at the top-of-canopy are modelled as contributing to the incident radiative flux. Leaf elements reflectance and transmittance properties are assumed equal at this stage of development with FLAIR inversion. (Further research will examine separating the foliage reflectance and transmittance within the multi-scattering model, important in the highly reflective near infrared region.)

For sunlit viewed canopy components, FLAIR inversion assumes that the direct beam intensity

dominates the downwelling incident flux incident on the sunlit surface. For the shaded proportions however, the two-stream model is applied to determine the apparent shaded reflectance factor (as defined in Section 2.1). As the absolute canopy component reflectance property does not change as a function of the downwelling irradiance, the ratio of shaded-to-sunlit apparent reflectance factors can be modelled using the relative intensity of the shaded irradiance determined via the two stream model.

4 THE FLAIR INVERSION ALGORITHM

FLAIR Inversion is presently being designed as a tool for the Imaging Spectrometer Data Analysis System (ISDAS) processing software [Stanz et al., 1998]. This tool will allow the user to highlight spatial regions of interest (ROI) from hyperspectral imagery. It would then invert observed BRF_{λ} for selected spectral bands to determine mean $eLAI$ and mean

spectral reflectance factor coefficients for the overstorey and background (including the apparent shaded spectral reflectance factors).

Inversion accuracy will depend in part on the homogeneity of the ROIs, the accuracy of the reflectance determination (atmospheric correction and sensor radiometric accuracy), as well as the range of spectral and angular variation available from the imagery. A flow chart highlighting the inversion procedure is provided in figure 2.

5 AGRICULTURAL TEST SCENE

Initially, FLAIR inversion was designed for multi-angle, single band applications. Testing of the single band inversion procedure were successfully performed using multi-angle acquisitions of forest scenes obtained during BOREAS 1994 campaigns [Sellers et al., 1995] using CASI, PARABOLA, and POLDER sensors [White et al., 2001; Leblanc et al., 2002; White et al., 2002].

Re-analysis of this boreal forest broadband BRF data, using the above multi-band procedure resulted in biophysical parameter and component reflectance extraction which better reproduced the concurrently measured field data [White et al., 2002].

In practice, hyperspectral image acquisitions seldom provides several distinct view angle observations of a region. Often, a sensor is flown only once, or if funds and atmospheric conditions permit, twice per study period. With satellite imagery, the acquisition is limited to the capability and orbital

constraints of the sensor, limiting the sun/view geometry. The present multi-band FLAIR inversion was tested on limited sun/view geometry hyperspectral imagery of agricultural scenes.

BRF_{λ} values were extracted from double pass airborne nadir imagery acquired over corn fields near Clinton, Ontario, using the Probe-1 sensor [Earth Search Sciences Inc., 2002] in July, 1999. The imagery consists of 128 spectral bands ranging from 430 to 2500 nm, with a pixel resolution of $5 \times 5 \text{ m}^2$. Acquisitions were 45 minutes apart, resulting in a change of solar zenith angle from 43° to 35° . In-field measurements of corn leaf reflectance and $eLAI$ were taken concurrently [Champagne et al., 2002].

To provide sufficient data for inversion, a ROI was defined outlining corn fields in the test image area known to be of similar age and subject to similar growing conditions. View/sun geometry for each pixel with the ROI was determined, and corn field BRF_{λ} extracted. FLAIR inversion was performed as outlined above. Sample results of the inversion procedure are provided in figure 3.

The inverse derived mean $eLAI$ of the validation corn field is within the standard error of the mean $eLAI$ measured in-field of 2.4 ± 0.3 [Pacheco, 2001] using a LI-COR LAI-2000 [LI-COR, 1992]. GER3700 Spectroradiometer [GER Corp., 2002] reflectance measurements of sunlit corn leaves measured at the Clinton sites are also reproduced by FLAIR inversion.

Visual inspection of the results easily reveal however that the sunlit background spectral

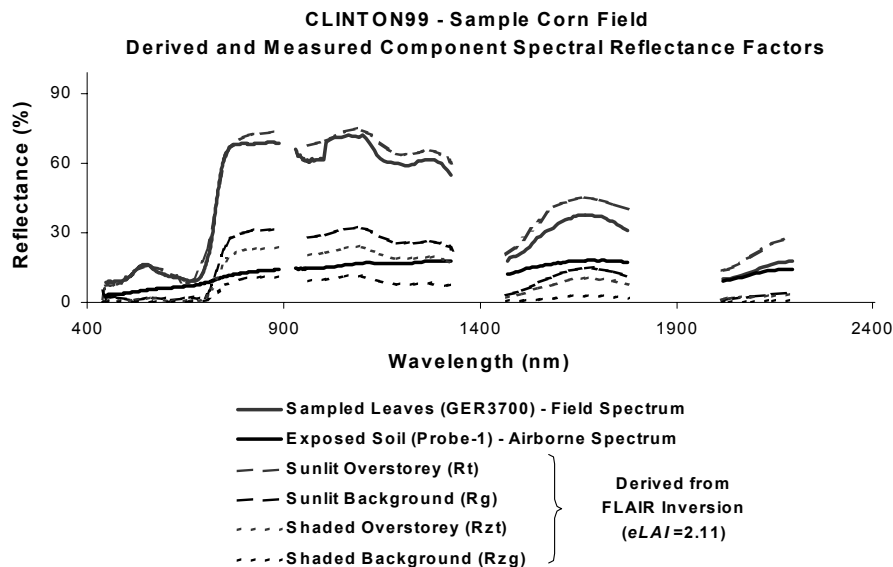


Figure 3: FLAIR inversion derived component spectral reflectance factor signatures of a Clinton test corn field. Field data spectral reflectance factors (GER3700) are provided for comparison.

reflectance factors do not match. While the magnitudes are similar, the inversion derived background reflectance maintains a vegetation-like signature not seen with the bare soil spectral nadir reflectance. This may be due in part to the existence of ground cover plants (weeds) and residue in the fields which were not present at the bare soil site used to obtain the sunlit soil spectral reflectance. Also of note, the selected sunlit bare soil site was not contaminated by contributions of foliage multi-scattering to the incident downwelling flux on not-shaded background locations, further research is required to determine the relative influence of this contribution to the observed reflectance. Shaded spectral reflectance derived by FLAIR inversion are also shown in figure 3.

One example application of utilizing hyperspectral inversion is sub-pixel unmixing, using a spectral mixing analysis. A previous analysis of this data [Pacheco et al., 2001] performed a constrained linear spectral unmixing of the Clinton corn fields to determine the percentage of crop per pixel. The aim was to identify areas of high and low yield and to compare unmixing results to measured *eLAI*.

Table 1: Endmember fractions using various analysis techniques of the Clinton test corn field from sample plot locations.

	From Vertical Photographs		Using Image Endmember Extraction		Using FLAIR Endmember Extraction	
	Soil	Corn	Soil	Corn	Soil	Corn
Site ID						
377-38	0.19	0.81	0.03	0.97	0.18	0.82
362-57	0.22	0.78	0.02	0.98	0.09	0.91
343-80	0.14	0.86	0.01	0.99	0.11	0.89
331-95	0.13	0.87	0.02	0.98	0.14	0.86
315-101	0.21	0.79	0.06	0.94	0.23	0.77
Scene Average	0.18	0.82	0.03	0.97	0.15	0.85

In that study, endmember spectra were selected by identifying areas of clear soil and dense foliage and extracting their spectral reflectance from the hyperspectral imagery. Table 1 shows pixel specific results of unmixing a Clinton test corn field using endmembers selected using the original field observed endmember spectra, as well as by using FLAIR inversion results as endmembers. For comparison, digital camera imagery analysis of the identified pixels are also shown. FLAIR endmembers included both shaded and sunlit spectral reflectance factors for the overstorey and background, for comparison to previous studies, the shaded and sunlit fractional components are combined in table 1.

4 DISCUSSION

This preliminary investigation demonstrates the potential of using *BRF_λ* inversion to determine average scene *eLAI*, component spectral reflectance factors, and shaded properties of agricultural corn crops. This analysis used the previously demonstrated (for forest canopies) FLAIR Model with the addition of a two-stream radiative transfer model to constraint the contribution of shaded components to the observed reflectance.

When the scene is sufficiently homogeneous in composition, such as an agricultural field, then the derived mean component spectral reflectance factors can be directly related to the foliage and background. This allows for the definition and separation of sunlit and shaded spectral signatures which can be used for such things as spectral unmixing and determining shaded light conditions at the understorey level.

More detailed investigation of this technique with other agricultural crops and more heterogeneous canopies will be pursued. Of specific interest will be the examination of how canopy *BRF* is influenced with respect to spectral features (such as the water index which relies on determining the accurate depth of liquid water absorption features [Peñuelas et al., 1986], the red-edge spectral features used for land cover mapping [Zarco-Tejada and Miller, 1999]) and the level of light intensity in shade within a vegetative canopy (significant for determining such properties as secondary growth success (weeds in agricultural crop) and successional processes (second generation tree growth in forests)).

5 REFERENCES

- Chen, J.M., Pavlic, G., Brown, L., Cihlar, J., Leblanc, S., White, H.P., Hall, R., Peddle, D., King, D., Trofymow, J., Swift, E., Van der Sanden, J., and Pellikka, P.K.E., 2002, Derivation and validation of Canada-wide coarse-resolution leaf area index maps using high-resolution satellite imagery and ground measurements. *Remote Sensing of Environment*, 80, 165-184.
- Bicheron, P. and Leroy, M., 1999, A method of biophysical parameter retrieval at global scale by inversion of a vegetation reflectance model. *Remote Sensing of Environment*, 67, 251-266.
- Badhwar, G.D., MacDonald, R.B., Metha, N.C., 1986, Satellite-derived leaf-area-index and vegetation maps as input to global carbon cycle models – a hierarchical approach. *International Journal of Remote Sensing*, 7, 265-281.

- Abuelgasim, A.A., Gopal, S., and Strahler, A.H., 1998, Forward and inverse modelling of canopy directional reflectance using a neural network, *International Journal of Remote Sensing*, 19(3), 453-471.
- Abuelgasim, A.A., Gopal, S., Irons, J.R., and Strahler, A.H., 1996, Classification of ASAS multiangle and multispectral measurements using artificial neural networks, *Remote Sensing of Environment*, 57, 79-87.
- Peddle, D.R., Hall, F.G., and LeDrew, E.F., 1999, Spectral mixture analysis and geometric-optical reflectance modelling of boreal forest biophysical structure, *Remote Sensing Environment*, 67, 288-297.
- Broge, N.H., and Leblanc, E., 2000, Comparing prediction power and stability of broadband and hyperspectral vegetation indices for estimation of green leaf area index and canopy chlorophyll density, *Remote Sensing Environment*, 76, 156-172.
- Goel, N.S., 1988, Models of vegetative canopy reflectance and their use in estimation of biophysical parameters from reflectance data, *Remote Sensing Reviews*, 32, 1-212.
- White, H.P., Miller, J.R., and Chen, J.M., 2002, Four-scale linear model for anisotropic reflectance (FLAIR) for plant canopies. I: Model description and partial validation, *IEEE Transactions on GeoScience and Remote Sensing*, 39(5), 1072-1083.
- Zarco-Tejada, P.J. and Miller, J.R., 1999, Land cover mapping at BOREAS using red edge spectral parameters from CASI imagery, *Journal of Geophysical Research*, 104(D22), 27921-27933.
- Earth Search Sciences Inc., 2002, Technology - About Probe-1, <http://www.earthsearch.com>
- Champagne, C.M., Staenz, K., Bannari, A., White, H.P., Deguise, J.-C., and McNairn, H., 2002, Estimation of plant water content of agricultural canopies using hyperspectral remote sensing, Proceedings of the 1st International Symposium Recent Advances in Quantitative Remote Sensing held in Valencia, Spain, on 16-20 September 2002.
- White, H.P., Miller, J.R., and Chen, J.M., 2002, Four-scale linear model for anisotropic reflectance (FLAIR) for plant canopies. II: Validation and inversion with CASI, POLDER, and PARABOLA data at BOREAS, *IEEE Transactions on GeoScience and Remote Sensing* – Invited paper, 40(5), 1038-1046.
- Chen, J.M. and Leblanc, S.G., 1997, A four-scale bidirectional reflectance model based on canopy architecture, *IEEE Transactions on Geoscience and Remote Sensing*, 35, 1316-1337.
- Hall, F.G., Townshend, J.R., and Engman, E.T., 1995, Status of remote sensing algorithms for estimation of land surface state parameters, *Remote Sensing of Environment*, 51, 138-156.
- Beaudet, M., Messier, C., Canham, C.D., 2002, Predictions of understorey light conditions in northern hardwood forests following parameterization, sensitivity analysis, and tests of the SORTIE light model, *Forest Ecology and Management*, 165, 235-248.
- Sabol Jr., D.E., Gillespie, A.R., Adams, J.B., Smith, M.O., and Tucker, C.J., 2002, Structural stage in Pacific northwest forests estimated using simple mixing models of multispectral images, *Remote Sensing of Environment*, 80, 1-16.
- Sellers, P.J., 1985, Canopy reflectance, photosynthesis and transpiration, *International Journal of Remote Sensing*, 6(8), 1335-1372.
- Sellers, P.J., 1987, Reflectance, photosynthesis, and transpiration. II. The role of biophysics in the linearity of their interdependence, *Remote Sensing of Environment*, 21, 143-183.
- Staenz, K., Szeredi, T. and Schwarz, J., 1998, ISDAS – A system for processing/analyzing hyperspectral data, *Canadian Journal of Remote Sensing*, 24(2): 99-113
- Chen, J.M., Black, T.A., and Adams, R.S., 1991, Evaluation of hemispherical photography for determining plant area index and geometry of a forest stand, *Agricultural and Forest Meteorology*, 56, 129-143.
- Vetterling, W.T., Teukolsky, S.A., Press, W.H., Flannery, B.P., 1990, Linear Programming and the Simplex Method, Numerical Recipes in C., Cambridge, U.K.: University Cambridge Press.

- Dickinson, R.E., 1983, Land surface processes and climate-surface albedos and energy balance, *Advanced Geophysics*, 25, 205.
- Sellers, P.J., Hall, F., Margolis, H., Kelly, B., Baldocchi, D., den Hartog, G., Cihlar, J., Ryan, M.G., Goodison, B., Crill, P., Ransonm K.J., Lettenmaier, D., and Wickland, D.E., 1995, The Boreal ecosystem-atmosphere study (BOREAS): An overview and early results from the 1994 field year, *Bulletin American Meteorological Society*, 76(9), 1549-1577.
- Leblanc, S.G., Chen, J., White, H.P., Latifovic, R., Fernandes, R., Roujean, J-L., Lacaze, R., 2002, Mapping leaf area index heterogeneity over Canada using directional reflectance and anisotropy canopy reflectance models, Proceeding of the Joint 24th Canadian Symposium on Remote Sensing / 2002 International Geoscience and Remote Sensing Symposium held in Toronto, Ontario, Canada 24-28 June 2002.
- White, H.P., Leblanc, S.G., Chen, J.M., Lacaze, R. and Roujean, J-L., 2001. Mapping biophysical parameters with modelled and inverted functions from directional satellite measurements, 23rd Canadian Symposium on Remote Sensing held in Ste. Foy, Quebec, Canada, 20-24 August, 2001.
- Pacheco, A., Bannari, A., Deguise, J-C., McNairn, H., and Staenz, K., 2001, Application of hyperspectral remote sensing for LAI estimation in precision farming, Proceedings of the 23rd Canadian Symposium on Remote Sensing held in Ste. Foy, Quebec, Canada, 20-24 August, 2001, pp. 281-287.
- LI-COR Inc., 1992, LAI-2000 Plant Canopy Analyser Operating Manual, LI-COR Inc., Lincoln Nebraska, USA.
- GER Corporation, 2002, The GER3700 Field Portable Spectrometer, <http://www.ger.com/3700.html>
- Peñuelas, J., Filella, I., Serrano, L., and Savé R., 1986, The reflectance at the 950-970 region as an indicator of plant water status, *International Journal of Remote Sensing*, 17(2), 373-382.

Mapping Vineyard Soil Surface Features by Very High Spatial Resolution Remote Sensing

T. Wassenaar¹, J.M. Robbez-Masson², F. Baret¹, P. Andrieux²

¹INRA CSE, Domaine Saint-Paul, 84914 Avignon Cedex 09, France,

Tel. +33 4 32 72 23 64, fax +33 4 32 72 23 62,

wassenaar@avignon.inra.fr, baret@avignon.inra.fr

²INRA Sol & Environnement, 2 place Pierre Viala, 34060 Montpellier Cedex 02, France,

robbez@ensam.inra.fr, patrick.andrieux@ensam.inra.fr

ABSTRACT- Spatially distributed hydrological modelling is required to understand and predict the erosion, flooding and pollution risks that affect the vine cultivated Mediterranean environment. Previous field studies have demonstrated the dominant influence of soil surface features on overland flow and they therefore constitute an essential input to the hydrological model. In this paper we propose a remote sensing based method to map vineyard soil surface features with an appropriate spatial and temporal resolution. Our goal was to classify each soil surface portion in accordance with a pre-established, field measured infiltration capacity based typology. The radiometric characteristics of each of these hydrological surface classes were measured in the field and their Bi-directional Reflectance Distribution Function (BRDF) was modelled. Vineyard sunlit soil surface pixels are automatically extracted from high spatial resolution scanned aerial colour photographs: First a per-field Fourier frequency analysis allows to recognise and describe vine cultivated fields, then a multi-scale analysis based segmentation procedure extracts the pixels of these fields corresponding to the sunlit soil surface. These pixels are radiometrically classified by comparison of their measured reflectance with BRDF-based reflectance ranges, predicted for each soil surface type and for the specific illumination and viewing geometry of each pixel.

Results show that our fuzzy classification approach and the simple radiometric information used, allow to identify the majority of the hydrological surface types. The method can easily be transposed in time and space. Its performance quite strongly depends on the radiometric and geometric accuracy of the input data. Significant improvements of the soil surface classification are expected from considering spatial context information and from monitoring the soil surface evolution.

1 INTRODUCTION

Hydrological studies conducted on farmed catchments in the Mediterranean area confirmed that the typical intense rainfall events combined with often discontinuous soil cover by crops cause intense overland flow and erosion (Llorens and Gallart, 1992; Wainwright, 1996). Previous studies have demonstrated the dominant influence of soil surface features on overland flows (Andrieux *et al.*, 1996) and pesticide transport (Lennartz *et al.*, 1997; Louchart *et al.*, 2001). Such soil surface features vary strongly in space, especially between fields, and evolve at variable rates in time, being determined by agricultural management practices difficult to foresee and a highly irregular rainfall regime (Léonard and Andrieux, 1998). Therefore spatially distributed hydrological modelling is required to understand and describe flooding events, agricultural pollution and water resource management (Moussa *et al.*, 2002). Such

spatial modelling, that have to include the temporal dimension, requires quantitative and easily accessible input information on soil surface variables at the scale of one or more catchments.

Remote sensing is often considered as the favourite tool to provide such spatial and temporal input information. For agricultural areas with spatially continuous crops, remote sensing has proven to provide information on various surface feature variables. Reviews like Blanchard *et al.* (1999) and Van de Griend & Engman (1985) summarise the results obtained over the last twenty years focusing on the use of remote sensing for hydrological modelling. They were mostly reporting the advances in surface roughness, humidity and soil organic matter characterisation.

However, these studies highlighted also the limits of remote sensing techniques for an operational use in hydrological modelling of a vineyard environment. Firstly, we note that the studies are generally focussing on only one single soil surface variable (Arrouays *et*

al., 1996; Cialella *et al.*, 1997; Mathieu *et al.*, 1997; Zhangshi and Lee, 1997), whereas the surface classes used by the hydrological models are defined by a whole set of variables. A second limiting aspect is the inadequacy between the spatial and temporal resolutions as provided by the available remote sensing devices and those required by the hydrological models (Blanchard *et al.*, 1999). Thirdly and lastly we observe that little effort has been directed towards sparse crops such as vineyards. Most of the few remote sensing studies applied to vineyards were focusing on the vegetation canopy rather than on the underlying soil surface. They generally exploit the spectral features of the radiometric signal while ignoring the influence of the spatial discontinuity (Wildman, 1979; Minden and Philipson, 1982; Trolier *et al.*, 1989 using Landsat TM; Johnson *et al.*, 1998; Carothers, 2000). The few studies that investigated the soil surface signal over vineyards are based either on hyperspectral data or on microwave data: Hill *et al.* (1994), used spectral unmixing techniques at a 20 m spatial resolution to estimate soil erosion risk of Mediterranean vineyards from AVIRIS hyperspectral sensor. Company *et al.* (1994; 1995), used airborne SAR and ERS data to describe soil surface roughness over Mediterranean vines. They were severely hampered by the effect of vine rows and their compass orientation on radar backscatter. It follows from these studies that satisfactory results may only be expected by directly assessing the soil surface signal.

Assessing this signal means to assess the surface's bi-directional reflectance, which requires to take into account its Bi-directional Reflectance Distribution Function (BRDF). BRDF models exist and are generally used for two types of applications (Chopping, 1998) : (1) reflectance normalisation (Hu *et al.*, 2000) and (2) information extraction from variation of reflectance upon changing pixel observation and illumination geometry (Lacaze *et al.*, 1999; Chopping, 2000; Scarth and Phinn, 2000).

This paper presents a series of quantitative and unsupervised procedures allowing in the end to detect the combined variables determining soil infiltration, on the basis of simple radiometric data. for this purpose, we used helicopter aerial photography that provides the required high spatial resolution (a pixel size of 0.25×0.25m) and flexibility to frequently repeat the observations.

In the following, we will first briefly describe the study area. Then the methods will be presented that allow to extract the pixels representing the vineyard's sunlit soil surface, taking profit of the spatial characteristics of a vine crop. After analysing the radiometric behaviour of the soil surface types to be distinguished, we will propose a method to classify the observed soil surface signal into pre-established

radiometric classes representing these groups based on simple BRDF features. After concluding, it will shortly be shown how the consideration of spatial and temporal information can improve the quality of the results obtained.

2 MATERIAL AND STUDY AREA

The small Roujan catchment (0.91 km²) is located in the Hérault valley, 60 km west of Montpellier, Southern France, was selected because it represents quite well the conditions encountered in the larger Peyne valley (about 100 km²). The valley of the Peyne river is a good paradigm of the Languedoc-Roussillon coastal vine cultivated region. Moussa *et al.* (2002) demonstrated that the hydrological behaviour of the Roujan catchment is largely determined by agricultural practices through their strong influence on the soil surface features. Former field studies and experiments allowed to establish a soil surface typology. Six soil surface classes (SSC) are distinguished. In a first group, "recently tilled soils", we distinguish, (i) SSC 0 : an tilled, non-crusted soil surface and (ii) SSC 1 : a soil surface with a structural crust (Valentin and Bresson, 1992) corresponding to a laboured surface, slightly sealed by the drop impact of a few rainfall events. In the second group, previously tilled or non-tilled soils, four classes are distinguished: (iii) SSC 2 : bare soil, with a structural or sedimentary crust; (iv) SSC 3 : at least 50 % of the (structural or sedimentary) crusted surface is grass covered ; (v) SSC 4 : at least 50 % of the surface is covered by stones (gravel and pebbles) and (vi) SSC 5 : at least 50 % of the mineral soil surface is covered by organic litter (leafs, twigs and humus). This typology was verified to be valid throughout the Peyne valley, an area of some 6000 ha comprising the Roujan catchment.

It is important to consider the impact of these definitions: within-class variation can induce a considerable change in its radiometric response, without having any impact on infiltration (a green or dry grass cover for example). And between-class radiometric differences can be expected to be most pronounced in intensity. It can therefore reasonably be stated that multi- or hyper-spectral remote sensing devices are not required for this work. On the contrary a very high spatial resolution is required to obtain pure pixels within vine rows. This is why aerial photography has been considered to be the best adapted remote sensing device. Moreover our device is flexible, allowing high temporal resolution data acquisition as required by the end users.

The aerial photographs were acquired around solar noon by a Canon EOS camera aboard a Hughes 300 helicopter at an altitude of about 1100 m. This camera was equipped with a 35 mm focal distance objective and a Fujichrome Provia 100 RDP-II film. Pictures

were taken with a short exposure time (1/250 s) and an aperture varying from 6.7 to 11. Selected slides were scanned with a Nikon LS-1000 slide scanner at a resolution of 2700 dpi, which is close to the resolving power of the emulsion and corresponds to a ground resolution of 20 to 25 cm. This was resampled by the nearest neighbour method upon georeferencing (triangulation) to a 25 cm resolution. Resulting mosaics were radiometrically calibrated by the classical empirical line method. An original aspect of this calibration was the use of an important number of radiometric ground control points and the consideration of their bi-directional behaviour that was known thanks to field measurements.

Concurrent CIMEL radiometric field measurements were made to study the spectral response of the surface classes at positions of the reflective solar spectrum comparable to those provided by the aerial photographs, and observed at about the same spatial resolution. For several SSCs the reflectance was expected to exhibit a strong anisotropic bi-directional behaviour. Especially the tilled soils, because of the potentially important portion of shadow within an image's pixel. Therefore, field measurements were made using the CIMEL radiometer mounted on a goniometer. The measurements were acquired in summer with solar zenith angles varying between 20° and 40°. The goniometer allowed for measurement series from -60° to 60° zenith view angle at 10° steps, in the solar plane as well as in the perpendicular plane. In summer 1999, such series of measurements have been obtained on a total of 37 sites distributed throughout the Peyne valley and achieved within a limited time interval during the day (from about 10:30 to about 16:30 local time). These sites were chosen by stratified sampling to represent the different SSC as well as their internal variability and the influence of the soil mineralogical composition throughout the study area on observed soil surface radiometry.

3 RECOGNISING VINEYARDS

We developed a method allowing to identify vine cultivated fields, based on the only characteristic that all vineyards have in common and that they do not share with any other land cover type occurring in the region: the periodic spatial pattern resulting from the planting and training scheme of this discontinuous crop. The high spatial resolution of our data allows to assess this pattern.

The method has been extensively described by Wassenaar *et al.* (2002-1). The red channel provides the best contrast between vine and soil surface (low reflectance of vegetation and high for mineral soil). Even if the soil surface is covered by grasses or residues of vine shoots, the surface signal remains

higher due to a large portion of shadow contained in vine vegetation pixels.

A wide variety of mathematical approaches exist to analyse local spatial patterns: morphology analysis, edge analysis and frequency analysis. This last group constitutes the most direct and robust approach, also allowing for the use of expert knowledge on the spatial pattern upon analysis. Periodic phenomena are best handled with the Fourier transform (Graps 1995), but Fourier analysis is based on global information which is not adequate for the study of compact or local patterns. This is why Gabor (1946) introduced a local Fourier analysis, taking into account a sliding Gaussian window. At the same time per-field analysis is more and more used in remote sensing studies (Mason *et al.* 1988, Smith *et al.* 1997) because of the development of GIS (Hinton 1996, Wilkinson 1996). The combination of local Fourier transform and per-field analysis appears to provide a pertinent solution to our problem. The Fourier power spectrum of each field is exploited using a knowledge based analysis to characterise each field's planting pattern, spacing and orientation.

3.1 Knowledge based frequency analysis

The frequency model is a translation of expert knowledge on stock spacing and training modes that can be encountered in French vineyards: a square grid with about 1.5×1.5m spacing between stocks, or slightly rectangular, i.e. 1.4×1.6m (Argillier 1989, Goma-Fortin *et al.* 1997). The other common spatial training mode is called 'wire-trained', i.e. rows of plants growing along two or more horizontal metal wires. The distance between the rows varies from 2.0 to 2.5m. This allows to identify the peaks in each field's frequency power amplitude spectrum that are typical of vineyards (figure 1). The frequency and location of these peaks moreover allow to precisely quantify crop spacing as well as the compass orientation of the pattern, which constitutes useful information for hydrologists as well as other users. Figure 1 shows the result of the model when applied to a non weeded goblet (grid pattern) field with grass growing in discontinuous patches and in-between a strongly contrasted crusted soil surface. We observe that our method is not disturbed by this heterogeneity.

3.2 Results and conclusion

Applying this model to a set of 400 fields with extremely varied field patterns and soil radiometry, resulted in a correct classification for 96% of these fields. Field checks allowed to demonstrate that vine stock spacing is determined with a precision of over 98% and that the mean error in determining compass orientation is only 1.6°. A minimum of frequency

information is required though, but only very small and especially very narrow fields (less than 4 rows) could be erroneously classified.

The method developed is therefore considered to provide a robust recognition of vineyards, allowing to accurately extract quantitative variables, handling the

complex and variable radiometry of the environment considered. Moreover the model can be transposed to other regions characterised by other (perennial) discontinuous crops with their own specific frequencies by a simple adjustment of criteria.

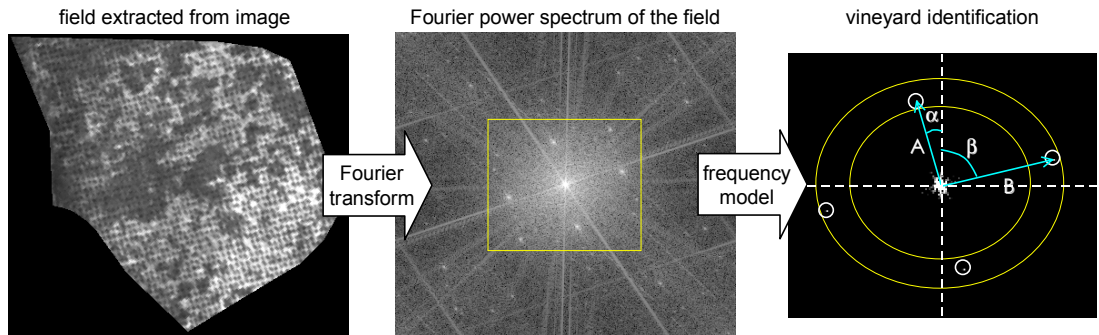


Figure 1 Vineyard identification by frequency analysis. The field on the left is automatically extracted from an image at 0.25m resolution using a digital land register. The image on the right corresponds to the (thresholded) central part of the central image. The ovals delimit the vine frequency area, within which perpendicular peak pairs are identified. The angles and vector lengths allow to obtain pattern orientation and spacing.

4 SUNLIT SOIL SURFACE EXTRACTION

Most studies applied to vineyards are focusing on crop rather than on the underlying soil surface. They generally exploit the spectral features of the radiometric signal ignoring the influence of the spatial discontinuity. Few studies have assessed the soil surface signal under vineyards. Hill *et al.* (1994), used AVIRIS data in an environmental study to estimate soil erosion risk of Mediterranean vineyards using spectral unmixing techniques at a spatial resolution of 20m. Company *et al.* (1994, 1995), used airborne SAR and ERS data to describe soil surface roughness under Mediterranean vines. They were severely hampered by the effect of vine rows and their compass orientation on radar backscatter. It follows from these studies that satisfactory results may only be expected by directly assessing the soil surface signal.

4.1 Multi-scale analysis

Traditional spectral thresholding does not provide an adequate solution to the problem. Even results from adaptive thresholding (Horaud & Monga, 1993) techniques are not satisfactory: local histograms do not allow for robust determination of a threshold because of the relatively important transitional zones between the objects; these techniques are not contrast invariant and may mix up vine and grass covered soil. To obtain satisfactory results, a spatial segmentation operation based on an image texture model approach is required, because it allows to incorporate the concept of 'object' (Mason *et al.*, 1988): There are only two objects of

interest: the sunlit soil surface, and the vine with its shadow. The sunlit soil surface is expected to be always at least slightly brighter in red reflectance than vine and/or shadow pixels. The object 'vine with shadow', of variable but very limited size (about 2 to 5 pixels wide and undetermined length) and very regular spacing (the centres of two identical and adjacent objects are 6 to 10 pixels apart), is superimposed on the soil surface background, having itself an internal variability at different scales. In between these two objects we find an important fringe of mixture pixels smoothing the borders.

Clearly such a model as basis for segmentation would provide erroneous results on fields other than vineyards, but those have been eliminated beforehand. The 'vine with shadow' object can best be isolated from its background by a method taking profit of this specific size and spacing, i.e. multiresolution analysis. Belonging to the image pyramids category, multiresolution analysis (Mallat, 1989) results from the embedded subsets generated by interpolations at different scales. Our object being coarser than the single pixel resolution, a smoothing is required to make the object stand out. A reliable identification of the object now depends on the selected scale and smoothing approach. Over the last decades a lot of interest has been put on obtaining the information at different scales by wavelet transforms. In our case however a multiresolution approach based on the median transform as proposed by Starck *et al.* (1998) provided better results (see Wassenaar *et al.*, 2001 for a detailed description).

The object 'vine and shadow' is identified, by looking at the change in level sets upon change of scale. The difference between the scales obtained by smoothing with a 3×3 and a 5×5 median filter appears to best delimit our object. The smallest window, needing to be as small as possible regarding the often small width of the object, provides the level sets delimiting the object. The larger window rises the level sets of the object 'vine with shadow' by incorporating edge information in the centre of the object and sunlit soil information near the edge of the object. At the same time level sets of the object 'sunlit soil' are lowered by inclusion of edge information in the centre and vine or shadow information near the edge. After this first location of the object a proper delimitation of the object 'sunlit soil' is obtained by applying a 'conditional erosion/dilatation' procedure.

4.2 Conclusion

A validation of the method, described by Wassenaar *et al.* (2001), shows its robustness with respect to crop orientation and training mode (goblet or wire-trained). Compared to manually produced masks considered 'true', we see that the vine and shadow cover estimation 'error' generally remains below 10%. The method proposed allows for a rapid and unambiguous identification of the majority of the sunlit soil surface, independent of its radiometry and variation. The radiometry of the pixels labelled "sunlit soil surface" can now be compared to the bi-

directional reflectance properties of the SSCs.

5 RADIOMETRIC SURFACE CLASSIFICATION

In the introduction we underpinned the need to take into account the BRDF when interpreting the soil surface radiometry. Figure 2 confirms the necessity to take into account the view and illumination geometry. For mineral soil surfaces this non-lambertian, or anisotropic bi-directional behaviour has already been described in some detail by Courault (1989) and Cierniewski & Verbrugghe (1997). Due to the often small focal distance, i.e. large within-scene view angle variation, this is known to cause problems when radiometrically interpreting imagery from aerial remote sensing, as observed for example Clevers and van Stokkum (1992) and King (1991). Figure 2 illustrates the difference in the BRDF of a tilled and that of a crusted soil surface situated a few meters from each other within the same soil unit. The absolute reflectance of the tilled surface is considerably lower than that of the crusted surface reflectance and strongly dependent on view and illumination geometry. Even the plane, crusted surface has stronger back scattering than forward scattering, but the darker tilled surface has a much more pronounced hot spot effect. Not taking into account this influence of geometrical configuration will make the distinction between these two very contrasted surfaces difficult if not observed under identical angles.

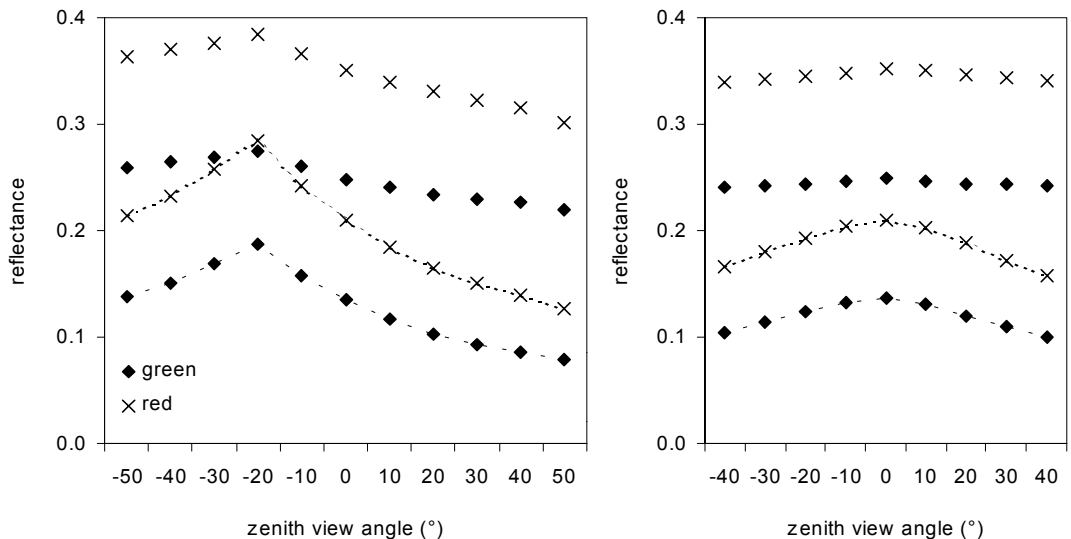


Figure 2 Series of red and green reflectances obtained by a goniometer mounted CIMEL radiometer on a tilled (symbols and dotted line) and crusted (symbols) soil surface situated at a few meters distance from each other in one and the same vine field and soil unit. Solar zenith angle was 20°. The diagram on the left shows the solar plane measurements, the one on the right the perpendicular plane measurements.

Soil hydro-radiometric class	Surface description	Indicative mean infiltration rates (mm/h)	Corresponding SSC
SHR 0	recently tilled soil surface	31	SSC 0
SHR 1	recently tilled but slightly crusted or stone layer	21-24	SSC 1 or 4
SHR 2	plane crusted surface	9	SSC 2
SHR 3	litter and/or dry weed covered surface	18-19	SSC 3 or 5
SHR 4	(green) weed covered surface	19	SSC 3
SHR 5	surface less than half covered by litter and/or dry weed	9-30	partial cover
SHR 6	surface less than half covered by (green) weed	9-30	partial green cover

Table 1 Summary of the soil hydro-radiometric classes and their mean saturated infiltration rates.

5.1 The BRDF model used

Amongst a wide variety of models, the model of Rahman *et al.* (1993) has been chosen for its simplicity (bi-directional radiometry is described by only three parameters) and its good performances over a wide range of different surfaces as reported by Kalluri *et al.* (1997) and Privette *et al.* (1997):

$$\rho(\theta_1, \phi_1; \theta_2, \phi_2) = \rho_0 \frac{\cos^{k-1} \theta_1 \cos^{k-1} \theta_2}{(\cos \theta_1 + \cos \theta_2)^{1-k}} \cdot F(g) \cdot [1 + R(G)] \quad (1)$$

where $\theta_1, \phi_1, \theta_2, \phi_2$ are the zenith and azimuth angles of res. illumination and observation. $R(G)$ accounts for the hot spot reflection peak and is a function of ρ_0 and G , where G is a geometric factor depending on illumination and view angles. $F(g)$ is a function determining the relative contribution of forward and backward scattering, defined as follows:

$$F(g) = \frac{1 - \Theta^2}{[1 + \Theta^2 - 2\Theta \cos(\pi - g)]^{1.5}} \quad (2)$$

where g is the phase function determined by the illumination and view angles. Three parameters remain: the coefficient ρ_0 is an arbitrary parameter characterising the intensity of the reflectance of the surface cover, k indicates the level of anisotropy of the surface and Θ controls the relative amount of forward ($0 \leq \Theta \leq +1$) and backward ($-1 \leq \Theta \leq 0$) scattering.

The CIMEL ground measurement series were used to adjust the three parameters of the BRDF model. This was performed for each site measured and the two spectral bands considered, using a multi-dimensional difference minimisation based on the downhill simplex method (Nelder and Mead, 1965).

The ratio between the red and the green reflectance does not depend on the geometrical configuration. Mineral soil reflectance spectra are ascending, which makes the distinction between mineral SSC based on reflectance intensity more easily separable at longer wavelengths (red with

respect to green). These two observations allowed us to summarise the radiometric behaviour of each measured site by four parameters : the ρ_0 , k and Θ of the red band, and the ratio between the red (R) and the green (G) reflectances. The latter was expressed by the colour index (CI, Mathieu *et al.*, 1997) for its resemblance with the NDVI:

$$CI = \frac{R - G}{R + G} \quad (3)$$

5.2 The radiometric classes

The radiometric behaviour of the different SSCs are more extensively described by Wassenaar *et al.* (2002-2). Upon plotting the BRDF parameters, the mineral soil SSCs show quite well defined clusters for each class, but intermediate situations cause more or less fuzzy boundaries. This corresponds to the actual gradual transition between soil surface features. Though some SSC classes could not be separated. This is why we introduced the concept of what could be called "soil hydro-radiometric" classes (SHR), i.e. classes that represent one or more SSCs and that have distinct hydrological as well as radiometric properties. For the correspondence between SSC and SHR classes see table 1. The radiometric properties of surfaces with a considerable although not dominant weed and/or litter cover (up to 50%) are strongly altered by this cover, allowing to define a distinct radiometric class (table 1). Although such a non dominant cover does not significantly alter the underlying surface's saturated infiltration properties, its radiometric impact prohibits the pixel from being affected to one of the SSCs. The hydrological signification of the SHR representing these surfaces is "unknown SSC, having a non dominant weed/litter cover". This information can be completed in a later stage when taking into account the other SHRs that have been identified in the pixel's field.

5.3 The classification technique

the spatial resolution of the aerial imagery is comparable to that of the radiometric field measurements on which the BRDF models were adjusted. The observation and illumination geometry of every image pixel was known thanks to special pre-processing steps, based on knowledge of camera position, focal distance, flight altitude and time of day and year, combined with DEM based slope and aspect information. The range of theoretical radiometric responses possibly resulting from a surface with a viewing and illumination geometry identical to that of the pixel under consideration and belonging to a particular SHR class, was calculated by considering all the BRDF model parameter triplets provided by the different field measurement sites belonging to that SHR class. After repeating this for all SHR classes, the sunlit soil pixel is affected to the SHR class whose predicted red reflectance range comprises the pixel's red reflectance value.

A complication results from the fact that the defined SHR classes, although having a distinct radiometric behaviour, do not always have a different theoretical directional reflectance under one given geometrical configuration. Theoretic reflectance ranges of different classes can very well have a more or less important portion in common. And due to the few measured sites defining each class, a uniform within range probability distribution was adopted. As a result, actual observed pixel reflectance values situated within the predicted reflectance ranges of

more than one SHR class, are affected with equal possibility to all classes concerned. This is illustrated by the hypothetical red reflectance pixel values A and B, observed under two geometrical conditions (figure 3). This figure also shows the strong dependence of the predicted reflectance ranges on this geometrical configuration: a pixel A with a red reflectance of 0.08 would be classified as a partial cover surface type (SHR 5/6) if this reflectance was measured in forward scattering direction, and would be classified as a litter or weed covered surface type (SHR 3) if this value represents the backscattered reflectance (i.e. a different classification result only upon changing viewing azimuth angle!). And if under both conditions a pixel reflectance of 0.24 (B) is observed, it would in one case be clear that the pixel belongs to the SHR class 1, whereas in the other case the same value could as well represent SHR class 1, class 0 or class 5! So the image classification results for an important portion of the sunlit soil pixels in a fuzzy classification.

Results (Wassenaar *et al.*, 2002-2) showed that crusted mineral soil surfaces as well as surfaces more than half covered by litter and/or weed could be unambiguously identified on the basis of this information. The separability of the other hydrologically important types of surfaces was shown to strongly depend on the viewing and illumination geometry. Two soil surface classes (tilled but slightly crusted surface and stone layer) that were difficult to separate had to be merged within one single soil hydro-radiometric class.

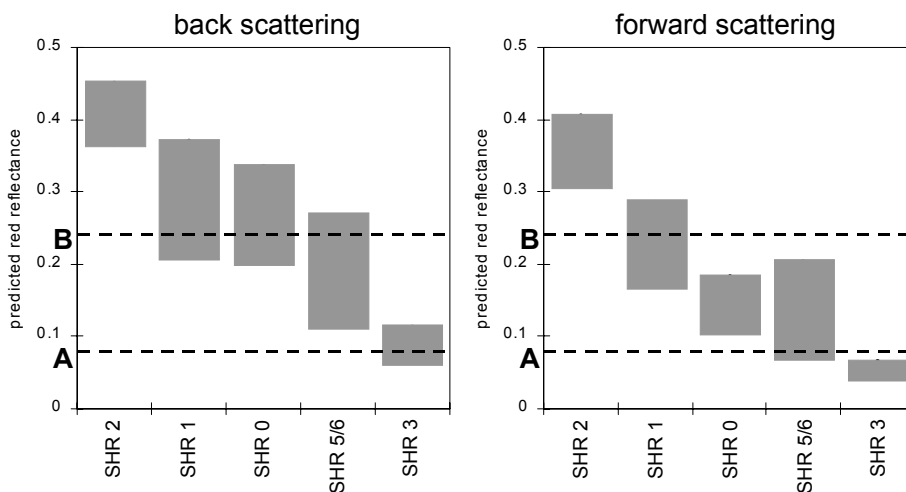


Figure 3 Predicted red reflectance ranges of all hydro-spectral classes for a horizontal surface illuminated under a sun zenith angle of 32°. The diagram on the left shows the ranges predicted in case the surface has been viewed at a 20° zenith angle in the solar plane in back scattering direction (view azimuth = sun azimuth). The diagram on the right represents the same situation but with a view azimuth opposite to the sun azimuth (forward scattering).

This classification method requires substantial amount of input information. The spectral as well as the geometric information is associated to uncertainties that impact on the accuracy of the final result. A sensitivity analysis was performed on one large image mosaic to investigate the effect of these uncertainties, showing a particularly high sensitivity to the radiometric quality of the images as well as to viewing orthogonality.

6 CONCLUSIONS

We demonstrated that several classes of soil surface features with a distinct infiltration rate can be distinguished on the basis of a simple radiometric information, acquired at a very high spatial resolution (0.25 m) but spectrally as well as directionally limited (two broad reflective bands and one direction). The methods developed represents well the hydrological information that can be obtained in a highly varying and fragmented vineyard environment by an operational, state of the art remote sensing system. Our remote sensing device and original methods present several advantages with respect to more traditional approaches:

- the remote sensing device allows for quick and precisely timed data acquisition, without a tedious preceding planning/programming. This is an important characteristic of information that is to be used within distributed hydrological modelling;
- once SHR classes have been defined, applying the unsupervised quantitative classification method does not require any assistance or expert knowledge and it does not depend on time of year;
- the method can easily be transposed to other regions, provided that the different soils surface feature classes are known and that their BRDF could be characterised in the field.

The predicted reflectance ranges corresponding to the soil hydro-radiometric classes are often close to each other. Therefore, the accuracy of the classification was shown to depend at different degrees, on the quality of the input data. Further, the validity of the classification is subjected to two important assumptions: (1) the spatial variation of the mineralogical composition of the soil surface throughout the study area should not induce a significant variation in red reflectance of the surface, otherwise soil hydro-radiometric classes will have to be defined for each geologically homogeneous area. (2) The soil surface film interacting with the optical solar radiation is supposed to be dry. This might not constitute a major problem in our Mediterranean environment: the soil surface dries quickly and when wet, the sky is generally cloudy so no data acquisition is possible. However, when applying the method to more temperate regions, an appropriate delay with

respect to the time elapsed since the last rainfall event should be respected. In temperate lowland areas with fine textured soils and high water tables this constraint could be too strong.

The results of this study have been obtained on the sole basis of variations exhibited by the two first dimensions but with a limited sampling. Temporal and spatial information dimensions constitute an important potential to improve classification precision, allowing to integrate expert knowledge on evolution of soil surface features. Upscaling to the field level will not only help to reduce classification fuzziness by expert knowledge on distribution and cooccurrence of classes, but will also allow to obtain the synthetic per-field surface description as required by the distributed hydrological model.

7 REFERENCES

- Andrieux, P., Louchart, X., Voltz, M. and Bourgeois, T., 1996, Déterminisme du partage infiltration-ruisellement sur parcelles de vigne en climat méditerranéen. *Documents du BRGM* **256**, 7-11.
- Argillier, J. P., 1989, Interdépendance des facteurs de la qualité. Montpellier, Chambre d'Agriculture de l'Hérault.
- Arrouays, D., King, C., Vion, I. and Le Bissonnais, Y., 1996, Detection of soil crusting risks related to low soil organic carbon contents by using discriminant analysis on Thematic Mapper data. *Geocarto International* **11**(4), 11-16.
- Blanchard, E., King, C., Le Bissonnais, Y., Bourguignon, A., Souchère, V., Desprats, J.-F. and Maurizot, P., 1999, Paramétrisation du potentiel de ruissellement des bassins versants au moyen de la télédétection et des systèmes d'information géographiques. Application à des bassins versants du Pays de Caux. *Étude et Gestion des Sols* **6**(3), 181-199.
- Carothers, J., 2000, The art of winemaking. *Imaging Notes* **15**(1), 18-21.
- Chopping, M. J., 1998, Linear semi-empirical kernel-driven bidirectional reflectance distribution function models in monitoring semi-arid grasslands from space. department of Geography. Nottingham, University of Nottingham, 501.
- Chopping, M. J., 2000, Testing a LiSK BRDF model with in situ bidirectional reflectance factor measurements over semiarid grasslands. *Remote Sensing of Environment* **74**(2), 287-312.
- Cialella, A. T., Dubayah, R., Lawrence, W. and Levine, E., 1997, Predicting soil drainage class using remotely sensed and digital elevation data. *Photogrammetric Engineering and Remote Sensing* **63**(2), 171-178.
- Cierniewski, J. and Verbrugge, M., 1997, Inferring soil surface roughness from soil bidirectional

- reflectance data. *International Agrophysics* **11**, 147-157.
- Clevers, J. G. P. W. and van Stokkum, H. T. C., 1992, The quantitative evaluation of false colour photography with application of a red filter. *International Journal of Remote Sensing* **13**(9), 1709-1733.
- Company, A., Delpont, G., Guillobez, S. and Arnaud, M., 1994, Potentiel des données radar ERS-1 pour la détection des surfaces contributives au ruissellement dans les vignobles méditerranéens du Roussillon (France). 6eme Symposium International "Mesures Physiques et Signatures en Télédétection", Val d'Isère, pp. 375-382.
- Company, A., King, C., Beaudoin, A. and Delpont, G., 1995, Using microwaves for the assessment of runoff risk over mediterranean soils : an experiment in the Réart catchment basin (Roussillon, France). International Symposium : "Remote sensing and GIS as tools for monitoring soils in the environment", Ouagadougou, pp. 151-167.
- Courault, D., 1989, Étude de la dégradation des états de surface du sol par télédétection. Thèse. *Sols* **17**, 239.
- Gabor, D., 1946, Theory of communication. *Journal of the IEE* **93**, 429-441.
- Goma-Fortin, N., Guerber, M., Halma, A., Planas, R. and Medina, E., 1997, La conduite du vignoble en Languedoc-Roussillon. Tome 1 : Respecter et disposer le feuillage pour une qualité optimale. Montpellier, Chambres d'Agriculture du Languedoc-Roussillon.
- Graps, A., 1995, An introduction to wavelets. *IEEE Computational Science and Engineering* **2**(2), 50-61.
- Hinton, J. C., 1996, GIS and remote sensing integration for environmental applications. *International Journal of Geographical Information Systems* **10**(7), 877-890.
- Horaud, R. and Monga, O., 1993, Vision par ordinateur, outils fondamentaux. (Paris: Hermès).
- Hu, B., Lucht, W., Strahler, A., Barker Schaaf, C. and Smith, M., 2000, Surface albedos and angle-corrected NDVI from AVHRR observations of South America. *Remote Sensing of Environment* **71**(2), 119-132.
- Johnson, L., Lobitz, B., Bosch, D., Wiechers, S., Williams, D. and Skinner, P., 1998, Of pixels and palates: can geospatial technologies help produce a better wine? 1st International Conference on Geospatial Information in Agriculture & Forestry, Lake Buena Vista FL.
- Kalluri, S. N. V., Zhang, Z., Liang, S., JaJa, J. and Townshend, J. R. G., 1997, Retrieval of bidirectional reflectance distribution function (BRDF) at continental scales from AVHRR data using high performance computing. IGARSS '97, pp. 174-176.
- King, D., 1991, Determination and reduction of cover type brightness variations with view angle in airborne multispectral video imagery. *Photogrammetric Engineering & Remote Sensing* **57**(12), 1571-1577.
- Lacaze, R., Roujean, J. L. and Goutorbe, J. P., 1999, Spatial distribution of Sahelian land surface properties from airborne POLDER multiangular observations. *Journal of Geophysical Research - Atmospheres* **104**(D10), 12131-12146.
- Lennartz, B., Louchart, X., Voltz, M. and Andrieux, P., 1997, Diuron and simazine losses to runoff water in mediterranean vineyards as related to agricultural practices. *Journal of Environmental Quality* **26**(6), 1493-1502.
- Léonard, J. and Andrieux, P., 1998, Infiltration characteristics of soil in Mediterranean vineyards in Southern France. *Catena* **32**, 209-223.
- Llorens, P., Gallart, F., 1992, Small basin response in a Mediterranean mountainous abandoned farming area: research design and preliminary results. *Catena* **19**, 309-320.
- Louchart, X., Voltz, M., Andrieux, P., Moussa, R., 2001, Herbicide transport to surface waters at field and watershed scales in a Mediterranean vineyard area. *Journal of Environmental Quality* **30**, 982-991.
- Mallat, S., 1989, A theory for multiresolution signal decomposition: the wavelet representation. *IEEE Transactions on Pattern Analysis and Machine Intelligence* **11**, 674-693.
- Mason, D. C., Corr, D. G., Cross, A., Hogg, D. C., Lawrence, D. H., Petrou, M. and Taylor, A. M., 1988, The use of digital map data in the segmentation and classification of remotely-sensed images. *International Journal of Geographical Information Systems* **2**(3), 195-215.
- Mathieu, R., King, C. and Le Bissonnais, Y., 1997, Contribution of multi-temporal SPOT data to the mapping of a soil erosion index. The case of the loamy plateaux of northern France. *Soil Technology* **10**, 99-110.
- Minden, K. A. and Philipson, W. R., 1982, Grapevine canopy reflectance and yield. 8th International Symposium on Machine Processing of Remotely Sensed Data, Purdue University, West Lafayette, Indiana, pp. 430-433.
- Moussa, R., Voltz, M., Andrieux, P., 2002, Effects of the spatial organization of agricultural management on the hydrological behaviour of a farmed catchment during flood events. *Hydrological Processes* **16**, 393-412.

- Nelder, J. A. and Mead, R. A., 1965, A simplex method for function optimization. *Computer Journal* **7**, 308-313.
- Privette, J. L., Eck, T. F. and Deering, D. W., 1997, Estimating spectral albedo and nadir reflectance through inversion of simple BRDF models with AVHRR/MODIS-like data. *Journal of Geophysical Research* **102**(D24), 29,529-29,542.
- Rahman, H., Pinty, B. and Verstraete, M. M., 1993-2, Coupled surface-atmosphere reflectance (CSAR) model. 2. Semiempirical surface model usable with NOAA Advanced Very High Resolution Radiometer Data. *Journal of Geophysical Research* **98**(D11), 20,791-20,801.
- Scarth, P. and Phinn, S., 2000, Determining forest structural attributes using an inverted geometric-optical model in mixed eucalypt forests, Southeast Queensland, Australia. *Remote Sensing of Environment* **71**(2), 141-157.
- Smith, G. M., Fuller, R. M., Amable, G., Costa, C. and Devereux, B. J., 1997, Clever mapping: an implementation of a per-parcel classification procedure within an integrated GIS environment. 23rd Annual Conference and Exhibition of the Remote Sensing Society: Observations & Interactions, Reading, Remote Sensing Society, pp. 21-26.
- Starck, J.-L., Murtagh, F. and Bijaoui, A., 1998, Image processing and data analysis, the multiscale approach. (Cambridge: Cambridge University Press).
- Troler, L. J., Philipson, W. R. and Philpot, W. D., 1989, Landsat TM analysis of vineyards in New York. *International Journal of Remote Sensing* **10**(7), 1277-1281.
- Valentin, C. and Bresson, L.-M., 1992, Morphology, genesis and classification of surface crusts in loamy and sandy soils. *Geoderma* **55**, 225-245.
- van de Griend, A. A. and Engman, E. T., 1985, Partial area hydrology and remote sensing. *Journal of Hydrology* **81**, 211-251.
- Wainwright, J., 1996, Infiltration, runoff and erosion characteristics of agricultural land in extreme storm events, SE France. *Catena* **26**, 27-47.
- Wassenaar, T., Andrieux, P., Baret, F. and Robbez-Masson, J.-M., 2002-2, Detection of soil surface infiltration capacity classes in a Mediterranean vine cultivated environment by radiometric classification of remotely sensed imagery based on measured BRDFs. *Catena* accepted.
- Wassenaar, T., Baret, F., Robbez-Masson, J. M. and Andrieux, P., 2001, Sunlit soil surface extraction from remotely sensed imagery of perennial, discontinuous crop areas; the case of Mediterranean vineyards. *Agronomie* **21**, 235-245.
- Wassenaar, T., Robbez-Masson, J. M., Andrieux, P. and Baret, F., 2002-1, Vineyard identification and description of spatial crop structure by per-field frequency analysis. *International Journal of Remote Sensing* **23**(17), 3311-3325.
- Wildman, W. E., 1979, Color infrared: a valuable tool in vineyard management. 7th Workshop on Color aerial Photography in Plant Sciences and Related Fields, Davis, California, pp. 229-238.
- Wilkinson, G. G., 1996, A review of current issues in the integration of GIS and remote sensing data. *International Journal of Geographical Information Systems* **10**(1), 85-101.
- Hill, J., Mehl, W. and Altherr, M., 1994, Land degradation and soil erosion mapping in a mediterranean ecosystem. *Imaging Spectrometry - a Tool for Environmental Observations*. J. Hill and J. M  gier. Brussels, Kluwer Academic Publishers. **4**, 237-260.
- Zhangshi, Y. and Lee, W., 1997, Obtaining spatial and temporal vegetation data from Landsat MSS & AVHRR/NOAA satellite images for a hydrological model. *Photogrammetric Engineering and Remote Sensing* **63**, 69-77.

Monitoring of Evapotranspiration and Irrigation in Arid Conditions in the Moroccan Atlas Using Optical Satellite Data

B. Duchemin, P. Maisongrande, F. Frappart, M. Magnac, G. Chehbouni, G. Dedieu, B. Mougenot,

Centre D'Etudes Spatiales de la Biosphère (CESBIO)

Unité Mixte de Recherche CNES, CNRS, IRD, UPS

18, Av. Edouard Belin 31401 Toulouse, France

benoit.duchemin@cesbio.cnes.fr

ABSTRACT - This paper presents approaches we developed for the spatial and temporal monitoring of evapotranspiration and irrigation of cereals in semi-arid regions surrounding the Mediterranean basin. The test site covers a 3 x 3 km² area located in the plain of Marrakech (Morocco) where wheat crops is dominant. Two methodologies of coupling evapotranspiration models and remote sensing data were compared. They result in estimate of plant maximal transpiration and water requirements corresponding to crop cycles observed by time series of satellite data. The two approaches were tested using eight high spatial resolution images acquired by HRVIR sensor onboard SPOT satellite during one agricultural season. The spatialisation method outlines the spatio-temporal patterns of crop development. The associated maps of seasonal evapotranspiration appear consistent with rainfall and irrigation features. These maps can provide with a suitable overview of plant water consumption as well as deficit in supply of irrigation water. The drawbacks and advantages of each approach are finally discussed, as well as the perspectives on improvement and validation of these first result.

1 INTRODUCTION

The SUD-MED project aims at monitoring water resources over Mediterranean semi-arid regions by coupling ground truth, process models and satellite measurements. The test area is the water catchment of Tensift river that covers about 30.000 km² around the Marrakech city in Morocco. The climate is arid : a low and irregular pluviometry (≈ 240 mm/year) contrasts with a very high potential evapotranspiration ($\approx 2,400$ mm/year). Hydrological processes – snow/rain partition, snowmelt, surface and sub-surface runoffs – stresses the water budget on the Atlas mountainous region, while vertical exchanges dominates in the plain. On irrigated areas covered with cereals and orchards (olive and orange trees), the important terms to be known are rainfall, irrigation, drainage and evapotranspiration.

This paper presents two methodologies we developed in order to monitor evapotranspiration of cereals crops in the flat open country surrounding Marrakech. We focus on the possibilities offered by time series of high spatial resolution (20 m) satellite data and coupling with evapotranspiration models. The analysis is performed from eight images acquired by the HRVIR sensor onboard SPOT-4 satellite over a 3 x 3 km² test site where wheat is predominant. Firstly, image classification was used to discriminate irrigated field

and cluster them according to crop cycle patterns. This processing also permits to extract major phenological features and track the intra- and inter-class variability in plant development. The impact of this variability is investigated using two models to monitor the surface water budget. One is based on a crop process model (STICS, Brisson et al. 1998) in order to simulate plant maximal evapotranspiration. The other was developed by the FAO (Allen, 1998) to assess crop water requirements. In both case, we present maps of cumulated evapotranspiration for the 2001-2002 agricultural season. These maps were established through remote sensing data by driving phenological stages and calibrating the time course of Leaf Area Index (case of STICS model). They are suitable to estimate the seasonal evapotranspiration averaged over field or countryside. In addition, they could indicate the level of extreme deficit in supply of irrigation water.

2 MATERIAL AND METHODS

2.1 Processing of Satellite Data

A 3 x 3 km² test site where wheat crops is predominant was selected within an area managed by the 'Office Régional de Mise en Valeur Agricole du Haouz' (ORMVAH, which is the regional authority for planning and irrigation of agriculture in the Marrakech plain). During the 2001/2002 agricultural season, a

programming request for the HRVIR sensor onboard SPOT-4 satellite resulted in the acquisition of eight high spatial resolution (20 m) optical data. Thanks to the flat topography of the test site, geometric corrections allowed superimposition of images possible with a good accuracy. Surface reflectances in red and near-infrared bands were calculated by performing calibration and atmospheric correction using a code adapted from the SMAC procedure (Rahman and Dedieu 1994). Finally, the Normalized Difference Vegetation Index (NDVI, Rouse et al. 1974) was computed.

An unsupervised classification of the eight NDVI images allowed to define 15 classes (Fig.1). One among them is predominant and covers up to 85% of the total surface. This class featured systematically low NDVI values (around 0.13). It includes crops that farmers could not irrigate this year and was removed of our analysis. A visual analysis of NDVI time series led to exclude two other minor classes (covering less than 2% of the total surface). These two classes exhibited very high and nearly constant values, which were found incompatible when compared to wheat typical seasonal signatures. Over the remaining 13%, the time courses of NDVI satisfy expected trajectories for irrigated cereals, although a wide range of patterns were observed. To track this variability, 12 classes were considered and, for each class, three scenario of crop development were built. Our idea is twofold : 1) consider a mean scenario in order to provide field and area averaged estimates of crop development and evapotranspiration, 2) analyse the difference between maximum and minimum scenario in term of extreme case of water deficit. Mean growth conditions were obtained by averaging the NDVI over the class, while minimal and maximal conditions correspond to the pixel of the class where the temporal sums of NDVI are respectively the lowest and the highest. This processing allows to define 36 cases that encompass all agricultural practices over the test site. Figure 2 illustrates the result of this processing for class 12 where the NDVI seasonal signature is characteristic of well-watered plants.

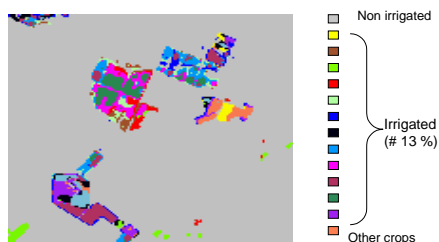


Figure 1. Classification of the test site based on the NDVI time series derived from SPOT/HRVIR

2.2 Approaches for Estimating Evapotranspiration

The first approach is based on the STICS model (Brisson et al., 1998-a and 2002), which was conceived as a simulation tool able to work under actual agricultural conditions. Although the model was chosen for its abilities to estimate yields and environmental budgets (water, fertilisers), we were interested here in the resistive scheme that estimates latent heat fluxes (Brisson et al. 1998-b Shuttleworth and Wallace 1985). A sensitivity analysis has pointed out the major parameters that act upon evapotranspiration : humidity at field capacity and at wilting point, apparent soil density, sowing date, date of maximum Leaf Area Index (LAI) and maximum rate of LAI setting up. The three latter can be derived from remote sensing data, since NDVI and LAI are highly correlated. Soils properties were determined through the analysis of soil maps provided by ORMVAH and pedo-transfert rules (Jensen 1990) : a high clay content was found, joined with a 15% value for the soil water content available for roots uptake. To run the model at a daily step, a climatology was built from three years (1999-2001) of data acquired at the ORMVAH weather station located 30 km North of the test site. Only rainfall data actually correspond to the period of simulation (October 2001 – June 2002).

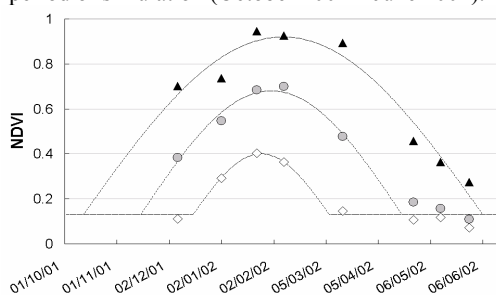


Figure 2. NDVI time series derived from SPOT/HRVIR images associated to minimum (diamonds), mean (circles) and maximum (triangles) scenario of crop development. The lines highlight sinus curves are together with sinusoidal curves that were fitted on NDVI time series (see the 2.3 section).

The second method, developed by FAO (Allen 1998), is based on the concept of reference evapotranspiration (ET₀) that allows to study the evaporative power of the atmosphere independently of crop type, crop development and agricultural practices. The reference surface is an 'hypothetical' extensive green grass actively growing (with adequate water) and completely shading the ground. This description is linked with assumptions on physical variables that

lead to unambiguous definition and derivation of ET₀ through the so-called FAO Penman-Monteith equation (after Penman 1948 and Monteith 1985). Only climatic parameters affect the reference evapotranspiration, which have been calculated from the above-mentioned weather data set. For other crops, the evapotranspiration under standard conditions (ETC) corresponds to disease-free and well-fertilised plants that ‘hypothetically’ grow under optimum soil water conditions for achieving full production. ETC is obtained by multiplying ET₀ with a cultural coefficient that varies according to phenological stages with the distinction of initial (from sowing to 10% growth cover), mid (from effective full cover to the start of maturity) and late season (until harvest or full senescence). Note that the effective full cover is also defined as the date when LAI reaches 3. Thus, it seems relevant that remotely-sensed optical data can contribute to infer crop coefficients and run the FAO model.

2.3 First analysis of satellite data

From the previous discussion, we reached the conclusion that two kinds of parameters – LAI and phenological stages – both appear crucial for modelling evapotranspiration and derivable from optical satellite data. In order to facilitate their retrieval and to drive the FAO approach at a daily step, sinus curves were fitted on each NDVI time series. The curves obtained for each growth scenario within class 12 are given in Fig.2. They are determined by three parameters : the date when NDVI begins to increase, which roughly corresponds to plant emergence ; the amplitude, which provides an index of maximum crop vigour ; the date when NDVI stops to decrease, which indicates harvest or full senescence. By comparing the latter with the day of emergence, the length of crop cycle can easily be estimated. Figure 3 (next page) displays maps where these three parameters were obtained class by class considering mean growth conditions (the sinus curves were fitted on time courses of NDVI after spatial averaging over each class). These maps provide a quick and synthetic overview of crop development on the test site for the 2001/2002 agricultural season. A simple analysis of this figures suggests that growth was weak and irregular. Amplitudes are always lower than 0.55, while the seasonal dynamics of NDVI may be generally higher for well-watered cereals (see the case of maximum growth condition for class 12 in Fig.2). Crop cycles are generally short, with a median value of 92 days to be compared with the values collected in Allen (1998) that ranges between 105 to 140 days. The probable cause is the severe droughts from years 2000 to 2002 that have limited dams filling and therefore

the supply of irrigation water. Furthermore, two different phenological patterns come up from the map of emergence dates, acknowledging the fact that NDVI starts to increase either in January-February or in March-April (blue/green or yellow/red colors in Fig.3). The first pattern corresponds to that encountered in the Marrakech plain when rainfall and irrigation-flooding events are normally distributed. The second one indicates a delay in emergence date due to unavailability of water for irrigation and late-season rainfall. 2.4 Spatialisation of evapotranspiration models

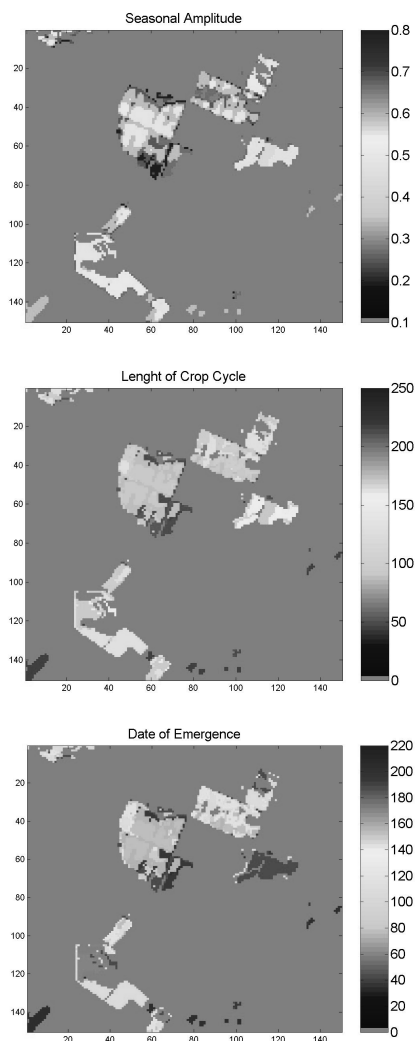


Figure 3. Features of crop development pattern extracted from the sinusoidal curves fitted on NDVI time series : seasonal amplitude (up, in NDVI units), length of crop cycle (middle, in days), date of plant emergence (bottom, in days).

The maps previously built from NDVI times series (see Fig.3) provide two useful phenological features in order to run the STICS model : 1) the day of maximum LAI, which can be taken as the middle between emergence and full senescence ; 2) the date of sowing, which can be assumed to occur 15 days before emergence according to Allen (1998). The most complex parameter to fit is the maximum rate of LAI setting up because the knowledge of LAI is required. However, sound relationships between NDVI and LAI have been established on wheat crops. We here calibrate the one given in Eq.1 (after Asrar et al. 1984), assuming that the pixel which displays minimal and maximal NDVI values (both spatially and temporally) corresponds respectively to bare soil ($NDVI_S = 0.13$ in Eq.1) and ‘infinitely’ dense vegetation ($NDVI_{\infty} = 0.94$ in Eq.1). Eq.1 allows us to derive LAI at SPOT-HRV acquisition dates. Retrieved LAI values are then used to optimise the maximum rate of LAI setting up by comparing satellite observation and STICS simulation through a Simplex Algorithm (Nelder and Mead 1965). After optimisation, the model was run at a daily step. Since the automatic irrigation mode was activated, plants are watered as soon as they are stressed. We also assume there is no deficit in soil nitrogen content in order to have plant maximal transpiration.

For the FAO approach, the issue to be addressed is the translation of NDVI curves into time dependent crop coefficients (K_c). Given Eq.1 and the hypothesis of linearity between LAI and K_c in the FAO method, we can suppose that the relationship between NDVI and crop coefficient is exponential. The problem is thus to determine two points where both NDVI and K_c are known in order to fit the $K_c = A \cdot e^{B \cdot NDVI}$ equation. Looking at the tables reported in Allen (1998), we chose the extreme ranges expected in K_c values for wheat in semi-arid conditions : the minimal value ($K_c=0.3$) corresponds to the initial stage from sowing to 10% growth cover, while the maximal one ($K_c=1.15$) is observed at mid-season when full cover is effective (ie. $LAI \approx 3$). The joined NDVI values (0.13 and 0.9) were determined by applying Eq.1 with LAI successively equal to 0 and 3. Once the relationship was established, NDVI sinusoidal curves were used to track the variability of phenology and determine the time course of crop coefficient as follow. From sowing to emergence (i.e. initial stage), K_c is assumed minimal. When the NDVI is larger than 0.9 (mid-season stage), K_c is assumed maximal. Otherwise (growing period and late-season stage), the exponential relationship between NDVI and K_c is applied.

3 RESULTS AND DISCUSSION

Fig. 4 (last page) displays seasonal evapotranspiration obtained with the FAO- and STICS-based approaches over the test site for the 2001/2002 agricultural season. The two approaches were successively applied for the three scenario of crop development within each class. For the FAO method, daily values have been cumulated between sowing and full senescence stages, and figure 4 furnishes seasonal crop water requirements. For the STICS-based approach, evapotranspiration is constrained by climate (rainfall) as well as irrigation practices as observed by remotely sensed-data through crop development. Thus daily values can be (and have been) cumulated during the whole simulation period. In this case, simulations end up with seasonal plant maximal transpiration for the observed LAI time course. Thus the difference with cumulated rainfall, which is close to 200 mm, estimates the minimum supply of irrigation water required to satisfy plant needs.

The hierarchy between the three scenario of crop development is clearly visible in Figure 4. The mean scenario, based on averaged NDVI per crop class, is the most suitable to estimate the average values on field and countryside. For the two approaches, it leads to values lower than those expected on arid regions.

$$NDVI = NDVI_{\infty} + (NDVI_S - NDVI_{\infty}) e^{-K \cdot LAI} \quad (1)$$

(with $K = 1$ after Baret et al. 1989)

This result is plausible since supply of irrigation water was limited. For the maximal scenario that corresponds to the plants that are the most watered, the highest values on the test area (600 mm for FAO, 450 mm for STICS) appears regular for wheat in arid condition. The minimum value provided by the STICS model corresponds to the value of cumulated rainfall. In this case, the crop development is low enough to be sustained by rainfall, and STICS simulates no irrigation.

When considering the FAO method, seasonal evapotranspiration can even in some case be under the amount of precipitation. The large differences between maximum and minimum scenario indicate the cases of extreme deficit in water consumption. Since we crossed two approaches and three scenario of crop development, we believe that the range of seasonal evapotranspiration displayed in Figure 4 is correct.

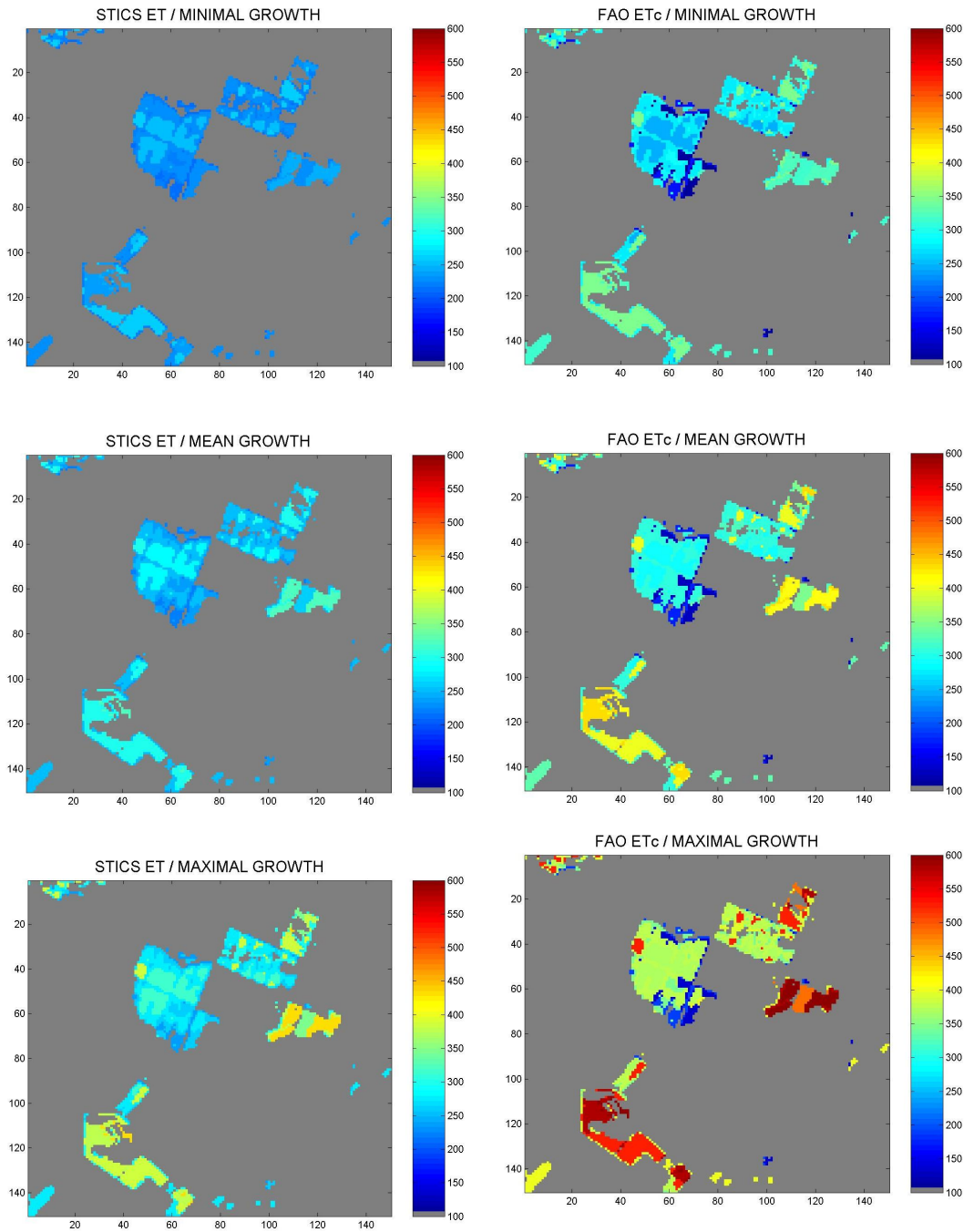


Figure 4. Estimate of crop water requirement (mm) during the agricultural season for the minimum (up), the mean (middle) and the maximum (bottom) scenario of crop growth. These results are obtained by cumulating the daily values obtained with STICS-based (left) and FAO-based (right) approaches.

There is nevertheless a strong need for ground data to analyse these first results. Therefore, our team plans to hold important experimental efforts during the 2002/2003 agricultural season. Local validation should permit quantitative analysis of the accuracy of both FAO- and STICS-based approaches.

A quite good correlation is observed between the results of the two methods (Fig.5). The explanation mostly lies in the fact that no stress was implemented in the STICS model. Consequently, the simulation ends up with maximal plant transpiration. However, the soil evaporation is reduced because the soil surface is rapidly drying after wetting events, while it is always assumed wet in the FAO approach. This partially explains the bias observed between FAO- and STICS-estimates. The second difference is due to the fact that the crop coefficient at full senescence was approximately taken equal to that of the initial stage.

The previous statements first point out the need for an improvement in coupling the FAO model and remote sensing data to better discriminate soil and vegetation latent heat fluxes and account for the decrease in water requirements during late-season. Improvements will be first proposed to separate growing and senescence periods as well as to revisit the fit of NDVI time series using physically-based models (with for instance phenology inferred by degree day approach with photoperiodic slowing, see Weir et al. 1984). Further effort will be paid to test the dual (soil and vegetation) crop coefficients developed by the FAO. Finally, the most important issue to be addressed concerns the driving of approaches designed with the assumption of well-watered plants with remotely-sensed data that observe fields in actual agricultural conditions. Developments should be done to cope with the monitoring of soil moisture in order to better account for the impact of water stress on crop development.

Despite the above-discussed limitations, our study points out the potential of remote sensing data to calibrate and spatialise evapotranspiration models. The spatial results we obtained using the STICS model in arid conditions and for a wide range of irrigation practices are consistent. This first analysis was necessary to take advantage of all the possibilities offered by the model, such as yield estimation. The range of evapotranspiration derived from our adaptation of the FAO-based approach is also satisfactory. This second approach appears promising since we conceived it as an operational tool, paying attention to simplicity in order to provide helpful information for decision makers and end-users

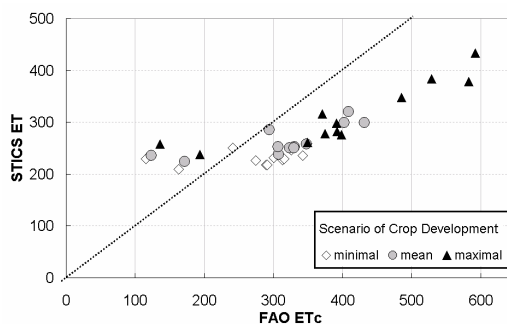


Figure 5. Comparison of seasonal crop water requirement estimated by the STICS model and the FAO method.

ACKNOWLEDGEMENTS

This study was conducted with support from the WATERMED project (WATER use Efficiency in natural vegetation and agricultural areas by Remote sensing in the MEDiterranean basin, see <http://www.uv.es/ucg/watermed/>), which have been funded by the European Union 5th Framework INCO-MED Programme. We thank the ISIS ('Incitation à l'utilisation Scientifique des Images SPOT' by 'Centre National D'Etudes Spatiales', see <http://medias.obs-mip.fr/isis/>) for providing us with satellite data. The authors are very grateful to ORMVAH and University Cadi Ayyad of Marrakech (Morocco), for their helpful scientific and technical help.

REFERENCES

- Asrar G., Fuchs M., Kanemasu E.T., Hatfield J.L., 1984. Estimating absorbed photosynthetic radiation and leaf area index from spectral reflectance in wheat. *Agron. J.* 76 : 300-306.
- Baret F., Guyot G., Major D.J., 1989 – a. Crop biomass evaluation using radiometric measurements. *Photogrammetria* 43 : 241-256.
- Brisson N., Mary B., Ripoche D., Jeuffroy M.H., Ruget F., Nicoulaud B., Gate P., Devienne-Baret F., Antonioletti R., Durr C., Richard G., Beaudoin N., Recous S., Tayot X., Plenet D., Cellier P., Machet J.M., Meynard J.M., Delécolle R., 1998 – a. STICS : a generic model for the simulation of crops and their water and nitrogen balances. I. Theory and parametrization applied to wheat and corn. *Agronomie* 18 :311-346.

- Brisson N., Ruget F., Gate P., Lorgeou F., Nicoullaud B., Tayot X., Plenet D., Jeuffroy M.H., Bouthier A., Ripoche D., Mary B., Justes E., 2002. STICS: a generic model for the simulation of crops and their water and nitrogen balances. II Model validation for wheat and maize. *Agronomie* 22:69-92.
- Brisson N., Itier B., L'Hôtel J.C., Lorendeau J.Y., 1998 – b. Parametrization of the Shuttleworth-Wallace model to estimate daily maximum transpiration for use in crop models. *Ecological Modelling* 107 : 159-169.
- Jensen M.E., Burman R.D., Allen R.G. (editors), 1990. ASCE manual and reports on engineering practice, No 70. Rahman H. and G. Dedieu, 1994. SMAC: a simplified method for the atmospheric correction of satellite measurements in the solar spectrum. *International Journal of Remote Sensing* 15:123-143.
- Monteith J.L., 1985. Evaporation from land surfaces: progress in analysis and prediction since 1948. *Proceedings of the ASAE Conference on Evapotranspiration*, Chicago, Ill, ASAE, St. Joseph, Michigan.
- Nelder J.A. and Mead R., 1965. A simple method for function minimization. *Computer Journal* 8:308-318.
- Penman H.L., 1948. Natural evaporation from open water, bare soil and grass. *Proc. Roy. Soc. London, A* 193, 120-146.
- Rouse J.W., Haas R.H., Schell J.A., Deering D.W., Harlan J.C., 1974. Monitoring the vernal advancement and retrogradation of natural vegetation. NASA/GSFC, Type III, Final report, Greenbelt MD : 1-371.
- Shuttleworth W.J., Wallace J.S. 1985. Evaporation from sparse canopy: an energy combination theory. *Quart. J. Royal Meteorol. Soc.* 111:839-855.
- Weir A.H., Bragg P.L., Porter J.R., Rayner J.H., 1984. A winter wheat crop simulation model without water or nutrient limitations. *Journal of Agric. Science* 102:371-382.

CLAMP: A Model of Leaf Clumping in Canopies

N. Rochdi⁽¹⁾, F. Baret⁽¹⁾, B. Combal⁽¹⁾, M. Chelle⁽²⁾

⁽¹⁾INRA, CSE, Site Agroparc Domaine St Paul Avignon 84914 cedex 9 France.

⁽²⁾INRA, EGC, F78850 Thiverval-Grignon, France.

Email : rochdi@avignon.inra.fr

ABSTRACT: Leaf clumping in plant canopies is investigated to better characterize the interactions between solar radiation and canopy elements. It affects the radiative regime of plant canopies through the expression of the gap fraction (P_0), a key variable that governs interception of solar beam by foliage elements. Two steps are considered here for studying relations between gap fraction and clumpiness. The first one corresponds to the design of generic 3D canopy architectures with a range of clumpiness. The second corresponds to the modelling of gap fraction P_0 . To describe different leaf organisations, 3D computer prototypes are generated considering various leaf area indices, leaf orientations, leaf shapes, leaf sizes, stem-leaf distances and sowing schemes. We assumed that the leaves are attracted to virtual vertical axes at a variable distance and that they don't cross themselves. Using the Zbuffer technique, monodirectional gap fractions are then computed as a function of the viewing geometry. The Poisson and Markov gap fraction models are evaluated by comparison with computed gap fraction. On this basis, results show that in the case of random sowing scheme, $P_0(\theta, \phi)$ decreases as function of zenith angle and leaf area index (LAI). The sensitivity to the leaf-stem distance becomes higher for the higher LAI values and for the small leaves. The comparison between the Poisson model and the computed gap fractions showed, as expected, a good agreement in the case of randomly distributed leaves. For highly clumped canopies and large LAI, the Markov model performs better than the Poisson one. The adjustment of the Markov parameters λ , ΔL show that ΔL could be fixed to 0.01. In the case of small leaves, the sensitivity of the clumping index λ to the zenith angle is established. The influence of the leaf-stem distance on λ becomes less significant for large leaves. The clumping index independence on the leaf orientation is also demonstrated.

1 INTRODUCTION

Gap fraction (or gap frequency) defines the probability that a beam penetrating inside the canopy will reach the ground without contact with the vegetation organs. Related to the geometrical structure such as plant location, orientation, size and shape of canopy elements, gap fraction governs the interactions between solar radiation and vegetation. Therefore, the gap fraction is explicitly used to simulate canopy reflectance (verhoef, 1984; Myneni, 1989). Within turbid radiative transfer models, canopies are considered as an infinite homogenous medium with very small phyto-elements randomly located. The gap fraction in such model is described by Poisson law (ROSS, 1981) as a function of leaf area index (LAI), leaf angle distribution and view configuration. Unfortunately, the Poisson assumption is only restricted to homogeneous dense canopies. It is violated in several actual canopies where leaves are clumped around stems (corn crop for instance) and have finite dimensions. Nilson 1971 used the theory of Markov chains to demonstrate the relation between gap fraction, leaf angle distribution and leaf position in the case of clumped canopies. Markov model assumes that the canopy is divided into N equal

horizontal layers where only zero or one contact (light-leaf) is possible. The probability of a contact (light-leaf) inside a given layer is determined by the state of the preceding layer. Therefore, this dependence between two consecutive layers was featured by the clumping index λ which turns to be a key variable of canopy structure. However, the main problem associated relies in the difficulty to measure physically λ and to characterize its relationship with other canopy variables. Because of the complexity of measurements, few experimental results were reported in the literature. A laboratory experiment was conducted by Andrieu 1993 on artificial canopies for a given canopy structure. However, the results don't explain the relation between λ , viewing geometry (θ, ϕ) and canopy variables.

The objective of this work is to describe the variation of the clumping index λ with direction (θ, ϕ) and other canopy variables. This will be achieved thanks to generic computer prototypes simulating canopies with various levels of clumpiness.

2 METHOD

2.1 Generic Clumped Canopy Architecture Model 'CLAMP'

In order to simulate a wide range of actual canopies, a generic clumped canopy 3D architecture model is developed. The choice of 3D prototype characteristics is based on 3 scales: leaf, plant and canopy. Therefore, the leaf is designed by a triangle with given shape and size; the plant is assumed to correspond to a virtual vertical axis on which leaves are associated. The canopy is an ensemble of plants sown either randomly or with a particular pattern.

To build the 3D prototype, we first sow axis with given density, then we distribute leaves randomly and we associate each leaves to the nearest axis. Afterward, leaves are oriented according to ellipsoidal leaf angle distribution (Campbell, 1990) and attracted to the axis with given translation factor. At last, some leaves are moved by azimuthal rotation in an horizontal plane with respect to the associated vertical axis. All the dimensions are relative to the height of the canopy (h).

Sowing density was chosen considering the relationship between density and canopy height. In fact, taking into account the cases of some canopies (wheat, corn, maritime pine...), the plants density was fixed to 100 axis/ h^2 . Four values of the leaf size relative to the canopy height $Size^*$ were defined "0.025, 0.1, 0.25, 0.4" that should cover a wide range of actual cases. Two leaf shape values 'Rap' (ratio basis/height of triangle) "0.25, 1" and three average leaf angles "30°, 58°, 70°" were considered assuming an ellipsoidal distribution. The distance leaf-plant was modulated using translation factor χ "0, 0.25, 0.5, 0.75, 1" (Figure1). To simulate contrasted canopies, low and high leaf area index values were introduced "0.5, 1, 3, 5". In the case of row sowing pattern, a structure index (ratio of distance between rows/distance between axis on the same row) was assumed to be equal to "6.25". This value is typical for many cultivated canopies.

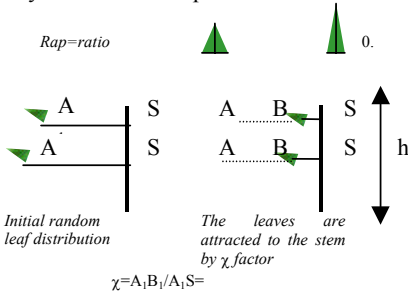


Figure 1: Schema describing the plant structure.

2.2 Gap fraction computation

Gap fraction was computed using the Zbuffer technique. This method consists to create an image corresponding to the canopy prototype projected in a given view direction. The window of projection considered has the same size as the prototype and the view zenith angles θ are sampled from -80° to $+80^\circ$, with a 5° step, the azimuth angle φ is equal to 0° . The precision of this technique depend on the view direction. Therefore, the RMSE of the gap fraction for zenith angle $\theta < 60^\circ$ is quite satisfying (about less than 10%).

2.3 Evaluation of the gap fraction models

As mentioned before, the Poisson model is simple but not always realistic because of the strong assumptions consisting in a random distribution of leaves and a small leaf size. The gap fraction is defined as :

$$P(\theta, \varphi) = \exp\left[\frac{-L \times G(\theta, \varphi)}{\mu}\right] \quad (1)$$

where θ, φ are respectively zenith and azimuth view angles, L is the leaf area index and $G(\theta, \varphi)$ is the projection of unit leaf area in the beam direction (θ, φ).

Contrary to the previous model, the Markov model takes statistically into account the leaf position (Nilson, 1971). The main assumptions are:

- (1) the canopy is divided into $N=L/\Delta L$ equal horizontal layers.
- (2) only zero or one contact (light-leaf) within a layer is possible.
- (3) the conditional probability of observing a contact within a layer ΔL is $\lambda_0 G \Delta L / \cos(\theta) \leq 1$ if there has been a contact in the above layer ΔL , and is $\lambda G \Delta L / \cos(\theta) \leq 1$ if there have been no contacts in the above layer ΔL . The probabilities of no contacts are respectively $1 - \lambda_0 G \Delta L / \cos(\theta)$ and $1 - \lambda G \Delta L / \cos(\theta)$. Here, $G \Delta L / \cos(\theta)$ is the unconditional probability of contact within the layer ΔL and the parameters λ and λ_0 describe the reciprocal dependence of leaf locations between two adjacent layers.

In the first layer (at the top of the canopy), the unconditional probability of no contact is $1 - G \Delta L / \cos(\theta)$. The probability that a solar beam penetrates both the top and adjacent bottom layers

without reaching leaves is $(1 - G\Delta L/\cos(\theta))(1 - \lambda G\Delta L/\cos(\theta))$. Then, by iterating this process up to the last bottom layer, the probability of no contacts into the whole canopy, i.e. the gap fraction for a given view direction θ_v, ϕ_v is defined as :

$$P(\theta, \phi) = \left[1 - \frac{G(\theta_v, \phi_v) \Delta L}{\cos(\theta_v)} \right] \times \left[1 - \frac{\lambda(\theta_v, \phi_v) G(\theta_v, \phi_v) \Delta L}{\cos(\theta_v)} \right]^{\left(\frac{L}{\Delta L} - 1 \right)} \quad (2)$$

The parameter λ is representative of the canopy structure: for regular canopies where leaves avoid each other and tend to fill the gaps, $\lambda > 1$; for clumped canopies with leaves concentrated around stems, $\lambda < 1$. For homogeneous canopies with randomly distributed small leaves as supposed in Poisson law, λ is fixed to 1. However, this last case is violated by most of the canopies because of their specific leaf spatial arrangement depending on plant species and sowing pattern. To quantify and reduce the bias induced by such assumption, the parameters λ and ΔL were adjusted from the Zbuffer gap fractions.

3 RESULTS

3.1 Generic Clumped Canopy Architecture

The combination of all input variables of the generic clumped canopy architecture model leads to design 160 3D computer prototypes. Only random sowing patterns of the vertical axes was considered here. In the case of prototypes with large $Size^*$ values ($= 0.1$), supplementary replicates were added to get the same order of uncertainty on the gap fraction computation achieved for the small leaves ($Size^*=0.025$). Figure 2 shows some examples of prototypes with $LAI=5$, leaf shape $Rap=1$ and leaf size $Size^*=0.025$. The nadir view on the prototypes show the gradual evolution of structure from turbid to clumped medium as a function of leaf-stem distance.

3.2 Sensitivity of gap fraction to canopy clumpiness.

Because of the random sowing pattern considered here, the view direction will be only characterized by the zenith angle

As showed in Figure 3, gap fraction depends on the view angle. Close to nadir view, the probability that a beam reaches the ground is maximal and the maximum of ground (soil) is seen in this direction. As the view zenith angle increases, the soil proportion (or the gap fraction) progressively

diminishes. Similarly, increasing LAI decreases the gap fraction for all view directions.

The effect of the χ parameter is significant for small leaves ($Size^*=0.025$) and large LAI values (Figure 3). The clumping effect is also very important for the nadir viewing directions, in relation to the attraction of the leaves by the vertical axes. For large leaves ($Size^*=0.1$), the impact of the χ parameter on the gap fraction is only marginal and the behaviour is close to that of turbid medium models. This effect of the leaf size could be explained by considering a large leaf with surface equivalent to that of n small leaf surfaces. If a given translation of the leaf to the stem is applied to both cases (small and large leaf), small leaves will tend to overlap each other and discover more the ground. On the opposite, large leaves movements will be relatively smaller.

3.3 Selection of a gap fraction models

The Poisson and Markov models were adjusted over the gap fractions computed with the Zbuffer technique over a range of different cases. The parameters λ for Poisson, and λ and ΔL for Markov models, were fitted using non-linear optimization techniques. Optimizations were performed by constraining λ (and ΔL) to be independent of LAI but to vary with other canopy structure variables and zenith angle.

The following combination of canopy structure variables was investigated $LAI=[0.5; 1; 3; 5]$, $Rap=[0.25; 1]$ and $Size^*=[0.025; 0.1]$. Results show that for turbid medium ($\chi=0$, $Size^*=0.025$) the gap fraction simulated with the Zbuffer from the prototypes canopies are very consistent with theoretical Poisson and Markov models. The λ parameter value is close to 1 for any zenith angle and ΔL remains very small ($\Delta L=0.01$) (Figure 4a and 4b). This high consistency with theory in the case of turbid medium, provides some confidence on the method used. For clumped canopies, the Poisson model tend to underestimate the gap fraction for larger LAI and χ values (Figure 4c). The Markov model performs better in these situations as attested by Figure 4d.

Such results confirm the restrictions of Poisson assumptions. Because of the hypothesis of the mutual dependence of leaf position, Markov model better takes into account the actual canopy structure. In the following, the Markov model was used with $\Delta L=0.01$, and λ adjusted to each direction and combination of canopy variables except LAI.

3.4 Variation of clumping parameter λ with canopy architecture

For large leaves (Figure 5), the λ parameter remains close to 1 whatever the value of χ . This is obviously in

good agreement with previous observations on the gap fractions of canopies with large leaves that behave like turbid medium. For the small leaves, the λ parameter depends strongly on χ and direction θ . The λ value decreases when χ increases, particularly when $\chi \geq 0.5$. We note that λ is very sensitive to χ for nadir viewing as pointed out earlier. For $\theta > 30^\circ$, λ keeps a value that is independent on the view angle θ .

In the previous computations, the leaf angle distribution was assumed to be spherical (average leaf angle $ALA = 57^\circ$). The possible effect of ALA on the clumping parameter, as

implemented on the Markov model, was investigated. We adjusted the Markov model on a range of situations ($LAI = [0.5, 1, 3, 5]$; $Rap = 0.25$; $Size^* = 0.025$; $\chi = [0, 0.25, 0.5, 0.75, 1]$; $ALA = [30^\circ, 58^\circ, 70^\circ]$). The adjustment was achieved either assuming that λ depends or not on ALA . Figure 6 shows the comparison between the residual of the adjustment in the two cases. It clearly appears that the residues are strongly correlated indicating that the assumption of a clumping parameter independent of the leaf inclination is valid.

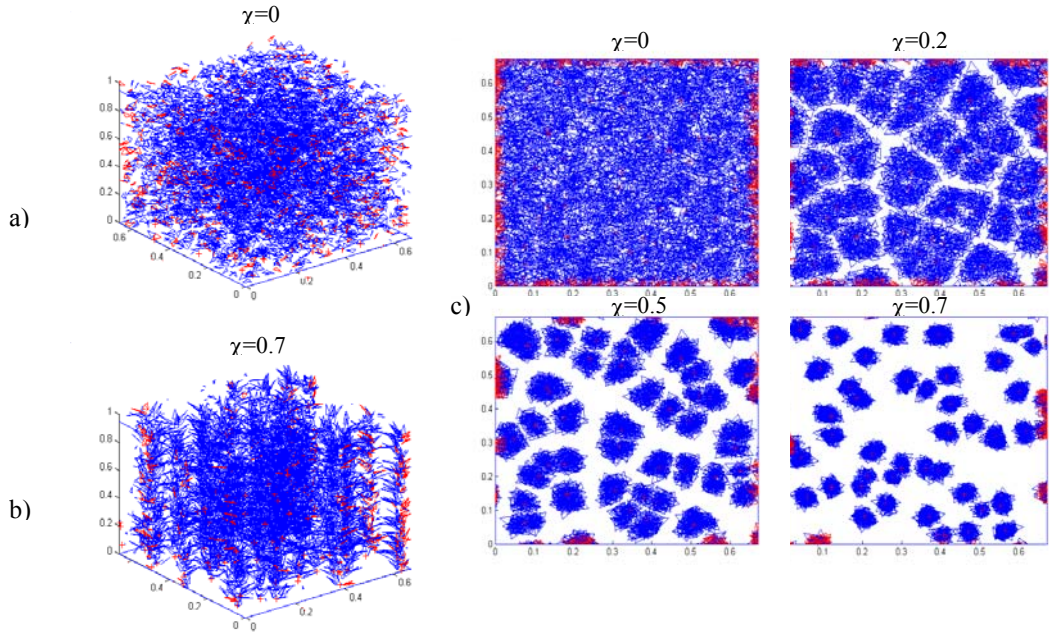


Figure 2. Examples of 3D computer prototypes with random sowing : (a) turbid medium, (c) clumped medium and (c) nadir view of prototypes with various levels of clumpiness. $Size^* = 0.025$, $LAI = 5$

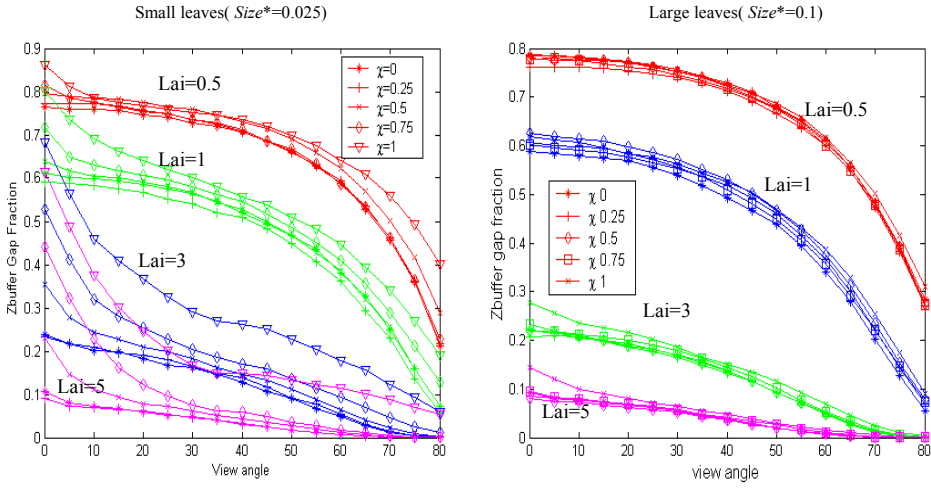


Figure 3. Zbuffer gap fraction as a function of view angle for all LAI and translation factors χ such as leaf size $Size^*=0.025$ (left) and $Size^*=0.1$ (right)

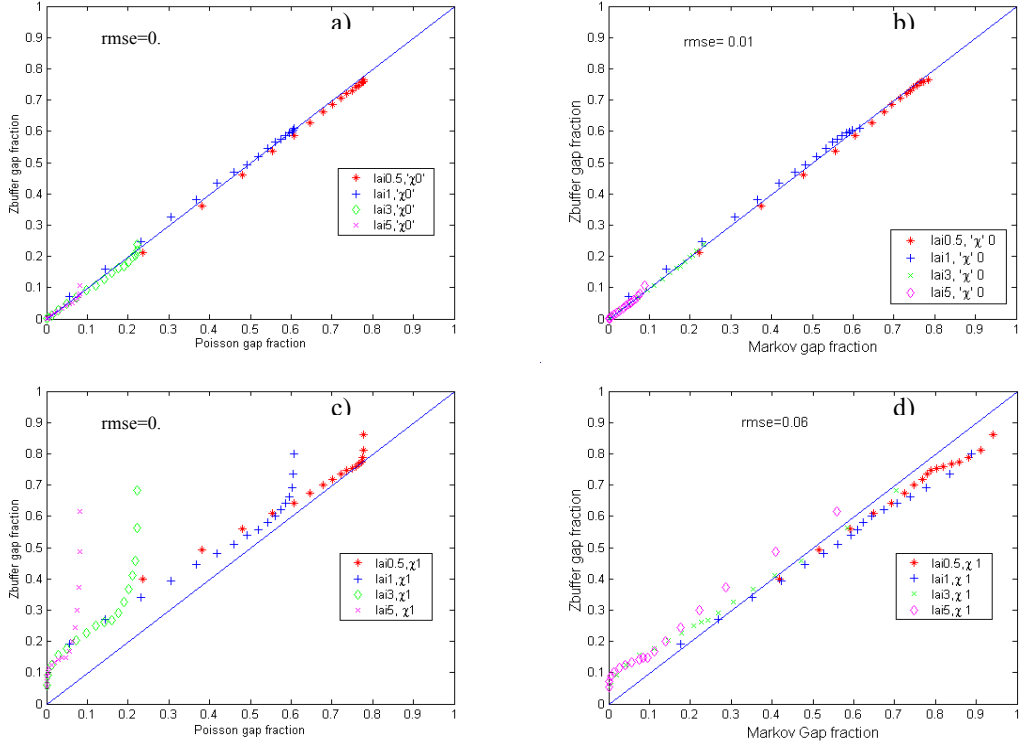


Figure 4. Comparison between gap fraction models and Zbuffer gap fraction for turbid and clumped prototypes ($Size^*=0.025$; $Rap=0.25$)

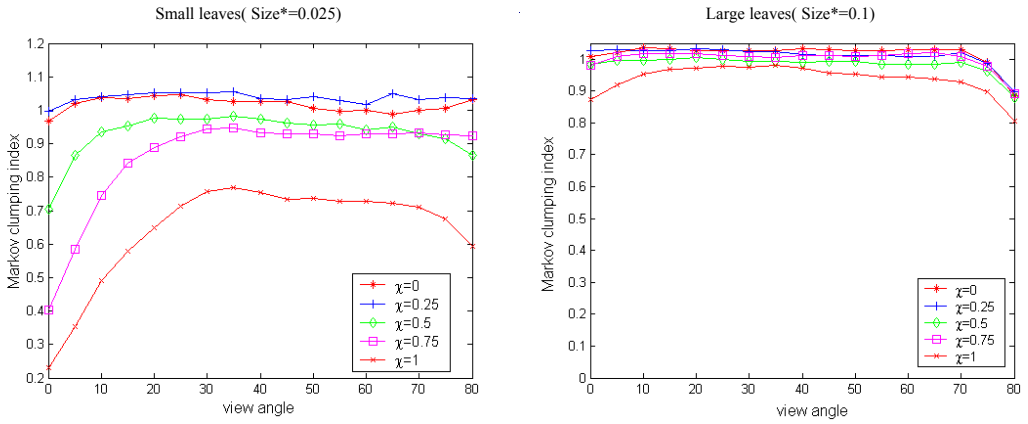


Figure 5. Clumping index as function of the view zenith angle for $Size^*=0.025$ and $Size^*=0.1$

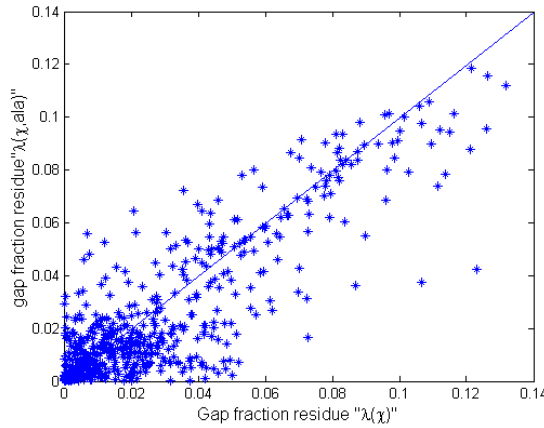


Figure 6. Gap fraction residues assuming that λ does not depend on leaf inclination distribution ($\lambda(\chi)$) as compared to the situation when λ depend on the leaf inclination distribution ($\lambda(\chi)$, ALA)

4 CONCLUSION

The relationship between canopy clumpiness, viewing geometry and other canopy structural variables was investigated in the case of random sowing pattern. The gap fraction was computed using the Zbuffer technique, based on 3D computer simulations representing various canopy architecture.

The sensitivity of the gap fraction to the view zenith angle and to the leaf area index was demonstrated. The gap fraction is also very sensitive to the leaf-stem distance for high LAI and small leaves.

For turbid medium, the adjustment of Poisson and Markov models with Zbuffer gap

fractions shows consistency with theory (clumping index $\lambda=1$). This agreement was obtained with Markov parameter ΔL fixed to 0.01. For clumped canopies, the Markov model performs better than the Poisson one.

The λ parameter sensitivity to leaf size and leaf-stem distance was also proved. For small leaves, λ is very sensitive to the leaf-stem distance χ and varies as a function of the zenith angle for $\chi \geq 0.5$. Around nadir, λ is very sensitive and becomes constant for $\theta > 30^\circ$. For large leaves, λ remains constant (around 1) for any χ and θ values, which correspond to the turbid medium situation.

Based on this conclusions, we will investigate a formulation of the λ parameter as a function of the zenith angle and the other canopy variables (leaf's size and leaf-stem distance). This formulation will be then validated on gap fractions measured on actual canopies with the hemispherical photographs. The effect of row sowing pattern on λ will also studied. Because the clumpiness effect affect the radiative transfer within plant canopy, the λ parameter will be implemented within 1D radiative transfer models (such as SAIL).

5 REFERENCE

- Andrieu B, Sinoquet H, 1993: Evaluation of structure description requirements for predicting gap fraction of vegetation canopies. *Agricultural and Forest Meteorology*, vol 65, pp. 207-227.
- Campbell GS., 1990: Derivation of an angle density function for canopies with ellipsoidal leaf angle distribution. *Agricultural and Forest Meteorology* vol 49, pp.173-176
- Myneni R. B., Ross J., and Asrar G., 1989: A review on the theory of photon transport in leaf canopies . *Agricultural and Forest Meteorology* vol 45, pp. 1-165.
- Nilson T, 1971: A theoretical analysis of the frequency of gaps in plant stands. *Agricultural Meteorology* vol 8, pp.491-503
- Ross J., 1981: The radiation regime and architecture of plants stands. Junk, The Hague, Netherlands, 391 pp.
- Verhoef W., 1984: Light scattering by leaf layers with application to canopy reflectance modeling: The SAIL model. *Remote Sensing of environment*. Vol 16. pp. 125-141

Assessing recent algorithms devoted to albedo estimation using the airborne ReSeDA / PolDER database.

F. Jacob ^{*}, A. Olioso ⁺

^{*} USDA / ARS / HRSR, Bldg 007, BARC-West, Beltsville, MD 20705-2350, USA.

⁺ INRA / CSE, Site Agroparc, Domaine St Paul, 84914 Avignon Cedex 9, France.

fjacob@hydrolab.arsusda.gov, olioso@avignon.inra.fr

ABSTRACT - This paper reviews investigations dealing with albedo estimation using recent algorithms devoted to multidirectional and multispectral remote sensing data. We focused on instantaneous value of visible and near infrared apparent albedo, as well as instantaneous value, diurnal course and daily value of shortwave apparent albedo. The considered algorithms were assessed using airborne PolDER data and ground based measurements collected during the ReSeDA experiment. We firstly focused on estimating hemispherical reflectance using BRDF kernel-driven models, the estimates having a relative accuracy of 10%. We secondly estimated the integrated albedos as linear combinations of hemispherical reflectances using several coefficient sets. The validation showed that adequate sets provided albedo estimates with a relative accuracy about 8%. We thirdly calibrated sets using ground based measurements. We could not obtained a relative accuracy better than 8%, whereas considering more bands than red and near infrared added more noise than information. Moreover, using nadir reflectance rather than hemispherical reflectance decreased the relative accuracy of 2%. Finally, we derived diurnal course and daily value of albedo using multidirectional observations at a single time of the day along with reciprocal BRDF kernel-driven models. Estimate quality was better when using the diurnal course rather an instantaneous value, with an absolute accuracy about 0.02. For all these investigations, we obtained better results with the "Li-Sparse / Ross Thick" variant of the Li-Ross kernel-driven model.

1 INTRODUCTION

Several applications require knowledge of surface albedo that is an important variable of surface radiative budget (Dickinson, 1992; Courault et al., 2001; Olioso et al., 1999; Jacob et al., 2002a). The required variable differ from an application to another, yielding to several subdefinitions according to both the considered spectral range and component of incoming solar radiation (Liang et al., 1999), or the time scale. The main difficulties encountered when dealing with albedo are the characterization of the Bidirectional Reflectance Distribution Function (BRDF) from a limited number of viewing directions, the spectral extrapolation of the integrated value of albedo over a given range from a limited number of waveband observations, and the temporal extrapolation of the diurnal course of albedo from observations at a given time of the day when focusing on sun-synchronous satellites. Several algorithms were developed these last two decades to remove these difficulties. In this paper, we assessed the most recent methods using the airborne PolDER

database collected simultaneously with field measurements in the framework of the ReSeDA European project. The benefit of this database is to allow validating these methods throughout one year while problems due to mixed were reduced.

We focused here on estimating instantaneous value of shortwave (SW), visible (VIS), near infrared (NIR) apparent albedo, and further on retrieving the diurnal course and daily value of SW apparent albedo from observations at a single time of the day. After a brief presentation of the data, we review the results we obtained when estimating hemispherical reflectance (or spectral albedo) from multidirectional measurements along with linear BRDF kernel-driven models. Next we assessed the accuracy it is possible to reach by first validating albedo estimates and second calibrating linear combinations to perform the spectral extrapolation. At this point we assess the interest of using either single directional or multidirectional data. Finally, we proposed to retrieve the diurnal course of albedo using the multidirectional observations collected at a single time of the day along with reciprocal BRDF

kernel-driven models.

2 DATA ACQUISITION & PREPROCESSING

The ReSeDA experiment lasted from December 1996 to December 1997, in the South East of France (N 43 ° 47 ', E 4 ° 45 '). The experimental site was a 5×5 km² agricultural region with corn, sunflower, wheat and alfalfa fields about 200×200 m² size (Prévoit et al., 1998; Oliso et al., 1998). In this study, we used both the airborne PolDER measurements and the field data of albedo. The following is an overview of the PolDER and *in-situ* data acquisition and preprocessing. More detailed descriptions are given by Leroy & Hauteceur (1999); Oliso et al. (2002); François et al. (2002); Jacob et al. (2002c).

The airborne PolDER sensor (Deschamps et al., 1994) flew approximately one or two times per month during the year 1997, on clear sky days, at a 3000 m altitude resulting in a 20 m nadir spatial resolution. Four flight lines parallel to the solar plane and one perpendicular were completed within 45 minutes centered around solar noon. The measurements were collected in four 40 nm width wavebands centered at 443 nm, 550 nm, 670 nm, and 865 nm. View zenith angle ranged from 0 to 50 °. The sensor calibration was performed by the Laboratoire d'Optique Atmosphérique (Lille, France) before, during and after the experiment. Atmospheric effects were corrected using the SMAC algorithm (Rahman & Dedieu, 1994). Image registration was performed using data provided by both a Global Positioning System and a gyroscopic central unit, according to a Lambert II projection that provided a 20 m spatial sampling of the study area.

Ground based observations of SW albedo were estimated as the ratio of reflected to incident solar radiation measurements. The incident solar radiation was measured using a Kipp & Zonen CM6B pyranometer setup at the meteorological site located at the center of the experimental area. The reflected solar radiation was measured on seven locations corresponding to alfalfa, wheat, and sunflower crops using either Kipp & Zonen CM6B pyranometers or Skye Instruments SP1110 silicon sensors. These routine data were collected with both a 15 s time step and a 20 mn period averaging. The corresponding footprint ranged from 1000 to 3000 m². The intercalibration of the Kipp sensors provided a residual error about 10 W.m⁻², which yielded a relative error on computed albedo of 1.5%. The Sky sensor spectral configuration required applying a correction that

was performed by expressing the corrected value as a linear combination of the measured value. The linear combination was calibrated over simulations of the SAIL model performed by François et al. (2002), and has a residual error about 0.003.

The diurnal course of both incoming and reflected solar radiation (direct + diffuse) observed on the seven fields showed that the measurements were fluctuating on two days, which was induced by atmospheric perturbations such as very thin clouds. Obviously, the diurnal course of the derived albedo was also perturbed. These daily data sets were therefore removed since the method used to retrieve the diurnal course of albedo did not account for the variations of meteorological conditions throughout the day. Besides, we observed that diurnal course of albedo computed from measurements collected over one of the sunflower field depicted a bell shape curve oriented towards the bottom whereas the other courses were oriented towards the top. Since this kind of shape was never observed before, we suspected the data quality that might be affected by the field heterogeneity around the *in-situ* measurements. We therefore decided to remove the data set acquired on this field. From these curves, we also observed asymmetries between morning and afternoon variations that could be explained by several factors such as morning dew, evaporation, wind and vegetation alignment (Minnis et al., 1997; Song, 1998).

3 ESTIMATING HEMISPHERICAL REFLECTANCE FROM MULTI-DIRECTIONAL OBSERVATIONS

A detailed discussion about the choice of the kernel-driven models used and the results obtained when assessing their performances is given by Jacob et al. (2002b) and Jacob et al. (2002c). Kernel-driven models allowed deriving the whole BRDF and next hemispherical reflectance using integration procedures. We only give here an overview of the most important results and some concluding remarks.

The chosen models were four classical three-kernel-driven models: Li-Ross in the "Li-Sparse / Ross-Thick" variant (Wanner et al., 1995), the semi-linearized version of MRPV (Engelsen et al., 1996), Roujean (Roujean et al., 1992), and the non reciprocal version of Walthall (Walthall et al., 1985). Model performances were assessed considering PolDER data acquired over the *in-situ* data locations. It was shown that the fitting performances were very close from a model to another, and mainly affected

by the aerosol diffusion since they increased with the wavelength. The comparison of hemispherical reflectance between models showed that the estimate agreement did not increase systematically with wavelength, as observed for BRDF fitting. This emphasized that hemispherical reflectance estimation was not only driven by fitting performance but also by extrapolation abilities. Finally, the inter-comparison of the estimates showed that the hemispherical reflectance values could be significantly different from one model to another, with a relative discrepancy of about 10% (discrepancy expressed as the ARMSD and RRMSD).

We next assessed the robustness of the model to provide realistic values regarding to experimental perturbations, i.e. values larger than 0 and lower than 1. Regardless of kernel-driven model, the rejection rate of unrealistic values decreased as the wavelength increased, which was ascribed to lower atmospheric perturbations. Regardless of PolDER waveband, Roujean model provided the largest rejection rate while the most robust models were Li-Ross and MRPV. As a consequence, the choice of a kernel-driven model should be partially driven by the ability of the model to provide realistic values when used in an operational manner. For further investigations, we selected PolDER data acquired over the *in-situ* data locations.

4 ESTIMATING BROADBAND ALBEDO FROM MULTISPECTRAL DATA

Regardless of subdefinition, albedo can be expressed as a weighted integration of hemispherical reflectance over the considered spectral range, where the hemispherical reflectance corresponds to the diffuse component, and / or the direct component of the incoming solar radiation. The narrowband to broadband conversion consists in expressing the integrated value as a linear combination of the waveband hemispherical reflectances. Since coefficient sets devoted to the airborne PolDER sensor did not exist, we selected among the several sets suggested in the literature some proposed in recent studies and devoted to atmospherically corrected data: 3 by Weiss et al. (1999) for generic sensors, 3 by Liang et al. (1999) and 3 by Liang (2000) for the MISR sensor. A detailed description of these coefficient sets is given in (Jacob et al., 2002c). We just note here that they were calibrated over several databases that included numerous types of surfaces, and that they differ on several points: simulated or collected data, bidirectional or hemispherical reflec-

tance, and spectral range. These sets were dedicated to the computation of SW, VIS and NIR apparent / inherent albedo.

The comparison of inherent or apparent SW albedos for a given coefficient set showed that the values were systematically close from one kernel-driven model to another. On the other hand, the estimates for a given kernel-driven model could be significantly different from one coefficient set to another when considering sets devoted to the apparent albedo. This emphasized that the method we used was more sensitive to the choice of a coefficient set than to the choice of a kernel-driven model. Moreover, the difference we obtained when comparing two sets dedicated to apparent albedo could be more important than the difference between inherent and apparent estimates. A possible explanation was the theoretical inaccuracy of the coefficient sets we used and / or both the theoretical and experimental inaccuracies of the hemispherical reflectance estimates.

The comparison of the airborne estimates against field measurements required accounting for the spatial, temporal and spectral features of both the PolDER and *in-situ* data. Accounting for the spatial features consisted in assessing the influence of the spatial variability over the 400 m² size PolDER estimates that were compared against 1000 to 3000 m² size field data. The coefficient of variation inside both 3×3 and 5×5 PolDER pixel windows ranged between 1 and 2%, which emphasized the negligible effect of the spatial variability around field measurement locations. The PolDER data extraction was therefore performed using 3×3 pixel windows. Accounting for the temporal features consisted in averaging the field data over the period of the PolDER data acquisition that was about 45 minutes. Accounting for the spectral features when validating PolDER VIS and NIR albedos against the SW field estimates consisted in weightily summing these values, the weights being respectively the ratio k of the incident radiation over the VIS spectral domain to the whole solar spectrum, and its complementary to unity. Following the results of Varlet-Grancher et al. (1982) and assuming that surface albedo is quite constant over the UV - VIS domain led us considering k values between 0.47 and 0.56.

The validation of airborne estimates against field measurements was analyzed considering the characteristics of the databases used to calibrate coefficient sets, in order to emphasize possible links between assumptions made during the calibration and validation results. However, we obtained different re-

sults when considering sets calibrated over the same database and similar results with sets calibrated over different databases. Consequently, it was not possible to isolate the errors induced by the assumptions made when calibrating sets (i.e. the choice of the spectral range to compute the broadband albedo, the use of a given sensor spectral configuration to compute wavebands estimates, the use of either bidirectional or hemispherical reflectance, and the consideration of either apparent or inherent albedo). This was ascribed to the experimental inaccuracies, i.e. 5% at least on the radiometric processing of POLDER data, and 10% of relative discrepancy over the estimates from the four kernel-driven models. The best validation result corresponded to set proposed by Liang et al. (1999) for the MISR sensor, with a RRMSE between airborne and ground based estimates of 8%.

The indirect validation of VIS and NIR albedo using a reconstructed SW albedo showed that regardless of the k value, the best estimates corresponded to the set proposed by Liang (2000) for the MISR sensor along with the Walthall model. Furthermore, it was difficult to conclude about the quality of the VIS and NIR estimates since the validation was indirect and depended on k values that varied according to the meteorological conditions. We could only mention that the best validation result corresponded to a k value about 0.55, which agreed with the value proposed by Varlet-Grancher et al. (1982) when considering the French national scale. Besides, the validation results varied significantly according to this ratio, with a RRMSE ranging from 8.5% ($k = 0.55$) to 15% ($k = 0.47$).

When focusing on validation results regarding to kernel-driven model, it was shown that the best estimates corresponded systematically to both Li-Ross and Walthall models, with slightly better results for Walthall. The results we obtained with Walthall were consistent with previous studies, and were explained by the model robustness when considering several land use situations (Strahler et al., 1996; Baret et al., 1997). The results we obtained with Li-Ross were also consistent with previous studies (Privette et al., 1997; Lucht, 1998; Lucht et al., 2000), and could be explained by the directional performances of the "Li-Sparse / Ross-Thick" variant over vegetative areas. Since Li-Ross was also one of the most robust model when assessing the ability to provided realistic hemispherical reflectance data, we can conclude that this model seems to be the most interesting, for both its accuracy and its feasibility.

5 CALIBRATING COEFFICIENT SETS FOR THE NARROW BAND TO BROADBAND CONVERSION

Since no proposition existing in the literature for the narrow band to broadband conversion from POLDER data, we calibrated some coefficient sets dedicated to the estimation of SW apparent albedo. This was performed considering both hemispherical and bidirectional reflectance. When dealing with bidirectional reflectance, we considered the nadir reflectance computed from kernel-driven models. The comparison of nadir reflectance estimates from the four kernel-driven models showed a relative discrepancy about 3.5%, which emphasized that this variable was estimated with a better quality than hemispherical reflectance (relative discrepancy about 10%).

Before performing the coefficient set calibration, we assessed the information provided by each POLDER waveband by calculating the intercorrelation coefficients between the waveband estimates. For both nadir and hemispherical reflectance and regardless of kernel-driven model, we observed that only the NIR channel was not correlated to the others: correlation coefficient ranging between 0.9 and 0.96 when intercomparing blue, green and red channels, and correlation coefficient ranging between -0.43 and -0.72 when comparing NIR channel against the others. This showed that regarding to the database we used, two channels should be sufficient to compute albedo, whereas the use of the NIR channel was absolutely necessary. Besides, the information over the VIS wavebands was either redundant or could not be discriminated because of noise over the database.

The calibration of the coefficient sets was performed using a pseudo-matrix inversion between the POLDER hemispherical / nadir reflectances and the field measurements of albedo. Moreover, we estimated the 90% confidence interval for the coefficients, as well as the residual error. The results we obtained using the Li-Ross model are listed in Table 1. We only reported the results corresponding to a unique selection among the blue, green and red channels. Indeed, the results with the other selections were very similar, which was consistent with the correlation coefficients between these three bands.

When dealing with the statistical confidence of coefficients according to the number of considered channels, we observed the same trend with both

reflectance	blue	green	red	NIR		ARMSE RRMSE
	coef	coef	coef	coef	offset	
	co. in.	co. in.	co. in.	co. in.	co. in.	
Nadir	-	-	0.2268	0.3055	0.0595	0.0202
	-	-	± 0.1082	± 0.0643	± 0.0318	10.38%
Nadir	-	-0.1355	0.3339	0.3162	0.0588	0.0202
	-	± 0.9018	± 0.7209	± 0.0965	± 0.0324	10.37%
Nadir	-0.0992	-0.0869	0.3509	0.3137	0.0579	0.0201
	± 0.5038	± 0.9435	± 0.7331	± 0.0983	± 0.0331	10.36%
Hemis	-	-	0.5912	0.3737	-0.0008	0.0155
	-	-	± 0.1199	± 0.0533	± 0.0291	8.04%
Hemis	-	-0.2659	0.8118	0.3978	-0.0025	0.0153
	-	± 0.4158	± 0.3651	± 0.0652	± 0.0292	7.94%
Hemis	-0.3867	-0.2205	1.0044	0.4122	-0.0114	0.0147
	± 0.3488	± 0.4066	± 0.3954	± 0.0648	± 0.0295	7.63%

Table 1: Values of the calibrated coefficients (coef) obtained from linear regressions between the field data of albedo and the PolDER estimates of both nadir (Nadir) and hemispherical (Hemis) reflectance. The associated 90% confidence intervals (co. in.) are given below the coefficients with the \pm sign. The corresponded residual errors as given through ARMSE and RRMSE.

nadir and hemispherical reflectances. The coefficient values were very stable from one model to another when using only two channels. Besides, the coefficient confidence interval ranged between 15 and 20% of the coefficient values, and the values were physically consistent (positive value with a sum close to one). When considering more than two PolDER channels, the results were worse despite a lower residual error. The confidence interval could be of about 100% of the coefficient itself. Moreover, adding the green and / or the blue channels increased significantly the uncertainty of the red coefficient, indicating that this added more noise than information. As a consequence, the multilinear regression provided some physically unrealistic coefficients such as negative values whereas the coefficient sum was not anymore close to one. Considering these observations, we concluded that using the red and NIR PolDER channels to compute albedo was the best solution.

We next compare the quality of the calibrated coefficients for the narrowband to broadband conversion when considering either hemispherical or nadir reflectance. It was shown that the absolute (respectively relative) residual error increased by 0.005 (respectively 2%) when considering nadir reflectance rather than hemispherical reflectance. This indicated

that the information loss was small as compared to the accuracy we could reach, i.e 8% in relative. As mentioned previously, nadir reflectance computation was more stable when comparing the estimates from a model to another. Consequently, we observed that the coefficient variability from a model to another was significantly lower with nadir reflectance than with hemispherical reflectance. Therefore, using this variables seemed at first sight more interesting than considering hemispherical reflectance. However, we noted that the confidence interval could be significantly higher with nadir reflectance. When considering red and NIR PolDER channels, we noticed that regardless of kernel-driven model, using nadir rather than hemispherical reflectance increased the confidence interval from 15 to 25% over the NIR channel, but especially from 18 to 48% over the red channel. This indicated a lower statistical quality of the calibrated coefficients when using the nadir reflectance, which could be explained by a lack of directional information.

6 ESTIMATING DIURNAL COURSE AND DAILY VALUE OF ALBEDO FROM SINGLE TIME OBSERVATIONS

The last part of this study dealt with the retrieval of the diurnal course and further the daily value of

SW apparent albedo using multidirectional observations at a single time of the day. This required using reciprocal kernel-driven BRDF models for which it is possible to switch the illuminating and viewing directions, yielding calibrated coefficient that do not depend on sun position. These models are therefore supposedly able to characterize the evolution of the BRDF as a function of sun position. A detailed discussion about the method we used and the results we obtained is given in Jacob & Oliso (2001).

The first step of the procedure was the inversion of reciprocal kernel-driven models, i.e. Li-Ross, MRPV and Roujean. The second step consisted of deriving the 20 mn diurnal course of hemispherical reflectance in the PolDER channels by feeding the inverted models with solar zenith and azimuth angles between sunrise and sunset (solar angles computed from astronomical rules using both the latitude-longitude of the site and the universal time). The calculations were actually limited to solar zenith angles ranging from 0 to 80° since the reciprocal kernel-driven models provided unrealistic estimates for higher zenith angles whereas we noted very low values of incoming solar radiation at such angles (about 10 W.m⁻² as compared to the 600 W.m⁻² around solar noon). The diurnal course of albedo was next derived from the diurnal course of hemispherical reflectance over the PolDER wavebands using the coefficient sets proposed by Liang et al. (1999) for the MISR sensor, since this set provided the best validation result when dealing with the instantaneous value around solar noon of SW apparent albedo. Finally, the daily value of albedo was derived from the diurnal course by weighting each instantaneous estimates with the corresponding incoming solar radiation.

We first compared the retrievals of both instantaneous albedo around solar noon and daily albedo against ground based measurements. The three reciprocal kernel-driven models provided similar estimates that agreed quite well with the reference. The best agreement corresponded to the Li-Ross model that provided the lowest scattering. The estimates of the daily value were not as good as those of the instantaneous value. This was explained by the assumptions made when using reciprocal kernel-driven models to retrieve the diurnal course of albedo. The quality of the daily value estimates was first correlated to the accuracy of the instantaneous albedo retrievals, with similar over- or underestimations according to the model. The underestimation of the instantaneous values observed with

Li-Ross was more pronounced when estimating the daily value. This was explained by the shape of the retrieved diurnal course of albedo, which was more flat with this model (see example in Figure 1). We should notice that the daily values were higher than the instantaneous ones at solar noon, with an averaged difference about 0.018 and a maximum of 0.03. This was explained by the albedo increase when solar zenith angle increases.

We next assessed the accuracy on the retrievals of the reflected solar when considering the diurnal course of albedo, the daily albedo and the instantaneous albedo at solar noon respectively. The results obtained with the Li-Ross model and the PolDER data are illustrated in Table 2. The retrievals were quite good, the best results being obtained when accounting for the diurnal course. The use of the instantaneous albedo at solar noon induced an underestimation of the reflected solar energy over the diurnal cycle since this albedo value was usually the lowest during the day. The resulting underestimation occurred mainly for intermediary solar zenith

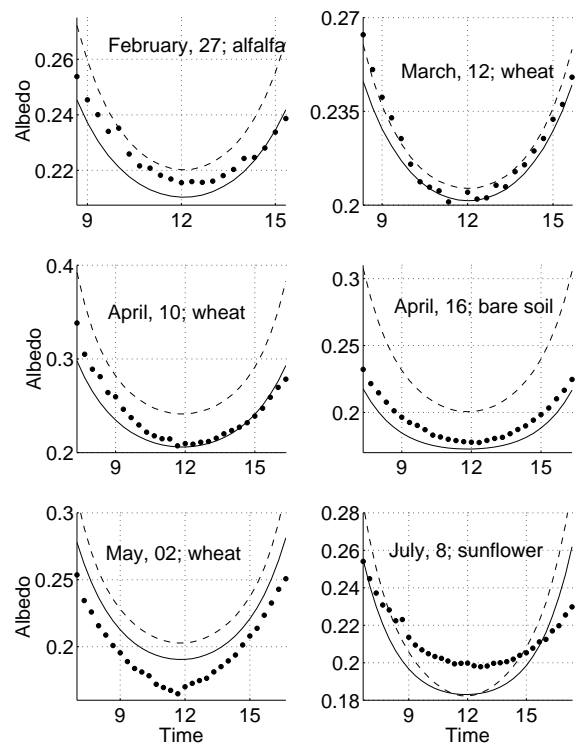


Figure 1: Comparison against field measurements (●) of the diurnal course of albedo retrieved from Li-Ross (—) and Roujean (- -).

Albedo	RMSE (W.m ⁻²)	Bias (W.m ⁻²)	RMSE _U (W.m ⁻²)
Diurnal course	11.47	-5.56	9.95
Daily Value	14.81	-5.50	12.84
Noon value	16.78	-12.48	11.10

Table 2: RMSE, Bias and $RMSE_U$ between retrievals from PolDER data with Li-Ross model and *in-situ* measurements of reflected solar radiation when considering the diurnal course, the daily mean value and the instantaneous value at solar noon of albedo respectively.

angles (the incoming solar radiation became low for higher angles). The use of the daily value induced a large scatter around solar noon. This was linked to the scatter occurring in the estimation of solar noon albedo combined to the fact that mean albedos were larger than noon albedos. The discrepancy obtained in the diurnal course of reflected solar radiation from the reconstitution of albedo throughout the day was linked to 1) the errors in noon retrievals, 2) the ability of the reciprocal kernel-driven models to reconstruct the diurnal course of the BRDF mainly at high solar zenith angles (Lucht, 1998), and 3) the influence of changes in atmospheric and surface conditions (Song, 1998).

7 CONCLUSIONS

This study assessed recent algorithms devoted to albedo estimation using the airborne PolDER / ReSeDA database. We focused on estimating instantaneous visible (VIS), near infrared (NIR) and short-wave (SW) albedos, as well as the diurnal course and the daily value of SW albedo. The hemispherical reflectance was estimated using four classical linear BRDF kernel-driven models. The intercomparison of the estimates showed a relative discrepancy of about 10%. Assessing model abilities to provide realistic values despite of noise occurring on database showed that Li-Ross and MRPV were the most robust models.

Integrated values of albedos was expressed as linear combinations of waveband hemispherical reflectances. We considered several coefficient sets proposed in the literature for different sensors. The validation of VIS and NIR and SW albedos showed that it was possible to reach a relative accuracy of 8%. However, the hemispherical reflectance dataset was not accurate enough to assess the uncertainties of the assumptions made when calibrating the sets. Regardless of coefficient sets, the best validation re-

sults corresponded to Li-Ross and MRPV. The calibration of coefficient sets devoted to the estimation of SW albedo from PolDER data showed that the database was not accurate enough to draw a general conclusion. Considering nadir reflectance rather than hemispherical reflectance increased the relative residual error of 2% only, but significantly decreased the statistical quality of the coefficients.

The diurnal course and the daily value of albedo, as well as the evolution of reflected solar radiation throughout the day, could be retrieved with a good accuracy using reciprocal kernel-driven models (especially the Li-Ross model). Besides, it was better to use the diurnal course of albedo rather than the daily albedo when describing the energetic exchanges with an hourly time step, especially when the daily value is computed from the diurnal course. In all cases, the use of an instantaneous value around solar noon would yield significant underestimations of reflected solar energy.

ACKNOWLEDGMENTS

This study was performed during a post-doctoral position funded by the ASTER project of NASA's EOS-Terra Program. Financial support was provided by EC in the frame of the WATERMED project (contract ICA3-CT-1999-00015). The Alpilles / ReSeDA project was funded by the EEC-DG XII (contract ENV4-CT96-0326-PL952071) and the French *Programme National de Télédétection Spatiale and Programme National de Recherches en Hydrologie*. The PolDER airborne sensor was provided by the *Laboratoire d'Optique Atmosphérique*, Lille, France.

References

- Baret, F., Weiss, M., Leroy, M., Hauteceur, O., Santer, R., and Bégue, A., 1997. Impact of surface anisotropies on the observation of optical imaging sensors, final report. ESA contract 11341/95/NL/CN, ESA, ESTEC, the Netherlands.
- Courault, D., Lacarrere, P., Clastre, P., Lecharpentier, P., and Jacob, F., 2001. Estimation of surface fluxes using remote sensing data and the MESONH model on the ALPILLES area. In: *Remote sensing and Hydrology Symposium, Montpellier, France*. Submitted.
- Deschamps, P.Y., Bréon, F.M., Leroy, M., Podaire, A., Bricaud, A., Buriez, J.C., and Sèze, G., 1994, The PolDER mission : instrument characteristics and scientific objectives. IEEE Transactions on Geoscience and Remote Sensing, 32, 598–615.
- Dickinson, R.E., 1992. *Land surface*. Cambridge University Press, New York.
- Engelsen, O., Pinty, B., Verstraete, M., and Martonchik, J.V., 1996. Parametric bidirectional reflectance factor models : evaluation, improvements and applications. Report EUR16426EN, European Commission,

- Joint Researches Center, Space Application Institute, ISPRa, Italy.
- François, C., Ottlé, C., Oliso, A., Prévot, L., Bruguier, N., and Ducros, Y., 2002, Conversion of 400 - 1100 nm vegetation albedo measurements into total short-wave broadband albedo using a canopy radiative transfer model. *Agronomie*. Accepted.
- Jacob, F., Gu, X.F., Hanocq, J.-F., and Baret, F., 2002a, Atmospheric corrections of single broadband channel and multidirectional airborne thermal infrared data. Application to the ReSeDA Experiment. *International Journal of Remote Sensing*. Accepted.
- Jacob, F. and Oliso, A., 2001, Derivation of diurnal courses of albedo and reflected solar radiation from PolDER data. *Journal of Geophysical Research*. Submitted.
- Jacob, F., Oliso, A., Weiss, M., Baret, F., and Hauteceur, O., 2002b, Mapping short-wave albedo of agricultural surfaces using airborne PolDER data. *Remote Sensing of Environment*, 80, 36–46.
- Jacob, F., Weiss, M., Oliso, A., and French, A., 2002c, Assessing the narrowband to broadband conversion to estimate visible, near infrared and shortwave apparent albedo from airborne PolDER data. *Agronomie*. Accepted.
- Leroy, M. and Hauteceur, O., 1999, Directional parameters, hemispherical reflectances and angle-corrected NDVIs derived at global scale by the spaceborne PolDER. In: CNES (ed.), *Proceedings of Alps 1999 conference, Méribel, France, January 18-22, 'Land surface' session*, pp. 1–4.
- Liang, S., 2000, Narrowband to broadband conversions of land surface albedo I Algorithms. *Remote Sensing of Environment*, 76, 213–238.
- Liang, S., Strahler, A.H., and Walthall, C.W., 1999, Retrieval of land surface albedo from satellite observations: A simulation study. *Journal of Applied Meteorology*, 38, 712–725.
- Lucht, W., 1998, Expected retrieval accuracies of bidirectional reflectance and albedo from EOS-MODIS and MISR angular sampling. *Journal of Geophysical Research*, 103, 8763–8778.
- Lucht, W., Schaaf, C.B., and Strahler, A.H., 2000, An algorithm for the retrieval of albedo from space using semi-empirical BRDF models. *IEEE Transaction on Geoscience and Remote Sensing*, 38, 977–977.
- Minnis, P., Mayor, S., Smith Jr., W.L., and Young, D.F., 1997, Assymetry in the diurnal variation of surface albedo. *IEEE Transactions on Geoscience and Remote Sensing*, 35, 879–891.
- Oliso, A., Braud, I., Chanzy, A., Ducros, Y., Gaudu, J.C., Gonzales-Soza, E., Lewan, L., Marloie, O., Ottlé, C., Prévot, L., Autret, H., Bethenod, I., Bonnefond, J.M., Brugier, N., Calvet, J.C., Chauki, H., Goujet, R., Jongschaap, R., Kerr, Y., Lagouarde, J.P., Laurent, J.P., McAneney, J., Moulin, S., Thony, J.L., Weiss, M., and Wigneron, J.-P., 2002, SVAT modeling over the Alpilles-ReSeDA experiment: experimental setup for monitoring energy and mass transfers. *Agronomie*. Submitted.
- Oliso, A., Chauki, H., Courault, D., and Wigneron, J.P., 1999, Estimation of evapotranspiration and photosynthesis by assimilation of remote sensing data into SVAT models. *Remote Sensing of Environment*, 68, 341–356.
- Oliso, A., Prévot, L., Baret, F., and Chanzy, et al., 1998, Spatial aspects in the Alpilles-ReSeDA project. In: *Scaling and modeling in forestry: application in remote sensing and GIS*, Ed. D.Marceau, Université de Montréal, Québec, pp. 92–102.
- Privette, J.L., Eck, T.F., and Deering, D.W., 1997, Estimating spectral albedo and nadir reflectance through inversion of simple BRDF models with AVHRR/MODIS-like data. *Journal of Geophysical Research*, 102, 29529–29542.
- Prévot, L., Baret, F., Chanzy, A., Oliso, A., and Wigneron, J.P. et al., 1998, Assimilation of multi-sensor and multi-temporal remote sensing data to monitor vegetation and soil: the Alpilles ReSeDA project. In: L. Tsang (ed.), *IGARSS'98 International Geoscience and Remote Sensing Symposium, IEEE, Institute of Electrical and Electronics Engineers, Piscataway (USA), Sensing and managing the environment*, vol. 5, pp. 2399–2401.
- Rahman, H. and Dedieu, G., 1994, SMAC : a Simplified Method for the Atmospheric Correction of satellite measurements in the solar spectrum. *International Journal of Remote Sensing*, 16, 123–143.
- Roujean, J.L., Leroy, M., and Deschamps, P.Y., 1992, A bidirectional reflectance model of the Earth's surface for the correction of remote sensing data. *Journal of Geophysical Research*, 97, 20455–20468.
- Song, J., 1998, Diurnal assymetry in surface albedo. *Agricultural and Forest Meteorology*, 92, 181–189.
- Strahler, A.H., Schaaf, C.B., Muller, J.-P., Wanner, W., Barnsley, M.J., d'Entremont, R., B., Hu, Lewis, P., Li, X., and Ruise De Lope, E.V., 1996, MODIS BRDF / Albedo product: Algorithm Theoretical Basis Document. NASA EOS-MODIS Doc. Incl. Update, version 4.0, NASA/GSFC, Greenbelt MD, USA.
- Varlet-Grancher, C., Bonhomme, R., Chartier, M., and Artis, P., 1982, Efficience de la conversion de l'énergie solaire par un couvert végétal. *Acta oecologica. Oecologica Plantarum*, 17, 3–26.
- Walthall, C.L., Norman, J.M., Welles, G., Campbell, G., and Blad, G.L., 1985, Simple equation to approximate the bidirectional reflectance from vegetative canopies and bare soil surfaces. *Applied Optics*, 24, 383–387.
- Wanner, W., Li, X., and Strahler, A.H., 1995, On the derivation of kernels for kernel-driven models of bidirectional reflectance. *Journal of Geophysical Research*, 100, 21077–21089.
- Weiss, M., Baret, F., Leroy, M., Bégué, A., Hauteceur, O., and Santer, R., 1999, Hemispherical reflectance and albedo estimate from the accumulation of across-track sun-synchronous satellite data. *Journal of Geophysical Research*, 104, 22221–22232.

Influence of spatial heterogeneity and scaling on leaf area index estimates from remote sensing data

S.Garrigues¹, D.Allard², M.Weiss³, F.Baret¹, S.Marni⁴, H.Jeanjean⁵

1. INRA, Avignon, France: sgarrig@avignon.inra.fr, baret@avignon.inra.fr
2. INRA-Biométrie, Avignon, France, allard@avignon.inra.fr
3. NOVELTIS, Toulouse, France, weiss@avignon.inra.fr
4. ALCATEL SPACE, Cannes, France, Sandrine.Marni@space.alcatel.fr
5. CNES, Toulouse, France, Herve.Jeanjean@cnes.fr

ABSTRACT –To monitor terrestrial surfaces, quantitative information like Leaf Area Index (LAI) are retrieved from remote sensing data. Because of technology constraints the sensors currently used have coarse resolution. Characterizing spatial heterogeneity at coarse resolution is important to improve LAI estimates. The aim of this study is to propose a methodology to characterize spatial structure of remote sensing data. Variogram models are fitted for different variables (RED and NIR reflectance, NDVI vegetation index and LAI) for four contrasted landscapes (crop, pine forest, Mediterranean vegetation and tropical forest). The comparison of the variogram model parameters (sill, range, integral range) between landscapes allows to draw a typology of spatial heterogeneity. Then spatial heterogeneity is related to scaling issue to emphasize the influence of resolution with application to the estimation of LAI.

1 INTRODUCTION

Terrestrial surfaces are observed frequently and globally by series of large swath sensors such as NOAA/AVHRR, VEGETATION, MERIS, MODIS, MISR and POLDER. To monitor phenological changes and dynamic processes such as primary production, studies have to be carried using high time frequency data. Because of technological constraints, these sensors are associated to coarse spatial resolution, *i.e.*, in the resolution from few hundreds of meters up to few kilometers. However, at these scales, spatial heterogeneity may have a great influence on land surface characteristics estimation from remotely sensed data (Leaf Area Index: LAI, vegetation cover, canopy chlorophyll content...), particularly if the relationship between the considered variable and the radiometric data are non linear, which is the case for LAI. Indeed the transfer function used to derive LAI from remote sensing data (reflectance, NDVI) is generally built to be applied to homogeneous surface whereas the remote sensing measurement is a spatial average of radiative signals over the pixel. Applying such transfer functions at coarse resolution to derive LAI does not account for the subpixel variation and leads to error on retrieving quantitative information LAI. Therefore the spatial heterogeneity issue has to be dealt with the problem of scaling and the non linearity of the transfer function.

Depending on the kind of study, spatial heterogeneity can have different meanings. In this work, spatial heterogeneity is related to a quantitative

information that characterizes the spatial structure of remote sensing data (vegetation description) for a given geographic domain (*ie* image). Spatial heterogeneity can be quantitatively characterized by different techniques. A first way consists in computing textural parameters (variance, covariance, skewness...) to characterize spatial data variation within an image (Haralick, 1996). Different authors show that geostatistical theory (Cressie, 1991) can be applied to remote sensing image to describe data spatial variation by variogram function (Woodcock *et al* 1987, Jupp *et al.* 1988a, Jupp *et al.* 1988b, Woodcock *et al* 1988, Atkinson 1997, Milne *et al.* 1999, Treitz 2000, Beaufort 2000...). Fractal dimension (Mandelbrot, 1983) was used to monitor spatial pattern change in multiscale analysis (De Cola 1989, Bian and Walsh 1993, Bian 1997, Xia *et al.* 1997, Cao 1997...). More recently wavelet transform is used in multiresolution analysis (Ranchin and Wald, 1993). However Chen (1999) underlines that contextual parameters (size and organization of the objects within the image) are more effective than textural parameter to describe the effect of spatial discontinuity on scaling. Moreover different studies characterize spatial heterogeneity with scaling issue. Bian (1997) uses fractal dimension to emphasize data aggregation influence on spatial pattern. Milne *et al.* (1999) used geostatistical theory to monitor data regularization evolution with resolution. Spatial heterogeneity is also studied as an influence on LAI error estimates at coarse resolution. Chen (1999) shows that the error estimates depends not only on the non linearity of the derivation algorithm but also on the mixed pixel spatial pattern organization. Friedl (1997) shows with a simulation study that the LAI

error estimates results from the interaction between spatial resolution of the sensor and the scale of spatial variation in the ground scene.

This study consists in developing a methodology to characterize quantitatively spatial heterogeneity for different variables (reflectance or biophysical variable derived from remote sensing) for different landscapes. To this purpose, the study objectives are:

1. describing spatial heterogeneity at high resolution (20m resolution) for different vegetation sites and variables
2. analyzing scaling effect in relation with spatial heterogeneity
3. observing heterogeneity influence on LAI error estimates at coarse resolution.

2 STUDIED DATA

2.1 Studied sites

The data come from the VALERI database (<http://www.avignon.inra.fr/valeri>, Baret *et al.* 2002). It consists in a network of sites used to validate large swath satellite biophysical products (including LAI). For each site, high resolution images (SPOT) are available. Four SPOT images of 4 contrasted landscape are used. The size of each image is the same: 3km*3km and the SPOT pixel resolution is 20m. Figure 1 shows the NDVI image at SPOT resolution for the different sites.

2.2 Studied variables

a) SPOT reflectances

NIR and RED bands will be investigated. Moreover the NDVI index is computed:

$$NDVI = \frac{NIR - RED}{PIR + RED} \quad (1)$$

The remote sensing data are not corrected from atmospheric effects, a cloud mask was applied only on Counami image, the acquisitions for the other sites being cloud free.

b) Biophysical variable

A LAI image of each site is performed by applying a semi-empirical expression (Baret and Guyot, 1991). The relationship is fitted on a learning data set composed of LAI variable and corresponding reflectance values. The data set was generated with SAIL radiative transfer model simulations (Weiss, 2002) for a wide range of simulations.

$$LAI = \frac{\log((NDVI - NDVI_{\infty}) / (NDVI_s - NDVI_{\infty}))}{-K_{lai}} \quad (2)$$

- K_{lai} is the extinction coefficient
- $NDVI_{\infty}$ is the asymptotic value of NDVI (corresponding to infinite LAI)
- $NDVI_s$ is the bare soil NDVI value

For each variable (LAI, NDVI, RED, NIR) and each site, different resolution images are computed by aggregating (arithmetic mean) the 20m resolution image.

3 METHODOLOGY

3.1 Geostatistical tools

Geostatistics (Cressie 1991, Wackernagel 1995) allow to characterize spatial distributions of one or more variables. Variable spatial distribution is characterized by the variogram function that measures the spatial dependence of neighbouring observations. Since the variable describes a spatial phenomenon, this variable is called regionalized variable. In our case the variable are reflectance or LAI derived from reflectance. Since reflectance values of an image are a function of spatial position they can be considered as regionalized variables. For this study, the variable support is the SPOT pixel that is a 20m*20m square. Although the value associated to the pixel is a spatial average of radiative signals over the square we will consider the value associated to the pixel as punctual. This induces the assumption of homogeneous SPOT pixels (intrinsic characteristics of VALERI site). Moreover since the pixel value results from a spatial averaging process (Point Spread Function) the remote sensing variable can be considered continuous on the image. Spatial variation and spatial dependence are described by the experimental semivariogram $\gamma_e(h)$ (commonly called experimental variogram) which is the mean squared deviation of a variable at locations separated by a given lag distance:

$$\gamma_e(h) = \frac{1}{2 \cdot N(h)} \sum_{i=1}^{N(h)} (z(x_i) - z(x_{i+h}))^2 \quad (3)$$

$z(x_i)$ is the variable at location i , $z(x_{i+h})$ is the variable value at lag h from x and $N(h)$ is the number of pairs of points separated by the distance h . Figure 2 presents the experimental variograms performed over the 3km*3km SPOT image for different variables and different sites. Two main parameters characterize the variogram:

- The total sill (σ^2) corresponds to the true variance of the data.

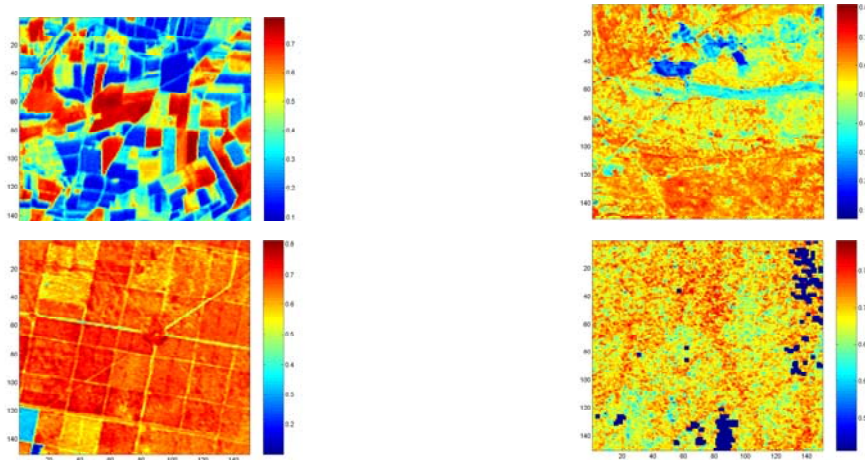


Figure1: NDVI images of the studied sites (3km*3km): a Alpilles, Crop Site (March), mean NDVI=0.41, std NDVI=0.19; b: Puechabon (France), Mediterranean Forest (June), mean=0.54, std=0.1; c: Nezer (France), Pine Forest (June), mean=0.65, std=0.06; d: Counami (French Guyana), Tropical Forest (October), mean=0.69, std=0.029

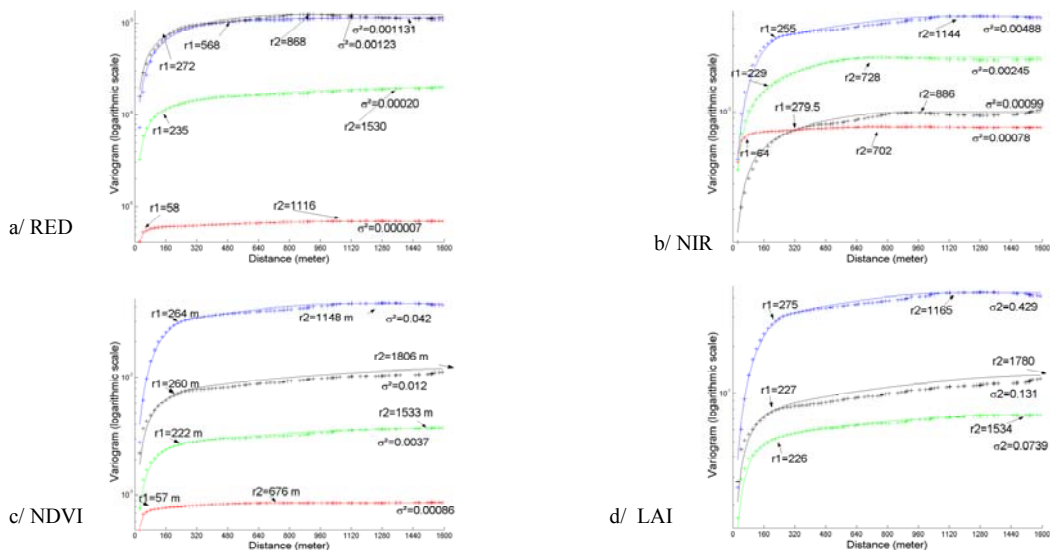


Figure 2: Experimental (crosses) and theoretical variograms (line) for the 4 landscapes studied: Alpilles (red), Puechabon (black), Nezer (green), Counami (red)

- The range (r) is the lag at which the variogram reaches the sill. Up to this distance data are spatially autocorrelated, beyond this distance samples are spatially independent.

As the regionalized variable $z(x)$ is difficult to model with a simple deterministic function, it is seen as an outcome of a random function $Z(x)$. In this context and assuming a second-order stationarity hypothesis for $Z(x)$, the theoretical variogram describing the spatial dependence and spatial variation of the random function is introduced:

$$\gamma(h) = 0.5 * E[(Z(x) - Z(x+h))^2] \quad (4)$$

In practice a theoretical model is fitted on the experimental variogram.

3.2 Theoretical variogram models:

Two kinds of basic variogram functions were used:

- *spherical model*:

$$\gamma(h) = \sigma^2 \left[1.5 \left(\frac{h}{r} \right) - 0.5 \left(\frac{h}{r} \right)^3 \right] \text{ for } h < r$$

$$= \sigma^2 \text{ for } h \geq r \quad (5)$$

- *exponential model*:

$$\gamma(h) = \sigma^2 \left[1 - \exp\left(-\frac{h}{r}\right) \right] \quad (6)$$

The fitted models used here are nested structure, *i.e.*, weighted sums of one or two simple models cited above. So each model is characterized by two or four parameters (σ_1^2 , σ_2^2 , r_1 , r_2). For each site and for each studied variable (RED, NIR, NDVI, LAI) one model is fitted (figure 2).

4 HETEROGENEITY CHARACTERIZATION

4.1 Vegetation type influence on spatial structure

The NDVI variograms allow to draw spatial structure differences between sites. Indeed the total sill ($\sigma_1^2 + \sigma_2^2$) value indicates the true variance and gives a first heterogeneity criterion. The Counami site (tropical forest) has the lowest sill value and is the most homogeneous site whereas the Alpilles site (crop) presents the highest value and appears as the most heterogeneous site. On the Counami site, the first structure has a very short range (70m) and accounts for most of the variance (σ_1^2 is 85% of the total sill). It can be considered that there is almost no spatial correlation after 70m. Hence it is the most spatially homogeneous site. The other sites present a first range at larger distances, between 200m and 300m. The Alpilles site and the Nezer site have patchy spatial patterns. Their first range variogram can be associated to the intra-field variability and the discontinuities

between fields. Moreover it might represent the mean size of the fields. On the one hand, on Alpilles, differences between field values is particularly high with a succession of crop field with high NDVI value and bare soil field with low NDVI values leading to a very high sill. On the other hand, Nezer presents a NDVI value distribution between fields more homogeneous leading to lower sill. Moreover the size and the shape of the fields are more regular for the Nezer site than those of the Alpilles site. This confirms Chen (1999) results, *i.e.*, the importance of accounting for contextual parameter (spatial pattern organization) to characterize spatial heterogeneity. Finally it is more difficult to characterize the second range of the model. It can represent:

- a large scale continuous phenomenon : for agricultural site like Alpilles it can be soil properties, for Puechabon the north west part presents different geomorphologic characteristics than the rest of the site.
- some image singularities: Puechabon presents a quarry at the north part of the site.

The variogram model was computed on the whole 3km*3km site without any mask. So it reflects the real spatial structure of the site including singularities like quarry, river... Variogram model do not reflect only the spatial structure of the vegetation making the site comparison more difficult. In addition some noise linked with the remote sensing chain processing can influence the variogram ranges (r_1, r_2): remaining non detected clouds, atmospheric effect, topography or view angles.

4.2 Integral range: a parameter derived from the theoretical variogram

The integral range (A) (Chiles, 1999) is a yardstick that summarizes the variogram range.

$$A = \left(\frac{1}{\sigma^2} \right) * \int_{R^2} C(h) dh = \int_{R^2} \left(1 - \frac{\gamma(h)}{\sigma^2} \right) dh \quad (7)$$

where $C(h)$ is the covariance function defined by:

$$C(h) = C(0) - \gamma(h) \quad (8)$$

By plotting the total sill of each model versus the integral range for the NDVI of each site, we can draw a first heterogeneity typology (figure 3): spatial heterogeneity increases from the tropical forest site and the pine forest site to the Mediterranean vegetation site and the agricultural site.

4.3 Variable effect on spatial structure

Figure 2 does not show important differences between NDVI spatial structure and LAI spatial

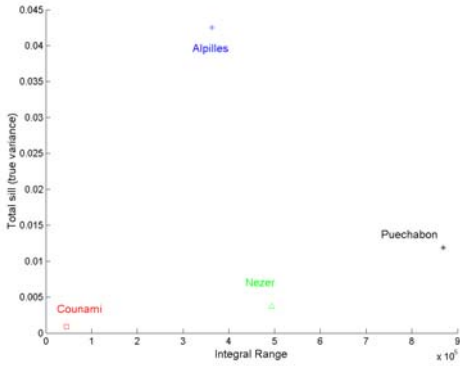


Figure 3: Integral Range versus total sill (σ^2) for NDVI variable

structure. No LAI variogram was fitted for the Counami site because of saturation problem with transfer function applied at high NDVI values. The main difference is between reflectance (NIR, RED) variables and NDVI. The first structure (r_1) is detected in both reflectance and NDVI variograms, but the level of variability (total sill) and the second range (r_2) scale differ. One of the reasons could be that NDVI characterizes the amount of surface vegetation whereas the reflectance variables are affected by several other factors. Therefore, it is more relevant to use NDVI variable to describe vegetation spatial structure.

5 SCALING EFFECT

5.1 Statistical parameters evolution with scaling

A first approach to explore scaling effect is to observe the evolution of the NDVI value distribution at different ranges of resolution. Figure 4 shows the NDVI histograms for the four sites at four resolutions: 20m, 100m, 300m, 500m. If the NDVI values were independent, standard results in statistics would show that the standard deviation of block averages would be inversely proportional to their area and that the distribution, properly standardized, would tend to a Normal distribution. However Alpilles site standard deviation decreases by 32 % from 20m resolution to 300m resolution whereas Counami site standard deviation decreases by 60 % from 20m resolution to 300m resolution. Except for Counami, the distribution shows low symmetrization with scaling up. These differences between NDVI distribution evolution

through scaling are explained by the difference between spatial autocorrelation range. Thus, to

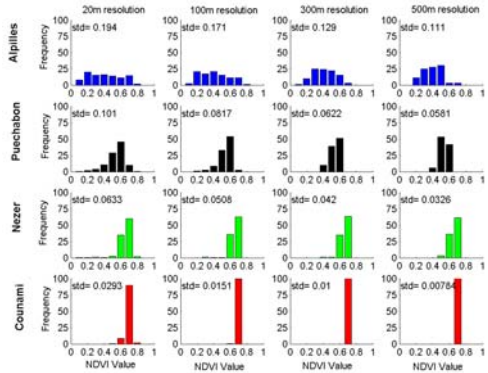


Figure 4: NDVI distribution for different sites at different resolutions

understand the scaling effect, the spatial structure has to be accounted for.

5.2 Dispersion variance

a) Dispersion Variance definition

An other way to explore the evolution of the spatial structure with resolution consists in observing the variable variance evolution of 20m SPOT pixel (x) within coarser block size (v). Calling V the entire domain image (3000m*3000m), V is decomposed in a union of n congruent subregions v ($v_1 \dots v_n$). We respectively call $Z(V)$ and $Z(v_i)$ the average variable value over V and the block v_i :

Spatial variability can be compared at three different scales (Friedl, 1997):

1. the variation of the pixel value (x) with respect to the regional average value on the whole image (V)

$$S^2(x, V) = \frac{1}{V} \sum_x (Z(x) - Z(V))^2 \quad (9)$$

\sum_x

represents the pixel sum over the whole image.

2. the variation of subregional average value (v block value) with respect to the regional average value on the whole image (V)

$$S^2(v,V)=\frac{1}{n} \sum_{i=1..n} (Z(vi)-Z(V))^2 \quad (10)$$

3. the average variation of the pixel values within block v

$$S^2(x,v)=\frac{1}{n} \sum_{i=1..n} \frac{1}{v} \sum_x (z(x)-Z(vi))^2 \quad (11)$$

$S^2(x,V)$ corresponds to the variance of the whole image, that can be seen as the variance of pixel values within blocks plus the variance of block values within the image (Krige relation, Wackernagel,1995):

$$S^2(x,V)=S^2(x,v)+S^2(v,V) \quad (12)$$

We called $S^2(x,v)$ the experimental dispersion variance of x within v. A theoretical dispersion variance can be derived from the variogram model and is obtained by taking the expectation (Wackernagel,1995):

$$\sigma^2(x,V)=E(S^2(x,V))=\sigma^2-C(v,v)=\gamma(v,v) \quad (13)$$

- b) Dispersion variance evolution with resolution

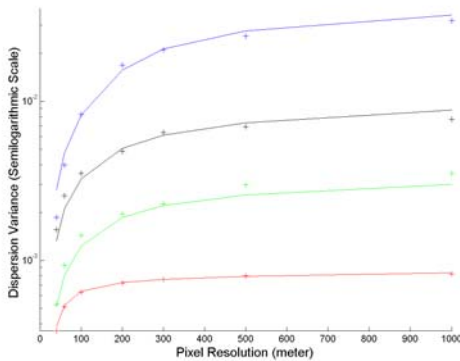


Figure 5:Dispersion Variance versus resolution

Figure 5 presents the evolution of experimental and theoretical dispersion variances versus the aggregation scale. As expected, the dispersion variance increases with the resolution. The comparison of the dispersion variance evolution with resolution for the four sites confirms the first observations made in §3 . Besides it allows to makes inferences on data regularization, *ie*, with increasing resolution, data becomes more spatially continuous which is reflected by changes in geostatistical properties (lower sill, more regular variogram at the origin, dispersion variance reaching the sill):

- Counami being the most homogeneous site, its dispersion variance reaches a sill very

rapidly: increasing the support leads to a rapid data regularization .

- The other sites do not reach a sill at 1000m resolution, meaning that no total regularization is reached at this scale, *ie*, data are still spatially autocorrelated. Alpilles is the most heterogeneous site, presenting high dispersion variance value. Puechabon site presents an important regularization at short distance.

Finally, the quite good fitting of the theoretical dispersion variance on experimental dispersion variance confirms the model fitting performances.

6 INFLUENCE OF HETEROGENEITY ON LAI ERROR ESTIMATES

The LAI variable is derived from remote sensing data by a semi empirical expression ($LAI=f(NDVI)$). However this transfer function derived from SAIL simulation is strictly valid for homogeneous surfaces. To obtain the “integrated” LAI_i value at coarser resolution, the right way consists in aggregating the LAI computed at the higher spatial resolution (20m):

$$LAI_i=f(ndvi) \quad (14)$$

However the LAI at coarse resolution can be approximated by applying the transfer function f over coarse resolution NDVI data, *ie*, for values aggregated at the coarse resolution: the “mean” LAI_i or “lumped” LAI is obtained as:

$$LAI_i=f(NDVI_i) \quad (15)$$

Where $NDVI_i$ is the integrated NDVI at coarse resolution.

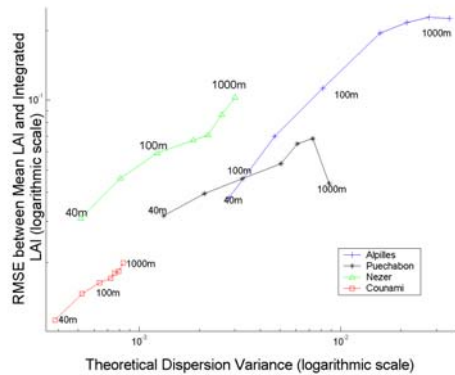


Figure 6: RMSE between integrated LAI and mean LAI versus dispersion variance .

Because of the non linearity of the transfer function an error is made in computing the lumped LAI_l. This error can be evaluated by the root mean square difference between the lumped variable and the distributed variable at a given resolution. Figure 6 presents a plot between the dispersion variance and the RMSE computed between lumped and integrated LAI for different resolutions. By increasing the resolution, the RMSE is increasing linearly with the dispersion variance in log-log scale. The four sites have RMSE ranges that increase according to their spatial heterogeneity degree confirming the spatial heterogeneity typology made on §3.2. However for the Puechabon site the RMSE value decreases at 1000 m resolution. Two hypothesis arise: On the one hand, a RMSE computed with 9 samples (at 1000m resolution) may not be statistically consistent. On the other hand, at 1000m resolution the Puechabon NDVI image is not stationary with some very homogeneous pixels and very heterogeneous pixels. Therefore since the NDVI range value changes with increasing resolution, the degree of non linearity of the transfer function is also changing and can influence the LAI error estimates. In conclusion, dispersion variance is a relevant parameter that reflects spatial heterogeneity importance at a given resolution and could be used to assess LAI error.

7 CONCLUSIONS AND PROSPECTS

Biophysical variable estimates error results from the non linearity of the transfer function and the spatial heterogeneity of the data. It will be important to account for these two features to improve biophysical variable estimate at coarse resolution. This study shows that geostatistical methodology allow to describe the spatial structure characteristics of different landscapes. By computing variograms, it is possible to make some inference on spatial heterogeneity between vegetation sites and to link the data autocorrelation with scaling issues. Dispersion variance provides an indication on the degree of heterogeneity for a given resolution. This parameter will be useful to account for spatial heterogeneity in biophysical variable estimates.

REFERENCES

- Aman, A., Randriamamantena, H P., Podaire, A., Frouin, R. (1992), Upscale Integration of Normalized Difference Vegetation Index: The Problem of Spatial Heterogeneity. *IEEE Transactions on Geoscience and Remote Sens.*, 30 (2):326-338.
- Atkinson, P.M. (1997), On estimating measurement error in remotely sensed images with the variogram. *Int. J. Remote Sens.*, 18:3075-3084.
- Baret, F. and Guyot, G., (1991), Potentials and limits of vegetation indices for LAI and APAR assessment. *Remote Sens. Environ.*, 35:161-173.
- Baret, F, Weiss, M., Garrigues, S ., Allard, D., et al., (2002), VALERI: a network of sites and a methodology for the validation of medium spatial resolution land satellite product. *Remote Sens. Environ.*, Submitted.
- Bian, L. and Walsh,, S.J. (1993), Scale dependencies of vegetation and topography in mountainous environment of Montana. *Prof. Geogr.*, 45,1.
- Bian, L. (1997), Multiscale Nature of Spatial Data in Scaling Up Environmental Models. In *Scale in Remote Sensing and GIS. Quattrochi and Goodchild Eds, Lewis Publisher, pp 13-26* .
- Cao,C. and Lam, N S. (1997), Understanding the Scale and Resolution Effects in Remote Sensing and GIS. In *Scale in Remote Sensing and GIS. Quattrochi and Goodchild Eds. Lewis Publisher, pp 57-72*.
- Chen, J.M. (1999), Spatial Scaling of a Remotely Sensed Surface Parameter by Contexture. *Remote Sens. Environ.*, 69 :30-42.
- Chilès, J.P. and Delfiner P. (1999), Geostatistics : Modeling Spatial Uncertainty. *Wiley, New-York*.
- Cressie, N. A. C. (1991), Statistics for Spatial Data, *Wiley, New York*.
- De Beaufort, L. (2000), Definition d'une méthode de cartographie d'indice foliaire destinée à la validation de produits de capteurs satellites. *Master report from ENSAR engineering school*.
- De Cola, L. (1989), Fractal analysis of a classified Lansat scene. *Photogr. Eng. Remote Sens.*, 55(5):601-610..
- Friedl, M A. (1997), Examining the effects of Sensor Resolution and Sub-Pixel Heterogeneity on Spetral Vegetation Indices: Implications for Biophysical Modeling. In *Scale in Remote Sensing and GIS., Quattrochi and Goodchild Eds., Lewis Publisher, pp 113-140* .
- Haralick, R.M. (1986), Statistical image texture analysis. In *Handbook of Pattern Recognition and Image Processing, T.Y. Yong and K.S. Fu, Eds., Academic, New York, pp 247-280*.
- Jupp, D. L. B., Strahler, A.H and Woodcock, C.E (1988a), Autocorrelation and regularization in digital images I: Basic Theory. *IEEE Trans. Geosci. Remote Sens.*, 26: 463-473.
- Jupp, D. L. B., Strahler, A.H and Woodcock, C.E (1988b). Autocorrelation and regularization in

- digital images II: Simple image models. *IEEE Trans. Geosci. Remote Sens.*, 27: 247-258.
- Mandelbrot, B. B. (1983), The fractal geometry of nature. *W.H Freeman and Company, New York*.
- Milne, B. T. and C., W. B. (1999), Multiscale Assessment of Binary and Continuous Landcover Variables for MODIS Validation, Mapping and Modelling Applications. *Remote Sens. Environ.*, 70: 82-90.
- Myers, D E. (1997), Statistical Models for Multiple-Scaled Analysis. In *Scale in Remote Sensing and GIS.*, Quattrochi and Goodchild Eds, Lewis Publisher, pp 273-294 .
- Ranchin, T. and Wald, L. (1993), The wavelet transform for the analysis of remotely sensed data. *Int. J. Remote Sens.*, 14(3) :615-619.
- Treitz, P. (2001), Variogram Analysis of High Spatial Resolution Remote Sensing Data: An Examination of Boreal Forest. *Int. J. Remote Sens.*, 22(18): 3895-3900.
- Wackernagel, H. (1995), Multivariate Geostatistics., *Springer-Verlag, Berlin, Heidelberg*, 256p.
- Weiss, M. and Baret, F. (1999), Evaluation of Canopy Biophysical Variable Retrieval Performances from the Accumulation of Large Swath Satellite Data. *Remote Sens. Environ.*, 70:293-306.
- Weiss, M., Baret, F., Leroy, M., Hauteceur, O., Bacour, C., Prevot, L., and Bruguier, N. (2002), Validation of Neural Net techniques to estimate canopy biophysical from remote sensing data. *Agronomie : Agriculture and Environnement, In press*.
- Woodcock, Strahler, Jupp (1988). The use of variograms in remote sensing: a/ scene models and simulated images b/ Real digital images. *Remote Sens. Environ.*, 25: 323-379.
- Woodcock, Strahler. (1987). The factor of Scale in remote sensing. *Remote Sens. Environ.*, 21: 311-332.
- Xia, Z-G. and Clarke, C. K. (1997) Approaches to scaling of Geo-Spatial Data. In *Scale in Remote Sensing and GIS.*, Quattrochi and Goodchild Eds, Lewis Publisher, pp 309-360.

The 3-D Scene Computer Simulation of the Field Crop Canopy

Menxin Wu¹ Qijiang Zhu¹ Lihong Su¹ Jindi Wang¹ Yueqin Xiang² Tang Shihao² Penxin Wang²

1 Beijing Key Laboratory for Remote Sensing of Environment and Digital Cities, Research Center for Remote Sensing and GIS, Dept. Geography, Beijing Normal University, 100875, Beijing, China

2 Institute of Geographical Science and Nature Resources Research, CAS, 100101, Beijing, China

E-mail: wumenxin@163.com Address: Dept. Geography, Beijing Normal University, 100875, Beijing

ABSTRACT—*The directional property of the spectrum is closely related to the spatial distribution and 3-D structure of crops in certain growth period. Based on the L-system, a new approach is developed to simulate the 3-D structure of field crop canopy. The 3-D simulation of the field crop can be divided into three processes, i.e. obtaining the data about the spatial distribution and the 3-D structure of the plant, processing the obtained data, and simulating the crop canopy. The approach for 3-D simulation of crop canopy can be used to establish an object-oriented database, which can easily produce the input file of L-system and clearly describe the structure of the plant.*

1 INTRODUCTION

Recent advances in the computer graphics have made it possible to generate images of 3-D objects on personal computer. It is technically applicable to evaluate the radiosity via relation between the 3-D structure of the objects and the electromagnetic radiation, which has become a new field in the quantitative remote sensing research on the vegetation. The research on the structure, spatial distribution and the 3-D characteristics of the vegetation has turned into an important part of the realistic structure model. In the research field, Mandelbrot discovered the self-similar characteristic of the structure of the plant and introduced the concept of the fractal to interpret the characteristic (Mandelbrot, 1972); Prusinkiewicz realized the fractal graphics on the computer screen (Prusinkiewicz, 1989); Lindermayer created the L-system, which defines a set of parallel re-writing system to describe the fractal feature of the plant in a simple way and becomes a new tool for studying the fractal of the plant. From then on, L-system has been improved from D0L to ELSYS. Now the ELSYS can be applied to generate 3-D graphics (N.S.Goel, 1991). Based on the extended L-system, a new approach is developed to simulate the realistic scene of the cropland, which connects the object-oriented program design and combines the parts of the scene.

2 OBTAINING DATA

The original properties of the cropland is composed of the following data: (1) the structure data on the plant, i.e. the property data on leaves---the leaf length and the leaf width, the property data on stem---the stem height and the stem width, and the relative location of leaves, (2) the spatial distribution of the plants, i.e. the plant distance, row distance, and the density of the plants. These property data are obtained through Kodak digital cameras and the rulers in the Luancheng Ecologic Experiment Station (LEES) of China Academy of Science (CAS), which is located in Luancheng, Hebei province, China.

3 OBJECTS COMBINING METHOD BASED ON L-SYSTEM

3.1 Objects Structure Analysis

The analysis method on farm cropland is from the whole to the parts at three levels. At the first level, the whole cropland is divided into the soil and the canopies; at the second level, the canopies are divided into separate plants; and at the third level, the plants are divided into leaves and stems whose properties are measured in fieldwork. However, the re-building of the 3-D scene is from parts to the whole, which is exactly the reverse process of the structure analysis of the cropland. The whole 3-D scene is restored by combination of those parts that can be described

accurately in mathematics on the computer screen.

3.2 Object-oriented Data Model

Since 1990's, object-oriented method and design have been widely used in system analysis. Based on the analysis on the structure of the cropland, an object-oriented data model is introduced to describe easily the process, which is from parts to the whole in re-building the 3-D structure. The idea can be realized by the abstract data type, which is provided by C++ language. The scattered data obtained will be organized and become the data of a specific subject. The object-oriented data has its own claimed advantages: encapsulation, inherit, polymorphism. the space facet is defined as the most basic spatial component unit, which other complex structures are based on, in the process of re-building the 3-D cropland scene. Applying the abstract data type, the data structure of the plant is expressed as the following:

```
class Plant
{
public:
    int leafnum;
    Leaf lf[LEAFCOUNT];
    Stem stm;
public:
    Plant();
    ~Plant();
    int plantproduce();
};
```

According to the above construct process, it is concluded that the next object is combined based on the combination of the previous objects (class Leaf and class Stem). The object-oriented data model is able to connect the data in different levels into a whole, which is expressed as the property of objects at different levels. The abstract data type is easily expanded and managed. The plant has some member functions that can executive the operation on the data.

3.3 ELSYS and Simulation of the cropland scene

L-system is a special program language, which has two particular features: parallel re-writing and graphics interpretation of the string. Once the strings are produced, the graphics can be generated. In ELSYS turtle state is represented by a quintuplet (P, H, L, U, c). The turtle can move from one location to another, and can also rotate around any of the three vectors defining its orientation. The turtle's movement is the graphics in 3-D space (N.S.Goel, 1991).

In fact, one will find it very complex in that its source code will have to be repeated many times if one wants to generate a none-fractal feature plant with direct L-system source code. Based on the design idea and input file format of ELYS, a new program is developed to generate L-system source code with application of object-oriented program technology.

Two object-oriented databases are designed in order to save the structure data and the spectrum data of the

leaf, the stem, the soil .etc. One C++ program module obtains these data then makes some small lsy-format files, the other module combines these generated lsy-format files, which correspond the different components of the plant respectively, into a integrated lsy-format file of the plant. The program produces an output, which is exactly the input of ELSYS. Thus, the original data can be directly processed to the necessary format and the 3-D structure can be easily obtained and displayed in ELSYS graphic model. According to the above the process, 3-D structure of corn field in different growth period is simulated in ELSYS. The result is in the appendix at the end of the paper.

4 THE RADIATION REGIME AND THE APPLICATION OF THE 3-D SIMULATION

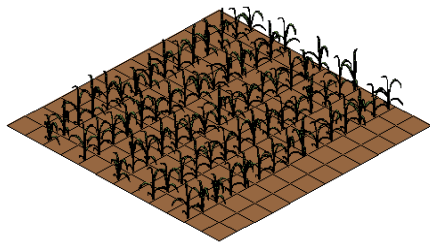
3-D simulation is the previous work of calculation of the BRF and the albedo. The radiation regime of a canopy can be described through the radiosity among the space facets. After the generation of the field crop canopy is accomplished, the visibility of a facet by sun or the viewer should be determined. Considering the multiple scattering among the facets, the visibility of one facet for another facet should be determined. DIANA model has brought up the algorithms for evaluating the visibilities. The radiosity of every facet can be expressed as:

$$B_i = E_i + \rho_i \sum_{j=1}^N B_j F_{ij} + \tau_i \sum_{k=1}^N B_k T_{ik} \quad (1)$$

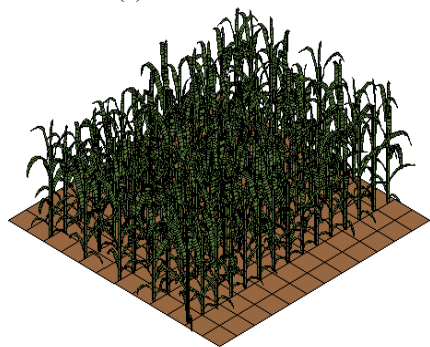
Where N is the number of the facets, ρ_i is the reflectance of the facet, B_i (B_j , B_k) is the flux density of the facet i (j , k), τ_i is the transmittance of the facet i , F_{ij} is the form factor between the facet i and the facet j . T_{ik} is the form factor between the backside of the facet i and the facet k . Through solving radiosity equations of the N facets, BRF and albedo expressions can be evaluated. Thus, the relation between the radiation regime and the 3-D structure is described by the mathematic formula accurately.

5 CONCLUSIONS AND DISCUSSION

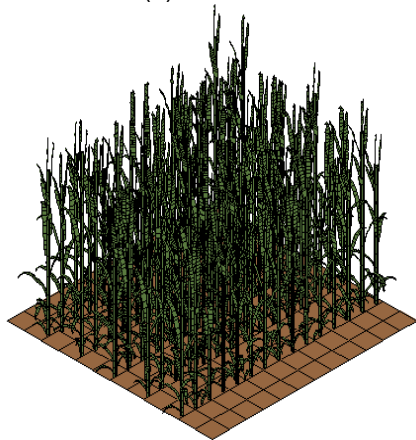
The approach applies more advanced design ideas and can generate the field crop canopy more effectively. It provides a method which is able to connect object-oriented program technology with ELSYS. It is a way to develop ELSYS further in order to make the simulation process easier. If a more realistic scene is expected, the further work will be done on illumination model, measure methods, and program optimization. The radiation regime based on the 3-D structure simulation will be further studied for universality and simplicity.



(a) $H=52\text{cm}$ $LAI=0.8$



(b) $H=124\text{cm}$ $LAI=3.2$



(c) $H=202\text{cm}$ $LAI=4.6$

Fig.1 the image on corn cropland scene in different growth period

6 ACKNOWLEDGMENTS

Subsidized by the Special Funds for Major State Basic Research Project (G20000779). Project supported by the National Natural Science Foundation of China (40171068). Project Subsidized by the National High Technology Research and Development program (2001AA131030).

We acknowledge the assistance of Wenhan, Qin in NASA.

REFERENCES

- N. S. Goel, Ivan Rozemal, Richard L. Thompson, 1991, A Computer Graphics Based Model for Scattering from Objects of Arbitrary Shapes in the Optical Region .Remote Sensing of Environment 36,73-104
- N. S. Goel, I. ROzehnal, 1992, A High Level Language for L-systems and Its Applications, New York Spring-verlag.
- Lihong Su, Xiaowen Li, and Jindi Wang, 2000, L System and 3D Landscape Graphics, *Computer Applications*, Vol.20, No.2, 1-4p.
- Przemyslaw Prusinkiewicz, Aristid Lindenmayer, 1991, Lindenmayer□System ,Fractals, and Plants. New York. Spring-verlag.
- Przemyslaw Prusinkiewicz, Aristid Lindenmayer, 1991, The Algorithmic Beauty of Plants. New York Spring-verlag.
- B.B.Mandelbrot, 1982, The fractal geometry of nature, W.H.Freeman, San Francisco

Validating LAI Using Hyperspectral Imagery Over Agricultural Canopies

Anna Pacheco^{1*}, Abdou Bannari¹, Karl Staenz², Heather McNairn² and Jean-Claude Deguise²

¹*Remote Sensing and Geomatics of Environment Laboratory, Department of Geography, University of Ottawa, P.O. Box 450, Stn. A, Ottawa (Ontario), Canada, K1N 6N5.*

²*Canada Centre for Remote Sensing, Natural Resources Canada, 588 Booth St., Ottawa (Ontario), Canada, K1A 0Y7.*

*corresponding author: anna.pacheco@ccrs.nrcan.gc.ca

ABSTRACT *Hyperspectral remote sensing has gone through rapid development over the past two decades and interest is growing in the application of hyperspectral data to precision farming. Defined as one half the total green leaf area per unit ground surface area, Leaf Area Index (LAI) is a key parameter controlling biophysical processes of the vegetation canopy. LAI can be estimated using different approaches but only hyperspectral remote sensing has the potential to distinguish effectively the crop from other field components. The objective of this study is to validate eLAI estimation of agricultural canopies from Probe-1 airborne hyperspectral data acquired over two agricultural sites in Canada, near Clinton (Ontario) and Indian Head (Saskatchewan) during the growing seasons of 1999 and 2000, respectively. Using the LAI-2000 (LI-COR), ground eLAI measurements were collected simultaneously to the image acquisitions on various crops (corn, white beans, wheat, canola and peas). Preliminary results indicate that hyperspectral data was sensitive to variability in ground eLAI values from different canopies and demonstrates encouraging results for future analysis.*

1 INTRODUCTION

Hyperspectral remote sensing has gone through rapid development over the past two decades and interest is growing in its application to precision farming. However, crop growth is very dynamic and monitoring the condition of agricultural crops is challenging. Leaf Area Index (LAI) is a key parameter used to assess biophysical processes of the vegetation canopy. Defined as one half the total green leaf area per unit ground surface area (Chen and Black, 1992), LAI is used to describe the percentage of vegetation cover and to estimate productivity or yield of the vegetation canopies. LAI can be estimated using different approaches such as destructive sampling, optical ground-based instruments and optical remote sensing imagery. The techniques associated with multispectral data consider the total amount of the vegetation canopy to estimate LAI. Within this context, it is essential for agricultural applications to distinguish the crop from the other vegetation such as weeds or volunteer crops present in a pixel in order to estimate a more accurate LAI. Hyperspectral data has the

advantage of discriminating different target materials within a pixel using spectral unmixing analysis.

The objective of this study is to validate LAI estimation of agricultural canopies using hyperspectral imagery in the context of precision farming. More specifically, this research paper will investigate the correlation between ground eLAI measurements estimated with the LAI-2000 (LI-COR), an optical instrument often used to measure LAI in agricultural and forest canopies, and eLAI values derived from hyperspectral imagery. As a result, a model developed by Staenz *et al.* (2002) for the estimation of LAI using hyperspectral data will be tested on various agricultural crops (white beans, corn, wheat, canola and peas). This model requires the input of crop endmember fractions, which are derived from spectral unmixing. This technique is successfully used in geological and environmental applications (Staenz *et al.*, 2000; Lévesque *et al.*, 2000; Nadeau, 2002) but has not been rigorously validated for agricultural applications. This study will also examine the potential of spectral unmixing to determine percent crop cover estimates on a crop-by-crop basis.

2 MATERIAL AND METHODS

LAI data and airborne hyperspectral imagery were acquired from two agricultural sites in Canada characterized by various crop types and site conditions. Field campaigns were carried out during the growing seasons in Clinton, Ontario (43° 40' N, 81° 30' W) in 1999 and in Indian Head, Saskatchewan (50° 33' N, 103° 36' W) in 2000.

At the Clinton site, six fields were chosen for ground validation measurements: three white bean (*Phaseolus vulgaris* L.) and three corn (*Zea mais* L.) fields. Surface cover in these fields included crop vegetation, residue from the previous crop and soil. In order to facilitate spectral unmixing analysis of the hyperspectral imagery, 20 m by 20 m pure patches of double seeded crop, soil and residue were established in some of the fields at the beginning of the season.

For the Indian Head site, fields used for ground validation purposes were located on the precision agricultural test farm of the Indian Head Agricultural Research Foundation (IHARF). Eight fields were selected for intense sampling: four wheat (*Triticum aestivum* L.), two canola (*Brassica napus* L.) and two pea (*Lathyrus aphaca* L.) fields. Crop vegetation, residue and soil constituted ground surface coverage for these fields. Similarly to the Clinton site, crop patches were selected within the aforementioned fields while soil and residue patches were established in an adjacent field.

Ground-based measurements and hyperspectral airborne data were acquired within a week to ensure both data sets were analogous for validation purposes. Between 9 and 13 sampling sites were selected per field in order to reflect within-field variability. These sites were chosen based on elevation and soil maps.

2.1 Ground Data Collection

Ground LAI measurements were collected using the LAI-2000 (Plant Canopy Analyser, LI-COR) which estimates LAI as a function of incoming diffuse solar radiation at the top and at the bottom of the vegetation canopy. These estimates were made at five zenith angles (7°, 23°, 38°, 56° and 68°) simultaneously (LI-COR, 1990). Therefore, the LAI-2000 was utilized during overcast conditions only. It is also important to consider that the instrument measures the effective LAI (eLAI) by making the assumption of a random spatial distribution of leaves (Chen and Cihlar, 1995). However, regular and equal spacing of crop plants in agricultural canopies reduces this effect considerably.

Three eLAI measurements were taken at each sampling site to minimise errors and thus, provide a representative eLAI average of the area.

Measurements were acquired along 2 m diagonal transects between two plant rows within an area of 2 to 3 m surrounding the centre of the sampling site. For each set of measurements, one reference was taken above the crop canopy and four measurements were acquired below. Five canopy transmittance values are then calculated from the five zenith angles of the optical sensor, which are utilised to determine foliage amount and orientation.

Percent ground cover was calculated from vertical photographs taken with a 35-mm camera equipped with a 28-mm lens. The camera was mounted on an overhead mast at a height of 2 m above ground. In this configuration, the camera viewed a ground area of approximately 4 m². Photographs were taken 3 to 4 m from the centre of the sample site locations. Three photographs were taken at each sampling site in order to obtain percent ground cover representative of the area covered by one hyperspectral imagery pixel.

2.2 Image Data Acquisition and Preprocessing

Airborne hyperspectral Probe-1 (Earth Search Sciences Inc., 2001) imagery were acquired on July 7, 1999 and on June 28, 2000 for the Clinton and the Indian Head test sites respectively. The Probe-1 is a "whiskbroom style" instrument that collects data in a cross-track direction by mechanical scanning and in an along-track direction by movement of the airborne platform. This sensor collects upwelling radiance from 128 bands in the visible and near infra-red (VNIR) and short-wave infra-red (SWIR) wavelength regions from 437.9 nm to 2056.7 nm almost continuously. The bandwidths at full width of half maximum (FWHM) varies from 13.3 nm to 22.3 nm with a spectral sampling interval of 10.7 nm to 19.8 nm. The aircraft was flown at an altitude of 2500 m above ground resulting in a swath width of 2.56 km (512 pixels) and a spatial resolution of 5 m at nadir.

The Probe-1 sensor was mounted on an active 3-axis gyro-stabilized real-time motion compensation system. A non-differential GPS was recording the location of the aircraft during the flight but no attitude measurements were made. To preserve the spectral integrity of each pixel in the imagery, no geometric correction of the Probe-1 data was made. A reversed image-to-image registration process was used to locate the Probe-1 pixels where ground samples were acquired. During the field campaign, all sampling site locations were accurately measured with a differential GPS unit. The position of these sites were digitally marked on a series of aerial ortho-photos of the area for the Clinton dataset and on a panchromatic ortho-rectified Ikonos image for the Indian Head site. The marked ortho-photos and the ortho-rectified Ikonos image were then registered using a polynomial fit to

the Probe-1 imagery. The pixel-line locations of the sampling site markers on the Probe-1 imagery were relocated by this reverse process and used for the correlations between the crop fractions and eLAI values derived from the hyperspectral data and the percent crop cover and ground eLAI measurements presented in this paper.

Image preprocessing was carried out using the Imaging Spectrometer Data Analysis System (ISDAS), a software package developed at the Canada Centre for Remote Sensing utilized for hyperspectral data processing and analysis (Staenz *et al.*, 1998). The Probe-1 raw digital numbers (DN) were first radiometrically calibrated using a reflectance-based vicarious calibration technique (Secker *et al.*, 2001). Reflectance spectra from a uniform target were acquired with a GER-3700 field spectroradiometer and used with this technique to generate a new set of gains to convert the DNs to radiance. A bare soil patch was selected as such a target for the Clinton site while an asphalt area was employed for the Indian Head site. These recalibrated radiance data were then converted to reflectance using the surface reflectance retrieval procedure implemented in ISDAS (Staenz and Williams, 1997).

3 ANALYSIS APPROACH

The vertical ground photographs were digitised in three channels (blue, green and red) and processed with PCI ImageWorks (PCI Geomatics, 1997) for classification purposes. An unsupervised classification was carried out using ten classes: three classes for soil, three for leaf cover, two for residue, one for soil shadow, and one for leaf shadow. These classes were then aggregated to form three major components: leaf, residue and soil cover. Once the classification was completed, percentages of leaf, soil and residue cover were determined for each photograph and averaged per sampling site to finally determine the percent ground cover.

Constrained linear spectral unmixing was performed on the hyperspectral data using an algorithm implemented in ISDAS (Staenz *et al.*, 1998). Endmember spectra were selected and manually extracted from the reflectance image data based on knowledge of the fields. For the Clinton data set, these spectra were extracted from the pure patches created intentionally for the purpose of endmember selection and from specific areas of the fields where there is a high pixel purity level. Crop density patches were not “pure” but did constitute about 80 % crop cover and the residue patch did contain a small amount of green grass. However, soil patches were 100 % soil. For the Indian Head site, only the soil patch was used for endmember extraction. Crop endmember spectra were retrieved from the fields where high crop

density had been identified and the residue endmember spectra was extracted from a very dense residue patch identified on one of the fields.

Spectral unmixing was conducted on the Probe-1 data using the full spectral range. For the Clinton site, only three endmembers categories were used to unmix the hyperspectral cube: crop vegetation according to the crop type of the field, soil and residue. For the Indian Head site, all fields are at the same location and thus, five endmembers were used to perform spectral unmixing on all fields at once: wheat, canola, pea, soil and residue. As a result, fraction maps of these endmembers were then derived from the hyperspectral Probe-1 data.

The eLAI values were estimated from the hyperspectral data using an algorithm implemented in ISDAS (Staenz *et al.*, 2002). Crop fractions from each of the fields were used as input to generate eLAI maps. eLAI can be calculated as follows (Ross, 1981):

$$eLAI = \frac{\cos \alpha}{G} (-\ln P), \quad (1)$$

where P is the probability of a beam of radiation at an incidence angle α passing through a horizontally uniform plant canopy with random leaf angular and spatial distribution and G is the mean projection coefficient of unit foliage area on a plane perpendicular to α .

To estimate eLAI from hyperspectral data, G (α) can be determined at 0.5 for plants, which have randomly distributed leaf angles such as agricultural crops (Norman, 1979). The incidence angle α corresponds to the sensor viewing zenith angle. Probe-1 is usually flown at a view angle of 0° (nadir looking). Also, P represents the gap (non-vegetation) fraction, which is determined by spectral unmixing as follows:

$$P = 1 - f_c, \quad (2)$$

where f_c is the fraction of the crop endmember. eLAI is then derived from hyperspectral data according to the following formula:

$$eLAI(f_c) = -2 \ln(1 - f_c). \quad (3)$$

For each sampling site, eLAI values were estimated from the hyperspectral imagery using a 3-by-3 pixel window average centred on the sampling site locations. Correlations were generated between the

eLAI estimates from the hyperspectral data and the ground eLAI measurement acquired with the LAI-2000.

4 RESULTS AND DISCUSSION

Results from both sets of correlations (percent crop cover versus crop fractions derived from the hyperspectral data and ground eLAI measurements versus Probe-1 eLAI values) are presented in Table 1. Correlation coefficients were calculated for each crop type and on pooled data from all crops. Correlations were not computed on a field-by-field basis since the number of sample points was too small and variability in eLAI values within a field was almost non-existent.

Correlation Coefficients (r)*		
Crop Canopies	Percent Crop Cover vs Crop Fractions	LAI-2000 eLAI Values vs Probe-1 eLAI Values
All Crops	0.728	0.690
Corn	0.696	0.695
White Beans	0.743	0.161
Wheat	0.741	0.597
Canola	0.875	0.568
Peas	0.645	0.589

* All correlations were significant at a probability level of <0.05.

Table 1: Correlation coefficients between percent crop cover and LAI-2000 eLAI values and crop fractions and eLAI values derived from hyperspectral Probe-1 data.

A good correlation was found between the Probe-1 derived crop fraction, and the percent crop cover acquired during the Clinton and Indian Head field campaigns. A correlation coefficient (R-value) of 0.728 was achieved when the crop fractions derived from spectral unmixing were regressed against percent crop cover calculated from the photographs. When correlations are examined on a crop specific level, correlations differ significantly from one crop to another. Overall, crop fractions were all positively correlated with the percent crop cover. Hence, these results indicate that spectral unmixing has the potential to provide information on the extent of crop ground cover. Although correlations are significant, it is clear that some variability is still unexplained. Spectral reflectance from 3-dimensional targets like crop canopies is also dependent upon canopy architecture. Thus, further analysis is planned utilizing more detailed crop measurements such as canopy architecture properties. The unexplained variance could also be related to limitations in the endmember

selection, and this requires further investigation. Endmembers were selected from double seeded patches or high-density areas of crop that were not exactly "pure".

As for the relationship between ground eLAI and eLAI derived from hyperspectral data, a correlation coefficient of 0.690 was found for all the data of both field campaigns. Similarly to the crop fractions and percent crop cover relationships, correlations vary considerably when they are observed at a crop specific level. Correlation coefficient for the white bean crops is low. This can be explained by the difference of growth stage between the corn and the white beans at the time of the Clinton field campaign. The white bean fields were not well developed and large gaps existed between the plant rows and between each of the plants along a row. Furthermore, plants were very small in certain areas of the fields, plant height was no more than 15 cm. Thus, errors might have occurred when ground eLAI measurements were acquired with the LAI-2000. In fact, it was noted that the standard error of the eLAI (SEL) values were considerably higher for white beans than for the rest of the crops. Furthermore, all limitations found in the spectral unmixing analysis process are carried to the eLAI estimation since the crop fraction is used as input to the eLAI algorithm.

Following a more precise examination of the regression plot for the eLAI Probe-1 values and the LAI-2000 eLAI values (Figure 2), it can be noticed that eLAI values derived from remote sensing data overestimate eLAI measured with the LAI-2000 instrument. The range of eLAI values is also greater for eLAI estimated from hyperspectral data than from the LAI-2000. Further investigation is necessary in order to improve the understanding of eLAI estimation from hyperspectral data. Nevertheless, preliminary results are very encouraging and this study demonstrates a large potential for the application of hyperspectral remote sensing to LAI estimation in agricultural crops.

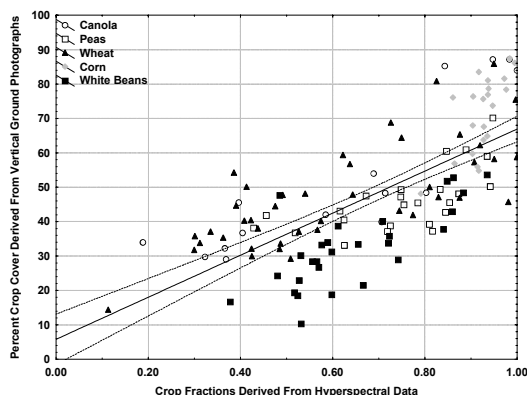


Figure 1: Correlation plot between percent crop cover calculated from vertical ground photographs and crop fractions derived from hyperspectral Probe-1 data.

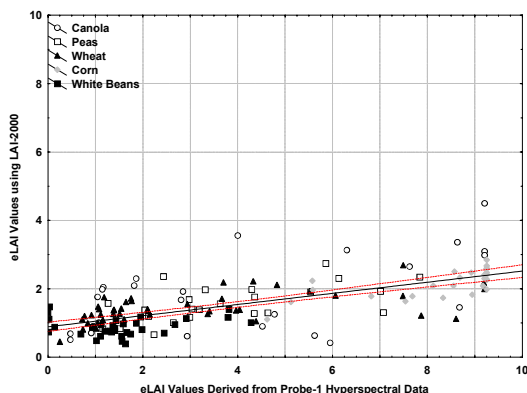


Figure 2: Correlation plot between ground eLAI values measured with the LAI-2000 and eLAI values derived from hyperspectral Probe-1 data.

5 CONCLUSIONS

Probe-1 hyperspectral data were acquired over the Clinton (Ontario) and the Indian Head (Saskatchewan) agricultural sites in 1999 and 2000, respectively. Various crops were used for the investigation: corn, white beans, wheat, canola and peas. Simultaneously to the Probe-1 acquisition, percent crop cover was derived from vertical ground photographs and eLAI measurements were taken using the LAI-2000 instrument. Crop fractions were generated using spectral unmixing analysis, which in turn, were used as input to the eLAI estimation. Validation of these map products using ground data indicated that crop fractions derived from spectral unmixing were correlated with percent crop cover. LAI-2000 eLAI and eLAI values estimated from the hyperspectral data also demonstrated a fair correlation. Thus, hyperspectral data was sensitive to variability in percent crop cover and ground eLAI values for different crop types and illustrates encouraging results for future analysis.

6 ACKNOWLEDGMENTS

The authors would like to thank Robin Smith from Woodroffe High School in Ottawa, for classifying all the ground cover photos and calculating the classification statistics for the Indian Head data set. Special thanks to Robert Hitchcock of Prologic Systems Ltd. for performing the atmospheric correction of the Probe-1 data. Thanks also goes to Jeff Secker of DRDC and Christian Nadeau of MDA

for implementing the eLAI algorithm module in ISDAS.

7 REFERENCES

- Chen, J.M. and Black, T.A., 1992, Defining Leaf Area Index for Nonflat Leaves. *Plant Cell Environment*, **13**, 2565-2581.
- Chen, J.M. and Cihlar, J., 1995, Plant Canopy Gap-Size Analysis: Theory for Improving Optical Measurements of Leaf Area Index. *Applied Optics*, **34** (27), 6211-6222.
- Earth Search Sciences Inc., 2001, About Probe-1. www.earthsearch.com/technology.
- LI-COR, 1992, LAI-2000 Plant Canopy Analyzer - Instruction Manual. LI-COR, Lincoln, Nebraska.
- Lévesque, J., Staenz, K. and Szeredi, T., 2000, The Impact of Spectral Band Characteristics on Unmixing of *casi* Data for Monitoring Mine Tailings Site Rehabilitation. *Canadian Journal of Remote Sensing*, **26**(3), 231-240.
- Nadeau, C., Neville R.A., Staenz K., O'Neill N.T., and Royer A., 2002, Atmospheric Effects on the Classification of Surface Minerals in an Arid Region Using SWIR Hyperspectral Imagery and a Spectral Unmixing Technique. *Canadian Journal of Remote Sensing* (in press).
- Norman, J.M., 1979, Modelling the Complete Crop Canopy. In Int. B.J. Barfield and J.F. Gerber (Editors), Modification of the Aerial Environment of Plants, *American Society of Agricultural Engineers*, St. Joseph, Michigan, pp. 249-277.
- PCI Geomatics, 1998. Using PCI Software, Version 6.3, PCI Geomatics: Richmond Hill, Ontario, 990 pages.
- Staenz, K. and Williams D.J., 1997, Retrieval of Surface Reflectance from Hyperspectral Data Using a Look-Up Table Approach. *Canadian Journal of Remote Sensing*, **23**(4), 354-368.
- Ross, J., 1981, The Radiation Regime and Architecture of Plant Stands, *Dr. W. Junk Publishers*.

- Secker, J., Staenz, K., Gauthier, R.P. and Budkewitsch, P., 2001, Vicarious Calibration of Airborne Hyperspectral Sensors in Operational Environments. *Remote Sensing of Environment*, **76**, 81-92.
- Staenz, K., Szeredi, T. and Schwarz, J., 1998, ISDAS - A System for Processing/Analyzing Hyperspectral Data, Technical Note. *Canadian Journal of Remote Sensing*, **24**(2), 99-113.
- Staenz, K., Nadeau, C., Secker, J. and Budkewitsch, P., 2000, Spectral Unmixing Applied to Vegetated Environments in the Canadian Arctic for Mineral Mapping. *Proceedings of XIX ISPRS Congress*, Amsterdam, The Netherlands, July 15-23, 8 p.
- Staenz, K., Deguise, J.-C., Chen, J.M. and McNairn, H., 2001, Estimation of Leaf Area Index (LAI) from Crop Fraction Using Hyperspectral Data (*submitted to the Canadian Journal of Remote Sensing*).

Potential of Getis Statistics to Characterize the Radiometric Spatial Uniformity and Temporal Stability of Test Sites Used for the Calibration of Earth Observation Sensors

A. Bannari ¹, K. Omari ¹, P.M. Teillet ^{1,2} and G. Fedosejevs ²

¹ Remote Sensing and Geomatics of Environment Laboratory, Department of Geography, University of Ottawa, Box 450, Stn. A, Ottawa (Ontario) K1N 6N5, Phone (613) 562-5800 (extension 1042), Fax (613) 562-5145

² Canada Centre for Remote Sensing, 588 Booth Street, Ottawa (Ontario) K1A 0Y7
Email: abannari@uottawa.ca

ABSTRACT - The calibration of airborne and satellite remote sensing sensors is a fundamental step for the rigorous validation of products derived from satellite data. Because of the inaccessibility of Earth observation satellites on orbit, the direct calibration method based on a test site with ground reference data is often considered necessary. However, the problem of radiometric spatial uniformity and temporal stability of test sites constitutes an important issue in the precision achieved in calibration operations and the long-term characterization of satellite sensor radiometry. Generally, the coefficient of variation and semi-variograms are the most widely used tools for evaluating the radiometric temporal uniformity of a calibration site. In this study, we analyze for the first time the potential of Getis statistics compared to the coefficient of variation for the study of the radiometric spatial uniformity and temporal stability of the Lunar Lake Playa, Nevada (LLPN) test site. The results obtained show the potential and the importance of the synergy generated by these two methods for analyzing the radiometric temporal stability of the LLPN site. Getis statistics provide an excellent spatial analysis of the site while the coefficient of variation provides complementary information on the temporal evolution of the site.

1. INTRODUCTION

During the last three decades, the demand for remote sensing products has increased tremendously, particularly for the management of natural resources and more generally for the environment. Digital remote sensing images are largely used in the areas of forestry, agriculture, meteorology, hydrology, geology, urban studies, etc. Moreover, the surveillance of the Earth's environment at the local, regional, continental or global scale using various sensors requires adequate radiometric calibration in order to have precise and reproducible geophysical and biophysical surveys through time. However, if the radiometric data are exploited in their raw form, changes in sensor response can incorrectly be attributed to changes in the geophysical and biophysical elements in the scenes under consideration (Bannari *et al.*, 1999). Consequently, gross errors can spread through all subsequent image processing operations, including vegetation indices, the designing and analysis of mosaics, spatial and multitemporal analyses,

classification techniques, etc. (Price, 1987; Teillet, 1994). For example, independently from the type of sensor used, the Normalized Difference Vegetation Index (NDVI) is the most widely used remote sensing index for the assessment of vegetation covers, the prediction of agricultural crop yields and the mapping of changes in the land cover. The index can vary considerably if the data are not calibrated radiometrically. The error introduced into the NDVI without radiometric sensor calibration can be on the order of 50 % (Goward *et al.*, 1991; Gutman, 1991). According to Teillet (1994), the NDVI extracted from AVHRR images increases by approximately 32% following absolute radiometric sensor calibration, where AVHRR is the Advanced Very High Resolution Radiometer that has flown repeatedly on a series of satellites by the U.S. National Oceanic and Atmospheric Administration (NOAA). However, to get the maximum from satellite and airborne data derived products, sensors must constantly be calibrated, the data validated, and the stability and quality of data ensured (Teillet *et al.*, 1997; Asrar, 1995).

In general, the calibration of instruments dedicated to Earth observation is not an easy task. To increase the accuracy of this operation, it is advisable to use several independent methods (Teillet *et al.*, 1990; Henry *et al.*, 1993). Different methods have been used for the relative and absolute calibration of optical sensors: calibration in laboratory before launch in a well controlled environment; on-board calibration using a lamp, a sphere, a solar diffusion panel or a solar sensor; calibration through Moon viewing; calibration using ground sites with simultaneous ground reference data; calibration using pseudo-invariant ground sites without ground reference data, inter-instrument and inter-band calibration (Dingirard and Slater, 1999; Slater *et al.*, 1987; Teillet *et al.*, 1990; Gu, 1991). Because of the inaccessibility of the satellite on orbit, the direct calibration method based on a ground site using simultaneous ground reference data is often considered a necessary step to ensure the best “accuracy versus investment” compromise (Slater *et al.* 1987; Gu, 1991). It is used successfully by NASA and the Centre national d'études spatiales (CNES), France, for the calibration of sensors such as Landsat TM (Thematic Mapper) and SPOT (Satellite Probatoire d'Observation de la Terre) HRV (Haute Résolution dans le Visible). The method has the advantage of reproducing the real conditions of image data acquisition. Its accuracy depends closely on the radiometric stability of the calibration site, the precise determination of the mean site reflectance and the accuracy of the atmospheric parameters measured at the time of image acquisition. In the best conditions of site and measurement stability, it ensures a calibration accuracy of $\pm 3\%$ (Dingirard and Slater, 1999).

Calibration sites are never chosen randomly and to be adequate they must satisfy a certain number of criteria (Slater, 1984; Slater *et al.*, 1987 et 1996; Leroy, 1990; Teillet *et al.*, 1997; Scott *et al.*, 1996). According to the literature, many test sites are used for the direct calibration of satellite and airborne sensors. The most popular sites are the alkali flats of the gypsum desert at White Sands in New Mexico (USA) (Slater *et al.*, 1987), the La Crau site in southern France (Gu, 1991; Santer *et al.*, 1992), and the Lunar Lake Playa and Railroad Valley Playa sites in central Nevada (USA) (Teillet *et al.*, 1995; Shepard *et al.*, 1991; Scott *et al.*, 1996).

Recently, new sites have been investigated, such as the Newell County Rangeland site in Alberta, Canada (Teillet *et al.*, 1997; Teillet *et al.*, 2001; Omari *et al.*, 2001), the Dunhuang site in Gansu province in China (Wu *et al.*, 1997), the Tinga Tingana site in the Strzelecki desert in south Australia, and the Uyuni Salt Flats site in Bolivia (Omari *et al.*, 2000). Other sites such as the Sonora site in north-west Mexico (Whitlock *et al.*, 1987), the desert sites of North Africa and the Arabian Peninsula have also been used for sensor calibration operations (Cosnefroy *et al.*, 1993 et 1996; Delphin *et al.*, 1991). However, the problems of radiometric spatial uniformity and temporal stability of test sites are very important for the calibration, inter-calibration and the long-term radiometric control of satellite sensor data. Evidently, each of these sites shows strengths and weaknesses (temporal stability, atmospheric stability, spectral stability and spatial homogeneity), which explains the existence of many sites. The problems affecting the optical properties and the radiometric stability of a test site are due to different factors such as site surface moisture variations and the capture of water in the upper surface layers, the presence of lichens and pebbles of different sizes, the presence of vegetation causing spectral variations, variations in the topography generating shade effects, the drying of the surface that transforms the landscape into squares of various sizes with fissures that trap light, the non-Lambertian character of the surface increasing bidirectional reflectance effects as well as atmospheric instability inducing important temporal variations (Slater, 1984; Slater *et al.*, 1987; Frouin et Gautier 1987; Markham *et al.*, 1990; Leroy, 1990; Thome *et al.*, 1993; Wheeler *et al.*, 1994; Teillet *et al.*, 1997; Scott *et al.*, 1996).

The references indicate that scientists often address the problems related to the analysis of the temporal variability of orbital sensor radiometry. However, although the analysis of the spatial uniformity and temporal stability of test site radiometry is fundamental, investigations of this problem are rare. In the framework of this study, we carried out such an analysis for the Lunar Lake Playa, Nevada (LLPN) site, often used for the calibration of satellite sensors with medium to high spatial resolutions. Generally, the coefficient of variation

and semi-variograms are the most widely used tools for evaluating the radiometric temporal uniformity of a calibration site. In this study, we analyze for the first time the potential of Getis statistics as compared to the coefficient of variation for the study of test site temporal uniformity. Towards this objective, Getis statistics and the coefficient of variation were programmed in relation to different window sizes varying from 3×3 to 9×9 pixels. Three SPOT HRV multispectral images acquired over the LLPN test site in 1997 and 1998 were used.

2. MATERIALS AND METHODS

2.1. Getis statistics

Spatial autocorrelation can be defined as the degree of dependence between the values of the same variable “X” associated with locations “j” close to each other (Derksen *et al.*, 1998). The measurement of this parameter requires taking into consideration both its location and the data attributed to it (Goodchild, 1986). In the case of image processing in remote sensing, locations “j” are the pixel coordinates and the attributed data “X” are the digital counts (DC) (Wulder, 1998). Remote sensing images portray landscapes in regularly spaced grids with cells of the same size, i.e., pixels (Fisher, 1987). It can be expected that pixels from similar land covers will generate clusters in image feature space that differ in intensity from pixel clusters from other land cover types. This clustering translates into a positive spatial auto-correlation when we have a cluster of similar DCs and a negative auto-correlation when we have a cluster of dissimilar values (Derksen *et al.*, 1998).

Spatial auto-correlation can be measured by using global or local statistics. Global indicators provide one single measurement summarizing all the spatial inter-relations of the entire study area. This measure can be of reduced reliability if the nature and the extent of the spatial auto-correlation vary significantly over the image. The LISA indicators (Local Indicators of Spatial Association) were developed by Anselin (1995) to find the discrete spatial regimes that are undetectable using global indicators (Wulder, 1998). LISA values are a measure of the extent

and nature of the concentration of DCs for a limited area within the entire study area (Wulder and Boots, 1998). Among these local indicators, there are the *Getis* statistics that come in two versions (Getis and Ord, 1992; Ord and Getis, 1995). The first version, denoted G_i , excludes the digital count attributed to the pixel “i” from the local sum while this value is included in the second version, denoted G_i^* . The latter is the most appropriate for remote sensing applications because it permits the calculation of statistics based on a user defined window size (Wulder and Boots, 1998). Recently, Wulder and Boots (2001) have shown that these statistics can be applied successfully to the digital analysis of Landsat TM images acquired over a forest cover presenting a mixture of different species. The potential of the method was clearly demonstrated for extracting information concerning the spatial structure of the forest cover and locating the different species. Moreover, by exploiting *Getis* statistics and image data acquired by the SSM/I sensor (Special Sensor Microwave/Imager) over snow-covered prairies, Derksen *et al.* (1998) identified the dominant configurations of the clusters and the influence of the latter on atmospheric circulation.

Getis statistics are defined as follows (Ord and Getis, 1995):

$$G_i^*(d) = \frac{\sum_j w_{ij}(d)x_j - W_i^* \bar{x}}{s[W_i^*(n - W_i^*) / (n - 1)]^{1/2}} \quad (1)$$

The matrix of spectral weights $\{w_{ij}(d)\}$ is both binary and symmetric with a weight equal to unity (w_{ij} equal to 1) for all the pixels found within distance “d” of pixel “i” considered and a weight equal to zero (w_{ij} equal to 0) for all the pixels found outside “d”. $\sum_j w_{ij}(d)x_j$ is the sum of the varying values “X” (DC in the case of images) within distance “d” of pixel “i” (i included), W_i^* is the number of pixels within the distance “d” (i included):

$$W_i^* = \sum_j w_{ij}(d) \quad (2)$$

$$\bar{x} = \sum_j x_j / n \quad (3)$$

$$s^2 = \sum_j x_j^2 / n - \bar{x}^2 \quad (4)$$

Where “n” is the total number of pixels, “ (\bar{x}) ” is the global mean of x and “s” is the variance of x . In equation (1), a cluster of pixels with high digital counts is indicated by largely positive G_i^* values, while a cluster of pixels with low digital counts is indicated by largely negative G_i^* values (Wulder and Boots, 1998). In the case of our study, G_i^* statistics were used for the first time for the characterization of calibration sites. It enabled us to analyze the spatial uniformity of the site, e.g., to select spatially heterogeneous or homogeneous areas. Towards this objective, G_i^* statistics and the coefficient of variation were calculated in relation to different window sizes (distances d), varying from 3×3 to 9×9 pixels. The resulting images permit the visualization and the analysis of the homogeneous or heterogeneous pixel clusters.

2.2. Coefficient of variation

Knowledge of the relative variation is indispensable for evaluating site radiometric uniformity. Among the tools often used to measure relative dispersal is the coefficient of variation, CV (Gu *et al.*, 1990; Teillet *et al.*, 1998). It is defined by the ratio of the standard deviation (σ) over the average (\bar{x}). The CV was used to characterize the radiometric spatial uniformity and the temporal evolution of the La Crau site in France by Gu *et al.* (1990) using SPOT HRV images. The authors set a 20 x 20 pixel window (an area of 400 x 400 m in the middle of the La Crau site) and they moved the window with a sampling step of one pixel on each of the raw images in order to derive images of the coefficient of variation. According to the authors, this method permitted the determination of the most spatially and spectrally homogeneous area on the La Crau site with a coefficient of variation of 2 %. Moreover, Teillet *et al.* (1998) calculated the coefficient of variation using SPOT HRV images acquired over the sites of Railroad Valley Playa, in Nevada (USA), and Newell County Rangeland in

Alberta (Canada), using a variable window size ranging from 3 km x 3 km to 20 km x 20 km with a sampling step of 1 km. The results obtained showed that the most homogeneous areas have a coefficient of variation of 2.5 % and 3 % respectively for the Newell County Rangeland and Railroad Valley Playa sites. Based on the results of the research work previously cited, in the framework of this study we will consider a site homogeneous when the coefficient of variation is 3 % or less.

2.3. Study site: Lunar Lake Playa, Nevada, USA

The Lunar Lake Playa, Nevada (LLPN) test site is located approximately 300 miles north of Las Vegas and 100 miles east of Tonopah in central Nevada (38° 23' N and 115° 59' W) at an altitude of 1750 m (Figure 1). The site area is approximately 2 by 4.5 km² with the topography varying from 1 to 2 meters. The climate is continental with a high ratio of clear days and is characterized by important variations in terms of mean precipitation (Teillet *et al.*, 1995). The central portion of the site (0.5 km by 0.5 km) presents a smooth and homogeneous surface characterized by a nearly Lambertian behaviour, by high brightness (superior to 0.5) and by spatial uniformity (Shepard *et al.*, 1991; Scott *et al.*, 1996). Unfortunately, these characteristics are transitory because of the temporal variations affecting the region (Teillet *et al.*, 1995). After each rainfall or snowstorm, the surface of the LLPN becomes inundated; modifying these characteristics while the surface dries up. These transformations are accentuated further by the high wind in these regions (Teillet *et al.*, 1995). The soil structure of LLPN is made up of compact lacustrine deposits rich in clay forming a surface composed of units varying in size from 20 cm to 30 cm in diameter in the south of the playa and from 10 to 20 cm in the north. The mineral composition of the site is constituted approximately by 90% smectites, kaolinites and vermiculites, and less than 10 % carbonates, quartz, feldspath and micas (Shepard *et al.*, 1991, 1993). These compositions are unevenly distributed over the whole of the site area. According to Van *et al.* (1993) and Teillet *et al.* (1998), this site is quite satisfactory for the calibration of high spatial

resolution sensors such as Ikonos, SPOT HRS and HRV, Landsat-5 TM, Landsat-7 ETM+, QuickBird, etc. Unfortunately, because of its reduced area, it cannot be used with reliability for low spatial resolution satellite sensors because of environmental effects (Scott *et al.*, 1996).

2.4. Image data

The characterization of test site radiometric uniformity through time and space requires image data acquired over a period of many years including different spatial and spectral resolutions and well distributed on a yearly scale or at least at the scale of the period where the site is usable. However, the objective of the study reported in this paper was mainly focused on the potential of *Getis* statistics and its synergy with the CV for analyzing test site temporal stability rather than towards the rigorous characterization of the site through too years time. Among the images archived by the Canada Centre for Remote Sensing and the University of Arizona (Tucson), we selected three cloud-free images that most closely met our objectives. Theses SPOT-HRV images were acquired on June 18, 1998, June 28, 1997 and March 10, 1997.

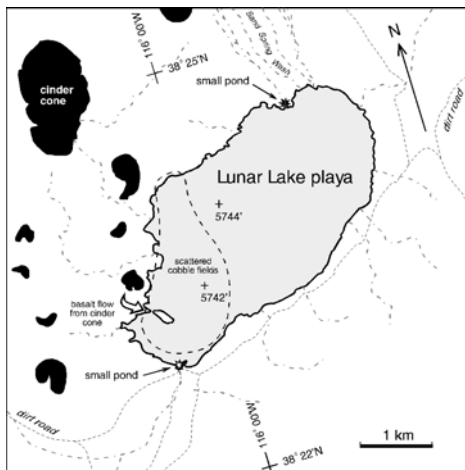


Fig. 1. Location map of the Lunar Lake Playa calibration site, Nevada.

3. ANALYSIS AND DISCUSSION

3.1 Characterization of spatial uniformity

In a first step, the spatial uniformity of the site was evaluated by calculating the coefficient of variation and the *Getis* G_i^* statistics for different windows ranging from 3x3 to 9x9. In each case, the window was moved by a step of 1 pixel over all the images. The results obtained show that a small window (3x3) permits the characterization of spatial homogeneity variability at the level of the central pixel of the window and limits its dependence to only the neighbouring pixels without considering others located further. When using a large window (9x9), this dependence widens in a space (180 m) that is too large. It is evident that the 7x7 and 9x9 windows hide a certain pixel variability calculated in relation to those surrounding it in the image. Consequently, we retained a medium size window (5x5) for all the data processing.

Figure 2 illustrates the results obtained using an HRV image acquired in March 1998. The CVs are very similar for the three bands of the HRV sensor. Also, the highest CVs are recorded on the southwest side of the playa, with values exceeding 25 %. The lowest CVs are recorded in the middle of the playa, with values on the order of 2 to 4% for the three bands). This low variation indicates good site spatial homogeneity. Also, the low CVs in the near infrared (Figure 2c) show that the site is free from vegetation. These findings agree with the findings of Shepard *et al.* (1993) indicating that the surface of the playa is very bright, notably in the middle of the site. Moreover, the authors highlighted the presence of basalt pebbles dispersed at the south end of the site, probably explaining the high CV values in that area.

Figure 3 presents an example of the results obtained with *Getis* statistics derived from HRV data (image acquired in March 1997). The sub-images of this figure reveal visible heterogeneities in the LLPN site. One can clearly distinguish many clusters of pixels of varying intensities in the three bands. Accordingly, the north and the southwest areas of the site are characterized by high brightness with high G_i^* values in all the images of

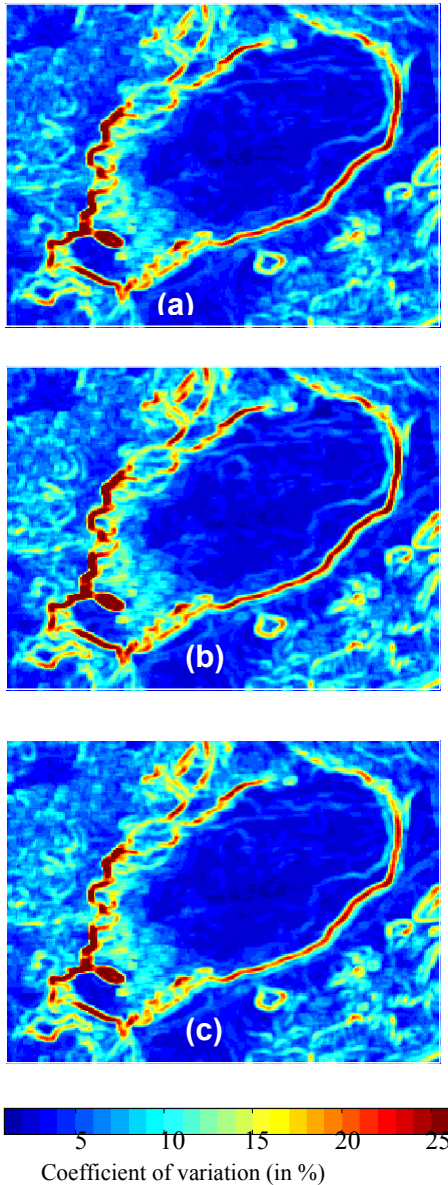


Fig. 2. Images of the coefficient of variation calculated using a 5x5 pixel window in the three bands (HRV1 (a), HRV2 (b) and HRV3 (c)) of a SPOT-HRV image acquired over Lunar Lake Playa in March 1997.

Figure 3 (yellow and red) and relatively low spatial uniformity. As to the northeast of the playa, it is less bright and heterogeneous (blue and yellow in the images of Figure 3). The main factor responsible for this behaviour is likely the soil moisture variation since March is in the rainy season in that area. Topography has no effect in this region since the Lunar Lake playa is perfectly flat and free from vegetation. The sub-images of this figure also show that Getis statistics are nearly identical independently from the spectral band used.

Contrary to the coefficient of variation showing that the Lunar Lake playa is a homogeneous and relatively uniform site, Getis statistics show the heterogeneous nature of the site. The statistics appear to be sensitive to surface moisture, which is quite variable in this area. However, the two methods have shown themselves to be relatively insensitive to spectral variation, insofar as the three broad spectral bands of SPOT HRV are a measure of the spectral dimension.

3.2 Multitemporal characterization

For the multitemporal characterization of the LLPN site, we calculated the coefficient of temporal variation for the site, on the one hand between the months of March and June of the same year (1997), and on the other hand, for the month of June in two different years (1997 and 1998). Figures 4 and 5 illustrate how the site surface reflectance has changed over these periods in the three SPOT HRV bands. According to Figure 4, the CV variation in the three bands is high, on the order of 30 % in the first band (green) and 27 % in the other two bands (red and near infrared). These results indicate that the LLPN site undergoes changes to its surface. It is thought that these changes are caused by variations in soil moisture resulting from atmospheric conditions that are quite variable in the region, but this hypothesis has not been validated. Figure 5 also indicates that this site has undergone a more significant variation, from approximately 22 % in the first band to more than 42 % in the third band.

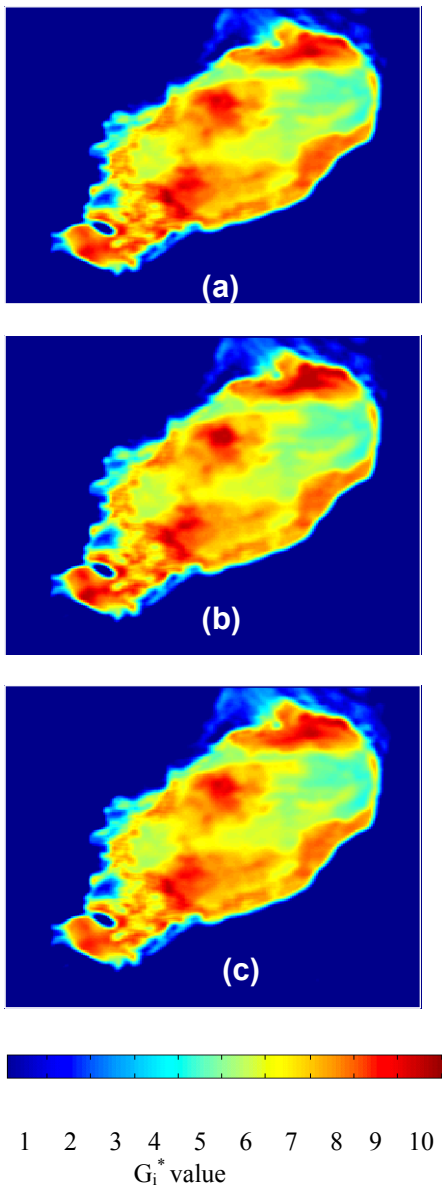


Fig. 3. Images of the Getis statistics calculated using a 5x5 pixel window in the three bands (HRV1: (a), HRV2: (b) and HRV2: (c)) of a SPOT-HRV image acquired over the Lunar Lake Playa in March 1997.

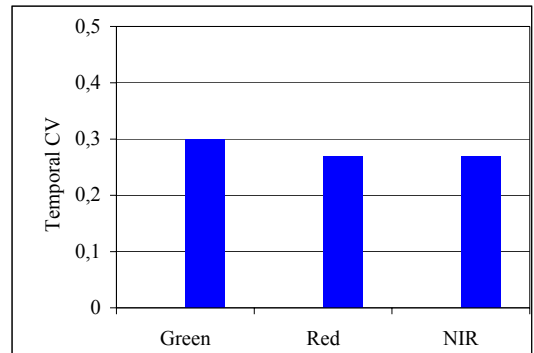


Fig. 4. Temporal evolution of the three HRV bands acquired over the Lunar Lake Playa for the month of June with reference to the month of March 1997.

To better characterize the temporal variation of the site, Figures 6 and 7 present sub-images of the coefficient of variation and of the Getis statistics derived from band 2 (red) of the three HRV images of LLPN. It must be noted that the site behaviour in the green and near infrared bands is the same as in the red band. According to Figure 6, CV has extracted the borders of the playa and the perimeters of the areas having undergone significant spatial variations. However, CV also indicates that the site may have generally remained homogeneous between the months of March and June in 1997. According to Figure 7, Getis statistics extracted spatially heterogeneous areas located in the middle of the site. Overall, the sub-images of both figures show the areas having undergone the most significant temporal variations. In 1997, the north and the southeast of the playa, possibly affected by moisture in March (Figures 6a, b and 7a, b), became relatively bright and dry in June (yellow to red in Figures 7a and b). However, the northeast region, very bright (red) and uniform in March, has become less homogeneous in June. Moreover, comparison between the two sub-images of the Gestis statistics (7a, b) clearly shows that the central portion of the playa has undergone an important change in June 1998 compared to the same period in 1997. Figure 7c shows that the region may be subject to high surface moisture, perhaps generated by the presence of standing water resulting from a rainstorm before the image acquisition date. The surroundings of this affected area

show a cluster of high G_i^* values indicating a dry and bright surface during this period.

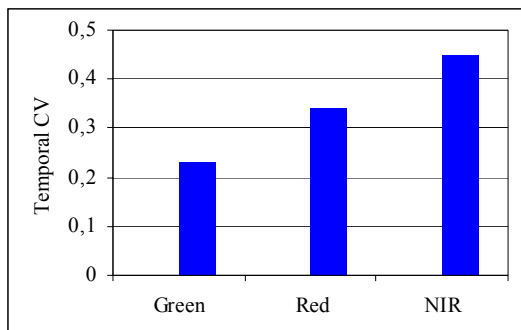


Fig. 5. Temporal evolution of the three HRV bands acquired over the Lunar Lake Playa for the month of June 1998 with reference to the month of June 1997.

Based on these results, it is clear that the LLPN site is subject to significant temporal variations, not only in terms of brightness but also in terms of spatial homogeneity. Moreover, using ERS-1 synthetic aperture radar data, Teillet et al. (1995) noted that the Lunar Lake Playa surface may be subject to temporal variations due to humidification and drying. One can also add the possibility of the redistribution of surface components generated by frequent winds in the region. Even if surface moisture is a transitory phenomenon depending both on the intensity of evaporation and soil hydrodynamic properties (capacity of the soil for diffusing its moisture), its effect must be taken into consideration when using this site for calibration operations.

4. CONCLUSIONS

The proper use of remote sensing data must be preceded by different data standardization operations, including a radiometric calibration specifically designed for the sensor. Although many Earth observation satellites have

onboard calibration systems, their use remains complex and fairly unreliable due to aging and other difficulties that have been documented in the literature. To address these concerns, measurement campaigns are organized periodically at test sites to evaluate the radiometric performance of satellite and airborne sensors.

As we have discussed in this paper, the sites used for calibration operations must meet a number of criteria, including the uniformity and stability of the site's radiometric properties in space and time, respectively. For studying this issues, we developed a methodology based on two types of statistics: the coefficient of variation, a classical tool already used in previous work, and Getis statistics that we used for the first time for the radiometric characterization of the LLPN site. The results demonstrated the synergy generated by using the two methods. Getis statistics provide an excellent spatial analysis of the test site independently from the spectral band used. They have shown high potential for the extraction of radiometric heterogeneities for a surface that appears to be homogeneous according to a widely used image processing tool, the coefficient of variation.

On the other hand, while the coefficient of variation does not adequately characterize the site spatially, it provides complementary information on the temporal evolution of the site. The synergy between the two methods provided an information on the radiometric uniformity and stability of the site. In spite of its apparent spatial homogeneity and its high brightness, we have shown that the surface of the LLPN site experiences temporal variations presumably controlled by climate that cause changes in the surface structure (presence of water, moisture variations and formation of lichens).

5. ACKNOWLEDGMENTS

The authors would like to thank the Natural Sciences and Engineering Research Council of Canada (NSERC) for its financial support, as well as the Canada Centre for Remote Sensing and the University of Arizona (Tucson) for the image data.

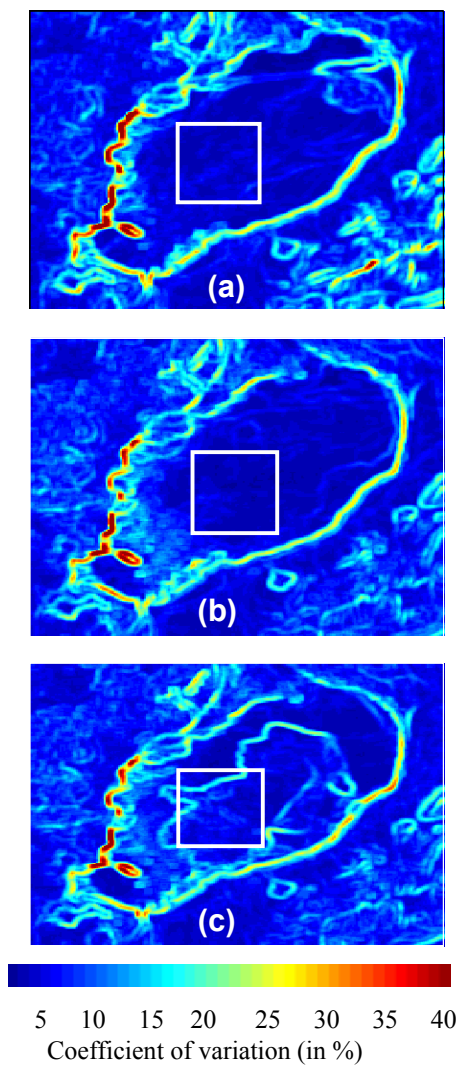


Fig. 6. Images of the coefficients of variation calculated using a 5x5 pixel window in the HRV red band HRV ((a) March 1997, (b) June 1997 and (c) June 1998).

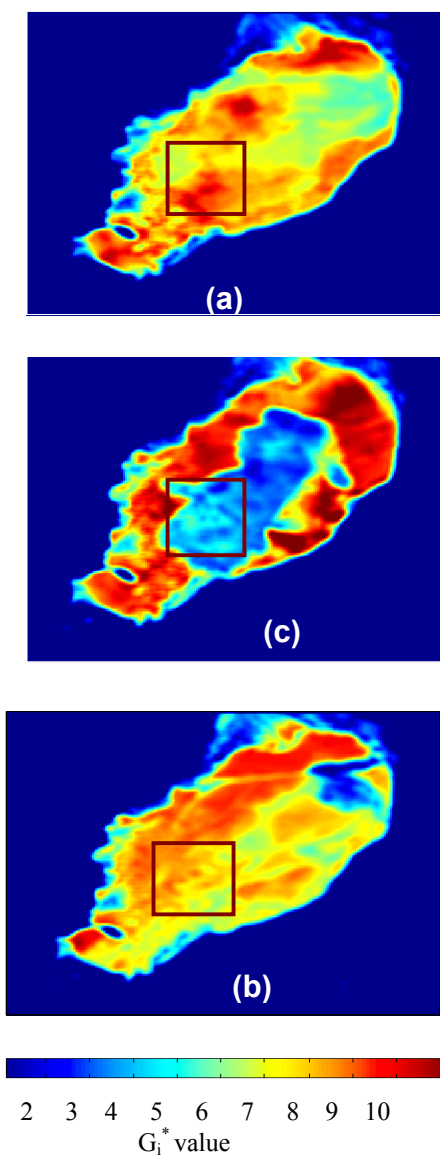


Fig. 7. Images of the Getis statistics using a 5x5 pixel window in the HRV red band ((a) March 1997, (b) June 1997 and (c) June 1998).

6. REFERENCES

- Asrar, G. (edit.) (1995) EOS Data Quality : Calibration, Validation, and Quality Assurance, in MTPE / EOS Reference Handbook. NASA-Goddard Space Flight Centre, (www.eospso.gsfc.nasa.gov/eso_reference/handbook95.pdf), p. 53-55
- Anselin, L. (1995) Local indicators of spatial association-LISA. **Geographical Analysis**, vol. 27(2), p. 93-115.
- Bannari, A., Teillet, P.M. and Richardson, G. (1999) Nécessité de l'étalonnage radiométrique et standardisation des images numériques de télédétection. **Journal canadien de télédétection**, vol. 25, no.1, p.45-59.
- Cosnefroy, H., Briottet, X. and Leroy, M. (1993) Characterization of Désert Areas With METEOSAT-4 Data for the Calibration of the Optical Satellite Sensors. **Proceedings of SPIE**, vol. 1938, p. 203-210.
- Delphin, L., Briottet, X., Vermote, E. et Leroy, L. (1991) Caractérisation des sites désertiques africains pour l'étalonnage relatif des capteurs optiques spatiaux a grand champ. Proceedings of the 5 th **International Colloquium. Physical Measurements and signatures in Remote Sensing**, Courchevel, France, p. 49-52.
- Derksen, C., Wulder, M., LeDrew, E. and Goodison, B. (1998) Associations between spatially autocorrelated patterns of SSM/I-derived prairie snow cover and atmospheric circulation. **Hydrological Processes**, vol. 12, p. 2307-2316.
- Dingirard, M. and Slater, P.N. (1999) Calibration of Space-Multispectral Imaging. **Remote Sensing of Environment**, vol. 68, p. 194-205.
- Fisher, P. (1997) The pixel: A snare and a delusion. **International Journal of remote sensing**, vol. 18, p. 679-685.
- Flittner, D.E. and Slater, P.N. (1991) Stability of Narrow-Band Filter Radiometers in the Solar-Reflective Range. **Photogrammetric Engineering and Remote Sensing**, vol. 57, No. 2, p. 165-171.
- Frouin, R. and Gautier, C. (1987) Calibration of NOAA-7 AVHRR, GOES-5, and GOES-6 VISSR/VAS Solar Channels. **Remote Sensing of Environment**, vol. 22, p. 73-101.
- Getis, A. and Ord, J. (1992) The analysis of spatial association by distance statistics. **Geographical Analysis**, vol. 24, p. 189-206.
- Goodchild, M. (1986) Spatial Autocorrelation. **Concepts and Techniques in Modern Geography**, vol. 47 (Norwich: Geo Books), p. 3-6.
- Goward, S.N., Markham, B., Dye, D.G., Dulaney, W. and Yang, J. (1991) Normalized difference vegetation index measurement from the Advanced Very High Resolution Radiometer. **Remote Sensing of Environment**, vol. 35, p. 257-277.
- Gu, X. (1991) Étalonnage et intercomparaison des données satellitaires en utilisant le site test de "La Crau" (appliqué aux images SPOT1-HRV, Landsat5-TM, NOAA11-AVHRR). **Thèse de doctorat de l'Université Paris VII**, 260 pages.
- Gu, X., Guyot, G. et Verbrughe, M. (1990) Analyse de la variabilité spatiale d'un site-test: exemple de "La Crau" (France). **Photo-interpretation**, vol. 90, no.1, Fasc. 5, p. 40-51.
- Gutman, G. G. (1991) Vegetation Indices from AVHRR : An Update and Future Prospects. **Remote Sensing of Environment**, vol. 35, p. 121-136.
- Henry, P., Dingirard, M. and Bodilis, M. (1993) SPOT calibration over désert areas. **Proceedings of SPIE**, vol. 1938, p. 67-76.
- Leroy, M.M. (1990) Modèles des systèmes de mesure imageurs optiques. In **École d'été en télédétection spatial: aspects physiques et modélisation**, CEPADUES Ed, Toulouse, France, p.311-363.
- Markham, B.L., Irons, J.R., Deering, D.W., Halthore, R.N., Irish, R.R., Jackson, R.D., Moran, M.S., Biggar, S.F., Gellman, D.I., Grant, B.G. and Palmer, J.M (1990) Radiometric Calibration of Aircraft and Satellite Sensors at White Sands, NM. **IGARSS**, p. 515-518.
- Omari, K., Bannari, A., Fedosejevs, G. et Teillet, P.M. (2000) Caractérisation de différents sites tests d'étalonnage radiométrique des capteurs d'observation de la terre. **Actes du 22^{ème} Congrès de la Société Canadienne de Télédétection**, Victoria, Colombie Britannique, pp. 733 – 744.
- Omari, K., Bannari, A., Fedosejevs, G. et Teillet, P.M. (2001) Analyse de l'uniformité spatio-temporelle du site-test "Newell County Rangeland" en Alberta (Canada) pour l'étalonnage radiométrique des capteurs d'observation de la terre. **Actes du 8^{ème} Symposium international des mesures et signatures en Télédétection**, Aussois, France, pp. 195 – 200.
- Ord, J. and Getis, A. (1995) Local spatial autocorrelation statistics: Distributional issues and an application. **Geographical Analysis**, vol. 27, p. 286-306.

- Price, J.C. (1987) Radiometric Calibration of satellite sensors in the visible and near-infrared: history and outlook. **Remote Sensing of eEnvironment**, vol. 22, p. 3-9.
- Santer, R., X.F. Gu, G. Guyot, J.L. Deuze, C.Devaux, E. Vermote, and M. Verbrughe. (1992) SPOT Calibration at the La Crau Test Site (France). **Remote Sensing of Environment**, vol. 41, p. 227-237.
- Scott, K.P., Thome, K.J. and Brownlee, M. (1996) Evaluation of the Railroad Valley Playa for Use in Vicarious Calibration. **Proceedings of SPIE Conference 2818**, Denver, Colorado, p.158-166.
- Shepard, M.K., Arvidson, R.E. and Guinness, E.A. (1991) Scattering behavior of Lunar Lake Playa determined from PARABOLA bidirectional reflectance data. **Geophysical Research**, vol. 18, no. 12, p. 2241-2244.
- Shepard, M.K., Arvidson, R.E. and Guinness, E.A. (1993) Specular scattering on terrestrial Playa and implications for planetary surface studies. **Journal of Geophysical Research**, vol. 98, no. E10, p. 707-718.
- Slater, P.N. (1984) A Review of Some Radiometric Calibration Problems and Methods. **II^e Colloque international des signatures spectrales d'objets en télédétection**, Bordeaux, France (Les colloques de L'INRA, no. 23), p. 391-405.
- Slater, P.N., Biggar, S.F., Holm, R.A., Jackson, R.D., Mao, Y., Moran, M.S., Palmer, J.M. and Yuan, B. (1987) Réflectance-and Radiance-Based Methods for In-Flight Absolute Calibration of Multispectral Sensors. **Remote Sensing of Environment**, vol. 22, p. 11-37.
- Slater, P.N., Biggar, S.F., Thome, K.J., Gellman, D.I. and Spyak, P.R. (1996) Vicarious Radiometric Calibrations of EOS Sensors. **Journal of Atmospheric and Oceanic Technology**, vol. 13, p. 349-359.
- Teillet, P.M., Slater, P.N., Ding, Y., Santer, R.P., Jackson, R.D. and Moran, M.S. (1990) Three Methods for the Absolute Calibration of the NOAA AVHRR Sensors In-Fight. **Remote Sensing of Environment**, vol. 31, p. 105-120.
- Teillet, P.M., Fedosejevs, G., Gautier, R.P., O'Neill, N.T., Thome, K.J., Biggar, S.F., Ripley, H. and Meygret, A. (2001) Generalized Approach to the Vicarious Calibration of Multiple Earth Observation Sensors Using Hyperspectral Data. **Remote Sensing of Environment**, vol. 77, p. 304 - 327.
- Teillet, P.M., Fedosejevs, G., Gautier, R.P. and Schowengerdt, R.A. (1998) Uniformity Characterization of Land Test Sites Used for Radiometric Calibration of Earth Observation Sensors. **Proceedings of the Twentieth Canadian Symposium on Remote Sensing**, Calgary, Alberta, p.1-4.
- Teillet, P.M., Horler, D. and O'Neill, N.T. (1997) Calibration, Validation, and Quality Assurance in Remote Sensing: A New Paradigm. **Canadian Journal of Remote Sensing**, vol. 23(4), p. 401 - 414.
- Teillet, P.M., Fedosejevs, G., Gautier, D., D'Iorio, M.A., Rivard, B., Budkewitsch, P. and Brisco, B. (1995) An Initial Examination of Radar Imagery of Optical Radiometric Calibration Sites. **Proceedings of the SPIE Europto Symposium on Advanced and Next-Generation Satellites, SPIE**, vol. 2583, p.154-165.
- Teillet, P.M. (1994) Vegetation Index Monitoring: Radiometric Considerations. **Remote Sensing in Canada**, vol. 22, no. 1, pp. 8-9.
- Thome, K. J., Gellman, D.I., Parada, R.J., Biggar, S.F., Slater, P.N. and Moran, S.M. (1993) In-flight radiometric calibration of Landsat-5 Thematic Mapper from 1984 to present. **Proceedings of SPIE vol. 1938**, Orlando, Florida, USA, p. 126-130.
- Wheeler, R.J., Lecroy, S.R., Whitlock, C.H., Purgold, G.C. and Swanson, J.S. (1994) Surface characteristics for the Alkali flats and dunes regions at the White Sands Missile Range, NM. **Remote Sensing of Environment**, vol. 48, p. 181-190.
- Whitlock, C.H., Purgold, G.C. and LeCroy, S.R. (1987) Surface Bidirectional Réflectance properties of Two South-Western Arizona deserts for wavelengths between 0,4 and 2,2 microns, **NASA TP 2643**.
- Wu, D., Yin, Y., Wang, Z., Gu, X., Verbrughe, M. and Guyot, G. (1997) Radiometric Characterisation of Dunhuang Satellite Calibration Test Site (CHINA) and First Test Using SPOT Data. **Seventh International Symposium on Physical Measurements and Signatures in Remote Sensing**, Courchevel, France.

- Wulder, M. and Boots, B. (2001) Local Spatial Autocorrelation Characteristics of Landsat TM Imagery of a Managed Forest Area, **Journal canadien de télédétection**, Vol. 27, No. 1, pp. 67-75.
- Wulder, M. and Boots, B. (1998) Local spatial autocorrelation characteristics of remotely sensed imagery assessed with the Getis statistic. **International Journal of Remote Sensing**, vol.19(11), p. 2223-2231.
- Wulder, M. (1998) Optical remote sensing techniques for assessment of forest inventory and biophysical parameters. **Progress in Physical Geography**, vol. 22, no. 4, p. 449-476.

Fusion of different spatial and spectral resolution images: development, application and comparison of new methods based on wavelets

M. González-Audicana¹, X. Otazu^{2,3,4,5}, O. Fors^{2,3}, R. García¹ and J. Núñez^{2,3}

¹ Department of Projects and Rural Engineering. E.T.S.I.A. Public University of Navarre. Campus Arrosadía s/n, 31006 Pamplona

² Department of Astronomy and Meteorology. University of Barcelona. C/Martí i Franquès 1, 08028 Barcelona

³ Fabra Observatory. Camí d'Observatori s/n, 08035 Barcelona

⁴ Computer Vision Center. Autonomic University of Barcelona. Campus UAB

⁵ Image Processing and Artificial Intelligence Department. Autonomic University of Barcelona. maria.audicana@unavarra.es; xotazu@am.ub.es; ofors@am.ub.es

ABSTRACT. During last years, Earth Observation Satellite images distribution companies, have been offering mixed products such as the SPOT 4 P+XI scenes offered by Spot Image or the 1 m Pan-Sharpener IKONOS images offered by Space Imaging. The present paper compares different fusion methods, such as the traditionally used IHS or PCA procedures, with more recent methods based on multiresolution analysis and wavelet transforms. Moreover, new methodological alternatives also based on wavelet transform are presented, applied and compared to the previous methods. All fusion procedures have been used to merge SPOT 4 XI (20 m) with SPOT 4 M (10 m) images and IKONOS MS (4 m) and Pan (1 m) images, all of them corresponding to irrigated areas of Navarre. Twelve methods have been compared using the resulting fused images. To assess the quality of the resulting images, these should be compared to the 'theoretic' images observed by the multispectral sensor if this would offer the spatial resolution of the panchromatic one. As these images are not available we worked with spatially degraded images. The comparison of the fused images is based on spectral and spatial characteristics and it is made visually and quantitatively, using statistical parameters and quantitative indexes. It is proved that methods based on wavelet transforms preserve the spectral characteristics of the multispectral image better than other methods and supply high spatial quality images. The merged images with the highest spectral and spatial quality have been obtained when the methodological alternatives based on wavelets proposed by this research group are used.

1. INTRODUCTION

During last years, companies that distribute Earth Observation Satellites images, have been offering mixed products with high spatial and spectral resolution. These are obtained by combination of the spatial detail information of the panchromatic images with the colour information of the multispectral images both of them acquired at the same time by sensors lodged at the same space platform. Two representative examples of that are the SPOT 4 P+Xi Scenes offered by *Spot Image* or the 1-meter Pan-Sharpener multispectral IKONOS images offered by *Space Imaging*.

Because of their complementary nature, multispectral and panchromatic image fusion is a widely used solution to obtain high spectral and spatial resolution images.

Some of the most common image fusion methods are those based on the Intensity-Hue-Saturation (IHS) transformation (Haydn *et al*, 1982; Welch and Ehlers,

1987; Carper *et al*, 1991) and the Principal Component Analysis (PCA) (Chavez *et al*, 1991; Shettigara, 1992). The main drawback of these procedures is the high distortion of the original spectral information that the resulting multispectral images show. This is an important problem if the merged images are going to be used to extract thematic information such as agricultural crop distribution, change detection or land uses mapping through a multispectral classification.

In the last few years, multiresolution analysis has become a suitable tool for the development of new image-fusion methods. Recently, several researchers (Yocky, 1995; Garguet-Dupont *et al*, 1996; Zhou *et al*, 1998; Núñez *et al*, 1999; Ranchin and Wald, 2000) have proposed different image fusion procedures using the multiresolution analysis based on the discrete wavelet transform, and proved that those methods provide an improved spatial resolution image, while keeping the spectral properties of the original multispectral data.

In this paper, new methodological fusion alternatives based on wavelet transforms are presented, applied and compared to the traditional IHS or PCA procedures, as well as to those methods proposed by the above mentioned researchers.

Twelve image-fusion methods have been compared analysing the quality of each resulting merged image.

To assess the quality of the resulting images, these should be compared to the 'theoretic' images observed by the multispectral sensor if this would offer the same spatial resolution than the panchromatic one. As these images are not available we decided to work with spatially degraded images.

Comparison of the fused images is based on spectral and spatial characteristics and it is performed visually and quantitatively using statistical parameters (correlation coefficients, means difference...) and quantitative indexes (such as the Relative Average Spectral Error, RASE, or the Relative Adimensional Error of the Fusion, ERGAS, proposed by Wald *et al* 1997)

All fusion methods have been used to merge SPOT 4 XI with SPOT 4 M images and IKONOS MS with Pan images, all of them corresponding to irrigated areas of Navarre (Spain).

2 MULTIREOLUTION ANALYSIS AND WAVELET TRANSFORM

Multiresolution analysis, based on the wavelet theory, allows to decompose bidimensional datasets into different frequency components, and to study each component with a resolution matched to its size. At different resolution, the details of an image, i.e. high frequency components, characterise different physical structures of the scene (Mallat, 1989). At a coarse resolution, these details correspond to the larger structures, while at a more detailed resolution, this information corresponds to the smaller size structures.

The wavelet transform provides a framework to decompose images into a number of new images, each of them with a decreasing degree of resolution, and to separate the spatial detail information of the image between two successive resolution degrees.

The continuous wavelet transform of a one-dimensional function, $f(x) \in L^2(R)$, respect to the *Mother Wavelet* $\psi(x)$ can be expressed as

$$W_f(a,b) = \langle f, \psi_{a,b} \rangle = \int_{-\infty}^{+\infty} f(x) \psi_{a,b}(x) dx \quad (1)$$

The wavelet base functions $\psi_{a,b}(x)$ are dilations and translations of the *Mother Wavelet* $\psi(x)$

$$\psi_{a,b}(x) = \frac{1}{\sqrt{a}} \psi\left(\frac{x-b}{a}\right) \quad (2)$$

where $a, b \in R$. Parameter 'a' is the dilatation or scaling factor, and parameter 'b' is called translation one.

For every scale a and location b , the wavelet coefficients $W_f(a,b)$ represents the information contained in $f(x)$ in that scale and position.

The original signal can be exactly reconstructed from the wavelet coefficients by:

$$f(x) = \frac{1}{C_\psi} \int_0^\infty \int_{-\infty}^{+\infty} W_f(a,b) \psi_{a,b}(x) db \frac{da}{a^2} \quad (3)$$

where C_ψ is the normalizing factor of the *Mother Wavelet*.

2.1 Mallat's and "à trous" algorithms.

The discrete approach of the wavelet transform can be done with several different algorithms.

We have used the Mallat's and the "à trous" discrete wavelet transform algorithms.

2.1.1 The Mallat's algorithm.

In order to understand the multiresolution analysis concept based on the Mallat's algorithm is very useful to represent the wavelet transform as a pyramid. The basis of the pyramid is the original image, with C columns and R rows. Each level of the pyramid, that is only accessible from the immediately lower level, is an approximation to the original image. When climbing up in the pyramid, the successive approximation images have a coarser spatial resolution. At the N^{th} level, the approximation image has $C/2^N$ columns and $R/2^N$ rows because a dyadic wavelet transform with downsampling is applied (Mallat, 1989)

These approximation images are computed using scaling functions related to the *Mother Wavelet* function $\psi(x)$ (Mallat, 1989; Daubechies, 1992). The difference of information between two successive levels of the pyramid, e.g. between the original image A_2^j at a resolution 2^j and the approximation image A_2^{j-1} at a resolution 2^{j-1} is given by the wavelet transform, and computed using the wavelet functions. Three wavelet coefficient images, DH_2^{j-1} , DV_2^{j-1} and DD_2^{j-1} pick up, respectively, the horizontal, vertical and diagonal detail that is lost between the images A_2^j and A_2^{j-1} and contains the structures with sizes comprised between 2^j and 2^{j-1} resolution. If the original image has C columns and R rows, the approximation and the wavelet coefficients images obtained applying this

multiresolution decomposition have $C/2$ columns and $R/2$ rows.

When the inverse wavelet transform is applied, the original image A_2^j can be reconstructed exactly from the approximation image A_2^{j-1} and the horizontal, vertical and diagonal wavelet coefficients DH_2^{j-1} , DV_2^{j-1} and DD_2^{j-1} .

For the practical implementation of the Mallat's algorithm, quadrature mirror filters are used instead of the scaling and wavelet functions. The 'h' filter, associated to the scaling function, is a one-dimensional low pass filter that allows to analyze low frequency data, while the 'g' filter, associated to the wavelet function, is a one-dimensional high pass filter that allows to analyze the high frequency components, i.e. the detail of the image being analyzed.

The number of parameters of these filters and the value of these parameters depend on the *Mother Wavelet* function used in this analysis. In this work, we have used the Daubechies four-coefficient wavelet basis. This leads to the following filters:

$$\begin{aligned} h: & \left\{ \frac{(1-\sqrt{3})}{4\sqrt{2}}, \frac{(3-\sqrt{3})}{4\sqrt{2}}, \frac{(3+\sqrt{3})}{4\sqrt{2}}, \frac{(1+\sqrt{3})}{4\sqrt{2}} \right\} \\ g: & \left\{ -\frac{(1+\sqrt{3})}{4\sqrt{2}}, \frac{(3+\sqrt{3})}{4\sqrt{2}}, -\frac{(3-\sqrt{3})}{4\sqrt{2}}, \frac{(1-\sqrt{3})}{4\sqrt{2}} \right\} \end{aligned} \quad (4)$$

2.1.2 The "à trous" algorithm.

Other discrete approach of the wavelet transform is the "à trous" algorithm (Holschneider and Tchamitchian, 1989; Starck and Murtagh, 1994).

In this case, the image decomposition scheme cannot be represented with a pyramid as in Mallat's algorithm but with a parallelepiped. The basis of the parallelepiped is the original image, A_2^j at a resolution 2^j , with C columns and R rows. Each level of the parallelepiped is an approximation to the original image, as in Mallat's algorithm. When climbing up through the resolution levels, the successive approximation images have a coarser spatial resolution but the same number of pixels as the original image. If a dyadic decomposition approach is applied, the resolution of the approximation image at the N^{th} level is 2^{j-N} .

These approximation images are computed using scaling functions. The wavelet planes, that represents the spatial detail lost when the approximation image A_2^{j-1} at a resolution 2^{j-1} is obtained from the original image A_2^j at a resolution 2^j , are computed as the difference between these consecutive levels of the parallelepiped.

In contrast to the Mallat's algorithm, the "à trous" algorithm allows a shift-invariant discrete wavelet decomposition. All the approximation images

obtained applying this decomposition have the same number of columns and rows as the original image. This is a consequence of the fact that the "à trous" algorithm is a nonorthogonal oversampled transform.

For the practical implementation of the "à trous" algorithm, a bi-dimensional filter associated to the scaling function is used. In this work, we use a scaling function which has a B_3 cubic spline profile. This function leads to the following low pass filter:

$$\frac{1}{256} \begin{pmatrix} \frac{1}{256} & \frac{1}{64} & \frac{3}{128} & \frac{1}{64} & \frac{1}{256} \\ \frac{1}{64} & \frac{1}{16} & \frac{3}{32} & \frac{1}{16} & \frac{1}{64} \\ \frac{3}{128} & \frac{3}{32} & \frac{9}{64} & \frac{3}{32} & \frac{3}{128} \\ \frac{1}{64} & \frac{1}{16} & \frac{3}{32} & \frac{1}{16} & \frac{1}{64} \\ \frac{1}{256} & \frac{1}{64} & \frac{3}{128} & \frac{1}{64} & \frac{1}{256} \end{pmatrix} \quad (5)$$

3 IMAGE FUSION METHODS

In order to apply any of the image-fusion methods described in this section, it is necessary that the multispectral and the panchromatic images can be accurately superimposed. Therefore, both images have to be co-registered and the multispectral image needs to be resampled to make its pixel size similar to that of the panchromatic.

Different image-fusion procedures have been analysed and compared in this work. Some of them are well known and others are firstly presented in this paper. We have grouped the twelve methodological alternatives under study in three groups:

3.1 Arithmetic combination methods.

Methods based on the arithmetic combinations of the multispectral and panchromatic images to fuse, such as the Brovey transform (Hallada and Cox, 1993) or the Pradines method (Pradines, 1986).

3.2 Components substitution methods.

The most popular image-fusion methods are those based on the IHS transformation and the PCA. Both mergers are based on the same principle: the dissociation of the spatial information of a multispectral image from its spectral information by means of linear transform.

3.2.1 The IHS merger.

The widespread use of these transformation to merge images lies in the fact that the IHS transforms can take apart the spectral information of an RGB composition in its two components H and S and isolate in the I component most of the spatial information (Pohl and Van Genderen, 1998). The panchromatic image, whose histogram has been

matched with that of the I, replaces that Intensity image. Applying the inverse IHS transform, we obtain the fused RGB image, with the spatial detail of the panchromatic image. Several algorithms have been developed to convert the colour RGB values into IHS values. We have used those based on the Smith's hexacone model and the Smith's triangle model (Smith, 1978). The first consider the I as the maximum value of R, G and B (hereafter IHS algorithm) while the second computed the I as the average of R, G and B (hereafter LHS algorithm).

3.2.2 The PCA merger.

Usually, when a PCA analysis is applied to a multispectral image, the first principal component (PC^1) collects the information that is common to all the bands, i.e. the spatial information, while the spectral information that is specific to each band is picked up in the other principal components. This PC^1 is substituted by the panchromatic image, whose histogram has previously been matched with that of the PC^1 . The inverse PCA analysis allows to obtain the new fused bands, with the spatial detail of the panchromatic image incorporated into them.

3.3 Structures Extraction and Injection methods

The basic idea of these methods is to extract the spatial detail from the panchromatic image to introduce it into the multispectral one. We grouped the methodological alternatives by the procedure used to extract the spatial information from the panchromatic image as well as by the procedure used to inject this spatial detail into the multispectral image.

3.3.1 High Pass Filter method.

Edge information is extracted from the panchromatic image using a high pass filter (HPF). The HPF results are added, pixel by pixel to the multispectral data set, in order to obtain a high spectral and spatial resolution image.

3.3.2 Additive Wavelet methods (AW)

In this case, discrete wavelet transforms are used to extract the spatial detail information from the panchromatic image. The main advantage of these methods compared with the HPF is the selective spatial detail extraction. When a multiresolution decomposition scheme is used, it is possible to extract from the panchromatic image just the spatial detail information non-present in the multispectral, to later insert that detail information into this multispectral image.

Both the extraction and injection of spatial detail is done using the Mallat's and the "à trous" wavelet decomposition algorithms.

3.3.2.1 Additive Wavelet method using the Mallat's algorithm.

The steps for merging multispectral and panchromatic images using this method are:

- 1.- Generate new panchromatic images, whose histograms match those of each band of the multispectral image.

- 2.- Apply the wavelet transform to the "histogram-matched" panchromatic images. Apply the same transform to each multispectral band, using the Daubechies four-coefficient wavelet basis. From each multispectral and panchromatic wavelet image decomposition, four half-resolution images are obtained. The first one is a low frequency version of the original image, and the other three images, the wavelet coefficients images.

- 3.- Introduce the detail of the panchromatic image into each multispectral band through the inverse wavelet transform.

This image fusion method has been used by Yocky, 1995; Gauguier-Duport *et al*, 1996; Zhou *et al*, 1998 and Ranchin and Wald, 2000, amongst others.

3.3.2.2 Additive Wavelet method using the "à trous" algorithm.

The steps for merging multispectral and panchromatic images using this method are:

- 1.- Generate new panchromatic images, whose histograms match those of each band of the multispectral image.

- 2.- Perform the wavelet transform only on the panchromatic images.

- 3.- Add the wavelet planes of the panchromatic decomposition to each band of the multispectral data set.

This image fusion method has been firstly used by Nuñez *et al*, 1999.

3.3.3 Additive Wavelet Intensity (AWI) and Additive Wavelet Principal Component (AWPC) methods.

When the spectral range of the panchromatic image does not embrace the spectral range of all the bands of the multispectral image, the AW methods would inject not-real spatial detail into the multispectral image. To solve this problem, this research group proposes the following methodological alternatives for the fusion of multispectral and panchromatic images.

The basic idea of these new methods is to use the IHS transformation and the PCA to insert, using a

discrete wavelet transform, just the spatial information of the panchromatic image not present in the multispectral one, into the later.

3.3.3.1 AWI and AWPC using the Mallat's algorithm.

The steps for merging images using these methods are the following:

- 1.- Apply the PCA or the IHS transform to the multispectral image. These transformations separate the spatial information of a multispectral image into the PC¹ or I components respectively.

- 2.- Generate a new panchromatic image, whose histogram matches the histogram of the PC¹ or I images.

- 3.- Apply the Mallat's decomposition algorithm to the PC¹ or I image and to the corresponding "histogram-matched" panchromatic one. Both decompositions are computed using the Daubechies four-coefficient wavelet basis. Extract the wavelet coefficients that pick up the horizontal, vertical and diagonal spatial detail present in the panchromatic image and missing in the multispectral one.

- 4.- Add this spatial detail information into the PC¹ or I image through the inverse wavelet transform.

- 5.- Insert the spatial information of the panchromatic image into the multispectral one through the inverse PCA or IHS transform. The result is a merged image with spectral and spatial resolution.

3.3.3.2 AWI and AWPC using the "à trous" algorithm.

The steps for merging images using these methods are:

- 1.- Apply the PCA or the IHS transform to the multispectral image and obtain the PC¹ or I image.

- 2.- Generate a new panchromatic image, whose histogram matches the histogram of the PC¹ or I images.

- 3.- Decompose only the "histogram-matched" panchromatic image and obtain the wavelet planes.

- 4.- Add the wavelet planes to the PC¹ or I images.

- 5.- Insert the spatial information of the panchromatic image into the multispectral one through the inverse PCA or IHS transform.

The AWI method was defined in Nuñez *et al*, 1999.

4 RESULTS

All the methods described above have been applied to merge SPOT 4 XI (20 m) and SPOT 4 M (10m) images, as well as, IKONOS MS (4 m) and Pan (1 m) images.

The spatial resolution ratio between the SPOT 4 M and the SPOT 4 XI images is 2:1 and the spectral range of the panchromatic sensor matches the spectral range of the Red band of the multispectral one. The spatial resolution ratio between the panchromatic and multispectral IKONOS images is 4:1 and the spectral range of the panchromatic sensor embraced the spectral range corresponding to all the bands of the multispectral one.

4.1 Spatial degradation.

The usefulness of each image-fusion method has been tested by the qualitative analysis of the different merged images. To assess the quality of the resulting merged images, these should be compared to the 'theoretic' images observed by the multispectral sensor if this would offer the same spatial resolution than the panchromatic one. As these images are not available we decided to work with spatially degraded images.

The SPOT XI and SPOT M images have been co-registered and degraded to 40 m and 20 m respectively. The resulting images are very close to what the corresponding sensor would have observed with a degraded resolution.

The IKONOS MS and Pan images have been co-registered and degraded to 16 m and 4 m respectively.

This approach allows us to assess the spectral and spatial quality of the SPOT and IKONOS merged images, comparing these to the original SPOT XI (20 m) and IKONOS MS (4 m) images.

4.2 Spectral quality of the merged images.

The SPOT or IKONOS merged images obtained by different methods have a spatial resolution of 20 m or 4 m respectively, so their spectral quality can be evaluated by comparing its spectral information to that of the original SPOT XI or IKONOS MS image.

In doing so, it is possible to determine which method produces high spectral quality images, that is, which method does not degrade the spectral information.

The spectral quality assessment procedure is based on visual inspection and the use of the following quantitative indicators:

- Difference between the means of the original and the merged images (or BIAS), in radiance. It should be as close as possible to 0.
- Standard deviation of the difference image, in radiance. It globally indicates the level of error at any pixel. Best values, near 0.
- The RASE index, Relative Average Spectral Error, expressed as percentage. It characterises the average performance of the method in the

considered spectral bands (Ranchin and Wald, 2000):

$$RASE = \frac{1}{M} \sqrt{\frac{1}{N} \sum_{i=1}^n RMSE^2(B_i)} \quad (6)$$

where M is the mean radiance of the N spectral bands (B_i) of the original multispectral image, and the $RMSE$ is the Root Mean Square Error computed following the expression:

$$RMSE^2(B_i) = BIAS^2(B_i) + S.DEV^2(B_i) \quad (7)$$

It should be as close as possible to 0

➤ The ERGAS index, (*Erreur Relative Globale Adimensionnelle de Synthèse*), or Relative Adimensional Global Error in the Fusion (Wald, 2000):

$$ERGAS = 100 \frac{h}{l} \sqrt{\frac{1}{N} \sum_{i=1}^n \left(\frac{RMSE^2(B_i)}{M_i^2} \right)} \quad (6)$$

where h is the resolution of the high spatial resolution image, l the resolution of the low spatial resolution image and M_i the mean radiance of each considered spectral band.

The lower the ERGAS values the better the spectral quality of the merged images.

4.3 Spatial quality of the merged images.

To evaluate the spatial quality of the merged images, we used the procedure proposed by Zhou. The panchromatic and the merged images are filtered using the Laplacian filter:

$$\begin{vmatrix} -1 & -1 & -1 \\ -1 & 8 & -1 \\ -1 & -1 & -1 \end{vmatrix} \quad (5)$$

A high correlation between the merged filtered image and the panchromatic filtered one indicates that many spatial information from the panchromatic image has been incorporated during the merging process (Zhou *et al*, 1998)

4.4 Image-fusion methods comparison.

In order to compare the usefulness of each image-fusion methods, the spectral and spatial quality of the resulting merged images have been jointly analysed. The next bar diagrams show graphically the values of the ERGAS index (spectral quality) as well as the correlation coefficients between the panchromatic and merged filtered images (spatial quality).

Although several quantitative parameters have been calculated to assess the spectral quality of the merged images, we present in these diagrams only the ERGAS index results because it embraced other parameters such as the bias or the standard deviation and it allows to estimate globally the spectral quality of a merged data set.

4.1 Spectral and spatial quality of the SPOT merged images

Table 1 shows the results obtained for the indexes described above when the SPOT XI^{40m} – SPOT M^{20m} merged images are compared to the SPOT XI^{20m} original image.

The bars diagram shows graphically the value of the spatial correlation coefficients (first plane) and the ERGAS index (second plane) for each merged image.

Table 1. Spectral and spatial quality of the SPOT merged images

	<i>Xdegrad</i>	<i>Brovey</i>	<i>Pradines</i>	<i>IHS</i>	<i>LHS</i>	<i>PCA</i>	<i>HPF</i>	<i>AW</i> 'à trous'	<i>AW</i> Mallat	<i>AWL</i> 'à trous'	<i>AWL</i> Mallat	<i>AWPC</i> 'à trous'	<i>AWPC</i> Mallat	<i>IDEAL</i>
Spatial correlation coefficient	0.6018	0.9835	0.7608	0.9012	0.9668	0.9709	0.9279	0.9213	0.9047	0.9174	0.8898	0.8786	0.8966	0.8731
	0.6529	0.9836	0.7753	0.9142	0.9729	0.9755	0.9306	0.9418	0.9135	0.9394	0.9367	0.9450	0.9286	1.0000
	0.1993	0.9138	0.6329	0.7263	0.8111	0.5139	0.8732	0.7533	0.5333	0.5209	0.5404	0.4936	0.4252	0.2763
	0.4930	0.9741	0.7110	0.9516	0.9472	0.9597	0.9127	0.8868	0.7914	0.8811	0.8343	0.8759	0.8369	0.6812
ERGAS	2.95	5.69	4.72	6.37	4.30	3.51	8.63	2.88	2.78	2.71	2.48	2.39	2.28	0

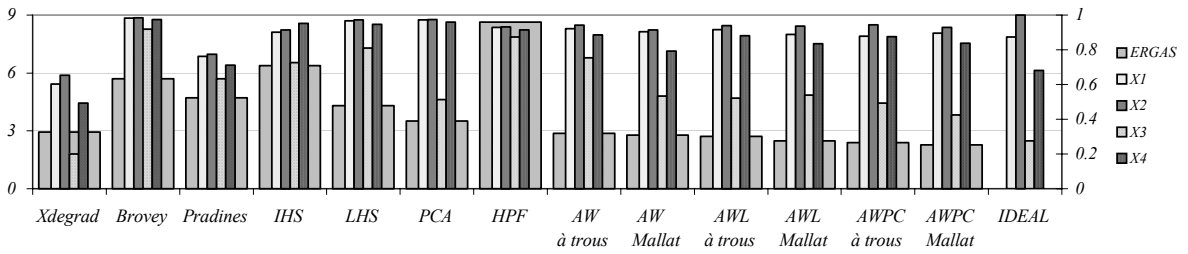


Figure 1. Spatial correlation coefficients and ERGAS values of the SPOT merged images

Higher ERGAS values than those showed in the first column indicate that the image-fusion procedure tends to modify the spectral information of the multispectral image, while lower ERGAS values imply that the fusion method used allows a 'high quality transformation of the multispectral content when increasing the spatial resolution'.

The first column, 'X_{degrad}' shows the results that refer to the comparison between the SPOT XI^{40m} spatially degraded image (initial multispectral image for the fusion) and the SPOT XI^{20m} original multispectral image (IDEAL merged image).

Spatial correlation coefficients close to those corresponding to the IDEAL situation indicates a high spatial quality of the merged images.

Brovey, Pradines, HPF, IHS and LHS methods give poor results both spectrally and spatially. There is an excessive incorporation of information from the panchromatic image into the multispectral one and this results in a low spectral quality of the merged image.

The PCA standard method performs better, but the spectral content of the merged image is significantly different from that of the SPOT XI original one. The ERGAS value is higher after the fusion than before (3.51 and 2.95 respectively). This fact can be observed in the colour of the river, left-bottom part Fig 3(d) in comparison with the same areas in Fig 3(c)

All the methods based on the discrete wavelet transform provide high spectral quality images. In all cases, the ERGAS values are lower after the fusion than before.

Spatially, the AWPC methods perform best. In the AW cases there is an excessive spatial detail incorporation in the NIR band.

Both discrete wavelet transform algorithms used, Mallat's and "à trous", lead to close merged images, both spectrally and spatially

4.2 Spectral and spatial quality of the IKONOS merged images

Table 2 shows the ERGAS values obtained when the merged IKONOS images have been compared to the IKONOS MS^{4m} original one, as well as the spatial correlation coefficients obtained when the merged images have been compared to the IKONOS Pan^{4m}.

Brovey, Pradines, HPF and IHS methods introduce spectral distortion during the fusion process as the high ERGAS values indicate.

When LHS and PCA methods are applied to merge the IKONOS MS and Pan images, the spectral and also, the spatial quality of the resulting merged images is good enough. The reason is in the spectral response function of the IKONOS Pan sensor, which overlaps the spectral response function of all the bands of the IKONOS MS sensor. This fact explains the high correlation coefficient between the IKONOS Pan image and the Intensity or PC¹ obtained when a LHS or PCA are applied to the multispectral image, and also, the high spectral quality of the merged images by these methods.

The AWL methods based on the "à trous" algorithm performs the best, both spectrally and spatially as shown in Fig 4, (at the end of the paper).

Once again, all the methods based on the discrete wavelet transform leads to the best spatial and spectral quality images.

Table 2. Spectral and spatial quality of the IKONOS merged images

	<i>Xdegrad</i>	<i>Brovey</i>	<i>Pradines</i>	<i>IHS</i>	<i>LHS</i>	<i>PCA</i>	<i>HPF</i>	<i>AW</i> <i>'à trous'</i>	<i>AW</i> <i>Mallat</i>	<i>AWL</i> <i>'à trous'</i>	<i>AWL</i> <i>Mallat</i>	<i>AWPC</i> <i>'à trous'</i>	<i>AWPC</i> <i>Mallat</i>	<i>IDEAL</i>
Spatial correlation coefficient	0.179	0.97	0.944	0.924	0.986	0.993	0.861	0.975	0.920	0.977	0.920	0.956	0.926	0.72
	0.195	0.958	0.946	0.926	0.985	0.996	0.863	0.975	0.922	0.961	0.912	0.958	0.928	0.78
	0.193	0.945	0.933	0.913	0.976	0.996	0.862	0.978	0.924	0.947	0.901	0.960	0.930	0.78
	0.204	0.945	0.96	0.96	0.973	0.949	0.865	0.965	0.917	0.949	0.903	0.917	0.897	0.75
ERGAS	2.16	5.40	2.68	2.71	1.87	2.20	5.55	1.81	1.91	1.70	1.81	1.72	1.88	0

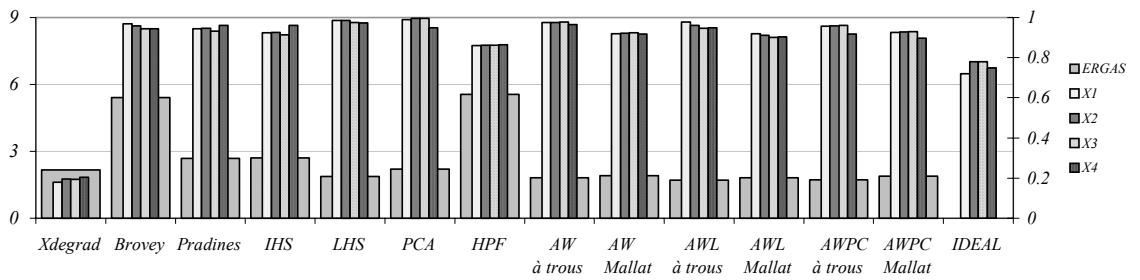


Figure 2. Spatial correlation coefficients and ERGAS values of the IKONOS merged images

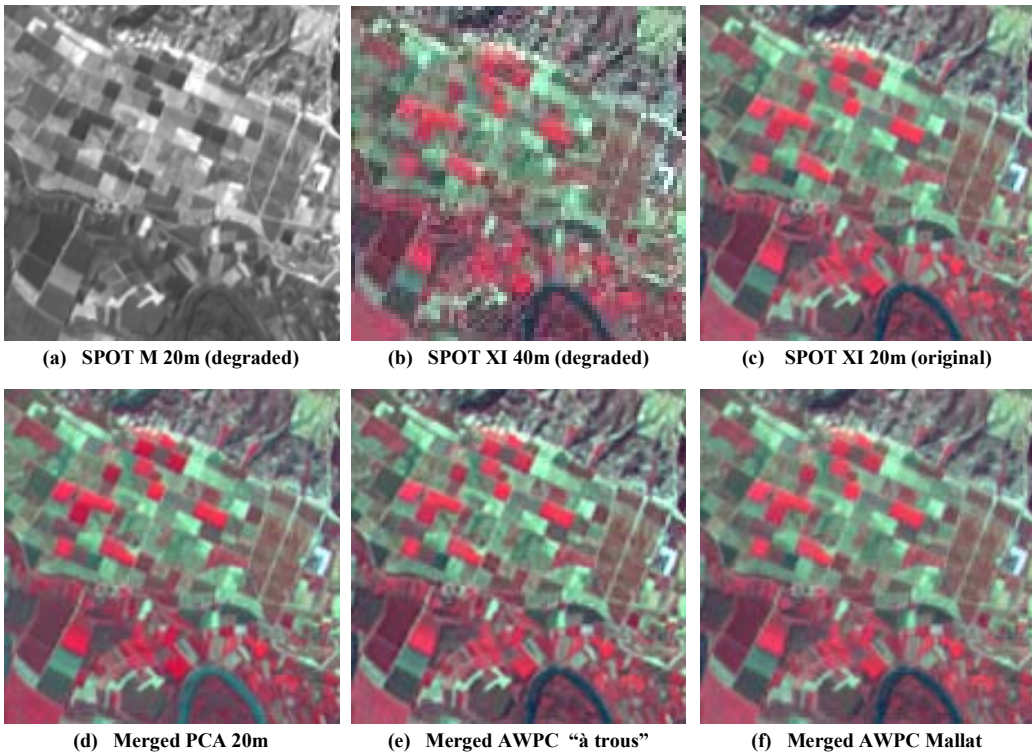


Figure 3. SPOT degraded, original and merged images.

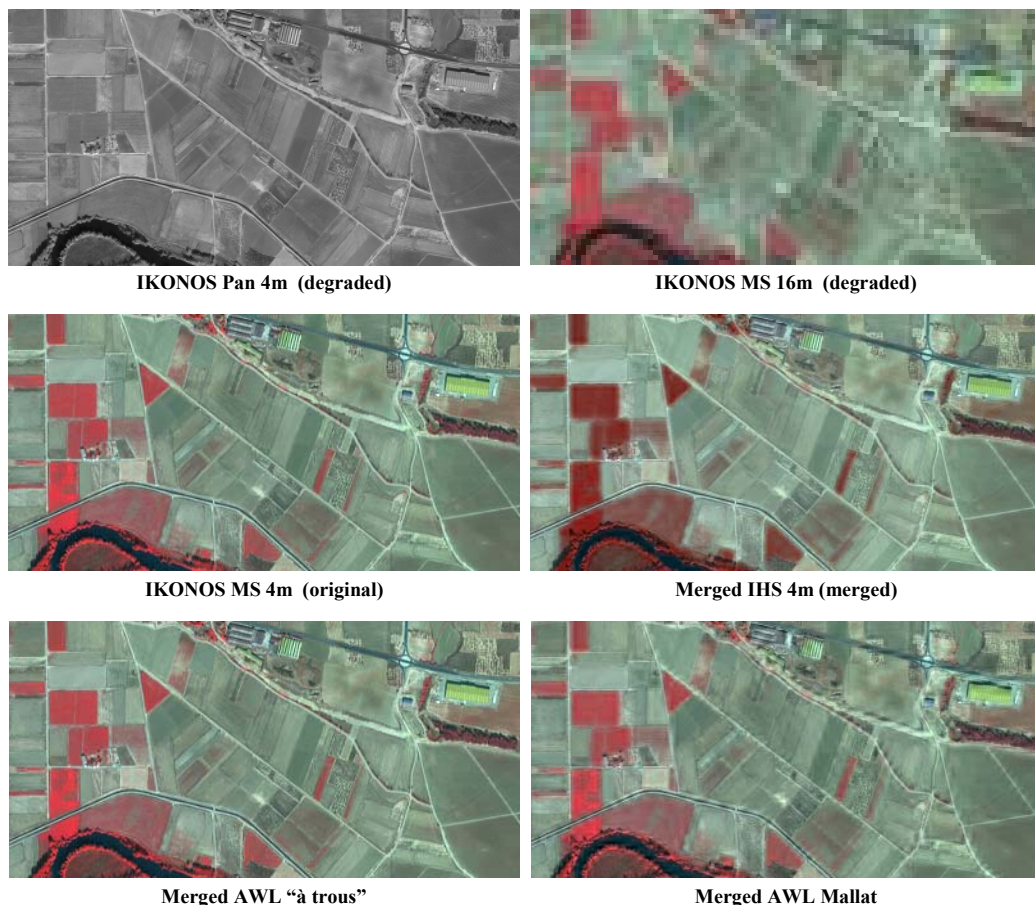


Figure 4. SPOT degraded, original and merged images.

5 CONCLUSIONS

The new multispectral and panchromatic image-fusion methods based on the discrete wavelet transform and proposed by this group (AWL and AWPC) are capable of enhancing the spatial quality of the multispectral image while preserving its spectral content.

The AWL and AWPC methods lead to better results than the AW methods when the spectral response function of the panchromatic sensor doesn't overlap the spectral response function of all the bands of the multispectral one, as it is shown in the SPOT merged images.

Both discrete wavelet transform algorithms used in this work, Mallat's and "à trous" algorithms, lead to merged images with similar spectral quality. Visually, the spatial quality of the SPOT and IKONOS merged images is better when the "à trous" algorithm is used.

6 REFERENCES

Carper, J., T.M. Lillesand and R.W. Kiefer, 1991, The use of intensity-hue-saturation transformations for merging SPOT panchromatic and multispectral image data. *Photogrammetric Engineering and Remote Sensing*, 56(4), 459-467.

- Chavez, P.S., J. Stuart, C. Sides and J.A. Anderson, 1991, Comparison of three different methods to merge multiresolution and multispectral data: Landsat TM and SPOT panchromatic. *Photogrammetric Engineering and Remote Sensing*, 57(3), 259-303.
- Garguet-Dupont, B., J. Girel, J.M. Chasseny and G. Pautou, 1996, The use of multiresolution analysis and wavelet transform for merging SPOT panchromatic and multispectral image data. *Photogrammetric Engineering and Remote Sensing*, 62(9), 1057-1066.
- Hallada, W.A.. and S. Cox, 1983, Image sharpening for mixed spatial and spectral resolution satellite systems. *Proceedings of 17th International Symposium on Remote Sensing of Environment*, 1023-1032.
- Haydn R., G.W. Dalke, J. Henkel and J.E. Bare, 1982, Applications of the IHS color transform to the processing of multisensor data and image enhancement. *Proceedings of the International Symposium on Remote Sensing of Arid and Semi-Arid Lands* held in El Cairo, Egipt, 559-616.
- Holschneider, M. and P. Tchamitchian, 1990, Régularité locale de la fonction non-différentiable de Riemann, in *Les Ondelettes* in 1989, P.G. Lemarié, Ed. Paris, France: Springer-Verlag, p.102
- Mallat, S.G., 1989, A theory for multiresolution signal decomposition: the wavelet representation. *IEEE Transaction on Pattern Analysis and Machine Intelligence*, 11(7), 674-693.
- Nuñez, J., X. Otazu, O. Fors, A. Prades, V. Palà and R. Arbiol, 1999, Multiresolution-based image fusion with additive wavelet decomposition. *IEEE Transactions on Geoscience and Remote Sensing*, 37(3), 1204-1211.
- Pohl, C and J.L. Van Genderen, 1998, Multisensor image fusion in remote sensing: concepts, methods and applications. *International Journal of Remote Sensing*, 19(5), 823-854.
- Pradines, D, 1986, Improving SPOT image size and multispectral resolution. *Proceedings SPIE Conference: Earth Remote Sensing using Landsat TM and SPOT Systems*, 660, 78-102.
- Ranchin, T. and L. Wald, 2000, Fusion of high spatial and spectral resolution images: the ARSIS concept and its implementation *Photogrammetric Engineering and Remote Sensing*, 66(1), 49-61.
- Smith, A.R, 1978, Color gamut transforms pairs. *Computer Graphics*, 12, 12-19.
- Starck, J.L. and R. Murtagh, 1994, Image restoration with noise suppression using wavelet transform. *Astronomy and Astrophysics*, 288, 342-348
- Shettigara, V.K., 1992, A generalized Component Substitution technique for spatial enhancement of multispectral images using a higher resolution dataset. *Photogrammetric Engineering and Remote Sensing*, 58(5), 561-567.
- Wald, L, T. Ranchin and M. Mangolini, 1997, Fusion of satellite images of different spatial resolution: Assessing the quality of resulting images. *Photogrammetric Engineering and Remote Sensing*, 63(6), 691-699.
- Welch, R. and M. Ehlers, 1987, Merging multiresolution SPOT HRV and Landsat TM data. *Photogrammetric Engineering and Remote Sensing*, 53(3), 301-303.
- Yocky, D.A., 1995, Image merging and data fusion by means of the discrete two-dimensional wavelet transform. *Journal Optical Society of America A.*, 12(9), 1834-1841.
- Zhou J., D.L. Civco and J.A. Silander, 1998, A wavelet transform method to merge Landsat TM and SPOT panchromatic data. *International Journal of Remote Sensing*, 19(4), 743-757.

Comparison between the different curvature models of terrain for determining the degree of soil humidity.

Porres de la Haza, M.J., Pardo Pascual, J.E.

Dpto. Ingeniería Cartográfica, Geodesia y Fotogrametría. Universidad Politécnica de Valencia

mporres@cgf.upv.es

ABSTRACT- *The curvatures are defined as the rate of change of the slope in a particular direction, the same being the curvature of the line that is the intersection of the topographical surface with any plane. The calculation of this parameter, using information obtained from a raster digital elevations model, theoretically permits the identification of areas where there is an accumulation or dispersion of surface or subterranean water and, in turn, can be an indicator of the areas where vegetation is more developed.*

This study compares, by means of correlation, the landform and the vegetation density. The landform is determined by different curvature parameters according to several algorithms proposed in the bibliography (profile curvature, plan curvature, tangent curvature, longitudinal convexity and cross-sectional convexity) and with different neighborhoods (only considering the four adjacent neighbors or the eight surrounding pixels). The vegetation density is characterized by the NDVI of Landsat ETM and TM images. The analysis is done in three Mediterranean calcareous environments but are slightly different in climate and geomorphology.

The results obtained show the small role that the landform, described by curvature parameters, has on the vegetation distribution in very permeable geological areas, as are those studied. The only areas in which relatively significant correlation levels have been found are those in which the curvature changes coincide with significant lithologic changes. That suggests that in calcareous Mediterranean environments the soil humidity distribution is not directly affected by the landform.

The results do not allow for a confident conclusion that there are some parameters that are more descriptive than others, although it appears that the curvature profile and the tangent curvature analyzed with eight neighbors obtain higher degrees of correlation than the rest of the parameters.

1. INTRODUCTION

The terrain curvature is defined by the rate of slope inclination and is determined mathematically as the second derivative of the function that determines the topographic area. It constitutes one of the most descriptive morphometric parameters of the landform, and there are many authors that propose it as a tool for locating the concentration or dispersion of water flow (Moore et al., 1991; Felicísimo, 1994; Florinsky, 1998; Wilson and Gallant, 2000) because the concave and convex areas of a region can be recognized.

The relationship between the landform and the distribution of humidity can be initially considered as direct. Thus, it is thought that the concave areas accumulate humidity to a higher degree, while convex areas favor the divergence of water, and will tend to be areas with less humidity.

To corroborate the significance that the landform has in the distribution of soil humidity, analyses about the relationship that exists between the terrain

curvature and the density of spontaneous vegetation have been done. The latter, at least in Mediterranean areas, is much related with the existence of sufficient soil humidity. Research like that of Florinsky & Kuryakova (1996) has shown that, in more humid regions, the relationship between the vegetation and the curvature of the terrain is high, thus the landform could be considered a determining factor in the distribution and development of vegetation. For the Mediterranean region, however, the research that has been conducted until now by the authors (Porres & Pardo, 2000; Pardo et al., 2001; Pardo et al. 2002) has shown that the relationship between the distribution of vegetation and the landform (established by the curvature parameters) is, in general, very small or insignificant compared to what happens with other topoclimatic parameters, such as potential direct radiation.

The parameterization of the terrain by the curvature is always complex and, in fact, there are several algorithms to define it. Various authors (Zevenbergen & Thorne, 1987; Moore et al., 1991;

Wood, 1996; Florinsky & Kuyakova, 1996) have made diverse proposals to characterize the different curvatures of the terrain whose values, actually, do not coincide (Porres et al., 2002).

In the present study we seek to explore the relationship that exists between the different curvatures - as they have been established by different authors- and the distribution of vegetation density as it relates to the average soil humidity.

To achieve that, three different regions were studied that correspond to calcareous areas that are more or less humid, although always in the Mediterranean climate zone. Specifically, small basins in the interior of the province of Valencia have been analyzed, ravines situated to the south of Muela de Cortes de Pallás, and ravines situated in the Maestrat region - province of Castelló de la Plana, close to Albocàsser - which are quite a bit more humid than those in the Muela de Cortes, as well as a small southern area of the Menorca island. Morphologically, in all cases areas formed by tabulated limestone fissured by deep ravines are analyzed. The bottoms of the Menorcan ravines were found to be full of fine sediment which differentiates them from the other two areas, in which the bottoms of the ravines correspond to areas that are also calcareous, but through which streams full of thick sediments flow.

2. MATERIAL USED

To carry out this research Landsat TM and ETM satellite images have been used, from which the NDVI was calculated. Specifically, the Cortes de Pallás region (Valencia) was studied using an image from June 1994, that of Albocàsser was from June 2000 and that of Menorca was taken on February 25th 2000. The images of Cortes de Pallás and Albocàsser were orthorectified and resampled to 25 m/pixel. The image of Menorca was rectified and resampled by the nearest neighbor at 10 m/pixel.

To determine the curvature parameters we began by using the digital elevation model (DEM). Raster models have been used to facilitate the comparison with the satellite images. Specifically, the DEM corresponding to the Muela de Cortes is from the Centro Geográfico del Ejército (with a grid step of 25 x 25 m). It is a DEM that was determined using a topographic cartography of 1:50,000. The DEM of Albocàsser was generated using a topographic cartography of 1:10,000 from l'Institut Cartogràfic Valencià, and using ArcView 3D Analyst initially to generate a TIN model that was later generalized to a raster with a grid step of 25 x 25 m. These two models have been used for the orthorectification of the images

as well as to determine the curvature models. The DEM of Menorca was generated using a topographic cartography of 1:5,000, also with ArcView 3D Analyst, but the raster model obtained has a grid step of 10 x 10 m.

3. PARAMETERIZATION OF THE CURVATURE

The curvature defined as the rate of slope change in a particular direction requires, in the first place, the definition of the surface using the information from the DEM. Secondly, it is necessary to establish a cutting plane, so that the curvature parameter determined is that of the line that emerges as the intersection of the surface with the cutting plane. As a result of this two issues emerge: the first is the definition of the surface from the altitude information of the DEM, and the second is the definition of the cutting plane derived from the curvature parameter which is significant for this study.

3.1. Establishing the topographic surface

There are various mathematical models used to determine the topographic surface using a raster DEM, whose complexity increases as the number of terms used in its equation increase. In our case, all of the topographic surfaces from which the curvature parameters are derived, are determined using second level polynomial equations or greater. In this study, the surface assumed by each curvature model is not specifically analyzed. Instead, the models proposed by various authors are analyzed directly as well as the manner with which they obtain the terms of the different equations.

Once the mathematical model used to characterize the surface is determined, the calculation of its coefficients depends directly on the altitude values of the neighborhood, as well as the number of neighbors that are included in the calculation. In our case, for the calculation of the curvatures using the DEM, two different procedures have been used for determining the topographic surface, which involves the use of a different number of pixels in the calculation. Although in both cases, neighborhoods of 3x3 were considered, the difference between the two procedures is that the first method involves all of the neighbors and the second only uses the pixels that are immediately adjacent to the central pixel, the cardinal pixels.

In previous studies (Porres et al., 2002) it is observed that the effect seen and results obtained when all of the members of the neighborhood are used for the calculation of the curvatures were smoother than using only adjacent pixels. In this study we will use once again the two forms of considering the neighborhood to try to calibrate which of the two

procedures is more descriptive in detecting the relationship that exists between the terrain curvatures and the vegetation distribution.

Nomenclature used by the authors in this study	Nomenclature proposed by the authors compared		
Profile Curvature <i>Pc</i>	Florinsky	K_v	<i>Profile convexity</i> <i>Profile curvature</i>
	Woods	prof c	
	Moore	K_p	
Plan curvature <i>SC</i>	Florinsky	-	<i>Plan convexity</i> <i>Plan curvature</i>
	Woods	planc	
	Moore	K_c	
Tangent curvature <i>C_{TAN}</i>	Florinsky	K_h	<i>Tangent curvature</i>
	Woods	-	
	Moore	K_t	
Longitudinal convexity <i>C_L</i>	Florinsky	-	<i>Longitudinal conv</i>
	Woods	long c	
	Moore	-	
Cross-sectional convexity <i>C_T</i>	Florinsky	-	<i>Cross-sectional conv</i>
	Woods	cross c	
	Moore	-	

Table 1. Terms used by the authors.

3.2. Definition of the curvature parameters

There are as many possible curvature parameters as there are intersecting planes on the surface. Nevertheless, the parameters referenced as good descriptors of concave and convex areas in the bibliography are basically reduced to five. In fact, there exists considerable conceptual and terminological confusion, given that not all of the authors give the same names and even, on occasion, establish identical denominations for different parameters. With the intention of facilitating comprehension of the multiple parameters proposed by different authors (Zevenbergen & Thorne, 1987 ; Moore et al., 1991 ; Wood, 1996 ; Florinsky & Kuryakova, 1996) Porres et al. (2002) used a common nomenclature which attempted to group together what had previously been described by other authors (Table 1) and analyzed the differences between the different parameters. For this study, five of the potentially more descriptive parameters have been selected. These are the following:

* The *profile curvature* (*Pc*). This parameter describes the curvature of the steepest line of a

surface, that is, the curvature of the line that emerges as the intersection of the surface with the vertical plane which contains the gradient vector. It is used to study the phenomena of transport and the sedimentation of materials by water flow which, in a certain way, have been directly linked to studies like the one which concerns us now. The resulting values are given, as in all the curvature parameters, in radians/m, and are deduced using the following equation:

$$P_c = \frac{g^2 d + 2 f g h + e h^2}{(g^2 + h^2) \left(\sqrt{g^2 + h^2} + 1 \right)^3} \tag{1}$$

in which the terms *g* and *h* refer to the altitude variations in the model in directions *x* and *y*, while *d*, *e* and *f* describe the variations of the slope on the *x*-axis, the *y*-axis and in a diagonal direction, as shown here:

$$d = \frac{\delta^2 z}{\delta x^2}; \quad e = \frac{\delta^2 z}{\delta y^2}; \quad f = \frac{\delta^2 z}{\delta x \delta y}; \quad g = \frac{\delta z}{\delta x}; \quad h = \frac{\delta z}{\delta y};$$

The *d*, *e*, and *f* parameters are calculated using the second derivatives, which makes them the most relevant in the curvature equation.

The result oscillates around the value of 0, showing the convex areas with negative values and the concave areas with positive values. In Figure 1 an example of the MDT of the profile curvature to which have been added the contour curves to facilitate its interpretation. The high values (whiter) are found at the concave contact area between the valley edges and the bottom of the ravine. The lesser values, on the other hand, correspond to the land inflexion seen on the upper edge of the valley walls.

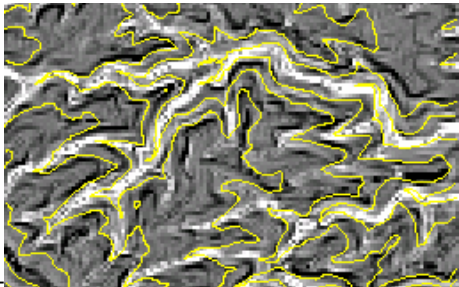


Fig. 1. Digital profile curvature model which corresponds to the area of Cortes de Pallás. Contour curves have been added to facilitate its interpretation.

* The *plan curvature*, (*Sc*). This parameter coincides with the curvature of the line that emerges as the intersection of the topographic surface with the horizontal XY plane that passes through the point.

That is, it describes the rate of change of the surface orientation along a horizontal line of the surface. It is, then, a curvature parameter complementary to the profile curvature, that is, the planes that determine the plan curvature and the profile curvature are orthogonal. Its use is justified in the studies about flow dispersion or convergence. It is determined using the following equation:

$$S_c = \frac{h^2 d - 2fgh + eg^2}{(\sqrt{g^2 + h^2})^3} \quad (2)$$

As in the case of the Pc the positive values are shown in concave areas and the negative in the convex areas. In the plan curvature model (Figure 2) the highest values are shown in the bottoms of the valleys and water beds, while the lowest are clearly shown to be in the watershed limits. This model, as observed in the figure, is particularly interesting as a morphological descriptor.

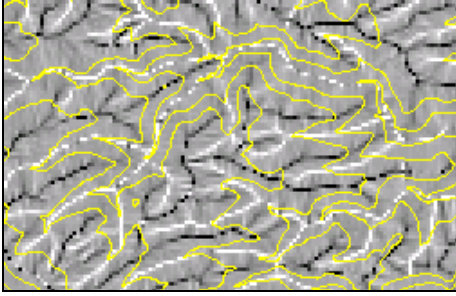


Fig. 2. Digital model of the plan curvature.

* The *tangent curvature* (C_{TAN}) coincides with the plan curvature but is multiplied by the sine of the slope to avoid excessively large values when the slope of the surface is small. The tangent curvature is a defined by a plane inclined perpendicularly to the line of maximum slope and to the surface. It is determined by the following equation:

$$C_{tan} = \frac{h^2 d - 2fgh + eg^2}{(g^2 + h^2)\sqrt{g^2 + h^2 + 1}} \quad (3)$$

It also involves a parameter that is complementary to the curvature profile. Moore et al. (1991) and Florinsky & Kuryakova (1996) show that its use is preferable to that of the Sc because it is by means of the C_{tan} that small irregularities are better noticed, while the Sc shows the evident features with more clarity, blurring the topographic irregularities of lesser significance. In figure 3 it is shown that the results are very similar, but here more nuances appear.

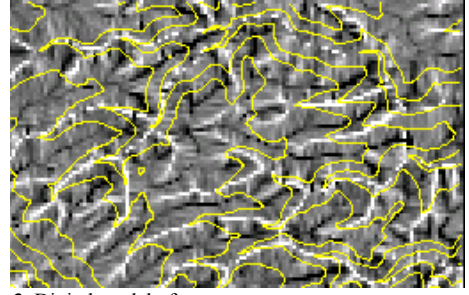


Fig. 3. Digital model of tangent curvature

* *Longitudinal curvature* (C_L) and *cross-sectional curvature* (C_c). Both are parameters defined mathematically, but without physical significance. The mathematical definition of the curvatures, as explained by Zevenbergen (1987) not only depends on the second derivatives, but also of the first, although these "false curvatures" explain the terrain in a similar way that the curvature profile and the plan curvature. The C_L is determined by the following equation proposed by Wood (1996):

$$C_L = \frac{-2(g^2 d + fgh + eh^2)}{g^2 + h^2} \quad (4)$$

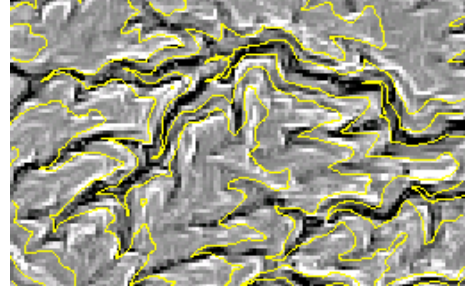


Fig. 4. Digital model of longitudinal convexity.

As can be seen in Figure 4, the result is very similar to that of the Pc , the difference being the change of the sign. Here the values of the convex shapes are positive while those of the concave shapes are negative. The cross-sectional convexity could be considered as the complementary curvature to the C_L and is determined by the equation:

$$C_T = \frac{-2(h^2 d - fgh + eg^2)}{g^2 + h^2} \quad (5)$$

As in the case of C_L , the sign has also been changed with respect to the previous examples, showing positive values for the watershed limits and negative values for the concave bottoms of the water beds and valleys (Figure 5).

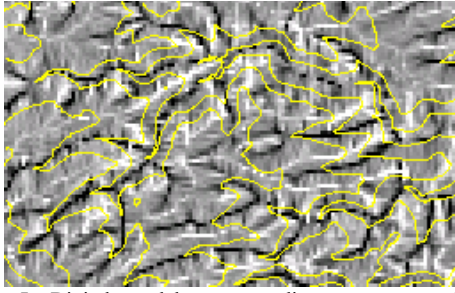


Fig. 5. Digital model corresponding to cross-sectional convexity.

4. METHODOLOGY USED

Given the objective of the study, to have the models of all the curvature parameters generated by the two procedures of neighborhood taken into consideration is a requirement, as is the NDVI that corresponds to common areas in the three zones of study.

To do this a tool has been programmed using IDL with which the different curvature parameters have been calculated, permitting the characterization of the terms d , e , f , g , and h using the eight surrounding neighbors at every pixel (Figure 6) or just the cardinal neighbors.

(a)			(b)		
Z1	Z2	Z3	Z1	Z2	Z3
Z4	Z5	Z6	Z4	Z5	Z6
Z7	Z8	Z9	Z7	Z8	Z9

Fig. 6. Notation given to the neighbors that are considered in the case of just the cardinals (a) and if all are included (b).

The terms d , e , f , g y h are calculated by determining the variations between the altitudes of the neighbor pixels, showing the difference between the two methods used lies in the number of pixels involved in the calculations.

In Table 2 the mathematical expressions used to deduce each of the terms in the curvature parameter equations in the case of using a type (a) neighborhood, that is, only the immediately adjacent pixels. In table 3 the expressions used to deduce these terms in a type (b) neighborhood:

$$d = \frac{Z_6 + Z_4 - 2Z_5}{L^2}$$

$$e = \frac{Z_8 + Z_2 - 2Z_5}{L^2}$$

$$f = \frac{(Z_3 + Z_7) - (Z_1 + Z_9)}{4L^2}$$

$$g = \frac{Z_6 - Z_4}{2L}$$

$$h = \frac{Z_2 - Z_8}{2L}$$

Table 2. Expressions to determine the terms if a type (a) neighborhood is used.

$$d = \frac{(Z_1 + Z_3 + Z_4 + Z_6 + Z_7 + Z_9) - 2(Z_2 + Z_5 + Z_8)}{3L^2}$$

$$e = \frac{(Z_1 + Z_2 + Z_3 + Z_7 + Z_8 + Z_9) - 2(Z_4 + Z_5 + Z_6)}{3L^2}$$

$$f = \frac{(Z_3 + Z_7) - (Z_1 + Z_9)}{4L^2}$$

$$g = \frac{(Z_3 - Z_1) + (Z_6 - Z_4) + (Z_9 - Z_7)}{6L}$$

$$h = \frac{(Z_1 - Z_7) + (Z_2 - Z_8) + (Z_3 - Z_9)}{6L}$$

Table 3. Expressions to determine the terms if a type (b) neighborhood is used.

The Landsat images that correspond to the Muela de Cortes and the Albocàsser area have been orthorectified. In previous studies (Porres & Pardo, 2000; Pardo et al., 2001, Pardo et al. 2002) the images compared had only been rectified and so it is possible that the low level of correlation is due to the existence of a certain geometric offset between the images. With the Menorca image, though, the orthoimage was unavailable and so the analyses have been done using the rectified image.

With all of this information a correlation analysis between the two data sets was carried out to establish the level of dependence that exists between the vegetation distribution and the landform and to determine which curvature parameter shows the clearest relationship between the two. The analyses have been carried out over small regions, limited only to the areas of spontaneous vegetation, the other areas were masked out.

5. RESULTS

The results obtained are partially shown in Tables 4, 5, and 6, and within which the slight or null correlation that exists between the curvatures and the vegetation distribution can be confirmed. A detailed analysis, however, permits nuances to be made in this first assertion and the extraction of some useful ideas to assess the interest in curvature in vegetation density distribution studies as well as the geographic distribution of soil humidity.

Focusing on the difference found between the use of type (a) or (b) neighborhoods, table 4 shows that it cannot be considered significant in any of the analyzed parameters. Attention should be brought to the result that shows a negative correlation in the case of P_c , Sc and C_{tan} , which indicates that in concave areas – valley bottoms – the vegetation decreases. Following the same logic, apparently incoherent, with the C_L and C_T models, the correlation is positive.

	8 neighbors	4 neighbors
P_c	-0.023	-0.020
Sc	-0.009	-0.011
C_{tan}	-0.005	-0.006
C_L	0.021	0.017
C_T	0.007	0.008

Table 4. Correlation coefficients between different curvature parameters and the NDVI for a part of the Cortes de Pallás areas.

Given this apparent lack of coherence it was decided that only one slope would be analyzed so that other variables – like solar radiation- would remain basically homogeneous. The result (Table 5) shows an improvement, although the relationship is still very low, at least the correlation sign removing the bottom of the watercourses is now coherent.

	8 neighbors	4 neighbors
P_c	0.062	0.056
Sc	0.040	0.032
C_{tan}	0.065	0.046
C_L	-0.061	-0.051
C_T	-0.073	-0.052

Table 5. Correlation coefficients between the different curvature parameters and the NDVI for a slope of the Cortes de Pallás.

Of the results shown in Table 5 it is worth emphasizing three significant ideas: (i) That although the study is based on a homogeneous area, as is a

slope, the correlation indices continue to be very low; (ii) Although they are low, it is shown that, in all cases, the correlation is somewhat larger if the curvature parameters determined using the eight pixels take into account only the four adjacent neighbors; (iii) While the P_c and C_L parameters have almost identical correlation indices, in the complementary parameters significant differences are observed, and that C_T and C_{TAN} show significantly higher degrees of correlation than Sc .

	Menorca	Albocàsser
P_c	0.222	-0.040
Sc	0.070	0.015
C_{tan}	0.034	-0.016
C_L	-0.165	-0.040
C_T	-0.062	0.013

Table 6. Correlation indices obtained by different curvature parameters, with type (2) neighborhoods with respect to the NDVI of the Menorca and Albocàsser images.

In Table 6 the correlation indices obtained from the Albocàsser and Menorca areas are shown. It is interesting to note that the values reached are very low and we see a similar incoherence to that observed in Cortes de Pallás (Table 2) in the case of Albocàsser. On the contrary, the results obtained for a small area corresponding to the south of Menorca show much better values, some of the parameters reaching a 22% correlation between the profile curvature and the NDVI which is more revealing, in this case the C_L shows a value of 16%.

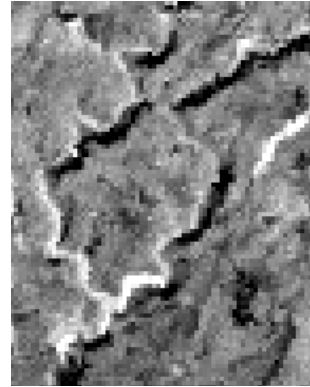


Fig. 6. NDVI that corresponds to an area of the ravines in southern Menorca, specifically the Barranc de Trabalúger.

In Figures 6 and 7 it can be observed that there are significant similarities in the area that corresponds to the ravines.

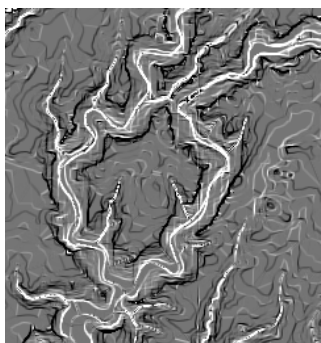


Fig. 7. Model of the profile curvature that corresponds to one of the ravines in southern Menorca. It is the same area that is shown in figure 6.

The image of the model of P_c shows the splitting lines of the slope: The convexities are shown in black while the concavities appear white (the inverse of what is seen with C_L) which explains why the correlation was positive in the case of P_c and negative for the C_L . The white lines show where the bottom of the ravine begins. This area coincides with a change in the type of material (it is full of fine material from the Holocene epoch) which in turn marks a sudden change in the vegetation, into being a bottom that is covered with vegetation. In fact, it is possible that the correlation indices that were obtained have been relatively undervalued due to the fact that the image is from the wintertime and the proportion of spaces with shadows at the edge and at the bottom of the canyons is very high, distorting the correlation results.

The morphing of the terrain of Albocàsser and Cortes is relatively similar. They are large units of tabular limestone, divided by deep valleys through which rocky streams flow. However, climatically, the Albocàsser area is significantly colder and more humid than that of the Cortes. The Menorcan ravines, also made of very permeable limestone, can be distinguished from those of the interior of Valencia because they are filled with fine sediment. The results obtained seem to suggest that, in very permeable environments, such as those that we are analyzing here, the factor of the change in vegetation is not as related to a topographical modification – a change in the slope or a concavity in the landform – nor with small climatic variations. Instead, it is related to a change in the type of materials which implies an alteration in the capacity to retain humidity by these materials.

6. CONCLUSIONS

The results show that in a Mediterranean environment with very permeable lithologies, such as those studied, the role of the terrain curvature in the

vegetation distribution is quite small compared to what happens in other geographical environments. The correlation indices between the NDVI and the curvature parameters are generally very low.

The low correlation does not appear to follow the methodological factors, but rather the physical factors that are associated with the features of the places. In fact, the correlation indices obtained have been low in all cases without considering: (a) That the NDVI was obtained from a orthorectified or simply a rectified image; (b) The specific parameter with which the curvature was calculated. If differences were found, they cannot be considered important enough to establish that one parameter is clearly more descriptive than another. It is possible that an analysis of areas where the landform has more direct significance in the humidity distribution would permit the identification of one parameter as more descriptive; (c) The fact that only 4 cardinal neighbors or the 8 adjacent ones were used for the calculations seems to have an influence, but cannot be said to be a determining factor.

The only result that shows a certain degree of correlation is that seen in Menorca, with a correlation of the NDVI with the curvature profile of 22% (and to a lesser extent the longitudinal curvature with 16%). The greatest correlation, more than that with the simple landform, seems to be associated with a change in the type of material that are in the canyon walls and bottom.

If the use of the curvatures seems to be inefficient for vegetation distribution analysis, its use in geomorphic study seems to be much more promising.

7. REFERENCES

- Florinsky, I.V. y Kuryakova, G.A. (1996): "Influence of topography on some vegetation cover properties", *Catena* 27, 123-141.
- Gallant J.C. y Wilson, J.P (2000): "Primary Topographic Attributes" . Wilson y Gallant *Terrain Analysis: Principles y applications*. NY: 2000, 3, pp.51-86
- Moore, I. D., Grayson, R.B. y Ladson, A.T. (1991): "Digital Terrain Modelling: A review of hydrological, geomorphological and biological applications" *Hydrological Processes*, 5 (1), 7-34.
- Pardo J.E., Porres M.J., Fernández Sarriá, A, Ruiz Fernández, L.A. (2001) *Influencia de la topografía en la regeneración de áreas quemadas*. Universidad de Lleida y editorial Milenium. pp.155-159

- Pardo Pascual, J. E, Fernández Sarría, A. Porres de la Haza, M. J. y Ruiz Fernández, L. A. (2002): Analysis of the regeneration processes of the vegetation canopy on different lithologies and their relationship with topoclimatic variables derived from a DEM, ESSC Congress Valencia 2000
- Porres de la Haza, M.J. y Pardo Pascual, J. E. (2000): Influence of topoclimatic variables derivated from digital terrain models over the vegetation regeneration processes in burned areas, IAPRS, vol. XXXIII, Amsterdam.
- Porres de la Haza, M.J., Pardo Pascual, J.E. , Ruiz Fernández, L.A. y Fernández Sarría, A. (2002): “Estudio comparativo de los métodos de obtención de las curvaturas del terreno para la descripción de los flujos hídricos subsuperficiales y superficiales” Actas de la 3ª Asamblea Hispano-Portuguesa de Geodesia y Geofísica. (En prensa). Valencia
- Woods, J. (1996) : “The geomorphological characterisation of Digital Elevation Models”, PhD Thesis, University of Leicester, UK. Ver también:
http://www.geog.le.ac.uk/jwo/research/dem_char/thesis
- Zevenbergen, L.W. and Thorne, C.R. (1987): “Quantitative analysis of land surface topography”. *Earth Surface Processes and Landforms* 12, pp.47-56.

6. ACKNOWLEDGEMENTS

This study has been developed within the research project “The generation of local thematic cartography and its analysis using geographical information systems”, PB98-1507-C02.

VEGETATION / SPOT4 data for use in meteorological models : surface albedo and land cover mapping.

L. Franchistéguy¹, JL Champeaux¹, S. Garrigues^{1,2}, R. Lacaze^{1,3}, JL Roujean¹

1. GAME/CNRS Météo-France, 42, Av. G. Coriolis, 31057 Toulouse Cedex, France

2. (present affiliation) INRA Bioclimatologie, Domaine St Paul, Site Agroparc, 85914 Avignon Cedex 9, France

3. (present affiliation) MEDIAS-France, CNES-BPI2102, 18 Av E. Belin, 31055 Toulouse Cedex, France

Corresponding author : laurent.franchisteguy@meteo.fr

ABSTRACT - *The soil-vegetation-atmosphere transfer scheme ISBA, implemented in atmospheric models of Météo-France, requires land surface parameters like albedo. So far, these parameters are specified as a function of vegetation type based on a land cover classification and look-up tables (LUT). The VEGETATION instrument on board SPOT4 provides measurements at 1 km which presents improvements compared to AVHRR. Those data sets are used in this study to improve and update land cover and surface albedo products over Europe.*

The land cover mapping over France is achieved in the framework of the Global Land Cover 2000 project. The objective of this latter project is to produce a global map at 1 km resolution using VEGETATION data for the year 2000. The classification method based on components analysis and clustering techniques was applied on daily multi-spectral VEGETATION data and ten days NDVI composites products. The validation of the map relies on CORINE land cover dataset. In parallel, land surface spectral albedo is calculated from the inversion of kernel-driven BRDF (Bidirectional Reflectance Distribution Function) model. Values of land surface albedo per vegetation units are compared to standard values regularly used or prescribed. Comparisons with other albedo data sets show good agreement.

Although the final objective is to provide spatially distributed products over Europe, results will be shown here on limited French areas. Future meteorological models will require better estimation of global surface parameters to reduce errors in the energy budget at the atmospheric boundary layer. The new generation of sensors system like POLDER, MODIS, MISR, MSG and VEGETATION will help to obtain such global products.

1 INTRODUCTION

In meteorological simulations, the interactions between the soil, the biosphere and the atmosphere are carried on with the SVAT (Soil Vegetation Atmosphere Transfer) model category. One of them, ISBA, has been successfully implemented in atmospheric models of Météo-France. Most of the land surface parameters that are required in ISBA (albedo, leaf area index, percentage of vegetation cover for example) were so far derived from LUT and an AVHRR land cover classification.

We study there the ability of the VEGETATION sensor (VGT) to improve the determination of these parameters. The VGT instrument on board SPOT4 provides measurements at 1 km sensor-resolution that are used to produce a land cover map and a land surface albedo data set over France. It presents improvements compared to actual AVHRR-derived products thanks to better radiometric and geometric resolutions.

2 DATA SET

VGT sensor provides a global observation of the world on a daily basis, at 1-km resolution, in four spectral bands : blue (430-470 nm), red (610-680 nm), near infra-red (780-890 nm) and short-wave infra-red bands (1580-1750 nm). Data were made available in the framework of VEGA2000 programme ('Vegetation data for the Millenium Ecosystem Assesment') and GLC2000 project (Global land Cover 2000). We processed time-series of VGT-S1 data (surface reflectance, daily synthesis) over France from November 1999 to December 2000. Geometric corrections were applied and data were corrected from atmospheric effects (water vapor content, ozone, aerosols).

3 LAND COVER MAPPING

3.1 Methodology

a) Eco-climatic stratification

The purpose of a stratification is to divide a large area in strata where phenology and land cover are homogeneous. Different types of climate (oceanic, Mediterranean, mountain, etc...) are present in France. As shown during the Pelcom project (Mucher et al, 2001), a stratified approach improves the accuracy and details of a classification, thereby reducing the number of misclassifications due to spectral confusion. The stratification over France was derived from the FIRS (Forest Inventory from Remote Sensing) ecosystem regions (EC, 1995) and 11 eco-climatic regions were defined.

b) Unsupervised classification using 10-days NDVI profiles

One of the most common method to map the landcover is to perform an unsupervised classification in order to cluster NDVI temporal profiles according to similar spectral signatures values in an iterative way.

The unsupervised classification performs well to distinguish in particular agricultural crops while sometimes it is difficult to separate pasture and forests. Areas with low vegetation such as vineyards are also difficult to detect.

Furthermore, the major problems of the unsupervised classification are the arbitrary selection of the number of classes and the labelling of these classes. The difficulties can be partly overcome when a large area, such as Europe, is processed but the method becomes hazardous when many small areas are considered for classification. In this case a complex patchwork is generated, each cluster determined by the algorithm does not necessarily represent a required land cover class, but represent an heterogeneous area of several land cover classes.

c) Principal component analysis on VGT-S1 data

At the opposite of the most commonly opinion of the land cover community to do composites before classification, we have taken the opportunity to use the primary information of the S1 channels to map the land cover.

However, some prerequisites are necessary : for each climatic area, we have selected a list of clear days (with less than 10% of cloudy pixels). Furthermore, we have verified that these days are free of atmospheric perturbations, do not present artifacts due to defective SWIR detectors, and are free of bi-directional effects. After this selection, we have

chosen days that represent the best the vegetative cycle. In general, the number of days varies between 10 to 30 days.

So, each pixel can be now defined by a vector $P_i = R_i(t, \lambda)$ where $R_i(t, \lambda)$ is the reflectance of the pixel P_i at the day t for the channel λ . To condense the information, we have performed a principal component analysis, selected the most informative components and then run an unsupervised classification on the selected components. Different tests with the n-uplets combinations of channels were computed and studied and the best combination was the triplet Red-Near-Infrared, SWIR.

3.2 Results

The region "Centre" of France was chosen to test the both methodologies as described above. To evaluate the quality (visually and by the mean of confusion matrix) of the different classifications, we have compared the results with the Corine dataset used as the reference. The CORINE legend distinguishes 44 classes grouped in a hierarchical nomenclature (CEC, 1993). In the region "Centre", the main classes are pastures, arable land and forests (figure 1).

First of all, we have performed an unsupervised classification in 12 classes using 28 10-days NDVI composites. Even if the main patterns are recognized (figure 2), the quality of this classification is very poor (accuracy lower than 50% for pastures and forests, of about 60% for crops). Some forests are missing and the distinction between coniferous and deciduous is not possible.

The second method applied to the daily reflectances (Red, NIR, SWIR) of 10 days distributed along the year leads to very good results (figure 3) and a good agreement with the Corine data. Very detailed patterns are well recognized and the accuracies comparing with Corine vary from 84% for urban dense areas, 85% for crops, 71% for pastures; for the forests even if the accuracy is globally high, the distinction of coniferous forests present lower accuracy (about 50%) due to a mixing of broadleaf and coniferous forests.

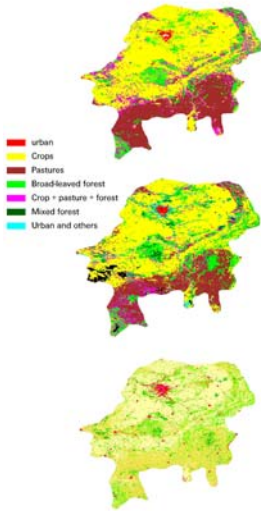


Figure 2: VGT classification using NDVI profiles

Figure 3: VGT classification using daily reflectances

The quality of the classification appears clearly on the zooms made on Paris for the VGT classification (figure 4) and the Corine Land Cover dataset (figure 5). For Paris area, the urban class and also the forest class are well detected. A sub-urban class can also be identified. It is important to notice that, unlike the NOAA/AVHRR data, the high accuracy of the multi-spectral and multi-temporal registration allows to really represent the landscapes at the 1km resolution.

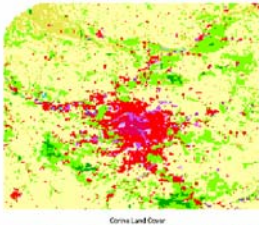


Figure 4 : Corine classification on Paris

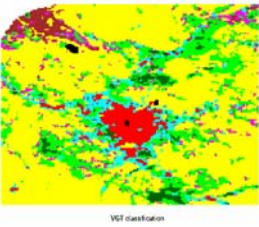


Figure 5 : VGT classification on Paris

3.3 Conclusion

Afterwards, these two methodologies were applied to the whole France. The first results shows a satisfactory mapping of the landcover. However, some problems are still present: bad detection of the permanent crops (vineyards), difficulties to discriminate in some cases coniferous and broad-leaved forests, discontinuities of landcover classes at the frontier of adjacent climatic regions.

4 SURFACE ALBEDO

4.1 Methodology

Cloud detection is operated on daily data by applying a cloud mask algorithm appropriate to the France domain. The operational cloud mask was replaced by a cloud mask based on new thresholds on blue and short wave infra-red surface reflectances. A dilatation of one pixel was also added.

Correction of directional effects and normalization of data are applied on cloud-free surface reflectances to avoid dependency on Sun-target-sensor geometry. The inversion of kernel-driven reflectance model of Roujean et al (1992) is used on a 30-days period of compositing and on a 10-days temporal window to obtain the parameters describing the Bi-Directional Reflectance Distribution Function (BRDF) :

$$\rho(\theta_s, \theta_v, \phi) = k_0 + k_1 * f_1(\theta_s, \theta_v, \phi) + k_2 * f_2(\theta_s, \theta_v, \phi).$$

The number of days defining the compositing period is in general coherent with the vegetation growth. A minimum of 6 cloud-free observations per pixel for each compositing period is required for the inversion. The processing of data is done on pixel basis in each spectral band. These 1-km BRDF parameters then serve to derive hemispherical reflectance product. Note that similar method has been retained for operational use on POLDER/ADEOS-I (Leroy, 1997) and MISR-MODIS/TERRA (Lucht, 2000).

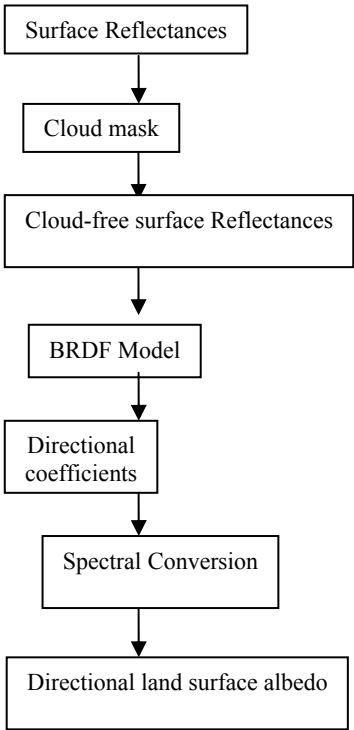


Figure 6 shows an example of noise reduction in measurements after correction of directional effects using several methods. Daily NDVI observed for an homogeneous pixel of the domain ('arable land', same land cover on 3*3 km area surrounding the pixel) are compared with NDVI computed with coefficient k_0 ($\theta_v=0$, $\theta_s=0$), MVC (Maximum Value Composite) and NDVI obtained with modelled reflectances ($\theta_v=0$, θ_s is the median of Solar Zenith Angles for the compositing period). The MVC method is robust (continuity in NDVI temporal profile), reduction of noise in measurements is improved using BRDF models.

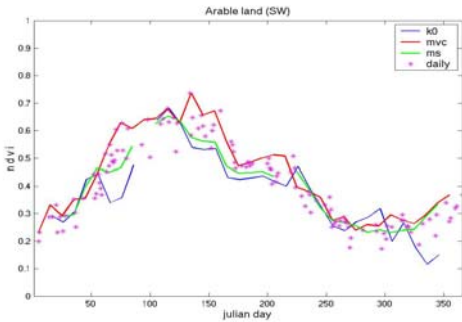


Figure 6: comparison of NDVI observed (daily), NDVI computed with coefficients k_0 , NDVI-MVC and NDVI obtained with modelled reflectances for an arable land pixel of the domain

4.2 10-Days spectral albedoes retrieval on southwest part of France

Spectral land surface albedoes (in near infra-red-NIR and visible-VIS channels) are computed at 1 km resolution and on a 10-day basis over southwest part of France. Spatial data sets of spectral albedo (400*400 km) and BRDF model parameters are generated for the entire year 2000. The transition between forests and pastures appears clearly (figure 7 - 8). NIR spectral albedo of Landes forest increases during the months of May and June while VIS spectral albedo is decreasing (growth of the vegetation, absorption of visible radiation).

Figure 7: NIR 10-days surface albedos. 05/05-24/06/2000

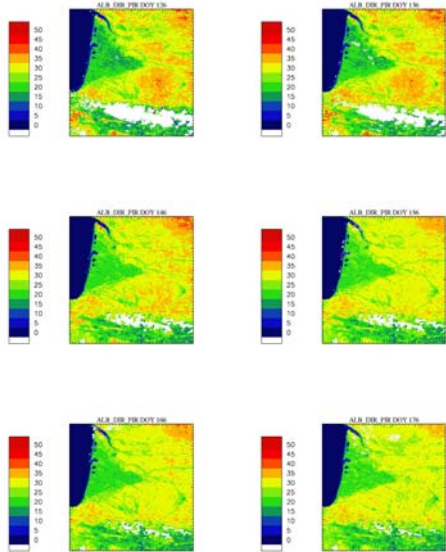
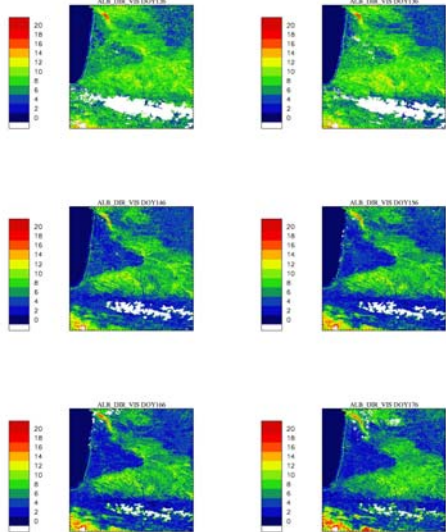


Figure 8: VIS 10-days surface albedos. 05/05-24/06/2000



4.3 Comparison of monthly spectral albedoes VGT with other datasets

Using 10-days directional surface albedoes, monthly spectral albedoes (VIS and NIR) are computed for the entire year 2000. The comparison is made on five homogeneous pixels of the domain (same land cover for 3*3 km area). The albedo datasets used for the comparison are projected on a common 6-km resolution. POLDER directional albedoes are only available from November 1996 to June 1997 and correction of aerosol effects was not applied to obtain this data set. Values of ECOCLIMAP albedos are inferred from a land cover map and the use of look-up tables (Masson, 2002).

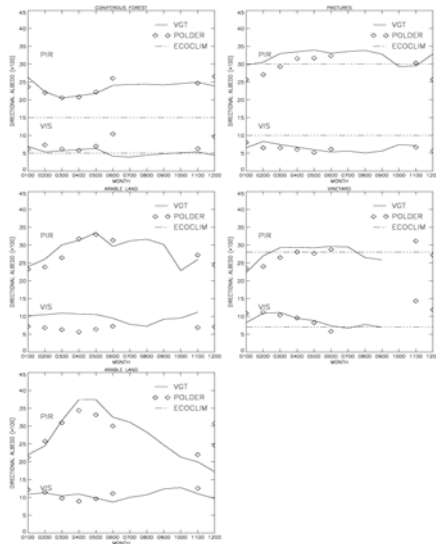


Figure 9 : comparison of monthly spectral albedo VGT with POLDER and ECOCLIMAP albedos for 5 homogeneous pixels (year 2000).

This comparison shows the good consistency of different datasets instead of differences between instruments (spectral bands, time of acquisition, methodology used to compute surface albedo). There exists very good agreement between POLDER and VGT albedoes despite their differences (time shift of 3 years, spectral bands) allowing to complete existing POLDER product with VGT product. This could complete the POLDER observations to derive an annual cycle of vegetation (see pixel 'Arable land').

We can notice the surestimation of coniferous forest albedos in NIR channel for VGT and POLDER.

4.4 Comparison of monthly broadband albedos VGT with other datasets

Monthly broadband albedoes VGT are computed with NIR and VIS monthly albedoes further compared to other data sets : POLDER, ECOCLIMAP, CMS (Météo-France CMS internal product obtained with Météosat) and GUTMAN atlas (AVHRR). The comparison is carried on with the homogeneous pixels selected in part 4.3.

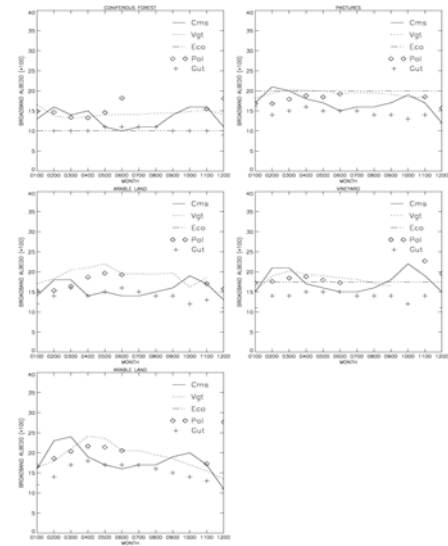


Figure 10 : comparison of monthly broadband albedos VGT with POLDER, ECOCLIMAP, CMS and GUTMAN albedos for 5 homogeneous pixels (year 2000).

There is a rather good consistency of different data sets instead of differences between instruments, year of acquisition and methods applied to obtain these data sets. Except for the 'coniferous forest' class, the difference between VGT, POLDER albedos on one side and ECOCLIMAP albedos on the other side is always less than 0.05.

4.5 Conclusion

This study has shown consistency of land surface albedo retrieval from VEGETATION data. Thanks to

better radiometric and geometric resolutions, VGT products present improvements compared to actual AVHRR derived products. Determination of a 10-day surface spectral albedo product over France will be done for the entire year 2000. This product will be then tested in atmospheric models. In the next years, Météo-France will develop a new meso-scale model with a resolution of 2-3 km over France. This model will require the best estimation of surface parameters at this scale and VGT products will meet these requirements.

5 REFERENCES

- CEC, CORINE Land Cover, 1993, technical guide. EUR 1285 EN, Office for Official Publications of the European Communities, Luxembourg.
- Champeaux, J.-L., 2002, Land cover mapping over France Using S1-S10 VEGETATION data, GLC2000 meeting in ISPRA, <http://www.gvm.sai.jrc.it/glc2000/defaultGLC2000.htm>
- Champeaux, J.L., Arcos, D., Bazile, E., Giard, D., Goutorbe, J.P., Habets, F., Noilhan, J. and Roujean, J.L., 2000, AVHRR-derived vegetation mapping over western Europe for use in numerical weather prediction models, *International Journal of Remote Sensing*, 21, 1183-1199.
- Holben, B.N., 1986, Characteristics of maximum-value composite images from temporal AVHRR data, *International Journal of Remote Sensing*, 7, 1417-1434.
- Lacaze, R., Roujean J.L. and Goutorbe J.P., 1999, Spatial distribution of Sahelian land surface properties from airborne POLDER multiangular observations, *Journal of Geophysical Research*, 104, 12, 131-12,146.
- Lucht, W., Schaaf, C. B. and Strahler, A. H., 2000, An algorithm for the retrieval of albedo from space using semiempirical BRDF model, *IEEE Transactions on Geoscience and Remote Sensing*, 38 (2), 977-998.
- Leroy, M., Deuzé, J.L., Bréon, F.M., Hautecoeur, O., Herman, M., Duriez, J.C., Tanré, D., Bouffies, S., Chazette, P. and Roujean, J.L., 1997, Retrieval of atmospheric properties and surface bi-directional reflectances over the land from POLDER/ADEOS, *Journal of Geophysical Research*, 102, 17023-17037.
- Masson, V., Champeaux, J.L., Chauvin, F., Meriguet, C., Lacaze, R., 2002, A global database of land surface parameters at 1 km resolution in meteorological and climate models, *Journal of Climate*, in revision.
- Mucher, C.A., Champeaux, J.L., Steinnocher, K. T., Gruiguolo, S., Wester, K., Heunks, C., Winiwater, W., Fessler, F.P., Goutorbe, J. P., Ten Brick, B., Van Katwijk V. F., Furberg, O., Perdiago, V. and Nieuwenhuis G.J.A., 2001, Development of a consistent methodology to derive land cover information on a European scale from remote sensing for environmental modeling, The Pelcom Report, Center for Geo-Information (CGI), Wageningen university, 160 pp.
- Roujean, J.L., Leroy, M., Deschamps, P.Y., 1992, A bidirectional reflectance model of the Earth's surface for the correction of remote sensing data, *Journal of Geophysical Research*, 97, 20, 445-20,468.
- Roujean, J. L., Lacaze, R., 2002, Global mapping of vegetation parameters from POLDER multiangular measurements for studies of surface-atmosphere interactions : pragmatic method and its validation, *Journal of Geophysical Research*, submitted.

6 ACKNOWLEDGMENTS

The work on determination of land surface albedo from VEGETATION received financial support from the Programme National de Télédétection Spatiale.

Land surface albedo retrieval via kernel-based BRDF modeling: statistical inversion method, models comparison, and an optimal design scheme for the angular sampling

Oleg Pokrovsky ⁽¹⁾ and Jean-Louis Roujean ⁽²⁾

⁽¹⁾ Voeikov Main Geophysical. Observatory, 7 Karbyshev Str., St.-Petersburg, 194021, Russia

⁽²⁾ GAME/CNRM (Météo-France/CNRS), 42, avenue Gaspard Coriolis, 31057 Toulouse, France

E-mail addresses: pokrov@main.mgo.rssi.ru ; roujean@meteo.fr

ABSTRACT – A new statistical inversion method is first presented in support to the application of kernel-based BRDF models for the calculation of the surface albedo. The proposed inversion method is innovative in that it provides the confidence intervals for each of BRDF model coefficients with a prescribed significance expressed by a probability level. The results show a strong dependence on the solar zenith angle (SZA) and the land cover type (LCT) for all candidate models. The implementation of the confidence interval technique shows that the BRDF model coefficients can be retrieved with an uncertainty of 20-30%, the more occurring in the case of forest. The corresponding albedo estimates could be characterized by an absolute uncertainty of 1-2% in the visible band and 5-10% in the near infrared band, or by 10-30% in relative values. The Fisher informative matrix is considered to circumscribe the optimal design problem to search for the best angular sampling. Two approaches are presented and discussed: one relates to the random noise term of the BRDF model and is independent on the land cover type (LCT); the other is operated by the residual term of the BRDF model and is determined by the reflectance peculiarities of the different LCT patterns. The optimal angular sampling distributions for ground-based multi-angular data sets over different LCT and known residual terms were determined. It was shown that the functions that are associated with the chosen criteria saturate after the selection of 5 or 6 observing geometries. A fast convergence rate is observed with angular measurements determined by the optimal design.

1. INTRODUCTION

The land surface albedo is a key parameter influencing the climate near the ground. Therefore, it must be determined with a sufficient accuracy. The last several years have seen a rapid growth in our understanding of both the potential and the limitations of semi-empirical BRDF modelling in the context of having to process large volumes of satellite data. Semi-empirical models for this purpose were first investigated more seriously in the early to mid 1990s after the 1980s had seen considerable advances in physical BRDF theory. As a consequence, today the first generation of major BRDF products from POLDER, MODIS, MISR and even AVHRR is based on semi-empirical BRDF models. The availability of global BRDF data products at a coherent time scale of the vegetation growth is just entering its operational phases. Nevertheless, there are several fundamental issues still to be resolved in kernel-based BRDF modelling. First of these is that there is still no sound theoretical framework for explaining why a BRDF may be developed into kernels. A summary paper by Lucht and Roujean (2000) shows that such vision of a linear decomposition of the radiometry into geometric and volume scattering effects may be supported by natural phenomena of three kinds: the scale partition from

micro-scale to macro-scale, the distinction of various entities of the landscape, namely soil and vegetation, and a separation between thin and thick optical media. Recent BRDF modelling developments was discussed by Gao et al. (2000).

The ambition in implementing the category of kernel-based models is to mimic as closely as possible all bi-directional signatures of land surface targets. The approach has been largely supported by the existence of repetitive angular signatures. On the other hand, different physical processes may share the same signatures. This latter still probably contributes to put a severe limit in the interpretation of the retrieved coefficients from the inversion of BRDF models. Likewise, the choice of the model is driven by its capability to reproduce the set of observations, provided that the model coefficients are robust enough with respect to the angular sampling. In this paper, the authors compare the performances of the model to restore the spectral BRDF. Previous efforts in attempting to recommend the use of a given model did not make to a clear decision (Privette et al., 1997). A main reason seems the lack of sufficient statistical criteria that could ultimately lead to a scientific consensus on the model recommendation. This explains the choice for considering different kernels in various existing projects since the models are sensitive

enough to the angular sampling to perform differently between the sensor orbital characteristics. Hence, it is the goal of this work to propose new elements of comparison, which could in a first round be used to select kernels, and further to select optimal angular data sets once the model has been implemented in the processing of satellite data. We examine two main causes of uncertainty affecting the predicted reflectance values. They are a contribution of the random noise term in the measurements and the model residual after adjustment. For such, we bring in both notions of experimental design for the angular sampling and kernel response function for an arbitrary set of angular measurements. The Fisher informative matrix is considered to circumscribe the optimal design problem to search for the best angular sampling (Pokrovsky, 1969, 1972). Two approaches are presented and discussed: one relates to the random noise term of the BRDF model and is independent on the land cover type (LCT); the other is operated by the residual term of the BRDF model and is determined by the reflectance peculiarities of the different LCT patterns. Additionally, we explore the residual terms as a function of the LCT and we analysed the sensitivity of the reflectance predicted by the various BRDF models to the kernel response function

2. BRDF KERNEL-DRIVEN MODELS

For the comparison study, five leading candidate models were chosen: 1) Roujean (R), 2) Li-Sparse non-reciprocal (LS), 3) Li-Sparse reciprocal (LSR), 4) Li-Dense (LD), 5) Walthall (W) model. According to the original idea of Roujean et al. (1992), a general form of kernel models has a following view:

$$\rho(\theta_v, \theta_s, \varphi, \lambda) = f_{iso}(\lambda) + f_{vol}(\lambda) * k_{vol}(\theta_v, \theta_s, \varphi) + f_{geo}(\lambda) * k_{geo}(\theta_v, \theta_s, \varphi) \quad (1)$$

where ρ is the reflectance at illumination and view zenith angles θ_s and θ_v , respectively, at relative azimuth angle φ , and at wavelength λ . Terms like k_{vol} and k_{geo} are geometrical expressions of basic BRDF types occurring in the problem of light scattering in vegetation and describe the bi-directional scattering of scene constituents. f_{iso} , f_{vol} and f_{geo} are the spectrally dependent model parameters to be retrieved from the measurements.

3. STATISTICAL INVERSION METHOD

The traditional regression model writes in the form

$$\mathbf{y} = \mathbf{A}\mathbf{c} + \boldsymbol{\varepsilon} \quad (2)$$

Having \mathbf{y} as an n -by-1 vector of responses, \mathbf{A} as an n -by- m matrix of predictors, \mathbf{c} as an m -by-1 vector of model coefficients to be estimated, $\boldsymbol{\varepsilon}$ as an n -by-1 vector of random disturbances. The model of (2) is

related to the minimization δ of the quadratic norm of residuals, that is:

$$\delta = \min_c \|\mathbf{y} - \mathbf{A}\mathbf{c}\|^2 \quad (3)$$

The standard system of normal equations could therefore provide the least square estimator of \mathbf{c} in the following matrix form:

$$\hat{\mathbf{c}} = (\mathbf{A}^T \mathbf{A})^{-1} \mathbf{A}^T \mathbf{y} \quad (4)$$

(‘ \mathbf{T} ’ is a sign of transpose and ‘ -1 ’ of inverse matrix). However, this definition has poor numerical properties. Particularly dubious is the computation of $(\mathbf{A}^T \mathbf{A})^{-1}$, which is both costly and imprecise. To avoid those difficulties, most prevalent methods are the singular value decomposition (SVD) and QR decomposition of \mathbf{A} : $\mathbf{A} = \mathbf{Q}\mathbf{R}$. Residual of model (2) $\mathbf{r} = \mathbf{y} - \mathbf{A}\hat{\mathbf{c}} = \mathbf{y} - \hat{\mathbf{y}}$ might be described by:

1) the degree of freedom, v , to be assigned as $v = n - m$;

2) the root mean square error $Rmse = \frac{\|\mathbf{r}\|}{\sqrt{v}}$,

3) the coefficient of determination (correlation) $r^2 = \frac{R_{ss}}{T_{ss}}$,

4) the regression sum of squares $R_{ss} = \|\hat{\mathbf{y}} - \bar{\mathbf{y}}\|^2$,

5) the total sum of squares $T_{ss} = \|\mathbf{y} - \bar{\mathbf{y}}\|^2$,

6) the Fisher statistics $F(v, m) = \frac{(n-m) \|\hat{\mathbf{y}} - \bar{\mathbf{y}}\|^2}{(m-1) \|\hat{\mathbf{y}} - \mathbf{y}\|^2}$.

The Fisher statistics is indeed of great practical importance because it simultaneously contains information on the redundancy of kernel matrix columns and the residual scale. The evaluation of an estimation uncertainty is of considerable value to judge if the retrieved model coefficients are dependable. The uncertainty half-band of the vector of regression of (2) can be assessed from the following expression:

$$\delta \hat{\mathbf{c}} = R_{MSE} T_{inv}(1 - \frac{\alpha}{2}, v) \mathbf{c}_R \quad (5)$$

where $T_{inv}(1 - \frac{\alpha}{2}, v)$ is the inverse Student's cumulative distribution function value for the significance level α and the degree of freedom v (see, e.g., Abramovitch and Stegun, 1964). The vector \mathbf{c}_R depends on the matrix \mathbf{R} of QR decomposition (Pokrovsky and Roujean, 2002a).

4. COMPARISON OF INVERSE PROBLEM SOLUTIONS FOR DIFFERENT BRDF MODELS AND LAND COVER TYPES

The statistical inversion method was tested with an *in situ* collection of BRDF measurements covering a wide variety of land cover surface types. Field experiments were performed in Maryland, northern Africa, and Virginia (Kimes, 1983). Amongst the set of eleven sampled land cover types (LCT), only the better documented were retained, including a plowed field, hard and irrigated wheat canopies, a soybean crop, and pine and deciduous forests. These measurement data encompass various landscape units deemed to be representative enough with the leaf area index (LAI) reaching the largest value of 4.6 for the soybean crop. Data have been acquired in the visible (0.58-0.68 μm) and the near infrared (0.73-1.1 μm) spectral bands using a Mark III radiometer equipped of a field of view of 12° . For each set of acquisitions, a given target was viewed under 3 values of the solar zenith angle θ_s , and for 41 view directions distributed every 15° interval for zenith angle θ_v , and every 45° interval for azimuth ϕ . It is necessary to note that, really, we have only 26 independent measurements because of azimuth symmetry feature of Kimes data sets. The total angular set for three solar zenith angle SZA in Kimes sample data therefore contains 78 measurements. The model of (1) was inverted against previous measurements in using the different kernels mentioned in Section 2. See some results at fig.1. In the visible spectral band, the Fisher statistic ranks the LCT in descending order (plowed field, hard wheat, irrigated wheat, pine forest), which coincides exactly with the same ascending ordering obtained by relative R_{MSE} . A similar LCT ordering based on the Fisher statistic can also be derived for the infrared spectral band: deciduous forest, plowed field, irrigated wheat, hard wheat. Therefore, the Fisher statistic is a good indicator of retrieval success for each of the LCT. Interestingly, the same models was never systematically preferred for the same vegetation type and the same value of θ_s , for either the visible or the near infrared reflectance data sets. The results reveal there is no universal model acting as the best for all LCT. Moreover, a model can only be qualified as the best relative to a certain range of θ_s . However, and as somewhat expected in regard to previous studies (Strahler and Muller, 1999), it appears that the three kernel-based models LS, LSR and R can be considered as the favorites in the current study. The most preferable SZA for the retrieval of grassland and crop field features lies in the high Sun position range, while a medium Sun position might be recommended for the inversion data related to pine and deciduous forests. The approach developed permits an investigation of

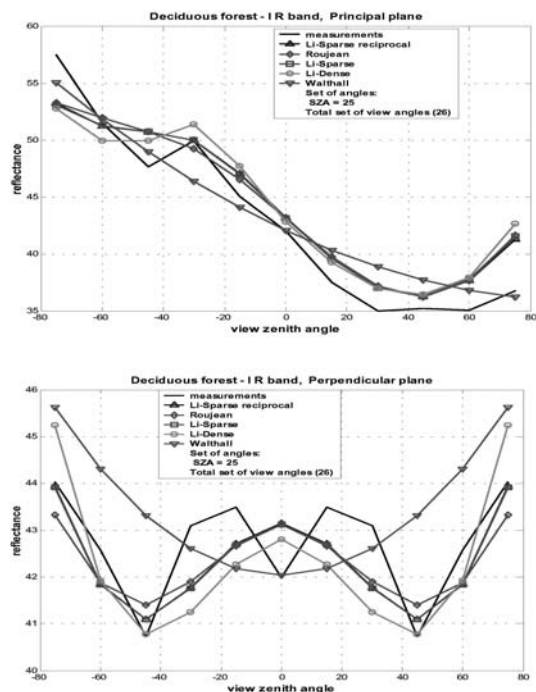


Fig.1. Models comparison from the inversion in the NIR band for a deciduous with SZA of 25° .

reflectance values predicted by the BRDF models. Let us consider some computational results for the LSR and R models (fig.2). The first angular data set comprises the triple array for the 3 values of θ_s and the second corresponds to a single θ_s , which represents 26 angular measurements. The results obtained for the irrigated wheat reflectance data sets in the visible band show that the predicted reflectance curve based on a single θ_s data set lies more close to the curve of the measured values in both the principal and perpendicular planes because the models are less severely constrained. One can notice that the curve of the measured values borders on the error bar domain. It is worth outlining that the error bars associated with the combination of the 3 values of θ_s are two or three times wider than for any angular data set of a single θ_s . This can be justified only by the dependencies of the model coefficients on θ_s . It is worth underlining this feature because it was only previously known that these coefficients are wavelength-dependent (see Strahler and Muller, 1999; Wanner et al., 1995).

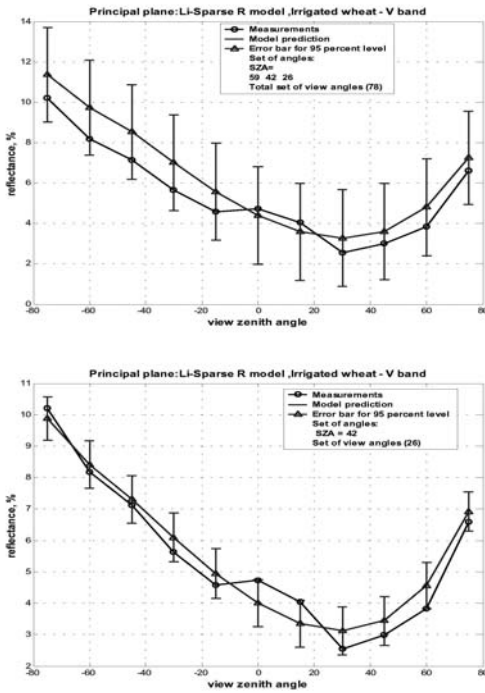


Fig.2. Uncertainties in the reflectance estimates obtained with the LSR model for the irrigated wheat crop in the visible band: three values of SZA (top); one value (bottom).

The results for other LCT and spectral bands support a similar conclusion, namely that the model inversion with a single θ_s value lead to a better approximation of the measurement curve and to narrower uncertainty bands. Owing to this, measurement data do not exceed the uncertainty area even at the hot spot angles. The key information extracted from the figures comparison is a very weak dependence of the results on the candidate BRDF models in relation to the criteria of the predicted reflectance values and the error bar widths. For instance, in the case of the soybean crop, the results were rather indifferent to the observing plane for a high Sun position, or small θ_s . These reflectance measurements have clearly demonstrated the benefit of a preferred data set attributable to optimal θ_s values on the inversion procedure. It confirms our previous learning to use preferably data corresponding to a preferred θ_s .

5. UNCERTAINTY ANALYSIS OF THE BRDF MODEL COEFFICIENTS

Our study demonstrates that the kernel model coefficients are estimated with some uncertainty rate described by their confidence intervals (see (5)). The 5%-th significance level is a very frequently used interval in applied statistical studies. The estimated

values of the R model coefficients along with error bars for 5%-th significance level for several LCT are now presented in Fig.3. We used here the total set of angular reflectance data obtained for the three different θ_s . There remains considerable uncertainty in all three models coefficients, more in the volumetric and geometric terms and less in the Lambert term. The highest coefficient uncertainties are attained for the case of deciduous and pine forests. The uncertainties on the Lambert term amount to 7-10%, to be compared with the 20-70% for the volumetric and the geometric terms.

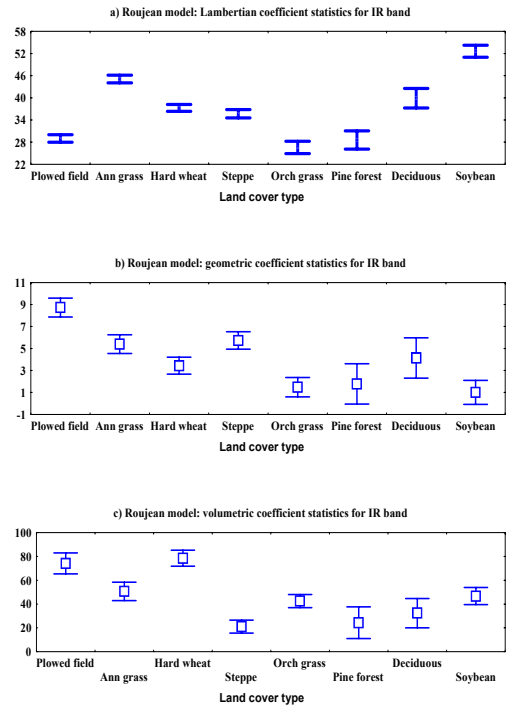


Fig.3. Statistics for Roujean model coefficients in NIR band.

The estimated values are spanning within 10-30% uncertainty band for both volumetric and geometric coefficients. Moreover, the uncertainties due to the Lambert term reach 10-15%. The range of uncertainty in estimating the BRDF model coefficients is of primary importance due the implications this yields for a further retrieval of other biophysical parameters like as albedo and LAI.

6. UNCERTAINTIES IN THE PREDICTED ALBEDO VALUES

The surface albedo is an important parameter determining the Earth's climate near the ground. Clearly, users' requirements impose severe criteria for the albedo algorithm development, production and dissemination of this parameter. Expert climate

modelers (Sellers et al., 1986) make reference to an accuracy assessment on albedo of 1-2% in terms of absolute values. The reflectance model of Roujean et al. (1992) was then selected to derive the hemispherical reflectance values. More recently, the MODIS group followed a similar route in opting for the LSR model as the geometric kernel (Strahler and Muller, 1999). In both cases, the results of an angular integration of the kernels were numerically approached via a polynomial fit involving the sun-view geometry characteristics. An albedo parameterization is obtained based solely on a combination of BRDF model coefficients in which the linear dependence on θ_s is optimized. From this, an albedo estimate can be given along with the corresponding confidence intervals for each θ_s and LCT.

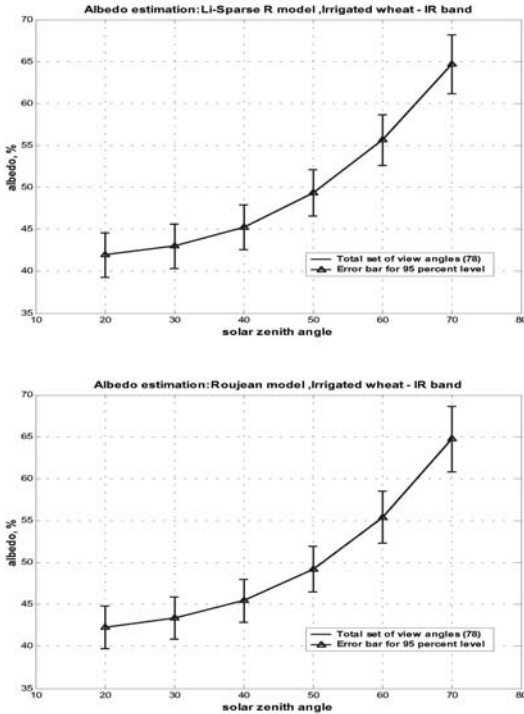


Fig.4. The uncertainty in NIR albedo estimates for irrigated wheat: Li-Sparse (top) and Roujean (bottom) models.

In this study, the results shown are restricted to the association of the three θ_s . The given examples outline a well-known feature of the diurnal cycle of albedo, varying monotonically from the minimum at noon to a maximum at sunrise and sunset. A large variability in daily albedo is obtained in the case of the irrigated wheat (Fig.4) with infrared angular variance reaching 20% in absolute units. The albedo derived from the R model gives, as a rule, some weaker dependence of albedo on θ_s and wider error bands than the albedo product based on the LSR

model. The lowest albedo SZA dependences can be seen for deciduous forest. In general, the uncertainties in retrieved albedo values can fluctuate from 1-2% in the visible range to 5-10% in the near infrared range. As a reminder, the present results were obtained under ideal conditions, which means complete angular data sets and absence of atmospheric disturbance factors and residual cloud contamination. In a real situation, the error bar that can be expected on albedo retrieval could be about a few more percent. This sustains the additional efforts remaining to be made to enhance the inversion technique and the reflectance model method. One of these efforts concerns the development of composite kernel-driven models, based on an optimal combination of existing kernels.

7. OPTIMAL ANGULAR SAMPLING

7.1. Statement of problem

Our task is to address the main advantages in achieving a model inversion at some specific peculiarities of a given problem in order to then accomplish a deeper insight in it. The inverse problem could in the most general form be written as the following functional equation:

$$y(s)=F(x,s)+\varepsilon(s) \quad (6)$$

In (6), $y(s)$ is the measured variable, $F(x, s)$ would stand for a model operator describing for instance here the characteristics of light scattering processes within a given medium, and $\varepsilon(s)$ is the random noise variable originating from the measurement errors. The three primary variables in (6) are a function of a secondary variable s of control incorporating all the useful information (the wavelength, the sun-view geometry, the spatial and temporal coordinates). The variable x represents the parameters to be retrieved. In an early paper, the three main principles for the solution of the inverse problem were formulated for (1) (Pokrovsky, 1969):

- *A priori* information on the solution x should be incorporated in the algorithm.
- An optimal set of control variables s has to be determined.
- A regularization algorithm is suitable to procure a physically interpretable solution.

Let us assume that we consider a linear problem (2) and the set of M control variables $\mathbf{s}_M=(s_1, \dots, s_M)$ have been selected for angular sampling and M is largely superior to the number n of estimated BRDF model coefficients. Rewrite (2) in following form:

$$\mathbf{y}(\mathbf{s}_k)=\mathbf{A}(\mathbf{s}_k) \cdot \mathbf{x}+\varepsilon(\mathbf{s}_k) \quad (7)$$

The angular set \mathbf{s}_k is a subset of full set \mathbf{s}_M . From that, we may formulate a problem of the best choice of the angular coordinate subset $\mathbf{s}_k=(s_{i1}, \dots, s_{ik})$ with

dimension k . We assume k to be quite small compared to M , but approximately the same as n . Lets call subset \mathbf{s}_k as the experiment design. The choice of \mathbf{s}_k would appear as a result of the optimum finding given some functional criteria based on Fisher information matrix. From the subset of angular measurements we obtain the next expression for the covariance matrix of the modeled reflectance:

$$\Sigma_{\hat{\mathbf{y}}(\mathbf{s}_M/\mathbf{s}_k)} = \mathbf{A}(\mathbf{s}_M) \cdot [\mathbf{A}(\mathbf{s}_k)^T \cdot \mathbf{A}(\mathbf{s}_k)]^{-1} \cdot \mathbf{A}(\mathbf{s}_M)^T \quad (8)$$

The equation (8) describes the conditional dispersions for the set of modeled reflectance values over the full angular domain \mathbf{s}_M in assuming that the measurements were only performed over the subset angular domain \mathbf{s}_k . An inverse matrix of the covariance matrix of (8) is considered to belong to the optimal design theory (Fyodorov, 1970). It is the Fisher informative matrix:

$$\mathbf{G}(\mathbf{s}_k) = \left\{ \mathbf{A}(\mathbf{s}_M) [\mathbf{A}(\mathbf{s}_k)^{-1} \cdot \mathbf{A}(\mathbf{s}_k)]^{-1} \cdot \mathbf{A}(\mathbf{s}_M)^T \right\}^{-1} \quad (9)$$

The Fisher informative matrix provides the functional criterion for the optimization study. As a matter of fact, several criteria exist for the optimization study (Fyodorov, 1970). Most widely used criteria refer to the two following functional forms: the D-optimization, which is based on the maximization of the determinant of the matrix \mathbf{G} , and the A-optimization, which is based on the maximization of the trace of the matrix \mathbf{G} . The D-optimization criterion is a product of the eigen-values of the matrix \mathbf{G} while the A-optimization criterion is a sum of the same values. Let denote any functional criteria as $\Psi(\mathbf{G}(\mathbf{s}_k))$. Then, the optimal design problem can be expressed as a problem of finding amongst the set \mathbf{s}_M the functional maximum value \mathbf{s}_k :

$$\mathbf{s}_k = \text{argmax} \{ \Psi(\mathbf{G}(\mathbf{s}_k)) \} \quad (10)$$

In this context, it appears questionable the appropriate choice for the size k of the experimental design and the numerical method to find the maximum value. The optimal choice of k is related to two aspects: the first one is the number of differently viewed clear scenes from satellite observation; the second one is the relevance of any additional information inferred from new measurements. The achievement of a numerical maximization is however a difficult task. For example, attempting to calculate the cost function in (10) is a long task. It is on the order of magnitude of M^k and would be high even in the simple case when $M=10^4$ and $k=10$. Pokrovsky (1969) proposed an efficient algorithm for the consecutive search of the optimal design point s_i . This method only requires about $M \cdot k$ times to calculate the cost function of (12). The basic idea of this method relies on a formula aimed at increasing the information content when incrementing the number k of measurements. This formula was initially developed for the treatment of an inverse problem with only one component (Pokrovsky, 1969),

and later with n components (Pokrovsky, 1972). The latter is of particular interest in the case of taking into account the impact of external perturbing factors like the atmospheric and anisotropic effects.

7.2. Response function

Let us come to the relationship for the response function after (Pokrovsky, 1972):

$$\mathbf{R}(s/\mathbf{s}_k) = \mathbf{a}(s) \cdot [\mathbf{A}(\mathbf{s}_k)^T \cdot \mathbf{A}(\mathbf{s}_k)]^{-1} \cdot \mathbf{a}(s)^T \quad (11)$$

Let call $\mathbf{a}(s)$ a raw of the matrix \mathbf{A} corresponding to the angular variable s . As a remind, we assumed that the noise term $\boldsymbol{\varepsilon}$ has a unity covariance matrix. That means each component of vector $\boldsymbol{\varepsilon}$ is an independent random value having a unit dispersion. The response function of (11) indicates the amplification rate of input unit noise on the uncertainty in the reflectance prediction at the view angle s provided the measurements were performed within the angular set \mathbf{s}_k . The concern is now to determine the best angular measurement conditions according to the LCT. As it was stated above, there is also another source of uncertainty in the reflectance prediction linked to the residual forms. It is easy to obtain (Pokrovsky and Roujean, 2002b) an expression for diagonal elements of the covariance matrix for the predicted reflectance:

$$\begin{aligned} \mathbf{Dy}(\mathbf{s}_M/\mathbf{s}_k) = & \text{diag} \{ \mathbf{A}(\mathbf{s}_M) \cdot [\mathbf{A}(\mathbf{s}_k)^T \cdot \mathbf{A}(\mathbf{s}_k)]^{-1} \cdot \mathbf{A}(\mathbf{s}_M)^T \} + \\ & + \text{diag} \{ (\mathbf{y}(\mathbf{s}_M) - \mathbf{A}(\mathbf{s}_M) \cdot \hat{\mathbf{x}}(\mathbf{s}_k)) \cdot (\mathbf{y}(\mathbf{s}_M) - \mathbf{A}(\mathbf{s}_M) \cdot \hat{\mathbf{x}}(\mathbf{s}_k))^T \} \end{aligned} \quad (12)$$

In contrast to (8) this formula contains a residual (second) term. This dispersion matrix yields the criteria for implementing an optimal design scheme as a function of LCT. In Fig.5, we computed the polar graphs of the response function in the particular case when available data sets span over the hemisphere according to the Kimes measurement protocol. The minimum value area of the response function expands over a wide angular domain for all models and slightly spreads with increasing SZA. The maximum value of the response function increases twice for the R model when SZA changes from 30 ° to 60 °. This area is asymmetric with respect to the perpendicular plane and demonstrates some advantage of non-zero azimuth planes due to more wideness in the zenith angular band. At SZA= 60 °, the response function of both models shows the largest zone of small values as compared to SZA=30° (Fig 5). In general, we dispose of few angular measurements, the extreme situation being to have a single datum. Even in this last case, the response function technique allows performing a sensitivity analysis to identify the angular areas that are the more sensitive to the input data set. To illustrate this, let consider the response function (11) when the reflectance is only measured at point $\mathbf{s}_k=s$. Corresponding polar graphs of the sensitivity function

for LS model is shown in Fig. 6. The most important result is that both response functions are everywhere beyond the value of 4, that is over the critical value of 1. This means that the inversion method amplifies the input data noise by several times, and thus is the solution to the inverse problem useless. The maximum values of the hot spot are observable with both models but are nonetheless more pronounced for LS model.

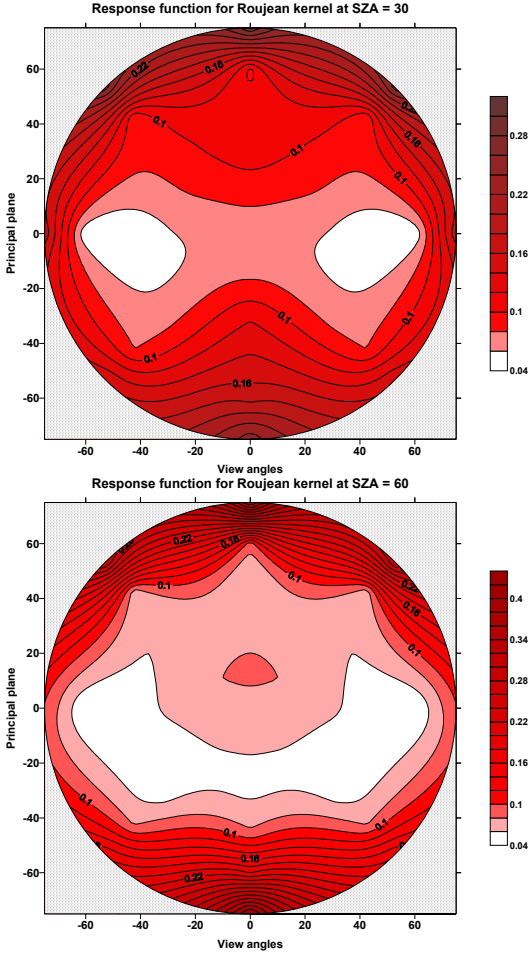


Fig.5. Response functions for Roujean kernel at SZA=30°(top), 60°(bottom).

Response function for Li-Sparse (Wanner) kernel at SZA = 30 in the case of one view angle

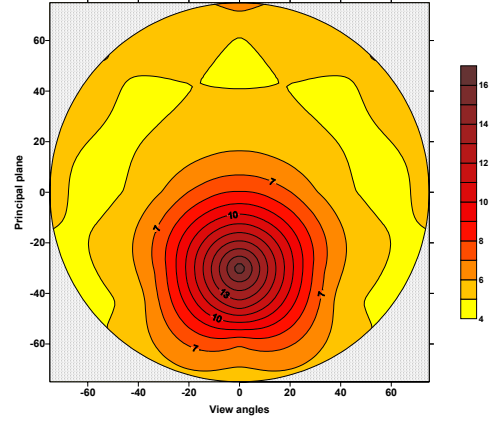


Fig. 6. Response functions for Li-Sparse model at SZA=30°.

7.3. Examples of an optimal design

The results that are presented hereafter aim at illustrating the advantages in applying the above inversion method. We bounded our search by the first 10 steps of the optimization algorithm. The useful points are concentrated along the principal plane, when criteria (9) was used. The angular points outside $\phi=0^\circ$ are selected only after 10 runs, except for the LS model. The angular averaged values of the response function calculated at each step of the optimization algorithm rapidly decrease for all BRDF models along with the number of the optimization steps. It reaches 0.3 after five steps and 0.2 after ten steps. The critical value of 1 is crossed at the third step. It is not surprising that during the first steps of the optimization algorithm, the major contribution to the functional criterion in (12) is provided just by the second term related to the residual impact. Our research of the cost function shows that the dependence on the number of the optimization step is even considerably more based on the criterion (12) than (9), as discussed above. It decreases from the maximal value to the steady state value in four to six steps for the different SZA values, LCT and BRDF models. It can be noticed that in case of (12) appear to be a lot of angular points located outside the principal plane, in particular at $\phi=135^\circ$. This is coherent with the residual signatures. The detailed ground data set gives the opportunity to perform a thorough simulation experiment to test the optimal designs obtained in the retrieval process and to compare the corresponding retrieval results with the full set of angular measurements. For all considered cases, the reduced optimal angular sampling including 4 or 5 angular points provide very similar results for when using full angular data sets with 26 measurements. In the cases of the hard wheat and plowed field, the reduction of

input data provides some improvement in the reflectance prediction in the hot spot area (Fig. 7).

7.4. Statistical diagnosis of the optimal design

We use here the meaningful set of the statistical diagnosis: the residual standard deviation, the Fisher and R-square statistics. We track the results of statistics during the optimization process in order to identify the points that vary the more when incrementing the number of the angular measurements. The most general feature is that all considered statistics have maximal changes within the first 3-6 steps of the optimization algorithm. The faster convergence for all statistics to the reference level corresponding to the full set of measurements (26) is observed for the irrigated wheat.

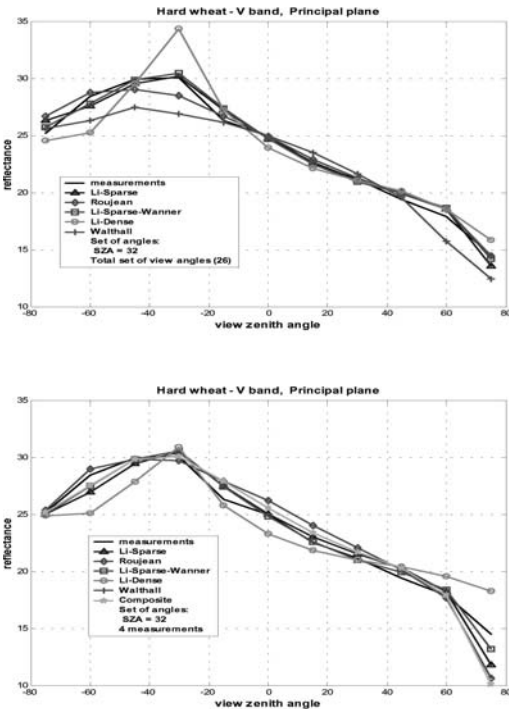


Fig. 7. Models comparison from the inversion against all angular measurement data in the visible band for a plowed field in the principal plane at SZ=26°: all data set (top); 4 optimal measurement data(bottom).

In this case, the optimal number of angular measurements is equal to 4, as demonstrated previously. A slower convergence is observed for the deciduous and pine forests (Fig. 8), when statistics reach saturation after 8 steps of optimization.

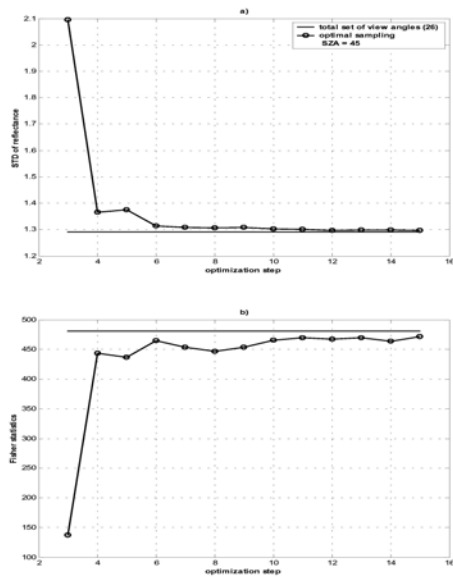


Fig. 8. Comparison of the convergence rate for the Roujean model inversion between all and the optimum angular data set for the pine forest at SZ=26°: residual standard deviation (top); Fisher statistics(bottom).

8. REFERENCES

- Abramovitch M. and I.A. Stegun, 1964, Handbook of mathematical functions. US Government Printing Office, 26.6.2, 651 p.
- Fyodorov V.V., 1976. Theory of optimal experiment (Moscow: Nauka).
- Gao F., X.Li, A. Strahler, C. Shaaf, 2000, Evaluation of the LiTransit kernel for BRDF modeling, *Remote Sensing Reviews*, v.19, p. 205-224 .
- Kimes, D.S., 1983, Dynamics of directional reflectance factor distribution for vegetation canopies, *Appl. Optics*, **22**,1364-1372.
- Lucht, W., et J.L. Roujean, 2000, Considerations in the parametric modeling of BRDF and albedo from multiangular satellite sensor observations, *Remote Sens. Rev.*, **18**, 343-379.
- Pokrovsky, O.M., 1969, Optimal design in remote sensing. *Izvestia:Physics of Atmosphere and Oceans*, (Boston: AGU), **5**,1169-1172.
- Pokrovsky, O.M., 1972, Optimal design in remote sensing: a multi-parameter case. *Izvestia:Physics of Atmosphere and Oceans*, (Boston: AGU), **8**, 445-450.
- Pokrovsky, O.M., and J.L. Roujean, 2002 a, Land surface albedo retrieval via kernel-based BRDF modeling: I. Statistical inversion method and models comparison, *Remote Sens. Environ.*, in press.
- Pokrovsky, O.M., and J.L. Roujean, 2002 b, Land surface albedo retrieval via kernel-based BRDF

- modeling: II. An optimal design scheme for the angular sampling, *Remote Sens. Environ.*, in press.
- Roujean, J.-L., Leroy, M. and Deschamps, P.Y., 1992, A bi-directional reflectance model of the Earth's surface for the correction of remote sensing data, *J. Geophys. Res.*, **97**, 20455-20468
- Privette J.L., T.F. Eck, D.W. Deering, 1997, Estimating spectral albedo and nadir reflectance through inversion of simple BRDF models with AVHRR/MODIS-like data, *J. Geophys. Res.*, **102**, 29529-29542.
- Sellers, P., Y. Mintz, Y. Sud and A. Duldres, 1986, Simple Biosphere (SiB), Model for Use Within General Circulation Models, *J. Atm. Sci.*, **43**, 505-531.
- Strahler A.H., and J.P. Muller, 1999, MODIS BRDF/Albedo Product: Algorithm Theoretical Basis Document version 5.0, 53 p.
- Wanner, W., Li, X. and Strahler, A.H., 1995, On the derivation of kernels for kernel-driven models of bidirectional reflectance, *J. Geophys. Res.*, **100**, 21,077-21,090.

Henry Flores Tovar^{1,2}, Jose M. Baldasano^{1*}, Nelson Vera¹, Pere Nadal³

¹ Laboratorio de Modelización Ambiental, UPC. Barcelona España.

² Instituto de Mecánica de Fluidos. UCV, Caracas Venezuela.

³ Govern Balear, Palma de Mallorca España.

E-mail: jose.baldasano@upc.es

RESUMEN - En el presente trabajo se emplea un modelo estadístico para la determinación de la radiación solar global superficial de las Islas Baleares a través de imágenes NOAA AVHRR, las cuales presentan una amplia cobertura conjuntamente con una adecuada resolución espacial. El proceso se divide en tres pasos, el primero consiste en un procedimiento de detección de nubes, en el segundo se obtiene el albedo planetario visible y se determinan los índices de nubosidad para cada píxel de la imagen de satélite, los cuales son utilizados en el tercer paso para la aplicación del modelo estadístico. Los coeficientes de regresión del modelo se determinaron a partir de los datos de estaciones de medición en superficie ubicadas en Cataluña. Este modelo fue comprobado para los 12 meses del año 1998, obteniéndose un coeficiente de determinación superior a 0.98 en todos los casos, con un error cuadrático medio entre 9.7% y 15.9% y un bias que varía entre -9.8% y 1.2%. Los resultados obtenidos mediante satélites son mucho más precisos que los obtenidos mediante interpolación de datos en superficie si las estaciones de medición se encuentran espaciadas más de 30 km una de otra. Mediante la aplicación del modelo para las Islas Baleares se obtienen valores máximos de la radiación solar global media horaria estimada por satélite entre las 14:00 y 15:00 h (LST) del orden de 3200 kJ/m²h para el mes de junio, y valores mínimos del orden de 1100 kJ/m²h en el mes diciembre.

ABSTRACT - A statistical model is presented for the determination of global solar radiation from NOAA AVHRR satellite data to Balearics Island, which provides wide coverage, together with adequate spatial resolution. The process is divided into three steps. The first step consists of a cloud detection procedure, the second determines the planetary albedo and the cloud index for each point on the satellite image, which is then used for the third step in the application of the global solar radiation statistical model. The coefficients for the model are determined by regression from the data obtained from 11 global surface solar radiation measurement stations. Once the coefficients have been determined, a surface interpolation is performed in order to obtain the entire coefficient field for the area under study with the objective of applying the model. The estimates obtained from the model were compared to data from another 10 ground radiation measurement stations in Catalonia (Spain). This model was tested for 12 consecutive months for the year 1998, with an excellent correlation being obtained between the estimate provided by the model and that data from the measurement stations, which resulted in a coefficient of determination greater than 0.98 in all cases, together with an rmse of between 9.7%-15.9% and a bias that varied from -9.8% to 1.2%. Concerning satellite-based method offers more exact spatial estimates for global solar radiation than do the interpolated estimates based on stations measurements, especially in regions where the stations network is sparse or not exist. By means of the application of the pattern for the Balearic Islands maximum values of the hourly global solar radiation are obtained estimated by satellite between the 14:00 and 15:00 h (LST) of the order of 3200 kJ/m²h for the month of June, and values minima of the order of 1100 kJ/m²h in December.

1 INTRODUCCIÓN

Para realizar los proyectos de aprovechamiento de la energía solar, ya sea por la conversión fototérmica en colectores planos o de concentración, como por conversión fotovoltaica por medio de células solares, hace falta el conocimiento de la cantidad y la distribución de la energía solar que incide en el lugar donde se instale el sistema de captación de energía y su variación temporal a lo largo de los ciclos anual y diario.

De acuerdo con las directivas de la Unión Europea, y el plan de fomento de las energías renovables, se prevé que al menos el 12% de la demanda total de energía en España para el año 2010, sea cubierto por fuentes de energía renovables (IDAE 1999).

A finales de 1998, la superficie de colectores solares de baja temperatura instalados en España era del orden de 341.000 m², en su mayor parte para la producción de agua caliente sanitaria en el sector doméstico y turístico. Mientras que había una

potencia instalada de 8.6 MW, asociados a aplicaciones de energía solar fotovoltaica.

Para cumplir con el objetivo general del plan de fomento de las energías renovables, se prevén nuevas aplicaciones y crecimientos muy importantes en las áreas de la energía solar.

En nuevas aplicaciones se estima la instalación de 200 MW de energía solar térmica y 144 MW de energía solar fotovoltaica. Paralelamente para la energía solar térmica de baja temperatura se estima la instalación adicional de 4.500.000 m², entre los años 1999 y 2010.

En el caso de las Islas Baleares se requiere aumentar de forma considerable el uso de fuentes de energía renovables, y entre ellas se esta prestando especial interés a la aplicación de tecnologías solares, por lo cual el Govern de les Illes Balears esta realizando estudios en detalle para conocer la cantidad y distribución de la energía solar en todas las islas, con la finalidad de aprovechar al máximo este recurso. Uno de esos estudios consiste en la determinación de la radiación solar superficial por medio de imágenes de satélites.

2 MODELO

El modelo empleado en este estudio es de tipo estadístico. Los datos de las estaciones de medición de radiación solar global en superficie, son usados para la determinación de los coeficientes de regresión del modelo, que luego son empleados para la determinación de la radiación solar global superficial.

Varias variables independientes deben ser introducidas en las ecuaciones de regresión; el coseno del ángulo cenital solar $\cos \theta$, que proporciona información de la radiación extraterrestre incidente en el tope de la atmósfera; el índice de nubosidad n , que describe la cantidad de cubierta nubosa para la zona de estudio; la transmisividad atmosférica $T(\theta)$, que tiene en cuenta la atenuación de la radiación solar producida por los diferentes componentes atmosféricos; brillo B , medido por el satélite, que proporciona información de la radiación solar ascendente emergente de la atmósfera (Irradiancia); brillo para cielo despejado o simplemente brillo B_0 , que proporciona información del albedo de la superficie terrestre; y el brillo máximo B_{max} , el cual proporciona información del albedo de las nubes.

El modelo desarrollado fue aplicado y validado en Cataluña para un año completo de registros, obteniendo una excelente correlación entre la estimación realizada por el modelo y la obtenida por las estaciones de validación, al obtenerse un coeficiente de determinación superior a 0.98 en todos los casos, conjuntamente con un error cuadrático medio entre 9.7% y 15.9% y un bias que varía entre -9.8% y 1.2% (Flores y Baldasano 2001b).

Zelenka et al. (1999) consideran que para cualquier aplicación que requiera datos específicos para un lugar y momento determinado, el usuario debe confiar plenamente en los datos de satélite, más que en los datos obtenidos por los alrededores de las estaciones de medición, si estas se encuentran espaciadas más de 20-30 km una de otra, es por ello que haciendo uso de esta propiedad y gracias a la cobertura espacial de las imágenes empleadas y a la determinación de los coeficientes de regresión del modelo para toda la cobertura espacial de la imagen NOAA, fue posible obtener los mapas de radiación solar de las Islas Baleares.

Un procedimiento similar al descrito en este trabajo ha sido empleado ampliamente por la Agence Française pour la Maîtrise de l'Energie (Diabaté et al. 1989) y por la European Solar Radiation Atlas (ESRA) (Beyer et al. 1997, Kasten et al. 1996) para la elaboración de mapas de radiación solar del continente Europeo, mediante la aplicación del método Heliosat.

El método Heliosat, desarrollado por Diabaté et al. (1989) produce mapas de radiación solar con una adecuada escala temporal (horaria) y espacial (del orden de 1 píxel de 5 km x 5 km de la imagen Meteosat), como los obtenidos por Cano et al. (1986).

La principal diferencia entre el modelo descrito en este trabajo y el desarrollado por el método Heliosat, consiste en la determinación de coeficientes mensuales de regresión del modelo dada su variabilidad tanto espacial como temporal, incluyendo variaciones estacionales, a diferencia del método Heliosat que considera un solo conjunto de coeficientes de regresión por hora, constantes en el tiempo y en el espacio a lo largo del año, o Cano et al. (1986) que considera los coeficientes de regresión constantes en el tiempo y en el espacio a lo largo del año, solo con una ligera variación estacional.

Otra diferencia la constituye la consideración del albedo variable de las nubes, a diferencia de Cano et al. (1986) y Diabaté et al. (1989) que establecen que el albedo de las nubes puede considerarse constante para determinados tipos de imágenes de satélites.

En la Figura 1 se muestra el diagrama correspondiente al procedimiento de cálculo para la obtención de la radiación solar global superficial a partir de datos de satélites. En primer lugar se aplica un algoritmo para la detección de nubes, el cual consiste en la aplicación de una serie de umbrales a distintas bandas de la imagen, tal como lo describe Flores y Baldasano (2001a), este algoritmo, originalmente desarrollado por Laine et al. (1999) utiliza la reflectividad del canal 1 (R_1) y la temperatura de brillo de los canales 3 y 4 (T_3 y T_4 respectivamente) de las imágenes NOAA, para separar nubes, nieve y suelo.

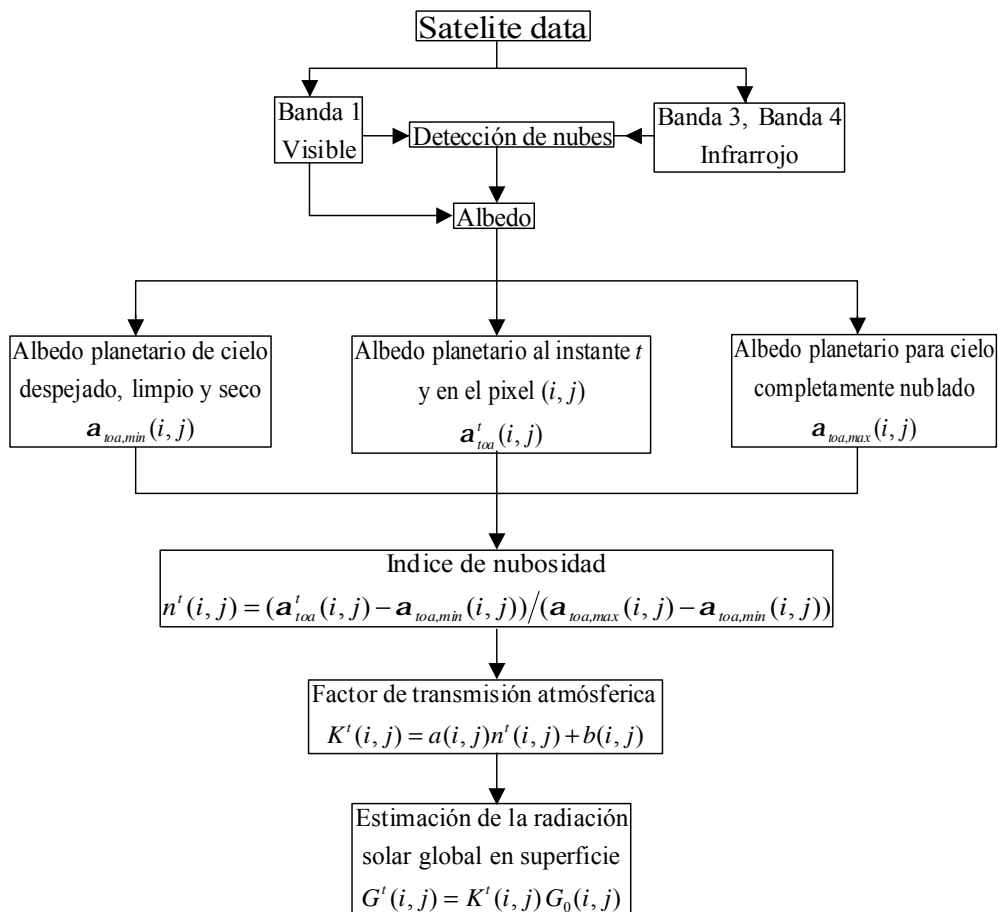


Figura 1. Diagrama de cálculo

Para las imágenes de satélite, el procedimiento consiste en tomar todas las imágenes del mes en estudio. Las imágenes visibles e infrarrojas son usadas para detectar las nubes, mientras que el canal visible se utiliza para determinar el albedo tanto de la superficie como de las nubes.

Cada imagen en el canal visible se normaliza dividiendo por el coseno del ángulo solar cenital local.

El índice de nubosidad se determina aplicando un procedimiento estadístico mediante el cual se toma en cuenta la posibilidad de que un píxel este o no contaminado de nubes. Se toman las imágenes diarias del mes en estudio y se retiene el valor mínimo de cada píxel, proporcionando información del albedo planetario para cielo despejado para cada píxel $a_{toa,min}(i, j)$.

De manera similar, el máximo valor de cada píxel en la serie analizada es retenido, el cual corresponde

al albedo planetario para cielo completamente nublado $a_{toa,max}(i, j)$. Luego el índice de nubosidad se determina para cada píxel mediante la aplicación de una ecuación estadística que determina el porcentaje de cobertura nubosa para cada píxel.

Los coeficientes del modelo se determinan definiendo una regresión lineal entre el factor de transmisión atmosférica calculado de las estaciones de medición en superficie y el índice de nubosidad en la misma ubicación determinado por el satélite.

Por último se relaciona la radiación solar global extraterrestre con el factor de transmisión atmosférica determinado previamente y se obtiene la radiación solar global superficial para toda el área en estudio (Figura 1). Los resultados obtenidos por el modelo fueron validados con otro conjunto de datos independientes provenientes de las estaciones de validación.

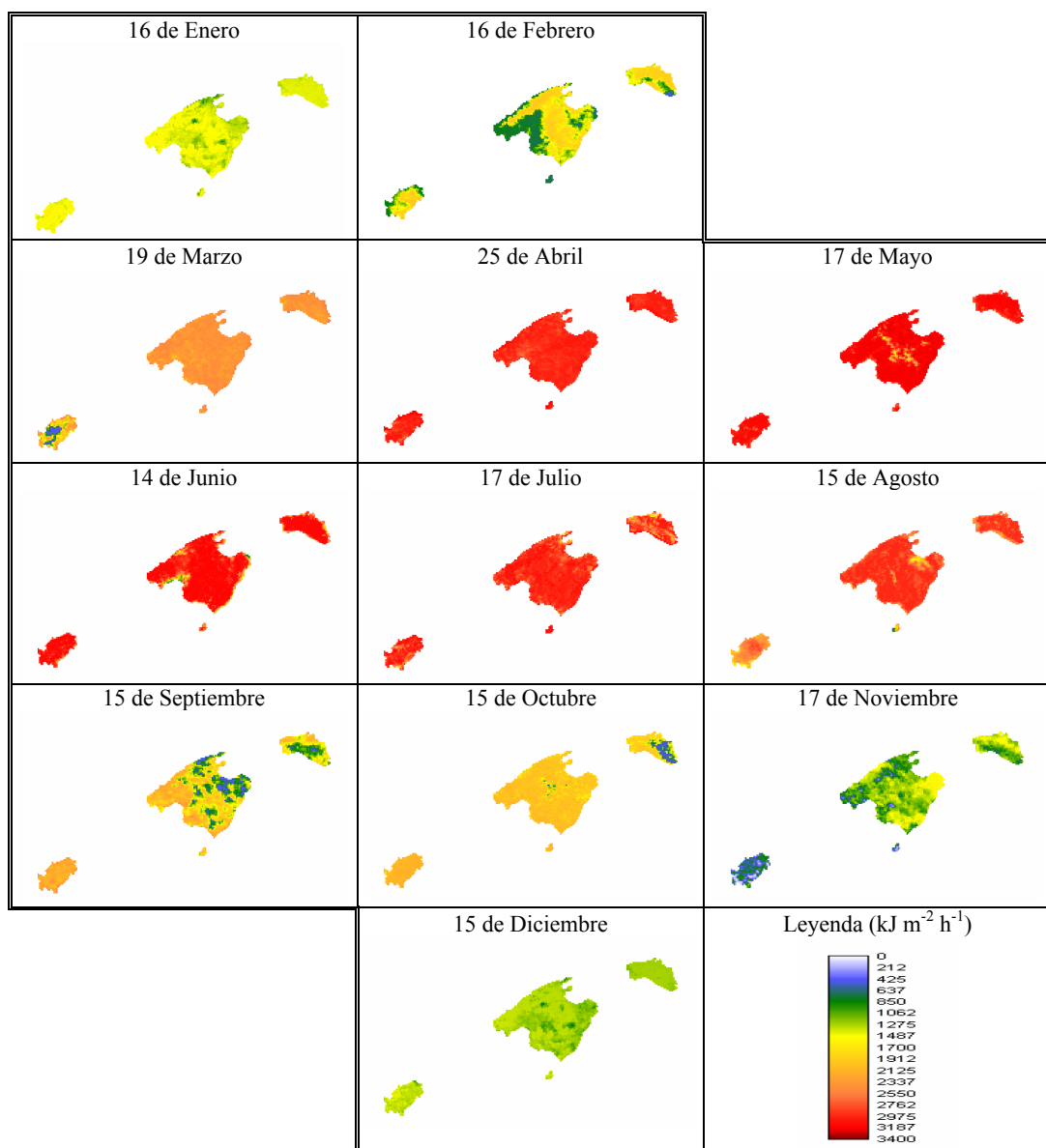


Figura 2. Mapa de radiación solar global horaria de las Islas Baleares entre las 14:00 y 15:00 h (LST), para el año 1998

2 PROCEDIMIENTO OPERACIONAL

2.1 Recopilación y filtrado de datos de las estaciones de medición

Los datos se obtuvieron a partir de 30 estaciones de medición de radiación solar global en superficie distribuidas por toda la geografía de Cataluña, y, pertenecientes a las redes del Instituto Nacional de

Meteorología (INM), Institut Català d'Energia (ICAEN) y el Departament d'Agricultura Ramaderia i Pesca (DARP), estas dos últimas pertenecientes a la red agri-meteorológica de la Generalitat de Catalunya. Las medidas se realizaron empleando piranómetros Kipp-Zonen, Siap y Campbell. Los datos consisten en valores promedio de irradiación cada 5 minutos, conjuntamente con insolación acumulativa diaria para el año 1998.

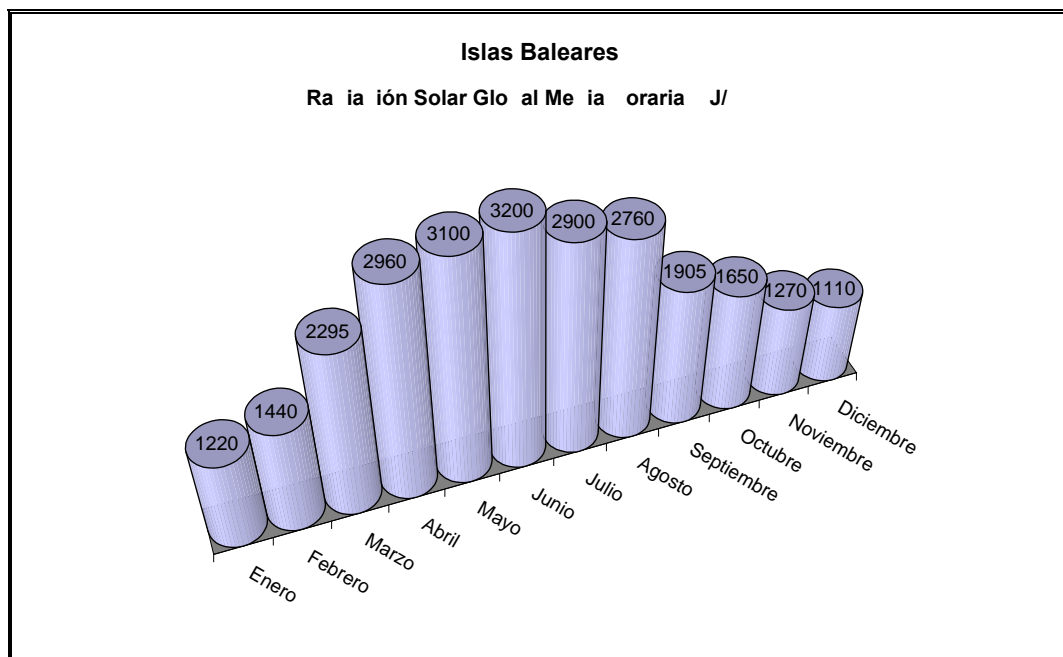


Figura 3. Radiación solar global media horaria para las Islas Baleares

A los datos obtenidos por los piranómetros, se le aplica un cuidadoso proceso de filtrado para corregir posibles errores de medición, por ejemplo: sensores planos, presencia de sombras, malas calibraciones etc. El método consiste en el análisis de los datos en función de dos criterios: coherencia temporal (valores de radiación dentro de rangos aceptables) y espacial de los datos (adecuada distribución espacial de los datos) siguiendo el procedimiento descrito por Santabàrbara et al. (1996) y Baldasano et al. (1999).

Después de la combinación de los dos criterios anteriores, algunos periodos de datos fueron eliminados. En algunos casos, los datos totales de una estación en particular fueron eliminados. Esto condujo a la eliminación de los datos de 9 estaciones de las 30 iniciales

2.2 Imágenes de satélite

Para este estudio se emplearon datos de satélite de órbita polar NOAA AVHRR, para ello se utilizaron 189 imágenes del año 1998, capturadas por la estación receptora del Departament de Medi Ambient de la Generalitat de Catalunya, mediante un receptor Dartcom HRPT system.

En cuanto a la resolución temporal, pueden obtenerse dos imágenes diarias aproximadamente a las 07:30 y 14:30 h (LST), que corresponden al paso consecutivo de un satélite matutino (NOAA-15) y al

de un satélite vespertino (NOAA-14) respectivamente. Sin embargo para este estudio solo estuvieron disponibles por razones técnicas, las imágenes correspondientes a las 14:30 h LST (NOAA-14).

2.3 Resultados del modelo para las Islas Baleares

En la Figura 2 se muestra la radiación solar global horaria estimada por satélite entre las 14:00 y 15:00 h (LST) para las Islas Baleares, para el periodo Enero - Diciembre de 1998. En ellas se ha tratado de representar en lo posible el día 15 de cada mes, el cual es tomado como representativo de la radiación solar global horaria del mes en cuestión. Todos los meses se han representado con la misma escala, de manera que son directamente comparables entre sí.

La secuencia de la Figura 2 muestra claramente la variación estacional de la radiación solar global horaria, en ella se observa que para el mes de diciembre se registran los mínimos absolutos anuales, asociados al solsticio de invierno. Los valores de radiación varían entre 800 y 1450 kJ/m²h, la distribución de la radiación es bastante uniforme y regular en casi todas las islas. Ibiza presenta los menores valores de radiación, mientras que Mallorca presenta unos mínimos relativos dispersos ubicados en la región central y sur este de la isla.

También se observan los valores máximos durante el mes de junio asociado con el solsticio de verano. El rango de variación de la radiación va de 1470 a 3210 kJ/m²h, la distribución de la radiación es bastante uniforme y regular en todas las islas.

En Menorca se aprecian núcleos dispersos de mínimos relativos esparcidos en la región central de la isla. En Mallorca se aprecian unos mínimos relativos en las costas de la Bahía de Pollença, mientras que en Ibiza se observan unos mínimos relativos en la región de San Antoni de Portmany y en los límites de la ciudad de Eivissa.

En la Figura 3 se representa el valor de la radiación solar global media horaria entre las 14:00 y 15:00 h (LST) estimada por el modelo para las Islas Baleares durante el año 1998.

En ella se observa claramente como aumenta la radiación solar global media horaria durante el verano, alcanzando un máximo de 3200 kJ/m²h para el mes de junio, y disminuye a medida que se aproxima el invierno, hasta alcanzar un valor mínimo de 1100 kJ/m²h en diciembre.

3 CONCLUSIONES

En el presente estudio se aplicó un modelo estadístico para la determinación de la radiación solar global horaria empleando datos NOAA AVHRR.

Los coeficientes del modelo se determinaron a partir de los registros de 11 estaciones de medición en superficie (estaciones de calibración), obteniendo altos coeficientes de determinación para el modelo de regresión.

Una vez determinados los coeficientes de regresión, se procede a la aplicación del modelo para obtener la radiación solar global horaria. Los resultados del modelo se compararon con datos de 10 estaciones de medición en superficie (estaciones de validación) independientes a las utilizadas para la determinación de los coeficientes, obteniéndose que la estimación realizada por el modelo se ajusta muy bien a las mediciones, presentando un coeficiente de determinación 0.98 en todos los casos, conjuntamente con un error cuadrático medio entre 9.7% y 15.9% y un bias que varía entre -9.8% y 1.2%.

Los valores de radiación solar global horaria determinados por satélite, producen estimaciones espaciales mucho más precisas que aquellas obtenidas mediante interpolación en superficie de los datos de las estaciones de medición, especialmente en regiones donde la densidad de estaciones de medición es muy escasa y por ende se encuentran muy retiradas unas de otras, y esto se debe a que los datos obtenidos por satélite toman en cuenta variaciones espaciales y locales de la radiación solar global, mientras que la interpolación en superficie de los datos de estaciones

de medición, al ser un proceso discreto no tiene en consideración, a menos que se posea una muy densa red de medición, con separaciones de unos 20 km entre una estación y otra y con características topográficas similares, en cuyo caso los resultados obtenidos por interpolación son de igual calidad que los obtenidos mediante satélites.

Estos resultados demuestran claramente que los datos de satélite pueden ser utilizados para producir mapas de radiación solar global y mapas de cobertura nubosa a escalas locales, regionales e incluso continentales.

El modelo aquí descrito está completamente operativo y los coeficientes fueron validados para un año completo de estudio, para la obtención de la radiación solar global horaria, por lo que dichos coeficientes pueden seguir siendo aplicados a imágenes NOAA de los años siguientes, si bien, convendría ir actualizándolos periódicamente mediante el procesamiento de nuevas imágenes y llegar a construir de esta manera una base de datos de imágenes lo suficientemente larga de manera de llegar a establecer los coeficientes climáticos del modelo en cuestión para la zona en estudio.

Este modelo puede ser empleado para obtener mapas detallados de radiación solar global para varios años de medición y datos de satélites, los cuales son altamente apreciados por científicos, ingenieros y usuarios en general dentro del campo de la energía solar, tanto para la evaluación y dimensionamiento de plantas y edificaciones con tecnología solar, y para su uso tanto en agricultura como en meteorología.

4 AGRADECIMIENTOS

Los autores desean expresar su agradecimiento al Govern Balear por el apoyo en la realización de este trabajo, al Departament de Medi Ambient de la Generalitat de Catalunya por la cesión de las imágenes y al Consejo de Desarrollo Científico y Humanístico de la Universidad Central de Venezuela por el apoyo prestado para la presentación de este trabajo.

5 REFERENCIAS

- Baldasano, J.M., C. Soriano and H. Flores, (1999): Atlas de radiació solar a Catalunya (Dades del període 1964-1997). *Institut Català d'Energia*, 71 pp.
- Beyer, H.G., G. Czeplak, U. Terzenbach and L. Wald, (1997): Assessment of the method used to construct clearness index maps for the new European Solar Radiation Atlas (ESRA). *Solar Energy*, **61** (6): 389-397.

- Cano, D., J.M. Monget, M. Albuisson, H. Guillard, N. Regas and L. Wald, (1986): A method for the determination of the solar radiation from meteorological satellite data. *Solar Energy*, **37** (1): 31-39.
- Diabaté, L., G. Moussu and L. Wald, (1989): Description of an operational tool for determining global solar radiation at ground using geostationary satellite images. *Solar Energy*, **42** (3): 201-207.
- Flores, H. y J.M. Baldasano, (2001a): Detección de nubes mediante imágenes NOAA AVHRR. IX Congreso Nacional de Teledetección. Universidad de Lleida, 19-21 de septiembre.
- Flores, H. and J.M. Baldasano, (2001b): Solar radiation mapping from NOAA AVHRR data in Catalonia (Spain). *J. Appl. Meteor.*, **40** (11), 1821-1834.
- IDAE (1999), Plan de fomento de las energías renovables en España, Instituto para la Diversificación y Ahorro de la Energía (IDAE), Madrid.
- Kasten, F., H.J. Golchert, R. Dogniaux and M. Lemoine, (1996): European solar radiation atlas. Editors Palz, W. and Greif, J., 3rd Ed. Springer-Verlag, Berlin Germany. 333 pp.
- Laine, V., A. Venäläinen, M. Heikinheimo, and O. Hyvärinen, (1999): Estimation of surface solar global radiation from NOAA AVHRR data in high latitudes. *J. Appl. Meteor.*, **38** (12), 1706-1719.
- Santabàrbara, J.M., J. Calbó, J.M. Baldasano, J. Esteve and A. Mitja, (1996): Month to month variation of global solar radiation in Catalonia (Spain). *Int. J. Climatol.*, **16**: 711-721.
- Zelenka, A., Perez, R., Seals, R. y Renné, D. (1999), Effective accuracy of satellite-derived hourly irradiances. *Theor. Appl. Climatol.*, **62**, 199-207.

Using NOAA-AVHRR and SPOT-VGT data to estimate surface parameters: application to a mesoscale meteorological model

Pineda⁽¹⁾, N., Jorba⁽²⁾, O., Jorge⁽¹⁾, J., Baldasano⁽²⁾, J.M.

⁽¹⁾ Department of Applied Physics, EUPM. Av. Bases Manresa 61-73, 08240 Manresa, SPAIN

Universitat Politècnica de Catalunya (UPC). Tel.++3493.877.72.75 Fax ++3493.877.72.02

⁽²⁾ Laboratory of Environmental Modeling, ETSEIB. Av. Diagonal 647, 08028 Barcelona, SPAIN

Universitat Politècnica de Catalunya (UPC).

E-mail address: npineda@fa.upc.es

ABSTRACT – *The mesoscale numerical weather prediction model MM5, the 5th generation Pennsylvania State University/NCAR Mesoscale Model, uses a global land-use map to set the physical parameters on the surface characteristics to model the soil-surface processes. These parameters are albedo, emissivity, thermal inertia, roughness length and soil moisture data. A new estimation of the physical soil parameters is done for the north-east of the Iberian Peninsula from a AVHRR data set of year 2000. The new values are introduced into MM5 via a new land-use map, the recent NATLAN 2000 - CORINE land-use map, in order to incorporate the last decade land-cover changes. The model is tested with the original and the CORINE land-use map to evaluate the sensitivity to land-use changes and new physical soil parameters definition. Results show clear local differences in some meteorological variables as wind fields or updraft movements, but comparisons with measurements don't lead to a clear improvement in the model general performance.*

1 INTRODUCTION

Correctly treating the land surface properties is becoming increasingly important for meteorological models to be able to capture local mesoscale circulation induced by land surface forcing (Chen and Dudhia, 2001). Several mesoscale models, like the fifth-generation Pennsylvania State University/NCAR Mesoscale Model (MM5) used in this study, rely on albedo, emissivity, thermal inertia, roughness length and soil moisture data sets derived from land-use maps. The simple surface parameters scheme of the model specifies them according to land use category and season. The accuracy of land-use information is important to obtain accurate simulations.

MM5 (Dudhia, 1993) uses the USGS global land-use map to set the physical parameters on the surface characteristics, a 10-year old land-use map that was created with a multitemporal 1-km AVHRR NDVI data (1992-1993) (Anderson et al., 1976). To incorporate the last decade land-cover changes, the recent CORINE land-use map of the European Environment Agency NATLAN information package

(EEA, 2000) was used in the simulations instead of the original map.

Geophysical surface parameters (albedo, emissivity and thermal inertia) were estimated for the working region from a AVHRR data set of year 2000, and mean values for the CORINE land-use classes were calculated for the four seasons. As soil moisture and roughness can not be estimated with optical remote sensing sensors, a category equivalence between land-use maps was established, in order to use the original MM5 tabulated roughness and moisture values with the new land-use map.

2 STUDY LOCATION

The location of the present study is situated in the north-east of the Iberian Peninsula (figure 1). This region is characterized with very complex topography, a high mountain range to the north of the area, with extend mountains to the south-west and an important river-valley canalisation going from the north-west to the east flowing into the Mediterranean sea. Mediterranean sea is another particularity of the region, with a large coast line.

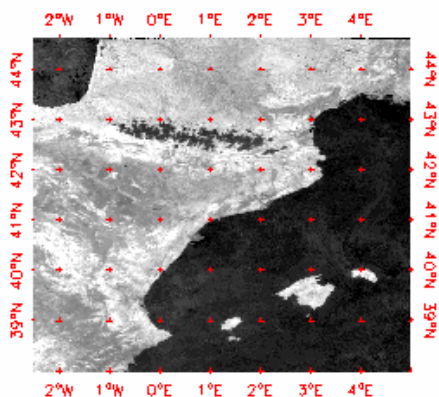


Figure 1. Estimated albedo for march 2000 in the D3 domain of MM5 over NE Spain.

3 SURFACE PARAMETERS ESTIMATION

3.1. AVHRR processing

A selection of 70 afternoon pass and 55 morning pass NOAA14-AVHRR images were used in this study. Such images were taken from an original set of 162 L1B images furnished by the *Centro de Recepción, Proceso, Archivo y Distribución de Imágenes de Observación de la Tierra* (CREPAD). Before surface parameters estimation some corrections were applied:

Step 1. Re-calibration. Because of sensor degradation after launch, it was necessary to apply time-dependent calibration gains and offsets, obtained from NOAA (1998), to derive the TOA (top of atmosphere) radiance for AVHRR 1 and 2 channels.

Step 2. TOA Reflectance for AVHRR channels 1 and 2. A lambertian correction (Teillet, 1992) was used to transform radiance to reflectance.

Step 3. Atmospheric correction. The SMAC algorithm (Rahman and Dedieu, 1994) was employed to convert TOA reflectance to surface reflectance of each image. SMAC input data, like water vapor content and columnar ozone content was derived from the NOAA-TOVS sensor, data furnished by the ATMOS User Center of the German Remote Sensing Data Center (DFD). Aerosol optical depth (at 550 nm) was obtained from the Aerosol Robotic Network (AERONET) (Holben et al, 1998).

For the thermal channels, a split-window technique was used. Day and night Land Surface Temperature (LST) were calculated with the Sobrino and Raussoni (2000) algorithm. Input data are the channels 4 and 5 brightness temperature, surface emissivity and water

vapor, obtained from the morning and afternoon passes of the NOAA-TOVS.

Step 4. Identification of cloud contaminated pixels and image compositing. In order to create cloud-free monthly mean images, clouds were filtered using a regional adaptation of the threshold procedure proposed by Derrien et al. (1993). Once clouds masked, monthly composites were calculated, applying the mean for the non-contaminated pixels, channel-by-channel. Geophysical surface parameters were estimated from these month composites

3.2. Geophysical surface parameters estimation

ALBEDO was estimated assuming lambertian reflection. To derive broad-band albedo from AVHRR, a narrow-band to broad-band conversion method (Saunders 1990) that combines weighted AVHRR channels 1 and 2 was used. From the channel weights proposed by different authors, the ones estimated for the Iberian Peninsula by Valiente et al. (1995) were used.

EMISSIONITY at 9 nm was calculated using the Valor and Caselles (1996) method, which derives emissivity from NDVI vegetation index images.

THERMAL INERTIA (TI) was estimated according to the simple formulation for calculating TI from remote sensing data, given by Price (1977). The Sobrino and El Kharraz (1999) Price's model adaptation was used. Calculated TI values with AVHRR were higher than USGS ones for all the land-use categories, specially in coastal and high altitude regions as shown in figure 2. Low altitude flat and continental regions are the most similar to MM5 global TI values. It seems that sea and mountains effects in TI are not contemplated in the MM5 tabulated TI values.

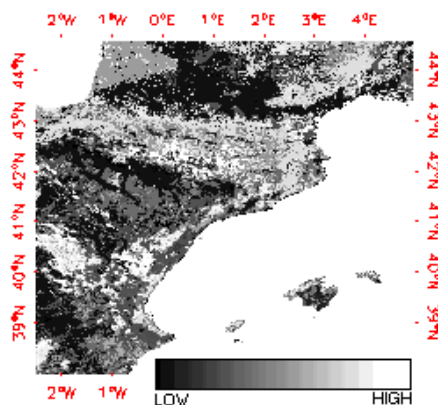


Figure 2. Differences between CORINE and USGS Thermal Inertia.

4. LAND-USE CATEGORIES EQUIVALENCE

Albedo, emissivity and Thermal Inertia were derived from the AVHRR data set, but roughness and soil moisture can not be estimated with optical sensors. To run the simulation in MM5 with the CORINE land-use map, it was necessary to obtain an estimation of these surface parameters for the CORINE categories.

Table 1. Surface parameters for CORINE land-use categories and equivalences with USGS land-use map. The third column is percent of category presence in the land surface of D3 domain. W: winter S: summer.

CORINE	Category Description	%	ALBEDO		MOISTURE		EMISSION		ROUGHNESS		THERMAL INERTIA		NATLAN	USGS	USGS Category Description	GOWER
			W	S	W	S	W	S	W	S	W	S				
1-11	Urban	0.43	16.8	17.8	10	10	93.5	93.7	50	50	0.055	0.069	1-11	1	Urban and Built-Up Land	6.2
12	Non-Irrigated Arable Land	21.77	18.4	20.7	60	30	96.0	95.8	5	15	0.049	0.056	12	2	Dryland Cropland and Pasture	15.2
13	Permanently Irrigated Land	3.23	19.7	20.5	50	50	95.4	96.5	5	15	0.037	0.056	13	3	Irrigated Cropland and Pasture	11.2
14	Rice Fields	0.18	15.7	17.0	50	50	92.8	97.5	5	15	0.063	0.095	14	3	Irrigated Cropland and Pasture	21.7
15	Vineyards	3.91	18.5	19.9	60	35	95.2	95.6	20	20	0.046	0.056	15	6		23.5
16	Fruit Trees And Berry Plantations	1.97	16.5	17.1	60	35	96.4	95.9	20	20	0.050	0.068	16	6	Crops/Wood mosaic	27
17	Olive Groves	0.51	15.8	17.1	60	35	96.4	95.3	20	20	0.048	0.061	17	6		15
18	Pastures	2.32	16.0	17.1	60	30	97.6	98.9	5	15	0.063	0.080	18	2	Dryland Cropland and Pasture	36.1
19	Annual Crops & Permanent Crops	0.50	18.5	20.4	60	35	97.1	93.7	20	20	0.050	0.058	19	6		22.6
20	Complex Cultivation Patterns	9.21	17.4	18.8	60	35	96.5	96.7	20	20	0.053	0.063	20	6	Crops/Wood mosaic	33.9
21	Mixed Agriculture & Natural Vegetation	5.94	17.8	19.4	60	35	95.7	95.0	20	20	0.044	0.053	21	6		24.5
22	Agro-Forestry Areas	0.08	17.8	19.4	60	35	95.7	95.0	20	20	0.044	0.053	22	6		19
23	Broad-Leaved Forest	10.03	14.4	16.1	60	30	97.1	98.5	50	50	0.066	0.078	23	11	Deciduous Broadleaf Forest	5.7
24	Coniferous Forest	12.56	14.1	14.3	60	30	97.3	97.4	50	50	0.057	0.071	24	14	Evergreen Needleleaf Forest	20.4
25	Mixed Forest	3.15	14.1	14.8	60	30	97.4	98.4	50	50	0.064	0.079	25	15	Mixed Forest	4.8
26	Natural Grassland	4.30	17.7	17.2	30	15	96.1	98.0	0.10	0.12	0.060	0.069	26	7	Grassland	42
27	Moors & Heathland	1.19	16.0	16.4	25	15	97.4	98.4	10	11	0.060	0.077	27	9		28.4
28	Sclerophyllous Vegetation	8.41	15.6	15.8	25	15	96.4	96.0	10	11	0.051	0.062	28	9	Mix Shrubland/Grassland	21.3
29	Transitional Woodland-Shrub	6.06	15.4	15.6	25	15	96.7	96.5	10	11	0.051	0.064	29	9		11.5
30	Beaches, Dunes & Sand Plains	0.06	16.8	17.1	5	2	94.5	96.9	10	10	0.066	0.066	30	19		66.4
31	Bare Rock	0.62	17.3	18.9	5	2	96.2	96.5	10	10	0.063	0.071	31	19		55.8
32	Sparsely Vegetated Areas	0.98	19.6	21.1	5	2	95.1	94.3	10	10	0.039	0.048	32	19	Barren or Sparsely Vegetated	72
33	Burnt Areas	0.19	13.3	13.8	5	2	97.0	96.4	10	10	0.048	0.052	33	19		113.2
34	Glaciers & Perpetual Snow	0.00	51.3	41.5	95	95	99.7	98.1	5	5	0.009	0.010	34	24	Snow or Ice	-
35-38	Inland Marshes, Peatbogs, Salines	0.06	14.7	15.5	75	60	94.6	95.8	20	20	0.067	0.080	35-38	17	Herbaceous Wetlands	-
39	Intertidal Flats	0.01	15.1	15.8	75	60	93.7	95.6	20	20	0.067	0.093	39	17		-
40-43	Inland Water	0.16	7.8	7.7	100	100	97.8	97.8	0.01	0.01	0.142	0.170	40-43	16	Water Bodies	-
44	Sea & Ocean	-	7.8	7.7	100	100	97.8	97.8	0.01	0.01	0.169	0.187	44	16		-

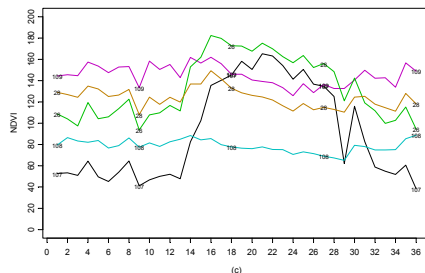
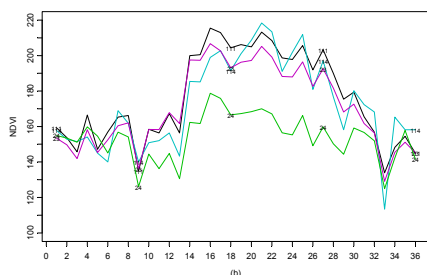
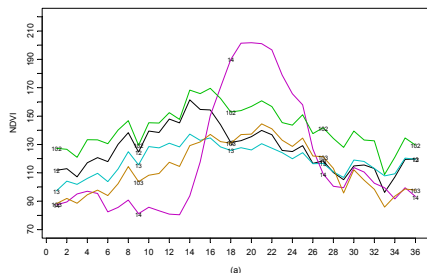


Figure 3. Annual NDVI cycles of some CORINE and USGS land-use categories.

For the land-use categories equivalence study, a set of 36 SPOT-VGT S_{10} NDVI images of the year 2000 was used. Nevertheless NDVI vegetation index can be calculated with AVHRR images, the VITO SPOT-VGT data set has more images (one each 10 days), better calibration and geographical quality than

AVHRR data, thus they are more suitable for annual vegetation cycle variations analysis. The ten-day synthesis (S_{10}) NDVI images are composites of the maximum NDVI value acquired during 10 day periods.

Calculated parameters for the CORINE categories are shown in table 1. Winter and summer periods correspond to three months periods. The equivalence between land-use categories is shown on the right part of table 1. The final column correspond to the Gower metric statistic (Gower, 1971), used to establish the categories annual NDVI cycle similarities. As Gower statistic value gets lower, the annual NDVI patterns between categories are more similar.

In figure 3 annual NDVI cycles of some CORINE and USGS land-use categories are represented. Cropland classes are represented in figure 3 (a). CORINE Non-Irrigated Arable Land (cat.12) has a similar NDVI annual pattern with its comparable class in USGS, dry crops (cat.102), but with higher NDVI values. The same occurs for the irrigated crops (CORINE cat.13 and USGS cat.103), but rice fields (CORINE cat.14) has a completely different NDVI annual pattern. According to the Gower statistic is more similar to USGS-103 (Gower: 21.7) than to 'dry crops' (Gower: 37.8), thus roughness and moisture values for rice fields were taken from USGS cat.103. Figure 2 (b) shows a good equivalence between USGS cat.111 'Deciduous Broadleaf Forest' and CORINE cat.23 'Broad-Leaved Forest' (Gower: 5.7) and a less good equivalence between USGS cat.114 'Evergreen Needleleaf Forest' and CORINE-24 'Coniferous Forest' (Gower: 20.4).

The CORINE 'Sclerophyllous Vegetation (cat.28)' (figure 3 (c)) seems theoretically to correspond to USGS 'Shrubland' (cat.108), but according to the NDVI pattern and the gower metric (21.3 for cat.109 and 45.3 for cat 108), it seems more appropriate to take values of roughness and moisture from class 'Mix Shrubland/Grassland (cat.109)' for the Sclerophyllous Vegetation category. Finally besides Shrubland categories, grassland (USGS cat.107) is represented. The NDVI is quite different between summer and winter periods, because of the snow presence between November to April. In the MM5 tabulated surface parameters for grassland in winter are quite different of the AVHRR calculated ones, because snow is not contemplated, and that can lead to important differences in winter simulations.

5 METEOROLOGICAL MODEL

The mesoscale meteorological model used in this study is MM5. It is a community mesoscale model widely used for numerical weather prediction, air

quality studies, and hydrological studies. On the smaller meso-beta and meso-gamma scales (2-200 km), MM5 can be applied to studies involving mesoscale convective systems, fronts, land-sea breeze, mountain-valley circulations, and urban heat islands (MMD/NCAR, 2001).

Two major changes were introduced into the model in order to evaluate some improvements in its performance. A new set of physical soil properties were introduced to MM5 via a more accurate land use map. Some modifications were carried out to adapt the new information to the model. These new parameters are tabulated in table 1 for winter and summer case.

To evaluate the behavior of MM5 with these modifications, two simulations were performed. A base case with the default values of physical soil properties and the land-use map of the USGS, and a simulation with the new parameters and the CORINE land-use map. Hereinafter the simulation with the CORINE land-use map and the new physical soil properties will be named CORINE simulation, and the simulation with the defaults values of MM5, USGS simulation.

5.1 Model configuration

Four nested domains were selected (figure 4), which essentially covered Europe (Domain 1, D1), the Iberian Peninsula (Domain 2, D2), NE of the Iberian Peninsula (Domain 3, D3) and Catalonia (Domain 4, D4). D1 has 50x35 grid points in the horizontal with 72-km grid-point spacing. D2 has 61x49 24-km cells. D3 has 93x93 6-km cells. D4 has 151x151 2-km cells. The vertical resolution consisted for all domains of 23 σ -layers, with the lowest one situated approximately at 36-m AGL.

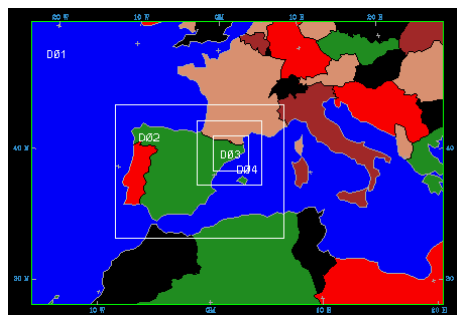


Figure 4. MM5 domains definition over Southern Europe.

The model uses the Mellor-Yamada scheme as used in the ETA model (Janjic, 1994) for the PBL parameterization, the Anthenis-Kuo and Kain-Fritsch (Kain and Fritsch, 1993) cumulus scheme for domain

1 and 2, and no cumulus parameterization for domain 3 and 4. A simple ice explicit moisture scheme, a cloud-radiation scheme, and the five-layer soil model are the rest of physical parameterizations used in these simulations.

Initialization and boundary conditions for the mesoscale model were introduced with analysis data of the ECMWF global model. Data were available at a 1-degree resolution (100-km approx. at the working latitude) at the standard pressure levels every 6 hours.

5.2 Meteorological situation

A synoptic situation was studied in order to evaluate the performance of the model working with a new land use map and physical parameters obtained with the methodology explained before. The meteorological case was August 14th of 2000. A situation with weak synoptic forcing was chosen, so that mesoscale phenomena, induced by the particular topography of the region, and the physical properties of the soil would be dominant.

Synoptic situation of August 14th corresponds to a typical summertime barometric swamp over the Iberian Peninsula. At surface, the high pressure area is centered over south Atlantic ocean, with the anticyclonic wedge affecting most part of the Iberian Peninsula, producing a typical barometric swamp along the easterly part of the Peninsula. Surface winds are low. This fact, and the strong daily solar heating, produced the development of mesoscale phenomena. These phenomena in the region are mainly sea-breezes, up-slope and down-slope winds and valley channeled winds. The heating during August 14th was so intense that a thermal low started to develop in the south-east of the Iberian Peninsula. In height, a zonal flow blows aloft the Peninsula veering to the south-east having northwesterly winds affecting the northeast of the Iberian Peninsula. The winds aloft exhibit the maximum velocities at north-west of the Peninsula.

6 MODEL RESULTS

The new land-use map and the physical soil parameters have been introduced to MM5. Three regions of domain 4 are described in order to illustrate the differences produced by those changes. The differences in moisture availability between the two model simulations are displayed in figure 5, with the location of three test regions (marked with a black square). A first area with an introduction of several urban zones around Barcelona city, a second one with a large extension of a land-use homogeneous change, and a third one comprising a couple of mountains ranging from 1000 to 3000 m (Pyrenees).

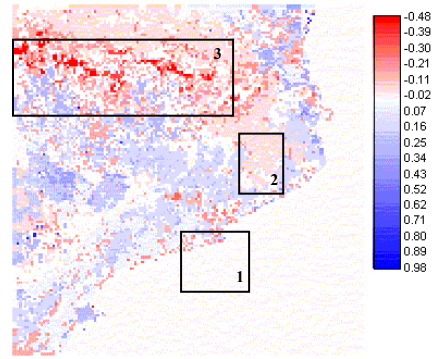
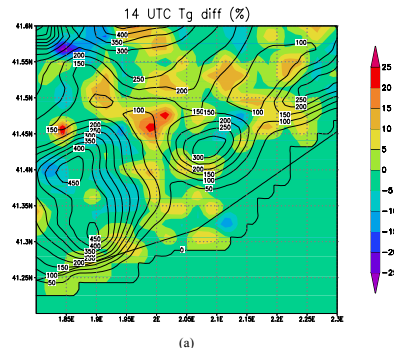


Figure 5. Differences in moisture availability between the two MM5 simulations (CORINE - USGS).

6.1 Geographical area of Barcelona

In figure 6 differences in ground temperature (CORINE-USGS) are displayed in top panel. The values are percentages relative to USGS ground temperature. The regions with a new reclassification of the land-use to urban soil appear to be warmer in CORINE simulation. The differences range varies from 25% to -25%. These differences in ground temperature affects the air temperature at the first layer of the model with differences between the two simulations (CORINE-USGS) in a lower way, with differences at 14 UTC ranging from 2.5% to -1.5%, bottom panel (figure 6 b).

These differences are produced due to the new definition of physical soil parameters and because a different results on cumulus simulation. The modifications of the surface properties are sufficiently important to produce variations in cloud developments, and as a result, precipitation patterns are slightly different.



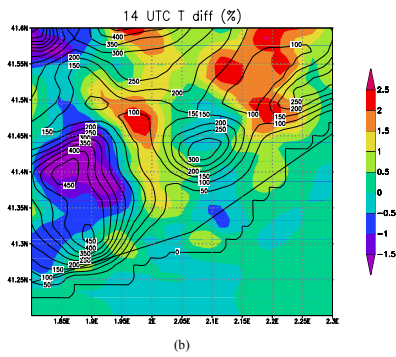


Figure 6. Differences in (a) ground temperature (CORINE-USGS) and (b) first level temperature.

The variation of surface budgets between the two simulations are able to change the surface and aloft wind fields in several regions of domain 4. Figure 7 (a) shows the surface wind field of the geographical area of Barcelona obtained with the USGS land-use map at 14 UTC (top panel). A sea breeze is well established, blowing inland over all the domain, with southerly winds veering southeasterly leeward the coast mountain range. The bottom panel (b) of figure 7 shows the differences between the two surface wind fields simulated by CORINE and USGS land-use map. The arrows are the wind field difference between CORINE and USGS, and the color shaded map are the differences of the wind's velocity. With the modifications introduced to MM5, the sea breeze is weaker inland, and over the sea has a more southwesterly component. The differences in the velocity magnitude are lower in comparison to the direction differences. It is important to note, that in other regions were convective flows are simulated, the surface winds can vary with values of 5 m/s. That's because the different placement of the vertical thermals that produce the cumulus clouds simulated by the model with different soil parameters.

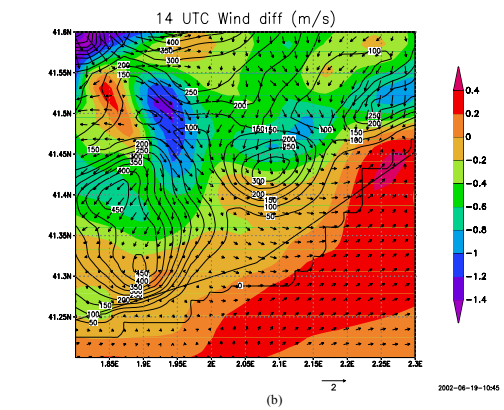
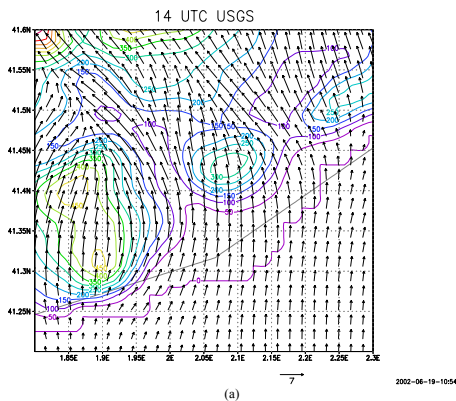


Figure 7. (a) Surface wind field of the base case, and (b) surface wind field difference (CORINE - USGS).

6.2 NE of domain 4

To the north-east region of domain 4, a general increase of thermal inertia, roughness length, emissivity and albedo, and a decrease of moisture availability are produced. These variations can be associate to the change of the land-use of that region. With USGS map, the land-use was classified as cropland-woodland mosaic, and with the implementation of the CORINE land-use map, that region was considered as broad-leaved forest. As can be seen, the CORINE land-use categories are more explicit, and the USGS ones more generic with mosaic classes. The values of the physical soil parameters with the two maps are tabulated in table 2.

The more important differences in physical parameters reside on thermal inertia and roughness length. With these values, a warmer layer near the ground should be simulated during night with CORINE map, and colder during the daytime. However, the model seems to be much sensible to moisture availability than to the rest of the other parameters.

Table 2 Variation of physical parameters in region 2.

	Albedo (%)	Moisture avail. (%)	Emissivity (% at 9 \square m)	Roughness length (cm)	Thermal inertia ($\text{cal cm}^{-2} \text{K}^{-1} \text{s}^{-1/2}$)
USGS-crop./woodland mosaic	16	35	93	20	0.04
CORINE-broad-leaved forest	17.11	30	98.29	50	0.0672

In figure 8, the evolution of the ground temperature at a location within the region is showed (a). Green line is the CORINE results and black one the USGS. At night, the ground temperature is higher with the

CORINE simulation due to the high values of thermal inertia associated to the land-use class of that point, nevertheless, during the daytime the temperature with CORINE continues over the USGS one. This performance can be explained due to the lower values of moisture availability, producing a decrease of the latent heat flux. In the evolution of the temperature (b) the two simulations have a similar behavior, with a faster response to a decrease of the incident short wave downward radiation by USGS case, because the lower value of T_l . The decrease of the incident radiation is caused by the clouds, with slightly variations in extension dimension between simulations.

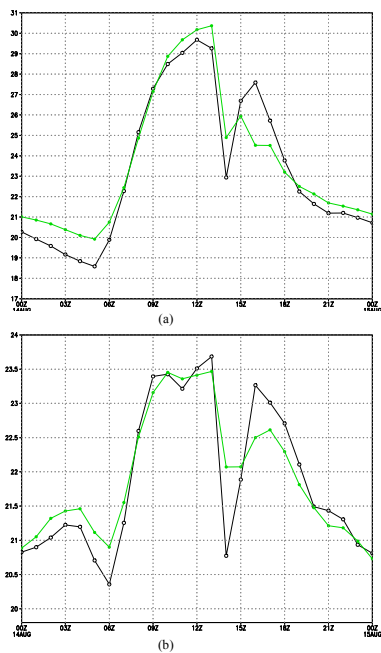


Figure 8. Daily evolution of (a) ground temperature and (b) first layer temperature at 42°45'N 2°6'E in region 2. Green line CORINE, black line USGS.

6.3 Pyrenees

With the CORINE land-use map and the new values of the physical soil parameters the model simulate higher ground temperatures in the Pyrenees mountain range during all the simulated period. These differences can reach values up to 90% of the value simulated with USGS. That behavior can be explained due to the low values of moisture availability associated to the high peaks of the Pyrenees with the new reclassification. Complex variations in the wind fields are produced within this region due to the high complexity of the topography and the variations introduced with the new parameters.

Note that depending on the location of cumulus development, the aloft winds can vary in an important way. A cross section of the wind field and the mixing ratio is displayed in figure 9, the top panel shows the cross section for the results of the CORINE simulation, and the bottom panel the cross section for the USGS simulation. Both cross sections at 15 UTC along 1.55°E.

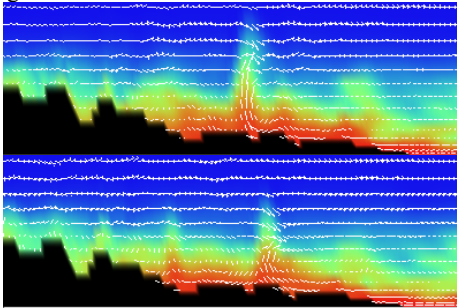


Figure 9. Cross section of the wind field and the mixing ratio along 1.55°E (CORINE upper, USGS bottom panel).

The differences are clearly evident, with an important updraft over the middle of the region injecting moist air aloft in the CORINE simulation. This updraft is less important in the USGS case, with a boundary layer warmer and dryer in comparison with the CORINE one.

6.4 Measurement comparison

An extensive net of surface measurements is available at the area of domain 4. Comparisons with these observations are done calculating the root-mean square error (RMSE), the BIAS and for the vector wind, the root-mean square vector error (RMSVE). The temperature at 2m and the wind at 10 m are evaluated. Figure 10 shows the evolution of the RMSE and the BIAS for the temperature at 2 m. Both statistics are calculated in basis to the observations.

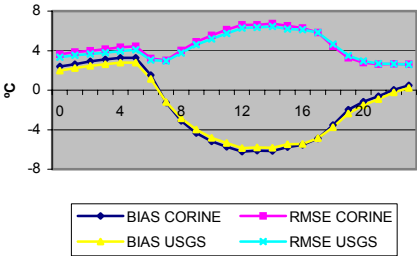


Figure 10. Evolution of the RMSE and the BIAS for the temperature at 2 m.

The errors in both simulations are nearly equals. The CORINE simulation is slightly warmer during night time, as can be appreciated with the bias evolution, and slightly colder during day time. The model is not able to reproduce the daily variations of the temperature, with an overestimation at night and subestimation during the day. With the modifications introduced, land-use map and surface properties, there is not an improve in the model performance. The comparison with the winds at 10 m gives similar results as can be observed in figure 11.

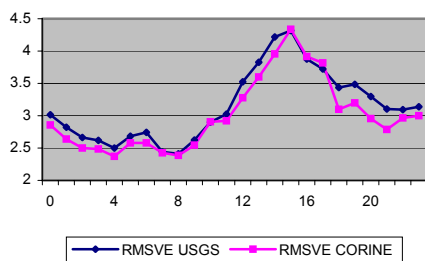


Figure 11. RMSVE for the winds at 10 m.

In both cases, the evolution of the RMSVE is similar with little differences. CORINE simulation gives little better results in RMSVE, but the RMSE of the magnitude of the velocity is slightly higher than with USGS results. The surface winds appear to be lower in CORINE simulation than in USGS one, and in both cases are lower than the observations during the daytime, and higher at night. The evolution of RMSE and RMSVE for the wind shows a little improvement in wind direction with the new land-use map.

7 SUMMARY

An updating of the local physical parameters used in MM5 was intended, in order to get a better performance of the model and to have better regional simulations. Remotely sensed data of the year 2000 was used, as well as a recent land-use map. Results show that differences in surface parameters basically rely on thermal inertia. Besides, land-use maps comparison had shown important differences between classifications which also affect the final composition of surface parameters that get into the model.

The new values of the physical soil parameters have been introduced to MM5 with a new land-surface map. These modifications have been enough important to produce variations in the performance of the model. The cloud development differs in the two cases basically in the location and dimensions of the clouds, that drives to a different superficial radiative budget

affecting the evolution of air temperature at low levels. The different results in cumulus simulation produced important differences in the surface wind field and the updrafts. The introduction of those changes are enough important to obtain slightly variations in the pattern of accumulated precipitations for the simulated period. Comparisons with measurements have been done. Similar errors are obtained with the two land-use maps and physical parameters, without a clear improvement in the performance of the meteorological model.

Acknowledgments. The authors thank the Environmental European Agency for providing the EEA NATLAN-2000 land-use information package; the CREPAD-INTA (Instituto Nacional de Técnica Aeroespacial, Spain) for the AVHRR data; the AUC-DLR center (German Aerospace Center) for the TOVS data; the VITO (Flemish Inst. Technological Research, Belgium) center for providing the SPOT-VGT S₁₀ images; the Spanish Meteorological Institute (INM) for providing data from the ECMWF; and the Catalan Meteorological Service (SMC) for providing surface station data for validation.

Simulations were run on an HP Exemplar V2500 belonging to CESCA (Centre de Supercomputació de Catalunya). This work was developed under projects IMPACTE and CICYT REN2000-1754-C02-01/CLI.

8. REFERENCES

- Anderson, J.R., Hardy, E.E., Roach J.T., and Witmer R.E., 1976, A land use and land cover classification system for use with remote sensor data: U.S. Geological Survey Professional Paper 964.
- Chen, F., Dudhia, J., 2001, Coupling an advanced land surface-hydrology model with the Penn State-NCAR MM5 Modeling System. Part I: Model implementation and sensitivity. *Monthly Weather Review*, 129, 569-585.
- Derrien, M., Farki, B., Harang, L., LeGléau, H., Noyalet, A., Pochic, D., Sairouni, A., 1993, Automatic cloud detection applied to NOAA-11/AVHRR imagery. *Remote Sensing of Environment*, 46, 246-267.
- Dudhia, J., 1993, A non-hydrostatic version of the Penn State-NCAR mesoscale model: Validation tests and simulation of an Atlantic cyclone and cold front. *Monthly Weather Review*, 121, 1493-1513.
- European Environment Agency, 2000, NATure/LANd Cover information package (CORINE Land Cover 1:100000)
- Gower, J.C., 1971, A general coefficient of similarity and its properties. *Biometrics*, 27, 857-871.

- Holben B.N., T.F.Eck, I.Slutsker, D.Tanre, J.P.Buis, A.Setzer, E.Vermote, J.A.Reagan, Y.Kaufman, T.Nakajima, F.Lavenu, I.Jankowiak, and A.Smirnov, 1998. AERONET - A federated instrument network and data archive for aerosol characterization. *Remote Sensing of Environment*, 66, 1-16.
- Mesoscale and Microscale Meteorology Division, National Center for Atmospheric Research, 2001, PSU/NCAR Mesoscale Modeling System Tutorial Class Notes and User's Guide: MM5 Modeling System Version 3, June 2001.
- NOAA, 1998, Polar Orbiter Data User's Guide (November 1998 version)
<http://www2.ncdc.noaa.gov/docs/podug/index.htm>
- Price, J.C., 1977, Thermal Inertia mapping: A new view of the earth, *Journal of Geophysical Research*, 82, 2582-2590.
- Saunders, R.W., 1990, The determination of broad band surface albedo from AVHRR visible and near-infrared radiances, *International Journal of Remote Sensing*, 11 (1), 49-67.
- Sobrino, J.A., El Kharraz, M.H., 1999(b), Combining afternoon and morning NOAA satellites for thermal inertia estimation. 2. Methodology and application, *Journal of Geophysical Research*, vol. 104(D8), 9455-9465.
- Sobrino, J.A., Raissouni, N., 2000, Toward remote sensing methods for land cover dynamic monitoring. Application to Morocco, *International Journal of Remote Sensing*, 20(2), 353-366.
- Teillet, P.M., 1992, An algorithm for the radiometric and atmospheric correction of AVHRR data in the solar reflective channels, *Remote Sensing of Environment* 41, 185-195.
- Valiente, J.A., Nunez, M., Lopez-Baeza, E. and Moreno, J., 1995, Narrow-band to broad-band conversion for Meteosat-visible channel and broad-band albedo using both AVHRR-1 and -2 channels, *International Journal of Remote Sensing*, 16 (6), 1147-1166.
- Valor, E. and V.Caselles, 1996, Mapping land surface emissivity from NDVI: Application to European, African, and South American areas, *Remote Sensing of Environment*, 57, 167-184.

Factor Analysis of Landsat-TM for vegetation cover quantification in a *dehesa* ecosystem

M.P. González Dugo¹, P. Fernández Rebollo², J.V. Giráldez Cervera³, J.E. Guerrero Ginell⁴

¹SCAI. Información del Territorio., E-mail: maria@uco.es

²Dept. Ingeniería Agroforestal. E-mail: palferrep@uco.es

³Dept. Agronomía, E-mail: aglgecej@uco.es. ⁴Dept. Producción Animal, E-mail: palgegi@uco.es. Universidad de Córdoba. Apto. 3048 CORDOBA

ABSTRACT. *The dehesa is a complex and multiple land use ecosystem for agricultural and cattle breeding purposes frequent in the Western Iberian Peninsula. A linear mixture model characterizes its different components. Previously the real dimension of a thematic mapper image taken in the region has been estimated to separate all the components of this system, following two methods. The analysis of the eigenvalues from a Principal Component transformation using both the Imbedded Error Function, IE, and the Factor Indication Function IND, discerns four factors from the original six TM bands. A Minimum Noise Fraction Rotation produced similar results. The four components can definitely model the main elements of the dehesa: oak trees, pasture and bare soil, while the fourth factor represents the illumination changes with a shade component.*

1 INTRODUCTION

The *dehesa* is one of the predominant landscape units in the Western Iberian Peninsula, especially in the Southwest. It is a combination of several vegetation layers maintaining an integrated livestock, agriculture and forest production. This complexity implies a difficulty for remote sensing studies. In this area most image pixels are mixtures of few elements, randomly distributed showing a different degree of coverage. These elements cannot no be detected in most multispectral images on the basis of spatial properties alone, because targets are smaller than image sampling units. However they can be detected under certain circumstances of spectral contrast, spectral sampling, and instrumental noise (Sabol et al., 1992). The spectrum of all sub pixel elements is a combined signal. An isolated pixel may not be retrieved in the spectrum through inversion of the combined signal. Nevertheless, it can be estimated using spectral mixture analysis when the spectral variance from pixel to pixel of a multispectral image is available.

The real dimension of an image, that is a crucial parameter for a posterior spectral mixture model, can be evaluated using the factor analysis. This method is applicable to the analysis of large areas studies avoiding the difficulties induced by the complexity of the *dehesa* coverage

2 THEORY

The number of components considered in the model depends on landscape elements, being limited by the real dimension of the original data. In the case of an image, that limit is the number of bands plus one, considering all of them as independent variables. The redundancy of image data with a high level of correlation between bands, have enforced to most studies with TM sensor to use a maximum of either four (Adams y col. 1995, García-Haro et al. 1996), or five components (van der Meer and Jong, 2000).

Because the experimental error is unknown, the determination of the real dimension of an image or the true factor is not a simple task. Various criteria have been developed for this purpose.

2.1 Eigenvalue analysis

The number c of eigenvalues obtained from a principal component analysis, PCA, can be grouped into two sets of eigenvalues. The first set with n members contains the largest values. The second set with $c-n$ members is composed of the experimental errors. Criteria must be chosen to deduce how many of the smallest eigenvalue belong to the latter set.

Several empirical methods are commonly used to deduce the factor space without a previous knowledge of the error, as it happens with remote sensing images. Malinowski (1991) suggested two functions based on the study of how errors weave into the factor analysis scheme.

The raw experimental data is a sum of a pure data matrix and an error matrix. The pure data are regenerated using the n primary eigenvectors only. There are then three data matrices differing in three theoretical errors: the difference between the pure data and the factor-analysis-generated data is measured by imbedded error, IE. The IE function can be used to determine the number of factors in a data matrix and is defined as

$$IE = \left(\left(rc(cn^{-1}-1) \right)^{-1} \sum_{j=n+1}^c \lambda_j^0 \right)^{1/2} \quad (1)$$

λ_j^0 are the secondary eigenvalues, r , the number of rows c the number of columns, and n the factor number. Because this information is always available during the performance of a factor analysis, IE is computed as a function of n , as n goes from 1 to c . The true number of factors is deduced exploring the behavior of IE as n varies. As stated by Malinowski (1991) the IE function should decrease with the number of primary eigenvectors in data regeneration. However, once the primary set is exhausted and the secondary set is used in the reproduction, the IE should increase.

The difference between the raw original data and the factor-analysis-regenerated data is estimated by the root-mean-square error, RMS.

$$RSD = \left((RMS)^{-1} \sum_{j=n+1}^c \lambda_j^0 \right)^{1/2} \quad (2)$$

When the experimental error is known, the eigenvalue whose RSD approximately equals the estimated error identifies the correct number of factors. The Factor indicator function, IND, is defined using RSD, but without relying on the experimental error

$$IND = \frac{RSD}{(c-n)^2} \quad (3)$$

The IND function reaches a minimum when the correct number of factors is employed.

In spite of the apparent similarity among the indices IE and IND, the latter has the advantage of being more sensitive for the selection of the appropriate factor number, (MALINOWSKI, 1991). The minimum of IE is easily found whenever the error

distribution function is uniform and the errors are truly random, but no in other cases.

2.3 Minimum Noise Fraction Transformation

The principal component transformation arranges the factors maximizing their variance. However in the case that any kind of noise show higher variance than that of the signals, especially among radiation bands, the reduction of the variance in the successive components of PCA does not necessarily imply a loss of quality in the image.

One method of arrangement of the multi-band image, according to a quality criterion, could be based on the maximization of their signal to noise ratio, SNR, or, alternatively, on the maximization of the noise fraction, using it in a reverse manner. With both methods result the same set of eigenvalues (Nielsen, 1994). The first authors that used this concept, (Green et al., 1988) chose the second option, giving in this way name to the technique, minimum noise fraction, MNF. There are two consecutive principal components transformation cascading once the covariance matrix of the noise has been computed. In addition to the estimation of the real dimension of the image, MNF transformation discriminates, and removes later, the noise from the signal, simplifying subsequent processing (Boardman y Kruse, 1994). The final result consists of a series of orthogonal bands arranged after their information content.

This method is very useful in the analysis of hyper spectral sensors data (Kruse, 1999; van der Meer, 1999), where its ability to reduce the dimension of data is more necessary, since there is more information than in other sensors data. Others authors applied it to Landsat-TM, (van der Meer and Jong 2000; Small, 2001).

In the MNF algorithm, the gray level in the original image is a linear combination of one signal and one noise components. If the raw data matrix is \mathbf{D} with c bands or columns, and the noise is additive

$$\mathbf{D} = \mathbf{S} + \mathbf{N} \quad (4)$$

where \mathbf{S} and \mathbf{N} are the signal and noise matrices, respectively. Consequently,

$$\mathbf{Z} = \mathbf{\Sigma}_S + \mathbf{\Sigma}_N \quad (5)$$

where $\mathbf{\Sigma}_S$ and $\mathbf{\Sigma}_N$ are the covariance matrices of \mathbf{S} and \mathbf{N} respectively. The method might be applied to the analysis of a multiplicative noise scheme, after previous logarithmic transformation of raw data. The SNR to be maximized is defined as (Lee et al., 1990; Nielsen and Larsen, 1994):

$$\begin{aligned}
\frac{\text{Var}\{\mathbf{a}_i^T \mathbf{S}\}}{\text{Var}\{\mathbf{a}_i^T \mathbf{N}\}} &= \frac{\mathbf{a}_i^T \Sigma_S \mathbf{a}_i}{\mathbf{a}_i^T \Sigma_N \mathbf{a}_i} = \\
&= \frac{\mathbf{a}_i^T (\mathbf{Z} - \Sigma_N) \mathbf{a}_i}{\mathbf{a}_i^T \Sigma_N \mathbf{a}_i} \\
&= \frac{\mathbf{a}_i^T \mathbf{Z} \mathbf{a}_i}{\mathbf{a}_i^T \Sigma_N \mathbf{a}_i} - 1 = \frac{1}{\lambda_i} - 1
\end{aligned} \tag{6}$$

with \mathbf{a}_i as the eigenvector matrix and λ_i as the eigenvalue of Σ_N with respect to \mathbf{Z} .

$$\frac{\mathbf{a}_i^T \Sigma_N \mathbf{a}_i}{\mathbf{a}_i^T \mathbf{Z} \mathbf{a}_i} = \lambda_i \tag{7}$$

Since what is maximized in this way is the noise fraction, the final results must be obtained in a reverse order.

The key problem of the method is the estimation of the noise. Among the proposed methods to estimate Σ_N the most widely accepted is the maximum/minimum correlation factor, MAF, described by Switzer and Green (1984). The basis of the method is the high correlation of a pixel signal with those of the neighbors, whereas the noise correlation is much lower. After some transformation of the original bands data a noise covariance matrix is estimated. Olsen (1993) discussed other methods. Some noise originated by sensor defects may have a high degree of spatial correlation. In this case they may be taken as signals, unless removed with a Fourier filter (Nielsen, 1994).

3 RESULTS AND DISCUSSION

Table 1 presents the PCA eigenvalues. Since the experimental error is unknown, it is not possible to compare the RSD values. Therefore the trends of the indices IND and IE will be examined. There is no a minimum value of IE in the Table. Consequently, the correct number of factors may not be found. This abnormal behavior might be attributed to a non-uniform error distribution, or to a lack of randomness of the error, due to the presence of a systematic error.

There is a gap in the evolution of IND, as n approaches 5, what could be accepted as an estimate of the correct number of factors, 4. The IND function smoothes the deformation caused in the non-uniform

distribution of the error by principal components analysis. Nevertheless as the behavior of this index is not perfectly known a third method will be used to confirm the proper number of factors.

MNF maximizes the SNR with a double transformation of principal components. The resulting eigenvalues estimate the signal fraction in the new axis. This analysis will be a good indicator of real dimension of the data, with the additional advantage of a coherence exploration of the images to detect the possible noise.

Fig. 1 shows an extract of the six resulting images after the MNF transformation with their respective eigenvalues. The images correspond to the one area of 36 km² in the study site. The last two images do not have any spatial coherence, with eigenvalues close to unity (1.75 and 1.23). This indicates that the images consist essentially of noise. The first four images contain coherent information with eigenvalues well above unity.

Considering this result what coincides with the IND information it is possible to accept that only four factors are required for the reconstruction of the data matrix.

Since one of the four components is due to the shadow, the other three factors are the dominant aspects of the study area, showing the outstanding spectral characteristic of the landscape: quercus tree cover, dry pasture and bare soil. The dry shrubs of some spots will be integrated in the tree cover. Many authors treat separately green and dry types in sparsely vegetated areas (Pech et al., 1986; Graetz et al., 1988; Roberts et al., 1993), assigning to the first type any kind of plant with photosynthetic activity. In the present case as the herbaceous vegetation was already dry, this distinction is not made. Where the vegetal species are clearly distinguishable and their spectra are distinct it is possible to assign individual factors for species, determining their proportion (Huguenin y col. 1997). However these examples are not abundant in the literature, what might be an indication of the involved difficulty of its analysis. The tree cover stratum of the area is a combination of species among them quercus, what increases the similitude spectral signature, although there are structural differences between species

Table 1. Eigenvalues and indices of the correlation matrix analysis. (3.133.219 rows and 6 columns)

FN	Eigenvalues	RSD	IND	IE
1	5.98668	2.92E-05	1.17E-06	1.19E-05
2	0.00750	2.15E-05	1.35E-06	1.24E-05
3	0.00373	1.49E-05	1.65E-06	1.05E-05
4	0.00133	1.09E-05	2.73E-06	8.93E-06
5	0.00050	8.36E-06	8.36E-06	7.63E-06
6	0.00022			

4 CONCLUDING REMARKS

•The IND function reaches a local minimum for $n=4$, which is not confirmed by the IE function results, with no minimum at all. The IE behavior can be explained by a no uniformity in the error distribution, or the existence of not truly random, systematic or sporadic errors.

•The MNF images and the values closer to one of the last two MNF AV corroborate the existence of four factors in the Landsat image.

•Four components can be defined in the *Dehesa* ecosystem as oak trees, pasture, bare soil, and a shade component to account for illumination changes. A linear spectral mixture model can therefore be developed from these components information using a Landsat-TM image.

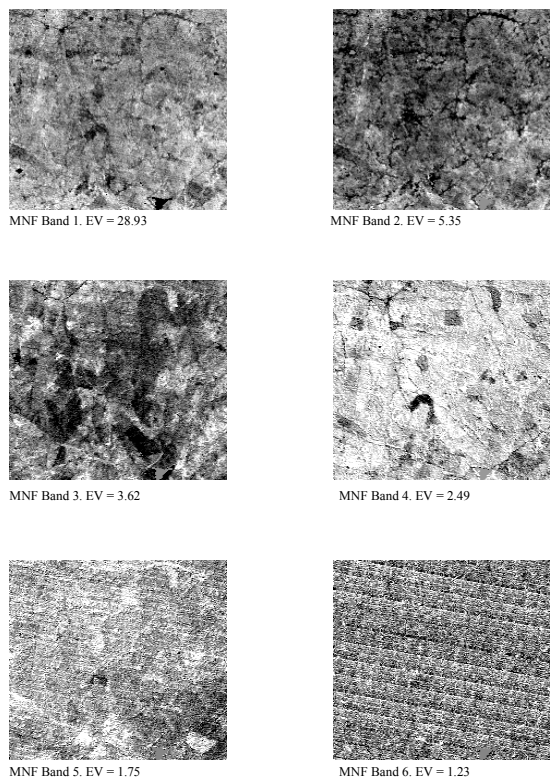


Figure 1. Images obtained after MNF transformation of a 200x200 pixels matrix of the study site. Images of the six eigenvectors and their associated eigenvalues, EV.

References

- Adams, J. B., D. E. Sabol, V. Kapos, R.A. Filho, D.A. Roberts, M. O. Smith and A. R. Gillespie, 1995. Classification of multispectral images based on fractions of end members: Application to land-cover change in the Brazilian Amazon. *Remote Sens. Environ.* **52**, 137-154.
- Boardman, J. W. and F. A. Kruse, 1994. Automated spectral analysis: a geologic example using AVIRIS data, north Grapevine Mountains, Nevada. Proc. 10th. thematic conference on geologic remote sensing. Environmental Research Institute of Michigan, Ann Arbor, Mich., pp. I-407 – I-418.
- García-Haro, F. J., M. A. Gilabert and J. Meliá. 1996. Linear spectral mixture modeling to estimate vegetation amount from optical spectral data. *Int. J. Remote Sens.* **17**, 3373-3400.
- Graetz, R. D., R. P. Pech and A. W. Davis, 1988. The assessment and monitoring of sparsely vegetated rangelands using calibrated Landsat data. *Int. J. Remote Sens.* **9**, 1201-1222.
- Green, A. A., M. Berman, P. Switzer, and M. D. Graig, 1988. A transformation ordering multispectral data in terms of image quality with implications for noise removal. *IEEE Trans. Geosci. Remote Sens.*, **26**, 65-74.
- Huguenin, R. L., M. A. Karaska, D. Van Blaricom and J. R. Jensen, 1997. Sub pixel classification of bald cypress and tupelo gum trees in thematic mapper imagery. *Photogram. Eng. Rem. Sens.* **63**, 717-725.
- Kruse, F. A. 1999. Visible-Infrared Sensors and Case Studies. Remote Sensing for Earth Science: ASPRS Manual of Remote Sensing. v. 3. ed: A. N. Renz.. Wiley, New York. pp: 567-611.
- Lee, J. B., S. Woodhyatt and M. Berman, 1990. Enhancement of high spectral resolution remote-sensing data by noise-adjusted principal components transform. *IEEE Trans. Geosci. Remote Sens.* **28**, 295-304.
- Malinowski, E. R., 1991. Factor Analysis in Chemistry. (Wiley, 2nd ed New York)
- Nielsen, A.A., 1994. Analysis of regularly and irregularly sampled spatial, multivariate, and multi-temporal data. PhD Dissertation. Institute of Mathematical Modelling. Lyngby. Demmark.
- Nielsen, A. A. and R. Larsen, 1994. Restoration of GERIS data using the Maximum Noise Fractions Transform. Proc. First Int. Airborne Remote Sens. Conf. (ERIM), Strasbourg, (ERIM, Ann Arbor), V. II, pp: 557-568.
- Olsen, S. L., 1993. Estimation of noise in images: an evaluation. *Graph. Models Image Proc.* **55**, 319-323.
- Pech, R. P., R. D. Graetz and A. W. Davis, 1986. Reflectance modelling and the derivation of vegetation indices for an Australian semiarid shrubland. *Int. J. Remote Sens.* **7**, 389-403.
- Roberts, D. A., M. O. Smith and J. B. Adams, 1993. Green vegetation, nonphotosynthetic vegetation, and soils in AVIRIS data. *Remote Sens. Environ.* **44**, 255-269.
- Small, C., 2001. Estimation of urban vegetation abundance by spectral mixture analysis. *Int. J. Remote Sens.* **22**, 1305-1334.
- Switzer, P. and A. A. Green, 1984. Min/Max autocorrelation factors for multivariate spatial imagery Tech. rep. 6. Stanford University.
- van der Meer, F, 1999. Iterative Spectral Unmixing (ISU). *Int. J. Remote Sens.* **20**, 3431-3436.
- van der Meer, F. and S. M. de Jong, 2000. Improving the results of spectral unmixing of Landsat Thematic Mapper imagery by enhancing the orthogonality of end-members. *Int. J. Remote Sens.* **21**, 2781-2797.

Advances in the use of DEMs for improved quantitative analysis of multiscale remote sensing data.

J. C. García^{1,2}, J. Moreno²,
DIELMO¹, University of Valencia².
dielmo@dielmo.com, jose.moreno@uv.es

ABSTRACT - *Slope estimation and the correction of direct illumination effects in satellite images is traditionally carried out by using a Digital Elevation Model (DEM) with the same resolution of the satellite image. In this paper we illustrate that the use of high resolution DEMs (10 or more times the spatial resolution of the image) improves the compensation of topographic effects and adds additional information for the analysis of remote sensing data. With this information we have performed the correction of the illumination effects produced by the terrain topography in the case of simulated MERIS data, by using different techniques that are compared to the ideal case.*

1. INTRODUCTION

The traditional use of a DEM with the same spatial resolution of the image introduces severe errors in the slope estimation, that depends on the working spatial resolution and on the level of the terrain topography. These errors are enhanced in the illuminated DEM, therefore the topographic compensation is not correct.

Using a high resolution DEM, we can in fact perform a slope estimation that does represent a quite accurate estimate at the spatial resolution of the image. With this information the illuminated DEM at the resolution of the image can be considered as highly correct, and we then perform a better correction of the topographic effects. Figure 1 shows the effect of the use of a DEM with 10 times the spatial resolution of the image in the analysis of local topographic effects.

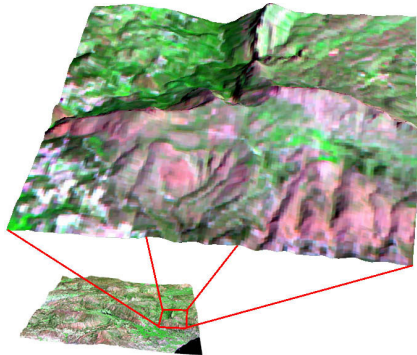


Fig. 1. Use of a high resolution DEM to account for local within-pixel topography.

Moreover, the high resolution DEM gives additional information, such as a measurement of the roughness [Zribi – 98] inside each pixel of the image, allowing the correction of the diffuse solar radiation and directional reflectance effects.

To illustrate it, we have selected a mountainous study area located in Alicante (Spain). We have used a 30 m resolution DEM and a Landsat scene of the study area. We use the Landsat image to simulate MERIS data (300 m local mode -FR- and 1200 m global mode -RR- [ESA – 95]), comparing the different techniques for the correction of the illumination effects. First we give a description of the techniques by using simulated MERIS FR mode and finally we will carry out some comparisons among the different methods discussed.

2. TRADITIONAL ESTIMATION OF SLOPE

In the traditional approach, for each pixel of the DEM the slope is estimated as a function of the heights of the nearest points. Using this procedure, we always will have uncertainties and probable errors in the estimation of pixel slope, that cannot be avoided in the lack of within-pixel information.

These errors affect the topographic correction and are more important with the increase of the topography and with the decrease in the spatial resolution of the DEM. Figure 2 shows an example of the slope estimation error.

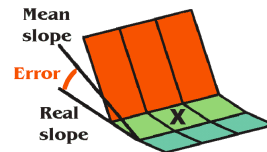


Fig. 2. Example of the errors in the traditional slope estimation.

Now we perform a comparison of the illuminated DEM obtained with the traditional method with a result considered as ideal. The illumination of the DEM is defined as the cosine of the angle (i) between the incident solar radiation and the normal on a pixel, representing the proportion of the direct solar radiation that arrives to a pixel. Figure 3 shows the

definition of these angles.

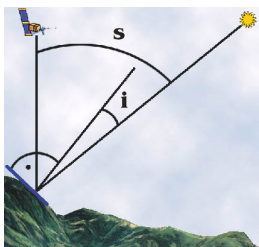


Fig. 3. Solar angles for the illumination of the DEM.

We assume that the ideal result for the illumination of the DEM is the obtained by illuminating it at 30 m resolution with the traditional method, using the average to obtain the result at 300m (Local Mode) and 1200m (Global Mode). In Figure 4 we compare the ideal result with the illumination obtained with the traditional method.

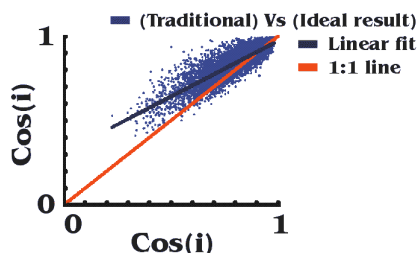


Fig. 4. Comparison of the ideal illuminated DEM with the obtained by means of the traditional method in the case of MERIS Local Mode (FR).

If the result obtained with the traditional method were perfect, in Figure 4 the linear fit will be superposed to the 1:1 line. As we can see, the result is not correct, as the points do not follow the 1:1 line and the linear fit gives a slope far away from such 1:1 line.

3. DIRECT RESAMPLING OF THE IMAGE

We have tested a possible improvement of the traditional method, consisting in the following steps:

- Resample the image from low (300m) to high (30m) spatial resolutions.
- Calculate the illumination of the high (30m) DEM and perform the correction in directly in high resolution mode.
- Resample the result of the correction from high (30m) to low (300m) resolution.

The figure 5 shows a diagram for this procedure.

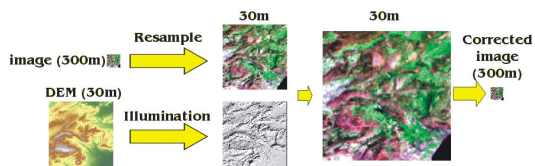


Fig. 5. Diagram of the correction with the direct resampling of the image.

The result is not accurate and it produces an overcorrection of topographic effects. Artefacts are due to the fact that the DEM contains more information about the topography than the actual information content of the 300m image.

4. WITHIN-PIXEL SLOPE METHOD

This new procedure consist in:

- Divide the DEM in areas with size equal to the desired final pixel resolution. In this case we want to obtain the illuminated DEM with $300 \times 300 \text{m}^2$ and it corresponds with 10×10 pixels in the 30m DEM.
- Adjust each one of these areas to a 2D plane (as shown in figure 6).

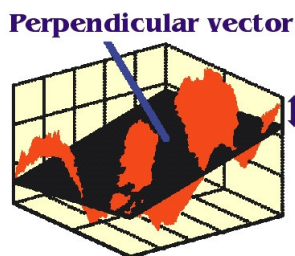


Fig. 6. Adjustment of the within-pixel elevation information to a 2D plane.

- Calculate the perpendicular vector of the plane (shown in figure 6).
- Calculate the cosine of the angle between the solar vector (Figure 3) and the perpendicular vector of the adjusted plane (Figure 6). This will be the value of the illumination factor for each 300m pixel.

The standard deviation of all the heights inside the pixel gives a measurement of the roughness for the $300 \times 300 \text{ m}^2$ area. This measurement allows the correction of the diffuse solar radiation and directional effects, that will be shown in future works.

Figure 7 shows the comparison of the ideal result with the illumination obtained with the within-pixel slope method. The result is quite better than the obtained

with the other methods, and the linear fit is almost superposed with the 1:1 line.

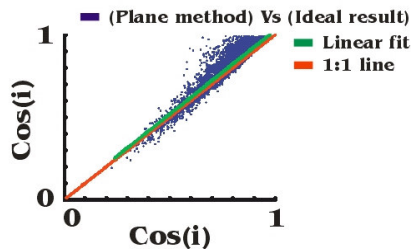


Fig. 7. Comparison of the ideal illuminated DEM with the obtained with the within-pixel slope method in the case of MERIS Local Mode (FR)..

5. MERIS SIMULATION

In the previous sections we have compared the corrections done for the MERIS Local Mode (FR). In the case of Global Mode the results are shown in Figures 8 and 9.

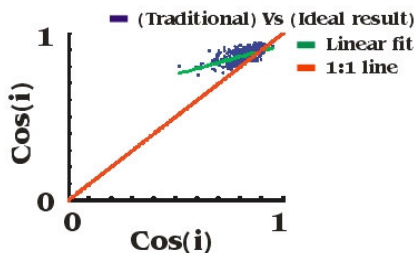


Fig. 8. Comparison of the ideal illuminated DEM with the obtained with the traditional method in the case of MERIS Global Mode (RR).

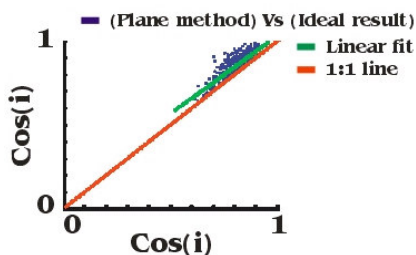


Fig. 9. Comparison of the ideal illuminated DEM with the obtained with the within-pixel slope method in the case of MERIS Global Mode (RR).

In the case of MERIS Global Mode (1200m) the results are similar to the obtained with the Local Mode resolution (300m), indicating the robustness of the approach.

Figures 7 and 9 indicate that with the within-pixel slope method we obtain good results independently of the working spatial resolution. In this case the most important is to have a DEM with more resolution than the image, and it is valid in all the cases, while with

the traditional method results get quite worse with a degraded spatial resolution in the DEM.

Now we can compare the visual effect of the topographic correction in the images. First, Figures 10 and 11 show the illuminated DEMs calculated for the two resolutions and with both methods.

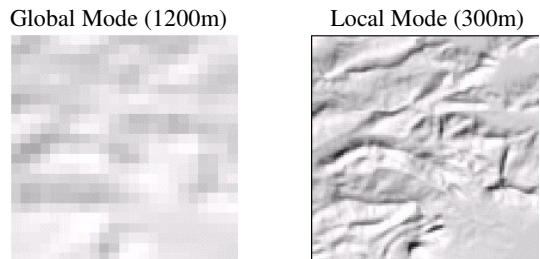


Fig. 10. Illuminated DEM for the Global and Local Modes using the traditional method.

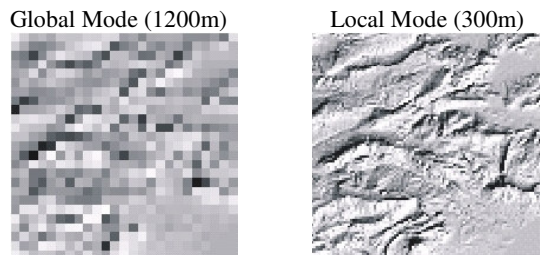


Fig. 11. Illuminated DEM for the Global and Local Modes using the within-pixel slope method.

In these figures we observe the fact that the illumination obtained with the traditional method is less contrasted (smooth illumination) than the obtained with the within-pixel slope method. In the last case we observe a better description of the shadows inside the image.

On the other hand, in the correction process the most important is to have a good result for the illuminated DEM. Independently of the sophistication of the method used to perform the topographic correction, to have a high-quality DEM, and to properly illuminate it, are necessary conditions to perform an adequate compensation of topographic effects.

Figure 12 shows the original images at 300 and 1200m resolution. If we compare these images with the ones shown in Figures 10 and 11, we can clearly distinguish the areas with shadows that have to be corrected. The main shadow is located in the right part of the image, near the center.

Global Mode (1200m)



Local Mode (300m)

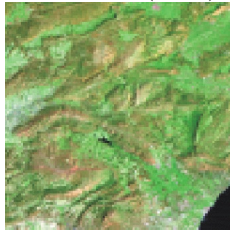


Fig. 12. Original Global and Local Mode images (colour figure in the appendix).

There are many different approaches to perform the correction of the illumination effects in optical satellites data. In [P. Meyer – 93] we can find a comparison of four classical methods: empirical – statistical correction, cosine correction, Minnaert correction, C – correction .

We here use the empirical – statistical method because it is the simplest method and it does not produce any artifact when $\cos(i)$ tends to zero. Remember that independently of the correction method that we use, the most important is to have a DEM with the sufficient quality, otherwise we will introduce more errors in the image rather than compensate for topographic disturbances.

Figures 13 and 14 shows the results of the illumination correction for the two resolutions and with both methods.

Global Mode (1200m)



Local Mode (300m)



Fig. 13. Corrected images for the Global and Local Modes using the traditional method (colour figure in the appendix).

Global Mode (1200m)



Local Mode (300m)



Fig. 14. Corrected images for the Global and Local Modes using the within-pixel slope method (colour figure in the appendix).

On one hand, comparing Figure 13 with Figure 12, we observe the fact that the shadows are not perfectly corrected. On the other hand, if we compare Figure 14 with Figure 12, we can see that the topographic effect disappears, and the regions under the shadows are compensated appropriately.

6. CONCLUSIONS

The traditional methods for slope estimation introduce errors in topographic corrections, especially for DEMs with same resolution as the working spatial resolution of the image. These errors translate into illumination artefacts. Moreover, local roughness effects cannot be accounted for by using traditional correction methods.

This paper illustrates that the within-pixel slope method, based on a high resolution DEM, is an adequate procedure to perform the slope estimation and the correction of the direct solar illumination effects. Moreover, the within-pixel slope method gives additional roughness information inside each low resolution pixel, allowing corrections of the directional illumination effects (surface BRDF).

The method is applicable at all scales, provided that a much more detailed DEM that the working image resolution is available.

7. REFERENCES

- C. Proy, D. Tanre, and D.Y. Deschamps, 1989, "Evaluation of topographic effects on remotely sensed data", *Remote Sens. Environ.*, vol. 30, pp. 21-32.
- C.O. Justice, S.W. Wharton, and B.N. Holben, 1981, "Application of digital terrain data to quantify and reduce the topographic effect on Landsat data", *Int. J. Remote Sensing*, vol. 2, pp. 213-230.
- ESA, 1995, "MERIS: The Medium Resolution Imaging Spectrometer", ESA Pub. SP-1184, Parts A and B, 62 pp., March 1995.
- F. Cavayas, 1987, "Modelling and correction of topographic effect using multi-temporal satellite images", *Canad. J. Remote Sensing*, vol. 13, pp. 49-67.
- J. Moreno, 1994, "Spectral/spatial integration effects on information extraction from multispectral data: multiresolution approaches", *EOS/SPIE European Symposium on Satellite Remote Sensing*, Rome, September 1994, SPIE Proc. vol. 3214, pp. 324-338.
- J. Moreno, 1996, "Radiometric corrections of visible/infrared satellite data over terrestrial environments: angular, atmospheric and topographic

effects", Proceedings IGARSS'96, Lincoln, Nebraska, May 1996, IEEE Pub. 96CH35875, vol. III, pp. 1823-1825.

P. Meyer, K. I. Itten, 1993, "Radiometric corrections of topographically induced effects on Landsat TM data in an alpine environment". ISPRS Journal of Photogrammetry and Remote Sensing, 48(4): 17-28.

R.J. Woodham, "Using digital terrain data to model image formation in remote sensing", Image Processing for Missile Guidance, Proceedings SPIE, vol. 238, pp. 361-369, 1980.

Análisis de corredores ecológicos a nivel comarcal, mediante clasificación supervisada de la imagen de satélite LANDSAT – TM. Caso particular de la sierra de ancares.

M. L. Gil¹ and A. González¹, I. Cañas².

¹*Departamento de Ingeniería Agroforestal, Universidad de Santiago de Compostela, Escuela Politécnica Superior de Lugo, España; e-mail: mlgild@correo.lugo.usc.es*

²*Departamento de Construcción y Vías Rurales, Universidad Politécnica de Madrid, Escuela de Ingenieros Agrónomos, España*

ABSTRACT

El presente trabajo tiene por objeto generar cartografía temática de vegetación arbórea a partir de la clasificación supervisada de la imagen de satélite Landsat – TM, que permita la identificación de corredores ecológicos a nivel comarcal (Escala 1:200.000) analizados como elementos lineales visibles, caracterizados por una vegetación arbolada que forman masas asociadas a las vías, de más de veinticinco metros de ancho. Se estudian los corredores asociados a las vías existentes en la sierra de los Ancares gallegos (Lugo – España), comarca con un alto interés y valor medioambiental ya que incluye varias zonas con reconocimiento legal como: la Reserva de Caza, el Área para la Recuperación del Oso Pardo y otros espacios naturales catalogados (Os Ancares, Monte Agüeira, A Pitinidoira, O courel y O Aciñeiral de Cruzul). En este contexto de áreas de interés natural independientes entre sí y de reducida extensión, es de gran importancia la existencia de corredores ecológicos que permitan la conectividad de los diferentes ecosistemas para asegurar su pervivencia y enriquecimiento. El establecimiento de corredores naturales asociados a otras funciones rurales como el transporte agrícola y forestal permiten un desarrollo integral rural sostenible y la integración de las vías como componentes de la estructura del paisaje. Mediante la teledetección se pueden analizar los corredores ecológicos a partir de la clasificación de la composición coloreada 4/5/3, identificando la vegetación arbórea respecto del resto de las cubiertas y permitiendo así el análisis global de contexto y la búsqueda de la mejor opción para crear, consolidar o mantener los corredores ecológicos. Del Mapa de corredores creado se extrae la información sobre la conectividad entre las zonas catalogadas o que tienen algún tipo de reconocimiento legal en la comarca de los Ancares Gallegos. El resultado de este trabajo muestra que la conexión entre espacios naturales en la sierra de los Ancares resulta muy insuficiente debido a la falta de corredores ecológicos continuos asociados a las vías de comunicación.

1. INTRODUCCIÓN Y OBJETO

En la actualidad, los bosques autóctonos existentes en el mundo desarrollado, han quedado reducidos a islas, generalmente ubicados en lugares inhóspitos y alejados, y alrededor los cuales la naturaleza ha sido profundamente alterada. La situación de aislamiento de estos ecosistemas repercute enormemente en la pervivencia de las especies de flora y fauna y permiten la conservación en ellos de especies exclusivas. No obstante, este aislamiento empobrece notablemente el ecosistema y agrava notablemente sus riesgos de extinción (Moore, 1962; Perez, 1992; Vales, 1987). Es por ello que resulta fundamental la conectividad entre áreas de interés natural o Reservas Naturales aprovechando, entre otros, aquellos márgenes de la red de vías que puedan funcionar como corredores ecológicos. Dentro del desarrollo integral rural es necesario un cambio de mentalidad y política para

dar oportunidad al establecimiento de corredores naturales asociados a otras funciones rurales como el transporte agrícola y forestal.

Se analizan las vías y la vegetación característica asociada a las mismas, como constituyentes de elementos lineales de la arquitectura del paisaje en sí mismos. Las vías pueden funcionar como corredores ecológicos, máxime cuando están asociadas a otros elementos lineales como un curso fluvial.

El estudio de corredores se realiza generalmente a partir de técnicas tradicionales (Cañas, 1996; Ruiz, 2001, Varios autores 1995) aunque también hay antecedentes del empleo de la teledetección para la identificación de los mismos (Goossens, 1991; Gulink, 1991; Klijn, 1988; Wulf, 1988). En el presente trabajo se elabora cartografía temática de vegetación arbórea a partir de la clasificación supervisada de la imagen de satélite. Se analizan los corredores como elementos lineales visibles, caracterizados por una

vegetación arbolada que forman masas asociadas a las vías, de ancho superior a veinticinco m.

El tratamiento digital de la imagen espacial permite la obtención de información relativa a la función de las vías como corredores, analizando cuáles pueden permitir la conectividad de los distintos espacios naturales existentes en la zona de estudio.

El objetivo de este trabajo es determinar si existe conexión entre la Reserva de Ancares y otros Espacios Naturales del entorno próximo a través de corredores ecológicos asociados a las vías de baja densidad de tráfico.

2. LA ZONA DE ESTUDIO

La Sierra de los Ancares se extiende por el extremo oriental de la provincia de Lugo constituyendo las estribaciones de la Cordillera Cantábrica. Es, así mismo, la que marca la divisoria entre las comunidades autónomas de Galicia (provincia de Lugo) y Castilla y León (provincia de León). Se encuentra situada al Noroeste de la Península Ibérica y está delimitada por las coordenadas geográficas siguientes: 42° 44' 24" y 42° 51' 02" de latitud Norte, 6° 50' 01" y 6° 58' 27" de longitud Oeste (Greenwich).

Los terrenos objeto de estudio constituyen la comarca de los Ancares Gallegos, una de las áreas geográficas mejor conservadas del territorio español.

Posee unas privilegiadas características naturales por su flora y fauna, y por la diversidad de paisajes que ofrecen su gran número de montañas y valles. Las instituciones europeas se han hecho eco de la importancia de conservar esta zona; así lo demuestran los planes de desarrollo que se acometen por distintas fundaciones, asociaciones y entidades, que desde los distintos organismos e instituciones públicas y privadas tratan de potenciar la comarca.

Sobre este espacio se sitúan varias zonas que tienen reconocimiento legal como son la Reserva de Caza, el Plan de Recuperación del oso pardo y otros espacios naturales catalogados (*Os Ancares*, *Monte Agüeira*, *A Pitinidoira*, *O courel* y *O Aciñeiral de Cruzu*). Son muchas, por tanto, las peculiaridades y valores naturales de los Ancares, por su gran interés biológico, científico, cultural y paisajístico (Perez, 1995).

3. LOS CORREDORES ECOLÓGICOS

3.1 Necesidad de los corredores ecológicos

En la actualidad, los espacios naturales legalmente protegidos constituyen los ecosistemas mejor conservados de la flora y la fauna. Aunque el tamaño del ecosistema – isla es esencial, puede

resultar preferible, o cuanto menos más práctico, la existencia de un mayor número de islas aunque de menor tamaño, y más próximas entre sí, de forma que sea más factible su intercomunicación haciendo que todo el sistema “archipiélago” funcione como un conjunto (Vales, 1987).

Dada la situación actual de fragmentación de la práctica totalidad de los hábitats naturales, siendo esta misma tendencia la previsible en el futuro, parece ser más viable la protección de la vida silvestre y una ordenación del paisaje según un modelo de “archipiélago” bien intercomunicado, que pretender una amplia restauración de grandes masas de bosque (Pérez, 1992).

Las islas estarían interconectadas por corredores de vegetación o corredores ecológicos, en el que tendrían un cometido importante las ripisilvas y otras áreas de protección y vegetación de borde, importantes no tanto por su valor sino por su contribución al paisaje y al valor global de todo el sistema.

Esta alternativa de ordenación, se dibuja en el paisaje como una retícula más o menos tupida, semejando un mosaico en el que se combinan piezas de distinta madurez y finalidad tejidas mediante la infraestructura ecológica.

3.2 Los corredores ecológicos en Europa

La larga historia rural de la ocupación y actividad humana ha alterado la población y hábitats de las especies salvajes. En muchas zonas de Europa existen reservas naturales, biotopos y bosques generalmente pequeños y aislados, por lo que el concepto de corredor está siendo promovido como un principio estratégico para la conservación de la naturaleza. Los usos de suelo tradicionales han originado considerables elementos de vegetación lineales que pueden ser considerados como parte de esta red estratégica.

Abordar el estudio de las vías desde esta perspectiva reviste en la actualidad un interés creciente. Las vías como redes de comunicación ecológica son cruciales para el desarrollo y la política de conservación de la naturaleza en Europa (Jongman, 1995).

En numerosas regiones de la Europa húmeda existe una densa red de comunicaciones con márgenes vegetales. Así por ejemplo en Bélgica dicha red está estimada en 3 Km/Km². La red de ríos, arroyos y cursos de agua es también densa pero altamente contaminada. Elementos lineales vegetales de diferentes clases (setos, caminos de carro, vegetación en cunetas y terraplenes) existentes en el paisaje agrícola, no son considerados en el desarrollo de la agricultura a gran escala: pesticidas, abonos, quemados, no tienen en consideración esta serie de elementos (Gulinck, 1991).

A finales del siglo diecinueve, el desarrollo tecnológico y económico llevó a un incremento de la pérdida de naturaleza en el noroeste de Europa. Al

mismo tiempo el interés por el medio ambiente y el reconocimiento de su importancia conlleva a una mayor sensibilidad e interés para su protección. La controversia entre su valoración y su pérdida ha servido de base para la definición de políticas para la conservación.

En muchos países la conservación de la naturaleza se realiza mediante la designación de reservas naturales y parques nacionales; en otros países se desarrollan nuevos conceptos como la restauración de áreas naturales y el desarrollo de corredores ecológicos. En Europa, los científicos y planificadores han propuesto una protección de la naturaleza coherente mediante la designación de una red de comunicación ecológica consistente en áreas - núcleo, zonas de corredor, zonas intermedias y, si es necesario, la rehabilitación de áreas para el restablecimiento de la naturaleza.

En la actualidad, la red ecológica Europea (Red Natura 2.000) es un nuevo fenómeno en el planeamiento de la conservación de la naturaleza. Tiene sus antecedentes en los años 20 en el sistema de parques de Estados Unidos. La situación en Europa, sin embargo, difiere bastante de la situación en el continente americano. En muchas áreas de Europa el tamaño de las áreas naturales es mucho más pequeño y su soporte depende de otras áreas circundantes no protegidas. Es en este contexto en donde tiene mayor importancia la intercomunicación entre las diferentes áreas de reserva natural (flora, fauna y paisaje).

3.3 Los corredores ecológicos en Galicia (España)

Existe en Galicia un tipo de corredor interligado a la arquitectura del paisaje cuyo ancho varía entre los cinco y veinticinco metros. Bordea los cultivos y son característicos de los caminos rurales tradicionales de no más de tres o cuatro metros de ancho y cuyas profundidades, debidas entre otras causas al propio uso continuado a lo largo del tiempo, van desde unos centímetros hasta varios metros. Estos corredores, así como los cierres que bordean los cultivos de las parcelas, suponen el bosque y refugio para numerosas especies.

En estos caminos tradicionales se puede encontrar fauna y flora como mamíferos depredadores o aves características. Los árboles, arbustos y herbáceas vienen determinados por un número complejo de factores bióticos y abióticos como: la historia de los usos de suelo, el aislamiento de cultivos adyacentes, el influjo de nutrientes, el microclima, el suelo y las prácticas de manejo. En óptimas condiciones de gestión y evitando el influjo de nutrientes, la diversidad florística es muy alta.

Los paisajes con estructuras en mosaico (propios del medio rural gallego) se caracterizan por la existencia de pequeños bosquetes o manchas de

arbolado entre los cultivos, en donde las ripisilvas y la vegetación de borde de fincas y caminos rurales tienen una gran importancia ecológica.

3.4 Evolución y perspectivas de los corredores ecológicos

La vegetación entre parcelas y cultivos en lindes van desapareciendo con la intensificación de la agricultura y los procesos de concentración parcelaria. La red de vías, por el contrario, se densifica por lo que sus márgenes pueden tomar el relevo a la función que antes realizaban los antiguos corredores.

Durante las últimas décadas, las malas prácticas de manejo y el cambio de las actividades agrícolas en los cultivos adyacentes han provocado un dramático empobrecimiento de la flora en muchos márgenes de las carreteras (Gulinck, 1991). Los usos de suelo están sujetos a las necesidades del hombre, sacrificándose continuamente el mundo natural en aras de la expansión humana.

Dentro del desarrollo integral rural es necesario un cambio de mentalidad y política para dar oportunidad al establecimiento de corredores naturales asociados a otras funciones rurales como el transporte agrícola y forestal. El desarrollo de una base cartográfica de los corredores asociados a las vías es un paso hacia esta política.

Las carreteras deben ser consideradas como un componente inherente de la estructura del paisaje. Los planes para la realización de nuevas vías deberían de ser diseñadas para optimizar la estructura del mosaico del paisaje (Miller, 1996).

3.5 Antecedentes del estudio de corredores a partir de la teledetección

Existen diferentes trabajos sobre teledetección y cartografía de corredores. Wulf (1988) utiliza datos Landsat -MSS (de 80 m de resolución espacial) para analizar corredores y hábitats de dimensiones superiores a la resolución de la imagen de satélite como los utilizados por el panda gigante. Más difícil es cartografiar los corredores de dimensiones próximas e inferiores a la resolución de la imagen, como ejemplo, Klijn (1988) utiliza Landsat - TM y realiza trabajos en Noruega para la detección de setos, y concluye que sólo pueden ser identificados un 50 % de los mismos.

Gulinck (1991) utiliza la banda visible del SPOT y el infrarrojo cercano para evaluar el papel de los datos de la teledetección para cartografiar corredores potenciales y actuales. Realiza la identificación de corredores arbolados a través del análisis y clasificación de la imagen de satélite. Investiga aspectos del paisaje que se consideran relevantes para la planificación como son el paisaje visual y las estructuras ecológicas del paisaje, ambos sometidos a importantes cambios debido a la presión humana. Realiza la identificación de corredores arbolados a través del análisis y clasificación

de la imagen de satélite SPOT pancromático y multispectral. Utiliza la teledetección para cartografiar elementos y formas que tienen un posible papel como corredor ecológico.

Gulinck define el corredor como el marco estructural para el movimiento y migración de los diferentes organismos. Selecciona las técnicas de procesamiento de imágenes útiles para el análisis de las propiedades estructurales del paisaje relacionados con los corredores arbolados en un contexto típico de paisaje rural sujeto a cambios económicos y ecológicos. Para cartografiar los corredores a partir de la imagen SPOT, tiene en cuenta las siguientes consideraciones: desde un punto de vista práctico, considera a los corredores como elementos lineales visibles con alta conectividad caracterizados, en muchos casos, por una vegetación arbolada; los elementos lineales arbolados de más de ocho metros de ancho pueden ser considerados como corredores funcionales para diversas especies.

Realiza la identificación y cartografía de elementos lineales del paisaje basándose en la clasificación por máxima probabilidad, de usos de suelo a partir de SPOT – XS identificando el 95% de los bosques existentes. El análisis visual de datos pancromáticos proporciona resultados satisfactorios en la identificación de elementos lineales arbolados en el 65% de los casos. Indica que los corredores están habitualmente asociados infraestructuras de vías o con remanentes de vegetación autóctona.

Goossens (1991) utiliza la imagen SPOT – XS para detectar la infraestructura ecológica o corredores a partir del tamaño y forma de los bloques del terreno (define bloque de terreno como la superficie con el mismo uso de suelo rodeado por al menos tres elementos lineales). Dentro de este estudio, analiza los tipos de elementos lineales que bordean a los bloques.

Mediante la aplicación de un filtro de realce de bordes, detecta los siguientes elementos lineales:

- Cierres de árboles y vegetación de borde (estructuras en desaparición con la modernización de la agricultura).
- Límites entre parcelas con usos distintos.
- Cursos de agua.
- Carreteras y caminos.

De entre los elementos indicados destacan por su importancia tres elementos fundamentales: carreteras, cunetas y árboles.

Los factores que influyen en la detectabilidad de los elementos lineales son:

- Los que coinciden con algún curso de agua o línea de drenaje.

- Las carreteras por su alto contraste con la vegetación.
- La combinación de elementos lineales como carreteras bordeadas de árboles.

4. MATERIAL Y MÉTODO

4.1. Material

Se dispone de las *ortoimágenes digitales* E 1:100.000 de la sierra de Ancares, se corresponden con las hojas del mapa topográfico nacional (MTN) 99, 100, 125 y 126. Las ortoimágenes han sido generadas por el Instituto Geográfico Nacional (IGN) a partir de la imagen del satélite Landsat-5, sensor Thematic Mapper (TM). La imagen utilizada es la escena número TM204-30-4 de fecha de adquisición 30 de Septiembre de 1986.

Las imágenes proporcionadas corresponden a las 6 bandas del Landsat-TM (no se dispone de la banda correspondiente al infrarrojo térmico).

La corrección geométrica inicial ha sido realizada por el IGN mediante funciones polinómicas de segundo grado y ajuste por mínimos cuadrados con residuo final menor de 2 píxeles. El método para la interpolación ha sido el de la convolución cúbica. Remuestreo a 25 m de tamaño de pixel final. Toma de puntos de control en cartografía 1/50.000. Sistema Geodésico de Referencia RE-50: Europea Datum (ED 50), Elipsoide Internacional Hayford 1924. Origen de longitudes: Meridiano de Greenwich. Proyección UTM. No se aplicó corrección de los efectos del relieve, ya que los algoritmos existentes en la época en que se realizó el trabajo no lo permitían para imágenes Landsat.

En este trabajo se emplea el programa de tratamiento de imágenes y creación de cartografía EASI/PACE y ACE de la compañía canadiense PCI Geomatics Group.

4.2. Metodología

4.2.1 Realización del mosaico de los ancares gallegos

Intervienen las 4 hojas de Landsat disponibles (99,100, 125 y 126 según fig.1) previamente georreferenciadas a partir de las coordenadas de las cruces del MTN. La escala de edición de este mosaico es 1:200.000.

Se realiza el mosaico mediante puntos de control en la zona de solape con interpolación por el vecino más próximo. El ajuste de la radiometría se realiza de forma manual.



Fig. 1- Distribución de hojas en el Mosaico de los Ancares Galaico –Leoneses.

Se muestra en la fig. 2 el resultado de la imagen que ha sido filtrada con filtro de paso alto 3 x 3 y realizada mediante realce lineal.

4.2.2. Identificación de masas boscosas

Se realiza una clasificación digital supervisada del mosaico formado con las imágenes Landsat - TM para determinar la conexión entre los espacios naturales existentes en la comarca de Ancares. Se utiliza la composición coloreada de las bandas 4/5/3 por ser una combinación reconocida por su interés para el estudio de usos de suelo por su utilización en el proyecto Corine – landcover.

La clasificación efectuada para identificar los posibles corredores ecológicos, se ha realizado a partir de la selección de la clase espectral que recoge la clase temática de “vegetación arborea”. Se han seleccionado, por tanto, dos categorías temáticas: terreno arbolado y resto de vegetación.

Se clasifica la imagen de satélite según los pasos que se indican a continuación:

1. Fase de entrenamiento: selección de una muestra de píxeles de la imagen, que representen, adecuadamente, las categorías de interés.
2. Clasificación supervisada de la composición 4/5/3, utilizando el algoritmo de máxima probabilidad.
3. Comprobación de la calidad de la clasificación mediante fotografía aérea a escala 1:18.000 y 1:20.000.

Se refleja el resultado de esta clasificación en la fig. 3. Las masas boscosas más importantes son las que aparecen en la Reserva de caza, fundamentalmente las situadas en las laderas orientadas al Norte. El principal interés no radica, sin embargo, en los corredores interiores a la Reserva sino en aquellos que la comunican con otras áreas naturales próximas.

El método empleado permite la identificación del 90 % de las masas arboladas de superficie superior al tamaño de pixel de la imagen (25 x 25).

5. RESULTADOS

La identificación de corredores ecológicos se realiza mediante el análisis visual de la clasificación supervisada de la composición 4/5/3 de la imagen Landsat - TM. Se elabora cartografía temática de vegetación arborea (fig. 3) a partir del análisis visual de los corredores definidos como elementos lineales visibles asociados a las vías, caracterizados por una vegetación arbolada de superficie superior al tamaño de pixel.

Se obtiene un mapa de corredores del cual se extrae la información sobre la conectividad de la Reserva de los Ancares con otras zonas catalogadas o que tienen algún tipo de reconocimiento legal. Este análisis se realiza a partir de las vías que pueden funcionar como corredores ecológicos:

- La carretera que constituye la salida Norte de la Reserva supone una buena conexión de la misma con el área afectada por el *Plan de Recuperación del Oso Pardo* que se prolonga hacia el Norte de la Reserva.
- La cadena montañosa que recorre el límite Este de la Reserva supone un límite natural de división y constituye una barrera natural a la comunicación con los Ancares Leoneses.
- La conexión de la Reserva por el Oeste se realiza fundamentalmente mediante dos vías asociadas a cursos fluviales que se unen en donde confluyen ambos ríos. Hasta ese punto dichos elementos lineales van asociados a masas arbóreas.

Estas vías pueden funcionar como corredores aunque pierden su asociación a masas arboladas con lo que pierde su función de corredor ecológico. Este hecho implica que no se llega a establecer la conexión de la Reserva con las áreas naturales denominadas *Monte Agüeira* y *O Aciñeiral de Cruzul* situadas más al Oeste.

- El área natural denominada *A Pintinidoira* situada a menos de 4 Km del Suroeste de la Reserva aparece mal enlazada con la misma, ya que no hay ninguna vía que pueda funcionar como corredor ecológico.
- Existe una gran desconexión con *O Courel*, espacio natural situado al Suroeste de la Reserva, no aparecen masas arboladas que conecten ambas zonas ya sea asociadas a las vías o de forma independiente.

Por todo lo anteriormente indicado se deduce que la conexión entre espacios naturales en la comarca de Ancares es muy deficiente.

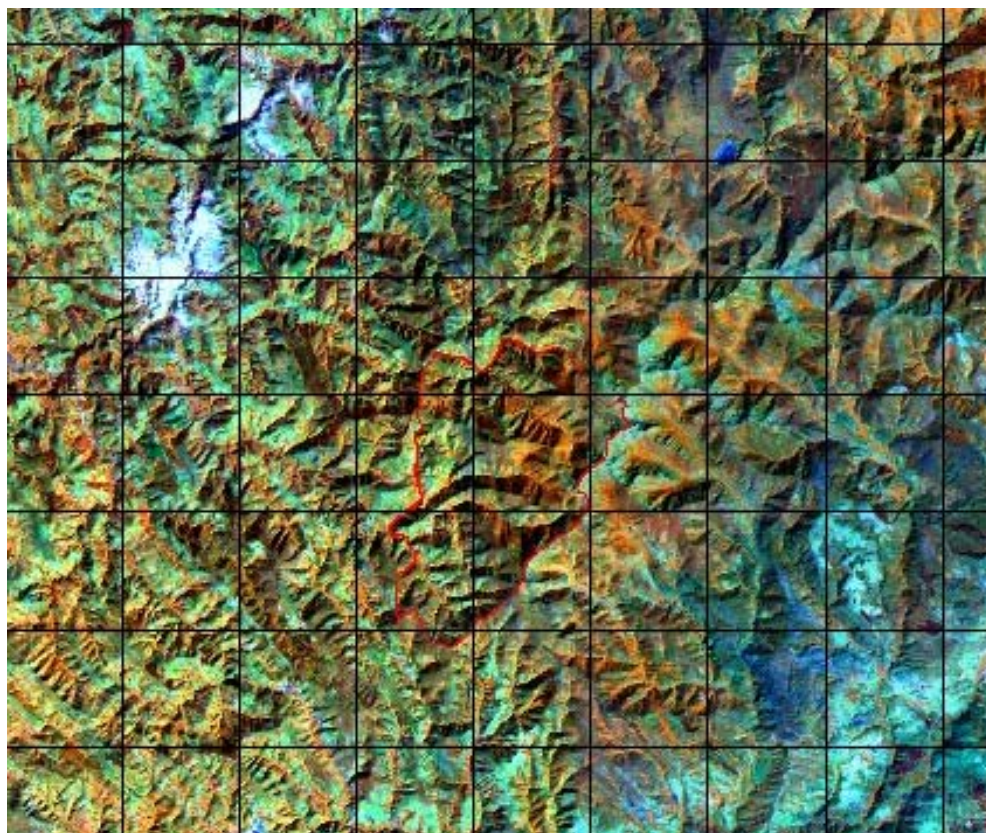


Fig. 2.- Imagen resultante de la Sierra de los Ancares gallegos. Composición coloreada 4/5/3.

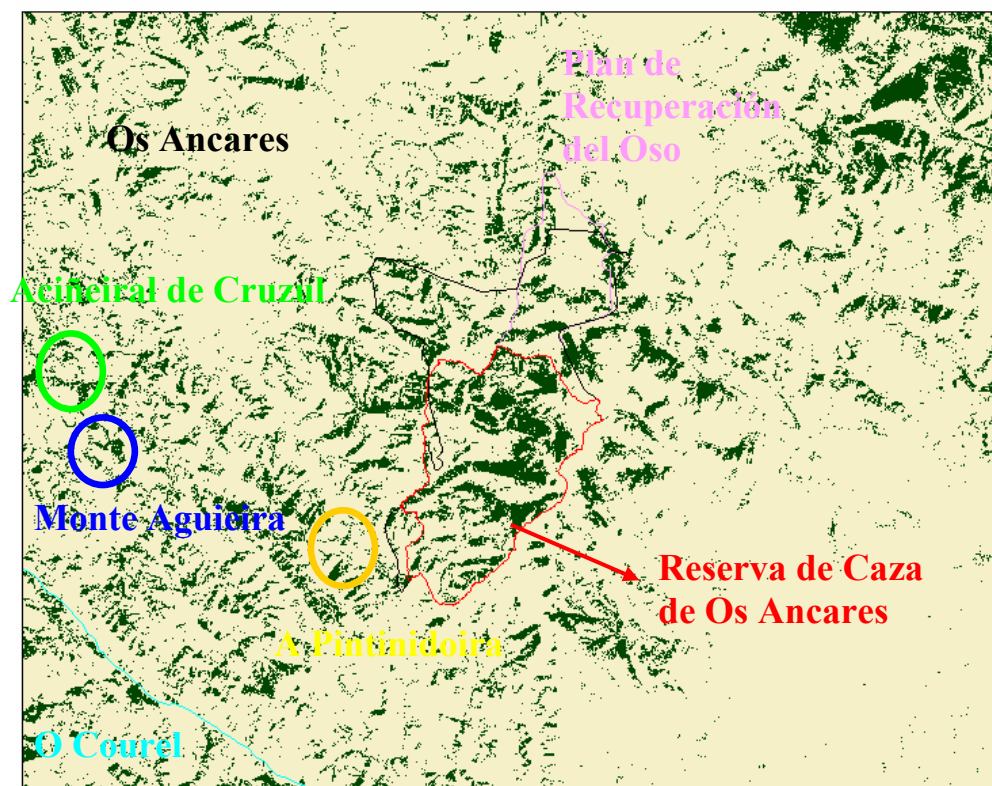


Fig. 3 - Mapa de masas boscosas de la Sierra de Ancares

6. CONCLUSIONES

Mediante la teledetección se pueden analizar los corredores ecológicos a partir de la clasificación de la composición coloreada 4/5/3, identificando de forma visual el bosque respecto del resto de las cubiertas y permitiendo así el análisis global de contexto y la búsqueda de la mejor opción para crear, consolidar o mantener los corredores ecológicos.

Las técnicas de extracción de la información de la imagen de satélite permiten la obtención de información relativa a la función de las vías como corredores ecológicos. Se podrá analizar qué corredores pueden facilitar la conectividad entre áreas naturales próximas. Proporciona además la oportunidad para la construcción y representación de corredores alternativos en el paisaje.

La teledetección permite, por tanto, realizar una triple aproximación a los corredores mediante su detección, cartografía y contexto dentro del paisaje o usos de suelo lo que supone una herramienta para la planificación.

Ayuda a la definición de estrategias para el planeamiento o protección de corredores a escala local y regional.

7. BIBLIOGRAFÍA

- CAÑAS GUERRERO, I; RUIZ, M^a. A; FANJUL ALONSO, M^a. J. 1996. "Las vías forestales y el medio ambiente". En *Actas del III Congreso Internacional de Ingeniería de Proyectos*. Vol. 2, págs. 736-743.
- GIL DOCAMPO, M^a. L; CAÑAS GUERRERO, I. 2001. "Aplicaciones de las imágenes espaciales al estudio del paisaje". En *Gestión sostenible de paisajes rurales*. Ed. Mundi-Prensa. Madrid. Págs 81-94.
- GIL DOCAMPO, M^a. L; 2001 "El empleo de imágenes Landsat -TM y SPOT - P para el estudio de las vías de baja densidad de tráfico. Caso particular de la Reserva de Caza de los Ancares Gallegos. Ed. Unidixital. Universidad de Santiago de Compostela. España
- GOOSSENS, R; D'HAULUIN, E; LARNOE, G. 1991. "Satellite image interpretation (SPOT) for the survey of the ecological infrastructure in a small scaled landscape (Kempenland, Belgium)." *Landscape Ecology*. Vol. 5, N° 3, págs.175-182.

- GULINCK, H; WALPOT, P; JANSSENS,P; DRIES, I. 1991. "The visualisation of corridors in the landscape using SPOT data". En *Nature conservation 2: the role of corridors*. Edit Denis A. Saunders and Richard J. Hobbs. Surrey Beatty and Sons. Págs. 9-17.
- JONGMAN, R. H. G. 1995. "Nature conservation planning in Europe: developing ecological networks". *Landscape and Urban Planning*. Nº 32, págs. 169-183.
- KLIJN, F. AND LIGHART, T.N. 1988. "The applicability of remote sensing in habitat network planning on a regional scale; a case study in the province of Groningen, the Netherlands" *Münstersche Geographische Arbeiten* 29; págs. 179 – 180.
- MILLER, J.R; JOYCE, L.L; KNIGHT, R. L; KING, R.M. 1996. "Forest roads and landscape structure in the southern Rocky Mountains." En *Landscape Ecology*. Vol. 11, Nº 2, págs. 115-127.
- MOORE, N. W. 1962. "The healths of Dorset and their conservation". *Journal of Ecology*, 50. Págs. 369 – 391
- PEREZ MOREIRA, R. 1992. *Ecología forestal e ordenación do bosque*. Ed. Do Castro. La Coruña. 261 págs.
- RUIZ, Mª A. CAÑAS GUERRERO, I; 2001. "Técnicas de estudio del impacto paisajístico de las infraestructuras lineales". En *Gestión sostenible de paisajes rurales*". Ed. Mundi-Prensa. Madrid. Págs 121-145.
- VALES VAZQUEZ, C. 1987. "Política forestal e conservación dos recursos biolóxicos". V Xornadas Agrarias Galegas. Ed. Xunta de Galicia. Consellería de Agricultura. 1989. Págs. 335-353.
- Varios autores. 1995. "Special Issue: Greenways" *Landscape and Urban Planning*. Nº 33. Págs. 1 - 481
- WULF, R. D; GOOSSENS, R; MACKINNONO, J Y SHEN CAI, W. 1988. "Remote sensing for wildlife management: Giant Panda habitat mapping from Landsat MSS images. *Geocarto International*. Págs. 41 – 50.

Installation set an reli inar res lts o a CIMEL CE31 2 in B rassot S ain

V. Estellés, J.L. Gómez-Amo, A. Segarra, M.P. Utrillas, J.A. Martínez-Lozano
Grupo de Radiación Solar. Dept. Termodinàmica, Universitat de València.
C/ Dr. Moliner, 50, 46100 Burjassot (SPAIN)
jmartine@uv.es, vestelle@uv.es

ABSTRACT - *In this paper we present the results obtained from ground-based measurements using a CIMEL sunphotometer during 27 selected clear days corresponding to the first six months of 2002 in Valencia, an urban coastal Mediterranean site. From the direct solar extinction data the spectral aerosol optical depth (AOD) and the columnar water vapour content have been retrieved. The spectral AOD has been used to obtain the Angstrom coefficients and the size distribution function from the King inversion algorithm. The results show the great dependence of the optical aerosol characteristics on the dominant winds in this area. This location is subject to winds which have either a land or Mediterranean origin which frequently mask the aerosols coming from the Atlantic or north Africa, respectively.*

1 INTRODUCTION

Recent years have seen significant advances in the knowledge of atmospheric components and the mechanisms that drive the Earth's radiation budget and, consequently, the Earth's global climate. This improvement has been particularly important in relation to the stratospheric ozone and the greenhouse gases. However, the direct and indirect effects of atmospheric aerosols upon global radiative forcing are highly uncertain (Houghton et al. 2001). Furthermore, for the new generation of satellites aerosol models which link aerosol properties to satellite-measured variables are desirable (Remer and Kaufman 1998). Better and more information about parameters like the aerosol optical and radiative properties and their spatial and temporal distribution are needed (Schwartz and Andreae 1996). Season and location are only partial predictors of aerosol optical properties, whilst the variation in aerosol size, for instance, can vary significantly from day to day at a single location (Remer and Kaufman 1998). Such day to day variations stem from meteorological variability rather than direct changes in the strength of aerosol sources. In particular the air mass residence times and the duration of stagnant conditions determine aerosol optical properties (Remer et al. 1999).

Aerosol optical depth (AOD) is the single most comprehensive variable to remotely assess the aerosol burden in the atmosphere from ground based instruments which are, in turn, the simplest, most accurate and easy to maintain monitoring systems. The AOD is used to characterise aerosols and, for example, to make atmospheric corrections to satellite remotely sensed data. Currently the Aerosol Robotic Network

(AERONET) (Holben et al. 1998) fills the gap left after previous measurement networks, whose results had been widely questioned (Dutton et al. 1994, WMO 1994) were closed down.

Since the beginning of the present year 2002, a CIMEL CE318-2 sunphotometer has been deployed in in Burjassot, Spain. Once the installation had been finished and checked, a preliminary analysis of the data was performed, to derive some magnitudes of interest. In this paper we present some results of these preliminary data (in particular the aerosol optical depth and size distributions) for selected days corresponding to the first six months of 2002.

2 SITE DESCRIPTION, INSTRUMENTATION AND MEASUREMENTS

The measurements were taken in the Solar Radiation Group measurement station, on the terrace of the Faculty of Physics, at Burjassot (latitude 39° 30' N, longitude 0° 25' W), 4 km from Valencia. The city of Valencia is located on the Spanish Mediterranean Coast. The metropolitan area has a population of 1.3 million inhabitants.

A commercial photometric system CIMEL CE318-2 for measuring direct solar and sky radiance was installed at this station in December 2001. This kind of instrument is described in detail by Holben et al. (1998). It measures in five channels nominally centred on 0.44, 0.67, 0.87, 0.936 and 1.02 μm , with a FWHM (full width at half maximum) of 0.01 μm . Three polarised filters provide additional measurements in the 0.87 μm channel. The 0.936 μm channel is used to derive the water vapour content of the atmosphere at the time of each direct

measurement. The scan of each series of eight channels lasts only 8s, although three direct measurement cycles are taken 20s apart for cloud discrimination and variability estimation. The sensor head, equipped with a 1.2° FOV (field of view) collimator, automatically points at the sun following a detailed time plan.

The calibration was performed through Langley plots (Shaw 1983, Schmid 1995) to extrapolate the reference signal $V_o(I)$ meaning signal on the top of the atmosphere, for a Sun-Earth distance of 1 U.A. Equation (1) shows the linear relationship derived from the Bouger-Lambert-Beer law.

$$\ln V(I) = \ln \left(V_o(I) R^2 \right) - \bar{t}(I) m(q) \quad (1)$$

where R is the Sun-Earth distance, $\bar{t}(I)$ the total mean optical depth for the considered time period, and $m(q)$ the optical mass, dependent on the zenith angle.

By plotting the logarithm of the signal as measured by the instrument against the air mass at the time of each observation, we could easily obtain $V_o(I)$ by linear fitting. The mass range used was limited between the values two and six to avoid possible variation in the AOD when the air mass varied slightly, coinciding with the times when the aerosol layer is more active. At the same time, this range avoided the higher air masses where the temporal variation and the indetermination in the value of the air mass (due to refraction) are more important. The air mass values were taken from Kasten and Young (1989) where only one value of air mass is assumed for all the atmospheric components.

Six stable and clear mornings or afternoons were used in the Langley plots, and the points that lay further than 2σ from the fitted line were removed. In this case, σ is the standard deviation of the fit calculated as the rms of the residuals.

The mean value of the calibration constants, $V_o^{mean}(I)$, was found through equation (2), where the daily $V_{oi}(I)$ is weighted by the rms of the fit residuals. For the error on the final $V_o^{mean}(I)$, the standard deviation for the set of daily constants was taken.

$$V_o^{mean}(I) = \frac{\sum_{i=1}^6 (V_{oi}(I) / s_i)}{\sum_{i=1}^6 (1/s_i)} \quad (2)$$

The measurements were taken during the first six months of 2002, and 27 cloudless days were analysed, although we only show the analysis of the two time series given in table I, because of their different

behaviour. Data is scarce in March, due to the temporary removal of the instrument for maintenance.

3 METHODOLOGY

Only the solar extinction measurements at each wavelength have been used in the present analysis. The error assumed for each data point and channel was calculated as the standard deviation of the three groups of direct sun measurements, so the errors are dependent on the wavelength and hour of the day. The measurements have been used to derive the AOD for four wavelengths (0.44, 0.67, 0.87, 1.02 μm). The measurements from the 0.936 μm channel were used to retrieve the precipitable columnar water vapour content (Bruegge et al. 1992, Halthore et al. 1997).

3.1 Spectral aerosol optical depth

From the direct solar extinction signal, $V(I)$, and the calculated calibration constant by the Langley plot method, $V_o^{mean}(I)$, the total atmospheric optical depth, $t_f(I)$, can be obtained using the Bouger-Lambert-Beer law:

$$V(I) = V_o^{mean}(I) R^2 \exp(-m(q) t_f(I)) \quad (3)$$

In turn, $t_f(I)$ can be written as the sum of several atmospheric process contributions:

$$t_f(I) = t_R(I) + t_a(I) + t_3(I) + t_2(I) \quad (4)$$

where $t_R(I)$, $t_a(I)$, $t_3(I)$ and $t_2(I)$ are, respectively, the optical depths due to molecular scattering (Rayleigh), aerosols extinction, and ozone and nitrogen dioxide absorptions.

The optical depth from the last two components could be neglected since the four CIMEL channels were selected in atmospheric windows. Nevertheless we preferred to include an ozone correction in order to consider absorption wing features inside our bands. For this purpose, the effective ozone absorption coefficients were calculated by a convolution of a gaussian profile over the absorption coefficients proposed by Anderson and Mauersberger (1992). Although for some days the ozone columnar content was available through the Solar Radiation Group's Microtops II measurement, on most of the days the value given in the Total Ozone Mapping Spectrometer (TOMS) web site was used (http://toms.gsfc.nasa.gov/teacher/ozone_overhead.html). For Rayleigh scattering, the approximation proposed by Bodhaine et al. (1999) was used. For the optical mass, an error of 0.1% was assumed. The values of the AOD error obtained here were similar to those presented by Eck et al. (1999).

3.2 Parametrisation of the spectral aerosol optical depth

We analysed the dependence of the aerosol optical depth on the wavelength, employing the power law relationship proposed by Angstrom (1929, 1930):

$$t_a(\lambda) = b\lambda^{-a} \quad (5)$$

where the wavelength is expressed in micrometers.

The turbidity coefficient b is the aerosol extinction coefficient corresponding to the 1 μm wavelength. This coefficient is related to the amount of aerosols present in the atmosphere and is widely used in meteorological observations to characterise the degree of air pollution, or turbidity. The wavelength exponent a is related to the aerosols' size distribution and is a first rough assessment of the aerosols' physical characteristics, i.e. the effective radius. According to Higurashi and Nakajima (1999) the characteristic dependence of the Angstrom exponent on the AOD is caused by a correlation between the accumulation mode and the large coarse particle mode.

To obtain values of a and b we adjusted equation (5) for each of the spectral measurement series, in a log-log plot.

3.3 Aerosol size distribution

The determination of the size distribution of the atmospheric aerosols from extinction measurements can be formulated in terms of a Fredholm integral equation of the first kind (Yamamoto and Tanaka 1969). The aerosol size distribution can be obtained from the shape of the spectral aerosol optical depth curve, $t_a(\lambda)$, solving the integral:

$$t_a(\lambda) = \int_0^{\infty} \pi r^2 Q_{\text{ext}}(r, \lambda, m_r) n_c(r) dr \quad (6)$$

where $Q_{\text{ext}}(r, \lambda, m_r)$ is the Mie extinction efficiency factor, m_r is the complex refractive index and $n_c(r)$ is the aerosol size distribution which corresponds to the number of particles per unit radius interval per unit area in a vertical column through the atmosphere.

To calculate the aerosol size distribution we used the inversion method proposed by King et al. (1978) and King (1982) which has been previously used by other investigators (Martínez-Lozano et al. 1999, Watson and Oppenheimer 2000). To guarantee the convergence of this method it is very important to choose properly the radius interval in which the equation is to be applied. Here all the inversions were performed assuming for the integral limits the 0.13 and 5.0 μm radius values, and using the four

wavelengths within their estimation error. For all the inversions we considered that the complex refractive index of the aerosol particles was both wavelength and size independent (Martínez-Lozano et al. 1999).

3.4 Water vapour content

To estimate the precipitable water vapour content, the 0.936 μm band extinction measurements were used. This channel is centered on a strong absorption feature of water vapour. In this case we could not use the standard Langley plots calibration because the functional form of the optical air mass is no longer valid.

Bruegge et al. (1992) proposed a modified Langley plot in the case of the 0.94 μm band, running LOWTRAN simulations over a range of masses in three different kinds of atmosphere, to find the functional form of the air mass. Equation (7) summarises the results obtained from LOWTRAN simulations:

$$T_{\text{wat}} = \exp(k(wm)^b) \quad (7)$$

where T_{wat} is the transmittance due to water vapour, and k and b are fitting parameters.

For the modified Langley plot, the product given by $t_a m$ is substituted by the sum of the scattering contributions to the 0.936 μm band ($t_R + t_a$) m plus the water vapour contribution $k(wm)^b$. Therefore the Langley plot for the water band can be described by:

$$\ln V + t_{\text{scat}} m = \ln(V_0/R^2) - k(wm)^b \quad (8)$$

Plotting $(\ln V + t_{\text{scat}} m)$ for each data point, against m^b , we can attempt a linear fit, which will give us both the calibration coefficient for this channel and the mean content of water vapour over the air mass interval considered. The more stable the water vapour content in the air mass interval, the better the calibration coefficient. The mean calibration coefficient is found through equation (2).

Once we knew the calibration coefficient, and all the variables (V , t_{scat} , m) were established, equation (8) was used to determine the columnar water vapour content for the 27 days.

The coefficients k and b proposed by Halthore et al. (1997) were used to solve equation (8). They analysed the influence of the position of the wavelength and the bandpass of the filter over these coefficient values, for a system identical to ours. The conclusion was that a 10 nm FWHM is a good choice. It seems that the exact position of the wavelength centre is not as important as the bandpass.

4 RESULTS AND DISCUSSION

4.1 Spectral aerosol depth and precipitable water vapour content

The eight cloudless days considered in this work are summarised in table I. For each of these days there are several series of data corresponding to channels centred at 0.44, 0.67, 0.87 and 1.02 μm . The methodology described above was applied, based on equations (3) and (4), and the corresponding AOD values were determined. The number of measurements taken in a whole day was variable, and depended both on the weather conditions and the day length. In table I this number is represented as n_d .

For the AOD spectra obtained for each four channel measurement set, the Angstrom law given by equation (5) was fitted, giving the a and b parameters. From these fits, t_{500} (aerosol optical depth for wavelength 0.5 μm) was calculated, taking its mean as a representative value for the day. t_{500} is the value usually employed to characterise the aerosols in remote sensing applications. In table I the mean values of the t_{500} and of the a and b fitted coefficients are shown. Each parameter has attached both the mean error (e) and the standard deviation (s).

The precipitable water vapour content has been obtained by applying the methodology described above, through equation (8). Like for the AOD case, starting from the data for each measurement point, daily mean values were calculated. These are shown in table I, with the corresponding mean error and standard deviation.

At the bottom of table I, mean monthly values, obtained from the daily mean values, are given for w , a , b and t_{500} . Although these results do not cover a sufficiently long time to give climatic evolution criteria, the mean monthly values can help us to see both time trends and comparisons with aerosol characteristics in other sites. In this respect the t_{500} results showed the same trends as other results obtained previously by the authors for this location (Pedrós et al. 1998), using different instruments and methodologies. Pedrós et al. (1998) analysed the annual evolution of turbidity indexes for Valencia and found out that the summer turbidity values are at least twice as high as the winter ones.

Validation of our work should be done in relation to the databases of other studies. Although our data is insufficient to obtain definitive conclusions they can help us to know whether the magnitude orders are similar when the comparison is made with stations with similar characteristics. Studying the stations included in the AOD database from the AERONET network, published to date (Holben et al. 2001), we found Greenbelt (Maryland) which has similar

geographical characteristics to Valencia, except the former is Atlantic and the latter is Mediterranean. The t_{500} and its standard deviation from both stations, for the extreme months of our data (January and June), were of the same order of magnitude. Mean values for Greenbelt, obtained after 7 years of measurements, are 0.10 for January and 0.37 for June.

Apart from these mean monthly values, the daily behaviour of the parameters was analysed, in particular, the daily evolution of water vapour content, the AOD for the four extinction channels, the calculated t_{500} , and the Angstrom parameters. To analyse them, we centred our attention on two different periods for which we had measurements on several consecutive days and for which similar atmospheric characteristics prevailed. These two time series covered intervals from 16 to 18 January, and 17 to 22 June, as shown in table I.

In relation to the a coefficient, it could be observed that it showed very different average values in the two periods, of the order of 1.2 for January and 0.5 for June, suggesting the presence of different types of aerosols and probably from different origins. In figure 1 the daily evolution is showed for both parameters, for 17 January and 18 June.

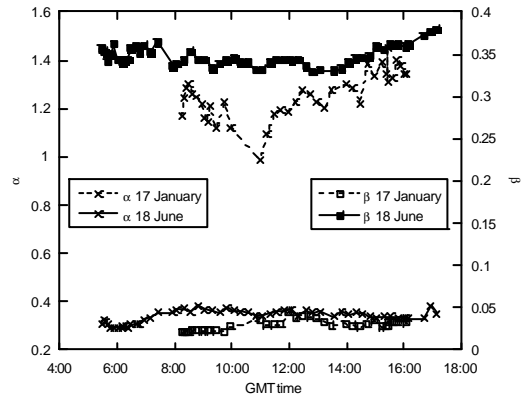


Figure 1: Daily evolution of a and b for 17 January and 18 June

4.2 Aerosol type: size distribution and air mass back-trajectories

In order to establish aerosol types we based our analysis on the back-trajectories of the air masses and in the size distributions.

Three-day back-trajectories computed with the HYSPLIT4 (Hybrid Single-Particle Lagrangian Integrated Trajectory) Model (courtesy of NOAA Air Resource Laboratory, <http://www.arl.noaa.gov/ready/hysplit4.html>) ending at 1200 GMT in Valencia were used to characterise the origin of the air masses arriving over the measurement site. Figures 2 and 3 show these back-trajectories. In these figures it is

possible to appreciate that during the period of January the air masses had a well defined Atlantic origin, which logically suggests the transport of aerosols of maritime origin. For the month of June, the air masses at high atmospheric levels proceeded from North Africa which, in principle would account for the presence of desert dust type aerosols over the measurement site.

The size distribution, as already noted, was obtained by solving equation (6) using the inversion method proposed by King et al. (1978), assuming for the integral limits the 0.13 and 5.0 μm radius values. We checked that a slightly different radius range do not affect the resulting size distribution. In all cases the curves have a clear bimodal form, with accumulation and coarse modes. The principal difference between the distributions corresponding to the two periods is that whilst in the winter both modes have equal weight, during the summer the coarse mode is clearly dominant.

To test the validity of the results, from the obtained distribution functions, the spectral AOD were reconstructed using equation (6). The experimental values of AOD and those obtained from (6) were compared using the relative rmsd. For the winter period the AOD values obtained from these curves showed deviations with respect to the experimental AOD values with a relative rmsd of about 7.2 % for the whole of the spectral range. For the summer period the deviations of the AOD values derived from equation (6) relative to the experimental values have a relative rmsd between 0.25 % and 2.6 %. The higher deviations are related to the shape of the AOD spectrum and the AOD value, with the AOD spectrum of 16 January being the most difficult to invert. This may be due to the uncertainty when the AOD is lower.

In order to analyse in more detail the characteristics of these distributions, we assumed that each of the modes can be represented by a lognormal distribution given by equation (9):

$$\frac{dV_{ol}}{d \ln r} = \frac{V_{ol}^0}{s\sqrt{2p}} \exp \left[-\frac{(\ln(r/r_m))^2}{2s^2} \right] \quad (9)$$

where $dV_{ol} / d \ln r$ is the volume distribution,

V_{ol}^0 is the column volume of the particles per cross-section of atmospheric column, r is the radius, r_m is the volume modal radius, and s is the standard deviation of the natural logarithm of the radius for the volume distribution. Figure 4 shows the fitted curves for the King size distributions inverted at three different times (morning, afternoon and solar noon) on 17 January and 18 June. Table II shows the fitting parameters of these curves.

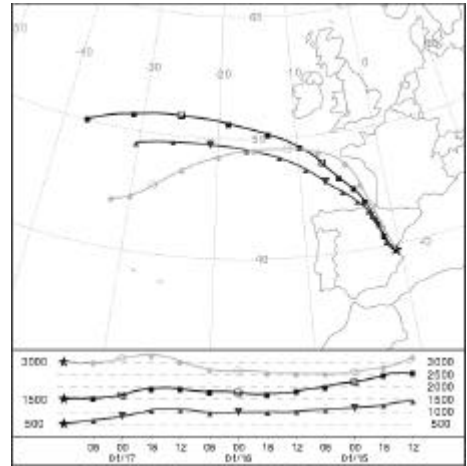


Figure 2: Three-day back-trajectories computed with HYSPLIT4 ending at 1200 GMT for 17 January

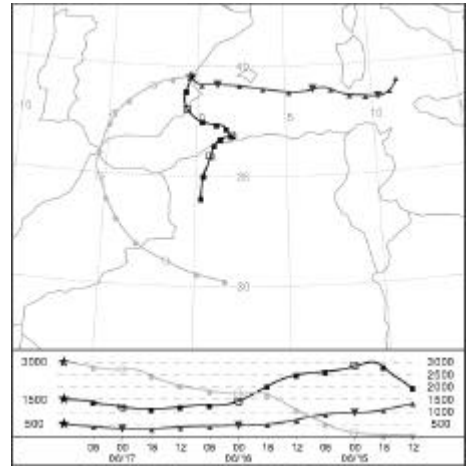


Figure 3: Three-day back-trajectories computed with HYSPLIT4 ending at 1200 GMT for 17 June

It can be seen that for 17 January the weights of the accumulation and coarse mode aerosols were of the same order of magnitude. In the accumulation mode an increase in the weight of the aerosols over the length of the day occurred, whilst the average radius remained practically constant at around 0.1 μm . For the coarse mode there was an increase during the morning followed by a decrease during the afternoon, whilst the average radius dropped from 6.9 μm at the beginning of the morning to 5.2 μm at the end of the afternoon, with a particularly sharp drop after midday. This behaviour was similar on the other days of this month. If we consider all the days together, the daily average radius corresponding to the coarse mode

Day	τ_{500}	σ_{τ}	ε_{τ}	α	σ_{α}	ε_{α}	β	σ_{β}	ε_{β}	w	σ_w	ε_w	n_d
1601	0.035	0.005	0.018	0.8	0.17	0.5	0.020	0.033	0.004	0.87	0.07	0.09	25
1701	0.070	0.016	0.018	1.3	0.10	0.2	0.029	0.006	0.003	0.93	0.07	0.09	38
1801	0.19	0.02	0.02	1.55	0.03	0.10	0.066	0.008	0.004	1.23	0.08	0.12	28
1706	0.31	0.011	0.02	0.37	0.03	0.07	0.242	0.007	0.005	2.0	0.07	0.2	67
1806	0.44	0.016	0.03	0.34	0.03	0.05	0.347	0.012	0.007	2.3	0.13	0.2	54
1906	0.40	0.013	0.02	0.33	0.018	0.06	0.319	0.010	0.007	2.2	0.06	0.2	44
2106	0.24	0.03	0.02	0.58	0.13	0.09	0.164	0.030	0.005	1.90	0.20	0.19	58
2206	0.25	0.02	0.03	1.00	0.06	0.11	0.127	0.007	0.006	2.4	0.09	0.2	48

Month	τ_{500}	σ_{τ}	ε_{τ}	α	σ_{α}	ε_{α}	β	σ_{β}	ε_{β}	w	σ_w	ε_w	n_m
Jan.	0.085	0.061	0.018	1.2	0.2	0.3	0.034	0.018	0.003	0.97	0.23	0.10	5
Feb.	0.12	0.10	0.02	1.0	0.4	0.3	0.052	0.031	0.004	0.87	0.21	0.09	7
Mar.	-	-	-	-	-	-	-	-	-	-	-	-	0
Apr.	0.18	0.02	0.03	1.49	0.12	0.15	0.064	0.010	0.005	1.47	0.20	0.15	4
May	0.08	0.02	0.03	1.23	0.33	0.03	0.034	0.006	0.006	1.43	0.29	0.14	4
June	0.28	0.11	0.03	0.78	0.50	0.10	0.189	0.117	0.006	2.2	0.2	0.2	7

Table I: Daily mean values of τ_{500} , water vapour content (w) expressed in gcm^{-2} , and Angstrom parameters (**a** and **b**) for the days considered (σ : standard deviation, ε associated error, n_d : number of measurements along a day, n_m : number of days used for the monthly mean).

decreased from 7.7 μm on 16 January to 2.1 μm for 18 January.

For the 18 June the curves shown in figure 4 practically overlay the experimental points, which at least in principal indicates great atmospheric stability (typical of anticyclonic conditions over this area at this time of year) with a greater weight of aerosols in the coarse mode than in the accumulation mode. If we analyse the values given in table II for this day we can see that the values of V_{ol}^0 for the accumulation mode were similar to those obtained in the previously analysed winter period, with an average radius steady around 0.1 μm . In the range of coarse particle the average radius varied between 29 and 37 μm , with an average daily value of approximately 33 μm . If we consider the five days of this month similar values were obtained for them all in the accumulation mode,

both for V_{ol}^0 and for r_m . However in the coarse mode different behaviour was seen on different days. During the first three days the value of V_{ol}^0 remained around the same order of magnitude as shown in figure 4, whilst the value of r_m evolved from 30 μm (17 June) to 38 μm (19 June). On the last two days of this period however there was a decrease both in V_{ol}^0 and r_m , with an average daily value of the latter of 20 μm for 21 June and of 7.4 μm for 22 June. For the last day V_{ol}^0 reached similar values in both modes.

All of the above appears to indicate that during the winter period studied there was a predominance of aerosol originating in the Atlantic whilst during the summer there were aerosols from North Africa until 21 June. This would be consistent with the air mass trajectories shown in figures 2 and 3.

Currently the parameter that best characterises the aerosol type (in the absence of experimental values of the refractive index) is the average radius of the modes, especially that corresponding to coarse particles. If we compare our results with the average

GMT Time	Mode 1			Mode 2		
	V_{ol}^0	σ	r_m	V_{ol}^0	σ	r_m
17 January						
0815	5.7 10 ⁶	2.8	0.11	1.9 10 ⁶	3.9	6.9
1200	1.0 10 ⁷	3.1	0.09	5.7 10 ⁶	3.9	6.5
1559	1.8 10 ⁷	3.5	0.10	2.9 10 ⁶	4.1	5.2
18 June						
0805	9.0 10 ⁶	5.3	0.11	2.9 10 ⁸	4.4	31.6
1204	8.4 10 ⁶	3.6	0.08	3.5 10 ⁸	4.1	29.5
1656	1.0 10 ⁷	6.1	0.24	3.8 10 ⁸	4.5	36.9

Table II: Model parameters and standard deviation derived from inversion of AOD using the King algorithm. V_{ol}^0 is the column volume of the particles per cross section of atmospheric column ($\mu m^3 cm^{-2}$); r_m is the modal radius of the volume distribution (μm).

values of the radii of this mode proposed by Hess et al. (1998) in the OPAC (Optical Properties of Aerosol and Clouds) database, we can see that they assign a value of $7.9\ \mu\text{m}$ for the sea salt coarse mode, and a value of $11\ \mu\text{m}$ for the mineral coarse mode, although for the latter the possible range of values reaches $60\ \mu\text{m}$. In the model of Hess et al. (1998) sea-salt particles consist of the various kinds of salt contained in seawater, and mineral particles are mineral aerosol or desert dust produced in arid regions. Kaufman et al. (1998) have presented a summary of the aerosol dynamic models in which they assign a radius r_m of $17\ \mu\text{m}$ for dust of continental origin.

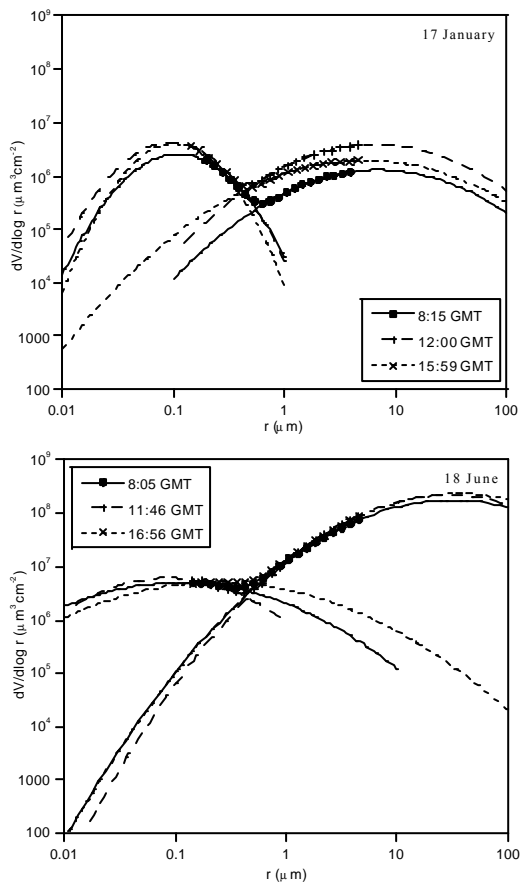


Figure 4: Bimodal lognormal fit for the three volume size distributions corresponding to the 17 January and 18 June

These values would confirm the presence of sea-salt particles over Valencia when the air masses come from the Atlantic, after crossing the Iberian Peninsula, and the presence of Saharan dust particles in the upper atmospheric layers when the synoptic conditions

favour the entry of air masses in altitude from Africa. These Saharan dust particles had radii in the coarse mode in the upper part of the range for this type of particles, indicating the closeness of the source of these emissions to the measurement site (Hess et al. 1998).

5 CONCLUDING REMARKS

Ground-based measurements using a CIMEL sunphotometer were taken during 27 clear days spread irregularly over the first six months of 2002. Based on the measurements of AOD made with the CIMEL the aerosol characteristics over Valencia, an urban coastal Mediterranean site, have been analysed for two typical synoptic conditions. The results showed the great dependence of the optical aerosol characteristics on the dominant winds in this area. When the western wind predominated in winter the atmospheric conditions were those of very clear skies (t_{500} of around 0.1), with an Angstrom α coefficient of 1.2 and a predominance of sea-salt type particles in the coarse mode. This west wind, often considered to be a continental wind, actually originated over the Atlantic and crossed the Iberian Peninsula before reaching the measurement site.

In spring and summer the AOD values were always greater than in winter with values of t_{500} greater than 0.4 being registered, and with an Angstrom α coefficient of 0.5. These values corresponded to east winds (Mediterranean) at the surface, with winds entering from Africa at altitude dragging Saharan dust over the measurement site. This Saharan dust had large size in the coarse mode with an average radius of the order of $30\text{--}40\ \mu\text{m}$.

Although the period analysed in this study is clearly insufficient to extract conclusions of a general character in relation to the annual variation of the aerosols present over Valencia, it nevertheless demonstrated that, in future, it will be difficult to establish an aerosol climatology for the site, which is apparently influenced by winds of both continental and Mediterranean origin which may, in many cases, hide aerosols originating in the Atlantic and North Africa respectively. Therefore our future work in the characterisation of the aerosols over this site must necessarily be accompanied by an analysis of the origins of the air masses at different altitudes.

ACKNOWLEDGEMENTS

The CIMEL 318-2 sunphotometer was acquired with funds from the Spanish Interministerial Commission for Science and Technology (CICYT). V. Estellés currently holds a research grant from the same commission, CICYT.

REFERENCES

- Anderson, S. M., and Mauersberger, K., 1992, Measurements of ozone absorption cross section in the Chappuis band, *Geophys. Res. Lett.*, 19, 933-936.
- Angstrom, A., 1929, On the atmospheric transmission of sun radiation and on the dust in the air. *Geografis. Annal.*, 11, 156-166.
- Angstrom, A., 1930, On the atmospheric transmission of sun radiation, *Geografis. Annal.*, 12, 130-159.
- Bodhaine, B. A., Wood, N. B., Dutton, E. G., and Slusser, J. R., 1999, On Rayleigh optical depth calculations, *J. Atmos. Oceanic Technol.*, 16, 1854-1861.
- Bruegge, C. J., Conel, J. E., Green, R. O., Margolis, J. S., Holm, R. G., and Toon, G., 1992, Water vapor column abundance retrieval during FIFE, *J. Geophys. Res.*, 97, 18759-18768.
- Dutton, E. G., Patrick, R., Ryan, S., and DeLuisi, J. J., 1994, Features and effects of aerosol optical depth observed at Mauna Loa, Hawaii: 1982-1992, *J. Geophys. Res.*, 99, 8295-8306.
- Eck, T. F., Holben, B. N., Reid, J. S., Dubovik, O., O'Neill, N. T., Slutsker, I., and Kinne, S., 1999, Wavelength dependence of the optical depth of biomass burning, urban and desert dust aerosols, *J. Geophys. Res.*, 104, 31333-31349.
- Halothore, R. N., Eck, T.F., Holben, B.N. and Markham, B., 1997, Sunphotometric measurement of atmospheric water vapor column abundance in the 940-nm band, *J. geophys. Res.* 102, 4343-4352.
- Hess, M., Koepke, P., and Schult, I., 1998, Optical properties of aerosol and clouds: the software package OPAC, *Bull. Am. Meteor. Soc.*, 79, 831-844.
- Higurashi, A., and Nakajima, T., 1999, Development of a two-channel aerosol retrieval algorithm on a global scale using NOAA AVHRR, *J. Atmos. Sci.*, 56, 924-941.
- Holben B. N., Eck, T. F., Slutsker, I., Tanré, D., Buis, J. P., Setzer, A., Vermote, E., Reagan, J. A., Kaufman, Y. J., Nakajima, T., Lavenu, F., Jankowiak, I., Smirnov, A., 1998, AERONET - A Federated instrument network and data archive for aerosol characterization, *Rem. Sensing Environ.*, 66, 1-16.
- Holben, B.N. et al. (23 authors), 2001, An emerging ground-based aerosol climatology: Aerosol optical depth from AERONET, *J. Geophys. Res.*, 106, 12067-12097.
- Houghton, J., Ding, Y., Griggs, D.J., Noguer, M., van der Linden, P.J., Dai, X., Maskell, K. and Johnson, C. A., 2001, (Eds.), *Climate Change: The Scientific Basis*, (New York: Cambridge Univ. Press).
- Kasten, F., and Young, M. T., 1989, Revised optical air mass tables and approximation formula, *Appl. Opt.*, 28, 4735-4738.
- Kaufman, Y. J., Tanré, D., Chu, A., Mattoo, S., and Remer, L., 1998, Algorithm for remote sensing of tropospheric aerosol from MODIS, MODIS ATBD, Product ID: MOD04.
- King, M. D., Byrne, D. M., Herman, B. M. and Reagan, J. A., 1978, Aerosol size distribution obtained by inversion of spectral optical depth measurements, *J. Atmos. Sci.*, 35, 2154-67.
- King, M. D., 1982, Sensitivity of constrained linear inversions to the selection of Lagrange multiplier, *J. Atmos. Sci.*, 39, 1356-69.
- Martínez-Lozano, J. A., Utrillas, M. P., and Tena, F., 1999, Retrieval of the aerosol size distribution from spectroradiometer measurements at a coastal site in the Mediterranean sea, *I. J. Remote Sensing*, 20, 2167-2182.
- Pedrés, R., Utrillas, M. P., Martínez-Lozano, J. A. and Tena, F., 1999, Values of broad-band turbidity coefficients in a Mediterranean coastal site, *Solar Energy*, 66, 11-20.
- Remer, L. A. and Kaufman, Y. J., 1998, Dynamic aerosol model: Urban/industrial aerosol, *J. Geophys. Res.*, 103, 13859-13871.
- Remer, L. A., Kaufman, Y. J. and Holben, B. N., 1999, Interannual variation of ambient aerosol characteristics on the coast of the United States, *J. Geophys. Res.*, 104, 2223-2231.
- Schmid, B., Wehrli, C., 1995, Comparison of Sun photometer calibration by use of the Langley technique and the standard lamp, *Appl. Opt.*, 34, 4500-4512.
- Schwartz, S.E. and Andreae, M.O., 1996, Uncertainty in climate change caused by aerosols, *Science*, 272, 1121-1122.
- Shaw, G. E., 1983, Sun Photometry, *Bulletin American Meteorological Society*, 64, 4-9.
- Watson, I. M. and Oppenheimer, C., 2000, Particle size distributions of Mount Etna's aerosol plume constrained by sun photometry, *J. Geophys. Res.*, 105, 9823-9829.
- WMO, 1994, Report on the measurements of atmospheric turbidity in BAPMoN, GAW Report No. 94.
- Yamamoto, G. and Tanaka, M., 1969, Determination of aerosol size distributions from spectral attenuation measurements, *Appl. Opt.*, 8, 447-53.

Quantitative analysis of cropland's BRDF anisotropy using airborne POLDER data

F. Camacho-de Coca, F. J. García-Haro and M. A. Gilabert.

Department of Thermodynamics, University of Valencia

C/Dr. Moliner, 50. 46100 Burjassot. Valencia.

fernando.camacho@uv.es

ABSTRACT- During the DAISEX campaigns of the ESA several flights over an agricultural area were performed with the POLDER instrument. In this work, a quantitative analysis of the BRDF anisotropy has been conducted using the anisotropy factor (ANIF) and the anisotropy index (ANIX). The influence of optical properties, sun zenith angle and canopy architecture on the BRDF anisotropy is examined. The analysis shows that the nadir reflectance increases up to 120% in the backscattering direction for a view zenith angle of 45°, whereas the decrease is typically 40% in the forward scattering region. The analysis shows that the anisotropy increase systematically when both sun zenith angle and absorbance increase. The ANIX, which represents the amplitude of the BRDF anisotropy, shows values ranging between 2 and 7 and provides useful information to discriminate the different cover types.

1. INTRODUCTION

Canopy structure plays a fundamental role in the interaction of solar radiation and thus for describing the three-dimensional radiation field in vegetation canopies. Besides, the right understanding of this radiation field scattered from vegetation canopies is necessary for interpreting properly remote sensing data, and for developing biophysical parameters retrieval techniques from remotely sensed information.

The basic magnitude to characterize the spectral and directional properties of reflectance is the Bidirectional Reflectance Distribution Function (BRDF). Traditionally, quantitative remote sensing techniques have relied on the exploitation of spatial, temporal and spectral domains of the BRDF. Nevertheless, the new generation of satellite sensors, such as the POLarization and Directonality of the Earth's Reflectance (POLDER) or the Multi-Angle Imaging Spectro Radiometer (MISR), have been conceived to acquire multi-view angle measurements. In addition, the synergistic use of these polar orbiting sensors and geostationary satellites sensors, like the Spinning Enhanced Visible & InfraRed Imager (SEVIRI) on Meteosat Second Generation (MSG), will increase the sampling of the directional domain by combining the sun varying with the view varying measurements.

To understand the canopy radiation regimen, three important features must be considered (Knyazikhin et al, 1998): (1) the canopy architecture; (2) the optical properties of vegetation elements and soil; and (3) the sun zenith angle, which determines joint to the atmospheric conditions the incident

radiation field. These features determine the sunlit and shadows areas observed in a scene. The variation of these areas with the sun and view angles results in a directional dependence of measured reflectance. Therefore, the anisotropy of the BRDF is linked to the 3D structure of the canopy and thereby it constitutes a potential source of information. For instance, the directional signature has been used to retrieve clumping index or foliage density (Lacaze et al. 2002). Nevertheless, the information contained in the directional domain is very influenced by the viewing geometry, optical properties and sun position.

Previous experiments have analysed the anisotropic behaviour of the BRDF (Kimes 1983, Deering et al. 1999, Sandmeier et al. 1998). Two effects are used to explain this behaviour: the gap effect and the backshadow effect. The gap effect is produced when increasing off-nadir view angle produces the increment in the proportion of illuminated upper canopy layers viewed from the sensor. This effect is clearly related to the vertical structure of the canopy and the spatial distribution of elements, which determines the fraction of soil, vegetation and shadows in the scene –for a specific sun zenith angle. Backshadow effect is related to the orientation of the canopy components and the irradiation condition derived from the cosine law and shadow's pattern. Thus, when the normal of the surface is pointing to the sun the surfaces are more irradiated. This effect is very strong in the soils due to the fact that the single scattering governs the dispersion of radiation, and the high contrast between shaded and sunlit areas.

In this work we perform a quantitative analysis of the anisotropy of BRDF of croplands as a function

of wavelength, sun zenith angle and structural parameters thanks to the wide BRDF sampling taken during the Digital Airborne Spectrometer EXperiment (DAISEX) campaign. This study has been undertaken in the framework of the ‘Scientific Analysis of the ESA Airborne Multi-Annual Imaging Spectrometer Campaign DAISEX’ project. The main goals have been: (1) to determine the influence of the canopy structure, optical properties and sun zenith angle in the anisotropy of BRDF with the aid of appropriate directional indices, and (2) to understand better the radiative transfer in this kind of herbaceous canopies as a previous step towards the implementation of an innovative directional mixture approach to retrieve structural parameters from multiangular information (García-Haro et al. *this issue*).

In section 2 we briefly present the experiment and methodology. Section 3 shows an example of the BRDF and the quantitative analysis of anisotropy. Finally, conclusions are summarised in section 4.

2 EXPERIMENT AND METHODOLOGY

DAISEX campaigns were performed during the summers of 1998, 1999 and 2000 to demonstrate the feasibility of retrieving biophysical parameters from imaging spectrometer data. The anisotropic effects in surface reflectance were widely considered during all the campaign including the acquisition of the hot spot effect (Camacho-de Coca et al., *this issue*).

The experiment site selected by ESA for the DAISEX campaigns is a 3 km by 3 km area centered at 39° 3' N, 2° 5' W, which is located 28 km from Albacete (Spain), close to the Barrax town (see figure 1 in Camacho-de Coca et al. *this issue*). A supervised classification of the area was made based on field information. The dominant cultivation in the area was approximately 53% dry land (29% barley, 24% fallow) and 42% irrigated land (15% corn, 11% alfalfa, 8% wheat; 2% legumes, 2% sugar beet, and 4% others) with a 5% of unclassified data. Hence, the study area involves different vegetated units, with its own structural characteristics and in its own phenological status. According to the percentage of coverage, barley, alfalfa, wheat and legumes presented full coverage, sugar beet medium coverage and corn, which only presented 3-5 leaves, a very sparse coverage. According to the structural parameters, wheat and barley presented similar characteristics: vertical structure, well-developed spikes, and similar height and LAI. However, the wheat canopy was still vigorous and photosynthetically active whereas the barley canopy was non-photosynthetically active due to its senescent stage. On the other hand, alfalfa and legumes were lower in height, with smaller leaf size and higher LAI than wheat and barley. Sugar beet and

corn were markedly row-distributed with large contribution of the bare soil. Vegetation *in-situ* measurements were taken during the campaign corresponding to major agricultural units. NDVI and structural parameters of the major cover types are shown in the next table. FVC was obtained using a variable endmember spectral mixture analysis (VMESMA) (García-Haro et al., 2002) from HyMAP data whereas LAI was derived from the SAVI vegetation index (ESA, 2001).

Table 1. NDVI and structural parameters of the dominant surface types in the study area. The asterisk refers to field data.

	NDVI	FVC (%)	LAI	Height (m)*
Soil	-	0	0	-
Corn	0,19	25	0,26	0,1-0,2
Sugar Beet	0,32	55	0,6	0,1-0,15
Barley	0,21	92	2,9*	0,55-0,65
Wheat	0,86	97	1,56	0,7-0,85
Legumes	0,76	100	2,22	-
Alfalfa	0,83	100	3,59	0,5-0,6

In the 1999 campaign, the directional capabilities of the POLDER instrument added a new dimension in the acquisition of BRDF measurements. The spectral filters of the POLDER instrument were centered at 443, 500, 550, 590, 670, 700, 720, 800, and 864 nm wavelength. The POLDER field-of-view (FOV) was along track and cross track of $\pm 43^\circ$ and $\pm 51^\circ$ respectively. This resulted in a ground FOV of $7.4 \times 5.6 \text{ km}^2$ for the flight altitude of 3000 m. At this altitude the spatial resolution was 20 m (Leroy et al. 2001).

Four flights with the ARAT plane carrying POLDER and LEANDRE instruments were performed in the 1999 campaign. They correspond to 3rd June at noon (from 11:29 to 12:31 UT), 4th June in the morning (from 7:16 to 8:15 UT) and in the afternoon (from 13:57 to 15:01 UT), and 5th June in the morning (from 6:57 to 8:02 UT). In this study we have used the data collected in the first three flights, neglecting the last because the time acquisition was very similar to the second one.

In each flight the POLDER instrument records around 140 spectral images, which constitutes a POLDER sequence. One image is acquired within 3 seconds, and the acquisition is repeated every 10 seconds, with an overlap between consecutives images. Thus, in a sequence, every pixel is observed with different viewing directions, typically between 30-60 covering a wide range of the directional space. This rich viewing sampling in addition to 9 spectral channels and three different sun positions allows a good BRDF characterization. The POLDER reflectance images were calibrated, geo-coded and

corrected for atmospheric effects as it is specified in Leroy et al (2001).

In order to analyze the influence of the anisotropy regarding the viewing geometry, a simple anisotropy factor (ANIF) or nadir normalized reflectance has been used (Sandmeier et al. 1998):

$$ANIF(\lambda, \theta_i, \varphi_i, \theta_r, \varphi_r) = \frac{R(\lambda, \theta_i, \varphi_i, \theta_r, \varphi_r)}{R_0(\lambda, \theta_i, \varphi_i)} \quad (1)$$

where R_0 is the reflectance factor acquired from nadir view.

In addition, to quantify spectrally the anisotropy's degree of the different samples the anisotropy index (ANIX) has been used. The ANIX gives the amplitude of the reflectance variation for a defined sun zenith angle and relative azimuth angle (Sandmeier et al. 1998):

$$ANIX(\lambda) = \frac{R_{\max}(\lambda)}{R_{\min}(\lambda)} \quad (2)$$

where R_{\max} is the maximum reflectance factor and R_{\min} the minimum. In this work, the ANIX values have been calculated in the principal plane where the anisotropy is manifestly enhanced.

3 RESULTS

3.1 Anisotropy Factor

Firstly, the results of the ANIF, which represents the variation of reflectance factor in percentage regarding the nadir value, are presented. Figure 1 shows the results obtained for two wavelengths, 670 and 800 nm, three different sun positions (17°, 37°, 56°) and four different samples (wheat, legumes, sugar beet and bare soil). The BRDF has been retrieved from a 3x3 pixel area (60x60 m²).

Regarding the optical properties we can observe that for 670 nm the major absorptivity of vegetation and soil translates into a higher anisotropy. The ANIF goes up to 2.2 in the morning for the wheat cover, which represents an increment of the 120% regarding the nadir value. However, at 800 nm the influence of the multiple scattering radiation smoothes the anisotropy of BRDF. The influence of optical properties is evident in dense vegetation canopies (figure 1a and figure 1b) due to the high spectral contrast between red and NIR region. However, for soils (figure 1d) there is no difference in the ANIF at 670 and 800 nm. Therefore, -as a consequence of the optical properties influence on the BRDF anisotropy- the directional information can be used in addition to the spectral information to discriminate soil and vegetation as was pointed in Camacho-de Coca et al (2001). It should be noted that the senescent vegetation (e.g. barley) could present similar optical

properties in red and infrared regions then showing a similar directional behavior than the soils.

The sun zenith angle position has a high influence in the anisotropy as it can be observed in the figure 1. When the sun position is nearby zenith, the irradiance of the sample is more homogeneous, resulting in a more isotropic behavior of scattered radiance. Consequently, the lesser variations of the ANIF take place at noon with values ranging typically between 0.8 and 1.2. However, when the sun zenith angle increases, the differences between the irradiance field in the top and bottom of the canopy becomes greater. This results in an increase the BRDF anisotropy. Hence, the ANIF increases systematically when the SZA increases. This variation is higher in the wheat cover. For the dense wheat cover, the vertical structure implies large differences between nadir reflectance, where the sensor's field-of-view observes the lower canopy layers, and the backscatter radiance, where the sensor mainly collects the radiance coming from the well-illuminated upper layers. In the case of the sparse sugar beet, the increasing SZA results in a lower nadir reflectance value due to the higher fraction of shaded soil.

Concerning the viewing geometry, the ANIF appears symmetric with respect to the solar principal plane, even for the row-distributed sugar beet crop. Conversely, the asymmetry is clearly manifested with respect to the orthogonal plane, and is maximum along the principal plane. In the forward scatter direction large shaded areas are seen resulting in a decreasing reflectance, whilst in the backscatter hemisphere the sunlit areas are predominant and thus the reflectance is enhanced. The maximum value of reflectance occurs in the hot spot geometry. The nadir reflectance increases in this domain up to 120% for a view zenith angle, whereas it decreases typically 20-40% in the forward scattering domain. It should be noted that at this directional resolution the hot spot peak is smoothed (see Camacho de Coca et al. *this issue*) and, consequently, the magnitude of the anisotropy.

Regarding the canopy geometry, the ANIF shows a different behavior that is linked to the influence of the 3D structure on the radiative transfer within the canopy. It is most noticeable at highest sun zenith angle as we can see in the figure 1. Figures 1a and 1b correspond to the ANIF of wheat and legumes cover respectively, both with very similar FVC and LAI values. The differences in the ANIF pattern are connected with the architecture of these samples. The wheat cover presents an erectophile distribution, whilst the legumes cover presents a phanophile distribution. An erectophile distribution favors the gap effect, increasing the anisotropy. This is generally manifested as an increase of reflectance when the off-nadir view angle increase, independently of the

azimuth plane, although this trend is reversed if the sun zenith angle is low, typically lower than 20°. The gap effect cause the typical bowl-shape of the BRDF, clearly manifested in the figures 1a corresponding to the NIR, as closed ANIF isolines.

The barley cover shows similar variation than the wheat cover, from 60% in the NIR to 80% in the blue region according with its optical properties. The sugar beet crop shows values from 30% in the NIR to 100% in the red channel, where the spectral contrast between soil and vegetation is more important. Finally, the bare soil shows the highest differences ranging between 100 and 200%. In this case, the low absorbance and the increment of dark shadows in the forward scatter region, produce a very important increment of the anisotropy. The ANIX rise from 2.3 at noon to 7.4 in the morning flight at 500 nm. This result demonstrates the important influence of the sun position in the anisotropy of the BRDF.

However, in the red region, the high absorbance favors also the backshadow effect, combining thus both effects. This results in a high anisotropy of the wheat cover, especially at high SZA in the red region.

The planophile alfalfa cover shows more isotropic values. Both gap and backshadow effects present low influence due to the vegetation is like a bidimensional mat, rather than a tridimensional surface. The different anisotropic behavior of these two covers of very similar structural parameters is well characterized by normalizing the nadir reflectance. Then, the ANIF allows identifying the influence of architecture on the anisotropy of BRDF. In the other two samples (figure 1c and 1d) the ANIF diagrams are influenced by the soil contribution. For soils, the directional behavior is determined by the backshadow effect. This effect is symmetric with respect to the principal plane, thus the isolines appears orthogonal to the solar plane. In addition, in the principal plane, the ANIF values decrease monotonally as the phase angle increase. For the Sugar Beet this effect is stronger in the red band, because of the high absorbance of the vegetation, and the large amount of shadows cast by the plants. Thereby, the ANIF shows the lowest values around 0.6 in the forward scattering region.

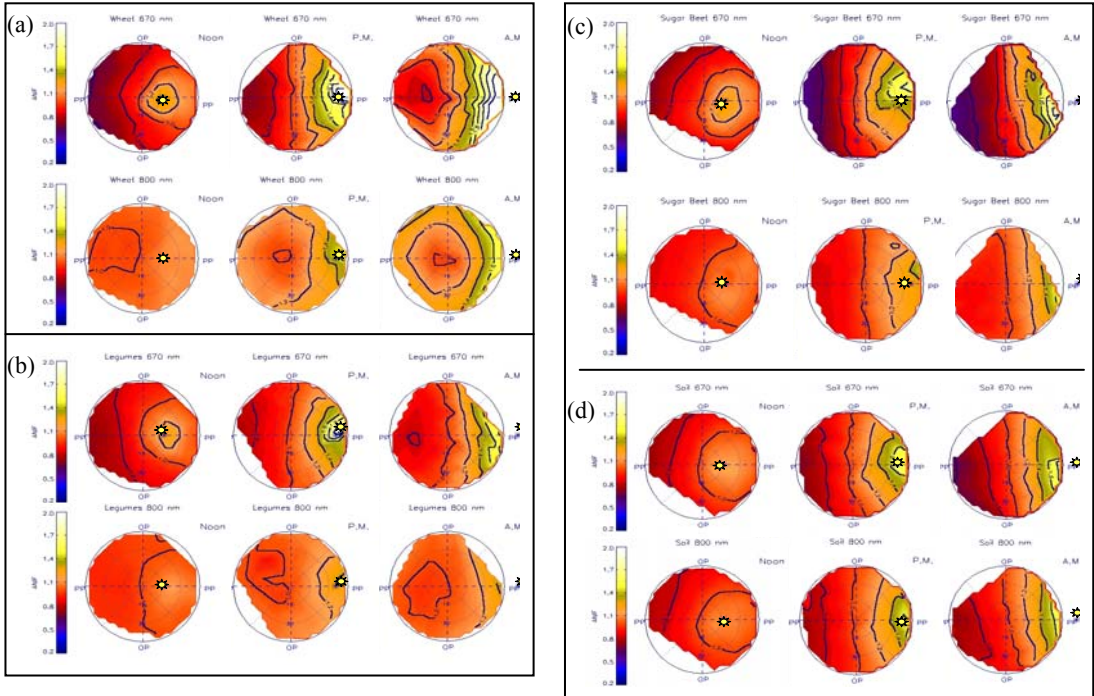


Figure 2. Anisotropy Factors at 670 and 800 nm for three sun zenith angles (17°, 37°, 56°): (a) Wheat , (b) Legumes, (c) Sugar beet and (d) Bare soil.

3.2 Anisotropy Index

In order to quantify the influence of the canopy geometry on the spectral BRDF anisotropy the ANIX was used. Figure 2 shows the results obtained for the major land cover types existing in the study area. In the noon flight (SZA=17°) the anisotropy index presents similar values for the samples considered. The values range typically between 2 and 3, and go up to 4 at shorter wavelengths. This result shows a small influence of the canopy cover type in the anisotropy index because of the sun position. However, when the sun zenith angle increase, the differences in the spectral anisotropy index between canopy types become more important. In the afternoon (SZA=37°) and in the morning (SZA=56°) flights, the ANIX ranges typically between 2 and 6, and goes up to 8 in the blue. Each canopy cover type presents a slightly different spectral trend, according with its optical properties and structural parameters. For example, sugar beet presents a marked peak in the red region, whereas soil and barley present a decreasing trend with the wavelength, conversely to the multiple scattered radiation. The soil presents the highest ANIX (except at 670 nm) in the morning, associated with the enlargement of the very dark shadows. These results show the influence of the canopy geometry in the anisotropy of the BRDF, showing also the potential of this kind of index to discriminate vegetation types in agricultural areas. Therefore, the ANIX could be considered as a spectral signature directly related with the anisotropic properties of vegetation canopies and, thus, with its optical and structural characteristics.

We have finally evaluated the relative increment of the ANIX when the sun zenith angle changes from 17° to 56°. This positive variation depends again of the cover type and optical properties and ranges between 30% and 200%. The lowest variation corresponds to the homogeneous legumes crops in the NIR region. For the dense wheat cover, the ANIX variation is twice than for legumes (typically 60%), showing the influence of the canopy architecture.

4. CONCLUSIONS

Using airborne POLDER data acquired during the DAISEX campaign, a quantitative analysis of the BRDF anisotropy has been performed by means of the ANIF and ANIX anisotropy indices. The ANIF quantify the variation of nadir reflectance with the viewing geometry, whilst the ANIX quantifies the amplitude of the anisotropy, computed as the ratio between the maximum and minimum values.

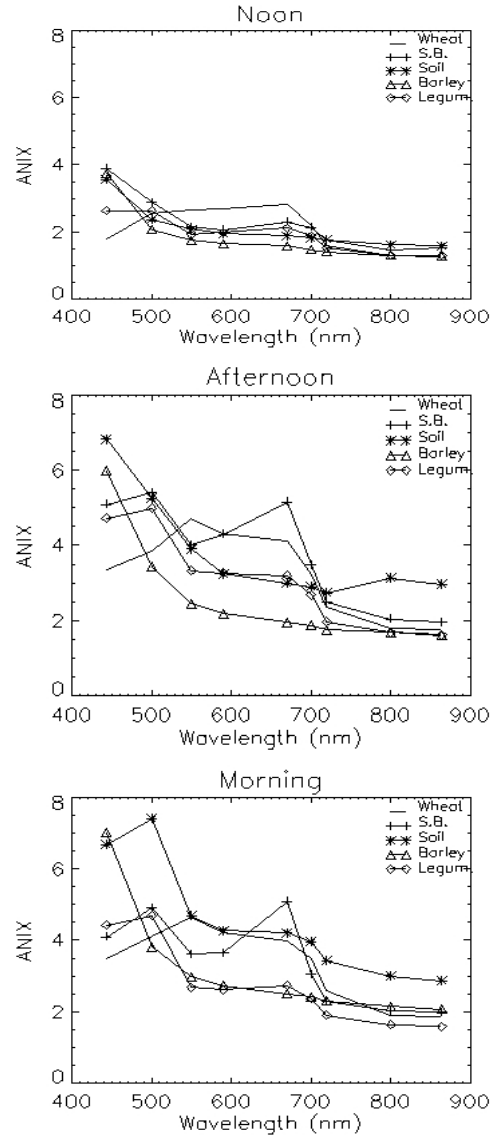


Figure 2. Anisotropy Index of the main cover types for three different SZA: Noon (SZA=17°), Afternoon (SZA=37°), Morning (SZA=56°).

The analysis has allowed evaluating the influence of the canopy structure, optical properties and sun zenith angle on the BRDF anisotropy. The main results were:

(1) The BRDF anisotropy is symmetrical regarding the principal plane. This fact allows us to reduce considerably the sampling necessary to exploit the directional domain. Unlike the orthogonal plane, the principal plane exhibits asymmetry and the highest anisotropy's degree. In this plane, the nadir reflectance

increases up to 120% in the backscattering, whereas it decreases around 20-40% in the forward scattering.

(2) The BRDF anisotropy is strongly dependent of the SZA showing a systematic increase with the SZA increase.

(3) Optical properties exert also a strong influence. In general, the multiple scattered radiation (NIR) smoothes the anisotropy whereas a high absorbance (VIS) increases the BRDF anisotropy.

(4) Finally, the structural parameters and the architecture of the canopy determine the anisotropy of the BRDF. The ANIX obtained in the principal plane has shown that the influence of the canopy architecture becomes more important for higher sun zenith angles. The ANIX values ranges between 2 and 7 in the morning (SZA=56°), revealing a very marked anisotropic behavior.

ACKNOWLEDGEMENTS

This work has been partially supported by the LSA SAF (EUMETSAT), the Scientific Analysis of the ESA Airborne Multi-Annual Imaging Spectrometer Campaign DAISEX and CICYT (CLI 99-0793) projects. J. García-Haro has currently a research position (Ramón y Cajal) from MCyT, Spain.

REFERENCES

- Camacho-de Coca, F., M.A. Gilabert, and J. Meliá, (2001). Hot Spot Signature dynamics in Vegetation Canopies with varying LAI. Proceedings of the 8th Symposium International on Physical Measurements and Signatures in Remote Sensing. Aussois, France. 8-12 Enero 2001
- Camacho-de Coca, F., M. Leroy, J.P. Gastellu-Etchegorry and F.J. García-Haro (2002). Measured Hot Spot Directional Signatures of Agricultural Crops during DAISEX'99. Proceeding of the 1st International symposium on Recent advances in quantitative remote sensing, (this issue).
- Deering, D.W., T.F. Eck and B. Banerjee, (1999). Characterization of the reflectance anisotropy of the three boreal forest canopies in Spring-Summer. Remote Sensing of Environment, 67, 205-229.
- ESA, 2001, Proceedings of the DAISEX final results workshop, ESA SP-499, ESA Publication Division, ESTEC, The Netherlands, July 2001 (277 pp).
- García-Haro F.J., F. Camacho-de Coca, and J. Meliá (2002). Retrieval of biophysical parameters using directional spectral mixture analysis. Proceeding of the 1st International symposium on Recent advances in quantitative remote sensing (this issue).
- García-Haro, F.J., S. Sommer and T. Kemper (2002). Variable multiple endmember spectral mixture analysis (VMESMA): a high performance computing and environment analysis tool, Remote Sensing of Environment, submitted.
- Kimes, D. S. (1983), Dynamics of directional reflectance factor distributions for vegetation canopies. *Applied optics*. 22:1364-1372.
- Knyazikhin, Y., J.V. Martonchik, R.B. Myneni, D.J. Diner, and S.W. Running (1998). Synergistic algorithm for estimating vegetation canopy leaf area index and fraction of absorbed photosynthetically active radiation from MODIS and MISR data. Journal of Geophysical Research, vol. 103, NO. D24, 32257-32275.
- Lacaze, R. J.M. Chen, J.L. Roujean and S.G. Leblanc (2002). Retrieval of vegetation clumping index using hot spot signatures measured by POLDER instrument. Remote Sensing of Environment, 79, 84-95.
- Leroy, M, O. Hatecoeur, F. Ponchaut, L. Alonso-Chorda, and J. Moreno, 2001, The airborne POLDER data in the DAISEX'99 campaign, ESA SP-499, ESA Publication Division, ESTEC, The Netherlands, July 2001, 13-22.
- Sandmeier, S., C. Müller, B. Hosgood, and G. Andreoli, (1998). Physical mechanisms in Hyperspectral BRDF Data of Grass and Watercress. Remote Sensing of Environment, 66: 222-223.

Distinguishing cover crops and bare soils in olive groves using remote sensing

Peña-Barragán J.M.*, López-Granados F.*, Atenciano S.*, Jurado-Expósito M.*, González-Andújar J.L.*, Sánchez-de la Orden M.***, García-Ferrer A.**, García-Torres L.*

* *Institute for Sustainable Agriculture, CSIC . Alameda del Obispo, s/n. 14080, Córdoba.*

** *Remote Sensing Department, University of Cordoba. Av.Menéndez Pidal, s/n. 14004, Córdoba.*

Email: pa2pebaj@uco.es; cs9logrf@uco.es; satenciano@cap.junta-andalucia.es; cs9disaj@uco.es; cs1goanj@uco.es; ig1saorm@uco.es; ir1gapoa@uco.es; m1lgatol@uco.es;

ABSTRACT - *This work aims to determine cover crop, bare soil and tree areas in olive (*Olea europea* L.) groves as affected by the season when images were taken, types of aerial photographs and estimated vegetation indexes. Conventional-colour and colour-infrared (CIR) aerial photographs were taken in spring and summer on three olive farms of about 75 to 100 ha, from a plane at 1525 m above the ground. Resulting images of an average scale of 1:10,000 were digitized, georeferenced and processed. Twenty-eight selected vegetation indexes were essayed for soil uses discrimination. Early summer is the most suitable time to enhance discrimination in between cover crops and olive trees since under Mediterranean conditions cover crop is desiccated and not consistently degraded yet. Conventional-colour photography was more adequate and economic material to discriminate the mentioned soil uses than colour-infrared photography. At spring, the blue (B, 400-500 nm) and red (R, 600-700 nm) wavelength reflectivity's and the vegetation index $(B+G+R)/3$, where G is green wavelength (500-600 nm), only showed good discrimination in between bare soil and vegetation, but not in between cover crop and olive trees. At summer, several vegetation indexes from conventional-colour photographs such as B/R , $B/(G+R)$ or $B/(B+G+R)$ and $R/(B+G)$ or $R/(B+G+R)$ satisfactorily discriminated cover crops and olive trees from the other soil uses, respectively.*

1 INTRODUCTION

Olive (*Olea europea* L.) crop is very important in the Mediterranean basin with a grown area of about 12.4-M ha, of which 2.4-M ha are in Spain (Barranco *et al.*, 2001). Traditionally, olive trees are separated 10 to 12 m each other and soil management is mainly based on plough-, disk- and harrow- tillage operations, which drastically alter the top layer of the soil. Therefore, soil coverage in between olive trees used to be very low throughout the year and consequently soil erosion very pronounced. For example, soil erosion rates from 40 to 80 tons ha⁻¹ year⁻¹ has been repeatedly reported (Laguna, 1989; Pastor-Muñoz and Castro-Rodríguez, 1997). To overcome this environmentally unacceptable situation a drastic change in olive groves soil management has been developed, globally named as conservation techniques. These mainly consist to alter the little the possible the natural soil profile, protecting it permanently with cover crop or crop residues (García-Torres, 1999, 2001). In olive groves, cover crops are about 4 to 6 m wide, placed in between tree rows. Generally, they consist in sowing grassy and legume seeds in September, growing throughout autumn and winter, and terminated / desiccated early spring by applying a non-residual systemic herbicide. So that, competition for water and nutrients in between cover crops and olive trees is

prevented throughout the rest of the spring and summer.

Over the past 30 years there has been increased emphasis on the potential utility of using remote sensing techniques to obtain real-time assessments of the agricultural landscape (Hatfield and Pinter, 1993), and particularly to distinguish and assess plants and crops. This was carried out using photographs (Everitt and Villarreal, 1987; Everitt *et al.*, 1992, 1993, 1994; Everitt and Deloach, 1990; Brown and Steckler, 1995), video imageries (Everitt *et al.*, 1992, 1993, 1994), digital sensors (Lamb and Weedon, 1998; Bajwa and Tian, 2001; Yang *et al.*, 2001), radar data (Hoozeboom, 1983; Chakraborty *et al.*, 1997), or satellite images (Oetter *et al.*, 2000; Everitt *et al.*, 1993; Bauer *et al.*, 1978). The purpose of these techniques varied; for example, in Menges *et al.* (1985) was to assess weeds from orange trees by using colour-infrared photography; in Peñuelas *et al.* (1995, 1997) to assess the reflectance of Mediterranean trees.

Recently, EU and European national administrations has developed regulations to subsidy the implementation of cover crops in between olive trees rows (EU Directives 1257 and 1259/ 1999; Spanish Real Decree 4/ 2001). The estimation of cover crop soil coverage on the ground is time-consuming, and consequently not feasible economically. Similarly, vehicle-mounted systems and real-time systems cover relatively small areas and are expensive when

compared with remote sensing systems (Bajwa and Tian, 2001). Therefore, the general objective of this study was to establish, using remote sensing techniques, a rapid, accurate and economic methodology to assess cover crops in olive, at a farm and regional level, for the follow-up of the previously mentioned administrative initiatives. Specific objectives were to determine: 1) the time of the year when aerial photographs should be taken; 2) types of photographic material; 3) selected vegetation indexes.

2 MATERIAL AND METHODS

2.1 Photography and Scanning

Conventional-colour (400–700 nm) and colour-infrared (700–1100 nm) aerial photographs were taken in spring and summer 2000 and 2001 on three olive farms of about 75 to 100 ha each, namely La Cubana, Cortijo del Rey and Matallana, located in Southern Spain. Cover crop species composition was predominantly made of *Hordeum murinum* and *Lolium*

rigidum in La Cubana, *Avena sativa* in Cortijo del Rey and *Hordeum sativum* and *Avena sativa* in Matallana, established for over 4 to 6 years in any location.

Photographs were taken from a turboprop twin-engine plane CESSNA 310 R, provided with an automatic pilot to handle the photographic equipment. The camera used was WILD RC-10, provided with an objective AF/15 UAG at a focal distance of 153.66 mm, and with a film AGFA AVIPHOT COLOUR H-100 PE-1. Average flight height was 1,525 meters over the land resulting photographs of average scale of 1:10,000. The images were taken with a longitudinal recovering between photographic prints of the 60%. Film was processed in the laboratory through automatic system COLENTA.

Spring images detected the cover crops with the typical green colour of the vegetative growing phase (Figure 1A), while in the summer picture cover crops were yellow-like colour due to have been desiccated previously (mid-April; Figure 1B).

Figure 1. (A) Cover crop with the typical green colour of the vegetative growing phase (in early Spring before herbicide use). (B) Cover crop with the yellow-like colour due to having been desiccated (after herbicide use).



Figure 1.A.



Figure 1.B.

The selected farms were visited near when photographs were taking in order to determine the cover crop vegetative development and odd land uses that could be clearly distinguished in the images. In addition, over 30 ground control points (GCPs) in each farm were georeferenced using the sub-meter differential GPS TRIMBLE PRO-XRS provided with TDC-1 unit, to fit the geographical coordinates of the images, as suggested by (Bajwa and Tian, 2001). Selected photographic prints were digitized using the Hewlett Packard Scan Jet 4C scanner taking 635 points per inch (PPI), resulting pixels of 40 cm x 40 cm, as the average scale of the photographs was of 1:10,000.

The method followed was similar to that developed by Andreasen *et al.* (1997), Everitt and Villarreal (1987), and Everitt *et al.* (1990, 1994). ILWIS 2.2 software was used for images processing. The digitized photographs were georeferenced by rectifying to the Universal Transverse Mercator (UTM).

2.2 Vegetation indexes used

Each pixel was characterized by a certain waveband reflectance or vegetation index value (DL or DV, from 0 to 255). Vegetation indexes are made up by waveband reflectance values combinations to enhance

soil uses discrimination while minimizing solar radiance and soil background effects (Jackson and Huete, 1991). Some vegetation indexes have been commonly applied by many authors, such as Normalized Difference Vegetation Index $NDVI = (NIR - R) / (NIR + R)$ (Rouse *et al.*, 1973; Jackson and Huete, 1991; Lamb and Weedon, 1998; Yang *et al.*, 2001), Ratio Vegetation Index $RVI = NIR / R$ (Tucker, 1979; Jackson and Huete, 1991; Everitt and Villarreal, 1987; Everitt *et al.*, 1993; Bajwa and Tian, 2001; Yang *et al.*, 2001), Simple Ratio Pigment Index $SRPI = B / R$ (Peñuelas *et al.*, 1995), $NG = NIR / G$ (Yang *et al.*, 2001), $RB = R / B$ (Everitt and Villarreal, 1987), $g = G / (B + G + R)$ (Andreasen *et al.*, 1997), Intensity $I = (B + G + R) / 3$ (Myers and Allen, 1968; Chuvieco, 1996).

In addition, in this work another new vegetation indexes ratios have been studied up to fourteen. For example, in conventional-colour photographs as following, B , G , R , B/R , G/B , R/G , $B/(G+R)$, $G/(B+R)$, $R/(B+G)$, $B/(B+G+R)$, $G/(B+G+R)$, $R/(B+G+R)$, $(B+G+R)/3$ and $(G-R)/(G+R)$, where B , G and R are the blue, green and red reflectivity values, respectively. Similarly, other fourteen in colour-infrared photographs: G , R , NIR , NIR/R , NIR/G , R/G , $NIR/(G+R)$, $R/(G+NIR)$, $G/(R+NIR)$, $NIR/(G+R+NIR)$, $R/(G+R+NIR)$, $G/(G+R+NIR)$, $(G+R+NIR)/3$ and $(NIR-R)/(NIR+R)$, where NIR is the near-infrared reflectivity digital value.

2.3 Vegetation indexes selection

The following selection procedure was performed:

a) Visual pre-selection at training plots (TP) of 500 x 500 pixels (about 200 x 200 m; Figure 2A and 2B). For each vegetation index, three TP were established by image cutting in several representative zones of each farms, testing which soil uses could be clearly discriminated. Selected indexes achieved good discrimination of at least one soil use in the three TP of each farm (Figure 2C); otherwise, the indexes were not considered for further studies (Figure 2D).

b) Numerical analysis at training subplots (TS) of 100 x 100 pixels (about 40 x 40 m). This was achieved in order to quantify the percentage of coincidence in

between the pixels classified as olive trees, cover crop and bare soils in the vegetative index and in the Ground Truth images. This was carried out in three TS obtained by image cutting in selected zones of each farm with different cover development. Previously, a Ground Truth Map (GTM) was edited using the computer, the boundaries in between soil uses were manually drawn over the original TS, and then each soil uses surface were converted into polygon-format and lately into raster-format map (Figure 2E and 2F), similarly as achieved by Lamb and Weedon (1998).

The GTM showed the soil uses of the original image, interpreted as the field reality created by the photointerpreter, and was used to check or verify index classification. On the other hand, each vegetation index map (VIM) classifies the soil uses by grouping the digital values (DV) according to the ranges, which characterize each soil use. To accomplish it, boundary digital values (BDV) were established according to the image analysis of the histogram values range of each soil use. This histogram thresholding technique separated crops and soil reasonably well, and were previously used by other authors (Jansen *et al.*, 1993; Andreasen *et al.*, 1997; Lamb and Weedon, 1998). Once the BDV are determined for each VIM, the pixels are grouped by the computer according the soil uses, creating a Slicing Classified Vegetation Index Map (SCVIM) (ILWIS, 1997). Selection of the BDV was based on an iterative process of measuring the Overall Accuracy (OA) (Congalton, 1991) of the SCVIM generated for all possible values of BDV between its ranges. The optimum BDV in each VIM was then selected as the one yielding the highest OA, and the corresponding SCVIM was used in the subsequent accuracy analyst, such as carried out by Lamb and Weedon (1998). So that, the confusion matrix (CM) (ILWIS, 1997) of each vegetative index was estimated in each TS, similarly as achieved by others authors (Menges *et al.*, 1985; Chuvieco, 1996; Chakraborty *et al.*, 1997; Lamb and Weedon, 1998; Oetter *et al.*, 2000).

A total of 99 different vegetative index images were analyzed and their CM calculated. Finally OA was estimated for each SCVIM. The final selection of indexes was based on the corresponding OA values for each soil use.

Figure 2. (A) and (B) Views of training (TP, 500 x 500 pixels) and sub-training plots (SP, 100 x 100 pixels) at Cortijo del Rey farm in summer and spring 2000, respectively. (C) and (D) Visually acceptable and rejected soil uses discrimination by the vegetation indexes B/(B+G+R) and B/R at Cortijo del Rey farm, in summer and spring 2000, respectively. (E) “Ground Truth Map” (GTM) TS manual vectorization of soil uses boundaries; and (F) Edition and rasterization of the GTM, where blue is olive tree, yellow is bare soil and red is cover crop.

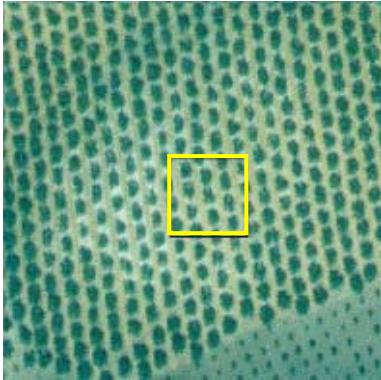


Fig. 2.A

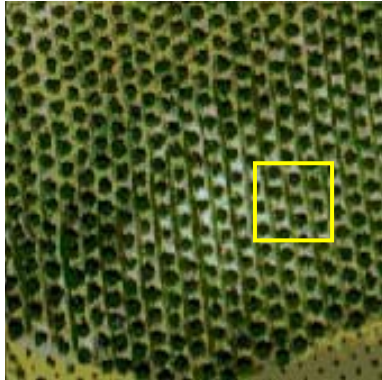


Fig. 2.B

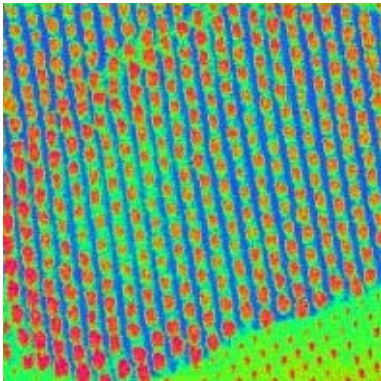


Fig. 2.C

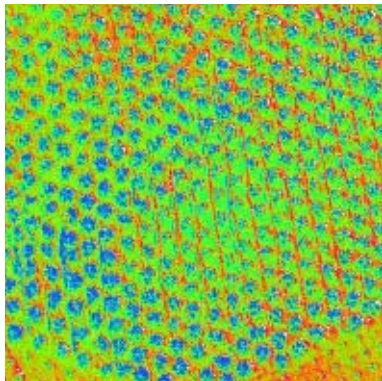


Fig. 2.D



Fig. 2.E

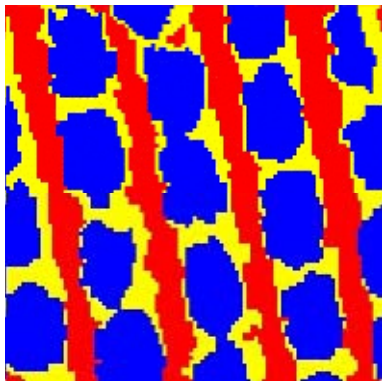


Fig. 2.F

3 RESULTS AND DISCUSSION

3.1 Season of the year

From conventional-colour photographs taken in summer three indexes were selected for cover crop discrimination and none from the same type of photographs taken in spring (Table 1). It should be pointed out that under Mediterranean conditions cover crops in olive groves are usually terminated by application of post-emergence non-residual herbicides

to prevent soil water competition with the olive groves (García-Torres, 2001) and that above soil cover biomass is decreasing since the time when it was desiccated onward. Therefore, in early summer cover crop exhibit high biomass completely desiccated with a typical yellow-like colour which enhance its discrimination with olive trees and the bare soil. Everitt *et al.* (1990, 1993) got similar results in Chinese Tamarisk (*Tamarix chinensis*) and in Shin Oak (*Quercus havardii*) groves.

Table 1. Overall Accuracy (OA) of visually pre-selected vegetation indexes

Season and Type of Photographs	Vegetation Index	Soil Use Discriminated	Farm			
			La Cubana	Cortijo del Rey	Matallana	Average
Summer 2000 Conventional Colour	R/(B+G)	Olive tree	94.1 ± 1.0	92.6 ± 0.8	90.7 ± 0.5	92.5 ± 1.7
	R/(B+G+R)	Olive tree	95.1 ± 0.9	91.5 ± 0.9	90.6 ± 0.8	92.4 ± 2.4
	B/R	Cover crop	81.9 ± 1.6	91.9 ± 1.4	83.8 ± 1.1	85.9 ± 5.3
	B/(G+R)	Cover crop	79.9 ± 1.9	91.8 ± 1.4	83.1 ± 1.1	84.9 ± 6.2
	B/(B+G+R)	Cover crop	80.4 ± 1.8	91.6 ± 1.9	82.6 ± 1.2	84.9 ± 5.9
Summer 2000 Colour Infrared	(G+R+NIR)/3	Cover crop	81.8 ± 2.6	82.1 ± 1.5	73.1 ± 1.2	79.0 ± 5.1
	G/(R+NIR)	Bare soil	74.7 ± 2.7	85.0 ± 1.6	64.5 ± 4.0	74.7 ± 10.3
	G/(G+R+NIR)	Bare soil	74.9 ± 3.4	84.5 ± 2.1	66.8 ± 4.2	75.4 ± 8.9
Spring 2001 Conventional Colour	(B+G+R)/3	Bare soil	83.5 ± 1.0	88.5 ± 1.9	87.9 ± 0.5	86.6 ± 2.7
	B	Bare soil	82.5 ± 0.9	87.5 ± 0.2	87.0 ± 0.7	85.7 ± 2.8
	R	Bare soil	80.5 ± 2.0	87.1 ± 2.9	85.7 ± 1.7	83.4 ± 3.5

3.2 Types of photographic material

In conventional-colour photographs taken in summer and spring 8 vegetation indexes out of a total of 14, were selected to discriminate at least one soil used in the three tested farms (Table 1). On the other hand, in colour-infrared photographs only three of the 14 vegetation indexes tested showed a visually acceptable discrimination in the TP; however none of these indexes shown consistency results from the numerical analysis. Consequently, it can be concluded that conventional-colour photography was more efficient and economic material to discriminate the mentioned soil uses than colour-infrared photography. This result is not in agreement with some authors such as Zwiggelaar (1998) that reported that CIR photograph was the most adequate to discriminate crops in general, or with Menges *et al.* (1985) that concluded that near-infrared was the most adequate band to distinguish weeds in crops. At the contrary, Everitt *et al.* (1990, 1992) obtained good results using conventional-colour to distinguish Chinese Tamarisk (1990) and Common (*Isocoma coronopifolia*) and Drummond Goldenweed (*Isocoma drummondii*) (1992).

3.3 Vegetation Indexes Selected

The indexes visually pre-selected and its CM values are shown in Table 1. From the conventional-colour photographs taken in summer, the vegetation indexes B/R, B/(G+R) and B/(B+G+R), out of a total of 14, were visually pre-selected to discriminated cover crop from the other soil uses. The averaged overall accuracy of these indexes were 85.9%, 84.9%, and 84.9%, respectively (Table 1). The index B/R showed slightly higher discrimination power for cover crop than the indexes B/(G+R) and B/(B+G+R). Overall accuracy of B/R for cover crop discrimination was 81.9%, 91.9% and 83.8% for La Cubana, Cortijo del Rey and Matallana, respectively (Table 1). Similarly, with the same type of photography and time of the year the indexes R/(B+G) and R/(B+G+R) discriminated olive crop from the others soil uses with an averaged overall accuracy of 92.5% and 92.4%, respectively. However, none of the 14 indexes tested was adequate for bare soil area determination in the summer, in some cases overestimating the occurrence of this soil use over 135% (greater coincidence than 135%). It should be pointed out that vegetation indexes made up blue band as dividend, generally, are the most suitable cover crop discrimination whereas those which the dividend is red band discriminated well olive tree.

The index B, R and (B+G+R)/3 were selected in conventional-colour photographs taken in spring for bare soil discrimination, with an averaged overall accuracy of 85.7%, 84.4% and 86.6%, respectively (Table 1). Furthermore, the index (B+G+R)/3 showed better discrimination of bare soil than the index B and R, with an OA of 83.5%, 88.5% and 87.9% in La Cubana, Cortijo del Rey and Matallana, respectively. Slight variation in the results can be attributed to the drawing of the overlaying map, which is carried out by the photointerpreters defining subjective boundary lines between soil uses. Other differences can also be attributed to the computer classification technique that is based on discrete spectral classes, wherein a decision is made concerning each pixel (Everitt *et al.*, 1994).

From colour-infrared at summer three vegetation indexes were first visually selected, namely (G+R+NIR)/3 for cover crop discrimination, and G/(R+NIR) and G/(G+R+NIR) for bare soil discrimination (Table 1). However, their averaged overall accuracy of any of these indexes were 79.0% 74.7% and 75.4%, respectively, and therefore comparatively lower than those selected for the same soil uses discrimination with conventional-colour. Therefore, none of the 14 indexes tested in colour-infrared photographs distinguished adequately each soil use from the others.

In spring, cover crop is actively growing, exhibiting an intense green colour similar to the olive trees, and therefore both soil uses can not be discriminated each other. Nevertheless, the estimation from conventional-colour photographs taken in spring of bare soil area (BSA) of a farm could be useful if olive trees area (OTA) was also known from previous determination. For example, OTA can be adequately estimated in summer photographs, which could be taken the previous year. The subtraction from the total area of BSA and OTA would result in the cover crop area (CCA).

4 CONCLUSIONS AND FINAL COMMENTS

In this study, airborne conventional-colour and colour-infrared photographs were taken in spring and summer, four spectral bands (blue, green, red and near-infrared) of each image processed and a total of 28 vegetation indexes defined. At summer, when cover crops are desiccated, exhibiting a yellow-like colour, conventional-colour photographs allow the assessment of cover crop areas using selected vegetation indexes, such as B/R, B/(G+R) or B/(B+G+R), with an accuracy of over 85%. However, colour-infrared did not adequately discriminate cover crop from olive grove. At spring, when cover crops are actively growing and exhibiting a green colour, only vegetation (olive tree and cover crop) could be discriminated from bare soil particularly by the index

B+G+R/3. However, at spring it was not feasibly the determination of cover crop areas separately from olive trees.

The use of near-infrared band is not recommended since it did not enhanced the discrimination in between the soil uses considered as compared with the visible spectrum bands. This can be considered an economic advantage to perform this works at high scale, since colour-infrared photographs are considerably more expensive and of more complicated development and maintenance than conventional-colour photographs.

It is expected in the coming years a consistent development of the Cover Crop Program in Perennial Crops, as part of the Agri-Environmental Measures subsidized by the EU and National administrations. Within these administrative programs the verification of the cover crop in selected/ sorted farms is needed. The results herein obtained can be considered very acceptable for implementing these remote-sensing techniques as an administrative tool for the following up of cover crops in olive farms and other tree groves under Mediterranean conditions. This would substitute the time-consuming and subjective observations from on-ground-farm visits. Furthermore, the following up the mentioned administrative program in large regions, i.e. Andalusia (Southern Spain), with aerial photographs just taken on a reduced number of selected/ sorted farms, is currently more economical and easy to handle than using satellite images. This is the case of the Quick Bird satellite, with spatial resolution of about 0.6 m but currently providing images for areas of about 64 km² or larger at very high cost.

5 ACKNOWLEDGMENT

This research was partly supported by the Spanish Ministry of Science and Technology (R + D Project AGL2001-2808), the Department of Agriculture and Fishery of Andalusian Government and the Spanish Association for Conservation Agriculture.

6 REFERENCES

- Andreasen, C., Rudemo M., and Sevestre, S., 1997, Assessment of weed density at an early stage by use of image processing. *Weed Research*, **37**, 5–18.
- Barranco, D., Fernández-Escobar, R., and Rallo, L., 2001, *El Cultivo del Olivo* (Madrid: Mundi-Prensa).
- Brown, R. B., and Steckler, J.-P. G. A., 1995, Prescription maps for spatially variable herbicide application in no-till corn. *Transactions of the ASAE*, **38**, 1659–1666.

- Bajwa, S. G., and Tian, L. F., 2001, Aerial CIR remote sensing for weed density mapping in a soybean field. *Transactions of the ASAE*, **44**, 1965–1974.
- Bauer, M. F., Hixson, M. M., Davis, B. J., and Etheridge, J. B., 1978, Area estimation of crops by digital analysis of Landsat data. *Photogrammetric Engineering and Remote Sensing*, **44**, 1033–1043.
- Chakraborty, M., Panigraphy, S., and Sharma, S. A., 1997, Discrimination of rice crop grown under different cultural practices using temporal ERS-1 synthetic aperture radar data. *ISPRS Journal of Photogrammetry and Remote Sensing*, **52**, 183–191.
- Chuvieco, E., 1996, Fundamentos de teledetección espacial (Madrid: Rialp).
- Congalton, R. G., 1991, A review of assessing the accuracy of classifications of remotely sensed data. *Remote Sensing of Environment*, **37**, 35–46.
- Everitt, J. H., and Villarreal, R., 1987, Detecting Huisache (*Acacia farnesiana*) and Mexican Palo-verde (*Parkinsonia aculeata*) by aerial photography. *Weed Science*, **35**, 427–432.
- Everitt, J. H., and Deloach, C. J., 1990, Remote sensing of Chinese Tamarisk (*Tamarix chinensis*) and associated vegetation. *Weed Science*, **38**, 273–278.
- Everitt, J. H., Alaniz, M. A., Escobar, D. E., and Davis, M. R., 1992, Using remote sensing to distinguish Common (*Isocoma coronopifolia*) and Drummond Goldenweed (*Isocoma drummondii*). *Weed Science*, **40**, 621–628.
- Everitt, J. H., Escobar, D. E., Villarreal, R., Alaniz, M. A., and Davis, M. R., 1993, Canopy light reflectance and remote sensing of Shin Oak (*Quercus havardii*) and associated vegetation. *Weed Science*, **41**, 291–297.
- Everitt, J. H., Richerson, J. V., Alaniz, M. A., Escobar, D. E., Villarreal, R., and Davis, M. R., 1994, Light reflectance characteristics and remote sensing of Big Bend Loco (*Astragalus mollissimus* var. *earlei*) and Wooton Loco (*Astragalus wootonii*). *Weed Science*, **42**, 115–122.
- García-Torres, L. (editor), 1999, Conservation Agriculture in Europe: Environmental, Economic and EU policy aspects (Brussels: European Conservation Agriculture Federation (ECAF)).
- García-Torres, L. (editor), 2001, Agricultura de conservación en el olivar: cubiertas vegetales (Cordoba: Asociación Española Agricultura de Conservación / Suelos Vivos (AEAC/SV)).
- Hatfield, J. L., and Pinter-Jr, P. J., 1993, Remote sensing for crop protection. *Crop Protection*, **12**, 403–413.
- Hoogeboom, P., 1983, Classification of agricultural crops in radar images. *IEEE Transactions of Geoscience and Remote Sensing*, **23**, 329–336.
- ILWIS Development, ITC., 1997, ILWIS 2.1. for Windows Reference Guide (Enschede: The International Institute for Aerospace Survey and Earth Sciences (ITC)).
- Jackson, R. D., and Huete, A. R., 1991, Interpreting vegetation indices. *Preventive Veterinary Medicine*, **11**, 185–200.
- Jansen, R. C., Reinink, K., and Van der Heijden, G. W. A. M., 1993, Analysis of grey level histograms by using statistical methods for mixtures of distribution. *Pattern Recognition Letters*, **14**, 585–590.
- Laguna, A., 1989, Estudio cuantitativo de la erosión del suelo. Ph. D. Thesis (Cordoba: Department of Agronomy, University of Cordoba).
- Lamb, D. W., and Weedon, M. M., 1998, Evaluating the accuracy of mapping weeds in fallow fields using airborne digital imaging: *Panicum effusum* in Oilseed Rape stubble. *Weed Research*, **38**, 443–451.
- Menges, R. M., Nixon, P. R., and Richardson, A. J., 1985, Light reflectance and remote sensing of weeds in agronomic and horticultural crops. *Weed Science*, **33**, 569–581.
- Myers, V. L., and Allen, W. A., 1968, Electrooptical remote sensing methods as nondestructive testing and measuring techniques in agriculture. *Applied Optics*, **7**, 1819–1838.
- Oetter, D.R., Cohen, W. B., Berterretche, M., Maersperger, and T. K., Kennedy, R. E., 2000, Land cover mapping in an agricultural setting using multiseasonal Thematic Mapper data. *Remote Sensing of Environment*, **76**, 139–155.
- Pastor-Muñoz, M., and Castro-Rodríguez, J., 1997, Sistemas de manejo de suelo en el olivar, In Agricultura de Conservación: Fundamentos Agronómicos, Medioambientales y Económicos, edited by L. García-Torres and P. González-Fernández (Cordoba: Asociación Española Agricultura de Conservación / Suelos Vivos (AEAC/SV), pp. 289–308.
- Peñuelas, J., Filella, I., Lloret, P., Muños, F., and Vilajeliu, M., 1995, Reflectance assesment of mite effects on apple trees. *International Journal of Remote Sensing*, **16**, 2727–2733.

- Peñuelas, J., Llusia, J., Piñol, J., and Filella, I., 1997, Photochemical reflectance index and leaf photosynthetic radiation-use-efficiency assessment in mediterranean trees. *International Journal of Remote Sensing*, **18**, 2863–2868.
- Rouse, J. W., Haas, R. H., Schell, J. A., and Deering, D. W., 1973, Monitoring vegetation systems in the Great Plains with ERTS, Third ERTS Symposium, Vol. I.
- Tucker, C. J., 1979, Red and photographic infrared linear combinations for monitoring vegetation. *Remote Sensing of Environment*, **8**, 127–150.
- Yang, C., Bradford, J. M., and Wiegand, C. L., 2001, Airborne multispectral imagery for mapping variable growing conditions and yields of cotton, grain sorghum, and corn. *Transactions of the ASAE*, **44**, 1983–1994.
- Zwiggelaar, R., 1998, A review of spectral properties of plants and their potential use for crop/ weed discrimination in row-crops. *Crop Protection*, **17**, 189–206.

2. SINERGIA/ SINERGY

On Estimation of Turbulent Heat Fluxes and Evaporation with Radiometric Measurements: Past, Present and Future

Z. Bob Su

Wageningen University and Research Centre, Alterra Green World Research, P.O. Box 47, 6700 AA Wageningen, The Netherlands

E-mail: B.Su@alterra.wag-ur.nl

ABSTRACT *Turbulent heat fluxes and evaporation are among the most important processes in land-atmosphere exchanges. Hence accurate estimation of these fluxes at large scales is imperative for research and applications in areas ranging from numerical weather forecast, climate research, water resources management, sustainable agricultural production and ecological preservation. Quantitative remote sensing is probably the only efficient and economically viable technology to provide regional to global radiometric observations of several physical quantities that are relevant to the estimation of these fluxes. This paper examines the physical principles underlying the turbulent heat fluxes and evaporation, along with exploring the difficulties and possibilities for estimation of these fluxes using radiometric measurements. Past efforts, recent progresses are reviewed and future research needs are identified. In particular, the Surface Energy Balance System (SEBS) recently developed in Wageningen are introduced and its strengths and weakness are analysed in view of future space-borne sensor systems. Several applications derived on the basis of SBES, including estimation of turbulent heat fluxes and actual evaporation, estimation of relative soil moisture and drought monitoring are discussed.*

INTRODUCTION

The international environmental sciences communities have seen a very rapid evolution over the last ten years. A new global, interdisciplinary science of the Earth System has emerged at the interface of science and policy development. Both the IGBP and the WCRP are in the process of reviewing past achievements and developing a new scientific strategy for the next decade. The need to bridge in a more focused way the gap between earth sciences and sustainable management of the terrestrial environment is already emerging as an overall priority. In this regard, understanding the interactions between terrestrial ecosystems and the atmosphere is a central requirement to address issues such as climate change and environmental degradation. Extensive scientific investigations over the past decades have demonstrated beyond doubt that the biosphere is tightly coupled to its physical environment, over a wide range of space and time scales, and the sensitivity of atmospheric circulation to land surface properties and to their variability in space and time is well documented in literature. Since turbulent heat fluxes and evaporation are among the most important processes in land-atmosphere exchanges, accurate estimation of these fluxes at large scales is imperative for research and applications in areas ranging from numerical weather forecast, climate research, water resources management, sustainable agricultural production and ecological preservation. Such importance may be viewed in the following context:

In dealing with climate - land Interactions – especially in studies concerning terrestrial water, energy and carbon cycles, models are often used to assist urgent policy decisions on environmental issues – but we must ask the following questions before the results derived from such models being used for further decision making processes:

- Is the interaction with a dynamic terrestrial biosphere in global models properly understood and described so that our forecasts of the long term evolution of climate are reliable ?
- Are processes at scales from global to local properly linked so that our assessment of the impacts of climate variability on land and water resources is reliable and scenarios on the evolution of the terrestrial biosphere are realistic ??
- Are the political decisions based on the current model simulations/predictions/scenarios well founded ???

To be able to answer these questions, there is a critical need to understand the feedback between the land surface and the atmosphere at various scales. As shown by recent works, the land component of the climate system must be viewed as an active participant in the coupled system, rather than a passive recipient of atmospheric forcing. In this view, accurate representation of land surface dynamics is more important than it had been thought previously. It has also been suggested that in the 2001 IPCC report, the role of land surface in modifying the climate has not been adequately considered and the effects of land-cover change on climate may be comparable to, and, perhaps larger than, the effects on climate due to

changes in atmospheric composition. The current level of scientific understanding in land-atmosphere interactions has been characterized as “very low”. Further, the current parameterizations of land processes in all Earth system models are based on simple conceptions that are representative, at best, for homogeneous flat land surfaces and few observation data sets over complex terrain exist to allow integrated long-term off-line testing that is essential to evaluate land surface parameterizations in climate models.

Currently, it has been recognized that observations of terrestrial carbon-cycle dynamics are a fundamental component of attempts to understand the global carbon cycle, which requires a combination of measurements and models, integrating observations (Earth observation and in situ), models (diagnostic and predictive), process and manipulative experiments and case studies in a ‘multiple constraint’ synthesis approach. Abilities to estimate turbulent heat fluxes and evaporation using radiometric measurements from satellite sensors will help to resolve the above mentioned uncertainties and difficulties.

Several processes at the land surfaces can be distinguished, including exchanges of radiation, heat, water and carbon and other gasses. More specifically we may consider: solar radiation, thermal radiation, sensible heat flux, latent heat flux including phase change, soil heat flux and advection, precipitation, water and vapor transport in soil, as well as biochemical processes in soil and canopy (see Fig. 1). The driving forces of these processes are solar radiation and wind. Since most of these processes vary continuously in space and time from local to global scale and from seconds to decades and centuries, their adequate quantification also requires measurements with corresponding spatial-temporal coverage. It is in this aspect that remote sensing can play an essential role. In the following, we will briefly review some progress made in estimation of turbulent heat fluxes and evaporation.

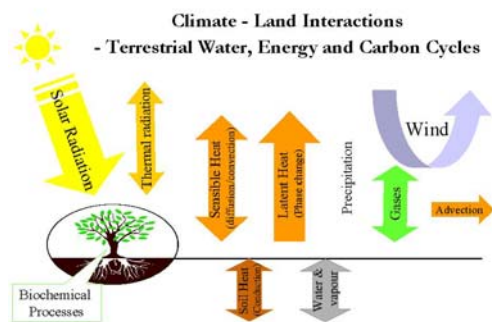


Fig. 1. Major land surface processes

A BRIEF HISTORY IN REMOTE SENSING OF TURBULENT HEAT FLUXES AND EVAPORATION

The estimation of atmospheric turbulent fluxes (or evapotranspiration when latent heat flux is expressed in water depth) at the land surface has long been recognised as the most important process in the determination of the exchanges of energy and mass among hydrosphere, atmosphere and biosphere (e.g. Bowen, 1926; Penman, 1948; Monteith, 1965; Priestly and Taylor, 1972; Brutsaert, 1982; Morton, 1983; Famiglietti and Wood, 1994; Sellers et al., 1996; Su and Menenti, 1999; Su and Jacobs, 2001). Conventional techniques that employ point measurements to estimate the components of energy balance are only representative of local scales and cannot be extended to large areas because of the heterogeneity of land surface and the dynamic nature of heat transfer processes. Remote sensing is probably the only technique which can provide representative measurements of several relevant physical parameters at scales from a point to a continent. Techniques using remote sensing information to estimate atmospheric turbulent fluxes are therefore essential when dealing with processes that can not be represented only by point measurements.

In general, we can distinguish two types of methodologies: analytical versus (semi-) empirical, the former takes into consideration detailed physical processes at the scale of interest but usually involves complicated relationships and demands various input variables including those which can be observed directly by radiometric measurements and meteorological variables at a proper reference height, while the later tries to employ empirical relationships and data available chiefly from remote sensing observations. Representative works of the first type include, among others, Jackson et al. (1981, 1988) that derived the so-called Crop Water Stress Index (CWSI) by applying the Penman-Monteith equation to radiometric measurements (Monteith, 1981); Choudhury et al. (1986) and Kustas (1990); Kalma and Jupp (1991) who utilized the dual-source model proposed by Shuttleworth and Wallace (1985) which by itself was an extension of the Penman-Monteith approach to take into account soil and canopy explicitly; Moran et al. (1994) further extended the CWSI approach to partial canopies (the so-called trapezoid-method); More recent work in the same line are those of Chehbouni et al. (2001) and Boegh et al. (2002) who thoroughly examined the CWSI concept using detailed field measurements collected in Denmark.

Other relevant works but of different concepts are those of Chanzy et al. (1995) for soil evaporation and Norman et al. (1995) and Anderson et al. (1997)

proposing a new type of dual-source model aiming at utilizing directional radiometric measurements. More recently Kustas and Norman (1999) applied actual soil and vegetation component temperatures to the same dual-source model but did not obtain better results than using only composite temperature without changing the applied Priestly and Taylor coefficient to a much high value. Efforts related to combined modeling and data assimilation have been reported by Olioso (1992) and Olioso et al. (2002) and will be not reviewed explicitly here.

As far as (semi-) empirical approaches are concerned, the earlier works of Jackson et al. (1977) and Seguin and Itier (1983) are representative and many more recent works still follow the same type of approaches. In addition, Menenti (1993), Carlson et al. (1995), Kustas and Norman (1996) and Zhang (1996) have provided excellent reviews to the then up-to-date approaches relative to their times of publications. Similarly the progress made in Wageningen, the Netherlands can also be mapped in the analytical versus (semi) empirical fashion.

The foundation of the analytical approaches were laid by Menenti (1984) proposing a two-layer combinational equation for a drying soil which was later shown by Menenti (1993) to be able to reduce to the Penman-Monteith combinational equation and was also shown by Stanghellini (1987) to be equally valid for a green-house canopy. In a further attempt, Menenti and Choudhury (1993) extended the CWSI concept to the so-called Surface Energy Balance Index (SEBI) approach. While the CWSI was based on surface meteorological scaling, the SEBI concept used Planetary Boundary Layer (PBL) Scaling. However the parameterization used in SEBI were limited to the then state-of-the-art concepts, namely the ratio between aerodynamic roughness and thermal dynamic roughness was taken as 10 and the stratification correction was taken as 2.9. Application of the SEBI concept to the Aral Sea by Menenti et al. (2001) revealed that the parameterization was probably not universal and caused some unexplained scatters in the results. More recently, Su (2001, 2002) have proposed the Surface Energy Balance System (SEBS) by extending the SEBI concept with a dynamic model for thermal roughness (Su et al. 2001) and the Bulk Atmospheric Similarity (BAS) theory of Brutsaert (1999) for PBL scaling and the Monin-Obukhov Atmospheric Surface Layer (ASL) similarity for surface layer scaling such that SEBS can be used for both local scaling and regional scaling providing a link for radiometric measurements and atmospheric models at various scales. Using SEBS, Jia et al. (2001) have successfully coupled large scale Numerical Weather Prediction model fields to radiometric measurements from the Along Track Scanning Radiometer (ATSR)

onboard of ERS-2. Rauwerda et al. (2002) have extended SEBS to a parallel source model and have showed significant improvement in estimated turbulent heat fluxes. On the application side, SEBS has been used to generate daily, monthly and annual evaporation in a semi-arid environment (Li, 2001) and for drought monitoring (Su et al., 2001, 2002). Another development is that of Jia et al. (2001) who have proposed a dual-source model for using component (soil and vegetation) temperatures such as those derivable from ATSR data. The scheme is similar to the Shuttleworth and Wallace (1985) dual-source model but employing the boundary resistance formulation of Stanghellini (1987) and showed much flexibility in dealing with heterogeneous surfaces.

On the empirical side, the work of Nieuwenhuis et al. (1985) was among the earliest attempts but was valid only for single crops. Later Bastiaansen (1995) proposed the Surface Energy Balance Algorithm for Land (SEBAL) that required simultaneous presence of absolute dry and wet pixels and has been used for many irrigation studies. Later on, Su et al. (1999) have made correction in SEBAL for a theoretical problem and added a scheme to include NWP fields with a up-scaling and down-scaling approach. Roerink et al. (2000) proposed a Simplified Surface Energy Balance Index (S-SEBI) by fitting dry and wet cases present in the spatial radiometric data and showed reasonable success for application to semi-arid areas.

In order to give a clear picture of the differences in various schemes encountered in turbulent heat fluxes parameterization, Fig. 2 summaries the single-source, dual-source, and parallel source schemes. The relevant atmospheric boundary layer that needs to be considered in different scaling is shown in Fig. 3.

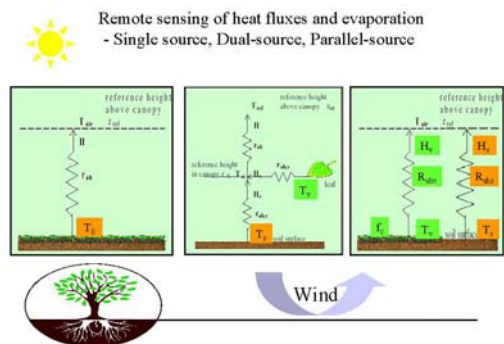


Fig. 2. Flux parameterization schemes

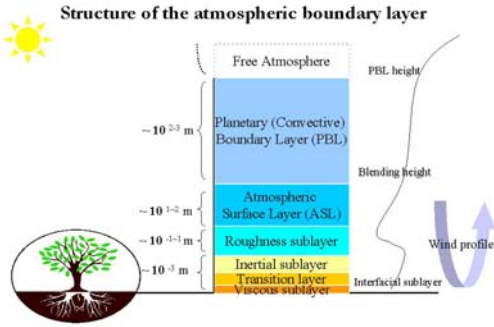


Fig. 3. Typical structure of the atmospheric boundary layer

THE SURFACE ENERGY BALANCE SYSTEM (SEBS) FOR ESTIMATION OF TURBULENT HEAT FLUXES AND EVAPORATION

In the following we will review the difficulties and the relationships between radiometric measurements and atmospheric boundary meteorological variables in estimation of turbulent heat fluxes and evaporation by means of SEBS (Su, 2001; 2002).

1) Surface energy balance terms

The surface energy balance in SEBS is written as

$$R_n = G_0 + H + \lambda E \quad (1)$$

where R_n is the net radiation, G_0 is the soil heat flux, H is the turbulent sensible heat flux, and λE is the turbulent latent heat flux (λ is the latent heat of vaporization and E is the actual evapotranspiration). The equation to calculate the net radiation is given by

$$R_n = (1 - \alpha) \cdot R_{swd} + \varepsilon \cdot R_{lwd} - \varepsilon \cdot \sigma \cdot T_0^4 \quad (2)$$

where α is the albedo, R_{swd} is the downward solar radiation, R_{lwd} is the downward longwave radiation, ε is the emissivity of the surface, σ is the Stefan-Boltzmann constant, and T_0 is the surface temperature. The equation to calculate soil heat flux is parameterized as

$$G_0 = R_n \cdot [\Gamma_c + (1 - f_c) \cdot (\Gamma_s - \Gamma_c)] \quad (3)$$

in which it is assumed that the ratio of soil heat flux to net radiation $\Gamma_c = 0.05$ for full vegetation canopy (Monteith, 1973) and $\Gamma_s = 0.315$ for bare soil (Kustas and Daughtry, 1989). An interpolation is then

performed between these limiting cases using the fractional canopy coverage, f_c .

From eqs. (1,2,3) we observe that radiometric measurements can provide measures for $\alpha, \varepsilon, T_0, f_c$.

2) Turbulent Flux terms

In SEBS the similarity theory is used to parameterize turbulent flux terms, in which a distinction is made between the Atmospheric Boundary Layer (ABL) or Planetary Boundary Layer (PBL) and the Atmospheric Surface Layer (ASL). ABL refers to the part of atmosphere that is directly influenced by the presence of the Earth's surface and responds to the surface forcings with a timescale of an hour or less, while ASL refers to usually the bottom 10% of ABL where turbulent fluxes and stress vary by less than 10% of their magnitude (Stull, 1988) but above the roughness sublayer (see Figure 3). The latter (or the interfacial layer) is the near surface thin layer of a few centimeters where the molecular transport dominates over turbulent transport. The thickness of the roughness sublayer is thought to be around 35 times of the surface roughness height, or 3 times of the vegetation height (Katul and Parlange, 1992). In ASL, the similarity relationships for the profiles of the mean wind speed, u , and the mean temperature, $\theta_0 - \theta_a$, are usually written in integral form as

$$u = \frac{u_*}{k} \left[\ln \left(\frac{z - d_0}{z_{0m}} \right) - \Psi_m \left(\frac{z - d_0}{L} \right) + \Psi_m \left(\frac{z_{0m}}{L} \right) \right] \quad (4)$$

$$\theta_0 - \theta_a = \frac{H}{ku_* \rho C_p} \left[\ln \left(\frac{z - d_0}{z_{0h}} \right) - \Psi_h \left(\frac{z - d_0}{L} \right) + \Psi_h \left(\frac{z_{0h}}{L} \right) \right] \quad (5)$$

where z is the height above the surface, $u_* = (\tau_0 / \rho)^{1/2}$ is the friction velocity, τ_0 is the surface shear stress, ρ is the density of air, $k = 0.4$ is von Karman's constant, d_0 is the zero plane displacement height, z_{0m} is the roughness height for momentum transfer, θ_0 is the potential temperature at the surface, θ_a is the potential air temperature at height z , z_{0h} is the scalar roughness height for heat transfer, Ψ_m and Ψ_h are the stability correction functions for momentum and sensible heat

transfer respectively, L is the Obukhov length defined as

$$L = -\frac{\rho C_p u_*^3 \theta_v}{kgH} \quad (6)$$

where g is the acceleration due to gravity, θ_v is the potential virtual temperature near the surface. For measurements performed at a height of a few meters above ground, the surface fluxes are clearly related to surface variables and variables in the atmospheric surface layer, calculations use the Monin-Obukhov Similarity (MOS) functions given by Brutsaert (1999). In order to relate surface fluxes to surface variables and the mixed layer atmospheric variables we use the Bulk Atmospheric Boundary Layer (ABL) Similarity (BAS) functions proposed by Brutsaert (1999) in the system of Eqs. (4-6). For stable conditions the expressions proposed by Beljaars and Holtslag (1991) and evaluated by van den Hurk and Holtslag (1995) are used for atmospheric surface layer scaling and the functions proposed by Brutsaert (1982, p.84) for atmospheric boundary layer scaling. The friction velocity, the sensible heat flux and the Obukhov stability length are obtained by solving the system of non-linear Eqs. (4-6).

Clearly we have to deal with the variables T_a, u, q that need to be determined from meteorological measurements and the variables z_{0m}, d_0, z_{0h} that need further parameterization. In SEBS a simplified model for estimation of thermal dynamic roughness proposed by Su et al. (2001) is used. By means of the energy balance at limiting (dry and wet) cases (Menenti and Choudhury, 1993), the turbulent heat flux terms are determined. Figure 4 shows the scheme used and figure 5 gives a summary of the SEBS basic equations. Full explanations are given in Su (2002).

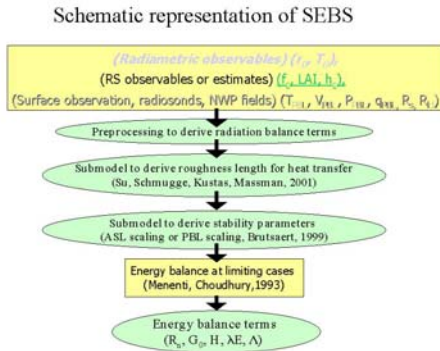


Fig. 4. SEBS Scheme

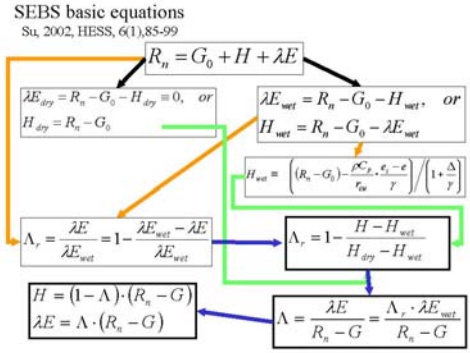


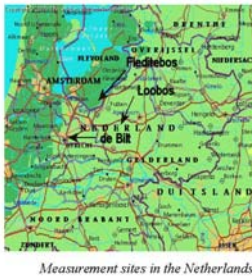
Fig. 5. SEBS basic equations.

DIFFICULTY IN DETERMINATION OF AERODYNAMIC ROUGHNESS HEIGHT

Aerodynamic roughness height (the displacement height is often related to it) influences greatly the turbulent characteristics near the surface where the heat fluxes originate. Currently, there are several methods that can be used for its determination as shown in Figure 6, including retrievals from wind profiles which is probably the most accurate method but is limited to the local topographic and canopy structure and varies with wind speed (different fetch) and direction (for heterogeneous terrain). Other methods are based on either vegetation height or land use classes and assigning each a nominal value, or using a relationship with vegetation index. One particular promising method is that of Hasagar and Jensen (1999) that is able to consider the dynamic flow characteristics and actual land use characteristics. Menenti and Richie (1994) showed that airborne LIDAR measurements of vegetation heights provided reliable determination of the aerodynamic roughness, so that a space borne LIDAR system when available might be quite promising. At any rate, despite great efforts in the past, the determination of aerodynamic roughness remains a challenging issue for large scale applications both for remote sensing of surface turbulent heat fluxes and meso-scale and global-scale atmospheric modelling. Figure 7 shows the spatial distribution of z_{0m} derived by two often employed methods and the discrepancy between is shown to be large.

Methods to determine Z0m

- Retrievals from wind profiles (point values)
- $Z_{0m} = 0.136 \cdot h$ (vegetation height)
- Land use + LUT table (Z_{0m} per class) (e.g. in atmospheric models)
- $Z_{0m} \sim VI$ relationships (e.g. $Z_{0m} = \exp(A+B \cdot NDVI)$)
- Land use + modelling (Hasagar, Jensen, 1999)
- LIDAR measurements (e.g. Menenti, Richie, 1994)
- Vegetation Canopy LIDAR ???



Measurement sites in the Netherlands

Fig. 6. Summary of some methods used to determine aerodynamic roughness

Uncertainties in Input Parameters -Z0m

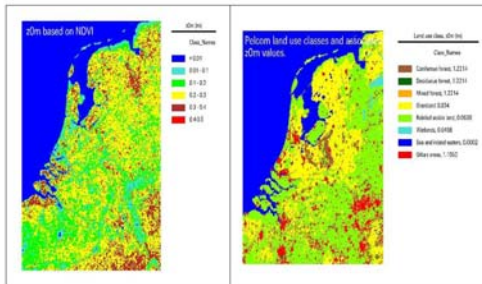


Fig. 7. Comparison of aerodynamic roughness height maps derived with two different methods

SINGLE-SOURCE SEBS VERSUS PARALLEL-SOURCE SEBS

Essentially, the parameterisation in single source SEBS and parallel SEBS (see Fig. 2 for details) are the same except in the case of the parallel source, we first set the fractional cover of vegetation as one and calculate the energy balance and turbulent heat flux terms, similarly we do the same for soil by setting the fractional cover of soil as one, and finally we sum up the fluxes terms weighted by their actual fractional coverage. Despite the simplicity of such a scheme, the results from the parallel-source SEBS are remarkably improved over the single-source SEBS as shown in Figs. 8-11 for three sites in Spain when compared the estimated turbulent heat fluxes to scintillometer measurements. Further details are given in Rauwerda et al. (2002).

3 Sites in SPAIN, ATSR data + meteorological data from nearest stations



Badajoz: alt. 168 m
large scale irrigation (wheat, corn, alfalfa, lettuce, olives beans, tomatoes)
scintillometer path 5250 m

Lleida: alt. 168 m
small scale irrigation (fruit trees, peaches, alfalfa)
scintillometer path 4650 m

Tomelloso: alt. 660 m
dry vineyard,
scintillometer path 1000 m

Fig. 8. Location of the three study sites and their characteristics in Spain

Single source vs parallel source - Badajoz, Sensible Heat Flux

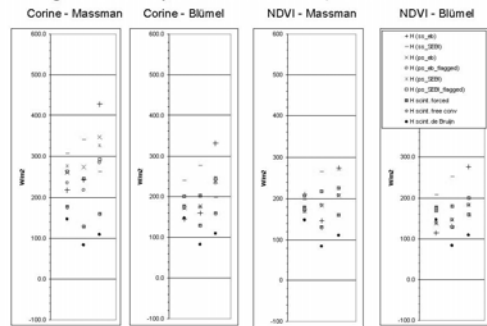


Fig. 9. Results derived from both single-source and parallel-source SEBS for Badajoz site (Corine refers to aerodynamic roughness derived from Corine land use map; Massman refers to the thermal dynamic roughness model of Su et al., 2001; Blümel refers to the thermal dynamic roughness model of Blümel (1999); NDVI refers to aerodynamic roughness derived with NDVI - Normalised Difference Vegetation Index; ss - single source; ps - parallel source; eb - sensible heat flux derived from the non-linear equation; sebi - sensible heat flux derived on the basis of the SEBI concept; flagged - energy limit is applied, i.e. maximum sensible heat flux is equal to available energy; scint. Forced, scint. Free convection, scint. de Buin refer to three different ways of estimation of sensible heat fluxes from scintillometer measurements)

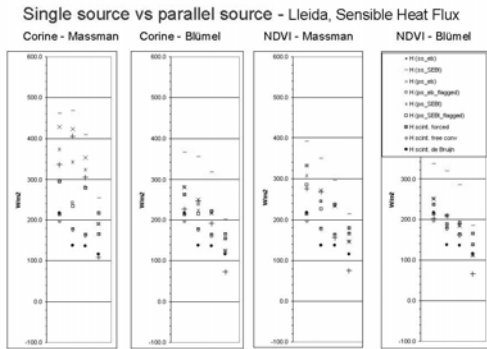


Fig. 10. Results derived from both single-source and parallel-source SEBS for Lleida site (explanation of symbols is the same as for in Figure 9)

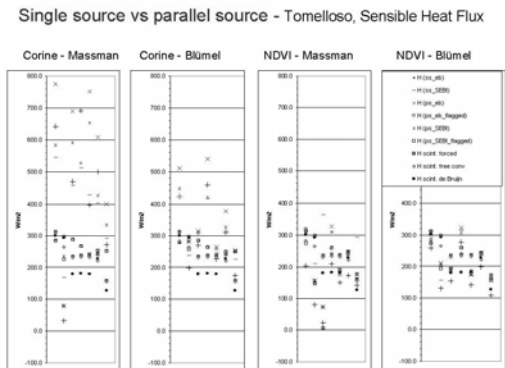


Fig. 11. Results derived from both single-source and parallel-source SEBS for Tomelloso site (explanation of symbols is the same as for in Figure 9)

SOME SEBS APPLICATIONS

Besides the results presented above, SEBS has been used for several studies conducted recently. Examples are estimation of actual evaporation in a semi-arid inland basin in Northwest China (Li, 2001), Drought monitoring (Su et al., 2001; 2002) and validation of atmospheric model simulations and data assimilation at regional scale (Jia et al., 2001). In all applications, clearly benefits when using radiometric measurements are demonstrated.

CONCLUSIONS

In this contribution, a brief history in estimation of turbulent heat fluxes and evaporation using radiometric observations is given. The Surface Energy Balance System (SEBS) is briefly introduced and it is shown that SEBS is scale invariant, so that it can be applied easily to different scales. Data of high or low spatial resolution from all sensors in the visible, near-

infrared and thermal infrared frequency ranges can be used in the system. Based on a set of case studies, SEBS was shown to be capable to estimate turbulent heat fluxes and evaporation from point to continental scale with acceptable accuracy for low vegetation. Further, it is shown that big uncertainty exists in estimation of aerodynamic roughness height, LIDAR measurements will be very helpful.

ACKNOWLEDGEMENTS

This work was jointly funded by the Dutch Remote Sensing Board (BCRS), the Dutch Ministry of Agriculture, Nature Management and Fisheries (LNV), and the Royal Netherlands Academy of Science (KNAW). Assistance and constructive comments from L. Jia, J. Wen, H. Rauwerda, G. Roerink, K. sintonen, C. Jacobs (Alterra), M. Menenti, Z.-L. Li (TRIO/ULP), B. van den Hurk (KNMI), W. Verhoef (NLR), J. Wang, Y. Ma (CAREERI/CAS), H. de Bruin, A. Moene (WU), R. Zhang, X. Sun (IGSNRR/CAS) and T. Schmugge and T. Jackson (USDA/ARS) are gratefully appreciated.

REFERENCES

- Bastiaanssen, W.G.M., (1995) Regionalization of surface flux densities and moisture indicators in composite terrain – A remote sensing approach under clear skies in Mediterranean climates. Ph.D. thesis, Wageningen Agricultural University, The Netherlands, 273 pp.
- Beljaars, A.C.M., and Holtslag, A.A.M., (1991) Flux parameterization over land surfaces for atmospheric models, *J. Appl. Meteor.*, 30, 327-341.
- Blümel, K., (1999) A simple formula for estimation of the roughness length for heat transfer over partly vegetated surfaces, *J. Appl. Meteorol.*, 38, 814-829.
- Bowen, I.S., (1926) The ratio of heat losses by conduction and by evaporation from any water surface, *Phys. Rev.*, 27, 779-787.
- Brutsaert, W., (1982) Evaporation into the atmosphere. D. Reidel, 299pp.
- Brutsaert, W., (1999) Aspects of bulk atmospheric boundary layer similarity under free-convective conditions, *Rev. Geophys.*, 37, 439-451.
- Carlson, T.N., O. Taconet, A. Vidal, R.R. Cillies, A. Olioso, K. Humes, (1995) An overview of the workshop on the thermal remote sensing held at La Londe les Maures, France, September 20-24, 1993. *Agric. Forest Meteorol.*, 77, 141-151.

- Chanzy, A., L. Bruckler, and A. Perrier, (1995) Soil evaporation monitoring: a possible synergism of microwave and infrared remote sensing, *J. Hydrol.*, 165, 235-259.
- Chehbouni, A., Y. Nouvellon, J.P. Lhomme, C. Watts, G. Boulet, Y.H. Kerr, M.S. Moran, D.C. Goodrich, (2001) Estimation of surface sensible heat flux using dual angle observations of radiative surface temperature. *Agric. Forest Meteorol.* 108, 55-65.
- Choudhury, B.J., Reginato, R.J. and Idso, S.B., (1986) An analysis of infrared temperature observations over wheat and calculation of latent heat flux, *Agric. Forest Meteorol.*, 37, 75-88.
- E. Boegh, H. Soegaard, A. Thomsen (2002) Evaluating evapotranspiration rates and surface conditions using Landsat TM to estimate atmospheric resistance and surface resistance, *Remote Sensing of Environment* 79, 329– 343.
- Famiglietti, J.S. and Wood, E.F., (1994) Multiscale modeling of spatially variable water and energy balance processes, *Wat. Resour. Res.*, 30, 3061-3078.
- Hasager, C., & Jensen, N. O. (1999). Surface-flux aggregation in heterogeneous terrain. *Quarterly Journal of the Royal Meteorological Society*, 125, 1–28.
- Jackson, R.D. R.J. Reginato, and S.B. Idso, (1977) Wheat canopy temperature: A practical tool for evaluating water requirements. *Water Resour. Res.* 13, 651-656.
- Jackson, R.D., Idso, S.B., Reginato, R.J., and Pinter Jr., P.J., (1981) Canopy temperature as a crop water stress indicator, *Water Resour. Res.*, 17(4), 1133-1138.
- Jackson, R.D., Kustas, W.P., and Choudhury, B.J., (1988) A re-examination of the crop water stress index, *Irrig. Sci.*, 9, 309-317.
- Jia, L., M. Menenti, Z. Su, V. Djepa, Z.-L. Li, Z.-L. and J. Wang (2001) Modeling sensible heat flux using estimates of soil and foliage temperatures: the HEIFE and IMGRASS experiments. In "Remote sensing and climate modeling: Synergies and Limitations", in "Advances in Global Change Research", edited by: M. Beniston and M. Verstraete, Kluwer Academic publisher, Dordrecht, The Netherlands.
- Jia, L., Z. Su, B. van den Hurk, A. F. Moene and M. Menenti (2001) Sensible and latent heat fluxes: Evaluation of the Surface Energy Balance System (SEBS) using ATSR and scintillometer measurements and RACMO PBL variables, in B.J.J.M. van den Hurk, Z. Su, W. Verhoef, G. Roerink and L. Jia, ENVISAT Land Surface processes Phase 2, Final report 4.2/AP-14.
- Kalma, J.D., and Jupp, D.L.B., (1990) Estimating evaporation from pasture using infrared thermometry: evaluation of a one-layer resistance model, *Agric. Forest Meteorol.*, 51, 223-246.
- Katul, G.G., and Parlange, M.B., (1992) A Penman-Brutsaert model for wet surface evaporation, *Water Resour. Res.*, 28(1), 121-126.
- Kustas, W. P., and Norman, J.M., (1999) Evaluation of soil and vegetation heat flux predictions using a simple two-source model with radiometric temperatures for partial canopy cover, *Agric. For. Meteorol.*, 94, 13-29.
- Kustas, W.P., (1990) Estimates of evapotranspiration with a one and two layer model of heat transfer over partial canopy layer, *J. Appl. Meteorol.*, 29, 704-715.
- Kustas, W.P., and Daughtry, C.S.T., (1989) Estimation of the soil heat flux/net radiation ratio from spectral data, *Agric. For. Meteorol.*, 49, 205-223.
- Kustas, W.P., and Norman, J.M., (1996) Use of remote sensing for evapotranspiration monitoring over land surfaces, *Hydrol. Sci. J.*, 41(4), 495-516.
- Li, X. (2001), Estimation of Urumqi River Basin Evaporation with Remote Sensing, M.Sc. Thesis in Hydrological Engineering, IHE, Delft.
- Menenti, M. (1993), Understanding land surface evapotranspiration with satellite multispectral measurements. *Adv. Space Res.*
- Menenti, M., (1984) Physical aspects of and determination of evaporation in deserts applying remote sensing techniques. Report 10 (special issue), Institute for Land and Water Management Research (ICW), The Netherlands, 202pp.
- Menenti, M., and Choudhury, B.J., (1993) Parametrization of land surface evapotranspiration using a location-dependent potential evapotranspiration and surface temperature range. In: Bolle, H.J. et al. (eds.). Exchange processes at the land surface for a range of space and time scales. *IAHS Publ. No. 212*: 561-568.

- Menenti, M., and J.C. Ritchie, (1994) Estimation of effective aerodynamic roughness of Wulnut Gulch watershed with laser altimeter measurements. *Water Resour. Res.*, 30, 1329-1337.
- Menenti, M., Choudhury, B.J., and Di Girolamo, N., (2001) Monitoring of actual evaporation in the Aral Basin using AVHRR observations and 4DDA results. in Su, Z., and Jacobs, C. (Eds.), *Advanced Earth Observation – Land Surface Climate*, report USP-2, 01-02, Publications of the National Remote Sensing Board (BCRS), pp79-83.
- Monteith, J.L., (1965) Evaporation and environment, *Sym. Soc. Exp. Biol.*, 19, 205-234.
- Monteith, J.L., (1973) Principles of environmental physics. Edward Arnold Press, 241 pp.
- Monteith, J.L., (1981) Evaporation and surface temperature. *QJR Meteorol. Soc.*, 107, 1-27.
- Moran, M.S., Clarke, T.R., Inoue, Y., and Vidal, A., (1994) Estimating crop water deficit using the relation between surface-air temperature and spectral vegetation index, *Remote Sens. Environ.*, 49, 246-263.
- Nieuwenhuis, G.J.A., E.A. Schmidt, H.A.M. Tunissen (1985) Estimation of regional evapotranspiration of arable crops from thermal infrared images. *Int. J. remote Sens.* 6, 1319-1334.
- Norman, J. M., Kustas, W. P., and Humes, K.S., (1995) A two-source approach for estimating soil and vegetation energy fluxes from observations of directional radiometric surface temperature, *Agric. For. Meteorol.*, 77, 263-293.
- Oliosio, A, I. Braud, A. Chanzy, J. Demarty, Y. Ducros, J.-C. Gaudu, E. Gonzalez-Sosa, E. Lewan, O. Marloie, C. Ottle, L.. Prevot, J.-L. Thony, H. Autret, O. Bethenod, J.-M. Bonnefond, N. Bruguier, J.-P. Buis, J.-C. Calvet, V. Casselles, H. Chauki, C. Coll, C. Francois, R. Goujet, R. Jonschaap, Y. Kerr, C. King, J.-P. Lagouarde, J.-P. Laurent, P. Lecharpentier, J. McAneney, S. Moilin, E. Rubio, M. Weiss, J.-P. Wigneron (2002) Monitoring energy and mass transfers during the Alpilles-ReSeDA experiment, *Agronomie* 22 (in press).
- Oliosio, A., 1992, Simulation des échanges d'énergie et de masse d'un couvert végétal, dans le but de relier la transpiration et la photosynthèse aux mesures de réflectance et de température de surface, Ph.D. Thesis, Université Montpellier II, 1992.
- Penman, H.L., (1948) Natural evaporation from open water, bare soil and grass, *Proc. Roy. Soc., A*, 193, 120-146.
- Priestly, C.H.B., and Taylor, R.J., (1972) On the assessment of surface heat flux and evaporation using large-scale parameters, *Mon. Weather Rev.*, 100(2), 81-92.
- Rauwerda, H., R. Reorink, Z. Su (2002) Estimation of Evaporative Fractions by the Use of Vegetation and Soil Component Temperatures determined by means of Bi-directional Remote Sensing, CGI report.
- Roerink, G.J., Z. Su, M. Menenti, (2000), S-SEBI: A simple remote sensing algorithm to estimate the surface energy balance, *Physics and Chemistry of the Earth*, 25, 147-157.
- Seguin, B. and B. Ittier (1983) Using midday surface temperature to estimate daily evaporation from satellite thermal IR data. *Int. J. Remote Sens.* 4, 371-383.
- Sellers, P.J., Randall, D.A., Collatz, G.J., Berry, J.A., Field, C.B., Dazlich, D.A., Zhang, C., Collelo, G.D., and Nounoua, L., (1996) A revised land surface parameterisation (SiB2) for atmospheric GCMS, part 1: model formulation, *J. Climate*, 9, 676-705.
- Stanghellini, C., (1987) Transpiration of greenhouse crops – an aid to climate management, Ph.D thesis, Agriculture University, Wageningen, The Netherlands.
- Stull, R.B., (1988) An introduction to boundary layer meteorology. Kluwer Academic Publ., pp. 670.
- Su, Z., (2001) A Surface Energy Balance System (SEBS) for estimation of turbulent heat fluxes from point to continental scale, in Z. Su and Jacobs, C. (eds.), *Advanced Earth Observation – Land Surface Climate*, Publications of the National Remote Sensing Board (BCRS), USP-2, 01-02, 184pp.
- Su, Z., (2002) The Surface Energy Balance System (SEBS) for estimation of turbulent heat fluxes, *Hydrology and Earth System Sciences*, 6(1), 85-99.
- Su, Z., G. Roerink, B.H. Gao, Y. Yang, X. Zhang, G. Lu, J.M. Wang, Y.B. He, Drought monitoring and prediction over continental China, -A perspective approach nased on satellite earth observation, atmospheric and hydrological

modelling, Paper presented at EGS XXVI General Assembly, Nice, France, 26 - 30 March 2001 (Geophysical Research Abstracts).

- Su Z., and Jacobs, C. (Eds.), (2001) Advanced Earth Observation – Land Surface Climate, report USP-2, 01-02, Publications of the National Remote Sensing Board (BCRS), 184pp.
- Su Z., and Menenti, M. (Eds.), (1999) Mesoscale climate hydrology: the contribution of the new observing systems, Report USP-2, 99-05, Publications of the National Remote Sensing Board (BCRS), 141pp.
- Su, Z., Pelgrum, H., Menenti, M., (1999) Aggregation effects of surface heterogeneity in land surface processes, Hydrol. Earth Sys. Sci., 3(4), 549-563.
- Su, Z., Schmugge, T., Kustas, W.P., Massman, W.J., (2001) An evaluation of two models for estimation of the roughness height for heat transfer between the land surface and the atmosphere, J. Appl. Meteorol. 40(11), 1933-1951.
- Su, Z., A. Yacob, J. Wen, G. Roerink, Y. He, B. Gao, H. Boogaard¹, C. van Diepen, (2002) Assessing Relative Soil Moisture with Remote Sensing Data: Theory and Experimental validation, (submitted to Physics and Chemistry of the Earth).
- van den Hurk, B.J.J.M., and Holtslag, A.A.M., (1995) On the bulk parameterization of surface fluxes for various conditions and parameter ranges. Boundary-Layer Meteorol., 82, 199-234.
- Zhang, R.H. (1996) Remote sensing models and ground surface foundation, The Science Press, Beijing,

Assimilation of remote sensing data into crop simulation models and SVAT models

Albert Olioso⁽¹⁾, Yoshio Inoue⁽²⁾, Jérôme Demarty^(1, 6), Jean-Pierre Wigneron⁽³⁾,
Isabelle Braud⁽⁴⁾, Samuel Ortega-Farias⁽⁵⁾, Patrice Lecharpentier⁽¹⁾, Catherine Ottlé⁽⁶⁾,
Jean-Christophe Calvet⁽⁷⁾, Nadine Brisson⁽¹⁾

(1) INRA-CSE, Domaine Saint-Paul, 84914 Avignon Cédex 9, FRANCE

olioso@avignon.inra.fr

(2) NIAES, Remote Sensing Laboratory, Tsukuba, JAPAN

(3) INRA, Bioclimatologie, Villenave d'Ornon, FRANCE

(4) LTRE (UMR 5564 CNRS, INPG, IRD, UJF), Grenoble, FRANCE and CEMAGREF, Lyon, FRANCE

(5) SIAR, Universidad de Talca, CHILE

(6) CETP, Vélizy, FRANCE

(7) CNRM, Météo-France, Toulouse, FRANCE

ABSTRACT: *Soil-Vegetation-Atmosphere Transfer models (SVAT) and Crop Simulation models describe physical and physiological processes occurring in crop canopies. Remote sensing data may be used through assimilation procedures for constraining or driving SVAT and crop models. We developed the coupling between crop, SVAT and radiative transfer models in order to implement assimilation procedures in various wavelength domains (solar, thermal and microwave). Simple assimilation tests are presented in order to illustrate the main techniques that may be used.*

1 INTRODUCTION

Crop models and Soil-Vegetation-Atmosphere Transfer models (SVAT models) have been designed for analyzing the interactions between plant canopy processes and the environment. They give priceless information for production and yield monitoring, water resources assessment and more recently for carbon cycle studies in relation with climate research. The use of such models over large areas is limited by our ability to provide them with the required input information. On one hand, it is almost impossible to obtain requisite plant and soil characteristics directly from networks of ground observations. On the other hand, remote sensing techniques can provide indirect information on plant canopy processes over large areas. This information is not direct because it results from the interaction of radiation with soil surface and plant canopy.

It is then necessary to use models for interpreting these interactions and for relating plant and soil characteristics to remote sensing measurements. Such models range from simple empirical relationships to complex radiative transfer models. For example, numerous relationships were established between spectral reflectances and plant characteristics such as LAI by means of vegetation indices; they can be used for estimating LAI that is then fed into process models. Such method has been described for examples by Delécolle et al. (1992) for driving crop

models or by Sellers et al. (1996b) for a SVAT model used as a land surface parameterization in an atmospheric general circulation model. Such methods have been termed as forcing method by Delécolle et al. (1992). They require that the driving variables are estimated from remote sensing data with a very fine time resolution close to the time step of the model (or interpolated).

However, many process models may be operated without a systematic use of remote sensing data; the model intrinsically provides the mean for interpolating fluxes or biomass production between remote sensing data acquisitions which maybe infrequent. Moreover, it might be possible to implement procedures to use data acquired by a large range of remote systems, differing in wavelength domains, acquisition time or geometry. For instance, it may be proposed to combine thermal infrared data from different sensors such as ATSR and AVHRR which provide mid-morning and mid-afternoon data, respectively. Data from Earth observation systems (SPOT-HRV, ERS, Radarsat) might also be combined to thermal data provided by meteorological sensor (e.g., AVHRR) despite their very different acquisition repetitivities. Another point is that, in many cases, plant and soil characteristics that are used in process models cannot be related in a simple way to remote sensing data. It is then necessary to apply more complex techniques that will directly combine the use

of the model for estimating 'hidden' quantities, such as intimate parameters that are related to physical processes or biological processes (stomatal conductance, phenological parameters, soil physic parameters, soil moisture in the root zone, specific leaf area ...).

Techniques that make it possible to integrate remote sensing information into process models will be termed as assimilation techniques. They are very numerous since aims in agronomy, hydrology or meteorology imply different use of data and models. SVAT and crop models give access not only to a limited number of final variables such as evapotranspiration or net primary production. They simulate intermediary variables linked to hydrological or physiological processes. Thus, they are often proposed to estimate soil moisture from remote sensing data and then used as an interface with other models, such as atmospheric or hydrological models.

Nowadays, a major problem is to analyze the possible synergy between various observing system and various models. Till now, most of the studies devoted to assimilation of remote sensing data into crop models focused on the use of visible and near infrared reflectances or radar measurements (Bouman, 1995, Moulin et al. 1998, Chauki et al. 2000). Indeed, these measurements give information on crop structure and biomass seasonal dynamics. One may think that thermal infrared (TIR) data can also provide significant information on crop processes when water limitations occur (Cayrol et al. 2000, Oliso et al. 2001). Conversely, the use of TIR with SVAT models has been investigated in details by many authors (e.g. Soer 1980, Taconet et al. 1986, Ottlé and Vidal-Madjar 1994, Gillies et al. 1997, Oliso et al. 1999a and b). No many studies analyze the possible complementary use of various wavelength (Ottlé and Vidal-Madjar 1994, Gillies et al. 1997, Oliso et al. 1999b, Cayrol et al. 2000).

2 CROP SIMULATION AND SVAT MODELS

2.1 Generality

Crop models describes the main processes that occur during plant growth and crop production (similar models have also been developed to describe productivity of natural ecosystems or forest): phenology, photosynthesis, dry matter production, water processes, nitrogen processes, biomass partition, organ building, solar radiation absorption. The typical time step of such models is the day which is in agreement with the time scale of the simulated processes (crop growth and phenology). **SVAT models** are mainly used for estimating evapotranspiration, surface energy exchanges and

water balance. Most of the transfer mechanisms (radiative, turbulent, and water transfers) and some physiological processes (stomatal regulation) are described. Their time resolution is less than 1 h in agreement with the dynamic of atmospheric and surface processes. Note that this fine time resolution is also interesting when they are combined with remote sensing data, which are acquired instantaneously.

Numerous crop and SVAT models have been developed (see reviews by Sinclair and Seligman 1996, Oliso et al. 1999a). They may have very different complexity level depending on the quantity and the detail of described processes. Recent advances in crop modeling make it possible to simulate a large variety of crops and a large variety of agricultural practices (Brisson et al. 2002). Specific description or parameterization may be required for each type of crops, even for models which aim to be generic. Such details are not available in SVAT models, even if the physical processes that are described (turbulent exchanges, water uptake) are not specific to plant species. However, as SVAT models have usually been designed for homogeneous surface, they are often difficult to use for describing heterogeneous systems such as orchards, vineyards, developing crops or savannah (cases in which they fail in the calculation of global turbulent exchange coefficients and global surface conductance for the vegetation layer). Another difficulty in the use of SVAT models results from a very low insight in the description of the vegetation phenology. Usually, vegetation dynamic is only considered as an input. Because of a new interest in the study of CO₂ fluxes in climatological and global change studies, some of the SVAT models have been extended to the simulation of photosynthesis (Carlson and Bunce, 1996; Sellers et al., 1996a, Oliso et al. 1996, Calvet et al. 1998). The introduction of photosynthesis makes it possible to simulate biomass production and then evolution of crop structure such as LAI (such models are sometime termed as vegetation-interactive model). In this study we used several types of models (described below).

2.2 The STICS crop model

STICS is a crop model developed in France to simulate a wide range of crops (Brisson et al. 1998, 2002). It simulates crop growth and development as well as soil water and nitrogen balances driven by daily climatic data. It calculates both agricultural variables (yield, production quality, input consumption) and environmental variables (water and nitrogen losses). From a conceptual point of view, STICS relies essentially on well-known relationships

or on simplifications of existing models. One of the key elements of STICS is its adaptability to various crops made possible by the choice of generic parameters and options for both crop physiology and crop techniques. It is a daily time-step crop model. The data required to run the model inform climate, soil (water and nitrogen initial profiles and permanent characteristics), crop management and species and varietal parameters. Soil is likened to a sequence of horizontal layers, each of which is characterized in terms of its water content, mineral nitrogen content and organic nitrogen content. Soil and crop interact via the roots, and these roots are defined with respect to root density distribution in the soil profile. Crop growth is driven by the plant carbon functioning: solar radiation interception by the foliage and then transformation into aboveground biomass that is directed to the harvested organs during the final phase of the cycle. According to the plant type, crop development is driven either by a thermal index or a photothermal index. The development model is used to i) make the leaf area index evolve and ii) define the harvested organ filling phase. Water stress and nitrogen stress, if any, reduce leaf growth and biomass accumulation, based on stress indices that are calculated in water and nitrogen balance modules.

2.3 ISBA and ISBA-Ags SVAT models

The **ISBA** SVAT model was developed at Météo-France for being implemented as a land surface scheme in atmospheric weather forecast model and GCM (Noilhan and Planton 1989, Noilhan and Mahfouf 1996). This model solves the surface energy balance and the soil water balance with a five minute time step. The force–restore scheme, presented by Deardorff (1978), is used and the soil is described by one bulk reservoir corresponding to the root zone (including a thin surface layer). The main surface variables simulated by ISBA are the surface temperature, the soil moisture in the root zone, the surface soil moisture and the energy fluxes. We may note that only one energy balance equation is solved, but that a separation of soil evaporation and plant transpiration is done on the basis of the vegetation fraction cover. This model requires meteorological variables, albedo, minimum stomatal resistance, LAI and vegetation height as inputs, as well as the soil texture, wilting point and field capacity.

In the **ISBA-Ags** version of ISBA (Calvet et al. 1998), the physiological stomatal resistance scheme proposed by Jacobs et al. (1994) is used to describe photosynthesis and its coupling with stomatal resistance at the leaf level. The computed net vegetation assimilation is used to feed a simple growth sub-model, and to predict the density of the

vegetation cover. Three main parameters are required to calibrate ISBA-Ags: leaf life expectancy (DE) and effective biomass per unit leaf area (B/LAI) to calibrate the growth sub-model, and a mesophyll conductance (gM). Once calibrated, the ISBA-Ags model is able to simulate water budget, fluxes (CO₂, sensible and latent heat fluxes, etc.) and leaf area index (LAI). Thus, the model is able to adapt the simulations of vegetation growth in response to changes in the environmental conditions (precipitation distribution, soil moisture in the root-zone, climatic conditions, etc.) and, in contrast to ISBA, ISBA-Ags can be considered as 'an interactive vegetation SVAT model'.

2.4 The SiSPAT SVAT model

In the **SiSPAT** model, heat and water transfers in the soil are described in more details than in ISBA (Braud et al. 1995). The vertical heterogeneity of the soil structure and texture may be accounted for, and a root distribution must be prescribed. Coupled transfers of moisture and heat in a partially saturated soil are described using the approach described in Milly (1982). The soil prognostic variables are the vertical profiles of temperature and soil matrix water potential. This approach requires more complex information on the soil characteristics than ISBA, such as retention curves and hydraulic conductivity as a function of soil moisture. The effect of vegetation above the ground is based on the solution of two energy budgets, one for the ground surface and another one for the vegetation layer. Basic radiative and turbulent transfer calculations are done inside the canopy in order to partition energy between the soil surface and the vegetation layer. They require to prescribe separately albedo, emissivity and aerodynamic resistances for the vegetation layer and for the soil surface. The circulation of water from the soil to the atmosphere through the plants and the soil water uptake by the roots follows an electrical analogue model. The stomatal conductance is described as a function of vapor pressure deficit, leaf temperature, incident radiation and leaf water potential.

2.5 Some simulations of surface processes

Figure 1 presents STICS, ISBA, ISBA-Ags and SiSPAT simulations of evapotranspiration, water reserve, biomass and LAI for a soybean crop in Avignon in 1990 (Olioso et al. 1996, 1999b). It shows that despite the differences between models, close results were usually obtained. Note that in this case, direct or indirect calibration of the models were done, either on the experimental data of water reserve and LAI or from the parameterization of a more complex model (SOYGROW) for STICS.

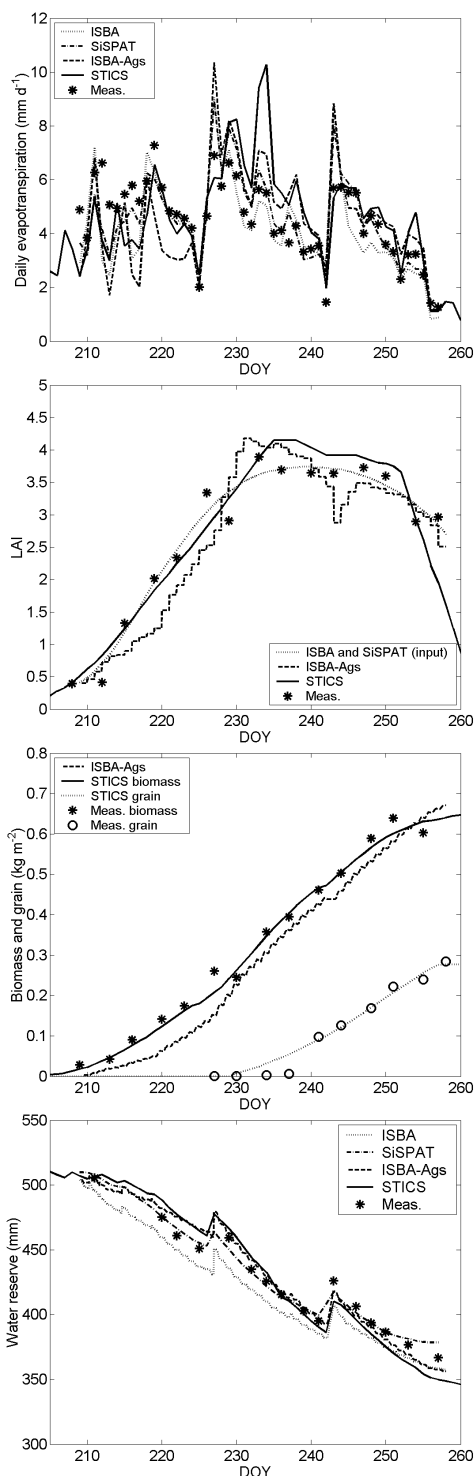


Figure 1. Simulations of surface variables using STICS, ISBA, ISBA-Ags and SiSPAT for a soybean crop in Avignon (1990).

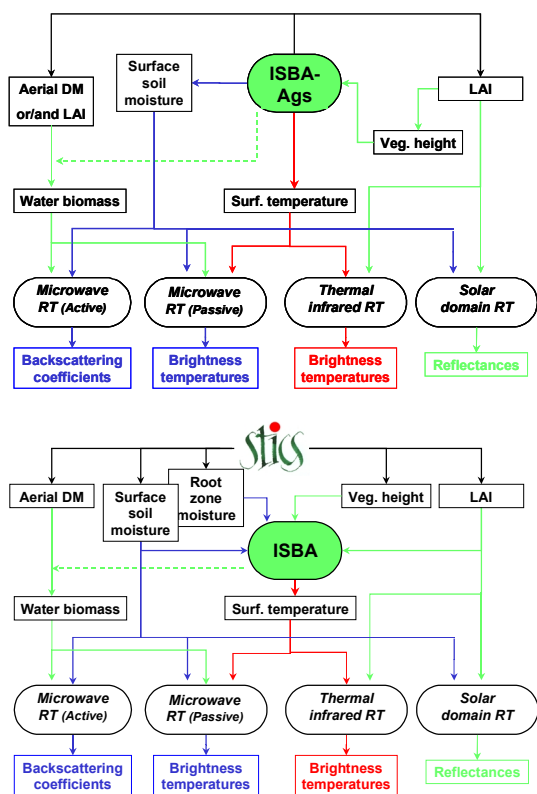


Figure 2. Scheme of coupling the different vegetation and radiative transfer models.

3 SIMULATIONS OF REMOTE SENSING DATA

In order to simulate remote sensing data, simple radiative transfer models were coupled to the process models (Fig. 2). This was almost direct for simulating reflectances and backscattering coefficients. A Beer-Lambert type model (Weiss and Baret 1999) was used for simulating NDVI from LAI simulated by STICS or ISBA-Ags. This model was calibrated on SAIL model simulations for various soybean canopies. Background effect of soil moisture was accounted for. A water cloud model was used in the microwave domain to relate the vegetation integrated water content (estimated from LAI or dry biomass) and the surface soil moisture to backscattering coefficients (Wigneron et al. 1999). Soil behavior in the microwave was accounted for using the IEM model.

In the case of thermal infrared and microwave emission, the coupling was more complex, at least for STICS. As this model did not describe the processes that determine surface temperature and as its daily time step was not compatible with the fast response of these processes, it was necessary to use ISBA as an

interface between STICS and radiative transfer models. For each simulation day, LAI and vegetation height were transferred from STICS to ISBA (Fig. 2). Surface and root zone soil moistures simulated by STICS were also transferred to ISBA to be used as initial values for each simulation days. As ISBA-Ags time step was adequate, no such interface was implemented. Simulation of thermal infrared brightness temperature from surface temperature simulated by ISBA or ISBA-Ags was done by using an emissivity model depending on LAI (adapted from Olioso 1995). The microwave emission was simulated from surface temperature using the τ - ω model proposed by Wigneron et al. (1995) using similar inputs as for active microwave simulations.

Note that SiSPAT has also been coupled to the SAIL radiative transfer model and to a simplified thermal model in order to simulate reflectances and thermal infrared signals by Demarty et al. (2002a and b); this version is called SiSPAT-RS.

Examples of remote sensing data simulations with the coupled models in the conditions of the 1990 soybean experiment in Avignon are displayed in Figure 3. They show an overall agreement between measurements and simulations of NDVI and maximum thermal infrared brightness temperature. The overestimations of NDVI at some periods were actually linked to the particular leaf movements that occurred as a response of water stress for this soybean cultivar (Labrador with a very short cycle). Simulations of microwave backscattering coefficients qualitatively agreed with the data presented by Wigneron et al. (1999) for an experiments on soybean in 1989 in Avignon (see below). Simulation of microwave brightness temperature were presented by Olioso et al. (2001) on soybean and Wigneron et al. (2002) on wheat.

4 ASSIMILATION TECHNIQUES

Various techniques have been proposed and used for assimilating data in dynamic vegetation process models (Delécolle et al. 1992, François et al. 2001). A first way consists in estimating model state variables from remote sensing data, and to directly introduce (force) them into the model (at occurrences compatible with the time step of the model). Other methods consist in correcting the course of model dynamic variables by comparing them to remote sensing measurements. In **sequential assimilation** techniques, the model is updated each time an observation is available. It is usually used for updating model prognostic variables.

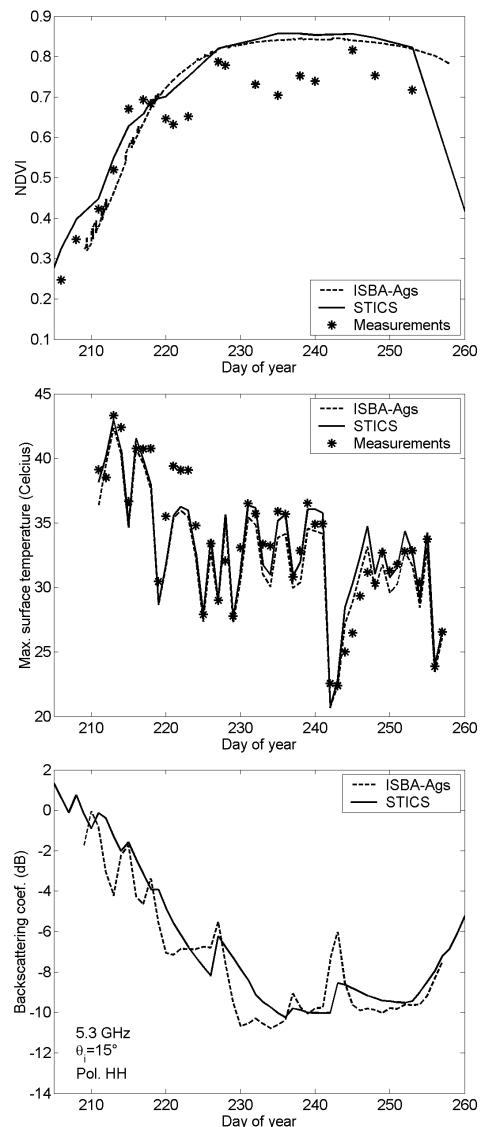


Figure 3. Simulation of remote sensing data with ISBA-Ags and STICS

In **variational assimilation** techniques, all the available observations for a certain period of time are processed together. They are usually used for retrieving model parameters or initial values of model variables (using model calibration techniques). Many different types of methodology and mathematical tools have been developed for implementing assimilation procedures. Many of them were employed in the fields of dynamic atmospheric modeling (in particular applied to numerical weather forecast) and at a lesser extent for hydrological modeling. Just to give some names here (we won't

say anything more about them after that), we can cite LSM, Kalman filter, 3D-VAR, 4D-VAR, adjoint model, linear tangent model. Here, simple examples of assimilation procedures are presented and applied to the assessment of surface processes with ISBA and ISBA-Ags for the 1989 soybean experiment in Avignon (a different experiment than the one used for testing the models in 1990). A stochastic method will also be briefly presented using the SiSPAT-RS model.

4.1 Forcing method

We estimated LAI from NDVI, and then forced it in ISBA and ISBA-Ags, short-cutting the LAI production module (Figure 4). The LAI-NDVI model was calibrated on data in Avignon in 1987 and 1990. ISBA and ISBA-Ags parameters (essentially linked to stomatal conductance) were calibrated on the 1990 experiment (Table 1). Simulated evapotranspiration (Table 2) was in nice agreement with the measurements despite a significant underestimation (mainly due to difficulties at low LAI).

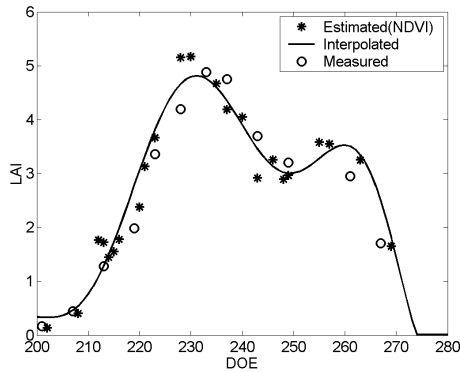


Figure 4. Estimation of LAI temporal profile from NDVI in 1989; comparison to the measured data.

Table 1. Calibrated ISBA-Ags coefficients on two datasets (from Calvet et al. 1998).

	gM (mm s ⁻¹)	DE (day)	B/LAI (g m ⁻²)
Hapex-Mobilhy	1	250	63
Avignon 1990	2.87	15	25

Table 2. performances of ISBA and ISBA-Ags retrieval of evapotranspiration.

	RMSE on ET (mm d ⁻¹)	Bias on ET (mm d ⁻¹)
LAI-forced ISBA	1.1	-0.7
LAI-forced ISBA-Ags	1.1	-0.5
Sequential-HAPEX	1.4	0.5
Sequential-Avignon	1.0	-0.1

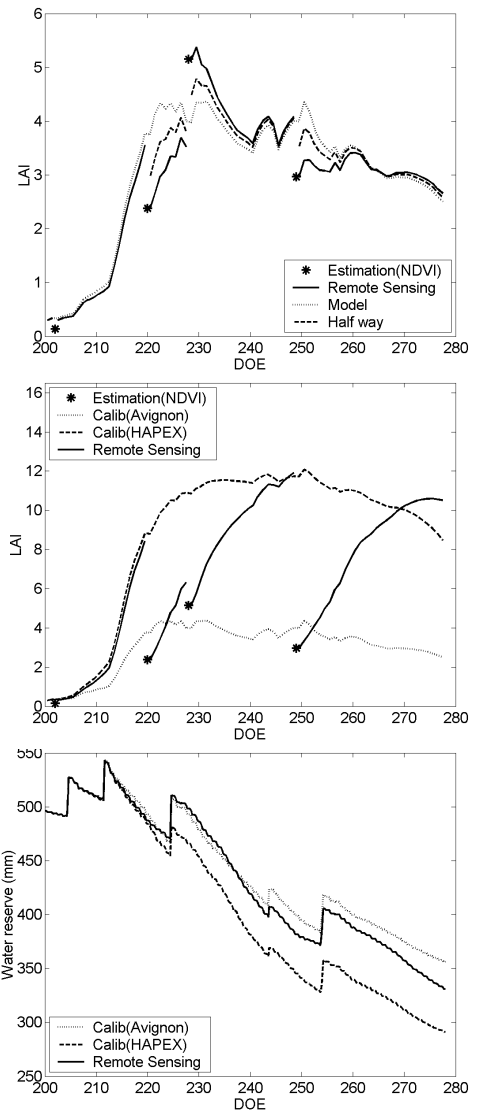


Figure 5. Sequential assimilation of LAI in ISBA-Ags. **Top graph:** using parameters calibrated on Avignon 1990 dataset: three correction levels of the simulations are displayed: full correction, no correction and half correction. **Two lower graphs:** using HAPEX-MOBILHY calibration (full correction, no correction and comparison to the Avignon calibration).

4.2 Sequential assimilation

LAI estimated from NDVI was used for correcting ISBA-Ags simulations. Two cases are presented: the mesophyll conductance (gM), the leaf life expectancy (DE) and the effective biomass per unit leaf area (B/LAI) were obtained from calibrations of ISBA-Ags on the Hapex-Mobilhy data set or on the Avignon 1990 experiment (see Calvet et al; 1998). The two sets of coefficients are very different (Table 1) implying large differences in simulations of LAI, ET and water reserve (Figure 5 and Table 2). In the case of Avignon calibration, the use of remote sensing data to correct the evolution of LAI had only a slight effect on ET and water reserve simulations. In the case of the HAPEX calibration, the correction of the LAI time course using NDVI had a large influence on model results. Simulated LAI showed very fast increases and high values when not corrected, generating a large water uptake. However, after assimilation, ISBA-Ags results were still not as good as with the parameters calibrated on the Avignon experiment.

4.3 Variational assimilation

In a first case, we used the ISBA-Ags model calibrated on Avignon-1990. Simulated remote sensing signals (NDVI, T_s , σ_0) were adjusted to their measurements by changing the initial water content. Figure 6 shows that RMSE for the different signals were reaching their lowest values for high values of initial water content, which resulted in almost similar estimation of LE (latent heat flux). LAI and soil reserve were also satisfactorily estimated, even if some time lags were noticed (Figure 7). **In a second case**, we tried to retrieve at the same time ISBA-Ags parameters for LAI production (DE and B/LAI) and the initial soil water content. This attempt was not converging. Then, we tried to retrieve ISBA-Ags parameters at various levels of initial soil moisture. RMSE for remote sensing signals had similar values whatever the initial soil moisture (Figure 6). Figure 7 shows that LAI was adequately simulated for each initial soil moisture, while soil reserve might be completely wrong. Evapotranspiration was also quite conservative. Retrieved parameters (DE and B/LAI) had very different values for each initial soil moisture in order to compensate the effect of water level and to produce a LAI in agreement with the measured remote sensing data. This example shows that the assimilation of remote sensing data into a surface process model makes it possible to describe energy balance and vegetation growth without an accurate knowledge of the soil process. Olioso et al. (1999a

and b) reached a similar conclusion using a very different model and a very different assimilation procedure. This was also due to compensations between parameters. This behaviour may be very interesting in some applications, but it will also generate large difficulties for applications in which both plant and soil parameters must be retrieved. We have also to notice in the two previous examples that the 3 types of remote sensing data we used provided very similar results. This illustrates that, at the scale of the whole crop cycle, the main surface processes are correlated with each others (plant growth, water processes, energy balance ...).

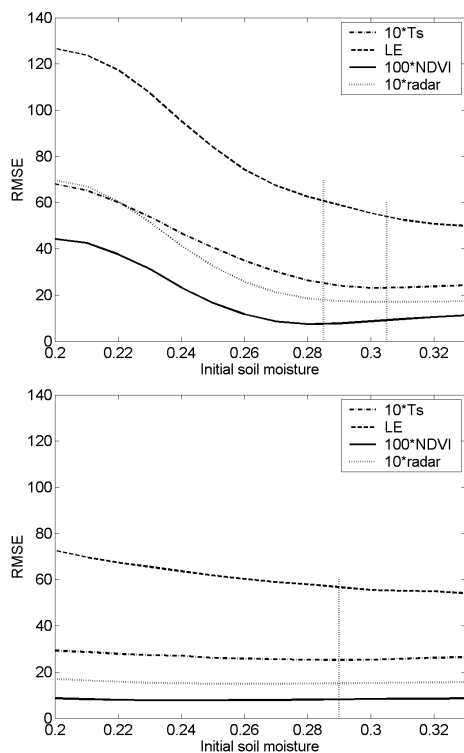


Figure 6. Evolution of latent heat flux and signals RMSE when changing initial soil moisture. In the top graph, only initial soil moisture was retrieved (first case of variational assimilation). In the bottom graph LAI production parameters were retrieved at each initial soil moisture (second case).

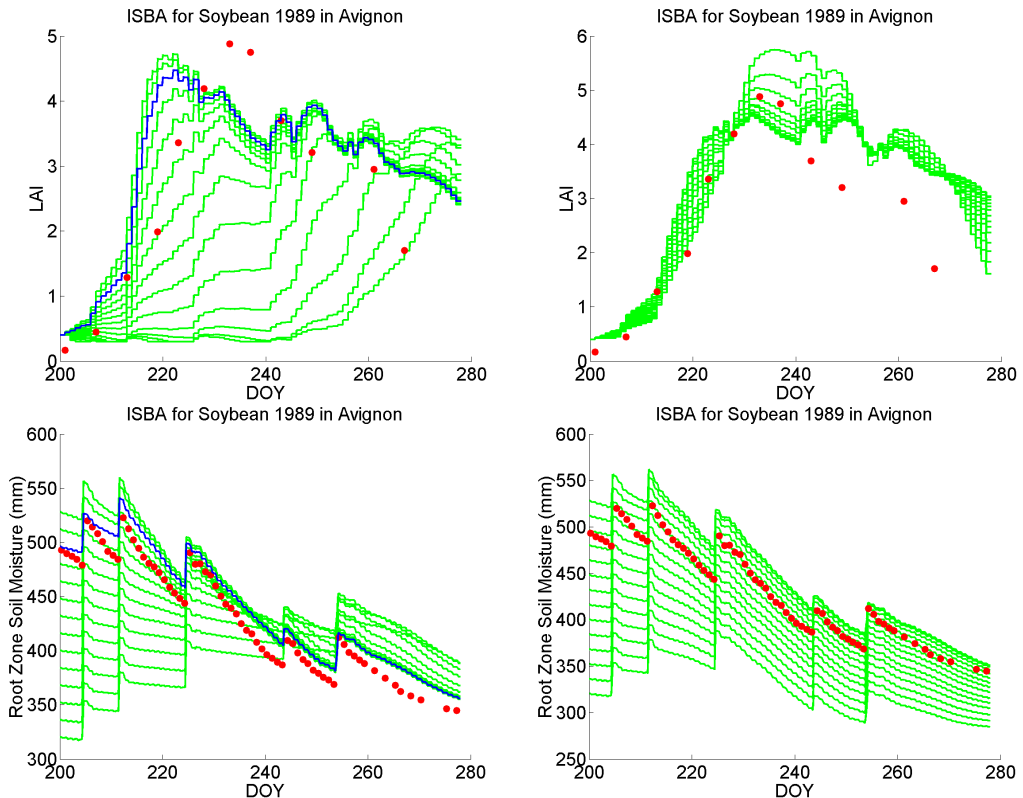


Figure 7. Evolution of LAI and soil water reserve at different level of initial water content. On the left: using the Avignon-1990 calibrated ISBA-Ags (first case of variational assimilation). On the right: calibrating the LAI production parameters at each initial soil moisture (second case).

4 STOCHASTIC ASSIMILATION IN SiSPAT

As shown in the previous example, the assimilation of data in vegetation process models is not always providing a single optimum parameter set (usually considered as allowing the “best” model simulations). This may be due to model errors, compensation between model parameters and uncertainties in the measurements. The multi-objective approach, proposed by Gupta et al. (1998), may be used to develop data assimilation procedures that overcome this problem. It is based on series of Monte Carlo simulations over a feasible parameter space. The partition of these simulations into an “acceptable” region and a “non-acceptable” region, according to their performance in terms of agreement between simulated and measured remote sensing signals, allowed to retrieve acceptable parameter sets and then to perform the assimilation (several signals may be used together). Demarty et al. (2002b) applied this stochastic calibration procedure on SiSPAT-RS

(SiSPAT coupled to Remote Sensing modules: Demarty et al. 2002a) using the water content of the upper five soil centimeters (instead of microwave data) and the surface temperature together. The optimization of 35 SiSPAT-RS parameters was performed combining information collected on two short temporal periods of a wheat field of the Alpilles-ReSeDA experiment. It allows to determine the parameter set that is possible to calibrate from remotely sensed observations in relation to the various environmental conditions and vegetation stages. In this sense, results showed particularly that the brightness temperature and the surface soil moisture provided complementary information about soil and vegetation parameters (retention curve, hydraulic conductivities, thermal properties and stomatal conductance).

5 CONCLUSION

After introducing some surface process models including SVAT and crop models, we presented simple examples illustrating various types of procedures to assimilate remote sensing data into surface process models. We showed that the assessment of surface fluxes, soil moisture and plant growth may be possible, at least in some conditions. However, when implementing assimilation procedures, it will be important to analyse carefully the compensations occurring between the different parameters or variables in the model in order to choose the quantities which will be retrieved through the assimilation process. This will be true also for defining the data that must be used and their accuracy requirements. Our examples showed that it is not easy to analyse the synergy that may exist between different types of remote sensed information: the analysis with SiSPAT-RS showed that complementary information were provided by the surface soil moisture and the surface temperature; conversely, the analysis with the ISBA-Ags model showed that reflectances, backscattering coefficients and surface temperature were providing very similar information. A possible synergy between wavelength domains may depend on the type of assimilation procedure and on the addressed problem. Nowadays, the use of assimilation procedures to drive surface models with remote sensing data is still at its beginning (François et al. 2001). Many assimilation techniques have been developed for assimilating meteorological data (and some remote sensing data) in atmospheric modelling for weather forecast or for assimilating soil moisture or water flow in hydrological modelling. At the moment, none of them has been applied with significant results to the analysis of surface processes. Making use of adequate procedures is one of the first challenge for developing a quantitative use of remote sensing information in agricultural and environmental issues in the next future.

6 ACKNOWLEDGEMENT

This work was partially founded by ECOS-CONICYT French-Chile cooperation program n° C99U04 and by the French ACI "Observation de la Terre".

7 REFERENCES

- Bouman, B.A.M., 1995, Crop modelling and remote sensing for yield prediction, *Nederlands Journal of Agricultural Science*, 43, 143-161.
- Braud, I., Dantas Antonino, A.C., Vauclin, M., Thony, J.-L., and Ruelle, P., 1995, A Simple Soil Plant Atmosphere Transfer model (SiSPAT): development and field verification, *Journal of Hydrology*, 166, 213-250.
- Brisson, N., Mary, B., Ripoche, D., et al., 1998, STICS: a generic model for the simulation of crops and their water and nitrogen balances. I. Theory and parameterization applied to wheat and corn, *Agronomie*, 18, 311-346.
- Brisson, N., Gary, C., Justes, E., et al., 2002b, An overview of the crop model STICS, *Submitted*.
- Calvet, J.-C., Noilhan, J., Roujean, J.-L., Bessemoulin, P., Cabelguenne, M., Olioso, A., and Wigneron, J.-P., 1998, An interactive vegetation SVAT model tested against data from six contrasting sites, *Agricultural and Forest Meteorology*, 92, 73-95.
- Carlson, T.N., and Bunce, J.A., 1996, Will a doubling of atmospheric carbon dioxide concentration lead to an increase or a decrease in water consumption by crops? *Ecological Modeling*, 88, 241-246.
- Cayrol, P., Kergoat, L., Moulin, S., Dedieu, G., and Chehbouni, A., 2000, Calibrating a coupled SVAT / vegetation growth model with remotely sensed reflectance and surface temperature. A case study for the HAPEX-Sahel grassland sites. *Journal of Applied Meteorology*, 39, 2452-2472.
- Chauki, H., Prévot, L., Troufleur, D., Brisson, N., Olioso, A., Baret, F., and Guérif, M., 2000, Assimilation of ERS and RadarSat SAR observations within STICS crop growth model. In *Proceedings of the CEOS SAR Workshop*. Toulouse, Oct. 1999. ESA SP-450, pp. 485-490.
- Deardorff, J.W., 1978, Efficient prediction of ground surface temperature and moisture, with inclusion of a layer of vegetation, *Journal of Geophysical Research*, 83, 1889-1903.
- Delécolle, R., Maas, S.J., Guérif, M., and Baret, F., 1992, Remote sensing and crop production models: present trends, *ISPRS Journal of Photogrammetry and Remote Sensing*, 47, 145-161.
- Demarty, J., Ottlé, C., François, C., Braud, I., and Frangi, J.P., 2002a, Effect of aerodynamic resistance modeling on SiSPAT-RS simulated surface fluxes, *Agronomie in press*.
- Demarty, J., Ottlé, C., François, C., Braud, I., Olioso, A., Frangi, J.P., Bastidas, L., and Gupta, H.V., 2002b, Multiobjective calibration of a physically based SVAT model in a context of remote sensing data assimilation, *submitted*.
- François, C., Cayrol, P., Kergoat, L., and Moulin, S., 2001, Assimilation techniques of remote sensing measurements into vegetation models: overview, limits and promises. In *Proc. of the 8th Internat. Symposium on Physical Measurements and Signatures in Remote Sensing*, 8-12 January 2001, Aussois, France, pp 649-658.

- Gillies, R.R., Carlson, T.N., Cui, J., Kustas, W.P., and Humes, K.S., 1997, Verification of the "triangle" method for obtaining surface soil water content and energy fluxes from remote measurements of the Normalized Difference Vegetation Index NDVI and surface radiant temperature, *International Journal of Remote Sensing*, 18, 3145–3166.
- Gupta, H.V., S. Sorooshian, and P.O. Yapo, Toward improved calibration of hydrologic models: Multiple and non-commensurable measures of information, *Water Resources Research*, 34 (4), 751–763, 1998.
- Gupta, H.V., L.A. Bastidas, S. Sorooshian, W.J. Shuttleworth, and Z.L. Yang, Parameter estimation of a land surface scheme using multicriteria methods, *Journal of Geophysical Research*, 104 (D16), 19,491–19,503, 1999.
- Jacobs, C.M.J., van den Hurk, B.J., and de Bruin, H.A.R., 1994, Stomatal behaviour and photosynthetic rate of unstressed grapevines in semi-arid conditions, *Agricultural and Forest Meteorology*, 80, 111–134.
- Milly, P.C.D., 1982, Moisture and heat transport in hysteretic inhomogeneous porous media: a matrix head-based formulation and a numerical model, *Water Resources Research*, 18, 489–498.
- Moulin, S., Bondeau, A., and Delécolle, R., 1998, Combining agricultural crop models and satellite observations: from field to regional scales. *International Journal of Remote Sensing*, 19, 1021–1036.
- Noilhan, J., and Planton, S., 1989, A simple parameterization of land surface processes for meteorological models, *Monthly Weather Review*, 117, 536–549.
- Noilhan, J., and Mahfouf, J.-F., 1996, The ISBA land surface parameterisation scheme, *Global Planetary Changes*, 13, 145–159.
- Olioso, A., 1995, Simulating the relationship between thermal emissivity and the Normalized Difference Vegetation Index. *International Journal of Remote Sensing*, 16, 3211–3216.
- Olioso, A., Carlson, T.N., and Brisson, N., 1996, Simulation of diurnal transpiration and photosynthesis of a water stressed soybean crop, *Agricultural and Forest Meteorology*, 81, 41–59.
- Olioso, A., Chauki, H., Courault, D., and Wigneron, J.-P., 1999a, Estimation of evapotranspiration and photosynthesis by assimilation of remote sensing data into SVAT models, *Remote Sensing of Environment*, 68, 341–356.
- Olioso, A., Chauki, H., Wigneron, J.-P., Bertuzzi, P., Chanzy, A., Bessemoulin, P., and Calvet, J.C., 1999b, Estimation of energy fluxes from thermal infrared, spectral reflectances, microwave data and SVAT modeling, *Physics and Chemistry of the Earth, Part B*, 24, 829–836.
- Olioso, A., Inoue, Y., Wigneron, J.-P., Ortega-Farias, O., Lecharpentier, P., Pardé, M., Calvet, J.C., and Inizan, O., 2001, Using a coupled crop-SVAT model to assess crop canopy processes from remote sensing data. In *IGARSS 2001*, July 2001, Sydney, Australie.
- Ottlé, C., and Vidal-Madjar, D., 1994, Assimilation of soil moisture inferred from infrared remote sensing in a hydrological model over the HAPEX-MOBILHY region, *Journal of Hydrology*, 158, 241–264.
- Sellers, P.J., Randall, D.R., Collatz, G.J., et al., 1996a, A revised land-surface parameterization (SiB2) for atmospheric GCMs. Part 1: Model formulation, *Journal of Climate*, 9, 676–705.
- Sellers, P.J., Los, S.O., Tucker, C.J., et al., 1996b, A revised land-surface parameterization (SiB2) for atmospheric GCMs. Part 2: The generation of global fields of terrestrial biophysical parameters from satellite data, *Journal of Climate*, 9, 706–737.
- Sinclair, T.R., and Seligman, N.G., 1996, Crop modeling: from infancy to maturity, *Agronomy Journal*, 88, 698–704.
- Soer, G.J.R., 1980, Estimation of regional evapotranspiration and soil moisture conditions using remotely sensed crop surface temperature, *Remote Sensing of Environment*, 9, 27–45.
- Taconet, O., Bernard, R., and Vidal-Madjar, D., 1986, Evapotranspiration over an agricultural region using a surface flux/temperature model based on NOAA-AVHRR data, *Journal of Climate and Applied Meteorology*, 25, 284–307.
- Weiss, M., and Baret, F., 1999, Evaluation of canopy biophysical variable retrieval performances from the accumulation of large swath satellite data, *Remote Sensing of Environment*, 70, 293–306.
- Wigneron, J.-P., Chanzy, A., Calvet, J.C., and Bruguier, N., 1995, A simple algorithm to retrieve soil moisture and vegetation biomass using passive microwave measurements over crop fields, *Remote Sensing of Environment*, 51, 331–441.
- Wigneron, J.-P., Ferrazzoli, P., Olioso, A., Bertuzzi, P., and Chanzy, A., 1999, A simple approach to monitor crop biomass from C-band radar data, *Remote Sensing of Environment*, 69, 179–188.
- Wigneron, J.-P., Chanzy, A., Calvet, J.-C., Olioso, A., and Kerr, Y., 2002, Modeling approaches to assimilating L-band passive microwave observations over land surfaces. *Journal of Geophysical Research*, 107 (D14), ACL 11-1 to ACL 11-14.

Active vegetation fluorosensing: present state and prospects

I. Moya, A. Ounis, Z.G. Cerovic and Y. Goulas

Equipe Photosynthèse et Télédétection, LURE/CNRS, Centre Universitaire Paris-Sud, B.P. 34, 91898 ORSAY Cedex, France.

moya@lure.u-psud.fr

ABSTRACT - Plant chlorophyll (Chl) is the only constituent of the terrestrial biosphere that exhibits fluorescence in the red (RF) and far-red (FRF) part of the spectrum. This makes red fluorescence a specific signature of vegetation. In addition to Chl fluorescence (ChlF), the UV part of the solar spectrum induces a blue-green fluorescence emission (BGF) of vegetation that originates from various phenolic compounds. The aim of this work is to highlight several new signatures of vegetation provided by active fluorescence remote sensing (fluorosensing) in both spectral regions:

- BGF/ChlF ratio. A high carbon-nutrient ratio stimulates the production of plant phenolics and increases this ratio,
- RF/FRF ratio can be used to monitor Chl content,
- Dual-wavelength Chl excitation. The RF/FRF ratio excited at two wavelength, differently absorbed by the chlorophyll, yields a double fluorescence ratio (DER) that allows a quantitative remote assessment of the leaf Chl content in a wider range.
- Chl fluorescence lifetime (τ). τ is an intensive parameter roughly proportional to the fluorescence yield. This technique also allows to determine the spatial position of leaves within the canopy.
- Imaging of laser-induced fluorescence. The use of spatial resolution of several fluorescence ratios reveals leaf or canopy fluorescence heterogeneity.
- Light-induced variable ChlF. Offers the possibility of a non-invasive monitoring of plant photosynthesis under field conditions over extended periods of time.

1 INTRODUCTION

Plants occupy a preponderant place in the biosphere, not only by producing biomass, but also due to their role in biogeochemical cycles and gas exchange with the atmosphere, particularly CO₂ uptake. Chlorophylls (Chl) are the photosynthetic pigments underlying the processes of primary production and the only constituent of the biosphere to fluoresce in the red (Fig. 1). The emission of fluorescence is produced after absorption of light by a mechanism directly in competition with the photochemical conversion. Although weak (less than 2% of absorbed energy) this emission is widely used to evaluate photosynthetic activity of leaves in the laboratory. In addition to chlorophyll fluorescence emission, the ultraviolet part of the solar spectrum also induces a blue-green fluorescence (BGF) of plants. This emission, which is not directly linked to chlorophyll or to photosynthesis, is species dependent and originates from several fluorophores, mainly from the phenylpropanoid family. As described in two recent reviews (Buschmann and Lichtenthaler 1998; Cerovic et al. 1999), BGF could be used at different levels for the identification and cartography of plant species, detection of stress or estimation of foliar temperature. New developments in laser sources have improved

the possibilities to detect plant fluorescence by remote sensing (fluorosensing). Lidars (Light Detection And Ranging) based on laser excitation have therefore been applied for the analyses of fluorescence signals emanating from aquatic or terrestrial vegetation (Hoge and Swift 1983). One limitation of fluorescence Lidar systems (FLIDAR) is that they measure fluorescence intensities, and by consequence, remain influenced by factors including distance, atmospheric transmission, geometry and movements of the plant. These limitations can be overcome by using emission or excitation ratios as fluorescence signatures.

This paper aims to examine these emergent techniques and evaluates their potential application for monitoring photosynthesis at different levels, from a single leaf to whole plant canopies.

2 THE EMISSION RATIO RF/FRF

The RF/FRF (or F685/F735) ratio was the first signature introduced by Lichtenthaler et al. (1986). It depends on the chlorophyll content of the leaf and on leaf anatomy. Owing to the selective re-absorption of red fluorescence by Chl molecules relative to far-red

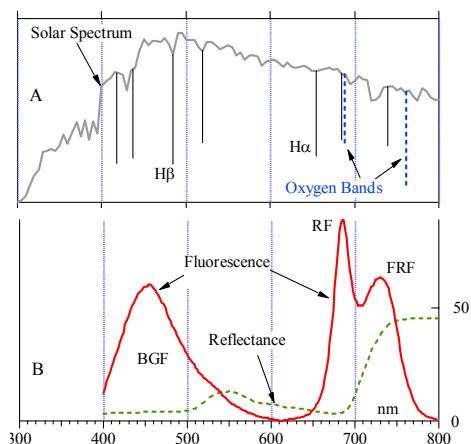


Fig. 1. A: Solar spectrum at sea level. Vertical lines represent the position and the intensity of the main absorption bands. Dashed lines: oxygen absorption bands due to terrestrial atmosphere. Continuous lines: Absorption bands due to the solar atmosphere. B: continuous line: fluorescence emission spectrum of a grapevine leaf excited at 355 nm. Dashed line: reflectance spectrum of the same leaf.

fluorescence, there is an inverse curvilinear relationship between this ratio and the leaf Chl content observed in many plant species (Gitelson et al. 1998). Gitelson et al. (1999) proposed to measure FR in the 700-710 nm range. As these wavelengths are intermediary between 685 nm (strong Chl absorption) and 735 nm (low Chl absorption) the accuracy and sensitivity of the RF/FRF method is highly improved.

The RF/FRF ratio can also show changes of small amplitude at constant Chl content. Changes in the RF/FRF ratio, have been detected during diurnal cycles (from 0.75 to 1.15) (Valentini et al. 1994; Agati et al. 1995) and under temperature stress (Agati et al. 1995; Agati et al. 1996; Agati et al. 2000). The dependence of this signature on irradiance indicates that these changes are due to a change in the level of non-photochemical quenching (NPQ) of Chl fluorescence.

3 TWO WAVELENGTH-EXCITATION OF CHL FLUORESCENCE

Phenolic compounds, mainly hydroxycinnamic acid esters and flavonoid glycosides, present in the cell walls and vacuoles, respectively, are good UV absorbers and will therefore efficiently screen the Chl located in the mesophyll (cf. Cerovic et al. 1999). As a consequence, Chl fluorescence excited below 400

nm is one to two orders of magnitude lower than when excited in the visible part of the spectrum (Cerovic et al. 1999).

But, this screening effect can also be exploited for a quantitative assessment of phenolic compounds, present mainly in the epidermis, by comparing leaf Chl fluorescence excited in the UV and visible part of the spectrum (Sheahan 1996; Bilger et al. 1997). New FLIDARs using double- (Ounis et al. 2001a) or multiple- (Samson et al. 2000) excitation wavelengths were designed and used to validate this approach for fluorosensing (Ounis et al. 2001a), and to follow the accumulation of phenolic compounds in nitrogen deficient maize plants (Samson et al. 2000) (Fig. 2).

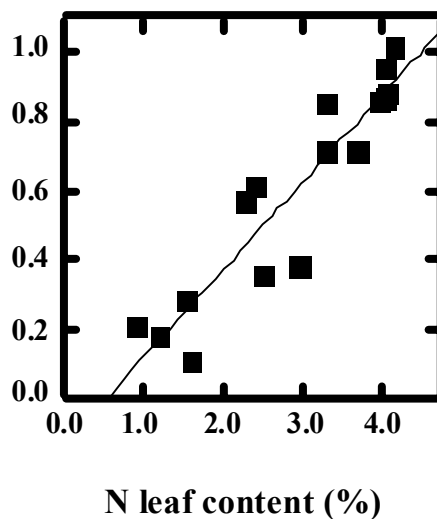


Fig. 2. Linear relationship ($R^2 = 0.93$) between the $FRF(ex360) / FRF(ex440)$ ratios and N contents in corn (measured at different times during its growth). From Samson et al. (2000).

In the work of Ounis et al. (2001a) and Ounis (2001), the DE-FLIDAR, for Dual-Excitation FLIDAR, was also used to check a new fluorescence signature that combines the double excitation and double emission approach. The double fluorescence ratio (DER), red (685 nm) to far-red (735 nm) fluorescence emission ratio, excited at 355 and 532 nm, was shown to be linearly depend on the leaf Chl content, for a large range, 20 to 70 $mg\ m^{-2}$, which is naturally found in leaves of most plant species (Fig. 3).

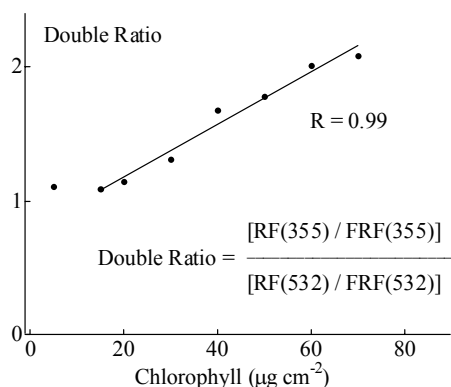


Fig. 3. The dual fluorescence emission ratio was linearly dependent on the Chl content. A linear fit gives a correlation coefficient of 0.99. From Ounis et al. (2000).

4 MEASUREMENT OF THE EMISSION RATIO BGF/RF (OR BGF/FRF)

An interesting approach to explain the changes of UV-induced fluorescence in nutrient-deficient plants is to use the frame of the carbon-nutrient balance hypothesis that is widely accepted by chemical ecologists (Bryant et al. 1987; Baas 1989; Price et al. 1989). According to this hypothesis, excess of fixed carbon relative to the plant's resources (high carbon-nutrient ratio) stimulates the shikimate pathway and therefore the production of plant phenolics (Price et al. 1989; Waterman and Mole 1994). Increases of total plant phenolics have indeed been observed in nutrient-deficient plants (Bryant et al. 1987; Price et al. 1989; Waterman and Mole 1994). The increases of the BG/ChlF ratios observed in N-deficient plants (Chappelle et al. 1984; Heisel et al. 1996; Corp et al. 1997; Buschmann and Lichtenthaler 1998) are also consistent with the carbon-nutrient balance hypothesis.

All this findings led us to propose in 1995 a new vegetation index based on fluorescence measurements — the Fluorescence Global Vegetation Index (FGVI) (Cerovic et al. 1995; Cerovic et al. 1999) (Fig. 4). This proposal to use a normalized fluorescence ratio (ChlF - BGF)/(ChlF + BGF) as a global vegetation index of nutrient shortage and presence of stress is now strengthened by the knowledge of the UV-screening effect of the secondary metabolites described above. Low FGVI or high simple BGF/ChlF ratio is a global indication of nutrient shortage induced either by an accumulation of fluorescing phenolics, which contribute to BGF increase, or accumulation of non-fluorescent phenolics, which by screening UV-excitation of Chl,

contribute to ChlF decrease. The FGVI would be interesting on the regional and global level, like the reflectance signature NDVI, but its practical application will depend on the development of airborne lidars at the regional level, and passive fluorosensing in the Fraunhofer lines for the global level (Moya et al. 1992).

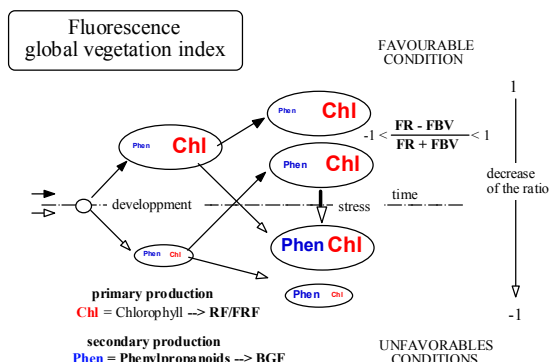


Fig. 4. Fluorescence global vegetation index (FGVI). The size of the oval surface symbolizes leaf development and expansion, and the size of abbreviation they encircle, Chl for chlorophyll, and Phen for phenylpropanoids, represent their respective content in the leaf. From Cerovic et al. 1999.

5 UTILIZATION OF CHL FLUORESCENCE LIFETIME

An alternative to the measurement of the Chl fluorescence yield (ϕ) is to use the mean fluorescence lifetime, τ . The use of τ in Chl fluorosensing is based on several studies showing that in most physiological situations, τ is roughly proportional to ϕ (Moya 1974; Cerovic et al. 1996). As τ is an intensive physical property of the fluorescence decay, it is independent of the geometry of the leaf, the concentration or the absorption of the fluorophore and of the atmospheric transmission. Importantly, τ has been shown to be almost insensitive to Chl fluorescence reabsorption (Terjung 1998), which greatly helps quantitative measurements on leaves.

A system for measuring the Chl fluorescence lifetime of plants from a distance (τ -FLIDAR) was successfully developed at LURE (Goulas 1992; Goulas et al. 1994; Moya et al. 1995; Goulas et al. 1997). It was based on the use of a laser delivering very short pulses (< 100 ps) and on the temporal analysis of fluorescence and backscattered signals detected by a fast photomultiplier and a digital transient recorder. The overall time response (0.35 ns) imposes to make use of deconvolution techniques.

When fluorosensing complex targets that contain several leaves at different surface planes and even stems in the field of view, a special two-step deconvolution program was developed to retrieve the lifetime parameter. A first deconvolution was applied to the backscattered laser light from the target, which provides the level and the relative area of leaves illuminated by the laser beam. In a second step, this information on the position of the illuminated leaves was used to calculate the mean Chl fluorescence lifetime (Camenen et al. 1996; Goulas et al. 1997).

The τ -FLIDAR was used on individual leaves from a distance of 15 m, to track the variation of the mean Chl fluorescence lifetime as a function of the plant water status (Cerovic et al. 1996). An important falloff of this work is the possibility to determine the spatial position of leaves within the canopy by analysing the backscattered signal after picosecond excitation. The structure of canopies is of particular interest for the evaluation of the intercepted radiation in radiative transfer models. Another set up for measuring the mean Chl fluorescence lifetime at distance has been developed by Sowinska et al. (1996).

Among other LIDAR techniques, remote sensing of the mean fluorescence lifetime appears to be the most robust method, at the cost, however, of a sophisticated and expensive technology.

6 IMAGING SYSTEMS

The FLIDAR imaging systems are based on bi-dimensional matrix detectors (Saito et al. 1999; Sowinska et al. 1999; Corp et al. 2000) or on "raster" systems that reconstitute the image pixel by pixel (Johansson et al. 1996). Their spatial resolution allows one to take into account the leaf or canopy fluorescence heterogeneity. Imaging FLIDARs use many emission fluorescence ratios. Of particular interest is the truck-based laser-induced fluorescence imaging system described by Sowinska et al. (1999) (Fig. 5). A remote sensing unit devoted to distance measurements records images of fluorescence excited at 355 nm and detected consecutively at four wavelengths (440, 520, 690 and 730 nm) through band pass filters. In addition, a second detection unit is installed inside the truck for measurements on detached leaves under laboratory-like conditions. The system was used to discriminate between wheat plants submitted to different fertilisation rates (Heisel et al. 1997).



Fig. 5. The truck-based FLIDAR imaging system described by Sowinska et al. (1999)

7 MICRO-FLIDARS

The method of saturating light pulses, introduced almost two decade ago by Schreiber (1986), allows precise measurements of variations of fluorescence yield under full daylight conditions, from which one can deduce the photosynthetic electron transfer rate (Genty et al. 1989). Although instruments based on this method are intended to operate at near contact, it can be modified for continuous monitoring of the steady state Chl fluorescence (F_s) at distance up to several meters. The Laser-PAM (Ounis et al. 2001b) is based on a regular PAM 101 detection unit (Heinz Walz, Effeltrich, Germany) equipped with a Fresnel lens and a laser diode emitting at 638 nm. However, in this transformation, the possibility to measure at distance has been obtained at the expense of the possibility to saturate Chl fluorescence.

Variable Chl fluorescence measurements by the light doubling method has also been shown to be possible at distances up to 5 meters thanks to a new fluorimeter, the FIPAM (Frequency Induced Pulse Amplitude Modulation) (Cavender-Bares et al. 1999; Flexas et al. 2000; Apostol et al. 2001). The FIPAM is a small laser diode-based FLIDAR, able to measure the steady state Chl fluorescence level (F_s) at a very low repetition rate (1 Hz) or the minimum level (F_o) in the dark.

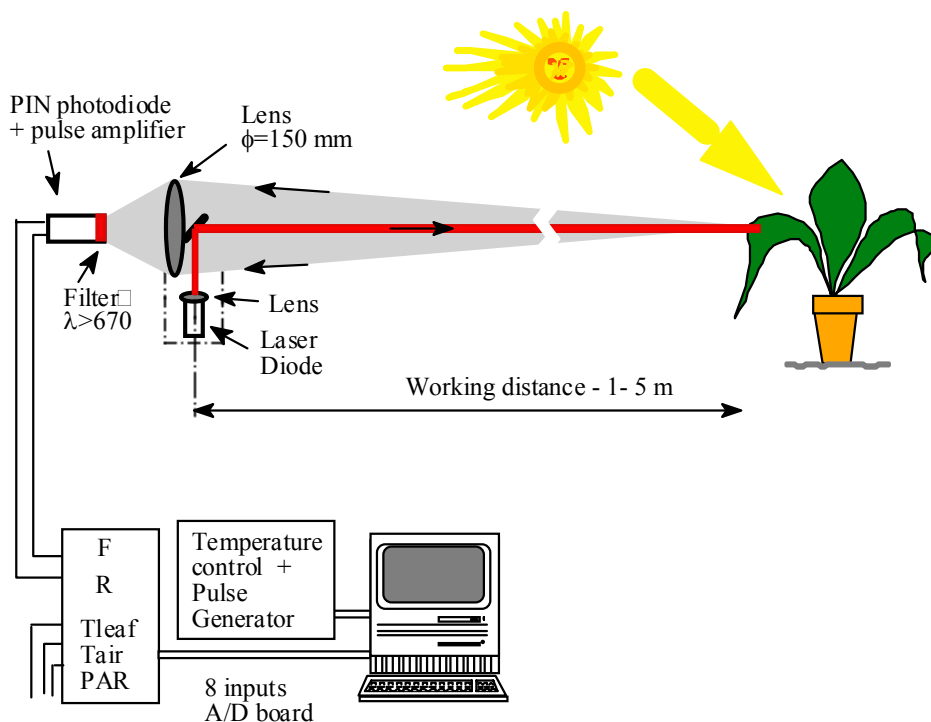


Fig. 6. Scheme of the FIPAM fluorimeter. A laser-diode beam at 635 nm is modulated at different frequencies with constant amplitude and duration (2 μ s) and focused on a leaf by a microscope objective. Working distances were adjustable in the range from 0.5 to 5 m. F_s (or F_o) are measured at 1 Hz, (average intensity of 0.05 μ mol photons $m^{-2} s^{-1}$). F_m (or F_m'), is induced by increasing the frequency to 100 kHz (average intensity ranges between 2000 and 10000 μ mol $m^{-2} s^{-1}$, depending on focusing). The induction kinetics can also be acquired, with a time resolution of 10 μ s. Leaf fluorescence signal (F) is collected by a lens and focused on a PIN photodiode, after passing through a high-pass filter ($\lambda > 670$ nm). In addition, a continuous signal (R) is recorded corresponding to the reflected light by the leaf. R is proportional to the PPFD at the exact area where F is measured. The instrument is controlled by a computer with a specially designed program, which allows continuous measurement over several days.

The maximum Chl fluorescence level (F_m) is obtained by increasing the frequency of repetition up to 100 kHz that saturates Chl fluorescence. Fig. 6 shows a scheme of the FIPAM principle. This system was intended as a reference tool for other lidars, or to calibrate passive fluorescence measurements.

The FIPAM was used to follow continuously F_s and F_m chlorophyll fluorescence parameters of a potted grapevine during 17 days of water-stress development. Fig. 7 shows the relationship between $\Delta F/F_m'$ and light intensity for the afternoon. Two different days, before and after water-stress development, were compared. It is observed that the stressed plants exhibit a lower capacity to recover after high light exposure. According to Cornic and

Briantais (1991), electron transport to O_2 should increase during the desiccation of the leaf. This alternative sink for electrons should be large enough to maintain high rates of electron transport during most of the day. By contrast to what happened under irrigated conditions, such an increase in electron transport to O_2 was not able to protect leaves from photoinhibition during drought stress, as witnessed by only a partial recovery of the afternoon quenching (see Fig. 7) (Flexas et al. 2000).

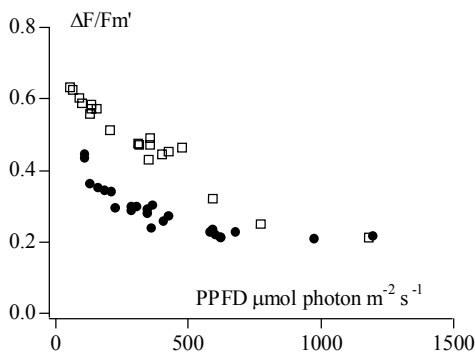


Fig. 7. $\Delta F/Fm'$ measurements plotted against PPFD. Afternoon data of a diurnal cycle of a potted vine plant (*Vitis vinifera* L.). Open squares: well watered plant; Closed circles: same plant after several days of withholder watering.

An instrument measuring at several tens of meters, based on the FIPAM principle, is technically feasible, however, the danger inherent to the use of high power focussed laser beams, necessary to saturate fluorescence, renders it harmful. This is why most of the applications of fluorescence, in field conditions, are based on the measurement of the F_s parameter.

Although lower than that of F_m , the variations of F_s can be up to 100% (Cerovic et al. 1996). Several studies have been devoted to the understanding of F_s changes in relation to the constraints to which plants are subjected (Cerovic et al. 1996; Rosema et al. 1998; Flexas et al. 2000). Fig. 8 shows that one can obtain a valuable information on the water status of a vine plant by a simple measurement of F_s as a function of natural light changes. In this experiment, the two parameters must be measured on exactly the same part of the leaf, which is one of the special features of the FIPAM.

The results shown in Fig. 8 can be interpreted as follows. When the stomata are open, photochemical quenching (Q_p) determines the actual fluorescence level. An increase in the light intensity modifies the equilibrium of the electron transport chain in the direction of a reduction, which is accompanied by an increase of Chl fluorescence. In a water-stressed plant, the stomata are closed. Electron transport to O_2 should be relatively increased during the desiccation of the leaf (Cornic and Briantais 1991). To dissipate the excess of absorbed energy, a mechanism of non-radiative dissipation (NPQ) takes place at the level of the PSII antennae, inducing a decrease of F_s . When this mechanism is reinforced following an increase of light, F_s decreases.

Reciprocally, F_s increases when the NPQ relaxes after a decrease of light.

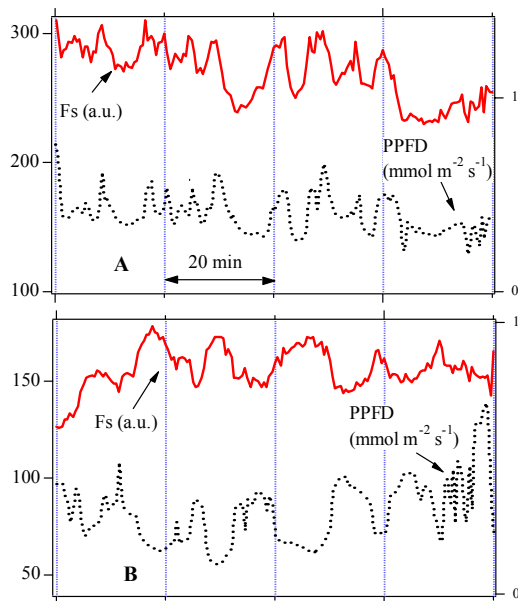


Fig. 8. Stationary Chl fluorescence (F_s) and PPFD of a potted vine plant (*Vitis vinifera* L.) as a function of time. Measurements were performed with the FIPAM fluorimeter at a distance of 1 m. PPFD variations are due to clouds. A. Well watered plant. B. Same plant after several days of withholder watering. Note the anti-parallel correlation between F_s and PPFD.

8 CONCLUSIONS

For a long time, Chl fluorescence studies remained confined to the laboratory and did not attain the status of a remote sensing signal, usable in an operational way. The main reason was the difficulty to understand the underlying mechanisms of Chl fluorescence changes under natural outdoor conditions. The situation has changed during the last decade, thanks to the increasing research work on the photosynthetic regulation mechanisms at the leaf level, which permitted a much better understanding of the significance of Chl fluorescence variations. New parameters, like excitation ratios or Chl fluorescence imaging, also contribute to renew the interest for active fluorosensing. The use of laser diode based or diode pumped solid state lasers also largely improved the reliability of FLIDAR systems. So the question arises if such instrumentation can be used to measure ground targets from a space platform. For example, a first estimation at an altitude of 258 km, based on a pulsed excitation and a detection time window of 20 ns, indicates that the minimum pulse energy needed to induce and detect

Chl fluorescence would be in the order of one Joule per pulse (Ounis 2001). But this was calculated for the case of night measurements. Under daylight conditions, however, much higher energies are required because of the contribution of ground albedo. At the present time, the use of such a powerful laser from a space platform seems unrealistic. With respect to long range remote sensing of Chl fluorescence, passive methods, based on the filling-in of the Fraunhofer lines (see Fig. 1) (Moya et al 1993, Moya et al 1998) seems to have the greatest potential.

9 ACKNOWLEDGEMENTS

We wish to acknowledge the support of the CNRS through the GDR 1536 "FLUOVEG". We thank also all the members of the team "Photosynthesis and Remote Sensing" of LURE for the data used in this manuscript.

10 REFERENCES

Agati G, Cerovic ZG and Moya I (2000) The effect of decreasing temperature up to chilling values on the *in vivo* F685/F735 chlorophyll fluorescence ratio in *Phaseolus vulgaris* and *Pisum sativum*: The role of the Photosystem I contribution to the 735 nm fluorescence band. *Photochem Photobiol* 72: 75-84

Agati G, Mazzinghi P, di Paola ML, Fusi F and Cecchi G (1996) The F685/F730 chlorophyll fluorescence ratio as indicator of chilling stress in plants. *J Plant Physiol* 148: 384-390

Agati G, Mazzinghi P, Fusi F and Ambrosini I (1995) The F685/730 chlorophyll fluorescence ratio as a tool in plant physiology: response to physiological and environmental factors. *J Plant Physiol* 145: 228-238

Apostol S, Briantais J-M, Moise N, Cerovic ZG and Moya I (2001) Photoinactivation of photosynthetic electron transport chain by accumulation of over-saturating light pulses given to dark adapted pea leaves. *Photosynth Res*: in press

Baas WJ (1989) Secondary plant compounds, their ecological significance and consequences for the carbon budget. In: Lambers H (Ed.) *Causes and Consequences of Variation in Growth Rate and Productivity of Higher Plants*, pp 313-340, SPB Academic Publishing, The Hague

Bilger W, Veit M, Schreiber L and Schreiber U (1997) Measurement of leaf epidermal transmittance of UV radiation by chlorophyll fluorescence. *Physiol Plant* 101: 754-763

Bryant JP, Chapin FSI, Reichardt PB and Clausen TP (1987) Response of winter chemical defense in Alaska paper birch and green alder to manipulation of carbon/nutrient balance. *Oecologia* 72: 510-514

Buschmann C and Lichtenthaler HK (1998) Principles and characteristics of multi-colour fluorescence imaging of plants. *J Plant Physiol* 152: 297-314

Camenen L, Goulas Y, Guyot G, Cerovic ZG, Schmuck G and Moya I (1996) Estimation of the chlorophyll fluorescence lifetime of plant canopies: validation of a deconvolution method based on the use of a 3-D canopy mockup. *Remote Sens Environ* 57: 79-87

Cavender-Bares J, Apostol S, Moya I, Briantais J-M and Bazzaz FA (1999) Chilling-induced photoinhibition in two oak species: Are evergreen leaves better protected than deciduous leaves? *Photosynthetica* 36: 587-596

Cerovic ZG, Goulas Y, Camenen L, Guyot G, Briantais J-M, Morales F and Moya I (1995) Scaling fluorescence signals from the chloroplast to the canopy level. In: Guyot G (Ed.), *Photosynthesis and Remote Sensing*, pp 21-27, Montpellier, France: EARSeL, Paris

Cerovic ZG, Goulas Y, Gorbunov M, Briantais J-M, Camenen L and Moya I (1996) Fluorescence of water stress in plants. Diurnal changes of the mean lifetime and yield of chlorophyll fluorescence, measured simultaneously and at distance with a τ -LIDAR and a modified PAM-fluorimeter, in maize, sugar beet and Kalanchoë. *Remote Sens Environ* 58: 311-321

Cerovic ZG, Samson G, Morales F, Tremblay N and Moya I (1999) Ultraviolet-induced fluorescence for plant monitoring: present state and prospects. *Agronomie: Agriculture and Environment* 19: 543-578

Chappelle EW, McMurtrey JE, Wood FM and Newcomb WW (1984) Laser-induced fluorescence of green plants. 2: LIF caused by nutrient deficiencies in corn. *Appl Opt* 23: 139-142

Cornic G and Briantais J-M (1991) Partitioning of photosynthetic electron flow between CO₂ and O₂ in a C₃ leaf (*Phaseolus vulgaris* L.) at different CO₂ concentrations and during drought stress. *Planta* 183: 178-184

Corp LA, McMurtrey JE, Chappelle EW, Daughtry CST and Kim MS (1997) UV band fluorescence (*in vivo*) and its implications to the remote assessment of nitrogen supply in vegetation. *Remote Sens Environ* 61: 110-117

Corp LA, Chappelle EW, McMurtrey JE, Mulchi, CL, Daughtry CST and Kim MS (2000) Advances in fluorescence systems for the remote assessment of nitrogen supply in field corn. In: IEEE P, NJ, USA (Ed.), *IEEE 2000 International Geoscience and Remote Sensing Symposium*, pp 351-353, Piscataway, NJ, USA: IEEE

- Flexas J, Briantais J-M, Cerovic ZG, Medrano H and Moya I (2000) Steady-state and maximum chlorophyll fluorescence responses to water stress in grapevine leaves: A new remote sensing system. *Remote Sens Environ* 73: 283-297
- Genty B, Briantais J and Baker N (1989) The relationship between the quantum yield of photosynthetic electron transport and quenching of chlorophyll fluorescence. *Biochim Biophys Acta* 990: 87-92
- Gitelson AA, Buschmann C and Lichtenthaler HK (1998) Leaf chlorophyll fluorescence corrected for re-absorption by means of absorption and reflectance measurements. *J Plant Physiol* 152: 283-296
- Gitelson AA, Buschmann C and Lichtenthaler HK (1999) The Chlorophyll Fluorescence Ratio as an accurate measure of the chlorophyll content in plants. *Remote Sens Environ* 69: 296-302
- Goulas Y. Télédétection de la fluorescence des couverts végétaux: Temps de vie de la fluorescence chlorophyllienne et fluorescence bleue [PhD thesis]. Université de Paris-Sud, 1992.
- Goulas Y, Camenen L, Briantais J-M, Schmuck G, Moya I and Guyot G (1994) Measurements of laser-induced fluorescence decay and reflectance of plant canopies. In: Guyot G (Ed.), *Physical Measurements and Signatures in Remote Sensing*, pp 937-944, Val d'Isère, France: CNES
- Goulas Y, Camenen L, Guyot G, Cerovic ZG, Briantais J-M, Schmuck G and Moya I (1997) Measurements of laser-induced fluorescence decay and reflectance of plant canopies. *Remote Sens Rev* 15: 305-322
- Heisel F, Sowinska M, Khalili E, Eckert C, Miehe JA and Lichtenthaler HK (1997) Laser-induced fluorescence imaging for monitoring nitrogen fertilising treatments of wheat. In: Narayanan RM and Kalshoven JE (Eds.), *Aerosense '97*, pp 10-21, Bellingham: SPIE
- Heisel F, Sowinska M, Miehe JA, Lang M and Lichtenthaler HK (1996) Detection of nutrient deficiencies of maize by laser induced fluorescence imaging. *J Plant Physiol* 148: 622-631
- Hoge FE and Swift RN (1983) Airborne dual laser excitation and mapping of phytoplankton photopigments in a Gulf Stream Warm Core Ring. *Appl Opt* 22: 2271-2281
- Johansson J, Andersson M, Edner H, Mattsson J and Svanberg S (1996) Remote fluorescence measurements of vegetation spectrally resolved and by multi-colour fluorescence imaging. *J Plant Physiol* 148: 632-637
- Lichtenthaler HK, Buschmann C, Rinderle U and Schmuck G (1986) Application of chlorophyll fluorescence in ecophysiology. *Radiat Environ Biophys* 25: 297-308
- Moya I (1974) Durée de vie et rendement de fluorescence de la chlorophylle in vivo. Leur relation dans différents modèles d'unités photosynthétique. *Biochim Biophys Acta* 368: 214-227
- Moya I, Goulas Y, Morales F, Camenen L, Guyot G and Schmuck G (1995) Remote sensing of time-resolved chlorophyll fluorescence and back-scattering of the laser excitation by vegetation. *EARSeL Adv Remote Sens* 3: 188-197
- Moya I, Guyot G and Goulas Y (1992) Remotely sensed blue and red fluorescence emission for monitoring vegetation. *ISPRS J Photogram Remote Sens* 47: 205-231
- Moya, I., Camenen, L., Latouche, G., Mauxion, C., Evain, S. and Cerovic, Z. G. (1998), An instrument for the measurement of sunlight excited plant fluorescence, In *Photosynthesis: Mechanisms and Effects* (G. Gorab, ed.), Kluwer Acad. Pub., Dordrecht, pp. 4265-4270.
- Ounis A. Télédétection de la fluorescence des couverts végétaux induite par laser : application des techniques de corrélation temporelle microseconde et nanoseconde [Ph.D.]. Université de Paris-Sud, 2001.
- Ounis A, Cerovic ZG, Briantais J-M and Moya I (2001a) Dual excitation FLIDAR for the estimation of epidermal UV absorption in leaves and canopies. *Remote Sens Environ* 76: 33-48
- Ounis A, Evain S, Flexas J, Tosti S and Moya I (2001b) Adaptation of a PAM-fluorometer for remote sensing of chlorophyll fluorescence. *Photosynth Res* 68: 113-120
- Price P, Waring GL, Julkunen-Titto R, Tahvanainen J, Mooney HA and Craig T (1989) Carbon-nutrient balance hypothesis in within-species phytochemical variation of *Salix lasiolepis*. *J Chem Ecol* 15: 1117-1131
- Rosema A, Snel JFH, Zahn H, Buurmeijer WF and Van Hove LWA (1998) The relation between laser induced chlorophyll fluorescence and photosynthesis. *Remote Sens Environ* 65: 143-154
- Saito Y, Saito R, Nomura E, Kawahara TD, Nomura A, Takaragaki S, Ida K and Takeda S (1999) Performance check of vegetation fluorescence imaging lidar through *in vivo* and remote estimation of chlorophyll concentration inside plant leaves. *Opt Rew* 6: 155-159
- Samson G, Tremblay N, Dudelzak AE, Babichenko SM, Dextraze L and Wollring J (2000) Nutrient

- stress of corn plants: early detection and discrimination using a compact multiwavelength fluorescent lidar. In: Proceedings of the 20th EARSel Symposium, Dresden, Germany:
- Schreiber U (1986) Detection of rapid induction kinetics with a new type of high-frequency modulated chlorophyll fluorimeter. *Photosynth Res* 9: 261-272
- Sheahan JJ (1996) Sinapate esters provide greater UV-B attenuation than flavonoids in *Arabidopsis thaliana* (Brassicaceae). *Am J Bot* 83: 679-686
- Sowinska M, Cunin B, Heisel F and Miehe JA (1999) New UV-A laser-induced fluorescence imaging system for near-field remote sensing of vegetation: characteristics and performances. In: Proceedings of the SPIE Conference on Laser Radar Technology, pp 91-102, Orlando Florida: The International Society for Optical Engineering
- Sowinska M, Heisel F, Miehe JA, Lang M, Lichtenthaler HK and Tomasini F (1996) Remote sensing of plants by streak camera lifetime measurements of the chlorophylla emission. *J Plant Physiol* 148: 638-644
- Terjung F (1998) Reabsorption of chlorophyll fluorescence and its effects on the spectral distribution and the picosecond decay of higher plant leaves. *Z Naturforsch C* 53: 924-926
- Valentini R, Cecchi G, Mazzinghi P, Scarascia-Mugnozza G, Agati G, Bazzani M, De Angelis P, Fusi F, Matteucci G and Raimondi V (1994) Remote sensing of chlorophyll *a* fluorescence of vegetation canopies: 2. Physiological significance of fluorescence signal in response to environmental stresses. *Remote Sens Environ* 47: 29-35
- Waterman PG and Mole S (1994) *Analysis of Phenolic Plant Metabolites*, pp 1-238 Oxford: Blackwell Scientific Publications

Land Cover Classification at a Regional scale in Iberia: separability in a multi-temporal and multi-spectral data set of satellite images

Agustín Lobo¹, Pierre Legendre², José Luis González Rebollar³, Jordi Carreras⁴ and Josep-Maria Ninot⁴

¹*Institut de Ciències de la Terra "Jaume Almera" (CSIC), Lluís Solé Sabarís s/n, 08028 Barcelona, Spain (alobo@ija.csic.es)*

²*Département des Sciences Biologiques, Université de Montréal, C.P. 6128 succ. A, Montréal, Québec, Canada H3C 3J7*

³*Estación Experimental del Zaidín (CSIC), Prof. Albareda 1, 18008 Granada, Spain*

⁴*Departament de Biologia Vegetal, Facultat de Biologia, Universitat de Barcelona, Diagonal, 645, 08028 Barcelona, Spain*

ABSTRACT. *Earth Observation at regional scales, such as the Iberian Peninsula or the Mediterranean Basin, is an important tool to understand the relationships between climate and surface properties. Among the different layers of information that can be derived from satellite imagery, Land Cover maps are important by themselves and as an aid to infer other variables. Land Cover legends at regional scales require finer categories than those used at a global scale, which implies processing multi-spectral imagery acquired by Earth Observing systems with daily acquisition rates. In this article we discuss several alternatives to analyze satellite image data sets that are both multi-temporal and multi-spectral, with spatial resolution of 1 km². In order to facilitate the interpretation of our results, we restrict our analysis to pixels that correspond to cells with a uniform and known cover on the ground, as described by a detailed vegetation map, in Catalonia (NE Spain). Our results indicate that canonical Redundancy Analysis is efficient at reducing the multi-spectral and multi-temporal space while keeping high statistical separability among habitat types. The small fraction of uniform pixels (~2 %) suggests that, at least for the Mediterranean Region, data fusion techniques would be convenient to increase spatial resolution in the data set, and that instruments keeping daily acquisition rates but with higher spatial resolution (~1 ha) should be considered.*

1 INTRODUCTION

Earth observation through remotely sensed imagery has an important role in Global Change research. Satellite images are used to assess the state of the surface, to parameterize some models and to validate results. Considering that these images are the only observations done at a scale close to the one intended for models, their analysis should suggest new approaches for modeling.

Among the applications of Remote Sensing on this field, Land Cover (LC) mapping holds a central place. Global Land Cover maps are critical information for monitoring changes of the Earth surface and also have an auxiliary role to estimate other surface variables. Historically, Land Cover mapping has used either multi-temporal or multi-spectral imagery depending on whether the study had global or continental extent with coarse resolution (typically using AVHRR data sets), or covered smaller areas with higher resolution (typically using LANDSAT and SPOT images).

Most work done with AVHRR data sets for global and continental Land Cover mapping reduce each multi-spectral image to one single layer of Normalized Difference Vegetation Index (NDVI), which is proportional, in a statistical sense, to the fraction of photosynthetically-active radiation that is intercepted by green tissue (fPAR). The multi-temporal and multi-spectral data set is thus simplified into a time sequence of NDVI layers. An early and important finding of Remote Sensing is that time series of NDVI are very good descriptors of vegetative phenology. Global and continental charts produced from AVHRR data sets are essentially based on the information provided by time series of NDVI, although different authors used different techniques for classification (Tucker et al. 1985, Townshend et al 1987, Lloyd 1990, Loveland 1991, Eidenshink 1992, Running et al. 1994, 1995, DeFries et al 1995, Ehrlich and Lambin, 1996, Loveland et al. 2000). A similar approach was used at a regional scale by Lloyd (1989) and Lobo et al. (1997).

While most work on Global Change has been conducted at a global scale, interest on modeling and assessing the impact at a regional scale is growing. A regional scale facilitates evaluation of results, and its detail is more appropriate to study the implications of Global Change for human populations. Current legend schemes of Land Cover classes are relevant information for studies at global and continental scales, but regional applications require more detailed classifications, which in turn require more spectral information. Newer recent satellite Earth observation systems with daily acquisition rates are equipped with more spectral bands than earlier NOAA systems.

A methodological problem arises when we decide to analyze time series of multi-spectral images and want to use more than one single index across time, as data from each cell becomes a multi-variate time series. In an analogous way as done with the older AVHRR imagery, it is, in principle, possible to identify specific features in time profiles of several indices, but little is known on the phenological behavior of indices other than NDVI and alike. Another approach is to stack spectral bands from images of successive dates, as if they were bands from other regions in the electromagnetic spectrum, to create a huge multi-spectral image). This approach simplifies the problem by ignoring its temporal aspect and subsuming it into its multi-spectral aspect. Such an approach would, however, severely affect the essence of the problem, since the time axis (the arrow of time) is of a different nature than the axes of the variables.

In this study, we describe the use of Canonical Redundancy Analysis (RDA) to transform the original space of n (cells) \times t (times) \times p (spectral variables) to a reduced space of n (cells) \times p (scores) which is subsequently submitted to discriminant analysis. As a first step and in order to facilitate the interpretation of our results, we restrict our analysis to pixels that correspond to cells with a uniform and known cover on the ground, using an annual set of SPOT-4 VEGETATION images and land-cover maps of Catalonia (NE Spain).

2 METHODS

2.1 Data

We have processed an annual (1999) set of 36 S10-VEGETATION images and 44 digital maps at the scale 1:50,000 from the series of Maps of Habitats of Europe for Catalonia (NE Spain). Each map covering an area of 28 km \times 18.5 km, we have screened a total of 22,792 km². S10-VEGETATION images are 10-day syntheses of daily calibrated and atmospherically corrected images produced through the Maximum Value Compositing method of Holben (1986). SPOT-4 VEGETATION has four spectral bands: 430 – 470,

610 – 680, 780 – 890 and 1580 – 1750 nm. The legend of the maps is based on the Corine Biotopes Manual (Devillers *et al.*, 1991) and the Directive 92/43 of the European Union with specific improvements for Catalonia (NE Spain) (Carreras & Vigo 1997). This system is very close to the more recent and comprehensive European Nature Information System (EUNIS) of the European Environment Agency, developed and maintained by the European Topic Center on Nature Protection and Biodiversity of the European Union. Rather than to *habitats* in the ecological sense, the legend corresponds to that of a land-cover map with emphasis on vegetation categories.

2.2 Analysis

We selected those 1-km² cells that had at least 90% of their surface in a single habitat patch (a total of 495 cells, 2.17% of all screened cells), and extracted the reflectance data and ancillary information from the sequence of S10-VEGETATION pixels that matched those cells. We organized the reflectance values as one data matrix for each selected pixel. The data matrices had time observations as rows (one observation for each S10 composite), while, as columns, we included the four spectral bands and two normalized difference (ND) indices: NDVI (which we call here ND(nir,red) for consistency) and ND(nir,mir).

We ran three approaches of analysis, aiming to discriminate the selected cells according to their habitat type. In all three approaches, we calculated the statistical separability of the different habitat categories in the transformed spaces using the Jeffries-Matutsita distance (Richards 1999). The use of the Jeffries-Matutsita distance as a measure of statistical separability in all cases let us compare the discriminant power of each approach.

The first approach used only the (univariate) time series of ND(nir,red) for each selected cell. Therefore, this approach focused on the temporal aspect of the data set. We selected the column of NDVI profiles from the data matrix of each selected cell, assembled a global data matrix with these profiles as row vectors, ran a PCA on the global data set, and selected the first four scores (accounting for > 96% of the total variance).

The second approach used the spectral space defined by the bands of the imagery for each period of synthesis, hence focusing on the spectral characteristics of the data set. We made a multi-variate table with the selected cells and their reflectance values in the four bands of the VEGETATION image for each period of synthesis, calculated the statistical separability for each table, and, finally, calculated a combined statistical separability matrix by selecting the highest separability value across time for each pair of habitats.

The third approach used the (multi-variate) time course of the spectral responses for each cell, attempting to combine both sources of information: temporal and spectral. We ran a RDA (Legendre and Legendre, 1998) on the multivariate table of all selected cells using bands B2, B3 and MIR plus the two ND indices as matrix of response variables, and a matrix of dummy variables coding for the cells as matrix of explanatory variables.

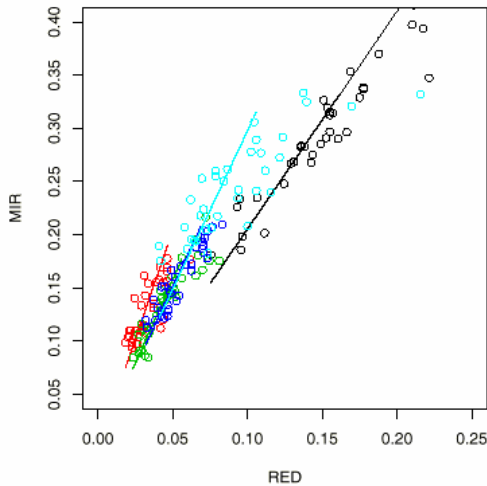


Figure 1. Examples of four robust fits of a regression line to the mir vs. red reflectance values of four selected cells, constraining the intercept to a 0 value. Black symbols, a non-irrigated cereal crop (code 30); red, evergreen oak forest (code 25) Catalonia (NE Spain).

2.3 Slope of the MIR vs. RED regression.

The relationship between values of red and medium-infrared reflectance is dependent upon both the structure and the humidity of the target. Most plots of the values of MIR vs. RED bands for a given target along an annual cycle are a cloud in which a linear

trend accounts for most of the variance (Fig. 1). Some outliers located well below the linear trend are likely due to recent rainfall events. We used a robust linear regression method to fit a line constraining the intercept to be 0 for each selected cell, and test the use of the slope as a characteristic feature of different habitats.

3 RESULTS

A plot of the selected cells in the plane of the first two principal components (PCs) of the ND(nir,red) time series (Fig. 2) indicates that the main source of variation is along an axis from the evergreen oak community (code 25, relatively flat plots of ND(nir,red), see Fig. 3) to the non-irrigated cereal fields (code 30, wave of ND(nir,red) peaking in early spring). Therefore, the main source of variation is due to the “degree of deciduousity” of the plants in the cell. A second axis of variation ordinales the ND(nir,red) time profiles from those with a narrow wave picking in spring to those with a narrow wave picking in summer (code 31, rice fields), with the flat profiles of evergreen communities and the wide waves of the *Genista purgans* shrubland (a pattern of discontinuous evergreen shrubs over an herbaceous background) at intermediate positions. The second main source of variation is thus related to the timing of the greenness peak.

Values of the Jeffries-Matusita index indicate that several habitat types cannot be adequately discriminated using the PCs of the ND(nir,red) time profiles. Particularly low values are found among the different Mediterranean shrub communities (codes 5, 6 and 7) and between those and *Pinus halepensis* woodlands (code 12). In some cases the low separability is a consequence of the definition of the habitat types. This is the case for *Rosmarinus* garrigue and *Pinus halepensis* woodlands over *Rosmarinus* garrigue (codes 12 and 13) and between the two types of *P. halepensis* woodlands (codes 12 and 13). As these woodlands can be very open, a substantial part of the reflectance actually comes from the understory.

The RDA ordination is essentially the same as the PCA ordination. Clustering within class 30 is more evident and, in general, cells tend to cluster by habitat type more than in the PCA ordination. As a consequence, discrimination among habitat types is enhanced in the RDA ordination. Separability reaches high values for classes 5 vs. 6 (1.96) and 5 vs. 7 (1.99), while classes 6 vs. 7 remain undiscriminated. Statistical separability of the Mediterranean shrublands (codes 5, 6 and 7) vs. the *P. halepensis* woodlands (codes 12 and 13) also achieves high values in this data set. Discrimination between the two evergreen oak forests (codes 25 and 26) is, however, even more difficult here, although the values of separability in the PCA-transformed data set were already too low. Despite a small increase, discrimination between *P. halepensis* (codes 12 and 13) and *P. uncinata* forests (code 23) is weak. An important increase of separability occurs between the Mediterranean shrublands (codes 5, 6 and 7) and the *P. uncinata* forests (code 23).

MIR vs. RED slopes calculated by robust linear regression with the constrain of null intercept show an interesting pattern (Fig. 4). Lowest values are found for rice fields, increase for cereal fields and attain a maximum for evergreen forests. Values for garrigue habitats are intermediate. Several other facts deserve being highlighted. First, while MIR vs. RED slopes do not discriminate between the two evergreen oak forests (*Quercus suber* and *Q. ilex*), they show a clear bimodal distribution for the case of *Q. suber* forests, with two distinct clusters. Cereal fields show also two clusters. Second, values from cells of *Cistus* garrigue are higher than those from cells of the other two garrigues. Third, conifer forests show intermediate values between the M-R slopes of evergreen forests and garrigues. Including M-R slopes as an additional variable for RDA increases separability, particularly between the *Rosmarinus* and *Cistus* garrigues. There is an increase between the two evergreen oak forests (*Quercus suber* and *Q. ilex*) as well, but this is a consequence of the presence of lower cluster of *Q. suber*. However, in both cases the increase is not sufficient to reach a good discrimination in these two pairs of habitats.

Despite the enhanced discrimination power, some habitat types still show poor separability. Two of the three Mediterranean shrublands cannot be discriminated between them, neither can be the two types of woodlands of *P. halepensis*. Furthermore, there is a weak separability between one of these two woodlands and one type of *P. uncinata* forest.

Combining the best spectral separability of each period of time does not improve discrimination within any of the pair of habitats with weak separability in the RDA-transformed data set. Searching the best discriminant period for each pair of habitat types also

has the problem of selecting an eventually high separability merely due to transient conditions (i.e., a recent rainfall) rather than to more stable characteristics. This risk is much reduced if the entire annual cycle is considered, as in the RDA approach.

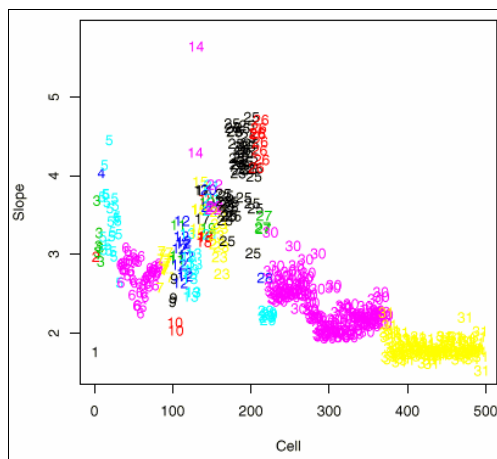


Figure 4. Values of the slope of the MIR vs. RED regression line with 0 intercept. Cells coded, and ordered, by habitat.

4 CONCLUSIONS

Direct RDA reduces a very complex multi-spectral and multi-temporal space and still keeps a high statistical separability among habitat types. Results using the RDA-transformed data set are better than those using NDVI time series and than those combining the best discriminant dates using all bands.

Some habitat types cannot be sorted out in the RDA-transformed data set. In some cases, the problem can be solved by going up one step in the hierarchical structure of the legend, and merging the indistinguishable types into a broader category, while still keeping an acceptable thematic detail. This is the case, for example, of the Mediterranean shrublands "*Rosmarinus* garrigue" and "*Cistus* and *Anthyllis cytisoides* garrigue" that can be lumped together into the category "Western garrigue" of the EUNIS classification scheme. However, in other cases, the indistinguishable types are not related in the hierarchical legend, and merging them together would create incoherent or too broader categories (i.e., "*P. halepensis* woodlands" and some "*P. uncinata* forests"). More research is required to discriminate these habitat types, with particular attention to including angular information.

The fraction of 1 km² pixels that are completely included within one single habitat patch is very low in our region of study (2.17%). Data fusion of imagery acquired by complementary systems might result into

products with the required intensity in both time and space. Also, Remote Sensing systems designed for the Mediterranean region and featuring spatial resolution close to 1 ha and daily acquisition should be contemplated.

ACKNOWLEDGEMENTS

This research has been conducted within the framework of project AMFIBER (REN2001-1841/GLO, *Programa Nacional de Ciencia y Tecnología* of Spain) and the Programa Nacional Ramón y Cajal (*Ministerio de Ciencia y Tecnología* of Spain), using imagery provided by the VEGETATION Preparatory Program.

REFERENCES

- Bartalev, S., Achard F., Erchov D., Gond. V., 2000. The potential contribution of SPOT 4/VEGETATION data for mapping Siberian forest cover at continental scale. Proceedings of the VEGETATION 2000 conference, 3-6 April 2000 Belgirate (Italia). <http://vegetation.cnes.fr:8080/>
- Braun-Blanquet, J., 1951, Pflanzensozioologie. 2ond. Ed. (Springer-Verlag. Viena).
- Carreras, J. and Vigo, J. 1997. Projecte de Cartografia dels Hàbitats a Catalunya. Report of the "Grup de Geobotànica i Cartografia de la Vegetació (Universitat de Barcelona)" for the "Departament de Medi Ambient de la Generalitat de Catalunya". Unpublished.
- Casanova, D. 1998. Quantifying the effects of land conditions on rice growth: a case study in the Ebro delta (Spain) using remote sensing. Thesis Landbouwniversiteit Wageningen, 219 pp.
- DeFries R.S. and Townshend, J.R.G. 1995, Global discrimination of land cover types from metrics derived from AVHRR Pathfinder data. . *Remote Sensing of Environment* **54**, 209-222.
- Devillers, P., Devillers-Terschuren, J. & Ledant, J.P. 1991. Corine Biotopes Manual. Habitats of the European Community. Commission of the European Communities. Luxembourg.
- Eidenshink, J.C., 1992. The 1990 conterminous US AVHRR data set. *Photogrammetric Engineering and Remote Sensing*, **58**, 809-813.
- Ehrlich, D. and Lambin, E.F., 1996. Broad scale land-cover classification and international climatic variability. . *International Journal of Remote of Remote Sensing*, **17**, 845-862
- Gao, B.-C., 1996, NDWI - a normalized difference water index for remote sensing of vegetation liquid water from space. *Remote Sensing of Environment*, **58**, 257-266.
- Holben, B.N., 1986. Characteristics of maximum-value composite images from temporal AVHRR data. *International Journal of Remote of Remote Sensing*, **7**, 1417-1434.
- Legendre, P. and Legendre, L. 1998. Numerical Ecology. 2nd edition (Amsterdam, Elsevier).
- Lloyd, D. 1989. A phenological description of Iberian vegetation using short wave vegetation index imagery. *International Journal of Remote of Remote Sensing* **10**, 827-833
- Lobo, A., Ibáñez-Martí, J.J. and Carrera Giménez-Cassina, C. 1997. Regional scale hierarchical classification of temporal series of AVHRR vegetation index. *International Journal of Remote Sensing*, **18**, 3167-3193.
- Loveland, T.R. and Belward, A.S. 1997. The IGBP-DIS Global 1 km Land Cover Data Set, DISCover First Results. *International Journal of Remote Sensing*, **18**, pp. 3289-3295
- Loveland, T., B. Reed, J. Brown, D. Ohlen, Z. Zhu, L. Yang and J. Merchant. 2000. Development of a Global Land Cover Characteristics Database and IGBP DISCover from 1-km AVHRR Data. *International Journal of Remote Sensing*, **21**, 1303-1330.
- Loveland, T.R., Merchant, J.M., Ohlen, D.O. and Brown, J.F. 1991. Development of a land cover characteristics for te conterminous US. *Photogrammetric Engineering and Remote Sensing*, **57**, 1453-1453.
- Richards, J. and Jia, X., 1999. Remote Sensing Digital Image Analysis. An Introduction. (Berlin, Springer).
- Running, S.W., Loveland, T.R., and Pierce L.L., 1994. A vegetation classification logic based in global biogeochemical models. *AMBIO*, **23**, 77-81
- Running, S.W., Loveland, T.R., Pierce L.L., Nemani, R.R. and Hunt, E.R., 1995. A vegetation classification logic for global land cover analysis. *Remote Sensing of Environment* **51**, 39-48.
- Spot Image 1998. *VEGETATION User's Guide*. http://www.spotimage.fr/data/images/vege/VEGETAT/book_1/e_frame.htm
- Townshend, J.R.G., Justice, C. and Kalb, V., 1987, Characterization and classification of Sout American land cover types using satellite data. . *International Journal of Remote Sensing*, **8**, 1189-1207
- Tucker, C.J., Townshend, J., and Goff, T.E., 1985. African land-cover classification using satellite data. *Science*, **227**, 369-375.

Remote Sensing Monitoring of Desertification, Phenology, and Droughts

Arnon Karnieli, Giorgio Dall'Omo,
J. Blaustein Institute for Desert Research
Ben-Gurion University of the Negev
Sede-Boker Campus 84990, ISRAEL
Tel: +972-7-6596855 Fax: +972-7-6596704
E-mail: karnieli@bgumail.bgu.ac.il

ABSTRACT Year-to-year fluctuations of rainfall in the northern Negev desert provide an opportunity to characterize and assess the temporal dynamics of desertification, phenology, and drought processes. Such information was retrieved and analyzed by combined use of satellite imageries in the reflectivity and thermal spectral bands.

Data covering four-years of coarse spatial resolution and images from a high revisit time satellite, namely the NOAA-I4, were used. The images were processed to produce the Normalized Difference Vegetation Index (NDVI) and the Land Surface Temperature (LST). These measures were applied to the sand field in the northwestern Negev (Israel), which is almost totally covered by biological soil crusts, and to an adjacent region in Sinai (Egypt), consisting mainly of bare dune sands. Various manipulations of the data were applied. Time series presentation of the NDVI and LST reveals that the NDVI values correspond to the reaction of the vegetation to rainfall and that LST values represent seasonal climatic fluctuation. Scatterplot analysis of LST vs. NDVI demonstrates the following: (1) The two different biomes (Sinai and the Negev) exhibit different yearly variation of the phenological patterns: two seasons in Sinai moving along the LST axis, and three seasons in the Negev - where the NDVI axis represents the growing season; (2) The Sinai has an ecosystem similar to that found in the Sahara, while the Negev, only a few kilometers away, has an ecosystem similar to the one found in the Sahel; (3) Drought indicators were derived by using several geometrical expressions based on the two extreme points of the LST – NDVI scatterplot. The later analysis led to a discrimination function that aims to distinguish between the drought years and the wet years in both biomes.

Results from the current study show that a great deal of information on dryland ecosystems can be derived from four, out of five, NOAA/AVHRR spectral bands. The NDVI is derived from the red and the near-infrared bands and the LST from the two thermal bands. Combined use of these two products provides more information than any product alone.

1 INTRODUCTION

The severe recurrence of droughts in the Sahel and other regions, as well as an apparent accelerated southward advance of the Sahara Desert, led to extensive international discussions and to the establishment of the United Nations Conference on Desertification (UNCOD). At this meeting, desertification was defined as “land degradation in arid, semi-arid, and dry sub-humid areas resulting mainly from adverse human impact” (UNEP, 1992).

The term phenology is usually defined as “the study of the timing of recurring biological phases, the cause of their timing with regard to biotic and abiotic forces, and the interaction among phases of the same or different species” (Lieth 1974). The current study deals with natural vegetation phenology, rather than that of agriculture.

Drought can be defined as a period of abnormally dry weather, which persists long enough to produce a serious ecological, agricultural, or hydrological imbalance (e.g., crop damage, water shortage, etc.). The severity of the drought depends upon the degree of moisture deficiency, the duration, and the size of the affected area. In this context, meteorological drought refers to lower than average precipitation for some time period (Wilhite and Glantz, 1985).

These three basic dryland processes, namely desertification, phenology, and drought, are strongly linked. Drought is part of the cause of desertification and certainly makes the situation worse. Mainguet (1994) states that desertification is “revealed by drought”. The phenology of natural plants is changed by either desertification or drought processes. It is expressed, for example, by changes between grasses and shrubs, C3 and C4 species, or palatable to

unpalatable species. The objective of the current paper is to characterize and assess the temporal dynamics of these three processes, by jointly analyzing reflective and thermal data acquired by satellite remote sensing means.

The Advanced Very High Resolution Radiometer (AVHRR), operated by the National Oceanic Atmospheric Administration (NOAA), with 1 km spatial resolution and high temporal resolution of about 1 day, plays a significant role in monitoring regional and global processes. The most important AVHRR-derived products for ecological applications are the Normalized Difference Vegetation Index (NDVI) and the Land Surface Temperature (LST).

The NDVI was formulated by (Rouse, 1974) as:

$$NDVI = (\rho_{NIR} - \rho_R) / (\rho_{NIR} + \rho_R) \quad (1)$$

where ρ is the reflectance in the red (R) and near-infrared (NIR) bands of the NOAA/AVHRR sensor. This index, as well as several other modifications of it that are less common, are based on the difference between the maximum absorption of radiation in the red - due to the chlorophyll pigment, and the maximum reflection of radiation in the NIR - due to the leaf cellular structure and the fact that soil spectra, lacking these mechanisms, typically do not show such a dramatic spectral difference. The NDVI has been proven to be well correlated with various vegetation parameters, such as green biomass (Tucker, 1979), chlorophyll concentration (Buschmann and Nagel, 1993), leaf area index (Asrar et al., 1984), foliar loss and damage (Vogelmann, 1990), photosynthetic activity (Sellers, 1985), carbon fluxes (Tucker et al., 1986), phenology (Justice et al., 1985), and others. Also, they have been found to be useful for a variety of image analyses like crop classification (Ehrlich and Lambin, 1996), green coverage (Elvidge and Chen, 1995), and change detection (Lambin and Strahler, 1994).

The retrieval of LST from NOAA-AVHRR data is achieved mainly through the application of so-called split window. Several split window algorithms have been developed on the basis of various considerations of the effects of the atmosphere and the emitting surface, derived from the equation of thermal radiation and its transfer through the atmosphere. However, the effect of the atmosphere is so complex, that any treatment is difficult. Therefore, various simplifications have been assumed for the derivation that has led to the establishment of different forms of split window algorithm (Qin and Karnieli, 1999). Thus, if T_4 and T_5 are the brightness temperatures in

bands 4 and 5 of AVHRR data, respectively, which are given by inverting Planck's equation for the radiation received by the sensor, the general form of split window algorithm can be expressed as:

$$LST = T_4 + A(T_4 - T_5) + B \quad (2)$$

where A and B are the coefficients affected by the atmospheric transmittance and surface emissivity in spectral bands 4 and 5 of AVHRR data. All temperatures in the equation are in degrees of Kelvin. The theoretical accuracy of the LST can reach $\pm 1.6^\circ\text{C}$.

2 STUDY AREA

Perhaps the most spectacular phenomenon connected with desertification vs. rehabilitation can be observed across the Israel-Egypt political border (Figure 1). Although the sand field of the Negev desert (Israel) represents the eastern extension of the Sinai (Egypt) fields from the geomorphological and lithological points of view, the area is artificially divided by the political borderline. The borderline is characterized by a sharp contrast; higher reflectance values (brighter) on the Egyptian side and lower reflectance values (darker) on the Israeli side. This contrast has long drawn the attention of many scientists. The traditional and popular explanation asserts that the contrast is mainly due to severe anthropogenic impact of the Sinai Bedouin - especially overgrazing by their black goat and sheep herds, as well as gathering of plants for firewood. The Israeli side of the border has been subject to a conservation of nature policy since the 1950s and especially, under an advanced rehabilitation process since 1982. This interpretation was pioneered by Otterman (1974) and summarized in Otterman (1996).

Classification based on satellite and aerial photographs revealed that the Sinai is dominated by bare sands (83.5%) while in the Negev, the sands are overlaid by soil biological crusts (71%) (Table I). Consequently, Sinai is characterized by shifting sand dunes while these dunes have been stabilized in the Negev. As a result, a new theory, recently proposed by Karnieli and Tsoar (1995) and Tsoar and Karnieli (1996), suggests that the contrast is not a direct result of severe overgrazing of higher vegetation but is caused by an almost complete cover of biological soil crusts on the Israeli side, while human and animal activities have prevented the establishment and accumulation of such crusts, as well as trampling and breaking up any existing crusts on the Egyptian side.



Figure 1: Location map based on NOAA-AVHRR image showing the study polygons on both sides of the border between Israel and Egypt. The high contrast across the borderline is due to almost complete cover of soil biological crusts in the Negev and absence of them in Sinai.

Table I: Percent ground cover of different ground features in the Negev (Israel) and Sinai (Egypt) (after Qin, 2001).

	Negev	Sinai
Playas / Bare Sands	%11	%83.5
Biological Soil Crusts	%71	%12
Perennials	%18	%4.5

Mean annual rainfall in the study area is 90 mm. The current project lasted four years from October 1995 to September 1999. Two of these years were relatively dry (drought) years - 1995/6 and 1998/9, with 32.3 and 31.2 mm rainfall, respectively. The other two years were relatively wet - 1996/7 and 1997/8 with 79.3 and 83.6 mm rainfall, respectively.

3 METHODOLOGY

The NOAA-AVHRR data were acquired in High-Resolution Picture Transmission (HPRT) format (~1X1 km) by the ground receiving station located at the Sede Boker Campus (Negev, Israel). NOAA-14

images were obtained for four-years from October 1995 to September 1999. The geometrical distortion introduced by the large scan angle was reduced by limiting the use of the images to those with a satellite zenith angle of 30° and by using only cloud-free images.

Three types of pre-processing were used in the study - radiometric, atmospheric, and geometric corrections. The processing of the data in the visible and NIR bands was based on post-launch calibration coefficients suggested by NOAA/NESDIS (Rao and Chen, 1998). Atmospheric correction of the top-of-atmosphere reflectances was carried out using the 6S code, including correction for molecular scattering, while geometry of the sensor and the sun was also applied (Vermote et al., 1997). This program also requires estimates of the water vapor, aerosol, and ozone contents in the atmosphere. The total precipitable water and aerosol optical thickness of the atmosphere were obtained from an automatic tracking sun photometer (CIMEL), installed at Sede Boker, about 50 km away from the study area (Holben et al., 2001). Ozone content in the atmosphere was based on climatology derived from the Total Ozone Mapping Spectrometer (TOMS) onboard the Nimbus-7 spacecraft between 1987 and 1993.

The images were geometrically corrected to a master image, using ground control points and applying a nonlinear second order transformation. The accuracy of the correction lies at the subpixel level. One subset of 150 pixels on each side of the border (about 15 X 10 km²) was extracted, assuming homogeneous areas from each image (Figure 1). The NDVI values were calculated from the surface reflectance values of the red and NIR bands of the AVHRR images.

Radiometric correction of the two NOAA AVHRR thermal bands, 4 and 5, was performed following Brown et al. (1995) and Weinreb et al. (1990). Geometric correction and subset extraction were applied to the red and NIR bands. These operations were necessary at this early step of the processing in order to later apply the local characteristics of the split window algorithm (Qin et al., 2001), used to correct the atmospheric influence on the thermal infrared bands. The algorithm used has a modified form of Equation 2 that requires total precipitable water and surface emissivity to compute the constants. The first constant was obtained from the CIMEL data, relative to the image date of acquisition; the second was estimated by laboratory analysis of soil samples taken in the study area (Qin 2001). Based on this work, the emissivity value of bare sand dunes (average value of 0.95) was assigned to the Sinai's polygon, while the emissivity value of

the biological soil crusts (average value of 0.97) for that of the Negev. The Maximum Value Composite (MVC) method (Holben 1986) was applied to the NDVI and LST values for a one-month composition period.

4 ANALYSIS AND RESULTS

4.1 Temporal dynamics of NDVI and LST

The temporal variations of the NDVI and the LST along the four hydrological years of the project are presented in Figure 2. Figure 2a shows that the Negev ecosystem, under an advanced rehabilitation process since 1982, shows higher values of vegetation index (mean NDVI for the whole data set = 0.124 ± 0.039) and high reactivity to rainfall (from 0.116 ± 0.033 during the dry period to 0.143 ± 0.045 in the wet period), especially during wet years (1996/97 and 1997/98). In contrast, the Sinai area, under desertified conditions, presents a very low reaction to rainfall (from 0.086 ± 0.014 during the dry period to 0.096 ± 0.015 in the wet period), maintaining approximately constant NDVI values (mean NDVI for the whole data set = 0.089 ± 0.015).

A slight increase in the vegetation index is visible only during the wet years. The differences between the mean NDVI values of Negev and Sinai can be as high as 0.1, following the rainy season of a wet year. Since it is well known that higher NDVI values are caused by a dark soil background (Huete, 1998), NDVI differences during the dry periods seem to be related to the brightness difference between the two sides of the border, due to the presence of the dark biological soil crusts and, to a lesser extent, the higher vegetation on the Israeli side (Karnieli and Tsoar, 1995).

Figure 2b demonstrates the monthly MVC values of the computed LST in the sampling polygons on both sides of the border. No clear differences in phase are evident. On the contrary, the cyclical temperature trends are similar in the Negev and in Sinai and follow the climatic variations throughout the four years. During the relatively wet winters, evaporation determines large losses of energy from the wet soil surface; low sun irradiance also contributes less significantly than in summer to the soil heat balance. Thus, the minimum LST values are always found in the rainy period during the winter, and can be as low as 20°C. In these seasons, the difference in the amplitude between the polygons is almost negligible. The maximum temperatures are found at the height of summer and can reach values of 58°C. The temperature differences between the two sides of the border can be as high as 7°C.

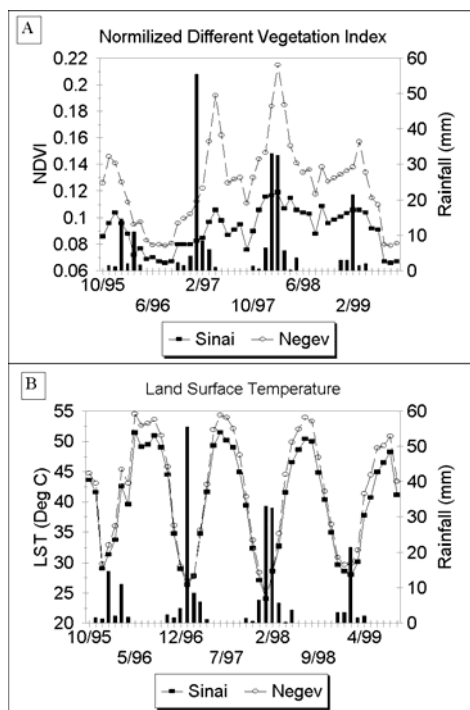


Figure 2: Temporal variations of NDVI (A) and LST (B) in Sinai and the Negev along the four hydrological years of research. The NDVI values correspond to the reaction of the vegetation to rainfall and that LST values represent seasonal climatic fluctuation.

The explanations for the amplitude differences evident in the dry period are addressed in Qin et al. (2001). Since the sand dunes on the Israeli side are almost completely covered by dark biological soil crusts, they absorb more incident radiation and emit stronger thermal radiation than the bare sand on the Egyptian side. Moreover, although more higher and lower vegetation is present on the Israeli side, these desert plants, due to their scarcity and dormancy in the hot, dry summer, contribute almost nothing to the regional evapotranspiration that cools the surface. Thus, in the dry season, the Israeli side presents higher values of surface temperatures than in the Sinai.

4.2 Desertification assessment

The combination of reflective and thermal data for determining soil water status or surface water availability has been reported in numerous studies (Goward and Hope, 1989; Nemani et al., 1993; Lambin and Ehrlich, 1996; 1997). This type of analysis has usually been undertaken by plotting LST against NDVI values (Figure 3a, after Lambin and Ehrlich 1996). Such a method is used in the current research in order to characterize the desertification

processes in the study area. A scatterplot of multi-year NDVI vs. LST values was created (Figure 3b). Applying a K-mean analysis of two clusters for the data, it was shown that the combined values of the Negev are significantly different from those of Sinai. Comparing the location of the clusters to the African continental scheme of Lambin and Ehrlich (1996), the current scatterplot demonstrates that the Sinai desertified ecosystem overlaps the area covered by the Sahara biome, while the Negev recovered side of the border, although located only a few kilometers away, exhibits characteristics similar to those of the Sahel biome (although it fits even better to that in the Southern African Hemisphere, discussed in the same paper).

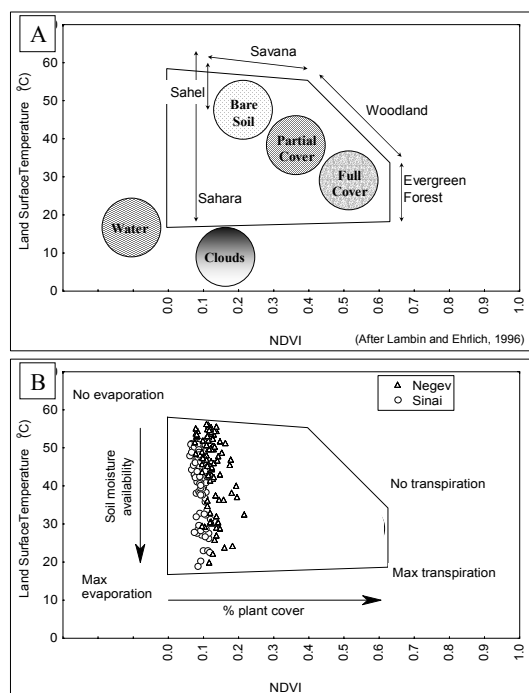


Figure 3: (a) Scatter diagram for schematic discriminating of different biomes in Africa as proposed by Lambin and Ehrlich (1996). (b) Data obtained for this study. The Sinai has an ecosystem similar to that found in the Sahara, while the Negev, only a few kilometers away, has an ecosystem similar to the one found in the Sahel.

4.3 Phenology

Results of the K-mean analysis reveal that 5 clusters characterize the study area (Figure 4). Statistics for each cluster are described in Table II. The Sinai area, under a desertification process, is characterized by just two clusters (1 and 2) corresponding to the dry and

wet seasons respectively, and defined by the fluctuations of land surface temperatures throughout the year. In this area, the biological activity is almost non-existent, therefore only the physical meteorological factors are responsible for the movement inside the LST-NDVI space. On the other hand, the recovered ecosystem of the Negev shows relatively intense biological activity and is characterized by movements over three clusters of the LST-NDVI space. In the Negev ecosystem, as in the Sinai, both dry and rainy seasons are evident (clusters 3 and 4) while the third cluster (number 5) represents the growing season, which is evident only on the Israeli side of the border and which includes the highest values of NDVI. Only a few points are presented inside cluster number 5, because it corresponds to the very short period of the year in which the desert reaches its maximum greenness due to the blooming of the annuals.

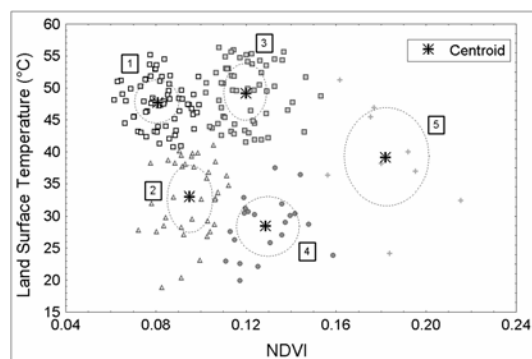


Figure 4: Groups obtained from the cluster analysis of NDVI and LST data. The numbers in the square boxes refer to the cluster numbers mentioned in the text and in Table II. The dashed lines represent one standard deviation from each centroid (after Dall'Olmo and Karnieli, 2002). The two different biomes (Sinai and the Negev) exhibit different yearly variation of the phenological patterns: two seasons in Sinai (clusters 1 and 2) moving along the LST axis, and three seasons in the Negev (clusters 3, 4 and 5) where the NDVI axis represents the growing season.

It is interesting to note that several points belonging to the Negev are located inside cluster 1, which represents the Sinai. The explanation for this fact can be found in Holling (1973). Natural arid land systems show a resilient character rather than a resistant one: their stability is not defined by a unique equilibrium state, but according to fluctuations of environmental parameters. Beyond certain limits, they can be associated with multiple-equilibrium states of a domain, inside which the ecosystem does not change its structure. This is the result of adaptation to the harsh desert environment. The overlapping points of cluster 1 are relative to the very dry years (1995/6 and

1998/9). In extremely dry periods, the recovered ecosystem is able to reduce its activity to the minimum needed for surviving in the area of the LST-NDVI space typical of desertified ecosystems. As soon as the precious resource of water is available again, it can immediately react and produce relatively high values of NDVI. However, the disturbed ecosystem shows the result of a man-made perturbation that has changed its structure: in wet years only an extremely limited response to rainfall is detected.

Table II: Description of the clusters obtained from the NDVI and LST data analysis (after Dall’Olmo and Karnieli, 2002).

Cluster	Season	# of Negev pixels	# of Sinai pixels	Mean NDVI (stdev.)	Mean LST (stdev.)
1	Dry	14	48	0.082 (0.010)	47.7 (3.6)
2	Rainy	4	33	0.095 (0.010)	33.0 (5.8)
3	Dry	51	7	0.120 (0.012)	49.2 (4.6)
4	Rainy	16	5	0.123 (0.013)	28.5 (4.6)
5	Growing	9	0	0.182 (0.018)	39.1 (8.1)

The multi-year average of the combined NDVI and LST values are presented in Figure 5 in terms of month-by-month trajectories. Phenology starts in October and ends in September of the following year. It is shown that the desertified Sinai ecosystem exhibits the highest variability mostly along the LST axis and is almost unaffected by the NDVI, except for a slight deviation from the straight line between April and July, most likely due to some greenness of perennials. On the other hand, the recovered Negev side of the border exhibits variability on both LST and NDVI axes. Here, the NDVI axis is dominant especially during the wet months (January – July) due to the greening of biological soil crusts, annuals, and perennials. During the summer months, the trajectory moves only along the LST axis.

4.3 Drought assessment

Figure 6 exhibits the breakdown of Figure 5 into the four hydrological years under investigation, to demonstrate the annual dynamics. In the Sinai, little difference can be seen between the wet and the dry years, with the same general trajectory shape - long, narrow, and with a vertical pattern along the LST axis. In the Negev, however, there is a considerable difference between the wet and dry years. During the wet years (1996/7 and 1997/8) the shape of the graphs is stretched towards the high NDVI values and the

phenological cycle is much more pronounced, whereas during droughts (1995/6 and 1998/9) the NDVI component is much less remarkable and the phenological cycle shrinks significantly.

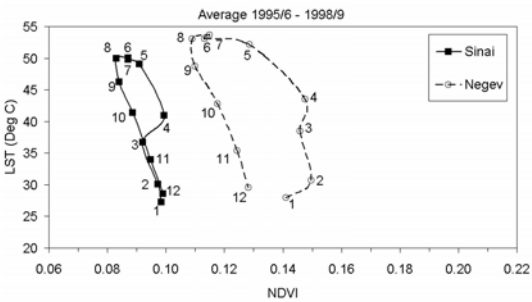


Figure 5: Multi-year average of the combined NDVI and LST values in terms of month-by-month trajectories. The desertified Sinai ecosystem exhibits the highest variability mostly along the LST axis and is almost unaffected by the NDVI. On the other hand, the recovered Negev side of the border exhibits variability on both LST and NDVI axes.

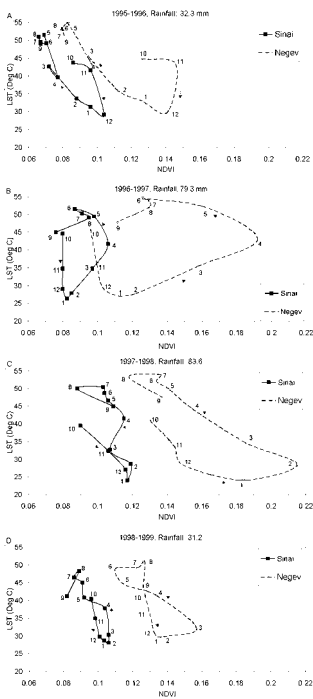


Figure 6: Trajectories of combined NDVI and LST values for each of the four hydrological years (October (10) → September (9)). Note differences between the drought years (1995/6 and 1998/9) and the normal years (1996/7 and 1997/8).

Figure 7 shows the lines connected between two points defined as (1) the maximum LST – minimum NDVI; and (2) minimum LST – maximum NDVI, for each of the hydrological years and for the Negev and Sinai ecosystems separately. It may be seen that the Sinai lines are very similar in terms of position and length; however, two groups can be distinguished between the Negev lines. The lines of the wet years are longer and with gentler slopes, whereas the dry-years lines are shorter and steeper. These characteristics can be quantified by three geometrical expressions as schematically illustrated in Figure 8:

$$\text{Angle} = \arctan(\Delta\text{LST}/\Delta\text{NDVI}) \quad (3)$$

$$\text{Area} = \Delta\text{NDVI} * 0.5\Delta\text{LST} \quad (4)$$

$$\text{Length} = [(\Delta\text{LST})^2 + (\Delta\text{NDVI})^2]^{0.5} \quad (5)$$

These three expressions can be used as indicators for quantifying drought years. Their calculated values are presented in table III. Evaluation of the three indicators was performed by applying the following Discrimination Function (DF) for each year (i) and for each region (j):

$$\text{DF}_{ij} = (\text{X}_{ij} - \text{X}_{\text{mean}j})/(\text{X}_{\text{max}j} - \text{X}_{\text{min}j}) \quad (6)$$

Where X_{ij} is the calculated value for each indicator, either in Sinai or in the Negev, in any particular year. X_{avg} , X_{max} , and X_{min} , are the yearly average, maximum and minimum values for each region, respectively. The objective of this function is to discriminate the drought years from the wet years on both sides of the border.

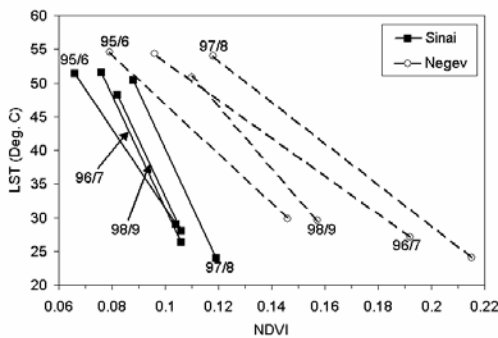


Figure 7: Lines connected between maximum LST – minimum NDVI and minimum LST maximum NDVI for the Sinai and the Negev. Note differences in slope and length of the lines between the two biomes and among years.

Table III: Calculated values for the three drought indicators

	Year	Sinai	Negev
Angle	6/1995	80.36	74.85
	7/1996	83.20	70.63
	8/1997	83.31	72.06
	9/1998	83.23	77.78
Area	6/1995	0.43	0.83
	7/1996	0.38	1.31
	8/1997	0.41	1.45
	9/1998	0.24	0.50
Length	6/1995	22.38	24.75
	7/1996	25.16	27.31
	8/1997	26.42	29.95
	9/1998	20.22	21.17

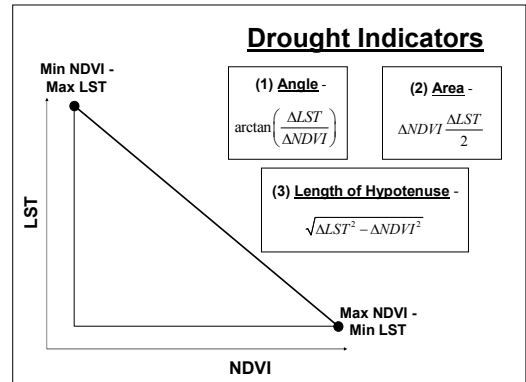


Figure 8: Schematic illustration of three geometrical expressions for indicating droughts.

Results of the discrimination function for each of the drought indicators are presented in Figure 9. It can be noticed that for the Negev, each of the indicators successfully separates the two drought years from the wet years, since the DF_{ij} receives either positive or negative values. However, for Sinai, only the “length” indicator is able to show this phenomenon. The other two indicators - slope and angle - produce mixed results. Consequently, the “length” indicator will be used for further analysis.

Using the “length” indicator, Figure 10 presents the DF_{ij} values as a function of the yearly rainfall of each year. Despite the fact that only 8

points are involved in the regression analysis, a clear trend is exhibited between the drought-year cluster (negative values) and the wet-year cluster (positive values). The crossing point between the regression line and the DF=0 line can be used to quantify the threshold between wet and drought years in terms of rainfall amount (54 mm in the current example).

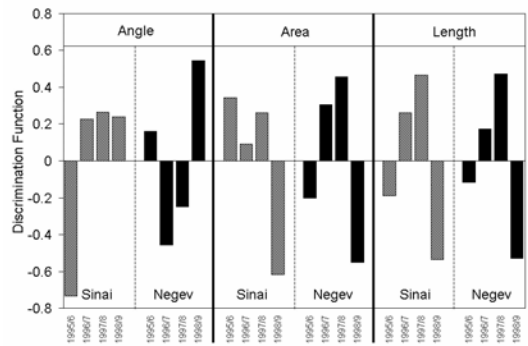


Figure 9: Results of the discrimination function procedure for each drought indicator. Note that the “length” indicator provides the best results in terms of discrimination between the drought years (1995/6 and 1998/9) and the normal years (1996/7 and 1997/8).

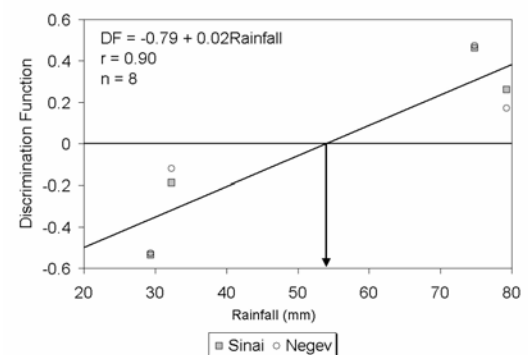


Figure 10: Discrimination function values vs. the yearly rainfall amounts of each year. The crossing point between the regression line and the DF=0 line can be used to quantify the threshold between wet and drought years in terms of rainfall amount.

5 SUMMARY AND CONCLUSIONS

Results from the current study show that desertification, phenology, and droughts processes can be detected and characterized by using four out of five NOAA/AVHRR spectral bands. The NDVI is derived from the red and the NIR bands and the LST from the two thermal bands. Combined use of these two products provides more information than any product alone.

Time series presentation of NDVI and LST reveals that the NDVI values correspond to the reaction of the vegetation to rainfall and that LST values represent seasonal climatic fluctuation. Scatterplot analysis of LST vs. NDVI demonstrates the following:

1. The two different biomes (Sinai and the Negev) exhibit different yearly variations of the phenological patterns: two seasons in Sinai moving along the LST axis, and three seasons in the Negev, where the NDVI axis represents the growing season;
2. The Sinai has an ecosystem similar to that found in the Sahara while the Negev, only a few kilometers away, has an ecosystem similar to that of the Sahel;
3. Drought indicators were derived in terms of three geometrical expressions based on the two extreme points of the NDVI - LST scatterplots. Evaluation of the suggested indicator shows only one that can successfully separate between the drought and the wet years. It is concluded that the AVHRR imagery can provide valuable information for drought monitoring and characterization.

6 ACKNOLADGMENT

I would like to thank Mr. Qin Zhihao for processing the thermal data.

7 REFERENCES

Asrar, G., Fuchs, M., Kanemasu, E.T., and Hatfield, J.L., 1984, Estimating absorbed photosynthetic radiation and leaf area index from spectral reflectance of wheat. *Agronomy Journal*, **76**, 300-306.

Buschmann, C., and Nagel, E., 1993, In vivo spectroscopy and internal optics of leaves as basis for remote-sensing of vegetation. *International Journal of Remote Sensing*, **14**, 711-722.

Dall’Olmo, G., and Karnieli, A., 2002, Following phenological cycles of desert ecosystems using NDVI and LST data derived from the Advanced Very High Resolution Radiometer. *International Journal of Remote Sensing*, (in press).

Goward, S.N., and Hope, A.S., 1989, Evaporation from combined reflected solar and emitted terrestrial radiation: Preliminary FIFE results from AVHRR data. *Advances in Space Research*, **9**, 239-249.

Ehrlich, D., and Lambin, E.F., 1996, Broad scale land-cover classification and interannual climatic variability. *International Journal of Remote Sensing*, **17**, 845-862.

- Elvidge, C.D., and Chen, Z.K., 1995, Comparison of broad-band and narrow-band red and near-infrared vegetation indexes. *Remote Sensing of the Environment*, **54**, 38-48.
- Holben, B.N., 1986, Characteristics of maximum-value composite images from temporal AVHRR data. *International Journal of Remote Sensing*, **7**, 1417-1434.
- Holling, C. S., 1973, Resilience and stability of ecological systems. *Annual Review of Ecology and Systematics*, **4**, 1-23.
- Huete, A., 1988, A soil-adjusted vegetation index (SAVI). *Remote Sensing of the Environment*, **25**, 295-309.
- Justice, C.O., Townshend, J.R.G., Holben, B.N., and Tucker, C.J., 1985, Analysis of the phenology of global vegetation using meteorological satellite data. *International Journal of Remote Sensing*, **6**, 1271-1318.
- Karnieli, A., and Tsoar, H., 1995, Spectral reflectance of biogenic crust developed on desert dune sand along the Israel-Egypt border. *International Journal of Remote Sensing*, **16**, 369-374.
- Lambin, E.F., and Ehrlich, D., 1996, The surface temperature-vegetation index space for land cover and land-cover change analysis. *International Journal of Remote Sensing*, **17**, 463-487.
- Lambin, E.F., and Ehrlich, D., 1997, Land-cover changes in Sub-Saharan Africa (1982-1991): application of a change index based on remotely sensed surface temperature and vegetation indices at a continental scale. *Remote Sensing of the Environment*, **61**, 181-200.
- Lambin, E.F., and Strahler, A.H., 1994, Change-vector analysis in multitemporal space: A tool to detect and categorize land-cover change processes using high temporal-resolution satellite data. *Remote Sensing Environment*, **48**, 231-244.
- Lieth, H., 1974, *Phenology and Seasonality Modeling*. Springer-Verlag, New York, 444 pp.
- Mainquet, M., 1994, *Desertification – Natural Background and Human Mismanagement*. Springer Study Edition, vol.1, 2e ed., Springer, Heidelberg, 314 pp.
- Nemani, R.R., Peirce, L., Running, S.W., and Goward, S., 1993, Developing satellite derived estimates of surface moisture status. *Journal of Applied Meteorology*, **32**, 548-557.
- Otterman, J., 1974, Baring high-albedo soils by overgrazing: a hypothesized desertification mechanism. *Science*, **186**, 531-533.
- Otterman, J., 1996, Desert-scrub as the cause of reduced reflectances in protected versus impacted sandy arid areas. *International Journal of Remote Sensing*, **17**, 615-619.
- Rouse, J.W., Haas, R.H., Schell, J.A., Deering, D.W., and Harlan, J.C., 1974, *Monitoring the Vernal Advancements and Retrogradation (Greenwave Effect) of Nature Vegetation*. NASA/GSFC Final Report, NASA, Greenbelt, MD, 371 pp.
- Price, J.C., 1984, Land surface temperature measurements from the split window channels of the NOAA-7 Advance Very High Resolution Radiometer. *Journal of Geophysical Research*, **89**, 7231-7237.
- Qin, Z., 2001, *A Study of Temperature Change on Both Sides of The Israeli-Egyptian Border: Remote Sensing and Micrometeorological Modeling*. Ph.D. thesis, Ben Gurion University of the Negev, Israel.
- Qin, Z., and Karnieli, A., 1999, Progress in the remote sensing of land surface temperature and ground emissivity using NOAA-AVHRR data. *International Journal of Remote Sensing*, **20**, 2367-2393.
- Qin, Z., Dall'Olmio, G., Karnieli, A., and Berliner, P., 2001, Derivation of split window algorithm and its sensitivity analysis for retrieving land surface temperature from NOAA-AVHRR data. *Journal of Geophysical Research*, **106**, 22,655-22,670.
- Sellers, P.J., 1985, Canopy reflectance, photosynthesis and transpiration. *International Journal of Remote Sensing*, **6**, 1335-1372.
- Tsoar, H., and Karnieli, A., 1996, What determines the spectral reflectance of the Negev-Sinai sand dunes?. *International Journal of Remote Sensing*, **17**, 513-525.
- Tucker, J.C., 1979, Red and photographic infrared linear combination for monitoring vegetation. *Remote Sensing of the Environment*, **8**, 127-150.
- Tucker, C.J., Fung, I.Y., Keeling, C.D., and Gammon, R.H., 1986, Relationship between atmospheric CO₂ variations and a satellite-derived vegetation index. *Nature*, **319**, 195-199.
- UNEP, 1992, *World Atlas of Desertification*. Edward Arnold Publishers, Sevenoaks.
- Vermote, E., Tanré, D., Deuze, J.L., Herman, M., and Morcette, J.J., 1997, Second Simulation of the Satellite Signal in the Solar Spectrum (6S). *IEEE Transactions in Geoscience and Remote Sensing*, **35**, 675-685.
- Vogelmann, J.E., 1990, Comparison between two vegetation indices for measuring different types of forest damage in north-eastern United States. *International Journal of Remote Sensing*, **11**, 2281-2297.
- Wilhite, D.A., and Glantz, M.H., 1985, Understanding the drought phenomenon: the role of definitions. *Water International*, **10**, 111-120.

The EuroSTARRS airborne campaign over land surfaces (SMOS mission): First results

Kauzar Saleh(1), Jean-Pierre Wigneron(2), Ernesto Lopez Baeza(1), Jean-Christophe Calvet(3), Thierry Pellarin(3), Michael Berger(4), Lester Simmonds(5)

(1) University of Valencia, Dr Moliner, 50. Burjassot, 46100 Valencia, Spain

(2) INRA Bioclimatologie, B.P. 81, 33883 Villenave d'Ornon CEDEX, France

(3) Météo France CNRM, 42 av G. Coriolis, 31057 Toulouse Cedex 1, France

(4) ESTEC/ESA - Land Surfaces Unit, P.O. Box 299, 2200 AG Noordwijk, The Netherlands

(5) University of Reading, PO Box 233, Whiteknights, Reading, UK

wigneron@bordeaux.inra.fr

ABSTRACT -. A number of experiments using ground based and airborne sensors have shown the high potential of L-band passive microwave radiometry for estimating and monitoring surface soil moisture. This has led to the Soil Moisture and Ocean Salinity (SMOS) mission, a European Space Agency (ESA) Earth Explorer Opportunity mission, which is currently being studied in phase B. SMOS has the objective to observe soil moisture over land and sea surface salinity over sea, both key parameters for predictive atmospheric, oceanographic and hydrologic models. In preparation of SMOS, the EuroSTARRS airborne campaign was carried out in November 2001. Multi-angular L-band measurements in vertical polarisation were acquired over several sites in Southern France, the Pyrenees and Eastern Spain. The chosen sites represent specific land conditions and vegetation canopies which need further investigation for the parametrization of passive microwave model (dense forests, shrubs and scrubland, mixture of different vegetation covers). This paper gives an overview of the experiment and provides preliminary results from measurements over forest sites. Measurements acquired over the Les Landes site display a decrease in the L-band emissivity as biomass increases for coniferous forests. This can be correctly simulated using a simple microwave emission model.

1 INTRODUCTION

Research across a wide range of disciplines indicates that knowledge of soil moisture (SM) is essential for understanding many environmental processes. In an accurate description of the soil-vegetation-atmosphere interface, soil moisture needs to be taken into account, as it influences the fluxes of energy, water, and CO₂ across this interface. Previous studies have demonstrated the capability of L-band (1.4 GHz) passive microwave radiometry for soil moisture monitoring (Jackson et al., 1995; Schmugge, 1998) and they are the basis for the definition of the *Soil Moisture and Ocean Salinity* Mission (SMOS) (Kerr et al., 2001). The main objective of this mission is to deliver two key parameters over land surfaces and oceans: soil moisture fields and sea surface salinity fields. SMOS is ESA's second Earth Explorer Opportunity mission and the SMOS satellite will be launched in 2006. The SMOS mission will make use of an L-band passive microwave radiometer (see also www.esa.int/livingplanet -- SMOS). The SMOS instrument (MIRAS: Microwave Imaging Radiometer by Aperture Synthesis) provides multi-angular viewing which is to be exploited in the simultaneous

retrieval of soil and canopy contributions to the observed microwave emission (Waldteufel *et al.*, 2000). Wigneron *et al.* (2000) proposed two-parameter (soil moisture w_s and vegetation optical depth τ) and three-parameter (w_s , τ and effective surface temperature T_s) retrieval algorithms from multi-angular L-band brightness temperatures for the SMOS mission. The advantage of such multi-parameter retrievals is that they remove the need for ancillary information about the canopy, (such as vegetation water content) in order to obtain information about near-surface soil moisture content. Key to the success of the interpretation of multi-angular measurements is a good understanding of the dependence of the vegetation optical depth on the sensor configuration (polarisation and observation angle). This needs further study, especially for forests and natural vegetation (shrubs and scrubland). An assessment on the effect of topography and heterogeneity within the observed pixel on the retrieval is also necessary (Njoku and Entekhabi, 1996; Kerr *et al.*, 2001).

To address these issues, the EuroSTARRS-2001 campaign was carried out in November 2001. Multi-angular vertical polarisation measurements were acquired by the L-band STARRS (Salinity Temperature and Roughness Remote Sensor) microwave radiometer from the Naval Research Laboratory (NRL, USA) over several sites: *Valencia Site* (Spain, variety of natural and agricultural vegetation covers), *Agre Forest Site* (near Toulouse, France, mixed deciduous and coniferous forests), *Nezer Site* (*Les Landes forest*, near Bordeaux, France, coniferous forest), Toulouse (France, urban area) and the *Pyrenees* (France-Spain, mountainous region). Low altitude flights were made over forests and urban sites. Combined low and high altitude flights were made at the *Valencia Site* to study the effects of heterogeneity.

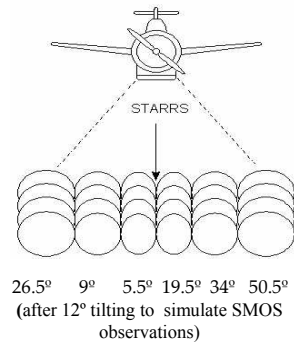
Over land surfaces, the main objective of EuroSTARRS was to improve the scientific understanding of L-band emissivity over a variety of surfaces. More specifically, (i) to characterise the dependence of the vegetation optical depth on the incidence angle for a variety of vegetation covers (in particular for forests and natural vegetation covers), (ii) to validate the soil moisture retrieval procedure over mixed pixels by using combined observations at low altitude and high altitude, (iii) to estimate the multi-angular signatures over urban areas, (iv) to estimate the multi-angular signatures over mountainous regions, (v) to evaluate the potential application of information on vegetation optical depth to determine forest characteristics such as branch biomass or total biomass (Ferrazzoli et al., 2001).

This paper presents a description of the EuroSTARRS-2001 campaign (section 2) together with some preliminary results (section 3). A principal component analysis based on the STARRS measurements allows a forest classification based on stand age over coniferous trees at *Les Landes*. The relationship between the vegetation microwave emission and forest biomass is investigated and a preliminary assessment of the performance of a simple emission model is carried out over coniferous forests. More information about the campaign can be found at Berger et al (2002), in the proceedings of this conference.

2 EXPERIMENTAL CAMPAIGN

2.1 The STARRS Instrument

Airborne observations were performed with the STARRS radiometer, provided by the Naval Research Laboratory (NRL, USA). For EuroSTARRS-2001, the sensor was operated aboard a Dornier 228 (DO-228) aircraft by DLR (German Aerospace Center), Oberpfaffenhofen. STARRS is an L-band (1.400-1.426 GHz) vertical polarisation radiometer with six independent antennae which were mounted perpendicular to the flight direction (push-broom configuration) (figure 1). As a result, the radiometer produces a 2-D image as the aircraft moves along track. In order to obtain a "SMOS-like" field of view up to 55° , the radiometer was tilted at an angle of 12° towards the starboard side of the aircraft, resulting in six observation angles at $\theta=5.5^\circ, 9^\circ, 19.5^\circ, 26.5^\circ, 34^\circ$ and 50.5° . The instrument also includes a two-band thermal infrared sensor, which was used to provide an estimate of the land surface temperature and a C-band radiometer operating in vertical polarisation at 5.18,



5.65 , 5.85 , 6.21 , 6.60 , and 7.05 GHz in the nadir direction. The L-band radiometer acquisition system collects data from the six receivers simultaneously. The antenna beamwidth at 3dB is about 16 degrees.

Fig.1. STARRS observation angles, STARRS sensor and STARRS mounted on DLR Dornier 228.

2.2. Sites description

Nezer Site

The *Nezer Site* ($44^\circ 35'N, 1^\circ 04'W$) of *Les Landes* forest is an experimental site of the French *Institut National de la Recherche Agronomique (INRA)*. The site consists of well-defined uniform stands of pine trees (*Pinus pinaster*) with a large range of ages (from seedlings to 50 years) and biomass (dry biomass varies from 0 to 160 Tons/ha). Trees are mostly arranged in rows within large homogeneous stands of approximately 500 m x 500 m over a nearly flat

surface. The soils are podzols and the percentage of sand in the A horizon generally exceeded 80%. As a result, soil moisture content is low and the contrast between soil and vegetation microwave emissivity is rather small. A few agricultural and bare soil fields can also be found near the site. STARRS performed low altitude measurements (300 m above surface) along 21 parallel flight lines of 11-km length separated by 150 m. The flights covered forest areas and fields of maize, carrots and bare soil. During the day of the flight, *in situ* ground measurements of the mean volumetric water content of the upper 6 cm of the profile were carried out using a *Delta-T ThetaProbe* (*Delta-T Devices, Cambridge, UK*) within about twenty selected plots. Air temperature, soil temperatures at 1, 3, 5, 10 and 50 cm depth, wind speed and air humidity were recorded at screen height at 3 meteorological stations located within the flight area.

The Agre Forest

Interest in the *Agre Forest Site* (near *Toulouse, France*, 43° 57'N, 1° 16'E) focused on the multi-angular signature of deciduous and coniferous forests at L-band. The *Agre Forest* consists of 145 stands representing 26 canopy types, including common tree species as Sessile oaks (*Quercus petraea*, 57% of total surface), Corsican pines (*Pinus nigra laricio*, 13%), English oaks (*Quercus robur*, 12%), etc. The site had a rolling topography with altitude varying between 100 m and 130 m. The flight altitude (300m above ground) was selected such that multi-angular measurements could be made over contrasting homogenous stands such that the footprints fell within the boundaries of the homogenous areas. The aircraft performed 16 parallel flight lines (200 m apart) of about 7 km in length. The ground sampling was carried out within 17 stands on the day of the flight. Measurements included soil temperature under the litter cover, volumetric surface soil moisture (gravimetric techniques and *ThetaProbe* readings) and litter water content.

Valencia Site

The main contribution of the *Valencia Site* (39° 32'N, 01° 6'W) to the EuroSTARRS-2001 campaign was to provide a dataset for natural vegetation cover (shrubs, scrubland) and natural forested areas. The dominant agricultural land use in the area is vineyards, (short stumps at the time of the flight). The area of study contains other representative ecosystems of semi-arid Mediterranean regions particularly shrubland incorporating a large number of species (such as *Quercus ilex rotundifolia*, *Quercus coccifera*, etc). The area contains also pine trees, mainly replanted pine trees (*Pinus halepensis*), with natural undergrowth vegetation. Some stands of olive trees were selected for the study as well. The landform within the study

area shows topography characterised by flat regions (slope < 2%) and undulated areas (8-15% slopes). The dominant soil texture is clay loam. The airborne measurements were made at two different altitudes in order to study the impact of the heterogeneity of the scene. Flight lines were parallel, separated by 200 m for the low altitude flights and 500 m for the high altitude flights, in order to observe the same target from different view angles. The aircraft performed 12 flight lines at low altitude (700m above the surface) and 4 high altitude flight lines at approximately 1900 m above the ground. Eleven homogeneous stands of 300 m x 300 m were selected for detailed study according to their vegetation cover (three stands of shrubs, two stands of olive and almond trees, three stands of vineyards, one stand of young pine trees and one stand of adult pine trees). Five of these stands were chosen as to define a 900 m x 900 m mixed pixel to be used to study the impact of heterogeneity on the observations from the high altitude flights. Samples of soil (0-6 cm depth) were collected from 16 locations within each of the stands to determine the gravimetric soil moisture, and the volumetric soil moisture (average 0-6 cm depth) was measured using *ThetaProbes*. Small shrubs and branches of trees were collected *in situ* in order to estimate the vegetation water content by oven drying. Soil texture within each of the stands was also determined.

Pyrenees

The transit from France to Spain followed the 0°30'E meridian and provided an opportunity to acquire brightness temperature data over a mountainous region that will be used to evaluate the modelling of L-band emission over mountainous areas. The chosen flight line crossed the highest part of the Pyrenees, through the Portillon and Oô lakes with altitude varying from 800 m to 2000 m. The first 10 km flight passed over a deep U-shaped valley with no or little vegetation. From 10 km to 20 km, forest was present on north-aspect slopes only. From 10 km to 15 km, the flight was parallel to the Oô valley, and from 15 km to 20 km perpendicular to the Larboust valley. The final 20 km consisted of numerous densely forested valleys with various orientations to the flight line.

Toulouse City

A single low altitude flight line (300 m above surface) over the city of Toulouse (France) provided the opportunity to measure brightness temperature over a large diverse urban area to analyse the microwave emission from different urban landscapes and to determine the impact of Radio Frequency Interference (RFI).

3.1. Principal component analysis

Over the *Nezer Site* and the *Agre forest*, relationships between the microwave emissivities at different look angles and frequencies and the forest categories, based on the age of trees, were investigated through a principal component analysis (PCA) technique as in Wigneron et al. (1997). The emissivity ϵ_v at vertical polarization (1) was computed as (Ulaby et al., 1986):

$$\epsilon_v = (T_{BP} - T_{B-SKY}) / (T_S - T_{B-SKY}) \quad (1)$$

where T_{BP} is the measured brightness temperature, T_{B-SKY} is the downwelling atmospheric emission, and T_S is the surface temperature, as measured using the STARRS thermal infrared radiometer. T_{B-SKY} was estimated as a function of the air temperature and site altitude (Ulaby et al., 1986). The emissivities at the six incidence angles at L band (denoted $\epsilon_{L5.5}$, ϵ_{L9} , $\epsilon_{L19.5}$, $\epsilon_{L26.5}$, ϵ_{L34} and $\epsilon_{L50.5}$) and the six C band frequencies (denoted $\epsilon_{C5.18}$, $\epsilon_{C5.65}$, $\epsilon_{C5.85}$, $\epsilon_{C6.21}$, $\epsilon_{C6.60}$ and $\epsilon_{C7.05}$) provide the variables for our analysis. An emissivity matrix E is defined from the emissivity vectors for each of the 10 classes of forest age and then normalised (mean=0, standard deviation=1). The forest stands have been classified according to the following categories, where the numbers denote the age in years: A.1, B.2, C.3-4, D.5-7, E.8-14, F.15-20, G.21-23, H.24-27, I.28-34, J.35-49. The eigenvectors of the covariance matrix calculated from E describe the variance of the emissivities associated with each incidence angle/frequency configuration to forest age. The PCA provides principal components according to their contribution to the total variance. A cross representation between different components produces diagrams of clusters of stands characterised by age, which illustrate the potential of different configurations to discriminate stand categories. Figures 2a-c illustrate the application of PCA to the coniferous stands at the *Nezer Site*. First, the PCA was performed using only the L-band emissivities. Figure 2a shows a significant sensitivity of emissivity to the age of stands, where three main age groups of 0-7, 8-14 and 15-49 years can be distinguished. The first principal component ($pc1$) is proportional to the sum of all emissivities at L-band ($pc1 = 0.42\epsilon_{L26.5} + 0.43\epsilon_{L9} + 0.42\epsilon_{L5.5} + 0.42\epsilon_{L19.5} + 0.42\epsilon_{L34} + 0.34\epsilon_{L50.5}$). In contrast, the second component ($pc2$) is related to the difference between the largest angle ($\theta = 50.5^\circ$) and smaller angles ($pc2 = 0.02\epsilon_{L26.5} + 0.16\epsilon_{L9} + 0.18\epsilon_{L5.5} + 0.30\epsilon_{L19.5} + 0.12\epsilon_{L34} - 0.92\epsilon_{L50.5}$). The inertia associated with the

first component is 89%, whereas the second and third component values are 7.9% and 1.7%, respectively. Hence the statistical analysis reveals thus a two-dimensional problem, as the inertia associated to the third axis is almost negligible.

It was also shown that the use of only three angles ($\theta = 9^\circ$, $\theta = 5.5^\circ$ and 50.5°) at L-band, i.e. the two lowest and the largest available angles, could provide very similar discrimination capabilities by comparison with the use of all available incidence angles (figure 2b). Inertia values in this case were 84.8%, 14.4% and 0.8% for the angles stated above, $pc1 = 0.60\epsilon_{L9} + 0.60\epsilon_{L5.5} + 0.52\epsilon_{L50.5}$ and $pc2 = 0.36\epsilon_{L9} + 0.37\epsilon_{L5.5} - 0.85\epsilon_{L50.5}$.

Including the emissivities at C-band did not provide a clear improvement in the stand discrimination (figure 2c). When using L and C bands, inertia values for the first three components were: 85.5%, 8.2% and 2.22% respectively. Again, the first component is proportional to the sum of all variables ($pc1 = 0.29\epsilon_{L26.5} + 0.30\epsilon_{L9} + 0.30\epsilon_{L5.5} + 0.30\epsilon_{L19.5} + 0.29\epsilon_{L34} + 0.20\epsilon_{L50.5} + 0.29\epsilon_{C5.18} + 0.30\epsilon_{C5.65} + 0.30\epsilon_{C5.85} + 0.30\epsilon_{C6.21} + 0.29\epsilon_{C6.60} + 0.28\epsilon_{C7.05}$), and the second component is related to the difference between the emissivities at L- and C-bands

($pc2 = 0.30\epsilon_{L26.5} + 0.19\epsilon_{L9} + 0.12\epsilon_{L5.5} + 0.08\epsilon_{L19.5} + 0.21\epsilon_{L34} + 0.69\epsilon_{L50.5} - 0.17\epsilon_{C5.18} - 0.21\epsilon_{C5.65} - 0.22\epsilon_{C5.85} - 0.24\epsilon_{C6.21} - 0.23\epsilon_{C6.60} - 0.32\epsilon_{C7.05}$). In summary, the preliminary results that were obtained over coniferous forests showed that the use of L-band emissivities at only two angles (almost at nadir ($\theta = 5.5^\circ$) and for a relatively large angle ($\theta = 50.5^\circ$)) could discriminate between three main categories of pines (A, B, C, D), (E) and (F, G, H, I, J), with age ranges respectively of 1 to 7 years, 8 to 14 years and 15 to 49. This discrimination capability was not improved by the use of emissivity data at the other incidence angles and/or frequencies.

The PCA was also applied to a dataset combining the emissivities from the *Nezer* and the *Agre Forest Sites*. Choosing separately only L-band or C-band measurements did not provide a clear classification of stands. However, it was found that by using both L-band and C-band data produced groups of stands characterised by the same vegetation type. For example, using two small angles at L-band (5.5° and 9°) and emissivities for two frequencies at C-band (smallest and largest available, 5.18 and 6.60 GHz), the two sites appeared relatively well separated when the PCA was applied (figure 2d). The first principal component distinguishes L-band from C-band: $pc1 = 0.5\epsilon_{L9} - 0.5\epsilon_{L5.5} + 0.5\epsilon_{C5.18} + 0.5\epsilon_{C6.60}$.

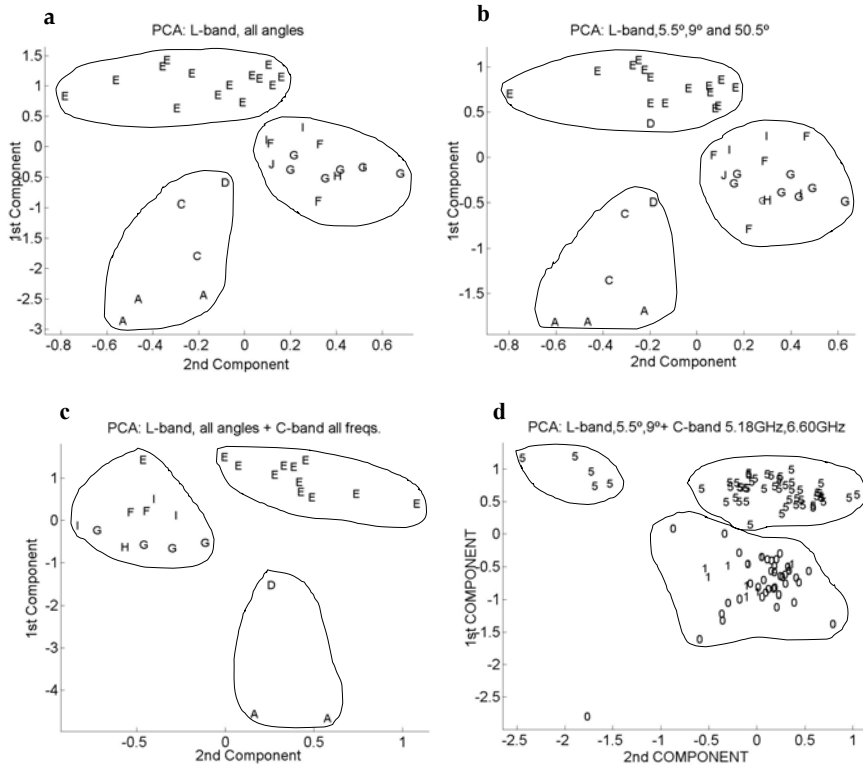


Fig.2: Scatter plot of the first (pc1) and second (pc2) components of the forest stands from (a) L-band emissivities for all angles at the Nezer Site, (b) L-band emissivities at 5.5°, 9° and 50.5° at the Nezer Site, (c) L-band emissivities for all angles and C-band emissivities for all frequencies at the Nezer Site, (d) L-band emissivities at 5.5°, 9° and C-band emissivities at 5.18 and 6.60 GHz at the Nezer and Agre sites.

The second component is almost proportional to the sum of emissivities: $pc2 = 0.5eL9 + 0.4eL5.5 + 0.5eC5.18 + 0.5eC6.60$. Inertia values for each component are 61.8%, 33.6%, 3.1% and 1.5%. Several combinations of configurations mixing L and C band data allow to differentiate the two experimental sites.

3.2. L-band sensitivity to forest biomass

In this section, we provide some preliminary results of the comparison between the microwave signature of coniferous forests as measured by STARRS at the *Nezer Site* and simulated using a very simple approach: the τ - ω model. The τ - ω model has been tested over crops with successful results in many studies (Ulaby et al., 1986; Wigneron et al., 1995). However, very few studies have investigated the use of simple models over forests. Ferrazzoli et al. (2002) performed a modelling study and analysed the microwave signature of coniferous forests using a discrete radiative transfer model accounting for multiple scattering effects. The authors showed that a

simple model, such as the τ - ω model (Wigneron et al., 1995), could be used to simulate the microwave forest signature provided there is effective parametrization for the canopy type of the vegetation optical depth (τ) and the single-scattering albedo (ω). The τ - ω model simulates the microwave brightness temperature emitted by a two-layer system representing the soil covered by a homogeneous vegetation layer. Attenuation and scattering effects are introduced by means of two effective parameters, the vegetation optical depth (τ) and the single scattering albedo (ω). The vegetation optical depth (τ) can be linearly related to the total vegetation water content (W_C , kg/m²) (Jackson and Schmugge, 1991) through a parameter (b) which depends mainly on the type of canopy and frequency ($\tau = b \cdot W_C$). Several studies have concluded that the vegetation parameter b depends also on the stage of vegetation growth (Wigneron, 1996), polarisation and incidence angle (Ulaby et al., 1986; Wigneron et al., 1996). As regards to forests, Ferrazzoli et al. (2002) found that the effective vegetation optical depth can be

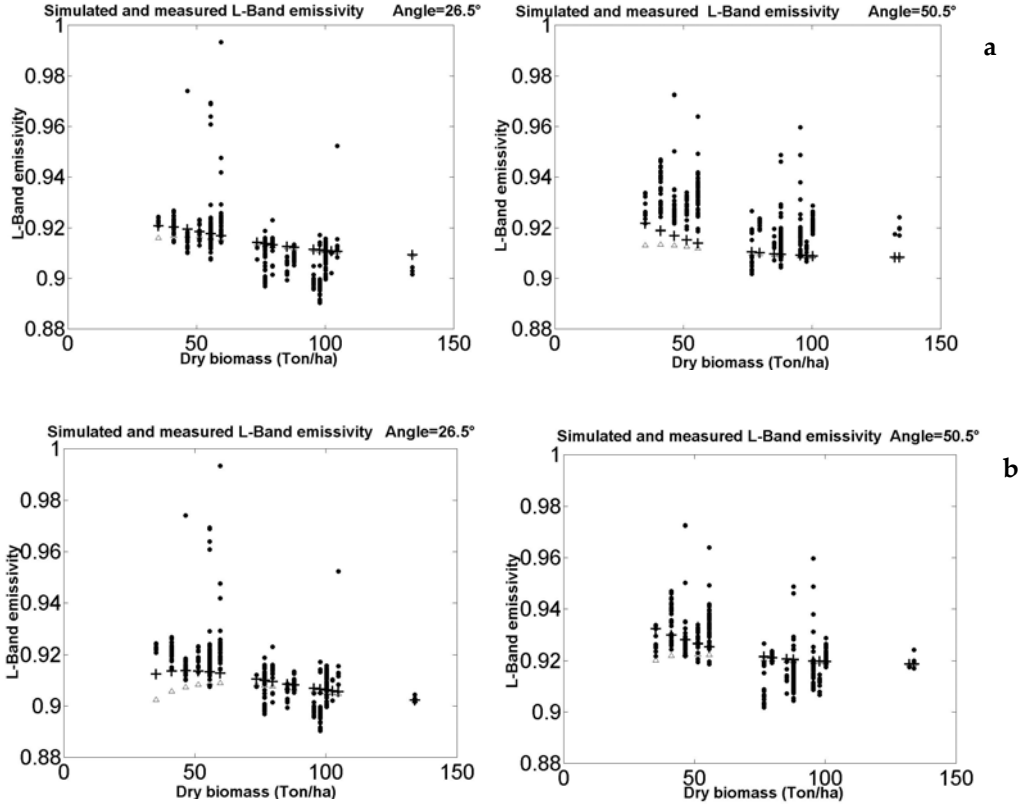


Fig.3: Comparison between emissivities derived from STARRS data and emissivities simulated with the τ - ω model. Single scattering albedo (ω) and vegetation parameter (b) values are best-fit and they are considered as (a) Top: independent of the observation angle, (b) Bottom: dependent on the incidence angle
(• STARRS data, + simulation for vertical polarisation, Δ simulation for horizontal polarisation)

expressed as a linear function of the total biomass (B_T) or of the branch water content (kg/m^2). In the present paper, as no measurement of the branch water content is available over the *Nezer site*, we make use of a relationship between the vegetation optical depth (τ) and the total dry biomass (B_S , Ton/ha) through the parameter b_{FDB} , where the subindex *FDB* stands for *Forest and Dry Biomass* ($\tau = b_{FDB} \cdot B_S$). Note that, as the gravimetric moisture content of the vegetation material is about 50% for both trunks and branches, the total dry biomass can be considered as linearly related to the total biomass ($B_S \approx 0.5 B_T$). In this study, dry biomass (Ton/ha) is approximated by a regression model based on stand age (in years) used in Wigneron et al. (1997) and derived from Karam et al. (1995) as shown in (2) :

$$\text{Dry biomass} = (463.85 \text{ Age} - 2938)^{1/2} \quad (2)$$

for Age > 8 years

STARRS microwave signatures measured at different incidence angles show that L-band emissivity decreased as biomass increased over coniferous forests. We investigated whether the τ - ω model could be used to reproduce this measured trend. The model requires a priori knowledge of the surface soil moisture and the calibration of an effective parameter (h_s) which accounts for soil roughness (Wigneron et al., 2001). The value of h_s ($h_s = 0.6$) was calibrated from measurements obtained by STARRS over bare soil surfaces within the *Nezer site*. The STARRS measurements were made just after rainfall and the soil moisture conditions were rather homogeneous over the *Nezer site*. The value of the volumetric soil moisture w_s ($w_s = 0.12 \text{ m}^3/\text{m}^3$) was taken to be the average across all of the stands of the ground-based *ThetaProbe* measurements made on the day of the flight. The soil dielectric constant was derived from w_s using a simple mixing model (Dobson et al., 1985).

Preliminary tests showed that the values of b_{FDB} and ω as obtained from the study of Ferrazzoli et al. (2002) did not provide a good fit to the measured emissivity. Therefore, the single scattering albedo and the vegetation parameter b_{FDB} were considered here as best-fit parameters that were obtained by minimising the error between experimental and simulated emissivity values. Two examples of simulations are presented for three observation angles 26.5° and 50.5°. First, the parameters b_{FDB} and ω are determined assuming they are independent of incidence angle. Obtained best-fit values are $\omega=0.09$ and $b_{FDB}=0.03$, and results of the simulations are compared with the STARRS measurements in figure 3a. In figure 3b, best-fit parameters are computed assuming they are angle dependent, thus improving the simulations. In particular best-fit values are $\omega=0.10, 0.08$ and $b_{FDB}=0.02, 0.03$ for $\theta=26.5^\circ$ and 50.5° respectively. These preliminary results are in agreement with the study of Ferrazzoli et al. (2002) as they show that the simple τ - ω model can be used to simulate the microwave signature of coniferous forests, provided both τ and ω are considered as effective parameters which should be calibrated. Simulations of the brightness temperature, using effective parameters for forests obtained in the study of Ferrazzoli et al (2002), reproduce a similar decreasing trend when emissivity is displayed versus branch water content. The EuroSTARRS dataset will enable a detailed analysis of the dependence of these effective parameters on the measurement configuration (i.e. the dependence on incidence angle and frequency) and on the canopy type (coniferous, deciduous, mixed forest, etc). Also, further analysis should reveal the relationship between the effective microwave parameters (τ and ω) and the vegetation characteristics such as age, dry and wet biomass, leaf area index, etc.

4 CONCLUSION

The EuroSTARRS experimental plan was the result a very fruitful international collaboration: ESA coordination, USA NRL instrument, DLR aircraft, three scientific teams (INRA Bordeaux, Météo-France, University of Valencia). The main objective of the campaign was to provide an experimental dataset to improve our knowledge of (i) the passive microwave signature of a variety of vegetation covers and (ii) passive microwave emission model performance over forests and natural vegetation areas. First, a statistical analysis based on a principal component analysis showed the potential of multi-angular L-band measurements for forest classification. The PCA identifies clusters of stands classified by age from emissivities obtained from STARRS at different angles. Then an example of modelling was presented

based on the τ - ω approach. This simple emission model, is very tractable for inversion problems, and it has been previously tested over crops with successful results. Hence there was an interest in estimating the performance of this model over a variety of other vegetation covers (such as forests, natural vegetation, etc.). Preliminary analysis of the EuroSTARRS dataset over coniferous trees indicate that L-band brightness temperature decreases as dry biomass increases. This trend could be reproduced by the τ - ω model using calibrated values of both the single scattering albedo and the vegetation optical depth.

In parallel to these studies further work will focus on the analysis of EuroSTARRS data over other types of vegetation covers, the assessment of the effect of undergrowth on the microwave signature for small angles, the effects of topography from EuroSTARRS data over the *Pyrenees*, and other issues such as the modelling of the L-band emission of urban areas.

ACKNOWLEDGEMENTS

This work has been carried out in the framework of the respective ESTEC-ESA n° 15949/02/NL/SF Contracts with Universitat de Valencia (Spain), INRA (Bordeaux, France) and CNRM (Toulouse, France). The authors wish to thank all the EuroSTARRS-01 campaign, from: CIDE (especially C.Antolin and F.Ferrer), Gener Valenciana and Ayuntamiento de Valencia, INRA Bordeaux and CNRM (Toulouse) teams.

REFERENCES

- Dobson M. C., F. T. Ulaby, M. T. Hallikainen and M. A. El-Reyes, 1985, Microwave dielectric behavior of wet soil- Part II: Dielectric mixing models', IEEE Tr. Geosc. Remote Sens. 23:35-46.
- Ferrazzoli, P., Guerriero L., and Wigneron J.P, 2001, Simulating L-band emission of forests in view of future satellite applications, IEEE Tran s. Geosc. Remote Sens. Environ., in press.
- Jackson T. J. and T. J. Schmugge, 1991, Vegetation effects on the microwave emission of soils, Remote Sens. Environ., 36:203-212.
- Jackson, T. J., Le Vine, D. M., Swift, C. T., Schmugge, and T. J., Schiebe, F. R., 1995, Large area mapping of soil moisture using the ESTAR passive microwave radiometer in Washita'92, Remote Sens. Environ., 53,27-37.

- Karam, M.A, Amar, F., Fung, A.K., 1995, A microwave polarimetric scattering model for forest canopies based on vector radiative transfer theory. *Remote Sens. Environ.*, 53 :16-30.
- Kerr, Y. H., Waldteufel, P., Wigneron, J.-P. , Font, J., and Berger, M., 2001, Soil Moisture Retrieval from Space: The Soil Moisture and Ocean Salinity (SMOS) Mission, *IEEE Trans. Geosc. Remote Sens.*, 39(8), 1729-1735.
- Njouku, E.G., and Entekhabi D.,1996, Passive microwave remote sensing of soil moisture, *J. of Hydrology*, 184,101-129.
- Schmugge, T., 1998, Applications of passive microwave observations of surface soil moisture, *J. of Hydrology* 212-213, 188-197.
- Ulaby F. T., R.K. Moore and A.K. Fung, 1986, *Microwave Remote Sensing - Active and Passive*, vol. 3., Artech House, Norwood, MA 02062.
- Waldteufel, P., Anterrieu, E., Goutoule, J. M., and Kerr, Y., 2000, Field of view characteristics of a microwave 2-D interferometric antenna, as illustrated by the MIRAS concept, in *Microwave radiometry and remote sensing of the Earth's Surface and atmosphere*, ed by P Pampaloni and S. Paloscia, VSP BV 2000, Utrecht, pp 477-483.
- Wigneron, J.P., A. Chanzy, J.-C. Calvet Aand N. Bruguier, 1995, A simple algorithm to retrieve soil moisture and vegetation biomass using passive microwave measurements over crop fields, *Remote Sens. Environ.*, 51, 331-341.
- Wigneron, J.P., Combal, B., Wegmüller, U., and Mätzler, M., 1996, Estimation of microwave parameters of crops from radiometric measurements, *Int J.of Rem. Sens.* 14:2875-2880.
- Wigneron, J. P., Guyon, D., Calvet J.C, Courier, G., and Bruguier N., 1997, Monitoring coniferous forest characteristics using a multifrequency (5-90GHz) microwave radiometer, *Remote Sens. Environ.*, 60, 299-310.
- Wigneron, J.P., . Waldteufel P., Chanzy A., Calvet J. C., and Kerr, Y. 2000, Two dimensional microwave interferometer retrieval capabilities over land surfaces (SMOS mission), *Remote Sensing Environ.*, 73, pp 270-282.
- Wigneron, J.-P., L. Laguerre, and Y. Kerr, 2001 Simple Modeling of the L-band Microwave Emission from Rough Agricultural Soils, *IEEE Trans. Geosc. Remote Sens.*, 39(8), 1697-1707

Mapping paleoflooded areas on evaporite playa deposits over sandy sediments (Tablas de Daimiel, Spain) using hyperspectral DAIS 7915 and ROSIS spectrometer data

A. Rianza*, R. Mediavilla*, E. Garcia-Meléndez**, M. Suarez**, A. Hausold***, U. Beisl***, H. Van der Werff****

(*) *Instituto Geológico y Minero de España (IGME), Rios Rosas 23, 28003 Madrid, Spain
Ph: 3491 3475907; Fax: 3491 4426216*

(**) *Departamento de Geología, Universidad de Salamanca, Pza. de la Merced s/n, 37008 Salamanca, Spain*

(***) *DLR_ German Aerospace Research Establishment, Remote Sensing Data Centre, Oberpfaffenhofen, Postfach 1116, 82230 Weßling, Deutschland*

(****) *International Institute for Aerospace Survey and Earth Sciences (ITC), P.O.Box 6, 7500 AA Enschede, The Netherlands*

a.rianza@igme.es, r.mediavilla@igme.es, egm@usal.es, msuarez@usal.es, Andrea.Hausold@dlr.de, ulrich.beisl@landshut.org, wdwerff@itc.nl

ABSTRACT- *Open-system lakes developing marshes are sensitive environments to climate changes. Mineralogical climate markers such as gypsum and dolomitized carbonate are spatially traced using hyperspectral imagery. Climate-dependent saline soils, carbonate, organic matter and iron oxide crusts have been mapped along different stages of flooding and emersion in the past 2000 years using DAIS and ROSIS spectrometer data. Spectral behaviour interacting and masking from various mineralogical components are described on laboratory spectra. Influence of landuse on the spatial spectral behaviour of paleoenvironments is discussed. A general outline of the past pools is drawn on the area surrounding the actual marsh, providing priceless data to use in further paleoclimate limnological research and in the development of new techniques for that research.*

1 INTRODUCTION

The Las Tablas de Daimiel Natural Park frames a lake at the head of the river Guadiana draining to the Atlantic, settled in the large plain of La Mancha in central Spain (fig.1). This continental dry plain is subject to a Mediterranean climate with dry summer and winter and relatively short rainy seasons in spring and autumn. Periods of drought are recurrent within the lapse of five years. It is a wetland with a linear morphology associated to an alluvial plain (Casado and Montes, 1995), resulting from two main interacting processes. First, the overflowing of the rivers Cigüela and Guadiana, which join at the Tablas de Daimiel. And second, the natural discharge of the underlying aquifer, through upwelling water at points locally termed “ojos” (eyes).

The recent sedimentological record of the Quaternary deposits in the area points to recent harsh paleoenvironmental conditions (2500-2300 years before present) with diminishing humidity and lowering of groundwater levels (García Antón et al, 1986). Intensive use of groundwater for cereal crop irrigation has produced a serious descent on the

groundwater level and cover, an already irreversible environmental problem. Today the Tablas de Daimiel has long since ceased to be an upwelling groundwater area and has instead become a big pool of artificial water inflow (Llamas, 1998).

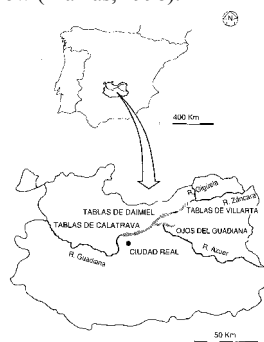


Fig 1. Geographical location of the Tablas de Daimiel wetland and natural park

Lakes are environments particularly sensitive to climate changes, both actual and paleoclimates. Open

system lakes fed by groundwater and seasonal runoff show a fluctuating shoreline.

The underlying most recent sediments are a system of sands deposited during the Holocene. The sand deposits present soil development of red-brown soils, considered remnants of old red soils now degraded (Pérez-González et al, 1983, Rodríguez García, 1998).

Organic sediments (peat) occur when the shallow channels excavated by the rivers overflow the adjacent floodplains with sediments loaded with clay, silt, sulphate, calcium and in lesser amounts, magnesium and chlorides. This favours the development of marshes on permanently flooded areas with abundant vegetation, where organic matter deposits occur. During the periods of draught, the groundwater level deepens, and the sediments are exposed developing saline soils with gypsum and dolomitization of carbonate. Water level fluctuations in open-system lakes cause much reworking of sediment in the nearshore zone (Allen and Collinson, 1978, in Reading, 1978).

Space and airborne imagery depicts subtle variations in the reflectance properties of desert surfaces, which are indicative of changes in mineralogical composition. The intensity of the red colour of sands in Namibia (Logan, 1960) has been used as an indication of age in the dunes. In Australia, the intensity of dune reddening resulted in information about the distance from the sand source area (El Baz, 1978; El Baz and Prestel, 1980).

The presence of hematite coatings on individual grains has been given as the cause of red colour in desert sands. Several studies indicate that the coating on sand grains is composed of kaolinite with powdery hematite, thus linking such reddening to desert varnish (Potter and Rossman, 1977). The hematite coating on quartz grains increases in thickness depending on the location of the deposit, and so the reddening of the sands increases with the transport distance (McCay et al, 1980). This way, the reddening property has been used to determine the relative ages of colour zones in the same sand field.

The effects of weathering processes on the spectral response of rocks exposed to the atmosphere has been evaluated both on sedimentary and igneous rocks on laboratory spectral measurements in the visible and nearinfrared (Riaza, 1992).

The mixtures of iron and clay minerals produced by weathering alteration associated to posthercynian erosion paleosurfaces in the Duero Basin (Central Spain) developed under different paleoclimates have been mapped using thematic mapper imagery (Riaza et al, 1997). Different image processing procedures helped to model sediment patterns on various stages of the evolution of the sedimentary basin (Riaza et al, 1995, 1997, 2000).

Iron bearing minerals, gypsum, carbonate and clays, have been used as the main mineral spectral references for the geological mapping of a carbonate area in the desert of Israel using the hyperspectral airborne spectrometer DAIS 7915 (Riaza et al, 1998).

Prior work has been focused on the spectral behaviour of playa evaporites both in the visible and nearinfrared (Crowley, 1991, 1993) and thermal infrared (Crowley, 1996). The influence of organic matter on soil colour is a long experienced relationship in spectrometry (Shields et al, 1968, Leone and Escadafal, 2001). Saline soils are recurrent on remote sensing studies because of their relationship with anthropic irrigation uses (Dehaan and Taylor, 2002; Koch et al, 2000). Various spectral libraries of minerals and rocks have been built, which are now in the public domain and well known by the geological community (Clark et al, 1993; Grove et al, 1992; Salisbury et al, 1992).

Areas flooded by water in the past which are nowadays exposed to the surface in the Tablas de Daimiel have changed the mineralogical and spectral aspect of the underlying Holocene sands, the most recent deposit hosting the wetland. The colour of the sand is darkened to grey, by influence of large amounts of organic matter deposited at the bottom of the flooded area. Meanwhile, peat and saline deposits are developed. Gypsum and carbonate precipitate (Arauzo et al, 1996), and new clays such as palygorskite and sepiolite occur. Such mineralogical changes can be spectrally detectable on the imagery.

2 METHOD

DAIS 7915 and ROSIS Spectrometer data were recorded on July 2000, aiming to minimum vegetation vigour and maximum soil exposure. The spatial resolution of 5 m for DAIS and 2 m for ROSIS was ensured at a flying altitude with maximum signal to noise ratio.

Non-coherent noise was corrected after in-flight calibration for DAIS (Strobl et al, 1996) to remove the sensor sensitivity effects on the 79 DAIS channels. Different spectral imaging processing tools were tested on atmospherically corrected data using a midlatitude summer profile (Richter, 1996; Richter et al, 2002) using field spectra from dark and light targets. ROSIS data with 115 channels in the visible 430-860 nm wavelength range, were corrected using a different procedure (Gege et al, 1998). Both sensors operated simultaneously at the same flight altitude. As a consequence, the area covered by ROSIS is a narrow belt centered along the DAIS central flightline (fig.12). The main interpretation procedures were focused on DAIS data. Particular nuances in the visible were contrasted with ROSIS data, with a 4 nm spectral resolution and 2 m spatial resolution compared to the 5 m DAIS spatial resolution.

Field spectra were collected for thematic analysis on geologically representative targets to be used for interpretative image processing with a GER Spectrometer. Non consolidated soil samples were collected at different stages during the interpretation of the imagery lead by hyperspectral image processing suggestions on mineralogy and sedimentology. Laboratory spectra were run on field soil samples using a Perkin-Elmer Lambda 6 Spectrometer in the visible and nearinfrared provided with an integrating sphere. Non consolidated rock samples were dry-sieved before measurement.

X-ray diffraction analysis was performed on selected non-consolidated rock samples to confirm field observations regarding mineralogical contents. Laboratory measurements were made on powdered samples after XRD aiming to ascertain spectral features which might appear on fine grained samples after separation of the clay fraction.

Image processing was conducted using ENVI hyperspectral modules and reference spectral libraries.

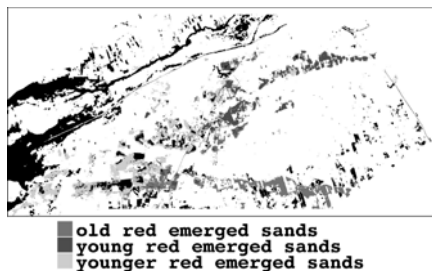


Fig.2. Geological map composed from DAIS images indicating the main sedimentary units

3 DIGITAL IMAGE PROCESSING

DAIS images were processed aiming to separate different sediments and minerals indicative of geological processes both of palustrine and fluvial environments (fig.2). Mosaics were composed with the two scenes for panoramic view of the area, and for selection of areas of interest (fig.3). Masks were built for densely vegetated areas using channels 17 and 13 for a red/nearinfrared ratio. Masks for water were also built using value 26 on channel 1 as threshold. A false colour composite with channels 19, 6 and 53 (BRG) was selected gathering both information on the three DAIS detectors on the visible and nearinfrared, and wavelength ranges which are critical for known reflectance absorptions diagnostic of minerals present in the area.

The six thermal infrared channels were used for a primary estimation of lithological variety (Riaza et al, 1998) (fig.3). Both Principal Components and Minimum Noise Fraction Transforms were useful

identifying the main lithological regions indicating further hyperspectral image processing. Masks were built using selected minimum noise fraction transforms from thermal infrared channels to isolate geological units on the sands (fig.2). Pixel Purity Index and n-dimensional analysis were run on selected masked areas, helping to understand the geological spectral meaning of the various statistical populations among the sands (Boardman et al, 1993; Boardman and Kruse, 1994).

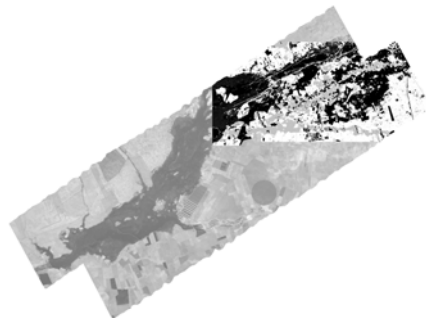


Fig.3. False colour composite with Principal components 1 (red), 2(green) and 3 (blue) computed from the six thermal infrared DAIS channels on the flight line mosaic after masking water and dense vegetation. Indication of the northeastern area selected for mapping.

Illumination Angle Effects jeopardised any subtle hyperspectral analysis on flightline mosaics. Image processing procedures were repeated for individual scenes and subsets, and maps were produced composing final results for the same geological units.

Field spectra taken with a GER Spectrometer were used with Spectral Angle Mapper (Kruse et al, 1993). Spectra showing iron absorption features were grouped into a library, and spectra showing carbonate absorptions were included into a different library. SAM was run on the 72 VIS-NIR DAIS channels on independent areas masked for the three main sandy areas: red emerged sands, depressions with organic matter, and flooded mudflats temporarily exposed developing saline soils (fig.4). The same procedure was used with the iron absorption library using first only the 29 VIS DAIS channels, and the library with spectra showing carbonate absorptions was used to compute maps on the 2000-2500 nm wavelength range on a second stage (fig.5). Six representative spectra were selected after several attempts, giving better spatial outline of geological paleoflooded regions (fig.6).

The resulting maps were quite noisy when using a reduced number of channels, so that only maps computed with the 72 VIS-NIR channels were used for analysis. All results were very similar on the drawn geological units, coinciding with the spectral signatures

coming from PPI and n-dimensional analysis. SAM was more sensible showing the deeper flooded areas richer both in carbonates and organic matter (fig.4).

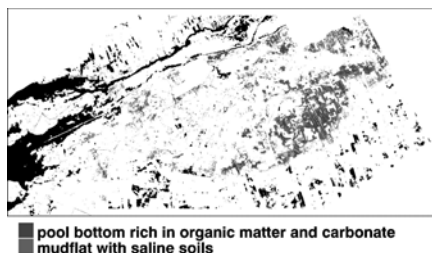


Fig.4. Map built using Spectral Angle Mapper on the grey mudflat "playa" sands on the 72 VIS-NIR DAIS channels using six selected field spectra taken with a GER spectrometer (fig.6). The deeper areas of the paleopool richer on organic matter and carbonate are isolated from the flooded mudflats on a fluctuating shore developing saline soils.

When using SAM on the red emerged areas (fig.5), a connecting channel among the two main paleopools is spectrally prominent. This connecting very shallow channel was not obvious on the prior analysis using mnf, ppi and n-dimensional analysis.

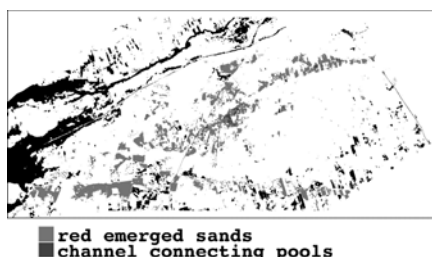


Fig 5. Map built using Spectral Angle Mapper on the red emerged sands on the 72 VIS-NIR DAIS channels using six selected field spectra taken with a GER spectrometer (fig.6). a channel connecting the two main paleopools is shown.

Laboratory spectra of nonconsolidated rock samples pointed to DAIS channels 33 (1520-1544 nm, gypsum), 34 (1565-1575 nm (gypsum), 40 (1777-1757, gypsum), 59 (2229-2225 nm, illite), 60 (2230-2240 nm, illite), 61 (2250-2253, gypsum, illite, palygorskite) and 64 (2298-2297 nm, sepiolite, dolomite) as critical showing absorptions related to minerals in the area (fig.8). Channels 41, 42 and 70 mineralogically sensitive to gypsum, goethite, calcite, illite and iron oxides, were rejected because of low signal quality. Hyperspectral image processing is impossible on this reduced number of channels, and more conventional image processing gives noisy results. However, useful

hints came from colour composites built with mnf213 and pc214 from such channels.

The same procedure was used for ROSIS, elaborating parcial maps to contrast with DAIS results.

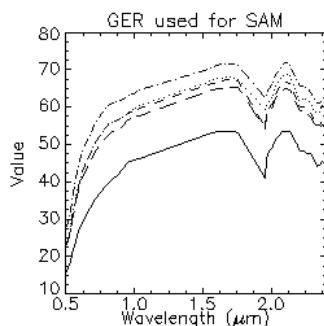


Fig 6. Field spectra taken with a GER spectrometer selected as depicting better geological units.

4 LABORATORY SPECTRA

Visual and mineralogical analysis of the fluvio-lacustrine system of the Tablas de Daimiel depicts a sulphate and carbonated water solution, being chloride absent. Intensive agricultural practices have destroyed any crusts which might have developed on the surface. Saline minerals are unstable mineralogical components, relying on subtle variations of temperature and humidity to precipitate or dissolve. Such physical parameters may change during daytime. Therefore, saline minerals excluding gypsum have not been used on the spectral interpretation, nor are crusts of any sort expected to be recorded by the imagery.

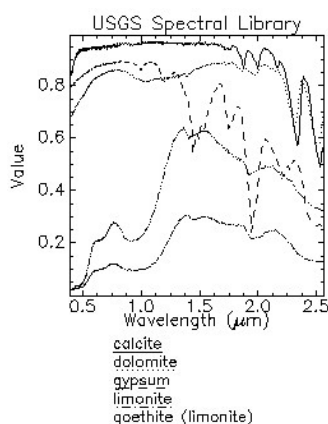


Fig.7. Spectra of the main minerals present on the sediments of the area of study related to palustrine and fluvial processes (United States Geological Survey Spectral Library).

The spectral response of mudflats around the former wetland are mineralogically dominated by gypsum and carbonate, whether calcite or dolomite (fig.7,8). Increasing dolomite contents would indicate an intensification of palustrine processes. Clays are not widely present in the area, nor does laboratory mineralogical analysis detect them.

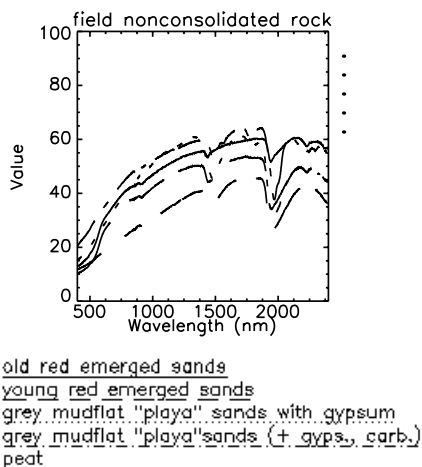


Fig.8. Laboratory Spectra from field nonconsolidated rock samples using a Perkin Elmer Lambda 6 Spectrometer on representative sediments, with expression of the minerals whose absorption features are present.

Laboratory spectra of peat is dominated by the presence of gypsum on typical shapes with minimum at 1477, 1520, 1565 and 2250 nm (Clark et al, 1992) (fig.7,8). The presence of carbonate appears as a weak 1975 nm minimum. Sepiolite and mainly dolomite are detected by the 2298 nm.

The holocene red sands are sediments composed of sand with quartz as a principal component. The overall reflectance of sands is higher than peat due to the influence of gypsum and saline minerals (fig.7,8). Clays are responsible for the 1438 nm minimum. Goethite contributes with a weak 1943 nm minimum and illite to the 2229-2230 nm and weak 2370 nm minimum. X-ray diffraction analysis showed no presence of clays on the red sands, but rather and widespread carbonate. Spectra run on clay size powder from soil samples showed the presence of carbonate on most red sands (fig.9). Grey sands which had been once flooded also show the same carbonate absorption.

Several systems of red sands have been spectrally identified based on different iron minerals related to variable time of exposure to the atmosphere and weather conditions. Three morphosedimentary surfaces can be distinguished by intensity of reddening directly related to age (fig.8,10,11). Intense reddening

occurs on older and topographically highest surfaces resulting on deeper iron absorptions in the visible and higher overall reflectance. Darker red colour on lower surfaces is associated to lower overall reflectance.

The grey sands, which have been once flooded by water present a dolomite 2298 nm minimum, absent on the rest of the sands (fig.8). XRD have revealed the presence of nesquehonite, a magnesium carbonate common as secondary mineral in saline playa deposits with high Mg/Ca ratios and high Mg concentration in water (Kelts and Hsü, 1978). The presence of dolomite is indicative of organic matter degradation, whether by oxidation liberating sulphur, or by increase of Mg in the system from runoff.

The spectral response of gypsum dominates grey sands, along with dolomite (fig.8). The displacement of a minimum from 1940 to 1970 nm indicates the transition from the temporarily flooded mudflat to the everemerged sands only subjected to reddening by iron coatings developed by exposure to the atmosphere. Spectra on powdered samples for X-ray diffraction analysis only display the gypsum absorption features when present. However, carbonate has been reported on the same samples. Gypsum dominates and hinders spectrally the presence of carbonate, both on soil samples and clay-size powdered samples (fig.8,9). The presence of gypsum on the grey sands increases geographically towards the river, indicating a likely progressive water salinity in comparatively recent times.

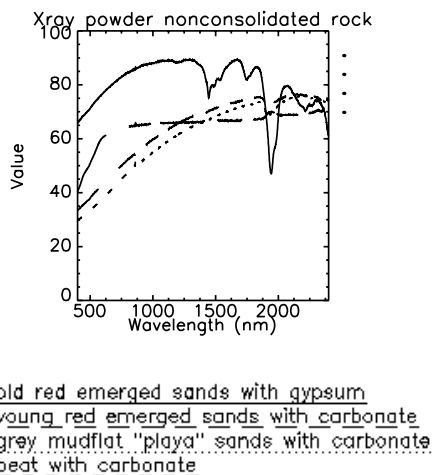


Fig.9. Laboratory Spectra from powder after X Ray Diffraction Analysis from field nonconsolidated rock samples, using a Perkin Elmer Lambda 6 Spectrometer on representative sediments, with expression of the minerals whose absorption features are present.

Peat, in spite of the high contents of organic matter, records spectrally the presence of gypsum

(fig.8). High contents of organic matter obliterates any spectral response from iron minerals (Galvao and Vitorello, 2001). Presence of carbonate is shown by spectra run on clay-size powdered samples for X-ray diffraction analysis (fig.9).

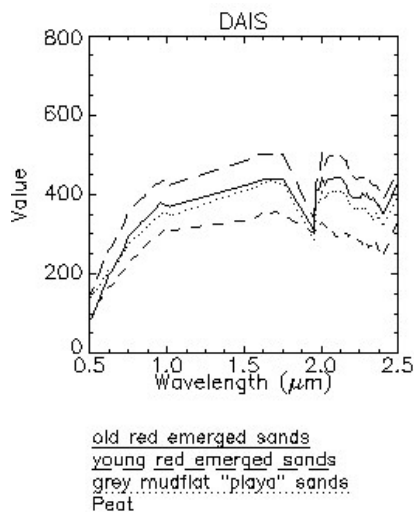


Fig.10. Z profiles from DAIS images from areas representing sedimentary units on maps built using digital image processing (fig.2 and 11).

Carbonate is widespread throughout the area, both in emerged and flooded areas. Imagery is quite noisy on the nearinfrared to be able to show carbonate-related absorption, relatively weak on the laboratory spectra. Hyperspectral profiles on DAIS imagery do not depict a clear spectral response due to the low energy available for the fourth detector on the 2000-2500 nm wavelength range. However, the topographically low areas where water was deeper and rich in gypsum should pop on the nearinfrared.

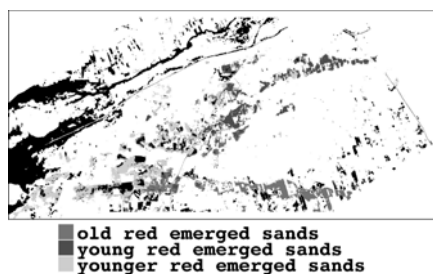


Fig.11. Geological map on red emerged sands built from DAIS imagery associated to three main morphosedimentary surfaces.

5 DAIS SPECTRAL RESPONSE

DAIS images present a distinguishing response from once flooded and everemerged areas (figs.10,11). All the emerged areas, whether sand deposits or continental aprons or fluvial deposits, show depressions in the visible due to the presence of iron bearing minerals.

The wide depression on red everemerged sands is more pronounced, consistent with their bright orange colour. In all of the mapped units, young red emerged sands display the highest overall reflectance. The areas which were once flooded are less expressive on the visible.

In the nearinfrared, the most distinguishing feature is the presence of a narrow absorption at 2.1 μm on areas which were flooded. Both bloedite $\text{Na}_2\text{Mg}(\text{SO}_4)_2 \cdot 4\text{H}_2\text{O}$, calcite and dolomite can be responsible.

The areas which are emerged display a shoulder centred between 2.2-2.3 μm non-existent on the flooded areas. This might suggest abundance of clays, which is not confirmed by XRD mineralogical analysis or by sedimentological expectations. Widespread carbonate can also contribute to this spectral feature.

DAIS imagery show differences inside the flooded areas due to the variable contents on organic matter, gypsum and saline minerals (fig.4). The deeper hydrologically closed areas, where standing water persisted longer to develop marshes and to precipitate organic matter in detectable amounts, seem to be richer also in gypsum. When the groundwater level lowers, marshes are exposed to the atmosphere developing saline soils.

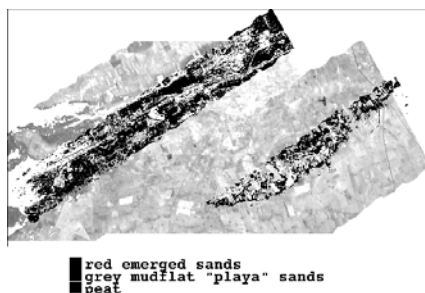


Fig. 12. Map built from ROSIS data using a similar procedure to former DAIS data, overlying over DAIS images, representing the main sedimentary units.

Preliminary analysis on DAIS imagery does not show distinctive absorptions among the mapped units, but Spectral angle Mapper using selected field spectra depicted subtle spectral variations (fig. 4). A depression on 2.3 μm is present on both peat and saline mudflats, whether due to gypsum or carbonate. The overall

reflectance is lower on the areas longer flooded due to more abundant organic matter.

6 ROSIS SPECTRAL RESPONSE

ROSIS data display a similar pattern of geological units when following the same digital image processing procedure used for DAIS (fig.12). Improved spatial resolution increases the spectral variability particularly on red emerged sands. Spectra do not display a very obvious iron absorption feature, due to the atmospherical correction system (fig.13).

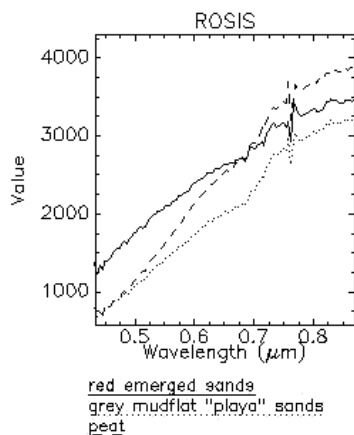


Fig. 13. Z profiles from ROSIS images from areas representing sedimentary units on maps built using digital image processing (fig. 12).

7 CONCLUSIONS

Hyperspectral imagery has been able to distinguish paleoflooded areas related to a receding wetland due to differential mineralogical contents associated with topography and palustrine and fluvial processes.

Gypsum, carbonate and organic matter are paleoclimate indicators spectrally recorded by the imagery in the VIS-NIR. Saline soils with gypsum both on occasionally overflowed areas adjacent to shallow river channels and on mudflats around standing water pools, have been recorded by the imagery. Originally deeper areas rich in organic matter where marshes develop at times of low water movement are also shown.

Gypsum masks the presence of carbonate on the spectral response. Only X-ray diffraction analysis has depicted the presence of carbonate when coexisting with gypsum. Therefore, carbonate may also be present in the geochemically central fluvio-lacustrine areas rich in gypsum.

Several systems of fluvial terraces with red sands have been shown by the imagery. Mineralogical variations on iron oxides and hydroxides developed when sediments are emerged in periods of drought are easily recorded in the visible wavelength range.

DAIS thermal infrared, particularly sensitive to topography, was first used to depict spectrally variable areas. From them, through successive hyperspectral image processing on selectively masked areas, a spatial map of the paleolake has been drawn from the imagery, orientating drill location for further palinological studies and paleoenvironmental analysis.

8 ACKNOWLEDGEMENT

The Fifth Framework Program, Improvement of Human Potential, Access to Research Infrastructures (contr. HPRI-CT-1999-00075, ref HS2000-ES1) funded data for this work. Thanks are due to S. Martín Alfageme and Iñigo Martín for software and hardware assistance (STIG, University of Salamanca). J. O'Malley reviewed the English version.

9 REFERENCES

- Allen, P.A. and Collinson, J.D., 1978, *Lakes. In., Sedimentary Environment and Facies*, edited by H.G. Reading (Oxford, London: Blackwell Scientific Publications), pp 63-282.
- Boardman, J. W., 1993, Automated spectral unmixing of AVIRIS data using convex geometry concepts. In *Summaries Fourth JPL Airborne Geoscience Workshop*, JPL Publication 93-26, v. 1, pp. 11 - 14.
- Boardman J.W. and Kruse, F. A., 1994, Automated spectral analysis: A geologic example using AVIRIS data, north Grapevine Mountains, Nevada: in *Proceedings, Tenth Thematic Conference on Geologic Remote Sensing*, Environmental Research Institute of Michigan, Ann Arbor, MI, pp. I-407 - I-418.
- Arauzo, M., Rubio, A., and Vicioso, J., 1996, El ambiente acuático: Hidroquímica, 70-90, in Alvarez Cobelas, M. y Cirujano, S., Ed., *Las Tablas de Daimiel, Ecología Acuática y Sociedad*, Ed. Organismo Autónomo Parques Nacionales, Madrid, 370 p.
- Casado, S. and Montes, C., 1995, *Guía de los lagos y humedales de España*, Reyero, Madrid, 255 p.
- García Antón, M., Morla, C., Ruiz Zapata, B., Sais Ollero, H., 1986, *Contribución al conocimiento del paisaje vegetal Holoceno en la Submeseta Sur Ibérica: análisis polínico de sedimentos*

- higroturbosos en el Campo de Calatrava (Ciudad Real, España), In: Quaternary Climate in Western Mediterranean (F. López Vera ed.), Universidad Autónoma de Madrid Publications.
- Clark, R. N., Swayze, G. A., Gallagher, A., King, T. V. V. and Calvin, W. M., 1993. The U.S. Geological Survey Digital Spectral Library: Version 1: 0.2 to 3.0 mm: U.S. Geological Survey, Open File Report 93-592, 1340 p.
- Crowley, J.K. and Hook, S.J., 1996, Mapping playa evaporite minerals and associated sediments in Death Valley, California, with multispectral thermal infrared images, *Journal of Geophysical Research*, vol.101, no. B1, 643-660, January 10.
- Crowley, J.K., 1993, Mapping playa evaporite minerals with AVIRIS data: A first report from Death Valley, California, *Remote Sensing of Environment*, 44, 337-356.
- Crowley, J.K., 1991, Visible and near-infrared (0.4-2.5 μ m) reflectance spectra of playa evaporite minerals, *Journal of Geophysical Research*, 96, 16.231-16.240.
- Dehaan, R.L. and Taylor, G.R., 2002, Field-derived spectra of salinized soils and vegetation as indicators of irrigation-induced soil salinization, *Remote Sensing of Environment* 80, 406-417.
- El Baz, f., 1978, The meaning of desert color in earth orbital photographs, *Photogrametric Engineering and Remote Sensing*, 44, 69-75.
- El Baz, F., Prestel, D.J., 1980, Desert varnish on sand grains from the Western Desert of Egypt: Importance of the clay component and implications to Mars. In : *Lunar and Planetary Science XI*, 1980, Houston, Texas: Lunar and Planetary Institute, 254-256.
- Galvao, L.S., and Vitorello, I., 1998, Role of organic matter in obliterating the effects of iron on spectral reflectance and colour of Brazilian tropical soils, *International Journal of Remote Sensing*, 19, n° 10, 1969-1979.
- García Antón, M., Morla, C., Ruiz Zapata, B., Sais Ollero, H., 1986, Contribución al conocimiento del paisaje vegetal Holoceno en la Submeseta Sur Ibérica: análisis polínico de sedimentos higroturbosos en el Campo de Calatrava (Ciudad Real, España), In: Quaternary Climate in Western Mediterranean (F. López Vera ed.), Universidad Autónoma de Madrid Publications.
- Gege, P., Beran, D., Mooshuber, W., Schulz, J., van der Piepen, H., 1998, System analysis and performance of the new version of the imaging spectrometer ROSIS, *Proceedings 1st Workshop on "Imaging Spectroscopy"*, Zürich, Switzerland, 6-8th October 1998, 29-36.
- Grove, C. I., Hook, S. J., and Paylor II, E. D., 1992. *Laboratory Reflectance Spectra of 160 Minerals, 0.4 to 2.5 Micrometers*: Jet Propulsion Laboratory Pub., 92-2.
- Kelts, K., and Hsü, K.J., 1978, Freshwater Carbonate Sedimentation, In Lerman, A., ed. "Lakes: chemistry, geology, physics", Springer Verlag, 1978, New York, 363 p.
- Koch, M., 2000, Geological controls of land degradation as detected by remote sensing: a case study in Los Monegros, north-east Spain, *International Journal of Remote Sensing*, 21-3, 457-474.
- Kruse, F. A., Lefkoff, A. B., Boardman, J. B., Heidebrecht, K. B., Shapiro, A. T., Barloon, P. J., and Goetz, A. F. H., 1993. The Spectral Imaging Processing System (SIPS) – Interactive Visualization and Analysis of Imaging Spectrometer Data, *Remote Sensing of Environment*, 44, 145-163.
- Leone, A.P., and Escadafal, R., 2001, Statistical analysis of soil colour and spectroradiometric data for hyperspectral remote sensing of soil properties (example in a southern Italy Mediterranean ecosystem), *International Journal of Remote Sensing*, 22, n°12, 2311-2328.
- Logan, R.F., 1960, The Central Namib Desert, National Academy of Sciences, National Research Council Publication 785, 162 p.
- Llamas, M.R., Conflicts Between Wetland Conservation and Groundwater Exploitation: Two Case Histories in Spain, 1988, *Environmental Geology and Water Science*, vol.11, n° 3, 241-251.
- Mathieu, R., Pouget, M., Cervelle, B. and Escadafal, R., 1998, Relationships between Satellite-Based Radiometric Indices Simulated Using Laboratory Reflectance Data and Typic Soil Color of an arid Environment, *Remote Sensing of Environment*, 66, 17-28.
- McCay, D., Constantonopolus, C., Prestel, D.J. and El Baz, F., Thickness of coatings on quartz grains from the Great Sand Sea, Egypt. In *Reports of*

- Planetary Geology Program- 1980, Washington D.C.: National Aeronautics and Research Administration, NASA TM-82385, 1980, 304-306.
- Pérez González, A., Aleixandre, A., Pinilla, J., y Gallardo, J., 1983, El pasaje eólico de la llanura aluvial de San Juan (llanura manchega central), *Actas de la VI Reunión del Grupo Español de Trabajo en el Cuaternario*, Galicia, 631-655.
- Portero García, J.M., Ancochea, E., y Gallardo, J., 1988, Memoria del Mapa Geológico a escala 1:50.000, Segunda Serie, hoja nº 760 (Daimiel).
- Potter, T.R. and Rossman, J.R., 1977, Desert varnish: the importance of clay minerals. *Science*, 196, 1446-1448.
- Riaza, A., 1992, Reflectancia en rocas en función de su litología y fábrica interna. II Cartografía de rocas ígneas en el Complejo de Burguillos del Cerro en el visible y el infrarrojo cercano: reflectancia espectral en el laboratorio y evaluación estadística de la misma en relación con imágenes thematic mapper, *Boletín Geológico y Minero*, 103, n.3, 3-26.
- Riaza, A., Mediavilla, R., Santisteban, J. L., Villar, P. and Martín Alfageme, S., 1995. Regolitos en una cuenca terciaria. Propiedades espectrales según su mineralogía en función de la evolución climática, Coloquio Internacional sobre propiedades espectrales y teledetección de los suelos y rocas del visible al infrarrojo medio, La Serena (Chile), 24-27 de Abril 1995, 100-104.
- Riaza, A., Mediavilla, R., and Santisteban, J.I., 2000, Mapping geological stages of climate-dependent iron and clay weathering alteration and lithologically uniform sedimentary units using Thematic Mapper imagery, *International Journal of Remote Sensing*, vol.21, nº5, 937-950
- Riaza, A., Mediavilla, R., Santisteban, J. L., Villar, P. and Martín Alfageme, S., 1997. Cartografía de formaciones geológicas litológicamente similares en zonas llanas cultivadas, V Reunión Científica de la Asociación Española de Teledetección, Las Palmas (Gran Canaria), 10-12 November 1993, 863-876.
- Riaza, A., Kaufmann, H., Zock, A. and Müller, A., 1998, Mineral Mapping in Maktesh Ramon (Israel) using DAIS 7915, *Proceedings 1st EARSeL Workshop on Imaging Spectroscopy*, Zürich, Switzerland, 6-8 October 1998, in press.
- Richter, R., 1996. Atmospheric correction of DAIS hyperspectral image data, *Computers & Geosciences*, vol.22, no.7, 785-793.
- Richter, R., Müller, A. and Heiden, U., 2002, Aspects of operational atmospheric correction of hyperspectral imagery, *International Journal of Remote Sensing*, vol.23, nº 1-10, 145-158.
- Rodríguez García, J.A., 1998, Geomorfología de las Tablas de Daimiel y del endorreísmo manchego centro-occidental, October 1998, MSc Thesis, University Complutense of Madrid, 164 p, unpublished.
- Salisbury, J. W., Walter, L. S., Vergo, N. and D'Aria, D. M. 1992. Infrared (2.1-25 µm) Spectra of Minerals, The John Hopkins University Press, Baltimore (Maryland, USA).
- Strain, P.L., El Baz, F.: 1982, Sand distribution in the Kharga depression of Egypt: Observations from Landsat images. *International Symposium on Remote Sensing of Environment*, 1982. Ann Arbor, Michigan: Environmental Research Institute of Michigan, First Thematic conference: Remote Sensing of Arid and Semi-arid Lands, Cairo, Egypt, ERIM, paper B-11, 101-102.
- Strobl, P., Richter, R., Lehman, F., Müller, A., Zhukov, B., Oertel, D., 1996. Preprocessing for the Digital Airborne Imaging Spectrometer DAIS 7915, *SPIE's AEROSENSE '96 Conference*, Orlando, Apr. 8-12, 1996, *SPIE Proc.* Vol. 2758.
- Shields, J.A., Paul, E. A., Arnaud, R.J.Sr. and Head, W.K., 1968, Spectrophotometric measurement of soil color and its relationship to moisture and organic matter, *Canadian Journal of Soil Science*, 48, 271-280.
- Walker, T.R., 1967, Formation of red beds in modern and ancient deserts. *Geological Society of America Bulletin*, 78, 353-368.

Soil-vegetation indices developed from spectral signatures recorded by various satellites

K. Dabrowska-Zielinska, W. Kowalik, M. Gruszczynska, A. Hoscilo K. Stankiewicz,
Institute of Geodesy and Cartography, Remote Sensing and Spatial Information Centre
Jasna 2/4, 00-950 Warsaw, Poland,
e-mail: kasia@igik.edu.pl

ABSTRACT *The investigation has been carried out for the wetlands in the Biebrza Basin, Poland, which is the best-preserved area of marshes, and swamps in Central Europe. In the valley of the Biebrza River, flooded heavily every spring natural plant communities grow in several zones. The investigation aimed at finding the best vegetation index to characterise marshland habitat. The indices were calculated on the basis of all considered spectral bands of low spatial resolution satellites as SPOT VEGETATION, ERS ATSR, and NOAA/AVHRR. The GEMI and EVI index calculated from SPOT VEGETATION was the best for distinguishing vegetation classes. The best correlation between LAI measured at the ground and the indices was with GEMI and EVI index. Soil moisture values calculated from ERS2. SAR well characterised marshland humidity classes.*

1 INTRODUCTION

The assessment and monitoring of grassland in the biggest area of the marshes in Europe have been very important tasks for proper management in order to maintain this unique environment and to slow down worsening environmental conditions due to deterioration and degradation of the area. Nowadays, most of the area (about 77%) is strongly moisture deficient. Decreasing water table and changes in soil moisture were caused by drainage due to irrigation ditches starting from early 19th century when excessive rainfalls occurred that time flooded the area. However, interruption of the hydrographic network led to the draining of 50% of the wetland (Okruszko and Byczkowski, 1996). Precipitation deficit in recent years intensified lowering of the water table. These factors caused mineralisation and decomposition of peat soils into peat-moorsh and caused changes in vegetation. In this aspect there is a strong need to get information about changes in vegetation cover by examining the use of various vegetation indices calculated from spectral reflectance registered by radiometers situated on the following EO satellites: NOAA/AVHRR, SPOT VEGETATION, ERS-2.ATSR, ERS-2.SAR, and Landsat ETM+. The advantage of using these observations is the delivery of inexpensive repetitive information about seasonal and long-term changes for proper protection and management of this unique, very often impenetrable area.

2 THE STUDY AREA

The research has been carried out in the test site situated in northeast part of Poland in the Biebrza

Valley. The geographic location of the test site is as follows:

UL: Lat. 53°38'20", Long. 22°51'28"

UR: Lat. 53°38'14", Long. 22°57'48"

LL: Lat. 53°22'58", Long. 22°51'20"

LR: Lat. 53°32'52", Long. 22°57'40"

Biebrza Valley wetland is one of the biggest in Europe natural rich biotope, important zone for nesting and wintering for fauna. This area is protected due to the large amount of unique species of flora and fauna. There are big problems noticed at the area: scrub encroachment, lowering of the water table, changes of the farming activity. It is the flat area with the prevailing soil types of peat, peat-moorsh and moorsh. The weather is one of the coolest in Poland; mean year daily temperature is equal to 7° C, and rather dry. The average precipitation is equal to 500 mm per year and is one of the lowest in Poland. The length of the growing season (air temperature above 5°C) is from 190 to 200 days per year and is one of the shortest in Poland.

3 DATA

Throughout each of the growing seasons simultaneously to satellite overpasses the measurements of soil and vegetation parameters were carried out at 150 plots, which were represented by point measurements chosen for different habitats. The point measurements were well distributed within the 1 km² pixel and averaged for each of the pixel. The following soil-vegetation parameters have been measured at the test site: volumetric soil moisture [%] using TDR method (TRIME-FM), Leaf Area Index (LAI) using Plant Canopy Analyser (LI-COR LAI-2000), height of the vegetation, development stage and growing condition. The historical data of

volumetric soil moisture were obtained from local IMUZ station. Ground measurements were used along with satellite data in statistical analyses to derive algorithms for soil moisture.

For the study area it was possible to receive the following satellite data for the same or very close date: Landsat ETM and SPOT VEGETATION for the date 16.05.2000, ERS ATSR for 17.05.2000, NOAA AVHRR for 16.05.2000, ERS ATSR for 02.05.2001, SPOT VEGETATION for 03.05.2001, and NOAA AVHRR for 04.05.2001. Different wave bands were

applied to calculate vegetation indices and then it was examined which index gives the most differentiation in the particular area. Table 1 presents the wavelength of particular radiometers which data were considered in this paper.

The six ERS-2.SAR historical data (from the years 1995 and 1997) were used for the derivation of algorithms for soil moisture estimation and ERS-2.SAR data registered on 18.05.2000 was used for calculation of soil moisture using corresponding to LAI values algorithms.

Table 1. Spectral characterisation of optical radiometers used in the research.

Satellite/Radiometer	Wavelength μm					
	Blue	Green	Red	NIR	SWIR	SWIR
Landsat ETM Spectral resolution	0.45-0.52 0.07	0.52-0.60 0.08	0.63-0.69 0.06	0.76-0.90 0.14	1.55-1.75 0.20	2.08-2.35 0.27
SPOT/VEGETATION Spectral resolution	0.43-0.47 0.04		0.61-0.68 0.07	0.78-0.89 0.11	1.58-1.75 0.17	
ERS2/ATSR Spectral resolution		0.54-0.56 0.02	0.64-0.66 0.02	0.86-0.88 0.02	1.45- 1.75 0.3	
NOAA/AVHRR Spectral resolution			0.58-0.68 0.10	0.72-1.1 0.38		

4 VEGETATION INDIES ESTIMATION USING REMOTELY SENSED DATA

The vegetation indices are calculated from remote sensing data taking into account jointly the features of vegetation responsible for reflection in various bands and combining this information from several spectral bands. They are usually easy to calculate without additional meteorological data.

Many authors presented the dependence of vegetation indices on biomass (Tucker and Sellers 1986, Asrar et al 1989), ground cover, canopy photosynthesis (Sellers 1985) Asrar et al 1986), stress detection, yield prediction and irrigation scheduling (Moran et al 1997). Development of spectral vegetation indices presented Qi, 2001. Teillet et al (1997) examined changes of NDVI regarding radiometric characteristics for forested regions with the conclusion that mostly red bandwidth is responsible for decrease in NDVI values. Optimum NDVI values were obtained when the width of red band was less than 50 nm.

The aim of the study was to find the best vegetation index, which gives the largest number of classes to present variation of vegetation due to moisture conditions in the marshland area. The following indices, which included different bands, were calculated: ARVI, GEMI, EVI, MI, and NDVI.

The Atmospherically Resistant Vegetation Index (ARVI, Kaufman and Tanre, 1992), which is

$$\text{ARVI} = \frac{\text{NIR} - \text{BLUE}}{\text{NIR} + \text{BLUE}} \quad \text{MI} = \frac{\text{SWIR} - \text{RED}}{\text{SWIR} + \text{RED}}$$

four times less sensitive to atmospheric effects than the NDVI, includes the spectral response of vegetation, which for our purpose was presented as follows:

$$\text{GEMI} = \frac{\eta(1 - 0.25\eta) - (\text{RED} - 0.125)}{1 - \text{RED}},$$
$$\eta = \frac{2(\text{NIR}^2 - \text{RED}^2) + 1.5\text{NIR} + 0.5\text{RED}}{\text{NIR} + \text{RED} + 0.5}$$

The Global Environment Monitoring Index (GEMI, Pinty and Verstraete, 1992), which includes near infrared and red band and accounts for standard atmospheric effects and soil effects is calculated as follows:

$$\text{EVI} = 2.0 \cdot \frac{\text{NIR} - \text{RED}}{1 + \text{NIR} + 6 \cdot \text{RED} - 7.5 \cdot \text{BLUE}}$$

In order to reduce the effect of atmosphere and soil Liu and Huete (1995) developed Enhanced Vegetation Index (EVI). This index presents the vegetation index product on MODIS (Huete et al, 1994).

The Medium Infrared Index (MI, developed by authors) takes into account the reflection in medium infrared band. This index was considered to be sensitive to moisture of marshland vegetation.

Normalized Difference Vegetation Index (NDVI) is well known and widely used for vegetation monitoring on a global and local scale. It is related to biomass by many authors. Also, it is known that is not corrected for the reflectance of soils what is important when vegetation is not dense. The weakness of NDVI is its sensitivity to atmospheric effect.

$$NDVI = \frac{NIR - RED}{NIR + RED}$$

Calculated from various satellite data indices were compared and the best vegetation index, which gives the largest number of classes to present variation of vegetation due to moisture conditions in the marshland area was found

5 RESULTS AND DISCUSSION

Results of the study are presented and discussed in the following section.

Figure 1 presents humidity of marshland habitats in the Middle Biebrza Basin created with phytoindication method (Okruszko et al. 1996). This method uses plants species as habitat moisture indicators.

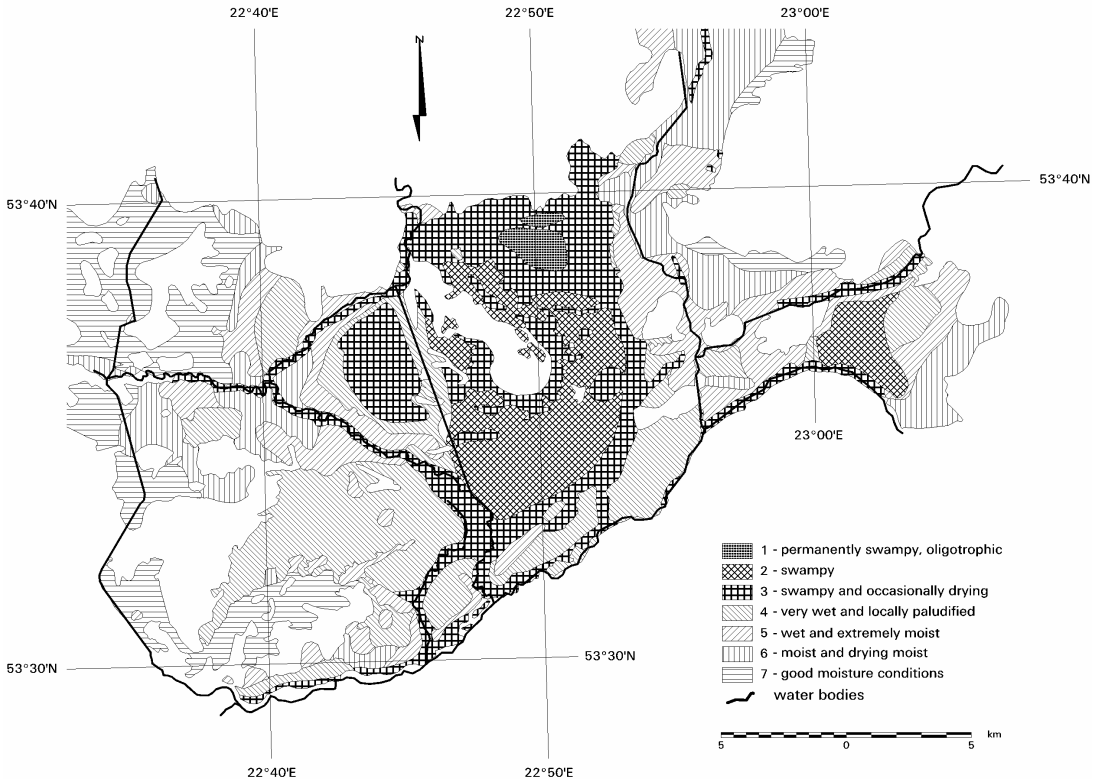


Figure 1. Humidity of marshland habitats in the Middle Biebrza Basin created with phytoindication method.

There are seven distinguished humidity classes of habitats, which differ from permanently swamp areas to good moisture conditions (Okruszko, 1996). The class (1) of permanently swamp conditions (plant species with high demand of water) covers the smallest area and can be observed in northern part of the area. Good grassland moisture conditions (7) are noticed mostly in western part of Middle Biebrza

Basin due to land reclamation (grasses and dicotyledons). Swampy occasionally drying marshland (3) exists in the middle part of the study area (reed, cattail, sedge, and moor-grass). Generally, south part of the study area is covered with very wet and locally paludified habitats (4) (canary, sedge) and east part is covered with moist and drying habitats (6) (grasses, herbs and weeds). The class (2) covers swampy habitat

and class (5) represents wet and extremely moist conditions.

The map of each index was overlaid on the map of humidity of marshland habitats in order to obtain the number of vegetation index classes in different areas.

The figure 2 a-e presents the number of values of vegetation index classes in each area of the marshland humidity class. The number of calculated EVI and GEMI classes is high. There are more than 150 different classes of EVI and GEMI calculated from VEGETATION (03.05.01) in the habitat class 3, 4 and 5. The number of calculated NDVI classes from the same sensors and for the same marshland humidity classes was about 80. The biggest number of indices classes in the class 3, 4 and 5 represent different group of vegetation, which occurs in these classes due to severe changes in moisture conditions.

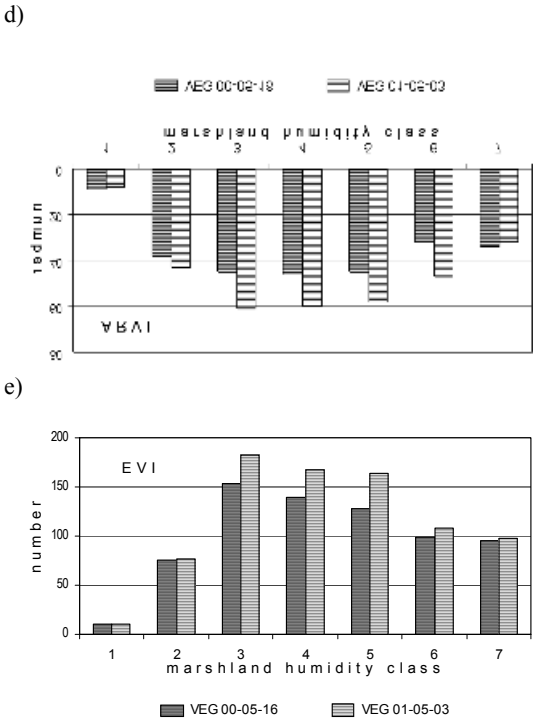
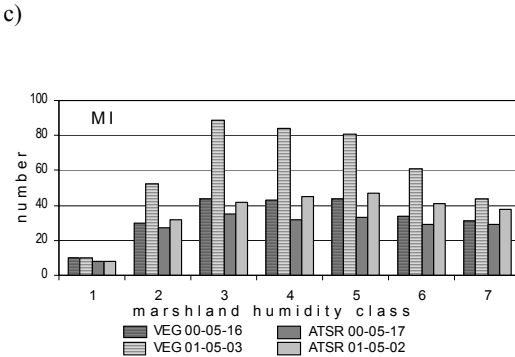
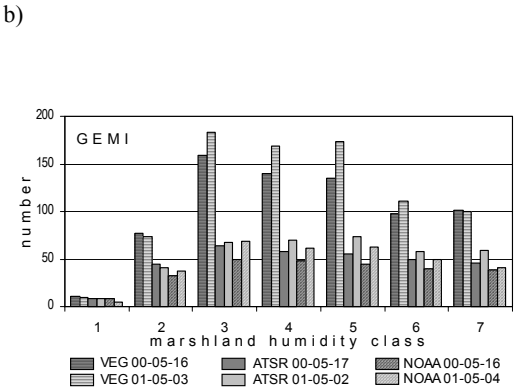
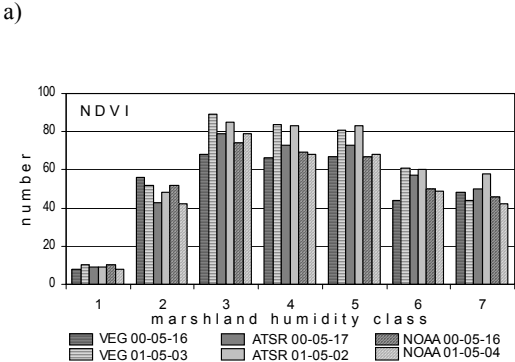


Figure 2 a-e. Number of classes of NDVI values within different marshland humidity areas.

It can be concluded that EVI and GEMI much better represent the variety of vegetation and its changes. In each of the habitats' humidity classes GEMI index calculated from VEGETATION gives more information about vegetation changes than GEMI calculated from ATSR. There is no big difference in the NDVI calculated from different sensors in the number of classes. However, the index calculated from VEGETATION and ATSR gives the biggest number of variety while index from NOAA/AVHRR gives less number of NDVI classes within most of habitat humidity. The index MI gives smaller amount of classes than NDVI. In the first class of habitat humidity the variation of all indices calculated from the sensors give the smaller amount of classes, as there is no variety of vegetation in this class.

The index GEMI characterises very well marshland habitat. The correlation between the indices calculated from the data from all sensors and averaged in each habitat humidity class give very good results in the correlation between the index values and humidity classes (figure 3 a-d). The correlation is linear; the highest GEMI index represents the class of good moisture conditions. Accumulation of green biomass is the highest in this class as moisture conditions are the best.

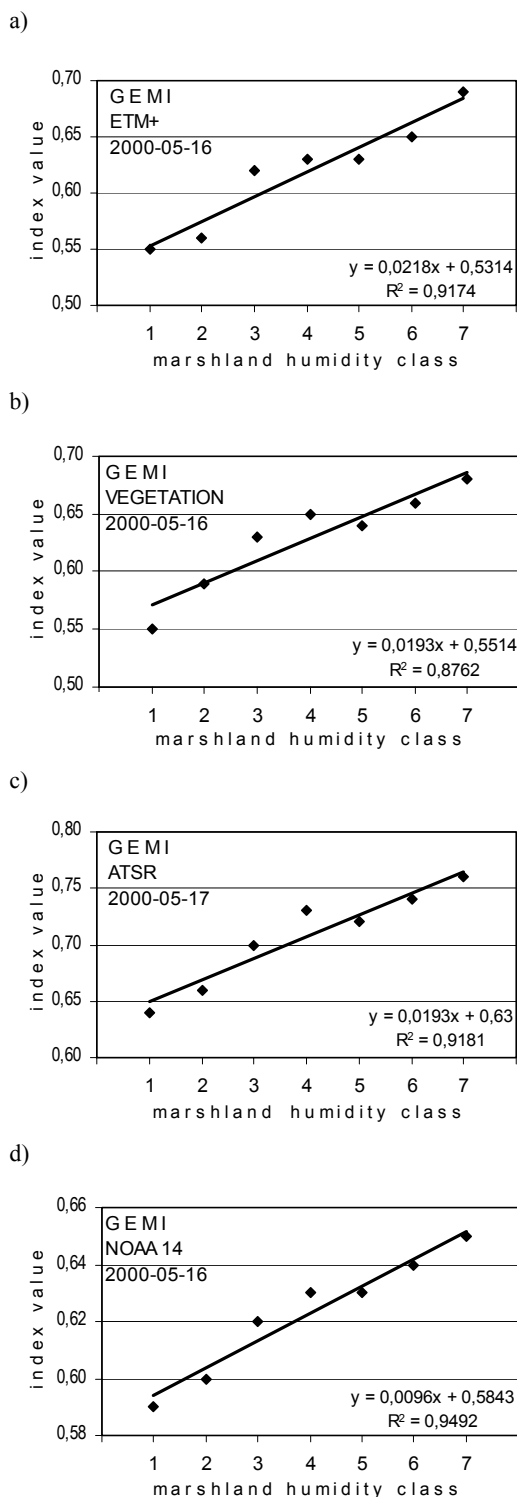


Figure 3 a-d. Relationship between the GEMI index and marshland humidity class.

The relationship between EVI and marshland humidity classes is also high, but lower than taking into account GEMI index (figure 4 a-b). Relationship between NDVI, MI and ARVI and marshland humidity classes is not so significant.

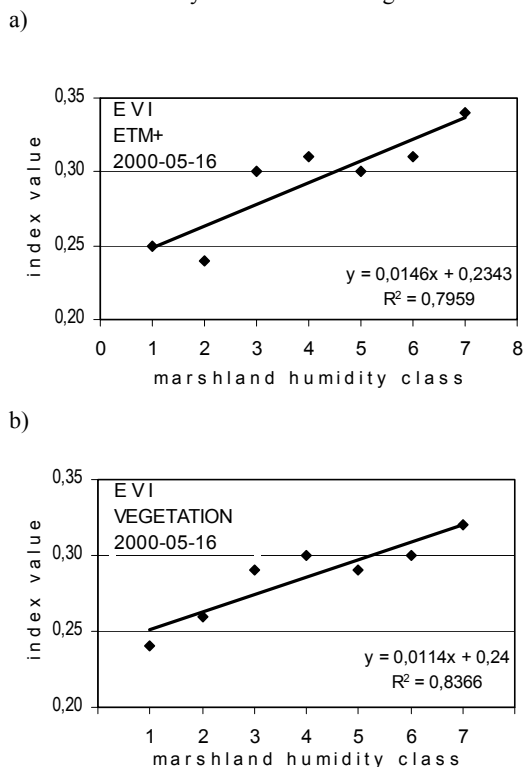


Figure 4 a-b. Relation between EVI index and marshland humidity class.

The Figure 5 shows distribution of GEMI index for the area of Middle Basin. Also the GEMI index was calculated from Landsat ETM data in its resolution. The areas with low values of indices on ETM image are distinguished by low values of indices calculated from the data provided by low spatial resolution satellites. The index GEMI (figure 5) calculated from ATSR had the highest values, but the distribution of values from VEGETATION and NOAA 14 follow better the values from ETM.

The ground measurements of LAI represented 43 of 1 km² pixels. Figure 6 a-f presents the best correlations between LAI values and each of the indices from calculated from the sensors. It is shown that the highest precision to obtain Leaf Area Index is to apply GEMI or EVI index from VEGETATION. The less precise in obtaining LAI was applying GEMI calculated from NOAA satellite (Figure 6 b).

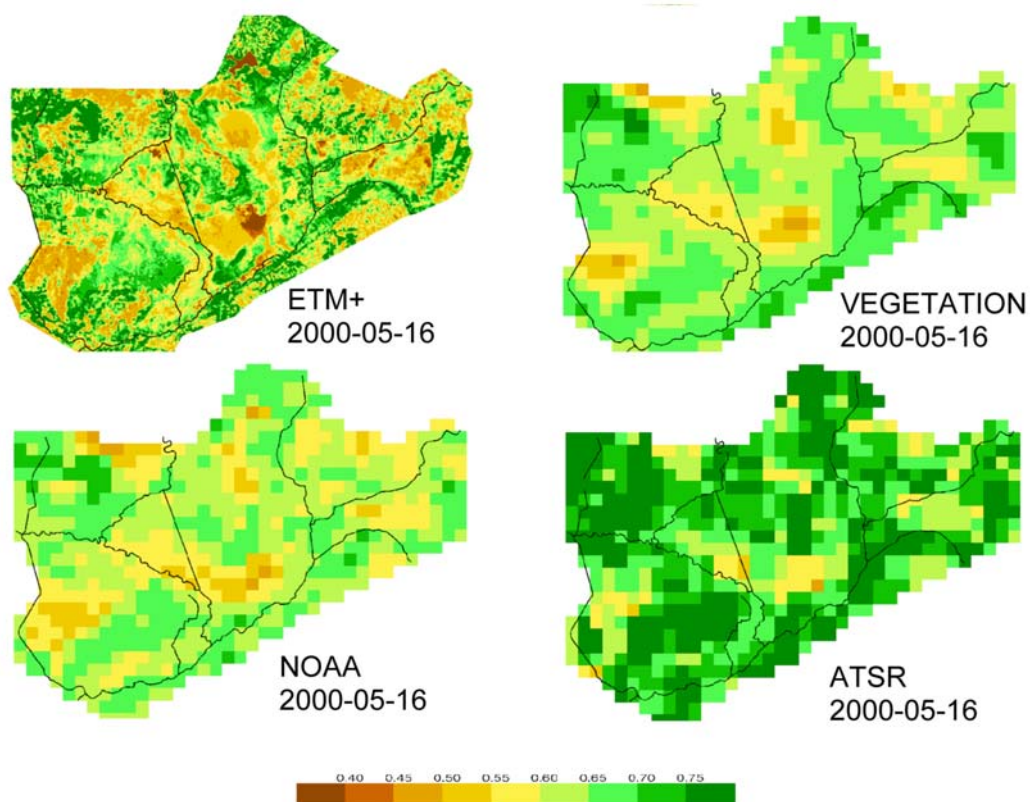
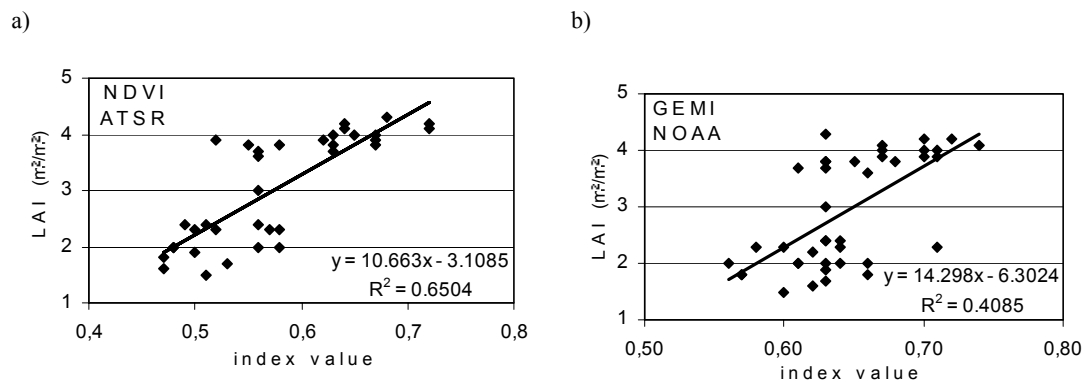


Figure 5. Distribution of GEMI from different satellites in the Middle Biebrza Basin.



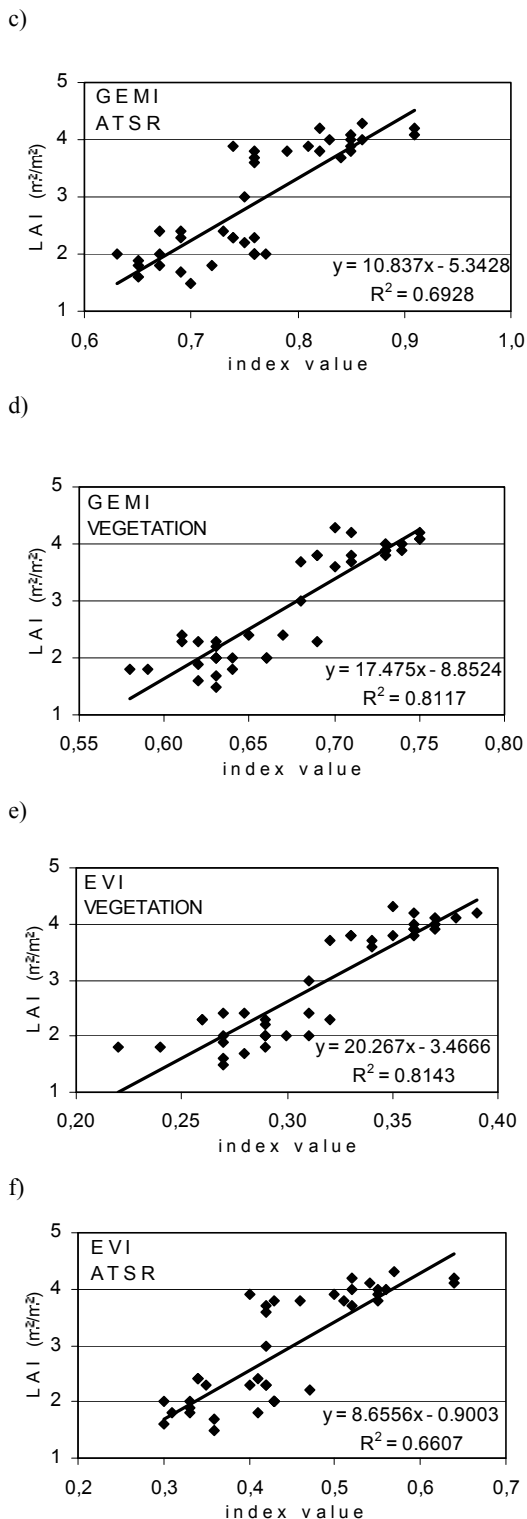


Figure 6 a-f. Relationship between LAI and various vegetation indices.

It was possible to integrate the microwave data from ERS2. SAR to obtain soil moisture and to relate soil moisture to habitat humidity classes. The backscattering coefficient calculated from SAR data values represents in active microwave the integrated respond of several soil – vegetation parameters as soil moisture, surface roughness and vegetation cover. One of the approaches that have been considered in this research was to match Leaf Area Index to surface roughness (Dabrowska – Zielinska et al 1997, Gruszczynska and Dabrowska – Zielinska 1998).

Leaf Area Index values were calculated for each of the marshland humidity habitats classes from the equation derived from the relationship of LAI and GEMI (figure 6 d). Then, surface roughness has been classified into three classes using the following LAI values: <2; 2-3; >3. From historical ERS-2.SAR images the backscattering coefficient was calculated and for the test site related to soil moisture within each of LAI classes. For each of the LAI classes the obtained correlations were high (Gruszczynska and Dabrowska 1998). Derived from the correlation algorithms were used to calculate soil moisture from SAR data. LAI classes were calculated in the function of GEMI index. Calculated soil moisture values were compared to marshland humidity classes.

The figure 7 shows the correlation between soil moisture derived from SAR and habitats humidity classes. The correlation is very high. The lowest moisture is considered in the class 7 (close to 30%), where the grassland moisture conditions are good.

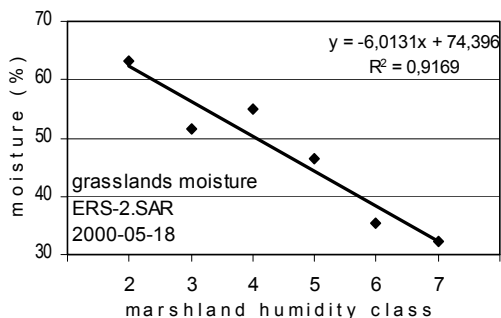


Figure 7. Relationship between soil moisture calculated from ERS-2.SAR and marshland humidity.

6 CONCLUSIONS

GEMI and EVI indices calculated from SPOT VEGETATION give the highest number of classes, which can characterise marshland habitat. The various soil-vegetation indices have been calculated using different spectral bands for obtaining LAI values. For this purpose, the best indices were GEMI and EVI from VEGETATION. Calculated LAI was used for

surface roughness classification needed for soil moisture estimation from ERS-2.SAR data. The possibility to use indices from low spatial resolution satellites is very beneficial for monitoring changes in marshland vegetation due to changes in soil moisture and habitat humidity.

ACKNOWLEDGEMENTS

We wish to acknowledge ESA for satellite images (AO-ID 122), Biebrza National Park for discussion and allowance for penetration the reserved area, Institute for Land Reclamation and Grassland Farming in Biebrza for discussion and historical ground truth data.

REFERENCES

- Asrar G., Fuchs, M. Kanemasu E.T., and Hatfield J.L., 1984, Estimating absorbed photosynthetic radiation and leaf area index from spectral reflectance in wheat, *Agronomy Journal*, 76, 300-306.
- Asrar G., Myneni R. M. and Kanemasu , E.T., 1989, Estimation of plant canopy attributes from spectral reflectance measurements, *Theory and Applications of Optical Remote Sensing*, G. Asrar (Ed), NY Wiley, 252-296.
- Dąbrowska-Zielińska K., M. Gruszczyńska, K. Stankiewicz, M. Janowska, U. Rączka, 1997, Soil moisture investigation for the different agricultural crops using ERS-1 and ERS-2 data, *Proc. of the 3rd ERS Symposium on Space at the service of our Environment*, Florence, Italy, 159-162.
- Gruszczyńska M., K. Dąbrowska-Zielińska, 1998, Application of microwave images from European Remote Sensing Satellites (ERS-1/2) for soil moisture estimates, *Journal of Water and Land Development*, No 2, 7-18.
- Huete A.R., Justice C., and H. Liu, 1994, Development of vegetation and soil indices for MODIS-EOS, *Remote Sens. Environ.*, 49, 224-234.
- Kaufman Y.J and Tanre D., 1992, Atmospherically resistant vegetation index (ARVI) for EOS-MODIS, *IEEE Transactions on Geoscience and Remote Sensing*, vol. 30, No 2, 261-270.
- Liu H.Q., and Huete A.R., 1995, A feedback based modification of the NDVI to minimize canopy background and atmospheric noise, *IEEE Transactions on Geoscience and Remote Sensing*, 33, 457-465.
- Moran M.S., Inoue Y., Barnes, E.M., 1997, Opportunities and limitations for image-based remote sensing in precision crop management, *Remote Sens. Environ.*, 61, 319-346.
- Okruszek H., A. Byczkowski, 1996, Osuszanie mokradeł w basenie środkowym Biebrzy w ujęciu historycznym, *Zeszyty Problemowe Postępów Nauk Rolniczych*, z. 432, 33-43.
- Okruszek H., Szuniewicz J., Kamiński J., and Chrzanowski S., 1996, Charakterystyka środowiska oraz zakres potrzeb jego renaturyzacji w Basenie Środkowym Biebrzy, *Zeszyty problemowe Postępów Nauk Rolniczych*, z. 432, 9-32.
- Pinty B., Verstraete, M. M., 1992, GEMI: A non-linear index to monitor global vegetation from satellites, *Vegetatio*, 101, 15-20.
- Qi , J., 2001, Interpretation of spectral vegetation indices and their relationship with biophysical variables: NIAES-STA, *International Workshop on Crop Monitoring and Prediction at Regional Scales*, 19-21 February Tsukuba, Japan.
- Sellers P.J., 1985, Canopy Reflectance photosynthesis and transpiration, *Int. Journal Rem. Sensing*, vol. 6, 1335-1341.
- Teillet P.M., Staenz K., Williams D.J., 1997, Effects of spectral, spatial and radiometric Characteristics on Remote Sensing Vegetation Indices of forested regions, *Remote Sensing Env.*, 61, 139-149.
- Tucker C.J., Sellers P.J., 1986, Satellite Remote Sensing of primary productivity, *Int. Journal of Remote Sensing*, vol. 7, 1395-1416.

Estimating foliar chlorophyll concentration at leaf and canopy level using a model- empirical synthesized method

Chunyan Yan, Qiang Liu, Zheng Niu, Changyao Wang

Larsis, Institute of Remote Sensing Applications, Chinese Academy of Sciences, Beijing, 100101, PRC

yanchunyan@hotmail.com

ABSTRACT- *Many ecological processes are related to foliar concentration of biochemicals like chlorophyll etc., so it is important to find a practical way to remotely sense the chlorophyll concentration. This paper investigated the applicability of Kokaly and Clark methodologies which used multiple stepwise regression and absorption depths, following continuum removal and normalization against band depth at the centre of the absorption feature to estimate foliar chlorophyll concentration. First, given some assumptions, PROSPECT and PROSPECT+SAIL models were employed to calculate reflectance spectra samples at leaf and canopy level respectively. Second, reflectance spectra samples were divided into calibration and validation data at leaf and canopy level. All the samples were continuum removed and normalized. Comparing the original reflectance curve with normalized absorption depths under same chlorophyll concentration while different other non-foliar parameters, it was found that the normalized absorption depths could largely reduce the non-foliar effects. Last, calibration data after continuum removed and normalized were multiple stepwise analyzed and the regression relationships were built. The regression relationships were applied to validation data to estimate chlorophyll concentration respectively at leaf and canopy level, good results were obtained at both levels with ($R^2 > 0.9$, RMSE/mean=0.0195 and $R^2 > 0.9$, RMSE/mean=0.019 at leaf and canopy level respectively) which implied that these methodologies does have the potential to be applied at remotely sensed data.*

1 INTRODUCTION

Many ecological processes are related to the foliar concentration of biochemicals like chlorophyll, water, nitrogen, lignin and cellulose (Peterson and Hubbard, 1992; Aber and Federer, 1992; Goetz and Prince, 1996). So it is important to obtain the content and spatial distribution condition of canopy biochemicals (Running et al., 1985; Peterson et al., 1988; Wessman, 1994; Dawson et al., 1999). Remote sensing provides a time- and labor-saving way to get information based on which the terrestrial ecosystem functioning can be better described and understood. Developments in airborne and even spaceborne hyperspectral imaging sensors are paving way for the operational quantifying of photosynthetic pigments even other biochemicals within vegetation over large scale. But before this operational work can really be implemented, there has yet much theoretical research work to be done.

During the past two decades, researchers have done quite a lot work over leaf, canopy and even air level to estimate foliar chlorophyll concentration. Generally, two different approaches have been developed, applied and revised widely.

1.1 Inversion of theoretical models.

In the forward mode, analytical leaf reflectance models (S. Jacquemoud, and Baret. F. 1990; Fourty et al., 1996; Barry D. Ganapol, et al., 1998; Dawson et al., 1998), usually containing a biochemical component, describe the interaction of photons with leaves. In the inverse mode, the biochemical content, which usually can not be expressed analytically, can be inverted through optimizing the merit function (S. Jacquemoud, and Baret. F. 1990; Fourty et al., 1996; S. Jacquemoud, et al., 1996; Baret and Fourty, 1997; Barry D. Ganapol, et al., 1998). Incorporated with canopy models, these models may be used to inverse the whole canopy biochemical concentration (Jacquemoud et al., 1995; Gitelson, A. A. et al., Dawson et al., 1999; V. Demarze and J. P. Gastellu-Etchegorry, 2000).

This work was supported by the grant of the Knowledge Innovation Program of the Chinese Academy of Sciences (KZCX1-SW-01), and subsidized by the China's Special Funds for Major State Basic Research Project (G2000077900).

1.2 Empirical and semi-empirical method.

One emphasis of the semi-empirical methods is laid on the developing of various indices with which the chlorophyll content is highly correlated. (Horler et al., 1983; Huete, 1988; Baret et al., 1994; Kupiec and Curran, 1995; Verstraete and Pinty, 1996). Many spectral indices have been developed and applied to estimate chlorophyll concentration at different levels (Chappelle et al., 1992; Peñuelas et al., 1995; Gitelson et al., 1997; Bisun Datt, 1998; Blackburn, 1998; Rosemary et al., 1999; Daughtry et al., 2000; Broge and Mortensen, 2002; Haboudane et al., 2002; Sims and Gamon, 2002)

One important component of empirical methods are laboratory-based near-infrared spectroscopy (NIRS) techniques (Dixit & Ram, 1985; Osborne Fearn, 1986; Williams and Norris, 1987; Card et al., 1988; Peterson et al., 1988; Marten et al., 1989; McLellan et al., 1991; Curran et al., 1992; Peñuelas, Baret, & Fillela, 1995; Barbara J. Yoder and Rita E. Pettigrew-Crosby, 1995). NIRS techniques perform quite well under controlled laboratory conditions and there indeed exists potential to extend these techniques to canopy, airborne and even spaceborne imaging spectrometer (Curran et al., 1989; Verdebout et al., 1994; Dungan et al., 1996; Curran et al., 1997; Gitelson & Merzlyzak, 1997).

However, when extending from controlled conditions of the laboratory to airborne studies, a number of perturbing effects are introduced, including variable solar illumination intensity and angle, viewing geometry, canopy structure, understory and atmospheric conditions. Under these conditions, these techniques may lose robustness and portability (Grossman et al., 1996; Dawson et al., 1999). Yet, on the other hand, the refinement of these techniques provides a possibility for the processing of data from field, airborne and eventually spaceborne imaging spectrometers.

Such refined methodologies were published in this journal (termed as K-C methodologies in this paper) (Kokaly & Clark, 1999; Kokaly, 2001).

2 METHODOLOGIES

Our work is to investigate the applicability of the K-C methodologies respectively at leaf and canopy level, furthermore, we found out which parameters have the greatest impact on this methodologies and which ones can be ignored. Leaf optical characteristic model PROSPECT was used to model the leaf spectra and later was incorporated with canopy model SAIL to model the canopy spectra.

2.1 Model introduction

2.1.1 Continuum removal

Continuum removal is a numerical method to estimate the absorptions not due to the band of interest and to remove their effects (Clark and Roush, 1984). Continuum-removed absorption features can be normalized to the band depth at the center of the absorption feature for comparisons (Kokaly & Clark, 1999; Kokaly, 2001; Curran et al., 2001). They can be given by the following expression:

$$D_n = (1 - (R/R')) / (1 - R_c/R'_c) \quad (1)$$

where D_n is the normalized band depth, R the sample reflectance, R' the reflectance of continuum line, R_c the sample reflectance at absorption feature center which is the minimum of the continuum-removed absorption feature and R'_c the reflectance of continuum line at absorption feature center.

2.1.2 PROSPECT-leaf model

Leaf reflectance $\rho(\lambda)$ and transmittance $\tau(\lambda)$ spectra were simulated with the PROSPECT model (Jacquemoud and Baret, 1990), which simulates upward and downward hemispherical radiation fluxes between 400 and 2400 nm. This is done by assuming that the leaf is a stack of N identical elementary layers separated by $N - 1$ air spaces. The number of layers mimics the scattering within the leaf. It is independent of the wavelength λ . Layers are defined by their refractive index $n(\lambda)$ and by an absorption coefficient $K(\lambda)$, which is a linear combination of the specific absorption coefficients K_i of each absorbing material i , weighted by its concentration C_i :

$$K(\lambda) = \sum_{i=1}^I K_i(\lambda) C_i \quad (2)$$

Actually, three C_i , i.e., chlorophyll a+b concentration $C_{ab}(\mu g\ cm^{-2})$, water depth $C_w(cm)$ and dry matter content $C_m(mg\ cm^{-2})$ are enough to be considered.

In the visible spectrum, the chlorophylls a+b are usually the most optically active component. Thus, in this domain we have

$$K(\lambda) = \sum K_{ab}(\lambda)C_{ab} \quad (3)$$

Both $n(\lambda)$ and K_i are assumed to be independent of time and leaf species, which implies that in the visible region, leaf reflectance $\rho(\lambda)$ and transmittance $\tau(\lambda)$ depend only on the wavelength λ , C_{ab} and N .

2.1.3 SAIL-canopy model

The radiative transfer model SAIL (Verhoef, 1984) describes four radiation fluxes in the canopy: ascending and descending fluxes of direct and diffuse radiation in a homogeneous layer. It represent the canopy structure in a simple way and requires only a few parameters, i.e., leaf reflectance $\rho(\lambda)$ and transmittance $\tau(\lambda)$, leaf area index (LAI), average leaf inclination angle $\theta_l(^{\circ})$, soil reflectance $\rho_s(\lambda)$, and the fraction of diffused incident solar radiation (skyl). Directional spectra could be modeled through modifying the measurement conditions, i.e., solar zenith angle $\theta_s(^{\circ})$, solar azimuth angle $\varphi_s(^{\circ})$, view zenith angle $\theta_v(^{\circ})$ and view azimuth angle $\varphi_v(^{\circ})$. The original SAIL model was adapted (Kussk, 1991) to take into account the effect of hot spot.

What should be pointed out is that here just gives the brief introduction of the models used, refer to the references cited in the paper for details if necessary.

2.2 Model parameter needed

In conclusion, spectral reflectance at leaf and canopy level (represented with $\rho(\lambda)$ and $R(\lambda)$ respectively) calculated by PROSPECT and PROSPECT+SAIL depends on the following parameters (all the units are as defined above):

2.2.1 Leaf level

Chlorophyll a+b concentration C_{ab} , layer number N .

2.2.2 Canopy level

Biophysical parameters: chlorophyll a+b concentration C_{ab} , layer number N , LAI, leaf inclination angle θ_l , and hot spot size S .

Soil spectral reflectance $\rho_s(\lambda)$ and the fraction

of diffused incident solar radiation (skyl) which is always replaced by horizontal visibility VIS (km).

Measurement parameters: solar zenith angle θ_s , solar azimuth angle φ_s , view zenith angle θ_v and view azimuth angle φ_v .

2.3 Analysis step

First, using PROSPECT and PROSPECT+SAIL, under different chlorophyll a+b concentration C_{ab} , at the same time modifying the other parameters, reflectance spectra samples at leaf and canopy level were calculated. Some data were used as calibration data, and the left were used as the validation data in the step Third.

Second, the sample reflectance data was put in the continuum-removal and normalization procedure to get the normalized absorption depth.

Third, through multiple stepwise analysis, the C_{ab} regression equation was built and through validation, the applicability of the K-C methodologies and the effect of every parameter has on the accuracy of chlorophyll a+b concentration estimation was investigated.

3 REFLECTANCE DATA MODELING

In the PROSPECT model, there are just 2 parameters, while in the PROSPECT+SAIL, there are 10 parameters altogether. If C_{ab} ranges from 10 ($\mu\text{g cm}^{-2}$) to 80 ($\mu\text{g cm}^{-2}$) with 1 ($\mu\text{g cm}^{-2}$) step, at the canopy level, even though every of the 9 other parameters only has 2 conditions, there would be 36352 samples! It is neither realistic nor necessary for of the 9 other parameters, some are correlative, some parameters' effects prevail over other's, what is more, 2 conditions can not describe the real situation at all. So, the advisable approach is to assign those unimportant or insensitive parameters common values. We fixed layer number N , hot spot size S , horizontal visibility VIS, solar zenith angle θ_s , solar azimuth angle φ_s , view zenith angle θ_v and view azimuth angle φ_v respectively at 2.0, 0.5, 50, 30, 0.0, 0.0 and 0.0. Soil was considered Lambertian and measured soil reflectance $\rho_s(\lambda)$ at low, medium and high water content was put in the model.

The left parameters are the main dominant factors, table 1 listed the parameter values used to calculate the

reflectance at leaf and canopy level. Parameter C_{ab} will be considered true chlorophyll concentration

compared with its counterpart estimated by multiple regression relationship (see Data analysis)

Table1 Parameter values used to calculate the reflectance

Model parameters	Leaf level	Canopy level
$C_{ab} (\mu g\ cm^{-2})$	From 10-80 with 1 step	From 10 to 80 with 1 step
LAI	--	0.5, 1, 2, 4, 8
$\theta_l(^{\circ})$	--	15, 30, 45, 60
$\rho_s(\lambda)$	--	Low, medium and high water content

With these parameter configurations, using the PROSPECT and PROSPECT+SAIL model, reflectance at leaf and canopy level was modeled from 400 to 800 nm with 5-nm wavelength intervals.

4. DATA ANALYSIS

After reflectance data was modeled, continuum-removal and normalization procedure was conducted respectively, and stepwise multiple regression analysis was done. We randomly chose one half of the samples as calibration data, the left as validation data.

4.1 At leave level

4..1 1 Continuum-removal and normalization

Calibration data was continuum removed and normalized to the band depth at the center, Fig.1 illustrates the leaf reflectance and its normalized absorption depth. Continuum started at 555nm and ended at 740 nm.

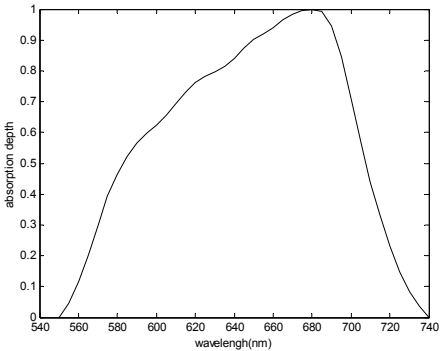
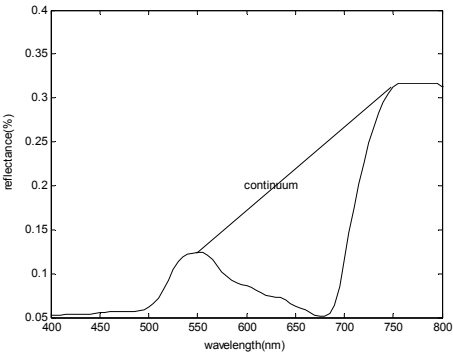


Figure 1 An example of the modeled leaf reflectance (top) and its normalized absorption depth (bottom) (taken $C_{ab} = 50$ as example).

4.1.2 Estimate chlorophyll concentration using stepwise multiple regression

Stepwise regression used on the calibration data to develop relationship between chlorophyll concentration and absorption depth. These relationship were then applied to the validation data to estimate their chlorophyll concentration. The estimated chlorophyll concentration was compared with the true values. The correlations between true C_{ab} and estimated C_{ab} were presented as Fig. 2. The validation showed good results with a high $R^2 > 0.9$ and low RMSE/mean=0.0195.

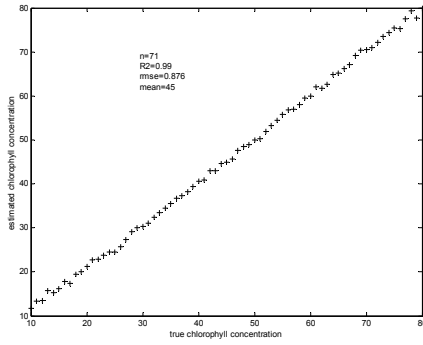


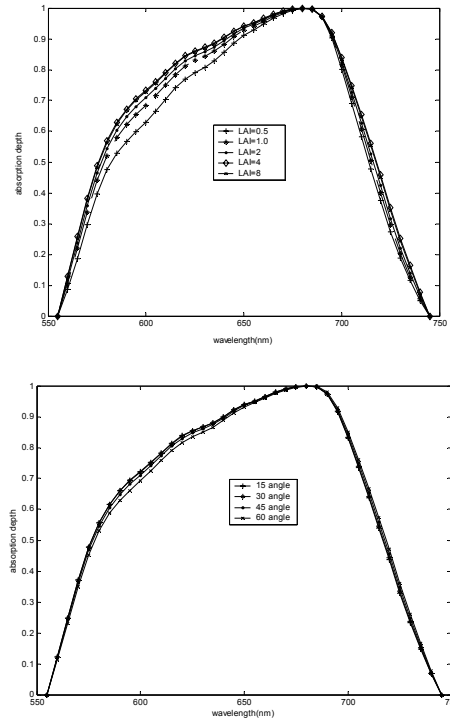
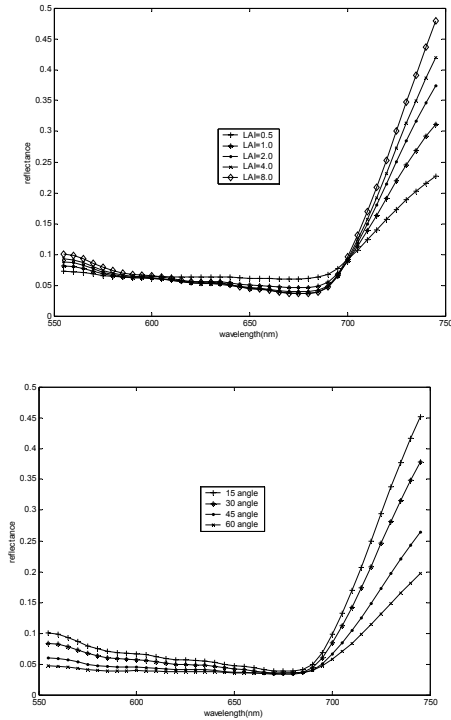
Fig. 2 . Corrologram between true and estimated C_{ab} .

4.2 At canopy level

4.2.1 Continuum-removal and normalization

Conditions at canopy level are more complex than at leaf level, factors except C_{ab} will greatly affect the

reflectance which means the reflectance spectra of two canopies will differ even if they hold the same C_{ab} , so in order to find a way to estimate the C_{ab} , the effects other than C_{ab} must be removed. Derivative spectra can partly decrease the effects, but still not promising. Kokaly and Clark showed in their paper (Kokaly & Clark, 1999) that the K-C methodologies reduced the nonfoliar influences. In this paper we further investigated whether K-C methodologies is sensitive to LAI, θ_l and $\rho_s(\lambda)$ which represents the effects of plant density, canopy structure and underlied soil. Fig. 3 represented the canopy reflectance and normalized absorption depth with different parameter LAI, θ_l and $\rho_s(\lambda)$. When one parameter changed (except C_{ab} was always fixed at 50 as examples), the others were fixed in order to discern which parameter was sensitive to the methodologies and which was not.



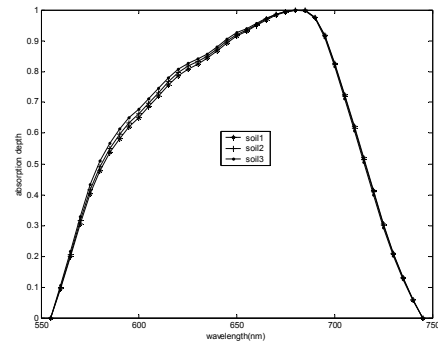
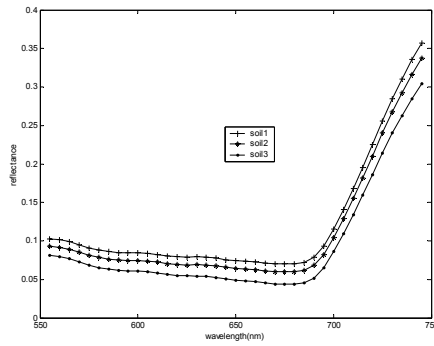


Fig. 3. Canopy reflectance and corresponding continuum removed and normalized absorption depth with leaf area index 0.5, 1.0, 2.0, 4.0, 8.0 while $\theta_l = 30^\circ$ and soil is medium water content (top two); with average leaf inclination $15^\circ, 30^\circ, 45^\circ$ and 60° while LAI=1.0 (middle two); with soil type being low, medium and high water content (soil1, soil2, soil3) while LAI=1.0 and $\theta_l = 30^\circ$ (bottom two).

From fig. 3, it could be seen that when C_{ab} was the same, LAI, θ_l and $\rho_s(\lambda)$ varied, the canopy's reflectance curves differed very much. After continuum removal and normalization, the transformed curves showed different performances.

As to LAI variation, it was noted that the absorption depth also differ a lot when LAI=0.5, 1.0 and 2.0. But it also noted that though reflectance curves at LAI=4 and 8 are much different, their transformed absorption depth curves were almost the same. It means that when the cover density is high, continuum removal and normalization can reduce the effect of LAI.

As to θ_l and $\rho_s(\lambda)$, it could be seen that though different θ_l and $\rho_s(\lambda)$ induced much differences in reflectance spectra, continuum removal and normalization largely reduced their effects.

4.2.2. Estimate chlorophyll concentration using stepwise multiple regression

The same stepwise multiple regression and validation procedure as at leaf level was applied at the normalized absorption depth at canopy level. Since as stated above, the low LAI effects could not be removed by continuum removal and normalization, so samples with low LAI were not used. The estimated chlorophyll concentration was compared with true values. The correlations between true C_{ab} and estimated C_{ab} were presented as Fig. 4. The validation showed good results with a high $R^2 > 0.9$ and low RMSE/mean=0.019 see Fig. 4 $\square R^2$.

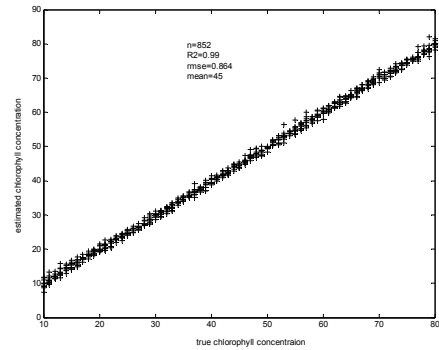


Fig. 4 . Correlogram between true and estimated C_{ab} .

5 CONCLUSION

Chlorophyll concentration estimation by physical models appear more robust but complex and currently can not be used operationally. Some empirical models are simple but it was evident that under same C_{ab} , if other parameter varied, the reflectance spectra showed great differences. So the original reflectance spectra can not be applied directly in empirical models. Even the derivative spectra reduces less the non-foliar effects (Kokaly and Clark, 1999).

In this paper we modeled the reflectance spectra at leaf and canopy level and afterwards, the reflectance spectra were continuum removed and normalized. It was found that continuum removal and normalization could reduce the non-foliar differences greatly especially at high LAI. Regression equations found by multiple stepwise regression were applied on validation data to estimate C_{ab} , good results were obtained. We

can say that the K-C Methodologies does have potential to estimate foliar biochemicals at leaf and canopy level.

When extended to air or space level, some other factors must be considered, this work has yet not referred to this.

REFERENCES:

- Aber, J. D., and Federer, C. A. (1992), A generalized, lumped-parameter model of photosynthesis, evapotranspiration and net primary production in temperate and boreal forest ecosystems. *Oecologia* 92, 463-474.
- Barbara J. Yoder and Rita E. Pettigrew-Crosby (1995). Predicting nitrogen and chlorophyll content and concentrations from reflectance spectra (400-2500nm) at leaf and canopy scales. *Remote Sens. of Environ.*, 53, 199-211.
- Baret, F., Vanderbilt, V. C., Steven, M. D., and Jacquemoud, S. (1994), Use of spectral analogy to evaluate canopy reflectance sensitivity to leaf optical properties. *Remote Sens. Environ.*, 48, 253-260.
- Baret, F., and Fourty, Th. (1997), The limits of a robust estimation of canopy biochemistry. In: G. Guyot, & Th. Phulpin (Eds.). *Physical measurements and signatures in remote sensing* (pp. 413-420). Rotterdam: A. A. Balkema.
- Barry D. Ganapol, Lee F. Johnson, Philip D. Hammer, Christine A. Hlavka, and David L. Peterson (1998), LEAFMOD: a new within-leaf radiative transfer model. *Remote Sens. Environ.*, 63, 182-193.
- Bisun Datt (1998), Remote sensing of chlorophyll a, chlorophyll b, chlorophyll a+b, and total carotenoid content in Eucalyptus leaves. *Remote Sens. Environ.*, 66, 111-121.
- Blackburn, G. A. (1998), Quantifying chlorophylls and carotenoids at leaf and canopy scales: an evaluation of some hyperspectral approaches. *Remote Sens. Environ.*, 66, 273-285.
- Broge, N. H. and Mortensen, J. V. (2002), Deriving green crop area index and canopy chlorophyll density of winter wheat from spectral reflectance data. *Remote Sens. Environ.*, 81, 45-57.
- Card, D. H., Peterson, D. L., & Matson (1988), Prediction of leaf chemistry by the use of visible and near infrared reflectance spectroscopy. *Remote Sens. of Environ.*, 26, 123-147.
- Chappelle, E. W., Kim, M. S., and McMurtrey, J. E., III, 1992, Ratio analysis of reflectance spectra (RARS): an algorithm for the remote estimation of the concentrations of chlorophyll A, chlorophyll B and the carotenoids in soybean leaves. *Remote Sens. Environ.*, 39, 239-247.
- Clark, R. N. and Roush, T. L. (1984), Reflectance spectroscopy: quantitative analysis techniques for remote sensing applications. *J. Geophys. Res.* 89, 6329-6340.
- Curran, P. J., Dungan, J. L., Macler, B. A., Plummer, S. E., & Peterson, D. L. (1992), Reflectance spectroscopy of fresh whole leaves for the estimation of chemical composition. *Remote Sens. of Environ.*, 39, 153-166.
- Curran, P. J., Dungan, J. L., Peterson, D. L. (2001), Estimating the foliar biochemical concentration of leaves with reflectance spectrometry: Testing the Kokaly and Clark methodologies. *Remote Sens. Environ.*, 76, 349-359.
- Daughtry, C. S. T., Walthall, C. L., Kim, M. S., E. Brown de Colstoun, and McMurtrey III, J. E. (2000), Estimating corn leaf chlorophyll concentration from leaf and canopy reflectance. *Remote Sens. Environ.*, 74, 229-239.
- Dawson, T. P., Curran, P. J., North, P. R. J., & Plummer, S. E. (1998), LIBERTY: modeling the effects of leaf biochemistry on reflectance spectra. *Remote Sens. Environ.* 65, 50-60.
- Dawson, T. P., Curran, P. J., North, P. R. J., & Plummer, S. E. (1999), The propagation of foliar biochemical absorption features in forest canopy reflectance : a theoretical analysis. *Remote Sensing of Environment*, 67, 147-159.
- Dixit, L., & Ram, S. (1985). Quantitative analysis by derivative electronic spectroscopy. *Applied Spectroscopy Reviews*, 21, 311-418.
- Dungan, J. L., Johnson, L., Billow, C. et al. (1996), High spectral resolution reflectance of Douglas fir grown under different fertilization treatments: experiment design and treatment effects, *Remote Sens. of Environ.*, 55, 217-228.
- Fourty, Th., & Baret, F., S. Jacquemoud, Schmuck, G., & Verdebout, J. (1996), Leaf optical properties with explicit description of its biochemical composition: direct and inverse problems. *Remote Sens. Environ.*, 56, 1104-117.

We are indebted to Dr. Stephane Jacquemoud for the FORTRAN code of the PROSAIL model.

- Gitelson, A. A., & Merzlyak, M. N. (1997), Remote estimation of chlorophyll content in higher plant leaves. *International Journal of Remote Sensing*, 18, 2691-2697.
- Goetz, S. J. and Prince, S. D. (1996), Remote sensing of net primary production in boreal forest stands. *Agricultural and Forest Meteorology*, 78: 149-179.
- Grossman, Y. L., S. L. Ustin, S. Jacquemoud, E. W. Sanderson, G. Schmuck, and J. Verdebout (1996), Critique of stepwise multiple linear regression for the extraction of leaf biochemistry information from leaf reflectance data. *Remote Sens. Environ.*, 56, 182-193.
- Haboudane, D., Miller, J. R., Tremblay, N., Zarco-Tejada, P. J., and Dextraze, L. (2002), Integrated narrow-band vegetation indices for prediction of crop chlorophyll content for application to precision agriculture. *Remote Sens. Environ.*, 81, 416-426
- Horler, D.N. H., Dockray, M., and Barber, J. (1983), The red edge of plant leaf reflectance. *Int. J. Remote Sens.*, 4, 278-288.
- Huete, A. R. (1988), A soil-adjusted vegetation index (SAVI). *Remote Sens. Environ.*, 25, 295-309.
- Kupiec, J. A., and Curran, P. J. (1995), Decoupling the effect of the canopy and foliar biochemical concentration in AVIRIS spectra. *Int. J. Remote Sens.*, 16, 1731-1739.
- Kokaly, R. F. and Clark, R. N. (1999), Spectroscopic determination of leaf biochemistry using band-depth analysis of absorption features and stepwise multiple linear regression. *Remote Sens. Environ.*, 67, 267-287.
- Kokaly, R. F. (2001), Investigating a physical basis for spectroscopic estimates of leaf nitrogen concentration. *Remote Sens. Environ.*, 75, 153-161.
- Kusk (1991), The hot spot effect in plant canopy reflectance, in *Photon-Vegetation Interactions. Application in Optical Remote Sensing and Plant Ecology*
- MaLellan, T. M., Aber, J. D., Martin, M. E., Melillo, J.M., and Nadelhoffer, K. J. (1991), Determination of nitrogen, lignin, and cellulose content of decomposing leaf material by near infrared reflectance spectroscopy, *Can. J. For. Res.*, 21, 1684-1688.
- Marten, G., Shenk, J., Barton II, F. E. (1989). Near infrared reflectance spectroscopy(NIRS): Analysis of forage quality, U. S. Dept. of Agric. Handbook 643, USDA, Washington, DC.
- Osborne, B. G., & Fearn, T. (1986), Near infrared spectroscopy in food analysis. Harlow: Longman.
- Peñuelas, J., Baret, F., & Fillella, I. (1995), Semi-empirical indices to assess carotenoids/chlorophyll a ratio from leaf spectral reflectance. *Photosynthetica*, 31, 221-230.
- Peterson, D. L., Aber, J. D., Matson, P. A., Card, D. H., Swanberg, N. A., Wessman, C. A., & Spanner, M. A. (1988), Remote sensing of forest canopy leaf biochemical contents. *Remote Sensing of Environment*, 24: 85-108.
- Peterson, D. L., and Hubbard, G. S. (1992), Scientific issues and potential remote sensing requirements for plant biochemical content, *J. Imaging Sci. Technol.* 36:445-455.
- Rosemary A. Jago, Mark E. J. Cutler, and Paul J. Curran (1999), Estimating canopy chlorophyll concentration from field and airborne spectra. *Remote Sens. Environ.*, 68, 217-224.
- Running, S. W., Aber, J. D., Peterson, D. L., Matson, P. A., and Vitousek, P. M. (1985), A simulated model integrating carbon, water and nitrogen cycles in forest, in *Proc. Symp. IUFRO Whole Plant Physiology*, Oak Ridge, TN.
- S. Jacquemoud, and Baret, F. (1990), PROSPECT: a model of leaf optical properties. *Remote Sens. Environ.* 34, 75-91.
- S. Jacquemoud, F. Baret, B. Andrieu, F. M. Danson, and K. Jaggard (1995), Extraction of vegetation biophysical parameters by inversion of the PROSPECT+SAIL models on sugar beet canopy reflectance data. Application to TM and AVIRIS sensors. *Remote Sens. Environ.*, 52, 163-172.
- Sims, D. A. and Gamon, J. A. (2002), Relationships between leaf pigment content and spectral reflectance across a wide range of species, leaf structures and developmental stages. *Remote Sens. Environ.*, 81, 337-354.
- Verdebout, J., S. Jacquemoud, and G. Schmuck (1994). Optical properties of leaves: modeling and experimental studies. *Imaging Spectrometry-Atool for Environmental Observations*. J. Hill and J. Megier, (Eds). Dordrecht, The Netherlands: Kluwe Academic Publishers. 4, 335p.

- Verhoef, W. (1985), Earth observation modeling based on layered scattering matrices. *Remote Sens. Environ.* 17, 165-178.
- Verstraete, M. M., and Pinty, B. (1996), Designing optimal spectral indexes for remote sensing applications. *IEEE Trans. Geosci. Remote Sens.*, 34, 1254-1265.
- V. Demarez and J. P. Gastellu-Etchegorry (2000), A modeling approach for studying forest chlorophyll content. *Remote Sens. Environ.*, 71, 226-238.
- Wessman, C. A. (1994), "Remote sensing and estimation of ecosystem parameters and functions," *Imaging Spectrometry-a Tool for Environmental Observations*, J. Hill and J. Megier, Eds. Dordrecht, The Netherlands: Kluwer, 39-56.
- Williams, P. C., and Norris, K. H., Eds. (1987), *Near-infrared technology in the agricultural and food industries*.

Flux estimation with the MESONH model over the Alpilles.

D. Courault¹, P. Lacarrère², F. Jacob³, A. Olioso¹, P. Clastre¹, P. Lecharpentier¹, O. Marloie¹, L. Prévot¹.

¹INRA, unité CSE, site agroparc, 84914 Avignon cedex 9, France.

²CNRM Météo-France, avenue Coriolis, Toulouse, France

³USDA-ARS, Hydrology and Remote Sensing Laboratory, Beltsville, Maryland, USA

courault@avignon.inra.fr

ABSTRACT - 3D models tend to account for surface processes with more and more accuracy to reproduce realistically meteorological events and climatological patterns. With the increasing satellite imagery resolution, identification of smaller areas with a well-pronounced contrast is a straightforward task. We have used such a model: MesoNH with a high spatial resolution (50m) to estimate surface fluxes over the Alpilles area. The land surface parameterisation schema used in MESONH is the ISBA model. All the surface parameters were provided from remote sensing data acquired during the experiment in 1997 at a high resolution (20m). Albedo, LAI and vegetation fraction were derived from the POLDER images. Simulations were done for the days where radio soundings were acquired over the site every 2 hours for two periods in April and June 1997. The simulated fluxes are strongly correlated to the surface parameters, as expected. Their large variability on the whole area is well reproduced by the model and is in accordance with the measurements. We have compared MESONH-simulated temperatures against remotely sensed temperatures acquired with the airborne thermal infrared camera INFRAMETRICS 760 and observed a good agreement between images and simulations. Instantaneous values estimated at 2m above the surface showed coherent structures due to the turbulence, which disappeared when the values were averaged at hourly scale. It was the first time that such structures are observed at this scale. The simulation performed at 50m with MesoNH provided more realistic lower boundary conditions to land surface schemes, which can help to improve the numerical simulation of the atmosphere.

1 INTRODUCTION

The evolution of Agriculture during these last years, such as irrigation of large areas or deforestation modifies not only the landscape but also the regional climate (De Ridder et Gallée, 1998). Numerous studies have shown the effect of the different surfaces on the atmospheric circulations (Segal *et al*, 1988, 1998). But until now, most of them dealt with large spatial scales (>100km²) using 3D atmospheric models where the various surfaces were represented with a grid mesh rarely below 200m, most of the time around 1km. At this spatial scale, it is not possible to consider the crop variability, which can present high contrasts, and consequently induce important variability in climate. This is particularly the case in the agricultural regions in the South East of France where the fields are often small but very contrasted with irrigated crops beside dry wheat or orchards. With the increasing resolution of pixel, remote sensing can provide useful information to identify the different types of crops.

- The aim of this paper was to show the influence of the different cultivated surfaces characterized by remote sensing data, on the variability of the air temperature and energy fluxes for a small region (<20km²). For this study, we worked with a 3D atmospheric model called MESONH (<http://www.aero.obs-mip.fr/~mesonh/>) usually applied to large areas (>1000km²). It was the first time that this model was used at a so fine spatial resolution (50m for the horizontal grid mesh to describe better the different crops). The input data were derived from different remote sensing data (POLDER, SPOT).

- The second aim of this study was to validate MESONH for this situation. We used the Alpilles – Reseda dataset (<http://www.avignon.inra.fr/reseda/>) corresponding to an intensive experiment, which took place in 1997 on a small area in the South East of Avignon. A lot of data were available both to calibrate and validate the model. We have analysed in particular the infrared thermal images acquired by an airborne camera during flights performed all along the experiment.

The next paragraph will present the main characteristics of this site and the measurements used, then a brief description of the model MESONH will be made. We will explain the different options chosen for the implementation to simulate the Alpilles area. Lastly, we will show the first results obtained for some days simulated and the comparison with ground measurements. A discussion about the turbulence will close this paper.

2 SITE AND DATASET

The Alpilles area is located around 30km South-East of Avignon. It is a flat area of 4 x 5 km, chosen for the ReSeDA project because of various types of crops and the field size was large enough (~4ha) for remote sensing studies. The aim of the project was to provide a substantial dataset for assessing crop and soil processes from remote sensing data in order to propose methods to estimate net primary production, evapotranspiration and crop yields (Prevot *et al.*, 1998). A lot of ground measurements were acquired over the year 1997: micrometeorological stations were set on seven fields (mainly wheat but also sunflower and alfalfa). The evolution of soil moisture and vegetation structure (LAI, crop height) was monitored during the crop cycle (details can be found in Oliso *et al.*, 2002). Different types of images were collected covering all wavelengths and for different spatial resolutions using space borne sensors (NOAA, SPOT ERS, RADARSAT) or airborne ones (IRT camera inframetrics 760, POLDER, ERASME). A specific part of the experiment was dedicated to the spatialization of surface processes (mapping) and to scaling (Oliso *et al.* 1998). In this frame, a CNRM team performed radio soundings in April and June every two hours from 4:00 am to 20:00 pm.

We have chosen to simulate precisely two days in each of these two periods (16,18/4; and 10,12/06/1997), because these days corresponded to different stages for crop development and at different climatic conditions (figure 1). In April, it was after a long dry period without rain, the soil surface was dry. Sunflower was recently sown and very low, like bare soil for some fields. Wheat was already grown and well green with a leaf area index (LAI) around 1-2 at 60 cm for crop height. The spring was exceptionally dry in 1997, so in June, sunflower (which was not irrigated) growth was very irregular for most of the fields, with sparse flowers. Wheat was dry, ready to be harvested. At this time only irrigated grasslands or alfalfa had not suffered from the water stress and showed green surfaces.

Figure 2 and table 1 show the main climatic characteristics of the four days studied. The highest

thermal contrast between surface and the atmospheric layers above was observed for the 18/4, where the wind speed was low, the sky very clear, while for the 16/4, there was a very strong wind from the north. The two days in June were partially covered by clouds.

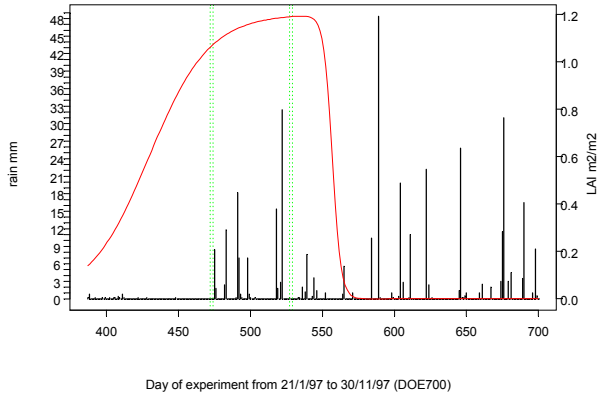


Figure 1. Rain and wheat LAI evolution during the Alpilles experiment. (The vertical dotted lines corresponded to the radio soundings performed by the CNRM and to the 4 days simulated with the 3D model, 16&18/04 and 10&12/06).

Table 1. Main climatic characteristics for the 4 days simulated by MESONH.

Days	Wind direction (degree)	Wind speed At 2m (m/s)	Air temperature at 12h (°C)
16/4	360 N (strong mistral)	6	17.6
18/4	30(weak windy, clear sky)	2	20
10/6	250 NE (cloudy windy day)	6	29
12/6	340 N (sparse clouds)	0,6	28.6

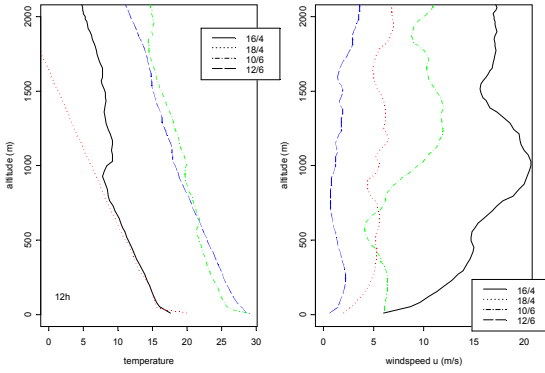


Figure 2. Radio soundings obtained for the four days simulated: 16&18/04 and 10&12/06, (a) temperature (b) wind speed.

3. MESONH MODEL

This model has been developed since several years by different teams, mainly by the CNRM and the LA¹ from Toulouse and is still evolving, in particular on the atmosphere chemistry part. It is a non-hydrostatic atmospheric model, which means no assumption on vertical wind speed gradients is made. Its complete description can be found at the following address: <http://www.aero.obs-mip.fr/~mesonh>.

It allows simultaneous simulations of several scales by the so-called interactive grid nesting. It allows also for the transport and diffusion of passive scalars to be coupled with a chemical module. This model is applicable from large (synoptic) to small (eddy) scales, but most of applications were on large scale (>200m).

There are different ways to use it according to the spatial and temporal scales. The model can simulate the cloud formation and takes into account orography and lakes. The different stages of water (ice, liquid water and vapour) can be chosen by options, as the turbulence schemes according to the scale (1D, 3D).

The radiative scheme comes from the ECMWF² and calculates the radiative fluxes (direct, diffuse components for long wave and short-wave ranges).

The surface interacts with the atmosphere via the energy fluxes applied at the base of atmospheric layers. By providing more realistic lower boundary conditions, land surface scheme can help to improve the atmosphere simulation.

3.1 The surface scheme

Here the land surface scheme is ISBA initially described by Noilhan and Mahlouf (1996), then completed by different authors, among them, Calvet *et al* (1998) for the stomatal resistance. ISBA simulates the surface fluxes and the evolution of surface variables using the force-restore method of Deardorff (1978). There are 5 prognostic equations for deep soil temperature (T_2), deep soil water content (w_2), surface temperature (T_s), soil water content (w_g), and interception water storage (w_r). The main surface parameters involved in the flux computation are the canopy albedo, the canopy emissivity, the momentum and thermal roughness (z_{0veg} and z_{0h}), LAI, and the stomatal resistance (r_s). Several models are proposed for the calculation of r_s , (Jarvi's model, or Jacob's model accounting photosynthesis). Only one energy balance is considered for the whole system ground vegetation. Latent heat flux is obtained by the sum of the evaporation of liquid water from both the soil surface (E_g) and vegetation (E_v). E_v is computed using classical equations, where veg is the fraction vegetation cover derived from LAI, h_v is the exchange coefficient depending on stomatal (r_s) and aerodynamical resistances (r_a).

$$LE = LE_g + LE_v$$

$$E_v = veg pa CH h_v [q_{sat}(T_s) - q_a]$$

$$h_v = (1 - \delta) r_s / (r_s + r_a) + \delta$$

δ is a power function of the moisture content of the interception reservoir (Deardorff, 1978).

3.2. Implementation of the model to simulate the Alpes area.

A good representation of land surface characteristics is necessary to reproduce real climatological patterns. Most of input data have been derived from remote sensing data acquired on the site at a fine spatial resolution (20m). They are summarized in the table 2.

- LAI and veg were computed from POLDER images, acquired by an airborne sensor at 3000 m above the surface (spatial resolution 20 m). First hemispherical and nadir reflectance at 443, 550, 670 and 865 nm were computed by inverting the Walthall kernel-driven model over the POLDER multi-angular data set (Jacob *et al.* 2002a). Next LAI and veg were calculated by feeding a Neural Network (NN) using nadir and hemispherical reflectance estimated in the PO₁ D₁ P₁

¹ Laboratoire d'aérologie TOULOUSE

² ECMWF : European center for Medium Range weather forecast

channels. The NN were previously calibrated over a database simulated with the SAIL model for a wide variety of crops and *LAI* as proposed by Weiss and Baret (1999). Validations were performed mainly on wheat by Weiss et al. (2002). The estimation of *veg* gave generally good results. *LAI* was slightly less good, but let us notice that the measurements of *LAI* were also debatable according to the various wheat fields. Nevertheless *LAI* estimation could be considered as reliable for our application.

- Visible and Near Infrared albedos were calculated by Jacob et al. (2002b) as linear combinations of POLDER hemispherical reflectances (ρ) using coefficient sets proposed by Liang et al, (1999).

$$\alpha_{vis}=0.3511\rho_{blue}+0.3923\rho_{green}+0.2603\rho_{red}$$

$$\alpha_{nir}=0.6088\rho_{red}+0.1442$$

The other surface parameters like emissivity, roughness (*z0veg*) and parameters linked to the computation of the stomatal resistance (γ , *rgl*, *rsm*) were derived from the land use map obtained from SPOT images. Values were assigned to each crop type according to its development (crop height and season).

All these surface parameters were provided as 2D maps at 20m resolution to the MESONH model which made then its own spatial interpolation according to the grid mesh defined (50m in our case) and to the geographical projection used (here degree, min for latitude and longitude).

The Alpilles area was represented by a box of 100x100 horizontal meshes of 50m and 31 vertical levels from 2 m from the surface to 4000 m altitude, the first levels being squeezed near the surface (5m). It has to be noticed that it was the first time that this model was used at a so fine resolution, and this was possible because of the input dataset of Alpilles. Also, due to this fine spatial resolution, the turbulence scheme must be the Large Eddy Simulation (LES) mode, that means, the mixing length depended on the mesh size. The time step must also be short. We have chosen 1 second.

Simulations were performed for 4 days initialised by a radio sounding measured at 10:00 am. The boundary conditions were cyclic. Neither grid nesting, nor nudging was used. We simulated 4 hours (from 10:00 to 14:00) without injecting atmospheric data like ARPEGE profiles. The model ran alone for 4 hours on a super computer at IDRIS (Institut Du Développement et des Ressources en Informatique Scientifique, ORSAY). One simulation lasted around 5 hours.

Table 2. Different remote sensing data sources used to derived input parameters for MESONH

Parameters	Sources	Model/ref
Visible albedo	POLDER	Liang <i>et al</i> , 1999
Near infrared albedo		Jacob et al., 2002b
LAI Veg=(1-F0)	POLDER	Weiss et al., 2002
Z0veg Z0h Emissivity Stomatal resistance min γ , Rgl CV	SPOT land use map	Values according to land use classes (bibliography)

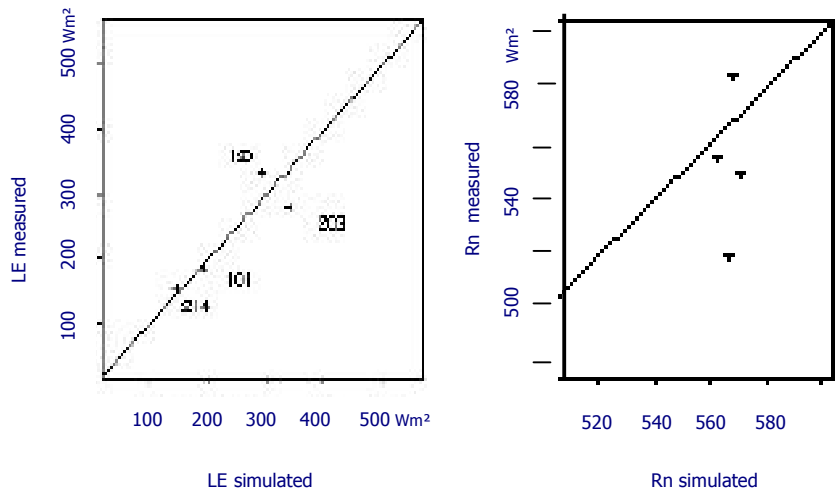
4. RESULTS

MESONH allows different types of outputs: instantaneous variables as 2D maps of temperature at each atmospheric level, wind speed (vertical and horizontal components)..., surface fluxes, or mean values of these same variables averaged for one hour. We can also extract vertical maps anywhere on the simulated area or atmospheric profiles for each variable.

4.1. Validation of the model

In a first time, we have analysed the 2D maps of the main energy fluxes at the surface (R_n , G , H , LE), and extracted the mean values for each field where micrometeorological measurements were performed in order to compare simulations to observations. Figure 3a and b shows the good correlations obtained for both the net radiation and latent heat flux on the 18/4/97 at 12:00am. High values (around 300W/m²) were observed for alfalfa (n°203) and wheat well irrigated (field 120) and the lowest values (100W/m² see figure 4) corresponded to sunflower or cornfields, which were like bare soils at this period. Wheat fields presented great variations between 150 to 250W/m², some ones were sown in spring (n°214) and less developed than others irrigated (n°120) or sown in November (n°101).

Figure 3. Correlations between simulations and measurements for latent heat flux (a) and net radiation (b) obtained for the 18/4/97 at 12:00UTM.



The comparison of the surface temperature simulated by MESONH to the thermal infrared image acquired by the inframetrics airborne camera gave also satisfactory results (figure 4b and c). High temperatures (in red) were observed for bare soils, and low values (in blue) for surfaces well supplied in water.

4.2. Turbulence phenomenon at fine spatial scale

For the clearest days with weak wind (ex:18/4), the map of instantaneous *LE* was well correlated with the surface parameters like *LAI* and *veg*, and the fields were well identified with clear shapes. While for windy or cloudy days (16/4, 10-12/6), these field boundaries were less visible on instantaneous maps, particularly for air temperature map, which seemed to be not correlated to the surface heterogeneity. For these situations, field boundaries could be recognized only on hourly averaged maps (Figure 5). The instantaneous values seemed to be particularly influenced by the vertical wind speed. At 2m above the surface, air temperature seemed to be already mixed with the above atmospheric layers. A vertical cut of the vertical wind speed (*w*) in the middle of the simulated area showed positive and negative values between 150 and 1500m (figure 6a). These patterns were observed for all days simulated and indicated that small convective cells appeared in the surface layer. The wavelength of these structures seemed to be in order of magnitude of the simulated area, e.g. around 4-5 km. Figure 6 b and c show these coherent structures according to horizontal cuts made at 100m above the surface in the atmosphere. We saw well the good correlation between spatial variations obtained for temperature and vertical wind speed. This turbulence phenomenon was not yet well known at this small spatial scale. Other simulations made by Lacarrere from Meteo-France have shown similar

figures for small scale (200m) in Florida, but more simulations and validation measurements are necessary to understand better their formation.

5. DISCUSSION - CONCLUSION

The first results obtained with the MESONH model used with a grid mesh of 50m were satisfactory. The spatial variability of the surface fluxes was well reproduced by the model, in comparison with the ground measurements. We have showed that, even at this small spatial scale, the crop types seemed to induce significantly variations, both on the temperature and on the surface fluxes. This was particularly when there was weak wind. The energy fluxes were strongly correlated to the surface parameters like *LAI*.

The spatial variations of air temperature at 2m above the ground were not negligible (around 2 degrees in April). This had direct consequences on the crop development and could explain the yield differences observed. Small convective cells appeared in the surface layer between 150 and 1500m. This could be due to these high thermal gradients induced by the different surfaces. Until now, this phenomenon not yet well analysed, will need more investigations to understand better its formation. Other simulations must be performed in order to confirm these results with various atmospheric conditions.

The high resolution chosen to describe the different crops allowed to better represent the exchanges between soil, plant and atmosphere by giving appropriate surface parameters for each type of crop. Remote sensing giving us data at a resolution of 20m was an indispensable tool to provide accurate inputs.

Acknowledgements

Special thanks to Juan Escobar and to Didier Gazen (LA Toulouse) for their help to use MESONH on IDRIS super computers. Maps of parameters were made available through the EC WATERMED project (contract ICA3-CT-1999-00015). The Alpilles dataset was acquired during the ReSeDA project, which was funded by the EEC-DG XII (contract ENV4-CT96-0326-PL952071) and the French *Programme National de Télédétection Spatiale* and *Programme National de Recherches en Hydrologie*.

6 REFERENCES

- Calvet JC, Noilhan J, Rougean JL, Bessemoulin P, Cabelguenne M, Olioso A., Wigneron JP, 1998. An interactive vegetation SVAT model tested against data from six contrasting sites. *Agricultural and Forest Meteorology*, 92, 73-95.
- Deardorff J.W., 1978. Efficient prediction of ground surface temperature and moisture with inclusion of a layer of vegetation. *Journal of Geophysical research*, vol83, 20, pp1889-1903
- De Ridder K., Gallée H., 1998. Land surface induced regional climate change in southern Israel. *Journal of applied meteorology*, 37, pp1470-1485.
- Jacob, F., Olioso, A., Weiss, M., Baret, F., and Hautecoeur, O., 2002a, Mapping short-wave albedo of agricultural surfaces using airborne POLDER data, *Remote Sensing of Environment*, 80, 36-46.
- Jacob, F., Weiss, M., Olioso, A., and French, A.N., 2002b, Assessing the narrow-band to broad-band conversion to estimate visible, near infrared and shortwave apparent albedo from airborne POLDER data, *Agronomie*, in press.
- Liang, S., Strahler, A.H., Walthall, C.W., 1999. Retrieval of land surface albedo from satellite observations: A simulation study. *Journal of Applied Meteorology*, 38, pp 712-725.
- Noilhan J., Mahfouf J.F., 1996. The ISBA land surface parameterisation scheme, *Global planetary change* 13, pp 145-159.
- Olioso, A., et al., 1998, Spatial aspects in the Alpilles-ReSeDA project, in: *Scaling and modeling in forestry: application in remote sensing and GIS*, Marceau, D. (ed.), Université de Montréal, Québec, 1998, pp. 92-102.
- Olioso, A., Braud, I., Chanzy, A., et al., 2002, Monitoring energy and mass transfers during the Alpilles-ReSeDA experiment, *Agronomie*, in press.
- Prévo L., Baret F., Chanzy A., et al, 1998. Assimilation of multi-sensor and multi-temporal remote sensing data to monitor vegetation and soil : the Alpilles Reseda project., in IGARSS'98, Seattle WA USA, Int Geoscience and remote sensing symp Ed
- Segal, Avissar, McCumber and Pielke, 1988. Evaluation of vegetation effects on the generation and modification of mesoscale circulations. *J of Atmospheric Sciences*, 45 (16), 2269-229
- Segal, Pan Turner and Takle, 1998. On the potential impact of irrigated areas in North America on summer rainfall caused by large-scale systems. *J of Applied Meteorology*, 37, 325-331.
- Weiss, M., and Baret, F., 1999, Evaluation of canopy biophysical variable retrieval performances from the accumulation of large swath satellite data, *Remote Sensing of Environment*, 70, 293-306.
- Weiss, M., Baret, F, Leroy, M., Hautecoeur, O., Bacour, C., Prévo L., and Bruguier, N., 2002. Validation of Neural Net techniques to estimate canopy biophysical variables from remote sensing data, *Agronomie* in press.

Xiaoguang Jiang¹, Lingli Tang¹, Changyao Wang², Cheng Wang³

¹China Remote Sensing Satellite Ground Station, CAS, 100086, Xgjiang@rsgs.ofg.cn

²LARSIS, Institute of Remote Sensing Applications, CAS, Beijing 100101

³Institute of Geography Science, Nanjing Normal University, Nanjing, 210097

ABSTRACT: *Hyperspectral remote sensing data with band-width of nm level has tens or even several hundreds channels and contains abundant spectral information. Different channels have their own properties and show the spectral characteristics of various objects in image. Rational feature selection from the varieties of channels is very important for the effective analysis and information extraction of hyperspectral data. This paper, taking Shunyi region of Beijing as a study area, comprehensively analyzed the spectral characteristic of hyperspectral data. On the basis of analyzing the information quantity of bands, correlation between different channels, spectral absorption characteristics of objects and object separability in bands, a fundamental method of optimum band selection and feature extraction from hyperspectral remote sensing data were proposed.*

Key words: *hyperspectral data, spectral characteristics, feature selection*

1. INTRODUCTION

Hyperspectral technology, i.e. imaging spectral technology, is one of the important leading research field of remote sensing. Since the first imaging spectrometer was produced in 1983, in less than 20 years, hyperspectral remote sensing technology has been successfully applied in many fields, and shown a great potential and bright prospect (Benediktsson J.A., Sveinsson J.R., and Arnason K., 1995). However, up to now the research on applications of hyperspectral remote sensing data has far fallen behind the research on sensor. Research on processing, analysis and information extraction of hyperspectral data should be strengthened to mine more and useful information, make full use of the advantage and potential of hyperspectral remote sensing technology and promote the development of the new and vital technology.

2. CHARACTERISTICS OF HYPERSPECTRAL REMOTE SENSING DATA

As known, the traditional remote sensing sensors, such as TM, ETM+ and Spot, acquire the spectral information of objects in only several discrete bands. Their band-widths are wider than 100 nm. While imaging spectrometer acquires the spectral information of objects in "continuous bands". Compared with traditional remote sensing data, the obvious characteristics of hyperspectral data are:

(1) High spectral resolution and much more bands

The band-width of hyperspectral remote sensing data is tens or even several nm. Different from the traditional remote sensing data, hyperspectral data has much more bands. It has as many as tens or several hundreds bands from visible light wave to infrared wave. For example, AVIRIS has 224 bands in 0.4 μm ~2.5 μm . The increase of band number and decrease of band-width mean that the spectral resolution of hyperspectral data is very high. This is the important advantage of hyperspectral data and the most evident difference of hyperspectral data from traditional remote sensing data (Dai C., Lei L., 1989).

(2) High correlation between bands

There is high correlation between bands, especially between adjacent bands (Amarsaikhan D., Ganzorig M., 1999). The data redundancy exists in hyperspectral data obviously. The information increases greatly with the increase of band number. Therefore, the number of image channel is not simply equal to the number of information dimension because of the existence of band correlation and data redundancy.

This paper concentrates on the study of spectral characteristic and feature selection of hyperspectral data in the area of Shunyi region, Beijing. The hyperspectral data consists of 32 bands. Its wavelength ranges from 0.44 μm to 2.4 μm . The spectral resolution of visible light wave and near infrared wave is 20 nm, and that of short wave infrared is 30 nm. The number

of band that can be used is 25 because something is wrong with the data of band 1, 9, 17, 22, 23, 25 and 32. The band 1~11 are visible light channels. The band 12~16 are near infrared and the band 18~32 are short wave infrared (table1).

Table1 Spectral Range of Hyperspectral Data of Shunyi

Band	Wave length (μm)	Band	Wave length (μm)
1	0.44-0.46	17	1.53-1.56
2	0.46-0.48	18	1.56-1.59
3	0.52-0.54	19	1.59-1.62
4	0.54-0.56	20	1.62-1.65
5	0.56-0.58	21	1.65-1.68
6	0.58-0.60	22	1.68-1.71
7	0.62-0.64	23	2.04-2.07
8	0.64-0.66	24	2.07-2.10
9	0.66-0.68	25	2.10-2.13
10	0.68-0.70	26	2.13-2.16
11	0.70-0.72	27	2.16-2.19
12	0.94-0.96	28	2.19-2.22
13	0.96-0.98	29	2.22-2.25
14	0.98-1.00	30	2.31-2.34
15	1.00-1.02	31	2.34-2.37
16	1.02-1.04	32	2.37-2.40

2.1 Analysis of correlation between bands

Correlation coefficient between bands shows the correlation of different bands. To know the correlation of different bands, correlation analysis was carried out. The result is shown in table 2(at the end of this paper). It can be known from the correlation matrix of Shunyi hyperspectral data that according to the correlation coefficients of hyperspectral data, the bands of data can be divided into three groups: visible light group (band 2~11), near infrared group (band 12~16) and short wave infrared group (band 18~31). The coefficients between bands in same group are very high. For example, the average coefficients of each group are 0.92, 0.98 and 0.83 respectively; while the coefficients between bands in different group are small. For example, the coefficients between the bands in visible light group and those in near infrared group is only 0.04~0.26. This indicates that the bands in same group have similar characteristic and different groups are relatively independent which should be taken into special account in the analysis and processing of hyperspectral data.

2.2 Analysis of information quantity

The information quantity contained in a band is an important parameter in evaluating band. The deviation and entropy are often used to shown information amount. Several statistical parameters of Shunyi hyperspectral data are listed in table 3 from which we can know that:

Table3 Statistical Parameters of Shunyi Hyperspectral Data

Band	Mean	Max	Min	Range	Deviation	Entropy
2	355	266	630	364	24.304	6.938
3	455	351	915	564	42.699	7.502
4	406	316	769	453	35.113	7.298
5	402	307	788	481	42.383	7.472
6	498	398	883	485	48.374	7.591
7	390	291	775	484	52.746	7.696
8	368	268	729	461	52.093	7.637
10	395	287	775	488	57.952	7.808
11	294	202	539	337	27.287	6.964
12	383	233	524	291	45.531	7.651
13	465	293	614	321	52.793	7.841
14	570	331	763	432	75.302	8.310
15	506	296	685	389	66.727	8.146
16	454	290	601	311	51.461	7.783
18	604	15	1391	1376	163.595	9.363
19	326	7	978	971	134.507	9.063
20	328	2	793	791	99.522	8.646
21	423	6	967	961	115.429	8.847
24	474	240	827	587	76.268	8.383
26	322	64	629	565	64.493	8.244
27	458	147	761	614	64.302	8.178
28	483	319	755	436	55.726	8.014
29	579	397	812	415	48.266	7.864
30	556	211	796	585	54.946	7.902
31	325	134	615	481	58.185	8.074

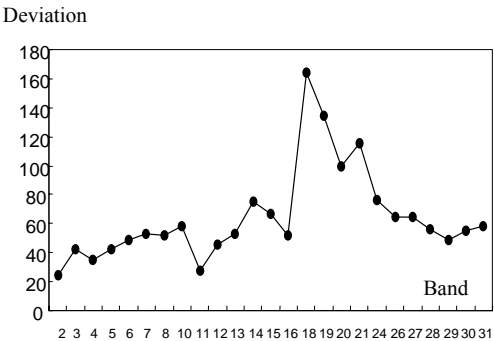


Fig.1 Relation of band and deviation

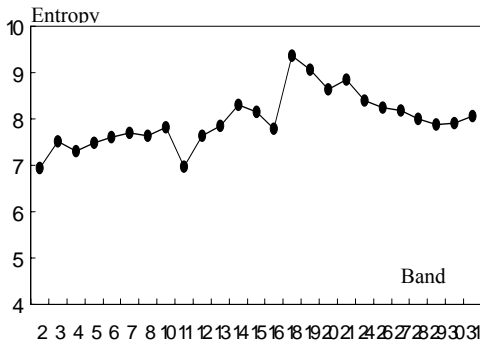


Fig.2 Relation of band and entropy

3. OBJECT ORIGINATED FEATURE SELECTION

Feature selection is one of the most important steps in recognition and classification of remote sensing image. It is impossible to classify image accurately and effectively without rational and efficient feature selection (Hsu P.H., Tseng Y.H., 1999). This is especially important for hyperspectral remote sensing data. Abundant in spectral information and powerful in distinguishing objects is the advantage of hyperspectral data. But, it doesn't mean that the more bands are used, the better results are obtained because: First, as discussed in 2.1, there is evident correlation between bands that will influence the classification accuracy. If all the bands are used in classification without selection, the classification precision will decrease instead of increase.

Second, the more bands are selected, the more training samples are needed to classify correctly (Mausel P.W., 1990). It is very difficult for hyperspectral data to find enough and correct training samples that can meet the demand of classifier if too many bands are chosen in classification.

Third, increase of band number in classification will inevitably result in the increase of processing time and cost that will reduce the processing speed and benefit.

Therefore, it is necessary to select feature before classification. The optimal features are those that can be used to distinguish objects easily and correctly. Three factors, the information quantity of bands, the correlation between bands and the spectral characteristic (e.g. absorption speciality) of classified objects in study area, are considered in our study. The features abundant in information, low in correlation and good in separability are optimum.

3.1 Band index

Let ρ_{ij} is correlation coefficient between band i and band j , hyperspectral remote sensing data is divided into k groups according to correlation of bands and the

number of band in each group is n_i ($i = 1, 2, \dots, k$). Defined band index as:

$$p_i = \frac{\sigma_i}{R_w + R_a} \quad (1)$$

where σ_i is deviation of i th band, R_a is the sum of absolute value of correlation coefficient between i th band and all other bands in different groups, R_w is absolute value of mean correlation coefficient between i th band and other bands in same group, i.e.

$$R_w = \frac{1}{n_k} \sum_{j=1}^{n_k} |\rho_{ij}| \quad (i \neq j) \quad (2)$$

Hyperspectral data has many bands that assemble in groups. This band index is designed according to this striking feature of hyperspectral data. Two factors, information quantity and correlation of band, are considered comprehensively in band index. The bigger the deviation is, the more information the band contains; the smaller the correlation coefficient of band is, the more independent the band is. Thus, the bands with higher band index are better.

Table 4 Order of Band Index in Group

Short Wave Infrared	Band Index	Visible Light	Band Index	Near Infrared	Band Index
18	25.807	10	5.988	14	22.051
19	21.754	7	5.488	15	18.913
21	16.829	8	5.391	13	16.150
20	14.571	6	5.190	16	14.807
24	9.262	3	4.949	12	13.943
27	8.290	5	4.801		
26	8.191	4	4.242		
30	8.097	11	3.163		
31	7.936	2	3.137		
28	7.568				
29	6.615				

The order of band index of different spectral groups is shown in table 4 from which it can be known that

(1) In short wave infrared group, the band index of bands with shorter wavelength (band 18~21) are higher than that of bands with longer wavelength. The difference of maximum and minimum is as high as 19.642. While in visible light group, the band index of bands with longer wavelength is higher and the difference is rather small.

(2) The band index of short wave infrared group and near infrared group are higher than that of visible light group. Band 18 has maximum band index and band 2 minimum.

3.2 Separability of objects in bands

Although band index is important parameter in evaluating band, it just reflects the total information and correlation of band. Since the final purpose of band evaluation is to distinguish objects, for a concrete application task, besides band index, the separability and spectral speciality of objects to be distinguished should be concerned to know the effective spectral scope of recognizing objects and to select the optimal bands. The separability of objects can be measured by Bhattacharya (BH) distance. By selecting the training samples of different types of objects in image and calculating their BH distance in multi-dimensions data space, the separability of objects (samples) in bands was got (table 5). We can see from the table 5 that the separability difference of objects in bands is evident. Thus, it is necessary to select proper feature before classification. The optimal bands are different for distinguishing different objects. There is no absolute optimum band for all objects.

3.3 KL transformation in spectral group

Different from traditional remote sensing data, for hyperspectral data, the number of bands after band selection is still much more. There are correlations between selected bands too. Some of them are even very high. To eliminate the correlation and reduce the number of data dimensions, feature extraction should be used after band selection. Generally, feature extraction is done by data transformation, such as KL transformation. Considering the bands of hyperspectral data in our study area assembly in three relatively independent groups, the KL transformation is performed in each group respectively. By feature extraction, the data is transformed from original data space to a new data space where the data information is redistributed and accumulated in less data dimension. In new data space, the correlation between features is eliminated, less data dimensions contain almost as much information as that the original data does, the distance within same type of object reduces and the distance between different types increases. As a result, the objects can be classified effectively and accurately in new data space.

The spectral characteristic of object is influenced by many factors and is very complicated. Therefore, optimal feature parameters for distinguishing some objects are probably not suitable for other objects. It is difficult to use complete same optimal feature parameters to distinguish all the objects in whole area, especially when the area is complicated or the spectral

characteristic of classified objects are similar. To solve this problem, method of multilevel feature selection is suggested. First, the spectral characteristic of objects in study area is studied comprehensively. Then, the course of feature selection and classification is divided into several sub-courses or levels. Finally, the object originated feature selection is done in each sub-courses respectively according to the spectral characteristic of distinguished objects. In this way, the complicated feature selection and classification course is simplified into several sub-courses. In every sub-course, optimum feature parameters are chosen to classify only less types of objects. This makes the feature selection more efficient and classification easier and accurate.

4. CONCLUSION

Hyperspectral remote sensing data has abundant spectral information. How to evaluate and select optimal feature parameters for a concrete application goal is very important for making full use of the information in hyperspectral data and recognizing objects effectively and accurately. This paper, on the basis of comprehensively analyzing and studying the correlation, information quantity and spectral characteristic of Shunyi hyperspectral remote sensing data, a method and procedure for feature selection are proposed. To verify this method, it was used in the hyperspectral data of Ningbo, Changzhou and Suzhou region too. The similar conclusion was obtained.

5 REFERENCES

- Amarsaikhan D., Ganzorig M., 1999, Different Approaches in Feature Extraction for Hyperspectral Image Classification, *Proceedings of the 20th Asian Conference on Remote Sensing*, Hong Kong, November 22-25, 1999, 434-438.
- Benediktsson J.A., Sveinsson J.R., and Arnason K., Classification and Feature Extraction of AVIRIS Data, *IEEE, Transactions on Geoscience and Remote Sensing*, (33)5:, 1995.
- Dai C., Lei L., 1989, The Spectral Characteristic and Optimal Band Combination of TM image. *Remote sensing of Environment (chinese)*, 4(4), 282-292.
- Hsu P.H., Tseng Y.H., 1999. Feature Extraction for Hyperspectral Image. *Proceeding of the 20th Asian Conference on Remote Sensing*, 405-410.
- Mausel P.W., 1990, Optimum band selection for supervised classification of Multispectral Data. *Photogrammetric engineering and Remote Sensing*, 56, 55-60.

Table2 Correlation Matrix of Shunyi Hyperspectral Data

Band	2	3	4	5	6	7	8	10	11	12	13	14	15	16	18	19	20	21	24	26	27	28	29	30	31
2	1.00																								
3	0.90	1.00																							
4	0.90	0.96	1.00																						
5	0.89	0.97	0.96	1.00																					
6	0.88	0.96	0.95	0.96	1.00																				
7	0.86	0.95	0.93	0.96	0.98	1.00																			
8	0.86	0.94	0.93	0.96	0.98	0.98	1.00																		
10	0.84	0.93	0.92	0.94	0.97	0.98	0.98	1.00																	
11	0.82	0.91	0.91	0.91	0.91	0.91	0.90	0.90	1.00																
12	-0.07	-0.11	-0.05	-0.15	-0.21	-0.24	-0.25	-0.25	0.05	1.00															
13	-0.08	-0.10	-0.05	-0.13	-0.20	-0.23	-0.24	-0.23	0.07	0.97	1.00														
14	-0.11	-0.11	-0.06	-0.14	-0.21	-0.25	-0.26	-0.24	0.06	0.97	0.98	1.00													
15	-0.12	-0.12	-0.08	-0.16	-0.23	-0.26	-0.27	-0.26	0.04	0.96	0.98	0.98	1.00												
16	-0.10	-0.12	-0.08	-0.17	-0.23	-0.26	-0.27	-0.26	0.04	0.98	0.98	0.98	0.98	1.00											
18	0.51	0.60	0.58	0.59	0.61	0.62	0.62	0.64	0.64	0.01	0.03	0.03	0.01	0.01	1.00										
19	0.49	0.56	0.55	0.56	0.58	0.59	0.59	0.60	0.62	0.04	0.06	0.06	0.04	0.04	0.88	1.00									
20	0.52	0.59	0.58	0.58	0.59	0.60	0.59	0.61	0.66	0.14	0.15	0.15	0.13	0.13	0.90	0.92	1.00								
21	0.50	0.58	0.56	0.57	0.57	0.58	0.58	0.60	0.65	0.16	0.18	0.18	0.16	0.16	0.91	0.89	0.96	1.00							
24	0.64	0.72	0.70	0.73	0.75	0.77	0.77	0.78	0.73	-0.16	-0.15	-0.15	-0.17	-0.17	0.83	0.75	0.76	0.77	1.00						
26	0.64	0.71	0.70	0.71	0.74	0.75	0.75	0.76	0.72	-0.11	-0.10	-0.11	-0.12	-0.12	0.82	0.75	0.78	0.78	0.90	1.00					
27	0.63	0.70	0.69	0.71	0.73	0.74	0.74	0.75	0.72	-0.09	-0.08	-0.09	-0.11	-0.11	0.84	0.76	0.79	0.79	0.91	0.92	1.00				
28	0.62	0.68	0.67	0.68	0.70	0.71	0.71	0.71	0.69	-0.06	-0.06	-0.07	-0.08	-0.08	0.82	0.75	0.79	0.87	0.88	0.90	0.90	1.00			
29	0.62	0.68	0.67	0.67	0.69	0.71	0.71	0.71	0.69	-0.05	-0.05	-0.06	-0.07	-0.07	0.82	0.75	0.78	0.78	0.88	0.89	0.91	0.90	1.00		
30	0.60	0.65	0.66	0.66	0.65	0.65	0.65	0.66	0.67	0.03	0.04	0.03	0.01	0.01	0.79	0.73	0.77	0.77	0.81	0.81	0.84	0.84	0.88	1.00	
31	0.61	0.67	0.66	0.67	0.69	0.70	0.71	0.71	0.68	-0.07	-0.06	-0.07	-0.09	-0.08	0.82	0.75	0.79	0.87	0.88	0.91	0.98	0.91	0.83	1.00	

Table5 Separability of Various Types of Objects

Band	Wheat & orchard	Band	Wheat & Forest	Band	Orchard & Forest	Band	Wheat & Corn	Band	Orchard & Vegetable
NDVI	1.941	14	1.915	21	1.175	NDVI	2.000	6	1.934
14	1.795	16	1.891	19	1.171	14	1.964	3	1.928
16	1.735	13	1.884	11	1.044	16	1.953	8	1.924
13	1.717	12	1.869	20	0.992	15	1.944	5	1.902
15	1.651	15	1.866	18	0.894	13	1.930	10	1.880
12	1.636	NDVI	1.687	30	0.858	12	1.925	7	1.865
24	1.148	21	0.385	14	0.748	24	1.837	4	1.838
27	1.042	11	0.251	27	0.702	8	1.805	NDVI	1.720
18	1.014	20	0.202	24	0.695	10	1.805	2	1.655
19	0.954	4	0.174	31	0.679	7	1.724	11	0.966
10	0.839	24	0.167	4	0.648	6	1.565	15	0.763
31	0.823	19	0.161	10	0.639	27	1.563	14	0.630
21	0.794	27	0.108	28	0.635	18	1.408	18	0.563
26	0.794	3	0.095	15	0.623	26	1.377	16	0.526
8	0.778	8	0.087	5	0.620	31	1.343	19	0.434
28	0.765	26	0.075	13	0.603	28	1.333	21	0.373
20	0.756	5	0.052	6	0.598	29	1.266	20	0.306
29	0.754	29	0.051	16	0.571	5	1.232	13	0.290
30	0.747	18	0.045	3	0.554	30	1.121	24	0.288
7	0.694	30	0.040	26	0.528	19	1.107	29	0.252
6	0.664	7	0.037	29	0.512	3	1.063	12	0.249
11	0.535	31	0.033	7	0.463	4	0.808	27	0.246
5	0.462	10	0.032	12	0.463	11	0.761	30	0.220
3	0.340	28	0.023	8	0.461	20	0.750	26	0.212
4	0.241	2	0.016	NDVI	0.135	21	0.679	28	0.200
2	0.056	6	0.008	2	0.070	2	0.578	31	0.175
Band	Paddy & Vegetable	Band	Paddy & Corn	Band	Vegetable & Corn	Band	Vegetable & Residential	Band	Corn & Residential
3	1.72636	18	0.697	3	1.181	21	1.572	24	0.791
5	1.71728	19	0.580	4	1.006	19	1.468	19	0.583
14	1.66709	24	0.553	5	0.945	20	1.290	27	0.542
13	1.66416	21	0.509	2	0.851	15	1.218	21	0.528
4	1.61028	20	0.479	6	0.804	18	1.166	26	0.516
15	1.59655	10	0.449	13	0.719	14	1.074	31	0.474
6	1.58594	14	0.411	14	0.654	13	1.021	20	0.471
8	1.54836	8	0.400	15	0.626	16	0.905	28	0.467
21	1.53939	28	0.390	12	0.555	5	0.764	18	0.446
10	1.52146	15	0.382	8	0.548	3	0.757	29	0.432
18	1.49373	11	0.360	11	0.508	12	0.734	30	0.361
11	1.46423	13	0.351	16	0.495	4	0.715	15	0.153
19	1.4564	31	0.345	10	0.493	6	0.607	16	0.100
16	1.41851	27	0.342	7	0.487	10	0.567	2	0.096
7	1.35181	16	0.341	24	0.424	11	0.555	NDVI	0.092
20	1.29802	29	0.326	21	0.407	8	0.541	14	0.090
12	1.26173	7	0.297	19	0.332	2	0.524	3	0.090
2	1.10987	30	0.296	18	0.302	7	0.465	13	0.057
26	0.26562	26	0.289	20	0.270	26	0.419	12	0.055
30	0.25107	6	0.232	29	0.140	27	0.340	4	0.052
27	0.17832	5	0.225	27	0.126	31	0.269	6	0.031
28	0.16957	12	0.207	28	0.122	30	0.266	5	0.028
29	0.13243	4	0.130	31	0.107	28	0.229	11	0.020
31	0.12936	3	0.122	30	0.089	24	0.217	10	0.010
24	0.08876	NDVI	0.032	26	0.068	29	0.189	8	0.002
NDVI	0.014	2	0.027	NDVI	0.036	NDVI	0.097	7	0.002

Brazilian Soybean Yield Prediction using Satellite Stress Indices

William T. LIU¹, André L. SOUZA² and Felix KOGAN³

¹ Universidade Católica Dom Bosco, Campo Grande, MS, BRAZIL, Email: will@ucdb.br;

² Departamento de Ciências Atmosféricas, Universidade de São Paulo, São Paulo, BRAZIL, Email: Andreifs@model.iag.usp.br; ³ Satellite Applications Laboratory, NOAA/NESDIS, Camp Spring, MD, USA. Email: Fkogan@nesdis.noaa.gov

ABSTRACT - This study is to present Vegetation Stress Index (VSI) and Temperature Stress Index (TSI) calculated from Temperature Condition Index (TCI) and Vegetation Condition Index (VCI) for developing Brazilian soybean yield prediction models. Nine models, including one country and 8 principal soybean production states were constructed using data of 1985 to 1995 (except 1994) and validated using data of 1996 to 1999. TSI/VSI models were compared to TCI/VCI models. The results showed that TSI/VSI models had R^2 of 0.51 to 0.87 and RMSE of 3% to 16%, while the TCI/VCI models had R^2 of 0.29 to 0.92 and RMSE of 4% to 25%. TSI/VSI models had 30 out of 36 cases with absolute errors within 10%, comparing to TCI/VCI models with 27 out of 36 cases. It is concluded that TSI/VSI models have improved slightly but are more stable comparing to the TCI/VCI models. It is suggested that the use of Landsat data to identify planting date in order to readjust the crop calendar each year and the use of surface temperature estimated from the Local Split-Window method to improve further the prediction accuracy.

1. INTRODUCTION

Unganai and Kogan (1998) used weighted VCI and TCI to construct models for African corn yield estimate. They demonstrated that the use of vegetation greenness surface inferred by VCI and surface coolness inferred by TCI to monitor regional drought as well as to predict crop yield. Equations (1) and (2) calculate VCI and TCI.

$$VCI = (NDVI - NDVI_{min}) / (NDVI_{max} - NDVI_{min}) * 100. \quad (1)$$

$$TCI = (BT_{max} - BT) / (BT_{max} - BT_{min}) * 100 \quad (2)$$

Where

NDVI = smoothed weekly NDVI;

NDVI_{max}, NDVI_{min} = multi-year maximum and minimum NDVI;

BT = NOAA AVHRR channel 4 weekly brightness temperature;

BT_{max}, BT_{min} = multi-year maximum and minimum BT;

Liu and Kogan (2002) presented statistical regression models using TCI and VCI to predict Brazilian soybean yield. From the validation of one national and 8 state models using 3 years independent data set, they have obtained 21 out of 27 cases of absolute errors lower than 10 %. Comparing to models presented by various researchers (Hayes and Decker, 1996, Rasmussen,

1997, Unganai and Kogan, 1998), the models of Liu and Kogan (2002) had better performance. Nevertheless, it was observed that the years with high errors often occurred in some wetter or dryer years. Summer rainstorm may result a temporal flood surface, which results a high TCI. In this case, the TCI value may be interpreted incorrectly as a cool vegetation surface, which presents favorable crop growth conditions. It is necessary to separate a high TCI caused by a water surface from a high TCI inferred optimum crop growth conditions. From analyzing the correlation between TCI and normalized crop yield, it was observed that the crop yield reached its maximum at a TCI value around 80 and reduced the crop yield in some years while the TCI increased from 80 to 100. Therefore, a TCI threshold value of 80 was used to establish two functions based on two ranges of TCI (0 to 80 and 80 to 100) for calculating TSI. TSI value is scaled from zero to 100 at TCI ranging from 80 to zero presented by equation (3). Within the TCI ranging from 80 to 100, the TSI value is scaled from zero to 40 presented by equation (4).

$$TSI = 100 - 1.25TCI \quad (\text{when } 0 \leq TCI \leq 80) \quad (3)$$

$$TSI = 100 - [1354.32 - 6.883TCI + 0.2338(TCI)^2] \quad (4) \\ (\text{when } TCI > 80)$$

Also a decrease of yield loss in a severe drought year may not be properly inferred by a linear decrease of VCI value since the impact of a severe drought on yield loss is higher than that of a mild drought. A polynomial equation expressed by equation (5) was

used to convert the linear effect of VCI on yield to a nonlinear VSI.

$$VSI = 100 - [2.145 + 3.9CI - 0.0725 (VCI)^2 + 6.716 \times 10^{-4} (VCI)^3 + 2.39 \times 10^{-6} (VCI)^4] \quad (5)$$

2. METHODS

2.1 Area of Study

The main soybean production region is concentrated in the southern part of Brazil, including 8 states: Rio Grande do Sul (RS), Paraná (PR), Santa Catarina (SC), Mato Grosso (MT), Mato Grosso do Sul (MS), Goiás (GO) Minas Gerais (MG) and São Paulo (SP). Figure 1 present locations, environmental resources and areas where satellite data were collected of these states. The eight states contribute up to 95% of the national total soybean production. Therefore, nine models were constructed in this study, including one model for each of the eight states counting for regional difference and one general country model taking the country as a whole.

2.2 Data Used

Soybean yield data provided by the Brazilian Geography and Statistics Institute (IBGE, 1999), trend yield models (equation 6) and TCI and VCI data set provided by Liu and Kogan (2002) were used in this study. For the satellite data to match the Southern Hemisphere meteorological and crop growing cycle, the soybean crop calendar year was reconstructed to stretch from July of the current year through June of the following calendar year. Week 1, therefore, refers to the first week of July, week 26 to the last week of December and week 52 to the last week of June in the following calendar year.

2.3 Trend Yield and Yield Departure Models

The model construction consists of two steps: modeling of trend yield and yield departure. The yield increases due to genetic and management improvement was estimated by a linear function of calendar year during a period of 1986 to 1995 (equation 6), which was named as trend yield model (Yt).

$$Y_t = a + b(y) \quad (6)$$

Where a = interception coefficient;
 b = slope of observed yield to year;
 y = calendar year - 1900.

After the annual yield has been separated from its trend yield, the model was constructed using the percentage of yield departure (dY) from its trend yield as dependent variable and TSI and VSI as independent variables. The dY is defined as following:

$$dY = 100\% * (\text{Observed Yield} / \text{Trend Yield}) \quad (7)$$

A multiple linear regression model using dY as dependent variable and TSI/VSI, as independent variables was constructed to estimate weather-related fluctuations expressed by dY for each studied region. In order to select candidate variables, correlation coefficient lower than 0.3 were excluded. One to two candidate models were then selected through the "STEPWISE" regression process available in the software SAS ("Statistical Analysis System"). Each model contains two variables using data period from 1986 to 1995.

The calculation of model predicted final yield was done, first, by calculating the model predicted dY in percentage divided by 100 and then multiplying the trend yield of the year under consideration to obtain the estimated yield. The yield unit was then corrected to its original unit of kg/ha by multiplying 100.

2.4 Model Validation

The model validation was done by applying independent TSI/VSI data of 1996 to 1999 to predict soybean yields by each model. For each studied region, four years of soybean yield were estimated. Soybean yields predicted by 9 TSI/VSI models were compared to 9 TCI/VCI models reported by Liu and Kogan (2000).

3. RESULTS AND DISCUSSION

3.1 Yield Models

Table 1 summarizes the TSI/VSI models. The results showed that TSI/VSI models had improved considerably the values of R^2 and RMSE), comparing to the TCI/VCI models. The R^2 values of TSI/VSI models range from 0.51 to 0.87, while the R^2 of TCI/VCI models range from 0.35 to 0.92. The TSI/VSI models had RMSE ranging from 3% to 16%, while the TCI/VCI models ranging from 4% to 25%.

From the comparison of these 9 TSI/VSI models and 9 TCI/VCI models presented by Liu and Kogan (2002), the inclusion of early growth and/or late maturity stage and the use of TSI/VSI for model construction, have improved the MT, MS, RS and BR models but did not show any improvement of the rest of the models, including GO, PR, SC, SP and MG. Although the TSI/VSI models showed some improvements, the development of sub regional models according to the regional soil property variation may be needed to improve further the model performance.

The model validation was done by applying an independent TSI/VSI data set of 1996 to 1999 to predict the yield and compare to the observed yield. By summing up 4 year estimates from 9 models, a total of 36 yield prediction cases were obtained. The results showed that the absolute errors were lower than or equal to 10% in 30 out of 36 cases tested (83% of success), comparing to 27 out of 36 cases (75% of success) for TCI/VCI models (Table 2). None of the TSI/VSI models had prediction error higher than 19% comparing to the TCI/VCI models with 2 cases of error over 24%. Within 9 TSI/VSI models, there were 5 models had absolute errors lower or equal to 10%, including MT, MS, PR, MG and BR. The GO model had one year with error of -14.7%, the SC model had one year with error of 15%, the RS model had two years with errors of -17% and 19% and the SP model had two years with errors of -11.3% and -15.6%. By comparing the models presented by Hayes and Decker (1996), Rasmussen (1997, 1998), Unganai and Kogan (1998), and Liu and Kogan (2002), the TSI/VSI models with absolute errors of lower than 20% obtained from an independent data set showed a significant improvement. Nevertheless attention should be made that besides the spatial variation of climate and soil type, the annual variation of crop planting date in each region may contribute to prediction error since the initial of rainy season, which recharges the soil moisture sufficiently for seeding, may differ from year to year.

4. CONCLUSION

It is concluded that TSI/VSI models have improved slightly but are more stable comparing to the TCI/VCI models. It is suggested that the use of Landsat data to identify planting date in order to readjust the crop calendar each year and the use of surface temperature estimated from the Local Split-Window method (Becker and Li, 1990; Valor and Caselles, 1996) to improve further the prediction accuracy.

ACKNOWLEDGEMENTS

The authors wish to thank Dr. Kogan, NESDIS/NOAA and IBGE for providing the crop and satellite data. This research work is the result of the research project financed by the FAPESP, São Paulo State, Brazil, under contact: Proc. N°. 1997/11568-3.

5. REFERENCES

- Becker, F. and Li, Z. L., 1990. Towards a local split window over land surfaces. *International Journal of Remote Sensing*, 11:369-393.
- Hayes M. J. and Decker, W.L., 1996. Using NOAA AVHRR data to estimate maize production in the United States Corn Belt, *International Journal of Remote Sensing*, 17, 3189-3200, and 1996.
- IBGE, 1999. Anuário Estatístico do Brasil. *Fundação Instituto Brasileiro de Geografia e Estatístico*, Rio de Janeiro, Brasil.
- Liu, W.T. and Kogan, F. N., 2002. Monitoring Brazilian Soybeans Production Using NOAA/AVHRR Based Vegetation Condition Indices. *International Journal of Remote Sensing*, 22:1161-1179.
- Rasmussen, M.S., 1997. Operational yield forecasting using AVHRR NDVI data: prediction of environmental and inter-annual variability. *International Journal of Remote Sensing*, 18:1059-1077.
- Unganai, L.S. and Kogan, F. N., 1998. Drought Monitoring and corn yield estimation in Southern Africa from AVHRR data, *Remote Sensing of Environment*, 63, 219-232.
- Valor, E. and Caselles V., 1996. Mapping land surface emissivity from NDVI: application to European, Africa and South American areas. *Remote Sensing of Environment*, 57: 167-184.

Fig. 1 - Administrative regions, annual total precipitation isoline (mm), monthly total precipitation (mm) and monthly potential evapotranspiration (mm) for selected stations in the Brazilian soybean production region.

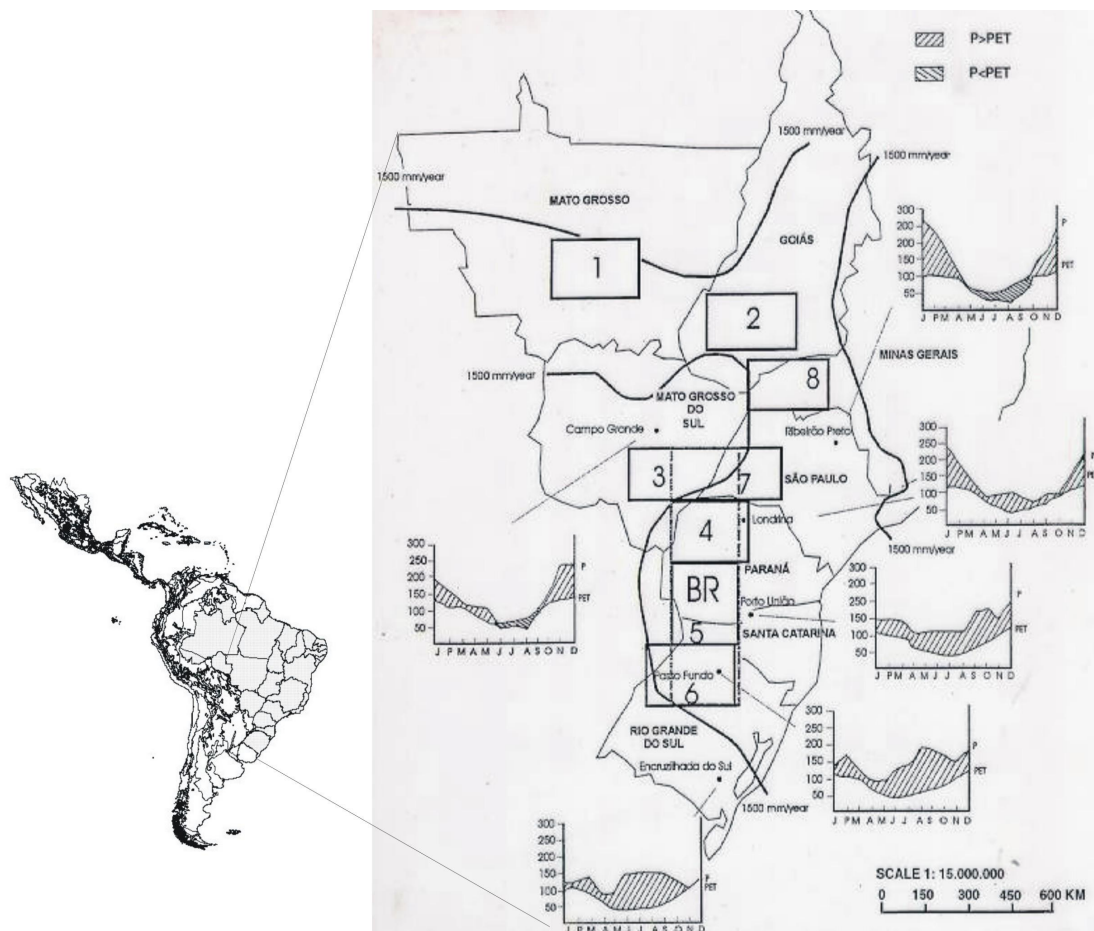


Table 1. Soybean yield prediction models and coefficient of determinant (R^2) and root mean square error (RMSE) for yield departure from the yield trend as a function of Temperature Stress Index (TSI) and/or Vegetation Stress Index (VSI) for Brazil and 8 principal soybean production states: Mato Grosso (MT), Goiás (GO), MS (Mato Grosso do Sul), Paraná (PR), Santa Catarina (SC), Rio Grande do Sul (RS), Sao Paulo (SP) and Minas Gerais (MG).

Region	State/country	Model*	R^2	RMSE
1	MT	$113.789 - 0.002754(T4)^2 - 0.10087(V3)^2$	0.82	3
2	GO	$92.5684 - 0.015382(T4)^2 + 1.10191T5$	0.87	5
3	MS	$108.810 - 0.152085(V4)^2 - 0.003652(T4)^2$	0.79	5
4	PR	$109.444 - 0.08198T2 - 0.00308(T3)^2$	0.56	9
5	SC	$110.654 - 0.51136V2 - 0.005091(T2)^2$	0.86	6
6	RS	$88.3764 + 7.74818V2 - 15.3132V3$	0.51	16
7	SP	$108.111 - 1.09873V2 - 0.002247(T2)^2$	0.64	6
8	MG	$97.1816 + 0.4493T2 - 0.007565(T2)^2$	0.86	4
9	BR	$114.201 - 0.004298(T3)^2 - 0.52393V4$	0.58	6

Independent variables are shown as following:

- For region 1: $T4 = (TSI_{36} + TSI_{37} + TSI_{38} + TSI_{39})/4$; $V3 = (VSI_{36} + VSI_{37} + VSI_{38})/3$.
- For region 2: $T4 = (TSI_{34} + TSI_{35} + TSI_{36} + TSI_{37})/4$;
- $T5 = (TSI_{34} + TSI_{35} + TSI_{36} + TSI_{37} + TSI_{38})/5$;
- For region 3: $V4 = (VSI_{23} + VSI_{24} + VSI_{25} + VSI_{26})/4$;
- $T4 = (TSI_{33} + TSI_{34} + TSI_{35} + TSI_{36})/4$;
- For region 4: $T2 = (TSI_{18} + TSI_{19})/2$; $T3 = (TSI_{28} + TSI_{29})/2$;
- For region 5: $V2 = (VSI_{35} + VSI_{36})/2$; $T2 = (TSI_{36} + TSI_{37})/2$;
- For region 6: $V2 = (VSI_{20} + VSI_{21})/2$; $V3 = (VSI_{32} + VSI_{33})/2$;
- For region 7: $V2 = (VSI_{35} + VSI_{36})/2$; $T2 = (TSI_{32} + TSI_{33})/2$;
- For region 8: $T2 = (TSI_{32} + TSI_{33})/2$;
- For region 9: $T3 = (TSI_{13} + TSI_{14} + TSI_{15})/3$; $V4 = (VSI_{35} + VSI_{36} + VSI_{37} + VSI_{38})/4$.

(Where the subscript number indicates the week number).

Table 2 Comparison of observed and TSI/VSİ based model and TCI/VCİ based model predicted
Brazilian soybean yield for the period of 1996 to 1999

State/Brazil	Year	Observed Yield		TCI/VCİ model		TSI/VSİ model
		(kg/ha)	(kg/ha)	error (%)	(kg/ha)	error (%)
MT	1996	2550	2484	-3	2520	-1.2
	1997	2766	2852	3	2539	-8.2
	1998	2702	2618	-3	2705	0.1
	1999	2838	2810	1	2752	-3.0
GO	1996	2270	1899	-16	2116	-6.8
	1997	2412	2240	-7	2056	-14.7
	1998	2467	2224	-10	2397	-2.8
	1999	2565	2260	-12	2438	-4.9
MS	1996	2408	2456	2	2348	-2.5
	1997	2467	2496	1	2290	-7.2
	1998	2091	2484	18	2164	3.5
	1999	2607	2394	-8	2345	-10.0
PR	1996	2677	2443	-9	2478	-7.4
	1997	2580	2583	1	2565	-0.6
	1998	2558	2630	3	2721	6.4
	1999	2801	2670	-3	2779	-0.8
SC	1996	2438	2185	-10	2296	-5.8
	1997	2324	2266	-2	2226	-4.2
	1998	2355	2266	-4	2121	-9.9
	1999	2143	2430	13	2464	15.0
RS	1996	1769	1907	8	1905	7.7
	1997	1613	1870	16	1574	-2.4
	1998	2088	2494	19	1963	-17.0
	1999	1459	1806	24	1736	19.0

SP	1996	2144	2320	8	2235	4.2
	1997	2450	2342	-4	2172	-11.3
	1998	1948	2438	25	2111	8.4
	1999	2730	2311	-15	2305	-15.6
MG	1996	1953	2065	6	2067	5.8
	1997	2201	2033	-8	2161	-1.5
	1998	2261	2188	-3	2188	-3.2
	1999	2325	2261	-3	2205	-5.2
BR	1996	2195	2284	4	2157	-1.7
	1997	2298	2209	-4	2227	-3.1
	1998	2360	2490	6	2492	5.6
	1999	2375	2340	1	2551	7.4

Parameterization of land surface heat fluxes over inhomogeneous landscape of Tibetan Plateau and arid area of inland satellite remote sensing applications

Y.M.MA¹, Zh.B.SU², M.MENENTI^{2,3}, Z.-L.LI³, O.TSUKAMOTO⁴, H.ISHIKAWA⁵, T.KOIKE⁶

1. Cold and Arid Regions Environmental and Engineering Research Institute, Chinese Academy of Sciences, China, Tel.: +86-931-4967079, Fax: +86-931-4967079, E-mail: yyma@ns.lzb.ac.cn
2. Alterra Green World Research, Wageningen University and Research Centre, The Netherlands
3. Centre National Dela Recherche, Université Louis Pasteur, 67400 Illkirch Strasbourg, France
4. Faculty of Sciences, Okayama University, Okayama 700, Japan
5. Disaster Prevention Research Institute, Kyoto University, Japan
6. Department of Civil Engineering, University of Tokyo, Japan

ABSTRACT Parameterization methods to derive the regional land surface heat fluxes over inhomogeneous landscape by using NOAA-14 AVHRR data, Landsat TM data and field observations have been proposed in this study. The methods are applied to the areas of GAME/Tibet (GEWEX Asian Monsoon Experiment on the Tibetan Plateau, 1996-2000) and HEIFE (HEIthe Field Experiment in northwest of China, 1989-1994). The distributions of net radiation, soil heat flux, sensible heat flux and latent heat flux have been determined over these two areas. The derived results have been validated by using the "ground truth", and it showed that the derived results are acceptable and comparable in two areas. A comparison between the former results (in which the land surface variables and surface heat fluxes were derived from Surface Energy Balance Algorithm for Land³SEBAL) and the results derived from new parameterization method in the HEIFE area has also been given in this study. The results shown that the new method is a better approach to get related air-land parameters over inhomogeneous landscape. At last, the use field of the new remote sensing parameterization methods and the recommendations of improving the scheme has been discussed.

1 INTRODUCTION

The regional distribution of land surface heat fluxes plays a very important role in the exchange processes of water and heat over land surface. The observational study of land surface heat fluxes (net radiation, soil heat flux, sensible heat and latent heat flux) is an important component in many land surface processes experiments, such as GEWEX (Global Energy and Water Cycle Experiment) Asian Monsoon Experiment on Tibetan Plateau (GAME/Tibet) and the HEIthe basin Field Experiment (HEIFE).

The intensive observational period (IOP) of GAME/Tibet was carried out in northern Tibetan Plateau area from May to September 1998. The experimental region, about 100×200 km², covers complex land surfaces with mainly a large area of grassy marshland, some desert areas, many small rivers and several lakes. At different landscapes, two basic comprehensive observation stations (Anduo and Naqu), two PAM (Portable Automated Meso-net) observation stations (MS3478 or NPAM and MS3637 or SPAM), five automatic weather stations (D66, D105,

D110-AWS110, Naqu and MS3608 or AWS3608), one 3D Doppler Radar, radiosonde system, tethered-sonde system, soil moisture and soil temperature net, rain gauge net and barometer net had been operated continuously for almost five months (figure 1).

The HEIFE observation was based in an inland river basin of northwestern China. The experimental area, about 70 × 90km², covers complex land surface conditions with mainly a large area of the Gobi, sand desert and various scales of oasis dispersed along the river and canals. During the experiment period, five basic micrometeorological stations, five automatic weather stations and four groundwater level stations were set up in oasis, sand desert and Gobi areas. Each basic micrometeorological station had a 20m-high profile tower (the tower in oasis is 40 high). Air temperature, humidity, wind velocity and wind direction were observed at 6 levels of the tower. Short-wave incoming radiation, reflective radiation, long-wave incoming and long-wave outgoing radiation and net radiation were recorded at surface level. Simultaneously ground surface temperature, soil temperature at 5 depths under the surface, soil heat fluxes at 2 layers were measured. During the experimental period,

meteorological data from three routine weather observation stations were collected. Surface runoff and sub-surface hydrological data from three routine hydrological stations in the experimental area were collected for providing the background information. The experiment has been operated successfully for more than two years (figure 2).

A large amount of data of surface observations has been collected during these experiments. Some interesting detailed studies concerning land surface heat fluxes have been reported (Wang and Mitsuta 1990; Tsukamoto et al. 1992; Wang and Mitsuta 1992; Hu et al. 1994; Maitani et al. 1995; Mitsuta et al. 1995; Tsukamoto et al. 1995; Sahashi 1995; Tamagawa 1996; Ma et al 2000; Tanaka et al 2001; Ma et al 2002).. However, those researches were on point-level or a local-pitch-level. To understand the land surface processes over the areas of GAME/Tibet and HEIFE the aggregation of the individual results into a regional scale is inevitable. Remote sensing from satellites offers the possibility to derive regional distribution of land surface heat fluxes.

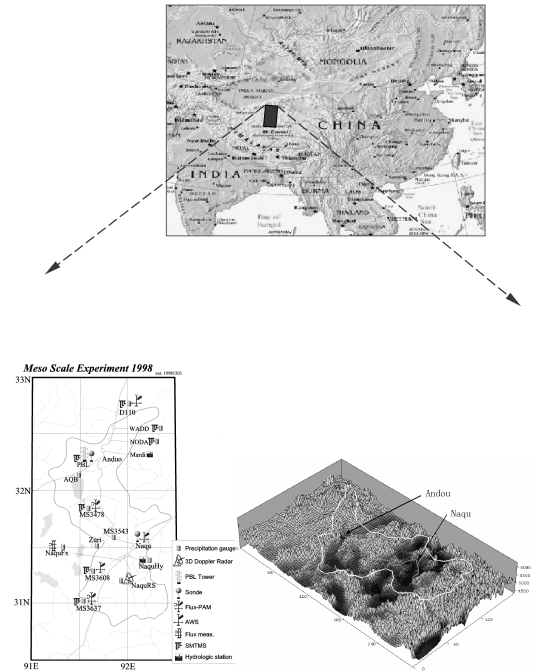


Figure 1. The geographic map and the sites layout during IOP of GAME/Tibet.

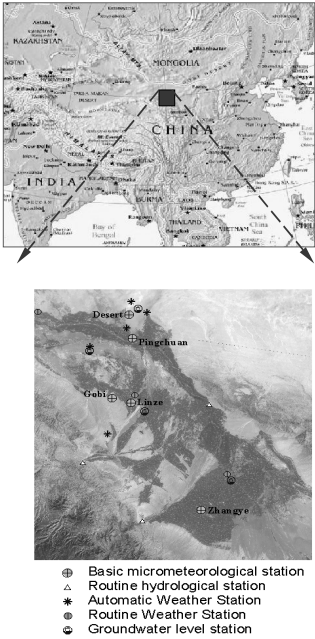


Figure 2. The geographic map and the sites layout during IOP of HEIFE, the red part is oasis or irrigated farm and the others are Gobi desert.

2. SATELLITE DATA AND FIELD OBSERVATIONAL DATA

Landsat Thematic Mapper (TM) provides a spectral radiance in seven narrow bands, with a spatial resolution of about $30 \times 30 \text{ m}^2$ for three visible bands (Band-1, -2, -3) and three near infrared bands (Band-4, -5, -7), and $120 \times 120 \text{ m}^2$ for the thermal infrared band (Band-6). Because of high spatial resolution of TM, the land surface variables, the vegetation variables and land surface heat fluxes estimated from TM data can be directly compared with the ground measurements (Wang et al. 1995; Bastiaanssen 1995; Ma et al. 1999). One TM images used in this study was taken at 10:00(local time) July 7, 1991 over the HEIFE area. This day was very clear when the Landsat TM over-passed the experimental area, and the IOP was just carried out in that day. It means that we have field observational data to calculate the regional surface heat flux and to validate the derived the results from the satellite remote sensing parameterization method.

The NOAA-14 Advanced Very High Resolution Radiometer (NOAA-14 AVHRR) provides spectral information in 5 narrow bands, with a spatial resolution of about $1 \text{ km} \times 1 \text{ km}$. one scenes of satellite data used in this study were collected at 15:43h(Beijing Standard Time, BST) June 12, 1998.

The most relevant field data, collected at the GAME/Tibet and the HEIFE surface stations to support the parameterization of land surface heat

fluxes and analysis of satellite images,, consist of surface radiation budget components, surface radiation temperature, surface reflectance, vertical profiles of air temperature, humidity, wind speed and direction measured at the PBL towers, sodar, radiosonde and tethered-sonde, turbulent fluxes measured by eddy-correlation technique, soil heat flux, soil temperature profiles, soil moisture profiles, and the vegetation state.

3. THEORY AND SCHEME

The general concept of the methodology of deriving land surface heat fluxes from the satellite data and field

observational data is shown in two diagrams (figure 3).

3.1 Net radiation

The regional net radiation flux can be derived from

$$R_n(x,y) = K_{\downarrow}(x,y) - K_{\uparrow}(x,y) + L_{\downarrow}(x,y) - L_{\uparrow}(x,y) \quad (1)$$

$$= (1 - r_0(x,y)) \bullet K_{\downarrow}(x,y) + L_{\downarrow}(x,y) - e_0(x,y) \sigma T_{sc}^4(x,y)$$

where surface emissivity of $e_0(x,y)$ is a function of vegetation coverage P_v , it can be derived from the model of Valor and Caselles (1996). K represents the

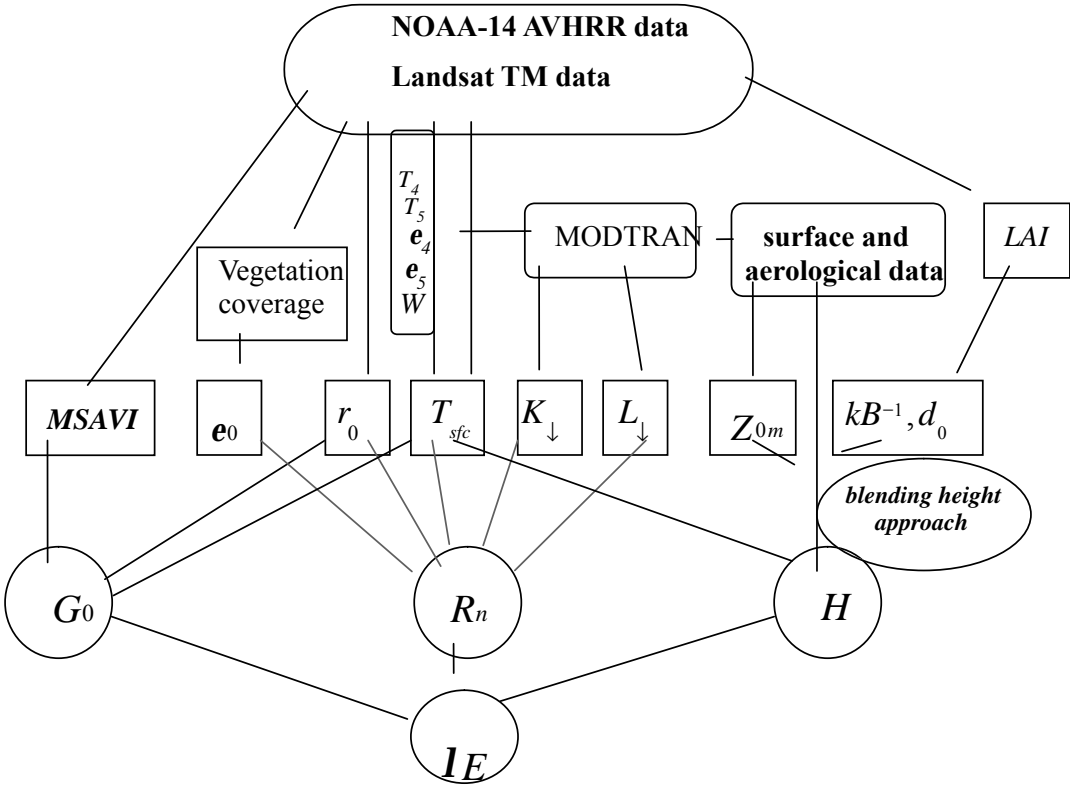


Figure 3. Diagram of parameterization land surface heat fluxes by combining NOAA-14 AVHRR data and Landsat TM data with field observations

short wave (0.3-3 μ m) and L the long wave (3-100 μ m) radiation components, respectively. The downward short-wave and long-wave radiation at the surface in Eq.(1) can be computed by using the radiative transfer model MODTRAN (Berk et al.1989; Ma 2001). The surface reflectance for short-wave radiation (r_0) can be retrieved from Landsat TM data with the atmospheric

correction by a four-stream radiative transfer assumption for atmospheric correction in solar spectral bands (Verhoef 1997) using aerological observation data. The surface reflectance $r_0(x,y)$ can also be derived from the channel-1 and channel-2 of NOAA-14 AVHRR data with the models of Paltridge and Mithchell(1990) and Valiebt et al (1995). The land surface temperature (T_{sc}) in HEIFE area can be

derived from Landsat TM data and aerological observation data (Ma 2001). The land surface temperature $T_{sfc}(x,y)$ in GAME/Tibet area can be retrieved from the brightness temperature of channels four and five of NOAA-14 AVHRR according to Becker and Li (1990 and 1995). We first assume that the T_{sfc} is expressed as

$$T_{sfc} = F(T_4, T_5, \mathbf{e}_4, \mathbf{e}_5, W, \mathbf{q}) \quad (2)$$

where T_4 and T_5 are the brightness temperatures of channels 4 and 5 of AVHRR; \mathbf{e}_4 and \mathbf{e}_5 are the spectral emissivities of channel 4 and 5 respectively; W is water vapor content, and \mathbf{q} represents the view angle of satellite

Equation (2) was expressed by different split window algorithms (Becker and Li, 1995). The algorithm proposed by Sobrino and Raissouni (2000) will be used in this study, i.e.

$$T_{sfc}(x,y) = T_4(x,y) + 1.40[T_4(x,y) - T_5(x,y)] + 0.28[T_4(x,y) - T_5(x,y)]^2 + 0.83 + (57 - 5W)(1 - \mathbf{e}) - (161 - 30W)\Delta\mathbf{e} \quad (3)$$

where $\mathbf{e} = (\mathbf{e}_4 + \mathbf{e}_5)/2$, $\Delta\mathbf{e} = \mathbf{e}_4 - \mathbf{e}_5$ (Li and Becker, 1993).

3.2 Soil heat flux

The regional soil heat flux $G_o(x,y)$ is determined through (Choudhury and Monteith 1988)

$$G_o(x,y) = \mathbf{r}_s C_s \frac{[T_{sfc}(x,y) - T_s(x,y)]}{r_{sh}(x,y)}, \quad (4)$$

where \mathbf{r}_s is soil dry bulk density, C_s is soil specific heat, $T_s(x,y)$ represents soil temperature of a determined depth, and $r_{sh}(x,y)$ stands for resistance of soil heat transportation. The regional soil heat flux $G_o(x,y)$ cannot directly be mapped from satellite observations through Eq.(4). Many investigations have shown that the mid-day G_o/R_n ratio, \mathbf{G} , is reasonably predictable from special vegetation indices (Daughtry et al. 1990). \mathbf{G} can be considered as a function F which relates G_o/R_n to other variables (Ma 2001). Some researchers have concluded that $G_o/R_n = \mathbf{G} = F(NDVI)$ (Clothier et al. 1986; Kustas and Daughtry 1990). A better ratio of $G_o/R_n = \mathbf{G} = F(r_o, T_{sfc}, NDVI)$ was also found (Choudhury et al. 1987; Menenti et al. 1991; Bastiaanssen 1995). A parameterization scheme based on $MSAVI$ has been found over the HEIFE area as

$$G_o(x,y) = R_n(x,y) \cdot [T_{sfc}(x,y)/r_o(x,y)] \cdot (0.00028 + 0.004364\bar{r}_o + 0.00846\bar{r}_o^2) \cdot [1 - 0.97892MSAVI(x,y)^4] \quad (5)$$

And a parameterization scheme based on $MSAVI$ has been found over the GAME/Tibet area as

$$G_o(x,y) = R_n(x,y) \cdot [T_{sfc}(x,y)/r_o(x,y)] \cdot (0.00029 + 0.004756\bar{r}_o + 0.00873\bar{r}_o^2) \cdot [1 - 0.98035MSAVI(x,y)^4] \quad (6)$$

where \bar{r}_o is surface reflectance averaged over the period when the soil is heated from the sun. Surface temperature T_{sfc} is expressed in degrees Celsius. $MSAVI(x,y)$ is derived from the band reflectance of Landsat TM as (Qi et al. 1994)

$$MSAVI(x,y) = \frac{2r_4(x,y) + 1 - \sqrt{[2r_4(x,y) + 1]^2 - 8[r_4(x,y) - r_3(x,y)]}}{2} \quad (7)$$

where r_3 and r_4 are the band reflectance of Landsat TM Band-3 and Band-4 on the land surface. $MSAVI(x,y)$ is derived from the band reflectance of NOAA-14 AVHRR as

$$MSAVI(x,y) = \frac{2r_2(x,y) + 1 - \sqrt{[2r_2(x,y) + 1]^2 - 8[r_2(x,y) - r_1(x,y)]}}{2} \quad (8)$$

where r_1 and r_2 are the band reflectance of NOAA-14 AVHRR Band-1 and Band-2 on the land surface.

3.3 Sensible heat flux

The regional distribution of sensible heat flux is calculated from

$$H(x,y) = \mathbf{r} C_p k^2 u(x,y) \cdot (T_{sfc}(x,y) - T_a(x,y)) / ((\ln \frac{z - d_o(x,y)}{Z_{om}(x,y)} + k B^{-1}(x,y) - \mathbf{y}_h(x,y)) \bullet (\ln \frac{z - d_o(x,y)}{Z_{om}(x,y)} - \mathbf{y}_m(x,y))) \quad (9)$$

One approach to simulate sensible heat flux on a large scale is to scale-up or aggregate the regional sensible flux by a weighted average of the contributions from different surface elements, based on the principle of flux conservation. A method of "blending height" is used to derive the regional sensible heat flux in this study. If the local-scale advection is comparatively small during the period of Landsat TM and NOAA-14 AVHRR observation taking place, the development of convection boundary layer may adjust the surface-disorganized variability at "blending height", where the atmospheric characteristics become proximately independent of the horizontal position. The corresponding 'effective' surface variables can be determined accordingly (Mason 1988, figure 4). This approach has been proved to be successful to calculate areally averaged surface fluxes in recent years (Lhomme et al. 1994; Bastiaanssen 1995; Wang et al. 1995; Ma et al. 1999). Based on this approach, the regional sensible heat flux $H(x,y)$ can be described as

$$H(x,y) = rC_p k^2 u_B \cdot (T_{sf}(x,y) - T_a(x,y)) / \left(\ln \frac{z_B - d_0(x,y)}{Z_{0m}(x,y)} + kB^{-1}(x,y) - y_h(x,y) \right) \cdot \left(\ln \frac{z_B - d_0(x,y)}{Z_{0m}(x,y)} - y_m(x,y) \right) \quad (10)$$

where Z_B is blending height and u_B is the wind speed at the blending height. In this study, Z_B and u_B are determined with the aid of field measurements of tether-sonde and sodar. $Z_{0m}(x,y)$ is the effective aerodynamic roughness length including the effect of topography and vegetation (e.g. crop field and grassy marshland). It is calculated by using Taylor's

model (Taylor et al. 1989). kB^{-1} is the excess resistance to heat transfer, which can be determined from leaf area index (LAI) by using a widely-used model (Qualls and Brutsaert 1995). d_0 is zero-plane displacement, which can be calculated from leaf area index (LAI) by using Raupach's model (Raupach 1994). $y_h(x,y)$ and $y_m(x,y)$ in Eq.(10) are the integrated stability functions. They can be derived by using Paulson's method (Paulson 1970) and Webb's method (Webb 1970). $T_a(x,y)$ in Eq.(10) is the regional distribution of air temperature at the reference height. Using an improved interpolation method it can be obtained (Ma 2001).

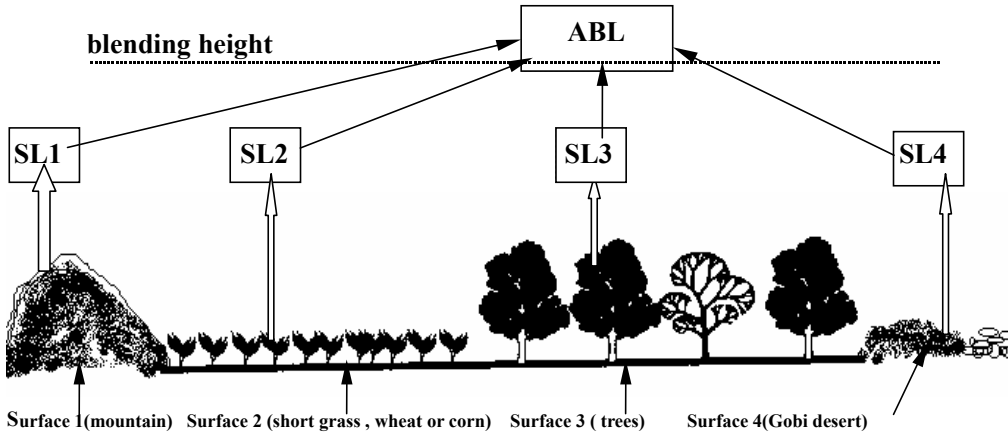


Figure 4. The approach of blending height. SL: surface layer.

3.4 Latent heat flux

The regional latent heat flux $IE(x,y)$ can be derived as the residual of the energy budget theorem for land surface based on the condition of zero horizontal advection at $z < z_{sur}$, i.e.

$$IE(x,y) = R_n(x,y) - H(x,y) - G_0(x,y) \quad (11)$$

4 CASE STUDY AND VALIDATION

Figure 5 shows the distribution maps of land surface heat fluxes over the HEIFE area based on 2600×2600 pixels with a size of about 30×30 m². Figure 6 shows the distribution maps of land surface heat fluxes over the GAME/Tibet area based on 180×51 pixels with a size of about 1×1 km². The derived land surface heat fluxes can be validated by field measurements. In Figure 7 the derived results are plotted against the measured values in the field for the four terms of the energy balance. The 1:1 line is also plotted in the graphs. Land surface heat fluxes derived from SEBAL (Wang et al. 1995; Ma et al. 1999) are plotted in Figure 7 as well. The results of another two cases (July 16, 1998 and Aug.21, 1998) in the GAME/Tibet area are

also plotted in figure 7. Since it is difficult to determine where the exact locations of the experimental sites are, the values of a 5×5 pixel rectangle, surrounding the determined Universal Transfer Macerator (UTM) coordinate, are compared with the field measurements. The mean absolute percent difference (MAPD) can quantitatively measure the difference between the derived results ($H_{derived(i)}$) and measured values ($H_{measured(i)}$) as

$$MAPD = \frac{100}{n} \sum_{i=1}^n \left(\frac{|H_{derived(i)} - H_{measured(i)}|}{H_{measured(i)}} \right) \quad (12)$$

It can be seen that: (1) the derived land surface heat fluxes over the HEIFE and the GAME/Tibet areas are in good accordance with the land surface status (figure 1 and figure 2). These parameters show a wide range due to the strong contrast of surface features. There are two peaks in the distribution maps over the HEIFE area, The first peak corresponds to the oasis and another one corresponds to the Gobi desert; (2) the derived net radiation over HEIFE area is very close to the field measurement with MAPD less than 5%.

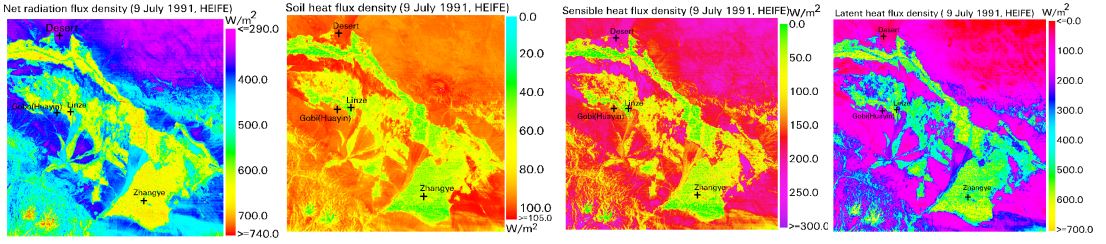


Figure 5. Maps of land surface heat fluxes for the HEIFE area. 10:00(LT), July 9, 1991

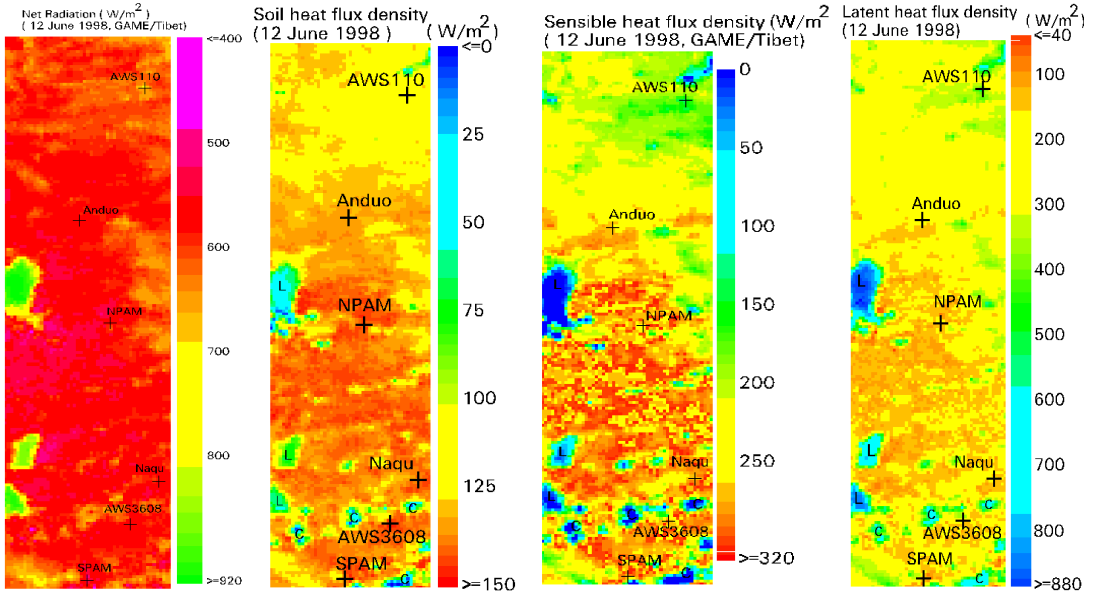


Figure 6. The distribution maps of surface heat fluxes for GAME/Tibet area (June 12, 1998). C: cloud, L: lake

It is better than the former results (Wang et al. 1995; Ma et al. 1999) due to the improvements in $r_0(x, y)$, $T_{sfc}(x, y)$, $e_0(x, y)$, $K_{\downarrow}(x, y)$ and $L_{\downarrow}(x, y)$. The derived net radiation over the GAME/Tibet area is also close to the field measurement with MAPD less than 7%. The net radiation flux over the GAME/Tibet area is higher than that in HEIFE area due to the high altitude (higher downward short wave radiation) and good land surface vegetation coverage (lower upward long wave radiation) in the area; (3) problems exist in the NDVI definition equation because of the external factor effect, such as soil back-ground variations (Huete et al. 1985; Huete 1989). To reduce the soil back- ground effect, Qi et al. (1994) proposed using MSAVI. Therefore, the parameterization method based on MSAVI for soil heat flux is better than it based on

NDVI on heterogeneous land surface. Although the derived regional soil heat flux based on MSAVI is a bit higher than the measured value in the HEIFE area, the MAPD gets smaller than the former derived value based on the NDVI (Wang et al. 1995; Ma et al. 1999). The derived soil heat flux over the GAME/Tibet area is closed to the measured values with MAPD less than 10%; (4) the derived regional sensible heat fluxes with MAPD less than 5% over the GAME/Tibet area are in good accordance with the field measurements. The derived regional sensible heat fluxes with MAPD of around 5% at four validation sites in the HEIFE area are in good accordance with the field measurements. The derived sensible heat flux by using improvement method is much better than the previous results (Wang et al. 1995; Ma et al. 1999) due to the improvement in calculating scheme of regional air temperature $T_a(x, y)$,

$kB^{-1}(x,y)$, $Z_{om}(x,y)$ and $d_0(x,y)$. The previous results derived from SEBAL (Bastiaanssen 1995) could be used over the Gobi and sand desert surface (MAPD=9.37% and MAPD=6.21%), but there is a large difference between the derived results and the field-measured values over oasis (MAPD=36.76% in Linze and MAPD=34.40% in Zhangye); (5) the derived regional latent heat fluxes, which is based on the energy balance equation, is acceptable for the whole HEIFE area. The value calculated from MAPD is less than 10% for the four validation sites; and (6) the derived latent heat flux in north PAM station is in

good agreement with the measured values (MAPD=1.95%), but there is big difference for latent heat flux between the derived value and the measured value at Anduo station with MAPD 59.3%. In other words, the method, which is based on the energy balance equation, may not be suitable to derive the latent heat flux over the GAME/Tibet area. The reason is that the energy is unbalanced for the whole area (Ma et al., 2000; Tanaka et al, 2001). Another reason may depend on the accuracy of the turbulence measurement sensors.

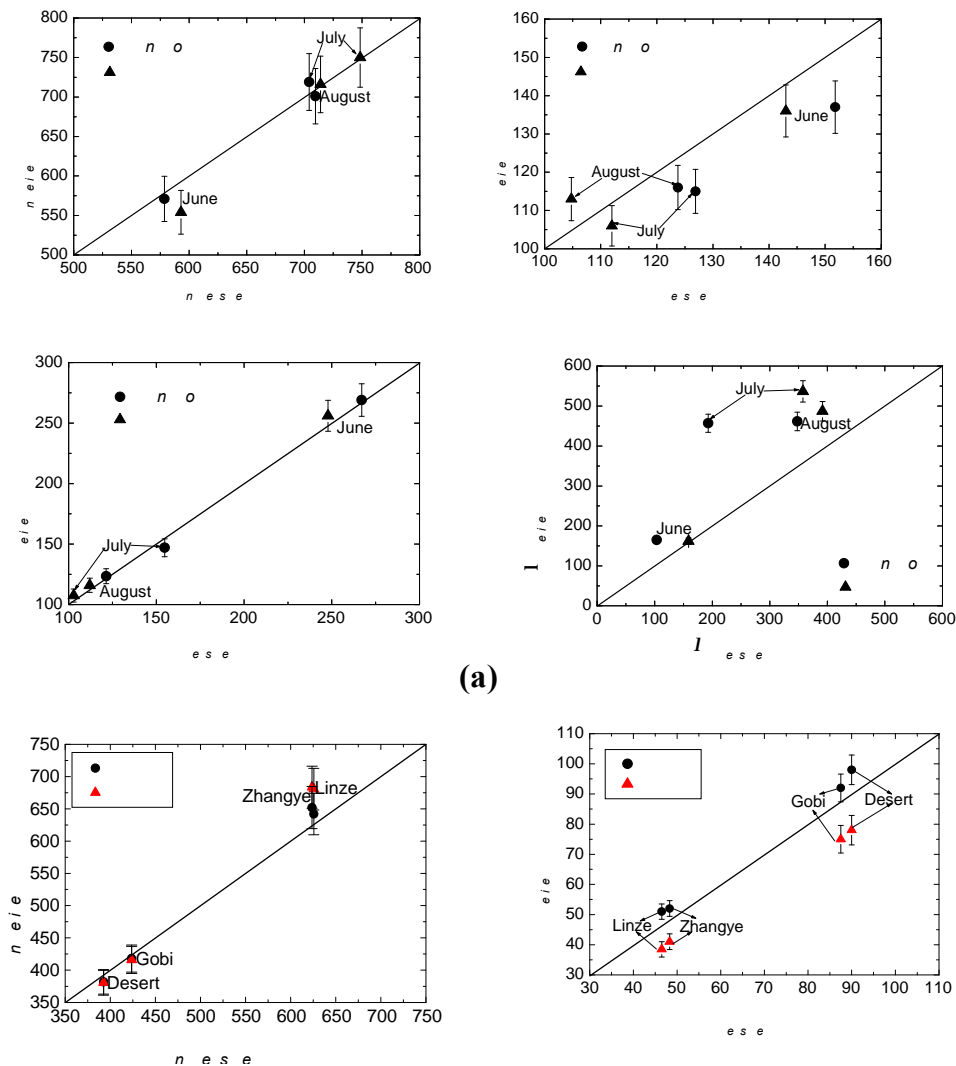


Figure 7. Validation of the derived results against the field measurements for land surface heat fluxes over the areas of GAME/Tibet and HEIFE, together with 1:1 line. (a) GAME/Tibet; (b) HEIFE, Cal.2: this study, Cal.1: Wang et al. 1995 and Ma et al. 1999.

5 CONCLUDING REMARKS

In this study, the regional distributions of land surface heat fluxes (net radiation, soil heat flux, sensible heat flux and latent heat flux) over heterogeneous areas of GAME/Tibet and HEIFE are derived with the aid of NOAA-14 AVHRR data, Landsat TM data and the field observational data. Compared with previous studies (Wang et al. 1995; Ma et al. 1999) and the “ground truth”, the new method has been proved to be a better approach to getting related air-land parameters over heterogeneous landscape due to the improvements in old parameterizations (Wang et al. 1995; Ma et al. 1999). This study forms a sound basis to study land surface fluxes over inhomogeneous landscape.

Dealing with the regional land surface heat fluxes over heterogeneous landscape is not an easy problem. The parameterization method presented in this research is still in developing stage: 1) From Eq. (9), it is better to use air temperature and wind speed at the reference height when we calculate the sensible heat flux. But we only propose one method to calculate regional air temperature at reference height in this research, therefore the “blending height” approach has to be used. The wind speed at the reference height over HEIFE area should be derived by using some numerical models, and the spatial resolution of the models should be 30m×30m and 1km×1km; 2) Only a single set of values at a specific time of specific day are used in this research. To reach more accurate regional land surface fluxes, more field observations and another satellite data such as GMS (Geo-stationary Meteorological Satellite) and ATSR (Along Track Scanning Radiometer) etc. have to be used. These research works will be done in the next step.

ACKNOWLEDGEMENTS

This work was under the auspices of the project of National Natural Science Foundation of China(40275003), the Chinese National Key Programme for Developing Basic Sciences (G1998040900) • the Innovation Project of Chinese Academy of Sciences (KZCX2-301), and the Innovation Project of Cold and Arid Regions Environmental and Engineering Research Institute, Chinese Academy of Science (CACX210072). Some parts of this study were done as cooperative research works in Disaster Prevention Research Institute, Kyoto University and the Alterra Green World Research, Wageningen UR, the Netherlands. The authors wish to acknowledge Profs. M.Maitani, E.Ohtaki, K.Sahashi, T.Koike and Dr. K.Ueno for their kind helps and useful discussions. The data used in this paper was obtained by the GAME-Tibet and the HEIFE projects supported by the Chinese Academy of Science (CAS), National Science Foundation of China, the Ministry of

Education, Science, Sport and Culture of Japan, the Science and Technology Agency of Japan, the National Space Development Agency of Japan, and the Frontier Research System for Global Change.

REFERENCES

- Bastiaanssen, W.G.M., 1995, Regionalization of surface fluxes and moisture indicators in composite terrain, • PhD thesis, Wageningen Agricultural University, Wageningen, the Netherlands, pp143–161.
- Becker, F and Li, Zh., 1990, Towards a local split window method over land surfaces, *International Journal of Remote Sensing*, **11**(3), 369~393.
- Becker, F and Li., Zh., 1995, Surface temperature and emissivity at various scales: definition, measurement and related problems, *Remote Sensing Review*, **12**, 225-253.
- Berk, A., L.S. Bernstein, and D.C.Robertson, MODTRAN, 1989, A moderate resolution model for LOTRAN 7, GL-TR-89-0122.
- Chodhury, B.J., Idso, S.B., and Reginato, R.J., 1987: Analysis of an empirical model for soil heat flux under a growing wheat crop for estimating evaporation by infrared-temperature based energy balance equation, *Agricultural and Forest Meteorology*, **39**, 283-297.
- Chodhury, B.J and J.L.Monteith, 1988, A four-layer model for the heat budget of homogeneous land surfaces, *Quarterly Journal of the Royal Meteorological Society*, **114**, 373-398
- Clothier, B.E., K.L.Clawson, P.J.Pinter, M.S.Moran, R.J.Reginato and R.D.Jackson, 1986, Estimating of soil heat flux from net radiation during the growth of alfalfa, *Agricultural and Forest Meteorology*, **37**, 319-329.
- Daughtry, C.S.T., Kustas, W.P., Moran, M.S., Pinter, P.J., Jackson, R.D., Brown, P.W., Nichols W.D., and Gay, L.W, 1990, Spectral estimates of net radiation and soil heat flux, *Remote Sensing of Environment*, **32**, 111-124.
- Hu, Y., Gao, Y., Wang, J., Ji, G., Shen, Zh., Cheng, L., Chen, J. and Li, Sh., 1994, Some achievements in scientific research during HEIFE, *Plateau Meteorology*, **13**, 225–236. (In Chinese with English abstract).
- Huete, A.R., Jackson, R.D., and Post, D.F., 1985, Spectral response of a plant canopy with different soil backgrounds, *Remote Sensing Environment*, **17**, 37-53.

- Huete, A.R., 1989, Soil influences in remotely sensed vegetation-canopy spectra, *Theory and Applications of Optical Remote Sensing* 107-141.
- Kustas, W.P., and C.S.T.Daughtry, 1990, Estimation of the soil heat flux/net radiation ratio from spectral data, *Agricultural and Forest Meteorology*, **39**, 205-223.
- Li, Zh-L., and Becker, F., 1993, Feasibility of land surface temperature and emissivity determination from AVHRR data, *Remote Sensing of Environment*, **43**, 67-85.
- Lhomme, J.-P., A.Chehbouni, and B.Monteny, 1994, Effective parameters of surface energy balance in heterogeneous landscape, *Boundary -Layer Meteorology*, **71**, 297-310.
- Ma, Y., Wang, J., Menenti, M., and Bastiaanssen, 1999, Estimation of fluxes over the heterogeneous land surface with the aid of satellite remote sensing and field observation, *ACTA Meteorologica Sinica*, **57**, 180-189. (In Chinese with English abstract).
- Ma, Y., O.Tsukamoto, X.Wu, I. Tamagawa, J.Wang, H.Ishikawa, Z. Hu, and H. Gao, 2000, Characteristics of energy transfer and micrometeorology in the surface layer of the atmosphere above marshland of the Tibetan Plateau area, *Chinese Journal of Atmospheric Sciences*, **24**(5), 715-722. (In Chinese with English abstract).
- Ma, Y., 2001, Parameterization of land surface heat fluxes over inhomogeneous landscape by combining satellite remote sensing with field observations (PhD thesis, Okayama University, Japan), pp1-195.
- Ma, Y., O.Tsukamoto, Wang, J., H.Ishikawa, and I. Tamagawa, 2002, Analysis of aerodynamic and thermodynamic parameters over the grassy marshland surface of Tibetan Plateau, *Progress in Natural Sciences*, **12**(1), 36-40.
- Maitani, T., Sahashi, K., Ohtaki, E., Tsukamoto, O., Mitsuta, Y., and Wang, J., 1995, Measurements of turbulent fluxes and model simulation of micrometeorology in a wheat field at Zhangye oasis, *Journal of the Meteorological Society of Japan*, **73**(5), 959-965.
- Mason, P., 1988, The formation of areally averaged roughness lengths, *Quarterly Journal of the Royal Meteorological Society*, **114**, 399-420.
- Mitsuta, Y., Tamagawa, I., Sahashi, K., and Wang, J., 1995, Estimation of annual evaporation from the Linze desert during HEIFE, *Journal of the Meteorological Society of Japan*, **73**(5), 967-974.
- Menenti, M., Bastiaanssen, W.G.M., Hefny, K., and Abd El Karim, M.H., 1991: Mapping of ground water losses by evaporation in the Western Desert of Egypt (DLO Winand Staring Centre, Report no.43, Wageningen, The Netherlands), pp.1-116.
- Paltridge, W., and Mitchell, Ross M., 1990, Atmospheric and viewing angle correction of vegetation indices and grassland fuel moisture content derived from NOAA/AVHRR, *Remote Sensing Environment*, **31**, 121-135.
- Paulson, C.A., 1970, The mathematic representation of wind speed and temperature profiles in the unstable atmospheric surface layer, *Journal of Applied Meteorology*, **9**, 856-861.
- Qi J., A. Chehbouni, A. R. Huete, Y. H. Kerr, S. Sorooshian, 1994, A Modified Soil Adjusted Vegetation Index, *Remote Sensing Environment*, **48**, 119-126.
- Qualls, R.J., and W.Brutsaert, 1995, The effect of vegetation density on the parameterization of scalar roughness to estimate spatially distributed sensible heat fluxes, *Water Resource Research*, **32**, 645-652.
- Raupach, M.R., 1994, Simplified expressions for vegetation roughness length and zero-plane displacements as functions of canopy height and area index, *Boundary -Layer Meteorology*, **71**, 211-216.
- Sahashi, K., 1995, A wet period in the desert station in HEIFE, *Journal of the Meteorological Society of Japan*, **73**(6), 1213-1217.
- Sobrino, J.A. and Raissouni, N., 2000, Toward remote sensing methods for land cover dynamic monitoring: application to Morocco, *International Journal of Remote Sensing*, **21**(2), 353-366.
- Tamagawa, I., 1996, Turbulent characteristics and bulk transfer coefficients over the desert in the HEIFE area, *Boundary -Layer Meteorology*, **77**, 1-20.
- Tanaka, K., H. Ishikawa, T. Hayashi and I. Tamagawa and Y.Ma, 2001, Surface Energy Budget at Amdo on Tibetan Plateau using GAME/Tibet IOP'98 Data, *Journal of the Meteorological Society of Japan*, **79**(1B), 505-517.
- Sykes and P.J.Mason, 1989, On the parameterization of drag over small scale topography in neutrally stratified Boundary flow, *Boundary -Layer Meteorology*, **48**, 409-422.

- Tsukamoto, O., Wang, J., and Mitsuta, Y., 1992, A significant Evening peak of vapour pressure at an oasis in the semi-arid region, *Journal of the Meteorological Society of Japan*, **70**(6), 1155-1159.
- Tsukamoto, O., Sahashi, K., and Wang, J., 1995, Heat budget and evapotranspiration at an oasis surface surrounded by desert, *Journal of the Meteorological Society of Japan*, **73**(5), 925-935.
- Valiente, J.A., Nunez, M., Lopez-Baeza, E., and Moreno, J.F., 1995, Narrow-band to broad-band conversion for Meteosat-visible channel and broad-band reflectance using both AVHRR-1 and -2 channels, *International Journal of Remote Sensing*, **16**(6), 1147-1166.
- Valor E. and V. Caselles, 1996, Mapping land surface emissivity from NDVI: Application to European, African and South American Area, *Remote Sensing Environment*, **57**, 167-184
- Verhoef W., 1997, Theory of radiative transfer models applied in optical remote sensing of vegetation canopies (PhD thesis, Remote Sensing Department of National Aerospace Laboratory, The Netherlands), pp.20-105
- Wang, J. and Y. Mitsuta, 1990, Peculiar downward water vapor flux over Gobi desert in the daytime, *Journal of the Meteorological Society of Japan*, **68**(3), 399-402.
- Wang, J. and Y. Mitsuta, 1992, An observation study of turbulent study of turbulent structure and transfer characteristics in Heihe oasis, *Journal of the Meteorological Society of Japan*, **70**(6), 1147-1154.
- Wang, J., Ma, Y., Menenti, M., W. Bastiaanssen and Y. Mitsuta 1995: The scaling-up of processes in the heterogeneous landscape of HEIFE with the aid of satellite remote sensing, *Journal of the Meteorological Society of Japan*, **73**, 1235-1244.
- Webb, E.K., 1970: Profile relationships: the log-liner range and extension to strong stability, *Quarterly Journal of the Royal Meteorological Society*, **96**, 67-90.

Multi-sensor flood crisis management and case-based database over the Moselle river (France)

J.-B. Henry, N. Tholey, P. De Fraipont,
Service Régional de Traitement d'Image et de Télédétection
Pôle API – Bd. Sébastien Brandt
67400 ILLKIRCH – FRANCE
Tel. +33(0)390.244.644 – Fax. +33(0)390.244.646
sertit@sertit.u-strasbg.fr – <http://sertit.u-strasbg.fr>

ABSTRACT – *Flood risk constitutes one of the major natural hazards affecting populations all over the world. In order to create new markets, many space agencies have initiated studies to promote and improve the integration of EO information within GIS, and more generally in decision making systems for flood management. The case-based approach is presented through two major involvements of SERTIT in flood risk management. The first is a case study, in an operational crisis management action, on behalf of ESA on the Moselle and Meuse rivers for the January 2002 flood ; and the second consists of R&D actions for the French Ministry of Research since December 2000, and that are still running, on well documented historical events on the river Moselle, NE France. Both optical and radar data are used in these two examples, with specified pre-processing levels for the quick production of cartographic information over a specific and occurring event. Combined with environmental datasets, remotely sensed data can feed a case-based system on flood events, to obtain the most complete description of each event.*

Obviously, this case-based approach supposes a large stability of the general runoff conditions over the whole river catchment. This is a very simplified hypothesis, but gives operational users elements to qualify a situation and evaluate the risk level facing a given population. Finally, this paper provides conclusions and viewpoints towards the future integration of remotely sensed information into flood crisis management and event mitigation, especially through the use of future high spatial and temporal resolution systems.

1. INTRODUCTION

Flooding often appears as the most devastating and frequent natural hazard. Flood events have a huge impact on human beings, settlements and ways of life. Always having dramatic impact on populations, their origins can vary from one region to another, and from season to season.

Several space agencies (ESA, CSA, CNES, ISRO, NOAA)¹ are currently working on crisis management support through imagery services and communication networks. Within this framework, several projects have been performed recently and many partnerships were established between these agencies, industrial companies, value-adder firms and National Civil Protection Services. For example, the International Charter on Space and Major Disasters has permitted many interventions during various events (<http://www.disasterscharter.org>). Through these

actions, space agencies aim to prove the efficiency of remotely sensed information for crisis management purposes.

This paper treats two case studies of Earth Observation (EO) data integration into geo-information systems (GIS) as an aid in the different phases of risk management. The first is SERTIT's involvement in crisis management over the Meuse and Moselle Rivers, for the January 2002 flood. Then, the case-based approach is explained, using the results from the crisis management phase.

2. EARTH OBSERVATION DATA AND RISK MANAGEMENT

Over many years, researchers have concentrated efforts in using remote sensing data in the different phases of risk management. Historically, the difficulties of scheduling satellite acquisitions over determined areas, the delay between acquisition and delivery to value-adder firms, and the processing delay after reception limited remote sensing techniques to prevention and modeling purposes. Nowadays, the increasing number of EO missions, progress in telecommunications, image processing, improved

¹ European Space Agency, Canadian Space Agency, Centre National d'Etudes Spatiales, Indian Space Research Organisation, National Oceanic and Atmospheric Administration.

technical and scientific know-how, and finally, better user awareness permit their use in the different phases of risk management.

2.1. Prevention, prevision, mitigation

EO datasets have been widely exploited in prevention studies as a cartographic tool, essentially for land use description. Many examples are given in the literature covering regional to local scale studies, depending on sensor resolution and swath. Earth observation systems provide adequate spatial and spectral resolutions, even if revisit frequency is lower (Baumgartner and Apfl, 1996) but this is improving.

On the other hand, forecasting also needs information over large areas to improve its predictions and requires much auxiliary information, that can issue from field measurement for the parameterization, calibration and validation of empirical models. Studies have developed simulation models that can account for various remotely sensed parameters such as terrain morphology descriptors (Beven and Kirkby, 1979), soil nature and related hydraulic properties (Müschen *et al.*, 2000), and land use to define boundary conditions for models (Bates *et al.*, 1997) by mapping vegetated areas which contribute to the evapo-transpiration process.

Soil moisture is difficult to quantify and monitor, because of its spatial and temporal variability, even if much progress has been made in microwave remote sensing (Dubois *et al.*, 1995; Engman and Chauhan, 1995; Fellah *et al.*, 1995), and through campaigns such as AGRISCAT, NOPEX, Washita, HAPEX-Sahel.

2.2. Crisis management

Studies have stressed the usefulness of different types of remote sensing and cartographic data (Tholey *et al.*, 1997; Profeti and Macintosh, 1997). Generally, information extraction from satellite datasets in a crisis situation employs change detection techniques, requiring an image of the event and an archive image.

Crisis management requires high temporal frequency data, to manage the event's dynamics, at a good spatial resolution. Current EO system resolutions still appear to be too coarse for an accurate operational use, even if they give useful results (Oberstadler *et al.*, 1997). However, this is changing with the new generation of satellites and their finer resolutions.

The main difference with the preceding phases is that speed is of the essence (Henry *et al.*, 2002). All retrieved data and mapping products are reusable for mitigation and prevention purposes (Yésou *et al.*, 2001).

3. CRISIS MANAGEMENT APPLICATION

In early January 2002, the Meuse and Moselle rivers burst their banks. Very high water table levels

and heavy rainfall coincided at the end of December, resulting in widespread flooding, starting in the upper basin on the 31st of December. Several major towns of North-Eastern France were threatened such as Verdun, Sedan and Charleville-Mézières.

3.1. Data transmission and pre-processing

The French Civil Protection Authorities activated the International Charter on Space and Major Disasters on the 31st of December as water levels rose in the upper Meuse basin. Operational coordination was entrusted to ESA. Satellite acquisitions were programmed on SPOT and Radarsat systems, whereas only scheduled ERS images were planned to be used. In parallel, archive images were sought and sent to SERTIT. During the delay between satellite activation and crisis data reception, the archive images were prepared in order to facilitate flood plain mapping. All raw data transfers were realized using a high bandwidth FTP protocol. For example, to retrieve PRI ERS-2 images (about 130 Mb) approximately 10 mins per image were required.

Sensor / Mode	Date
SPOT HRVIR / Xi-XS	02/01/02
	03/01/02
	04/01/02
	05/01/02
ERS-2 SAR / PRI	01/01/02
	04/01/02
RADARSAT SAR / STD1	05/01/02
	06/01/02

Table 1. Flood crisis data management over the Meuse and Moselle rivers January 2002 flood.

Because of exceptional weather conditions and because of the ability of 3 satellites, this event was widely covered by SPOT data. However, radar data still proved their usefulness in mapping flood extents.

Geometric and radiometric corrections are then performed in order to produce interpretable mosaics. All data were referenced to the national cartographic system. Thus, geometric coherence was obtained and GIS integration for map production is facilitated.

3.2. Information extraction

Data dependant algorithms are used to extract flood extents. Difference or ratio algebra between archive images and the flood image, combined with an appropriate threshold can be applied both on optical and radar datasets (Figure 1a). For radar data, the overall process appears to be more efficient when both images are acquired under similar conditions, i.e. resolution, incidence angle, season, imaging mode...

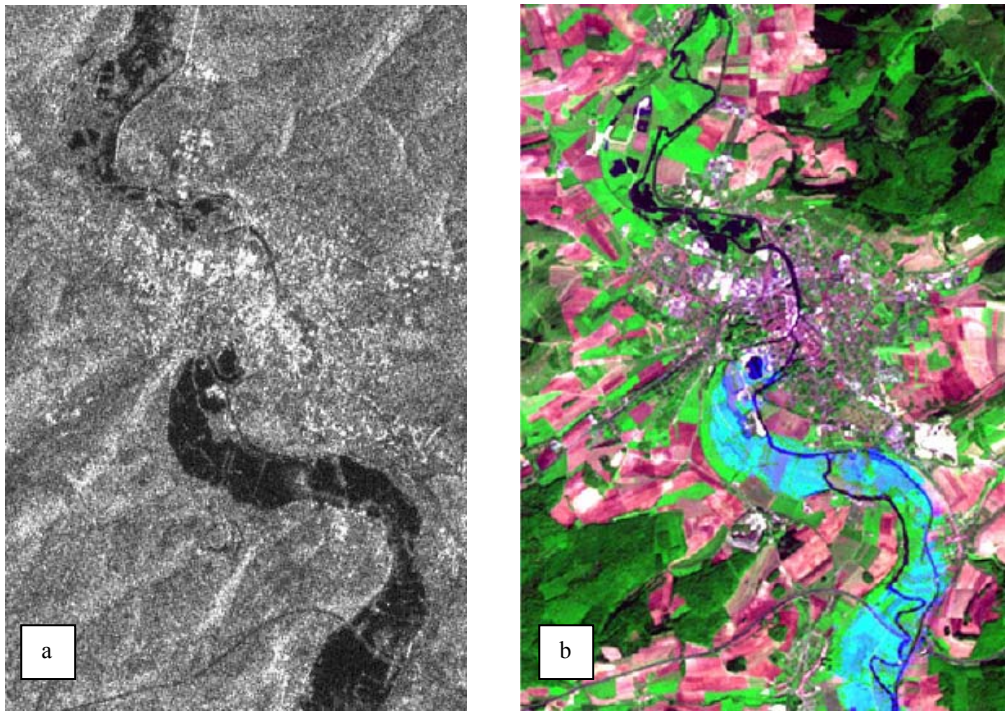


Figure 1. Observed flood extent on ERS image (a) and fusion with a natural color image (b)

During this case, to extract flood extents a non-negligible part of photo-interpretation was necessary to ensure automatic process validation.

Flood extents are mapped as binary overlays, which are plotted within a pseudo-natural colour image (Figure 1b). During other events, this kind of information presentation was the most appreciated by end users. This product gives a visual appreciation of flood impact, even if no more specific processing are necessary.

However, the plotting of flood extents on standard cartographic products, such as ordnance survey maps (IGN), appears to be a much more interesting product for operational users. Field operators are more used reading this type of information than satellite derived maps. Unfortunately, in many European countries such as France, cartographic information and the related databases are very expensive. Consequently, given time delay and financial requirements, alternatives have to be found to propose efficient cartographic production.

3.3. Cartographic outputs

One of the major goals of the International Charter on Space and Major Disasters is to furnish EO derived cartographic products to operational services. Therefore, time delay is the key factor of this kind of

production chain. These rapid flood mapping products are delivered within 6 hours. Thus, final products are e-mailed to operational users to speed up, once again, the information's availability.

Cartographic web servers would be the next enhancement to provide dynamic broadcasting and customizable map products. The new technologies of information and communication appear to be a very efficient means in providing a wide, but secure, access to cartographic information. However, the development of flexible interfaces needs to be performed, because operational users do not have much time for information retrieval.

4. CASE-BASED APPROACH

The case-based approach aims to propose a synthetic vision of a flood event. Combining many geographical data, such as flood extents or land use maps, with meteorological and gauge data, a case is defined by the synergistic analysis of each component and its contribution to the event's intensity. Thus, the database consists of a GIS fed with geographical and environmental data layers.

4.1. Area and database

This study is centered on the area of Metz-Thionville, on the Moselle river, in North-Eastern

France. This area was chosen for the PACTES program (Prévention et Anticipation des Crues au moyen des Techniques Spatiales) because of its high urban density.

The project database contains a large variety of earth observation data. It comprises optical data from SPOT, IKONOS, KVR, CORONA systems for optical and radar data from ERS-1/2, RADARSAT, airborne X-Band SAR and JERS-1 systems. Completed with ancillary data such as topographic and cartographic databases, it constitutes a considerable dataset.

This diversity aims to evaluate the contribution of the new generation of earth observation systems like ENVISAT or COSMO-SKYMED to flood risk management. Much hope is placed in their new imaging abilities and especially, in the multi-incidence and multi-polarization modes (Xia, 1996).

4.2. Geographical dataset

This layer is constituted of two main information layers. Firstly, it is important to obtain a good description of the landscape. This is possible by the numerical and visual interpretation of optical data, creating land use maps. These maps are elaborated with a precise nomenclature, which is highly detailed in urban areas. A feature data fusion performed on actualized and historical classification products allows a study of land use dynamics, and especially urban dynamics. This process can emphasize urbanization trends, in or close to frequently inundated areas. The analysis performed for 1962, with CORONA data, to 2000, with SPOT-P data clearly shows vulnerability evolution.

Secondly, analysis performed on optical and radar images acquired during flood events permit an instantaneous flood extent cartography, using the same extraction methods as in a crisis situation. When successive images are available, their intersection leads to a flood dynamic cartography, permitting flood duration and frequency mapping (Tholey *et al.*, 1997).

These two geographical components can be easily combined to precisely assess the impact of an event on urban areas. It is thus possible to evaluate local land planning policies and how they account for a known hazard.

Moreover, radar data analysis enables the consideration of soil moisture variations, through the backscatter coefficient. Even if it is taken into account in very few models, monitoring the moisture content of the upper soil layers appears to be a useful parameter to characterize each situation. The strong correlation between moisture and backscattering coefficient has already been widely studied in the literature, using many types of data, and they all stress on the importance of field validations.

A further effort has to be made to link backscatter coefficient measures with the real soil water content, obtained by piezometric *in-situ* measurements. Thus, for the chosen area, it will be possible to quantitatively monitor this variable.

4.3. Environmental dataset

Contrary to the geographical dataset, this second layer is comprised of variables measured at point sources, i.e. precipitation, water levels, soil water contents and regional water balance. Time series of rainfall and hydrometric measurements are available for each event. A quick analysis shows that a standard integration period, of 10 days in our study, enables the efficient description of an event, its intensity, and thus the elaboration of a synthetic overview (GENESIS, 2000). The water balance's utility is to provide a global appreciation of the hydrologic state of the catchment, assuming that the same rainfall would not have the same consequences on hydrometry depending on soil moisture.

In practice, the composition of the environmental dataset involves the building of a geo-information attributes table locating measurement stations. For each variable (precipitation, river flow...), the table is elaborated with raw measurements and time-integrated values.

4.4. Case description

The case description is the final step of the database's development. It uses its different layers and highlights, as far as possible, the correlation between a given rainfall, flood extent and observed river flow. It is founded on the simple assumption of cause and effect. Hence with equivalent conditions, the same causes will produce the same effects. Even if reductive, this hypothesis allows the analysis of an occurring event by a quick comparison with historical cases.

Finally, the main idea is to give operational users elements with which to qualify a majority of the events they have to face. In this way, the knowledge of each component of observed events is important and useful. This constitutes the loop back, from the mitigation to the prevention process and is susceptible to be used by many user communities: hydrologists, environment analysts as well as local administrations and insurance companies.

Thus, the availability of a highly detailed database on the Moselle area enables them to consider the different product types that can be produced using earth observation systems.

5. DISCUSSION

As the intensity and frequency of flood events cannot be fully controlled, solutions must be found to

limit their impact on human beings. The development of crisis action frameworks using advanced space technologies is a first step, which needs to be completed by further studies to improve the knowledge of the natural processes involved. Thus, the case-based approach aims to synthesize all information acquired during an event. Through this simple assumption of cause and effect, a quick quantification of any flood situation might be enabled.

Permanent monitoring of the environment and its major variables seems to be one of the most important challenges over the next few years. ENVISAT's capabilities will greatly help in achieving these goals, but it will be necessary to adapt our view of what kind of information is pertinent and useful for the different phases of flood risk management.

Moreover, the use of EO data appears to be taking hold in flood risk management phases. The production of EO derived cartographic data on natural hazards, over large areas, is widely appreciated by scientists, crisis management services, land planners and insurance companies. Future developments aim to improve the synergistic use of remotely sensed information with other geographical ancillary data. This would trend towards EO systems being completely integrated into flood hazard management chains.

6. ACKNOWLEDGMENTS

This work is part of the PACTES program (Prévention et Anticipation des Crues au moyen des Techniques Spatiales) which is financed by the French Ministry of Research and coordinated by the CNES (Centre National d'Etudes Spatiales).

7. REFERENCES

- Bates P. D., Horritt M. S., Smith C. N. and Mason D., 1997, Integrating remote sensing observations of flood hydrology and hydraulic modeling. *Hydrological Processes*, **11** (14), 1777-1795.
- Baumgartner M.F. and Apfl G.M., 1996, Remote sensing and geographic information systems. *Hydrological Sciences Journal*, **41** (4), 593-607.
- Beven K.J. and Kirkby M.J., 1979, A physically-based variable contributing area model of basin hydrology. *Hydrological Sciences Bulletin*, **24**, 27-53.
- Dubois P.C., Van Zyl J. and Engman T., 1995, Measuring soil moisture with imaging radars. *IEEE Transactions on Geosciences and Remote Sensing*, **33** (4), 915-926.
- Engman E.T. and Chauhan N., 1995, Status of Microwave Soil Moisture Measurements with Remote Sensing, *Remote Sensing Environment*, Vol. 51, pp. 189-198.
- Fellah K., Bally P., Besnus Y., Meyer C., Rast M. and de Fraipont P., 1995, Impact of SAR radiometric accuracy in hydrological and agro-environmental applications, *Proceedings of Retrieval of bio- and geophysical parameters from SAR data for land applications*, Toulouse 17-20 October, pp. 337-346.
- GENESIS, 2000, Geospatial Emergency Management Network for Support by Imagery Services, European Commission, DG XIII-C26401-B, TEN TELECOM Program.
- Henry J.-B., Fellah K., Clandillon S., Allenbach B. and De Fraipont P., 2002, Earth observation and case-based systems for flood risk management, *Proceedings of IGARSS'02*.
- Müschen B., Flügel W.-A., Hochschild V., Steinnocher K., De Fraipont P., Fellah K., Rodolfi G., Colpaert A., Krzywinski K. and Quiel F., 2000, Parameterization of Hydrological, Erosion and Solute Transport Models by Remote Sensing Techniques and GIS Analyses in European Catchments, *Proceedings of the 28th Int. Symposium on Remote Sensing of Environment*, Capetown 27-31 March, 4p.
- Oberstadler R., Hönsch H. and Huth D., 1997, Assessment of the mapping capabilities of ERS-1 SAR data for flood mapping: a case study in Germany, *Hydrological Processes*, **11** (10), pp. 1415-1425.
- Profeti G. and Macintosh H., 1997, Flood management through LANDSAT TM and ERS SAR data: a case study, *Hydrological Processes*, **11** (10), pp. 1397-1408.
- Tholey N., Clandillon S. and De Fraipont P., 1997, The contribution of spaceborne SAR and optical data in monitoring flood events: examples in northern and southern France, *Hydrological Processes*, **11** (14), pp. 1409-1413.
- Xia Z.G., 1996, Applications of multi-frequency, multi-polarization and multi-incident angle SAR systems in urban land use and land cover mapping, *Proceedings of IGARSS'96*, **4**, pp. 2310-2314.
- Yésou H., Chastanet P., De Fraipont P., Dossmann P., Stock N. and Béquignon J., 2001, Mapping floods in France, *Backscatter*, **12** (3), pp. 23-26.

Dart: a 3-D model for simulating Satellite images and surface radiation budget

Martin E., Gastellu-Etchegorry J.P., Gascon F., Gentine P. and Belot A.

Centre d'Etudes Spatiales de la BIOsphère

Paul Sabatier University - CNES - CNRS

18 av. Ed. Belin (bpi 2801) 31401 Toulouse - France

☎: (33) 5 61 55 61 30 Mail: gastellu@cesbio.cnes.fr

ABSTRACT - *DART (Discrete Anisotropic Radiative Transfer)* is a radiative transfer model that simulates remotely acquired images. It was originally developed to work in the short wavelengths ($0.3\mu\text{m}$ - $3\mu\text{m}$) within 3D natural scenes that are represented as matrices of rectangular cells containing trees, shrubs, grass, soil, etc. DART was recently improved in order to get a better accuracy and a larger range of applications. Presently, it works with natural and urban landscapes, on the whole optical domain (thermal infrared included), with a multispectral approach that uses optical data bases from $0.3\mu\text{m}$ up to $15\mu\text{m}$. Moreover, it simulates radiative transfer in the whole "Atmosphere - Earth" system and it accounts for the instrumental transfer function. The paper presents these new capabilities and describes how multiple scattering simulation was modified to improve DART accuracy.

1 INTRODUCTION

Modeling the interaction of radiation with terrestrial surfaces is more and more a prerequisite for conducting research activities in several scientific domains. This is typically the case of vegetation studies using remotely acquired information. In many situations, retrieving information from remotely sensed data would benefit of the use of three dimensional (3-D) models that simulate accurately the spectral behavior of bi-directional reflectance (BRDF) and temperature (BTDF) distribution functions of Earth's surfaces. This is the case when it is intended to derive physical (e.g. albedo and temperature) and structural (e.g. Leaf Area Index, LAI) characteristics of ground targets from remote sensing information. It is also the case when one expects to associate signal characteristics (e.g. BRDF and/or BTDF anisotropy) with some conditions of these targets. Indeed, 3-D models have the potential to account for the spectrally dependent anisotropic behavior of vegetation canopies (Syren, 1994). Usually, this anisotropy is a serious constraint for studying vegetation with remote sensing data acquired under different experimental conditions, i.e. view and illumination conditions. Associated errors depend on sun - view conditions, and on target characteristics; e.g. the albedo of a canopy with an anisotropic BRDF may be underestimated by as much as 45% if it is computed with nadir reflectance only (Kimes and Sellers, 1985). Thus, 3-D models are more and more necessary tools because they better account for the 3-D nature of Earth surfaces than other models.

Quantification of vegetation functioning is another important domain of application of 3-D radiative transfer models when these are coupled with leaf physiological models. Indeed, vegetation development is directly influenced by the within stand radiation regime and the photosynthesis function of vegetation elements. The expected advantage of 3-D radiative transfer models is to provide an accurate 3-D distribution of the radiative energy that is intercepted and absorbed by natural vegetation.

DART is a 3-D radiative transfer model (Gastellu-Etchegorry *et al.*, 1996) that was designed with these two objectives in mind. The 1996 initial DART version simulates BRDFs, remote sensing images and the radiation budget of 3D natural landscapes (e.g., trees, roads, grass, soil, water) in the visible and short wave infrared domains. For that, it uses simplifying hypotheses for simulating landscapes and for modeling multiple scattering mechanisms. It was successfully tested against reflectance measurements (Gastellu-Etchegorry *et al.*, 1999) and used in various studies (Guillevic and Gastellu-Etchegorry, 1999).

This paper introduces recent improvements of DART for broadening its domain of application (urban landscapes and the atmosphere over the whole optical domain) and for increasing its accuracy.

2 DART

DART simulates radiative transfer in 3D landscapes with the exact kernel and discrete ordinate approaches. Landscapes are simulated as rectangular matrices of

parallelepipedic cells, *i.e.* building block for simulating larger scenes. Radiation is restricted to propagate in a finite number of directions (Ω_i) with ($\Delta\Omega_i$) being the width (sr) of its angular sector. Any set of N discrete directions can be selected ($\sum_{n=1}^N \Delta\Omega_n = 4\pi$). Radiation that propagates along direction (Ω_i) at a position r is called a source vector $W(r, \Omega_i)$.

Irradiance incident on a scene has 2 components:

- direct sun source vectors $W(\Omega_s) = E_s(\Omega_s) \cdot |\mu_s| \cdot \Delta x \cdot \Delta y$ propagate along direction (Ω_s).
- atmospheric radiation $W_a(\Omega_n) = L_a(\Omega_n) \cdot |\mu_n| \cdot \Delta x \cdot \Delta y \cdot \Delta\Omega_n$

that originate from a fictitious cell layer at the top of the scene. $\Delta x \cdot \Delta y$ is the area of DART cell faces, $\mu_s = \cos\theta_s$, $\mu_n = \cos\theta_n$, $E_s(\Omega_s)$ is the sun constant at the top of the scene, Ω_s is the solar incident direction, and $L_a(\Omega_n)$ is the atmospheric specific intensity along direction (Ω_n), with $n \in [1, N']$, where N' is the number of downward discrete directions. Practically, the knowledge of $L_a(\Omega_n)$ requires an atmospheric model.

Let $W(l, \Omega_s)$ be a source vector that crosses (Figure 1) a turbid vegetation cell i along direction Ω_s , with $l \in [0, \Delta l_i]$ the path length from the entrance point (A) of cell i , and Δl_i the within cell path length. Propagation of $W(l, \Omega_s)$ leads to scattered source vectors $W_1(\Delta l_i, \Omega_s \rightarrow \Omega_v)$ along directions Ω_v , $v \in [1, N]$. Cell scattering along (Ω_v) is computed with the assumption that $W_1(\Delta l_i, \Omega_s \rightarrow \Omega_v)$ is calculated with an origin, called middle point (M_s), different from the cell center, whereas the geometric path of scattered radiation that exits the cell is simulated from the cell center. (M_s) is defined as the point along the path ($\Delta l_i, \Omega_s$) such that 50% of the total radiation $W_{int}(\Delta l_i, \Omega_s)$ intercepted along Δl_i is intercepted before (M_s). Thus, path length Δr_i between (M_s) and the entrance point (A) of cell i verifies:

$$W_{int}(\Delta r_i, \Omega_s) = \frac{1}{2} \cdot W_{int}(\Delta l_i, \Omega_s)$$

$$\Rightarrow \Delta r_i = \frac{\ln 2 - \ln[1 + \exp(-u_f(i) \cdot G(j, \Omega_s) \cdot \Delta l_i)]}{u_f(i) \cdot G(j, \Omega_s)} \quad \text{Eq. 1}$$

$G(j, \Omega_s)$ is the mean projection of a unit foliage area in cell i onto a surface unit normal to direction (Ω_s).

Because several source vectors cross any cell, we use the gravity center of all (M_s) within each cell, weighted by the energy intercepted. For a cell i of type j , we have:

$$W_1(\Delta l_i, \Omega_s \rightarrow \Omega_v) = W_{int}(0, \Omega_s) \cdot T(j, \Omega_s, \Omega_v)$$

$$= \iint_{\Delta\Omega_v} \int_{\Delta l_i} W(l, \Omega_s) \cdot u_f(i) \cdot |\Omega_s \cdot \Omega_l| \cdot \frac{g(j, \Omega_l)}{2\pi} \cdot f(j, \Omega_l, \Omega_s \rightarrow \Omega_v) \cdot d\Omega_l \cdot dl \cdot d\Omega_v$$

$$\text{with } [T(j, \Omega_s, \Omega_v)] = \frac{\int_{\Delta\Omega_v} \int_{\Delta\Omega_s} \frac{g(j, \Omega_l)}{2\pi} \cdot |\Omega_s \cdot \Omega_l| \cdot f(j, \Omega_l, \Omega_s \rightarrow \Omega_v) \cdot d\Omega_l}{G(j, \Omega_s)} \cdot d\Omega_v$$

where $f(j, \Omega_s \rightarrow \Omega_v)$ is the leaf scattering phase function for vegetation of type j . It is assumed to be the sum of a lambertian component $f_d(j, \Omega_l, \Omega_s \rightarrow \Omega_v)$ and a specular component $f_s(j, \Omega_l, \Omega_s \rightarrow \Omega_v)$. The $N \times N$ matrix $[T(j, \Omega_s, \Omega_v)]$ is the scattering transfer function of turbid cells of type j . It is pre-computed for minimizing repetitive computations. Each matrix $[T(j, \Omega_s, \Omega_v)]$ may be anisotropic and rotationally variant. It has two components that are dependent and independent of leaf mesophyll information.

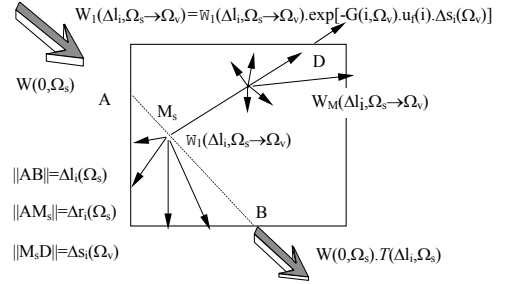


Figure 1: Within cell single and multiple scattering.

Single-scattering radiation $W_1(\Delta l_i, \Omega_s \rightarrow \Omega_v)$ that escapes cell i along Ω_v corresponds to the attenuation of $W_1(\Delta l_i, \Omega_s \rightarrow \Omega_v)$ within cell i after a propagation length $\Delta s_i(\Omega_v)$ from the middle point (M_s).

$$W_1(\Delta l_i, \Omega_s \rightarrow \Omega_v) = W_1(\Delta l_i, \Omega_s \rightarrow \Omega_v) \cdot \exp[-G(j, \Omega_v) \cdot u_f(i) \cdot \Delta s_i(\Omega_v)]$$

Within cell multiple scattering source vectors $W_M(\Delta l_i, \Omega_s \rightarrow \Omega_v)$ that escape any cell i are computed with energy $W_{1,int}(\Delta l_i, \Omega_s \rightarrow \Omega_v)$ intercepted along the path $\Delta s_i(\Omega_v)$ and with the approximation that within cell multiple scattering is nearly isotropic. Total source vector scattered by a cell i along direction (Ω_v) is: $W_1(\Delta l_i, \Omega_s \rightarrow \Omega_v) + W_M(\Delta l_i, \Omega_s \rightarrow \Omega_v)$

DART computes accurately first order scattering. For that, it stores direct sun radiation that is intercepted by scene elements, for computing scattering with an exact expression in the first iteration. Use of this method for simulating multiple scattering in further iterations would demand a huge computer memory capacity for storing the intensity of the intercepted radiation, for each cell and incident direction. Thus, an approximation was used: for each interception, radiation scattering is exactly computed and its distribution is represented by a spherical expansion of coefficients $C_{lm}(i)$. This is well adapted to relatively smooth functions defined on the sphere, and to the incremental computation of

scattered radiation due to successive impinging interaction mechanisms, in any cell i : calculation of the scattered radiation angular distribution, computation of associated $C_{lm}(i)$ coefficients and adding them to the already accumulated $C_{lm}(i)$ coefficients. This approach being accurate but very computational intensive, we adopted a much faster method: multiple scattering is computed with the intercepted energy under the hypothesis that the originally incident radiation is isotropic. This proved to be accurate with homogeneous landscapes; *i.e.* turbid scenes (Demarez, 1997).

The 1996 DART model projects the 4 upper corners of the scene onto the sensor plane for simulating sensor images with a digital image processing software. The need of an additional software is a constraint, similar to the need of an atmospheric model for taking into account the atmosphere.

3 CAPABILITY OF THE NEW DART MODEL

As already mentioned, DART domain of application was recently broadened. Its additional features are:

- Radiative transfer simulation in urban landscapes,
- Simulation of thermal infrared (TIR) radiative transfer,
- Radiative transfer simulation in the atmosphere,
- Simulation of images in the plane of the sensor,
- Account of the sensor transfer function (ASCII file),
- Development of a graphic user interface (GUI).

3.1 Simulation of urban landscapes and topography

Now, DART simulates all landscape elements (*e.g.*, rivers, roads, buildings, tree trunks), except vegetation, as the juxtaposition of plane surfaces (*i.e.*, triangles and parallelograms) (Mathiaud, 2000; Benech, 2000). Thus, DART cells can be empty or filled with either turbid media or plane surfaces. The latter ones can be larger or smaller than DART cells. They are mostly used to simulate topography and urban elements (*e.g.*, houses and buildings) with or without topography. Buildings are the superimposition of generic shapes (Figure 2) characterized by any 8 points. Thus, their shapes can be very complex.

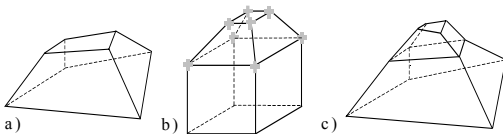


Figure 2: Generic shape (a) to build up houses (b,c).

Plane surfaces BRDFs are modeled with parametric reflectance models (1 up to 9 parameters) to account for possible specular and backscattering components.

Within cell radiative transfer is now more complex because cells can contain several plane surfaces. For example, radiation must be emitted or scattered only from points on the external surface of plane figures.

3.2 TIR radiative transfer simulation

DART simulates TIR radiative transfer with a method (*i.e.*, exact kernel method, discrete ordinate approach, etc.) similar to 1996 DART model. Emitted energy is calculated on a cell per cell basis as the integration of the Planck law over the selected spectral band.

For cells with plane surfaces, the emitted energy is proportional to the apparent areas of the within cell plane surfaces. It propagates from points that belong to a grid that samples the cell volume.

For leaf cells, the emitted energy depends on the cell LAI and LAD. It is computed with an integration over the cell volume. Radiation is emitted from points that belong to grids that sample the 6 cell faces. The location of the emission point P (Figure 3) depends on the emission direction and on the cell face.

Plane surfaces and leaf cells can have any temperature within predefined intervals. Temperature is calculated through an illumination stage in the visible spectral domain (Guillevic, 1999; Boyat, 2001).

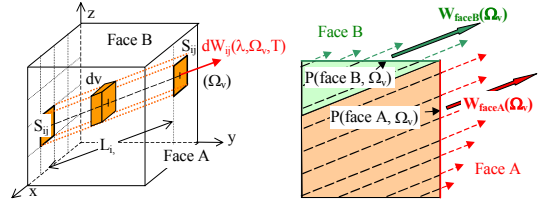


Figure 3: Thermal emission of a leaf cell.

3.3 Atmospheric radiative transfer

Atmosphere affects scene reflectance and images at different levels. For example, it determines the incident illumination (direct sun and atmospherically scattered radiation). Atmospheric radiation has two components: radiation yet and not yet reflected by the Earth. Atmospheric models are needed for simulating these components. However, knowledge of the atmospheric component that has already been reflected by the Earth requires to couple an atmospheric and an earth radiative transfer models. This stresses the interest to simulate radiative transfer in the "atmosphere - earth" system with a unique model.

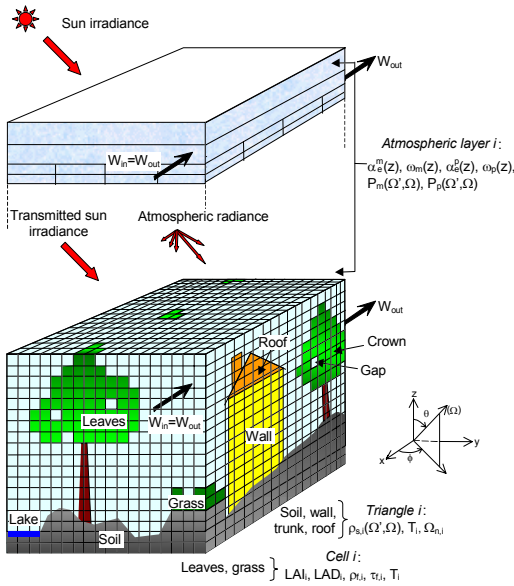


Figure 4: "Atmosphere + Earth" DART scene.

Now, DART simulates the "earth - atmosphere" system (Figure 4) and its coupling effects in the optical domain with the exact kernel and discrete ordinate methods (Gascon, 2001; Dallest, 2001). Aerosol and gas characteristics are input as optical depths and scale heights or profiles (gas extinction coefficient $\alpha_e^m(\lambda, z)$ and spherical albedo $\omega_m(\lambda, z)$, aerosol extinction coefficient $\alpha_e^p(\lambda, z)$ and spherical albedo $\omega_p(\lambda, z)$), with gas $P_m(\lambda, \Omega', \Omega)$ and aerosol $P_p(\lambda, \Omega', \Omega)$ phase functions. They are given by the operator or extracted from a data base ([0.3 15 μ m]) derived from the Modtran atmospheric model, for a few typical atmospheres.

Ferran (2001) showed that DART gives atmospheric reflectance, transmittance and apparent temperature very close to those of the 6S and Modtran atmospheric models with lambertian horizontal Earth surfaces.

3.4 Simulation of sensor images

DART simulates sensor images (Gentine, 2002) with:

- image projection onto the sensor plane. Geometric correction is done with an interpolation procedure that oversamples the sensor plane. It accounts for the apparent area of emitters and scatterers for improving the image geometry, especially in presence of 3D architecture (e.g., city, topography).
- signal convolution with the sensor impulse response.
- signal conversion into a number of electrons N_e .
- addition of a positive radiometric noise.
- conversion of the image into digital values.

3.5 Graphic User Interface (GUI)

A graphic user interface (GUI) was developed to ease the task of the operator. It provides:

- interactive specification of input parameters,
- display of computer scenes, which allows one to verify that the DART scene is correctly simulated.
- display of simulation results.

3.6 Examples of DART simulations

Two types of DART images are shown here:

- color composites of a Toulouse district (France) for a sensor below and above the atmosphere (Figure 5). They were simulated by CNES (French Space Agency) for selecting the spectral domain of the future high spatial resolution PLEIADES-HR satellite sensor (Gascon *et al.*, 2001).
- color composite and thermal infrared image (Figure 6) of a natural cover (South West France) (Boyat, 2001).

4 IMPROVEMENT OF DART ACCURACY

4.1 Detection of inaccuracies

Recently, DART was compared with 3-D reflectance models (*Flight*: North, 1996, *Sprint*: Thompson and Goel, 1998, Raytran: Govaerts and Verstraete, 1998) in the RAMI (Radiation transfer Model Intercomparison) experiment (Pinty *et al.*, 2001). Only BRDFs were compared because only DART simulates images.

A "soil + trees" scene (Figure 7, table 1) was used in this work. All models are close in the visible domain (Figure 8). However, DART differs from the other models in the near infrared (NIR) domain. Maximal difference ($\approx 11\%$) occurs for sun zenith angle $\theta_s = 20^\circ$.

Thus, we deeply analyzed DART approximations for improving them without increasing computational time. Three major sources of errors emerged:

- inaccurate position of the middle point (M_s).
- multiple scattered radiation is assumed to be due to an isotropic incident radiation.
- inaccurate location of the origin of scattered radiation.

Parameter	Value	
LAI (leaf area index)	5 (per tree)	
LAD (leaf angle distribution)	spherical	
Leaf reflectance (ρ_f) and transmittance (τ_f)	VIS	$\rho_f = 5.5\%$ $\tau_f = 1.5\%$
	NIR	$\rho_f = 49.6\%$ $\tau_f = 44.1\%$
Soil reflectance (ρ_{sol})	VIS	12.7 %
	NIR	15.9 %
Sun zenith angle (θ_s)	20° and 50°	

Table 1: RAMI landscape parameters (Figure 7).

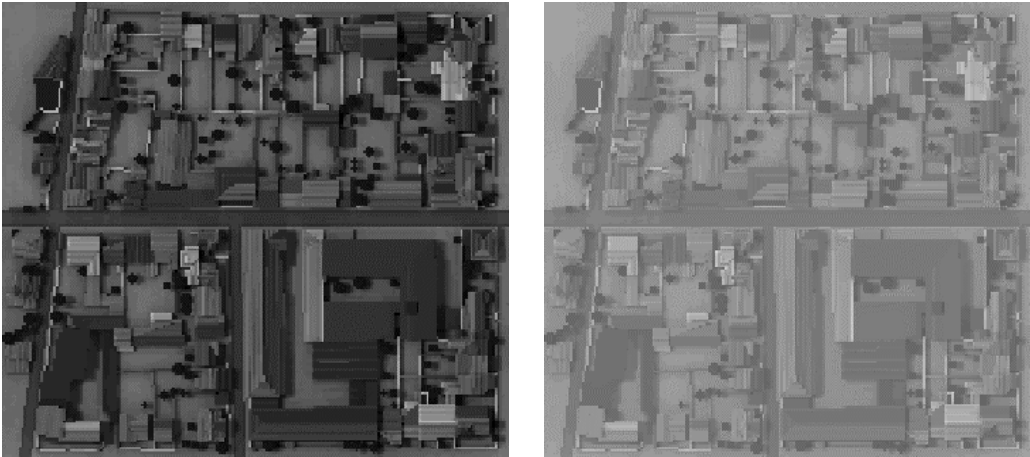


Figure 5: Bottom (left) and top of the atmosphere (right) DART simulations of a Toulouse district.

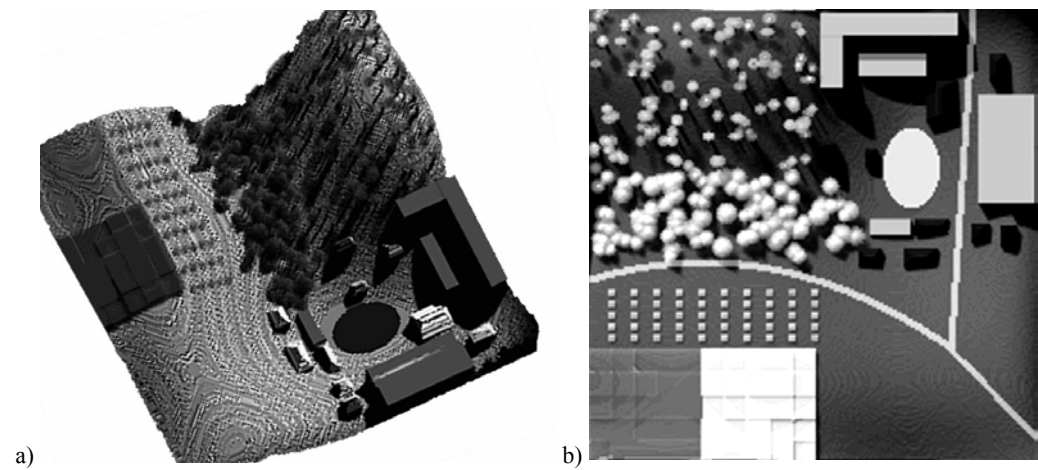


Figure 6: DART simulation of a natural landscape (South west France). Colour composite (a). Thermal infrared (b).

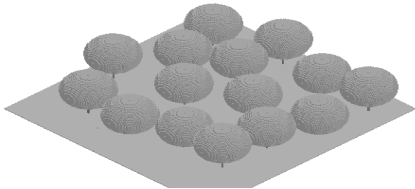


Figure 7: RAMI landscape (soil + trees).

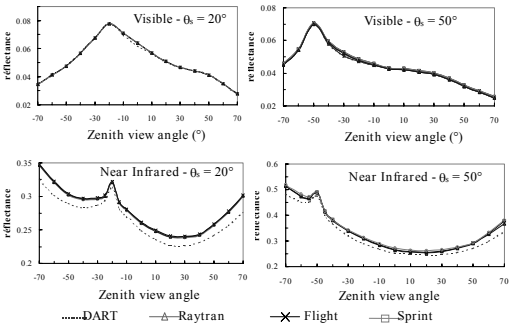


Figure 8: Comparison of DART and three 3D reflectance models with the RAMI scene (Table 1).

4.2 Position of the middle point M_s

First, we assessed the error due the position of the center of gravity (noted M_s here) of middle points. For that, we compared the first order source vectors $W_1(\Omega_s \rightarrow \Omega_v)$ of a turbid layer (Figure 9) simulated by DART, $W_{1M_s} = W_1(\Delta z, \Omega_s \rightarrow \Omega_v)$, with an exact analytical expression, $W_{1\text{exact}} = W_1(\Delta z, \Omega_s \rightarrow \Omega_v)$. This turbid layer was characterized by its height Δz , its LAD, its LAI and leaf optical properties (ρ_f , τ_f). Directions of the incident and scattered source vectors are noted (Ω_s) and (Ω_v), respectively.

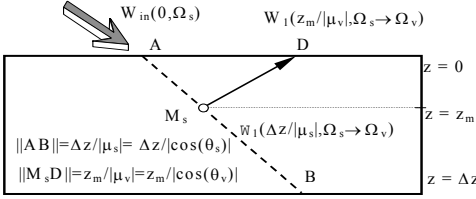


Figure 9: First order scattering by a turbid layer.

Let z_m be the altitude of M_s , $G_s = G(\Omega_s)$ and $G_v = G(\Omega_v)$.

- upward directions (i.e., $\mu_s < 0$ and $\mu_v > 0$):

$$W_{1\text{exact}} = \int_0^{\Delta z} W_{in}(\Omega_s) \cdot T(\Omega_s, \Omega_v) \cdot G_s \cdot u_f \cdot \exp[G_s u_f \frac{z}{|\mu_s|}] \cdot \exp[-G_v u_f \frac{z}{|\mu_v|}] \cdot \frac{dz}{|\mu_s|}$$

$$= W_{in}(\Omega_s) \cdot T(\Omega_s, \Omega_v) \cdot \frac{-G_s \mu_v}{G_v \mu_s - G_s \mu_v} \cdot [1 - \exp[u_f \Delta z \cdot (\frac{G_s}{\mu_s} - \frac{G_v}{\mu_v})]]$$

$$W_{1M_s} = W_{in}(\Omega_s) \cdot [1 - \exp[-G_s u_f \frac{\Delta z}{|\mu_s|}]] \cdot T(\Omega_s, \Omega_v) \cdot \exp[-G_v u_f \frac{z_m}{|\mu_v|}]$$

- downward directions (i.e., $\mu_v < 0$), with $\theta_s \neq \theta_v$:

$$W_{1\text{exact}} = W_{in}(\Omega_s) \cdot T(\Omega_s, \Omega_v) \cdot \frac{G_s \mu_v \exp[u_f \frac{G_v}{\mu_v} \Delta z]}{G_v |\mu_s| - G_s |\mu_v|} \cdot [1 - \exp[u_f \Delta z \cdot (\frac{G_v}{|\mu_v|} - \frac{G_s}{|\mu_s|})]]$$

$$W_{1M_s} = W_{in}(\Omega_s) \cdot [1 - \exp[-G_s u_f \frac{\Delta z}{|\mu_s|}]] \cdot T(\Omega_s, \Omega_v) \cdot \exp[-G_v u_f \frac{\Delta z - z_m}{|\mu_v|}]$$

- sun direction ($\theta_s = \theta_v$):

$$W_{1\text{exact}} = W_{in}(\Omega_s) \cdot T(\Omega_s, \Omega_v) \cdot G_v u_f \cdot \exp[-u_f G_s \frac{\Delta z}{|\mu_s|}] \cdot \frac{\Delta z}{|\mu_s|}$$

$$W_{1M_s} = W_{in}(\Omega_s) \cdot [1 - \exp[-G_s u_f \frac{\Delta z}{|\mu_s|}]] \cdot T(\Omega_s, \Omega_v) \cdot \exp[-G_s u_f \frac{\Delta z - z_m}{|\mu_s|}]$$

Relative error $\varepsilon_1 = \frac{W_{1M_s} - W_{1\text{exact}}}{W_{1\text{exact}}}$ depends on scattering direction (Ω_v), incident direction (Ω_s), and layer LAD and LAI ($u_f \Delta z$). It does not depend on the scattering transfer function $T(\Omega_s, \Omega_v)$ and $\Delta \Omega_v$. Use of middle point (Figure 10) implies an overestimate of nadir reflectance ($\varepsilon_1 \leq 2\%$) and an underestimate of the energy scattered along the vertical downward direction ($\theta_v = 180^\circ$). Actually, ε_1 decreases if the number of cells used to build up the layer increases.

The error due to M_s is removed if we use a middle point $M_s(\Omega_v)$ per scattering direction that satisfies:

$$W_{1\text{exact}}(\Delta z, \Omega_s \rightarrow \Omega_v) = W_{1M_s}(\Delta z, \Omega_s \rightarrow \Omega_v)$$

For upward directions, the height of M_s is:

$$z_{m\text{exact}}(\Omega_v) = -\frac{|\mu_v|}{G_v u_f} \ln \left[\frac{\frac{G_s |\mu_v|}{G_v |\mu_s| + G_s |\mu_v|} [1 - \exp[-u_f \Delta z \cdot (\frac{G_v}{|\mu_v|} + \frac{G_s}{|\mu_s|})]]}{[1 - \exp[-G_s u_f \frac{\Delta z}{|\mu_s|}]]} \right]$$

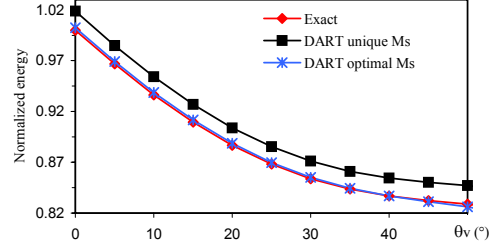


Figure 10: Exact and DART unique M_s and optimal $M_s(\Omega_v)$. $\theta_s = 70^\circ$. LAI = 1. Spherical LAD.

Second order expansion of z_{mM_s} and $z_{m\text{exact}}$ expressions

with the hypothesis $[\frac{G(\Omega_s)}{|\mu_s|} + \frac{G(\Omega_v)}{|\mu_v|}] u_f \Delta z \ll 1$, gives:

$$z_{mM_s} = \frac{\Delta z}{2} - \frac{G(\Omega_s) u_f \Delta z^2}{8 |\mu_s|}$$

$$z_{m\text{exact}}(\Omega_v) = \frac{\Delta z}{2} - \frac{2 G(\Omega_s) |\mu_v| + G(\Omega_v) |\mu_s|}{24 |\mu_s| |\mu_v|} u_f \Delta z^2$$

Thus, a unique M_s is exact at order one and inexact at order two. With a spherical LAD ($G(\Omega) = 0.5 \forall \Omega$), z_m is underestimated if $\theta_v < \theta_s$, which implies $W_{1\text{exact}} < W_{1M_s}$. As expected, $z_{m\text{exact}}$ and $z_{mM_s} \rightarrow 0$ if $u_f \rightarrow \infty$, then. Then, for upward directions (expressions are similar for downward directions):

$$W_{1\text{exact}}(\Delta z, \Omega_s \rightarrow \Omega_v) \rightarrow W_{in}(\Omega_s) \cdot T(\Omega_s, \Omega_v) \cdot \frac{G(\Omega_s) |\mu_v|}{G(\Omega_v) |\mu_s| + G(\Omega_s) |\mu_v|}$$

$$W_{1M_s}(\Delta z, \Omega_s \rightarrow \Omega_v) \rightarrow W_{in}(\Omega_s) \cdot T(\Omega_s, \Omega_v) \cdot \exp[-\frac{G(\Omega_v) |\mu_s| \ln(2)}{G(\Omega_s) |\mu_v|}]$$

Ideally, $z_{m\text{exact}}$ must be computed for each direction (Ω_v) and for each cell of the scene, which causes an unacceptable computational constraint due to the large number of scattering directions. A solution could be found because $z_{m\text{exact}}$ varies smoothly with θ_v : we define 2 mean points $M_s(z_{m\uparrow})$ and $M_s(z_{m\downarrow})$ for upward and downward directions, respectively. These points are exact only for specific upward $\Omega_{m\uparrow}$ and downward $\Omega_{m\downarrow}$ directions: $z_{m\uparrow} = z_{m\text{exact}}(\Omega_{m\uparrow})$ and $z_{m\downarrow} = z_{m\text{exact}}(\Omega_{m\downarrow})$. The sign of $[z_{m\text{exact}}(\Omega) - z_{m\text{exact}}(\Omega_m)]$ changes for $\theta = \theta_m$. Thus, W_1 is overestimated or underestimated if θ is larger or smaller than θ_m . When dealing with remote sensing

images, ε_1 must as small as possible for upward directions that are not too oblique. This depends on the choice of directions $\Omega_{m\uparrow}$ and $\Omega_{m\downarrow}$. For example, with $\theta_{m\uparrow}=40^\circ$, ε_1 is smaller than 0.3% for all directions with $\theta_v < 50^\circ$ (Figure 10). We found that optimal $z_{m\uparrow}$ and $z_{m\downarrow}$ are for $\theta_{m\uparrow}=20^\circ$ and $\theta_{m\downarrow}=160^\circ$. Thus, as expected, the use of two points M_s instead of only one improves the accuracy of scattering modeling.

4.3 Directional distribution of intercepted radiation

The assumption that multiple scattering radiation is due to an isotropic incident radiation implies that the vector source scattered along (Ω_v) is:

$$W_{\text{scat}}(\Omega_s, \Omega_v) = W_{\text{int}} \int_{4\pi} T(\Omega_s, \Omega_v) \cdot d\Omega_s$$

$$\text{Actually, it is: } W_{\text{scat}}(\Omega_s, \Omega_v) = \int_{4\pi} W_{\text{int}}(\Omega_s) \cdot T(\Omega_s, \Omega_v) \cdot d\Omega_s$$

Thus, simulations are erroneous except if DART scattering transfer function $T(\Omega_s, \Omega_v)$ is isotropic. We developed a method that improves this situation without increasing memory and computational time requirements. This method uses a schematic representation of the directional distribution of intercepted radiation. It partitions the space of propagation (4π) directions into N_{sect} angular sectors ($\Delta\Omega_{\text{sect},i}$). Indeed, any intercepted radiation $W_{\text{int}}(\Delta\Omega_{\text{sect},i})$ belongs to one of these sectors (Figure 11).

$$W_{\text{scat}}(\Omega_v) = \sum_{i=0}^{N_{\text{sect}}} \int_{\Delta\Omega_{\text{sect},i}} W_{\text{abs}}(\Omega_s) \cdot d\Omega_s \cdot \int_{\Delta\Omega_{\text{sect},i}} T(\Omega_s, \Omega_v) \cdot d\Omega_s$$

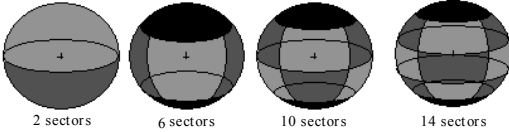


Figure 11: Partition of the space of propagation directions into 2, 6, 10 and 14 angular sectors ($\Delta\Omega_{\text{sect},i}$).

We studied how DART accuracy varies with N_{sect} . For that, we tested DART against a DART modified model that works with the Monte Carlo approach and the same landscape representation (Colas, 1998). This latter model is more accurate than DART because it computes multiple scattering as successive single scattering but its computational time is much larger.

First, tests took place in terms of RMSE (*Root Mean Square Error*) and ME (*Maximal Error*) with an homogeneous turbid medium. As expected, stronger differences occur if LAI layer is large and/or if

scattering transfer function is anisotropic (e.g., planophile LAD with $\rho_f \gg \tau_f$) with a very small soil reflectance ρ_s . Figure 12 shows RMSE and ME for an unfavorable case. As expected, errors decrease if N_{sect} increases, especially between $N_{\text{sect}}=1$ (i.e., incident isotropic radiation) and $N_{\text{sect}}=2$ (i.e., incident radiation along vertical upward and downward directions only).

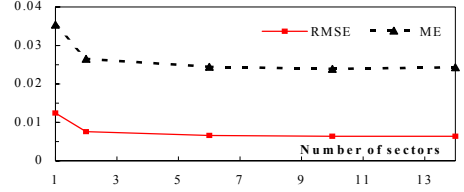


Figure 12: DART RMSE and ME, with N_{sect} from 1 to 14. $\theta_s = 20^\circ$. Homogeneous turbid layer with LAI=2, planophile LAD, $(\rho_f, \tau_f)=(45\%, 0\%)$ and $\rho_s=0\%$. Nadir reflectance $\approx 21\%$.

After one scattering, radiation angular distribution (Figure 13) is very anisotropic with very large values for θ close to 0° and very small for θ close to 180° . A similar anisotropy occurs for all odd scattering orders. Conversely, for even scattering orders (2, 4, 6, ...), upward radiation is weak whereas downward radiation is still large. The repetitive pattern of tendencies for odd and even scattering orders is mainly due to the planophile LAD and $\tau_f = 0$. At first scattering order, a minimum occurs in the principal plane for the *hot-spot* direction because rays single scattered along this direction are not intercepted by leaf turbid cells. This invalidates the hypothesis that multiple scattered radiation is isotropic. The associated error depends on many factors (e.g., LAD, LAI and canopy height). Figure 14 shows the incident radiation angular distribution at a leaf cell located at mid altitude in the canopy in the case $\{\theta_s = 0^\circ, \rho_f = \tau_f = 45\%, \text{LAI} = 2, \text{spherical LAD}\}$. Compared to the previous case study with a planophile LAD, the angular distribution of single scattered radiation is much more isotropic. Moreover, there is a vertical symmetry because sun radiation is vertical. Azimuthal variations are very small. Two maxima occur along directions $\theta = \pm 90^\circ$, because the number of interceptors increases along these directions. Moreover, the angular distribution of the absorbed radiation is constant for scattering orders larger than 3. Thus, results stress the need to account for the original direction of intercepted radiation for simulating scattering mechanisms with a good accuracy. Moreover, the choice of $N_{\text{sect}}=2$ proved to be a good trade-off (RMSE<0.01).

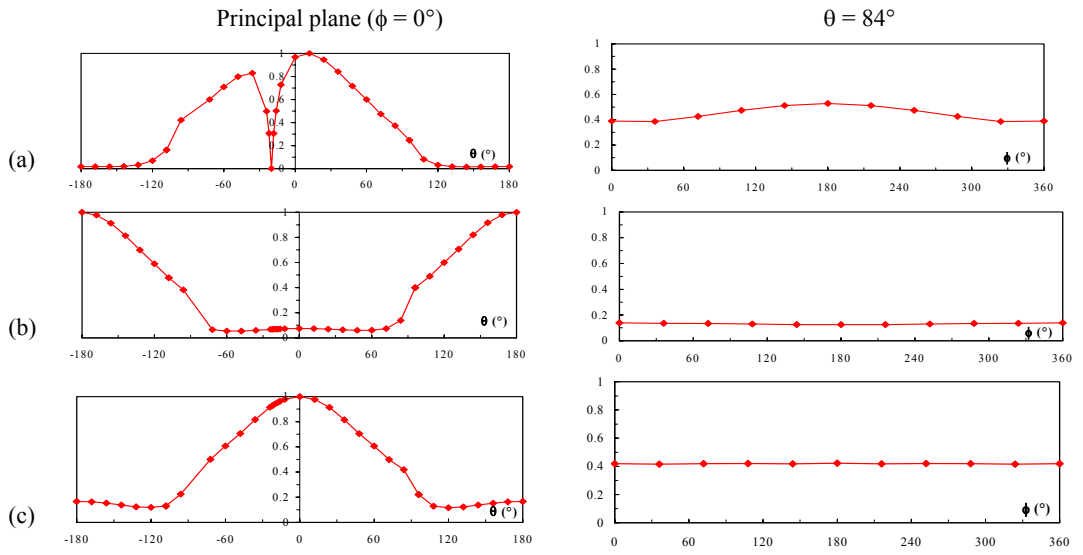


Figure 13: Normalized angular distribution of intercepted radiation after 1 (a), 2 (b) and 3 (c) scattering in the principal plane (left) and directions with a zenith angle " $\theta = 84^\circ$ ".

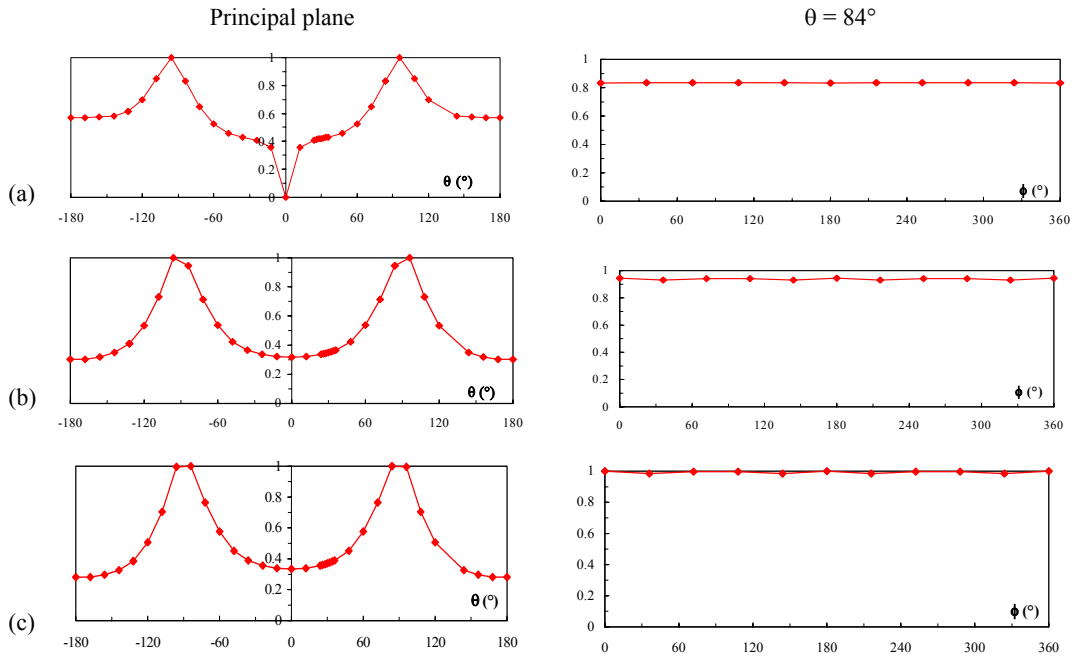


Figure 14: Normalized distribution of absorbed radiation after scattering orders 1 (a), 2 (b) and 3 (c) in the principal plane (left) and directions with a zenith angle $\theta = 84^\circ$.

For 3-D canopies with trees (*Figure 15*), the use of two sectors leads to larger errors (RMSE et ME), which implies the need to use a larger number of angular sectors. Indeed, the angular distribution of intercepted radiation is much more anisotropic. This is shown here for a leaf cell located on the external surface of a tree crown (*Figure 16*). Finally, simulations stressed that $N_{\text{sect}}=6$ is a good trade off between accuracy and computation time.

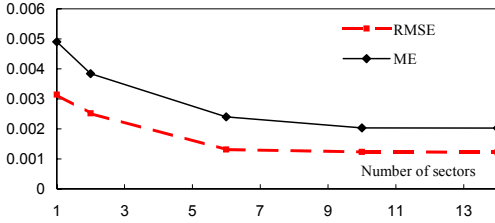


Figure 15: DART RMSE and ME, with the number of angular sectors. $\theta_s = 20^\circ$. Scene parameters in table 1. Nadir reflectance is $\approx 25.3\%$.

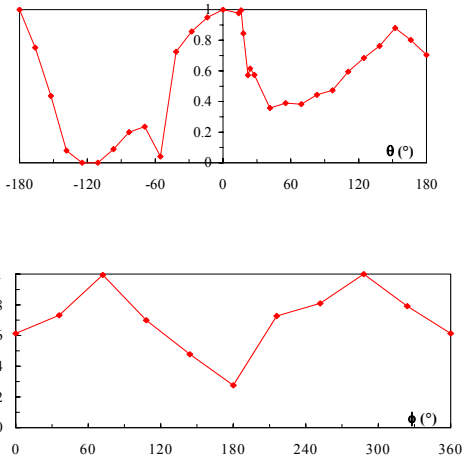


Figure 16: Normalized distribution of absorbed radiation after scattering orders 1 in the principal plane (up) and directions with a zenith angle $\theta = 84^\circ$ (down).

4.4 Geometric origin of scattered rays

In the 1996 DART model, leaf cells scatter rays from cell centers with an intensity computed as if rays come a unique middle point. The use of the center cell as the origin of rays allows one to pre-compute all possible paths which reduces a lot computational times.

However, this is a source of error because cell centers can be far from middle points, especially for very oblique rays (*Figure 17*).

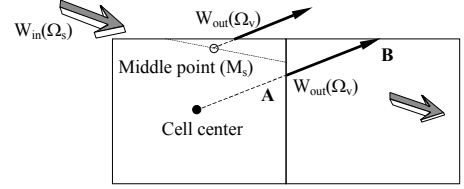


Figure 17: Error on scattered ray path.

Instead of the exact scattered ray $W_{\text{out}}(\Omega_v)$, the effective ray is attenuated along the path AB

This problem can be solved if we decrease the size of cells of the DART scene. Unfortunately, a decrease by a factor N increases a lot computational time. This becomes $T_{\text{comp}} \approx N^3 \cdot (D_1 + n \cdot D_n) + N \cdot (I_1 + n \cdot I_n + S_1 + n \cdot S_n)$ instead of $T_{\text{comp}} \approx D_1 + n \cdot D_n + I_1 + n \cdot I_n + S_1 + n \cdot S_n$, where n is the number of directions, D_1 and D_n are computational times for simulating scattering mechanisms at iterations 1 and n ($n > 1$) respectively, I_1 and I_n are computational times for simulating radiation interception at iterations 1 and n ($n > 1$) respectively. Terms S_1 and S_n are computational times for simulating radiation propagation at iterations 1 and n ($n > 1$) respectively. We adopted a solution that improves accuracy without increasing computational time: the point from which a ray originates is the closer point of M_s among a set of N_{sc}^3 nodes (P) that sample the cell (*Figure 18*). It pre-computes all ray paths for all N_{sc}^3 nodes. The associated computer memory requirement is not much increased because ray paths are computed as two successive ray paths:

- path from point P up to the next horizontal plane that comprises the upper or lower horizontal cell face.
- path from one of the N_{sf}^2 nodes that sample any horizontal cell face.

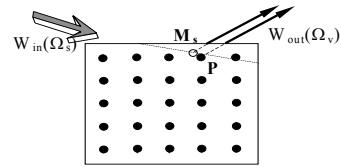


Figure 18 : Grid of points used as the origin of rays that are scattered by a turbid cell. The origin of the ray $W_{\text{out}}(\Omega_v)$ is (P) instead of (M_s)

This cell sampling with a set of points P is also used for simulating radiation propagation from cells associated to urban landscapes and topography.

Energy intercepted within these cells is scattered from the point P that is the closer to the actual interception point on the present opaque plane figure (Figure 19).

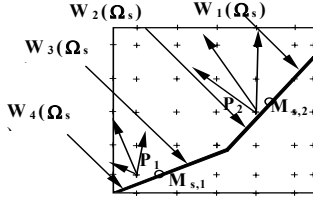


Figure 19: Interception of 2 rays by 2 opaque figures at points $M_{s,1}$ and $M_{s,2}$. Effective scattering originates from nodes P_1 and P_2 .

Tests were conducted to assess how DART accuracy varies if N_{sc} varies. Figure 20 shows results with $N_{sc} = 1, 3, 5$ and 7 . It stresses that the use of points P is always interesting if cell LAI is larger than one and if N_{sc} is larger than 3. Relative error can be decreased by more than 60%. Similar results were obtained with 3D covers such as forests. This illustrates the interest of points P as the origin of ray paths. Moreover, several tests stressed that the best trade-off is $N_{sc}=5$.

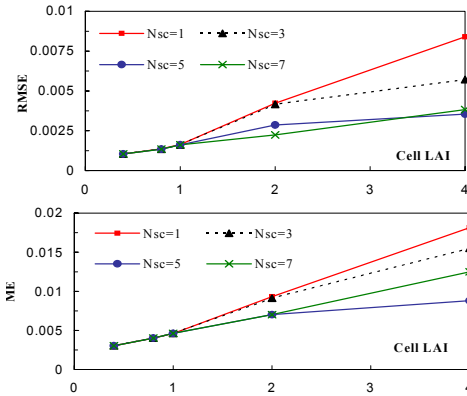


Figure 20: Scattering accuracy (RMSE and ME) of a turbid cell (erectophile LAD) with $N_{sc} = 1, 3, 5$ and 7 . Visible spectral domain. $\theta_s = 50^\circ$.

4.5 Accuracy improvement

With the aim to assess how the above mentioned improvements increased DART accuracy, the new DART model was compared to the 3-D reflectance models of the RAMI experiment (Figure 8). Figure 21 shows that differences decreased by a factor 3 in the NIR. For example, maximal difference decreased from 9.6% down to 3.0% for $\theta_s = 20^\circ$ and from 11.1% down to 3.2% for $\theta_s = 50^\circ$. This stresses the importance of the improvements that were brought to DART.

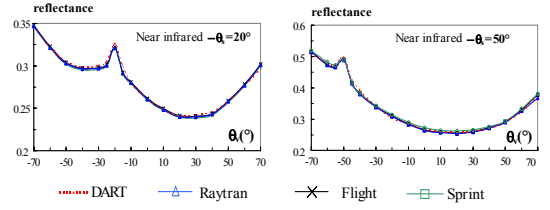


Figure 21: Comparison of the new DART model with three 3-D reflectance models. RAMI scene (Table 1). NIR case. $\theta_s = 20^\circ$ (left). $\theta_s = 50^\circ$ (right).

5 CONCLUSION

The 1996 version of the DART model was recently improved for broadening its domain of application. Presently, DART simulates radiative transfer simultaneously in the atmosphere and urban/vegetation landscapes, with or without topography. Urban landscapes (*i.e.*, houses, buildings, roads, etc.) and topography are simulated with plane elements (*i.e.*, triangles and parallelograms). DART works in the whole optical domain, including the mid infrared region around $3\mu m$. It does no more require the use of an atmospheric model because it simulates directly atmospheric radiative transfer. Atmosphere can have variable gas, aerosols and water profiles. A major feature of DART is to simulate images in the plane of the sensor, for different altitudes from the bottom to the top of the atmosphere. The simulation accounts for the sensor transfer function.

An important effort was dedicated to the improvement of DART accuracy. This was done thanks to a more accurate simulation of multiple scattering, with a sub-discretization scheme of the cells of the DART cell matrix and a better account of the original direction of radiation that is subsequently multiple scattered.

DART is now an efficient and accurate tool for studying 3-D natural and urban with remote sensing images acquired in the optical domain from the visible to the thermal infrared domain. In order to be also a computational effective tool, an industrial version of DART is planned to be developed next year.

References:

- Benech N., 2000, Modélisation des zones urbaines. DESS Multimédia, 125p, Univ. Bordeaux I, France.
- Boyat P., 2001, Modélisation du transfert radiatif dans le thermique. Rpt ENSICA, 115p, Toulouse, France.

- Dallest T., 2001, Modélisation du transfert radiatif atmosphérique dans l'infrarouge thermique. Rpt ENSHMG, 135p, France.
- Demarez V., 1997, Modélisation du transfert radiatif et télédétection hyperspectrale pour le suivi temporel de la teneur en chlorophylle d'une Forêt tempérée, PhD, Université Paul Sabatier, 156p, Toulouse, France.
- Gascon F., 2001, Modélisation physique d'images de télédétection optique, PhD, 156p, Univ. Paul Sabatier, Toulouse, France.
- Gascon F., Gastellu-Etchegorry J.-P., Lefevre M.J., 2001, Radiative Transfer Model for simulating High-Resolution Satellite Images. IEEE Transactions on Geoscience and Rem. Sens., 39(9), 1922-1926.
- Gastellu-Etchegorry JP, Demarez V, Pinel V, Zagolski F, 1996, Modeling radiative transfer in heterogeneous 3-D vegetation canopies, Rem Sens Envir, 58, 131-156.
- Gastellu-Etchegorry J.P., Guillevic P., Zagolski F., Demarez V., Trichon V., Deering D., Leroy M., 1999, Modeling BRF and radiation regime of tropical and boreal forests. Rem. Sens. Envir, 68, 281-316.
- Govaerts Y., and Verstraete M.M., 1998, Raytran : A Monte Carlo ray tracing model to compute light scattering in three-dimensional heterogeneous media. IEEE Trans. Geosc. and Rem. Sens., 36, 493-505.
- Guillevic P., Gastellu-Etchegorry J.P., 1997, Modeling BRF and radiation regime of Tropical and Boreal Forests, PAR regime. Rem. Sens. Envir, 68, 317-340.
- Kimes DS. and Sellers P.J., 1985, Inferring hemispherical reflectance of the Earth's surface for global energy budgets from remotely sensed nadir or directional radiance values. Rem. Sens. Environ., 18, 205-223.
- Mathiaud V., 2000, Modélisation Physique d'Images de Télédétection. Rpt Sup Aero, 115p, Toulouse, France.
- North P.R.J., 1996, Three-dimensional forest light interaction model using a Monte Carlo method, IEEE Trans. on Geoscience and Rem. Sens., 34, 946-956.
- Pinty B., Gobron N., Widlowski J.L., Gerstl S.A.W., Verstraete M.M., Antunes M., Bacour C., Gascon F., Gastellu-Etchegorry J.P., Jacquemoud S., North P., Qin W., Thompson R., 2001, Radiation transfer model intercomparaison (RAMI) exercice, J. Geophysical Research, 106, D11, 11937-11956.
- Syren P., 1994, Reflectance anisotropy for nadir observations of coniferous forest canopies. Rem. Sens. Envir., 16, 125-141.
- Thompson R.L. and Goel N.S., 1998, Two models for rapidly calculating bidirectional reflectance: Photon spread (ps) model and statistical photon spread (sps) model. Remote Sensing Reviews, 16, 157-207.

Development and Application of the SiSPAT-RS SVAT Model at Field Scale During the Alpilles-ReSeDA Experiment: Multiobjective Calibration in a Context of Remote Sensing Data Assimilation

J. Demarty (1,2,3), C. Ottlé (1), I. Braud (4), A. Olioso (2) and J.P. Frangi (3)

(1) CETP, 10-12 Avenue de l'Europe, 78140, Vélizy, FRANCE

(2) INRA-CSE, Avignon, FRANCE

(3) LED, Paris, FRANCE

(4) LTRE, Grenoble FRANCE and CEMAGREF, Lyon, FRANCE

jdemarty@avignon.inra.fr

ABSTRACT: *The Simple Soil-Plant-Atmosphere Transfer–Remote Sensing (SiSPAT-RS) model was developed for remote sensing data assimilation objectives. This version of the physically based SiSPAT model simulates (1) the main surface processes (energy fluxes, soil water content profiles, temperatures) and (2) remote sensing data in the visible, infrared and thermal infrared spectral domains. The model potentialities were investigated on a wheat field of the Alpilles-ReSeDA (Remote Sensing Data Assimilation) experiment. Then, a multiobjective approach was particularly performed in a context of remote sensing data assimilation in order to determine the parameters sets leading to a good simulation of the in situ brightness temperature and the surface soil water content. This methodology allows to combine both a sensitivity analysis and a calibration procedure. The sensitivity analysis results revealed different influential parameters according to the contrasted environmental conditions. In the calibration phase, it was showed that it was possible to optimise simultaneously several input parameters, notably soil hydrodynamic parameter. Moreover, the consequences of the calibration procedure on the simulated surface fluxes were particularly investigated. Results allowed for the use of the physically based SVAT model without a priori information about soil hydrodynamic properties.*

1 INTRODUCTION

Soil Vegetation Atmosphere Transfer (SVAT) models describe energy and water exchanges between the soil, the vegetation and the atmosphere. The understanding and the quantification of these biophysical processes are important for meteorological, agronomical and hydrological purposes. SVAT models require a large set of input parameters and initial state variables that are spatially and temporally distributed. In general, model complexity and the number of parameters increase simultaneously. Because of parameter uncertainties and model structure errors, SVAT models need to be calibrated and regularly corrected. The remote sensing ability to provide information about surface properties is an attractive tool for this purpose. It requires the coupling of the SVAT model with radiative transfer models in order to simulate both surface processes and remotely sensed data, such as directional reflectances, thermal infrared brightness temperatures, passive microwave brightness temperatures or radar backscattering coefficients. Assimilation of remote

sensing data in SVAT models has been investigated in recent studies. For instance, Burke et al. (1997, 1998) calibrated soil hydraulic properties from L band passive brightness temperature measurements in a soil water and energy budget (SWEAT) model, coupled with a microwave emission model (MICRO). Calvet et al. (1998) and Calvet and Noilhan (2000), investigated on the use of microwave remote sensing data, for retrieving initial soil water content by assimilation of surface soil moisture measurements in the ISBA model (Noilhan and Planton, 1989; Noilhan and Mahfouf, 1996).

This paper presents part of different research efforts carried out to assimilate remotely sensed data into a SVAT model. The Simple Soil Plant Atmosphere Transfer – Remote Sensing (SiSPAT-RS) model was developed for this purpose. It simulates soil-vegetation-atmosphere energy and water transfers as well as remote sensing measurements at the field scale, in visible-infrared and thermal infrared spectral domains. The aim of this study was to perform model calibration with little a priori information about soil and vegetation properties. A common step towards this

objective was the determination of influential parameters for given environmental and climatic conditions. To assess the model sensitivity to variations or uncertainties on its main input parameters, we used a multiobjective framework (Gupta *et al.*, 1998) in a context of remote sensing data assimilation. This methodology was applied on the SiSPAT-RS model, with data collected on a wheat field of the Alpilles-ReSeDA (Remote Sensing Data Assimilation) experiment.

2 MULTIOBJECTIVE CALIBRATION AND SENSITIVITY ANALYSIS

The calibration in land surface modeling is generally considered as the determination of a single optimum parameter set, allowing the "best" simulation of several output variables. Due to errors in model structure and parameter uncertainties, the determination of a such optimum single set is generally impossible. Relatively, little work focused on the errors caused by parameter uncertainty (Leplastrier *et al.*, 2002). In this objective, the multiobjective framework was developed by Gupta *et al.* (1998). It was already applied in many recent applications (Gupta *et al.*, 1999; Bastidas *et al.*, 1999; Madsen, 2000; Boyle *et al.* 2000, 2001; Houser *et al.*, 2001, Leplastrier *et al.*, 2002, Demarty *et al.*, 2002 b; 2002 c).

In the multiobjective framework, the model calibration is envisaged on series of Monte Carlo simulations. That is conducted by randomly sampling over a feasible parameter space defined by establishing upper and lower limits for the possible values of each parameter. The model performances are then determined estimating the distance between observations and the simulated variables, i.e. defining one or many objective functions.

The next step consists to partition the simulation the sample into two regions, called "acceptable" and "non-acceptable" regions. In the case where only one objective function is considered, that can simply be done choosing a threshold value for single objective function. In the case of multiobjective approach, however, many objective functions are considered. It becomes necessary to introduce two main notions. First, the notion of Pareto set allows to isolate in the sample the particular parameter sets which cannot be distinguished in terms of model performance. In this particular set, also called the "solution set", none of the set is better than the other in terms of all objective functions in a mathematical sense. In other terms, each solution of Pareto set improves one or several criterion while causing deterioration of another. However, in a physical sense, it is important to note that the particular solutions of the Pareto set which privilege single criteria to the detriment of the others ones can

be less attractive. It is possible to avoid these solutions of the Pareto set choosing threshold values for each single criteria. Leplastrier *et al.* (2002) used this methodology to isolate simulations of the Pareto set that lead best compromise between single criteria. Representative threshold values can be chose according to the errors in observations. Second, the notion of Pareto ranking (Goldberg, 1989) allows to assign a rank to each points of the sample, representing their individual superiority in the multicriteria sense. Setting aside a Pareto set (combining or not with threshold values) and attributing the rank 1, it consisted to determine the new Pareto set of the remaining set and to attribute rank 2. Finally, all the points of the sample can be ranked following the same procedure. Examples of the Pareto set and the Pareto ranking can be found in many papers (Gupta *et al.*, 1998; Bastidas *et al.*, 1999; Houser *et al.*, 2001; Demarty *et al.*, 2002 b and c).

Finally, the choice of a Pareto rank as threshold allows to partition the sample into final acceptable and non-acceptable regions. The statistical analysis of each parameter distributions between these two sets allows to assess model sensitivity to its input parameters (Bastidas *et al.*, 1999), but also to perform model calibration, optimizing each sensitive parameters. For instance, Demarty *et al.* (2002 b) calibrated the SiSPAT-RS model using a manual optimization of many sensitive parameters on their associated preferred range. However, the detected preferred ranges of sensible parameters can still be relatively large and the number of parameters can be important. That implies that the manual optimization can be relatively complex and subjective. Previous authors reduced the dimensionless of the optimization problem considering *a priori* specification of retention curves parameters on their respective preferred ranges. As a consequence, Demarty *et al.* (2002 c) proposed to use a simple iterative procedure in order to both avoid complex manual calibration and simultaneously optimize all the sensible parameters, as the retention curve parameters. It consists to repeat the above-described steps; i.e. (1) generate a set of simulations, (2) perform the model sensitivity analysis and finally (3) determine the preferred range of sensitive parameters in order to generate a new set of simulations accounting for the new parameters ranges. The implementation of a such procedure is quite simple. Moreover, it allows to estimate the model error due to parameter uncertainties after each iteration. For instance, in the context of this study where only potential remotely sensed variables will be considered to calibrate the model, it will be particularly interesting to determine the impact of this calibration procedure in terms of simulated surface fluxes.

3. CASE STUDIES

This multiobjective calibration procedure was applied on the SiSPAT-RS model in a context of remote sensing data assimilation. Thus, only the water content of the upper five soil centimeters (W_{05}) and the local directional brightness temperature (T_b) were retained as single criteria to calibrate the SVAT scheme. The calibration was performed on the wheat field numbered 101 of the Alpilles-ReSeDA experiment. Objective functions associated to each individual variable were defined as the RMSE (see Eq. 1.) between observed and model-simulated variables, from 7am to 4pm.

$$RMSE(\theta) = \sqrt{\frac{1}{n} \sum_{i=1}^n (Z(\theta, t) - O(\theta, t))^2} \quad (1)$$

where Z represents the modeled variable, O the observations, n the total number of available observations and θ a particular set of model parameters. Observations can be issued from ground measurements, remote sensing data or a reference simulation.

In this work, two successive multiobjective approaches were particularly conducted. First, in order to analyze model sensitivity in different context, the multiobjective calibration were first applied on two specific time periods related to the available ground observations. The main goals of this step was to determine parameters that are possible to retrieve from remotely sensed observations in relation to the various environmental conditions and vegetation stages. The first period (DOE 440-460; March 15 to April 4, 1997), corresponds to a regular soil drying, without precipitation, during the wheat-growing period. A very dry soil and a well-developed canopy characterize the second sub-period (DOE 505-517; May 19-31). Then, the second step consisted to test the iterative calibration procedure on the 20 days first period (DOE 440-460), notably accounting for the preferred range whose found in the previous step.

3.a. Soil-Vegetation-Atmosphere Transfer model

The SiSPAT model (Braud *et al.*, 1995; Braud, 2000) with a Remote Sensing (SiSPAT-RS) module (Demarty, 2001, Demarty *et al.*, 2002 a) was especially used in this study. It is composed by the coupling of SiSPAT with two radiative transfer models in the visible-infrared spectral domain and in the thermal infrared domain. The SVAT model describes vertical heat and water exchanges within the soil-plant-atmosphere continuum. It is a two-layers (soil and vegetation) SVAT model (Figure 1). The soil column is described as a juxtaposition of horizontal horizons, characterized by different thermal and

hydraulic properties. Each horizon is divided in several soil layers. The module solves the coupled heat and mass transfer equations including vapor phase and water extraction by roots (Milly, 1982). Specifications of retention curve and hydraulic conductivity parameterizations for each horizon in terms of volumetric water content are necessary. Water extraction from the soil is parameterized using a resistance model developed by Federer (1979), considering that plant transpiration equals the root extraction. The vegetation is composed by a green and a layer vegetation layers, each of them being described by optical properties and an Organ Area Index. It was assumed that the yellow vegetation layers does not contribute to the plant transpiration. The sensible and latent heat fluxes (respectively H and LE) are expressed using an electrical analogy. The bulk stomatal resistance (r_s) is computed following Jarvis (1976) in terms of environmental factors, as incoming solar radiation, vapor pressure deficit and leaf water potential. The three required aerodynamic resistances (r_{as} , r_{bv} , r_a) are determined using wind profile parameterizations inside and above the canopy proposed by Shuttleworth and Gurney (1986). For a more complete description of the SiSPAT model, see Braud *et al.* (1995) and Braud (2000).

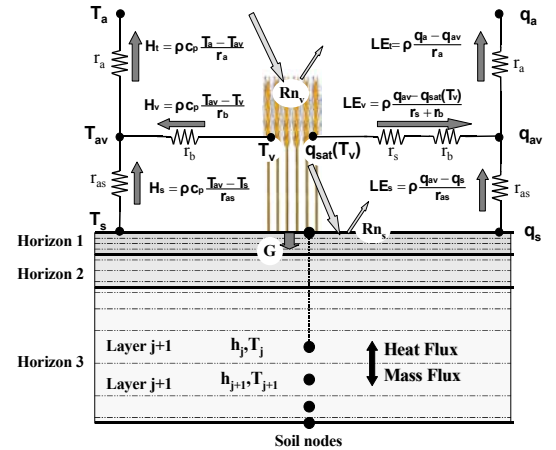


Figure 1: Schematic representation of the energy processes in SiSPAT model: Net radiation (R_n), soil heat conduction (G), sensible and latent heat fluxes (H and LE), bulk stomatal resistance (r_s) and aerodynamic resistances (r_{bv} , r_{as} , r_a), temperatures (T) and specific humidity (q). Subscript s , v and tot refer to the soil, vegetation and total contributions respectively, a to the reference height measurements above the canopy and av to the fictive level inside the canopy

3.b Data set

The data set collected on wheat field numbered 101 of the Alpilles-ReSeDA experiment (Oliosio *et al.*, 2001; 2002) was especially used in this study. This experiment focused on agricultural land and practices. Therefore, a small agricultural area characterized by a large diversity of crops (wheat, sunflower, alfalfa) was instrumented and monitored during one year to document the whole crop cycle. It was located near Avignon, France, (N43°47', E4°45') and the experiment lasted from October 1996 to November 1997. A very flat area, with large enough agricultural fields (200m by 200m) characterized the site. Atmospheric forcing was measured in the middle of the experimental area, over a bare soil surface with a 15 seconds time step and an averaging period of 20 minutes. More specifically to the wheat field 101, soil properties were estimated at several depths along the soil profile, including particle size data analysis, infiltration tests and dry bulk density measurements. The Organ Area Index (OAI) and the cover height were acquired regularly during the crop cycle and daily interpolated. Several initial and modeled output variables were observed, such as soil moisture down to a depth of 140cm, energy and mass fluxes and local thermal infrared brightness temperatures. Eddy correlation and Bowen ratio methods were implemented to assess latent and sensible heat fluxes. The first method was used to validate the second one, and was only implemented over the short period studied. Unfortunately, "failures in the Bowen ratio method instrumentation were frequent, generating error in the system for measuring vapor and temperature gradients which did not allow to compute fluxes with a good accuracy" (Oliosio *et al.*, 2002).

3.c Modeling strategy

According to Demarty *et al.* (2002 b), the soil column was modeled by 3 different soil horizons, corresponding to the 0-10 cm soil depth (denoted H1 hereafter), 10-30 cm (H2) and 30-200cm (H3). The retention and hydraulic conductivity curves were parameterized using the Van Genuchten (1980) model and the Brooks and Corey (1964) model. The model sensitivity to the variations of 60 parameters and initial variables were particularly investigated in Step 1; see Demarty *et al.* (2002 b). However, in Step 2 (testing of the iterative procedure), we particularly chose to impose the cover height, the green and yellow OAI and the root profile to the ground observations, in order to focus principally on the calibration of soil hydraulic properties and vegetation parameters. Consequences of a such assumption will be particularly discussed in the section 5. As a consequence, only 35 parameters (23 for soil, 12 for

vegetation) were particularly investigated in Step 2. List of the 35 parameters and their associated boundary range can be found in Demarty *et al.* (2002 c).

4 RESULTS

4.1. First step results: Periods 440-460 and 505-517

Figure 2 presents the model sensitivity to the 35 parameters considered in Table 1 for the two time periods. The top and bottom subplots show results for the joint multiobjective analysis (Pareto ranking + threshold values) and the single-objective analyses, respectively. A vertical bar indicates the relative sensitivity in terms of probability result of the K-S test. The horizontal dashed lines indicate the considered transition levels between "high" (top part), "medium" (intermediate part) and "low" (bottom part) model sensitivity (Bastidas *et al.*, 1999).

Concerning the first period (Figure 2a), multi-objective sensitivity results (top) show 9 sensitive parameters, of which 5 are related to soil (W_{sa1} , K_{s3} , La_1 , La_2 , $Emis$) and 4 are related to the vegetation (R_{sm} , R_p , PFC , $Emif$). In relation to the environmental and climatic conditions, we found a significant impact of parameters controlling stomatal regulation and water exchanges on the deep soil layers. On the other hand, it is important to note that the model is particularly insensitive to retention curve parameters. That is due to the fact that the surface fluxes are no considered as single-objective criteria in the sensitivity analysis (Demarty *et al.*, 2002 b). This lack of sensitivity is partially compensated by single-objective sensitivity analyses (bottom part). For example, the model is sensitive to the soil properties (hg_1 , n_3 , K_{sa1}).

For the second period (Figure 2b), multiobjective sensitivity subplot indicates 10 sensitive parameters, of which 8 are related to the soil (W_{sa1} , hg_1 , n_1 , K_{s1} , La_1 , La_2 , La_3 , $Emis$) and only 2 are related to the vegetation (R_{sm} , $Emif$). The predominance of these parameters is consistent with the climatic and environmental conditions. In general, all the soil parameters of horizon 1 induced a high model response. More specifically, the parameter n_B becomes a predominant parameter in the retention curve and the hydraulic conductivity functions according to the observed dry conditions. Concerning vegetation parameters, the minimum stomatal resistance have a high influence. Single-objective sensitivity analysis shows that it play a role on the simulation of the brightness temperature. Finally, on this period, the account of $\{T_b\}$ and $\{W_{05}\}$ as single criteria allows to assess water exchanges near underlying soil surface as well as in deeper soil layers.

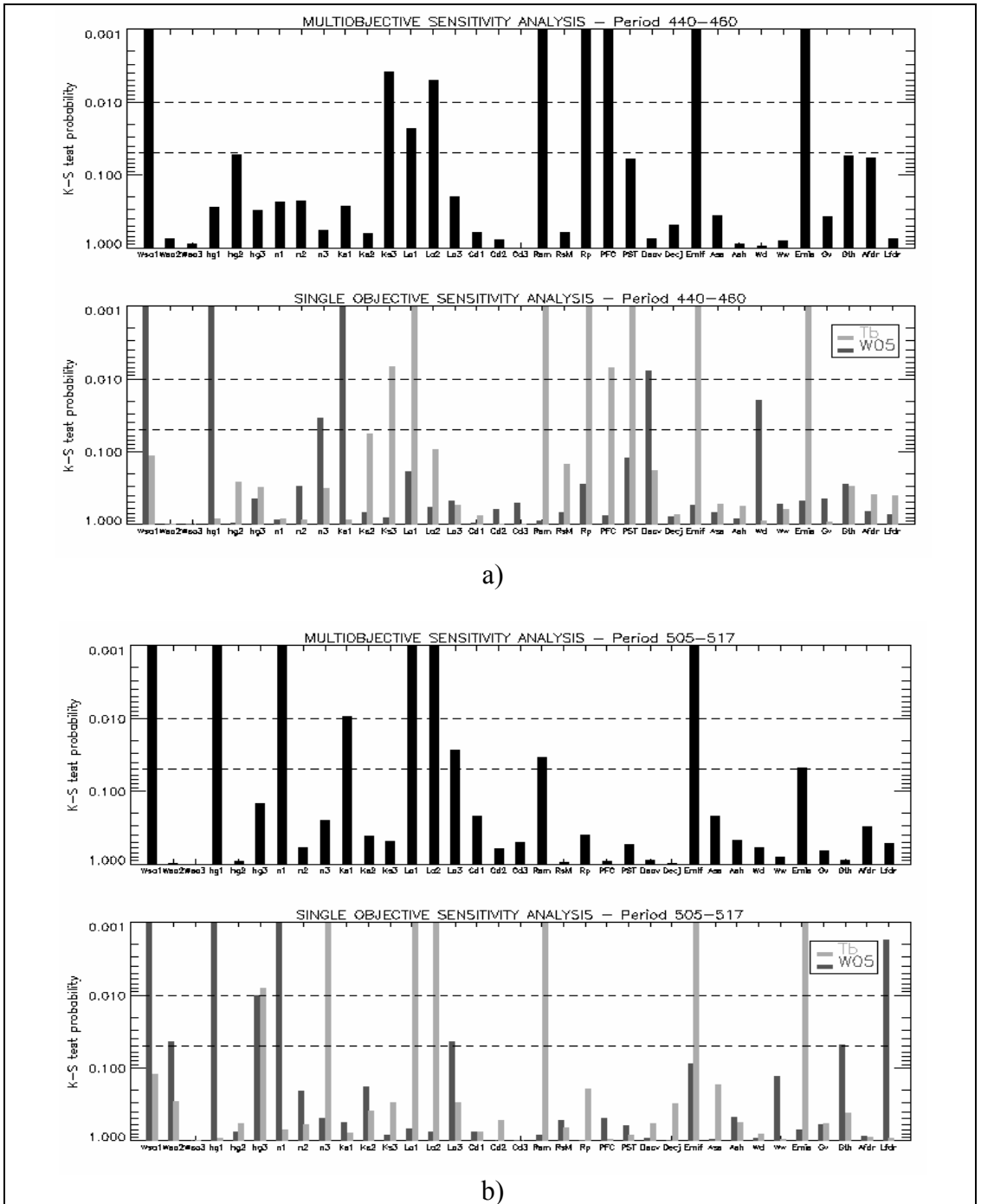


Figure 2: Multiobjective SiSPAT-RS model sensitivity to the 35 parameters considered in the calibration procedure on the periods DOE 440-460 (a) and DOE 505-517 (b). Vertical bars indicate relative sensitivity of parameters in terms of probability result of the K-S test. Horizontal dashed lines indicate transition levels between "high" (above 0.01), "medium" (between 0.01 and 0.05) and "low" (under 0.05) sensitivities.

4.2. Second step results: Iterative procedure on period 440-460

The iterative procedure was tested on the first period 440-460 to perform better optimization of the 35 parameters. In this context, two new samples were successive done, representing respectively the second and the third iterations of the calibration procedure.

4.2.1 Iterative calibration procedure performance

Figure 3 presents calibration procedure results in terms of the RMSE of the upper five soil centimeters (W_{05}) and of the local brightness temperature (T_b). On each subfigure, "acceptable" (black asterisk *) and "non acceptable" (gray square) simulations obtained after the Pareto ranking and threshold step are distinguished. Considered threshold values for T_b and W_{05} are also observable (1.2 K and $0.025 \text{ m}^3.\text{cm}^{-3}$). Two main results are shown on Figure 3. First, the performance of the procedure increases in relation

to the successive iterations. For the third iteration, the 2000 simulations provide comparative results in terms of RMSE, indicating that the number of iteration realized is enough. The second result concern the systematic low RMSE obtained for T_b for each iteration (around 0.9 K). The origin of this systematic error can not be attributed to parameter uncertainties, but exclusively to observations or model structure errors. In oppose sense, many sets of parameters lead a very low RMSE of W_{05} (near $0.0 \text{ m}^3.\text{m}^{-3}$). It seems relatively much easy to control this variable, especially since both the initial water content are known and the studied simulation period is relatively short and characterized by a regular soil drying.

4.2.2. Consequences on the simulated surface fluxes

Figure 4 presents the results in terms of the RMSE of the sensible (H) and latent (LE) heat fluxes on the period 440-460, for each iteration. The simulated surface fluxes H and LE improve in relation

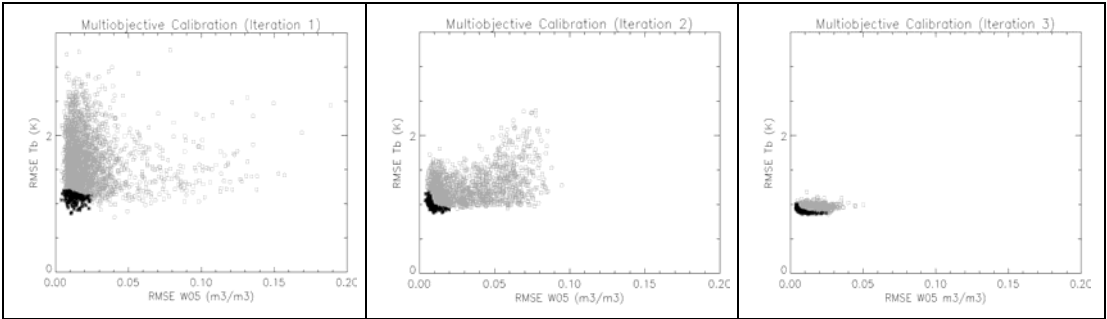


Figure 3: Multiobjective calibration results in terms of RMSE of the surface water content (W_{05}) and the local brightness temperature (T_b).

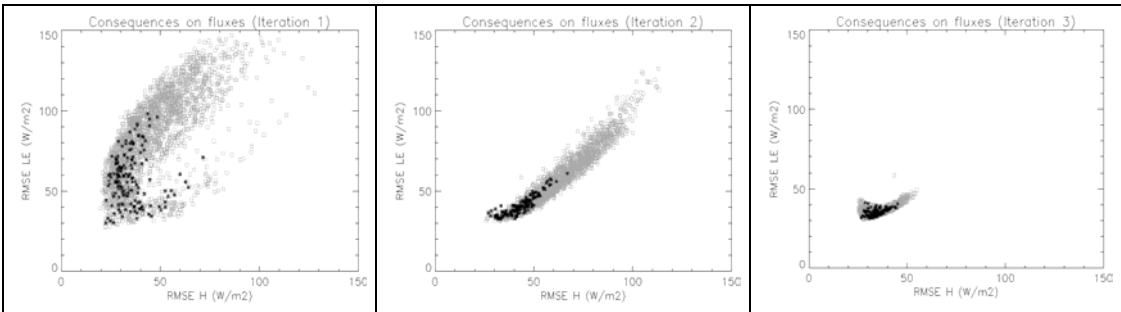


Figure 4: Consequences of the multiobjective calibration on the RMSE of the sensible (H) and latent (LE) heat fluxes.

to the iterations. In relation with the climatic conditions, it is clearly shown that the calibration of the surface water content and the brightness temperature using ground observations allow to improve the simulation of the surface fluxes. Quantitatively, the dispersion of the RMSE of the acceptable simulations (black asterisks) move from 50-70 W.m⁻² to 10-20 W.m⁻². Nevertheless, a systematic RMSE comprised between 20-30 W.m⁻² was obtained on H and LE.

5 CONCLUSION

This paper focused on physically based SVAT model calibration at field scale in a context where (1) no *a priori* parameter information was available, especially for soil description and (2) only calibration variables are brightness temperature and surface soil water content. To achieve this objective, the Simple Soil Plant Atmosphere Transfer – Remote Sensing (SiSPAT-RS) SVAT model was developed to simulate main surface processes (energy fluxes, soil water content, temperatures) and remote sensing observations in the visible-infrared and thermal infrared spectral domains. The calibration procedure of the SiSPAT-RS model was performed using a multiobjective approach. In this sense, the methodology proposed by Gupta *et al.* (1999) and Bastidas *et al.* (1999) was adapted to SiSPAT-RS. It permitted to determine parameter sensitivity on many simulated variables. Also it allowed a significant reduction in the associated uncertainty ranges of sensitive parameter for the model calibration. This methodology was applied on a short period of ReSeDA wheat field number 101. Finally, results indicated that it is possible to calibrate a rather complex model without *a priori* information on soil structure. Notably, the iterative calibration procedure permits to optimize simultaneously several sensitive parameters. Moreover, the brightness temperature and the surface soil water content provide complementary information on soil and vegetation properties, notably for the soil retention parameters which have a high spatial variability and play an important role in physically based SVAT models.

6 ACKNOWLEDGEMENTS

The authors would like specially to thank all the partners of the ReSeDA program for providing ground truth data. This work was supported by the INSU/CNRS French national programs (PNRH and PNTS).

7 REFERENCES

- Bastidas L.A., Gupta H.V., Sorooshian S., Shuttleworth W.J. and Yang Z.L., Sensitivity analysis of a land surface scheme using multicriteria methods, *Journal of Geophysical Research*, 104 (D16), 19,481-19,490, 1999.
- Boyle D.P., Gupta H.V., Sorooshian S., toward improved calibration of hydrologic models: combining the strengths of manual and automatic methods, *Water Resources Research*, 36, 12, 3663-3674, 2000
- Boyle D.P., Gupta H.V., Sorooshian S., Koren V., Zhang Z. and Smith M., Toward improved streamflow forecasts: Value of semidistributed modeling, *Water Resources Research*, 37, 11, 2749-2759, 2001
- Braud I, SiSPAT, a numerical model of water and energy fluxes in the soil-plant-atmosphere continuum. Version 3.0, SiSPAT user's manual, 107 p, 2000, (<http://www.lthe.hmg.inpg.fr>)
- Braud I., A.C. Dantas-Antonino, M. Vauclin, J.L. Thony, and P. Ruelle, A simple soil-plant-atmosphere transfer model (SiSPAT) development and field verification, *Journal of Hydrology*, 166, 213-250, 1995a.
- Brooks, R.H., and A.T. Corey, Hydraulic properties of porous media, Colorado University, Fort Collins, 1964.
- Burke E.J., R.J. Gurney, L.P. Simmonds, and P.E. O'Neill, Using a modeling Approach to Predict Soil Hydraulic Properties from Passive Microwave Measurements, *IEEE Transactions on Geoscienc and Remote Sensing*, 36 (2), 454-462, 1998.
- Burke, E.J., R.J. Gurney, L.P. Simmonds, and J.T. J., Calibrating a soil water and energy budget model with remotely sensed data to obtain quantitative information about the soil, *Water Resour. Res.*, 33, 1689-1697, 1997.
- Calvet J.-C., J. Noilhan, and P. Bessmoulin, Retrieving the Root-Zone Soil moisture from Surface Soil moisture or temperature Estimates: A Feasibility Study Based on Field Measurements, *American Meteorological Society*, 1998.
- Calvet, J.C., and J. Noilhan, From near-surface to root-zone soil moisture using year-round data, *Journal of Hydrometeorology*, 1, 393-411, 2000.
- Deardorff, J.W., Efficient prediction of ground surface temperature and moisture, with inclusion of a layer of vegetation, *Journal Geophys. Res.*, 83, 1889-1903, 1978.
- Demarty J., Otlé C., François C., Braud. I and Frangi J.P., Effect of aerodynamic resistance modeling on SiSPAT-RS simulated surface fluxes, *in press, Agronomie*, 2002 a
- Demarty J., Otlé C., François C., Braud. I, Frangi J.P., Bastidas L. and Gupta H.V., Using a

- multiobjective sensitivity analysis to calibrate the SiSPAT-RS model, *submitted in Journal of Hydrology*, 2002 b
- Demarty J., Otlé C., François C., Braud. I, Frangi J.P., Bastidas L. and Gupta H.V., Multiobjective calibration of a physically based SVAT model in a context of remote sensing data assimilation, *to be submitted in Water Resources Research*, 2002 c
- Federer C.A., A Soil-Plant-Atmosphere Model for Transpiration and Availability of Soil Water, *Water Resources Research*, 15 (3), 555-562, 1979.
- Fuentes, C., R. Haverkamp, and J.Y. Parlange, Parameter constraints on closed-form soil water relationships, *Journal of Hydrology*, 134, 117-142, 1992.
- François, C., The potential of directional radiometric temperatures for monitoring soil and leaf temperature and soil moisture status, *Remote Sens. Environ.*, 79, 1-12, 2001.
- Goldberg, D.E., *Genetic algorithms in Search. Optimization and Machine Learning*, Addison-Wesley, Reading, Mass., 1989
- Gupta, H.V., L.A. Bastidas, S. Sorooshian, W.J. Shuttleworth, and Z.L. Yang, Parameter estimation of a land surface scheme using multicriteria methods, *Journal of Geophysical Research*, 104 (D16), 19,491-19,503, 1999.
- Gupta, H.V., S. Sorooshian, and P.O. Yapo, Toward improved calibration of hydrologic models: Multiple and non-commensurable measures of information, *Water Resources Research*, 34 (4), 751-763, 1998.
- Jarvis, P.G., The interpretation of the variations in leaf water potential and stomatal conductance found in canopies in the field, *Philos. Trans. R. Soc. London, Ser.B*, 273: 593-602, 1976
- Milly, P.C.D., Moisture and Heat Transport in hysteretic inhomogeneous porous media: a matrix head-based formulation and a numerical model, *Water Resources Research*, 18, 489-498, 1982.
- Noilhan J., and J.-F. Mahfouf, The ISBA land surface parameterisation scheme, *Global and Planetary Change*, 13, 145-159, 1996.
- Noilhan J., and S. Planton, A simple parameterization of land surface processes for meteorological models, *Mon. Wea. Rev.*, 117, 536-549, 1989.
- Olioso, A., Braud, I., Chanzy, A., Demarty, J., Ducros, Y., Gaudu, J. C., Gonzales-Sosa, E., Jacob, F., Lewan, L., Marloie, O., Otlé, C., Prévot, L., Thony, J. L., Autret, H., Bethenot, O., Bonnefond, J. M., Bruguier, N., Buis, J.P., Calvet, J.C., Caselles, V., Chauki, H., Coll, C., Gouget, R., Jongschaap, R., Kerr, Y., King, C., Lagouarde, J. P., Laurent, J. P., Mc Aneney, J., Moulin, S., Rubio, E., Weiss, M. and Wigneron, J. P. SVAT modeling over the Alpillles-ReSeDA experiment : Experimental setup for monitoring energy and mass transfers, *submitted to Agronomie*, 2002 a
- Olioso, A., Braud, I., Chanzy, A., Courault, D., Demarty, J., Kergoat, L., Lewan, E., Otlé, C., Prévot, L., Zhao, W., Calvet, J.C., Cayrol, P., Jongschaap, R., Moulin, S., Noilhan, J. and Wigneron, J.P. SVAT modeling over the Alpillles-ReSeDA experiment: Comparison of SVAT models, first results on wheat, *submitted to Agronomie*, 2002 b
- Olioso, A., Y. Inoue, J.P. Wigneron, S. Ortega-Farias, P. Lecharpentier, M. Pardé, J.C. Calvet, and O. Inizan, Using a coupled crop-SVAT model to assess crop canopy processes from remote sensing data, in *IGARSS, Sydney, Australia*, 2001.
- Shuttleworth W.J., and R.J. Gurney, The theoretical relationship between foliage temperature and canopy resistance in sparse crops, *Q. R. J. Meteorol. Soc.*, 116, 497-519, 1990.
- Van Genuchten M.T., A Closed Equation for Predicting the Hydraulic Conductivity of Unsaturated Soils, *Soil Sci. Soc. Am. J.*, 44, 892-898, 1980.
- Verhoef, W., Light scattering by leaf layers with application to canopy reflectance modelling: the SAIL model, *Remote Sens. Environ.*, 16, 125-141, 1984.
- Verhoef, W., Earth Observation Modeling based on layer scattering matrices, *Remote Sens. Environ.*, 17, 165-178, 1985.
- Weiss, M., D. Troufleau, F. Baret, H. Chauki, L. Prévot, A. Olioso, N. Bruguier, and N. Brisson, Coupling canopy functioning and radiative transfer models for remote sensing data assimilation, *Agricultural and Forest Meteorology*, 108, 113-128, 2001.

Mapping surface sensible heat flux from thermal infrared and reflectances data using various models over the Alpilles test site

A. Olioso⁽¹⁾, C. Hasager⁽²⁾, F. Jacob⁽³⁾, T. Wassenaar⁽¹⁾, A. Chehbouni⁽⁴⁾, O. Marloie⁽¹⁾, P. Lecharpentier⁽¹⁾, D. Courault⁽¹⁾

⁽¹⁾ INRA-CSE, Domaine Saint-Paul, 84914 Avignon Cedex 9, FRANCE; olioso@avignon.inra.fr

⁽²⁾ Risoe National Laboratory, Wind Energy Department, Roskilde, DANEMARK

⁽³⁾ USDA/ARS Hydrology and Remote Sensing Laboratory, Beltsville, MD, USA

⁽⁴⁾ CESBIO (CNES-CNRS-IRD-UPS), Toulouse, FRANCE

ABSTRACT: Maps of surface sensible heat flux were generated from remote sensing images over the Alpilles test site in the South of France using various models : a direct flux equation using surface temperature, air temperature, wind speed and surface roughness; the SEBAL model (Bastiaanssen et al. 1998a) which computed the wind speed and the air temperature by using the spatial variation of albedo and surface temperature; a microscale aggregation model (Hasager and Jensen 1999) which consists in a linearized version of the atmospheric flow equation in two dimensions in the horizontal domain. It is shown that most of the differences between model results were due to differences in the way surface parameters and meteorological variables were obtained. Among these inputs, momentum and thermal roughness lengths, as well as air temperature had the most significant impact on flux estimations.

1 INTRODUCTION

Mapping surface energy fluxes is an important step for the estimation of evapotranspiration or for assessing the water status of plant canopies and soils over agricultural landscapes. Many of the land surface properties that drive the energy exchanges at the soil - vegetation - atmosphere interface can be obtained using remote sensing systems: surface temperature, albedo, fraction of vegetation cover and Leaf Area Index (e.g. Jacob et al. 2002a, b and c, Weiss and Baret 1999). If these variables are used as input of models that describe the energy balance of the terrestrial surface, it becomes possible to map the energy transfers (e.g. Soer 1980, Kustas et al. 1994, Courault et al. 1994, Gillies et al. 1997, French et al. 2002). Many models have been developed to estimate surface energy fluxes from remote sensing data according to the available information (see Zhan et al. 1996, Olioso et al. 1999).

In this study, three models of sensible heat flux that differ either by the parameterization of flux or by the way of prescribing input parameters are compared over the Alpilles experimental site.

2 THE ALPILLES EXPERIMENT

2.1 General description

The Alpilles-ReSeDA experiment lasted from December 1996 to November 1997 over a small agricultural area (5 km X 5 km) near Avignon (South-

East of France). The main crops were wheat, sunflower, vegetables, orchards, corn, grassland and alfalfa. A detailed map of land use has been established by combining supervised classification of multi-temporal SPOT data, photogrammetric analysis of IR aerial photographs and ground survey (Figure 1).

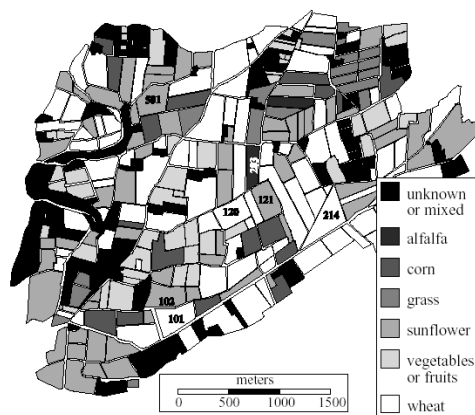


Figure 1. Land use map of the Alpilles experimental site in 1997. Energy balance measurements were done on the numbered fields (101, 102, 120, 121, 203, 214 and 501).

Concise descriptions of the experiment were given by Prévot et al. (1998) and Olioso et al. (1998) (see also <http://www.uv.es/ucg/watermed/avignon.htm> and <http://www.avignon.inra.fr/reseda>). Among the

numerous satellite, airborne and field measurements collected, the main data used in this study were obtained from airborne sensors (reflectances and thermal infrared data) and ground measurements (sensible heat fluxes).

2.2 Ground data

Field measurements of both meteorological variables, surface energy fluxes, LAI, albedo and surface temperature were acquired in several fields (see a detailed description of the ground segment by Oliso et al. 2002 and for some parts by Jacob et al. 2002c). Micrometeorological field measurements were performed on seven points located on alfalfa, wheat, and sunflower crops: energy balance (using both Bowen ratio and combined fluctuation systems), thermal brightness temperature over the [8-14] μ m window, wind speed, reflected solar radiation, plant structure, ...). An improved meteorological site was set near the centre of the experimental zone (incoming radiations, air temperature, wind speed and direction...).

2.3 Airborne data

Remote sensing measurements were acquired over the visible and the near infrared using the airborne POLDER sensor and over the thermal infrared domains with an Inframetrics 760 video camera (see Jacob et al. 2002a, b and c). Both instruments flew on days with clear sky around solar noon and approximately one or two times per month at altitudes of 3000 m and/or 1500 m. Twenty seven flight acquisitions were performed between March and October (corresponding to 18 different days). After spatial registration and atmospheric correction, the spatial resolution of the images was 20 m. As both instruments acquired multi-directional data, specific procedures were used for generating bi-directional reflectance distribution functions from POLDER images and nadir thermal infrared brightness temperature from the Inframetrics camera.

3 THE FLUX MODELS

3.1 The standard mono-dimensional model

The standard mono-dimensional model consists in the following simple equation for computing the sensible heat flux (H):

$$H = \rho c_p h_a (T_s - T_a) \quad (\text{eq. 1})$$

where ρ is the density of air, c_p its heat capacity (at constant pressure), T_s the aerodynamic surface temperature, T_a the air temperature, and h_a a turbulent exchange coefficient. This last coefficient is computed

using the Monin-Obukhov theory as a function of wind speed (u_a), momentum roughness length (z_{0m}), thermal roughness length (z_{0h}), and accounting for the effect of thermal stratification. Then mapping the sensible heat flux required maps of roughness lengths, air temperature and surface temperature, as inputs, as well as wind speed.

3.2 The microscale aggregation 2D model

It was described by Hasager and Jensen (1999). The aggregation model solves the linearized atmospheric flow equations by Fast Fourier Transforms. This solution makes the model computationally fast. The model equations include an iterative calculation for non-neutral stability and it is assumed that the ratio of the roughness length for heat z_{0h} to the roughness length for momentum z_{0m} is of the order of 0.1 to 0.001 (Hasager and Jensen 1999, Hasager et al. 2001). The necessary model inputs are wind speed, wind direction and air temperature at the computational level from meteorological observations at masts or radiosoundings (Batchvarova et al. 2001) and maps of surface roughness and land surface temperature.

3.3 The SEBAL model

The Surface Energy Balance Algorithm for Land model (SEBAL) was described by Bastiaanssen et al. (1998a and 1998b). This model uses Equation 1 for computing H . By considering the spatial variability induced by hydrological and energetic contrasts, it is able to retrieve the atmospheric variables (wind speed and air temperature) at the same time as the energy fluxes. This approach relies on the assumption of the simultaneous presence of dry areas and wet areas over the study site and on specific calculations of energy balance on these areas (net radiation and ground heat flux must be computed). The required inputs are incoming radiations, surface temperature map, NDVI and albedo maps (NDVI is used for computing emissivity, roughness length and ground heat flux to net radiation ratio).

4 MODEL INPUTS

The 3 models required the same type of input maps: surface temperature maps and roughness maps. In the specific case of SEBAL maps of albedo and NDVI are also required. Concerning the meteorological inputs, air temperature and wind speed are required as inputs of the 1D model and the 2D model. In the case of SEBAL, these quantities are internally computed by the model. Incoming solar and thermal radiations are required for running SEBAL. Emissivity maps were required in order to obtain surface temperature maps from thermal infrared brightness temperature maps provided by the Inframetrics camera.

4.1 NDVI and albedo maps

Polder images provided BRDF samplings in four channels (443 nm, 550 nm, 670 nm, 865 nm) that were used for fitting BRDF models such as Li-Ross model or Walthall model (see Jacob et al. 2002a). From this fitting, images of hemispherical and nadir reflectances were computed. Nadir reflectances in the red and the near-infrared channels were used for computing NDVI (Jacob et al. 2002c). Hemispherical reflectances in all the channels were linearly combined to obtain albedo (Jacob et al. 2002b).

4.2 Emissivity maps and surface temperature maps

Maps of thermal infrared brightness temperature at nadir were obtained by selecting the median of closest data to nadir in the directional sampling provided by the Inframetrics 760 camera. The calibration of the instrument performed at the laboratory was found inadequate for the in-flight measurements. Then we re-calibrated the data by using the thermal infrared brightness temperatures that were continuously measured at the ground level in different fields (3 to 5 simultaneous ground measurements). To obtain surface temperature, it was necessary to correct the data for the effects of surface emissivity and atmospheric radiation in the measurement waveband. We used the procedure given by Olioso (1995a) that expressed the surface temperature as a function of the brightness temperature, the emissivity and the atmospheric radiation.

Emissivity maps were derived from NDVI maps using either the relationship obtained by van de Griend and Owe (1993) or using a simplified model based on the analysis done with the SAIL model by Olioso (1995b) and the measurements performed by Coll et al. (2002) during the experiment. The first relation was used in SEBAL. It generated emissivity values between 0.92 and 1. The second relation was used in the 1D model and the microscale aggregation model: the derived emissivities ranged between 0.96 for bare soil and 0.99 for well-developed canopies.

4.3 Roughness maps

Two ways were used for deriving roughness maps. In SEBAL, we used an empirical relationship with NDVI calibrated by Bastiaanssen et al. (1998a) over a data set collected in a Mediterranean semi-arid region. Roughness length for heat was set to 1/10 times roughness length for momentum ($kB^{-1} = 2.3$).

For the 1D and the microscale aggregation models, roughness maps were derived from the land use map

(Figure 1) and ground measurements of vegetation height. Evolution of vegetation height was recorded on wheat, sunflower, alfalfa and maize crops. Mean values were affected to all the similar fields in the area. Two types of wheat fields, (winter and spring wheat) and two types of sunflower fields (early and late sowing) were considered on the basis of NDVI time profiles. No height measurements were performed on orchards, woods and vegetable fields. Orchard height was estimated at 3 meters on the basis of a multiyear ground survey in similar areas. Wood height was estimated from later ground survey. Vegetable crop heights were estimated from the type of crops (tomato, artichoke, salad), NDVI time profiles and expertise knowledge. Eventually, aerodynamic roughness was estimated as 0.13 times vegetation height (Figure 2). For the 1D and the microscale aggregation models, we assumed a value of $kB^{-1} = 4.6$.

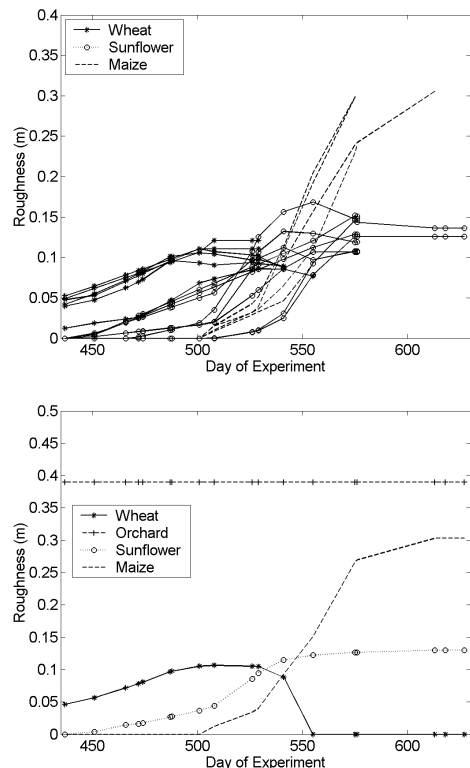


Figure 2. Time evolution of roughness length for several wheat, sunflower and maize fields (top graph) and mean values of roughness length used for generating roughness maps from land use map (bottom graph). The Day of Experiment referred to the number of days since 1996 January 1st.

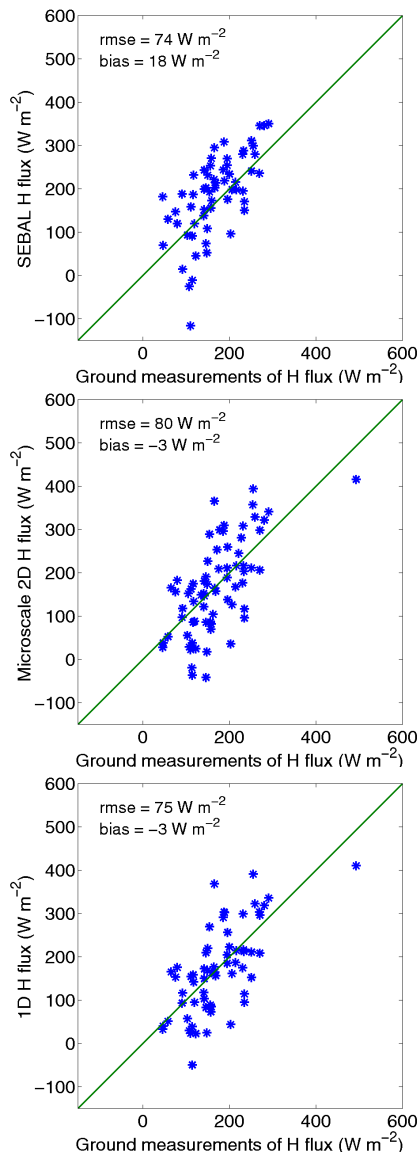


Figure 3. Comparison of sensible heat flux simulations to ground measurements for the 3 models. rmse is the root mean square error.

4.4 Air temperature and wind speed

For the 1D and the microscale aggregation model, in order to avoid the influence of surface conditions on meteorological parameters (see for example Courault et al. 1996), we chose to use T_a and u_a values derived at 25 m height from the re-analysis of the Numerical Weather Prediction (NWP) model Arpège run at Météo-France on an operational basis. The meteorological parameters at this height were assumed

to be horizontally homogeneous (assuming that a blending height was reached at this level).

SEBAL included specific procedures that allowed the computation of a regional value of wind speed and spatialized values of T_a (see Jacob et al. 2002c). A mean value of wind speed at the atmospheric reference level was calculated from the aerodynamic properties of an effective layer between the surface and the blending height. These aerodynamic properties were inverted from the characterisation of the sensible heat transfer through the atmospheric layer considering aggregated surface temperatures, roughness lengths and sensible heat flux over the dry areas (allocated from a surface temperature versus albedo diagram). In these calculations, the original SEBAL model described by Bastiaanssen et al. (1998a) was modified in order to account for an ill-posed problem and we used an improved variant proposed by Su et al (1999a and b). In this improved variant, the regional resistance for heat is determined using the potential air temperature at the blending height. Air temperature was obtained as a linear relation of surface temperature $T_a = a T_s + b$. This linear relationship was calibrated by inverting the sensible heat flux over wet areas on one side (assuming $T_s - T_a = 0$) and dry areas (assuming no latent heat flux). These areas were selected considering respectively minimum and maximum surface temperatures over the study site.

5 COMPARISON OF OUTPUTS

5.1 Comparison of model results to field measurements of sensible heat flux

Figure 3 shows the comparison of the 3 models to the ground measurements of H flux. To do this comparison, only the locations of field measurements were selected on the images (actually the mean flux in 3 by 3 pixel windows centred on the position of micrometeorological masts). The 3 models had global performances close to each other: RMSE around 70 – 80 W m^{-2} and small bias; just note that SEBAL had a larger (positive) bias than the two other models.

5.2 Comparison of model results to each others

Figure 4 shows a comparison of heat flux simulations by the different models. This comparison is presented only on the location of ground measurements and not on the whole images. The 1D and the microscale aggregation models gave almost exactly the same results while large differences existed between these two models and SEBAL.

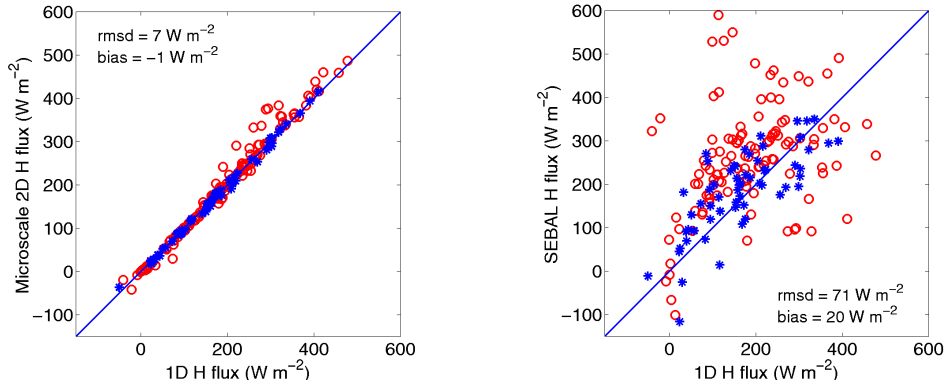


Figure 4. Comparison of sensible heat flux simulated by the different models (the circles correspond to simulations without corresponding ground measurements). rmsd is the root mean square difference.

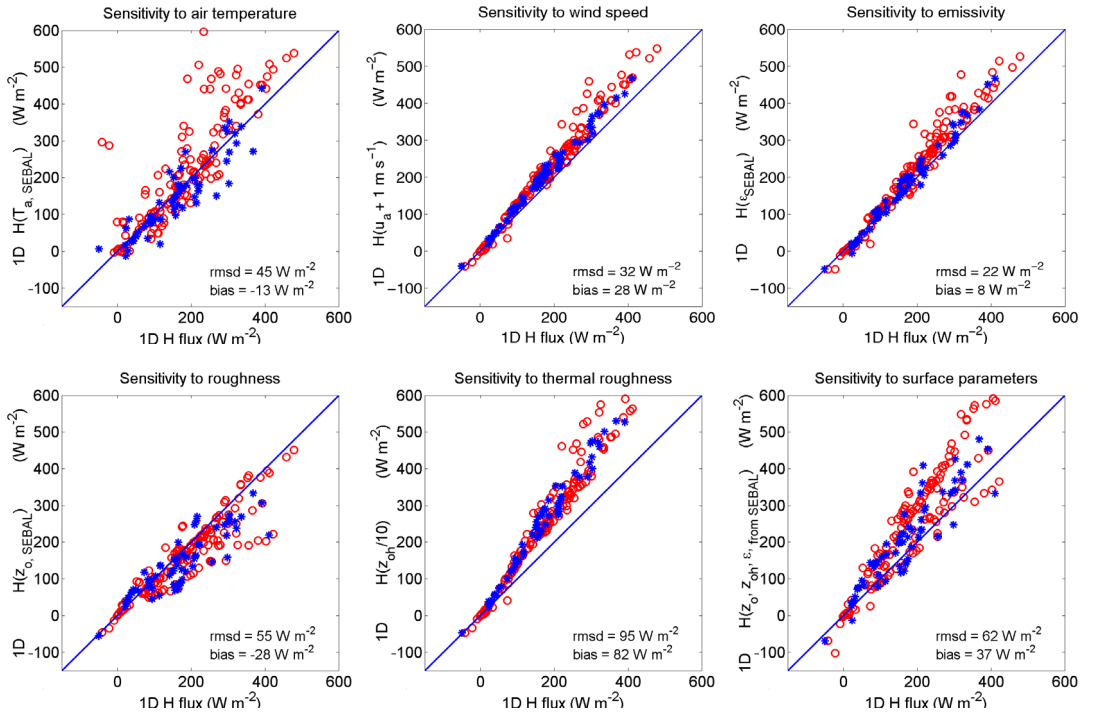


Figure 5. Sensitivity of the 1D model to various input parameters (the circles correspond to simulations without corresponding ground measurements). rmsd is the root mean square difference.

6 SENSITIVITY ANALYSIS

In order to explain the differences between SEBAL and the two other models, we performed a sensitivity analysis of the sensible heat flux calculation. We tested the effect of changing model inputs using the

standard 1D model. We only used this model because *-i)* it gave similar results as the microscale aggregation 2D model with the same inputs (on the locations of ground measurements); *-ii)* the same flux equation was used in SEBAL and then it is possible to assume that the differences between SEBAL and the 1D model were only related to differences in Eq. 1

inputs. The comparison of the 1D model calculations to the calculations using the same inputs as in SEBAL are presented in Figure 5.

Effect of air temperature: in the 1D model and the microscale aggregation model we used air temperatures computed at 25 meters by the Arpège NWP model, while in SEBAL, air temperatures were derived from the surface temperature maps. It was not possible to directly compare these two temperature sets since the air temperature used by SEBAL was computed in the lower layers of the atmosphere for each pixel. However, we have done calculations with the 1D model setting the minimum temperature that was derived in SEBAL for each image at the same atmospheric level as the Arpège analysis, i.e. 25 m. The differences between the two temperature estimations were significant (Figure 6). The effect on H was important with a large scatter ($\text{rmsd} = 45 \text{ W m}^{-2}$). However, it looked like a large part of the differences were associated with a few specific dates for which large underestimation of air temperatures were obtained with SEBAL.

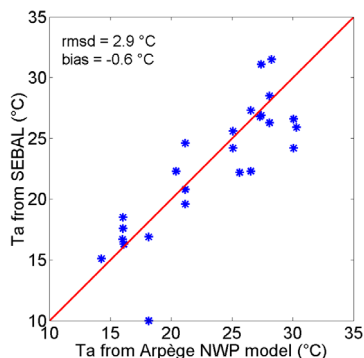


Figure 6. Differences between the two sets of estimated air temperature.

Effect of wind speed: in the 1D model and the microscale aggregation model we used wind speeds computed at 25 meters by the Arpège NWP model, while in SEBAL, the wind speeds were derived from energy balance calculations on dry pixels. Jacob et al. (2002c) showed that the estimation of wind speed at 2 m high above the surface was done with a $\text{rmsd} = 0.9 \text{ m s}^{-1}$. Then we changed the wind speed as input of the 1D model by 1 m s^{-1} generating an error around 30 W m^{-2} mainly due to a large bias.

Effect of emissivity: two equations were used for computing emissivity (O95 obtained from Olioso et al. (1995b) in the 1D and 2D model and GO93 from van de Griend and Owe (1993) in SEBAL). For developed canopies, they were giving almost similar values at moderate values of NDVI (0.5 – 0.65). For higher

NDVI, GO93 gave higher values than O95: differences as high as 0.01 were obtained. At low NDVI values, the differences were larger up to 0.05 (OG93 giving lower values). This was due to a calibration site effect: GO93 was established over an area in Botswana in which the soil type (loamy sand) was very different from the soil types in the Alpilles area (silty clay, silty clay loam or silt loam). Sand has usually the effect of decreasing soil emissivity and then canopy emissivity at low vegetation cover. The resulting effect on sensible heat flux was not very large (root mean square difference = 22 W m^{-2}).

Effect of momentum roughness z_{om} : in the 1D model, roughness was estimated from the land use map, while in SEBAL an equation proposed by Bastiaanssen et al. (1998a) over a dataset collected in a Mediterranean semi-arid area. In order to test the effect of roughness estimation, we run the 1D model using the roughness maps from SEBAL. Jacob et al. (2002c) showed that this equation may lead to errors in the estimation of momentum roughness as large as 200 % for green canopies in our study area. Lagouarde et al. (2002) found errors higher than 1000 % for senescing canopies, which was explained by changes in NDVI while aerodynamic properties were almost unchanged. The effect on the simulation of sensible heat flux was large ($\text{rmsd} = 55 \text{ W m}^{-2}$) mainly linked to underestimation of roughness by the equation used in SEBAL.

Effect of thermal roughness z_{oh} : in the SEBAL model, the thermal roughness was estimated as 1/10th of the momentum roughness, while it was 1/100th in the case of the 1D model. Using the SEBAL ratio in the 1D model resulted in a very large increase of the sensible heat flux (bias = 82 W m^{-2}).

Effect of surface parameters: we combined together the effects of the different estimations of emissivity, momentum roughness and thermal roughness. This resulted in a significant overestimation of the sensible heat flux (bias = 37 W m^{-2}) and a large scatter ($\text{rmsd} = 62 \text{ W m}^{-2}$), showing that the effect of thermal roughness estimation was predominant. This effect counterbalanced the effect of the underestimation of momentum roughness, while the effect of emissivity was low. The effect of surface parameters was higher than the effect of atmospheric variables.

7 DISCUSSION AND CONCLUSION

We compared three models for estimating the sensible heat flux from thermal infrared remote sensing measurements. These three models differed either in the resolution of turbulent exchange equations (1D and SEBAL compared to the microscale aggregation

model) or in the way of acquiring surface and meteorological input data (1D and the microscale aggregation model compared to SEBAL). The three models had similar performances, but large differences occurred between SEBAL and the 1D model. There was almost no difference between the 1D model and the microscale aggregation model showing that both resolutions of turbulent transfer equations were equivalent. However, the comparison was only shown for the location of energy balance ground measurements, which were chosen in order that fetch conditions were not affecting flux measurements. In these conditions it was rather reassuring to have similar results. Differences existed closer to field edges.

It was possible to assume that simulation differences between SEBAL and the 1D model were due to the prescription of input quantities since both models used the same equation for computing sensible heat flux. Our sensitivity analysis showed that variations in flux simulations linked to model input variations had a similar magnitude to model performances. Then we can conclude that the way these inputs were obtained had a significant impact. SEBAL only used remote sensing information in order to derive all its input parameters; these parameters were significantly different from those used for driving the 2 other models. The effect of emissivity estimation was small and will be easily corrected in the future. The problem of roughness estimation is more complex since it will be almost impossible to derive this parameter from reflectances without ancillary data on vegetation type and phenology; other remote sensing technique (LIDAR) might be used, but not so easily; however, we should notice that error lower than 100 % on z_{om} had a limited effect on flux estimation (lower than 20 % most of the time: see Oliosio et al. 2001). For most of crop types in our area, it will be easy to derive an accurate enough momentum roughness by analyzing NDVI time profile over the crop season, as soon as the crop type is known. The estimation of thermal roughness length is still problematic; new parameterizations are currently being tested by several research teams (see Su et al. 2001, Hasager et al. 2002). Over our area, Hasager et al. (2002) showed that it maybe possible to obtain an estimation of thermal roughness length using remote sensing measurements of LAI and a flow dependant equation. Meteorological inputs (air temperature and wind speed) derived from remote sensing data in SEBAL might be less satisfactory than those derived from NWP (Arpège) model; a comparison to in-situ measurements at the ground and by radiosoundings is undergoing in order to understand why and in which situations SEBAL estimations of atmospheric variables were erroneous. Despite these

misestimations, temperatures and wind speeds derived by SEBAL were quite nicely estimated, since a large part of the discrepancies were due to a few wrong days. Moreover, the effect of atmospheric variables was lower than the effect of surface parameters in the sensitivity analysis. It is also interesting to notice that the effects of input parameters were in the same order as the errors in comparing models to ground data of sensible heat flux.

8 ACKNOWLEDGEMENT

Financial support for this study was provided by EC in the frame of the WATERMED project (contract ICA3-CT-1999-00015). The Alpilles dataset was acquired during the ReSeDA project, which was funded by the EEC-DG XII (contract ENV4-CT96-0326-PL952071) and the French *Programme National de Télédétection Spatiale* et *Programme National de Recherches en Hydrologie*.

9 REFERENCES

- Bastiaanssen, W.G.M., Menenti, M., Feddes, R.A., and Holtslag, A.A., 1998a, A remote sensing surface energy balance algorithm for land (SEBAL). I: Formulation, *Journal of Hydrology*, 212-213, 198-212.
- Bastiaanssen, W.G.M., Pelgrum, H., Wang, J., Ma, Y., Moreno, J.F., Roerink, G.J., van der Wal, T., 1998b, A remote sensing surface energy balance algorithm for land (SEBAL). II: Validation, *Journal of Hydrology*, 212-213, 213-229.
- Batchvarova, E., Gryning, S.-E., and Hasager, C.B., 2001, Regional fluxes of momentum and sensible heat over a sub-arctic landscape during late winter, *Boundary-Layer Meteorology*, 99, 489-507.
- Coll, C., Caselles, V., Rubio, E., Valor, E., Sospedra, F., Baret, F., Prévot, L., and Jacob, F., 2002, Temperature and emissivity extracted from airborne multi-channel data in the ReSeDA experiment, *Agronomie*, in press.
- Courault, D., Clastre, P., Guinot, J.P., and Seguin, B., 1994, Analyse des sécheresses de 1988 à 1990 en France à partir de l'analyse combinée de données satellitaires NOAA - AVHRR et d'un modèle agrométéorologique, *Agronomie*, 14, 41-56.
- Courault, D., Cauchy, P., Clastre, P., and Bloser, B., 1996, Analyse des variations spatiales de la température de l'air en fonction de l'occupation de surface, *Photo Interpretation*, 3-4, 19-60.
- French, A.N., Schmugge, T.J., and Kustas, W.P., 2002, Estimating evapotranspiration over El Reno, Oklahoma with ASTER imagery. *Agronomie*, 22, 105-106.
- Gillies, R.R., Carlson, T.N., Cui, J., Kustas, W.P., and Humes, K.S., 1997, Verification of the "triangle" method for obtaining surface soil water content and

- energy fluxes from remote measurements of the Normalized Difference Vegetation Index NDVI and surface radiant temperature, *International Journal of Remote Sensing*, 18, 3145–3166.
- Hasager, C.B., and Jensen, N.O., 1999, Surface-flux aggregation in heterogeneous terrain, *Quarterly Journal of the Royal Meteorological Society*, 125, 2075–2102.
- Hasager, C.B., Jensen, N.O., Boegh, E., Soegaard, H., Schelde, K., and Thomsen, A., 2001, Scaling-up evapotranspiration from field to regional scale based on optical remote sensing scenes, In the *Proceedings of the Symposium on Remote Sensing and Hydrology 2000*, Santa Fe, New Mexico, USA, April 2000, IAHS Publication N° 267, 292–295.
- Hasager, C.B., Jensen, N.O., and Oliso, A., 2002, Land cover, surface temperature and leaf area index maps from satellites used for the aggregation of momentum and temperature roughnesses, in *this proceedings*.
- Jacob, F., Oliso, A., Weiss, M., Baret, F., and Hautecoeur, O., 2002a, Mapping short-wave albedo of agricultural surfaces using airborne POLDER data, *Remote Sensing of Environment*, 80, 36–46.
- Jacob, F., Weiss, M., Oliso, A., and French, A.N., 2002b, Assessing the narrow-band to broad-band conversion to estimate visible, near infrared and shortwave apparent albedo from airborne POLDER data, *Agronomie*, in press.
- Jacob, F., Oliso, A., Gu, X.F., Su, Z., and Seguin, B., 2002c, Mapping surface fluxes using airborne visible, near infrared, thermal infrared remote sensing data and a spatialized surface energy balance model, *Agronomie*, in press.
- Kustas, W.P., Moran, M.S., Humes, K.S., Stannard, D.I., Pinter Jr., P.J., Hipps, L.E., Swiatek, E., and Goodrich, D.C., 1994, Surface energy balance estimates at local and regional scales using optical remote sensing from an aircraft platform and atmospheric data collected over semiarid rangelands, *Water Resources Research*, 30, 1241–1259.
- Lagouarde, J.-P., Jacob, F., Gu, X.-F., Oliso, A., Bonnefond, J.-M., Kerr, Y., McAnneny, K., and Irvine, M., 2002, Spatialization of sensible heat flux over a heterogeneous landscape, *Agronomie*, in press.
- Oliso, A., 1995a, Estimating the difference between brightness and surface temperatures for a vegetal canopy, *Agricultural and Forest Meteorology*, 72, 237–242.
- Oliso, A., 1995b, Simulating the relationship between thermal emissivity and the Normalized Difference Vegetation Index, *International Journal of Remote Sensing*, 16, 3211–3216.
- Oliso, A., et al., 1998, Spatial aspects in the Alpilles-ReSeDA project, in: *Scaling and modeling in forestry: application in remote sensing and GIS*, Marceau, D. (ed.), Université de Montréal, Québec, 1998, pp. 92–102.
- Oliso, A., Chauki, H., Courault, D., and Wigneron, J.P., 1999, Estimation of evapotranspiration and photosynthesis by assimilation of remote sensing data into SVAT models, *Remote Sensing of Environment*, 68, 341–356.
- Oliso, A., Jacob, F., Hadjar, D., Lecharpentier, P., and Hasager, C., 2001, Spatial distribution of evapotranspiration and aerodynamic roughness from optical remote sensing, in: *Workshop on landscape heterogeneity and aerodynamic roughness: modeling and remote sensing perspectives*, October 2001, Anvers, Belgique, 2001.
- Oliso, A., et al., 2002, Monitoring energy and mass transfers during the Alpilles-ReSeDA experiment, *Agronomie*, in press.
- Prévo, L., et al., 1998, Assimilation of multi-sensor and multi-temporal remote sensing data to monitor vegetation and soil: the Alpilles ReSeDA project, in: *IGARSS'98*, IEEE, volume 5, pp. 2399–2401.
- Soer, G.J.R., 1980, Estimation of regional evapotranspiration and soil moisture conditions using remotely sensed crop surface temperature, *Remote Sensing of Environment*, 9, 27–45.
- Su, Z., Menenti, M., Pelgrum H., van den Hurk B.J.J.M., and Bastiaanssen W.G.M., 1999a, Remote sensing of land surface fluxes for updating numerical weather predictions, in: *Operational Remote Sensing for Sustainable Development*, Nieuwenhuis, Vaughan and Molenaar Eds, Balkema, Rotterdam, pp. 393–402.
- Su, Z., Pelgrum, H., Menenti, M., 1999b, Aggregation effects of surface heterogeneity in land surface processes, in: *Hydrology and Earth Science System* (Eds. Z Su, M Menenti), volume 3, pp. 549–563.
- Su, Z., Schmugge, T., Kustas, W.P., and Massman, W.J., 2001, An evaluation of two models for estimation of the roughness height for heat transfer between the land surface and the atmosphere. *Journal of Applied Meteorology*, 40, 1933–1951.
- van de Griend, A.A., and Owe, M., 1993, On the relationship between thermal infrared emissivity and the Normalized Difference Vegetation Index for natural surfaces, *International Journal of Remote Sensing*, 14, 1119–1131.
- Weiss, M., and Baret, F., 1999, Evaluation of canopy biophysical variable retrieval performances from the accumulation of large swath satellite data, *Remote Sensing of Environment*, 70, 293–306.
- Zhan, X., Kustas, W.P., and Humes, K.S., 1996, An intercomparison study on models of sensible heat flux over partial canopy surfaces with remotely sensed surface temperature, *Remote Sensing of Environment*, 58, 242–256.

ESTIMATION OF EVAPOTRANSPIRATION ON HETEROGENEOUS PIXELS

Wassenaar, T.⁺, Olioso, A.⁺, Hasager, C.^{*}, Jacob, F.[#], Chehbouni, A.[§]

⁺ INRA Bioclimatologie, Domaine Saint-Paul, Avignon, France, F-84914 Avignon Cedex 9, France, tel. +33 4 32 72 24 06, fax +33 4 32 72 23 62,

wassenaar@avignon.inra.fr

^{*} Risoe National Laboratory, Windenergy Department, Atmospheric Physics, Roskilde, Denmark charlotte.hasager@risoe.dk

[#] USDA/ARS Hydrology and Remote Sensing Laboratory, Beltsville, MD, USA

fjacob@hydrolab.arsusda.gov

[§] CESBIO (CNES-CNRS-IRD-UPS), Toulouse, France

ghani@cesbio.cnes.fr

ABSTRACT - Various models have been derived for estimating evapotranspiration from remote sensing data. These models have usually been designed for homogeneous canopies which are considered as having homogeneous characteristics at local scale. At a larger scale, landscape heterogeneity and model non-linearity can lead to substantial errors in the estimation of evapotranspiration (Bougueraz, 1999). In this work, the linearity of the simplified relationship model (as proposed by Seguin and Itier, 1983) is investigated. Namely, we consider a pixel region covered with various homogeneous cover types for which the evapotranspiration can be calculated. Aggregated calculations are used to define heterogeneous pixel radiances and landscape evapotranspiration. This analysis has been applied to the Alpilles dataset which includes high resolution maps of surface temperature and spectral reflectances over a small agricultural area. The results showed that the non linearity effect on evapotranspiration induces an error of several tenths of mm/day at a given surface temperature. This effect is mainly linked to the non-linearity of the simplified relationship toward aerodynamic roughness. The way of estimating roughness over heterogeneous pixels has also a very significant influence on the results. In a second step, in order to analyse the effect of roughness, a two-dimensional boundary layer model was used for estimating the aerodynamic roughness at the pixel scale.

1 INTRODUCTION

Daily evapotranspiration is an important factor for monitoring water requirements of crops and water consumption at a regional scale. The integrated evapotranspiration through the whole phenological cycle is also closely related to the crop final productivity. Many attempts have been made in the past for estimating evapotranspiration using remote sensing (for a review see Olioso and Jacob 2002). Semi-empirical and more deterministic approaches have been developed. Most evapotranspiration estimations from remote sensing are residual approaches based on the assessment of the energy balance. Evapotranspiration corresponds to the latent heat flux (LE), which can be calculated as the residual of the net radiation (Rn) minus the soil and sensible heat fluxes (G and H):

$$LE = Rn - G - H \quad (1)$$

Rn and H are calculated by a series of variables, some of which can be estimated instantaneously by remote sensing (albedo, emissivity and radiometric surface temperature). Recently, some operational applications have even been implemented (ex. EARS),

although some important fundamental problems still remain to be solved. Major difficulties in obtaining more precise and more useful, distributed LE estimates are (1) the estimation of daily flux values on the basis of instantaneous measurements; (2) fulfilling the need for (distributed) micrometeorological data (like wind speed and air temperature); (3) the application of physical equations with only local validity to heterogeneous pixels, a still largely ignored problem.

This paper mainly focuses on the last mentioned problem. Since the early eighties, experimental studies use coarse spatial resolution remote sensing in order to obtain regional evapotranspiration estimates (Vidal *et al.*, 1987; Lagouarde & Brunet, 1989). At the same time it is common knowledge that the physical equations used are only valid for homogeneous and continuous land cover types. This makes the use of coarse remote sensing data like the often used AVHRR (1 km² resolution), especially on fragmented agricultural areas, a very delicate operation. This is though not only due to the non-linearity of the physical equations, but also to the difficulty of estimating some parameter values at levels where they are no more homogeneous (like estimating the

aerodynamic roughness length of a composite area made up for example of bare soil, sunflower, wheat and forest).

2 METHODS

Our assessment is based on the consistent experimental data set which has been acquired during the ReSeDA program over the Alpilles test site in the South-East of France in 1997. This flat area of 5×5km is well suited to study the scale change problem, because it's divided into rather small fields with varying land use. Main crops are wheat and sunflower, but alfalfa, maize, vegetables and orchards are also present. The data set comprises continuous micrometeorological field measurements and optical and infrared remote sensing data, acquired throughout the cultural season at different resolutions by a series of sensors (airborne Inframetrics760 and PolDER, spaceborne SPOT, Landsat and AVHRR). These data have already been used in the past for deriving physical variables that are used in our work (ex. diurnal albedo, Jacob *et al.*, 2002; Jacob & Olioso, 2002).

The effect of scale change is assessed by calculating the energy fluxes, first using high spatial resolution input data and a second time using a spatially degraded version of these input data. Then the resulting high resolution energy fluxes are integrated to the level of the coarse resolution energy flux estimations, allowing for comparison.

The spatially distributed input variables are provided at a 20m resolution by the airborne sensors. This means that most pixels cover surfaces that can reasonably be considered as a continuous and homogeneous cover, thereby allowing for energy flux estimations respecting the physical principles.

2.1 Estimating energy fluxes

The net radiation flux density R_n , i.e. the budget governing the energy fluxes at the surface, can be computed from incident radiation, surface albedo (α), emissivity (ϵ) and surface temperature. Incident radiation is provided by the micrometeorological ground station, α is obtained from multi-directional PolDER data (Jacob *et al.*, 2002) and ϵ is estimated using the PolDER nadir estimates based NDVI (Olioso, 1995b). Surface temperature is calculated following the approach of Olioso (1995a), using the Inframetrics760 (8-14 μ m spectral band) brightness temperature (T_b) and ϵ .

The instantaneous sensible heat flux H of the surface cover is defined as follows:

$$H = \rho c_p h_a (T_s - T_a) \quad (2)$$

where ρ and c_p are respectively the air density and specific heat at constant pressure, h_a the turbulent exchange coefficient and T_a the air temperature at a given reference height. To avoid spatial variation we used midday T_a at 25m above the ground provided by the French meteorological numerical weather prediction model *Arpège*.

h_a is determined by the classical equation of Brutsaert (1982) where h_a is a function of u_a at the reference height (so no spatialisation required! Provided by *Arpège*), the aerodynamic roughness length z_{0m} (commonly a simple fraction of crop height), the roughness length for heat transfer z_{0h} , and the Monin-Obukhov length L . z_{0h} is taken to be 1% of z_{0m} .

A spatialised estimate of G is hard to obtain as there is no direct relation with remotely sensed radiation. Daily G is often considered to equal zero.

2.2 A residual approach for estimating daily LE

To obtain a daily evapotranspiration estimate, we are now confronted to the fundamental problem of relating instantaneous measurements to daily estimates as stated in the previous paragraph. Remote sensing typically provides only instantaneous radiation measurements. Some more or less strong hypothesis (notably a constant H/R_n ratio throughout the day and a daily G close to zero) allow to obtain a daily LE estimate for clear sky days.

The solution we adopted is based on the so-called *simplified relationship*: As originally observed by Jackson *et al.* (1977), the difference between instantaneous surface and air temperature can statistically be related to daily LE if daily R_n is known:

$$LE_d - R_{n_d} = A - B(T_{s_i} - T_{a_i}) \quad (3)$$

Seguin & Itier (1983) proposed to use this relationship to obtain regional LE_d estimates using satellite measured midday T_{s_i} , with ground measured R_{n_d} and T_{a_i} being considered constant throughout the more or less homogeneous area studied. The statistically determined parameters A and B can give a good estimate for a given clear sky day and homogeneous R_{n_d} and T_{a_i} , provided that the instantaneous H/R_n ratio remains constant throughout the day. For operational use, A and B are considered to be constant and characteristic of the area studied, which adds one more hypothesis: the midday ratio R_{n_d}/R_{n_i} should be constant throughout the year.

Many authors have used this relationship ever since and tried to propose a more analytical, but operational, parameterisation either by a theoretical analysis (Riou *et al.*, 1988) or using SVAT models (Vidal *et al.*, 1987; Lagouarde, 1991; Carlson *et al.*,

1995). This has resulted in several semi-deterministic models to estimate A and B. In fact the offset A corresponds to an average daily soil heat flux G_d and is therefore generally considered to equal zero. Regression slope B is often defined as a “mean exchange coefficient”. Because B is found to depend on the surface roughness z_0 , its dependence upon land cover type is since long recognised by the scientific community.

But the definition of B as a “mean exchange coefficient” contains a contradiction in terms. B indeed is related to the instantaneous sensible heat flux and can be defined as:

$$B = c \cdot \overline{\rho c_p h_a} \quad (4)$$

where the average concerns the crop season average and c being the constant Rn_d/Rn_i ratio. But h_a , and so B, is determined by the highly variable u_a , z_0 and the atmospheric stratification (expressed by L). So B can vary strongly from day to day, which is why Seguin & Itier (1983) advised to sum results over two to four week periods. But still then the evolution of crop height versus a fixed B value induces an error.

On the other hand the examination of the ReSeDA micrometeorological ground measurements database revealed that the clear sky day midday Rn_d/Rn_i ratio is not constant neither, but shows a considerable evolution (figure 1). This same figure also shows that the daily soil heat flux cannot be neglected. This daily soil heat flux is variable, but a general annual tendency can be discerned.

So affecting unique A and B values to each field, generally on the basis of land cover information only (Courault *et al.*, 1996) will not provide a precise estimation of LE.

We therefore adopted a more mechanistic way to estimate daily LE, reducing the fundamental hypotheses to the number of two:

- 1) the classical hypothesis stating that the instantaneous H/Rn ratio remains constant throughout clear sky days;
- 2) the hypothesis that the value of A is not zero, but spatially constant and equal to the daily G_d flux that can be approximated by a yearly sinusoidal evolution (figure 1):

$$G_d = 17 \sin\left(\frac{2\pi(D+100)}{365}\right) \quad (5)$$

where G_d is the daily soil heat flux (W/m^2) and D the Julian day. This is a coarse approximation, but it reduces the error with respect to the zero flux hypothesis.

Instantaneous and local values of B are calculated through the distributed midday h_a and Rn_d/Rn_i values. The daily Rn , the remaining unknown, is calculated by

considering diurnal values for α as provided by Jacob & Olioso (2002) and a daily longwave upward radiation estimated by the daily integration method proposed by Lagouarde *et al.* (1991).

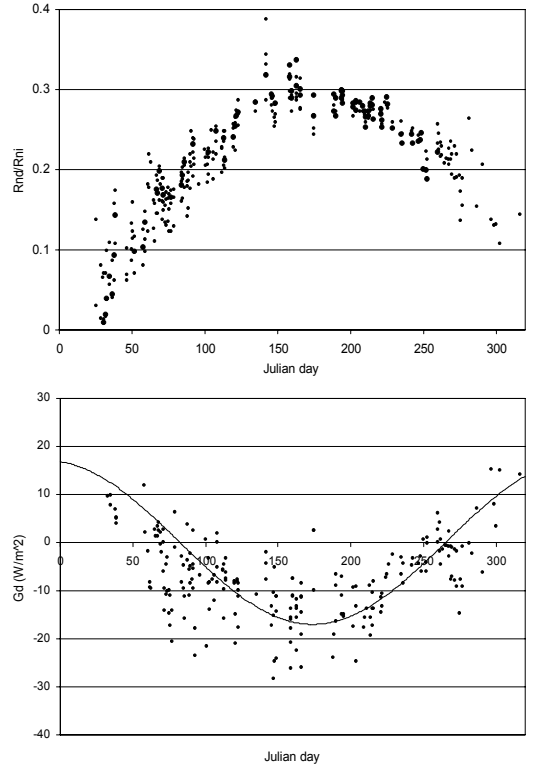


Figure 1 ReSeDA field measured energy fluxes from 7 sites pooled together. 1a (top) shows the annual evolution of the Rn_d/Rn_i ratio; 1b (bottom) shows the daily integrated measured soil heat flux.

2.3 Upscaling of input variables

Let us now consider the spatially distributed variables required as input for calculating Rn , H and LE : albedo, NDVI based emissivity, T_s and crop height (linearly determining d_0 , z_{0m} and z_{0h}). These variables are available at a 20 m resolution, allowing for individual flux calculations for each crop and land cover type. To evaluate the effect of non linearity by calculating these fluxes on input data with heterogeneous pixels, we performed a scale change on these input variables, degrading them from 20 m down to a 1 km resolution. Corresponding to the resolution of AVHRR data, the differences found will be an indication of the error that can be committed by AVHRR based flux estimates in comparable areas.

Bougueraz *et al.* (1999) showed that albedo is almost insensitive to heterogeneity, because expressed as a quasi linear function of red and near infrared

reflectances. The upscaled 1 km² resolution albedo could therefore be considered to correspond to the average of the 50×50 20 m resolution pixels. Upscaled emissivity is calculated using the aforementioned relation with NDVI. NDVI in turn was calculated using upscaled red and near infrared reflectances.

Things become more complicated when considering Ts. In fact temperature has to be transformed back into an energy flux; the radiation emitted by the surface. After upscaling (averaging) we retransform the result into temperature.

A final but crucial difficulty is how to determine crop height for pixels covering crops of varying height. Theoretical studies on determining effective roughness length z_{0m}^{eff} resulted in different models that have recently been compared by Bottema *et al.* (1998). They found important differences between model predictions (as did Klaassen & Claussen, 1995) and concluded that the choice of the model parameters remains a major point of concern. Having the opportunity to confront these models to real data, we tested different upscaling methods. The roughness length at 20 m resolution is a function of the crop (obtained by multi-temporal image classification) and its observed general seasonal evolution. As first approximations we used the crop weighted roughness length average, the crop roughness length mode (height of the dominant crop) and the average of the logarithm as proposed by Taylor (1987):

$$z_{0m}^{eff} = e^{\overline{\ln(z_{0m})}} \quad (6)$$

We also estimated surface roughness, both at 20 m and 1 km resolution, from NDVI by the empirical relationship as used by evapotranspiration models such as the SEBAL model (Jacob *et al.*, 2002):

$$z_{0m} = e^{(6.38NDVI - 6.665)} \quad (7)$$

A more mechanistic method uses the logarithmic wind profile:

$$u_a(z) = \frac{\langle u_* \rangle}{k} \left(\ln \left(\frac{z}{z_{0m}^{eff}} \right) - \Psi_m(z/L) \right) \quad (8)$$

where k is the Von Karmann constant and Ψ_m the atmospheric stability correction function for momentum. $\langle u_* \rangle$ is the effective friction velocity which is taken as the root mean square of the high resolution u_* provided upon calculation of h_a . Resolution of the equation provides the effective roughness length.

A last and still more sophisticated method to estimate z_{0m}^{eff} at the 1 km² pixel scale followed the same approach but this time based on the high

resolution u_* provided by a two-dimensional boundary layer model (Hasager & Jensen, 1999).

In all cases effective z_{0h} is continued to be set to 1% of effective z_{0m} (§ 2.1). The last two nearly complete parameterisations of z_{0m} have also been used in combination with a proper parameterisation of z_{0h} through the temperature profile (similar to the wind profile used for z_{0m}).

3 RESULTS

3.1 Impact of non-linearity on emissivity and surface temperature

Figure 2 shows the impact of pixel heterogeneity on these variables for one specific day. Table 1 provides a summary for all data acquisition dates.

For comparison with upscaled estimates, observed emissivity on homogeneous sub-elements can be integrated to the lower scale level in two ways depending on its use. This results in a directional e-emissivity and a directional r-emissivity as defined by Norman & Becker (1995). e-emissivity is to be used to calculate Ts when used to estimate the sensible heat flux and r-emissivity should be used in the longwave radiation absorption term of R_n . In both cases, comparison with the 1km² resolution NDVI based emissivity shows that the latter somewhat overestimates heterogeneous pixel emissivity. The effect of the scale change of Tb is shown by comparison with the per pixel averaged Tb. Although such an averaging does not have a real physical meaning, this allows us to notice that Tb has a near linear behaviour. The combined effect of the Tb and emissivity non-linearities on Ts is assessed through their impact on the longwave upward radiation term. Comparison with the per pixel means suggests that upscaled emissivity counterbalances the slight non-linearity of Tb, resulting in a negligible non-linearity for Ts.

Table 1 shows the scale change errors for these variables remain very small. Tb estimation error increases somewhat up to 0.5K with absolute temperature rise in summer, but remains acceptable. More so since the combined effect of Tb and ϵ on Ts results in a negligible error (less than 1W/m² for a flux of about 400 to 500W/m²).

This result is related to the characteristics of the study area. To provide a preliminary answer to the question whether our findings would have been very different on other areas, we artificially modified the high resolution input data: bare ground emissivity was lowered to 0.85, increasing the influence of NDVI, and thereby the spatial contrast, especially in the beginning of the growing season. Tb contrast was increased by applying a sigmoidal transform to the 20m resolution data.

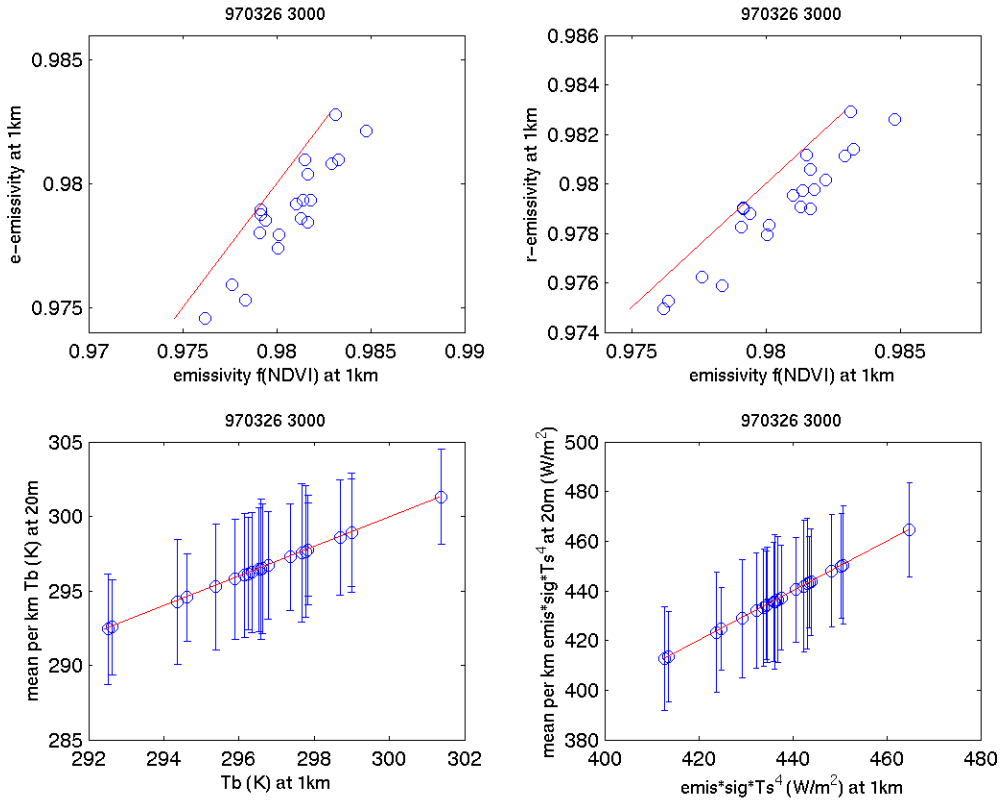


Figure 2 Non-linearity of input parameters for March 26th 1997 : NDVI based emissivity compared to e-emissivity (upper left) and r-emissivity (upper right), Tb compared to the per km mean (and standard deviation in error bar, bottom left), $\epsilon\sigma T_s^4$ compared to the per km mean and standard deviation.

Acquisition date	Tb (K)	ϵ (vs. r- ϵ)	ϵ (vs. e- ϵ)	$\epsilon\sigma T_s^4$ (W/m ²)
970312	0.091	0.001	0.002	0.278
970326	0.105	0.002	0.002	0.345
970410	0.188	0.002	0.002	0.493
970416	0.13	0.002	0.002	0.328
970502	0.109	0.001	0.002	0.359
970522	0.141	0.001	0.001	0.34
970609	0.058	0.001	0.001	0.307
970708	0.334	0.001	0.002	0.745
970729	0.523	0.001	0.002	1.344
970904	0.202	0.001	0.001	0.544
970918	0.082	0.001	0.001	0.255
total	0.254	0.001	0.002	0.618

Table 1 RMSE for the four scale change errors illustrated by figure 2, summarised for all data acquisition campaigns realised at 3000m flight height. The general average also includes 1500m flight height campaigns.

The resulting increased within pixel (1km resolution) variation induces larger scale change effects. As the range of emissivity values increased, the absolute error

also did. Tb RMSE now varies through time from some tenths of K to over 2K and the general RMSE is 1.2K. Finally, the effect on Ts as shown by $\epsilon\sigma T_s^4$ remains very small for the simulated extreme case: $\epsilon\sigma T_s^4$ RMSE varies through time from 0.5 to 4.5 W/m².

3.2 Impact of scaling on roughness and fluxes

Using these upscaled input data allowed us to run the flux estimation models on heterogeneous pixels, using the different ways for upscaling z_0 as described in section 2.3.

As discussed in this same section, the only spatially distributed and non-linear variables influencing daily net radiation are Ts and ϵ . Comparing 1km² means of “locally” estimated R_n with the 1km resolution estimates in the same way as done in figure 2 showed that the slight non-linearity of these input parameters does not have a measurable impact (an average relative RMSE of 0.2%).

Sensible heat flux calculation additionally requires the roughness length z_0 . The upscaled versions of z_{0m} as obtained by equation 8 and the temperature profile based z_{0h} are considered to be the true effective roughness lengths, because they are made to fit the measured heat flux. Figure 3 illustrates for one date (March 26th) the considerable discrepancies with these “true” values as caused by the other upscale methods. The area weighted roughness mean gives a considerable overestimation, especially for z_{0h} . The other two illustrated methods underestimate z_{0m} . The NDVI based roughness only provides acceptable estimates at very low roughness values, whereas the 1% logarithmic average z_{0m} (eq. 6) gives a surprisingly good fit to effective z_{0h} .

The impact of scale change on the heat flux estimate is illustrated by using these data (and those of figure 2) as input for calculation. In figure 4 the resulting values are compared to the 20m resolution estimates integrated to the 1km resolution level. The results clearly are strongly influenced by the roughness upscaling method used. As expected, the use of equation 8, with u^* from the one or two dimensional boundary layer models, provides a near perfect fit. Dominant roughness (mode) based H estimates are worst, but H based on NDVI or area average roughness also shows unacceptable errors. The latter structurally gives an overestimation, whereas the former underestimates H . Regarding the non negligible discrepancies in figure 3 for the logarithmic average roughness estimate, the resulting low upscaled H estimation error is surprising. These results appear to be representative of the results obtained on other days. On all dates, the NDVI based roughness estimate results in a considerable underestimation of H (-34 W/m² on average), while

the inverse is true for area weighted roughness average (+57 W/m² on average). The mode based roughness estimate gives a very variable H estimation error and a structurally high RMSE (88 W/m² on average). The use of the logarithmic average roughness always gives a very slight underestimation, but this error is nearly negligible (-4.7 W/m² on average), confirming the structural character of the observations made on figure 4. The corresponding RMSE is higher than that for the estimations based on complete parameterisations of roughness, but the difference remains very small (res. 12.9 and 9.5 W/m²). Best results are always provided by the 2D boundary layer based roughness estimate, but the improvement is insignificant in our case. It is important to notice here that the quality of the estimations based on complete parameterisations of roughness (e and f) appear to be strongly influenced by upscaling of z_{0h} : estimating z_{0h} as 1% of the equation 8 based z_{0m} caused a considerable bias to appear.

As the other input variables for estimating daily evapotranspiration (§ 2.2) are either non spatialised (A , T_a) or demonstrate a near linear behaviour (Rn_d , Rn_i , T_s). It is therefore not surprising that the evolution of the daily evapotranspiration estimation scale change error (table 2) follows the same trend as H . Of course ET_d is overestimated there where H_i was underestimated and vice versa. Table 2 shows the magnitude of the impact of the H_i estimation error on ET_d : about 0.5mm or more when H_i was based on one of the little accurate effective roughness estimations, an RMSE of only 0.1mm for logarithmic average roughness based H_i , i.e. as weak as those originating from the fully parameterised roughness based H_i estimations.

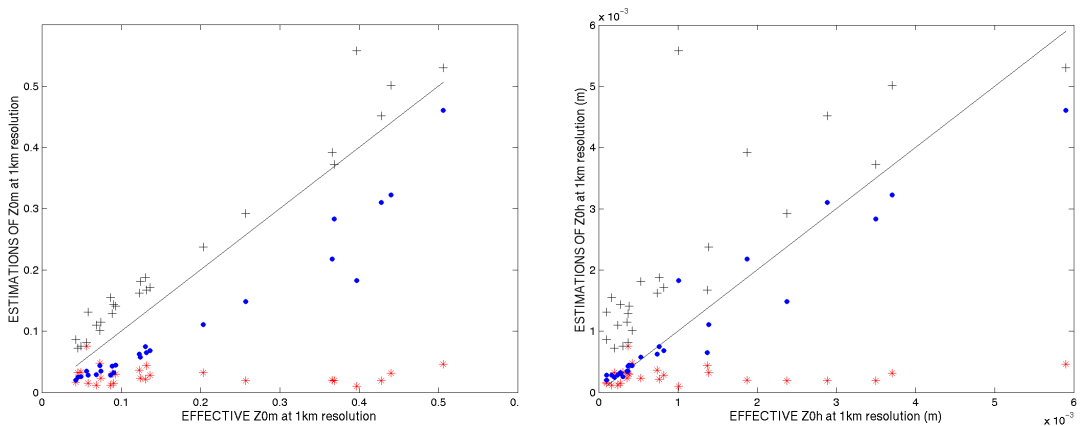


Figure 3 Comparison between estimations of z_{0m} (left) and z_{0h} (right), based on the weighted average (+), on equation 6 (dots), on equation 7 (*) on one side (with $z_{0h} = 0.01z_{0m}$), and the results of the effective roughness (equations 8 for z_{0m}) on the other. The 1km² data of March 26th 1997 are used.

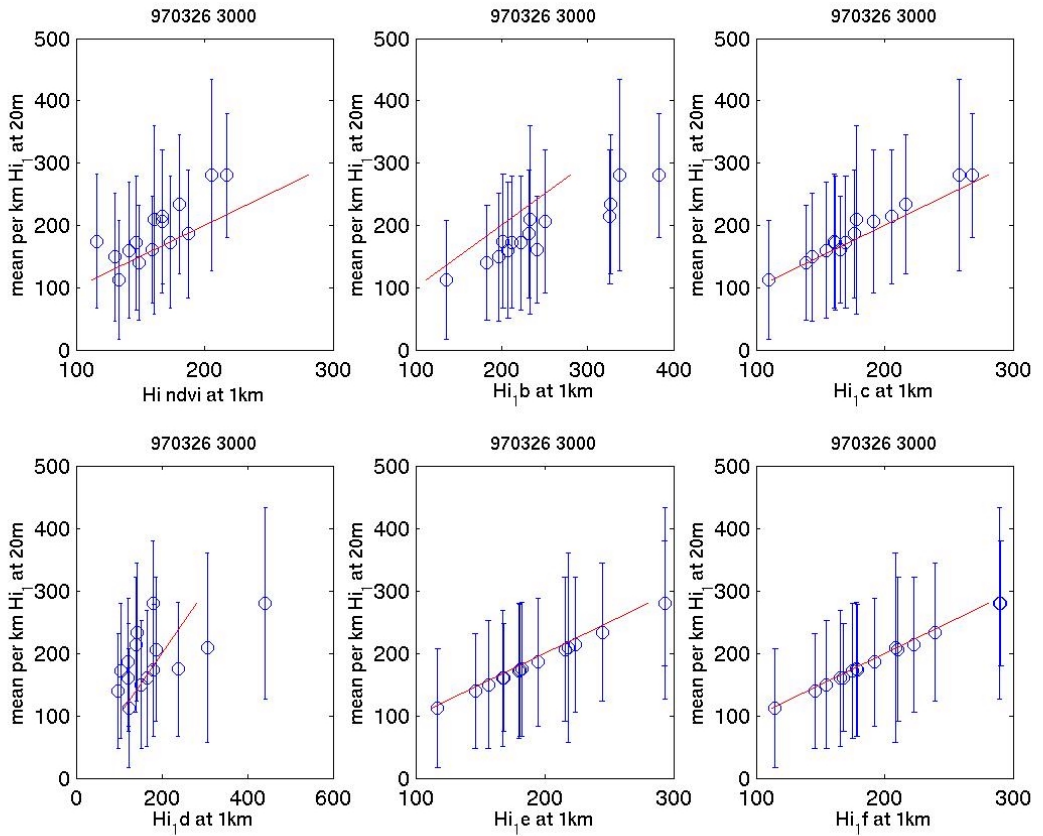


Figure 4 Midday heat flux estimates at 1km resolution on March 26th 1997, as obtained when based on the different roughness upscaling methods (x axis), compared 20m resolution fluxes integrated to 1km² areas (y axis, with standard deviation in error bars). H flux plotted on x axis are based on: ndvi based z_{0m} (upper left, H a); the area weighted average z_{0m} (H b); eq. 6 (H c); mode of z_{0m} at 20m level (H d); z_{0m} from eq. 8 and similarly parameterised z_{0h} (H e); as H e, with u^* from a 2D boundary layer model (H f).

Day	ET a		ET b		ET c		ET d		ET e		ET f	
	mean E	RMSE	mean E	RMSE	mean E	RMSE	mean E	RMSE	mean E	RMSE	mean E	RMSE
970312	0.17	0.24	-0.26	0.28	0.07	0.08	0.03	0.35	-0.04	0.04	-0.03	0.04
970326	0.16	0.24	-0.36	0.40	0.05	0.08	0.05	0.45	-0.07	0.07	-0.05	0.05
970410	0.27	0.38	-0.58	0.63	0.02	0.09	-0.53	0.98	-0.10	0.10	-0.09	0.09
970416	0.25	0.34	-0.41	0.48	0.02	0.08	-0.16	0.60	-0.11	0.11	x	x
970502	0.32	0.42	-0.52	0.58	0.07	0.12	-0.37	0.81	-0.12	0.12	-0.08	0.08
970522	0.59	0.62	-0.47	0.54	0.04	0.09	-0.45	0.78	-0.13	0.13	-0.09	0.09
970609	0.32	0.34	-0.11	0.13	0.05	0.05	-0.11	0.25	-0.04	0.05	-0.03	0.04
970708	0.20	0.31	-0.65	0.70	0.04	0.11	-0.03	0.92	-0.11	0.11	-0.08	0.08
970729	0.41	0.57	-1.43	1.54	-0.04	0.20	0.25	1.52	-0.17	0.20	-0.14	0.17
970904	0.30	0.36	-0.54	0.58	0.03	0.08	0.22	0.63	-0.09	0.09	-0.06	0.07
970918	0.21	0.23	-0.26	0.28	0.03	0.06	0.15	0.34	-0.04	0.04	-0.03	0.03
total	0.29	0.40	-0.53	0.70	0.02	0.12	-0.07	0.78	-0.09	0.11	-0.05	x

Table 2 1km resolution daily latent heat flux estimation errors, summarised for all data acquisition campaigns realised at 3000m flight height. The general average (bottom) also includes 1500m flight height campaigns. *mean E* gives the mean absolute error (mm). RMSE is also given in mm. The suffixes a to f refer to the different upscaled roughness estimation methods (Fig. 4). x: not available.

4 CONCLUSIONS

The impact of non-linearity on flux estimations was studied, using different scenarios for upscaling input parameters. In all cases this impact was measurable. Net surface radiation (R_{n_d} , R_{n_i}) was shown to have a near linear behaviour. H_i and ET_d on the contrary exhibit a significant non linearity, strongly depending upon the way effective surface roughness is estimated. For the fragmented, cultivated area studied, area weighted average, dominant land cover and NDVI based effective roughness estimates induce considerable instantaneous heat flux errors. The logarithmic average results in heat flux estimates of a quality nearly as high as nearly entirely mechanistic estimates.

Using a mechanistic adaptation of the simplified relationship, the impact of this non-linearity on daily evapotranspiration estimates could be quantified. Using the logarithmic average for effective surface roughness the impact of non-linearity was limited to about 0.1mm on average.

Model results appeared to be very sensitive to effective roughness length for heat transfer, z_{0h} . Further study is required to evaluate the role of the $0.01z_{0m}$ rule used to determine z_{0h} , in the good results provided by the effective z_{0m} based on logarithmic averaging. The ratio z_{0m}/z_{0h} is known to differ between homogeneous and heterogeneous surfaces (Hopwood, 1995) and forcing it to remain constant maybe partially compensates the z_{0m}^{eff} estimation error when based on the logarithmic average.

5 ACKNOWLEDGEMENTS

Financial support for this study was provided by the EC in the frame of the WATERMED project (contract ICA3-CT-1999-00015).

6 REFERENCES

- Bottema, M., Klaassen, W. and Hopwood, W. P., 1998, Landscape roughness parameters for Sherwood forest - Validation of aggregation models. *Boundary-Layer Meteorology* **89**, 317-347.
- Bougueraz, F. A., Olioso, A. and Raffy, M., 1999, Modelling radiative and energy balance on heterogeneous areas from remotely sensed radiances. *Canadian Journal of Remote Sensing* **25**(4), 412-424.
- Brutsaert, W., 1982, *Evaporation into the Atmosphere, Theory, History and Applications*. (Dordrecht: Reidel Publishing Co.).
- Carlson, T. N., Capehart, W. J. and Gillies, R. R., 1995, A new look at the simplified method for remote sensing of daily evapotranspiration. *Remote Sensing of Environment* **54**, 161-167.
- Courault, D., Aloui, B., Lagouarde, J.-P., Clastre, P., Nicolas, H. and Walter, C., 1996, Airborne thermal data for evaluating the spatial distribution of actual evapotranspiration over a watershed in oceanic climatic conditions - application of semi-empirical models. *Int. Journal of Remote Sensing* **17**(12), 2281-2302.
- Hasager, C. B. and Jensen, N. O., 1999, Surface-flux aggregation in heterogeneous terrain. *Quarterly Journal of the Royal Meteorological Society* **125**(558), 2075-2102.
- Hopwood, W. P., 1995, Surface transfer of heat and momentum over an inhomogeneous vegetated land. *Quarterly Journal of the Royal Meteorological Society* **121**, 1549-1574.
- Jackson, R. D., Reginato, R. J. and Idso, S. B., 1977, Wheat canopy temperature: a practical tool for evaluating water requirements. *Water Resources Research* **13**(3), 651-656.
- Jacob, F. and Olioso, A., 2002, Derivation of diurnal courses of albedo and reflectef solar radiation from PolDER data. submitted.
- Jacob, F., Olioso, A., Gu, X. F., Hanocq, J. F., Hautecoeur, O. and Leroy, M., 2002, Mapping surface fluxes using visible-near infrared and thermal infrared data with the SEBAL algorithm. submitted.
- Klaassen, W. and Claussen, M., 1995, Landscape variability and surface flux parameterization in climate models. *Agricultural and Forest Meteorology* **73**, 181-188.
- Lagouarde, J.-P., 1991, Use of NOAA-AVHRR data combined with an agrometeorological model for evaporation mapping. *International Journal of Remote Sensing* **12**, 1853-1864.
- Lagouarde, J.-P. and Brunet, Y., 1989, Spatial integration of surface latent heat flux and evaporation mapping. *Advanced Space Research* **9**(7), (7)259-(7)264.
- Lagouarde, J.-P., Brunet, Y., Kerr, Y. and Imberson, J., 1991, Estimating the daily upward longwave radiation from NOAA-AVHRR data for mapping net radiation. *Advanced Space Research* **11**(3), (3)151-(3)161.
- Norman, J. M. and Becker, F., 1995, Terminology in thermal infrared remote sensing of natural surfaces. *Agricultural and Forest Meteorology* **77**, 153-166.
- Olioso, A., 1995a, Estimating the difference between brightness and surface temperatures for a vegetal canopy. *Agricultural and Forest Meteorology* **72**, 237-242.
- Olioso, A., 1995b, Simulating the relationship between thermal emissivity and the Normalized Difference Vegetation Index. *International Journal of Remote Sensing* **16**(16), 3211-3216.
- Olioso, A. and Jacob, F., 2002, Estimation de l'évapotranspiration à partir de mesures de télédétection., *La Houille Blanche*, 62-67.
- Riou, C., Itier, B. and Seguin, B., 1988, The influence of surface roughness on the simplified relationship between daily evaporation and surface temperature. *International Journal of Remote Sensing* **9**(9), 1529-1533.
- Seguin, B. and Itier, B., 1983, Using midday surface temperature to estimate daily evaporation from satellite thermal IR data. *International Journal of Remote Sensing* **4**(2), 371-383.
- Taylor, P. A., 1987, Comments and further analysis on the effective roughness length for use in numerical three-dimensional models. *Boundary-Layer Meteorology* **39**, 403-419.
- Vidal, A., Kerr, Y., Lagouarde, J.-P. and Seguin, B., 1987, Télédétection et bilan hydrique: utilisation combinée d'un modèle agrométéorologique et des données de l'IR thermique du satellite NOAA-AVHRR. *Agricultural and Forest Meteorology* **39**, 155-175.

Land cover, surface temperature and leaf area index maps from satellites used for the aggregation of momentum and temperature roughnesses

Charlotte B. Hasager*, Niels Otto Jensen*, Albert Olioso⁺

*Risø National Laboratory, Wind Energy Department, Roskilde, Denmark

⁺INRA Bioclimatologie, Domaine Saint-Paul, Avignon, France

charlotte.hasager@risoe.dk, n.o.jensen@risoe.dk, olioso@avignon.inra.fr

ABSTRACT- A new concept for aggregation (area-averaging) of the roughness lengths for the momentum and sensible heat flux is described. The result are the so-called effective roughness values that are useful for the calculation of the surface energy balance and surface fluxes at larger scales e.g. in climate models, weather forecasts and hydrological modelling in heterogeneous landscapes. Typically a ratio between the momentum roughness, z_0 and temperature roughness, z_{0t} , of the order of 1 or 10 is assumed. In the current work the roughnesses are directly calculated based on a set of linearized atmospheric flow equations. The equations are solved by Fast Fourier Transforms and iteratively solved in regard to stability (Monin-Obukhov similarity scaling), viscous sub-layer resistance and water roughness (Charnock). The microscale model calculates the area-average of $\langle z_0 \rangle$ and $\langle z_{0t} \rangle$ for each large grid cell containing a number of local microscale patches of the size order of 30-1000 m. At this horizontal length scale the non-linear advective effects are highly significant. The results from a case study in the Alpilles area in France are presented. The model inputs are surface temperature maps, leaf area index maps and land cover maps based on high-resolution optical satellite or airborne scenes. The local roughness length for momentum is assigned per pixel based on land cover type and vegetation height. For bare soil, water and urban area there is a constant ratio between the local values of z_0 and z_{0t} but in vegetated areas the ratio is dependent upon vegetation type and leaf area index. Therefore $\langle z_0 \rangle$ and $\langle z_{0t} \rangle$ are no longer proportional.

1 INTRODUCTION

There is a need to calculate the aggregated, i.e. non-linearly area-averaged, values of the roughness lengths for momentum and scalars because these effective values are necessary input to many regional and global scale atmospheric models used for weather prediction, climate simulations as well as in hydrological applications. Microscale heterogeneities, i.e. surface changes in the spatial domain of the order of 100 m to 1000 m, are very important for the total grid averaged surface stress and the grid averaged surface heat fluxes. The need to find practical and fast aggregation routines for the roughnesses is a well-known problem (e.g. Viterbo 1996, Sellers et al. 1996). Area-averaging the roughness by simple area-weighted averaging is not physically sound. This is due to the highly non-linear turbulent responses of the atmospheric flow.

Recently an objective, physically-based model that takes the turbulent response of the atmospheric flow into account for every roughness step change in the terrain was developed. The solution is numerical fast because the linearized flow equations are solved by

Fast Fourier Transforms (Hasager and Jensen, 1999). The model is a so-called microscale surface-flux aggregation model in 2-dimensions in the horizontal domain.

Briefly described the microscale aggregation model needs input of high-resolution maps of roughness, land cover type, leaf area index (LAI) and surface temperature and a known wind speed, wind direction and air temperature at the computational level (e.g. the lowest level of the Météo France Arpège model at 25m). The flow equations include correction for atmospheric stability (Monin-Obukhov similarity scaling). This is iteratively calculated in every pixel. The friction velocity and sensible heat flux is calculated pixel-wise in the domain and area-averaged non-linearly to the desired grid cell size of low-resolution satellite data such as NOAA AVHRR 1 km grid cells (Wassenaar et al. 2002) or mesoscale climate models (Hasager et al. 2002a).

The model outputs are 1) the effective roughness length for momentum, $\langle z_0 \rangle$ that always will be larger than a logarithmic average due to the added effect of non-equilibrium flow conditions, 2) the effective

scalar roughness length, $\langle z_{0t} \rangle$ (for heat, water vapour and passive scalars) that generally will be smaller than for equilibrium conditions (Wood and Mason, 1991), 3) the friction velocity map, 4) the scalar scale map and 5) the sensible heat flux map. The maps have the same spatial resolution as the input maps.

It is seen as an advantage to calculate $\langle z_{0t} \rangle$ directly instead of estimating it as a fraction of $\langle z_0 \rangle$ for surface-flux calculation.

The logarithmic ratio between the two roughness values is named the kB^{-1} value. For homogeneous surfaces with porous vegetation a value of 2.3 is often assumed valid (see Hasager, 1997), but worldwide experimental evidence shows a very large variation (e.g. Mölders et al., 1998).

The overall goal of calculating the effective roughness for scalar transport is to achieve very precise area-averages of the surface fluxes. For very large patches equilibrium conditions will apply, but for shorter horizontal length scales typical for instance in the Alpilles area in France, non-equilibrium conditions is expected to dominate the scalar surface fluxes.

2 THEORETICAL PART

In surface-layer profile relations it has been customary to take the roughness length for temperature z_{0t} equal to z_0 for momentum. However, especially if z_0 includes the effect of separated flow over orography this can lead to quite erroneous results for the heat flux. In the following we will assume that z_0 is the micrometeorological roughness, but as we will show below, z_{0t} is in general less than z_0 . How much smaller depends on the type of the surface, and unfortunately also on the value of the friction velocity u_* . Recently the formal dependence was presented by Jensen et al. (2002) and is described in detail in the following. Note, we reserve brackets e.g. $\langle z_0 \rangle$ to signify spatial averages as opposed to z_0 for local values.

Per definition we have

$$u_* r_a = \frac{u}{u_*} = \frac{1}{\kappa} \left(\ln \frac{z}{z_0} - \Psi_M \left(\frac{z}{L} \right) \right) \quad (1)$$

where u_* is the friction velocity, r_a is the aerodynamic resistance, u is the mean wind speed, κ the von Kármán constant (≈ 0.4), z is the height above the displacement distance of the vegetation, and z_0 is the aerodynamic roughness.

The correction function, Ψ_M which depends on atmospheric stability expressed by the Monin-Obukhov length

$$L = \frac{u_*^2}{\kappa \frac{g}{T} \theta_*} \quad (2)$$

is an empirically determined function (fitted analytical function). While r_a is the only limiting resistance for “deposition” of momentum, scalars¹ such as temperature and humidity have an additional resistance r_b because they are also limited by molecular diffusion through the viscous sub-layers that blanket all surfaces. Thus for temperature

$$u_* (r_a + r_b) = \frac{\theta - \theta_0}{\theta_*} = \frac{1}{\kappa} \left(\ln \frac{z}{z_{0t}} - \Psi_H \left(\frac{z}{L} \right) \right) \quad (3)$$

where θ is the temperature at height z , θ_0 is the surface temperature and θ_* is a scale for the temperature fluctuations ($\theta_* u_*$ is the sensible heat flux, H). z_{0t} is the roughness for temperature and Ψ_H is the Monin-Obukhov function for heat flux. Implicitly, eq. (3) assumes that the von Kármán constant as well as the displacement distance are the same for a scalar as for momentum. From eqs.(1) and (2) it follows that

$$u_* r_b = \frac{1}{\kappa} \left[\ln \frac{z_0}{z_{0t}} - \left(\Psi_H \left(\frac{z}{L} \right) - \Psi_M \left(\frac{z}{L} \right) \right) \right] \quad (4)$$

This equation establishes the intimate connection between r_b and z_{0t} . In the following we shall neglect the subtle difference between Ψ_H and Ψ_M which then leads to the simple relationship

$$z_{0t} = \frac{z_0}{\exp(\kappa u_* r_b)} \quad (5)$$

For smooth surfaces z_0 and z_{0t} in eq.(4) are replaced by the molecular sub-layer thickness ν/u_* and D/u_* respectively, leading to a fixed ratio between the momentum and temperature roughness and

$$z_{0t} = \frac{z_0}{Pr} \quad (6)$$

where Pr is the Prandtl number (≈ 0.7) equal to the kinematic viscosity ν ($\approx 1.5 \cdot 10^{-5} \text{ m}^2 \text{ s}^{-1}$) divided by the molecular heat conductivity D ($\approx 2 \cdot 10^{-5} \text{ m}^2 \text{ s}^{-1}$). In practice this will occur only over water surfaces under low wind conditions (at about $u_* < 0.1 \text{ m s}^{-1}$ or u_{10m} less than 3.3 m s^{-1}).

¹ although temperature and humidity have some influence on buoyancy they are for some practical purposes regarded as passive contaminants

The above implies that $u_* r_b$ is constant for smooth surfaces. However, in general this product is not a constant but is in itself a function of u_* . Hence it is immediately seen from eq.(5) that z_{0t} is not a property of the surface alone but depends on the flow.

2.1 Expressions for the additional resistance: r_b

As mentioned above $u_* r_b$ is not in general a constant. It is customary to describe its variation in relation to the roughness Reynolds number

$$Re = \frac{z_0 u_*}{\nu} \quad (7)$$

Figure 1, adapted from Garratt and Hicks (1973), shows such dependencies. The striking thing is the difference between rough surfaces consisting of bluff elements and rough surfaces consisting of plants (fibrous canopies).

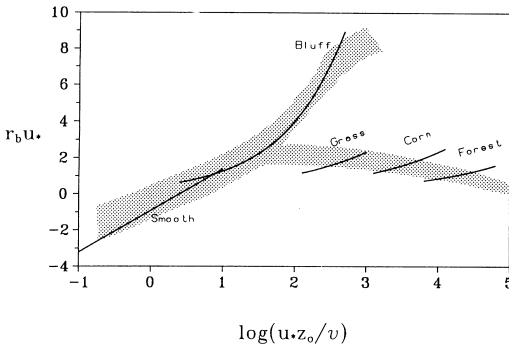


Figure 1 Adapted from Garratt and Hicks (1973). Note that there is an error in the label on the ordinate axis. It should have been $\kappa_b u_*$.

The bluff body branch on the figure can be described by the relation

$$\kappa_b u_* = c \text{Pr}(Re)^{1/2}. \quad (8)$$

The types of land cover categories where this equation applies ranges from water bodies that are aerodynamically rough ($u_* > 0.1$ m/s) over ice, snow and bare soils to cities. However, it turns out that for large z_0 values, the values of z_{0t} become unrealistically small (e.g. 10^{-40} m). So it is concluded that the relation in eq. (8) is not realistic for large values of Re . Therefore a modified expression is sought.

It is suggested to express Re as a function of the length scale of typical materials over which the development of laminar layers at the urban surfaces takes place, e.g. bricks, roof materials etc. In fact the method is similar in concept to the one applied for plant canopies by Jensen and Hummelshøj (1995). In other words, the laminar layers do not scale with the height of the

buildings but rather with the smaller scale features of the urban surfaces, e.g. roof tiles, windows, etc.

$$Re = \frac{l u_*}{\nu} \quad l = \begin{cases} z_0 & \text{if } z_0 < 0.05m \\ 0.05 & \text{if } z_0 \geq 0.05m \end{cases} \quad (9)$$

Thus by combining eqs. 5 and 9 we get

$$\ln \frac{z_0}{z_{0t}} = c \text{Pr} \left(\frac{l u_*}{\nu} \right)^{1/2}. \quad (10)$$

The factor $c \text{Pr}$ in the above equation is assessed to be about 0.4.

In the MKS unit system we thus have the following practical expressions for non-vegetated land surfaces

$$z_{0t} = \frac{z_0}{\exp(100 \sqrt{z_0 u_*})} \quad \text{for } z_0 < 0.05 \text{ m} \quad (11)$$

and

$$z_{0t} = \frac{z_0}{\exp(22 \sqrt{u_*})} \quad \text{for } z_0 \geq 0.05 \text{ m} \quad (12)$$

Figure 2 shows the variation of z_{0t} as a function of z_0 for non-vegetated surfaces and it is seen that z_{0t} varies several orders of magnitude.

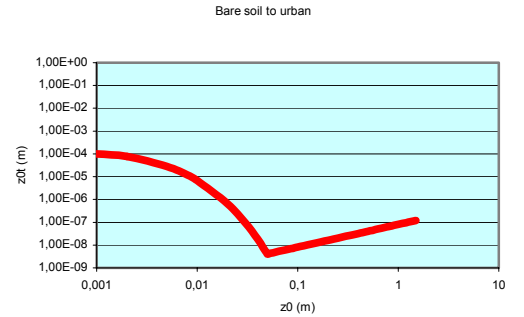


Figure 2 z_{0t} in m as a function of z_0 for non-vegetated surfaces for $u_* 0.5 \text{ m s}^{-1}$.

Over water the description is complicated by the fact that the roughness z_0 depends on u_* through Charnock's formula (Charnock, 1955)

$$z_0 = \alpha \frac{u_*^2}{g} \quad (13)$$

where g (9.81 m s^{-2}) is the constant of gravity and $\alpha \approx 0.015$ but where the exact value actually depends on the wave age, the fetch length and probably also the water depth at least over shallow water.

For smooth water, i.e. for $u_* < 0.1$

$$z_{0t} = z_0; \quad z_0 = 0.1 \nu / u_* \quad (14)$$

$$\nu \approx 1.5 \cdot 10^{-5} \text{ m}^2 \text{ s}^{-1}.$$

For rough water, i.e. for $u_* > 0.1$

$$z_{ot} = \frac{z_o}{\exp(100(z_o u_*)^{1/2})}; \quad z_o = 0.015 \frac{u_*^2}{g} \quad (15)$$

The plant canopy branch (see Figure 1) on the other hand has literally no dependence on Re . It was shown by Jensen and Hummelshøj (1995) that this is because the length scale z_o is not relevant. For example z_o for a forest is very large but what controls r_b , or more precisely the thickness of the viscous sub-layers is the dimensions l of the fibrous elements. For plant canopies Jensen and Hummelshøj (1997) give

$$r_b u_* = c \frac{Pr}{LAI^{2/3}} \left(\frac{l u_*}{\nu} \right)^{1/3} \quad (16)$$

where LAI is the leaf area index, the Prandtl number has already been defined and c here is a constant of about 5. The length scale l is around $3 \cdot 10^{-3}$ m for grass, grains and conifer forest and around $3 \cdot 10^{-2}$ m for deciduous forest in leaves.

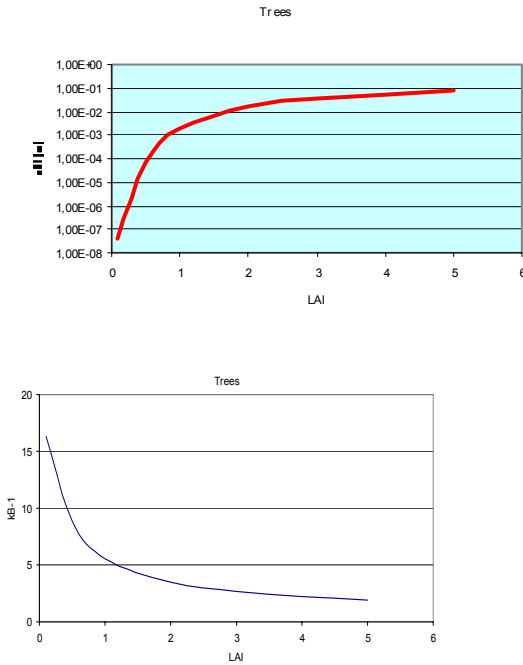


Figure 3 a) z_{0t} in m as a function of LAI and b) kB^{-1} as a function of LAI for forest with z_o 0.5 m.

For vegetated land

$$z_{ot} = \frac{z_o}{\exp\left(\frac{5.85}{LAI^{2/3}} u_*^{1/3}\right)} \quad (17)$$

Figure 3a and b show the variation of z_{0t} and kB^{-1} as a function of LAI for forest, respectively. The value of

z_{0t} varies several orders of magnitude and for large values of LAI the value of kB^{-1} approaches 2.3.

3 THE AGGREGATION PROGRAMME

The new model development is an explicit calculation of the effective roughness for temperature $\langle z_{0t} \rangle$. The approach is to apply a set of equations valid for local conditions for the different land cover types in the terrain for z_{0t} and iteratively solve these.

The model runs on pc and the calculation for a 512×512 domain (e.g. a 15 km * 15 km region with an input of 30 m * 30 m resolution) is achieved typically in less than 10 seconds computational time. Figure 4 shows a schematic of the model components.

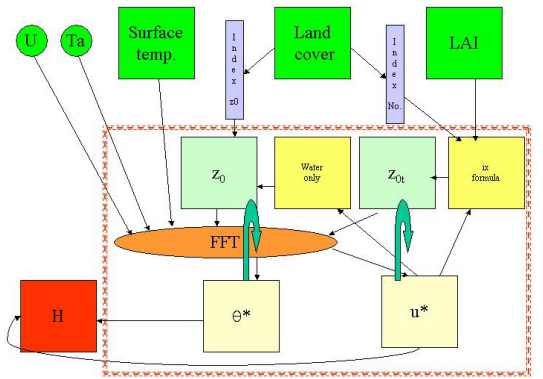


Figure 4 Schematic of the surface-flux microscale aggregation model. The inputs are mean wind speed (u) and direction, air temperature (T_a) at the computational level and maps of surface temperature, land cover classes and LAI from satellite or airborne Earth observation data. The aerodynamic roughness map (z_0) is generated from an index list except for water bodies where the Charnock's relationship is used. The index number and z_{0t} -equation (ix-formula) are prescribed for each land cover type to provide the initial z_{0t} map (eqs.11, 12, 14, 15 and 17). The model runs within the dotted line. The linearized atmospheric flow equations are solved by FFT. The output maps are the friction velocity (u_*), the temperature scalar (θ_*), the roughness map (z_0) and the scalar roughness map (z_{0t}) all of which are found through iteration (indicated by the curved arrows). The iteration is due to the stability function (Monin-Obukhov similarity scaling) and the Charnock's relationship. The final outputs are a map of the sensible heat flux (H) and the effective roughness for momentum $\langle z_0 \rangle$ and for scalar transport $\langle z_{0t} \rangle$ calculated directly.

4 ALPILLES CASE STUDY

4.1 Experimental site and remote sensing data

The experimental site in the Alpilles area is located in the south of France (N43°47', E4°45') and the measurement campaign was from October 1996 to November 1997. The ground-based study involved surface-flux observations in various crops e.g. wheat, sunflower, maize, alfalfa (Oliosio et al. 2002a). Other dominant land cover types within the 5 km by 5 km study area are orchards and forest.

The airborne observations include POLDER and thermal scenes (Jacobs et al. 2002). The thermal scanner was flown at 1500 m and 3000 m height on a total of 18 days. The thermal images were calculated into radiant surface temperature maps including correction for emissivity and the roughness maps were produced from combining land cover information and vegetation height from field studies (Oliosio et al. 2002b). The *LAI* maps were retrieved from airborne POLDER NDVI data by neural network analysis (Weiss et al. 2002) and the land cover type map was retrieved from SPOT satellite scenes and field observations through a supervised classification analysis (Oliosio et al. 2002b).

4.2 The meteorological data

The upper boundary atmospheric conditions are from local radiosoundings for three days and from the Arpège meteorological model for 18 days. The Arpège meteorological model results from Météo France may not represent the local area of the Alpilles very well due to the coarse horizontal grid resolution of around 30 km. However comparison of the Arpège grid air temperatures to the local radiosounding observations shows a good correspondance. The Arpège air temperatures are slightly higher than the radiosounding observations in all cases. This is reassuring as the radiosoundings are probed higher (53, 42 and 46 m) in the atmosphere than the Arpège grid level.

The local air temperatures at the 2 m level measured in a well-watered alfalfa field are also compared successfully to the Arpège temperatures (Fig. 5). In this well-watered alfalfa field *H* is low and the atmospheric condition – very locally – has near-neutral stability. Therefore it is to be expected that the 2m air temperature will be quite similar to the temperature aloft.

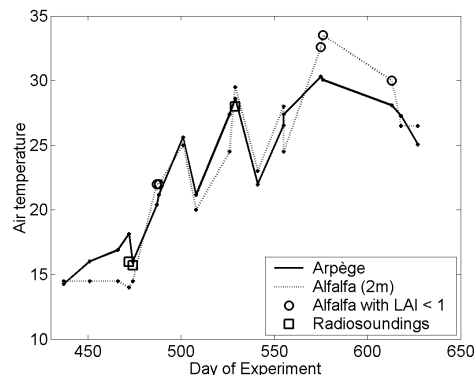


Figure 5 The Arpège meteorological air temperatures at 25 m and the surface air temperature at 2 m in a well-watered alfalfa field at the Alpilles site.

Furthermore the Arpège air temperatures are compared to the average and minimum surface temperatures in the airborne surface temperature maps. As all cases were acquired around noon in the growing season in the southern part of France, the average land surface temperature was always hotter than the average air temperature aloft (unstable conditions). The minimum surface temperature was determined from the *NDVI-Ts* minimum method.

The minimum surface temperature was on average around 10 °C cooler than the average surface temperature in the thermal maps. The minimum surface temperature in the maps was most often found in forest but sometimes in well-watered crops. In the case of near-neutral static stability the air temperature aloft would be close to the minimum surface temperature. The Arpège air temperature is lower (-1.6 °C) than the minimum surface temperature in only one case and within 2 °C in 11 cases out of 23 cases. This indicates that there typically is not local inversions (as expected) and that the minimum surface temperature may be found aloft at a (much) higher level in the atmosphere.

The wind speeds from the Arpège meteorological model, local field observations and radiosoundings in the Alpilles area are successfully compared in figure 6 at the times of thermal image data acquisition. The difference in wind speed between the Arpège data and field observations are on average 0.7 m s⁻¹ with a maximum of 3 m s⁻¹ and a standard deviation of 1.45 m s⁻¹.

Comparing wind speeds between Alpilles observations and Arpège results

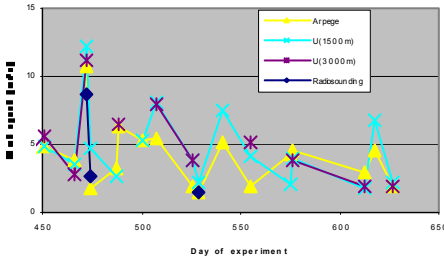


Figure 6 Comparing wind speeds from the Arpège meteorological model at 25 m grid level, field observations at 2m and radiosounding observations at 53, 42 and 46m in the Alpilles area at the times of thermal image data acquisition of 1500 m and 3000m flight levels.

4.3 Microscale aggregation model results

Previously the microscale aggregation model has been run with a fixed ratio between the effective roughness lengths of 0.1, 0.01 and 0.001 on the Alpilles data set. It was found that a ratio of 0.01 (kB^{-1} of 4.6) gave the best correspondence between field based H observations and aggregation model results (Hasager et al. 2002b). The bias was near zero and the rmse around 80 W m^{-2} . The model results on H were better with input of radiosounding data indicating that these locally are more precise than the Arpège data.

The new aggregation model results on kB^{-1} is shown in figure 7. The directly calculated values of kB^{-1} range from 5 to 9, i.e. they are somewhat larger than previously found (kB^{-1} 4.6).

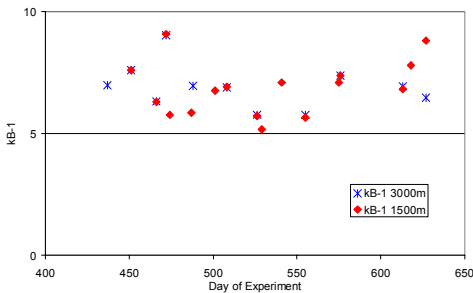


Figure 7 The kB^{-1} values calculated directly by the aggregation model for the cases in the Alpilles site.

The comparison between in-situ ground measurements of H and the new model results are graphed in figure 8a and b for input of radiosounding data and Arpège data, respectively. It is seen that there is a bias around 30 W m^{-2} for both but that the rmse is lower for input of radiosounding (around 70 W m^{-2}) than for Arpège data (around 85 W m^{-2}). This means that there is not obtained any significant improvement on the calculation of H compared to the results in Hasager et al. (2002b). It is however a great advantage that the ratio between the roughness for momentum and scalar fluxes did not have to be guessed.

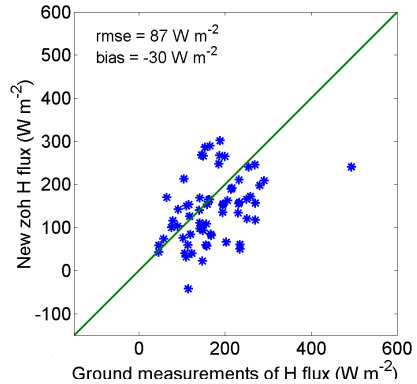
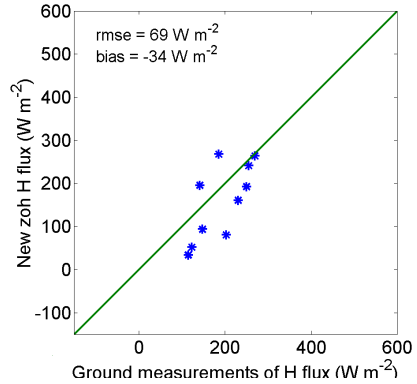


Figure 8 a) Comparison of in-situ ground observations of sensible heat (H) flux to the new aggregation model results for local radiosounding input, b) for Arpège data.

The new H results are compared to the previous H model results (Hasager et al. 2002b) for all data points corresponding in space to ground flux observations and the comparison is shown in figure 9. It seems that two sets of observations each belonging to a different linear regression line exits. The results are preliminary as no in-depth study has been carried out yet to explain this result.

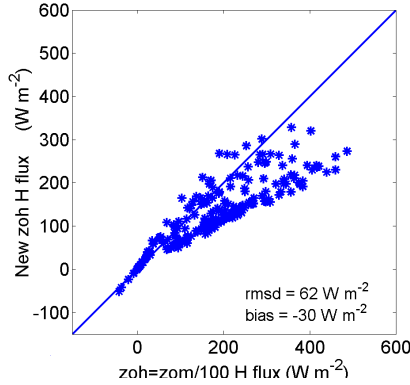


Figure 9 Comparison of sensible heat flux (H) from assuming kB^{-1} 4.6 and the new H result with direct calculation of kB^{-1} for all data points corresponding in space to ground flux observations.

For non-vegetated surfaces there is a constant ratio between the local values of z_0 and z_{0t} but for vegetated surfaces the ratio is dependent upon vegetation type and LAI . Therefore $\langle z_0 \rangle$ and $\langle z_{0t} \rangle$ are no longer proportional in (partly) vegetated terrain. This effect is demonstrated for the Alpilles area for day of experiment 487 where the mean LAI was 1.123. It is now (artificially) assumed that the whole area possess this value of LAI as well as mean values ranging from 0.5 to 6.0 LAI . The effective $\langle z_{0t} \rangle$ values are graphed as a function of LAI in figure 10.

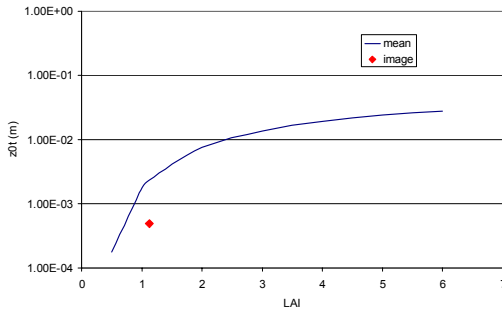


Figure 10 The $\langle z_{0t} \rangle$ value calculated directly by the aggregation model for mean LAI values assumed to range from 0.5 to 6.0 at the Alpilles site. The result for the actual spatial variation is also shown ('image').

It is found that $\langle z_{0t} \rangle$ including the actual (real) spatial variations in LAI is lower than assuming a mean LAI value. For large values of LAI , $\langle z_{0t} \rangle$ levels off to a nearly constant value whereas for decreasing values of LAI $\langle z_{0t} \rangle$ rapidly decreases. This indicates that $\langle z_{0t} \rangle$

is very variable in areas of relatively low LAI values. Furthermore it demonstrates that the spatial variations of LAI are of great importance.

5 CONCLUSION

A new version of the physically-based surface-flux microscale aggregation model (original model described in Hasager and Jensen, 1999) is presented theoretically and applied on the Alpilles data set. The new development include the additional input of land cover type and LAI maps to the model in order to calculate not only the effective roughness for momentum $\langle z_0 \rangle$ but also the effective roughness for scalars $\langle z_{0t} \rangle$ directly. It is shown that the logarithmic ratio between $\langle z_0 \rangle$ and $\langle z_{0t} \rangle$ ranges from 5 to 9 for the 18 days studied at the Alpilles site based on airborne thermal images, LAI maps from airborne POLDER NDVI, land cover maps from SPOT and air temperatures, wind speed and wind direction from local radiosoundings and Arpège data. A value of kB^{-1} 2.3 is often assumed valid (in homogeneous terrain) but experimental data (from heterogeneous sites) have shown much larger values (e.g. up to 25). The new directly calculated values confirms the general experimental evidence that kB^{-1} is much larger than 2.3 in heterogeneous terrain.

Comparison of in-situ surface sensible heat flux from ground observations in various crops in the Alpilles area to the new aggregation model results shows a bias around 30 $W m^{-2}$ and rmse around 70 $W m^{-2}$ for radiosounding observation input and rmse around 85 $W m^{-2}$ for Arpège data input. This is not significantly better than if assuming kB^{-1} 4.6 but the great advantage is that no assumption has to be taken. The results for the Alpilles site are preliminary as further investigation is on-going.

6 OUTLOOK

After ascertaining that the local H flux estimates are in accordance with in-situ observations, it is possible to area-average the flux at the 1 km grid scale comparable to NOAA AVHRR resolution. Sensible heat flux estimated from the microscale aggregation model at the larger scale may then be used as a guideline for the applicability of certain simpler surface-flux calculation methods at that scale.

Acknowledgements

The EC 5th framework WATERMED project funding ICA3-CT-1999-00015 for application of the aggregation model to the Alpilles data set and the SAT-MAP-CLIMATE project funding from the

Danish Research Agency, Space Research Grant 5006-00-0063, for development of the new model version is gratefully acknowledged.

REFERENCES

- Charnock, H. 1955 Wind stress on a water surface. *Quart. J. Royal Met. Soc.*, 81, 639-640
- Garratt J.R. and B.B. Hicks (1973) Momentum heat and water vapour transfer to and from natural and artificial surfaces. *Q.J.R.Met.Soc.*, **99**, 680-687.
- Hasager C.B. 1997. Surface fluxes in heterogeneous landscape. *Ph.D. dissertation. Risø-R-922(EN)*, 177p
- Hasager, C.B. & Jensen, N.O. 1999 Surface-flux aggregation in heterogeneous terrain, *Quart. J. Roy. Met. Soc.* **125**, 2075-2102.
- Hasager, C.B., Nielsen, N.W., Jensen, N.O., Christensen, J.H., Dellwik, E., Soegaard, H., and Boegh, E. 2002 Effective roughness calculated from satellite-derived land cover maps and hedge information and used in a weather forecasting model. *Boundary-Layer Meteorology* (submitted).
- Hasager, C.B.; Olioso, A.; Jacob, F., 2002b Parametrisation of aggregated roughness and sensible heat flux from field scale to hydrological scale by microscale modelling in the Alpilles experiment in France. EGS 2002, 27. General assembly, Nice (FR), 21-26 Apr 2002. *Geophys. Res. Abstr.* (CD-ROM) (2002) 4. See [abstract](#) and [poster](#)
- Jacob, F., Olioso, A., Gu, X.F., Su, Z., and Seguin, B., 2002, Mapping surface fluxes using airborne visible, near infrared, thermal infrared remote sensing data and a spatialized surface energy balance model. *Agronomie*, 22, in press.
- Jensen, N.O., Hasager, C.B. and Larsen, S.E. 2002 Aggregation of momentum and temperature roughnesses based on satellite data. European Geophysical Society 2002, XXVII General Assembly, Nice, France, 21-26 April, *Geophys. Research Abstracts*. (CD-ROM) See [abstract](#)
- Jensen N.O. and P. Hummelshøj (1995) Derivation of canopy resistance for water vapour fluxes over a spruce forest, using a new technique for the viscous sublayer resistance. *Agri. and Forest Met.*, **73**, 339-352.
- Jensen N.O. and P. Hummelshøj (1997) Erratum to "Derivation of canopy resistance for water vapour fluxes over a spruce forest, using a new technique for the viscous sublayer resistance". *Agri. and Forest Met.*, **85**, 289.
- Mölder, M., Sugita, M., Hiyama, T., and Bergstrom, H.: 1998, 'Regional Sensible Heat Flux and Thermal Roughness Length of an Inhomogeneous Landscape', *Hydrological Processes* 2115-2131
- Olioso, A., Braud, I., Chanzy, A., Demarty, J., Ducros, Y., Gaudu, J.-C., Gonzalez-Sosa, E., Lewan, E., Marloie, O., Ottlé, C., Prévot, L., Thony, J.-L., Autret, H., Bethenod, O., Bonnefond, J.-M., Bruguier, N., Buis, J.-P., Calvet, J.-C., Caselles, V., Chauki, H., Coll, C., François, C., Goujet, R., Jongschaap, R., Kerr, Y., King, C., Lagouarde, J.-P., Laurent, J.-P., Lecharpentier, P., Mc Aneney, J., Moulin, S., Rubio, E., Weiss, M., and Wigneron, J.-P., 2002, Monitoring energy and mass transfers during the Alpilles-ReSeDA experiment. *Agronomie*, 22, in press.
- Olioso, A., Hasager, C., Jacob, F., Wassenaar, T., Chehbouni, A., and Marloie, O., 2002, Mapping surface sensible heat fluxes from thermal infrared and reflectances data using various models over the Alpilles test site. First International Symposium on Recent Advances in Quantitative Remote Sensing, 16-20 September 2002, Valencia, Spain.
- Sellers P.J., D.A.Randall, G.J.Collatz, J.A.Berry, C.B.Field, D.A.Dazlich, C.Zhang, G.D.Collelo and L.Bounoua, 1996, A revised land surface parameterization (SiB2) for atmospheric GCMs. Part I. Model formulation., *J.Climate* Vol 9, no 4, p676-705
- Viterbo, P., 1996, The representation of surface processes in general circulation models, European Centre for Medium-Range Weather Forecasts, Reading, UK, pp201
- Wassenaar, T., Olioso, A., Hasager, C., Jacobs, F., Chehbouni, A. 2002 Estimation of evapotranspiration on heterogeneous pixels. In: *Proceedings of 1st international conference on Recent Advances in Quantitative Remote Sensing* (this issue)
- Weiss, M., Baret, F., Leroy, M., Hauteceær, O., Bacour, C., Prévot, L., Bruguier, N. 2002 Validation of neural net techniques to estimate canopy biophysical variables from remote sensing. *Agronomie* 22
- Wood N. and P.Mason, 1991. The influence of static stability on the effective roughness lengths for momentum and heat transfer, *Q.J.R.Meteorol.Soc.* 117, 1025-1056

F. Jacob, A. French, T. Schmugge, K. Ogawa, B. Kustas

USDA/ARS Hydrology and Remote Sensing Laboratory,
Bldg 007, BARC-West, Beltsville, MD 20705-2350, USA

fjacob@hydrolab.arsusda.gov, anfrench@hsb.gsfc.nasa.gov, schmugge@hydrolab.arsusda.gov

ABSTRACT - *This paper reviews investigations focused on the comparison of two surface energy balance models using ASTER imagery. The main difference between the models we compared is the description of the soil - vegetation - atmosphere by discriminating or not the soil and vegetation components. The comparison was performed over two different areas, a grazing landscape located in OK, USA and a semi-arid region in the northern Chihuahuan desert, NM, USA. The benefit of using ASTER imagery is to consider a 90 m spatial scale that reduces problems due to mixed pixels. We first assessed model assumptions. It was shown that the models relied on contradictory hypotheses when dealing with albedo. Nevertheless, the differences in net radiation computations were similar to errors reported in the literature when performing validations. Overall, the comparison of the four components of surface energy balance could provide very close results or significant differences according to both the study site and the date. We did not observe any systematic correlation between the differences in intermediary variables and the differences in surface energy fluxes. On the other hand, the models provided some systematic differences, which underlined that they presented some similarities in their behaviors.*

1 INTRODUCTION

Knowledge of surface energy balance is of prime interest for several applications such as meteorology, hydrology and agronomy. In order to provide maps of surface energy fluxes at different temporal and spatial scales, several investigations have focused these last few years on using surface energy balance models along with remote sensing data. The remaining difficulty is then to derive some variables driving energetic exchanges that can not be retrieved directly from remote sensing, such as micrometeorological and aerodynamic variables or soil thermal properties. Numerous models have been proposed, aiming at either retrieving indirectly these variables or avoiding their use. These models differ on several points: the considered mechanisms and their description level, the use of absolute or spatial / temporal differential approaches, and the differentiation or not of the surface components that do not have the same biophysical properties.

A possible way to distinguish these models is considering or not soil and vegetation components, commonly labeled "one source" and "two source" approaches. This distinction is important since it results in significantly different descriptions of Soil - Vegetation - Atmosphere (SVA) interface

when dealing with radiative and aerodynamic properties, as well as energy balance components. The resulting assumptions are more or less realistic regarding to environmental conditions the models are applied. A possible way to assess the robustness and the limitations of a given method is to validate against ground measurements. However, model validations are restricted by the environmental conditions of the considered experiments. Another possibility is to intercompare model estimates over entire scenes acquired by a given sensor, the benefit being to account for the numerous situations included in a given scene. In this case, the goal is to confront the model assumptions and to assess the agreement between their physical statements.

The goal of this study was to perform an intercomparison of one source and two source approaches using ASTER scenes. As compared to other sun-synchronous sensors such as Landsat, Spot, AVHRR, Vegetation or MODIS, the benefit of the ASTER sensor is to provide multispectral measurements from visible to thermal infrared with a spatial resolution ranging between 15 and 90 m. Using such a spatial scale reduces problems due to mixed pixels when comparing different models. We considered two surface energy balance models that were previously validated and that aimed at ac-

counting for the spatial variability depicted by natural landscapes. After the presentation of the data and the models, we present the results we obtained when comparing them. The comparison includes several variables that describe the surface radiative and aerodynamic properties, and finally the energy fluxes.

2 THE MODELS

The two models we considered were the SEBAL (Surface Energy Balance Algorithm for Land) algorithm (Bastiaanssen et al., 1998) and the TSEB (Two Source Energy Balance) model (Norman et al., 1995). TSEB and SEBAL were previously validated considering different kinds of situations (see the reviews by French et al. (2000) and Jacob et al. (2002a) respectively). Both models use resistance network approaches and provided estimates of net radiation R_n , soil heat flux G_0 , sensible and latent heat fluxes H and LE . They compute at the same resolution and at the same time instantaneous estimates of several surface properties and energy fluxes. We give here overviews of the model. Detailed descriptions can be found in Norman et al. (1995); French (2001), and Bastiaanssen et al. (1998); Su et al. (1998, 1999); Jacob et al. (2002a) for TSEB and SEBAL, respectively.

2.1 The TSEB model

The main characteristic of TSEB is to use a two source approach that discriminates the soil and vegetation components. This aims at better describing heterogeneous surfaces when dealing with radiative and aerodynamic properties, as compared to the one source approach. The model requires as input information maps of kinetic temperature, Normalized Difference Vegetation Index (NDVI), land use, incoming solar and thermal radiation, as well as micrometeorological measurements of air temperature / humidity / pressure and wind speed. As suggested by Choudhury et al. (1994), Fractional Vegetation Cover (FVC) is computed using a scaled NDVI. Leaf Area Index is deduced from FVC using a logarithmic function. Vegetation height is deduced from the land use map along with a Look Up Table calibrated from field observations. Radiative properties of the canopy are computed using the Divergence of Net Radiation method (DNR, see Campbell & Norman (1998)) along with radiative properties of soil and vegetation that are set to nominal values. Roughness length for momentum is set to $1/8 \times$ vegetation height.

Radiative transfer inside canopy is modeled considering the multiple scattering between the soil and vegetation. R_n , H and LE are computed for both soil and vegetation. G_0 is computed as a fraction of soil net radiation, the fraction being set to a nominal value. Using a two-source remote sensing approach along with single directional observations such as ASTER data, requires adding some assumptions to compute soil and vegetation temperatures. This is performed deducing the vegetation latent heat flux from vegetation net radiation using the Priestley-Taylor relation. Further, composite radiative temperature is expressed as a weighted sum of vegetation and soil temperatures, the weights being the fractional vegetation cover and its complementary to unity, respectively. Finally, vegetation sensible heat flux and soil latent heat flux are computed as the residues of vegetation and soil energy balance respectively.

2.2 The SEBAL model

SEBAL is a one layer approach that computes surface energy fluxes without discriminating soil and vegetation components. Its main characteristic is to retrieve wind speed and air temperature using the information contained in the spatial variability of convective fluxes that is linked to the hydrological contrast depicted by the study area. The model does not need ancillary information, and requires as input maps of kinetic temperature, surface albedo, NDVI, incoming solar and thermal radiation. The computations are performed using both semi-empirical relationships and simplifications of energy balance formulation over dry areas (no evapotranspiration) and wet areas (no sensible heat transfer). The surface temperature versus albedo diagram that results from evaporative and radiative processes is used to both verify the existence of hydrological contrasts and allocate wet and dry areas, respectively.

R_n is computed as the algebraic sum of shortwave and longwave radiative budget using solar and thermal incoming radiations, albedo, broadband emissivity and surface radiometric temperature. G_0 is expressed as a fraction of R_n , the fraction being a semi-empirical function that depends on surface radiometric temperature, NDVI, instantaneous and daily albedo. The estimation of H requires three steps. First, roughness length for momentum is deduced from NDVI using an exponential shaped empirical relationship and roughness length for heat is set to $1/10$ times roughness length for momentum. Second, the radiative and aerodynamic properties of

the dry areas are used along with an aggregation scheme to compute a mean value of wind speed. Third, air temperature is assumed to be linearly related to surface temperature, the coefficients of the linear relation being calibrated by inverting sensible heat flux expression over dry and wet areas. Finally, LE is computed as surface energy budget residue.

3 DATA ACQUISITION & PREPROCESSING

In order to perform the intercomparison by accounting for different situations, we considered two study areas. The first area is the Jornada Experimental Range, a semi-arid region located in the northern Chihuahuan desert, New Mexico, USA. The second area is the El Reno Grazing land, a grassland located in Oklahoma, USA. The selection of these two areas was driven by the availability of ground based measurements to validate the models and the significant difference between the two areas about the meteorological conditions and the type of vegetation. We selected four ASTER scenes collected around solar noon: two over El Reno (June 10, 2001 and April 01, 2002) and two over Jornada (May 12, 2001 and May 15, 2002). The ASTER sensor is a nadir single directional sensor that collects data in the Visible (VIS), Near Infrared (NIR), Shortwave infrared (SWIR), and Thermal Infrared (TIR) domains. The resolution is 15 m from 0.55 to 0.87 μm , 30 m from 1.65 to 3 μm and 90 m between 8.25 and 11.3 μm . Instrumental corrections were performed by the ASTER team.

VIS - NIR - SWIR data were atmospherically corrected using the 6S radiative transfer code (Vermote et al., 1997), along with radiosoundings launched from the closest meteorological stations (<http://raob.fsl.noaa.gov/>) and estimates of the Aerosol Optical Thickness at 550 nm deduced from the closest sun photometer measurement in the framework of the AERONET (<http://aeronet.gsfc.nasa.gov:8080/>). TIR data were atmospherically corrected using the MODTRAN radiative transfer model along with the radiosounding aforementioned. Since the information used to perform atmospheric corrections did not coincide spatially and temporally with the satellite overpass, a sensitivity analysis was performed. It was shown that the resulting inaccuracies on VIS-NIR-SWIR reflectances were not significant, with a relative discrepancy lower than 5% over the wavebands we considered for further investigations. On the other hand, the resulting inaccuracy over the TIR wavebands was of about 2 °C. This was a significant er-

ror as compared to the required accuracy, i.e. lower than 1 °C. A detailed discussion about these investigations is given in Jacob et al. (2002b). Finally, the VIS-NIR-SWIR data were resampled to a 90 m spatial resolution using an averaging procedure. We considered for further investigations the whole ASTER scenes over El Reno and the left side of the scenes over Jornada. The selection over Jornada was driven by the necessity to remove the San Andres Mountain chain since SEBAL computes a mean value of wind speed by assuming an atmosphere homogenization from the surface to the blending height (i.e. around 100 m above the surface).

The ground based measurements for the Jornada Range were incoming solar radiation, air pressure / temperature / humidity, and wind speed data collected at the New Mexico State University / Leyendecker Plant Science Research Center (LPSRC / NMSU), 10 km southeast of the site; as well as R_n , G_0 , H and LE data collected at the Jornada Range. The ground based measurements for the El Reno grazing land were incoming solar radiation, air pressure / temperature / humidity, wind speed, R_n , G_0 , H and LE data collected at the Fort Reno SCAN site of the United State Department of Agriculture / Natural Resources Conservation Service / National Weather and Climate Center (USDA / NRCS / NWCC). H and LE were estimated using the Bowen Ratio method. The data were collected with a 1 hour time step, and we selected the estimates closest to the satellite overpasses.

4 ESTIMATING MODEL INPUTS

The preprocessed ASTER data were used to compute next surface kinetic temperature, surface albedo NDVI and land use. Surface kinetic temperature was deduced from ASTER multispectral measurements using the Temperature Emissivity Separation (TES) algorithm (Schmugge et al., 1998), that was previously calibrated over the MODIS / ASTER spectral libraries. Surface albedo was computed using the Narrowband To Broadband (NTB) conversion that consists of expressing the integrated value of albedo as a linear combination of waveband nadir reflectances. NDVI was computed as the normalized difference between nadir reflectances over the ASTER band 2 and 3. Detailed discussions about the calibration of the TES method, the choice of a coefficient set to compute albedo, the theoretical accuracy of the computations regarding experimental condi-

tions, and the validation of these product against ground based measurements are given in Jacob et al. (2002b).

Incoming atmospheric radiation over the thermal spectral range was deduced from field measurements of air temperature and humidity using the Stefan-Boltzmann relation along with the Brutsaert formulation of air emissivity (Brutsaert, 1982). The land use maps were computed considering the 90 m spatial resolution ASTER bands 2, 3, 4, 11 and 13 (i.e. red, NIR, SWIR and TIR data) along with an unsupervised isodata classification and knowledge from ground observations.

5 ASSESSING AND COMPARING MODEL ASSUMPTIONS

The radiative transfer inside canopy is simulated by TSEB considering a nominal value about 0.2 for soil albedo and a canopy albedo computed using the DNR method aforementioned. Consequently, soil albedo is set to a uniform value and canopy albedo is spatially variable (we observed values ranging between 0.16 and 0.2 over both El Reno and Jornada). We compare this hypothesis against the SEBAL input maps of albedo calculated using the NTB conversion. Figure 1 displays the evolution of surface albedo from NTB conversion against the Fractional Vegetation Cover (FVC) from the scaled NDVI over the El Reno site on June, 10, 2001. We observed very similar results regardless of the day and of the study area. It was shown that NTB albedo ranged between 0.15 and 0.2 over vegetative areas (high FVC values), which was consistent with the values observed for canopy albedo and mentioned previously. On the other hand, it was shown that NTB albedo over bare soil was significantly variable in space, with values ranging from 0.15 to 0.3. This observation emphasized the contradiction between the ASTER observations and the TSEB hypothesis. Since there was no possibility to validate either ASTER NTB conversion or TSEB DNR albedos, we could only conclude that the models relied on converse hypotheses when dealing with albedo. Consequently, the difference between TSEB and NTB albedos was important over Jornada (Relative Root Mean Square Difference RRMS about 30%) since the study area included mainly bare soils. Conversely, the difference over El Reno was lower (RRMS about 10%) since the ASTER scene included grazing lands.

SEBAL assumes there is a relation between surface albedo and temperature that results from hydro-

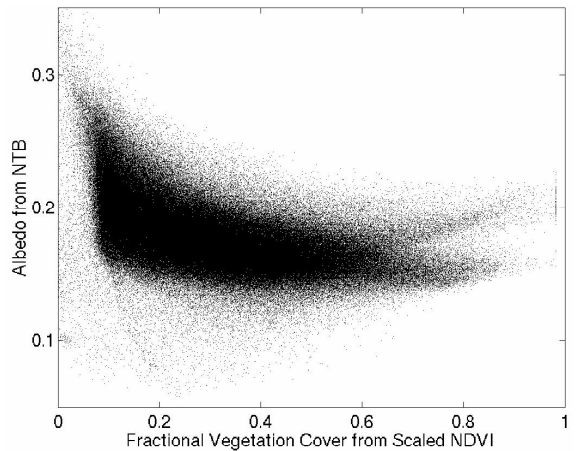


Figure 1: Evolution of the NTB conversion albedo as a function of fractional vegetation cover from scaled NDVI over El Reno site on June, 10, 2001.

logical contrasts inside the study area. This assumption was verified by several previous studies (see the reviews by Bastiaanssen et al. (1998) and Jacob et al. (2002a)). We first assessed the existence of this assumption. Figure 2 displays an example of the evolution of radiometric temperature versus albedo. It appeared that over Jornada, the classical temperature versus albedo diagram was quite verified. This was explained by the simultaneous presence of dry areas (the Jornada LTER area) and wet areas (the agricultural regions around the Rio Grande River). Nevertheless, as shown on Figure 2, the scatterplots depicted significant discrepancies whereas most of the plots corresponded to dry areas with intermediate albedo values. When considering the El Reno site, it was shown that the relation was not verified. Indeed, we noted that the radiative branch of the temperature versus albedo diagram (corresponding to the negative derivative of the temperature - albedo polynomial function) did not exist. This was explained by the absence of dry areas inside the El Reno scene that included mainly grazing lands. These observations emphasized that the assumption SEBAL relies upon was not systematically valid.

6 COMPARING MODEL SIMULATIONS

We first compared the estimation of roughness length, computed by SEBAL as a empirical logarithmic shaped relationship of NDVI, and as $h_c/8$ by TSEB, where h_c is the vegetation height de-

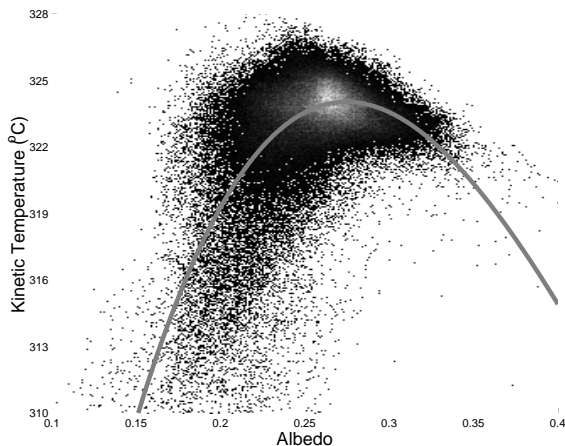


Figure 2: Evolution of the surface radiometric temperature versus NTB conversion albedo over the Jornada site on May, 15, 2002. The evolution is given as as Probability Density Function. The gray line is the third order regression used to determine the albedo threshold value corresponding to the null derivative of the temperature versus albedo function, the threshold value being further used to allocate dry and wet pixels.

duced from the classification previously presented. Over Jornada, we observed significant differences, with a RRMS about 200% and an overestimation from the TSEB estimates. The difference over El Reno was significantly lower (RRMS around 80%), with an overestimation from the SEBAL estimates. The TSEB computations were supposed to be better since the estimation of roughness length from vegetation height was validated by several previous study whereas the SEBAL semi-empirical relation was already invalidated by Jacob et al. (2002a). Nevertheless, the accuracy of the vegetation height estimation depended on the accuracy of both the classification and the ground truth information used to set a nominal value to a given class. The consequences for sensible heat flux computations will be assessed further.

Figure 3 displays an example of comparison between TSEB and SEBAL R_n estimates. The cluster corresponding to TSEB R_n around 600 W.m^{-2} was ascribed to water bodies that were processed by TSEB in a specific way. The estimates were very close over El Reno and quite different over Jornada (see table 1). This was consistent with the observations previously mentioned when comparing albedo. Indeed, TSEB overestimation of low albedo values

Date & site	ARMS	RRMS	ABias	RBias
	W.m^{-2}	%	W.m^{-2}	%
06/10/01, ER	20.3	03.7	07.4	1.3
04/01/02, ER	23.3	04.8	-13.9	-2.9
05/12/01, JO	57.8	13.5	53.3	12.5
05/15/02, JO	67.3	16.2	61.6	14.7

Table 1: Absolute (A) and Relative (R) Root Mean Square Difference (RMS) and bias between TSEB and SEBAL estimates of R_n when considering the four ASTER scene: two over El Reno (ER) and two over Jornada (JO).

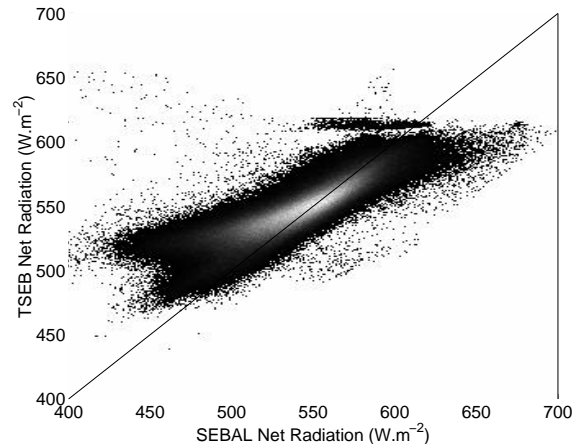


Figure 3: Comparison of SEBAL and TSEB R_n estimates over El Reno on June, 10, 2001. The Comparison is given as as Probability Density Function.

induced TSEB underestimation of high R_n values, and vice versa. The comparison over both sites gave quite satisfactory results as compared to validation results reported in the literature that ranged ranged between 30 and 60 W.m^{-2} (Moran et al., 1994; Kustas et al., 1994). Indeed, both models compute net radiation in very different ways, and they rely upon different assumptions. We should note that the validation results observed over Jornada depicted a systematic error.

Figure 4 displays an example of comparison between TSEB and SEBAL estimates of G_0 . We notice low G_0 range regardless of considered ASTER scene. Despite significant discrepancies as displayed in Figure 4, the comparisons showed low differences since most of the plots were located close to the 1:1 line. Indeed, the differences over the whole

Date & site	ARMS	RRMS	ABias	RBias
	W.m ⁻²	%	W.m ⁻²	%
06/10/01, ER	10.08	11.7	-4.49	-05.24
04/01/02, ER	21.01	32.2	19.12	29.38
05/12/01, JO	11.47	13.0	-9.78	-11.11
05/15/02, JO	08.81	09.9	-5.01	-05.64

Table 2: Absolute (A) and Relative (R) Root Mean Square Difference (RMS) and bias between TSEB and SEBAL estimates of G_0 when considering the four ASTER scene: two over El Reno (ER) and two over Jornada (JO).

scenes ranged between 10 and 20 W.m⁻² (see Table 2). This was explained by the similarity of the approaches used by both models to compute this variables. TSEB estimates G_0 as a fraction of soil net radiation. SEBAL uses a semi-empirical relation to first characterize the fraction G_0/R_n over a bare soil, and second account for the extinction of incoming solar radiation by the canopy. The evolution of the difference between both estimates as a function of the fraction vegetation cover did not emphasize any trend over Jornada, the difference ranging between ± 20 W.m⁻² as FVC ranged between 0 and 1. On the other hand, the difference varied as a function of FVC over El Reno, from approximately 40 to -20 W.m⁻² as FVC increased from 0 to 1. This showed that the two methods did not characterize in the same way both the fraction of R_n to G_0 over bare soil and the canopy extinction. Moreover, the results were different from a site to another, which emphasized that the characterization was land use dependent. It is interesting to note that we observed a good (respectively bad) agreement between net radiation estimates over El Reno (respectively Jornada), whereas it was the converse for G_0 . This indicated that some error compensation occurred when computing G_0 .

An example of sensible heat flux comparison is given in Figure 5. This example is the best case we observed. Indeed, the other comparison results indicated significant differences as shown in Table 3. No factor was isolated to explain the significant variation for a given site. We assessed the possible consequences of roughness length estimation by checking the evolution of the difference in sensible heat flux as a function of the difference between roughness lengths. We did not observe any correlation. The same procedure was investigated considering air temperature estimation through the difference

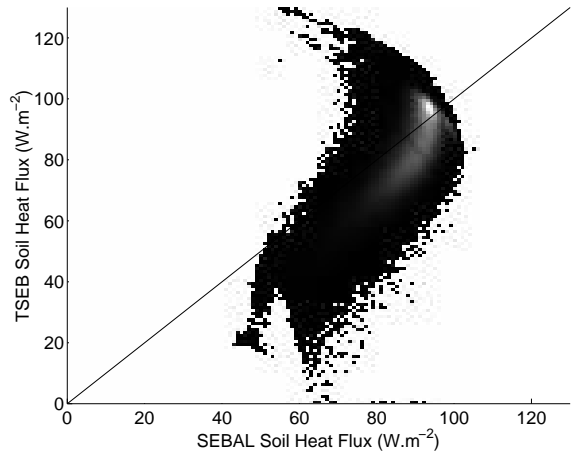


Figure 4: Comparison of SEBAL and TSEB G_0 estimates over El Reno on June, 10, 2001. The Comparison is given as as Probability Density Function.

between the SEBAL estimates and the air temperature recorded at the meteorological station that was used as a TSEB input. Over Jornada, we did not note any correlation. Over El Reno, we observed a correlation only on June, 10, 2001 but this trend was not physically consistent: as the air temperature difference from decreased 0 to -15°C, the sensible heat flux difference increased from 0 to 150 W.m⁻²; whereas it decreased from 150 W.m⁻² to 25 W.m⁻² as the air temperature difference decreased from 15 to 20 °C. These observations indicated that the differences in sensible heat flux computations were not mainly driven by the differences in either roughness length or air temperature computations. Several other parameters could influence the calculations, especially inside the TSEB framework that relies on several assumptions to compute the 7 components of surface energy balance in a two layer scheme.

An illustration of latent heat flux comparison is given in Figure 6, that corresponds to one of the best cases we observed. As mentioned previously when dealing with sensible heat flux calculations, the results could be significantly different from a site to another and from a date to another. Besides, the best agreement did not correspond to the best agreement in sensible or latent heat flux. This could be explained by the difference in the model schemes: latent heat flux is computed as the surface energy balance residue by SEBAL whereas TSEB computes as energy budget residues both vegetation sensible heat and soil latent heat fluxes.

Date & site	ARMS	RRMS	ABias	RBias
	W.m ⁻²	%	W.m ⁻²	%
06/10/01, ER	186.66	71.5	-178.67	-68.4
04/01/02, ER	050.71	20.2	-025.41	-10.1
05/12/01, JO	102.14	41.3	097.81	39.6
05/15/02, JO	068.13	24.7	055.69	20.2

Table 3: Absolute (A) and Relative (R) Root Mean Square Difference (RMS) and bias between TSEB and SEBAL estimates of sensible heat flux when considering the four ASTER scene: two over El Reno (ER) and two over Jornada (JO).

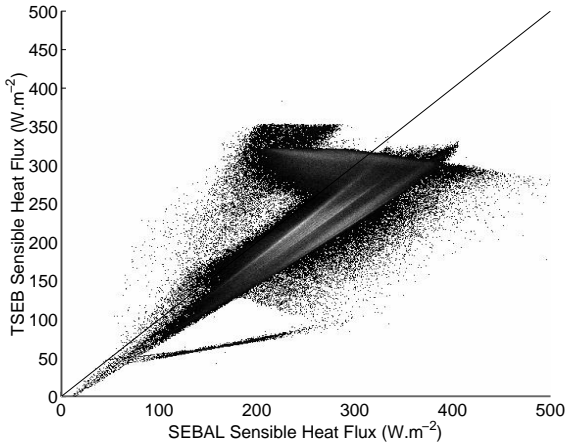


Figure 5: Comparison of SEBAL and TSEB sensible heat flux estimates over El Reno on April, 01, 2002. The Comparison is given as as Probability Density Function.

Date & site	ARMS	RRMS	ABias	RBias
	W.m ⁻²	%	W.m ⁻²	%
06/10/01, ER	196.7	100.23	190.63	97.1
04/01/02, ER	045.7	027.67	-07.60	-04.6
05/12/01, JO	052.9	057.82	-34.69	-37.8
05/15/02, JO	054.5	102.08	11.03	20.6

Table 4: Absolute (A) and Relative (R) Root Mean Square Difference (RMS) and bias between TSEB and SEBAL estimates of latent heat flux when considering the four ASTER scene: two over El Reno (ER) and two over Jornada (JO).

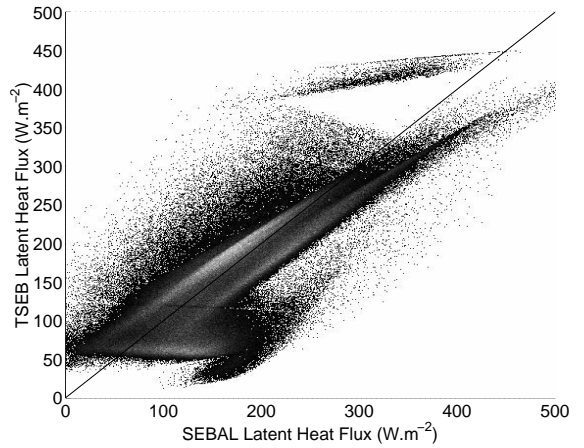


Figure 6: Comparison of SEBAL and TSEB latent heat flux estimates over El Reno on April, 01, 2002. The Comparison is given as as Probability Density Function.

The whole set of observations reported here indicated that the models provided mainly systematic differences, especially when comparing H and LE . This emphasized the realism of the underlying assumptions for both models. Moreover, these systematic differences corresponded to given groups of scatterplots that belonged probably to given types of surface (3 to 5 groups). Locating these scatterplots on ASTER scenes should be useful to understand the differences between models according to the land use. We also noted that agreement between both model assumptions depend on land use and meteorological situations. Besides, differences between convective fluxes could be lower than differences between net radiation. This indicated than some compensation differences occurred, which requires sensitivity studies for a better understanding of model behaviors. The large differences we observed over Jornada could also be explained by poor performances of TSEB over dry areas since the model was not designed to be applied in such environmental conditions. An improvement could be performed by accounting for ASTER observations when setting nominal values as inputs of the DNR method. Finally, a validation procedure over the El Reno site on June, 10, 2001 showed good agreement between both model calculations and field measurements (differences about 20 W.m⁻² on sensible heat flux and 25 W.m⁻² on latent heat flux). This emphasized the interest of model intercomparison since the validation showed good agreement whereas in-

tercomparison over whole scenes showed larger differences.

7 CONCLUSION

This paper reports investigations focused on the comparison of two surface energy balance models using 90 m spatial resolution ASTER imagery. The two models we considered were the one source SEBAL and the two source TSEB models. The comparison was performed over two study sites that corresponded to semi-arid region and grazing lands. Assessing the model assumptions showed that they relied on some contrary hypotheses when computing the albedo, a prime variable of the radiative budget. Consequently, we noted significant differences in net radiation when considering areas with many bare soils such as the Jornada Range semi-arid region. In this case, we suspected the performances of TSEB when calculating albedo. It should be possible to improve the method that computes net radiation by using ASTER observations rather than nominal values. The soil heat flux computations provided very close results. However, we observed that larger differences in net radiation could induced lower differences in soil heat flux. Consequently, we suspected some difference compensations, and we therefore could not conclude about the methods used. When dealing with sensible heat flux, we could not observe any link between differences in surface fluxes with differences in intermediary variables such as roughness length or air temperature. Nevertheless, the convective flux comparison scatterplots showed systematic differences that corresponded to given groups of plots. Further investigation focused on locating these groups over ASTER scenes will be useful to understand the differences in calculations as combinations of land use and model assumptions.

ACKNOWLEDGMENTS

This study was supported by the ASTER Project of NASA's EOS-Terra Program.

REFERENCES

- Bastiaanssen, W.G.M., Menenti, M., Feddes, R.A., and Holtslag, A.A.M., 1998, A remote sensing surface energy balance algorithm for land (SEBAL). I: Formulation. *Journal of Hydrology*, 212-213, 198–212.
- Brutsaert, W., 1982. *Evaporation into the atmosphere*. International geophysics series. Reidel Ed., San Diego.
- Campbell, G.S. and Norman, J.M., 1998. *An introduction to environmental biophysics*. second edition. Springer-Verlag, New York, USA.
- Choudhury, B.J., Ahmed, N.U., Idso, S.B., Reginato, R.J., and Daughtry, C.S., 1994, Relation between evaporation coefficients and vegetation indices studied by model simulations. *Remote Sensing of Environment*, 50, 1–17.
- French, A., 2001. *Scaling of surface energy fluxes using remotely sensed data*. Phd thesis, 273 pp, University of Maryland.
- French, A., Schmugge, T.J., and Kustas, W.P., 2000, Estimating surface fluxes over the SGP site with remotely sensed data. *Physics and Chemistry of the Earth(B)*, 25, 167–172.
- Jacob, F., Olioso, A., Gu, X.F., Su, Z., and Seguin, B., 2002a, Mapping surface fluxes using visible, near infrared, thermal infrared remote sensing data with a spatialized surface energy balance model. *Agronomie*. Accepted.
- Jacob, F., Schmugge, T., Ogawa, K., A., French, and Ritchie, J., 2002b. The potentialities of ASTER to retrieve radiative properties over semi-arid regions. In: *First International Symposium on Recent Advances in Quantitative Remote Sensing*.
- Kustas, W.P., Moran, M.S., Humes, K.S., Stannard, D.I., Pinter, P.J., Hipps, L.E., Swiatek, E., and Goodrich, D.C., 1994, Surface energy balance estimates at local and regional scales using optical remote sensing from an aircraft platform and atmospheric data collected over semiarid rangelands. *Water Resources Research*, 30, 1241–1259.
- Moran, M.S., Kustas, W.P., Vidal, A., Stannard, D.I., Blanford, J.H., and Nichols, W.D., 1994, Use of ground-based remotely sensed data for surface energy balance evaluation of a semiarid rangeland. *Water Resources Research*, 30, 1339–1349.
- Norman, J.M., Kustas, W.P., and Humes, K.S., 1995, Two source approach for estimating soil and vegetation energy fluxes in observations of directional radiometric surface temperature. *Agricultural and Forest Meteorology*, 77, 263–293.
- Schmugge, T.J., Hook, S.J., and Coll, C., 1998, Recovering Surface Temperature and Emissivity from Thermal Infrared Multispectral Data. *Remote Sensing of Environment*, 65, 121–131.
- Su, Z., Menenti, M., Pelgrum, H., van den Hurk, B.J.J.M., and Bastiaanssen, W.G.M., 1998. Remote sensing of land surface fluxes for updating numerical weather predictions. In: *Operational Remote Sensing for Sustainable Development*, Nieuwenhuis, Vaughan and Moleenaar Eds, 1999 Balkema, Rotterdam.
- Su, Z., Pelgrum, H., and Menenti, M., 1999. Aggregation effects of surface heterogeneity in land surface processes. In: Z. Su & M. Menenti (eds.), *Hydrology and Earth Science System*, vol. 3, pp. 549–563.
- Vermote, E., Tanré, D., Deuzé, J.L., and Morcrette, J.J., 1997, Second simulation of the satellite signal in the solar spectrum: an overview. *IEEE Transactions on Geoscience and Remote Sensing*, 35, 675–686.

Using LANDSAT TM imagery to detect landslides impact on montane forests of NW Argentina

L. Paolini#, J. A. Sobrino* and J. C. Jiménez-Muñoz*

Laboratorio de Investigaciones Ecológicas de las Yungas, Universidad Nacional de Tucuman, CC 34, Yerba Buena, 4107, Argentina

* *Unidad de Cambio Global, Departamento de Termodinámica, Universidad de Valencia, Burjassot, 46100, España*

ABSTRACT - Remote sensing technics applied to environmental studies has been used succesfully to identified, mapping and analyzing the spatial and temporal ecosystem dynamics. In studies of natural disturbances, such fires and landslides, the remote sensing approach can be used to asses the impact of thees disturbances at broad spatial and temporal scale. Using 1986 and 2001 Landsat TM images we detected landslides accured on Norwest Argentina subtropical forests, and we evaluated their impact on natural communities. Using supervised classifications, we diferenciaded landslides from others land cover units with an overall accuracy of 91% in the 1986 image and 89% in the 2001 image. Landslides studies based on remote sensing technics can help to a better understanding of this kind of disturbance, in terms of their impact on the subtropical forests and their relationship with the climate change (spetially precipitation) registered in the zone.

1 INTRODUCTION

Remote sensing techniques has become a very useful tool to carry out spatial and temporal large-scale environmental studies. In particular, Landsat TM imagery caracteristiques (7 bands of spectral resolution, 28.5 m x 28.5 m pixel size, 180 km x 180 km spatial coverage of each scene and the temporal availability of the images since 1982) enable to identify relatively small environmental alteration, to evaluate their effects on a regional scale and to determine change rates over the past decades. Several environmental studies have successfully use Landsat TM image analysis to identify natural and anthropogenic disturbances such as deforestation, fires or tornados (Grau 2001; Mukai and Hasegawa 2002; Almeida-Filho and Shimaukuro 2002), to determine land use change (Helmer *et al* 2000; Song *et al* 2001; Watson and Wilcok 2001; Rogan *et al* 2002) and to mapping vegetation coverage (Towsend 2000; Pax-Lenney *et al* 2001) in several different ecosystems. In other study of landslides carry out in the mountain forest of Bolivia(Yungas), Blodgett (1998) could identify and quantify the impact of this kind of disturbance on the Yungas, using Landsat TM images supervised classifications.

The Yungas of Bolivia ar part of the same montane forests or Yungas in Norwest Argentina. These forests have some particular advantages in terms of image analysis studies, in comparison with other environments such as cloudy forests and deserts. By one hand, the montane forests of NW Argentina represent a continuous and uniform matrix of vegetation cover, in which fresh, not colonized, landslides are more conspicuous. On the other hand, the strong seasonality of these forests make possible to

work with images of the dry season, when the atmosphere is almost could free, which improve visualization. Studies of large-scale environmental changes are fundamental to understand how ecosystems work. The strong relationship between climate, disturbances and vegetation have a major effects in determining the structure and dynamics of natural communities. The climate affects the vegetation in a direct way, by conditioning the establishment and growth of the species and, in an indirect way, by modifying the kind, frequency, extension and magnitude of the disturbances (Prentice 1992; Beniston & Fox 1996). The disturbances, by the other hand, produce an important resource release that favour the establishment and/or developing of the species better adapted to those sites. In mountainous areas, the regional climate fluctuations, specially precipitation fluctuations, can alter and modify the landslides dynamic, specially under the consideration that exist a very close relationship between landslide occurrence and the amount of water in the soil (Keefer & Johnson 1983; Iverson & Mair 1987; Bovis & Jones 1992). One of the effects that landslides have in the ecology of mountain cloudy forests is that they alter the structure and function of these ecosystems (Veblen & Ashton 1978; Garwood *et al* 1979; Guariguata 1990). In the same way, Grau & Brown (1995) found that in he upper part of the Yungas in NW Argentina, where the slope are pronounced and the precipitation reach the maximum for the area, landslides are one of the disturbances of more impact, because its favour the establishment of pioneer species in the old growth forest, increasing the richness and delaying the succession (Guariguata 1990). The climate change associated to the future global warming is expect to modify the disturbances regimen, causing alterations

in the forests structure due to the an increase of forest patches with early succession stages (Overpeck *et al* 1990). Landslide as a disturbance not only affects the vegetation communities dynamics but also have an impact on human activities. Due to big populated areas and major cities in NW Argentina are very close related to mountains, this kind of studies will be very important to understand and evaluate the future impact of landslides on people lives. By knowing how landslides respond to precipitation changes could estimate the future alterations in water quality, the sedimentation rates in rivers and lakes and the risk levels of flood and mudflows for populations on the foothills.

Climate studies based on instrumental records (Minetti & Vargas 1997) and on tree ring analysis (Villalba *et al* 1998) shows an important increase in precipitations on NW Argentina, since the last 50 years. In this way, we expect an increase in the number, size and frequency of landslides in the last decades. The main objective of this study is to identify landslides in the mountain forests of NW Argentina, by using Landsat TM images. Furthermore, we evaluated the area affected by landslides in 1986 and 2001, and we estimate the change rate between these years.

2 METHODS

The study site is located in NW Argentina (Fig.1 A & B) and represent a portion of the subtropical mountain forests or Yungas (23° 58' SL – 65° 28' WL; 24° 4' SL – 64° 49' WL; 25° 10' SL – 65° 52' WL; 25° 16' SL – 65° 13' WL). The area have a monsoon climate with dry-cool winters and wet-warm summers, and abundant precipitations (1500 – 2000 mm a year) mainly concentrated between December and March. The vegetation is abundant with very big trees arranged in a continuous forests matrix, mainly placed on the eastern slopes of the Sierras Subandinas, that are displaced in north-south direction. For this study we use two Landsat TM images, scene 231/077 (11/09/1986 & 03/08/2001), Georeferenced with UTM south zone 20. In each one of the images the spectral data was in DN values mainly because it is not strictly necessary to transform those values or to perform an atmospheric correction to carry out a multitemporal comparison between images (Song *et al* 2001; Foody 2002). We made an image-to-image coregistration by using 25 ground controls points (GCPs), second degree polinomy calculations and nearest neighbourhood resampling method. In each one of the scenes we choose an analysis area trying to include as much as possible of forested areas, and we perform a supervised classification (Fig. 1 C). With images displayed in RGB false colour (bands 5, 4 & 2) to improve the landslides visualization (Blodgett 1998), we visually identify 25 different landslides in 1986

image and 28 different landslides in 2001 image. Beside the landslides, and based mainly on our knowledge of the area, we could identify other terrain units, which we will use as training classes for the supervised classification. We used two independent separability index, Jeffries-Matusita and Transformed Divergence, to statistically determine the spectral separation between training classes (Richards & Jia 1999). Those index compute the degree of spectral differences for all the possible class pair combinations. Higher spectral separation mean less classes superposition and minor classification error. Due to that both index values vary between 0 and 2, we decided to classify the images only if the defined classes has at least one of the index major to 1.85 and no one of the index minor to 1.55. By doing this we reduce the probability of error classification to < 0.05 (Richards & Jia 1999). Based on the defined training classes we made a Maximum Likelihood supervised classification (Threshold: $p < 0.05$) on each one of the images. Both images classifications were evaluated by the analysis of their confusion matrix. To analyse the overall impact of landslides on the forests, we chose four different woody areas where we did evaluate the total area occupied by landslides on each image. To improve our analysis and avoid misinterpretations of the results we discard single-lonely pixels and take in account for the analysis just group of 9 or more pixels were all of them has at least 4 neighbours classified as landslide. We determine the overall change of the area affected by landslides between 1986 and 2001 by measuring the total hectares occupied by this disturbance in each one of the classified images.

3 RESULTS

The mean square error for the image-to-image spatial coregistration was 0.7 (21 m). We define 11 diferents training classes, all of it are composed by more than the 10 N (where N=number of bands) minimum number of pixels recommended (Swain & Davis 1978; in: Richard & Jia 1999). For all the pair classes, the separability indexes are acceptable (>1.6) (Table 1), which indicate that the spectral overlapping of the classes are enough small to minimize the probability of classification error. The confusion matrix analysis shows good accuracy and kappa values, and low error levels for both classifications (Table 2). For the 1986 image the overall accuracy is 91% and the kappa coefficient value of 0.89, and for the 2001 image the overall accuracy is 90% with a kappa coefficient of 0.87. The total area occupied by landslides, on the four woody areas, in 1986 was 3104 Ha., that correspond to 1.35 %, meanwhile in the year 2001 the total woody area affected by landslides rise to 3448 Ha, which is the 1.5 %. This difference mean an increase of 343 Ha., 0.15% of the area occupied by the forests under study (Fig. 1, D & E).

Table 1. Region of interest separability (JM= Jeffries-Matusita index, DT= Transformed Divergente index) for 1986 (shadow values) and 2001.

Pi els	Plot	Cit		Ri er	Fire	ater	S a o		A ti e lant.	Ina ti e lant.	i o ntain	Forest	Lan sli.		Grass
		JM	DT				JM	DT					JM	DT	
217	Cit	2.	2	1,90;1,98	2,00;2,00	2,00;2,00	1,99;2,00	1,99;2,00	1,99;2,00	1,86;1,99	1,99;2,00	1,99;2,00	1,95;1,99	1,99;2,00	
1507	Ri er	1,91;1,99	2.	2	1,99;2,00	1,99;2,00	1,99;2,00	1,99;2,00	1,99;2,00	1,98;1,99	1,99;1,99	1,99;2,00	1,97;1,99	2,00;2,00	
1204	Fire	1,99;2,00	1,99;2,00	1,99;2,00	2	2	1,99;2,00	1,99;2,00	1,99;2,00	1,97;1,99	1,99;1,99	1,99;1,99	1,90;1,98	1,99;1,99	
11074	ater	1,99;2,00	1,99;2,00	1,99;2,00	1,98;2,00	2	2	2,00;2,00	2,00;2,00	2,00;2,00	1,99;2,00	1,99;2,00	2,00;2,00	2,00;2,00	
854	S a o	1,99;2,00	2,00;2,00	2,00;2,00	1,99;2,00	1,96;1,99	2	2	2,00;2,00	1,99;2,00	1,99;2,00	1,99;1,99	1,99;2,00	2,00;2,00	
3167	A it e .	1,99;2,00	1,99;2,00	1,99;2,00	1,99;2,00	2,00;2,00	2,00;2,00	2	2	1,99;2,00	1,99;2,00	1,99;1,99	1,99;1,99	1,99;1,99	
3391	Ina t. .	1,99;1,99	1,99;1,99	1,99;1,99	1,98;1,99	2,00;2,00	2,00;2,00	1,99;2,00	1,99;2,00	2	2	1,96;1,99	1,71;1,96	1,99;1,99	
7923	. o nt.	1,98;2,00	1,99;1,99	1,99;1,99	1,99;1,99	1,99;2,00	1,99;2,00	1,99;2,00	1,99;2,00	1,90;1,99	2	2	1,77;1,93	1,84;1,99	
5959	Forest	1,99;1,99	1,99;2,00	1,99;2,00	1,99;2,00	1,99;2,00	1,99;2,00	1,97;1,99	1,97;1,99	1,98;2,00	1,99;2,00	2	2	1,99;1,99	1,98;1,99
1246	Lan sli e	1,98;1,99	1,97;1,99	1,97;1,99	1,99;1,99	1,99;2,00	1,99;2,00	1,99;1,99	1,99;1,99	1,65;1,91	1,62;1,80	1,97;1,99	2	2	1,82;1,99
607	Grass	1,99;2,00	2,00;2,00	2,00;2,00	1,99;1,99	2,00;2,00	2,00;2,00	1,99;1,99	1,99;1,99	1,99;1,99	1,97;1,99	1,92;1,97	1,75;1,99	2	2

Table 2. Confusion matrix resume.

Year Classes	1986 Overall Accuracy: 91 %; Kappa: 0.89		2001 Overall Accuracy: 90 %; Kappa: 0.87	
	Productor Accuracy (%)	User Accuracy (%)	Productor Accuracy (%)	User Accuracy (%)
City	88.02	97.95	95.39	97.64
River	86.60	99.92	98.74	100.00
Fire	90.12	97.22	98.83	99.65
Water	99.70	100.00	90.86	99.95
Shadow	91.10	98.11	86.82	70.08
Active p.	99.18	99.94	95.52	99.86
Inactive p.	82.31	99.89	98.84	98.23
H. mount.	76.23	99.74	98.75	99.90
Forest	95.94	99.88	72.65	99.21
Landslide	78.21	80.03	80.25	99.94
Grass	83.03	62.53	36.09	84.75

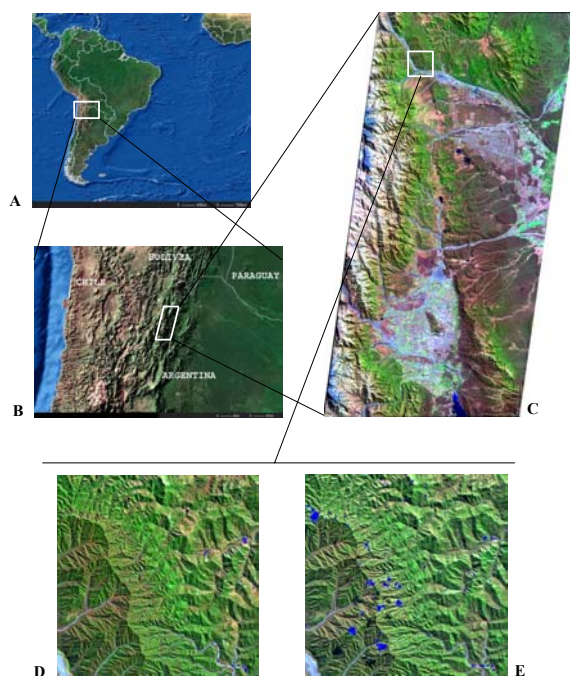


Figure 1. Geographic location of the study area and análisis of landslides changes between 1986 and 2001. Argentina in Southamerica (A). Northwestern Argetina (B). Study area (C). Fresh landslides (in blue) in 1986 (D) and 2001 (E).

4 CONCLUSIONS

Results shows that it is possible to differentiate landslides and to evaluate their impact on subtropical mountain forests, with a good accuracy. Furthermore, we found that it is possible to estimate the overall change in the area affected by landslides during the last decade. The high separability values between classes may be mainly due to our previous knowledge of the study area, which allow us to choose true spectral differentiated land cover types as training classes. The low spectral separability that landslides show with the “inactive plantation” and “high mountain” classes, in comparison with other classes, did not affects our results because we focus the impact analysis in the four forest areas describes before. The high separability values obtained between landslides and forest improve the classification, as show the low classifications errors in the confusion matrix.

Using Maximun Likelihood Supervised Classifications allow to make a good land cover characterization and make possible to distinguish fresh landslides. Although the increase in the area occupied by landslides between 1986 and 2001 is important, do not necessary represent a real change rate, mainly because the lack of intermediate years images that allow to perform a more accurate multitemporal analysis. Despite this, the analysis demonstrate that it is possible to evaluate temporal changes in landslide regimen and to obtain a broad picture of the behaviour of this kind of disturbance in global change scenarios.

The main limitation of this study is that just could identify fresh-not colonized landslides inside the forest matrix, what limit the knowledge of the landslide evolution, in special the colonization process, expansion of the affected area and the probability of landslide reactivation. Further studies related with these topics will make possible to have a broader understanding of the interaction between disturbances and vegetation dynamics, and will make possible to estimate the future characteristics of these ecosystems under the future global change scenarios proposed by the General Circulations Models. Landslides detection at regional scale is the first step toward the study of the disturbances regimen change in NW Argentina. Inside the actual and future global change phenomenon, this kind of study have a great potential to understand the operation of the ecosystem from a dynamic point of view. This knowledge will be fundamental to estimate future changes and to improve the management of protected areas.

5 ACKNOWLEDGEMENTS

This project was founded by the Consejo Nacional de Investigaciones Cientificas y Tecnicas (CONICET), Argentina and by the Unidad de Cambio Global, University of Valencia, Spain. We spetially thank to

Dr. Ricardo Grau for their contributions and comments.

6 REFERENCES

- ALMEIDA-FILHO, R. and SHIMABUKURO, Y. E., 2002, Digital Processing of Landsat TM time series for mapping and monitoring degraded areas caused by independent gold miners, Roraima State, Brazilian Amazon, *Remote Sensing of Environment*, 79:42-50.
- BENISTON, M., and FOX, D. G., 1996, Impacts of Climate Change on Mountain Regions. In: R.T. Watson, M. C. Zinyowera, R. H. Moss (eds), *Cimate Change 1995. Impacts, adaptations and mitigation of climate change: scientific-technical analyses*. Cambridge, UK, Cambridge University Press pp. 191-213.
- BLODGETT, T. A., 1998, Erosion Rate on the NE Escarpment of the Eastern Cordillera, Bolivia Derived from Aerial Photographs and Thematic Mapper Images, Cornell University. Ph. D. Thesis.
- BOVIS, M. J., and JONES, P., 1992, Holocene history of earthflow mass movements in south-central British Columbia: the influence of hydroclimatic changes, *Canadian Journal of Earth Sciences*, 29:1746-1755.
- FOODY, G. M., 2002, Status of land cover classification accuracy assessment, *Remote Sensing of Environment*, 80:185-201.
- GARWOOD, N. C., JANOS, D. P. and BROKAW, N., 1979, Earthquake-caused landslides: A major disturbance to tropical forests, *Science*, 205: 997-999.
- GRAU, H. R. and BROWN, A. D., 1995, Los deslizamientos de ladera como condicionantes de la estructura y composición de la selva subtropical de montaña, En: Brown, A. D. y H. R. Grau, (eds.). *Investigación, conservación y Desarrollo en Selvas Subtropicales de Montaña*, pp. 79-84.
- GRAU, H. R., 2001, Regional-scale spatial patterns of fire in relation to rainfall gradients in sub-tropical mountains, NW Argentina, *Global Ecology and Biogeography*, 10:133-146.
- GUARIGUATA, M. R. 1990, Landslide disturbance and forest regeneration in the upper Luquillo mountains of Puerto Rico. *Journal of Ecology*, 78: 814-832.

- 2000, Mapping mountain tropical forest successional stage and land use with multi-date Landsat imagery, *International Journal of Remote Sensing*, 21(11):2163-2183.
- IVERSON, R. M., and MAJOR, J. J., 1987, Rainfall, ground-water flow, and seasonal movement at Minor Creek landslide, northwestern California: physical interpretation of empirical relation, *Geological Society of America Bulletin*, 99:579-594.
- KEEFER, D. K., and JOHNSON, A. M., 1983, Earthflow, morphology, mobilization, and movement, *United States Geological Survey*, Professional Paper 1264.
- MIENTTI, J. L., and VARGAS, W. M., 1997, Trends and jumps in the annual precipitation in South America, south of the 15 S. *Atmósfera*, 11: 205-221.
- MUKAI, Y. and HASEGAWA, I., 2002, Extraction of damaged areas of windfall trees by typhoons using Landsat TM data, *International Journal of Remote Sensing*, 21(4):647-654.
- OVERPECK, J. T., RIND, D., and GOLDBERG, R., 1990, Climate-induced changes in forest disturbance and vegetation, *Nature*, 343: 51-53.
- PAX-LEANNY, M., WOODCOCK, C. E., MACOMBER, S. A., GOPAL, S. and SONG, C., 2001, Forest mapping with a generalized classifier and Landsat TM data, *Remote Sensing of Environment*, 77: 241-250.
- PRENTICE, C. I., 1992, Climate change and long-term vegetation dynamics. In: D. C. Glenn-Lewin, R. K. Peet and T. T. Veblen (eds), *Plant Succession: Theory and prediction*. Chapman and Hall, London, pp. 293-239.
- RICHARDS, J.A. and JIA, X., 1999, *Remote Sensing Digital Image Analysis: an introduction*, Springer-Verlag, Berlin.
- ROGAM, J., FRANKLIN, J. and ROBERTS, D. A., 2002, A comparison of methods for monitoring multitemporal vegetation change using Thematic Mapper imagery, *Remote Sensing of Environment*, 80:143-156.
- SONG, C., WOODCOCK, C. E., SETO, K. C., PAX-LENNY, M. and MACOMBER, S. A., 2001, Classification and change detection using Landsat TM data: when and how to correct atmospheric affects?, *Remote Sensing of Environment*, 75:230-244.
- SWAIN, P. H. and DAVIS, S. M. (eds.), 1978, *Remote sensing: the quantitative approach*, N.Y., McGraw-Hill.
- TOWNSEND, P. A., 2000, A quantitative fuzzy approach to assess mapped vegetation classification for ecological applications, *Remote Sensing of Environment*, 72:253-267.
- VEBLER, T. T. and ASHTON, P., 1978, Catastrophic influences on the vegetation of the Andean Andes, Chile, *Vegetatio*, 36(3):149-167.
- VILLALBA, R., GRAU, H. R., BONINSEGNA, J. A., JACOBY, G. C., and RIPALTA, A., 1998, Tree-Ring Evidence for Long-Term Precipitation Changes in Subtropical south America, *International Journal of Climatology*, 18:1463-1478.
- WATSON, N. and WILCOCK, D., 2001, Preclassification as an aid to the improvement of the thematic and spatial accuracy in land cover maps derived from satellite imagery, *Remote Sensing of Environment*, 75:267-278.

Semi-Supervised Method For Crop Classification Using Hyperspectral Remote Sensing Images

L. Gómez-Chova¹, J. Calpe¹, E. Soria¹, G. Camps-Valls¹, J.D. Martín¹, J. Moreno²,

⁽¹⁾ GPDS, Department of Electronics Engineering, University of Valencia

⁽²⁾ Department of Thermodynamics, University of Valencia

luis.gomez-chova@uv.es ; <http://gpds.uv.es/>

ABSTRACT - This work is a contribution to the DAISEX project, funded by the ESA during 1998, 1999, and 2000. Three data acquisition campaigns were carried out under controlled conditions in the area of Barrax (Spain). We have used six hyperspectral images acquired with the HyMap spectrometer during the DAISEX-99 campaign, in order to benchmark traditional classifiers and propose a new method for crop cover recognition. We propose a procedure to reduce dimensionality while preserving relevant information. Posterior classification is based on a combined strategy of supervised and unsupervised learning methods.

1 INTRODUCTION

This work is a contribution to the *Digital Airborne Imaging Spectrometer Experiment* (DAISEX) project, funded by the European Space Agency (ESA) within the framework of its Earth Observation Preparatory Program during 1998, 1999, and 2000 [DAISEX, 2000]. Three data acquisition campaigns were carried out under controlled conditions in the area of Barrax (Spain). We have used six hyperspectral images acquired with the HyMap spectrometer during the DAISEX-99 campaign, in order to benchmark traditional classifiers and propose a new method for crop cover recognition.

The information contained in the hyperspectral images allows the reconstruction of the energy radiated by the terrestrial surface throughout the electromagnetic spectrum. The properties of reflection, absorption and emission of the materials in certain wavelengths, due to their composition and molecular structure, make possible the characterization and identification of the observed materials from their spectral curve.

Summarizing the analysis of hyperspectral images, the data set can be interpreted as a 4-D hypercube where two dimensions represent the spatial coordinates of the image, a third one corresponds to the spectral coordinate, and the fourth is radiance. Therefore we have a complete image for each band. The values for a given point in the hypercube represent the reflectance at a given wavelength as measured by the sensor for that pixel. The last objective will be to process these data in order to extract the underlying structure in data. Pattern recognition methods [Duda, 2000] have proven to be effective techniques in this kind of applications.

1.1 Analysis And Classification In Hyperspectral Imaging

The objective of this work is to use the hyperspectral aerial images to implement crop cover classifiers and to obtain a thematic map of the crops on the scene. However, one of the main problems with hyperspectral image processing is the huge amount of data involved. In addition, pattern recognition methods are sensitive to problems associated to high dimensionality features spaces (referred to as Hughes phenomenon or curse of dimensionality [Hughes, 1968]). The close relation between classifier complexity and the size of the training set suggests the idea of a prior reduction of input space.

Classical and advanced techniques have proved well-suited in this sort of classification tasks but some problems are encountered:

- a) The main problem with supervised methods is that the learning process heavily depends on the quality of the training data set. Consequently, small number of samples compared to data dimensionality, or the poor representativity of these samples are main issues to be addressed [Fukunaga, 1989]. In hyperspectral image processing these problems are even more severe given the high cost of true sample labelling, the high number of spectral bands, and the high variability of the earth surface.
- b) Unsupervised methods are not sensitive to the number of labelled samples since they work on the whole image. In addition, they are able to detect all the classes even though they are not previously known. Nevertheless, they build clusters attending to data similarity criteria that may depend on spectral characteristics that are

not related to the discriminative information among crops. Therefore, relationship between clusters and classes is not ensured.

2 HYPERSPECTRAL DATA

The hyperspectral images used in this work were acquired with the HyMap spectrometer. It is a 128-band scanner with a discontinuous spectral range from 0.4 μm to 2.5 μm .

The HyMap images acquired in the DAISEX'99 campaign correspond to two consecutive days. Each flight consisted on two overpasses, one in North-South direction and the other East-West direction which yielded six images of the same area. The calibration in the reflecting region of the HyMap spectrometer was made during the flight and using the vicarious calibration [Müller, 2001]. The atmospheric correction was based on MODTRAN atmospheric model with the software package ATCOR-A (atmospheric correction, airborne version) by the Deutsches Zentrum für Luft- und Raumfahrt (DLR) [Richter, 2001]. Simultaneously to the aerial campaign, another one was made on the ground level [Moreno, 2001] with the acquisition of atmospheric measurements, spectral measurements in the surface, measures of temperature, and samples of vegetation. All of them were analyzed by the remote sensing laboratory of the University of Castilla la Mancha. A Global Positioning System (GPS) enabled an accurate geocoding of the HyMap images and the construction of a training set.

For classification purposes, six different classes were considered in the area: corn, wheat, sugar beet, barley, lucerne, and bare soil. A 900 samples training set and another 900 samples verification set were defined for classification purposes considering spectra of ground checked points to assure its certainty. The number of samples among each class was taken equal for the six classes (25 samples per image and per class \rightarrow 150 samples per class). The last step was to use a true map of the scene in order to verify the classification results on the complete images. In each one of the six images (700x670 pixels), the total number of test samples is 327336 (corn 31269; sugar beet 11322; barley 124768; wheat 53400; lucerne 24726; and ground 81851) and the rest is considered *unknown*.

3 REDUCTION OF DIMENSIONALITY

The first aim is to reduce dimensionality while preserving relevant information for posterior classification. This is achieved with techniques that reduce redundant information by correlation criteria and select features that contain the highest discriminative capabilities. These methods are referred to as feature extraction techniques.

3.1 Redundant Information

The great amount of redundant information is due to the high spectral resolution of the instruments. This redundant information aggravates the problems related to the curse of dimensionality since crop classification results do not improve beyond ten bands.

We use the correlation matrix between all the spectral bands (no class labelling was assumed) in order to identify similarities and redundant information (see Fig. 1). High correlation between subsets of bands can be observed. In the same figure, we represent blocks of correlated contiguous spectral bands after applying a 0.99 threshold.

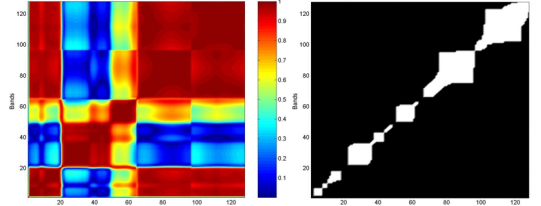


Fig. 1. **Left:** Correlation coefficients matrix among all the spectral bands. **Right:** Blocks of correlated contiguous spectral bands to each other after applying a 0.99 threshold.

The information contained in each set of the correlation matrix principal diagonal (over the threshold) is contained in one of those bands. In order to select the more discriminative spectral band between classes we look for the one that separates more the distribution of classes using the Bhattacharyya distance between the distributions of the classes, which is given by

$$J_B = \frac{1}{4}(\mu_2 - \mu_1)^T [\Sigma_1 + \Sigma_2]^{-1} (\mu_2 - \mu_1) + \frac{1}{2} \log \left(\frac{|\Sigma_1 + \Sigma_2|}{2(|\Sigma_1||\Sigma_2|)^{1/2}} \right) \quad (1)$$

This distance performs better than other metrics since it considers the first and second order statistics of the data (variability inside each class) and it is not scale dependent (Fig.2).

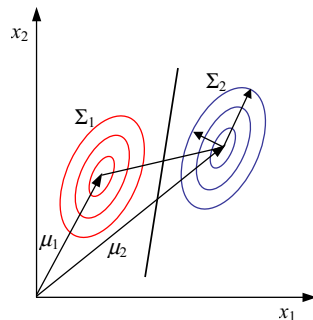


Fig. 2. Bhattacharyya probabilistic distance between two Gaussian distributions.

3.2 Feature Selection

After eliminating redundant information, we obtain a set of self-contained information bands. At this moment, the task becomes to identify those bands that better discriminate among classes. A two-stage feature selection algorithm is followed: firstly, a search strategy for feature group selection is carried out, and secondly, the objective function that evaluates the different subgroups is calculated [Doak, 1992].

A feature selection stage based on the *Sequential Floating Forward Selection* (SFFS) algorithm which maximizes the mean probabilistic distance between classes is used. We chose this method due to the following characteristics:

- Sequential:** Sequential algorithms present reasonable computational requirements than exponential algorithms which perform an exhaustive search. The latter are infeasible when working with 128 spectral features. Random search algorithms have the advantage of avoiding local minima in the objective function.
- Floating:** A floating sequential search process is more versatile since it is adapted during the process based on the criterion.
- Forward:** The forward search begins with one variable and continues adding features. It presents a couple of practical advantages with regard to the backward search. Firstly, if the initial dimension is very high, the calculation of the criterion can be complex or impossible (for example the estimation of the covariance matrix from few samples). Secondly, if the search process is long and interrupted, the best sets of variables for small dimensions are already obtained.
- Selection:** Feature selection is better than extraction since obtained results can be directly interpreted and extrapolated to other sensors [SmartSpectra, 2002].

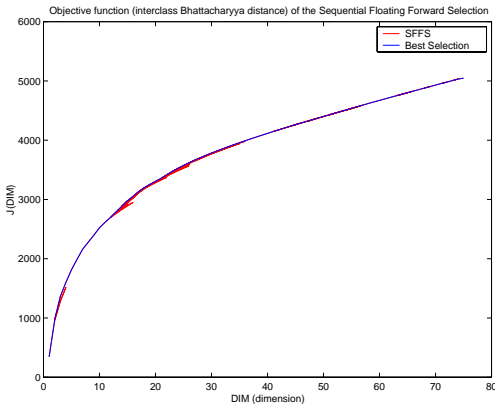


Fig. 3. Selection criteria attending to the considered number of features.

This method produces a hierarchy of feature subsets with the best selection for each dimension. We can represent the value of the objective function for each number of features (Fig. 3) and check monotonicity (no local minima).

4 SEMI-SUPERVISED CLASSIFICATION METHODOLOGY

We propose a methodology that complements the labelled samples with non-labelled samples in order to increase the training set (semi-supervised learning [Landgrebe, 2002]). This method simplifies the analysis and classification tasks in hyperspectral imaging. Supervised learning applied to crop classification is combined with unsupervised learning techniques in order to classify the rest of the image, extracting the natural clustering among data. Figure 4 shows the stages of the proposed semi-supervised classification method with the used algorithms (block arrows) and the intermediate results (boxes).

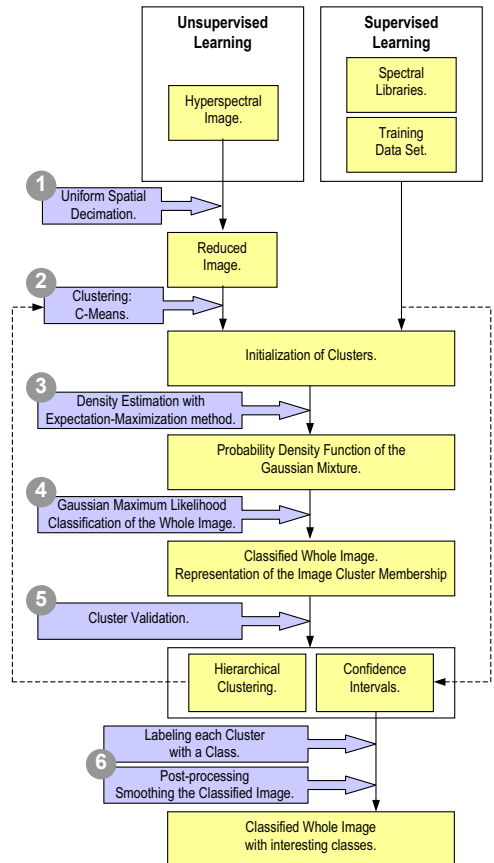


Fig. 4. Block diagram of the proposed semi-supervised classification method. The used algorithms are shown with block arrows and the intermediate results in boxes.

In the learning process we want to extract information of the acquired data. In the unsupervised case we only have the hyperspectral image (hypercube in Fig. 5). The supervised learning requires an additional previous knowledge of the problem that allows to label part of the data (this training set is represented in Fig. 6 by the spectral signature of each crop).

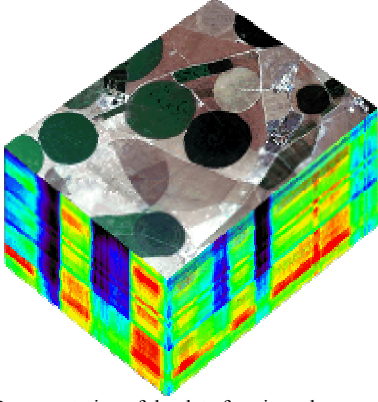


Fig. 5. Representation of the data forming a hypercube.

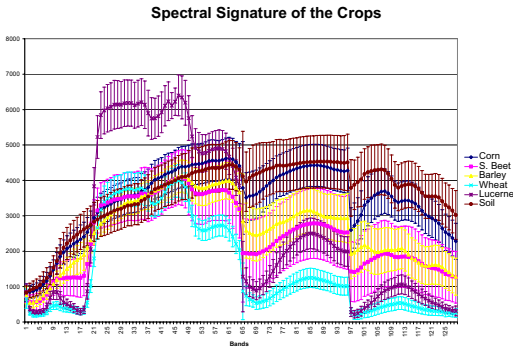


Fig. 6. Spectral curves of the crops to be classified for he training data set

In the next subsections, we briefly describe the stages of our proposal. Results provided by each algorithm are used in the following stage.

4.1 Uniform Spatial Decimation

The unsupervised learning use raw data from the image in order to extract the information of the clusters. The problem is the amount of data of the whole hyperspectral image. A first stage may be the reduction of the number of pixels through uniform spatial decimation of the image. The reduction factor is related to the spatial resolution but is no critical since the information of the classes relies on the spectra and does not on the spatial distribution.

4.2 Clustering: C-Means

The familiar *C*-Means algorithm is used to obtain a first approach to the structure of the data in clusters. It is applied to the reduced image and obtains an approximation of the clusters on the scene. This algorithm only needs the number of clusters C to be found and minimizes the Euclidean distance of the samples in one cluster to its mean. The M samples $x_k \in \mathfrak{R}^N$ are vectors containing the N spectral bands for each pixel. *C*-Means algorithm finds the clusters in an iterative procedure which computes the mean of the cluster (Eq. 2) and updates the membership of the samples to the clusters (Eq. 3). This procedure is iteratively performed until centers do not change [Alpaydin, 1998].

$$\mu_i = \frac{\sum_{k=1}^M p_{ki} x_k}{\sum_{k=1}^M p_{ki}} \quad (2)$$

$$p_{ki} = \begin{cases} 1 & \text{if } \|x_k - \mu_i\| = \min_j \|x_k - \mu_j\| \\ 0 & \text{otherwise} \end{cases} \quad (3)$$

4.3 Density Estimation: Expectation-Maximization

Once we have an initialization of the clusters in the image, we employ it as the starting point for the Expectation-Maximization (E-M) algorithm. These clusters are necessary to initially estimate the distributions of the present classes in the image. However, if a training set is available we can directly estimate the distribution of the classes of interest in a supervised way and add them to the detected clusters. Another possibility is to initialize the mean of the clusters with the spectral signature of the class (crop) of interest from a spectral library. We applied the E-M algorithm in an iterative procedure on the pixels of the decimated, reduced image. In this way, this method adapts the distributions of the specified classes to the peculiarities of the specific analyzed image.

The E-M algorithm [Dempster, 1977] considers the data set as a mixture of normal distributions (Eq. 4) and provides the maximum likelihood estimation of the probability density function (p.d.f.) of the Gaussian mixture (for each component of the mixture it estimates the mixture coefficient α_i , the mean μ_i and the covariance matrix Σ_i). This p.d.f. describes both the classes of interest and the non-identified clusters which are present in the image. Figure 7 shows the p.d.f. of the mixture of the six classes of interest using 10 Gaussian components.

$$P(x) = \sum_{i=1}^C \alpha_i P(x|\theta_i) = \sum_{i=1}^C \alpha_i P(x|\Sigma_i, \mu_i) \quad (4)$$

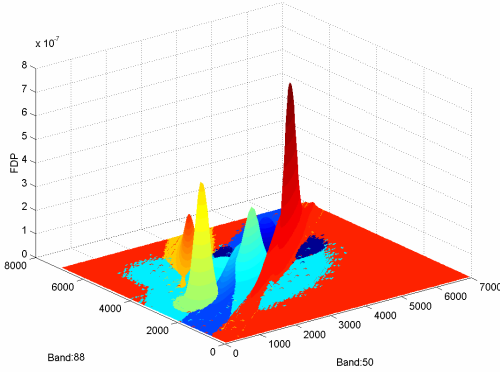


Fig. 7. Probability density function of the Gaussian mixture of the classes.

4.4 Classification: Gaussian Maximum Likelihood

Once we know the Gaussian components of the probability density function of the data we perform a Gaussian maximum likelihood classification on the whole image. The algorithm assigns the pixel to the cluster with the maximum *a posteriori* probability generating a map with the clusters in the image (Fig. 8).

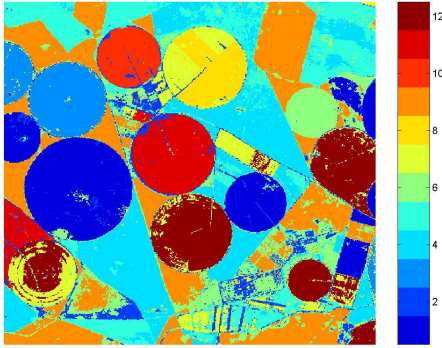


Fig. 8. Map containing the labels of the clusters in the whole image.

In addition, at this stage, we may obtain, for each cluster, a representation of the cluster membership for each pixel in the image. This kind of representation contains useful information about the spatial distribution of clusters in the scene. Fig. 9 shows two clusters which represent two subclasses of the same crop. In this figure, we can observe the mixture of pixels of both clusters in the same field.



Fig. 9. Representation of the image cluster membership of the pixels for the clusters 4 and 5 (high membership in dark areas).

4.5 Cluster Validation

Once the clusters of the image are obtained, it is necessary to assign them a class label from a well-known crop. This requires a training set or an spectral library to compare the spectral signatures with the clusters. One possibility is to use distances such as the Mahalanobis distance. However, relative measures always assign the nearest class, which does not assure trustable results in our problem. For this reason, we used confidence intervals of the normal distribution.

The confidence interval of the normal distribution can not be calculated analytically, but can be derived from tables obtained by numerical methods for the univariate normal distribution case [Lapin, 1983]. For its calculation, it is strictly necessary to transform the feature space into a system of coordinates with (a) the origin into the mean of the cluster distribution and (b) the axes oriented in the directions of the covariance matrix eigenvectors of the cluster distribution. In this system, the covariance matrix of the distribution is diagonal, therefore, the variance of the characteristics and the densities of probability of each component are independent (Eq. 5). This enables us to calculate the interval of confidence in each direction (calculation of the probability $1-[F(a)-F(-a)]$), and, to obtain the total probability for all the distribution by means of a productory:

$$f(x) = \frac{1}{(2\pi)^{N/2} |\Lambda|^{1/2}} \exp \left[-\frac{1}{2} x^T \Lambda^{-1} x \right] \quad (5)$$

$$= \prod_{i=1}^N \left\{ \frac{1}{(2\pi)^{1/2} \lambda_i^{1/2}} \exp \left[-\frac{1}{2} \cdot \frac{x_i^2}{\lambda_i} \right] \right\}$$

We do not know the class of clusters that does not accomplish the confidence interval but we know their distribution (mean spectra and covariance), and their position in the scene. This yields better results that the introduction of an *unknown* class as supervised methods do, and may improve our knowledge.

In the proposed methodology, the user only specifies one parameter. This parameter indicates the

number of clusters in the image, which is unknown *a priori*. We want to find, at least, the number of classes of interest. In this sense, we propose to specify a higher number of clusters than classes of interest for two reasons:

- a) We want to find all the classes of interest, assuming that other cover types may exist in the whole image.
- b) When the number of crops in the scene is higher than the specified number of clusters then we obtain a bad class p.d.f. estimation. On the other hand, if the number of crops in the scene is lower than the specified number of clusters then several clusters will represent the same class (subclasses).

However, the estimation of the class distribution improves if the correct number of clusters is assigned. For this reason, we propose a hierarchical clustering of the Gaussian components of the distribution mixture to identify and validate the number of clusters. In each step of the hierarchical clustering we join the most similar components of the mixture. Equations (6) show the parameters of the new cluster.

$$\begin{aligned}\mu &= \frac{\alpha_1 \cdot \mu_1 + \alpha_2 \cdot \mu_2}{\alpha_1 + \alpha_2} \\ \Sigma &= \frac{\alpha_1 \cdot \Sigma_1 + \alpha_2 \cdot \Sigma_2}{\alpha_1 + \alpha_2} \\ \alpha &= \alpha_1 + \alpha_2\end{aligned}\quad (6)$$

This fast and straightforward validation technique obtains all the possible classifications attending to the number of clusters. Two advantages can be drawn:

- a) It provides a dendrogram where the structure of the clustering and the similarity among clusters is indicated. This allows to establish an objective criterion to determine the suitable number of clusters (Fig. 10).
- b) As the clusters are joined a hierarchical sequence of maps with the new classification is generated. This allows the analyst to quickly verify the results and to aid in the decision of which is the suitable number of clusters. This advantage would be lost if the space distribution of the clusters in the image did not follow any pattern.

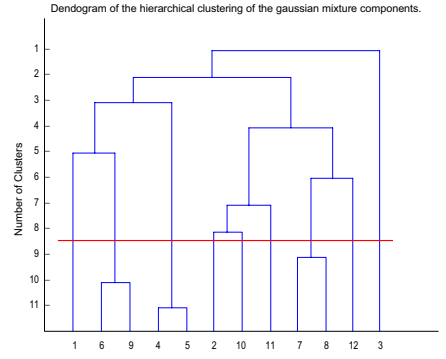


Fig. 10. Dendrogram of the hierarchical clustering of the found clusters in the hyperspectral image.

4.6 Post-Processing

The last stage of the image classification methodology is a post-processing stage to smooth the classified image using a spatial average in the *a posteriori* probability maps (Fig. 11).

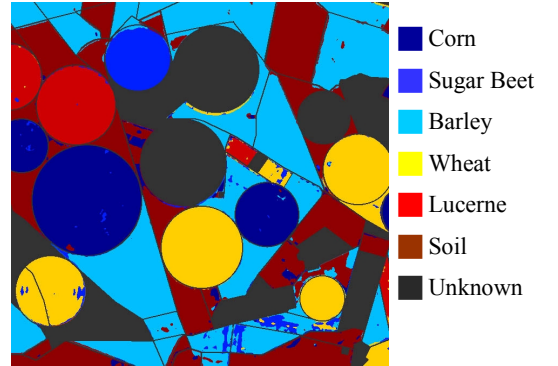


Fig. 11. Map with the labels of the classes of interest of the whole image.

5 RESULTS

In a first stage we have studied the need of reducing the input space dimension. Fig. 12 shows how the classification success rate falls as data dimension increases. Results do not improve beyond 20 bands due to the dimensionality of the spectral information. But the results get worse over 100 bands due to the Hughes phenomenon (a covariance matrix of dimension 100 is estimated with only 150 samples).

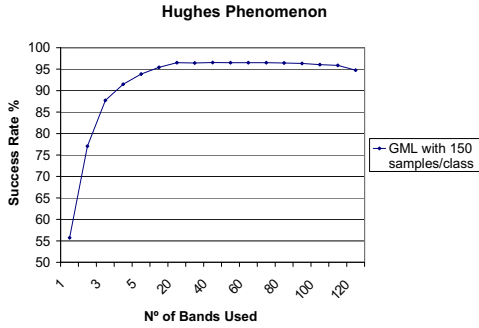


Fig. 12. Hughes phenomenon in a Gaussian Maximun Likelihood (GML) Classifier considering the data set for different numbers of bands uniformly distributed in the spectrum.

With the procedure explained in section 2 we reduce the dimension of the data. The set of the 6 most discriminative bands is used with all the classifications methods. Table I benchmarks the methods in terms of the average classification performance and its standard deviation for the six available images. All models were developed in MATLAB[®] environment (Mathworks, Inc). Since the computational burden was very high in some cases, *m-files* were translated to MEX-files and programs were run on fast workstations. Statistical analysis was carried out using S-Plus 2000[®] (MathSoft, Inc).

Classification Method	Success Rate	Standard Deviation
C-Means	66.6%	5.7%
ISODATA	64.6%	6.1%
Learning Vector Quantization	84.3%	1.2%
Gaussian Max. Likelihood	94.4%	1.1%
Expectation-Maximization	91.4%	2.6%
Semi-Supervised Method	96.7%	1.5%
Multilayer Perceptron	95.3%	1.0%

Table I. Average classification performance and standard deviation of the proposed methods for the six images.

The main features extracted from this table are:

- The proposed semi-supervised method, whenever it has supervised information to initialize the clusters, outperforms the rest of methods.
- Expectation-Maximization method gives better results than other unsupervised methods and the LVQ (supervised), that uses a poor metric to consider the variability of the data (Euclidean distance).
- Unsupervised methods present higher standard deviation between images due to their random initialization of clusters (no training set force a distribution of the classes in data).

6 CONCLUSIONS

In this communication, we have proposed a procedure to reduce dimensionality while preserving relevant information for posterior classification based on a combined strategy of supervised and unsupervised learning methods.

This feature selection procedure yields the following benefits:

- Increases the performance of the classifier by mitigating the Hughes phenomenon.
- Reduces the amount of data. This allows to make the calculations faster and also makes possible the training of iterative methods, such as artificial neuronal networks.
- The selected bands optimize the class separation. It allows to easily recognize the natural structure in data.
- We can identify the physical meaning of the selected spectral bands and interpret the results.

With regard to the proposed semi-supervised method of image classification, its main advantages and disadvantages are:

- ✓ Presents higher robustness to changes in external conditions of acquisition since it uses the data of the whole analyzed image.
- ✓ Allows to incorporate previous knowledge if no supervised information of the data set is available.
- ✓ Learning consists on the estimation of the probability density function of a Gaussian mixture with simple and fast calculations.
- ✓ Only requires two parameters that are important but not critical for the results.
- ✓ Takes advantage of spectral and spatial information of the data set.
- ✓ Provides a great amount of additional information in order to understand results.
- ✗ Has the advantages of unsupervised methods but requires a selection of the discriminative features.
- ✗ Is useful for classes that present a Gaussian mixture distribution [Gómez-Chova, 2001].
- ✗ Is automatic in its execution but requires a validation of the obtained results supervised by the analyst.
- ✗ Uses the spatial relation between pixels so its application is restricted to image pattern recognition.

ACKNOWLEDGMENTS

This research has been partially supported by the Information Society Technologies (IST) programme of the European Community. The results of this work will be applied in the "Smart Multispectral System for

Commercial Applications" project (Contract n°: IST-2001-37306).

This research has been partially supported by the European Space Agency. All the used data were acquired in the Scientific Analysis of the ESA Airborne Multi-Annual Imaging Spectrometer Campaign DAISEX (Contract n°: 15343/01/NL/MM).

BIBLIOGRAPHY

Alpaydin, E. (1998). "Soft vector quantization and the EM algorithm." *Neural Networks* 11: 467-477

DAISEX. (2000). "Digital Airborne Imaging Spectrometer Experiment" Project Home Page: <http://io.uv.es/projects/daisex/>. ESA, 2000.

Dempster, A. P., Laird, N.M., Rubin, D.B. (1977). "Maximum likelihood from incomplete data via the EM algorithm." *J. R. Stat. Soc. Ser. B*(39): 1-38.

Doak, J. (1992). "Intrusion Detection: The Application of Feature Selection, A Comparison of Algorithms, and the Application of a Wide Area Network Analyzer." Master's thesis, University of California, Davis, Dept. of Computer Science.

Duda, R.O., Hart, P.E., Stork, D.G. (2000). "Pattern Classification". Second Edition. John Wiley and Sons, New York.

Fukunaga, K., Hayes, R.R. (1989). "Effects of sample size in classifier design." *IEEE Trans. Pattern Analysis and Machine Intelligence* 11(8): 873-885

Gómez-Chova, L., Calpe, J., Soria, E., Moreno, J., González, M.C., Alonso, D., Martín, J.D. (2001). "Improvements in land surface classification with hyperspectral HyMap data at Barrax". Final Results Workshop on DAISEX, ESA/ ESTEC, Noordwijk, The Netherlands, ESA Publications Division.

Hughes, G.F. (1968). "On The Mean Accuracy Of Statistical Pattern Recognizers." *IEEE Transactions on Information Theory* (14-1): 55-63

Landgrebe, D. (2002). "Hyperspectral Image Data Analysis as a High Dimensional Signal Processing Problem," Special Issue of the *IEEE Signal Processing Magazine*, Vol 19, No. 1 pp. 17-28, January 2002.

Lapin, L.L. (1983). "Probability and statistics for modern engineering", Duxbury Press. PWS Publishers.

Moreno, J., Caselles, V., Martinez-Lozano, J.A., Melia, J., Sobrino, J., Calera, A., Montero, F., Cisneros, J.M. (2001). "The measurement programme at Barrax". Final Results Workshop on DAISEX, ESA/ ESTEC, Noordwijk, The Netherlands, ESA Publications Division.

Müller, A., Richter, R., Heiden, U. (2001). "Vicarious calibration of imaging spectrometers in the reflective region". Final Results Workshop on DAISEX, ESA/ ESTEC, Noordwijk, The Netherlands, ESA Publications Division.

Richter, R. (2001). "Atmospheric correction methodology for imaging spectrometer data". Final Results Workshop on DAISEX, ESA/ ESTEC, Noordwijk, The Netherlands, ESA Publications Division.

SmartSpectra (2002). "Smart Multispectral System for Commercial Applications", SmartSpectra Home Page: <http://www.smartspectra.com>. Information Society Technologies Programme. (Contract no.: IST-2001-37306).

The VALENCIA ANCHOR STATION: A Reference Cal/Val Area For Low-Resolution Remote Sensing Data And Products

E. López-Baeza(1,2), C. Antolín Tomás(2), A. Bodas Salcedo(1), J. F. Gimeno Ferrer(1), K. Saleh Contell(1), F. Ferrer(2), N. Castell Balaguer(1,3), C. Doménech García(1), and M. A. Sanchez Alandí(1), A. Velázquez Blázquez(1)

(1) *Climatology from Satellites Group, Remote Sensing Unit, Department of Thermodynamics*

(2) *Centre for Desertification Studies Research (CIDE)*

(3) *Centre for Mediterranean Environmental Studies (CEAM)*

University of Valencia

Ernesto.Lopez@uv.es

ABSTRACT - This paper introduces the VALENCIA Anchor Station site that has recently been installed in the Utiel-Requena Plateau, near Valencia (Spain), with the main objective of developing and providing a Calibration/Validation (Cal/Val) test area principally dedicated to large-scale low-spatial resolution remote sensing missions. Together with the description of the station and of its instruments, the paper presents the proposed methodology to characterise an area of more than 50 x 50 km² which is about the size of a GERB (Geostationary Earth Radiation Budget) pixel, onboard the recently launched METEOSAT Second Generation (MSG) satellite, or that of the forthcoming Soil Moisture and Ocean Salinity (SMOS) Mission planned for early 2006. The station is robustly equipped with conventional standard meteorological instruments, situated at two different levels in the atmosphere, and also in the soil, and with specialised measurements of all radiation components and of soil moisture content. The station includes instruments and facilities to carry out mobile measurements along and across the whole area. The site is reasonably homogeneous from different viewpoints such as topography, land use, and other climatic elements.

Specifically, the tasks to be carried out at the VALENCIA Anchor Station will be:

- Definition of a large scale validation area for low-spatial resolution missions
- Definition and characterisation of a large scale reference pixel
- Time Interpolation and Spatial Averaging. Study of scaling issues. Criteria for aggregation and disaggregation

Besides GERB and SMOS, it is expected that the VALENCIA Anchor Station may also be useful in the framework of SEVIRI, ENVISAT (AATSR), CERES, and AMSR.

1 INTRODUCTION

The requirements for data records and information products derived from Earth Observation technology are consistent quality, precision and accuracy. Besides, in order to produce reliable measurements as input to the geophysical parameter retrieval, a basic requirement is that the spaceborne instruments are properly calibrated. This ensures that the retrieval algorithms are independent of instrument errors and establishes confidence in the geophysical parameter estimates. For climate measurements, for example, changes of only a few percent in geophysical parameters are of critical interest.

The activity that endeavours to ensure that remote sensing products are highly consistent and reproducible is known as calibration and validation, or "cal/val". This is an evolving discipline that is becoming increasingly important as more long-term

studies on global change are undertaken, and new satellite missions are launched. *Calibration* is the process of quantitatively defining the system responses to known, controlled signal inputs. *Validation* is the process of assessing, by independent means, the quality of the data products derived from the system outputs. These definitions are internationally accepted and are most often used in the remote sensing context to refer specifically to sensor radiometric calibration and geophysical data product validation. Agencies usually undertake the calibration of their respective mission satellite systems, however to extend this beyond the *commissioning phase* is potentially very difficult. Therefore, well-instrumented benchmark test sites and data sets for calibration should be supported, in particular for terrestrial applications, to provide calibration information to supplement or substitute for on-board calibration, in a coordinated way, and ensuring continuity, and

reliability to access to their data with minimal delay. These sites could well receive rotating support from agencies with the agency (or company) with the most recent satellite launch funding the site during the *commissioning phase*.

Besides a history of long data records, the ideal requirements for these test sites include that they are large, flat homogenous areas, with nearly Lambertian and nearly flat spectral reflectance, and with high percentage of clear skies and dry conditions. They should primarily be bright targets, including a few low reflectance targets as well. Besides having year-round availability, the test site should somehow have "controlled" human disturbance as well.

The primary objective of validation is to assess the quality, and as far as possible to quantify the accuracy of remote sensing data products. Ideally, validation activities seek to compare the data products with more accurate independent measurements of the same quantity over a statistically significant number of samples and wide variety of situations. The problem is that the space and time scales of the *in-situ* data and the satellite data are rarely directly comparable. Typically, there are insufficient *in-situ* measurements to cover a satellite field of view, whether the field of view is some meters (high resolution imagers, for example), or several km (broadband radiometers, L-band radiometers, etc). Thus, even a perfect remote sensing measurement will be expected to differ from an *in-situ* verification measurement because of the inability to match the observations in time or space. *In-situ* measurements are invariably taken at small space and time scales, while a satellite overpass is a few second snapshot of a large area. For broadband radiometers, a common example is the comparison of a surface flux radiometer to a satellite based estimate for the radiometer field of view. The matching error can be reduced (but not eliminated) by increasing the number of surface observations within the field of view (level 2 data) or grid box (level 3 data). This error can also be minimized by using very large ensembles of matched data.

Field campaigns are best for process studies and hypothesis formation. They provide the most complete case study data, but provide very limited statistical significance. Dedicated sites, BSRN (*Baseline Surface Radiation Network*) surface sites, and other long-term sites are considered the best strategy for validation of cloud and radiation data.

In many geophysical fields, the region of the earth viewed by a satellite observation rarely matches exactly that viewed by the surface radiometer. Recourse must be made to statistical intercomparisons in order to reduce the sampling noise induced by the different space and time sampling characteristics of satellite and surface data. The special character of remote sensing measurements to correspond to area integrated values, obliges independent *in situ*

measurements to be representative of zones of a minimum number of pixels of the sensor under consideration. The large pixel size of some satellite missions such as GERB, EarthCARE (*Earth Clouds, Aerosols and Radiation Explorer*), CERES (*Clouds and the Earth's Radiant Energy System*), etc., introduces a number of scientific issues that make it relevant and even necessary to develop a specific methodology and carry out specific measurements over large extended areas. These regions should be well controlled from the viewpoint of other complementary measurements, also at a large scale.

The University of Valencia has recently set up a robust automatic meteorological station located towards the North-West part of the Valencia region, in the *Utiel-Requena Plateau*, at about 80 km from the city of Valencia. The main objective of the *VALENCIA Anchor Station* is to define and characterise a large, reasonably homogeneous and flat area, mainly dedicated to vineyards, as reference for Cal/Val activities in low-resolution large-scale pixel size satellite sensors, as those corresponding to the missions mentioned above. The area is well documented and has previously been used in other projects. It is desirable that the *VALENCIA Anchor Station* area, together with the Central Spain area where the University of Castilla-La Mancha has three other twin stations operational, could define a still larger and reasonably homogeneous region of about 300 x 200 km², in order to be able to count with a minimum number of large size pixels of the order of 50 x 50 km² (Figure 1).

2 SCIENTIFIC OBJECTIVES OF THE *VALENCIA ANCHOR STATION*

The specific scientific objectives of the tasks to be carried out at the zone mainly in relation to the missions mentioned above are (Lopez-Baeza et al., 2001):

2.1 Definition of a large scale validation area for low spatial resolution missions:

Valuable requirements for a test site are the information on the area, basic documentation, availability of retrospective measurements and maintenance and attention of the site. These conditions are especially accomplished in this case, both for the University of Valencia site, that is, the *VALENCIA Anchor Station*, and for the University of Castilla-La Mancha sites, that is the *Tomelloso, El Bonillo and Barrax Anchor Stations*.

On the one hand, the Regional Ministry for Public Works, Land Planning and Transports of the Regional Government of Valencia scientifically documented the territory from the viewpoint of soil as a natural resource, and provided physiography maps, maps of

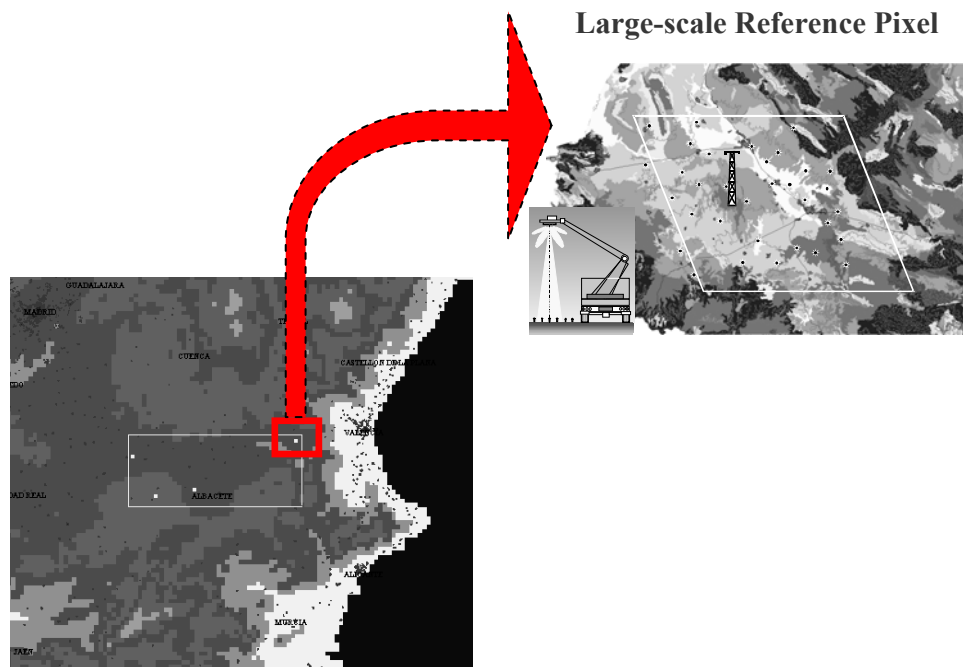


Figure 1. The VALENCIA Anchor Station area

soils, land capability, potential erosion and actual erosion (Antolin, 1998).

These maps may be obtained in a Geographical Information System environment, perfectly documented.

On the other hand, the Castilla-La Mancha region has thoroughly been studied in previous well-known international projects such as:

- a) EFEDA (ECHIVAL Field Experiment in a Desertification-Threatened Area)
- b) ECHIVAL-EFEDA PHASE II Project no. 5: Remote Sensing and Radiometric Properties of the Surface: Assessment of Desertification From Space
- c) RISMOP (Radiometric Impact of Surface Moisture on Precipitation)
- d) RESMEDES (Remote Sensing of Mediterranean Desertification and Environmental Stability)
- e) RESYSMED (RESMEDES Synthesis of Change Detection Parameters Into a Land-

Surface Change Indicator for Long-Term Desertification Studies)

Besides, the area has currently been used as the vicarious validation area for METEOSAT. The University of Castilla-La Mancha holds information on soils, vegetation, land use classifications, etc.

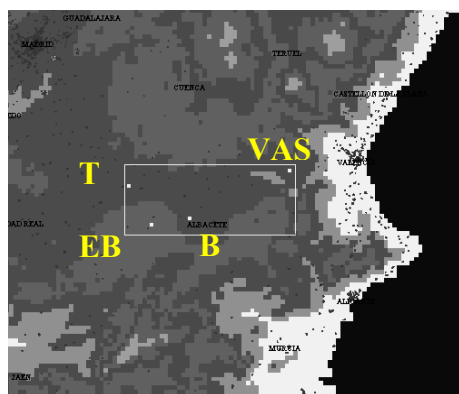


Figure 2.- Relative situation of the 4 Anchor Stations: VAS: Valencia Anchor Station; T: Tomelloso; B: Barrax; EB: El Bonillo. Consecutive colours drawn at 200 m altitude steps. Red dots indicate urban areas

The overall area proposed may be defined from the available information mentioned above, taking into account the characteristics of soils, climate, physiography, etc. It does then result a large extended area, more than 300 km wide, reasonably homogeneous taking into account the low spatial resolution of the remote sensing instruments under consideration. The first principal task to be undertaken should be to homogenize the large quantity of information available and complete intermediate zones by means of interpolation methods based on spatial statistical techniques (*kriging* and *co-kriging*) and by using remote sensing techniques. It may be stated that there does not exist in Europe an area of similar characteristics, especially as large and homogeneous, and located in a climatic area of so much scientific interest from many different viewpoints.

2.2 Definition and characterisation of a large scale reference pixel:

Complementarily to the previous objective, it is also planned to carry out specific tasks to facilitate the preparation of future Cal/Val activities of the missions mentioned earlier. This is a valuable objective that both the GIST (*GERB International Science Team*) and the *SMOS Science Team* have positively valued by accepting the *VALENCIA Anchor Station* site as one of the basic areas to carry out this kind of activities. This objective includes several planned tasks starting from the classification of different *homogeneous environmental units* in the large pixel area. The plan is to select an area of about 50 km wide around the actual *Anchor Station* site, approximately of the size of a GERB or a SMOS pixel where to design and carry out a number of distributed measurements of soil moisture content, soil temperature, surface

temperature, reflectance, albedo, and net radiation and some meteorological parameters in every homogeneous environmental unit defined (Figure 3).

Large Scale Reference Pixel

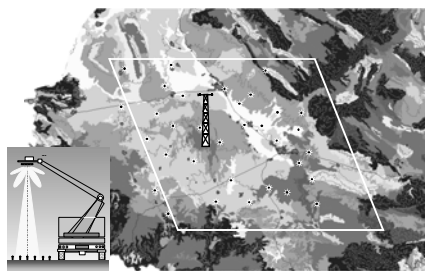


Figure 3.- The *VALENCIA Anchor Station* Site

Non-homogeneities within every unit may be characterised by defining transects and using mobiles instrumentation. As far as surface reflectance is concerned, the *Climatology from Satellites Group* may count on the collaboration of the *Field Radiometry Group*, both included in the *Remote Sensing Research Unit* of the University of Valencia. It would be desirable to be able to also count on the collaboration of other groups to carry out angular measurements by using L-band radiometers as well (Figure 4).

It is planned that this characterisation be made firstly in an area of about 5 km diameter, and then scaling up to 10 km, 20 km, etc, until covering the whole zone. It will also be carried out under different meteorological and climatological conditions along the year, minimally during a dry period and immediately after a significant rain event, and accounting for spatial variability and topographic effects.



Figure 4.- Mobile equipment of the *VALENCIA Anchor Station*. Left hand side: mobile radiation and meteorological station. Right hand side: Truck with a 15 m boom for reflectance measurements

2.3 Study of scaling issues. Criteria for aggregation and disaggregation. Time Interpolation and Spatial Averaging

With no doubt, the large size, not only of the whole area, but also of the reference pixel, makes it necessary to study in detail the change of scale processes to be able to compare measurements proceeding from so different sources at different scales, namely point measurements, aircraft observations, different spatial resolution acquisitions from different satellite platforms, etc., and establish criteria for aggregation and disaggregation to get different area averages and validate large scale pixels. Similarly, time interpolation, that is, handling the time dependent diurnal cycles or getting monthly averages of surface temperature, solar zenith angle albedo dependence, and cloud property diurnal cycles, to name a few examples is also a difficult task except for geostationary satellites.

3 VALENCIA ANCHOR STATION DESCRIPTION

The *VALENCIA Anchor Station* (39°34'15''N, 1°17'18''W, 813 m) is placed in the *Requena-Utiel Plateau*. This is an extensive undulated plain formed by quaternary sediments surrounded by mountainous regions at the Northern and Eastern sides and the *Gabriel River Basin* at the Western and Southern sides. The landform shows erosion and depositional footslopes and topography characterised by flat regions (slope <2%) and undulated areas (8-15%). The major soils of the region - *Calcareous Cambisol* and *Haplic Calcisol*- are deep soils with carbonate accumulations and equilibrated textures, and low organic matter amounts. The dominant land use in the plateau is dedicated to vineyards, however, the *Anchor Station* surrounding area contains representative ecosystems of the Mediterranean arch, typical of semi-arid regions, including *Alepo* pine forests and Mediterranean shrubs.

In principle, the *VALENCIA Anchor Station* as such is a robust meteorological station where measurements are made at different levels both in the atmosphere and in the soil in order to be able to derive surface energy fluxes.

Table 1.- *VALENCIA Anchor Station*'s instruments.

Parameter	Instrument	Resolution	Range	Model	Maker
Wind Speed at 2 and 15 m	Anemometer	0.1 m ⁻¹	0 - 50 m s ⁻¹	VV-200	Geónica
Wind Direction at 15 m	Weather Vane	1°	0 – 360°	DV-200	Geónica
Air Temperature at 0.5 m	Temperature Sonde	0.1°C	-50 - +50 °C	STA-212-PVC	Geónica
Air Temperature and Humidity 2 and 15 m (tbc)	Integrated T and H Transmitter	T: 0.1°C H: 5 %	-50 - +50 °C 0 - 100%	44212/50-U	Vaisala
Atmospheric Pressure	Barometer	1 mb	600 – 1100 mb	SPA-900	Druck Limited
Downwelling Reflected and Net SW Radiation	Albedometer	1 W m ⁻²	0 – 1500 W m ⁻²	CM 14	Kipp & Zonen
Downwelling Emitted and Net LW Radiation	Pyrgeometer	1 W m ⁻²	0 – 1500 W m ⁻²	CG 1/2	Kipp & Zonen
Soil Temperature	Temperature Sonde	0.1°C	-50 - +50 °C	STS-212-PVC	Geónica
Soil Heat Flux	Soil Heat Plate	1 W m ⁻²	0 – 1500 W m ⁻²	RIMCO HP3/CN3	RIMCO Middleton Synchotac
Soil Moisture Content	Delta-T Profile Probe	±0.5 m ³ m ⁻³	0-10 m ³ m ⁻³	PR 1/4 – 1/6	Hoskin Scientific LTD
Evaporation	Evaporimeter	0.76 mm	0 – 254 mm	255-100	Nova Lynx Corp.
Precipitation	Pluviometer	0.1 mm	0 – 26 cm	52202/52203	Young

Table 1 shows the parameters that are operationally measured at different levels together with the characteristics of those measurements (instrument, resolution, range, model and range). Brand names are given just for information and do not mean any special endorsement from the authors. The station is composed of two masts. One holds conventional meteorological instruments at the atmospheric levels of 2 and 15 m, and -10, -20 and -40 cm in the soil. Air temperature is also measured at 0.5 m. The second mast is dedicated to the measurement of the four radiation components at 2 m above the ground. Table 2 shows the mobile instruments that can be used to measure specific parameters and some meteorological quantities in the whole *Anchor Station* area by means of transects performed with the vehicles shown in figure 4. There are two mobile meteorological stations that measure air temperature and humidity, global irradiance, surface albedo and net radiation at 2 m above the ground and soil temperature profile and soil heat flux at different levels within the soil.

Table 2.- *VALENCIA Anchor Station's instruments.*

Parameter	Instrument
Net Radiation	2 Middleton pyrrometers
Global Irradiance	2 Kipp and Zonen pyranometers
Surface Albedo	2 Kipp and Zonen albedometers
Soil Heat Flux	4 Middleton heat flux plates
Soil Temperature Profile	Campbell Pt-100 Temperature probes
Surface Radiometric Temperature	Raynger MX4 Howholst
Atmospheric Transmissivity	EKO Sunphotometer MS-110
Soil Dielectric Constant	Tektronic TDR 1502C
Soil Moisture Content	ThetaProbe type ML2X
Surface Spectral Reflectance (Field Radiometry Group)	GER-SIRIS and GER-3700 Spectroradiometers
Band Reflectance (Field Radiometry Group)	EXOTECH Radiometer
LAI (Field Radiometry Group)	LICOR-2000 Plant Canopy Analyser
Chlorophyll (Field Radiometry Group)	Minolta SPAD-502

The specific parameters mentioned earlier refer mainly to surface reflectance and brightness temperature and some vegetation parameters, together with other soil

characteristics such as soil moisture content and soil dielectric characteristics. Atmospheric transmissivity may also be measured. There are other instruments planned to be acquired in the short future to improve atmospheric and cloud measurements, as well as a singular and unique instrument to determine atmospheric radiation divergence.

4 ACKNOWLEDGEMENTS

The *VALENCIA Anchor Station* is the result of an infrastructure project co-financed by the Regional Government of the Valencia Region and the University of Valencia. We acknowledge the support provided by the Regional Ministry for Environment for the maintenance of the station. The land is indefinitely lent by Bodegas Iranzo and we also acknowledge the support provided by the Town Halls of Utiel and of Caudete de las Fuentes.

There are presently two Spanish Research Programme Projects on Space Research that are being developed in the framework of the *VALENCIA Anchor Station*, namely MIDAS (Lopez-Baeza, 2001) and SCALES (Lopez-Baeza, 2002). Both include tasks addressed to the characterisation of the whole *VALENCIA Anchor Station* area, respectively with respect to soil moisture content (MIDAS in the context of the SMOS Mission) and to radiation and cloud studies (SCALES in the context of GERB and SEVIRI onboard MSG).

We also acknowledge the confidence and scientific support from the GIST (*GERB International Science Team*) and the SMOS Science Team who count on the *VALENCIA Anchor Station* as a reference station for their validation activities.

5 REFERENCES

- Antolín, C., 1998, Soil as a Natural Resource in the Valencian Autonomous Community. Vol. I . Colección Territori 8, Regional Ministry for Urbanism, Planning and Public Works (C.O.P.U.T). (Generalitat Valenciana, Regional Government of the Valencian Autonomous Community)., Valencia, 187 pp. Idem. Vol.II 4 pages. Foldable maps. 74 pages. of plates. + 1cd-rom.
- López-Baeza, E., 2001, MIDAS (Medidas Radiométricas en Microondas y Desarrollo de Algoritmos para la Misión SMOS, *Microwave Radiometric Measurements and Algorithm Development for the SMOS Mission*). Spanish Ministry for Science and Technology, National Programme on Space Research (28-12-2001 to 27-12-2003)

- López-Baeza, E., 2002, SCALES (Area De Calibración/Validación para Experimentos de Campo en Gran Escala con SEVIRI/GERB, *SEVIRI & GERB Cal/Val Area for Large-scale Field Experiments*). Spanish Ministry for Science and Technology, National Programme on Space Research (01-10-2002 to 30-09-2005)
- López-Baeza, E., C. Antolín, A. Bodas, N. Castell, F. Ferrer, J.F. Gimeno, J. Rausell et K. Saleh, 2001, La Station de Référence *VALENCIA ANCHOR STATION* de Données et de Produits de Télédétection à Grande Échelle. XIV COLLOQUE INTERNACIONAL DE CLIMATOLOGIE. Sevilla 12-15 Septembre 2001

Information Content of HyMap Hyperspectral Imagery

Cédric Bacour¹, Frédéric Baret¹, Stéphane Jacquemoud²

¹INRA-CSE, site Agroparc, domaine Saint-Paul, 84914 Avignon Cedex 09

²LED-Université Paris 7, CP 7071 - 2, place Jussieu, 75251 Paris Cedex 05

cbacour@avignon.inra.fr, baret@avignon.inra.fr, jacquemo@ccr.jussieu.fr

ABSTRACT- *Hyperspectral characteristics of the HyMap airborne instrument are used to determine the minimum number of wavebands useful for accurate retrieval of canopy biophysical variables. The information content of a reflectance spectrum indicates the number of independent variables that explain its variance. It is usually determined statistically and leads to the identification of the spectral regions the most sensitive to variations of these variables. Here, a sensitivity analysis of the PROSPECT+SAIL model is performed with the aim of determining the most informative HyMap spectral bands on the dynamics of the canopy biophysical variables. The relevance of such optimal wavelengths is then assessed in inverse mode, where the variables are estimated from real reflectance spectra acquired during the DAISEX 1999 (Digital Airborne Spectrometer EXperiment) campaign. Emphasis is on the estimation of the leaf chlorophyll content C_{ab} and the leaf area index LAI.*

1 INTRODUCTION

Inversions of canopy reflectance models have spread during the last decade to estimate vegetation characteristics. In comparison with empirical or semi-empirical methods, physically-based models better account for the interdependence between canopy state variables. Nevertheless, the non-unicity of the solution turns out to be a limiting factor for reliable estimates. Recent efforts to develop computationally efficient inversion techniques such as neural networks and look-up tables, and to regularize the inverse problem by introducing prior information on the variables, have only partially overcome this issue. A further approach may take advantage of optimal sampling configurations which i) express the best adequacy between the models and "reality" (i.e., between the input variables and the "real" canopy state variables; between the simulated and the measured reflectances), and ii) carry as much information as possible.

The inverse problem consists here in determining the set of model variables such that the simulated reflectances comply the best with observations. The search for an optimal set of canopy variables, by all the acceptable solutions, implicitly supposes that there is a particular combination of reflectances associated to it. The aim of this study is to determine the best choice of N observations, among M available (N being smaller than M), that leads to the best estimation of the canopy biophysical variables. The determination of such optimal configurations of observation is in progress (Kimes et al., 2000) and is advanced by spatial agencies (CNES, ESA, NASA) to

improve the quality of remote sensing products and the definition of new instruments.

In remote sensing, the concept of *information content* of a reflectance spectrum has been first introduced by the pioneers of imaging spectroscopy applied to soils and plant canopies, even though this issue was not considered for inversion purposes. It measures the number of independent variables that explain most of the observed variability. Its determination is inseparable from the identification of the spectral regions the most sensitive to these variables (Price, 1975). Typically, five dimensions satisfactorily described the variability of radiometric signals measured over vegetation (Price, 1992; Curran, 2001): two in the visible, one in the near infrared, and two in the middle infrared. The selection of a limited number of wavebands for the estimation of plant canopy characteristics is generally made statistically (multiple regression analysis for instance).

In this paper, we propose an alternative approach based on the sensitivity analysis of a canopy reflectance model (the issue of adequacy between model and reality is not considered here since we assume that the model *is* reality). The PROSPECT+SAIL model is used in the observation configuration of HyMap to determine the best wavelengths for the estimation of canopy biophysical variables, in particular the leaf chlorophyll content C_{ab} and the leaf area index LAI that are the two most relevant biophysical variables that reveal vegetation state and functioning.

Then, inversions of the coupled canopy reflectance model on HyMap reflectance spectra acquired during

the DAISEX99 campaign enable to validate these preliminary results.

2 SENSITIVITY ANALYSIS

2.1 The model

The SAIL radiative transfer model (Verhoef, 1984, 1985) is widespread in the remote sensing community for the estimation of vegetation biophysical variables. It calculates the canopy reflectance, provided the leaf optical properties and a limited number of variables describing its architecture: the leaf area index LAI , the mean leaf inclination angle ALA , assuming an ellipsoidal distribution of foliage elements (Campbell, 1990), the hot spot parameter s_l , and a soil brightness parameter α_{soil} .

It is coupled with the PROSPECT model in order to account for the leaf optical properties. The version used here requires the leaf structure parameter N , the chlorophyll a and b content C_{ab} ($\mu\text{g}\cdot\text{cm}^{-2}$), the equivalent water thickness C_w (cm), the dry matter content C_m ($\text{g}\cdot\text{cm}^{-2}$), and the brown pigment concentration C_{bp} (Jacquemoud and Baret, 1990; Baret and Fourty, 1997), to simulate leaf reflectance and transmittance spectra in the optical domain.

2.2 Experimental design

Design of numerical experiments recently emerged in the field of remote sensing for sensitivity analyzes of complex computational models (Bacour et al., 2002). They allow better sampling of the parameter space in a limited number of simulations where all the input variables vary simultaneously (Benoist et al., 1994). We used such an method to study the influence of each variable of the model within its range of variation.

The space of canopy realizations is determined after a Hyper Graeco Latin Geometric sampling scheme, the resolution of which allows full investigation of all interactions between two variables. The companion experimental design is made of 2401 simulations corresponding to different combinations of the eight PROSPECT+SAIL input variables, each of them taking one over seven values equidistributed within its definition range (Table I). As the simulations are conducted in the principal plane where the hot spot parameter has very little influence, the latter is fixed to 0.25.

The observation configurations comply with those of the HyMap instrument used in the DAISEX99 campaign (see §3.1): sun zenith angle θ_s of 17° , view zenith angle θ_v varying from 0° to 25° with a 5° step, and relative azimuth angle ϕ equal to 100° and 280° . 89 over 128 wavebands are used. They cover the solar spectrum from 457 to 2271 nm.

		Lower bound	Upper bound
Leaf	N	1	3
	C_{ab}	1	100
	C_m	0.002	0.02
	C_w	0.04	0.04
	C_{bp}	0	1
Canopy	LAI	0	8
	ALA	30	85
	α_{soil}	0.5	3

Table I. Variation of the PROSPECT+SAIL input parameters used in the experimental design.

2.3 Sensitivity analysis

The effects and contributions of the model variables are assessed from the whole set of simulations (for more details, see Bacour et al., 2002). The mean effect of a variable v represents the distance between the mean values of the model responses when v is on level n , $\bar{\rho}_n$, and the general mean $\bar{\rho}$. They are expressed as a percentage:

$$E_{vn} = \frac{\bar{\rho}_n - \bar{\rho}}{\bar{\rho}} \times 100 \quad (1)$$

Since the results present only a slight dependence with the view zenith angle, we will deal with directional averaged values hereafter. The spectral sensitivity of the model variables is summarized in Figure I: given a wavelength, the tangent to the effect surface expresses the ability of the model to link variations of reflectance levels to variations of the biophysical variables: a positive (respectively, negative) slope means that increasing the value of a variable translates into an increase (respectively, decrease) of the reflectance; moreover, the sharper the slope is, the more sensitive the reflectance is to variations of the considered variable. One can observe a quasi-exponential decrease of C_{ab} , C_w , and LAI effects on their definition range, with a noticeable reversal for the leaf area index in the green (where increasing biomass tends to increase the reflectance). On the other hand, effects of the other variables turn out to be almost linear.

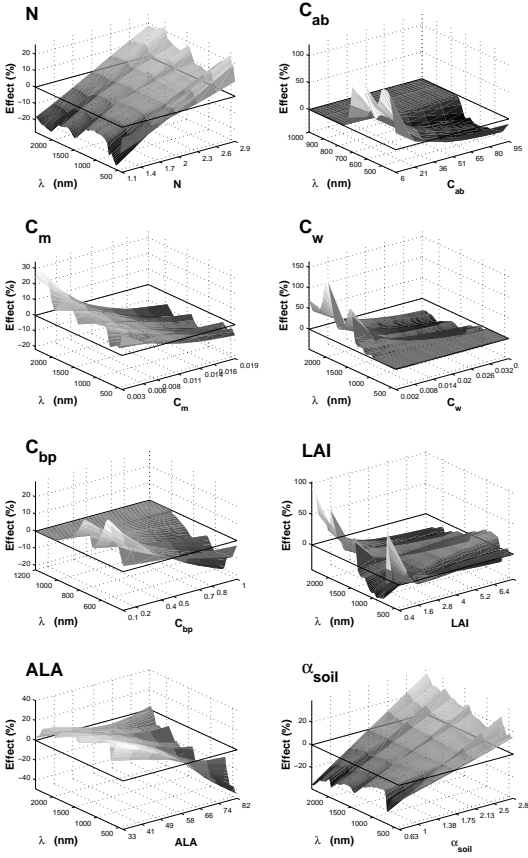


Figure I. Mean effects of the PROSPECT+SAIL variables as a function of the wavelength: N , C_{ab} , C_m , C_w , C_{bp} , LAI , ALA , and α_{soil} .

Whereas the study of the variable effects reveals their sensitivity, the determination of their relative contribution helps organizing their own influence on the canopy reflectance into a hierarchy. For each variable, the contribution index C_v characterizes the variance it explains:

$$C_v = \frac{\frac{N}{n} \sum_{1 \leq m \leq n} [\rho_{vm} - \bar{\rho}]^2}{\sum_{1 \leq k \leq N} [\rho_k - \bar{\rho}]^2} \times 100 \quad (2)$$

for $N = 2401$ simulations and $m = 7$ levels taken by each variable.

As illustrated by Figure II, the total contribution of the variables and their interactions almost equal 100%; the residues are attributed to inherent computational errors and should be regarded as noise. Figure II clearly shows the spectral influence of each variable:

in the visible, the chlorophyll content drives about 50% of the reflectance variations, with a weaker contribution near 550 nm; in the near-infrared, the most important variables are the leaf angle parameter and the leaf area index; the middle infrared confirms the strong influence of light absorption by the leaf water content around 1450 and 1940 nm.

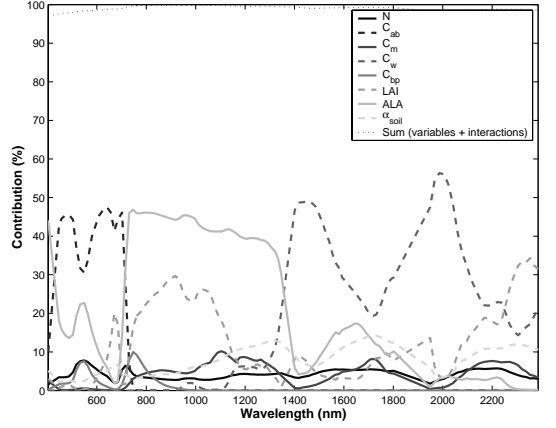


Figure II. Spectral variation of the contribution of the PROSPECT+SAIL variables.

2.4 Definition of optimal wavebands

In order to determine optimal wavebands for the estimation of C_{ab} and LAI , let us define sensitivity S_v and optimality I indices which combine both the sensitivity and contribution of the variables:

$$S_v = \sum_{1 \leq m \leq n} \sqrt{\Delta(E_{vm})^2} \quad (3)$$

and

$$I = (S_{Cab} + S_{LAI}) \times (C_{Cab} + C_{LAI} - \sum_{i=1}^m I_{Cab/LAI}^i) \quad (4)$$

S_v expresses the cumulative magnitude of the sensitivity of the variable v (i.e. the slope of its mean effects) on the range of variation. In the definition of the optimality index, the impact of the interactions where C_{ab} and/or LAI are involved, has been taken into account so as to reduce possible compensations between variables during inversions. Each wavelength has been attributed such indices. Then, the selection of optimal spectral bands is only based on the values of I . Because of the distribution of the latter in the solar

spectrum – the maximum values are all located in the near infrared – we decided to split it into three domains: the visible (400-700 nm), the near infrared (700-1300 nm), and the middle infrared (1300-2300 nm). Also, another hierarchy has been established to account for correlations between the wavelengths: for each wavelength λ_0 , the optimality index I is weighted by a factor that depends of the value of the correlation of λ_0 with the other wavebands comprised within a given correlation length (that is, every spectral band λ_i verifying $\text{corr}(\lambda_0, \lambda_i) \geq 1/e$). The goal was to spread the information of adjacent wavebands on the solar spectrum with respect to physical assumptions (Figure III).

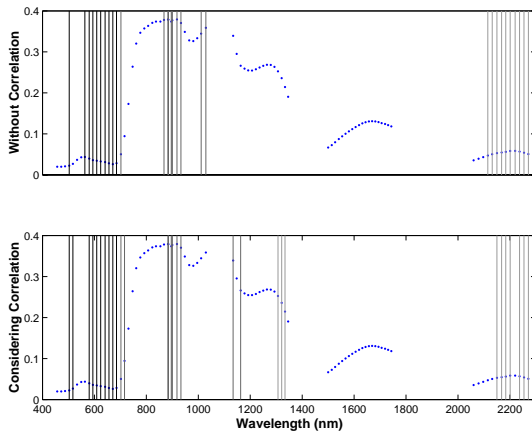


Figure III. Position of the eight most optimal wavelengths in the visible (400-700 nm), near infrared (700-1300 nm), and middle infrared (1300-2300 nm) domains, together with an experimental wheat reflectance spectrum, whether the correlation between wavebands is taken into account (top) or not (bottom).

3 CANOPY BIOPHYSICAL VARIABLE ESTIMATION

The relevance of the optimality indices determined previously is appraised with HyMap measurements, and illustrated with the leaf area index for which the ground truth was available. The aim is to assess whether the use of the selected wavebands determined as above improves the estimation of LAI or not, by comparison with inversions performed with the whole radiometric information.

3.1 The DAISEX99 campaign

The scientific goal of DAISEX (Berger et al., 2001; Müller et al., 2001; Moreno et al., 2001) was to

demonstrate the retrieval of geo- bio-physical variables from imaging spectrometers. In this context, the Barrax (Spain) test site – an agricultural flat area of $3 \text{ km} \times 3 \text{ km}$ centered on $39^\circ 3' \text{N}$, $2^\circ 5' \text{W}$ – was monitored the 3rd of June 1999 with HyMap and *in situ* to determine some biophysical variables including the leaf area index of corn (*Zea mays* L.), sugar beet (*Beta vulgaris* L.), and barley (*Hordeum vulgare* L.).

3.2 Inversions

Inversions of PROSPECT+SAIL are conducted by means of a quasi-Newton algorithm to minimize the misfit function S^2 that characterizes the gap between measured R_{mes} and simulated R_{mod} reflectances:

$$S^2 = \sum_{i=1}^N [R_{mes}^i - R_{mod}^i]^2 \quad (5)$$

The routine E04JYF of the Numerical Algorithm Group library allows fixing the upper and lower bounds of variation of the nine variables estimated simultaneously (the eight ones defined in Table I plus the *hot spot* parameter). Also, 10 sets of variables, with values drawn randomly according to a uniform distribution, are used as initial guess of the inversion process. In the following, the estimated LAI values are averages of these 10 estimates.

3.3 Studied cases

Different combinations of optimal wavelength selections have been studied for the estimation of the leaf area index (Table II). In each case, the estimations were made with the previously selected wavelengths, considering or not the correlation, as well as with randomly drawn wavelengths.

The use of such a limited radiometric information for inferring biophysical variables by inversion rises the question of determination of the optimization problem. Theoretically, solving the inverse problem imposes the system to be over-determined, i.e. the number of variables M to estimate must be at most equal to the number of measurements N ; the solution is therefore not unique. However, from a statistical point of view, the higher the number of available data is (considering they are noise free), the more consistent the estimation is. The ratio N/M is therefore an indicator of the confidence one can expect in the estimates.

	Number of wavebands				Ratio N / M
	VIS	NIR	MIR	Total	
# 1	16	36	37	89	9.9
# 2	16	36	—	52	5.8
# 3	8	10	—	18	2
# 4	10	10	—	20	2.2
# 5	6	6	6	18	2

Table II. Different cases tested for the estimation of the leaf area index with HyMap.

Results of the *LAI* estimations are gathered in Figure IV. Reducing the spectral information generally leads to debase the estimates of low *LAI* values (below 1), as illustrated by #2 to #5. This trend may result from different soil conditions between the model and real crops: in the experimental designed simulations, the soil is assumed Lambertian; in the inversions, it is anisotropic and characterized by the SOILSPECT model (Jacquemoud et al., 1992) whose input parameters were estimated on a bare soil from HyMap spectra. For higher *LAI* values, the estimates better match the *in situ* measurements, even when few radiometric data are available (#3, #4, and #5). The introduction of spectral correlations in the determination of the optimal wavelengths does not improve the estimations. Moreover, inversions performed at the "optimal" wavelengths led to better results, with regard to the ground truth, than when using random ones, pointing out a certain relevance of the concept of optimal configuration.

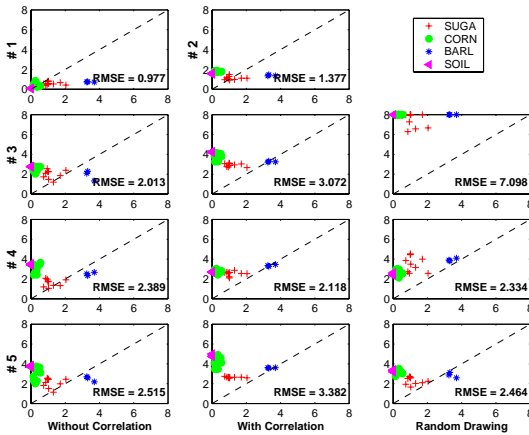


Figure IV. Estimated values of the leaf area index (y-axis) against the *in situ* measurements (x-axis) for different selections of the wavebands (see Table II).

4 CONCLUSION

Improved estimation of canopy biophysical variables through inversion of a radiative transfer model may be obtained by taking advantage of optimal sampling configurations i) carrying as much information as possible, and ii) providing the best adequacy between the models and "reality". The first point was investigated in this paper with the PROSPECT+SAIL model.

In a first step, a sensitivity analysis of the model enables to point out some spectral features where the influence of the leaf area index and the chlorophyll a plus b content is prominent as compared to the other variables. On this basis, different sets of optimal wavelengths were determined. These were then employed in inversion on HyMap hyperspectral reflectance spectra acquired during the DAISEX99 campaign. It appeared that, even for limited radiometric information, high *LAI* values were consistently estimated when compared to the ground truth (results were even better than when using all the reflectances). Conversely, lower *LAI* values (<1) were poorly retrieved, probably because of different soil characteristics between simulations and actual canopies. The hypothesis of a homogeneous canopy is also no more valid in that case.

These preliminary results point out that the relevance of the "optimal" wavelengths derived in this study still remains ambiguous. Their validation in the inversion process is limited by the number of canopies considered and the lack of information on the experimental errors (for the radiometric part as well as for the *LAI* ground truth). It also appears that most of the wavebands retained are contiguous, i.e. their information content is correlated. Other choices in the empirical determination of the optimality indices may have lead to different results: more emphasis could have been put on either the sensitivity or the contribution, different weights could have been laid to the parameter interactions, etc. Finally, their use in the prospect of estimation of canopy biophysical variables with model inversion is restricted by the determination of the inverse problem (i.e. the number of variable to estimate vs. the number of available data). Quite obviously, the potentiality of exploiting optimal wavelengths should be enhanced by addition of directional information.

ACKNOWLEDGMENTS: The authors greatly thank Yves Tourbier, Renault - Direction de la Recherche, who provided the Hyper Graeco Latin Geometric experimental design used in the study.

REFERENCES

- Bacour, C., Jacquemoud, S., Tourbier, Y., Dechambre, M., Frangi, J.-P., 2002, Design and analysis of numerical experiments to compare four canopy reflectance models. *Remote Sensing of Environment*, **79**, 72-83.
- Baret, F., Fourty, T., 1997, Radiometric estimates of nitrogen status in leaves and canopies. In *Diagnosis of the Nitrogen Status in Crops*, edited by G. Lemaire (Springer, Berlin), pp. 201-227.
- Benoist, D., Tourbier Y., Germain-Tourbier, S., 1994, Plans d'expériences : construction et analyse (Tec & Doc, Lavoisier, Paris), 700 pp.
- Berger, M., Moreno, J., Mueller, A., Beisl, U., Richter, R., Schaepman, M., Strub, G., Stoll, M. P., Nerry, F., Leroy, M., Rast, M., Wursteisen, P., Attema, E., 2001, The DAISEX campaigns in support of a future land surface processes mission. *ESA Bulletin*, accepted for print.
- Campbell, G. S., 1990, Derivation of an angle density function for canopies with ellipsoidal leaf angle distribution. *Agricultural and Forest Meteorology*, **49**, 173-176.
- Curran, P. J., 2001, Imaging spectrometry for the study of vegetation canopies. In *Proceedings of the International Workshop on Spectroscopy Application in Precision Farming*, Freising-Weihestephan, Germany, on January 16-18 2001, pp. 7-8.
- Jacquemoud, S., Baret, F., 1990, PROSPECT: A model of leaf optical properties spectra. *Remote Sensing of Environment*, **34**, 75-91.
- Jacquemoud, S., Baret, F., Hanocq, J.-F., 1992, Modeling spectral and bidirectional soil reflectance. *Remote Sensing of Environment*, **41(2-3)**, 123-132.
- Kimes, D. S., Knyazikhin, Y., Privette, J. L., Abuelgasim, A. A., Gao, F., 2000, Inversion methods for physically-based models. *Remote Sensing Reviews*, **18**, 381-439.
- Moreno, J., Casalles, V., Martinez-Lozano, J. A., Melia, J., Sobrino, J., Calera, A., Montero, F., Cisneros, J. M., 2001, The measurement programme at Barrax. In *Proceedings of the Final Results Workshop on DAISEX*, ESTEC, Noordwijk, the Netherlands, on March 15-16 2001, pp. 43-52.
- Müller, A., Hausold, A., 2001, The airborne imaging spectrometer data acquisition programme in 1998, 1999, 2000. In *Proceedings of the Final Results Workshop on DAISEX*, ESTEC, Noordwijk, the Netherlands, on March 15-16 2001, pp. 7-12.
- Price, J. C., 1975, Information content of Iris spectra. *Journal of Geophysical Research*, **80(15)**, 1930-1936.
- Price, J. C., 1992, Variability of high-resolution crop reflectance spectra. *International Journal of Remote Sensing*, **13(14)**, 2593-2610.
- Verhoef, W., 1984, Light scattering by leaf layers with application to canopy reflectance modeling: the SAIL model. *Remote Sensing of Environment*, **16**, 125-141.
- Verhoef, W., 1985, Earth observation modeling based on layer scattering matrices. *Remote Sensing of Environment*, **17**, 165-178.

Passive vegetation fluorosensing using atmospheric oxygen absorption bands

Evain S.¹, Ounis A.^{1*}, Baret F.², Goulas Y.¹, Louis J.¹, Cerovic Z.G.¹ and Moya I.¹

¹*Equipe Photosynthèse et Télédétection, LURE/CNRS, Centre Universitaire Paris-Sud, B.P. 34, 91898 ORSAY Cedex, France.*

²*INRA-Bioclimatologie, Domaine St. Paul, Site Agroparc, 84914 AVIGNON Cedex 9, France.*

(*) ounis@lure.u-psud.fr

ABSTRACT- *Two passive instruments based on the Fraunhofer line principle applied to the atmospheric oxygen absorption bands, at 760 and 687 nm, were used to monitor maize canopies under stress conditions. Sunlight-induced chlorophyll fluorescence (ChlF) and reflectance signals were acquired continuously and remotely in the field. The reflectance signals at 687 and 760 nm were used to calculate the NDVI, and the reflectance at 531 and 570 nm, available from additional detecting channels, allowed us to follow also the PRI index. Two stress conditions were progressively generated: the inhibition of photosynthetic electron flow by a herbicide (DCMU), and the water stress induced by withholding watering. Photosynthetic assimilation and stomatal conductance were acquired daily on several representative leaves using an infrared gas analyser. Additional measurements of the chlorophyll (Chl) content, and of the variable ChlF were recorded on the same leaves with a chlorophyll-meter and a portable fluorometer.*

The DCMU study clearly showed a substantial increase in the ChlF yield, when the canopy was treated by the herbicide. This increase in fluorescence was also confirmed by active measurements and was related to the inhibition of photosynthesis and to stomatal closure.

The PRI and NDVI recorded on maize canopy under water stress were only correlated with the decrease in Chl content, when the stress became severe. However, we proposed a new passive ChlF index (NDFI) that uses fluorescence measurements, at 687 and 760 nm, which is sensitive to water stress, but also to changes in Chl content.

1 INTRODUCTION

Chlorophyll (Chl) fluorescence (ChlF) is widely used as a powerful signal to monitor photosynthetic activity or to detect stress conditions on vegetation (for reviews, see Lichtenthaler, 1988; Krause and Weis, 1991; Schreiber et al., 1994). However, this signal remains difficult to detect by passive fluorescence remote sensing (fluorosensing), since it represents only 1 to 2% of the reflected sunlight by the vegetation. Therefore, ChlF signal can only be quantified at particular wavelengths where the solar spectrum is attenuated by atomic absorption of the solar atmosphere, or by molecular absorption of the terrestrial atmosphere. The Fraunhofer Line Principle (FLP), which compares the depth of an absorption line in the solar irradiance to the depth of the same line in the radiance of the target, was first introduced to vegetation fluorosensing using the H α absorption line (656.28 nm) (Plascyk, 1975; Plascyk and Gabriel, 1975). The FLP was successfully applied to study water stress in Citrus (McFarlane et al., 1980) and to determine the relationship between ChlF at 656.28 nm and the net photosynthetic rate in Pinus taeda (Carter

et al., 1990). Carter et al. (1996) extended the FLP to the atmospheric oxygen B band, at 687 nm, and investigated ChlF changes induced by herbicide (DCMU). More recently, Moya et al. (1998) and Evain et al. (2001) further extended the FLP to both atmospheric oxygen bands A (760 nm) and B, and performed simultaneous measurements on small canopies. Compared to the H α line, the A and B absorption bands are much wider and deeper, and are closer to the ChlF maxima at 685 and 735 nm.

The aims of this paper is to present recent results of passive fluorescence measurements on maize canopies using the FLP in both oxygen bands. In-field measurements of ChlF and reflectance on vegetation under DCMU treatments and water stress are presented. Comparison of ChlF signatures to NDVI (Normalized Difference Vegetation Index), PRI (Physiological Reflectance Index), net CO₂ assimilation and stomatal conductance are discussed.

2 MATERIALS AND METHODS

Measurements of ChlF and reflectance on maize canopies were performed in Avignon (France) (4° 49' longitude East, 43° 56' latitude North), between the 24th September and 13th October 2001.

Maize (*Zea mays* L.) was chosen because of its C4 metabolism, and absence of the photorespiration. Thus, CO₂ assimilation can be directly related to the electron transport. Maize plants were grown outdoors in soil-filled pots (50 pots, two plants per 3-L pot). All pots were watered daily. Two canopies of approximately 3 m² each were assembled for the experiments.

Sunlight-induced ChlF and canopy reflectance were acquired daily during 3 weeks on both canopies, from 09:00 to 18:00 h UT. Measurements were performed at distance using two FLP-based sensors. The bidetector instrument (Moya et al., 1998) was used to monitor ChlF and reflectance changes at 760 nm (A band) over a canopy area of 40 × 30 cm, at a distance of 7.4 m, from a scaffold, with a detection angle of 50°. The second instrument, a passive multi-parameter sensor, was used to monitor ChlF and reflectance changes at both 687 (B band) and 760 nm (A band) (Evain et al., 2001). This detector was mounted on a 9-m high tower, and the measurements were performed over a canopy area of 85 × 65 cm, with a detection angle of 40°, from a distance of 12 m. Thanks to two additional channels available on this sensor, at 531 and 570 nm, it was also possible to monitor the PRI=(R531-R570)/(R531+R570), where R531 and R570 are the canopy reflectances at 531 and 570 nm, respectively (Gamon et al. 1992). Using the canopy reflectance at 687 and 760 nm, we also calculated the NDVI. A white flat panel installed beside both canopies was used as a reference surface. The reflectance of this panel was calibrated using a standard white panel (Spectralon, Labsphere, North Dutton, N.H.). The bidetector and the passive multi-parameter sensor were south-to-north and north-to-south oriented, respectively, for comparative purposes.

Two stress conditions were progressively generated: a photosynthetic electron flow interruption by the addition of a herbicide (DCMU, (3,4-dichlorophenyl)-1,1-dimethylurea), and a water-stress induced by withholding watering. Five days after the beginning of the measurements, the first canopy was treated with DCMU (80 ml per pot, 800 g L⁻¹). This canopy was daily watered during all the campaign to prevent any other stress. The second canopy was subjected to a progressive water-stress by withholding watering at the beginning of the experiment.

Climatic parameters were recorded with a micro-meteorological station. Photosynthetic assimilation (A) and stomatal conductance (g) were

daily acquired on several representative leaves (6 leaves situated around the target area for each canopy) using an infrared gas analyser (LI-6400, Li-Cor Inc., Lincoln, NE, USA). Additional measurements of the Chl content and variable ChlF were carried out on the same leaves with a Chl-meter (SPAD-502, Minolta, Carrière-Sur-Seine, France) and a portable active fluorometer (PAM-2000, Walz, Effeltrich, Germany). All these data were acquired daily at noon under full sunlight.

Unless indicated, all presented data recorded with the passive sensors were performed under full sunlight (1600 μmol photons m⁻² s⁻¹) and averaged from 11:00 to 14:00 h UT to minimise the effect of canopy structure.

3 RESULTS AND DISCUSSION

3.1 DCMU treatment

Midday measurements of net CO₂ assimilation (A) and stomatal conductance (g), from 27th September to 04th October, are presented in Figure 1a. They could be compared to the passive and active ChlF measurements performed with the bidetector and the portable fluorometer on the same maize canopy (see

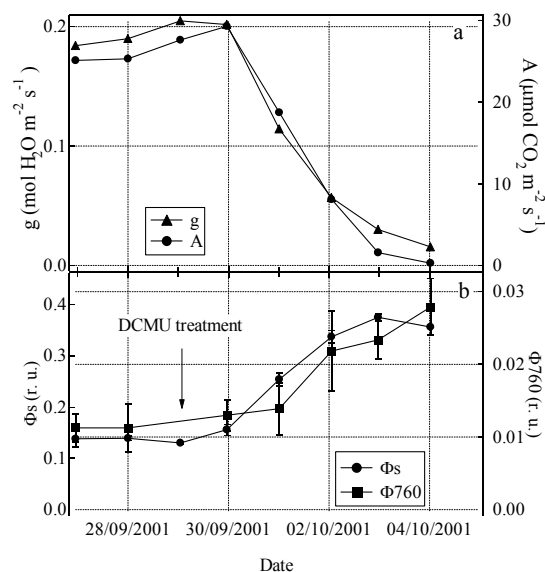


Figure 1. Daily measurement of ChlF and gas exchanges on a maize canopy following a treatment with DCMU. (a) Variation of net CO₂ assimilation (A) and stomatal conductance (g). (b) Responses of the sunlight-induced ChlF yield (φ₇₆₀) and the ChlF yield measured with the portable fluorometer (Φ_s). Vertical lines denote standard deviation. See text for details.

Figure 1b). Sunlight-induced ChlF, at 760 nm, was

inhibition of the electron transfer. Under these

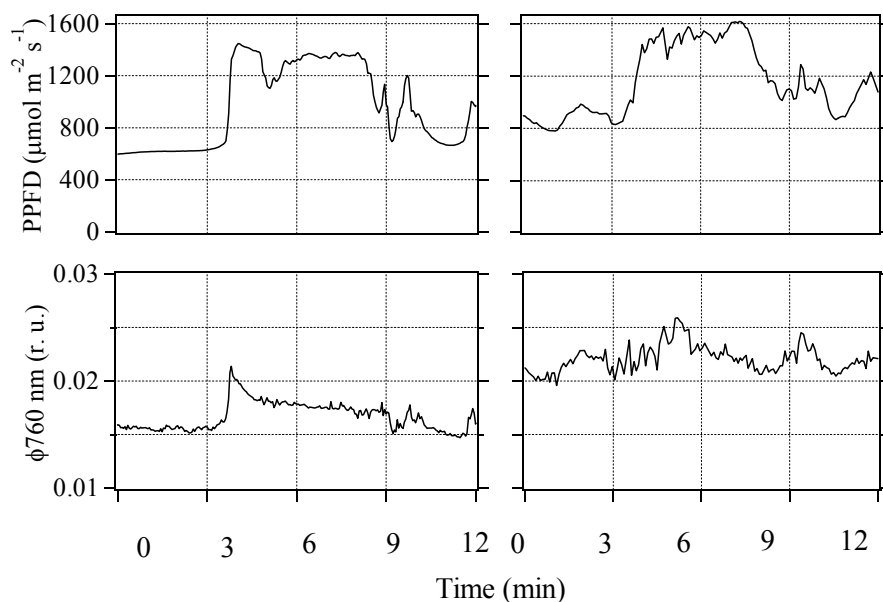


Figure 2. Effect of DCMU on sunlight-induced ChlF kinetics (fluorescence yield at 760 nm) induced by a rapid light transition (PPFD, Photosynthetic Photon Flux Density).

divided by the canopy reflectance at the same wavelength to obtain an apparent ChlF yield (Φ_{760}) that can directly be compared to the active steady-state ChlF measurements.

Two days after the addition of DCMU, period that corresponds to the penetration of the herbicide in the plant, both A and g started to decrease rapidly towards a zero value attained after five days, indicating total inhibition of PSII (Lichtenthaler and Rinderle, 1988). Both passive and active ChlF yield measurements showed the same variations. In addition, these variations are well correlated with the variation of A and g: the ChlF yield increasing to a maximum (3 times the initial value) while A and g decreasing. Indeed, ChlF is in direct competition with the photochemical conversion. Therefore, a reduction of the photosynthetic electron transport leads to an increase in dissipative processes, including ChlF.

Using the bidetector, we also analysed the effect of DCMU treatment on ChlF induction kinetics induced by sunlight transitions during cloudy days (Figure 2). Before herbicide treatment, a transition in sunlight produced an induction in ChlF yield (Figure 2 left). However, four days after the treatment, nearly the same transition of sunlight did not produce any changes in ChlF yield (Figure 2 right). This absence of rapid increase in ChlF was the consequence of the

conditions, the steady-state ChlF level is increased to the maximum attained without the inhibition. The signal was much noisier in that day due to a high wind speed (15 m s^{-1}).

3.2 Water stress

Figure 3a shows time-evolution of A, g and Chl content during the progressive induction of drought on maize canopy, from 25th September to 13th October. Decrease in A and g starting from 30th September witnessed a closure of stomata due to an increased water deficit. Meanwhile, the Chl content remained constant, and decreased only after several days of severe water stress (Figure 3a).

The NDVI and PRI, recorded with the passive multi-parameter sensor, remained unchanged as long as the Chl content did not change (Figure 3b). This absence of changes in PRI under moderate water stress has already been observed on sunflower leaves (Gamon et al. 1992). Actually, PRI changes are related to chloroplast conformational changes associated with an increased ΔpH and the de-epoxidation of xanthophylls (Gamon et al., 1990). Both NDVI and PRI started to decrease with the Chl content decrease.

The steady-state ChlF, recorded both by the passive multi-parameter sensor and by the PAM-2000 fluorometer, did not show any significant variation

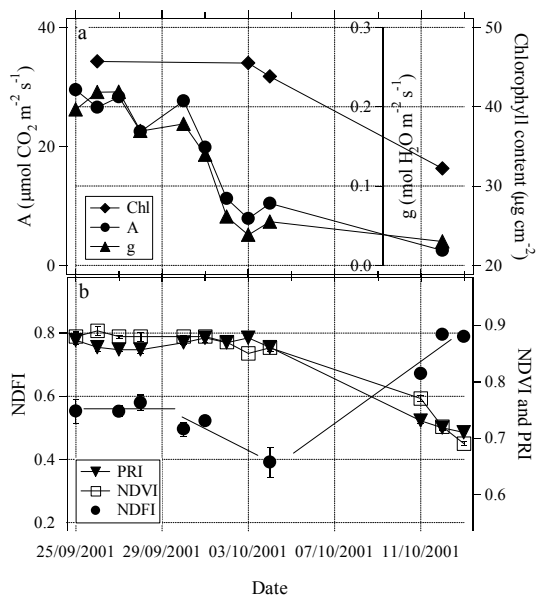


Figure 3. Daily measurement of gas exchanges and optical parameters on a maize canopy under the establishment of progressive water stress. (a) Variation of net CO₂ assimilation (A), stomatal conductance (g) and Chl content. (b) Evolution of PRI, NDVI and NDFI indexes. Vertical lines denote standard deviation.

directly correlated to water stress effect (data not shown). However, a Normalized Difference Fluorescence Index defined as $\text{NDFI} = (\text{F687} - \text{F760}) / (\text{F687} + \text{F760})$, where F687 and F760 represent ChlF at 687 and 760 nm respectively, followed g and A changes. Indeed, stomatal closure and the decrease in photosynthesis was accompanied by a substantial

decrease in NDFI (see Figure 3b). These changes in NDFI could be the result of a rearrangement in canopy structure as shown in Figure 4. Therefore, F687, which is more sensitive to the canopy structure in comparison to F760, because of the reabsorption effect, reduced the NDFI. Later, when the Chl content decreased, the reabsorption of ChlF at 687 nm became weaker and F687 increased. On the other hand, F760 decreased because it is directly proportional to the Chl content. Thus, NDFI increased subsequently as a result of the chlorosis induced by prolonged water stress.

4 CONCLUSIONS

Thanks to our new sensors based on the FLP, applied to the atmospheric oxygen absorption bands, at 687 and 760 nm, we were able to follow physiological modifications on maize canopies under stress conditions by passive fluorosensing. Using the bidetector, a substantial (3 fold) increase in the fluorescence yield was seen, when the canopy was treated with the DCMU herbicide. This increase in ChlF was also confirmed by active measurements and could be linked to stomatal closure and photosynthesis inhibition.

On the other hand, the presence of water stress did not induce any significant change on the stationary ChlF yield measured at the canopy level. The PRI and NDVI measured with the passive multi-parameter sensor decreased only after the Chl content decrease as a consequence of a prolonged water-stress. We proposed in this study a new ChlF index (NDFI) based on the measurement of passive ChlF signals at 687 and 760 nm. This index is clearly sensitive to moderate water stress, but also to changes in Chl content. The NDFI seems to be mainly sensitive to ChlF reabsorption effects, and then to changes in canopy structure. However, the influence of other phenomena,



Figure 4. Photograph of an irrigated maize canopy (left), and the same canopy under water stress (right).

like StateI-StateII transitions should not be excluded, and therefore awaits further investigations.

4 REFERENCES

- Carter, G. A., Jones, J. H., Mitchell, R. J. and Brewer, C. H. (1996), Detection of solar-excited chlorophyll a fluorescence and leaf photosynthetic capacity using a fraunhofer line radiometer, *Remote Sens. Environ.*, 55:89-92.
- Carter, G. A., Theisen, A. F. and Mitchell, R. J. (1990), Chlorophyll fluorescence measured using the Fraunhofer line-depth principle and relationship to photosynthetic rate in the field, *Plant Cell Environ.*, 13:79-83.
- Evain, S., Camenen, L. and Moya, I. (2001), Three channels detector for remote sensing of chlorophyll fluorescence and reflectance from vegetation, In *8th International Symposium: Physical Measurements and Signatures in Remote Sensing*, (M. Leroy, ed.) Aussois, France, 2001, CNES, pp. 395-400.
- Gamon, J. A., Field, C. B., Bilger, W., Bjorkman, O., Fredeen, A. L. and Penuelas, J. (1990), Remote sensing of xanthophyll cycle and chlorophyll fluorescence in sunflower leaves and canopies, *Oecologia*, 85:17.
- Gamon JA, Penuelas J and Field CB (1992) A narrow-waveband spectral index that tracks diurnal changes in photosynthetic efficiency. *Remote Sens Environ* 41: 35-44
- Krause, G. and Weis, E. (1991), Chlorophyll fluorescence and photosynthesis: The basics, *Annu. Rev. Plant Physiol. Plant Mol. Biol.*, 42:313-349.
- Lichtenthaler, H. K. (1988), In vivo chlorophyll fluorescence as a tool for stress detection in plants, In *Applications of Chlorophyll Fluorescence* (H. K. Lichtenthaler, ed.), Kluwer Academic Publishers, Netherlands, pp. 129-142.
- Lichtenthaler, H. K. and Rinderle, U. (1988), The role of chlorophyll fluorescence in the detection of stress conditions in plants, *CRC Crit. Rev. Anal. Chem.*, 19:29-85.
- McFarlane, J. C., Watson, R. D., Theisen, A. F., Jackson, R. D., Ehrler, W. L., Pinter, P. J., Idso, S. B. and Reginato, R. J. (1980), Plant stress detection by remote measurement of fluorescence, *Appl. Optics*, 19:3287-3289.
- Moya, I., Camenen, L., Latouche, G., Mauxion, C., Evain, S. and Cerovic, Z. G. (1998), An instrument for the measurement of sunlight excited plant fluorescence, In *Photosynthesis: Mechanisms and Effects* (G. Gorab, ed.), Kluwer Acad. Pub., Dordrecht, pp. 4265-4270.
- Plascyk, J. A. (1975), The MK II Fraunhofer line discriminator (FLD-II) for airborne and orbital remote sensing of solar-stimulated luminescence, *Opt. Eng.*, 14:339-346.
- Plascyk, J. A. and Gabriel, F. C. (1975), The Fraunhofer line discriminator MKII -An airborne instrument for precise and standardized ecological luminescence measurements, *IEEE Trans. Instrum. Meas.*, 24:306-313.
- Schreiber, U., Bilger, W. and Neubauer, C. (1994), Chlorophyll fluorescence as a noninvasive indicator for rapid assessment of in vivo photosynthesis, In *Ecophysiology of Photosynthesis* (E. D. Schulze, M. M. Caldwell, eds.), Springer-Verlag, Berlin, pp. 49-70.

Evaluation of texture analysis techniques to characterize vegetation

Luis A. Ruiz, Alfonso Fdez.-Sarría, Jorge Recio

Dpto. Ingeniería Cartográfica, Geodesia y Fotogrametría. Universidad Politécnica de Valencia.
Camino de Vera s/n, 46022-Valencia (Spain).

laruiz@cgf.upv.es

ABSTRACT

The extraction of numeric features to characterize textures on images takes special relevance in certain satellite and aerial images classification processes. The wide range of the methodological approaches used and their applications in the earth observation (i.e., vegetation analysis, urban distribution and growing, landscape analysis, etc.) makes difficult the appropriate selection of the method in each particular case. In this work, several texture analysis techniques were evaluated: statistical features extracted from the *grey level co-occurrence matrix*, methods based on *energy filters* and the *edgeness* factor, and the most recent based on the *wavelets* decomposition theory. In addition, different methodological parameters were tested, the most relevant being the neighbourhood size chosen for the determination of the texture features, as well as the distance between pixels and the number of grey levels used.

The wavelets based methods offer a wide range of options, specially regarding the type of mother wavelets used, or if the feature extraction is made from images that result from the standard decomposition or from the decomposition and further reconstruction using the inverse transform. Several types of mother wavelets and both decomposition options were tested. One of the best advantages of this methods is that multiresolution analysis allows the combination of features from different levels of resolution.

The evaluation was carried out using a mosaic of real images, with the goal of discriminating between different types of crops. The results show that the combination of the original and wavelet features together yields a better performance when the appropriate wavelet is chosen. The wavelets with higher support, such as the Coif-24, generated better results, and most of the texture information of the tested vegetation classes is contained in the lower levels of decomposition.

1. INTRODUCTION

Texture analysis methods have been used with positive results in many remote sensing applications, such as mapping and analysis of urban expansion, classification of forests, characterization of vegetation to study regeneration processes, or landscape analysis. The texture of an image is related to the distribution of grey levels in the image, so we can consider microtextures, when a small neighbourhood is analysed for the distribution of values, or macrotextures, when the analysed area is larger.

The features used to describe the texture can be obtained by several methods. The most traditional are the statistical approaches, which are based on the measurement of the occurrences of each grey level value in a particular neighbourhood, known as first-order statistics, or on the cooccurrences of the different grey levels between two pixels of the neighbourhood, as described by Haralick et al. (1973), and called second-order statistics. Other approaches are based upon filtering the image and then computing the energy for

each pixel or for each pixel neighbourhood (Laws), or by computing the edgeness of a region by applying gradient filters. Autocorrelation measures, Fourier transform based features (), Gabor filters banks (Turner, 1986), Gauss-Markov random fields (Kashyap et al., 1982), or fractals models (Pentland, 1984), among others, are also techniques that have been used to characterize textures in different applications.

Most recently, the development of the theory of wavelets has supposed the beginning of the application of this technique in order to improve the results of texture classification processes. The use of a pyramid-structured wavelet transform for texture analysis was first suggested by Mallat (1989). Since the texture of an image is a function of the scale, an advantage of wavelet decomposition is that provides a unified framework for multiscale texture analysis. Due to the wide range of possibilities and variations that wavelet decomposition offers, these studies have been usually focused on specific methodologies. Thus, for instance, Chang and

Kuo (1993) used wavelet packets, and Unser (1995) a variation of the discrete and overcomplete wavelet decomposition. In addition, some comparative studies have been done, testing different combinations of internal parameters of texture analysis methods based on the wavelet transform (Fatemi-Ghomi et al., 1996), or comparing more traditional filtering approaches with some variations of wavelet based methods (Randen and Husoy, 1999). In all cases, the testing data sets used were composed of standard images, usually obtained from the Brodatz database (Brodatz, 1966), which is valid for comparison purposes, but particular real problems often render unequal performances, so they need to be specifically tested. In fact, the results obtained do not lead to an optimum methodology or a unique combination of parameters to be used.

The wavelet transform decomposes the original image into a low-resolution image and several detail images. The low-resolution images are obtained by iteratively low-pass filtering the original image, and the detail images contain the information lost in the process. In general, the *energy* and *variance* of the detail images are the most common features extracted for texture classification. However, Van de Vover et al (1999) used, as texture features, histogram and cooccurrence signatures computed from the same detail images. They noticed that the results obtained with the first-order set (histogram) and with the second-order set (cooccurrence) of features were different depending on the specific class considered. This result reinforces the former statement that the method, texture features and parameters used should be specifically chosen for each application or group of applications.

The texture of an image becomes an important property for the classification of vegetation units. On one side, it provides spatial information about the density and distribution of spontaneous vegetation, useful in forestry applications such as classification of landscape units in forested environments (Marceau et al., 1994), or determination of forest canopy densities for regeneration studies (Ruiz and Fdez.-Sarria, 2000). In addition, it provides information about the spatial arrangement of plants and trees in orchards for agricultural applications like crop classification, using high spatial resolution images as initial data for the extraction of texture features.

In this paper, we evaluate three main groups of texture analysis methods (statistical, filtering and wavelet based) to discriminate agricultural landscapes using high resolution images from central Spain. The experiments are focused on testing the variations of several parameters related with texture analysis from wavelet decomposition, like the window size, the type of

mother wavelet used, the influence of the decomposition level, the convenience to work with the decomposed detail images or with the reconstructed ones, or the selection of the most discriminant features. The classification results obtained from the different variations of the wavelet parameters are compared to the results obtained from the best statistical and filtering features.

The classification of images by textures is always limited by the *edge effect*, or the high missclassification rate produced in the transition areas between classes, due to the fact that the classification of each pixel is determined by the values of its neighbourhood, so the pixels from the border areas will be affected by the pixels values of the adjacent classes. The effect will increase when larger window sizes are used to compute the texture features. In this sense, all of the classification results should be referred to the internal and external areas of the texture classes (Ruiz et al., 2001, Ferro and Warner, 2002).

2. METHODS

In this section we will describe the experimental procedure followed for the evaluation of different texture methods for the characterization of vegetation. First, we will explain the image data used and the texture classes defined. In the next three sections, we will describe the feature extraction methods used: grey levels cooccurrence matrix features, filtering, and wavelet decomposition analysis. Finally, a description and discussion of the experimental tests is made attending to the different parameters considered, as well as the classification process used to obtain the final results.

2.1. Experimental data

The image data used for the study were extracted from a series of aerial photographs from a large region of central Spain, dominated by a diverse agricultural landscape including extensive and intensive crops, sometimes combined with disperse oak trees forming *dehesas*. Some urban areas were included to increase the diversity in the classification problem.

The initial aerial photographs, with an approximate scale of 1:30.000, were digitised to obtain 2 m. spatial resolution images. Then, several areas were extracted to form a mosaic image with the criterium of preserving a high variety of significant texture classes and reducing the amount of data to decrease the computing time on the tests. The final mosaic was composed of six subimages as shown in figure 1.

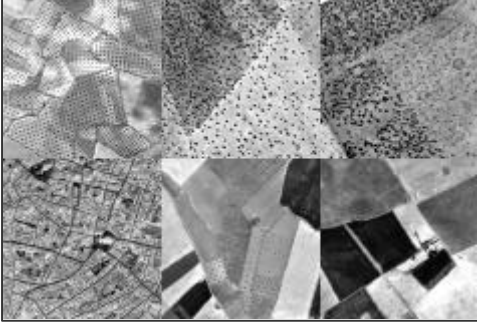


Figure 1. Mosaic image used for the texture analysis tests.

A total of 12 texture classes were defined, 6 of them may be considered as fine textures: *Vineyards* (V); *Non-Harvested Cereal* (CN); *Harvested Cereal* (CC); *Alfalfa* (A); *Harvested Alfalfa* (AC); and *Maize* (M). The other 6 correspond to coarse textures: *Vineyards combined with Olive trees* (VO); *Olive trees* (O); *Dehesa combined with Cereal* (DC); *High density Dehesa* (DA); *Low density Dehesa* (DB); and *Urban areas* (U) (figure 2).

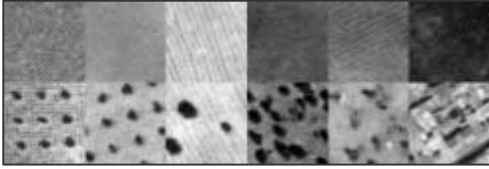


Figure 2. Image samples of the 12 texture classes. Fine textures in upper row (from left to right): V, CN, CC, A, AC and M. Coarse textures in lower row (from left to right): VO, O, DC, DA, DB and U.

The extraction of texture features from the mosaic image was accomplished using three different methods: features derived from the grey level cooccurrence matrix, energy filters, and wavelet decomposition based features.

2.2. Cooccurrence features

These features are based on the computation of the grey level cooccurrence matrix (GLCM) in the neighbourhood of each pixel. A generic element of this matrix, $p(i,j)$, represents the relative frequency in which two grey levels, i and j , occur in that neighbourhood between two pixels separated a distance d in a given direction q :

$$p(i, j) = \frac{P(i, j)}{\sum_{i=0}^{N_g-1} \sum_{j=0}^{N_g-1} P(i, j)}$$

where N_g is the number of grey levels. The neighbourhood is defined by the window size, which is an important parameter to be considered. Since the defined texture classes do not follow any particular orientation, the results of four directions were averaged for this test. After the results obtained in former experiments (Ruiz, 1998 and 2000), the distance between pixels (d) used was always 1 pixel.

A total of 8 texture features were initially computed from the GLCM (Haralick et al., 1973):

$$\text{Uniformity: } \sum_{i=0}^{N_g-1} \sum_{j=0}^{N_g-1} p(i, j)^2$$

measures the homogeneity, with high values when the spatial distribution of the grey levels is almost constant.

$$\text{Entropy: } - \sum_{i=0}^{N_g-1} \sum_{j=0}^{N_g-1} p(i, j) \cdot \log[p(i, j)]$$

is a measure of the randomness of the intensity distribution.

$$\text{Contrast: } \sum_{i=0}^{N_g-1} \sum_{j=0}^{N_g-1} (i - j)^2 \cdot p(i, j)$$

is related to the spatial frequency of the neighbourhood. High values of contrast are indicative of high grey level values off the principal diagonal of the matrix.

$$\text{Mean: } \mathbf{m} = \sum_{i=0}^{N_g-1} i \cdot p_x(i)$$

$$\text{where } p_x(i) = \sum_{j=0}^{N_g-1} p(i, j)$$

provides information about the overall intensity level in the neighbourhood.

$$\text{Variance: } \sum_{i=0}^{N_g-1} \sum_{j=0}^{N_g-1} (i - \mathbf{m})^2 \cdot p(i, j)$$

is a measure of heterogeneity, with higher values when the grey levels differ from the mean.

$$\text{Inverse difference moment} : \sum_{i=0}^{N_g-1} \sum_{j=0}^{N_g-1} \frac{p(i, j)}{1 + (i - j)^2}$$

is inversely related to the *contrast*.

$$\text{Product moment} : \sum_{i=0}^{N_g-1} \sum_{j=0}^{N_g-1} (i - m) \cdot (j - m) \cdot p(i, j)$$

is a measure of local homogeneity. Finally, if the *product moment* is normalized (divided) with respect to the variance, the *correlation* is obtained, which represents the eighth cooccurrence feature computed.

2.3. Filters

The filtering approaches are based on the application of convolutions to the original image and then computing some basic indices, such as energy, over the neighbourhood of each pixel.

The textural energy features are based on the convolution of the initial image I with a variety of kernels g_1, g_2, \dots, g_N , yielding N new images $J_n = I * g_n$ ($n = 1, \dots, N$). Each filter is designed to enhance a different texture property on the image. Two sizes of filters were used, 5x5 and 7x7, considering that they were the most appropriate for the type of elements present in our texture classes.

We used 6 filters (figure 3) proposed by Laws (1985): *Level (L)*, that gives information of the average grey level in the neighbourhood; *Gradient (E)* is and edge enhancing filter; *Shape (S)* enhances certain shapes on the grey level dimension; *Wave (W)*; *Ripple (R)*, and *Oscillation (O)*, that enhance different waving shapes on the image. In addition, the *Laplacian of a Gaussian filter (LoG)* was also computed.

7 x 7									5 x 5							
L =	[1	6	15	20	15	6	1]	[1	4	6	4	1]
E =	[-1	-4	-5	0	5	4	1]	[-1	-2	0	2	1]
S =	[-1	-2	1	4	1	-2	-1]	[-1	0	2	0	-1]
W =	[-1	0	3	0	-3	0	1]	[-1	2	0	-2	1]
R =	[1	-2	-1	4	-1	-2	1]	[1	-4	6	-4	1]
O =	[-1	6	-15	20	-15	6	-1]	[]

Figure 3. 1D representation of the 7x7 and 5x5 filters used on the tests (Laws, 1985).

A problem that arises with this approach is the introduction of significant errors along the boundaries

between different textures in the image, formerly called the *edge effect*. It might be the case of obtaining energy values, in the areas located on the boundaries, that are closer to a third texture than to the ones included in the 7 x 7 window, with the subsequent error in classification. To reduce this effect, a new level of processing was applied, as proposed by Hsiao and Sawchuk (1989): for each pixel on the textural energy image J_n , the mean and variance of the four neighbourhoods for which the pixel is the corner are computed, and the new pixel takes the value of the mean of the quadrant that has the smallest variance (figure 4).

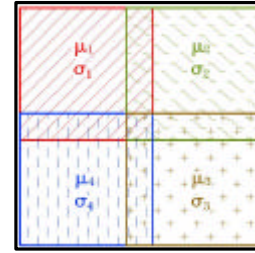


Figure 4. Diagram that represents the further processing level on the energy features to reduce the *edge effect*.

Another texture feature computed that can be included into the filtering methods is the *edgeness*, based on the idea of Sutton and Hall (1972), in which texture is conceived in terms of edgeness per unit area and represented by the gradient (the sum of the absolute value of the differences between neighbouring pixels) as a function of the distance between the pixels. For a given distance d (tested as a variable texture parameter) and subimage I , defined over a neighbourhood N , the *edgeness* is computed with the following expression:

$$g(i, j, d) = \sum_{(i, j) \in N} \{ |I(i, j) - I(i + d, j)| + |I(i, j) - I(i - d, j)| + |I(i, j) - I(i, j + d)| + |I(i, j) - I(i, j - d)| \}$$

where $g(i, j, d)$ represents the edgeness per unit area for a generic pixel (i, j) in the image, and d is a variable parameter to be studied for each particular group of textures.

2.4. Wavelet based texture analysis

A wavelet is a scaled and translated version of an elemental function called a *mother wavelet*

$$\mathbf{y}_{s,u}(x) = \frac{1}{\sqrt{s}} \mathbf{y} \left(\frac{x-u}{s} \right) \quad u \in \mathbb{R} \quad s \in \mathbb{R}^+$$

where s is the scale parameter and u the translation parameter. The wavelet decomposition of a function can be computed by applying each of these wavelets to the function itself

$$Wf(s,u) = \int_{\mathbb{R}} f(x) \frac{1}{\sqrt{s}} \mathbf{y}^* \left(\frac{x-u}{s} \right) dx$$

In practice, the extension to a 2-D discrete function is usually performed by means of a product of 1-D low-pass and high-pass filters (Walker, 1999). The original image is thus decomposed into a set of subimages at several scales, some of them contain the *averages* of the original image at a particular scale, and the other subimages represent the *details*. Since most relevant texture information is removed by iteratively low-pass filtering, the *average images* are not usually considered to obtain texture features (Van de Wouwer, 1999).

The technique used for the application of a discrete wavelet transform consists of the convolution of the digital image with a smoothing filter (*scaling*) and a band-pass filter (*wavelets*) along two orthogonal directions. The combination of these two filters along the vertical and horizontal directions renders four new output images for each level of decomposition, denoted by a , h , v , and d . The first one represents the *average* and the rest represent the first-order horizontal, vertical and diagonal *details*, respectively. It is important to mention that the wavelet decomposition entails the downsampling of the image by a factor of two, so each level of decomposition represents a lower scale or spatial resolution than the original image.

The application of the inverse transform of each output *detail* image produces a reconstructed version of the horizontal, vertical and diagonal *details*, denoted by H , V , and D , that contain high frequency information on different scales depending on the level of decomposition of the *detail* images. The reconstruction process, named *multiresolution analysis*, entails the upsampling of the images to the original size (figure 5). Considering that at each level of decomposition we are representing a down-scaled version of the image, the original image may be understood as a 0-level image, containing information at the original scale. This is an important aspect because the texture is a scale-dependent property, and each particular texture class usually has an optimum scale or resolution level for representation and feature extraction.

Once the decomposed and reconstructed images of the details were obtained, several texture features were computed for every output image. The features were selected among the statistical and filter based texture variables proposed on sections 2.2 and 2.3, on the basis of a separability criterium.

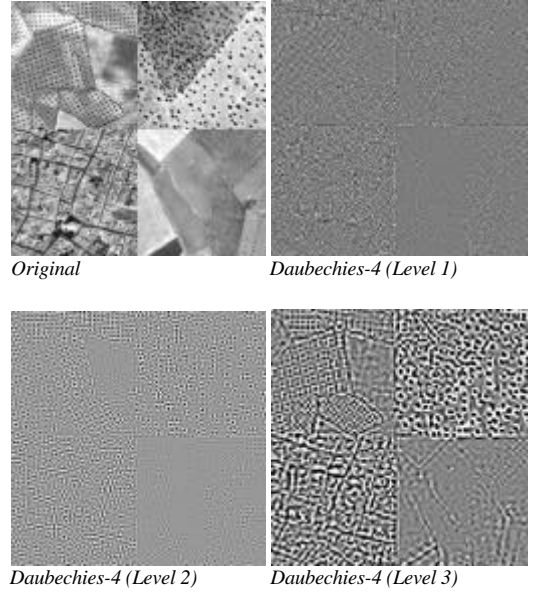


Figure 5. Detail of the original image before and after the respective three levels of wavelet decomposition and further reconstruction using only the *detail* components (V, H and D). The mother wavelet used is the Daubechies-4.

2.5. Experimental procedure

An important issue in texture analysis, especially when the wavelet decomposition method is used, is the selection of the most appropriate set of methodological parameters for each specific problem of texture classification. In this study, different variations of the following parameters were tested:

- *Window size*, or the neighbourhood to be considered to compute the values of the texture features for each pixel.
- The *texture features* that provide a better discrimination between classes. The selection was made between 8 statistical and 7 filtering features, as described above.

- *Type of mother wavelet* used. Six different wavelets were tested: Haar, Daubechies 4 and 8, Coiflets 6, 12 and 24.
- Influence of the *wavelet decomposition level*. Three levels were tested.
- Whether to use the *decomposed* or the *reconstructed detail* images to compute the texture features.
- Whether to use the *independent detail* images or the *sum of details* (H+V+D) for each level of decomposition.

Additional parameters, such as the *distance* between pixels (*d*) to compute the cooccurrence matrix or the *edgeness*, and the *number of grey levels* used, were studied in previous works for similar classification problems (Ruiz, 1998).

A pre-selection of two parameters, the influence of the *decomposition level* and the use of *independent details* or the *sum of the details*, was made by means of a statistical separability analysis using the Jeffries-Matusita distance. The rest of the parameters were directly evaluated by means of the classification process.

The classification method used to assign a texture class to each pixel on the image was based on the Bayesian maximum likelihood rule. Three different sampling sets were defined: the first was used as the learning set to obtain the decision functions, the other two were testing sets, one to evaluate the errors on the internal areas of the different textures, and the last set was used to evaluate the errors within the boundaries between classes, which are particularly high in texture classifications, due to the *edge effect*.

3. RESULTS AND DISCUSSION

Attending to the classification results, the first conclusion that should be pointed is that the classes with finer texture (cereal, alfalfa, maize,...) have a lower producer's classification accuracy on the external areas (boundaries between classes) than the classes with coarser textures (olive trees, dehesas, urban,...). Therefore, the default error in assigning classes to those pixels that are located on the borders of the texture areas is higher for finer textures, probably because the combination of two or more fine textures is more likely to be confused with heterogeneous or coarse textures, due to the higher dispersion of the texture signatures that the coarse textures naturally present.

From the 15 different texture features computed, the best classification results were obtained using 6 of them: variance, contrast, inverse difference moment,

correlation, edgeness and energy. A window size of 21 x 21 pixels was selected taking into account to preliminary results and the type of classes, considering a trade-off between the classification accuracies of the internal and external areas. In general, the increase of the window size provides better results in internal areas and worse in external areas of the texture regions.

The separability tests showed that the generation of texture features for each of the independent *detail* images in the wavelet decomposition process does not increase the overall separability distance between classes, but multiplies by 3 the number of variables to compute. Therefore, the final classification results were obtained by using the sum of the horizontal, vertical and diagonal *detail* images.

In order to determine the influence of the wavelet decomposition level, the 6 most relevant features were computed for all the images derived from decomposition levels 1, 2 and 3, and for level 0 (original image without decomposition). A series of separability analysis were carried out to find the best 6 variables from a set of features from the 4 levels. The average results are shown on table 1, ordered by the percentage of time that a variable from a particular level was selected. About half of the times, the best variables were from level 0 (without wavelet decomposition), and the relevance of the variables was progressively lower as the level increased. In addition, the overall accuracies of four classifications using the wavelet Daubechies-4, with features of levels 0, 1, 2 and 3 were 86.1%, 74.7%, 57.0% and 46.2%, respectively. Therefore, in this case most of the texture information is included in the higher resolution levels.

Table 1. Influence of the decomposition level of the wavelet transform, expressed as the percentage of variables from different levels included among the best discriminant features.

<i>Decomp. Level</i>	0	1	2	3
<i>% of var. included</i>	48%	24%	18%	10%

Regarding the use of the decomposed or the reconstructed *detail* images to compute the texture features, two classifications were compared using the wavelet Daubechies-4. The overall accuracy was 65.7% when the decomposed images of the 3 levels were used, and 77.8% using the reconstructed ones.

Finally, figures 6 and 7 show the overall accuracies of a series of classifications to compare the influence of the type of wavelet and the convenience to use features computed from the original image (level 0), from the wavelet transforms with three level of decomposition

(levels 1+2+3), or from the combination of all of them (levels 0+1+2+3).

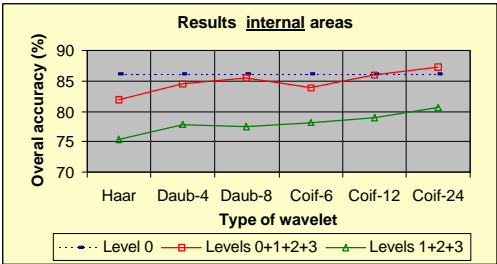


Figure 6. Classification results for **internal** areas using different types of wavelets and 3 different sets of features (level 0 means original image).

Figure 6 shows the results for the internal areas, without consideration for the *edge effect*. In those areas, the use of the original image always yields better results (86.1%) than the wavelet transform images. However, the combination of the original (level 0) and the wavelet features together produces a better performance when the appropriate wavelet is chosen. Thus, while the Haar wavelet has a relatively poor performance, the Coiflets work better, especially when the support is increased. The wavelet Coif-24 combined with the original image provide the best results of the tests (87.2%).

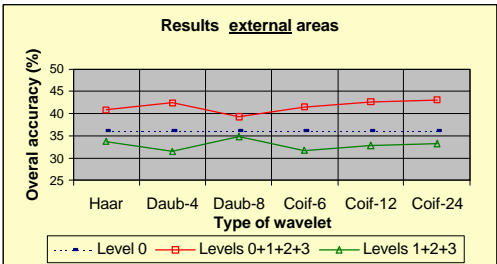


Figure 7. Classification results for **external** areas (*edge effect*) using different types of wavelets and 3 different sets of features (level 0 means original image).

The same tendency is observed in the external areas (figure 7), those in which the edge effect makes the accuracy of the classification decrease sharply. The combination of the features from the original image with the wavelet features provides better results with all the types of wavelets tested, but specially with the Coif-24, where the classification accuracy for those areas is increased by 6.4% with respect to that obtained only from the original image.

Figure 8 shows an example of the classified image used in the tests, where 12 texture classes were defined.

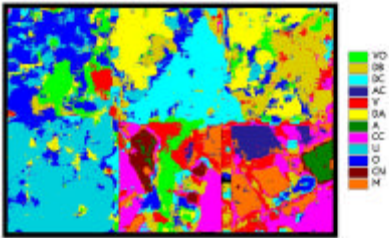


Figure 8. Classification of the mosaic image on figure 1 in 12 agricultural classes using texture features.

CONCLUSIONS

Texture classification of agricultural landscape images is a useful method to identify crops using traditional statistical features, though the edge effect inherent to these methods usually produces poor results on the boundaries between classes.

The combination of these features with those obtained from wavelet decomposition of images on several levels may increase the accuracy of the classification when the mother wavelet used in the transformation is properly chosen. Most of the texture information is contained in the lower levels of decomposition, and the reconstructed images (H, V and D) applying the inverse wavelet transform seem to provide better results than the decomposed images (h, v, and d).

In general, the wavelet approach provides a better performance for those areas that are on the boundaries between different textures. Therefore, the methods based on wavelets seem to reduce the *edge effect* of the classification.

The type of wavelet used is an important parameter. In our tests, the wavelets with higher support, such as the Coif-24, generated better results. However, further experiments should be done, using a wide variety of wavelets, in order to select the most appropriate type for each application.

REFERENCES

Brodatz, P., 1966. Textures: A photographic album for artists and designers. Dover, New York.

- Chang, T. and Kuo, C.J., 1993. Texture analysis and classification with tree-structured wavelet transform. *IEEE Trans. Image Processing*, vol. 2, pp. 429-441.
- Fatemi-Ghomi, N., Palmer, P.L., Petrou, M., 1996. Performance of texture segmentation algorithms based on wavelets. *Technical Report. Electronic and Electrical Engineering Department. University of Surrey*.
- Ferro, C.J. and Warner, T.A., 2002. Scale and texture in digital image classification. *Photogrammetric Engineering and Remote Sensing*, vol. 68, no. 1, pp. 51-63.
- Haralick, R.M., K Shanmugam and Dinstein, 1973. Texture features for image classification. *IEEE Transactions on Systems, Man, and Cybernetics*. SMC-3 : 610-622.
- Hsiao, J.Y. and A.A. Sawchuk, 1989. Unsupervised image segmentation using feature smoothing and probabilistic relaxation techniques. *Computer Vision, Graphics and Image Processing*, vol. 48, pp. 1-21.
- Kashyap, R.L., Chellapa, R., Khotanzad, A., 1982. Texture classification using features derived from random fields models, *Patt. Recogn. Lett.*, vol. 1, pp. 43-50.
- Laws, K.I., 1985. Goal-directed texture image segmentation. *Applications of Artificial Intelligence II*, SPIE vol.548, pp. 19-26.
- Mallat, S.G., 1989. A theory of multiresolution signal decomposition: The wavelet representation. *IEEE Trans. Patt. Anal. Machine Intell.*, vol. 11, no. 7, pp. 674-693.
- Marceau, D.J., Gratton, D.J., Fournier, R.A., Fortin, J., 1994. Remote sensing and the measurement of geographical entities in a forested environment. *Remote Sensing of Environment*, vol. 49, pp. 105-117.
- Pentland, A.P., 1984. Fractal-based description of natural scenes. *IEEE Trans. Patt. Anal. Machine Intell.*, vol. 6, pp. 661-674.
- Randen, T. and Husoy, J.H., 1999. Filtering for texture classification: A comparative study. *IEEE Trans. Patt. Anal. Machine Intell.*, vol. 21, no. 4, pp. 291-310.
- Ruiz, L.A., Iñán, I., Baridón, J.E., Lanfranco, J.W., 1998. Combining multispectral images and selected textural features from high resolution images to improve discrimination of forest canopies. *Image and Signal Processing for Remote Sensing IV*. SPIE Vol. 3500: pp. 124-134.
- Ruiz, L.A. and Fdez.-Sarría, A., 2000. Analysis of image segmentation of multisource data in mountain environments. *International Archives of Photogrammetry and Remote Sensing*. XIX ISPRS Congress, pp 469-475.
- Ruiz, L.A., Acosta, P., Fdez.-Sarría, A., Porres, M.J., Pardo, J.E., 2001. Mejora de la eficiencia en la segmentación de imágenes por texturas mediante filtros de energía. *Teledetección: Medio Ambiente y Cambio Global. Proceedings del IX Congreso Nacional de Teledetección*, Lleida.
- Sutton, R.N. and E.L. Hall, 1972. Texture measures for automatic classification of pulmonary disease. *IEEE Transactions on Computers*, vol. C-21, pp. 667-676.
- Turner, M.R., 1986. Texture discrimination by Gabor functions. *Biol. Cybern.*, vol. 55, pp. 71-82.
- Unser, M., 1995. Texture classification and segmentation using wavelets frames. *IEEE Trans. Image Processing*, vol. 4, no. 11, pp. 1549-1560.
- Van de Vover, G., Scheunders, P., Van Dyck, D., 1999. Statistical Texture Characterization from Discrete Wavelet Representations. *IEEE Trans. on Image Process.*, vol. 8, No. 4, pp. 592-598.
- Walker, J.S., 1999. A Primer on Wavelets and their Scientific Applications. Chapman & Hall/CRC.

Remote Sensing Monitoring Crop Growth

A. Calera*, J. González-Piqueras*, and J. Melia**

* Remote Sensing and G.I.S. Unit-I.D.R. University of Castilla-La Mancha, Campus of Albacete. 02071 Albacete. Spain

**Dep. Of Thermodynamics, University of Valencia, Campus of Burjassot, 46100, Valencia, Spain.

Alfonso.Calera@uclm.es ; Jose.Gonzalez@uclm.es ; Joaquin.Melia@uv.es

ABSTRACT:

Vegetation indices have been used for operational quantitative monitoring of vegetation. Here, corn and barley cultures have been used to relate meaningful biophysical parameters as dry biomass and Crop Growth Rate (CGR) to the well-established Normalized Difference Vegetation Index (NDVI). We explain these relationships by means of the use of the Light Use Efficiency (LUE) models, based on positive relation between primary production and Absorbed Photosynthetically Active Radiation. In these models we introduce NDVI as lineal estimator of f_{APAR} . Experimental data over corn and barley show that dry biomass is lineally related to the Time-Integrated of the NDVI (ITNDVI). The characteristic plateau stage of NDVI coincides temporarily with the lineal growth phase. During this stage both NDVI and maximum CGR remains constant for well-watered crops. Water status of vegetation is a relevant parameter because it can modify substantially the relationship between CGR and NDVI. Under this assumption can be established that NDVI on plateau stage, represents an estimator of the potential rate of dry matter accumulation, dependant on crop and environmental variables.

1 INTRODUCTION

A traditional interest has been established to link biophysical variables to vegetation indexes, because it supposes an operational quantitative monitoring of vegetation by means of Remote Sensing. Vegetation monitoring requires describing crop's growth by the most meaningful growth analysis term for crop canopies, known as the accumulation of dry matter per unit of land area and per unit of time, or the Crop Growth Rate (CGR) (Gardner et al, 1990).

Relationship between biomass and vegetation indexes has been usually formulated by two ways. First, by establishing an empirical relationship between biomass and vegetation index (Gilabert et al, 1996; Anderson et al., 1993).

A second way is by using Monteith's model (Monteith, 1977) which is based on the fact that the rate of growth of many crops is almost proportional to the rate at which radiant energy is intercepted by the foliage. Models based on positive relation between primary production and Absorbed Photosynthetically Active Radiation are known as Light Use Efficiency (LUE) or ϵ -model (Gower et al, 1999). Primary production, P (Kg/m^2), defined as dry biomass by unit

of surface, can be estimated by using the Fraction of Absorbed Photosynthetically Active Radiation, f_{APAR} , and the incident radiation, PAR , as:

$$P = \epsilon \int f_{APAR} PAR dt \quad (1)$$

where ϵ is the efficiency to convert radiant energy into dry biomass.

On a similar way, Asrar et al, (1989) established that the primary production of dry biomass is related to the fraction of absorbed radiation by the expression,

$$P = \int_0^t f_{APAR} \cdot PAR \cdot \epsilon \cdot W \cdot dt \quad (2)$$

where W is the water stress index defined as the ratio between the evapotranspiration of the plant in real conditions, ET , and the evapotranspiration under optimal conditions, ET_m . The differences between equations (1) and (2) are on the introduction of coefficient W , and on its temporal variation.

The NDVI is introduced on equations (1) and (2) by using a lineal function such as (Asrar et al, 1989),

$$f_{APAR} = a \cdot NDVI + b \quad (3)$$

Wiegand et al (1991) consider that bias and gain on eq. (3) depend on the crop and suggest using constant values in each crop stage: growth, reproductive maturation and senescence. Although some authors such as Ridao et al, (1999) suggest non linear relationship between f_{APAR} and NDVI, theoretical works by Sellers et al. (1997) provides solid foundation to eq. (3). Including expression (3) into (2) we can obtain,

$$P = \int_0^t (a \cdot NDVI + b) \cdot PAR \cdot \varepsilon \cdot W \cdot dt \quad (4)$$

Assuming that parameters ε , PAR, and W are constant for each development stage, the expression (4) enables to introduce the concept of Time-Integrated value of NDVI (ITNDVI). ITNDVI is defined as the area under the curve described by NDVI with the time (Yang et al., 1998). In this case primary production can be expressed as:

$$P = m \text{ ITNDVI} + n. \quad (5)$$

This expression was used to estimate the primary production of an ecosystem at moderate and global scales (Rasmussen, 1998).

In this work it is performed an experimental analysis of models expressed on equation (2) and (3) to obtain expression (5). For this purpose a relationship between ITNDVI and biomass is used for representative crops such as barley and maize under different water conditions on field.

The crop's growth dynamic is studied by establishing an experimental relationship between the NDVI and CGR following LUE's model as exposed before. So, deriving equation (4), CGR can be expressed on the form:

$$CGR = dP/dt = (aNDVI+b) \varepsilon PAR W_i \quad (6)$$

Equation (6) shows that NDVI can be related to the rate of the dry matter accumulation. In this work, it is

discussed eq. (6) on the basis of experimental field data.

2 MATERIALS AND METHOD

Two representative crops were selected to perform this study: barley and corn. Barley experience was carried out during winter-spring in 1998 in the area of Casa Alcocer in Tarazona de la Mancha (Albacete). Three water levels were established based on the water supply to the barley plots. The first of them are the so-called *irrigated plots* under optimal water conditions with water supply indicated by the Advisory Irrigation Service (SAR, *Servicio Asesoramiento de Riegos*) in the Regional Agronomic Institute (ITAP, *Instituto Técnico Agronómico Provincial*). Water supply is calculated by FAO procedure (Allen et al, 1998). The second water level is the *semi-irrigated plots* with half of the estimated optimal water supply. And the third level is the *unirrigated or dry plots* with only water supply by rain. Along this experience a variety of irrigated barley has been used under optimal nutrient and water conditions as reference crop. Biomass was measured cutting a representative area of 0.5 x 0.5 m² for each plot; the weights of these samples are their wet biomass. Introducing them on an oven at 105 °C for 5 days the water is removed to obtain the dry biomass. The average height of plants had a great variability due to the inclination of structure caused by the weight of the ears. LAI measurements were taken by using a LICOR-LAI 2000, and phenological stage was determined referencing to Keller-Bagliolini scale.

Corn experience was carried out during spring-summer in 2001 in the area of Las Tiesas, in Barrax (Albacete). There was a plot of corn spotted on a weight lysimeter centred on an area of 1 ha. This corn crop was maintained under optimal water conditions, following the water supply indications of SAR. Biomass samples were taken with and interval of 7 to 10 days surrounding the selected plot. Other biophysical variables were measured such as plant height, green cover fraction, LAI and phenological stage. LAI was determined by using a destructive method: taking a representative sample of 1x1 m², out of the lysimeter area and measuring the total leaf area. The fraction of green cover was estimated using a digital camera following procedure described by Calera et al. (2001)

The radiometric measurements over barley and corn were taken with a GER-3700 spectroradiometer, with spectral range in 300-2500 nm and maximum spectral

resolution of 1.4 nm. The observation height in both cases was 5 m over crop canopy and the instantaneous field of view (IFOV) was 3°, which represents a circular observation area of 70 cm in diameter. In case of barley this IFOV included several rows. For corn each measurement covers a transect of 6 samples. Measurements were taken under nadir observation and avoiding clouds. Before performing radiometric measurements over vegetation a reference radiometric measurement over Spectralon (Lab sphere) panel was taken following the methodology proposed by Gilabert et al. (1996) to estimate the reflectance. Besides, the temporal interval of acquisition was set to 7-10 days to monitor crop's growth. Finally, the bands reflectance was calculated using the ETM+ sensor spectral responses to compute NDVI.

3 RESULTS

Figures 1a and 1b show the temporal evolution of the NDVI, and the phenology for barley and corn respectively. In the experience over barley, measurements started on DOY 91. Three barley plots started at the same point at the beginning of the experience (DOY 90), taking in account that they were under some conditions of water and nutrients until DOY90. Since DOY 90, barley plots were differentiated by water supply. Fig. 1a displays the characteristic NDVI plateau for all plots. Plateau length is related to water supply. The NDVI starts declination in coincidence with the beginning of the maturity stage. The beginning of the ageing, yellowing, indicates the commencement of maturity or senescence of leaves. This stage starts before in less watered plots than in more watered ones. It is due because more water stress on dry barley plot produces earlier crop wilting; as consequence water supply modifies the behaviour of the NDVI.

Corn measurements were taken during all the phenological cycle of the crop. Starting on DOY 149 the NDVI increases rapidly reaching its maximum on DOY 190, both reproductive and forming ears stages fall into this plateau. The maximum is located approximately on flowering, starting the NDVI declination on DOY 230 and locating the final stage on DOY 290. During all phenological cycle, the water status of corn was maintained under optimal conditions.

Analogous results in the temporal evolution of NDVI have been obtained in other experiences for corn and other crops (Gilabert et al. 1996; Fisher, 1994)

NDVI and Biomass.

Several authors considering different ranges of application have interpreted the relationship between NDVI and biomass. Anderson et al., (1993) establishes a correlation between dry biomass and NDVI for low ranges of biomass, of good applicability in cases of sparse vegetation like prairies. Gilabert et al. (1996) established a logarithmic expression between NDVI and biomass for maize. In both cases calculations were made under restrictions that depends on site and crop. Experimental data of biomass and NDVI for barley and corn are represented in fig. 2a, 2d.

The behaviour of biomass shows the well-established curve of crop growth (Gardner et al, 1990), with a good representation in case of maize. It is characterized by a first stage of exponential growth

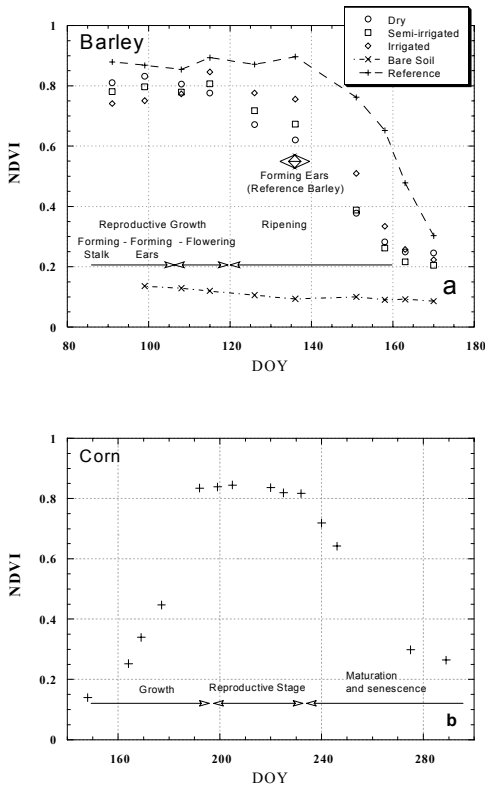


Figure 1. Representation of NDVI versus DOY for both experiences (a) barley and (b) corn.

until DOY 180, followed by a stage with lineal growth, with an accumulated dry matter at maximum constant rate. After this stage crop growth rate falls (DOY230) reaching a stationary state (physiological maturity). Behaviour of NDVI along time shows a first exponential stage reaching a plateau on DOY 180-190, until DOY 230, followed by the commencement of maturity. The plateau stage of NDVI is concurrent with a constant accumulated biomass rate. For barley plots, measurements were taken during constant accumulated rate of biomass stage corresponding to the plateau of the NDVI.

Maximum growth rate occurs when NDVI reaches the plateau stage, just when crop is at full effective cover point. At the beginning of this stage corn crop has a dry biomass of 0.3 kg/m² with 1.2 m of plant height, and at the end dry biomass is of 2.5 Kg/m² with a 2.3 m of plant height. For this period, while the NDVI remains constant, the dry biomass and height experience the most important change in the crop

cycle. For barley, the behaviour is the same, with different values for NDVI and biomass.

By this fact it is not recommended a direct analysis between NDVI and biomass, except in cases of sparse vegetation with a range of low green cover. For these cases the relationship NDVI-fraction of green cover (Calera et al, 2001) can be essential to explain the relationship between NDVI and biomass on these first development stages, being the NDVI also affected by the presence of soil.

It seems more adequate to analyse NDVI vs. biomass to apply equation (5) obtained from LUE's model i.e. to explore the relationship between biomass and the ITNDVI

ITNDVI and Biomass.

Estimations of ITNDVI are made by lineal interpolation of the NDVI values and by integrating the area under the curve, thus the ITNDVI units are

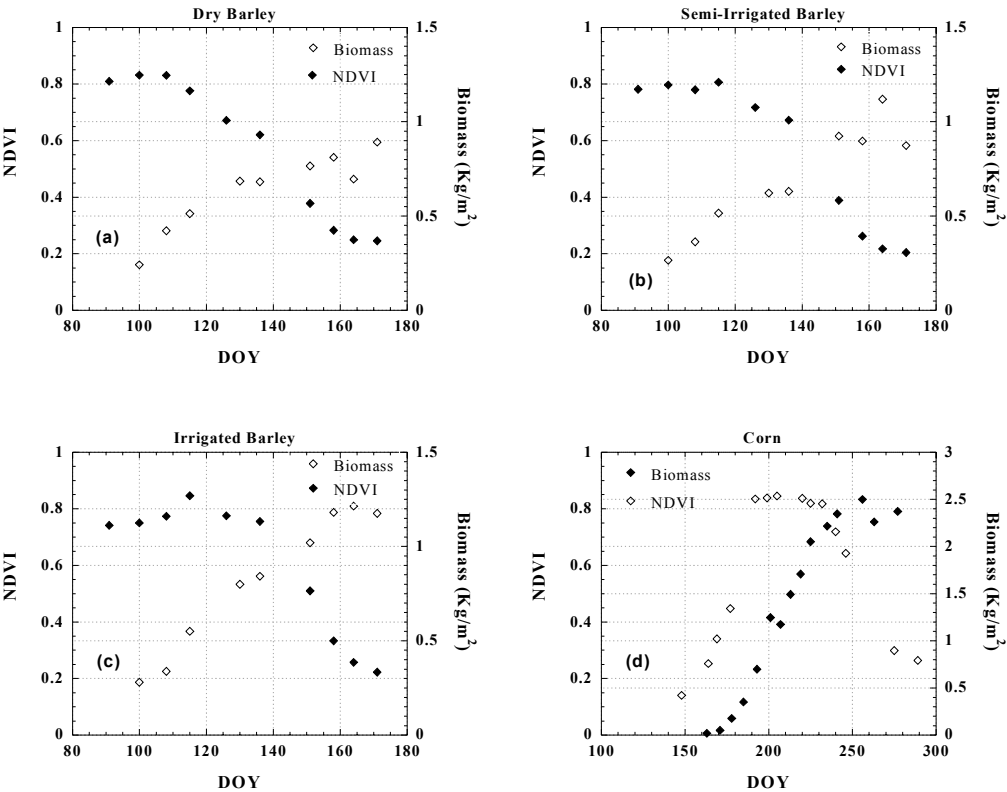


Figure 2. Biomass and NDVI versus DOY for (a) dry, (b) semi-irrigated, (c) irrigated barley, and (e) corn.

NDVI-day. First day to calculate for barley has been DOY 91 and DOY 148 for corn. Results are represented in figure 3a for barley and 3b for corn. For barley plots we can observe that similar results are obtained differing by their water supply. So, starting at same point, the trend of ITNDVI curves is similar to cumulated dry biomass curves.

For corn, the relation between ITNDVI and dry biomass shown in fig 3b is similar to barley. So, on first stage a lineal regression to DOY can be set, corresponding to initial and medium growth. On ripening stage (DOY 170 for barley and 240 for corn), this tendency is not well defined. It can be observed in both cases a parallel behaviour for the biomass and the ITNDVI in all range of phenological cycle.

If we consider the values of ITNDVI and biomass during the growing and reproductive stages a lineal relationship between them can be established. Under this assumption, applying a lineal regression we obtain the next equations: (6) for dry, (7) semi-irrigated, (8) irrigated barley and (9) for corn:

$$B = 0.19 + 0.015 \cdot \text{ITNDVI} \quad R^2 = 0.96 \quad (6)$$

$$B = 0.15 + 0.017 \cdot \text{ITNDVI} \quad R^2 = 0.94 \quad (7)$$

$$B = 0.14 + 0.020 \cdot \text{ITNDVI} \quad R^2 = 0.98 \quad (8)$$

$$B = 0.07 + 0.036 \cdot \text{ITNDVI} \quad R^2 = 0.96 \quad (9)$$

Where B is the biomass in Kg/m² and the ITNDVI is expressed in NDVI-day. Considering equation (4) and assuming average values for PAR, W and ϵ , this relationship can be expressed as,

$$B = C + \epsilon_{\text{average}} \cdot \text{ITNDVI} \quad (10)$$

where parameter $\epsilon_{\text{average}}$, is the averaged value of $\epsilon \cdot \text{PAR} \cdot W$.

All barley plots have been under same climatologic conditions, the only difference is due to water supply, it differentiates plots along their development (figure 2). It can be observed that coefficient $\epsilon_{\text{average}}$ increases with the water content of the culture. In plants like corn, under optimal water conditions and similar environment than barley, coefficient $\epsilon_{\text{average}}$ is larger; this can be explained because its efficiency for conversion of photosynthetic active radiation to dry matter is greater (Gower et al., 1999). Another relevant difference between irrigated barley and corn is the air temperature, higher in summer just during

the growth and development of the corn than during barley cycle. Differences due to value of PAR during corn and barley cycle must be considered also.

Results obtained by other authors show that for maize (Calera, A. 2000;) the value of coefficient $\epsilon_{\text{average}}$ is in agreement with the result showed in equation (9).

NDVI and CGR.

The Crop Growth Rate (CGR) shows the capability of crops to generate biomass, Gardner et al. (1990) establishes that this is a basic parameter in the description of the growth and development of crops. Direct calculations of CGR from dry matter measurements shows an important dependence on the

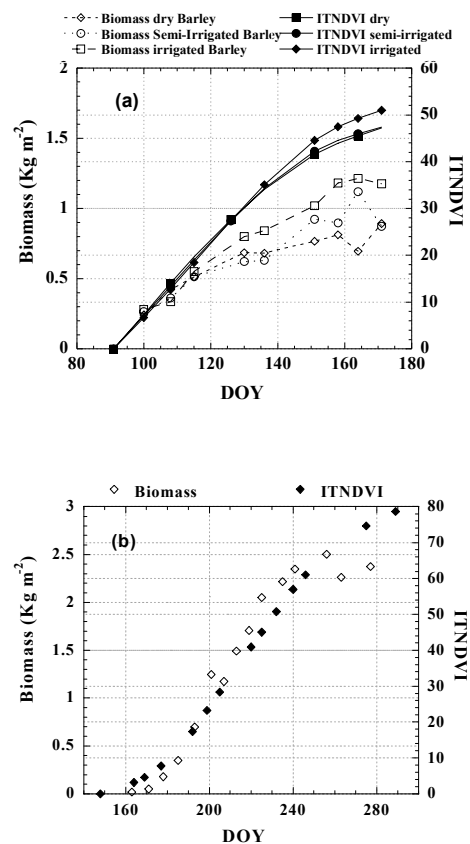


Figure 3. ITNDVI (NDVI*day) and Biomass (Kg/m²) versus DOY for (a) barley under three different water conditions and (b) corn.

spatial variability of the field samples. One of the functions typically used to adjust biomass data and DOY are third degree polynomials. Deriving this function CGR can be obtained. The application of this function must be done adequately taking into account the important variation in slope when derivation is made. In this case, by deriving third degree polynomials, a second degree polynomial function is obtained that does not fit well with the behaviour of idealistic CGR (Gardner et al., 1990) showed on figure 5, because a parabolic function have not the characteristic plateau of CGR, corresponding to a linear growth phase.

If we compare the temporal evolution of NDVI for maize and for idealistic CGR, fig. 2e and fig. 5, we find a high degree of shape coincidence, and most important, temporal coincidence.

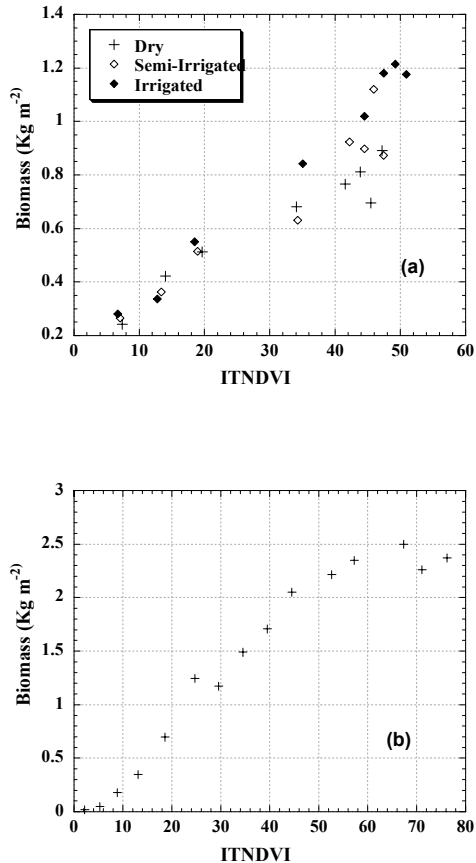


Figure 4. Values of Biomass (Kg/m²) and ITNDVI (NDVI-day) calculated in experience of (a) barley and (b) corn.

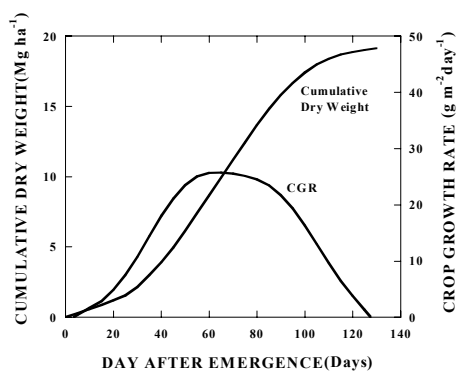


Figure 5. Idealistic representation of Cumulative dry weight and Crop Growth Rate (After Gardner et al., 1990).

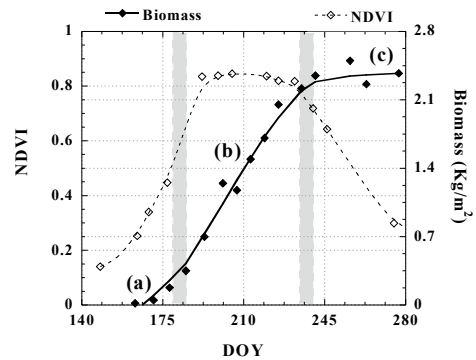


Figure 6. Differential rates of growth over cumulative dry weight for corn. (a) exponential growth phase; (b) lineal growth ; (c) falling stage. It is represented temporal evolution of NDVI for corn.

As mentioned before there is not a mathematical function fits well with CGR behaviour during all cycle, alternative way is to consider separately the different stages of the rate of cumulative dry matter. These phases have been represented on figure 6.

A first step is to analyse the phase of lineal rate growth in which CGR reaches a maximum and constant value. On agronomical practice this value is used as representative value of CGR (Gardner et al, 1990). This stage is simultaneous with the plateau stage of NDVI versus DOY (figure 6), indicating a relationship between the NDVI and the CGR. The values for maize and irrigated barley are showed in table 1. Each one supposes an averaged value estimated on a 50 days

interval for corn and irrigated barley. Notice that crop growth rate of corn is larger by a factor 2 than for barley maintaining the same range for vegetation index values.

For irrigated barley and corn, water stress index W will be near 1. In this case the NDVI on the plateau stage represents the maximum value of growth rate for a crop maintaining variables on equation 6: a , ϵ , and PAR , constant. Then, with no water stress NDVI value on plateau stage can be seen as a potential growth estimator for a vegetal canopy, depending on crop and environmental conditions described by parameters in eq. 6.

Table 1. - Averaged values of CGR and NDVI corresponding to maximum growth rate stage and NDVI plateau.

Crop	CGR (Kg/m ² / day)	NDVI
Corn	0.039	0.85
Barley (Irrigated)	0.019	0.75

In case of crops under water stress, the constant rate stage is not well defined and it remains for a shorter period of time, as exposed before. Behaviour of NDVI and CGR in time are similar because the NDVI falls, in coincidence with falling the slope of biomass and vice versa (figures 2d and 5). A maximum potential on crop growth can be supposed due to NDVI values reached on plateau stage, but water stress can limit the corresponding maximum growth, as is shown by equation 6. As consequence of water stress the vegetation could wilt to adjust it's growth at the new environmental conditions, diminishing the values of NDVI. In other cases like forests, reaction to water stress can be to close stomas maintaining NDVI values, although diminishing rate growth.

9. CONCLUSIONS

It is not recommended to use direct relationship between NDVI and dry biomass: while NDVI is on plateau stage with a near constant value, the dry matter accumulation is at maximum rate. So, in the case of corn during this stage, while NDVI value remains constant at 0.85, dry biomass ranges from 0.2 to 2 Kg/m².

It seems more adequate in order to describe the relation between biomass and NDVI to use models proposed by Monteith (1977) and Asrar (1989), known as Light Use Efficiency or epsilon model (Gower et al, 1999). In these models NDVI is introduced as a good estimator of f_{APAR} .

Application of these LUE's model establishes a lineal relationship between dry biomass and Time-Integrated value of NDVI, ITNDVI, obtaining good agreement with experimental data for barley and corn analysed in this work. Differences showed on the dry biomass and ITNDVI relation for same crop under different water stress levels show the relevant role of water stress coefficient into the model.

In coherence with these LUE's models, NDVI is related to dry biomass growth rate, CGR. Accordingly with our experimental data, the NDVI temporal evolution and the idealistic temporal evolution of CGR, display similar behaviour over growing season for corn. The characteristic plateau stage of NDVI coincides temporarily with the lineal growth phase; at this lineal phase dry matter increases at constant rate. During this stage both NDVI and maximum CGR remains constant for well-watered crops.

So, under non-water stress, NDVI on plateau stage can be seen as an estimator of the dry matter accumulation rate, depending on crop and environmental variables. It establishes a relationship between NDVI and CGR, that agrees with the idea that considers NDVI as an estimator of the canopy photosynthetic power. On this way, Monteith and Unsworth (1990), consider that vegetation index can be legitimately be used to provide and estimate of growth rate.

Water status of vegetation is a relevant parameter because it can modify substantially the relationship between CGR and NDVI. With this assumption we can establish that NDVI on plateau stage, represents an estimator of the potential rate of dry matter accumulation, depending on crop and environmental variables; this potential growth rate is a maximum value; it coincides with real growth rate when the crop is on optimal conditions. Out of optimal conditions, i.e. water stress, growth rate will be lower. This fact is of great importance when using ITNDVI to estimate primary production by means of equation 5, especially on semiarid climates where vegetation can be most of time under water stress. In these cases the coefficients on this equation will be different according to water stress of vegetation.

10. REFERENCES

- Allen, R.G., Pereira, L.S., Raes, D., Smith, M., 1998. Crop evapotranspiration. Guidelines for computing crop water requirements. *FAO Irrigation and Drainage Paper*. 56.
- Anderson, G.L., Hanson, J.D., Haas R.H., 1993. Evaluating Landsat Thematic Mapper derived vegetation index for estimating above.ground

- biomass on semiarid rangelands. *Remote Sensing of Environment* 45:165-175.
- Asrar, G., Mineny, R. B., Kanemasu, E.T. 1989. Estimation of plant-canopy attributes from spectral reflectance measurements. In *Theory and applications of optical remote sensing*. Asrar G. (Ed.) John Wiley & Sons. Pp.: 252-292.
- Baret, F. and Guyou, G., 1991. Potentials and limits of vegetation indices for LAI and APAR assessment. *Remote Sensing of Environment*. 35:161-173.
- Calera, A., 2000. Seguimiento mediante teledetección de la cubierta vegetal de los cultivos de secano y su relación con variables climáticas en Castilla-La Mancha. Tesis Doctoral. Universidad de Valencia.
- Calera, A.; C. Martinez; J. Meliá (2001) : A procedure for obtaining green plant cover: relation to NDVI in a case study for barley. *Int. J. Remote Sensing*, vol 22, no. 17, 3357-3362
- Choudhury, B.J., Ahmed N.U., Idso S.B., Reginato R.J., Daughtry C.S.T., 1994. Relations between evaporation coefficients and vegetation indices studied by model simulations. *Remote Sensing of Environment*. 50, 1-17.
- Delgado, J.A., Terrab, R., Illera, P., Casanova, J.L., 1997. Estimación del rendimiento de la cosecha de cereal mediante imágenes NOAA y datos meteorológicos. En *Teledetección aplicada a la gestión de recursos naturales y medio litoral marino*. Hernández, C. y Arias J.E. (Ed.). Asociación Española de Teledetección y Universidad de Santiago de Compostela.
- Fischer A., 1994. A simple model for the temporal variations of NDVI at regional scale over agricultural countries. Validation with ground radiometric measurements. *Int. J. Remote Sensing* 15,7, 1421-1446.
- Gardner, F.P., Brent, P.R., Mitchell, R.L. 1990. *Physiology of Crop Plants*. Iowa State University Press: Ames.
- Gilabert, M.A., Gandia, S., Melia, J. 1996. Analyses of spectral-biophysical relationships for a Corn Canopy. *Remote Sensing of Environment*. 55:11-20.
- Gilabert, M.A., Gonzalez-Piqueras, J., García-Haro, J., 1997, Acerca de los índices de vegetación. *Revista de Teledetección*. 8:35-45.
- Gonzalez-Piqueras, J., 1999. GESAVI: A Generalized Soil Adjusted Vegetation Index. *Trabajo de Investigación* Universidad de Valencia.
- Gower, S.T.; C. J. Kucharik; J. H. Norman 1999 Direct and Indirect Estimation of Leaf Area Index, fAPAR, and Net Primary Production of Terrestrial Ecosystems. *Remote Sensing of Environment*, vol70; 29-51
- Kumar, M and J.L. Monteith, 1981: Remote sensing of crop growth. In *Plant and the Daylight Spectrum* (Ed. by H.G. Smith) pp: . Academic Press
- Monteith, J.L. 1977. Climate and the efficiency of crop production in Britain. *Phil. Trans. R. Soc. Lond. B*. 281, 277-294
- Monteith, J.L., and Unsworth, M. 1990. *Principles of Environmental Physics*. 2nd Ed. Arnold. London
- Rasmussen, M.S. 1998. Developing simple operational consistent NDVI-vegetation models by applying environmental and climatic information. PartI: Assesment of net primary production. *Int. J. Remote Sensing* 19, 1, 99-118.
- Ridao, E.; Conde, J.R., Minguez, M.I., 1998. Estimating fAPAR from nine vegetation indices for irrigated and nonirrigated faba bean and semileafles pea canopies. *Remote Sensing of Environment*. 66: 87-100.
- Sellers, P.J., Dickinson, R.E., Randall, A., Betts, A.K., Hall, F.G., Berry, J.A., Collatz, G.J., Denning, A.S., Mooney, H.A., Nobre, C.A., Sato, N., Field, C.B., Henderson-Sellers A., 1997. Modelling the exchanges of energy water and carbon between continents and the atmosphere. *Science*. Vol 275 502-509.
- Wiegand, C.L., Richardson, A.J., Escobar, D.E., Gerbermann, A.H., 1991. Vegetation Indices on Crop Assesments. *Remote Sensing of Environment*. 35, 105-119.
- Yang L., Wylie, B.K., Tieszen, L.L., Reed, B.C., 1998. An analysis of relationships among climate forcing and time-integrated NDVI of grasslands over the U.S. Northern and Central Great Plains. *Remote Sensing of Environment*. 65:25-37.

St o t e lan se an es e e ts on t e e a otrans iration in entral S ain sin re ote sensin te ni es

S. Lanjeri*, D. Segarra*, A. Calera** and J. Meliá*

**Department of Thermodynamics, Faculty of Valencia, University of Valencia*

Dr. Moliner 50, 46100 - Burjassot, València, Spain.

** *University of Castilla-La Mancha*

Instituto de Desarrollo Regional

Campus universitario s/n

02071 Albacete

E-mail: Siham.Lanjeri@uv.es

ABSTRACT *The work deals with an analysis of the evapotranspiration variation in the study area within a surface of about 3500 km². This area is located in Castilla-La Mancha (Spain), where intense land use changes have taken place during the last twenty years mainly due to irrigated cultures. Landsat TM imagery has been used for classification purposes and for vegetation cover scenarios construction. The analysis has been carried out during 1982-2000 period and concerning the main vegetation cover types in the zone. The results obtained are extrapolated to different realistic scenarios, according the socio-economic evolution of the region.*

1 INTRODUCTION

The work is continuation of the studies initiated in 1991 in an extensive zone of Castilla-La Mancha (Bolle, 1997, Lanjeri, 1998, Lanjeri et al., 2001) and is being done in the frame of many projects: CICYT "Evaluación por Teledetección de la incidencia de los cambios de la cubierta vegetal del suelo en los flujos de agua y energía" (CLI99-0793), landSAF (EUMETSAT), Land Water MED (Geo-information for sustainable management of Land and Water resources in the MEDiterranean region) (ICA3-ct-1999-00015).

Vegetation change detection is a powerful application of remote sensing, in that the spectral and temporal resolution of multi-sensor approaches can be used to advantage in monitoring both significant and subtle land cover changes over time at global scale (Munyati, 2000). The importance of mapping, quantifying, and monitoring the changes in physical characteristics of land cover has been widely recognized in the scientific community as a key element in the study of global change (IGBP 1990, Henderson-Sellers and Pitman 1992).

In this paper, we take advantage of the availability of high resolution, multiband imagery from the Landsat TM and ETM+ to obtain many maps of the zone study over the last 20 years. It allows us to monitor the irrigated crops surface area which has undergone an increment during period 1982-2000. Therefore, it affect specially the land cover evapotranspiration,

because of the difference in the soil water content availability.

In fact, evapotranspiration (E_c) is an important boundary condition for regional scale hydrological and climatological modeling. A large number of more or less empirical methods has been developed over the last fifteen years by numerous scientists to estimate the evapotranspiration from different climatic variables.

Further studies have been undertaken by the FAO working group (Itier, 1996; Jensen, 1994) to evaluate the utility of FAO Penman-Monteith method in determinating the evapotranspiration when limited meteorological data are available. Smith et al. (1996), recommended the FAO Penman-Monteith equation as the standard method for estimating reference and crop evapotranspiration, E_o and E_c . It is method with strong likelihood of correctly predicting E_o in a wide range of locations and climates and has provision for application in data-short situations. In this paper we take advantage of the method to calculate both magnitudes.

Furthermore, using both Landsat imagery and evapotranspiration data, we were able to generate evapotranspiration scenarios of the study area.

2 STUDY AREA

The study zone called "Albacete" is situated in the experimental region -Castilla-La Mancha- of the projects mentioned above, and it is located in central Spain delimited by the following UTM coordinates X (m): 566900, 616050 and Y (m): 4291575, 4362225

(see figure1). The study area was originally selected due to its flat morphology, thus minimising the complications introduced by topography, and because the presence of large, uniform man-made different units of vegetation. The climate is of Mediterranean type, with heaviest rainfalls in spring and autumn and lowest in summer, high thermic oscillations in all season between the maximum and minimum daily temperatures. There are different types of vegetation land cover presented in the study area: Irrigated winter and summer crops, dry cereal, vineyard, sunflower, natural vegetation, fallow.

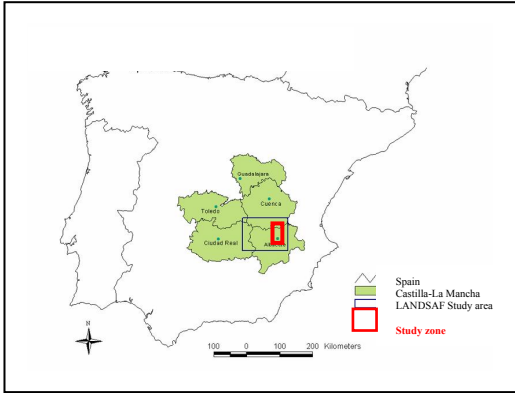


Figure1. Location the study area in Castilla-La Mancha and Spain.

3 LAND VEGETATION COVER EVOLUTION DURING 1982-2000 PERIOD

For this purpose, we used serie of Landsat images, acquired from different sensors, MSS, TM and ETM+. The availability of Landsat imagery from 1982 to 2000 allow us to obtain many maps of the study zone, making empahsize on the irrigated areas and its evolution during the last two decades. Vegetation cover maps for 1982 to 1986 period and for 1996 and 2000 have been obtained using the multitemporal masking classification method (Lanjeri et al., 2001). For 1982-1986 period, only Irrigated winter and summer crops are considered (see figure2).

The analysis of the results are presented in the tables 1 and 2. First, we analyse the actual situation of the land cover vegetation in the Albacete zone (the period 1996-2000). Then, the analysis data will be extended to the whole period 1982-2000 according to the evolution of the irrigated areas.

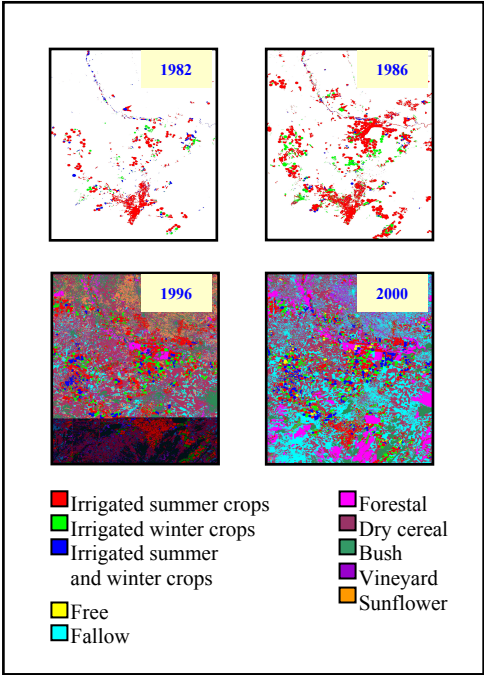


Figure2. Land cover maps of the Albacete zone for period 1982-2000, obtained using the Landsat MSS, TM and ETM+ imagery.

	1996 (ha)	1996 (%)	2000 (ha)	2000 (%)
Dry crops	178.271	51.3	211.751	61
Irrigated crops	60.409	17.4	66.835	19,2
Forestal/Bush	91.374	26,3	50.085	14,4
Vineyard	17.490	5	18.873	5,4

Table1. Land vegetation cover surface area in ha and % in Albacete zone for 1996-2000 period.

The table 1 shows that the irrigated surface area increases with percentage of 0.1% during 1996-2000 period. The dry crops and vineyard has been also increased in surface area with 0.2% and 0.08% successively. While natural vegetation has been decreased in surface area with 0.5%.

In the table2, we present the summer and/or winter irrigated surafce area in ha and % in the study area among the years of study.

Table2. Irrigated surface area in ha and % in Albacete zone for 1982-2000 period.

	1982 (ha)	1983 (ha)	1984 (ha)	1985 (ha)	1986 (ha)	1996 (ha)	2000 (ha)
Summer irrigated	12.717	12.925	24.011	30.023	32.273	32.611	26.350
Winter irrigated	1.897	1.478	3.193	4.706	7.138	16.834	18.754
Other irrigated	2.663	938	1.153	3.122	2.256	8.094	21.731
Total	17.277	15.341	28.357	37.851	41.667	57.539	66.835
% of total surface (347.544 ha)	5,0	4,4	8,2	10,9	12,0	16,6	19,2

The table2 shows that the irrigated summer and/or winter surface area have been increased with percentage of about 3% during the last 20 years. Thus, the land surface system can be extremely influenced in terms of the water requirements. This also affect the land water balacies.

4 ANALYSIS OF THE EVAPOTRANSPIRATION CROPS DATAEvapotranspiration is determinated by the crop coefficient approach whereby the effect of the various weather conditions are incorporated into Eo and the crop characteristics into the Kc coefficient. The effect of both crop transpiration and soil evaporation are integrated into a single crop coefficient.

The calculation procedure for crop evapotranspiration, Ec, consists of:

- (i) Constructing the crop coefficient curve, in order to allow us to determine Kc values for any period during the growing period.
- (ii) Calculating the reference evapotranspiration crop Eo using the Penman-Monteith equation (Monteith, 1981) recommended by the FAO (Smith et al , 1992).
- (iii) Calculating Ec as the product of Eo and Kc:

$$Ec = Kc * Eo$$

Changes in vegetation and ground cover mean that the crop coefficient Kc varies during the growing period. The trends in Kc during the growing period are represented in the crop coefficient curve.

In our case, the crop coefficient Kc is determinated for all the vegetation land cover presented in the study area using the Kc values proposed by the ITAP (Instituto Técnico Agronómico Provincial) of Albacete.

In the figure 3 we present the Kc coefficient of the land cover vegetation presented in the study area

(ITAP). The summer and the winter irrigated crops coefficient are determinated by combining the pondered Kc of summer or winter crops. The ponderation depends on the year of study, because it represents the crop surface area in %.

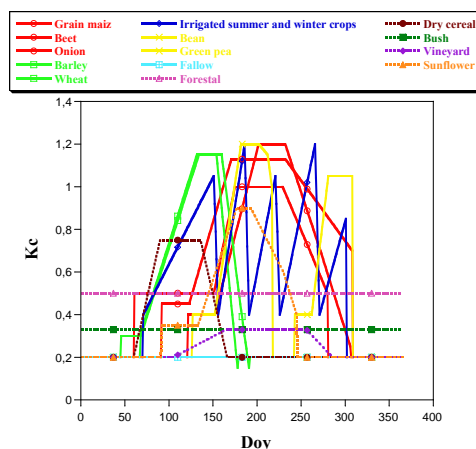


Figure3. Crop coefficient Kc curves for different vegetation land cover presented in the study area (ITAP).

Figure4 shows the crop coefficient Kc curves for different vegetation land cover presented in the study area for 2000.

The Kc coefficient obtained for the irrigated areas are more real than that obtained for the dry crops. Therefore, we assume that the dry crops coefficient Kc is an orientative value, because it overcomes the Kc values which experiment the dry crops in reality.

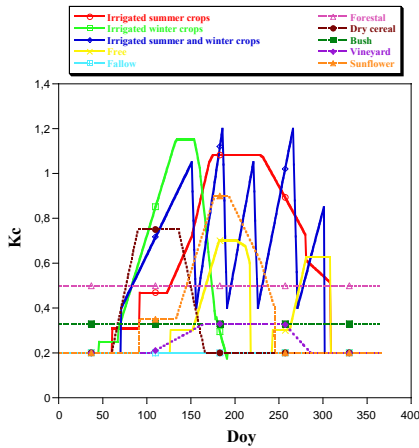


Figure4. Crop coefficient K_c curves for the vegetation land cover presented in the study area for 2000.

As previously commented, the FAO Penman-Monteith method is recommended as the sole E_o method for determining reference evapotranspiration. It is calculated using the following equation:

$$ETo = \frac{0.408\Delta(R_n - G) + g \frac{900}{T + 273} U_2 (e_a - e_d)}{\Delta + g(1 + 0.34U_2)}$$

ETo = reference evapotranspiration (mm day^{-1})

R_n = net radiation at the crop surface ($\text{MJ m}^{-2} \text{day}^{-1}$)

G = soil heat flux density ($\text{MJ m}^{-2} \text{day}^{-1}$)

T = mean daily air temperature at 2 m height ($^{\circ}\text{C}$)

U_2 = wind speed at 2 m height (ms^{-1})

$(e_a - e_d)$ = saturation vapour pressure deficit (KPa)

Δ = slope vapour pressure curve ($\text{Kpa } ^{\circ}\text{C}^{-1}$)

γ = psychrometric constant ($\text{Kpa } ^{\circ}\text{C}^{-1}$)

The E_o values have been obtained using the equation indicated above, where all the parameters are measured at the Barrax site (situated in the west of the province of Albacete). The parameters measurements are acquired with good accuracy and E_o values are considered as constant over the study area.

Then, we have established climatic curves using the reference evapotranspiration data for four years (1997 to 2000).

In the figures 5 and 6 we represent successively the reference crop Evapotranspiration E_o and accumulated E_o climatic curves type obtained by polynomial adjustment of E_o data corresponding to four years (from 1997 to 2000).

The obtained climatic curves for both reference evapotranspiration E_o and accumulated evapotranspiration can be considered as an important input data in order to obtain climatic scenarios of the study area.

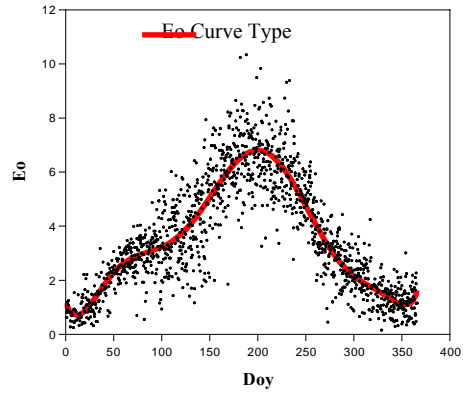


Figure5. Reference crop Evapotranspiration E_o climatic curve type obtained by polynomial adjustment of E_o data corresponding to four years (from 1997 to 2000).

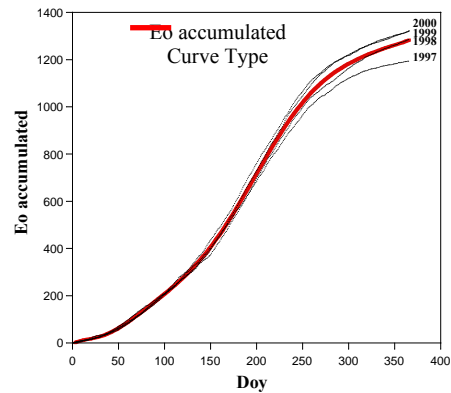


Figure6. Accumulated Reference crop Evapotranspiration E_o curves for four years (1997 to 2000). In red, we present the accumulated E_o climatic curve type obtained by polynomial adjustment of E_o data corresponding to years indicated above.

The accumulated E_o for 1997 to 2000 is 1193 l/m^2 , 1285 l/m^2 , 1319 l/m^2 , 1322 l/m^2 , successively. The E_o variation among four years is about 0.1%. This increase in the accumulated E_o can affect mainly the

irrigated cultivated areas, thus, can be stood out in terms of the crop water requirements.

In the figure 7 we present the accumulated evapotranspiration vegetation cover curves type. To obtain these curves; first, we have obtained the evapotranspiration curves type for each land cover, as multiplication of the crop coefficient of each land cover and the reference evapotranspiration E_o curve type (presented in red in the figure5).

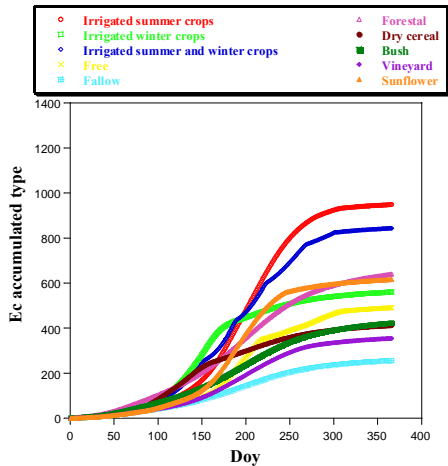


Figure7. Accumulated evapotranspiration vegetation cover curves type.

5 ANALYSIS OF THE DATA CORRESPONDING TO THE YEAR 2000

To carry out this study, we have used the land vegetation cover map obtained for 2000, and the evapotranspiration data also corresponding to the same year.

Some analysis have been made to obtain the evapotranspiration E_c values for each land cover during and outside its phenological development. The total evapotranspiration E_c have been also calculated in order to make an comparative analysis between the vegetation land cover presented in the study area.

Introducing the surface area in ha for each vegetation land cover, we were able to calculate the water consumption in hm^3 and %. The results are presented in the figure 8.

As indicated in the figure 8 (graphic (a)), the dry cereal with fallow present of about 60% of the total surface area. While, irrigated crops and natural vegetation present 22% and 14% successively. Finally, vineyard presents only 5%.

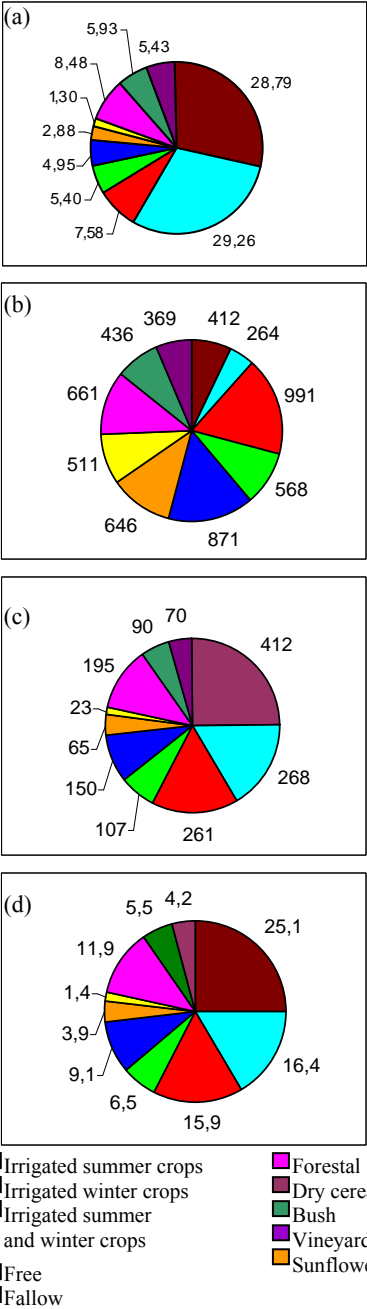


Figure8. Analysis of the evapotranspiration data for 2000. The graphics (a) and (b) represent successively the surface area in % occupied by each vegetation cover in the study area in 2000 and the total land cover evapotranspiration (l/m^2). While graphics (c) and (d) show the total water consumption by each land cover in hm^3 and % successively.

The analysis of the graphics b, c and d points out the following:

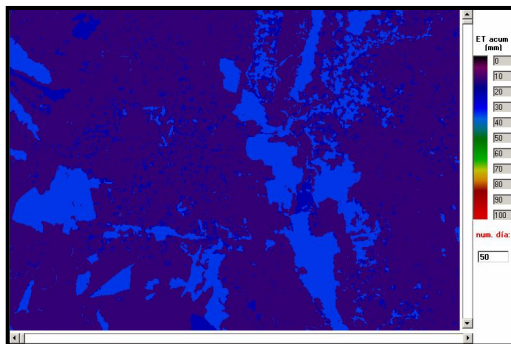
- The total water consumption estimated from the evapotranspiration calculations is 1.640 hm^3 for the total surface area of 347.531 ha .
- The fallow surface presents less consumption with value 264 l/m^2 .
- Comparing the total evapotranspiration of the cultivated zones, vineyards areas is considered as those of smaller consumption, with 369 l/m^2 .
- Considering that fallow and dry cereal present the same crop unity, according to the habitual agricultural practices, we would have an average value of 338 l/m^2 .
- The water consumption of the irrigated areas during its phenological development is of 549 hm^3 .
- Both Vineyard and fallow areas present values of total evapotranspiration of 369 and 338 l/m^2 , similar to the annual precipitations.
- If we suppose that the annual precipitation average is about 400 l/m^2 , we deduce that the annual precipitation value is 1390 hm^3 . Comparing this value with the total E_c of 1640 hm^3 , we obtain an annual deficit of 251 hm^3 .

6 MONITORING SPATIAL DISTRIBUTION OF ACCUMULATED EVAPOTRANSPIRATION CROPS IN ALBACETE AREA AT DIFFERENTS DATES OF THE YEAR 2000

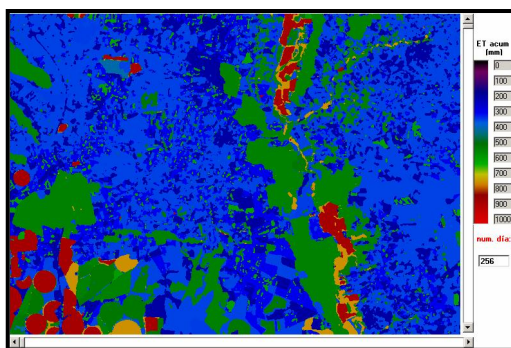
The analysis of the evapotranspiration made previously have allowed to generate maps of the accumulated evapotranspiration data.

For this purpose, we have made program which introduce as input data, the evapotranspiration E_o , the crop coefficient K_c and the land vegetation cover map of the study area. All the input data correspond to the year 2000.

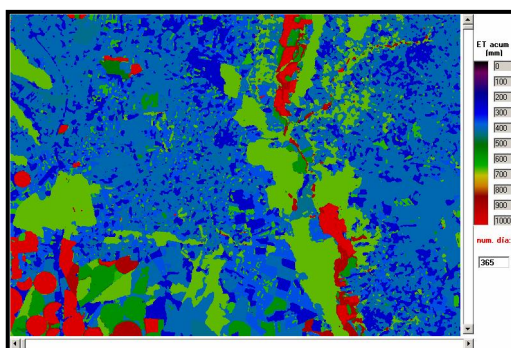
In the figure 9 we present the spatial distribution of the accumulated evapotranspiration crops at three dates of 2000, and which correspond to region of 10000 ha selected from the study area.



(a) February 19th



(b) September 12th



(c) December 30th

Figure9. Spatial distribution of the accumulated evapotranspiration crops at three dates of 2000, and which correspond to region of 10000 ha selected from the study area.

REFERENCES

- Bolle, H. J., (editor), 1997, Desertification processes in the Mediterranean area and their interlinks with the global climate. Sub-grup V: Remote Sensing and Radiometric properties of the surface: Assessment of desertification from space (EV5V-CT93-0284), Final Report. Free University of Berlin.
- Henderson-Sellers, A., and Pitman, A. J., 1992, Land-surface schemes for future climate models: specification, aggregation, and heterogeneity. *J. Geophys. Res.*, 97, 2687-2696.
- IGBP (International Geosphere Biosphere Programme), 1990, The international Geosphere Biosphere Programme: A study of global change, The Initial Core Projects Report No. 12. International council of Scientific Unions, Stockholm, Sweden.
- Itier, B., 1996, Measurement and Estimation of Evapotranspiration. "In: Sustainability of Irrigated Agriculture, edited by Pereira, L. S. et al., NATO ASI Series, 312, 171-191.
- Jensen, M. E., 1994, Adjusting Canopy Resistance in the Penman-Monteith equation. Report submitted to FAO/AGL, Rome.
- Lanjeri, S., 1998, Análisis mediante teledetección de los cambios en el uso agrícola del suelo relacionados con el viñedo en zonas amenazadas de desertificación en Castilla-La Mancha. Doctoral Thesis. Universitat de València.
- Lanjeri, S., Melia, J., and Segarra, D., 2001, A multi-temporal masking classification method for vineyard monitoring in central Spain. *International Journal of Remote Sensing*, 22, 3167-3186.
- Monteith, J. L., 1981, Evaporation and surface temperature. *Quarterly Journal of the Royal Meteorological Society*, 107, 1-27.
- Munyati, C., 2000, Wetland change detection on the Kafue Flats, Zambia, by classification of a multitemporal remote sensing image dataset. *International Journal of Remote Sensing*, 21, 1787-1806.
- Smith, M., Allen, R., and Pereira, L., 1996, Revised FAO Methodology for Crop Water Requirements. Proceedings of the ASAE International Conference on Evapotranspiration and Irrigation. 3-6 November, 1996. San Antonio (Texas). USA.
- Smith, M., Allen, R., Monteith, J. L., Perrier, A., Pereira, L., and Segeren, A., 1992, Report on the Expert Consultation for the Revision of FAO methodologies for the crop water requirements. Land and Water Development Division. FAO. Rome.

ACKNOWLEDGMENTS

We thank the ITAP "Instituto Técnico Agrónomo Provincial de Albacete". Thanks also go to the Spanish Agency of International Cooperation, Institute of Cooperation with the Arab World (AECI-ICMAPD) for their contribution with a grant. This work was supported by the CYCYT project "Evaluación por Teledetección de la incidencia de los cambios de la cubierta vegetal del suelo en los flujos de agua y energía".

Satellite remote sensing of drought conditions and vegetation monitoring in Spain during the period 1987-2001

F. González-Alonso⁽¹⁾, A. Calle⁽²⁾, J.L. Casanova⁽²⁾, A. Romo⁽²⁾ and J.M. Cuevas⁽¹⁾

⁽¹⁾Remote Sensing Laboratory, CIFOR-INIA, Crta. La Coruña km 7, 28040 Madrid, Spain

⁽²⁾LATUV, University of Valladolid, Dpt. Applied Physics I. Faculty of Sciences, 47071 Valladolid, Spain

alonso@inia.es; abel@latuv.uva.es

ABSTRACT- Droughts are a very recurrent phenomenon in Spain which causes severe damages in the agriculture reducing in a very important way the production of cereal crops and natural pastures. The aim of the present work is to carry out a comparative study on the way droughts have affected Spain during the period extending from 1987 to 2001, as deduced by the analysis of images registered by the AVHRR sensor in the NOAA satellite series. The results obtained have been able to evaluate in an objective way the impact caused by the drought in different Spanish regions during the period 1987-2001, revealing how useful the spatial Remote-Sensing can be in these kinds of applications. Taking into account the long period of time comprising the study, the results obtained can be considered quite strong.

1 INTRODUCTION

Drought are a very recurrent phenomenon in Spain which causes severe damages in the agriculture reducing in a very important way the production of cereal crops and natural pastures. With respect to the environment, its consequences are also very significant and highly serious: the presence of droughts has been proved to increase dramatically the number of forest fires as well as the surface affected by them.

Drought are a very complex natural phenomenon for which there is not a universally accepted definition. There are many different definitions, but in general terms, a drought is considered to exist when the rainfall in a determined period of time is inferior to the mean rainfall for the same period of time calculated in a series of reference years.

More specifically, we can talk of a meteorological drought, agricultural drought, hydrological drought and a socio-economic drought depending on the aspect which is highlighted.

Droughts are a natural disaster whose effects are greater today than 30 years ago due to a higher population rate on the Earth, which makes it more vulnerable specially in the underdeveloped and developing countries.

Since 1967, 2,800 million people have suffered the consequences of meteorological disasters according to estimations made by the World Meteorological Association, half of which were affected by droughts.

Between 1967 and 1997, droughts caused the death of 1.3 million people worldwide in a direct or indirect way (Obasi 1994). In the decade of the 90's, droughts affected large areas in Europe, Africa, Australia and

America (North, Central and South). In 1988, a drought caused \$40,000 million worth of losses to the USA economy. During the period 1991-1992, the agricultural production in southern and eastern Africa was the lowest in the whole century affecting 24 million people. In Kajastan, there were also very significant droughts in 1991 and 1995 with losses of over 40% in the production of grain.

Spain is a country specially affected by droughts since between the period 1880-1980 more than half of the years have been classified as dry or very dry. In Spain, during the decade of the 80's, seven years were considered dry or very dry and during the 90's five years have been classified in the same way. According to Agricultural Associations, the losses in the sector caused by droughts were superior to a 9-10⁹ euros during the period 1992-1995.

For more than a decade, several authors have been using remote-sensing techniques to carry out the identification and monitoring of the drought-affected areas on a regional, national and global scale. Results have been quite satisfactory so far. (Tucker and Choudhury 1987, Gutman 1990, Teng 1990, Kogan 1997).

The Remote Sensing Laboratories of the INIA and of the University of Valladolid have been working jointly in the study of drought in Spain through spatial Remote-Sensing techniques since 1996. As a result of this work, a database of NOAA-AVHRR images has been generated consisting of 4,500 images. The aim of the present work is to carry out a comparative study on the way droughts have affected Spain during the period extending from 1987 to 2001, as deduced by the analysis of images registered by the AVHRR sensor in the NOAA satellite series. The methodology

carried out is based upon the following of the evolution of the Normalized Vegetation Index (NDVI), deduced out of the AVHRR images, in the period of time comprising the 1987-2001 study. The results obtained have been able to evaluate in an objective way the impact caused by the drought in different Spanish regions during the period 1987-2001, revealing how useful the spatial Remote-Sensing can be in these kinds of applications. Taking into account the long period of time comprising the study, the results obtained can be considered quite significant. They can be a highly useful reference for a large number of important applications in the subject of forest, agricultural and environmental management (farm insurance, risk of forest fires, etc).

2 METHODOLOGY

Methodology followed to obtain results is:

- Radiometric calibration and atmospheric correction of channels 1 and 2 of the AVHRR sensor.
- Daily determination of the Normalized Difference Vegetation Index (NDVI) calculated from channels 1 and 2.
- Geometric correction of the NDVI's images.
- Generation of the image corresponding to the maximum NDVI value (MNDVI),for each ten –day period from February to September.
- Generation of a multitemporal file for all the ten –day periods with the MNDVI images corresponding to the years 1987-2001.
- Calculation of the ratio between the MNDVI value of every ten days period in the year of study and the mean value of all the corresponding periods of the time serie 1987-2001.
- Expression of the previous ratio as a percentage.

Characterization of the drought incidence for each year of the period 1987-2001 as the mean percentage of all the ten days periods from February-September. Values of this mean percentage below 100 indicate drought conditions (negative anomaly).

3 RESULTS AND CONCLUSIONS

The first result is the analysis of NDVI values during the period 1987-2001. Figure 1 a) shows the averaged NDVI values for 1987-2001 period. More interesting is the regression analysis for all NDVI images. Figure 1 b) shows an slope image of NDVI values for 1987-

2001 period and finally, figure 1 c) shows the yearly increase (in percent) of NDVI referred to 1987

The results achieved, showed in figure 2, show the level of impact caused by drought in the different Spanish regions, in a objective way, during the 1987-2001 period. Particularly the larger part of Spanish territory was affected by the huge drought conditions observed in 1989-1992 period.

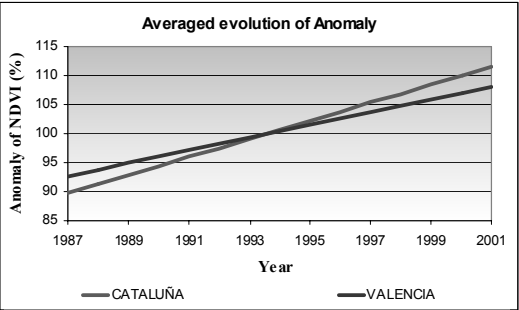


Figure 3. Regression analysis for the two extremes autonomous communities in Spain: Cataluña, the best and Valencia, the worst

	Slope (m)	Correlation (r)
CAST.Y LEON	1.254	0.541
GALICIA	1.368	0.803
NAVARRA	1.414	0.65
ARAGON	1.489	0.642
CATALUÑA	1.554	0.784
VALENCIA	1.093	0.556
ANDALUCIA	1.279	0.595
MURCIA	1.129	0.435
EXTREMAD	1.196	0.564
MADRID	1.221	0.563
LA RIOJA	1.354	0.606
CAST.MANCH	1.286	0.578
BALEARES	1.393	0.606
CANTABRIA	1.182	0.677
ASTURIAS	1.286	0.747
PVASCO	1.25	0.677

Table 1. Regression analysis of anomalies for all autonomous communities in Spain

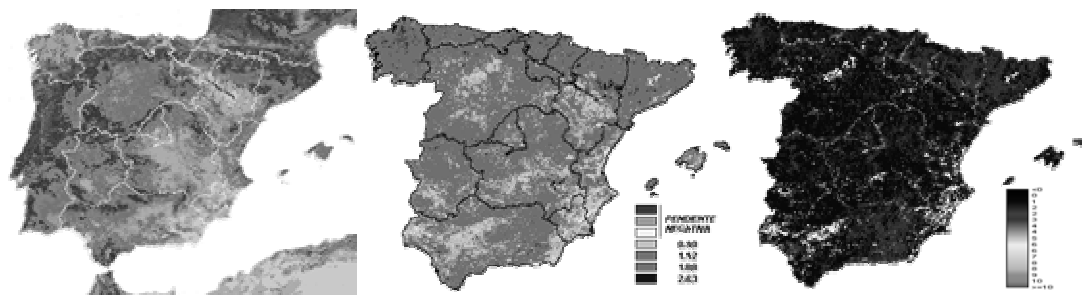


Figure 1. a) Averaged NDVI values for 1987-2001 period; ; b) SLOPE image of NDVI values for 1987-2001 period; c) Yearly increase (%) of NDVI referred to 1987

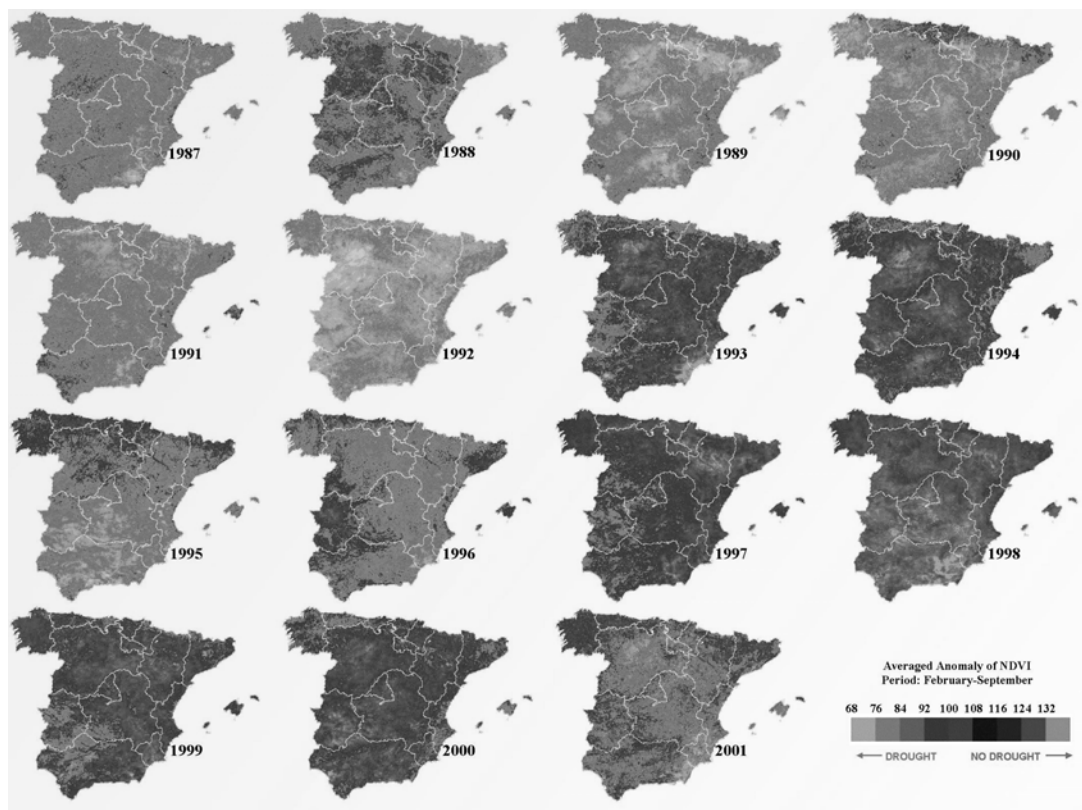


Figure 2. Serie of images of anomaly for Spain, on the period 1987-2001

In a drought trend basis, the regression analysis of the MNDVI anomalies over the analysed period (1987-2001) show a positive evolution in every Spanish region (see table 1).

While the best evolution (higher slope) of MNDVI anomalies was observed in Cataluña region, the one related to Valencia was the worst. Rising temperatures, longer vegetative periods and precipitation increased since 1996, could explain the previous trendy results. This result can be observed on figure 3

The obtaining of remote sensing series of data over longer periods of time, will make it possible to improve the accuracy and strength of this methodology with a view to obtaining a truly effective system for early detection and prevention of drought.

Utilisation of this data base will be useful to carry out the carbon content evaluation into the vegetation cover; control referred to Kyoto Protocol.

4 REFERENCES

- Gutman, G., 1990. Towards monitoring droughts from space. *Journal of Climate*, 2: 282-295.
- Kogan, F.N., 1997. Global drought watch from space. *Bulletin of the American Meteorological Society*, 78: 621-636.
- Obasi, G.O.P., 1994. WMO's Role in the international decade for natural disaster reduction. *Bulletin of the American Meteorological Society*, 75: 1655-1661.
- Teng, W.L. 1990. AVHRR monitoring of U.S. crops during the 1988 drought. *Photogrammetric Engineering and Remote Sensing*, 56: 1143-1146.
- Tucker, C.J. and Choudhury, B.J., 1987. Satellite remote sensing of drought conditions. *Remote Sensing of Environment*, 23: 243-251

Me ora en los to os e re istro e i enes SPOT en n ión e las ara ter sti as el terreno

Martín F.J., Pinilla C. y Ariza F.J.

Grupo de Investigación en Ingeniería Cartográfica.

Universidad de Jaén.

C/ Virgen de la Cabeza, 2. 23071-Jaén. Spain.

cpinilla@ujaen.es

RESUMEN. *Una imagen bruta Spot no es un documento cartográfico debido a las diversas distorsiones que presenta. La corrección geométrica de estas imágenes puede ser abordada mediante dos métodos claramente diferenciados: polinómicos y orbitales. Los desplazamientos acusados debido al relieve invalidan la utilización de polinomios simples en aquellas zonas donde su presencia se pone de manifiesto. En este trabajo se utiliza una imagen Spot de una zona con un amplio rango de altitudes, con el fin de establecer qué polinomios de menor complejidad proporcionan un mejor ajuste y absorben la componente sistemática del error. Además, los resultados de estos métodos son comparados con los resultados de métodos orbitales realizados con software comercial. Se estudia también la influencia del número de puntos de control en el RMS resultante.*

ABSTRACT. *A raw Spot image cannot be considered as a cartographic document because of several distortions. Geometric correction of this images can be approached by means of two main procedures: polynomial methods and parametric methods. Relieve displacements marked, depending on terrain altitude and plot distance to the satellite trace, are not allowed to the use of simples polynomial functions. A Spot image with a wide range of altitude changes has been used in order to develop the less degree polynomial adjustment with the possibility of to absorb the systematic error component. In addition, the polynomial method results are compared versus the orbital method results obtained by means of the ENVI algorithm. The influence of the GCPs number on RMS is also studied.*

Key Words: *register, ground control points -GCPs., check points -CPs., geometric distortions.*

INTRODUCCIÓN

Son numerosas las causas de distorsión en las imágenes orbitales, por ejemplo, las causadas por la oscilación de la plataforma, la rotación y la curvatura terrestre, los desplazamientos debidos al relieve, etc. Los procedimientos de corrección geométrica se engloban en dos grandes grupos: polinómicos y paramétricos u orbitales. En este trabajo se comparan los resultados obtenidos con algunos de dichos métodos cuando el relieve es muy acusado.

Se partió de una imagen Spot pan HRV2 con resolución espacial de 10 m. correspondiente a la zona suroeste de la provincia de Jaén (España), que presenta un amplio rango en altitud, con valores comprendidos entre 190 m. en el valle del Guadalquivir hasta altitudes máximas de 2160 m. en la zona de Sierra Mágina.

Posteriormente se compararon las diferentes imágenes georreferenciadas a través de 100 GCPs. que describían adecuadamente la morfología de la zona y cuyas coordenadas terreno fueron tomadas de la Gerencia Provincial del Catastro (ortofotografías a escala

1:5.000) y del Modelo Digital de Elevaciones DEM20 del Instituto de Cartografía de Andalucía. Previamente se comprobó la calidad posicional de dichas fuentes de información a través de 21 CPs. medidos en campo mediante GPS. Además, estos últimos se utilizaron para comprobar a posteriori la calidad de las diferentes imágenes georreferenciadas tanto para los métodos polinómicos como orbitales. En ambos métodos se abordó la georreferenciación mediante una transformación indirecta.

Con el fin de estudiar el comportamiento del RMS en función del número de GCPs. se redujo la muestra inicial de 100 a 80, 60 y 30 GCPs.

Como aplicación práctica se desarrolló una aplicación en C++ que permite planificar para una determinada zona en el terreno y para una imagen de satélite Spot/Landsat concreta, qué zonas habrán de ser corregidas del efecto del relieve. De esta forma puede conocerse a priori dónde se hace obligado el uso de polinomios complejos que tienen en cuenta el relieve ó correcciones orbitales para llevar a cabo la georreferenciación.

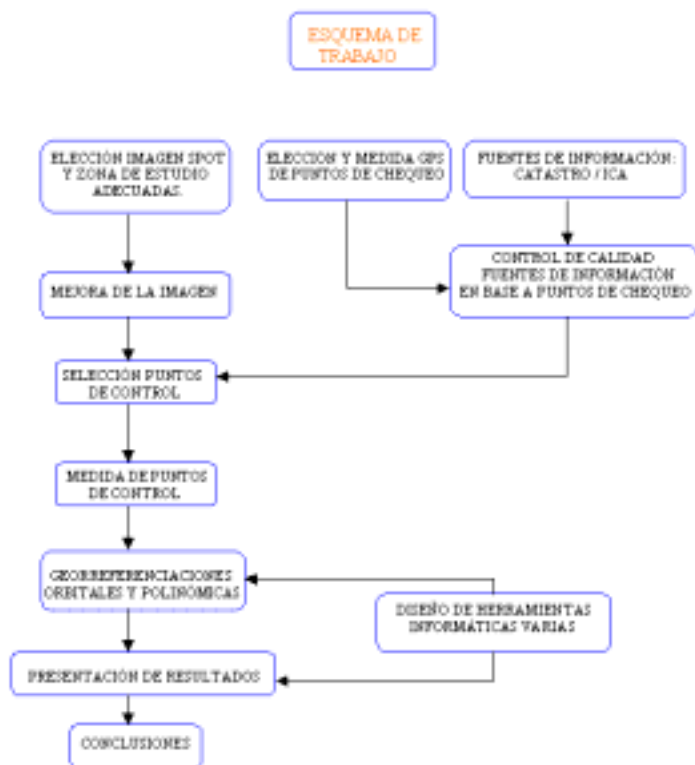


Figura 1.- Esquema de trabajo.

FUNDAMENTOS

Errores geométricos.

Aparte de las distorsiones puramente geométricas de una imagen digital de satélite causadas por la oscilación de la plataforma, la oblicuidad de las líneas debida al tiempo de barrido en los sensores de espejo y otras como la panorámica, este trabajo se centra en las distorsiones geométricas derivadas de la morfología de la superficie. Debido a que las imágenes Spot muestran una perspectiva cilíndrica, será pues a lo largo de cada fila y en sus extremos, donde el efecto será más acusado. Su expresión en el sistema imagen, siempre positiva hacia los extremos de la escena, presentará la siguiente forma:

$$dr_x = \frac{fL^3}{2R(H-z)^2} \approx \frac{fL^3}{2RH^2} \quad (1)$$

donde f es la distancia focal nominal, H es la altitud plataforma, L es la distancia a la línea nadiral, R es el radio terrestre y z es la altitud punto de superficie terrestre

La expresión en el espacio imagen para las columnas se verá, pues, modificada en la forma

$$\begin{aligned} x'_{\text{imagen}} &= x_{\text{imagen}} + dr_x = f_1(a_0, a_1, \dots, a_i, X_T, Y_T, Z_T) \\ y'_{\text{imagen}} &= y_{\text{imagen}} = f_2(b_0, b_1, \dots, b_i, X_T, Y_T, Z_T) \end{aligned} \quad (2)$$

o para transformaciones orbitales:

$$\begin{aligned} x'_{\text{imagen}} &= x_{\text{imagen}} + dr_x = f_1(f, m_{11}(t), \dots, m_{33}(t), X_0(t), Y_0(t), Z_0(t), X_T, Y_T, Z_T) \\ y'_{\text{imagen}} &= y_{\text{imagen}} = f_2(f, m_{21}(t), \dots, m_{33}(t), X_0(t), Y_0(t), Z_0(t), X_T, Y_T, Z_T) \end{aligned} \quad (3)$$

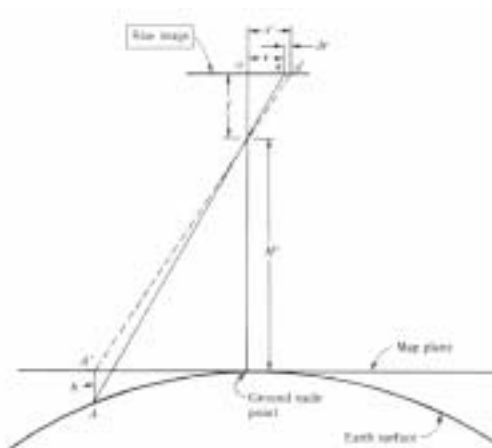


Figura 2.- Efecto de curvatura terrestre para cada fila de la imagen

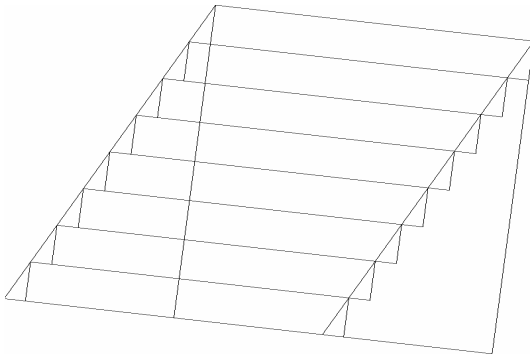


Figura 3.- Adquisición escena Spot bajo Distorsión por rotación terrestre.

En fotografía aérea dicho efecto debe tenerse en cuenta a partir de escalas inferiores a 1/40.000. La

dirección del error es radial y hacia el punto nadiral. En sensores remotos espaciales dicha corrección es muy acusada para NOAA y satélites geoestacionarios, pero en el caso de Spot-pan no ha de tenerse en cuenta. Así, para una distancia máxima mitad del lado de la escena (30 km.) y valores nominales de 832 Km. y 1.082 m. de altura orbital y focal respectivamente, se obtiene un error del orden de 1 μ m, muy por debajo del valor al que habría de tenerse en cuenta (2/3 de la resolución del píxel).

La inclinación orbital Spot es de 8.77° respecto al meridiano local. Las filas de la escena habrían de situarse ortogonales a la línea nadiral al ser éste un sensor de empuje, aunque el efecto de la distorsión por rotación terrestre provoca el efecto de la Figura 3.

En imágenes Landsat debe tenerse en cuenta además el fenómeno de distorsión por oblicuidad según muestra la Figura 4. Para este caso, la dirección de adquisi-

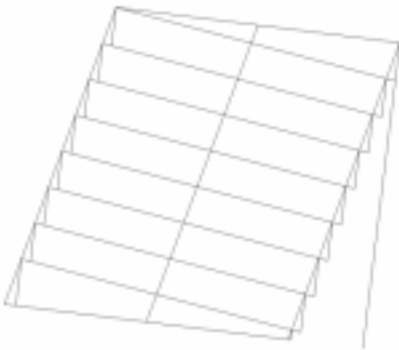


Figura 4.- Adquisición escena Landsat bajo distorsión por rotación terrestre.
ción de cada fila no es ortogonal a la línea nadiral.

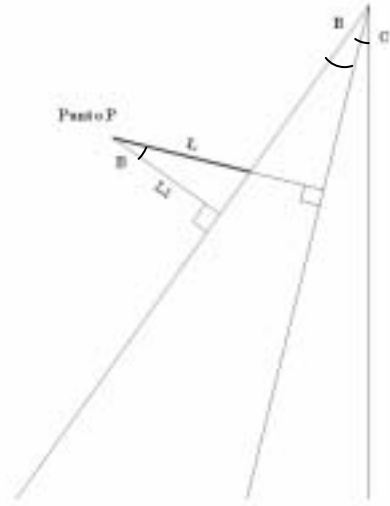


Figura 5.- Cálculo de distancia a la traza para Spot. .B: ángulo de rotación terrestre. C: inclinación orbital. D: Ángulo de distorsión por oblicuidad en el tiempo de barrido.

La expresión simplificada para la distorsión por desplazamiento debido al relieve para un modelo plano

obedece a:

$$dp = \frac{Lz}{H} \quad (4)$$

Las nuevas ecuaciones para la imagen serán de la forma

$$\begin{aligned} x'_{imagen} &= x_{imagen} + dp_x = f_1(a_0, a_1, \dots, a_i, X_T, Y_T, Z_T) \\ y'_{imagen} &= y_{imagen} + dp_y = f_2(b_0, b_1, \dots, b_i, X_T, Y_T, Z_T) \end{aligned} \quad (5)$$

o para transformaciones orbitales

$$\begin{aligned} x'_{imagen} &= x_{imagen} + dp_x = \\ &= f_1(f, m_1(t), \dots, m_{33}(t), X_o(t), Y_o(t), Z_o(t), X_T, Y_T, Z_T) \\ y'_{imagen} &= y_{imagen} + dp_y = \\ &= f_2(f, m_2(t), \dots, m_{33}(t), X_o(t), Y_o(t), Z_o(t), X_T, Y_T, Z_T) \end{aligned} \quad (6)$$

La distancia a la traza para el caso de Spot se puede calcular según la Figura 5 en base a:

$$L = \frac{L_1}{\cos(B)} \quad (7)$$

siendo para Landsat

$$L = \frac{L_1}{\sin(D+B)} \quad (8)$$

Regresión Multilineal.

Los modelos de regresión lineal múltiple tienen por expresión general:

$$= (\text{ }_0 + \text{ }_1 \text{ }_1 + \dots + \text{ }) + \text{e} = \text{ } + \text{e} \quad (9)$$

Realizando un ajuste mínimo-cuadrático se puede deducir fácilmente el siguiente sistema normalizado (Caridad 2000):

$$\begin{pmatrix} \sum \text{ }_{11} & \sum \text{ }_{12} & \dots & \sum \text{ }_{1k} \\ \sum \text{ }_{21} & \sum \text{ }_{22} & \dots & \sum \text{ }_{2k} \\ \vdots & \vdots & \ddots & \vdots \\ \sum \text{ }_{k1} & \sum \text{ }_{k2} & \dots & \sum \text{ }_{kk} \end{pmatrix} \begin{pmatrix} 0 \\ 1 \\ \vdots \\ 1 \end{pmatrix} = \begin{pmatrix} \sum \text{ }_{11} \\ \sum \text{ }_{21} \\ \vdots \\ \sum \text{ }_{k1} \end{pmatrix} \quad (10)$$

(k+1, k+1) (k+1, 1) (k+1, 1)

El coeficiente de determinación para la variable dependiente 3 en función de las independientes 1,2 (k=2) es:

$$R^2_{3/1,2} = \frac{r^2_{13} + r^2_{23} - 2r_{12}r_{13}r_{23}}{1 - r^2_{12}} \quad (11)$$

donde r_{ij} :coeficiente de correlación lineal simple. La expresión para el coeficiente de correlación multilineal es:

$$r = \sqrt{R^2} \quad (12)$$

MATERIALES Y MÉTODOS

Una vez elegida una imagen digital SPOT-Panc HRV2 correspondiente a una zona de trabajo con grandes diferencias de altitud en su orografía se procedió a comprobar la calidad posicional de las fuentes de

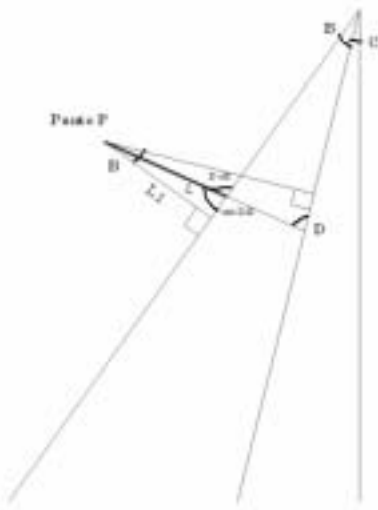


Figura 6.- Cálculo de distancia a la traza para Landsat.

información para la toma de coordenadas-objeto de puntos GCPs., así como para comprobar los errores en las imágenes georreferenciadas tanto en los métodos de corrección polinómicos como orbitales. Para ello se seleccionaron 21 puntos mediante GPS con características heterogéneas atendiendo a distancias respecto a la traza y altitud, y número suficiente como para asegurar la aleatoriedad de la muestra. Se utilizó un método estático relativo partiendo de forma diferencial del vértice de referencia con coordenadas precisas conocidas.

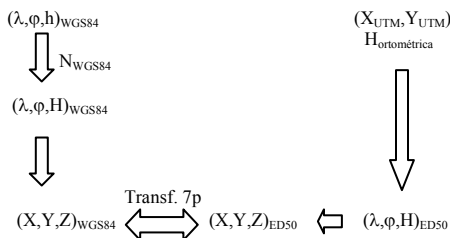
La expresión para el cálculo de la altitud ortométrica (H) obedece a la siguiente expresión

$$H = h - N = h_{WGS84} - N_{WGS84} = h_{ED50} - N_{ED50} \quad (13)$$

en la que tanto la ondulación del Geoide (N) como la altura elipsoidal (h) dependen del elipsoide utilizado.

Para el cálculo de N se utilizó la superficie del Cuasi-geoide correspondiente a la provincia de Jaén (GIL A. J., 2001) caracterizada por una precisión relativa de 1ppm.

El esquema seguido para la obtención de coordenadas objeto en proyección, y puesto que se disponía de la ondulación en el sistema global GPS, fue el siguiente.



Con el propósito de calcular unos parámetros de transformación adaptados a cada zona local, se subdividió la Red Regente en 5 sectores según la Figura 7.

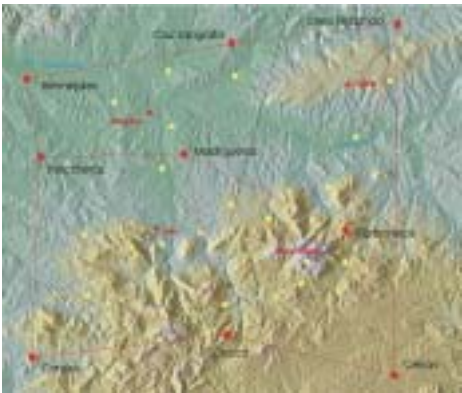


Figura 7.- Distribución en zona de estudio de 21 puntos CPs. (en amarillo) por sectores, para el cálculo de los parámetros de transformación, utilizando los vértices de la Red Regente. C.I.

El error en el sistema global WGS84 se obtiene como componente cuadrática del error de observación GPS y de ondulación. Para la obtención del error en el sistema local ED50 (\mathcal{E}_{wi}) se estudió la propagación de errores en el proceso de transformación, teniendo en cuenta las incertidumbres de los parámetros según:

$$\begin{pmatrix} w_x \\ w_y \\ w_z \end{pmatrix} = \begin{pmatrix} v_x + x_0 \\ v_y + y_0 \\ v_z + z_0 \end{pmatrix} + \begin{pmatrix} K & t_z & -t_y \\ -t_z & K & t_x \\ t_y & -t_x & K \end{pmatrix} \cdot \begin{pmatrix} v_x - X_G \\ v_y - Y_G \\ v_z - Z_G \end{pmatrix} \quad (14)$$

Sin embargo estas incertidumbres no son definitivas. Para estudiar cómo se propaga el error en el paso de coordenadas locales ED50 a proyección UTM se aplican las ecuaciones de transformación a las coordenadas cartesianas ED50 afectadas del error estimado en el apartado anterior. El RMS finalmente obtenido fue de 61.5, 22.5 y 27 cm. en X_{UTM} , Y_{UTM} , H_{ort} respectivamente, en cualquier caso inferiores al metro. Se puede, pues, dar por válida la precisión alcanzada en base a los objetivos perseguidos.

Las fuentes de información elegidas para la toma de coordenadas objeto fueron las ortofotos 1:5.000 pertenecientes a la Gerencia Provincial del Catastro, así como el DEM10 obtenido por interpolación bilineal a partir del DEM20 del Instituto de Cartografía de Andalucía.

La altimetría es tenida en cuenta en base a cómo afecta en las posiciones planimétricas X,Y. De esta forma se plantea qué precisión mínima en altitud será exigible al DEM para que el error en XY no sea apreciable. Para dar respuesta a esta cuestión se estudia la expresión (4) bajo condiciones desfavorables, validando la simplificación del error

$$d(dr) \cong \sqrt{\left(\frac{\partial dr}{\partial L}\right)^2 dL^2 + \left(\frac{\partial dr}{\partial h}\right)^2 dh^2} \quad (15)$$

Aceptando un error máximo de desplazamiento $d(dr)$ de 2/3 del lado del píxel Spot-Panc para las condiciones más desfavorables, se puede obtener el error máximo en altitud del DEM a utilizar:

$$dh = \frac{\sqrt{H^2(d(dr))^2 - h^2 dL^2}}{L} = 194m. \quad (16)$$

El DEM utilizado fue el DEM20-ICA interpolado bilinealmente a 10 m., con un error cuadrático medio altimétrico máximo de 10 m., mucho menor que el límite de 194m. Se puede, pues, afirmar que *a priori* es válido para los fines perseguidos. No obstante habrá de ser ratificado tras un adecuado Control de Calidad.

Se aplicó el Test de Calidad Posicional EMAS (ASPRS 1989) a las 3 componentes X,Y, H_{ortm} por separado, asignando desviaciones históricas de 1/3 del

píxel Spot-pan para X,Y y 10 m. en H_{ortm} , valores superiores a las incertidumbres de nuestras coordenadas terreno tomadas en campo. Previamente a la realización del Test, se comprobaron los supuestos de normalidad y aleatoriedad a través de los Tests de Kolmogorov-Smirnov y Wald-Wolfowitz respectivamente, concluyendo que las fuentes de información utilizadas son válidas con una desviación teórica de 3 m. en X,Y y 10 m. en altitud, valores suficientes para nuestros propósitos.

Para la obtención del fichero de correspondencia se eligieron 100 GCPs. tomándose sus coordenadas objeto de las fuentes de información anteriormente validadas y sus coordenadas imagen a partir del software Envi 3.2. (Figura 8).

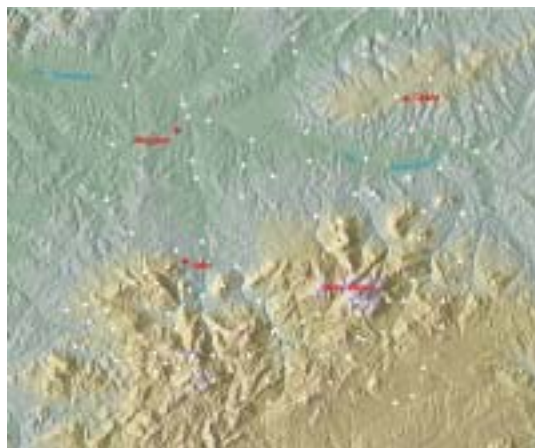


Figura 8.- Elección de 100 GCPs. atendiendo a la morfología del terreno.

A continuación se realizaron las georreferenciaciones polinómicas simples (grado 1,2,3) y polinómicas complejas (teniendo en cuenta el relieve). El polinomio Palà-Pons de grado 1 (Palà V. and Pons X., 1995) se caracteriza por la transformación

$$\begin{aligned} x_i &= [a_0 + a_1 X_T + a_2 Y_T] + a_3 Z_T + a_4 X_T X_T + a_5 Y_T Y_T \\ y_i &= [b_0 + b_1 X_T + b_2 Y_T] + b_3 Z_T \end{aligned} \quad (17)$$

Con el fin de conseguir un mejor modelado se dedujo por extensión el correspondiente polinomio Palà-Pons grado 2:

$$\begin{aligned} x_i &= [a_0 + a_1 X_T + a_2 Y_T + a_3 X_T Y_T + a_4 X_T^2 + a_5 Y_T^2] + a_6 Z_T + \\ &+ a_7 Z_T X_T + a_8 Z_T Y_T + a_9 X_T^2 Y_T + a_{10} X_T Y_T^2 + a_{11} Z_T Y_T^2 \\ y_i &= [b_0 + b_1 X_T + b_2 Y_T + b_3 X_T Y_T + b_4 X_T^2 + b_5 Y_T^2] + b_6 Z_T \end{aligned} \quad (18)$$

Por otro lado se llevó a cabo una georreferenciación orbital utilizando datos coetáneos a la toma de la escena obtenidos a partir del fichero de metainformación asociado a la imagen Spot. Éste proporciona



Figura 9.- Imagen binaria de Desplazamiento debido al relieve en nuestra zona de trabajo y para nuestra imagen Spot concreta.

valores discretos de Posición/Velocidad lineal referidos al sistema geocéntrico del Elipsoide Internacional 1980 así como velocidades angulares (INS) cada 125 ms. con un error estándar de $6.25 \cdot 10^{-5}$ grados/s. La

relación entre el espacio imagen y objeto obedece al modelo de colinealidad de la forma

$$0 = -f \frac{m'_{11}(X_i - X_c^t) + m'_{12}(Y_i - Y_c^t) + m'_{13}(Z_i - Z_c^t)}{m'_{31}(X_i - X_c^t) + m'_{32}(Y_i - Y_c^t) + m'_{33}(Z_i - Z_c^t)} \quad (19)$$

$$S_i y_i = -f \frac{m'_{21}(X_i - X_c^t) + m'_{22}(Y_i - Y_c^t) + m'_{23}(Z_i - Z_c^t)}{m'_{31}(X_i - X_c^t) + m'_{32}(Y_i - Y_c^t) + m'_{33}(Z_i - Z_c^t)}$$

X_i, Y_i, Z_i : coordenadas terreno del punto de control i .
 m'_{11}, \dots, m'_{33} : en función de $\omega^t, \varphi^t, \kappa^t$.

X_c^t, Y_c^t, Z_c^t : parámetros orbitales en el tiempo t .

S : factor de escala para CCD rectangular.

Uno de los modelos de polinomios utilizados (Torbjörn, 1990) para describir las efemérides/orientación a lo largo de la escena obedecen a las expresiones lineales:

$$\begin{aligned} X_c^t &= X_0 + X_1 t & \omega^t &= \omega_0 + \omega_1 t & \varphi &= \varphi_0 + \varphi_1 & \kappa &= \kappa_0 + \kappa_1 \end{aligned} \quad (20)$$

Una vez calculados los coeficientes

$X_0, Y_0, Z_0, X_1, \dots, \kappa_0, \kappa_1$ por ajuste mínimo cuadrático y en función del tiempo dentro de la escena, pueden conocerse los parámetros externos mediante (20) y así poderlos sustituir en (19) para realizar la georreferenciación orbital mediante una transformación inversa. Ésta se llevó a cabo mediante Envi 3.2. y se comprobó la veracidad de dicha georreferenciación mediante la comparación de coordenadas terreno CPs. obtenidas en campo y a partir del ajuste orbital.

Con el fin de extraer conclusiones se implementó en C++ una aplicación para la obtención de una imagen binaria de similares dimensiones y tamaño de píxel al

DEM utilizado, la cual proporciona para una escena concreta Spot/Landsat las zonas (píxeles) que habrán de ser corregidas por el desplazamiento debido a los efectos del relieve, según un umbral de binarización previamente seleccionado (en este caso la resolución espacial Spot) según la Figura 5 y la ecuación (7).

Con el objeto de extraer posibles conclusiones para el sentido de los vectores residuo, se obtuvo una imagen de pendiente unidireccional en la dirección media de éstos. La imagen resultante (Figura 10) es de similares dimensiones y resolución a la del DEM seleccionado

en la que cada píxel contiene el signo y módulo de su pendiente en la dirección anteriormente mencionada.

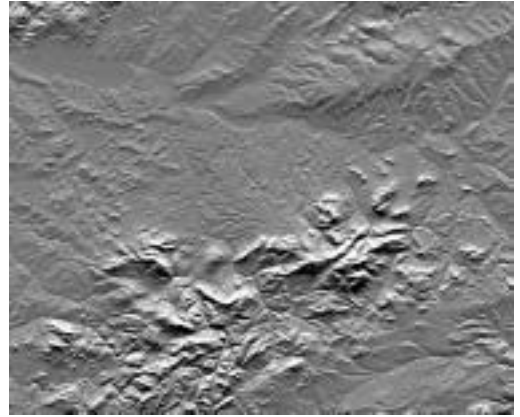


Figura 10.- Mapa de pendiente unidireccional en la dirección media de los vectores residuo grado 1 (349° x+) para nuestra zona de trabajo.

Podremos así obtener los valores para nuestros 100 puntos GCPs. Para su cálculo se utilizó una vecindad 3x3 y la media ponderada entre los 2 píxeles que afectan en el cálculo de cada uno de los extremos de la línea unidireccional.

Nuestro valor de dirección media para los vectores residuo del polinomio grado 1 fue de 349° a partir del eje x positivo, dirección sensiblemente coincidente con la normal a la traza sin rotación terrestre. Esta diferencia se podría atribuir a la componente aleatoria del error.

RESULTADOS Y DISCUSIÓN

Si representamos gráficamente aquellos dos ejemplos que mejor describen la diferencia entre Polinomios simples y complejos, apreciamos para el caso de grado 1 módulos residuales muy superiores a la circunferencia de escalado de radio 10 m. (resolución píxel Spot-pan) según Figura 11. En ella también se representa la imagen binaria (sombreado) debido al desplazamiento por desplazamiento por relieve.

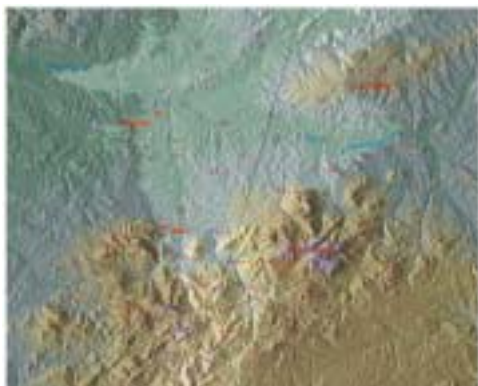


Figura 11.- Representación de residuo polinomio grado 1 junto a línea nadiral e imagen de desplazamiento debido al relieve..



Figura 12.- Representación gráfica de residuo polinomio Palà-Pons grado 1 junto a línea nadiral e imagen de desplazamiento debido al relieve..

En la Figura 12, en cambio, los módulos residuales para el polinomio complejo Palà-Pons grado 1 permanecen por debajo de la misma circunferencia de referencia, caracterizándose sus direcciones por el fenómeno de aleatoriedad.

Los resultados del estudio del RMS a priori en el espacio imagen para ambas componentes x e y por separado son los siguientes:

RMSx (u.píxel)				
	30 GCPs.	60 GCPs.	80 GCPs.	100 GCPs.
g1	5.87	6.21	6.14	5.78
g2	5.46	6.02	5.98	5.72
g3	4.26	5.87	5.84	5.48
PPg1	0.61	0.71	0.72	0.68
PPg2	0.61	0.72	0.73	0.69

RMSy (u. píxel)				
	30 GCPs.	60 GCPs.	80 GCPs.	100 GCPs.
g1	0.57	0.63	0.61	0.61
g2	0.56	0.63	0.61	0.61
g3	0.54	0.6	0.58	0.59
PPg1	0.55	0.58	0.56	0.57
PPg2	0.56	0.58	0.57	0.57

Una vez realizadas las distintas Georreferenciaciones se estudia la desviación estándar entre las coordenadas terreno en éstas y las obtenidas en campo, para los 21 puntos CPs. A su vez los resultados polinómicos se podrán contrastar con los orbitales. Dicha comparación es realizada exclusivamente para aquellas georreferenciaciones más relevantes.

Desv. estándar del error en X (m.)				
GCPs.				
	100	80	60	30
g1	78			80
g2	77			82
PPg1	12			11
Orbital	10	10	11	12

Desv. estándar del error en Y (m.)				
GCPs.				
	100	80	60	30
g1	23			21
g2	22			22
PPg1	10			11
Orbital	9	11	11	12

Pero el sentido para los residuos de los Polinomios simples, como muestra la Figura 11, no presenta un sentido exterior con respecto a la traza como cabría esperar, aunque sí sensiblemente orientados en la dirección perpendicular a ésta. Se decidió, pues, cruzar a la variable residuo las variables altitud, pendiente unidireccional-349° (dirección media de los residuos) y distancia a la línea nadiral, con el fin de vaticinar algún tipo de correlación. Su existencia pone en evidencia que el sentido para dichos residuos no obedece a una toma errónea de puntos GCPs. Dado el comportamiento aleatorio para el caso de Polinomios Complejos el estudio sólo se lleva a cabo para Polinomios Simples.

Se confeccionó así una tabla con los 100 puntos GCPs. cuyas columnas estaban formadas por una variable simple de las mencionadas anteriormente: z (altitud), P (pendiente unidireccional), L (distancia a la

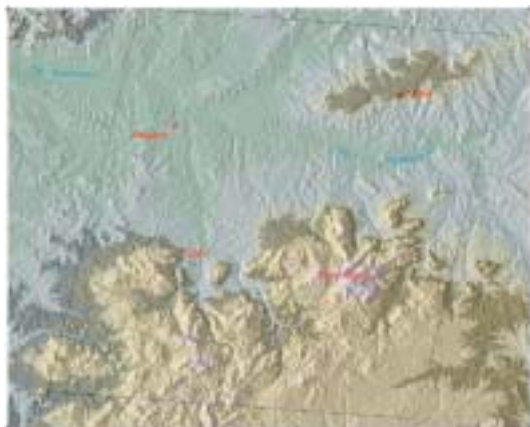


Figura 13.- Zonificación $V=1$ sombreado en negro. Polinomio grado 1.

traza), $Vg1$, $Vg2$ y $Vg3$. Únicamente las variables altitud y residuo presentan correlación lineal simple de alrededor del 70% para grado 1, 2 y 3, apreciándose

píxel. Será en estas zonas donde podremos prescindir de polinomios complejos (Palà-Pons grado 1) ó métodos paramétricos-orbitales. Para llevar a cabo dicha tarea se representó el residuo respecto de la altitud y de la distancia a la traza mediante la primera ecuación de (21) y los coeficientes obtenidos en la correlación multilíneal. Se obtuvo, así, una imagen de zonificación residual para cada polinomio simple de similares dimensiones y resolución al DEM seleccionado. Para su obtención se fue leyendo z del DEM píxel a píxel a la vez que se calculaba la distancia a la traza L , sustituyendo los coeficientes del plano de regresión calculados según cada caso, para así obtener el valor de v para dicho píxel. La imagen binaria así obtenida (Figura 13) tiene una configuración similar para grado 1,2,3 salvo pequeños cerramientos en la zona suroeste. Dicha imagen muestra para qué zonas el módulo del residuo es inferior al píxel.

Como se puede observar, la superficie sombreada de negro en el ejemplo se adapta perfectamente a la morfología del terreno. Además, las zonas más bajas correspondientes al valle del río Guadalquivir, y en contra a lo que cabría esperar, no aparecen como zonas donde se permita la utilización de Polinomios Simples. Esto puede ser debido a que el ajuste es general para toda el área, haciendo que las zonas más altas (parte sur de la zona de estudio) fueren el desplazamiento de las zonas en la que es posible su utilización a altitudes medias y no a las más bajas. Este hecho se pone en evidencia si se calculan numéricamente valores para la distancia a la traza según distintos valores de 1 y -1 en residuo mediante

GRADO 1				
$v=b_0+b_1Z+b_2L$		$Z(m.)$	$L(V=1)$	$L(V=-1)$
		100	-122480	-162287
b_0	8.2716	600	-11221	-51028
b_1	-0.0112	1100	100039	60231
b_2	0.0001	1600	211298	171491
		2100	322557	282750
		2600	433816	394009

correlación multilíneal de la variable residuo respecto a las variables altitud y distancia a la traza, así como altitud y pendiente unidireccional según planos de regresión de la forma

$$v = a_0 + a_1Z + a_2L \quad v = b_0 + b_1Z + b_2P \quad (21)$$

Es conveniente plantearse en qué zonas del ensayo, y para un polinomio simple concreto (grado 1,2,3), el residuo del ajuste global se mantiene por debajo del

$$L = \frac{v - b_0 - b_1Z}{b_2} \quad (22)$$

Como puede observarse, para valores residuales de $V = 1$ y -1 en unidades píxel y para valores de altitud con sentido físico en nuestra imagen Spot (altitudes comprendidas entre 190 y 2160 m.), los valores para la distancia a la traza L (intervalo comprendido entre -30 y 30 km) están comprendidos dentro del intervalo de altitud entre 600 y 1000 m. aproximadamente. Es éste el intervalo de uso teóricamente permitido para polinomios simples.

CONCLUSIONES

1. Como cabría esperar para una toma de coordenadas correcta, las direcciones de los residuos siguen, como pauta general y para el caso de Polinomios simples, una dirección sensiblemente perpendicular a la línea nadiral original (sin corregir del efecto de rotación terrestre). En cuanto a su sentido, los resultados de la correlación multilíneal muestran que alrededor de un 70% de los casos están relacionados directamente con la altitud.
2. El ensayo realizado para el polinomio Palà-Pons grado 2 no aporta una mejora apreciable con respecto al polinomio Palà-Pons grado 1.
4. Para las zonas más bajas de la escena estudiada, el uso de polinomios simples a nivel local es óptimo. Si por el contrario se realiza un ajuste global en un amplio rango de altitudes, las zonas más bajas no aparecen como áreas donde se permita utilizar polinomios simples.

5. Para la dirección "y" el comportamiento es análogo en todos los casos, no siendo así para el caso de la componente "x". Así, para los casos de polinomios simples y al nivel global el valor para RMSx es incluso superior a 5 píxeles, lo cual prohíbe la utilización de dichos polinomios en la escena completa si existen amplios rangos de altitud. Tan sólo son válidos, para permanecer con un error por debajo del píxel, los resultados de los polinomios de Palà-Pons y la corrección orbital rigurosa.

REFERENCIAS

- ASPRS 1989. Accuracy standards for large-scale Line Maps. *PR&RS*, Vol 56, N°7.
- Caridad, J.M. 2000. Estadística Aplicada II. Universidad de Córdoba. Córdoba.
- Chen and Lee. 1993. Rigorous Generation of Digital Orthophotos from SPOT Images. *PE&RS* Vol. 59, No. 5, pp. 655-661.
- Gil, A. J. 2001. A Gravimetric Geoid Computation and Comparison with GPS Results in Northern Andalusia (Spain). *Studia geoph. et geod.* 45, 55-66.
- Palà V. and Pons X. 1995. Incorporation of Relief in Polynomial-Based Geometric Corrections. *PE&RS* Vol. 61, No. 7, pp. 935-944.
- Pinilla, C. 1995. Elementos de Teledetección. RA-MA.. Madrid.
- Poli, D. 2001. Direct georeferencing of multi-line images with a general sensor model ISPRS Workshop "High resolution mapping from space 2001". Hannover.
- Torbjörn, W. 1990. Precision rectification of SPOT imagery. *PE&RS* Vol. 56, No. 2, pp. 247-253.
- Wolf, P. R. 1983. Elements of Photogrammetry. McGraw-Hill. New York.

Comparación de matrices de confusión pixel a pixel mediante el bootstrap

Ariza, F.J., Pinilla, C., García, J.L.
Grupo de Investigación en Ingeniería Cartográfica.
Universidad de Jaén.
C/ Virgen de la Cabeza nº 2, 23071-Jaén (Spain)
fjariza@ujaen.es

RESUMEN. *Este trabajo presenta cómo aplicar la simulación para poder realizar contrastes de hipótesis, celda a celda, entre dos matrices de confusión. Junto con las bases estadísticas del bootstrapping se presenta un ejemplo numérico que permite entender el alcance de los resultados que se pueden obtener con esta metodología.*

ABSTRACT. *This paper presents how the simulation can be applied in order to carry out hypothesis contrasts, pixel to pixel, between two confusion matrices. A numeric example is shown basing on the bootstrapping statistical technique to understand the extent of the results that it can be obtained with this methodology.*

INTRODUCCIÓN

En Teledetección, el análisis de la calidad de los trabajos de clasificación se suele acometer mediante el uso de la matriz de confusión, las cuales presentan una visión general de las asignaciones correctas (en la diagonal) e incorrectas (errores de omisión y comisión, en los valores fuera de la diagonal) (Pinilla, 1995). No obstante, el uso directo de la matriz de confusión tiene algunos inconvenientes, de los cuales, los más destacados pueden ser:

q La matriz es un conjunto de valores, por lo que resulta más cómodo el uso de índices, como el porcentaje de acuerdo "Pa" o el índice de acuerdo "Kappa", que dan una visión global de todo el proceso.

q En caso de querer comparar dos trabajos, el uso de sus respectivas matrices de confusión como base para la comparación no es tarea cómoda.

Respecto al primer inconveniente, poco se puede hacer. La matriz da una visión general que no puede ser sintetizada, sin pérdida de información, por un índice global. La solución común en los trabajos es, pues, acompañar al índice con la matriz y a la matriz con el índice.

El segundo de los inconvenientes señalados muestra, sin embargo, la necesidad de métodos capaces de permitir una comparación más cómoda de matrices de confusión.

En esta última línea, destacan los trabajos de Feinberg y Holland (1970), que proponen el uso normalizado de dichas matrices, lo cual significa que todos los valores

presentes en la matriz se muestran en tantos por uno. Esto presenta ventajas (Hardin, 1997):

q Para todas las clases, los valores presentes en la diagonal dan idea directa de los errores de comisión y omisión dado que tras la normalización las marginales¹, valen la unidad.

q Facilita la labor de comparación de matrices obtenidas por diversos métodos o fuentes (Zhuang, 1992, Congalton, 1998).

q Facilita la comparación, celda a celda, entre distintas matrices.

La normalización consiste en un proceso iterativo de compensación en el que se va consiguiendo el valor unidad en las marginales, tanto en filas como en las columnas. Por este motivo algunos autores denominan el proceso *margfit* (Congalton, 1998) de *marginal fitting*.

Lo ventajoso de la aplicación del método es que las celdas de la matriz así obtenidas son directamente comparables, unas con otras y con otras matrices, y los valores obtenidos fuera de la diagonal dan una mejor idea de los errores de omisión y comisión presentes. En este proceso se modifican los valores de los parámetros de tipo global que se pueden derivar de la matriz (por ejemplo, el porcentaje de acuerdo), pero también de parámetros tradicionales como la exactitud del usuario o del productor.

¹ Las marginales son la suma de todos los elementos de una fila o columna de la matriz de error.

Si bien los valores normalizados son más fáciles de comparar que los valores originales, desgraciadamente no se conoce la función de distribución de los mismos, por lo que no existe método estadístico paramétrico para decidir si existen o no diferencias celda a celda. No obstante, dado que las matrices de error no son en sí mas que un suceso aleatorio, convendría realmente disponer de un número adecuado de matrices de error para poder así derivar conclusiones con significación estadística.

El *bootstrapping* es la técnica estadística adecuada para alcanzar la meta planteada en el párrafo anterior: con un único muestreo —la matriz de confusión con la que se trabaja— se pueden derivar —simular— distintas matrices de confusión, lo que permite estimar las funciones de distribución de los valores presentes en cada una de las celdillas y proceder, de esta forma al análisis de la existencia de diferencias significativas mediante test estadísticos (Hardin, 1997).

En este trabajo se muestran las bases teóricas del *bootstrapping*, la manera de implementarlo en algoritmos sobre matrices de confusión, y un ejemplo de uso que permite aclarar las ventajas de su uso: con todo ello se pretende abrir las puertas a métodos de control de calidad de mayor rigor estadístico y de mayor capacidad de análisis y decisión.

BASES DEL BOOTSTRAPPING

El *Bootstrapping* es un método de Monte Carlo que permite estimar la distribución muestral de un estadístico cuando no existe un estimador paramétrico. Consiste en el remuestreo aleatorio de la muestra original un elevado número de veces, de forma que en cada iteración el estadístico de interés es calculado y almacenado. Así se consigue obtener una aproximación de la distribución, que vendrá dada por la distribución frecuencial del estadístico, y se podrá estimar, por ejemplo, la desviación típica.

El proceso de *Bootstrapping* puede resumirse en los siguientes pasos (Hardin y Shumway, 1997):

q Extraer aleatoriamente una muestra de tamaño n a partir de la población utilizando una estrategia de muestreo apropiada.

q Extraer m muestras aleatorias a partir de la muestra original, siendo m elevado ($m > 200$). Cada muestra también debe ser de tamaño n .

q Determinar el estadístico de interés en cada muestra. Ordenar el conjunto de m valores del estadístico para crear una distribución, que será una aproximación a la distribución muestral del estadístico.

Como se deduce de lo anterior, se trata de un método de simulación que permite el remuestreo. Este proceso requiere poco análisis pero, sin embargo, necesita un

importante esfuerzo computacional, de manera que interviene la simulación para facilitar el cálculo; además, este método es interesante en el análisis de resultados de la simulación (Ríos y Col, 1997). Es una técnica adecuada para el cálculo de errores medios cuadráticos (ECM) como se puede observar en diversas referencias (Ross, 1999; Ríos y Col, 1997).

Veamos su base analítica utilizando el caso del EMC. Sea una muestra A_1, \dots, A_n independiente procedente de una variable aleatoria A con función de distribución de probabilidad F , que depende de un parámetro desconocido q , que se pretende estimar mediante una función dependiente de la muestra $h(a_1, \dots, a_n)$. Para estudiar su bondad como estimador, se calcula su error cuadrático medio según:

$$ECM(F) = E_F[(h(a_1, \dots, a_n) - q_F)^2] \quad (1)$$

Si la distribución F fuera conocida, se podría calcular, sin problemas, el error cuadrático medio, pero dicha distribución es desconocida. Pero cuando el tamaño de la muestra n es grande, la función de distribución F se puede aproximar mediante su función de distribución empírica, definida como:

$$F_n(a) = \frac{\text{número de valores muestrales} \leq a}{n} \quad (2)$$

Entonces, el parámetro $q_{F_n} = q_n$ está próximo a q_F y el $ECM(F)$ se aproxima mediante la técnica de *bootstrap* del error cuadrático medio, dado por:

$$ECM(F_n) = E_{F_n}[(h(a_1^*, \dots, a_n^*) - q_n)^2] \quad (3)$$

donde (a_1^*, \dots, a_n^*) es una muestra aleatoria simple de F_n .

Debido a la construcción de F_n , el vector (a_1^*, \dots, a_n^*) tiene la misma probabilidad de tomar cualquiera de los n^n valores posibles $(a_{i_1}, \dots, a_{i_n})$ para $i_j \in \{1, \dots, n\}$, $j=1, \dots, n$, por lo que:

$$ECM(F_n) = \sum_{i_n} \dots \sum_{i_1} \frac{(h(a_{i_1}, \dots, a_{i_n}) - q_n)^2}{n^n} \quad (4)$$

lo cual necesita la suma de n^n términos, que es imposible para n grande.

Pero se puede calcular el promedio de un gran número de términos mediante simulación, generando n variables aleatorias independientes $(a_{1_i}^*, \dots, a_{n_i}^*)$ cada una con distribución F_n , y después calcular:

$$b_i = \left[h(a_{i_1}^*, \dots, a_{i_n}^*) - q_n \right]^2 \quad (5)$$

De esta forma, se repite el proceso, hasta obtener las variables b_1, \dots, b_r ($r=100$ se suele considerar suficiente para obtener una buena aproximación). Entonces, se puede estimar el error cuadrático medio mediante el promedio de las variables b :

$$E\hat{CM}(F_n) = \frac{\sum_{i=1}^r b_i}{r} \quad (6)$$

BOOTSTRAPPING APLICADO A LAS MATRICES DE CONFUSIÓN

Como se ha explicado anteriormente, el disponer de los valores normalizados de la matriz de confusión facilita la comparación celda a celda. Sin embargo, dado que no se conoce la función de distribución de los mismos, no existe método estadístico paramétrico para decidir si las diferencias existentes son estadísticamente significativas (Ariza, 2002; Hardin y Shumway, 1997), por lo que el usuario queda limitado a la inspección visual.

La utilidad de la aplicación del método de bootstrapping a las matrices de confusión reside en la posibilidad de estimar la distribución de cada una de las celdas, con lo que ya se pueden contrastar posteriormente hipótesis estadísticas que permitan saber si es significativa la diferencia entre una misma celda en dos matrices diferentes.

El proceso a aplicar para una determinada celda de la matriz sería el siguiente:

A) Obtener la matriz de confusión procedente de la elaboración de cartografía temática, utilizando una técnica de muestreo apropiada (ver ejemplo en Tabla 1).

Tabla 1.- Ejemplo de matriz de confusión

	1	2	3
1	4	1	2
2	1	5	0
3	2	1	3

B) Convertir la matriz de confusión en una lista donde el número de elementos es igual a n . Cada celda de la matriz introduce en la lista tantos elementos como el valor de la celda. Cada elemento debe tener asociado un indicador de la fila y columna a la que pertenece en la matriz de confusión (ver ejemplo en Tabla 2 donde cada elemento de la lista es de la forma fila-columna).

C) Extraer una muestra aleatoria con reemplazo de tamaño n de la lista y construir una nueva matriz de confusión sirviéndose de los indicadores de fila y columna.

D) Aplicar a la matriz el método de pseudoceros (Feinberg y Holland, 1970).

E) Normalizar la matriz usando el método de Feinberg y Holland (1970).

F) Guardar el valor de la celda.

G) Repetir los pasos C a F m veces, siendo m un número lo suficientemente elevado.

H) Ordenar los valores almacenados de la celda para construir el histograma de frecuencias, que será la estimación de la distribución.

I) Contrastar la normalidad de la distribución estimada.

J) Estimar la desviación típica de la celda.

Una vez se conocen las desviaciones típicas en dos celdas de dos matrices que se pretende comparar, se puede aplicar un contraste de hipótesis de igualdad de valores:

$$Z = \frac{x_{i,j_1} - x_{i,j_2}}{\sqrt{\hat{S}_{i,j_1}^2 + \hat{S}_{i,j_2}^2}} \quad (7)$$

siendo:

Z el estadístico para contrastar la hipótesis.

x_{i,j_1} el valor original de la celda (i,j) en la matriz 1.

x_{i,j_2} el valor original de la celda (i,j) en la matriz 2.

\hat{S}_{i,j_1}^2 la desviación típica estimada para la celda (i,j) en la matriz 1.

\hat{S}_{i,j_2}^2 la desviación típica estimada para la celda (i,j) en la matriz 1.

EJEMPLO DE APLICACIÓN

Se va a considerar la existencia de tres matrices de confusión (Tabla 3) relativas a una misma situación pero que proceden de tres trabajos de control distintos. La calidad global de cada trabajo puede estimarse mediante el Porcentaje de Acuerdo (ver última fila Tabla 3). De esta forma, el estudio de la similitud estadística de los niveles de calidad alcanzados en los trabajos puede realizarse utilizando este índice y planteando un contraste de hipótesis para verificar si el comportamiento global de las tres matrices es similar, dos a dos. La Tabla 4 presenta el resultado de este análisis.

Lo apuntado hasta ahora supone una aproximación global al problema cuando el Bootstrapping permite, justamente, descender a nivel de lo que ocurre en cada celda. La simple observación de las matrices (Tabla 3) nos permite afirmar que los Casos A y B son bastante similares en cuanto a los valores numéricos que se presentan en las celdas; sin embargo, la matriz correspondiente al Caso C presenta en sus celdillas, respecto a los Casos A y B, una variación de valores sensible-

mente mayor que la observada en la comparación anterior. Conviene advertir que, en este caso, la apreciación anterior se puede realizar cómodamente dado que las tres matrices que se presentan (Tabla 3) tienen en sus celdillas valores en un mismo orden de magnitud, en caso contrario, la normalización de las matrices podría ser una técnica útil de comparación celda a celda

Tabla 2.- Matriz de confusión de la Tabla 1 en forma de lista																	
1-1	1-1	1-1	1-1	1-2	1-3	1-3	2-1	2-2	2-2	2-2	2-2	2-2	2-2	3-1	3-1	3-2	3-3

Tabla 3.- Matrices de confusión relativas a XXX																				
Caso A: Matriz Original							Caso B: Matriz con poca variación							Caso C: Matriz con mucha variación						
326	10	0	0	3	80	0	326	10	0	0	2	80	0	296	9	0	1	2	80	0
18	805	0	0	70	150	5	18	813	0	0	71	148	5	16	813	2	0	74	144	5
0	0	51	1	0	0	0	0	0	49	1	0	0	0	0	0	45	1	1	0	0
0	4	0	3	0	1	5	0	4	0	3	0	1	5	1	4	1	3	0	7	5
3	99	1	0	210	0	0	3	100	2	0	209	0	0	0	110	4	0	215	0	0
70	127	0	3	30	555	0	70	118	0	4	30	555	0	103	106	0	4	20	554	0
1	2	0	5	1	0	3	1	2	0	5	1	0	3	2	4	0	4	1	0	2

Tabla 4.- Igualdad estadística de los comportamientos globales de tres matrices de confusión			
	Caso A	Caso B	Caso C
Caso A	---		
Caso B		---	
Caso C			---
Contraste de hipótesis:			
o	so		so
	so	1	so
Nivel de significación $\alpha = 5\%$ ($Z_{\text{tabla}} = 1,96$)			

Tabla 5.- Matriz normalizada (Caso A: Original)						
0,8265	0,0146	0,0006	0,0001	0,0094	0,1486	0,0002
0,0277	0,6386	0,0008	0,0002	0,1195	0,1626	0,0505
0,0001	0,0002	0,9778	0,0221	0,0001	0,0002	0,0000
0,0002	0,0376	0,0001	0,3548	0,0001	0,0129	0,5942
0,0106	0,1755	0,0199	0,0001	0,7927	0,0010	0,0002
0,1175	0,1147	0,0007	0,0341	0,0582	0,6745	0,0002
0,0175	0,0188	0,0001	0,5885	0,0200	0,0002	0,3548
Pa = 65.99; Sigma Pa = 0.03206						

Tabla 6.- Matriz normalizada (Caso B: poca variación)						
0,8273	0,0148	0,0004	0,0001	0,0067	0,1504	0,0001
0,0271	0,6430	0,0006	0,0002	0,1234	0,1593	0,0464
0,0002	0,0002	0,9707	0,0286	0,0001	0,0002	0,0000
0,0002	0,0409	0,0001	0,3488	0,0002	0,0140	0,5959
0,0102	0,1733	0,0277	0,0001	0,7876	0,0010	0,0001
0,1162	0,1072	0,0005	0,0413	0,0597	0,6749	0,0002
0,0188	0,0205	0,0001	0,5808	0,0223	0,0002	0,3572
Pa = 65.85; Sigma Pa = 0.03212						

Tabla 7.- Matriz normalizada (Caso C: mucha variación)

0,7841	0,0165	0,0003	0,0253	0,0084	0,1652	0,0002
0,0203	0,6348	0,0080	0,0003	0,1302	0,1365	0,0699
0,0002	0,0004	0,9272	0,0621	0,0097	0,0003	0,0001
0,0103	0,0265	0,0321	0,2896	0,0002	0,0555	0,5858
0,0006	0,1802	0,0321	0,0002	0,7859	0,0009	0,0002
0,1544	0,1030	0,0003	0,0567	0,0439	0,6414	0,0003
0,0300	0,0387	0,0001	0,5659	0,0217	0,0002	0,3435

Pa = 62.95, Sigma Pa = 0.03332

Tabla 8.a.- Matriz de Valores medios del Caso A

0,8258	0,0139	0,0000	0,0000	0,0096	0,1507	0,0000
0,0269	0,6402	0,0000	0,0000	0,1199	0,1620	0,0509
0,0000	0,0000	0,9709	0,0292	0,0000	0,0000	0,0000
0,0000	0,0371	0,0000	0,3544	0,0000	0,0143	0,5942
0,0103	0,1737	0,0291	0,0000	0,7869	0,0000	0,0000
0,1137	0,1135	0,0000	0,0411	0,0575	0,6730	0,0012
0,0233	0,0217	0,0000	0,5752	0,0261	0,0000	0,3537

Tabla 8.b.- Matriz de desviaciones típicas del Caso A

0,0017	0,0004	0,0000	0,0000	0,0007	0,0015	0,0000
0,0005	0,0026	0,0000	0,0000	0,0015	0,0016	0,0030
0,0000	0,0000	0,0028	0,0027	0,0000	0,0000	0,0000
0,0000	0,0025	0,0000	0,0151	0,0000	0,0025	0,0141
0,0006	0,0020	0,0028	0,0000	0,0026	0,0000	0,0000
0,0012	0,0011	0,0000	0,0022	0,0006	0,0024	0,0010
0,0024	0,0021	0,0000	0,0148	0,0036	0,0000	0,0155

Tabla 9.a.- Matriz de Valores medios del Caso B

0,8256	0,0144	0,0001	0,0000	0,0061	0,1536	0,0002
0,0258	0,6439	0,0006	0,0006	0,1196	0,1559	0,0536
0,0000	0,0001	0,9487	0,0473	0,0029	0,0009	0,0001
0,0005	0,0370	0,0268	0,3325	0,0006	0,0159	0,5866
0,0093	0,1770	0,0235	0,0000	0,7889	0,0000	0,0013
0,1128	0,1086	0,0003	0,0445	0,0587	0,6736	0,0015
0,0261	0,0190	0,0000	0,5751	0,0232	0,0000	0,3567

Tabla 9.b.- Matriz de desviaciones típicas del Caso B

0,0019	0,0005	0,0003	0,0000	0,0006	0,0019	0,0007
0,0006	0,0027	0,0006	0,0008	0,0019	0,0016	0,0038
0,0001	0,0002	0,0052	0,0052	0,0010	0,0004	0,0007
0,0009	0,0029	0,0060	0,0195	0,0011	0,0020	0,0195
0,0007	0,0026	0,0028	0,0000	0,0024	0,0001	0,0018
0,0018	0,0012	0,0004	0,0022	0,0010	0,0022	0,0011
0,0033	0,0021	0,0000	0,0190	0,0034	0,0000	0,0200

Tabla 10.a.- Matriz de valores medios del Caso C

0,7913	0,0174	0,0001	0,0157	0,0081	0,1665	0,0009
0,0199	0,6369	0,0095	0,0003	0,1334	0,1349	0,0651
0,0000	0,0003	0,9225	0,0680	0,0081	0,0000	0,0011
0,0100	0,0301	0,0301	0,3003	0,0000	0,0601	0,5693
0,0001	0,1743	0,0364	0,0000	0,7873	0,0000	0,0018
0,1519	0,1025	0,0002	0,0541	0,0466	0,6385	0,0062
0,0267	0,0383	0,0011	0,5616	0,0166	0,0000	0,3556

Tabla 10.b.- Matriz de desviaciones típicas del Caso C						
0,0024	0,0009	0,0003	0,0037	0,0010	0,0019	0,0016
0,0006	0,0022	0,0024	0,0005	0,0023	0,0029	0,0037
0,0000	0,0003	0,0096	0,0092	0,0015	0,0000	0,0024
0,0018	0,0027	0,0075	0,0191	0,0000	0,0042	0,0175
0,0002	0,0023	0,0026	0,0000	0,0024	0,0000	0,0020
0,0015	0,0019	0,0004	0,0035	0,0017	0,0025	0,0020
0,0022	0,0043	0,0025	0,0170	0,0045	0,0000	0,0182

Las Tablas 5, 6 y 7 presentan los resultados de la normalización de las matrices correspondientes a los tres casos bajo consideración. El proceso se ha realizado con el programa CTem (Ariza y Col, 2002) mediante un proceso de 100 iteraciones). Mediante esta técnica todas las celdas presentan ya valores en el intervalo [0, 1] y de esta forma resulta bien fácil la comparación, vis a vis, de una celda *i,j* de un trabajo con la misma celda *i,j* de otro trabajo. Si los valores de las celdas de las matrices que se presentan en las Tablas 5, 6 y 7 se multiplican por 100, las diferencias entre ellos son tantos por ciento de discrepancia entre los trabajos para esa posición *i,j* de la matriz. Por ejemplo, para la celda *i=1; j=1*, se tiene:

Diferencia Caso A/Caso B: 82,65 - 82,73 = -0.008 %

Diferencia Caso A/Caso C: 82,65 - 78,41 = 4.24 %

Diferencia Caso B/Caso C: 82,73 - 78.41 = 4.32 %

Las Tablas 8a y 8b; 9ª y 9b; 10ª y 10b presentan los resultados del bootstrapping cuando se aplica a las matrices normalizadas (Tablas 5, 6 y 7) con un número de iteraciones en el bootstrap de 50. Al igual que en el caso anterior, el proceso se ha realizado con el programa CTem. Como se observa, aquí se presentan parejas de tablas pues se muestran los valores medios y las desviaciones de cada celda.

Dado que las Tablas 8, 9 y 10 caracterizan estadísticamente el comportamiento de cada celda, se puede plantear una comparación celda a celda. Esto es lo que se ha realizado en las Tablas 11, 12 y 13. Cada una de ellas representa el valor del estadístico calculado según la ecuación 7 anterior.

Se puede plantear el siguiente contraste para cada pareja de celdas de igual índice entre cada una de las Tablas 8, 9 y 10:

$$H_0: a_{ij} - a'_{ij} = 0; (a_{ij} = a'_{ij})$$

$$H_1: a_{ij} - a'_{ij} \neq 0;$$

Tomando un nivel de significación $\alpha = 5\%$, en este caso el test es a dos colas, por lo que la regla de decisión es: H_0 se rechaza si $Z^3/|Z_{a2}| = 1,96$. Las Tablas 11, 12 y 13 presentan en colores el resultado de este contraste:

- Color verde: supone un comportamiento similar.
- Color rojo: supone que no existe un comportamiento similar desde un punto de vista estadístico.
- Sin color: no se puede decir nada.

El simple análisis visual de las Tablas 11, 12 y 13 es claro en cuanto a la similitud estadística, celda a celda, de las matrices de confusión que se presentan en la Tabla 3, en las Tablas 4, 5 y 6 de manera normalizada, cuando se comparan dos a dos.

Aquí no cabe ya la intuición del intérprete, ahora si el valor que aparece en cada celda, $Z_{observado}$ de las matrices presentadas en las Tablas 11, 12 y 13 supera el umbral marcado por el estadístico correspondiente al nivel de significación, $Z_{observado}^3 \geq 1,96 = |Z_{0,025}|$, se puede considerar que $a_{ij} \neq a'_{ij}$. En este caso el valor representado en las celdas a_{ij} del las matrices de las Tablas 11, 12 y 13 son valores absolutos, pero su inclusión con signo podrían servir para aportar mayor información sobre los problemas de desajuste que existen entre las matrices que se comparan.

Tabla 11.- Valor del estadístico para la diferencias entre los Casos A y B						
0,0784	0,7809	0,3333	--	3,7963	1,1980	0,2857
1,4084	0,9871	1,0000	0,7500	0,1239	2,6958	0,5577
0,0000	0,5000	3,7589	3,0892	2,9000	2,2500	0,1429
0,5556	0,0261	4,4667	0,8880	0,5455	0,4998	0,3158
1,0847	1,0060	1,4142	--	0,5652	0,0000	0,7222
0,4160	3,0100	0,7500	1,0928	1,0290	0,1843	0,2018
0,6862	0,9091	--	0,0042	0,5856	--	0,1186

Tabla 12.- Valor del estadístico para la diferencias entre los Casos A y C						
11,7304	3,5537	0,3333	4,2432	1,2288	6,5269	0,5625
8,9626	0,9689	3,9583	0,6000	4,9164	8,1821	2,9811
--	1,0000	4,8400	4,0467	5,4000	--	0,4583
5,5556	1,9023	4,0133	2,2220	--	9,3704	1,1080
16,1276	0,1969	1,9105	--	0,1130	--	0,9000
19,8861	5,0104	0,5000	3,1447	6,0462	9,9551	2,2361
1,0443	3,4689	0,4400	0,6034	1,6485	--	0,0795

Tabla 13.- Valor del estadístico para la diferencias entre los Casos B y C						
11,2053	2,9139	0,0000	4,2432	1,7150	4,8009	0,4008
6,9532	2,0099	3,5976	0,3180	4,6258	6,3404	2,1683
0,0000	0,5547	2,3997	1,9588	2,8844	2,2500	0,4000
4,7206	1,7414	0,3436	1,1797	0,5455	9,5015	0,6603
12,6372	0,7778	3,3761	--	0,4714	0,0000	0,1858
16,6875	2,7145	0,1768	2,3222	6,1349	10,5400	2,0591
0,1513	4,0331	0,4400	0,5295	1,1702	--	0,0407

CONCLUSIONES

En esta trabajo se ha presentado una metodología de aplicación de las técnicas de bootstrapping para la mejora en los análisis basados en celdas de la matriz de confusión. Junto a la metodología anterior se ha desarrollado un caso numérico para ejemplizar, de una forma muy simple, los resultados y aportación que se obtienen con el método propuesto.

Los contrastes de hipótesis planteados en el ejemplo numérico lo son para celdas de iguales índices i, j de dos matrices de confusión distintas, pero el bootstrapping puede también servir para plantear hipótesis sobre cotas a valores suma en los errores de omisión/comisión de una matriz dada y cualquiera otra hipótesis estadística que se quiera probar tomando como base los valores medios y desviaciones calculados. Esto da una gran flexibilidad en el uso práctico del método.

Las matrices de valores medios, desviaciones derivadas del bootstrap y los resultados de los contrastes de hipótesis no han de considerarse como los elementos únicos en un análisis en el que se comparen dos matrices de confusión, más bien deben entenderse como elementos cuantitativos que permiten entender y apoyar otras hipótesis más generales sobre la realización del trabajo y del comportamientos de clases particulares.

Desde un punto de vista operativo, la simulación que supone el bootstrap no suele estar incorporada en ningún programa de teledetección ni de análisis estadístico (p.e. SPSS, StatGraphics, etc.) pero su programación es bastante inmediata.

BIBLIOGRAFÍA

- Ariza, F.J. 2002. *Calidad en Producción Cartográfica*. Ed Ra-Ma, Madrid.
- Ariza, F.J.; García, J.L.; Atkinson, A. 2002. *Ctem: Control de Calidad Temática*.
- Congalton, R.; Green, K. 1998. *Assesing the accuracy of remotely sensed data: Principles and Practices*. Lewis Publishers.
- Feinberg, S. E; Holland 1970. An iterative procedure for estimation in contingency tables. *Annals of Mathematical Statistics*, 42(3).
- Hardin, P. 1997. Statistical significance and normalized confusion matrices. *Photogrammetric Engineering & Remote Sensing*, 63(6).
- Pinilla, C. 1995. *Elementos de Teledetección*. Ed. Ra-Ma, Madrid.
- Ríos, D.; Ríos, S., Martín, J. 1997. *Simulación, métodos y aplicaciones*. Ed Ra-Ma, Madrid.
- Ross, S. 1999. *Simulación* (2ª Edición). Pearson-Prentice Hall. México.
- Zhenkul, M. 1995. Tau Coefficients for Accuracy Assessment of Classification of Remote Sensing Data. *Photogrammetric Engineering and Remote Sensing*, 61(4): 435-439.
- Zhuang, M. 1992. Accuracy of Spatial Data Used in Geographic Information Systems. *Photogrammetric Engineering and Remote Sensing*, 58(6): 835-841.

A simple model to estimate reference evapotranspiration from satellite data in the Azul River basin, Buenos Aires, Argentina

R. Rivas^{1,2}, V. Caselles², E. Valor²

¹ Instituto de Hidrología de Llanuras, CIC-Univ. Nacional del Centro de Buenos Aires, Argentina, rrivas@faa.unicen.edu.ar

² Departamento de Termodinámica, Facultad de Física, Universidad de Valencia, España, vicente.caselles@uv.es

ABSTRACT: A simple model to obtain the reference evapotranspiration (ET_o) from NOAA-AHVR data is exposed. The model is based on the following linear relationship:

$$ET_o = a \cdot T_s + b$$

where ET_o (mm day^{-1}), T_s is the surface temperature ($^{\circ}\text{C}$), and a ($\text{mm day}^{-1} \text{ } ^{\circ}\text{C}^{-1}$) and b (mm day^{-1}) are specific parameters of the study area.

The proposed model was applied to the Azul river basin, located at the centre of the Buenos Aires province, Argentina. A total of 58 NOAA-AVHRR images were used to get T_s . Values for the a and b parameters were obtained from the T_s and ET_o data at the reference meteorological station, given all image available and a linear fit using least squares. A coefficient determination (r^2) between T_s and ET_o of 0,86 was obtained. The proposed model was applied to a series of weekly T_s images. Finally, the values measured in the meteorological station (Azul station) were compared with the results obtained from the application of the model.

INTRODUCTION

This paper aims at assessing the spatial variation of ET in an area of scarce data. A linear model that combines remote sensing data with the Penman-Monteith evapotranspiration equation was used to estimate ET_o at the pixel level.

The model requires to have available enough meteorological information to compute ET with the Penman-Monteith equation (Allen et al., 1998), as well as series of T_s images to adjust its parameters.

METHODOLOGY

The model is based on the following linear relationship:

$$ET_o = a \cdot T_s + b \quad (1)$$

where ET_o (mm day^{-1}), T_s is the surface temperature ($^{\circ}\text{C}$), and the a ($\text{mm day}^{-1} \text{ } ^{\circ}\text{C}^{-1}$) and b (mm day^{-1}) are parameters specific of the study area.

The estimation of the ET_o (mm day^{-1}) was done by employing the Penman-Monteith-FAO equation (Allen et al., 1998). T_s has been calculated using the quadratic split window equation proposed by Coll and Caselles (1997), that accounts for the difference in bands 4 and 5 of the AVHRR-NOAA sensor.

Values for a and b parameters were obtained from the $T_s - ET_o$ data at the reference weather station, given all the images available and a linear fit using least squares.

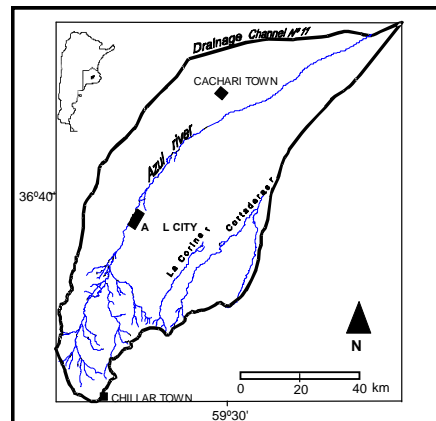


Figura 1: Location of study area.

The study area corresponds to the Azul River basin, located at the centre of Buenos Aires Province, Argentina (Figure 1). It covers about 6.000 km^2 . Essentially a flat-land landscape with the mean regional slope is less than 1 %, even reaching values as low as 0,2 % at the northern portion. The climate is humid, with low to null water deficit, a mean annual precipitation of 950 mm and a mean annual ET of 915 mm (Varni et al., 1999).

RESULTS

Figure 2 shows the linear fit of $T_s - ET_o$ values and a and b parameters obtained. The fit is acceptable ($r^2 = 0,88$), with an estimation error of $\pm 0,6 \text{ mm day}^{-1}$ (17 W m^{-2}).

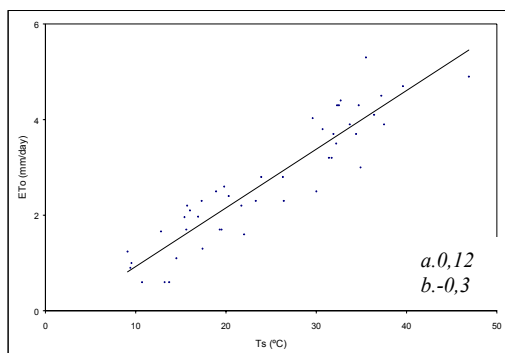


Figure 2. Linear fit of T_s - ET_0 data.

The following equation contains the a and b parameters coming from the linear fitting of the points in Figure 2 (using least-squares):

$$ET_0 = 0,12 \cdot T_s - 0,3 \quad (2)$$

The proposed model (equation 2) was applied to a series of weekly T_s images from 1992 to 1996. Figure 3 shows the results for period December to April 1993. Table 1 show the results measured in the Azul station and calculated by applied model

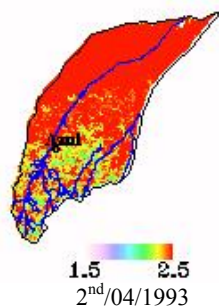
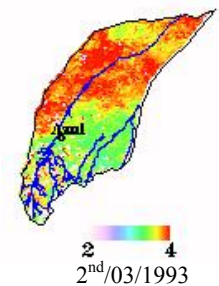
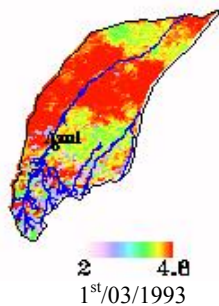
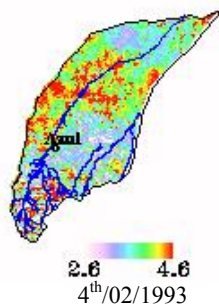
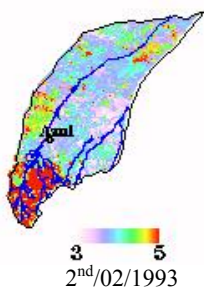
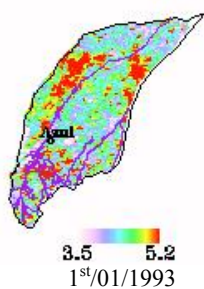
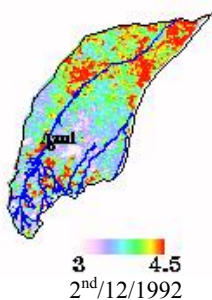


Figure 3. Daily value of ET_0 (mm day^{-1}) obtained by applying the model corresponding to December, January, February, March and April 1993.

Week	ET _o station (mm day ⁻¹)	ET _o model (mm day ⁻¹)
2 nd /12/1992	3,5	3,6
1 st /01/1993	4,5	4,2
2 nd /02/1993	4,3	3,8
4 th /02/1993	3,9	3,7
1 st /03/1993	3,9	4,2
2 nd /03/1993	3,8	3,4
2 nd /04/1993	2,4	2,1

Table 1. Measured and calculated values for Azul station (ET_o).

CONCLUSIONS

The model presented allows the estimation of weekly ET_o from the T_s information retrievable from the AVHRR-NOAA sensor.

As an example, the model has been applied to the Azul River basin, Buenos Aires Province, Argentina. The parameters were fitted by a function with a r² of 0,88, and an estimation error of $\pm 0,6 \text{ mm day}^{-1}$ (17 W m^{-2}).

Finally, the values measured in the meteorological stations were compared with the results obtained from the application of the model which are close enough to reveal a good performance (Table 1).

REFERENCES

- Allen, R. G., Pereira, L. S., Raes, D. and Smith, M. 1998, Crop evapotranspiration-Guidelines for computing crop water requirements-FAO. Irrigation and Drainage Paper 56. Water Resources, Development and Management Service, Rome.
- Boegh E., Soegaard H. and Thomsen A. 2002. Evaluating evapotranspiration rates and surface conditions using Landsat TM to estimate atmospheric resistance and surface resistance. Remote Sensing of Environment, 79, 329-343.
- Coll, C. and Caselles, V. 1997. A split window algorithm for land surface temperature from advanced very high resolution radiometer data: Validation and algorithm comparison. Journal of Geophysical Research, vol. 102, 14, 16697-16713.
- Varni, M., E. Usunoff, P. Weinzettel, and Rivas, R. 1999. The groundwater recharge in the Azul aquifer, central Buenos Aires Province, Argentina. Physics and Chemistry of the Earth 24 (4), 349-352.

Wavelet transform as a tool to detect land degradation from remotely sensed data

Jaume F. Gimeno-Ferrer, María A. Gilabert, Joaquín Meliá

Remote Sensing Unit, Department of Thermodynamics, University of Valencia, Spain

Jaume.F.Gimeno@uv.es

ABSTRACT—Vegetation dynamics can be considered as a good indicator of land degradation and is often studied by means of the temporal evolution of vegetation indices. This specific case implies the study of signals over long time periods to derive information about both the trend and the variability of the series. These analysis are usually performed making use of mathematical tools such as Fourier decomposition of the input signal, maybe with an application of low-pass or high-pass filters afterwards. Fourier transform is widespread in many scientific fields, including remote sensing, because of its conceptual simplicity, computational speed and quite general mathematical conditions of validity. Nonetheless, two important restrictions must be taken into account: Fourier analysis assumes linear and stationary data. Therefore, it should be cautiously applied to data that does not fit these conditions to avoid deriving wrong conclusions. This is commonly the case of satellite data, because of the intrinsically non-stationary nature of the monitored system or due to the lack of time series long enough to cover the stationarity period of the data. Moreover, Fourier transform performs a spectral analysis of data in the frequency space, thus losing temporal information in the spectrum as a consequence of the assumed stationarity in the data. In accurate change analysis it is the time evolution of the frequency content of the data what matters, so that a spectral technique preserving both frequency and time information, as the wavelet transform, would be more convenient. In this work wavelet transform has been applied to study land degradation over the Iberian Peninsula. Time series of NDVI since 1981 from NOAA-AVHRR and since 1998 from SPOT-VGT have been used. Wavelet analysis decomposes the data in low- and high- frequency time functions to describe both the trend and the variability of the time series at different time scales. In addition, this technique reveals itself to be robust under variations in surface scene, in the sense that it can describe very different surface types ranging from dense vegetation to desert regions. After wavelet transform has been performed over the individual pixels of a series of images, key descriptive statistics may be applied to form change trends and variability images.

1 INTRODUCTION

Desertification has become nowadays a serious threat in very different areas in the planet, affecting increasingly large extensions. Thus, systems and methodologies to study these processes must be developed and put into practice. In this context, remote sensing has turned out to be the only technique suitable for monitoring land degradation and desertification processes in a global or regional scale and over long time periods. Thus, methodologies to treat remote sensing data should be developed to be applied to this concrete field. In this sense, several approaches can be used to study the evolution of land properties to monitor desertification processes. For this purpose, NDVI is a good indicator of the vegetation canopy state, and surface temperature also presents some dependence on the vegetation content.

In this paper, a preliminary algorithm to assess land degradation from remotely sensed data is presented and applied over the Iberian Peninsula. The proposed strategy only makes use of shortwave

information, i.e., studies NDVI evolution, since surface temperature also presents daily cycles and other dependences that would make necessary further assumptions and normalisations of longwave data. In addition, requiring just one kind of information makes the proposed algorithm more flexible from an operative viewpoint.

Next section describes the data used to develop and apply the methodology here proposed, which is presented in section 3. Furthermore, some preliminary results are shown and discussed in section 4 and, finally, some conclusions are drawn in section 5.

2 NDVI DATA

The data to be analysed consists on long time series of NDVI. With these data, we intend to monitor desertification processes and land degradation, studying vegetation dynamics over long time periods. The remotely sensed data are low resolution images of NDVI coming from the AVHRR and VEGETATION sensors, onboard NOAA and SPOT platforms respectively.

The AVHRR data is contained in the Pathfinder AVHRR Land (PAL) database (Townshend, 1994; Smith *et al.*, 1997). This set of data contents NDVI images composited every 10-day period with a spatial resolution degraded to 8 km, covering the time period from July 13, 1981 to December 31, 1999, with an empty gap from September 1, 1994 since 1995.

On the other hand, in the VEGETATION data, NDVI images are also provided every 10 days after a compositing method based on the selection of the best measurement over the period (maximum NDVI). The spatial resolution is maintained at the nominal pixel size of 1 km, and the covered time period extends from April 1, 1998 to August 31, 2001. Hence, long time series of NDVI are available, especially of AVHRR data, although this data set presents a coarser spatial resolution.

3 METHODOLOGY OF ANALYSIS

3.1 Wavelet transform

The objective to be fulfilled is the detection of land degradation and desertification processes monitoring from space with remotely sensed data. These phenomena imply the progressive loss or change of the vegetative canopy, so this fact can be exploited to study the evolution of desertification. Vegetation cover exhibits two different kinds of variations: short-term variability due to seasonal cycles and long-term trend, which contents information about changes.

For the particular purpose of detecting desertification, both short and long-term variations are important: the former informs about the state of vegetation and the latter about changes in its quantity. Thus, methodologies to extract variations at different time scales would be useful for our study. This is the core of the proposed algorithm: a spectral analysis of the time series data, so that its information can afterwards be rebuilt at different scales. A widespread kind of spectral analysis is Fourier transform, which switches the data from time to frequency domain and is easily and efficiently implemented. Nonetheless it has an important drawback: time information is lost and it should not be applied to non-stationary data. Precisely, we are interested in the detection of changes that are non-stationary phenomena for which the location of events in time is important, so we should use a more suitable spectral analysis technique.

Wavelet transform much better fits our requirements (Strang, 1993; Perrier *et al.*, 1995). It conserves information in both time and frequency domains and is applicable to non-stationary data. The mathematical aspects of wavelet transform are conceptually somehow similar to those of Fourier analysis: it is performed convolving the time series f with an analysing function ψ to extract the energy W

contained in the signal at concrete time scales (a) and locations (τ) (Daubechies, 1990):

$$W(a, \tau) = \frac{1}{\sqrt{a}} \int_{-\infty}^{\infty} f(t) \psi\left(\frac{t-\tau}{a}\right) dt \quad (1)$$

The advantage of wavelet transform is that the analysing functions are located in time, in contrast to sines and cosines used in Fourier analysis. This allows us to keep time information while extracting spectral features by convolving the signal with expanded and shifted versions of the analysing function (mother wavelet). The concept of frequency does not appear as such in the wavelet transform. Instead, it is replaced by the related concept of scale of the analysis (a in Eq. 1), which is a more suitable way to describe features found in natural series.

We use wavelet transform to extract the long-term trends and the seasonal variability respect to that trend from the NDVI time series. This can be more efficiently accomplished by using the discrete wavelet transform (DWT) approach (Rioul and Duhamel, 1992), which performs the convolutions in (1) at a discrete number of optimised values for a and τ .

$$a = a_0^j > 0, \quad \tau = a_0^j k \tau_0, \quad j, k \in \mathbf{Z} \quad (2)$$

where a_0 and τ_0 are the discretization intervals, which usually take the values 2 and 1 respectively. This way, the mother wavelets are scaled by powers of 2 (dyadic scales) and are shifted by integers, so (1) can be written as:

$$W_{DWT}(j, k) = \int_{-\infty}^{\infty} f(t) \psi_{jk}(t) dt \quad (3)$$

for the DWT, where

$$\psi_{jk}(t) \equiv 2^{-j/2} \psi(2^{-j}t - k) \quad (4)$$

This algorithm allows us to implement a so-called multiresolution signal analysis (MRA) to decompose the NDVI time series in trend and variability respect to the trend series (Jawerth and Sweldens, 1993). The key parameter associated with MRA is the maximum level of the analysis, which establishes the threshold time scale between trend and variability. In our case, some time scale higher than one year should be taken to distinguish interannual and seasonal variations in the vegetation cover.

3.2 Proposed algorithm

The algorithm that has been developed is based on the wavelet transform of the NDVI time series available over the individual pixels of our data sets, in the form of MRA. With this procedure we obtain two functions (trend and variability) for each pixel on the images, so a reduction of these data must be applied to be able to interpret the results. Key descriptive statistics are used for this purpose. The algorithm can be summarised as follows:

1. Filtering and gap filling of the time series of NDVI over the individual pixels,
2. Wavelet-based MRA of the aforementioned modified time series for every pixel in the image set,
3. Extraction of trend and noiseless variability time series over each individual pixel, and
4. Reduction of these functions with key descriptive statistics.

The modification of the original time series is needed to eliminate extreme and spurious values due to low quality measurements, and to fill the empty gaps, since wavelet analysis requires a complete set of equally spaced data. NDVI values are removed when their deviation from the mean of the series is higher than three times its standard deviation. The empty gaps are filled afterwards using a linear interpolation scheme.

Regarding the MRA, a discrete approximation of the Meyer wavelet was taken as the mother wavelet. The maximum level of the analysis was fixed to 6, thus establishing a threshold time scale between trend and variability of 2.65 years. Level 1 variabilities, with time scales lower than one month, were removed from the extracted time series to suppress noisy behaviors.

4 RESULTS OVER THE IBERIAN PENINSULA

4.1 Pixel-by-pixel analysis

The first stage of the proposed algorithm implies the analysis of the NDVI time series over individual pixels. Figs. 1 and 2 show the trend series extracted at different analysis levels of the MRA over two different scenes, namely, the Albufera Natural Park and the Guadalentin Basin, along with the analysed NDVI time series (from the PAL database). The first one corresponds to a cropland area with a very important seasonal component in the vegetation cover, while the second one is a degraded semiarid area with few vegetation content. Both kinds of surfaces exhibit very different physical properties, but their analysis turns out to extract trend series in a similar way. Thus, wavelet-based MRA applied to these data series reveals itself as a robust tool for the analysis of the evolution of land properties for single pixels, even successfully removing extreme values appearing in the original series.

4.2 Single-pixel data reduction

At this point of the algorithm we dispose of trend and variability series for every pixel in the data set. This information is valuable, but a interpretation of the results over spatial scales greater than a few pixels necessarily requires a further reduction of this data. The approach that has been adopted consists on the

application of descriptive statistics on the extracted time series. Quite a high number of statistics have been applied to test their capability to keep the key information contained in the time series. Figs. 3 to 6 show the preliminary results obtained for the

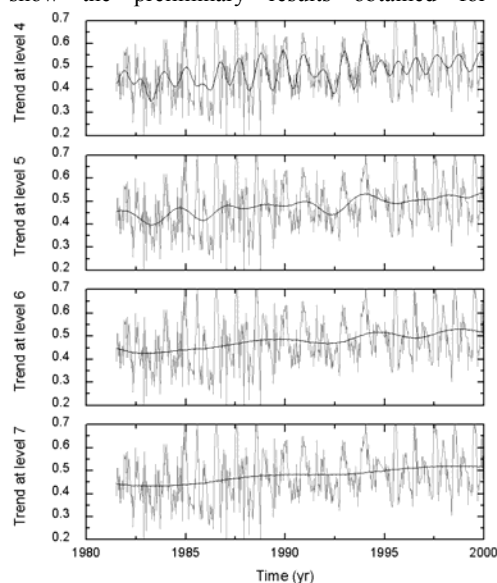


Figure 1. NDVI time series and trends extracted with wavelet-based MRA at different levels of analysis over the Albufera Natural Park.

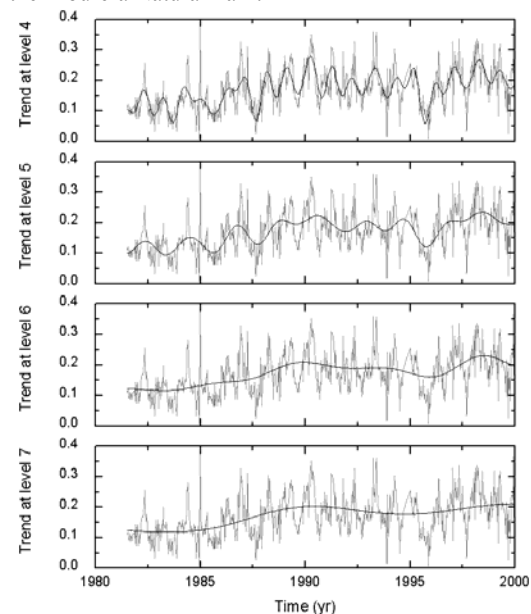


Figure 2. Same as Figure 1, but over the Guadalentin Basin.

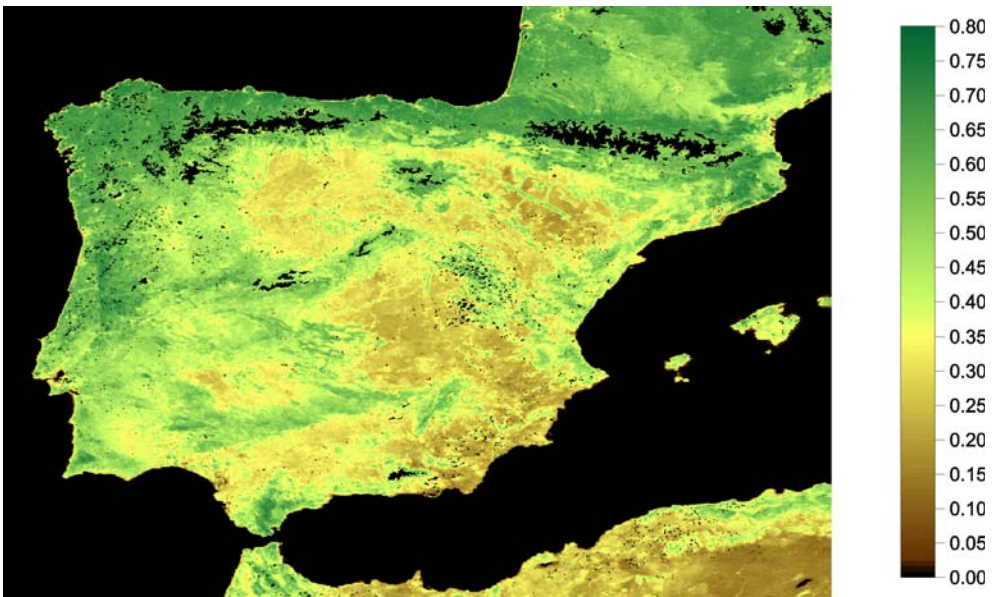


Figure 3. Mean of the trend series extracted with wavelet analysis from the VEGETATION NDVI time series.

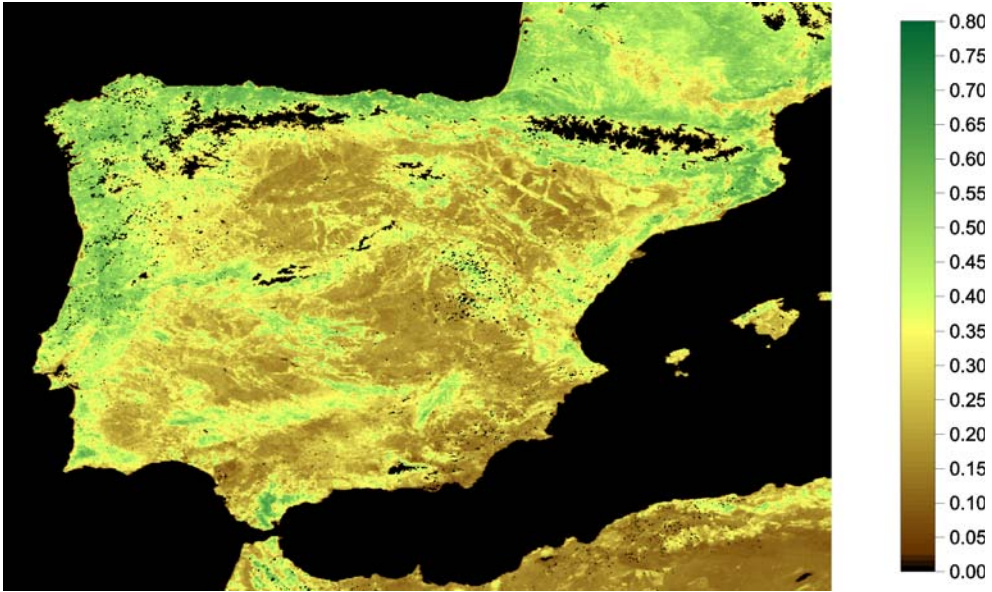


Figure 4. Percentile 10% of the sum of the trend and variability series extracted with wavelet analysis from the VEGETATION NDVI time series.

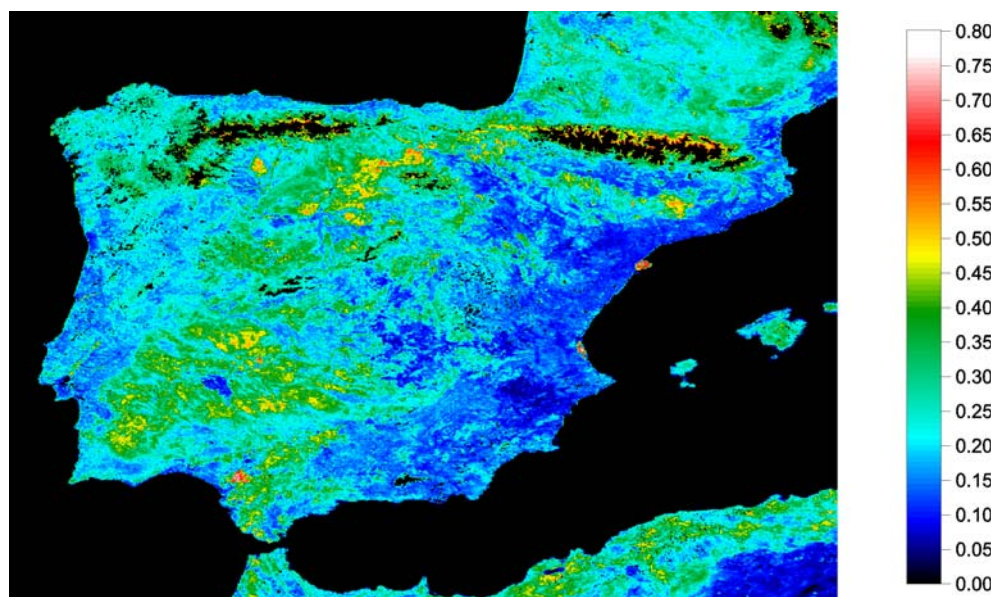


Figure 5. Difference of the percentiles 90% and 10% of the variability series extracted with wavelet analysis from the VEGETATION NDVI time series.

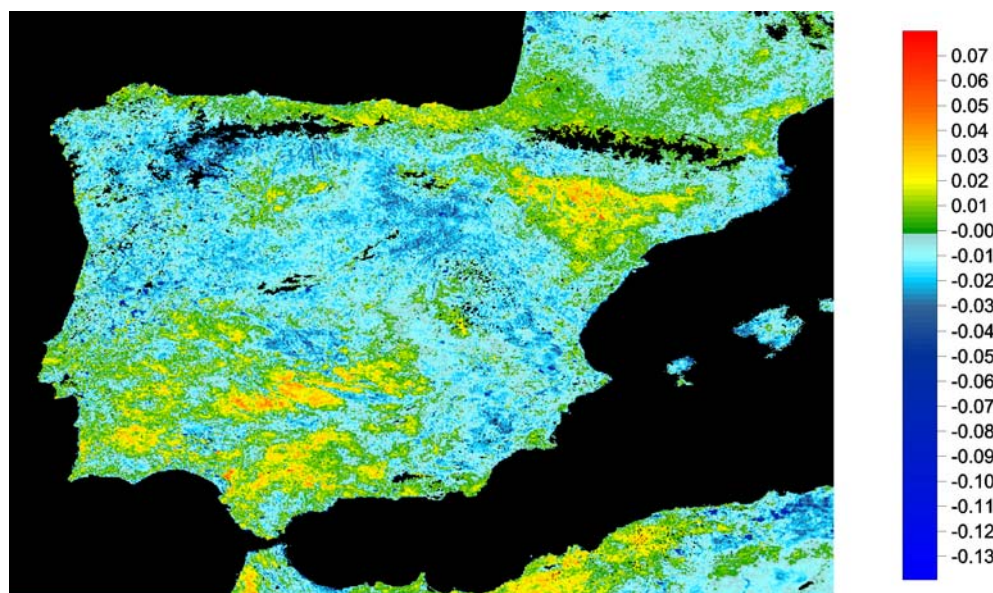


Figure 6. Linear slope of the trend series extracted with wavelet analysis from the VEGETATION NDVI time series.

VEGETATION data with some of these statistics: mean of the trend, percentile 10% of the sum of trend and variability, difference of percentiles 90% and 10 % of the variability, and the slope of a linear regression performed on the trend. The inclusion of percentiles in the analysis is due to the fact that, in this way, more

robust estimators are obtained. The percentile 10% of the sum of trend and variability is equivalent to the minimum NDVI in the studied time period, although by using the percentile we get a value less sensitive to outliers that can also be considered to average the minimums of the seasonal cycles. The same

considerations would apply to the relationship between the amplitude of the seasonal cycle and the difference of percentiles 90% and 10% of the variability.

Each of the applied statistics contains some physical information of interest. The mean of the trend informs about the average state of the surface within the analysed time period. The linear slope of the trend reflects the drifts occurred in the vegetation cover. On the other hand, the rest of statistics have the aforementioned physical interpretations. The detailed interpretation of Figs. 3 to 6 should lead us to the identification of the main zones affected by desertification over the Iberian Peninsula.

5 CONCLUSIONS

A study for developing a methodology for the monitoring of land degradation processes and desertification from remotely sensed data has been carried out. The algorithm is based in a wavelet transform of long time series of NDVI over individual pixel of a set of images, followed by a reduction of the results with key descriptive statistics.

The procedure has turned out to be robust under scene variations and provides physically meaningful information that can be interpreted afterwards to derive adequate conclusions about desertification in critical areas. The monitoring of desertification and land degradation processes is a complex task that requires the combination of different kinds of information, like those obtained from the statistics presented here, which are physically meaningful.

ACKNOWLEDGEMENTS

This work is funded by *Ministerio de Ciencia y Tecnología* project HISPASED (Desertification Alert and Monitoring Procedures in Spain, REN2000-1507-C03-02). One of the authors, J. F. Gimeno-Ferrer, holds a predoctoral grant within the aforementioned project.

REFERENCES

- Daubechies, I., 1990, The wavelet transform, time-frequency localization and signal analysis. *IEEE Transactions on Information Theory*, **36**, 961-1005.
- Jawerth, B., and Sweldens, W., 1993, An overview of wavelet based multiresolution analyses. *SIAM Review*, **36**, 377-412.
- Perrier, V., Philipovitch, T., and Basdevant, C., 1995, Wavelet spectra compared to Fourier spectra. *Journal of Mathematical Physics*, **36**, 1506-1519.
- Rioul, O., and Duhamel, P., 1992, Fast algorithms for discrete and continuous wavelet transforms. *IEEE Transactions on Information Theory*, **38**, 569-586.
- Smith, P. M., Kalluri, S. N. V., Prince, S. D, and DeFries, S. R., 1997, The NOAA/NASA Pathfinder AVHRR 8-km land data set. *Photogrammetric Engineering and Remote Sensing*, **63**, 13-31.
- Strang, G., 1993, Wavelet transforms versus Fourier transforms. *Bulletin of the American Mathematical Society*, **28**, 288-305.
- Townshend, J. R. G., 1994, Global data sets for land applications from the Advanced Very High Resolution Radiometer: an introduction. *International Journal of Remote Sensing*, **15**, 3319-3332.

Retrieval of biophysical parameters from dais data

J. C. Jiménez-Muñoz¹, M. Gómez¹, J. A. Sobrino¹, G. Soria¹, J. El-Kharraz¹, and J. Labed-Nachbrand²

¹Global Change Unit, Dpt. of Thermodynamics, Faculty of Physics, University of Valencia, C/ Dr. Moliner 50, 46100 Burjassot, Spain.

²GRTR/LSIT, 5 Boulevard Sebastien Brant, 67400 Illkirch, France

E-mail : juancar.jimenez@uv.es

ABSTRACT - In this paper, a methodology is presented to extract surface temperature, surface emissivity and heat fluxes from the different DAIS (Digital Airborne Imaging Spectrometer) channels in the framework of the DAISEX (Digital Airborne Imaging Spectrometer Experiments) campaign that were carried out in 1999 over the Barrax (Spain) site. To obtain surface temperature from DAIS thermal channels 74 (8.747 μm), 75 (9.648 μm), 76 (10.482 μm), 77 (11.266 μm), 78 (11.997 μm) and 79 (12.668 μm), a single-channel and two-channel methods have been used, while for extracting surface emissivity five methods have been considered to obtain relative values and three methods to obtain absolute ones. They are Temperature-Independent Spectral Indices method (TISI), REference channel method (REF), emissivity NORmalization method (NOR), emissivity RE-normalization method (RE) and ALPHA emissivity method (ALPHA) for relative emissivity, and the NDVI THresholds Method (NDVI^{THM}), the Normalized Emissivity Method (NEM) and Temperature/Emissivity Separation method (TES) for absolute emissivity. A comparison between temperature and emissivity values measured in situ and the ones extracted for different plots from DAIS images are also analysed. The final results show that algorithms that use DAIS channels 77 and 78 give the best results for surface temperature, with a root mean square deviation of around 1.5 K. For extracting absolute emissivity values, NDVI^{THM} gives the best results for vegetation plots, and NEM gives the best ones for bare soil and water plots, with an error of around 1 % in both cases. TISI and NOR relative methods give the same relative emissivity values within less than 0.4 %, confirming their superiority against the other relative methods.

1 INTRODUCTION

The European Space Agency (ESA) carries out a number of airborne campaigns to support geophysical algorithm development, calibration/validation and the simulation of future spaceborne Herat observation missions. The Digital Airborne Imaging Spectrometer Experiment that has been achieved in 1998 (DAISEX-98), 1999 (DAISEX-99) and 2000 (DAISEX-00) in Barrax (Spain) and Colmar (France) are two samples of these campaigns (Müller and Hausold, 2001). In these campaigns the Digital Airborne Imaging Spectrometer (DAIS) (see Figure 1) has been used onboard the aircraft Do228 (Müller et al., 2001).



Figure 1. The DAIS sensor.

The seventy-nine DAIS channels are seen to include coverage from the Visible to MIR (Medium InfraRed) and TIR (Thermal InfraRed) channels (see Figure 2).

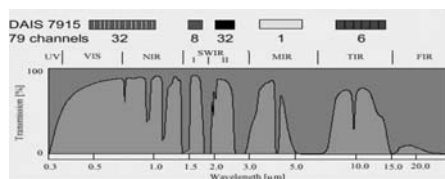


Figure 2. The seventy-nine DAIS channels.

In this paper is presented a methodology to obtain land surface temperature and emissivity from re-calibrated DAIS data obtained from a linera ground calibration fo the DAIS thermal channels using two validation targets (water and bare soil). To estimate land surface temperature, a single-channel and two-channel methods have been considered. To extract land surface emissivity, the TISI (Temperature-Independent Spectral Indices), REF (REference channel), NOR (emissivity NORmalization), RE (emissivity RENormalization) and ALPHA methods (Li et al., 1999) have been considered relative emissivity values, and the NDVI^{THM} (NDVI

THresholds Method) (Sobrino et al., 2001a), NEM (Normalized Emissivity Method) and TES (Temperature/Emissivity Separation) methods (Gillespie et al., 1999) have been considered to obtain absolute emissivity values. These methodologies have been applied to the DAIS images to obtain maps of different biophysical parameters such as land surface temperature, emissivity and NDVI.

2 LAND SURFACE TEMPERATURE ESTIMATION

2.1. Single-Channel Equation

On the basis of radiative transfer equation, the radiance (L_{sensor}) measured from space or aircraft in channel i may be written with a good approximation as (Li et al., 1999)

$$L(\theta)_{\text{sensor},i} = L(\theta)_{\text{surface},i} \tau(\theta)_i + L(\theta)_{\text{atm},i}^{\uparrow} \quad (1)$$

where θ is the observation angle, τ_i is the channel total transmission of the atmosphere in channel i , $L_{\text{atm},i}^{\uparrow}$ is the upwelling atmospheric radiance in channel i and $L_{\text{surface},i}$ is the channel radiance observed in channel i at ground level given by

$$L(\theta)_{\text{surface},i} = \varepsilon(\theta)_i B(\theta)_i(T_s) + (1 - \varepsilon(\theta)_i) L(\theta)_{\text{atm},i}^{\downarrow} \quad (2)$$

In this expression, ε_i is the channel emissivity, is $L_{\text{atm},i}^{\downarrow}$ the downwelling hemispheric atmospheric radiance in channel i , and $B_i(T_s)$ is the channel radiance which would be measured if the surface were a blackbody (=1) at temperature T_s .

When the at-surface radiances (L_{surface}) are known, it is possible to obtain the land surface temperature (T_s) using a single infrared channel. So, taking into account the equation (2), it is easy to check that

$$T_s = B_i^{-1} \left[\frac{L_{\text{surface},i} - (1 - \varepsilon_i) L_{\text{atm},i}^{\downarrow}}{\varepsilon_i} \right] \quad (3)$$

with B_i^{-1} indicating the inversion of Planck law. The advantage of this method is that only one thermal channel is required to obtain the surface temperature value. This value can be also obtained with more than one thermal channel. In this case, the maximum temperature calculated with the different thermal channels can be chosen as the land surface temperature. Alternatively, a mean effective temperature for all the thermal channels ($\langle T_s \rangle$) can be obtained as land surface temperature using the following expression:

$$\langle T_s \rangle = \frac{1}{\Delta \lambda_{i,j}} \int_j^i T(\lambda) d\lambda \quad (4)$$

with i and j the first and last thermal channel respectively.

The results obtained for the validation of this method are shown in Table 1, with a rmsd (root mean square deviation) values of 1.41 K using equation (4) to obtain the final value for land surface temperature. This validation has been carried out in the framework of the DAISEX (Digital Airborne Imaging Spectrometer Experiment) campaigns at Barrax site (Albacete, Spain), in which in-situ surface radiometric temperatures and emissivity measurements were made and in-situ radiosoundings were launched (González et al., 2001).

Table 1. Validation for the single-channel equation.

(LT: Local Time, σ : standard deviation, rmsd: root mean square deviation)

DATE - LT	PLOT	T_s^{situ} (K)	$T_{\text{max}} - T_s$ (K)	$\langle T \rangle - T_s$ (K)
3/6/99 - 13:52	bare soil*	322.21	0.00	0.00
3/6/99 - 13:52	Alfalfa	295.97	3.83	2.86
3/6/99 - 13:52	water*	295.02	0.01	0.00
3/6/99 - 13:52	Barley	314.19	-0.40	-1.05
3/6/99 - 14:08	bare soil*	323.07	0.00	0.00
3/6/99 - 14:08	water*	295.02	-0.01	-0.02
3/6/99 - 14:08	Barley	313.57	5.96	4.74
4/6/99 - 10:01	barley1	298.62	-0.59	-1.41
4/6/99 - 10:01	water*	291.88	0.01	0.00
4/6/99 - 10:01	bare soil*	303.35	0.01	0.00
4/6/99 - 10:01	barley2	298.56	-0.53	-1.29
4/6/99 - 10:16	barley1	298.63	2.57	1.73
4/6/99 - 10:16	water*	291.81	0.00	0.00
4/6/99 - 10:16	bare soil*	307.28	0.00	0.00
4/6/99 - 10:16	barley2	298.70	1.91	0.33
4/6/99 - 16:58	bare soil*	320.08	0.01	0.00
4/6/99 - 16:58	water*	293.65	0.00	0.00
4/6/99 - 16:58	Barley	313.26	-0.41	-1.11
4/6/99 - 17:11	bare soil*	320.36	0.00	0.00
4/6/99 - 17:11	Water*	293.23	0.00	0.00
4/6/99 - 17:11	Barley	312.83	1.05	-0.03
		mean	0.64	0.23
		σ	1.64	1.39
		rmsd	1.76	1.41

(*) These plots have been chosen as calibration points, so their bias is exactly zero.

2.2 Two-channel technique

The basis of the two-channel technique (or split-window when is applied in the region 10-12.5 μm) is that the atmospheric attenuation suffered by the surface emitted radiance is proportional to the difference between the at-sensor radiances measured simultaneously in two different thermal channels (McMillin, 1975). Many papers have used this technique to extract sea surface temperature (Deschamps and Phulpin, 1980; McClain et al., 1985; Sobrino et al., 1993, etc.) and land surface temperature (Price, 1984; Becker and Li, 1990b; Sobrino et al., 1991; Prata, 1993; Sobrino et al., 1994, etc.). In this paper is proposed the following two-channel algorithm, which takes into account the emissivity and water vapour effects:

$$T_s = T_i + a_0(T_i - T_j) + a_2(T_i - T_j)^2 + (a_3 + a_4 W)(1 - \varepsilon) + (a_5 + a_6 W)\Delta\varepsilon + a_1 \quad (5)$$

where T_s is the surface temperature (in K), T_i and T_j are the at-sensor brightness temperatures of the thermal DAIS channels (in K), $\varepsilon = (\varepsilon_i + \varepsilon_j)/2$ and $\Delta\varepsilon = (\varepsilon_i - \varepsilon_j)$ are the mean effective emissivity and the emissivity difference, W is the total atmospheric water vapour (in g/cm^2) and finally, a_i are the numerical coefficients of the two-channel algorithm. These coefficients and the uncertainty of the algorithm can be obtained carrying out a simulation of the sensor measurements (Sobrino et al., 2001b). Table 2 shows the results for the validation with the best combinations of the DAIS thermal channels (from 74 to 79) and the plots given in Table 1. To obtain land surface temperature from equation (5), in-situ values of water vapour (W) and emissivity have been considered. The at-sensor radiometric temperatures (T_i , T_j) have been extracted from re-calibrated DAIS images considering an average value for a 5x5 pixels plot.

Table 2. Validation of the two-channel algorithm for the plots given in Table 1 (values in K, σ : st. dev., rmsd: root mean sq. dev.).

CHANNELS	bias	σ	rmsd	rmsd*
74-79	-0.80	1.74	1.92	1.50
75-78	-1.67	2.25	2.81	2.70
75-79	-1.26	1.72	2.13	1.73
76-77	-0.23	1.90	1.91	1.60
77-78	1.39	2.30	2.69	1.54
77-79	1.09	2.27	2.51	2.18
78-79	-0.16	2.42	2.43	1.64

(*) Values obtained only for the calibration points (water and bare soil).

3 SPECTRAL EMISSIVITY RETRIEVAL

3.1 Relative Emissivity

To obtain relative emissivity values with respect to another emissivity reference value, five methods (TISI, NOR, REF, RE, ALPHA) have been considered and applied to DAIS data (Sobrino et al., 2001c). A detailed development of these methods can be found in Li et al. (1999). Figure 3 shows the graph of the difference between the relative methods against the REF method for bare soil and alfalfa and for the different DAIS thermal channels. TISI and NOR methods give slightly the same difference against the REF method, confirming the superiority of these both methods compared to the others.

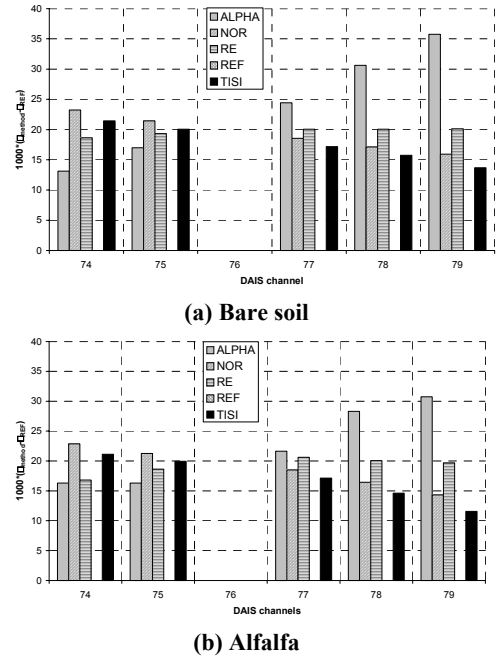


Figure 3. Graph of the difference between the relative methods against the REF method for (a) bare soil and (b) alfalfa.

3.2 Absolute Emissivity

Three different methods have been considered to obtain the absolute spectral emissivity from DAIS thermal channels: the NDVI^{THM} (Sobrino et al., 2001a), the NEM and the TES method (Gillespie et al., 1999).

The NDVI^{THM} is a simplified method based on the estimation of emissivity, ε , using atmospherically corrected data in the visible and near infrared channels, which considers three different

types of pixels depending on the NDVI value: bare soil pixels ($NDVI < 0.2$), mixed pixels ($0.2 \leq NDVI \leq 0.5$) and fully vegetation pixels ($NDVI > 0.5$). The $NDVI^{THM}$ have been adapted to the DAIS thermal channels 74 to 79 using the methodology proposed by Sobrino (2000) for rough and non-homogenous surfaces with the help of Salisbury's spectra (Salisbury and D'Aria, 1992) and the DAIS filter functions to obtain the appropriate expressions to estimate absolute emissivity. The NDVI value have been calculated with the well-known equation that uses reflectivity values from the Red region (ρ_{red}) and Near InfraRed (ρ_{nir}) region, according to:

$$NDVI = \frac{\rho_{red} - \rho_{nir}}{\rho_{red} + \rho_{nir}} \quad (6)$$

The DAIS channels 10 ($0.659 \mu m$) and 22 ($0.868 \mu m$) have been used for ρ_{red} and ρ_{nir} respectively. The final expressions obtained for this method are for bare soil pixels ($NDVI < 0.2$),

$$\varepsilon_{74} = -0.378 \rho_{red} + 1.002 \quad (7a)$$

$$\varepsilon_{75} = -0.209 \rho_{red} + 0.986 \quad (7b)$$

$$\varepsilon_{76} = -0.094 \rho_{red} + 0.984 \quad (7c)$$

$$\varepsilon_{77} = -0.081 \rho_{red} + 0.988 \quad (7d)$$

$$\varepsilon_{78} = -0.063 \rho_{red} + 0.988 \quad (7e)$$

$$\varepsilon_{79} = -0.066 \rho_{red} + 0.991 \quad (7f)$$

for mixed pixels ($0.2 \leq NDVI \leq 0.5$),

$$\varepsilon_{74} = 0.963 + 0.025 P_v \quad (8a)$$

$$\varepsilon_{75} = 0.972 + 0.016 P_v \quad (8b)$$

$$\varepsilon_{76} = 0.982 + 0.008 P_v \quad (8c)$$

$$\varepsilon_{77} = 0.985 + 0.006 P_v \quad (8d)$$

$$\varepsilon_{78} = 0.987 + 0.004 P_v \quad (8e)$$

$$\varepsilon_{79} = 0.988 + 0.002 P_v \quad (8f)$$

and for vegetation pixels ($NDVI > 0.5$),

$$\varepsilon_{74} = \varepsilon_{75} = \varepsilon_{76} = \varepsilon_{77} = \varepsilon_{78} = \varepsilon_{79} = 0.990 \quad (9)$$

with P_v being the vegetation proportion, given by

$$P_v = \frac{NDVI - NDVI_{min}}{(NDVI_{max} - NDVI_{min})^2} \quad (10)$$

The constraint of this method is that it can not be used to extract water emissivity values because it is not possible to apply the NDVI and P_v equations for water pixels.

Figure 4 illustrates the reflectivity spectrum for different plots with their NDVI value obtained with the equation (6), while Figure 5 shows the graph of the spectral emissivity obtained with the $NDVI^{THM}$ for different plots. For plots with NDVI value higher than 0.5, a constant values of 0.99 is assigned, so the alfalfa plot gives a constant spectrum. Bare soil gives the lowest values, as is expected, while corn and non-irrigated barley plots give a similar spectrum.

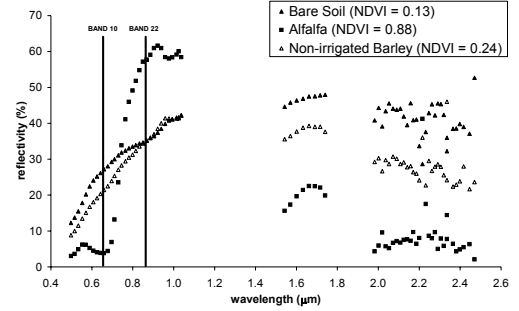


Figure 4. Reflectivity spectrum obtained with the DAIS visible, near-infrared and medium-infrared channels (from 1 to 70) for bare soil, alfalfa and non-irrigated barley plots. NDVI values have been obtained with channels 10 and 22.

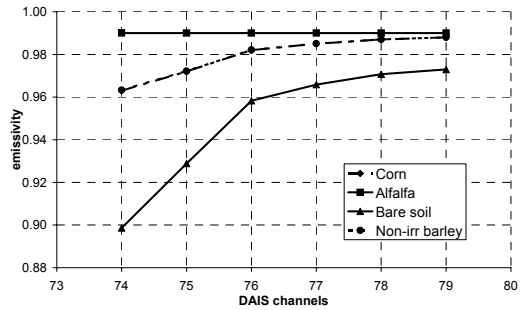


Figure 5. Spectral emissivity obtained with the $NDVI^{THM}$ for different plots (corn, alfalfa, bare soil and non-irrigated barley).

With the **Normalized Emissivity Method (NEM)** thermal images obtained from DAIS sensor are inverted to extract an emissivity value for every pixel image and for every thermal DAIS channel. Using this method some iterations have been made until the downwelling radiance between two consecutive iterations reaches a convergence of $0.05 \text{ W m}^{-2} \text{ sr}^{-1} \mu\text{m}^{-1}$. The method also needs an initial emissivity value to recalculate the final emissivities. In our case, we have made only one iteration and we

have chosen an initial emissivity value of 0.99. Note that this method is similar to the NOR method shown in the next section, with the iterative process being the difference between both methods.

The **Temperature/Emissivity Separation Method (TES)** algorithm uses the NEM to estimate temperature, from which emissivity ratios are calculated. These ratio values are the NEM emissivities normalized by their average value. The ratio spectrum preserves the shape, but not the amplitude, of the actual emissivities. To recover the amplitude, and hence a refined estimate of the temperature, the spectral contrast (MMD) is calculated and used to predict the minimum emissivity. For this purpose, the Salisbury's spectra with the DAIS filter functions have been used to obtain the following equation with a correlation coefficient of 0.996:

$$\epsilon_{\min} = 0.9843 - 1.0616 \text{ MMD} \quad (11)$$

A similar expression for ϵ_{\min} and MMD can be found in Gillespie et al. (1999) for ASTER sensor onboard NASA's TERRA satellite. Equation (11) is used to calculate TES emissivities for DAIS thermal channels.

Due to the fact that the downwelling radiances are known (using the radiosoundings as input data in the MODTRAN code and executing it in thermal radiance mode) we only require one iteration when applying the NEM and TES methods. Furthermore the initial emissivity value selection is not very relevant, the values differ only by 0.001 by choosing 0.98 or NDVI emissivity as initial emissivity. The reader interested in a more detailed study of the NEM and TES methods can consult Gillespie et al. (1999).

In Figure 6 the NEM and TES results for absolute spectral emissivity are presented. Both methods give slightly the same values, with better spectrum shapes for the different plots and higher values for the DAIS thermal channels 74 and 75 compared with the NDVI^{THM} ones. The validation from in-situ emissivity measurements shows a rmsd values of 0.012, 0.013 and 0.014 for NDVI^{THM} , NEM and TES method respectively.

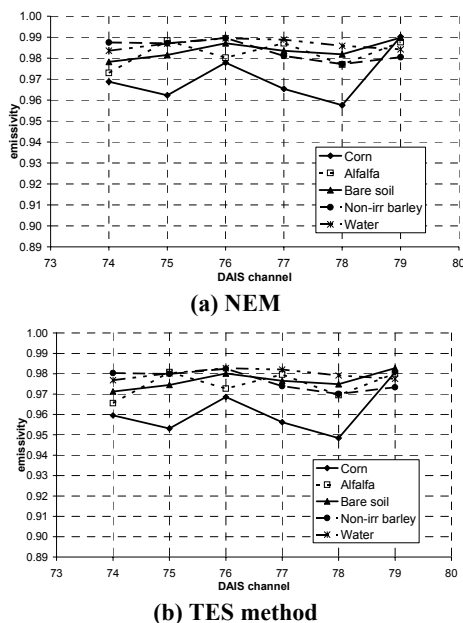
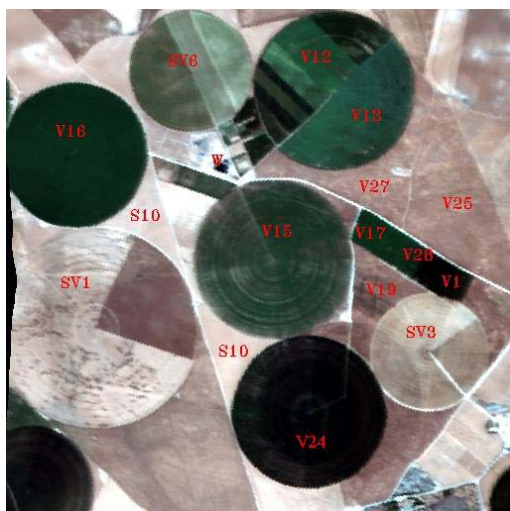


Figure 6. Spectral emissivity obtained with the (a) NEM and (b) TES method for different plots (corn, bare soil, non-irrigated barley and water).

4 APPLICATION TO DAIS IMAGES

The methodology proposed in sections 2 and 3 can be applied to the DAIS images to obtain maps of land surface temperature and emissivity. Other biophysical parameters can be also obtained from DAIS images, as for example NDVI maps. In Figure 7 it is shown a resized DAIS image centered at the study area with the different plots in the DAISEX notation, while Figure shows the maps of NDVI, relative emissivity with the NOR method, absolute emissivity with the NEM method and land surface temperature. The NDVI map has been obtained using the equation (6), the NOR and NEM maps have been obtained using the methodology showed in the section 3, and the land surface temperature map has been obtained using the equation (5) using as emissivity values the emissivity image obtained with the NEM.



PLOTS

S10: Bare soil
 SV1: Corn (two leaves)
 SV3: Corn (five leaves)
 SV6: Beet
 V1 : Wheat
 V12: Experimental plot
 V13: Experimental plot
 V15: Alfalfa (cut)
 V16: Alfalfa
 V17: Alfalfa
 V19: Non-irrigated barley
 V24: Irrigated wheat
 V25: Non-irrigated barley
 V27: Non-irrigated barley
 V28: Legume
 W : Water

Figure 7. The Barrax test site. False color composite (RGB) using DAIS bands 10 (0.659 μm), 4 (0.553 μm) and 1 (0.498 μm).

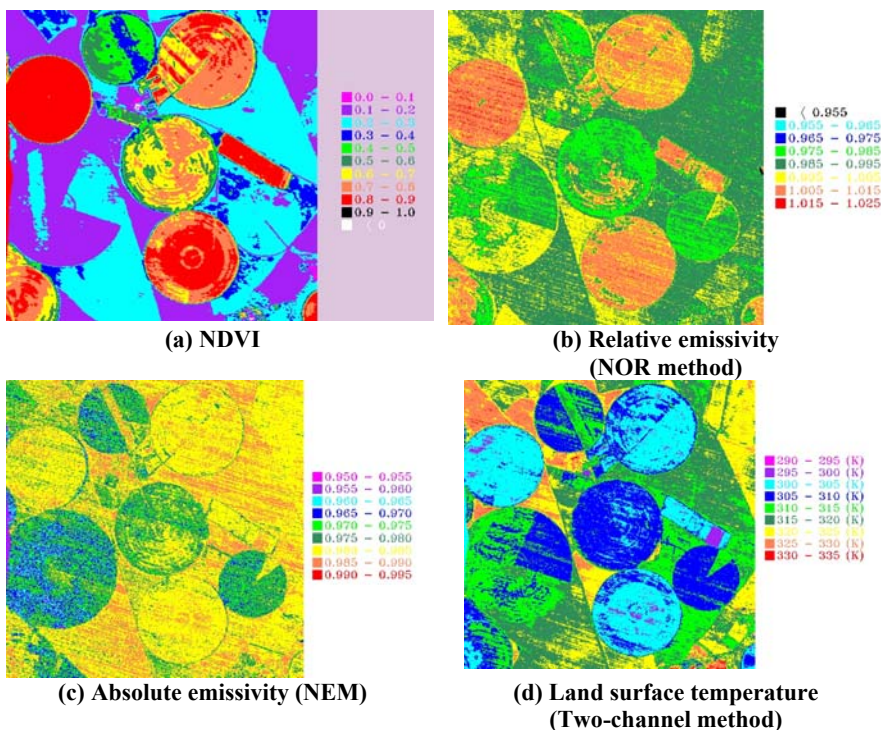


Figure 8. Biophysical parameters maps from DAIS data: (a) NDVI map, (b) relative emissivity map applying the NOR method, (c) mean absolute emissivity map applying the NEM and (d) land surface temperature using a two-channel method and the emissivity image obtained with the NEM.

5 CONCLUSIONS

Land surface temperature, land surface emissivity and evapotranspiration have been estimated from DAIS data. To obtain land surface temperature, a single-channel and two-channel method have been used, with rmsd (root mean square values) values of around 1.5 K. Five methods have been considered to obtain relative emissivity values: TISI, REF, NOR, RE and ALPHA. The results show that TISI and NOR give the same values within less than 0.4%, confirming their superiority against the other methods. The NDVI^{THM}, NEM and TES method have been considered to extract absolute emissivity, with rmsd values of 0.012, 0.013 and 0.014 respectively. Finally, some maps of land surface temperature, emissivity and NDVI have been obtained from DAIS images.

6 ACKNOWLEDGMENTS

We wish to thank to the ESA (European Space Agency) for the financial support (projects ESA-ESTEC 13053/NL/GD and 13390/NL/GD) and the DLR (German Optoelectronic Institute) for providing us with the DAIS images. We would also like to thank the European Union (WATERMED, Project No. ICA3-ct-1999-00015) and the Ministerio de Ciencia y Tecnología (project REN2001-3105/CLI).

7 REFERENCES

Gillespie, A.R., Rokugawa, S., Hook, S.J., Matsunaga, T. and Kahle, B., 1999, Temperature/Emissivity Separation Algorithm Theoretical Basis Document, Version 2.4, *Document Prepared under NASA Contract NAS5-31372*.

González, M. C., Fortea, J. C., Martínez-Lozano, J. A., Utrillas, M. P., Pedrós, R., Moreno, J., Cisneros, J. M., y Manzano, J. L., 2001, *Measurement of Atmospheric Constituents (Ozone, Water Vapour) at Barrax*, DAISEX Final Results Workshop, SP-499, ESA Publications Division, pp. 53-61.

Li, Z.-L., Becker, F., Stoll, M. P., y Wan, Z., 1999, *Evaluation of Six Methods for Extracting Relative Emissivity Spectra from Thermal Infrared Images*, Remote Sensing of Environment, vol. 69, pp. 197-214.

McMillin, L. M., 1975, *Estimation of sea surface temperature from two infrared window measurements with different absorption*, Journal of Geophysical Research, vol. 80, pp. 5113-5117.

Müller, A., y Hausold, A., 2001, *The Airborne Imaging Spectrometer Data Acquisition Programme in 1998, 1999 and 2000*, DAISEX Final Results Workshop, SP-499, ESA Publications Division, pp. 7-11.

Müller, A., Gege, P., y Cocks, T., 2001, *The Airborne Imaging Spectrometers Used in DAISEX*, DAISEX Final Results Workshop, SP-499, ESA Publications Division, pp. 3-6.

Sobrino, J. A., Raissouni, N. and Z.-L. Li, 2001a, A comparative study of land surface emissivity retrieval from NOAA data, *Remote Sensing of Environment*, 75:256-266.

Sobrino, J. A., Jiménez, J. C., Nerry, F., and Laporta, S., 2001b, Split-Window Methods for Surface Temperature Estimation from DAIS Data, DAISEX Final Results Workshop, SP-499, ESA Publications Division, pp. 125-131.

Sobrino, J. A., Raissouni, N., Labed, J., Nerry, F., Li, Z.-L., and Jiménez, J. C., 2001c, Land Surface Emissivity Retrieval From Remote Sensing Data, 8th International Symposium Physical Measurements & Signatures in Remote Sensing, CNES series, pp. 531-536.

3. INFRARROJO TERMICO / THERMAL INFRARED

Quality assessment and validation of the MODIS global land-surface temperature

Zhengming Wan^a, Yulin Zhang^a, Qincheng Zhang^a, and Zhao-liang Li^b

^a ICESS, University of California, Santa Barbara, CA 93106-3060, USA

^b TRIO/LSIIT/ENSPS, Parc d'Innovation, 5 Bd. Sebastien Brant, 67400, France

ABSTRACT -This paper presents the evaluation of the Earth Observing System (EOS) Moderate Resolution Imaging Spectroradiometer (MODIS) thermal infrared bands and the status of Land-Surface Temperature (LST) version-3 standard products retrieved from Terra MODIS data. The accuracy of daily MODIS LST products has been validated in more than twenty clear-sky cases with in-situ measurement data collected in field campaigns in 2000-2002. The MODIS LST accuracy is better than 1°C in the range from -10 to 50 °C. Refinements and improvements were made to the LST algorithm for using both Terra and Aqua MODIS data. The major advantages of Using both Terra and Aqua MODIS data for the LST retrieval improves the quality of the LST product and the diurnal feature in the product due to better temporal, spatial and angular coverage of clear-sky observations.

1. INTRODUCTION

As a part of the NASA-centered international Earth Observing System, two MODIS instruments (Salomonson et al. 1989) have been launched to provide information for global studies of atmosphere, land, and ocean processes. The first one was launched on 18 December 1999 on the morning platform called Terra, and the second one was launched on 4 May 2002 on the afternoon platform called Aqua. The strengths of the MODIS instrument include its global coverage, high radiometric resolution and dynamic ranges, and accurate calibration in visible, near-infrared and thermal infrared bands. The Terra MODIS data have been used to generate science data products for more than two years and these science data products are available to public free of charge. A consistent reprocessing has been made for Terra MODIS data since November 1999 to generate science data products (in version 3) in either provisional quality or validated quality. Science data products based on Aqua MODIS data will also be available after the testing and evaluation stage.

LST is one of the key parameters in the physics of land-surface processes on regional and global scales. It combines the results of all surface-atmosphere interactions and energy fluxes between the atmosphere and the ground (Mannstein 1987, Sellers et al. 1988). The LST retrieved from satellite data may be used to validate and improve the global meteorological model prediction after appropriate aggregation and parameterization (Price 1982, Diak and Whipple 1993). The remotely sensed LST has been used in land cover and land-cover change analysis (Ehrlich and Lambin 1996, Lambin and Ehrlich 1997), and in the production of the MODIS land cover product. It has

been also used in monitoring drought and estimating surface soil moisture (Feldhake et al. 1996, McVicar and Jupp 1998), evaluating water requirements of wheat (Jackson et al. 1977), and determining frosts in orange groves (Caselles and Sobrino 1989).

We present the evaluation of the MODIS thermal infrared (TIR) bands used for LST retrieval, a brief summary of the MODIS LST algorithms, validation status of the MODIS LST product, new refinements and improvements made to the operational LST code (version 4), and the major advantages of using Terra and Aqua MODIS data for the LST product in the following sections.

2. PERFORMANCE OF MODIS TIR BANDS

The specification and estimated performance of the TIR bands in the MODIS Proto-Flight Model (PFM) flown on Terra are shown in Table 1. The channel-dependent noise and systematic error in MODIS TIR channel data were evaluated with early MODIS data over lake and ocean sites in clear sky days acquired with the A-side of scan mirror and electronics before the end of October 2000 (Wan 2002). In 14 cases of sub-area sites with a size of 10 lines by 16 pixels each line, where the brightness temperature in band 31 changes within $\pm 0.1\text{K}$, average and standard deviation values of brightness temperatures in ten channels (consisting of a ten-element linear detector array) of 16 MODIS TIR bands show the channel-dependent noise and systematic errors. It is found that the ninth channel in bands 21 and 24, and the fourth channel in band 22 are too noisy to use, and that the specification of noise equivalent temperature difference (NEDT) is reached or nearly reached in all other channels of the 16 MODIS TIR bands as shown in column 5 of Table 1.

Table 1. Specifications of the Terra MODIS TIR bands, and its estimated performance in the A-side configuration before 31 October 2000 (Wan et al., 2002) and the new A-side configuration after 3 July 2001.

band	bandwidth (μm)	IFOV	NEDT Specified (K)	NEDT (K) Estimated (Wan, 2002)	calibration bias estimated (K) (before 2000/10/31)	calibration bias estimated (K) (after 2001/07/03)
20	3.660-3.840	1km	0.05	0.06	0.60	0.63
21	3.929-3.989	1km	2.00	0.64	0.46	0.70
22	3.929-3.989	1km	0.07	0.07	0.55	0.15
23	4.020-4.080	1km	0.07	0.05	0.40	-0.08
24	4.433-4.498	1km	0.25	0.13		
25	4.482-4.549	1km	0.25	0.08		
27	6.535-6.895	1km	0.25	0.12		
28	7.175-7.475	1km	0.25	0.09		
29	8.400-8.700	1km	0.05	0.03	0.03	-0.12
30	9.580-9.880	1km	0.25	0.08		
31	10.780-11.280	1km	0.05	0.03	0.12	0.09
32	11.770-12.270	1km	0.05	0.05	-0.19	0.05
33	13.185-13.485	1km	0.25	0.16	0.55	(0.98)
34	13.485-13.785	1km	0.25	0.27		
35	13.785-14.085	1km	0.25	0.23		
36	14.085-14.385	1km	0.35	0.41		

The absolute radiometric accuracy of MODIS TIR channel data was evaluated with in-situ data collected in a vicarious calibration field campaign conducted in Lake Titicaca, Bolivia, during May 26 and June 17, 2000 (Wan et al 2002). The comparison between MODIS TIR data produced by the new Level-1B code (version 2.5.4) and the band radiances calculated with atmospheric radiative transfer code MODTRAN4.0 (Berk et al 1999) based on lake surface temperatures measured by five IR radiometers deployed in the high-elevation Lake Titicaca, and the atmospheric temperature and water vapor profiles measured by radiosondes launched on the lake-shore on 13 and 15 June 2000, calm clear-sky days, shows good agreements in bands 29, 31 and 32 (within an accuracy of 0.5%) in daytime overpass cases. Sensitivity analysis indicates that the changes on the measured atmospheric temperature and water vapor profiles result in negligible or small effects on the calculated radiances in bands 20-23, 29, and 31-32. Therefore, comparisons for these bands were made for cases when lake surface temperature measurements were available but no radiophone data were available, and in sub-areas of 10 by 16 pixels where there was no in-situ measurement but MODIS brightness temperatures in band 31 vary within $\pm 0.15\text{K}$ by using the validated band 31 to determine lake surface temperatures. These comparisons show that the specified absolute radiometric accuracy of 1% is reached or nearly reached in MODIS bands 21, 29 and 31-33, and that there is a calibration bias of 2-3% in bands 20, 22, and 23, as shown in column 6 of Table I.

The MODIS sensor was reconfigured on 31 October and 1 November 2000 to the B-side Science

Mode from the A-side Science Mode. By transitioning to latest focal plane bias voltage in the B-side configuration, the three originally noisy detector elements returned to normal performance. The MODIS instrument experienced a Power Supply 2 shutdown anomaly and did not take science data during the time period of June 15 to July 2, 2001. The MODIS instrument was reconfigured to the A-side Science Mode with the same focal plane bias voltage used in the B-side mode on 3 July 2001. The MODIS data in this configuration are referred as new A-side data. To evaluate the calibration accuracy of the new A-side data, we conducted a field campaign in Walker Lake, Nevada in mid October 2001. The estimated calibration bias is less than 1% in bands 22-23, 29, and 31-32, as shown in column 7 of Table I (Wan et al 2002).

The relative spectral response (RSR) functions of Terra and Aqua MODIS instruments in bands 20, 22, 23, 29, 31-33 are shown in Figure 1. The effects of the difference between Terra and Aqua MODIS RSR functions are less than 0.1K in these seven bands.

We use the Terra and Aqua MODIS data over Lake Titicaca on June 26, 2002 to estimate the NEDT and calibration accuracy of the early Aqua MODIS TIR bands. Their granule IDs are MOD021KM.A2002177.0300 and MYD021KM.A2002177.0600, respectively. A sub-area with a size of 10 lines by 16 pixels each line was searched for a smallest variation in the brightness temperatures in band 31 within the lake in these two granules. The standard deviation values in brightness temperatures are used to estimate the NEDT. The average brightness temperatures are used to estimate

the calibration bias under the following three assumptions: 1) there is no significant change in the atmospheric condition during the three hours of the Terra and Aqua overpass time difference; and 2) the change in lake surface temperature during three hours is small enough to adjust with the average brightness temperatures in band 31; 3) there is no significant

change in the calibration accuracy of the Terra MODIS TIR bands in the period from October 2001 to June 2002 so that we can use the estimated values in the last column of Table I. The comparisons of NEDT and calibration bias between Terra and Aqua MODIS TIR bands are shown in Figure 2.

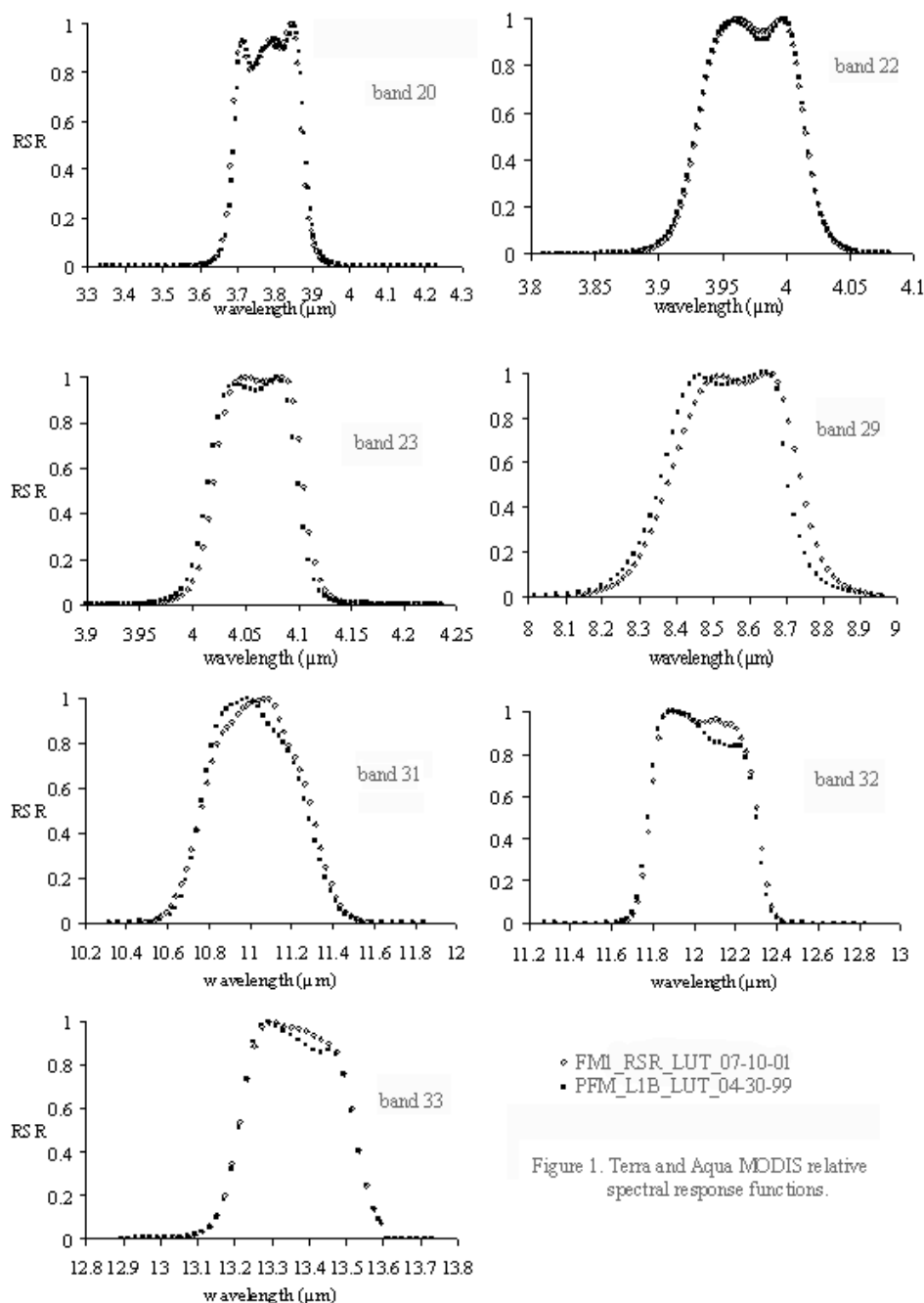


Figure 1. Terra and Aqua MODIS relative spectral response functions.

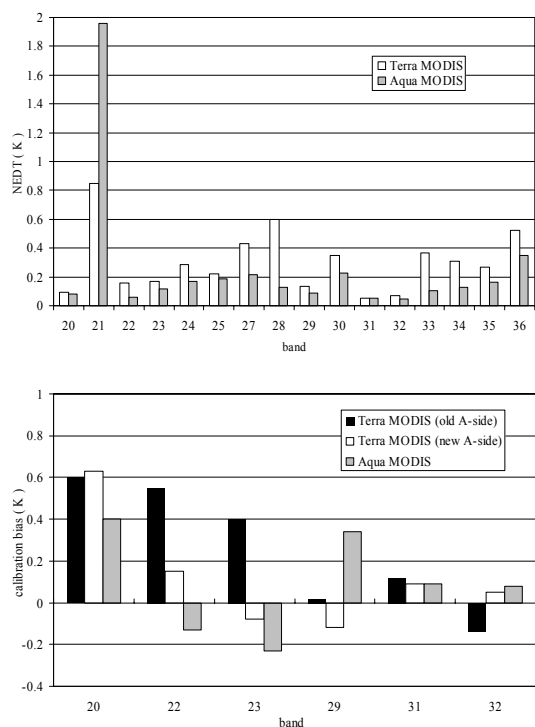


Figure 2 The comparisons of NEDT and calibration bias between Terra and Aqua MODIS TIR bands

3. MODIS LST ALGORITHMS

3.1 Basic Considerations

LST is retrieved from MODIS TIR data only in clear-sky conditions so that LST is not mixed with cloud-top temperature. Because TIR signals cannot penetrate clouds and the probability of cloudy conditions is often larger than 50% at the regional and global scales, cloudy pixels must be skipped in the LST processing.

LST is defined by the radiation emitted by the land surface observed by MODIS at the instant viewing angle. The land surface is canopy in vegetated areas or soil surface in bared areas. Instant MODIS TIR data do not contain information at other viewing angles due to weak scattering of the TIR signals in the clear-sky atmosphere. We recognize that applications may need LST at different angles (nadir in some cases or 50° in other cases). Referring LST at other angles from the value at a given viewing angle requires detailed information of the surface proportions and structures, which is not available at the global scale.

Appropriate resolution of the land-atmosphere coupling is the key in retrieving surface and atmospheric properties. Although advances have been

made in the integrated retrieval (Ma et al. 2000, 2002), this approach is very computing time consuming. It is not practical to implement the integrated retrieval of the surface and atmospheric properties at a spatial resolution of several kilometers into the operational at this time. Instead, we use multiple bands in the atmospheric windows for the LST retrieval. The values of atmospheric temperature and water vapor are useful to improve the LST retrieval. However, there may be large errors in these values. Therefore, we use them as indicators of ranges or initial guess values only.

3.2 The Generalized Split-Window LST Algorithm

The LST of clear-sky pixels in MODIS scenes is retrieved from brightness temperatures in bands 31 and 32 with the generalized split-window algorithm (Wan and Dozier 1996). The coefficients used in the split window algorithm are given by interpolation on a set of multi-dimensional look-up tables (LUT). The LUTs were obtained by linear regression of the MODIS simulation data from radiative transfer calculations over wide ranges of surface and atmospheric conditions. Improvements for the generalized split-window LST algorithm incorporated in the establishment of the LUTs include: 1) view-angle dependence, 2) column water vapor dependence, and 3) dependence on the atmospheric lower boundary temperature. The view-angle dependence is kept in one dimension of LUTs for a set of viewing angles covering the whole MODIS swath so that LST can be retrieved at higher accuracies for pixels at both small and large viewing zenith angles, and at best accuracies for pixels at nadir and small view angles. The column water vapor dependence is kept in another dimension of LUTs for a set of overlapping intervals of column water vapor so that the information of water vapor provided in the MODIS atmospheric product is used as the most likely range of the water vapor rather than its exact value because the uncertainties in the atmospheric water vapor may be large. Similarly, the information of the atmospheric lower boundary temperature provided in the MODIS atmospheric product is also used to improve the LST retrieval accuracy. The LST accuracy can be improved further by iterations with the information of difference between LST and the surface air temperature.

The band emissivities, also called classification-based emissivities (Snyder et al 1998) are estimated from land cover types in each MODIS pixel through TIR BRDF and emissivity modeling (Snyder and Wan 1998). A simple linear correction is made to the band emissivities to account for the viewing angle effect in the emissivities when the viewing angle is larger than 45 degrees for some land cover types. In the at-launch MODIS LST processing, the University of Maryland IGBP-type land-cover based on AVHRR data

(Townshend et al 1994) is used to provide global land cover information at 1km grids. Since June 2001, the MODIS land-cover product (Muchoney et al 1999) is used in the MODIS LST processing. Note that errors and uncertainties in the classification-based emissivities may be large in semi-arid and arid regions because of the large temporal and spatial variations in surface emissivities and lack of knowledge on the emissivity variation with viewing angle.

3.3 The MODIS Day/Night LST Algorithm

A physics-based day/night algorithm (Wan and Li, 1997) was developed to retrieve surface spectral emissivity and temperature at 5km resolution from a pair of daytime and nighttime MODIS data in seven TIR bands, i.e., bands 20, 22, 23, 29, and 31-33. The inputs to this algorithm include the MODIS calibrated radiance product (MOD021KM), geolocation product (MOD03), atmospheric temperature and water vapor profile product (MOD07), and cloud mask product (MOD35). To our knowledge, this day/night algorithm is the first operational LST algorithm capable of adjusting the uncertainties in atmospheric temperature and water vapor profiles for a better retrieval of the surface emissivity and temperature without a complicated complete retrieval of surface variables and atmospheric profiles simultaneously (Ma et al. 2000, 2002). Because we use a pair of daytime and nighttime MODIS data in seven bands, we have 14 observations. In the day/night algorithm, there may be maximum of 14 unknown variables. The minimal set of the surface variables includes 7 band emissivities, and daytime and nighttime surface temperatures. There are only five unknowns left for atmospheric variables. Because of the close coupling between land surface and atmosphere, uncertainties in surface emissivities may result in large errors in the atmospheric temperature/water vapor retrieval (Plokhenko and Menzel 2000). These errors could exist in the shape of the retrieved temperature/humidity profile, and in the values of atmospheric temperature at the surface level (T_a) and column water vapor (cwv). Atmospheric radiative transfer simulations show that the MODIS radiances in the above seven TIR bands are relatively less sensitive to changes in the shapes of temperature and water vapor profiles. Therefore, we set four atmospheric variables (T_a and cwv, for daytime and nighttime, respectively). Then there is only one unknown left for the anisotropic factor of the solar beam BRDF at the surface. This anisotropic factor is defined by the ratio of the surface-reflected solar beam at the view direction of the MODIS sensor to the radiance that would have resulted if the surface reflected isotropically (such a surface is called Lambertian surface). Bidirectional reflectance measurements of sands and soils (Snyder et al. 1997) show that

although there are quite strong spectral variations in surface reflectance for most terrestrial materials in the 3.5-4.2 μ m wavelength range, their BRDF anisotropic factor in this wavelength range has very small variations on the order of 2%. Therefore, we can use a single anisotropic factor for bands 20, 22, and 23. Besides we assume: 1) The surface emissivity changes with vegetation coverage and surface moisture content. However, it does not significantly change in several days unless rain and/or snow occurs during the short period of time - particularly for bare soils in arid and semi-arid environments, for which the surface of the ground is normally dry (Kerr et al. 1992). 2) Atmospheric radiative transfer simulations show that in clear-sky conditions the surface-reflected diffuse solar irradiance term is much smaller than the surface-reflected solar beam term in the thermal infrared range, and the surface-reflected atmospheric downward thermal irradiance term is smaller than surface thermal emission. So the Lambertian approximation of the surface reflection does not introduce significant error in the 3-14 μ m thermal infrared region. Then we can link hemispherical directional reflectance $r(\theta)$ to directional emissivity $\varepsilon(\theta)$ by $r(\theta) = 1 - \varepsilon(\theta)$ according to Kirchhoff's law. All the atmospheric and solar terms in the algorithm can be given by numerical simulations of atmospheric radiative transfer. The set of 14 nonlinear equations in the day/night algorithm is solved with the least-squares fit method (Wan and Li 1997).

Considering the angular variation in surface emissivity, we separate the whole range of MODIS viewing zenith angle into sub-ranges, and use one emissivity in each of the sub-ranges. In the day/night LST processing, we select a pair of clear-sky daytime and night MODIS observations at view angles in a same sub-range whenever it is possible. If there is no such pair of day/night observations available in a reasonable short period of time but there is a pair of day/night observations in different sub-ranges of view angle, we use this less favorable pair for surface emissivity and temperature retrieval and set a lower quality for the retrieved results. Sometimes we have to make a tradeoff between a favorable period of time and a favorable pair of view angles for temporal variations versus angular variations in surface emissivities. If the time difference between daytime and nighttime observations is too long, the chance for a large change in surface emissivity will be high. In the new product generation executive (PGE) code (version 3), the whole range of MODIS viewing zenith angle is separated into four sub-ranges (0°- 40°, 40°- 52°, 52°- 60°, 60°- 65°, respectively), instead of two sub-ranges in the earlier beta version.

4. STATUS OF THE MODIS LST PRODUCT

The level-2 MODIS LST product (MOD11_L2) in version 3, available from EDC DAAC (<http://edcdaac.usgs.gov/modis/dataproduct.html>), is retrieved with the generalized split-window algorithm in the product generation executive (PGE) LST code (Wan and Dozier 1996) from the calibrated radiance data of bands 31 and 32 data in the MODIS Level-1B 1km resolution (MOD021KM) product. Other inputs to this algorithm include MODIS geolocation product (MOD03), cloud mask product (MOD35), and atmospheric temperature and water vapor profile product (MOD07). The physics based day/night algorithm (Wan and Li 1997) was used to retrieve surface spectral emissivity and temperature at 5km resolution for the MODIS LST level-3 MOD11B1 product from a pair of daytime and nighttime MODIS data in seven TIR bands, i.e., bands 20, 22, 23, 29, and 31-33.

The daily 1km resolution level-3 MOD11A1 LST product is constructed with the results in the MOD11_L2 products of a day through mapping the science data sets of all pixels in the MOD11_L2 products onto grids in the integerized sinusoidal projection and averaging the values in each grid.

Detailed descriptions of the science data sets and their attributes in MODIS LST daily products MOD11_L2, MOD11A1, MOD11B1, and the 8-day product MOD11A2 are given at <http://www.ices.ucsb.edu/modis/LstUserGuide/userguide.html> in "MODIS Land Surface Temperature Products User's Guide".

The accuracy of daily MODIS LST product at 1km resolution generated by the generalized split window algorithm, was validated in eleven clear-sky cases with in-situ measurement data collected in field campaigns in 2000 and 2001. The MODIS LST accuracy is better than 1K in the range from 263K to

300K over Lake Titicaca in Bolivia, Mono Lake, Bridgeport grassland, and a rice field in Chico, California, and Walker Lake, Nevada, in the atmospheric column water vapor range from 0.4 to 3.0cm. In six cases over a silt playa in Railroad Valley, Nevada, the 1km MODIS LSTs are a few Kelvin degrees lower than the in-situ measured LSTs because the surface emissivities inferred from land cover types in the split-window LST method are often overestimated in semi-arid and arid regions. After a correction with the difference between the 5km LST retrieved by the day/night LST method and the LST aggregated from 1km LSTs retrieved by the split-window method, the MODIS LSTs agreed with in-situ measured LSTs within $\pm 1K$ in the range from 263K to 322K for the six cases in Railroad Valley and one case of snow cover in Bridgeport, California (Wan et al. 2002).

In order to validate the LST product in wet atmospheric conditions, we conducted field campaigns in the low Mississippi River basin late June - August 2002. Five radiometers were deployed a soybean field, and three in a rice field, Greenville, Mississippi and plan to conduct field campaigns to validate the MODIS LST product with in-situ measurements in crop fields near Greenville, Mississippi. The validation results are given in Table 2 and Figure 3. Note that a part of the larger difference between the LST and in-situ values at viewing zenith angle near 40° may be due to the uncertainty in estimated surface emissivities. We will measure the LST at multiple angles in the future field campaigns.

In summary, the collection-3 MODIS LST products since 1 November 2000 were validated at multiple sites in relatively wide ranges of surface and atmospheric conditions. More ground-based measurements will be made to validate the LST products, especially for the products retrieved from Aqua MODIS data.

Table 2. Comparison between the MODIS LSTs and in-situ measured LSTs in validation field campaigns conducted in a soybean field (33.08263 °N, 90.7866 °W), Mississippi, in 2002. The atmospheric column water vapor (cwv) comes from MOD07_L2

case no.	granule ID	date & time (month/day hh:mm)	view zenith (°)	atmos. cwv (cm)	in situ Ts from radiometers (K)	MODIS Ts (δ Ts) (K)	MODIS – in situ Ts (K)
1	A2002199.0415	7/17 23:16 CDT	6.99	3.5	296.8	297.0 (0.15)	0.2
2	A2002215.0415	8/02 23:16 CDT	6.62	3.3	298.3	298.3 (0.17)	0.0
3	A2002217.0400	8/04 23:04 CDT	18.17	3.0	297.6	297.2 (0.20)	-0.4
4	A2002220.0430	8/07 23:35 CDT	38.85	3.5	294.5	293.6 (0.30)	-0.9
5	A2002222.0420	8/09 23:22 CDT	18.68	3.3	295.7	295.5 (0.28)	-0.2

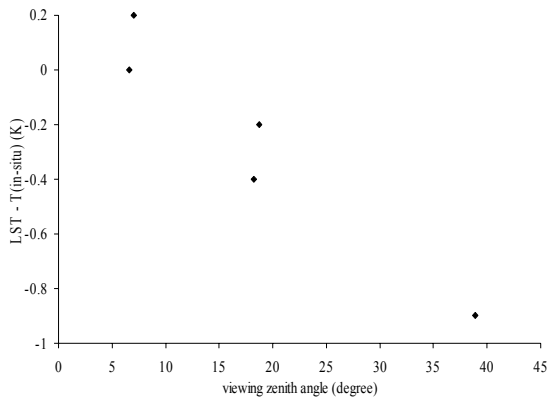


Figure 3 LST error in function of viewing zenith angle

5. IMPROVEMENTS OF THE MODIS LST PGE

The following new refinements and improvements were made to the version-4 MODIS LST product generation executive (PGE) code: 1) update of the look-up tables (LUT) used in the day/night LST algorithm, 2) processing lake pixels in clear-sky at a confidence of 66% and higher, 3) using BRDF Albedo Parameters of the MODIS 16-day BRDF product (MOD43B1C) as input, 4) separating the range of viewing zenith angles into five sub-ranges (0-24°, 24-38°, 38-49°, 49-58°, and 58-65°) instead of four, 5) parallel processing of data in odd and even days to double the production rate and the storage of interim results for the day/night algorithm, 6) an option to jointly use the Terra and Aqua MODIS data, 7) incorporating a split-window method into the day/night algorithm to ensure that the retrieved emissivities can be used by split-window algorithms.

The size of the LUT for the solar radiation terms used in the day/night LST algorithm was increased by 50% in order to better describe their variations with the changes in atmospheric temperature and water vapor profiles. The size of the LUT for the thermal infrared terms was increased by 80% in order to better describe their variations with the changes in atmospheric conditions and the viewing angle.

In a new option added to the MODIS LST PGE code, if the BRDF Albedo Parameters for band 7 (at 2.13 μm) in MOD43B1C in the previous 16-day period are available, they will be used to provide a better initial value for the anisotropic factor of the solar beam BRDF at the surface in the day/night LST algorithm. This anisotropic factor is used for bands 20, 22, and 23 (in the spectral region of 3.6-4.1 μm). Although the reflectance values in these two spectral regions may be different for terrestrial materials, they vary in similar regions (Salisbury et al. 1991). Because

BRDF parameters depend on the surface materials and structure, there should be a strong correlation between the BRDF parameters in these two spectral regions. With this new option, the knowledge of the BRDF parameters in the short wave TIR spectral region (in band 7 at 2.13 μm) is used to provide a better initial value of the anisotropic factor to the solution of the day/night LST algorithm. Because of the non-linearity of the day/night LST algorithm, a better initial value will lead to a better solution of the algorithm, i.e. more accurate surface emissivities and temperatures could be retrieved.

The MODIS LST PGE code is also modified to add an option for the use of both Terra and Aqua MODIS data in the day/night LST algorithm for better solutions of the surface emissivities and temperatures. By the combining use of Terra and Aqua MODIS data, the chance of clear-sky observations will be roughly doubled, and the chance to have a pair of daytime and nighttime observations at viewing angles in the same sub-ranges will be significantly increased so that the accuracy of the retrieved surface emissivities can be improved.

In the version 4 reprocessing scheduled for November 2002, the accuracies of retrieved LST and surface emissivities will be improved due to the improvements in the qualities of input MODIS products including calibrated radiance, atmospheric temperature/water vapor profile, cloud mask, land cover and snow cover.

Terra and Aqua MODIS data collected in the early Aqua mission (June 25-26 and July 4-9, 2002) have been processed at the science computing facility of the UCSB MODIS LST group with the version-4 PGE code. In figure 4, the retrieved daytime and nighttime LSTs averaged in this period of time show spatial distribution of the LST diurnal variation in the regions of Europe, North Africa, and Mid East. The retrieved surface emissivities are shown in figure 5 in color composite image with emissivities in bands 29, 22, and 20 as RGB components (figure 5a), and that with emissivities in bands 29, 31, and 32 enhanced by the equalization histogram method as RGB components (figure 5b). The comparison between retrieved surface emissivities over the Sahara Desert and those measured from sand samples in the laboratory is shown in figure 6a. Three of the sand samples were brought from store and another one was collected from the beach near UCSB. The comparison between retrieved surface emissivities in Caspian Sea and the theoretical emissivity values of the sea water is shown in figure 6b

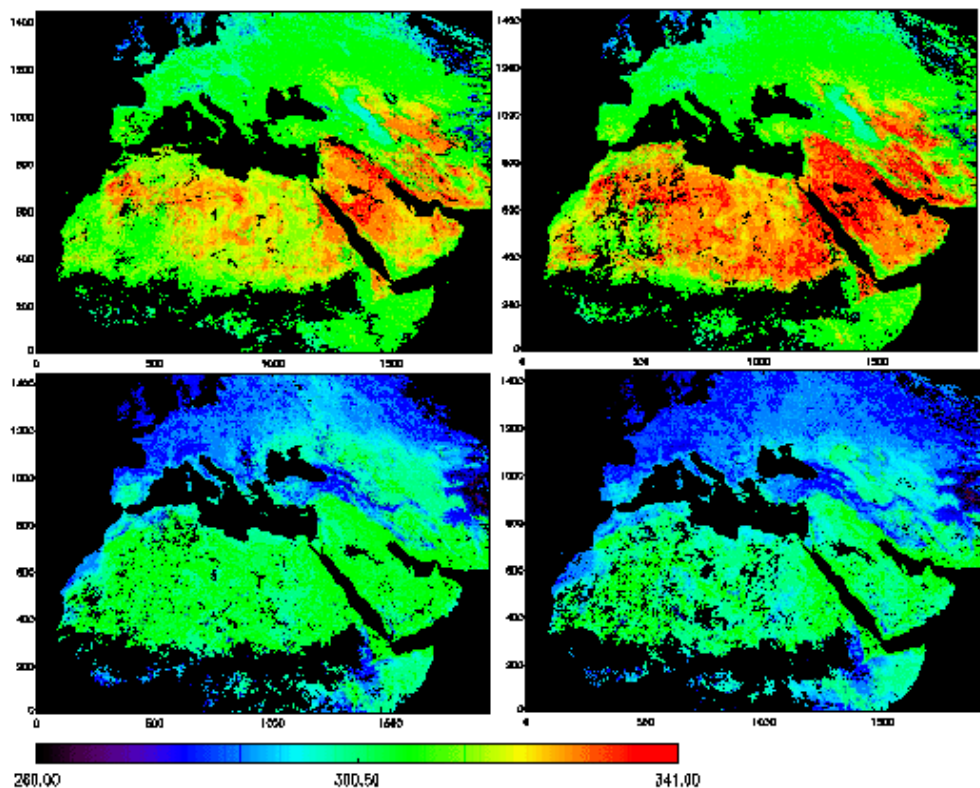


Figure 4 spatial distribution of the LST diurnal variation in the regions of Europe, North Africa, and Mid East

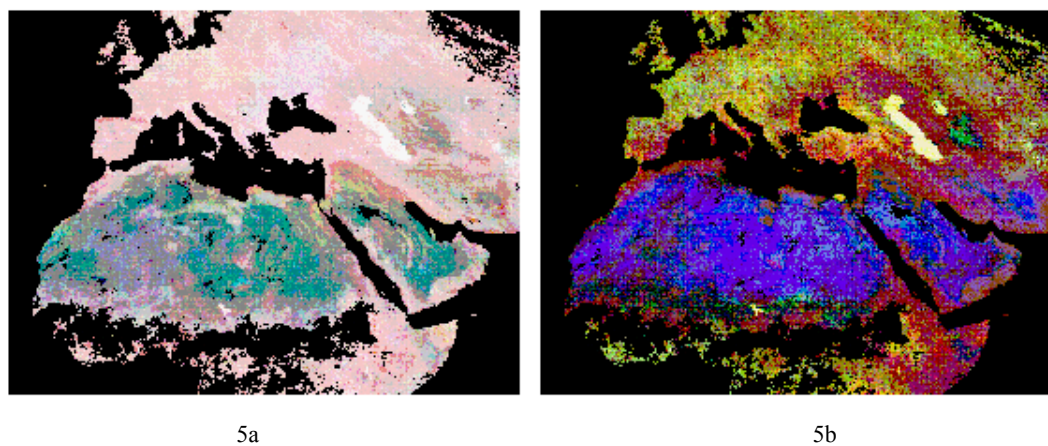
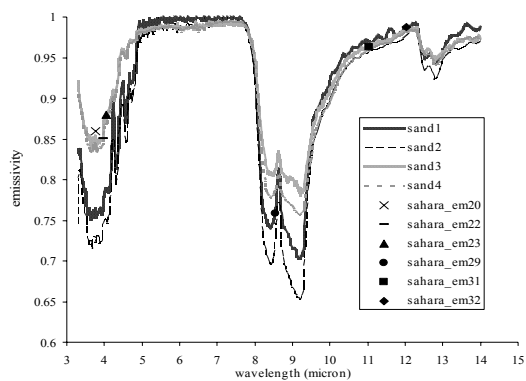
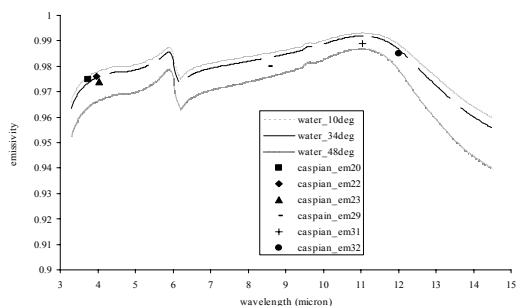


Figure 5. Color composite image of the retrieved surface emissivities (a) bands 29, 22, and 20 as RGB components, (b) bands 29, 31, and 32 enhanced by the equalization histogram method as RGB components



(a)



(b)

Figure 6a Comparison between retrieved surface emissivities over the Sahara Desert and those measured from sand samples in the laboratory. Figure 6b Comparison between retrieved surface emissivities in Caspian Sea and the theoretical emissivity values of the sea water.

6. CONCLUSIONS

The MODIS LST products have been validated within 1K in multiple validation sites in relatively wide ranges of surface and atmospheric conditions. Refinements and updates were made to improve the quality of the LST product and to use both Terra and Aqua MODIS data in the LST retrieval. The major advantages of the additional Aqua MODIS data for the LST product include the increase in quantity and the improvement in quality of the surface emissivity and temperature science data over the global land due to the increasing number of MODIS observations in clear-sky conditions. With the MODIS observations at least four times a day for nearly every spot on the Earth and more frequently in high latitude regions, a much better information of the diurnal cycle will be kept in the LST product. Because of the Aqua overpass time around 1:30pm, the afternoon LSTs retrieved from the MODIS data will be more close to the maximum temperature of the land surface so that it is more suitable for regional and global change studies, especially in applications for estimating soil

moisture condition and water requirements of crops, and for monitoring drought.

ACKNOWLEDGMENT

This work was supported by research contract NAS5-31370 of the National Aeronautics and Space Administration.

REFERENCES

- Berk A., G. P. Anderson, L. S. Bernstein, P. K. Acharya, H. Dothe, M. W. Matthew, S. M. Adler-Golden, J. H. Chetwynd, Jr., S. C. Richtmeier, B. Pukall, C. L. Allred, L. S. Jeong, and M. L. Hoke, "MODTRAN4 radiative transfer modeling for atmospheric correction," *Optical Spectroscopic Techniques and Instrumentation for Atmospheric and Space Research III, Proc. SPIE*, vol. 3756, pp. 348-353, 1999.
- Caselles V., and J. A. Sobrino, "Determination of frosts in orange groves from NOAA-9 AVHRR data," *Remote Sens. Environ.*, vol. 29, no. 2, pp. 135-146, 1989.
- Diak G. R. and M. S. Whipple, "Improvements to models and methods for evaluating the land-surface energy balance and effective roughness using radiosonde reports and satellite-measured skin temperature data," *Agricul. and Forest Meteorol.*, vol. 63, no. 3-4, pp. 189-218, 1993.
- Ehrlich D. and E. F. Lambin, "The surface temperature-vegetation index space for land cover and land-cover change analysis," *Int. J. Remote Sens.*, vol. 17, no. 3, pp. 463-487, 1996.
- Feldhake C. M., D. M. Glenn, and D. L. Peterson, "Pasture soil surface temperature response to drought," *Agron. J.*, vol. 88, no. 4, pp. 652-656, 1996.
- Jackson R. D., R. J. Reginato, and S. B. Idso, "Wheat canopy temperature: a practical tool for evaluating water requirements," *Water Resour. Res.*, vol. 13, pp. 651-656, 1977.
- Kerr Y. H., J. P. Lagouarde, and J. Imbernon, "Accurate land surface temperature retrieval from AVHRR data with use of an improved split window algorithm," *Remote Sens. Environ.*, vol. 41, no. 2-3, pp. 197-209, 1992.
- Lambin E. F. and D. Ehrlich, "Land-cover changes in sub-Saharan Africa (1982-1991): Application of a change index based on remotely sensed surface temperature and vegetation indices at a continental scale," *Remote Sens. Environ.*, vol. 61, no. 2, pp. 181-200, 1997.
- Ma X., Z. Wan, C. C. Moeller, W. P. Menzel, L. E. Gumley, and Y. Zhang, "Retrieval of geophysical parameters from Moderate Resolution Imaging Spectroradiometer thermal infrared data: evaluation of a two-step physical algorithm," *Appl. Optics*, vol. 39, no. 20, pp. 3537-3550, 2000.

- Ma X.-L., Z. Wan, C. C. Moeller, W. P. Menzel, and L. E. Gumley, "Simultaneous retrieval of atmospheric profiles and land-surface temperature/emissivity from Moderate Resolution Imaging Spectroradiometer thermal infrared data: extension of a two-step physical algorithm," *Appl. Optics*, vol. 41, no. 20, pp. 909-924, 2002.
- Mannstein H., "Surface energy budget, surface temperature and thermal inertia," in *Remote Sensing Applications in Meteorology and Climatology*, ed. R. A. Vaughan and D. Reidel, NATO ASI Ser. C: Math. Phys. Sci. Vol. 201, pp. 391-410, Dordrecht, Netherlands: A Reidel Publishing Co., 1987.
- McVicar T. R. and D. L. B. Jupp, "The current and potential operational uses of remote sensing to aid decisions on drought exceptional circumstances in Australia: a review," *Agricultural Systems*, vol. 57, no. 3, pp. 399-468, 1998.
- Muchoney D. M., J. S. Borak, H. Chi, M. Friedl, J. Hodges, N. Morrow, and A. Strahler, "Application of the MODIS global supervised classification model to vegetation and land cover mapping of Central America," *Int. J. Remote Sens.*, vol. 21, no. 6/7, pp. 1115-1138, 1999.
- Plokhenko Y. and W. P. Menzel, "The effects of surface reflection on estimating the vertical temperature-humidity distribution from spectral infrared measurements," *J. Appl. Meteorol.*, vol. 39, pp. 3-14, 2000.
- Price J. C., "On the use of satellite data to infer surface fluxes at meteorological scales," *J. Appl. Meteor.*, vol. 21, pp. 1111-1122, 1982.
- Salisbury J. W., L. S. Walter, N. Vergo, and D. M. D'Aria, *Infrared (2.1-25 μ m) spectra of minerals*, Baltimore and London: The Johns Hopkins University Press, 1991.
- Salomonson V., W. Barnes, P. Maymon, H. Montgomery, and H. Ostrow, "MODIS: advanced facility instrument for studies of the Earth as a system," *IEEE Trans. Geosci. Remote Sens.*, vol. 27, no. 2, pp. 145-153, 1989.
- Sellers P. J., F. G. Hall, G. Asrar, D. E. Strebel, and R. E. Murphy, "The first ISLSCP Field Experiment (FIFE)," *Bull. Amer. Meteorol. Soc.*, vol. 69, no. 1, pp. 22-27, 1988.
- Snyder W., Z. Wan, Y. Zhang, and Y.-Z. Feng, "Thermal infrared (3-14 μ m) bidirectional reflectance measurements of sands and soils," *Remote Sens. Environ.*, vol. 60, pp. 101-109, 1997b.
- Snyder W., Z. Wan, Y. Zhang, and Y.-Z. Feng, "Classification-based emissivity for land surface temperature measurement from space," *Int. J. Remote Sens.*, vol. 19, no. 14, pp. 2753-2774, 1998.
- Snyder W. and Z. Wan, "BRDF models to predict spectral reflectance and emissivity in the thermal infrared," *IEEE Trans. Geosci. Remote Sens.*, vol. 36, no. 1, pp. 214-225, 1998.
- Townshend J. R. G., C. O. Justice, D. Skole, J.-P. Malingreau, J. Cihlar, P. Teillet, and S. Ruthenberg, "The 1km resolution global data set: needs of the International Geosphere Biosphere Programme," *Int. J. Remote Sens.*, vol. 15, pp. 3417-3441, 1994.
- Wan Z. and J. Dozier, "A generalized split-window algorithm for retrieving land-surface temperature from space," *IEEE Trans. Geosci. Remote Sens.*, vol. 34, no. 4, pp. 892-905, 1996.
- Wan Z. and Z.-L. Li, "A physics-based algorithm for retrieving land-surface emissivity and temperature from EOS/MODIS data," *IEEE Trans. Geosci. Remote Sens.*, vol. 35, no. 4, pp. 980-996, 1997.
- Wan Z. "Estimate of noise and systematic error in early thermal infrared data of the Moderate Resolution Imaging Spectroradiometer (MODIS)," *Remote Sens. Environ.*, vol. 80, no. 1, pp. 47-54, 2002.
- Wan Z., Y. Zhang, Z.-L. Li, R. Wang, V. V. Salomonson, A. Yves, and R. Bosseno, "Preliminary estimate of calibration of the Moderate Resolution Imaging Spectroradiometer (MODIS) thermal infrared data using Lake Titicaca," *Remote Sens. Environ.*, vol. 80, no. 3, pp. 498-515, 2002.
- Wan Z., Y. Zhang, Q. Zhang, and Z.-L. Li, "Validation of the land-surface temperature products retrieved from Terra Moderate Resolution Imaging Spectroradiometer data," *Remote Sens. Environ.*, vol. 83, no. 1-2, pp. 163-180, 2002.

Quantitative Estimates of Soil Emissivity from ASTER Data

Thomas Schmugge¹, Frederic Jacob¹, Andrew French² and Kenta Ogawa¹

¹USDA Hydrology & Remote Sensing Lab, Beltsville, MD 20705, USA

²Hydrological Sciences Branch, NASA Goddard Space Flight Center

Tel: 301-504-8554, FAX: 301-504-8931, email: schmugge@hydrolab.arsusda.gov

ABSTRACT: *With the successful launch of the Terra satellite in December 1999 a new tool for observing land surface properties became available, i.e. multispectral thermal infrared data from the Advanced Spaceborne Thermal Emission and Reflection (ASTER) radiometer. ASTER has 5 channels in the 8 to 12 micrometer wave band with 90 meter resolution. These data can be used to assess the spectral variations of surface emissivity. Knowledge of the surface emissivity is important for determining the radiation balance at the land surface. This is significant for arid lands with sparse vegetation because the emissivity of the exposed soils and rocks is highly variable. The results we will present are from ASTER data acquired over the Jornada Experimental Range in New Mexico during 2000 and 2001, a total of 9 scenes. The Jornada site is typical of a desert grassland where the main vegetation components are grass and shrubs with a large fraction of exposed soil. The Temperature Emissivity Separation (TES) algorithm is used to extract the temperature and 5 emissivities from the 5 channels of ASTER data. TES makes use of an empirical relation between the range of observed emissivities and their minimum value. In spite of the 90 m resolution, the results appear to be in quantitative agreement with laboratory measurements of the emissivity for the quartz rich soils of the site with values < 0.85 for the 8 - 9 micrometer channels. For the longest wavelength channel little spatial variation of the emissivity was observed with values of 0.96 ± 0.005 over large areas. The White Sands National Monument with its dunes of gypsum sand was also within several of the scenes. Emissivity values from May, 2000 through May, 2002 scenes for the gypsum at White Sands were in good agreement with values calculated from the lab spectra for gypsum and with each other. The results for vegetated targets show little or no spectral variation with emissivities > 0.97. Ground TIR brightness temperature measurements were made in 7 x 7 grids with 5 m spacing using broadband radiometers at several sites. The resulting average temperatures were in good agreement with those derived from the ASTER data.*

1 INTRODUCTION

The Advanced Spaceborne Thermal Emission and Reflection radiometer (ASTER) (Yamaguchi et al., 1998) on the Terra satellite provides a new tool for studying the earth's surface. The multichannel thermal infrared (TIR) band makes it possible to extract both surface temperature and spectral emissivity from the data. The Temperature Emissivity Separation (TES) (Gillespie et al., 1998) algorithm is used to extract the temperature and 5 emissivities from the 5 channels of ASTER TIR data. TES makes use of an empirical relation between the range of observed emissivities and their minimum value. This approach will be demonstrated with data acquired over the Jornada Experimental Range in New Mexico. Knowledge of the surface emissivity is important for determining the radiation balance at the land surface. For heavily vegetated surfaces there is little problem since the emissivity is relatively uniform and close to one. However, for arid lands with sparse vegetation the problem is difficult because the emissivity of the exposed soils and rocks is highly variable. This is shown in Fig. 1 where laboratory measurements of emissivity for several relevant soils are presented. In particular note the strong variations of emissivity in the

8 to 9 μ m region. The results we will present are from ASTER data acquired over the Jornada Experimental Range and the White Sands National Monument in New Mexico between May 2000 and May 2002. The Jornada site is typical of a desert grassland where the main vegetation components are grasses and shrubs.

2.1 JORNADA SITE

The Jornada Experimental Range lies between the Rio Grande flood plain (elevation 1190 m) on the west and the crest of the San Andres mountains (2830 m) on the east. The Jornada is 783 km² in area and is located 37 km north of Las Cruces, New Mexico on the Jornada del Muerto Plain in the northern part of the Chihuahuan Desert. The larger Jornada del Muerto basin is typical of the Basin and Range physiographic province of the American Southwest and the Chihuahuan Desert.

Several sites in the Jornada were chosen for analysis to cover a range of vegetation conditions from grassland to shrub dominated (mesquite or creosote). The sites are: grass, mesquite, transition and creosote. The grass site is in a fairly level area where black grama grass dominates and encompasses an enclosure where grazing has been excluded since 1969. Honey mesquite on coppice dunes dominates a shrub site. The dunes vary in height from 1 to 4 m with honey mesquite bushes on

each dune. Bare soil dominates the lower areas between these coppice dunes with most of this area covered by a darker soil with a consolidated crust. The transition site is between the grass and mesquite site and represents the degradation from a good grassland to the shrub dominated mesquite area. The creosote site is also fairly level with the shrubs being smaller and closer together than those at the mesquite site.

A portion of the interdunal area at the mesquite site is covered by a bright quartz-rich sand. Samples of these two soils were taken to the Jet Propulsion Laboratory for measurements of their emissivity spectra. The results are shown in Fig. 1 along with the ASTER spectral response functions and the emissivity spectra for the gypsum sand from the White Sands area. It is clear that there will be a significant variation of the emissivity for the 5 ASTER channels for these soils with the longer wavelength ones ($8 < \lambda < 9.5\mu\text{m}$) having noticeably lower emissivities.

2.2 ASTER

ASTER has 5 thermal infrared channels between 8 and 12 μm as seen in Fig. 1. The central wavelengths of the channels are: 8.29, 8.63, 9.08, 10.66 and 11.29 μm . These channels have a spatial resolution of 90 m. The radiance at the satellite is given by

$$L_j(\text{surf}) = (L_j(a/c) - L_j(\text{atm}\uparrow)) / \tau_j \quad (1)$$

where the values of τ_j and $L_j(\text{atm}\uparrow)$ can be calculated using an atmospheric radiative transfer model, e.g. MODTRAN-4, with atmospheric profile data from NCEP. The profile was adjusted for the surface temperature and humidity conditions observed on the Jornada. The remaining problem is to relate these radiances to the surface emissivity in the 5 channels without direct knowledge of the temperature, T_{grd} using the relation:

$$L_j(\text{surf}) = \epsilon_j \text{BB}_j(T_{\text{grd}}) + (1 - \epsilon_j) \cdot L_j(\text{atm}\uparrow) \quad (2)$$

where $\text{BB}(T)$ is the Planck equation for the radiation from a black body. These radiances are used in the TES algorithm (Gillespie, et al., 1998) to extract the surface temperature and the 5 emissivities. The approach has been successfully demonstrated with data from multispectral thermal infrared data onboard aircraft platforms for this site (Schmugge et al., 2002).

3. RESULTS AND CONCLUSIONS

The radiances for a 2 by 2 pixel area (~ 180 by 180 m) from White Sands were analyzed for the May dates and the emissivity results are presented in Fig. 2 for 3 days of observation in May 2000 and May 2001. The solid circles are the results from laboratory measurements.

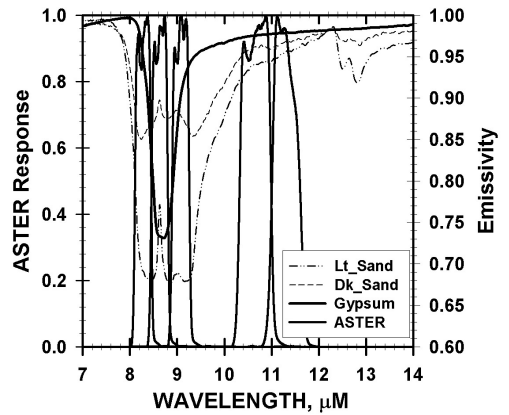


Fig. 1 Plots of the spectral emissivity for 3 soils from New Mexico and the response functions for the 5 ASTER thermal infrared channels. Note that the emissivity curve for the light sand is the one that goes below 0.70.

The ASTER results show excellent agreement with the laboratory results and with each other for the center 3 bands. The latter were obtained for each ASTER channel by integrating the product of the ASTER response and gypsum emissivity curve shown in Fig. 1. The agreement is particularly clear for the low emissivity 8.6 μm channel. Bands 10 (8.29 μm) and 14 (11.29 μm) show the biggest differences. These are the bands with the strongest atmospheric effects and may indicate inadequate correction. The open symbols are the results from a CIMEL 312 (Legrand et al., 2000) radiometer which has approximately the same 5 spectral bands as ASTER. The shortest wavelength band of the CIMEL is a little longer than that of the ASTER band and as a result shows a much lower emissivity than those observed by ASTER band 10. For the other channels the agreement is very good.

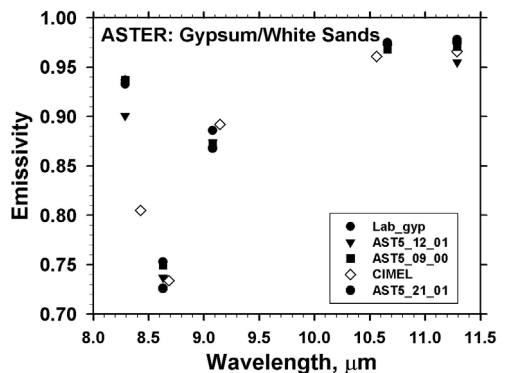


Fig.2. ASTER emissivity results for a gypsum site.

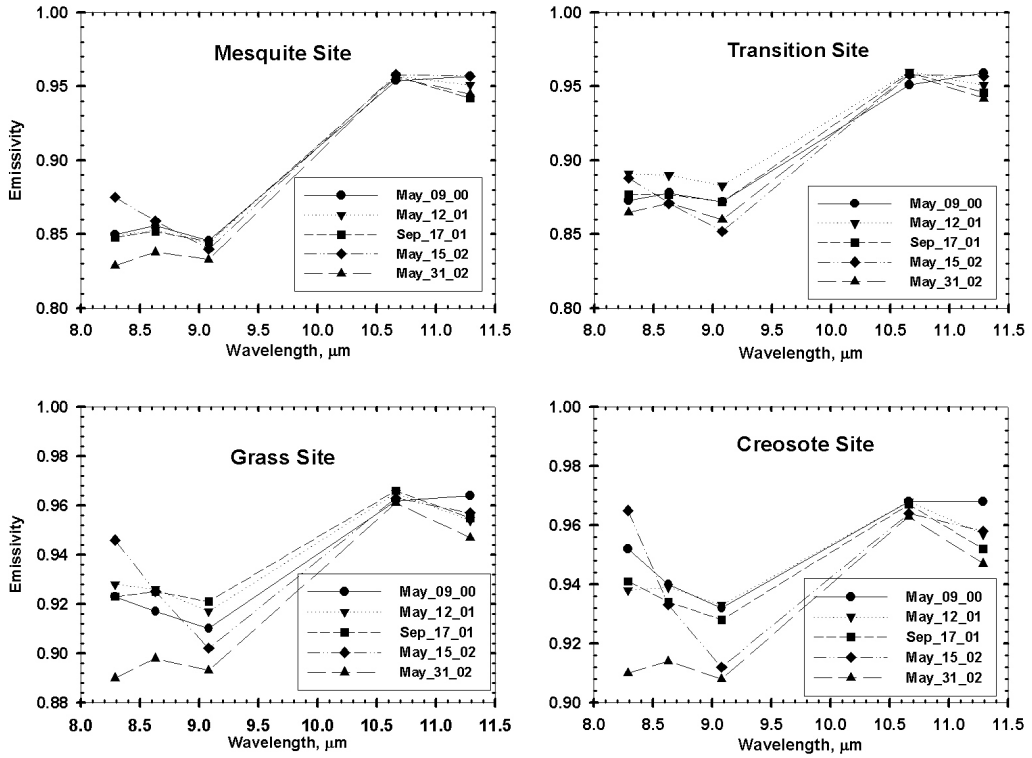


Fig. 3. ASTER results for the 4 sites at the Jornada from 5 observations between 5/09/00 and 5/31/02.

The results from the four Jornada sites for 5 dates from May 9, 2000 to May 31, 2002 are given in Fig. 3. There is good agreement amongst the ASTER results for all 5 channels for both the mesquite and transition sites. In these cases there is a small difference between the lab results (not shown) and the ASTER results, e.g. < 0.03 for the 5 channels. At the mesquite site we made field measurements with the CIMEL 312 radiometer and found that there was good agreement between the ground measurements for the dominant dark soil and the ASTER results. As seen in the figure there is reasonable consistency amongst the the ASTER results for the 5 different days.

The results from the grass and creosote sites show reasonably good agreement for the 3 dates in 2000 and 2001. However the two dates in 2002 show consistently lower emissivity values, especially for the long wavelength channels. At the present time we do not have an explanation for this difference, but we suspect that it could be due lower vegetation cover resulting from the drier than normal conditions.

Ground measurements of surface brightness temperature, T_B , were made on a 7×7 grid with 5 meter spacing using a broadband, 7 to $14 \mu\text{m}$, radiometer at these sites. A summary of the results are given in Fig.

4 for the four dates on which we have nearly coincident ground measurements and an ASTER overpass. The ground data are presented in boxplots at the times bracketing the overpass, i.e. 11:30 and 12:30 MDT, or coincident with the overpass (about 12:00 MDT) for the four sites. The box shows the range for 50% of the observations and bright line in the box indicates the median for the data. The line represent outliers in the measurements beyond that expected for a normal distribution indicated by the brackets. The range of T_B for the 5 ASTER channels is presented by the up and down triangles. It is expected that the broadband emissivity for the ground measurements would be within the range of those for the 5 ASTER channels, and thus the average ground T_B should be within the ASTER T_B range as seen in Fig. 4. It is seen that there is reasonable agreement but the ASTER data are a bit cooler.

These results indicate that the TES algorithm appears to work as well with the data from space as it did with the aircraft data presented earlier (Schmugge, et al., 2002). This is encouraging for the application of the technique for mapping emissivity over large areas. An example of this is shown in Fig. 5 where we have plotted an estimate of the broadband (3 - $14 \mu\text{m}$) emissivity from a linear combination of the emissivities

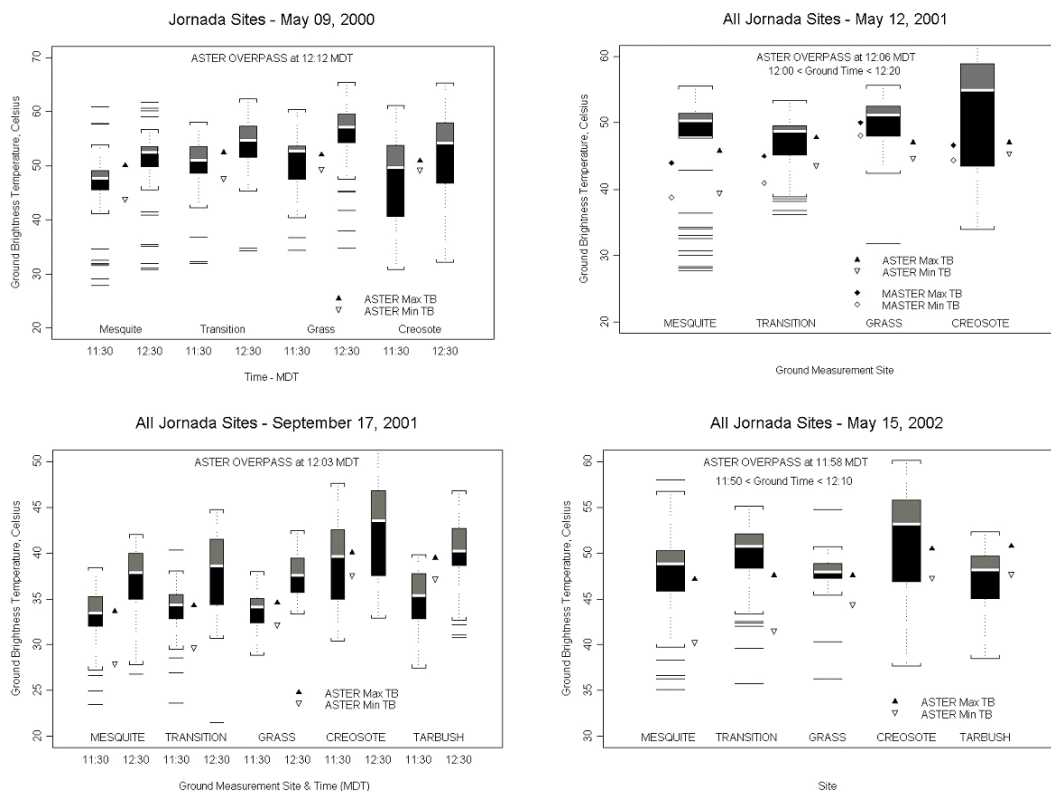


Fig. 4. ASTER brightness temperatures at the surface compared with nearly coincident ground measurements.

for the 5 ASTER bands (Ogawa et al., 2002). This result is for the May 12, 2001 for the Jornada. The range of emissivities is from 0.92 to about 0.98, with the low values being for the exposed soils and the gypsum of White Sands which is at the upper right. The high emissivity areas are along the San Andreas mountain ridge running roughly north - south through the scene and irrigated agricultural fields along the Rio Grande.

As noted above, there was also good agreement between the ASTER brightness temperatures and ground measurements

4. ACKNOWLEDGMENT

This research was supported by the ASTER project of NASA's EOS-Terra program. The laboratory emissivity measurements were made by Cindy Grove of the Jet Propulsion Laboratory. The NCEP profiles were provided by Ron Alley of JPL.

5. REFERENCES

Gillespie, A., S. Rokugawa, T. Matsunaga, J. S. Cothorn, S. Hook, and A. B. Kahle, 1998. A temperature and emissivity separation algorithm for Advanced Spaceborne Thermal Emission and

Reflection Radiometer (ASTER) images. *IEEE Transactions on Geoscience and Remote Sensing*, vol. **36**, pp. 1113-1126, 1998.

Legrand, M., C. Pietras, G. Brogniez, M. Haefelin, N.K. Abuhassan and M. Sicard, 2000. A High-accuracy multiwavelength radiometer for in situ measurements in the thermal infrared. Part 1: Characterization of the instrument. *Journal of Atmospheric & Oceanic Technology*, vol. **71**, pp. 1203-1214, 2000.

Ogawa, K., Schmugge, T., A. French, Jacob, F. 2002. Estimation of broadband land surface emissivity from multi-spectral thermal infrared remote sensing. To be published in *Agronomie*, **22**.

Schmugge, T., A. French, J.C. Ritchie, A. Rango, and H. Pelgrum, 2002. "Temperature and emissivity separation from multispectral thermal infrared observations." *Remote Sensing of Environment*, vol. **79**, pp. 189 - 198, 2002.

Yamaguchi, Y., A. B. Kahle, H. Tsu, T. Kawakami, and M. Pniel, 1998. Overview of Advanced Spaceborne Thermal Emission and Reflection Radiometer (ASTER). *IEEE Transactions on Geoscience and Remote Sensing*, vol. **36**, pp. 1062-1071, 1998.

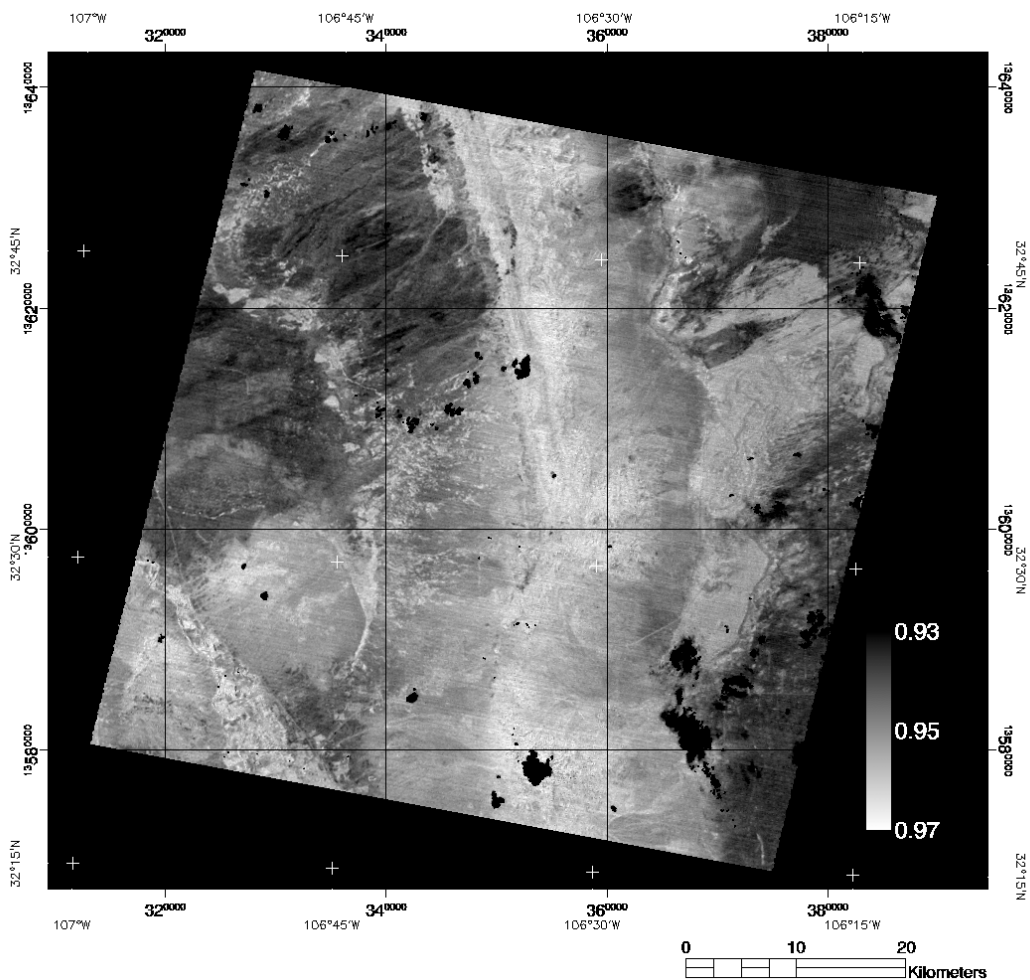


Fig. 5. Broadband emissivity map of the Jornada experimental range area in south central New Mexico. The White Sands National Monument is the low emissivity area at the upper right. The irrigated fields along the Rio Grande are in the high emissivity area in the lower left.

Relati it o Isot er al De inition an Its S alin E e ts in antitati e T er al In rare Re ote Sensin

Ren-Hua Zhang¹, Zhao-Liang Li², Xinzhai Tang¹, Xiaomin Sun¹, Hongbo Su¹, Caiying Zhu¹, Zhilin Zhu¹

¹ Institute of Geographic Sciences and Natural Resources Research, CAS, Beijing, 100101, China.

Email: zhangrg@igsnr.ac.cn, Fax: 86-10-64858099

² TRIO/LSIIT (CNRS UMR 7005), 5 Bld. Sebastien Brant, 67400 Illkirch, France

ABSTRACT *Three definitions of emissivity for non-isothermal pixel are evaluated, and their differences are analyzed. On the basis of the experimental data and numerical simulation, a generalized formula is established to scale for land surface emissivity, reflectance, and others variables between pixel scale and sub-pixel scale. Finally, it is pointed out that isothermal concept of land surface temperature and homogeneous concept of some other parameters in one spatial scale is relative according to human's capability of measurement and heterogeneity in a spatial scale is absolute in natural world.*

1. INTRODUCTION

With the further development of earth system science exploration technology, human begins to study the natural processes of earth surface more and more in the regional scale and even in planet scale, such as global change, estimation of crop yields in large area, regional water balance. The instruments of acquiring data, however, are still limited to the measurement in rather small scale, which we usually call it point measurement. For most usually used biophysical parameters such as surface temperature, soil moisture, leaf area index (LAI), the observations of these items are mostly restricted to local points. Among them, the observation of land surface temperature from meteorological and ecological stations generally employs glass thermometer of which the sensor bulb has a diameter less than 1cm. As well known, observation resulting from this method lacks regional representation. It is a challenge to overcome contradiction between the need and the supply for geo-scientific information in the exploration of nature. Since the emergence of the technology of remotely measuring temperature using thermal infrared radiometer, the average radiometric temperature of about 1 square meter can be measured by thermal infrared radiometer on ground. Once the thermal infrared radiometer is mounted on airborne or space-borne, it can measure the average temperature for an area of several hundreds or thousands of square

meters. Thermal infrared scanning radiometer thus can measure the distribution of temperature in two dimensions by mechanical or electronic scanning. It should be noted that the sensor can only give an average value on a pixel scale. Because the earth surface parameters are almost always heterogeneous distributed in the area of a pixel, how to understand the average value in pixel scale becomes an interesting research field.

In the first part of this paper, we shall focus our discussion on several definitions of emissivity for pixels with non-isothermal surface. Their validation will be performed by means of a special designed experiment in the second part. In the third part of this paper, a general scaling rule from sub-pixel to pixel will be put forward. Finally conception of the relativity of isothermal surface will be discussed.

2. DEFINITIONS AND CONCEPTIONS OF SCALING FOR EMISSIVITY

Non-isothermal pixel can be regarded to be composed of many isothermal sub-pixels with different temperatures. To understand the sub-pixel information from pixel scale, currently, there have been some definitions of emissivity for non-isothermal pixel (Dozier and Warren 1982, Becker and Li 1995, Norman and Becker 1995, Li et al. 1999). What is called definition of emissivity for non-isothermal pixel, in fact, is a simple algorithm to express effective emissivity on pixel scale using sub-pixel information.

It involves some important conceptions in scaling.

First, definition of r -emissivity will be discussed. It is based on the Kirchhoff's law and the opacity of objects in thermal infrared band. Its most advantage is that it is measurable from space. For a flat pixel composed of two homogeneous sub-pixels, if sub-pixel information is known, the emissivity for this pixel can be expressed as the function of the sub-pixel emissivities ($\varepsilon_1, \varepsilon_2$), i.e.

$$\varepsilon = a_1\varepsilon_1 + a_2\varepsilon_2 \quad (1)$$

where a_1 and a_2 are the area proportion of sub-pixel in the whole pixel, $a_1 + a_2 = 1$, according to the Kirchhoff's law, for an opaque surface, $\varepsilon + \rho = 1$, equation (1) can be rewritten as

$$\varepsilon = a_1(1 - \rho_1) + a_2(1 - \rho_2) = 1 - \rho \quad (2)$$

If sub-pixel information is not known, emissivity in a pixel scale can only be defined through reflectivity on the basis of the Kirchhoff's law

$$\varepsilon = 1 - \rho \quad (3)$$

According to the radiative energy conservation, $\rho = a_1\rho_1 + a_2\rho_2$, equation (3) becomes

$$\varepsilon = 1 - (a_1\rho_1 + a_2\rho_2) = a_1\varepsilon_1 + a_2\varepsilon_2 \quad (4)$$

Since equations (1) and (4), (2) and (3) are identical, emissivities for a whole pixel defined by these two approaches are indifferent.

Another definition of emissivity is e -emissivity. Assuming that there is an equivalent black body, which has an identical temperature distribution with non-isothermal pixel, e -emissivity is defined as the ratio of the radiance from the pixel to that from the equivalent black body (Norman and Becker 1995).

$$\varepsilon = \frac{a_1\varepsilon_1 B_\lambda(T_1) + a_2\varepsilon_2 B_\lambda(T_2)}{a_1 B_\lambda(T_1) + a_2 B_\lambda(T_2)} \quad (5)$$

where $B_\lambda(T_1)$ and $B_\lambda(T_2)$ are radiance of black body with temperature T_1 and T_2 respectively. The numerator and denominator of equation (5) are respectively the weighted sum of radiance emitted by each sub-pixel and their corresponding black body radiance. It should be noted that the equivalent black body introduced in e -emissivity definition does not exist because the radiations emitted by the composite of different blackbodies do not have the behaviors of a

blackbody due to the non-linearity of the Planck function with temperature, and the e -emissivity defined by equation (5) depends on the temperature of each sub-pixel. In order to make the radiance emitted by the equivalent black body following the Planck law, Li et al. (1999) proposed another emissivity definition.

$$\varepsilon = a_1\varepsilon_1 + a_2\varepsilon_2 + (a_2\varepsilon_2\Delta T_2 - a_1\varepsilon_1\Delta T_1) \frac{dB_\lambda(T)}{dT} \bigg|_{T=T_0} \quad (6)$$

where T_0 is a reference temperature for the whole pixel, it may take average value of temperatures in the whole pixel. ΔT_1 and ΔT_2 are temperature differences between T_0 and T_1 , between T_0 and T_2 respectively.

Three definitions listed above are all to deal with scaling between the whole pixel and sub-pixels. Some questions should be put forward: 1. What are basic factors, which result in the differences of these definitions for effective emissivity from sub-pixel to pixel scales? 2. How to validate some important conception concerning with isothermal surfaces? These questions imply some important conception in scaling not only for emissivity but also for other parameters in quantitative remote sensing. To answer these questions and validate these conceptions in scaling from sub-pixel to pixel, we design and conduct an experiment to fulfill such a goal.

3. EXPERIMENT AND VALIDATION OF SOME CONCEPTIONS

3.1 Design of the Experimental Device and Conditions

To study the emissivity scaling between isothermal sub-pixel and non-isothermal pixel, the experiment should enable the measurement of r -emissivity in different scales and supply as much as possible the true surface temperature, which is required for the validation of some classical emissivity definitions. Thus, the idea of this experiment is to construct a whole pixel with four area identical sub-pixels (boxes) as showed in figure 1. The upper surfaces of these four boxes have different combination of emissivity and temperature: high surface emissivity with high temperature, high surface emissivity with low temperature, low surface emissivity with high temperature and low surface emissivity with low temperature. The boxes are aluminum containers that can be filled by water. Water filled inside can make the box surface an isothermal surface. Surface temperature

of box is controlled by water with different temperatures. The upper surfaces of two boxes were polished to gray-white body with an average surface roughness of 2 to 5 μm , which can give low emissivity without specular reflection. High emissivity surface is the aluminum board that was sprayed a layer of black lacquer.

Low irradiance of sky in clear day and relatively high irradiance of a field tent above the boxes can supply two different environmental irradiances, which is a prerequisite to measure directly emissivity from emission of surface in both laboratory and field. Sensor we employed is a non-frozen thermal camera, its sensitivity is 0.1°C. Upper surfaces of the four square-boxes can be regarded as sub-pixel surfaces and combining the upper surfaces of these four boxes can form a square surface we call it pixel through the whole paper. Putting the four boxes inside and outside of the tent alternately, the thermal camera can produce the thermal images with different environmental irradiances. As shown in the next sub-section, surface emissivity can be derived from four measurements corresponding to target in tent, target out of tent, sky and inside surface of tent.



Figure 1. Photos of the experiment setup taken at different angles

3.2. Effective Emissivity Measurements at Two Different Scales

Radiometric temperatures of four sub-pixels and the whole pixel can be measured with thermal camera.

Figures 2 shows the radiometric temperatures of these four sub-pixels. The effective radiometric temperature of the irradiance from the tent (T_p) and sky (T_{sky}) can also be obtained from camera measurements. On the basis of the radiative transfer equation, the radiance M_{li} of target i (i represents either one of four sub-pixels or the whole pixel) measured out of tent can be written as (Wan and Li 1997)

$$M_{li} = \varepsilon_i B(T_{si}) + (1 - \varepsilon_i) B(T_{sky}) \quad (7)$$

and the radiance M_{2i} of target i in the tent can be expressed as

$$M_{2i} = \varepsilon_i B(T_{si}) + (1 - \varepsilon_i) B(T_p) \quad (8)$$

Eliminating the radiance emitted by target itself from equations (7) and (8), the r -emissivity of a whole pixel and emissivities of sub-pixels can be obtained from

$$\varepsilon_i = 1 - \frac{M_{2i} - M_{li}}{B(T_p) - B(T_{sky})} = 1 - \rho_i \quad (9)$$

It should be noted that the denominator of equation (9) is identical for sub-pixel as well as for the whole pixel, therefore, area weighted average emissivity of the two scales will be the same. The rule of scaling will be discussed in the section 4. The method of emissivity determination agrees with r -emissivity definition

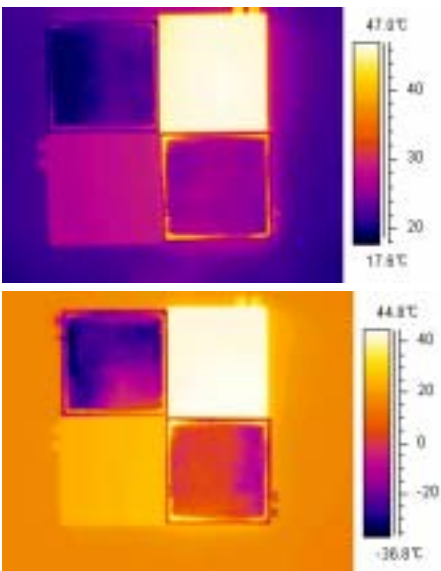


Figure 2: radiometric temperatures of four sub-pixels upper image: in tent, right image: out of tent

3.3. Correction of Radiometric Temperature

Because the temperature of target and that of the environment are different, there exists the energy exchange between them before reaching the status of energy equilibrium. Lower temperature is increasing while higher temperature is decreasing. The speed of temperature change is dependent on the heat balance of the surface. The correction of radiometric temperature or emittance plays a key role in improving the accuracy of emissivity measuring. Within the interval of the two measurements of environmental irradiance, the temperature of object can be corrected as $\frac{T_{Ti} + T_{Ti+1}}{2} - T_{Ei}$ and $T_{Ti} - T_{Ei}$ or $T_{Ei+1} - T_{Ei}$, where the T_{Ti} and T_{Ti+1} are the i th and $(i+1)$ th radiometric temperatures of object under the irradiance of tent. T_{Ei} and T_{Ei+1} are the i th and $(i+1)$ th radiometric temperatures of object under the irradiance of sky. The experiment points out that this kind of correction method is and feasible and useful for improving measuring precision of the emissivities.

3.4. Experimental Results

As shown in the previous subsections (see also figures 1 and 2), emittance and environmental irradiances required in equation (9) for each sub-pixel and for the whole pixel can be obtained from the thermal camera measurements. Therefore, emissivity at two spatial scales (sub-pixel and pixel scales) can be determined using different definitions. The goal of this experiment is to understand the difference of emissivity resulting from different definitions and to study the rules of scaling.

With camera measurements, emissivities for four sub-pixels are first derived using equation (9), and then emissivity for a whole pixel is obtained by the area weighted average of sub-pixel emissivities (equation (1)). This emissivity for a whole pixel called *r*-emissivity should be equal to that determined by

equation (9) as demonstrated by equations (3) and (4). *e*-emissivity is also derived using the data collected in this experiment with equation (5). Table 1 shows the derived emissivity for each sub-pixel and the emissivities for a whole pixel derived using different definitions with/without correction of temperature change during the period of measurements as discussed in subsection 3.3.

From this experiment, some remarks can be made:

1. The experiment shows that emissivity can only be measured by changing the irradiance of environment according to the conception of *r*-emissivity (equation 9). The emissivity at pixel scale measured by a thermal camera from equation (9) does not conflict with general physical conception.
2. Because of the change of environmental irradiance, there exists a fluctuation in temperature of target. The surface temperature should be corrected before emissivity calculation. The computed emissivity is reduced by 0.013-0.038 after temperature correction. Therefore the emissivity derived after temperature correction is used in the following discussion.
3. According to equation (9), the emissivities of sub-pixels are 1.009 for high emissivity with high temperature, 1.000 for high emissivity with low temperature, 0.236 for low emissivity with low temperature and 0.314 for low emissivity with high temperature. Considering the emissivity value derived for sub-pixel having high emissivity with high temperature, the accuracy of emissivity determination is less than 0.009.
4. As for emissivity of a whole pixel, it equals 0.640 for *r*-emissivity definition (equation 1). But it is 0.686 and 0.690 respectively for *e*-emissivity (equation 5) and T_0 -emissivity (equation 5). Their differences result from different emissivity scaling.

Table 1. Results of Experiment for Emissivity Scaling

Emissivity	Sub-pixel Scale (eq. 9)				Pixel scale		
	(I)	(II)	(III)	(VI)	<i>r</i> - ϵ (eq. 1)	<i>e</i> - ϵ (eq. 5)	T_0 - ϵ (eq. 6)
T without Correction*	0.993	0.249	1.038	0.332	0.653	0.700	0.703
T with Correction**	1.009	0.236	1.000	0.314	0.640	0.686	0.690
(I). High ϵ High T; (II). Low ϵ Low T; (III). High ϵ Low T; (VI) Low ϵ High T							

*The radiometric temperature without correction means that there is no correction of the surface temperature change under different environmental irradiance.

**The radiometric temperature with correction means the corrections are considered.

3.5. Validation of the Definitions and Some Conceptions

Further analysis on the essentials of the emissivity definitions and some conceptions should be made. The calculation method of sub-pixels in our experiment conforms to the first definition of emissivity (the same with r -emissivity determination), which is applicable when the information of sub-pixels is available or not available, because r -emissivity determination does not need to know sub-pixel information as shown in equation (3), we use only reflectance to calculate emissivity, this is why we call it r -emissivity. The method of e -emissivity determination on pixel scale (equation (5)) is applicable only in the situation that the information of sub-pixels must be available.

Therefore, the two definitions of emissivity are examined through the experiment. The difference between them is due to spatial scaling, which will be discussed in next section. The third definition of emissivity (equation 6) needs to find an average temperature (T_0) although the temperatures of sub-pixels (T_1 and T_2) are unknown. Starting with the area weighted average of radiances, i.e.

$$\varepsilon_{A3}B(T_0) = a_1\varepsilon_1B(T_1) + a_2\varepsilon_2B(T_2) \quad (10)$$

where ε_{A3} is emissivity defined for a whole pixel by Li et al. (1999).

Dividing $B(T_0)$ on the two sides of equation (10), one gets

$$\varepsilon_{A3} = a_1\varepsilon_1 \frac{B(T_1)}{B(T_0)} + a_2\varepsilon_2 \frac{B(T_2)}{B(T_0)} \quad (11)$$

By analogue, r -emissivity (denoted ε_{A1}) defined in equation (1) can be rewritten as

$$\varepsilon_{A1} = a_1\varepsilon_1 \frac{B(T_1)}{B(T_1)} + a_2\varepsilon_2 \frac{B(T_2)}{B(T_2)} \quad (12)$$

Moreover, considering that $a_1 + a_2 = 1$, equation (11) can be rewritten in the same form of equation (5) (e -emissivity) as

$$\varepsilon_{A3} = \frac{a_1\varepsilon_1B(T_1) + a_2\varepsilon_2B(T_2)}{a_1B(T_0) + a_2B(T_0)} \quad (13)$$

Comparing equations (12) with equation (11), and equation (13) with equation (5), we note that their difference is just that T_1 and T_2 are replaced by T_0 in the denominator and the definition given in equation (6) can be a chain between the r -emissivity (equation (1)) and the e -emissivity (equation (5)) if the black

body temperatures (denominators) of sub-pixels are identical. The transformation will be discussed in section 4.

Subtracting equation (11) from equation (1) yields the difference of emissivity ($\Delta\varepsilon$) resulting from two definitions,

$$\Delta\varepsilon = \varepsilon_{A1} - \varepsilon_{A3} = a_1\varepsilon_1\left[1 - \frac{B(T_1)}{B(T_0)}\right] + a_2\varepsilon_2\left[1 - \frac{B(T_2)}{B(T_0)}\right] \quad (14)$$

Seven parameters including a_1 , a_2 , ε_1 , ε_2 , T_1 , T_2 , and T_0 have to be known to get the difference of emissivities given by two different definitions. In our experiment, $a_1 = a_2 = 0.5$, ε_1 and ε_2 are determined by the experiment because of its invariance with temperature. What are left to be determined are surface temperatures T_1 , T_2 , and T_0 . Because the upper surface of the container which was sprayed a layer of black lacquer has high emissivity closed to unit and water inside the container has a very high heat capacity, the radiometric temperature measured by the thermal camera is therefore very closed to the true surface temperature T_1 . Two containers with different surface emissivity are filled with water with identical temperature. Thus, sub-pixel (container) having low emissivity has the same true surface temperature (T_1) as the high emissivity one (true at least when water is just filled in). The low temperature of the two other containers is achieved by filling water with temperature approximately equal to the atmospheric temperature, which will produce a stable temperature for a longer period of time by reducing the heat exchange between the surface and atmosphere. Thus, the radiometric temperature measured by thermal camera for high emissivity with low temperature surface will be equal to its surface temperature (T_2). Because the low emissivity with low temperature container is filled with water with the same temperature, the low emissivity surface will have the same temperature T_2 . Knowing T_1 , and T_2 , $B(T_1)$ and $B(T_2)$ in the bandwidth of thermal camera can be calculated using numerical integration of Planck function in the bandwidth from 8 to 14 μ m. T_0 is computed from T_1 and T_2 by weighted average of energy flux. Then $B(T_0)$ can be obtained. Calculation results show that for $\varepsilon_1=0.236$, $\varepsilon_2=1.00$, according to equation (14), the difference of emissivity, $\Delta\varepsilon$, is equal to 0.05. The magnitude of $\Delta\varepsilon$ depends on (T_1 - T_0) and T_1 .

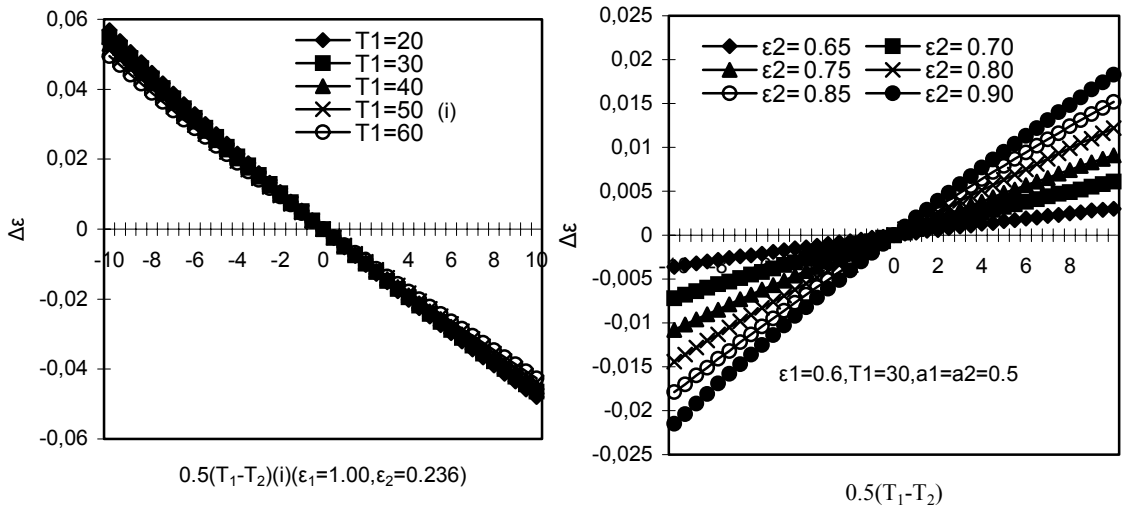


Figure 3. Quantitative relationship among $\Delta\epsilon$, emissivity and temperature difference of two sub-pixels

Figure 3 shows the relationship among T_1-T_0 , T_1 and $\Delta\epsilon$ when $\epsilon_1=1.00$, $\epsilon_2=0.236$ using the simulated data. From this figure, we can see that $\Delta\epsilon$ increases with increase of T_1-T_0 and it is almost independent on T_1 . The variance of $\Delta\epsilon$ is asymmetrical over the zero point. When the (T_1-T_0) is -10°C , the $\Delta\epsilon$ can reach 0.06. Therefore, the $\Delta\epsilon$ must be evaluated to fulfill the emissivity scaling and to conform to the physical conceptions..

4. SCALING RULE BETWEEN SUB-PIXEL AND PIXEL SCALES

The experimental results of scaling for emissivity enlighten us to search for scaling rule between sub-pixel and pixel scales for any parameters with generalized meaning. In the classical theoretical calculation of emissivity (equations (5) and (6) or (13)), emittance of both target and blackbody were obtained by integrating the Planck function over a certain bandwidth in terms of true temperature. Knowing the emittance of sub-pixels and that of the corresponding black body, the ratio of the two radiances is called emissivity (In fact, there must be a particular instrument to determine the radiances instead of theoretical calculation). Notice that the two emittances can be only obtained separately, and what is calculated is a ratio of the two emittances. This is important condition to establish the scaling rule below. For n sub-pixels, equations (1) and (5) can be

expressed in terms of the radiance M_i ($i=1,..n$) emitted by the sub-pixel i and the emittance M_{Bi} emitted by a black body having the same surface temperature than that of sub-pixel i :

$$\epsilon_{A1} = \sum_{i=1}^n a_i \frac{M_i}{M_{Bi}}, \text{ and} \quad (15)$$

$$\epsilon_{A2} = \frac{\sum_{i=1}^n a_i M_i}{\sum_{i=1}^n a_i M_{Bi}} \quad (16)$$

where $M_i = \epsilon_i M_{Bi} = \epsilon_i B(T_{si})$ and $\sum_{i=1}^n a_i = 1$.

The difference between above two equations is obvious.

Another case is the measurement of spectral reflectance by a spectrometer. Generally, the reflectance ρ in visible and near infrared band is calculated from the definition of reflectance, i.e.

$$\rho = \frac{R}{E} \quad (17)$$

The procedure of measurement is that the reflected radiance R in each band is measured firstly, then, the irradiance E in that band is calculated via the reference board. As noted above, the reflected radiance and the irradiance are measured separately. There are two methods to calculate reflectance for a broadband from narrow bands measurements. Assuming the bandwidth

of narrow band is equal and their weighted coefficient is $1/n$, then as done for equations (15) and (16), one gets

$$\bar{\rho}_{A1} = \frac{1}{n} \left(\frac{R_{\lambda 1}}{E_{\lambda 1}} + \frac{R_{\lambda 2}}{E_{\lambda 2}} + \dots + \frac{R_{\lambda n}}{E_{\lambda n}} \right), \quad (18)$$

$$\bar{\rho}_{A2} = \frac{\sum_{i=1}^n R_{\lambda i}}{\sum_{i=1}^n E_{\lambda i}} = \frac{\sum_{i=1}^n \rho_i E_{\lambda i}}{\sum_{i=1}^n E_{\lambda i}} \quad (19)$$

where λ denotes wavelength, Since our sensor can only detect the total energy fluxes, that is to say, the spectral resolution is too coarse to measure the narrow band, we have to use the formula given by equation (19) to determine reflectance for a broad band.

The experiment and results of analysis above raise a question, is there a generalized rule in the algorithm to calculate the average value of surface parameters from the heterogeneous sampling data set? In order to answer this question, let us suppose that there is a series of variables (fractions) as

$$\frac{x_1}{y_1}, \frac{x_2}{y_2}, \frac{x_3}{y_3}, \dots, \frac{x_n}{y_n},$$

then, the weighted averaging value of the this series F_1 should be:

$$F_1 = \left(a_1 \frac{x_1}{y_1} + a_2 \frac{x_2}{y_2} + a_3 \frac{x_3}{y_3} + \dots + a_n \frac{x_n}{y_n} \right) = \sum_{i=1}^n a_i \frac{x_i}{y_i} \quad (20)$$

where a_i is the weight and $\sum_{i=1}^n a_i = 1$.

However, sometimes we can only obtain the weighted sum of x series and the weighted sum of y series separately, and what we are interested is the ratio of these two quantities, F_2

$$F_2 = \frac{a_1 x_1 + a_2 x_2 + a_3 x_3 + \dots + a_n x_n}{a_1 y_1 + a_2 y_2 + a_3 y_3 + \dots + a_n y_n} = \frac{\sum_{i=1}^n a_i x_i}{\sum_{i=1}^n a_i y_i} \quad (21)$$

Then difference of F_1 and F_2 is given by

$$\Delta F = F_1 - F_2 = \frac{\sum_{i=1}^n a_i \frac{x_i}{y_i} \sum_{i=1}^n a_i y_i - \sum_{i=1}^n a_i x_i}{\sum_{i=1}^n a_i y_i} \quad (22)$$

From this equation, we notice that $F_1 = F_2 = 0$ if

y_i in the denominator remains constant, which implies that no difference exists between equations (20) and (21). For an isothermal system, the emittance of the corresponding black body is the same for all sub-scales. It is consistent with the conditions discussed above. Therefore the first two definitions of emissivity (equations (1) and (5) or equations (15) and (16) are quite identical. Consequently, if variable is in the form of fraction, such as emissivity, reflectance, SR, regardless of the complexity of the denominator and numerator, the generalized formula (equation (22)) can always be used to predict the difference in scaling.

According to the generalized formula (equation (22)) of the difference in two methods of average. If the variant x in numerator keeps constant, the relationship between the mean variant error of variable y in denominator will be an increasing function. If average variant error of y is zero, then difference of F_1 and F_2 becomes zero too.

The faction of sub-pixel's emittance and black body can solve the emissivity. We can study the emissivity difference of two scales by numerical simulation, and also calculate the averaged emissivity using the equation (1). This average emissivity falls into the category of F_1 discussed above. If we can calculate the sum of emittance for all sub-pixels and that for the black body with the same structure and temperature with the sub-pixels, the ratio of the two values is an emissivity in the category of F_2 . If the T_0 assumed in the third definition is equal to the temperature inverted from the radiance of the total pixel, $\Delta \varepsilon$ will be the emissivity difference between two scales.

5. RELATIVITY OF ISOTHERMAL FOR LAND SURFACE TEMPERATURE

We have discussed the rules of emissivity scaling between non-isothermal pixel and isothermal sub-pixels. The ideas can be extended to some other land surface parameters such as reflectance and simple ratio SR and NDVI vegetation index. These parameters are searched for quantitative remote sensing.

An important question is how to judge whether surface temperature is isothermal surface and how to judge whether the land surface parameters are homogeneous in a certain spatial scale. According to experiments and experiences, the criteria are dependent on the sensor's radiometric resolution, spectral resolution and spatial resolution. In the

following, we will discuss respectively these three kinds of resolutions.

5.1. Effect of Spectral Resolution:

According to equations (18) and (19), obviously, there exists difference of reflectance between narrow and broad bands. The analysis of the relationship between reflectance in broad band and that in narrow band shows that if a narrow band measurement $R_{\lambda 1}$ can still be divided into m narrower bands measurements $R_{\lambda 11}, R_{\lambda 12}, \dots, R_{\lambda 1m}$ by an advanced spectrometer, the reflectance $R_{\lambda 1}$ for a narrow band 1 can be derived from m narrower bands measurements as done in equation (19) for a broad band:

$$\frac{R_{\lambda 1}}{E_{\lambda 1}} = \frac{\sum_{i=1}^m R_{\lambda 1i}}{\sum_{i=1}^m E_{\lambda 1i}},$$

This means that whether the bandwidth is broad or narrow is dependent on the spectral resolution of sensor used.

5.2. Effect of Radiometric Resolution

Whether the pixel is of isothermal concept is dependent on the sensitivity and accuracy of the sensor, i.e. thermal radiometric resolution. In practice, the so-called isothermal means that the sensor cannot detect the temperature difference among the sub-pixels. For non-isothermal, it is on the contrary. Similar to the analysis of reflectance, the criteria of isothermal in temperature are related to the sensor's sensitivity. For a sensor with a sensitivity of 0.1C, 0.19C and 0.15C will be regarded as no difference in temperature. For a sensor with a sensitivity of 0.01C, 0.19C and 0.15C will belong to non-isothermal concept. But 0.019C and 0.015C still belong to isothermal. From these examples, we can see that the isothermal concept cannot be separated from the spatial and spectral resolution of the sensor. Actually, the conception of isothermal is relative and dynamic. When the radiometric resolution is improved, the status of isothermal may be changed, because the sensor can detect the difference among the sub-pixels. Therefore, the isothermal is not absolute.

5.3. Effect of Spatial Resolution

The conception of isothermal surface for an area is also relative in natural world. A pixel of NOAA-AVHRR is about 1 square kilometer, which are

composed of many Landsat TM pixels (with an resolution of 120mx120m) with different temperatures. A pixel of TM itself consists of many smaller pixels with different temperatures in airborne thermal image. When we use thermal infrared radiometer, it can detect the temperatures of the sub-pixels in a pixel from airborne image. When it comes a more micro scale, a thermal infrared radiometer with a broad field of view can measure the temperature of flat soil without big clump under sunlight with a spatial resolution of several centimeters. Generally, the measurement results of this scale are thought to be homogeneous and isothermal. In addition, we can find that the temperatures are not homogeneous at all in the thermal image of a thermal camera with high spatial resolution, because the sunlit and shadowed soil shows completely different temperatures in the image.

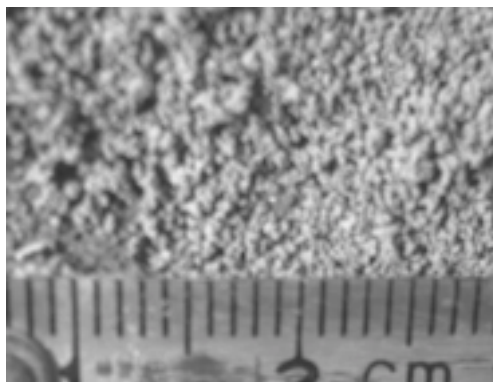


Figure 4, Temperatures of sands present isothermal in pixel scale and heterogeneity in sub-pixel scale. The ruler in picture has a minor mark of 1mm. There are 2 to 3 sand grains in sunlight or shadow in every 1 square millimeter

Some scientists thought prudently that if the number of sub-pixels is more than 30, the range of temperature variance is not too much and the independent temperatures follows the Gaussian distribution, the whole pixel could be treated as an isothermal one. In fact, only if conditions of the sub-pixel number and distribution are met, the non-thermal pixel can be handled as an isothermal one. From the figure 6, it can be seen that the temperature difference of sunlit and shadowed sands is more than 10°C, whereas a thermal infrared radiometer with a wide field of view can only detect the average energy flux for the whole pixel.

With the improvement of the spatial resolution of sensors, the temperature distribution of sub-pixels in the field of view will be nearly the Gaussian distribution. Statistic analyses for a huge amount samples cannot be deemed inaccurate or approximate. Plank Law can be derived from statistical physics based on a huge amount of molecules with different average kinetic energy.

According to above analyses, the conception of temperature is the result of statistical average. When we discuss the isothermal conception of temperature, also should consider it is a results of statistics and relativity, which has a close relation with certain scale. With the guidance of this thought, we want to discuss the essence of emissivity for pixel with non-isothermal (heterogeneous temperature).

The above definitions of emissivity for pixel with non-isothermal surface are common in that they all try to define an average emissivity based on the isothermal sub-pixels. When the information of sub-pixels is not available, some models are adopted to separate the sub-pixels from data in pixel scale. The reason why the temperature of sub-pixels is used to analysis the emissivity in pixel scale is that it will be more precise in physics conception. It also demonstrates that man can be able to study in a scale of higher resolution than the sensor's capability. It's positive and valuable in theoretical research. If the definition can not be measured in practice, its application and value, however, will be limited. After the sensor can measure the ground in a higher spatial resolution and detect the sub-pixels or the sub-pixels' temperature can be separated from the mixed temperature of pixel by multi-angle and multi-time data, the sub-pixel can be treated directly as a homogeneous pixel.

In a word, isothermal in one scale is dependent on human's capability of measurement. Heterogeneity in a spatial scale is absolute in natural world, while isothermal is relative. With the change of scale, isothermal may turn into non-isothermal.

6. CONCLUSIONS

In this paper, we discussed scaling from isothermal sub-pixel to non-isothermal pixel through introducing some definitions of emissivity for pixels with non-isothermal surface.

In order to study scaling of emissivity between sub-pixel and pixel, we designed special device in a experiment not only for r-emissivity that use directly measurable data to obtain emissivity but also for e-emissivity and T_0 -emissivity that can not directly use measurable data but must calculate based on Plank law through true surface temperature to get emissivity.

According to the experiment some points were presented:

1. It was validated that r-emissivity is measurable directly and invariable from sub-pixel to pixel; e-emissivity and T_0 -emissivity are not directly measurable and variable from sub-pixel to pixel.
2. We validated the difference among three definitions to express effective emissivity in isothermal pixel and found their chain.
3. Based on experimental data and numerical simulation, a generalized formula was established to scaling for land surface emissivity, reflectance, and simple ratio vegetation index between pixel scale and sub-pixel scale.
4. The experiment inspires us to conclude that isothermal concept of land surface temperature and homogeneous concept of some other parameters in one spatial scale is relative according to human's capability of measurement. Heterogeneity in a spatial scale is absolute in natural world.

The conclusions of this paper are preliminary. Quantitative remote sensing and scaling is a strong challenging research field where there are more practical and theoretical problems waiting for us.

ACKNOWLEDGEMENTS.

This work was supported by Key-Important Project of NSFC (Grant No. 49890330), National Key-Important Basic Research Plan Project (Grant No. 2000077900), and Knowledge Innovation Project of IGSNRR, CAS (Grant No CXIOG-C00-05-02 and CXIOG-E01-01, 04).

REFERENCES

- BECKER, F., and LI, Z.-L., 1995, Surface temperature and emissivity at various scales: definition, measurement and related problems. *Remote Sensing Reviews*, 12: 225-253.
- DOZIER, J., and WARREN, S.G., 1982, Effect of viewing angle on the infrared brightness temperature of snow. *Water Resources Research*, 18(5): 1424-1434.
- LI, X., STRAHLER, A., and FRIED, M., 1999, A conceptual model for effective directional emissivity for non isothermal surface. *IEEE Transactions on Geoscience and Remote Sensing*, 37(5): 2508-2517.
- NORMAN, J.M., and BECKER, F., 1995, Terminogy in thermal infrared remote sensing of natural surface, *Agriculture and Forest Meteorology*, 77:153-176.
- WAN, Z., and LI, Z.-L., 1997, A physics-based algorithm for retrieving land surface emissivity and temperature from EOS/MODIS data. *IEEE Transactions On Geoscience and Remote Sensing*, 35(4): 980-996.

Retrieval of plant and soil temperature by AMTIS Data

Fan Wenjie¹, Zhang Yuanzhen², Xu Xiru³

1, Institute of Remote Sensing of Peking University, Beijing, China

2, The Training Center of National Meteorology Administration (NMAC) of China, Beijing, China

3, Center of Remote Sensing and GIS of Beijing Normal University, Beijing, China

Email: fanwj@urban.pku.edu.cn

ABSTRACT Remote sensing of land surface temperature (LST) is significant to deeply understand the circulation of water and energy and to improve the studies such as drought and long-term weather forecast, and so on. If the emissivity or temperature of components is obvious different, the information of components' temperature can be extracted from the multi-angle radiance data. In this paper, we construct the matrix model of infrared radiance, analyze the correlation of $(w_{k,j})$, choose the optimal viewing angles and select the parameters that can be retrieved. Then based on data of the airborne sensor AMTIS that developed in China, through geometrical and atmospherical correction, the plant and soil temperature in mixed pixel are separated using matrix retrieval method. The results and the error analysis shows that the accuracy of retrieved plant and soil temperature is good, but the problem of correlativity among angles always affect the accuracy of retrieval.

1 INTRODUCTION

Remote sensing of land surface temperature (LST) is significant to deeply understand the circulation of water and energy and to improve the studies such as drought and long-term weather forecast, and so on. The mixed pixels wildly exist in the land surface, so it is difficult to retrieve the components' temperature of land surface accurately. Separating component's temperature of pixel always plays an important role in thermal infrared studies. If the emissivity or temperature of components is obvious different, the information of component's temperature can be extracted from the change of multi-angle radiant brightness (Xu X., etc., 2001, pp367-p372; Li Z., etc., 2000, pp27-p38). Extracting components temperature of pixel always play an important role in thermal infrared studies. The Chinese High Technique Research Project supported a new multi-angular sensor – AMTIS (Airborne Multi-angular TIR/VNIR Imaging System) (Li X., etc, 2001, pp154-p166; J.F. Wang, 2000), it provide the new multi-angle infrared data for us.

2 DATA ACQUISITION OF AMTIS

2.1 Introduction of AMTIS data

The wavelength of AMTIS infrared sensor is from 7.5 to 13 μ m, the radiometric resolution of it is

from 0.2 to 0.4K. The AMTIS instrument acquires multi-angular images with a rolling device, which rolls along the direction of the track and acquires images of 9 different viewing angles (Figure 1, Table 1)(Liu Q., etc., 2002, pp299-p306). The design maximum inclination angle of the instrument is about 45 degree when amounted to airplane and flight in a height of 4000m and velocity of 70m/s, the spatial resolutions are respectively 2.7meters. there will be overlap about 40% between two neighboring nadir-view images. And there will be even more overlap for neighboring off-nadir-view images. So, there are usually 15—20 angular observations for every ground pixel near the track.

2.2 Experiment site

The field was observed by the airborne AMTIS in Shunyi County, Beijing, in April 11th, 2001. The latitude of experiment site is N40°09'—40°15', the longitude is E116°24'—116°54. It is a flat area and large enough to extract pure pixel, the main crops are the winter wheat sown in row. During the airborne experiment, the measurement of vegetation structure and components temperature was regularly performed on the selected fields. Other measured parameters included: Leaf emissivity, soil emissivity, atmosphere characteristics and so on.

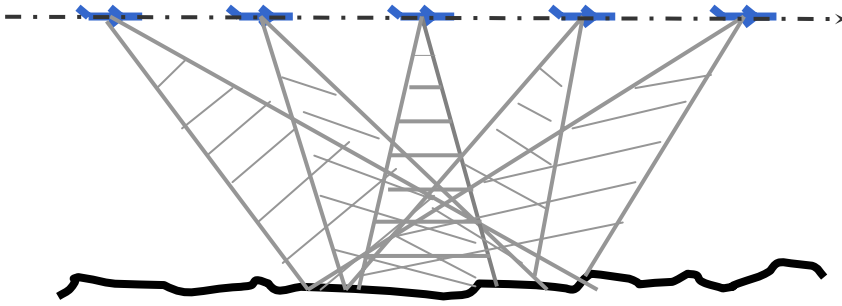


Figure (1) The multi-angle observation principium of AMTIS

Table 1 The designed and actual observe angles of AMTIS

No	Design Zenith (Degree)	Retrieved Zenith (degree)			Design Azimuth (Degree)	Retrieved Zenith (degree)		
		Axis 1	Axis 2	Axis 3		Axis 1	Axis 2	Axis 3
1	45	46.882	46.113	48.81	90	92.68	95.58	95.29
2	33.75	38.854	37.262	40.567	90	92.42	94.48	94.83
3	22.5	28.141	27.383	29.879	90	91.48	93.25	94.2
4	11.25	17.51	16.777	18.919	90	88.54	90.28	91.74
5	0	6.4556	5.6941	7.8294	-----	76.45	80.92	84.42
6	11.25	3.7277	4.9086	3.1185	270	308.79	297.91	316.57
7	22.5	13.33	13.55	11.471	270	284.31	284.48	289.58
8	33.75	23.784	24.207	22.135	270	281.37	282.01	283.44
9	45	34.056	34.473	32.529	270	279.726	280.95	280.95
Azimuth	270	275.69	277.51	276.81	-----			

3 ATMOSPHERIC CORRECTION AND GEOMETRICAL CORRECTION OF AMTIS

Before retrieval calculation, the atmospheric correction and geometrical correction must be done to the image of AMTIS.

3.1 Geometrical correction

The amount of airborne AMTIS data is large, and the resolution of it is high. We matched VNIR AMTIS images to Georeferenced spot images, and then matched infrared images to VNIR AMTIS images. We always matched the images that observed vertically, and then match the images of other angles to it. Because scenes that have irregular elevation distortion of image observed from large viewing zenith is extremely localized. Choosing B-spline as

warping function enables us to correct local distortion

3.2 Atmospheric correction

The radiation reaching the sensor includes three parts are respectively the surface radiation, the hemispheric downwelling radiation reflected to the sensor and the atmospheric upwelling radiation between the ground surface and the sensor.

With the radio sounding atmosphere profile data, we can calculate the atmospheric transmittance and the atmospheric upwelling radiation between the ground surface and the sensor with simulation of MODTRAN 4.0 program. As the weather condition was good when the flight experiment was carried out, it is reasonable to assume that the atmosphere is horizontally homogenous. So we assume that the atmospheric parameters only depend on the view angle and are

independent of the azimuth angle.

4 RETRIEVED METHOD OF COMPONENTS TEMPERATURE

The relationship between multi-angle thermal infrared radiance of non-isothermal mixed pixel and black body's radiance of components can be expressed by the matrix formula (Xu X., etc., 2002, pp654-p661):

$$\bar{L}_\lambda(\theta_k) = (\mathbf{w}_{k,j}) \bar{L}_{bb}(\mathbf{T}_j) \quad (1)$$

Here λ represents wave length of electronic magnetic wave, θ_k means zenith angle of view direction, $L_\lambda(\theta, T)$ means the measured radiance, $(\mathbf{w}_{k,j})$ is called the matrix of system's effective emissivities, T means the temperature in K degree, $L_{bb}(T)$ means the radiance of black body described by plank function. k means the number of view angle, j represents the rank number of part of field of view. Based on the principle of the least square error, we have got the formulas for retrieved components temperature and absolute error (formula 2)(E. R. Malinowski, 1980, pp80-p81). The super script "T" means the transpose of matrix.

$$\bar{L}_{bb}(\mathbf{T}_j) = |(\mathbf{w}_{k,j})^T (\mathbf{w}_{k,j})|^{-1} (\mathbf{w}_{k,j})^T \bar{L}(\theta_k) \quad (2)$$

If $\bar{\delta}(\mathbf{T}_j)$ represents the absolute output error vector of retrieved component temperature. The formula of absolute error propagation should be (E. R. Malinowski, 1980, pp80-p81; Zeng Q., 1974, pp71-p77; Wen S., 2001, pp103-p106):

$$\bar{\delta}(\mathbf{T}_j) = |(\mathbf{w}_{k,j})^T (\mathbf{w}_{k,j})|^{-1} (\mathbf{w}_{k,j})^T \bar{E}(\theta_k) \quad (3)$$

We have proved that the high correlativity does exist among multi-angle thermal infrared data. The accuracy of retrieved component temperature is seriously affected by it, because various kinds of errors are unavoidable. The number of retrievable parameters is not equal to the number of angles used to retrieval. So we must find the number of retrievable parameters and to evaluate the retrieval error at first.

Based on the theory of relative errors

propagation of matrix (Wen S., 2001, pp103-p106), we have:

$$\frac{\|\delta L_b(\mathbf{T}_j)\|}{\|L_b(\mathbf{T}_j)\|} \leq \frac{\|\mathbf{w}_{k,j}^{-1}\| \|\mathbf{w}_{k,j}\| \left[\frac{\|\delta \mathbf{w}_{k,j}\|}{\|\mathbf{w}_{k,j}\|} + \frac{\|\delta L(\theta_k)\|}{\|L(\theta_k)\|} \right]}{1 - \|\mathbf{w}_{k,j}^{-1}\| \|\delta \mathbf{w}_{k,j}\|} \quad (4)$$

Here the symbols " $\|\cdot\|$ " denote the norm of a vector or matrixes. $\frac{\|\delta L_b(\mathbf{T}_j)\|}{\|L_b(\mathbf{T}_j)\|}$ represents the relative error of retrieved values, $\frac{\|\delta \mathbf{w}_{k,j}\|}{\|\mathbf{w}_{k,j}\|}$ and $\frac{\|\delta L(\theta_k)\|}{\|L(\theta_k)\|}$ represent the relative errors from modeling and measurements respectively. We call $\|\mathbf{W}_{k,j}^{-1}\| \|\mathbf{W}_{k,j}\|$ the conditional number. It determined the number of retrievable parameters.

If the relative errors of modeling and measurements are not larger than 0.1% and the relative accuracy of retrieved values are expected within 0.3%-0.5%, then the number of retrievable parameters should be two, because $\left(\frac{\lambda_1}{\lambda_2}\right)^{\frac{1}{2}} = 2.15 \sim 2.43$.

If the relative errors of modeling and measurements are not larger than 0.05%, then the number of retrievable parameters may reach 3, because

$$\left(\frac{\lambda_1}{\lambda_3}\right)^{\frac{1}{2}} = 3.294 \sim 3.742.$$

5 RETRIEVAL OF SOIL AND PLANT TEMPERATURE BY AMTIS DATA

According to the experiment test, we choose winter wheat sown in line as example to retrieve components temperature. Fig.2 show the sectional drawing of winter wheat field. As measured in experiment, the parameter W (=5cm), D (=10cm), and H (=13.7) represent the swath, the distance between swath and the height of crop respectively. We simply suppose the cross section of crop swath taking rectangular shape full of gaps. The model with three independent components' temperatures had been designed: vegetative canopy temperatures T_v , the

shadowed soil surfaced temperature T_{ss} and the lighted soil surface temperature T_{sl} . If the parameters LAI (leave area index)=1.5, LAD (leave angle distribution) is erect type, ϵ_v (emissivity of single leaf) =0.98 and ϵ_s (emissivity of the soil surface) =0.95 are

known according to the field test, $(w_{k,j})$ can be calculated using Monte-Carlo method (Xu X., etc., 2002, pp654-p661).

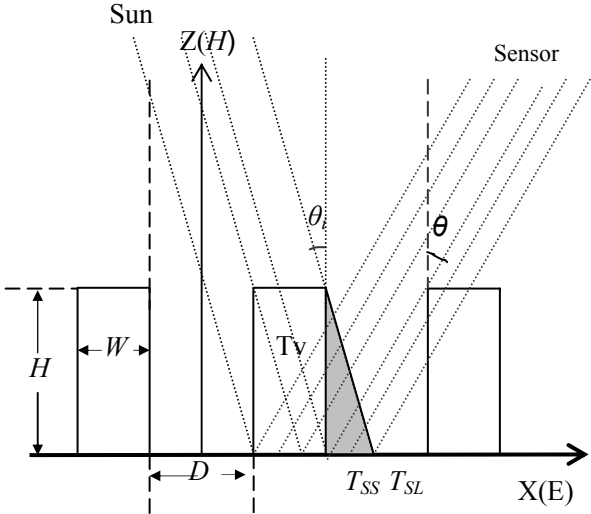


Figure (2) The sectional drawing of winter wheat field

Before retrieval, we classified the image of AMTIS and chosen the pixels of winter wheat sown in line as target. Because the view zenith and azimuth of each pixel in AMTIS image is different, the $(w_{k,j})$ must be calculated for each pixel. The retrieval speed was very slow. So we choose twenty samples which plant canopy is well distributed in the field of test (Figure 3), calculated the average view zenith and azimuth of each sample, then calculated $(w_{k,j})$ respectively. We retrieved the temperature of vegetation, lighted soil and shadowed soil by the five angles radiance value of AMTIS. The retrieved result was shown in Table 2.

Compared with the soil and plant temperatures measured in the field, the retrieved errors of soil temperature is 1~1.5K, but the retrieved precision of plant temperature is not good enough, the SSE of retrieved plant temperature is 3.41K, because in this test the Leave Area Index (LAI) is on the low side, the information of plant is low too. The results show that the component temperature can be retrieved from the thermal infrared multi-angle data of AMTIS in principle. But it was simulated that when LAI=3.0 and the input error reaches $\pm 0.5k$, the retrieved error of

plant temperature was still larger than 1 because of the correlation $(w_{k,j})$.

Figure (3) Distribution of sample in the ground synchronism test area.
(The black line is the flight course and the black boxes are the samples)

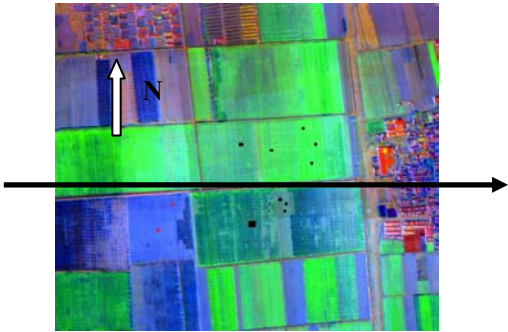


Table 2 The retrieval result of soil and plant temperature (°C)

Components	Temperature of field	Average retrieved components temperature	Maximum error	Minimum error	SSE of retrieval
Tsl	24	24.61	1.72	0.57	0.98
Tss	15.7	15.89	2.11	1.01	1.42
Tv	15.8	13.15	6.25	0.76	3.41

6 RESULTS AND DISCUSSION

Based on the matrix formula of thermal infrared radiance, we find a new method of retrieving components temperature. We also proposed that “the number of retrievable parameters” and relative errors propagation must be calculated before retrieval.

The accuracy of retrieved component temperature is seriously affected by the high correlation among multi-angle thermal infrared data. Various kinds errors are unavoidable, the correlation is the major obstacle for improving the retrieved accuracy.

In different growth season of crop, the accuracy of retrieval is different, even the retrievable components temperature also can change, so the choice of angle and retrieval strategy is changed correspondingly.

ACKNOWLEDGEMENT This paper is supported by the Hi-Tech Research and Development program of China(Grant No. 2001AA135110), the Special Funds for Major State Basic Research Project (Grant No. G2000077900), Fund of National Nature Science of China (40171073) and Fund for Doctor Station from Ministry of Education. Many thanks to Professor Li Xiaowen for his helpful suggestion.

7 REFERENCES

- E. R. Malinowski, 1980, Factor analysis in chemistry, NewYork, 80-81
- Fan Wenjie, Xu Xiru, 2002, The correlation of multi-angle thermal infrared data and the choice of optimal view angles, Science in China, Series D, in press.
- J.F. Wang, 2000, “The Study of Airborne Multi-angle TIR/VNIR Imaging System”, Proc. IWMMM-2, Ispra, Italy.
- Liu Qiang, Liu Qinhua, Xiao Qing, et. al, 2002, Study on Geometric Correction of Airborne Multiangular Imagery, Science in China, Series D (in Chinese, and English version will be published soon), 32(4):299-306.
- Li Xiaowen, Wang Junfa, Wang Jindi, Liu Qinhua. 2001, Multiangular Observation and Thermal Infrared Remote Sensing for Land Surface, Chapter 5: Theoretical Basis, Feature and Capability of AMTIS. Chinese Science Publisher. P154-166.
- Li Zhaoliang, M.P.Stroll, Zhang Renhua, et. Al, 2000, Extract soil and vegetative temperature by ATSR data, Science in China (Series E), 30(Supplement), 27-38.
- Wen Shipeng, 2001, Applied numerical analysis, Beijing, Petroleum Industry Press, 103-106.
- Xu Xiru, Chen Liangfu, Zhuang Jiali, 2001, Gennetic inverse algorithm for retrieval of component temperature of mixed pixel by multi-angle thermal infrared remote sensing data. Science in China (Series D), 44(4): 363-372.
- Xu Xiru, Fan Wenjie, Chen Liangfu, 2002, Matrix expression of thermal radiative characteristics for an open complex, Science in China, Series D, 45(7), 654-661.
- Zeng Qingcun, 1974, The theoretical problems of infrared remote Sensing of atmosphere[M], Beijing, Science Press, 71-77.

The component temperature of mixed pixel retrieved by multi-angle combined multi-time thermal infrared remotely sensed data

Xu Xiru¹, Fan Wenjie², Zhang Yuanzhen³

1, Center of Remote Sensing and GIS of Beijing Normal University, Beijing, China

2, Institute of Remote Sensing of Peking University, Beijing, China

3, The Training Center of National Meteorology Administration (NMAC) of China, Beijing, China

Email: fanwj@urban.pku.edu.cn

ABSTRACT We had proven the distribution of thermal radiance in half space of an arbitrary open complex could be expressed by $\bar{L}_\lambda(\theta_k) = |W_{k,j}| \bar{L}_{b\lambda}(T_j)$. Here $\bar{L}_\lambda(\theta_k)$ means the measured radiance of view angle of θ_k , $\bar{L}_{b\lambda}(T_j)$ means the radiance of black body of component's temperature T_j , $|W_{k,j}|$ is a matrix with $K \times J$ dimensions which is a function of emissivities and area ratio of components within field of view of sensor. But we cannot retrieve T_j straightforward from $\bar{L}_{b\lambda}(T_j) = |W_{k,j}|^{-1} \bar{L}_\lambda(\theta_k)$, even if $K=J$ and $|W_{k,j}|^{-1}$ exists, because the high correlativity among raw vectors (or column vectors) of $|W_{k,j}|$ will make the solution highly sensitive to various kind of errors. So we deal with this kind ill-posed inverse problem by reducing the error contained by data matrix at one hand and performing the orthogonal transform for matrix equation on the other hand, because any solution of inverse problem essentially contains the contents of decorrelation. If multi-angle data combined with multi-time data together, we have $|L_\lambda(\theta_k, t_n)| = |w_{k,j}| |\bar{L}_{b\lambda}(T_j, t_n)|$, here t_n represents the time series. Then we can retrieve the multi-time components' temperature at the same time. Good results had been gained by this way.

1 INTRODUCTION

The remote sensing of land surface temperature (LST) is essentially different from the remote sensing of sea surface temperature (SST). The targets of LST generally owns 3-D structure and belong to inhomogeneous, non-isothermal mixed pixel category. The sea surface can be treated approximated by a flat, homogeneous isothermal plane, therefore the average temperature of a pixel is meaningful for SST. Oppositely, only the component temperature of LST has definite meaning and practical value, the concept of average temperature of LST pixel is ambiguous. So many people had investigated this problem for a long time, some new concept had been raised (J.Norman, F.Becker, 1995, pp153-176; Wan, J.Dozier, 1996, pp892-p905). Some good results had been gained also (J.A.Sobrino, etc., 1996, pp2089-p2114). Let us take winter wheat field as an example, the temperature of vegetative canopy (T_v) or the temperature of soil surface (T_s) is obviously more important than the average temperature of mixed pixel. The multi-angle thermal

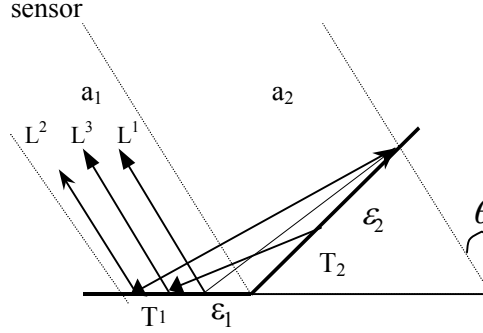
infrared data are more favorable for retrieval of component temperature than multi-band data because the former contains 3-D structural information, the radiance of vegetative canopy and soil surface take different weight within total measured radiance, as the viewing zenith angle changes. The different value offers us a possibility to retrieve component temperature from mixed pixel. So the first important thing is to know the law of radiance distribution in half space of non-isothermal mixed pixel the second one is how to tackle the ill-posed problem, since the measured radiance from different viewing angle are highly correlated, the retrieved component temperature are sensitive to various kind errors. There are two ways to tackle this problem. One is to find some methods that are insensitive to errors, we can list some of them, such as reiterated method, statistical method and so on. The other way is to reduce errors from data, then to keep the instability of retrieved values within limits. The component temperature retrieved by multi-angle combined with multi-time thermal infrared data is an example of this idea.

2 THE DIRECTIONAL DISTRIBUTION FUNCTION OF THERMAL INFRARED RADIANCE OF NON-ISOTHERMAL MIXED PIXEL

In spite of what kinds of material is used to form an inner wall of a cave, the radiative behavior of aperture of this cave can be approximated by black body. This fact tells us that the inner multi-scattering

will raise the emissivity value of system.

If we demand the error of retrieved component temperature less than 1K, then under the circumstance of earth surface, the change of emissivity within 0.003~0.004 may cause the errors of temperature about 1K. Even though the emissivity of leaves as large as 0.98, the multi-scattering among leaves and soil surface must be count in.



L1 represents the emitting radiance of component 1 directly received by sensor, it should be $L^1 = \varepsilon_1 L_{b\lambda}(T_1)$. L2 represents the emitting radiance of component 1 through multi-scattering, at last reflected by component 1 itself and received by sensor, it should be $L^2 = \Delta\varepsilon_{1,1} L_{b\lambda}(T_1)$. L3 represents the radiance emitted by of component 2 through multi-scattering, at last reflected by component 1 and received by sensor, it should be $L^3 = \Delta\varepsilon_{1,2} L_{b\lambda}(T_2)$.

Figure (1) The dual complex system

Based on these points of view, we may express the radiative behavior of dual system (Figure 1) as (1)

$$L_{\lambda}(\theta) = (a_1(\theta), a_2(\theta)) \begin{pmatrix} \varepsilon_1 + \Delta\varepsilon_{11} & \Delta\varepsilon_{12} \\ \Delta\varepsilon_{21} & \varepsilon_2 + \Delta\varepsilon_{22} \end{pmatrix} \begin{pmatrix} L_{b\lambda}(T_1) \\ L_{b\lambda}(T_2) \end{pmatrix} \quad (1)$$

Here θ means zenith angle of view direction, $L_{\lambda}(\theta)$ represents the measured radiance of the dual system, and $a_1(\theta)$ and $a_2(\theta)$ represent area ratio of components within field of view of sensor, ε_1 and ε_2 mean the material emissivity of components respectively. $\Delta\varepsilon_{i,j}$ means the increment of emissivity caused by inner multi-scattering, T1 and T2 represent component temperature, their corresponding black body radiance can be expressed by $L_{b\lambda}(T_1)$ and $L_{b\lambda}(T_2)$. It is easy to expand this expression from one angle to K angles and

from two components to j components.

$$\text{Let } \overline{W} = (a_1(\theta), a_2(\theta)) \begin{pmatrix} \varepsilon_1 + \Delta\varepsilon_{11} & \Delta\varepsilon_{12} \\ \Delta\varepsilon_{21} & \varepsilon_2 + \Delta\varepsilon_{22} \end{pmatrix},$$

then

$$\overline{L}_{\lambda}(\theta_k) = \overline{W}_{k,j} \overline{L}_{b\lambda}(T_j) \quad (2)$$

If we know the material emissivity of component and the inner geometrical structure of system, then the value of matrix $\overline{W}_{k,j}$ can be known by Monte-Carlo simulation.

The formula (2) shows us the distribute function of radiance of non-isothermal mixed pixel always has a linear relationship with black body radiance of components in despite of its complexity.

It means that it is easy to retrieve component

temperature by

$$\overline{L_{b\lambda}}(T_j) = |W_{k,j}|^{-1} \overline{L_{\lambda}}(\theta_k) \quad (3)$$

When $J=K$, $|W_{k,j}|^{-1}$ exists. Or when $K \neq J$,

$$\overline{L_{b\lambda}}(T_j) = |W_{k,j}|^T |W_{k,j}|^{-1} |W_{k,j}|^T \overline{L_{\lambda}}(\theta_k) \quad (4)$$

Here $|W_{k,j}|^T$ represents the transposition of matrix $|W_{k,j}|$. In fact, in many cases, we can't use (3) or (4) to retrieve component temperature accurately, because row (or column) vector of matrix $|W_{k,j}|$ are highly correlated, so (3) and (4) are ill-posed equations.

3 RETRIEVING COMPONENT TEMPERATURE BY MULTI-ANGLE COMBINED WITH MULTI-TIME DATA

In principle, there are two ways to tackle the ill-posed problem, one is to get rid of formula (3) or (4), in order to find out new ways to retrieve component temperature, such as reiterated method, statistical method and so on, anyway they must be insensitive of errors. The other way is to reduce errors from data matrix dramatically. What does the "ill-posed" mean? The solution are sensitive to errors, so if errors reduced, the effect of "ill-posed" will be kept within limit. The content of this paper belongs to this category, the time series data should be included into formula(2).

$$|L_{\lambda}(\theta_k, t_n)| = |W_{k,j}| |L_{b\lambda}(T_j, t_n)| \quad (5)$$

Here t_n represents the time series.

$$\text{Let } L'_{\lambda}(\theta_k, t_n) = L_{\lambda}(\theta_k, t_n) - \overline{L_{\lambda}}(\theta_k, t_n)$$

$$L'_{b\lambda}(T_j, t_n) = L_{b\lambda}(T_j, t_n) - \overline{L_{b\lambda}}(T_j, t_n)$$

Here $\overline{L_{\lambda}}$ and $\overline{L_{b\lambda}}$ represent the average values.

$$\text{Then } |L'_{\lambda}(\theta_k, t_n)| = |W_{k,j}| |L'_{b\lambda}(T_j, t_n)|$$

$$\text{Let } |z| = |L'_{\lambda}(\theta_k, t_n)|^T |L'_{\lambda}(\theta_k, t_n)|$$

$$|z|Q_n = \lambda_n Q_n$$

Here Q_n is the eigenvector corresponding to eigenvalue λ_n . $|Q_n|$ represents an eigenvector matrix consisted of all eigenvectors with $N \times N$ dimensions. In fact, only T_1, T_2, \dots, T_J really exist, so only $Q_1, Q_2, Q_3, \dots, Q_J$ are meaningful (Malinowski, E.R., 1980, 72-86; Ortega, J.M., 1990). The rank of matrix $|Z|$ is equal to J . $Q_{J+1} \dots Q_N$ consist of noise only. We discard all eigenvectors from Q_{J+1} to Q_N and form a new matrix with $N \times J$ dimensions, using $|Q^*|$ to express it.

$$|L'_{\lambda}(\theta_k, t_n)| = |L_{\lambda}(\theta_k, t_n)| |Q| |Q|^{-1} = |L_{\lambda}(\theta_k, t_n)| |Q| |Q|^T$$

$$\text{Let } |R^*| = |L_{\lambda}(\theta_k, t_n)| |Q^*|$$

$$|L'^*_{\lambda}(\theta_k, t_n)| = |R^*| |Q^*|^T$$

It is obvious, $|L'^*_{\lambda}(\theta_k, t_n)|$ contains less errors than $|L'_{\lambda}(\theta_k, t_n)|$.

$$|L'^*_{\lambda}(\theta_k, t_n)| = |W_{k,j}| |L'_{b\lambda}(T_j, t_n)|$$

$$|L'^*_{\lambda}(\theta_k, t_n)|^T = |L'_{b\lambda}(T_j, t_n)|^T |W_{k,j}|^T \quad (6)$$

$$\text{Let } |Z^*| = |\overline{L'^*_{\lambda}}(\theta_k, t_n)| |\overline{L'^*_{\lambda}}(\theta_k, t_n)|^T, K=J$$

$$|Z^*| Q'_k = \lambda'_k Q'_k, |Q'|^{-1} = |Q'|^T$$

$$\text{Let } |R^+| = |L'^*_{\lambda}(\theta_k, t_n)|^T \bullet |Q'|$$

$$|L'^*_{\lambda}(\theta_k, t_n)|^T = |R^+| |Q'|^T = |R^+| |T|^{-1} |T| |Q'|^T \quad (7)$$

Here $|T|$ is a matrix with $K \times K$ dimensions called transform matrix.

$$\text{Let } |W_{k,j}|^T = |T| |Q'|^T$$

$$|T| = |W_{k,j}|^T |Q'|$$

If you compare (7) with (6), we will find out

$$|L'_{b\lambda}(T_j, t_n)|^T = |R^+| |T|^{-1}$$

4 THE FIELD EXPERIMENTS

The winter wheat field was chosen as an experiment target. The multi-angle and multi-time thermal infrared radiance measurements were carried out in shunyi county, Beijing, from 10th April to 19th May, 2001. The radiometer is made by Chinese, its band width is from 8 μ m to 14 μ m. The error of measurement is within (brightness temperature) 0.4K. The T_v and T_s also were measured at the same time with both semiconductor point thermometer and radiometer. The average values were taken as a reference temperature. During this season total sets data were gain, because the location of radiometer is very close to the target, so the atmospheric effect was neglected. Using three time and three angles data, the differences between retrieved temperature and measured temperature of T_s are within 1.08 K(average), the maximum difference value is 1.85K.

ACKNOWLEDGEMENT

This paper is supported by the Hi-Tech Research and Development program of china(Grant No. 2001AA135110), the Special Funds for Major State Basic Research Project (Grant No. G2000077900), Fund of National Nature Science of China (40171073) and Fund for Doctor Station from Ministry of Education. Many thanks to Professor Li Xiaowen for his helpful suggestion.

5 REFERENCES

- Malinowski, E.R., 1980, Factor analysis in chemistry, John Wiley & Sons Inc., 72-86.
- Norman, J., Becker, F., 1995, Terminology in thermal infrared remote sensing of natural surface, Agriculture and Forest Meteorology, 77:153-176.
- Ortega, J.M., 1990, *Numerical Analysis*, A second Course, Soc. For Indust. And Appl. Math., Philadelphia, Pa.
- Sobrino, J.A. Z.L.Li, M.P.Stroll, F.Becker, 1996, Multi-channel and multi-angle algorithms for estimating sea and land surface temperature with ATAR data, International Journal of remote sensing, 17(11): 2089-2114.
- Wan Z., Dozier J., 1996, A generalized split-window algorithm for retrieving land-surface temperature from space. IEEE Trans on Geoscience and Remote Sense, 34(4): 892-905.

Integrating VNIR and TIR Information in Inversion of Land Surface Component Temperature

Qiang Liu, Liangfu Chen, Qing Xiao, Qinhua Liu and Guoliang Tian,
LARSIS, Institute of Remote Sensing Application, Chinese Academy of Sciences

Email: toliuqiang@263.net

P.O. Box 9718Beijing, 100101, China

ABSTRACT - *The goal of this paper is to retrieve component temperatures from remote sensing data. A major problem in land surface temperature inversion is that there are too many unknown variables, especially when the pixel is a complex mixture of several land cover types. To increase information of target surface, inversion results from visible and near infrared (VNIR) observations can be introduced into thermal infrared (TIR) inversion. There are three kinds of parameters that are invariant with respect to wavelength: 1) mixing ratio for the several land cover types in one TIR pixel; 2) structural parameters which define how each typical land cover is composed by components; 3) properties that describe component material, such as soil moisture. These parameters can be retrieved from VNIR data. Then, in the TIR model, all these parameters are represented by component effective emissivity (CEE), and thermal radiance from the pixel can be expressed as linear sum of blackbody radiances weighted by the CEEs. So, only the component temperatures are unknowns in TIR model. With less unknown variables and proper a priori constraints, the TIR model can be inverted and component temperature retrieved. We tested the algorithm with two kinds of data. The multi-angular data were acquired by airborne multi-angular TIR/VNIR sensor, and inversion results are partly validated by simultaneous ground measurement. The multi-channel data are ASTER images, and inversion results are within reasonable range.*

1 INTRODUCTION

Great advances have been achieved in recent years in quantitatively using thermal infrared (TIR) remote sensing data in land surface researches. Efforts are focused on atmospheric correction, temperature and emissivity separation (Gillespie et al., 1998; Paul et al., 2001), coupled inversion of atmospheric and surface parameters (Wan et al., 1997; Chen et al., 2002), and component temperature inversion (Kimes, 1983; Li Z-L et al., 2000). Although each work focuses on different aspect of the subject, a common difficulty that challenges all these researches is the mixed pixel problem. Natural land surface is usually composed of several land cover types, and each land cover type is composed of several components. Average temperature and emissivity cannot describe of the complex thermal state of mixed pixel, thus are not sufficient for many applications.

Inversion of component temperature is appreciated in ecological and agricultural applications. However, to separate the pixel into components will greatly increase number of unknowns in the model, thus make component temperature inversion an ill-posed problem. If all the unknowns are put together into model, inversion will be practically impossible.

In order to retrieve component temperature from thermal infrared (TIR) observations, extra sources of information are necessary. One of the most convenient information sources is the visible and near infrared (VNIR) observations that are simultaneous to TIR observations. Many physical parameters are invariant with respect to the spectral difference between VNIR and TIR. The most frequently used ones are structural parameters and material parameters. When co-registered, VNIR data usually have advantage over TIR data in its high spectral and spatial resolution. So, structural and material parameters derived from VNIR channels usually are much more accurate than that derived from TIR channels.

Plank Law is originally defined on isothermal surface. It states that thermal radiation is determined by two independent parameters: temperature and emissivity. For structured and non-isothermal pixel, the simple form of Plank Law cannot maintain (Li Xiaowen et al., 1999). However, using the concept of component effective emissivity (CEE), we can still disentangle component temperature from effect of other parameters, and effects of all other parameters can be represented by CEE (Chen et al. 2000). So, inversion of other parameters can be separated from inversion of component temperature; the whole algorithm can be modularised and made simple.

This study is supported by China's Special Funds for Major State Basic Research Project (2000077900) and Knowledge Innovation Project (KZCX2-312).

In this paper, we present a component temperature inversion algorithm, which integrate VNIR and TIR

information together in the frame of CEE model. The algorithm is tested with multi-angular data and multi-channel data, and results are partly validated.

2 SURFACE THERMAL EMISSION MODEL

2.1 Component effective emissivity model

After correction for atmosphere path radiance and transmittance, the surface leaving radiance can be written as:

$$L_{Grd}(\lambda, \theta) = \bar{\varepsilon}(\lambda, \theta) \cdot L_b(\lambda, \bar{T}) + \alpha(\lambda, \theta) \cdot L_{\downarrow}(\lambda) \quad (1)$$

Where L_{Grd} is the observed surface leaving radiance, it is a function of wavelength λ and view angle θ . $\bar{\varepsilon}$ denotes the mean emissivity for the pixel, and \bar{T} is the corresponding pixel-mean temperature. $L_b(\lambda, \bar{T})$ is the blackbody radiance in temperature \bar{T} . L_{\downarrow} denotes atmospheric downward radiance. And α is the spherical-directional reflectance of the pixel.

This equation is based on the assumption of pixel-mean emissivity and temperature. However, natural land surface is usually mixed and non-isothermal. Theoretic analysis indicates that definition of pixel-mean temperature and emissivity can not satisfactorily describe the true state of the surface, thus become hindrance to further improvement of model accuracy. To relate pixel radiance with subpixel components enables us to construct more accurate model. A major objective of model research is to reduce complexity of model while maintain accuracy as much as possible. In TIR band, multiple reflection plays minor role in comparison to direct emission. So, we emphasize the term of direct emission and write the equation as:

$$L_{Grd}(\lambda, \theta) = \sum_{i=1}^n (a_i(\theta) \cdot \varepsilon_i(\lambda, \theta) + \Delta\varepsilon_{mi}(\lambda, \theta)) \cdot L_b(\lambda, T_i) + \alpha(\lambda, \theta) \cdot L_{\downarrow}(\lambda) \quad (2)$$

Here, ε_i is the material emissivity for the i th component, and a_i is the fraction of visible area for this component. $\Delta\varepsilon_{mi}$ denotes the emissivity increment because of multi-scattering for the i th component. It is defined as the ratio of photons emitted from the i th component, scattered at least once, and finally reached the sensor.

We can see from eq. (2) that ε_i , a_i and $\Delta\varepsilon_{mi}$ are independent to component temperature. So we define a new parameter, and call it as “component effective emissivity” or “CEE”. Its definition is:

$$w_i(\lambda, \theta) = a_i(\theta) \cdot \varepsilon_i(\lambda, \theta) + \Delta\varepsilon_{mi}(\lambda, \theta) \quad (3)$$

CEE is only related to material emissivity of the component and pixel structure. It can be calculated through a physical BRDF model or Monte-Carlo simulation (Chen et al. 2000). With the concept of CEE, Eq. (2) can be shortened as:

$$L_{Grd}(\lambda, \theta) = \sum_{i=1}^n w_i(\lambda, \theta) \cdot L_b(\lambda, T_i) + \alpha(\lambda, \theta) \cdot L_{\downarrow}(\lambda) \quad (4)$$

In eq. (3), the items contain temperature, i.e., $L_b(\lambda, T_i)$ are separated from items contain other parameters. This separation can be seen clearer in the matrix expression (Xu et al., 2001), in which the original form of Plank Law can be maintained. We can also derive the relation between CEE and spherical-directional reflectance α of the pixel by:

$$\alpha(\lambda, \theta) = 1 - \sum_{i=1}^n w_i(\lambda, \theta) \quad (5)$$

2.2 Hierarchical structure of mixed pixel

The most important aspect in remote sensing modelling is to parameterise the structure of the pixel. Here we will decompose the problem into two steps. First a remote sensing pixel is decomposed into several subpixel land cover types. This step is necessary for application of TIR data because of the relatively coarse resolution. In the second step, each land cover type is further decomposed into components.

Models for each subpixel land cover types are usually nonlinear because they need to describe the complex 3D structural. These nonlinear subpixel models need to be combined into pixel model in order to apply to remote sensing data. Here, it is assumed that land cover types inside the pixel are distributed in 2D surface. That means their area ratio inside the pixel will not change with observation angle, so the combination are linear sum weighted by their area ratio. Accordingly, the CEEs of mixed pixel are weighted linear average for CEEs of each subpixel land cover types.

In our region of interest, there are 4 major land cover types: cropland, bare soil, village and woods. We choose SAIL model for description of cropland (Verheef, 1984). There are two components in SAIL model, i.e., leaf and soil. For woods and village, we use Li-Strahler GO model (Li Xiaowen and

Strahler,1992), and there are 4 components: sunlit vegetation, shaded vegetation, sunlit ground and shaded ground. Bare soil is assumed to be single component and Lambert.

3 MODEL INVERSION

We take two steps to invert eq. (4) for component temperature, the first step is to derive CEEs, the second step is to retrieve component temperature. In the first step, TIR remote sensing data is not involved, information source is VNIR remote sensing data and spectra library measured from laboratory, and output is CEE. In the second step, information comes from TIR remote sensing data and *a priori* knowledge, and output is component temperature.

3.1 To derive component effective emissivity

VNIR remote sensing data usually have much higher spatial resolution than TIR data. That means, one TIR pixel correspond to several VNIR pixels. In the sense of approximation, we can assume that each VNIR pixel is of pure coverage type, so the area ratio of subpixel land cover types inside the TIR pixel can be approximated by the number of VNIR pixels of certain cover type divided by the number of total VNIR pixels inside the TIR pixel. That means, we will first classify the co-registered VNIR image into typical land covers, then count the pixels of each cover type to derive subpixel area ratio for TIR image.

In the case that VNIR data is of low resolution, the VNIR pixel could also be mixed. If there are multi-spectral channels, we will use spectral unmixing procedure to derive detailed area ratio for VNIR pixels.

Many cover types have 3D structure that will cause significant directionality in reflectance and thermal radiance. So we need to get the structural parameters in the first place. For example, cropland can be characterized by, LAI, LAD and crop height; forest be characterized by average tree density, tree radius and average height. Information of structural parameters can be retrieved by inversion of BRDF models. Multi-angular remote sensing data is of advantage for this purpose. When multi-angular observation is not available, only the most sensitive parameter (like LAI or vegetation coverage) can be retrieved, other parameters will be set to optimal value.

Another important aspect for CEE model is component material emissivity. With empirical model, component material emissivity can be related to physical and chemical properties of the component, and properties of components can be related to component spectra in VNIR band. Our strategy is to integrate parameters of component properties into

surface BRDF model, and invert them simultaneous to structural parameters. After component properties are known, we can find the corresponding component material emissivity from spectra library.

For each VNIR pixel, we choose a RT or GO or Monte Carlo model according to its cover type, then, structural parameters and component emissivity are put into the model so that CEEs are derived. In the last step, CEEs in the scale of TIR pixel are derived from the several VNIR pixels that correspond the TIR pixel.

3.2 To retrieve component temperature

After component effective emissivity is derived, we can invert equation (4) for component temperature from atmospherically corrected TIR observations. There are two possible situations. In the first case, multi-angular dataset is available, and, to simplify question, we assume that the sensor has only one TIR channel. Because equation (3) is linear with respect to $L_b(T_i)$, we can use standard linear regression or optimisation method to invert $L_b(T_i)$, and further derive T_i with Plank Law.

In the second case, only nadir-view observation is available, but the sensor has multiple channels in the TIR region. So, the group of equations are of different wavelength. Because equation (3) is non-linear with respect to the unknowns T_i , a quasi-Newton regression method is adopted for inversion of T_i .

Another problem is that inversion of the equation is ill-posed even when CEEs are known. For a complex mixed pixel, there can be more unknown component temperatures than observations. Even if number of unknowns are less than number of observations, there still exist the noise in data and correlation of equations, and they may cause large error to the solution. To solve the ill-posed problem, *a priori* knowledge of component temperature is used here as constraints to the solution. *A priori* knowledge is a concept in Bayes inversion theory; it refers to knowledge about the unknown variables before inversion. Source of *a priori* knowledge usually is physical bounds of the variable or statistics from similar cases. *A priori* knowledge provides reasonable constraints to unknown variables, thus can significantly improve stability of inversion. In this paper, *a priori* knowledge is expressed as Gaussian distribution and parameterised by its *a priori* mean and std. deviation.

4 ERROR ANALYSIS.

There are 3 sources of noise that introduce error into

results of component temperature inversion. They are: i) noise in structural parameters, this is due to uncertainties in classification (or spectra unmixing) and BRDF model inversion; ii) noise in component material emissivity, this is due to uncertainties in inverted component property or in spectral library; iii) error in TIR observation, this is due to sensor noise and uncertainties in atmospheric and geometric correction. The extent of these sources of noise can be as large as several percent in many cases. And noise usually tends to be enlarged in inversion procedure because of the ill-posed nature of the problem. So the error analysis here does not intend to guarantee good accuracy, but rather to indicate the factors that are relevant to accuracy improvement.

Error analysis is performed on simulation of a typical example. In this example, land cover of the pixel is wheat field, average LAI is 1.5, LAD is parameterised from field measurement in discrete form as in SAIL model, VNIR and TIR spectra of leaf and soil are measured from laboratory. First, simulation is performed in forward direction; “true” TIR observations are derived with CEE model and measured component temperature. Then, in the inversion process, random noises are added into TIR observation, structural parameter or component material emissivity, and errors in the resulted component temperature are recorded. Because *a priori* knowledge plays important role in the inversion process, we also tested effect of different *a priori* knowledge setting on inversion result.

Details of the analysis will not be shown in this short paper. One major conclusion of the analysis is that multi-angular data provide much more information for component temperature than 1-angle-multi-channel data. Inversion results for multi-angular data are relatively stable while, inversion results for 1-angle-multi-channel data are more sensitive to noises. It is shown that 1 percent of noise in TIR observation can cause 1.2C° average absolute error in component temperature for of 5-angle-1-channel data set, and 2.6C° average absolute error for 1-angle-5-channel data set. For structural parameters, several percent of noise are tolerable for both kind of data set. In comparison, noise of component material emissivity is tolerable for multi-angular data, but tends to be amplified for 1-angle-multi-channel data. So accurate measurement for component material emissivity is important for inversion with multi-channel data set.

Another conclusion of the analysis is that accurate *a priori* knowledge can significantly improve inversion results. For example, when the *a priori* mean value for component temperatures is accurate and *a priori* std. deviation set to $\pm 30\text{C}^\circ$, 1 percent of noise in TIR

observation can cause 1.2C° average absolute error in component temperature for of 5-angle-1-channel data set, and 2.6C° average absolute error for 1-angle-5-channel data set. If *a priori* std. deviation is decreased to $\pm 5\text{C}^\circ$, the same noise will only cause 0.45C° average absolute error for 5-angle-1-channel data set, and 0.22C° average absolute error for 1-angle-5-channel data set.

5 EXAMPLES AND RESULTS

5.1 Temperature inversion with AMTIS data

AMTIS is an airborne sensor capable for multi-angular VNIR/TIR observation (Wang et al., 2000). AMTIS has 3 channels, i.e., VIS, NIR, TIR. View zenith angles of AMTIS range from nadir to more than 50 degree. A typical pixel in AMTIS database has about 20-30 angular observations. After registration and atmospheric correction, AMTIS VNIR data is re-sampled to 2.72m, while TIR data is re-sampled to 5.44m.

Directional reflectance and thermal radiance for cropland is described by SAIL model, which assumes horizontal homogeneous canopy and gives good consideration for LAD and multi-scattering inside the canopy. The model is inverted in VNIR band to retrieve LAI and soil moisture, then extended into TIR band (Liu et al, in press) to predict CEEs for leaf and soil.

Li-Strahler GO model is adopted for woods and village. The model describes the scene as ellipsoids randomly distributed on flat ground. For woods, the ellipsoids are tree crowns. For village, the ellipsoids are mixtures of trees and houses. The ground is assumed to be Lambert and its spectra is approximated by sandy soil spectra. Structural parameters of the model are inverted from VNIR multi-angular data. Multiple scattering is ignored in GO model, so CEE equals to the visible area ratio of corresponding component multiply its material emissivity.

There are 7 components in our experiment field, so the outputs of CEE model inversion are 7 maps; each corresponds to temperatures distribution of one component. If a pixel does not provide any information for certain component, its temperature is set to *a priori* mean, and this situation is indicated in the uncertainty index.

Fig. 1 shows the classification map of our experiment field, which locates in Shunyi district near Beijing, and the date was Apr 11th. Fig.2 shows LAI distribution for cropland. Pixels that are not classified as crop are left as blank. Fig.3 and Fig. 4 show the leaf and soil temperature distribution for cropland.

Ground-based experiment was carried out simultaneous to the airborne observation. Component temperatures for leaf and soil of wheat field were measured by contact thermometer. Canopy average temperature was measured by TIR radio-thermometer. The airplane flew overhead many times during the experiment, component temperatures were measured every 2 hours. Each time we measured 10 points randomly scattered inside one field. In each point, component temperatures were repeatedly measured till we felt confident on the average value. A comparison

of the statistics of measured and inverted component temperature is shown in Table 1. The inverted canopy average temperature is derived from eq. (1) with pixel-mean emissivity set to the sum of all CEEs. Because the time that airborne data were actually acquired was between two ground-based measurements, the comparison is not strictly simultaneous. We can see that measured temperatures are lower in the first time than that of the second time, and inverted temperatures are between these two measurements. This result can be explained by the temperature raise during morning.

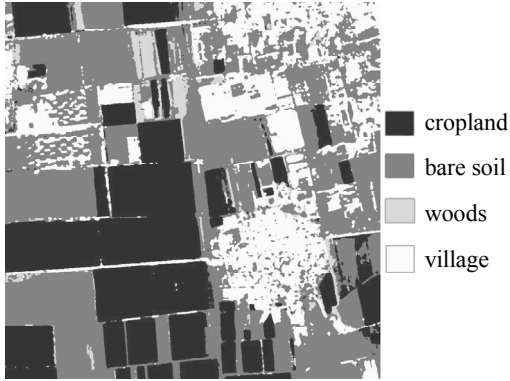


Fig. 1 Classification map of AMTIS experiment field.

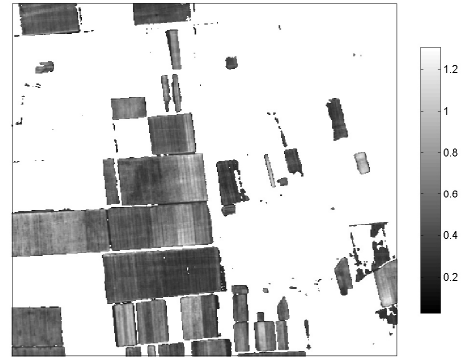


Fig. 2 Inverted LAI for AMTIS experiment field.

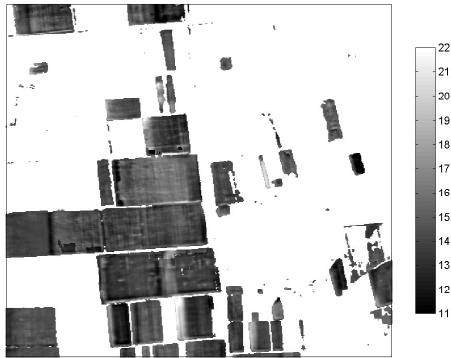


Fig. 3 Inverted leaf temperature for AMTIS experiment field.

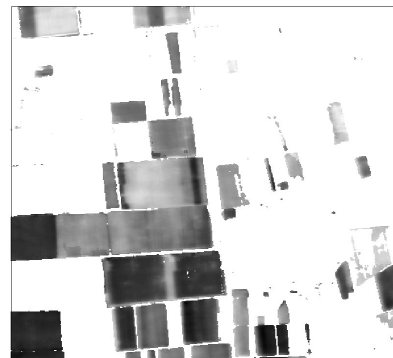


Fig. 4 Inverted soil temperature for AMTIS experiment field.

Table 1 Comparison of inverted component temperature from AMTIS data with quasi-simultaneous ground-based measurement.

	Ground-based measurement				Inversion result	
measure time	9:00 - 9:15		11:10 - 11:30		10:16	
statistics	mean	std. dev.	mean	std. dev.	mean	std. dev.
leaf temperature	14.031	0.7870	16.472	0.7685	14.03	0.5321
soil temperature	14.668	1.5028	21.792	1.5763	16.73	0.5235
canopy temperature	16.400	0.8446	18.390	1.2569	16.26	0.5084

5.2 Temperature inversion with ASTER data

ASTER is a sensor onboard EOS-Terra. It has 3 VNIR channels and 5 TIR channels (Yasushi Yamaguchi et al., 2000). One characteristic of ASTER data is that the spatial resolution of VNIR channels is 15m while that of TIR channels is 90m. The great difference between spatial resolution of VNIR and TIR channels emphasis the need of unmixing TIR pixel with VNIR pixel. So, our first work here is to built classification map in VNIR resolution, then to derive the mixing ratio for each TIR pixel. The ASTER experiment field is classified into 4 cover types: cropland, bare soil, tree shadow and waterbody. Because ASTER is nadir view and has only 3 VNIR channels, we can only retrieve the most significant parameters from ASTER VNIR data. We invert LAI and soil moisture for cropland; area ratio for shadow and vegetation for tree shadow; soil moisture and sand/soil ratio for bare soil.

Fig. 5 shows classification map of our experiment

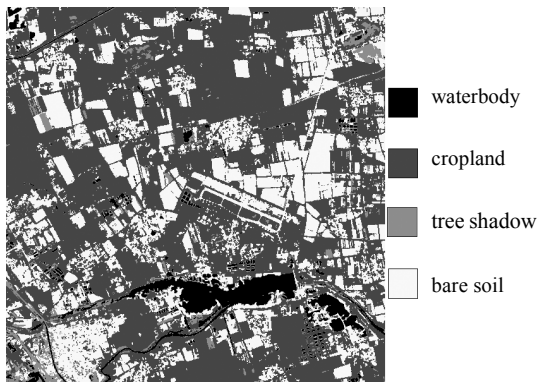


Fig. 5 Classification for ASTER VNIR image.

field. , Fig.6 shows distribution of LAI for cropland. Fig.7 and Fig. 8 show the temperature distribution for leaf and soil in cropland.

Although we made ground-based measurement simultaneous to ASTER observation, our experiment field is outside ASTER image. Our measured leaf temperature ranged from 31C° to 35C°, soil temperature from 33C° to 43C°, air temperature about 33C°. Most of the inversion results are within this range.

6 CONCLUSION:

Land surface component temperature is very useful parameter, but its inversion is difficult because of the too many unknown variables appeared in the model. The CEE model is of advantage for component temperature inversion because it separates the effect of component temperature from effects of other parameters. By splitting inversion process into two steps, we greatly simplified the algorithm of component temperature inversion, thus

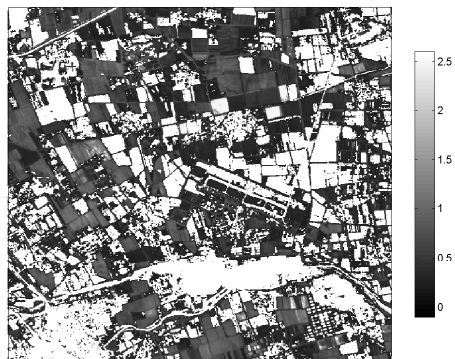


Fig. 6 Inverted LAI for ASTER experiment field.

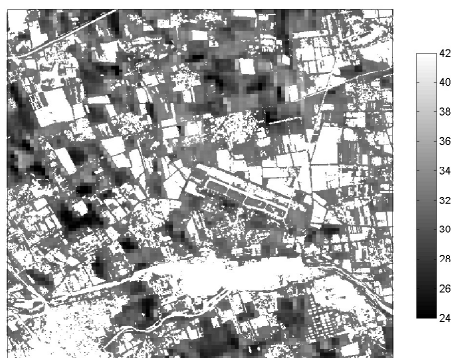


Fig. 7 Inverted leaf temperature for ASTER experiment field.

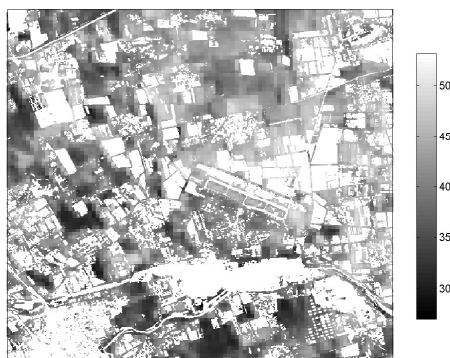


Fig. 8 Inverted soil temperature for ASTER experiment field.

made it practical to be applied to image data.

Error analysis indicates that random noise in TIR observation tends to be amplified during the inversion process. Although the signal-to-noise ratio is greatly improved for the new generation of sensors, the after atmospheric correction error can still be more than 1K. So the accuracy of component temperature inversion is limited. However, when we set proper *a priori* constraints, inversion results are greatly improved and become tolerable.

Because we assume that atmospheric effect can be satisfactorily corrected and component material emissivity is available through ground experiment, our algorithm applies only to regional studies in which ground-based measurement is possible. However, even in such favourable case, validation is still very preliminary. The main difficulty in validation is that description and measurement for component temperature in the scale of remote sensing pixel is problematic even on the ground. Because component temperature inversion is a new and prospective research subject, it will be worthwhile to bestow more efforts on it and eventually solve these problems.

REFERENCES

- Chen L-F, Zhuang J-L, Xu X-R, Niu Z., Zhang R-H, Xiang Y-Q, 2001, The concept of effective emissivity of non-isothermal mixed pixel and its test. *Chinese Science Bulletin*, vol. 45(7), pp. 788-795.
- Chen Liangfu, Liu Qinhuo, Li Zhaoliang, Xu Xiru, 2002, The couple-inversion of atmospheric profile and surface temperature and emissivity from MODIS data. Proceedings of IGARSS'02, Toronto. Xu Xiru, Fan Wenjie and Chen Liangfu, 2002. Matrix expression of thermal radiative characteristics for an open complex. *Science in China (Series D)*, vol. 45(7), pp. 654-661.
- Gillespie A R, Rokugawa S, Matsunaga T, et al., 1998, A temperature and emissivity separation algorithm for Advanced Spaceborne Thermal Emission and Reflection Radiometer (ASTER) images. *IEEE Transactions on Geoscience and Remote Sensing*, vol. 36(4), pp. 1113-1126.
- Kimes D. S., 1983, Remote sensing of row crop structure and component temperatures using directional radiometric temperatures and inversion techniques. *Remote Sensing of Environment*, vol. 13, pp. 33-55.
- Li Xiaowen and A. H. Strahler, 1992, Geometric-optical bidirectional reflectance modeling of mutual shadowing effects of crown in a forest canopy. *IEEE Transactions on Geoscience and Remote Sensing*, vol. 30(2), pp. 276-292.
- Li, Xiaowen, A. Strahler and M. Friedl, 1999, A conceptual model for effective directional emissivity from non-isothermal surface. *IEEE Transactions on Geoscience and Remote Sensing*, vol. 37(5), pp. 2508-2517.
- Li Z-L, Stoll M.P., Zhang R-H, Bob Su, Jia L., 2001, On the separate retrieval of soil and vegetation temperatures from ATSR data. *Science in China (Series E)*, vol. 44(suppl.), pp. 97-111.
- Liu Qiang, Chen Liang-fu, Liu Qin-huo and Xiao Qing, in press, A radiation transfer model to predict canopy radiation in thermal infrared band. accepted by *Journal of Remote Sensing* (in Chinese).
- Paul M., Ingram and A. Henry Muse, 2001, Sensitivity of iterative spectrally smooth temperature/emissivity separation to algorithmic assumptions and measurement noise. *IEEE Transactions on Geoscience and Remote Sensing*, vol. 39(10), pp. 2158-2167.
- Verhoef, W., 1984, Light scattering by leaf layers with application to canopy reflectance modelling: the SAIL model. *Remote Sensing of Environment*, vol. 16, pp. 125-141.
- Wang Junfa, 2000, An airborne multi-angle TIR/VNIR imaging system. *Remote Sensing Reviews*, vol. 19(1-4), pp. 161-170.
- Wan, Z., Li, Z., 1997, A physics-based algorithm for retrieving land-surface emissivity and temperature from EOS/MODIS data. *IEEE Transactions on Geoscience and Remote Sensing*, vol. 35(4), pp. 980-996.
- Yasushi Yamaguchi, Anne B. Kahle, Hiroji Tsu, Toru Kawakami, and Moshe Pniel, 1998, Overview of advanced spaceborne thermal emission and reflection radiometer (ASTER). *IEEE Transactions on Geoscience and Remote Sensing*, vol. 36(4), pp. 1062-1071.

Development of a Remote Sensing Method for Soil and Vegetation Thermal Inertia Separation

Ren-Hua Zhang¹, Xiao-Min Sun¹, Zhao-Liang Li², Zhi-lin Zhu¹, Hong-Bo¹ Su, Xin-Zhai Tang¹

¹ Institute of Geographic Sciences and Natural Resources Research, CAS, Beijing, 100101, CHINA

² LSIIST, CNRS, FRANCE

zhangrh@igsnr.ac.cn,

ABSTRACT Time process information (TPI) of radiometric temperature for soil and vegetation is also called multi-temporal information. Two kinds of utilities for the TPI are discussed in this paper. One is to separate surface temperature into soil surface and canopy surface temperatures. The other is to develop a differential thermal inertia (DTI) according to the TPI of radiometric temperature. And soil evaporation of bare soil can be obtained using Bowen Ratio (BR) that derived from DTI. The model of the use of DTI does not require air temperatures and wind speed data that cannot obtain using remote sensing method.

1 INTRODUCTION

Much attention has been given to the estimation of regional land surface fluxes by applying remote sensing approaches in the last decade. Several models by remotely sensed information have been put forward to determine the distribution of land surface fluxes in two dimensions.

We demonstrated how to develop and apply time process information (TPI) of radiometric temperature in this paper. TPI for soil and vegetation is also called multi-temporal information. Two kinds of utilities for the TPI are discussed in this paper.

First of all, we discussed how to separating surface temperature using TPI of radiometric temperature. The separation of temperature in a mixed pixel (i.e. mixed surface) is a vital step and also the only way to extract crop transpiration information in the two-layer evapotranspiration model. People used to multi-angular remote sensing data to separate mixed pixel temperature. ATSR satellite is the only one that can give two angular data. But the data over the whole Chinese territory are difficult to obtain. Here we put forward another method to separate surface temperature in mixed pixels into that of soil and that of canopy with multi-temporal data.

Second part in the paper, we would like to discuss how to develop a new way for inverting surface flux using TPI of radiometric temperature. The new way is to create a differential thermal inertia (DTI) according to the TPI of radiometric temperature. And soil evaporation of bare soil can be obtained using Bowen Ratio (BR) that derived from DTI without NRSP that can hardly be obtained by remote sensing technology, which can be estimated only by interpolating the data from meteorological station and synchronously

observed data from ecological station. What we are trying to do is to figure out a simple but practical new way on soil evaporation inversion only by remote sensing information.

2 SEPARATING SURFACE TEMPERATURE USING TPI

Expressions of temperatures at noon (with subscript p) and in the early morning (with subscript a) can be as follows:

$$\begin{aligned} T_{mp} &= fT_{vp} + (1-f)T_{sp}, \\ T_{ma} &= fT_{va} + (1-f)T_{sa} \end{aligned} \quad (1).$$

where T_{sp} , T_{vp} and T_{mp} are radiometric temperatures of soil surface, crop canopy surface and mixed pixel surface at noon respectively; T_{sa} , T_{va} and T_{ma} are radiometric temperatures of soil surface, crop canopy surface and mixed pixel surface in the early morning respectively; $T_{sp}-T_{sa}$, $T_{vp}-T_{va}$ and $T_{mp}-T_{ma}$ are the diurnal amplitude (DA) (DA, the difference between the values in early morning and at noon for any parameter, which belongs to TPI) value of surfaces for soil, crop canopy and mixed pixel, respectively. Basing on the fact that soil and canopy surface radiometric temperatures are very close to each other at the time when net radiation is equal to zero we can get the expression of radiometric temperature difference between soil and canopy at noon by subtraction of one of the equations above from the other as

$$T_{sp} - T_{vp} = [(T_{sp} - T_{sa}) - (T_{mp} - T_{ma})] \frac{1}{f}. \quad (2)$$

From equation (2) we can see that radiometric temperature difference between soil and mixed pixel at noon, $T_{sp}-T_{vp}=\delta T_p$, is equal to the difference between

DA of radiometric temperature of soil and that of canopy divided by f , which is the coverage degree (CD) or percentage of vegetation cover. (PVC). The DA of radiometric temperature is an important index of soil thermal inertia while that (the DA of radiometric temperature) in mixed pixel is also a key index for moisture availability^[1] or crop water stress index^[2,3]. The value of δT_p not only reflects the difference for comprehensive effect in heat balance between surfaces of soil and crop canopy, but also gives the difference of information about soil moisture expressed by thermal inertia and by crop water stress index.

A important phenomenon fact is that $T_{sa}-T_{va}=\delta T_a$ is close to zero in early morning and evening when the net radiation flux is zero. Radiometric temperatures of soil, canopy and mixed pixel are identical approximately. Introducing the expression of apparent thermal inertia into eq. (2), we have

$$\begin{aligned} T_{sp} - T_{vp} &= (T_{sp} - T_{mp}) \frac{1}{f} \\ &= [(T_{ma} - T_{mp}) + \frac{1}{P(S, D, \alpha_s, \Delta t)}] \frac{1}{f}. \end{aligned} \quad (3)$$

where P is the apparent thermal inertia (PTI) of soil, Δt is the time span between the extreme values of diurnal change in soil radiometric temperature, other symbols are the same as in previous equations.^[4] The theoretical expression equation (3) resembles the experimental one that has been given before^[5].

In practice, the relationship between the DA of radiometric temperatures of soil and DA of mixed pixel readings can be found by experiment. It is closely related to the PVC. Certainly δT is nonexistent in the extreme cases where PVC equals 0 or 1. Through simultaneous thermal infrared images with high spatial resolution we can find out the radiometric temperature of bare soil in mixed pixel as well as its diurnal amplitude for low-resolution images. It can also be approximately estimated in a mixed pixel of the neighboring bare soil. However, better way is to adopt DA of mixed temperature and experimental value of ATI in equation (3).

Considering the linear relationship between DA of radiometric temperature of soil and that mixed pixel, i.e.

$$T_{sp} - T_{sa} = A' [T_{mp} - T_{ma}] + C', \quad (4)$$

we have

$$T_{sp} - T_{vp} = A [T_{mp} - T_{ma}] + C, \quad (5)$$

where A' , C' , A and C are the coefficients to be determined, which should be functions of PVC and differences between surfaces of soil and canopy in optical and physical properties.

From the above analysis, it is seen that the temperature difference between soil surface and

canopy is in linear relation to DA of radiometric temperature of mixed pixel when PVC is not changing. This linear relationship is also the relation between DA of radiometric temperatures of soil and mixed pixel.

3 DEVELOPING DTI USING TPI

According to heat transfer equation at ground surface and its initial and boundary conditions, an analytical solution can be got. First term is taken (high-degree terms are neglected) approximately^[4]. And net radiation flux is used instead of ground (soil) heat flux; because the net radiation flux can be obtain from remote sensing method^[6]. To increase Signal-to-Noise, the period of time Δt_i is calculated in the interval when from zero of net radiation flux of soil surface appears to the i -th moment. And phase sign i is used instead of trigonometric function in the solution. ATI, thus, can be expressed approximately:

$$\begin{aligned} P_i &\approx \frac{\Theta(R_{ni} - R_{nmin})_i \Delta t_i}{\sqrt{\Delta t_i (T_i - T_{min})}} \\ &= \frac{\Theta R_{ni} \sqrt{\Delta t_i}}{(T_i - T_{min})} = \frac{\Theta R_{rei}}{\sqrt{\Delta t_i (T_i - T_{min})}}, \end{aligned} \quad (6)$$

where i is ATI, Δt_i is the interval when from zero of net radiation flux of soil surface appears to the i -th moment. $T_i - T_{min}$ and $R_{ni} - R_{nmin}$ are radiometric temperature difference and net radiation flux difference between time i and at the moment when zero of net radiation flux of soil surface appears. Θ is a transferring coefficient (no dimension). Due to $R_{nmin}=0$, the simplified formula is shown in (6). This definition is different from the one stated by Price in two points: net radiation flux substituting solar direct radiation flux, radiation temperature at any time replacing the highest radiation temperature. It should explain that dimension of R_{nmin} is $\text{cal}\cdot\text{cm}^{-2}\cdot\text{s}^{-1}$, but R_{rei} is $\text{cal}\cdot\text{cm}^{-2}$.

ATI and $(\rho)^{1/2}$ have identical dimension and physical meaning. Initial definition for thermal inertia of ground objects is: $P = (c\rho k)^{1/2}$, c , ρ , and k are specific heat ($\text{cal}\cdot\text{g}^{-1}\cdot^\circ\text{C}^{-1}$), density ($\text{g}\cdot\text{cm}^{-3}$) and heat conductivity of ground objects ($\text{cal}\cdot\text{cm}^{-1}\cdot\text{s}^{-1}\cdot^\circ\text{C}^{-1}$) respectively. However ATI can be calculated using remote sensing data. Physical meaning of ATI is that measures of the temperature increase at the surface of an object in response to the gaining heat for the object within extraction time of a period and a unit area. The physical meaning can be extended. ATI also is a measure of the temperature decrease at the surface of an object in response to the losing heat for the object within extraction time of a period and a unit area. ATI

is a function with time. ATI at moment is comprehensive result from the period. The surface temperature must be decreased if the net radiation flux has decreased when ATI keeps on the same.

The explicit mathematical description between Bowen ratio and soil moisture availability gives us a clue to assume a possible function between Bowen ratio and ATI. From physical point of view, quantitative conjunction of thermal inertia and soil moisture availability is much weaker than its differential value over time. During a certain period, e.g. twelve hours, soil physical parameters such as soil property cannot change abruptly, their differential value over time equals to zero. Because soil moisture among soil physical parameters changes fast, the change of thermal inertia with time is mostly result from the change of soil moisture. This statement has been clearly explained by the following differential equation of thermal inertia.

$$\frac{\partial P_{co}}{\partial t} = \frac{\partial (P_{wa} + P_{so} + P_{ai})}{\partial t} = \frac{\partial P_{wa}}{\partial t},$$

$$\int_{t_1}^{t_2} \frac{\partial P_{co}}{\partial t} dt = \int_{t_1}^{t_2} \frac{\partial P_{wa}}{\partial t} dt = P_{wa}(t_1) - P_{wa}(t_2), \quad (7)$$

where P_{co} , P_{wa} , P_{so} , P_{ai} are total soil thermal inertia, soil moisture thermal inertia, dry soil thermal inertia, and air thermal inertia in the soil respectively. The first formula of (7) is the soil total thermal inertia differential coefficient, integrating from t_1 to t_2 , we get the difference of thermal inertia between two temporal phases which is crucial for model establishing. It should be mentioned that the difference has no relation with dry soil thermal inertia and air thermal inertia in the soil, indicating the model based on the difference of soil thermal inertia between two temporal phases could be applied universally.

As remote sensing is the science based on experiments, field measurement and experiment are the most convincing way for model establishment. Large daily change of thermal inertia and relatively homogeneous soil surface are preferable for Bowen ratio inversion by thermal infrared remote sensing images of two temporal phases. Desert after rain could meet the requirement. A field experiment was conducted at Shapotou Station located in Tengeli Desert, Northwest of China during the last ten-day of June, 2000. After an occasionally heavy rainfall in Tengeli Desert on 20th, June, a sunny fine day is found on 21st characterized by clear atmosphere and high value of net radiation flux. Strong evaporation in the desert dried up moisture at soil surface gradually. The conditions concerning soil surface moisture, homogeneity of soil surface and the local weather are suitable for carrying out experiment. Equipment is

able to measure ATI and Bowen ratio. The automatic thermo-infrared radiometer and Bowen ratio system used in the field are a set of thermal inertia detecting system developed by our research group.

Let's first analyze the measured data in the Tengeli Desert in 2000. The trend of the curves of Bowen ratio and ATI are opposite. The kernel of apparent thermal in smaller while the value of Bowen ratio is getting larger.

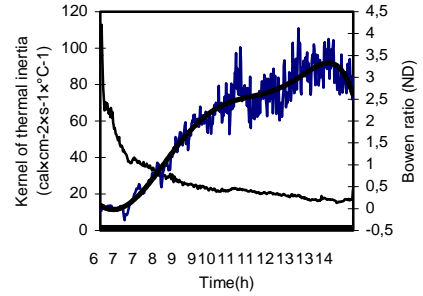


Fig. 1. Daily curves of the kernel of soil ATI and Bowen ratio after rain.

Relative Thermal Inertia (RTI), or called as Normalized Thermal Inertia (NTI), and Relative Residual Thermal Inertia (RRTI), or Normalized Residual Thermal Inertia (NRTI) are defined as follows:

$$RTI = ATI_i / ATI_{max}$$

The nominator means the ATI at any moment i , and the denominator means the ATI when soil surface is sufficiently wet;

$$RRTI = (ATI_{max} - ATI_i) / ATI_{max}$$

RTI is more applicable than ATI, further more, its relativity eliminates the noise of a certain signals, the precision of inversion can be improved accordingly. Fig. 4a illustrates the correlative relationship between RRTI and Bowen ratio. The physical meaning of the definition of RRTI is different approach from that of the crop water stress index, but equally satisfactory in result. And the latter equals to one minus the soil moisture availability.

The sensitivity of Bowen ratio and RRTI is non-linear as shown in Fig. 4a. The change of Bowen ratio is rather insensitive when RRTI ranges between 0.1 and 0.6, Bowen ratio begins to increase when RRTI value is over 0.6, more over, the increasing rate is non-linear.

Bowen ratio of saturated water surface is not zero. The value depends on the difference of molecular diffusion between dry air and water vapor and difference of transport coefficient between heat and

water vapor. After the very heavy rainfall, the sandy soil surface is almost saturated. The automatic data logging indicated that it was night when Bowen ratio was close to zero. To build a transforming model between Bowen ratio and RRTI, it is reasonable to neglect the data at night. (Fig.1)

As discussed before, Bowen ratio is dependent on the soil moisture availability. The higher the RTI, the bigger the soil moisture availability, and the higher the latent heat flux (LE). The bigger the RRTI, the smaller the moisture availability, and the higher the sensible heat flux (H). Physical relation between Bowen ratio and RTI is, to the fundamental, the relation between soil moisture content and evaporation. According to heat balance principal and the mechanism of sensible heat flux and latent heat flux, the ratio of upward going heat from soil surface to the consumed energy of water vapor should equal to Bowen ratio under the dynamic and thermal forces. Their conversion is non-linear. Assuming: 1. sensible heat fluxes is the product of non-linear convert function of sensible heat $\Psi(\Omega)$, RRTI, and net radiation flux (the difference between net radiation flux and soil heat flux to be exactly); 2. latent heat flux is the product of non-linear convert function of latent heat $\omega(\Omega)$, RTI and latent evaporation^[7-9]. 3. when ATI reaches maximum, soil surface is saturated. The Bowen ratio is equal to

$$\beta = \frac{\Delta + \gamma - \alpha\Delta}{\alpha\Delta} \quad [10]$$
 In this way, Bowen ratio may be expressed as follows:

$$\begin{aligned} \beta &= \frac{\Psi(\Omega) \left(\frac{P_{\max} - P_i}{P_{\max}} \right) (R_n - G)}{\omega(\Omega) \frac{P_i}{P_{\max}} LE_0} + \frac{\Delta + \gamma - \alpha\Delta}{\alpha\Delta}, \\ &= \frac{\Psi(\Omega)}{\omega(\Omega)} \left(\frac{P_{\max} - P_i}{P_i} \right) \frac{(R_n - G)}{LE_0} + \frac{\Delta + \gamma - \alpha\Delta}{\alpha\Delta}, \end{aligned} \quad (8)$$

where Ω is the transport variable of turbulent flow. $\Psi(\Omega)$ and $\omega(\Omega)$ are non-linear converting functions, however, according to the similarity theory, they should have the same non-linear kernel. So $\Psi(\Omega)/\omega(\Omega) = \zeta$, ζ is an experimental coefficient, expressing linear or constant relationship between dry air and water vapor to some extent. Suppose no influence of advection involves, then, $R_n - G = LE$, and the formulae (8) can be simplified only by remote sensing information:

$$\beta = \zeta \left(\frac{P_{\max} - P_i}{P_i} \right) + \frac{\Delta + \gamma - \alpha\Delta}{\alpha\Delta}, \quad (9)$$

where P_i, P_{\max} are ATI at moment i and ATI when soil surface is sufficiently wet. According to the definition, RTI and RRTI can be stated as P_i / P_{\max} and $(P_{\max} - P_i) / P_{\max}$ respectively.

When total soil ATI changes, soil property does not change. Equations (7) and (8) can expressed the differential thermal inertia in expression (6). Using difference of actual computation to substitute the differentiation and integration. Within a certain period, the difference of ATI at two temporal phases, independent of the regional soil surface parameters, such as soil type, etc., equals to the difference of moisture thermal inertia at two temporal phases. The experiment demonstrates that ζ is close to psychrometric constant, namely, ζ equals to 0.66. The converting model between ATI and Bowen ratio is thus established. Fig. 4b presents the model simulated relationship between Bowen ratio and RRTI.

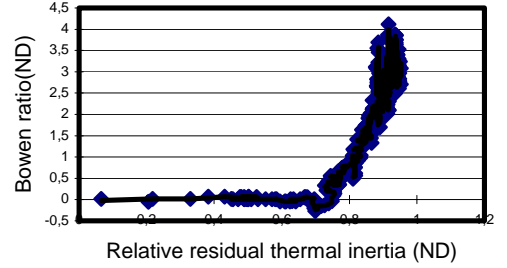


Fig. 2 Correlation between measured Bowen ratio and RRTI

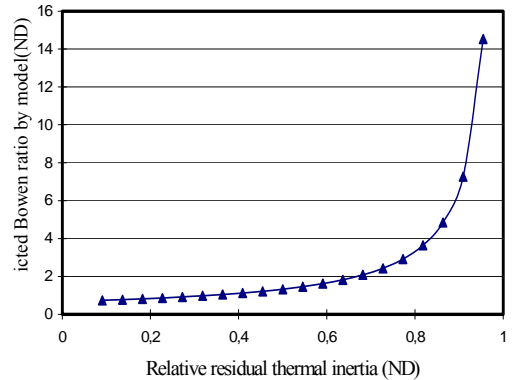
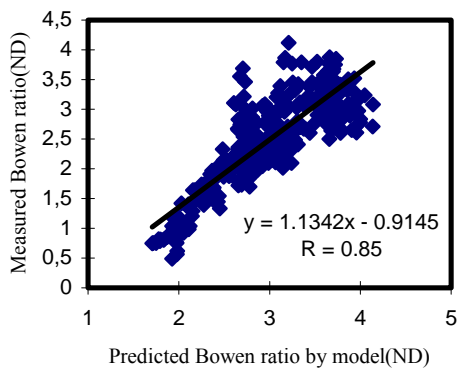


Fig. 3 Relation between simulated Bowen ratio and RRTI

Fig. 4 tells us that when ζ equals to 0.66, the predicted Bowen ratio and the measured one is consistent basically among the data over four hundred groups with a correlation coefficient of 85 percent, which reflects the hypothesis is basically in accordance with the reality. Mean time it shows that with the increase of Bowen ratio, the uncertainty increases accordingly due to the intensity increase of turbulent flow, and the error is getting obvious. The reason for the occurrence of the error should be further studied in the future.



3 RESULTS AND MODEL VERIFICATION

3.1 Validation for separating surface temperature by TPI

It was validated by monitoring the radiometric temperature of wheat field in the spring of 2000 at the Yucheng Comprehensive Experimental Station (YCES). We also found this relation to hold by thermal camera in Shunyi experiment in 2001. Fig. 1 shows the relation between radiometric temperature difference (for soil surface and wheat canopy) and the DA of radiometric temperature of mixed pixels. The linear correlation coefficient is as high as 0.98. It can be explained by the invariance of PVC in the field of view of the thermal infrared radiometer. So the PVC did not work in the measurements, and the relationship was stable from March to May in 2000 at YCES.

In addition, according to the data of measurement, the relationship of surface temperature difference between soil and canopy with DA of total radiation on the mixed surface is less obvious than the DA of radiometric temperature of mixed pixel, which proves the reasoning given above. Although the difference in surface temperature between soil and wheat canopy is controlled by components of heat balance and their analytical expression is complex, and so is DA of the radiometric temperature given by mixed pixel, the two kinds of information are similar.

Therefore the simplification from equation (1) to equations (2) (3) as well as this linear relationship proved correct by theory and experiments. Differences between controlling factors of heat balance between soil surface and crop canopy result in the relationship is relatively high according to the measurements, it is possible to solve the equation so as to get the slope and intercept based on the previous knowledge once PVC is determined.

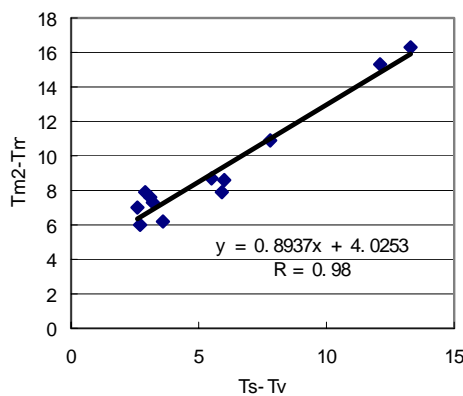


Fig. 5. Relationship between the radiometric temperature difference (for surfaces of soil and wheat canopy) and DA radiometric temperature of mixed pixels at YCES.

3.2 Validation for DTI using TPI

The model and the algorithm discussed above are based on the temporal change of ATI within a day. Applying temporal-dependent model to calculate spatial distribution of water vapor fluxes, the first problem to be identified is the applicable range of the model. From the ATI distribution image, it is known that the change of ATI in each pixel is either caused by the sequence of temporal phase or the spatial heterogeneity. No matter what reason it might be, the objective result is the same. Therefore it can be inferred that the difference of ATI due to spatial heterogeneity equals to that due to the temporal phase from saturated soil surface to completely dry surface. In this way, the temporal-dependent model and the coefficient fitted the experiment could be applied to calculate spatial distribution of ATI. ATI in situation for soil moisture sufficiently wet, could also be used in a model computing spatial distribution.

Soil heat flux is the function of net radiation flux and daily amplitude of soil surface temperature (the highest temperature minus the lowest one). The measured data at Shapotou demonstrates the non-linear relationship between heat flux and net radiation flux of sandy soil. Growing rate of heat flux of sandy

soil decreases with the increase of net radiation flux. Besides, heat flux of sandy soil is related to the heat transport coefficient of soil and soil temperature gradient vertically. To make full use of remote sensing information, heat flux of sandy soil should be linked with thermal amplitude of soil surface temperature, as shown in Fig. 6a and Fig. 6b. Applying net radiation flux and daily amplitude of surface temperature of sandy soil on 21st and 22nd of June, the following non-linear equation can be derived:

$$G_i = [0.00521(T_i - T_{\min}) - 0.0017]R_{ni} - \left[0.0011(T_i - T_{\min})^{\frac{1}{2}} + 0.0039\right]R_{ni}^2 + 3.17(T_i - T_{\min}) - 85.00, \quad (10)$$

where G_i , R_{ni} , T_i and T_{\min} are soil heat flux, net radiation flux and radiometric temperature of soil surface at the moment i , and the last, the minimum change of soil surface temperature.

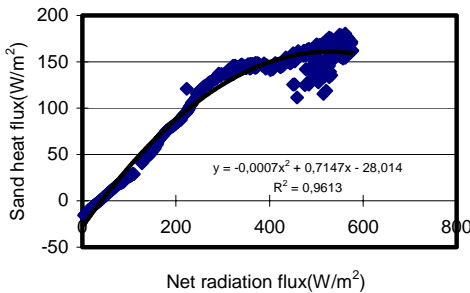
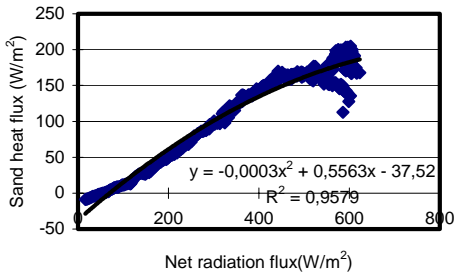


Fig. 6a and Fig. 6b Correlation between heat flux and net radiation flux of sandy soil



After obtaining soil heat flux of bare soil, latent heat flux can be calculated by net radiation flux, soil heat flux, and Bowen ratio. The procedure to quantitatively estimate evaporation with remote sensing information has been simplified. The main advantage of the algorithm is the removal of NRSP, i.e. air temperature, wind velocity and the atmospheric dynamic resistance at referred height. Without the influence of advection, the latent heat flux of soil surface can be estimated by Bowen ratio based algorithm. Bowen ratio based algorithm is a well-recognized method, expressed as:

$$LE = \frac{R_n - G}{1 + \beta}, \quad (11)$$

According to the model, the inversion of soil surface evaporation can be summarized as the following steps: 1. based on the remote sensing image and ground measured data synchronously (applying MODTRAN4 algorithm and split window technology if possible) to retrieve soil surface albedo and soil surface radiometric temperature of each pixel, including hemispherical albedo converted by directional reflectivity and the real temperature for soil surface converted by directional radiometric temperature; 2. to deduce NDVI from visible-near infrared band of the image, then using NDVI to calculate fractional canopy coverage and leaf area index; 3. to calculate net radiation flux of each pixel by direct solar radiation flux, sky-diffusive radiation flux measured during experiment, albedo and real temperature of soil surface obtained in step 1; 4. to estimate Bowen ratio of each pixel based on the soil surface temperature, net radiation flux at two temporal phases and the model put forward in the paper; and 5. to invert the latent heat flux of each pixel, net radiation flux, soil heat flux and Bowen ratio. The inversion process of Bowen ratio and soil heat flux have been presented and discussed in detail in this paper. The quantitative inversion of net radiation flux by remote sensing information will not be introduced here; the procedure has been presented in other papers written by the authors [10,11].

Using five-band NOAA-AVHRR data and synchronously measured ground data at two temporal phases, we get 9 images on the distribution of soil surface parameters and soil surface fluxes including the net radiation flux and the latent heat flux of Shabotou, which are shown in Fig. 7

Fig. 6a and Fig. 6b Correlation between heat flux and net radiation flux of sandy soil

After obtaining soil heat flux of bare soil, latent heat flux can be calculated by net radiation flux, soil heat flux, and Bowen ratio. The procedure to quantitatively estimate evaporation with remote sensing information has been simplified. The main advantage of the algorithm is the removal of NRSP,

i.e. air temperature, wind velocity and the atmospheric dynamic resistance at referred height. Without the influence of advection, the latent heat flux of soil surface can be estimated by Bowen ratio based algorithm. Bowen ratio based algorithm is a well-recognized method, expressed as:

$$LE = \frac{R_n - G}{1 + \beta}, \quad (11)$$

According to the model, the inversion of soil surface evaporation can be summarized as the following steps: 1. based on the remote sensing image and ground measured data synchronously (applying MODTRAN4 algorithm and split window technology if possible) to retrieve soil surface albedo and soil surface radiometric temperature of each pixel, including hemispherical albedo converted by directional reflectivity and the real temperature for soil surface converted by directional radiometric temperature; 2. to deduce NDVI from visible-near infrared band of the image, then using NDVI to calculate fractional canopy coverage and leaf area index; 3. to calculate net radiation flux of each pixel by direct solar radiation flux, sky-diffusive radiation flux measured during experiment, albedo and real temperature of soil surface obtained in step 1; 4. to estimate Bowen ratio of each pixel based on the soil surface temperature, net radiation flux at two temporal phases and the model put forward in the paper; and 5. to invert the latent heat flux of each pixel, net radiation flux, soil heat flux and Bowen ratio. The inversion process of Bowen ratio and soil heat flux have been presented and discussed in detail in this paper. The quantitative inversion of net radiation flux by remote sensing information will not be introduced here; the procedure has been presented in other papers written by the authors^[10,11].

Using five-band NOAA-AVHRR data and synchronously measured ground data at two temporal phases, we get 9 images on the distribution of soil surface parameters and soil surface fluxes including the net radiation flux and the latent heat flux of Shabotou, which are shown in Fig. 7

Model verification is not only very important, but is concerned by readers. As regional multi-points verification demands large investment, single-point verification has been performed up to now. The procedure of model verification has been carried out as described below: Bowen ratio measurement was conducted in homogeneous soil surface selected at the experimental field within ten minutes before or after the satellite overpasses the field, the data were collected every two minutes, 5 groups of data have been taken. The latitude and longitude of the corresponding point where Bowen ratio measurement was taken can be found in Fig.7 with the aid of GPS, the value of latent heat flux of the pixel can be read

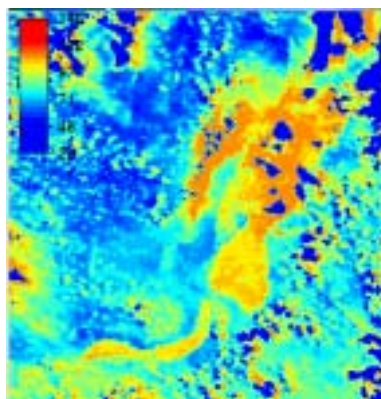


Fig. 7 Images of latent heat flux inverted by the model using differential thermal inertia parameter.

directly. As the image matching could cause an error of 0.5 to 1 pixel, therefore, the values of the neighboring pixels, the upper, the lower, the left and right, together with the middle pixel located by GPS, 5 groups in all, have been compared with the measured data. The relative error between the calculated evaporation and the measured value ranges from 10 to 15 percent. The result is rather satisfactory. However, if another point is chosen, the relative error might be larger. Error can be caused in each step mentioned above. The errors could be added or eliminated each other. We carried out validations for each step using ground truth and simultaneous measurements. Nice inverting methods and priori knowledges should be adopted^[14-16]. It would be more desirable if multi-point verification can be performed. Here, we just wish to share our idea with readers and the colleagues who are interested in this field. Further modification for the model proposed in this paper is discussed below:

Although the verified area is bare soil near Shabotou, the selected region must have covered the oasis or agricultural regions where applying Bowen ratio algorithm will cause errors, and the reason can be explained by the distinction of equation (2) and equation (5). Soil moisture availability and ATI are different functions in T.Carlson's numerical simulation, but he didn't figure out the converting function. We think the vegetation type and the depth of roots absorbing water cause the distinction. The non-linear linkage and the conversion of the two functions are rather complicated which will be an important research aspect in the future. After the problem can be solved, the inversion precision can then be improved. In this way, the model can not only be applied to bare soil and sparse canopy coverage, but also be used in oasis and agricultural region. Disturbance of soil surface fluxes inversion by NRSP can be resolved thoroughly.

4 CONCLUSIONS

1. It is seen that the temperature difference between soil surface and canopy is in linear relation to DA of radiometric temperature of mixed pixel when PVC is not changing. This linear relationship is also the relation between DA of radiometric temperatures of soil and mixed pixel.
2. The paper demonstrates that the Bowen ratio can be obtained by model conversion and function conversion between ATI and the Bowen ratio. Bowen ratio can be used to derive the change of net radiation flux and soil heat flux, and at last, to obtain the surface evaporation flux. The thought is feasible in terms of bare sandy soil and sparse canopy area. The disturbance of using soil surface fluxes inversion by NRSP can be resolved basically.
3. As ATI can't be applied in the soil surface covered by vegetation, the model and the algorithm proposed in this paper demand further research for densely vegetative oasis and agricultural region. Research contents should be extended in two aspects: ATI should be applied to soil surface covered by vegetation, forming General Apparent Thermal Inertia; water stress index for vegetation should be extended to bare soil surface, forming General Water Stress Index. The discussion upon this topic needs more study in terms of quantitative remote sensing or microclimatology.

Acknowledgements This work was supported by the Key Project of the National Natural Science Foundation of China (Grant No. 49890330), the National Basic Research Project (Grant No. 2000077900), and the Knowledge Innovation Project of Institute of Sciences and Natural Resources Research, Chinese Academy of Sciences (Grant Nos. CXIOG-C00-05-02 and CXIOG-E01-01, 04).

5 REFERENCES

- Carlson, T.N., Regional-mscale estimates of surface moisture availability and thermal inertia using remote thermal measurements. *Remote Sensing Review*, 1986, Vol.1, 197–247.
- Jackson, R. D., Idiso, S. B., Reinator, R. J., et al., Canopy temperature as a crop water stress indicator. *Water Resources Res.*, 1981, 17 (4): 1133–1138.
- Price, J. C., Thermal inertia mapping, a new view of the earth, *Journal of Geophysical Research*, 1982, 87:2582–2590.
- Priestley, C.H.B. and R.J. Taylor, on the assessment of surface heat fluxes and evaporation using large scale parameters, *Monthly Weather Review*, 1972, 100:.(2), 81–92.
- Wetzel, P.J. and Atlas, D., Inference of soil moisture from geo-synchronous satellite infrared observation, *Proceedings of the AMS Conference on Agriculture and Forest Meteorology*.1983,.23: 375–391
- Zhang Renhua, Model of experiment remote sensing and the soil surface base, Beijing: Science Press, 1996.
- Zhang Renhua, Sun Xiaomin, Zhu Zhilin et al., A remote sensing model of CO₂ flux for wheat and studying of regional distribution. *Science in China (Series D)* 1999,. 42. (3), 325–336.
- Zhang Renhua ,SUN Xiaomin, LIU Jiyuan, SU Hongbo, TANG Xinzhai & ZHU Zhilin Determination of regional distribution of crop transpiration and soil water use efficiency using quantitative remote sensing data through inversion, *Science in China (Series D)*,2002,in press.
- Zhang Renhua, Inertia model of soil moisture and its application, *Chinese Science Bullentin*,1991 36: 12, 924-927.
- Z. Su, Schmugge, T., Kustas, W.P., Massman, W.J., Advanced algorithms for estimation of surface feat fluxes, Su Z. and Roerink, G.J. edited “ENVISAT-Soil Surface Processes” BCRS,ISBN 9054113561, 2001, 55–80.

Definition of component effective emissivity for heterogeneous and non-isothermal surfaces and its Monte Carlo calculation

Liangfu Chen¹, Zhao-Liang Li², Qinhua Liu¹, Shuisen Chen³, Yong Tang¹, and Bo Zhong¹

¹Laboratory of Remote Sensing Information Sciences, Institute of Remote Sensing Applications, Chinese Academy of Sciences P.O. Box 9718, Beijing 100101, China. Email: lfchen@irsa.irsas.ac.cn; qhliu@irsa.irsas.ac.cn

²TRIO, Laboratoire des Sciences de l'Image, de l'Informatique et de la Teledetection (UMR 7005), 5 Bld. Sebastien Brant, 67400 Illkirch, France. Email : li@sepiu.u-starsbg.fr

³ Guangzhou Institute of Geography, Guangzhou, 510070 China

ABSTRACT Measurement of land surface temperature faces a lot of problems. For example, each pixel over land surface is likely to be heterogeneous and non-isothermal with both vegetation canopy and background soil, and the three-dimensional structure of canopy often makes the canopy radiation angular dependent. It is difficult to define an overall land surface temperature and emissivity at the scale of pixel for heterogeneous and non-isothermal surfaces. After having recalled several definitions of effective emissivities, component effective emissivity is defined in this paper under the conditions of local thermal equilibrium and a constant material emissivity for surface temperature variation in normal Earth environment. Component effective emissivities make it possible to retrieve the component temperature based on multi-directional measurements. The sum of component effective emissivities is equal to the overall effective emissivity, which can be used to inverse pixel-averaged effective temperature. Taking continuous plant/soil system as an example, Monte Carlo method is used to simulate the effective emissivities. Monte Carlo simulated results show that the sum of direct-line emission and single scattering effective emissivity is close to overall effective emissivity when soil and leaf are set to be 0.94 and 0.98.

1 INTRODUCTION

One of the methods to determine the surface heat fluxes from space requires the measurement of land surface temperature (Becker and Li 1995). Different from the sea surface temperature retrieval, retrieval of land surface temperature faces several additional problems: Firstly, each pixel over land surface is likely to be heterogeneous and non-isothermal with both plant and soil system. Secondly, three-dimensional structure of canopy often makes the radiation emitted from canopy a function of view angle (Paw U 1991). For heterogeneous and non-isothermal surfaces, the effective emissivity has been proposed to calculate the effective temperature (Sutherland and Bartholic 1977, Becker and Hechinger 1978, Becker 1981, Price 1982, Caselles et al. 1988). If the flat surface consists of N components with individual directional emissivity

$\varepsilon_{\lambda k}(\Omega)$ and area fraction S_k ($\sum_{k=1}^N S_k = 1$), Becker and Li (1995) scaled the local scale up to the pixel scale by defining the overall emissivity $\varepsilon_{\lambda e}(\Omega)$ as

$$\varepsilon_{\lambda e}(\Omega) = \sum_{k=1}^N \varepsilon_{\lambda k}(\Omega) S_k(\Omega) \quad (1)$$

leading to the overall effective temperature

$$T_{se,\lambda} = B_{\lambda}^{-1} \left[\sum_{k=1}^N \varepsilon_{\lambda k}(\Omega) B_{\lambda}(T_{sk}) S_k(\Omega) / \varepsilon_{\lambda e}(\Omega) \right] \quad (2)$$

where T_{sk} is the surface temperature of element k . However the effective temperature $T_{se,\lambda}$ is wavelength dependent (Becker and Li 1995, Norman and Becker 1995).

For rough surfaces, the multi-scattering should be considered. Dozier and Warren (1982) developed a model to compute the overall effective emissivity for isothermal snow. Becker and Li (1995) defined the overall effective emissivity for heterogeneous and non-isothermal rough surfaces from Kirchhoff's law as

$$\varepsilon_{\lambda e}(\Omega) = 1 - \rho_{\lambda e}(\Omega) \quad (3)$$

where $\rho_{\lambda e}(\Omega)$ is the overall hemispherical-directional reflectance. Norman and Becker (1995) called it r-emissivity. Besides, Norman and Becker (1995) also proposed another emissivity: e-emissivity, which was defined as the ratio of the radiance of natural non-isothermal surface to the radiance emitted from the blackbody with the same distribution of temperatures. The definition itself raises a problem that it is difficult to find the same temperatures distribution of ensemble

as a natural non-isothermal surface (Norman and Becker 1995, Li et al. 1999). Based on the Dozier's model, Li et al. (1999) proposed a new conceptual model of emissivity for non-isothermal pixel. This model introduces the "apparent increment of effective emissivity" (Li et al. 1999) resulted from the differences of sub-element temperatures to a mean temperature.

In this paper, a component effective emissivity is introduced in the second section. The sum of component effective emissivities is equal to the overall effective emissivity defined previously. In the third section, the continuous vegetation/soil system is taken as an example, and the Monte Carlo method is used to calculate the component effective emissivities. Then an analytical expression of the component effective emissivities including single scattering is put forward in the fourth section. Taking spherical leaf angle distribution as an example, the component effective emissivities are respectively calculated by Monte Carlo algorithm and AEE in the fifth section. The final part is the conclusions of this paper.

2. DEFINITION OF COMPONENT EFFECTIVE EMISSIVITY

The effective emissivities defined previously are the overall pixel effective emissivity, and they can be used to retrieve the effective temperature at pixel scale. In this section, a component effective emissivity will be defined to get both the component effective temperatures and the overall effective temperature. Supposing that a pixel is composed of two different elements (sub-pixels) with two different temperatures T_1 and T_2 , and the elements are Lambertian with emissivities of $\varepsilon_{\lambda 1}$ and $\varepsilon_{\lambda 2}$ (see figure 1), the sensor measures the sum of direct-line emission $L_{\lambda d}(\Omega)$ and multi-scattering radiance $L_{\lambda m}(\Omega)$ emitted from the rough surface.

$$L_{\lambda}(\Omega) = L_{\lambda d}(\Omega) + L_{\lambda m}(\Omega) \quad (4)$$

with

$$L_{\lambda d}(\Omega) = S_1(\Omega)\varepsilon_{\lambda 1}B_{\lambda}(T_1) + S_2(\Omega)\varepsilon_{\lambda 2}B_{\lambda}(T_2), \text{ and}$$

$$L_{\lambda m}(\Omega) = \Delta s_{\lambda 1}(\Omega)\varepsilon_{\lambda 1}B_{\lambda}(T_1) + \Delta s_{\lambda 2}(\Omega)\varepsilon_{\lambda 2}B_{\lambda}(T_2),$$

where $S_1(\Omega)$ and $S_2(\Omega)$ are the fractions of elements satisfying the relationship $S_1(\Omega) + S_2(\Omega) = 1$, $\Delta s_{\lambda 1}(\Omega)$ and $\Delta s_{\lambda 2}(\Omega)$ are coefficients describing the contribution of multi-scattering emitted respectively from elements "1" and "2" but reflected from both the elements to the sensor.

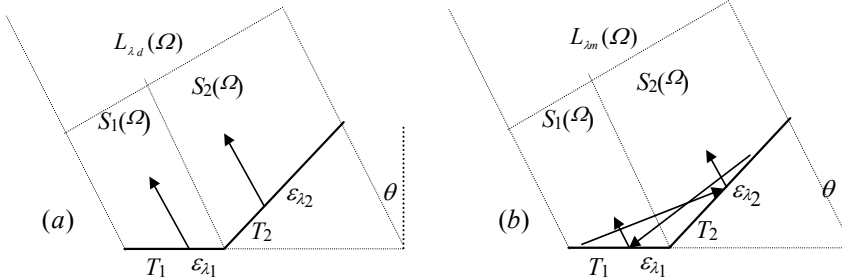


Fig. 1 Sketch map of radiance of simple 3D non-isothermal target (a: part of direct emission, b: part of scattering emission)

Equation (4) can be arranged to

$$L_{\lambda}(\Omega) = [S_1(\Omega) + \Delta s_{\lambda 1}(\Omega)]\varepsilon_{\lambda 1}B_{\lambda}(T_1) + [S_2(\Omega) + \Delta s_{\lambda 2}(\Omega)]\varepsilon_{\lambda 2}B_{\lambda}(T_2) \quad (5)$$

If the system satisfies the local thermodynamic equilibrium, Kirchhoff's law may be applied to each local isothermal surface, thus the component reflectance becomes,

$$\rho_{\lambda k}(\Omega) = 1 - [S_k(\Omega) + \Delta s_{\lambda k}(\Omega)]\varepsilon_{\lambda k} = 1 - F_k(\Omega)\varepsilon_{\lambda k} \quad (6)$$

with $F_{\lambda k}(\Omega) = [S_k(\Omega) + \Delta s_{\lambda k}(\Omega)]$.

Therefore, the overall hemispherical-directional

reflectance of the surface in direction Ω becomes

$$\rho_{\lambda e}(\Omega) = 1 - \sum_{k=1}^2 F_{\lambda k}(\Omega)\varepsilon_{\lambda k} = 1 - \varepsilon_{\lambda e}(\Omega) \quad (7)$$

which yields $\varepsilon_{\lambda e}(\Omega) = \sum_{k=1}^2 F_{\lambda k}(\Omega)\varepsilon_{\lambda k}$ and

$$\varepsilon_{e\lambda k} = F_{\lambda k}(\Omega)\varepsilon_{\lambda k} \quad (8)$$

$\varepsilon_{e\lambda k}$ is called as effective emissivity of component k (Chen et al. 2000), and the sum of component effective emissivities is equal to the overall effective emissivity, which can be expressed as

$$\varepsilon_{\lambda e}(\Omega) = \sum_{k=1}^2 \varepsilon_{e\lambda k}(\Omega) \quad (9)$$

Correspondingly, equation (5) changes to

$$L_{\lambda}(\Omega) = \sum_{k=1}^2 \varepsilon_{e\lambda k}(\Omega) B_{\lambda}(T_k) \quad (10)$$

Equation (10) shows the relationship between the directional radiance $L_{\lambda}(\Omega)$ and the component temperature T_k , and this equation can be used to retrieve the component temperature based on the multi-directional measurements.

If the field of view is composed of N components with different temperatures, the ensemble emissivity of the heterogeneous and non-isothermal rough surfaces can be expressed as the same form as equation (1),

$$\varepsilon_{\lambda e}(\Omega) = \sum_{k=1}^N F_{\lambda k}(\Omega) \varepsilon_{\lambda k} = \sum_{k=1}^N \varepsilon_{e\lambda k}(\Omega) \quad (11)$$

For rough surface, $\Delta s_{\lambda k}(\Omega) > 0$ (if the materials are not black body), thus $\sum_{k=1}^N F_{\lambda k}(\Omega) > 1$. When the rough surface

changes into flat surface, $\Delta s_{\lambda k}(\Omega) = 0$ and $\sum_{k=1}^N F_{\lambda k}(\Omega) = 1$.

Difference between equation (11) and equation (1) comes from cavity effects induced by three-dimensional structure

$$C_{\lambda}(\Omega) = \sum_{k=1}^N \Delta s_{\lambda k}(\Omega) \varepsilon_{\lambda k} \quad (12)$$

where $C_{\lambda}(\Omega)$ is cavity effects, it depends on structure of rough surface and component emissivities

According to equations (8), (10) and (11), the sum of component effective emissivities can be used to calculate the pixel-averaged effective temperature

$$T_{se,\lambda} = B_{\lambda}^{-1} \left[\sum_{k=1}^N \varepsilon_{\lambda k} B_{\lambda}(T_k) F_{\lambda k}(\Omega) / \varepsilon_{\lambda e}(\Omega) \right] \quad (13)$$

3 COMPONENT EFFECTIVE EMISSIVITY CALCULATIONS FOR CONTINUOUS CANOPY

3.1 Principle of Monte Carlo method

Monte Carlo method has been widely used to simulate BRDF due to its easy simulating photon transmitting in crown medium (House and Avery 1969, Smith and Oliver 1974, Szwarzbaum and Shaviv, 1976, Gerstl and Simmer 1986, Antyufeev and Marshak 1990). In thermal infrared domain, the components are not only the reflectors for thermal radiation but also the mainly emitters. In this study, we assume that the vegetation

forms a uniform layer with height of H . This layer and its underlying soil have constant temperatures T_v and T_s . Furthermore, we assume that leaf and soil surfaces are Lambertian with emissivity $\varepsilon_{\lambda v}$ and $\varepsilon_{\lambda s}$. The thermal radiance emitted from the plant/soil system is a function of canopy geometry, spatial distribution of component temperatures and sensor view angle. In the local thermal equilibrium condition, the Kirchhoff's law can be used in this system (Francois et al. 1999), the emissivity of non-metal does not change with temperature in the earth environment condition, the absorptance of element is equal to its emittance in the non-isothermal plant and soil system.

3.2 The stochastic process of Monte Carlo calculation

To precisely describe the stochastic process of photon transmitting in crown medium, the key step is the use of Monte Carlo method to calculate the effective emissivity of continuous vegetation canopy. Generally, the leaves of crown are assumed to be uniformly distributed in azimuthal direction. The motion directions of photons are measured by a polar coordinate, the Monte Carlo calculation is summarized as follows.

a) Based on the principle of reciprocity, one photon with a unit weight "1" is initialized above the canopy from source direction Ω driving to canopy.

b) Generating a uniformly distributed random number r_1 between 0 and 1 to calculate the free path length l , l is the distance traveled by photon between collisions. If the probability density function of non-collision for an optical distance l is $P(l) = e^{-l}$, the probability that no collision occurs in the range of optical distance from 0 to l is

$$r_1 = \int_0^l P(l') dl' = 1 - e^{-l} \quad (\text{House and Avery 1969}).$$

c) Calculating the distance l_{max} photon driven in crop system along its moving direction. If $l_{max} > l$, photon collides with a leaf, a portion of the photon weight absorbed by the element equals to " α ", where " α " is absorbance of leaf at wavelength λ , the remaining portion is $(1-\alpha)$.

d) After a collision, the direction of scattering in the leaf coordination system may be calculated based on the normal of leaf. For Lambertian surface, the scattering zenith angle θ_1^l can be determined according to the accumulated probability function

$$Q(\theta_1^l) = \int_0^{\theta_1^l} \eta(\theta_1^l) d\theta / \int_0^{\pi/2} \eta(\theta_1^l) d\theta \quad (14)$$

where $\eta(\theta_1^l) = \sin 2\theta_1^l$, $Q(\theta_1^l)$ ranges from 0 to 1 when

θ_1^l changes from 0 to $\pi/2$. So giving a random number r_2 between 0 and 1 to be set to $Q(\theta_1^l)$, we can get the photon's zenith angle θ_1^l based on equation (14). The azimuthal angle φ_1^l of scattering can be gotten according to random number r_3 between 0 and 1, $\varphi_1^l = r_3 2\pi$.

e) The photon direction $(\theta_1^l, \varphi_1^l)$ in the leaf coordination system will be converted into the real direction (θ_1, φ_1) in uniform polar coordinate using the matrix of transformation:

$$\begin{bmatrix} \sin\theta_1 & -\cos\theta_1 & 0 \\ \cos\theta_1 \cos\varphi_1 & \cos\theta_1 \sin\varphi_1 & -\sin\theta_1 \\ \sin\theta_1 \cos\varphi_1 & \sin\theta_1 \sin\varphi_1 & \cos\theta_1 \end{bmatrix}$$

where (θ_1, φ_1) is the direction of leaf normal in uniform polar coordinate.

f) Go to step b) to judge whether the photon continuously goes on colliding with elements or escapes from the crop system after collision. If it will collide with background, the $(1-\alpha)\beta$ will be absorbed by soil surface with absorbance β , then the remaining weight of the photon changes into $(1-\alpha)(1-\beta)$. If the photon has respectively collided with plant element and soil for “i” and “j” times, the remaining portion is only $(1-\alpha)^i(1-\beta)^j$. When this portion is less than a given small threshold, for example 10^{-5} , or the photon escapes from the canopy, the photon is dead.

g) Accumulating the weight fractions of one photon respectively absorbed by plant and soil, noted as $\varsigma_{\lambda v1}(\Omega)$ and $\varsigma_{\lambda s1}(\Omega)$. Repeat from step a) to g) and trace the history of each photon from “birth” to “death”. Accumulating all the weights absorbed by plant and soil respectively for a big number of photons (e.g. one million photons), we can get the effective absorbed coefficients through following equation,

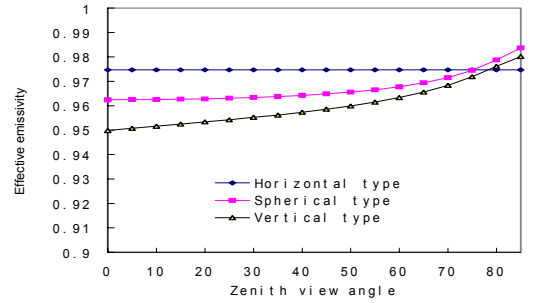
$$\varsigma_{\lambda\omega}(\Omega) = \frac{1}{m} \sum_{k=1}^m \varsigma_{\lambda\omega k}(\Omega), \omega = v, s \quad (15)$$

where $\varsigma_{\lambda vk}(\Omega)$ and $\varsigma_{\lambda sk}(\Omega)$ mean the weight fractions absorbed from number “k” photon by plant and soil respectively, “m” represents the total weight of all photons, and $\varsigma_{\lambda v}(\Omega)$ and $\varsigma_{\lambda s}(\Omega)$ mean the plant and soil effective absorbances. $\varsigma_{\lambda v}(\Omega)$ and $\varsigma_{\lambda s}(\Omega)$ are related to wavelength, view direction Ω and plant structure. Because of the local thermal equilibrium condition, $\varsigma_{\lambda v}(\Omega)$ and $\varsigma_{\lambda s}(\Omega)$ are equal to plant and soil effective emissivities $\varepsilon_{\lambda v}^{MC}(\Omega)$ and $\varepsilon_{\lambda s}^{MC}(\Omega)$, their sum is the overall effective emissivity. We can write them as

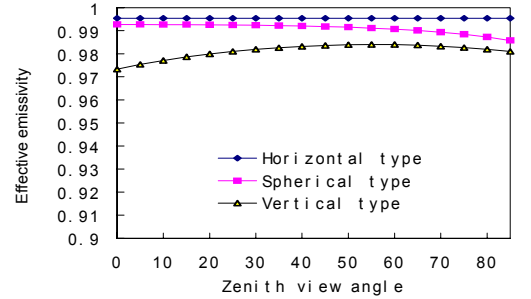
$$\begin{aligned} \varepsilon_{\lambda v}^{MC}(\Omega) &= \varsigma_{\lambda v}(\Omega) \\ \varepsilon_{\lambda s}^{MC}(\Omega) &= \varsigma_{\lambda s}(\Omega) \\ \varepsilon_{\lambda}^{MC}(\Omega) &= \varepsilon_{\lambda v}^{MC}(\Omega) + \varepsilon_{\lambda s}^{MC}(\Omega) \end{aligned} \quad (16)$$

4 RESULTS

In order to illustrate the effects on overall effective emissivities by different LAD, three kinds of LAD (Nilson,1970) are cited here. The leaf angle distribution functions and G-functions are as follows: (1)horizontal foliage: $g = \delta(\mu_l - 1)$, $G = |\mu|$, (2)spherical distribution of foliage normals: $g=1$, $G=0.5$ and (3)vertical foliage with no preferred orientation: $g = \delta(\mu_l - 0)$, $G = 2\sin\varphi_l/\pi$. The emissivities of leaf and soil surface are set to be 0.98 and 0.94 respectively, and LAI is set to be 0.5 and 4, then we get the results expressed in figure 2.



(a) LAI is set to be 0.5



(b) LAI is set to be 4

Figure 2. The variation of overall effective emissivities with view zenith angle and different LADs when soil and leaf emissivities are set to be 0.94 and 0.98 respectively. (a) LAI=0.5, (b) LAI=4.

In the following text, only the spherical distribution of foliage was taken as an example. When $\varepsilon_v=0.98$, $\varepsilon_s=0.94$ and LAI are set to be 1.0 and 3.0, we get the variation of crown and soil effective

emissivities $[\varepsilon_{e\lambda v}^{MC}(\Omega), \varepsilon_{e\lambda s}^{MC}(\Omega)]$ with view angle (see figure 3). The component effective emissivity mainly depends on the gap probability, which decreases with LAI and view angle. When LAI is small, the bigger gap probability (see figure 4) makes more contribution from, so the soil effective emissivity is larger than that of plant.

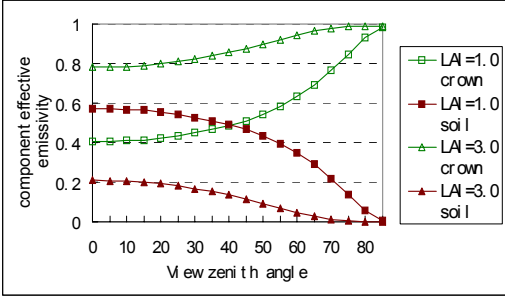


Figure 3. Variation of component effective emissivities as function of zenith view angle when LAI is set to be 1.0 and 3.0, the legends “crown” stands for $\varepsilon_{e\lambda v}^{MC}(\Omega)$ and “soil” stands for $\varepsilon_{e\lambda s}^{MC}(\Omega)$

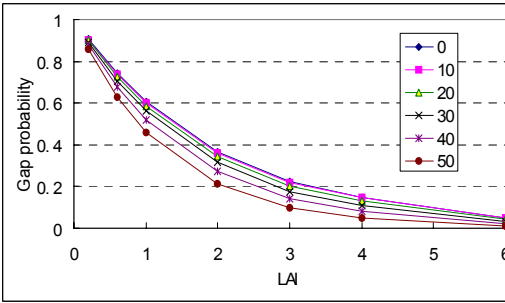


Figure 4. Variation of gap probability with LAI at different view zenith angle.

Figure 5 shows the variation of overall effective emissivity with view zenith angle when LAI ranges from 0.2 to 6. Since the soil emissivity is less than leaf emissivity, it indicates increases with LAI . When LAI is up to 3, the overall effective emissivity increases slowly. It also indicates that the overall effective emissivity increases with view zenith angle when LAI is equal or less than 2.0. Otherwise it changes slowly with view zenith angle. Figure 5 depicts the effect of single and multiple scattering on the overall effective emissivity (cavity effect). From this figure, we notice that the cavity effect increase when LAI decreases to a threshold value, then decreases when LAI continue to drop down from this threshold value. Generally, the cavity effect decreases with increase of view angle, in our case, the effect of cavity is less than 0.025.

The effective emissivity calculated by Monte Carlo method includes direct-line emission and multi-scattering contribution from vegetation and soil system. Figure 7 shows that the difference of effective emissivity with and without multiple scattering at different view zenith angles is less than 0.0005, when soil and leaf emissivities are set respectively to be 0.94 and 0.98 and LAI range from 0.2 to 6.0. This proves that the multiple scattering in thermal infrared region is negligible.

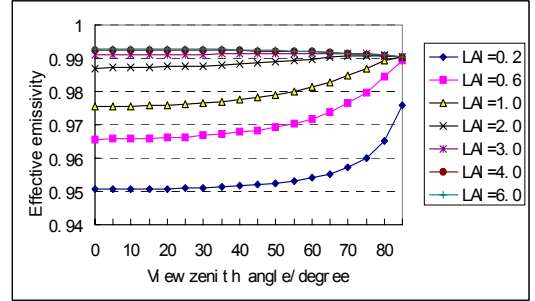


Figure 5. Variation of overall effective emissivity of vegetation and soil system calculated by Monte Carlo method as function of the zenith view angle for LAI ranging from 0.2 to 6.0. Soil and leaf emissivities are set respectively to be 0.94 and 0.98 in this simulation.

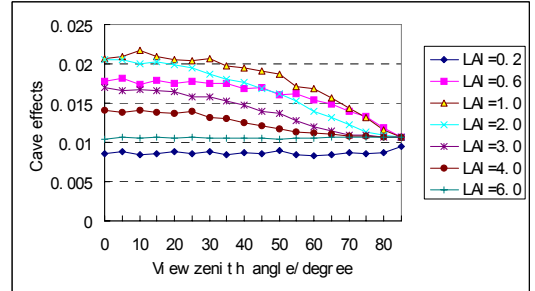


Figure 6. Cavity effect (single plus multiple scattering contribution) calculated using Monte Carlo method for different LAI and view zenith angle. Soil and leaf emissivities are set respectively to be 0.94 and 0.98 in this simulation.

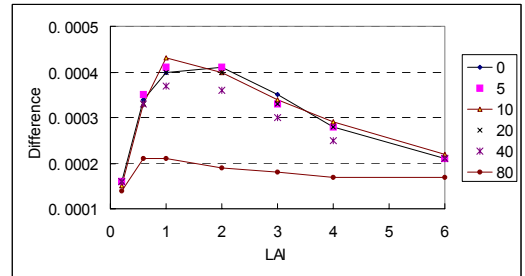


Figure 7. The variation of difference of the overall effective emissivity with and without multiple scattering as function of LAI at different view zenith angle, when soil and leaf emissivity are set to be 0.94 and 0.98. In this figure, the “0, 5, 10, 20, 40 and 80” stand for different zenith view angles.

5 CONCLUSIONS

Under the conditions of local thermal equilibrium and material emissivity unchangeable with temperature in Earth environment, this paper gives a new definition of non-isothermal surface overall effective emissivity $\varepsilon_{\text{ae}}(\Omega)$ and component effective emissivity shown in equation (8). The sum of component effective emissivities has the similar effects as other assemble emissivities (Becker and Li 1995, Norman and Becker 1995, Francois et al. 1997, Li et al. 1999), which can be used to calculate pixel effective temperature. The definition of component effective emissivity makes the component temperatures inversion possible based on the multi-angle measurements because it links the radiance of a system to component temperatures. Taking continuous plant and soil system as an example, Monte Carlo method is introduced to calculate the overall and component effective emissivities. Then an analytic expression equation (AEE) has been developed to calculate the effective emissivity in this paper.

The results of Monte Carlo calculation reveal that the sum of direct-line emission and single scattering effect is close to overall effective emissivity. The effective emissivity calculated by Monte Carlo method has the same effects as “canopy emissivity” (Francois et al. 1997).

Acknowledgments

This work was supported by the China's National 863 Plan (Grant no. 2001AA135050-3). The authors are indebted to Prof. Xiru XU for discussions concerning Monte Carlo algorithm and other related ideas.

References

- Antyfeev, V.S., and Marshak, A.L., 1990, Monte Carlo method and transport equation in plant canopies. *Remote Sensing of Environment*, 31,183-191.
- Becker, F., and Hechinger, E., 1978, Potentialites de la teledetection pour l'etude des mecanismes de transfert et la mesure des flux echanges entre sol et atmosphere. EERM Meteorologie Nationale, Noulogne-Billancourt, III20-52.
- Becker, F., 1981, Angular reflectivity and emissivity of natural media in the thermal infrared bands. In First International Colloquium on Spectral Signatures of Objects in Remote Sensing (G. Guyot and M. Verbrugge, eds.). Avignon, INRA 5, pp.57-72.
- Becker, F., and Li Z-L., 1995, Surface temperature and emissivity at various scale: definition, measurement, and related problem. *Remote Sensing Review*, 12, 225-253.
- Caselles, V., Sobrino, J.A., and Becker, F., 1988, Determination of the effective emissivity and temperature under vertical observation of a citrus orchard. Application to frost nowcasting. *Internal Journal of Remote Sensing*, 9(4),715-727.
- Chen L., Zhuang J., Xu X., Niu Z., Zhang R., and XIANG Y., 2000, The Concept of effective emissivity of non-isothermal mixed pixel and its test. *Chinese Science Bulletin*, 45(7),788-795.
- Dozier, J., and Warren, S.G., 1982, Effect of viewing angle on infrared brightness temperature of snow, *Water Resources Research*, 18, 1424-1434.
- Francois, C., Ottle, C., and Prevot, L., 1997, Analytical parameterization of canopy directional emissivity and directional radiance in the thermal infrared. application on the retrieval of soil and foliage temperatures using two directional measurements. *Internal Journal of Remote sensing*, 18,2587-2621.
- Gerstl, S.A.W., and Simmer, C., 1986, Radiation physics and modeling for off-nadir satellite sensing of non-Lambertian surface. *Remote Sensing of Environment*, 20, 1-29.
- House, L., and Avery, L., 1969, The Monte Carlo technique applied to radiative transfer. *Journal of Quantitative Spectroscopy and Radiative Transfer*, 9, 1579-1591.
- Nilson, T., 1970, A Theoretical Analysis of the Frequency of Gaps in Plant Stands. *Agricultural Meteorology*, 8, 25-38.
- Norman, J., and Becker, F., 1995, Terminology in thermal infrared remote sensing of natural surface. *Agriculture and Forest Meteorology*, 77,153-176.
- Ottnerman J., Brakke, T.W., and Susskind, J., 1992, A model for inferring canopy and underlying soil temperatures from multi-directional measurements. *Boundary-Layer Meteorol.* 61:81-97.
- Li, X., Strahler, A.H., and Friedl, M.A., 1999, A conceptual model for effective directional emissivity from non-isothermal surfaces. *I.E.E.E. Transactions and Geoscience and Remote sensing*, 37,2508-2517.
- Li, Z-L., Stoll, M.P., Zhang, R.H., Jia L., and Su, Z., 2001, On the separate retrieval of soil and vegetation temperatures from ATSR data. *Science in China (Series D)*, 44(2),97-111.

- Kimes, D.S., 1980, Effects of vegetation canopy structure on remotely sensed canopy temperature., *Remote Sensing Environ.*, 10, 165-174.
- Paw U, K. T., 1991, Dense canopy albedo as a function of illumination direction. *Theoretical Applied Climatology*, 43, 3-16.
- Price, J.C., 1982, On the use of satellite data to infer surface fluxes at meteorological scales. *Journal of Applied Meteorology*, 21,1111-1122.
- Ross, J., and Nilson, T., 1966, A mathematical model of the radiation regime of vegetation, in:V.K. Pydmaa (Ed.), *Actinometry and atmosphere of productive systems*, Israel Prog. Sci. Transl. Jerusalem, Israel, pp.86-99.
- Smith, J. A., and Oliver, R. E., 1974, Effects of changing canopy directional reflectance on feature selection. *Applied Optics*,13,1599-1604.
- Sobrino, J.A., and Caselles, V., 1990, Thermal infrared radiance model for interpreting thermal radiation from a terrestrial surface. *Journal of Applied Meteorology*, 18, 759-763.
- SUTHERLAND, R.A., and BARTHOLIC, J.F., 1977, Significance of vegetation in interpreting thermal radiation from a terrestrial surface. *Journal of Applied Meteorology*, 16(8),759-763.
- Szwarchbaum I., and Shaviv, G., 1976, A Monte carlo model for the radiation field in plant canopies. *Agriculture Meteorology*,7(5),333-352

Derivation of Land Surface Temperatures from MODIS Data Using General Split-Window Technique

Mito C. O, Laneve G., Castronuovo M. M

University of Rome "La Sapienza",

Via Salaria 851, 00138 Rome, Italy.

Email: collins@psm.uniroma1.it

ABSTRACT- *A study has been carried out using FASCODE (Fast Atmospheric Signature Code), a line – by – line radiative transfer program, to simulate MODIS (Moderate Resolution Imaging Spectroradiometer) data at 11.03- and 12.02- μm wavelengths, in order to ascertain how accurately the land and sea surface temperature (LST, SST) can be inferred, by split window technique (SWT), for a wide range of atmospheric and terrestrial conditions. The approach starts from the Ulivieri's algorithm, originally applied to AVHRR (Advanced Very High Resolution Radiometer) channels 4 and 5. This algorithm proved to be very accurate compared to several others and takes into account the atmospheric effects, in particular the water vapor column (WVC) amount and a non-unitary surface emissivity. Extended simulations allowed the determination of new coefficients of this algorithm appropriate to MODIS bands 31 and 32, using different atmospheric conditions. Moreover, it has been improved by removing some of the hypothesis on which its original expression was based. This leads to the addition of a new corrective term that allows to take into account the interdependence between water vapor and non-unitary emissivity values and their effects on the retrieved surface temperature. The LST products were validated within 1 K with in situ LSTs in 11 cases.*

1 INTRODUCTION

The extensive requirement of LST for environmental studies and management activities of the Earth's resources has made the remote sensing of LST an important academic topic during the last two decades. Many studies have been devoted to establish the methodology for the retrieval of LST from channels 4 and 5 of AVHRR data. The most popular form of split-window algorithm is $T_s = T_4 + A(T_4 - T_5) + B$, where T_s is land surface temperature, T_4 and T_5 are the brightness temperatures of AVHRR channels 4 and 5, A and B are coefficients related to atmospheric effects, viewing angle and ground emissivity.

The retrieval of surface temperatures from AVHRR measurements over land has shown that the problem is well understood from the theoretical point of view. Due to inherent sensor noise and the lack of adequate data on the atmospheric state as well as on the surface emissivity, however, AVHRR derived land surface temperatures are currently subject to uncertainties.

This situation may substantially improve with the availability of new instruments with better performances both for the ground observation and the atmosphere sounding. Such instruments should preferably be mounted all on the same platform in order to assure contemporary measurements. Some of these platforms and sensors capable of such high quality measurements have recently been designed as, for example, the satellite series in the frame of Earth Observing System (EOS) of NASA, the Meteosat

Second Generation (MSG) satellite, and the ENVISAT platform of ESA.

MODIS is an EOS instrument that serves as the keystone for global studies of atmosphere, land, and ocean processes. It scans $\pm 55^\circ$ from nadir in 36 bands, with bands 1-19 and band 26 in the visible and near infrared range, and the remaining bands in the thermal infrared from 3-15 μm . The specifications of MODIS bands can be found in MODIS Level 1B Algorithm Theoretical Basis Document, 1995, NASA/GSFC, Greenbelt, MD.

The bands in transparent atmospheric windows are designed for the remote sensing of surface properties. Other bands are mainly for atmospheric studies. MODIS provides images of daylight reflection and day/night emission of the Earth, repeating global coverage every one to two days. It uses 12 bits for quantisation in all bands. The thermal infrared (TIR) bands have an Instantaneous Field-Of-View (IFOV) of 1 km at nadir. MODIS is particularly useful because of its global coverage, radiometric resolution and dynamic ranges, and accurate calibration in multiple thermal infrared bands (better than 1% absolute) designed for retrieval of SST, LST, and atmospheric properties.

Specifically, all atmospheric channels of MODIS are used to retrieve atmospheric temperature and water vapour profiles. Band 26 detects cirrus clouds, and thermal infrared bands 20, 22, 23, 29, 31-33 correct atmospheric effects and retrieve surface emissivity and temperature. Taking advantage of the seven TIR bands

of the MODIS instrument, a day-night algorithm has been proposed based on pairs of co-located measurements to retrieve simultaneously the surface temperature and the spectral emissivity without the knowledge of atmospheric temperature and WVC, Wan (1999). As a constraint this algorithm has augmented probability of no cloud free conditions because retrieval is based on two images. This reduces, obviously, the portion of Earth areas suitable for its application.

Fig. 1 shows the absorption corresponding to water vapour (H₂O), Ozone (O₃) and carbon dioxide (CO₂) in the 750-1050 cm⁻¹ spectral range together with the relative response functions of AVHRR channels 4 (Ch4.) and 5 (Ch5.) and MODIS bands 31 (Ba. 31) and 32 (Ba. 32). These calculations were done for a typical scenario for the equatorial region, using PcLnWin Radiative Transfer (RT) Program in a clear-sky (23-km visibility), with total water vapour content of 4.2 g cm⁻² at nadir.

It is evident how MODIS bands 31 and 32 reproduce well the AVHRR channels 4 and 5 which have been used in the past to develop split-window / “adapted” split-window technique algorithms. The spectral ranges (Fig. 1) of the two bands are closer to each other compared to AVHRR and therefore, the usual assumption of linearisation of the Planck function is more justified for any split-window technique algorithm development. This assumption requires that the measurements be made in two spectral ranges close to each other, such that one of the measured radiances may be expressed as a linear function of the other.

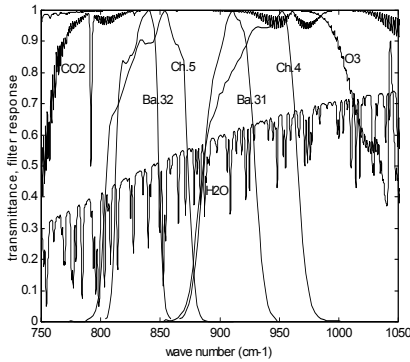


Fig. 1. Absorption of the atmospheric constituents and filter response of AVHRR / 2 and MODIS.

2 THEORETICAL BASIS OF THE ALGORITHM

When the surface reflectance $\rho_v = 1 - \varepsilon_v$ is not negligible, the total radiance I_v emerging at the top of a nonscattering cloud-free atmosphere is given, in

any selected radiometric band centred in ν , by the relationship:

$$I_v = \varepsilon_v \tau_v B_v(T_s) + \overline{B_v}(1 - \tau_v) + (1 - \varepsilon_v)(1 - \tau_v) \tau_v \overline{\overline{B_v}} \quad (1)$$

where:

B_v is the Planck intensity (watt cm⁻² sr⁻¹ μm⁻¹),

T_s is the surface temperature (K),

ε_v the spectral surface emittance,

τ_v the total atmospheric spectral transmittance,

$\overline{B_v}$ and $\overline{\overline{B_v}}$ the upwelling and downwelling atmospheric mean radiance.

Equation (1) may be rewritten in a more convenient form by introducing the quantities:

$$\begin{cases} E_i = \varepsilon_i \tau_i \\ A_i = [1 + (1 - \varepsilon_i) \tau_i z_i](1 - \tau_i) \end{cases} \quad (2)$$

where: $z_i = \overline{\overline{B_i}} / \overline{B_i}$. Substituting these expressions in (1) the equation for the remotely - sensed radiance at the satellite sensor becomes:

$$I_i = E_i B_i(T_s) + A_i \overline{B_i} \quad (3)$$

The philosophy of GSWT is based on a suitable combination of the relations derived from equation (3) for two adjacent spectral channels.

This may be achieved by expanding (3) around a reference temperature. However, following McMillin (1975, 1980), it is considerably more accurate, especially when the wavelengths are close to each other, to expand the Planck's function at a reference wavelength. Adapting McMillin's results to the formalism of (3) the following system is found:

$$\begin{cases} I_1 = E_1 B_1(T_s) + A_1 \overline{B_1} \\ B_1(T_2) = B_1(T_s) E_2 (1 - \alpha) + B_1(\overline{T_2}) A_2 \end{cases} \quad (4)$$

where subscripts 1 and 2 indicate the split window channels, centred at the lower (taken as reference) and higher wavelength, $\overline{T_1}$ and $\overline{T_2}$ are the atmospheric brightness temperatures in the two thermal channels, T_2 is the corresponding brightness temperature of I_2 and $B_i(\overline{T_i}) \equiv \overline{B_i}$ with $i=1, 2$. In (4) α is a shifting correcting term whose origin has been discussed in detail by Ulivieri and Cannizaro (1985a).

If the linearized Planck's function around T_1 is used (Ulivieri *et al.*, 1994), the corresponding brightness temperature equation yields:

$$T_s = T_1 + \beta(a_1 - 1)T_1 + a_2(T_1 - T_2) + a_3(T_s - T_{air}) \quad (5)$$

where coefficients a_j ($j = 1, 2, 3$) are functions of the surface spectral emittances, the atmospheric water vapour content and the temperature profile of the atmosphere, their expressions are reported elsewhere (Ulivieri *et al.*, 1994) and β , which does not vary greatly over temperature and spectral ranges of interest, is a term resulting from linearization and is given by:

$$\beta = \frac{T_1}{C_2 \nu_1} [\exp(C_2 \nu_1 / T_1) - 1] / \exp(C_2 \nu_1 / T_1) \quad (6)$$

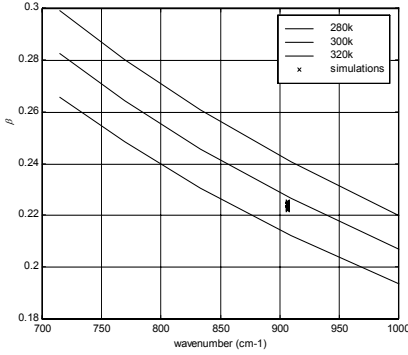


Fig. 2. The β term for the 700-1000 cm^{-1} atmospheric window for typical values of scene temperatures and the MODIS simulated results.

Fig. 2 shows the weak dependence of β on typical scene temperatures for the 700–1000 cm^{-1} atmospheric window together with the results obtained by accurate simulations of MODIS measurements. The simulations for the atmospheric effects in this work have been performed using PcLnWin software package. It allows the prediction of atmospheric transmittance and radiance at high spectral resolution, since the atmospheric calculations are based on FASCODE and the HITRAN (atlas of high resolution molecular spectroscopic data) 96 database. The standard built-in atmospheric profiles in FASCODE together with the atmospheric conditions obtained by periodic radiosounding (once a week) performed at the Broglio Space Centre (BSC) in Malindi, Kenya, were used. The coefficients a_j were computed for a range of water vapour content between 0.4 and 5.4 g cm^{-2} (Fig. 3) for the MODIS bands 31 and 32. It can be observed that a_2 is more sensitive to the surface

emittance effect than a_1 and a_3 . Analogously a_2 and, to a lesser degree, a_3 are significantly influenced by water vapour absorption. Regressive relationships for the two values of mean surface emittance are respectively:

$$\begin{cases} a_2'(\bar{\varepsilon} = 1) = 0.34w + 1.53 \\ a_3'(\bar{\varepsilon} = 1) = 0.02w - 0.01 \\ a_2'(\bar{\varepsilon} = 0.9) = 0.39w + 1.71 \\ a_3'(\bar{\varepsilon} = 0.9) = 0.023w - 0.01 \end{cases} \quad (7)$$

For $\varepsilon_1 = \varepsilon_2 = \bar{\varepsilon} = 1$ and $T_s \cong T_{air}$ the first and the third corrective terms of equation (5) are zero; the resulting split window algorithm is analogous to that proposed by most authors. They assume a_2' as a constant over a wide range of w ; it is evident from equation (7) that this approximation may cause a significant relative error on a_2' . Furthermore, Ulivieri (1984) showed how the a_2' values proposed in the SWT approaches give an overestimation of the water vapor effect, which compensates for the small surface emittance effect of water bodies.

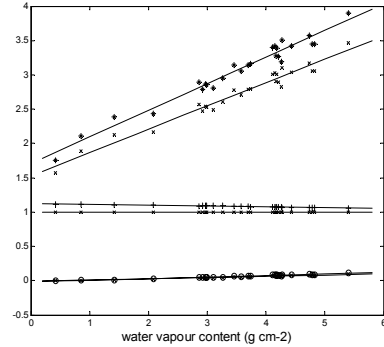


Fig. 3. Coefficients of Eq. 5 vs. total water vapour content for two values of mean surface emittance: $\bar{\varepsilon} = 0.9$ (+) a_1 , (*) a_2 , (o) a_3 ; $\bar{\varepsilon} = 1$ (x) $a_{1,2,3}'$.

3 ASSESSMENTS OF THE EFFECTS

If strong $T_s - T_{air}$ differences occur, (e.g., for arid lands) the term containing a_3 must be considered since it can contribute up to a 25% corrective action in surface temperature determination, (Ulivieri and Cannizaro 1985b).

For the sake of simplicity, T_s can be assumed equal to T_{air} , being the corresponding corrective term almost independent of the other two. Then, if T'_s is the retrieved surface temperature for $\varepsilon_1 = \varepsilon_2 = 1$, equation (5) reduces to:

$$T'_s = T_1 + a'_2(T_1 - T_2) \quad (8)$$

and the surface emittance effect can be evaluated by:

$$T_s - T'_s = \beta(a_1 - 1)T_1 + (a_2 - a'_2)(T_1 - T_2) \quad (9)$$

Given $\delta\varepsilon = \varepsilon_1 - \varepsilon_2$ and $\varepsilon_1 + \varepsilon_2 = 2\bar{\varepsilon}$, it results:

$$T_s = T'_s + H_1(1 - \bar{\varepsilon}) + H_2\delta\varepsilon + H_3\left\{(1 - \bar{\varepsilon})^2 - (0.5\delta\varepsilon)^2\right\} \quad (10)$$

where:

$$H_1 = \frac{G_1}{D}, \quad H_2 = \frac{G_2}{D}, \quad H_3 = \frac{G_3}{D}$$

$$G_1 = -\beta\left\{A'_2E'_1(A'_1Z_1 - 1)c + A'_1E'_2(1 - A'_2Z_2)\right\}T_1 - a'_2\left\{A'_2(E'_2Z_2 - E'_1(1 + Z_1E'_1))c + A'_1E'_2(1 - A'_2Z_2)\right\}(T_1 - T_2)$$

$$G_2 = 0.5\left\{\beta\left[A'_2E'_1(A'_1Z_1 - 1)c - A'_1E'_2(1 - A'_2Z_2)\right]T_1 + a'_2\left[A'_2(-E'_2Z_2 - E'_1(1 + Z_1E'_1))c - A'_1E'_2(1 - A'_2Z_2)\right](T_1 - T_2)\right\}$$

$$G_3 = -\beta\left\{E'_1E'_2\left[A'_2Z_2(A'_1Z_1 - 1)c + A'_1Z_1(1 - A'_2Z_2)\right]\right\}T_1 - a'_2\left\{E'_1E'_2\left[A'_2Z_2(A'_1Z_1 - 1)c + A'_1Z_1(1 - A'_2Z_2)\right]\right\}(T_1 - T_2)$$

$$D = cA'_2 - A'_1 + \left\{A'_2\left[E'_2Z_2 - E'_1(1 - A'_1Z_1)\right]c + A'_1\left[E'_2(1 - A'_2Z_2) - E'_1Z_1\right]\right\}(1 - \bar{\varepsilon}) + 0.5\left\{A'_2\left[E'_2Z_2 + E'_1(1 - A'_1Z_1)\right]c + A'_1\left[E'_2(1 - A'_2Z_2) + E'_1Z_1\right]\right\}\delta\varepsilon + \left[A'_2E'_1E'_2Z_2(A'_1Z_1 - 1)c + A'_1E'_2E'_1Z_1(1 - A'_2Z_2)\right]\left\{(1 - \bar{\varepsilon})^2 - (0.5\delta\varepsilon)^2\right\}$$

where $E'_i = \tau_i$, $A'_i = 1 - \tau_i$, and c is a correlation coefficient discussed elsewhere (Ulivieri *et al.*, 1994).

3.1 Estimation of H_1 , H_2 and H_3

The following mathematical procedure has been used to determine the approximate values of H_1 , H_2 and

H_3 . The idea is to set up as many simultaneous equations as possible using known values of emissivity and estimate the values of these functions for every atmospheric condition used in the simulations. This leads to having more linear equations than unknowns and it is impossible to find an exact solution, which satisfies all the equations in such a situation. The method discussed, hereafter, attempts to solve this problem by seeking for a solution, which approximately satisfies all the equations.

Let **a** and **c** be known and **h** be unknown in the following set of equations where there are more equations than unknowns:

$$\begin{bmatrix} a_{11} & a_{12} & \dots & a_{1m} \\ & a_{21} & a_{22} & \\ & & a_{31} & \\ & & & \ddots \\ & & & & h_m \\ & & & & & \ddots \\ & & & & & & a_{n1} & \dots & a_{nm} \end{bmatrix} \begin{bmatrix} h_1 \\ h_2 \\ \vdots \\ h_m \end{bmatrix} \approx \begin{bmatrix} c_1 \\ c_2 \\ \vdots \\ c_n \end{bmatrix} \quad (11)$$

This is the matrix form of equation (10) that would result by changing the emissivity conditions where:

$$a_{i1} = (1 - \bar{\varepsilon})_i, \quad a_{i2} = (\delta\varepsilon)_i, \quad a_{i3} = \left\{(1 - \bar{\varepsilon})^2 - (0.5\delta\varepsilon)^2\right\}_i \\ h_1 = H_1, \quad h_2 = H_2, \quad h_3 = H_3, \quad c_i = (T_s - T'_s)_i, \\ i = 1, 2, \dots, n.$$

In this case, n is the total number of known sets of emissivity conditions we want to consider in solving the three variables for every atmospheric profile and c_i is the combined emissivity effect obtained by simulations.

Since there will be no set of h_m which exactly satisfies equation (11), let us define an error vector e_i by:

$$\begin{bmatrix} a_{11} & a_{12} & \dots & a_{1m} \\ & a_{21} & a_{22} & \\ & & a_{31} & \\ & & & \ddots \\ & & & & h_m \\ & & & & & \ddots \\ & & & & & & a_{n1} & \dots & a_{nm} \end{bmatrix} \begin{bmatrix} h_1 \\ h_2 \\ \vdots \\ h_m \end{bmatrix} - \begin{bmatrix} c_1 \\ c_2 \\ \vdots \\ c_n \end{bmatrix} = \begin{bmatrix} e_1 \\ e_2 \\ \vdots \\ e_n \end{bmatrix} \quad (12)$$

The development can be simplified by rewriting equation (12) as:

$$\begin{bmatrix} -c_1 & a_{11} & a_{12} & \dots & a_{1m} \\ -c_2 & a_{21} & a_{22} & & \\ -c_3 & a_{31} & & & \\ \vdots & & & & \\ -c_n & a_{n1} & \dots & a_{nm} \end{bmatrix} \begin{bmatrix} 1 \\ h_1 \\ h_2 \\ \vdots \\ h_m \end{bmatrix} = \begin{bmatrix} e_1 \\ e_2 \\ \vdots \\ e_n \end{bmatrix} \quad (13)$$

Equation (13) may be abbreviated as:

$$\mathbf{B}\mathbf{h} = \mathbf{e} \quad (14)$$

where \mathbf{B} is the matrix containing \mathbf{c} and \mathbf{a} . The i th error may be written as a dot product and either vector may be written as the column:

$$e_i = [b_{i1} \ b_{i2} \ \dots] \begin{bmatrix} 1 \\ h_1 \\ h_2 \\ \vdots \end{bmatrix} = [1 \ h_1 \ \dots] \begin{bmatrix} b_{i1} \\ b_{i2} \\ \vdots \end{bmatrix}$$

We then try to minimize the sum-squared error E defined as:

$$E = \sum e_i^2 = \sum_i [1 \ h_1 \ \dots] \begin{bmatrix} b_{i1} \\ b_{i2} \\ \vdots \end{bmatrix} [b_{i1} \ b_{i2} \ \dots] \begin{bmatrix} 1 \\ h_1 \\ h_2 \\ \vdots \end{bmatrix} \quad (15)$$

By bringing the summation inside the constants the following results:

$$E = [1 \ h_1 \ h_2 \ \dots] \left\{ \sum_{i=1}^n \begin{bmatrix} -c_i \\ a_{i1} \\ a_{i2} \\ \vdots \end{bmatrix} \begin{bmatrix} -c_i & a_{i1} & a_{i2} & \dots \end{bmatrix} \right\} \begin{bmatrix} 1 \\ h_1 \\ h_2 \\ \vdots \end{bmatrix} \quad (16)$$

The matrix in the centre, which we can call r_{ij} , is symmetrical. It is a positive (more strictly, nonnegative) definite matrix because it is not possible to find a value of h for which E is negative, since E is a sum of squared e_i . We find the h with minimum E by requiring:

$$\partial E / \partial h_1 = 0, \quad \partial E / \partial h_2 = 0, \quad \dots, \quad \partial E / \partial h_m = 0$$

Let us specialize equation (16) to three unknowns, as is the case in our situation:

$$E = [1 \ h_1 \ h_2 \ h_3] \begin{bmatrix} r_{00} & r_{01} & r_{02} & r_{03} \\ r_{10} & r_{11} & r_{12} & r_{13} \\ r_{20} & r_{21} & r_{22} & r_{23} \\ r_{30} & r_{31} & r_{32} & r_{33} \end{bmatrix} \begin{bmatrix} 1 \\ h_1 \\ h_2 \\ h_3 \end{bmatrix} \quad (17)$$

Setting to zero the derivative with respect to h_1 we get:

$$0 = \frac{\partial E}{\partial h_1} = [0 \ 1 \ 0 \ 0] R \begin{bmatrix} 1 \\ h_1 \\ h_2 \\ h_3 \end{bmatrix} + [1 \ h_1 \ h_2 \ h_3] R \begin{bmatrix} 0 \\ 1 \\ 0 \\ 0 \end{bmatrix} \quad (18)$$

$$\text{where: } R = \begin{bmatrix} r_{00} & r_{01} & r_{02} & r_{03} \\ r_{10} & r_{11} & r_{12} & r_{13} \\ r_{20} & r_{21} & r_{22} & r_{23} \\ r_{30} & r_{31} & r_{32} & r_{33} \end{bmatrix}$$

Since $r_{ij} = r_{ji}$, both terms on the right are equal. Thus equation (18) may be written as:

$$0 = \frac{\partial E}{\partial h_1} = 2[r_{10} \ r_{11} \ r_{12} \ r_{13}] \begin{bmatrix} 1 \\ h_1 \\ h_2 \\ h_3 \end{bmatrix} \quad (19)$$

Analogously, differentiating with respect to h_2 and h_3 and combining the three equations we get:

$$\begin{bmatrix} 0 \\ 0 \\ 0 \end{bmatrix} = \begin{bmatrix} r_{10} & r_{11} & r_{12} & r_{13} \\ r_{20} & r_{21} & r_{22} & r_{23} \\ r_{30} & r_{31} & r_{32} & r_{33} \end{bmatrix} \begin{bmatrix} 1 \\ h_1 \\ h_2 \\ h_3 \end{bmatrix} \quad (20)$$

that is we have three equations with three unknowns. One may write equation (20) in a more conventional form as:

$$\begin{bmatrix} r_{11} & r_{12} & r_{13} \\ r_{21} & r_{22} & r_{23} \\ r_{31} & r_{32} & r_{33} \end{bmatrix} \begin{bmatrix} h_1 \\ h_2 \\ h_3 \end{bmatrix} = - \begin{bmatrix} r_{10} \\ r_{20} \\ r_{30} \end{bmatrix} \quad (21)$$

The matrix of equation (20) lacks only a top row to be equal to the matrix of equation (17). We may augment equation (20) by:

$$\nu = r_{00} + r_{01}h_1 + r_{02}h_2 + r_{03}h_3 \quad (22)$$

where equation (22) may be regarded as a definition of a new variable ν . Combining equation (22) and equation (20) we get:

$$\begin{bmatrix} \nu \\ 0 \\ 0 \\ 0 \end{bmatrix} = \begin{bmatrix} r_{00} & r_{01} & r_{02} & r_{03} \\ r_{10} & r_{11} & r_{12} & r_{13} \\ r_{20} & r_{21} & r_{22} & r_{23} \\ r_{30} & r_{31} & r_{32} & r_{33} \end{bmatrix} \begin{bmatrix} 1 \\ h_1 \\ h_2 \\ h_3 \end{bmatrix} \quad (23)$$

The solution of h of equation (21) or (23) is that set of h_k ($k = 1, 2, 3$) for which E is a minimum. To get an interpretation of ν , we may multiply both sides by $[1 \ h_1 \ h_2 \ h_3]$, getting:

$$\nu = [1 \ h_1 \ h_2 \ h_3] \begin{bmatrix} \nu \\ 0 \\ 0 \\ 0 \end{bmatrix} = [1 \ h_1 \ h_2 \ h_3] R \begin{bmatrix} 1 \\ h_1 \\ h_2 \\ h_3 \end{bmatrix} \quad (24)$$

Comparing equation (24) with equation (17) we see that ν is the minimum value of E . It is convenient to have equation (16) in partitioned matrix form i.e.,

$$E = \begin{bmatrix} \cdot & \cdot & \cdot \\ \mathbf{1} & \cdot & \mathbf{h} \\ \cdot & \cdot & \cdot \end{bmatrix}^T \begin{bmatrix} -\mathbf{c}^T \\ \cdot \\ \cdot \\ \mathbf{A}^T \end{bmatrix} \begin{bmatrix} \cdot \\ \cdot \\ \cdot \\ -\mathbf{c} \end{bmatrix} + \begin{bmatrix} \cdot \\ \cdot \\ \cdot \\ \cdot \end{bmatrix} \begin{bmatrix} \mathbf{1} \\ \cdot \\ \cdot \\ \mathbf{h} \end{bmatrix} \quad (25)$$

The final equation (23) then splits into:

$$\nu = \mathbf{c}^T \mathbf{c} - \mathbf{c}^T \mathbf{A} \mathbf{h} \quad (26)$$

$$0 = -\mathbf{A}^T \mathbf{c} + \mathbf{A}^T \mathbf{A} \mathbf{h} \quad (27)$$

where equation (27) represents simultaneous equations to be solved for h .

Equation (27) was set up for 21 sets of emissivity conditions as shown in Table 1. The variations of H_1 , H_2 and H_3 with water vapor content are illustrated in Fig. 4. It is evident how they are insignificantly influenced if water vapor content is $\leq 3.0 \text{ g cm}^{-2}$ and the following modified split window algorithm can be adopted to retrieve land surface temperature:

$$T_s = T_s' + 58.87(1 - \bar{\epsilon}) - 119.59\delta\epsilon + 46.13 \left\{ (1 - \bar{\epsilon})^2 - (0.5\delta\epsilon)^2 \right\} \quad (28)$$

where $H_1 = 58.87$, $H_2 = -119.59$ and $H_3 = 46.13$ are the calculated mean values of these functions and T_s' is evaluated for a calculated mean value of $a_2' = 2.23$ in this water vapour range.

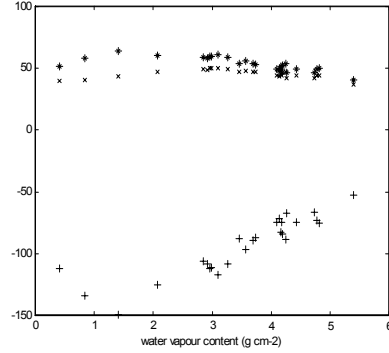


Fig. 4. The H_1 (*), H_2 (+) and H_3 (x) functions, vs. water vapour content.

For water vapour content above 3.0 g cm^{-2} the following regressive relationships hold:

$$\begin{cases} H_1 = -7.61w + 82.69 \\ H_2 = 24.35w - 182.22 \\ H_3 = -4.81w + 65.12 \end{cases} \quad (29)$$

4 VALIDATION RESULTS

In the MODIS LST processing, the data in MODIS Calibrated Radiance (MOD021KM) and Geolocation (MOD03) products were used together with the emissivity product from (MOD11_L2) to retrieve the LST pixel by pixel. The LST validation results are given in Tables 2a-2c. All the *in situ* data used in the LST validation were obtained from the field campaigns conducted by the MODIS Land Discipline Group during the year 2000 and 2001 and reported in the MODIS Science Team Meeting of Dec. 18, 2001 (<http://www.icess.ucsb.edu/modis/modis-lst.html>).

For validation of the algorithm over the sea, the field campaign conducted by Consiglio Nazionale delle Ricerche (CNR) of Italy was the only available source of data. A sample of 8 coincident ground measurements and EOS MODIS cloudless observations in December 2001 was considered for the Mediterranean Sea. The SST products were validated within $0.3 \text{ }^\circ\text{K}$ with *in situ* measurements (Mito, 2002).

TABLE 1 Emissivity data set used in the estimation of H_1 , H_2 and H_3

$\bar{\varepsilon}$	ε_1	ε_2	$(1 - \bar{\varepsilon})$	$\delta\varepsilon$	$(1 - \bar{\varepsilon})^2 - (0.5\delta\varepsilon)^2$
0.98	0.99	0.97	0.02	0.02	0.00030000
	0.985	0.975		0.01	0.00037500
	0.9825	0.9775		0.005	0.00039375
	0.98	0.98		0.0	0.00040000
	0.9775	0.9825		-0.005	0.00039375
	0.975	0.985		-0.01	0.00037500
	0.97	0.99		-0.02	0.00030000
0.94	0.95	0.93	0.06	0.02	0.00350000
	0.945	0.935		0.01	0.00357500
	0.9425	0.9375		0.005	0.00359375
	0.94	0.94		0.0	0.00360000
	0.9375	0.9425		-0.005	0.00359375
	0.935	0.945		-0.01	0.00357500
	0.93	0.95		-0.02	0.00350000
0.9	0.91	0.89	0.10	0.02	0.00990000
	0.905	0.895		0.01	0.00997500
	0.9025	0.8975		0.005	0.00999375
	0.9	0.9		0.0	0.01000000
	0.8975	0.9025		-0.005	0.00999375
	0.895	0.905		-0.01	0.00997500
	0.89	0.91		-0.02	0.00990000

TABLE 2a Validation of the 1 KM MODIS LST product (I)-In lake sites

Case n°	Site	Lat. Long.	Date (m/d/y)	Time (UTC)	CWV (cm)	<i>In situ</i> T_s (°K)	$\bar{\varepsilon}$	$\delta\varepsilon$	T_{modis} (°K)	$T_{\text{modis}} - T_s$ (°K)
1	A	37.9930°N 118.9646°W	07/25/00	19:18	2.1	296.01	0.989	0.006	295.8100	-2000
2	A	38.0105°N 118.9695°W	10/06/00	19:11	1.4 (0.62)	290.17	0.989	0.006	290.6641	0.4941
3	B	38.6972°N 118.70802° W	10/18/01	18:57	0.81 (0.95)	290.56	0.990	0.004	290.2904	-2696

A - Mono Lake, California; B - Walker Lake, Nevada

TABLE 2b Validation of the 1 KM MODIS LST product (II)-Over grassland and rice field

Case n°	Site	Lat. Long.	Date (m/d/y)	Time (UTC)	CWV (cm)	<i>In situ</i> T_s (°K)	$\bar{\varepsilon}$	$\delta\varepsilon$	T_{modis} (°K)	$T_{\text{modis}} - T_s$ (°K)
4	A	38.2202°N 119.2693°W	07/30/00	05:57	2.4	283.24	0.988	-0.004	282.7110	-.5290
5	B	39.5073°N 121.8107°W	07/30/00	05:57	3.0	293.02	0.988	-0.004	293.0480	0.0280
6	C	38.2199°N 119.2683°W	03/12/01	06:36	0.4	263.50	0.988	-0.004	264.0254	0.5254

A - Bridgeport, grassland; B - Rice field, California; C - Bridgeport, snow cover

TABLE 2c Validation of the 1 KM MODIS LST product (III)-Over silt playa

Case n°	Site	Lat. Long.	Date (m/d/y)	Time (UTC)	CWV (cm)	<i>In situ</i> T _s (°K)	$\bar{\varepsilon}$	$\delta\varepsilon$	T _{modis} (°K)	T _{modis} -T _s (°K)
7	A	38.4617°N 115.6927°W	07/18/01	18:35	1.25 (0.86)	321.2	0.968	-0.008	320.5721	-.6279
8	A	38.4617°N 115.6926°W	07/20/01	06:21	0.64	287.4	0.968	-0.008	287.1168	-.2832
9	A	38.4617°N 115.6926°W	07/21/01	05:26	0.69	289.7	0.967	-0.006	289.0860	-.6140
10	A	38.4630°N 115.6930°W	07/21/01	19:05	0.68 (0.92)	320.1	0.9680	-0.008	319.0526	-1.0474
11	A	38.4630°N 115.6930°W	07/24/01	05:57	1.01	290.7	0.9670	-0.006	290.4274	-.2726

A – Silt playa in Railroad Valley, Nevada

5 CONCLUSIONS

A simple extension of the SWT for land surface temperature determination has been set up; it is in fact, theoretically possible to express LST as a combination of the brightness temperatures in two spectrally adjacent channels, also separating the atmospheric absorption and the surface emittance if the water vapour amount is less than 3.0 g cm^{-2} . For any realistic value of the atmospheric water vapor content above 3.0 g cm^{-2} the error on the temperature estimate depends strongly on the accuracy in the knowledge of atmospheric water vapor content, and the algorithm takes the advantage of the NIR / IR MODIS bands, which allow the estimation of this parameter (MOD05_L2) with a 5 – 10% error. In both cases the algorithm should be used in association with the emissivity information from the reflective bands in order to retrieve surface temperature.

The LST product has been validated within 1K, with *in situ* LSTs in 11 cases over land in the atmospheric WVC range of $0.4 - 3.0 \text{ g cm}^{-2}$. It is expected that the combined use of Terra and Aqua MODIS data will improve the LST quality significantly. As a future work we expect to validate the LST products with *in situ* data from the tropical region. In this way the accuracy of the algorithm can be ascertained for this type of atmosphere where water vapour concentration higher than 3.0 g cm^{-2} can be usually expected. This will allow the exploitation of the MODIS images to be acquired in future at BSC Equatorial Station (Malindi – Kenya) for LST and SST estimate in the Central – East Africa area.

REFERENCES

- McMillin, L.M. (1975): Estimation of sea surface temperatures from two infrared window measurements with different absorption. *Journal of Geophysical Research*, 80 (36), 5113-5117.
- McMillin, L. M. (1980): The split window algorithm for sea surface temperature derived from satellite. In *Remote Sensing of Atmospheres and Oceans*, edited by A. Deepak (London: Academic Press), 437-455.
- Mito C. O., (2002): Retrieval of land and sea surface temperatures using MODIS data with improved split window technique. Ph.D. Thesis, University of Rome "La Sapienza".
- Ulivieri C., (1984): Minimization of atmospheric water vapour and surface emittance effects on remotely sensed sea surface temperatures, *IEEE Trans. Geosci. Remote Sensing* 22, 622-628.
- Ulivieri, C., and Cannizzaro G., (1985a): Land surface temperature retrievals from satellite measurements. *Acta Astronautica*, 12, 977-985.
- Ulivieri, C., and Cannizzaro G., (1985b): The influence of surface-air temperature difference on the estimate of remotely sensed surface temperatures. *Proc. Int. Con. of the Remote Sensing Society and CERMA*, London, II, 173-178.
- Ulivieri, C., Castronuovo, M. M., Francioni, R., and Cardillo, A (1994): A split window algorithm for estimating land surface temperature from satellites. *Advances in Space Research*, 14, 59-65.
- Wan, Z., (1999): MODIS Land Surface Temperature Algorithm Theoretical Basis Document (LST ATBD). Version 3.3 Contract Num. NAS5-3137

The Urban Heat Island Effect in the São Paulo Metropolitan Region By AVHRR and The Influence In The Human Health¹

Souza, L. F. A², Massambani, Oswaldo
Instituto de Astronomia, Geofísica e Ciências Atmosféricas
Rua do Matão, 1226, Cidade Universitária
05508 – 900 São Paulo – SP, Brazil
andrefls@model.iag.usp.br; omassamb@model.iag.usp.br

1 Research financed by Fundacion MAPFRE

2 Processo FAPESP: 99/07632-3

ABSTRACT - One period was selected to evaluate the urban heat island effect in São Paulo Metropolitan Region (SPMR) through satellite and its effect in the morbidity. The period was limited through the May and June months. The transition months between the autumn and the winter seasons (May and June) is when happened a better configuration of this phenomenon in SPMR. In other months this effect occurs, but not present the same characteristics, mainly the atmospheric moisture patterns. The dataset were supplied by several sources (IAG/USP, INMET, CETESB, SUS and EDC-NOAA) and several parameters were collected such as precipitation rate, global solar transmission, relative moisture, air temperature, morbidity and parameters generated by remote sensing dataset, as vegetation index (NDVI) and land surface temperature. The land surface temperature must be evaluated jointly with vegetation index and surface albedo for this case, due the emissivity variation. Every data evidence that the configuration of the heat island phenomenon has its formation and maintenance associated with phenomenons of great and local scale. The geographical position of SPMR is also a factor of great importance and influence in this configuration and the effect of the thermal gradient can be observed through the remote sensing, by the vegetation index and the land surface temperature.

1. OBJECTIVE

This work has as main objective assess the satellite dataset such as, vegetation indexes and land surface temperature. The intend is evaluate that forms the improvement the estimate of mentioned parameters. This dataset can contribute the studies of the heat island effect, mainly its interaction with the climatic conditions. The interaction between the climatic parameters generators of the heat island phenomenon and the air quality is very important, because the influence in the breathing system diseases, denominated by morbidity rate.

2. INTRODUCTION

The São Paulo Metropolitan Region (SPMR) is located in the most demographic density and also presents the largest urbanization rate and industrial activities (Figure 1).

In this context, the "heat islands effect" are created by the trees remotion and construction of high buildings, as well as the soils pavimentation. During the day, the dark materials as the asphalt and the roofs also absorb and store heat. After sunset, these materials maintain the temperature of the urban ranches more discharges than the rural areas. This phenomenon is peculiar in urban areas, and is characterized by a fast increase of the temperature in the urban atmosphere, an increase

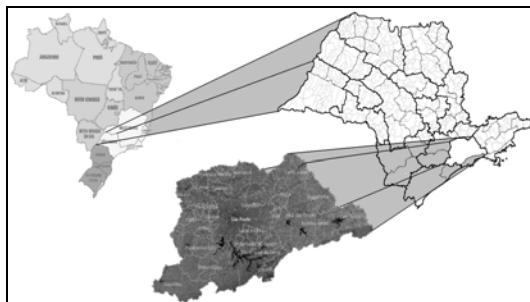


Figure 1: São Paulo Metropolitan Region (SPMR), by LANDSAT (Source: DSI/INPE).

of the concentration of the atmospheric pollutants and a decrease in the atmospheric moisture.

The thermal behavior of the "urban islands" is different from that can be observed in the rural atmospheres, because the temperature on the urban space is function of the air temperature, that in the form of brightness temperature (radiant energy) interage with the most varied surfaces that composes the urban way and it propitiates the formation that can be called in the literature of "urban heat island" (Conde, 1999).

The urban heat island corresponds an area where the surface temperature is higher than in its nearby, providing the rising of local circulations due to reduction of the evaporation, increase of the roughness and the thermal properties of the buildings and the materials used in the roads pavement (Lombardo, 1984). In the central of the urban areas, with the vegetation reduction, the temperatures reach maximum values. On the other hand, the minimum values are registered in green areas and reservoirs of water. The heat island effect can modify the wind currents and the precipitation, but this should be analyzed by means of other factors as for example the type of time, the geographical position, the buildings structures. The roughness effect of the constructions and the ascending hot air can increase the aerosols concentration and provoke the increase precipitation (Lombardo, 1984).

The energy and radiation budget in the urban zone as a consequence of the alterations promoted by the substitution of the natural surfaces by pavements and constructions, that store part of the incident energy in the surface that it would be used in the evaporation of the moisture of the surface, heats up the urban atmosphere, turning it hotter than outlying areas (Landsberg, 1981). In this way, knowing the ideal conditions of the inhabitants' of the great urban centers, the life can come to be investigated through the thermal discomfort and the morbidity rate provoked by the "heat island effect ". All the topographic complexity associated with the neighbourhood of the ocean and the intense urbanization on the area influence the pattern of the atmospheric circulation creating peculiar situations in SPMR. (CETESB, 1993).

Climatic Conditions

The topography effects in the local circulations are strongly controlled by the latitudinal position (Fast and McCricle, 1990). In low latitudes, the diurnal heating is well distributed along the whole year. However, direct circulations induced by the differential heating (mountain - valley and ocean - land) must be more intense and persistent. The geographical location of SPMR sustains the generation of different patterns of circulation, mainly for the thermal effect associated with the topography (Silva Dias and Machado, 1997; Karam and Pereira, 2000).

In agreement with Cabral (1997) it was consisted that an increase tendency in the air temperature and the consequent decrease of the relative moisture cannot, in association with the bad air quality, generate situations of bad thermal confort and also to provoke damages to

the local inhabitants health. The climatic factors and associated with antropogenic are: simultaneous periods of excess of heat, low values of the relative moisture, stability atmospheric and high indexes of the air pollution. The pollution also concentrates with larger intensity on the heated up city areas and with smaller indexes of green spaces, showing the existent relationship directly between the heat island phenomenon and the atmospheric pollution. In a general way, Titarelli (1982) verified that there is a periodic alternation in the episodes of bad air quality, mainly in the autumn-winter seasons, associating the same ones to the pre-front systems.

3. MATERIAL

The feature of the "urban heat island" effect by satellite should have as base the characterization of this phenomenon through surface data, supplied by the most several sources. In this work, the dataset used was supplied by the following agencies:

- ❑ Mirante de Santana Meteorological Station - National Institute of Meteorology (INMET): daily precipitation, wind velocity, frequency of the thermal inversions;
- ❑ Água Funda Meteorological Station (IAG/USP): clouds types, atmospheric pressure, air temperature, air moisture and precipitation;
- ❑ Company of Environmental Technology for Clean Up (CETESB): Monthly distribution of favorable and unfavorable number days for the dispersion pollutants in the atmosphere, in the SPMR, from 1988 to 1992;
- ❑ Water and Energy Department (DAEE): Daily precipitation in the SPMR;
- ❑ Public Health System / International Disease Classification (SUS/IDC): Morbidity occurs in the SPMR, in according of IDC (International Disease Classification) for patient admission caused by disease for breathing apparel and other diseases of the breathing apparel;
- ❑ AVHRR Dataset (National Oceanic and Atmospheric Administration): radiance eand bright temperature (channels 1, 2, 4 e 5), with 1 km x 1 km of spacial resolution (Eidenshink and Faundeen, 1997).

The 1992 year was chosen based in the supplied dataset. The May and June months are characterized by the end of the autumn and beginning of the winter seasons. In this period the main atmospheric components that characterize the influence on the heat island effect in the inhabitants health of the SPMR, as the thermal inversions, atmospheric stagnation, high pollutants concentrations and low precipitation rates and entrance of the front systems.

4. METODOLOGY

The surface data supplied by INMET, IAG/USP, CETESB and SUS should be used to detect the favorable conditions for the formation of the heat urban island phenomenon, as well as the increase of the morbidity, in particular diseases of the breathing apparel. The data obtained through remote sensing should also be used to detect the surface conditions, through bioclimatics and physics as normalized difference vegetation index (NDVI), albedo and land same ones reflect the true conditions observed in the surface.

The normalized difference vegetation index (NDVI) its obtained in the following way:

$$NDVI = (Ch2 - Ch1) / (Ch2 + Ch1) \quad (1)$$

Where: NDVI → Normalized difference vegetation; index; Ch1 → Reflectance channel 1; Ch2 → Reflectance channel 2.

In the reflectance generation of the channels 1 and 2, the NOAA dataset radiometric and geometric calibrations follow the proposal of Rao and Chen (1995, and 1996), should be used together with the algorithm of atmospheric correction proposed by Paltridge and Mitchell (1990). The channels 1 and 2 are: 0,55 to 0,68 μm (visible band) and 0,725 to 1,1 μm (near infrared band), respectively. The NDVI reflects a environmental effect that limit the ecosystems growth. This index has been showing high correlations with vegetation parameters as: green leaves, biomass production and leaf area index, showing considerable discrimination of coverings, besides being related the conditions of hydric stress (excess or deficit) (Myers, 1983; Justice et al, 1985), being applied this index for SPMR, it is waited that the values of NDVI are minimum for two reasons, the main is that this is an extremely urbanized area, therefore, we will have a larger answer of the several types of surfaces (asphalt new and old, and plenty concrete).

For the Plank law, all material presents an only characteristic signature, emitting eletromagnetic energy., and a simplified way, the radiant energy emitted in long wave, or bright temperature, links with the temperature through the relationship of Stephan – Boltzman (2), in the following way:

$$R = \sigma \epsilon T^4 \quad (2)$$

Where: R = Long wave spectral radiance; ε = Emissivity; σ = Stephan-Boltzman coefficient, $5,67 \times 10^{-8} \text{ Wm}^{-2} \cdot \text{K}^{-4}$; T = temperature in K.

surface temperature. The estimate of these parameters will be a tool that will be used in the detection of the surface conditions observed through the surface data.

The importance on using data obtained through the satellites is that the derived parameters of these sources collect the whole terrestrial space. This is the great advantage in using this source data. However, some calibrations should be applied in these data so that the

The satellites, captured the surface informations through the digital number, that its transformed in radiance and brightness temperature by the (3)

$$T_i(RAD_i) = \frac{C_2 * v_c}{\ln(1 + \frac{C_1 * v_c^3}{RAD(v)_i})} \quad (3)$$

Where: $T_i(RAD_i)$ – brightness temperature, C_1 e C_2 – Plank constants, v_c - wave central number, $RAD(v)_i$ – Radiance in a specific band.

The land surface temperature is obtained through split window technique (SW), that assumes to be linear the relationship between the temperature and the emissivity. This method bases on the effect of diferencial absorption among the channels 4 and 5, due of these channels be located in the "atmospheric window" between 10,5 and 12,5 μm (Becker and Li, 1990). The land surface temperature is obtained by:

$$T_S = A_0 + P * [(T_4 + T_5)/2] + M * [(T_4 - T_5)/2] \quad (3)$$

Where:

$$A_0 = 1,274; P = 1 + 0,15616 * [(1 - \epsilon)/\epsilon] - 0,482 * (\Delta\epsilon / \epsilon^2); \\ M = 6,26 + 3,98 * [(1 - \epsilon)/\epsilon] - 0,482 * (\Delta\epsilon / \epsilon^2); \\ \epsilon = 1,0094 + 0,047 * (NDVI); \Delta\epsilon = 0,016;$$

The emissivity is obtained by Griend and Owe (1993) and Kerdilles and Grondona (1996) methods. Ming and Liu (1998), observed that in general the estimate of the land surface temperature suggested for the Valor and Caselles (1996) method, not limiting the surface emissivity and also using the reflectance variation to the channels 1 and 2 as weights modulators for the variability presented by emissivity.

5. RESULTS

5.1. Surface stations

Two meteorological stations were used, presenting historical datasets of the climatological series, and this

data was obtained with maximum efficient collection, obeying the international norms. The stations are: Mirante de Santana (INMET), located in Santana's neighborhood, in the North Zone of the São Paulo capital and the Água Funda (IAG/USP), located inside the State Park of the Ipiranga's Water Source, in the South Zone of the São Paulo capital.

The both surface stations (Mirante de Santana and Água Funda) captured the patterns presented by the climate variation. The May and June months presented as characteristics, a reduction of the precipitation rate and the relative moisture. The wind speed in surface also presented an reduction on the intensity. The number of thermal inversions presented an increase. All these characteristics favor the configuration of the urban heat island phenomenon and it also increase the pollutants concentration in SPMR.

Some decadal periods of the May and June months are stand out. They are: second decadal period from May; first and second decadal periods from June, 1992. In these periods it can be observed the urban heat island phenomenon in SPMR (Figure 2). These months are characterized by the increase of the patient admission due to the increase of the morbidity rate.

During the summer season and one month before, there is a pattern modification on the environmental conditions, such as temperature, moisture, surface wind and also in the pollutants concentration. Thus, even with an increase of the land surface temperature configuring an urban heat island, the increase of the atmospheric moisture doesn't allow that the characteristics patterns of the heat island settle down and affect the morbidity rate.

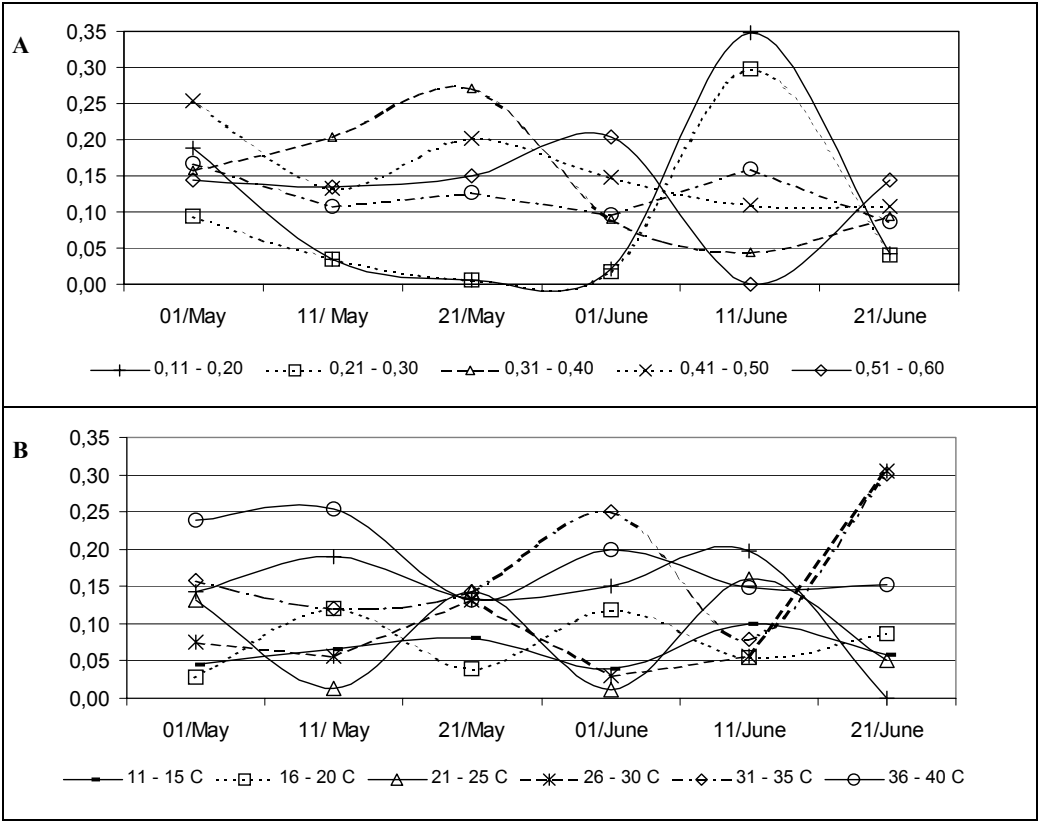


Figure 2: Normalized frequency concentration from SPMR to decadal vegetation index (NDVI) and land surface temperature.

5.1. Derived satellite parameters

The figure 2A and 2B, show the normalized frequency distribution for the vegetation index and land surface temperature, where the pixels of each image are

concentrated on each strip. This data were selected due the heat island effect configuration in the SPMR. For the vegetation index pixels we can concentrate our analyses among the strips of 0,11 to for 0,50. For land surface temperature our analysis will be concentrated

on the strips between 26 and 40 °C. Through these illustrations we can observe that a larger concentration happens in lower values of the vegetation index when there is the configuration of the heat island effect in RMSP (Figure 4). The same effect observed in the vegetation index can be viewed on the temperature, that also presents high values to pixels concentration.

Through the illustration (Figure 2), it can be observed that to the long selected periods (May and June months) there is a particular variation in the pixels concentration that configures the urban heat island effect, the lowest values, in the vegetation index, and in the values high, in the case land surface temperature. This supplies us a valuable tool in the image analysis obtained through remote sensing

In the Figure 3 (A, B, C and D), it can be observed that the periods were a great variation, particularly in the pixels concentration that determine the heat island effect, where the lowest values, to the vegetation index, and the highest values, to land surface temperature. This give us a valuable tool in the image analysis obtained by remote sensing, confirming the visual analysis. The second decadal period from May, and the second and third decadal period from June showed the major evidence of the studied effect with more pixels concentration and more admission patient in hospitals in the SPMR.

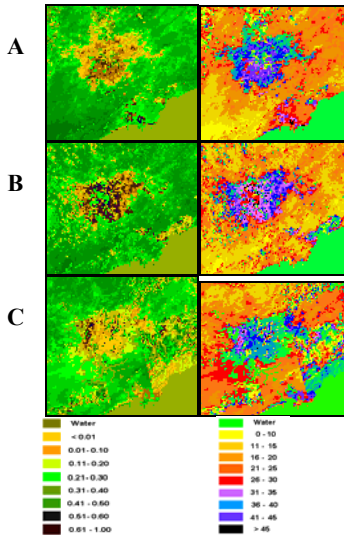


Figure 3: Vegetation index (NDVI), and land surface temperature for: (a) second decadal period from May, 1992.; (b) and (c) for first and second decadal periods from June, 1992.

To summarize what it was obtained through the analysis of the satellite dataset, we can verify that in the cases where there is less atmospheric moisture

available (after the passage of high pressure systems), the land surface temperature tends to come larger in SPMR. This can be due to great urbanization rate, that does the surfaces store a larger amount of solar energy during the days, and liberate them at night. It could also be observed that the heat island effect stays during the hottest months (november, december and january), however with smaller intensity. The NDVI show that this index presented quite significant increments when the precipitation events happened, and the inverse behavior happened with the land surface temperature. The behavior of the temperature can be explained in the following way: with the summer, there was an increase on the precipitation events and the atmospheric moisture in great scale. This parameter is obtained in the infrared bands (channels 4 and 5) that is sensitive to the water vapor in the atmospheric column and also to the surface emissivity.

The topography influences the climatic patterns directly that they determine the conditions of the environment captured through satellite, playing a fundamental part in the climate of SPMR. The marine breeze penetration and the cold fronts provide the moisture for the SPMR area. This humidity is also the responsible for the decrease of the land surface temperature, through the emissivity capted by remote sensing. The vegetation indexes evidence this surface dryness. However, the permanence of these conditions doesn't provoke extending the stress conditions.

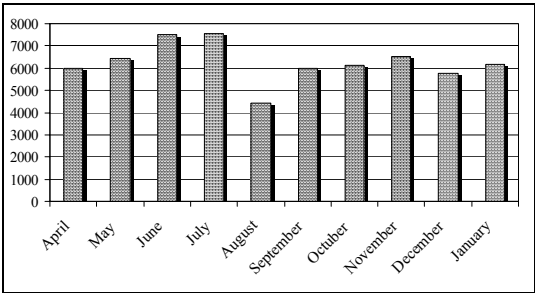


Figure 4: Patient admission for São Paulo Metropolitan Region by Morbidity (Brieth Disease Apparel and Others Diseases Apparel) for April/1992 to January/1993 (Source: Public Health System from São Paulo State).

5.2. Public health system / international disease classification

These data consist of the patient admission for breathing apparel diseases and other breathing apparel diseases, denominated as morbidity. Its is not part of this study to verify that type of diseases are defined as morbidity. The morbidity types supplied by this health

agency were chosen how the referring the breathing diseases due to increase of suffer influence on the effects attributed to the urban heat island effect.

The morbidity data were observed in the others periods that not used in this study, as the april, july, august, september, october and january months. Through these data, is observed that the May, June and July months presented the largest morbidity rates. Among the studied periods, the June month presented the most favorable conditions to the sensitive related to the breathing system and other diseases of the breathing apparel are plotted. These data refers to SPMR. It can be observed in this picture a sensitive increase in the patient admission number, presenting larger incidence in the initial months on the winter beginning.

6. CONCLUSIONS

Through the analyses of all parameters used in the characterization of the urban heat island phenomenon can be observed that factors of another space scales influence in a direct way in the formation and maintenance of the climatic patterns. Allies to these factors of great scale, there is interaction with peculiar patterns of the topography and location of SPMR in the context of the Southeast Region from Brazil and also in the São Paulo State. The use of dataset obtained through remote sensing as study and analysis tool comes high potentiality, that together with other sources they can be used in the identification of these conditions so that preventive measures the public health can be taken. Through the vegetation index and land surface temperature dataset and also the pixels frequency, a real idea can be obtained on the form by the which the temperature and the atmospheric moisture are distributed on SPMR. This indirectly can determine the potential areas where can observe larger pollution concentrations and also to supply an estimate of the impact of these parameters in the morbidity rates, that are a lot of susceptible to these environmental conditions.

ACKNOWLEDGE

The authors would like to thank the Fundação de Amparo a Pesquisa do Estado de São Paulo (FAPESP), wich had financed our projects, Ph.D and Themathic, on the IAG/ USP, and also the Distributed Active Archive Center (Code 902.2) at the Goddard Space Flight Center, Greenbelt, MD, 20771, for producing the data in their present form and distributing them. The original data products were produced under the NOAA/NASA Pathfinder program, by a processing team headed by Ms. Mary James of the Goddard Global Change Data Center; and

increment of the morbidity rate. Factors as the low moisture, low precipitation rate and the passage of few front systems should also have been providing this increment in the morbidity.

The main objective to be reached with these data is verifying that during the months when the heat island effect is better configured, there is also the largest incidence of patients admision related to the morbidity rate of the breathing apparel disease. This can be observed in the illustration 3, where the morbidity rate the science algorithms were established by the AVHRR Land Science Working Group, chaired by Dr. John Townshend of the University of Maryland. Goddard's contributions to these activities were sponsored by NASA's Mission to Planet Earth program.

REFERENCES

- BECKER, F. and Z-H. LI, 1990. Temperature-Independent Spectral Indices in Thermal Infrared Bands. *Rem. Sens. Envir.* 32: 17 - 33.
- CABRAL, E. 1997. Análise da Alterações Climáticas da Cidade de São Paulo (1887 - 1995) no Contexto da Expansão de sua Mancha Urbana. Dissertação de Mestrado. Departamento de Geografia. Faculdade de Filosofia, Letras e Ciências Humanas – USP. p. 278.
- CETESB – Companhia de Tecnologia de Saneamento Ambiental – Relatório de Qualidade do Ar no Estado de São Paulo – 1992. Governo do Estado de São Paulo – Secretaria do Meio Ambiente.
- CONDE, F.C, 1999. “Estudo da Correlação entre a Quantidade de Veículos e a Temperatura do Ar na Área Urbana de Belém – PA”.UFPA – Universidade Federal do Pará. Trabalho de conclusão de curso.
- EIDENSHINK, J.C. and J.L. FAUNDEEN, 1997. The 1 km AVHRR global land data set: first stages in implementation. *Int. J. Rem. Sens.* 51: 39 – 56.
- FAST, J. D. and M.D. MCCORCLE, 1990. A Two-Dimensional Numerical Sensivity Study of the Great Plains Low-Level Jet. *Monthly Weather Review*, 118, 151 – 163.
- GRIEND, A. A. V. and M. OWE, 1993. On the relationship between thermal emissivity and the normalized difference vegetation index for natural surfaces. *Int. Jour. Rem. Sens.* 14, 6:1119-1131.

- JUSTICE, C.O.; J.R.G. TOWNSHEND; B. N. HOLBEN, and C. J. TUCKER, 1985. Analysis of phenology of global vegetation using meteorological satellite data. *Int. J. Rem. Sens.* 8: 1271 – 1318.
- KARAM, H.A. and A.P. OLIVEIRA, 2000. Patterns of Local Circulation Induced by Topography: Observation and Numerical Modeling. (article submitted to *Boundary-Layer Meteorology*).
- KERDILLES, H., and M. O. GRONDONA, 1996. NOAA-AVHRR NDVI decomposition and subpixel classification using linear mixing in the Argentina Pampa. *Int. J. Rem. Sens.* 16: 1303 – 1325
- LANDSBERG, H.E., 1981. *The Urban Climate*. New York. Academic Press.
- LOMBARDO, M.A., 1984. *The Heat Urban Island of Paulistan Metropolis*. Pd.D Degree. Instituto de Geografia – USP.
- MING, T. C; and LIU, W. T. H., 1998. Comparação de Três Métodos de Estimativa de Temperatura da Superfície Terrestre Utilizando Dados de AVHRR. X Congresso Brasileiro de Meteorologia. VIII Congresso da FLISMET. . 26 a 30 de outubro. Brasília-DF.
- MYERS, V.I., 1985. Remote sensing applications in agriculture in *Manual of remote Sensing*. 2^a ed. 2. American Meteorological Society of Photogrammetry. 1985. 2724 pp.
- PALTRIDGE, G.W., and R.M. MITCHELL, 1990. Atmospheric and viewing angle correction of vegetation indices and grassland fuel moisture content derived from NOAA/AVHRR. *Remote Sensing for Environment*, 31:121-135.
- RAO, C.R.N., and J. CHEN, 1995. Inter-satellite calibration linkages for the visible and near-IR channels of the AVHRR on the NOAA-7, -9 and -11 spacecraft. *International Journal of Remote Sensing*, 16 (11):1931-1942.
- RAO C.R.N. and J. CHEN, 1996. Post- launch calibration of the visible and near-IR channels of the AVHRR on the NOAA-14 spacecraft. *Int. J. Rem. Sens.*, 17(14):2743-2747.
- SILVA DIAS, M. A. and A. J. MACHADO, 1997. The Role of Local Circulations in Summertime Convective Development and Nocturnal Fog in São Paulo, Brazil. *Boundary-Layer Meteor.*, 82, 135 – 157.
- TITARELLI, A.H.V., 1982. Alterações do Clima Local nos Centros Urbanos: Efeitos Adversos da Urbanização. *Caderno Prudentino de Geografia*. Presidente Prudente, 3, p. 28 – 35.
- VALOR, E. and V. CASELLES, 1996. Mapping land surface emissivity from NDVI: Application to European, Africa and South American areas. *Rem. Sens. Environ.* 57: 167 -184.

The use of HIRLAM climate predictions and AVHRR data for the calculation of evapotranspiration rates in Denmark

E. Boegh¹, H. Soegaard¹, J. H. Christensen², C. B. Hasager³, N. O. Jensen³, N. W. Nielsen² and M. S. Rasmussen¹

¹*Institute of Geography, Oester Voldgade 10, 1350 Copenhagen K, Denmark*

²*Danish Meteorological Institute, Lyngbyvej 100, 2100 Copenhagen Ø, Denmark*

³*Risø National Laboratory, Frederiksborgvej 399, 4000 Roskilde, Denmark*

evb@geogr.ku.dk, hs@geogr.ku.dk, jhc@dmi.dk, charlotte.hasager@risoe.dk, n.o.jensen@risoe.dk, nwn@dmi.dk, msr@geogr.ku.dk

ABSTRACT *In order to calculate the spatial distribution of evapotranspiration rates in Denmark, grid-based predictions of weather conditions are combined with remote sensing based estimates of surface temperature, global albedo and vegetation index. The climate predictions were calculated by the high-resolution limited area resolution model, HIRLAM, at 5 km grid resolution to represent the atmospheric conditions in Denmark. The predictions were used both for atmospheric correction of satellite imagery and as inputs for the calculation of evapotranspiration rates. The evapotranspiration rates were calculated at the 1 km² resolution of the AVHRR data and validated using landscape scale atmospheric fluxes of sensible and latent heat recorded for an agricultural region, a beech forest and a conifer forest.*

1 INTRODUCTION

Evapotranspiration rates constitute a sensitive linkage of atmospheric and hydrological processes. While the land surface feedback of heat and water vapour is important for an accurate prediction of atmospheric circulations, the net input of precipitation (precipitation minus evapotranspiration) is important for the evaluation of water resources on Earth. Since an increase in the global temperature of several degrees is anticipated in the present century, accurate methods for evaluating the interactions between the atmosphere and the land surface have become acutely important. Because Earth observations can be used to quantify the spatial distribution of evapotranspiration rates, they constitute an important extrapolation tool in support of field measurement based studies and modelling activities within the fields of meteorology and hydrology.

One constraint for remote sensing based flux estimation at the larger scale is the spatial representativity of the applied meteorological data. Field measurements of global radiation, air temperature and air humidity, which are needed for calculating the evapotranspiration rates, may vary significantly within the area monitored by satellites. Because of the difficult and expensive access to spatial representative meteorological field data, in this study, a high-resolution regional weather forecasting model, HIRLAM, is used to provide spatially distributed inputs of weather conditions to facilitate the

atmospheric correction of satellite imagery and the subsequent calculation of evapotranspiration rates.

2 METHODS

2.1 Climate predictions

The High Resolution limited Area Model (HIRLAM) is a routine weather forecast model used in Denmark, Sweden, Finland, Iceland, Ireland, the Netherlands and Spain. The model system consists of three nested models operating at different horizontal resolutions (50 km, 15 km and 5 km). The 50 km resolution model receives lateral boundary conditions from the European Centre for Medium-Range Weather Forecast (ECMWF) every 6 hours. The 15 km resolution model then receives the predictions from the low resolution model, and it provides the 5 km resolution HIRLAM model version with hourly predictions. Predictions are given 4 times a day by the high resolution HIRLAM model (at 0.00 GMT, 6.00 GMT, 12.00 GMT and 18.00 GMT). The 5 km resolution predictions of air temperature and air humidity at 12.00 GMT were extracted for use in the present study.

2.2 Satellite processing

All midday/afternoon NOAA satellite passages in the year 1998 and in the period 15th April-15th May 2000 were downloaded from the NOAA HRPT receiving station facilities at the Institute of Geography, Copenhagen. The data set was cloud screened and images with extreme off-nadir view-angles were

detached. The image processing was conducted using the software WinCHIPS (www.geogr.ku.dk/chips) which includes a NOAA module for unpacking, geo-registration, calibration and calculation of the spectral surface albedo and the surface temperature.

While the estimation of the surface temperature (T_s) uses the split-window technique, the calculation of the spectral surface albedoes includes HIRLAM predictions of integrated atmospheric water vapour content to facilitate the atmospheric correction of the satellite data. Atmospheric correction of the data recorded by the AVHRR sensors onboard the NOAA satellites was conducted using the 5S-SMAC radiative transfer model (Rahman and Dedieu, 1994). The optical depth (τ) was estimated using visibility observations and the Dark Dense Vegetation (DDV) approach (ie Kaufmann and Sendra, 1988). Details on the processing is described in Boegh et al. (2002a).

2.3 Global albedo and net radiation

Calculation of the global albedo (α) is based on a conversion of the narrow-band red (0.57-0.7 μm) and near-infrared (0.72-0.99 μm) albedoes computed from the NOAA-AVHRR channels into a broad-band (0.3-2.5 μm) albedo (Valiente et al., 1995). The net radiation (R_n) is then calculated

$$R_n = R_s(1-\alpha) + R_l(1-\epsilon_s) - \epsilon_s \sigma T_b^4 \quad (1)$$

Where R_s is global radiation, R_l is incoming longwave radiation which is calculated (Idso et al., 1981) using the HIRLAM predictions of air temperature and air humidity, ϵ_s is the surface emissivity, σ is the Stefan-Boltzman coefficient and T_b is the brightness temperature recorded by the satellite.

2.4 Soil heat flux

The soil heat flux (G) is estimated using an empirical linear relationship between G/R_n and NDVI (Kustas and Daughtry, 1990) where the coefficients were obtained by stretching the full range of observed NDVI's towards a full range of G/R_n fractions. It is assumed that G/R_n is 0.4 for bare soil and 0.05 for dense vegetation.

2.5 Evapotranspiration rate

The evapotranspiration rate (E) is calculated by

$$\lambda E = (\rho c_p / \gamma) (e_s^* - e_a) / (r_{ac} + r_s) \quad (2)$$

where λ is the latent heat of vapourization, ρc_p is the volumetric heat capacity, γ is the psychrometric constant, e_s^* is the saturated vapour pressure at the evaporating front which is evaluated at the temperature of the saturated evaporation front (T_s^*), e_a is the air humidity at the atmospheric reference level (the lower boundary level in HIRLAM), r_{ac} is the atmospheric resistance between the surface and the atmospheric reference level and r_s is the surface resistance. For a wet or densely vegetated soil, $T_s^* = T_s$, but for a dry soil, the effective source of water vapour is below the surface so that $T_s^* < T_s$. In this case (Boegh and Soegaard, 2002),

$$(T_s - T_s^*) = B(T_s - T_a) \quad (3)$$

where $B = \rho c_p z_d (G/H) / (r_{ac} k_s)$ with H being the sensible heat flux, z_d is the thickness of the upper dry soil layer and k_s is the thermal conductivity of dry soil. Assuming G/H to be constant (ie. Berkowicz and Prahm, 1982), the factor B remains dependent on variations in z_d and r_{ac} . Because the transition from energy-limited to soil-limited evaporation is usually abrupt and accompanied by an increase in T_s (Amano and Salvucci, 1999), literature values of the maximum thickness of the upper dry soil layer (Yamanaka and Yonetani, 1999) is used to assess the factor B . For a sandy loam (80 % sand, 10 % silt, 10 % clay), $B = 1.2$ can be used as a proxy in Equation 3 for estimating T_s^* when $(T_s - T_a) > 5$ K (Boegh and Soegaard, 2002). For $(T_s - T_a) \leq 5$ K, T_s and T_s^* are assumed to be equal.

The r_{ac} is calculated by

$$r_{ac} = \rho c_p [(T_s - T_a) + (e_s - e_a) / \gamma] / (R_n - G) \quad (4)$$

and r_s is calculated as

$$r_s = r_{ac} (e_s^* - e_s) / (e_s - e_a) \quad (5)$$

The vapour pressure at the surface (e_s) is estimated using an empirical expression (Boegh et al., 2002b),

$$e_s = A \Omega e_s^* + (1 - \Omega) e_a \quad (6)$$

where $A = 0.9$ and $\Omega = (\Delta / \gamma + 1) / (\Delta / \gamma + 1 + r_s / r_{ac})$ is the decoupling coefficient (Jarvis and McNaughton, 1986) (Δ is the slope of the temperature-saturation vapour pressure curve). High atmospheric turbulence facilitates a close coupling between the surface and the air ($\Omega \rightarrow 0$) in which case $e_s \rightarrow e_a$ (Equation 6). In contrast, when $\Omega \rightarrow 1$, there is a poor atmosphere-

surface coupling which causes water vapour to accumulate at the surface, thus approaching $A_{e_s}^*$. Equations 4, 5 and 6 are solved using Newton-Raphson iteration.

3 FIELD DATA

Atmospheric fluxes of latent and sensible heat were available for 3 experimental sites; ie. an agricultural region located in affinity to the Institute of Agricultural Sciences in Foulum, a beech forest (EUROFLUX site) located near Soroe which is close to the centre of the major island (Zealand) in Denmark, and a conifer forest which is located at an extensive sandy outwash plain close to the Western shoreline (Ulborg site). All flux measurements were recorded using the eddy covariance technique. Field measurements of global radiation, air temperature and air humidity were also made available for the study. Further description of field data is given by Boegh et al. (2002a).

4 RESULTS

4.1 Weather predictions

The predicted weather conditions at 12 GMT were used as proxies for the air temperature and air humidity at the time of satellite passage (12.30 – 15.00 GMT). The root mean square error (rmse) of the assessed (proxy) air temperature was 1.9 °C (Boegh et al., 2002a) which is lower than the rmse of 3-5 °C which have been reported for remote sensing based estimates of in situ air temperature (ie. Prince et al., 1998). Generally, the temperature predictions tended to be lower than the field measurements. This may well be explained by the difference between prediction level (approximately at 30 m height) and measurement level (a few meters above the canopy). For the air humidity, the rmse is 204 Pa. This is comparative to the accuracy with which air humidity can be assessed using microwave remote sensing observations above the ocean (Schüssel et al., 1995). Remote sensing based estimation of air humidity in heterogeneous landscapes is not yet feasible (Czajkowski et al., 2002). Except for the Ulborg site in West Jylland, the HIRLAM predicted (proxy) air humidity tended to be underestimated.

4.2 Evapotranspiration rates

An example on the HIRLAM and satellite inputs for calculating the evapotranspiration rates is shown in Figures 1 and 2. Figure 1 shows the HIRLAM predicted air temperatures (degrees Celsius) and air humidities (g m^{-3}) for Denmark on 29th April 2000 at 12.00 GMT. Due to the encirclement by sea shorelines, there is a significant spatial variation in the

weather conditions in Denmark. In particular, the effect of the sea breeze circulation system is responsible for the intrusion of cooler air temperatures along the shorelines. This effect is stronger on the shorelines located in the upwind direction (Eastern winds prevail on 29th April 2000). Inland, the air temperature is up to 3 degrees higher (Fig. 1). With respect to the air humidity, the larger values in the Southern part of the country agree with the presence of clouds in the satellite data (Fig. 2).

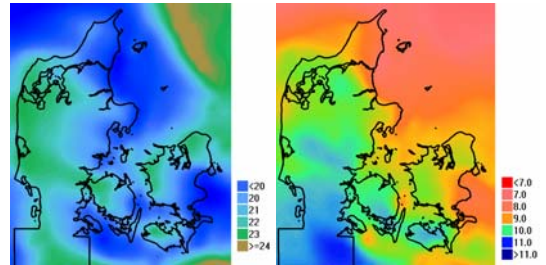


Fig. 1. HIRLAM predicted air temperature in degrees Celsius (left) and air humidity in g m^{-3} (right). Denmark, 29th April 2000 at 12.00 GMT.

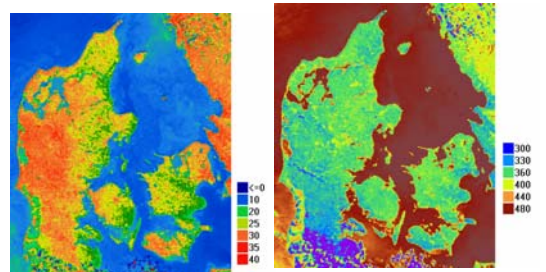


Fig. 2. Surface temperature in degrees Celsius (left) and net radiation in W m^{-2} (right) calculated from NOAA-AVHRR. Denmark, 29th April 2000 at 14.00 GMT. The dark blue dots in the lower part of the surface temperature image (left) illustrates very low temperatures due to cloud coverage.

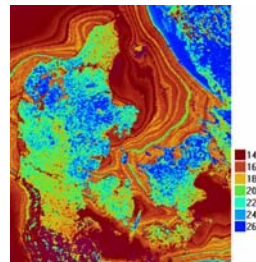


Fig. 3. Evapotranspiration rates in W m^{-2} calculated using HIRLAM weather predictions and NOAA-AVHRR observations. Denmark, 29th April 2000 at 14.00 GMT.

Figure 2 shows the surface temperature (degrees Celsius) and the net radiation (W m^{-2}) which are calculated on the basis of the satellite data. The surface temperature is generally highest in West Denmark because of the location of an extensive sandy outwashed plain in this part of the country. Because of a low surface albedo, the net radiation is also relatively high for this geomorphological unit.

Combining the weather predictions and the satellite data, it appears that the intrusion of cooler air temperature by the sea breeze circulation system increases the sensible heat flux and suppresses the evapotranspiration rates (Boegh et al., 2002a). The effect of cooler air temperature on the evapotranspiration rate is most pronounced in the Northern and Eastern parts of Denmark in Fig. 3 while, in South Denmark, the high atmospheric humidity also works to suppress the evapotranspiration rate. Because of the high surface temperatures of the drier sandy outwashed plain in West Jylland, the evapotranspiration rates are also lower in this part of the country. The spatial pattern of the calculated evapotranspiration rates at sea are governed mainly by the HIRLAM predicted air temperature.

The comparison between calculated and measured atmospheric heat fluxes in Foulum (agriculture), Sorø (beech forest) and Ulborg (conifer) disclosed a linear relationship with a rather large degree of scattering. The root mean square errors were found to be 67 W/m^2 and 80 W/m^2 for the latent and sensible heat fluxes, respectively (Boegh et al., 2002a). Improved accuracies in both the weather (proxied) predictions and the processed satellite image quality are warranted to advance the presented approach for calculating evapotranspiration rates at larger scale. In order to improve satellite data quality, spatially distributed information on atmospheric conditions should be allowed as inputs for the atmospheric correction of satellite (instead of single values representing all Denmark).

5 SUMMARY

The importance of using spatially distributed weather conditions for remote sensing based calculation of evapotranspiration rates at larger scale were testified, and the benefits of using meteorological predictions by a regional weather forecast model for 1) atmospheric correction of satellite imagery and 2) calculation of evapotranspiration rates were highlighted.

The weather predictions at 12 GMT were found to be reasonable proxies for the atmospheric conditions at the time of satellite passage, and the feasibility of using HIRLAM predictions for the atmospheric correction of satellite imagery was encouraging. Therefore, the combination of the weather predictions

and timeseries of atmospheric corrected satellite observations were useful for the calculation of evapotranspiration rates in Denmark. In Denmark, the sea breeze effect and the distinct (observed) surface properties of the sandy outwash plain in West Jutland had significant impact on the spatial distribution of evapotranspiration rates in Denmark. The scatter between predicted and measured evapotranspiration rates is expected to reduce with increased accuracies in both the weather predictions and the satellite observations.

ACKNOWLEDGEMENTS

The study was financed by the Danish research project SAT-MAP-CLIMATE. The guidance provided by Ebba Dellwik and Dr. Kim Pilegaard (Risø National Laboratory) with respect to data extraction from the Risø databases is gratefully acknowledged.

REFERENCES

- Amano, E., and Salvucci, G. D., 1999, Detection and use of three signatures of soil-limited evaporation. *Remote Sensing of Environment*, 67, 108-122.
- Berkowicz, R., and Prahm, L. P., 1982, Sensible heat flux estimated from routine meteorological data. *Journal of Applied Meteorology*, 21, 1845-1864.
- Boegh, E., and Soegaard, H., 2002, Remote sensing based estimation of evapotranspiration. *International Journal of Remote Sensing*, submitted.
- Boegh, E., Soegaard, H., Christensen, J. H., Hasager, C. B., Jensen, N. O., Nielsen, N. W., and Rasmussen, M. S., 2002a, Combining weather predictions and remote sensing data for the calculation of evapotranspiration rates in Denmark. *International Journal of Remote Sensing*, submitted.
- Boegh, E., Soegaard, H., and Thomsen, A., 2002b, Evaluating evapotranspiration rates and surface conditions using Landsat TM to estimate atmospheric resistance and surface conditions. *Remote Sensing of Environment*, 79, 329-343.
- Czajkowski, K. P., Goward, S. N., Shirey, D., and Walz, A., 2002, Thermal remote sensing of near-surface water vapour. *Remote Sensing of Environment*, 79, 253-265.
- Idso, S. B., 1981, A set of equations for full spectrum and 8- to $14 \mu\text{m}$ thermal radiation from cloudless skies. *Water Resources Research*, 17(2), 295-304.

- Jarvis, P. G., and McNaughton, K. G., 1986, Stomatal control of transpiration: scaling up from leaf to region. *Advances in Ecological Research*, 15, 1-49.
- Kaufmann Y. J., and Sendra, C., 1988, Algorithm for automatic atmospheric corrections to visible and near-IR satellite imagery. *International Journal of Remote Sensing*, 9(8), 1357-1381.
- Kustas, W. P., and Daughtry, C. S. T., 1990, Estimation of the soil heat flux/net radiation ratio from spectral data. *Agricultural and Forest Meteorology*, 49, 205-223.
- Prince, S. D., Goetz, S. J., Dubayah, R. O., Czajkowski, K. P., and Thawley, M., 1998, Inference of surface and air temperature, atmospheric precipitable water and vapor pressure deficit using AVHRR satellite observations: comparison with field observations. *Journal of Hydrology*, 212-213, 231-250.
- Rahman, H., and Dedieu, G., 1994, SMAC: a simplified method for the atmospheric correction of satellite measurements in the solar spectrum. *International Journal of Remote Sensing* 15(1), 123-143.
- Schüssel, P., Schanz, L., and Englisch, G., 1995, Retrieval of latent heat flux and longwave irradiance at the sea surface from SSM/I and AVHRR measurements. *Advanced Space Research*, 16(10), 107-116.
- Valiente, J. A., Nunez, M., Lopez-Baeza, E., and Moreno, J. F., 1995, Narrow-band to broad-band conversion for Meteosat-visible channel and broad-band albedo using both AVHRR-1 and -2 channels. *International Journal of Remote Sensing*, 16(6), 1147-1166.
- Yamanaka, T., and Yonetani, T., 1999, Dynamics of the evaporation zone in dry sandy soils. *Journal of Hydrology*, 217, 135-148.

Atmospheric correction of IR satellite data using neural networks

Frank-M. Göttsche, Folke-S. Olesen,

Forschungszentrum Karlsruhe – IMK, Postfach 3640, D-76021 Karlsruhe, Germany

E-mail: frank.goettsche@imk.fzk.de

folke.olesen@imk.fzk.de

ABSTRACT - Land surface temperature (LST) is an important component of the energy-budget of the surface. In order to determine LST from IR satellite data the atmospheric influence on the measured radiance has to be accounted for. Provided that the current state of the atmosphere (vertical moisture and temperature profiles) and the surface emissivity are sufficiently well known, it is possible to use a single channel method to calculate the atmospheric corrections: the method utilises explicit radiative transfer calculations, e.g. with MODTRAN-3, and does not linearise the atmospheric effect. Variations of surface emissivity, elevation, and view angle are readily incorporated into the method. However, radiative transfer calculations are very expensive in terms of computing time and, therefore, not well suited to correct large quantities of data. In order to overcome this limitation, MODTRAN-3 is substituted by a neural network (NN). The main advantage of using a NN is its high computational speed: it is estimated to be around 10^4 times faster than MODTRAN-3 and, therefore, it allows to correct historically valuable single channel IR data, e.g. the 25 years of METEOSAT data. The NN was developed using the evolutionary algorithm "Evolutionärer Netzwerk Optimierer" (ENZO) in combination with the Stuttgart Neural Network Simulator (SNNS). The training and validation data consist of MODTRAN-3 calculations for TOVS Initial Guess Retrieval (TIGR) profiles. Results for the validation data and for verification data, which were obtained by simulating atmospheric situations described by ECMWF re-analyses, are presented.

1 INTRODUCTION

Atmospheric corrections of satellite data with split-window techniques (SWT) require at least two channels in the terrestrial IR (TIR) window (8-13 μm). Such channels are available on several sun-synchronous satellites, e.g. National Oceanic and Atmospheric Administration (NOAA) and European Remote Sensing (ERS) polar-orbiters and Earth Observation Satellite (EOS) - Terra, and also on some geostationary satellites, e.g. Meteosat Second Generation (MSG). SWT with "fixed" coefficients use linear approximations of the aggregated atmospheric effect, which in the TIR is mainly controlled by the amount and the temperature of water vapour and surface emissivity. The high variability of surface emissivity as well as of the atmosphere, which over land surfaces can change substantially over mesoscale distances (~10 km), necessitates schemes with locally adjusted SWT-coefficients (Sobrino et al., 1991; Becker and Li, 1990; Sun et al. 2002).

Atmospheric corrections can also be performed using 'single channel methods': these methods explicitly calculate the atmospheric effect on the radiance emitted by the surface, e.g. by using the radiative transfer models Moderate Transmittance Code "MODTRAN-3" (Kneizys et al., 1996). Unfortunately, precise radiative transfer models (RTMs) are computationally very expensive: therefore,

the single channel method cannot be applied to large data volumes, e.g. to several months or years of Meteosat data. In order to overcome these speed limitations, linear approximations of the atmospheric effect on the outgoing long-wave radiance from the land surface, e.g. as performed by SWTs, are dismissed here and the RTM is approximated by a neural network (NN). The NN readily incorporates all variables entering the RTM: atmospheric profiles, LST, surface emissivity, and path through the atmosphere (given by surface elevation and view angle). Once the NN is developed, it is also able to generalise to untrained input data and does not require explicit interpolation schemes during application (Göttsche and Olesen 2002).

2 THE RADIATIVE TRANSFER EQUATION

Generally, in the TIR window region the following assumptions are valid: (1) up to about 50-70 km the atmosphere is at local thermodynamic equilibrium, (2) scattering is negligible for clear-sky, non-hazy conditions, and (3) Earth's surface approximates a Lambertian reflector (Dash et al., 2001). The influence of the variable composition (water vapour most relevant in the TIR) and thermal structure of the atmosphere on outgoing radiance from Earth's surface can then be calculated using the radiative transfer equation:

$$\begin{aligned}
L_i^{sat} = & \int_{\lambda_1}^{\lambda_2} f_i(\lambda) \varepsilon(\lambda) B(\lambda, T_S) \tau(\lambda) d\lambda \\
& + \int_{\lambda_1}^{\lambda_2} \int_0^p f_i(\lambda) B(\lambda, T_p) \frac{d\tau}{dp} dp d\lambda \\
& + \int_{\lambda_1}^{\lambda_2} \int_0^{\pi/2} \int_0^{2\pi} (1 - \varepsilon(\lambda)) f_i(\lambda) L^\downarrow(\lambda, \theta, \phi) \tau(\lambda) \sin 2\theta d\lambda d\theta d\phi
\end{aligned} \quad (1)$$

where L_i^{sat} : radiance measured by a satellite sensor in channel i , λ : wavelength and λ_1 and λ_2 lower and upper spectral limits of the channel, f_i : normalised response function of the sensor, $\varepsilon(\lambda)$: surface spectral emissivity, B : Planck function, T_S : surface temperature, $\tau(\lambda)$: spectral atmospheric transmission, p : pressure, p_s : pressure at Earth's surface, T_p : temperature at pressure p , $L^\downarrow(\lambda, \theta, \phi)$: downwelling atmospheric radiance, θ : zenith angle, and ϕ : azimuth angle.

The first term in Eq. (1) denotes the contribution of the surface attenuated along the upward path, the second term is the atmospheric contribution along the upward path, and the third term gives atmospheric radiance reflected by the surface and attenuated along the upward path. MODTRAN-3 solves Eq. (1) numerically and calculates spectral radiance at satellite level. Specific atmospheres can be defined, e.g. temperature and humidity profiles from radiosondes. MODTRAN-3 also has to be supplied with surface emissivity, LST, surface elevation, and the location of the sensor and the target. Applying the response function of a satellite sensor to the calculated radiances and using calibration information yields satellite brightness temperature (BT). Atmospheric corrections (LST – calculated satellite BT) obtained for a range of parameters and atmospheres can be interpolated to match a given satellite BT. This forms the basis of the ‘single channel method’ of Reutter et al. (1994).

3 ATMOSPHERIC CORRECTION WITH THE SINGLE CHANNEL METHOD

Forward calculations with MODTRAN are carried out for a range of surface temperatures and ground heights, where the state of the atmosphere is characterized by the actual ECMWF humidity and temperature profiles and surface emissivity is assumed to be known or set to 0.975. Due to their small temporal variability and their small effect in the TIR the distribution of all atmospheric absorbers apart from water vapor, e.g. carbon dioxide, ozone, nitrous

oxide, etc., are taken from standard profiles. Then, LST is determined for each atmospheric profile location from the actual satellite measurement in the TIR for the known ground height from a Digital Elevation Model by interpolation of the results from the forward calculations. The corrections in the neighbourhood of each satellite pixel location, e.g. for the nearest 6 profiles, are spatially (Schroedter et al., 2001) and temporally (Göttsche and Olesen, 2001) interpolated to obtain corrections for all IR measurements. For typical LSTs, the standard atmospheric profiles mid-latitude summer and winter, and a surface emissivity of $\varepsilon = 0.975 \pm 0.025$ the associated maximum temperature error is estimated to be about ± 1.4 K (see Figure 1).

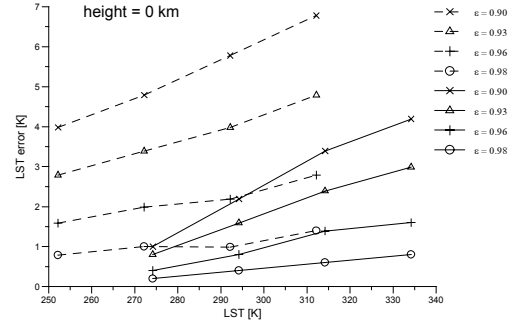


Figure 1. Retrieved error in LST using the single channel method for mid-latitude summer (solid) and winter (broken) for different emissivities (Schädlich et al. 2001).

Taking also into account the maximum error of 0.7 K of MODTRAN-3 the maximum error of the single channel method for the above situation is estimated to be about ± 2.1 K. For the same situation and with a well defined surface emissivity ($\Delta\varepsilon = \pm 0.005$) the maximum error of the method is estimated to be about ± 1 K.

4 NEURAL NETWORKS AND EVOLUTION

Fully connected, feed-forward NNs with multilayer perceptron (MLP) structure are the most commonly used type of NN. The most simple feed-forward NN consists of an input and an output layer, but usually it also features at least one hidden layer. In feed-forward NNs information is strictly passed from the input layer via the hidden layer(s) to the output layer (hence the name). The output of each neuron is specifically weighted for each connection to the neurons of the following layer; for these the weighted outputs serve as input. During training the error of the

NN is minimised by adjusting its weights according to a learning rule, e.g. Back-Propagation developed by Rummelhart et al. (1986). During training the ability of the NN to generalise is tested by observing its outputs for a validation data set, which is a subset of the training data (not used for training).

As no deterministic algorithm to determine NN topology (layers and neurons) exists, it is usually determined by trial and error. Here, the evolutionary optimisation scheme “Evolutionärer Netzwerk-optimierer (ENZO)” is utilised to determine a NN which is close to the global optimum (Braun and Ragg, 1996). Evolution of NNs can be regarded as a multi-point search: starting from N points, where N is the size of the population, the algorithm searches for the optimum topology. In each evolution cycle new offsprings are created by mutation and (optionally) crossover. The selection of parents is random but biased according to a user defined fitness criterion, i.e. fitter individuals produce more offsprings. This increases the average fitness of the population. Each offspring is trained using Resilient Propagation (RProp) with weight-decay (Riedmiller and Braun, 1993), which ENZO accesses via the Stuttgart Neural Network Simulator (SNNS) (Zell, 1994).

4.1 Training and validation data

“Adequate” data sets for training and validation have to cover the whole bandwidth of situations which might be encountered during the application phase with a sufficiently small sampling interval – otherwise the network cannot be expected to approximate the relationship underlying the data. Here, atmospheric situations are described by 84 profiles extracted from the TOVS Initial Guess Retrieval (TIGR) library (1761 globally distributed, quality checked and representative radiosondes; see Chedin et al. (1984)). The profiles were taken from within 45.0 N and 55.0 N latitude (Vollmer, 2000). The 40 pressure levels in the TIGR library were reduced to 14 (1000, 850, 700, 500, 400, 300, 250, 200, 150, 100, 70, 50, 30, 10 hPa) in order match atmospheric profiles extracted from Global Circulation Model (GCM) analyses performed by the European Centre of Medium-Range Weather Forecasts (ECMWF). These analyses are available globally for long periods of time, e.g. ECMWF re-analyses “ERA-15” for 15 years, and have a spatial resolution of 1.1 degree (T106 spectral data). MODTRAN-3 calculations for the 84 profiles were performed for 4 LSTs, 4 surface elevations, and 3 scan angles (Table 1). This yields 4032 pairs of input / output patterns for training and validation. Emissivity was set to $\varepsilon = 0.975$.

LST	Elevation	Scan angle
$T_{1000} - 10^{\circ}\text{C}$,	110 m,	$\delta(x-3^{\circ})$,
T_{1000} ,	1000 m,	$\delta(x)$,
$T_{1000} + 10^{\circ}\text{C}$,	2000 m,	$\delta(x+3^{\circ})$
$T_{1000} + 20^{\circ}\text{C}$	3000 m	x: profile latitude

Table 1. Variation of parameters used for the forward calculations with MODTRAN-3 (T_{1000} : air temperature at 1000 hPa).

BTs corresponding to the simulated Meteosat-IR measurements and atmospheric corrections were derived as described in section 2. The data was split into training data (68 profiles, 3264 patterns) and validation data (16 profiles, 768 patterns), which were used to detect under- and over-fitting.

4.2 Optimising neural networks

A manually optimized NN (“Manual-NN”; Table 2) served as reference for the creation of an initial population of NNs.

Layer	Manual-NN	ENZO-NN
Input	45 neurons	31 neurons
Hidden 1	44 neurons	22 neurons
Hidden 2	18 neurons	4 neurons
Output	1 neurons	1 neurons
Weights	2790	286

Table 2. The NNs determined manually (Vollmer, 2000) and using ENZO.

The weights of the initial population were set to random values. The size of the population and the maximum number of evolution cycles (generations) was set to 30. Each generation 10 offsprings were produced. A results for a desired rms. error of 0.5 K is shown in Figure 2; higher accuracy leads to NNs with more hidden neurons and weights (Göttsche and Olesen 2002). The input neurons shown as white boxes in Figure 2 are neurons which were disconnected by ENZO: they are redundant (to achieve the desired accuracy).

After evaluating some results, the 14 neurons representing the altitudes of the atmospheric pressure levels were identified as redundant and removed from the input data. Using the same parameters as above, a population of NNs with a reduced input layer of 31 neurons was evolved. The NN determined by ENZO for a desired rms. error of 0.3 K (“ENZO-NN” in Table 2) has 58% fewer hidden neurons and ca. 90% fewer weights than the manually determined NN. The computation time for the evolution of the NNs was about 6 days on a SUN Ultra-Sparc with 450 MHz.

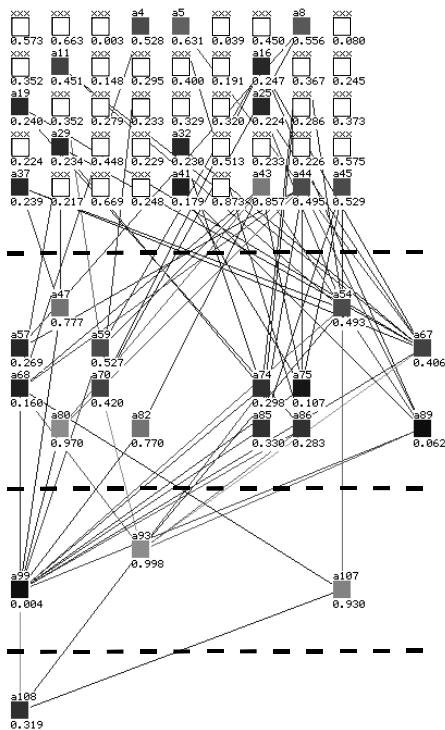


Figure 2. NN automatically generated by ENZO for a desired rms. error of 0.5 K. Boxes and lines represent neurons and weights, respectively. The broken lines separate the layers (top to bottom): input (45 neurons) – hidden 1 (14 neurons) – hidden 2 (3 neurons) – output (1 neuron).

4.3 Verification of the neural network

In order to verify the NN determined by ENZO, it is tested with an independent data set. The data set was generated analogously to the training data but for atmospheric profiles extracted from analyses performed for the ECMWF GCM. 6 ECMWF analyses representing different seasons and times of the day were considered: 10.03.96 – 12 hours, 12.04.96 – 06 hours, 15.06.96 – 06 hours, 20.07.96 – 18 hours, 18.09.96 – 00 hours, and 26.10.96 – 12 hours. From each of these analyses 25 profiles (grid cells) from the area covered by the TIGR profiles (training patterns) were selected. Varying surface parameters as described in section 4.1, MODTRAN-3 was used to generate a verification data set of 1200 situations for each analysis. Figure 3 shows the rms. temperature errors for the 6 data sets.

For the cloud-free grid cells of the ECMWF GCM, which were identified using cloud-masks derived from Meteosat data (Schädlich et al., 2001), the rms. error ranges from 0.26 K to 0.44 K.

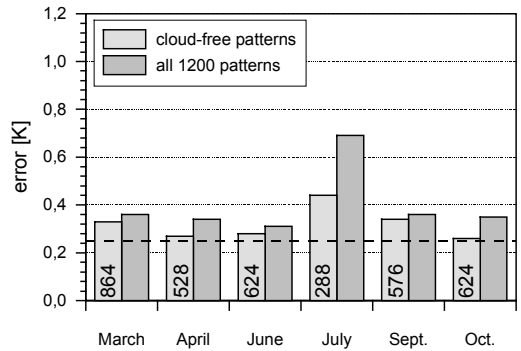


Figure 3. Rms. errors of the NN “ENZO-NN” in Table 2 for the verification data (see text). Dashed line: rms. validation error (untrained TIGR data) of 0.25 K.

The corresponding rms. errors for all grid cells (no cloud-clearing) range from 0.31 K to 0.69 K. The maximum error is observed in July, which is caused by high water vapour concentrations due to clouds in this specific analysis; this is reflected by the low number of cloud-free situations (numbers in the light grey bars in Figure 3). The rms. validation error (untrained TIGR data) of the NN developed by ENZO is 0.25 K (desired rms. error: 0.3 K) and the rms. verification error is 0.31 K (cloud-free ECMWF analyses): this indicates the good generalisation capability of the impressively small “ENZO-NN” (Table 2). Furthermore, in spite of the different structure of the ECMWF analyses compared to the TIGR radio-soundings, which were used to train the network, the errors are smaller than the intrinsic maximum error of MODTRAN-3.

5 CONCLUSIONS AND OUTLOOK

It was shown that NNs can substitute radiative transfer models in the TIR, which were performed for a broad range of atmospheres, LSTs, and path lengths, i.e. surface elevations and view angles. The NNs were trained and validated using MODTRAN-3 results for 84 atmospheric profiles from the TIGR library and verified using MODTRAN-3 results for profiles extracted from ECMWF analyses, which have quite a different structure.

The NNs developed by the evolutionary algorithm ENZO are superior to the manually developed NN. For a desired rms. error of 0.3 K compared to the radiative transfer calculations the final NN has 58% fewer hidden neurons and about 90% fewer weights than the manually developed NN. Due to ENZO’s ability to identify redundant input parameters the input neurons could also be reduced. The NN is more robust and the rms. verification error of 0.31 K (ECMWF analyses) is slightly smaller than

for the manually developed NN: this means that the NN developed by ENZO also generalises better. A practical advantage of ENZO is the fast development of the NN (6 days without user interaction). Radiative transfer calculations with the NN developed by ENZO are estimated to be of the order of 10^4 times faster than with MODTRAN-3: this allows atmospheric corrections of long time series of IR satellite data, e.g. the 25 years of Meteosat single channel IR data.

6 REFERENCES

- Becker, F. and Li, Z-L. 1990, Towards a local split window method over land surface. *International Journal of Remote Sensing*, 11, 369-394.
- Braun, H., and Ragg, T. 1996, ENZO: Evolution of neural networks, Internal report (1996, 21). University of Karlsruhe, Institute for logic, complexity, and deduction systems, Germany.
- Chedin, A., Scott, N.A., Wahiche, C., and Moulinier, P. 1984, The improved initialisation inversion method: a high resolution physical model for temperature retrievals from satellites of the TIROS-N series. *J. Climate Appl. Meteor.*, 24, 128-143
- Dash, P., Göttsche, F.-M., Olesen, F.-S., and Fischer, H. 2001, Land surface temperature and emissivity estimation from passive sensor data: theory and practice; current trends. *International Journal of Remote Sensing*, 23(13), 2563-2594.
- Göttsche, F.-M., and Olesen, F.-S., 2002, Evolution of neural networks for radiative transfer calculations in the terrestrial infrared. *Remote Sensing of Environment*, 80(1), 157-164.
- Göttsche, F.-M., and Olesen, F.-S., 2001, Modelling of diurnal cycles of brightness temperature extracted from METEOSAT data. *Remote Sensing of Environment*, 76(3), 338-349.
- Kneizys, F.X., Abreu, L.W., Anderson, G. P., Chetwynd, J.H., Shettle, E. P., Berk, A. L., Bernstein, S., Robertson, D. C., Acharya, P., Rothman, L. S., Selby, J. E. A., Gallery, W. O. and Clough, S. A. 1996, The Modtran 2/3 report and Lowtran 7 model. Philipps Laboratory, Hanscom, USA.
- Riedmiller, M., and Braun, H. 1993, A direct adaptive method for faster back-propagation learning : The RProp algorithm. Proc. of the IEEE Int. Conf. on Neural Networks (ICNN 93), San Francisco, USA, 1, 586-591
- Rummelhart, D.E., Hinton, G.E., and Williams, R.J. 1986, Learning internal representation by error propagation, In: D.E. Rummelhart and J.L. McClelland (Editors), *Parallel Distributed Processing: Explorations in the Microstructures of Cognition*, MIT Press, Cambridge, MA, USA, pp. 318-362.
- Schädlich, S., Göttsche, F.-M., and Olesen, F.-S. 2001, Influence of land surface parameters and atmosphere on METEOSAT brightness temperatures and generation of land surface temperature maps by temporally and spatially interpolating atmospheric correction. *Remote Sensing of Environment*, 75(1), 39-46.
- Schroedter, M., Olesen, F.-S., and Fischer, H. 2001, Determination of land surface temperature distributions from single channel IR measurements: An effective spatial interpolation method for the use of TOVS, ECMWF and radiosonde profiles in the atmospheric correction scheme. *International Journal of Remote Sensing* (in press)
- Sobrino, J. A., Cool, C. and Caselles, V. 1991, Atmospheric correction for land surface temperature using NOAA-11 AVHRR channels 4 and 5. *Remote Sensing of Environment*, 38, 19-34.
- Sun, Yi-Yi, Göttsche, F.-M., Olesen, F.-S., and Fischer, H., 2002, Retrieval of land surface temperature from combined AVHRR data. *Annales Geophysicae*, 20(8), 1257-1259.
- Vollmer, M., 2000, Korrektur des atmosphärischen Einflusses in IR-Satellitenmessungen mit neuronalen Netzen. Final thesis, University of Karlsruhe (TH), Germany.
- Zell, A., 1994, Simulation neuronaler Netze. Book, Oldenbourg-Verlag, München, Germany.
- Reutter, H., Olesen, F. S. and Fischer, H. 1994, Distribution of the brightness temperature of land surfaces determined from AVHRR data. *International Journal of Remote Sensing*, 15, 95-104.

Comparison of Meteosat-7 and (A)ATSR Data Over Land: A Sensitivity Analysis

E. J. Noyes, J. J. Remedios, D. T. Llewellyn-Jones, M. C. Edwards

EOS Group, Department of Physics & Astronomy, University of Leicester, University Road, Leicester, LE2 7RH, UK.

E. J. Noyes: ejn2@le.ac.uk J. J. Remedios: jjr8@le.ac.uk D. T. Llewellyn-Jones: dlj1@le.ac.uk M. C. Edwards: mcel@le.ac.uk

ABSTRACT- Low-Earth orbiting satellites such as the European Remote Sensing –2 (ERS-2) offer the opportunity to obtain measurements of land surface temperature (LST) at high spatial resolution (e.g. 1 km²) but with a temporal resolution that is not suitable for monitoring the diurnal temperature range over land. Estimates of LST from instruments such as the Along-Track Radiometer-2 (ATSR-2), onboard ERS-2, and the Advanced ATSR (AATSR) onboard Envisat, can be achieved to accuracies of 1-3 K (Prata, 2000) using split-window algorithms which utilise data from more than one channel. Meteosat is a geostationary satellite with one thermal infrared channel that has also been used to retrieve LST (e.g. Reutter et al., 1996). Images are obtained every 30 minutes but with a low spatial resolution (5 km² at the sub-satellite point). A combination of thermal data from both the (A)ATSR series of instruments and Meteosat would provide a data set that has the temporal resolution of the latter and spatial resolution of the former. Data from the two instruments is comparable as the Meteosat IR channel bandwidth (10.5 µm to 12.5 µm) is very similar to the combined bandwidth of the (A)ATSR 11 and 12 micron channels. Initially, a sensitivity analysis is carried out to compare the response of each instrument to changes in surface temperature and emissivity, with a view to developing a methodology based on the results and later comparisons with real (A)ATSR and Meteosat data.

1. INTRODUCTION

Land surface temperature, (LST) has been recognised by a number of researchers to be an important parameter used to monitor global environmental change. It may be considered to be a representative radiative temperature of the skin surface of the Earth over a specific area (e.g. 1 km pixel).

Applications for the use of LST data include the study of land surface changes as it is sensitive to vegetation and soil moisture (Dash et al., 2002), and surface and atmosphere long-wave radiation exchange (Prata, 2000).

Thermal infrared data from satellites can be used to derive LST, due to the wide-scale availability of the data from several different instruments, and its spatial and temporal coverage.

Surface temperature retrieval methods are based on the Radiative Transfer Equation (RTE) where the radiance measured by a sensor is defined to be (Susskind et al, 1983):

$$L_i^{sat} = \int_{\lambda_1}^{\lambda_2} f_i(\lambda) \epsilon(\lambda) B(\lambda, T_s) \tau(\lambda) d\lambda + \int_{\lambda_1}^{\lambda_2} \int_{p=0}^{p_s} f_i(\lambda) B(\lambda, T_p) \frac{d\tau}{dp} d\lambda dp + \int_{\lambda_1}^{\lambda_2} \int_{\theta=0}^{\pi/2} \int_{\phi=0}^{2\pi} (1 - \epsilon(\lambda)) f_i(\lambda) L^\downarrow(\lambda, \theta, \phi) \tau(\lambda) \sin 2\theta d\lambda d\theta d\phi \quad (1)$$

where i is channel; λ is wavelength; λ_1 and λ_2 are the respective lower and upper limits of spectral range;

$f_i(\lambda)$ is normalised channel response function; $\epsilon(\lambda)$ is surface spectral emissivity; $B(\lambda, T)$ is the Planck function (temperature T); T_s is the temperature at the Earth's surface; $\tau(\lambda)$ is the spectral atmospheric transmissivity; p is pressure; p_s is the pressure at the Earth's surface; θ is zenith angle; ϕ is azimuth angle and L^\downarrow is downwelling atmospheric radiance (downwelling irradiance divided by π).

The first term of equation (1) represents the radiation emitted by the surface attenuated along the upward path; the second term the atmospheric contribution along the upward path and the third term is the atmospheric irradiance that has been reflected from the surface and attenuated along the upward path (Dash et al., 2002).

In order to calculate the surface temperature it can be seen from equation (1) that the following parameters must be known: (a) radiances measured by the satellite instrument over n channels, (b) the normalised channel response function(s), (c) auxiliary atmospheric data (from which the atmospheric transmissivity and the contribution from the last two terms of the equation can be determined) and (d) the emissivity of the surface. Parameters (a) and (b) are easily obtained and an approximation for (c) is generally achieved by utilising global atmospheric data sets or radiosonde data, for example. (d) can be difficult to determine since it is dependent on the nature of the surface in question (e.g. surface

composition and roughness) and can be spectrally dependent.

For n channels, n equations can be constructed, where n is the number of channels of the radiometer. Surface temperature is a constant quantity between each of the equations but emissivity may not be, thus $n+1$ unknowns are generated.

In the case of sea surface temperature (SST) retrieval, the situation is comparatively simple since the surface can be considered to be homogeneous over the scale of the footprint of the satellite (e.g. 1-5 km²) and temperature has very little spatial variation on this scale of measurement. This is simplified further by the fact that the emissivity of seawater is often well known and close to one with very little spectral variation. Furthermore, the spatial scale of atmospheric variations can be relatively large compared to the atmosphere over land. It is widely recognised that SST is an excellent way of monitoring global temperature change and substantial work has been carried out on SST retrievals. For these reasons, values can be obtained up to an accuracy of ± 0.3 K.

In comparison, land surfaces are heterogeneous and LST varies considerably over space and time, making it a very difficult parameter to measure. Variations of as much as 10 K have been observed over a scale of a few metres and with a diurnal temperature range of up to 50 K (Prata, 1994). The main influences on LST retrieval from satellite data are the atmosphere and surface emissivity, and without correcting for these effects, errors of up to 12 K may result (Sobrino et al., 2000). The emissivity of land is highly variable and often spectrally dependent. Atmospheric conditions also vary considerably over land and are thus much more difficult to correct for in the field of LST retrieval, in comparison to satellite-based SST retrievals. It is therefore an interesting topic to pursue and researchers are currently working on methods to improve accuracies in LST determination.

2 SATELLITE DATA USED IN LST RETRIEVAL

Two types of satellites that have previously been used in surface temperature retrieval are polar-orbiting and geostationary satellites. Polar-orbiting satellites such as the Advanced Very High Resolution Radiometer (AVHRR) and the Along Track Scanning Radiometer (ATSR) series of instruments are preferred because of their high spatial resolution (typically 1 km²), but they lack the temporal coverage required to monitor diurnal LST change. Geostationary satellites, such as Meteosat-7, can provide data with a much higher temporal coverage but at a much lower spatial resolution (typically 5-6 km²), which can be problematic for land-based studies due to the high spatial variability of LST.

Instruments such as the ATSR have been

successfully used for SST retrieval, as a very high temporal resolution is not vital due to the relative stability of SST. At present, there is no instrument that has both the spatial and temporal resolution that is required for land-based studies. However, Reutter et al., 1996, have combined data from the AVHRR and Meteosat to produce a data set that has both the temporal resolution of the latter and the spatial resolution of the former (approximately 2.5 km). It is proposed in this paper that a similar type of study may be carried out using data from the (A)ATSR and Meteosat-7.

2.1 The ATSR

The ATSR-2 is an imaging radiometer onboard the European Space Agency's (ESA) European Remote Sensing -2 (ERS-2) satellite. It is the successor to the now-redundant ATSR-1, and became operational in 1995. Its successor, the Advanced ATSR (AATSR) was launched onboard ESA's Envisat satellite, in March 2002. Table 1 shows the spectral channels on both these instruments.

Nominal Channel	Centre λ	B'width	Primary Application
0.55 μm	0.555 μm	20 nm	Chlorophyll
0.66 μm	0.659 μm	20nm	Vegetation Index
0.87 μm	0.865 μm	20 nm	Vegetation
1.6 μm	1.61 μm	0.3 μm	Cloud Clearing
3.7 μm	3.70 μm	0.3 μm	SST Retrieval
11 μm	10.85 μm	1.0 μm	SST Retrieval
12 μm	12.00 μm	1.0 μm	SST Retrieval

Table 1: ATSR-2 and AATSR spectral channels (Llewellyn-Jones et al., 2001)

Primarily designed to measure SST to a high degree of accuracy, the (A)ATSR also has dual viewing geometry, nadir and forward views, that allow for an accurate atmospheric correction to be made as radiation is measured along two atmospheric path lengths (Figure 1). The (A)ATSR has a spatial resolution of 1 km² with two overpasses occurring each day (e.g. at 10.30 and 22.30 local time for ATSR-2).

The ATSR-2 SST retrieval methodology commonly utilises data from both viewing geometries and two or three of the channels (the 3.7 micron channel data can only be used at night as it is saturated with back-scattered short-wave infra-red radiation during the day). This is called the split- or triple-window technique. The split-window formula for SST retrieval can be approximated by equation (2):

$$SST_{ret} = a_0 + \sum_i^n a_i T_i \quad (2)$$

where n is the number of channels used and T_i is the brightness temperature (BT) obtained from channel i . Different sets of coefficients, a_i , are required depending on whether a dual- or single-view retrieval is being carried out, and whether a split- or triple-window technique is employed. They account for the effect of the atmosphere and surface emissivity, thus different sets of coefficients must also be used for different areas of the globe. Values can be derived in a variety of different ways based on the RTE (e.g. modelling of BTs) or statistical methods (comparison of observed BTs with observed surface temperatures).

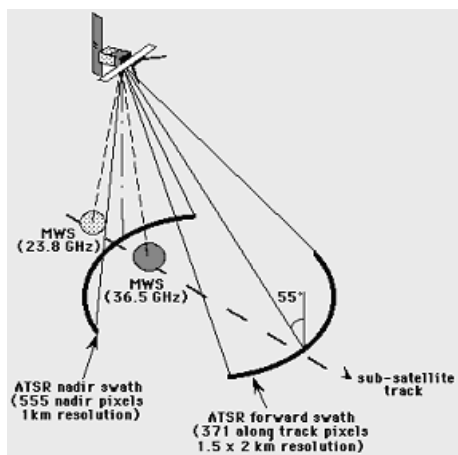


Figure 1: (A)ATSR viewing geometry
(URL, <http://earth.esa.int/ERS1.5>)

The split- and triple- window technique applied to ATSR and other polar-orbiting satellite data (such as the AVHRR) has been adapted for LST retrieval by a number of researchers. Algorithms have been developed that can achieve accuracies of 1-3 K with improved accuracies (close to 1 K) usually being achieved at night when there is no ‘differential surface heating’ (Prata, 2000). Problems may also arise when using the dual-view algorithms as the two fields of view are not measured simultaneously (Prata, 2000) and LST can change significantly over a very short period of time. Emissivity also varies with viewing angle, which may pose problems in LST retrieval.

2.2 Meteosat-7

The European Organisation for the Exploitation of Meteorological Satellite’s (EUMETSAT) Meteosat-7 became the operational geostationary satellite at 0° in June 1997. It is primarily used for weather forecasting and has three imaging channels as shown in table (2).

Channel	Centre λ	B’width
Visible (VIS)	0.7 μm	0.4 μm
Infrared water vapour absorption band (WV)	6.4 μm	1.4 μm
Thermal infrared (window) band (IR)	11.5 μm	2.0 μm

Table 2: Meteosat-7 spectral channels
(EUMETSAT, 2001)

The VIS channel has a spatial resolution of 2.5 km² at the sub-satellite point, whereas for the WV and IR channels the resolution is only 5 km². A complete scan is completed every 30 minutes, thus producing 48 full-disc images in every 24-hour period.

As Meteosat-7 only has one thermal imaging channel, split-window algorithms cannot be applied to retrieve surface temperature. Furthermore, since Meteosat-7 only has one viewing geometry, atmospheric effects cannot be corrected for in the same way as for the ATSR. However, some researchers have used Meteosat data to calculate surface temperature, as its temporal resolution makes this an attractive data set to utilise in this field of research.

3 COMPARING METEOSAT-7 AND (A)ATSR DATA: A SENSITIVITY ANALYSIS

It can be seen from tables 1 and 2 that the combined bandwidth of the ATSR 11 and 12 micron channels is almost identical to the Meteosat-7 IR channel. However, a direct comparison between the two sets of channels is not a simple procedure as radiometers have a response that varies with wavelength. This response is called the instrument filter function, or response curve. The measured signal in each channel is the signal flux at the top of the atmosphere integrated over the appropriate response function. The instrument response curves for the (A)ATSR and Meteosat thermal channels are shown in figures 2 and 3 respectively.

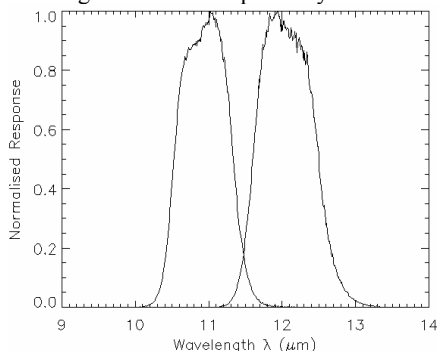


Figure 2: (A)ATSR 11 and 12 micron channel filter functions

(URL, <http://www.atrs.rl.ac.uk/documentation/docs/filterfunctions/index.shtml>)

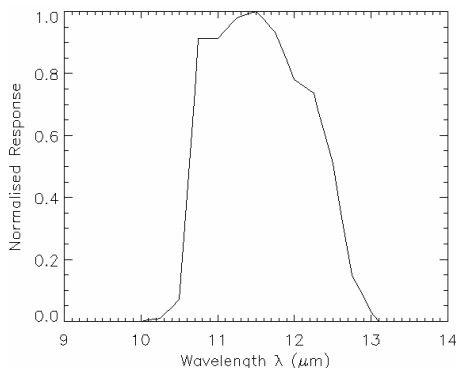


Figure 2: Meteosat IR channel filter function
(URL, <http://www.eumetsat.de/en/index.html?area=left7.html&body=/en/dps/mpef/calibration.html&a=730&b=1&c=700&d=700&e=0>)

Initially, a sensitivity analysis was carried out to examine the response of each channel to changes in surface temperature and emissivity for constant atmospheric conditions. This was performed by modelling the signal measured at the top of the atmosphere (TOA) over the bandwidth of each of the three channels for a range of emissivities and temperatures. These radiances can then be compared for their response to changes due to these parameters.

3.1 The Oxford Reference Forward Model (RFM)

The RFM, a line-by-line radiative transfer model developed in Oxford, UK, was used in this study. The model assumes specular diffuse reflection for radiance. Surface temperature, surface emissivity and atmospheric profiles (via a list of gases) are specified by the user and input spectral line data are taken from the HITRAN database 2000. The spectral data are output at a resolution of 0.01 cm^{-1} (user-specified) and are then integrated over the spectral bandwidth of each channel to give the simulated radiance for each channel. It should be noted that only the nadir view has been considered at this stage in the study due to the problems that may result from using the forward view in LST retrieval (section 2.1) and to avoid complications due to emissivity variations with satellite viewing angle.

3.2 The Libyan Desert: A Validation Site

Although this study is still in the theoretical stages, a land site was chosen so that real values of surface temperature, emissivity and atmospheric data could be considered for the sensitivity analysis.

Established sites are commonly used to compare geophysical parameters derived from satellite data with *in situ* measurements to validate the former. Such sites are commonly referred to as validation sites and may or may not have instruments (such as ground-based radiometers) that run continuously so that data can be compared quickly and easily. The other advantage of having established validation sites is that other geophysical parameters that may affect the quantity(ies) of interest can be well documented. For example, for LST retrieval, emissivity and atmospheric conditions must be known in order to perform an accurate retrieval.

LST validation sites are usually chosen for their homogeneity – the sites should be as topographically flat and the surface type as uniform as possible, so that surface emissivity can be accurately measured and variations neglected. Ideally, the site should also be dry and remote so that atmospheric conditions remain stable. In addition, the location should also be cloud-free as satellite-based surface temperature retrievals can only be done in clear conditions (as clouds typically cause a drop in the observed BT). The dimensions of the site is also an important consideration as it must accommodate several satellite pixels, e.g. for (A)ATSR validation, the site must be several km square.

For this study, the Libyan Desert was chosen for the reasons outlined above. It also provides an excellent location to make a comparison between data, as the diurnal temperature range can be as much as 50 K. Emissivity of an arid desert region can be variable. Snyder et al., 1998 suggest an emissivity range of approximately 0.95-0.98 for ‘arid bare soil’ for the Moderate Resolution Imaging Spectrometer (MODIS) band 31, which is approximately equivalent to the (A)ATSR 11 micron channel.

4. SENSITIVITY ANALYSIS USING THE RFM

Using the model data, several processing steps were embarked upon:

(i) Graphs of radiance versus emissivity were plotted for constant temperatures over the range $T_s=283\text{--}323 \text{ K}$ at intervals of 10 K, for each of the (A)ATSR and Meteosat thermal channels. Similarly, plots of radiance versus temperatures for constant emissivities in the range $\epsilon=0.95\text{--}0.99$ at intervals of 0.01, were generated. As changes in atmospheric conditions were not being considered at this stage of the study, an equatorial reference atmosphere, originally designed for use with the Michelson Interferometer for Passive Atmospheric Sounding (MIPAS), onboard ESA’s Envisat was used (Remedios, 1999). Second degree polynomial equations were fitted to the graphs as described by equations (3) and (4):

$$R_i(\varepsilon) = a_\varepsilon + b_\varepsilon \varepsilon + c_\varepsilon \varepsilon^2 \quad (3)$$

$$R_i(T_s) = a_{T_s} + b_{T_s} T_s + c_{T_s} T_s^2 \quad (4)$$

where $R_i(\varepsilon)$ and $R_i(T_s)$ are the sum of the radiances over the channel bandwidths, normalised by the sum of the channel filter function, and a , b and c are the polynomial coefficients for each equation. (Coefficients were also calculated over a smaller range of surface temperatures ($T_s=302-310$ K) at intervals of 1 K to compare for linearity over a more limited range). Figure 4 shows an example of a plot of $R(\varepsilon)$ versus ε for a surface temperature of 303 K.

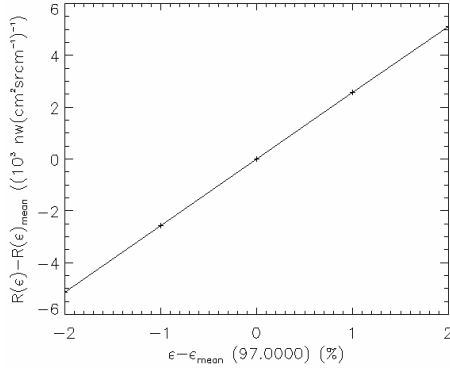


Figure 4: Graph of $R(\varepsilon)$ versus ε for (A)ATSR 11 micron channel for $T_s=303$ K.

(ii) Equation (4) was differentiated and graphs of $\delta R(T_s)/\delta T_s$ versus ε and $\delta R(\varepsilon)/\delta \varepsilon$ versus T_s were plotted. This allowed the response of each instrument channel to be compared over the given temperature and emissivity ranges. Figure 5 shows the results for $\delta R(T_s)/\delta T_s$ for $T_s=303$ K – the shape of the graph of $\delta R(\varepsilon)/\delta \varepsilon$ versus T_s is almost identical.

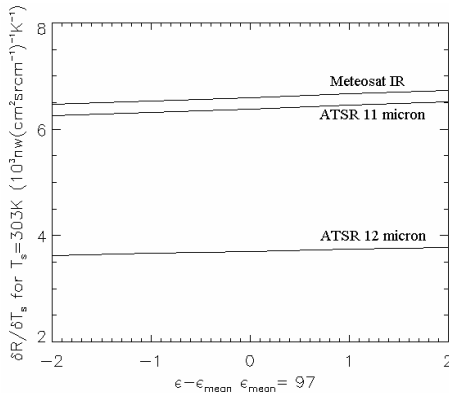


Figure 5: Graph of $\delta R(T_s)/\delta T_s$ for $T_s=303$ K versus ε for all channels.

(iii) By equating δR for equations (3) and (4) the following equation can be derived:

$$\delta T_s = \frac{(b_\varepsilon + 2c_\varepsilon \varepsilon)}{(b_{T_s} + 2c_{T_s} T_s)} \cdot \delta \varepsilon \quad (5)$$

Using equation (5) values of δT_s were plotted against ε for the different values of T_s . With $\delta \varepsilon$ set to 0.01, the deviation from temperature T_s that will cause the equivalent change in measured radiance can be obtained for each channel (figures 6-8). Values for b_{T_s} and c_{T_s} were taken from those coefficients associated with the mean emissivity used in the study, in this case 0.97. Using alternative coefficients (derived using different values for the emissivity) only resulted in a change in δT_s of less than 0.03 K.

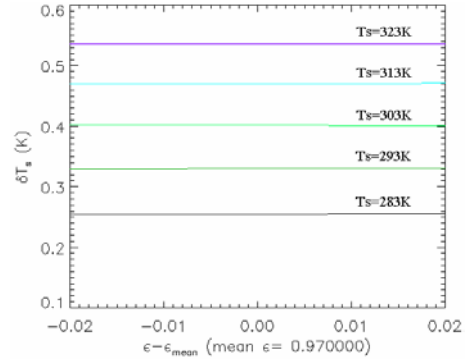


Figure 6: Graph showing δT_s versus ε for ATSR 11 micron channel. $\delta \varepsilon=0.01$.

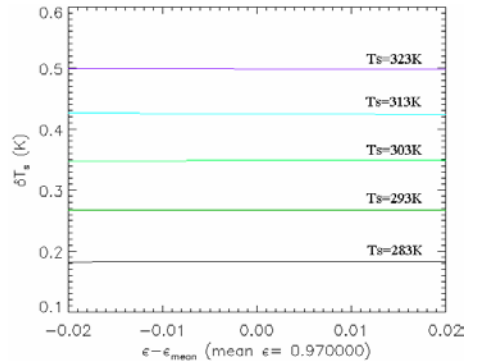


Figure 7: Graph showing δT_s versus ε for ATSR 12 micron channel. $\delta \varepsilon=0.01$.

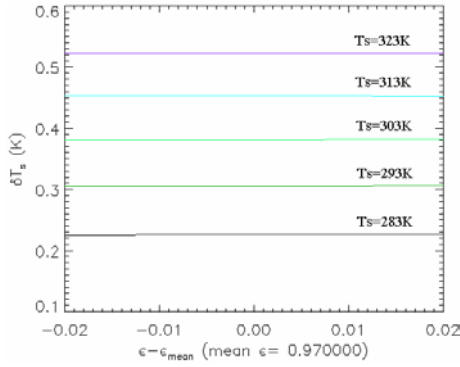


Figure 8: Graph showing δT_s versus ε for Meteosat IR channel. $\delta\varepsilon=0.01$.

5. RESULTS

The results from stage (i) confirmed linearity over the temperature and emissivity ranges of interest.

The results from stage (ii) of the sensitivity analysis are interesting as they imply that there is a strong similarity in the response to changes in surface emissivity and temperature between the (A)ATSR 11 micron and Meteosat-7 thermal channels. In other words, a change in surface temperature or emissivity will cause a similar change in measured radiance for the (A)ATSR 11 micron and Meteosat IR channels, but a much lower change in the (A)ATSR 12 micron channel. The other notable feature of these plots is that the changes in radiance caused by changes in emissivity or temperature is linear and the lines for each channel have very similar gradients. The gradients of the graphs are also positive which indicates that the measured change in radiance increases with increasing emissivity for a constant temperature, and increases with increasing temperature for a constant emissivity.

The findings from stage (iii) of the analysis are the most interesting because they suggest that a change in emissivity of 0.01, results in the same change in measured radiance caused by a temperature change of approximately 0.18-0.54 K, where the exact values increase with increasing surface temperature. This may first appear to contradict equation (5) since T_s is in the denominator. However, it must be remembered that the coefficients b_ε and c_ε vary for different values of T_s . The b_ε coefficients, which increase considerably with increasing T_s , are of the order of 100 times greater than the corresponding c_ε coefficients (since the lines from which they are derived from are almost perfectly straight (figure 4)). In addition, the c_ε coefficient is multiplied by a number that is of the order of 0.01. The resulting effect is that the numerator of equation (5) is dominated by the b_ε term, which is why we also see very little change in the

gradients of the lines in figures 6, 7, and 8.

Göttsche et al., 2000, suggest that a temperature error of ca. ± 1.4 K is associated with $\varepsilon=0.975 \pm 0.025$, for mid-latitude summer and winter, based upon their findings using the radiative transfer model MODTRAN-3. From equation (5) it can be seen that δT_s is directly proportional to $\delta\varepsilon$, thus the equivalent approximation using the RFM for an uncertainty in emissivity of 0.025 is 0.45-1.4 K. Although the figures are very close, discrepancies may be attributed to (a) the differences between the locations considered (thus different atmospheric profiles were probably used) and (b) the differences between the resolutions of the two models (MODTRAN-3 is 1 cm^{-1} (Göttsche et al., 2000) and the RFM calculations were performed at 0.01 cm^{-1}).

An obvious feature of the results shown on figures 6-8 is that the differences between the responses of each of the three channels to changes in emissivity are only small, with the y-intercept values for the Meteosat IR channel lying virtually halfway between those for the (A)ATSR 11 and 12 micron channels.

6. DISCUSSION AND FURTHER WORK

Assuming known constant atmospheric conditions over the scale of a Meteosat pixel, the BT of one pixel recorded by each of the (A)ATSR 11 and 12 micron channels is a function of a representative emissivity and surface temperature for the area covered by that pixel. The BT of one pixel recorded by the Meteosat IR channel may be considered to be a function of the emissivities and surface temperatures of the (A)ATSR pixels that are covered by that Meteosat pixel. This may be described mathematically as:

$$BT(11\mu)_j = F_{11}(\varepsilon_{11j}, T_{sj}) \quad (6)$$

$$BT(12\mu)_j = F_{12}(\varepsilon_{12j}, T_{sj}) \quad (7)$$

$$BT(IR)_k = F_{IR}(\varepsilon_{11j=1,x}, \varepsilon_{12j=1,x}, T_{sj=1,x}) \quad (8)$$

where $BT(11\mu)_j$ and $BT(12\mu)_j$ are the BTs measured by the (A)ATSR for a pixel j that lies within the area covered by Meteosat pixel k ; $BT(IR)_k$ is the BT recorded by Meteosat for pixel k ; F_{11} , F_{12} and F_{IR} are functions; x is the total number of (A)ATSR pixels included in Meteosat pixel k ; ε_{11} and ε_{12} are the representative emissivities of pixel j for the (A)ATSR 11 and 12 micron channels, respectively, and T_s is the representative surface temperature of (A)ATSR pixel j .

Equation (8) is valid because the Meteosat IR channel bandwidth approximately spans the (A)ATSR 11 and 12 micron channels.

Stage (ii) of the sensitivity analysis indicates that a change (or uncertainty) in emissivity or surface temperature will produce a change in radiance measured by the sensor. The magnitudes of the

changes in measured radiances for the (A)ATSR 11 micron and Meteosat IR channels are very similar, whereas for the (A)ATSR 12 micron channel, the values are smaller. However, the relative responses between each channel are similar, as the lines are virtually parallel. At first, this appears to contradict the results from stage (iii) as they suggest that the responses to changes in emissivity are almost identical for all three channels. To explain this apparent difference, we must consider equation (5). This equation can be re-written as:

$$\begin{aligned}\frac{\delta T_s}{\delta \varepsilon} &= \frac{\delta R(\varepsilon)}{\delta \varepsilon} \times \frac{\delta T_s}{\delta R(T_s)} \\ \Rightarrow \frac{\delta T_s}{\delta \varepsilon} &= \frac{\delta R(\varepsilon) / \delta \varepsilon}{\delta R(T_s) / \delta T_s}\end{aligned}\quad (9)$$

As $\delta R(T_s)/\delta T_s$ and $\delta R(\varepsilon)/\delta \varepsilon$ for the (A)ATSR 12 micron channel are both smaller than for the (A)ATSR 11 micron and Meteosat IR channels, it is possible that equation (9) may yield very similar values for $\delta T_s/\delta \varepsilon$, which is what can be seen in figures 6-8.

The implication of the sensitivity analysis may be considered in two parts. Firstly, the change in the radiance measured by the sensor for both the (A)ATSR 11 micron and Meteosat IR channels are very similar. This implies that the observed BTs over a region for the Meteosat IR and (A)ATSR 11 micron channel should change by similar amounts in response to changes in emissivity or surface temperature. Secondly that the error in surface temperature associated with an uncertainty in emissivity is virtually identical for each of the channels.

It is intended that these results will be used in establishing a method for combining Meteosat and (A)ATSR thermal data. Future work to be carried out should include a study using the (A)ATSR forward view and the responses of the three channels under different atmospheric conditions. In addition, it is intended that real data should be examined over the Libyan Desert to determine whether the relationships observed between the three thermal channels can be related to the model results.

7. CONCLUSIONS

- A combined data set from the (A)ATSR 11 and 12 micron and Meteosat IR channels could provide the temporal and spatial resolution required to resolve the diurnal temperature range over land.
- The behaviour of each of these three channels to changes in surface temperature and emissivity is linear over the ranges of interest ($T_s=283-323$ K, $\varepsilon=0.95-0.99$) and has a positive gradient (i.e. measured radiances increase with increasing

emissivity and surface temperature).

- The change in measured radiance increases with increasing temperature and emissivity, and similar values are observed between the (A)ATSR 11 micron and Meteosat IR channels, with the (A)ATSR 12 micron channel having lower values of $\delta R(T_s)/\delta T_s$ and $\delta R(\varepsilon)/\delta \varepsilon$. The gradients of the lines are very similar.
- The error in surface temperature associated with an uncertainty in emissivity of 0.01 is 0.18-0.54 K, where the error increases with increasing surface temperature.
- Further studies involving the (A)ATSR forward view, and examining the response of each of the channels under different atmospheric conditions should be carried out. In addition, real data should be studied and compared to the model results.

REFERENCES

- Dash, P., Göttsche, F.-M., Olesen, F.-S. and Fischer, H., 2002, Land surface temperature and emissivity estimation from passive sensor data: theory and practice-current trends. *International Journal of Remote Sensing*, v23, n13, 2563-2594.
- Göttsche, F.-M. and Olesen, F.-S., 2000, Thermal land-surface-parameters from METEOSAT-IR data, *Workshop on Climatic Indices in Africa and Research in Global change in the Mediterranean, Casablanca, 27 Feb 2000*
- Llewellyn-Jones, D. T., Edwards, M. C., Mutlow, C. T., Birks, A. R., Barton, I. J., Tait, H., 2001, AATSR: Global-Change and Surface Temperature Measurements from Envisat. *ESA Bulletin*, 105, 10-21.
- Prata, A. J., 1994, Land surface temperatures derived from the advanced very high resolution radiometer and the along-track scanning radiometer 2. Experimental results and validation of AVHRR algorithms. *Journal of Geophysical Research*, v99, no.D6, 13,025-13,058.
- Prata, A. J., 2000, Land Surface Temperature Measurement from Space: AATSR Algorithm Theoretical Basis Document, *Contract report to ESA, CSIRO Atmospheric Research, Aspendale, Victoria, Australia*, 34pp.

- Olesen, F.-S., Kind, O., and Reutter, H., 1995, High resolution time series of IR data from a combination of AVHRR and METEOSAT, *Advances in Space Research*, 16(10), (10)141-(10)146.
- Reutter, H., Olesen, F.-S. and Fischer, H., 1996, Determination of Land Surface Temperatures from AVHRR and METEOSAT Data. In: *Heat, Moisture and Mass Exchange Processes on a Regional scale in a Non Homogeneous Terrain, Final Report, Environment*
- Snyder, W. C., Wan, Z., Zhang, Y., and Feng, Y.-Z., 1998, Classification-based emissivity for land surface temperature measurement from space, *International Journal of Remote Sensing*, v19, n14, 2753-2774.
- Sobrino, J. S. and Raissouni, N., 2000, Toward remote sensing methods for land cover dynamic monitoring application to Morocco, *International Journal of Remote Sensing*, v21, n2, 353-366
- Susskind, J., Rosenfield, J., and Reuter, D., 1983, An accurate radiative transfer model for use in the direct physical inversion of HIRS2 and MSU temperature sounding data. *Journal of Geophysical Research*, 88, 8550-8568.

Additional References:

- EUMETSAT, 2001, Meteosat High resolution Image Dissemination, Technical Description, Revision 6.
- Remedios, J. J., 1999, MIPAS equatorial atmospheric data set designed for use with the Oxford RFM.
- Rothman, L. S., Rinsland, C. P., Goldman, A., Massie, S. T., Edwards, D. P., Flaud, J.-M., Perrin, A., Camy-Peyret, C., Dana, V., Mandin, J.-Y., Schroeder, J., McCann, A., Gamache, R. R., Wattson, R. B., Yoshino, K., Chance, K. V., Jucks, K. W., Brown, L. R., Nemtchinov, V., and Varanasi, P., 1996, The HITRAN Molecular Spectroscopic Database and HAWKS (HITRAN Atmospheric Workstation), 1996 Edition, *Special Issue of the Journal of Quantitative Spectroscopy and Radiative Transfer*, v60, pp. 665-710 (1998).*
- * The actual database used in this study was the updated HITRAN 2000 database, an updated version of the 1996 release.

Using MODIS land surface temperature and normalized difference vegetation index products for monitoring drought in the southern Great Plains, USA

Peng-xin WANG (1, 2), Zheng-ming WAN (1), Xiao-wen LI (2, 3)

1. *Institute for Computational Earth System Science, University of California, Santa Barbara, CA 93106, USA. Email: pengxinwang@263.net; wan@icess.ucsb.edu.*

2. *Research Center for Remote Sensing and Department of Geography, Beijing Normal University, Beijing 100875, PR China.*

3. *Department of Geography and Center for Remote Sensing, Boston University, Boston, MA 02215, USA. Email: lix@thames.bu.edu.*

ABSTRACT -A near-real time drought monitoring approach is developed using Terra-MODIS normalized difference vegetation index (NDVI) and land surface temperature (LST) products. The approach is called vegetation temperature condition index (VTCI) which integrates land surface reflectance and thermal properties. VTCI is not only related to NDVI changes, but is also related to LST changes. It is defined as the ratio of LST differences among pixels with a specific NDVI value in a sufficiently large study area. The numerator is the difference between maximum LST of the pixels and LST of one pixel, while the denominator is the difference between maximum and minimum LSTs of the pixels. VTCI is lower for drought and higher for wet conditions. The ground-measured precipitation data from a study area covering parts of the States of Texas and Oklahoma in the southern Great Plains, USA are used to validate the drought monitoring approach. Linear correlation analysis between VTCI, and total monthly precipitation and departure from normal monthly precipitation shows that VTCI is not only closely related to recent rainfall events but is also related to past rainfall amounts, and indicates that VTCI might be a better and a near-real time drought monitoring approach.

1 INTRODUCTION

Drought is a slow-onset natural disaster, an insidious, creeping phenomenon; it occurs in virtually all climatic regimes. Drought is also related to the timing and the effectiveness of the rains, thus, each drought year is unique in its climatic characteristics and impacts. Therefore, it is not possible to make a definition of drought that can be universally accepted (Li and Xiao, 1992; Wilhite, 1993). Drought can be described by three characteristics: intensity, duration and spatial coverage (Wilhite and Glantz, 1985; American Meteorological Society, 1997). Intensity refers to the degree of precipitation shortfall and is closely linked to duration in the determination of its impacts. To some extent, drought occurs with uncertainty at a micro-scale, and drought occurrence sites vary from time to time when studying spatial distributions of drought (Wang and Wei, 1998). Meteorologically based drought monitoring refers to point-based analyses which might include simple presentations of specific events relative to their long-term historical averages (often denoted as 'normal'). The point-based drought indices have been used extensively for monitoring drought and for making operational water management decisions. The Palmer indices are based on a monthly water balance accounting scheme that involves precipitation, evapotranspiration, runoff and soil moisture (Palmer, 1965). The standardized precipitation index (SPI)

based only on precipitation gives a better representation of abnormal wetness and dryness than the Palmer indices (McKee *et al.*, 1993, 1995; Guttman, 1999). The SPI is probability based and was designed to be a spatially invariant indicator of drought that recognizes the importance of time scales in the analysis of water availability and water use.

The impacts of drought are usually first apparent in agriculture. Agriculture production is closely linked to actual crop evapotranspiration, which is usually monitored by the water balance of the whole crop growth cycle. Therefore, a drought index, which closely describes temporal and spatial variations of crop water use status, is suitable for drought monitoring. Satellite remotely sensed data offer considerable advantages and should be an integral part of monitoring drought, especially for the temporal and spatial evolution of drought. Since 1981, Advanced Very High Resolution Radiometer (AVHRR) data collected from the National Oceanic and Atmospheric Administration (NOAA) series of satellites have been used to generate vegetation indices such as the normalized difference vegetation index (NDVI) and to retrieve land surface temperature (LST). NDVI not only maps the presence of vegetation on a pixel basis, but also provides measures of the amount or condition of vegetation within a pixel. LST is a good indicator of the energy balance at the Earth's surface because it is one of the key parameters in the physics of land-surface processes on regional and global scales.

AVHRR NDVI was applied successfully to classify land vegetation types (Menenti *et al.*, 1993), and monitor vegetation growth conditions from excellent to stressed (Kogan, 1990; Prince, 1991). AVHRR NDVI and/or LST time series plots have been used to identify and monitor drought evolution (Kogan, 1990, 1995; Liu *et al.*, 1994; Chen *et al.*, 1994; Lozano-Garcia *et al.*, 1995; Liu and Kogan, 1996). Liu and Ferreira (1991) reported a good correlation between monthly total rainfall and monthly cumulative NDVI with a time lag of one month. Di *et al.* (1994), through a simulation approach, found a good correlation between daily rainfall and daily NDVI with a time lag of 15 to 23 days. Wilks (1995) suggested that, due to the obvious seasonal variation of climatic events, the use of standardized anomaly data instead of mean values was more suitable for investigating the annual NDVI departure from the normal. Chen *et al.* (1994) developed the anomaly vegetation index (AVI) for monitoring drought occurrence in China.

Associated with the drought, land surface temperatures increase slightly earlier than plant cover decreases (McVicar and Jupp, 1998). During dry conditions (there are less soil moisture available), rising leaf temperatures are good indicators of plant moisture stress and precede the onset of drought. This thermal response can occur even when plants are green, as stomata close to minimize water loss by transpiration resulting in a decreased latent heat flux. At the same time, due to the requirement that the energy flux must balance, there will be an increase in the sensible heat flux which may result in increased leaf temperatures. This increase in leaf temperature can be used for stress detection in crops. This land surface energy flux balance results in high land surface temperatures.

Goetz (1997) reported that the negative correlation between LST and NDVI, observed at scales from 25m² to 1.2km², was largely due to changes in vegetation cover and soil moisture, and indicted that the surface temperature can rise rapidly with water stress. Nemani *et al.* (1993) found the slope of LST versus NDVI to be negatively correlated to a crop-moisture index. Therefore, the ratio of LST/NDVI increases during times of drought. Advances are currently being made to use LST vs NDVI plot combined with meteorological data and process based models to provide a more meaningful interpretation of the remotely sensed data (McVicar and Bierwirth, 2001). There are two methods currently being put forward. The first is a progression from the slope of LST vs NDVI approach which describes the data as falling into a triangle (Price, 1990; Carlson *et al.*, 1994; Gillies and Carlson, 1995; Gillies *et al.*, 1997). The second, the vegetation index/temperature trapezoid (VITT) (Moran *et al.*, 1994; Yang *et al.*, 1997), is an evolution of the crop water stress index (CWSI) (Jackson *et al.*, 1981), which promotes the ideas of

data falling into a trapezoid. Based on AVHRR NDVI and brightness temperature, vegetation condition index (VCI) and temperature condition index (TCI) have been developed and used for monitoring drought (Kogan, 1990, 1995). On the basis of the triangular space of LST and NDVI, the vegetation temperature condition index (VTCI) approach was proposed for monitoring drought occurrence at a regional level (Wang *et al.*, 2001), and the temperature-vegetation dryness index (TVDI) approach was developed for assessing soil surface moisture status (Sandholt *et al.*, 2002).

Since meteorological data, such as precipitation and land air surface temperature, collected by surface observation stations often possess poor spatial resolution, especially in remote regions with difficult access and in some developing countries, remotely retrieved NDVI and LST data may provide a valuable source of information for monitoring drought. As mentioned above, the drought monitoring approaches of satellite remotely sensed data are based on NDVI and LST (or brightness temperature), and a simple ratio of LST and NDVI. It becomes critical to develop more complicated and physically based drought monitoring approaches by integrating remotely sensed LST and NDVI products.

The Moderate Resolution Imaging Spectroradiometer (MODIS) is a keystone instrument on the Terra satellite launched in December 1999. The MODIS remotely sensed data have been used to generate the NDVI product (van Leeuwen *et al.*, 1999) and the LST product (Wan and Dozier, 1996; Wan and Li, 1997).

In this paper, the VTCI drought monitoring approach is further developed by using the Terra-MODIS LST and NDVI products, and applied to monitor drought at a study area in the southern Great Plains, USA. Determination of the 'warm edge' and 'cold edge' of the triangular space of LST and NDVI is discussed. Ground measured meteorological data of total monthly precipitation and departure from normal monthly precipitation are used to validate the approach.

2 STUDY AREA AND DATA

It is important to monitor agricultural and hydrological droughts in much of rural U.S.A., particularly in areas such as the southwest and throughout the Great Plains where variability in annual rainfall is high. The Great Plains extend through the mid west from eastern Montana and North Dakota in the north to Texas in the south. This region is characterized by temperature extremes and erratic rainfall from year to year (White *et al.*, 2001). The 500mm rainfall isohyet closely follows the 100 degree west meridian, separating the high plains grazing lands from vast areas under crop. The 1011×853km² study area in the southern Great Plains which covers parts of the States of Texas and

Oklahoma is selected for validating VTCI approach. The central latitude and longitude of the study area are set to 32.5°N and 98.5°W. The area covers 10 climatic regions in Texas, from High Plains to Low Rolling Plains, from Edwards Plateau to Upper Coast. A part of the Trans-Pecos climatic region in Texas is excluded due to sparse meteorological stations there. Most of the study area is covered by grasslands and croplands. Other land cover types are savannas and sparsely vegetated land etc.

Monthly meteorologically measured surface data are obtained from the National Climatic Data Center. The data include elevation, latitude and longitude of the meteorological stations, total monthly precipitation (TPCP), and departure from normal monthly precipitation (DPNP). The selected stations should have records of precipitation for at least 30 years, and have fully recorded data for every month from January 2000 to December 2001.

The Terra MODIS 16-day composite of NDVI and LST images (daytime) are selected for the study. The compositing period is from May 25 to June 9, 2001 (day 145 to 150 of the year), and the spatial resolution of the composite data is 4.63km per grid.

3 METHODS AND DATA PROCESSING

3.1 VTCI Definition

Vegetation temperature condition index is defined as:

$$VTCI = \frac{LST_{NDVIi,max} - LST_{NDVIi}}{LST_{NDVIi,max} - LST_{NDVIi,min}} \quad (1)$$

where

$$\begin{aligned} LST_{NDVIi,max} &= a + bNDVI_i \\ LST_{NDVIi,min} &= a' + b'NDVI_i \end{aligned} \quad (2)$$

where $LST_{NDVIi,max}$ and $LST_{NDVIi,min}$ are maximum and minimum land surface temperatures of pixels which have same $NDVI_i$ value in a study region, respectively, LST_{NDVIi} denotes land surface temperature of one pixel whose NDVI value is $NDVI_i$.

a , b , a' and b' are coefficients and can be estimated from an area large enough where soil moisture at surface layer should span from wilting point to field capacity at pixel level. In general, the coefficients are estimated from the scatter plot of LST and NDVI in the area. The shape of the scatter plot is normally a triangular at a regional scale (Gollies *et al.*, 1997; Wang *et al.*, 2001) if the study area is large enough to provide wide range of NDVI and surface moisture conditions.

VTCI is not only related to NDVI changes in the region, but is also related to LST changes of pixels with a specific NDVI value. It can be physically explained as the ratio of temperature differences among the pixels (figure 1). The numerator of the

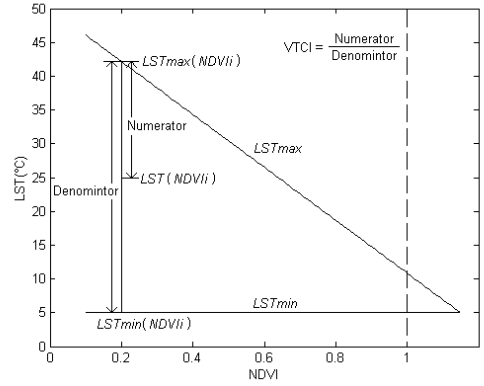


Figure 1. Schematic plot of the physical interpretation of VTCI. The vertical dashed line denotes the maximum NDVI value (NDVI = 1).

equation (1) is the difference between maximum LST of the pixels and LST of one pixel, while the denominator of the equation (1) is the difference between maximum and minimum LSTs of the pixels. In figure 1, LST_{max} can be regarded as the 'warm edge' in which there are less soil moisture available and growing plants are under dry conditions, LST_{min} can be regarded as the 'cold edge' where there are no water restrictions for plant growth (under wet conditions) (Gollies *et al.*, 1997; Wang *et al.*, 2001). The value of VTCI ranges from 0 to 1, the lower the value of VTCI is, the higher the occurrence of drought is.

3.2 Data Processing

We ordered the 16-day MODIS VI product (MOD13A2) and daily LST product (MOD11B1) covering the continental US, free of charge, from the NASA EOS Data Gateway (<http://redhook.gsfc.nasa.gov/~imswwww/pub/imswelcome/>). The NDVI data at 1km (actual size is 0.93km) grids in the VI product were aggregated to 4.63km grids. We shifted the NDVI and LST grids in the integerized sinusoidal map projection so that the grids at longitude 80°W are kept in the same column. Then subsets of the NDVI and LST images were selected to cover the study area. For the retrieved LST and NDVI data, extractions are made for 3×3 grids around the meteorological stations. This size of 3×3 grids is big enough for the accuracy of geo-referencing but small enough for a similar rainfall amount. We apply the average values of LST and NDVI over the square of 3×3 grids for statistical analysis. We selected only those squares where the mean square root of the variation in LST is less than 1.7 °C, and the NDVI variance is less than 0.005.

General linear correlation analysis is applied to study the relations between precipitation, and NDVI,

LST, LST/NDVI ratio and VTCI. The precipitation data are set to TPCP and DPNP in April 2001 and May 2001, and their combinations for 2, 3, 6, 9 and 12 month intervals ended in May 2001, respectively. The analysis is carried out to the whole study area (all land cover types), the croplands, and the grasslands, respectively.

4 RESULTS AND DISCUSSION

4.1 Relations Between Precipitation and NDVI, LST, LST/NDVI Ratio

Linear correlation analysis between NDVI and TPCP shows that NDVI is related to monthly cumulative precipitations (TPCP combinations) for 3, 6, 9 and 12 month intervals for the whole study area, the croplands, and the grasslands, respectively (table 1). For the croplands, the coefficients are relatively higher. The coefficients between TPCP in April 2001 and NDVI are greater than those between TPCP in May 2001 and NDVI for the whole study area and the grasslands. These results show that there is about a month time lag between precipitation and NDVI. Since there is a

certain time lag between NDVI and precipitation, the decrease in NDVI associates with the decreasing amounts of plant cover, therefore, NDVI may not be a good index for monitoring drought without concerning the time lag.

There are negative correlations between LST and TPCP in May 2001 and their combinations for the whole study area (table 1). For the croplands and the grasslands, the linear correlation coefficients are higher for 2 and 3 month combinations than those for 9 and 12 month combinations.

There are negative linear correlations between LST/NDVI ratio and TPCP combinations for 3, 6, 9 and 12 month intervals, respectively. A site with less cumulative precipitation has higher LST/NDVI value, and there is a high probability of drought occurrence. It can be concluded the LST/NDVI ratio is also related to TPCP amount in the early months.

In the traditional point-based drought monitoring approaches, both short-term and long-term precipitations are often applied at the same time in order to give a better description of drought intensity, duration and spatial distribution. With satellite remotely sensed data, suitable and near-real time drought monitoring approaches might be developed by integrating land surface reflectance and thermal properties.

Table 1. Linear correlation coefficients between TPCP, and NDVI, LST, LST/NDVI ratio and VTCI in the study area.

TPCP†	NDVI	LST	LST/ NDVI	VTCI
The whole study area (n = 122)				
May(01)	0.211	-0.482	-0.278	0.638
Apr.(01)	0.498	-0.400	-0.447	0.130
Apr.(01)-	0.351	-0.584	-0.401	0.653
Mar.(01)-	0.633	-0.672	-0.582	0.448
Dec.(00)-	0.727	-0.656	-0.619	0.318
Sept.(00)-	0.770	-0.620	-0.640	0.198
Jul.(00)-	0.764	-0.657	-0.648	0.288
Croplands (n = 17)				
May(01)	0.047	-0.626	-0.259	0.610
Apr.(01)	0.149	0.053	-0.033	-0.097
Apr.(01)-	0.100	-0.583	-0.261	0.551
Mar.(01)-	0.816	-0.598	-0.842	0.009
Dec.(00)-	0.777	-0.438	-0.752	-0.129
Sept.(00)-	0.807	-0.264	-0.723	-0.338
Jul.(00)-	0.747	-0.312	-0.684	-0.234
Grasslands (n = 37)				
May(01)	0.191	-0.524	-0.316	0.650
Apr.(01)	0.413	-0.292	-0.369	0.055
Apr.(01)-	0.272	-0.587	-0.391	0.668
Mar.(01)-	0.396	-0.586	-0.468	0.549
Dec.(00)-	0.571	-0.600	-0.563	0.403
Sept.(00)-	0.613	-0.447	-0.524	0.124
Jul.(00)-	0.615	-0.490	-0.533	0.190

† May(01) means the TPCP in May 2001, and Apr.(01)- means the TPCP amount in the period from April 2001 - May 2001 (also called the TPCP combination for 2 month interval in this paper).

4.2 Relations Between VTCI and Precipitation

4.2.1 Determination of the 'warm edge' and 'cold edge'

One important issue of using VTCI approach for monitoring drought is to determine whether the study area is large enough to provide wide range of NDVI and surface soil moisture conditions. Soil moisture should comprise the whole span of its contents, from wilting point to field capacity. In the study area, the main land cover types are grasslands and croplands, other land cover types include savannas and sparsely vegetated lands etc. In general, some of lands along the river valleys and coastlines, and some of the irrigated croplands are under wet conditions, and some of the sparsely vegetated lands, and rainfed croplands and grasslands are under dry conditions. Another method to analysis the wet and dry conditions is to use the scatter plot of LST and NDVI. The scatter plots of the MODIS 16-day composite NDVI and LST values over the whole study area, the croplands and the grasslands are shown in figure 2. The spatial distributions of the NDVI and LST are shown in figure 3 (a) and (b). The same straight lines are drawn in the scatter plots based on the scatter plot of the whole study area shown in figure 2(a), the upper limits of the scatter plots represent the 'warm edges' (LST_{max}), where water supply is limited, and the lower limits of the scatter plots represent the 'cold edges' (LST_{min}), where there are no water restrictions.

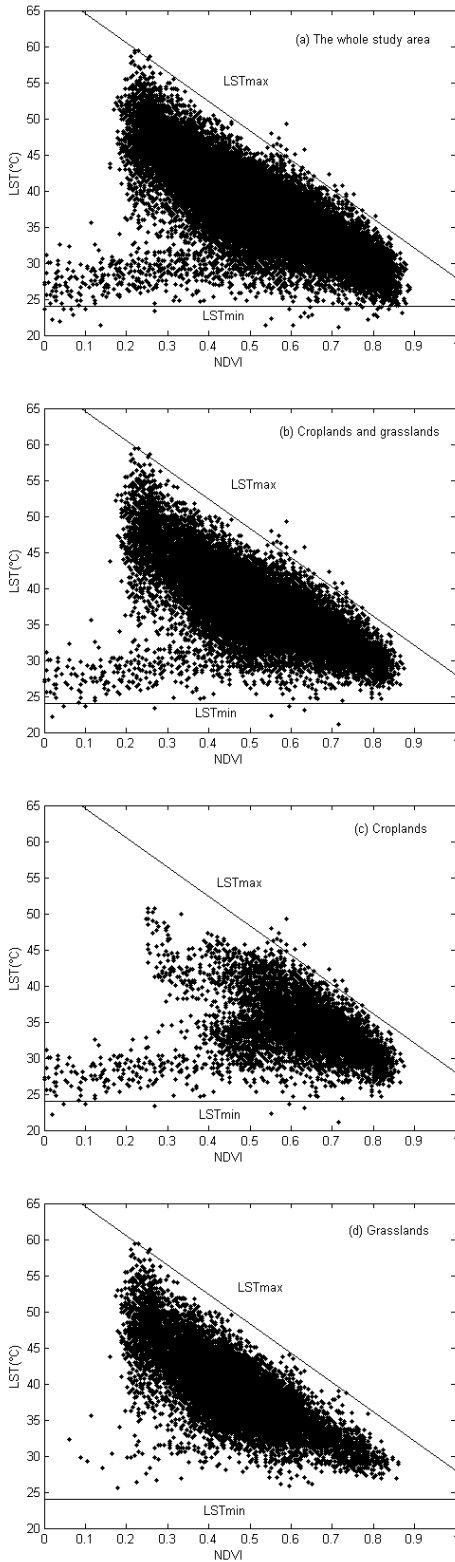


Figure 2. Scatter plots of LST versus NDVI for (a) the whole study area, (b) croplands and grasslands, (c) croplands, (d) grasslands, and (e) other lands. Note that the whole study area means all land cover types in the area, and other lands means land covered by other vegetations except for the croplands and grasslands in the study area.

All the 'warm edges' in the scatter plots in figure 2 seem to be well defined. For the 'cold edges', the whole study area, the croplands and other lands seem to have a similar edge. The 'cold edge' for the grasslands in figure 2(d) is a bit of lower, this may be partly because the grasslands are under rainfed conditions. Therefore, it becomes difficult to determine the wet conditions for the grasslands if we analyze the grasslands alone. On the whole, the same 'warm edge' and 'cold edge' are used for calculating VTCI for all land cover types in the study area.

The coefficients a , b , a' and b' can be approximately estimated from the selected 'warm edge' and 'cold edge', we get:

$$\begin{aligned} LST_{NDVI_i, max} &= 68.66 - 40.66NDVI_i \\ LST_{NDVI_i, min} &= 24.0 + 8 \times NDVI_i \end{aligned} \quad (3)$$

VTCI has been calculated for the study area for each pixel by using equations (3) and (1). The VTCI image of the study area is showed in figure 3(c).

4.2.2 Analyzing relations between VTCI and precipitation

There is significant linear correlation between VTCI and TPCP in May 2001 as shown in table 1. The VTCI value is higher for a higher TPCP value, indicating lower occurrence of drought. There is no significant relation between VTCI and TPCP in April 2001. VTCI is also significantly correlated with cumulative TPCP amount in April 2001 and May 2001. Compared to the croplands, VTCI for the grasslands is also closely related to TPCP combination for 3 and 6 month intervals. These results suggest that VTCI is not only closely related to recent rainfall events but is also

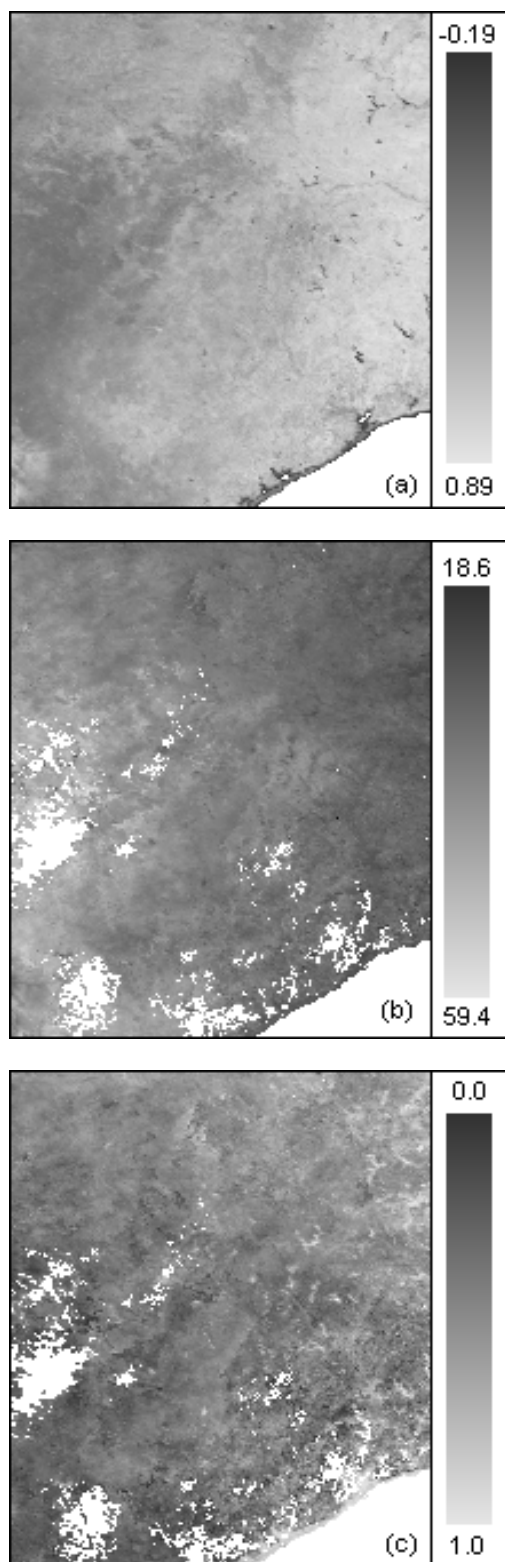


Figure 3, NDVI, LST and VTCI images of the study area: (a) NDVI, (b) LST (°C) and (c) VTCI. The compositing period is from May 25 to June 9, 2001. The size of the images is 218 pixels×184 pixels and the spatial resolution is 4.63km. The central latitude and longitude are set to 32.5°N and 98.5°W. Note that pixels in white are water body and land without LST values due to clouds.

related to past rainfall amount, and indicate that VTCI might be a better drought monitoring approach.

Departure from normal precipitation (DPNP) at a specific period is an important parameter for point-based drought monitoring indices. After applying the linear correlation analysis, we find that the correlations between DPNP and NDVI, LST and LST/NDVI ratio for the whole study area, the croplands, and the grasslands, are not in good agreement. As shown in table 2, for the croplands, NDVI and LST/NDVI ratio are related to DPNP combinations for 3, 6 and 9 month intervals, LST are related to DPNP in May 2001 and their combinations in 3 and 6 month combinations. While for the grasslands, the correlations seem to rely on 9 and 12 month cumulative DPNP values. The important finding is that VTCI is closely related to DPNP in May 2001 and to the DPNP combination of April 2001 and May 2001 for the whole study area, the croplands and the grasslands, respectively. These comparisons show that VTCI is a near-real time drought monitoring approach.

After applying VTCI approach to the study area, more drought occurrence is found in the Southwest, while small fractions in the Northeast and along the coastlines are under wet conditions as shown in figure 3(c).

5 CONCLUSIONS

VTCI can be physically interpreted as the ratio of LST differences among the pixels with a specific NDVI value in an area large enough to provide wide range of NDVI and to comprise the whole span of soil moisture at surface layer. The VTCI drought monitoring approach integrates the remotely sensed land surface reflectance and thermal properties, and gives the emphasis on both LST changes and NDVI changes over a region. A case study is carried out to validate VTCI approach by using ground measured precipitation data over the study area covering parts of the States of Texas and Oklahoma in the southern Great Plains, USA. Our case study shows that VTCI is not only related to recent rainfall events, but is also related to past rainfall amount. Another finding is that VTCI might be only related to recent DPNP amount which is an important parameter for point-based drought monitoring approaches. These results indicate VTCI is a near-real time drought monitoring approach.

Table 2. Linear correlation coefficients between DPNP, and NDVI, LST, LST/NDVI ratio and VTCI in the study area.

DPNP†	NDVI	LST	LST/ NDVI	VTCI
The whole study area (n = 122)				
May(01)	-0.034	-0.254	-0.062	0.518
Apr.(01)	-0.343	0.305	0.250	-0.160
Apr.(01)-	-0.143	-0.138	0.023	0.432
Mar.(01)-	-0.122	0.001	0.043	0.111
Dec.(00)-	0.236	-0.314	-0.267	0.274
Sept.(00)-	0.381	-0.299	-0.367	0.060
Jul.(00)-	0.335	-0.308	-0.352	0.162
Croplands (n = 17)				
May(01)	-0.054	-0.571	-0.150	0.626
Apr.(01)	-0.373	0.264	0.415	0.077
Apr.(01)-	-0.216	-0.366	0.061	0.568
Mar.(01)-	0.582	-0.441	-0.614	0.042
Dec.(00)-	0.617	-0.526	-0.656	0.136
Sept.(00)-	0.638	-0.142	-0.552	-0.299
Jul.(00)-	0.554	-0.157	-0.489	-0.197
Grasslands (n = 37)				
May(01)	0.071	-0.398	-0.213	0.564
Apr.(01)	-0.129	0.072	0.085	0.006
Apr.(01)-	0.040	-0.360	-0.184	0.532
Mar.(01)-	0.049	-0.261	-0.162	0.367
Dec.(00)-	0.277	-0.445	-0.350	0.442
Sept.(00)-	0.515	-0.409	-0.470	0.167
Jul.(00)-	0.552	-0.449	-0.495	0.191

† May(01) means the DPNP in May 2001, and Apr.(01)- means the DPNP amount in the period from April 2001 to May 2001.

VTCI is time-dependent and usually region-specific, and is better to be used during plant growing seasons. One issue of applying VTCI approach is how to determine its 'warm edge' and 'cold edge', future development of this drought monitoring approach should focus on the feasible ways to determine the edges and on validation of the approach in other regions.

ACKNOWLEDGEMENTS

This research was supported by the National Aeronautics and Space Administration (NASA Contract NAS5-31370) and the China Special Funds for Major State Basic Research Project (Contract G2000077900). The authors would like to thank Drs. Jiaya GONG and Jindi WANG for their contributions to this work.

REFERENCES

- American Meteorological Society, 1997, Policy statement: Meteorological Droughts. *Bulletin of American Meteorological Society*, **78**, 847-849.
 Carlson, T. N., Gillies, R. R., and Perry, E. M., 1994,

- A method to make use of thermal infrared temperature and NDVI measurements to infer soil water content and fractional vegetation cover. *Remote Sensing Reviews*, **9**, 161-173.
 Chen, W. -Y., Xiao, Q. -G., and Sheng, Y. -W., 1994, Application of the anomaly vegetation index to monitoring heavy drought in 1992 (In Chinese). *China Remote Sensing of Environment*, **9**, 106-112.
 Di, L. -P., Rundquist, D. C., and Han, L., 1994, Modeling relationship between NDVI and precipitation during vegetative growth cycles. *International Journal of Remote Sensing*, **15**, 2121-2136.
 Gillies, R. R., and Carlson, T. N., 1995, Thermal remote sensing of surface soil water content with partial vegetation cover for incorporating into climate models. *Journal of Applied Meteorology*, **34**, 745-756.
 Gillies, R. R., Carlson, T. N., Cui, J., Kustas, W. P., and Humes, K. S., 1997, A verification of the 'triangle' method for obtaining surface soil water content and energy fluxes from remote measurement of the Normalized Difference Vegetation Index (NDVI) and surface radiant temperature. *International Journal of Remote Sensing*, **18**, 3145-3166.
 Goetz, S. J., 1997, Multi-sensor analysis of NDVI, surface temperature and biophysical variables at a mixed grassland site. *International Journal of Remote Sensing*, **18**, 71-94.
 Guttman, N. B., 1999, Accepting the standardized precipitation index: a calculation algorithm. *Journal of the American Water Resources Association*, **35**, 311-323.
 Jackson, R. D., Idso, S. B., Beginato, R. J., and Pinter Jr, P. J., 1981, Canopy temperature as a crop water stress indicator. *Water Resources Research*, **17**, 1133-1138.
 Kogan, F. N., 1990, Remote sensing of weather impacts on vegetation in non-homogeneous areas. *International Journal of Remote Sensing*, **11**, 1405-1419.
 Kogan, F. N., 1995, Application of vegetation index and brightness temperature for drought detection. *Advances in Space Research*, **15**, 91-100.
 Li, S. -X., and Xiao, L., 1992, Distribution and management of dryland in the People's Republic of China. *Advances in Soil Science*, **18**: 148-278.
 Liu, W. T., and Ferreira, A., 1991, Monitoring crop production regions in the Sao Paulo State of Brazil using normalized difference vegetation index. Proceeding of the 24th International Symposium on Remote Sensing of Environment, Rio de Janeiro, May 27-31, Vol. 2 (Chicago: ERIM), pp. 447-455.
 Liu, W. T., and Kogan, F. N., 1996, Monitoring regional drought using the Vegetation Condition

- Index. *International Journal of Remote Sensing*, **17**, 2761–2782.
- Liu, W. T., Massambani, O., and Nobre, C., 1994, Satellite recorded vegetation response to drought in Brazil. *International Journal of Climatology*, **14**, 343–354.
- Lozano-Garcia, D. F., Fernandez, R. N., Gallo, K. P., and Johannsen, C. J., 1995, Monitoring the 1988 severe drought in Indiana, U.S.A. using AVHRR data. *International Journal of Remote Sensing*, **16**, 1327–1340.
- McKee, T. B., Doeskin, N. J., and Kleist, J., 1993, The relationship of drought frequency and duration to time scales. Proceedings of 8th Conference on Applied Climatology, American Meteorological Society, January 17–23 1993 (Boston), pp. 179–184.
- McKee, T. B., Doeskin, N. J., and Kleist, J., 1995, Drought monitoring with multiple time scales. Proceeding of 9th Conference on Applied Climatology, American Meteorological Society, January 15–20 1995, (Boston), pp. 233–236.
- McVicar, T. R., and Bierwirth, P. N., 2001, Rapidly assessing the 1997 drought in Papua New Guinea using composite AVHRR imagery. *International Journal of Remote Sensing*, **22**, 2109–2128.
- McVicar, T. R., and Jupp, D. L. B., 1998, The current and potential operational use of remote sensing to aid decisions on drought exceptional circumstances in Australia: a review. *Agricultural System*, **57**, 399–468.
- Menenti, M., Azzali, S. A., Verhoef, W., and van Swol, R., 1993, Mapping agroecological zones and time lag in vegetation growth by means of Fourier analysis of time series of NDVI images. *Advances in Space Research*, **13**, 233–237.
- Moran, M. S., Clarke, T. R., Inoue, U., and Vidal, A., 1994, Estimating crop water deficit using the relation between surface-air temperature and spectral vegetation index. *Remote Sensing of Environment*, **49**, 246–263.
- Nemani, R. R., Pierce, L. L., Running, S. W., and Goward, S. N., 1993, Developing satellite derived estimates of surface moisture status. *Journal of Applied Meteorology*, **28**, 276–284.
- Palmer, W. C., 1965, Meteorological Drought. Research Paper No. 45, U.S. Department of Commerce Weather Bureau, Washington D.C., 58 pp.
- Price, J. C., 1990, Using spatial context in satellite data to infer regional scale evapotranspiration. *IEEE Transactions on Geoscience and Remote Sensing*, **28**, 940–948.
- Prince, S. D., 1991, Satellite remote sensing of primary production: comparison of results for Sahelian grassland 1981–1988. *International Journal of Remote Sensing*, **12**, 1301–1312.
- Sandholt, I., Rasmussen, K., and Anderson, J., 2002, A simple interpretation of the surface temperature/vegetation index space for assessment of the surface moisture status. *Remote Sensing of Environment*, **79**, 213–224.
- van Leeuwen, W. J. D., Huete, A. R., and Laing, T. W., 1999, MODIS vegetation index compositing approach: A prototype with AVHRR data. *Remote Sensing of Environment*, **69**, 264–280.
- Wan, Z. -M., and Dozier, J., 1996, A generalized split-windows algorithm for retrieving land surface temperature from space. *IEEE Transactions on Geoscience and Remote Sensing*, **34**, 892–905.
- Wan Z. -M., and Li Z. -L., 1997, A physics-based algorithm for retrieving land surface emissivity and temperature from EOS/MODIS data. *IEEE Transactions on Geoscience and Remote Sensing*, **35**, 980–996.
- Wang, P. -X., Li, X. -W., Gong, J. -Y., and Song, C. -H., 2001, Vegetation temperature condition index and its application for drought monitoring. Proceedings of IGARSS 2001 International Geoscience and Remote Sensing Symposium, July 9–14 2001 (Sydney, Australia).
- Wang, P. -X., and Wei, Y. -M., 1998, Research, Demonstration and Extension of Sustainable Farming Systems for Rainfed Agriculture (UNDP-CPR/91/114 Project Final Report), (Xi'an, PR China: World Publishing Corporation).
- White, D. H., Wilhite, D. A., O'Meagher, B., and Hammer G. L., 2001, Highlights of drought policy and related science in Australia and the U.S.A. *Water International*, **26**, 349–357.
- Wilhite, D. A., 1993, Drought Assessment, Management, and Planning: Theory and Case Study, (Boston: Kluwer Academic).
- Wilhite, D. A., and Glantz, M. H., 1985, Understanding the drought phenomenon: the role of definitions. *Water International*, **10**, 111–120.
- Wilks, D. S., 1995, Statistical methods in the atmospheric sciences. International Geophysics Series, Vol. 59 (New York: Academic).
- Yang, X., Zhou, Q. and Melville, M., 1997, Estimating local sugarcane evapotranspiration using Landsat TM image and a VITT concept. *International Journal of Remote Sensing*, **18**, 453–459.

Change analysis of land surface temperature in china using NOAA-AVHRR data

Changyao Wang, Hao Yan, and Zheng Niu

LARSIS, Institute of Remote Sensing Applications, Chinese Academy of Sciences, Beijing 100101, tel: 86-10-64889561, fax: 86-10-64889786

wangchangyao@hotmail.com, yanhaon@hotmail.com

ABSTRACT *Temperature change is one of the research focuses of global change. In addition to air temperature, land surface temperature (LST) is also an important factor to study global change. Moreover, as a major solution to retrieve LST from NOAA-AVHRR data on a large scale, split-window algorithm was used to calculate yearly and monthly LST in China from 1982 to 1992. Further, comparing calculated LST with 0cm surface temperature of the same period, land temperature change over China was analyzed and some spatial and temporal change features were got. The results of this paper showed that, (1) both LST and 0 cm surface temperature tended to increase during these ten years; (2) spatial variation of cloudless LST in China was consistent with that of 0cm surface temperature; (3) from the beginning of 1980's to the beginning of 1990's, different regions presented different features of temperature change, some areas increased, and some areas decreased. Furthermore, the same regions in different season probably showed different properties of temperature change; (4) the increase value of annual LST had good positive correlation with its corresponding area of temperature increase. This paper indicated that it is a feasible way to study the change of LST using thermal infrared bands of NOAA-AVHRR. The distribution and change of Chinese land surface temperature was of great indicative significance in the study of the impact of global change in China and the change of land cover in China.*

1 INTRODUCTION

It has been the research focus of global change study in China how the temperature changed in whole China and whether the changes were the same in different areas of China. Generally, meteorological data was used to study the change of land surface temperature, and the number of ordinary meteorostations is 336 in China. However, for their different distribution, for example, more stations are densely distributed in the eastern part of China, the trend of air temperature must be affected, especially in some important areas, such as Tibetan Plateau which due to lack of ample meteorostations, it is difficult to deduce the change of temperature. Now, remote sensing can aid to quantitatively retrieve the land surface temperature (LST) on a large scale, and this technology can be classified into two ways: experimental method and theoretical one. Experimental method (Pu Jinguan, 1997) is to build the regression equation between raw data of satellite image and radiative energy emitted by land surface by

measuring the land surface temperature when the satellite overpasses the ground. Theoretical method (Qin yi, 1994) removes the atmospheric influence and gets land surface temperature by calculating the radiance transfer equation.

One important theoretical method for LST retrieval is split-window algorithm. Traditional split-window method succeeded in the retrieval of sea surface temperature (SST), and its error is less than 0.7°C (McClain, 1985). The main reason is that the property of sea surface is almost homogeneous and the emissivity almost equals to 1 in the research channel. However, as to land surface temperature, the error of the retrieval is higher than 1°C for the atmospheric infection and the emissivity differs much in different kinds of land surfaces during different seasons. Now a new method has been developed (Becker, 1990; Price, 1984) in which the error between the retrieved LST and the LST measured on the spot is less than 2°C (Gupta, 1997) provided some reasonable hypothesis is made and the influence of atmosphere and emissivity is simplified.

2 METHODS

2.1 Data

The Satellite Data used in this study was NOAA-AVHRR data set from 1982 to 1992 (total ten years, lack of 1984). The spatial resolution is 8km and the temporal resolution is 10 days. The method is maximum NDVI compositing (MVC). The retention of the highest NDVI value during the compositing period (ten days) reduces the number of cloud-contaminated pixels and the pixels nearest to nadir were selected (Holben, 1986). In addition, threshold method (Saunders, 1986) was used to detect the cloud and remove the cloud-contaminated pixels.

The channels used were Ch1 (visible 0.58-0.68 μ m), Ch2 (near infrared 0.725-1.10 μ m), Ch4 (thermal infrared 10.5-11.3 μ m) and Ch5 (thermal infrared 11.5-12.5 μ m). In addition, Ch1 and Ch2 were expressed as land reflectance in Percent, Ch4 and Ch5 were expressed as brightness temperature in Kelvin at the top of the atmosphere.

In accordance with the remote sensing data, the weather data including air temperature and 0cm surface temperature of the meteorostations at the same time, namely, monthly data of ten years were collected.

2.2 Retrieval procedure of LST from NOAA-AVHRR data

Retrieval procedure of LST was made up of the following three steps.

a) Calculation of NDVI

$$NDVI = (Ch2 - Ch1) / (Ch2 + Ch1) \quad (1)$$

Where, Ch1 is red channel, Ch2 is near infrared channel.

NDVI ranges from -1 to +1, and the higher value of NDVI means more green vegetation.

b) Calculation of emissivity ϵ

One method to calculate ϵ is from NDVI. With ground-based experiments, it was found that NDVI and ϵ had good correlation, with a correlation coefficient of 0.941 (Van De Griend, 1993). Thus NDVI can be used as approximate parameter to calculate the effective thermal emissivity of pixels.

The equation is:

$$\epsilon = 1.0094 + 0.047 \ln(NDVI) \quad (2)$$

However, the modified split-window algorithms use the spectral emissivity, so Josef et al (1997) calculated ϵ_4 and $\Delta\epsilon$ of AVHRR based on the previous work (Van De Griend, 1993; Salisbury, 1994).

The equation is:

$$\epsilon_4 = 0.9897 + 0.029 \ln(NDVI) \quad (3)$$

$$\Delta\epsilon = \epsilon_4 - \epsilon_5 = 0.01019 + 0.01344 \ln(NDVI) \quad (4)$$

c) Calculation of land surface temperature T_s

Under cloudless condition, the satellite-observed radiation at the top of the atmosphere can be expressed as

$$B_i(T_i) = \tau_i(\theta) [\epsilon_i B_i(T) + \rho_i R_i^\downarrow(hem)] + R_i^\uparrow(\theta) \quad (5)$$

Where B is Plank's function for channel i, T_i is the brightness temperature measured at satellite for channel i, $\tau_i(\theta)$ is the atmospheric transmittance for channel i at zenith observation angle θ , ϵ_i is the emissivity of channel i, T is the true land surface temperature, ρ_i is the channel bidirectional reflectivity of the surface, $R_i^\downarrow(hem)$ is the hemispheric downward atmospheric radiance for the waveband of channel i, $R_i^\uparrow(\theta)$ is the upward radiance emitted by the atmosphere in the waveband of channel i in the direction of θ .

However, it is difficult to directly calculate the parameters of the equation (6). During the course of atmospheric absorption in thermal channels, water vapor is the most important factor to influence the radiance transfer; so many researchers have deduced some modified split-window algorithms (see table 1) on the basis of their simplifying assumption of the radiance transfer.

$$T_s = 1.274 + (T_4 + T_5) / 2 \left\{ 1 + \left[0.15616(1 - \epsilon) / \epsilon \right] - 0.482 \left(\Delta\epsilon / \epsilon^2 \right) \right\} + (T_4 - T_5) / 2 \left\{ 6.26 + \left[3.98(1 - \epsilon) / \epsilon \right] + 38.33 \left(\Delta\epsilon / \epsilon^2 \right) \right\} \quad (6)$$

Furthermore, the error induced by using equation (3) and (4) to calculate ϵ from NDVI was analyzed in table 1. Two types of land cover were selected, they were forest field and agriculture field. The test condition of forest field was $T_4=300.29k$, $T_5=297.88k$, and when NDVI ranged from 0.48 to 0.58 (interval 0.01), the LST ranged from 36.41 to 35.91. And the test condition of agriculture field was $T_4=277.05$, $T_5=277.39$, and when NDVI ranged from 0.168 to 0.268 (interval 0.01), the LST ranged from 8.93 to 7.43. In all, table 3 showed that when NDVI changed 0.1, LST maximally changed less than 2k, LST was not so sensitive to the change of NDVI in equation (3) and (4).

Table 1 Sensitivity test of LST to NDVI

Forest Field		Agriculture Field	
NDVI	LST (°C)	NDVI	LST (°C)
0.48	36.40726	0.168	8.930439
0.49	36.35311	0.178	8.741476
0.5	36.30017	0.188	8.563651
0.51	36.24831	0.198	8.395741
0.52	36.19758	0.208	8.236727
0.53	36.14783	0.218	8.08576
0.54	36.09912	0.228	7.94206
0.55	36.05135	0.238	7.805014
0.56	36.00449	0.248	7.674044
0.57	35.95854	0.258	7.548643
0.58	35.91341	0.268	7.428368

Becker (1987) pointed out that the error analysis can be expressed as:

$$\Delta T = 50[(1 - \varepsilon)/\varepsilon] - 300[\Delta \varepsilon/\varepsilon] \quad (7)$$

The error between the split-window algorithm and the measurement in site was 2-4°C (Kalluri, 1995; Stowe, 1988).

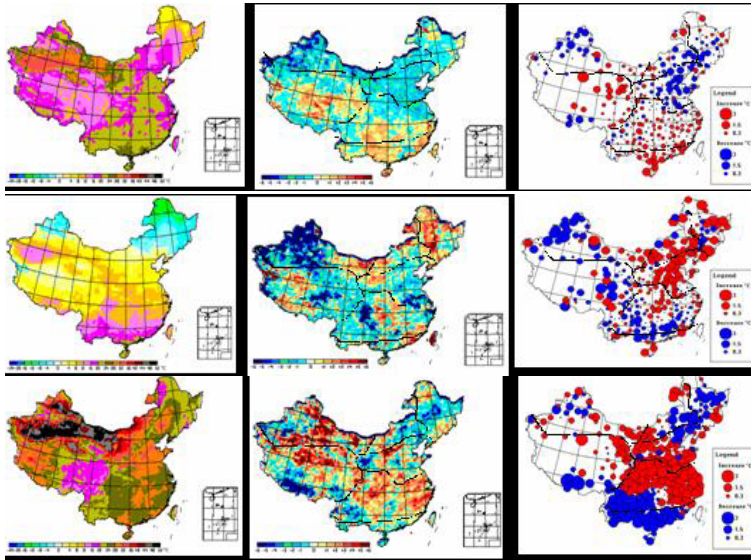
2.3 Calculation of temperature data for comparison

Using Becker and Li algorithm(Becker and Li, 1990), total Ts of every ten days in one year was 36, and every three Ts of the same month were averaged to monthly mean LST, then monthly mean LST of the same year were averaged to annual LST.

Similarly, 0cm surface temperature of every month was averaged to get annual 0cm surface temperature.

Then simple differentiation which is one of the more accurate change detection techniques (Woodwell et al, 1983;Singh, 1989) was applied to get the value of temperature change. To remove the accidental factors' influence of a single year, the temperature data of 1982 and 1983 were averaged as the data of the beginning of 1980's and that of 1991 and 1992 were averaged as the data of beginning of 1990's. Using the equation (8), we subtracted the annual data, January data and July data of the beginning of 1980's from the data of the beginning of 1990's to get the temperature change map (figure 1 to figure 9).

$$T_c = (T_{1991} + T_{1992})/2 - (T_{1982} + T_{1983})/2 \quad (8)$$



Figures 1,2,3

Figures 4,5,6

Figures 7,8,9

Figures 1-9: 1) The map of annual LST.2)The annual change map of LST.3)The annual change map of 0cm surface temperature. 4)The map of average LST in January. 5)The change map of average LST in January. 6)The change map of average 0cm surface temperature in January. 7)The map of average LST in July. 8)The change map of average LST in July. 9)The change map of average 0cm surface temperature in July.

3 RESULTS AND ANALYSIS

In order to describe the change of LST clearly, and according to the difference of weather and terrain, China was regionalized into seven natural divisions on the basis of previous work (Zhao Songqiao, 1983). These natural divisions were (1) Temperate humid & subhumid Northeast China, (2) Warm-temperate humid & Subhumid North China, (3) Subtropical humid Central China, (4) Tropic humid South China, (5) Temperate grassland of Inner Mongolia, (6) Temperate & warm temperate desert of Northwest China and (7) Tibetan Plateau (figure 10).

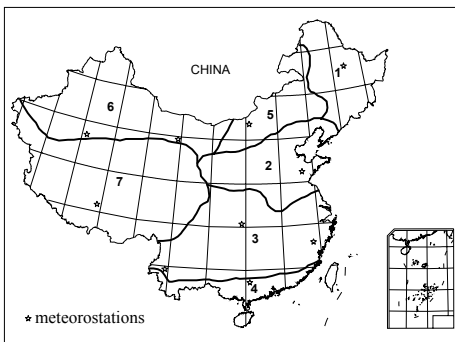


Figure10 Map for comprehensive regionalization in China (Zhao Songqiao, 1983) and meteorostation location.

3.1 Seasonal mean LST change

Base on analysis in figure 1, spatial distribution feature of annual mean LST indicated that China showed one high temperature region with LST ranged from 24°C - 40°C , which was temperate & warm temperate desert area of Northwest China (division 6); two low temperature regions, which were temperate humid & Northeast China (division 1) with LST ranged from 4°C - 20°C and Tibetan Plateau (division 7) with LST ranged from 12°C - 20°C ; other divisions of figure 10 belong to middle temperature region. This situation was differ from annual air temperature spatial distribution, which clearly followed the latitude change from south of division 4 with 25°C to North of division 1 with -5°C , the air temperature was over 36°C , but the biggest LST difference value appeared in Northwest China (division 6) and Northeast China (division 1). This results indicated that LST was more

synthetically affected by land surfaces, such as vegetation, soil, and topography, etc.

In China, annual LST also showed seasonal change features. Taking January as a key month in winter, figure 4 showed that LST gradually deceased from south to north with obvious gradient. LST in south region was high as 28°C and LST in north region was low as -16°C , moreover, the LST difference of south region and north region was 44°C in January. LST in Tibet plateau changed from 0 to 12°C , and 0°C isotherm of LST extended along latitude 40 degrees north.

In summer, taking July as a key month, LST (figure 7) reached its summit. The highest LST was located in arid region of Northwest China with 48°C and the lowest LST was in eastern part of Tibet plateau (division 7) with 14°C . Moreover, the LST in eastern part of Tibet plateau was 18°C , but the LST in western part of Tibet plateau was higher as 30°C . This situation also relied on the land surface difference. The west Tibet had more bare rock and east Tibet had more vegetation.

3.2 The change of LST from the beginning of 1980's to the beginning of 1990's

As to the change of annual temperature, the comparison of figure 2 and 3 identically showed that the temperature in Tibet (division 7) and South China (division 4) tended to increase, the temperature raised 1°C - 2°C there. The temperature in Northeast China (division 1), eastern part of North China (division 2) and Northwest China (division 6) tended to decrease, among them LST in Northwest China (division 6) decreased 2°C . 0cm surface temperature showed similar temperature change trend in this period.

As to the change of temperature in January, the comparison of figure 5 and 6 identically showed that the temperature in Northeast China (division 1), Inner Mongolia (division 5) and the middle of central China (division 3) tended to increase, and there existed a belt of temperature decrease from western part of Northwest China (division 6) to South China (division 4). 0cm surface temperature showed similar temperature change trend, except there was little LST increase in east part of North China (division 2).

As to the change of temperature in July, the comparison of figure 8 and 9 identically showed that the temperature of most part of China increased. LST

and 0cm surface temperature presented a similar spatial distribution feature, which showed that North China (division 2), most part of central China (division 3), Northwest China (division 6), and Tibetan Plateau (division 7) tended to increase; but Northeast China (division 1), South China (division 4), Southern part of central China (division 3) and southern part of Tibet (division 7) tended to decrease.

The analysis above indicated that from the beginning of 1980's to the beginning of 1990's, the 0cm surface temperature and cloudless LST showed a similar trend of temperature change in China, but the range of temperature change were different, LST changed much more. And the range of temperature change in different years was smaller than that in January and July of the same year.

3.3 Temperature change trend of LST, air temperature and 0cm surface temperature from 1982 to 1992

In order to analyze the change trend and relation of these above three kind of temperature during the ten years, ten ordinary meteorostations which represent different land cover and different climate types (figure 11) were selected for comparison. Further, annual temperature of LST, air temperature and 0cm surface temperature of ten stations were calculated and there linear fit were also conducted (figure 12). The result showed that LST, air temperature and 0cm surface temperature tended to increase, but air temperature and 0cm surface temperature increased more significantly during these ten years.

Moreover, the relation of the three kind of temperature was computed. The correlation between LST, air temperature and 0cm surface temperature is illustrated in figure 13. The correlation coefficient of LST and 0cm surface temperature was 0.65823 at a 0.01 level of significance, and the correlation coefficient of LST and air temperature is 0.54796 at a 0.01 level of significance. This result indicated that LST in China had close correlation with 0cm surface temperature than air temperature, so that LST can be used to study land surface temperature change in continental scale.

3.4 Relationship analysis of the increase value and the corresponding area of annual LST in China

Take the average of annual temperature of 1982 and 1983 as the baseline, we might compute the subsequent 7 years' temperature change map and get the scatterogram (figure 12) by calculating the increase value(°C) of annual LST and its

corresponding area (%) in China. It showed that if annual LST at the beginning of 1980's was used as the

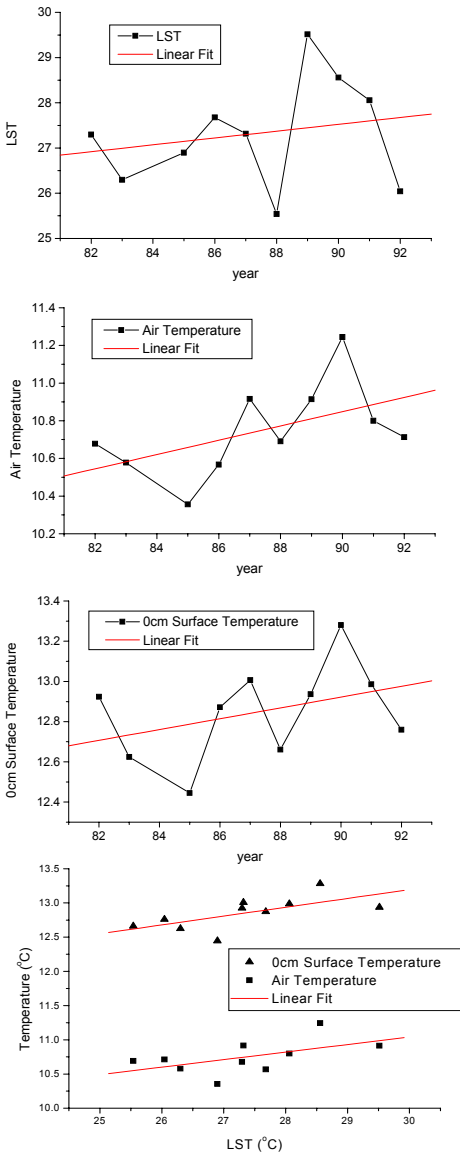


Figure 11 the trend and relation of annual temperature of LST (°C), air temperature (°C) and 0cm surface temperature (°C) of ten stations in China

baseline, four years' temperature increased (1986,1987,1989 and 1991), and three years' temperature decreased (1985,1988 and 1992). Further, from the beginning of 1980's to the beginning of 1990's, the increase value (°C) and the corresponding

area (%) of annual LST in China had good positive correlation, with a correlation coefficient of 0.9179 at a 0.01 level of significance. Namely, if the annual LST of China increases 3 °C, then the temperature of approximate 90% area in China increases. This paper also used Ulivieri algorithm to make validation, the result was approximately identical.

4 CONCLUSION AND DISCUSSION

Based on the analysis of the change of LST in China from the beginning of 1980's to the beginning of 1990's, it can be concluded that,

a) Spatial variation of cloudless LST in China was consistent with that of 0cm surface temperature.

b) From the beginning of 1980's to the beginning of 1990's, different regions had different property of temperature change. Some parts increased, and some parts decreased. Furthermore, the same region in different season probably had different property of temperature change. Generally temperature decrease was in temperate& warm temperate desert of Northwest China and North China, and temperature increase was in Tibetan Plateau and South China, where temperature increased 1-2°C.

c) The increase value (°C) and the corresponding area (%) of annual LST had good positive correlation.

d) Both LST and 0cm surface temperature tended to increase during the ten years.

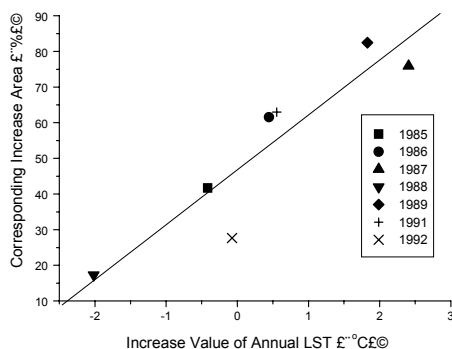


Figure 12 the scatterogram between the increase value (°C) and the corresponding area (%) of annual LST in China

e) When using cloudless LST and 0cm surface temperature in China to make comparative analysis, some errors surely existed, because the temporal resolution of LST is ten days and that of 0cm surface temperature is one day, which must induce error when

using the average yearly and monthly temperature. But the method, which uses the difference of different years and months' temperature to study change, must reduce the influence of some uncertain factors further.

f) This paper indicated that using thermal infrared bands of NOAA-AVHRR is feasible to study land temperature change. Furthermore, the temperature change in large scale is a key factor to study land use and vegetation change as well as global change.

5 Acknowledgments

The authors gratefully acknowledge the support of the China's Special Funds for Major State Basic Research Project (G 200077900), and the Knowledge Innovation Program of the Chinese Academy of Sciences (KZCX1-SW-01).

6 REFERENCES

- Becker, F., 1987, The Impact of Spectral Emissivity on the Measurement of Land Surface Temperature from a Satellite. *International Journal of Remote Sensing*, 8, 1509-1522.
- Becker, F., and Li, Z.L., 1990, Towards a Local Split Window Method over Land Surface. *International Journal of Remote Sensing*, 11, 369-393.
- Gupta, R.k., Prasad, S., Sesha sai, M.V.R., and Viswanadham, T.S., 1997, The Estimation of Surface Temperature over an Agricultural Area in the State of Haryana and Panjab, India, and its Relation with the Normalized Difference Vegetation Index (NDVI), using NOAA-AVHRR Data. *International Journal of Remote Sensing*, 18, 3729-3741.
- Holben, B.N., 1986, Characteristics of Maximum-Value Composite Images for Temporal AVHRR Data. *International Journal of Remote Sensing*, 7, 1435-1445.
- Josef Cihlar, Hung Ly, Zhanqing Li, Jing Chen, Hartley Pokrant, and Fengting Huang., 1997, Multitemporal, Multichannel AVHRR Data Sets for Land Biosphere Studies-Artifacts and Corrections. *Remote Sensing of Environment*, 60: 35-57.
- Kalluri, S. N. V., and Dubayah, R. O., 1995, Comparison of Atmospheric Correction Models for Thermal Bands of the Advanced Very High

- Resolution Radiometer. *Journal of Geophysical Research*, 100,25411-25418.
- McClain,E.P.,Pichel,W.G., and Walton, C.C., 1985,Comparative Performance of AVHRR based Multichannel Sea Surface Temperatures. *Journal of Geophysical Research*, 90(C6),11587-11601.
- Price, J. C., 1984, Land Surface Temperature Measurements from the Split Window Channels of the NOAA-7 AVHRR. *Journal of Geophysical Research*, 89, 7231-7237.
- Pu Jinguan,Dong Weidong,Guan Yanning,Qu Xiuxia, 1997,Study on the Ecological Environment of Douhe Reservoir. *Journal of Remote Sensing China*, 1(4),290-297.
- Qin yi,Tian Guoliang, 1994,A Research on the Method and Computer Program of Correction of Atmospheric Effects on NOAA-AVHRR Image.*Remote Sensing of Environment China*, 9(1),11-20.
- Salisbury,J.W.,and D'Aria,D.M. Emissivity of Terrestrial Material in the 3-5mm Atmospheric Window. *Remote Sensing of Environment*,1994, 47: 345-361.
- Singh,A.,1989,Digital Change Detection Techniques using Remotely-sensed Data. *International Journal of Remote Sensing*, 10, 989-1003.
- Stowe, L. L., Wellemeyer, C. G., Eck, T. F., Yeh, H. Y. M., and the Nimbus-7 Cloud data Processing Team, 1988, Nimbus-7 Global Cloud Climatology, Part 1, Algorithms and Validation. *Journal of Climate*, 1, 445-470.
- Saunders,R.W., and Kriebel,K.T.,1988,An Improved Method for Detecting Clear Sky and Cloudy Radiances from AVHRR Data. *International Journal of Remote Sensing*, 9, 123-150.
- Ulivieri, C. M. M., Castronuovo, R. F., and Cardillo, A., 1994, A Split-Window Algorithm for Estimation Land Surface Temperature from Satellites. *Advances in Space Research*, 14, 59-65.
- Van De Griend, A. A., and Owe, M., 1993,On the Relationship between Thermal Emissivity and the Normalized Difference Vegetation Index for Natural Surfaces. *International Journal of Remote Sensing*, 14, 1119-1121.
- Woodwell,G.M.,Hobie,J.E.,Houghton,R.A.,Melillo, J.M.,Peterson,B.T.,Shaver,G.R.,Stone,T.A.,Moore,B., and Park,A.B.,1983,Deforestation Measured by Landsat:Step towards a method. *Report No.DOE/EV/10468-1,Department of Energy, Washington,DC*.
- Zhao Songqiao, 1983,A New Scheme for Comprehensive Regionalization in China. *Acta Geographica Sinica*, 38,1-10.

Experimental setup for the multidirectional thermal emission of natural surfaces

Zhao-Liang Li^{1,2}, Renhua Zhang², Xiaomin Sun², Hongbo Su², Xinzhai Tang², Zhiling Zhu² and Jose A. Sobrino³

¹ TRIO/LSIIT, 5 Bld Sébastien Brant, 67400 Illkirch, France, email: li@sepia.u-strasbg.fr

² Institute of Geography Science and Natural Resource Research, Beijing 100101, China

³ Department of Thermodynamics, Faculty of Physics, University of Valencia, 46100Burjassot, Spain

ABSTRACT A new automatic experimental system was designed to improve the accuracy of the multidirectional thermal infrared measurements. This experimental system mainly consists of two identical thermal cameras operating in 8-13 μ m, one metal ring to keep the constant view area for different view angles and a goniometer, which is composed of 1) an half circle roadway of 2m diameters to change the observation angle in the azimuth direction, 2) an elevator of 1m high to adjust the measuring level to the target level. 3) a rotating arm installed one thermal camera for changing the observation angle in the zenith direction, and 4) a fixed arm equipped with another thermal camera at nadir to record the target temperature variation with time during the measurements. The system can be disassembled for easy transport and all of the data acquisition procedures are automatically monitored. For a given azimuth angle, the system needs about 2 minutes to make the directional measurements from about -70° to 70° and for completing one hemispheric measurement, it needs about 20 minutes if the multidirectional measurements are conducted by a step of 30° in the azimuth direction. The experiments show that the multidirectional data acquired by our new system are largely improved and present some regular directional distribution and can be used quantitatively to study the directional thermal emission of the natural surfaces.

1. INTRODUCTION

Anisotropy of Thermal InfraRed (TIR) radiance exists and is observed for many natural surfaces, particularly for three-dimensional (3D) vegetated areas (Fuchs et al., 1967; Kimes et al., 1980; Balick and Hutchinson, 1986; Balick et al., 1987; Paw U et al., 1989, Lagouarde et al., 1995). The magnitude and sign of this anisotropy depend, on one side, on macroscopic structural parameters and thermal heterogeneities, on the other side, on canopy geometric structure, density, and optical properties (Kimes and Kirchner, 1983; McGuire et al., 1989). It is also time dependent because of sun illumination effects and sensitivity to ambient conditions (Lagouarde et al., 1995). This anisotropy, on the one hand, brings a difficulty in obtaining a reliable surface temperature measurement, on the other hand, provides an opportunity to extract component temperatures of the surface elements (Kimes, 1981; Kimes, 1983; Ottermann, 1992; Menenti et al., 2001). Several experimental studies have been conducted to document this anisotropy over a wide range of surfaces and to validate different models developed to interpret observations of anisotropic thermal infrared radiance (Caselles et al., 1992; Norman et al., 1994). However, actual existing experimental systems designed to measure the anisotropic TIR radiance with TIR radiometer in field suffer from two major difficulties: 1) the projected area on the surface for a constant instantaneous field

of view of the radiometer changes with different view angles, for a thermally heterogeneous surface, this implies that different elements and different proportions of the elements are viewed in different view angles. 2) since multidirectional measurements in field often take several to thirty minutes, the heat balance on the surface, i.e. surface temperature, changes during the period of the measurement due to the variations of atmospheric turbulence and of local meteorological conditions. These two difficulties have hampered largely the understanding the mechanism of directional thermal radiation and quantitatively modeling of the directional TIR radiation. In this paper, a new experimental system will be designed to tackle the two difficulties mentioned above, consequently to improve the accuracy of the multidirectional TIR measurements. The second part of this paper is devoted to the detail presentation of our new experimental system. Some experimental results for bare soil and wheat are showed in the third part of this paper for illustration.

2. EXPERIMENTAL SYSTEM SETUP AND MEASURING PROCEDURES

2.1 Experimental Setup

As mentioned in Introduction, directional TIR measurement conducted by the actual existing experimental systems is greatly affected by changes of both surface temperature during the time of

measurement and the observed area on the surface with change of view angles for a constant radiometric field of view. In order to tackle these problems, a new automatic experimental system was designed as shown in figure 1. This system mainly consists of two identical thermal cameras operating in 8-13 μ m, one metal ring to keep the constant view area for different view angles and a goniometer. The goniometer is composed of

- 1) an half circle roadway of 2m diameters to change the observation angle in the azimuth direction,
- 2) a rotating arm installed one thermal camera for changing the observation angle in the zenith direction,
- 3) an elevator of 1m high to adjust the measuring level to the target level,
- 4) a small vehicle with two motors, one is used to drive the vehicle on the half circle roadway to change the observation angle in the azimuth direction, another is used to pivot the rotating arm

to change the observation angle in the zenith direction,

- 5) a fixed arm equipped with another thermal camera at nadir to record the target temperature variation with time during the measurements.

Moreover, a syntonc reducer is used to supply a moment of 400kgcm to rotate a 2m long arm and the 1.5kg thermal camera installed on it. Two identical thermal cameras are used to conduct the radiometric measurements simultaneously, one camera is mounted on a rotating arm (arm OA and AB in figure 1) to measure directional TIR temperatures at different zenith view angles, another camera is installed on a fixed arm at nadir to record the target temperature variation with time, and subsequently will be used to correct the temperature variation measured by the first one. A metal ring made of some low emissivity metal, such as aluminum and iron, which is easily recognized on the thermal image, is used to keep the constant view area for different view angle. The experimental system can be disassembled for easy transport and all of the data acquisition is automatically monitored.

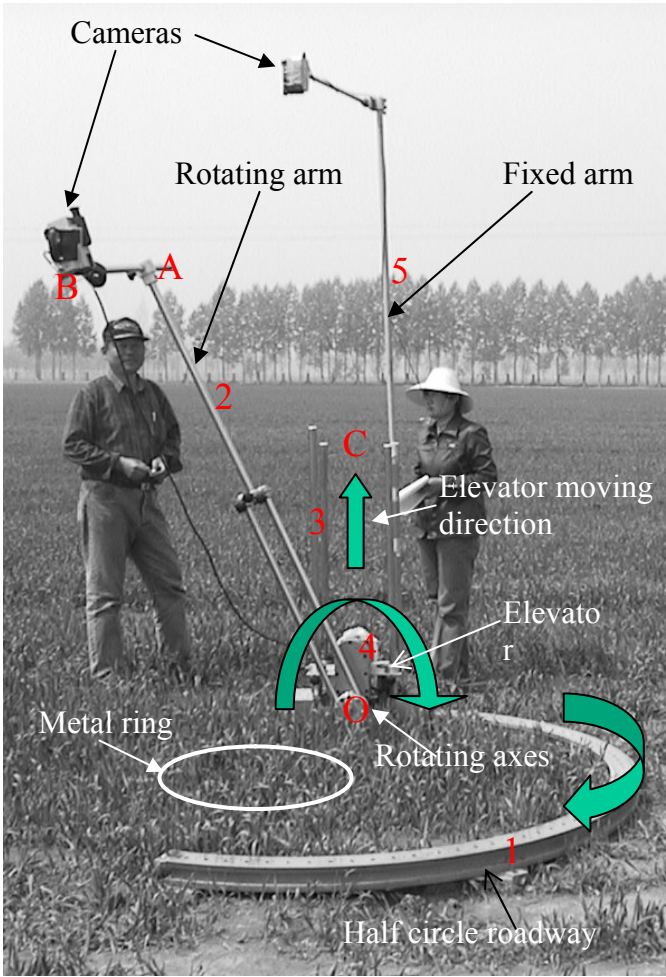


Figure 1 Photo of the new automatic field experimental setup for multidirectional thermal infrared radiance measurement

- 1: an half circle roadway of 2m diameters to change the azimuth view angle.
 - 2: a rotating arm (OA=2m and AB=1m) for changing the observation angle in the zenith direction.
 - 3: an elevator of 1m high (OC=1m) to adjust the measuring level to the target level.
 - 4: a small vehicle with two motors, one is used to drive the vehicle on the half circle roadway, another is used to drive the rotating arm.
- Observed target is the target inside the metal ring.

2.2 Measuring Procedures

The procedures to conduct the directional TIR measurements using the new automatic experimental system are described step by step in the following

1. Setting up the automatic experimental system as shown in figure 1 and then laying it in the opposite side of sun (see figure 2) to guarantee the shadow of the experimental system being out of the observed target, i.e. the shadow is beyond the metal ring in figure 1,
2. Adjusting the measuring level to the target level by moving the rotating axes O towards the direction C as indicated in figure 1,
3. Moving the vehicle on the half circle roadway to a given position, for example position C in figure 2, whose azimuth angle from north is ϕ , then the corresponding azimuth view angle φ should be $\varphi = \phi + 90$ (direction AB perpendicular to the line through the center of measured target to the position of the rotating axes C) as indicated in figure 2,

4. Conducting the directional measurements at different zenith view angles θ from about -70 to 70 degree by pivoting the rotating arm at position C. Small open squares laid on the line AB in figure 2 represent the positions of the directional measurements in the polar coordinate for an azimuth view angle $\varphi = \phi + 90$. Negative zenith view angle means the opposite azimuth ($\varphi = \phi + 270$),
5. Moving the vehicle to another position, for example C' in figure 2, in this case, the multi-directional measurements will be conducted in the direction A'B' as indicated in figure 2, and then repeating step 4 until it moves to the end of the half circle roadway, in this way, directional measurements over hemisphere are completed.

In general, it takes about 2 minutes to make the measurements from -70 to 70 degree in step of 5 degree and about 20 minutes to complete one hemispheric measurement in step of 30 degree in azimuth direction.

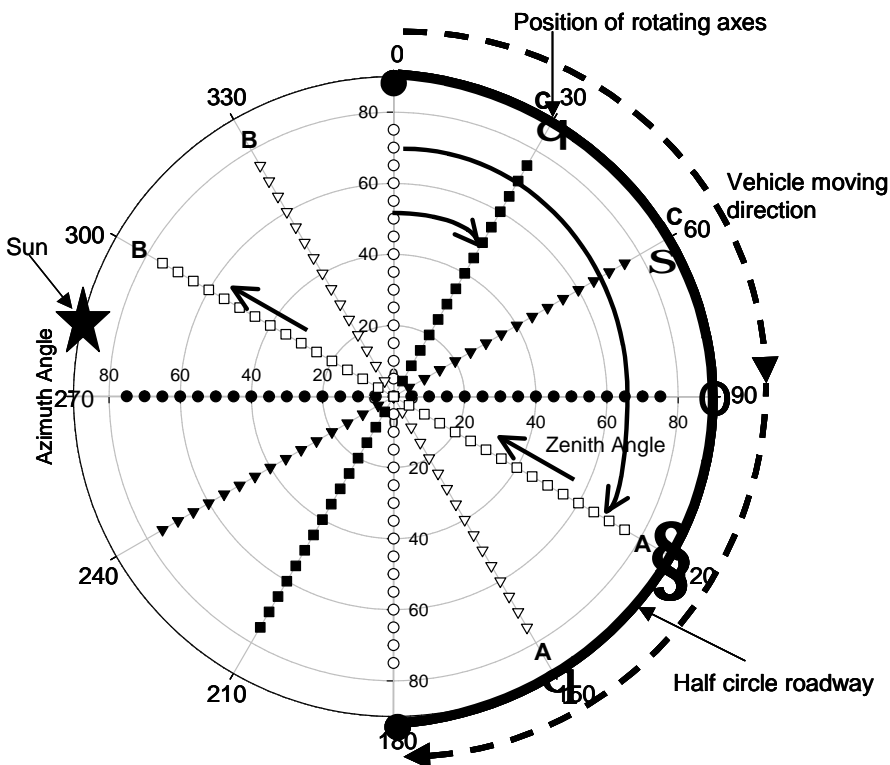


Figure 2. Illustration of the way to complete the hemispheric measurement with the new experimental system in polar coordinate. When the vehicle moves to the position C along the half circle roadway, the directional measurements at different view angles in the azimuth direction AB are conducted by pivoting the rotating arm at position C.

3. EXPERIMENTAL RESULTS

In order to test the data quality acquired by the proposed experimental system, a field campaign was conducted on April 15th 1999. In this experiment, surface brightness temperatures in different view angles and different azimuth angles were made for two types of surfaces, one type is bare soil with different surface roughness: a) smooth fine soil, b) rough soil and c) very rough soil, another is winter wheat with different Leaf Area Index (LAI): a) LAI=1.0, b) LAI=1.5, and c) LAI=3.0.

A portable non-frozen Agema thermal camera working within 8-13 μ m was mounted on the rotating arm as indicated in figure 1. This thermal camera has

resolution of 320 \times 240 pixels. Its sensitivity is 0.1 K and its absolute accuracy is better than 2 degrees. The response time of this camera varies between 1/50s and 1/60s. Instead of using another Agema thermal camera as required on a fixed arm, an infrared portable radiometer with wavelength ranging from 8-13 μ m was used to correct the variation of surface temperature with time during the multi-directional IRT measurements with Agema thermal camera. In order to keep the constant view area for different view angle, an aluminum ring of 1m diameter was used in this experiment. As seen in figure 3, this ring is easily recognizable on the thermal image, particularly on the images over bare soil.

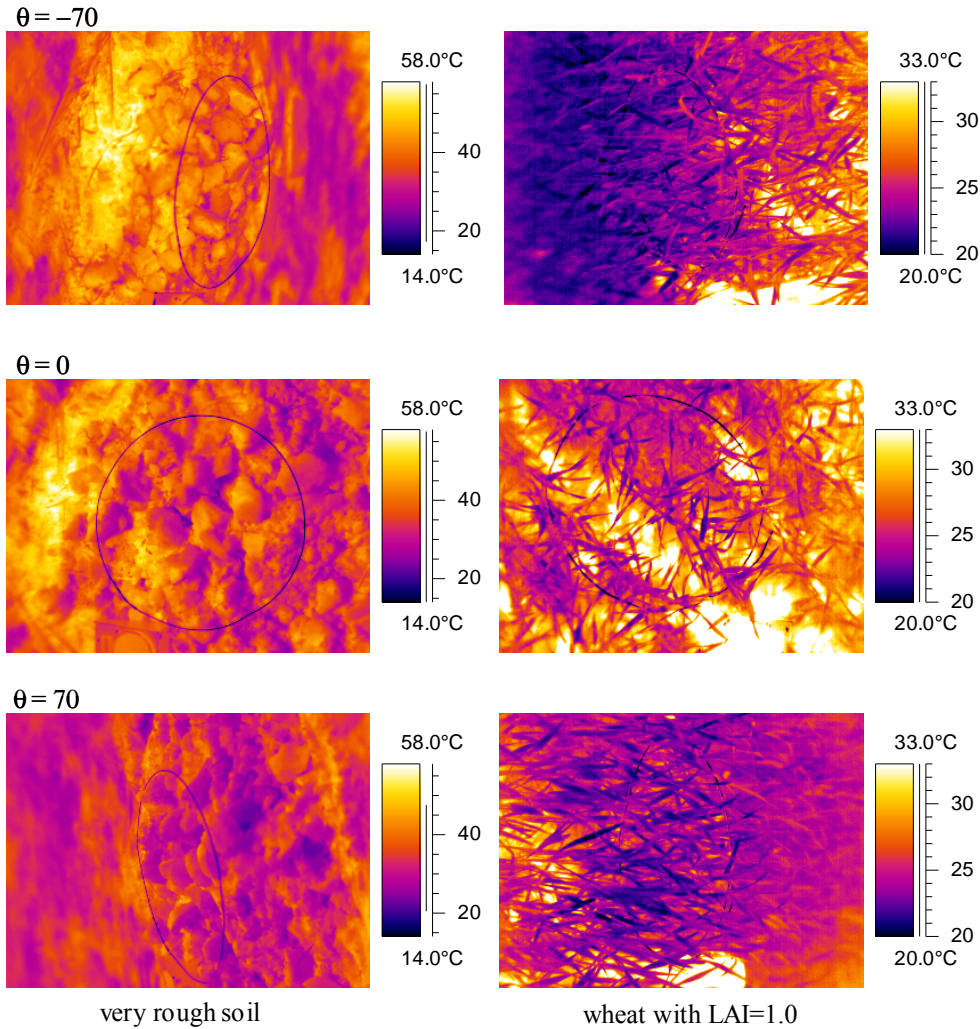


Figure 3. Illustration of thermal images for different view angles with different surface types. The metal ring is recognizable and varies with view angle on the image.

As an example, figure 4 shows the angular variation of surface brightness temperatures observed for bare soil with different surface roughness: a) smooth fine soil, b) rough soil and c) very rough soil. The angular measurements were made for different azimuth view angle. Table 1 gives the beginning and ending time associated with solar zenith angle for each type of surfaces.

Table 1. Measuring time and corresponding solar zenith angle for different types of surfaces.

Type of surfaces	Beginning time	Ending time	Solar zenith angle
Smooth fine bare soil	10h30	10h44	32
Rough bare soil	11h00	11h11	30
Very rough bare soil	11h20	11h35	29
Wheat with LAI=1.5	13h10	13h25	31
Wheat with LAI=3.0	13h45	14h00	35
Wheat with LAI=1.0	14h15	14h30	39

At the first glance, angular variation of surface brightness temperature is maximum for the principle plan, $\Phi = 0$ and 180 , where Φ is the azimuth angle difference between azimuth view angle ϕ and azimuth solar angle ϕ_s , i.e. $\Phi = \phi - \phi_s$, and this angular variation reaches its minimum for the perpendicular plan, $\Phi = 90$ and 270 . Moreover, for rough and very rough surfaces (figures 4b and 4c), angular variation of surface brightness temperature with respect to nadir view is always positive and directional surface brightness temperature increases almost monotonously with view angle when observer is on the same side of sun (negative view angle in figure 4), and contrarily when observer is on the opposite side of sun (positive view angle in figure 4). It looks like that there is no hot spot observed as in visible and near infrared bands. Figure 5 shows the angular variation of surface brightness temperatures observed for winter wheat with different LAI: a) LAI=1.0, b) LAI=1.5 and c) LAI=3.0. The measuring time and corresponding solar zenith angle are given in table 1. Since the component surface temperature for wheat is lower than that for background (soil) during the daytime and more wheat is viewed when view angle increases, the angular variation of surface brightness temperature with respect to nadir view should be negative as shown in figure 5.

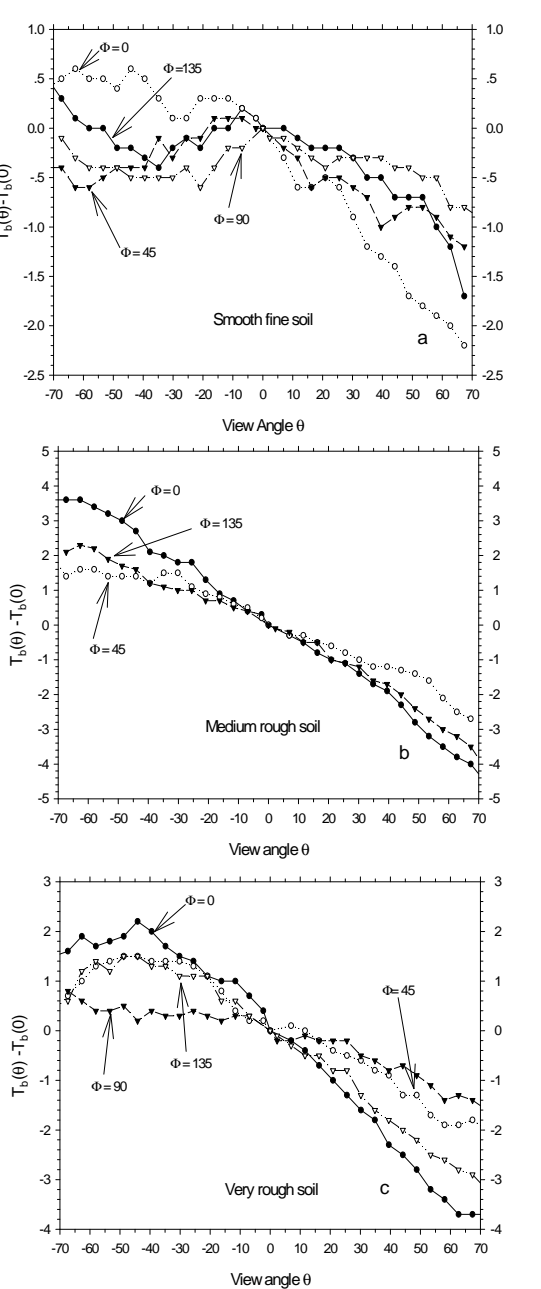


Figure 4. Angular variation of surface brightness temperatures observed for bare soil with different surface roughness: a) smooth fine soil, b) rough soil and c) very rough soil. Here Φ is the azimuth angle difference between azimuth view angle ϕ and azimuth solar angle ϕ_s , i.e. $\Phi = \phi - \phi_s$. Negative view angle in the figure means the observer (thermal camera) being on the same side of sun.

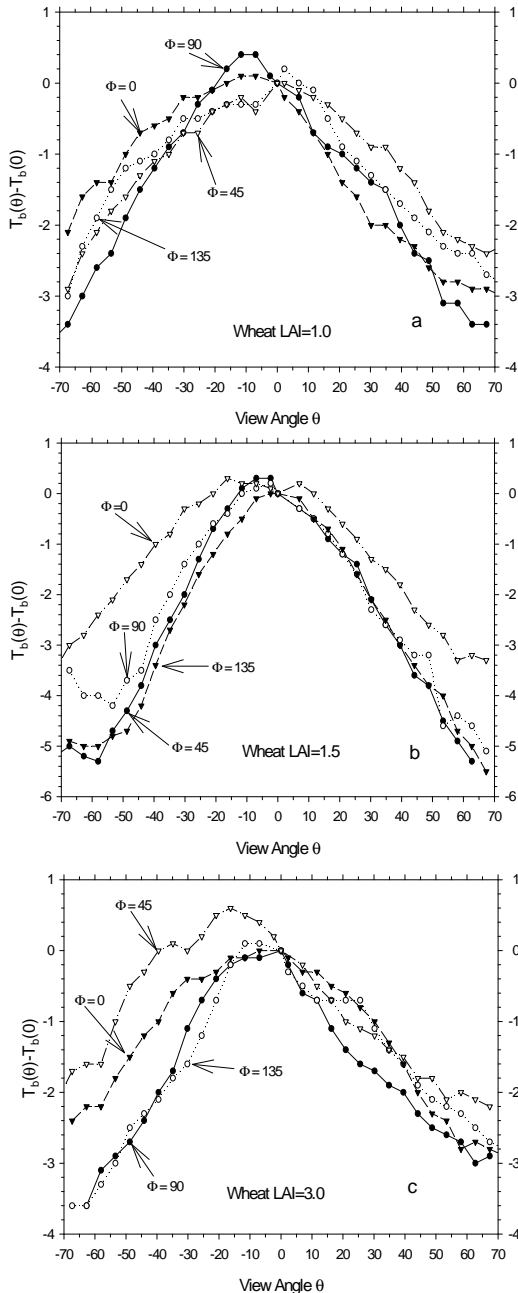


Figure 5. Same as figure 4, but for winter wheat with different LAI: a) LAI=1.0, b) LAI=1.5 and c) LAI=3.0

We notice from this figure that the directional surface brightness temperature decreases with view angle regardless of the relative position of the observer to the sun and the behaviours of the angular variation are

different depending on thermal heterogeneities, canopy geometric structure and so on.

More detail studies of directional thermal emission for natural surfaces are planned in the near future using the proposed experimental system.

4. CONCLUSION

A new automatic experimental system has been designed to study and document the anisotropy of TIR radiance of natural surfaces. The experimental system uses two identical thermal cameras to conduct the radiometric measurements simultaneously, one camera is used to measure directional TIR temperatures at different zenith view angles, another camera is employed to record at nadir the target temperature variation with time to correct the temperature variation measured by the first one. A metal ring made of aluminum is adopted to keep the constant view area for different view angle. The preliminary data acquired using the proposed system on bare soil and winter wheat are displayed and analyzed. The results show that the angular variation of surface brightness temperature is measurable and the magnitude and behaviours of this angular variation are different for different types of surfaces. It looks like that there is no obvious hot spot observed as in visible and near infrared bands. More detail studies of directional thermal emission for natural surfaces are planned in the near future using the proposed experimental system.

REFERENCES

- Balick, L.K., and Hutchison, B.A., 1986, Directional thermal infrared exitance distributions from a leafless deciduous forest. *IEEE Transactions on Geoscience Remote Sensing*, 24(5):693-698.
- Balick, L.K., Hutchison, B.A., Smith, J.A., and McGuire, M.J., 1987, Directional thermal exitance distributions of a deciduous forest in summer. *IEEE Transactions on Geoscience Remote Sensing*, 25(3):410-412.
- Fuchs, M., Kanemasu, E.T., Kerr, J.P., and Tanner, C.B., 1967, Effect of viewing angle on canopy temperature measurements with infrared thermometers. *Agronomy Journal*, 59: 494-496.
- Kimes, D.S., Idso, S.B., Pinter, P.J., Reginao, R.J., and Jackson, R.D., 1980, View angle effects in the radiometric measurement of plant canopy temperature. *Remote Sensing of Environment*, 10: 273-284.
- Kimes, D. S., 1981, Remote sensing of temperature profiles in vegetation canopies using multiple view angles and inversion techniques. *IEEE transactions on Geoscience and Remote Sensing*, 19(2):

- Kimes, D.S., 1983, Remote sensing of row crop structure and component temperatures using directional radiometric temperatures and inversion techniques. *Remote Sensing of Environment*, 13: 33-55
- Kimes, D.S., and Kirchner, A., 1983, Directional radiometric measurements of row-crop temperatures. *International Journal of Remote Sensing*, 4(2):299-311.
- Lagouarde, J.P., Kerr, Y., and Brunet, Y., 1995, An experimental study of angular effects on surface temperature for various plant canopies and bare soils, *Agricultural and Forest Meteorology*, 77: 167-190.
- Menenti, M., Jia, L., Li, Z.-L., Djepa, V., Wang, J., Stoll, M.P., Su, Z., and Rast, M., 2001, Estimation of soil and vegetation temperatures from directional thermal infrared observations: The HEIHE, SGP'97, IMGRASS experiments, *Journal of Geophysical Research*, 106(D11): 11997-12010.
- Ottermann, J., Brakke, T.W., and Susskind, J., 1992, A model for inferring canopy and underlying soil temperatures from multi-directional measurements. *Boundary-Layer Meteorol.* 61:81-97.
- Paw U, K.T., Ustin, S.L., and Zhang, C., 1989, Anisotropy of thermal infrared exitance in sunflower canopies. *Agricultural and Forest Meteorology*, 48: 45-58
- Caselles, V., Sobrino, J.A., and Coll, C., 1992, A physical model for interpreting the land surface temperature obtained by remote sensors over incomplete canopies. *Remote Sensing of Environment*, 39:203-211
- Norman, J.M., Castello, S., and Balick, L.K., 1994, Directional infrared temperature and emissivity of vegetation: measurements and models. *Proceedings of the 6th Symposium on Physical Measurements and Signatures in Remote Sensing* 17-21 Jan., Val d'Isère, France. CNES ED., pp 749-758.

Sensitivity of TIR remote sensing to soil water content and LAI in the soil-vegetation-atmosphere system

L. Jia¹, M. Menenti² and Z.-L. Li²

1. Alterra Green World Research, WUR, Droevendaalsesteeg 3, 6700 AA Wageningen, The Netherlands; 2. LSIT/TRIO, Université Louis Pasteur, France

L.Jia@Alterra.wag-ur.nl

ABSTRACT - The exploration of the full potential of multi - angular thermal infrared measurements is hampered by the scarcity of accurate and representative data sets. Acquisition of actual data has several constraints, including lack of a suitable airborne sensor system. Development and evaluation of algorithms requires detailed and accurate radiometric data, which have to be collected in a very short time to limit noise due to the temporal variability of surface temperature controlled by the local heat balance within the canopy. Several canopy properties have to be determined, e.g. Leaf Area Index (LAI), Leaf Inclination Distribution, in addition to soil and foliage temperature. A data set for validation studies should comprise a range of canopies and canopy conditions.

We have coped with these difficulties by using a detailed comprehensive model (CUPID) of the soil - plant - atmosphere system to produce synthetic data sets over a wide range of canopies and hydro - meteorological conditions. These data have been used to assess the sensitivity of the anisotropy in TIR radiance to LAI and to the soil water content. It was shown that dry topsoil and a wet root zone imply that the brightness temperature is highest at nadir viewing, opposite to the condition with a wet top soil and a drier root zone. The relative magnitude of the directional change in surface temperature compared with the difference between soil and foliage temperature was evaluated in detail over a range of LAI - values.

1 INTRODUCTION

Recent years have seen a renewed interest for the directional signature of soil - vegetation mixtures in the thermal infrared region (Kimes, 1983; Francois, 1992; Li et al., 2000; Menenti et al, 2001). This feature is particularly important because it provides a unique opportunity to distinguish between the temperatures of the background soil and of the overlying plant canopy. Such component temperatures are very useful to improve parameterization of heat exchange between landsurface and atmosphere (Kustas and Norman, 1997, 1999; Jia et al, 2001) and NWP model performance (Van den Hurk, 2002).

The change in brightness temperature of soil - vegetation mixtures is relatively small. Accurate measurements of surface brightness temperature are needed, therefore, to observe changes with view angle. Moreover, accurate TIR measurements of soil and foliage are required to validate the inversion model for retrieving component temperatures. Precise TIR measurements has never been an easy task due to the rapid temporal variability of surface temperature. This is because the surface brightness temperatures, as well as the ones of soil and foliage, depend on many processes and conditions of canopies and the interaction of canopy with the atmosphere. Exchanges of energy within the soil-vegetation system are

intimately linked. Canopy structure and soil moisture are the two major factors which affect significantly the component temperatures of soil - vegetation mixture. The canopy structure determines the behavior of radiative transfer and of heat exchange within the canopy. The soil water content determines the partitioning of absorbed energy by the canopy, hereafter controls the soil and foliage temperature in soil-canopy system.

One of the solutions to cope with such impediment is to use a process model to perform numerical experiments. In this study, a detailed comprehensive model (CUPID) of the soil - plant - atmosphere system proposed by Norman (1982) was used to produce synthetic data sets over a wide range of canopies and hydro-meteorological conditions. As a further step, these data sets were used to evaluate the sensitivity of anisotropy in TIR radiance to Leaf Area Index (LAI), to Leaf Inclination Distribution Function (LIDF), and to soil water content.

2 METHODOLOGY

2.1 Model description

The comprehensive soil - plant - atmosphere model CUPID proposed by Norman (1982) can predict plant - environment processes such as water budgets of crops, canopy light-use efficiency, water-use

efficiency, radiative energy distribution in the canopy and canopy energy budgets, etc.. Canopy environment processes are affected by canopy properties such as physiological characteristics (photosynthesis, stomatal conductance and respiration), canopy architecture (height, LIDF, LAI, etc.), soil characteristics (heat and water properties). Boundary conditions at the bottom and at the top of the soil – vegetation system have also considerable influences. In the CUPID model, the soil-plant-atmosphere vertical continuum is divided into layers which can be classified into four types: (1) the layers above the canopy; (2) the canopy layers; (3) the above ground layers; and (4) the layers below the soil surface. All the balance equations are solved simultaneously for all the layers. Fig.1 gives the outline of CUPID model.

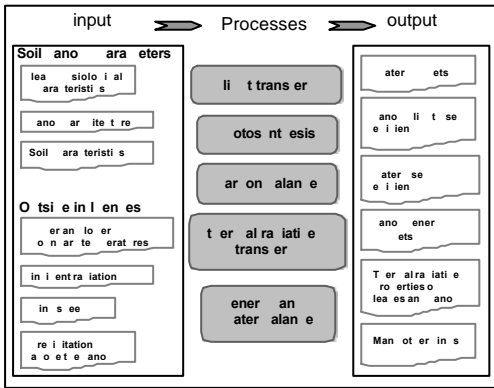


Fig. 1 Basic processes dealt by CUPID model and the necessary input and major output from it.

The angular distributions of emittance can be simulated by CUPID on the basis of radiative transfer and energy balance above and within the canopy.

In this paper, we recall briefly the theory of CUPID most relevant to our study. For a full description, the reader is referred to Norman (1979), Norman (1982) and Norman and Campbell (1983).

2.1.1 Radiative transfer within the canopy

Vertically heterogeneous canopies are described by partitioning the canopy in layers of varying thickness, with equal leaf area in each layer. Leaves are therefore described as randomly distributed in each layer.

The radiance incidents into a canopy will be attenuated due to the absorption and scattering of the leaves inside the canopy. For a canopy of N layers with the equal leaf area index increments ΔL , the probability of a beam of radiation passing through the canopy in the direction (θ, ϕ) to the leaf in the canopy layer j without being intercepted is

$$P_B(\theta, \phi) = \exp[-\alpha(N-j)\Delta L/\cos\theta] \quad (1)$$

where α is the extinction coefficient and depends on LIDF.

Diffuse radiation penetrating through a single layer of thickness ΔL is expressed approximately as

$$P_D = 2 \sum_i \{ \exp(-\alpha \cdot \Delta L / \cos\theta_i) \sin\theta_i \cos\theta_i \Delta\theta_i \} \quad (2)$$

where i represent an index over all possible incident zenith angle θ from which diffuse radiation originates. The penetration of emitted radiation has the same form as Eq.(2).

2.1.2 Water and heat exchange in the soil - vegetation system

The heat and water vapor balance of the air in the canopy space is expressed by:

$$\rho c_p \frac{\partial T}{\partial t} = \frac{\partial}{\partial z} \left(K(z) \frac{\partial T}{\partial z} \right) + Q_H \quad (3)$$

$$\frac{\rho e}{p} \frac{\partial e}{\partial t} = \frac{\partial}{\partial z} \left(\frac{\epsilon K(z)}{c_p p} \frac{\partial e}{\partial z} \right) + Q_E \quad (4)$$

where T and e are temperature and water vapor pressure of air respectively, $K(z)$ is the eddy thermal conductivity ($\text{J m}^{-1} \text{s}^{-1} \text{°C}^{-1}$), and $\epsilon K(z)/(c_p p)$ is the eddy conductivity for water vapor ($\text{kg m}^{-1} \text{s}^{-1} \text{Pa}^{-1}$), Q_H (W m^{-2}) and Q_E ($\text{kg m}^{-3} \text{s}^{-1}$) is the source or sink of heat respectively water vapor.

The heat and water balance in soil is described by similar equations, obtained by replacing all the state variables and the properties with analogous properties of the soil volume in the root zone.

In the soil, the hydraulic conductivity $K_w(z)$ is a function of soil type and water content. The soil heat capacity is mainly a function of water content. The heat sources in the soil are zero except at the soil surface where the heat source is the residual between net radiation just above the soil surface and the soil surface latent heat flux due to evaporation. Root water uptake is estimated for each soil layer from the product of root resistance in that layer (Norman and Campbell 1983).

In the canopy, the source or sink distributions of heat and water vapor are derived from the leaf (denoted by l) energy balance equations layer j and leaf angle k :

$$R_{n,l}(j,k) = H_l(j,k) + \lambda E_l(j,k) + 2\epsilon_l \sigma [T_l(j,k)]^4 \quad (5)$$

where $R_{n,l}(j,k)$ is net radiation absorbed by leaves, $H_l(j,k)$ and $\lambda E_l(j,k)$ are the sensible and latent heat flux, respectively, ε_l is the leaf emissivity, σ is Stefan-Boltzman constant ($5.668 \times 10^{-8} \text{ W m}^{-2} \text{ K}^{-4}$), $T_l(j,k)$ is the surface temperature of leaf (K).

To solve leaf energy and water balance equations for each leaf angle class in each canopy layer, the profiles of wind-speed, air temperature and air vapor pressure through the canopy are necessary. These air temperature and humidity profiles, in turn, depend on the wind speed in and above the canopy, the heat and water source-sink distribution defined by the leaf energy balance, and the soil as a source or sink of heat or moisture. Finally, all the balance equations for a) canopy air space, b) vegetation mass and c) root zone must be solved simultaneously.

2.1.3 The angular signature of the canopy

Above the canopy, the TIR radiance captured by the radiometer is angular dependent. The contributions of various leaf layers and soil are appropriately weighted by the proportion of each component occupied in the FOV in the particular view direction.

For a canopy of randomly distributed leaves, conditions met in each layer as defined above, the fraction of leaf and soil in the FOV can be computed from the leaf angle distribution, leaf area index and view zenith angle and declines exponentially with depth in the canopy. For j of the N ($=\text{TotalLAI} / \Delta L$) layers, the fraction of leaf area in the view direction (\hat{e}_v, \hat{o}_v) is written as

$$f(j, \theta_v, \phi_v) = [1 - \exp(-\alpha \cdot \Delta L \cdot \cos \theta_v)] \exp[-\alpha(j-1) \cdot \Delta L \cos \theta_v] \quad (6)$$

Then, the fraction of leaf area for the entire canopy in the direction (θ_v, ϕ_v) is the sum of the fractions of leaf area in each layer, and the total fractional vegetation cover is

$$f_c = 1 - \exp\left(-\frac{\alpha \cdot \text{LAI}}{\cos \theta_v}\right) \quad (7)$$

The fraction of soil is the complement of f_c , i.e. $f_s = 1 - f_c$.

3 DATA AND SENSITIVITY STUDY SET-UP

The data needed in the input to CUPID were collected during DAISEX'99 in Barrax site in Spain (see Moreno et al, 2001 for detailed description of the experiment and data). The landcover in Barrax is various crops with bare soil dispersed in between crops patterns. Two crops were taken in this study that

were maize and alfalfa with the mean leaf inclination angle 68.7° and 45° , and LAI were 2.0 and 2.2, respectively. In this paper, we refer to these two crops as erectophile respectively uniform leaf inclination distribution types. In the visible and near-infrared region, leaf spectral reflectance and transmittance of these two crops and soil reflectance were measured during DAISEX'99. The meteorological variables (wind speed, air temperature, humidity, solar radiation) were observed at 10 meters height.

The aim of the sensitivity study is to investigate how the canopy structure and soil water content affect the anisotropy of emittance for a heterogeneous vegetation canopy. As shown in Eqs.(1) and (2), both canopy structure (in term of LIDF) and LAI affect the radiation transfer within the canopy. At the same LAI, the fractional vegetation cover may not be identical due to different LIDF, which results in that the radiation arrived at a given canopy layer and the soil surface varies with LIDF. Soil water content plays an important role in determining the partitioning of available energy for the canopy. In general, soil moisture near surface layer controls the soil temperature, while the foliage temperature is mainly affected by water content at the deeper layer, e.g. at root zone, from where the foliage abstracts water to compensate transpiration.

Based on these considerations, the situations considered in this study are defined by all the possible combinations of LAI, LIDF and soil water content:

1. LAI ranges from 0.5 to 4.5 with interval of 1;
2. Two types of leaf inclination distribution have been considered, which are erectophile and uniform.
3. Two soil water conditions (Fig. 2):
 - upper soil layer is drier than root zone (named 'dry-surface');
 - upper soil layer is wetter than root zone (named 'wet-surface').

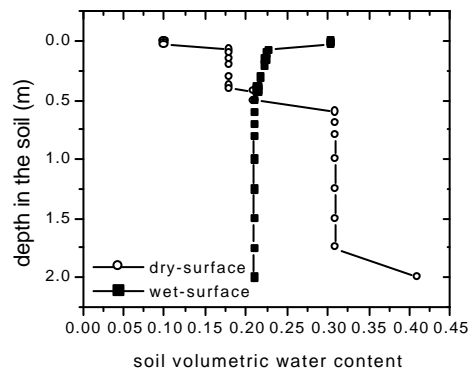


Fig. 2 Soil water content profiles used in the sensitivity study.

4 RESULTS

4.1 Influence of LAI and canopy structure on the anisotropy of thermal emittance

The values of LAI represent the canopy density and surface cover conditions in some degrees. When the surface is moderately drier than the root zone, the directional TIR signature is significant under low LAI (Fig. 3). The directional TIR signature decreases when LAI increases. At very high LAI, the directional signature is weak and difficult to interpret. In some cases, the radiometric surface temperature at off-nadir view is even higher than the one at nadir view. This is because that radiometer captures more upper foliage at larger zenith view angle than at nadir viewing. When LAI is higher the leaves in deeper canopy layers and the soil under the foliage may be cooler than leaves in the upper canopy layer due to the shelter.

It is obvious to see that canopy structure has an important influence on the directional signature of radiometric surface temperature. The maximum difference (up to about 4 °C in this study) of surface temperature between nadir and off-nadir appears with erectophile leaf inclination distributions comparing to uniform ones at given LAI value. With uniform LIDF, directional TIR signature reduces rapidly with LAI increasing, it can only be observed when LAI is smaller than 1.5. The LAI value, at which angular change becomes not significant, strongly depends on the canopy structure in terms of LIDF as well.

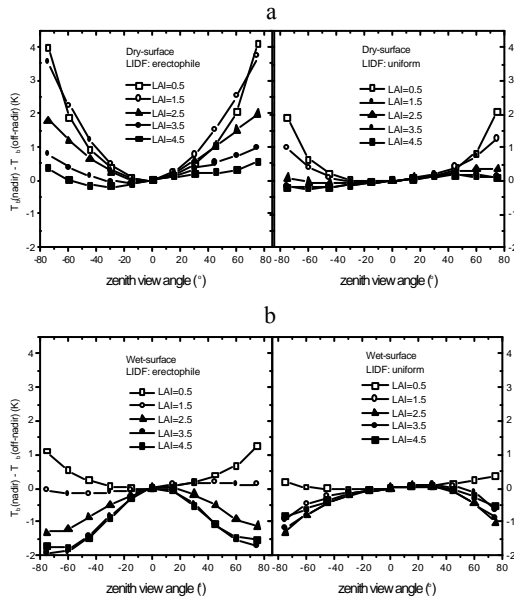


Fig.3. Variability of angular signatures due to the changes of LAI and soil water content at erectophile and uniform leaf inclination distribution conditions.

4.2 Influence of soil water content on the anisotropy of thermal emittance

Soil moisture profile shows important influence on the patterns of directional TIR signature when comparing Fig.3a (surface is drier than root zone) and Fig.3b (surface is wetter than root zone). Under the 'dry-surface' condition, surface temperature observed at nadir is larger than off-nadir ones in most of LAI conditions both for erectophile and uniform LIDF. Contrariwise, under 'wet - surface' condition, nadir vs. off-nadir surface temperature differences are generally negligible and even negative for several combinations of LAI and LIDF.

The soil water content exerts a most important role in determining the shape and the magnitude of TIR angular signature as shown in Fig.3. It is interesting to explore the details corresponding to those curves in Fig.3 where surface brightness temperature at nadir is lower than at off-nadir angles.

4.3 Component temperatures

Evaluation of simulated component temperatures under the same conditions considered above leads to similar conclusions (Fig.4).

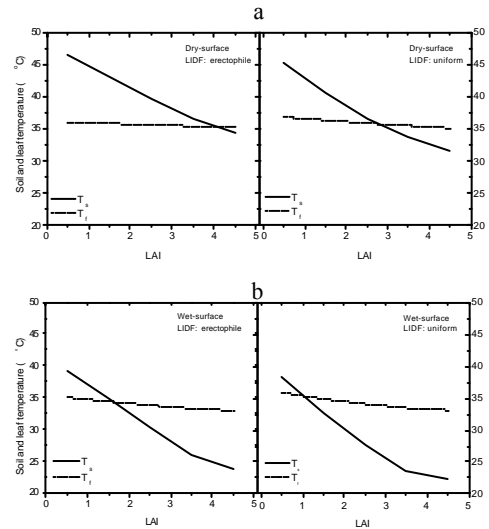


Fig. 4 Component temperatures under various LAI and soil water content conditions.

At lower LAI fractional vegetation cover is also small, the soil in the soil-vegetation system can receive higher solar radiation than in the case of a complete vegetation canopy at larger LAI values. When the surface is dry, most radiation absorbed by soil is used to heat the soil surface. If deeper soil layers are wetter, leaves withdraw efficiently water from the root zone for transpiration and the leaves are

cooler than the soil surface (Fig.4a). This will enlarge the difference of radiometric surface temperatures at nadir and off-nadir as shown in Fig 3. The LIDF of canopy exerts additional effects on the angular pattern and the relation between T_s and T_f may change sign when LAI arrives at some relatively low value.

In the 'wet-surface' case (irrigation case for instance), it is quite interesting to see that soil is rather cooler than soil in the 'dry-surface' case, even lower than foliage temperature even though LAI is rather low (Fig.4b). This is because most radiation absorbed by soil is used for evaporation rather than to heat the soil surface. Leaves are warmer due to the consequences of absorbing radiation and abstracting less water for transpiration from the root zone.

The impacts of LIDF on the component temperatures are illustrated in Fig. 5 explicitly. The root mean square difference (RMSD) for soil temperature between the two LIDF is 2.3 K, while RMSD is 0.5 K for foliage temperature. This implies that LIDF has less impact on mean foliage temperature, while it is more important for soil temperature in any soil water content conditions.

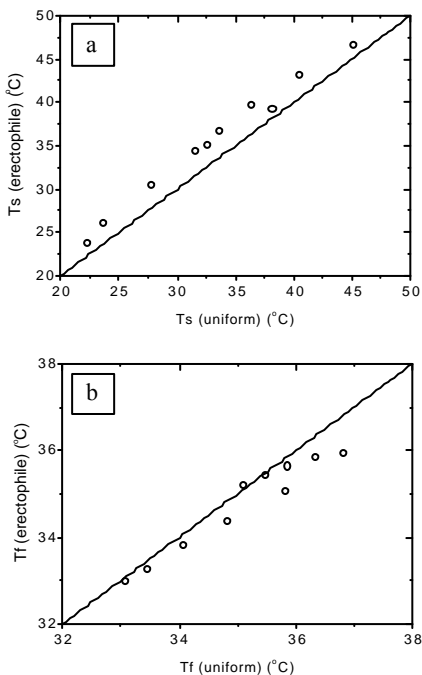


Fig. 5 Comparisons of (a) T_s ; (b) T_f under different LIDF under the considered soil water content conditions.

5 CONCLUSIONS

The canopy structure affects obviously the angular signature. Under the same LAI and the soil water content conditions, erectophile type of canopy shows larger angular signature than the uniform canopy. At moderate soil water content in the root zone, surface moisture plays a more important role. The drier the soil surface, the larger the angular signature in thermal infrared radiation from the soil-vegetation canopy. The maximum angular signature occurs under conditions of drier surface and sufficient water supply in root zone when LAI is low.

One should pay attention on the influences both by canopy structure and by soil water content profile when applying directional TIR signature to the relevant issues, such as inferring component temperatures. Particularly, when using Eq. (7) type of formulation to estimate fractional vegetation cover from LAI, the different attenuation coefficient should be used corresponding to the associated LIDF. It may not be practical in applying such formula to large scale, because with current capability of satellite observations the information of canopy LIDF are not available indeed. Moreover, LIDF is well defined for homogeneous targets, while it is not for a heterogeneous footprint, which is very often the case when observing the land surface.

The relationship between the directional TIR signature (in the other word the component temperatures) and soil water content may provide useful information for study of soil moisture in deeper depth in the soil and of water use by the soil-vegetation system. We note that the neither the "dry - surface" or the "wet - surface" case make the estimation of component temperatures of soil and foliage unfeasible, if a linear mixture model describes correctly the observed radiance (Menenti et al., 2001).

References

- Francois, C., Ottle, C., Prévot, L., 1997, Analytical parameterization of canopy directional emissivity and directional radiation in the thermal infrared. Application on the retrieval of soil and foliage temperature using two directional measurements, *Int. J. Remote Sensing*, 18(2): 2587-2621.
- Jia, L., Menenti, M., Su, Z., Djepa, V., Li, Z.-L. and Wang, J., 2001, Modeling of sensible heat flux using estimates of soil and vegetation temperatures: the HEIFE and IMGRASS experiments, In "Remote sensing and climate modeling: Synergies and Limitations" in "Advances in Global Change Research", edited by Beniston, M. and Verstraete, M., (Kluwer academic publishers, Dordrecht, The Netherlands), pp23-49.

- Kimes, D. S., 1983, Remote sensing of row crop structure and component temperatures using directional radiometric temperatures and inversion techniques, *Remote Sens. Environ.*, 3: 33-55.
- Kustas, W. P., and Norman, J. M., 1997, A two-source approach for estimating turbulent fluxes using multiple angle thermal infrared observations, *Water Resource Research*, 33, 1495-1508.
- Kustas, W. P., and Norman, J. M., 1999, Evaluation of soil and vegetation heat flux predictions using a simple two-source model with radiometric temperatures for partial canopy cover, *Agric. For Meteorol.*, 94, 13-29.
- Li, Z.-L., M. P. Stoll, R. H. Zhang, L. Jia and Z. Su, 2000, On the separate retrieval of soil and vegetation temperatures from ATSR2 data, *Science in China E*, 30: 27-38.
- Menenti, M., Jia, L., Li, Z.-L., Djepa, V., Wang, J., Stoll, M.P., Su, Z., and Rast, M., Estimation of soil and vegetation temperatures with directional thermal infrared observations: the IMGRASS, HEIFE and SGP'97 experiments, *J. Geophys. Res.*, 106 (D11), 11,997-12,010, 2001.
- Moreno, 2001, The measurement program at Barrax, Proceedings of the DAISEX Final Workshop, ESTEC-ESA, 15-16 March 2001, ESA SAP-499, pp.43-51.
- Norman, J. M., 1979, Modeling the complete crop canopy, In: Modification of the aerial environment of crops, edited by Harfield B. J and Gerbert J. F., ASAE, St. Joseph, MI, 538pp.
- Norman, J. M., 1982, Simulation of microclimates. In Biometeorology in integrated pest management, edited by J. L. Hatfield and I.J. Thomason (Academic Press, New York), pp. 65-99.
- Norman, J. M., and Campbell, G., 1983, Application of a plant-environment model to problems in irrigation, In: Advanced in irrigation, 2, edited by D. Hillel, (Academic Press, New York), pp.155-188.
- Van den Hurk, B.J.J.M., Jia, L., Jacobs, C., Menenti, M., Li, Z.-L., 2002, Assimilation of land surface temperature data from ATSR in an NWP environment - a case study, *Int. J. Remote Sensing*, in press.

Retrieval of optical properties of materials in the 3.5-14 μm infrared atmospheric window using a multi-temporal regression method

Françoise Nerry^a, Marc-Philippe Stoll^a and Alain Malaplate^b

^aLSIIT/TRIO, UMR 7005, bd Sébastien Brant, F-67400 Illkirch

^bFGAN-FOM, Gutleuthausstr.1, 76275 Ettlingen, Germany

Francoise.Nerry@mail-grtr.u-strasbg.fr

ABSTRACT- This work deals with combined use of bands II (MIR) & III (TIR), where band III is used for surface temperature determination, and focuses on the retrieval of MIR target's emissivity using a multi-temporal regression method.

Two cameras (band II & band III) were used in outdoor conditions, to image an artificial scene composed of various materials. Acquisitions were made at different times of day to vary the solar contribution and the surface temperature, while a screen was used to cast shadow on targets.

The first part deals with radiometric issues related to instrument filter, non black-body targets, and accurate handling of the measured band integrated radiances. Usual band integrated quantities, such as the band integrated emissivity, that are appropriate for narrow band sensors, have to be carefully redefined. In this work, different formulations, that correspond to different levels of approximation.

The second part addresses the extraction of the band II target's emissivity from actual time series of band II & III radiances. First, bi-directional reflectivity signatures of materials are obtained by means of band II sun/shadowed radiances leading to form factor determination. Then band II emissivity is obtained through multi-temporal regression using shadowed and /or sun lit band II radiances, with band III measurements as complementary information allowing for surface temperature determination. Comparisons are made with emissivities from lab measurements.

1 INTRODUCTION

There is a growing interest in infrared imaging sensors working in the MIR atmospheric window [3-5 μm], alone or in association with the TIR [8-14 μm] window (in the following, band II stands for MIR, band III for TIR). Band III is traditionally the most used especially when dealing with surface temperature. The less frequent use of band II in remote sensing comes from the complexity of the signal in this band which combines ground emitted and reflected solar radiation. Nevertheless, even if it is not easy dissociating these two contributions, band II contains an additional information that plays a key role in determining surface properties. Thus, this work aims at exploring ways to exploiting band II signal and extracting surface parameters. Methods to deal with remotely sensed TIR radiance address emissivity and surface temperature retrieval, either separately or simultaneously, most often based on band III multi-channel data. Most airborne and satellite-borne infrared sensors operate in the TIR [8-14 μm] atmospheric window for imaging of terrestrial surfaces

and surface temperature retrieval. However, the growing interest in the use of the MIR [3-5 μm] infrared window have to do with the additional information on surface optical characteristics brought along by band II where in this band a non negligible reflected solar radiation is in addition to ground emitted radiation. Thus, band II has much interest for detecting target against terrestrial background, an application that would require high spatial resolution. Another application based on combined use of bands II and III, recently developed, is high temperature events detection and analysis (H. Jahn & al, 1996). An issue of concern is the lack of knowledge of the surface properties (emissivity and reflectivity) of natural backgrounds as well as embedded targets. This work deals with the combined use of bands II and III image data and focuses on fieldwork for the retrieval of surface characteristics.

Two cameras (band II & band III) were used in outdoor conditions to image an artificial scene composed of various natural and man made materials. Acquisitions were made at different times of the day to vary the solar reflected contribution and the surface

temperature, while a screen was used to cast shadow on targets whenever necessary. Part 2 addresses radiometric issues, encountered with wide band sensors, related to instrument filter, non-blackbody targets, and accurate handling of the measured band-integrated radiances for inversion purposes. Part 3 presents the experimental data which will be used. The results of the inversion applied on the data are given in part 4 with a focus on the multi-temporal inversion method.

2 RADIOMETRIC ISSUES

At the sensor's window, the spectral radiance at wavelength λ (unit: $\text{Wm}^{-2}\text{sr}^{-1}\mu\text{m}^{-1}$), in view direction with zenith angle θ_v , is given by

$$L_i^{\text{sensor}}(\mathbf{q}_v) = [\mathbf{e}_i(\mathbf{q}_v) L_i^0(T_s) + \mathbf{r}_{h,i}(\mathbf{q}_v) L_{\text{atm},i}^{\downarrow} + \mathbf{r}_{b,i}(\mathbf{q}_v, \mathbf{q}_s) E_{\text{sun},i}(\mathbf{q}_s)] \mathbf{t}_i(\mathbf{q}_v) + L_{\text{atm},i}^{\uparrow}(\mathbf{q}_v) \quad (1)$$

Where

- $L_i^0(T)$: Planck function at T temperature
- $L_{\text{atm},i}^{\downarrow}$ and $L_{\text{atm},i}^{\uparrow}$: downwelling and upwelling atmospheric radiation
- $\mathbf{t}_i(\mathbf{q}_v)$: the atmospheric transmission
- $E_{\text{sun},i}(\mathbf{q}_s)$: the solar irradiance at ground level
- $\mathbf{e}_i(\mathbf{q}_v)$: directional emissivity
- $\mathbf{r}_{h,i}(\mathbf{q}_v)$: directional hemispherical reflectivity
- $\mathbf{r}_{b,i}(\mathbf{q}_v, \mathbf{q}_s)$: bi-directional reflectivity

As is well known, since even in the Lambertian case and irrespective of the solar reflected contribution, the pixel's ground radiance $L_i^{\text{ground}}(\mathbf{q}_v)$ is a function of two unknowns (spectral emissivity and surface temperature), it is not possible to solve for one of them unless an *a priori* information is used or an independent measurement is made of one of both quantities. For a daytime measurement in band II, in addition to those two unknowns, the directional properties (BRDF) of the surface, also unknown, come into play. Many efforts have been made toward solving this problem and several methods have been developed, mainly for band III multi-channels (wavelengths) measurements and natural media (Gillespie & al, 1998), (Li & al, 1999). The principle

$$L_i^{\text{sensor}} = \mathbf{e}_i \frac{\int \mathbf{e}_i L_i^0(T_s) f_{i,i} \mathbf{t}_i dI}{\int \mathbf{e}_i f_{i,i} \mathbf{t}_i dI} + \mathbf{r}_{h,i} \frac{\int \mathbf{r}_{h,i} L_{\text{atm},i}^{\downarrow} f_{i,i} \mathbf{t}_i dI}{\int \mathbf{r}_{h,i} f_{i,i} \mathbf{t}_i dI} + \mathbf{r}_{b,i}(\mathbf{q}_s, \mathbf{q}_v) \frac{\int \mathbf{r}_{b,i}(\mathbf{q}_s, \mathbf{q}_v) E_{\text{sun},i}(\mathbf{q}_s) f_{i,i} \mathbf{t}_i dI}{\int \mathbf{r}_{b,i} f_{i,i} \mathbf{t}_i dI} + L_{\text{atm},i}^{\uparrow} \quad (5)$$

of such an approach relies on an empirical relationship, used to constrain the inversion, and found to apply for most natural surfaces. The average emissivity value is hence linked to the amplitude of its spectral variation across the whole band III. For heterogeneous sparsely vegetated land surfaces, the empirical relationship links vegetation index and emissivity (Van de Griend, 1993). Such relationships do not hold for band II.

Since the focus of this work is on the determination of the target's band II emissivity and bi-directional reflectivity and not in priority on the surface temperature, it is assumed that in one way or another band III measurements, in simultaneity with band II measurements, provide access to the surface temperature. Although special methods, based on combinations of band II and band III measurements have been proposed, they do not readily apply to the situation relevant to this work and will not be discussed (Li et Becker, 1990), (Goïta et Royer, 1997). Once a value has been given to T_s , and if the approximation of Lambertian surface has been made equation(1) can be inverted to give emissivity:

$$\mathbf{e}_i(\mathbf{q}_v) = \frac{(L_i^{\text{sensor}}(\mathbf{q}_v) - L_{\text{atm},i}^{\uparrow}) / \mathbf{t}_i - L_{\text{atm},i}^{\downarrow} - E_{\text{sun},i}(\mathbf{q}_s) / p}{L_i^0(T_s) - L_{\text{atm},i}^{\downarrow} - E_{\text{sun},i}(\mathbf{q}_s) / p} \quad (2)$$

If T_s is assumed the same, when shadowing the surface or not, the difference between sunlit and shadowed target's radiance is directly proportional to the bi-directional reflectivity:

$$\mathbf{r}_{b,i}(\mathbf{q}_s, \mathbf{q}_v) = \frac{L_i^{\text{sensor sun}}(\mathbf{q}_s, \mathbf{q}_v) / \mathbf{t}_i - L_i^{\text{sensor shd}}(\mathbf{q}_v) / \mathbf{t}_i}{E_{\text{sun},i}(\mathbf{q}_s)} \quad (3)$$

Actual imaging sensors, apart from high spectral resolution spectro-radiometers, operate in one or several channels (i) with finite bandwidth, defined by their filter function $f_{i,i}$. The measured radiance (unit: $\text{Wm}^{-2}\text{sr}^{-1}$) is now the sum over the bandwidth of the spectral radiance (1)

$$L_i^{\text{sensor}} = \int L_i^{\text{sensor}} f_{i,i} dI \quad (4)$$

Considering the spectral integration of the equation (1) we obtain:

Let us consider the emitting part in equation (5) of the radiometric signal for a band II instrument:

$$L_{II}^{emi} = e_{II} \frac{\int e_{I1} L_I^0(T_s) f_{II,1} t_{I1} dI}{\int e_{I1} f_{II,1} t_{I1} dI} \quad (6)$$

A first approximation consists in factorizing the spectral emissivity but keeping the spectral transmission inside the integral. That is what we will call the transmission weighted approximation.

$$L_{II}^{emi} = e_{II} \frac{\int L_I^0(T_s) f_{II,1} t_{I1} dI}{\int f_{II,1} t_{I1} dI} \quad (7)$$

The second approximation, which is actually the usual way of dealing with the spectral radiometric signal is the standard approximation

$$L_{II}^{emi} = e_{II} t_{II} \frac{\int L_I^0(T_s) f_{I,1} dI}{\int f_{I,1} t_{I1} dI} \quad (8)$$

In a case of a narrow filter, all the definitions are equivalent. The following figure shows two examples of calculation of L_{II}^{emi} in the exact and standard cases for two different samples (concrete and Fontainebleau sand) and for the band II camera. We notice that the difference between both formulations depends on the spectral signature of the sample (see §3). The concrete presents a rather flat signature whereas the signature of the Fontainebleau sand has a high variability.

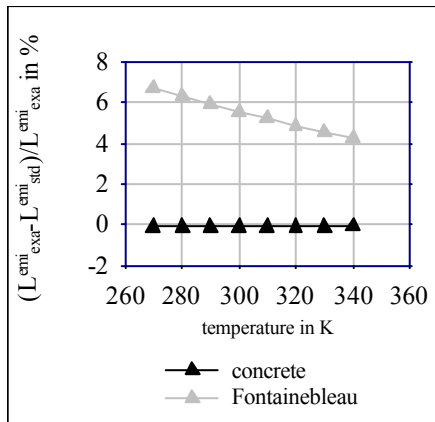


figure (1) relative difference in % between exact and standard formulation

3 EXPERIMENTAL WORK

The objectives of the experimental work are to check the feasibility of the determination of the band II target's optical properties from infrared images acquired in simultaneity in both bands II and III, to

compare the different ways presented in part 2 and to assess the accuracy attainable and identify the limitations. The measurements were carried out in outdoor conditions at the ONERA-PIRRENE test site, between 19th and 28th of June 2000. Artificial scenes composed of natural and man-made materials were built. The scenes included up to 12 different materials.



Figure (2) natural and man made elements of the artificial scene

The directional-hemispherical reflectivity $\rho_h(0)$ of all samples were measured in the laboratory at high spectral resolution over the infrared domain (from 2.5 to 25 μ m) using an integrating sphere. For the reference diffuse reflector (flame sprayed aluminum) partial BRDF under normal incidence was also measured in the laboratory. Figure (3) presents for a few samples the reflectivity signatures in band II.

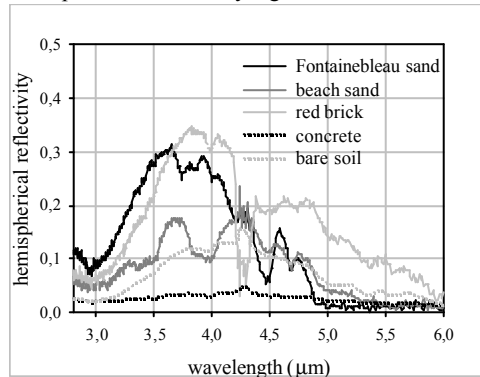


Figure (3) reflectivity signatures in band II

Two infrared cameras were used: one for band III (AGEMA 760), one for band II (INFRAMETRICS SC1000). The cameras were installed 5m above ground (scene) level, looking vertically. Several band III single channel radiometers were used at ground level to monitor the brightness temperature of selected targets in order to provide a means of comparison. The imaged scene also included a water body equipped with two Pt-100 temperature probes very close to the surface of the water. This water body was meant to provide a reference target for calibration purposes and was found to be more reliable in field conditions than blackbodies with controlled temperature incorporated in the scene.

A meteorological station was used in close proximity of the scene to record air temperature, relative humidity, wind speed and direction as well as global radiation. Balloon radio soundings were also made four times per day on June 26 and June 27 in order to fully characterize the atmospheric profiles. The data analyzed and discussed in this work pertain to those two days. As mentioned in part 2, the sensor's filter function is a key element for quantitative interpretation of the measurements. Figure (4) shows the filter function of the cameras together with the transmission of the 5m thick air layer as obtained with the MODTRAN-4.0 atmospheric code (Kneizys & al, 1996) fed with the meteorological parameters and atmospheric profiles of June 26/00 at 10:36 UT.

In band III, for such a small distance, the main absorber responsible for reduced transmission is water vapor. From figure (4) it can be anticipated that for the used band III camera the transmission is only weakly affected by atmospheric water vapor, which implies that the radiation emitted by the air layer directly to the sensor is weak too. In band II, figure (4) shows that the filter function of the used camera is such that water vapor has practically no influence on the transmission. However, the transmission takes very low values in the region of the very strong CO₂ absorption band centered at 4.26μm.

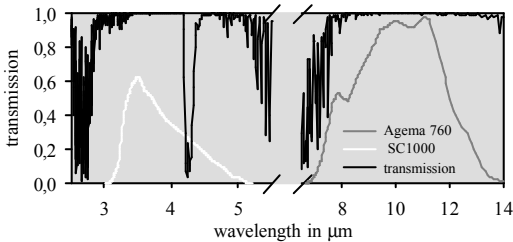


Figure (4) spectral filters functions of both cameras and spectral atmospheric transmission

4 RESULTS

As already mentioned, this work focuses on the determination of the optical properties in band II, here notably emissivity, not on surface temperature. Equation (2), spectrally integrated on band II camera filter becomes:

$$e_{II}(q_v) = \frac{\{[L_{II,I}^{sensor}(q_v) - L_{II}^{atm}(q_v)] - \langle L_{II,I} \rangle - F^{target}(q_s, q_v) \langle L_{II,I} \rangle\}}{\{\langle L_{II,I} \rangle - \langle L_{II,I} \rangle - F^{target}(q_s, q_v) \langle L_{II,I} \rangle\}} \quad (9)$$

The problems which are to be resolved before being able to reach the emissivity values are the determination of

- T_s
- atmospheric parameters
- form factor

T_s will be determined using camera band III measurement in conjunction with the knowledge of the spectral signature in this band.

Radiosondes data in coincidence with the measurement will feed a radiative transfer code (MODTRAN) to derive the atmospheric quantities.

The form factor, $F^{target}(q_s, q_v) = pr_b(q_s, q_v)/r_h(q_s)$ will be determine with a sun/shadow method where $r_b(q_s, q_v)$ is given by

$$r_b(q_s, q_v) = \frac{\Delta L_{II} |_{shd}}{E_{sun,II}} \quad (10)$$

The following figure exhibits the bidirectional reflectivity for several samples in the configuration of the exact formulation. Two cases are distinguished. In one case a correction of ΔT has been performed to take into account the existence of a difference in surface temperature of the sample in shadow or at sunlit. The figure shows that this correction tends to stabilize the angular behavior.

From this figure it can be seen that at first approximation, the considered samples behave as quasi Lambertian reflector. So, in the following, a form factor of unity will be taken for these materials.

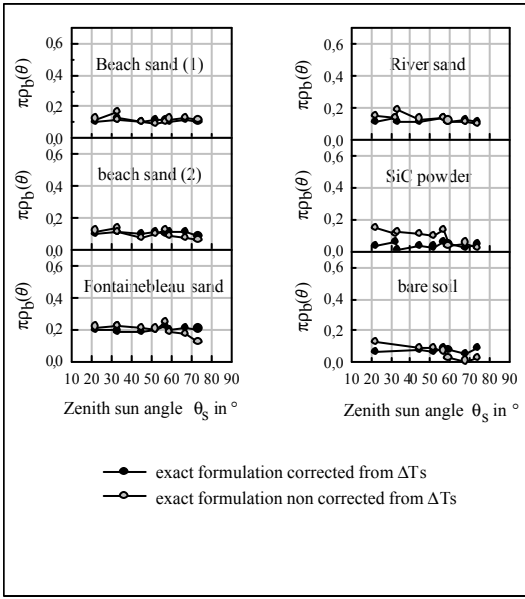


Figure (5): bidirectional reflectivity of different samples corrected and non-corrected of ΔT_s

Emissivity determination

1. direct inversion

The following figure shows for different times of the day the retrieval of the emissivity using equation (9) and demonstrates that a direct inversion leads to unstable results. Emissivity here is compared to an emissivity reference value from spectral signatures. As we can see the retrieved emissivity as a function of the time may take even totally unphysical values.

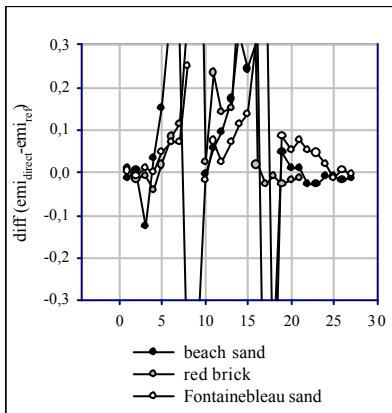


Figure (6) Direct inversion of band II ground radiance

2. Multi-temporal regression

The following figure presents multi temporal regression of the actual data of the Fontainebleau sand, the red brick and the beach sand where numerator and denominator are those from equation (9). The data presented are for the exact formulation in order to concentrate on radiometry rather than on spectral integration problems. Since the laboratory values of emissivity are used for the purpose of comparison, the reference slope is drawn as a guide line.

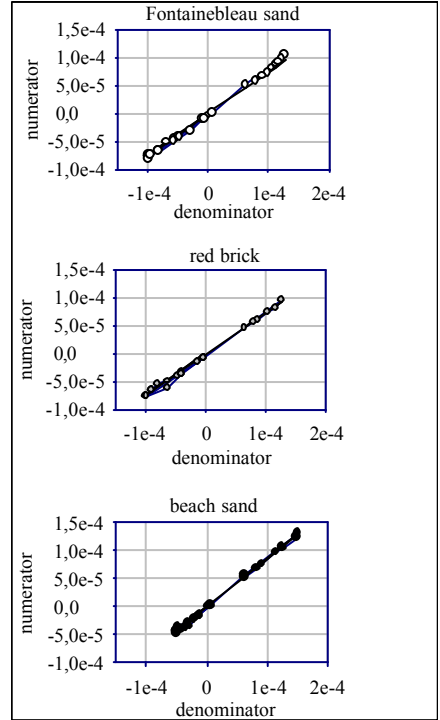


Figure (7) numerator in function of denominator in the exact formulation

Detailed results of the regression (slope, offset, correlation coefficient) for the exact formulation are summarised in table (1) for the different samples. As pointed out in previous sections, use of exact formulation allows obtaining results which are independent of a particular instrument and allows evaluating the goodness of the experimental radiometry and handling of data. Several observations follow from Table (1): 1) reproducibility is, on the average, better than 2%. 2) correlation coefficient is always very high. Regarding the absolute value of emissivity it appears that the retrieved value (regression slope), but for two targets, is systematically higher than the laboratory value taken

as reference. Finally Table (1) demonstrates that the proposed multi-temporal regression method has good measuring potential with an experimental retrieval error in the order of 2%.

target	slope	offset	R2	Lab. Emi
Beach (SP)	0.869	- 2.209 E-06	0.9973	0.860
Beach (BP)	0.879	- 3.862 E-06	0.9981	0.860
Fireproof brick	0.779	- 3.146 E-06	0.9948	0.753
Fontainebleau sand	0.784	- 9.388 E-07	0.9970	0.747
Red brick	0.742	- 2.891 E-06	0.9952	0.735
River sand	0.861	- 1.312 E-06	0.9977	0.820
Sic powder	0.920	- 2.933 E-06	0.9931	0.936
Bare soil	0.910	- 4.783 E-06	0.9974	0.888
concrete	0.901	- 3.520 E-06	0.9984	0.963

Table (1): slope, offset, correlation coefficient and laboratory emissivity for the different samples

5 CONCLUSION

This work demonstrates that direct inversion of the radiometric equation is totally unstable and unreliable. Thus, a new approach is proposed and evaluated in this work: the multi-temporal regression method such that the slope of the linear regression worked out on measurements made at different temperatures is the searched emissivity. In out-doors conditions, the way to vary the temperature is to make measurements at different times of day. If it is possible to cast shadow on the target, shade measurement play the role of night-time measurements. For day-time conditions, the same multi-temporal regression method has been applied in two steps. In step 1 the bi-directional reflectivity is retrieved from the combination of sunlit and shadow measurements made at different times of day and thus for different sun zenith angles. This allows obtaining the form factor of the target, a quantity that measures the deviation from a Lambertian behaviour. Once the form factor is known, the radiometric signal can be inverted in term of only emissivity and the regression method applied.

The regression approach was assessed on shade data, sunlit target data and both data together.. Very high correlation coefficients are obtained and good (<2%) reproducibility was found for the retrieved emissivity

(slope). Compared to the emissivity determined in the laboratory via directional-hemispherical reflectivity measurements, the retrieved emissivity exhibits a quasi systematic, a few %, positive bias. Such a slightly higher value may well be attributed to moisture affecting the target's material in outdoors conditions.

Although the proposed regression method requires a sequence of measurements over the day and accurate characterisation of all atmospheric quantities, the results obtained demonstrate that the method has good measuring potential and may be helpful for documenting band-2 radiative parameters of terrestrial backgrounds and imbedded materials.

References

- H. Jahn, K. Briess, E. Lorenz, M.v. Schoenermark, D. Oertel, V. tank, P. Haschberger & B. Zhukov, „FOCUS“: science objectives, ESA Symposium Proceedings on „Space Station Utilisation“, ESOC, Darmstadt, Germant 30 Sept.-2 Oct., SP-385 (Dec. 1996), 1996
- A.R. Gillespie, S. Rogugawa, T. Matsunaga, J.S. Cobern, S. Hook and A.B. Kahle, 1998. A temperature and emissivity separation algorithm for Advanced Space-borne Thermal Emission and Reflection Radiometer (ASTER) images, IEEE Trans. Geosc. Rem. Sensing, 36, 1113-1126
- Z.-L. Li, F. Becker, M. P. Stoll and Z. Wan, 1999 Evaluation of six methods for extracting relative emissivity spectra from thermal infrared images, Remote Sensing of Environ. 69, 197-214
- A. van de Griend and M. Owe, 1993. On the relationship between thermal emissivity and normalized difference vegetation index for natural surfaces. Int. J. Rem. Sensing, 15(6), 1119-1131
- Z.-L. Li and F. Becker, 1990. Feasibility of land surface temperature and emissivity determination from AVHRR data, Remote Sensing of Envir., 43, 67-85
- K. Goita and A. Royer, 1997. Surface temperature and emissivity separability over land surface from combined TIR and SWIR AVHRR. IEEE Tran. Geosc. Rem. Sensing, 35(3), 718-733
- F.X. Kneizys L.W. Abreu, G.P. Anderson, J.H. Chetwynd, E.P. Shettle, A. Berk, L.S. Bernstein, D.C. Roberston, P. Acharya, L.S. Rothman, J.E.A. Selby, W.O. Gallery & S.A. Clough, 1996 The MODTRAN 2/3 Report and LOWTRAN 7 MODEL, Phillips Laboratory, Geophysics Directorate, PL/GPOS, Hanscom AFB, Ma 01731-3010, November 1996.

Estimating land surface temperature in south america from NOAA-AVHRR images and reanalysis data

Luis J. Morales⁽¹⁾, Juan C. Parra⁽²⁾, J.A. Sobrino⁽³⁾

(1) Dpt. de Ciencias Ambientales y Recursos Naturales. Casilla 1004, Santiago de Chile. Facultad de Ciencias Agronomicas. Universidad de Chile, Chile. lmorales@uchile.cl.

(2) Dpt. de Ciencias Físicas. Casilla 54-D, Temuco. Facultad de Ingeniería, Ciencias y Administración. Universidad de La Frontera, Chile. jparra@ufro.cl.

(3) Dpt. de Termodinámica. C/ Dr. Moliner 50, 46100, Burjassot. Universidad de Valencia, España.. sobrino@uv.es.

RESUMEN

En este trabajo se expone un método para estimar la temperatura de la superficie de América del Sur desde imágenes NOAA-AVHRR a partir de datos del reanálisis, s un proyecto conjunto del NCEP (National Centers for Environmental Prediction) y el NCAR (National Center for Atmospheric Research) El método que proponemos se basa en corregir las imágenes del efecto atmosférico y de la emisividad, a partir de dos canales térmicos. Los perfiles atmosféricos, son obtenidos desde los datos medios mensuales climatológicos del reanálisis. Los datos de emisividad son obtenidos a partir de datos de NDVI publicados por el ISLSCP (International Satellite Land Surface Climatology Project), que poseen una resolución espacial igual al reanálisis. El modelo propuesto esta basado en la ecuación de transferencia radiativa y contempla la dependencia atmosférica y de emisividad superficial en los coeficientes del split-window.

ABSTRACT

In this work a method to estimate the surface temperature of South America from NOAA-AVHRR images and from reanalysis data, a joint project between (NCEP) and National Center for Atmospheric Research (NCAR), is presented. Our method consists in correcting the images both by the atmospheric effect and emissivity based on two thermal channels. Atmospheric profiles are obtained from the mean monthly climatological data of the reanalysis. Emissivity data are obtained from NDVI data published by the International Satellite Land Surface Climatology Project (ISLSCP) which have a space resolution similar to that of reanalysis. The proposed model is based on the equation of radiative transfer and it contemplates dependence on the atmosphere and surface emissivity in the split-window coefficients.

1 INTRODUCTION

De todas las variables que configuran el clima en una región determinada, la temperatura de la superficie terrestre (T_s) se constituye en uno de los parámetros claves en el seguimiento de la mayoría de los fenómenos medioambientales (desertificación, ciclo hidrológico, entre otros). En la práctica la estimación de la T_s es llevada a cabo mediante termómetros o termistores, y por lo tanto, con la problemática asociada de la escasa representatividad de la misma, limitada a una pequeña cobertura espacial alrededor del instrumento de medición. No obstante, para sustituir las medidas tradicionales de temperatura por las realizadas por satélites será necesario que la técnica de medida proporcione una T_s con una adecuada precisión, 2°K para estimar flujos de energía, mientras que para detectar cambios climáticos se requieren precisiones de hasta 0.3°K (Barton, 1992). Para lograr este objetivo será necesario, por tanto, resolver los

diferentes problemas que plantea la determinación de la T_s desde satélites, como el calibrado de los sensores utilizados, es decir, transformación de los valores digitales proporcionados por el satélite en valores de radiancia. Además la detección y eliminación de nubes, pues estas son prácticamente opacas a la radiación térmica, por lo que en presencia de nubes la radiancia detectada por el sensor es la de la parte superior de la nube y no la de la superficie del suelo, por ello habrá que detectar la presencia de nubosidad y en su caso eliminarla. Finalmente la corrección de los efectos atmosféricos y de emisividad.

1.1 Efecto de la emisividad

Las radiancias medidas por los sensores son transformadas en temperaturas suponiendo que son emitidas por un cuerpo negro (emisividad=1). Sin embargo, esta hipótesis no es estrictamente válida si se tiene en cuenta que gran parte de los elementos que componen una escena en la imagen de satélite

(vegetación, cuerpos de agua, suelos, etc) tienen una emisividad menor a la unidad. A este respecto, se estima que por cada 1% de diferencia de la emisividad respecto de la unidad, la diferencia entre la temperatura real y la aparente es de aproximadamente de 0.6°K (Sobrino y Caselles, 1989).

1.2 Efecto atmosférico

La atmósfera es, en general, un medio absorbente, emisor y dispersor, resultando prácticamente opaca en gran parte del infrarrojo. Tan sólo en ciertos intervalos espectrales (3.5-4.2 μm y 10.5-12.5 μm), denominados ventanas atmosféricas, es posible la observación de la Tierra desde el espacio, ya que la transmisividad es relativamente alta (Figura 1). Aún en estas ventanas existe una absorción apreciable que es debida casi por entero al vapor de agua, cuya concentración en la atmósfera es altamente variable tanto espacial como temporalmente (Varanasi, 1988), de forma que en la práctica se suele considerar como el único gas absorbente, salvo para atmósferas contaminadas donde la influencia de los aerosoles es importante. De esta manera, parte de la radiancia emitida por la superficie es absorbida por el vapor de agua, que a su vez actúa como emisor de radiación térmica a la temperatura a la que se encuentra en la atmósfera.

1.3 Ecuación de transferencia radiativa

El estudio de la transmisión de la radiación electromagnética en un medio material se basa en la ecuación de transferencia radiativa (Chandrasekhar, 1960). Suponiendo una atmósfera sin nubes y aerosoles, y en equilibrio termodinámico local, la solución de la ecuación de transferencia radiativa a través de la atmósfera proporciona la radiancia $R_{i\theta}$ medida desde cualquier punto del espacio en el canal i bajo un ángulo de observación cenital θ como la suma de tres términos: (a) radiación emitida por la superficie que es atenuada por la atmósfera, (b) la radiación ascendente emitida por la atmósfera hacia el sensor, y (c) la radiación descendente emitida por la atmósfera que incide en la superficie y luego es reflejada hacia el sensor, esto es

$$R_{i\theta} = B_i(T_{i\theta}) = \varepsilon_{i\theta} B_i(T_s) \tau_{i\theta} + R_{atmi\theta\uparrow} + R_i(ref) \tau_{i\theta} \quad (1)$$

En la ecuación anterior todas las cantidades van referidas a una integración espectral sobre el ancho de banda del canal i , B_i es la función de Planck, $T_{i\theta}$ es la temperatura radiométrica medida a nivel del satélite con un ángulo de observación cenital θ , $\varepsilon_{i\theta}$ es la emisividad de la superficie vista desde el ángulo

cenital θ , $B_i(T_s)$ es la radiancia que sería medida si la superficie fuera un cuerpo negro con la temperatura de superficie T_s , $\tau_{i\theta}$ es la transmisividad del camino atmosférico total desde el ángulo cenital θ , $R_{atmi\theta\uparrow}$ es la radiancia atmosférica ascendente desde el ángulo θ , que viene dada por (Sobrino et al., 1991)

$$R_{atmi\theta\uparrow} = (1 - \tau_{i\theta}) B_i(T_{atmi}) \quad (2)$$

donde T_{atmi} representa la temperatura media de la atmósfera existente entre la superficie del suelo y el sensor y siendo $R_i(ref)$ la radiancia atmosférica reflejada, dada por Sobrino et. al. (1996), de acuerdo con

$$R_i(ref) = (1 - \varepsilon_{i\theta}) (1 - \tau_{i53}) B_i(T_{atmi}) \quad (3)$$

El término $(1 - \tau_{i53}) B_i(T_{atmi})$ representa la radiancia emitida por la atmósfera en la dirección correspondiente a 53° con la vertical. Esta expresión se ha obtenido considerando que la transmisividad de la radiación difusa es cuantitativamente equivalente a la transmisividad de la radiación directa a la misma masa de materia absorbente pero a 53° (Kondratyev, 1969).

De esta forma, la ecuación (1), puede reescribirse como

$$B_i(T_s) = \frac{B_i(T_{i\theta}) - [(1 - \tau_{i\theta}) + (1 - \varepsilon_{i\theta})(1 - \tau_{i53}) \tau_{i\theta}] B_i(T_{atmi})}{\varepsilon_{i\theta} \tau_{i\theta}} \quad (4)$$

de modo que invirtiendo la función de Planck ponderada para el canal i , se obtiene la temperatura de la superficie. Sin embargo, el inconveniente de este método radica en que necesita además de conocer la emisividad de la superficie, del conocimiento preciso de los perfiles verticales de temperatura y humedad de la zona a estudiar, necesarios para determinar T_{atmi} y la transmisividad en el canal considerado, lo que requiere utilizar radiosondeos meteorológicos a la hora de paso del satélite y no siempre es frecuente disponer de los mismos.

1.4 Algoritmos de corrección de split-window

El método Split-Window consiste en combinar los datos obtenidos simultáneamente por dos anchos de banda en la misma ventana de transmisión atmosférica adquiridos por el sensor. Así, se tiene en cuenta las diferentes absorciones de la radiación por parte de la atmósfera para dos longitudes de onda distintas, y

evaluando tales absorciones es posible dar cuenta de la absorción de radiación por parte de la atmósfera. En contraste con otros métodos, numerosos han sido los trabajos utilizando esta técnica, para obtener la temperatura de la superficie del mar (Prabhakara et al., 1974; Descamps y Phulpin, 1980; Mc Clain et al., 1985; Sobrino et al., 1993b) como la terrestre (Price, 1984; Becker y Li, 1990; Sobrino et al., 1991; Prata, 1993; Sobrino et al., 1994). La aplicación de esta técnica ha sido llevada extensamente con la utilización de los datos procedentes del satélite NOAA (National Oceanic and Atmospheric Administration Satellite). Los principales sensores a bordo de los satélite NOAA son el TOVS (TIROVS Operational Vertical Sounder) y el AVHRR (Advanced Very High Resolution Radiometer), el cual es elegido para el desarrollo de este trabajo.

Para el sensor AVHRR es posible obtener una expresión para la T_s y aplicada a las bandas 4 y 5 del sensor AVHRR, es decir

$$T_s = T_4 + A(T_4 - T_5) - B_0 \quad (5)$$

$$+ (1 - \varepsilon)B_1 - \Delta\varepsilon B_2$$

donde T_4 y T_5 son las temperaturas radiométricas medidas en los canales 4 y 5 del sensor AVHRR, ε es la emisividad media en los canales 4 y 5, y $\Delta\varepsilon$ son respectivamente, la medida efectiva y la variación espectral de la emisividad y A , B_0 , B_1 y B_2 son los coeficientes dados por Sobrino et al., 1996. Cuando se trata de obtener la temperatura de la superficie de la tierra ($\varepsilon \neq 1$), la aplicación de la ecuación (5) es muy dependiente de la información que se posea: contenido total en vapor de agua de la atmósfera y/o transmisividad (datos necesarios para conocer los coeficientes A , B_0 , B_1 y B_2), la emisividad de la superficie terrestre y su variación angular y/o espectral.

En un sentido estricto la ecuación (5) no presenta un carácter global, siendo válida para una atmósfera dada. Lo anterior, implicará que su aplicación a escala mundial necesitará de una adecuada evaluación de los coeficientes. Este inconveniente se evita usualmente determinado los coeficientes mediante regresión estadística de la datos reales de la TST frente a temperaturas radiométricas proporcionadas por el satélite, como lo hace la NOAA para el caso de la determinación de la TSM. Sin embargo, en el caso de la determinación de la TST, que es el problema que nos ocupa, no existe en la actualidad un importante volumen de datos reales de TST de calidad suficiente que sean coincidentes con las medidas de temperatura radiométrica proporcionadas por los sensores. Una solución operativa a este problema es dada por

Sobrino et al. (1996), donde se procede a linealizar los coeficientes A , B_0 , B_1 y B_2 en función del contenido en vapor de agua existente en la atmósfera, W , que es una magnitud no espectral y que representa la cantidad total de vapor de agua atmosférico. La incorporación de la dependencia en vapor de agua de los coeficientes se basa en el hecho que los algoritmos no pueden operar correctamente con un conjunto de coeficientes constantes para todas las situaciones atmosféricas. La estimación de las temperaturas radiométricas, es obtenida por simulación a través del programa LOWTRAN-7 con los filtros apropiados de los canales 4 y 5 del AVHRR-NOAA y para un total de 60 radiosondeos extraídos de la base TIGR (TOVS Initial Guess Retrieval) (Scott y Chédin, 1981). Estos radiosondeos cubren una gran variabilidad de la temperatura (250°K a 320°K), y de la concentración de vapor de agua en la atmósfera (0.15 a 6.7 gr/cm²). La atenuación de la radiancia de la superficie se ha considerado de acuerdo al procedimiento seguido por Sobrino (1993a), añadiendo los perfiles de los gases incluidos en las atmósferas estándar del LOWTRAN-7 (CO₂, N₂O, O₃, CO y CH₄), al perfil de los radiosondeos. Para cada radiosondeo se han considerado 5 temperaturas de superficie $T-5$, $T+5$, $T+10$, y $T+20$ (T es la temperatura del primer nivel del radiosondeo), dos ángulos de observación (0° y 53°), y 11 emisividades para cada canal, desde 0,90 a 1. De esta forma se tienen un total de 600 situaciones diferentes (60 atmósferas x 5 temperaturas x 2 ángulos) para cada superficie. Para simplificar el problema no se consideraron los aerosoles, lo cual implica que, para poder aplicar el algoritmo, se deberían eliminar los datos de satélite contaminados por aerosoles. Esto podría hacerse de acuerdo a la metodología de Rao et al. (1989).

De esta forma se tiene el siguiente algoritmo Split-Window, para la estimación de la temperatura de la superficie terrestre (Sobrino, 2000)

$$T_s = T_4 + 1.4(T_4 - T_5) - 0.32(T_4 - T_5)^2 \quad (6)$$

$$+ 0.83 + (57 - 5W)(1 - \varepsilon) - (161 - 30W)\Delta\varepsilon$$

La validación de este algoritmo ha sido realizada con la serie de datos CSIRO (Australia Commonwealth Scientific and Industrial Organization) suministrada por Prata (1994a y 199b). Dicha serie consta de 300 datos tomados en dos regiones semiáridas de Australia, con un clima bastante seco. La base de datos CSIRO nos ha proporcionado valores de temperatura de superficie terrestre medidos in situ con sus correspondientes valores de emisividad, vapor de agua, proporción de vegetación y temperaturas de los canales 4 y 5 del AVHRR.

2 DETERMINACION DE LOS COEFICIENTES

Los coeficientes dependientes del vapor de agua y de la emisividad en la ecuación (6) puede ser escritos de tal forma que la ecuación adopte la estructura

$$T_s = T_4 + 1.4(T_4 - T_5) - 0.32(T_4 - T_5)^2 + 0.83 + a_w(1 - \varepsilon) - b_w \Delta \varepsilon \quad (7)$$

donde a_w y b_w corresponden a

$$a_w = 57 - 5W \quad b_w = 161 - 30W \quad (8)$$

Los coeficientes de la ecuación (8), para América del Sur, a_w y b_w son calculados a partir de datos provenientes del reanálisis (NCEP/NCAR Reanalysis Project) y los valores de ε y $\Delta \varepsilon$ son estimados a partir de datos de NDVI publicados por el ISLSCP(International Satellite Land Surface Climatology Project). Esto se debe fundamentalmente a que ambas fuentes de información se encuentran a la misma resolución espacial y proyección cartográfica.

2.1.- Agua precipitable(W)

El agua precipitable en un perfil atmosférico o contenido de vapor de agua en una columna vertical de base unitaria extendida desde la altura z hasta una altura dada h , es calculada como

$$W(h, z) = \int_z^h \rho(z') dz' \quad (9)$$

donde $\rho(z')$ es la densidad del vapor de agua a una altura z' .

El contenido total del vapor de agua en la columna atmosférica puede ser obtenido a partir de perfiles de densidad de vapor de agua o por bases de datos generadas por organismos de meteorología. Una de estas bases de datos más importante es la generada por un proyecto en conjunto entre NCEP y NCAR cuyo propósito es generar diversos análisis del estado de la atmósfera usando los datos disponibles, tanto históricos (desde 1948) como actuales. Estos se presentan en datos medios diarios como mensuales, y abarcan todo el planeta con una resolución de 2.5 grados. Para cada uno de los puntos de la grilla, existen perfiles de temperatura, presión, humedad específica, entre algunos. De esta forma el uso de estos datos permitirá lograr el objetivo propuesto en este artículo.

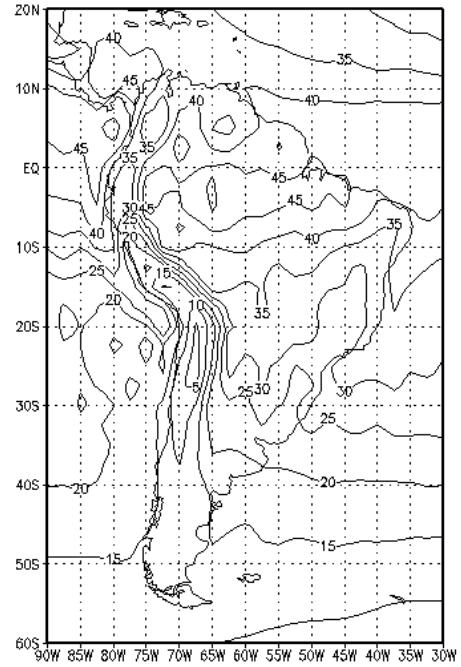


Figura 1.- Valores medios anuales de la distribución espacial del agua precipitable en kg m-2 para América del Sur.

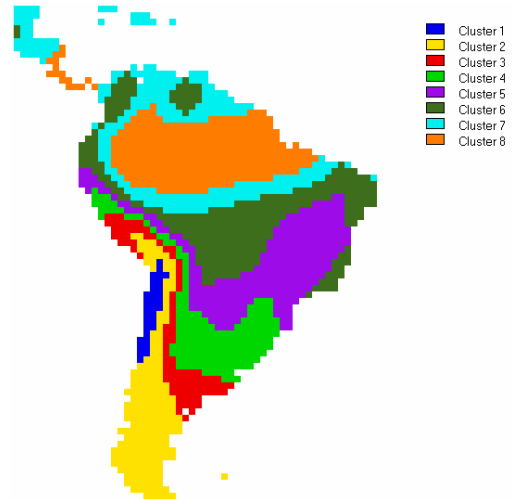


Figura 2.- Resultado del análisis de cluster sobre los valores medios mensuales de W utilizando la distancia euclidiana como medida de similitud

La figura (1) muestra la climatología de la distribución espacial del agua precipitable en kg m^{-2} , representada por su valor medio, para el cono sur de América. En esta figura es posible apreciar que el agua precipitable sigue una tendencia espacial bien definida, y al parecer asociada a los centros de acción meteorológica más importantes como el centro de bajas presiones en el Amazonas, el centro de baja polar, y los anticiclones del Pacífico y del Atlántico. Esta configuración se presenta también en los valores medios mensuales, lo que hace suponer que su distribución espacio temporal es también regular y puede ser obtenida a partir de análisis de tipologías o de cluster. La idea central es aplicar algoritmos de clasificación al conjunto de datos espacio temporales de W con el objetivo de organizarlos en grupos homogéneos y de esta forma poder obtener coeficientes generalizados de la ecuación (7) para cada cluster.

La figura (2) muestra el análisis de cluster utilizando la distancia euclidiana como medida de similitud. La similitud es calculada a partir de vectores espacio temporales asociados a los elementos de una matriz espacial de W para cada mes del año, de forma tal de poder agrupar por este concepto. Además en esta figura observamos claramente ocho zonas homogéneas que son comparables con la tipología de Köeppen para América del Sur. A partir de esta última matriz de áreas homogéneas de W es posible obtener los valores medios para cada cluster y poder de esta forma calcular los coeficientes de la ecuación de split-window. La tabla (1) muestra los valores medios mensuales de W para cada cluster de la Figura (2). En esta tabla es posible apreciar que el método utilizado para obtener las áreas homogéneas de W es aceptable en la discriminación de áreas homogéneas. Variación temporal de los valores medios mensuales del agua precipitable para cada cluster de la Figura 2. En la Figura (3) se aprecia claramente que el análisis de tipología, dado en la figura (1) y cuyos datos están en la tabla (1), se muestra aceptable en la identificación de áreas homogéneas.

Tabla 1.- Valores medios mensuales de W para cada cluster de los mostrados en la figura 2.

M es	C1	C2	C3	C4	C5	C6	C7	C8
1	1.054	1.573	2.263	2.934	3.484	3.763	3.849	4.510
2	1.020	1.594	2.255	2.954	3.515	3.818	3.860	4.532
3	0.872	1.501	2.184	2.803	3.452	3.838	3.931	4.598
4	0.589	1.292	1.850	2.424	3.143	3.724	4.068	4.709
5	0.448	1.111	1.548	2.067	2.731	3.473	4.135	4.722
6	0.401	0.938	1.328	1.817	2.414	3.153	4.027	4.516
7	0.373	0.889	1.233	1.713	2.232	2.870	3.757	4.220
8	0.391	0.907	1.284	1.765	2.311	2.875	3.752	4.143
9	0.436	0.988	1.421	1.934	2.617	3.171	3.913	4.241
10	0.496	1.094	1.623	2.214	2.995	3.518	4.053	4.390
11	0.650	1.278	1.841	2.424	3.212	3.703	4.088	4.547
12	0.854	1.445	2.083	2.704	3.414	3.772	3.965	4.559

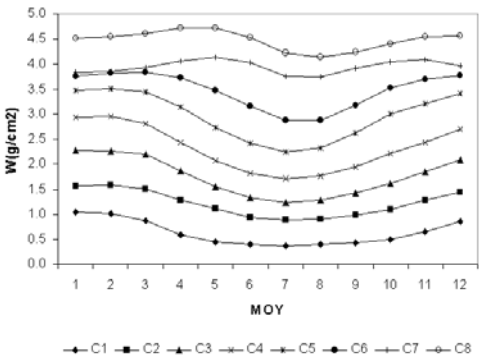


Figura3.- Variación temporal de los valores medios mensuales del agua precipitable para cada cluster de la figura 2. En esta figura se aprecia claramente que el análisis de tipología se muestra aceptable en la identificación de áreas homogéneas.

2.2.- Emisividad(ϵ)

Cuando se comparan los espectros de emisión de un cuerpo cualquiera y de un cuerpo negro a la misma temperatura se observa que la curva de emitancia correspondiente al cuerpo negro está siempre por encima de la relativa a un cuerpo natural. Lo anterior, ha llevado a introducir la noción de emisividad espectral hemisférica, que se define a partir del cociente entre la energía emitida por el cuerpo a una temperatura T dada y longitud de onda λ y la energía que emitiría un cuerpo negro a igual T y λ ., es decir:

$$\epsilon_{\lambda} = \frac{M_{\lambda}(T)}{M_{n\lambda}(T)} \tag{10}$$

la emisividad total de un cuerpo natural es por tanto,

$$\epsilon(T) = \frac{\int_0^{\infty} M_{\lambda}(T) d\lambda}{\int_0^{\infty} M_{n\lambda}(T) d\lambda} = \frac{\int_0^{\infty} \epsilon_{\lambda}(T) M_{n\lambda}(T) d\lambda}{\sigma T^4} \tag{11}$$

donde σ es la constante de Stefan - Boltzman ($5.67 \times 10^{-8} \text{ W/m}^2 \text{ }^{\circ}\text{K}^4$). Para superficies naturales, en general, la emisividad tiene una componente direccional dada por la expresión:

$$\varepsilon_{\lambda}(T) = \frac{1}{\pi} \int_0^{2\pi} d\phi \int_0^{\frac{\pi}{2}} \varepsilon_{\lambda}(\theta, \phi, T) \cos \theta \sin \theta d\theta \quad (12)$$

si la superficie es lambertiana $\varepsilon_{\lambda}(T) = \varepsilon_{\lambda}(\theta, \phi, T)$.

Para poder encontrar la emisividad ε y el la diferencia de las emisividades en los canales 4 y 5 de NOAA $\Delta\varepsilon$, en la ecuación (7), se recurre a las bases de datos de NDVI publicados por el ISLSCP(International Satellite Land Surface Climatology Proyect) y la utilización del método de umbrales (Sobrino et al, 2001).A partir de este método es posible estimar la emisividad para intervalos de índice de vegetación de diferencia normalizada (NDVI), de tal forma que una superficie dada puede ser considerada como una mezcla de suelo desnudo y vegetación, de manera que se puede expresar la emisividad como

$$\varepsilon_i = \varepsilon_{vi} P_v + \varepsilon_{si} (1 - P_v) + C_i \quad (13)$$

donde ε_{vi} y ε_{si} son las emisividades que se asignan a la vegetación y al suelo desnudo, respectivamente, para el canal i ($i = 4, 5$); P_v es la proporción de vegetación y C_i es un término que depende de las características de la superficie y tiene en cuenta las reflexiones internas (efectos de cavidad). Su valor es próximo a cero para valores extremos del NDVI, correspondientes a suelos desnudos y a pixeles cubiertos totalmente de vegetación. Así se tiene;

$$0.2 \leq \text{NDVI} \leq 0.5$$

Sobrino et al. (1990) proponen una aproximación lineal, que relaciona el término de reflexión, C_i , con P_v

$$\varepsilon_{8-14} = 0.971 + 0.019 P_v \quad (14)$$

$$\Delta\varepsilon = 0.006(1 - P_v) \quad (15)$$

En particular, para los canales 4 y 5 del AVHRR los valores del término C_i son:

$$\varepsilon_4 = 0.968 + 0.021 P_v \quad (16)$$

$$\varepsilon_5 = 0.974 + 0.015 P_v \quad (17)$$

donde el término P_v puede ser obtenido a partir de la imagen de NDVI(Carson y Ripley, 1997)

$$P_v = \frac{(\text{NDVI} - 0.2)^2}{0.09} \quad (18)$$

$$\text{NDVI} < 0.2$$

Los valores de NDVI inferiores a 0.2 son considerados como suelos desnudos y rocas, de tal forma que es posible estimar los valores de las emisividades de los canales 4 y 5 mediante el método desarrollado por Rubio et al (1997), obtiene la emisividad en los canales 4 y 5 mediante la emisividad en el intervalo 8-14 μm , esto es

$$\varepsilon_4 = 0.7395 + 0.2355 \varepsilon_{8-14} \quad (19)$$

$$\varepsilon_5 = 0.9150 + 0.6250 \varepsilon_{8-14} \quad (20)$$

$$\Delta\varepsilon = 0.173 \varepsilon_{8-14} - 0.1750 \quad (21)$$

$$\text{NDVI} > 0.5$$

Este es el caso cuando todos los pixeles están cubiertos con vegetación y las emisividades son estimadas a partir de

$$\varepsilon_4 = 1.6190 \varepsilon_{8-14} - 0.6080 \quad (22)$$

$$\varepsilon_5 = 1.4670 \varepsilon_{8-14} - 0.4580 \quad (23)$$

$$\Delta\varepsilon = 0.1520 \varepsilon_{8-14} - 0.1510 \quad (24)$$

Finalmente la emisividad en el intervalo 8-14 μm está dada por (Morales, 1997)

$$\varepsilon_{8-14v} = 0.9585 + 0.0357 \text{NDVI} \quad (25)$$

La figura 4 muestra el índice de vegetación NDVI medio anual para América del Sur. Esta configuración espacial del NDVI se superpone a las regiones climáticas, así se aprecia claramente el Desierto de Atacama, la zona semiárida de Chile y Argentina hasta la Patagonia, y la gran cuenca del Amazonas.

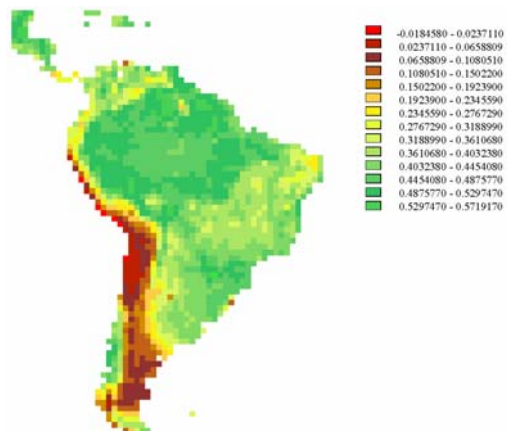


Figura4.- Valores medios de NDVI para América del sur.

A partir de esta información de NDVI y las ecuaciones (14) a la (25), se calculó la emisividad media y en los canales 4 y 5 de NOAA. Esta información anexada a la encontrada para el agua precipitable W , es la requerida para el calculo de los coeficientes de la ecuación de Split –Window dada por la ecuación (7).

2.3.- Coeficientes a_w , b_w , ϵ y $\Delta\epsilon$

Los coefientes a_w , b_w son calculados a partir de la tabla (1), ya que solo dependen del valor del agua precipitable. Los valores de estos coeficientes son mostrados en la tabla (2) y (3) respectivamente. Estos coeficientes permiten para cada cluster contar con la ecuación de split-window mas apropiada y que permita obtener de una forma más precisa la temperatura de superficie a partir de datos AVHRR de NOAA.

Tabla 2.- Valores medios mensuales de a_w para cada cluster de los mostrados en la figura 2.

M es	C1	C2	C3	C4	C5	C6	C7	C8
1	51.7	49.1	45.7	42.3	39.6	38.2	37.8	34.5
2	51.9	49.0	45.7	42.2	39.4	37.9	37.7	34.3
3	52.6	49.5	46.1	43.0	39.7	37.8	37.3	34.0
4	54.1	50.5	47.8	44.9	41.3	38.4	36.7	33.5
5	54.8	51.4	49.3	46.7	43.3	39.6	36.3	33.4
6	55.0	52.3	50.4	47.9	44.9	41.2	36.9	34.4
7	55.1	52.6	50.8	48.4	45.8	42.7	38.2	35.9
8	55.0	52.5	50.6	48.2	45.4	42.6	38.2	36.3
9	54.8	52.1	49.9	47.3	43.9	41.1	37.4	35.8
10	54.5	51.5	48.9	45.9	42.0	39.4	36.7	35.1
11	53.8	50.6	47.8	44.9	40.9	38.5	36.6	34.3
12	52.7	49.8	46.6	43.5	39.9	38.1	37.2	34.2

Tabla 3.- Valores medios mensuales de b_w para cada cluster de los mostrados en la figura 2.

M es	C1	C2	C3	C4	C5	C6	C7	C8
1	129	114	93	73	56	48	46	26
2	130	113	93	72	56	46	45	25
3	135	116	95	77	57	46	43	23
4	143	122	106	88	67	49	39	20
5	148	128	115	99	79	57	37	19
6	149	133	121	106	89	66	40	26
7	150	134	124	110	94	75	48	34
8	149	134	122	108	92	75	48	37
9	148	131	118	103	82	66	44	34
10	146	128	112	95	71	55	39	29
11	142	123	106	88	65	50	38	25
12	135	118	99	80	59	48	42	24

Los coefientes ϵ y $\Delta\epsilon$ son calculados a partir de la la matriz de clusters de agua precipitable. El procedimiento consiste en calcular los valores medios de NDVI para cada cluster de W . Esto se realiza mediante las matrices de NDVI publicados por el ISLSCP. A partir de esos datos se obtienen valores medios mensuales de ϵ y $\Delta\epsilon$ para cada cluster. Los valores de estos coeficientes son mostrados en la tabla (4) y (5) respectivamente. Es interesante mencionar que en ausencia de valores estimados de emisividad desde imágenes NOAA, es posible utilizar los valores dados por las tablas (4) y (5), con el fin de obtener una ecuación de split window para cada área, representada por un cluster, y para cada mes del año.

Tabla 4.- Valores medios mensuales de $(1-\epsilon)$ para cada cluster de los mostrados en la figura 2.

M es	C1	C2	C3	C4	C5	C6	C7	C8
1	0.030	0.028	0.027	0.022	0.022	0.022	0.021	0.020
2	0.030	0.027	0.026	0.021	0.020	0.022	0.022	0.019
3	0.030	0.028	0.025	0.021	0.021	0.021	0.022	0.019
4	0.030	0.028	0.025	0.020	0.019	0.021	0.023	0.019
5	0.030	0.028	0.027	0.021	0.019	0.020	0.021	0.019
6	0.030	0.028	0.028	0.025	0.021	0.021	0.022	0.022
7	0.030	0.028	0.028	0.026	0.023	0.022	0.022	0.022
8	0.030	0.029	0.028	0.025	0.026	0.022	0.019	0.018
9	0.030	0.029	0.028	0.023	0.027	0.026	0.021	0.019
10	0.030	0.029	0.026	0.021	0.025	0.024	0.021	0.018
11	0.030	0.028	0.026	0.023	0.021	0.022	0.021	0.019
12	0.030	0.027	0.027	0.021	0.020	0.021	0.021	0.021

Tabla 5.- Valores medios mensuales de $\Delta\epsilon$ para cada cluster de los mostrados en la figura 2.

M es	C1	C2	C3	C4	C5	C6	C7	C8
1	-0.017	-0.009	-0.004	-0.001	-0.001	0.000	0.000	-0.001
2	-0.019	-0.008	-0.002	-0.001	-0.001	0.001	0.001	0.000
3	-0.018	-0.009	0.000	0.000	-0.001	0.000	0.001	0.000
4	-0.018	-0.009	0.000	0.000	0.000	0.000	0.001	0.001
5	-0.018	-0.005	0.000	0.002	0.001	0.001	0.001	0.000
6	-0.017	-0.009	-0.004	0.004	0.002	0.001	0.000	-0.001
7	-0.017	-0.009	-0.004	0.003	0.003	0.002	0.000	-0.001
8	-0.016	-0.011	-0.005	0.001	0.004	0.003	0.001	0.000
9	-0.016	-0.012	-0.007	0.001	0.002	0.000	0.001	0.001
10	-0.016	-0.010	-0.004	0.001	0.004	0.002	0.001	0.001
11	-0.017	-0.010	-0.005	0.000	0.002	0.000	0.001	0.001
12	-0.017	-0.008	-0.004	0.000	0.000	0.000	0.000	-0.001

3 CONCLUSION

Al disponer de dos bandas ubicadas en diferentes regiones del infrarrojo térmico, los satélites NOAA se presentan como una alternativa muy ventajosa para obtener la temperatura de la superficie terrestre. Es por ello que el método de split-window ha sido el más utilizado para este propósito. Sin embargo, para América del Sur no se contaba con una serie de coeficientes que permitiera contar con una ecuación de split-window adecuada para cada región climática. En el presente trabajo se han encontrado estos coeficientes a partir de datos climatológicos provenientes del reanálisis y datos de NDVI del ISLSCP, ambos a una escala de resolución de 2.5° en latitud y longitud. A partir de estos datos se pudieron obtener los coeficientes que dependen del agua precipitable. De esta forma la ecuación de split-window seleccionada se puede aplicar a esta región. Finalmente a partir de las tablas (3) a la (6) y la ecuación (7) se puede construir un algoritmo de split-window específico para cada área de interés.

4 REFERENCIAS

- Anding D. and Kauth R., 1970. Estimation of sea surface temperature from space. *Remote Sens. of Environ.*, 1:217-220.
- Barton I., 1983. Dual channel satellite measurements of sea surface temperature. *Quar. J. R. Meteor. Soc.*, 109: 365-368.
- Becker F. and Li Z. (1990). Towards a local split-window method over land surfaces. *Int. J. Remote Sens.*, 11: 369-394.
- Chandrasekhar S., 1960. Radiative transfer. Doer Publications, New York.
- Deschamps P. and Phulpin T., 1980. Atmospheric correction of infrared measurements of sea surface temperature using channels at 3.7, 11 and 12 mm. *Bound. Layer Meteorology*, 18: 131-143.
- Kondratyev K., 1969. Radiation in the atmosphere. Academic Press.
- Kneizys F.X., Shettle E.P., Abreu L.W., Anderson G.P., Chetwynd J.H., Gallery W.O., Selby J.E., Clough S.A., 1988. Users Guide to LOWTRAN-7. Technical Report AFGL-TR-88-0177, Optical/Infrared Technology Division, U.S. Air Force Geophysics Laboratory, Hanscom Air Force Base, Massachusetts.
- Mc. Clain E., Pichel W. and Walton C., 1985. Comparative performance of AVHRR based multichannel sea surface temperatures. *J. Geoph. Res.*, C6: 11587 - 11601.
- Masuda K., Takashima T. and Takayama Y., 1988. Emissivity of pure and sea waters for the 80% model sea surface in the infrared window regions. *Remote Sens. of Environ.*, 24:313-329.
- Maul G. and Sidran M., 1972. Comment on Anding and Kauth. *Remote Sens. of Environ.*, 2:165-169.
- McMillin L., 1975. Estimation of sea surface temperatures from two infrared window measurements with different absorption. *J. Geoph. Res.*, 36: 5113-5117.
- Morales L., 1997. Evaluación y zonificación de riesgo de heladas mediante modelización topoclimática. Tesis Doctoral. Universidad de Concepción. Chile.
- Prabhakara C., Dalu G. and Kunde G., 1974. Estimation of sea surface temperature from remote sensing in the 11-13 mm window region. *J. Geoph. Res.*, 79: 5039-5044.
- Prata A.L., 1993. Sea surface temperatures derived from the AVHRR and ATSR I: Theory. *Journal of Geophysical Research*, 98D9, 16, pp 16689-167702.
- Price J.C., 1984. Land surface temperature measurements from the split-window channels of the NOAA 7 AVHRR. *J. Geoph. Res.*, D5: 7137-7231.
- Raissouni N., 1999. Análisis multi-temporal de imágenes NOAA-Pathfinder AVHRR land para el estudio de la dinámica de la cobertura terrestre: Aplicación a la Cuenca Mediterránea. Tesis doctoral. Universidad de Valencia, España, pp 220.
- Rao C.R., Stowe L., McCalin E.P., 1989. Remote sensing of aerosols over oceans using AVHRR data. Theory, Practice and Applications. *International Journal of Remote Sensing*, vol 10, pp 743-749.
- Rothman L.S., 1992. The HITRAN molecular database: Editions of 1991 and 1992. *J.Q. Spect. Rad. Trans.*, N° 48, pp 469.
- Rubio E., Caselles V., Badenas C., Emissivity measurements of several soils and vegetation types in the 8-14 μm wave band: Analysis of two fields methods. *Remote Sensing of Environment*. 59:490-521.

- Saunders, P.M., 1967. Aerial measurements of sea surface in the infrared. *Journal of Geophysical Research*, 16, 4109-4117.
- Sobrino J. and Casselles V., 1989. Medida mediante el método de la caja de la emisividad en la banda espectral de los 8-14 mm de algunos suelos agrícolas y de la vegetación. *Anales de Física. Serie B*: 220-227.
- Sobrino J., Coll A., Casselles V., 1991. Atmospheric correction for land surface temperature using NOAA11-AVHRR channels 4 and 5. *Remote Sens. Environ.*, 38:19-34.
- Sobrino J., Coll A., Casselles V., 1993. La medida de la temperatura desde satélites. EN: *La teledetección en el seguimiento de los fenómenos naturales. Climatología y Desertificación*. Universitat de Valencia. España.
- Sobrino J.A., Li Z-L., Stoll M.P., 1993b. Impact of the atmospheric transmittance and total water vapor content in the algorithms for estimating satellite sea surface temperature, I.E.E.E., *Transactions on geoscience and remote sensing*, 31, 946-952.
- Sobrino J., Li Z-L, Stoll M.P. and Becker F., 1996. Multi-channel and multi-angle algorithms for estimating sea and land surface temperature with ATSR data. *International Journal of Remote Sensing*, Vol 17, No. 11, pp 2089-2114.
- Sobrino J.A., Olmeda M., Raissouni N., 1998. Aplicación de la técnica de composición del máximo NDVI al seguimiento de la cobertura terrestre en la Península Ibérica. *Revista Española de Teledetección*, 10:19-29.
- Sobrino J.A., 2000 (editor). *Teledetección*. Universitat de Valencia. España, pp 467.
- Sobrino J.A., Raissouni N., 2000. Toward remote sensing methods for land cover dynamics monitoring: Application to Morocco. *International Journal of Remote Sensing*, vol 21, N° 2, 353-366.
- Sobrino J.A., Raissouni N., Zhao-Lianh Li, 2001. A Comparative study of land surface emissivity retrieval from NOAA data. *Remote Sensing of Environment*. 75:256-266.
- Scott N.A., Chedin A., 1981. A fast line by line method for atmospheric absorption atlas. *Journal of Applied Meteorology*, vol. 20, pp 802-812.
- Ulivieri C., Castronuovo M, Newcomb W., 1992. a split window algorithm for estimating land surface temperature from satellite. *COSPAR*, 27, Washington, DC USA.
- Varanasi P., 1988. Infrared absorption by water vapor in the atmospheric window. *SPIE 928. Modeling of the atmosphere*, 213-230.

Sea surface temperature assessment during the wind and salinity experiment (WISE)

V. Caselles¹, R. Niclòs¹, E. Rubio¹, C. Coll¹, A. Camps² and J. Font³

¹Department of Thermodynamics, Universitat de València, C/. Doctor Moliner, 50. 46100. Burjassot (València). Spain, Tel: 3121, Fax:3385.

²Department of Signal Theory and Communications, Universitat Politècnica de Catalunya, Barcelona, Spain.

³CSIC, Institut de Ciències del Mar, Barcelona, Spain.

Vicente.Caselles@uv.es, Raquel.Niclos@uv.es

ABSTRACT- The final aim of the Wind and Salinity Experiment (WISE) is to obtain the salinity from L-band sea surface emissivity with a precision of ± 0.1 psu. This supposes a temperature precision of at least ± 0.3 K and our paper demonstrates that it is a feasible and reliable objective. Thus, using a thermal infrared radiometer (CE 312), the sea surface temperature (SST) is determined with a precision of ± 0.13 K.

1 INTRODUCTION

The WISE campaigns, sponsored by the ESA, were carried out at Repsol Company's Casablanca oilrig (Camps et al., 2002). The SST was obtained by means of a CE 312 radiometer under the geometric and spectral conditions defined by the methodology described below.

2 METHODOLOGY

2.1 The Radiative Model for The Sea Surface

Radiative transfer equation for an i sensor channel located h height measuring in an observation direction (θ, ϕ) is expressed by the following equations:

$$R_i(\theta, \phi, h) = R_s(\theta, \phi, 0) \tau_i(\theta, 0, h) + L_i^{\uparrow atm}(\theta) \quad (1)$$

$$R_s(\theta, \phi, 0) = \varepsilon_i(\theta, \phi) B_i(SST) + R_\rho(\theta, \phi) \quad (2)$$

$$R_\rho(\theta, \phi) = [1 - \varepsilon_i(\theta, \phi)] L_i^{\downarrow atm}(\bar{\theta}_r, \phi) \quad (3)$$

where $B_i(SST)$ = Planck's radiance for the sea surface temperature SST ; $\varepsilon_i(\theta, \phi)$ = emissivity of seawater, obtained by the model of Masuda et al. (1998); $\tau_i(\theta, 0, h)$ = atmospheric transmittance; $L_i^{\downarrow atm}(\bar{\theta}_r, \phi)$ ($L_i^{\uparrow atm}(\bar{\theta}_r, \phi)$) = downwelling (upwelling) sky radiance; and $\bar{\theta}_r = \pi - \theta$ (Sidran, 1981).

2.2 Spectral and Geometric Measurement Conditions

The optimum spectral region and view geometry for the SST determination will be where the atmosphere transmittance and surface emissivity are the highest and the sky radiances are the lowest.

Table 1 shows the spectral dependence of the atmospheric effects by means of the average magnitudes simulated for an elevation angle of 25° with the MODTRAN radiative transfer code (Berk et al., 1999) and integrated for the atmospheric layer transmittance, τ , the upwelling sky radiance, $L^{\uparrow atm}$, and the downwelling sky radiance, $L^{\downarrow atm}$ (both in $W/m^2 sr \mu m$).

Figure 1 shows the spectral and the angular dependence of the emissivity. Sea surface emissivity calculated by the model of Masuda et al. (1988) is displayed by means of: (a) the integrated values for each CE 312 channel against the surface wind speed, U (m/s), and using an elevation angle of 25° ; and (b) the CE 312 channel 1 (8-14 μm) emissivity against the elevation angle for several surface wind speed values. Now, PL indicates the case of plane surface, with completely specular water surface. Thus, we analyse: (a) the spectral dependence of the sea surface emissivity and (b) its angular dependence.

Both, spectral and angular analysis prove the best measurement conditions are: (i) a view zenith angle between 5° and 25° , and a (ii) spectral region within the band 10.5 - 11.5 μm (CE 312 channel 3).

CE 312 Channels

	Ch 1 (8-14 μm)	Ch 2 (11.5-12.5 μm)	Ch 3 (10.5-11.5 μm)	Ch 4 (8.2-9.2 μm)
τ (W2000)	0.984	0.987	0.994	0.982
τ (W2001)	0.979	0.981	0.992	0.977
$L^{\uparrow}\text{atm}$ (2000)	0.000116	0.000140	0.000050	0.000096
$L^{\uparrow}\text{atm}$ (2001)	0.000163	0.000213	0.000077	0.000135
$L^{\downarrow}\text{atm}$ winter	0.001046	0.001234	0.000543	0.000632
$L^{\downarrow}\text{atm}$ summer	0.003613	0.005807	0.003233	0.002237

Table 1.- Average magnitudes simulated for an elevation angle of 25° with the MODTRAN radiative transfer code and integrated for the atmospheric layer transmittance, τ , the upwelling sky radiance, $L^{\uparrow}\text{atm}$, and the downwelling sky radiance, $L^{\downarrow}\text{atm}$ (both in $\text{W}/\text{m}^2 \text{ sr } \mu\text{m}$).

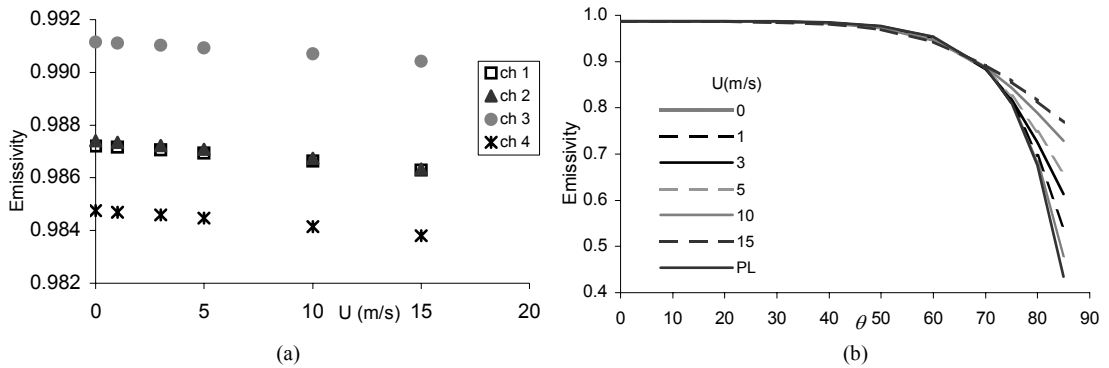


Figure 1.- (a) Emissivity integrated for each CE 312 channel against the surface wind speed, U (m/s), and using an elevation angle of 25° . (b) Angular dependence of the sea surface emissivity for the CE 312 channel 1 (8-14 μm). It shows emissivity against the elevation angle for several surface wind speed values. PL indicates the case of plane surface, with completely specular water surface.

2.3 Radiometric Data Corrections

It is necessary to correct the radiometric data in order to obtain the SST. There are three main effects to take into account:

Calibration process: A calibration process on the measurement system (protective camera-sensor), before and after each campaign, was made. In this way, an average error of ± 0.12 K for the CE 312 channel 3 brightness temperature was obtained.

Emissivity correction: Emissivity has been extracted by means of the model of Masuda et al. (1988) and using the surface wind speed as the only input.

Atmospheric correction: Table 2 indicates the temperature errors that would be committed if we neglected the effect of the downwelling atmospheric radiance and the atmospheric layer between surface and sensor (32 m height).

	Temperature differences (K)			
	Ch 1	Ch 2	Ch 3	Ch 4
Downward direction	-0.2	-0.3	-0.12	-0.19
Upward direction	0.12	0.04	0.03	0.14

Table 2.- Average temperature difference between taking into account the downwelling atmospheric radiance (downward direction) and the upwelling atmospheric layer effect (upward direction) or not in the radiative transfer equation (eq. 1 – 3).

This independent study of the upwelling and downwelling atmospheric effects confirmed the necessity of taking direct measurements of the downwelling sky radiance, however the upwelling contribution could be negligible.

2 RESULTS

The SST was obtained from WISE thermal-infrared radiometric measurements in the spectral band 10.5-11.5 μm with a view angle of 25° (sea surface) and 155° (sky) and modelling the emissivity against the measured surface wind speed.

The SST precision achieved by the method was $\pm 0.13 \text{ K}$. This is the average value of taking into account all the possible error sources (radiometric sensor error, calibration process, sensor pointing and wind surface speed determination).

The SST accuracy was $0.0 \pm 0.2 \text{ K}$. This is the average difference between oceanographic buoys temperature (reference temperature due to surface effect non-existence) and the SST retrieved from CE 312 radiometric data.

Figure 2 presents a histogram of the differences between the temperature observations registered by oceanographic buoys (Tb) and the SST retrieved from the CE 312 radiometric measurements (Tce). Figure 3 shows a detail of the inter-comparison between both temperatures. The histogram distribution results almost symmetrical around zero, therefore any systematic error is rejected and the good concordance between both data (Figure 2 and 3) validates the method.

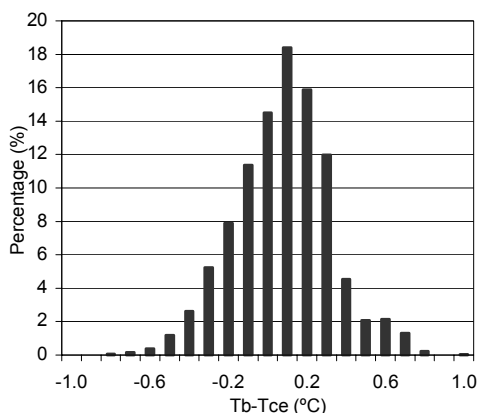


Figure 2.- Percentage histogram of the differences between the SST observations registered by oceanographic buoys (Tb) and the retrieved from the CE 312 radiometric measurements (Tce).

3 CONCLUSIONS

The sea surface temperature needs to be known with a precision at least of $\pm 0.3 \text{ K}$ in order to carry out the global climate request in salinity precision ($\pm 0.1 \text{ psu}$). Our purpose was the design of a methodology that permit us to obtain this temperature precision from radiometric thermal infrared data.

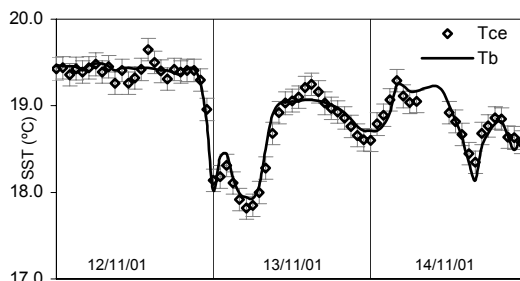


Figure 3.- Detail of the inter-comparison between the SST observations registered by the oceanographic buoys (Tb) and the retrieved from the CE312 radiometric measurements (Tce).

With this aim, we have determined the best measurement conditions as a view zenith angle between 5 and 25° and the 10.5 - 11.5 μm spectral region (CE 312 channel 3).

The application of the methodology developed to the WISE 2000 and WISE 2001 campaigns data has permitted us to obtain the sea surface temperature with a precision of $\pm 0.13 \text{ K}$ and an accuracy of $0.0 \pm 0.2 \text{ K}$.

Taking into account the SST precision (accuracy) attained, we could obtain the sea surface salinity with a precision (accuracy) of about $\pm 0.04 \text{ psu}$ ($\pm 0.06 \text{ psu}$). This satisfies the requirements imposed for the global climate studies within the SMOS Mission.

4 REFERENCES

- Berk, A., Anderson, G.P., Acharya, P.K., Chetwynd, J. H., Bernstein, L. S., Shettle, E.P., Matthew, M.W. and Adler-Golden, S.M., 1999, MODTRAN4 user's manual. Air Force Research Laboratory, Space Vehicles Directorate, Air Force Materiel Command, Hascom AFB, MA 01731-3010.
- Camps, A., Font, J., Etcheto, J., Rubio, E., Weill, A., Corbella, I., Vall-llossera, M., Duffo, N., Torres, F., Villarino, R., Enrique, L., Julià, A., Gabarró, C., Boutin, J., Caselles, V., Reising, S.C., Wursteisen, P., Martín-Neira, M. (2001) Sea Surface Emissivity Observations at L-band: First Results of the Wind and Salinity Experiment WISE-2000. *IEEE Trans. Geosc. Rem. Sens.* (submitted October 2001).
- Masuda, K., Takashima, T., and Takayama, Y., 1988, Emissivity of pure sea waters for the model sea surface in the infrared window regions. *Remote Sensing of Environment*, 48, 302-308.
- Sidran, M., 1981, Broadband reflectance and emissivity of specular and rough water surfaces. *Applied Optics*, 20, 3176-3183.

4. MICROONDAS / MICROWAVES

Recent progress in estimating snow properties using Synthetic Aperture Radar (SAR)

Jiancheng Shi

Institute of Remote Sensing Applications, Chinese Academy, Beijing China, & Institute for Computational Earth System Sciences, University of California, Santa Barbara. U.S.A
shi@icess.ucsb.edu

ABSTRACT - Seasonal snow cover is an important component in investigations of land-surface climate and hydrology. This study summarizes the recent progresses of using multi-parameter SAR in estimating snow properties. These progresses include 1) mapping snow cover, 2) estimating snow wetness, 3) estimating snow density, and 4) estimating snow depth and grain size. We demonstrate these progresses using SIR-C/X-SAR image data that was taken in 1994 in Mammoth Mtn., California.

1 INTRODUCTION

The most important attributes of the snow cover that are necessary for modeling runoff and climate in alpine areas are: snow water equivalence, snow covered area, free liquid water content, and spectral albedo. Because of rough, irregular topography, all these attributes exhibit large spatial variability over alpine drainage basins. Except area extent, those snow physical parameters have not been generally used in snow melting prediction because it is difficult and costly to measure on a routine basis over large areas.

The Shuttle Imaging Radar-C and X-Band Synthetic Aperture Radar (SIR-C/X-SAR), as an example, was a cooperative experiment between the National Aeronautics and Space Administration (NASA), the German Space Agency (DARA), and the Italian Space Agency (ASI). The SIR-C/X-SAR system was flown onboard NASA's Space Shuttle on two 10-day missions in April and October 1994. SIR-C provides radar polarimetric digital images simultaneously at two wavelengths, L-band (24 cm), and C-band (5.6 cm). These polarimetric data allows derivation of the complete scattering matrix on a pixel-by-pixel basis and more detailed information about the geometric structure and dielectric property of a target (Van Zyl *et al.*, 1987 and Evans *et al.*, 1988). X-band (3 cm) with VV polarization results in a three-frequency capability. The resolution of this system ranged between 10-m and 40-m, and it collected image swaths between 15 km and 90 km wide.

This study summarizes our current understanding of radar interactions with snow cover. We demonstrate our recent progresses of the algorithm developments on 1) mapping snow covered area, 2) inferring snow wetness, 3) estimating snow density, and 4) estimating snow depth and grain size. The examples will be given by using the SIR-C/X-SAR imagery obtained during

its first mission in April, 1994 over one of our test site - Mammoth Mt., California.

2 MAPPING SNOW COVER

Several methods have been developed to map snow cover in alpine regions. (1) using single pass, single frequency and polarization SAR image (Rott, *et al.*, 1988, Shi and Dozier, 1993); (2) using single pass but polarization properties (Shi, *et al.*, 1994); (3) using single frequency and polarization with repeat passes (Rott and Nagler, 1993); and (4) using single pass but multi-frequency and polarization (Shi and Dozier, 1997). Except the last technique, all above methods are restricted to mapping wet snow-cover since it is difficult to discriminate dry snow cover with bare ground and short vegetation. In a recent study using SIR-C/X-SAR data to map snow cover (Shi and Dozier, 1997), it was found that wet snow cover had very similar backscattering intensity and polarization characteristics to smooth bare surface at C-band and X-band. For instance, the backscattering from wet snow-cover is very similar to smooth dry soil, alluvial surfaces, and relatively rough water surfaces. At a large drainage basin or regional scale, where many different targets are within a scene, those techniques might not be reliable. For similar reasons, change detection measurement, are more unreliable since the similar change in backscattering could be caused by different natural environment changes. In order to develop a large-scale snow mapping technique other measurement are required to discriminate between snow and other targets.

Interferometric radar techniques for topographic mapping of surfaces promise the high-resolution digital elevation models; but they also permits inference of changes in the surface over the orbit repeat cycle from the correlation properties of the radar echoes. Measurements of interferometer

correlation describe processes occurring on the time scales of the orbit repeat time and size scales on the order of a radar wavelength, such as vegetation growth, glacier motion, permafrost freezing and thawing, and soil moisture induced effects. The coherence measurement between two repeat-passes, therefore, provides a useful measurement in addition to backscattering intensities in each scene and their changes between two passes, and makes it possible to develop an algorithm for mapping both dry and wet snow covers over large area.

We evaluated the coherence measurements between two repeat-pass SIR-C image data from its first mission in April (has snow) and second mission in October (without snow), 1994. This measurement indicates that the ground is completely undisturbed between viewings the signals will be highly correlated. Otherwise, the decorrelation will occur. Figure 1 (left) shows the coherence measurements of L-band VV polarization as y-axis and VH polarization ratio of L-band to C-band as x-axis from 5 targets - snow as shown by character *s*, lake - *w*, bare surface - *b*, short vegetation - *v*, and forest - *f*. The reason why we select the VH polarization ratio of L-band to C-band is that this measurement can be obtained without requiring terrain correction and also provide a good separation between the bare surface, short vegetation, and forest. It can be clearly seen that lake and snow cover have very low coherence between two data-takes with and without snow cover. For the lake, the decorrelation between two data-takes is mainly due to the changes of the lake surface roughness characteristics, because of different windy conditions, such as wind speed and direction. For the dry snow case, the dominant scattering at L-band is from the snow-ground interface. In addition to the change of the dielectric contrast from the air-ground to snow-ground, existing dry snow cover will result in large decorrelation. This is due to change in local incidence angle when radar signal passes through snow layer will cause a spatial baseline decorrelation. We also expect that the radar echoes will be close to completely decorrelated when measuring correlation between wet snow-cover and bare ground passes. This is because the radar signal in snow-covered pass can only penetrate a few centimeters so that the radar senses two different targets. The coherence measurements from the bare surface are significantly higher than those from lake. For the bare surface, a change of soil moisture will result in a decorrelation. However, the amount of decorrelation is expected to be smaller because radar senses a same target with a same scattering mechanism (only change in magnitude). The short vegetation (mainly sagebrush and grass in our study area) has very similar coherence measurements to the bare

surface mainly due to the dominant scattering source is from the ground surface at L-band. However, the coherence measurements from forest can have very low values - similar to those from snow and lake, especially from dense forest.

Therefore, the coherence measurement between a snow covered scene and one without snow and provide a very good separation between snow cover and bare surface as well as short vegetation. These two targets are most difficult to discriminate with snow cover. Thus, the correlation measurement provides a significant information to map snow covered area. We could use the coherence measurements to discriminate forest, open water, and snow with short vegetation and bare ground. Then using backscattering intensities to separate forest and open water with snow.

We used decision tree classifier (DTC) to establish a pixel-based classifier based on training sets. In order to verify the classification results, we acquired a cloud-free Landsat Thematic Mapper scene on April 14, 1994 (the SIR-C/X-SAR data-take on April 13, 1994). We classified the TM data using same technique. The geocoded the TM classification map was then projected (or co-registered) to the slant range presentation of the SAR images by using the Shuttle ephemeris data and ground control points. In the classification of the TM scene, there are only four target categories: lake, snow, forest, and range land, which includes bare ground and short vegetation. Figure 1 shows the SAR classification map (right) and the TM classification map (left). The comparison estimation of this two results indicated that at 86 % accuracy can be obtained for snow cover area under consideration of the TM classification map as the ground truth.

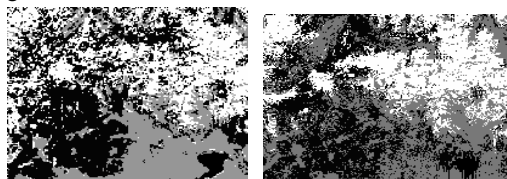


Figure 1. Comparison of SAR (right) and TM (left) derived classification maps. Black - Forest and Lake, grey - bare surface and short vegetation, white - snow.

3 ESTIMATION OF SNOW WETNESS

3.1 Current Understanding

Generally, SAR backscattering measurements from wet snow are affected by two sets of parameters: (1) sensor parameters, which include the frequency, polarization, and viewing geometry, and (2) snow parameters, which include snow density, liquid water

content, particle sizes and shapes of ice and water inclusions, type of the correlation function, and surface roughness. At C-band, the backscattering is controlled by snow volume backscattering and the surface backscattering at air - snow interface.

Surface roughness also affects the relationship between the backscattering coefficients and snow wetness. As snow wetness increases the backscattering decreases rapidly for low wetness (< 3%) conditions because volume scattering albedo decreases. When wetness is low, the dielectric contrast between air and snow is small and volume scattering dominates, so backscattering is not sensitive to surface roughness. As snow wetness further increases, backscattering becomes sensitive to surface roughness. This is because the surface scattering component becomes dominating, resulted from rapidly increasing surface scattering component and decreasing volume scattering component.

The relationship between backscattering and snow wetness is controlled by the scattering mechanism. When the surface is smooth, volume scattering dominates. Hence as snow wetness increases, both the volume scattering albedo and the transmission coefficients greatly decrease, resulting in a negative correlation between the backscattering and snow wetness. When the surface is rough, increasing snow wetness causes surface scattering to dominate, resulting in a positive correlation between the backscattering and snow wetness. Moreover, the relationship between co-polarization and snow wetness can be either positive or negative, depending on snow characteristics and surface roughness and on incidence angle. This complexity of the relationship between the backscattering and snow wetness makes it unrealistic to develop an empirical relation between the SAR signal and field measurements.

3.2 Algorithm to Estimate Snow Wetness with C-band Polarimetric SAR Measurements

An algorithm has been developed for snow wetness retrieval using C-band polarimetric SAR imagery (Shi and Dozier, 1995). This algorithm is based on a first-order scattering model that considers both surface and volume scattering.

A simplified surface backscattering model was obtained from the numerical simulations by using IEM model for the conditions of most seasonal wet snow covers. Through the property of the volume scattering ratio in co-polarizations which is only a function of snow permittivity and the simplified surface backscattering model, the inverse model by using

three measurements \mathbf{S}_t^{vv} , \mathbf{S}_t^{hh} , and \mathbf{S}_t^{vvhh} can be written as

$$M_1[a_{vx} \text{Re}[\mathbf{a}_{vv} \mathbf{a}_{hh}^*] \times (a_{vix} D_{RS} - D_{TS}) + b_{vx} M_2] \\ = M_2 \left[a_{vx} \text{Re}[\mathbf{a}_{vv} \mathbf{a}_{hh}^*] + \frac{b_{vx} M_2}{a_{vix} D_{RS} - D_{TS}} - D_{TV} |\mathbf{a}_{vv}|^2 \right] \quad (1)$$

with

$$M_1 = \mathbf{S}_t^{vvhh} - D_{TV}(\mathbf{q}_i, \mathbf{e}_s) \times \mathbf{S}_t^{vv} \quad (1.1)$$

$$M_2 = \mathbf{S}_t^{vv} + \mathbf{S}_t^{hh} - D_{TS} \times \mathbf{S}_t^{vvhh} \quad (1.2)$$

$$D_{TS} = \frac{D_{TV}(\mathbf{q}_i, \mathbf{e}_s) + D_{TH}(\mathbf{q}_i, \mathbf{e}_s)}{D_{TV}(\mathbf{q}_i, \mathbf{e}_s) \times D_{TH}(\mathbf{q}_i, \mathbf{e}_s)} \quad (1.3)$$

$$D_{RS} = \frac{|\mathbf{a}_{vv}(\mathbf{q}_i, \mathbf{e}_s)|^2 + |\mathbf{a}_{hh}(\mathbf{q}_i, \mathbf{e}_s)|^2}{\text{Re}[\mathbf{a}_{vv}(\mathbf{q}_i, \mathbf{e}_s) \mathbf{a}_{hh}^*(\mathbf{q}_i, \mathbf{e}_s)]} \quad (1.4)$$

Where $\mathbf{S}_t^{vvhh} = \text{Re}[\mathbf{S}_t^{vv} \mathbf{S}_t^{hh*}]$ is the real part of the cross product of VV and HH complex scattering elements, \mathbf{a}_{vv} and \mathbf{a}_{hh} are the polarization amplitudes (Ulaby, et al., 1982). $a_{vx}(\mathbf{q}_i)$, $a_{vix}(\mathbf{q}_i)$, and $b_{vix}(\mathbf{q}_i)$ are coefficients derived from statistical analyses and depend only on incidence angle.

They are given in (Shi and Dozier, 1995) $D_{TV}(\mathbf{q}_i, \mathbf{e}_s)$ and $D_{TH}(\mathbf{q}_i, \mathbf{e}_s)$ denote the volume backscattering ratios for $\text{Re}[\text{VVHH}^*]$ to VV and $\text{Re}[\text{VVHH}^*]$ to HH which are only depending on the local incidence angle and the dielectric constant of a wet snow pack.

This concept is from the first-order volume backscattering model for an inhomogeneous dielectric half space medium:

$$\mathbf{S}_v^{pp} = \frac{3}{4} \mathbf{W} T_{pp}^2 \cdot \exp[-2s^2(k_1 \cos(\mathbf{q}_i) - k_2 \cos(\mathbf{q}_i))^2] \quad (2)$$

T_{vv} and T_{hh} are power transmission coefficients for a plane interface for vertical and horizontal polarization. s is the standard deviation of the random surface height. The loss factor $\exp[-2s^2(k_1 \cos(\mathbf{q}_i) - k_2 \cos(\mathbf{q}_i))^2]$ is the rough surface effect on the power transmission coefficient. \mathbf{W} is the volume scattering albedo, which depends on snow density, wetness, particle size, size variation and shape.

Under the assumption of spherical grains or randomly orientated particles, the volume scattering albedo is independent of the polarization. Therefore, the ratio for the first-order volume backscattering signals of VV

and HH polarizations can be represented as a function of the local incidence angle and dielectric constant:

$$D_{TH}(\mathbf{q}_i, \mathbf{e}_s) = \frac{\mathbf{s}_v^{vvhh}}{\mathbf{s}_v^{hh}} = \frac{\text{Re}[T_{vvhh}(\mathbf{q}_i, \mathbf{e}_s)]^2}{T_{hh}^2(\mathbf{q}_i, \mathbf{e}_s)} \quad (2.1)$$

and

$$D_{TV}(\mathbf{q}_i, \mathbf{e}_s) = \frac{\mathbf{s}_v^{vvhh}}{\mathbf{s}_v^{vvh}} = \frac{\text{Re}[T_{vvhh}(\mathbf{q}_i, \mathbf{e}_s)]^2}{T_{vv}^2(\mathbf{q}_i, \mathbf{e}_s)} \quad (2.2)$$

The algorithm derived above requires no information about the volume scattering albedo or the surface roughness parameter. With known local incidence angle, it involves only the calculation of snow pack permittivity, which can be directly related to snow wetness. This algorithm is applicable to the situations of incidence angle from 25° to 70° , and the snow surface roughness - rms height < 0.7 cm and correlation length < 25 cm.

3.3 Validation from SIR-C's C-band Image Data

To test the algorithm for measuring snow wetness over a large area, we first mapped snow-covered area. Then we determined the Stokes matrix by the mean value within a 5×2 window to reduce image speckle, and applied the terrain correction. After the terrain correction, we determined the backscattering coefficients from the single-scattering components which was decomposed by Cloude's method from the averaged Stokes matrix. Then the algorithm was applied. Due to large variations of the surface orientation in alpine regions, the average processing of Stokes matrix to reduce the image speckle is, in general, limited to the scale of available DEM data in order to obtain a maximum information of the surface orientation for terrain correction. The image speckle might still cause the fluctuations in backscattering coefficients and decrease the measurement accuracy. In addition, the errors from model simplification and terrain correction, due to uncertainty in calculation of the local incidence angle, will also cause errors in estimation of snow wetness but they are more associated with at the scales of a pixel to tens pixels. We expect that snow wetness cannot be estimated for some pixels and that there is some uncertainty in the estimated snow wetness value. In post-processing, an average value from surround pixels within a 5×5 window was applied to fill in missing values and to reduce uncertainties. Notice this post-processing will only reduce the errors as mentioned above. The errors resulted from the antenna thermal noise and image data calibration are only associated with whole image scale. In other words, they will cause an overall under-estimation or over-estimation of snow wetness.

Figure 2 shows the comparison between the field measurements and the derived snow wetness for the locations where the ground measurements were available. Those included eight snow pits and two transects. The SAR-inferred snow wetness values were obtained from an average value of 3×3 windows around the snow pit locations. Snow wetness measurements from the transects were also averaged to 100 m scales and the inferred snow wetness from SAR was determined from a mean value of 4×2 windows along the transect measurements. Most SAR-derived snow wetness agreed well with estimates of snow wetness. The standard deviation of absolute error was about 1.3% by volume which gives 2.5% error bars at 95 % confidence interval for absolute error. The algorithm performed well on both local and regional scales and provided a quantitative estimate of spatial distribution of snow wetness at the top snow layer.

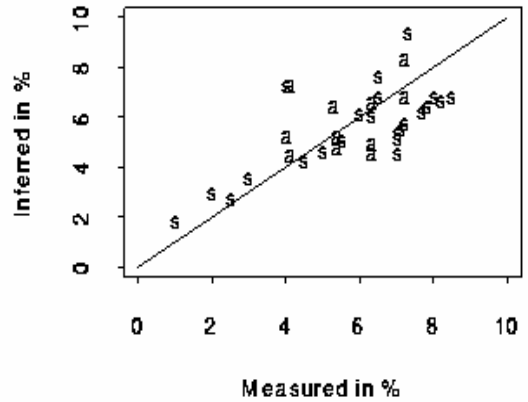


Figure 2. comparison between the field measurements and the derived snow wetness using C-band SIR-C's polarimetric SAR data.

4 ESTIMATION OF SNOW DENSITY WITH L-BAND MULTI-POLARIZATION SAR

4.1 Current Understanding

Snow density and depth are generally not highly correlated, so they must be considered as independent variables in field surveys of the spatial distribution of snow and in the study of snow's microwave backscattering properties. During the past two decades, little attention has been paid to microwave interactions of snow pack at L-band (1.25 GHz) frequencies or lower, while much work has been done at C-band (5.5 GHz) or higher frequencies (Rott *et al.*, 1988, Ulaby, *et al.*, 1982, Stiles and Ulaby, 1980,

Ulaby and Stiles, 1980, Ulaby *et al.*, 1984, Rott and Matzler, 1987). Because snow grains are much smaller than incident L-band wavelengths, no significant volume scattering can be generated by a snowpack. At C-band or higher frequencies, however, snow density affects the magnitude of the volume scattering and the surface scattering properties at the snow-ground interface.

Volume scattering and extinction from dry snow are small at L-band. At microwave frequencies, the absorption coefficient (the imaginary part of the dielectric constant) of ice is small, and snow grains are also small compared to an incident L-band wavelength (24 cm). Therefore, we can simplify the backscattering model by considering a dry, homogeneous snowpack over a bare soil or rock surface.

Two sets of parameters control surface backscattering from a random surface with no orientation of features: The *sensor* parameters include frequency, polarization, and incidence angle, and the *surface* parameters include the dielectric constant and surface roughness (roughness is generally described by an autocorrelation function and standard deviation of surface roughness height).

When the electromagnetic wave passes through the snowpack, versus directly striking the ground, the following differences occur:

§ Because of refraction within the snow, the incidence angle at the snow-ground interface is smaller.

§ The incident wavelength at the snow-ground interface is shorter because the snow is dielectrically thicker than air.

§ The snow layer reduces the dielectric contrast at the snow-ground interface, which in turn reduces the reflectivity at snow-ground interface.

§ The power loss at the air-snow interface reduces the total energy incident on the snow-ground interface.

The first two factors result in a change of the sensor observing parameters. Assuming the snowpack has no significant volume scattering at L-band, we can calculate

$$\mathbf{S}_{pp}^t(k_0, \mathbf{q}_i) = T_{pp}^2(\mathbf{q}_i) \mathbf{S}_{pp}^g(k_1, \mathbf{q}_r) \quad (3)$$

Note that the dielectric contrast ϵ_g/ϵ_s should be used instead of ϵ_g and that k_1 should be used instead of k_0 when calculating the backscattering \mathbf{S}_{pp}^g at the snow-ground interface. Since most natural terrain has a small rms height and random surface slope, single scattering will dominate over multiple scattering in most situations. In this study, the single-scattering

IEM model is used because it allows for a much wider range of surface roughness conditions than the traditional surface backscattering models (Fung, 1984).

The shift in wavenumber $k_1 = k_0 \sqrt{\epsilon_s}$ (or wavelength $\lambda_0 = \lambda_1 \sqrt{\epsilon_s}$) is a function of snow density. For the range of snow densities considered—100 to 550 kg m⁻³—the L-band propagation wavelength in snow ranges from 21 to 16 cm, compared to 24 cm in air. Because the surface roughness effect depends on its size relative to the incident radar wavelength, the shortening of the incident wavelength for higher snow densities will result in the soil surface appearing rougher than it would if the snow were absent. This causes an increase in the surface backscattering signal and is especially strong for a nearly smooth surface. However, this effect caused by the wavelength shift becomes smaller when the surface is rougher or the incident frequency is higher.

Snell's law specifies the change in incidence angle: $\sin(\mathbf{q}_i) = \sin(\mathbf{q}_r) \sqrt{\epsilon_s}$. The incidence angle at the snow-ground interface depends only on the incidence angle at the snow surface and the dielectric constant of snow, not on its thickness, thus it is a function of snow density. For a given incidence angle at the snow surface, a greater snow density causes a greater change in the incidence angle at the snow-ground interface. For a given snow density, however, a larger incidence angle at the snow surface results in a greater change in the refractive angle in the snow layer. Therefore, a greater increase in the backscattered power at larger incidence angles is expected than that at smaller incidence angles.

Furthermore, comparison of HH and VV polarizations shows a smaller increase in VV polarization than in HH polarization for the same snow density and ground surface properties. The backscattering of VV polarization as a function of incidence angle declines more slowly than that of HH polarization when the surfaces are not too rough. Therefore, the changes in VV polarization are smaller than that of HH polarization. However, for a very rough surface, the angular dependence is smaller than that for a smooth surface, and the difference between VV and HH polarization is smaller.

In summary, while a dry snowpack does not absorb or scatter the radar signal at low frequencies, it nevertheless affects the magnitude of the backscattering from the underlying rock or soil and the relationship between HH and VV polarization. The

magnitude of the effect depends on the radar incidence angle, snow density, roughness and dielectric properties of the soil. Snow is more likely to enhance the backscattering magnitude of a smooth soil than a rough soil. These factors enable development of an algorithm for inferring snow density using L-band SAR measurements.

4.2. Algorithm to Estimate Snow density

To find a manageable inversion algorithm that can handle a large volume of SAR data, we need to characterize the dependence of the surface backscattering on both the incidence angle and the wavelength, since the surface backscattering model in Equation (4) is generally complicated. For this purpose, we first simulated the surface backscattering components \mathbf{s}_{hh}^g and \mathbf{s}_{vv}^g using the IEM model [6] over a wide range of incidence angles, dielectric and roughness conditions, and incidence wavenumbers, corresponding to a range of snow densities from 100 to 550 kg m⁻³.

Secondly, we characterized the relationship of HH and VV backscattering signatures with the wide range of surface dielectric and roughness conditions at each incidence angle and wavenumber, using regression analysis to find coefficients to parameterize this relationship:

$$\begin{aligned} \log_{10} \left[\sqrt{\mathbf{s}_{hh}^g} + \sqrt{\mathbf{s}_{vv}^g} \right] &= a(\mathbf{q}_r, k_1) \\ &+ b(\mathbf{q}_r, k_1) \log_{10} (\mathbf{s}_{hh}^g + \mathbf{s}_{vv}^g) + c(\mathbf{q}_r, k_1) \log_{10} (\mathbf{s}_{hh}^g) \\ &+ d(\mathbf{q}_r, k_1) \log_{10} \left(\frac{\mathbf{s}_{hh}^g}{\mathbf{s}_{vv}^g} \right) + e(\mathbf{q}_r, k_1) \log_{10} \left(\frac{\mathbf{s}_{hh}^g}{\mathbf{s}_{vv}^g} \right)^2 \end{aligned} \quad (4)$$

Eq. (4) represents a relationship between the surface backscattering coefficients \mathbf{s}_{hh}^g and \mathbf{s}_{vv}^g at a given incidence angle and wavenumber for a wide range of random rough surfaces. The form of the relationship minimizes its sensitivity to the surface dielectric and roughness properties, while maximizing its sensitivity to the incidence angle and wavenumber. The coefficients a , b , c , d and e in Eq. (4) depend only on incidence angle and wavenumber at the ground surface. They are given in (Shi and Dozier, 2000).

By placing Eq. (3) in Eq. (4), we derive the algorithm for estimation of snow density by using only \mathbf{s}_{hh}^t and \mathbf{s}_{vv}^t SAR measurements:

$$\begin{aligned} \log_{10} \left[\frac{\sqrt{\mathbf{s}_{hh}^t}}{T_{hh}(\mathbf{q}_i, \mathbf{e}_s)} + \frac{\sqrt{\mathbf{s}_{vv}^t}}{T_{vv}(\mathbf{q}_i, \mathbf{e}_s)} \right] &= a(\mathbf{q}_r, k_1) \\ &+ b(\mathbf{q}_r, k_1) \log_{10} \left[\frac{\mathbf{s}_{hh}^t}{T_{hh}^2(\mathbf{q}_i, \mathbf{e}_s)} + \frac{\mathbf{s}_{vv}^t}{T_{vv}^2(\mathbf{q}_i, \mathbf{e}_s)} \right] \\ &+ c(\mathbf{q}_r, k_1) \log_{10} \left[\frac{\mathbf{s}_{hh}^t}{T_{hh}^2(\mathbf{q}_i, \mathbf{e}_s)} \right] \\ &+ d(\mathbf{q}_r, k_1) \log_{10} \left[\frac{\mathbf{s}_{hh}^t T_{vv}^2(\mathbf{q}_i, \mathbf{e}_s)}{\mathbf{s}_{vv}^t T_{hh}^2(\mathbf{q}_i, \mathbf{e}_s)} \right] \\ &+ e(\mathbf{q}_r, k_1) \log_{10} \left[\frac{\mathbf{s}_{hh}^t T_{vv}^2(\mathbf{q}_i, \mathbf{e}_s)}{\mathbf{s}_{vv}^t T_{hh}^2(\mathbf{q}_i, \mathbf{e}_s)} \right]^2 \end{aligned} \quad (5)$$

In Eq. (5), T_{pp} depends on the polarization pp , the incidence angle \mathbf{q}_i at the air-snow interface, and the dielectric constant of the snowpack \mathbf{e}_s . \mathbf{e}_s is the only unknown; \mathbf{q}_i can be calculated from a combination of the Space Shuttle orbital data and a digital elevation model. Therefore, for a given L-band SAR measurements of \mathbf{s}_{hh}^t and \mathbf{s}_{vv}^t , we can estimate \mathbf{e}_s numerically by varying the coefficients of a , b , c , d , and e to find the root of Eq. (5). It does not require *a priori* knowledge of the dielectric and roughness properties of the soil under the snow.

Furthermore, snow density can be estimated from Looyenga's semiempirical dielectric formula (Looyenga, 1965), which provides a good fit to Polder and van Santen's physical formula (Matzler, 1987).

$$\mathbf{e}_s = 1.0 + 1.5995 \mathbf{r}_s + 1.861 \mathbf{r}_s^3 \quad (6)$$

5 ESTIMATION OF SNOW DEPTH and GRAIN SIZE WITH C- and X-BAND MULTI-POLARIZATION SAR

5.1 Current Understanding

Field experiments using ground scatterometer data have shown different relationships between radar backscattering and SWE. For example, Ulaby and Stiles (1980) showed that backscattering at 8.2 and 17.0 GHz had a positive relation with SWE. Similarly, a positive relationship was also observed by an experiment over a smooth subsurface at 5.3 and 9.5 GHz (Kendra et al., 1998). However, this positive relationship existed only over a frozen subsurface, with no correlation over the unfrozen subsurface (Bernier and Fortin, 1998).

On the other hand, negative relationships have been observed at similar frequencies, 5.3 and 9.6 GHz (Strozzi, 1996). In addition, Rott and Mätzler (1987)

observed no significant difference between snow-free and dry snow covered regions at 10.4 GHz. Each field experiment represented particular snow and ground conditions.

The existence of both positive and negative relationships between radar backscattering and snow water equivalence indicates that this relationship is quite complex. The confusion may result from varying combinations of snow and ground properties, because backscattered power received by the radar over dry snow depends not only on the total snow mass but also on the snow's density, grain size, structure, and stratification, along with the dielectric and roughness properties of the underlying surface. Understanding this relationship is essential to the development of a reliable algorithm for estimating snow water equivalence.

A physically based backscattering model can directly explain the relationship. For simplicity, we discuss this relationship using a "cloud model" in which the interaction terms between the ground surface and the snow volume are ignored. The first derivative of this model with respect to snow depth d represents the slope of the backscattering curves in response to snow depth; it can be written as

$$\frac{\partial \mathbf{s}_{pp}^t(\mathbf{q}_i)}{\partial d} = T_{pp}^2 \frac{2\mathbf{k}_e}{\mathbf{m}_t} \exp(-2\mathbf{k}_e d / \mathbf{m}_t) \cdot \left(\frac{3}{4} \mathbf{w}\mathbf{m}_t - \mathbf{s}_{pp}^g \right) \quad (7)$$

The ground surface backscattering signal has a great impact on the relationship between the backscattering and snow depth. The sign of the bracketed term in (7) determines whether the relationship between the measured backscattering signal and snow depth is positive or negative. If $\mathbf{s}_{pp}^g > \frac{3}{4} \mathbf{w}\mathbf{m}_t$, the slope is negative. Physically, this means that the attenuated subsurface scattering signal, after it passes through the snowpack, is larger than the backscattering signal generated by the snowpack. It is possible for the bracketed term to be zero, in which case there is no correlation between backscattering and snow depth. In this case, the attenuated amount of the subsurface scattering signal is the same as that of the backscattering signal generated by snowpack. Even for the same snowpack, a positive relationship to snow depth may be observed over a smooth surface but a negative relationship will be observed over a rough surface.

Moreover, the sensitivity of the backscattering signal to snow depth depends not only on the snow properties, but also on the incidence angle, and the magnitude of the subsurface backscattering. From (7),

we can also see that as the snow depth increases, the change in backscattering will decrease. Therefore, we expect that the change in the backscattering measurements is more sensitive to shallow snow than to thick snow. The extinction coefficient and volume scattering albedo are positively correlated to the sensitivity of backscattering to snow depth. For a given snow depth, the larger these parameters, the greater the changes that will be expected. Similarly, the sensitivity is also proportional to the angle of incidence, which indicates that a large incidence should be more effective than a small incidence for the purpose of monitoring snow depth. Note that the parameters, such as the ground dielectric and roughness properties in the ground-surface and snow-volume interaction terms, also affect the relationships. The combinations of all parameters control the overall result.

From our understanding, the backscattering signal from a seasonal natural snow cover and the signal's relationship to snow depth are affected by three sets of parameters: 1) Sensor parameters, which include the frequency, polarization, and incidence geometry; 2) Snowpack parameters including snow density, particle size and size variation, free liquid water content, characteristics of particle spatial distribution (stickiness), and stratification, and 3) subsurface parameters that include the dielectric and roughness properties at the snow - ground interface. These complex relationships make it implausible to characterize the parameters from the limited field experiment measurements and to derive an empirical model for estimating snow depth or water equivalence from SAR measurements. To estimate snow depth and thereby water equivalence, we must separate the varying backscattering signals of the subsurface or minimize the effect of the backscattering signal generated by the snow-ground interface.

5.2 Algorithm to Estimate Snow Depth and Grain Size

It is clear that estimating the snow depth requires a physically based inversion model that considers all important scattering terms and a technique to separate the backscattering components of the snowpack itself from those of the air-snow and snow-ground interfaces. The model can be rewritten using the backscattering coefficient

$$\mathbf{s}_{pp}^t(f) = \mathbf{s}_{pp}^a(f) + \mathbf{s}_{pp}^v(f) + \mathbf{s}_{pp}^{gv}(f) + T_{pp}^2 \exp[-2\mathbf{k}_e(f)d / \mathbf{m}_t] \mathbf{s}_{pp}^g(f) \quad (8)$$

where σ_{pp}^g is the surface backscattering at the snow-ground interface. To carry out a forward simulation of a dry snow covered terrain (8) requires a total of 13

surface and snow parameters. The six snowpack parameters include snow depth, density, ice particle size, size variation, stickiness, and temperature. In addition to the dielectric constant of the ground, the six surface roughness parameters include RMS height, correlation length, and the two-parameter correlation functions at the air-snow and the snow-ground interfaces. It is difficult to estimate snow properties directly by using only the three SIR-C's SAR measurements.

However, we can use L-band SAR measurements to estimate the snow density ρ_s , ground dielectric constant ϵ_g , and surface RMS height s . From these parameters, we can obtain ϵ_s , q , k_i , T_{pp} , and ground reflectivity R_{pp12} . The remaining unknowns in (8) are the surface backscattering components $\sigma_{pp}^s(f)$ from the snow-ground interface and $\sigma_{pp}^a(f)$ from the air-snow interface, the extinction coefficients $\kappa_e(f)$, the volume scattering albedo $\omega(f)$, and the snow depth d .

To derive the snow parameters, we first simulated the backscattering coefficients at C- and X-band, using (8) with wide ranges of both the subsurface conditions and the snowpack parameters shown. Through analyses of the simulated data, we developed techniques for estimating snow depth and ice particle size using SIR-C C-band and X-SAR measurements, based on the following approaches:

§ *Semi-empirical models to characterize the snow-ground interaction terms.* These models represent the snow-ground interaction components more realistically than formulas developed under the assumption of independent scattering. Natural surfaces in alpine regions are quite rough. Therefore, a significant contribution to the snow-ground interactions from non-coherent components is expected. The semi-empirical models are developed explicitly in terms of snowpack volume scattering albedo, optical thickness, ground reflectivity, and surface RMS height. They are easy to implement in the inverse algorithm.

§ *Semi-empirical model to characterize the relationships between the ground surface backscattering components at C-band and X-band.* With L-band SAR estimates of the ground dielectric constant and RMS height, the relationships between the ground surface backscatterings at C-band and X-band can be well characterized. Thus, the unknowns in the ground surface backscattering formulation can be reduced to one.

§ *Parameterizing the relationships between snowpack extinction properties at C-band and X-band.* Because the extinction properties are highly correlated, we developed analytical forms for the extinction relationships at C-band and X-band. Using

these relationships, the number of unknowns in backscattering components from the snowpack can be reduced to two: the volume scattering albedo w and the optical thickness t .

From the developments in the above, the number of unknowns has been reduced to three in (8), that is τ , ω and the surface component : $\sigma_{vv}^s(X)$. Thus, these three unknowns can be solved numerically at each pixel by using (8) with three SAR measurements: $\sigma_{vv}^t(C)$, $\sigma_{hh}^t(C)$, and $\sigma_{vv}^t(X)$.

Furthermore, the absorption coefficient and $k_a(X)$ and snow depth can be estimated by

$$k_a(X) = 1.334 + 1.2182 \log(V_s) - 3.4217 \log \left(\frac{t(X)[1-w(X)]}{t(C)[1-w(C)]} \right) \quad (9)$$

$$d = \frac{t(X)[1-w(X)]}{k_a(X)} \quad (10)$$

V_s can be derived from the estimated snow density at each pixel by using L-band measurements.

By taking one step further, we develop a formula for estimating the optically equivalent particle size, defined as a particle size at which the extinction properties from a natural snow volume equal those obtained from an ideal snow volume with a uniform distribution of ice particles (Shi et al., 1993). This optically equivalent particle size can be represented by the weighted mean size with respect to the scattering properties for a natural snowpack and can be estimated by

$$\bar{r}_s = \left(\frac{0.01 k_s(X)}{2V_s S_f (2.8332 + 6.6143V_s)} \right)^{\frac{1}{3}} \quad (11)$$

where \bar{r}_s is in cm. $k_s(X)$ can be obtained from the estimated $k_a(X)$ and $w(X)$ at each pixel.

6 VALIDATION SNOW DENSITY, DEPTH, AND GRAIN SIZE WITH SIR-C/X-SAR DATA

We used three processed data-takes from the first mission SIR-C/X-SAR in April 1994. The three data-takes were acquired in the early morning around 6:00 a.m., while the snow pit measurements taken at 11:00 a.m. showed no signs of liquid water in the snow, even at 2,850 m elevation. Thus the imaged snowpacks were dry. The SIR-C calibration team at the Jet Propulsion Laboratory (JPL) performed radiometric calibrations for each data-take. Using the Space Shuttle orbital geometry data and a digital elevation model, we derived the terrain radiometric calibration

factor and local incidence angle images corresponding to the SIR-C image data. The terrain radiometric correction factor is $\sin q_0 / \sin q_i$, where q_0 is the incidence angle used in the initial SAR data processing under a flat surface assumption and q_i is the actual local incidence angle.

To estimate snow density, the subsurface dielectric constant, and rms height, we first averaged the Stokes matrix over 5×1 or 5×2 windows to form multi-look imagery with larger azimuth (25.1 m) and slant range (13.3 m) pixel spacing. Then we made the terrain correction. Based on the snow classification results derived from SIR-C/X-SAR's image data, we masked out the snow-free pixels.

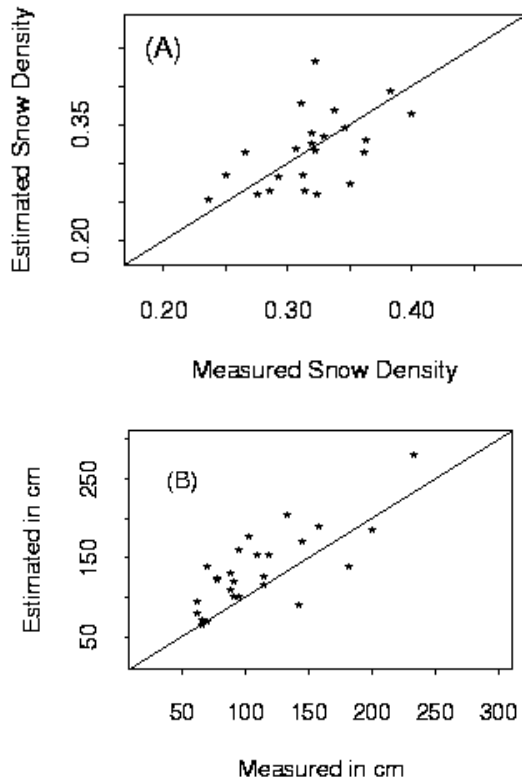


Figure 3. Compares of the field measurements (x-axis) with SIR-C/X-SAR's L-band image data (y-axis) derived snow density in (A) and C- and X-band derived snow depth in (B).

Figure 3. (A) shows the compares of the field measurements (x-axis) with SIR-C's L-band image data derived snow density (y-axis). The RMSEs are 42 kg m^{-3} and 13% for absolute and relative errors, respectively. The estimated snow density should represents the mean value from the snowpack's top

and bottom layers. This is because the backscattering signal is mainly controlled by two factors: 1) The snow density at the top layer near the surface mainly affects the power transmissivity at the air-snow interface. 2) The snow density at the bottom layer controls the incidence angle and wavenumber at the snow-ground interface. Figure 3. (B) shows the comparison of the field measurements with the depths estimated from the SIR-C/X-SAR image data. The algorithm inferred the overall trend of the snow depths, with an RMSE of 34 cm. During the SIR-C/X-SAR overflights, we dug 19 snow pits and made grain size measurements with detailed vertical profiles at depth intervals of 5 to 10 cm. Each individual ice particle size was measured by taking average values from three cross diameters with direction differences of 60° . There were more than 200 grains measured in each snow pit. Figure 4. compares the snow particle radius between the ground measurements and those estimated from the SIR-C/X-SAR image data. The estimated snow particle sizes were obtained from a mean value of 3×3 window at corresponding snow pit locations on the SAR images. The algorithm performed quite well. It inferred the overall trend of the snow particle sizes, with an RMSE of 0.27 mm.

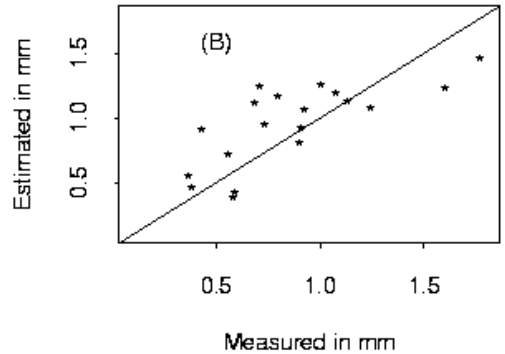


Figure 4. Compares of the field measurements of snow particle radius with SIR-C/X-SAR's C- and X-band image data derived grain size.

7 CONCLUSION

We demonstrated the utility of SAR on mapping snow in an alpine region by means of the repeat pass measurements. For large scale snow mapping, the major problem is topographic effect since accurate high resolution DEM data are not available for many parts of world. Mapping snow in remote alpine regions by a conventional SAR backscattering measurements

requires topographic information in order to remove their effects on the radiometric properties measured from SAR imagery. With the coherence measurements of repeat passes (with and without snow cover), both dry and wet snow can be mapped without requiring any topographic information. The validation, compared with TM classification result, indicates that a good accuracy can be achieved.

Although the L-band radar signal passes easily through dry snow, snow density affects the backscattering signal. Algorithms for estimating dry snow density and the dielectric constant and roughness of the underlying soil or rock use backscattering measurements with VV and HH polarization at L-band frequency (1.25 GHz). Comparison with field measurements of snow density during the first SIR-C/X-SAR overpass shows absolute accuracy of 42 kg m⁻³ (13% relative error).

The relationship between snow water equivalence (SWE) and SAR backscattering coefficients at C- and X-band (5.5 and 9.6 GHz) can be either positive or negative. Therefore, discovery of the relationship with an empirical approach is unrealistic. Instead, we estimate snow depth and particle size, using SIR-C/X-SAR imagery, from a physically based first-order backscattering model through analyses of the importance of each scattering term and its sensitivity to snow properties. Using numerically simulated backscattering values, we develop semi-empirical models for characterizing the snow-ground interaction terms, the relationships between the ground surface backscattering components, and the snowpack extinction properties at C-band and X-band. With these relationships, snow depth and optical equivalent grain size can be estimated from SIR-C/X-SAR measurements. Validation using three SIR-C/X-SAR images shows that the algorithm performs usefully for incidence angles greater than 30°, with root mean square errors of 34 cm and 0.27 mm for estimating snow depth and ice optical equivalent particle radius, respectively.

ACKNOWLEDGMENTS

This work is supported by Institute for Remote Sensing Applications, Chinese Academy.

REFERENCES

- Bernier, M. and J. P. Fortin, The potential of time series of C-band SAR data to monitor dry and shallow snow cover, 1998, *IEEE Trans. Geosci. Remote Sens.*, 36:226-243.
- Evans, D., T. G. Farr, J. J. van Zyl, and H. A. Zebker, 1988, Radar polarimetry: analysis tools and applications, *IEEE Transactions on Geoscience and Remote Sensing*, 26:774-789.
- Fung, A. K., 1994, in *Microwave scattering and emission models and their applications*, Artech House Inc., Norwood, MA.
- Haefner, H., F. Holecz, E. Meier, D. Nusch, and J. Piesbergen, 1993, Capabilities and limitations of ERS-1 SAR data for snow cover determination in mountainous regions, *Proceedings, Second ERS-1 Symposium*, ESA PS 353-359.
- Kendra, J. R., K. Sarabandi, and F. T. Ulaby, 1998, Radar measurements of snow: Experiment and analysis, *IEEE Trans. Geosci. Remote Sens.*, 36:864-879.
- Looyenga, H., 1965, Dielectric constant of heterogeneous mixtures, *Physica*, 21:401-406.
- Mätzler, C., 1996, "Microwave permittivity of dry snow," *IEEE Trans. Geosci. Remote Sens.*, 34:573-581.
- Rott, H., and C. Mätzler, 1987, Possibilities and limits of synthetic aperture radar for snow and glacier surveying, *Ann. Glaciol.*, 9:195-199.
- Rott, H., C. Mätzler, D. Strobl, S. Bruzzi, and K. B. Lenhart, 1988, Study on SAR land applications for snow and glacier monitoring, Technical Report 6618/85/F/FL(SC), European Space Agency.
- H. Rott and T. Nagler, 1993, Capabilities of ERS-1 SAR for snow and glacier monitoring in alpine areas, *Proceedings, Second ERS-1 Symposium*, pp. 1-6.
- Shi, J., R. E. Davis, and J. Dozier, 1993, Stereological determination of dry snow parameters for discrete microwave modeling," *Ann. Glaciol.*, 17: 295-299.
- Shi, J. and J. Dozier, 1993, Measurements of snow- and glacier-covered areas with single polarization SAR, *Annals of Glaciology*, 17: 72-76.
- Shi, J., J. Dozier, and H. Rott, 1994, Snow mapping in alpine regions with synthetic aperture radar, *IEEE Trans. Geosci. Remote Sens.*, 32(1): 152-158.

- Shi, J. and J. Dozier, 1995, Inferring snow wetness using C-band data from SIR-C's polarimetric synthetic aperture radar, *IEEE Trans. Geosci. and Remote Sensing*, 33(4): 905-914.
- Shi, J. and J. Dozier, 1997, Mapping Seasonal Snow with SIR-C/X-SAR in Mountainous Areas, *Remote Sensing Environment*, 59(2):294-307.
- Shi, J. and J. Dozier, 2000, Estimation of Snow Water Equivalence Using SIR-C/X-SAR, Part I: Inferring snow density and subsurface properties, *IEEE Trans. Geosci. Remote Sens.*, 38(6): 2465-24748.
- Shi, J. and J. Dozier, Estimation of Snow Water Equivalence Using SIR-C/X-SAR, Part II: Inferring snow depth and particle size, *IEEE Trans. Geosci. Remote Sens.*, 38(6):2475-2488.
- Stiles, W. H., and F. T. Ulaby, 1980, The active and passive microwave response to snow parameters, 1, Wetness, *J. Geophys. Res.*, 85:1037-1044.
- Strozzi, T., 1996, Backscattering measurements of snow covers at 5.3 and 35 GHz, Ph.D. Thesis, Institute of Applied Physics, University of Bern.
- Ulaby, F. T., and W. H. Stiles, 1980, The active and passive microwave response to snow parameters, 2, Water equivalent of dry snow, *J. Geophys. Res.*, 85:1045-1049.
- Ulaby, F. T., R. K. Moore and A. K. Fung, 1982, *Microwave Remote Sensing: Active and Passive*, 2, *Radar Remote Sensing and Surface Scattering and Emission Theory*, Reading, MA, Addison-Wesley.
- Ulaby, F. T., W. H. Stiles, and M. Abdelrazik, 1984, Snowcover influence on backscattering from terrain, *IEEE Trans. Geosci. Remote Sens.*, GE-22:126-132.
- Van Zyl, J. J., H. A. Zebker, and C. Elachi, 1987, Image radar polarization signatures: theory and observations, *Radio Science*, 22(4): 529-543.

Estimation of soil moisture and surface roughness using two radar configurations

Mehrez Zribi*, Monique Dechambre* and Nicolas Baghdadi&

* CETP, 10/12, Avenue de l'Europe, 78140, Vélizy, France

& BRGM, 3, avenue C. Guillemin – B.P. 6009 – 45060 Orléans cedex 2, France

Tel : 33 1 39 25 48 23, Fax : 33 1 39 25 49 22, E-mail : zribi@cetp.ipsl.fr

ABSTRACT

A new empirical model for retrieving soil moisture (M_v) and surface roughness (s) over bare soils is proposed from radar measurements. The derivation of this model is based on the results of three experimental radar campaigns conducted over bare agricultural fields. Radar data were acquired by means of two C-band spaceborne (SIR-C and RADARSAT) and helicopter borne ERASME sensors. This model is more specifically developed using the backscattering coefficient σ^0 in HH polarization and for an incidence angle of 39° ($\sigma_{HH,39}^0$), and the differential backscattering coefficient $\Delta\sigma^0$ defined as $\sigma_{HH,23}^0 - \sigma_{HH,39}^0$, in terms of an original roughness parameter, Z_s , and M_v . An inversion technique is proposed to retrieve Z_s and M_v from radar measurements. The approach is tested with an another data set (Floodgen '98).

1 INTRODUCTION

It has been shown in the recent years (Beven et al., 1996) that the knowledge of soil surface conditions, namely the soil moisture content and roughness, is of the highest importance in hydrological or climatic studies. Indeed, the soil moisture content plays a critical role in the surface energy balance at the soil-atmosphere interface and can be considered as a key state variable that influences the distribution of the radiant energy, the runoff generation and the percolation of water into the soil. On the other hand, the surface roughness effect is involved in the separation of water flow into infiltration and runoff. Therefore, the capacity of measuring soil surface characteristics on a large scale from space, with a complete and frequent coverage, seems to be extremely attractive, and a considerable effort has therefore been devoted, over the last two decades, to develop and improve active and passive microwave techniques as well as interpretation tools (Jackson et al., 1996).

Active sensors measure, particularly SAR (Synthetic Aperture Radar) offering high resolution images (<100m), the backscattering coefficient σ^0 of soil surfaces (Ogilvy, 1991) which depends on both roughness and moisture characteristics. Many studies and derived methods have been undertaken in radar remote sensing research in order to understand the backscattering response from natural surfaces and to retrieve the surface parameters.

Analytical electromagnetic backscattering models like the physical optics model (PO), the geometrical

optics (GO) and Small Perturbation Model (SPM) have been developed with this objective, but their range of validity is limited (Ogilvy, 1991, Fung, 1994) and they are not applicable for most agricultural surfaces. Afterwards, Fung (Fung et al., 1992) developed the Integral Equation Model (IEM) which brings a new contribution in theoretical simulations. However, comparisons of IEM simulations and data acquired during several radar campaigns have shown the limits of applicability of this model, i.e. smooth soils with small slope (Zribi et al., 1997, Zribi et al., 2000). In recent years, different improvements of this model were proposed (Chen et al., 2000, Wu et al., 2001).

The difficulties in simulating radar signals over natural surfaces are mainly attributed to 2 factors: first, the physical approximations introduced in a model are not always *a posteriori* verified (Fung, 1994), and secondly, the mathematical description of natural surfaces is not a straightforward task and so far, has not been solved in an entirely satisfactory way. For instance, many studies have tried to introduce new approaches in the description of soil surface (Davidson et al., 2000, Zribi et al., 2000). These works have brought an actual improvement in the understanding of backscattering mechanisms over bare soils. However, these approaches involve more complicated soil descriptions with other roughness parameters like fractal dimension, and here again, difficulties remain for inverting the radar signal.

For all these reasons, roughness and moisture inversion procedures are not yet valid when using these analytical approaches.

Numerical approaches have also been used to study the backscatter radar signal (Chen et al., 1989). Their good simulation of backscattering level depends also on roughness description which is still as for analytical models not yet satisfactory.

Simultaneously, many empirical and semi-empirical models have been developed since the beginning of SAR studies with applications to land surfaces (Oh et al., 1992; Dubois et al., 1995). The most popular semi-empirical model is a linear one, which characterizes the relation between surface moisture and radar signal. This linear relation has been validated using data acquired over many agricultural watersheds (Cognard et al., 1995; Quesney et al., 2000). However, the slope of this linear law is not exactly constant from one watershed to the next, and must be calibrated each time it is applied; furthermore, the roughness effects are neglected, thus limiting the use of this kind of models to large areas.

Our purpose in this paper is to present a new empirical model that aims at retrieving the surface parameters from radar measurements. In section 2, the experimental data sets of radar and ground measurements are described. In section 3, IEM simulations used to study the effect and influence of the system and soil parameters on the backscatter behavior are presented. In section 4, an empirical model characterizing the relation between soil surface parameters (described in an original manner) and the radar measurements is proposed. Finally, section 5 presents the new proposed inversion approach.

2 EXPERIMENTAL MEASUREMENTS

In this study, data acquired during 4 experimental radar campaigns carried out over agricultural watersheds are used (Orgeval'94, Pays de Caux'94 and Alpilles-Reseda, Floodgen'98). For three ones, in addition to spaceborne SAR data (ERS, SIRC, RADARSAT), some helicopter-borne data acquired with the scatterometer ERASME operating in C and X bands (5.35 and 9.25 GHz) complement the radar data base.

2.1 Orgeval'94

The objective of this experimental campaign was to characterize the effect of soil roughness on radar measurements. The Orgeval watershed is located in the East of Paris (France). The Orgeval'94 campaign was conducted concurrently with the SIRC/XSAR (1.25 GHz, 5.3GHz and 9.25 GHz) missions (Zribi et al., 1997).

The radar measurements were performed by 2 sensors: SIRC/X-SAR and ERASME which operate with incidence angles ranging from 25° to 57°. The watershed extends over a total area of about 8 by 8 km². The soil texture is relatively constant over the whole basin : clay 17%, silt 78%, sand 5%.

Simultaneous ground measurements were carried out in 6 fields which were selected to represent different crop practices: sowing of peas eroded by rain resulting in a smooth crusted top layer (one field), and different ploughed soil practices for future crops (five fields). As a result of a heavily rainy winter, during the 5 days (12-17 April 1994) of SAR surveys, the soil moisture content remained high and constant over the watershed (about 0.35 cm³/cm³), so that the soil roughness and practices were the main factors of the radar variability.

2.2 Pays de Caux'94

The Pays de Caux'94 experimental campaign aimed at characterizing the agricultural soil roughness and its effects on erosion and runoff in the North of France.

The test site is the Blossesville watershed located in the Pays de Caux in Northern France. The loamy soils of the northern European loess belt are mainly sensitive to soil structure degradation and commonly exposed to erosion caused by concentrated runoff. In that context, an important research program was carried out in the region of the Pays de Caux. The site's soil features are : (1) a very homogenous loamy texture (clay 13%, silt 65%, sand 22,5%), (2) of which approximately 50% are bare, or nearly bare. Radar measurements were performed in February 1994 over 10 large test fields (more than 100m x 100m each).

ERASME operated with incidence angles ranging from 15° to 40° off nadir. The campaign took place in winter, the soil moisture remains high and constant over the whole watershed (about 0.35 cm³/cm³) so that, similar to the Orgeval campaign, the soil roughness and practices were the remaining factors of the radar variability.

2.3 Alpilles-ReSeDA

The Alpilles – ReSeDA project aimed at improving methods for interpreting remote sensing data for a better evaluation of soil and vegetation functioning. Among different remote sensing techniques conducted, radar observations over a complete crop cycle were regularly acquired. The Alpilles-ReSeDa experiment took place from October 96 to November 97, with once-a-month radar acquisitions. The monitored site is a flat agricultural area whose dimensions are approximately 4km x 5km, located in the Rhone Valley near Avignon (France). The ground measurements were made in different test fields. Large variations of the volumetric moisture content were observed, ranging from 2% to 48%. Most of the soil textures are 40% clay, 54% silt and 6% sand particles.

Twelve RADARSAT images were acquired. The modes of SAR images acquisition have allowed incidence angle of about 23° (Standard S1, six images), and 39° (Fine F1, six images). In addition, the ERASME radar are operated, not exactly at the

same dates, at incidence angles ranging from 20° to 40°.

2.4 Flodgen'98

This campaign aimed at studying the effect of agricultural soil roughness in excessive runoff and erosion conditions in the test site. This site is situated in France, Normandie : longitude 0°50' West et latitude 49°47' North). It is characterized by high problems of erosion due to intensive agricultural practices. The measurements are made in the context of the European project FLOODGEN. Simultaneously to radar measurements acquired by RADARSAT and ERS2 satellites, different ground truth measurements were made during the period of 8-24 February 1998. For different test fields, roughness and surface moisture were measured. During the campaign, the soil moisture remained high and approximately constant over the whole watershed (about 0.3-0.4 cm³/cm³).

2.5 Roughness measurement results

The rms height (s) and the correlation length (l) are extracted from the correlation function computed from the measured soil profiles (Rakotoarivony et al., 1996). Results illustrated in Figure 1 show many types of agricultural soils for s ranging from 0.36 cm to 3.84 cm and l ranging from 1.5 cm to 11.79 cm. Different correlation lengths are observed for nearly the same rms heights of the test fields. The complementarities between the different data bases can also be seen, particularly between Alpilles-ReSeDa and the others in terms of roughness and moisture values.

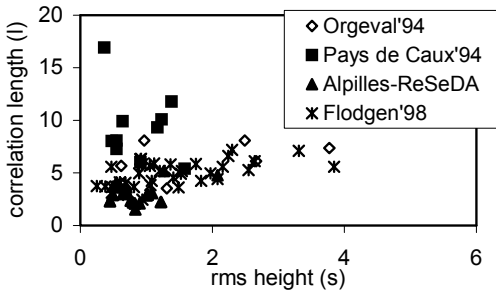


Figure 1 - Roughness parameter description.

3 INTRODUCTION OF A NEW Z_s PARAMETER

3.1 IEM simulations

The study will now focus on a particular radar configuration : 2 incidence angles i.e. 23° and 39°, HH polarization, C band (5.3 GHz) operating mode. In fact, our aim is to adapt our study to existing or future SAR operating configurations, particularly RADARSAT and ASAR-ENVISAT.

The objective of this section is to study the sensitivity of these radar configurations to surface parameters. Therefore, the IEM model is used as a reference to simulate the respective backscattering coefficients.

This IEM version introduces the transitional function proposed by Wu et al., 2001, in which the Fresnel reflection coefficient $R_p(T)$ is not evaluated for an incidence angle θ_i , but for an angle ranging from θ_i to the normal incidence.

It is written as:

$$R_p(T) = R_p(\theta_i) + [R_p(\theta_{sp}) - R_p(\theta_i)] \gamma_p; p = h, v \quad (1)$$

where $R_p(\theta_i)$ is the Fresnel reflection coefficient calculated at the incidence angle θ_i , $R_p(\theta_{sp})$ is the Fresnel reflection coefficient calculated at the specular angle θ_{sp} and γ_p is a transition function dependent on polarization, incidence angle, and surface parameters.

The IEM input parameters are the dielectric constant derived from the surface volumetric moisture content and the soil texture, and the correlation function of surface heights or its corresponding spectrum. Many studies have been carried out in order to derive a good and realistic description of the correlation function's shape (Shi et al., 1997). However, in the case of agricultural soil studies, an exponential correlation function will generally give a good fit to the majority of experimental surfaces:

$$\rho(x) = s^2 \exp\left(-\frac{x}{l}\right) \quad (2)$$

3.2 Introduction of Z_s

In many empirical studies, the effect of the correlation length l on the backscattering coefficient σ° is neglected and only the rms height s is tentatively inverted. This approximation could lead to large errors in the estimation of the backscattering coefficient. Nevertheless, inverting the two parameters s and l separately seems to be a very difficult task. For all these reasons, we propose in this work to introduce a new roughness parameter Z_s with the objective to mix the effects of s and l on the values of σ° , using only one parameter. The proposed parameter Z_s is:

$Z_s = s^2 / l$. The underlying idea is to introduce a slope effect which is an important soil feature in estimating σ° . Figure 2 illustrate the evolution of Z_s function of s and l . It shows for example that with small s , Z_s is generally small.

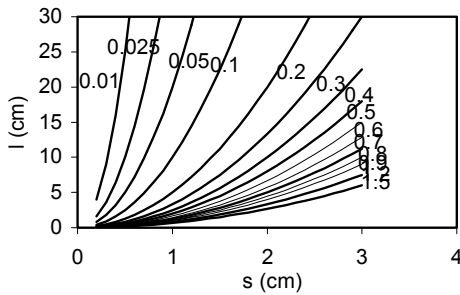


Figure 2 – Z_s parameter as a function of s and l .

In order to study the effect of roughness parameters on radar backscattering, IEM simulations are performed in a HH polarization and 39° radar configuration. Several surface parameters are chosen (rms heights $s=0.3$ cm, $s=0.4$ cm, $s=0.5$ cm, $s=0.6$ cm, $s=0.7$ cm, $s=0.8$ cm, $s=0.9$ cm, correlation lengths $l=3$ cm, $l=5$ cm, $l=7$ cm and $l=10$ cm and constant volumetric moisture $M_v=35\%$). Results of IEM simulations and the corresponding curve fitting are plotted in Figure 3. A real improvement can be seen when using $\ln(Z_s)$, (figure 3-b), instead of $\ln(s)$, (figure 3-a) in the proposed regression. The correlation coefficient R^2 increases from 0.85 to 0.97.

Figure 3-c shows IEM simulations of Z_s parameter for HH and VV polarizations and an incidence angle of 23° . These simulations confirm the good correlation of radar signal to Z_s parameter.

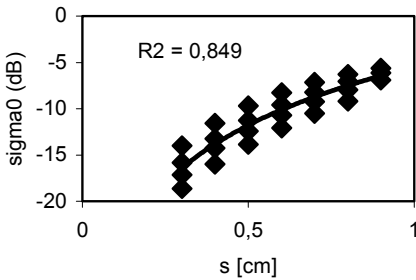


Figure 3.a - Relationship between s and simulated σ° for the configuration (HH , 39°).

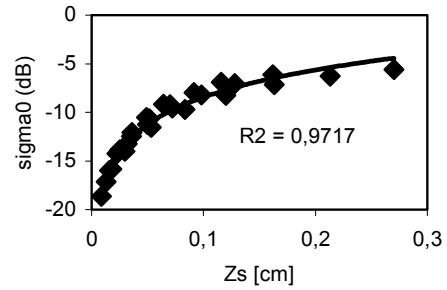


Figure 3.b - Relationship between Z_s and simulated σ° for the configuration (HH , 39°).

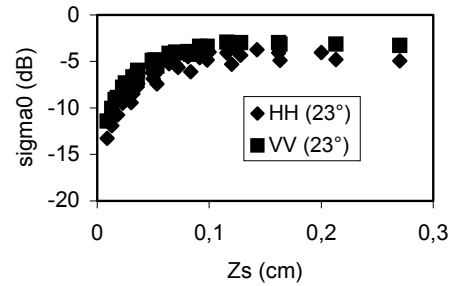


Figure 3.c - Relationship between Z_s and simulated σ° at 23° .

The question is now how to derive Z_s . Different studies have underlined the weak dependence of the soil moisture on the σ° difference (in dB, HH polarization) between a small incidence angle and a large one (Wegmuller et al., 1989), for instance $\Delta\sigma^\circ = \sigma^\circ_{HH,23} - \sigma^\circ_{HH,39}$. However, many experimental studies have shown the difficulty to observe a high correlation between $\Delta\sigma^\circ$ and s (Chanzy et al., 1998). IEM simulations are realized in order to calculate $\Delta\sigma^\circ$ with the same surfaces as used before. Figure (4-a) illustrates the variations of $\Delta\sigma^\circ$ with s , and Figure (4-b), the variations of $\Delta\sigma^\circ$ with Z_s . The correlation coefficients using s or Z_s increasing from 0.61 to 0.995. Thus, parameter Z_s enables a better description of the relation of $\Delta\sigma^\circ$ with surface roughness.

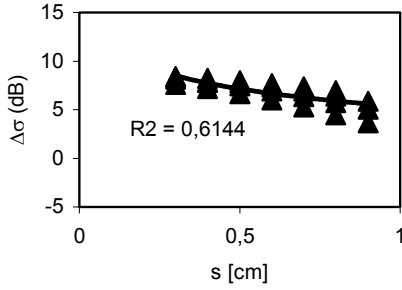


Figure 4.a - Relationship between s and simulated $\Delta\sigma^\circ$.

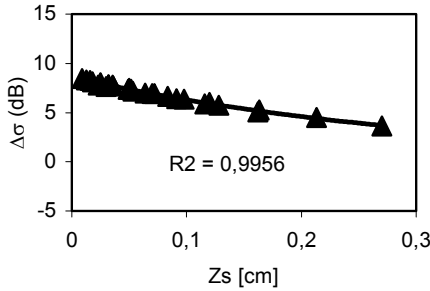


Figure 4.b - Relationship between Z_s and simulated $\Delta\sigma^\circ$.

4 THE EMPIRICAL MODEL

4.1 Methodology

The objective of this section is to present a new algorithm, based on the results presented in the previous section, and developed in order to retrieve the surface roughness characteristics and the soil moisture content from radar measurements.

Different experimental studies (Quesney et al., 2000) have shown that the moisture effect on the radar signal acquired over soil surface is approximately linear up to large volumetric moisture values (35% to 40%). Using the IEM model to simulate σ° at 39° and for HH polarisation, we observe a very fast saturation of the radar signal as a function of M_v (the saturation starts approximately from $M_v = 20$ to 25%). For M_v values ranging from 5% to 20%, IEM simulations could be approximated by a linear law with a slope of about 0.22 dB/1%, independent of the roughness. An empirical model deduced from IEM simulations is proposed for predicting the radar signal (HH polarization and 39°), which can be written as:

$$\sigma_{HH,39}^0 = 0.22M_v + f(\text{roughness}) \quad (3)$$

The Orgeval data and Pays de Caux data are used to calibrate the relation between Z_s and σ° , ($f(\text{roughness})$), independently of the moisture content values.

A good correlation is observed between σ° and Z_s with a correlation coefficient $R^2=0.75$.

Then, an empirical model linking Z_s and σ° at 39° ($M_v=35\%$) could be written as:

$$\sigma_{HH}^0 = 1.56 \ln(Z_s) - 5.6 \quad (4)$$

Finally, for all moisture and roughness values, $\sigma_{HH,39}^0$ could be written as:

$$\sigma_{HH}^0 = 1.56 \ln(Z_s) + 0.22M_v - 13.3 \quad (5)$$

As seen in the previous section if σ° is measured at two different incidence angles and in same soil moisture conditions, values of Z_s similar to those observed in the example presented in Figure 4-b can be derived.

Concerning the data sets used to build our inversion model, the Pays de Caux data set as well as the Alpilles-ReSeDa base contain ERASME σ° data measured at angles ranging from 15° to 40° , and RADARSAT σ° data (Alpilles database only) measured at 23° and 39° , but with a time delay of 3 days between the 23° and 39° acquisitions. In our study, we use data for which the variations of the volumetric moisture content is less than 1.5%.

A good correlation between experimental Z_s and $\Delta\sigma^\circ$ is observed in figure 5. We then propose to fit the experimental relation between $\Delta\sigma^\circ$ and Z_s with:

$$\Delta\sigma^0 = 6.48 \exp(-3Z_s) \quad (6)$$

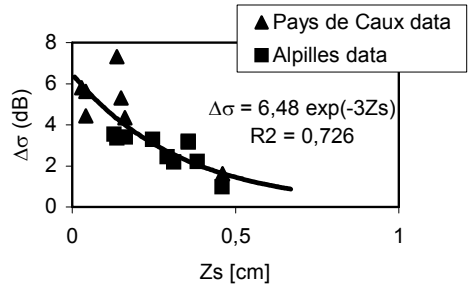


Figure 5 - $\Delta\sigma^\circ$ calculated from radar measurements as a function of Z_s for different test fields in Pays de Caux'94 and Alpilles-ReSeDa.

4.2 Application of the direct model

In order to validate the model (3), two data bases are used, the first one is extracted from Alpilles-ReSeDa data, the second one corresponds to Floodgen'98 measurements.

a) Data set 1

Data extracted from the Alpilles-ReSeDa data base for different values of M_v ranging from 7% to 38 % and different values of roughness are used. Figure 6 shows a good agreement between model simulations and ERASME data.

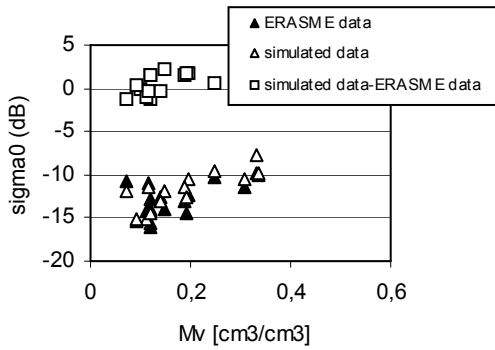


Figure 6 - Comparison between radar measurements and simulated data for test fields on Alpilles-ReSeDa.

b) Data set 2

The Floodgen'98 data set is characterized by different roughness values and very high moistures (between 30% and 40%). Figure 7 shows the evolution of real radar signals function of Z_s parameter with approximately constant moisture and for three radar configurations (VV23°, HH39°, HH47°). The three configurations show the same tendency with a increasing of σ^0 with Z_s .

Figure 8 illustrates the comparison between simulated and real backscattering values for HH39° configuration. We observe satisfactory results with an rms error equal to 2.2dB. However, an overestimation of the model is observed (less than 5 dB). This could be explained by the fact that values of moisture are in the limit of validity of this model which considers a linear relationship between moisture and radar signal up to moisture values around 35%.

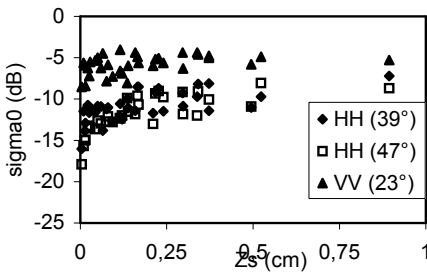


Figure 7 - Radar measurements for different configurations on Floodgen'98 as a function of Z_s .

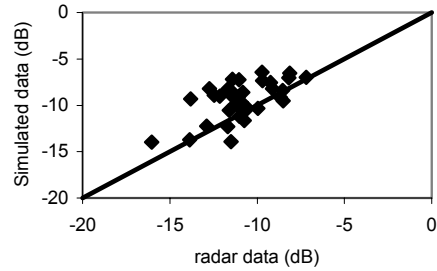


Figure 8 - Comparison between radar measurements and simulated data for test fields on Floodgen'98.

5 APPLICATION OF THE INVERSION MODEL

The data used in this application of the proposed inversion model are obviously different from those used for the derivation of the inversion model.

In Figure 9, a comparison of the estimated Z_s values and the measured ones is presented for different test fields. A very good agreement between simulated and measured data is observed (the residual rms error=0.8 mm). A very good agreement between simulated and measured data is again observed in Figure 9 (the residual rms error =4%).

These results show the potential of this algorithm to invert both the introduced soil roughness parameter Z_s and the soil moisture parameter M_v with a good accuracy. However, it would be advisable to conduct additional experimental measurements over a wider range of roughness and moisture conditions, in order to corroborate these promising results.

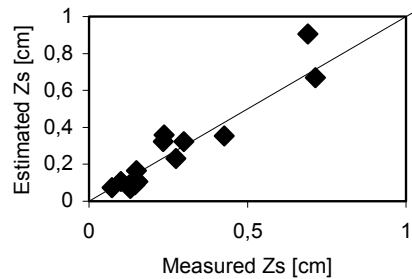


Figure 9 - Comparison between estimated and measured Z_s .

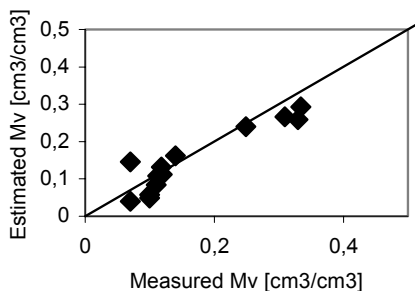


Figure 9 - Comparison between estimated and measured Mv.

REFERENCES

- Beven, K., J., and Fisher, J. (1996), Remote sensing and scaling in hydrology, scaling in hydrology using remote sensing, Edited by J. B. Stewart, E. T. Engman, R., A. Feddes and Y. Kerr.
- Chanzy, A., King, C., Prévot, L., Remond, A., Wigneron, J-P., Calcagno, P., Zribi, M., Desprats, M. (1998), Comparison of ERS and multi-angle RADARSAT measurements on bare soils: first results, *International Workshop on Retrieval of Bio & Geo-physical Parameters from SAR Data for Land Applications*, 21-23 October 1998.
- Chen, K-S, Wu, T, D, Tsay, M, K and Fung, A., K. (2000), A note on the multiple scattering in an IEM model, *IEEE Transactions on Geoscience and Remote Sensing*, 38, No. 1: 249:256.
- Chen, M. F., Chen, K. S., and Fung, A. K., A. (1989), study of the validity of the Integral Equation Model by moment method simulation - cylindrical case. *Remote Sensing of Environment*, 29: 217-228.
- Cognard, A, L, Loumagne, C, Normand, M, Olivier, P, Ottele, C, Vidal-Madjar, D, Louahala, S and Vidal, A. (1995), Evaluation of the ERS1/synthetic Aperture radar capacity to estimate surface soil moisture: two year results over the Naizin watershed. *Water Resource Research*, vol.31: 975-982.
- Davidson, M. W. J., Le Toan, T., Mattia, F., Satalino, G., Manninen, T., and Borgeaud, M. (2000), On the characterisation of agricultural soil roughness for radar remote sensing studies. *IEEE Transactions on Geoscience and Remote Sensing*, 38: 630:640.
- Dubois, P.C., Van Zyl, J. and Engman, T. (1995), Measuring soil moisture with imaging radars, *IEEE Transactions on Geoscience and Remote Sensing*, 33(4):915-926.
- Fung, A.K., Li, Z. and Chen, K.S. (1992), Backscattering from a randomly rough dielectric surface, *IEEE Transactions on Geoscience and Remote Sensing*, 30(2):356-369.
- Fung, A. K. (1994), *Microwave Scattering and Emission Models and their Applications*, Artech House.
- Jackson, T-J, Schmugge, J and Engman, E-T. (1996), Remote sensing applications to hydrology: soil moisture, *Hydrological Sciences*, 41 (4):517-530.
- Oh, Y., Sarabandi, K., and Ulaby, F.T. (1992), An empirical model and an inversion technique for radar scattering from bare soil surfaces, *IEEE Transactions on Geoscience and Remote Sensing*, 30(2):370-381.
- Ogilvy, O. (1991), *Theory of Wave Scattering from Random Rough Surfaces*, Adam Hilder.
- Quesney, A., Le Hégarat-Masclé, S., Taconet, O., Vidal-Madjar, D., Wigneron, J.P., Loumagne, C., and Normand, M. (2000), Estimation of watershed soil moisture index from ERS/SAR data, *Remote Sensing of Environment*, 72:290-303.
- Shi, J., Wang, J., Hsu, A. Y., O'Neill, P. E., Engmann, T. (1997), Estimation of Bare Surface Soil Moisture and Surface Roughness Parameter Using L-Band SAR Image Data, *IEEE Transactions on Geoscience and Remote Sensing*, Vol.35, No.5: 1254-1265.
- Wegmuller, U., Matzler, C., and Schanda, E. (1989), Microwave signature of bare soil, *Adv. Space Res.*, 9 (1): 307-316.
- Wu, T, D, Chen, K, S, Shi, J and Fung, A, K. (2001), A transition model for the reflection coefficient in surface scattering, *IEEE Transactions on Geoscience and Remote Sensing*, Vol.39, No.9: 2040-2050.
- Zribi, M., Taconet, O., Le Hégarat-Masclé, S., Vidal-Madjar, D., Emblanch, C., Loumagne, C. and Normand, M. (1997), Backscattering behavior and simulation comparison over bare soils using SIRC/XSAR and ERASME 1994 data over Orgeval, *Remote Sensing of Environment*, 59:256-266.
- Zribi, M., Ciarletti, V., Taconet. (2000), O., Validation of a rough surface model based on fractional brownian geometry with SIRC and ERASME radar data over Orgeval site, *Remote Sensing of Environment*, 73: 65-72.

MODEL BASED FOREST HEIGHT ESTIMATION FOR FOREST BIOMASS ESTIMATION

K.P. Papathanassiou, I. Hajnsek, T. Mette, and S.R. Cloude*

*German Aerospace Center (DLR),
Institute of Radio Frequency Technology and Radar Systems,
P.O. Box 1116, D-82230 Wessling, Germany
Tel: +49 / (0) 8153 28 2367, Fax: +49 / (0) 8153 28 1135
Email: kostas.papathanassiou@dlr.de, irena.hajnsek@dlr.de*

**AEL Consultants,
26 Westfield Avenue, Cupar, KY15 5AA, Scotland, UK
Tel: +44 (0)1334 653958, Fax: +44 1334 653958
E-mail: scloude@aelc.demon.co.uk*

ABSTRACT - *In this paper, the role of model based inversion of multi-parameter interferometric SAR data for the estimation of forest biomass is evaluated. The allometric relation between forest height and forest biomass allows the estimation of biomass even in high biomass forest ecosystems, where conventional techniques saturate. Different remote sensing approaches for the estimation of forest height are reviewed and the potential of model based forest height estimation from multi-parameter interferometric data is discussed with respect to forest biomass estimation.*

1 INTRODUCTION

Forest biomass is today one of the most unknown parameters in dynamic ecosystem change especially with respect to a reliable global Carbon-flux modelling. In many regions of our planet even a mere forest classification is missed. Parallel to the ecological dimension, and under the light of the Kyoto protocol, this problem has also a political dimension that increases the responsibility of the scientific community to provide exact answers.

The fact that biomass information is especially missed in remote areas (i.e. tropical and boreal forest ecosystems) combined with the fact that these ecosystems contain the biggest amount of forest biomass make remote sensing techniques a challenge. However, optical remote sensing sensors are in general not capable of measuring forest biomass or monitoring the dynamics of deforestation and biomass regeneration. There are two main reasons for this: 1) insufficient sensitivity to forest structure and above-ground biomass and 2) inadequate temporal observation frequency as a result of atmospheric conditions in tropical and boreal ecosystems. On the other hand, conventional Synthetic Aperture Radar (SAR) remote sensing methods based on the evaluation of backscattering amplitudes for the quantification of forest biomass are limited to biomass

levels below 150 tons/ha and thus, do not allow biomass inventory in boreal and tropical forest ecosystems. Recently, an alternative allometric approach for the estimation of above ground forest biomass from forest height estimates has been proposed (Papathanassiou, 2002; Mette, 2002). The main advantage of this approach is that the estimation of above ground forest biomass from forest height is widely unsaturated allowing the mapping of forest ecosystems with high biomass levels (see Table 1). In the following we review the potential remote sensing approaches for the estimation of forest height.

2 FOREST HEIGHT ESTIMATION FROM MULTIPARAMETER SAR INTERFEROMETRY

Given the importance of forest height for the allometric estimation of above ground forest biomass (Mette, 2002) we consider now the potential remote sensing techniques to measure forest height. Quantitative forest parameter estimation from SAR data is in general not trivial due to the fact that the radar measurables are in general not directly related to the desired parameters. There are two main approaches followed over the last years, direct estimation methods intending to measure directly forest height and model based estimation approaches which obtain estimates of forest height from the inversion of a scattering model that relates the measurables to forest height.

	Biomass Saturation Limit [tons / ha] [kg / m ²]		% of Earth's Vegetated Area	% of Total Above Ground Biomass
Backscatter Saturation C-band	20	2	25	4
Backscatter Saturation L-band	40	4	35	8
Backscatter Saturation P-band	120-150	12-15	60	20-30
Forest Height	> 400	> 40	> 90	> 95

Table 1. Biomass saturation values for different radar remote sensing techniques.

2.1 Direct Forest Height Estimation Methods

Laser Altimetry (Lidar scanning):

Laser altimeters measure the roundtrip time for a laser pulse (usually at the near infrared frequency band) to travel between the sensor and the scatterer. The incident pulse interacts with the canopy and/or the ground and is scattered back to the sensor. The forest height can be extracted from the time difference between the canopy (first) and the ground (last) return. The estimation accuracy depends theoretically only on the digitalisation rate of the returned signal (down to values on the order of centimeters). Atmospheric conditions can limit the temporal resolution of the acquisitions. However, the main limitation is the “visibility” of the ground scattering echo that is needed for an accurate height determination. Due to the inability of EM-waves at these frequencies to penetrate even thin canopy layers, the forest height estimation relies on canopy openings. For high canopy forests only a fraction of the returned samples may come from the ground. In dense forest ecosystems with high canopy closure the ability of laser altimeters to recover forest height becomes critical (Drake, 2002; Drake, 2002).

Dual-Frequency interferometry:

The operation of a dual frequency SAR interferometer at a low (e.g. P-band) and a high (e.g. X-band) frequency were proposed in order to obtain a direct separation of ground and canopy scattering. The idea is based on the assumption that at the low

frequency the canopy extinction is low (in the ideal case zero), so that the scattering occurs predominantly on the ground and on the other hand, at the high frequency the canopy extinction is high (in the ideal case infinity) so that the wave do not penetrate significantly into the canopy. Accordingly, the low frequency interferogram corresponds to the ground topography while the high frequency interferogram to the canopy top, and the forest height is obtained as the difference between the two interferograms. However, several experimental results demonstrated that both frequencies (X- and P-band) are affected by volume decorrelation. This indicates that even at higher frequencies there is a significant penetration into the canopy volume while at the same time canopy scattering contributions are not negligible at the lower frequencies especially in the presence of topographic variation. Consequently, in the most cases this approach leads to an underestimation of the vegetation height due to the fact that neither the higher frequency measures the top of the vegetation nor the vegetation layer is transparent at the lower frequency (Schwaebisch, 1999; Ulbricht, 2002).

2.2 Model Based Forest Height Estimation Methods

The absence of any direct relation between physical forest parameters (e.g. forest height, density, etc.) and interferometric observables, necessitates the consideration of model based estimation approaches. Model based parameter inversion may be regarded as a two-step procedure: In a first step, a (coherent) scattering model [M] that relates the scattering parameters to the interferometric observables has to be established:

$$\begin{bmatrix} \text{Interferometric} \\ \text{Observables} \end{bmatrix} = [M] \begin{bmatrix} \text{Scattering} \\ \text{Parameters} \end{bmatrix} \quad (1)$$

Then, in a second step, the scattering parameters can be estimated from the interferometric observables from the inversion of the scattering model as

$$\begin{bmatrix} \text{Scattering} \\ \text{Parameters} \end{bmatrix} = [M]^{-1} \begin{bmatrix} \text{Interferometric} \\ \text{Observables} \end{bmatrix} \quad (2)$$

The scattering model is essential for the accuracy of the estimated parameters. On the one hand the model must contain enough physical structure to interpret the radar observables, while on the other hand it must be simple in terms of parameters in order to be determinable with a limited number of observables, (Schwaebisch, 1999). This trade off is mirrored in the literature where both, direct and statistical modelling approaches have been addressed.

- Direct models are based on a detailed description of the scatterer in terms of discrete particle or equivalent dielectric constant distributions and model the radar observables by solving the corresponding Maxwell equations. As a detailed description of the scatterer's structure can be incorporated in terms of particle size, shape and orientation, direct models they are characterised by precise structural vegetation description paying the price of a large number of over-parameterisation.
- Statistical models – as already indicated by their name – use macroscopic statistical and/or symmetry derived properties of the scatterer to state about its scattering behaviour. They are not so detailed as direct models but have the advantage to be describable by a significant smaller number of parameters.

Direct models are in general too complex in terms of parameters and lead in general to underestimated inversion problems. They can be solved unambiguously only by introducing simplifying assumptions or *a priori* information and have therefore a constrained applicability. However, direct models can play an important role in concerning the understanding and parameterisation of scattering processes in forest environments and thus in the development of accurate simplified inversion models.

For the quantitative parameter estimation from multi-parameter interferometric SAR data, statistical models have been proved to be more robust leading to promising results and will be investigated in the following.

Random-Volume-over-Ground Scattering Model:

In the case of forest scattering at lower frequencies, a realistic scattering model has to consider both the vegetation layer and ground interactions. A simple statistical model to describe such a scenario is the random volume over ground scattering model (Hagberg, 1995; Askne, 1997; Treuhaft, 2000; Papathanassiou, 1999; Papathanassiou, 1999). Accordingly, the vegetation is modelled as a single layer of thickness h_V containing a volume with randomly oriented particles and scattering amplitude per unit volume m_V . This random volume, as shown schematically in Fig. 1, is located over a ground scatterer positioned at $z=z_0$ with scattering amplitude m_G . The ground is seen through the vegetation layer by an interferometric system operating at wavelength λ with physical baseline B under a mean incident angle θ_0 . In this case, the

complex interferometric coherence $\tilde{\gamma}$ after range spectral filtering, may be written as

$$\tilde{\gamma}(\vec{w}) = \exp(i\varphi_0) \frac{\tilde{\gamma}_V + m(\vec{w})}{1 + m(\vec{w})} \quad (3)$$

$\tilde{\gamma}_V$ denotes the complex coherence for the volume alone, which depends on the extinction coefficient sigma for the random volume, and its thickness h_V as

$$\begin{aligned} \tilde{\gamma}_V &= \frac{I}{I_0} \quad \text{where} \\ I &= \int_0^{h_V} \exp(ik_z z') \exp\left(\frac{2\sigma z'}{\cos\theta_0}\right) dz' \\ I_0 &= \int_0^{h_V} \exp\left(\frac{2\sigma z'}{\cos\theta_0}\right) dz' \end{aligned} \quad (4)$$

φ_0 is the phase related to the ground topography and m the effective ground-to-volume amplitude ratio accounting for the attenuation through the volume

$$m(\vec{w}) = \frac{m_G(\vec{w})}{m_V(\vec{w})I_0} \quad (5)$$

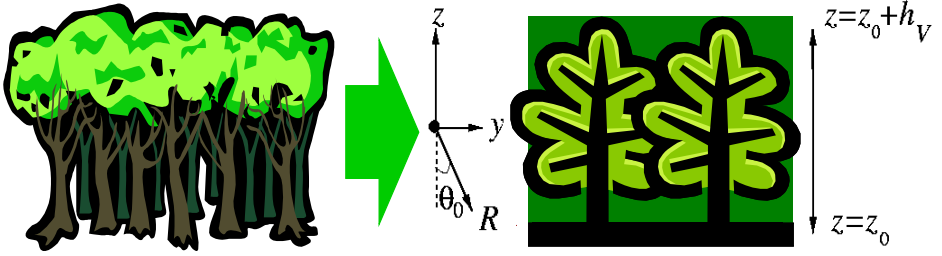


Figure 1: Scheme of the random volume over ground scattering model.

The extinction coefficient corresponds to a mean extinction value for the vegetation layer, and is a function of the density of scatterers in the volume and their dielectric constant. κ_z is the effective vertical interferometric wavenumber after range spectral filtering, which depends on the imaging geometry and the radar wavelength

$$\kappa_z = \frac{\kappa \Delta \theta}{\sin(\theta_0)} \quad (6)$$

$\Delta \theta$ is the incidence angle difference between the two interferometric images induced by the baseline. According to Eq. (3), the effective scattering center is located above the ground at a height that depends on the ground-to-volume amplitude ratio m as well as the attenuation length of the vegetation layer.

Equations (3-6) address the coherent random volume over a ground scattering problem as a four parameter problem regarding: 1) the volume thickness h_V (in meters), 2) the volume extinction coefficient σ (in dB/m), 3) the effective ground-to-volume amplitude ratio m , and, 4) φ_0 the phase (in radians), related to the underlying topography.

Note that, even this simple model leads to an underestimated inversion problem for a single-channel single-baseline interferometric system. Consequently, in the absence of *a priori* information and/or simplifying assumptions, multi parameter interferometric configurations are needed for its inversion. The random volume over ground scattering model can be inverted by a single frequency, fully

polarimetric, single baseline configuration or by a single frequency, single polarisation, multi-baseline configuration.

Multi-Baseline Single Frequency Single Polarisation Interferometry:

Multi-Baseline approaches were the first ones addressed in the literature concerning model-based inversion of vegetation parameters from interferometric data. Based on multi-baseline ERS-1/2 data the problem of vegetation height estimation from interferometric data was addressed for the first time [7-8]. Temporal decorrelation - affecting especially repeat pass interferometry at higher frequencies - was the main limitation of this approach leading to biased height estimates.

Latter investigations based on dual-baseline interferometric data acquired simultaneously, where successful in estimating tree height, canopy extinction, and underlying topography (Treuhaft, 2000). By varying the baseline all four model parameters (Height, Extinction, Underlying Topography and Ground to volume amplitude ratio) remain the same. The only parameter that changes is the effective vertical wavenumber (κ_z). So, any additional baseline offers two more observables while at the same time do not introduce additional unknowns. Accordingly, the inversion of the RVoG scattering model can be (in principal) performed using only two baselines, in form of a non-linear optimisation problem with four unknowns and four observables:

$$\begin{bmatrix} \text{Forest Height} \\ \text{Canopy Extinction} \\ \text{Underlying Topography} \\ \text{Ground/Volume scattering} \\ \text{amplitude} \end{bmatrix} = [M]^{-1} \begin{bmatrix} \text{Interferometric Phase and Coherence} \\ \text{from two (or more) Baselines} \end{bmatrix} \quad (7)$$

The availability of more baselines allows potentially the estimation of vertical vegetation structure profiles (Treuhaft, 2000; Cloude, 2002). However, in order to obtain two baselines a well-conditioned inversion problem, the two baselines have to be significantly different. The use of long baselines implies a loss in interferometric coherence due to volume decorrelation that can be compensated only at the expense of spatial resolution. Furthermore, the realisation of large baselines at airborne single-pass implementations – especially at lower frequencies (i.e., L- or P-band) – can be difficult and feasible only with high technological effort. The acquisition in repeat pass mode introduces temporal decorrelation effects that limit the performance or even the applicability of the approach.

Single-Baseline Single Frequency Fully Polarimetric Interferometry:

The second way to invert the RVoG model is by using polarisation diversity instead of baseline diversity. As the propagation through the volume is scalar, i.e. the extinction coefficient σ is independent of polarisation, the random volume contribution on the interferometric coherence $\tilde{\gamma}$ is polarisation independent. Polarisation influences the interferometric coherence only through the variation of the ground/volume amplitude ratio m . Accordingly, any additional polarimetric channel operating in a single baseline interferometric mode increases the number of observables by two, but at the same time introduces one additional unknown parameter: the ground-to-volume amplitude ratio for the new polarisation. Consequently, the inversion of the RVoG scattering scenario using a single baseline requires at

least three independent polarisations, and therefore, fully polarimetric interferometric data (Cloude, 1998; Papathanassiou, 1999).

Unfortunately, this six-dimensional optimisation problem has in general no unique solutions (Cloude, 2002), and a regularisation is required in order to establish uniqueness (Cloude, 2002; Brandfass, 2001). One way to overcome this problem without increasing the number of available baselines is to force the smallest $m = 0$ ($m_1 > m_2 > m_3, m_3 = 0$). Regarding the forest height estimation, the effect of this assumption is not serious (Papathanassiou, 2002), as the errors introduced by the assumption are compared to the intrinsic uncertainties in the data. Fig.2 shows a tree-height map obtained from the inversion of single-baseline single frequency fully polarimetric interferometric data from the Fichtelgebirge test site in Germany. The estimation accuracy lies in the order of 90% (Papathanassiou 2002; Papathanassiou, 2002).

There are main advantages of the single-baseline fully polarimetric mode compared to the multi-baseline single polarisation approach. The first one is that additional to the volume parameters, the inversion of polarimetric interferometric data provides also estimates about the effective ground-to-volume amplitude ratio at the different polarisations. This information about the ground scattering under the vegetation layer may open the way for the parameter estimation of vegetation covered terrain. The second one is that it requires only a single baseline. This can be essential regarding space-borne implementation scenarios.

$$\begin{bmatrix} \text{Forest Height} \\ \text{Canopy Extinction} \\ \text{Underlying Topography} \\ \text{Ground/Volume scattering} \\ \text{amplitude for each polarisation} \end{bmatrix} = [M]^{-1} \begin{bmatrix} \text{Interferometric Phase and Coherence} \\ \text{in three Polarisations} \end{bmatrix} \quad (8)$$

3 RVoG SCATTERING MODEL VALIDATION

The significance of any scattering model depends on its ability to fit experimental observations. Therefore, it is essential for any model-based parameter estimation to ascertain about the validity of the underlying model. One of the big advantages of the RVoG model is that it is possible to prove its validity from single-baseline polarimetric interferometric data without the need of any other information. The key for this is hidden in the geometrical interpretation of the model.

One key steps in understanding the role of polarisation in the RVoG scattering model is its geometrical interpretation. To obtain a geometrical interpretation of Eq. (3), it is important to recognise that the only parameter that varies with polarisation is the ground-to-volume amplitude ratio m . Thus Eq. (3) can be rewritten as

$$\tilde{\gamma}(\vec{w}) = \exp(i\varphi_0) \left[\tilde{\gamma}_V + \frac{m(\vec{w})}{1+m(\vec{w})} (1 - \tilde{\gamma}_V) \right] \quad (9)$$

This is the equation of a straight line in the complex plane, generated by the real parameter m . The line is going through the constant point $\exp(i\varphi_0) \tilde{\gamma}_V$

with direction $\exp(i\varphi_0)(1 - \tilde{\gamma}_V)$. Accordingly, the RVoG model predicts that the variation of the complex coherence as a function of polarisation is along a straight line inside the complex unit circle (Papathanassiou 2001; S.R. Cloude, 2002). In other words, by changing the polarisation state of the two interferometric images forming the interferogram, the loci of the corresponding complex coherences lie on a line inside the complex unit circle. The movement along a direction on the line corresponds to a monotonic (increasing or decreasing) change in m . Hence, a direct assessment of the validity of the RVoG model is possible by forming interferograms using different polarisations, plotting their complex coherences on the complex unitary circle and measuring their deviation from a straight line (Isola, 2001). This can be performed by means of chi-square statistics. Using N different polarisations for forming a

interferogram one obtain N complex coherence values

$\tilde{\gamma}_i$. If the RVoG model is valid then the real and

imaginary parts of $\tilde{\gamma}_i$ have to satisfy

$$\text{Im}\{ \tilde{\gamma}(\vec{w}) \} = A \text{Re}\{ \tilde{\gamma}(\vec{w}) \} + B \quad (10)$$

To measure how well the data satisfy this condition accounting for the intrinsic variance of amplitude and phase of the estimated complex

coherences when $|\tilde{\gamma}_i| \leq 1$ a chi-square merit function can be used which in this case is

$$\chi^2(A, B) = \sum_{i=1}^N \frac{\text{Im}\{ \tilde{\gamma}(\vec{w}_i) \} - A \text{Re}\{ \tilde{\gamma}(\vec{w}_i) \} - B}{\sigma_{\text{Im}i}^2 + A^2 \sigma_{\text{Re}i}^2} \quad (11)$$

$\sigma_{\text{Re}i}^2$ and $\sigma_{\text{Im}i}^2$ are the standard deviations of

the Real and Imaginary part of $\tilde{\gamma}_i$ respectively, and can be estimated directly from the data. Minimisation of Eq. (11) by setting the partial derivatives of $\chi^2(A, B)$ with respect to A and B to be zero, allows a least-squares determination of A and B ,

$$\partial \chi^2 / \partial A = 0 \quad \text{and} \quad \partial \chi^2 / \partial B = 0 \quad (12)$$

Note that while the condition - and thus the resulting equation - for the intersection point is linear, the condition for the slope is non-linear, due to the appearance of A in the denominator of Eq. (11). The agreement between the data and the model can be expressed by the “goodness” of the fit given by the probability Q

$$Q = \Gamma\left(\frac{N-2}{2}, \frac{\chi^2}{2}\right) \quad \text{with} \quad 0 \leq Q \leq 1 \quad (13)$$

where $\Gamma(\dots)$ is the incomplete gamma function. Large Q values indicate a good agreement between data and model while low Q values make the application of the RVoG model questionable.

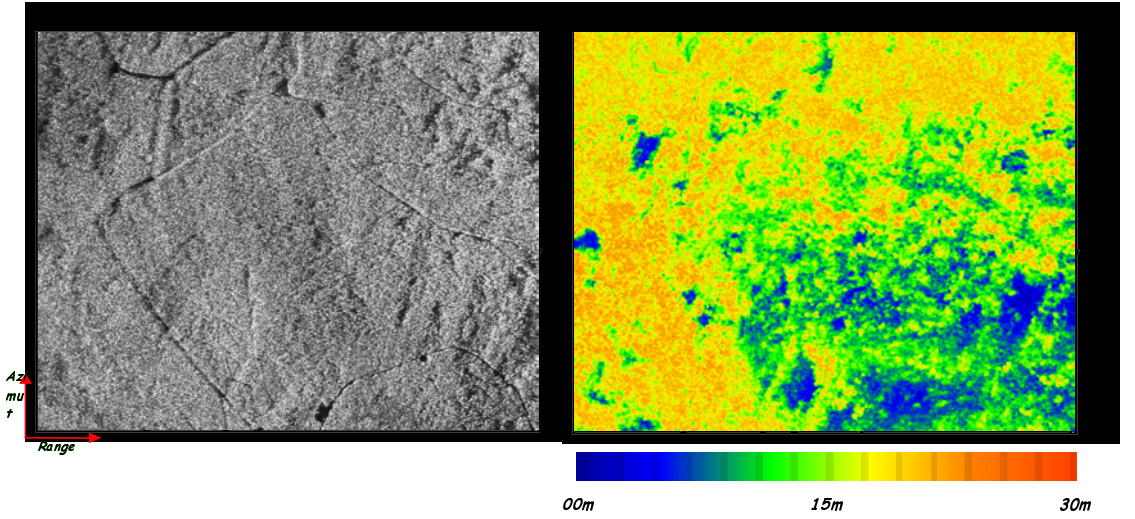


Figure 2: Left: L-band SAR Image. Right: Corresponding Forest Height Map

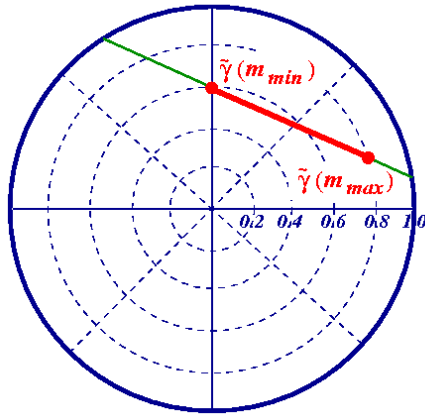


Figure 3: Geometrical Interpretation of the RVoG Scattering Model

Using this simple but essential concept a variety of polarimetric interferometric data sets acquired over different test sites – by different sensors - can be evaluated with respect to the validity of the RVoG model. Fig. 4 shows the Q maps obtained over the Fichtelgebirge/Germany test site (E-SAR/L-band) as a representative site of temperate central european forest. A very high agreement between model and data

is obtained over the whole forested region – independent from topographic variations. In Fig. 5, the corresponding Q map for a boreal forest from the Kudara/Russia test site (SIR-C/L-band) indicates also the validity of the RVoG model. Finally, also for a tropical rain forest in Amazon/Brazil (AeroSensing/P-band) the validity of the model is given as seen in Fig. 6 presented in the Q map.

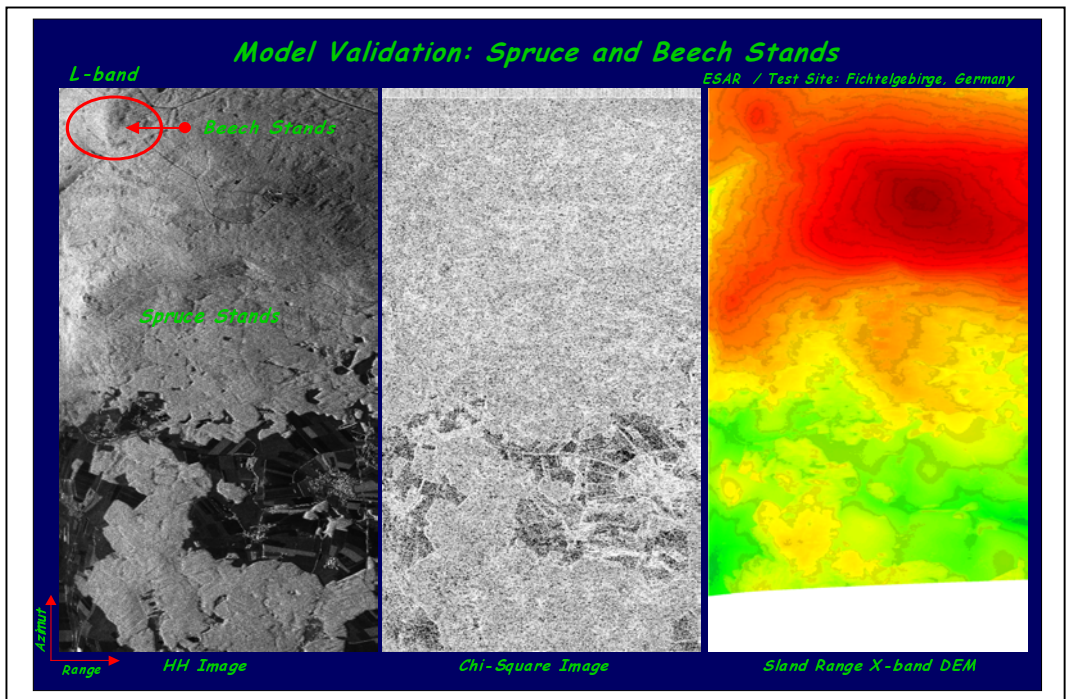


Figure 4: Left: SAR Image, Middle Q Map (white $Q=1$, black $Q=0$), Right DEM of the Fichtelgebirge Test Site

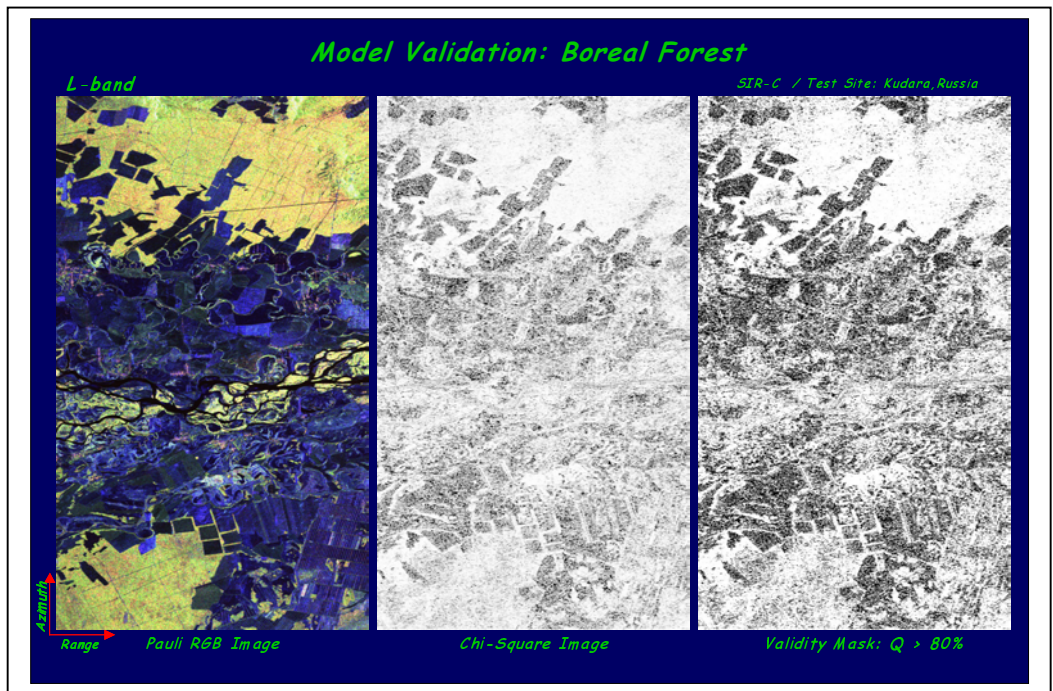


Figure 5: Left: SAR Image, Middle Q Map, Right Mask for $Q > 80\%$ for the Kudara Test Site

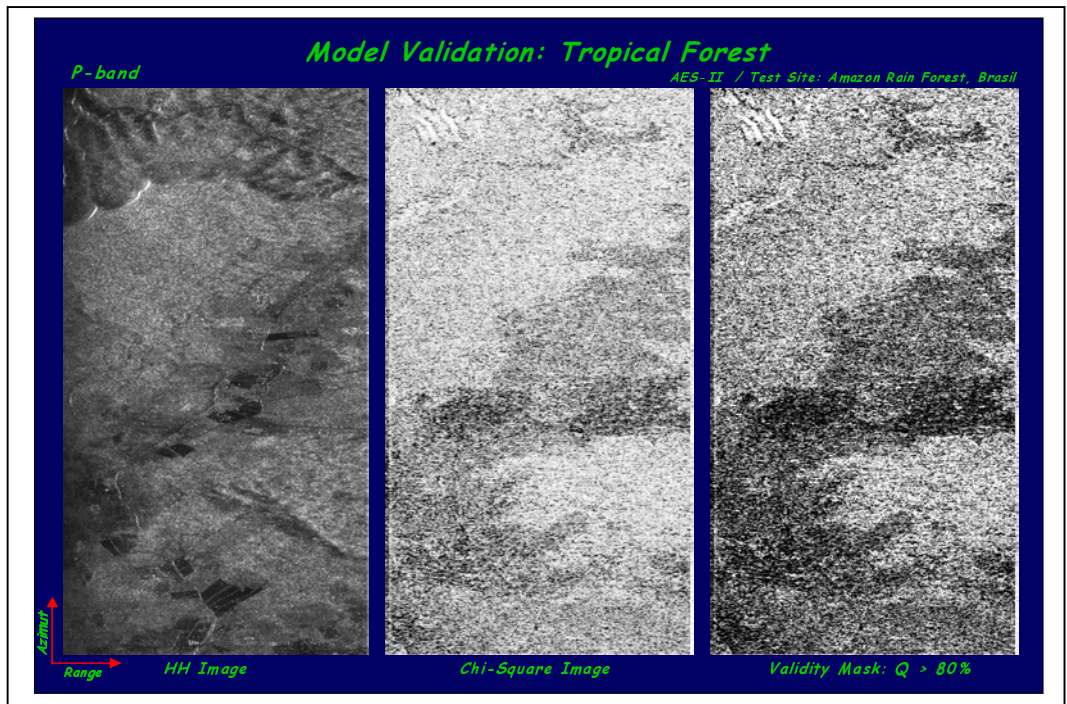


Figure 6: Left: SAR Image, Middle Q Map, Right Mask for $Q > 80\%$ for the Amazon Test Site

4 DISCUSSION AND CONCLUSIONS

In this paper the main approaches for model-based forest height estimation from multi-parameter interferometric radar remote sensing data have been discussed with respect to biomass estimation and in comparison to direct estimation approaches. The RVoG scattering model and the possible ways to invert it using multi-parameter interferometric data have been treated. Finally the question of validity of the RVoG has been addressed and the obtained results sketch out a wide validity for all important forest types including temperate, boreal, and, tropical forests in different terrain conditions.

5 REFERENCES

- J. Askne, P.B. Dammert, L.M. Ulander, and G. Smith, „C-Band Repeat-Pass Interferometric SAR Observations of the Forest“, IEEE Transactions on Geoscience and Remote Sensing, Vol. 35, No. 1, pp. 25-35, 1997.
- M. Brandfass, C. Hofmann, J.C. Mura, J. Moreira, and K.P. Papathanassiou, „Parameter estimation of Rain Forest Vegetation via Polarimetric Radar Interferometric Data“, Proceedings of SPIE 2001, Toulouse, France, August 2001.
- S.R. Cloude, and K.P. Papathanassiou, „Polarimetric SAR Interferometry“, IEEE Transactions on Geoscience and Remote Sensing, Vol. 36, No. 5, pp. 1551-1565, 1998.
- S.R. Cloude, and K.P. Papathanassiou, „A 3-Stage Inversion Process for Polarimetric SAR Interferometry“, Proceedings of European Conference on Synthetic Aperture Radar, EUSAR'02, pp. 279-282, Cologne, Germany, 4-6 June 2002.
- S.R. Cloude, „Robust Parameter Estimation using Dual Baseline Polarimetric SAR Interferometry“, Proceedings IGARSS'02 (cd-rom), Toronto, Canada, 22-26 June 2002.
- J.B. Drake et al, „Estimation of Tropical Forest Structural Characteristics using Large-Footprint Lidar“, Remote Sensing of Environment, Vol. 79, pp. 305-319, 2002.

- J.B. Drake et al, "Sensitivity of Large-Footprint Lidar to Canopy Structure and Biomass in a Neotropical Forest", *Remote Sensing of Environment*, Vol. 81, pp. 378-392, 2002.
- J.O. Hagberg, L.M. Ulander, and J. Askne, "Repeat-Pass Interferometry over Forested Terrain", *IEEE Transactions on Geoscience and Remote Sensing*, vol. 33, no. 2, pp. 331-340, 1995.
- M. Isola and S.R. Cloude, "Forest Height Mapping using Space-Borne Polarimetric SAR Interferometry", *Proceedings of the IGARSS'01*, 9-13 July, Sydney, Australia, 2001.
- T. Mette, K.P. Papathanassiou, I. Hajnsek, and R. Zimmermann, "Forest Biomass Estimation using Polarimetric SAR Interferometry", *Proceedings IGARSS'02* (cd-rom), Toronto, Canada, 22-26 June 2002.
- K.P. Papathanassiou, A. Reigber, and S.R. Cloude, "Vegetation and Ground Parameter Estimation using Polarimetric Interferometry - Part I: The Role of Polarisation", *Proceedings CEOS SAR Workshop*, Toulouse, 26-29 October 1999.
- K.P. Papathanassiou, A. Reigber, and S.R. Cloude, "Vegetation and Ground Parameter Estimation using Polarimetric Interferometry Part II: Parameter Inversion and Optimal Polarisations", *Proceedings CEOS SAR Workshop*, Toulouse, 26-29 October 1999.
- K.P. Papathanassiou and S.R. Cloude, "Single baseline Polarimetric SAR Interferometry", *IEEE Transactions on Geoscience and Remote Sensing*, Vol. 39, No. 11, pp. 2352-2363, 2001.
- K.P. Papathanassiou, I. Hajnsek, A. Moreira and S.R. Cloude, "Forest Parameter Estimation using a Passive Polarimetric Micro-Satellite Concept", *Proceedings of European Conference on Synthetic Aperture Radar, EUSAR'02*, pp. 357-360, Cologne, Germany, 4-6 June 2002.
- K.P. Papathanassiou, T. Mette, I. Hajnsek, G. Krieger and, A. Moreira, "A Passive Polarimetric Micro-Satellite Concept for Global Biomass Mapping", *Proceedings of the PI-SAR Workshop* (cd-rom), Tokyo, Japan, 29-30 August 2002.
- M. Schwaebisch, C. Hofmann, J. Moreira, C. Wimmer and S. Oh, "Operational Processing of Airborne P-band InSAR Data for Ground Topography Estimation", *Proceedings IGARSS'99*, Hamburg, Germany, 28 June – 2 July, 1999.
- R.N. Treuhaft, and P.R. Siqueira, "The Vertical Structure of Vegetated Land Surfaces from Interferometric and Polarimetric Radar", *Radio Science*, Vol. 35, No. 1, pp. 141-177, 2000.
- R.N. Treuhaft, B.E. Law, G.P. Asner, and S. Hensley, "Vegetation Profile Estimation from Multialtitude, Multifrequency, Radar Interferometric and Polarimetric Data", *Proceedings IGARSS'00*, Honolulu Hawaii, 24-28 July 2000.
- Ulbricht, A. Reigber, R. Horn, A. Potsis, and A. Moreira, "Multifrequency SAR Interferometry: DEM Generation in L- and P-band and Vegetation Height Estimation in Combination with X-band", *Proceedings of EUSAR 2000*, pp. 51-54, Munich, Germany, 23-25 May 2000.

Monitoring land surface soil moisture from L-band microwave radiometry: Retrievals from multi-angular observations

J.-P. Wigneron⁽¹⁾, Y. Kerr⁽²⁾, J.-C. Calvet⁽³⁾, T. Pellarin⁽³⁾, M. Pardé⁽¹⁾, S. Schmidl Søbjaerg⁽⁴⁾

⁽¹⁾ INRA Bioclimatologie, B.P. 81, 33883 Villenave d'Ornon CEDEX, France

Tél: (33) 5 57 12 24-19 Fax: (33) 5 57 12 24-20 wigneron@bordeaux.inra.fr

⁽²⁾ CNES / CESBIO, 31401 Toulouse Cedex 4, France

⁽³⁾ Météo France / CNRM, 42 av G. Coriolis, 31057 Toulouse Cedex 1, France

⁽⁴⁾ Oersted-DTU / Electr. Syst. Section, Technical University of Denmark (TUD), Lyngby, Denmark

ABSTRACT - L-band passive microwave remote sensing sensors are able to provide estimates of surface soil moisture (SM), on both spatial and temporal scales, compatible with applications in the fields of meteorology and hydrology. Based on this concept, the SMOS mission was proposed to the European Space Agency (ESA) in the framework of the Earth Explorer Opportunity Missions and was selected for a tentative launch in 2006. The radiometer will enable a frequent and global coverage and has dual-polarization and multiangular capabilities. It is likely that these characteristics are very significant assets in the retrieval process of surface soil moisture, especially over vegetation-covered areas. A number of studies have been carried out to investigate this aspect, and also, incidentally, to help defining the best suited multi-angular configuration of the SMOS instrument. In the present paper, a short review of soil moisture retrieval approaches is given. Then two examples of soil moisture retrieval analyses are presented. The first example concerns the implementation of statistical inversion methods at global scale, based on simulated data sets. The second example concerns tests of two- and three parameter retrieval methods over experimental data sets (PORTOS-93 over wheat and AVIGNON-2001 over corn). A discussion of most significant results is given in this paper.

1 INTRODUCTION

Surface soil moisture (hereafter referred to as w_s) is a key variable of water and energy exchanges at the land surface / atmosphere interface. This variable is of crucial importance for several reasons: in hydrology and meteorology, the water content of the surface soil layer is a pertinent descriptor of water exchanges between the surface and the atmosphere. Also, soil moisture is an important variable for estimating the distribution of precipitation between storm runoff and storage, and for computing several key variables of land surface energy and water budget (albedo, hydraulic conductivity, etc.).

Soil moisture is highly variable both spatially and temporally in the natural environment as a result of inhomogeneity of soil properties, topography, land cover, and the nonuniformity of rainfall and evapotranspiration. Remotely sensed data, which can provide frequent and spatially comprehensive estimates of land surface characteristics, arouse great interest. L-band passive microwave remote sensing sensors are able to provide estimates of surface soil moisture (SM), on both spatial and temporal scales, compatible with applications in the fields of meteorology and hydrology (Schmugge et al., 1994;

Njoku and Entekhabi, 1996; Jackson et al., 1999, Kerr, 2001).

Retrieving soil moisture over bare soils, e.g. in semi-arid and arid regions, is rather simple, since there is a direct link between T_b and soil moisture (m^3/m^3) (Schmugge et al., 1994). Over vegetation-covered areas however, retrieving SM is more complex, as it is necessary to account for the effect of vegetation. Usually, estimates of the vegetation attenuation term (e.g. optical depth τ) are derived from the vegetation water content W_C (kg/m^2) (Jackson and Schmugge, 1991). Values of W_C can be estimated from vegetation indices derived from remote sensing observations (Jackson et al., 1995) with substantial uncertainty. However, it is also possible to retrieve simultaneously both SM and τ from dual-polarization, multi-angular L-band data as has been demonstrated by Wigneron et al. (1993, 2000). Retrieving directly both SM and τ is a major potential asset as: (i) there is no need for ancillary W_C values to estimate τ (ii) the retrieved parameter τ may turn out to be a very useful product by itself: actually this variable could be a meaningful index for monitoring vegetation dynamics as well as for estimating forest characteristics.

A radiometric system with multi-angular viewing capabilities and relying on a deployable structure using

antenna synthesis methods has led to the Soil Moisture and Ocean Salinity (SMOS) mission. The SMOS mission was proposed to the European Space Agency (ESA) in the framework of the Earth Explorer Opportunity Missions and was selected for a tentative launch in 2006. The radiometer will enable a frequent (3-day revisit) and global coverage (ground resolution of 50 km). It is likely that the SMOS dual-polarization and multiangular capabilities are very significant assets in the retrieval process of surface soil moisture, especially over vegetation-covered areas. A number of studies have been carried out to investigate this aspect, and also, incidentally, to help defining the best suited multiangular configuration of the SMOS instrument. Recent studies have addressed various aspects of the soil moisture retrievals in the framework of the SMOS mission.

In the present paper, first, a short review of soil moisture retrieval approaches is given. Then two examples of soil moisture retrieval studies are presented. The first example concerns the implementation of statistical inversion methods at global scale, based on simulated data sets in 1987-1988 (Pellarin et al., 2002a-b-c). The objective of this study was to evaluate the retrieval methods over mixed pixels and to provide some first estimates of the accuracy in the soil moisture retrievals at global scale. The second example concerns tests of two- and three parameter retrieval methods over experimental data sets (PORTOS-93 over wheat and AVIGNON-2001 over corn, Pardé et al., 2002a). The objective of this study was to analyze how the vegetation structure, which depends mainly on vegetation type and phenological stage, may affect the soil moisture retrieval process. Several methods, accounting for these effects were evaluated. A short summary of these studies and a discussion of most significant results is given in the following.

2. REVIEW OF SOIL MOISTURE RETRIEVAL APPROACHES

An exhaustive review of soil moisture retrieval approaches was made by Wigneron et al. (2002) in the framework of the ESA-ITT 3652. The review shows that there are a fairly wide variety of approaches which have been used to retrieve soil moisture from microwave radiometry. Also, it appears that it is often difficult to strictly classify the approaches into a given category. Most of the studies have demonstrated the considerable potential of low frequency observations at L-band (~1.4GHz) for soil moisture retrievals. At higher frequencies (i.e. 6.6 GHz and higher), the sensitivity to soil moisture becomes very low when the vegetation water content exceeds about 1.5 kg/m² (Njoku and

Li, 1999), which corresponds roughly to a leaf area index (LAI) of about two for crops. Therefore, it seems that the use of C-band observations for soil moisture retrievals is limited to semi-arid regions (Van de Griend and Owe, 1994; Chanzy et al., 1997; Njoku and Li, 1999; Magagi et al., 2000) with low levels of vegetation biomass. However, Owe et al. (2001) have investigated the capability of dual polarization C-band observations for monitoring soil moisture over test sites in Illinois (mostly farms with cropland, grasses and woodland) and rather satisfactory retrieval results could be obtained. However, as reliable spatially averaged surface moisture data cannot be obtained easily, validation studies have still to be conducted. The authors considered that "field experiments with the express purpose of gathering such data should be designed and implemented as a research priority".

Over bare soils, e.g. in semi-arid and arid regions, the retrieval methodology for soil moisture w_s is simple, since there is a direct link between T_b and w_s (Schmugge et al., 1994; Chanzy et al., 1997). Over vegetation-covered areas however, retrieving w_s is more complex and requires ancillary data, as it is necessary to account for the effect of vegetation. Four main types of algorithms could be roughly distinguished. The distinction is made depending on the way vegetation and temperature effects are accounted for:

- (1) Parameters and variables used to correct for vegetation effects are derived from land cover classification maps (vegetation type, estimates of VWC, etc.)
- (2) Vegetation effects are computed, independently of soil moisture, from ancillary remote sensing indexes (microwave measurements from other channels, visible and near infrared observations, etc.)
- (3) Two-parameter retrievals: both soil moisture and vegetation optical depth (or VWC) are retrieved simultaneously from the microwave observations. Effective surface temperature is estimated from additional microwave or thermal infrared remote sensing observations.
- (4) Three-parameter retrievals: soil moisture, vegetation optical depth (or VWC) and the effective surface temperature are retrieved simultaneously from the microwave observations.

Most of the studies corresponding to Approach 1 are based on mono-configuration observations, in terms of frequency, polarization and view angle. This approach is well suited to a very accurate analysis of airborne observations over well-defined and well-controlled areas. For satellite applications, when detailed information on the types and water content of vegetation cannot easily be obtained, other approaches (2, 3 or 4) are generally more appropriate. Relatively satisfactory retrieval results have been obtained using

Approach 2. However, the approaches based on indices may have some disadvantages. For instance, indices based on visible and near infrared signatures (NDVI, for instance) are sensitive to cloud screening, atmospheric absorption and scattering effects. Microwave vegetation indices based on high frequency measurements are also highly sensitive to atmospheric effects. Moreover, the sensitivity of vegetation indices to biomass strongly depends on the frequency channel due to the fact that the penetration depth within the vegetation layer strongly decreases as frequency increases. For instance, estimates of optical depth from C-band indexes may saturate when vegetation water content exceeds about 1.5 kg/m².

The two-parameter retrievals (Approach 3), *i.e.* the capability of simultaneously retrieving soil moisture (w_s) and vegetation characteristics (τ or VWC) from the passive microwave observations was demonstrated by several studies: using dual-polarization multi-frequency observations (Van de Griend and Owe, 1994; Davis et al., 1995; Wigneron et al., 1995, 1996; Chanzy et al., 1997; Njoku and Li, 1999; Liou et al., 2002) or from dual-polarization multi-angular L-band observations (Wigneron et al., 1993, 1995, 2000; Liou et al., 2002; Pellarin et al., 2002b). The two-parameter retrieval is a major potential asset in comparison with Approach 1 because (Wigneron et al., 2000):

i) There is no need for ancillary information about the vegetation water content (VWC) and the b parameter to compute the optical depth (τ). The multi-angular approach considerably improves the retrieval process since estimating these two parameters on a large spatial scale from ancillary remotely sensed data is not easy. Vegetation water content may change significantly at a time scale of a few weeks, and no means is currently available to map or simulate these time changes. The b parameter was found to be sensitive not only to vegetation moisture content but also to canopy structure, which depends on the canopy type and on phenology (Wigneron et al., 1996; Levine and Karam, 1996; Pardé et al., 2002).

(ii) The retrieved variable τ may turn out to be a very useful product by itself. Actually, this variable is a meaningful index for monitoring vegetation dynamics (development and senescence) at a global scale (Choudhury, 1990; Van de Griend and Owe, 1993) as well as for estimating forest characteristics. This variable was found to be closely related to the vegetation water content for crops and to the total branch water content for forests (Ferrazzoli et al., 2002). Also, it seems that the use of the two-parameter retrievals (Approach 3) may

lead to significantly improved accuracy in the soil moisture retrievals as opposed to Approach 2 (Van de Griend et al., 1994).

The three-parameter retrievals (Approach 4), *i.e.* the capability of simultaneously retrieving three parameters: soil moisture (w_s), optical depth (τ) and the effective surface temperature from the passive microwave observations, is very promising but has not been clearly demonstrated. Calvet et al. (1995, 1996) and Njoku and Li (1999) showed that simultaneous retrievals of both soil moisture and surface temperature may be difficult for wet soil conditions. The theoretical study of Wigneron et al. (2000) showed that good estimates of soil moisture w_s and optical depth τ can be obtained from three-parameter retrievals in the central part of the FOV from multi-angular SMOS L-band data (associated errors are less than 0.04 m³/m³ and 0.06 for w_s and τ , respectively). The retrieval error for surface temperature T_s may be large for wet soil conditions. Therefore, the main conclusions of the study are:

(i) the three-parameter approach is very promising: its particular advantage is that no ancillary information about surface temperature or vegetation biomass is required to retrieve soil moisture.

(ii) rather good estimates of both soil moisture and optical depth could be obtained when the available angular range is sufficiently large.

(iii) accurate estimates of surface temperature should not be expected from the three-parameter approach (especially for wet soil conditions).

Three-parameter retrievals based on experimental observations have to be carried out to confirm these theoretical results.

Two- or three-parameter retrievals based on multi-channel observations (in terms of frequency f , polarization P and view angle θ) appeared to be very promising. However, the use of these approaches requires a good parameterization of the dependence of optical depth on the configuration parameters (f , P and θ). For instance, simultaneous retrievals based on multi-frequency observations require a good characterization of the ratio between the optical depth for the different frequency channels (Wigneron et al., 1995; Magagi et al., 2000). As an example, in the study of Wigneron et al. (1995), based on combined L- and C-band observations, the retrieval accuracy was found to be highly sensitive to the ratio, $\tau_{(5\text{GHz})} / \tau_{(1.4\text{GHz})}$. However, very little information is available at this time about the dependence of this ratio on view angle and polarization for different vegetation types. As noted above, the problem of using several frequencies is that the penetration depth within soil and/or vegetation strongly depends on the frequency. For instance, when using combined L- and C-band observations, empirical corrections have to be applied to account for the different sampling depths within soil at both L- and C-

band (Wigneron et al., 1995; Magagi et al., 2000). It is very difficult to define general relationships between the topsoil moisture over different depths (about 3 cm at L-band and 1 cm at C-band) that could be valid over a large range of soil and climatic conditions. Similarly, simultaneous retrievals based on multi-angular and/or dual polarization observations require a good characterization of the ratio τ_H/τ_V and of the angular dependence of optical depth τ , for both polarizations (Van de Griend and Owe, 1994; Wigneron et al., 1995). Several studies showed that optical depth (or the related b parameter) may strongly depend on polarization and incidence angle, especially for vegetation canopies with a dominant vertical structure (stem dominated canopy such as cereal crops) (Brunfeldt et al., 1984; Ulaby et al., 1986; Wigneron et al., 1995). As noted by Owe et al. (2001), vegetation elements are randomly orientated for most crops and naturally occurring vegetation and it is likely that optical depth (τ) is polarization-independent on a satellite scale. Validation of this hypothesis was made using satellite observations and it was shown that when retrieved τ_H and τ_V were plotted together, they fell very close to the 1:1 line. However, additional validation of these preliminary results is required. On a satellite scale, very few studies (if any) investigated the angular dependence of optical depth (τ). As for polarization, it is likely that this dependence is rather low if the optical depth is expressed in terms of its nadir component τ_0 . Future studies will have to address this key issue for retrievals based on the multi-angular microwave signatures.

3. APPLICATION OF INVERSION METHODS OVER HETEROGENEOUS PIXELS AT GLOBAL SCALE

As no L-band observations from spaceborne systems are currently available, the different soil moisture retrieval approaches could not be tested at global scale and during large time periods. The studies of Pellarin et al. (2002b-c-d), which were developed in the framework of ESA-ITT 3652, were based on a global data set of synthetic brightness temperatures (T_B) at L-band developed during two years: 1987 and 1988 (Pellarin *et al.*, 2002a). Note that contrasting El-Niño/La-Niña climatic conditions prevailed in 1987 and 1988, respectively. The T_B observations were simulated at the half-degree resolution, which is in good agreement with the SMOS spatial resolution (this resolution is expected to range between 20 and 60 km depending on the incidence angle, for various incidence angles and both polarizations (Horizontal and Vertical). The simulations were carried out for various land cover

types (different forest types, herbaceous canopies, bare soils, crops, etc.) and for a variety of climatological conditions encountered at global scale (frozen soils, snow cover overlaying vegetation, snow cover under forest, etc). In addition, because of the large spatial scale considered in this study, the pixel heterogeneity had to be accounted for in the T_B simulations.

3.1 General Method and Data Set

The data set has been developed from simulations based on a two-step process. First, a land surface scheme, the Interactions between Soil, Biosphere and Atmosphere (ISBA) model, was used at global scale to simulate the time variations in the surface state characteristics (e.g. soil temperature and moisture content at the surface and at depth, snow moisture content, etc.) needed by the T_B simulation model. The simulations were based on a two-year atmospheric forcing derived from the Global Soil Wetness Project (GSWP) and on a detailed global surface database: ECOCLIMAP (Pellarin et al., 2002a), which consists in land cover maps and climatic maps at 1km resolution. Second, a simple model (L-MEB, L-band Microwave Emission of Biosphere) based on the radiative transfer equations, was used to produce multi-temporal T_B maps from the ISBA outputs as well as from information derived from the thematic maps and the atmospheric forcing database. The brightness temperatures were computed at five different incidence angles (0, 20, 30, 40 and 50°) and two polarizations (H and V).

The synthetic L-band T_B were simulated at the half-degree resolution and at this rather coarse spatial resolution, there are very few "homogeneous" pixels. Therefore, the sub-pixel heterogeneity was accounted for by using a "multi-patch" version of ISBA. This version is able to simulate distinct water and energy budgets in the same pixel for the three main surface types which were considered in this study (namely bare soil, woody vegetation and herbaceous vegetation). The obtained synthetic global T_B data set was a very useful reference to develop and test methods for retrieving soil moisture in the framework of near-future spatial missions such as the SMOS mission. Based on these T_B data, the objective of the present study was to test inversion algorithms for soil moisture monitoring. Two different statistical methods based on simple regression analysis were investigated. The first approach (referred to as the global regression model GRM) relies on a single regression model which is used to retrieve surface soil moisture over the whole continental area. The second approach (referred to as the local regression model LRM) relies on independent regression models which are calibrated over each pixel.

Based on the state of the art knowledge in the field of passive microwave remote sensing, the results of these retrieval studies provide an exhaustive evaluation of the

SMOS capabilities for soil moisture monitoring, at global scale and during a two year period.

3.2 Statistical Retrieval Method

The evaluation and the comparison of the local and global statistical methods was made at global scale for both contrasted 1987 and 1988 years. The accuracy in the values of the retrieved soil moisture was also computed for various approaches in calibrating the regression model. Also, the influence of different instrumental noise levels on T_B was evaluated (1, 2 and 3 K). These values of noise correspond roughly to the range of values for individual SMOS observations, depending on the view angle, which is expected for SMOS (Kerr et al., 2001). The simple regression approach used in the study can be written as:

$$wg^* = a_0 + a_1 IND_1 + a_2 IND_2 + \dots + a_q IND_q \quad (1)$$

where wg^* is the estimated soil moisture, a_0, a_1, \dots, a_q are the regression coefficients and $IND_0, IND_1, \dots, IND_q$ the selected indices presented in Table 1.

The reference surface soil moisture wg which is used in the study is computed for each pixel as:

$$wg = (f_B \cdot wg_B + f_F \cdot wg_F + f_H \cdot wg_H) / (f_B + f_F + f_H) \quad (2)$$

where f_B, f_F, f_H represent the bare soil, forest and herbaceous fractions which were considered within the pixel, respectively, and wg_B, wg_F, wg_H correspond to the soil moisture of the bare soil, forest and herbaceous fractions of the pixel, respectively.

Slightly modified version of GRM were calibrated over 90% and 80% of the continental surfaces (methods referred to as GRM-20% and GRM-10%). This was made by excluding 10% or 20% of the worst pixels, which correspond to pixels where higher values of the RMS errors were obtained in the retrieval process of wg . For a 1K noise level, it was found that best retrieval results were obtained by using the LRM method (Figure 1). This method provided much better results than GRM-20%: the mean global RMS error value is equal to $0.029 \text{ m}^3 \text{ m}^{-3}$ in 1987 and $0.030 \text{ m}^3 \text{ m}^{-3}$ in 1988. The accuracy of the LRM soil moisture retrieval is better than $0.04 \text{ m}^3 \text{ m}^{-3}$ over about 90 % of the global continental area for both years, while this proportion is only about 40 % for GRM-20% (Figure 2).

However, both GRM and LRM approaches were found to be strongly sensitive to the noise level. For a 2K noise level, the proportion of continental pixels where the accuracy in the LRM soil moisture retrieval is better than $0.04 \text{ m}^3 \text{ m}^{-3}$ decreased very significantly from 90% to less than 30 %. Therefore, noise levels higher than 2K are significantly detrimental to the quality of the soil moisture retrievals presented in this study. However, as

mentioned in introduction, the SMOS radiometer should be able to carry out observations for a large number of view angles. By using simple statistical processing, the effect of the radiometric noise on the multiangular signature of the land surfaces should be probably reduced and thus, the 1 K noise level can probably be considered as a reference value of the radiometric noise for the SMOS observations.

The spatial distribution of the a_1, a_2 and a_3 coefficients used in the LRM method were found to be very coherently related to the physiographic maps used in the forward simulation. This result is very interesting for an operational use of the LRM in the retrieval process of the SMOS data. It is likely that semi-empirical relationships could be computed between these coefficients and the surface characteristics, providing a way to derive the regression coefficients at any location and for any spatial resolution.

These two aspects (sensitivity to the noise level, and relationships between the regression coefficients and the surface characteristics) should be investigated further in future studies.

3.3 Conclusions

The results of the study made at global scale (Pellarin et al., 2002a-b-c) showed that statistical approaches can provide very good retrieval results. For instance, the accuracy of the LRM method in soil moisture retrieval is better than $0.04 \text{ m}^3 \text{ m}^{-3}$ over about 90 % of the global continental area. The LRM approach consists of calibrating a regression model based on microwave indices over each pixel. The spatial distribution of the regression coefficients used in this method were found to be very coherently related to the physiographic maps used in the forward simulation. It is likely that relationships could be computed between these coefficients and the surface characteristics, providing a way to derive the regression coefficients at any location and for any spatial resolution.

3-parameter retrievals (results not shown here) could not provide accurate results over rather heterogeneous pixels. Therefore, this type of approach should be constrained using ancillary information. For instance, estimates of the surface temperature computed from meteorological models, or estimates of the surface fraction of the different cover types, could be used in the retrieval process. These different approaches are currently evaluated at a more local scale over a 40×40 km pixel South-West of France.

4 APPLICATION OF TWO- AND THREE-PARAMETER RETRIEVAL APPROACHES OVER EXPERIMENTAL DATA SETS

The objective of the study was to analyse how the vegetation structure, which depends mainly on vegetation type and phenological stage, may affect the

soil moisture retrieval process (Pardé et al., 2002). Also, several methods, accounting for these effects were evaluated. Preliminary studies showed that the vegetation effect (emission, scattering and attenuation) may depend strongly on incidence angle, polarization, and also on the stage of development of the vegetation canopies. This dependence was found for crops with a vertical (stem-dominated) structure such as cereals (Ulaby and Wilson, 1985, Wigneron et al, 1995, 1996), but it may be significant for other vegetation types. To date very few studies investigated in detail this dependence, and how it may affect soil moisture retrievals. A detailed study of these two questions was carried out over a wheat field based on the PORTOS-93 data set obtained during a three-month experiment at the INRA Avignon test site in 1993. A second and very similar study, was based on measurements acquired over a corn crop during a four month experiment on the new Avignon test site in 2001. The corn canopy is also made of vertical stems, but the effects due to the large leaves are expected to be more significant than over the wheat crops.

4.1 PORTOS-93 experiment

4.1.1 Characterizing the dependence of the vegetation parameters on θ , polarization and time

The values of τ were computed from the brightness temperature measured during PORTOS -93. The τ values at H polarization are almost constant, while they increase very significantly with view angle at V polarization. For vertical-stem dominated vegetation, a simple formulation based on the Cpol formulation was proposed by Wigneron et al. (1995) to model the dependence of τ_p on view angle and polarization. The Cpol formulation is given by the equation:

$$\begin{aligned}\tau_V / \tau_H &= \sin^2 \theta + C_{POL} \cos^2 \theta \\ \tau_H &= \tau_H(\theta=0) = \text{constant}\end{aligned}\quad (3)$$

In this approximation, τ for H-polarization (τ_h) is assumed to be independent on the incidence angle θ . Simulations of τ using the Cpol parameterizations were compared with the values of τ retrieved for each view angle and both polarizations. The use of Cpol was found to be very efficient, since (i) the use of the Cpol approach led to a very low values in the rms error between measurements and simulations of Tb (ii) the Cpol parameterization is a very convenient approach since only two parameters (Cpol and $\tau_h(0)$) are required to simulate τ as a function of view angle and polarization.

The values of the two parameters Cpol and $\tau_h(\theta=0)$ were computed for each day, by minimizing the rms

error between measured and simulated Tb. We can note that Cpol increase almost linearly during the wheat growth until the vegetation is well-developed. This increase can be related to the growth of the vertical stems which have high attenuation properties at V-polarization. At the beginning of the crop development (~DoY 120), stems are very short and the vegetation is leafy (associated values of Cpol are close to one, which correspond to the case of no dependence of τ on view angle and polarization). Then, the increase in the value of Cpol is simultaneous to the development of the stems.

Similarly the b parameter was also retrieved from the T_B observations. The time variations in the values of bp are plotted in figure 3 at $\theta=40^\circ$. These values were obtained by dividing the time variations in τ values by the vegetation water content. At H polarization, we can note a very significant decrease (from 0.15 to 0.02) in the values during the crop growth. The large values of bp at the beginning of the crop growth ($b_p \approx 0.15$) corresponded to a stage of leafy vegetation. Then, as the vegetation began to be dominated by the vertical stems, the values of bp decreased down to values in the range 0.07-0.12. Finally during senescence, the values of bp went on decreasing down to values in the range 0.05-0.02. At V polarization, the values of bp increased during the stem development and then decreased during the wheat senescence stage. Figure 3 clearly showed that it is difficult to assign a value to the bp parameter for the wheat crop, since the value of bp strongly depends on view angle, polarization, but also on the stage of vegetation during the crop cycle.

4.1.2 Comparison of different soil moisture retrieval approaches

The values of bp strongly depend also on view angle and polarization and it was found that the Cpol parameterization was an accurate parameterization of this dependence. Based on these results, different soil moisture retrieval approaches were tested and compared. In the most classical retrieval approach, it is considered that the vegetation water content can be estimated from ancillary information (with an associated uncertainty), and the optical depth is calculated using the bp parameter from $\tau_p = b_p \cdot W_C$. The study is made for observations acquired at one angle ($\theta=0^\circ$, approach A1a) or for several view angles ($\theta=0, 10, 20, 30, 40, 50^\circ$, approach A1b). The results are compared with the two- and three- parameter approaches (approach A2a-d, A3, A4) as defined in a theoretical study by Wigneron et al. (2000). As, the dependence of τ on view angle and polarization was found to be significant for wheat, two other approaches were tested. The Cpol parameter was retrieved concurrently with optical depth and soil moisture (approach A3) and with optical depth, soil moisture and

surface temperature (approach A4). For all the above configurations, the land surface variables were retrieved for all the dates of radiometric observations, and the retrieved soil moisture was compared with the gravimetric measurements made in the 0-2 cm layer.

First, the “classical” retrieval approaches (approaches A1a-b) were implemented assuming that the b_p parameter was constant and $b_p=0.12$ (best fit value) and the surface temperature was known. The RMSE between the retrieved soil moisture and the measurements (for the 0-2 cm layer) computed during the entire growing cycle (DoY 110-DoY 186) is $0.054 \text{ cm}^3/\text{cm}^3$ for approach A1b. If we consider only the time period before the stage of vegetation senescence (DoY 110-DoY 167) the RMSE is much lower ($\sim 0.03 \text{ cm}^3/\text{cm}^3$). Therefore, it appears that if the vegetation water content is known, the retrieval algorithm based on the use of a unique parameter b_p can provide rather accurate results as long as the general geometry of the vegetation canopy do not change much. Conversely, over a rather long time period, the value of b_p may change significantly as a function of the vegetation phenology and this approach is less efficient to retrieve soil moisture.

The two- and three- parameter retrieval approaches based on multi-angular and dual polarization were then tested. The use of $C_{pol}=1$ (i.e. $\tau_v = \tau_h$) produced a lower accuracy in the retrieved values of soil moisture in comparison with the use of $C_{pol}=4$. Therefore, accounting for the dependence of τ on both incidence angle and polarization seemed to be important in the retrieval process. As the correction parameter C_{pol} was found to vary significantly with time, it was retrieved simultaneously with the other vegetation variables in approaches A3 and A4. The soil moisture retrievals are illustrated for approach A3 in Figure 4. The rms error in soil moisture retrievals was about 0.05 and $0.06 \text{ m}^3/\text{m}^3$ for approaches A3 and A4, respectively. Thus relatively similar accuracy was obtained in SM retrievals for both classical approaches (A1) and 2-, 3- and 4-P retrievals. In figure 4, we can see that the soil moisture is slightly underestimated, especially during the first period of the crop growth. It seems that this underestimation in the soil moisture values is balanced by an underestimation in the optical thickness.

4.2 AVIGNON'01 experiment: accounting for the effects of corn structure

A very similar study to that made over wheat was carried out using the measurements made over a corn crop during a four-month experiment at the Avignon test site in 2001. The observations were

made by a L-band radiometer developed by the Technical University of Denmark (TUD) in Copenhagen (Figure 6). The dependence of τ on view angle was also found to be significant at V polarization. However, contrary to what was obtained over wheat fields, it was very uneasy to find a simple parameterization to model this dependence. Retrieval approach A1 and the two- and three- parameter retrieval methods were implemented on the corn data set. As before it is found that rather similar results were obtained using classical approach (A1) and the two- and three- parameter methods. However, as the dependence of τ on view angle could not be modeled, a lower accuracy was generally obtained in the retrieval of soil moisture for the different approaches implemented. First results of soil moisture retrievals computed on the AVIGNON'01 experiment are given in Figure 5.



Figure 6: Polarimetric L-band TUD radiometer at INRA-Avignon-2001 experiment. The set up is mounted on a crane boom, moving over several fields, and allowed changes in azimuth and incidence angle

4.3 Discussion and Conclusion

The dependence of the vegetation parameters on view angle, polarization and time were found to be significant over two types of crops (wheat and corn), especially at V polarization. Contrary to the wheat crop, it was very uneasy to find a simple parameterization to model the dependence of τ on θ for the corn crop. For both crops, the two- and three-parameter retrieval methods provided satisfying results. The accuracy in the soil moisture retrieval was about $0.04\text{-}0.06 \text{ m}^3/\text{m}^3$. A relatively similar accuracy was obtained in SM retrievals for both classical approaches (A1) and 2-, 3- and 4-P retrievals. In comparison with the classical approaches, the main interest in using N-P retrievals ($N \geq 2$) is that no ancillary information on the vegetation water content W_c , the b parameter and surface temperature (for a $N \geq 3$) are required in the inversion

process. Note that for the wheat and corn canopies, for which the dependence of the vegetation parameters on view angle and time was found to be significant at V polarization, good retrieval results were also obtained by using the H polarization only. Also, these results clearly showed that classical

approaches (A1a-b) provide lower retrieval accuracy when the vegetation structure changes with time (in relation with vegetation development, senescence, ...). Both two- and three-parameters approaches should be used in that case.

Index	Name	Definition
$AR_{p,\theta,\beta}$	Angular Ratio	$T_B(p,\theta)/T_B(p,\beta)$
PR_θ	Polarization Ratio	$(T_B(v,\theta)-T_B(h,\theta))/(T_B(v,\theta)+T_B(h,\theta))$
$PD_{p,\theta}$	Polarization Difference	$(T_B(v,\theta)-T_B(h,\theta)) \cdot T_B(v,\theta)$
$AD_{p,\theta,\beta}$	Angular Difference	$T_B(p,\theta)-T_B(p,\beta)$
$APR_{p,\theta,\beta}$	Angular Polarization Ratio	$(T_B(p,\theta)-T_B(p,\beta)) / T_B(p,\beta)$

Table 1 - Microwave indices. p, θ and β , denote the polarisation (V or H) and two incidence angles

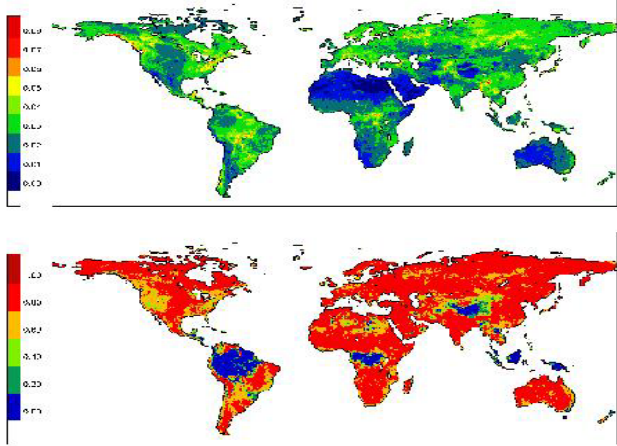


Figure 1 Spatial distribution of the scores in soil moisture retrievals using LRM, for a 1 K noise level, in 1988: (top) RMS error, (bottom) efficiency. (Pellarin et al., 2002b).

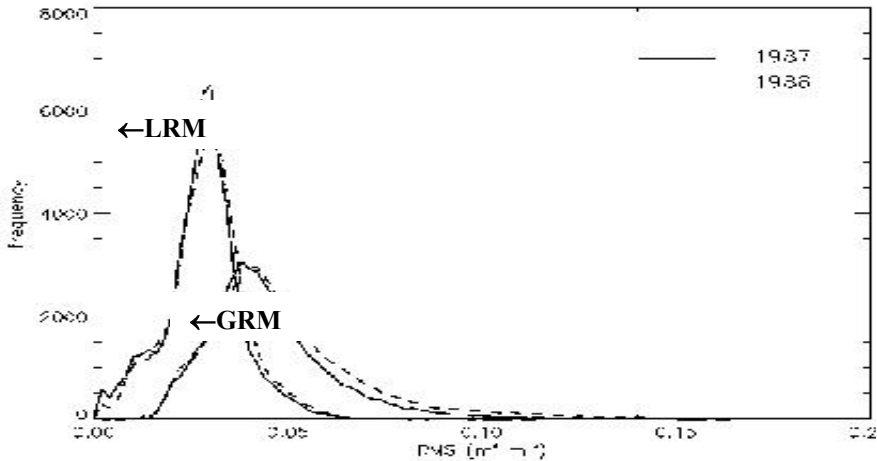


Figure 2 Probability density function of the RMS error on surface soil moisture (1987 and 1988) for LRM and GRM -20% (1 K noise level).(Pellarin et al., 2002b).

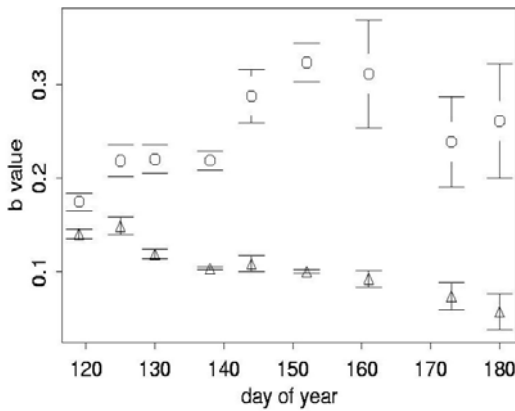


Figure 3: Retrieved b_p parameter during the wheat cycle (PORTOS-93 V(o), H(Δ) at $\theta=40^\circ$). (Parde et al., 2002a)

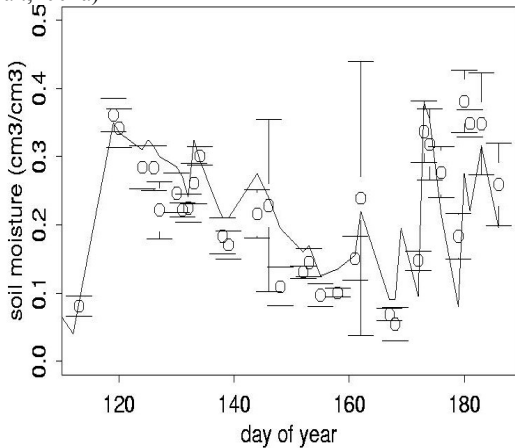


Figure 4: Time variations in retrieved soil moisture, (o) 2-P ret., (—) meas., PORTOS-93. (Parde et al., 2002a)

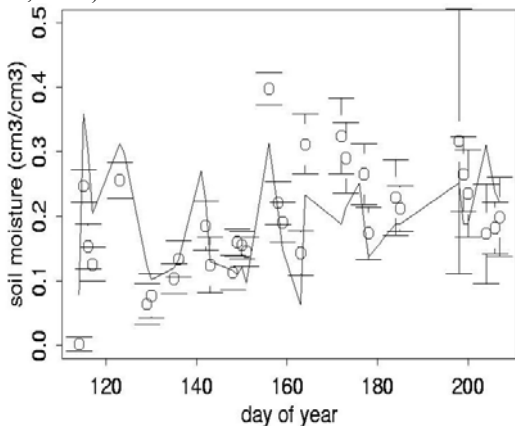


Figure 5: Time variations in retrieved soil moisture, (o) 2P-ret., (—) meas. (AVIGNON-01)

5. CONCLUSION

Different retrieval approaches based on multi-angular and dual-polarization observations have been investigated in recent studies. Significant results have been obtained from both experimental (over crop fields) and simulated (at global scale) data sets. More studies should be carried out to better defining operational methods. For instance, studies should be made over a variety of vegetation canopies, in particular over herbaceous and natural vegetation, to better evaluate the performance of the N-Parameter retrieval methods ($N \geq 2$). Also, to date, the use of N-P retrievals has been mainly tested from observations made over "homogeneous" covers. Over mixed pixels this type of approach should be constrained using ancillary information. For instance, estimates of the surface temperature computed from meteorological models, or estimates of the surface fraction of the different cover types, could be used in the retrieval process. Also, it is expected that at rather large scales, the SMOS pixels are very heterogeneous, and that in mixed pixels the dependence of τ on view angle is not as significant as over crops.

REFERENCES

- Brunfeldt, D. R., and F. T. Ulaby, Measured microwave emission and scattering in vegetation canopies, *IEEE Trans. Geosci. Remote Sensing*, 22, 520-524, 1984.
- Calvet, J.-C., J.-P. Wigneron, A. Chanzy, and D. Haboudane, Retrieval of surface parameters from microwave radiometry over open canopies at high frequencies, *Remote Sens. Environ.*, 53, 46-60, 1995.
- Calvet, J.-C., A. Chanzy, and J.-P. Wigneron, Surface temperature and soil moisture retrieval in the Sahel from airborne multifrequency microwave radiometry, *IEEE Trans. Geosc. Remote Sens.*, 34(2), 588-600, 1996.
- Chanzy, A., T. J. Schmugge, J.-C. Calvet, Y. Kerr, P. van Oevelen, O. Grosjean, and J. R. Wang, Airborne microwave radiometry on a semi-arid area during Hapex-Sahel, *J. Hydrol.*, 188-189, 285-309, 1997.
- Choudhury, B. J., Monitoring arids lands using AVHRR-observed visible reflectance and SMMR-37GHz polarization difference, *Int. J. Remote Sensing*, 11(10), 1949-1956, 1990.
- Davis, D. T., Z. Chen, J.-N. Hwang, L. Tsang, and E. Njoku, Solving inverse problems by Bayesian iterative inversion of a forward model with applications to parameter mapping using SMMR remote sensing data, *IEEE Trans. Geosc. Remote Sens.*, 33(5), 1182-1192, 1995.

- Ferrazzoli, P., L. Guerriero, and J-P Wigneron, Simulating L-band emission of forests in view of future satellite applications, *IEEE Trans. Geosc. Remote Sens.*, submitted, 2002.
- Jackson, T. J., and T. J. Schmugge, Vegetation effects on the microwave emission of soils, *Remote Sens. Environ.*, 36, 203-212, 1991.
- Jackson, T. J., D. M. Le Vine, C. T. Swift, T. J. Schmugge, and F. R. Schiebe, Large area mapping of soil moisture using the ESTAR passive microwave radiometer in Washita'92, *Remote Sens. Environ.*, 53, 27-37, 1995.
- Jackson, T. J., D. M. Le Vine, A. Y. Hsu, A. Oldak, P. J. Starks, C. T. Swift, J. D. Isham, and M. Haken, Soil moisture mapping at regional scales using microwave radiometry: the Southern Great Plains Hydrology Experiment, *IEEE Trans. Geosc. Remote Sens.*, 37, 2136-2150, 1999.
- Kerr, Y. H., P. Waldteufel, J.-P. Wigneron, J. Font, and M. Berger, Soil Moisture Retrieval from Space: The Soil Moisture and Ocean Salinity (SMOS) Mission, *IEEE Trans. Geosc. Remote Sens.*, 39(8), 1729-1735, 2001.
- Le Vine, D. M., and M. A. Karam, Dependence of attenuation in a vegetation canopy on frequency and plant water content, *IEEE Trans. Geosc. Remote Sens.*, 34, 1090-1096, 1996.
- Liou, Y.-A., S. F. Liu, W. J. Wang, J. B. Lee, and J.-P. Wigneron, Retrieval of crop biomass and soil moisture from measured 1.4 and 10.65 brightness temperatures, *IEEE Trans. Geosc. Remote Sens.*, in press, 2002.
- Magagi, R. D., Y. H. Kerr, and J.-C. Meunier, Results of combining L- and C-band passive microwave airborne data over the Sahelian area, *IEEE Trans. Geosc. Remote Sens.*, 38(4), 1997-2008, 2000.
- Njoku, E. G., and D. Entekhabi, Passive microwave remote sensing of soil moisture, *J. of Hydrology*, 184, 101-129, 1996.
- Njoku, E. G., and L. Li, Retrieval of land surface parameters using passive microwave measurements at 6-18 GHz, *IEEE Trans. Geosc. Remote Sens.*, 37(1), 79-93, 1999.
- Owe, M., R. de Jeu, and J. Walker, A methodology for surface soil moisture and vegetation optical depth retrieval using the microwave polarization difference index, *IEEE Trans. Geosc. Remote Sens.*, 39(8), 1643-1654, 2001.
- M. Pardé J.-P. Wigneron, A. Chanzy, P. Waldteufel, Y. Kerr, S. Huet, Using passive multi-angular and bi-polarization microwave measurements to retrieve soil moisture over a wheat field, Comparison of different methods, *IEEE Trans. Geosc. Remote Sens.*, to be submitted, 2002.
- T. Pellarin, J.-P. Wigneron, J.-C. Calvet, P. Ferrazzoli, H. Douville, E. Lopez-Baeza, P. Waldteufel, J. Pulliainen, L. P. Simmonds, M. Berger, Y. H. Kerr, Two-Year global simulation of L-band brightness temperatures over the land surfaces, *IEEE Trans. Geosc. Remote Sens.*, submitted, 2002a.
- T. Pellarin, J.-C. Calvet, J.-P. Wigneron, 'Surface Soil Moisture Retrieval from SMOS: a Global Regression Study', *IEEE Trans. Geosc. Remote Sens.*, submitted, 2002b.
- T. Pellarin, J.-C. Calvet, J.-P. Wigneron, 'Comparison of different retrieval methods based on a Two-Year global data set of L-band brightness temperatures over the land surfaces', *TGARS*, submitted, 2002c.
- Schmugge, T., and T.J. Jackson, Mapping soil moisture with microwave radiometers, *Meteorol. Atmos. Phys.*, 54, 213-223, 1994.
- Ulaby F. T. and E. A. Wilson, 'Microwave attenuation properties of vegetation canopies', *IEEE Trans. Geosc. Remote Sens.* 23:746-753, 1985.
- Ulaby, F. T., R.K. Moore, and A.K. Fung, *Microwave Remote Sensing - Active and Passive*, vol I, II, Addison-Wesley Publishing Company, 1981-82; vol III, Artech House, Norwood, MA, 1986.
- Van de Griend, A. A., and M. Owe, Determination of microwave vegetation optical depth and single scattering albedo from large scale soil moisture and Nimbus/SMMR satellite observations, *Int. J. Remote Sensing* 14(10), 1875-1886, 1993.
- Van de Griend, A. A., and M. Owe, The influence of polarization on canopy transmission properties at 6.6GHz and implications for large scale soil moisture monitoring in semi-arid environments, *IEEE Tr. Geosc. Remote Sens.*, 32, 409-415, 1994.
- Wigneron, J.-P., Y. Kerr, A. Chanzy, and Y. Q. Jin, Inversion of surface parameters from passive microwave measurements over a soybean field, *Remote Sens. Environ.*, 46, 61-72, 1993b.
- Wigneron, J.-P., A. Chanzy, J.-C. Calvet, and N. Bruguier, A simple algorithm to retrieve soil moisture and vegetation biomass using passive microwave measurements over crop fields, *Remote Sens. Environ.*, 51, 331-341, 1995.
- Wigneron, J.-P., J.-C. Calvet, and Y. Kerr, Monitoring water interception by crop fields from passive microwave observations, *Agric. Forest Meteor.*, 80, 177-194, 1996.
- Wigneron, J.-P., P. Waldteufel, A. Chanzy, J.-C. Calvet, and Y. Kerr, Two-D microwave interferometer retrieval capabilities of over land surfaces (SMOS Mission), *Remote Sens. Environ.*, 73, 270-282, 2000.

An Improved Estimation Technique for Rainfall Over Land Surfaces Using Active and Passive Microwave Satellite Data

Jörg Schulz¹ and Peter Bauer²

¹*Meteorological Institute of the University of Bonn, Germany*

²*ECMWF, Shinfield Park, Reading, UK*

joerg.schulz@uni-bonn.de, p.bauer@ecmwf.int

ABSTRACT - Rainfall estimation from satellite data over land surfaces still represents a challenge because neither at visible/infrared nor at microwave wavelengths do raindrops provide significant contributions to the total signal to allow a direct estimation of rain rate. Additionally, surface emissivity models for land surfaces in the microwave are still of quasi empirical character. Thus Bayesian approaches based on radiance libraries constructed from cloud resolving model results are still difficult to realise. Because of all this difficulties empirical algorithms over land surfaces are still popular. The combination of TRMM's TMI and PR sensors provide an excellent tool for the evaluation of available rainfall detection and estimation techniques as well as for new developments. The rain detection part of the presented new algorithm whose fundamentals are based on a methodology developed by Conner and Petty, consists of a two-stage approach to distinguish precipitation signatures from other effects: (1) Contributions from slowly varying parameters (surface type and state) are isolated by comparing observed brightness temperatures to those obtained from previous orbits only containing rain-free observations. (2) Effects of more dynamic parameters, i.e., surface temperature and moisture, are reduced by successive subtraction from the observations by means of principal component analysis. For this purpose, the general signatures of both temperature and moisture variations are deduced from radiative transfer simulations. The technique is first applied to TMI observations and compared to co-located measurements of PR over regions in Africa, North and South America, India as well as Australia. To quantitatively estimate the rain water content Heidke skill scores as a function of rain water content and brightness temperature range are used to efficiently calibrate the near surface rainfall intensities with a polynomial fit where the coefficients depend on location and time. Application to TMI data and comparison with the TRMM 2A12 V5 product indicates an improved performance of detecting rain water contents lower than 0.1 gm^{-3} . A comparison with the 2A25 product over a ten month period (Mar – Oct 2000) showed that the algorithm is able to explain ~65% of the variance of the PR estimated rainfall. However, remaining rms errors between the new algorithm and the PR for instantaneous estimates of the rain water content remain high at ~100% for rain water contents less than 0.1 gm^{-3} , decreasing to 25% - 50% for rain water contents up to 1 gm^{-3} .

1 INTRODUCTION

The estimation of rainfall over land surfaces is an ongoing challenge because neither at VIS/IR wavelengths nor at microwave wavelengths do raindrops provide significant contributions to the total signal to allow a direct estimation of rain rate. Principally, cloud top temperature and reflectivity is related to space-time averages of surface rainfall in those methods. The loose physical connection between these quantities prohibits an instantaneous estimate. At microwaves, surface emissivity is high and spatially variable which increases the uncertainty of the atmospheric contribution estimate compared to estimates over ocean surfaces. The main information over land surfaces comes from scattering by

precipitating ice particles. However, since the beginning of remote sensing both wavelength regions were exploited (Petty, 1995) and recent accuracy assessments indicate average errors of at best 50-100% with strong dependence on season and region as well as dataset resolution (Smith et al., 1998). Thus, algorithm improvements may only be achieved if local surface conditions are accounted for and if the signal to rain rate relationship is based on data which is more representative of global rainfall system variability.

With the launch of the Tropical Rainfall Measuring Mission in November 1997, the first spaceborne precipitation radar (PR) became available (Kummerow et al., 1998). It is a single frequency (13.8 GHz), electronically scanning radar with nominal resolutions of 4.3 km and 0.25 km in the horizontal and vertical dimensions, respectively. The

cross-track scan pattern covers a 215 km swath consisting of 49 beams along a scan angle of $\pm 17^\circ$. Its sensitivity is specified with 0.17 mm h^{-1} with a calibration accuracy of $\sim 0.8 \text{ dB}$. A microwave radiometer is available on the same platform (TRMM Microwave Imager, TMI) providing measurements at 10.65, 19.35, 21.3, 37.0, and 85.5 GHz on a conical scan with a nearly constant surface incident angle of 52.8° and a swath width of 760 km. All channels measure vertically and horizontally polarised radiances (expressed as blackbody temperatures, TB) except the 21.3 GHz channel which only measures vertically polarised radiances. Since only one antenna is used for all channels the spatial resolution of the effective field of view (EFOV) depends on frequency and ranges from $37 \text{ km} \times 63 \text{ km}$ at 10.65 GHz to $5 \text{ km} \times 7 \text{ km}$ at 85.5 GHz. The TRMM orbit is not sun-synchronous and covers latitudes between 38°N and 38°S . Thus the combination of both sensors provides an excellent tool for the evaluation of available rainfall detection and estimation techniques as well as for new developments. The difficult microwave signal interpretation over land surfaces has favoured somewhat the implementation of empirical algorithms which make use of co-located satellite and ground based (radar) observations to derive a calibration of satellite measurements by reference data (e.g. Ferraro and Marks, 1995). For large scale regional or even global applications this approach is hampered by the limited representativity of available calibration data sets. Thus co-located radiometric and radar measurements from TRMM provide an outstanding data source covering the tropical and subtropical latitudes over various climatological regimes.

The technique used in this paper follows the ideas of Conner and Petty (1998) and uses the methodology described in Bauer et al. (2001a) to combine TMI and PR measurements by using Heidke Skill score diagrams. Section 2 provides a brief summary of the methodology and describes the calibration of the precipitation index (PI) to a rain intensity by using PR data. Section 3 examines the application of the algorithm to a case of a meso-scale convective cluster over northwest Africa. The derived product is compared to the TRMM standard product 2A12 which delivers surface rainfall and 3D structure of hydrometeors and latent heating over the TMI swath (Kummerow et al., 2000). Additionally, the calibrated PI is compared to the calibration source (2A25) which gives an estimate of the remaining errors after the

calibration. All data used in this study are version 5 data, so the TMI brightness temperatures are calibrated as described in Kummerow et al. (2000). The paper is concluded by a summary and discussion.

In the following, rainfall intensity is always treated in terms of rain liquid water content (LWC) to avoid uncertainties imposed by the somewhat uncertain drop size distributions and the dependence of rainfall rate calculations on fallspeed parameterisation. Additionally, both scattering ($\propto D^6$) and emission ($\propto D^3$) are closer related to liquid water and ice volume densities (where D denotes the particle diameter).

2 METHODOLOGY

The methodology used has been described in detail in Bauer et al. (2001a). Fig. 1 is showing a flow chart depicting the main features of the algorithm. The technique used here makes use of a first order approach to remove seasonally varying surface contributions from instantaneous TMI measurements by generating maps of clear sky temporal averages of brightness temperatures using the screening technique of Ferraro et al. (1998) over 5 different regions, i.e. Africa, South America, North America, India, and Australia. The averages are running 10 day means up to the day for which the rainfall should be estimated, e.g. the average for the first July includes the last nine days in June and the first of July. The averaging was carried out for a period of 10 month (March – October) in the year 2000 and the resulting brightness temperatures are mapped onto a grid with a spatial resolution of $0.4^\circ \times 0.4^\circ$. Features of the background maps are rather smooth with variations introduced by water surfaces and snow in the mountains as well as undetected clouds and precipitation. To restrict the investigation to homogenous surfaces only those pixels are used for which the standard deviation at 10.65 GHz is less than 10 K.

Brightness temperatures (TB) at different wavelengths are usually positively correlated in particular over land surfaces where the background signal is rather strong. Only in case of scattering by precipitating ice the higher frequency measurements are negatively correlated to those at lower frequencies. The full set of available channels carries therefore some redundant information. Thus, the dimension of the input data set (9 for the TMI) may be reduced by means of principal components.

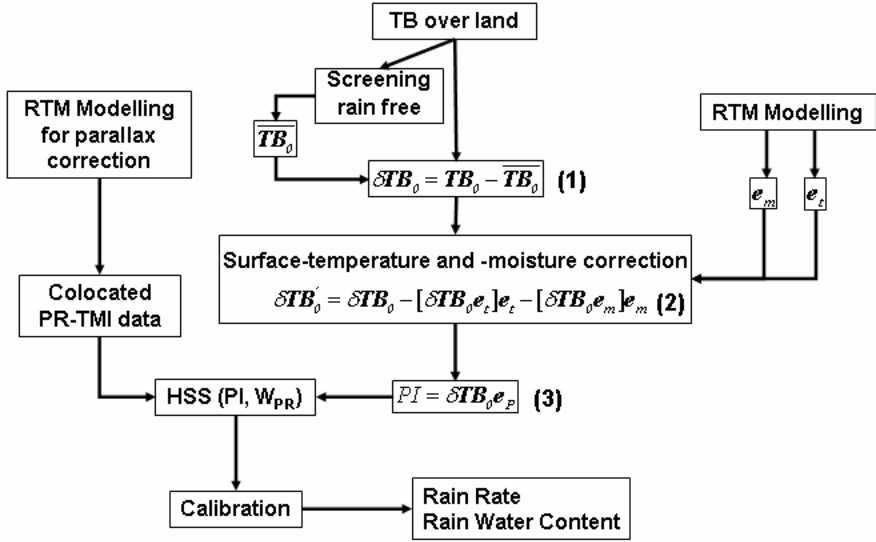


Figure 1: TMI algorithm flow, details are described in the text. Bars over symbols denote temporal averages and [...] denote inner products.

The idea of surface effect correction by generating datasets where either temperature or moisture dominate the signal and which are subtracted from the actual observation signal by orthogonalisation follows the approach by Conner and Petty (1998) (equation (2) in Fig.1). Bauer et al. (2001a) used radiative transfer simulations to derive the correction eigenvectors e_t and e_m . This approach is followed here because both eigenvectors are supposed to show only the signature of either temperature or moisture. If the correction datasets are constructed from measurements as in Conner and Petty (1998) then they may contain unscreened precipitation which would suppress the precipitation signal in later analysis. The first eigenvectors with respect to temperature and moisture explain 89% and 86% of the variance in either simulation so only those are used for the correction. After this correction, eigenvectors e_p which are assumed now to contain the precipitation signal can be computed. As Bauer et al. (2001a) already showed, e_p has the common feature to decrease with frequency in the first EOF which is fairly independent of time and region. This finding is confirmed by computing all e_p for the ten month period March – October 2000.

However, if the explained variance of the first EOF is considered as a function of time a strong dependence on region and period is obvious. Fig. 2 shows time series of the explained variances for the first three eigenvectors for all five regions. Over all regions, except India the explained variance of the first EOF is

rather high (~80%) with the smoothest time series over South America because of the most homogenous terrain. The eigenvector for India shows a clear depression during the Indian summer monsoon where the explained variance of the first eigenvector drops down to 60%, whereas that of the second is enhanced to 30%. A possible explanation is the high variability in cloud water and water vapour which is indicated by positive e_p at lower frequencies and negative e_p at 85.5 GHz for the second eigenvector. The highest explained variances are found over Australia reaching values up to 90% during the winter months July and August. Finally, the precipitation signal can be obtained from e_p by equation (3) in Fig. 1, where PI represents an index (in units of K) which is positively correlated to rain intensity (rather to ice water path).

For the calibration of the PI into rain water contents a co-location procedure of TMI and PR pixel values which are recorded along different scan geometries and resolutions is performed. For the TMI a reference resolution was defined which is set to the resolution of the 19 GHz channel. The effective field of view (EFOV) is enlarged by a factor of 2.5 to cover the area of which ~98% of the signal is received. The EFOVs are approximated by ellipses and the antenna gain function by Gaussian functions following the orientation of the real EFOVs along the TMI scan. PR pixels at a height of 2 km with valid PR retrievals covering more than 80%

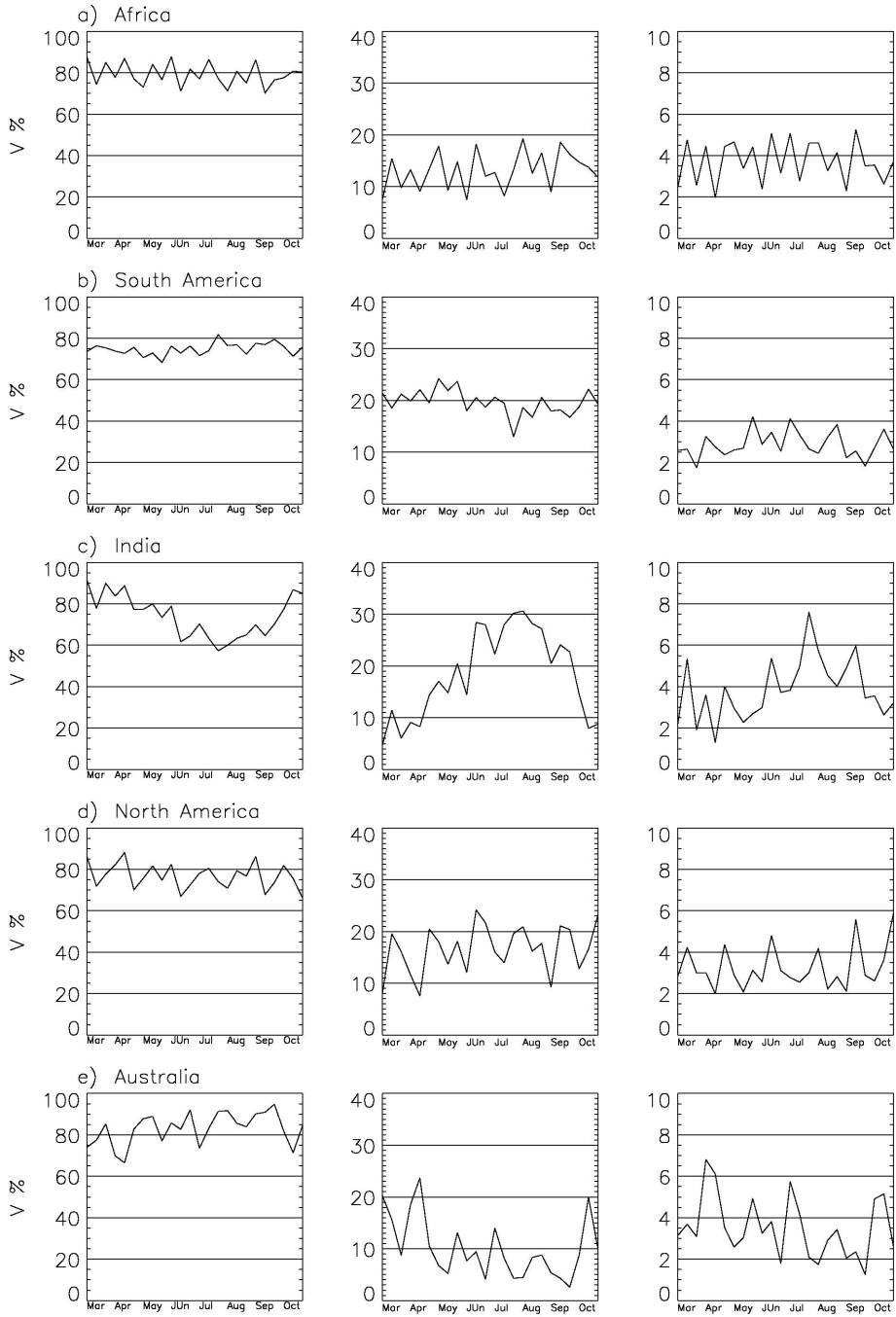


Figure 2: Time series (March – October 2000) of explained variances for the first three eigenvectors e_p for five different regions.

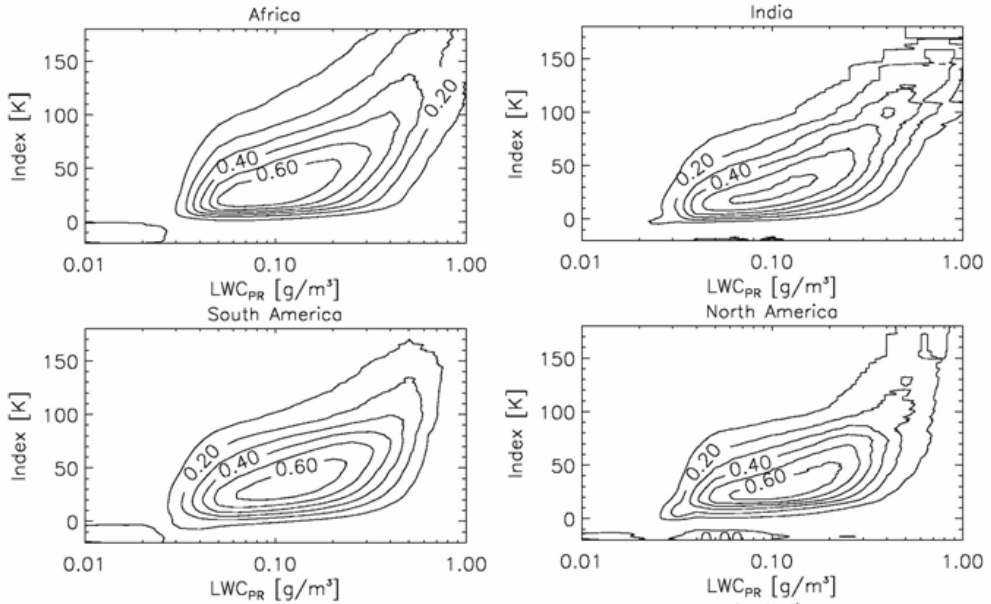


Figure 3: Heidke skill score diagrams for the period 09/11/2000 – 09/20/2000 used for the calibration on 09/20/2000 for four different regions.

of the TMI EFOV were used to minimise sampling problems. Before the averaging a parallax correction (Bauer et al., 2001a) is applied if the centre of gravity of the weighting function gives values larger than 5 km. This is important because in those cases where the signal contribution originates from higher altitudes, the comparison to radar data at the TMI footprint location may lead to errors in the calibration data set.

As in Bauer et al. (2001a) Heidke skill scores were employed to quantify the accuracy of rain detection from both TMI and PR and to give a calibration tool. The skill scores are computed for classes of rain intensity with a lower threshold resulting in skill score diagrams as presented in Fig.3 for an example period of 10 days in September 2000. To build up statistics it is necessary to sample at least ten days of data to fill the diagram which is important for a stable calibration. Thus it is chosen that the skill score diagrams were build for each day and region sampling the nine days before and the day of the actual TMI overpass. Comparing those diagrams for different regions exhibit some common features like there is almost no skill in determining rain water contents less than 0.03 gm^{-3} . The skill over India is generally ~ 0.1 smaller due to the less explained variance in the first eigenvector. Differences can also be seen at the high end where a maximum index in Africa is related to a PR-derived rain water content of 0.8 gm^{-3} whereas it is

only 0.6 gm^{-3} over South America. However, examining 10 months of data it was decided to use a polynomial fit along the maximum Heidke skill score to convert the precipitation index into rain water content. This was done for each 10 day running mean Heidke skill score diagram in each region ending up with a fit for each day and region. The errors of the fit itself are varying with time between 0.02 gm^{-3} and 0.06 gm^{-3} where higher errors occur if singular events dominate the skill score diagram.

3 EXAMPLES AND UNCERTAINTY ESTIMATION

Fig. 4 presents a typical example of the results obtained by using the polynomial fits to calibrate the PI into rain water contents. The case represents the passage of a meso-scale convective cluster over southern parts of northwest Africa. The measurement was taken in the decaying stage of most of the convective cells. Comparing the 2A12 with the 2A25 product it is obvious that 2A12 doesn't detect rain water contents lower than 0.2 gm^{-3} which lead to a significant smaller rain area. The calibrated precipitation index represents the PR swath data relatively well, e.g. between 8°E and 10°E and 10°N – 12°N . However, it is also not able to detect the very small rain water contents in the south western

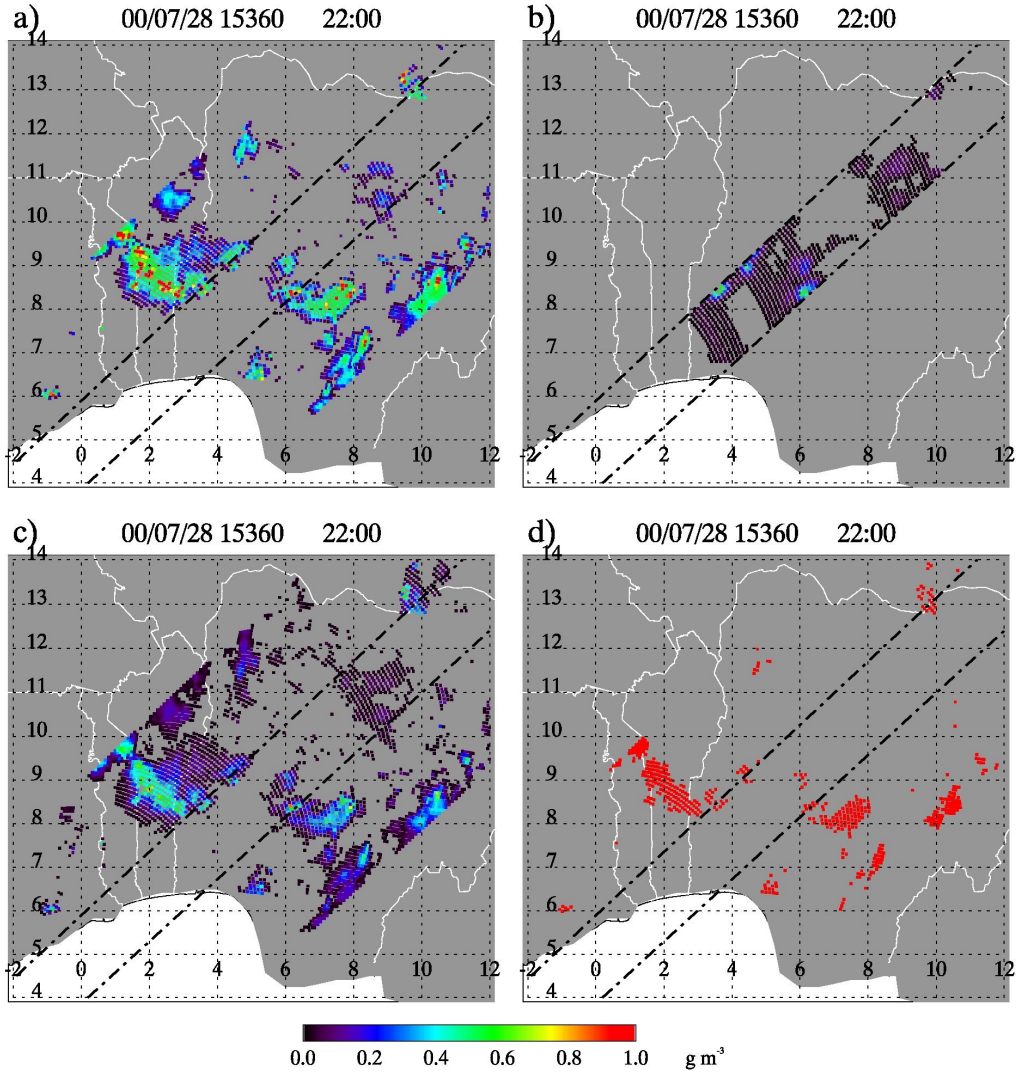


Figure 4: Distributions of retrieved rain water content for orbit 15360 on 28. July 2000 over Benin and Nigeria from (a) 2A12 V.5 algorithm, (b) PR estimates averaged to TMI reference resolution, (c) calibrated estimates from PI, and (d) pixels where the Ferraro et al. (1998) scattering index indicates rain.

part of this scene. In the Ferraro scattering index only the convective cores are well represented. Compared to 2A12 the calibrated PI shows a very similar structure at medium and high rain intensities but it exhibits a large negative bias in the convective cores which is introduced by the use of the PR as the calibration source.

Fig. 5 shows scatter plots for the orbit considered in Fig 4. In Fig. 5 (a) the scatter between 2A12 and the calibrated PI is increasing with decreasing rain water content. Other cases not shown here reveal that the spatial correlation between 2A12 and PI is relatively high (>0.7) for rain water contents larger than 0.1 g m^{-3} but the negative bias for the PI was found in any case considered.

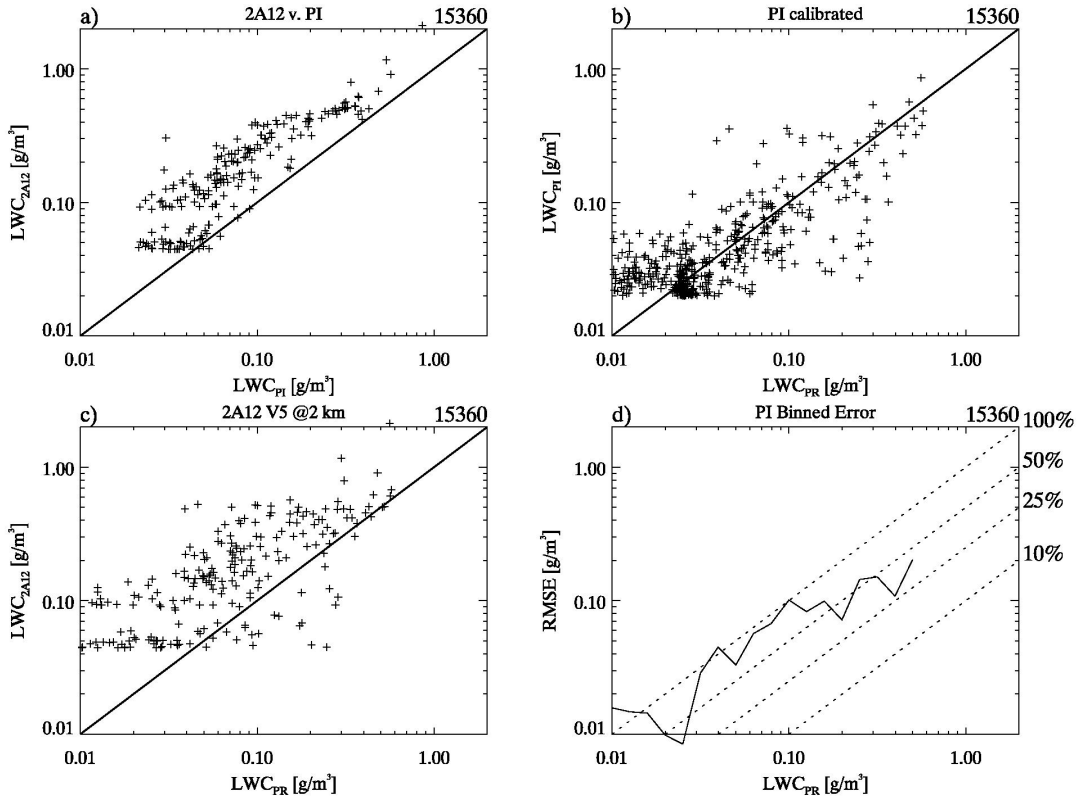


Figure 5: Scatter plots of (a) calibrated PI estimates versus 2A12 V.5 estimates, (b) calibrated PI estimates versus averaged PR estimates, (c) 2A12 V.5 versus averaged PR estimates, and (d) remaining standard deviation between calibrated PI and averaged PR pixels for the same case as in Fig. 3.

This bias is also obvious in Fig 5 (c) showing the comparison between 2A12 and 2A25 where also the scatter is considerable larger than between 2A12 and the PI. The comparison of PI to its calibration source in Fig 5 (b) and (d) shows an overestimation of the PI at rain water contents lower than 0.03 gm^{-3} which is a common feature of all investigated cases. For greater rain water contents there is almost no bias but still a large scatter. This is also obvious in the remaining rms error between 2A25 and the PI which is still around 100% at rain water contents below 0.1 gm^{-3} and decreasing to 25-50% above 0.1 gm^{-3} .

The large scatter around values of 0.1 gm^{-3} is potentially caused by the large area chosen to build the Heidke skill score diagrams for the calibration. Together with the time average over 10 days variability is suppressed finally causing the scatter in

the comparison. A second dynamical calibration like in the PATER ocean algorithm (Bauer et al., 2001b) could be envisaged but is not necessarily expected to improve the calibration very much.

To consider the development of errors over time, Fig 6 is showing 4 error measures for the period March – September 2000 for Africa. Fig. 6 (a) shows the relative number of pixels which fell outside the valid range of the PI and are therefore not to calibrate. This is varying between almost zero to a maximum of 4% where most values were below -20 K and only few above 180 K. The bias shown in Fig. 6 (b) as the ratio of rain water content PR to rain water content PI is varying between 93% and 107% showing largest biases at the beginning and the end of the rain season in northwest Africa. Fig 6 (c) shows the efficiency, defined as:

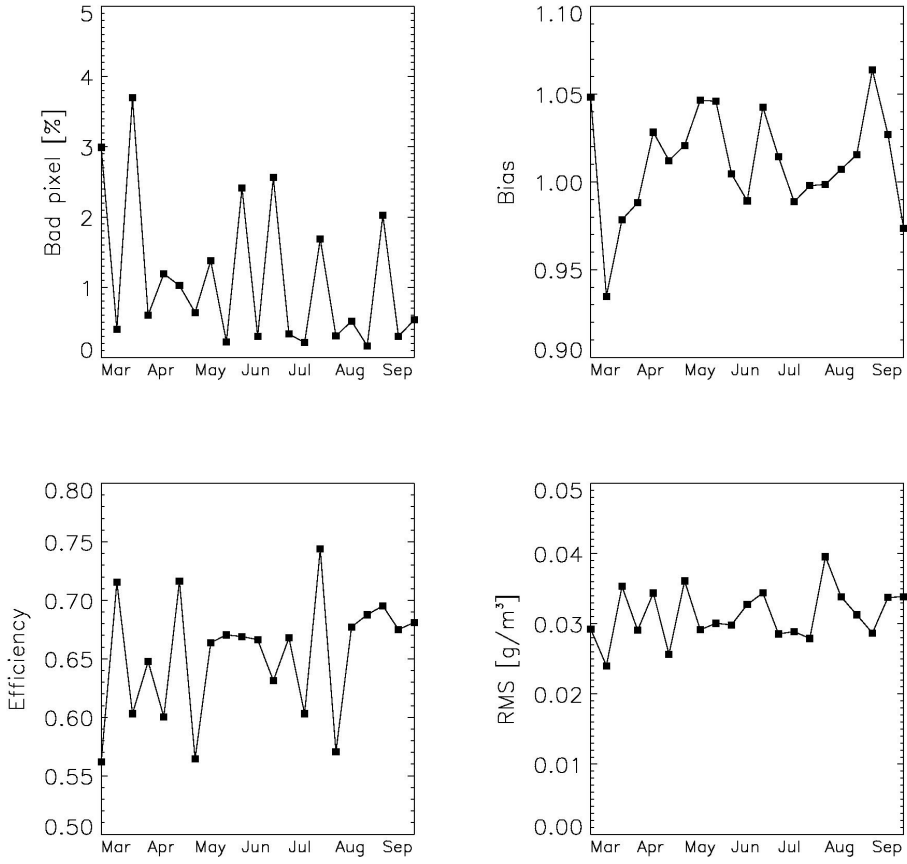


Figure 6: Time series of error measures for the African region, (a) percentage of pixels falling outside the calibrated PI range $[-20, 180]$, (b) bias between calibrated PI estimates and averaged PR estimates, (c) efficiency, and (d) rms error.

$$E = 1 - \frac{\sum_{i=1}^N (LWC_{PR} - LWC_{PI})^2}{\sum_{i=1}^N LWC_{PR}^2} \quad (4)$$

which is giving an estimate of the explained variability of the PR pixels by the calibrated PI values. E is showing values between 0.55 and 0.75 with the most values located around 65%. The largest variations are from April to May and in July and August where the low efficiencies probably reflect events with low rain

water contents distributed over large areas. The overall rms error Fig. 6 (d) is around 0.03 gm^{-3} which is dominated by the concentration of the pixel values at low rain water contents and may be somewhat misleading for judging the error at higher intensities as Fig 5 (d) has shown.

4 SUMMARY AND CONCLUSIONS

The presented method corrects brightness temperature departures from running 10 day rain free averages for small scale influences by surface temperature and moisture. Heidke skill scores were used to calibrate the resulting precipitation index into a rain water content. For different regions and seasons the same

type of calibration can be used. However, the coefficients of the calibration have to be adjusted every day using Heidke skill score diagrams accumulated over the same ten days as the background map.

Comparisons of the calibrated PI to TRMM standard products reveal a better potential for detecting low rain water contents than standard indices like SI and the 2A12 product. The calibrated PI usually exhibits a low bias in convective cores when compared to 2A12 but only a small positive bias at rain water contents below 0.04 gm^{-3} to 2A25. The PI shows a larger rain area than 2A12, mostly due to the improved detection of light rain. Otherwise the spatial features of 2A12 and PI are very similar. Remaining rms errors between the calibrated PI and PR are around 100% for rain water contents below 0.1 gm^{-3} but decreasing to 25-50% for larger rain water contents. Due to the use of large areas and running ten day averages for the calibration a large part of the variability given in the PR data is not captured. This might be improved by choosing smaller areas and a longer integration time. A more detailed error analysis should analyse the resulting probability density functions of the different products and their errors. Also a stratification of errors in terms of different meteorological regimes with the help of rain gauge and radar data in Benin will help to characterise the errors better. Further improvements can be expected from the consideration of rain (e.g. Olsen et al., 2001) and cloud classification as well as the additional use of microphysical properties of clouds derived from measurements of the SEVIRI instrument onboard of the Meteosat Second Generation satellite.

Further studies will focus on finding ways how the algorithm can be transferred to other passive microwave instruments, e.g. SSM/I, SSMIS, and AMSR to produce an inter-calibrated passive microwave multi-satellite product which is needed for the calibration of geostationary satellite data. This strategy is targeting at the planned Global Precipitation Mission which consists of a core satellite carrying a radar and a passive microwave radiometer which is accompanied by a constellation of several drone satellites carrying only passive microwave radiometers. This mission will deliver passive microwave rain estimates every three hours at any place on earth. It is planned by NASA and NASDA and will be supported by ESA with one Earth Explorer Opportunity Mission called EGPM.

ACKNOWLEDGEMENTS

The authors are grateful for free access to TRMM data through the NASA TRMM program. This research was supported by the Federal German Ministry of Education and Research (BMBF) under grant No. 07 GWK 02 and by the Ministry of Education, Science and Research (MSWF) of the federal state of Northrhine-Westfalia under grant No. 514-21200200.

REFERENCES

- Bauer, P., D. Burose, J. Schulz, 2001a, Rain detection over land surfaces using passive microwave satellite data. *Meteorologische Zeitschrift*, 11, 37-48.
- Bauer, P., P. Amayenc, C. D. Kummerow, E. A. Smith, 2001b, Over-ocean rainfall retrieval from multisensor data of the Tropical Rainfall Measuring Mission. Part II: Algorithm implementation.
- Conner, M. D. and G. W. Petty, 1998, Validation and intercomparison of SSM/I rain-rate retrieval methods over the continental United States. *J. Appl. Meteor.*, 37, 679-700.
- Ferraro, R. R., E. A. Smith, W. Berg, G. J. Huffman, 1998, A screening methodology for passive microwave precipitation retrieval algorithms. *J. Atm. Sci.*, 55, 1583-1600.
- Ferraro, R. R. and G. F. Marks, 1995, The development of SSM/I rain-rate retrieval algorithms using ground-based radar measurements. *J. Atm. Ocean. Technol.*, 12, 755-770.
- Kummerow, C., J. Simpson, O. Thiele, W. Barnes, A. T. C. Chang, E. Stocker, R. F. Adler, A. Hou, R. Kakar, F. Wentz, P. Ashcroft, T. Kozu, Y. Hong, K. Okamoto, T. Iguchi, H. Kuroiwa, E. Im, Z. Haddad, G. Huffman, B. Ferrier, W. S. Olson, E. Zipser, E. A. Smith, T. T. Wilheit, G. North, T. Krishnamurti, and K. Nakamura, 2000, The status of the Tropical Rainfall Measuring Mission (TRMM) after two years in orbit. *J. Appl. Meteor.*, 39, 1965-1982.
- Kummerow, C., D., W. Barnes, T. Kozu, J. Shiue, J. Simpson, 1998, The Tropical Rainfall Measuring Mission (TRMM) sensor package. *J. Atm. Ocean. Technol.*, 15, 809-817.

- Petty, G. W., 1995, The status of satellite-based rainfall estimation over land. *Rem. Sens. Environ.*, 51, 125-137.
- Smith, E. A., J. E. Lamm, R. Adler, J. Alishouse, K. Aonashi, E. Barrett, P. Bauer, W. Berg, A. Chang, R. Ferraro, J. Ferriday, S. Goodman, N. Grody, C. Kidd, D. Kniveton, C. Kummerow, G. Liu, F. Marzano, A. Mugnai, W. Olson, G. Petty, A. Shibata, R. Spencer, F. Wentz, T. Wilheit, E. Zipser, 1998, Results of WetNet PIP-2 project. *J. Atmos. Sci.*, 55, 1483-1536.

Sea Surface Salinity and Wind Speed Retrieved from a Tower-Based L-Band Radiometer in the NW Mediterranean

C. Gabarró¹, J. Font¹, A. Camps², M. Vall-llossera²

¹Institut de Ciències del Mar CMIMA - CSIC

²Departament de Teoria del Senyal i Comunicacions, UPC

cgabarro@icm.csic.es, jfont@icm.csic.es, camps@tsc.upc.es, merce@tsc.upc.es

ABSTRACT - In May 1999, the European Space Agency (ESA) selected SMOS as an Earth Explorer Opportunity mission (Kerr, 1998). One of its goals is the generation of global Sea Surface Salinity (SSS) maps. The sensor embarked is an L-band interferometric radiometer with full-polarimetric capability called MIRAS. The retrieval of SSS from microwave measurements is based on the fact that the brightness temperature (T_B) of seawater is a function of the dielectric constant, temperature and sea surface state (roughness, foam,...). The sensitivity of T_B to SSS is maximum at L-band, but it is necessary to quantify the other effects to have a reliable SSS retrieval. In order to improve the present understanding of these effects on T_B , ESA sponsored the WISE (Wind and Salinity Experiment) 2000 and 2001 field campaigns. These experimental results are of great importance for the development of sea surface emissivity models that will be used in the future SMOS SSS retrieval algorithms. This paper presents the influence of the emissivity models on the derived SSS from the data obtained in both campaigns. It also presents the impact of using in-situ measured or satellite-derived wind information, or even to compute simultaneously the wind speed (from the measured multi-angular T_B), on the retrieved SSS.

1. INTRODUCTION

The brightness temperature of the sea at L-band is dependent on the sea surface salinity (SSS), in particular on the dielectric constant (Klein and Swift, 1977), as well as on other factors like the sea roughness (mainly produced by wind stress), the sea surface temperature (SST), the presence of foam, the incidence angle, etc. Even though the sensitivity of the brightness temperature (T_B) on the SSS is maximum at L-band, it is quite low: ~ 0.5 K/psu at SST = 20 °C, decreasing to ~ 0.25 K/psu at SST = 0° (Skou, 1995; Lagerloef et al., 1995; 1998). The sensitivity of T_B to SST is about the same order, 0.2 - 0.4 K/°C (Swift and McIntosh, 83) and the sensitivity to wind speed (WS) is in the range of 0-0.4 K / ms⁻¹ depending on the incidence angle (Hollinger, 1971; Webster and Wilheit, 1976; Lerner and Hollinger, 1977). These numbers indicate that it is important to have a good knowledge of all the variables that impact on T_B to retrieve with good accuracy the salinity from radiometric measurements.

To improve the present understanding of these effects on T_B , the European Space Agency (ESA) has sponsored the WISE (Wind and Salinity Experiment) 2000 and 2001 field campaigns. This paper describes the results on salinity retrieval from WISE data, using wind and SST data measured in situ and also from satellite measurements. Furthermore, it is studied the possibility of retrieving simultaneously both the wind

speed and the SSS from the multi-angular T_B measurements.

2. CAMPAIGNS DESCRIPTION

The WISE experiments were held in the Casablanca oil platform at 40Km from the coast of Tarragona (Spain), in the NW Mediterranean sea, (40.72°N 1.36°E). Both experiments took place in autumn where usually there are high winds in the region. WISE 2000 campaign was held from November 16th to December 18th 2000 and continued during January 9th to 15th, meanwhile WISE 2001 campaign was held from October 23th to November 22th 2001.

The WISE participants were: the Polytechnic University of Catalonia (UPC, Barcelona, Spain, prime contractor with ESA), the Institute of Marine Sciences (ICM-CSIC, Barcelona, Spain), the Laboratoire d'Océanographie Dynamique et Climatologie (LODYC, Paris, France), the University of València (UV, València, Spain), the Centre d'Études Terrestres et Planétaires (CETP, Paris, France) and the University of Massachusetts (UMass, Amherst, USA) as a guest institution. The deployed instruments were:

- A L-band polarimetric radiometer – LAURA (L-band AUTomatic RADiometer) (UPC),
- A Ka-band polarimetric radiometer (UMass),
- A stereo-camera to determine surface topography and rms slopes of the sea surface (CETP),

- Four oceanographic and climatological buoys for near-surface salinity, temperature, wind speed and direction, wave height and period, etc. (ICM-CSIC and LODYC),
- A portable meteorological station with atmospheric pressure, air temperature, relative humidity and rain rate (UPC),
- A video camera mounted on the L-band radiometer pedestal to determine sea surface foam coverage (UPC),
- An IR radiometer to determine sea surface temperature estimates (UV).

Additionally, during WISE 2000, temperature and salinity were recorded from the platform at 5 m below the sea level, and simultaneously ocean color, wind vector and sea surface temperature were acquired by different satellites.

A full description of the performed measurements can be found in (Camps et al., 2000; 2001a). During the WISE 2000 campaign the SST ranged between 16.3°C and 13.6°C, and in WISE 2001 between 16.0°C and 22.5°C, due to the seasonal variation. The SSS remained close to 38 psu in both occasions. The 10 m wind speed varied widely reaching up to 18.4 m s⁻¹ at surface in 2000 and 25.5 m s⁻¹ in 2001. This so high value was measured during a strong storm on November 15th.

In the WISE campaigns the brightness temperatures in both (horizontal and vertical) polarizations were acquired by the radiometer LAURA. Three modes of measurement were implemented:

- 1) Mode 1, fixed observation: Long observations (1 h.) at fixed incidence and azimuth angles to study the stability time scale of the sea state and its consequences on L band emissivity.
- 2) Mode 2, azimuth scan: 6 angular positions in 140° at a fixed incidence angles. 20 min. long measurements.
- 3) Mode 3, elevation scan: 5 or 9 angular positions from $\theta_i = 25^\circ$ to 65° at fixed azimuth. 20 min. long measurements. These mode 3 data have been used for the work presented here.

Systematic tip-curve calibrations at the radiometer were done every 100 minutes approximately (Camps et al., 2002a).

3. SALINITY RETRIEVAL

This is the first time that an L-band radiometer measures at open sea with moored buoys measuring simultaneously the environmental conditions for a long period of time. WISE campaigns data will then be very useful to validate different theoretical sea surface

emissivity models that exist in the literature for L-band. A new empirical model based on these data has already been derived. It can not be forgotten that the data have been obtained for the West-Mediterranean conditions, and the derived results may not be directly extrapolated to other ocean environments.

The algorithm used here to retrieve the salinity from T_B data is a recurrent least squares fit called Levenberg-Marquardt (Press et al., 1992). It has been chosen for its easy implementation and computational efficiency. The T_B is computed setting an initial guess for SSS into the direct emissivity model. This value is compared with the T_B measured by the radiometer and then an increment ΔSSS is added to the initial salinity. This recursive system is stopped when the difference between the measured and the computed T_B is smaller than a specified threshold.

3.1. Emissivity models

In the past years, improved methods have been developed to model the polarimetric emission of the sea surface (Gasiewsky and Kunkee, 1994; Yueh et al., 1997; Laursen and Skou, 2001; Camps and Reising, 2001). However, these models have been developed or tuned at higher frequencies than 1.4GHz, typically 19 and 37 GHz. Additionally, the sea foam effects at L-band are hard to model since they have never been measured. According to recent results (Reuil and Chapron, 2001) only sea foam thicker than 2 cm may produce an increase of the L-band brightness temperatures, but experimental verification is still required.

The emissivity models, based in different approaches, take into account that power measured at the radiometer antenna follows equation (1), as it is described in (Ulaby et al., 1981).

$$T_{AP} = (T_B + T_{SC})/L_A + T_{UP}, \quad (1)$$

where T_B is the terrain emission, T_{SC} is the radiometric temperature of energy scattered by the terrain. The primary source of T_{SC} is the downward-emitted atmospheric radiation (T_{DN}), although it also may have a component due to extraterrestrial radiation incident upon the terrain (T_{EBT}). L_A is the atmosphere attenuation and T_{UP} is the atmospheric self-emission

Four different emissivity models have been studied in this work:

- 1) *NOAA model* : This is a semi-empirical model used in (Goodbertlet and Miller, 1997) as a linear regression

of Hollinger's derived wind speed sensitivities (Hollinger, 1971). When adapting it to our conditions (radiometer located at 33 m above sea level), the effects of L_A and T_{UP} can be neglected. Then the equation (1) can be reduced to (2),

$$T_B = \epsilon(SSS, SST, \theta_i) \cdot SST + \Delta T_{w,p}(\theta, U_{10}), \quad (2)$$

where the first term is due to the flat surface itself and the second one is the brightness temperature variation produced by the surface roughness. The ocean emissivity, $\epsilon(SSS, T_s, \theta)$, can be calculated from the Fresnel power reflection coefficients at horizontal and vertical polarisation as shown in equation (3).

$$e_H = 1 - \frac{\left| \cos(\theta_i) - \sqrt{\epsilon - \sin^2(\theta_i)} \right|^2}{\left| \cos(\theta_i) + \sqrt{\epsilon - \sin^2(\theta_i)} \right|^2}, \quad (3)$$

$$e_v = 1 - \frac{\left| \epsilon \cdot \cos(\theta_i) - \sqrt{\epsilon - \sin^2(\theta_i)} \right|^2}{\left| \epsilon \cdot \cos(\theta_i) + \sqrt{\epsilon - \sin^2(\theta_i)} \right|^2}.$$

The dielectric constant ($\epsilon = \epsilon' + i \epsilon''$) is calculated following (Klein and Swift, 1977), and θ_i is the incidence angle. $\Delta T_{b,p}$ is the brightness temperature due to the roughness of the surface and U_{10} is the wind speed at 10 m height. This is defined in this model as shown in equation (4)

$$\begin{cases} \Delta T_h = 0.2 \cdot (1 + \theta_i / 55^\circ) \cdot U_{10} \\ \Delta T_v = 0.2 \cdot (1 - \theta_i / 55^\circ) \cdot U_{10} \end{cases} \quad (4)$$

for incidence angles, θ_i , smaller than $\theta_i < 55^\circ$.

2) *UPC Model*: This is a modified version of the NOAA model where the wind dependence is now derived from WISE 2001 data (Camps et al., 2002a). The equation is shown in (5).

$$\begin{cases} \Delta T_h = 0.23 \cdot (1 + \theta / 70^\circ) \cdot U_{10} \\ \Delta T_v = 0.23 \cdot (1 - \theta / 50^\circ) \cdot U_{10} \end{cases} \quad (5)$$

3) *Yueh Model*: This is a two scale emissivity model that uses (Durden and Vesecky, 1985) spectrum multiplied by a factor of 2 (Yueh et al., 1997). This model has been recently found to compare well with brightness temperature measurements made at higher frequencies. The input values to the model are SSS, SST, WS, azimuth incidence angle and elevation angle θ_i .

4) *SSA Model*: This model follows the Small Slope Approximation theory for free-foam rough surfaces (Voronovich, 1994) with the wave spectrum derived by Elfouhaily (Elfouhaily et al., 1997). The input values to the model are SSS, SST, WS, azimuth and incidence angle, as well.

None of those models considers the foam effects. All of them have been implemented with the Klein & Swift dielectric constant model because, after some studies at L-band than the Ellison dielectric constant model (Ellison et al., 1996). Both dielectric constant models have been used to retrieve salinities from WISE data and the best results were, also, obtained with Klein and Swift model.

3.2. Results

Three different aspects have been studied in this work. The first one is the retrieval of SSS with different emissivity models, and the comparison with the in situ SSS measurements during WISE campaigns close to the radiometer field-of-view by the oceanographic buoys. The second part studies the impact of errors on the ancillary data (wind speed and sea surface temperature) in the retrieved salinity. The third part presents a study on other observed dependencies.

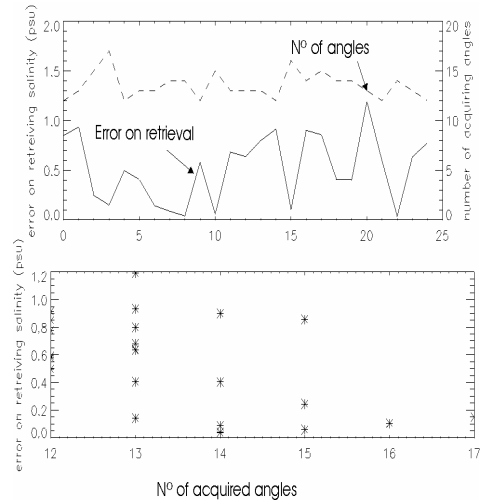


Figure 1: a) Error in the retrieved salinity (left axis) and number of elevation angles in the 25 cases analysed (right axis). b) Retrieval errors as function of the number of acquisition angles. The computations have been done with the UPC model.

The measurements performed in elevation scan (mode 3) are the best suited to study the retrieval problems. Figure 1 compares the results when using different number of acquisition angles. 25 experiments are plotted (abscise axis in figure 1a). In this plot only measurements in 9 different angles have been used. The number of incidence angles acquired in the plot means 9 different acquisitions angles per 2 polarisations minus the discarded measurements. Measurements were discarded when the level of RFI, constant during the whole measurement or part of it, led to too large σ_B values. It is clear that the SSS retrieval quality increases with the number of acquisition angles used in the retrieval. For the following work only the measurements with the largest number of incidence angles have been considered.

Analysis of the results using different models

The four models described above were run over 25 different measurements. They were acquired in different days and, consequently, under different wind and temperature conditions. In order to run the different algorithms for retrieving the salinity, in addition to the measured T_B , it is necessary to introduce as input the wind speed and SST. Those variables were measured by the oceanographic buoys simultaneously to T_B (measured by the radiometer LAURA). Data acquisition accuracy can be found in the WISE experimental plan (Camps et al., 2000a ; 2002a).

Figure 2 shows the difference between the retrieved salinity and the salinity measured in situ, in absolute value, for all the models. It is clear that the one that best fits with the campaign measurements is the UPC version of the NOAA model, as it could be expected.

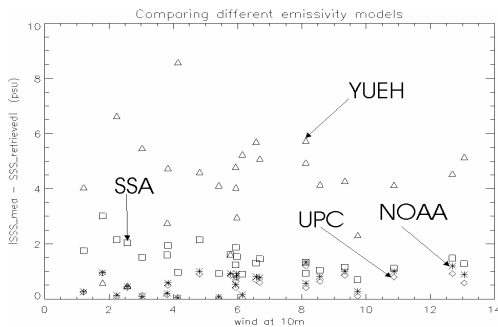


Figure 2: Error on the retrieved salinities using different emissivity models

Yueh's model is always highly underestimating the salinity. This problem is due to a weak wind dependence that forces the algorithm to decrease the salinity to increase the T_B .

SSA model overestimates the salinity, that is the wind dependence is too high. From figure 3 it can be observed that the retrieved salinity accuracy is poorer for events with low wind speed and small waves than in other conditions. This is in accordance with (Voronovich and Zavorotny, 2002), because they conclude that the Elfouhaily spectrum over-estimates the probability of having short waves, in 2-4 dB in the cross-wind direction. The results show that this model is not recommendable for low wind events. On the other hand it should be mentioned that this model is computationally much faster than the Yueh's two scale model.

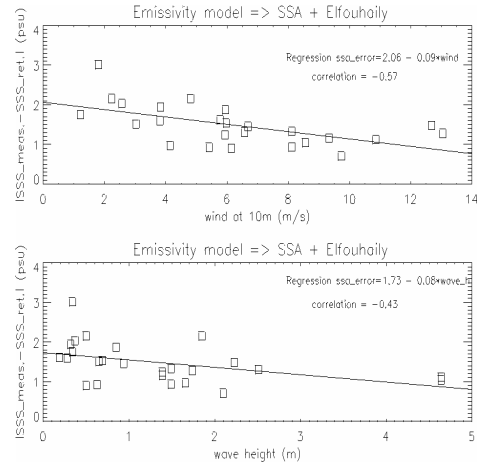


Figure 3: Error on the retrieved salinity for the SSA + Elfouhaily model as a function of wind speed and significant wave height (defined as the average of the highest third of the waves).

The mean and the variance of the errors on the retrieved salinity for the 25 measurements have been calculated and they are presented at table 1.

Table 1: Mean and variance of the retrieved salinity error for different models, considering $\Delta SSS = |SSS_{insitu} - SSS_{retrieved}|$.

	Mean (ΔSSS)	$\sigma_{\Delta SSS}$
NOAA model	0.63 psu	0.15 psu
UPC model	0.52 psu	0.12 psu
Yueh + Durden & Veseky *2	-4.28 psu	3.18 psu
SSA + Elfouhaily	1.48 psu	0.27 psu

From these results it can be concluded that the best model to use in order to retrieve salinities from WISE data is the one proposed by UPC. Yueh model gives results that are strongly biased. Consequently, the work presented below has been done using the the UPC model.

Impact on the retrieved SSS due to errors on ancillary data

To retrieve salinity from SMOS other variables (wind and SST) are needed as much simultaneously as possible in time and space to the radiometer measurement. At the first SMOS proposal, a second frequency radiometer to measure wind speed was foreseen. But this initial idea was cancelled due to budget reduction. There is the possibility to retrieve wind speed and direction from the L-band measurements themselves (3rd and 4th Stoke parameters), but this is under study at the moment. Another possibility is to obtain these data from other sensors embarked on a satellite with similar orbit, but these measurements will have instrumental errors (accuracy) and non-simultaneously orbit errors.

In this section the errors on the retrieved salinity produced by errors on the wind speed and SST measurements from satellite are quantified. Only errors in the accuracy of the data have been considered. Errors due to the time and space lag of both sensors should be considered in a future.

QuickScat satellite measurements during WISE campaigns were obtained. This scatterometer has an accuracy of 2 m s^{-1} and a spatial resolution of $25 \times 25 \text{ km}^2$. SST measurements were obtained from AVHRR with an accuracy of $0.3 \text{ }^{\circ}\text{C}$ and a spatial resolution of $1 \times 1 \text{ km}^2$.

Figure 4 shows the errors on the retrieved salinity for 3 different sources of wind speed; wind measured in situ by an anemometer, wind from QuickScat satellite, and finally leaving the wind as an unknown parameter and allowing the inverse algorithm to converge to a value of wind speed and salinity. For this last situation the algorithm uses an initial guess for both wind speed and salinity values.

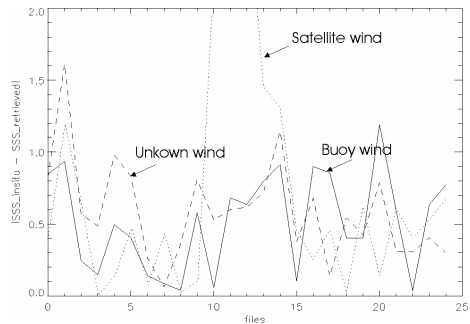


Figure 4: Retrieving salinity using three different methods of measuring wind speed.

It is noticeable that when the wind measured by the satellite has big errors (achieving the accuracy value or higher) (cases 10-14) the retrieved salinity increases excessively. The option of leaving the wind as a free parameter seems to retrieve with reasonably good accuracy both the salinity and the wind. The dependence of the initial wind and salinity values on the results has, also, been studied. It has been found that the results are highly independent to those initial values. It has to be considered that the wind speed has a wide spectrum of values, and QUICKSCAT wind speed measurement could be used as a first guess.

Table 2 shows the mean and the variance of the errors of 25 retrieved salinities using the UPC model with three different wind sources. It can be concluded that it is better to leave the wind variable as a free parameter to retrieve, than having an average error of 2 m s^{-1} on the wind measurements.

Table 2: Mean and variance of the retrieved salinity error for different wind sources, considering $\Delta\text{SSS} = |\text{SSS}_{\text{insitu}} - \text{SSS}_{\text{retrieved}}|$ and $\Delta\text{WS} = |\text{WS}_{\text{insitu}} - \text{WS}_{\text{retrieved}}|$.

	mean (ΔSSS)	$\sigma_{\Delta\text{SSS}}$	mean (ΔWS)	$\sigma_{\Delta\text{WS}}$
In situ wind measurement	0.52 psu	0.12 psu	-	-
QUICKSCAT wind meas.	0.77 psu	0.72 psu	2.63 ms^{-1}	10.12 ms^{-1}
Wind unkown parameter	0.59 psu	0.12 psu	1.15 ms^{-1}	0.54 ms^{-1}

Figure 5 compares the errors on the retrieved salinity when using SST measured by the in situ buoy and using the same SST plus the accuracy of a sensor $0.3 \text{ }^{\circ}\text{C}$. It is observable that errors on SST does not produce high errors on the retrieved SSS, maximum 0.1 psu . It has to be underlined that the SST measured by a satellite has a reasonable high accuracy, $0.3 \text{ }^{\circ}\text{C}$. The mean and the variance computation of the error on the retrieved salinities for the 25 files are shown in table 3.

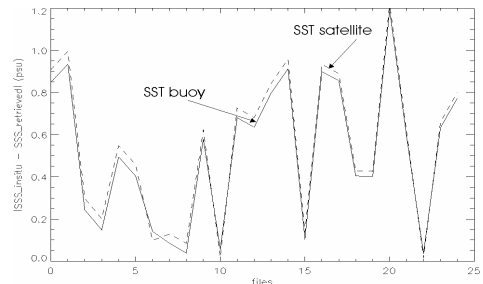


Figure 5: Retrieving salinity using two different SST.

Table 3: Mean and variance of the retrieved salinity error for different SST measurement, considering $\Delta SSS = |SSS_{insitu} - SSS_{retrieved}|$.

	mean (ΔSSS)	$\sigma_{\Delta SSS}$
SST in situ meas.	0.52 psu	0.12 psu
SST _{in situ} + 0.3 (accuracy AVHRR)	0.55 psu	0.12 psu

Other observed dependencies

Figure 6 shows a tendency to increase the error on the retrieved salinity with increasing wind. This effect can be explained by the fact that the foam effect has not been taken into account in models. Normally, the foam coverage increases with wind and its effect can be considered negligible only below wind speeds of 10 m s⁻¹. The foam increases the brightness temperature. If this ΔT_{Bfoam} is not expressed in the model equations, the inversion algorithm will decrease the salinity to compensate for this increment on T_B . This is exactly what can be seen in the results. It happens the same when considering the wave height. Figure 6 shows a linearly increasing dependence of the error of the retrieved salinity with increasing wave height.

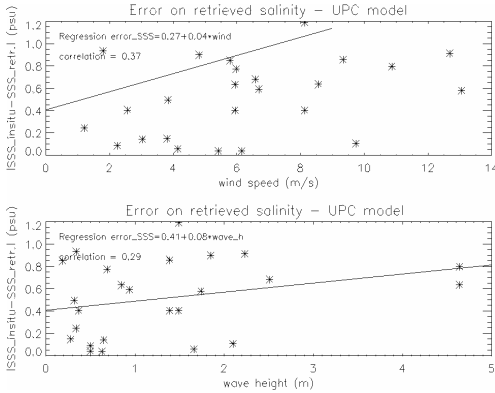


Figure 6: Relation between error on retrieved salinity and wind speed and wave height.

The dependence with the wind direction has also been analysed, but no specific dependence has found (figure 7).

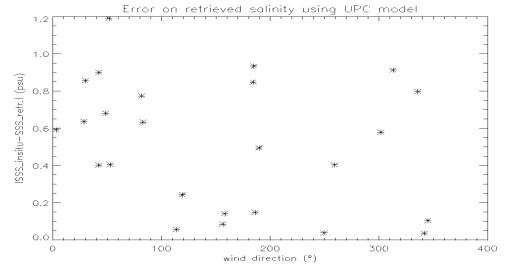


Figure 7: Error on retrieved salinity vs wind direction.

Another way to obtain the retrieved salinity is using a model that considers the sea surface roughness term as function on the significant wave height beside the wind speed. The advantage of this dependence should be that the wave height is not as variable as the wind. In addition, surface roughness can be due to the swell and not to wind waves. The spectrum models are usually only dependent on the local wind and they neglect the swell effect. In this work the retrieval computation have been done using the wave height dependence derived from WISE 2000 and 2001 data by the UPC group (Camps et al., 2002a), and presented in equation (7).

$$\begin{cases} \Delta T_h = 1.09 \cdot (1 + \frac{\theta}{142^\circ}) \cdot SWH_{(m)} \\ \Delta T_v = 0.92 \cdot (1 - \frac{\theta}{51^\circ}) \cdot SWH_{(m)} \end{cases} \quad (7)$$

being SWH the significance wave height (defined as the average of the highest third of the waves) measured by one of the moored buoy. Figure 8 presents the comparison of the retrieved salinity errors using the wind speed dependence with the wave height dependence. The results considering the wave height appear to be worse than using the wind dependence. The increment of the error for high winds (foam effect) can be appreciated here as well (figure 8). The computation of the mean and the variance of the 25 files in both cases have been computed and are shown in table 4.

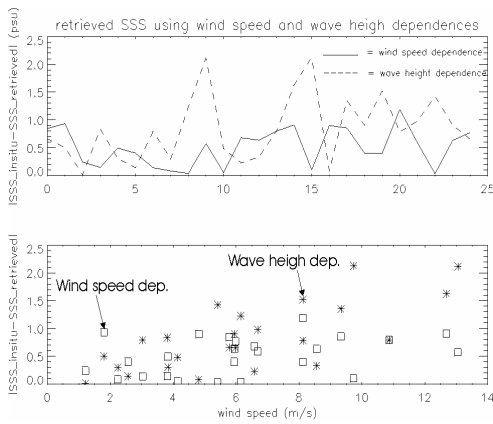


Figure 8: Comparison of the retrieval errors using wind and wave height dependence model.

Table 4: Mean and variance of the retrieved salinity error when using wind speed dependence and wave height dependence, considering $\Delta SSS = |SSS_{insitu} - SSS_{retrieved}|$.

	mean (ΔSSS)	$\sigma_{\Delta SSS}$
Wind speed dependence	0.52 psu	0.12 psu
Wave height dependence	0.84 psu	0.35 psu

When the MIRAS instrument for the SMOS mission will be launched, the necessary wind information may be provided by another space-borne sensor, with time and space lags between the measurements of the two satellites. In that case, the use of the SWH must be re-analyzed because this value present smoother changes than the wind speed. Further work should be done on this line.

4. CONCLUSIONS

WISE 2000 and 2001 campaigns have provided new data to better understand the emissivity process of the sea at L-band. The results of this work confirm that it is feasible to retrieve salinity with good accuracy from this measurements. The results emphasize that errors on the wind measurement produce large errors on the salinity retrievals.

Inverse algorithm applied to the brightness temperature measured by the LAURA radiometer and for different emissivity models indicate that the most realistic model is the one with the wind dependence derived from WISE, as it should be expected. This fact must be check with measurements in other sea conditions. It shows, also, that the Yueh model (2-

scales with Durden & Vesecky multiplied by 2 wave spectrum) gives poor results: the retrieved salinities have a bias of about 4 psu higher. The SSA model with Elfouhaily spectrum seems to work quite well for high wind speed (high waves) conditions, but for low wind conditions the retrieved salinity errors are important. As it was expected in this work we have demonstrated that the best retrieved salinities are obtained for the occasions where T_B has been measured with more different incidence angles.

On the other hand, we conclude that it is necessary to study the effect of the foam at L-band, because it may be important for wind speeds higher than 10 m s^{-1} . In these conditions the retrieved data with UPC model were underestimated. This is the way the inverse algorithm has to compensate for the increment on the emissivity due to the foam.

The study of the errors on the retrieved salinity due to errors on the ancillary data concludes that errors of 2 m s^{-1} on the wind speed (accuracy of a normal scatterometer on a space-borne) produce unacceptable errors in the retrieved salinity. To allow the inverse algorithm to find a value of wind speed as well as salinity is a potential solution. Errors on the SST does not produce an important impact on the retrieved salinity.

The attempt to retrieve salinity using a wave height dependence model (instead of wind speed dependence) gives quite good results, although they are worse than using wind speed dependence.

Further research has to be focused on studying the effect of the spatial and temporal lags between ancillary data and SMOS T_B measurements. Also further work has to be done on studying the possibility to have good retrieval salinities using wave height models beside wind speed models, because wave height has a slower variability than wind speeds.

REFERENCES

- Camps, A., I. Corbella, M. Vall-llossera, F. Torres, J. Font, A. Julià, C. Gabarró, J. Etcheto, A. Weill, E. Knapp, C. Swift, E. Rubio, V. Caselles, 2000, 'Wind and Salinity experiment 2000. Experiment Plan. ESTEC RFQ/3-9650/99/NL/DC, July 21st 2000.
- Camps, A., I. Corbella, M. Vall-llossera, F. Torres, J. Font, A. Julià, C. Gabarró, J. Etcheto, A. Weill, E. Knapp, C. Swift, E. Rubio, V. Caselles, 2001a, Wind and Salinity Experiment 2001. Experiment Plan. ESTEC RFQ/3-9650/99/NL/DC.

- Camps, A., I. Corbella, M. Vall-llossera, F. Torres, R. Villarino, L. Enrique, J. Miranda, J. Arenas, J. Font, A. Julià, C. Gabarró, J. Etcheto, J. Boutin, S. Contardo, Weill, A., R. Niclós, V. Caselles, P. Wursteisen, M. Berger and M. Martín-Neira, 2002a, Sea surface radiometric Observations at L-Band: Wind Speed Sensitivity Derived From WISE 2000 and 2001. Proceedings of the URSI (International Union of Radio Science) general assembly, Maastricht, The Netherlands.
- Camps, A., J. Font, J. Etcheto, V. Caselles, A. Weill, I. Corbella, M. Vall-llossera, N. Duffo, F. Torres, R. Villarino, L. Enrique, A. Julià, C. Gabarró, J. Boutin, E. Rubio, S.C. Reising, P. Wursteisen, M. Berger, M. Martín-Neira, 2002b, Sea Surface Emissivity Observations at L-band: First Results of the Wind and Salinity Experiment WISE-2000. Radio Science. (In press).
- Camps, A., J. Font, J. Etcheto, A. Weill, V. Caselles, I. Corbella, M. Vall-llossera, F. Torres, N. Duffo, R. Villarino, L. Enrique, J. Miranda, A. Julià, C. Gabarró, J. Boutin, R. Niclós, P. Wursteisen, M. Berger and M. Martín-Neira, 2002c, L-band Sea Surface Emissivity Radiometric Observations under High Winds: Preliminary Results of the Wind and Salinity Experiment WISE-2001, Proceedings of the IGARSS 2002, (CD_ROM), Toronto, Canada.
- Camps, A., and S.C. Reising, 2001, Wind Direction Azimuthal Signature in the Stokes Emission Vector from the Ocean Surface at Microwave Frequencies. Microwave and Optical Technology Letters, Vol 29, No 6, 426-432.
- Durden, S.L., and J. F. Vesecky, 1985, A Physical Radar Cross-Section Model for a Wind-Driven Sea with Swell. IEEE Journal of Oceanic Engineering, vol. OE-10, 445-451.
- Elfouhaily, T., B. Chapron, K. Katsaros, and D. Vandermark, 1997, A Unified Directional Spectrum for Long and Short Wind-driven Waves. Journal of Geophysical Research, Vol. 102, 15781-15796.
- Ellison, W.J., Balana, A., Delbos, G., Lamkaouchi, K., Eymard, L., Guillou, C., Prigent C., 1996, Study and Measurement of the Dielectric Properties of the Sea Water. European Space Agency contract N° 11197/94/NL/CL.
- Gasiewski, A.J., and D.B. Kunkee, 1994, Polarized Microwave Emission from Water Waves. Radio Science, Vol. 29, No. 6, 1449-1466.
- Goodberlet, M., Miller, J., 1997, NPOESS Sea surface Salinity. NOAA contract # 43AANE704017, FINAL REPORT.
- Hollinger, J.P., 1971, Passive Microwave Measurements of Sea Surface Roughness. IEEE Transactions on Geoscience Electronics, GE-9, 3, 165-169.
- Kerr, Y. 1998, SMOS - Soil Moisture and Ocean Salinity, Proposal in answer to call for Earth Explorer Opportunity Missions. Ref: COP 16. Nov 30th.
- Klein, L. and Swift C.T, 1977, An improved model for the dielectric constant of sea water at microwave frequencies. IEEE Transactions on Antennas and Propagation, Vol. AP-25, No 1, 104-111.
- Lagerloef, G. S. E., Swift, C.T. and LeVine D. M. 1995, Sea surface salinity: the next remote sensing challenge. Oceanography, vol. 8, No 2, 44-50.
- Lagerloef, G. S. E., 1998, Report of the First Workshop, Salinity Sea Ice Working Group. La Jolla, USA, 7-8 Feb.
- Lagerloef, G. 2001, Oral Communication at 3rd SMOS Workshop. Oberpfafenhofen Germany.
- Laursen, B., and N. Skou, 2001, Wind direction over the ocean determined by an airborne, imaging, polarimetric radiometer system. IEEE Transactions on Geoscience and Remote Sensing, Vol. 39, No. 7, 1547-1555.
- Lerner, R. M. And Hollinger, J. P., 1977, Analysis of 1.4 GHz radiometric measurements from Skylab. Remote Sensing Env., 6, 251-269.
- Press, W., S. Teukolsky, W. Vetterling, B. Flannery, 1992, Numerical Recipes in C. The Art of Scientific computing, 2nd edition (Cambridge University Press).
- Reuil, N. and B. Chapron, 2001, Foam Emissivity at L-band. ESA Salinity Requirement Study, WP1300 Report.
- Skou, N., 1995, An overview of requirements and passive microwave radiometer options, in Consultative Meeting on Soil Moisture and Ocean Salinity measurement requirements and

radiometer techniques (SMOS). Noordwijk, ESA 41-48.

Swift C.T, and McIntosh R.E. 1983, Considerations for Microwave Remote sensing of Ocean-Surface salinity. IEEE Transactions on geoscience Electronics, Vol GE-21 No 4, 480-491.

Ulaby, F., R. Moore and A. Fung, 1981, 'Microwave Remote Sensing. Active and Passive' Volume I. 1st edn, (Reading, Massachusetts: Addison-Wesley Publishing Company).

Voronovich, A. G., 1994, Small-slope approximation for electromagnetic wave scattering at rough interface of two dielectric half-spaces. Waves in random Media, 4, 337- 367.

Voronovich, A. G., Zavorotny, V.U., 2001, Modelling of backscattering of radar signals from sea surface at Ka- and C- bands. Proceedings of the URSI General Assembly (CD ROM), Maastricht, The Netherlands.

Webster, W. J. And Wilheit T.T., 1976, Spectral characteristics of the microwave emission from wind driven foam coverage sea. Journal of Geophysics Research, 81, 3095- 3099.

Yueh, S. H., W. J. Wilson, F. K. Li, S. V. Nghiem, and W. B. Ricketts, 1997, Polarimetric Brightness Temperatures of the Sea Surface Measured with Aircraft K- and Ka-Band Radiometers. IEEE Transactions of Geoscience and Remote Sensing, Vol. 35, No 5, 1177-1187.

ACKNOWLEDGEMENTS

The WISE campaigns have been sponsored by the European Space Agency under ESTEC Contract No 14188/00/NL/DC. The numerical simulations have been performed under ESTEC Salinity study contract 14273/00/NL/DC. We thank S. Contardo for computational support at LODYC. The implementation of the L-band radiometer at the Polytechnic University of Catalonia has been supported by the Spanish government under grant CICYT TIC99-1050-C03-01. The French moorings were supported by the Centre National d'Études Spatiales. We thank Météo-France for the help in the buoy data handling. Last, but not least, the authors very much appreciate all the cooperation and help provided by the personnel of Repsol Investigaciones Petrolíferas – Base Tarragona – Plataforma Casablanca during the campaign.

Quantitative comparison of IEM calculations with L-band SAR measurements in agricultural areas

Jiancheng Shi¹, M. Herold², & C. C. Schmullius³

¹*Institute of Remote Sensing Applications, Chinese Academy, Beijing China, & Institute for Computational Earth System Sciences, University of California, Santa Barbara. U.S.*

²*Department of Geography, University of California, Santa Barbara. U.S.A.,*

³*Remote Sensing Unit, Department of Geography, Friedrich Schiller University of Jena, Germany*

shi@icess.ucsb.edu

ABSTRACT – *Soil moisture is an important component in investigations of land-surface climate and hydrology. This study investigates issues and problems in modeling surface backscattering signal for soil moisture radar remote sensing in agricultural areas as part of the International Surface Parameter Retrieval Collaboration (SPARC). The study is based on E-SAR's L-band multi-polarization data, Integral Equation Model (IEM), and intensive field measurements of soil moisture and surface roughness. The comparison of SAR measurements with the IEM model calculations shows that 1) co-polarization signals can be modeled quite well, 2) the type of surface correlation function plays also an important role, and 3) cross-polarization signal can be realistically modeled by the semi-empirical model.*

1 INTRODUCTION

Soil moisture is a key parameter in numerous environmental studies, including hydrology, meteorology, and agriculture. It plays an important role in the interactions between the land surface and the atmosphere, as well as the partitioning of precipitation into runoff and ground water storage. Therefore, the spatial and temporal dynamics of soil moisture are important parameters for various processes in the soil-vegetation-atmosphere-interface. In spite of its importance, soil moisture has not found a widespread application in the modeling of hydrological and biogeochemical processes and related ecosystem dynamics, in part because soil moisture is a difficult parameter to measure on a large area, cost-effective, and routine basis. However, recent advances in microwave remote sensing have demonstrated the potential to measure soil moisture quantitatively on bare and short vegetated surfaces. This raises the feasibility of developing algorithms for the retrieval of this important parameter through microwave remote measurements.

Radar backscattering response of soil surface can be used to retrieve the soil moisture and surface roughness parameters. The sensitivity of this response to the soil moisture and surface roughness has been extensively studied over the past years. Several theoretical models have been used for this purpose. The small perturbation method (SPM) and Kirchhoff approximation (KA) are traditional theories of wave scattering of rough surfaces which have the limited range of validity (Fung, 1994, Ulaby et al., 1982). SPM is validated for the small roughness surface and KA is applied for the rough surface with large surface

curvature. There are a few methods developed to overlap these two methods such as the small slope method (SSM) (Voronovich, 1994) and the integral equation model (IEM) (Fung, 1994). It has been shown that SPM and KA can be obtained from the recent developed integral equation model (IEM) under some restrictive hypothesis (Fung, 1994) and the IEM has more broad roughness range of validity (Chen et al., 2000, Wu et al., 2001).

Applying the IEM to the natural soil surfaces, however, there are still some inconsistencies comparing with the experimental measurements (Zribi et al., 1997). To retrieve the soil moisture and surface roughness, some empirical formulas were also developed based on the field measurements (Oh et al., 1992, 1994, 2002 and Dubois et al., 1995). The empirical models developed from a limited number of observations might have site-specific problem due to the nonlinear response of backscattering to the soil moisture and surface roughness parameters. Indeed, some inconsistencies between the measurements and empirical formula have been reported (Zribi et al., 1997).

Radar backscattering response of soil surface is determined by both the soil moisture and surface roughness. To obtain the correct backscattering response of soil surfaces, one depends upon the theoretical model itself, the other depends upon how to describe the statistical properties of soil surface correctly. Traditional description of random rough surface is generally assumed as a stationary process (Ogilvy, 1991). They are described by the height probability distribution function and surface correlation function (Ogilvy, 1991). The height probability distribution function of random rough

surfaces is usually assumed as Gaussian function. The commonly used surface correlation functions are either Gaussian or exponential correlation functions. However, the actual correlation functions from field measurements are very complicated. Some of field measurements have shown that the correlation functions of natural soil surfaces are close to the exponential for the smooth surfaces and Gaussian for the very rough surfaces (Oh et al., 1992). The others showed that the correlation functions of natural soils usually vary between Gaussian and exponential functions only for lag distances close to the origin. Away from the origin the experimental trends are extremely variable. In particular, values of below zero for the experimental correlation functions have been often observed.

The problems in mapping soil moisture with radar remote sensing approaches in heterogeneous landscapes result from several reasons such as the insufficient availability of adequate SAR-data, from errors in the processing and retrieval approaches and problems with the acquisition and comparison of field data and remote sensing data (Davidson et al., 2000).

In this study, we evaluate IEM model with the intensive field measurements and the multi-polarization L-band SAR data for soil moisture mapping in agricultural areas. The investigations are part of the international using radar data from the German Experimental SAR system (E-SAR). The analysis were focused on the comparison of SAR measurements with the surface backscattering models calculations for

- IEM model prediction for co-polarization signals
- Semi-empirical model for cross-polarization

Next section describes the background of IEM modeling approach that we are taken in this study. Section 3 explains the field measurements and SAR data processing. The Comparisons of IEM model with SAR measurements for co-polarization are shown in section 4. Section 5 evaluates the semi-empirical model prediction for the cross polarization signals and followed by conclusion in section 6.

2 BACKGROUND ON IEM MODELING

For completeness, the backscattering coefficient of the IEM is given in the following (Fung, 1994).

$$\sigma_{pp}^0 = \frac{k^2}{2} \exp[-2k_z^2 h^2] \cdot \sum_{n=1}^{\infty} h^{2n} |I_{pp}^n|^2 \frac{W^{(n)}(-2k_x, 0)}{n!}, \quad p = h, v \quad (1)$$

where $k_z = k \cos \theta_i$, $k_x = k \sin \theta_i$, θ_i is incident angle, k is the radar wave number, and h is the rms height of rough surfaces, and I_{pp}^n is a function determined by incidence angle, permittivity, rms height, and Fresnel reflection coefficient. In the original IEM (Fung, 1994), Fresnel reflection coefficient is evaluated at the incidence angle of θ_i . To extend the range of validity of the IEM, a modified IEM with transitional function is proposed (Chen et al., 2000, and Wu et al., 2001). In which, the Fresnel reflection coefficient is not evaluated at the incidence of θ_i instead they are evaluated at the angle between θ_i and normal incidence depending on the surface roughness parameters. It has been shown that IEM with transitional function can provide very good results of backscattering coefficients for wide range of surface roughness parameters by comparing with the results of Monte-Carlo simulations and Lab controlled microwave experimental measurements (Chen et al., 2000 and Wu et al., 2001). Therefore, we choose the IEM with transition function to simulate the backscattering coefficients of random rough surfaces.

Li, et al., (2002) described a generalized power law spectrum to characterize the random rough surfaces. Both analytic expressions of spectra and correlation functions are given. It has been shown that it naturally reduces to Gaussian and exponential spectra by adjusting the power index of the spectrum. Unlike other spectra, the generalized power law spectrum provides wider range coverage for the natural surfaces.

The generalized power law spectrum for 2-D rough surface is

$$W(k) = \frac{h^2 l^2}{4\pi} (p-1) \frac{a_p^2}{b_p^2} \left[1 + \frac{a_p^2}{b_p^2} \frac{k^2 l^2}{4} \right]^{-p} \quad (2)$$

The corresponding correlation function for isotropic rough surface is given by

$$C(\rho) = \frac{h^2}{2^{p-2} \Gamma(p-1)} \left[\frac{2b_p}{a_p} \frac{\rho}{l} \right]^{p-1} K_{p-1} \left[\frac{2b_p}{a_p} \frac{\rho}{l} \right] \quad (3)$$

Where

$$a_p = \frac{\Gamma(p-0.5)}{\Gamma(p)} \quad (4)$$

and b_p is determined by

$$\left[\frac{2b_p}{a_p} \right]^{p-1} K_{p-1} \left[\frac{2b_p}{a_p} \right] = 2^{p-2} \Gamma(p-1) e^{-1} \quad (5)$$

so that the values of coefficients a_p and b_p can guarantee parameter h is rms height and l is correlation length. For the given value of power index, b_p can be found by solving equation (5) numerically. The rms slope is given by

$$s = \sqrt{\frac{2}{p-2} \frac{b_p}{a_p} \left(\frac{h}{l} \right)} \quad (6)$$

for $p > 2$. Again, there is no rms slope exists for the power index of $p \leq 2$.

In equation (1), $W^{(n)}(-2k_x, 0)$ is the Fourier transform of the n th power of the surface correlation function and the generalized power law spectrum is given by,

$$W^{(n)}(K) \approx \frac{(l/n^{fp})^2}{2} (p-1) \frac{a_p^2}{b_p^2} \cdot \left[1 + \frac{a_p^2}{b_p^2} \frac{K^2 (l/n^{fp})^2}{4} \right]^{-p} \quad (7)$$

Where fp is a function of power index p and is in the range of 1.0 and 0.5 for $1.5 \leq p \leq \infty$. The relationship between fp and p is

$$fp = 0.5 \left[1 + \left(\frac{1.5}{p} \right)^2 \right] \quad (8)$$

3 DATA AND PROCESSING

3.1 Ground Measurements

The comprehensive field measurements were conducted during the experiment. They are summarized in Table 1.

These surface roughness and soil volumetric moisture measurements obtained by

- 199 surface soil moisture measurement points using TDR method (3 measurements at each point in 2 m radius)
- 45 roughness measures using scaled 1 m boards and digital processing for roughness parameter calculation (RMS height and Autocorrelation length, 1 cm sampling density).

Nearly all investigated fields were flat and bare soil with different roughness conditions due to agricultural utilization that ranges from very smooth seedbed fields to fresh ploughed areas. The roughness parameters

were estimated on the field basis by averaging all measurements perpendicular and parallel to the flight line. This approach assumes a consistent cultivation or rather homogenous roughness condition on each field. The soil moisture values range from mainly 15 to 40 vol.% in most parts of the area. Some areas show significantly higher values due to a wetland located in the center of the test site.

roughness Category (field-ID)	# of profiles	rms (cm)	ACL (cm)	# of TDR	Mv (%)
Seed bed (field-1)	17	1.08	13.82	16	22-33
Fresh ploughed (field-2)	17	3.0	13.18	3	35-36
Ploughed (field-3)	6	1.91	9.83	11	22-35
Seed bed (field-4)	4	1.28	14.00	23	23-36
Seed bed (field-5)	6	1.24	22.33	23	25-40

Table 1. Summary of the field surface roughness and soil moisture Mv measurements during the experiment.

These surface roughness and soil volumetric moisture measurements obtained by

- 199 surface soil moisture measurement points using TDR method (3 measurements at each point in 2 m radius)
- 45 roughness measures using scaled 1 m boards and digital processing for roughness parameter calculation (RMS height and Autocorrelation length, 1 cm sampling density).
-

3.2 SAR Data and Processing

A polarimetric (L-band) E-SAR data acquired on 28th of March 2000 is used in this study. The processing of the SAR data included the calculation of the radar backscatter parameters such as sigma-nought, the polarimetric decomposition (Cloude and Pottier, 1996) and the derivation of the interferometric coherence. The data were geometrically corrected and geocoded. For the accurate comparison between field measurements and SAR-data the sigma-nought and polarimetric parameter images were homogenized using speckle reduction and smoothing filters. Furthermore the spatial resolution was degraded from originally 1 m to 4 m using an averaging algorithm. The SAR backscatter values for every soil moisture

field measurement were extracted in a 2 by 2 pixel neighborhood (8m x 8m area) due to soil moisture sampling circle of 2 m and point mapping accuracy in the field.

5 COMPARISON IEM SIMULATION WITH L-BAND SAR MEASUREMENTS OF CO-POLARIZATIONS

The study by Herold et. al., (2001) indicated several problems in analyses of this data-set. The comparison of soil moisture and SAR backscatter for different fields shows a fair amount of variation in the data that cannot be related to soil moisture changes. This problem was investigated by a spatial analysis of the residuals of the linear regression between soil moisture and L-band backscatter intensity for every field. Points with high residuals represent possible problematic measurements. The results of the analysis show that errors found for these points result from three major problems:

1. Most of the points with high residuals are located on field or land cover borders. The high errors of the points can be justified by the fact that the surrounding land cover objects (such as trees or driveways) influence the backscatter at these pixels.
2. The fields contain backscatter heterogeneities that are not caused by soil moisture. These can result from different roughness conditions or other artifacts that produce a higher local backscatter. This indicates that there are some problems with the assumptions that agricultural field can be considered as homogenous areas concerning surface roughness, especially considering that surface roughness is the dominant backscatter signal in L-band.
3. Problems also occur if the soil moisture measurements represent a spatial heterogeneity that is not acquired by the spatial resolution of the radar data. The comparison of field measures and SAR data was done for 8m x 8 m area. If two measurements with different moisture are in between this radius the soil moisture variations cannot be separated by the radar signal.

This analysis excluded areas in wetland due to insensitivity of the radar signal to high soil moisture values and some points that show additional backscatter influences, i.e. from other land cover objects at field borders.

In this study, the backscatter signal of L-HH and L-VV was modeled using a modified IEM model with transitional function for five different fields. In order to demonstrate the sensitivity of radar backscattering to the type of surface correlation functions, we simulated the backscattering coefficients with 4 different type of the surface correlation functions: 1) gauss, 2) 1.5 power, 3) exponential, and 4) the generalized power law correlation functions. Figure 1, 2, and 3 show the comparisons of SAR measurements (x-axis) and predictions of IEM model with transition function (y-axis) for gauss, 1.5 power, and exponential correlation functions, respectively. Their corresponding the roughness power spectrum are given by (Fung, 1994) for gauss (9), 1.5 power (10), and exponential (11) as:

$$W(\theta) = 0.5 \cdot (kl)^2 \cdot \exp\left(-(\sin(\theta) \cdot kl)^2\right) \quad (9)$$

$$W(\theta) = (kl)^2 \cdot \exp(-2 \sin(\theta) \cdot kl) \quad (10)$$

$$W(\theta) = (kl)^2 / \left(1 + (2 \sin(\theta) \cdot kl)^2\right)^{1.5} \quad (11)$$

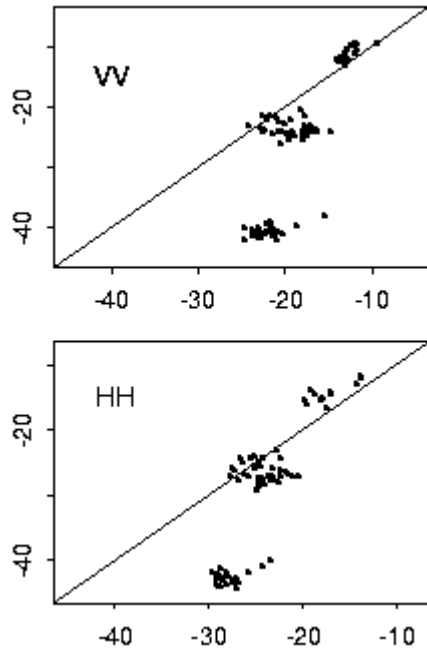


Figure 1. Comparison SAR measurements and the predictions of IEM model with transition function for the Gaussian correlation function.

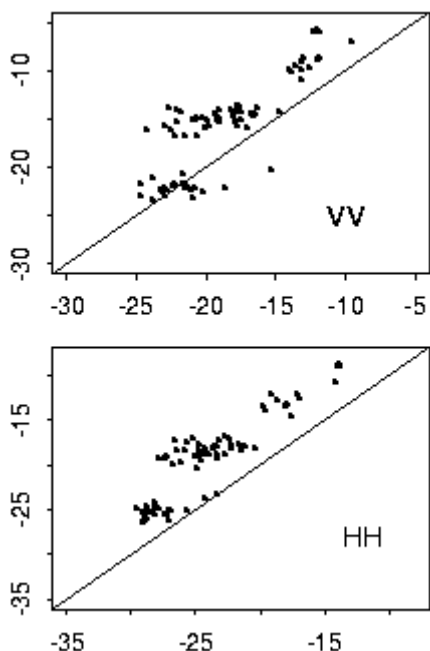


Figure 2. Comparison SAR measurements and the predictions of IEM model with transition function for the 1.5 power correlation function.

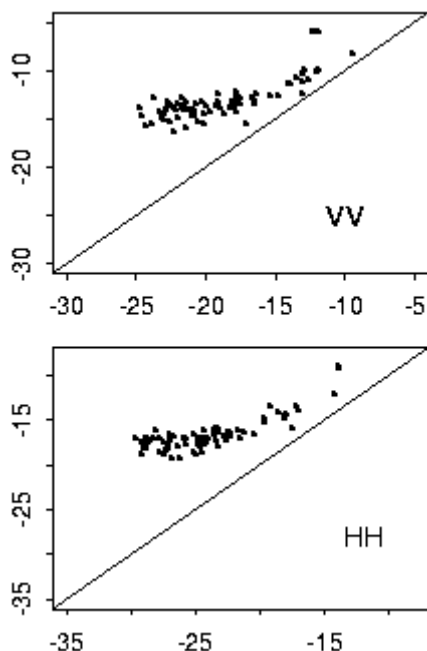


Figure 3. Comparison SAR measurements and the predictions of IEM model with transition function for the exponential correlation function.

For the generalized power law correlation function in equation (2), the power indexes in equation (7) are obtained by minimizing the overall differences of backscattering coefficients at each test field for both VV and HH polarization at different incidence angles that ranged from 42° to 54° (in the most of test fields) between the IEM simulation and SAR measured data. They are summarized in Table 2 below.

Field ID	1	2	3	4	5
Power index p	5	28	10	3	3

Table 2. Power index p in each corresponding field.

In the Figure 4, the comparisons of the backscattering coefficients between the experimental measurements and IEM simulations are plotted as for VV (top) and HH (middle) polarization, and the ratio of HH/VV (bottom), respectively.

In comparison of the SAR measurements and IEM simulation with the gauss correlation function as shown in Figure 1, the overall accuracies are 10.89 dB and 8.54 dB for VV and HH polarizations, respectively. The major problem is from the field-5 that has the rms height 1.24 cm and correlation 22.3 cm. The differences between the modeled and measured values are at 13 db to 22 dB range. It has been recognized that the gauss correlation function poorly describes the random rough surfaces when the correlation length is large or small random surface slope, especially at large incidences. For the rough surfaces (test fields-2&3), it has very good agreements with only a few dB differences for both VV and HH polarizations between modeled and measured values. It indicates that both rough surface test fields can be described as the gauss random surface. The estimated power indexes with 28 and 10 for these two rough fields are also very large – close to that for the gauss correlation function. As shown in the study (Oh, et al., 1992), the trend exists that the natural rough surfaces are better described by the gauss correlation function and that the smooth surfaces are more close to the exponential correlation function. Our results support this observation in conception.

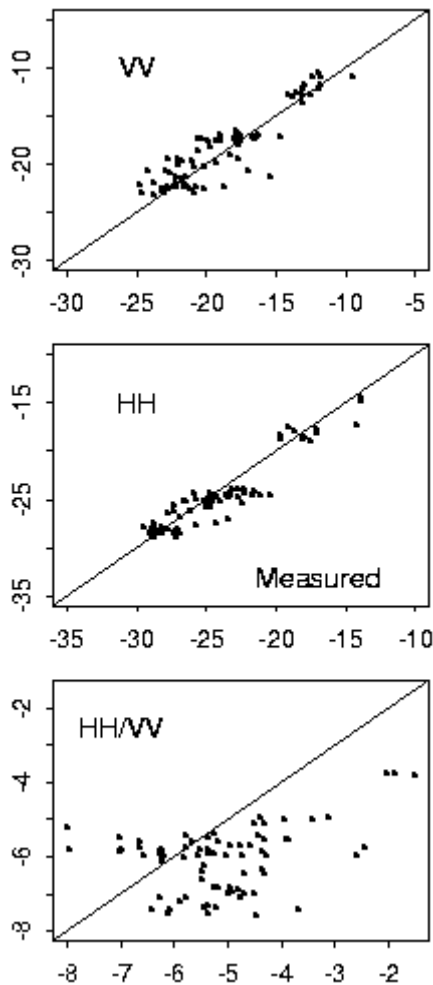


Figure 4. Comparison SAR measurements and the predictions of IEM model with transition function for the generalized power law correlation function.

As shown in Figure 2, the 1.5 power correlation function gives the better overall results in comparison with that from either the gauss (Figure 1) or exponential (Figure 3) correlation functions. The overall accuracies are 4.05 dB and 5.22 dB for VV and HH polarizations, respectively. It has quite well predictions for the smooth field-5. No extreme cases (very large errors) are found. The maximum error for both VV and HH polarization is smaller than 10 dB from all test fields. For the predictions with the exponential correlation function as shown in Figure 3, the model over-estimated the backscattering coefficients with the overall accuracies of 6.33 dB and 8.0 dB for VV and HH polarizations, respectively. It indicates that the exponential correlation function is a poor description and can't be used to characterize

the rough surface property of our test fields. However, by justifying the power index for each test field, IEM predictions the generalized power law correlation function as shown in Figure 4 have a very good agreement with SAR measurements with the overall accuracies of 1.6 dB and 1.4 dB for VV and HH polarizations. In recognizing that unlike the fixed the gauss, 1.5 power, and exponential correlation function for all test fields, there is a free parameter – the power index p which allows to justify the correlation functions for each test field in the simulations of using the generalized power law correlation function. However, it does indicate that the surface backscattering are very sensitive not only to the surface dielectric and roughness properties of rms height and correlation length but also to the type of the correlation function. Table 3 bellow summarizes the results of the comparisons between IEM predictions for each correlation function and SAR measurements in term of the Root Mean Square Error (RMSE) in dB.

Correlation function	Gaussian	1.5 power	Exponential	Power Law
RMSE-VV	10.89	4.05	6.33	1.6
RMES-HH	8.54	5.22	8.00	1.4

Table 3. Summary of RMSE in dB for each correlation function.

As shown in Figure 4, the backscatter differences between the fields (caused by roughness) are well represented by the model. However, as indicated in (Herold et al., 2001) problems can be found for the description of the within field variability. For most fields this variability is around 5-6 dB in the measured backscatter. The model just predicts around 2-3 dB of this variability. The moisture-varying symbol size in Figure 4 indicates that areas with low moisture are over predicted, whereas moister areas tend to be underestimated by the model. This fact is very important considering that the soil moisture is an objective of the analysis. Indeed, not all inaccuracies can be explained by this solution. There is also a clear indication of the roughness properties within field variability since our model simulation used only the field average surface roughness parameters. It can be seen in the bottom plot of Figure 4, the ratio of HH and VV polarizations is poorly predicted as this measurement is very sensitive to the surface roughness property especially to the surface rms height. They can be explained by local backscatter differences caused by surface roughness or other structural features.

5 EVALUATION OF THE SEMI-EMPIRICAL MODEL FOR CROSS-POLARIZATION

In contrast to IEM predictions for co-polarized backscattering coefficients, the cross-polarized signals are poorly predicted. The significant under-estimation by the theoretical models including IEM model have been commonly found in comparison with SAR measurements. In this study, we evaluate the feasibility of using the semi-empirical models as an alternative approach to predict the cross-polarization signals of the bare surfaces for future study of active microwave remote sensing of soil moisture using multi-polarization measurements.

Currently, there are three semi-empirical models that have been developed by Oh et al., (1992, 1994, and 2002) using the field experiments data. These semi-empirical models describe the relative relationship between the cross-polarization VH and one of the co-polarization VV as a function of the incidence angle, frequency, the surface reflectivity and roughness parameter – rms height. They represented in the form of $q = \text{VH/VV}$ ratio and given as

$$q = \frac{\sigma_{vh}}{\sigma_{vv}} = 0.23 \cdot \sqrt{\Gamma^0} \cdot [1 - \exp(-kl)] \quad (12)$$

(Oh et al., 1992) and

$$q = 0.25\sqrt{\Gamma^0} \cdot (0.1 + \sin^{0.9}\theta) \cdot \left[1 - \exp\left(-(1.4 - 1.6\sqrt{\Gamma^0}) \cdot kl\right)\right] \quad (13)$$

as in (Oh et al., 1994) and

$$q = 0.1\sqrt{\Gamma^0} \cdot (s/l + \sin(1.3\theta))^{1.2} \cdot \left[1 - \exp(-0.9 \cdot kl^{0.8})\right] \quad (14)$$

as in (Oh et al., 2002). Where s and l are the surface rms height and correlation length, respectively.

Our test is to evaluate the above relative relationships so that we can simulate the bare surface cross-polarization signals with the known VV polarization signals. In other words, it is evaluated as

$$\sigma_{vh} = q \cdot \sigma_{vv} \quad (15)$$

Through our analyses with VV polarization from the SAR measurements, we found in general

- the equation (12) resulted in slightly under-estimation
- the equation (13) resulted in an under-estimation
- the equation (14) resulted in an over-estimation

Among above three semi-empirical models, the equation (12) gives a best result with RMSE 1.6 dB.

However, it slightly under-estimates in most of the cases.

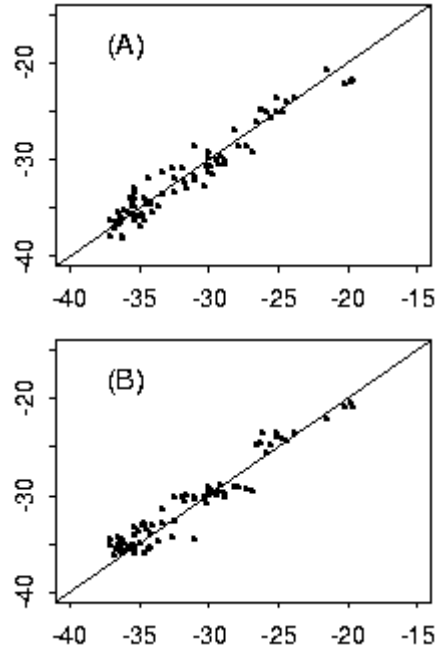


Figure 5. Comparison SAR measurements and the predictions of IEM model with transition function for the generalized power law correlation function

The best fitting, however, is from the average q of all three semi-empirical models. Figure 5 shows the comparison of the measured (x-axis) and predicted (y-axis) VH polarization signals with VV polarization from the measurements in (A) and that from IEM model prediction in (B). The average q from the equations (12-14) is calculated from the field measurement data. As we can see that both tests show an extremely well agreement with SAR measurements. The RMSEs are 1.22 dB and 1.27 dB, respectively. Therefore, it is possible to simulate the bare surface cross-polarization signals by using IEM model to simulate co-polarization signals and then by using above semi-empirical model to simulate the cross-polarization signals.

6 CONCLUSIONS

Surface backscattering is very sensitive to the correlation length and the type of correlation function. The commonly used correlation functions may poorly predict the backscattering without knowing surface condition. IEM model with transition function + the generalized power law correlation function can be used to predict the surface co-polarization signals with good accuracy.

The Oh's semi-empirical model does provide an alternative approach to simulate the cross-polarization signals. Our validation shows a very good agreement can be achieved by using this model. Therefore, it is possible to simulate surface multi-polarization signals with co-polarization from IEM and cross-polarization from the semi-empirical model realistically.

ACKNOWLEDGMENTS

This work is supported by Institute for Remote Sensing Applications, Chinese Academy.

REFERENCES

- Chen, K.S., T.D. Wu, and J. Shi, 2000, "A model-based inversion of rough surface parameters from radar measurements," *J. Electromagnetic Waves and Applications*, 15:173-200.
- Cloude, S. R. and E. Pottier, 1996, "A review of target decomposition theorems in Radar polarimetry", *IEEE Trans. Geosci. Remote Sensing*, 34(2):498-518.
- Davidson, M. W. J., T. L. Toan, F. Mattia, G. Satalino, T. Manninen, M. Borgeaud, 2000, "On the characterization of agricultural soil roughness for radar remote sensing studies," *IEEE Trans. Geosci. Remote Sensing*, 38(2):630- 640.
- Dubois, P. C. , J. van Zyl, and T. Engman, 1995, "Measuring soil moisture with imaging radars," *IEEE Trans. Geosci. Remote Sensing*, 33(4):915-926.
- Fung, A. K., 1994, in *Microwave scattering and emission models and their applications*, Artech House Inc., Norwood, MA.
- Li, Q., J. Shi, and K. S. Chen, 2002, "A Generalized Power Law Spectrum and Its Applications to the Backscattering of Soil Surface on the Integral Equation Model", *IEEE Trans. Geosci. and Remote Sens.*,40(2):271-280.
- Ogilvy, J. A., 1991, in *Theory of Wave Scattering from Random Rough Surfaces*, Adam Hilger: Bristol.
- Oh, Y., K. Sarabandi, and F. T. Ulaby, 1992, "An empirical model and inversion technique for radar scattering from bare soil surface", *IEEE Trans. Geosci. and Remote Sens.*, 30(2):370-381.
- Oh, Y., K. Sarabandi, and F. T. Ulaby, 1994, "An inversion algorithm for retrieving soil moisture and surface roughness from polarimetric radar observation", *Procedings IGARSS'94*, Pasadena, IEEE Catalog Number 94CH3378-7, vol. III, pp. 1582-1584.
- Oh, Y., K. Sarabandi, and F. T. Ulaby, 2002, "Semi-empirical model of the ensemble-averaged differential Mueller matrix for microwave backscattering from bare soil surfaces", *IEEE Trans. Geosci. and Remote Sens.*, 40(6):1348-1355.
- Ulaby, F. T., R. K. Moore and A. K. Fung, 1982, *Microwave Remote Sensing: Active and Passive, 2, Radar Remote Sensing and Surface Scattering and Emission Theory*, Reading, MA, Addison-Wesley.
- Voronovich, A. G., 1994, in *Wave scattering from rough surfaces*, Berlin: Springer-Verla,.
- Wu, T. D., K. S. Chen, J. Shi and A. K. Fung, 2001, "A Transition Model for the Reflection Coefficient in Surface Scattering", *IEEE Trans. Geosci. and Remote Sens.*, 39(9):2040-2050.
- Zribi, M., O. Taconet, S. Hegarat, D. Vidal-Madjar, 1997, "Backscattering behavior and simulation comparison over bare soils using SIR-C/X-SAR and ERASME 1994 data over Orgeval," *Remote Sens. Environ.*, 59:256-266.

Offshore wind resources quantified from satellite SAR: methodology and technical aspects

Charlotte B. Hasager¹, Birgitte R. Furevik², Sara C. Pryor^{3,1}, Rebecca J. Barthelmie¹

¹ Risø National Laboratory, Wind Energy Department, Roskilde, Denmark

² Nansen Environmental and Remote Sensing Centre, Bergen, Norway

³ Indiana University, Atmospheric Science Program, Geography, Bloomington, USA

charlotte.hasager@risoe.dk, birgitte.furevik@nrsc.no, spryor@indiana.edu,

r.barthelmie@risoe.dk

ABSTRACT *For the planning of offshore wind farms, the offshore wind resource is a key parameter. Satellite SAR-based wind speed mapping may be used for estimating the wind resource either in feasibility studies or in combination with meteorological mast observations to investigate spatial patterns along coastlines. The wind power potential is proportional to the third power of wind speed and therefore the demand on accuracy on wind speed mapping is very high. The current study investigates the technical aspects on quantitative wind speed mapping relating to the precision in ERS SAR as well as the accuracy in C-band algorithms used for wind speed mapping including the error estimation due to uncertainty on wind directions. Wind direction may be found from SAR streaks or taken from other sources e.g. meteorological observations. Comparison to in-situ offshore mast observations is done by footprint analysis, a method that effectively integrates the upwind source area to a wind sensor at a given height above sea level. Finally, the biases inherent in current satellite-based wind speed maps are discussed in relation to wind resource calculation, i.e. wind statistics (1st to 4th moment).*

1 INTRODUCTION

The offshore wind resource is one of the renewable energy sources that have attracted an increasing commercial interest during the last decade. The first offshore wind farm to be installed was the Vindeby wind farm in Denmark in 1991. Since then a number of offshore wind farms e.g. Tunø Knob and Middelgrunden (DK) and Bockstigen, Utgrunden and Stengrund (S) have started operation. Currently the largest offshore wind farm is under construction at Horns Rev (DK) and several more are underway e.g. Rødsand and Samsø (DK) and some in England, Ireland, Germany and the Netherlands.

Prior to investment in an offshore wind farm, it is a necessity to calculate the potential wind power output. The cost of installation and operation is very high and the investment should be balanced by the economical profit of the wind farm. The wind power potential is proportional to the cube of the mean wind speed. Hence in the early phase of an offshore wind farm project, there is a strong need for an accurate mapping of the local and regional wind climate.

The classical method of calculation of the wind resource is based on meteorological time-series of at

least one years duration. It is costly to collect such data.

Therefore satellite SAR-derived wind speed and wind direction observations may become an attractive alternative or additional source of observations for offshore wind resource calculation. The SAR C-band observations are available from ERS-1 and -2 SAR, ENVISAT ASAR and RADARSAT. The historical archives contain large numbers of scenes for most of the globe. It is clear however that with a relatively low sampling rate e.g. 3 per month, the total number of scenes may be rather limited. For ENVISAT ASAR it will be necessary to pre-order the scenes in advance. The SAR scenes have to be calibrated. Then a CMOD algorithm has to be applied to the scene e.g. CMOD4 (Stoffelen and Anderson, 1993) or CMOD-IFR2 (Quilfen et al., 1998) to derive the wind speed. Prior to applying the CMOD models, the wind direction has to be known e.g. from SAR wind streak analysis (Furevik et al., 2002) or in-situ observations (Hasager et al., 2002a).

Statistic on wind speed and wind direction from the SAR imagery may then be used in a wind resource calculation tool, i.e. a software that translates the 10 m wind speed to the typical hub-height of wind turbines and include the actual coastal terrain effects. Even very modest coastal topography may have a significant

impact on the calculated potential wind power (Hasager et al., 2002b).

A typical met-observation time-series consists of hourly mean values from one (or more) years, i.e. 8769 observations on wind speed and wind direction per year. For SAR-based wind resource estimation the number of samples will be much less, dependent on available SAR scenes as well as the economy (price per scene). It has been tested how much error may be expected from a very reduced set of observations (Barthelmie and Pryor, 2002; Pryor et al., 2002). The findings support the applicability of using SAR scenes in offshore wind resource estimation, however with a significantly lower accuracy and confidence level as compared to classical meteorological observations. It is shown that approx. 60-70 SAR wind speed maps should be collected for obtaining reliable statistical results (eg. 10% significance at 90% confidence level) for wind resource estimation (assuming no error in the SAR wind speed maps (Pryor et al., 2002)). An advantage of the SAR-derived wind speed maps is that spatial patterns are directly mapped rather than modelled.

2 ON SAR-DERIVED WIND SPEED MAPPING

In the current study only ERS-2 SAR scenes are analysed. These are C-band VV polarized data.

2.1 Calibration

The SAR imagery has to be in precision image mode (PRI). It is then possible by use of the ESA SAR tool box (http://earth.esa.int/stb/documentation/manual/stb_x_v-5_5.html) to calibrate the images.

2.2 CMOD wind speed retrieval

The CMOD models can be applied to the calibrated SAR scenes. The CMOD models originate from scatterometer data, buoy data and ECMWF (European Center of Medium-Range Weather Forecasting). The CMOD4 is based on correlation analysis between ERS AMI-SCAT and ECMWF ocean wind speeds (Stoffelen and Anderson, 1993) and the CMOD-IFR2 is based on NOAA buoy data (Quilfen et al., 1998). The functions for scatterometer are adjusted for wind speed in the interval 1-28ms⁻¹ with a precision of ±2ms⁻¹ and for wind directions ±20°. Outside the wind-speed interval the functions are modelled by extrapolation. The model functions are defined for wind speeds between 0-60 ms⁻¹ and for incidence angles between 16-60°. For the ERS SAR the incidence angle interval is very narrow from 21-26°.

The SAR wind speeds are valid for 10 m above sea level.

The relationship between the measured backscatter in each resolution cell and wind speed is given in eq. 1.

$$\sigma^0 = B_0(1 + B_1 \cos(\phi) + B_2 \cos(2\phi)). \quad (1)$$

Here σ^0 (dB) is the normalised radar cross section (backscatter coefficient) in each resolution cell. It is dependent upon the relative wind direction, ϕ ($\phi = 0^\circ$ for a wind blowing against the radar), the local radar beam incidence angle, θ , of the illuminated area and the wind speed, U . The coefficients B_0 , B_1 , B_2 depend on θ and U (Quilfen et al., 1998).

From eq.1 it is clear that the geometry between the local radar incidence angle and wind direction is of importance. The relationship is graphed in Figure 1 for the CMOD-IFR2 algorithm. It is clear that uncertainty on the relative wind direction gives a large effect especially for high wind speed.

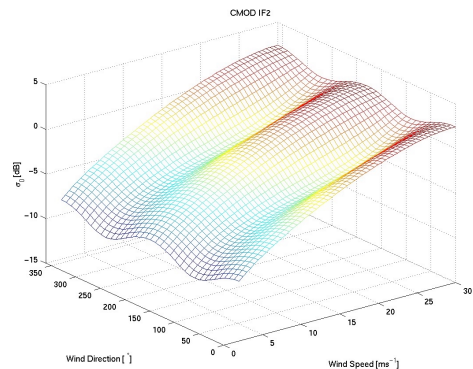


Figure 1. The dependence between backscatter coefficient, wind speed and relative wind direction for the CMOD-IFR2 algorithm.

For a relative wind direction of 0° and an incidence angle of 23°, the relationship between wind speed and backscatter coefficient is shown in figure 2 for the CMOD4 and CMOD-IFR2 models. In the current study the CMOD-IFR2 is used as this model gave the best results when comparing research ship met-observations to SAR-derived ocean wind speeds (Furevik et al., 2002).

Obviously the absolute precision in the SAR imagery is of importance. The radiometric accuracy of ERS-1 and -2 SAR's is within ±0.4dB (Attema et al., 2000)

that translates to approximately $\pm 0.7 \text{ ms}^{-1}$. For very high wind speeds with around 0 dB, the error may be larger dependent on the calibration procedure (Horstmann et al., 2000).

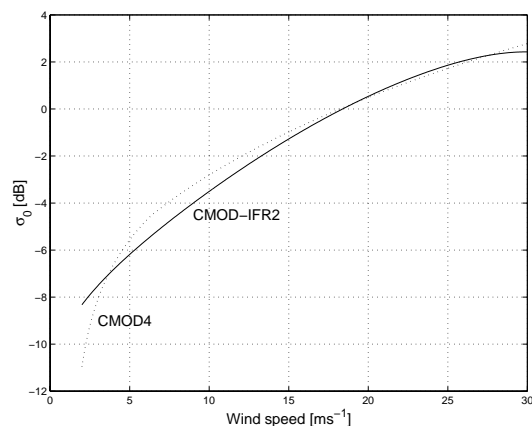


Figure 2 The model functions of the CMOD4 and CMOD-IFR2 are shown for a relative wind direction of 0° and an incidence angle of 23° .

3 THE STUDY SITE

The study site is Horns Rev in the North Sea where the worlds largest offshore wind farm is under construction in the summer of 2002. The wind farm (<http://www.hornsrev.dk/>) belongs to ELSAM and the collection of meteorological observations is performed by Tech-wise (Neckelmann and Petersen, 2000). The in-situ observations are from a tall meteorological mast located 14 km offshore from the coast, see figure 3. The observations studied are from the period May 1999 to June 2000, i.e. collected prior to the installation phase of the wind farm.

4 ANALYSIS RESULTS

4.1 On SAR wind fields

A total of 16 ERS-2 SAR scenes are analysed with respect to wind speed and wind direction accuracy. The mean wind speed in the SAR wind speed maps are calculated for a simple ellipse-shaped area upwind of the mast and compared case by case to the in-situ observations, see an ellipse in figure 3. The size of the ellipse is a function of height (here 10m) and the ellipse is located in the upwind direction of the mast. It is a simple footprint area-averaging method where all pixels in the footprint are weighted equally.

It is found that the linear regression result is $y = 1.038x - 1.785$ with $R^2 = 0.882$ on SAR wind speed and in-situ wind speed for wind direction taken a priori from the in-situ observations and used in the CMOD-IFR2. This result is for the 10 m wind speed.

Intercomparison of in-situ wind directions and SAR streak directions derived from 2D-FFT functions shows a linear regression of $y = 1.11x - 31.57$ with $R^2 = 0.95$. The accuracy on wind speed and wind direction compares to other studies e.g. (Vachon and Dobson, 1996).

The wind direction is relatively well defined from the wind streaks, however using the wind streak directions in the CMOD-IFR2 algorithm seem to introduce more uncertainty in the wind speed retrieval. This is found from the linear regression $y = 1.102x - 2.126$ with $R^2 = 0.768$ for a set of SAR wind speed maps calculated from a priori wind direction from the streaks and compared to in-situ wind speed (Hasager et al., 2002a).

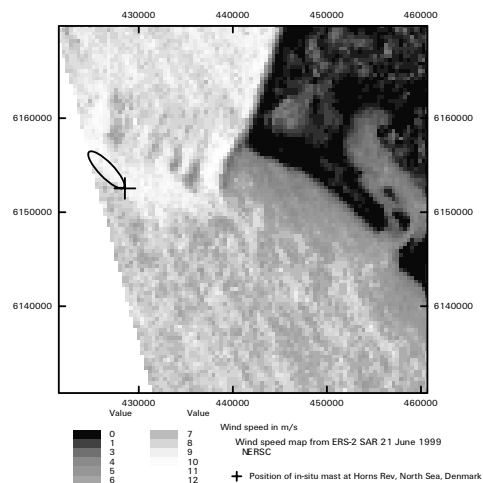


Figure 3 Wind speed map from the Horns Rev in the North Sea calculated by the CMOD-IFR2 model based on a ERS-2 SAR satellite scene.

4.2 On offshore wind statistics and sampling

In a study based on offshore in-situ meteorological data from two Danish sites, Horns Rev as mentioned above, and the Vindeby site, an analysis is undertaken to answer the question: 'Can satellite sampling of offshore wind speeds realistically represent wind speed distributions?' At both sites tall met-mast with long-term high-quality time-series are available. The investigation deals with the statistical properties of the

wind speed distributions. In order for wind resources to be calculated the 1st to 4th moments are needed.

Based on the data analysis and assuming an uncertainty of $\pm 10\%$ at a confidence level of 90% is acceptable then of the order of 60-70 randomly selected samples (SAR images) are required to characterize the mean wind speed and Weibull c parameter, while of the order of 150 images are required to obtain a variance estimate, and nearly 2000 are needed to obtain an energy density (or Weibull k) estimate. The finding is based on perfect accuracy of the image wind speed retrieval, a criteria that cannot be fulfilled. Furthermore the SAR scenes cannot be selected randomly in time as the satellite orbital parameters place a limit on availability in time. For the given cases (Horns Rev and Vindeby) the daily variations in mean wind speed was reasonably well-represented from the local recording times of the ERS-2 SAR (around 10.30 and 21.30 UTC) (Barthelmie and Pryor, 2002; Pryor et al., 2002).

The above-mentioned statistical limits at uncertainty bound and confidence level are chosen as an example, rather than a strict guideline. In feasibility studies the goal for predicting the offshore wind resource may be site specific, hence the SAR wind speed maps may offer a valuable information content in certain cases.

5 DISCUSSION

The accuracy needed for feasibility studies on wind resource mapping may be obtained from ERS-2 SAR wind speed maps. In order to reduce the uncertainty to an acceptable level, a large number e.g. 60-70 scenes will have to be used. This is possible in some parts of the world as the SAR scenes are stored in archives from the ESA satellites ERS-1 and ERS-2 SAR as well as the Canadian Radarsat satellite. Currently ERS-2 SAR, ENVISAT ASAR and RADARSAT are collecting SAR observations and these may be pre-ordered for a site of interest. The cost of SAR scenes for commercial purposes may however limit the use (e.g. 1200 Euro per ERS SAR scene). The cost should however be compared to the expenses necessary to obtain wind speed measurements and the time involved. In remote areas wind speed observations may not be readily available from airports, met-offices and the like. Hence it may be necessary to operate a met-mast at the site. Such operation involves a planning phase (e.g. legislation to erect the mast), logistical consideration and technical work. The met-observation collection phase itself is minimum one year to obtain a climatological record.

The advantages of SAR wind speed maps are that they are readily available and only image processing is necessary (office work). Furthermore SAR wind speed maps may directly indicate local wind phenomenon that atmospheric models may not necessarily capture accurately. This spatial information could be useful for exact geo-positioning of a proposed offshore wind farm.

The disadvantages of SAR wind speed maps are that the accuracy is far less accurate than high-quality wind speed observation (e.g. less than 1 % error on the in-situ wind speed observations from cup anemometers at Horns Rev) and that the number of samples may be rather limited due to cost.

A prototype tool for wind resource calculation based on SAR wind speed maps is under development. It is based on a footprint methodology of area-averaging the SAR wind speeds and classical methods in wind resource estimation extrapolating from the 10m level to hub-height (60-80m) of modern offshore wind turbines. So far a full validation on the SAR wind speed map methodology for offshore wind resource mapping has not been possible due to the limited number of satellite scenes but work is ongoing to achieve this.

5 CONCLUSION

The accuracy on SAR-derived wind speed maps is by careful processing less than the $\pm 2\text{ms}^{-1}$ and the accuracy on wind direction retrieval around $\pm 20^\circ$. The number of satellite scenes (samples) that would give a 10% significance at the 90% confidence level for wind resource estimation (assuming no error in the SAR wind speed maps) is around 60-70 scenes. Hence it is concluded that the accuracy will be less than this statistical output, however probably still acceptable in some offshore wind resource feasibility studies.

ACKNOWLEDGEMENTS

We are thankful to EC for the WEMSAR ERK6-CT1999-00017 contract, to ESA for the AO3-153 project granting the ERS-2 SAR scenes and to Tech-wise for the meteorological observations at Horns Rev.

REFERENCE LIST

- Attema, E., Desnos, Y.-L., and Duchossiois, G.: 2000, 'Synthetic Aperture Radar in Europe: ERS, Envisat, and Beyond', *John Hopkins APL Technical Digest*, **21**, 155-169

- Barthelmie, R. J. and Pryor, S. C.: 2002, 'Can Satellite Sampling of Offshore Wind Speeds Realistically Represent Wind Speed Distributions?', *Journal of Applied Meteorology* (accepted)
- Furevik, B., Johannessen, O., and Sandvik, A. D.: 2002, 'SAR-Retrieved Wind in Polar Regions - Comparison With in Situ Data and Atmospheric Model Output', *IEEE Transactions on Geoscience and Remote Sensing* **40**, (to appear August)
- Hasager, C. B., Dellwik, E., Nielsen, M., and Furevik, B.: 2002a, 'Validation of ERS-2 SAR Offshore Wind-Speed Maps in the North Sea', *International Journal of Remote Sensing* (submitted)
- Hasager, C. B., Frank, H. P., and Furevik, B. R.: 2002b, 'On Offshore Wind Energy Mapping Using Satellite SAR', *Canadian Journal of Remote Sensing*, **28**, 80-89
- Horstmann, J., Lehner, S., Koch, W., and Tonboe, R.: 2000, 'Computation of Wind Vectors Over the Ocean Using Spaceborne Synthetic Aperture Radar', *John Hopkins APL Technical Digest*, **21**, 100-107
- Neckelmann, S. and Petersen, J.: 2000, 'Evaluation of the Stand-Alone Wind and Wave Measurement Systems for Horns Rev 150KW Offshore Wind Farm in Denmark In: *Proceedings of OWEMES offshore wind energy in Mediterranean and other European Seas*, 13-15 April 2000, Sircusa, Sicily, Italy. ATENA/ENEA, Rome.
- Pryor, S. P., Barthelmie, R. J., and Hasager, C. B.: 2002, 'Can Satellite Sampling of Offshore Wind Speeds Represent Wind Speed Distributions?', In: *Proceedings Global Windpower Conference and Exhibition*, Paris (FR), 2-5 Apr 2002. (European Wind Energy Association, Brussels) CD-ROM, p.5
- Quilfen, Y., Chapron, B., Elfouhaily, T., Katsaros, K., Tournadre, J., and Chapron, B.: 1998, 'Observation of Tropical Cyclones by High-Resolution Scatterometry', *Journal of Geophysical Research*, **103**, 7767-7786
- Stoffelen, A. and Anderson, D. L. T.: 1993, 'Wind Retrieval and ERS-1 Scatterometer Radar Backscatter Measurements', *Advance Space Research*, **13**, 53-60
- Vachon, P. W. and Dobson, F. W.: 1996, 'Validation of Wind Vector Retrieval From ERS-1 SAR Images Over the Ocean', *Global Atmosphere and Ocean System*, **5**, 177-187

Seasonal Changes of Polarimetric Parameters from Crops – a Comparison of Different Decomposition Approaches at L-Band

Tanja Riedel, Christiane C. Schmullius

Remote Sensing Unit, Institute of Geography, Friedrich-Schiller-University (FSU) Jena, Loebdergraben 32, D-07743 Jena

Tanja.Riedel@geogr.uni-jena.de

ABSTRACT – *The objective of this study is analyse and interpret the seasonal changes of polarimetric parameters derived by different decomposition theorems. Furthermore, it should be investigated whether the results of the diverse approaches are in concordant with each other. The analyses were carried out on polarimetric E-SAR data at L-band. Between June and July the total power of the radar signal decreases for most crops. The seasonal changes in backscattering behaviour differ for cereals and broad-leaf crops. The effective scattering mechanism of green, full developed grains strongly depends on the local incidence angle. The model based decomposition approach indicates dominant double bounce interactions in near range, whereby in far range surface scattering prevails. Contrary, the eigenvector theorem signifies the predominance of volume scattering for low incidence angles. When the cereals get ripe multiple scattering becomes dominant for nearly all fields. For broad-leaf crops, such as potatoes, corn and rape, only little seasonal changes in scattering mechanisms were found. They are characterized by dominant volume scattering or double bounce interactions. The entropy H , which is a measure for the number of effective scattering mechanisms, is relative high. Contrary, the model based decomposition theorem signifies the predominance of one strong scattering mechanism.*

1. INTRODUCTION

One important application field of radar remote sensing is the interpretation of SAR data from agricultural areas. Radar polarimetry provides the unique possibility to extract information about the scattering mechanisms of the target, which mainly depend on the dielectrical and structural characteristics of the objects. The understanding of the scattering mechanisms, that contribute to the received radar signal is a major problem in analysing polarimetric data. Regarding backscattering from agricultural areas, usually the following scattering mechanisms considered to be important (Skriver et al., 1999 and Brisco et al., 1998):

- 1.) direct backscattering from the underlying soil, including multiple scattering;
- 2.) direct backscattering from the vegetation constituents such as leaves, stems, heads, including multiple scattering;
- 3.) double-bounce reflections between the soil surface and the crop canopy.

In recent years many studies have been published investigating the scattering processes of crops. Few authors analysed the seasonal changes of polarimetric parameters from crops and their residue, e.g. the phase difference, the correlation coefficient, the circular backscatter and the pedestal height (Mc Nairn, 2002; De Matthaeis et al, 1994; Baronti et al., 1995 and Skriver et al., 1999). Others used vegetation models to improve the understanding of the physical interaction of microwaves with the vegetation and the underlying

soil (Chiu et al., 2000 and Stiles et al., 2000). The application of such models usually is limited by the fact, that they are very complex and require a lot of input parameters. Another approach to derive information about the relevant scattering mechanisms is the application of target decomposition theorems. In recent years several decomposition techniques have been proposed. A review of the different approaches is given by Cloude et al. (1996).

2. STUDY SITE

The test site of this study covers a 2x3 km area located around 25 km southwest of Munich, Germany. The region is characterized by a flat terrain. Only in the north of the study area there is an older moraine formation with significant topography. This region is used for forestry and agriculture. South of the moraine there is a wetland mainly cultivated by pasture and meadow. The sedimentary plain in the south of the test site represents a typical rural landscape with small-scale agricultural land use pattern. As shown in Figure 1, the main crop types are cereals (wheat, rye, oat, winter and summer barley), corn, potatoes, rape and sugar peas.

3. EXPERIMENTAL DATA

The investigation were carried out using polarimetric L-band data from the airborne E-SAR system of the German Aerospace Center (DLR). The radar scenes were recorded in March, June and July 2000. The local

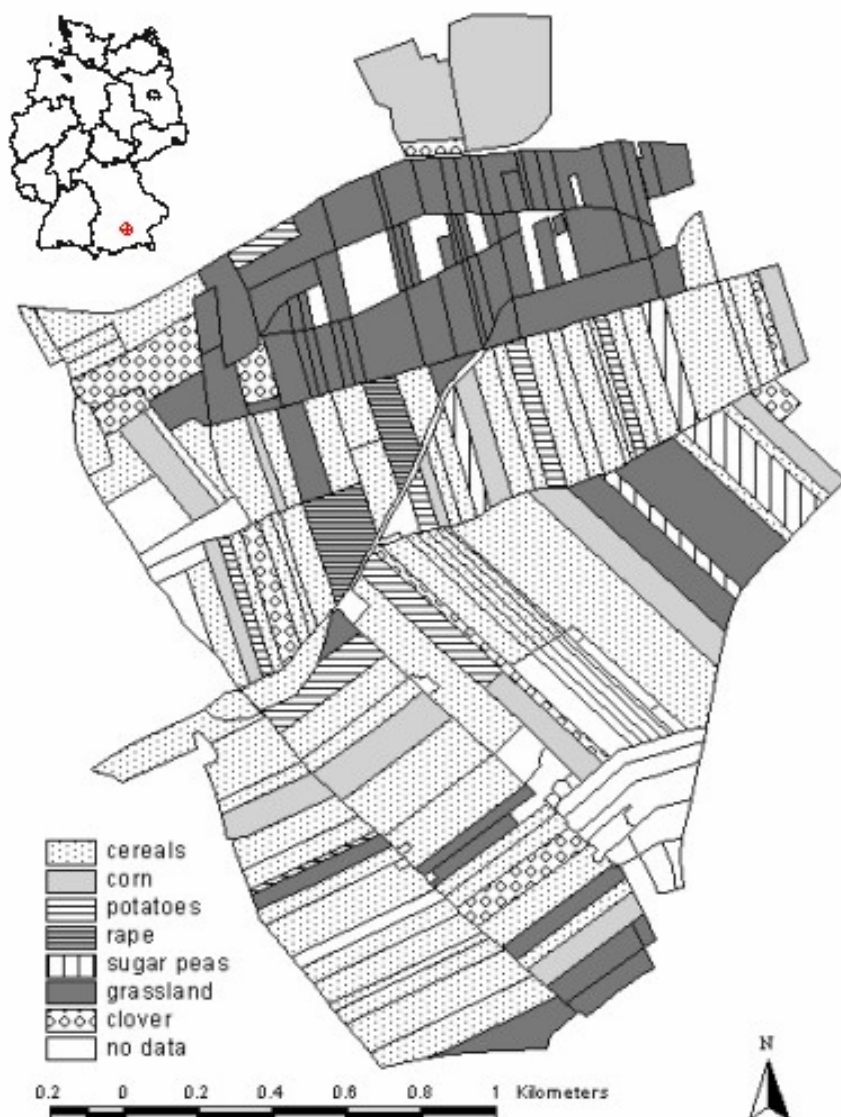


Fig. 1: Location and land use of the study area

4. METHODS

incidence angles of the observed fields varies between 30 and 55°.

During all flight campaigns extensive field data were collected. Soil moisture measurements were taken along profiles applying gravimetric and Time Domain Reflectometry (TDR) methods. Additionally, in March and July surface roughness data were collected on bare fields. Furthermore, land use information and different vegetation parameters such as vegetation height, row spacing, fractal cover and leaf area index were acquired.

In the framework of this study three different target decomposition theorems were applied to the polarimetric E-SAR data at L-band, namely the coherent, eigenvector and model based approach.

A widely used coherent decomposition theorem is the Pauli spin matrix decomposition. Pauli spin matrices originally were used in quantum mechanics. The decomposition approach express the scattering matrix $[S]$ as the complex sum of Pauli spin matrices (Cloude et al., 1996):

$$[S] = a \cdot \begin{bmatrix} 1 & 0 \\ 0 & 1 \end{bmatrix} + b \cdot \begin{bmatrix} 1 & 0 \\ 0 & -1 \end{bmatrix} + c \cdot \begin{bmatrix} 0 & 1 \\ 1 & 0 \end{bmatrix} + d \cdot \begin{bmatrix} 0 & -i \\ i & 0 \end{bmatrix} \quad (1)$$

The first component could be interpreted as single scattering from a plane surface. The second matrix is characteristic for even bounce reflection. Volume scattering is represented by the third component. The final element is not required for backscatter problems. The Pauli decomposition usually is used for visual interpretation only (Cloude, 1992, Cloude et al., 1996 and Titin-Schnaider, 1999).

The eigenvector decomposition approach is based on the decomposition of the 3x3 coherency matrix $[T]$ into three independent coherency matrices $[T_i]$, whereby each matrix represents a single scattering process. Its contribution to the received radar signal is given by the appropriate eigenvalue (λ_i). Based upon the eigenvector target decomposition theorem three important roll-invariant parameters could be derived. The entropy H is defined by the logarithmic sum of the eigenvalues:

$$H = \sum_{i=1}^3 -P_i \log_3(P_i); \text{ where } P_i = \lambda_i / \sum_{j=1}^3 \lambda_j \quad (2)$$

This parameter is an indicator for the number of effective scattering mechanisms, whereby $H = 0$ belongs to deterministic scattering and $H = 1$ to totally random scattering. The second physical feature, the anisotropy A , describes the proportions between the secondary scattering mechanisms:

$$A = \frac{\lambda_2 - \lambda_3}{\lambda_2 + \lambda_3} \quad (3)$$

A only yields additional information for medium values of H . High A signifies, that besides the first scattering mechanism only one secondary process contributes to the radar signal. For low A both secondary scattering processes play an important role.

Finally, another important polarimetric parameter is α , which represents the type of scattering mechanism and ranges between 0 and 90°. It is evaluated as:

$$\alpha = P_1\alpha_1 + P_2\alpha_2 + P_3\alpha_3 \quad (4)$$

Thereby $\alpha = 0$ indicates surface scattering. As α increases, the surface becomes anisotrop. An α -value of 45° represents a dipole. If α reaches 90° the scattering process is characterised by double bounce interactions (Hellmann et al., 1998 and Pottier et al., 1999).

The third decomposition approach, the three-component scattering model was previously developed by Freeman and Durden. Surface scattering is

modelled by the first-order Bragg model. Double bounce interactions are represented by scattering from a dihedral corner reflector. Finally, the volume scattering component is modelled by scattering from randomly oriented dipoles. This results in the following model for the total backscatter:

$$\begin{aligned} \langle |Shh|^2 \rangle &= fs|\beta|^2 + fd|\alpha|^2 + fv \\ \langle |Svv|^2 \rangle &= fs + fd + fv \\ \langle ShhSvv^* \rangle &= fs\beta + fd\alpha + fv/3 \\ \langle |Shv|^2 \rangle &= fv/3 \\ \langle ShhShv^* \rangle &= \langle ShvSvv^* \rangle = 0 \end{aligned} \quad (5)$$

For dominant surface scattering $\alpha = -1$ and for double bounce scattering $\beta = 1$. Thus, the model equations could be solved. The contribution of each scattering mechanism to the radar signal is (Freeman et al., 1998):

$$\begin{aligned} P &= P_s + P_d + P_v = \\ &= f_s(1 + |\beta|^2) + f_d(1 + |\alpha|^2) + 8f_v/3 \end{aligned} \quad (6)$$

Finally, for all derived polarimetric parameters the field mean values were calculated and the seasonal trends were analysed.

5. RESULTS

Generally it could be stated, that the seasonal changes in scattering mechanisms differ for broad-leaf crops and cereals. Table 1 as well as Figure 2 show the observed polarimetric parameters for agricultural crops derived by the eigenvector and the model based decomposition theorem. In the following the backscattering behaviour of the different crop types will be discussed in detail.

Bare soil:

In March, backscattering is dominated by strong surface scattering from bare fields and from pads covered by low vegetation (< 15 cm in height). This is indicated by all decomposition theorems. The α -angles and H -values derived by the eigenvector decomposition approach are low. For bare fields only, the analyses showed an increase of α from 24° in near range up to 37° in far range. This results are in agreement with the coherent decomposition. The model-based decomposition shows no dependence from the local incidence angles for rough fields, which were ploughed in autumn. Contrary, for harrowed pads

a decrease in all scattering mechanisms in range was found.

The different scattering behaviour of the single fields could be regarded to varying soil moisture and surface roughness conditions, whereby the influence of soil moisture on the backscattering signal is reduced at larger incidence angles (Mc Nairn et al., 2002). In the test site significant changes in soil moisture content within one field could be found in the sedimentary plain south of the wetland. The soil moisture increases about 10% from south to north. But for most fields only bad correlations between the polarimetric parameters and the soil moisture measurements were found. This is not exceptionally, because these fields are characterized by relative high soil moisture contents (25 – 40%) and high incidence angles ($> 50^\circ$).

Rape:

Former studies showed, that the backscattering behaviour of rape in the early season is characterized by surface scattering and double bounce interactions between the soil surface and the vertical stems. The radar signal of developed rape plants, which are relative large and dense, is dominated by backscattering from the vegetation. The proportion of the soil on the total backscatter is low. In comparison to other crops, former study reported the highest contribution of volume scattering processes to the radar signal (Skriver et al., 1999).

In March, the rape plants are around 10 cm in height. Their scattering behaviour differs significantly from those observed for all other crops. Thus, for the identification of rape fields at L-band radar scenes recorded early in the season are most advisable. Regarding the polarimetric parameters derived by the eigenvector decomposition it was found, that the observed α - ($\sim 51^\circ$) and H-values (~ 0.7) are relative high. This indicates the presence of three scattering mechanisms, whereby the dihedral component dominates. The model based decomposition signifies dominant volume scattering and high double bounce interactions, whereas the contribution of surface scattering processes to the radar signal is low. The visual and statistical interpretation of the Pauli-components indicate dominant double bounce interactions and strong surface scattering, which is in agreement with previous studies.

In June, the plants are around 1.35 m in height. The α -values indicate dominant volume scattering. All three scattering mechanisms contribute significant to the radar signal, as denoted by the relative high H-values. Contrary, the model based decomposition signifies a low contribution of surface scattering and double bounce interactions (both around -21 dB). The received radar signal is strongly dominated by volume scattering (around -8 dB). According to the Pauli components the proportion of volume scattering is also very high. Only for potatoes similar high values could be found.

In July, the rape was already harvested and surface scattering dominates according to the eigenvector and the Pauli decomposition approaches. Due to 40 – 50 cm high rape stubble on one field the contribution of the other scattering mechanisms is relative high. In contrast, the model-based decomposition indicate dominant volume scattering.

Corn:

At L-band the backscattering of corn is characterized by strong double bounce interactions between the stem and the soil. Often the other scattering mechanisms even contribute significant to the radar signal (De Mattheis et al., 1994). Furthermore, the backscattering behaviour of corn at L-band is strongly affected by the row direction. Brunfeldt & Ulaby (1984) documented, that fields with row direction perpendicular to the look direction have significant higher brightness values than those with parallel row direction. Moreover, for perpendicular row direction the brightness temperature of V-polarization is higher than for H-polarization.

According to the eigenvector decomposition the backscattering in June from corn, which is about 0.8 m in height, is dominated by volume scattering or double bounce interactions. The α -values vary between 45 and 57° . As indicated by the relative high H-values (~ 0.7), all three scattering mechanisms contribute to the radar signal. This is in agreement with the results of the model-based approach, which also indicates dominant volume scattering and strong double bounce interactions. The visual interpretation of the Pauli-decomposition also indicates strong double bounce interactions.

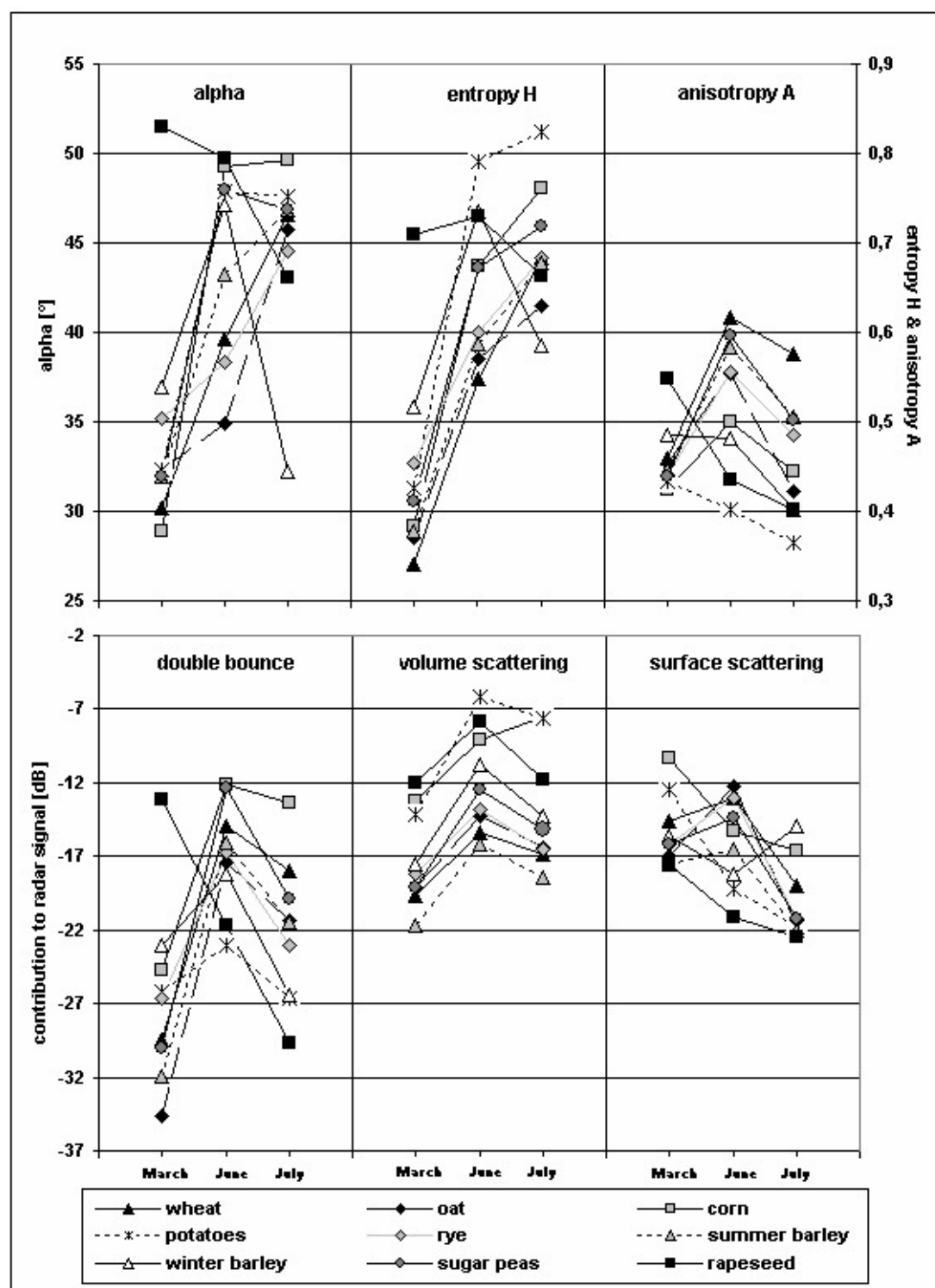


Fig. 2: Polarimetric parameters derived by the eigenvector (top) and model based (down) decomposition

Crop type	Month	LIA [°]	Eigenvector D.			Model based D.			
			alpha [°]	H	A	span	Pd [dB]	Pv [dB]	Ps [dB]
Rape	June	47,6	50,4	0,73	0,44	-7,3	-20,3	-7,7	-21,4
	July		harvested						
Corn	June	38,0	49,6	0,69	0,53	-5,9	-10,3	-9,1	-14,2
	July		51,7	0,78	0,44	-5,3	-13,4	-6,2	-18,2
Potatoes	June	43,5	48,8	0,80	0,40	-5,6	-21,7	-5,9	-19,2
	July		48,1	0,83	0,36	-8,4	-25,5	-8,6	-22,8
Sugar peas	June	50,0	49,6	0,68	0,61	-9,0	-12,9	-13,1	-15,7
	July		45,9	0,73	0,47	-12,5	-21,2	-14,1	-20,0
Wheat	June	32,7	46,4	0,55	0,64	-9,0	-12,4	-15,4	-14,0
	July		47,4	0,78	0,46	-11,8	-20,9	-13,1	-20,8
	June	48,9	33,8	0,53	0,58	-9,3	-17,5	-15,2	-11,5
	July		43,1	0,58	0,64	-13,4	-18,2	-19,7	-17,1
Rye	June	34,3	49,8	0,55	0,69	-10,1	-12,3	-17,6	-16,8
	July		45,0	0,75	0,52	-14,0	-23,1	-16,5	-21,3
	June	47,4	32,0	0,58	0,59	-9,4	-18,1	-14,8	-11,7
	July		43,9	0,71	0,55	-14,3	-20,2	-18,2	-19,1
Summer barley	June	38,8	51,5	0,57	0,61	-11,4	-14,1	-16,1	-20,1
	July		44,2	0,67	0,53	-15,8	-21,4	-19,6	-20,9
	June	49,2	35,6	0,57	0,54	-11,0	-18,9	-15,7	-14,1
	July		51,5	0,67	0,49	-14,1	-18,7	-16,6	-24,4
Oat	June	40,7	35,8	0,54	0,58	-9,6	-16,5	-15,4	-12,3
	July		50,4	0,60	0,43	-14,9	-18,6	-18,0	-25,4
Winter barley	June	37,2	47,4	0,76	0,45	-9,1	-18,9	-10,2	-18,8
	July		harvested						

Tab. 1: Scattering behaviour of crops on June 16 derived by the eigenvector and model based decomposition theorem

Between June and July the vegetation height of the corn increases from around 0.8 to 2.3 m. According to the eigenvector decomposition theorem the scattering behaviour of corn changes only little. Volume scattering dominates the radar signal for all fields. Furthermore, the two secondary scattering mechanisms becomes more important, as indicated by an increase in H and a decrease in A. The model based decomposition signifies an increase in volume scattering between June and July. Consequently, the proportion of the other scattering mechanisms, especially of the double bounce interactions, decreases. This is in agreement with the results obtained for the Pauli decomposition, which show an increase in volume scattering and a simultaneous decrease in double bounce interactions for most fields.

The influence of the row direction on the backscattering behaviour was studied on two corn fields in the north of the test site. Both fields are separated only by a small way. The row direction on the western field is parallel to the look direction,

whereas on the eastern field the row direction is perpendicular to the look direction. With respect to the received radar signal the parallel row direction results in obvious lower backscatter values at VV-polarization (~ 5 dB). The polarimetric analyses of the SAR scenes from June showed higher H- (parallel: 0.71; perpendicular: 0.58) and α -values (parallel: 51°; perpendicular: 45°) for this fields. That means, that the contribution of the secondary scattering mechanisms to the radar signal is higher for fields, those row direction is parallel to the look direction. The analysis of the model based decomposition showed for the perpendicular row direction obvious higher surface scattering (parallel: -18.9 dB; perpendicular: -9.2 dB). The contribution of double bounce interactions even shows a slight increase. In consequence volume scattering becomes more important, when the row direction is parallel to the look direction. The visual interpretation of the Pauli decomposition even indicates stronger volume scattering processes on the western field. However, in the whole test area there is

only one field, whose row direction is nearly parallel to the flight direction. The investigations indicate, that in July the influence of the row direction on the radar signal and the polarimetric parameters is less important.

Sugar pea:

In contrast to the other broadleaf crops cultivated in the study area, sugar pea fields are characterized by a relative high fractal cover and a low row distance. In June the plants have nearly reached their maximum height (up to 80 cm).

Backscattering from sugar peas in June is dominated by volume scattering, as indicated by α ranging between 47 and 50°. The secondary scattering mechanisms also play an important role, as indicated by the H-values. The model based approach even signifies, that the contribution of the secondary scattering mechanisms is relative high, whereby volume scattering or double bounce interactions prevail. The Pauli decomposition indicate strong surface and double bounce scattering, whereas the proportion of volume scattering is low in comparison to the other broad-leaf crops.

In July on all fields dominant volume scattering was observed by the eigenvector and the model based decomposition theorem. The polarimetric parameter H shows an increase, whereas A decreases between both SAR data acquisition times. This indicates, that the proportion of the second and the third scattering mechanism on the radar backscatter increases. This is in contrast to the model based approach, which indicates, that the proportion of the dominant volume scattering processes increase, whereas the contribution of the secondary scattering mechanisms decreases. The Pauli decomposition also shows an increase in volume scattering mechanisms between June and July.

Potatoes:

Former studies showed, that backscattering of potato fields at L-band is dominated by stem scattering at all polarizations. Beyond this stem-soil interactions play an important role at L-band (De Mattheis et al., 1994, Ferrazzoli & Guerriero, 1994 and Srivier et al., 1999). De Mattheis et al. (1994) found, that volume scattering from tillers, sprays and twigs are prevalent for potatoes. In comparison to other crops, developed potatoes are characterized by very high backscattering values at cross-polarization (Ferrazzoli, 2001).

In the test site the potato plants were around 45 cm height in June and 65 cm in July, respectively. Typically they have a low stem density and a low fractal cover.

Regarding all polarimetric parameters derived for the potatoes fields in June and July, one striking fact is, that the inter-field variability is extremely low. No significant differences could be found due to different

incidence angle, row direction and other crop parameters. Bouman & Hoekman (1993) found higher γ -values for fields with perpendicular row direction to the radar beam.

All decomposition approaches signify, that the scattering behaviour between June and July remained nearly unchanged, whereas the total power of the received radar signal shows a slight decrease. The eigenvector and the model based approach indicate dominant volume scattering processes. For potatoes, all scattering mechanisms strongly contributes to the radar signal, as indicated by the very high H-values (~0.8) in comparison to other crops. This is in contrast to the results obtained for the model based decomposition. This approach signify, that the contribution of the secondary scattering mechanisms to the radar signal is relative low for potatoes. The Pauli components indicate the presence of three strong scattering mechanism, whereas the volume component dominate.

Cereals:

As already stated, many studies have been published investigating the scattering of wheat fields, especially at C-band. At HH- and crosspolarized C-band the radar signal is dominated by ground scattering for all incidence angles. For VV-polarization the soil is dominant only for angles less than 35° (Brown, 2001). Due to the higher penetration depth at L-band it could be expected, that ground scattering dominates the radar signal even at high incidence angles at all polarizations. Analyses of polarimetric parameter at L-band showed the dominance of surface scattering processes (De Mattheis et al., 1994). Touré (1994) stated, that it is possible to derive soil moisture conditions in wheat fields for local incidence angles ranging from 20° to 50°. Contrary, Stiles (2000) model no significant contribution of ground scattering to the radar signal. Ferrazzoli (2001) stated, that at L-band the backscatter behaviour of wheat is strong dependent from the plant density. Regarding the backscattering behaviour of barley and rye at L-band only few investigations were carried out. Ferrazzoli (2001) points out, that due to the similar crop structure the general behaviour of barley signatures at C-band is similar to those observed for wheat. In contrast to wheat, barley and rye have long awns. Moreover, the ear bending is more enhanced. Bouman & Hoekman (1993) found, that lodging of wheat results in an increase in γ -values of about 0 – 3 dB for all incidence angles at L-HH.

One important fact, which must be considered when analysing the backscattering from cereals at L-band, is the strong dependence of the backscatter signal from the row direction (Stiles, 2000). Especially for fields, whose row direction is perpendicular to the flight direction, strong coherence effects have to be

expected. These effects are especially strong for high resolution sensors. In the study site the fields south of the wetland are characterized by the lowest azimuthal look angles ($\sim 21^\circ$), whereby 0° indicates, that the row directions is perpendicular to the flight direction. Thus, no strong coherence effects would be expected.

In the test area following cereals were cultivated: wheat, rye, oat, winter and summer barley. In June, winter barley was yellow, dried out and the ears were bending. The other cereals were green and had already reached their maximum height. In July the winter barley fields were harvested. The soil moisture conditions were similar during all SAR data acquisitions.

The influence of the local incidence angle on the scattering mechanisms of cereals were investigated for wheat, rye and barley. Oat fields could not included in the study, because there were only three oat fields with nearly identical local incidence angles in the whole test site. As already stated, for bare soil and fields covered by low vegetation respectively, an increase in α in range was found. Contrary, the tall green grain in June show a strong decrease in α with increasing local incidence angles (Fig. 3). That means, that in near range volume scattering processes are dominant, whereas in far range surface scattering dominates. The

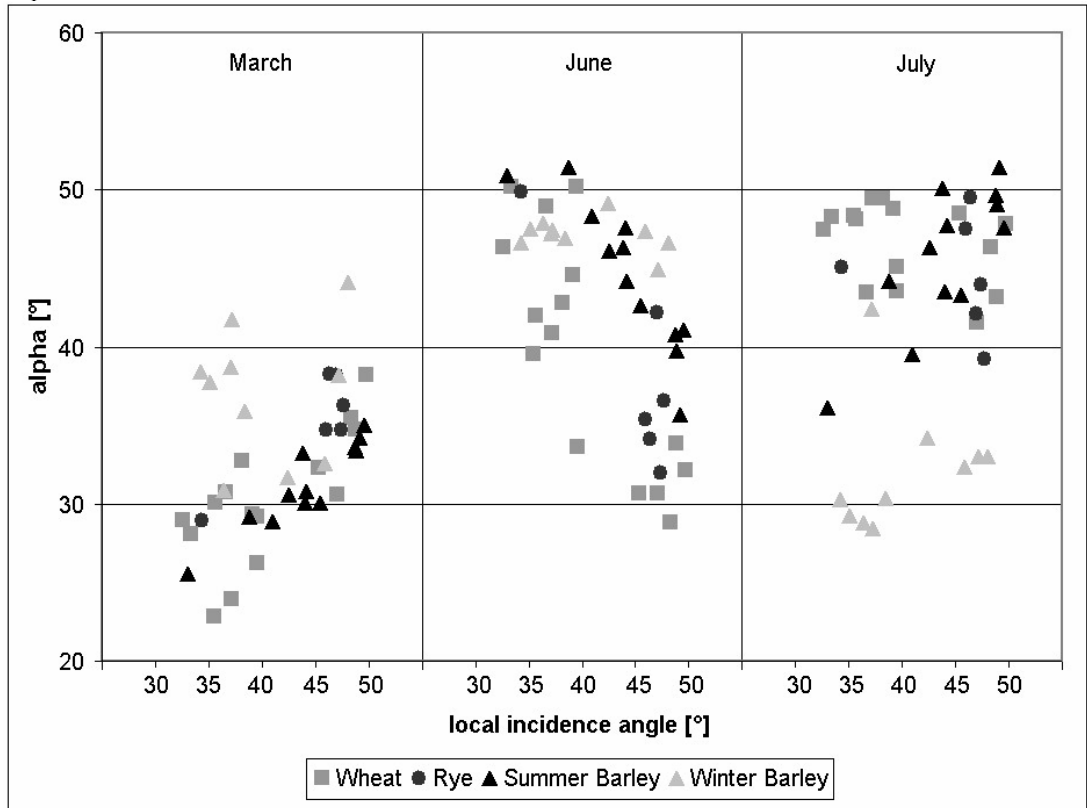


Fig. 3: Dependence of the dominant scattering mechanism of cereals from the local incidence angle

other parameters derived by the eigenvector decomposition show no significant variations for different incidence angles. This is in contrast to the results obtained by the model based decomposition approach, which indicates relative low volume scattering at all incidence angles, except for few summer barley fields in far range. For summer barley dominant double bounce interactions were found for fields with an local incidence angle lower than 45° . For higher incidence angles dominant surface or volume scattering was found. The same tendency was determined for wheat and rye, whereby for wheat double bounce interactions are dominant for local

incidence angles lower than 35° . In far range surface scattering processes strongly dominate the radar response. The analysis of the Pauli decomposition also show increasing surface scattering and decreasing double bounce interactions in range. Altogether, the backscattering behaviour of green, full developed cereals is totally different from those observed for bare fields. This signifies, that the received radar signal is dominated by backscattering from the vegetation. Maybe, the strong surface scattering in far range is due to direct scattering from the ears and stalks.

For ripe cereals, like winter barley fields in June as well as wheat, rye, oat and summer barley in July,

volume scattering processes became dominant for most fields, whereas the total power decreases. This is indicated by the eigenvector and the model-based decomposition theorems. Regarding the dependence from the local incidence angles, the scattering behaviour of ripe cereals is totally different from those observed for green, full developed plants (Fig. 4). Ripe wheat, rye and winter barley show no dependence from the local incidence angle. Summer barley fields even show an increase in α and a decline of the contribution of surface scattering in range. This scattering behaviour in range was found for fields in March and probably indicates the predominance of scattering from ground due to the decrease of the attenuation of the vegetation layer for ripe cereals. An increase in ground scattering is also indicated by the rise of double bounce interactions in far range between June and July.

All together, the polarimetric signatures are quite similar for all cereals. Indeed, the analysis of the eigenvector decomposition indicates, that summer barley in June is characterised by higher α -angles in comparison to wheat, rye and oat (Fig. 4). The model-based decomposition approach shows, that for summer barley fields the proportion of volume scattering processes to the received radar signal is higher and that the surface scattering component is less important. This is in agreement with the analysis of the Pauli decomposition.

6. CONCLUSIONS

The investigations have shown, that the dominant scattering mechanism derived by either the eigenvector or the model based decomposition approach is identical in most cases. Significant differences between both approaches especially were found for green, full developed cereals. The eigenvector decomposition signifies, that α decreases with increasing incidence angles. Thus, the dominant scattering mechanism of cereals changes from volume scattering in near range to surface scattering in far range. The model based decomposition as well as the Pauli decomposition also show an increase of surface scattering processes in range. But in near range double bounce interactions mainly contribute to the radar signal. Their proportion to the total backscatter declines with increasing incidence angles. Volume scattering is always relative low. For broad leaf crops only little seasonal changes in scattering mechanisms were found. They are characterized by dominant volume scattering or double bounce interactions.

With respect to the polarimetric parameter H , which is an indicator of the number of effective scattering mechanisms, the investigations showed great differences between the eigenvector and the model based decomposition approach. For example,

for crops with high H -values such as potatoes, the model-based decomposition indicate the dominance of only one scattering mechanism.

7. ACKNOWLEDGEMENT

The SAR data from March and July were provided by the "Surface Parameter Retrieval Consortium" (SPARC) organised by the QuinetiQ and the DLR. The scenes from June are part of the data base of the TerraDew Project, which is funded by the German Ministry of Education and Research (BMBF, FKZ 50EE0035).

8. REFERENCES

- Baronti, S., Del Frate, F., Ferrazzoli, P., Paloscia, S., Pampaloni, P., and Schiavon, G., 1995, SAR polarimetric features of agricultural areas. *International Journal of Remote Sensing*, **14**, 2639 - 2656.
- Bouman, B. A. M., and Hoekman, D. H., 1993, Multi-temporal, multi-frequency radar measurements of agricultural crops during the Agriscatt-88 campaign in The Netherlands. *International Journal of Remote Sensing*, **8**, 1595 - 1614.
- Brisco, B., and Brown, R. J., 1998, Agricultural applications with radar. In *Manual of Remote Sensing - Principles & Applications of Imaging Radar*, Third Edition, Vol. 2, edited by F. M. Henderson and A. J. Lewis (New York: John Wiley & Sons, Inc.), pp. 381 - 406.
- Brown, S. C. M., Quegan, S., Morrison, K., Bennett, J. C., and Cookmartin, G., 2001, High resolution measurements of scattering in wheat canopies - implications for crop parameter retrieval. Third International Symposium Retrieval of Bio- and Geophysical Parameters from SAR Data for Land Applications held in Sheffield, UK, on 11-14 September 2001, SP-475 (Paris: European Space Agency), pp. 57 - 62.
- Brunfeldt, D.R., and Ulaby, F. T., 1984, The effect of row direction on the microwave emission from vegetation canopies. *Proceedings of IGARSS'84 Symposium held in Strasbourg, France, on 27-30 August 1984*, ESA SP-215, pp. 125 - 129.
- Chiu, T., and Sarabandi, K., 1999, Electromagnetic scattering from short branching vegetation. *IEEE Transactions on Geoscience and Remote Sensing*, **2**, 911 - 925.
- Cloude, S. R., 1992, Uniqueness of target decomposition theorems in radar polarimetry. In *Direct and Inverse Methods in Radar Polarimetry*, Part 1, edited by Boerner, M. (Kluwer Academic Publishers), pp. 267 - 296.
- Cloude, S. R., and Pottier, E., 1996, A review of target decomposition theorems in radar polarimetry.

- IEEE Transactions on Geoscience and Remote Sensing*, **2**, 498- 518.
- De Matthaeis, P., Schiavon, G., and Solimini, D., 1994, Effect of scattering mechanism on polarimetric features of crops and trees. *International Journal of Remote Sensing*, **14**, 2917 – 2930.
- Ferrazzoli, P., and Guerriero, L., 1994, Interpretation and model analysis of MAESTRO 1 Flevoland data. *International Journal of Remote Sensing*, **14**, 2901 – 2915.
- Ferrazzoli, P., 2001, SAR for agriculture: advances, problems and prospects. Proceedings Third International Symposium Retrieval of Bio- and Geophysical Parameters from SAR Data for Land Applications held in Sheffield, UK, on 11-14 September 2001, SP-475 (Paris: European Space Agency), pp. 47-56.
- Hellmann, M., and Krätzschar, E., 1998, Interpretation of SAR-data using polarimetric techniques, Proceedings 2nd International Symposium Retrieval Bio- and Geophysical Parameters from SAR Data for Land Applications, ESTEC, 21. – 23. Oct. 1998.
- McNairn, H., Duguay, C., Brisco, B., and T.J. Pultz, T. J., 2002, The effect of soil and crop residue characteristics on polarimetric radar response. *Remote Sensing of Environment*, **80**, 308 – 320.
- Pottier, E., and Lee, J. S., 1999, Application of the « $H/A/\alpha$ » polarimetric decomposition theorem for unsupervised classification of fully polarimetric SAR data based on the Wishart distribution. CEOS SAR Workshop held in Toulouse, France, on 26-29 October 1999.
- Skriver, H., Svendsen, M. T., and Thomsen, A. G., 1999, Multitemporal C- and L-band polarimetric signatures of crops. *IEEE Transactions on Geoscience and Remote Sensing*, **5**, 2413 – 2429.
- Stiles, J.M., Sarabandi, K., and Ulaby, F. T., 2000, Electromagnetic scattering from grassland – part II : measurement and modelling results. *IEEE Transactions on Geoscience and Remote Sensing*, **1**, 349 – 356.
- Titin-Schnaider, C. 1999, Radar polarimetry for vegetation observation. CEOS SAR Workshop held in Toulouse, France, on 26-29 October 1999.
- Touré, A., Thomson, K. P. B., Edwards, G., Brown, R. J., and Brisco, B. G., 1993, Adaption of the MIMICS backscattering model to the agricultural context – wheat and canola at L and C bands. *IEEE Transactions on Geoscience and Remote Sensing*, **1**, 47 – 61.

Effects of environmental factors on multi-frequency and full-polarization backscatter signatures over paddy field

Yoshio INOUE¹, Takashi KUROSU², Hideo MAENO², Toshiaki KOZU², and Seiho URATSUKA²

¹ National Institute for Agro-Environmental Sciences, Tsukuba, Ibaraki, 305-8604, Japan
Phone: +81-298-38-8220, Fax: +81-298-38-8199, E-mail: yinoue@niaes.affrc.go.jp

² Communications Research Laboratory, Tokyo, Japan

ABSTRACT *The effects of environmental factors such as wind and rain on backscattering coefficients σ_0 in paddy rice were investigated, based on a unique dataset consisting seasonal σ_0 measurements at all combinations of five frequencies (Ka, Ku, X, C, and L), all polarizations (HH, VH, HV, and VV), and four incident angles (25°, 35°, 45°, and 55°). Relationships of σ_0 with NDVI and fAPAR as affected by the environmental factors were also analysed. The daily deviation of σ_0 from the seasonal trend curve suggested that higher frequency (Ka and Ku) bands were sensitive to the environmental conditions, while the lower frequency bands (C and L) were less sensitive. Windy but non-rainy conditions decreased σ_0 over the canopy in most measurement configurations. The effect of wind was larger at higher frequency bands, and small at lower frequencies, presumably because of different sensitivity to canopy geometry. The effect of rain was not clear in our results. Rain, especially with high windspeed, might reduce the σ_0 in higher frequency bands that were more sensitive to geometrical change of rice canopy. Nevertheless, in general, apparent σ_0 measurements by various microwave sensors over rice canopies would include the effects of wind and rain. The Ka, Ku, and X bands had little correlation with both NDVI and fAPAR, while both of them were closely related to σ_0 in C and L bands at smaller incident angles; the VV polarization and larger incident angle was not effective for their estimation. The NDVI was better correlated with C band while fAPAR was with L band. The effect of environmental factors on the estimation of fAPAR from σ_0 at L band was negligible. Backscattering coefficients at C band provides equivalent information as NDVI, and L band is related robustly to fAPAR in the canopy of paddy rice.*

1 INTRODUCTION

Because of the “all-weather” feature, microwave remote sensing has great potential, especially in monsoon Asia, where optical observations are often hampered by cloudy conditions. SAR images are useful for classifying rice paddy fields, because of the unique specular feature of flooded conditions (Kurosui et al., 1997). Le Toan et al. (1997) and Ribbes et al. (1999) clearly showed the potential of ESR-1 SAR backscatter data for rice crop monitoring based on both satellite and ground-based scatterometer measurements. They also suggested further quantitative and complete studies on the interactions between backscatter signatures and rice plant variables, as well as on the effects of weather conditions and cultivation practices since they could affect apparent σ_0 measurements acquired by various sensors.

Inoue et al. (2002) obtained season-long daily measurements of backscatter signatures in Ka, Ku, X, C and L bands over a paddy field using a multi-frequency and full-polarization scatterometer. They showed intimate interactions between backscattering

coefficients and rice canopy variables such as biomass, leaf area index (LAI), stem density, canopy height and so forth. For example, LAI, fresh biomass, and head weight were well correlated with the backscattering coefficients in C, L, and Ku bands, respectively. These results would provide useful information for wide-area monitoring of rice growth using space-borne SAR data in monsoon Asia. In their analyses, they assumed stable relationships between backscattering coefficients and biological canopy variables, because plant variables such as biomass, leaf area index (LAI) and water content could never change rapidly or drastically at diurnal or daily duration. That is, backscattering coefficients derived from the smoothed trends were used as representative values for each day. However, the day-to-day fluctuations in backscattering coefficients, i.e., deviations from the smoothed line, cannot be negligible, but rather large in some conditions. In irrigated paddies, soil moisture and surface roughness are rather consistent, but environmental factors such as wind and rain can be changing in a dynamic manner. They can affect dielectric constant and geometry of the canopy, that is, canopy backscattering coefficients. However, a few experimental observations have been

reported concerning the effects of dew, rain and wind (Sofko et al., 1989; Gillespie et al., 1990; Brisco et al., 1998, Wood et al., 2002). They commonly suggest that rain and dew will increase backscattering coefficients, and such effects will impact on a number of applications to variable degree depending on vegetation conditions.

Thus, it may be useful to investigate the effects of wind and rain on the backscattering coefficients of the rice canopy based on the season-long measurements of multi-frequency backscattering coefficients, plant variables and micrometeorological data. The fAPAR (fraction of absorbed photosynthetically active radiation) is often related to optical reflectance such as vegetation indices (e.g., Asrar et al., 1989; Baret et al., 1991); however, it would be rather useful if the microwave backscattering coefficient provide equivalent information on fAPAR as vegetation indices. Thus, a comparative study was also conducted using optical and microwave measurements to investigate the relationship between backscattering coefficient and fAPAR and vegetation index as affected by environmental factors.

2 MATERIALS AND METHODS

A multi-frequency polarimetric scatterometer (developed by Communications Research Laboratory, Japan; Kozu et al., 1997) was used for the experiment. The system was equipped with Ka (35.25 GHz), Ku (15.95 GHz), X (9.6 GHz), C (5.75 GHz), and L (1.26 GHz) bands, and with all combinations of horizontal (H) and vertical (V) polarization (HH, HV, VV and VH). The incident and azimuth angles were changeable between 20° and 60°, and -60° and +60°, respectively. The system consists of antennas (horn ones for Ka and Ku; parabolic ones for X, C and L bands), RF front-end, network-analyser, and personal computer. Time-domain function of the network-analyser was adopted for measuring the range-gated target. Switching of frequency bands, polarization of antennas, setting of incident angle and azimuthal scan, signal-control of the network-analyser, and data storage can be controlled automatically by the computer; the system is programmable so that backscatter data could be taken at any combination of frequency, polarization, and incident and azimuth angles. The level of white noise was -95, -95, 105, -110, and -95 dB for Ka, Ku, X, C, and L band, respectively. The system obtained nine independent signals for each combination of frequency, polarization, and incident and azimuth angles, among which the maximum signal was used for processing. The antennas were mounted on an extension boom, and their height was adjustable up to five meters.

The system was installed at the side of an experimental paddy field at the National Institute for Agro-Environmental Sciences (Tsukuba, Japan; 36.0° North, 140.1° East, 25 m above sea level) before the growing season in 1999. For this particular experiment, incident angles were set to 25°, 35°, 45°, and 55°, and azimuth angles to -28°, -14°, 0°, 14°, and 28°. We collected backscatter data at all combinations of the five frequency bands, four polarizations, four incident angles, and five azimuth angles over the paddy field once each day. It took about seven hours (from 11:00 to 18:00 LST) to take the entire daily set of measurements. This time window was chosen to avoid the effect of morning dew, which disappeared by 10:00 at the latest. The power data were converted to σ_0 signatures (dB) using the calibration data. The antennas were 5 m high, while the maximum canopy height was about 0.8 m.

The experiment lasted for about five months; starting before transplantation of the rice seedlings, when the paddy was flooded, and ending after harvest of the mature rice crop. As is normal for rice cultivation in Japan, the paddy field was first flooded, and transplanted with rice seedlings (*Oryza sativa* L. *japonica*, Variety: Nipponbare) about 15 cm long. Sets of three seedlings were planted at 30 x 14 cm spacing, i.e., the average planting density was 23.8 hills m⁻². Biophysical and agronomic data for the rice canopy, such as LAI, wet and dry biomass, stem density, and canopy height were taken once every week by destructive sampling. Soil moisture and weather conditions were recorded every 15 minutes with an automated MAPS weather station. The soil moisture content was consistent (75 ± 3 %) since the paddy field was waterlogged during the entire growing season except a drainage period. Optical measurements, such as the hyperspectral reflectance between 380 and 2500 nm using FSFR1000 (ASD Inc.), directional extinction coefficients with the LAI2000 system (Li-Cor Inc.), and the fAPAR (fraction of absorbed photosynthetically active radiation) for the canopy, were also measured throughout the season.

3 RESULTS AND DISCUSSION

A season-long data set of backscattering signature, plant and micrometeorological measurements was obtained (Inoue et al., 2002). Figure 1 shows the seasonal change in plant variables for the rice canopy. Stem density and LAI reached their maximum values at DOY221 and DOY232, respectively. The average heading date when 50% of the heads were totally emerged from their leaf sheath was at DOY239. Since the coefficient of plant-to-plant variation in each plant variables was less than 5 %, and all plant variables changed in a very smooth manner, we applied spline fitting to estimate the their values on each date of

backscattering data acquisition. It may be reasonable to assume that all plant variables changed in very smooth manner during the entire period. Adverse weather conditions, such as typhoons and thunderstorms, occurred several times during the season, but the rice canopy suffered no serious damage, except for provisional changes in geometry.

The scatterometer system was suspended for a few days during typhoons and heavy rainstorms. A daily set of measurements took seven hours, but diurnal change in plant variables was presumed to be negligible since the paddy rice has no geometrical leaf adjustment and little change in plant water content during each daily cycle. The dynamic changes in wind and rain were recorded every 15 min. For the present analysis, measurements in five azimuth directions were averaged to obtain representative values of backscattering coefficients for the canopy. Since the correlation between the HV and VH coefficients was high along the one-to-one line for all frequencies and incident angles, data from both cross-polarizations were averaged for each set of measurements.

We excluded data on several days when the study area was obviously disturbed by management practices, such as transplanting, fertilizing, harvesting, and cultivating. After excluding such data, the remaining data were smoothed using spline fitting to estimate the seasonal change in the canopy backscattering coefficient without environmental disturbance.

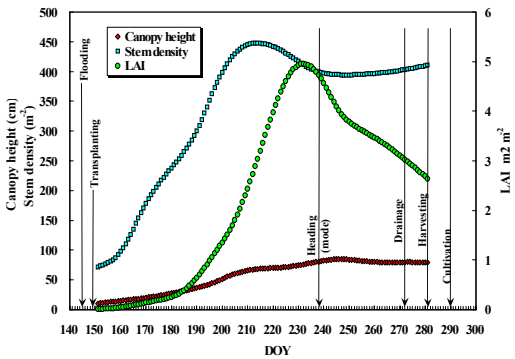
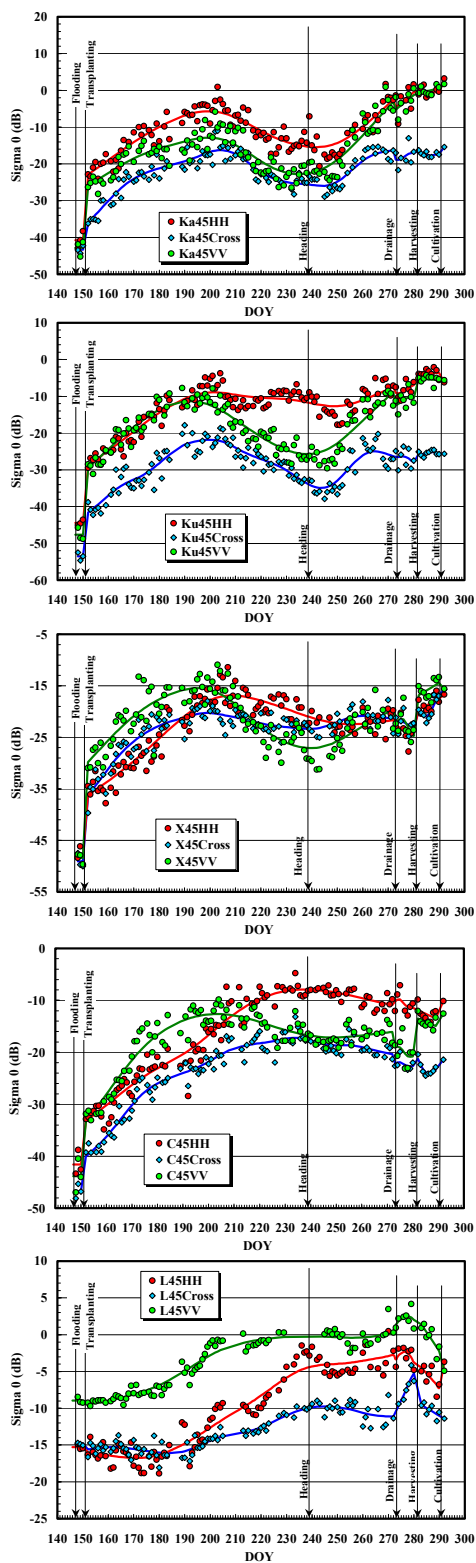


Fig. 1. Seasonal change of plant variables determined by destructive sampling. Daily data were derived by the smoothing-spline method, using weekly sampling data that changed in a smooth manner for the entire season.

Fig. 2. Time course change of microwave backscattering coefficients at Ka, Ku, X, C, and L bands. Data shown are only for the incident angle of 45°.



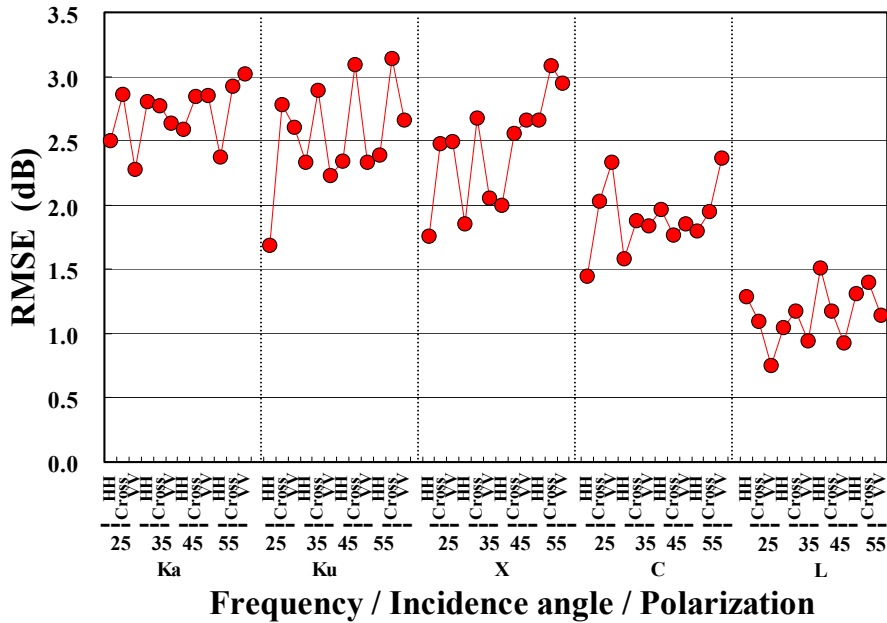


Fig. 3. Day-to-day fluctuation of backscattering coefficients represented by the root mean square error (RMSE) for smoothing spline curves. The RMSE was calculated for the data during DOY 152-280.

A part of seasonal data is presented in Figure 2. The day-to-day fluctuation in the original values of σ_0 was assumed to be caused by environmental factors such as wind and rain. The daily deviation from the smoothed seasonal curve will be related systematically to wind and rain events, although they include some electric noise inherent to the system. Figure 3 shows the summary of daily deviations in backscattering coefficients under all configurations. The RMSE may represent the sensitivity of backscattering coefficient to wind and rain conditions. The averaged values of RMSE are 2.7 dB for Ka, 2.5 dB for Ku, 2.4 dB for X, 1.9 dB for C, and 1.4 dB for L band. The higher frequency (Ka and Ku) bands may be sensitive to the environmental conditions, while the lower frequency bands (C and L) may be less sensitive.

3.1 Effect of wind on backscattering coefficients

In order to infer the effect of windspeed only, we first eliminated data on all rainy days, and then selected several sets of consecutive dates with different windspeed. We assumed all the other conditions including plant variables were same in each set of two consecutive dates. Consequently,

seven pares of such consecutive dates with different windspeed were selected for the entire period; each pare contains backscattering measurements under windy and less windy conditions. The average windspeed for the period of measurements (11:00–18:00 LST), and the differential of backscattering coefficients at high and low windspeed conditions were calculated for comparison.

Figure 4 shows the summary of such data set in the axis of LAI. The Y-axis indicates the differential backscattering coefficient $\Delta\sigma_0$ ($= \sigma_{0_{\text{windy condition}}} - \sigma_{0_{\text{less windy condition}}}$). It is obvious that the $\Delta\sigma_0$ is negative in all cases except for the dates when the windspeed differential was small. The decrease in $\Delta\sigma_0$ ranged from zero to several dB. Another trend is that the $\Delta\sigma_0$ is small in lower frequencies, especially in L band. In general, the wind may reduce the surface roughness of rice canopy, and may reduce backscattering coefficient over the canopy, although the degree of decrease depends on LAI and windspeed. The effect of wind may be larger at higher frequency bands, while it may be negligible at L band.

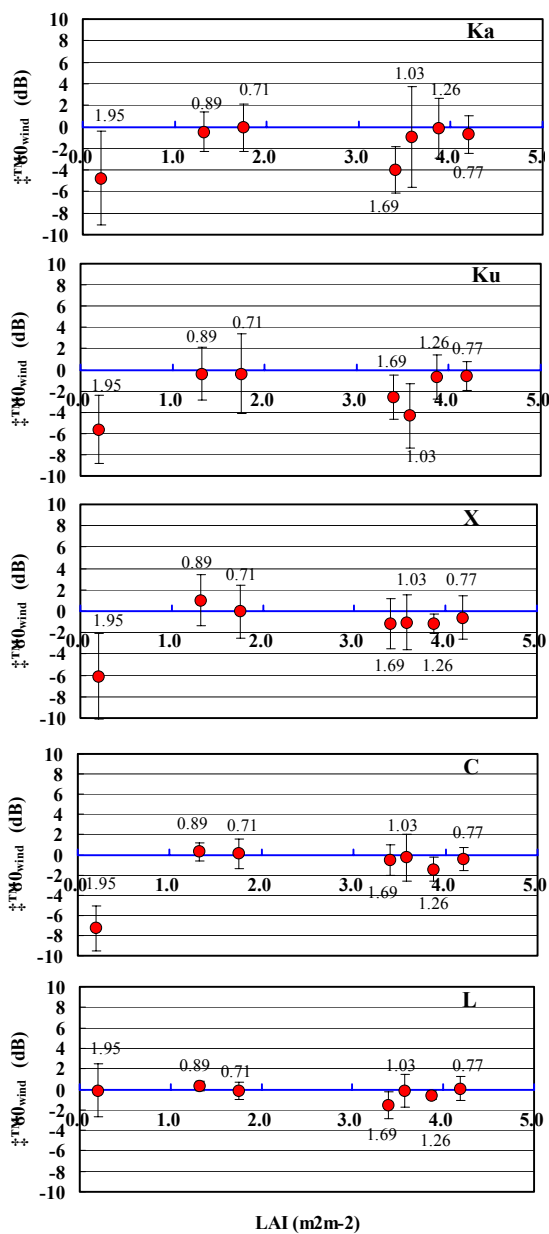


Fig. 4. Effect of wind on backscattering coefficient in Ka, Ku, X, C, and L bands at various leaf area index. The y-axis ($\Delta\sigma_{0_wind}$) indicates the difference in backscattering coefficients under windy and less windy conditions. The values at error bars indicate differences in windspeed during the time of measurements, respectively.

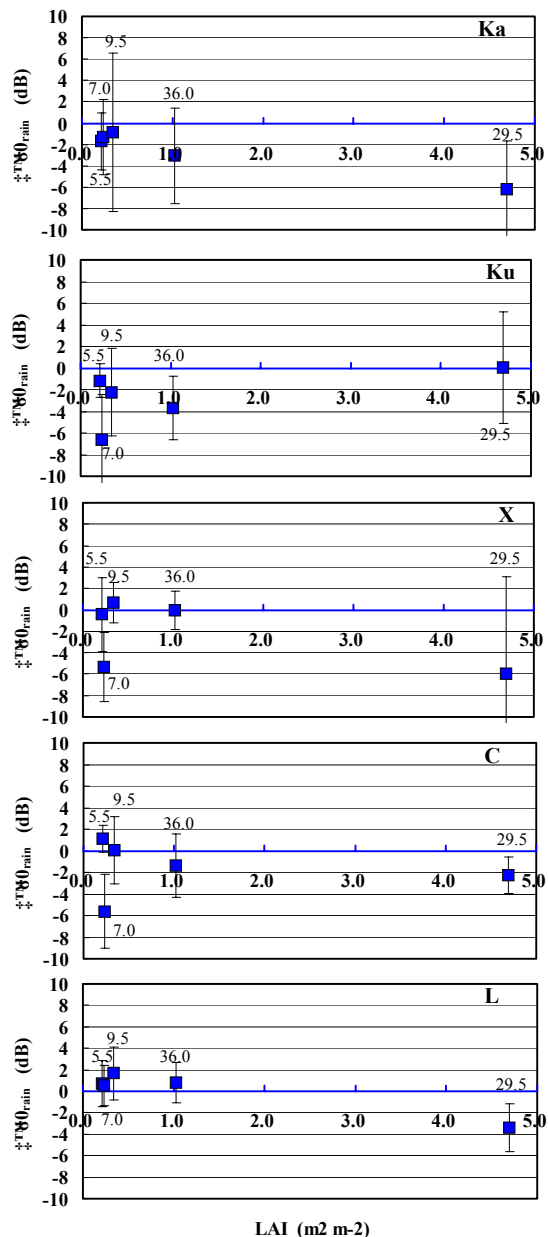


Fig. 5. Effect of rainfall on backscattering coefficient in Ka, Ku, X, C, and L bands at various leaf area index. The y-axis ($\Delta\sigma_{0_rain}$) indicates the difference in backscattering coefficients with and without rainfall. The values near error bars indicate the rainfall (mm) during the time of measurements, respectively. The windspeed differential during the measurements was -0.5, 1.3, 1.5, -1.2, and 1.0 m s⁻¹ from left to right, respectively.

The effect of wind only on the backscattering coefficient may have to be interpreted via the effect on canopy geometry. The geometry of rice canopy may have little effect on backscattering of L band.

3.2 Effect of rain on backscattering coefficients

A pair of consecutive dates with and without rainfall were selected for the entire period. Only five pairs were selected because the “rainy” condition was limited to such that it was continuously rainy during the period of measurements i.e., 11:00-18:00 LST. Since rain was often accompanied with wind, windy condition was also included in the data sets. The amount of rain during the period of measurements (11:00-18:00 LST), and the differential of backscattering coefficient under rainy condition from that under non-rainy condition were calculated for comparison.

Figure 5 shows the summary of such data set in the axis of LAI. The y-axis indicates the differential backscattering coefficient $\Delta\sigma_{0\text{rain}}$ ($= \sigma_{0\text{rainy condition}} - \sigma_{0\text{non-rainy condition}}$). The $\Delta\sigma_0$ is negative in most configurations in Ka and Ku bands while positive in several configurations in C and L bands. In general, the effect of wetness over the plant surface may be positive due to the change in dielectric constant. There are several reports that dew or artificial spraying increased the backscattering coefficients canopies by 2-4 dB (Sofko et al., 1989; Gillespie et al., 1990; Wood et al., 2002). Nevertheless, such increase was not clear in our results, but rather negative in many configurations.

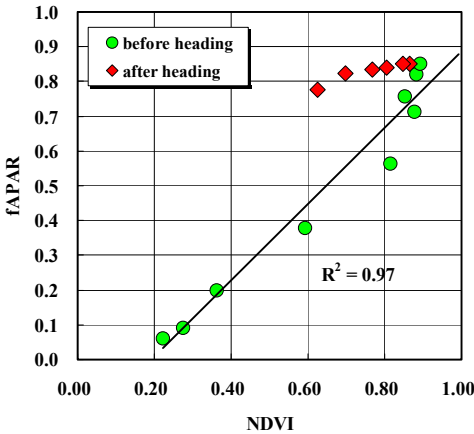


Fig. 6. Relationship between fAPAR of the rice canopy and vegetation indices NDVI for the entire growth period.

Hence, although the effect of wetness alone may increase the backscattering coefficient via the change in dielectric constant of the canopy, heavy rain or rain with wind may have different effects on backscattering coefficient via geometrical changes in a rice canopy. Rain, especially with high windspeed, may reduce the backscattering coefficient in higher frequency bands such as Ka and Ku that are more sensitive to geometrical change on rice canopy. Such dynamic changes in the canopy geometry also have spatial variations due to spatial variations of wind and rain. In case of SAR measurement, such variations may be masked by the averaging effect. In any case, results suggest that some bias may be included in apparent σ_0 measurements by various sensors.

3.3 Relationship of microwave backscattering coefficients with NDVI and fAPAR.

The fAPAR is an important canopy parameter for estimation of plant productivity, and is often used in growth models (Inoue et al., 1998). It is well known that fAPAR is closely related to spectral vegetation indices such as NDVI (e.g., Asrar et al., 1989; Baret et al., 1991; Leblon et al., 1991). Figure 6 shows the relationship between fAPAR and NDVI for the rice canopy. The reflectance values at red (655-665 nm) and near infrared (830-850 nm) wavelengths were extracted from the hyperspectra. The NDVI is closely related with fAPAR except the period after heading. It is also well-known that the fAPAR-NDVI relationship greatly change after heading for several crops (Asrar et al., 1989; Inoue et al., 1997). Since the conventional method to measure fAPAR is based on radiation budget for a canopy, the fAPAR include the radiation absorbed by non-photosynthetic part of the canopy that is not negligible especially in the period after heading, i.e., senescence phase. Thus, fAPAR-NDVI relationship for vegetative period may be applied to the senescence period to estimate realistic fraction of PAR absorbed by green leaves. Otherwise, growth models have to use very low value of radiation use efficiency (RUE) just after the time of heading.

Since the availability of optical data is limited, it will be useful for such applications if microwave backscattering is effectively related to fAPAR.

The correlation of backscattering coefficients with NDVI and fAPAR is summarised in Figure 7. The higher frequency bands, Ka, Ku, and X have little correlation with both NDVI and fAPAR.

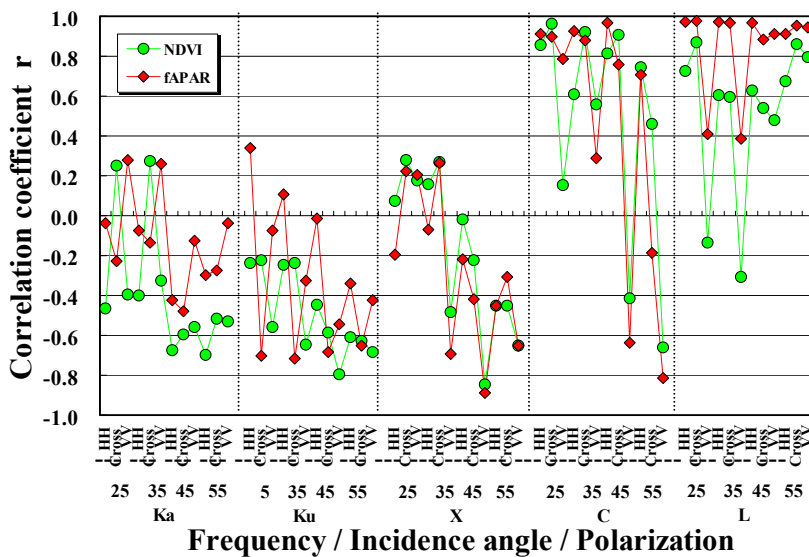


Fig. 7. Relationship of backscattering coefficients with NDVI and fAPAR. This calculation is based on the data during DOY152-280.

Contrarily, both NDVI and fAPAR are closely related to the C band backscattering coefficients at smaller incident angles ($r=0.90-0.96$); the VV polarization and larger incident angle are less well correlated. The fAPAR is best correlated with L band coefficient at almost all configurations except VV polarization ($r=0.95-0.98$), while NDVI is not the case. In general, NDVI is better correlated with C band while fAPAR is with L band. It is also obvious that the VV polarization is less sensitive to both fAPAR and NDVI in most configurations. This may be attributed

to the structure of the rice canopy that consists of thin vertical stems and leaf blades. The relationships between NDVI and backscattering coefficient at C25Cross, and between fAPAR and backscattering coefficient at L25HH are shown in Figures 8 and 9, respectively. The C25Cross is linearly related to NDVI, that is, the relation between L25Cross and NDVI, that is, the relation between L25Cross and fAPAR is similar for NDVI as in Figure 6. The C25Cross may provide the equivalent information on the canopy as NDVI. The backscattering coefficient at L25HH shows quasi-linear relationship with fAPAR.

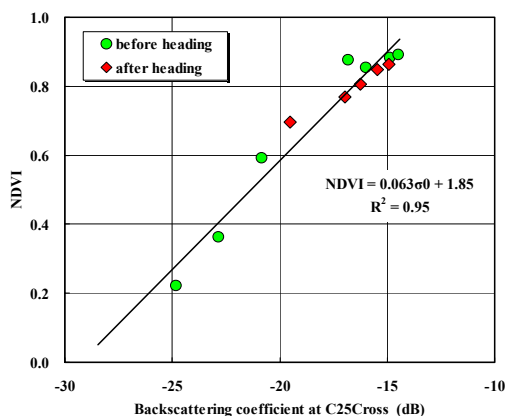


Fig. 8. Relationship between backscattering coefficients at C25Cross and NDVI for the rice canopy.

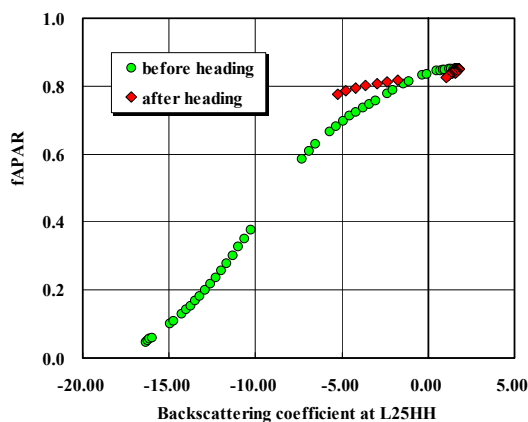


Fig. 9. Relationship between backscattering coefficients at L25HH and fAPAR for the rice canopy.

Their relationship change before and after heading, which is similar to that in the NDVI-fAPAR relationship in Figure 6. In rice canopy, backscattering coefficient at C band is closely related with LAI, while L band is more closely related to above-ground phytomass (Inoue et al., 2002). Since the fAPAR is estimated by PAR budget of the canopy, it is affected more by above-ground phytomass than LAI. Therefore, fAPAR may be better estimated by backscattering coefficient at L band than C band; NDVI is more closely related with C band. Thus, as far as the conventional estimates of fAPAR is concerned, backscattering coefficient in L band may provide better results than NDVI or C band. In principle, the fraction of PAR that is absorbed by photosynthetic part of plant canopy should be better related with optical measurements, since microwave backscattering is not related with greenness but only with the amount and structure of scattering elements in the canopy. Nevertheless, this close relationship would be useful enough to estimate the parameter.

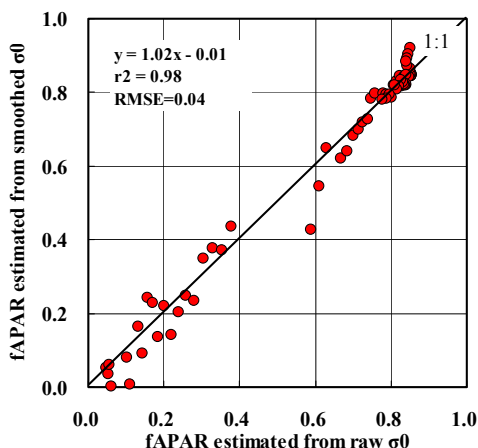


Fig. 10. The effect of environmental factors on fAPAR estimation from backscattering coefficients at L25HH. The fAPAR estimates from the smoothed σ_0 and raw σ_0 using the same regression equation are compared.

The effect of environmental factors on the estimation of fAPAR from backscattering coefficient at L25HH is shown in Figure 10. The relationship between values of fAPAR estimated from smoothed line and from raw measurements is close to 1:1 line with high correlation coefficients. The scattering includes both the day-to-day changes due to environmental factors, and system errors, but they both seem negligible in the estimation fAPAR. This result agrees well with those in Figures 3, 4 and 5. The backscattering coefficient at L band may be robustly related to fAPAR of rice canopy.

4 CONCLUSIONS

The unique data set consisting season long daily measurements of microwave backscattering, micrometeorological and plant data allowed the simple analysis on the effects of environmental factors on backscattering coefficient of a rice canopy.

It may be reasonable to assume that the day-to-day fluctuation in the original values of σ_0 is caused by environmental factors such as wind and rain since plant variables such as biomass, LAI, stem density, water content and so forth change very smoothly. The degree of daily deviation from the smoothed seasonal curve suggests that higher frequency (Ka and Ku) bands are sensitive to the environmental conditions, while the lower frequency bands (C and L) are less sensitive.

Windy but non-rainy conditions may decrease backscattering coefficient over the canopy in most measurement configurations, although the degree of decrease depends on LAI and windspeed. This effect may be attributed to the change in surface roughness caused by wind. The effect of wind may be larger at higher frequency bands, while it may be small at L band; the geometry of rice canopy may have little effect on backscattering of L band.

In spite of previous reports that dew or artificial wetness may increase the backscattering coefficient from crop canopies, such increase was not clear in our results, but rather negative under many measurement configurations. Rain, especially with high windspeed, may reduce the backscattering coefficient in higher frequency bands such as Ka and Ku that are more sensitive to geometrical change in the rice canopy. Heavy rain or rain with wind may have different effects on backscattering coefficient via geometrical changes in a rice canopy. In general, apparent σ_0 measurements by various microwave sensors over rice canopies would include the effects of wind and rain.

The higher frequency bands, Ka, Ku, and X have little correlation with both NDVI and fAPAR, while both of them are closely related to the C band backscattering coefficients at smaller incident angles. The VV polarization and larger incident angle may not be effective for their estimation. The NDVI is better correlated with C band while fAPAR is with L band. The C25Cross is linearly related to NDVI, thus may provide the equivalent information on the canopy as NDVI. The backscattering coefficient at L25HH shows quasi-linear relationship with fAPAR. Since fAPAR is estimated by PAR budget of the canopy,

backscattering coefficient in L band may provide better results than NDVI. The effect of environmental factors on the estimation of fAPAR from backscattering coefficient at L25HH may be negligible. Results suggest that backscattering coefficients at C and L bands can be used efficiently in growth models for paddy rice (Leblon et al., 1991; Inoue et al., 1998).

5 REFERENCES

- Asrar, G., Myneni, R.B. & Kanemasu, E.T. 1989. Estimation of plant-canopy attributes from spectral reflectance measurements. In G. Asrar ed., *Theory and Application of Optical Remote Sensing*. Wiley Interscience, New York. 252-296.
- Baret F. & Guyot G. 1991. Potentials and limitations of vegetation indices for LAI and APAR assessment. *Remote Sensing of Environment* 35: 161-173.
- Brisco, B. & Brown, R. J. (1998). Agricultural applications with radar. In: F. M. Henderson, & A. J. Lewis (Eds), *Principles and Applications in Imaging Radar* (pp. 381-406). New York: John Wiley & Sons, Inc.
- Gillespie, T. J., Brisco, B., Brown, R. J., & Sofko, G. J. (1990). Radar detection of a dew event in wheat. *Remote Sensing of Environment*, 33: 151-156.
- Inoue, Y., Moran, M. S., & Horie, T. (1998). Analysis of spectral measurements in Rice paddies for predicting rice growth and yield based on a simple crop simulation model. *Plant Production Science* 1: 269-279.
- Inoue, Y., Kurosu, K., Maeno, H., Uratsuka, S., Kozu, T., Dabrowska-Zielinska, K., & Qi, J. (2002). Season-long daily measurements of multi-frequency (Ka, Ku, X, C, and L) and full-polarization backscatter signatures over paddy-rice field and their relationship with biological variables. *Remote Sensing of Environment* 81: 194-204.
- Kurosu, T., Fujita, M., & Chiba, K. (1997). The identification of rice fields using multi-temporal ERS-1 C band SAR data. *International Journal of Remote Sensing* 18: 2953-2965.
- Le Toan, T., Ribbes, F., Wang, L., Floury, Ding, N. K., Kong, J. A., Fujita, M., & Kurosu, T. (1997). Rice crop mapping and monitoring using ERS-1 data based on experiment and modeling results. *IEEE Transactions on Geoscience and Remote Sensing* 35: 41-56.
- Leblon B., Guerif M. & Baret F. 1991. The use of remotely sensed data in estimation of PAR used efficiency and biomass production of flooded rice. *Remote Sensing of Environment* 38: 147-158.
- Ribbes, F., & Le Toan, T. (1999). Rice field mapping and monitoring with RADARSAT data. *International Journal of Remote Sensing* 20: 745-765.
- Sofko, G. J., Sloboshan, J., McKibben, M., Koehler, J., & Brisco, B. (1989). Variation of microwave radar cross-section of wheat during the early hours of a rainfall. In: IGARSS '89/12th Canadian symposium on remote sensing, Vancouver, BC (pp. 1191-1194). Canadian Remote Sensing Society.
- Wood, D., McNairn, H., Brown, R.J., & Dixon, R. (2001). The effect of dew on the use of RADARSAT-1 for crop monitoring - Choosing between ascending and descending orbits. *Remote Sensing of Environment* 80: 241-247.

Regional mapping of sahelian herbaceous production from a combined use of ERS Scatterometer data and a water balance model with an evolution strategies algorithm

Jarlan L.¹, Mazzega P.², Mougin E.¹, Duchemin B.¹, Tracol Y.¹, Frison P.L.³, Schoenauer M.⁴, Hiernaux P.⁵

¹ Centre d'Etudes Spatiales de la Biosphère

CNES / CNRS / UPS

18 avenue Edouard Belin

31401 Toulouse Cedex 4 - France

Fax : (33) 5.61.55.85.00 e-mail : jarlan@cesbio.cnes.fr

² Laboratoire d'Etude en Géophysique et en Océanographie Spatiales

18 avenue Edouard Belin

31401 Toulouse Cedex 4 - France

e-mail : ciamp@boreal-ci.cst.cnes.fr

³ Université de Marne la Vallée

Laboratoire des géomatériaux - IFG

5, boulevard Descartes

77454 Marne la Vallée Cedex 2

e-mail : frison@univ-mlv.fr

⁴ Projet FRACTALES - I.N.R.I.A. Rocquencourt

B.P. 105 - 78153 LE CHESNAY Cedex - France

e-mail : Marc.Schoenauer@inria.fr

⁵ International Livestock Research Institute

Centre Sahélien de l'ICRISAT, NIAMEY NIGER

e-mail : P.Hiernaux@cgnet.com

ABSTRACT - *Although originally designed to measure wind characteristics over the ocean, ERS wind scatterometers instruments have shown great potentials to monitor terrestrial vegetation. Over semi-arid areas, the measured backscattering coefficient shows a marked seasonality linked to the drastic changes of both soil and vegetation dielectric properties associated to the alternating dry and wet seasons. This study presents results of the combined use of a simple water balance model, a backscattering model and remote sensing data to produce map of herbaceous mass at a regional scale. For lack of direct observations of soil moisture, METEOSAT rainfall estimates (produced for the Family Early Warning System) are used to calculate temporal series of water content of the upper soil profile with the help of the water balance model. This a priori information is used as input of the backscattering model. Afterwards, an inversion algorithm is applied to retrieve vegetation characteristics from the ERS windscatterometer (WSC) data. Because of the non linear feature of the inverse problem at hand, the inversion is performed using a global stochastic non-linear inversion method (an evolutionary strategy algorithm). Thanks to ground measurements of herbaceous mass performed in the Malian Gourma, the retrieved values of herbaceous mass are compared to this ground data set over several sites covering the rainfall gradient of the African Sahel. The algorithm is then applied to a regional area located in the Gourma and Seno regions (700*500 km²). The obtained herbaceous maps show a general consistency with the vegetation index NDVI acquired in the optical domain by the VEGETATION instrument.*

1 INTRODUCTION

Since the nowadays famous drought of 1972-74 and 1983-85, the African Sahel is often pointed out as one of the most affected region by desertification process (GIEC, 2001). This drought is one

manifestation of the west african climate variability extending over many temporal and spatial scales. Many theoretical and empirical studies have recently shown that surface conditions have a strong impact in rainfall variability. Since the launch of the Wind Scatterometer instrument on board ERS-1 satellite

(ERS WSC) in 1991, many studies have underlined the potentiality of low resolution radar data (>25 km) to monitor surface biophysical characteristics over Sahel through the inversion of a theoretical radiative transfer model. Nevertheless, both soil (through its water content and roughness) and vegetation (through its water content and “density”) contribute to the backscattering response of a sahelian landscape. Within this frame, the work of Jarlan et al. (2002b) shows that the simultaneous retrieval of soil water content (SWC) and vegetation biomass (B_m) with the sole WSC data set is untractable for lack of sufficient constraint brought by the data on the radiative model.

This study presents results of the combined use of WSC data, METEOSAT rainfall estimates, a radiative transfer model and a simple water balance model to produce maps of herbaceous mass at a regional scale. For lack of a direct observation of soil water content, METEOSAT rainfall estimates are used to force a simple water balance model. This a priori calculated SWC is used as input of the radiative model. An inversion procedure is then applied to retrieve vegetation characteristics from the WSC data set. The minimisation of the resulting cost function is performed using an evolution strategies algorithm. The stochastic feature of this optimisation method allows to recover the time evolving distribution of admissible solutions from which an error bar is calculated. Retrieved solutions are then compared to ground measurements performed over four sites in the Malian Gourma during years 1999 and 2000. Finally, maps of herbaceous production over a 700*500 km² area are computed and compared to sum of NDVI images of the same region, a nowadays well known method to estimate production of the sahelian ecosystem.

The paper is organised as follows. In the second part, data and models are briefly presented. In the third part, the algorithm implementation is described. In the fourth part, results are discussed. Finally, conclusions and perspectives are drawn.

2 DATA AND MODELS

2.1 Data

ERS WSC data

ERS WSC operates at C-band (5.3 GHz) with VV polarization. The actual resolution is about 50 km, with an estimated radiometric accuracy of about 0.55 dB. Across the swath, local incidence angles range from 18° to 59°. Radar responses observed at large incidence are expected to be related to the vegetation cover. Accordingly, in the following sections, only measurements acquired between 40° and 55° of

incidence angles are taken into account and linearly normalised at 45°. Over the study period, the average number of $\sigma^0(45)$ measurements is around 1.8 / decade (10 days period).

METEOSAT rainfall estimates

The rainfall algorithm uses an empirical relationship between the occurrence duration of cold cloud tops over a region and the global telecommunication system (GTS) observational data (Arkin and Meisner, 1987). The resulting estimated rainfall, expressed in mm of water by decade, is distributed by the Family Early Warning System (<http://www.edcintl.cr.usgs.gov/adds/adds.html>) with a 8 km resolution. Because of the convective nature of most of sahelian rainfall events, the confrontation between low spatial resolution METEOSAT products and local rain gauge measurements is difficult in practice and precludes from a precise assessment of METEOSAT rainfall estimates accuracy. The spatial resolution is downgraded to the scatterometer pixel dimension (0.25°*0.25° \approx 3*3 pixels) by averaging rainfall amount by decade.

The study region

The study transect is located in the Malian Gourma and Seno region which is a sahelian pastoral zone with low cultivated surfaces. It extends from 6°W and 1°E in longitude and from 13.5°N and 18.5°N in latitude. Our validation sites consist of four windows of 25 km side, one in the saharo-sahelian zone named *Rharous*, and located at a latitude of about 16.5°N, two in the sahelian zone proper named *Gossi* and *Hombori* located at 16°N and 15.3°N respectively, and one in the sudano-sahelian zone named *Seno* at about 14.6°N. Within each window, several measurements of herbaceous mass are performed on sample areas of 1 km² (Hiernaux and Justice, 1986) and averaged together to get a representative value at the scale of a validation site. Because of an apparent stochastic heterogeneity of the sahelian landscape, errors on measurements at this large scale are difficult to estimate. In this study, relative error is taken to be around 30%.

2.2 Models

The radiative transfer model (RBM)

The radiative backscattering model simulates the interaction between the electromagnetic wave and the surface components (soil and vegetation) and relies on the backscattering coefficient acquired by the WSC instrument to the surface variables of interest. This backscattering model estimates the backscattering coefficient of the illuminated ground surface, given three input parameters, namely the herbaceous mass

B_m , the vegetation water content VWC and the soil moisture H_v . For a given incidence, the estimated backscattering coefficient of the illuminated scene, $\hat{\sigma}_{scene}^0$, is written as a weighted sum of contributions from the soil, σ_{soil}^0 , and vegetation, $\sigma_{vegetation}^0$:

$$\hat{\sigma}_{scene}^0(B_m, VWC, H_v) = [1 - v_c(B_m)[1 - L^2(B_m, VWC)]] \sigma_{soil}^0(H_v) + v_c(B_m) \sigma_{vegetation}^0(B_m, VWC) \quad (1)$$

The soil contribution, σ_{soil}^0 , only depends on the soil humidity H_v through its dielectric constant. The surface roughness is assumed to be constant. The vegetation term, $\sigma_{vegetation}^0$, as well as canopy transmission factor L depend on the above-ground herbaceous mass B_m and the vegetation water content H_p . The cover fraction v_c is related to B_m through an empirical relationship. Accordingly, the predicted backscattering coefficient, $\hat{\sigma}_{scene}^0$, depends only on the instantaneous biomass B_m , vegetation water content VWC and soil humidity H_v (see Frison et al., 1998 and Jarlan et al., 2002a for details).

The water balance model

The water balance model is a simple water bucket with four layers. In this study, we are only interested in the water content of the upper soil profile (2 cm depth). The soil hydrodynamical characteristics are measured

3 INVERSION ALGORITHM IMPLEMENTATION

The overall approach is summarised in figure 1.

The time series of soil water content are calculated a priori from the METEOSAT rainfall estimates and the water balance model. This information is used as input of the backscattering model. Then an evolutionary algorithm is used to minimise a cost function measuring the distance between predicted and measured backscattering coefficient during the vegetation growth period. Every solution satisfying the admissibility criterion are kept.

3.1 Computing the SWC time series

Because of a high global ray and a low field capacity of sahelian sandy soils, the decadal information provided by the METEOSAT rainfall estimates is not sufficient to allow a realistic description of the SWC temporal evolution. Accordingly, a semi-stochastic method is used to transform the decadal rainfall estimates in daily events. This daily information is used as input of the water balance model and a temporal averaging process over a 14-day window is applied to the water balance model outputs in order to fit the WSC data.

3.2 The cost function

The retrieval of surface parameters from remote sensing observations is generally solved by an optimisation process searching for those variables of the radiative model that better “explain” the satellite data time series. The distance between the n sensor observations at time t_i $\sigma^0(t_i)$ and the corresponding

model prediction $\hat{\sigma}_{scene}^0[B_m^i, VWC^i]$ is estimated using the following cost function :

$$J[B_m, VWC] = \left[\frac{1}{2} \cdot \sum_{i=1}^n \left\| \hat{\sigma}_{scene}^0[B_m^i, VWC^i] - \sigma^0(t_i) \right\|^2 \right]^{\frac{1}{2}}$$

where B_m and VWC represents the n -vector of herbaceous mass values and vegetation water content values describing their seasonal evolutions. As such

$[B_m, VWC]$ belongs to the parameter space $X \subset \mathfrak{R}^{2n}$.

$\hat{\sigma}_{scene}^0(B_m^i, VWC^i)$ depends on herbaceous mass B_m^i value and vegetation water content VWC^i at time t_i through the RBM. The better the solution, the lower the cost value. As explained in Jarlan et al. (2002b), in the case of noisy data and non-linear dynamics, we are not only interested in the optimal solution but also in characterising the whole time evolving distribution of the admissible solution (defined as those solutions with an associated cost lower than twice the data error standard deviation).

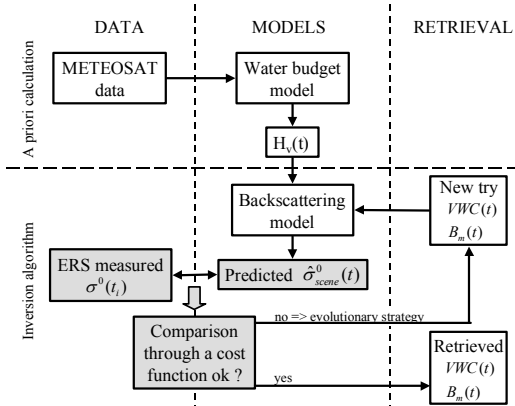


Figure 1: general scheme of the inversion algorithm.

over sandy soils in the study sites and taken to be constant over the whole region (see for a complete description : Mougin et al., 1995).

3.3 The evolution strategies algorithm

We use an evolution strategies (ES) algorithm developed by the evolutionary computation team of the Ecole Nationale polytechnique de Paris (named 'EvolC', Schoenauer et al., 1995). These algorithms work on a population of individual, each representing a search point in space X of potential solutions. The population is arbitrarily initialised and evolves towards better and better regions of the search space through the application of processes of selection, mutation, and recombination (Schwefel, 1981). Evolution strategies have received a lot of attention regarding their potential for real optimisation problem (Bäck and Schwefel, 1993).

3.4 Parameterisation of the sough variables

Preliminary computations have shown that approaching the inverse problem by directly trying to recover the variable discrete time series is not tractable. The ERS scatterometer data set doesn't allow to properly constrains the time evolution of the herbaceous mass [$B_m(t_i); i=1..n$] and vegetation water content [$VWC(t_i); i=1..n$] (even by using non-stationary covariance matrices in the cost function). Within this work, we look for a parsimonious parameterisation of the herbaceous mass time series $B_m(t)$ and vegetation water content time series $VWC(t)$ that would be adequate for any year to be used in the inversion algorithm.

Herbaceous mass parameterisation

A 15-years ground data base, extending from 1984 to 1993 and from 1999 to 2001 and over 15 sandy sites located in the Malian Gourma (e.g. 241 measurements), is used to compute the parameterization. In this study we are only interested in the period of vegetation growth, starting from near zero herbaceous mass to its maximum peak, which is usually a monotonic function of time (allowing the retrieval of the ecosystem production). The Fourier decomposition is used for the parameterisation. A Fast Fourier Transform discrete algorithm is applied to any herbaceous mass curve (corresponding to one site and one year). In most cases, we observed that the Fourier coefficient are naturally arranged in decreasing order in amplitude with increasing index k . This ordering means that slower time variations (low frequencies) of the herbaceous mass are more energetic than faster modes. This allows to truncate the Fourier decomposition. By fixing the $k < K_{max}=5$, the average tolerated misfit is 93% (in variance). In the inverse problem, the retrieval of the 5 Fourier coefficients and the 4 Fourier phases (the phases associated to the first coefficient is arbitrary set up to 0) completely

determines the herbaceous mass temporal evolution (usually an increasing function of time).

Vegetation Water Content parameterisation

The overall seasonal variation of VWC is roughly known for sahelian species (Guerin et al., 1991). VWC is at a maximum at emergence (young shoots) at the very beginning of the growing season reaching about $VWC^{max} = 80 \pm 10\%$ depending on species. Then, without any rainfall shortage the VWC decreases linearly to about 40 % in mature plants at the time of maximum herbaceous mass. Good results have been obtained with such a parameterisation with regards to forward backscattering simulations (Frison et al., 1998; Jarlan et al., 2002a). It is interesting to note that this variable can be linked to hydric stress but, presently, ERS repetitivity doesn't allow to recover such biological events. Finally, the only parameter to retrieve is VWC^{max} , ponderal humidity at early stages.

3.5 Algorithm implementation

$Hv(t)$ is calculated for each considered pixel and, as explained in the $B_m(t)$ parameterization, only WSC observations corresponding to the growth period are kept for the optimisation process (Jarlan et al., 2002b). The 10 unknown parameters describing the seasonal evolution of $B_m(t)$ and $VWC(t)$ are then estimated from ERS WSC data by optimisation of the cost function with the evolution strategies algorithm. From the numerous tries of the evolution strategies algorithm, the solutions leading to a cost lower than twice the data noise level are kept and considered as acceptable.

Prior to the application to real data, the algorithm robustness is theoretically verified using a simulated inversion experiments procedure. Such approach consists in generating an artificial data set by a forward application of the backscattering model from a known parameter vector p^i which will have to be retrieved. From the computed simulated backscattering coefficient time series, which are considered free of measurement errors, the synthetic seasonal variations of $B_m(t)$ and $VWC(t)$ are retrieved successfully with a cost lower than 1.10^{-2} dB.

4 RESULTS AND DISCUSSION

Our goal is to retrieve the time series of the observable vegetation parameters over a map (partitioned in independent scenes with geographical co-ordinates $r=[\phi, \theta]$). Firstly, the algorithm is evaluated over the four study sites during growing season 1999 and 2000 (8 cases) where we have field measurements to compare our retrieval with. Results for a representative particular case (Hombori in 2000) is analyzed in details with an error propagation study associated to the

incertitude on SWC estimation. Afterwards, a spatial extent is performed over the whole study region.

4.1 Study sites inversion

Keeping track of individual fitness in the model populations evolved by the ES algorithm, we get a sampling distribution of admissible solutions.

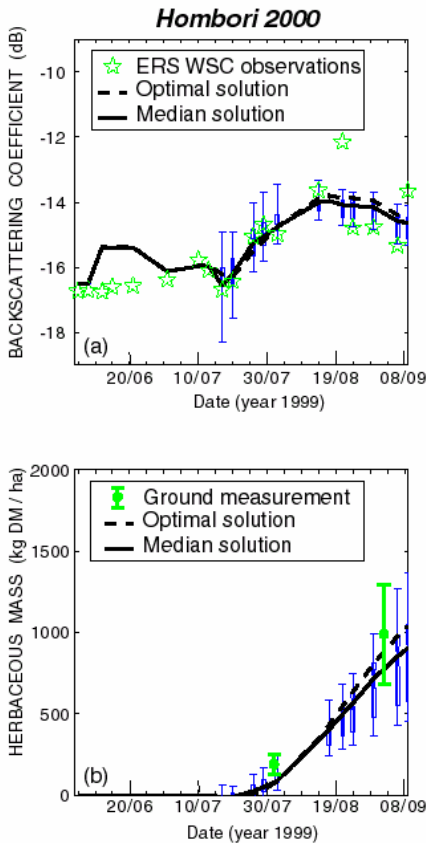


Figure 2 : Detailed analysis of retrieval results for Hombori in 2000 : seasonal evolutions of backscattering coefficient (a) and herbaceous mass (b). The distribution of solutions is summarized by a whisker plot with the minimum, first quartile, median, third quartile and maximum values. The optimal solutions found by the ES algorithm is also plotted (--).

In figure 2, we have plotted the time series of observed and predicted backscattering coefficient (2a) and the inversion results in terms of herbaceous mass curves (2b) for Hombori site during the growing season 2000. During season 2000, two ground measurements are available on the Hombori site.

As the minimisation criterion rely on satellite observations, retrieved model predictions of the scene backscattering coefficient are always in good agreement with the WSC measurements (figure 2a) or stated differently, the inversion algorithm always finds

acceptable solutions. The value of measured herbaceous mass is well estimated. Both the median and the optimal solution go through the nearest vicinity of the ground measurement (figure 2b). For Hombori 2000, retrieved herbaceous mass curves exhibit a slight delay as compared to ground measurements. The distribution is quasi-uniform and narrowed for Hombori 2000. The strong constraints on ponderal humidity temporal evolution curtail the search space on this variable and the retrieved distribution are obviously narrow (not shown here). Several trials performed in order to allow a larger range of shapes than this linear decrease showed that no significant improvement were noticed. According to the good results obtained on herbaceous mass retrieval, the average curve used in this study seem however to be a good approximation.

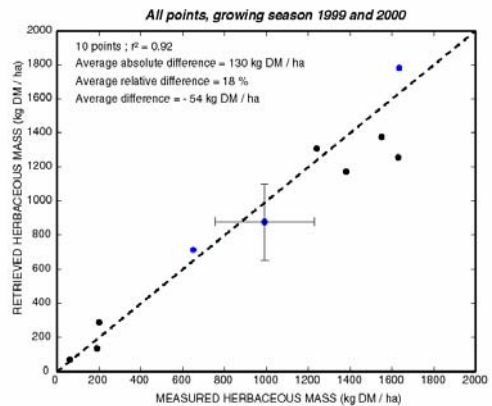


Figure 3 : Comparison between optimal inverse solutions and ground measurements of maximum herbaceous mass for all sites (Period 1999-2000).

From the 8 cases analyse (not shown here), the optimal retrieved value of herbaceous mass appears to be better than the other acceptable solutions when compared to ground measurements. Figure 3 is a scatter plot of herbaceous mass ground measurement versus inverse optimal solutions at the measurement date for the four sites during growing season 1999 and 2000. With an associated absolute error of 130 kg DM / ha and a correlation coefficient $r^2 = 0.92$, results are satisfying. The illustrative error bar is for an average B_m value of 990 kg DM / ha occurring in Hombori during the growing season 2000. On the measured herbaceous mass, it corresponds to 30% of the measured value. The calculation of error on the retrieved value is explained in the following paragraph. The slight under-estimation of inverse optimal solution (around -54 kg DM / ha) as compared to ground measurements may be explained by the optimisation criterion that is built in such a way that the algorithm finds backscattering model

predictions that fit, on average, the WSC data over the whole growing period. The number of WSC observations around the backscattering peak, that partly determine the maximum herbaceous mass value, is quite low because of the temporal resolution of this instrument. The inversion algorithm may produce solution that deviate from this particular values. Nevertheless, trials aiming at giving more weight to satellite observations around the backscattering peak by adding non-stationary covariance matrix of data errors were unsuccessful.

4.2 Error assessment

The algorithm critical point concerns the semi-stochastic estimated SWC time series. The low field capacity of the upper sandy soil layer leads to a quasi absence of SWC sensitivity to rainfall amount. In contrast, SWC is very sensitive to rainfall events distribution within the decade. In order to study the impact of the unknown distribution on herbaceous mass retrieval, 500 different SWC time series are generated following the stochastic method used in paragraph 3.1 and the inversion algorithm is ran for each time series. Figure 4 show the distribution of the 500 associated optimal solution for Hombori in 2000. The remainders follow a quasi-normal distribution of mean 850 kg DM / ha (near the ground measurement of 990 kg DM / ha) and of standard deviation 221 kg DM / ha). The low underestimation is due to the delay previously underlined. The quite high standard deviation illustrates the sensitivity of C band radar to the soil contribution (mainly driven by SWC) that represents more than 40% of the total backscattering over Sahel (Jarlan et al., 2002a).

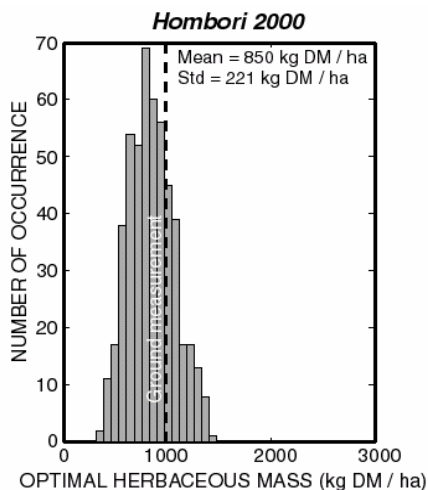


Figure 4 : Mono-pixel inverse optimal herbaceous mass distribution retrieved from ERS data associated to 500 different SWC time series at the ground measurement date (Hombori 2000).

4.3 Mapping of sahelian vegetation parameters

The inversion algorithm is applied to the whole study region (delimited by 18.5°N and 13.5°N in latitude and -6°W and 1°E in longitude that is around 500*700 km² = 350 000 km²) at a spatial resolution of 0.25° (e.g. 20*28=560 pixels). Preliminary test have shown that the inverse optimal solution doesn't evolve after the 25th generation. The number of generation for the ES algorithm is reduced to 25 generation because of computation time constraints. The inversion is computed independently from one pixel to an other. The herbaceous mass production maps are compared to a sum of NDVI which is a nowadays classical empirical method to estimate herbaceous mass over sahelian areas (Hiernaux and Justice, 1986).

Figure 5 shows the computed herbaceous production map at 0.25° from the inverse optimal solutions at the herbaceous mass peak during season 1999 (figure 5a) and the associated integrated NDVI images from the VEGETATION/SPOT 4 sensor downgraded at the same spatial resolution (figure 5b). The spectral index NDVI takes advantages from the spectral response difference of green leaves between the red and infra-red channel. Typical value of NDVI are comprised between 0 and 1 over vegetated area. The higher the NDVI value, the higher the green vegetation density. Nevertheless, due to the qualitative kind of information provided by integrated NDVI images, it cannot be considered as a validation. In this study, NDVI images are only used to verify the global consistency of retrieved vegetation mass spatial distribution.

The herbaceous maps show a vegetation spatial distribution coherence. The north-south gradient is particularly well depicted. The highest production areas are located towards the south of the transect, in the vicinity of the Douentza city, whereas at the Sahara border the production is nil. It is interesting to note that the high herbaceous productions encountered at the southern area (below 14°N) is surely the resulting contribution of both grass and trees that may be non negligible over these north sudanian savannah. Further investigation will be performed in a near future after an intensive ground campaign planned in winter 2003.

The integrated NDVI images and the herbaceous maps show an overall consistency associated to a significant correlation $r^2=0.71$ and $r^2=0.72$ for 1999 and 2000, respectively. A few common spatial features may be underlined. The occurrence of several low production isle (south-east of Gossi or east of Gourma-Rharous for example). Such isolated low production areas correspond to dismantled lateritic soils where production is low. They are quite well depicted both by the NDVI and by the WSC retrieval. The Iforas Adrar appears clearly at the extreme north east of both

images during season 1999. Although quite high in latitude, this region is characterised by a favourable climate that allows a good vegetation development. At the left bank of the Niger river, between 17°N and 18°N, these pre-saharian desertic zones exhibit a low production on the two images.

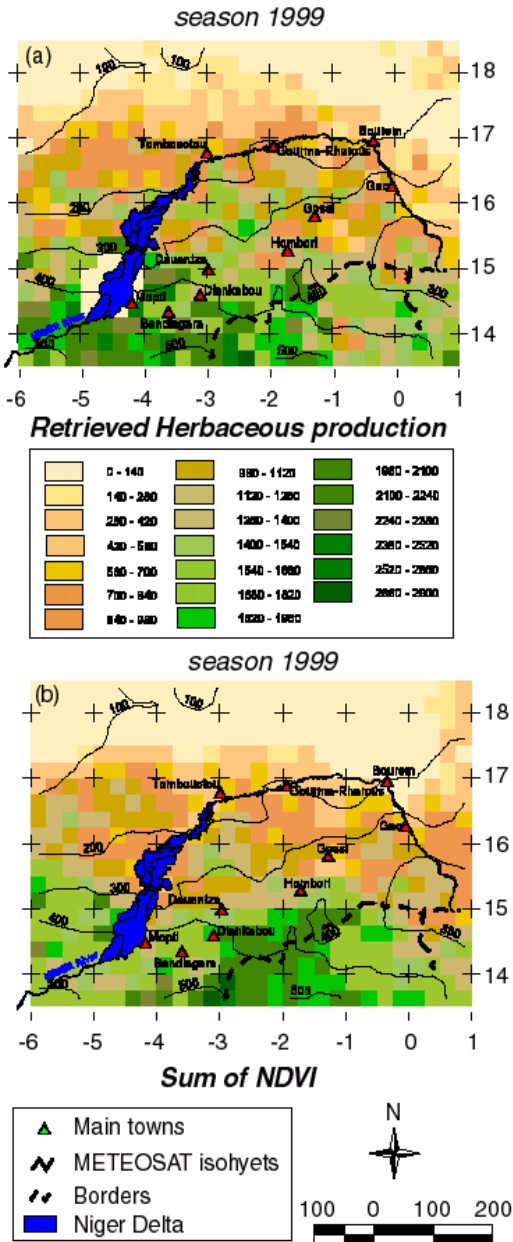


Figure 5 : Herbaceous production map estimated from the WSC data set during and the associated colorbar (a). NDVI sum acquired by the VEGETATION instrument on board SPOT4 (b). Isohyets computed from METEOSAT rainfall estimates and a mask delimiting the Niger river and delta have been added.

The most striking differences occur around the Niger delta. Both spaceborne signals are contaminated by these lands inundated most part of the year. On one hand, NDVI over water areas is negative leading to erroneous low integrated NDVI. On the other hand, the ERS retrieval algorithm is built in such a way that only vegetation parameters from short development cycle species can be retrieved (such area are masked on figure 6a and 6b). Around the Niger Delta, irrigated areas exhibit too long vegetation development cycle. Another interesting feature concerns the high latitude areas of low production (above Timbuktu). WSC retrieval algorithm detects herbaceous production of less than 300 kg DM / ha whereas the detection threshold of NDVI is reached at such low vegetation cover fraction.

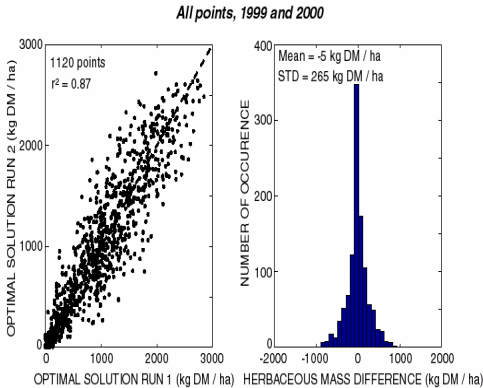


Figure 6 : Comparison between two optimal herbaceous mass maps retrieved from ERS data associated to two different SWC time series (both season 1999 and 2000 : 2*560 =1120 points). (a) scatter plot (b) differences distribution.

The sensitivity of retrieved production to SWC time series estimation previously underlined over the whole region is evaluated in a different way here. Because of time computing constraints, the calculation of mono pixel distributions such as those shown in figure 4 for the whole map is not conceivable in practice. Herbaceous production maps for year 1999 and 2000 are recomputed with new SWC time series generated stochastically and compared to the initial ones. Figure 6 show the scatter plot (6a) and distribution of differences (6b) for the one map 560 pixels for year 1999 and 2000 together. The two retrievals are obviously significantly correlated with a correlation coefficient $r^2=0.87$ (figure 6a). The remainders follow a nearly normal distribution with quasi zero mean and a standard deviation of 265 kg DM / ha. This standard deviation takes into account various conditions in terms of not only SWC estimation but also geomorphology spatial variability and vegetation development scenarii. The normal behaviour of both

production differences between two retrieved maps (figure 6) and mono pixel retrievals (figure 4) illustrates that the error propagation is similar over the whole study region. This last comment allow the assignment of an error bar of around 270 kg DM / ha to each retrieved solution.

5 CONCLUSIONS AND PERSPECTIVES

This study presents results of the quantitative mapping of West African Sahel vegetation variables from ERS scatterometer data through the inversion of a radiative backscattering model. The vegetation characteristics of interest are the vegetation water content and the herbaceous mass. The inverse problem is constrained by the a priori calculation of the soil water content time series and the parameterization of the time evolving vegetation variables to retrieve from a ground data base extending from 1984 to 2001. The inverse problem is then solved using an evolution strategies algorithm. Firstly the inversion algorithm is evaluated over four sites where we have ground measurements of herbaceous mass to compare our retrieval with. The confrontation of retrieved and measured herbaceous mass is good (130 kg DM / ha of average error and $r^2=0.92$). The time evolving admissible solution distributions show the good constraint brought by both ERS scatterometer data and soil water content estimation to retrieved vegetation characteristics with a reasonable accuracy. The critical point concerns the soil water content estimation. The inversion is performed for 500 different soil water content time series. The resulting optimal solution distributions have a quasi normal behaviour with a mean in the neighbouring the ground measurement and a standard deviation comprised between 220 kg DM / ha and 271 kg DM / ha. These quite high uncertainties underline the necessity to dispose of a precise estimation of SWC that could be assessed from remote sensing data (SMOS project; Kerr et al., 2000). The algorithm is then applied to a regional area of around 350000 km². The retrieved herbaceous production show an overall coherence with integrated NDVI images acquired by the VEGETATION instruments on board SPOT 4. In a following paper, we intend to apply the retrieval algorithm to the whole sahelian strip from 1991 to 2000.

A precise description of the surface functioning (humidity at different depth, energy and mass fluxes) cannot however be provided by the sole use of remote sensing data. A vegetation functioning model coupled to a soil-vegetation-atmosphere transfer model is necessary. With new remote sensing data provided by recently launched sensor (QUICKSCAT, MODIS on board TERRA, ASAR and MERIS on board ENVISAT, VEGETATION on board SPOT5) in different wave length domain, spatial and

temporal resolution, we intend to evaluate the potentiality of the different data set following the methodology described here. Afterwards, a control method, that takes advantages of information provided by both satellite and ground data, will be developed to constraint the numerals processes involved in the surface functioning. The resulting spatialised information on variables such as evaporative fluxes or vegetation cover fraction is of prime interest for GCM limit conditions setting within the frame of the AMMA project.

REFERENCES

- Arkin P.A. and Meisner B.N., 1987, The relationship between large-scale Convective Rainfall and Cold Cloud over the Western hemisphere during 1982-1984, *Monthly Weather Review*, 115, 51-74.
- Bäck T. and Schwefel H.P., 1993, An Overview of Evolutionary Computation for parameter optimization, *Evolutionary Computation*, 1(1):1-23.
- Frison, P.L., Mougin, E. and Hiernaux, P. 1998, Observations and Interpretation of Seasonal ERS-1 Wind Scatterometer Data over Northern Sahel (Mali), *Remote Sens. Environ.*, 693:233-242.
- Guerin H., Friot D., Mbaye N. and Richard D., 1991, Alimentation des ruminants Domestiques sur pâturages Naturels Sahéliens et Sahelo-soudanien : Etude Méthologique dans la région du Ferlo au Sénégal, I.E.M.V.T., 115 p.
- Hiernaux P.H.Y. and Justice C.O., 1986, Suivi du développement végétal au cours de l'été 1984 dans le Sahel Malien, *Int. J. Remote Sensing*, vol. 7, n° 11, 1515-1531.
- Jarlan L., Mougin E., Frison P.L, Mazzega P., Hiernaux P., 2002a, Analysis of ERS Wind Scatterometer time series over Sahel (Mali), *Remote Sensing of Environment*, 81, 404-415.
- Jarlan L., Mazzega P., Mougin E., 2002b, Retrieval of land surface parameters from ERS scatterometer data: A brute-force method. *IEEE Trans. Geosci. Remote Sens (in press)*.
- Kerr et al., 2000, Soil Moisture and Ocean Salinity, Proposal in answer to the Call for Earth Explorer Opportunity missions.
- Mougin, E., Lo Seen, D., Rambal, S., Gaston, A., and Hiernaux, P. (1995), A regional Sahelian grassland model to be coupled with multispectral satellite data. I. Description and validation. *Remote Sens. Environ.*, 52:181-193.
- Schoenauer et al., 1995, EvolC User Manual, Technical Report, EEAAX, Ecole Polytechnique, <http://www.eark.polytechnique.fr/EvolC.html>.
- Schwefel H.P., 1981, numerical optimization in computer models, John Wiley and sons Eds, NY.

Merging of airborne laser altimeter data and radarsat data to develop a digital elevation model

N. Baghdadi, B. Bourguine, S. Cavelier, J.-P. Chilès, C. King, P. Daniels, J. Perrin, and C. Truffert

Bureau de Recherches Géologiques et Minières (BRGM), French Geological Survey

3 avenue C. Guillemin, B.P. 6009 - 45060 Orléans cedex 2, France

Tel.: 33 2 38 64 32 02 - Fax: 33 2 38 64 33 99

E-mail : n.baghdadi@brgm.fr

ABSTRACT - *A Digital Elevation Model (DEM) has been developed for a site in French Guiana by merging airborne laser altimeter data with a stereo-radargrammetric DEM. Merging involved the combination of two types of kriging: (1) kriging of the difference between DEM elevations and airborne data, which is then subtracted from the radargrammetric DEM, and (2) direct kriging of airborne data when radargrammetric DEM elevations are unsatisfactory. Merging significantly improved the accuracy of the radargrammetric DEM. The standard deviation of elevation errors fell from 25 m to 17 m or from 19 m to 10 m, depending on the validation source adopted.*

1 INTRODUCTION

Topographic maps are a prerequisite to thematic mapping aimed at providing geological and environmental information. A feasibility study has been undertaken to create a Digital Elevation Model (DEM) by merging satellite radar data (SAR images) and airborne laser data. The originality of this work lies (1) in that it concerns a context of dense equatorial forest, where optical methods cannot operate due to constant cloud cover and fieldwork conditions are harsh, and (2) in that referencing satellite data is done without using any topographic map.

After presenting the context of the study and the available data, we describe the building of a preliminary satellite DEM by referencing the satellite images using only airborne data. In a second step, this preliminary DEM is combined with airborne data using different types of kriging, based on a geostatistical analysis of airborne and satellite data, to obtain an improved version of the DEM. Finally, the quality of this improved DEM is validated and we demonstrate that the satellite DEM can be significantly improved by taking into account airborne data.

2 CONTEXT OF STUDY AND AVAILABLE DATA

2.1 Study area

A study area measuring 45 x 55 km was selected in an equatorial environment to the south of Cayenne in French Guiana (long. 51°50'W to 52°30'W and lat. 4°20'N to 5°00'N) (Fig. 1). French Guiana is entirely covered by Amazonian forest. Elevation ranges from 0 to about 400 m a.s.l. (e.g. Kaw

mountain), although the majority of the area is flat or slightly undulating.



Figure 1 – Location of the study area.

2.2 Airborne data

During the geophysical survey of 1996, which covered 4/5th of French Guiana and combined magnetism and spectrometry, elevations were recorded with two altimeters, one radar and the other laser. Elevation accuracy is considered better than that of navigational barometric altimeters, which is approximately 5 m.

Flight lines oriented N30° with a 500-m spacing, complemented by transverse flight lines oriented N120° with a 5-km spacing, guaranteed the coherence of the flight programme. Sampling density along flight lines was approximately 70 m for the radar and 7 m for the laser.

The available laser data correspond to the first pulse returned, i.e. the first obstacle encountered. The radar altimeter operating in C band (4.3 GHz) was calibrated by comparing radar and laser altimeter recordings from several flights over the Atlantic off the French Guiana coast. In such a forest environment, the canopy is penetrated by only a few meters.

2.3 Satellite data

Two RADARSAT images were acquired on the 21 and 24 April 2001 with decreasing orbit in Standard (S2) and Fine (F5) modes respectively. The standard- and fine-mode images were processed in ground range format, with a pixel spacing of 6.25 x 6.25 m and 12.5 x 12.5 m respectively. The difference in incidence between the two images is about 19°.

2.4 Validation data

Most of our study area is covered by 1:25,000-scale IGN (Institut Géographique National) maps providing the elevation of many spot heights. Considering that this study aims at simulating the case where no map data are available, the latter were only used to evaluate the accuracy of the method. For validation purposes, a 10 x 10 km DEM acquired by airborne laser is also available for the southern part of our study area. The airborne DEM is located in an area entirely covered by thick forest. It provides, over a regular 20 x 20 m grid, ground elevations with an accuracy of a few tens of centimeters.

3 FILTERING THE AIRBORNE DATA

We had access to 1,338,379 laser (Z laser) elevations and 140,572 radar (Z radar) elevations for our study area. Statistics undertaken on the two data sets show that laser elevations are on average 3 m higher than radar elevations, which is consistent with a slight penetration of the vegetation cover by the radar. The laser and radar data show a strong correlation coefficient of 0.987. We nevertheless observe major differences in Z laser and Z radar elevations locally, which can vary from about -70 m to 160 m. These are probably measurement anomalies (laser or radar), and the corresponding points are discarded.

In addition, along a single flight line, major differences are observed in Z between one measurement point (n) and the next (n+1). We calculated these differences in Z along each flight line, and found that radar and laser elevations can vary by more than 150 m from one point to the next. This is again due to measurement errors and the corresponding points are discarded.

In conclusion, the laser and radar data are marred by anomalies that need filtering. For this, we must

discard values that seem anomalous, and extract those points that probably correspond to the tree tops.

The first filtering stage consists in eliminating those points with an elevation difference that is obviously too high, whether between two successive points issued from the same altimeter (laser or radar), or between laser and radar elevations for a single point. Note that DZ_{rad} is the difference in Z between two successive radar measurements and DZ_{las} is the difference in Z between two successive laser measurements. To prevent eliminating too many data, we chose a threshold of 25 m for DZ_{las} . With this filter, 5% of the data are eliminated. Radar points with a $DZ_{rad} > 50$ m for two neighbouring points were also eliminated. The variogram obtained with this threshold is almost identical to the Z radar variogram without filtering. Only 0.2% of the points (i.e. 250 points) have a $DZ_{rad} > 50$ m. Similarly, we simultaneously compared known laser and radar points so as to eliminate those without a maximal difference of 25 m between laser and radar data.

After eliminating the 'anomalous' points, the remaining points still displayed major fluctuations according to whether the point in reality corresponds to a tree top, a branch at intermediate level, or even a stream or the ground. We should bear in mind that radar sensors in C band do not penetrate dense vegetation cover, and consequently, elevations extracted by stereo-radargrammetry correspond to the top of the canopy (Z SAR).

So as to obtain airborne elevations of a similar nature to the Z SAR elevations for future comparative purposes, a second filtering was carried out. This second filtering consisted in selecting only the points that are local maxima, based on the assumption that these probably correspond to the top of the canopy. With a 9-point moving window, it is possible to conserve a third of the measurement points. Average elevation of the retained laser points is 50.1 m, compared to 42.7 m for the corresponding radar points. This result suggests that average penetration of the airborne radar is about 7.5 m, rather than 3 m as suggested prior to data filtering. After filtering, we are left with a laser data point every 25 m on average.

The quality of the filtered airborne data was assessed by examining the errors at flight-line intersections (lines N30° and N120°). Assuming that the errors related to linear interpolation carried out in the vicinity of flight-line intersections are insignificant in flat terrain where elevation < 10 m, then elevation accuracy for the filtered data is about 2 m.

4 CREATING A RADAR GRAMMETRIC DEM (SAR DEM)

4.1 Referencing the satellite data

For localisation purposes in an environment where operational conditions are difficult and reference data are inexistent, airborne data represent a source of ground control points (GCPs) for the stereoscopic pair. During extraction of the radargrammetric DEM, accurate geographical coordinates must be attributed to certain points identifiable on SAR images (Toutin 1999).

Matching between SAR images and airborne data is thus necessary but problematic: the former show mapping elements of the area and the latter, of which there are only a few, provide elevations with mapping shapes that are barely recognisable.

For satisfactory matching, the RADARSAT F5 image was referenced with respect to the airborne data (mainly laser data). Only rivers constitute easily identifiable calibration points common to both images (SAR and airborne), characterised on the SAR image by their specific radiometry, and on the airborne laser image because they correspond to the lowest elevations.

Referencing quality was assessed using 40 check points common to both the referenced F5 image and the IGN maps. The obtained results indicate an accuracy of approximately 16 m for X and Y.

4.2 Creating a preliminary SAR DEM

The radargrammetric DEM was created using the StereoSAR DEM module of the ERDAS IMAGINE software from ESRI. The first step consists in attributing geographical coordinates (X,Y,Z) to the ground control points (GCPs) well distributed spatially over the SAR pair. The coordinates are selected by combining both X,Y spatial data issued from the referenced RADARSAT image and Z elevations derived from the airborne data. A second step consists in reducing speckle on the SAR images. A Gamma-Map filter was adopted with a 3×3 window. A third step consists in identifying equivalent points with lowest and highest elevations on the two SAR images, enabling definition of the upper and lower limits of the parallaxes encountered. The stereoSAR DEM is then used for an automatic correlation of the two SAR images. Pixel size of the resulting radargrammetric DEM was set at 50×50 m (Fig. 2).

4.3 Validating and correcting the SAR DEM

The DEM's elevation accuracy was assessed on the basis of 224 check points from the IGN maps. The average error observed is 35 m (Table 1). Standard

deviation of the errors is 26 m, with a maximum error of 161 m and a minimum error of -42 m. We also note that elevations are overestimated in hilly terrain and underestimated in mountainous terrain, demonstrating that radargrammetry has a smoothing effect on relief. Similarly, the results obtained for the savannah are quite anomalous because radargrammetry portrays relief, of up to 70 m elevation, that is inexistent. This is due to poor correlation in such homogeneous environments. Furthermore, marked elevations, both negative and positive, are observed along the coast, and which can probably be explained by a lack of coherence related to swell or tide.

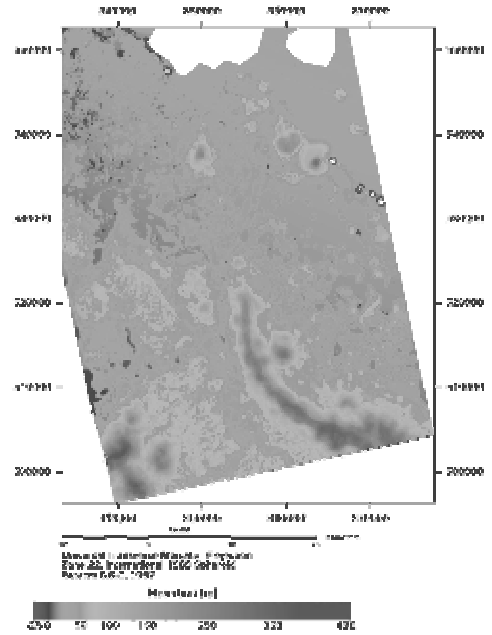


Figure 2 – Corrected SAR DEM.

A slight tilting was observed with the SAR DEM reflected by a shallow slope. To eliminate this tilting effect, we modelled the difference between SAR elevations and airborne elevations using a first-order polynomial defined by $Z_{\text{SAR}} - Z_{\text{laser}} = aX + bY + c$. The polynomial is then subtracted from the SAR DEM, thus giving a DEM corrected for slope and offset effects. This method enables a global correction of the DEM without changing its form. After correction, the quality of the SAR DEM is significantly improved. RMSE (root mean square error) decreases from 43 to 30 m (Table 1), whereas standard deviation is unchanged. An average overestimation of about 18 m is observed between the SAR DEM and the IGN maps, which probably corresponds to average canopy height (savannah + forest). Nevertheless, the corrections made to the SAR DEM do not, for example, account for major local

errors in the savannah. Kriging of the SAR DEM and the airborne data is thus necessary.

Validation source	(1) Uncorrected SAR DEM	(2) Corrected SAR DEM	
	IGN MAP	IGN MAP	Heliborne DEM
Number of points	224	224	3416
Mean Bias Error (m)	35	18	27
Standard Deviation (m)	26	25	19
Mean Absolute Error (m)	37	23	29
Root Mean Square Error (m)	43	30	33
Maximum Error (m)	161	146	111
Minimum Error (m)	-42	-54	-44

Table 1 - Statistics for elevation errors of the radargrammetric DEM: (1) unprocessed SAR DEM without correction, (2) SAR DEM after correction for tilting and offset effects.

We also calculated statistics for the heliborne DEM using all the points common to the heliborne DEM and the SAR DEM. The average of the errors reveals the existence of a bias of 27 m (Table 1). This is due to the fact that the SAR DEM gives canopy height, whereas the heliborne DEM corresponds to ground level. Figure 3 shows the close correlation between elevations from the airborne laser and those from the heliborne DEM, with a mean difference of approximately 30 m. We note that the offset between the SAR DEM and the heliborne DEM is clearly related to canopy height in dense forest, which is 30 m on average. Elevation accuracy of the SAR DEM is estimated at about 19 m using the heliborne DEM.

5 MERGING

5.1 Methodology

The starting point is to use the DEM derived from the SAR images, which provides large variations in relief, and model detailed fluctuations using laser data. For this we define a residual R equal to the difference between SAR elevation (Z_{SAR}) and airborne laser elevation (Z_{laser}):

$$R = Z_{\text{SAR}} - Z_{\text{laser}} \quad (1)$$

R was calculated at measurement points along laser profiles considering only the subset of points corresponding to the top of canopy (see §3). Kriging of the residual makes it possible to rectify the SAR

DEM along the flight lines whilst maintaining the shape between the profiles. We consider the remote sensing data to be of insufficient quality when the variance of the residual is much greater than the variance of the laser data.

We have access to two elevation databases, both of which provide the top of the canopy. The first is essentially composed of data derived from the airborne laser and are very well referenced, but irregular and rather sparse. The second database contains a radargrammetric DEM extracted from RADARSAT images on a regular grid of 50×50 m. Elevation accuracy of the laser data is some 2 m, compared to about 20 m (25 m with the IGN maps and 19 m with the heliborne DEM) for the SAR DEM. The aim is to merge these two databases whilst taking into account a) the high accuracy of the laser data, and b) the better density of the SAR data.

We relied on geostatistical techniques (Chilès and Delfiner, 1999) for the merging. In the case of the study of a single variable denoted Z , the basic geostatistical tool is the variogram $\gamma(h)$, which is a function of the distance h between two points:

$$\gamma(h) = \frac{1}{2} \times \frac{\sum_{i=1}^{N(h)} [Z(x_i + h) - Z(x_i)]^2}{N(h)} \quad (2)$$

Where: $N(h)$ is the number of pairs of points separated by a distance h , $Z(x_i)$ and $Z(x_i+h)$ the values of Z measured at points x_i and x_i+h .

The variogram characterises the spatial variability of a phenomenon. The advantage of the geostatistical approach is that it allows optimal interpolation of the variables based on the kriging technique. Kriging takes the spatial structure of the studied phenomenon into consideration and provides a measurement of the interpolation error.

Kriging consists in interpolation through linear combination of the data $Z(x_i)$. The value interpolated at point x , known as $Z_k(x)$, is given by:

$$Z_k(x) = \sum_{i=1}^N \lambda_i Z(x_i) \quad (3)$$

The weights λ_i are subjected to the condition $\sum_{i=1}^N \lambda_i = 1$, which avoids problems of bias.

These factors are selected so as to minimise the variance of estimation.

5.2 Local variographic analysis according to relief.

Analysis of the correlation cloud linking the two variables Z SAR and Z laser (Fig. 3) shows that for low elevations (Zlaser up to 30 m), SAR can provide elevations of up to 400 m. For elevations greater than 30 m, however, the two variables are relatively well correlated. We conclude that the quality of the SAR DEM data depends strongly on the relief (or rather the difference in elevation) of the zone.

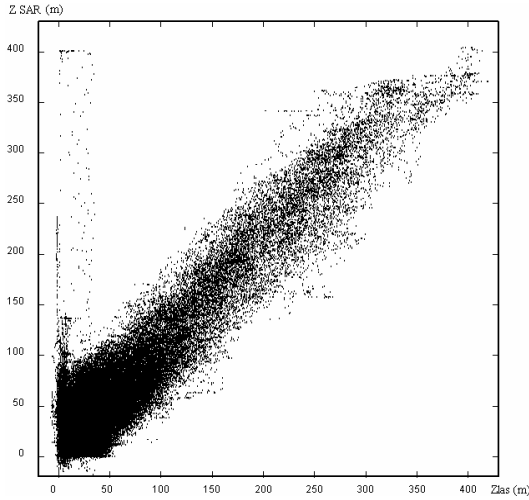


Figure 3 - Correlation cloud linking the variables Z SAR and Z laser.

A variographic study was undertaken according to the different relief zones. Variograms were calculated for the laser data (Z laser), the radargrammetric DEM (Z SAR) and the residual R (Z SAR – Z laser). Relief zones were identified over the study area using airborne laser data (assumed to be accurate) filtered by a median 2×2 km filter and selected as appropriate for zoning the relief encountered in our study area:

- sea: elevation ≤ 2 m
- flat terrain: elevation between 4 and 8 m
- “hilly” terrain: elevation between 10 and 30 m
- “mountainous” terrain: elevation ≥ 40 m

The boundaries of the relief zones are defined empirically, and a transition zone is set between each zone. The variograms (Fig. 4) show that:

- for flat terrain and the sea, the variogram of the residual is much higher than that of the airborne data (which is nearly null). It is also higher than the variogram of SAR data. This means that it is better to rely only on laser data, which are more stable, in order to build the final DEM. This will also lead to a lower estimation variance. In fact, as can be seen on the far

left of the correlation cloud (Fig. 3), remote sensing has an inconsistent response in the lower zones.

- for “mountainous” terrain, the level of the variogram of the residual is much lower than that of the variograms of individual variables (Z SAR and Z laser). In this case, it is preferable to interpolate the residual, which is more stable and leads to a lower estimation variance.
- for “hilly” terrain, the three variograms are similar. We can thus adopt a combination of the previous methods.

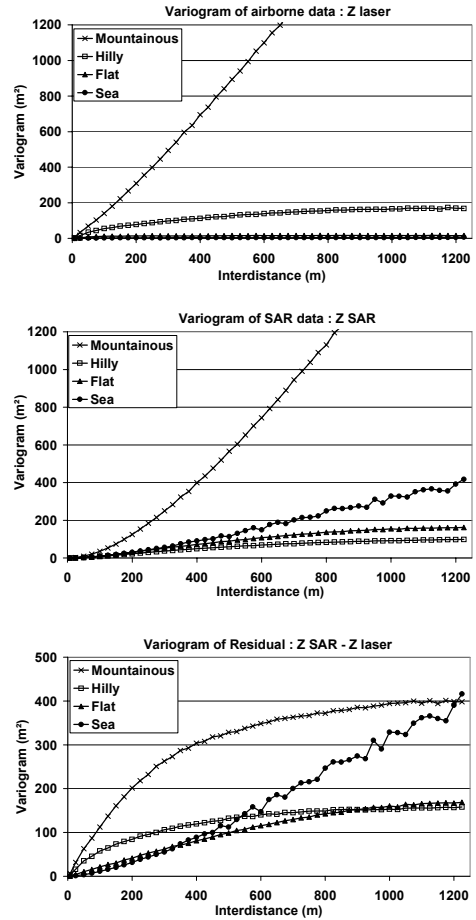


Figure 4 - Variograms of airborne laser data, remote sensing data (SAR DEM), and the residual (difference between SAR DEM and laser data).

- The final DEM is then computed as follows:
- for flat terrain and the sea :

$$\text{Final DEM} = Z \text{ laser}_k \quad (4)$$

- for mountainous terrain:

$$\text{Final DEM} = Z_{\text{SAR}} - R_k \quad (5)$$

- for hilly terrain :

$$\text{Final DEM} = \text{combination of (4) and (5)} \quad (6)$$

Where Z_{laser_k} and R_k are the values of Z_{laser} and R , using the appropriate variogram model fitted for each type of terrain.

5.3 Results and Discussion

The quality of the merging of a radargrammetric DEM derived from the S2/F5 pair with airborne laser data (Fig. 5) has been assessed according to two approaches: 1) comparison between the final DEM and either the IGN maps or the heliborne DEM; 2) construction of a DEM based on a subset of laser data, and assessment of the quality of the results using the remaining laser data. During analysis of the results, we must bear in mind that the IGN maps and the heliborne DEM provide a ground elevation, whereas the SAR DEM data correspond to the top of the canopy. A visual analysis of the kriged DEM shows minor errors along certain flight lines (Fig. 5), clearly visible in flat terrain. They are related to the airborne laser profiles and are probably due to GPS drift. These errors don't exceed few meters and are much lower than those recorded in the same terrain with the satellite DEM (few tens of meters).

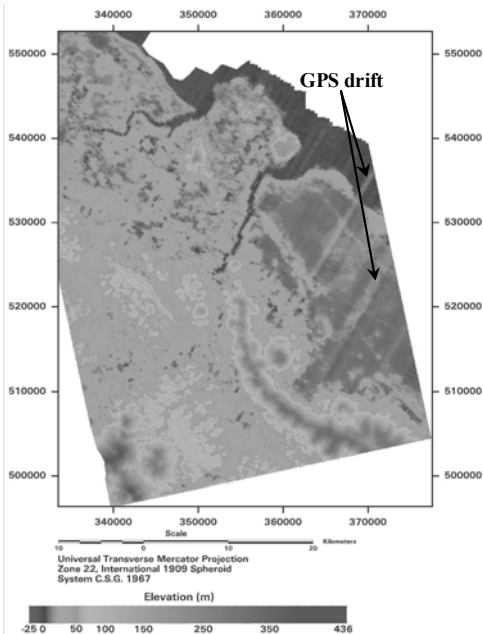


Figure 5 – Final DEM obtained by merging a radargrammetric DEM and airborne laser data.

• Validation of the final DEM using either the IGN maps or the heliborne DEM

Tables 2 and 3 give the statistics obtained for the corrected SAR DEM and the final kriged DEM compared respectively to the IGN maps and the heliborne DEM. Where the heliborne DEM is the validation source, the points used in the error analysis correspond to all the points common to the kriged DEM and the heliborne DEM (for each pixel of the kriged DEM, we average the elevations of the heliborne DEM located within the pixel). The analysis reveals a marked improvement of the radargrammetric DEM (corrected for slope effects): the standard deviation of the errors is reduced from 25 m to 17 m with respect to the IGN maps and from 19 m to 10 m with respect to the heliborne DEM.

A bias of the order of 17 m is observed between the SAR DEM and the IGN maps and about 33 m between the SAR DEM and the heliborne DEM. The height of the canopy had previously been calculated, during statistics involving airborne data and the heliborne DEM, at about 33 m. Consequently, in the presence of thick forest, we would expect a difference in elevation derived from the SAR DEM and that provided by the IGN maps to be of the order of 33 m. In an area devoid of vegetation or characterised by savannah, a less striking difference is expected. The bias of 17 m observed between the SAR DEM and the IGN maps is probably related to the diversity of vegetation cover: zones with a thick canopy, zones without a canopy and zones with savannah-type vegetation. Compared with the heliborne DEM, the observed errors on the kriged elevation vary from -2 to 69 m (-44 to 111 m before kriging), i.e. about -35 to 36 m if we include the height of the canopy.

	Corrected SAR DEM	Final DEM
Number of points	224	224
Mean Error	18	17
Standard Deviation	25	17
Mean Absolute Error	23	18
RMSE	30	24
Maximum Error	146	113
Minimum Error	-54	-37

Table 2: Statistics on elevation errors between the two available DEMs and IGN maps.

Error = $Z_{\text{DEM}} - Z_{\text{IGN}}$; RMSE = Root Mean Square Error. Corrected SAR DEM = SAR DEM corrected for slope effects. Final DEM = DEM obtained after merging corrected SAR DEM and airborne laser data.

	Corrected SAR DEM	Final DEM
Number of points	3416	3323
Mean Error	27	33
Standard Deviation	19	10
Mean Absolute Error	29	33
RMSE	33	35
Maximum Error	111	69
Minimum Error	-44	-2

Table 3: Statistics on elevation errors between the two available DEMs and the local airborne DEM. Error = Z DEM – Z Heliborne. Other notations are the same as in Table 2.

Merging reduces the smoothing of relief observed on the satellite DEM. For example, in valleys, after subtracting a canopy height of 33 m, the SAR DEM overestimates the elevation by about 19 m (compared to the IGN maps). After merging, this overestimation drops to 12 m. Symmetrically, in mountainous terrain, elevation after subtracting the height of the canopy, is underestimated by about 29 m with the SAR DEM and by only 19 m after merging.

The improvement gained through merging is also reflected by the standard deviation of the errors, which is almost halved compared to the SAR DEM.

Figure 6 shows the elevation errors before and after merging according to elevations from the heliborne DEM. We note, after merging, that the errors are less scattered (-2 to 69 m compared to -44 to 111 m before merging) and less dependent on elevation (the regression line has a slope of 2.9% compared to 8.1% before merging).

• Validation of the merged DEM using part of the airborne laser data

According to this approach, merging is carried out using flight lines oriented N30° with a 500-m spacing, and merging quality is assessed using measurement points along transverse flight lines oriented N120° with a 5-km spacing. The height of the canopy does not come into play during this comparison. Figure 7, representing the distribution of errors before and after merging, clearly illustrates the improvement gained through merging. After merging, about 90% of the tested points have an error between -15 and 15 m, compared to only 50% before merging.

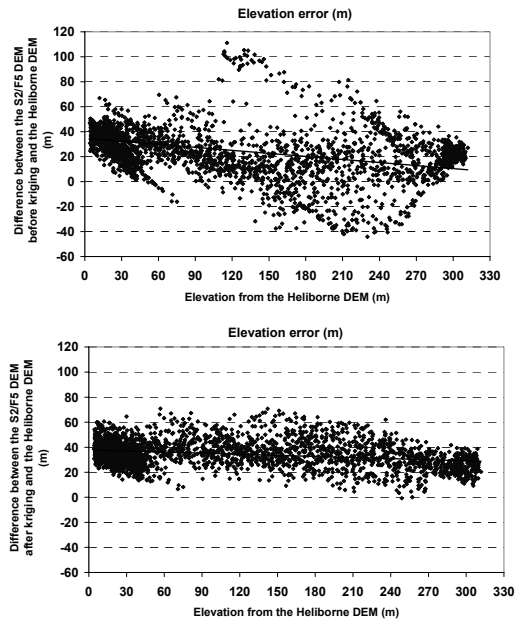


Figure 6 – Distribution of elevation errors according to elevations from the Heliborne DEM (before and after merging).

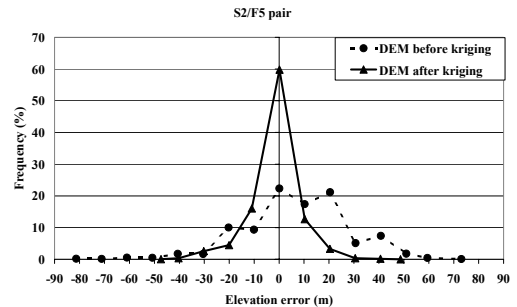


Figure 7 – Histogram of elevation errors for the S2/F5 pair before and after merging. Merging was performed using flight lines oriented N30°, whereas merging quality was assessed using measurement points on transverse flight lines oriented N120°.

• Qualitative assessment of the merged DEM based on section analysis

For an improved assessment of the merging results, several cross sections were drawn up (Fig. 8).

Based on these, we can see that it is necessary to krig the laser data in flat terrain, and to disregard the SAR. Merging based on the elevation criterion, i.e. relief zones, is thus essential. The section selected at sea confirms the results obtained for flat terrain. The section through mountainous terrain shows a smoothing of relief on the SAR DEM. However, the

shape of the SAR DEM is relatively good, hence the necessity to use it between flight lines to retrieve elevation.

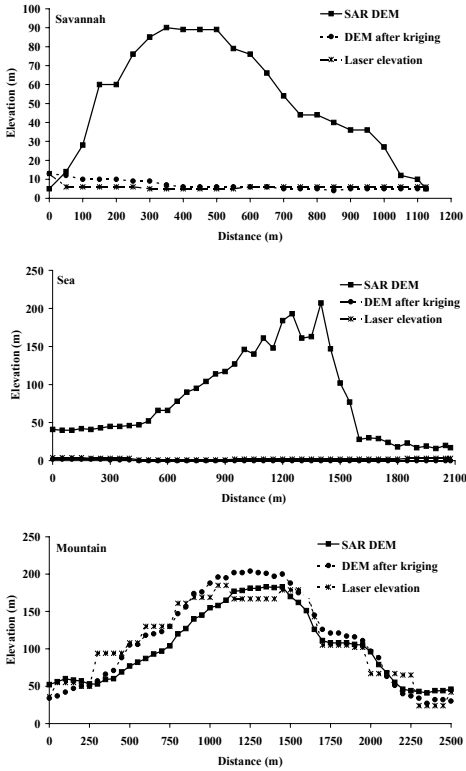


Figure 8 - Comparison of elevations from the SAR DEM, the interpolated laser data at 200 x 200 m, and the merged DEM (savannah, sea, mountain).

6 CONCLUSION

We have studied the feasibility of a Digital Elevation Model (DEM) constructed over a study area in French Guiana based on RADARSAT images and airborne elevation data.

The data were merged by kriging, taking into consideration the behaviour of the variables with distance, i.e. statistic and variographic characteristics of the variables. Two types of kriging were carried out: kriging of the difference between SAR elevations and laser elevations, then subtracted from the SAR DEM, and direct kriging of laser data when the SAR DEM yielded unsatisfactory results. Elevation was adopted as a criterion to divide the study area into several relief zones of homogeneous elevation in terms of variography, because variable behaviour is affected by elevation. Elevation accuracy (error std. dev.) was

improved from 25 m to 17 m and from 19 m to 10 m, depending on the validation source adopted (IGN maps and heliborne DEM, respectively). We thus demonstrate that the merging of DEM SAR and airborne laser data significantly improves results.

We also demonstrate, in a context where field operations and access are difficult and where traditional optical methods cannot be used, that the solution combining SAR images and airborne elevation data yields highly promising results. The scope of this method could be broadened to include other forms of data, such as radarclinometric and interferometric DEMs, and thus be applied to sites, whether in French Guiana or elsewhere, where DEMs are lacking in accuracy or even non-existent.

Acknowledgements.

The present study was jointly funded by BRGM (Bureau de Recherches Géologiques et Minières) and CNES (Centre National des Etudes Spatiales). The RADARSAT data were provided free of charge as part of the ADRO2 programme of the Canadian Space Agency. The heliborne DEM used was built by the company ALTOA on behalf of the mining company ASARCO.

7. REFERENCES

- Chilès J.P., Delfiner P., 1999, *Geostatistics: Modeling Spatial Uncertainty*. Wiley, New York.
- Toutin Th., 1999, Error tracking of radargrammetric DEM from RADARSAT images, *IEEE-Transactions on Geoscience and Remote Sensing*, Vol. 37, No. 5, pp. 2227-2238.

The Retrieval of Aerodynamic Surface Roughness from SAR Remote Sensing Image

Zhu Caiying^{1,2} Zhang Renghua², Wang Jingfeng², Xu Qing¹, Jin Guowang¹

1, The Zhengzhou Institute of Surveying and Mapping, Henan, China

2, The National Key Laboratory of Resource and Environment Information System,
Institute of Geographic Science and Resources, Chinese Academy of Sciences, Beijing

Email: zhucy@lreis.ac.cn, zcy63@371.net, zhangrh@igsrr.ac.cn

ABSTRACT This paper presents a new method to retrieval the aerodynamic surface roughness from SAR (Synthetic Aperture Radar) image. According to the theory of microwave backscattering, the pixel backscattering coefficient of SAR image is the function of the parameters of the SAR imaging system and the physical and geometrical properties of the experimental field area. There is a relationship between the pixel backscattering coefficient and aerodynamic surface roughness. This paper presented a series of process to extract the pixel backscattering coefficient from SAR image pixel values. A retrieval model of aerodynamic surface roughness from SAR image was built. Comparing the result obtained from the retrieval model with the SAR image to the results obtained from an experiment of field wind speed surveying, it is found that the outputs of the retrieval model are consistent. The developed retrieval model is valid.

1 INTRODUCTION

The interaction between earth surface and atmosphere is one of the most important topics in the domain of quantitative geographical sciences research. The information of the earth surface fluxes such as air onflow and water evaporation is largely related to the recent developments on geographical sciences research such as global changing, regional water balance and regional carbon balance, regional drought forecast etc. To retrieve earth's surface fluxes from remote sensing data is the breakthrough of the quantitative geographical sciences research during the recent decades. However the fluxes retrieval model from remote sensing data needs some parameters such as surface momentum, heat and impedance of evaporation, which are the functions of the aerodynamic surface roughness.

Aerodynamic roughness z_0 is the height above a surface at which a wind profile assumes zero velocity under the condition of neutrosphere stabilization. It is strongly influenced by size and spacing of surface roughness elements (e.g. tree, vegetation, house) and plays an important part in the interaction between atmosphere and underlying surface. It is often traditionally measured by field wind speed surveying. However, because of the complexities in field surveying, the traditional measurement consumes much time and it can not be operated in large scale.

Aerodynamic roughness z_0 and the pixel backscattering coefficient σ^0 of SAR image are both the function of submeter topography. The correlations

between z_0 and σ^0 have been developed from space borne SAR image (RADARSAT). It means that z_0 can be estimated with radar within large areas.

The center point of the experimental C-band SAR image is at the north latitude 40.23 degree and east longitude 116.43 degree. The image was obtained on April 22, 2002 by RADARSAT system, its pixel ground resolution is about 4.5m*4.5m. The field surveying was taken simultaneously around April 22, 2002. The heights of roughness elements relative to the ground and the coverage of the roughness elements in a certain area were surveyed in field work. Based on geocoding, the corresponding aerodynamic surface roughness was obtained both from the retrieval model from the SAR image and the field experiment of in North China.

Because of the specific advantages of SAR imaging, this will largely improve the technique for surveying the aerodynamic surface roughness. It is very useful for inverting surface fluxes.

2 THE MEASUREMENT OF PIXEL BACKSCATTERING COEFFICIENT FROM SAR IMAGE.

2.1 The Measurement of Pixel Backscattering

A distributed object corresponding to a pixel of SAR image has several independent scattering elements. When these elements interact with the SAR microwave, each one contributes a backscattering wave $e^{i\phi}$ with a

phase and amplitude change. The total returned incident wave is:

$$Ae^{i\phi} = \sum_{k=1}^N A_k e^{i\phi_k}.$$

The pixel value of SAR image is the mean value of total backscattering result weighted by the SAR PSF (Point Spread Function) under a particular imaging condition. For calibrated SAR image in db ---- $10\log_{10}(A^2)$, the pixel value corresponds to a linearly scaled estimate of the coefficient of backscattering σ^0 .

If the parameters of the SAR imaging system are not changed, the ground parameters ---- the standard deviation of a homogenous distributed surface height and its height correlation length, the constant of complex dielectric and the density of the material under the surface, whether or not hard object, are the direct factors which influence on the coefficient of backscattering σ^0 . Most of these factors influence on aerodynamic surface roughness too. The relationship between coefficient of backscattering σ^0 and aerodynamic surface roughness was built in this paper.

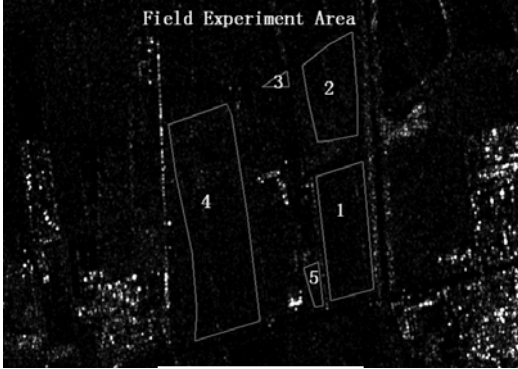


Figure (1)

2.2 The Estimate of Pixel Coefficient of Backscattering σ^0

According to the principle of the measurement of SAR backscattering, we know that the pixel value surveyed by SAR is the result of the interference among the microwave with different phase returned from the distributed object. As a result, SAR image shows speckle effect. The multiplicative SAR speckle model $I = \sigma \cdot n$ was used to describe the relationship among the pixel observed value ($I = A^2$), the

estimate (σ) of coefficient of backscattering and speckle noise (n) in this paper. For L-looks image, the pixel observed value I has a Gamma distribution and its PDF (Probability Density Function) (Chirs Oliver etc. 1997 pp94-p95) is :

$$P_I(I) = \frac{1}{\Gamma(L)} \left(\frac{L}{\sigma} \right)^L I^{L-1} e^{-LI/\sigma}, I \geq 0 \quad (1)$$

values of a pixel surveyed by N times under the same condition should be used to estimate the pixel coefficient of backscattering with Bayes criterion relating the observed I to the estimate σ . But it is difficult to obtain N values of a pixel under the complete same condition. According to the similarity of the contiguity of a pixel, the estimate (σ) is assumed constant over some neighborhood surrounding the pixel of interest. N values of a pixel are replaced by values of N pixels of the contiguity to implement the calculation in this paper. The Gamma MAP (Maximum A Posteriori — MAP) estimating method was used to obtain the estimate(σ) from the SAR speckle model $I = \sigma \cdot n$ (Chirs Oliver etc., 1997, p165-p166).

Figure (1) is a section of the RADARSAT C band original intensity image. its equivalent number of looks $L=1.5$. where the polygons circled by the red lines were the homogenous distributed areas and the digital number marked in a polygon center is the experimental station No.

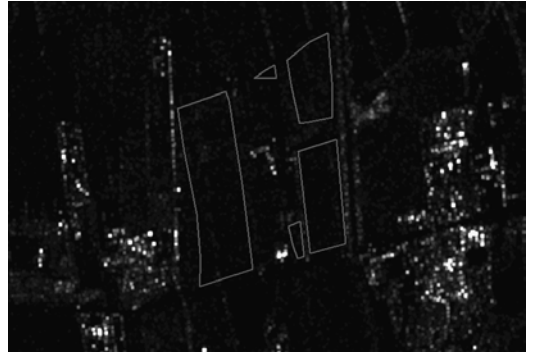


Figure (2)

The image of the estimate(σ) is shown as figure (2). We can find that many speckles in figure (1) have been filtered in the figure (2). Because the image intensity value I has a long range, the textures of figure (1) and figure(2) are not shown very clearly.

2.3 The Correction for Pixel Coefficient of Backscattering by Imaging System Parameters

The parameters and arithmetic used in correction for a SAR image pixel coefficient of backscattering are different from another one. For RADARSAT SLC formatted SAR image produced by CDPF(Canadian Data Processing Facility), the formulas to convert pixel observed value σ to pixel coefficient of backscattering σ^0 are listed as follows (Nick Shepherd, 2000):

$$\beta_j^0 = 10 * \log_{10} (\sqrt{\sigma_j} / A2_j)^2 \quad (\text{DB}) \quad (2)$$

$$\sigma_j^0 = \beta_j^0 + 10 * \log_{10} (\sin(IN_j)) \quad (\text{DB}) \quad (3)$$

where, σ_j is the estimated coefficient of backscattering of the j th pixel in a scan line corresponding to its observed value I_j , which can be obtained by above procedure “2.2”; β_j^0 is regarded as the brightness of the DB image ; $A2_j$ is the scaling gain value for j th pixel and it is obtained by linear interpolation of gain values given in the auxiliary data of the image data file; IN_j is the incident angle of the j th pixel.

Figure (3) is the corrected DB image, more details have been shown than the above intensity image.

The average σ^0 of each polygon was extracted statistically. These values are listed in table 1.



Figure (3)

3 THE FIELD MEASUREMENT OF AERODYNAMIC SURFACE ROUGHNESS FOR HOMOGENOUS DISTRIBUTED OBJECT.

Under the condition of neutrosphere stabilization, aerodynamic roughness parameters of a homogenous distributed object can be surveyed by the field measurement of a wind profile. According to reference (John L. Monteith, 1973), the relationship between height and wind speed above a homogenous distributed object is described as follows:

$$u(z) = a [\ln(z - d) - \ln z_0] \quad (4)$$

where, z_0 (unknown) is the aerodynamic surface roughness length; z (known) is the height above the ground surface at which wind speed is surveyed; $u(z)$ (known) is the observed wind speed; d (unknown) is displacement of the ground altitude, when $u(z) = 0$, $z_0 = z - d$; a (unknown) is a aerodynamic parameter.

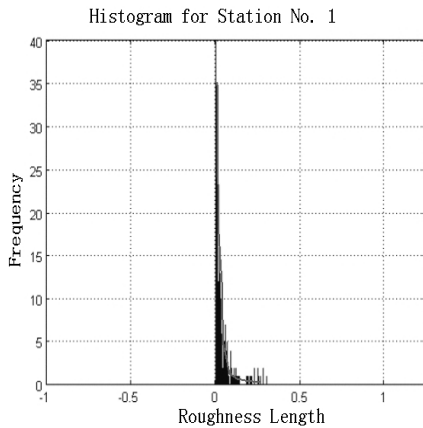
Equation (4) tells us that if more than 3 speeds at different height above a homogenous distributed object were surveyed, the parameters z_0 and d could be calculated.

Table 1 - The Average Coefficient of Backscattering of the Experiment Areas

Station No.	1	2	3	4	5
Style of Area	Dry Bareness	Wet Barness	Little Grass	Wheat	Disturbed Brick
Average σ^0	48.743553	50.976067	46.43121	50.91192	50.972931

Table 2 - Field Surveying for Aerodynamic Surface Roughness unit: M and %

Station No.	Style of ground	Standard Deviation of Soil Height (M)	Vegetable Height (M)	Vegetable Coverage (%)	Water Content Factor	z_0 (M)	d (M)
1	Area of Dry Bareness	0.0351	0	0	1.0	0.0035	0
2	Area of Moisture Bareness	0.0167	0	0	1.065	0.0015	0
3	Area of Little Grass	0.0050	0.05	20	1.0	0.0005	0
4	Area of wheat	0.0050	0.35~0.5	90	1.0	0.0242	0.34
5	Area of brick piles	0.3500	0	0	1.0	0.0235	0

**Figure (4)**

The experiment in this paper surveyed 5 wind profiles within 5 flat, homogenous distributed areas, which location and sizes have been drew in the figure (1). Each wind profile was observed continuously about 2 hours. The time interval between 2 records of the wind speeds is 10 seconds and each record at a time is consisted of 6 wind speeds observed at 6 different heights. The basic field surveyed situation and calculated results were listed in table 2.

The final results calculated under a condition of empirical climate correction have the most frequency among all calculated results. The values of column

7—“ z_0 ” and column 8—“ d ” in table 2 calculated by equation (4) were determined with the most frequency. For example, for the “station No. 1”, the histogram of the “Roughness Length” frequency is as figure (4). The histogram is worked out by “MATLAB” tool, where the red line is artificial. Then the value of “Roughness Length” can be read “0.0035” from its magnified figure. The values of column 6 — “Water Content Factor” in table 2 are determined empirically. Because only the polygon with “station No. 2” was irrigative in this field experiment, its “Water Content Factor” is given 1.065 and other polygon’s values are given 1.0

4. THE RETRIEVAL MODEL FOR AERODYNAMIC ROUGHNESS FROM SAR IMAGE

The relationship model between aerodynamic surface roughness and RADARSAT C_band F3 mode SLC formatted image pixel coefficient of backscattering has been built in this paper:

$$\log_{10} z_0 = \frac{\sigma^0}{W} \cdot k_1 - k_2 \quad (5)$$

where, parameters W —the “Water Content Factor” can be read from table 1, k_1, k_2 are empirical coefficients previously derived form RADARSAT data and field wind data. Using the data of “Station No. 1” and “Station No. 4” in the table 1 and table 2, the parameters is defined as $k_1 = 0.387271768, k_2 = 17.33293390$.

Table 3 Retrieval Calculated z_0 Compared to Field Surveyed z_0

Station No.	1	2	3	4	5
Style of Area	Dry Bareness	Wet Bareness	Little Grass	Wheat	Disturbed Brick
Average σ^0	48.743553	50.976067	46.43121	50.91192	50.972931
Field z_0	0.0035	0.0015	0.0005	0.0242	0.0235
Retrieval z_0	0.003500	0.001599	0.000445	0.024200	0.02555

Finally, the aerodynamic roughness length parameters calculated by the retrieval model with the pixel backscattering coefficient of the SAR image are listed as table 3 .

The displacement of ground altitude d is scaled with the height of roughness elements. A traditional formula (John L. Monteith, 1973) was established based on a large number of measurements of d :

$$\log d = 0.9793 \log h - 0.1536 \quad (6)$$

Where h is the height of vegetables. Using formula (6), the displacement of the ground altitude d at "Station No. 4 " is between 0.228 meters and 0.327 meters. This value is very close to the value in the table 2.

However the more accurate relationship also depends on the density and the hardness of the roughness elements.

5. CONCLUSION

The aerodynamic surface roughness z_0 of 5 homogenous distributed areas in pixel scale has been calculated by the retrieval model —formula (5). To compare the fourth row data to the fifth row data in table 3, it is found that the output of the retrieval model is matched with the field surveyed value.

The study in this paper has demonstrated that using the SAR DB image acquired by the space borne RADARSAT SAR imaging system to retrieval the aerodynamic surface roughness parameters in large extent and at pixel scale is possible. These parameters play an important part in the surface fluxes, which are an important process in the interaction between atmosphere and underlying surface.

6. REFERENCES

David J. Archer, Geoff Wadge, 1998, On the Use of Theoretical Models for the Retrieval of Surface Roughness from Playa Surfaces.
<http://www.estec.esa.nl/conferences/98c07/papers/p0>

[11.pdf](#)

J.F.McHone, R.Greeley, D.G.Blumberg, 1997, COMPARISON OF AERODYNAMIC ROUGHNESS (Z-0) VALUES FROM WIND MEASUREMENTS AND SRL RADAR; WESTERN U.S AND NAMIBIAN DESERTS. Lunar and Planetary Science, <http://www.lpi.usra.edu/meeting/LPSC97/PDF/1507.PDF>

John L. Monteith,1973, *Principles of Enviromental Physiscs*. Published by Edward Arnold 1973, Limited 25 Hill Street,London, WIX.8LL,pp78-99

Chirs Oliver, Shaun Quegan, 1997, *Understanding Synthetic Aperture Radar Images*. International Standard Book Numeber 0-89006-850-X, Library of Congress Catalog Card Number: 97-41709, Published with permission of the Controller of Her Britannic Majesty's Stationery Office.

Zhang Renhua, 2001, *Modeling of Experiment Quantitative Remote Sensing and Its Ground Surface Base*. Scientific Press, China, April, 1996

Zhang Renhua etc, 2001, Determination of regional distribution of crop transpiration and soil water use efficiency using quantitative remote sensing data through inversion. Journal of Science in China, Vol.31,(11),2001.

Nick Shepherd ALTRIX Systems, 2000, *Extraction of Beta Nought and Sigma Nought from RADARSAT CDPF Products*. 37 Belgrave Road, Ottawa, Ontario, Canada K1S0L9,28 April 2000.

K.K.Williams and R.Greeley, 1998, AERODYNAMIC ROUGHNESS ESTIMATES OF RADAR-DARK WIND STREAKS ON VENUS. Lunar and Planetary science 1207.pdf
<http://www.lpi.usra.edu/meetings/lpsc98/pdf/1207.pdf>

On-Board medium resolution SAR processing for fast image generation

Ana Vidal-Pantaleoni, Miguel Ferrando,

Departamento de Comunicaciones, Universidad Politécnica de Valencia

Camino de Vera s/n E-46022 Valencia, Tel: +34 963879710, Fax: +34 963877309

avidal@dcom.upv.es

ABSTRACT - *Spaceborne Synthetic Aperture Radar (SAR) instruments are becoming a very important source of information for Earth Observation. But these systems produce a great amount of data to be stored and extensively processed on ground. However, recent technological developments concerning microprocessors and solid state memories will enable the possibility of on-board SAR data processing. In this scenario, efficient algorithms for generating SAR images are demanded. This new situation requires specially designed algorithms for the processing stages because high-resolution approaches to SAR image generation are still too computationally expensive. There have been some studies in this direction in the past. This work makes a revision of the possible processing techniques to be used and presents some conclusions about the first and limited methods that could be implemented on-board the platform. In this work, we compare and analyze a very efficient SAR processing method for reduced resolution images called Spectral Analysis (SPECAN) and its variants. Nevertheless, range and azimuth data require different processing features that have to be carefully studied. Therefore, this work identifies the computational cost demanded by SPECAN in range and azimuth. Overall processing evaluation is validated in a simulation environment using ERS raw data. The conclusion obtained from this study is that SPECAN and especially some variants of it are very appropriate candidates for processing SAR data not only in azimuth but also in range. The results show that these new developments are very promising for obtaining fast and simple SAR image generation and they could be suitable candidates for a potential on-board implementation.*

1 INTRODUCTION

Earth Observation is an area of great interest. Governments and space agencies are investing a great amount of effort in developing Spaceborne platforms that carry Synthetic Aperture Radar (SAR) systems. SAR provides continuous and global monitoring of the Earth surface at all weather and illumination conditions. However, SAR systems produce highly correlated raw data that demands further processing. SAR focusing stages are carried out digitally by ground powerful computers (Curlander and McDonough 1991). Only limited computing resources are expected in the first on-board processing systems and consequently, just reduced resolution images could be generated. In this context, there is a need of advanced algorithms capable to process medium resolution SAR data. Efficient and modest algorithms are also very interesting due to their computational benefits for fast image generation.

The scenario where this kind of algorithms could be appreciated would be on-board SAR imaging or ground fast image generation for browsing purposes before high precision processing takes place. On-board SAR processing opens a several fields for real-time applications. SAR data dissemination usually suffers long delays and costly ordering procedures. It will

offer important savings in downlink data rate and will enable direct delivery to potential users. Medium resolution imagery is based on processing a decimated image without loss of quality if multilooking is also carried out. Consequently, the final data volume is lowered and further reduction is possible by image compression.

The Spectral Analysis (SPECAN) SAR processing algorithm and its variations are very appropriate for efficient SAR processing in both range and azimuth, when no full resolution is demanded. However, several problems arise due to the spectral analysis operation and its practical implementation. Matched filtering for range processing presents a different scenario related to SPECAN processing because the signal contains a fixed quadratic phase, but different amplitude envelope. This work studies the processing of raw SAR data by the SPECAN techniques in both range and azimuth dimensions. The main contributions of this study are the analysis of the signals and the identification of their practical limitations related to SPECAN processing. The results show that SPECAN is a very promising method for efficient two-dimensional ScanSAR image generation when no special care should be taken about the decimation ratio of the image.

The most relevant candidates to be taken into account for efficient processing have been also implemented for comparison. These are those based on fast convolution in the frequency domain and the unfocus technique (Curlander and McDonough 1991) for azimuth data. The objective is to identify an efficient yet good enough algorithm to be implemented on-board using a low capacity digital signal processor.

Some limitations concerning SPECAN processing have been identified in the past. It presents some serious drawbacks concerning output scaling that have been alleviated by the development of variations of the technique. For that purpose, SPECAN using the Chirp-Z Transform (Oppenheim and Schaffer 1989) as a spectral estimator (CZT-SPECAN) was proposed simultaneously by Vidal and Ferrando (1998) and Lanari et al. (1998) at the same international conference. This spectral analysis technique is a natural interpolator like the Chirp Scaling Algorithm (Moreira et al. 1996a, 1996b) and for that reason is a very valuable tool for designing efficient algorithms avoiding interpolators. Interpolators are either inaccurate if they have short kernels or inefficient when employing long kernels.

2 MEDIUM RESOLUTION SAR IMAGING

The digitised raw data need further processing in order to cancel the redundancy introduced by the SAR system response. Consequently, the processing chain plays a very important role in the complete SAR system. In a general case, SAR systems and their associated digital processing stages are very complex because many effects have to be considered and a rigorous mathematical analysis must be accomplished for obtaining a very accurate result. However, medium resolution or browsing images can be processed by taking some approximations without large impact on the final quality.

A trade-off between processing accuracy and computational efficiency must hence play the most important role. If the purpose of generating SAR images on-board the spacecraft is to monitor or distribute the images at near real time, then computational cost is the main driver for the processor design. The model must be simplified and some phenomena discarded for the processing stages depending on the available configuration. A quadratic approximation for the Doppler phase history and the transmitted waveform has been adopted. SAR processors need a Doppler parameter estimator that has not been taken into account. In case of medium resolution SAR image generation, range migration effect is often neglected because the larger pixel spacing in range usually compensates for the range migration. Since the data is digitised, if the

contribution of range migration is less than the decimated pixel size, then correction may be unnecessary. This fact simplifies the algorithms allowing the processing to be performed by one-dimensional deconvolution processes. This is a common approach taken in medium resolution processing.

Multilooking is the operation that reduces the amount of Speckle noise in a SAR image. It improves the radiometric resolution of the image at the cost of the spoiled geometric resolution, processing different bands of the spectrum in range and azimuth to obtain several images that can be averaged.

The possibility of producing reduced resolution SAR images on-board the orbiting platforms appears feasible for the near future as it was pointed out by Liu and Arens (1989). Once this possibility has been identified, some suitable algorithms capable of efficiently producing reduced resolution images need to be defined and assessed. The authors showed the efficiency and quality comparison for various medium resolution SAR processors in the frame of ERS-1 scenario and image generation of 160 m pixel spacing (Vidal-Pantaleoni and Rosello 1996). In that study, it was shown that for such an scheme the best performance was offered by the SPECAN techniques applied in both range and azimuth. However, that study did not take into account posterior developments in the field of SPECAN processing (Vidal-Pantaleoni and Ferrando 1998, Lanari et al. 1998). An optimum algorithm should be flexible enough to adapt to the changing conditions. It must also present capability to be efficiently implemented in a determined architecture. Finally, it should be able to cope with the different operating modes of the SAR system.

3 PROCESSING METHODS

The Range-Doppler algorithm is one of the most widely used methods and it is a good reference for comparison. The convolution with the reference template (Curlander and McDonough, Schreier 1993) may be practically implemented in the spectral domain taking into account the Convolution Theorem (Oppenheim and Schaffer 1989). Fast Frequency Convolution (FFC) is an efficient implementation of convolution in the frequency domain by means of the Fast Frequency Transform (FFT). It performs forward Fast Fourier Transform (FFT), reference multiplication and inverse FFT in smaller sets that usually correspond to different looks. The FFT data length must be at least as large as the corresponding reference templates (impulse response) and as large as possible for efficiency reasons, since a number of non-valid processed samples must be discarded depending on the FFT size and the template length. Therefore, FFC involves the use of large corner-turn memory blocks.

This requirement can be relieved by filtering and downsampling the incoming data, but this operation is also very time consuming and it does not bring much benefit apart from reducing the initial size of the FFTs, as it is shown in following sections. The FFC method allows efficient multilook extraction and spectral windowing for improving side-lobe amplitude level. These windows usually consist of a raised cosine with a variable coefficient depending on the desired performance (Curlander and McDonough 1991). In this paper, this method has been used to obtain the high quality multilook SAR image.

The unfocused processing is a special kind of azimuth SAR processing (Curlander and McDonough 1991) that does not fully exploit the phase content of the synthetic aperture. It integrates incoherently portions of the aperture by filtering in order to produce a reduced resolution azimuth signal. The best available azimuth resolution is expressed by:

$$\delta x = \sqrt{R \lambda / 2} \quad (1)$$

where R is the slant range distance and λ the carrier wavelength. The resolution restriction is the principal disadvantage of this simple method, in which the azimuth lines that form the unfocused aperture are merely weighted and added. The weighting window consists of a band pass filter. Azimuth multilooking may also be realized by a filter bank consisting of different Doppler bands. Nevertheless, increasing phase errors in looks located far from the Doppler centroid restrain this strategy.

Another technique that was introduced in SAR processing by Sack et al. (1985) and it is often involved in processing Chirp modulated signals is called Spectral Analysis (SPECAN). It is based in the deramping property of quadratic phase signals which appear in several Radar based instruments. It first performs multiplication by a reference chirp isolating target positions at different frequency tones. An efficient spectral estimator like the FFT is then applied using small windows in order to get the target position. This method also allows multiple look extraction by the original method developed previously by the authors (Vidal-Pantaleoni and Ferrando 1998) called continuous deramping. SPECAN processing may be applied for range compression if a pure quadratic Chirp is used and to azimuth processing if the azimuth phase history is sufficiently modelled with the second order term of the Taylor expansion (Curlander and McDonough 1991). This usually applies unless the SAR instrument is operating in a high squint angle mode. Efficient ScanSAR processing using the SPECAN method was proposed in the frame of fast image generation for browsing purposes or for the first prototypes of on-

board SAR processors (Vidal-Pantaleoni and Ferrando 1998). Moreover, it has also been studied in combination with other techniques like Chirp Scaling Algorithm for obtaining high precision SAR images (Moreira et al. 1996b).

The main drawback of this approach in the case of azimuth processing is the system dependence on range and velocity, which varies along the satellite orbit. For a fixed choice of FFT length, the output data rate and the inter-look pixel mismatch depend on the decimation rate d_{SPECAN} given by (2), where k is the frequency modulation rate and N_{FFT} is the number of samples used to carry out the Fast Fourier Transform (FFT).

$$d_{SPECAN} = \frac{k}{f_s^2} N_{FFT} \quad (2)$$

In the case of SPECAN azimuth processing, the sampling frequency f_s equals PRF and k is equivalent to the frequency modulation rate. Therefore, the decimation in azimuth does not only depend on the user choice but also on the orbit parameters. This problem can be solved by interpolation, which is not considered in the study for computation and complexity reasons.

In the case of range processing, the decimation can be freely chosen and it is only limited by the number of looks that are extracted from the signal. The most usual case is that the user adjusts the decimation ratio in order to obtain a square pixel in ground range and azimuth. SPECAN for range processing is appropriated because it operates on smaller data blocks than standard convolution algorithms. However, if multilook is carried out, then output pixels from different blocks must match an integer number of inter-pixel distances. That means that the expression in (3) must be accomplished, where N_R is the distance between input data blocks expressed in number of samples.

$$\frac{k}{f_s^2} N_R N_{FFT} \in \mathbb{Z} \quad (3)$$

The value in (3) is equivalent to the number of output valid samples per look and burst (Sack et al 1985, Vidal-Pantaleoni and Ferrando 1998b). It has to be obviously an integer value because looks have to be sampled at the same frequency points for valid look summation. For standard SPECAN without interpolation, only a limited set of decimation ratios and number of looks can be employed. The problem is that it is difficult to design the system in such manner that could avoid the interpolation stage.

CZT SPECAN introduced by Vidal-Pantaleoni and Ferrando (1998a) and Lanari et al. (1998) gives a

much more flexible algorithm. Its decimation choice does not depend so critically on the system characteristics. The procedure obtains equidistant spectrum samples at any arbitrary spectrum band and the decimation ratio choice is only limited by the system resolution. The time between bursts in samples is freely chosen by the user and the decimation d_{CZT} is given by (4).

$$d_{CZT} = \frac{N_R}{N_{out}} \quad (4)$$

The implemented techniques do not integrate any amplitude compensation thanks to the joined process of continuous deramping and multilooking that Vidal-Pantaleoni and Ferrando (1998) introduced. Slight amplitude modulation can be observed in the SPECAN images obtained in the simulation because no antenna pattern compensation has taken place.

3 RESULTS

This section presents the main experimental outputs from the software development. The SAR processing techniques mentioned above have been tested over ERS-1 real data and simulated point targets. The selected raw data set represents an area of approximately 70 by 80 Km acquired over the Flevoland test site in the Netherlands. This scene is chosen because it is a standard test image used to evaluate SAR algorithms and several man-made targets (dykes, roads, fields) are present.

A test has been performed in order to compare the different available techniques for medium resolution image generation. All the algorithms operate on the same data set and they provide similar output images concerning pixel spacing and number of looks. First, a high quality image obtained from the same scene is shown in figure 1. Four algorithms have been isolated for comparison: azimuth unfocused processing with range FFC in figure 2, azimuth SPECAN with range FFC in figure 3, SPECAN in range and azimuth shown in figure 4 and CZT-SPECAN in range and azimuth shown in figure 5. In order to perform a proper comparison, the same number of looks and close decimation ratios have been selected. Decimation ratios from 39 to 41.5 (six looks) in azimuth and from 6.7 to 8 (six looks) in range have been used for table 1. The resulting multilook image has a pixel spacing in the order on 190m in azimuth and ground range. SAR processing is rapidly generated and it can be used as a browsing tool or as an on-board fast algorithm. The scene that is presented in figure 2 to figure 5 has been generated on a Pentium-III machine running at 500 MHz. The scene covers approximately 70 km in range by 80 km in azimuth. Therefore, it is a fast and flexible tool for the

potential operator that can help in the dissemination of medium resolution SAR images.

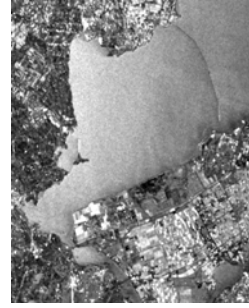


Figure 1. High quality Flevoland image processed with FFC method in range and azimuth.

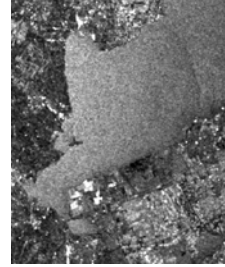


Figure 2. Flevoland image processed with FFC method in range and unfocus method in azimuth.

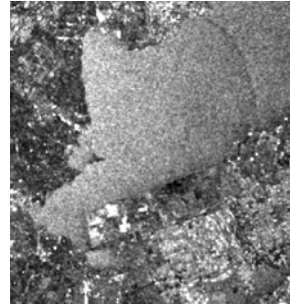


Figure 3. Flevoland image processed with FFC method in range and SPECAN method in azimuth.

Sea small windows in the Flevoland processed image were selected and the content of Speckle noise was estimated measuring the statistics of the signal and averaging the result of the different areas. The Equivalent Number of Looks (ENL) evaluates the multilook effectiveness. The results of this test are also shown in table 1. In all the cases, the measured value

is very close to the processed value (36 looks). The best result is acquired for SPECAN-2D, which is actually the most accurate method, but very close values are obtained for the rest of methods.

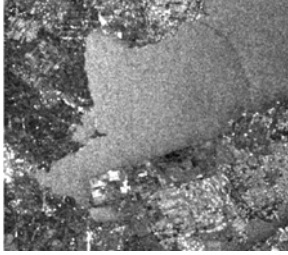


Figure 4. Flevoland image processed with SPECAN method in range and azimuth.

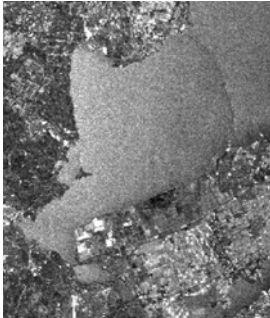


Figure 5. Flevoland image processed with CZT-SPECAN method in range and azimuth.

The visual evaluation shows a similar result for the same processing conditions (resolution and speckle removal). Since it is difficult to visualize other algorithm features, a more detailed point target analysis is carried out. In medium resolution imagery, a point target response is spread over a larger pixel grid than the one used in the full resolution case. Therefore, the calibration transponders present in ERS-1 test areas are not valid for point-target analysis because their energy contribution is low compared to the background clutter. Hence, a synthetic point target was simulated and analysed and its results are summarised in table 1. The simulated point target has been processed using the different algorithms. FFC in range and unfocus in azimuth is shown in figure 6, range FFC and azimuth SPECAN is shown in figure 7, range and azimuth SPECAN is shown in figure 8 and range and azimuth CZT-SPECAN is shown in figure 9. Then, the results are evaluated by the measured spatial resolution and Integrated Side Lobe Ratio (ISLR). First, the point target area is isolated and

interpolated using a cubic spline. Then, the point target was analysed in both dimensions by the beam width and the side lobe levels.

SPECAN algorithm produces better image quality concerning radiometric accuracy and CZT-SPECAN presents the best results in spatial resolution as it can be seen in table 1. Unfocus provides clearly the poorest result concerning radiometric and spatial resolution. Nevertheless, all of them show similar quality, that is due to the much coarser grid produced by the decimation compared to the high resolution case. From that analysis, it is shown that similar quality is offered by the different SAR techniques. It is also shown that the best spatial resolution is achieved for SPECAN algorithm although most values are in the same range. In that way, a proper algorithm choice should be mainly based on the computational efficiency offered by the proposed methods and their flexibility to adapt to the changing conditions (different spatial resolutions, different number of looks, different Doppler history, ScanSAR processing).

Therefore, the computational assessment is the most important factor in the selection of the most suitable algorithm for on-board purposes. A theoretical estimation of SAR processing computation cost is given in figure 10. As it is shown by Vidal-Pantaleoni and Rosello (1996), SPECAN techniques provides the best trade-off between computational cost and quality. In this paper, CZT-SPECAN has also been taken into consideration for the comparison.

Nevertheless, each algorithm is specially efficient under different conditions. More particularly, the unfocused method is not very convenient for azimuth multilooking, which turns it into a very time-consuming procedure. The processing cost required by a range and azimuth FFC method is also shown for reference. A comparison of the algorithm performances over a broad range of spatial resolutions illustrated in figure 10 shows that SPECAN techniques are the least time consuming and FFC is the most expensive method. That is due to the total spectrum computation that FFC produces independently of the desired number of looks. On the contrary, SPECAN methods carry out a much more efficient multilook extraction.

The number of complex multiplications needed for range processing (per input point and input line) are approximately estimated. The efficiency of the processing (valid samples out of input samples) is also included in these figures and the best case for FFC FFT lengths is chosen. In case of SPECAN techniques, only one small FFT is carried out, compared to the two large sized FFT's of the FFC algorithm. In the case of CZT-SPECAN, two FFT operations on small size data blocks are needed. This

is a very remarkable fact and it helps to turn the algorithms into almost real-time procedures. The high input data throughput is relieved and no large data blocks must be handled with corner-turn access.

Processing time can be estimated by the number of real multiplications per input line needed to implement the algorithms (final square root operation is not considered). The total amount of computation is measured by the average number of floating point multiplications needed for processing incoming lines at the rate that the SAR system produces. The rough figure of Mega Floating Point Operations per Second (Mflops) is computed considering only real multiplications and assuming a PRF of 1678.713 Hz and incoming lines of 4096 samples. This is only an approximate estimate. Therefore, it only represents an order of magnitude for assessing the feasibility of such on-board implementation. Overhead operations for initialisation (generation of matching templates and I/O functions) are not taken into account. The number of floating point multiplications is a good indicator of the total amount of computation required for DSP implementation and it also provides an estimate for a personal computer environment. In the case of the DSP, some parallelism is possible for floating point operations and the additions may be joined to the multiplications in one cycle under certain conditions. For a program running on a standard PC, the multiplication is a very time consuming task, so it properly models the total amount of computation if no other expensive tasks take place in the loops.

The general comparison among the selected algorithms is shown in figure 10. The theoretical figures for the Mflops needed for obtaining a constant number of looks in the final image are plotted versus pixel spacing variation. From this graph, it is concluded that the techniques that give the best performance in terms of computation are based on the SPECAN principle. Moreover, the high throughput front-end interface is relieved by rejecting incoming data and the amount of memory is also reduced.

High resolution processing dramatically increases the computational burden on SPECAN algorithms. On the contrary, for reduced resolution processing SPECAN technique for range compression always offers the best result. It has been verified that SPECAN range compression achieves the best efficiency result when decimation passes certain threshold. On the other hand, if we assume that some speckle reduction is going to be carried out, then there will exist a decimation ratio at least as high as the desired number of independent looks to be processed. Therefore, CZT-SPECAN range processing will probably give the best choice for medium resolution SAR image generation. Moreover, since the Chirp parameters are fixed, range SPECAN does not suffer

from the main drawbacks (scalloping, inter-pixel mismatch) that azimuth processing presents.

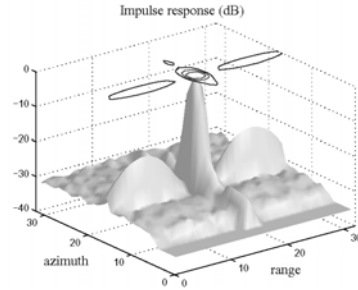


Figure 6. FFC method in range and unfocus method in azimuth point target response.

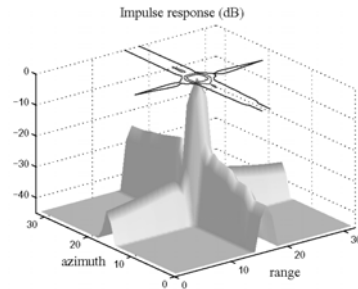


Figure 7. FFC method in range and SPECAN method in azimuth point target response.

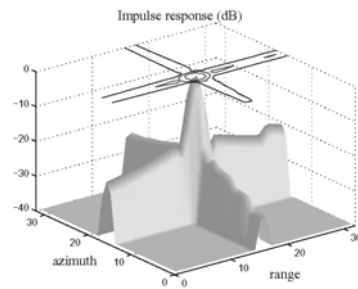


Figure 8. SPECAN method in range and azimuth point target response.

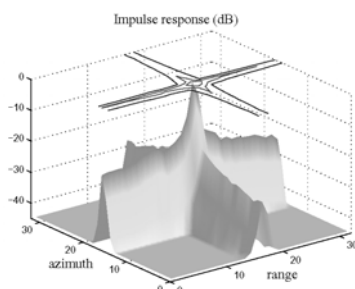


Figure 9. CZT-SPECAN method in range and azimuth point target response.

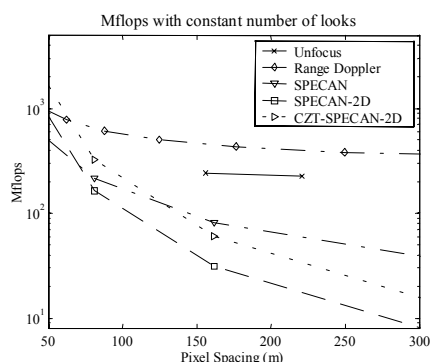


Figure 10. Computation cost in terms of Mflops for real time processing for constant number of looks and different mean spatial resolution for the implemented algorithms and the standard FFC method for range and azimuth shown for comparison.

5 CONCLUSIONS

The main purpose of this paper has been to identify and to evaluate several algorithms for on-board medium resolution imagery. Standard FFC techniques are accurate, but they require high computation efforts and a large amount of memory. On the contrary, unfocused processing offers a very simple method when restricted resources are available, although it presents main limitations on resolution and multilooking. Finally, SPECAN and CZT-SPECAN offer the best compromise between quality and computational cost. They are the most promising approach to achieve on-board real time image generation. They process data not only efficiently but also reducing the memory requirements. Moreover,

they are able to deal with ScanSAR data as well. They do not require large storage, need fewer number of operations and offer acceptable image quality. This processing may be applied to both dimensions and it turns out to be the most suitable choice for on-board imagery or browsing algorithm.

It is concluded that on-board SAR medium resolution image generation, producing an important data rate reduction and direct image distribution, will be feasible with the new technology developed by ESA. The next step in the development of an on-board SAR system will be the definition of an architecture based on four DSP's and the implementation of the selected algorithm.

The development of a algorithm based on CZT-SPECAN processing for range and azimuth processing is described. In this work, special emphasis is made on the practical considerations when applying SPECAN and CZT-SPECAN on range and azimuth data. The previous comparisons with other algorithms given in the literature is then complemented with the new introduction of the new method developed by the authors previously (Vidal-Pantaleoni and Ferrando 1998). The critical factors are the decimation ratio, number of looks and other SPECAN processing parameters. Some relations between them are presented through mathematical expressions for the case of SPECAN and CZT-SPECAN. The selected technique CZT-SPECAN has been shown as an example of SAR image generation that is efficiently carried out for browsing purposes and avoiding interpolation. The final product gives enough quality to distinguish spatial features and it is rapidly generated in a general purpose computer at very low computational cost.

ACKNOWLEDGEMENTS

The authors want to thank the European Space Agency for the kind provision of ERS-1 raw data.

REFERENCES

- Curlander, J. C. and McDonough, R., 1991, Synthetic Aperture Radar Systems and Signal Processing, (John Wiley and Sons Inc.: New York).
- Lanari, R., Hensley, S., and Rosen, P., 1998, Modified SPECAN algorithm for ScanSAR data processing. In Proceedings of IGARSS'98 (Piscataway, NJ: IEEE), pp 636-639.
- Liu, K., L. and Arens, W. E., 1989, Spacecraft on-board SAR image generation for EOS-type missions. *IEEE Transactions on Geoscience and Remote Sensing*, **27**(2), 184-192.

- Moreira, A., Scheiber, R. and Mittermayer, J., 1996a, Azimuth and range scaling for SAR and ScanSAR processing, In Proceedings of IGARSS'96, pp. 1214–1216.
- Moreira, A., Mittermayer, J., and Scheiber, R., 1996b, Extended chirp scaling algorithm for air- and spaceborne SAR data processing in stripmap and ScanSAR imaging modes. *IEEE Transactions on Geoscience and Remote Sensing*, **34**(5), 1123–1136.
- Oppenheim, A. V. and Schafer, R. W., 1989, Discrete-Time Signal Processing, (Prentice-Hall: London).
- Schreier, G., 1993, SAR Geocoding: Data and systems, Wichmann, Karlsruhe.
- Vidal-Pantaleoni, A. and Rosello, J., 1996, Comparison of medium resolution algorithms for spacecraft on-board SAR image generation. In Proceedings of IGARSS'96 (Piscataway, NJ: IEEE), pp. 1224-1226.
- Vidal-Pantaleoni, A. and Ferrando, M., 1998, A new spectral analysis algorithm for ScanSAR and medium resolution SAR data processing without interpolation. In Proceedings of IGARSS'98 (Piscataway, NJ: IEEE), pp. 639-641.
- Vidal-Pantaleoni, A. and Ferrando, M., 1998, A comparison of SAR processing SPECAN techniques for efficient ScanSAR image generation. In Proceedings of the SPIE, SAR Image Analysis, Modelling, and Techniques (Bellingham, WA: SPIE), **3497**, pp. 31–42.

	Unfocus	SPECAN-1D	SPECAN-2D	CZT-2D
ISLR (dB)	-33.37	-31.14	-32.57	-30.7
Range spatial resolution (pixels)	1.26	1.25	1.4	1.04
Azimuth spatial resolution (pixels)	1.28	1.26	1.25	0.9
Range decimation (m)	8	8	6.7	8
Azimuth decimation (m)	39	41.46	41.46	40
Number of looks (range x azimuth)	6 x 6	6 x 6	6 x 6	6 x 6
Mean ENL in uniform zones	22.7	28.33	33.66	22.9

Table 1 Comparison of quality analysis and processing parameters.

Comparison of different Speckle reduction techniques in SAR images using Wavelet transform

Ana Vidal-Pantaleoni, David Martí,

Departamento de Comunicaciones, Universidad Politécnica de Valencia

Camino de Vera s/n E-46022 Valencia, Tel: +34 963879710, Fax: +34 963877309

avidal@dcom.upv.es

ABSTRACT - *Speckle noise is a undesired characteristic effect in Synthetic Aperture Radar (SAR) images. It is important to reduce it before the information is extracted from the image. Many methods that reduce Speckle noise while preserving texture and detail have been presented before. In this paper, a methodical comparison of different methods using Wavelet decomposition is performed and new improvements for traditional methods are introduced. These techniques are: Wiener filtering, classical soft threshold, a new adaptive soft threshold and Bayesian reconstruction. First, Speckle noise in a SAR image has been analysed statistically. Then, a simulated image following these characteristics is created in order to evaluate noise reduction. The mean squared error is classified depending on the spatial characteristics of a local region. This tool gives valuable information for algorithm assessment. In the comparison, the new adaptive soft threshold method provides excellent results concerning noise reduction and detail preservation compared to classical soft threshold and Wiener. Besides, it gives as much noise reduction as the most sophisticated Bayesian method, but much more efficiently. So, the adaptive version of soft thresholding outperforms the other techniques. This study also presents a rigorous framework for noise reduction evaluation.*

1 INTRODUCTION

Synthetic Aperture Radar (SAR) images contain several sources of noise that are undesired and make image exploitation more difficult to achieve. The usual thermal noise given by electronic equipment is given, but there is also another source of error that is characteristic in SAR systems. This effect is called Speckle noise, because there is a similar effect in laser imaging (Dainty 1984, Curlander and McDonough 1991). The origin of Speckle in laser optics, ultrasonic imaging and microwave Radar is the same. It is caused by the high coherence of the illumination source that causes phase interference from random scattering points. The relatively narrow bandwidth combined with the surface roughness at the wavelength scale produces a pattern of interference that results in a grainy appearance (Curlander and McDonough 1991). Although it is a systematic effect, Speckle is generally considered a distortion factor and many efforts are made in order to reduce it. Noise affects severely automatic post-processing applications like segmentation and classification. For that reason, it is important to reduce it before feature extraction takes place. Despite of that, there are some situations that prefer to exploit an original SAR image rather than a despeckled one because denoising methods cancel out Speckle noise, which is undesired, but also texture data, which is the key information in some classification processes.

There are several approaches towards the problem of Speckle reduction. A comparison of several speckle reduction procedures is described by Schwarz et al. (1997). Simard et al. (1998a) applied Wavelet decomposition to normalised SAR images instead of logarithmically transformed images, which is the usual approach. Walessa and Datcu (2000) study Speckle reduction and texture preservation using Gauss Markov random fields because they take into account local statistics. As an alternative approach, Zeng and Cumming (2001) use a non standard Wavelet decomposition similar to Wavelet packet theory in order to preserve image texture.

In general, Speckle reduction techniques may be classified into two types. The first approach is devoted to the reduction of the noise variance by averaging. This method is called multilook and it may be implemented by different procedures. One of them is to obtain several acquisitions of the same imaged area by processing a number of antenna subapertures or spectrum bands. Then they are added and since the images are statistically independent, the variance is reduced by a factor that is related to the number of subimages (Curlander and McDonough 1991). This method carries a spatial resolution degradation because full resolution is only obtained when all the spectrum band is processed. Multilook may also be carried out by window averaging. It smoothes the image again at the cost of spatial resolution and produces poorer results.

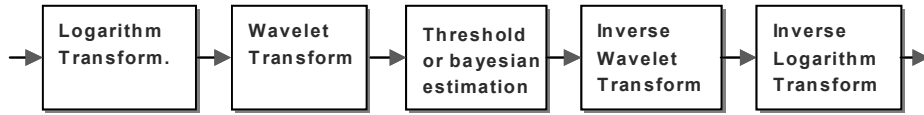


Figure 1. Speckle noise reduction block diagram.

The second technique that is used for speckle reduction is SAR postprocessing or image processing. It includes all sorts of local filters and transformations. Some of them are based on statistical locally adapted filters and recently, methods based on multiresolution decomposition have appeared in the literature (Datcu et al. 1996, Zeng and Cumming 1998, Simard et al. 1998a, Simard 1998b). In principle, this approach does not affect the original spatial resolution of the image as Multilooking does.

In this paper, the objective is to assess some techniques based on Wavelet decomposition. Some of them have been originally developed for normal additive white Gaussian noise. Therefore, they have been adapted to the new problem. In this work, Speckle noise should be reduced meanwhile preserving detail and edges on the image. Texture is not preserved, because the final objective is to get a good estimate of the reflectivity information for classification purposes. Logarithmic transform and Wavelet transform are assumed through the paper.

A method based on Wavelet decomposition with a new adaptive approach is presented. It combines the characteristics of additive noise reduction of soft thresholding (Donoho 1995) with the localization of information in the coarsest levels of the Wavelet transform (Mallat 1989), being its main contribution to adapt the effective threshold to the level of decomposition. A new Bayesian estimator with some variations compared to the traditional approach is also introduced. Finally, a comparison of all proposed algorithms is presented.

2 SPECKLE NOISE

Dainty (1984) and Arsenault and April (1976) give a very good description of laser Speckle. SAR Speckle noise is produced by coherent contributions of the terrain scattering points through an interference mechanism. However, there have been several attempts to establish a simplified model that could be considered as a good simple model of the real Speckle formation process. An approximation is to consider the Speckle formation as a random walk process in the complex domain with many contributions from many elementary scattering points, which are statistically independent in amplitude and phase. Then, the complex image is modelled with a complex independent stochastic process with Gaussian distribution. Under such assumption, Dainty (1984)

shows that the amplitude of the SAR image is Rayleigh distributed and the intensity of the SAR image is exponentially distributed. In general, noise contribution depends on the reflectivity, since bright areas present higher contributions of Speckle noise than dark regions. Besides, a local correlation due to the fully developed Speckle pattern is present in the image (Simard et al. 1998a). This dependence on the reflectivity is a severe drawback when programming a noise reduction algorithm. The well known local statistical filter introduced by Lee (1980) and the adaptive smoothing filter (Kuan et al. 1985) are two approaches that operate directly on the image domain, as they adapt the smoothing property of the filter to the local signal statistics.

As an alternative approach, Speckle can be considered noise contribution with a multiplicative model. Consequently, the image could be easily transformed to turn multiplicative noise into additive noise. That direction may be provided by a simple homomorphic transformation (Arsenault et al. 1976) that approximately turns the Speckle noise into a signal independent standard additive noise (Sadjadi 1987, Pascasio and Shrinzi 1996, Zeng and Cumming 1998, Zeng and Cumming 2001). However, the logarithmic transformation is not a linear procedure and it would affect the signal statistics and the signal-noise separation (Sadjadi 1987, Simard et al. 1998a). Another method that can be used for turning multiplicative noise into an additive model is normalisation by a smooth version of the image (Simard et al. 1998a). However, this method presents other drawbacks like the lack of linearity and the estimation of the smooth image. Normalisation using a low pass filtered image has been tested in this study, but homomorphic transformation has achieved the best results concerning noise reduction in the tests and it has been selected for this simulation.

The first stage in figure 1 is the logarithmic transformation following the multiplicative noise Speckle model introduced by Arsenault and April (1976). The digitised SAR reflectivity is represented by the image intensity $y(i,j)$, where the indices i and j are omitted in the rest of the paper. The intensity y in (1) is formed by the unknown reflectivity x and a multiplicative noise n . The possible additive thermal noise is neglected because it would complicate the study.

$$y = xn \quad (1)$$

$$\log(y) = \log(x) + \log(n) \quad (2)$$

$$\tilde{y} = \tilde{x} + \tilde{n} \quad (3)$$

$$\tilde{y} = \log(y), \quad \tilde{x} = \log(x), \quad \tilde{n} = \log(n) \quad (4)$$

In (2) a logarithmic transformation turns multiplicative noise n into additive noise \tilde{n} , which is the additive transformed speckle contribution that has been described (Zeng and Cumming 1998, Arsenault and April 1976) as a signal independent additive Gaussian noise. In this work, the validity of this model has been tested using a SAR image, that has been taken as a noise free image due to the high number of looks used in the SAR processing algorithm (484 looks). Another image of the same area but processed with only 24 looks is taken as a noisy observation. Then, a logarithmic transformation is applied and the corresponding transformed noise is analysed. It has been observed that this noise is not well characterised by a white Gaussian model. The noise statistics are Gaussian in different subbands, but they present different noise power at each level of decomposition. That means that the Gaussian model is well fitted to each level, but logarithmic Speckle noise is not white. For that reason, the Speckle source used for the simulation process in the following sections is a Gaussian distribution specially adapted to each subband.

3 WAVELET TRANSFORM

Wavelet transform (Daubechies 1988, Mallat 1989) is a tool that performs hierarchical decomposition of the signal space into a nested sequence of approximation spaces. This transformation takes information from the signal by filtering and scaling. One of the most profitable properties is that it gives coefficients related to spectral contents but also with good spatial localisation. It has been applied successfully (Datu et al. 1996) to the processing and interpretation of images and SAR data. In the field of Speckle reduction, promising results in the application of Wavelet decomposition have been reported in the literature (Wei et al. 1995, Odegard 1995, Simard et al. 1998a, Zeng and Cumming 1998, 2001).

The direct and the inverse wavelet transformation of the continuous one-dimensional signal $y(t)$ are calculated using the following expressions:

$$y_n^m = \int_{-\infty}^{\infty} y(t) \Psi_n^m(t) dt \quad (5)$$

$$y(t) = \sum_n \sum_m y_n^m \Psi_n^m(t) \quad (6)$$

where $\Psi_n^m(t)$ represents a set of basis functions that are dilations and translations of a single function called mother wavelet.

SAR images are discrete two-dimensional signals and the corresponding transformation is the two-dimensional Discrete Wavelet Transform (DWT). This transformation operates in a two dimensional discrete domain and the implementation of the transformation has been carried out through the efficient tree decomposition described by Mallat (1989). Filtering and decimation progressively decompose the original image by a scheme that creates a pyramid of lower resolution approximations.

Since DWT is a linear transformation, then the expression (7) applies. However, DWT is not a space invariant transformation due to the decimation stages. The statistics of the Wavelet and logarithmic transformed noise N are assumed to be Gaussian at each subimage as described by Zeng and Cumming (1998) and confirmed by a previous study using real SAR images.

$$\text{DWT}(\tilde{y}) = \text{DWT}(\tilde{x}) + \text{DWT}(\tilde{n}) \quad (7)$$

$$Y = X + N \quad (8)$$

$$Y = \text{DWT}(\tilde{y}), X = \text{DWT}(\tilde{x}), N = \text{DWT}(\tilde{n}) \quad (9)$$

Wavelet transformation has an interesting property of simultaneous space and frequency localisation. For that reason, features are preserved through the decomposition tree. Therefore, detail information may be kept and threshold application can reduce noise without edge distortion. An illustration of a two-dimensional DWT transformed image is shown in figure 2. In the decomposition tree, low pass information is progressively analysed and three high pass subimages are kept at each resolution level. High pass subimages usually contain information about directional edges.

There are several families of Wavelet functions that are useful for different applications. In this work, DWT has been applied with three levels of decomposition using an orthonormal family with 16 vanishing moments (Daubechies 1988). This wavelet family is widely used because it provides compactly supported orthonormal bases. Besides, 16th order gave the best noise reduction in a previous study.

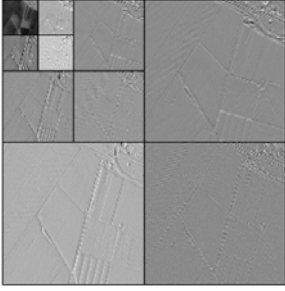


Figure 2. Wavelet transform of an image with three levels of decomposition.

4 THRESHOLDING

The combination of hierarchical Wavelet decomposition and adaptive shrinkage has been reported in the literature (Odegard et al. 1995, Donoho 1995). However, the special characteristics of SAR images and the statistical model of Speckle noise introduce new factors in those algorithms. First of all, an homomorphic transformation is carried out in order to make noise independent from the signal itself. That fact has been carefully evaluated in this study and some important results have been deduced from it. The basic idea for Wavelet noise reduction is to apply some kind of processing to the Wavelet coefficients that are obtained at different levels of decomposition.

Threshold application can be implemented by different techniques and the most common are soft and hard thresholds shown in figure 3. Hard threshold is the simplest one: coefficients above a certain value are kept and those below it are just set to zero. Donoho (1995) first proposed a more sophisticated technique that was called soft thresholding. It was originally developed for reducing additive Gaussian noise in a Wavelet decomposed signal. Hard thresholding typically yields the minimum mean squared error (MSE), but soft thresholding gets almost the minimax MSE with the property that it achieves a final result as least as smooth as the true solution. As a consequence, in the first case the operation is smoother and it gives the best results in SAR imagery (Odegard et al. 1995). The soft threshold is expressed in (10) and classical hard threshold is described in (11).

$$Y' = \begin{cases} \text{sign}(Y) \cdot (|Y| - T) & |Y| > T \\ 0 & |Y| \leq T \end{cases} \quad (10)$$

$$Y' = \begin{cases} Y & |Y| > T \\ 0 & |Y| \leq T \end{cases} \quad (11)$$

Donoho (1995) showed that soft thresholding outperformed the classical hard thresholding implementation in the case of Gaussian additive noise. Odegard et al. (1995) applied it successfully to SAR images after a logarithmic operation.

One of the key aspects is the choice of the threshold value T . This is the most critical step in the Wavelet shrinkage operation, since a poor adjustment may provide a distorted image or unnoticeable noise reduction. In Odegard et al. (1995) and Wei et al. (1995), the proposed threshold is proportional to the noise variance estimation and it is constant for all Wavelet coefficients except for the low pass image, that is not modified since it retains most of the information. The novelty in this paper is related to the threshold choice, which is computed taking into account subimage statistics and the level of decomposition in the Wavelet Transform and introducing the philosophy of locally adapted statistical methods.

The standard Wavelet soft threshold T applied to each wavelet coefficient is computed following (12).

$$T = T_{ef} \sigma \quad (12)$$

where T_{ef} depends on the number of pixels in the image and the chosen Wavelet family (Donoho 1995, Zeng and Cumming 2001) and σ is a noise standard deviation estimate.

The first innovation to the standard algorithm is to apply different thresholds T to different subimages and to use a subimage Signal to Noise Ratio (SNR) estimate to increase or decrease T_{ef} . That version is called in the simulation soft thresholding.

The second variation is to take also into account the level of decomposition in a two-fold modified shrinkage operation. Coefficient processing is carried out independently in each detail subimage and only those coefficients are taken into consideration for the computation of the standard deviation. Secondly, T is also different for each subimage and depends on the level of decomposition according to the following equation, that is a modified version of (12)

$$T = \gamma^{(N-i-1)} T_{ef} \sigma \quad (13)$$

where i is the decomposition level, N is number of levels, T_{ef} is the SNR adjustment parameter and γ is a processing parameter that has to be fixed. The level of decomposition is defined as the depth in the pyramid decomposition tree and it equals one for the coarsest level. This new method is called adaptive soft threshold.

There is no threshold application for the low pass subimage, following the strategy described in Odegard et al. (1995) and Wei et al. (1995). The low pass

smooth subimage retains most of the information and distortion effects would be more severe than possible noise reduction. The SNR of the transformed image increases with the level of the decomposition and that effect has been measured analysing the statistics of the image and Speckle noise. For that reason, the threshold is locally adapted to the resolution level. In summary, this new adaptive soft threshold noise reduction gets an adjustment, not only to the particular statistics of the sub-image (standard deviation), but also to the SNR of the resolution level.

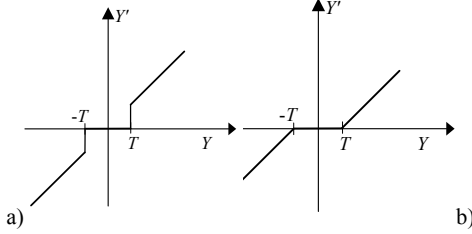


Figure 3. Threshold application: (a) hard threshold and (b) soft threshold.

5 BAYESIAN MODEL

Bayes theory for noise reduction is theoretically based on additive and signal independent noise. It provides an integral rule that can estimate a noise free signal from the noisy observation. For that purpose, it uses the noisy observations and the probability density function for both signal and noise (Simoncelli and Adelson 1996, Zeng and Cumming 1998). Since the amount of information about both signal and noise is higher than in the case of threshold application, it is obvious that more computation will be required for signal estimation. If the model for transformed signal plus noise described in (8) is taken, then Bayes provides us with an estimate $\hat{X}(Y)$ of the uncorrupted transformed signal X if probability distribution functions are known for the signal and noise.

Mallat (1995) proposed a model for Wavelet coefficients that is based on a two parameter generalised Laplacian distribution. Only the significant terms are shown in the expression. Parameters p and s can be estimated from the second and fourth moment of signal X as described by Simoncelli and Adelson (1996) and Schroder et al. (1999). Obviously, there is not a direct access to the noise free signal. Therefore, if we assume that noise is additive Gaussian noise, then p and s may be computed directly from the variance and kurtosis of the noisy signal as described by Simoncelli and Adelson (1996) with a blind Bayesian estimator.

Bayes theory is used in this paper for two purposes. The first one is to characterise SAR images

and Speckle noise. The second one is to use Bayes integral rule to perform Wavelet shrinkage. However, the expression with analytic probability distribution functions should be solved in order to get an estimate for X . If the distributions for signal and noise were Gaussian, then the solution would be simple scaling of the X samples using Wiener theory. In the case of considering Laplacian functions, then Simoncelli and Adelson (1996) show that integrals have to be solved numerically.

Logarithmic and Wavelet transformed noise has been modelled by a Gaussian distribution and noise variance estimation is assumed throughout the paper. From this study, it was concluded that SAR signal statistics are well fitted to a squared root exponential function and si in (14) is the only signal parameter that needs to be estimated.

$$\hat{X}(Y) = \frac{\int X e^{-\left(\frac{Y-X}{sr}\right)^2} e^{-\sqrt{\frac{X}{si}}} dX}{\int e^{-\left(\frac{Y-X}{sr}\right)^2} e^{-\sqrt{\frac{X}{si}}} dX} \quad (14)$$

Another Bayesian algorithm that has been developed in this paper is based on an adaptive version of the last Bayesian estimator operating in subimages with Gaussian noise distribution and squared root exponential SAR signal distribution. In this case, a Sobel edge detector is applied and the smoothing capacity of the Bayes estimator is also adapted to the presence of edges in the image. Therefore, parameter sr is computed taking into account the edge mask information. It has been detected that this algorithm is much more convenient when the amount of noise increases. In that case, the edge error cancellation increases when compared to the non adaptive Bayes estimator using the same models.

6 SIMULATION RESULTS

In the experimental simulation, the first stage is to evaluate the statistical characteristics of SAR images with and without Speckle noise. It is important to have a good statistical characterization of the noise and the signal in the logarithmic and Wavelet domain in order to apply Bayesian theory. For that reason, a study has been performed for obtaining a practical model for Speckle noise. The main drawback is that no noise free source can be available for a SAR image. Alternatively, a multilook image with high number of looks (484) shown in figure 4a is taken as a noise free image. Then, a multilook image of 24 looks shown in figure 4b is taken as a Speckled image. From this study, it has been concluded that logarithmic Speckle noise in different Wavelet levels presents Gaussian

distribution at each subimage and significant noise power differences through the levels of decomposition. This is an aspect that makes the equivalent additive transformed noise to be different from a Gaussian model, which preserves noise variance through the decomposition levels. The noise free SAR image has been also studied and the squared root exponential probability distribution function (14) has given the best fit for the SAR image.

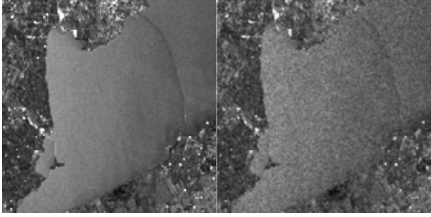


Figure 4. Multilook SAR image processed with: (a) 484 looks assumed as noise free SAR image and (b) 24 looks assumed as noisy image.

The most critical aspect in threshold application is the threshold choice, which involves an estimation for the noise power without knowing the amount of actual noise (blind estimation). In the case of the Bayesian estimators, even more information has to be extracted from the noisy data. Statistical parameters are obtained mainly from the second and fourth moment of the subimage. The evaluation of the threshold algorithms has been done varying the values of the effective soft threshold T_{ef} in (12) and (13) that are adjusted according to the image SNR and varying also the parameter γ (13). From the results using different processing parameters, the best ones are chosen for the following experiment. In a real scenario, parameters should be adapted in a blind procedure and further investigation should be carried out in this direction in order to achieve always the best results.

The experimental simulation has been carried out using an optical aerial image corrupted with multiplicative noise following Speckle statistics taken from the previous study. The original and the noisy image are shown in figure 5. The noisy signal presents a SNR of 13dB.

The algorithms have been tested on the simulated image and the results we have obtained are shown in figure 6 for the case of Wiener filtering, soft thresholding and adaptive soft thresholding. Bayesian techniques are presented in figure 7. The analysed methods use a Gaussian model for noise and a squared root exponential for image data and an adaptive version of the previous technique in figure 7.

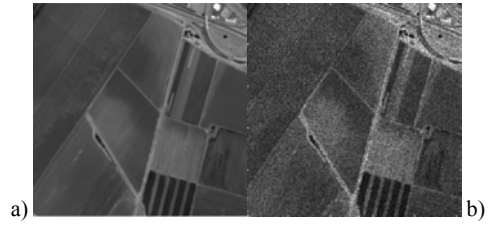


Figure 5. Simulation images: (a) optical noise free image and (b) simulated Speckled image with a SNR of 13 dB.

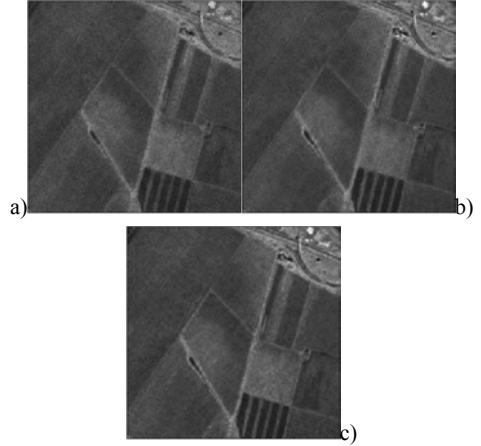


Figure 6. Reconstructed simulated images using: (a) Wiener filter, (b) soft thresholding and (c) adaptive soft thresholding.

It is difficult to evaluate the methods from visual inspection. Therefore, the results are also presented in figure 8 and figure 9 in terms of cancelled mean square error, which is an indicator of noise reduction. A test environment has then been created for comparing the performance of different Speckle reduction methods, and the analysis has taken into account edge preservation. The mask is provided by a smoothed Sobel edge detector. Therefore, the total error with respect to the original optical image can be easily evaluated, and it can be also classified through the mask into two categories: uniform region error and edge error. Figure 9 shows the amount of cancelled edge error versus cancelled uniform error. The proposed new adaptive soft threshold presents clearly the best results when compared to Wiener and non adaptive soft threshold.

The comparison of Bayesian methods has been also carried out using the same procedure in figure 9, which summarizes the algorithm performance of two selected techniques. It also shows edge error cancellation in relation to the achieved uniform error

cancellation. Bayesian techniques were expected to provide the best results taking into account that more prior information about the image is considered in the noise reduction process. However, the best result, which is given by the adaptive Bayesian estimator, just reaches the percentages in cancelled error given by soft thresholding as it was shown in figure 8. Besides, the process is much more time consuming. For that reason, the new adaptive soft threshold application is selected as the best technique in this study.

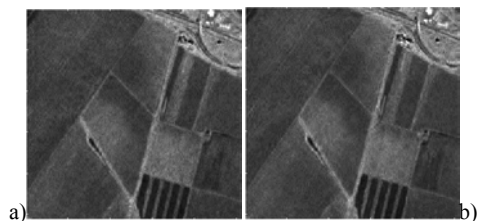


Figure 7. Reconstructed simulated images using Bayesian estimators: (a) Gaussian noise and squared root exponential image and (b) adaptive Gaussian noise and squared root exponential image.

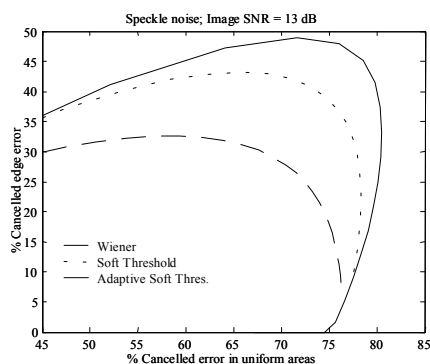


Figure 8. Comparison of error cancellation for Wiener and thresholding using the simulated image.

Once the performance of the new method has been shown on a simulated image, another test using real SAR data has been carried out. The result using adaptive soft thresholding is shown in figure 10. Speckle noise is noticeably reduced while edges and details like roads and dykes are preserved.

7 CONCLUSIONS

A rigorous analysis of different Speckle reduction techniques based on the Wavelet transformation has been performed. First, Speckle statistics have been studied and then the results have been applied to denoising techniques. Then, some improvements on the classical implementations have been identified and implemented. Besides, a method for the correct

evaluation of the different techniques which takes into account not only noise reduction in uniform areas but also edge preservation has been used. In this evaluation, error in the reconstruction process has been classified into error committed in uniform areas and error committed in edges.

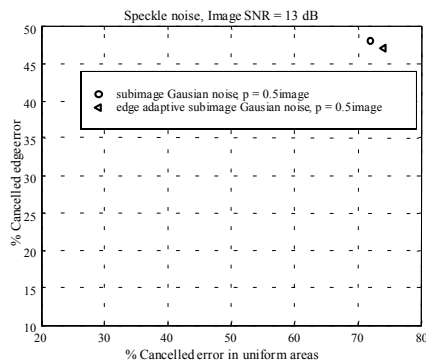


Figure 9. Comparison of error cancellation for Bayesian estimators using a simulated image.

Some conclusions concerning the statistical characterisation are obtained in this paper. First, a strong relation for the subimage SNR with the level of decomposition of the Wavelet transform has been identified. Secondly, Speckle noise statistics have been identified. There is a good agreement of the Speckle histogram of the image after logarithm transformation with Gaussian noise for each subimage. Finally, SAR images without Speckle noise are well modelled by a Laplacian function after logarithmic transformation. However, the best fit is achieved for a squared root exponential probability distribution model.

In this work, we have also implemented different techniques that achieve SAR Speckle reduction applied to the logarithm and Wavelet transformed simulated image. As final conclusion, adaptive soft thresholding has outperformed the other methods in quality results. It gives visually almost the same quality that standard soft thresholding for both simulated and real SAR images, but the detailed measurement of the edge preservation and noise cancellation shows that the new version gives a more accurate result.

ACKNOWLEDGMENTS

The authors want to thank the European Space Agency for the kind provision of ERS-1 raw data.

REFERENCES

- Arsenault, H. H. and April, G., 1976, Properties of Speckle integrated with a finite aperture and logarithmically transformed. *Journal of the*

- Optical Society of America*, **66(11)**, pp. 1160-1163.
- Curlander, J. C. and McDonough, R. N., 1991, *Synthetic Aperture Radar systems and signal processing* (New York: Wiley).
- Dainty, J. C., 1984, *Laser Speckle and related phenomena* (New York: Springer-Verlag).
- Datcu, M., Luca, D. and Seidel, K., 1996, Multiresolution analysis of SAR Images. *Proceedings of the European Conference on Synthetic Aperture Radar EUSAR'96* (Berlin: VDE Verlag), pp. 375-378.
- Daubechies, I., 1988, Orthonormal bases of compactly supported Wavelets. *Communications on Pure Applied Mathematics*, **441**, pp. 909-996.
- Donoho, D. L., 1995, De-noising by soft thresholding. *IEEE Transactions on Information Theory*, **41**, pp. 613-627.
- Kuan, D. T., Sawchuk, A. A., Strand, T. C. and Chavel, P., 1985, Adaptive smoothing filter for images with signal-dependent noise. *IEEE Transactions on Pattern Analysis and Machine Intelligence* **7(2)**, pp. 165-177.
- Lee, J. S., 1980, Digital image enhancement and noise filtering by use of local statistics. *IEEE Transactions on Pattern Analysis and Machine Intelligence*, **2**, pp. 165-168.
- Mallat, S. G., 1989, A Theory for multiresolution signal de-composition. *IEEE Transactions on Pattern Analysis and Machine Intelligence*, **11**, pp. 674-693.
- Odegard, J. E., Guo, H., Lang, M., Burrus, C. S., Wells, R. O., Novak, L. M. and Hiett, M., 1995, Wavelet-based SAR Speckle reduction and image compression. In *Proceedings of the SPIE, Algorithms for Synthetic Aperture Radar Imagery II*, **2487** (Bellingham, WA: SPIE), pp. 259-271.
- Pascasio, V. and Schrinzi, G., 1996, Reduction of multiplicative noise in SAR imaging by Wiener filtering. In *Proceedings of the IGARSS'96* (Piscataway, NJ: IEEE), pp. 1577-1579.
- Sadjadi, F. A., 1987, A perspective on techniques for enhancing speckled imagery. In *Proceedings of the SPIE, 829, Applications of Digital Image Processing X*, (Bellingham, WA: SPIE), pp. 158-164.
- Schwarz, G., Walessa, M. and Datcu, M., 1997, Speckle reduction in SAR images: techniques and prospects. In *Proceedings of the IGARSS'97* (Piscataway, NJ: IEEE), pp. 2031-2034.
- Simard, M. and DeGrandi, G., 1998a, Analysis of Speckle noise contribution on Wavelet decomposition of SAR images. *IEEE Transactions on Geoscience and Remote Sensing*, **36(6)**, pp. 1953-1962.
- Simard, M., 1998b, Extraction of information and Speckle noise reduction in SAR images using the Wavelet Transform. In *Proceedings of the IGARSS'98* (Piscataway, NJ: IEEE), pp. 4-6.
- Simoncelli, E. P., Adelson, E. H., 1996, Noise removal via Bayesian coring. 3rd IEEE International Conference on Image Processing, 16 September 1996, (Piscataway, NJ: IEEE), pp. 379-382.
- Schroder, M., Seidel, K., Datcu, M., 1999, Bayesian modeling of remote sensing image content. In *Proceedings of the IGARSS'98* (Piscataway, NJ: IEEE), pp. 1810-1812.
- Walessa, M. and Datcu, M., 2000, Model-based despeckling and information extraction from images. *IEEE Transactions on Geoscience and Remote Sensing*, **38(5)**, pp. 2258-2269.
- Wei, D., Guo, H., Odegard, J. E., Lang, M. and Burrus, C. S., 1995, Simultaneous Speckle reduction and data compression using best wavelet packet bases with application to Synthetic Aperture Radar (SAR) based ATD/R. In *Proceedings of the SPIE, 2491, Algorithms for Synthetic Aperture Radar Imagery II*, (Bellingham, WA: SPIE), pp. 1131-1141.
- Zeng, Z. and Cumming, I., 1998, Bayesian Speckle noise reduction using the discrete wavelet transform. In *Proceedings of the IGARSS'98*, (Piscataway, NJ: IEEE), pp. 7-9.
- Zeng, Z. and Cumming, I., 2001, SAR image data compression using a tree-structured Wavelet Transform. *IEEE Transactions on Geoscience and Remote Sensing*, **39(3)**, 546-552.

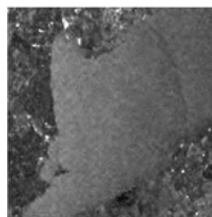


Figure 10. Reconstructed SAR image using adaptive soft thresholding.

Characterizing the vegetation microwave parameters dependence on view angle and polarization (SMOS mission)

M. Pardé, J.-P. Wigneron, A. Chanzy and P. Ferrazzoli

M. Pardé, J.-P. Wigneron are with the Bioclimatologie Laboratory, INRA (Institut nationale de recherche agronomique), BP 81, 33 883 Villenave d'Ornon cedex, France ,

A. Chanzy are with the CSE unity of INRA, Site Agroparc, Domaine Saint-Paul, 84914 Avignon Cédex 9, France

P. Ferrazzoli is with the Università Tor Vergata, Dipartimento di Informatica Sistemi e Produzione, Rome, Italy.

correspondence to mparde@bordeaux.inra.fr

ABSTRACT- *The value of the vegetation microwave parameters of the τ - ω model and their dependence on view angle, polarization and time are estimated for several vegetation crops in this study. To this end, we use three experimental data sets, BARC 1981 and PORTOS 1991 and 1993. During these campaigns, radiometric (L-band) passive measurements were made over corn, grass, alfalfa (for BARC), soybean (for PORTOS 1991) and wheat (PORTOS 1993). We used simple methods based on several consecutive measurements to estimate the vegetation parameters, for each configuration, by non linear regression. Results showed that for the H polarization, the estimated b parameter seems to be almost constant with view angle, but depends highly on the vegetation type. At V polarization, the time variations in the b parameter may be very significant during the crop cycle. For a wheat crop, it was shown that the use of a formulation based on a C_{pol} parameter provide good results in modelling the dependence of the b parameter on incidence angles and polarization. Concerning this crop, good agreement was found between the estimated values of the b parameter and those computed with a discrete radiative transfer model*

1 INTRODUCTION

Soil moisture, and its spatio-temporal evolution, is a key variable in the hydrologic cycle, for numerical weather and climate models. The most direct way to access to soil moisture is through the use of L-band (1.4 GHz, 21cm) microwave radiometer systems. The SMOS (Soil Moisture and Ocean Salinity) mission will use such a system and will make multiple measurements of the brightness temperature (T_b) at many view angles (θ) and two polarizations, with a high temporal frequency. Over the continents, the main objective of this mission is to monitor the surface soil moisture. However, the main difficulty in the estimation of the soil moisture arise from the presence of overlying vegetation. In fact, the canopy total microwave emission results from different effects: the soil emission, the effect of the vegetation on soil emission and the vegetation emission itself. Very few studies have investigated to date the vegetation microwave signature, including the angular and the polarization dependence. It was often considered that the vegetation parameters are independent on view angle and polarization effects. This work aims at characterizing the vegetation microwave parameters dependence, on view angle, polarization and time. The

model we used for simulating the vegetation emission is the τ - ω model (Wigneron, 1995) which is a zeroth-order solution of the radiative transfer equations in a vegetation layer.

To perform this study, we used experimental radiometric data sets over corn, alfalfa and grass (BARC data set, Wang, 1981), over soybean (PORTOS 1991, Chanzy, 1994) and over wheat (PORTOS 1993, Wigneron et al., 1995). A simple approach was used to compute the microwave parameters (the optical thickness τ , and the simple scattering albedo, ω) for each crop canopy. The approach is based on measurements which are acquired for several days during the vegetation growth. Therefore, the values of the classical b parameter (Jackson, 1991), which is the slope between the vegetation water content and the optical thickness, can easily be computed.

For crops with a vertical structure, a formulation using a single parameter (C_{pol}) was proposed by Wigneron et al. (1995) to parameterize the dependence of τ on view angle and polarization. We tested here the validity of this formulation over the wheat crop (which is a vertical-stem dominated crop) and we showed that it was a good way to simulate the dependence of the τ parameter on the viewing configuration.

Finally, in order to validate our results, we used a discrete radiative transfer model (Ferrazzoli, 2000) to estimate the vegetation microwave parameters, b and ω , and their dependence with view angle, polarization and time.

2 MATERIALS AND METHODS

2.1 Experimental Data

The microwave vegetation parameters estimation was done using three different data sets collected during the last two decades. The first one was acquired in 1981 on the BARC test site (Wang, 1981), over corn, grass and alfalfa. Three microwave radiometers at the frequencies of 1.4 GHz, 5 GHz and 10.7 GHz were mounted on a mobile tower. These radiometers were of the Dicke type and measured the thermal microwave emission in both vertical and horizontal polarization. The second and third data sets were obtained during the PORTOS experiments (Chanzy, 1994), in 1991 and 1993, over soybean and wheat, respectively. These experiments were conducted on a plot located on the INRA (Institut National de Recherches Agronomiques) Avignon test site (43°55 N, 4°53 E). The sensor was the multi-frequency passive microwave radiometer PORTOS (1.4, 5.05, 10.65, 23.8, 36.5 and 90 GHz) designed by CNES (Centre National d'Études Spatiales, France) and Matra Marconi in 1990. The radiometer was hanged on a 20-m crane boom, and observations were carried out at different incidence angles (from 0° to 50° over a 40 x 60m field). In the present study, the look direction was parallel to the row direction for the wheat measurements and orthogonal to the row direction for corn measurements (BARC data set). Only brightness temperature acquired at L-band (H and V polarization) were considered here.

The soil and vegetation variables were sampled regularly during the four campaigns. Concurrently with radiometric measurements, soil moisture (m_v) profiles were obtained from gravimetric measurements and soil temperature (T_s) was automatically measured at different depth. Many times during the crop growth, measurements of dry and wet biomass were performed and the values of the vegetation water content (Wc) were then calculated.

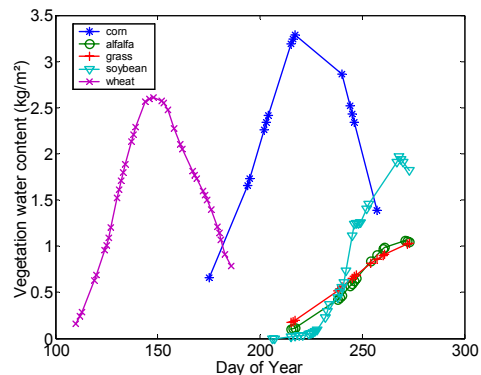


Figure 1. Vegetation water content (Kg/m²) for every crop considered in this paper. The symbols (x, o, ...) refer to the dates of brightness temperature measurements.

The time variations in the vegetation water content for each crop are plotted on Figure 1. For the wheat and the corn crops, we show here that the radiometric measurements were done during the entire crop cycle, but there were no measurements before the crop emergence, on bare soil; over the grass, the alfalfa and the soybean canopies, measurements were done only during the vegetation growth.

2.2 Calculation of the vegetation parameters

2.2.1 The τ - ω model

The model that we used is the τ - ω model (Wigneron, 1995). The p-polarized brightness temperature T_{bp} can simply be written as a function of the single scattering albedo $\omega(\theta, p)$, the optical depth $\tau(\theta, p)$, the soil reflectivity $\Gamma^s(m_v, \theta, p)$ and the effective temperature (for soil and vegetation) T_s^E :

$$T_{bp} = (1 - \omega)(1 - \gamma)(1 + \Gamma_s \gamma)T_v + (1 - \Gamma_s)T_s^E \gamma \quad (1)$$

where $\gamma(\theta, p, t)$ is the p-polarized transmittivity of the vegetation layer which can be expressed as a function of the optical thickness $\tau(\theta, p, t)$ and the incidence angle θ :

$$\gamma = e^{-\frac{\tau}{\cos(\theta)}} \quad (2)$$

The effective temperature T_s^E of the soil (we assume that the vegetation temperature and the soil temperature are equal) layer was computed from the radiative transfer theory:

$$T_s^E = \int_0^\infty T_s(z) \alpha(z) \exp\left(-\int_0^z \alpha(z') dz'\right) dz \quad (3)$$

where $T_s(z)$ is the soil temperature at depth z , and the attenuation coefficient $\alpha(z)$ is related to the soil dielectric constant as

$$\alpha(z) = \left(\frac{4\pi}{\lambda}\right) \frac{\epsilon_s''(z)}{2(\epsilon_s'(z))^{1/2}} \quad (4)$$

where λ is the wavelength of observation, and ϵ_s' and ϵ_s'' are the real and imaginary part, respectively, of the soil dielectric constant.

In this study, we will evaluate the assumption that the optical thickness τ is linearly related to the vegetation water content Wc (kg/m²) (Jackson, 1991) :

$$\tau_p = b_p Wc \quad (5)$$

where b_p is a factor which is mainly dependent on the frequency, the canopy type and the vegetation dielectric constant (the subscript p refers to the H or V polarization). The values of b for different vegetation types were evaluated by (Jackson, 1991). However, very few studies investigated the dependence of b on polarization and look angle. Moreover, the validity of the assumption that the vegetation water content and τ are linearly related remain questionable (Le Vine, 1996).

Another formulation will be considered in this paper. Wigneron et al. (Wigneron, 1995) developed a simplified parameterization for crops with a vertical structure, based on the *Cpol* parameter. This parameterization describes the dependence of τ on the viewing configuration, and is defined by:

$$\frac{\tau_v}{\tau_h} = \cos(\theta)^2 + C_{pol} \sin(\theta)^2 \quad (6)$$

$$\tau_h(\theta) = \text{constant}$$

This formulation is based on two unknown parameters: *Cpol* and $\tau_h(0)$. We tested here this parameterization for the wheat field only. Once we showed that it is an appropriate formulation to compute the values of τ for each time period, we estimated the values of *Cpol* and $\tau_h(0)$ for each day of radiometric measurements.

Before estimating the vegetation parameters, we have to compute the soil reflectivity $\Gamma^s(m_v, \theta, p)$. It is calculated using a modified Fresnel reflection formulation (Wang, 1980). This formulation is based on two semi-empirical parameters h_r and Q , which

model the intensity of the roughness effects and the polarization-mixing effects, respectively :

$$\Gamma^s(\theta, p) = [(1-Q)\Gamma^{SPC}(\theta, p) + Q\Gamma^{SPC}(\theta, q)] \cdot \exp(-h_r \cos(\theta)^n) \quad (7)$$

where $\Gamma^{SPC}(m_v, \theta, p)$ is the p -polarized specular reflectivity which is derived from computations of the soil dielectric properties using a dielectric mixing model (Dobson, 1985).

2.2.2 A simple method to compute b and ω

The vegetation parameters were computed using the non linear regression estimation. The non linear model can be written in the general form:

$$T_b = f(m_v', T_s^E, Wc, \omega_p'(\theta), b_p'(\theta)) + \varepsilon \quad (8)$$

where t is the time, $p=H$ or V polarization, $T_b=(T_{b1}, \dots, T_{bn})$ is a n vector of microwave signatures, $f()$ is the τ - ω equation, and $\varepsilon = (\varepsilon_1, \dots, \varepsilon_n)$ are the independent and identically normally distributed errors, with a constant variance σ^2 ; m_v , T_s^E and Wc are the variables, ω and b are the unknown parameters.

In this model, for the purpose of computing the parameters dependence on time polarization and view angle, the data set was indented in different time periods (*Int*). As these time periods are rather short it could be assumed that the vegetation structure does not change much during a given time period. Therefore, it can be assumed that ω remain constant, and that τ and the vegetation water content Wc can be linearly related during these periods. The following relationships can thus be assumed (Wigneron, 1996):

$$\begin{cases} \omega^i(\theta, p) = \omega^i(\theta, p) \text{ for } i \in \text{Int} \\ \frac{Wc1}{Wc2} = \frac{\tau^{t1}}{\tau^{t2}} \text{ for } t1 \text{ and } t2 \in \text{Int} \end{cases} \quad (9)$$

The subscripts 1 and 2 refer to two dates of measurements within the time period *Int*. In this model, there are two unknown parameters for each angle and each polarization, and the number of equations is the number of brightness measurements within the time period. The minimisation routine was based on the generalised least-square iterative algorithm of Gauss-Marquardt (Marquardt, 1963). The routine provided theoretical estimates of the standard deviations on the retrieved parameters.

2.3 The discrete model

A discrete radiative transfer model was used to compute values of the canopy emissivity $\epsilon(\theta, p)$ for the PORTOS 93 data set (Ferrazzoli, 2000). The aim is to estimate the previous vegetation parameters using a

more complex radiative transfer model, and compare results with those obtained with the τ - ω model. This model assumes the soil as a half space with uniform permittivity and an upper rough interface, while the overlying vegetation is described as an ensemble of discrete lossy scatterers, representing the plant constituents. The electromagnetic properties of the scatterers, are described by the absorption cross section and the bistatic scattering cross sections. To represent these constituents, we used discs for leaves and cylinders for stems and ears. The size, the density and the water content of these elements were derived from ground data. The permittivity of the vegetation elements was calculated using models developed by (El-Rayes, 1987) and (Mätzler, 1994).

The values of τ and ω were calculated according to:

$$\begin{cases} \tau = -\cos(\theta) \ln(\gamma) \\ \omega = 1 - \frac{e}{1-\gamma} \end{cases} \quad (10)$$

e is the emissivity and γ is the transmittivity of the cover. These values, calculated as a function of view angle, can be compared with those we retrieved from measurements over the wheat field.

3 RESULTS

3.1 The soil emission

To evaluate the vegetation parameters, we first computed the soil reflectivity corresponding to all the observations made during the campaign. In equation (7), the roughness parameters H , Q and n are unknown, and should be estimated from ground observations. As few information were available and no radiometric measurements were done over bare soil before the crop emergence, we chose to set the values of these parameters equal to zero. Note that low values of Q and n are generally used, (Wang, 1983) and these parameters can be set equal to zero at L-band (Wigneron et al., 2001). The assumption that H is equal to zero implies that we underestimate the soil emission. The main effect is that the vegetation emission and the vegetation b parameter, will be overestimated. However, the dependence of these parameters on view angle and on polarization should not be significantly affected. The time variations in the soil roughness could affect the time variations in the vegetation parameters. But as we have no information about time changes in the soil roughness characteristics, we assume that the roughness parameters are constant. Note that for the wheat field (PORTOS 1993) we estimated the value of the H parameter using brightness temperature measurements over a bare soil with similar soil roughness characteristics ($H=0.06$).

3.2 The dependence of the b and ω parameters on view angle.

For each type of vegetation, corn, alfalfa, grass, soybean and wheat, we plotted the values of the b parameter dependence on view angle for each polarization in Figures 2, 3, 4, 5 and 6 respectively.

For all above estimations (except for the soybean and wheat crop, where ω was set equal to zero) we plotted the values of retrieved single scattering albedo for all view angles and both polarizations.

First, we can note that for the three first crops the values of the ω parameter are close to zero for relatively low view angles and both polarizations. For higher view angles ($\theta > 30^\circ$), the value of ω can be rather large ($\omega \approx 0.1$). The assumption that the albedo is not significant is often used (Jackson, 1991, Wigneron, 1995) and seems to be confirmed here only for low view angles. For the corn crop, we note that the values of b at H polarization do not vary with view angle and this trend can be seen during the whole corn growth. The values of b at V polarization increase first with the view angle, and after about $\theta = 30^\circ$, they decrease. This difference between the two polarizations was observed when the corn was mature while during the corn growth period, the values of b for the two polarizations are similar.

The values of b for the alfalfa and the grass (Figure 3 and Figure 4) are similar. There is no significant difference between the two polarizations, and the angular variations are weak. This shape is almost constant with time for both crop types.

In Figure 5, we plotted the angle variations of b for H and V polarizations for soybean. For this crop, the b_h parameter is almost constant for θ lower than 30° and then increase slightly with the view angle (this shape is the same for all the dates of measurements). At V polarization the shape is quite different for the different days: during the crop growth, this parameter is constant for θ lower than 30° and then decrease with view angle. At the end of the crop growth, the values of b_v increase with θ .

The Figure 6 show the angular variation of the wheat b_v and b_h parameters. We plotted the values of b computed using the Cpol formulation (equation (6)) on the same figure. We show here that the values of b are almost constant with view angle for the H polarization, and that b increase significantly with θ for the V polarization. This shape is well predicted by the Cpol formulation and the use of the Cpol parameter may be useful in inversion problems (Pardé et al., 2002).

3.3 Dependence of b on time

The time variations of the b parameter are presented in figures 7, 8, 9, 10 and 11 for all the crops and for both polarizations. For the corn, the alfalfa and the grass, we show here that this parameter do not change much during the campaign. For the corn and the grass, the difference between the both polarizations remains weak during the whole campaign. For alfalfa, soybean and wheat, this difference change with time: for the soybean, the difference is low at the beginning of the campaign, and increase at the end of the crop growth.

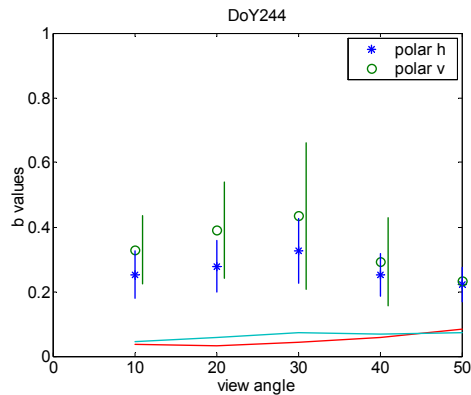


Figure 2. Values of b (o and *) and ω (-) vs θ and polarization for corn

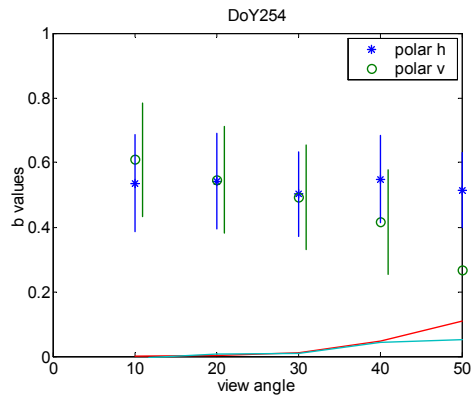


Figure 3. Values of b (o and *) and ω (-) vs θ and polarization for alfalfa (BARC)

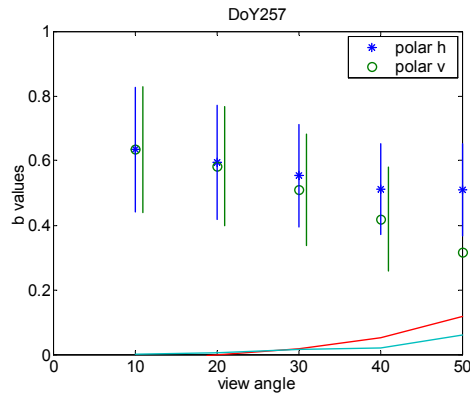


Figure 4. Values of b (o and *) and ω (-) vs θ and polarization for grass (BARC)

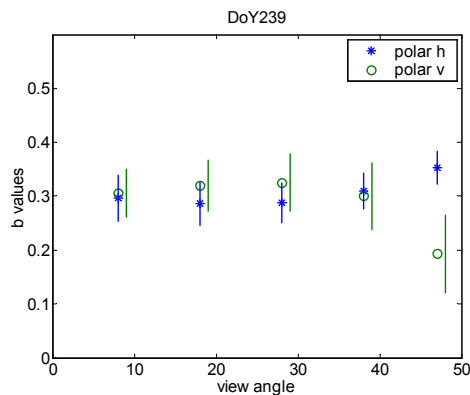


Figure 5. Values of b (o and *) vs view angle and polarization for soybean (PORTOS 1991)

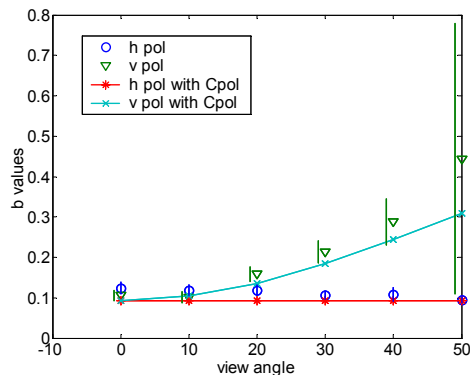


Figure 6. The b parameter for wheat estimated as a function of view angle on DoY 144 (PORTOS 1993) in comparison with the results obtained with the C_{pol} parametrization (Pardé, 2002).

For wheat, the b_h parameter remains constant during the growth and the senescence while b_v increase (from 0.2 to 0.3) during the wheat growth and remains constant during the senescence.

3.4 The Cpol formulation

In Figure 6, we showed that the Cpol formulation is appropriate to estimate the values of the b parameter dependence on view angle and polarization for the wheat crop. As there is only two unknown parameters ($Cpol$ and $\tau_h(0)$), we retrieved these parameters for each day of measurement. We plotted the time variation in these two estimated parameters $Cpol$ and $\tau_h(0) \times 10$ (Pardé, 2002) in Figure 12 for each day of radiometric measurements. The values of $Cpol$ increase during the crop growth and they are almost constant during the crop fall.

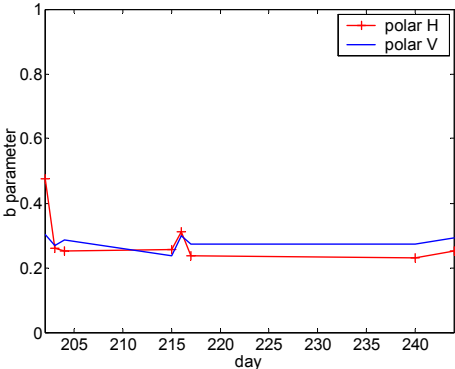


Figure 7. Time variations in b ($\theta = 40^\circ$) for the corn crop

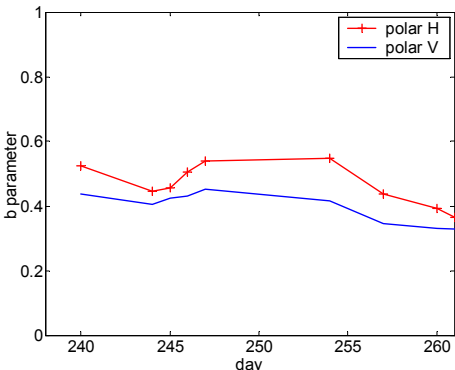


Figure 8. Time variations in b ($\theta = 40^\circ$) for alfalfa .

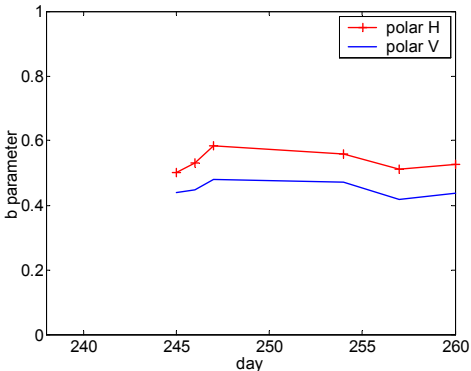


Figure 9. Time variations in b ($\theta = 40^\circ$) for grass.

They seems to be well correlated to the wheat height, at least during the crop growth. In the meantime, values of $\tau_h(0)$ increase during the crop growth and then decrease during the crop fall. It seems that these values are well correlated with the vegetation water content.

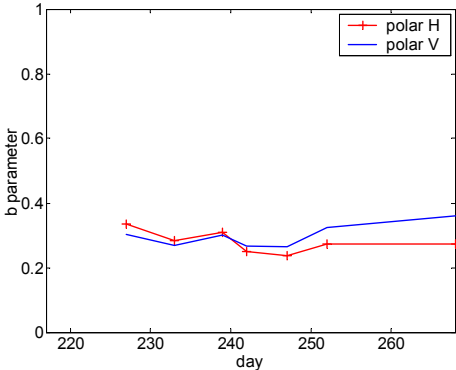


Figure 10. Time variations in b ($\theta = 40^\circ$) for soybean.

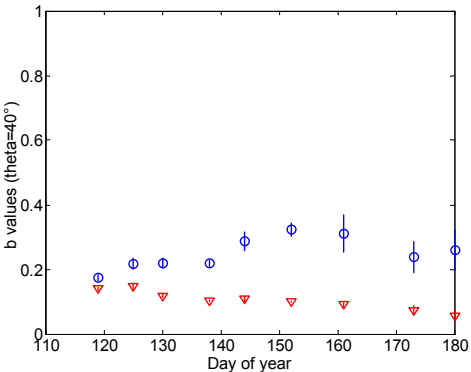


Figure 11. Time variations in b ($\theta=40^\circ$) for the wheat crop (PORTOS 1993 experiment) (V(o), H(∇)).(Pardé,2002)

3.5 Estimation of b and ω with the discrete model

Finally, we estimated the values of the vegetation parameters using the discrete model (Ferrazzoli et al., 2000). The values of the dependence of the b parameter on view angle are plotted in Figure 13, and those of the single scattering albedo in Figure 14. The values of the b parameter for the H polarization do not vary much with the view angle. At V polarization, this parameter increase regularly from values of 0.1 at nadir to 0.5 at 50° (this shape is the same during the whole crop growth). The values of ω are constant with the view angle for all the dates of measurements, and remains at values between 0.01 and 0.02 during the whole crop growth.

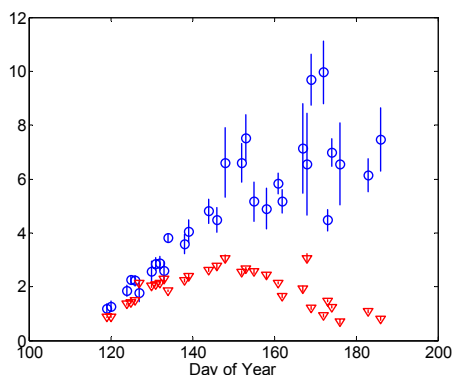


Figure 12. Time variation in C_{pol} (o) and $\tau_h(0) \times 10$ (V) parameters for the wheat crop (Pardé, 2002).

4 DISCUSSION AND CONCLUSION

These results show that the value of the b parameter can be very different depending on the crop type. For instance, the values of b for the grass and the alfalfa ($b_h \approx 0.45$) is about two times larger than for the corn ($b_h \approx 0.25$) and about four times larger than for the wheat ($b_h \approx 0.1$). These values could be overestimated for the corn, alfalfa and grass fields, as the effects of soil roughness were assumed to be negligible. However, as the soil surface was relatively smooth for the BARC fields (Wang, 1981), it is reasonable to think that the overestimation is not significant. The difference between values of the b parameter for the different crop types was found to be relatively significant. This can be explained by the canopy structure: the volume density of the grass and of the alfalfa is very high and the high density of the roots acts similarly to an increase of the soil roughness. However, Figure 1 indicates that radiometer data were available for a small portion of grass and alfalfa cycle, and the dynamic range in Wc was very limited. These limits in the available data could have reduced the reliability of our retrieval process, for these two

vegetation types. Also we showed that the values of the simple scattering albedo are weak (for low view angles) and that their dependence on polarization and time are low.

The dependence of b on view angle and polarization is very different for the different crop types. For the alfalfa, the grass and the soybean, the estimated values of the b_h and b_v parameters are very close, and they do not depend much on the view angle. For the wheat and the corn crops, we showed that the dependence of b on view angle and polarization is relatively strong: for wheat, the values of b at V polarization are low at nadir ($b \approx 0.1$) and are high at $\theta = 40^\circ$ ($b \approx 0.4$). These variations of b with view angle and polarization can be related to the vertical structure of the wheat canopy (Wigneron, 1995). For the corn crop, the variations of b vs θ and polarization are more complex, and we did not find any explanation in the decrease of b at V polarization for high view angles. For wheat, we compared these results with those given with the Cpol parameterization (equation (6)).

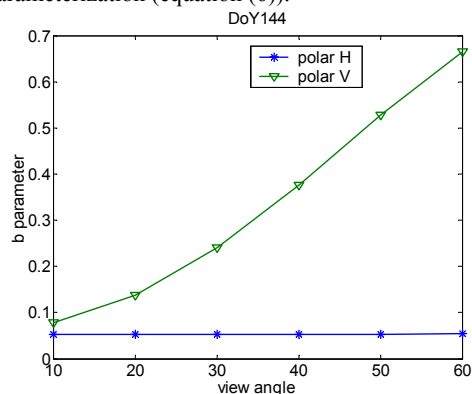


Figure 13. The b parameter computed with the discrete model for wheat (DoY = 144)

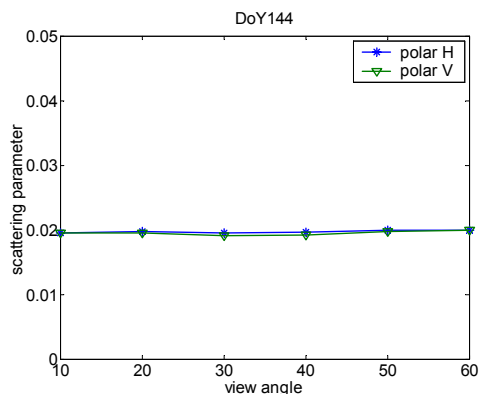


Figure 14. Single scattering albedo computed with the discrete model for the wheat crop (DoY 144)

It appears that this formulation is appropriate and could be used to characterise the attenuation effects for this crop type. The *Cpol* parameter was retrieved during the whole crop cycle, and its time variations were found to be highly correlated to the stem growth: the *Cpol* value is about one at the beginning of the crop growth and it increases continuously as the stems developed up to values which ranged between 5 and 10. The time variations in retrieved optical depth at nadir ($\tau(\theta=0)$) were strongly correlated with the vegetation water content *Wc*. The interest of this formulation is that only two parameters (*Cpol* and $\tau(\theta=0)$) are required to parameterize the dependence of τ on view angle and polarization; the correlation with the crop height and the water content should be studied in the view of retrieving vegetation variables in the case of the inverse problem.

Also, the values simulated by the discrete model (Figure 13 and Figure 14) are in close agreement with those shown in Figure 6. The discrete model seems to be an adequate tool to model the effects of the crop structure in the view of a better understanding of the interactions between the canopy and the microwave radiation. This tool could be used to simulate the effects of the corn structure in order to explain the dependence of the b_v parameter on view angle.

This study provides several new results about the effects of vegetation structure on the canopy microwave emission. We showed that the angular and the polarization dependence of vegetation parameters are very different depending on crop type and that the model using a constant *b* parameter is not adequate for wheat crop. The use of the *Cpol* parameter seems to be a good approach to model the dependence of the optical thickness on θ and polarization. Finally, we showed that discrete models can be useful tools to understand and estimate the vegetation effects on canopy microwave emission.

REFERENCES

- Chanzy A., Haboudane D., Wigneron J.-P., Calvet J.-C., and Grosjean O., 1994, Radiométrie micro-onde sur divers types de couverts végétaux: influence de l'humidité du sol, in 6th Int. Symp. Physical Measurements and Signatures in Remote Sensing, CNES, Toulouse.
- Dobson M. C., F. T. Ulaby, M. T. Hallikainen, and M. A. El-Reyes, 1985, Microwave dielectric behavior of wet soil-Part II: Dielectric mixing models, IEEE Trans. Geosc. Remote Sens. 23:35-46.
- El-Rayes M.A. and Ulaby F.T., 1987, Microwave dielectric spectrum of vegetation-Part I: Experimental observations, IEEE Trans. Geosc. Remote Sens., GE-25:541-549
- Ferrazzoli P., Wigneron J.-P., Guerriero L., and Chanzy A., 2000, Multifrequency emission of wheat: modelling and applications, IEEE trans. on geosc. and remote sensing, GE-21(1):2598-2607
- Jackson T. J., and T. J. Schmugge, 1991, Vegetation effects on the microwave emission of soils, Remote Sens. Environ., 36:203-212.
- Le Vine D.M., and Karam M.A, 1996, Dependence of attenuation in a vegetation canopy on frequency and plant water content, IEEE trans. on geosc. and remote sensing, 34(5):1090-1096.
- Marquardt, D.W., 1963, An algorithm for least-squares estimation of nonlinear parameters, Journal of the Society for Industrial and Applied Mathematics, 11:431-444.
- Mätzler C. , 1994, Microwave (1-100 GHz) dielectric model of leaves, IEEE trans. on geosc. and remote sensing, 32:947-949.
- Pardé M., Wigneron J.-P, Chanzy A., Waldteufel P., Kerr Y. and Huet S., 2002, Using passive multi-angular and bi-polarization microwave measurements to retrieve soil moisture over a wheat fields, Comparison of different methods, Remote Sens. Environ., to be published.
- Wang J. R., Jackson T.J., Engman E., Gould W., Juchs J., Glazer W., O'Neill P., Schmugge T., and McMurtrey J., 1981, Microwave radiometer experiment of soil moisture sensing at BARC test site during summer 1981, NASA, Goddard Space Flight Center Greenbelt, Maryland 20771.
- Wang J. R., P. E. O'Neill, T. J. Jackson, and E. T. Engman, 1983, Multifrequency measurements of the effects of soil moisture, soil texture, and surface roughness, IEEE Trans. Geosc. Remote Sens 21:44-51.
- Wang J. R., and T. J. Schmugge, 1980, An empirical model for the complex dielectric permittivity of soils as a function of water content, IEEE Trans. Geosc. Remote Sens., 18(4) :288-295.
- Wigneron J.-P, Chanzy A., Calvet J.-C and Bruguier N., 1995, A simple algorithm to retrieve soil moisture and vegetation biomass using passive microwave measurements over crop fields, Remote Sens. Environ, 51: 331-341.
- Wigneron J.-P, Combal B., Wegmüller U. and Mätzler C., 1996, Estimation of microwave parameters of crops from radiometric measurements, Int. J. Remote Sensing, 17(14):2875-2880.
- Wigneron J.-P , Waldteufel P., Chanzy A., Calvet J.-C and Kerr Y., 2000, Two dimensional microwave interferometer retrieval capabilities over land surfaces (SMOS-mission). Remote Sens. Environ, 73:270-282.

Land Surface Monitoring Using a Combination of Active and Passive Microwave and Optical Satellite Sensors

Lizbeth N. Guijarro^{1,2}, Venkat Lakshmi¹, Yann H. Kerr², Ghani Chehbouni²

¹Department of Geological Sciences, University of South Carolina, Columbia, SC 29208,

²Centre d'Etudes Spatiales de la Biosphère, 18 Av. Edouard Belin, 31401 Toulouse, France

¹lguijarro@geol.sc.edu, ¹vlakshmi@geol.sc.edu, ²Yann.Kerr@cesbio.cnes.fr,

¹Ghani.Chehbouni@cesbio.cnes.fr

ABSTRACT - *The aim of this study is to conduct a synergistic evaluation of remotely sensed data from active and passive satellite sensors for the evaluation of land surface dynamics. The variables of interest are soil moisture, vegetation amount, surface temperature, snow depth, and precipitation. The passive microwave satellite data were acquired by the Special Sensor Microwave Imager (SSM/I) mounted on the Defense Meteorological Satellite Program (DSMP) F13 platform, and the active microwave satellite data by the wind scatterometer (WSC) on board the European Remote Sensor 2 (ERS-2). This study focuses on algorithm development and validation for regions of Illinois and Oklahoma from 1998 to 1999. In situ soil moisture was measured at 19 stations in Illinois and 115 stations in Oklahoma with a neutron probe calibrated with gravimetric observations. The first stage of this study compares the SSM/I and WSC data with the observed soil moisture data for Oklahoma and Illinois. The Normalized Difference Vegetation Index (NDVI) from the Advanced Very High Resolution Radiometer (AVHRR) is used to estimate and quantify the changes of vegetation over time. The goal of this study is to provide useful results for the retrieval of soil moisture in larger scales.*

1 INTRODUCTION

Soil moisture, snow water content, surface temperature, and precipitation are variables that play a significant role in determining our climate. Active and passive microwave satellite sensors have been developed to observe weather and aid our understanding of the interaction of these parameters. The microwave region of the electromagnetic spectrum offers a promising avenue of monitoring the temporal evolution of these parameters, in particular soil moisture. Microwave satellite sensors have characteristics such as different spatial resolutions, multi polarizations, multi frequencies, multi angles, and varying time of day overpasses that are useful for land surface monitoring. These allow for disaggregation and diurnal variability studies. Furthermore, there is little atmospheric interference for the wavelengths used by these sensors, which allows reliable image acquisitions and analysis algorithms at any weather conditions. In addition, microwave satellite sensors have the capability to provide their own illumination regardless of local weather; thus, they can be accurately calibrated (Kerr 1999).

Accurate estimation of soil moisture changes on a regional scale is important for global climate modeling because of the significant influence it has on land-atmosphere coupling and monitoring (Woodhouse 2000). Microwave satellite sensors have proven to be

effective for soil moisture sensing because of the large contrast between the dielectric properties of liquid water and those of dry soil (Schmugge 1985). Therefore, they can provide a valuable contribution to global climate studies.

Soil moisture plays a key role in surface hydrology since it controls the partition of rainfall into runoff and infiltration. Additionally, by controlling the partition of available energy at the surface into sensible and latent heat flux, soil moisture plays a crucial role in boundary layer development and therefore in surface atmospheric interaction. In addition to soil moisture, proper characterization of land surface interaction also requires accurate estimates of:

1. Surface temperature
2. Vegetation amount
3. Snow depth and cover
4. Precipitation

The objective of this study is to carry out a synergistic approach using remotely sensed data for the evaluation of land surface dynamics using multiple sensors such as the Special Sensor Microwave Imager (SSM/I), European Remote Sensing 2 (ERS-2) windscatterometer (WSC), and the Normalized vegetation Index derived from the Advanced Very High Resolution Radiometer (AVHRR). The variables included in this study are soil moisture of the upper

layer of soil (0 – 10 cm), vegetation amount, surface temperature, snow depth and cover, and precipitation.

The motivation of this study stems from the lack of actual data at the appropriate time-space scale and the limitations associated with the retrieving algorithms of these land surface variables with the use of one satellite sensor. The utility of using satellite passive microwave observations to measure soil moisture over large regions has been examined by Vinnikov et al. (1999a). In their study, they used the Scanning Multichannel Microwave Radiometer (SMMR) and in situ soil moisture observations for the state of Illinois, United States. Their results suggested that the microwave indices, which use frequencies less than or equal to 18 GHz have a real utility for use as a soil moisture information source in regions with grass or crops where the vegetation is not too dense. Temporal crosscorrelations of soil moisture and vegetation still need to be used in physical models to improve the quality of soil moisture.

The work by Magagi and Kerr (2001) can be regarded as an effective step towards the retrieval of soil moisture using active microwave data. They made use of the multiple angles of the European Remote Sensing 2 (ERS) windscatterometer (WSC) on a new retrieval algorithm of soil moisture. Magagi and Kerr arrived at a best estimation of soil moisture under wet conditions with the use of the copolarization ratios derived from fore and mid beam configurations.

A comparison of the use of passive and active data for vegetation monitoring was the work of Frison et al. (2000). In their study, they performed a temporal analysis of the polarization difference and of the backscattering coefficient, and they showed that both datasets coincide in the minimum and maximum values of green biomass. Through a semi empirical model, Frison et al. demonstrated that the temporal signature of the polarization difference depended on various parameters such as physical soil temperature, air temperature, integrated water vapor content, vegetation cover fraction, and canopy volume fraction. They concluded that the SSM/I response was mainly sensitive to soil parameters, which are indirectly linked to vegetation biomass through bare soil fraction and the WSC response was directly sensitive to vegetation parameters.

This research is modeled after the methodology developed by Kerr et al. (1999) using active and passive microwave data to derive land surface parameters such as surface temperature, vegetation and snow depth. This paper investigates the possibility of achieving a better characterization of land

surface variables through the combination of passive and active microwave and optical remotely sensed data. The areas for this study comprise two networks for regions of Illinois and Oklahoma from 1998 to 1999. The first part of this study aims to understand the relationship between the variables derived from each sensor. It assesses the potential and limitation of using measurements from individual sensors to characterize surface variables. Secondly, this study assesses the advantage of combining measurements from different sensors to characterize the same surface variables. Lastly, it tests the performance of existing semi-empirical models for inverting surface variables.

The study areas and datasets are presented in section 2 of this paper. Section 3 shows the times series of microwaves indices and soil moisture. Section 4 is dedicated to the models. Discussion and future work are addressed in sections 5 and 6, respectively.

2 DESCRIPTION OF DATASETS

2.1 Satellite Data

2.1.1 Special Sensor Microwave Imager (SSM/I)

The Special Sensor Microwave Imager (SSM/I) is a passive microwave radiometric system. In this study, it is applied to obtain observations of Oklahoma and Illinois, United States. The SSM/I is a seven-channel, linearly polarized system, which measures atmospheric, ocean, and terrain microwave brightness temperatures, T_{BS} . SSM/I operates at frequencies of 19.35 GHz, 22.235 GHz, 37.0 GHz, and 85.5 GHz. The data produced at the 22.235 GHz channel are only vertical polarized. The other channels operate in both vertical and horizontal polarization. The brightness temperatures are measured across a 1400 km swath width at 53.1° of incidence angle. The spatial resolution of the 19.35 GHz channel is 43 x 69 km² and the 37 GHz channel it is 28 x 37 km². The 22.235 GHz channel will not be used in this study due to its single polarization configuration. The SSM/I daily data used for this study was reprocessed onto a global, equal-area SSM/I Earth (EASE) projection in a 25-km cell resolution grid at the National Snow and Ice Data Center (NSIDC) in Colorado. The inherent resolutions of each of the channels are presented in Table 1.

2.1.2 European Remote Sensor 2 (ERS-2)

The European Remote Sensing Satellite 2 (ERS-2) wind scatterometer is an active satellite sensor that

measures the backscattering coefficient, σ^0 , with the use of three antennas at different incidence and azimuth angles. The data used for this study are from the fore (22° – 50°), mid (16° – 42°) and aft (22° – 50°) antennas (Francis et al. 1991). The ERS-2 wind scatterometer has a nominal ground resolution cell of 50 km in diameter and it is sampled on a 25-km grid. It operates on C-band at a frequency of 5.3 GHz. The scatterometer is a single polarized (VV) radar with a swath width of approximately 500 km. The signal measured by this active microwave remote sensing instrument is sensitive to soil moisture variations (Wagner 2000).

2.1.3 Vegetation Data

Normalized Vegetation Index (NDVI) data is derived from visible and near-infrared Advanced Very High Resolution Radiometer (AVHRR). This vegetation index (Eq. 1) uses two satellite channels, one in the visible region (VIS i.e. band 1) and one in the near infrared (NIR, i.e. band 2), then

$$NDVI = \frac{(NIR - VIS)}{(NIR + VIS)} \tag{1}$$

where band 1 is the energy received in the visible spectrum at a wavelength of 0.58 – 0.68 μm , and band 2 is the energy received in the near infrared at a wavelength of 0.725 – 1.10 μm by the AVHRR radiometer.

The NDVI data used in this study is produced bi-weekly on an 8-km continental scale. Sensor degradation and aerosol attenuation have been corrected by the Global Inventory Monitoring and Modeling Studies (GIMMS). NDVI data is used to estimate, monitor, and quantify changes in the vegetation cover over time. The data is compared to polarization differences obtained with the brightness temperatures from the SSM/I sensor and the microwave vegetation index (MWVI), which is obtained by combining ERS-2 WSC and SSM/I data.

SENSOR	VARIABLES	FREQUENCY / POLARIZATION / EFOV
Special Sensor Microwave Imager (SSM/I)	T _B , brightness temperatures, in tenths of Kelvin	19.35 GHz V & H, 69 x 43 km 22.235 GHz V, 60 x 40 km 37.0 GHz V & H, 37 x 28 km 85.5 GHz V & H, 15 x 13 km resampled on a 25 km grid
European Remote Sensor (ERS-2) wind scatterometer (WSC)	σ^0 , backscatter index	5.3 GHz frequency VV, 50 km pixel spacing resampled on a 25 km grid
Tropical Rainfall Measuring Mission (TRMM) TRMM μ wave Imager (TMI)	T _B , brightness temperatures	10.65 GHz V & H, 63.2 x 9.1 km 19.35 GHz V & H, 30.4 x 9.1 km 21.3 GHz V, 22.6 x 9.1 km 37.0 GHz V & H, 16 x 9.1 km 85.5 GHz V & H, 7.2 x 4.6 km
Advanced Very High Resolution Radiometer (AVHRR) Normalized Difference Vegetation Index (NDVI)	Amount of green vegetation	Ch. 1 at $\lambda = 0.58 - 0.68 \mu\text{m}$ Ch. 2 at $\lambda = 0.725 - 1.10 \mu\text{m}$ Bi-weekly on a 8 km scale

Table 1. Variables retrieved and Effective Field of View (EFOV) of satellite sensors.

2.2 Soil and Meteorological Datasets

2.2.1 Illinois Soil Moisture Data

In situ observations of soil moisture from 1998 to 1999 at 19 Illinois Climate Network stations (Figure 2.1) are utilized to complement and to validate the satellite passive and active microwave observations from the ERS-2 WSC and SSM/I sensors. Soil moisture is measured with a Troxler Neutron Depth Probe. This instrument is calibrated with direct

gravimetric measurements at each site. The random error of the surface probe calibration is approximately 4.5 % by volume and smaller for the top meter of soil (Vinnikov et al., 1999a). The first data measurement is taken from the upper 10 cm layer of soil, and then every 20 cm thereafter down to a depth of 2 m. During the warmer months (which in Illinois last from March to September) the observations at each station are made at the middle and at the end of the month. During the colder months (October to February), only one measurement is made during the last week of the month (Vinnikov et al., 1999a). The average soil

moisture station spacing is about 93 km (Vinnikov et al., 1999b).



Figure 2.1 Map of Illinois, United States, with the 19 soil moisture stations.

The soil moisture stations are located mainly on loess soils of varying thickness, which are the main agricultural soils in Illinois. The stations in the southern one third of the state have a dense layer of soil approximately 0.5 m below the surface, which limits root development below 0.5 m. Stations in the northern two thirds of the state do not have any root-restricting zones above 2 m.

2.2.2 Oklahoma Soil Moisture Data

Direct soil moisture observations in the state of Oklahoma are used in addition to the in situ observations in Illinois. The data delivery is the product of a combined effort by the soil moisture research team and the Mesonet team at the Oklahoma Climatological Survey (OCS). The research team used raw measurements provided by the Mesonet sensors to develop procedures to estimate soil water potential and soil water content.

The soil water content data is derived from gravimetric and neutron probe samples at depths of 5 cm, 25 cm, 60 cm, and 75 cm. The Matric Potential Sensor used to take the soil moisture measurements is identical to that used in the two other Southern Great Plain Networks (the ARM/SWATS and the ARS/SHWMS network). Figure 2.2 shows the approximate location of the 114 soil moisture measurement stations in the state of Oklahoma. The average station spacing is 32 km.

In 1996 and 1997, approximately 60 stations comprised the initial station network where soil moisture sensors were installed. During the year

1999, soil moisture sensors were installed at approximately 40 additional sites. Thus, the data record for these 40 new sites does not span the entire calendar year. The stations are predominantly located on four soil types, which are loams, sandy loams, silty loams, and silty clayey loams (OCS 2001).

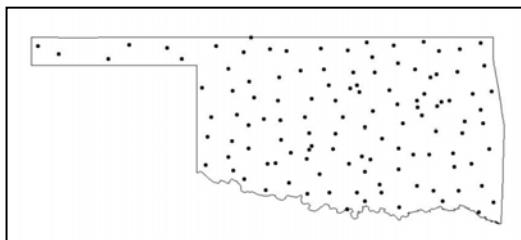


Figure 2.2 Map of Oklahoma, United States, with the 114 soil moisture stations.

2.2.3 Oklahoma Precipitation Data

Ancillary GCIP/ EOP Surface Oklahoma Mesonet precipitation data is also used in this study. The datasets were derived by the Joint Office of Science Support / University Corporation for Atmospheric Research from the Oklahoma Mesonet. The datasets were retrieved electronically from the JOSS Data Management Center via the CODIAC system. The observation frequency of the precipitation data for the Oklahoma Mesonet soil moisture stations is every 15 minutes.

2.2.4 Illinois Precipitation Data

The precipitation data for all Illinois soil moisture stations was obtained from EarthInfo's National Climate Data Center (NCDC), National Oceanic and Atmospheric Administration (NOAA)-Summary of the Day Datasets. The observation frequency of the precipitation data for the Illinois soil moisture stations is hourly.

3 TIME SERIES OF MICROWAVE INDICES AND SOIL MOISTURE

3.1 Polarization Difference Ratio (PR)

Several indices were used in this study for satellite remote sensing of soil moisture. The polarization difference ratio of brightness temperatures (T_{BP}) is a passive microwave index. The polarization index is a ratio of the vertical polarized channel minus the horizontal polarized channel, divided by the sum of these two polarized channels (Eq. 2). The polarization difference ratio was calculated using the brightness

temperatures of the 19 GHz channel. This polarization ratio is given by the expression:

$$PR = \frac{2(T_{BV} - T_{BH})}{(T_{BV} + T_{BH})} \quad (2)$$

Figures 3.1 and 3.2 show the evolution of PR and the upper soil moisture layer for Illinois and Oklahoma. The soil moisture signal gets stronger with decreasing frequency. It is best represented at 19 GHz.

3.2 Brightness Gradient (BG)

The spectral gradient index of brightness temperatures takes the difference between the value of a parameter for two different frequencies of the SSM/I sensor. The frequency channels used are 37 GHz and 19 GHz in vertical and horizontal polarizations. This index is given by the expression,

$$BG = T_{B37P} - T_{B19P} \quad (3)$$

where T_B is the brightness temperature for polarization P. Figures 3.3 and 3.4 show the evolution of BG and the upper soil moisture for Oklahoma and Illinois. The spectral gradient carries a recognizable soil moisture signal as well.

3.3 Radar Backscatter Index (RBSI)

A pseudo-vegetation radar backscatter index, RBSI, is derived from the relationship $\sigma^0 = f(\theta)$ in (Wismann et al. 1996). The backscattering coefficients are related to view angles, θ , azimuth angles, latitudes, and longitudes (Kerr et al. 1997). Because the backscattering coefficient has no dependence on the azimuth angles, all measurements from the fore, mid and aft antennas of the sensor are considered. Thus, the RBSI is estimated with the backscattering coefficients for incidence angles between 40 and 57 degrees divided by the slope index, α (Kerr et al. 1997), whereby α is computed by a linear regression between $\log(\sigma^0)$ and θ . This index is given by the expression,

$$RBSI = \frac{\sigma^0(40^\circ) - \sigma^0(57^\circ)}{\alpha} \quad (4)$$

Figures 3.5 and 3.6 compare the RBSI and NDVI for one selected station in Illinois and Oklahoma. The RBSI for Altus station in Oklahoma does not fit the temporal evolution of NDVI. The RBSI for Stelle station in Illinois follows the same NDVI pattern. The

peaks indicate when the vegetation is at maximum development stage.

3.4 Microwave Vegetation Index (MWVI)

Due to the limitations of the polarization difference ratio and the radar backscatter index, a microwave vegetation index (MWVI) is estimated by combining data measurements from SSM/I and WSC (Kerr et al. 1997). This index uses the backscatter index, RBSI and the polarization ratio, PR. The PR was derived from the SSM/I at 19 GHz as vegetation index. This index is used to detect vegetation and quantify the amount of biomass. Thus, based on these indexes, the microwave vegetation index is obtained as follows:

$$MWVI = \frac{\ln(1 + RBSI)}{(0.1 + 12.5PR_{19})} \quad (5)$$

Figures 3.7 and 3.8 show the MWVI and NDVI for one station in Illinois and Oklahoma. The MWVI carries a good soil moisture signal and it is comparable to the NDVI pattern.

After comparing the variables

4 EMPIRICAL ALGORITHMS

The algorithms used in this study are defined as follows:

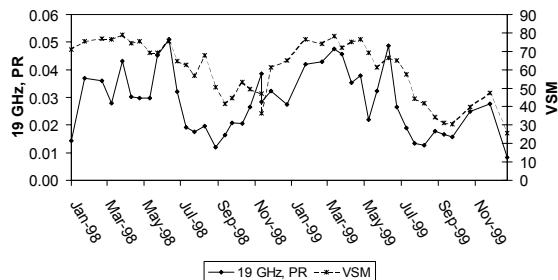
4.1 Physical Temperature

An empirical algorithm expressed by Kerr et al. (1999) is used to estimate physical temperatures from the SSM/I sensor. The vertical and horizontal polarizations of the 19 GHz channel, T_{B19P} , are used to estimate this temperature. The k parameter, which is used to weight the vertical and horizontal polarization contributions from the sensor, is set at 1.95. The ex parameter is an equivalent emissivity. This parameter depends on the actual H and V emissivities and the k factor, and it is set at 1.00. The algorithm is given by the equation,

$$T_{phys} = \frac{[kT_{B19V} - (k-1)T_{B19H}]}{ex} \quad (6)$$

Figure 4.1 shows the (modeled) physical temperature and the upper 5 cm soil temperature layer for Oklahoma. The correlation coefficient is 0.94.

Polarization ratio and upper 10 cm soil moisture layer for Illinois five most representative stations



Oklahoma average polarization ratio and upper 5 cm soil moisture layer

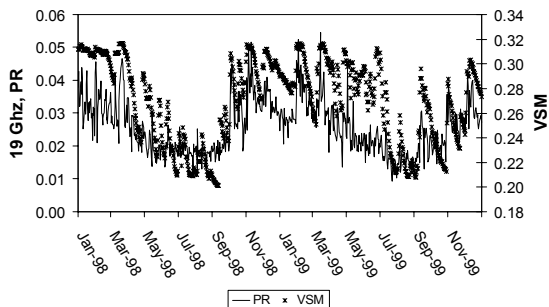
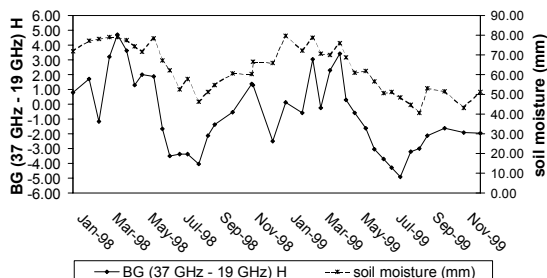


Figure 3.1 & 3.2 . Time series of the polarization ratio (19 GHz) and upper soil moisture layer for Illinois five most representative stations and Oklahoma, USA, 1998-1999.

Illinois average spectral gradient of brightness temperatures and upper 10 cm soil moisture layer



Oklahoma average spectral gradient of brightness temperatures and upper 5 cm soil moisture layer

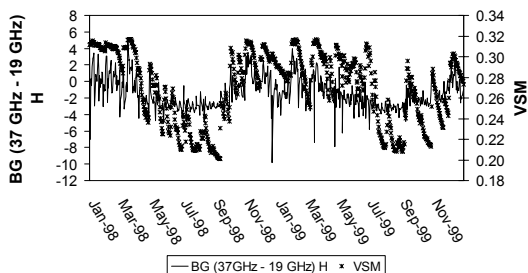
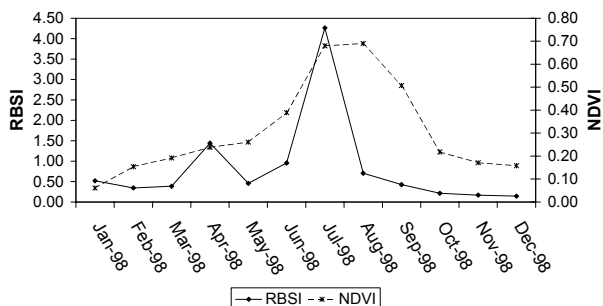


Figure 3.3 & 3.4. Time series of the spectral gradient of brightness temperatures and upper soil moisture layer for Illinois and Oklahoma, USA, 1998-1999

Radar Backscatter Index (RBSI) and Vegetation Index (NDVI) at Stelle station, Illinois



Radar Backscatter Index (RBSI) and Vegetation Index (NDVI) at Altus station, Oklahoma

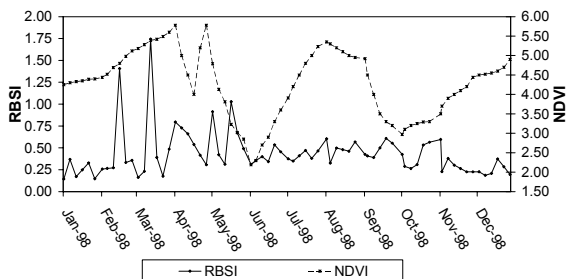


Figure 3.5 & 3.6. Time series of the radar backscatter index (RBSI) and vegetation index (NDVI) at Stelle station, Illinois (40.95° N, 88.17° W), and at Altus station, Oklahoma (34.58° N, 99.33° E), 1998.

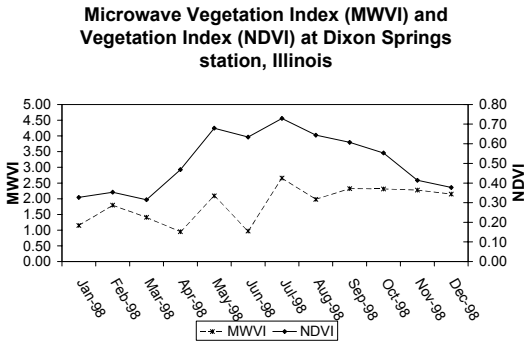


Figure 3.7. Time series of the microwave vegetation index (MWVI), and vegetation index (NDVI), at Dixon Springs station, Illinois (37.45° N, 88.67° W), 1998.

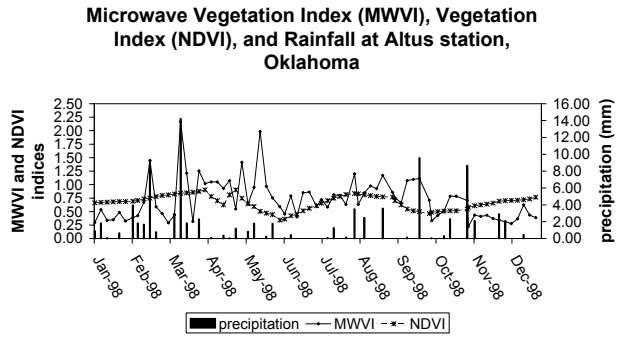


Figure 3.8. Time series of the microwave vegetation index (MWVI), vegetation index (NDVI), and rainfall at Altus station, Oklahoma (34.58° N, 99.33° E), 1998.

4.2 Snow Depth

crystals. A correction has to be implemented when vegetation is present (Kerr et al. 1999).

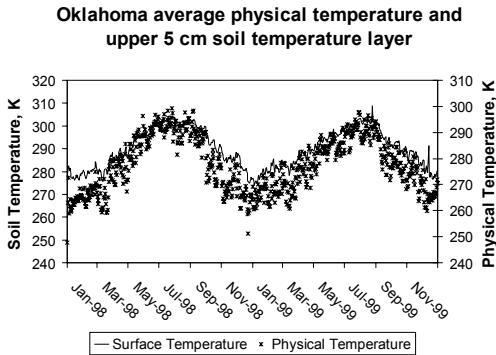


Figure 4.1. Time series of the physical temperature and upper 5 cm soil temperature layer for Oklahoma, USA. 1998-1999.

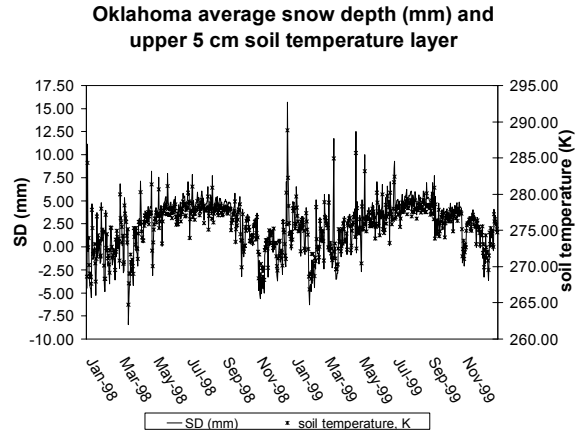


Figure 4.2. Time series of the snow depth (mm) and upper 5 cm soil temperature layer for Oklahoma. USA. 1998-1999.

The algorithm to retrieve the snow depth uses Chang et al. (1987) model. This is defined as the difference between the brightness temperatures of the 19 GHz and the 37 GHz channels for vertical or horizontal polarization multiplied by the 1.59 coefficient. It is expressed as follows:

$$SD(mm)=1.59(T_{B119H}-T_{B37H}) \quad (7)$$

Figure 4.2 compares (the modeled) snow depth and the upper 5 cm soil temperature for Oklahoma. The correlation coefficient is 0.94.

Equation 7 is an estimate of the amount of snow on bare ground for snow crystals, which assumes an averaged diameter of 0.3 mm of radius and snow depth between 10 cm and 1 m. The coefficient 1.59 mm/°K depends on the averaged size of the snow

5 DISCUSSION

The first stage of this study compared the SSM/I data and ERS data with the observed soil moisture data for Oklahoma and Illinois. Time series plots show the evolution of these variables and how well or poor these variables follow the soil moisture pattern.

The various algorithms mentioned in section 4 (Empirical Algorithms) are applied to the datasets to obtain estimations of the variables of interest: surface physical temperature, vegetation content, and snow depth and cover content. It is well known that vegetation has almost the same seasonal variation as soil moisture and temperature. Hence, it is difficult to

determine with accuracy variations within the microwave indices. Nonetheless, the microwave indices are used along with meteorological observations not only to demonstrate their quality of carrying the soil moisture signal, but also to aid in the interpretation of the observed variations of these indices. Due to the qualitative aspect of these results, the utilization of a model to invert soil moisture is needed to quantify the stages and dynamics of surface variables.

6 FUTURE WORK

1. Use and validate already existing models of SSM/I and ERS-2 to help in the retrieval of soil moisture. The first model is a bare-soil empirical model by Oh et al. (1992). It is applied to the measured backscattering coefficient from the ERS sensor. The other model is a physical model used by Jackson (1997). This model utilizes the brightness temperatures from the SSM/I sensor. These models will be adapted, if needed, for the vegetation regimes of the study area. Thereafter, an intercomparison will be made of the results of the soil moisture retrievals of these two models.

2. Investigate the spatial and temporal small-scale variability of soil moisture. Currently, there is no meteorological information or models that can reproduce the small-scale variability of the soil moisture field (Vinnikov, 1999a). Spatial and temporal autocorrelation will be applied to the observed soil moisture data for Illinois and Oklahoma for 4 years (1998 to 2001).

3. The final goal of this research is to provide useful results for the retrieval of soil moisture in larger scales and longer terms. For that, additional approaches are still being considered to reach this goal. One such approach is to incorporate other network soil moisture stations continentally or intercontinentally for validation of this remotely sensed data.

REFERENCES

- Chang, A.T.C., J.L. Foster & D.K. Hall (1987). Nimbus 7 SMMR-derived global snow cover parameters, *Annals of Glaciol.*, **9**, 39-44.
- Estimation of soil moisture for CYs 98 and 99 from the Oklahoma Mesonet Oklahoma Mesonet, Oklahoma Climatological Survey, Version 3.0, May 2001.
- Francis, R., G.Graf, P.G. Edwards, M. McCaig, C. McCarthy, P. Dubock, A. Lefebvre, B. Pieper, P.Y. Pouvreau, R. Wall, F. Wechsler, J. Louet, & R. Zobl. (1991). The ERS-1 spacecraft and its payload, *ESA Bulletin*, **65**, 27-48.
- Jackson, T. J., Soil moisture estimation using special satellite microwave/imager satellite data over a grassland region, *Water Resources Res.*, **33**, No. 6, 1475-1484, June 1997.
- P.L. Frison, E. Mougin, L. Jarlan, M.A. Karam, & P. Hiernaux. (2000). Comparison of ERS Wind-Scatterometer and SSM/I Data for Sahelian Vegetation Monitoring, *IEEE Transactions on Geoscience and Remote Sensing*, **38**, no. 4, 1794-1803.
- Kerr, Y.H., N.M. Mognard, S. Baillarin, J.C. Meunier, & S. Kalag dew. (1999). Combined use of passive and active microwave data to monitor seasons over high latitude continental regions, *Nordic Hydrology*, 1-40.
- Magagi, R.D., & Y.H. Kerr. (2001). Estimating Surface Soil Moisture and Soil Roughness From ERS-1 Wind-scatterometer Measurements Over Semi-Arid Areas: Use of the Co-Polarization Ratio, *Remote Sensing of the Environ.*, **75**, 432 – 445. CESBIO. Toulouse, France.
- Magagi, R.D., & Y.H. Kerr. (1997). Characterization of Surface Parameters Over Arid and Semi-Arid Areas by Use of ERS-1 Wind-scatterometer, *Remote Sensing Reviews*, **15**, 133-155.
- Oh, Y., Sarabandi, K., & Ulaby, F.T. (1992). An empirical model and inversion techniques for radar scattering from bare surfaces. *IEEE Transactions on Geoscience and Remote Sensing*, GE-30 (2), 370-381.
- Schmugge T.. (1985). Remote Sensing of Soil Moisture, Hydrological Forecasting, John Wiley & Sons Ltd., 100-125.
- Vinnikov K.Y., A. Robock, S. Qiu, J.K. Entin, M. Owe, B. J. Choudhury, S. Hollinger, & E. Njoku. (1999a). Satellite remote sensing of soil moisture in Illinois, United States, *J. Geophys. Res.*, **104**, No. D4, 4145 – 4168.
- Vinnikov K.Y., A. Robock, S. Qiu, & J.K. Entin. (1999b). Optimal design of surface networks for observation of soil moisture, *J. Geophys. Res.*, Vol. 104, No. D16, 19,743 – 19749.
- Wagner, W., & K. Scipal. (2000). Large-Scale Soil Moisture Mapping in Western Africa Using the ERS Scatterometer, *IEEE Transactions on Geoscience and Remote Sensing*, **38**, no. 4, 1777-1782.
- Wismann, V., A. Cavanie, D. Hoekman, I. Woodhouse, K. Boehnke, & C. Schmullius. (1996). Land surface observations using ERS-1 windscatterometer, ifars, ESA Contract, 11103/94/NL/CN.
- Woodhouse I.H. & D.H. Hoekman. (2000). A Model-Based Determination of Soil Moisture Trends in Spain With the ERS-Scatterometer, *IEEE Transactions on Geoscience and Remote Sensing*, **38**, no. 4, 1783-1793.

5. PROYECTOS RECIENTES Y MISIONES DE OBSERVACIÓN DE LA TIERRA / RECENT PROJECTS AND EARTH OBSERVATION MISSIONS

Monitoring Global Climate Change: The Advanced Along Track Scanning Radiometer (AATSR)

M.C.Edwards¹, D.Llewellyn-Jones¹ and D. Smith²

¹Space Research Centre, University of Leicester

² Rutherford Appleton Laboratory, Oxford

mce1@le.ac.uk, dlj1@le.ac.uk, d.l.smith@rl.ac.uk

ABSTRACT - Global sea surface temperature (SST) is potentially a useful and accurate indicator of global climate change. Observations of SST from space are essential in order to provide the necessary coverage and continuity, which will enable unambiguous and sensitive detection of global change to be made. The Advanced Along Track Scanning Radiometer (AATSR), a satellite sensor specifically designed to measure SST to the appropriate levels of accuracy for climate change research, was launched on board ESA's research satellite Envisat, on 1st March 2002. It continues the work of ATSR and ATSR-2, and will lead to a SST data record of longer than fifteen years. Following a successful launch, a comprehensive validation programme is underway to ascertain the quality of AATSR data. Activities include algorithm verification, and the comparison of SST measurements from AATSR with those collected from precision radiometers, buoys and modelled SST analysis fields. Visible channels will be validated over land and cloud targets. Validation results will be fed back into the AATSR operations programme, thus contributing to the successful commissioning of the instrument in the six-month period after launch. This paper describes the AATSR sensor and data products, and the validation programme.

1 INTRODUCTION

With increasing supporting evidence, the subject of global climate change is high on the international political agenda. In the United Kingdom, the Hadley centre for Climate Prediction and Research is committed to providing an up-to-date expert assessment of natural and anthropogenic changes in the global and regional climate. Climate models are used to simulate climate variability on a range of scales and make predictions as to future climates. For these models, a number of sources of data are needed. Satellite observations are one of the most important (Donlon et al 2002).

On March 2002, the European Space Agency launched Envisat, the largest satellite for Earth observation ever built in Europe. A sun-synchronous polar orbiting satellite, Envisat carries ten instruments designed to measure a range of environmental parameters. One of the instruments on board is the Advanced Along Track Scanning Radiometer, AATSR. The third in a series, the primary function of AATSR is to support the programme of research into climate change by providing high precision, high accuracy measurements of sea surface temperature.

This paper describes the AATSR instrument, and with the Envisat mission well underway, gives some

of the early results. Details of the validation programme, in place for AATSR, as with all Envisat instruments, are also given. Figure 1 shows one of the first global maps of AATSR data.

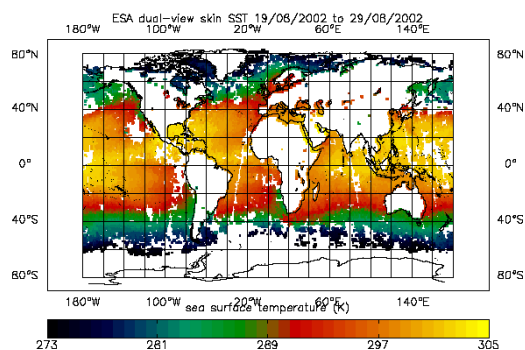


Figure 1: Spatially averaged, global SST data derived from AATSR data (Source: UK Met Office)

2. THE AATSR INSTRUMENT

The AATSR instrument is an imaging radiometer, designed to measure sea surface temperature (SST) to the degrees of accuracy and precision required for monitoring climate trends and research into climate

prediction (better than $0.3K \pm 1$ sigma limit). With wavebands in the visible and near infrared channels, it also provides data to support applications in the fields of oceanography, land surface studies and atmospheric science. The characteristics of the instrument are given in Table 1.

Spectral Bands (µm)	0.545-0.565 (chlorophyll) 0.649-0.669 (vegetation index) 0.855 –0.875 (vegetation index) 1.58 – 1.64 (cloud clearing) 3.55 – 3.93 (SST) 10.4 – 11.3 (SST) 11.5 – 12.5 (SST)
Spatial resolution	1 x 1 km at nadir
View Zenith	Nadir (nadir view) 55° (forward view)
Swath Width	500 km

Table 1: Specifications of the AATSR sensor

2.1 Funding and Heritage

The AATSR was built by a consortium of companies, lead by Astrium UK. It is funded by the UK Department for Environment, Food and Rural Affairs (DEFRA), with contributions from the Australian government and the UK Natural Environment Research Council.

The AATSR is the third in a series of instruments, following ATSR-1, launched on ERS-1 in July 1991 and ATSR-2, launched on ERS-2 in April 1995. Together, this family of instruments will provide a dataset of accurate SST measurements on a global scale of longer than fifteen years.

2.2 Accurate measurement of SST

In order to measure SST to the degrees of accuracy and precision required, the AATSR has a number of unique features.

a) Along Track Scanning

The (A)ATSR series of instruments offer a unique view of the Earth using along track scanning. Using a conical scan mechanism, every point on the Earth’s surface is viewed twice, first at an angle of 55° (the forward view) and then at an angle close to vertical (the nadir view) as the satellite moves forward. The two observations, separated in time by 150 sec, or approximately 1000km on the ground, provide two

views through the atmosphere, which are used to make a good atmospheric correction.

b) Stirling Cycle Coolers

The AATSR also uses closed cycle mechanical coolers to maintain the thermal environment necessary for the optimal operation of the infrared detectors. The thermal focal plane assembly (FPA) is cooled to 80 K whilst the visible FPA is maintained at ambient temperature. ATSR was the first environmental sensor to carry such a cooler into space.

c) On-board Calibration

In orbit, AATSR provides continuous on board calibration of both the thermal and the visible channels, thus again leading to accurate measurement of SST.

Calibration of the thermal channels is achieved using two on board blackbodies, basically cylindrical cavities with non-reflecting interior coatings and good insulation. One blackbody is maintained at a temperature of 305 K, just above the maximum expected to be observed over marine scenes, whilst the other is unheated, floating at a temperature close to the ambient temperature of the instrument enclosure, ~ 256 K (Llewellyn-Jones et al. 2001, Smith 2001).

The visible channels use a system whereby once per orbit, a brief view of the sun is taken, illuminating a Russian opal tile. Light enters the detector field of view at a suitable point in the scan cycle and calibration of the visible channels can be achieved.

Figure 2 shows the AATSR flight model, showing the aperture for visible calibration and the two blackbodies used for calibration of the thermal channels.

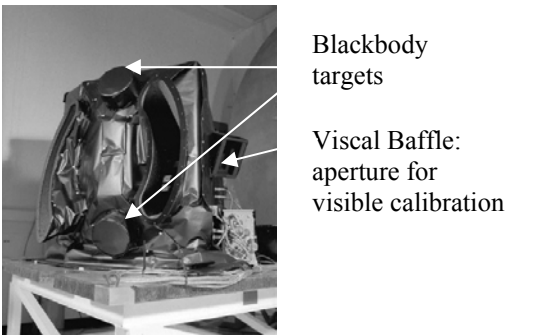


Figure 2: The AATSR Flight Model (Source: RAL)

3. AATSR DATA PRODUCTS

Table 2 details the set of AATSR products available (Llewellyn-Jones et al, 2001). When they are made available to the scientific community, these can be browsed and ordered through the ESA Payload Data Segment services facility.

Validation activities focus on the GBTR, GST and Meteo products, with the primary objective being to validate the geophysical parameter SST over land. Over land, AATSR does not currently offer any geophysical retrievals at level 2 other than the NDVI. Therefore, over land, validation focuses on the vicarious validation of the GBTR over land and cloud.

Name	Description
Level 0	Instrument source packet. Not available to users.
GBTR	Gridded Brightness Temperature/Reflectance. Full resolution TOA BT/Reflectance
Browse Product	3-band colour composite derived from 4*4 km sampling of GBTR.
Gridded Surface Temperature (GST)	Full resolution nadir only and dual view SST over sea. Full resolution 11 μ m BT and NDVI over land.
Averaged Surface Temperature (ATS)	Spatially averaged ocean, land and cloud parameters. Spatially averaged TOA BT/reflectance.
Meteo Product	Subset of spatially averaged SST and TOA BT at 10-arc min resolution.

Table 2: Summary of AATSR data products

4. AATSR COMMISSIONING

Following Envisat launch, every instrument enters a Switch On and Data Acquisition Phase (SODAP), where the instrument is switched on and checked out. A number of initial tests are performed to characterise and commission the instrument in orbit. Following the SODAP, algorithm verification and validation activities start.

The switch on for AATSR was performed on March 9th, and the main activities of the SODAP were completed by 19th May. Results from the early

commissioning phase are good, indicating that overall the instrument is performing well and all the mechanisms are functioning nominally.

In terms of the specific instrument features designed to produce an accurate measurement of SST, results indicate that the mechanisms are working well. The overall thermal performance of the instrument is good, and both the thermal and the visible calibration systems are functioning according to specifications.

Table 3 shows baseplate sensor readings from the hot and cold blackbodies. PRT6 is located on the baffle and is not included in the baseplate average. Temperature gradients are low and uniform indicating that the thermometry is good and stable. The results compare well with pre-launch tests.

	+XBB		-XBB	
	Reading	Diff.	Reading	Diff.
Baseplate Average	301.522		262.897	
PRT1	301.513	-0.009	262.898	0.001
PRT2	301.518	-0.004	262.899	0.002
PRT3	301.526	0.004	262.897	0.000
PRT4	301.525	0.003	262.892	-0.005
PRT5	301.530	0.008	262.897	0.000
PRT6	301.905	0.383	262.882	-0.015

Table 3: Base plate sensor readings for the AATSR hot and cold blackbodies

The visible calibration system is also performing as expected (see Figure 3), with a good signal showing 90 seconds of 100% illumination. The signal increases sharply when the sun is viewed.

In terms of radiometric performance, the Ne δ T is below 50 mK for the infrared channels, with dark noise for the visible channels being below digitisation levels. Frequency analysis on the blackbody signal shows no significant pickup below 3Hz from the cooler or other mechanisms. In general, it can be said that the radiometric performance is good and comparable to ATSR-2 levels.

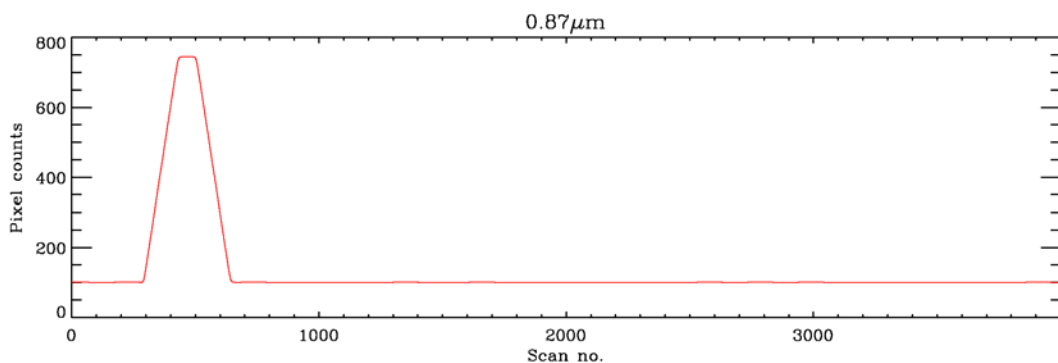


Figure 3: Plot showing 0.87 micron channel mean VISCAL count for orbit 1101 on 17 May 2002 (lower scale is relative time in mins)

5. THE AATSR VALIDATION PROGRAMME

Once the AATSR instrument is commissioned, attention turns to focus on the AATSR data itself. The AATSR validation programme, in particular, aims to:

- Determine whether the AATSR instrument is returning an acceptable global skin SST.
- Make an initial assessment of the quality of the AATSR SST data products in a number of sites and seasons.
- Assess the accuracy of AATSR data collected over land.

To achieve these goals, over 15 projects involving scientists from over 10 institutions worldwide will take place during the first 9 months of AATSR operations. As the mission progresses, this number will increase as validation is undertaken in more sites, over a wider variety of environmental conditions. New products will also be validated as they become available.

Validation activities can be described in 3 categories – algorithm verification, SST validation and validation of the visible/near infrared channels over land. Many of the activities, particularly those involving custom built radiometers, build on the validation work of the ATSR and ATSR-2 instruments (Barton and Skirving 1999, Minnett et al, 2001, Parkes et al 2000).

5.1 Algorithm Verification

Algorithm verification is an important activity to ‘commission’ the AATSR processors, characterise the performance of the algorithms used and evaluate the quality of the L1b and L2 products. It is being carried out by A. Birks at the Rutherford Appleton Laboratory.

5.2 SST validation

The AATSR validation programme has 3 levels of SST validation.

a) Global Buoy Comparisons

The UK Met Office is comparing AATSR SST data with data from buoys and SST analysis fields on a global scale, on a daily basis. This is designed to give an early indication of gross errors in the AATSR SST data.

Acquiring the AATSR METEO product in near real time, this activity started in August 2002. Although only preliminary results are available, early indications from this activity are that there is good agreement between the in situ/satellite measurements on a global scale.

The global buoy comparison by the Met Office gives an indication as to how well the AATSR SST measurements compare to *in situ* bulk SST measurements. With bulk SST typically varying from the skin SST in temperature by up to several degrees, measurement of the *in situ* skin SST is needed to complement these results (Parkes et al 2000). This is

achieved through use of custom built, high accuracy radiometers. These can either run autonomously on a merchant ship or ferry or by an expert on board a ship-of-opportunity.

b) Autonomous Measurements

There are four autonomous instruments measuring SST involved in the AATSR validation programme.

The Infrared Sea surface skin temperature (ISAR-5-IR), operated by Southampton Oceanography Centre, is a precision, autonomous, self-calibrating radiometer. It has been running on passenger ferries since the start of AATSR operations, and has collected a number of *in situ* validation measurements for AATSR.

Similarly, two radiometers are running on ferries in Australia waters, one on a ferry taking tourists from Townsville (Barton and Skirving 1999), and one on a ferry operating from the coast of Perth.

Lake Tahoe has been studied in detail for a number of years (e.g. Pearl et al 1975). Autonomous radiometers are currently deployed on the lake on four rafts for the validation of a number of satellite sensors including AATSR.

c) Precision measurements

AATSR validation is also being carried out using custom built radiometers, operated by experts, on ships-of-opportunity. With operators on hand to record conditions and perform a level of near real time quality control, these *in situ* measurements should be the most accurate. The accuracy of both the autonomous and precision radiometers used for AATSR Validation was assessed through an intercomparison exercise held in Miami in 2001. All radiometers showed they were of the accuracy required (Barton et al 2002).

To date, three dedicated cruises have taken place, one using the SISTeR instrument in the Indian Ocean (operated by T. Nightingale of RAL) and two in Australian waters using the DAR011 instrument (operated by I. Barton of CSIRO). The MAERI instrument operated by the University of Miami has also been continuously deployed on a cruise liner in the Caribbean (Minnett et al 2001). More validation cruises are planned for the period September-December 2002, before the Envisat validation workshop.

5.3 Validation of the visible/near infrared channels

For validation of the visible/near infrared channels, AATSR will be compared to other instruments such as

ATSR-2, MERIS and SCIAMACHY over land and cloud. These measurements will be enhanced by *in situ* measurements taken over land sites in Australia (CSIRO).

6. SUMMARY AND CONCLUSIONS

Early results from the AATSR mission indicate that the AATSR instrument is functioning well and operating within specifications. Preliminary validation results suggest that SST measured by AATSR shows a good comparison to *in situ* SST measurements, on a global scale. In order to make a more detailed assessment of the accuracy of AATSR, further validation results on a variety of scales are needed. A comprehensive validation programme is in place to provide these measurements, both in the short term and throughout the Envisat mission.

7. ACKNOWLEDGEMENTS

Marianne Edwards works as the AATSR Validation Scientist, David Llewellyn-Jones is the AATSR PI and David Smith is the AATSR instrument scientist. All 3 posts are supported by DEFRA in the UK. The authors would like to thank Hannah Tait of VEGA, ESA, and members of the AATSR validation team for their work for the AATSR validation programme.

8. REFERENCES

- Barton, I.J., and W. J. Skirving, W.J., 1999, "Satellite-derived sea surface temperature intercomparison: A case study" in *Advances in Space Research* Vol 23. No. 8 pp 1517-1523
- Barton, I. J., Minnett, P. J., Maillet, K. A., Donlon, C. J., Hook, S. J., Jessup, A. T and T. J. Nightingale, 2002. The Miami2001 infrared radiometer calibration and inter-comparison: 2. Ship board results. Submitted Journal of Atmospheric and Oceanic Technology.
- Donlon, C.J., Minnett, P.J., Gentlemann, C., Nightingale, T.J., Barton, I.J., Ward, B., and Murray, M.J., 2002, Toward improved validation of satellite sea surface skin temperature measurements for climate research, *Journal of Climate*, 15, pp 353-369.
- Llewellyn-Jones, D., Edwards, M.C., Mutlow, C.T., Birks, A.R., Barton, I.J., and Tait, H., 2001, AATSR: Global change and surface temperature measurements from Envisat, ESA Bulletin 105, February 2001, pp 10-21

- Minnett, P.J., Knuteson, R.O., Best, F.A., Osborne, B.J., Hanafin, J.A., Brown, O.B., 2001, "The Marine-Atmospheric Emitted Radiance Interferometer: A high-accuracy, seagoing infrared spectroradiometer", *Journal of atmospheric and oceanic technology* 18 no 6, pp 994-1013
- Parkes, I.M., Sheasby, T.N., Llewellyn-Jones, D.T., Nightingale, T.J., Zavody, A.M., Mutlow, C.T., Yokoyama, R., Tamba, S., and Donlon, C.J., 2000, The Mutsu bay Experiment: validation of ATSR-1 and ATSR-2 sea surface temperature, *International Journal of Remote Sensing*, Vol. 21. No. 18 pp 3445-3460
- Pearl, H.W., Richards, R.C., Leonard, R.L., Goldman, C.R., 1975, Seasonal nitrate cycling as evidence for complete vertical mixing in Lake Tahoe, California-Nevada, *Limnology and Oceanography*, Vol. 20. pp 1-8
- Smith, D.L., Delderfield, J., Drummond, D., Edwards, T., Mutlow, C.J., read, P.D., and Toplis, G.M. 2001, Calibration of the AATSR Instrument, *Advances in Space Research*, 28. No. 1 pp 31-39

Simulation of SPECTRA like scenes in order to learn and anticipate radiative transfer models

Heike Bach¹, Wout Verhoef²

¹ VISTA Geowissenschaftliche Fernerkundung GmbH,
Luisenstrasse 45, D-80333 Munich, Germany
tel. 0049-89-52389802, fax 0049-89-52389804
e-mail: bach@vista-geo.de

² National Aerospace Lab. NLR, P.O.Box 153, 8300 AD Emmeloord, The Netherlands
tel. 0031-527-248253, fax 0031-527-248210
e-mail verhoef@nlr.nl

ABSTRACT - Future remote sensing satellite missions, like SPECTRA (Surface Processes and Ecosystem Change Through Response Analysis), that has been nominated as a candidate Earth Explorer Mission by the European Space Agency, will feature advanced hyperspectral and directional optical imaging instruments. Given the complex nature of the data to be expected from these missions, a thorough preparation of their use is essential and this can be accomplished by realistic simulation of the expected imagery data years before the actual launch. Based on given spectral and directional capabilities of the planned SPECTRA instrument, and in combination with biophysical land surface properties obtained from existing imagery, the spectral and directional responses of several types of vegetation and bare soil were simulated pixel by pixel for a real scene using radiative transfer models.

Canopy reflectances were modelled using GeoSAIL, a two-layer version of the SAIL model which incorporates a sub-model for the effect of soil moisture on the soil's background spectrum. In the GeoSAIL model two spectrally different leaf types (e.g. green and brown leaves) are divided over both layers in different proportions, so as to mimic the vertical leaf colour gradient often seen in crops like wheat. The spectra of green and brown leaves were modelled using PROSPECT. By combining the models PROSPECT and GeoSAIL, the major aspects related to optical observation of vegetation and realistic modelling of directional canopy reflectance spectra were covered. However, the result represents the reflectance spectrum as it would have been measured on the ground, not what a sensor would observe from space. Therefore, the coupling of the surface reflectance model to an atmospheric radiative transfer model also needs to be addressed. For this, the model MODTRAN4 was selected, for computing of absorption and scattering in the terrestrial atmosphere at high spectral resolution over the solar-reflective and thermal windows. In this respect, MODTRAN4 was treated as a black box and an "interrogation" technique was applied in order to derive six effective atmospheric parameters from the outputs of three different MODTRAN runs.

In this paper the modelling methodologies for image simulation in the solar-reflective spectral window are described, as well as the study area, the set-up of the simulations and the results. As test site Barrax in Spain, where already a lot of land surface processes research was carried out, was selected for the simulation of imagery to be expected from the SPECTRA mission.

1 INTRODUCTION

The SPECTRA mission (Surface Processes and Ecosystem Change Through Response Analysis) (ESA 2001) was nominated as a candidate Earth Explorer Mission by the European Space Agency ESA for the study of land surface processes. This will be accomplished by means of a hyperspectral and directional optical imaging instrument that also includes two thermal bands, allowing simultaneous

and co-registered observation of targets in the solar-reflective as well as the thermal spectral window (see Tab.1).

In order to prepare the user community for SPECTRA imagery it is important to carry out realistic simulations, which include all aspects playing a significant role for this mission, such as its hyperspectral and directional observation capability,

its dedication to mainly vegetated land areas, and its expected spatial resolution. For this purpose Barrax in Spain was selected for the simulation of imagery to be expected from the SPECTRA mission. It is a site, where already a lot of land surface processes research was carried out..

Tab.1: SPECTRA main system parameters and observation capabilities (ESA, 2001)

Spectral characteristics (Region 1)	400 – 2400 nm 10 nm sampling interval
Spectral characteristics (Region 2)	TIR1: 10.3 to 11.3 μm TIR2: 11.3 to 12.3 μm
Spatial width	< 5m nadir < 150 m for 70° BRDF angle in Region 1 < 150 m for 55° BRDF angle in Region 2
Image swath and length	50 km
Observation angle	7 zenith angles (programmable, 0 to 60°)
Across-track depointing	+/-35° (=> capability for 3 days access)

Advanced hyperspectral sensors on board future earth-exploring satellites such as SPECTRA will at the same time be capable of measuring complete radiance spectra from selected targets on earth and of observing these targets under several viewing directions. In this way it will be possible to obtain detailed spectral and directional information on the reflectance properties of the target. This enables the accurate retrieval of land surface parameters that are important inputs for models describing the cycles of carbon, nitrogen and water, as well as for numerical weather prediction models and global climate models. Also for regional applications one can expect that hyperspectral and directional observations can provide a lot of useful additional information.

2 METHODOLOGY

Based on the given spectral and directional capabilities of the planned SPECTRA instrument, and in combination with biophysical land surface properties obtained from existing imagery, the spectral and directional responses of several types of vegetation and bare soil were simulated pixel by pixel using the radiative transfer models PROSPECT (for hyperspectral leaf reflectance and transmittance), GeoSAIL (for two-layer canopy bidirectional spectral reflectance of pixels), and MODTRAN4 (for atmospheric hyperspectral and directional effects). In

this way one obtains realistically simulated hyperspectral and directional top-of-atmosphere spectral radiance images. They include all major radiative effects, such as heterogeneity of the landscape, non-Lambertian reflectance of the land surface, the atmospheric adjacency effect and the limited spatial resolution of the instrument. A simplified illustration of the applied methodology and the model interactions are given in Fig. 1.

The model PROSPECT (Jacquemoud & Baret, 1990) computes spectra of the reflectance and transmittance of single leaves from chlorophyll concentration, water content and a structural leaf mesophyll parameter. In a more recent version (Baret, pers. comm. 1997) dry matter and brown pigment were added as biochemical substances. For the spectral range from 400 to 2400 nm and a sampling distance of one nm, absorption spectra of all substances, plus an effective index of refraction, are used as input to the model in order to compute spectra at a high resolution, that are then resampled using the spectral response functions of each SPECTRA band.

The canopy reflectance model is a two-layer version of the SAIL model (Verhoef, 1984) specially developed in the ESA GeoBIRD study (Bach *et al.*, 2001). Fig. 2 shows the 4 stream approach and input parameters of GeoSAIL. The two-layer model developed for GeoBIRD is based on SAIL, but it includes the hot spot effect as described in Verhoef (1998). In GeoSAIL it is assumed that the LIDF is the same for both layers, as well as the size parameter of the hot spot effect.

The partitioning of green and brown over the two layers is governed by two parameters, the fraction brown leaf area f_B and a dissociation factor D . For $D = 1$ all brown leaves are supposed to be located in the bottom layer and all green leaves in the top layer, whereas for $D = 0$ both leaf types are supposed to form a homogeneous mixture in both layers. This dissociation factor plays an important role in the model. Especially when brown leaves are covered by green leaves in the top layers of the canopy, their impact on the canopy reflectance spectrum can easily be overestimated if a homogeneous mixture of green and brown leaves is assumed.

Another important feature of GeoSAIL is that a sub-model for soil reflectance is incorporated (Bach & Mauser, 1994). This sub-model describes the influence of soil moisture in the top layer of the soil on its reflectance spectrum over the entire solar-reflective range. The input to this model consists of the reflectance spectrum under dry conditions plus the influence of surface soil moisture.

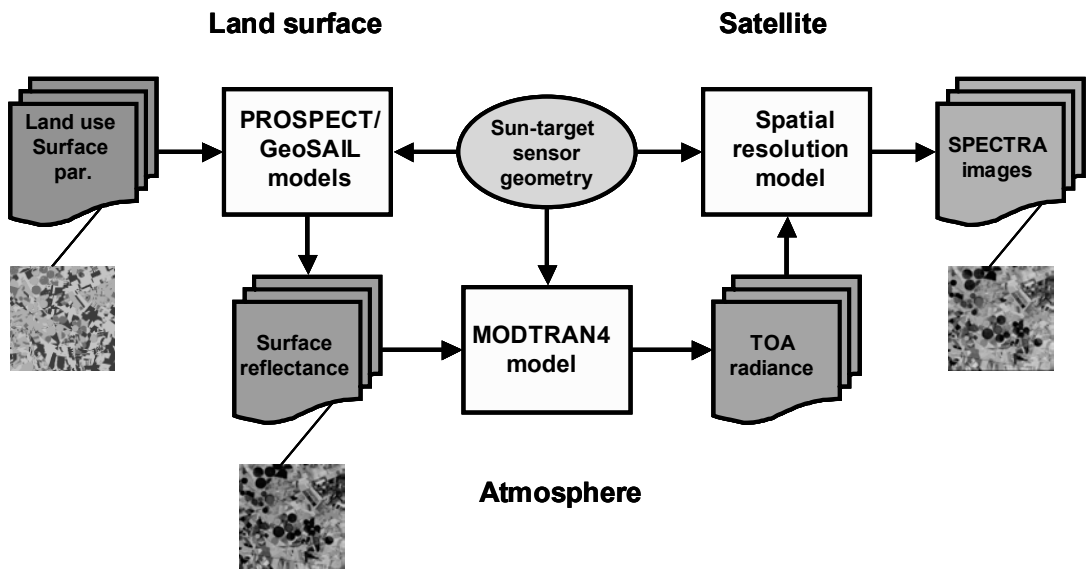


Fig. 1: Flow-chart of the applied methodology to simulate SPECTRA-like scenes

For image simulations in order to maintain the natural variations within vegetated fields and bare soil parcels, a model inversion technique, that was also used in Bach et al. (2000), was applied to an atmospherically corrected TM-image so as to modulate the initial values of canopy LAI and surface soil moisture. Using a land use map and the retrieved spatial distribution of leaf area and surface soil moisture, images of surface reflectance were simulated in the SPECTRA bands.

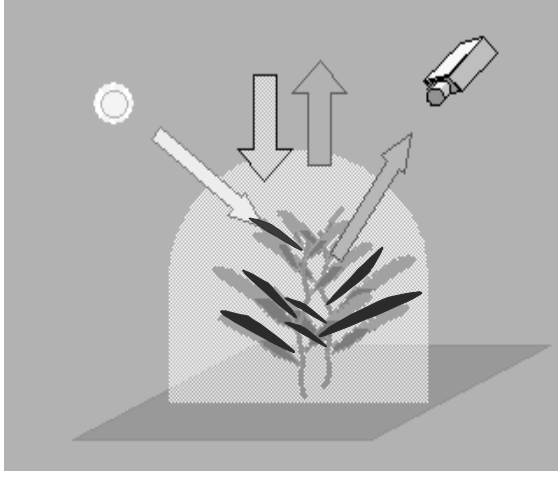
The whole model approach is entirely modular. First PROSPECT was run for the combination of leaf parameters that occurred, next the GeoSAIL input maps were generated from the land use and the Landsat TM model inversion results, and then GeoSAIL was run to produce the surface reflectance maps. These surface reflectance maps consist of four parameters describing for each pixel the non-Lambertian reflectance for the given directions of the sun and observation. Two of the four surface reflectance maps are spatially filtered for the adjacency effect.

To couple the surface reflectance model to an atmospheric radiative transfer model MODTRAN4 (Berk et al., 2000) was selected. With MODTRAN4 high spectral resolution absorption and scattering in the terrestrial atmosphere was calculated over the solar-reflective and thermal windows.

The MODTRAN4 model is run for three surface albedos (assuming 0%, 50%, and 100%) for the given sun-target-observer configuration and for the spectral range and resolution of the SPECTRA mission. An “interrogation” technique was applied in order to derive six effective atmospheric parameters from the outputs of three different MODTRAN runs. The six effective parameters derived for each wavelength describe the interaction of the whole atmosphere with the land surface, and in essence they can totally replace MODTRAN for a realistic forward modelling of top-of-atmosphere observations influenced by non-Lambertian surface reflection and landscape heterogeneity.

The combination of the six effective atmospheric parameters with the surface reflectance maps according to Eq. 1 results in top of atmosphere (TOA) radiances.

The last step is applying the spatial filtering and resampling required to simulate the spatial resolution of the sensor for the along-track and across-track pointing angles necessary to view the site.



Input parameters to GeoSAIL:

LAI - leaf area index
Average leaf slope parameter a
LIDF bimodality parameter b
Hot spot parameter q
Fraction brown leaf area fB
Layer dissociation factor D

structural

Reflectance green & brown leaves
Transmittance green & brown leaves
Fraction diffuse sky irradiance
Dry soil reflectance & soil moisture

spectral

Solar zenith angle
Viewing zenith angle
Relative azimuth angle

observational

Four-stream canopy reflectance model:

1. Direct solar flux
2. Diffuse downward flux
3. Diffuse upward flux
4. Direct observed flux (radiance)

Fig. 2: Four stream canopy reflectance model GeoSAIL and used input parameters

$$r_p = \rho_{so} + \frac{\overline{\tau_{ss} r_{sd}} + \overline{\tau_{sd} r_{dd}}}{1 - \overline{r_{dd} \rho_{dd}}} \tau_{do} + \frac{\overline{\tau_{sd} + \tau_{ss} r_{sd} \rho_{dd}}}{1 - \overline{r_{dd} \rho_{dd}}} r_{do} \tau_{oo} + \tau_{ss} r_{so} \tau_{oo} \quad (1)$$

where

r_{so} = target bidirectional reflectance

r_{do} = target directional reflectance for diffuse incidence

r_{sd} = average surroundings diffuse reflectance for solar incidence

r_{dd} = average surroundings diffuse reflectance for diffuse incidence

ρ_{so} = TOA atmospheric bidirectional reflectance

ρ_{dd} = BOA spherical albedo of the atmosphere

τ_{ss} = direct atmospheric transmittance in the direction of the sun

τ_{oo} = direct atmospheric transmittance in the direction of viewing

τ_{sd} = diffuse atmospheric transmittance for solar incidence

τ_{do} = directional atmospheric transmittance for diffuse incidence

r_p = TOA (planetary) reflectance

3 SIMULATION RESULTS

SPECTRA like scenes were simulated for the Barrax site. The acquisition scenario is illustrated in Fig.4 for an along track case. The Barrax site (Berger *et al.*, 2001) is situated in the west of the Province of Albacete, Spain. The landscape in the area is very flat. The soils are poorly developed and shallow. About 35% of the area is under irrigation, with maize, barley and alfalfa being the main land uses. In the non-irrigated areas dry crops (e.g. winter cereals) are grown, or they are left fallow.

In order to simulate hyperspectral and directional images with a realistic spatial distribution of vegetated areas and bare fields over the scene, a Landsat Thematic Mapper image of Barrax in Spain of June 28th 2000 was taken as input, and a land use classification result obtained from it by the University of Valencia, in combination with the results of ground measurements of biophysical parameters (Luis Alonso-Chorda, 2001; <http://io.uv.es/projects/daisex>) was applied to translate each soil or vegetation class into a basic set of model input parameters.

A realistic spatial distribution of plant parameters and moisture estimates for the partially irrigated fields was obtained by using an atmospherically corrected TM scene for the retrieval of leaf area index and surface soil moisture. The same optical model (PROSPECT-GeoSAIL) simulating LANDSAT-TM bands was applied for this task in an inverse mode. The inversion procedure is described in Bach *et al.* (2000).

With the resulting maps of leaf area and surface soil moisture the heterogeneity of a landscape could be represented with the detail necessary to a realistically modelling of SPECTRA-like scenes. In combination with the land use map this provides a complete set of input parameters for each pixel.

As part of the DAISEX campaign (Berger *et al.*, 2000), airborne hyperspectral images from the HyMap imaging spectrometer acquired on June 29th were also available. As these images were already atmospherically corrected and accurately calibrated into surface reflectances, they were used for the extraction of soil spectra and to validate preliminary model calculations (Fig.3) with the combination PROSPECT-GeoSAIL.

Based on the land use map, the PROSPECT derived leaf optical properties were assigned to each pixel. In a next step GeoSAIL was run using the pixel wise land surface parameterisations in order to simulate surface reflectances.

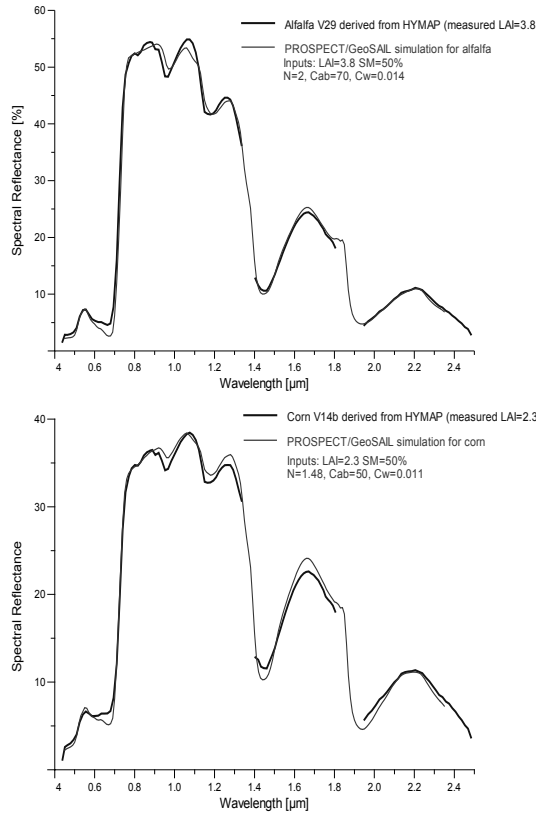


Fig. 3: Surface reflectance modelling validation results for alfalfa and corn

A result of this procedure is shown in Fig. 5. The complete data cube contains 191 spectral bands (450 nm – 2350 nm in 10 nm steps), as can be seen in the spectra plotted from selected pixels of different land use types.

Based on the surface BRDF components and the six effective atmospheric parameters, in a next step the TOA radiances were simulated by applying Eq. (1) for each pixel. Spectral results of this processing step are illustrated in Fig. 6 for 2 different atmospheric visibilities. The differences of the BOA surface reflectances with different observation geometry become less distinct after passing through the atmosphere. This effect is further strongly dependent on the aerosols in the atmosphere. As can be expected, for clear atmospheres with a visibility of 40 km the BRDF of the surface stays better observable. For low visibilities of 5 km the increase of radiances with increased viewing angles especially in the short wavelength region is evident.

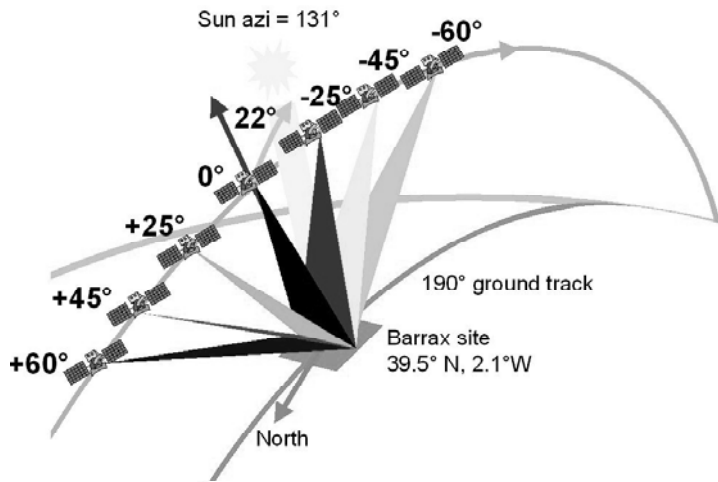


Fig. 4: Simulation cases for a realistic (along-track) SPECTRA acquisition scenario

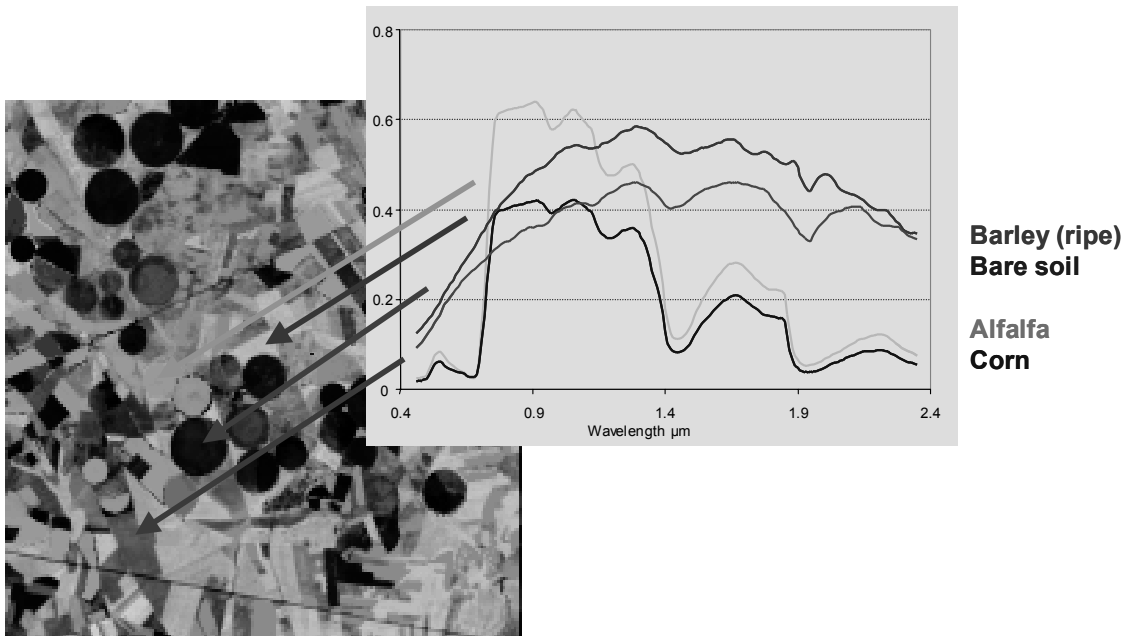


Fig. 5: Simulated SPECTRA scene for nadir view and spectra from 4 pixels of alfalfa, corn, dry crop and soil

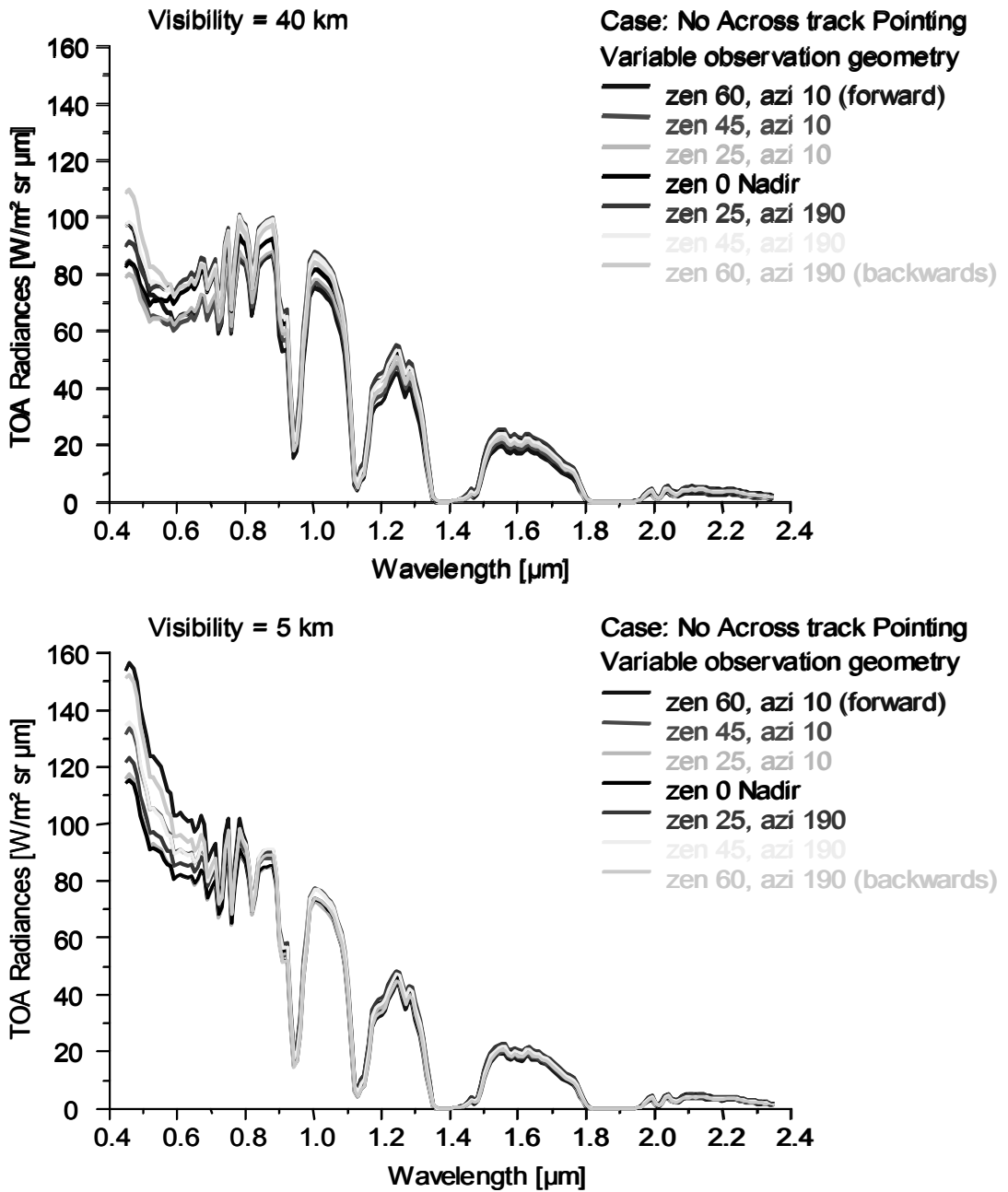


Fig. 6 Simulated spectra of TOA radiances for a clear and hazy atmosphere and a barley pixel

CONCLUSIONS

The feasibility of using the combination of the radiative transfer models PROSPECT, GeoSAIL and MODTRAN4 for realistic hyperspectral and directional radiance image simulation of SPECTRA scenes in the VIS-SWIR region has been demonstrated. These models were coupled in a chain of successive operations and a four-stream approximation was applied to describe the complex interaction of the 2-D heterogeneous and non-Lambertian land surface with the atmosphere in an effective yet realistic manner. In this respect, an "interrogation" technique was successfully applied to MODTRAN4 model outputs in order to extract spectra of the six effective parameters characterising the optical behaviour of the atmosphere.

The chain of radiative transfer models, coupled to GIS-info, will be used to (1) demonstrate capabilities of future earth observation concepts dedicated to vegetation monitoring and biophysical parameter retrieval, (2) optimise instrument specifications and image acquisition scenarios and (3) experiment with advanced site-oriented data assimilation procedures.

According to the simulations the atmospheric adjacency effect is considerable and its interaction with scene heterogeneity necessitates incorporation of the 2-D structure of the landscape into model inversion and data assimilation schemes.

Bidirectional effects are clearly noticeable and may provide additional biophysical information, especially on crop architectural parameters like LAI, leaf angle distribution and relative leaf size. In combination with hyperspectral observations this provides ways to improve the accuracy of biophysical parameter retrievals from multidirectional hyperspectral radiance images.

ACKNOWLEDGEMENTS

The results presented here were obtained in the framework of the DAASCEES study (Data Assimilation And Scaling for the Candidate Earth Explorer core mission SPECTRA), performed under ESA Contract No. 15164/01/NL/SF, with Mike Rast (ESA ESTEC) as study manager.

The authors want to express their sincere thanks to José Moreno, Luis Alonso-Chorda and Alfonso Calera of the University of Valencia, for their support regarding the ground truth and airborne data of the Barrax site. Frédéric Baret of INRA, Avignon, kindly provided us with the latest PROSPECT code plus leaf optical parameters.

REFERENCES

- Bach, H., Mauser, W., 1994, "Modelling and model verification of the spectral reflectance of soils under varying moisture conditions", Proceedings of IGARSS'94, Pasadena, IEEE, Vol. 4, pp. 2354-2356
- Bach, H., Verhoef, W., Schneider, K., 2000, "Coupling remote sensing observation models and a growth model for improved retrieval of (geo)biophysical information from optical remote sensing data", Remote Sensing for Agriculture, Ecosystems and Hydrology, SPIE Vol. 4171, pp. 1-11
- Bach, H., Schneider, K., Verhoef, W., Stolz, R., Mauser, W., Van Leeuwen, H., Schouten, L., Borgeaud, M., 2001, "Retrieval of geo- and biophysical information from remote sensing through advanced combination of a land surface process model with inversion techniques in the optical and microwave spectral range", Proceedings of the 8th International Symposium "Physical measurements and signature in remote sensing", Aussois, CNES, pp. 639-647
- Berger, M., Rast, M., Wursteisen P., Attema, E., Moreno, J., Müller, A., Beils, U., Richter, R., Schaepmann, M., Strub, G., Stoll, M.-P., Nerry, F., Leroy, M., 2001, "The DAISEX Campaign in Support of a Future Land-Surface-Processes Mission", ESA bulletin, No.105, Feb. 2001, pp. 101-111
- Berk A., G.P. Anderson P.K. Acharya, J.H. Chetwynd, L.S. Bernstein, E.P. Shettle, M.W. Matthew, .M. Adler Golden, 2000, "MODTRAN4 USER'S MANUAL", AFB, MA 01731-3010, 97 p.
- ESA, 2001, "SPECTRA Surface Processes and Ecosystem Change Through Response Analysis", SP-1257(5)
- Jacquemoud, S., Baret, F., 1990, "PROSPECT: A model of leaf optical properties spectra", Rem. Sens. Environ., 34, pp. 75-91
- Verhoef, W., 1984, "Light scattering by leaf layers with application to canopy reflectance modeling: the SAIL model", Remote Sens. Environ., Vol. 16, pp. 125-141
- Verhoef, W., 1998, "Theory of radiative transfer models applied in optical remote sensing of vegetation canopies", PhD Thesis, Wageningen Agricultural University, 310 p

Preparados para el lanzamiento del MSG-1

E. Oriol-Pibernat

European Space Agency, Italy

eoriol@esa.int

ABSTRACT- *Following one of its objectives, to demonstrate Earth Observation applications, the European Space Agency (ESA) started in the early seventies the Meteosat series of geostationary satellites, now operated by Eumetsat. Following this success, ESA has cooperated again with Eumetsat by developing a new series designed to obtain meteorological information from the same orbit. The new satellites, of second generation, have increased the number of spectral bands (from 3 to 12), a better resolution (1 km in the broad band) and double repeat cycle (every 15 minutes instead of 30 minutes). The satellite embarks an instrument aimed to measure the Earth radiation, GERB to study the climate, and an S&R transponder for humanitarian purposes.*

MSG-1, that had been stored during 2001 at Alcatel Space, Cannes-F, was sent to Kourou in French Guiana in May 2002, and successfully launched from the spaceport by Ariane 5 on 29 August 2002. The satellite was in the Early Orbit Phase Operations by ESOC at time of the conference

1 PUESTA AL DIA

El lanzamiento del MSG-1 tuvo lugar el 29 Agosto 2002 desde la base de Kourou en la Guyana Francesa a las 0:45 centro-Europeas. Ariane 5 (vuelo 155) llevaba a bordo dos satélites: Atlantic Bird (situado arriba del lanzador) y Meteosat Second Generation MSG-1. El lanzamiento se retrasó un día debido a un problema técnico entre el centro de control y la lanzadora. La separación del MSG-1 se produjo 36 minutos después.

La llamada LEOP (launch and Early Orbit Phase) fue realizada por ESA/ESOC (Darmstadt, Alemania), contratado por Eumetsat. Consistió en varias fases: primero se llevó el satélite desde la órbita de transferencia hasta la geostacionaria de casi 36000 Km, mediante motores de apogeo. Esto se hizo en 4 tiempos, el último el 5 Septiembre.

El 6 Septiembre se alineó el satélite con el eje de rotación terrestre. Después se quitaron las tapas del radiómetro y refrigerador. Al cabo de una semana se llevó el satélite a 10.5 grados Oeste para empezar las pruebas de comisión.

2 ESA Y EUMETSAT

El primer Meteosat fué lanzado por ESA en 1977. Lo siguieron una serie de otros seis satélites geoestacionarios meteorológicos que durante casi 25 años han proporcionado imágenes del tiempo y de los sistemas que afectan los continentes Europeo y Africano.

Eumetsat es una organización Europea creada en 1986 para la explotación de satélites meteorológicos. Eumetsat opera Meteosat desde 1995.

Está financiada por los servicios meteorológicos de 18 países.

ESA, como experta en sistemas espaciales y Eumetsat, que representa las necesidades de los usuarios meteorológicos, han colaborado de nuevo en la puesta a punto de los satélites MSG.

3 ¿QUE ES EL MSG?

MSG quiere decir Meteosat de Segunda Generación. Es una serie de (3 ó 4) satélites, destinados a reemplazar los conocidos Meteosat, desde el mismo punto de observación situado a 0 grados de longitud sobre el Golfo de Guinea.

Los satélites MSG han sido construidos por Alcatel Space industries, en Cannes-F. Han participado más de 50 industrias Europeas, incluyendo España.

3.1 El SEVIRI

MSG tiene un radiómetro llamado SEVIRI (Spinning Enhanced Visible and Infrared Imager) mucho más ambicioso que el que usa Meteosat:

- Imágenes detectadas en 12 canales espectrales (en vez de 3).
- Imágenes con 1 (VIS banda ancha) y 3 (el resto) km resolución (en vez de 2.5 y 5 km).
- Barre el disco terrestre de Sur a Norte cada 15' (Meteosat cada 30').
- La retransmisión pasa de 333 kbps a 3.2 Mbps.

3.2 Canales del SEVIRI

VIS 0.6 & 0.8 μm : usado por AVHRR en satélites NOAA. Fundamental para detectar nubes, seguir nubes, identificación de escenas, aerosoles, suelos y monitoreo de vegetación (sólo un canal en Meteosat).

NIR 1.6 μm : usado en ATSR en los satélites ERS. Discrimina entre nubes/nieve, nubes con hielo/agua, da información sobre aerosoles. (nuevo)

IR 3.9 μm : usado en AVHRR. Primordialmente para detectar niebla y nubes bajas. También proporciona información sobre la temperatura de suelo y mar por la noche. (nuevo)

WV 6.2 & 7.3 μm : para observar vapor de agua y vientos. Ayuda a determinar la altura de nubes semitransparentes. (sólo un canal en Meteosat)

IR 8.7 μm : usado por HIRS en satélites NOAA. Información acerca de cirrus delgados y discriminación entre nubes de hielo/agua. (nuevo)

IR 9.7 μm : absorción O₃. Usado en los satélites HIRS y GOES. Las radiancias del Ozono pueden usarse como entrada en modelos numéricos de predicción. También puede utilizarse para determinar movimientos en la baja estratosfera, identificando patrones. Util para la evolución del campo total de Ozono. (nuevo)

IR 10.8 & 12.0 μm : usado en AVHRR. Esencial para medir las temperaturas del mar, suelo y cima de nubes. También puede detectar cirrus. (solo uno en Meteosat)

IR 13.4 μm : absorción CO₂. Usado en los GOES anteriores. Ayuda a localizar la altura de cirrus tenues. En areas sin nubes, contribuye a la información para estimar la inestabilidad atmosférica. (nuevo)

3.3 Productos del MSG

El segmento terreno de Eumetsat está organizado de forma que dicha Organización recibirá los datos brutos del MSG en su estación de recepción y los procesará en su sede central de Darmstadt (Alemania). Los productos previstos son:

- Análisis de capas de nubes con cobertura, altura y tipo (mejorado con respecto a Meteosat). Vectores de movimiento atmosférico a varias alturas (mejorado).
- Humedad troposférica en niveles medio y alto (mejorado).

- Temperatura Superficial del Océano Atlántico (mejorado).
- Altura cima nubes imágenes (mejorado).
- Radiancias en cielo despejado (mejorado).
- Inestabilidad de la masa de aire, (nuevo). Flujos de radiación superficiales en el Atlántico (nuevo). Datos climáticos, (mejorado) a petición. Índice Precipitación, (nuevo) a petición. Ozono total (nuevo) a petición. Datos ISCCP, imágenes de baja resolución para el proyecto International Satellite Cloud Climatology Project (nuevo) a petición.

Otros productos serán obtenidos en las llamadas Satellite Application Facilities (SAFs) de Eumetsat. Una de ellas está encabezada por el Instituto Nacional de Meteorología.

3.4 El GERB

MSG contribuirá al seguimiento del clima mediante el instrumento Geostationary Earth Radiation Budget (GERB) proporcionado por un consorcio Europeo liderado por el Rutherford Appleton Laboratory (UK). Se embarcará en los tres satélites MSG.

GERB tiene una resolución espacial media de 44 km, con una resolución temporal elevada de una imagen completa del disco cada 15 minutos. La precisión radiométrica es de 1% para las ondas cortas y 0.5% para las largas.

Este instrumento mide el Balance de Radiación de la Tierra ERB (Infrarrojo y visible) desde un punto de vista primicia: geostacionario. En cada rotación del MSG, toma datos en una cinta de 256 pixel N-S.

GERB se lanzó encendido para proteger los mecanismos. Una hora después del lanzamiento, se hicieron pruebas rápidas de la telemetría, y luego se apagó. Las medidas eran nominales. El instrumento se ha enfriado hasta 17 grados para evitar la contaminación durante las maniobras del satélite.

4 OTROS INSTRUMENTOS

MSG participará en una misión humanitaria, gracias a un emisor S&R. MSG también hará de relay de información medioambiental de plataformas.

ANUNCIO DE OPORTUNIDAD DEL MSG

ESA y Eumetsat organizaron en 1998 un Research Announcement of Opportunity, dedicado a los investigadores de todo el mundo, para proponer proyectos innovativos con los datos del MSG y de los satélites de Observación de la Tierra de la ESA. Se aceptaron 43 propuestas, en los que participan unos 250 científicos: una de las propuestas, para detectar incendios, es Española (Universidad de Valladolid e INIA). La Universidad de Valencia está involucrada en la propuesta GIST (GERB International Science Team). El primer taller de los Investigadores Principales del MSG (PI) fué en Bologna en Junio 2000, en el CNR. El próximo será después de la Comisión.

6 COMISION DEL MSG-1

De acuerdo con los planes publicados por Eumetsat, la comisión del MSG se hará en dos fases:

- Finales Septiembre 2002 – empieza la fase A (GERB, IQGSE, Imagen, Calibración & Dry-runs de productos).
- Octubre 2002 – primera imagen.
- Finales 2002 – Distribución imágenes nivel 1.5, basadas en IQGSE (rectificadas).
- Finales Marzo 2003 – fin fase A.
- Abril 2003 – empieza fase B (Pruebas Core Imaging y pruebas Imagen, Calibración & Validación productos).
- Septiembre 2003 – fin fase B, empiezan operaciones.

Durante un cierto período, se operarán MSG-1 y Meteosat simultaneamente. La comisión del GERB se prevé a fines de Noviembre, cuando el sol estará fuera del campo de visión.

7 CONCLUSIONES

Los satélites MSG no sólo continuarán y mejorarán la misión de los Meteosat para meteorología operacional y seguimiento del clima, sino que también contribuirán a la investigación en muchos aspectos de Ciencias de la Tierra.

Ahora que se ha lanzado con gran éxito el primer MSG, hay que reconocer el papel de la ESA como pionera e impulsadora de la meteorología satelitaria en Europa.

Asimismo, gracias a la acertada combinación de las dos organizaciones ESA y Eumetsat, Europa se abre a una nueva era de aplicaciones satelitarias, que se verá complementada a partir del 2005 con los

satélites meteorológicos Europeos de órbita polar MetOp, fruto de una colaboración similar.

Más información del MSG se puede obtener a través del sitio:

<http://www.esa.int/export/esaMI/MSG/>

en el que se han podido también seguir las novedades del lanzamiento. Otros sitios de interés son:

<http://www.esa.int/>

<http://www.eumetsat.de>



Figura 1.- El primer Meteosat fue lanzado por ESA el 23/11/1977



Figura 2.- Lanzamiento del MSG-1 desde Kourou el 29/08/2002



Figura 3.- El MSG-1 instalado en la lanzadora Ariane 5

Estudio del fenómeno migratorio de la mariposa monarca en las sierras de San Geronimo

María-Luisa España-Boquera⁽¹⁾, Frédéric Baret⁽²⁾, Jean-François Hanocq⁽²⁾

(1) Instituto de Investigaciones Agropecuarias y Forestales (IIAF), Universidad Michoacana de San Nicolás de Hidalgo (UMSNH), Avd. Acueducto y Tzintzuntzan sn, colonia Matamoros, C.P. 58240, Morelia, Michoacán, México. Teléfono y FAX: (52) (443) 3 15 60 01.

(2) Unité Climat, Sol et Environnement, Institut National de la Recherche Agronomique (INRA). Bâtiment Climat, Domaine Saint Paul – Site Agroparc-84914 Avignon cedex 9, France.. Teléfono: (33) 04 32 72 23 60, FAX: (33) 04 32 72 23 62.

E-mail : boquera@zeus.umich.mx, baret@avignon.inra.fr, hanocq@avignon.inra.fr

RESUMEN – Al llegar el invierno, las mariposas monarca parten desde Estados Unidos y Canadá hacia México, donde llegan a mediados de noviembre y permanecen hasta el mes de marzo. Los lugares de hibernación, denominados “santuarios”, se encuentran entre los estados de Michoacán y México, en bosques cuya altitud media es de más de 3,000 metros y donde las temperaturas son cercanas a los 0 grados centígrados. La vegetación de estos bosques está dominada por oyameles (*Abies religiosa*, L.). Actualmente los santuarios de la mariposa monarca forman parte de un área natural protegida de 65,259 ha, con carácter de reserva de la biosfera. El presente trabajo busca establecer los sitios, dentro de la reserva de la mariposa monarca, que por sus características de altitud, orientación, vegetación, presencia de agua, etc., son susceptibles de acoger a las mariposas durante su hibernación, a fin de establecer un mapa de santuarios potenciales. Para ello se realiza la caracterización de la vegetación de la zona de estudio, a partir de la clasificación de imágenes satelitales Spot de la zona y otros datos complementarios, como mapas y modelos de elevación del terreno, cursos de agua, tipo de suelo, etc. Se busca así facilitar la detección de la llegada de las mariposas y prever en lo posible sus desplazamientos en el interior de la reserva, para apoyar los programas de preservación y de turismo de la zona. Se espera además ayudar a esclarecer los numerosos interrogantes que se formulan en torno a la tradicional llegada de las mariposas a estos bosques.

ABSTRACT- When arriving the winter, the monarch butterflies leave from United States and Canada toward Mexico, where they arrive by the middle of November and they remain until the month of March. The hibernation places, denominated "sanctuaries", are between the states of Michoacán and Mexico, in forests whose half altitude is of more than 3,000 meters and where the temperatures are near to the zero centigrade grades. The vegetation of these forests is dominated by "oyameles" (*Abies religiosa*, L.). At the moment the sanctuaries of the monarch butterfly are part of a protected natural area of 65,259 ha, with character of the biosphere reservation. The present work looks for to establish the places, inside the reservation, that for its characteristics of altitude, orientation, vegetation, witnesses of water, etc., are susceptible of welcoming the butterflies during their hibernation, in order to establish a map of "potential sanctuaries". I order to achieve this objective, a characterization of the vegetation of the study area is carried out, starting from the classification of Spot images of the area and other complementary data, as maps and models of elevation of the land, courses of water, floor type, etc. It is looked for this way to facilitate the detection of the arrival of the butterflies and to foresee its displacements as much as possible inside the reservation, to support the preservation and tourism programs of the area. It is also hoped to help to clarify the numerous queries that are formulated around the traditional arrival from the butterflies to these forests.

1 INTRODUCCIÓN

En los bosques de asclepia cercanos a la frontera entre Estados Unidos y Canadá, tres generaciones de mariposas monarcas (*Danaus plexippus plexippus* L.) se suceden durante los meses de primavera y verano. Pero las mariposas que emergen como adultas en los meses de septiembre y octubre encuentran temperaturas demasiado frías y una vegetación demasiado pobre para vivir y reproducirse en estos lugares durante el invierno que comienza. Es esta generación de mariposas la que parte hacia latitudes más cálidas. Se conocen tres rutas migratorias: una hacia California, cerca de San Diego, la segunda hacia Carolina y la Florida, hasta Cuba, y la tercera, hacia México.

Las mariposas que parten a México llegan a mediados de noviembre y permanecen hasta el mes de marzo. Durante la mayor parte de su estancia en tierras mexicanas, se encuentran en un estado de semi-targo, sin reproducirse, ya que las condiciones climáticas (fotoperiodo y temperatura) no les permiten llegar a la madurez sexual hasta finales de febrero. A mediados de marzo, cuando las temperaturas comienzan a ser demasiado elevadas, parten de nuevo hacia el norte, pero permanecen al sur de los Estados Unidos, donde las hembras fecundadas en México ponen los huevos que dan lugar a una nueva generación de mariposas. Después de dos o tres generaciones, hay un regreso hacia el norte, con lo que se cierra el ciclo, constituido así de cinco generaciones de mariposas, de las cuales una habita en México durante casi cinco meses.

Los lugares de hibernación de las mariposas monarca en México, denominados *santuarios*, se encuentran entre los estados de Michoacán y México, en bosques situados alrededor de los 3,000 metros sobre el nivel del mar y donde las temperaturas son cercanas a los cero grados centígrados. La vegetación de estos bosques está dominada por los oyameles (*Abies religiosa*, L.), lo que les confiere un aspecto de bosque alpino. Las mariposas ocupan siempre las laderas sur y sur-oeste de las colinas y procuran la proximidad de pequeños riachuelos, asegurando así la disponibilidad de agua.

En cada santuario se estima que se reúnen entre siete y veinte millones de mariposas, que se desplazan en función de las condiciones de luz y temperatura, así como de la velocidad del viento. Durante la noche se agrupan en los árboles para preservar la temperatura y

escapar del frío extremo. No es extraño que las ramas de los árboles se rompan por el exceso de peso, lo que produce la muerte por congelación de las mariposas que caen. Esta es la principal causa de mortalidad, si bien, a pesar de la toxicidad de su cuerpo, sufren el ataque de algunos depredadores (*Icterus parisorum*, *Icterus abeilli* y *Pheucticus melanocephalus*, principalmente). Se calcula que sólo cerca de la mitad de la población consigue sobrevivir el periodo de hibernación, lo que supone la pérdida de millones de individuos. En este sentido, se calcula que para asegurar una temperatura aceptable para las mariposas, los árboles deben ser adultos y la densidad no debe ser inferior a 400 árboles por hectárea (Secretaría del medio ambiente, recursos naturales y pesca. 2000).

Los santuarios mexicanos no fueron descubiertos hasta 1975. La protección oficial empezó en 1980 (Diario Oficial de la Federación, 9 de abril de 1980.) y la declaración de área natural protegida (ANP), por decreto presidencial, llegó en 1986 (Diario Oficial de la Federación, 9 de octubre de 1986).

Se trataba de 16,110 ha divididas en cinco santuarios:

- Santuario Cerro Altamirano : (8,55%) 245 ha de núcleo y 1,133 ha de zona de amortiguamiento.
- Santuario Sierra Chincua : (16.73%) 1,060 ha de núcleo y 1,636 ha de zona de amortiguamiento.
- Santuario Sierra el Campanario : (11.73%) 901 ha de núcleo y 989 ha de zona de amortiguamiento.
- Santuario Chivatí-Huacal : (12.5%) 940 ha de núcleo y 989 ha de zona de amortiguamiento.
- Santuario Cerro Pelón : (50.47%) 1,345 ha de núcleo y 6,787 ha de zona de amortiguamiento.

En noviembre del año 2000 se declaró área natural protegida, con el carácter de reserva de la biosfera, ampliándose la superficie a 65,259 ha, integradas por una zona núcleo de 13,551 ha y una zona de amortiguamiento de 42,707 ha (Diario Oficial de la Federación, 10 de noviembre de 2000.).

Los santuarios de la mariposa monarca están despertando un interés creciente a nivel estatal, nacional e internacional. La migración anual de las

mariposas hacia tierras michoacanas y mexiquenses es un fenómeno natural único y sorprendente, que se ha repetido durante milenios, al resguardo de miradas indiscretas y de intervenciones que lo pongan en riesgo. Sin embargo, desde el descubrimiento de los santuarios en 1975, este maravilloso espectáculo natural, del que ahora podemos disfrutar, se encuentra por lo mismo en peligro de desaparecer.

El fenómeno migratorio de las mariposas monarca ha sido estudiado desde numerosos puntos de vista, principalmente en lo que respecta al ciclo de vida de las mariposas, a la clasificación botánica de las especies de la zona y a la problemática socioeconómica de los habitantes de la región. Con este proyecto se pretende abordar una nueva perspectiva: Utilizando técnicas de teledetección se busca localizar las zonas reales y potenciales de presencia de las mariposas, con el fin de delimitar con la mayor precisión los santuarios conocidos y, quizá, descubrir otros. Se espera así contribuir a esclarecer el porqué de la elección milenaria de estas tierras por las mariposas, para su hibernación. Además con este trabajo se contribuye a un mayor conocimiento de los bosques de oyamel, que constituyen, por sí mismos, un valioso tesoro ecológico.

2 MATERIALES Y MÉTODOS

2.1 La zona de estudio

El presente estudio abarca toda la reserva de la mariposa monarca, declarada como área natural protegida con carácter de reserva especial de la biosfera. Esta zona queda incluida en un rectángulo cuyos vértices tienen las siguientes coordenadas geográficas: 19°45'N, 100°26'W (superior izquierdo) y 19°20'N, 100°10'W (inferior derecho).

La región presenta en general un clima Cw (según la clasificación de Köppen, modificada por García), templado subhúmedo con lluvias en verano, caracterizado por temperaturas medias anuales de 8° a 22°C y mínimas para el mes más frío entre -3° y 18°C; las precipitaciones promedio van de 700 a 1,250 mm. Es importante señalar que debido a la presencia de montañas y lo escarpado del relieve, que da lugar a cambios contrastados en altitud, exposición o pendiente, hay importantes variantes microclimáticas en distancias relativamente cortas.

La concentración de las precipitaciones en el verano da lugar a una marcada diferencia climática entre dos épocas del año: la época de *secas* (de octubre a mayo) en la que, aunque puede haber algo de nubosidad, es

muy inusual que llueva, y la época de lluvias, o de *aguas* (de mayo a septiembre) en la que las precipitaciones son casi diarias. Esta estacionalidad de las lluvias se traduce en importantes diferencias en la vegetación, tanto agrícola como forestal, en estos dos periodos: en las zonas en las que no se cuenta con agua de riego, la agricultura es de temporal, es decir, se siembra (principalmente maíz) durante las lluvias y los campos permanecen sin cultivar durante las secas; esto ocurre, en particular, en muchas zonas deforestadas, en las que las pendientes tampoco permitirían otro tipo de aprovechamiento agrícola. En cuanto a la vegetación forestal, existen en la región bosques caducifolios, que permanecen en reposo vegetativo mientras las temperaturas son bajas y las precipitaciones escasas. No es el caso, no obstante de la reserva de la mariposa monarca, cuya vegetación está dominada por oyameles (*Abies religiosa*, L.), pinos y encinos, todos ellos perennifolios; sin embargo, sí hay diferencias importantes en lo que concierne a la vegetación baja.

En la vegetación de la zona se distinguen cinco tipos principales (Madrigal X., 1967, Vázquez Collazo I., 2002):

- Bosques de oyamel (hábitat característico de la mariposa monarca).
- Bosque de pino y oyamel.
- Bosque de pino.
- Bosque de encino.
- Bosque de cedro.

Salvo en las cabeceras municipales, la población de la zona es de bajos recursos económicos, dedicada fundamentalmente a la agricultura y ganadería de subsistencia. La presión demográfica, la pobreza y las inadecuadas formas de manejo forestal están dando lugar a graves problemas de deforestación, que se traducen en la desaparición anual de más de 2,000 ha de bosque. Esta difícil situación socio-económica ha sido la causa, en gran medida, del fracaso del establecimiento de programas de manejo forestal y de protección de los santuarios en la reserva (Chapela G., 1995).

2.2 Imágenes satelitales

Para la realización del presente trabajo se contó con dos imágenes satelitales Spot 4, correspondientes a las siguientes fechas: 8 de enero de 1999 (existente en catálogo) y 23 de octubre de 2001 (programada).

Todas estas imágenes beneficiaron de los apoyos otorgados por el Centre National des Études Spatiales (CNES) en el marco del programa ISIS.

Ante la estacionalidad climática propia de la zona de estudio, se decidió trabajar con imágenes correspondientes a las dos épocas del año (*aguas y secas*), a fin de establecer más claramente los diferentes tipos de vegetación y en particular separar los bosques de oyameles de su entorno. En efecto, en la imagen de enero se distingue muy claramente la mancha boscosa de los bosques perennifolios, con respecto a las parcelas de cultivo, que presentan una escasa actividad vegetativa. Esta diferencia no es tan marcada en la imagen de octubre, por encontrarse las zonas agrícolas en plena producción. En esta imagen de octubre de 2001 aparecen algunas nubes sobre la zona de estudio.

2.3 Datos toponímicos y vectoriales

Se adquirieron los siguientes datos correspondientes a la zona de estudio, pertenecientes a la base generada por el Instituto Nacional de Estadística, Geografía e Informática (INEGI) de México (cartas topográficas escala 1:50,000, formato dxf):

- Altimetría
- Hidrografía e infraestructura hidráulica
- Localidades y rasgos urbanos
- Instalaciones diversas e industriales
- Tanques de almacenamiento, conductos y vías de transmisión
- Comunicación y transporte
- Áreas protegidas y sitios de interés histórico

Para cubrir la zona de estudio se necesitaron 4 cartas en cada caso.

Asimismo se utilizaron modelos digitales de elevación, generados por INEGI a partir de las curvas de nivel de la carta topográfica escala 1:50,000. El intervalo entre elevaciones es de 50 metros; la proyección es Universal Transversa de Mercator (UTM).

2.4 Recorridos de campo

Se realizaron varios recorridos de campo con el objetivo de familiarizarse con la zona de estudio, en particular con la vegetación y la topografía. Durante la

época de presencia de las mariposas se visitaron los cerros del Rosario y de Sierra Chincua.

2.5 Clasificación de la vegetación

El tratamiento de los datos se realizó con el software ENVI, versión 3.5.

Para la caracterización de la vegetación (especies, densidades, etc) se contó con la colaboración profesores de la Facultad de Biología de la UMSNH y del Dr. Guillermo Ibarra Manríquez, del Departamento de Ecología de los Recursos Naturales, del Instituto de Ecología de la Universidad Nacional Autónoma de México, en Morelia.

Se obtuvo una primera clasificación muy general de la vegetación a partir de la imagen de 1999, por requerir la imagen de 2001 de algunas correcciones geométricas. Se realizó una clasificación supervisada según el algoritmo de máxima semejanza, definiendo las regiones de interés a partir de un mapa de ocupación del suelo proporcionado por la Comisión Forestal de Michoacán (COFOM), y recorridos de campo. Se consideró un umbral de probabilidad de 0.6 para todas las bandas. Se distinguieron dos tipos de vegetación en los bosques (predominio de oyamel y de otras especies arbóreas, respectivamente), que fueron previamente separados de las zonas agrícolas y urbanas.

2.6 Determinación de los santuarios potenciales

En la imagen clasificada se seleccionó la zona correspondiente a los bosques de oyamel y se le superpusieron los cursos de agua y las curvas de nivel correspondientes a una altitud superior a los 3,000 m, obtenida a partir del modelo de elevación de terreno de INEGI. Fue necesaria la corrección de las coordenadas geográficas de este último para obtener una correcta superposición.

2.7 Datos infrarrojos

Partiendo de la hipótesis de que existe una diferencia de temperatura observable entre las mariposas y la vegetación que las rodea y considerando el elevado número de mariposas, se pensó en la posibilidad de distinguirlas en el dominio térmico, con ayuda de una cámara infrarroja. Así, se realizaron medidas locales para evidenciar la diferencia de temperaturas entre las mariposas y su entorno. Estas medidas se realizaron en Sierra Chincua, en diciembre del 2001, tanto en el día como en la noche.

3 RESULTADOS

3.1 Clasificación de la vegetación

La clasificación que se obtuvo de la vegetación es muy general y únicamente permite distinguir, dentro de las zonas forestales, los bosques de oyamel, pero sin separar los de oyamel puro, de los de pino-oyamel, ni distinguir los diferentes tipos de vegetación baja. Se encuentra, sin embargo, un buen acuerdo con respecto a la zona declarada como núcleo de la reserva.

3.2 Conformación de un mapa de santuarios potenciales

La superposición de la curva de nivel correspondiente a los 3,000 m de altitud, sobre la clasificación de la vegetación permite constatar un buen acuerdo entre bosques de oyamel y altitudes superiores a la señalada.

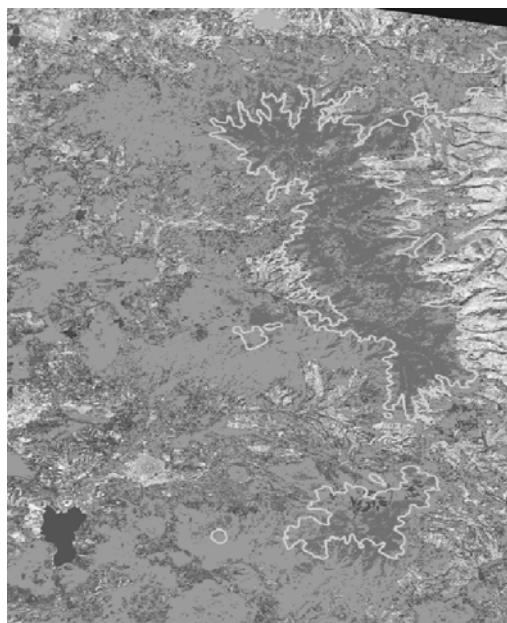


Figura 1: Imagen SPOT de la reserva de la mariposa monarca, del 18 de enero de 1999. En verde, superposición de la clasificación de la vegetación forestal: verde oscuro, bosque de oyamel; verde claro, otros tipos de bosque. En amarillo, superposición de la curva de nivel correspondiente a 3,000 metros de altitud. (ver anexo en color).

Los cursos de agua son muy abundantes en la zona, por lo que no parecen una limitante muy importante para el establecimiento de las mariposas.

De esta forma se obtuvo un mapa de los lugares dentro de la reserva que cumplen con las principales características que se cree que requieren las mariposas para hibernar, y que incluye el núcleo de la reserva.

3.3 Datos infrarrojos

En las observaciones realizadas con cámara infrarroja a mariposas situadas en los troncos o las ramas de los árboles, tanto en el día como en la noche, no fue posible distinguirlas de su entorno. Esto se puede explicar por el hecho de tratarse de animales de sangre fría, que adaptan su temperatura corporal a la del medio que los rodea. Sin embargo, en mariposas recogidas y puestas en una situación de semicautiverio, se observó un proceso de calentamiento gradual de la cabeza, que se podría explicar como una consecuencia del estrés causado por la manipulación y el encierro.

4 CONCLUSIONES Y PERSPECTIVAS

Debido a la pronunciada pendiente del terreno en la zona de estudio, parece necesario, para conseguir una buena clasificación de la vegetación, corregir los valores de reflectancia con respecto a la altitud. Para ello se utilizará el programa ATCOR3.

De esta forma se espera generar mapas más detallados y precisos que los existentes, en los que se puedan localizar correctamente los santuarios potenciales. En una segunda etapa de este trabajo se espera además superponer a estos mapas información real de los lugares en los que se ha registrado la presencia de mariposas en los últimos años. Esto permitirá verificar la exactitud de las teorías que pretenden explicar la ubicación de las mariposas en función de luz, temperatura y disponibilidad de agua. Por otra parte, se espera afinar las clasificaciones de la vegetación, con ayuda de un mayor número de datos de campo.

En cuanto a las observaciones en el infrarrojo, resulta claro que no es posible la observación directa de las mariposas, por no ser contrastante su temperatura con la del medio que las rodea. Todo apunta, sin embargo, a la existencia de un umbral de frío, por debajo del cual las mariposas mueren. Esto podría explicar algunas características de su comportamiento: el mismo fenómeno migratorio, motivado por la necesidad de escapar de los rigurosos inviernos de las altas latitudes en las que viven el resto del año, la aglomeración en los troncos o las ramas de los árboles,

la muerte por congelación de las mariposas que caen en la noche, etc. Este umbral se situaría, probablemente, algunos grados por debajo de 0°, lo que explicaría ciertos casos curiosos de mariposas que han quedado enterradas en la nieve y, al fundir ésta, han salido volando. Muchos interrogantes siguen, sin embargo, sin aclararse: ¿Por qué estas montañas, tan lejanas a su tierra natal, y en las que, a pesar de todo, hace frío y *mueren de frío*? ¿Cómo saben llegar, si nunca antes vinieron, ni ellas ni sus padres? Quizá nunca se encontrará una respuesta científicamente aceptable... *Pero, como quiera..., que sigan llegando...*

Vázquez Collazo I., Madrigal Huedo S., Pérez Morales A., García Zarco J., 2002. Diagnóstico fitosanitario en Sierra de Chincua. Ciencia Nicolaita, 30, 61-70.

5 AGRADECIMIENTOS

Ingenieros de la PROFEPA por las facilidades ofrecidas en los recorridos de campo.

Ingenieros de la COFOM por su disponibilidad para facilitarnos información sobre la zona de estudio.

Biólogo Eligio García Serrano, responsable de la Reserva de la mariposa monarca, por su apoyo en el campo.

CIC-UMSNH y PROMEP-SEP por el financiamiento de este trabajo.

Programa ISIS por las facilidades ofrecidas para la adquisición de las imágenes Spot.

6 BIBLIOGRAFIA

Chapela G. Y Barkin D., 1995. Monarcas y campesinos. Centro de Ecología y Desarrollo, A.C. Multidiseño Gráfico. 1ª. Ed., México.

Diario Oficial de la Federación, 9 de abril de 1980.

Diario Oficial de la Federación, 9 de octubre de 1986.

Diario Oficial de la Federación, 10 de noviembre de 2000.

Madrigal X., 1967. Contribución al conocimiento de los bosques de oyamel en el Valle de México. Instituto de Investigaciones Forestales, boletín técnico n°18. México.

Secretaría del medio ambiente, recursos naturales y pesca. Comisión nacional de áreas naturales protegidas, dirección general de ordenamiento ecológico e impacto ambiental. Julio, 2000. Estudio previo para justificar la recategorización y redelimitación del área natural protegida “mariposa monarca” en los estados de México y Michoacán. Reporte interno.

VEGETATION/SPOT

An Operational Mission for the Earth Monitoring

Presentation of New Standard Products

P. Maisongrande, B. Duchemin and G. Dedieu

CESBIO (unité mixte de recherche CNES-CNRS-UPS-IRD)

18, Avenue Edouard Belin, bpi. 2801, 31401 Toulouse Cedex 4 - FRANCE

Philippe.Maisongrande@cesbio.cnes.fr

ABSTRACT - *The VEGETATION instrument is the starting point of a European earth monitoring system that was developed jointly by France, the European Commission, Belgium, Italy and Sweden. Since April 1998, VEGETATION has provided a high quality global monitoring of the day to day land cover dynamics at 1 km resolution. The whole dataset is now available free of charge to the broad range of potential users and applications. The quality of delivered products in term of radiometry, geometry and additional processing for directional and atmospheric effects stands VEGETATION as an optimal tool for the monitoring of surface hydrology, crops, forest and land cover. Surface reflectances that are delivered by the operational VEGETATION system are corrected for molecular and aerosol scattering, for water vapor, ozone and other gas absorption. So far, the only well known MVC technique was used in the construction of 10 day synthesis. An additional enhanced composite product is now available, which evaluates the atmospheric optical depth and normalizes angular, sun-target-sensor variations. After presenting the VEGETATION instrument and products, this article introduces the new compositing schemes (Duchemin and Maisongrande 2002 and Duchemin et al.2002) and presents samples of the new products.*

1 INTRODUCTION

The recent successful launch of VEGETATION2 onboard SPOT5 on May the 4th 2002, has extended for a minimum of 5 additional years the ongoing earth monitoring by VEGETATION that began in April 1998 with SPOT4/VEGETATION1. This granted continuity will make possible the construction of 11 years of consistent long term Earth observation devoted to inter-annual global vegetation monitoring.

The two VEGETATION instruments offer an unprecedented look at terrestrial behavior for a wide community of users throughout the world. These operationally delivered information find potential application in the modeling of carbon and water fluxes between agro-ecosystems and the atmosphere. The VEGETATION instrument family is designed (wide spectral range from Blue to Short Wave Infra Red, 1km spatial resolution) to monitor the surface of the Earth with a near daily global coverage.

Besides the quality of the VEGETATION payload, a special effort is made on the data processing chain in the production line at CTIV (Centre de Traitement des Images VEGETATION). Initially, the correction for aerosol effects was made accounting for a fixed latitudinal distribution of aerosol amounts and the resulting reflectances at surface were selected through

a classical Maximum Value Composite criteria in the construction of 10-days synthesis.

In the frame of the European 'Project for Improvement and Continuity of the VEGETATION Mission', new algorithmic schemes were implemented at CTIV in order to improve the evaluation of Aerosol Optical Thickness (to be used in the atmospheric correction) and to remove directional patterns in compositing methods.

This document presents the VEGETATION Mission and the results of the new processing schemes for atmospheric and directional effects on the products that are currently delivered by the production entity at CTIV. A further detailed description and performance characterization of these new products is developed in Duchemin and Maisongrande (2002), and Duchemin *et al.* (2002).

2 CURRENT VEGETATION PRODUCTS

The VEGETATION products fall into 3 main categories that are VGT-P (Primary), VGT-S (Synthesis) and VGT-D (Directional) (see Table below).

PRODUCTS	P: Primary	S: Synthesis		D: Directional
		S1 : 1 day	S10: 10 days	D10: 10 days
Segment along an orbit	✗			
Merged segments		✗	✗	✗
Atmospheric component	✗			✗
Sun-target-Sensor Geom.	✗	✗	✗	Normalized geometry
Surface reflectances		✗	✗	✗
NDVI		✗	✗	✗
Archive	✗		✗	✗
Catalogue order (ie already acquired products)	✗		✗	✗
Suscription order(*)	✗	✗	✗	✗
HDF format	✗	✗	✗	✗

(*)Free products only concern catalogue orders

VGT-P products are for scientific applications requiring specific processing. They provide Top of the Atmosphere reflectances as seen by the sensor at each orbit pass. Both radiometric corrections (instrument calibration effects are corrected using a linear model that normalizes CCD response) and geometric corrections (for inherent system effects like satellite location and orientation) are applied to enhance the product quality. P products are delivered in various standard map projections that can be specified by the user. Auxiliary data supplied with this product make possible personal original processing (e.g. atmospheric and directional correction).

VGT-S products are mainly geared to straight operational and scientific use. Derived from P products they provide daily and 10-day MVC syntheses (Maximum Value Composite, Tarpley 1984, Holben 1986), that are corrected for atmospheric effects. Indeed, data acquired by optical sensors are disturbed by scattering and absorption due to gases and aerosols. The correction for atmospheric effects, applied to the current nominal products are based on a modified version of the SMAC code (Rahman and Dedieu 1994). This function represents absorption and scattering processes by semi-empirical equations whose coefficients are determined on the basis of

fitting reference computations regarding the 6S radiative transfer codes (Vermote *et al.* 1997).

VGT-D products consist in 10-day synthesis that normalize the surface radiances for directional effects. This enhanced composite has been designed within the European 'Project for Improvement and Continuity of the VEGETATION Mission'. In this project, CESBIO has handled investigations on new algorithmic schemes for an improved evaluation of Aerosol Optical Thickness (AOT to be used in the atmospheric correction) and for the introduction of directional models in a new compositing method. Part of the same project, a complementary effort was made at VITO, devoted to the improvement of cloud filtering. Having been approved by the VEGETATION Steering Committee, these recent innovative processing now operate at CTIV, the production line. Improvements resulting of these new schemes are presented in the next 3 paragraphs.

3 DETAILS ON NEW PRODUCTS

3.1 New cloud filtering

Kempeneers *et al.* (2000) have proposed a new 4 levels cloud mask on the basis of relevant multi-spectral thresholds. These 4 levels (clear, uncertain, cloudy and shadow) correspond with specific flags in a standard Status Map. Since the 11th of May 2001, this new improved filtering has been taken into account in the processing of S products that are delivered by CTIV with corresponding status map delivered both at the S and P level.

This upgrade was made simultaneously with the replacement of latitudinal dependent optical thickness by a real time calculated atmospheric opacity (method presented hereafter).

3.2 Atmospheric correction accounting for realistic optical thickness

In order to improve the correction for molecular effects, the prelaunch phase of the VEGETATION Preparatory Program recommended the use of ozone climatology and of numerical weather prediction analysis for water vapor content. So far, for aerosol effects, a crude correction was made using fixed aerosols amount per band of latitude.

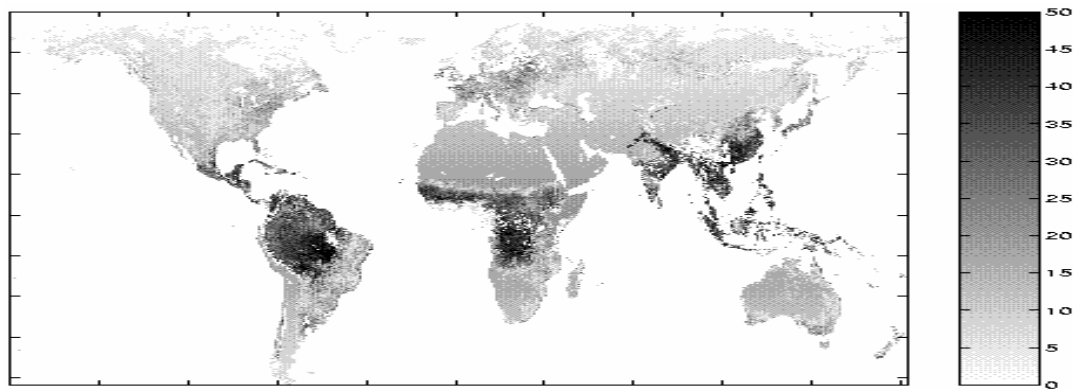


Fig. 1. Aerosol Optical Thickness ($100 \times \text{AOT at } 550\text{nm}$) calculated by the new CTIV processing. This map presents the average AOT calculated from the clear data from the 21/09/2001 to the 30/09/2001. The daily calculation of the AOT is applied in the correction for atmospheric effects.

Taking advantage of the VEGETATION spectral range, Maisongrande *et al.* (2001), proposed a new approach for the AOT retrieval. This procedure is based on the use of a **time and target dependent** ratio between blue and SWIR reflectances. The single SWIR channel of VEGETATION being too restrictive to make possible a direct application of the “dark target technique” (Vermote *et al.* 1997), we apply a method that relies on the assumption of a NDVI dependent SWIR/Blue relationship. For every reliable TOA reflectance, an Aerosol Optical Thickness is calculated when NDVI is higher than an aridity threshold. Otherwise the processing scheme considers the classical latitudinal dependant AOT value that was used by the initial processing chain. Then, resulting AOT's (Fig. 1.) are applied for atmospheric correction with SMAC. Correcting any kind of atmospheric opacity, this procedure reduces drastically the noise observed on reflectances and NDVI time series due to undetected semi transparent clouds and aerosols events.

3.3 New Bidirectional compositing

Due to the non lambertian properties of reflecting surfaces, the radiances measured by large field-of-view optical sensors present a dependency on the ‘source-target-sensor’ geometry. Although these directional effects are decreased by the NDVI calculation ($\rho_{\text{NIR-pred}}/\rho_{\text{NIR+pred}}$), a residual noise artefact still appears on time series and MVC syntheses. An new method which takes into account and normalizes this effect was conceived by CESBIO. The method (called BDC for Bi-Directional Compositing) can be summarized as follows :

- adjustment of Bidirectional Reflectance Distribution Function (BRDF) model;
- use of the BRDF model to normalize the cloud-free data of exactly the last 10 days in a standard angular configuration (nadir view and tabulated mean solar elevation during the considered 10 day period).
- Then, the new 10-day composite is calculated by an average of these corrected reflectances.

In order to ensure the same processing rate as the MVC technique, the BDC method manages to provide an adjusted BRDF for each 10 days period. Therefore, a constant number N of reference radiances (that are used to fit the BRDF) are stored regardless to their acquisition date. This strategy makes the BDC concept as productive as MVC. Fig. 2 presents a comparison between MVC and BDC syntheses.

Besides the efficiency of BDC itself, its combined effects with good cloud filtering, and correction for the actual atmospheric opacity strongly improves the quality of the VEGETATION products. This algorithm is now implemented at CTIV where 10-day BDC syntheses are currently produced simultaneously with the classical 10-day MVC (S10 products).

- gathering of the N (about 10) last cloud-free data (regardless to their date of acquisition);

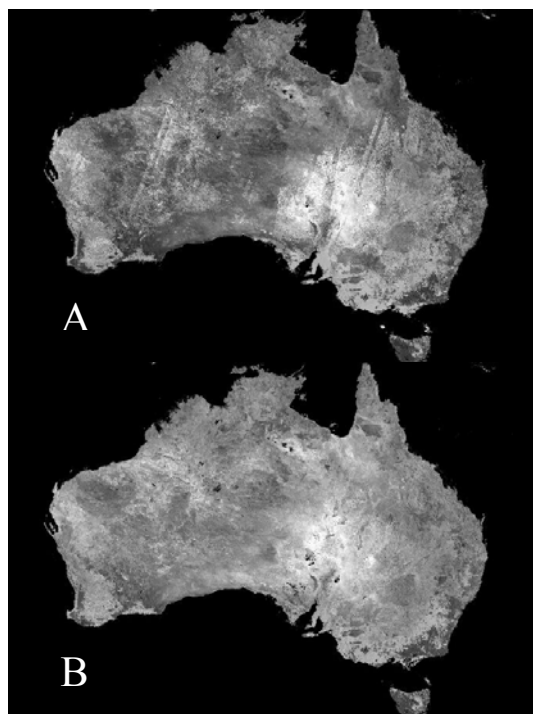


Fig. 2. 10-day MVC synthesis (A) vs 10-day BDC synthesis (B) comparison illustrated on a SWIR_NIR_Blue composite image of Australia (01/10/2001). The directional artifact displayed by the MVC image are removed after directional normalization. This correction does also improve the smoothness of normalized time series (not shown here).

3 CONCLUDING REMARKS

In scientific studies involving both remote sensing and modeling (e.g. assimilation and/or forcing strategies), the quality and accuracy on delivered reflectances and VIs is of prime significance. (see for example proceedings of the VEGETATION 2000 workshop at <http://VEGETATION.cnes.fr/>)

The VEGETATION program, dedicated to the daily observation of the land biosphere, makes possible a broad range of application addressing global change (land use and land cover) and environmental issues (agriculture, forest monitoring, surface hydrology). A typical example of application of the VEGETATION data is the incorporation of the 10-day composites in the FAO Global Information and Early Warning System.

Among existing and potential other applications involving VEGETATION the synergy between high and low resolution through disaggregation techniques is of great interest. Since the entire VEGETATION system was build in complement of the existing high spatial resolution capabilities of the SPOT series, the

combination of the SPOT HRVIR low-frequency and high resolution imagery with the VEGETATION high frequency and low resolution global monitoring makes this system a privileged tool for multi-temporal and multi-scale studies of terrestrial surfaces.

Today, the entire set of VEGETATION products are freely available for scientific purposes and demonstration activities at (<http://free.vgt.vito.be/>), providing to users of VEGETATION a panel of data that takes the earth observation to a new quality level, which is required by scientific and decisional applications.

The launch of VEGETATION 2 onboard SPOT 5 in April 2002 further guarantees the continuation of the VEGETATION mission for years to come.

Acknowledgements

This work was funded by the CNES project “European Project for the Improvement of the VEGETATION Mission” (part of the European contract ENV4-CT-98-0732). The authors acknowledge Béatrice Berthelot, François Cabot, Patrice Henry, Olivier Hagolle, Marc Leroy, Xavier Passot, Jean-François Reulet and Gilbert Saint for their helpful technical and administrative support. We are also grateful to our colleagues of VITO, Peter Kempeneers, Gil Lissens, Freddy Fierens and Jan Van Rensbergen, for their very fruitful and pleasant collaboration during the project.

4 REFERENCES

- B. Duchemin and P. Maisongrande, “Normalisation of directional effects in 10-day global synthesis derived from VEGETATION/SPOT-4 : I. Investigation of concepts based on simulation”, *Remote Sensing of Env.*, vol 81, issue 1, pp 90-100, 2002.
- B. Duchemin, B. Berthelot, G. Dedieu, M. Leroy and P. Maisongrande, “Normalisation of directional effects in 10-day global synthesis derived from VEGETATION/SPOT-4 : II. Validation of an operational method on actual data sets”, *Remote Sensing of Environment*, vol 81, issue 1, pp 101-113, 2002.
- B. N. Holben., “Characteristics of maximum-value composite images from temporal AVHRR data”, *Int. J. Remote Sens.* 7:1417-1434, 1986.

- P. Kempeneers, G. Lissens, F. Fierens and J.V. Rensbergen., "development of a cloud, snow and cloud shadow mask for VEGETATION imagery", *Proceedings of symposium VEGETATION 2000 "two years of operation to prepare the future", Lake Maggiore, Italy, 3-5 April 2000*, Edited by G. Saint, published by the Joint Research Center of the European Commission, Ispra, Italy, p.p. 303-306, 2000.
- P. Maisongrande, B. Duchemin, B. Berthelot, C. Dubegny, G. Dedieu and M. Leroy, "New composite products derived from the SPOT/VEGETATION mission", 8th Symposium on Physical Measurements and Signatures in Remote Sensing of International Society for Photogrammetry and Remote Sensing (ISPRS), Aussois, France, p.p. 239-248, Jan. 2001.
- H. Rahman and G. Dedieu, "SMAC : A simplified method for the atmospheric correction of satellite measurements in the solar spectrum", *International Journal of Remote Sensing*, Vol. 15, N°1, p.p. 123-143, 1994.
- E.F. Vermote, N. El Saleous, C.O. Justice, Y.J. Kaufman, J.L. Privette, L. Remer, J.C. Roger, and D. Tanré, "Atmospheric correction of visible to middle-infrared EOS-MODIS data over land surfaces : background, operational algorithm and validation", *Journal Geophysical Research* , 102, 17,131-17,141, 1997.
- E.D. Vermote, J.L. Tanré, M. Deuzé, M. Herman, J. J. Morcrette, "Second simulation of the satellite signal in the solar spectrum, 6S: An overview", *IEEE transactions on geoscience and remote sensing*, Vol 35, n 3, p.p. 675-686, 1997.

Preliminary pigment retrieval results from a sparse-canopy poplar plantation in northern Italy using hyperspectral data

C. Panigada ⁽¹⁾, J.R. Miller ⁽²⁾, M. Meroni ^(3,5), T. Noland ⁽⁴⁾, M. Boschetti ⁽³⁾, R. Colombo ⁽¹⁾, C.M. Marino ⁽¹⁾, Maara Packalen ⁽⁴⁾

⁽¹⁾ UNIMIB-DISAT, Department of Environmental Sciences, University of Milano-Bicocca, Piazza della Scienza 1, 20126 Milan - Italy

⁽²⁾ Department of Physics and Astronomy, York University, 4700 Keele St., Toronto M3J1P3- Canada

⁽³⁾ CNR-IREA, Institute for Electromagnetic Sensing of the Environment, Via Bassini 15, 20133 Milan - Italy

⁽⁴⁾ OFRI, Ontario Forestry Research Institute, 1235 Queen St.E., Sault Ste. Marie P6A2E5 - Canada

⁽⁵⁾ UNITUS-DISAFRI, Forest Ecology Lab, University of Tuscia, V. De Lellis s.n.c, 01100 Viterbo, Italy

cinzia.panigada@unimib.it, jrmiller@yorku.ca, michele.meroni@unimib.it, tom.noland@mnr.gov.on.ca, boschetti.m@irea.cnr.it, roberto.colombo@unimib.it, carlo.marino@unimi.it, maara.packalen@mnr.gov.on.ca

ABSTRACT - Successful retrieval of leaf pigment content in closed forest canopies is only recently being reported. Nevertheless, forestry continues to pose significant challenges to quantitative biochemical variable retrieval due to problems associated with the structural complexity in common open canopies, conifer canopies or sparse canopies. This research was focused on a poplar plantation in the northern Italy where hyperspectral data were acquired in summer 2001 by different airborne hyperspectral sensors: DAIS (Digital Airborne Imaging Spectrometer) and ROSIS (Reflective Optics System Imaging Spectrometer). The approach investigated for the prediction of chlorophyll content from the airborne hyperspectral data is the numerical inversion of coupled canopy and leaf reflectance models. The ecological properties of the poplar plantation, characterised by low LAI values, open and sparse canopy and an accompanying presence of a thick layer of understory vegetation, represented a challenging issue to the application of simple canopy modelling for interpretation. In this study we have evaluated the influence of understory vegetation on biochemical constituent estimation by inversion of a red edge slope optical index through a comparison of the overstory leaf pigment retrieval results from a poplar stand area in which understory was harvested, before the sensor overpass, relative to the non-tilled part of the poplar stand.

1.0 INTRODUCTION

The spatial distribution of leaf pigments in forest ecosystems is useful information for vegetation monitoring. In fact, canopy chlorophyll concentration is considered a bio-indicator of forest health status providing guidelines for natural forest and agro-forestry ecosystems management (Mohammed *et al.*, 1997).

Leaf pigment estimation from hyperspectral images through numerical inversion of coupled leaf canopy radiative transfer modelling has been studied (Demarez *et al.*, 2000) and recently demonstrated successfully in forests (Zarco-Tejada *et al.*, 2001a). In particular, inversion based on narrow-band vegetation indices (VI) has shown promising results both in forestry and agricultural applications (Dawson, 2000,

Zarco-Tejada, 2001a , Haboudane, 2001, Haboudane, 2002).

This paper investigates leaf pigment retrieval in a poplar plantation characterised by structural complexity: sparse, open and thin canopy and an accompanying presence of dense vegetated background. The influence of vegetated understory on chlorophyll (a+b) estimation has been evaluated through an experiment conducted in two poplar stands in which understory was partially harvested, before the sensor overpass. The approach used was scaling up and the numerical inversion of models coupled PROSPECT (Jacquemoud, 1990, Jacquemoud, 1993) and SAILH (Verhoef, 1984, Kuusk, 1991) using a simple ratio vegetation (VI) as a merit function to investigate its performance in minimising effects like shadows, resulting from the complex structure of the

plantation canopy. Results from the tilled understory area relative to the non-tilled area were compared

2.0 STUDY AREA

The study area is a poplar (*populus nigra*) plantation located north-west of Pavia in Lombardia region, Italy; it is a CARBOEUROFLUX investigation site managed by the Joint Research Centre (J.R.C.) at Ispra, Italy. The poplar plantation (*Kyoto forest or fast growing forest*) is composed of hybrid poplar trees planted in rows 6 meters apart, in order to maximise the plant growth. This plantation scheme defines an open and sparse canopy situation in juvenile or stressed stands.

3.0 DATA COLLECTION

3.1 AIRBORNE DATA

Hyperspectral images were acquired on July 2001 by DLR (German Aerospace Centre) with the ROSIS (*Reflective Optics System Imaging Spectrometer*) sensor, in the frame of the DARFEM (DAIS and ROSIS for Forest Ecosystem Monitoring) experiment (Brivio *et al.*, 2001). ROSIS images were collected in the principal plane in 115 channels, ranging from 430nm to 850nm (FWHM=7.5nm) and a spatial resolution of about 1m*1m. The processing of the remotely sensed data, including atmospheric and geometric corrections, were performed by the *Imaging Spectroscopy Team* of the DLR centre.

3.2 FIELD DATA AND TEST AREA

The ecological and forestry properties of the study area were characterised, in order to evaluate the variability of the poplar stands, by aerial photo interpretation and forestry measurements: tree height, diameter and crown radius. Additional SPAD 502 *Chlorophyll Meter* (Minolta, Osaka - Japan) measurements were conducted to define plots characterised by homogeneous health *status*, represented by similar leaf pigment content. Four different stands were defined and five leaves for each plot were sampled from the top of poplar tree crowns for laboratory analysis (leaf radiometric measurements and pigment extraction).

Ground measurements included: (i) optical depth for atmospheric corrections using a MS-120 Eko sunphotometer, (ii) LAI measurements of overstory and understory, using the Li-Cor plant canopy analyser LAI-2000, (iii) understory optical reflectance characterisation using a Fieldspec FRTM spectrometer, (iv) leaf reflectance and transmittance measurements using an integrating sphere (Li-Cor 1800-12S) coupled

to the Fieldspec FRTM. Leaf samples were stored in plastic bags and kept frozen for the biochemistry analysis: leaf chlorophyll-a and -b content was extracted in the laboratory by the Ontario Forestry Research Institute (OFRI, Sault St. Marie, Canada) team.

Two test areas (test site A and test site B) were selected from different homogeneous stands to evaluate the influence of different understory typology on sensor reflectance. For this purpose, in each test site a 24m*24m area was tilled before the sensor overpass. Stands properties are shown in Table 1.

TEST SITE	LAI _o (m ² /m ²)	LAI _u (m ² /m ²)	F _{co} (%)	F _{cu} (%)	Cd (m)
A	2.33	2.88	90	99	3.94
B	1.50	2.57	60	97	2.95

Table 1 - Test site ecological characteristics (LAI_o and LAI_u = LAI overstory and understory, f_{co} and f_{cu}= fractional cover overstory and understory, Cd = crown diameter).

4.0 ANALYSIS

4.1 RED EDGE INDICES INVESTIGATION

Recent research in pigment retrieval at canopy level has shown promising results through scaling up techniques and numerical inversion of physically-based coupled leaf and canopy radiative transfer models. Simple turbid-medium canopy models like SAILH have been successfully applied in closed canopy forests (with LAI>3) minimising the effects of canopy structure, in particular effects of shadows, by using a simple ratio vegetation index defining the red edge slope in the inversion procedure (Zarco-Tejada, 2001a).

In contrast, the poplar plantation study area in this experiment is characterised by an open and sparse canopy structure in addition to low LAI values (LAI<3) and the presence of dense vegetated background. Variation in spectral signatures between visible and NIR wavelengths, observed in test areas A and B associated with tilled and non-tilled crowns pixels (Fig.1, Fig.2), demonstrate the understory contribution on canopy reflectance.

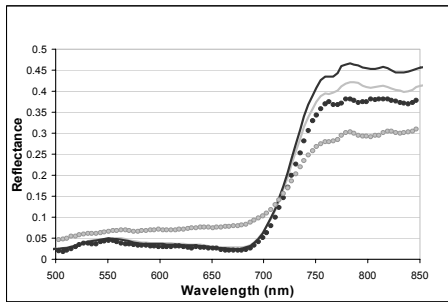


Fig. 1 - ROSIS poplar crown spectra extracted from tilled (black full line) and non tilled (grey full line) test area A and relative background spectra (dotted lines).

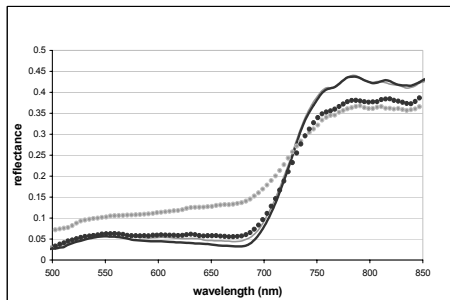


Fig. 2 - ROSIS poplar crown spectra extracted from tilled (black full line) and non tilled (grey full line) test area B and relative background spectra (dotted lines).

Red edge indices, in particular the ratio (R_{740}/R_{720}) relatively unresponsive to shadows (Zarco-Tejada *et al*, 2001), were investigated with respect to its dependency on background optical properties. With this goal, two profiles were defined on ROSIS imagery across tilled and non-tilled test areas A and B. Ratio (R_{740}/R_{720}) variations were observed between crown pixels in tilled and non tilled areas (Fig.2). Therefore, we expect that pigment retrievals using the R_{740}/R_{720} ratio as a merit function will be also be affected if nominal background spectra are used in the inversion procedure.

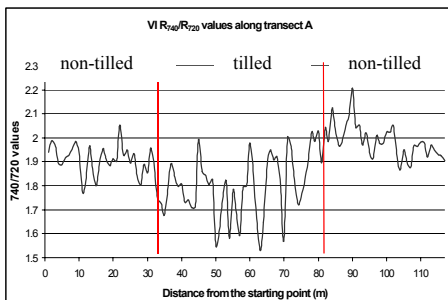


Fig. 3 - Ratio R_{740}/R_{720} values along profile A.

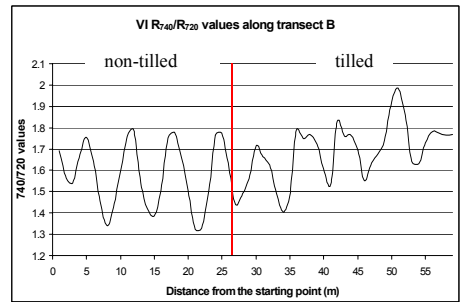


Fig. 4 - Ratio R_{740}/R_{720} values along profile B.

4.2 LEAF AND CANOPY REFLECTANCE SIMULATION

Relationships between chlorophyll (a+b) and the ratio R_{740}/R_{720} , derived from canopy reflectance simulated through PROSPECT and SAILH (PROSAILH), were used to estimate pigment content along the two profiles A and B for varying LAI values.

Leaf biochemical input parameters were assigned average nominal values estimated by PROSPECT inversion on reflectance and transmittance spectra of poplar leaves sampled in the study area ($N = 1.35$, $C_w = 0.009$ cm, $C_m = 0.006$ g/cm²). The hotspot and Mean Tilt Angle (MTA), were assigned nominal values, an average of the available field measurements (hotspot = 0.05, MTA = 45°). Spectra were simulated for various LAI (test area A - LAI range: 2.2 - 3.8; test area B - LAI range: 1.4 - 3.0 with a step increment of 0.4), and leaf chlorophyll content ranging from 10 µg/cm² to 55 µg/cm² with an increasing step of 5 µg/cm². Finally, local understory spectra, measured in the field by a Fieldspec FR spectrometer, were used in simulations to reproduce canopy reflectance properties of test areas A and B in natural ecological condition (non-tilled).

It is observed that chlorophyll retrieved along Profile B strongly depends on LAI for low values (LAI < 2.6), therefore precluding the simple use of nominal values in the PROSAILH numerical inversion procedure in presence of thin canopy. Moreover, influence of understory optical properties are evident along the profile: chlorophyll estimated tend to decrease in correspondence to the tilled area compared to the non-tilled area. The chlorophyll trend estimated along Profile A shows that dense vegetated understory influences the pigment retrievals even for higher LAI values and more closed canopy.

4.3 UNDERSTORY INFLUENCE

Pigment retrieval through numerical inversion of the PROSAILH model was attempted in order to quantify the understory influence on overstory pigment estimation when LAI is low. High resolution ROSIS data allowed separation of the problem concerned with low LAI values from complexity associated to sparse canopy structure, since it was possible to target crown pixels in ROSIS imagery.

In particular, spectra were extracted from nine crowns, four pixels each, defined in test areas A and B. The experiment hypothesis was that overstory poplars from tilled and non-tilled area have same biophysical characteristics, therefore differences in pigment retrievals are a response to local understory influence.

Leaf biochemical parameters, canopy structure parameters and sensor-target geometry, previously used in the direct simulations, were assigned nominal values in the inversion procedure. LAI poplar crown were calculated, taking into account the relative overstory Fc of the two test areas (Table 2), from local LAI values estimated by numerical inversion of PROSAILH model on multi-angular DAIS (Digital Airborne Imaging Spectrometer) observations (Meroni *et al.*, 2002).

TEST SITE	LAI* (m2/m2)	Fco (%)	LAIc (m2/m2)
A	2.45	90	2.7
B	1.2	60	1.8

Table 2 - LAI* = LAI retrieved from DAIS, Fc = fractional cover, LAIc = calculated crown LAI.

Inversion results using a nominal soil spectra for tilled and non-tilled area are compared with results obtained using local understory optical information (Table 3).

Chlorophyll values retrieved from poplar crowns in tilled and non-tilled areas show an average difference of 6.2 $\mu\text{g}/\text{cm}^2$ when a nominal background is used in the inversion procedure, while no significant differences are observed when local background optical properties are used.

TEST PLOT		Average Cab Values ($\mu\text{g}/\text{cm}^2$)			
		Nominal background		Known local background	
		Mean	Std	Mean	Std
A	Tilled	39.0	3.16	39.0	3.16
	Non-tilled	45.2	2.12	39.6	1.94
B	Tilled	35.4	3.67	35.4	3.67
	Non-tilled	41.7	3.68	36.0	3.23

Table 3 - Pigment retrieval in test areas A and B using nominal soil background spectra and local background spectra in the inversion procedure.

4.0 COARSER RESOLUTION RESULTS

Implications for coarser spatial resolution that would not allow targeting crowns were investigated averaging spectra of 20*20 m² defined in the tilled and non-tilled test areas.

PROSAILH numerical inversions were performed setting model input variables as before. Chlorophyll (a+b) concentration estimated are shown in Table 4 comparing the results using a nominal soil and local understory optical properties in the inversion procedure.

TEST PLOT		Average Cab values ($\mu\text{g}/\text{cm}^2$)	
		Nominal background	Known local background
A	Tilled	34.5	34.5
	Non-tilled	46.7	39.5
B	Tilled	37.7	37.7
	Non-tilled	64.2	38.7

Table 4 - Pigment retrievals in test areas A and B simulating a low spatial resolution sensor.

Chlorophyll values retrieved from poplar crowns in tilled and non-tilled areas, when nominal background is used, show an average difference of 20 $\mu\text{g}/\text{cm}^2$, in contrast to results by Zarco-Tejada (2001b), presumably due to the lower LAI canopies. Significantly less evident differences in pigment estimation (3.6 $\mu\text{g}/\text{cm}^2$) are observed when local background optical properties are used in the inversion procedure.

Even though effects like shadows, that affect the canopy reflectance, have been successfully overcome by using simple ratio VI as merit function in closed canopies, results here show that problems concerning open and sparse canopy still represent a challenging issue for accurate pigment retrievals at coarser spatial resolution.

5.0 CONCLUSION

This research has shown that vegetated understory has a clearly observable contribution on the canopy reflectance, in turn affecting the overstory pigment retrieval when the LAI has low values and the canopy is sparse and open. These ecological characteristics are typical of poplar plantations (*Kyoto forest or fast growing forest*) where stands are juvenile or stressed, therefore compromising the use of estimates of absolute chlorophyll content as bio-indicator in vegetation monitoring in these situations. However, the complete harvesting of the understory may be viewed as a rather extreme unknown in an operational programme of monitoring of these plantations.

The use of red edge slope as a merit function in the inversion procedure can improve the pigment estimation in canopy with complex structure by overcoming effects like shadows, but still show sensitivity to background optical properties and LAI values, affecting the accuracy of chlorophyll estimation. Nevertheless, the estimated relative pigment content appears to correctly identify test areas with relatively different leaf pigment content, and stand condition. In addition, the errors in pigment estimates in the overstory canopy introduced by such issues must be considered relative to the accuracies of pigment retrieval ($\sim 5 \mu\text{g}/\text{cm}^2$) under more ideal condition (Zarco-Tejada *et al.* 2001a).

Problems associated with the challenges to accurate overstory leaf pigment retrievals can be overcome by high spatial resolution data used in radiative transfer models when numerical inversion procedures are performed with known LAI values and local understory optical properties. Field campaigns can give the necessary understory characterisation and LAI values. Accurate LAI maps can also be achieved by multi-angular data analysis, if available.

Simulations of coarser spatial resolution suggest that pigment retrievals in open and sparse canopies, through numerical inversion of radiative transfer models, cannot be performed with results consistent with typical RMSE ranges in recent retrievals for closed canopy forests.

ACKNOWLEDGEMENTS

This study was supported by the EU-funded project HySens coordinate by DLR-Germany. The authors gratefully acknowledge G. Seufert (JRC-IES, Ispra, Italy) and his unit, P. Zarco-Tejada (Universidad de Valladolid), S. Jacquemoud, C. Bacour (Université Paris 7 - Laboratoire Environnement et

Développement), the optical laboratory staff (York University, Toronto) and the Remote Sensing Unit of DISAT (Università di Milano Bicocca).

REFERENCES

- Brivio P. A., M. Meroni, and C. Giardino, 2001, Monitoring forest ecosystems using hyperspectral and directional observations, *ESA Workshop on "SPECTRA", Nordwijk (The Netherlands) 12-13 June 2001, ESA-ESTEC (in press)*.
- Dawson T.P., 2000, The potential for estimating chlorophyll content from a vegetation canopy using MERIS, *Int. J. of Remote Sensing* 21: 2043 – 2051.
- Demarez, V., Gastellu-Etchegorry, J.P., 2000, A modeling approach for studying forest chlorophyll content, *Remote Sens. Environ.* 71: 226-238.
- Meroni, M., Colombo, R., Boschetti M., Panigada, C., Rossini, M., Brivio, P.A., Miller, J.R., 2002, LAI retrieval from multi-angle and hyperspectral observations in an intensive poplar plantation, *these conference proceedings*.
- Mohammed, G.H., Sampson, P.H., Colombo, S.J., Noland, T.L., Miller, J.R., 1997-. Bio-indicators of forest health and sustainability: development of a forest condition rating system for Ontario, Forest research information paper No. 137, Ontario Forest Research Institute, Sault Ste. Marie, Ontario-Canada
- Haboudane, D., Miller, J.R., Tremblay, N., Zarco-Tejada, P., Dextraze, L., Viau, A. 2001, Heterogeneity of CASI-estimated leaf chlorophyll in corn: assessment and comparison with ground truth from L'Acadie GEOIDE experimental site, *Proceedings of the 23rd Canadian Symposium on Remote Sensing and 10th Congress of the Quebec Remote Sensing Association, Université Laval, University Sainte-Foy, Quebec Canada, 21-24 August 2001*.
- Haboudane, D., Miller, J.R., Tremblay, N., Zarco-Tejada, P., Dextraze, L., 2002, Integrated narrow-band vegetation indices for prediction of crop chlorophyll content for application to precise agriculture. *Remote Sens. Environ.*, 81:416-426.
- Jacquemoud S., Baret F., 1990, PROSPECT: a model of leaf optical properties spectra, *Remote Sens. Environ.* 34: 75 – 91.
- Jacquemoud S., 1993, Inversion of the PROSPECT + SAIL canopy reflectance model from AVIRIS equivalent spectra: Theoretical study, *Remote Sens. Environ.* 44: 281 – 292.
- Kuusk A., 1991, The hot-spot effect in plant canopy reflectance, in *Photon-Vegetation Interactions; Application in Optical Remote Sensing and Plant Ecology (R. Mynemi and J. Ross, Eds.)*. Springer-Verlag, New York, 139 – 159.

- Verhoef W., 1984, Light scattering by leaf layers with application to canopy reflectance modeling: the SAIL model, *Remote Sens. Environ.* 16:125 – 141.
- Zarco-Tejada P., Miller, J.R., Noland, T.L., Mohammed, G.H., Sampson, P.H., 2001a, Scaling-up and model inversion methods with narrow band optical indices for chlorophyll content estimation in closed forest canopies with hyperspectral data. *IEEE Transactions on Geoscience and Remote Sensing*, 39, 1491-1507.
- Zarco-Tejada P., Miller, J.R., 2001b Minimisation of shadow effects in forest canopies for chlorophyll content estimation using red edge optical indices through radiative transfer: implication for MERIS. *Proceedings of the IEEE International Geoscience and Remote Sensing Symposium (IGARSS'01)*, July 9 - 13th, 2001, in Sydney, Australia

Effects of chlorophyll concentration on green LAI prediction in crop canopies: Modelling and assessment

Driss Haboudane¹, John R. Miller^{1,2}, Elizabeth Pattey³, Pablo J. Zarco-Tejada⁴ and Ian Strachan⁵

1) Centre for Research in Earth and Space Science (CRESS), Petrie Science Building, York University, 4700 Keele St., Toronto - Ontario M3J 1P3, Canada, driss@terra.phys.yorku.ca

2) Department of Physics and Astronomy, York University, Toronto, ON, M3J 1P3, Canada, jrmiller@yorku.ca

3) Agriculture and Agri-Food Canada, Central Experimental Farm, K. W. Neatby room 209I, 960, Carling ave., Ottawa, Ontario, K1A 0C6, Canada, PatteyE@agr.gc.ca

4) Grupo de Optica Atmosferica (GOA-UVA), Escuela Técnica Superior de Ingenierias Agrarias, Campus de La Yutera, Universidad de Valladolid, Avda. de Madrid, 44, Palencia, 34004 Spain, pzarco@iaf.uva.es

5) Department of Natural Resource Sciences, Macdonald Campus of McGill University, 21111 Lakeshore Rd., Ste. Anne de Bellevue, Qc, H9X 3V9, Canada, ian.strachan@mcgill.ca

ABSTRACT—A growing number of studies have focused on evaluating vegetation indices in terms of their sensitivity to vegetation biophysical parameters as well as to external factors affecting canopy reflectance. In this context, leaf and canopy radiative transfer models have provided a basis for understanding the behaviour of such indices, particularly their resistance to external perturbing effects related to soil background, illumination, and atmospheric conditions. But, so far no studies have thoroughly assessed the impact of leaf chlorophyll concentration changes on the ability of spectral indices to predict green leaf area index (LAI). Because the variables LAI and chlorophyll content have similar effects on canopy reflectance in the visible and red edge portions of the solar spectrum, there is a need to uncouple these effects in order to accurately assess each of these variables. In the present work we used PROSPECT and SAILH models to simulate a wide range of crop canopy reflectances which were used to study the sensitivity of a set of vegetation indices to LAI variability. The aim of the paper was to present a method for minimizing the effect of leaf chlorophyll content on the prediction of vegetation green LAI, and to propose an index that adequately predicts the LAI of crop canopies. Accordingly, we have developed new algorithms that proved to be the best predictor of green LAI with respect to potentially confounding leaf chlorophyll concentration effects. The technique has been validated using CASI hyperspectral reflectance images acquired on different dates (1999, 2000, 2001), over fields with various crops (corn, wheat, and soybean) at different growth stages, containing plots with various fertilization treatments. Maps of predicted LAI were generated and corresponding statistics were compared to ground truth data. Evaluation of predictions revealed good agreement with field measurements.

1 INTRODUCTION

Green leaf area index (LAI) is one of the canopy parameters that plays a major role in vegetation physiological processes, and ecosystems functioning; it has been frequently used by agronomists and crop physiologists to assess crop conditions and growth. Its estimation from remote sensing data has motivated the

development of various approaches and techniques for LAI mapping at local, regional, and global scales (Baret and Guyot, 1991; Daughtry et al., 1992; Chen et al., 2002; etc.). While some studies have focused on model inversion (Jacquemoud et al., 2000), and spectral mixture analysis (Hu et al., 2002; Peddle and Johnson, 2000; Pacheco et al., 2001), others have expended considerable effort to develop relationships between green LAI and spectral vegetation indices

(Spanner *et al.*, 1990; Chen and Cihlar, 1996; Fassnacht *et al.*, 1997). Though these indices were well correlated with green LAI, studies have demonstrated that they were as well very responsive to other vegetation descriptors such as canopy cover, chlorophyll concentration and absorbed photosynthetically active radiation (Broge and Leblanc, 2000; Broge and Mortenson, 2002; Daughtry *et al.*, 2000; Gitelson *et al.*, 2001; Haboudane *et al.*, 2002a). Consequently, to meet the requirements related to prediction accuracy and consistency, there is a need for the design of specific spectral indices that are ideally sensitive exclusively to a vegetation/canopy descriptor of interest. For instance, Daughtry *et al.* (2000) and Haboudane *et al.* (2002) have each suggested index-based approaches to estimate leaf chlorophyll content with minimal confounding effects due to LAI.

The objective of the present study is to evaluate the potential of selected spectral indices in terms of quantifying green LAI of crop canopies. Indices were assessed regarding their sensitivity to chlorophyll concentration changes, and their linearity and saturation with green LAI increase. As a part of the study, a new index is suggested and its LAI predictions are compared to ground truth data.

2 DATA COLLECTION AND PROCESSING

The study area is located near Ottawa, Canada at the former Greenbelt Farm. Over three successive years, different crops (soybean, corn, wheat) were grown on a 30-ha field with a drained clay loam soil as well as on adjacent fields operated by a private producer. The experiments consisted of dividing the main field into four regions receiving various nitrogen treatments: 100% of the recommended fertilization (155 kg ha^{-1}) over a flat region, 100% of recommended nitrogen over a region with a gentle topographic slope, 60% of the recommended rate, and no nitrogen application (0%). They were thus laid out to promote development of remote sensing techniques for detection of plant stresses in precision agriculture, particularly stresses due to nitrogen deficiency, water deficit, and topographic influence. Within each region, a grid of georeferenced points spaced every 25 m was established on a representative section of $150 \text{ m} \times 150 \text{ m}$. These locations were used to monitor crop biophysical parameters during the growing season, particularly during intensive field campaigns coinciding with image acquisition. Details on the experimental site are presented in Pattey *et al.* (2001).

Hyperspectral images were acquired by the Compact Airborne Spectrographic Imager (CASI), operated by the Centre for Research in Earth and Space Technology (CRESTech). Simultaneously, a set

of field and laboratory data were collected for biochemical and geochemical analysis, along with optical and biophysical measurements. Ground truth measurements included: (i) collection of leaf tissue for laboratory determination of leaf chlorophyll concentration, (ii) crop leaf reflectance and transmittance measurements using an integrating sphere (Li-Cor model 1800-12) coupled with a single mode optical fibre to a spectrometer (GER1500, GER, Millbrook, NY), (iii) chlorophyll meter (Minolta SPAD 502) measurements, (iv) leaf area index (LAI) measurements using the Plant Canopy Analyzer (Li-Cor model LAI-2000) and an area meter (LI-3100, Li-Cor, Lincoln, NE), and (v) crop growth measures.

During 2000 and 2001 growing seasons, CASI hyperspectral images were collected in three different deployments, using two modes of operation: the *multispectral mode*, with 1 m spatial resolution and 7 spectral bands suitable for sensing vegetation properties (489.51, 554.98, 624.63, 681.42, 706.12, 742.31, and 776.69 nm); and the *hyperspectral mode*, with 2 m spatial resolution and 72 channels covering the visible and near infrared portions of the solar spectrum from 408 to 947 nm with a bandwidth of 7.5 nm. Acquisition dates were planned to coincide with different phenological development stages, providing image data covering the earliest, middle and latest periods of the growth season.

The hyperspectral digital images collected by CASI were processed to at-sensor radiance using calibration coefficients determined in the laboratory by CRESTech (Centre for Research in Earth and Space Technology). Then the CAM5S atmospheric correction model (O'Neill *et al.*, 1997) was used to transform the relative at-sensor radiance to absolute ground-reflectance. To perform this operation, an estimate of aerosol optical depth at 550 nm was derived from ground sun-photometer measurements. Data regarding geographic position, illumination and viewing geometry as well as ground and sensor altitudes were derived both from aircraft navigation data recordings and ground GPS measurements.

Reflectance curves derived from processed CASI images showed the presence of spectral anomalies associated with atmospheric absorption features at specific wavelengths. Although we applied model-based atmospheric corrections, the calculated reflectances are still affected by spectrally-specific errors owing mostly to an under-correction of some atmospheric components effects (oxygen and water vapour absorption). These imperfections in reflectance data cube retrieval are a problem common to hyperspectral systems due to limitations in the performance of atmospheric correction models and to variations across the detector array in nominal imager characterisations in spectral registration and

bandwidth. The flat field calibration is a correction technique used to remove the residual calibration-induced noise and atmospheric effects from hyperspectral reflectance image cubes. Its aim is to improve overall quality of spectra and provide apparent reflectance data that can be compared with laboratory spectra (Boardman, and Huntington, 1996). It requires the presence, and identification in images of spectrally-flat uniform areas where the spectral anomalies can be unambiguously attributed, in narrow spectral ranges, to atmospheric effects and the solar spectrum. In CASI images, these features were observed over asphalt and concrete areas within the same image where the reflectance spectra are assumed to be flat or nearly flat over these features. Using signatures of such scene elements, we calculated coefficients that adequately compensated for the effects of atmospheric water and oxygen absorption. After those coefficients were applied to the entire image, but only in the specific spectral ranges affected, we checked the signatures of different components of the image and found that observed residual features have been successfully removed.

3 CANOPY REFLECTANCE SIMULATIONS

Leaf optical properties were simulated using the PROSPECT model (Jacquemoud and Baret, 1990; Jacquemoud *et al.*, 1996), which simulates upward and downward hemispherical radiation fluxes between 400 and 2500 nm, and relates foliar biochemistry and scattering parameters to leaf reflectance and transmittance spectra. It requires the leaf internal structure parameter N , the chlorophyll $a + b$ content C_{ab} ($\mu\text{g cm}^{-2}$), the equivalent water thickness C_w (cm), and the leaf dry matter content C_m (g cm^{-2}) to determine leaf reflectance and transmittance signatures in the optical domain.

Canopy reflectance spectra were simulated using a variant of the SAIL (Scattering by Arbitrary Inclined Leaves) model (Verhoef, 1984) called SAILH. It was adapted to take into account the hotspot effect or the multiple scattering in the canopy (Kuusk, 1985). It is a turbid-medium model that approximates the canopy as a horizontally uniform parallel-plane infinitely-extended medium, with diffusely reflecting and transmitting elements. Typical SAILH inputs are: canopy architecture defined by the leaf area index (LAI) and the leaf angle distribution function (LADF), leaf reflectance and transmittance spectra for given chlorophyll content per unit area, underlying soil reflectance, and the illumination and viewing geometry (solar zenith and sensor viewing angles).

4 LAI AND CHLOROPHYLL EFFECTS ON CANOPY REFLECTANCE

The chlorophyll content effect on canopy reflectance is presented in **Figure 1** for a preliminary analysis of SAILH simulated spectra. It shows reflectance differences induced by changes in leaf chlorophyll concentration ($5 - 70 \mu\text{g cm}^{-2}$) for a known medium LAI ($=3$). The relative spectral difference is performed between spectra representing various chlorophyll contents and the spectrum corresponding to $50 \mu\text{g cm}^{-2}$. Wavelength regions that are the most sensitive to leaf pigment variability are centered on 550 nm in the green and 715 nm in the red edge. The narrow peak observed at 715 nm seems to be shifted to longer wavelength when leaf chlorophyll concentrations increase. This corresponds to the transition from chlorophyll absorption processes in the red wavelengths to within-leaf scattering in the near-infrared region (Munden *et al.*, 1994). In fact, an increase of chlorophyll content induces a broadening of chlorophyll absorption feature in the red (670-680 nm) and, therefore, moves the red-edge position to longer wavelengths (Daughtry *et al.*, 2000) as seen on **Figure 1**. The relatively wide window of sensitivity to pigment variation in the green is due to the canopy reflectance decrease generated by the increase in leaf chlorophyll concentration.

In contrast, major LAI effects on canopy reflectance occur around 685 nm and beyond 740 nm (**Figure 2**). Unlike chlorophyll concentration, LAI generates weak variations of reflectance spectrum at 550 nm and at 720 nm. It can be seen that high differences in the red region (685-690 nm) are observed only for low LAI values (0.1, 0.5, and 1.0). This phenomenon could be associated with the influence of non-photosynthetic materials and dry biomass on canopy reflectance when green biomass represents a relatively small proportion. The major variations induced by LAI in the near-infrared are due to the canopy structural development and multiple scattering which is particularly important at these wavelengths. Based on these simulations, it can be seen that chlorophyll interactions with radiation are limited to the optical domain ranging from 400 nm to 725 nm, while LAI influences are observed over the red and near-infrared portions. Their combined effects occur over the red edge region where LAI and chlorophyll density increasingly contribute to the shift of the red edge position.

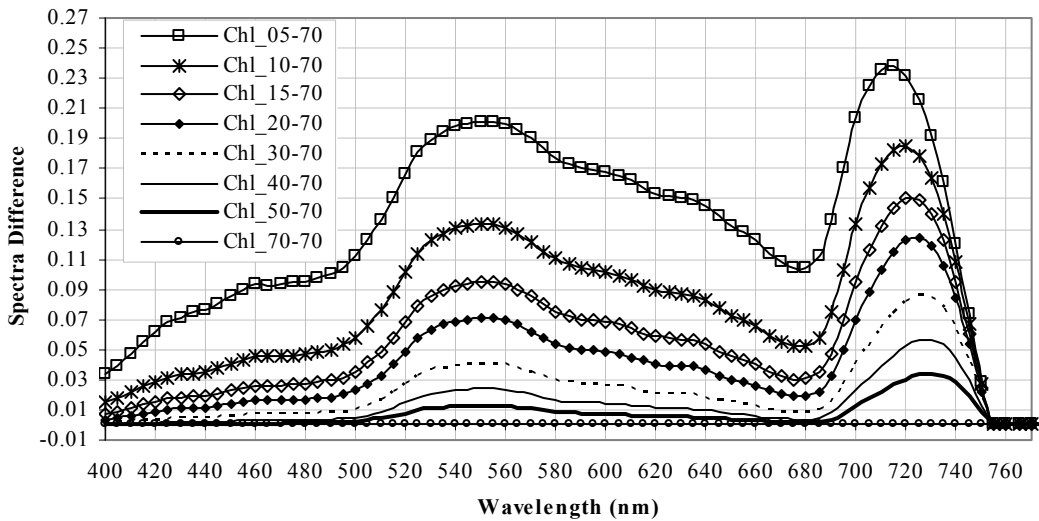


Figure 1 Relative canopy reflectance differences (difference between spectra representing various chlorophyll contents and the spectrum corresponding to $70 \mu\text{g cm}^{-2}$) for an LAI of 3. In the legend, Chl40-70 represents the difference between spectra corresponding to chlorophyll contents 40 and $70 \mu\text{g cm}^{-2}$.

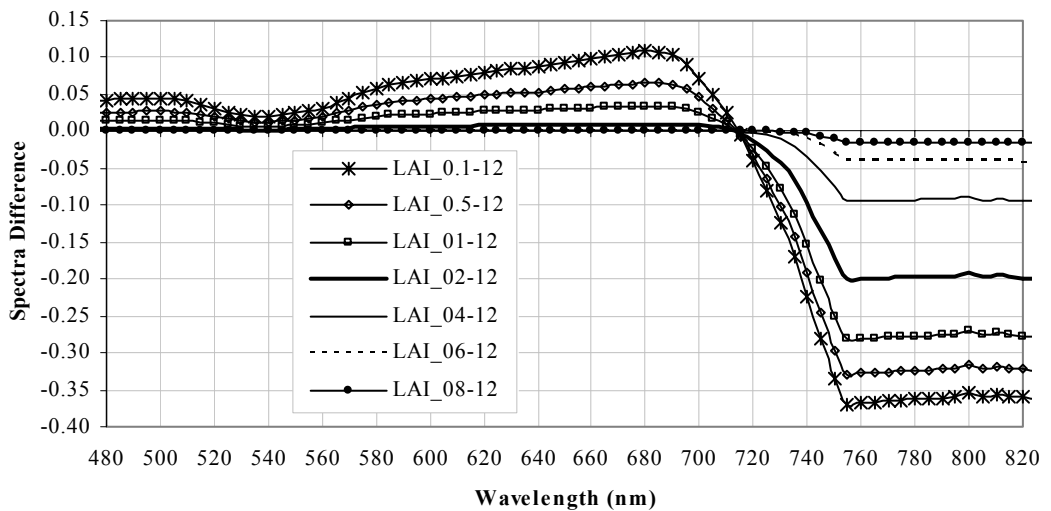


Figure 2 Relative canopy reflectance differences (difference between spectra representing various LAI values and the spectrum corresponding to LAI = 12) for a chlorophyll content of $35 \mu\text{g cm}^{-2}$. In the legend, LAI_04-12 represents the difference between spectra corresponding to LAI values 4 and 12.

5 LAI ESTIMATION: MODELLING AND PREDICTION

Different techniques have been developed in order to improve green LAI estimation over large areas, mainly through the use of spectral indices, model inversions (Jacquemoud et al., 2000), and spectral mixture

analysis (Hu *et al.*, 2002; Peddle and Johnson, 2000; Pacheco *et al.*, 2001). The widely used approach was to establish relationships between ground-measured LAI and vegetation indices (Spanner *et al.*, 1990; Chen and Cihlar, 1996; Fassnacht *et al.*, 1997). Consequently, a large number of relationships were developed, with a wide range of determination coefficients ($0.05 < r^2 < 0.66$) between satellite-

derived spectral indices and LAI (Baret and Guyot, 1991; Chen, 1996; Brown *et al.*, 2000).

Several optical indices have been reported in the literature and have been proven to be well correlated with various vegetation parameters such as LAI, biomass, chlorophyll content, and photosynthetic activity. Efforts focused on improving vegetation indices and rendering them insensitive to variations in illumination conditions, observing geometry, and soil properties. Thus, the performance and the suitability of a particular index are generally determined by its sensitivity to a characteristic of interest. Consequently, only a few of the most common vegetation indices were presented in this paper aiming to study leaf chlorophyll concentration effects on LAI predictions.

Their formulae and references are provided in **Table 1** below where G, R and NIR denote canopy reflectance in the green (550 nm), red (670 nm), and near-infrared (800 nm), respectively. A detailed discussion on some spectral indices can be found in Zarco-Tejada (2000), Broge and Leblanc (2000) and Haboudane *et al.* (2002a).

Evaluation of the performance of these indices was based on canopy reflectance spectra simulated with the radiative transfer models PROSPECT and SAILH. It was conducted with consideration of the following criteria: index sensitivity to chlorophyll effects, its saturation level when LAI increases, and the linearity of its relationship with LAI.

Table 1 Information about the spectral indices evaluated in the present research.

Acronym	Name	Formula	Reference
NDVI	Normalized difference vegetation index	$(NIR - R)/(NIR + R)$	(Rouse <i>et al.</i> , 1974)
MSAVI	Modified second soil-adjusted vegetation index	$\frac{1}{2} \left[2 * NIR + 1 - \sqrt{(2 * NIR + 1)^2 - 8 * (NIR - R)} \right]$	(Qi <i>et al.</i> , 1994)
MCARI1	Modified chlorophyll absorption ratio index	$2 * [(NIR - R) - 0.2 * (NIR - G)]$	(Haboudane <i>et al.</i> , 2002a)
MCARI2	Modified second chlorophyll absorption ratio index	$\frac{1.35 * [1.9 * (NIR - R) - 0.52 * (NIR - G)]}{(0.8 + NIR * NIR + R * R)}$	(Haboudane <i>et al.</i> , 2002a)

6 RESULTS AND ANALYSIS

To understand the chlorophyll effect on LAI estimation from reflectance data, we plotted spectral indices against green LAI as a function of chlorophyll concentration (**Figure 3**). For each index, the number of the curves expresses the variation of chlorophyll content from 10 to 100 $\mu\text{g cm}^{-2}$ with an increment of 5 $\mu\text{g cm}^{-2}$. As a preliminary analysis, it can be seen that all indices behave logarithmically rather than linearly with LAI. NDVI and MSAVI show a similar resistance to chlorophyll content changes, with clear sensitivity only to chlorophyll concentrations in the lower range (10 to 25 $\mu\text{g cm}^{-2}$). The main difference between these two indices is that NDVI reaches a

saturation level when LAI exceeds 2, while MSAVI shows a better dynamic response even extending to high LAI levels (up to 6) (**Figure 3**). The best behaviour in terms of both insensitivity to pigments variation and responsivity to LAI changes is given by MCARI1 and MCARI2. They offer the advantage of being the most resistant to chlorophyll changes and the least sensitive to the saturation phenomena. Indeed, MCARI1 and MCARI2 have almost unique relationships with green LAI independent of chlorophyll content changes. Because it has the advantage of including a soil adjustment term, MCARI2 was used to develop a predictive equation for estimation of canopy green LAI based on these model simulations for use with remotely sensed data.

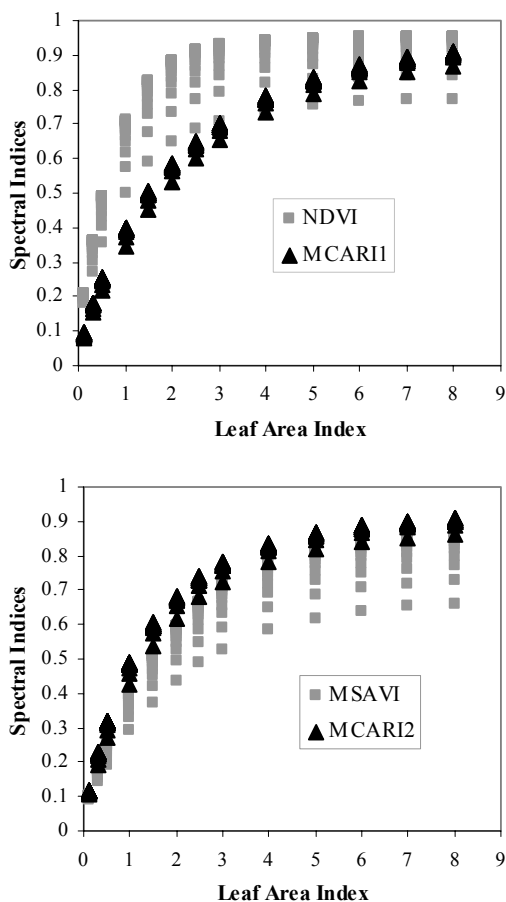


Figure 3 Effects of chlorophyll content on the relationships between spectral indices and green LAI. Application to canopy reflectance simulated using PROSPECT and SAILH. The curves correspond to various chlorophyll contents ranging from 5 to 100 $\mu\text{g cm}^{-2}$ in steps of 5 $\mu\text{g cm}^{-2}$.

For analyses of the linearity between spectral indices and green LAI, real reflectance data were extracted from CASI hyperspectral images. The latter were acquired in intensive field campaigns carried out in 1999, 2000, and 2001 over soybean, corn and wheat canopies. Indices under evaluation in this study were calculated from these data, then, plotted against the NIR reflectance as shown in **Figure 4**. The choice of NIR reflectance is due to the fact that above-canopy reflectance in the NIR is drastically affected by vegetation structural changes rather than by pigments concentration variations (**Figures 1 and 2**).

As can be seen in **Figure 4**, vegetation indices show different trends when plotted as a function of NIR reflectance. NDVI offered the weaker dynamic

range, and saturated quickly with the increase of NIR reflectance. In contrast, MSAVI and MCARI2 appeared to be more sensitive to NIR reflectance changes, however, their behaviour is characterised by a gentle asymptotic trend at high NIR reflectance values. The overall best linear relationship is offered by MCARI1, but further analyses have shown that it results in an overestimation at high LAI values.

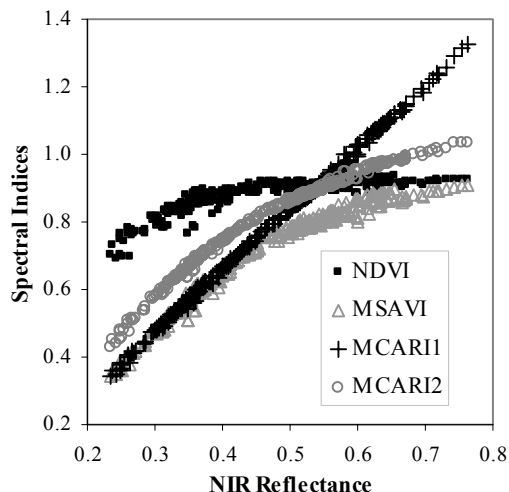


Figure 4 Relationships between evaluated spectral indices and the near-infrared (NIR) reflectance from CASI hyperspectral images collected over various crops.

A predictive relationship has been established to make green LAI estimations as a function of MCARI2 (**Figure 5**). The overall best fit was given by an exponential curve with a coefficient of determination (r^2) exceeding 0.98. One can see that, for a wide range of chlorophyll concentrations (15 to 100 $\mu\text{g cm}^{-2}$), there is a unique relationship between MCARI2 and green LAI. A corresponding predictive equation has been retrieved and successfully applied to CASI hyperspectral images to map green LAI status over agricultural fields seeded with corn, wheat, and soybean (**Figure 6**). Results of comparison between estimates using remote sensing and measurements in the field and laboratory are summarised in **Table 2** below.

Table 2 Comparison estimated-measured LAI: determination coefficient and RMSE.

Crop	Determination coeff. (r^2)	RMSE
Corn	0.82	0.87
Wheat	0.92	0.76
Soybean	0.96	0.87

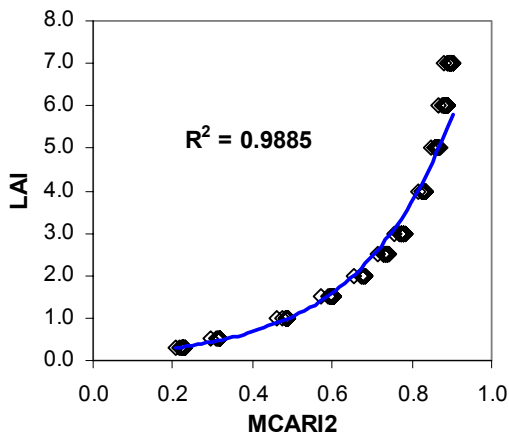


Figure 5 Relationships between Green LAI and MCARI2, for chlorophyll content varying from 15 to 100 $\mu\text{g cm}^{-2}$ and green LAI ranging from 0.3 to 7.

Spatial distribution of green LAI in corn, wheat, and soybean canopies is illustrated by the map in **Figure 6**. It represents the early growth stage as observed during the first intensive field campaign in summer 2001 (June 13). It shows two important features: (i) growth differences between fields of corn, wheat, and soybean, and (ii) effects of soil texture, topography, and fertilization on wheat conditions. Indeed, at this early stage, wheat has reached an advanced growth level, with LAI ranging from 0.2 to 7, in comparison to corn and soybean with LAI values not exceeding 0.4. LAI variability within the wheat field is controlled by nitrogen treatments, soil texture, and drainage conditions. Thus, high LAI levels observed in the north-eastern portion of the field (reddish tones) are associated with high nitrogen supply and the presence of a sandy soil, while low LAI values (blue and cyan tones) present in the north-western portion of the field result from deleterious topographic effects. Lack of nitrogen supply caused the low LAI levels (cyan, bright green tones) encountered in the south-western portion of the field.

7 CONCLUSION

The study presented in this paper has focused on developing a remote sensing approach to estimate green LAI of crop canopies, with minimum effects from chlorophyll concentration variations. Estimates based on modeling (PROSPECT & SAILH) and indices-based approach have shown that the pattern of crop LAI had responded to the spatial variability of various surface attributes such as: soil texture, topography features, soil nitrogen content. The

research has demonstrated the potential of airborne CASI reflectance data for detecting and characterizing the spatial heterogeneity of LAI of interest to precision agriculture. Moreover, it has shown the important role of linked leaf-canopy models (PROSPECT and SAILH used in this case) in developing and testing various spectral indices, as well as understanding effects of key vegetation biochemical and structural parameters on canopy reflectance.

8 ACKNOWLEDGEMENTS

The authors are very grateful for the financial support provided by GEomatics for Informed Decisions (GEOIDE), the Canadian Space Agency (CSA) and Agriculture and Agri-Food Canada. We thank Lawrence Gray, Phil Brasher and Heidi Beck of Aviation International for making CASI airborne field campaigns work efficiently. The field support of Lynda Blackburn, Dave Dow, Mathew Hinthner and Dave Meredith was greatly appreciated.

9 REFERENCES

- Baret, F., and Guyot, G. (1991), Potentials and limits of vegetation indices for LAI and APAR assessment. *Remote Sens. Environ.* 35:161-173.
- Boardman, J. W., and Huntington, J.F. (1996), Mineral mapping with AVIRIS data, in "the Summaries of the 6th Annual JPL Airborne Earth Science Workshop", JPL Publication 96-4, Pasadena, California. 1: 9-11.
- Broge, N. H., Leblanc, E. (2000), Comparing prediction power and stability of broadband and hyperspectral vegetation indices for estimation of green leaf area index and canopy chlorophyll density. *Remote Sens. Environ.* 76:156-172.
- Broge, B.H., and Mortensen, J.V. (2002), Deriving green crop area index and canopy chlorophyll density of winter wheat from spectral reflectance data. *Remote Sens. Environ.* 81:45-57.
- Brown, L., Jin, M. C., Leblanc, S. G., and Cihlar, J. (2000), A shortwave infrared modification to the simple ratio for LAI retrieval in boreal forests: an image and model analysis. *Remote Sens. Environ.* 71:16-25.
- Chen, J., and Cihlar, J. (1996), Retrieving leaf area index of boreal conifer forests using Landsat Thematic Mapper. *Remote Sens. Environ.* 55:153-162.
- Daughtry, C. S. T., Gallo, K. P., Goward, S. N., Prince, S. D., and Kustas, W. D. (1992), Spectral estimates of absorbed radiation and phytomass production in corn and soybean canopies. *Remote Sens. Environ.* 39:141-152.

- Daughtry, C. S. T., Walthall, C. L., Kim, M.S., Brown de Colstoun, E., and McMurtrey III, J. E. (2000), Estimating corn leaf chlorophyll concentration from leaf and canopy reflectance. *Remote Sens. Environ.* 74: 229-239.
- Fassnacht, K. S., Gower, S. T., MacKenzie, M. D., Nordheim, E. V., and Lillesand, T. M. (1997), Estimating the leaf area index of north central Wisconsin forest using Landsat Thematic Mapper. *Remote Sens. Environ.* 61:229-245.
- Gitelson, A., Rundquist, D., Derry, D., Ramirez, J., Keydan, G., Stark, R., and Perk, R. (2001), Using remote sensing to quantify vegetation fraction in corn canopies. *Proc. Third Conference on Geospatial Information in Agriculture and Forestry*, Denver, Colorado, 3-7 November 2001.
- Haboudane, D., Miller, J. R., Tremblay, N., Zarco-Tejada, P. J., and Dextraze, L. (2002). Integrated narrow-band vegetation indices for prediction of crop chlorophyll content for application to precision agriculture, *Remote Sens. Environ.* 81:416-426.
- Haboudane, D., Miller, J. R., Pattey, E., Zarco-Tejada, P. J., and Strachan, I. (2002a). Hyperspectral vegetation indices and novel algorithms for predicting green LAI of crop canopies: modeling and validation in the context of precision agriculture. *Remote Sens. Environ.* (submitted).
- Hu, B., Miller, J. R., Chen, J. M., and Hollinger, A. B. (2002). Retrieval of the canopy leaf area index in the BOREAS flux tower sites using linear spectral mixture analysis. *Remote Sens. Environ.* (in press).
- Huete, A. R. (1988), A soil vegetation adjusted index (SAVI). *Remote Sens. Environ.* 25:295-309.
- Jacquemoud, S., Bacour, C., Poilve, H., and Frangi, J.-P. (2000), Comparison of four radiative transfer models to simulate plant canopies reflectance: Direct and inverse mode. *Remote Sens. Environ.* 74: 417-481.
- Kuusk, A. (1985), The hot spot effect on a uniform vegetative cover. *Sov. J. Remote Sens.* 3: 645-658.
- Munden, R., Curran, P. J., and Catt, J. A. (1994), The relationship between red edge and chlorophyll concentration in the Broad-balk winter wheat experiment at Rothamsted. *Int. J. Remote Sens.* 15: 705-709.
- O'Neill, N.T., Zagolski, F., Bergeron, M., Royer, A., Miller, J.R. and Freemantle, J. (1997), Atmospheric correction validation of CASI images acquired over the BOREAS southern study area. *Can. J. Remote Sens.* 23: 143-162.
- Pacheco, A., Bannari, A., Deguise, J.-C., McNairn, H., and Staenz, K. (2001), Application of hyperspectral remote sensing for LAI estimation in Precision Farming. 23rd Canadian Symposium on Remote Sensing – 10^e Congrès de l'Association Québécoise de Télédétection, Quebec City, Canada, 21-25 August 2001.
- Pattey, E., Strachan, I. B., Boisvert, J. B., Desjardins, R. L., and McLaughlin, N. (2001). Effects of nitrogen application rate and weather on corn using micrometeorological and hyperspectral reflectance measurements. *Agric. and Forest Met.* 108: 85-99.
- Peddle, D.R. and Johnson, R.L. (2000). Spectral Mixture Analysis of Airborne Remote Sensing Imagery for Improved Prediction of Leaf Area Index in Mountainous Terrain, Kananaskis Alberta. *Can. J. Remote Sens.* 26: 176-187.
- Qi, J., Chehbouni, A., Huete, A. R., Keer, Y. H., and Sorooshian, S. (1994), A modified soil vegetation adjusted index. *Remote Sens. Environ.* 48:119-126.
- Rouse, J. W., Haas, R. H., Schell, J. A., Deering, D. W., and Harlan, J. C. (1974). Monitoring the vernal advancements and retrogradation of natural vegetation. NASA/GSFC, Final Report, Greenbelt, MD, USA, pp. 1-137.
- Verhoef, W. (1984), Light scattering by leaf layers with application to canopy reflectance modeling: The SAIL model. *Remote Sens. Environ.* 16: 125-141.

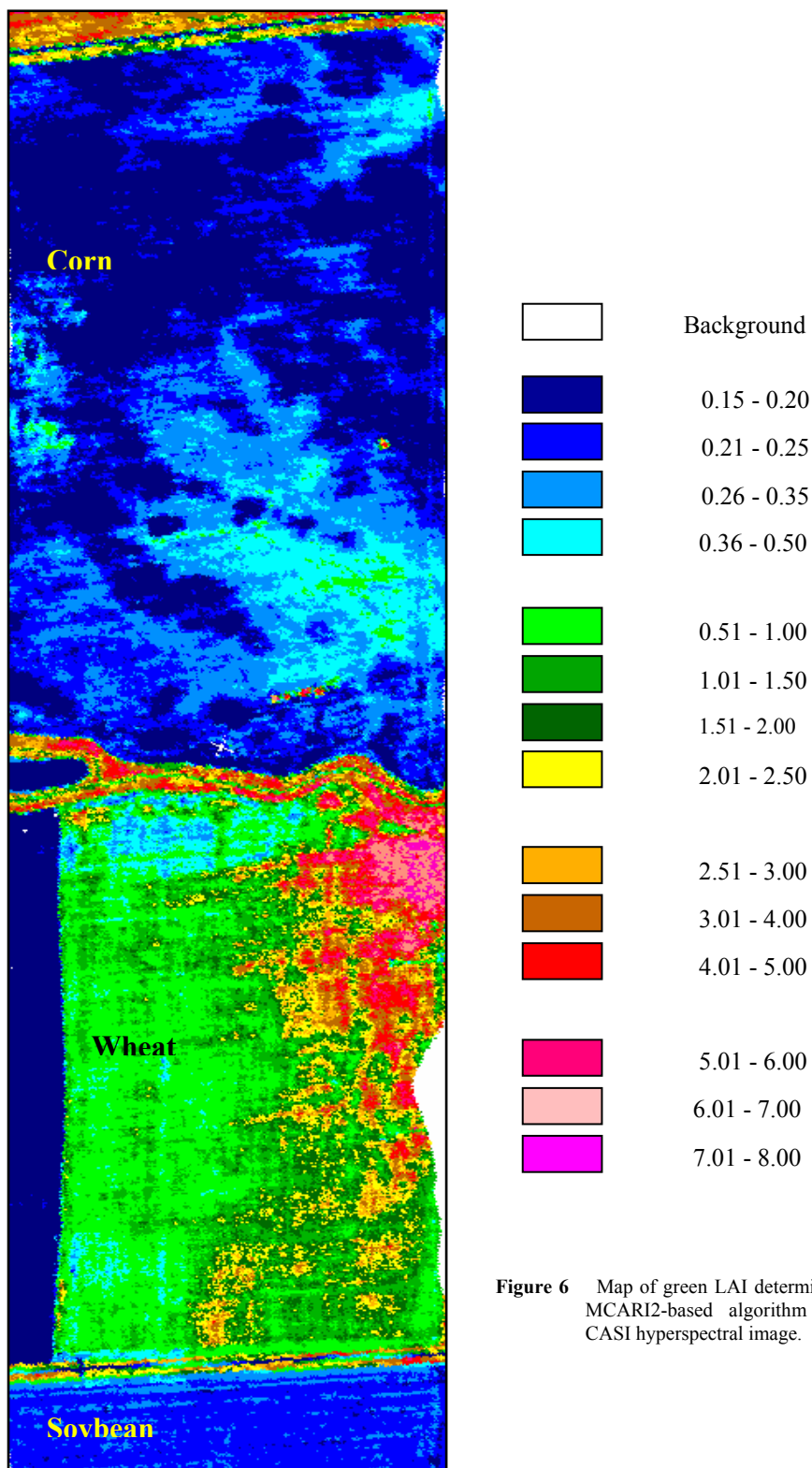


Figure 6 Map of green LAI determined with MCARI2-based algorithm from a CASI hyperspectral image.

LAI retrieval from multi-angle and hyperspectral observations in an intensively-managed poplar plantation

M. Meroni^(1,3), R. Colombo⁽²⁾, M. Boschetti⁽¹⁾, C. Panigada⁽²⁾, M. Rossini⁽²⁾, P.A. Brivio⁽¹⁾, J.R. Miller⁽⁴⁾

⁽¹⁾ CNR-IREA, Institute for Electromagnetic Sensing of the Environment, Via Bassini 15, 20133 Milan, Italy

⁽²⁾ UNIMIB-DISAT, Department of Environmental Sciences, University of Milano-Bicocca, Piazza della Scienza 1, 20126 Milan, Italy

⁽³⁾ UNITUS-DISAFRI, Forest Ecology Lab, University of Tuscia, V. De Lellis s.n.c, 01100 Viterbo, Italy

⁽⁴⁾ Department of Physics and Astronomy, York University, 4700 Keele St., Toronto M3J1P3, Canada

michele.meroni@unimib.it, roberto.colombo@unimib.it, boschetti.m@irea.cnr.it, cinzia.panigada@unimib.it, micolrossini@libero.it, brivio.pa@irea.cnr.it, jrmiller@yorku.ca

ABSTRACT – LAI is retrieved from airborne hyperspectral and multi-view-angle DAIS data (Digital Airborne Imaging Spectrometer) by numerical inversion of coupled leaf and canopy radiative transfer models. The effects of LAI and leaf Mean Tilt Angle (MTA) interactions are discussed and the magnitude of the error in LAI estimation associated with fixing the MTA to its mean value is provided by an uncertainty analysis of the inversion method. The effects of the background spectral signature are discussed and a technique for background assignment is proposed. Inversion method results are assessed comparing LAI estimates with field measurements and are compared to VI-based semi-empirical regression model results.

1 INTRODUCTION

Leaf Area Index (LAI) is usually estimated from remote observations through semi-empirical regression models (e.g. Dawson, 2000). Such models use statistical relationships in which a limited number of *in situ* measurements of the biophysical parameter examined are usually correlated with a spectral vegetation index (e.g. Rondeaux, 1995). The robustness of these relationships is influenced by many factors: the contribution of background reflectance, the structural and biochemical canopy characteristics, and finally the viewing geometry. An alternative to the semi-empirical approach is offered by the use of radiative transfer models in inverse mode. It consists of numerically minimizing the difference between remote observations and the spectral reflectances modelled for a set of biophysical parameters of interest. This technique allows the estimation of both biochemical and structural parameters in predictive mode, without requiring parameterisation (Bicheron and Leroy, 1999; Jacquemoud, 1993).

The capability to acquire nearly contemporary observations with different view angles, offered by airborne sensors is expected to improve the accuracy

of vegetation structural parameter estimation (Verstraete and Pinty, 2001).

2 STUDY AREA

The study area (Fig. 1) is an intensively-managed poplar plantation located North-East of the city of Pavia on the west bank of the Ticino river.

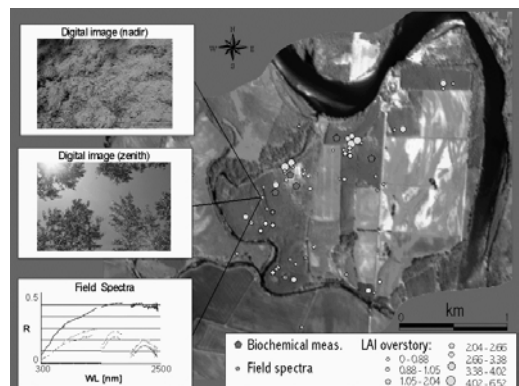


Fig. 1: Study area GIS of the field measurements (see Table 1).

The plantation (I-214 clones, spacing 6 x 6 m), composed by different stands with tree age ranging from two to ten years (about 120 ha in total), is a permanent experimental site of CARBOEUROFLUX net managed by IES-JRC (Ispra, Italy).

3 LAI FIELD MEASUREMENTS AND RS DATA ACQUISITION

Overstory LAI and mean tilt angle (LAI_o, MTA) were estimated with Li-Cor LAI2000-PCA (Li-Cor, 1992). Neglecting the effects of the non-random distribution of the foliage (with clumping index Ω close to 1 in broadleaf canopy), the only correction applied was to remove the contribution of stems and branches by repeating the measurements in winter-time. This corrected estimate, egLAI_o (effective green LAI of the overstory), will be referred to as gLAI_o in the remainder of this paper.

On 20/06/01, from 10.30 to 11 a.m. (local solar time), 4 and 3 stripes were acquired by DAIS (*Digital Airborne Imaging Spectrometer*) and ROSIS (*Reflective Optics System Imaging Spectrometer*) sensors (DLR-Germany), respectively. Geometric parameters of the data take and spectral characteristics of the sensors are reported in Fig. 2.

Flight-lines were designed with the aim of maximizing the number of DAIS directional observations (in the principal solar plane) of the target area. Three parallel stripes along the orthogonal solar plane and one along the principal solar plane were acquired.

Processed RS data were provided by DLR using ATCOR4 (Richter, 2000) at the correction level 2b.

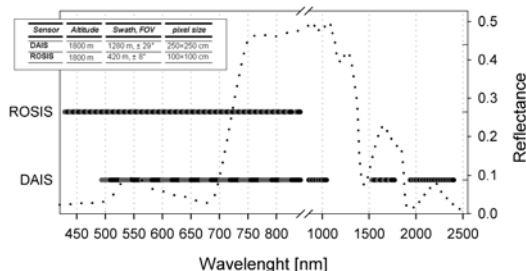


Fig. 2: Position and width of DAIS and ROSIS bands. Data take geometric characteristics are reported.

4 INVERSION OF RADIATIVE TRANSFER MODELS

Radiative transfer models used in this work are the canopy reflectance model SAILH (Verhoef, 1984, modified after Kuusk, 1991) and the leaf optical properties model PROSPECT (Jacquemoud and Baret, 1990).

PROSPECT and SAILH model coupled (PROSAILH in the following) were inverted on hyperspectral and directional DAIS data. Spectral reflectance was averaged over a spatial window of 3x3 pixels in order

to remove canopy cover discontinuities. All the available directional observations for every pixel (ranging from 2 to 4) were used simultaneously in the inversion process. Among the set of the parameters, two were fixed to a nominal value: N, the leaf structure parameter (PROSPECT) and MTA (SAILH). The N nominal value was set to 1.33 as estimated by PROSPECT inversion on leaf reflectance and transmittance spectra (Meroni *et al.*, 2002). MTA was set to its measured mean value (for a discussion on the error committed see the paragraph 4.3, Effect of LAI and MTA interaction).

The spectral domain of the merit function was selected from the available DAIS bands. Some bands were discarded due to noise and the spectral domain selected was: 808-923nm \cup 1020-1033nm \cup 1541-1639nm \cup 1995-2291nm. In the inversion process the merit function (Δ^2) was defined as follows:

$$\Delta^2 = \sum_{\text{do}} \sum_{\lambda} [R_{\text{obs}}(\text{VA}, \lambda) - R_{\text{mod}}(\text{VA}, \lambda, P)]^2$$

where,

- \sum_{do} refers to the summation over the available directional observations;
- \sum_{λ} refers to the summation over the wavelengths of the merit function spectral domain;
- $R_{\text{obs}}(\text{VA}, \lambda)$ is the observed reflectance for a given view angle (VA) and wavelength (λ);
- $R_{\text{mod}}(P)$ is the modelled reflectance for a given view angle, wavelength and set of model parameter (P).

A quasi-Newton algorithm (NAG library, routine E04YAF) was used to minimize the merit function.

4.1 Effect of the background spectral signature

Part the poplar canopy present in the study area is characterised by a layer of understory vegetation that varies in species composition and density as a function of ecological conditions at ground level (soil type and humidity, radiation, time since the last tillage, etc.).

This “understory effect” was found when inverting PROSAILH on those reflectances resulting from a mixture of canopy and underlying understory, yielding an overestimation of gLAI_o when a soil spectral signature was provided to the model as the background signature.

Providing the inversion with the proper background signature (collected in-field with a spectroradiometer, ASD-FieldSpec Pro) resulted in more accurate gLAI_o estimation in all sites where a field spectrum was available. A further analysis of the dataset (gLAI_o, field spectra and inversion estimates) showed that the LAI retrieval procedure accuracy is not compromised if only the type of background signature provided in terms of broad categories: bare soil, sparse understory vegetation and dense understory.

In order to automatically extract this information (type of background) from RS images a neural network (NN) approach (e.g. Binaghi *et al.*, 2000) was used to

produce a map of the background. NN is able to integrate the contextual information of a high geometric resolution panchromatic image generated from ROSIS data - high-resolution imagery (1 m pixel size) - with the spectral information of a selection of lower geometric resolution hyperspectral bands from DAIS.

4.2 Effect of LAI and MTA interaction

The analysis of a preliminary set of inversions evidenced that LAI and MTA were not easily separable.

A possible solution to the LAI-MTA interaction problem is to estimate separately the parameters of interest introducing constraints such as the knowledge of one parameter (Jacquemoud, 1993). An uncertainty analysis was performed in order to quantify the magnitude of the error in LAI retrieval introduced by fixing, in the inversion process, the MTA to its field mean value calculated from LAI2000 measurements.

The uncertainty analysis was performed using SimLab (SimLab 1.1, 2001), software capable of global quantitative analysis, designed for Monte Carlo analysis.

The sample set (50 arrays of input factors) was created with a stratified sampling method (*latin hypercube* sampling) in order to achieve a better coverage of the sample space of the input factors. Each element of the sample set created is supplied to the PROSAILH as input, and the model is run in direct mode 50 for each of the 3 level of LAI value considered. The results of each model evaluation are used as input in the inversion of PROSAILH: two input parameters, N and MTA, are assigned to their mean value, while the remaining is kept free. LAI estimated by inversion is the model outcome that is used for uncertainty study (Table 1).

Even if significant errors arise from the largest LAI value considered, an analysis of the error in LAI estimation as a function of the deviation of the assigned MTA from the true MTA reveals that, in the range of one SD of the measured MTA, the error is rather limited.

	LAI=1	LAI=2	LAI=3
<i>SDEP</i>	0.08	0.17	0.30
<i>Mean</i>	0.99	1.99	2.99
<i>SD</i>	0.08	0.17	0.30

Table 1: Standard Deviation Error in LAI Prediction (SDEP) caused by fixing the MTA; statistics of the predicted values in one SD of the measured MTA are reported for the three levels of LAI considered.

5 INVERSION RESULTS

Our results show that, supplying a plausible background signature to the inversion, PROSAILH provides an accurate estimation of the green LAI of

the overstory. The accuracy of the estimates was evaluated in terms of SDEP (Standard Deviation Error in Prediction) calculated on the basis of all the available LAI field measurements in the test area (n=35). LAI was ranging from 0.45 to 3.15 m²m⁻² (mean=1.53 m²m⁻², SD=0.81 m²m⁻²)

Assigning the spectral signature of a bare soil as a background signature resulted in a gLAIo SDEP of 0.91 m²m⁻². When the NN map (paragraph 4.2), was used as a criterion to assign the background signature (3 background classes: bare soil, sparse understory, dense understory) the gLAIo SDEP was limited to 0.48 m²m⁻², an accuracy that seems reasonable for most of the environmental applications.

6 A COMPARISON WITH SEMI-EMPIRICAL REGRESSION MODELS

A number of studies demonstrated that it is possible to obtain LAI estimations through statistical regressions based on optical vegetation indices (VIs) obtained from remote sensing data of various kinds (e.g. Franklin, 1986; Spanner et al., 1990). Among all the proposed LAI-VIs relationships we will refer here to the widely used LAI-NDVI regression model.

Assuming that the model hypotheses are satisfied, that a single regression may be used to estimate LAI in the study area, and that measurements are not affected by random errors, the following exercise was designed in order to compare the accuracies of PROSAILH and a typical LAI-NDVI regression model (DAIS data from flightline in the principal solar plane were used).

Regression SDEP was calculated partitioning the measurement set (n = 35) in one subset for the regression coefficients computation (70% of the measurements) and a second subset to test the regression (SDEP computation).

The results of this exercise are shown in Fig. 3: multiple SDEP values for a given number of calibration samples are due to the repeated random extraction of the calibration sample elements.

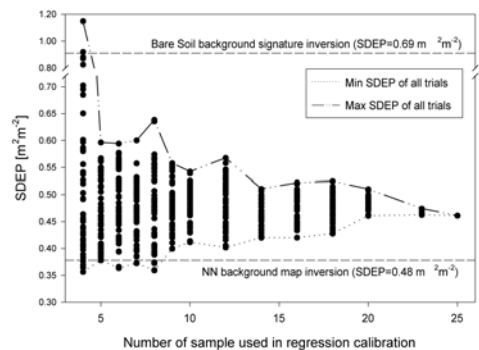


Fig. 3: SDEP of regression models (as a function of the number of sample used in calibration), and of MVA PROSAILH model inversions, calculated on the same dataset (10 test samples).

Regressions show a large SDEP variation when they are calibrated using a limited sample number. This is due to the proportion of green LAI overstory/green LAI not included in the calibration set dynamically considered, together with the soil reflectance and leaf biochemistry variability, etc. Such calibration sample set may indeed be, or not be, representative of the variability present in the testing set. When the number of sample used in regression calculations is increased, a lower SDEP variation is observed, indicating that regression predictions are insensitive to the composition of the particular sample used.

6 CONCLUSIONS

In this work, coupled PROSPECT and SAILH models were inverted to estimate the leaf area index with an acceptable accuracy, the availability of a background map seems crucial to the LAI retrieval accuracy.

A comparison exercise between regression models and inversion of PROSAILH model showed that regressions calibrated with a limited number of LAI-NDVI pairs provide an accuracy that is highly variable depending on the particular sample chosen.

PROSAILH estimate accuracy is comparable with that of regression models (higher when a map of the background type is used in the selection of the background reflectance to be provided to the inversion algorithm).

ACKNOWLEDGEMENTS

DAIS and ROSIS data were provided by DLR-Germany in the framework of the EU-funded HySens project. The authors gratefully acknowledge G. Seufert and the Climate Change unit staff (JRC-IES, Ispra), S. Jacquemoud, C. Bacour (LED - Université Paris 7), S. Tarantola (IPSC-JRC, Ispra, Italy), for their contributions and suggestions.

The understory map analysis is current research conducted by I. Gallo (CNR-ITBA, Italy) and E. Binaghi (University of Insubria, Italy) in collaboration with remote sensing department of IREA-CNR.

REFERENCES

Bicheron P., Leroy M., 1999, A method of biophysical parameter retrieval at global scale by inversion of a vegetation reflectance model, *Remote Sens. Environ.*, 67: 251 – 266.

Binaghi E., Brivio P.A., Gallo I., Pepe M., Rampini M., 2000, Soft computing techniques for high accuracy Remote Sensing data classification, in Recent Developments in Pattern Recognition Research, B. Chandrasekaran, M.D. Levine, C.H. Chen, Transworld Research Network Publishing, 89 - 112.

Dawson T.P., 2000, The potential for estimating chlorophyll content from a vegetation canopy

using MERIS, *Int. J. of Remote Sensing* 21: 2043 – 2051

Frankin, J., 1986, Thematic mapper analysis of coniferous forest structure and composition, *Int. J. Of Remote Sensing* 10: 1287 - 1301.

Jacquemoud S., Baret F., 1990, PROSPECT: a model of leaf optical properties spectra, *Remote Sens. Environ.* 34: 75 – 91.

Jacquemoud S., 1993, Inversion of the PROSPECT + SAILH canopy reflectance model from AVIRIS equivalent spectra: Theoretical study, *Remote Sens. Environ.* 44: 281 – 292.

Kuusik A., 1991, The hot-spot effect in plant canopy reflectance, in Photon-vegetation interactions; Application in optical remote sensing and plant ecology (R. Mynemi and J. Ross, Eds.). Springer-Verlag, New York, 139 – 159.

Li-Cor, 1992, LAI-2000 plant canopy analyzer instruction manual, LI-COR, Inc., Lincoln, Nebraska

Meroni M., Panigada C., Colombo R., Boschetti M., Brivio P.A., Marino C.M., 2002, Osservazioni remote iperspettrali e multiangolari per la stima dei parametri biofisici della vegetazione: parte II – tecniche di telerilevamento. Submitted to *Rivista Italiana di Telerilevamento*.

Richter R., 2000, ATCOR4 user manual, DLR-IB 564-04/2000.

Rondeaux G., 1995, Vegetation monitoring by remote sensing: a review of biophysical indices, *Photo-Interpretation* 3: 197 – 216.

SimLab 1.1 Version 1.1 Reference Manual, 2001, POLIS ISIS-JRC.

Spanner, M.A. Pierce, L.L., Peterson, D.L. and Running, S.W., 1990, Remote sensing of temperate coniferous forest leaf area index. The influence of canopy closure, understory vegetation and background reflectance, *Int. J. of Remote Sensing* 11: 95 - 111.

Verhoef W., 1984, Light scattering by leaf layers with application to canopy reflectance modeling: the SAILH model, *Remote Sens. Environ.* 16:125 – 141.

Verstraete M.M., Pinty B., 2001, Introduction to special section: Modeling, measurement, and exploitation of anisotropy in the radiation field, *J. of Geophysical research*, 106(11): 903 – 907.

Radiometric Saturation of Landsat-7 ETM+ Data Over the Negev Desert (Israel): Problems and Solutions

Arnon Karnieli*, Eyal Ben-Dor**, Bayarjargal Yunden*, Rachel Lugasi**

* *The Remote Sensing Laboratory, Jacob Blaustein Institute for Desert Research, Ben Gurion University of the Negev, Israel*

** *Department of Geography and Human Environment, Tel-Aviv University, Israel*

E-mail: karnieli@bgumail.bgu.ac.il

ABSTRACT - *Unsuccessful efforts to interpret and analyze several sets of images acquired over Israel by Landsat-7 during the first two years of its operation (August 1999 – August 2001) provided the motivation to examine the hypothesis that image data produced over the desert regions along the climatic transition zone of Israel were subject to radiometric saturation. The objectives of the current study are to characterize the saturation phenomenon, by inspecting different images of Landsat-7, and to suggest a statistically based methodology for solution. Entropy analysis was also performed on these images in order to compare the information content of the Landsat-7 ETM+ sensor with that of the Landsat-5 Thematic Mapper (TM) over the desert environment. The study reveals that radiometric saturation affected different ETM+ bands (especially band 3). Consequently, in terms of entropy, less information can be extracted from the saturated bands relative to equivalent bands of Landsat-5 TM. A statistical solution, based on multivariate correlation analysis among all spectral bands, is proposed to overcome the saturation problem. Satisfactory results were achieved by applying the statistical methods on several samples of saturated scenes. However, an operational revision in the spectral radiance range and the gain setting, applied to Landsat-7 ETM+ with effect from July 1, 2000, has improved the saturation phenomenon over the region.*

1 INTRODUCTION

One of the improvements of the Landsat-7 Enhanced Thematic Mapper Plus (ETM+) instrument over the previous TM one, for enhancing radiometric precision, and consequently for better land-cover discrimination, is its capability to scan in either a low- or high-gain state. This improvement was required since images are acquired over different surface albedo, including dark water bodies, tropical forests, agricultural lands, bare soils, and very bright ice seas. Consequently it was necessary to design a sensor that covers the entire dynamic range that would accommodate this extensive surface brightness variety.

Practically, the ETM+ gain is switched by the Mission Operation Center (NASA, WWW1), for any specific scene, between low and high states as a function of the combination between the surface brightness and sun elevation. Consequently, brighter surfaces are scanned in the low gain mode and darker surfaces in the high gain mode (NASA, WWW1). Six Earth surface cover categories are involved in the gain setting operational rules, namely: (1) Land (non-desert, no-ice); (2) Desert; (3) Ice/Snow; (4) Water; (5) Sea Ice; and (6) Volcano/Night. Since the current paper is dealing only with the first two categories, namely land and desert, their corresponding gain

setting rules are presented in table 1. From this table it can be noticed that, for the Land category, only band 4 can be switched between high and low gains. The latter is set where the Sun elevation is greater than 45° in order to avoid dense vegetation (reflectance >0.66) saturation. At this sun angle, high gain in band 4 saturated at a reflectance of about 0.66. As such, switching to low gain prevents targets at this reflectance or below from saturating. Desert surfaces are relatively bright due to sparse vegetation (if any) as well as low water, organic, and iron oxides contents. Therefore, in the Desert category low gains are set with respect to sun elevation to avoid bright desert target saturation when reflectances are higher than 0.66, 0.71, 0.65, 0.66, 0.70, and 0.68 in bands 1, 2, 3, 4, 5, and 7, respectively.

Entropy has been applied as one of the methods to evaluate and compare the information content of different systems. Mathematically, entropy (E) can be defined as:

$$E = -\sum_{i=0}^N p(i) \log_2 p(i) = -\frac{1}{\ln 2} \sum_{i=0}^N p(i) \ln p(i) \quad (1)$$

where $p(i)$ is the probability of occurrence of a DN between 0 and N (i.e., between 0 and 255 in Landsat's 8-bit system). Practically, the DN values are extracted

from the scene's grey level histogram. Therefore, entropy is a measure for characterizing image signals. In a specific spectral band, $E=0$ and $E=8$ represent zero and maximum information content, respectively, in units of bits/pixel.

Table I: Gain setting rules for the Land and Desert surface cover categories. H stands for sun elevation (Compiled from NASA, WWW3)

Band	Land	Desert
1	High	High for $H < 28^\circ$ Low for $H \geq 28^\circ$
2	High	High for $H < 28^\circ$ Low for $H \geq 28^\circ$
3	High	High for $H < 28^\circ$ Low for $H \geq 28^\circ$
4	High for $H < 45^\circ$ Low for $H \geq 45^\circ$	High for $H < 45^\circ$ Low for $H \geq 45^\circ$
5	High	High for $H < 38^\circ$ Low for $H \geq 38^\circ$
7	High	High for $H < 38^\circ$ Low for $H \geq 38^\circ$

2 STUDY AREA

Figure 1 presents a mosaic image of Israel composed of 3 Landsat-7 ETM+ scenes, band 3, overlaying by 50-years rainfall mean annual isohyets. Basically, Israel is a dryland that covers a 400 km cross-section of climatic zones from hyper-arid (25 mm mean annual rainfall in the south) to sub-humid (up to 900 mm in the north). The isohyetal belt between 200 and 300 mm is considered to be the desert boundary of Israel. In the Negev Desert, rainfall amounts decrease gradually from north to south with respect to the distance from the Mediterranean Sea. However, the Judean Desert lies in the rain shadow and is characterized by steep declining rainfall going towards the east. In mountainous areas, even in southern Israel, as the rising air masses become cooler, relative humidity increases. Therefore, these mountain ranges receive more precipitation.

Observing the Landsat-7 image in figure 1, it is clearly evident that the 200 to 300 mm isohyetal belt separates desert regions (such as the Negev and Judean Deserts) from the non-desert parts of Israel with a sharp contrast. The non-desert regions are characterized by dark tones where different ground albedo features (such as cultivated fields, settlements, cities, etc.) can be recognized. In contrast, the other side of the belt is dominated by very bright tones, mostly totally white, and no details can be resolved.

The sparse darker features are the relatively more humid mountains discussed above. Wide bright areas can also be observed in the surrounding deserts such as the Sinai and the deserts in Jordan and Syria.

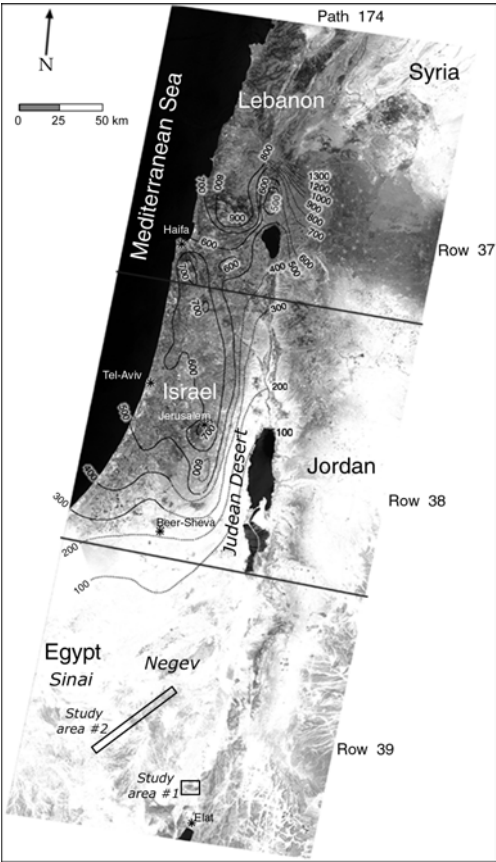


Figure 1: Landsat-7 ETM+ scenes covering Israel (path/row=174/37,38,39) overlaid with rainfall isohyets. Note the brightness contrast between the north and south sides of the 300 mm isohyet. Two study areas are marked. The image represents the Landsat-7 ETM+ band 3 data acquired on May 21, 2000.

3 OBJECTIVES

Because of the unsuccessful efforts to interpret and analyze several sets of Landsat-7 images acquired over Israel during the first two years of the Landsat-7 operation (August 1999 – August 2001) it was hypothesized that the desert regions along the transition zone of Israel are subject to radiometric saturation in the ETM+ sensor. The objectives of the current paper are to characterize the saturation phenomenon, to determine the extent of its occurrence by examining different images acquired since the start of operation of Landsat-7, and to suggest a methodology for partial solution.

3 DATA SETS

Eight Landsat-7 scenes were examined in the current project. As shown in figure 1, images of path 174 rows 37, 38, and 39 correspond to three different climatic zones - sub-humid, semi-arid, and arid (respectively, from north to south). Two pairs of these images were acquired on August 7, 1999 and May 21, 2000. Two single images, path/row=174/39, were acquired on October 10, 1999 and August 27, 2001. The latter image was selected in order to determine if the changes in the spectral radiance range and the gain setting, applied by NASA on July 1, 2000 (NASA, WWW2), have improved the saturation phenomenon over the region.

Surface cover brightness is progressing from north to south across the rainfall isohyets as discussed above. The northern part of Israel (row 37) is characterized by pronounced darker tones than the southern part (row 39). Indeed, information provided by NASA (NASA, WWW3) indicates that images 174/38 and 174/39 are categorized as "Desert". It should be pointed out that along the study area the annual precipitation mentioned is obtained mainly during a short period of time, namely between November and April, while during May to September, the period is considered dry.

In addition, one Landsat-5, path/row= 174/39, from September 21, 1995 was selected as a reference image (especially for the Landsat-7 174/39 image of October 10, 1999 due to the seasonal similarity). This image represents an end-of-summer image since we hypothesize that inter-annual variations are minimal after the long dry spell in the Negev desert.

4 ANALYSIS AND RESULTS

4.1 Pre-processing

The images specified above were purchased as level 1G product and were subject to radiometric, atmospheric, and geometric corrections. Table 2 presents the gain states that were set according to the rules described previously. It was found that in the Desert images (row 39) most of the bands were set to high gain instead of low before July 1, 2001. After that date, the gain setting was revised and all bands were changed to low gain except for band 4 when the Sun elevation is lower than 45° . Bearing in mind that scene 174/39 should be defined as Desert, it is assumed that wrong settings were selected in the images of August 7, 1999 and October 10, 1999 in all spectral bands as well as in bands 1, 2, and 3 of the image of May 21, 2000. The gain setting of the latest image in the current research, July 27, 2001, was set to low and hence is supposed to be correct for the desert area of Israel.

4.2 Saturation recovery

After the above-described step-by-step procedure and visual examination of the images, saturation can be observed on the earlier three row 39 images listed in table 2, in terms of bright tones, as demonstrated in figure 1. Saturation occurs almost all over the image except the high mountain ranges. For further investigation of the phenomenon, a preliminary study was conducted based on earlier sources that found high correlations among spectral bands for a similar ground feature (e.g., soil, vegetation, or water) (e.g., Price 1995; Karnieli et al. 2001).

Since desert landscape is usually composed of relative homogeneous coverage (mostly bare soils or rocks with scare amount of vegetation) it is expected that correlation does exist in the hyper spectral domain and may be also existed in the ETM+ multi spectral domain. These relationships can be used for correcting the saturation phenomena. In order to examine this hypothesis, reflectances were extracted from the same image along a sampling area in each of the row 39 images, a total of 15,480 pixels (figure 1, denoted hereby as Study area #2). This sampling area, about 80 km long, covers both relatively bright and relatively dark pixels. Profiles of reflectances along the sampling area (figure 2) show the difference between the high values over the bright part versus the lower values over the darker part (demonstrated on the image of May 21, 2000; path/row=174/39). The saturation of band 3, characterized by plateaus at $L^*=0.34$, can be recognized in the bright part along the sampling area.

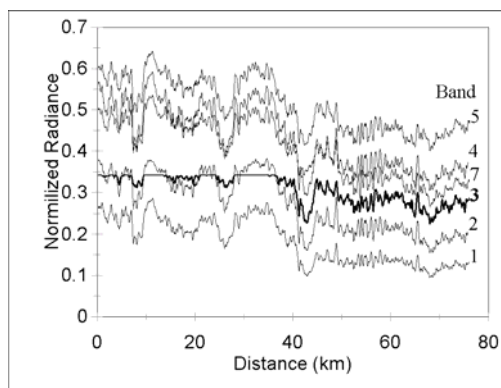


Figure 2: Profiles of reflectances along the study area #2 marked on figure 1 for the May 21, 2000 image. Note the unexpected high location of the band 3 profile (in bold) along with the long plateaus over the brighter area.

Table II: Gain settings (H=high, L=low) for the ETM+ images involved in the project along with the respective sun elevation angles, in degrees. (source: USGS, WWW5)

	Aug. 7, 1999			Oct. 10, 1999	May 21, 2000			Jul. 27, 2001
	174/37	174/38	174/39	174/39	174/37	174/38	174/39	174/39
	Sub-humid	Semi-arid	Arid	Arid	Sub-humid	Semi-arid	Arid	Arid
Band 1	H	H	H	H	H	H	H	L
Band 2	H	H	H	H	H	H	H	L
Band 3	H	H	H	H	H	H	H	L
Band 4	H	H	H	H	L	L	L	L
Band 5	H	H	H	H	H	H	L	L
Band 7	H	H	H	H	H	H	L	L
Sun Elevation	62.1526	62.6416	63.066	48.1659	66.0291	66.4188	66.7281	63.5711

In the current paper the saturation recovery proposed procedure is demonstrated on the image of May 20, 2001. Frequency histograms of the reflectances for the row 39 image are presented in Figure 3. From this figure it appears that image saturation exists in bands 2 and 3.

A statistical procedure is suggested for overcoming the saturation problem in the reflective bands of the ETM+ based on the correlation hypothesis demonstrated above. However, this correlation becomes worse when saturation occurs. In order to test this suggestion, a multivariate correlation analysis was performed on the Landsat-5 image of the Negev (path/row=174/39). Table 3A presents the statistical results that confirm the hypothesis. However, similar multivariate correlation analysis, performed on the Landsat-7 image of May 21, 2000, reveals lower correlations between the saturated band 3 and the other spectral bands (table 3B).

Table III: Correlation matrix (r^2) among reflectances of the reflective spectral bands (A) Landsat-5, path/row=174/39, September 21,1995; (B) Landsat-7, path/row=174/39, May 21,2000. Note the extremely low correlation coefficients associated with Landsat-7 band 3.

A

Bands	Landsat-5					
	1	2	3	4	5	7
1	1.00					
2	0.98	1.00				
3	0.96	1.00	1.00			
4	0.92	0.98	0.98	1.00		
5	0.85	0.88	0.90	0.90	1.00	
7	0.86	0.88	0.88	0.88	0.94	1.00

B

Bands	Landsat-7					
	1	2	3	4	5	7
1	1.00					
2	0.92	1.00				
3	0.45	0.58	1.00			
4	0.91	0.92	0.53	1.00		
5	0.83	0.83	0.49	0.91	1.00	
7	0.78	0.79	0.45	0.80	0.89	1.00

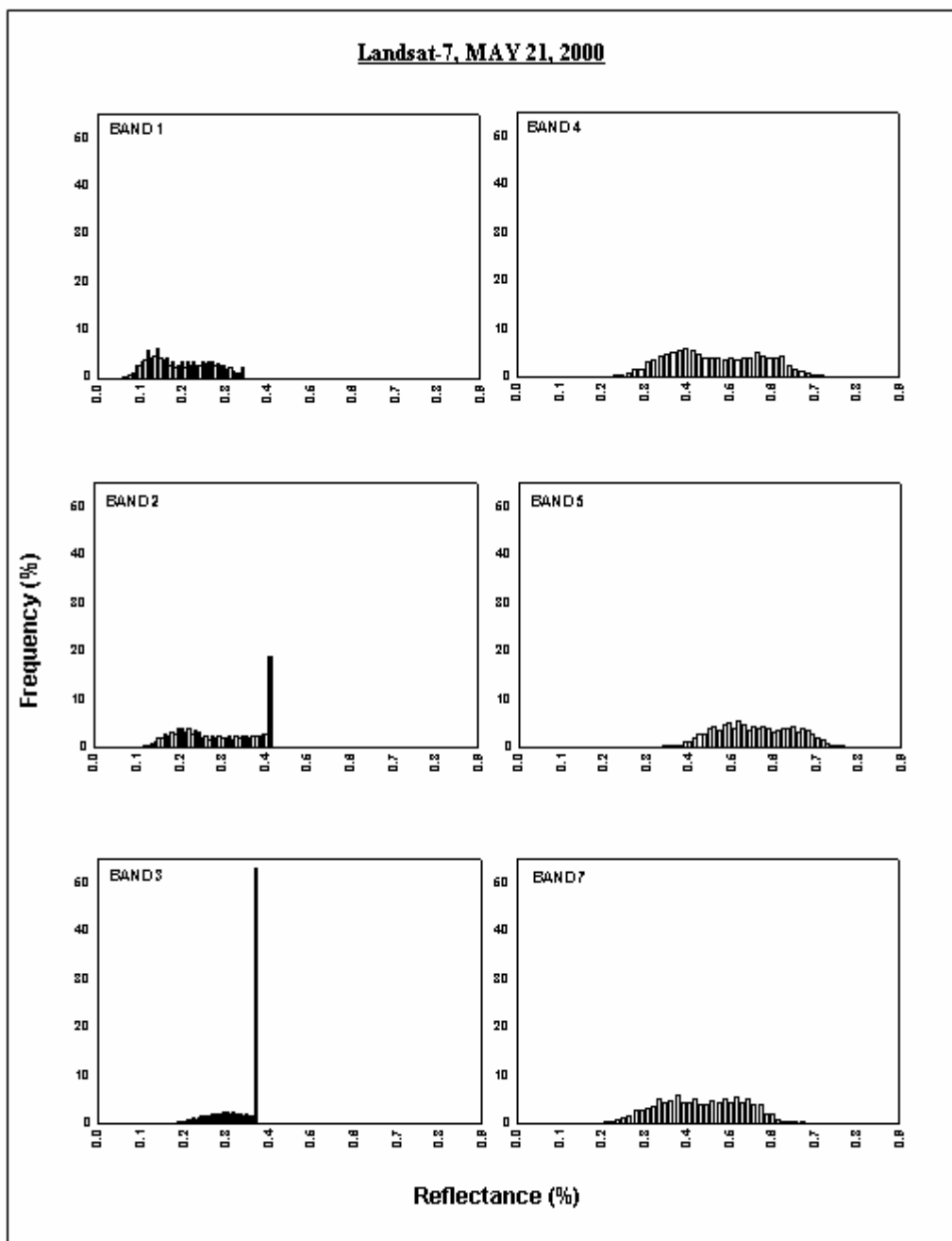


Figure 3: Reflectance histograms of the May 21, 2000 image, path/row=174/39. Data obtained from the study area #2 shown in figure 1.

The following section is aimed at proposing a procedure for reconstructing saturated bands by using the reflectances of their unsaturated parts along with those of the other unsaturated bands. In the first stage bands 3 (saturated) and 4 (unsaturated) of the May 21, 2000 row 39 image are used as an example. The following steps are proposed for achieving the close-to-reality recovery:

- (1) Start by observing the saturation on the image histogram as shown in figure 3;
- (2) Present the scatterplot of the saturated band as a function of another unsaturated band (figure 4A). In the present data set the saturation part of band 3 can be seen when the reflectance points are concentrated along a horizontal line rather than along the expected continuous correlation line;
- (3) Eliminate the pixels within the saturation zone from the data set and calculate a new set of regression parameters (figure 4B); and
- (4) Perform extrapolation, based on the new linear regression parameters, for relocating the eliminated pixels along the extension of the regression line (figure 4C).
- (5) Apply the correction equation on a pixel-by-pixel basis on the entire image, and thus recovering the values of the saturated pixels.

For more accurate results, it is proposed that all bands be involved in the process, using a multiple regression analysis. In the multivariate case, the linear equation contains the reflectances of the saturated band (ρ_s) as a dependent variable and the reflectances of the remaining five ETM+ bands (ρ_n) as independent variables. The linear multiple regression equation has the form:

$$\rho_s = a + b_1 \rho_1 + b_2 \rho_2 + \dots + b_n \rho_n \quad (2)$$

where ρ_1, \dots, ρ_n are the reflectances of the n unsaturated bands, and a and b_1, \dots, b_n are the multiple regression parameters. Figure 5 presents a comparison between the raw band 3 image of May 21, 2000 and its corrected version as generated from the multivariate regression analysis. The difference in sharpness and in observed details are remarkable. It is important to note that the regression parameters for correcting any given data set must be performed for the data in question and cannot be transferred from one data set to another. This is basically due to the fact that different atmospheric correction techniques can be used by different users, different illumination conditions may be introduced in different data sets, area coverage may differ from one season to another, and different sensor sensitivity may be obtained in different duration. This leads to the conclusion that the correction factors are scene-data

dependent and strictly need to be extracted from a specific set.

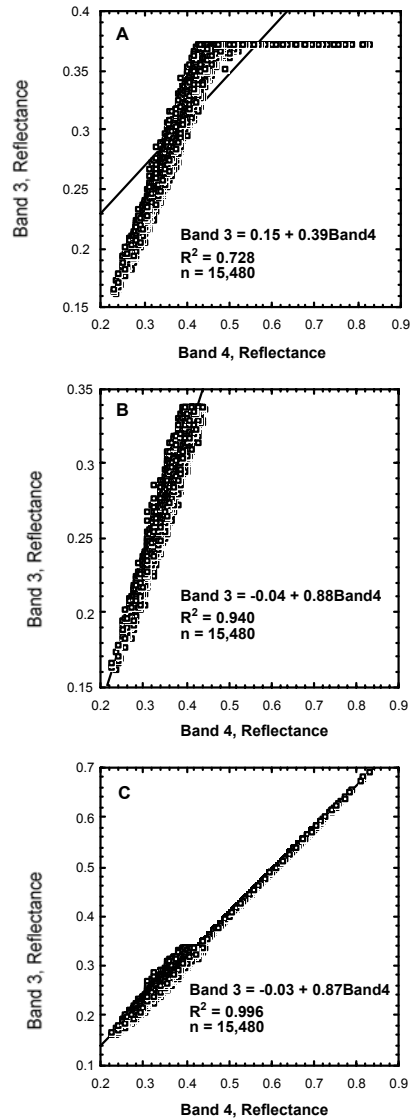


Figure 4: An example of the statistical procedure for recovering a saturated band. (A) Scatterplot of band 3 vs. band 4. The saturation part of band 3 is obvious where the reflectance points are concentrated along a horizontal line rather than the expected inclined correlation line; (B) The same relationships without the saturated points. A new regression equation is calculated; (C) Correction of the saturated pixels by extrapolation along the extension of the regression line.

4.3 Entropy analysis

Results of the entropy analysis for the Landsat-5 TM and Landsat-7 ETM+ spectral bands, for different acquisition dates, are presented in figure 6 and table 4A. Data obtained from the study area #2 represent the hyper-arid zone of the Negev and are characterized by relatively bright tones (figure 1) due to the saturation phenomenon as discussed earlier. Table 4B shows the difference in information content between the Landsat-7 data sets and those of the Landsat-5 used as reference. In all Landsat-7 images, band 1 has similar information content as Landsat-5. Band 2 exhibits a greater information content (0.67 – 0.82 bits/pixel) relative to the Landsat-5 TM sensor except for the May 21, 2000 image when it was saturated. Band 3 suffered from saturation on all dates prior to July 1, 2000 and therefore shows less information content on those days relative to the TM sensor. On

the image of August 27, 2001 entropy of band 3 shows increased information content of 0.45 bits/pixel. Band 4 in all four images has a relatively small increase in information content of 0.2 – 0.5 bits/pixel. Band 5, in all Landsat-7 images, shows a worse performance than Landsat-5 of 0.2 – 1.7 bits/pixel. Even the gain setting change, from high to low, on the latest two images did not improve this situation. Lastly, band 7 reveals a stable improvement compared to the TM sensor of about 0.2 – 0.6 bits/pixel.

The total image entropy values of the Landsat-7 data sets produced mixed results compared to those of Landsat-5 (table 4). However, it can be seen that the latest image (August 27, 2001) has higher values than Landsat-5. It is important to point out the improvement in the results after applying the proposed saturation correction procedure. The problematic bands 2 and 3 exhibited an increased information content of 0.8 and 3.0 bits/pixel, respectively.

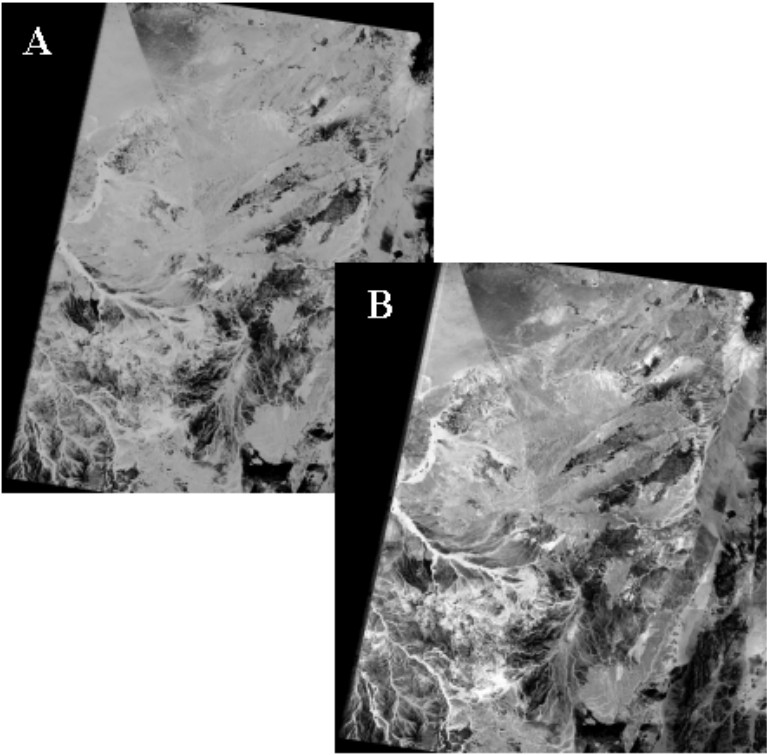


Figure 5: Results of the multivariate regression analysis procedure for reconstructing reflectance over saturated pixels demonstrated on the Landsat-7 ETM+ image of May 21, 2000, path/row=174/39, RGB = 4,3,2. (A) Raw image; (B) Corrected image.

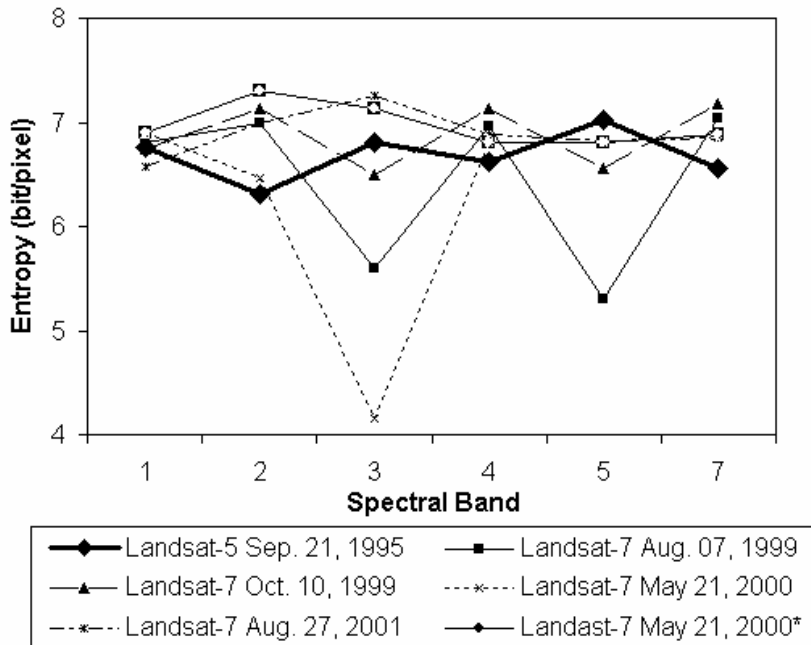


Figure 6: Entropy analysis for Landsat-7 ETM+ spectral bands of different acquisition dates in comparison to those of Landsat-5 TM. Data obtained from the study area #2 are shown in figure 1. Note that the line for May 21, 2000 that is marked with * was created after the saturation correction that had been applied on bands 2 and 3.

Table IV: Comparison of the information content of data from Landsat-5 TM and Landsat-7 ETM+ over the desert environment, in terms of entropy. (A) Entropy values (bits/pixel); (B) Difference in information content between the different ETM+ scenes and the TM.

A		Entropy (bit/pixel)						
		Band 1	Band 2	Band 3	Band 4	Band 5	Band 7	Total
Landsat-5	Sep. 21, 1995	6.754	6.316	6.802	6.624	7.028	6.564	40.089
Landsat-7	Aug. 07, 1999	6.803	6.992	5.592	6.955	5.304	7.042	38.688
Landsat-7	Oct. 10, 1999	6.737	7.136	6.494	7.129	6.563	7.183	41.243
Landsat-7	May 21, 2000	6.892	6.458	4.152	6.811	6.808	6.880	38.001
Landsat-7	Aug. 27, 2001	6.570	6.988	7.252	6.889	6.823	6.855	41.378
*Landsat-7	May 21, 2000	6.892	7.299	7.137	6.811	6.808	6.881	41.828

B		Entropy Differences (bit/pixel)						
		Band 1	Band 2	Band 3	Band 4	Band 5	Band 7	Total
Landsat-7	Aug. 07, 1999	0.049	0.675	-1.210	0.331	-1.724	0.477	-1.401
Landsat-7	Oct. 10, 1999	-0.018	0.820	-0.308	0.505	-0.465	0.619	1.153
Landsat-7	May 21, 2000	0.138	0.141	-2.651	0.187	-0.220	0.315	-2.088
Landsat-7	Aug. 27, 2001	-0.184	0.672	0.450	0.265	-0.205	0.291	1.288
*Landsat-7	May 21, 2000	0.138	0.982	0.335	0.187	-0.220	0.316	1.739

* Results after the saturation correction that was applied on bands 2 and 3.

5 DISCUSSION

The radiometric calibration of Landsat-7 ETM+ is supposed to have less uncertainty than that of the Landsat-5 TM (Markham, B. pers. comm.). The two-gain states along with the six Earth surface categories constitute significant improvements in the Landsat-7 ETM+ sensor over the TM. They are believed to provide the user with more radiometric precision and consequently with the ability to achieve better results with land-use and land-cover characterization for fulfilling the mission goals.

This paper has highlighted two problems: The first question is the reliability of the Landsat-7 ETM+ absolute calibration and the gain setting. Since no other saturation difficulties have been evidenced from other parts of the world and the vicarious calibration campaigns have generally revealed positive results, apparently, the saturation problem exists mainly along the desert transition zones where part of the scene can be defined as "Land" while the other as "Desert" as in the case of the images over Israel. The early Landsat-7 images over the region show no consistency in the saturated bands and no consistency in the saturation locations associated with the reflectances. The proposed statistically based procedure provides a reasonable solution for any saturated band.

It is currently believed that radiometric saturation difficulties occurred only during the first year of operation. These are probably the result of using the pre-launch calibration. About a year after operation, the revision of the spectral radiance range (L_{min} 's or L_{max} 's values) and a new gain setting were announced at NASA's web site. Normally, there is no need to change these values unless something drastic happens on the instrument or the sensitivity of the instrument increases, which is not expected. If the sensitivity decreases, the L_{max} values can be increased, and by so doing, the usable dynamic range of the product is increased. The changes that have taken place after a year of operation are mostly due to the adoption of the "improved" pre-launch gains for the instrument that have, in effect, "increased" its sensitivity (Markham, B. pers. comm.).

Calculations of the entropy analysis are generally similar to those presented by Maset et al. (2001), however the following differences can be counted: (1) These authors sampled seven of the most typical land-cover categories but desert; (2) They did not apply atmospheric correction before the entropy analysis; (3) They used an ETM+ image of July 28, 1999 that was acquired in high gain mode.

The current results, prior to July 1, 2000, do not completely agree with those of Maset et al. (2001). This is mainly due to the saturation phenomenon that influences the performance of bands 3 and 5. If we accept the assumption that the change in band setting from high- to low- gain along with the change of the

spectral radiance range after July 1, 2000 have led to a better performance of the ETM+ sensor, from the entropy analysis, it is evident that there has been an improvement of between 0.26 and 0.67 bits in bands 2, 3, 4, and 7, but a slight decrease in information content (about 0.2 bits) in bands 1 and 5. However, this research, over the desert environment, has never reached 1 bit of extra data as noted by Maset et al. (2001).

6 SUMMARY

The currently implemented gain setting strategy for Landsat-7 ETM+ consists of a fixed categorization of the earth's surface cover types. Gain setting rules, which are based on surface cover and sun angle, are aimed at improving the interpretation of land-use and land-cover in the changing environment. However, efforts to analyze these images over the Negev desert of Israel show that the detectors are subject to saturation. This phenomenon occurred at least during the first year of operation. Revisions in the spectral radiance range and the gain setting, implemented on July 1, 2000, seems to have reduced the saturation phenomenon over the region, but this still needs to be tested on more images. Nevertheless, a statistically based procedure is proposed in order to overcome the difficulties and to improve the saturated scenes.

7 ACKNOWLEDGEMENT

The authors would like to thank Dr. Yoram Kaufman (NASA/GSFC) for his important comments and Dr. Charles Ichoku (NASA/GSFC) for editing the manuscript. This research is partially supported by the Survey of Israel.

8 REFERENCES

- Karnieli, A., Kaufman, Y.J., Remer, L.A., Ward, A. 2001. AFRI – Aerosol free vegetation index. *Remote Sensing of Environment*, 77, 10-21.
- Masek, J.G., Honzak, M., Goward, S.N., Liu, P., & Pak, E. (2001). Landsat-7 ETM+ as an observatory for land cover - Initial radiometric and geometric comparisons with Landsat-5 Thematic Mapper. *Remote Sensing of Environment*, 78, 118-130.
- Price, J.C. (1995). Examples of high resolution visible to near-infrared reflectance spectra and a standardized collection for remote sensing studies. *International Journal of Remote Sensing*, 16, 993-1000.

9 URL ADDRESS

- http://ftpwww.gsfc.nasa.gov/IAS/handbook/handbook_htmls/chapter6/chapter6.html
- http://ftpwww.gsfc.nasa.gov/IAS/handbook/handbook_htmls/chapter11/chapter11.html
- <http://ftpwww.gsfc.nasa.gov/IAS/ascii/desert.lst>

The potential of the TERRA ASTER sensor to retrieve radiative properties over semi arid regions

F. Jacob, T. Schmugge, K. Ogawa, A. French, J. Ritchie

USDA/ARS Hydrology and Remote Sensing Laboratory,
Bldg 007, BARC-West, Beltsville, MD 20705-2350, USA

ffjacob@hydrolab.arsusda.gov, anfrench@hsb.gsfc.nasa.gov, schmugge@hydrolab.arsusda.gov

ABSTRACT - *This paper reviews investigations focused on the use of the TERRA - ASTER sensor to map radiative properties over the Jornada Long Term Ecological Range located in the northern Chihuahuan Desert, NM, USA. We focused on estimating surface kinetic temperature and albedo from single directional and multispectral observations. We considered data collected by both ASTER and its airborne version MASTER. We investigated the accuracy of retrieved brightness temperature and bidirectional reflectance. The consequences of the inaccuracy of the atmospheric characterization were assessed through a sensitivity study. We next performed a two step validation by comparing ASTER measurements with MASTER data and MASTER data with ground based measurements. Computing kinetic temperature and surface albedo was performed using the TES algorithm and the NTB conversion, respectively. The use of these methods is discussed according to the accuracy of the data preprocessing.*

1 INTRODUCTION

Knowledge of radiative properties is of prime interest when assessing the energetic status of land surfaces since it allows estimating several key variables that drive the energy transfers between soil, vegetation and atmosphere. Data acquired over the Visible (VIS) - Near Infrared (NIR) - Shortwave Infrared (SWIR) domain are used to retrieve radiative properties such as albedo (Weiss et al., 1999; Jacob et al., 2002b), as well as biophysical properties such as Fractional Vegetation Cover and Leaf Area Index (Weiss & Baret, 1999; French, 2001). Thermal infrared (TIR) measurements are used to retrieve surface emissivity and kinetic temperature (Schmugge et al., 1998). These variables are then used along with different models to simulate energy exchanges (Brasa-Ramos et al., 1998; Olioso et al., 1999; Jacob et al., 2002a; French et al., 2000).

Supplying models with remote sensing data assumes subpixel homogeneity of the variables. However, this is often far from the actual situation and requires therefore an understanding of aggregating processes which occurs when using data with a spatial resolution of approximately one kilometer. This requires scaling up studies based on the use of high spatial resolution sensors such as ASTER on board the TERRA satellite (Yamaguchi et al., 1998). In the framework of the EOS-TERRA project, the

MODIS / ASTER Airborne Simulator (MASTER) sensor was developed to support scientific studies such as validating the in-flight performances of the spaceborne sensor for both radiometric accuracy and quality of derived products by upscaling estimate comparisons from *in-situ* data to satellite products (Hook et al., 2001).

Several study sites on the Jornada experimental range in southern New Mexico, USA, provide a unique opportunity to perform long term ecological studies over semi-arid rangelands (Havstad et al., 1991). In the framework of the Jornada Experiment (JORNEX) program, remote sensing data have been acquired since 1995 in order to assess and improve the use of such observation techniques for monitoring vast desert areas. Simultaneously, field data have been acquired to validate remotely sensed data. In 1997, the site was selected as an EOS and ASTER validation site. Since then, MASTER data as well as ground measurements were collected twice a year, in spring and fall, at the time of ASTER overpass.

The objective of this study was to assess the quality of both ASTER measurements and the derived products collected over Jornada. A sensitivity study was conducted to evaluate the accuracy of atmospheric corrections compromised by a lack of information when characterizing the atmosphere (aerosol optical thickness, ozone concentration and profile of temperature and water vapor density). A two

step validation was performed by comparing, firstly, ASTER against MASTER surface reflectance and surface brightness temperature (SBT) and, secondly, MASTER against ground based data. We focused on estimating surface kinetic temperature and albedo from single directional and multispectral measurements. These variables are estimated using the Temperature Emissivity Separation (TES) algorithm and coefficient sets for the Narrow band To Broadband (NTB) conversion. We investigated the choice of coefficient set and the calibration of the TES method to be applied to ASTER data according to spectral performances of the ASTER data preprocessing.

2 DATA ACQUISITION

The Jornada experimental range is located north of Las Cruces, New Mexico (N 32.739 °, E - 106.892 °, mean altitude above sea level ASL: 1340 m). The climate is characteristic of a semi-arid area with abundant sunshine and low precipitation. Ground and aircraft remote sensing data are collected twice a year in the southwestern region of the area during a three day period around an ASTER overpass. Four sites are studied for the dominant vegetation: Creosote site (C), Grass site (G), Mesquite site (M) and Transition site (T).

2.1 Airborne and spaceborne remote sensing data

The airborne MASTER sensor Hook et al. (2001) on a small plane flew at 2500 m ASL, corresponding to a relative altitude above ground level (AGL) of 1200 m that yielded a nadir spatial resolution about 3 m. The sensor collected data over 25 bands between 0.45 and 2.5 μm , and 10 bands between 7.75 and 12.9 μm . View Zenith Angle (VZA) ranged between 0 and 40 °. We considered MASTER data acquired on May, 12, 2001 with ground based measurements simultaneously collected over the four study sites. The spaceborne sensor (Yamaguchi et al., 1998) on the EOS-Terra platform collects data over 9 bands between 0.5 and 2.5 μm , and 5 bands between 8 and 11.5 μm . VZA range is between 0 and 7 °. Nadir spatial resolution is about 15 m, 30 m and 90 m over VIS - NIR, SWIR and TIR domains, respectively. We considered data collected between May, 9, 2000 and June, 23, 2002. Both ASTER and MASTER data were collected at 18:00z that correspond to 10:30 local solar time. The data we considered were geometrically and radiometrically corrected by the EOS project.

2.2 Ground data

In-situ measurements were performed to validate VIS - NIR - TIR measurements. The VIS-NIR ground based data were collected using an Analytical Spectral Device (ASD) hyperspectral radiometer. Reflected incoming solar radiation was measured with a nadir viewing between 0.35 and 2.5 μm with a 0.005 μm step. The surface reflectance was calculated as the ratio of the solar radiation reflected by the land surface to the solar radiation reflected by a reference panel. For comparison with MASTER data, we calculated from these ASD hyperspectral measurements waveband averaged bidirectional reflectance using the MASTER spectral response functions. Each site was sampled using a 30×30 m² grid that included 49 measurements with a 5 m grid. This sampling scheme was also used to acquire the ground based TIR measurements. Data were collected using Apogee radiometers that provided SBT estimates over the 7 - 14 μm spectral range. Measurements were automatically corrected from the internal sensor temperature using a FLUKE thermometer. Both ASD and Apogee instruments had a footprint of a few cm².

2.3 Atmosphere characterization

There were no radiosoundings that coincided spatially and temporally with the ASTER / MASTER data collection. The available information were either radiosoundings provided by NOAA meteorological network or simulated NCEP profiles. When dealing with the NOAA / RAOB network, we selected radiosoundings launched inside a 3×3 ° latitude / longitude window. These radiosoundings were collected 6 hours before and after the satellite overpass from two meteorological stations located 200 km north (Albuquerque, NM) and 30 km southeast (El Paso, TX) of the study area. When dealing with NCEP simulated profiles, we considered the spatially interpolated profile over the Jornada site location on May, 12, 2001 at the same time the satellite passed by (18:00 z).

The integrated value over the whole atmosphere of aerosol optical thickness at 550 nm $AOT@550$ was derived from sun photometer measurements collected at the Sevilleta site, which is located at N 34.4 °, i.e. 200 km north of the Jornada site. Measurements were performed over 7 wavebands ranging from 400 to 1000 nm with approximately a 100 nm step. Pre and post field calibration, cloud clearing and manually inspection were performed

by John Van de Castle (U.S. LTER Network Office) in the framework of the AERONET project (<http://aeronet.gsfc.nasa.gov:8080/>). This processing provided aerosol optical thickness over the 7 wavebands.

3 ATMOSPHERIC CORRECTIONS

3.1 Methods

The VIS - NIR and TIR data were atmospherically corrected using the 6S code (Vermote et al., 1997) and MODTRAN 4 code (Berk et al., 1998), respectively. 6S requires atmospheric profiles of pressure, temperature and humidity (P, T, U); aerosol optical thickness at 550 nm $AOT@550$, and ozone concentration $[O_3]$. MODTRAN 4 inputs are atmospheric profiles (P, T, U). These profiles were either the radiosoundings measurements or NCEP simulations. When considering the radiosoundings provided by the NOAA/RAOB, we used the profiles in their original configuration as is the case for operational atmospheric corrections. However, the NCEP profiles ranged between sea level and 10 km in their original configuration. Therefore, we reconstructed atmospheric profiles considering both meteorological measurements collected at the experimental site and the NCEP profile values with an altitude ASL higher than that of the experimental site. $AOT@550$ was deduced from estimates at 670 and 500 nm using a linear interpolation by considering the data temporally closest to the satellite overpass. $[O_3]$ was estimated using the 6S climatological data base.

The 6S outputs for a given waveband j and given solar / view zenith and azimuth angles were three coefficients a_j , b_j and c_j , used along with the following relation to estimate surface reflectance ρ_j from the incoming radiance at the sensor level L_j^\uparrow :

$$\rho_j = (a_j L_j - b_j) / [1 + c_j (a_j L_j - b_j)] \quad (1)$$

Processing the airborne data required the knowledge of ozone concentration $[O_3]$, atmospheric water vapor W and $AOT@550$ between the surface and the sensor. This was calculated by 6S code for $[O_3]$ and W integrating the US 62 standard profile extrapolated from surface values, whereas $AOT@550$ was derived by integrating a 2 km exponential profile deduced from the value integrated over the whole atmosphere.

MODTRAN 4 was used to simulate atmospheric transmittance τ_j , atmospheric upwelling L_j^\uparrow and

downwelling L_j^\downarrow radiances. Next, τ_j and upwelling radiance L_j^\uparrow over the channel j were used to estimate surface outgoing radiance L_j^{sur} from the incoming radiance at sensor level L_j^{sen} by inverting the atmospheric radiative equation:

$$L_j^{sur} = (L_j^{sen} - L_j^\uparrow) / \tau_j \quad (2)$$

When performing the atmospheric corrections on the TIR data set acquired with the MASTER multidirectional sensor, the computation time was reduced by linearizing the atmospheric transmittance and upwelling radiance as first order functions of view zenith angle θ_v :

$$\tau_j, L_j^\uparrow = a + b / \cos(\theta_v) \quad (3)$$

3.2 Sensitivity to atmosphere characterization

The atmospheric radiative transfer model inputs characterized atmospheres that were not spatially and temporally coincident with the sensor overpasses. To assess the resulting inaccuracies on ASTER / MASTER products, we performed a sensitivity study. When considering the representativeness of radiosoundings, we processed the data by considering several atmospheric profiles that were available. When considering the representativeness of $AOT@550$ and $[O_3]$, we processed the data by varying these two variables $\pm 10\%$ around the nominal value. Next, we estimated for each channel j the mean value of the pixel by pixel variability over the corrected data. When dealing with the VIS - NIR - SWIR infrared data, we characterized the variability of bidirectional reflectance using the Relative Range expressed as:

$$RR_j = 100 * (\rho_j^{max} - \rho_j^{min}) / (\rho_j^{mean}) \quad (4)$$

where ρ_j^{max} , ρ_j^{min} and ρ_j^{mean} are the maximum, minimum and averaged values, respectively, of bidirectional reflectance over the several estimates. When dealing with the TIR data, we characterized the variability of SBT using the Absolute Range expressed as:

$$AR_j = SBT_j^{max} - SBT_j^{min} \quad (5)$$

where SBT_j^{max} and SBT_j^{min} are the maximum and minimum values, respectively, of SBT over the several estimates.

Figure 1 displays the evolution of the Relative Range over bidirectional reflectance (top) and Absolute Range over SBT (bottom) for the ASTER /

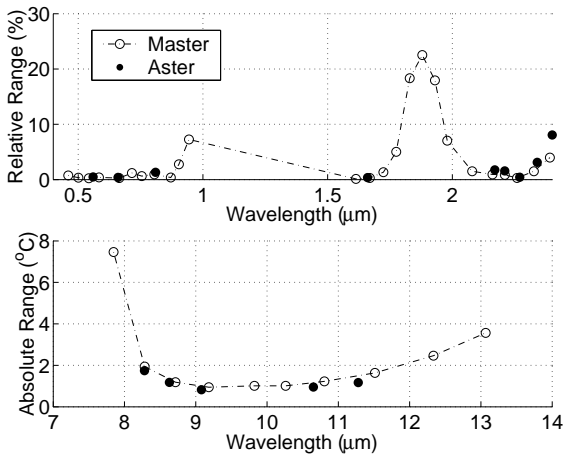


Figure 1: Evolution according to the wavelength of the Relative Range of the bidirectional reflectance (top) and Absolute Range of SBT (bottom) when using several radiosoundings to process ASTER/MASTER data.

MASTER channels when considering the data collected on May, 12, 2001. We observed the largest values over the $[1.7 - 2.1] \mu\text{m}$ spectral range. This was explained by a very low signal to noise ratio induced by a very low incoming solar radiation because of absorption by atmospheric water vapor. For the same reason, large values also occurred at 0.95 and $2.5 \mu\text{m}$. As a consequence, when deriving radiative properties using these data, one should avoid the use of these channels. When considering the other wavebands, it was shown that the lack of information on atmospheric characterization did not affect significantly the accuracy of surface bidirectional reflectance, with a relative range ranging between 0 and 3%. It was shown that the sensitivity of MASTER bands 41, 49 and 50 to atmospheric correction resulted in inaccuracy larger than 2°C . When considering the other MASTER and ASTER bands, the variability ranged between 1 and 2°C . The large inaccuracies observed on MASTER bands 41, 49 and 50 were ascribed to significant atmospheric effects occurring over the corresponding wavelengths. Therefore, it would be better to avoid using these bands when computing radiometric temperature.

The results we obtained when assessing the sensitivity to $AOT@550$ and $[O_3]$ estimates showed that the resulting error was not significant. When considering the sensitivity to $AOT@550$, the relative range decreased from 0.6 to 0.2% between 0.5 to $2.5 \mu\text{m}$,

which was explained by larger signal to noise ratio since the atmospheric diffusion by aerosol decreased as the wavelength increased. When considering the sensitivity to $[O_3]$, the relative range was around 1.2% between 0.5 and $0.8 \mu\text{m}$, which was explained by the ozone peak absorption centered at $0.6 \mu\text{m}$. The difference we observed between the sensitivities of ASTER and MASTER data processing to $AOT@550$ and $[O_3]$ could be explained by both sensor spectral responses and observation altitudes since these atmospheric components are distributed throughout the atmosphere.

Finally, we have to note that the results discussed here were observed when considering data collected on May, 12, 2001. It was shown that the sensitivities of both sensors were very similar. However, when considering all ASTER scenes available over the Jornada site, the results could be significantly different. Over the VIS - NIR - SWIR domain, the results were quite similar, the significant difference we observed being an increase of inaccuracy up to 10% at $2.4 \mu\text{m}$ (ASTER band 9). Over the TIR domain, the absolute range of brightness temperature increased to the $[1.5 - 3]^\circ\text{C}$ range. This emphasized that the atmosphere spatial or /and temporal variability, as well as the consequences on data processing accuracy could be significantly different. Further investigations are required to separate temporal and spatial variability and assess their respective consequences.

4 TWO STEP VALIDATION

4.1 Method

The next part of this study dealt with a two step validation of ASTER / MASTER both bidirectional reflectance and SBT. The procedure consisted of comparing ASTER and MASTER data, and MASTER data against ground based measurements. In this case, we considered ASTER and MASTER data atmospherically processed using the NCEP profile. To compare ASTER and MASTER images, MASTER images were registered to be superimposed onto ASTER scenes. In this case, we considered the MASTER scene acquired over the Mesquite site. The 3 m spatial resolution MASTER image was registered using control points selected on the ASTER scene along with a bilinear interpolation resampling at a 15 m spatial resolution. Master images over the SWIR (respectively TIR) spectral range were next degraded to a 30 m (respectively 90 m) spatial resolution. We compared ASTER and

MASTER bands as following (given as: spectral domain: ASTER / MASTER bands):

- Vis-NIR: 01/03, 02/05, 03/08,
- SWIR: 04/13, 05/21, 06/22, 07/23, 08/24, 09/25,
- TIR: 10/42, 11/43, 12/44, 13/47, 14/48.

4.2 Spatial analysis of data sets

To compare MASTER data against ground based measurements, we extracted data from 10×10 pixel windows. We next compared the spatial variability of bidirectional reflectance for each waveband over MASTER and ASD data sets by considering the Coefficient of Variation (CV), i.e. the ratio of standard deviation to the mean value. For the Creosote and Grass sites, there was no correlation between the spectral variations of MASTER and ASD CV, (CV values were low and constant for the MASTER data set). For the Mesquite and Transition sites, spectral variations were correlated, and the ASD values were twice as large. Overall, ground and MASTER data had Coefficient of Variations ranging between 10 and 50% and 2 and 25%, respectively.

When considering SBT estimates, we compared the spatial variability of broadband and single spectral field measurements with waveband and multispectral MASTER measurements. We observed similar trends. First, the spatial variability of MASTER data was lower for the Grass site as compared to Mesquite and Transition sites. Second, the standard deviation was larger for field data (between 4.5 and 7 °C) as compared to MASTER data (between 1 and 5 °C). From these observations, we noted that the spatial variability observed in the data sets was large. However, of greater importance was that the spatial information contained in both data sets was significantly different since they did not depicted the same spatial variability. This could be explained by the difference in scales, with a footprint about few centimeters for ASD and a 3 m spatial resolution for MASTER. Such differences in spatial information increased the difficulties in comparing these sets for validation purposes.

4.3 Comparing ASTER and MASTER data

The comparison between VIS - NIR - SWIR ASTER and MASTER images at a 15 m spatial resolution provided poor results. The Absolute Root Mean Square Difference (ARMSE) ranged from 0.02 to 0.06, which corresponded to a Relative Root Mean Square Difference (RRMSD) between 9 and

18%. Moreover, we observed that ASTER data underestimated MASTER data except over the green channel, with a Absolute Bias (ABias) ranging from 0.02 to 0.05, which corresponded to a Relative Bias (RBias) between 6.5 and 13%. We did not observe any trend regardless of waveband: the underestimation could either occur over the range of values, or corresponded to lowest or largest values. Besides, we noted both significant systematic error (over or underestimation) and unsystematic error (random discrepancy). We assessed a possible effect of viewing angle since MASTER data were collected with a View Zenith Angle (VZA) ranging between 0 and 40 ° whereas ASTER provided nadir observations. The comparison of ASTER and MASTER nadir data did not show significantly better results, the RRMSD decreasing of 2%. Then, we assessed a possible effect of registration inaccuracy, by degrading the spatial resolution to 90 and 180 m. This did not result in better validation results, the RRMSD decreasing of 3%.

When comparing the TIR data, we also obtained poor results, with a ARMSE ranging between 1.5 and 3 °C. The largest ARMSE occurred at 10.63 μm (MASTER band 47 / ASTER band 13), which did not correspond to the waveband with the largest atmospheric effects, i.e. ASTER band 10. We could not determine a trend regardless of waveband: ASTER data underestimated (respectively overestimated) MASTER data for bands 10, 11 and 12 (respectively band 13 and 14) about 0.5 °C (respectively 2°C). As mentioned previously when dealing with VIS - NIR - SWIR data, intercomparing the data by either selecting nadir observations or degrading the spatial resolution did not decrease the ARMSE significantly. To conclude, these observations showed that the significant differences we observed between ASTER and MASTER data did not result from registration inaccuracy, viewing conditions or atmospheric corrections. We therefore suspected sensor intercalibration, which requires further investigations.

4.4 Validation against ground based data

VIS - NIR - SWIR MASTER were validated against ground based measurements considering the four sites. Since the ASTER / MASTER intercomparison data did not provided satisfactory results, we included ASTER estimates in the comparison. In this case, we extracted over the considered site ASTER data using 2×2 pixel windows for bands 1 to 3 (15 m spatial resolution) and 1 pixel for

bands 4 to 9 (30 m spatial resolution). An example of the comparison results for the Mesquite site is given in figure 2. We observed the same trend among the four sites, i.e. a good agreement of the three data sets between 0.4 and 0.9 μm , some larger differences for larger wavebands, and a better agreement between ASTER and ASD measurements. It is interesting to note that we observed contradictory results when performing ground based validation and intercomparing airborne and spaceborne data. Indeed, the differences between ASTER and MASTER estimates were larger at shorter wavelengths whereas the converse was true when validating against ground based measurements. This emphasized the benefit of using a multi-scale and multi-sensor validation via airborne observations to ensure the validity of the observed trends. Finally, it was difficult to draw a conclusion since the spatial information contained in both MASTER and ASD data sets was significantly different. We observed large differences between MASTER and ASTER data, and ASTER estimates were closer to ASD measurements than MASTER data. Besides, the absence of spectral variation of the Coefficient of Variation for the Creosote and Grass sites led us to suspect the quality of the MASTER data.

TIR MASTER data were validated against ground based measurements by considering three sites, i.e. Grass, Mesquite and Transition. Indeed, the field measurements over the Creosote site did not temporally coincide with the MASTER data. We also considered the ASTER data by extracting one pixel from ASTER scenes. In this case, the comparison results have to be considered with many care since the validation consisted of comparing $30 \times 30 \text{ m}^2$ ground data with 90 m spatial resolution ASTER data. We observed that airborne and spaceborne measurements depicted the same spectral variation with different values. The MASTER data validation was performed considering a mean value of the waveband surface brightness temperatures without considering band 41 that was significantly perturbed by atmospheric effects. The ASTER data validation was performed considering a mean value over the 5 wavebands. The results are displayed in Figure 3. The ARMSE between airborne and ground based data was of 1.5 $^{\circ}\text{C}$, with an underestimation (respectively an overestimation) of field data for the Grass site (respectively Mesquite and Transition sites). The ASTER data agreed well with the ground based measurements, the RMSE being about 0.5 $^{\circ}\text{C}$. It was difficult to conclude about these results since

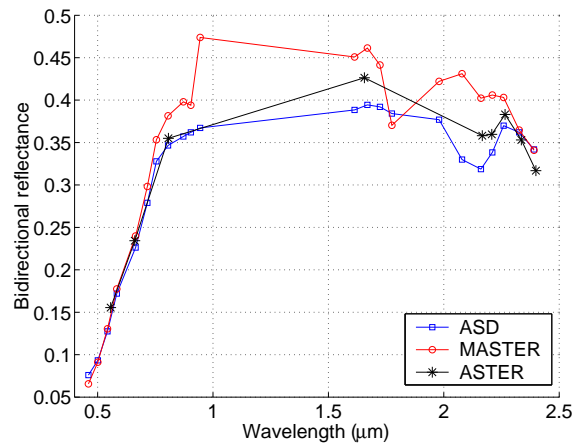


Figure 2: Comparison of the ASD / MASTER / ASTER estimates of bidirectional reflectance over the Mesquite site.

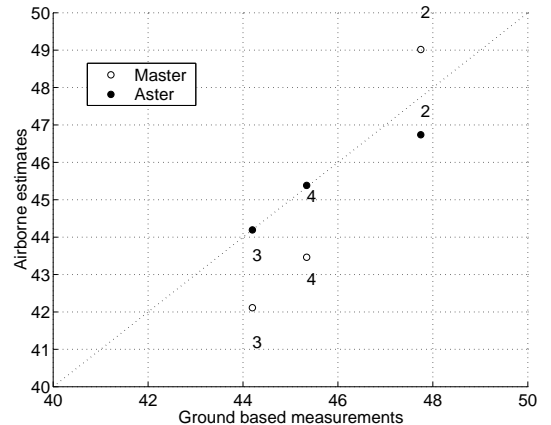


Figure 3: Comparison of the ground based / MASTER / ASTER estimates of broadband brightness temperature over Grass(2), Mesquite(3) and Transition(4) site.

the spatial resolutions of the data sets were significantly different, especially for ASTER data. Nevertheless, the observations we made when validating both VIS - NIR - SWIR and TIR data led us to suspect the MASTER data quality.

5 ALBEDO ESTIMATION

Albedo estimation was investigated using the ASTER scene collected on May, 12, 2001 at a 90 m spatial resolution. Expressing albedo as a linear

combination of waveband estimates assumes that the considered channels provide the necessary and non-redundant information. We therefore computed the correlation coefficients between the 9 ASTER bands by selecting pixels over the Jornada experimental range to avoid complications induced by clouds and nearby landscape features. The correlation coefficient matrix showed that wavebands 4 to 9 (wavelengths ranging between 1.6 and 2.5 μm) were significantly correlated, with correlation coefficients ranging between 0.95 and 0.99. It was therefore not necessary to consider the whole data set, thus it was possible to avoid the use of band 9 for which significant atmospheric perturbations were observed. Besides, the band 2 (0.661 μm) was correlated with bands 4 to 9, the correlation coefficient ranging between 0.75 and 0.8. We also noted a significant correlation between bands 1 (0.556 μm) and 2 (correlation coefficient of about 0.8), and no correlation between band 2 and 3 (0.806 μm) (correlation coefficient of about 0.23). From these observations, we could conclude that firstly, non redundant information was included in two bands, i.e band 2 and 3. Also, according to the correlation between band 2 and 4, further investigations are required to assess the benefit of using observations at 1.6 μm by assessing the added amount of information and / or noise.

Albedo was computed using several coefficient sets proposed in the literature for different sensors and devoted to the estimation of shortwave apparent albedo. These coefficient sets were either dedicated to ASTER and MISR (Liang, 2000), to generic sensors according to the number of considered band (Weiss et al., 1999), and to POLDER considering either nadir and hemispherical reflectance (Jacob et al., 2002b). We compared the set devoted to ASTER against other sets since 1) Liang (2000) considered the band 9 over which we observed significant atmospheric perturbations and 2) no field data were available. These sets were chosen since the related sensors had very similar spectral configurations. Good agreement was found (RRMSE between 2.5 and 8%) between coefficient sets proposed by Weiss et al. (1999) when considering green, red and NIR wavebands, Liang (2000) for both ASTER and MISR, and Jacob et al. (2002b) when considering hemispherical reflectance. It was not possible to conclude about the quality of the estimates since no validation was possible. Nevertheless, we should note that the agreeing sets were calibrated using databases that significantly differed on seve-

ral points. Moreover, the strong atmospheric perturbations occurring for ASTER band 9 did not induced significant differences since the set proposed by Liang (2000) was among the sets that provided similar results.

6 KINETIC TEMPERATURE ESTIMATION

The surface kinetic (or radiometric) temperature is operationally computed using the TIR ASTER measurements along with Temperature Emissivity Separation algorithm (TES). A detailed description of TES is given by Schmugge et al. (1998). The algorithm relies on the assumption that one of the wavebands emissivities is close to unity. Rather than considering a nominal value for the maximum brightness temperature, TES is based on a differential approach that is supposed to reduce instrumental and preprocessing errors: the minimum value of emissivity is linked to the emissivity variation over the sensor wavebands. Consequently, the algorithm requires previously a calibration of the relationship between the minimum emissivity ε_{min} and the variation characterized by the Minimum Maximum Difference MMD (the ratio of the difference between maximum and minimum values to the mean value): $\varepsilon_{min} = A - B \times MMD^C$. In the last part of this study, we investigated the calibration of this relation for both ASTER and MASTER by considering the performance of the algorithm according to the number of selected bands. This aimed at compromising between 1) using the spectral information necessary to well characterize land surface emissivity, and 2) avoiding wavebands strongly perturbed by the atmosphere. The theoretical error of TES was estimated using Planck's law simulations: an error on 0.015 on emissivity induced an error of about 1 $^{\circ}\text{C}$ on retrieved temperature.

The calibration was performed using the ASTER and MODIS spectral libraries generated by the University of Santa Barbara, the Jet Propulsion Laboratory, the United State Geological Survey and the John Hopkins University. Among the several spectra included in the libraries, we considered samples collected over rocks, soil, water and vegetation. We also considered few other spectra acquired over agricultural and semi arid areas. When the data corresponded to reflectance ρ_{λ} , we deduced emissivity ε_{λ} by considering the Kirchhoff's law at thermodynamical equilibrium, i.e. $\varepsilon_{\lambda} = 1 - \rho_{\lambda}$. From these spectral libraries, we computed a database of ASTER and MASTER waveband emissivities using the sensor spectral response functions. Next, the em-

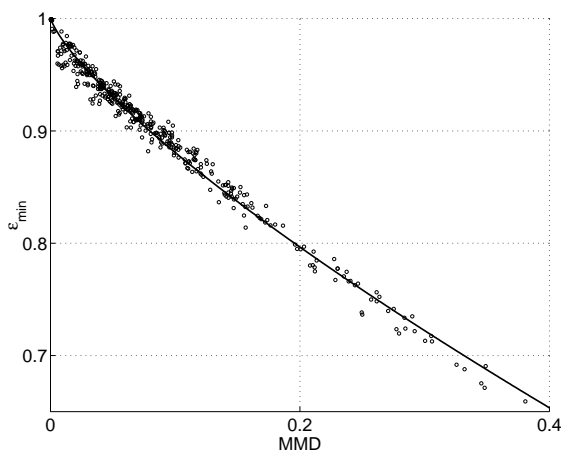


Figure 4: Calibration of the TES based empirical relationship $\varepsilon_{min} = A - B \times MMD^C$ using the spectral libraries when considering the ten MASTER bands .

irical relationship aforementioned was calibrated as shown in Figure 4, and its accuracy was assessed through the residual error. When dealing with MASTER and according to the wavebands performances of atmospheric corrections (see Figure 1), we considered 4 cases: bands 41 to 50, bands 42 to 50, bands 42 to 48 and bands 43 to 48. When dealing with ASTER, we considered three cases: band 10 to 14, bands 11-14 and bands 12-13. In all cases, we observed a residual error lower than 0.015 that increased as the number of bands decreased. The error ranged between 0.0081 to 0.0126 for MASTER, and from 0.0101 to 0.0139 for ASTER. According to both these results and the performances of the atmospheric corrections, it is recommended to consider only bands between 8.5 and 11.5 μm to reach an accuracy around 1 $^{\circ}\text{C}$.

ACKNOWLEDGMENTS

This study was supported by the ASTER Project of NASA's EOS-Terra Program. ASTER spectral library was provided by the Jet Propulsion Laboratory, California Institute of Technology, Pasadena, California, USA. Thanks to Carole Ritchie for reviewing the English.

References

Berk, A., Bernstein, L.S., Anderson, G.P., Acharya, P.K., Robertson, D.C., J.H., Chetwynd, and Adler-Golden, S.M., 1998, MODTRAN cloud and multiple scattering upgrades with application to AVIRIS. *Remote Sensing of Environment*, 65, 367–375.

Brasa-Ramos, A., De Santa Olalla, F.M., Caselles, V., and Jochum, A.M., 1998, Comparison of evapotranspiration estimates by NOAA-AVHRR images and aircraft

flux measurements in a semiarid region of Spain. *Journal of Agricultural Engineering Research*, 285-294, 70.

French, A., 2001. Scaling of surface energy fluxes using remotely sensed data. Phd thesis, 273 pp, University of Maryland.

French, A., Schmugge, T.J., and Kustas, W.P., 2000, Estimating surface fluxes over the SGP site with remotely sensed data. *Physics and Chemistry of the Earth(B)*, 25, 167–172.

Havstad, K.M., Kustas, W.P., Rango, A., Ritchie, J.C., and Schmugge, T., 1991, jornada Experimental Range: a unique arid land location for experiments to validate satellite system. *Remote sensing of Environment*, 53, 13–25.

Hook, S.J., Myers, J.J., Thome, K.J., Fitzgerald, M., and Kahle, A.B., 2001, The MODIS/ASTER airborne simulator (MASTER) - a new instrument for Earth science studies. *Remote Sensing of Environment*, 76, 93–102.

Jacob, F., Olioso, A., Gu, X.F., Su, Z., and Seguin, B., 2002a, Mapping surface fluxes using visible, near infrared, thermal infrared remote sensing data with a spatialized surface energy balance model. *Agronomie*. Accepted.

Jacob, F., Weiss, M., Olioso, A., and French, A., 2002b, Assessing the narrowband to broadband conversion to estimate visible, near infrared and shortwave apparent albedo from airborne POLDER data. *Agronomie*. Accepted.

Liang, S., 2000, Narrowband to broadband conversions of land surface albedo I Algorithms. *Remote Sensing of Environment*, 76, 213–238.

Olioso, A., Chauki, H., Courault, D., and Wigneron, J.P., 1999, Estimation of evapotranspiration and photosynthesis by assimilation of remote sensing data into SVAT models. *Remote Sensing of Environment*, 68, 341–356.

Schmugge, T.J., Hook, S.J., and Coll, C., 1998, Recovering Surface Temperature and Emissivity from Thermal Infrared Multispectral Data. *Remote Sensing of Environment*, 65, 121–131.

Vermote, E., Tanré, D., Deuzé, J.L., and Morcrette, J.J., 1997, Second simulation of the satellite signal in the solar spectrum: an overview. *IEEE Transactions on Geoscience and Remote Sensing*, 35, 675–686.

Weiss, M. and Baret, F., 1999, Evaluation of Canopy Biophysical Variable Retrieval Performances from the Accumulation of Large Swath Satellite Data. *Remote Sensing of Environment*, 70, 293–306.

Weiss, M., Baret, F., Leroy, M., Bégué, A., Hautecoeur, O., and Santer, R., 1999, Hemispherical reflectance and albedo estimate from the accumulation of across-track sun-synchronous satellite data. *Journal of Geophysical Research*, 104, 22221–22232.

Yamaguchi, Y., Kahle, A.B., Tsu, H., Kawakami, T., and Pniel, M., 1998, Overview of Advance Spaceborne Thermal Emission and Reflection Radiometer (ASTER). *IEEE Transactions on Geoscience and Remote Sensing*, 36, 1282–1289.

Assimilation of remote sensing SPOT data into vegetation process models in the ADAM project in Romania.

C. Lauvernet¹, F.X. Le Dimet², F. Baret¹,

H. Deboissezon³, J.C. Favard³, R. Vintila⁴, C. Lazar⁵, A. Badea⁶

¹INRA, CSE, Avignon, France

⁴ICPA, Bucarest, Romania

²LMC-IMAG, Grenoble, France

⁵ICCPT, Fundulea, Romania

³CNES-QTIS, Toulouse, France

⁶ASR, Bucarest, Romania

mail : claire.lauvernet@avignon.inra.fr

Francois-Xavier.Le-Dimet@imag.fr

baret@avignon.inra.fr

ABSTRACT - *The objective of this study is to develop a methodology for estimating canopy state variables in time and space using assimilation of high temporal frequency SPOT data into vegetation process models. This work is part of the ADAM (Assimilation of spatial Data within Agronomic Models) project, a franco-romanian partnership which experiment provided a complete scientific database of remote sensing and ground data products. The canopy functioning model chosen is STICS (Simulateur multiDisciplinaire pour les Cultures Standard) which was developed to simulate a wide range of crops evolution and is particularly well suited for wheat crops. First, the calibration of STICS was performed on Romanian wheat cultivar with help of the ADAM database. The forthcoming stage, that will consist in the data assimilation itself, is then described. Among many kinds of data assimilation techniques, a variational method has been chosen in the prospect of obtaining the adjoint model of STICS. This tool will enable to perform a sensitivity analysis, with regard to the observations and to the input parameters, to finally investigate the effects of high temporal frequency.*

1 INTRODUCTION

For fifty years, crop functioning models grew in number and in performance to better describe the state and evolution of vegetation, and to characterize water and nitrogen exchanges between the Earth surface and the atmosphere more reliably. These models use soil, climate and vegetation related data as input parameters. Some of these characteristics vary in space and time and are thus difficult to evaluate. Remote sensing observations would allow to better quantify them through assimilation techniques.

Data Assimilation (DA) (LeDimet, 2001) includes the techniques used for coupling Data and Models in order to get the best estimation (in a sense to be defined) of the geo-bio-physical fields in the past (analysis) or in the future (prediction). During the last decade, DA has known an increasing development, especially in meteorology (LeDimet and Talagrand, 1985) and oceanography (Benett, 2002). There is now a strong demand for DA applications to vegetation over land surfaces, as highlighted by a recent trend towards

assimilating remote sensing data into canopy functioning models (François et al., 1995; Guérif, 1995; Prévot et al., 2001).

However, a recent work (Weiss et al., 2001) showed that actual assimilation techniques into agronomic models still need improvement, because the results are very sensitive to the increasing of uncertainties, on the model or on the observations. The aim of this study is to develop a new assimilation technique, more robust, close to the ones used in meteorology. Based on a variational method, it will allow to calculate the adjoint of the agronomic model, a solid tool to perform sensitivity analysis and deal with model and observation uncertainties.

This study is conducted in the frame of the ADAM project, resulting from a Franco-Romanian partnership supervised by CNES (Centre National d'Etudes Spatiales), INRA (Institut National de la Recherche Agronomique), ESAP (Ecole Supérieure d'Agriculture de Purpan) and ASR (agentia spatiala româna), ICCPT (Institutul de Cercetari pentru Cereale si Plante Tehnice), ICPA (Institutul de Cercetari pentru

Pedologie si Agrochimie), CRUTA (Centrul Roman pentru Utilizarea Teledetectiei in Agricultura). Its objective is to develop and evaluate a method to obtain reliable agronomical information on crops (such as yield, water or nitrogenous status, etc.), required to optimize cultural practices and to estimate the productions.

First, the ADAM experiment is described. The STICS model, on which DA will be applied, is then presented and its parameters are discussed with the aim of choosing the ones to be assimilated. Finally, the variational assimilation theory is introduced, from a mathematical and a computational point of view, with the prospect of assimilating data into canopy functioning models.

2 THE EXPERIMENT

The project experiment mainly concerns wheat crops. It took place in the Danube Plain of Romania from October 2000 to July 2001. 42 wheat crops units of 1000m² each have been intensively investigated with space borne sensors and in the field (10 units of calibration, 32 units of validation). SPOT 1, 2 and 4, satellites provided 39 images throughout the whole growing season, concurrently with radar (ERS, Radarsat), Hyperion and ASTER images.

Ground measurements of biomass, humidity, leaf area index (LAI), etc., were made frequently on each unit to characterize the soil and the vegetation. Additionally, climate variables (such as wind speed, rainfall, temperatures, etc.) were also measured on the experimental site.

From October 2001 to July 2002, another experiment, including a SPOT5 image, was performed in order to validate the assimilation method and the calibration of the model.

All these data will be put on a web server and freely accessible to any scientist. The ADAM database is considered as the largest one in the world regarding the number of satellite images collected for agronomic research purposes along with the associated ground truth.

3 THE STICS VEGETATION MODEL

3.1 The model

STICS (Brisson et al., 1998) is a simulating model targeting both **agronomic** and **environmental** purposes. It is a dynamic canopy functioning model that aims at simulating the effects of climate variations and soil and crop management on the crop production and on the environment.

The simulated object is a cultural situation, that means

a soil-crop system and a given set of cultural practices.

STICS takes into account the climate (air humidity, wind speed, temperature, rainfall, etc.) and soil (water contents, clay and limestone contents, etc.) characteristics, the crop properties (cultivar), and the cultural practices (sowing date, irrigation, residues, etc.).

The simulated processes are growth and development of the crop, and water and nitrogenous balance of the soil-crop system.

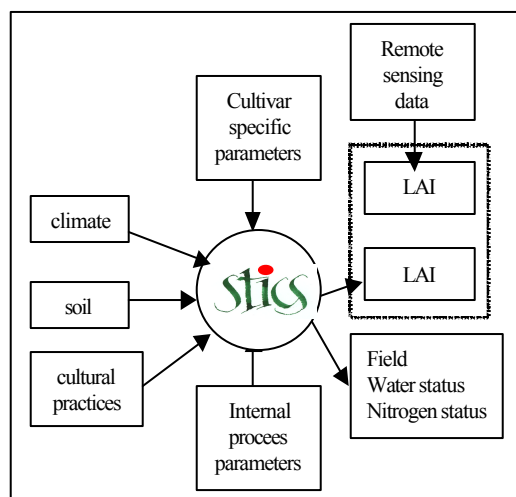


FIGURE 1 : Schematic description of the STICS model

The leaf area index is a key variable of vegetation functioning because it is related to the biomass production: it is defined as the number of equivalent layers of leaves the vegetation displays relative to a unit ground area. LAI governs and is driven by the above processes. Because LAI can be estimated from remote sensing data, this will be the link between space observations and crop modelling.

3.2 STICS parameters

Two types of parameters can be distinguished : some are cultivar specific, and other depend directly on the situation.

a. Cultivar dependent parameters

The parameters that can be related to cultivar differences in STICS are (Brisson et al., 2002):

- the development parameters: STICS considers the different growth stages, like emergence (LEV), 1cm

ear (AMF), maximal LAI (LAX), flowering (DRP) and senescence (SEN);

- the vernalization requirements, i.e. the requirements in low temperature for wheat development;
- the yield components: the maximal grain weight, the number of grains, the carbon harvest index;
- some characteristics of the roots: depth and density.

These cultivar specific parameters have to be calibrated on the two types of wheat studied in the ADAM project

- Dropia and Flamura. (see § 3.3)

b. Situation dependent parameters

Some parameters vary between the different units, and thus wheat crops may not have the same behaviour of growth and development, even if they are the same cultivars under same climate conditions. These parameters are the following:

- SOIL parameters: organic nitrogen, field capacity, density;
- cultural techniques: dates of sowing or emergence, organic residues from the previous crop, dates and types of fertilization, sowing density.

These crucial parameters are not always easy to asses. Moreover, they may vary spatially between fields. Data assimilation is therefore a valuable method to adjust them.

3.3 Calibration

In order to be as close as possible to a good basis before starting the assimilation process, we had to adjust STICS to the Dropia and Flamura cultivars. These cultivars are Romanian, and thus have a very different behaviour from the French cultivars like Thesee or Talent, that were used for initialising the simulations, and for which the values of the cultivar dependant parameters are known.

We used several ADAM experiment units, together with the Romanian climate and soils, combined with another experiment made in Avignon (France), corresponding to the same cultivar but with the French climate and soils characteristics. By this way, it was possible to calibrate on very different situations.

The calibration first concerned the phenology: the earliness of stem elongation (between LEV and AMF) and the ear emergence (between AMF and LAX), as well as the vernalization requirements. The aim was to vary the vernalization days (JVC) and to choose those that minimizes the standard deviation between the different phenologies on French or Romanian units, for the Flamura cultivar.

Figure 2 shows the variations of the length between LEV and AMF calculated by STICS as a function of the number of vernalization days, for different Romanian (U05, 01, 08) and French (U92) units of the experiment. Figure 3 points out that the standard deviation is minimum for a JVC equal to 35.

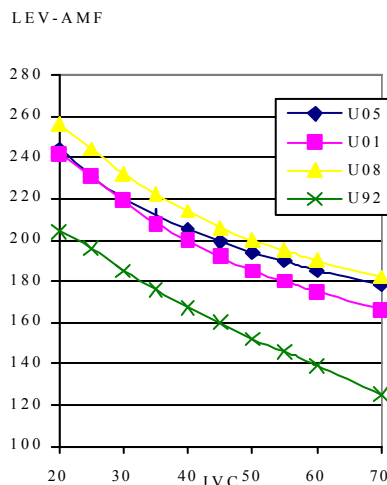


FIGURE 2 : variations of LEV-AMF as a function of vernalisation requirements

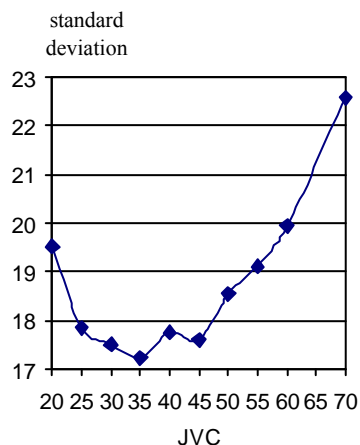


FIGURE 3: standard deviation of JVC between different units.

Finally, another calibration was made to improve the LAI simulations: on the leaves life length and on the density, using a least squares method.

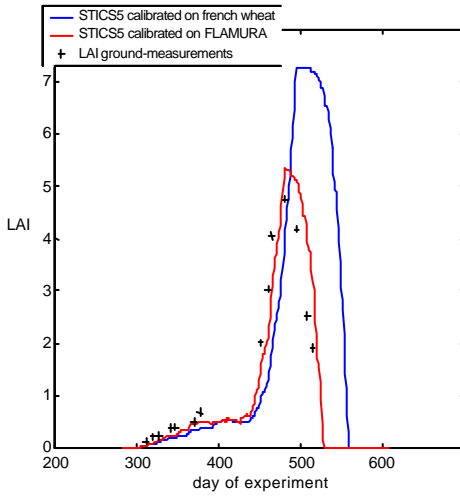


FIGURE 4 : LAI simulations by STICS

Figure 4 shows that even if the LAI simulations are closer to the observations after the calibration on the development stages and the other parameters, this is far from the reality (the RMSE is of 0.78 for Flamura, against an RMSE of 2.27 for Thesee). The disagreement between observed and simulated LAI values indicates that other parameters have to be tuned. This will be the challenge of assimilating data within such canopy process model.

4 DATA ASSIMILATION

4.1 Principle

Four types of information are available: information on physiological processes represented by the model (imperfect), information about the climate and the soil represented by the corresponding variables that were measured (with noise), remote sensing data, and *a priori* information on the parameters. Assimilation is the art of mixing all these different information.

There are two basic approaches for DA: the deterministic approach, based on Optimal Control Theory, and Stochastic methods based on the theory of Statistical Estimation and Kalman filter.

The second method requires to handle huge covariance matrices. For the time being they cannot be applied to realistic models. Conversely, the first method requires to calculate the adjoint model, which is a very powerful tool for parameters identification and also for coupling models. Finally, with an adjoint model it is easy to carry out sensitivity analysis in only one run.

Therefore in the following we will focus on the first method: variational assimilation, which is part of control theory.

4.2 General theory of variational assimilation

The general variational assimilation theory will be first presented, in order to apply it to STICS later on. It requires :

- **A state variable** which describes the fields : in this case, the state variable X is the leaf area index that is closely related to the crop growth.

- **An observation** X_{obs} , distributed in time and space. The observations X_{obs} come from the ADAM project experiment, first from ground measurements, then from remote sensing observations, with the help of a radiative transfer model.

- **Control variables** : U and V are the inputs which have to be provided to the model to get a unique solution between time 0 and time T . V is the set of initial parameters: water, nitrogen and organic matter in the soil, sowing date, residues quality, fertilisation, length of development stages, etc. U represents the error which provides from the model, and can be expressed by boundary conditions for example.

- **A model** which can be written:

$$\frac{dX}{dt} = F(X) + B.U$$

$$X(0) = V$$

B is a mathematical operator (a matrix for instance) used to map U in the same space as the output of F

- **A cost function** J which estimates the discrepancy between the solution of the model and the observations.

$$J(U,V) = \frac{1}{2} \int_0^T \|C.X - X_{obs}\|^2 dt + \frac{\mathbf{e}}{2}(NU,V)$$

$$\nabla J_v(U, V) = -P(0)$$

$$\nabla J_u(U, V) = -\left[\frac{\partial F}{\partial V}\right]^T P + NU$$

Because the variable X and the observations X_{OBS} are not in the same mathematical space, we will consider C mapping the mathematical space into a physical space. C plays here the same role as B in the error model term.

ε is a term we will vary to limit the error. The second term in the cost function is useful for the regularisation of the inverse problem in Tykhonov sense. It also works as a penalization criterion and avoids to consider large errors in observation adjustment. N is a definite positive operator, usually an approximation of the inverse of the covariance error matrix. It is a way for considering statistical information in the analysis.

Take into account the observation error, more than the error due to the model, is made possible by determining the sensitivity to the observations. This type of problem requires a second order derivation of the model, and will be done in a second step.

The problem is therefore: determine U^* and V^* minimizing J , i.e. we look for the model input parameters that lead to the model solution the closest to the observations. Therefore the closure of the model is stated as a problem of unconstrained optimisation for which there are many known efficient algorithms.

It is clear that U^* and V^* are characterized by the optimality condition:

$$\nabla J_u = 0$$

$$\nabla J_v = 0$$

The gradient of the cost function J has to be provided as input to the optimisation algorithms. Its computation is performed with the help of the **Adjoint Model**. We introduce P the “adjoint variable”. It has the same dimensionality as X and is the solution of the adjoint model:

$$\frac{dP}{dt} + \left[\frac{\partial F}{\partial X}\right]^T P = C^T (CX - X_{obs})$$

$$P(T) = 0$$

Then it can be seen that the gradient of J is given by:

Therefore the gradient is obtained by a backward integration of the adjoint model.

For this type of problem, an algorithmic solution exists: an iterative descent-type method is applied. At each iteration an evaluation of the model and of the gradient is required. The complexity of the adjoint model is of the same order of magnitude as the direct model. Its determination is done numerically, involving a computational cost in terms of writing and of computer resources. The help of automatic differentiation allows reducing time expenses.

4.4 Automatic differentiation

Automatic differentiation is a technique to evaluate the derivatives of a function defined by a computer program. The basic idea is to start from the last statement of the direct code and going up in the direct code, and to derive and to transpose each statement of the direct model (Corliss et al., 2001; Griewank, 1988).

Automatic differentiation will be performed by the TAPENADE software (INRIA Sophia-Antipolis, France). It takes the computer source program as an input. Then, it builds and returns the differentiated source program, that is used to evaluate the required derivatives, and finally computes the adjoint model.

Even though the help of automatic differentiation, the process is long and painful, all the more when the model is not differentiable, like STICS. An error in the adjoint model will lead to a wrong gradient inhibiting the optimization algorithm. The adjoint model should therefore be carefully checked.

5 CONCLUSION

The calibration of the STICS model was undertaken on Romanian wheat cultivar, with the ADAM 2000-2001 database, a complete agronomical dataset composed of *in situ* measurements and remote sensing products.

This study reported the disagreement between observed and simulated LAI values and pointed out the need for determining other parameters like soil characteristics, cultural practices and cultivar

specificities more reliably. It is the aim of the ADAM project to improve this kind of agronomic parameters, in order to optimize the cultural techniques and to better determine the production estimations.

Consequently, we consider here a new method that derives from the variational assimilation theory, and that will be specifically adapted to STICS. The adjoint model of the latter will be computed with the automatic differentiator TAPENADE software, carefully taking into account the non-differentiability of STICS.

Then, a sensitivity analysis will be performed in order to take into account the observations errors and to investigate the effects of high temporal frequency. Finally, the assimilation process will be validated on ADAM 2001-2002 data.

6 REFERENCES

Benett, A., 2002, Inverse Modeling of the Ocean and Atmosphere, *Cambridge University Press*.

Brisson, N., et al., 2002, STICS: a generic model for simulating crops and their water and nitrogen balances. II. Model validation for wheat and maize. *Agronomie* 22 (2002) pp 69-92.

Brisson N. et al., 1998, STICS : a generic model for the simulation of crops and their water and nitrogen balances. *Agronomie* 18 (1998), pp 311-346.

Corliss, G., Faure, C., Griewank, A., Hascoet, L., Naumann, U., 2001, Automatic differentiation of Algorithms, from simulation to optimization, *Springer*.

Delecolle, R., Baret, F., Guérif, M., Maas, S. J., 1991, L'utilisation conjointe de la télédétection et des modèles d'estimation des productions agricoles : tendances actuelles. *Proceedings of the 5th International colloquium -Physical measurements and signatures in remote sensing, Courchevel, France (14-18January 1991)*, pp 529-534.

François, C., Cayrol, P., Kergoat, L., Moulin, S., 1995, Assimilation techniques of remote sensing measurements into vegetation models : overview, limits and promises. *Actes de l' Ecole - Chercheurs INRA en bioclimatologie, Le Croisic, 3-7 Avril 1995*, INRA, pp 649-658.

Guérif, M., Courault, D., Brisson, N., 1995, Assimilation des données de télédétection dans les modèles de fonctionnement des cultures. *Actes de l' Ecole - Chercheurs INRA en bioclimatologie, Le Croisic, 1995, INRA, pp 169-190*.

Griewank, A., 1988, On Automatic differentiation, *Mathematics and computer science division*, Preprint ANL/MCS-P10-1088.

LeDimet, F-X., Blum, J., 2001, Assimilation de données pour les fluides géophysiques. *Matapli n°67-janvier2002*.

LeDimet, F-X., Talagrand, O., 1985, Variational algorithms for analysis and assimilation of meteorological observations : theoretical aspects. *Tellus* 38A (1986), pp 97-110.

Prevot, L., Chauki, H., Troufleau, D., Weiss, M., Baret, F., Brisson, N., 2001, Assimilating optical and radar data into the STICS model for wheat crops: preliminary results, *to be published in Physics and Chemistry of the earth*.

Weiss, M., Baret, F, 2001, *DAASCEES Progress review Assimilation of RS data, Noordijk, 5-10-2001*.

Localización de construcciones rurales en la imagen de satélite ikonos y gestión de las mismas mediante un sistema de información geográfica

M. L. Gil and A. González

Departamento de Ingeniería Agroforestal, Universidad de Santiago de Compostela, Escuela Politécnica Superior de Lugo, España; e-mail: mlgild@correo.lugo.usc.es

And I. Cañas.

Departamento de Construcción y Vías Rurales, Universidad Politécnica de Madrid, Escuela de Ingenieros Agrónomos, España

ABSTRACT

En este trabajo se desarrolla una metodología de tratamiento digital de la imagen del satélite IKONOS para la elaboración de inventarios de construcciones rurales y para el estudio de sus características constructivas, orientada a incorporar estos datos a un Sistema de Información Geográfica (SIG). Para el cálculo de la densidad de edificaciones se propone un método basado en el recuento de edificaciones sobre la composición 4/3/2 RGB convenientemente filtrada y realzada. El resultado del inventario se muestra en forma de mapa temático, de manera que puede ser incorporado a un SIG como cartografía temática. Para el cálculo de la densidad de construcciones industriales se propone el recuento sobre la composición 2/4/1 RGB; este parámetro constituye un reflejo del grado de alteración del medio natural.

La composición 4/3/2 RGB filtrada mediante filtro de realce de bordes y realzada permite analizar algunas características constructivas de las edificaciones: desarrollo volumétrico, forma en planta, materiales de cubierta, número de faldones, deterioros. Estos atributos se incorporan a la base de datos del SIG para su posterior análisis.

Esta metodología de trabajo, basada en el análisis digital de imágenes de altísima resolución espacial, permite ahorrar costes en la inventariación de edificaciones, en especial en zonas de hábitat disperso. No obstante sería interesante investigar en el futuro una metodología que permita inventariar las características de las construcciones de forma automática.

1. INTRODUCCIÓN Y OBJETO

Las actividades encaminadas a la ordenación y planificación territorial necesitan echar mano de la cartografía, instrumento que facilita el conocimiento físico del territorio. Cartografía y sistemas de información geográfica (SIG) han convergido en los últimos años (Fritsch, 1998). Los SIG se han consolidado como instrumentos fundamentales para la organización y el almacenamiento de datos territoriales en formato digital, pudiendo además realizar con los datos operaciones de análisis y tratamiento que permiten transformarlos y presentarlos gráficamente (o cartográficamente) (Lorenzo; 2001). Los SIG se han convertido en herramientas imprescindibles para la gestión de la información territorial, la protección del medioambiente, optimización de infraestructuras, planificación urbana, etc. Los SIG empleados en planificación y gestión territorial se construyen a partir de gran variedad de clases de información geográfica, entre ellas la relativa a las edificaciones y al patrimonio cultural.

La teledetección se consolida como una de las principales fuentes de información territorial, de aquí su utilidad para la los SIG y la cartografía. En concreto las imágenes de muy alta resolución, como las del satélite Ikonos, que genera imágenes pancromáticas de un metro de resolución y cuatro canales multispectrales de cuatro metros de resolución, son susceptibles de ser empleadas en el estudio de edificaciones. Así lo confirma un estudio reciente de Fraser, Baltsavias y Gruen (2002).

El principal objetivo de este trabajo consiste en desarrollar una metodología de tratamiento digital de la imagen para la elaboración de inventarios de construcciones rurales y delimitación de áreas urbanas y rurales a partir de las imágenes del satélite IKONOS. Asimismo, se pretende estudiar las posibilidades que dichas imágenes ofrecen en cuanto a la identificación de características constructivas de las construcciones rurales. Todo ello con el fin último de integrar dicha información en un SIG. De esta forma se conseguirá utilizar la potencia de la teledetección como fuente de información territorial junto con la capacidad de análisis de los SIG.

La primera cuestión que se plantea a la hora de abordar este estudio es el concepto de construcción rural. Hay diversas definiciones según autores. Dado que este estudio pretende servir de base para la caracterización de la arquitectura de áreas rurales, nos hemos centrado en aquellas construcciones presentes en el medio no urbano, ya sean estrictamente tradicionales o modernas de uso industrial.

El primer problema que surge a la hora de estudiar las edificaciones rurales de un lugar es su localización (Ortiz, 2001). Gracias a la alta resolución de la imagen, muchas edificaciones, en especial las de gran extensión (naves industriales), son visibles a simple vista sin necesidad de aplicar previamente tratamiento digital alguno. No obstante, las construcciones pequeñas pasan desapercibidas fácilmente, ya sea porque están parcialmente ocultas por vegetación, por mimetizarse con el entorno o por confundirse con las edificaciones adyacentes. Por ello se tratará de encontrar un tratamiento digital que permita visualizar en pantalla lo más claramente posible todas las construcciones.

Una vez localizadas, abordaremos la forma de estimar la densidad de construcciones, entendida como número de edificios por unidad de superficie. Datos cuantitativos sobre densidad urbana son útiles en el estudio de cambios en el medio urbano (Pineda, 2001). Este tipo de datos se incorporarán a un SIG como base cartográfica temática.

Se estudiará en qué medida pueden caracterizarse las construcciones a partir de la imagen Ikonos: se tratará de encontrar un tratamiento digital que aplicado a ella permita, en la medida de lo posible, caracterizar las edificaciones según los parámetros propuestos por Ortiz (2001) y De Llano Cabado (2000), descritos en la tabla 1. Estos datos pueden incorporarse a la base de datos del SIG.

Tabla 1. Análisis de las edificaciones (Ortiz Sanz, 2001; De Llano Cabado, 2000).

Edificación interior		
<i>Desarrollo volumétrico</i>	Simple	Prolongación de cubierta Unión perpendicular Mixtos
	Complejo	
<i>Forma en planta</i>		
		Cuadrangular
		ELE
		U
		Anillo
		T
		Otras

El desarrollo volumétrico de una edificación alude a la agrupación de volúmenes de la misma. Será simple cuando conste de un único volumen, compleja

en caso contrario. La planta del edificio puede tener forma cuadrangular, en “L”, en “U”, en “T”, en anillo, u otras.

Además se estudiarán los materiales de las cubiertas.

2. MATERIAL

2.1. Área de estudio

El área de estudio es la zona del Palmar (500 ha de superficie aproximadamente), pedanía perteneciente al ayuntamiento de Murcia, situada entre las ciudades de Murcia y Alcantarilla, y cuyo límite Sur se extiende hasta las estribaciones de la Sierra de la Cresta del Gallo. Pertenecce a la denominada región del bajo Segura, muy cerca del mar Mediterráneo, en el sureste de la Península Ibérica. Esta región es predominantemente agrícola; en ella se dan cita secanos y regadíos, garrigas y pastizales ralos, peñascales y algún bosque. Hay edificaciones rurales e industriales dispersas, y pequeños asentamientos.

2.2. Material

La imagen con la que hemos trabajado combina digitalmente las imágenes pancromáticas de 1 metro de resolución con las imágenes multispectrales de 4 metros, resultando una fusión que cuenta con una resolución espacial de 1 metro y con la alta resolución espectral de las bandas del visible e infrarrojo.

Esta es una ortoimagen con precisión métrica; el proceso de ortorectificación elimina las distorsiones introducidas por la variabilidad y geometría del relieve. La imagen está referida a la Proyección Universal Transversa de Mercator, elipsoide de Hayford, Datum Europeo 1950.

3. METODOLOGÍA

3.1. Visualización de las construcciones

El objetivo inmediato del tratamiento digital de la imagen consiste, como hemos indicado, en localizar las construcciones para poder efectuar el recuento de las mismas y posteriormente analizar sus características constructivas. Las construcciones adyacentes tienen una problemática particular, que se enfrenta a los siguientes problemas:

- Al no haber separación espacial entre ellas no hay superficies intermedias con comportamiento espectral diferente al de los materiales de cubierta. Es, pues, una sucesión continua de tejados, a veces del mismo material (en similares o diferentes estados de conservación).
- A veces la extensión de la planta de una de las edificaciones es pequeña. El efecto de borde (interferencia con las cubiertas vecinas) hace que

la cubierta no presente una respuesta espectral clara ni homogénea.

- Las cubiertas de algunos edificios están formadas por varios faldones con diferente inclinación; cada uno de ellos tiene un comportamiento espectral distinto.

3.1.1. Mejora de la visualización de las edificaciones

Las composiciones coloreadas y las técnicas de realce del contraste son útiles para hacer destacar las edificaciones de las áreas de entorno. Sobre cada una de las composiciones coloreadas se ensayan los realces que propone el programa EASI/PACE: expansión lineal del histograma, realce cuadrático, realce adaptado, ecualización del histograma.



Fig. 1. Composición 4/3/2 RGB realzada mediante expansión lineal del contraste.

Del análisis visual de las composiciones efectuadas se concluye que la composición 4/3/2 RGB realzada mediante expansión lineal del contraste (fig. 1) es la composición más apta para la localización de edificaciones y para el estudio de las características de las edificaciones. En ella la vegetación destaca inconfundiblemente sobre otros tipos de cubiertas. Dado que fuera de los núcleos de población las construcciones están mayoritariamente rodeadas de vegetación, ya sean campos de cultivo, jardines, o vegetación arbórea, las edificaciones se reconocen fácilmente. Resta tan solo poner cuidado en la interpretación de la imagen para no confundir una construcción con otras superficies como áreas asfaltadas, de suelo desnudo, metálicas, superficies de agua, etc.



Fig. 2. Composición 2/4/1.

En la composición 2/4/1 (fig. 2) tan solo las construcciones con cubiertas metálicas y/o de fibrocemento, tienen un color diferente (azul) del

general de la imagen (verde). He aquí un tratamiento que permite aislar un tipo de material de cubierta.

Estudiando en detalle la imagen, concretamente la composición 4/3/2 RGB, se observa que es posible identificar la mayor parte de las edificaciones. No obstante, existen ciertas dificultades: debido a que cada faldón de cubierta tiene un comportamiento espectral diferente derivado de su peculiar inclinación y orientación, a veces no resulta fácil establecer cuándo dos faldones pertenecen a la misma edificación y cuándo se trata simplemente de viviendas adyacentes; hay que tener en cuenta que algunas viviendas tienen tejados a un agua y otras a dos aguas; algunas incluso combinan faldones y terraza.

La observación de las sombras proyectadas por los elementos de la imagen puede resultar de gran ayuda. Los edificios son estructuras elevadas sobre el suelo y por consiguiente proyectan una sombra en alguna dirección. La vegetación arbórea también proyecta sombras, pero las de unos y otra difieren en la forma. La vegetación proyecta sombras irregulares, redondeadas a veces (debido a la forma de las copas), mientras que los edificios proyectan sombras de formas geométricas, regulares, continuas. Así pues, la observación de las sombras puede ayudar a la localización e incluso discriminación de edificios (en dos faldones separados por una sombra podremos reconocer dos construcciones diferentes con diferentes alturas).

3.1.2. Mejora de la nitidez de la imagen

El filtro de realce de bordes es una buena herramienta para hacer los contornos de las cubiertas más nítidos. La aplicación de este filtro en tamaño de matriz 3x3 sobre cada una de las bandas que componen una composición seleccionada mejora la nitidez de la imagen y la visualización de las construcciones (fig. 3). Tamaños mayores suponen una alteración excesiva de los niveles digitales originales que puede alterar la interpretación de la imagen.



Fig. 3. Composición 4/3/2 RGB filtrada mediante filtro de realce de bordes 3x3 y realzada mediante expansión lineal del contraste.

3.2. Estudio de la densidad de construcciones

Proponemos una metodología para estimar el número de edificios por unidad de superficie que consiste en lo siguiente:

- Se selecciona la composición coloreada más apta para la identificación de edificaciones: composición 4/3/2 RGB.
- Se aplica un filtro de realce de bordes 3x3 a cada una de las bandas.
- Se aplica un realce lineal a la composición.
- Se carga sobre la imagen la malla de coordenadas geodésicas UTM. Se toma cada cuadrícula como unidad de superficie (200 x 200 m). En cada una se cuenta el número de edificaciones.
- Se establecen clases de densidades (clases de cuadrículas). Ej: <5; 5-14; 15-24; 25-49; >50. A cada cuadrícula se le asigna una clase de densidad.
- Muestra de resultados:
 - Imagen original con información de contexto (fig. 4).
 - Mapa con los edificios marcados (fig. 5).
 - Mapa de densidades por cuadrículas (fig. 6).
 - Resultados y conclusiones.



Fig. 4. Detalle de la composición 4/3/2 RGB de Ikonos realzada mediante expansión lineal del histograma.

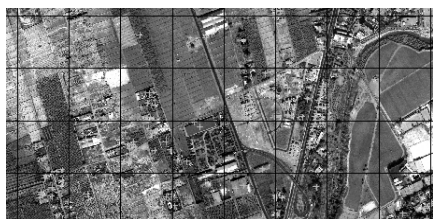


Fig. 5. Detalle del mapa de los edificios marcados sobre composición 4/3/2 RGB de Ikonos realzada mediante expansión lineal del histograma.

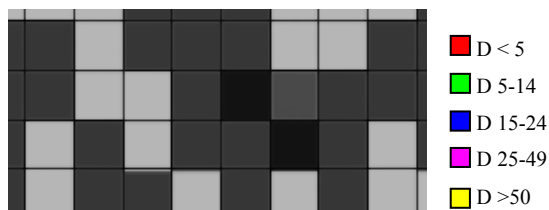


Fig. 6. Mapa de densidades por cuadrículas. A cada color lo corresponde una clase de densidad.

La clave para un buen recuento reside en una adecuada interpretación de la imagen, y ello requiere una concienzuda familiarización con el comportamiento espectral de cada uno de los tipos de cubiertas; será preciso tener en cuenta lo indicado más arriba referente a la variabilidad de comportamientos espectrales de un mismo tipo de cubierta debido a las diferentes inclinaciones y orientaciones de los faldones.

La densidad de edificios constituye un indicador del grado de ocupación y transformación del territorio, puesto que la actividad humana estratégica ocurre en o en asociación con algún tipo de edificio (Selvarajan, 2001). No obstante no necesariamente densidades bajas corresponden a áreas naturales poco alteradas, especialmente en esta región, donde los cultivos agrarios ocupan grandes extensiones de terreno. Además, las viviendas rurales no sólo no empobrecen el paisaje y el entorno, sino que lo enriquecen y configuran. Por ello a la hora de evaluar el grado de alteración del medio y del paisaje a través de la densidad, resulta más revelador el recuento de naves industriales.

Para ello basta con tomar como base la composición 2/4/1 en la que, como se apuntó más arriba, aparecen destacadas las construcciones con cubiertas metálicas y de fibrocemento, cubiertas propias de las naves industriales; su gran extensión permite además diferenciarlas de forma inequívoca de cobertizos y otras cubiertas metálicas no correspondientes a naves industriales.

3.2. Análisis y caracterización de las construcciones

Las características constructivas propuestas por Ortiz (2001) (Tabla 1) se introducen como campos en la base de datos del SIG de construcciones rurales: forma de la planta y desarrollo volumétrico (Tabla 2). La imagen 4/3/2 RGB realzada mediante expansión lineal del contraste y filtrada mediante filtro de realce de bordes 3x3 permite caracterizar las construcciones de acuerdo con estos atributos: se distinguen claramente las construcciones de desarrollo volumétrico simple de aquellas que presentan desarrollo volumétrico complejo; en éstas se puede llegar a especificar si los módulos están unidos perpendicularmente o bien si se combinan por prolongación de cubierta.

Se ha observado que en la composición 4/3/2 RGB tratada de la forma indicada es posible además identificar el material de la cubierta, contar el número de faldones que la componen e incluso detectar deterioros en las cubiertas metálicas. Estos atributos se introducen como nuevos campos en la base de datos del SIG (Tabla 3).

Tabla 2. Atributos del SIG de construcciones rurales fácilmente caracterizables a través de la imagen de satélite Ikonos.

Shape Id	Desarrollo volumétrico	Forma en planta
0	Complejo (unión perpendicular)	U
1	Complejo (unión perpendicular)	Anillo
2	Simple	Cuadrangular
3	Mixto	T

Tabla 3. Atributos del SIG de construcciones rurales caracterizables en la composición 4/3/2 RGB filtrada mediante filtro de realce de bordes 3x3 y realizada mediante expansión lineal del contraste.

Material de cubierta	Número de faldones de cubierta	Deterioros en cubierta
Teja árabe	3+4+2+4+3	No
Teja alicantina	2+2+2+2+2	No
Teja alicantina	4+4	No
Teja árabe	3	No

Creados los campos relativos a los atributos que pretenden estudiarse, se procede a especificar las características propias de cada edificación. Así por ejemplo, en la construcción identificada con el código 3 (shape Id 3; tabla 2) (fig. 7) el desarrollo volumétrico es complejo con prolongación de cubierta; la planta de la edificación tiene forma de “T”, la cubierta está formada por teja árabe, tres faldones componen la cubierta y no hay deterioros aparentes en ella.

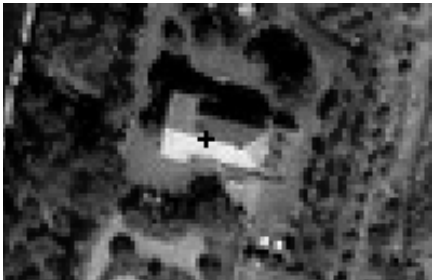


Fig. 7. Edificación codificada como “Shape Id 3” en la base de datos del SIG.

La introducción de las características específicas de cada construcción en la base de datos del SIG es una labor lenta dado que debe realizarse manualmente. No obstante, una vez introducidos los datos, el SIG permite realizar análisis globales de los atributos incluidos en la base de datos de forma rápida y cómoda. Así, por ejemplo, si interesa conocer la abundancia de las cubiertas de teja alicantina basta con solicitar del SIG que seleccione aquellas construcciones que tengan este material de cubierta.

Tabla 4. Análisis de los datos contenidos en el SIG.

Query

Apply query to ☒ All ☐ Selected Shapes Only

Query "Material de cubierta" = "Teja alicantina"

Al ejecutar la búsqueda, el SIG selecciona en la base de datos todas aquellas construcciones que tienen este material de cubierta (tabla 5); también en la imagen aparecen dichas construcciones señaladas.

Tabla 5. Resultado de la búsqueda en el SIG.

Shape Id	Material de cubierta
0	Teja árabe
1	Teja alicantina
2	Teja alicantina
3	Teja árabe
4	Teja árabe
5	Teja árabe
6	Teja árabe
7	Teja alicantina
8	Teja alicantina
9	Teja árabe

4. RESULTADOS

La metodología propuesta para el recuento de edificios, consistente en contar el número de edificios incluidos en cuadrículas de 200 m de lado, ha permitido extraer el mapa de densidad cualitativo para la pedanía del El Palmar (fig. 8).

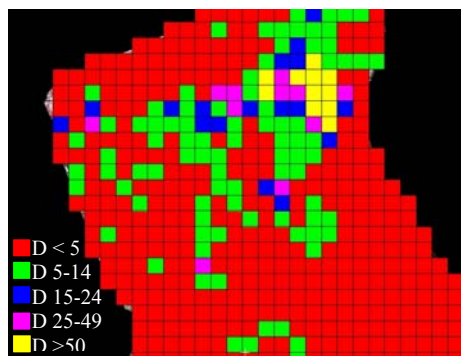


Fig. 8. Mapa de densidad de edificaciones para la pedanía de El Palmar (Murcia).

En este mapa se observa que tan solo el núcleo de población que da nombre a la pedanía, El Palmar, tiene una densidad superior a las 50 viviendas por cuadrícula, lo cual equivale a una vivienda por cada 800 m². La mayor parte de la pedanía corresponde a tierras de cultivo o espacios verdes (sierra) con densidades inferiores a las 5 viviendas por cuadrícula, es decir, menos de una construcción por cada hectárea de terreno. Puede concluirse, pues, que la densidad de edificios constituye un indicador fiable del grado de ocupación del territorio. El mapa de densidades se incorpora al SIG como cartografía temática.

El recuento de naves industriales sobre la composición 2/4/1 RGB da como resultado un mapa análogo de densidad. No cabe duda de que la abundancia de construcciones industriales conlleva una actividad económica intensa; esto tiene consecuencias en el tráfico de las carreteras de la región (vehículos pesados, circulación abundante), en la apariencia del paisaje (un paisaje industrial tiene menos valor que un paraje natural), en el grado de alteración del medio (ya se deba a que la actividad que allí se desarrolla explota alguno de los recursos naturales del medio, o a la propia alteración del medio que supone adecuar áreas para albergar naves industriales). Por ello la densidad de construcciones industriales constituye un reflejo del grado de alteración de la apariencia tradicional del paisaje.

En cuanto a las tipologías constructivas de la región, hay que decir que se han encontrado construcciones con desarrollo volumétrico simple (fig. 9), y con desarrollo volumétrico complejo de unión perpendicular (fig. 10).



Fig. 9. Edificación de desarrollo volumétrico simple.



Fig. 10. Edificación de desarrollo volumétrico complejo con unión perpendicular.

Se han encontrado edificaciones con planta de forma cuadrangular (fig. 11), rectangular (fig. 12), en "U" (fig. 13), en "L", en "T", en anillo simple y doble (fig. 14). No obstante, predominan las formas más simples.



Fig. 11. Construcción de planta cuadrangular.



Fig. 12. Construcción de planta rectangular.



Fig. 13. Construcción de planta en U.



Fig. 14. Cubierta de teja alicantina.



Fig. 15. Cubierta de teja árabe.

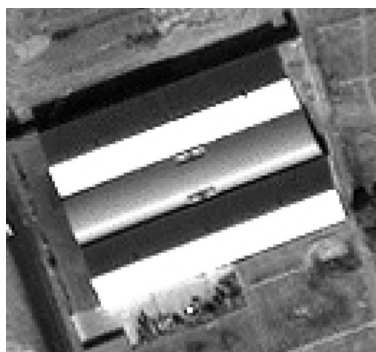


Fig. 16. Cubierta metálica.



Fig. 17. Cubierta de pizarra.

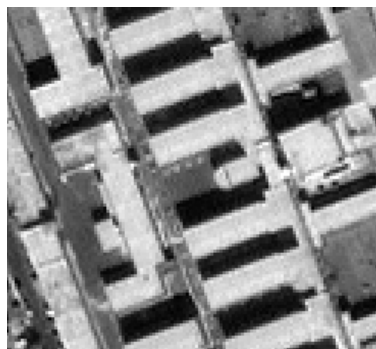


Fig. 18. Cubierta de terraza.



Fig. 19. Deterioro en cubierta metálica.

Los tipos de cubiertas que se han podido discernir son: teja alicantina (fig. 14), teja árabe (fig. 15), cubiertas metálicas (fig. 16), de pizarra (fig. 17), de terraza (fig. 18) y de fibrocemento. Se pueden detectar incluso deterioros en las cubiertas metálicas (fig. 19).

Este tipo de características son interesantes para establecer las tipologías dominantes. En esta región predominan las cubiertas de teja árabe. En núcleos urbanos predominan las terrazas. En cuanto a la forma de la planta y el desarrollo volumétrico, puede concluirse que en los núcleos de población predominan los desarrollos simples y formas cuadrangulares o rectangulares. En viviendas aisladas predominan desarrollos complejos con formas variadas.

5. CONCLUSIONES

La imagen Ikonos permite generar cartografía temática relativa a la densidad de construcciones, información que puede ser directamente incorporada a un SIG. El método propuesto se basa en el recuento del número de edificaciones en cuadrículas de 200 m de lado; el recuento se efectúa sobre la composición 4/3/2 RGB filtrada mediante filtro de realce de bordes 3x3 y realzada por expansión lineal del contraste. La densidad constituye un buen indicador del grado de ocupación del territorio.

Si se emplea como imagen de base para el recuento la composición 2/4/1, se obtiene la densidad de las construcciones industriales. Este parámetro refleja el grado de conservación de la apariencia tradicional del paisaje.

Para el análisis de las características constructivas de las edificaciones se trabaja sobre la composición 4/3/2 RGB. Esta imagen permite reconocer la forma de la planta, el desarrollo volumétrico, el material de la cubierta, el número de faldones de la cubierta y ciertos deterioros en cubiertas. Las características específicas de cada edificación relativas a estos atributos se incorporan a la base de datos del SIG de construcciones rurales, quedando así almacenados y disponibles para ser consultados en el momento preciso. El SIG permite realizar análisis globales relativos a las características constructivas de las edificaciones de la región. Así por ejemplo, permite identificar de forma inmediata las edificaciones con algún deterioro en la cubierta, lo cual puede ser útil en la gestión urbanística del municipio.

Esta metodología de trabajo, basada en el análisis digital de imágenes de altísima resolución espacial, permite ahorrar costes en la inventariación de edificaciones, en especial en zonas de hábitat disperso, ya que disminuye notablemente la labor de campo. No obstante, sería interesante investigar la forma de automatizar el reconocimiento de las características constructivas de las edificaciones.

6. REFERENCIAS

- Fraser, C. S.; Baltsavias, E.; Gruen, A. (2002). *Processing of Ikonos imagery for submetre 3D positioning and building extraction*. ISPRS Journal of Photogrammetry and Remote Sensing. Vol. 56 pp. 177-194.
- Fritsch, D. (1998). Technical Commission IV – “Mapping and Geographic Information Systems”. International Society for Photogrammetry and Remote Sensing (ISPRS). www.ifp.uni-stuttgart.de/comm4.
- Gil Docampo, M. (2001). *El empleo de imágenes Landsat y Spot-P para el estudio de las vías de baja densidad de tráfico. Caso particular de la Reserva de Caza de Los Ancares gallegos*. Tesis doctoral. Escuela Politécnica Superior de Lugo. Universidad de Santiago de Compostela.
- Lorenzo, R. M. (2001). *Cartografía, urbanismo y desarrollo inmobiliario*. CiE.
- Ortiz Sanz, J.; Rego Sanmartín, T. (2001). *Técnicas de estudio de los edificios tradicionales de una comarca*. Gestión sostenible de paisajes rurales. Técnicas e Ingeniería. Fundación Alfonso Martín Escudero.
- Pineda, N; Jorge, J. (2001). *Textura y urbanismo en la ciudad de Rosario (Argentina)*. Teledetección, Medio Ambiente y Cambio Global. IX Congreso Nacional de Teledetección. Lleida.
- Selvarajan, S.; Weng Tat, C. (2001). *Extraction of man-made features from remote sensing imageries by data fusion techniques*. 22nd Asian Conference on Remote Sensing. Singapore.

Land cover change monitoring in the Mediterranean Basin using NOAA-Pathfinder time series (1981-2001): WATERMED project.

J. A. Sobrino, J. El-Kharraz, M. Romaguera, M. Gómez, J. C. Jiménez-Muñoz & G. Sòria.
*Global Change Unit. Dept. of Thermodynamics, University of Valencia, C/ Dr. Moliner 50,
46100 Burjassot, Spain.*
sobrino@uv.es

ABSTRACT- *The WATERMED project (2000-2004) is founded by the European Union (INCO-med project) and contributes to the international efforts in analysing efficiency in water use, in particular for the Mediterranean Basin countries. The general objective of the WATERMED project is to develop a comprehensive method for the study of the water use and the resistance to the drought of the natural and irrigated vegetation in the Mediterranean Basin, by means of a combined historical and current space-based remote sensing database, vegetation models and field measurements. The Mediterranean basin was selected as the area of study thanks to its high environmental diversity. This area is clearly affected by the risk of the advance of the desert. Analysing multi-temporal data from the NOAA/NASA Pathfinder AVHRR land (PAL) dataset is taking place as part of the WATERMED project. The main objective of this study is to map, and monitor land-cover change in the Mediterranean basin between 1981 and 2001. The study consists in combining both the information in the visible/near-infrared bands in terms of Normalised Difference Vegetation Index (NDVI) and in the thermal-infrared bands in terms of Land Surface Temperature (LST). The space-temporal dynamics of these parameters have been sought by analysing seasonal and inter-annual variability. Finally, we analyse the evolution of LST and NDVI for the months of April and July by the use of the Land Cover Dynamic (VCLD) method.*

1 INTRODUCTION

They have been numerous investigations in the field of cartography and analysis on land cover changes considering only the temporal analysis of Normalized Difference Vegetation Index (NDVI) (Tucker et al. 1985; Townshend et al. 1987; Loveland et al. 1991; Lambin & Strahler, 1994). However, few papers introduced the Land Surface Temperature (LST) parameter obtained from satellite data to study the land cover changes (Lambin & Ehrlich, 1996; Raissouni & Sobrino, 1998; Sobrino & Raissouni, 2000). One of the motives is the difficulty of obtaining this parameter. Nevertheless, at present it is possible to determine LST within a precision of 1 K. Land cover classification and change detection using temporal series of LST and NDVI requires a good knowledge of the relationships between these biophysical parameters in different ecological conditions (Nemani & Running, 1989; Goward et al. 1985; Nemani et al. 1993; Friedl & Davis, 1994). Recently, we have developed two methods for the land cover dynamic monitoring in arid zones using satellite data: the Method of the Area of the Triangle (MAT) and the slope method (Sobrino & Raissouni, 2000). The MAT method is based on the form described by the annual evolution of LST and NDVI and the slope method analyses the slope of the line defined by the months of the maximum NDVI and the minimum LST. In this paper we apply the method

of Vector of Land Cover Dynamic (VLCD) (Sobrino et al., 2001) developed for the multi-temporal monitoring in the whole of the Mediterranean Basin.

2 ALGORITHMS

LST retrieval from satellite data is mainly influenced by the atmosphere and surface emissivity. If both effects are not corrected for the error in LST may be very large (up to 12 K). In order to obtain accurate estimations of LST, we have applied the following split-window algorithm (Sobrino & Raissouni, 2000) with an error of estimation of 1.3 K.

$$LST = T_4 + 1.4 (T_4 - T_5) + 0.32 (T_4 - T_5)^2 + 0.83 + (57 - 5W) (1 - \epsilon) - (161 - 30W) \Delta\epsilon \quad (1)$$

where T_4 and T_5 are the brightness temperatures measured in AVHRR Channels 4 and 5 respectively, ϵ is the average effective emissivity in both channels, $\Delta\epsilon$ is the spectral variation of emissivity and W is the total amount of atmospheric water vapour (g cm^{-2}) obtained applying the Split-Window Covariance-Variance Ratio (SWCVR) method (Sobrino et al. 1999).

$$W = 0.26 - 14.253(\cos\theta \ln R_{54}) - 11.649(\cos\theta \ln R_{54})^2 \quad (2)$$

where θ is the satellite observation angle and R_{54} is the ratio of the spatial covariance and the variance of

image brightness temperatures in the split-window Channels 4 and 5. The estimated error is 0.5 g cm^{-2} . To obtain ε we have applied the NDVI Threshold Method (NDVITHM) (Sobrino & Raissouni, 2000; Sobrino et al. 2001). This method integrates a wide spectral data set of bare soil reflectivity measurements in the band of $0.4\text{--}14 \text{ }\mu\text{m}$ and uses different approaches in function of NDVI.

3 AREA OF STUDY AND SATELLITE DATA

The study area is the Mediterranean Basin, located between 23.75° N and 46.25° N latitude and between 36.25° E and 17.5° W longitude. This particular geographical position gives the area a great bioclimatic diversity. The Mediterranean climate of the area is characterized essentially by two seasons: a hot and dry summer and a short winter with concentrated precipitation. The climate is also variable according to region and marked by strong annual and inter-annual irregularity. The area is also subjected to a significant problem with regard to desertification. The Pathfinder AVHRR Land (PAL) has been used to monitor this area. NOAA and NASA are the sponsors of the PAL project responsible of producing a set of global data calibrated and processed regularly for the investigation on climatic change. Approximately 20 years of global AVHRR data are now available. The AVHRR data used are the Global Area Coverage GAC (Towshend, 1994) with a resolution at nadir view of 4 Km . In this paper we have used the images from July 1981 through April 2001. The data are accessible via FTP (daac.gsfc.nasa.gov) from the Goddard Distributed Active Archive Centre.

4. MULTI-TEMPORAL ANALYSIS SOFTWARE USED

4.1 Zones of interest definition

In order to avoid monitoring land cover dynamics per pixel, which is time consuming and difficult to interpret, we have analysed the evolution of varied landscapes of the study area. The different zones of interest were defined using as mapping criterion the image of the Total Average of (TANDVI) for the whole period. Following this procedure we defined a total of six zones (Table 1) in order to yield zones that match the different climatic zones in the study area (see Fig. IV.12 in (Raissouni, 1999)) according to the classification of Köppen and Geiger based on monthly and annual precipitation and temperature quantities. Figure 1 represents the total average of albedo. The values of albedo over the arid regions (zones 1 and 2) are higher than those over the rest of zones (superior to 0.25), while in zones 5 and 6 they are lower (up to 0.15).

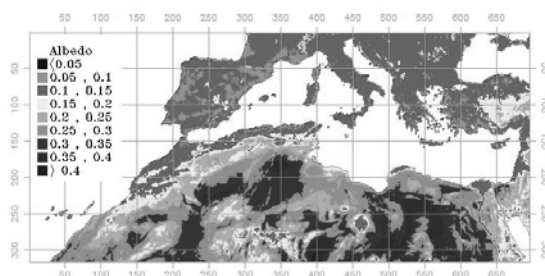


Figure 1.- Image of the Total Average of albedo.

4.2 Monthly evolution

Fig. 2a shows the results of the monthly evolution in terms of the NDVI in each of the defined zones. The arid zones (1 and 2) show small variations; with a maximum of 0.05 during spring and a minimum of -0.03 and 0 respectively during summer. Zones 3 and 4 reach the minimum in October and November (0.1 for zone 3 and 0.15 for zone 4), zones 5 and 6 achieve their minimum in December (0.25). For these last zones, the months of June and July show a maximum NDVI ($0.4\text{--}0.6$) during summer. Fig. 2b is similar to Fig. 2a but for LST evolution. The maximum ($> 320 \text{ K}$) is produced during summer and the minimum ($< 290 \text{ K}$) in winter. Thermal amplitude in the study area, between zone 1 and zone 6, is of about 23 K during July and 14 K during January. To distinguish between zones is better to work with summer data (July). Finally, Fig. 2c is similar to the previous ones but for emissivity evolution. Thus, zone 6 reaches a maximum of 0.988 during summer and a minimum of 0.976 during winter. Zone 5 shows a similar behaviour to the previous one with a maximum of 0.982 during summer and a minimum of 0.976 during winter. Zone 4 presents a maximum of 0.976 during spring and a minimum of 0.974 around the end of summer. Zone 3 presents an opposite behaviour that zone 4, a maximum of 0.976 is produced during winter and a minimum of 0.973 is produced during summer. The arid zones (1 and 2) show a similar evolution to the previous zone, but with low values; a maximum of 0.973 in December and a minimum of 0.968 in July.

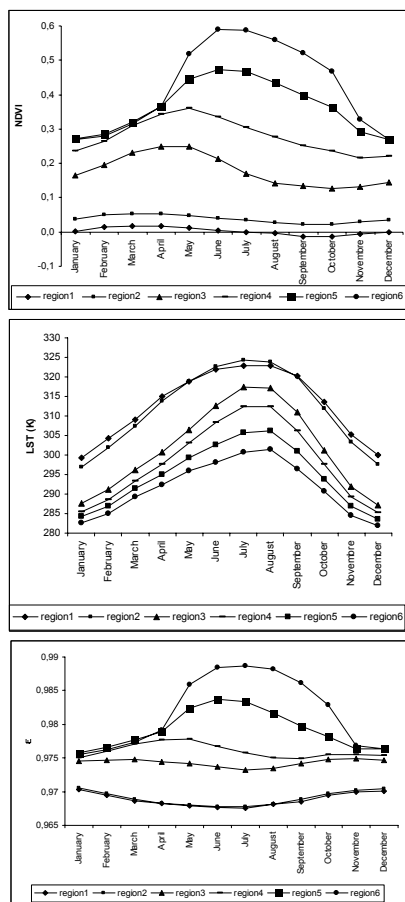


Figure 2.- Plot of the monthly evolution of (a) NDVI, (b) LST and (c) ϵ in each zone.

4.3 Annual evolution

Fig. 3a shows the results of the evolution in terms of NDVI for the whole period. In 1983, all the zones reach their minimum values, a decrease is observed during 1985 and 1992 for the zones 3, 4 and 5, and an important increase for the same zones is observed since 1994 which corresponds to the launch of NOAA-14. Arid zones (1 and 2) remain the same behaviour over the whole period except for the last years from 1995 in which an increase is observed. Fig. 3b is similar to Fig. 3a but for LST evolution. It is seen that the evolution hierarchy is conserved throughout the whole period. The arid zones (1 and 2) show the higher values of LST (about 313 K). The thermal amplitude in the Mediterranean basin between arid zones and those with abundant vegetation is of about 19 K. In Fig. 3b, the difference between zones 3, 4, 5, and 6 in terms of LST is between 2 and 4 K, while this

difference is greater between arid zones (1 and 2) and zone 3 which achieves 10 K. Finally, Fig. 3c shows the annual evolution of emissivity. Here, zones 3 and 4 are the most stable between 1981 and 1994, but since 1994, the difference between these zones increases as zone 3 decreases and zone 4 increases significantly. Zones 1 and 2 have the same behaviour over all the period, and a decrease is observed over its curve since 1994 which is explained by the increase of NDVI in the same period, while for zones 5 and 6 which have the higher values of emissivity, converge towards the same values since 1994.

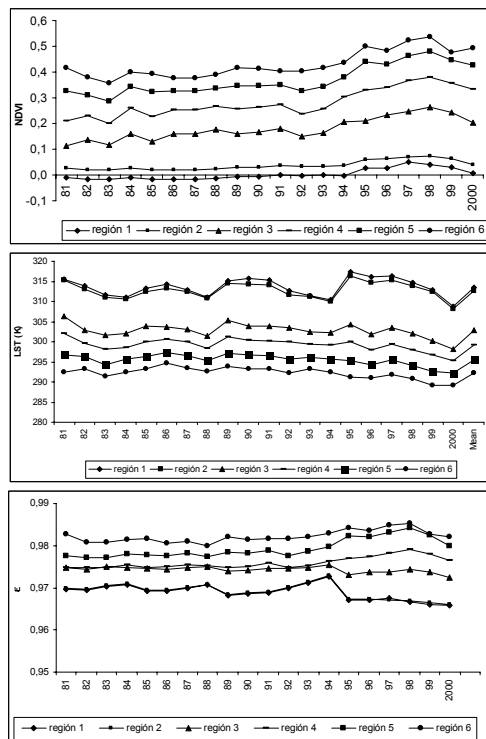


Figure 3.- Plot of the annual evolution of (a) NDVI, (b) LST and (c) ϵ in each zone.

5. VLCD METHOD

Even though in the previous paragraphs the evolution in the time of LST and NDVI separately is represented. Our objective is to analyse the evolution of both parameters conjointly to the aim of obtaining more information. With this end, we defined the method of the Vector of Land Cover Dynamic Monitoring method (VLCD) in Fig. 4. Certainly, it is difficult to have a conclusion studying separately the arctangent and the module without taking into account the information provided by both at the same time.

Therefore, the proposed method is based in the representation of both parameters in a bi-dimensional space whose axes are defined by both parameters. The definition of the module and the arctangent of the VLCD are given in the figure. Both parameters introduce thermal amplitude and NDVI amplitude corresponding to the months of April and July. Fig. 5 represents for each zone and for the whole period (20 years), the module and the arctangent of the corresponding VLCD. The zones are well separated and distributed in three regions: vegetation (zones 5 and 6, $\arctan < 75^\circ$), semi-arid (zones 3 and 4, $\arctan > 75^\circ$ and $\text{module} > 12.5$), and finally arid (zones 1 and 2, $\arctan > 75^\circ$ and $\text{module} > 12.5$).

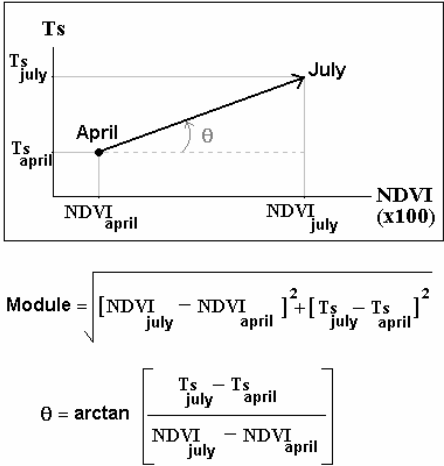


Figure 4.- Definition of the VLCD.

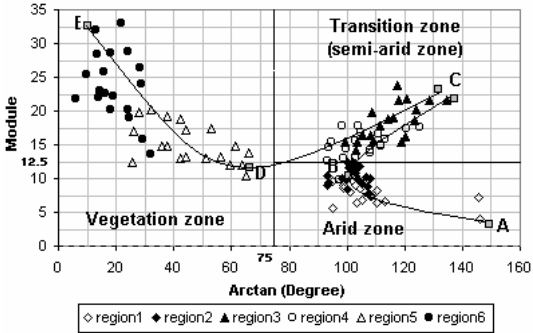


Figure 5.- Representation of the VLCD for the study area.

The VLCD method has the advantage of characterizing the temporal trajectories and the separation of the different zones according to the evolution of the vegetative systems. Fig. 5 permits

defining four evolution trajectories: AB, showing the evolution of zones 1 and 2 in the arid region; BC and CD, the evolution of zones 3 and 4 in the semi-arid region; and finally DE, showing the evolution of zones 5 and 6 in the vegetation region. An evolution throughout AB, CD and DE with a convergence toward the point B, D and E respectively, would mean a positive evolution of the zone. The case defined by the path BC, would correspond to an evolution from arid to semi-arid zone. Otherwise, due to different causes i.e.; drought, desertification, forest fires, climatic changes, etc. the evolution would correspond logically to a negative evolution of the zones. An application to our case has shown that the positive evolution (P_E) for zone 1 was during 1982 and 1999, and the negative evolution (N_E) was during 1988. For zone 2, P_E was during 1990 and 1992 and N_E was during 1993. For zone 3, P_E was during 1996 and 1999 and N_E was during 1983 and 1997. For zone 4, P_E was during 1996, and N_E was during 1997. For zone 5, P_E was during 1984, 1993 and 1996 and N_E was during 1982 and 1997. Finally, for zone 6, P_E was during 1984, 1990, 1991, 1996 and 1998 and N_E was during 1982.

Furthermore, the application of the VLCD method allowed us to give the average images of the arctangent and the module over the whole period considered (20 years), these means were obtained from all the months of April and July. Interestingly, from these images and the considerations relieved on the evolution of each region throughout the studied period, we could give the image application of the VLCD method (see Figures 6 and 7) for the Mediterranean Basin. Consequently, we could distinguish and define the limits of the arid zone, vegetation zone and transition zone. The central issue in knowing the limits of the transition zone is to study the evolutions of the ecotones over the time, because it is the most fragile area to climate and/ or human induced changes.

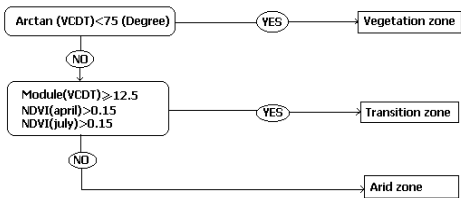


Figure 6.- Algorithm for the application of the VLCD to the characterization of region per pixel.

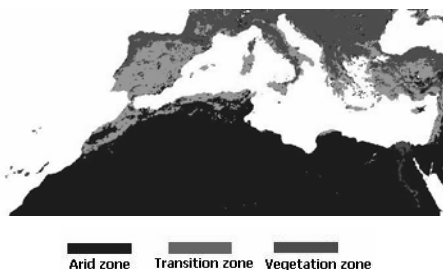


Figure 7.- Image result of the application of the VLCD method to the study area.

6. CONCLUSIONS AND PERSPECTIVES

A preliminary study on land cover dynamic monitoring in the Mediterranean basin has been carried out over 20 years (1981-2001). A method for the multi-temporal analysis called Vector of Land Cover Dynamic (VLCD) was applied. This method analyses the evolution of the slope and the module of the line which extremities are defined by LST and NDVI in April and July. The method permits characterizing the temporal trajectories and the evolution of the vegetative systems. Finally, among the future perspectives, we are interested to provide a classification map of the Mediterranean basin using the VLCD method and to apply the method to other future sensors data such as AATSR, MODIS, etc.

ACKNOWLEDGEMENTS

This research was supported in part by the European Union (WATERMED, Project No. ICA3-ct-1999-00015). The data used by the authors in this study include data produced through funding from the Earth Observing System Pathfinder Program of NASA's Mission to Planet Earth in cooperation with National Oceanic and Atmospheric Administration. The data were provided by the Earth Observing System Data and Information System (EOSDIS), Distributed Active Archive Centre at Goddard Space Flight Centre which archives, manages, and distributes this data set. The authors would like also to thank Dr. N. Raissouni for (1981-1994) data processing.

REFERENCES

Friedl, M. A., and Davis, F. W., 1994, Sources of variation in radiometric surface temperature over a tallgrass prairie, *Remote Sens Env*, **48**, 1-17.

Goward, S. N., Cruickshanks, G. D., and Hope A. S., 1985, Observed relation between thermal emission and reflected spectral radiance of a

complex vegetated landscape, *Remote Sens Env*, **18**, 137-146.

Lambin, E. F., and Strahler, A. H., 1994, Indicators of land-cover change for change-vector analysis in multi-temporal space coarse spatial scales, *International Journal of Remote Sensing*, **15**, 2099-2119.

Lambin, E. F., and Ehrlich, D., 1996, The surface temperature-vegetation index space for land cover and land-cover change analysis, *International Journal of Remote Sensing*, **17**, 463-487.

Loveland, T. R., Merchant, J. W., Ohlen, D. O., and Brown, J., 1991, Development of a land-cover database for the conterminous, U. S., *Photo Eng Remote Sens*, **57**, 1453-1463.

Nemani, R., and Running, S. W., 1989, Estimation of regional resistance to evapotranspiration from NDVI and Thermal-IR AVHRR data, *J Appl Met*, **28**, 276-284.

Nemani, R., Pierce, L., Running, S., and Goward, S., 1993, Developing Satellite-derived Estimates of Surface Moistures Status, *J Appl Meteo*, **32**, 548-557.

Raissouni, N., and Sobrino, J. A., 1998, Land cover dynamic monitoring in the Southwest Mediterranean Basin using the Global Land 1-KM AVHRR project data set, Proceedings of the "Satellite-based observation: A tool for the study of the Mediterranean basin" symposium, Tunis, on 23-27 November.

Raissouni, N., 1999, Análisis Multi-Temporal de Imágenes NOAA- Pathfinder AVHRR Land Para el Estudio de la Dinámica de la Cobertura Terrestre: Aplicación a la Cuenca Mediterránea. (in Spanish), pp. 230. Faculty of Physics, University of Valencia.

Sobrino, J. A., Raissouni, N., Simarro, J., Nerry, F., and Petitcolin, F., 1999, Atmospheric Water vapor content over land surfaces derived from The AVHRR Data. Application to the Iberian Peninsula, *IEEE, Trans Geo Remote Sens*, **37**, 1425-1434.

Sobrino, J. A., Raissouni, N., 2000, Toward remote sensing methods for land cover dynamic monitoring. Application to Morocco, *International Journal of Remote Sensing*, vol. **21**, 2, 353-366.

- Sobrino, J. A., Raissouni, N., Labed, J., Nerry, F., and Li, Z-L., Nerry, F., 2001, Land surface emissivity retrieval from coarse and high resolution satellite data, In Proceedings of the 8th International Symposium on Physical Measurements and Signatures in Remote Sensing. January, Aussois, France. CNES, ISPRS. CNES, Toulouse. 531-536.
- Sobrino, J. A., Cuenca, J., El-Kharraz, J., Gómez, M., Jiménez-Muñoz, J. C., Raissouni, N., and Soria, G., 2001, Multi-Temporal Analysis Using NOAA-Pathfinder AVHRR Land Imagery for the study of the land cover dynamic in the Mediterranean Basin. First International Workshop on the analysis of Multi-Temporal Remote Sensing images. Joint Research Centre European Commission. University of Trento, Trento, Italy, September.
- Townshend, J. R., 1994, Global data sets for land applications from the Advanced Very High Resolution Radiometer, *International Journal of Remote Sensing*, **15**, 3319-3332.
- Tucker, C. J., Townshend, J. R., and Goff, T. E., 1985, African land-cover classification using satellite data, *Science*, **227**, 369-375.

Water vapour retrieval from MODIS data.

J. El-Kharraz, J. A. Sobrino, M. Gómez, J. C. Jiménez-Muñoz & G. Sòria.

Global Change Unit. Dept. of Thermodynamics, University of Valencia, C/ Dr. Moliner 50, 46100 Burjassot, Spain.

jauad@uv.es

ABSTRACT- Launched on December 18, 1999, TERRA began collecting science data on February 24, 2000. The Moderate Resolution Imaging Spectroradiometer "MODIS" is a key instrument aboard the TERRA satellite. The MODIS Instrument views the entire Earth's surface every 1 to 2 days, with instantaneous fields-of-view (IFOVs) of 250 m (channels 1-2), 500 m (channels 3-7), and 1km (channels 8-36), and a scan angle of +/- 55° from nadir, acquiring data in 36 spectral channels. In this work, operative algorithms for retrieving atmospheric water vapour content using MODIS data are proposed. In order to attain this goal, the MODTRAN 3.5 radiative transfer code was used to predict near-IR solar radiation reflected by the land surface or by clouds for MODIS channels 2, 5, 17, 18 and 19. Techniques employing ratios of water vapour absorbing channels at 0.905, 0.936, and 0.94 μm with atmospheric window channels at 0.865 and 1.24 μm are used. Two kinds of algorithms based on 2- channel ratio and 3- channel ratio technique have been developed to produce water vapour amount, with a standard deviation of 0.13 and 0.15 g cm^{-2} . Finally, these algorithms have been validated, by comparing radiosoundings data provided by meteorological stations of Spain, and MODIS images of the same days, which has given errors lower than 0.5 g cm^{-2} .

1 INTRODUCTION

The inclusion of the total water vapour content in LST algorithms allows the elimination of an important error source in the estimation of LST. The knowledge of the total atmospheric water vapour content is necessary to improve the precision of the estimates of LST obtained from satellite data by means of split window algorithms. One way to obtain it consists of using coincident satellite overpasses and atmospheric radiosonde observations. However, this is not always possible, especially in the case of historical satellite databases. Also, in numerous areas of our planet radiosonde observations are not carried out in a systematic way. To overcome this inconvenience, numerous methods that allow us to estimate the total atmospheric water vapour content have been developed in recent years using data given by sensors, such as the Advanced Very High Resolution Radiometer (AVHRR) (Sobrino et al., 1999), and MODIS (Gao and Goetz, 1990; Kaufman and Gao, 1992). A good method should satisfy the following requirements: 1) low sensibility to the noise due to the statistical errors of the channels, 2) low sensibility to the variability of the other components of the atmosphere, and 3) low sensibility to the variability of the characteristics of the surfaces. In order to take these requirements into account the ratio technique was selected.

2 RATIO TECHNIQUE

The ratio technique consists of detecting the attenuation that reflected solar radiation suffers due to water vapour absorption after it has transferred down to the surface and back up through the atmosphere. The total vertical amount of water vapour can be derived from a comparison between the reflected solar radiation in near infrared non-absorption channels. In order to derive column water vapour from measurements of solar radiation reflected by the surface, the absorption and scattering properties of the atmosphere and the surface near 1 μm must be taken into account. The radiance at a downward-looking satellite sensor can be written in a simplified form, as (Hansen and Travis, 1974; Fraser and Kaufman, 1985),

$$L_{\text{Sensor}}(\lambda) = L_{\text{Sun}}(\lambda)\tau(\lambda)\rho(\lambda) + L_{\text{Path}}(\lambda) \quad (1)$$

where λ is the wavelength, $L_{\text{Sensor}}(\lambda)$ is the radiance at the sensor, $L_{\text{Sun}}(\lambda)$ is the solar radiance above the atmosphere, $\tau(\lambda)$ is the total atmospheric transmittance, which is equal to the product of the atmosphere transmittance from the Sun to the Earth's surface and that from the surface to the satellite sensor, $\rho(\lambda)$ is the surface bi-directional reflectance, and $L_{\text{Path}}(\lambda)$ is the path scattered radiance that we assume can be treated approximately as an unspecified fraction of direct reflected solar radiation when the aerosol

concentrations are low. This assumption allows the derivation of column water vapour amounts from satellite data without the need to model single and multiple scattering effects. The feedback effect was neglected because aerosol optical thickness are typically small in the near-IR region. The first term on the right hand side of Equation (1) is the direct reflected solar radiation. L_{Direct} is used to represent this component. $L_{Sensor}(\lambda)/L_{Sun}(\lambda)$ is defined as the apparent reflectance. The reflected solar radiation in the absorption band, without the water vapour effect, has to be estimated from the nearby channels. The main uncertainties in this method are the spectral characteristics of the surface in the near IR. Table 1 shows the spectral characteristics of MODIS near IR channels used in this paper to derive the total atmospheric water vapour amount.

Table 1. Spectral Characteristics of MODIS near IR channels used in water vapour retrieval algorithms.

Band Number	Band Centre(μm)	Bandwidth(μm)
2	0.865	0.04
5	1.24	0.02
17	0.905	0.03
18	0.936	0.01
19	0.94	0.05

The development and simulation of the ratios technique, are based on surface reflectance. For some surface covers the reflectance varies almost linearly with wavelength and for this type of cover the best technique is based on linear interpolation of the surface reflectance between two channels around the water absorption channel. We cannot get the water vapour transmittances (see Equation 1) from radiances of individual absorption channels. However, if the surface reflectances are constant with wavelength, a 2-channel ratio of an absorption channel with a window channel gives the water vapour transmittance of the absorption channel. Ratio technique using 2-channels was applied in this paper to derive atmospheric transmittances of the absorption channels, and subsequently the total atmospheric water vapour content. The ratios will be calculated from radiances MODIS channels 2, 5, 17, 18, and 19 centred at 0.865, 1.24, 0.905, 0.936 and 0.94 μm respectively. These channel ratios are approximately equal to the

atmospheric water vapour transmittances in the sun-surface-sensor ray path (Kaufman and Gao, 1992; Gao and Goetz, 1990) The values of 2-channel ratios and total atmospheric water vapour content were generated using MODTRAN 3.5. Examples of some reflectance values are tabulated in Table 2 together with the reflectance ratio of channels 2 (0.865 μm) and 19 (0.94 μm).

Table 2. Surface reflectance values and ratio $\rho_{0.865}/\rho_{0.94}$ for different surfaces extracted from Salisbury and D’Aria (1992).

Surface	$\rho_{0.865}$	$\rho_{1.24}$	$\rho_{0.905}$	$\rho_{0.936}$	$\rho_{0.94}$	$\rho_{0.865}/\rho_{0.94}$
0015	0.81	0.68	0.79	0.79	0.78	1.03
86p4603	0.22	0.35	0.23	0.25	0.25	0.87
87p313	0.20	0.30	0.21	0.22	0.22	0.91
87p325	0.23	0.31	0.24	0.24	0.24	0.93
87p4264	0.32	0.43	0.34	0.35	0.35	0.90
87p707	0.34	0.42	0.35	0.36	0.36	0.95
89p1793	0.36	0.42	0.36	0.36	0.36	0.98
Conifers	0.52	0.44	0.51	0.51	0.50	1.03
Deciduous	0.55	0.51	0.55	0.55	0.55	1.01
Drygrass	0.57	0.67	0.60	0.62	0.61	0.93
Gneiss1	0.73	0.80	0.73	0.73	0.73	0.99
Granith1	0.16	0.15	0.16	0.16	0.16	1.01
Grass	0.50	0.49	0.51	0.51	0.51	0.98
Limesth1	0.41	0.50	0.41	0.42	0.42	0.98
Marbleh1	0.33	0.31	0.33	0.32	0.32	1.04
Sandsth1	0.49	0.59	0.50	0.51	0.51	0.97
Schisth1	0.25	0.34	0.25	0.25	0.25	1.02
Shaleh1	0.27	0.30	0.27	0.28	0.28	0.98
Siltsth1	0.29	0.28	0.28	0.29	0.29	1.00
Slateh1	0.17	0.17	0.17	0.17	0.17	1.01
Mean	-	-	-	-	-	0.97
Std dev	-	-	-	-	-	0.047

Figure 1 shows a polynomial relationship between total atmospheric water vapour content and transmissivity.

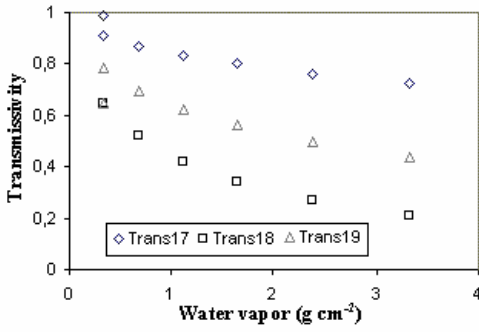


Figure 1. Transmissivity in channels 17, 18 and 19 versus the total atmospheric water vapour content.

3 ALGORITHMS

We have defined the following ratios G_{17} , G_{18} , and G_{19} as:

$$G_{17} = \frac{L_{17}}{L_2} \quad (2)$$

$$G_{18} = \frac{L_{18}}{L_2} \quad (3)$$

$$G_{19} = \frac{L_{19}}{L_2} \quad (4)$$

where L_i are radiances obtained by simulation for MODIS channels 2, 17, 18, and 19 with MODTRAN 3.5 using six standard atmospheres and 10 types of surfaces : fresh snow, forest, farm, desert, ocean, cloud deck, old grass, decayed grass, maple leaf, and burnt grass. The simulated amount of water vapour was varied between 0.3 and 3.3 g cm⁻². Figure 2 shows the radiance ratios versus the total water vapour amount, a polynomial behaviour is observed;

$$W_{17} = 26.314 - 54.434 G_{17} + 28.449 G_{17}^2 \quad (5)$$

$$W_{18} = 5.012 - 23.017 G_{18} + 27.884 G_{18}^2 \quad (6)$$

$$W_{19} = 9.446 - 26.887 G_{19} + 19.914 G_{19}^2 \quad (7)$$

where W_{17} , W_{18} , and W_{19} are the water vapour values for MODIS channels 17, 18, and 19, respectively. A mean water vapour value (W) could be obtained according to the following equation;

$$W = f_{17}W_{17} + f_{18}W_{18} + f_{19}W_{19} \quad (8)$$

where f_{17} , f_{18} , and f_{19} are weighting functions defined according to

$$f_i = \frac{\eta_i}{(\eta_1 + \eta_2 + \eta_3)} \quad (9)$$

$$\text{with } \eta_i = \frac{|\Delta\tau_i|}{|\Delta W|}$$

where ΔW is the difference between the maximum and minimum water vapour content from the six standard atmospheres and $\Delta\tau_i$ corresponds to the difference between the transmissivities for the maximum and the minimum water vapour amount obtained in channel (i).

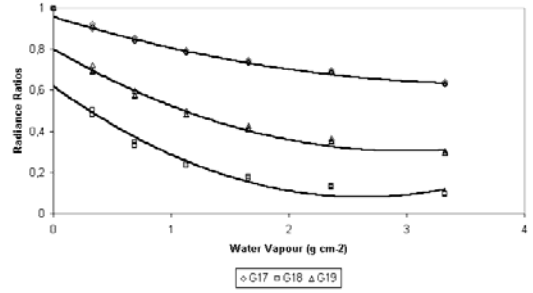


Figure 2. Radiance Ratios plotted versus the total water vapour amount.

The values obtained for f_i and η_i are $f_{17}=0.192$, $f_{18}=0.453$, $f_{19}=0.355$, $\eta_{17}= 0.062$, $\eta_{18}= 0.147$ and $\eta_{19}= 0.115$ respectively. So the equation (8) can be written as,

$$W = 0.192 W_{17} + 0.453 W_{18} + 0.355 W_{19} \quad (10)$$

Equation (10), is the algorithm that we proposed to obtain the total water vapour from MODIS images. the advantage of this algorithm is its simplicity as it is derived directly from radiance measurements. Finally Figure 3 shows the total water vapour content image constructed by applying the equation 10 to the MODIS image of Spain-Morocco of August 31, 2000.

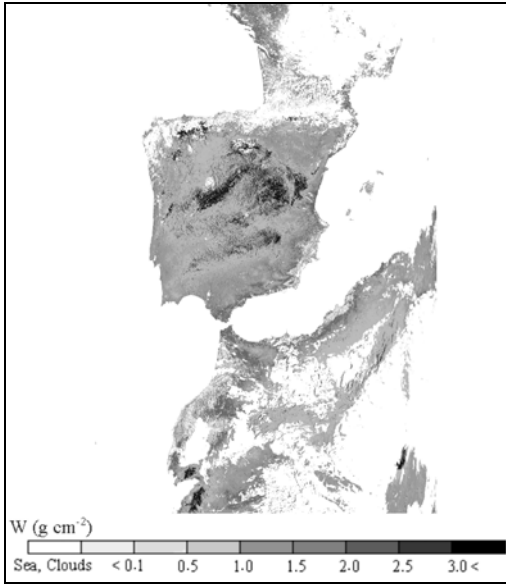


Figure 3. Water vapour content image of the study area for August 31, 2000.

3.1. Accuracy

In this section, an analysis of sensitivity has been made. To this end, we apply the error theory to equation 8, according to

$$\sigma_{\text{Total}}(W) = \sqrt{\sum_{i=1}^3 f_i \Delta W_i^2} \quad (11)$$

where $\Delta W_i = a_i G_i \Delta G_i + b_i \Delta G_i$, with $a_{17}=56.90$, $a_{18}=55.77$, $a_{19}=39.83$, $b_{17}=54.43$, $b_{18}=23.02$, and $b_{19}=26.89$. ΔG_i is obtained according to Kaufman and Gao (1992) as,

$$\Delta G_i = \frac{\sigma \left[G_i (3.32 \text{ g cm}^{-2}) \right]}{G_i (3.32 \text{ g cm}^{-2}) - G_i (0.33 \text{ g cm}^{-2})} \quad (12)$$

where $\sigma[G]$ is the standard deviation of G for the surface covers considered, and the denominator is the difference between the G_i functions estimated for extreme conditions, humid (3.32 g cm^{-2}) and dry atmospheres (0.33 g cm^{-2}). Sensitivity analysis applied to equation (24) gives a standard deviation and a bias of 0.13 and 0.40 g cm^{-2} respectively.

3.2. Evaluation

In this section a validation of equation 10 is included. Different radiosonde observations realised at 12 h on June 29, August 31, September 7, September 9, and September 14, from different meteorological stations of Spain (La Coruña, Santander, Gibraltar, Madrid, Murcia, Zaragoza, and Palma de Mallorca) and over Barrax (Spain) on June 29. In Figure 4, we show total atmospheric water vapour content obtained by radiosonde observations versus total atmospheric water vapour content obtained applying the proposed algorithm to the corresponding MODIS images, for these dates and places. The results of the comparison between the total water vapour content derived from the proposed algorithm and the obtained by the radiosonde observations gives a standard deviation of 0.45 g cm^{-2} and a Bias of 0.09 g cm^{-2} . This result is similar (a standard deviation of 0.41 g cm^{-2} and a bias of 0.09 g cm^{-2}) to the obtained considering the water vapour content product given by NASA (provided to us by Dr. Ridgway), and called MOD05_L2.

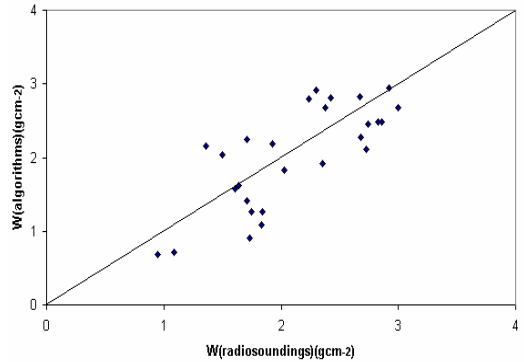


Figure 4. Plot of water vapour content obtained from radiosonde observations versus water vapour content obtained from the proposed algorithm.

4 CONCLUSIONS

In this paper, we have used ratio techniques to give operative algorithms to retrieve water vapour content. An algorithm was proposed and gives a standard deviation below 0.13 g cm^{-2} . This algorithm was validated by radiosoundings data and MODIS images, and we have obtained errors below 0.5 g cm^{-2} , and comparison with MODIS product has given an error of 0.89 g cm^{-2} . We are looking forward to validating our algorithms in more regions and in different conditions.

ACKNOWLEDGEMENTS

We wish to thank Dr. Gail Andersson from the Air Force Research Laboratory, Hanscom (USA) for providing us with the MODTRAN 3.5 program, Dr. Z. Wan and Dr. B. Gao for their appreciated and constructive comments, and Dr. Bill Ridgway for providing us MODIS images. We would also like to thank the European Union for the financial support (WATERMED, Project No. ICA3-ct-1999-00015). This work has been carried out while Jauad El Kharraz was in receipt of a grant from the WATERMED project.

REFERENCES

- Abreu L. W., and Anderson G. P., 1996, The MODTRAN 2/3 Report and LOWTRAN 7 Model, Prepared by Ontar Corporation for PL/GPOS.
- Carlson, T. N. and Ripley, D. A., 1997, On the relation between NDVI, Fractional Vegetation Cover, and Leaf Area Index. *Remote Sensing of Environment*, Vol. **62**, pp. 241-252.
- Caselles, V. and Sobrino, J. A., 1989, Determination of frosts in orange groves from NOAA-9 AVHRR data, *Remote Sens. Environ.*, vol **29**, no. 2, pp. 135-146.
- Chesters, D. C., Uccellini, L. W., and Robinson, W. D., 1983, Low level water vapour fields from the VISSR Atmospheric Sounder (VAS) "split-window" channels, *J. Clim. Appl. Meteor.*, **22**, 725-743.
- Fraser, R. S. and Kaufman, Y. J., 1970, The relative importance of American soils, *Photogramm. Eng.*, **36**, 955-965.
- Gao, B. C. and Goetz, F. H., 1990, Column Atmospheric Water Vapour and Vegetation Liquid Water Retrievals From Airborne Imaging Spectrometer data, *J. Geophys. Res.*, **95**, 3549-3564.
- Guenther, B., Godden, G. D., Xiong, X., Knight, E. J., Qui, S.-Y., Montgomery, H., Hopkins, M. M., Khayat, M. G., and Hao, Z., 1998, Prelaunch algorithm and data format for the level 1 calibration product for the EOS-AM1 Moderate Resolution Imaging Spectroradiometer (MODIS), *IEEE Tans. Geosci. Remote Sensing*, **36** (4), 1142-1151.
- Hansen, J. E. and Travis, L. D., 1974, Light scattering in planetary atmospheres, *Space Science Reviews*, **16**, 527-610.
- Kaufman, Y. J., and Gao, B. C., 1992, Remote sensing of water vapour in the near IR from EOS/MODIS, *IEEE Tans. Geosci. Remote Sensing*, **30**, 1-27.
- Kimura, F. and Shimura A.P., 1994, Estimation of sensible and latent heat fluxes from soil surface temperature using a linear air land heat transfer model, *J. Appl. Meteorol.*, vol. **33**, no. 4, pp. 477-489.
- Kneizys, F. X. et al., 1988, User's guide to LOWTRAN 7. Air Force Geophysics Laboratory.
- Rothman L. S. et al., 1992, The HITRAN molecular database: Editions of 1991 and 1992, *J. Q. Spect. Rad. Trans*, no. **48**, pp. 469-.
- Salisbury, J. W. and D'Aria, D. M., 1992, Emissivity of terrestrial materials in the 8-14 mm atmospheric window, *Remote Sens. Environ.*, vol. **42**, pp. 83-106.
- Saunders, R. W. and Kriebel, K. T., 1988, An Improved Method for Detecting Clear Sky and Cloudy Radiances from AVHRR Data. *International Journal of Remote Sensing*, Vol. **9**, pp. 123-150.
- Sellers, P. J., Hall, F. G., Asrar, G., Strebel, D. E., and Murphy, R. E., 1988, The first ISLSCP Field Experiment (FIFE), *Bull. Amer. Meteorol. Soc.*, vol. **69**, no. 1, pp. 22-27.
- Sobrino, J. A., Li, Z.-L., Stoll, M. P., and Becker, F., 1994, Improvements in the split-window technique for the land surface temperature determination. *IEEE Transactions on Geoscience and Remote Sensing*, Vol. **32** No. 2, pp. 243-253.
- Sobrino, J. A., Li, Z.-L., Stoll, M. P. and Becker, F., 1996, Multi-channel and multi-angle algorithms for estimating sea and land surface temperature with ATSR data, *International Journal of Remote Sensing*, 17, No. **11**, 2089-2114.
- Sobrino, J. A., Raissouni, N., Simarro, J., Nerry, F. and François, P., 1999, Atmospheric Water Vapour Content Over Land Surfaces Derived from The AVHRR Data. Application to the Iberian Peninsula. *IEEE Transactions and Geoscience and Remote Sensing*, **37**, pp. 1425-1434.
- Sobrino, J. A. and Raissouni, N., 2000, Toward remote sensing methods for land cover dynamic monitoring: application to Morocco, *International Journal of Remote Sensing*, vol. **21**, no. 2, 353-366.
- Sobrino, J. A., Raissouni, N., and Z.-L., Li, 2001, A comparative study of land surface emissivity retrieval from NOAA data. *Remote Sensing of Environment*, **75**, pp. 256-266.
- Vining, R. C. and Blad, B. L., 1992, Estimation of sensible heat flux from remotely sensed canopy temperatures, *J. Geophys. Res.*, vol. **97**, no. D17, pp. 18951-18954.

Angular Variation of Thermal Infrared Emissivity for Some Natural Surfaces on the Orbital and Field Measurements

J.A. Sobrino, J. Cuenca, G. Soria

Global Change Unit. Department of Thermodynamics, University of Valencia, c./ Dr. Moliner, 50, 46100 Burjassot, Spain. Tel.: 34-963983115; Fax: 34-963983099; <http://www.uv.es/~ucg>,

sobrino@uv.es, juan.cuenca@uv.es, guillem.soria@uv.es

ABSTRACT-Multi-angle algorithms for estimating sea and land surface temperature with AATSR (Advanced Along Track Scanning Radiometer) data require a precise knowledge of the angular variation of surface emissivity in the thermal infrared. Currently, very few measurements of this variation exist. In this work an experimental investigation of the angular variation of the infrared emissivity in one thermal infrared broad-band (8-13 μm) and three narrower bands (8.2-9.2 μm , 10.3-11.3 μm and 11.5-12.5 μm) of some representative samples (clay, sand, loam, gravel, grass) has been made at angles of 0°-60° (at 5° increments) to the surface normal. The results show a general decrease of the emissivity with increasing viewing angles. Finally, we include an evaluation of the impact that the data of the band 10.3-11.3 μm can produce on the dual angle algorithm for determining land and sea surface temperature.

1. INTRODUCTION

A precise knowledge of surface emissivity is necessary for an accurate surface temperature (ST) estimation from remote sensing in the thermal infrared (TIR) spectrum region. A deep study of the behaviour of this relevant parameter has to include the variations it suffers with the observation angle of the sample and with the working wavelength. The last sensor generations (ATSR and AATSR) operate in biangular mode, technique that allows the use of dual angle algorithms for obtaining the surface temperature. Dual angle algorithms have been demonstrated to be more adequate for obtaining ST in homogeneous areas than split window algorithms (Sobrino et al., 1996). For these algorithms, the knowledge of the angular behaviour of emissivity becomes critical importance. Actually, very few studies in this matter are to be found in the scientific bibliography (Masuda et al., 1988, Rees and James, 1992, Labed and Stoll, 1991, Snyder et al., 1997, Sobrino and Cuenca, 1999). In this work we have carried out an experimental study of the infrared emissivity in one thermal infrared broad-band (8-13 μm , what we call channel 1) and three narrower bands (11.5-12.5 μm , channel 2, 10.3-11.3 μm , channel 3 and 8.2-9.2 μm , channel 4) of some representative samples (clay, sand, loam, gravel, grass) at angles of 0°-60° (at 5° increments) to the surface normal.

2. THEORY

The work was planned to obtain the absolute (Eq. 1) and the relative to nadir (Eq. 2) emissivities of the samples:

$$\epsilon_{0,i} = \frac{B_i(T_{\theta,i}) - B_i(T_{\text{atm},i})}{B_i(T_s) - B_i(T_{\text{atm},i})} \quad (1)$$

$$\epsilon_{r,\theta,i} = \frac{\epsilon_{\theta,i}}{\epsilon_{0,i}} = \frac{B_i(T_{\theta,i}) - B_i(T_{\text{atm},i})}{B_i(T_{0,i}) - B_i(T_{\text{atm},i})} \quad (2)$$

In these expressions the parameters express:

- i makes reference to the used channel (i ranges from 1 to 4).
- θ is the observation angle.
- r is for relative to nadir emissivity.
- $B_i(T_{\theta,i})$ is Planck's radiation function for the surface, at channel i.
- T_s is the ground temperature measured in K.
- $B_i(T_s)$ is Planck's radiation function for the surface.
- $T_{\text{atm},i}$ is the surroundings equivalent temperature, measured at channel i.
- $B_i(T_{\text{atm},i})$ is the downwelling hemispherical radiance.
- 0 refers to nadir view.
- $B_i(T_{0,i})$ is the Planck's function evaluated at nadir view, and in channel i.

So, for simplicity, calling $\alpha = C_2/\lambda_{\text{eff},i}$, where $C_2 = 14388 \text{ K } \mu\text{m}$ and $\lambda_{\text{eff},i}$ is the effective wavelength in each channel, and according to all the considerations made at Sobrino and Cuenca (1999), we can write the operational expressions used to retrieve the angular absolute and relative emissivity at channel i as:

$$\varepsilon_{\theta,i} = \frac{\exp(-\alpha/T_{\text{rad},i}) - 1.3 \exp(-\alpha/T_{\text{atm0},i})}{\exp(-\alpha/T_s) - 1.3 \exp(-\alpha/T_{\text{atm0},i})} \quad (3)$$

$$\varepsilon_{r,\theta,i} = \frac{\exp(-\alpha/T_{\text{rad},i}) - 1.3 \exp(-\alpha/T_{\text{atm0},i})}{\exp(-\alpha/T_{\text{rad0},i}) - 1.3 \exp(-\alpha/T_{\text{atm0},i})} \quad (4)$$

3. EXPERIMENTAL PROCEDURE

The two basic materials used for doing all the present work are a infrared radiometer and a goniometric system. Besides, for taking the thermometric temperature of the samples, we used a thermocouple in the case of water and a thermistor for the other samples.

The radiometer is a portable infrared radiometer CIMEL 312 that has an instantaneous field of view of 10° . The instrument operates in four bands: 8-13 μm (channel 1), 11.5-12.5 μm (channel 2), 10.3-11.3 μm (channel 3) and 8.2-9.2 μm (channel 4). The sensitivity of the instrument is 8 mK for channel 1 and 50 mK for the rest of channels.

The goniometric system consists on a half-circle metallic frame. The radius of the half circle is 1.5 meters. With this distance, the spot diameter on the sample at nadir is 52 cm. The thermocouple used was a TES 1310 Type K. It has a sensibility of 0.1 K and was used for measuring the water temperature due to the possibility of sinking it in water. It was calibrated in our laboratory with the aid of a precision bulb

thermometer Siebert&Kuhn with a sensibility of 0.05 K. Several pairs of resistance and temperature values were taken and the obtained curve was adjusted. The accuracy for this instrument is better than 0.1 K. The samples studied were sand, clay, loam, gravel, water and grass. Sand, clay and loam were reduced as fine as possible, gravel was composed by 8-10 mm stones, and grass was 6-8 cm high.

The procedure consists in taking several measurements series in different conditions with the aim of having representative mean values of the emissivities. We were especially carefully with the weather conditions. We only took measurements the days with clear sky because clouds are determinant to have a great error in the atmospheric downwelling radiance. Another important experimental condition to be taken into account is that the samples need to be thermally stabilised. Related to this condition is the necessity of not taking measurements with the samples exposed to the sun or to winds. Another important aspect is to take the measurements in a time shorter than two minutes, approximately the time between the data acquisition forward-nadir of the ATSR. So we started in nadir (angle 0°) taking data and we measured temperature for each surface type at angles up to 60° (at 5° increments) to the surface normal. This is what we call a data series. We took several series for each sample. Before and after taking the data series we measured the sky temperature at nadir angle.

4. RESULTS

In this section we present the obtained results. Figures 1, 2 and 3, display in each case the angular emissivity dependence, for the calculated relative-to-nadir emissivities and for the absolute emissivities, specifying the spectral channel used. The graphics have been constructed with the arithmetical mean values of the several measured series.

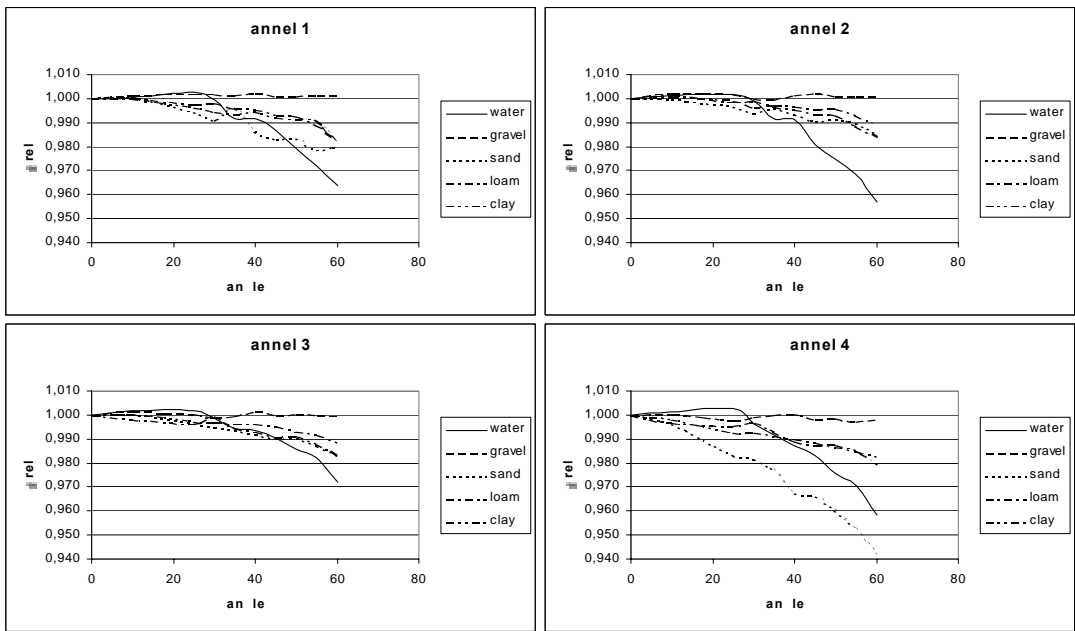


Figure 1: Angular variation of relative-to-nadir emissivity of all samples.

Some interesting results can be observed from this Figure 1. Firstly, channel 4 shows greatest dependence. Secondly, gravel is the sample that has

shown less dependence in all channel. Grass graphics are not shown in the figures because we did not find variations in its behaviour.

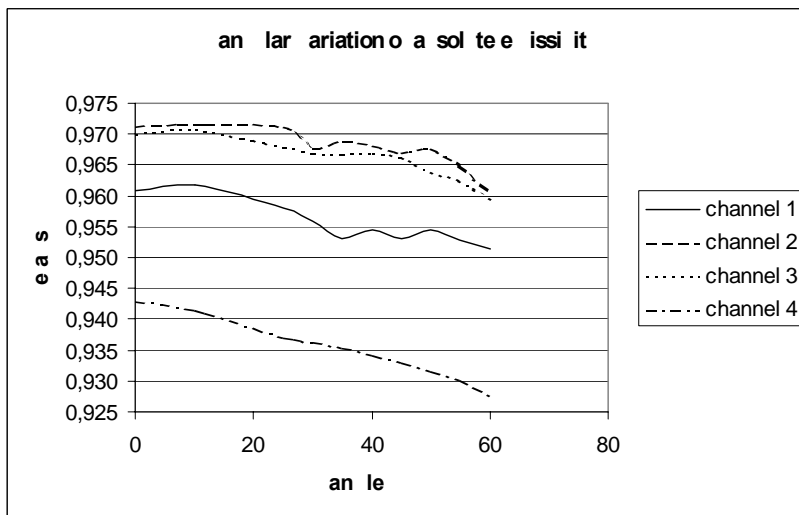


Figure 2: Angular variation of absolute emissivity for clay.

Figure 2 shows the angular variation of absolute emissivity for clay. At nadir, the emissivity varies from 0.943 at channel 4 to 0.971 at channel 2. The behaviour at channels 2 and 3 is very similar.

Finally, Figure 3 shows the comparison between Masuda et al.'s results (1988) and the present work for water. It is clear the similarity of both data

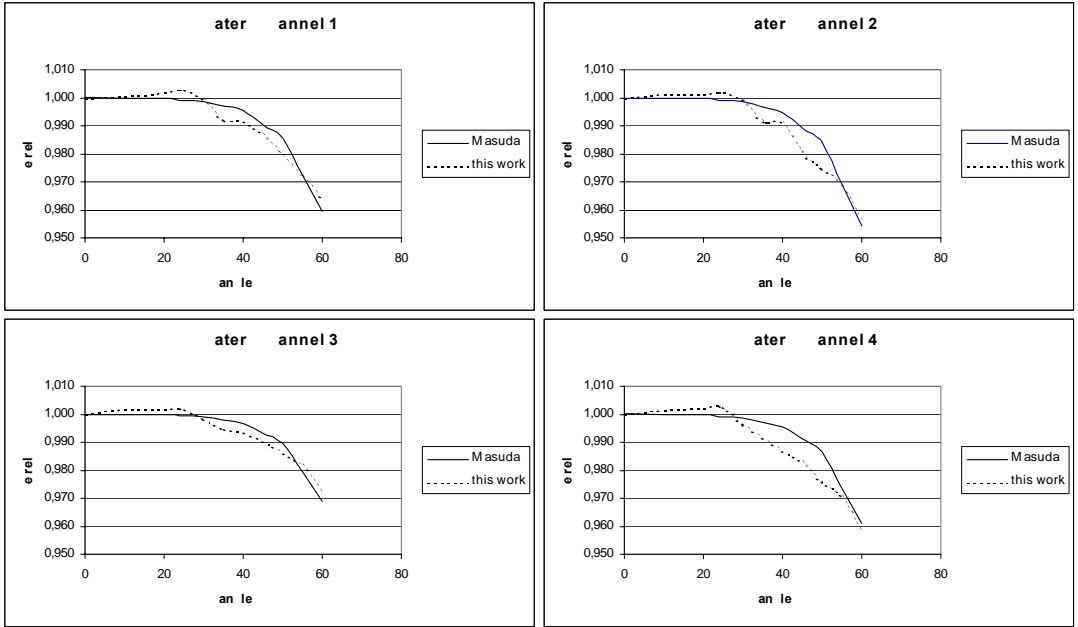


Figure 3: Comparison between Masuda et al. (1988) results and ours.

For water, there is no significant difference from 0 to 30°. After this, the emissivity declines progressively and both curves fall together. Masuda et al.'s results are corroborated by our measurements, and also the present results confirm the obtained by Sobrino and Cuenca (1999).

5. IMPACT IN SURFACE TEMPERATURE DETERMINATION

A main objective in the study of angular variation of emissivity is to proportionate adequate values for applying dual angle algorithms. With this aim, we have applied our results to the algorithm proposed by

Sobrino et al. (1996) for surface temperature determination with ATSR data at 11 μm wavelengths. From this algorithm, the expression of the error in the surface temperature estimation when the angular variation of emissivity is not considered is given by:

$$\Delta T_{s_e} = (57-7W) (1-\varepsilon_0) + (84-15W) (\varepsilon_0 - \varepsilon_\theta) \quad (5)$$

being W the total atmospheric water vapour content at nadir, and ε_0 and ε_θ the emissivities in the nadir and forward views, respectively. To this end, we have constructed Table 1, in which three different water vapour values are considered.

Table 1: Error in the surface temperature estimation, ΔT_{s_e} , $\Delta T_{s_e} = T_{s_e}(\Delta \varepsilon = 0) - T_{s_e}(\Delta \varepsilon_{55^\circ})$, when the angular variation of emissivity at channel 3 is not considered.

sample	ε	$\Delta \varepsilon_0$	W (g cm ⁻²)	ΔT_s (K)
water	0.977	0.014	1	2.1
			3	1.4
			5	0.6
gravel	0.972	0.002	1	1.5
			3	1.1
			5	0.6
sand	0.976	0.01	1	2.1
			3	1.3
			5	0.6
loam	0.989	0.012	1	1.4
			3	0.9
			5	0.3
clay	0.97	0.007	1	2
			3	1.4
			5	0.7

From Table 1 we can extract some conclusions. Firstly, the impact of the angular variation of emissivity in the determination of the surface temperature decreases with increasing contents of water vapour in the atmosphere. Referring to water, we can say that not considering the angular variation of emissivity can lead to errors exceeding of 2 K in the sea surface temperature, which is unacceptable in climatic studies, since 0.3 K constitutes the accuracy requirement needed in the climatic applications of the international Tropical Oceans Global Atmosphere (TOGA) programme (Barton, 1992).

6. CONCLUSIONS

In the present work we have studied the behaviour of the emissivity of several substances under different angles of view and at several spectral TIR intervals. We have seen that in general do exist a decreasing dependence of this parameter when the observation angle grows up for a fixed interval. We observe that the pattern of the curve corresponding to a concrete sample is conserved if operating at different wavelengths but changing the absolute values, so here is to be seen the spectral dependence of the emissivity. Part of our results confirms the very few preexistent

ones, and the rest are new introduced now in the scientific bibliography. We suggest to take into account the angular variation of emissivity in land surface temperature determination using a double angle method. Particularly, the working method is useful for ENVISAT, which carry on board AATSR sensor that operates with an angle of 53° in aperture to the nadir view.

In relation to the experimental technique we should remark the importance of being very careful with the condition of the thermal stabilisation of the samples to be studied. The weather conditions have to be homogeneous in all senses: clear sky (necessary to have reliable hemispheric downwelling radiances), absence of wind and to have temperature not influenced by external agents).

ACKNOWLEDGEMENTS

The authors wish to express their gratitude to the European Union (*WATERMED* Project, ICA3-ct-1999-00015) and to the Spanish Ministerio de Ciencia y Tecnología (Project REN2001-3105/CLI) for the financial support.

REFERENCES

- Barton, I. J., 1992, Satellite-Derived surface temperatures - A comparison between operational, theoretical and experimental algorithms. *Journal of Applied Meteorology*, **31**, pp. 432-442.
- Labeled, J. and Stoll, M. P., 1991, Angular variation of land surface spectral emissivity in the thermal infrared: laboratory investigations on bare soils. *International Journal of Remote Sensing*, **12**, No. 11, pp. 2299-2310.
- Masuda, K., Takashima, T. and Takayama, Y., 1988, Emissivity of pure sea waters for the model sea surface in the infrared window regions. *Remote Sensing of Environment*, **24**, pp. 313-329.
- Rees, W. G. and James, S. P., 1992, Angular variation of the infrared emissivity of ice and water surfaces. *International Journal of Remote Sensing*, **Vol. 13, No. 15**, 2873-2886.
- Snyder, W. C., Wan, Z., Zhang, Y. and Feng, Y.-Z., 1997, Thermal infrared (3-14 μm) bidirectional reflectance measurements of sands and soils. *Remote Sensing of Environment*, **60**, 101-109.
- Sobrino, J. A. and Cuenca, J., 1999, Angular variation of emissivity for some natural surfaces from experimental measurements. *Applied Optics*, Vol. 38, No. 18, 3931-3936.
- Sobrino, J. A., Li, Z.-L., Stoll, M. P. and Becker, F., 1996, Multi-channel and multi-angle algorithms for estimating sea and land surface temperature with ATSR data. *International Journal of Remote Sensing*, **Vol. 17, No. 11**, 2089-2114.

Surface temperature retrieval from AATSR data: multichannel and multiangle algorithms

G. Sòria¹, J. A. Sobrino¹, J. Cuenca¹, A. J. Prata², J. C. Jiménez-Muñoz¹, M. Gómez¹ & J. El-Kharraz¹.

¹ Global Change Unit. Dept. of Thermodynamics, University of Valencia, C/ Dr. Moliner 50, 46100 Burjassot, Spain.

guillem.soria@uv.es

²CSIRO Atmospheric Research, PMB 1 Aspendale, Vic. 3195, Australia.

ABSTRACT - A study has been carried out using MODTRAN 3.5 simulations of the Advanced Along-Track Scanning Radiometer (AATSR) data at 3.7, 11 and 12 μm wavelengths to give a range of operative and accurate multichannel and multiangle algorithms for estimating sea and land surface temperature (SST and LST). Making use of the dual-angle viewing capability of the AATSR, algorithms based on dual-angle, split-window and mixed structure have been considered. Although all the methods to estimate LST assumed that emissivity is a known parameter, in reality, emissivity must be determined. To build the simulated data base, angular (from in situ measurements) and spectral (from bibliography) emissivity values have been used. The proposed algorithms have been applied to a series of satellite images acquired by the CSIRO in Australia, retrieving LST with a standard deviation less than 0.6 K if the satellite data are error free; in this case, the emissivity and temperature values necessary to retrieve the ST have been acquired from CSIRO in situ data.

1 INTRODUCTION

The Advanced Along-Track Scanning Radiometer (AATSR) is a passive optical imaging instrument measuring radiation emitted and reflected from the Earth's surface. This instrument improves the technological characteristics of the (A)ATSR series on the European Remote Sensing Satellite (ERS), ensuring a surface temperature at an accuracy level of 0.3 K or better. AATSR have four mid/thermal infrared channels, together with three visible/NIR channels. The technical characteristics of the AATSR allow the use of the two-angle viewing method, which will be used to achieve accurate atmospheric corrections and improve the radiometric precision (0.05 K in front of the 0.12 K of AVHRR). The main aim of this paper is to show algorithms to estimate surface temperature from AATSR data to get the most accurate algorithm in each situation. With this intention, a large simulation data base has been made with MODTRAN 3.5 code to get the coefficients of the proposed algorithms and, finally, evaluate and validate them using the error theory and in situ data from a region of Australia.

2 ALGORITHMS

The structure of the algorithms has been obtained from the radiative transference equation:

$$T_s = T_i + A(T_i - T_j) - B_0 + (1 - \varepsilon_i)B_1 - \Delta\varepsilon_0 B_2 \quad (1)$$

where i and j are two different channels with the same view angle, split-window (SW) technique, or the same channel with two different view angles, dual-angular (DA) technique, in accordance with Sobrino et al., (1996). From all the evaluated combinations, Table 1 shows those SW and DA algorithm with the best statistical values. In order to simplify the reading of the tables, we will use the following notation: n : nadir view; SW: Split-Window Method (two spectral channels at the same observation angle); DA: Dual-Angle Method (one channel at two observation angles); QUAD: algorithm that includes a squared dependence on $(T_i - T_j)$; (1): ATSR-2 Channel 1 (12 μm); (2): ATSR-2 Channel 2 (11 μm); W: algorithm with water vapor content dependence; ε : algorithm with emissivity dependence; $\Delta\varepsilon$: algorithm including spectral or angular emissivity difference.

3 SIMULATION

In the preceding section we introduced the algorithm structures for obtaining ST from AATSR data. To apply these algorithms, apart from the surface emissivity, atmospheric temperature and transmissivity must be known in the area studied and for each atmospheric situation. To give operational algorithms, the determination of the dual-angle and split-window coefficients has been made using simulations because there is not yet a sufficient volume of high quality *in situ* measurement of ST (LST and SST) coincident with

Table 1.- Split-window (SW_i) and Dual-angle (DA_i) algorithms proposed for estimating ST from AATSR data.

Num.	NAME	EXPRESSION
SW 1	SW n, Quad:	$T_s = T_{2n} + a_0(T_{2n} - T_{1n}) + a_1(T_{2n} - T_{1n})^2 + a_2$
SW 2	SW n, Quad, ϵ :	$T_s = T_{2n} + a_0(T_{2n} - T_{1n}) + a_1(T_{2n} - T_{1n})^2 + a_2 + a_3(1 - \epsilon)$
SW 3	SW n, Quad, ϵ , $\Delta\epsilon$:	$T_s = T_{2n} + a_0(T_{2n} - T_{1n}) + a_1(T_{2n} - T_{1n})^2 + a_2 + a_3(1 - \epsilon) + a_4\Delta\epsilon$
SW 4	SW n (W), ϵ , $\Delta\epsilon$, W:	$T_s = T_{2n} + (a_0 + a_1W)(T_{2n} - T_{1n}) + (a_2 + a_3W) + (a_4 + a_5W)(1 - \epsilon) + (a_6 + a_7W)\Delta\epsilon$
SW 5	SW n, Quad, ϵ , $\Delta\epsilon$, W:	$T_s = T_{2n} + a_0(T_{2n} - T_{1n}) + a_1(T_{2n} - T_{1n})^2 + a_2 + (a_3 + a_4W)(1 - \epsilon) + (a_5 + a_6W)\Delta\epsilon$
SW 6	SW n, Quad(W), ϵ , $\Delta\epsilon$, W:	$T_s = T_{2n} + (a_0 + a_1W)(T_{2n} - T_{1n}) + (a_2 + a_3W)(T_{2n} - T_{1n})^2 + (a_4 + a_5W) + (a_6 + a_7W)(1 - \epsilon) + (a_8 + a_9W)\Delta\epsilon$
DA 1	DA (11) Quad:	$T_s = T_{2n} + a_0(T_{2n} - T_{2f}) + a_1(T_{2n} - T_{2f})^2 + a_2$
DA 2	DA(11) Quad, ϵ :	$T_s = T_{2n} + a_0(T_{2n} - T_{2f}) + a_1(T_{2n} - T_{2f})^2 + a_2 + a_3(1 - \epsilon_{2n})$
DA 3	DA(11) Quad, ϵ , $\Delta\epsilon$:	$T_s = T_{2n} + a_0(T_{2n} - T_{2f}) + a_1(T_{2n} - T_{2f})^2 + a_2 + a_3(1 - \epsilon_{2n}) + a_4\Delta\epsilon_0$
DA 4	DA(11) W, ϵ , $\Delta\epsilon$, W:	$T_s = T_{2n} + (a_0 + a_1W)(T_{2n} - T_{2f}) + (a_2 + a_3W) + (a_4 + a_5W)(1 - \epsilon_{2n}) + (a_6 + a_7W)\Delta\epsilon_0$
DA 5	DA (11) Quad, ϵ , $\Delta\epsilon$, W:	$T_s = T_{2n} + a_0(T_{2n} - T_{2f}) + a_1(T_{2n} - T_{2f})^2 + a_2 + (a_3 + a_4W)(1 - \epsilon_{2n}) + (a_5 + a_6W)\Delta\epsilon_0$
DA 6	DA(11) Quad(W), ϵ , $\Delta\epsilon$, W:	$T_s = T_{2n} + (a_0 + a_1W)(T_{2n} - T_{2f}) + (a_2 + a_3W)(T_{2n} - T_{2f})^2 + (a_4 + a_5W) + (a_6 + a_7W)(1 - \epsilon_{2n}) + (a_8 + a_9W)\Delta\epsilon_0$

AATSR temperatures, to permit a good determination of the coefficients. The band model MODTRAN 3.5 is used to calculate the brightness temperatures expected at the satellite for 60 different situations. The brightness temperatures have been calculated for a large gradient of temperatures between the near surface temperature and ground surface, consisting of five surface temperatures T-5, T, T+5, T+10, and T+20, (T is the first boundary layer temperature of the atmosphere) and four angles (0°, 11.2°, 24.7° and 53.8°) Furthermore, we have used 27 different emissivities obtained from the Salisbury and D'Aria, (1992) emissivity spectral responses of several types of surface (grass, dry grass, conifers, deciduous, sea, sand, clay, etc). These types of surfaces chosen are representative of the 90% of the Earth's landcover. The emissivities corresponding to the AATSR filters were obtained by integration of the response functions with the appropriate emissivity spectrum. Angular dependence of surface emissivities has been taken into account. The emissivities at forward view have been calculated using the factors defined by: Labed and Stoll, (1991) and Sobrino and Cuenca, (1999). These factors give a relation between emissivities at nadir view and forward view.

4 NUMERICAL COEFFICIENTS

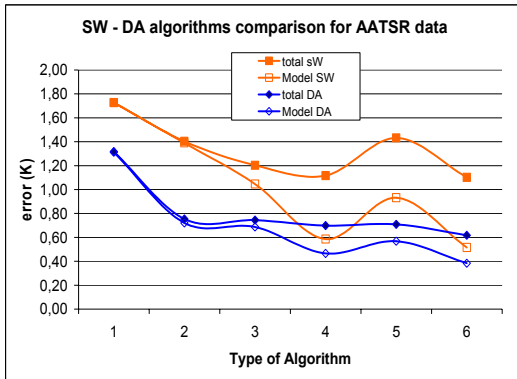
Once the structures of the algorithms have been determined, we selected the appropriate simulation data sets to derive the constant coefficients in the algorithms. The method used to minimize the

objective function is the Levenberg-Marquardt method. Table 2 summarizes the structures of the algorithms with the final values of the coefficients calculated by the minimization process. After having obtained the numerical expressions of the different algorithms proposed, our main goal was to give the sensitivity of each one of them in order to permit a comparison of algorithms. Error theory has been applied to all of the algorithms studied. The results of using the Levenberg-Marquardt minimization procedure and of applying the error theory are also given in Table 2.

The errors considered are the residual atmospheric error, σ_{mod} , which gives an idea of the possible accuracy in ST determination. The error owing to the noise (σ_{noise}) in the measurement process in the satellite instrument assuming a noise temperature of 0.05 K for the AATSR channels. It should be noted that σ_{noise} depends on the atmospheric water vapour content, in the process of computing the value of this error, a value of $W=1 \text{ g cm}^{-2}$ has been taken. The error associated with the water vapor column determination (σ_w), considering a water vapor content uncertainty of 0.5 g cm^{-2} , that error has a dependence with $(T_{4n} - T_{5n})$, ϵ_n , and $\Delta\epsilon_0$. To evaluate this error, we have taken for T_s the mean value of the database and we have chosen some representative values from the complete database for ϵ_n , and $\Delta\epsilon_0$. The error associated with the uncertainty in the value of the emissivity (σ_ϵ) is set at 0.005. The total error has been calculated, considering the different errors. Table 2 shows that the error of the model is smaller when the algorithm has more degrees of freedom.

Table 2.- Numerical coefficients and errors for the Split-window and Dual-angle algorithms proposed.

NAME	EXPRESSION	σ_{mod} (K)	σ_{noise} (K)	σ_{ϵ} (K)	σ_{WV} (K)	σ_{total} (K)
SW 1	$T_s = T_{2n} + 0.61(T_{2n}-T_{1n}) + 0.31(T_{2n}-T_{1n})^2 + 1.92$	1,73	0,07	—	—	1,73
SW 2	$T_s = T_{2n} + 0.76(T_{2n}-T_{1n}) + 0.30(T_{2n}-T_{1n})^2 + 0.10 + 51.2(1-\epsilon)$	1,39	0,07	0,18	—	1,40
SW 3	$T_s = T_{2n} + 1.03(T_{2n}-T_{1n}) + 0.26(T_{2n}-T_{1n})^2 - 0.11 + 45.23(1-\epsilon) - 79.95\Delta\epsilon$	1,05	0,09	0,59	—	1,20
SW 4	$T_s = T_{2n} + (1.01 + 0.53W)(T_{2n}-T_{1n}) + (0.4-0.85W) + (63.4-7.01W)(1-\epsilon) - (111-17.6W)\Delta\epsilon$	0,59	0,10	0,83	0,45	1,12
SW 5	$T_s = T_{2n} + 1.35(T_{2n}-T_{1n}) + 0.22(T_{2n}-T_{1n})^2 - (0.82-0.15W) + (62.6-7.2W)(1-\epsilon) - (144-26.3W)\Delta\epsilon$	0,93	0,11	1,06	0,20	1,43
SW 6	$T_s = T_{2n} + (1.97+0.2W)(T_{2n}-T_{1n}) - (0.26-0.08W)(T_{2n}-T_{1n})^2 + (0.02-0.67W) + (64.5-7.35W)(1-\epsilon) - (119-20.4W)\Delta\epsilon$	0,52	0,15	0,89	0,37	1,10
DA 1	$T_s = T_{2n} + 1.36(T_{2n}-T_{2f}) + 0.18(T_{2n}-T_{2f})^2 + 1.78$	1,31	0,11	—	—	1,32
DA 2	$T_s = T_{2n} + 1.56(T_{2n}-T_{2f}) + 0.15(T_{2n}-T_{2f})^2 - 0.34 + 51.9(1-\epsilon_{2n})$	0,72	0,12	0,18	—	0,75
DA 3	$T_s = T_{2n} + 1.57(T_{2n}-T_{2f}) + 0.15(T_{2n}-T_{2f})^2 - 0.11 + 51.7(1-\epsilon_{2n}) - 25.8\Delta\epsilon\theta$	0,69	0,13	0,26	—	0,74
DA 4	$T_s = T_{2n} + (1.62+0.3W)(T_{2n}-T_{2f}) + (0.18-0.52W) + (70.1-7.18W)(1-\epsilon_{2n}) - (35.4-3.67W)\Delta\epsilon\theta$	0,47	0,13	0,35	0,36	0,70
DA 5	$T_s = T_{2n} + 1.92(T_{2n}-T_{2f}) + 0.12(T_{2n}-T_{2f})^2 - (0.39+0.09W) + (71-7.55W)(1-\epsilon_{2n}) - (35.8-3.88W)\Delta\epsilon\theta$	0,57	0,15	0,36	0,17	0,71
DA 6	$T_s = T_{2n} + (2.67-0.07W)(T_{2n}-T_{2f}) - (0.29-0.09W)(T_{2n}-T_{2f})^2 - (0.31+0.28W) + (72.5-7.9W)(1-\epsilon_{2n}) - (35.8-4.1W)\Delta\epsilon\theta$	0,38	0,20	0,37	0,24	0,62

**Figure 1.-** Comparative analysis of split-window and dual-angle algorithm. The type of the algorithms is:

- 1: "SW n, QUAD" and "DA(2), QUAD";
- 2: "SW n, QUAD, ϵ " and "DA(2), QUAD, ϵ ";
- 3: "SW, n, QUAD, ϵ , $\Delta\epsilon$ " and "DA(2), QUAD, ϵ , $\Delta\epsilon$ ";
- 4: "SW, n(W), ϵ , $\Delta\epsilon$, W" and "DA (2), (W), ϵ , $\Delta\epsilon$, W";
- 5: "SW, n, QUAD(W), ϵ , $\Delta\epsilon$, W" & "DA(2), QUAD (W), ϵ , $\Delta\epsilon$, W";

However, in some situations, when the errors associated with W , ϵ and T_1 are considered, the total error can be higher than that obtained for algorithms with lower input parameters. The dual-angle in channel 2 gives better accuracy than in channel 1 and also better than the split-window that have the same structure (see Table 1). There is one interesting aspect of the values given in this Table: the water vapor dependent algorithms give better results than the other ones, even after including the effect of uncertainty in water vapor content error. Another way of representing the comparison between the split-window and the dual-angle algorithms is shown in Figure 1. Here, the behaviour of the algorithms in terms of their errors can be seen. The results are similar for both dual and split-window models when the simplest algorithm (less input parameters) is considered; however the differences increase when increasing the input parameters. The Figure also shows the effect due to the uncertainties in the input parameters that can reach up to 0.7 K.

Table 3.- Validation of algorithms proposed.

NAME	$\sigma_{\text{theor.}}$ (K)	$\sigma_{\text{validat.}}$ (K)	Bias (K)	RMSD (K)
SW 1	1.73	1.51	1.59	2.19
SW 2	1.40	1.56	1.48	2.15
SW 3	1.20	1.66	1.28	2.09
SW 4	1.12	1.93	1.28	2.31
SW 5	1.43	1.81	1.13	2.13
SW 6	1.10	2.06	1.17	2.36
DA 1	1.32	1.24	0.36	1.29
DA 2	0.75	1.29	0.02	1.29
DA 3	0.74	1.29	0.02	1.29
DA 4	0.70	1.25	-0.21	1.27
DA 5	0.71	1.39	-0.35	1.43
DA 6	0.62	1.28	-0.39	1.34

5 VALIDATION

The proposed algorithms have been applied to real data to be verified. These data consist of *in situ* measurements of temperature, atmospheric radiosoundings and satellite data (ATSR-2) acquired by the CSIRO (Commonwealth Scientific and Industrial Research Organisation of Australia). The studied area is an uniform region from New South Wales, Australia. The latitude and longitude of the central point is 34.392 °S and 145.305 °E respectively, with 110 m elevation. The site consists of a very uniform region approximately 900 km² within the largest plain in Australia. The landcover is Mitchell grass that is seasonally and rainfall dependent. The data was obtained between January and November of 1999. From the original collection of measurements, a mean of 6 images per month have been selected and the data have been filtered carefully to exclude the cloudy ones. In the validation process we calculate the surface temperature for every of the analyzed days from the proposed algorithms using satellite data and comparing these values with the ones measured *in situ*. Some measurements of the spectral emissivity have been made in the validation region and these values have been obtained from them: $\varepsilon_{1n}=0.967$, $\varepsilon_{1r}=0.958$; $\varepsilon_{2n}=0.961$ y $\varepsilon_{2r}=0.952$. Table 3 shows the values of the theoretical and experimental standard deviation, bias and RMSD. The conclusions of the theoretical analysis are confirmed: dual-angular algorithms show smaller errors on the estimation of the surface temperature than split-window ones.

6 CONCLUSIONS

A serie of dual-angle and split-window algorithms to estimate land surface temperature from AATSR data has been proposed. Its coefficients have been obtained from MODTRAN 3.5 simulations. A thorough comparison using real surface data suggests better results from the dual-angle algorithms than from the split-window ones. Anyway, the results belong to situations of relatively low content of water vapor (less than 2 g cm⁻²) and homogeneous regions. The non homogeneity of the surface will have more influence on dual-angle algorithms than on split-window algorithms, due to the different field of view of AATSR sensor between nadir and forward views. The effects of the angular variation of the emissivity values with the angle of vision have been included in the algorithms. At the moment the importance of this effect is being studied (Sobrino y Cuenca 1999; McAtee y Prata, personal communication).

7 ACKNOWLEDGEMENTS

This paper was partially sponsored by the European Union (Project WATERMED, under contract ICA3-ct-1999-00015), by the European Space Agency (Project: AO-ID 384) and to the Ministerio de Ciencia y Tecnología (REN2001-3105/CLI).

8 REFERENCES

- Labeled J. and Stoll, M. P., 1991, Spatial variability of land surface emissivity in the thermal infrared band: spectral signature and effective surface temperature. *Remote Sensing of Environment*, **38**, 1-17.
- McAtee B. and Prata, A. J. The angular behaviour of emitted infrared radiation (8–12 μm) at a semi-arid site in Australia: Implications for land surface temperature retrieval using wide field-of-view satellite instruments. In press.
- Salisbury J. W. and D'Aria, D. M., 1992, Emissivity of terrestrial materials in the 8-14 μm atmospheric window. *Remote Sensing of Environment*, **42**, pp. 83-106.
- Sobrino, J. A., Li, Z.-L., Stoll, M. P. and Becker, F., 1996, Multi-channel and multi-angle algorithms for estimating sea and land surface temperature with ATSR data. *International Journal of Remote Sensing*, **17**, 2089-2114.
- Sobrino J. A. and Cuenca, J., 1999, Angular variation of thermal infrared emissivity for some natural surfaces from experimental measurements. *Applied Optics*, **38**, 3931-3936.

Study of the Radiance to Flux Inversion within the Framework of the EarthCARE Mission

Alejandro Bodas Salcedo, Jaume F. Gimeno Ferrer, Ernesto López Baeza, and J. P. V. Poiares Baptista*

Climatology from Satellites Group, Remote Sensing Unit, Department of Thermodynamics, University of Valencia.

**European Space Agency, Earth Sciences Division.*

E-mail: Alejandro.Bodas@uv.es

ABSTRACT - The BBR (*Broad Band Radiometer*) is designed within the future ESA EarthCARE (*Earth Clouds, Aerosols, and Radiation Explorer*) mission framework to accurately measure SW (0.2–4 μm) and LW (4–50 μm) radiances exiting the Earth-Atmosphere system. From these radiances, it is expected to derive TOA (Top of Atmosphere) fluxes (SW and LW) to an accuracy of 10 W/m^2 , and for that, the aid of an Angular Distribution Model (ADM) is needed to account for the anisotropy of the radiance field. This is achieved thanks to the pointing capability of the BBR that observes along the scanning track with three views, namely a nadir view and two symmetric off-nadir views near 55°. Because the EarthCARE BBR only observes a short swath near the orbital track, this instrument is not suited for global monitoring of TOA radiation budget components. Its main objective however, is to provide a constraint for the derivation of vertical profiles of those components within the atmospheric column in order to test cloud and aerosol parameterisations in numerical models.

With the aid of a scene database specifically designed and built that contains radiances and fluxes corresponding to different geometrical, surface, atmospheric, and cloud conditions, the whole inversion procedure has been simulated in order to analyse the best possible BBR configuration regarding the off-nadir viewing zenith angle (VZA). That has been done by building the ADMs, both in shortwave and longwave, and studying their performance as function of the VZA.

The results show that the best selection for the VZA is around 55°, where the flux retrieval in SW is optimised, and in LW is also obtained with very good accuracy. Since the final error budget in longwave channel does not represent a problem, the main discussion is focused on the shortwave one.

1. INTRODUCTION

Predictions of global warming for 2100 range from 1.4 to 5.8 K, depending on the scenarios and models considered (IPCC, 2001).

Although all the models considered predict an increase in the global mean surface temperature, the uncertainty in the predictions is very high. A large part of this uncertainty comes from the limited knowledge in atmospheric sciences, specially with regard to the interaction of clouds and aerosols with radiation.

An example of this lack of knowledge has been provided by the Atmospheric Model Intercomparison Project (AMIP) (<http://www-pcmdi.llnl.gov/amip/>), which has shown the large differences in the zonal averages of cloud water content used in several climate models, if monthly means TOA fluxes are kept to be compatible with those measured from satellites.

Those results arise two questions. Firstly, parameterisations of interactions between clouds and aerosols with radiation are not adequately addressed in present climate models. Secondly, those results also show that present TOA Earth Radiation Budget databases, like ERBE (*Earth Radiation Budget Experiment*), are not sufficient to validate those

parameterisations in present climate models. Therefore, there is the need to obtaining not only TOA measurements, but also vertical profiles that provide us the ability to validating models. That will be the role of the EarthCARE mission.

EarthCARE has been defined (ESA, 2001) with the aim to determining, for the first time, and in a consistently radiative manner, global distribution of vertical profiles of cloud and aerosol field characteristics, to provide basic essential input data for numerical modelling and global studies of:

- The divergence of radiative energy
- The aerosol-cloud-radiation interaction
- The vertical distribution of water and ice and their transport by clouds
- The vertical cloud field overlap and cloud precipitation interactions

Radiative effects of clouds and aerosols depend on a number of different parameters, like macroscopic cloud structure (cloud fraction, cloud height, cloud overlap, etc), cloud water content, cloud particle effective radius, aerosol particle size and composition, etc.

To achieve these objectives, EarthCARE will measure many of these parameters in a radiatively consistent manner for a global sample of clouds and aerosols.

Two active and three passive instruments will flight onboard EarthCARE:

- **ATLID (Atmospheric Lidar)**: it is required to measure vertical profiles of optically thin cloud and aerosol layers. It is designed to provide vertical soundings with 100 m of vertical resolution.
- **CPR (Cloud Profiling Radar)**: it will provide vertical profiles of cloud structures along the satellite track with a vertical resolution of 500 m.
- **MSI (Multi-Spectral Imager)**: it will obtain images in 4 solar bands and in 3 thermal infrared bands. It will provide clouds and aerosol products, and the identification of the scene over a 150 km swath. It will have a horizontal resolution of 500 m at nadir.
- **BBR (Broad-Band Radiometer)**: the BBR will provide estimates of the TOA shortwave (0.2-4 μm) and longwave (4-50 μm) fluxes, with a constant resolution of 10 km in along-track observing configuration, with the nadir view and two off-nadir views with VZA of 55 degrees in forward and backward directions.
- **FTS (Fourier Transform Spectrometer)**: it will provide longwave fluxes with high spectral resolution, and vertical profiles of temperature and water vapour above the cloud top or with clear sky.

Figure 1 shows the EarthCARE objectives in a schematic way.

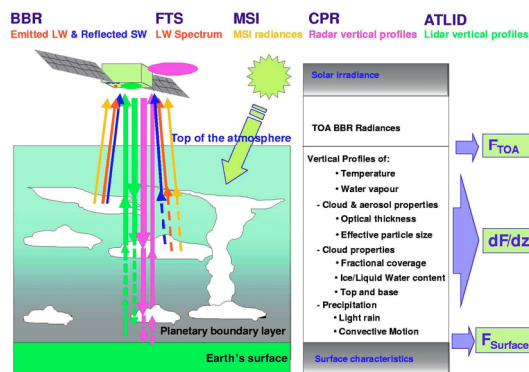


Figure 1. Mission objectives of EarthCARE.

All the measurements and products obtained from the mission have the restriction of an overall accuracy of 10 W/m^2 in TOA instantaneous fluxes. This restriction has established the particular accuracy of each instrument.

As the TOA fluxes will be independently measured with the BBR, it will provide the essential TOA boundary condition for the rest of the instruments.

Unfortunately, due to the fact that narrow field of view radiometers measure radiances, which are directional measurements, an inversion process has to be applied

in order to obtain the desired fluxes, which are hemispherical values (Raschke, 1973). That inversion process usually relies in ADMs, which represent the discrepancy of the radiance field with respect to the lambertian behaviour.

We now present a study carried out to optimise the BBR, based on theoretical ADMs built with a plane-parallel radiative transfer code.

To study the theoretical performance of the inversion procedure, a radiance database has been generated for a wide range of atmospheric conditions, and angular models have been built from that database. Then, the flux retrieval error has been studied as function of the observing geometry.

These results have helped in the design of the BBR, where the main idea is not to monitor the TOA Earth Radiation Budget (ERB) on a global scale, but to obtain accurate instantaneous TOA ERB measurements as a constraint to derive atmospheric profiles from the active instruments (ATLID and CPR). For this purpose, along-track configurations are very good candidates because the flux retrieval can be optimised by using different views of the same pixel from the same platform.

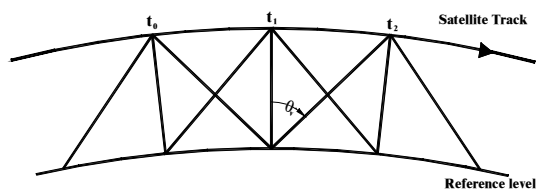


Figure 2. Diagram of the BBR along-track configuration with three views.

Figure 2 shows a diagram of an along-track observing configuration with three fixed views, one nadir, and two symmetric off-nadir views. This allows us to obtain three views of the same target at almost the same time. Other along-track configurations with a dense angular sampling were studied, but this paper will focus especially on the configuration shown in Figure 2, with only three views. This latter configuration was finally implemented in pre-phase A EarthCARE optimisation studies (López-Baeza et al., 2001).

The outline of the paper is as follows: the next section introduces the need of angular models to retrieve TOA fluxes, and briefly explains how they are built. Section 4 describes the database generated to carry out this work, and Section 5 presents the results of the optimisation study. Finally, we summarise the results and draw some conclusions.

2. NEED OF ANGULAR MODELS

One of the main error sources when measuring the ERB is the lack of knowledge of the anisotropy of the

observed radiance field (Suttles et al., 1988; 1989). Great efforts have been done for the last years to build and improve ADMs.

To obtain the final flux estimate, three main steps have to be carried out:

- *Calibration*: it consists on the conversion of the electronic signal from the sensor to the filtered radiance (e.g. Lee III et al., 1998).
- *Unfiltering Process*: it takes into account the spectral response of the optical components and the spectral distribution of the observed scene to provide the unfiltered radiance that reaches the satellite (e.g. Smith et al., 1986; Loeb et al., 2001).
- *Radiance to Flux Inversion*: this step converts the radiance into a flux estimate with the aid of an ADM (e.g. Raschke et al., 1973; Smith et al., 1986).

In addition to these three steps, in order to optimise unfiltering and radiance to flux inversion, a scene identification is needed. That introduces another error source in the general inversion process (Smith and Manalo-Smith, 1995). We shall focus our study on the last step, the radiance to flux inversion, assuming a perfect unfiltered radiance as input, and also a perfect scene identification.

The TOA radiance field is described by the spectral radiance $L_\lambda(\theta, \theta_v, \phi)$, with units of $\text{Wm}^{-2}\text{sr}^{-1}\mu\text{m}^{-1}$.

The angles θ , θ_v , ϕ , are the solar zenith angle (SZA), VZA, and relative azimuth (RAZ), respectively, and λ is the wavelength.

Therefore, the integrated radiance over a spectral range, Λ , is

$$L_\Lambda(\theta, \theta_v, \phi) = \int_\Lambda L_\lambda(\theta, \theta_v, \phi) d\lambda. \quad (1)$$

For the BBR, the interval Λ can be the solar part of the spectrum (SW), or the terrestrial emission (LW). Due to the fact that our input is always the broad-band unfiltered radiance, we will not use the subscript Λ .

Figure 3 shows the reference frame that defines the observing geometry. The origin of the relative azimuth is in the forward scattering direction, ranging from 0 to 180 degrees. Both zenith angles range from 0 to 90 degrees.

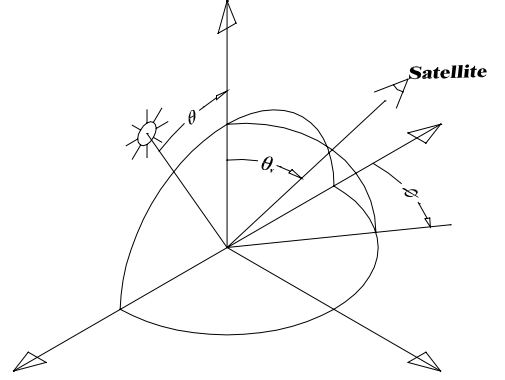


Figure 3. Observation Geometry.

The TOA flux is obtained by integrating the radiance field over the upper hemisphere:

$$F(\theta) = \int_0^{2\pi} d\phi \int_0^{\pi/2} L(\theta, \theta_v, \phi) \cos\theta_v \sin\theta_v d\theta_v. \quad (2)$$

This equation is telling us that we would need several sensors observing the same point at the same time from different satellites in order to provide enough angular sampling to compute that integral. Of course, that approach is unaffordable, and inversion algorithms have to be developed to estimate the flux from only one radiance. That inversion is carried out by means of an ADM. To build it, two mainly steps are required:

- Definition of scenes
- Mean radiance field for each scene

Each radiance must belong to one and only one scene type. For instance, a very simple scene definition would consist of only two classes, ocean and land.

Once the scene definition is done, the set of radiances can be *sorted in angular bins* (Taylor and Stowe, 1984) for each of those scene types. That is, we start

from a set of radiances L_{ijkl}^m , where the subscripts i, j , and k denote intervals in θ , θ_v , and ϕ , respectively, and l denotes different scenes. The index m distinguishes different measurements. Then, the anisotropic model is computed as

$$R_{ijkl} = \frac{\pi \bar{L}_{ijkl}}{F_{il}}, \quad (3)$$

where the overbar denotes averaging.

Finally, the flux estimate is computed by inverting that equation,

$$\hat{F}_{ijkl}^m = \frac{\pi L_{ijkl}^m}{R_{ijkl}}. \quad (4)$$

Although this inversion procedure is valid for any design concept because it makes use of only one radiance, more sophisticated algorithms can be developed with the aim to taking advantage of the multiangular concept of the BRR (Bodas-Salcedo et al., 2002a).

3. DATABASE

To generate the database, we have used the plane parallel radiative transfer code *Streamer 2.5p* (Key, 1998). The number of radiance fields generated have been 5760 for SW, and 2100 for LW.

Table 1 describes the scenes and angular bins used in the present study.

Table 1. Scene and angular bin definitions. C is the cloud cover fraction, in %.

Parameter	Range
SZA	[0-25, 25-35, 35-45, 45-55, 55-65, 65-70]
VZA	[-60, 60] 5-degree intervals
RAZ	[0-10, 10-30, 30-60, 60-90]
Surface	Ocean, Vegetation, Desert
C (%)	[0-1, 1-25, 25-50, 50-75, 75-99, 99-100]

Clouds at three different levels have been included in the computations, with their altitude depending on the standard atmosphere used in each case, as shown in Table 2. Low and middle clouds are comprised of cloud droplets, and high clouds of ice crystals. The labels defining the atmospheres are: TRO, MLS, MLW, SAS, and SAW for tropical, mid-latitude summer, mid-latitude winter, sub-artic summer, and sub-artic winter, respectively.

Table 2. Cloud top altitude (in km) used for different standard atmospheres.

Atmosphere	Low	Middle	High
TRO	2	6	14
MLS	2	5	12
MLW	2	5	10
SAS	2	5	10
SAW	2	5	8

Figure 4 shows the angular model for overcast ocean as a polar contour plot. It should be noted how the field is highly anisotropic, mainly in the forward scattering direction.

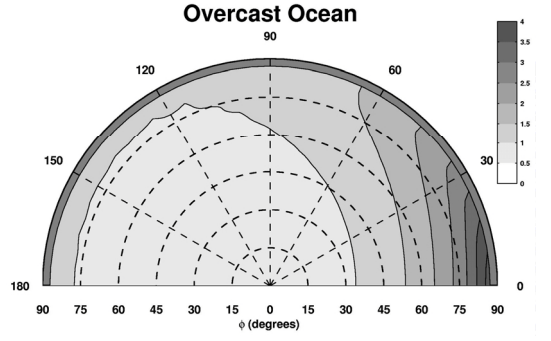


Figure 4. ADM for overcast ocean.

4. RESULTS

With the ADMs built from the radiance database, the performance of the inversion error has been studied by analysing the root mean square error (RMSE) for every angular bin and scene type,

$$RMSE_{ijkl} = \sqrt{\frac{1}{N_{ijkl}} \sum_{m=1}^{N_{ijkl}} (\hat{F}_{ijkl}^m - F_{ijkl}^m)^2}. \quad (5)$$

The actual flux, F_{ijkl}^m , is obtained by direct integration of the TOA radiance field in the database. This procedure allows to study the performance of the SW inversion RMSE as function of the observing geometry, as shown in Figure 5. To simplify the plots, negative VZAs are used when RAZ is greater than 90 degrees. For instance, a radiance with VZA=40° and RAZ=160° will now have VZA=-40° and RAZ=20°. This figure shows how a preferred inversion region appears in the range of VZAs between 50 and 60 degrees, both in forward and backward scattering regions, independently of the underlying surface and RAZ. Although not shown here, this behaviour is found when the signal is dominated by clouds, being the cloud cover greater than 50%. The differences between different surfaces can be attributable to different surface albedo.

The main reason for the different behaviour at different observing angles is due to the lack of linearity in the F-L relationship. If this linearity fails, as it does for example at nadir view, the performance of the inversion should be worse, even if by construction the inversion model is unbiased.

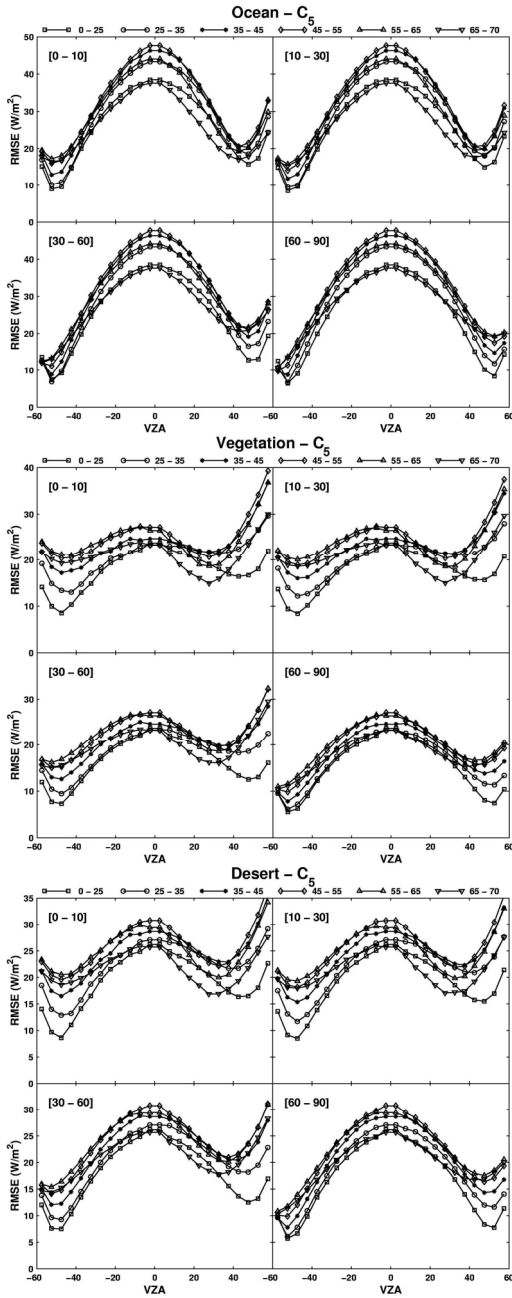


Figure 5. Shortwave flux retrieval algorithm RMSE under mostly cloudy conditions over ocean, vegetation, and desert. as function of VZA. Within a particular surface, each plot correspond to a different RAZ interval. The legend shows SZA intervals.

This lack of linearity is clearly noticed in Figure 6, which shows the comparison between real (F) and estimated (F_e) fluxes, and the probability density function (PDF) of the differences (error). Vertical dashed lines in the PDF plot correspond to the RMS error. The comparisons are shown for the results of Figure 5, but only to those over ocean, and for three VZAs, namely 0, -30, and -55 degrees, that is for nadir, and 30 and 55 degrees in the backward scattering direction.

We see in Figure 6 that for $VZA = -55^\circ$, the hypothesis of proportionality between radiance and flux assumed in the inversion model is well conserved. However, that is not the case for smaller VZAs, where the probability distributions are highly asymmetric, although with zero mean by construction. For the case of $VZA = -55^\circ$, the error distribution is almost symmetric, with the maximum close to the mean value, being this the best-behaved inversion. The other two distributions show their maxima in the negative portion of the x axis, with a large number of errors below zero (underestimation). Those underestimated values are compensated by the long positive tail, reaching errors of more than 100 W/m^2 in some cases.

To improve the inversion error for angles below 40/50 degrees, the scene definition must be stratified in other parameters than cloud cover. Additional computations have been done by stratifying the scene definition in cloud optical depth. It is observed that a very good scene identification is needed to reach the same inversion error at nadir and at -55 degrees for optically thick clouds. For instance, the RMSE with a perfect cloud optical depth retrieval algorithm for clouds with optical depth of 30 is 18 W/m^2 , and for a $VZA = -55^\circ$ without distinction of cloud optical depth is 13 W/m^2 , still better. That means that good accuracy can be reached by selecting the proper observing configuration, with a very simple scene definition.

The same computations have been done for LW, showing similar behaviour, with preferred inversion angles close to 50/55 degrees (Bodas-Salcedo et al., 2002a), although they are not shown here.

All these results have been validated with the aid of CERES/TRMM data (Bodas-Salcedo et al, 2002b). That validation supports the existence of that preferred inversion region for both LW and SW bands. Only in forward and backward scattering directions in SW do not appear the preferred inversion region, maybe due to the greater influence of three dimensional effects for those observing directions in real clouds (Várnai, 2000).

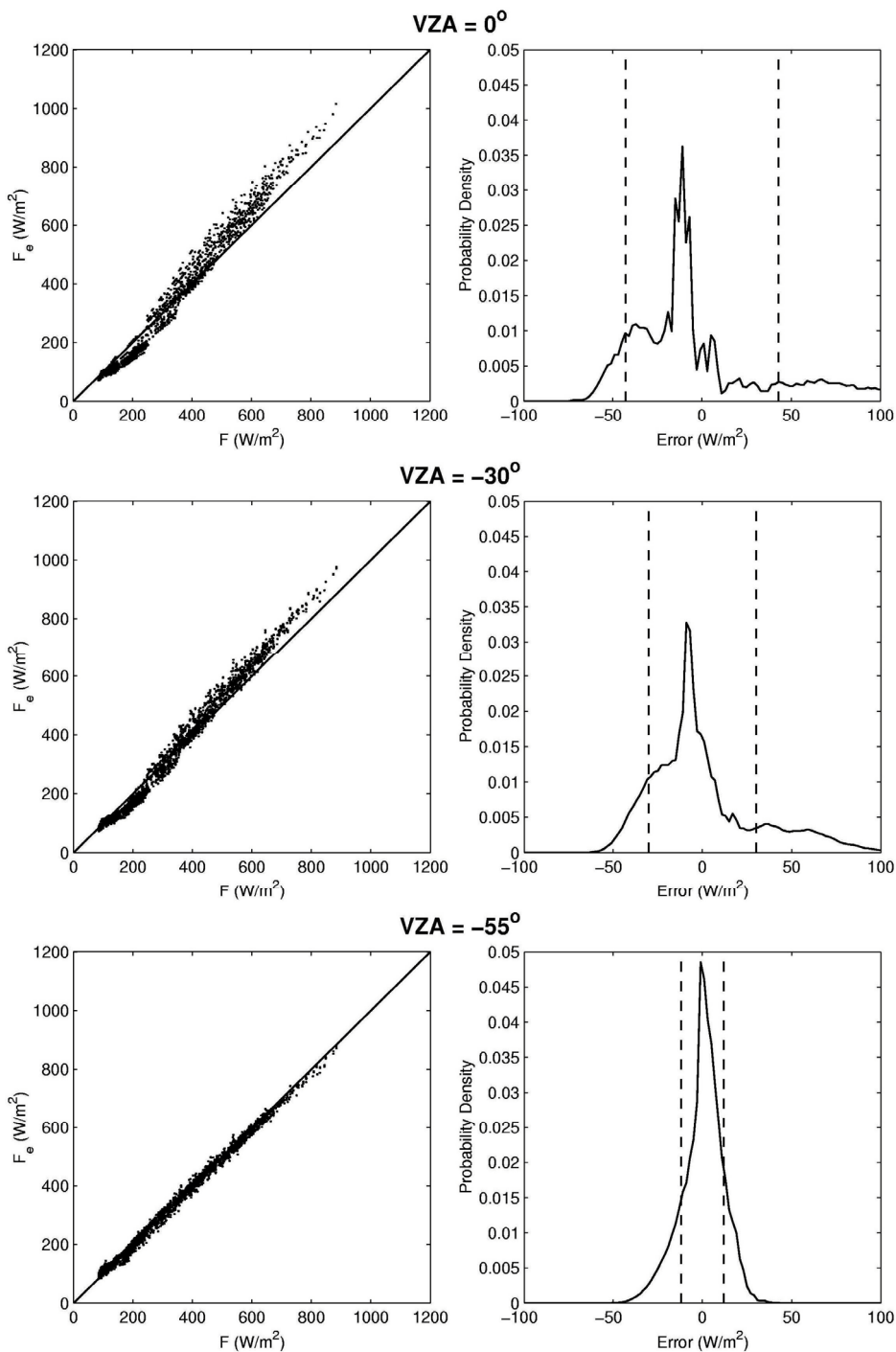


Figure 6. Comparisons between estimated and actual flux over ocean, with cloud cover between 75 and 99%, for three different VZAs, namely, 0° , -30° , and -55° . Vertical dashed lines show the \pm -RMSE range.

5. CONCLUSIONS

Taking as starting point a radiance database especially built with the aid of a radiative transfer code, different ADMs have been constructed. This has allowed us to study the impact of the observing geometry on the flux retrieval error.

Two different parallel studies have been developed, one for the shortwave band and another for the longwave band. Both of them show similar behaviour with respect to the VZA, although only SW results are shown here because the inversion error is larger in SW than in LW, and therefore the optimisation of the radiometer design has to be based mainly on SW results.

It has been observed that a preferred observing region appears for VZAs between 50 and 60 degrees, both in SW and LW. This is independent of the SZA, RAZ, and surface considered. This region is only observed when clouds dominate the signal reaching the sensor.

This study shows that an along-track design concept seems to be the best option to measure instantaneous TOA fluxes with high accuracy, because the VZA can be selected *a priori* for every pixel. Although this type of configurations do not provide global spatial coverage, they can be very powerful complements as boundary conditions for atmospheric profile measurements consisting of downward looking active instruments, like the ATLID and CPR onboard EarthCARE.

6. ACKNOWLEDGEMENTS

This work has been carried out in the framework of the ESA-ESTEC contract n°14685/00/NL/JSC.

One of the authors, A. Bodas Salcedo, holds a predoctoral grant funded by *Conselleria de Educació i Cultura de la Generalitat Valenciana*.

7. REFERENCES

- Bodas-Salcedo, A., J. F. Gimeno-Ferrer, and E. López-Baeza, 2002a, Flux Retrieval Optimisation with a Non-Scanner Along-Track Broad-Band Radiometer, *J. Geophys. Res.*, (submitted).
- Bodas-Salcedo, A., E. López-Baeza, and G. L. Smith, 2002b, Study of the Flux Retrieval Error Behaviour with CERES/TRMM Data, in *9th International Symposium on Remote Sensing, SPIE*, Crete, Greece, 22-27 September.
- ESA, 2001, The five candidate Earth Explorer Core Missions – EarthCARE – Earth Clouds, Aerosols, and Radiation Explorer. ESA SP-1257(1), 2001.
- IPCC, 2001, Intergovernmental Panel on Climate Change, Third Assessment Report, WG I Climate Change 2001: The Scientific Basis, Summary for Policy Makers. IPCC, 2001.
- Key, J., 1998, Streamer User's Guide, Technical Report 96-01, Department of Geography, Boston University, 90 pp.
- Lee III, R. B., B. R. Barkstrom, H. C. Bitting, D. A. H. Crommelynck, J. Paden, D. K. Pandey, K. J. Priestley, G. L. Smith, S. Thomas, K. L. Thornhill, and R. S. Wilson, 1998, Prelaunch Calibrations of the Clouds and the Earth's Radiant Energy System (CERES) Tropical Rainfall Measuring Mission and Earth Observing System Morning (EOS-AM1) Spacecraft Thermistor Bolometer Sensors, *IEEE Trans. Geosci. Remote Sensing*, **36**, 1173-1185.
- Loeb, N. G., K. J. Priestley, D. P. Kratz, E. B. Geier, R. N. Green, B. A. Wielicki, P. O'Rawe Hinton, and S. K. Nolan, 2001, Determination of Unfiltered Radiances from the Clouds and the Earth's Radiant Energy System Instrument, *J. Appl. Meteor.*, **40**, 822-835.
- López-Baeza, E., A. Bodas-Salcedo, and J. F. Gimeno-Ferrer, BBR Optimisation Study, Final Report, ESA Contract No. 14685/00/NL/JSC, ESA, 2001.
- Raschke, E., T. H. Vonder Haar, W. R. Bandeen, and M. Pasternak, 1973, The Annual Radiation Balance of the Earth-Atmosphere System During 1969-70 From Nimbus 3 Measurements, *J. Atmos. Sci.*, **30**, 341-364.
- Smith, G. L., R. N. Green, E. Raschke, L. M. Avis, J. T. Suttles, B. A. Wielicki, and R. Davies, 1986, Inversion Methods for Satellite Studies of the Earth's Radiation Budget: Development of Algorithms for the ERBE Mission, *Reviews Geophys.*, **24**, 407-421.
- Smith, G. L., and N. Manalo-Smith, 1995, Scene Identification Error Probabilities for Evaluating Earth Radiation Measurements, *J. Geophys. Res.*, **100**, 16377-16385.
- Suttles, J. T., R. N. Green, P. Minnis, G. L. Smith, W. F. Staylor, B. A. Wielicki, I. J. Walker, D. F. Young, V. R. Taylor, and L. L. Stowe, 1988, Angular Radiation Models for Earth-Atmosphere System. Volume I-Shortwave Radiation. NASA RP-1184.
- Suttles, J. T., R. N. Green, G. L. Smith, B. A. Wielicki, I. J. Walker, V. R. Taylor, and L. L. Stowe, 1989, Angular Radiation Models for Earth-Atmosphere System. Volume II-Longwave Radiation. NASA RP-1184.
- Taylor, V. R., and L. L. Stowe, 1984, Reflectance Characteristics of Uniform Earth and Cloud Surfaces Derived from NIMBUS 7 ERB, *J. Geophys. Res.*, **89**, 4987-4996.
- T. Várnai, 2000, Influence of Three-Dimensional Radiative Effects on the Spatial Distribution of Shortwave Cloud Reflection, *J. Atmos. Sci.*, **57**, 216-229.

Retrieval of biophysical parameters using directional spectral mixture analysis

F. J. García-Haro, F. Camacho-de Coca and J. Meliá
Department of Thermodynamics, University of Valencia.
C/Dr. Moliner, 50. 46100 Burjassot. Valencia, Spain.
J.Garcia.Haro@uv.es

ABSTRACT

In this study, we propose a modeling scheme to assess angular variation in discontinuous canopies, relating these variations with the main optical and structural parameters. The reflectance of an individual pixel is assumed to consist of an area weighted linear combination of the soil and vegetation radiances. Canopy geometrical effects are considered in the first order scattering. Hot spot kernels are used to model the joint probability of viewed and sunlit components. The model makes a simple treatment of the multiple scattering effect using an approximate analytical solution to the radiative transfer problem. The model formalism and the volume scattering formulation is similar to the GHOST model (Lacaze and Roujean, 2001). However, the between-crown gap probability is formulated in terms of the FVC and a geometric variable (η) associated with the shape of plants. The invertibility of the model to retrieve FVC and LAI was tested using airborne POLDER measurements corresponding to cropland. Although the model is less suited for homogeneous canopies, it has provided reasonable results, similar to accurate BRDF models of homogeneous canopies like NADIM (Gobron et al., 1997).

1 INTRODUCTION

Within the frame of the LSA SAF Project (Satellite Application Facility on Land surface analysis), we are aimed to develop robust and operational algorithms for retrieving biophysical parameters from the future Meteosat Second Generation (MSG) and European Polar System (EPS) satellites. The synergistic use of SEVIRI/MSG and AVHRR-3/EPS datasets will offer innovative angular capabilities for determining vegetation products over Europe and Africa thanks to concomitant multiple viewing and illumination geometries (Van-Leeuwen and Roujean, 2002). Our main concern is to retrieve fractional vegetation cover (FVC) and leaf area index (LAI) corrected from the effects of the sun-target-sensor geometry. These parameters play a critical role in the description of and land-atmosphere interactions.

Remotely sensed BRDF data is the unique way for monitoring the vegetation on a global scale. Linear mixture is the basis hypothesis in some simple BRDF models (e.g. GO models or kernel-driven models) for simulation of scene reflectance or in remote sensing algorithms, e.g. spectral mixture analysis (SMA). However, the degree of validity of this assumption depends on (Qin and Gerstl, 2000): (1) the presence of multiple scattering, (2) the difficulty to determine optical properties of scene elements, (3) directional effects which can be expressed by variations of downwelling and upwelling radiative fluxes as a function of the solar and viewing directions, and (4) the scale size. For example, at a shrub scale the linear assumption is incorrect, specially in the NIR

wavelengths. When the size is increased to the magnitude of kilometers, such as AVHRR and SEVIRI sensors, the linear mixture theory is approximately applicable. Furthermore, in this case the contribution of shadows is rather small (<5%), although the total fraction can be considerably higher (e.g. 18%). These results imply that at a large scale both GO and kernel-driven model are generally applicable.

SMA methods usually ignore the fact that proportions of viewed and shaded components depend on the view-sensor geometry. Only a few works have addressed these directional effects (Asner et al., 1997; Scarth and Phinn, 2000). Another assumption of SMA is that plants are modeled as Lambertian opaque surfaces. Crown transparency is thus ignored and, therefore, information related with canopy structural parameters (LAI, leaf angle distribution (LAD), etc.) is regarded as a source of noise which may introduce a bias in the solution. On the other hand most BRDF inversion methods utilize one-dimensional models, implying thus surface homogeneity within an image pixel. Hence they are limited to address mixed landcovers pixels, which are common in coarse resolution satellites. This study aims to develop a simple, fast and operational approach to deconvolve the angular reflectance into single landcovers reflectances, attempting to solve the inconsistencies of 1-D models and linear mixture approaches. We propose an hybrid model, which combines the geometric optics of large scale canopy structure with principles of radiative transfer for volume scattering within individual crowns.

Different hybrid models have been developed in the recent years to describe the radiation regime in forest canopies (Li et al., 1995; Chen and Leblanc, 1997). These models assume a medium consisting of gaps and regions idealized by a turbid volume with a foliage density of small leaves. Gap probability is calculated based upon a geo-statistical distribution of stems. More recently, the GHOST model (Lacaze and Roujean, 2001) has been developed to address the local scale angular structure of the hot spot, which can be judged relevant for patch and regional scales.

In our model, reflectance of an individual pixel is assumed to consist of an area weighted linear combination of the soil and vegetation radiances. Canopy geometrical effects are considered in the first order scattering. The model makes a simple treatment of the multiple scattering effect using an approximate analytical solution to the radiative transfer equation. The volume scattering formulation is similar to the GHOST model. However, the between-crown gap probability is formulated in terms of the FVC and a geometric variable (η) associated with the shape of plants. The invertibility of the model to retrieve FVC and LAI has been demonstrated using airborne POLDER measurements corresponding to cropland. Model performance was also evaluated by comparing it with an accurate BRDF model of homogeneous canopies like NADIM (New Advanced DIScrete Model) (Gobron et al., 1997). The next section describes the model formulation in detail. The inversion algorithm is presented in section 3. The model is validated in section 4. Finally, the conclusions and future prospects are presented in section 5.

2. MODEL FORMULATION

The reflectance of an individual pixel is assumed to consist of an area weighted linear combination of the soil and vegetation contributions:

$$R = R_v + R_s \quad (1)$$

The vegetation reflectance is expressed as a sum of single scattering (ss) and multiple scattering (ms) reflectances (Hapke, 1981; Lacaze and Roujean, 2001):

$$R_v = \frac{\omega}{4 \mu_s \mu_v} \cdot \{P(\xi) I_{ss} + [H(\mu_s) H(\mu_v) - 1] I_{ms}\} \quad (2)$$

where ω is the leaf scattering albedo, i.e. the sum of the leaf reflectance (ρ) and transmittance (τ), $\mu_{s,v} = \cos \theta_{s,v}$, ξ is the phase angle, and the factors I_{ss} and I_{ms} model the proportion of radiation flux which is single/multiple scattered by foliage elements on the downgoing and outgoing optical pathways as a whole. The Chandrasekhar function $H(\mu_{s,v})$ is used to compute multiple scattering (Hapke, 1981). $P(\xi)$ is a

turbid medium phase function (Ross, 1981). The G-function controls the volume component depending on the within-crown element distribution, whereas the external geometric component depending on the crown shape and dimension is evaluated using an average theory of the gap probability.

2.1 Volume component

The proposed model assumes that the geometrical component and the volume component of the radiation fluxes can be decoupled in such a way that the flux interception of radiation can be expressed as follows:

$$I_{ss} = I_{ss,vol} \cdot I_{ss,geo} \quad I_{ms} = I_{ms,vol} \cdot I_{ms,geo} \quad (3)$$

The volume single/multiple scattered component can be described using the Beers' law:

$$I_{ss,vol} = \frac{1}{\Delta} [1 - \exp(-\Delta LAI \Omega_E \gamma / g_c)] \quad (4)$$

$$I_{ms,vol} = \frac{1}{\Delta'} [1 - \exp(-\Delta' LAI \Omega_E \gamma / g_c)] \quad (5)$$

where Ω_E is the clumping index of the shoots, which quantifies the level of foliage aggregation within the tree crown. LAI is the scene leaf area index defined as half the total needle area per unit ground surface area, g_c denotes the fractional vegetation cover and γ is a band-specific factor, which was assumed to be dependent on the leaf transmittance (e.g. Bégué, 1992). Assuming plants with similar foliar density in the scene, LAI/g_c represents an average value of the LAI of individual plants. This term is more pertinent to describe crown trees transparency than scene LAI. Δ denotes the (bidirectional) normalised extinction coefficient for singly scattered radiance. The model adopts the analytical expression derived by Roujean (2000) to the hot spot effect, i.e. coupling the downgoing and outgoing optical pathways:

$$\Delta = \sqrt{\frac{G_s^2}{\mu_s^2} + \frac{G_v^2}{\mu_v^2} - 2 \frac{G_s}{\mu_s} \frac{G_v}{\mu_v} \cos \xi} \quad (6)$$

where G is the well-known function defined by Ross (1981) to represent the mean monodirectional projection of a unit foliage area, which depends on the LAD. For the multiple scattered component the hot spot phenomenon is usually ignored (Qin and Goel, 1995), i.e.:

$$\Delta' = \frac{G_s}{\mu_s} + \frac{G_v}{\mu_v} \quad (7)$$

2.2 Geometric component

The geometric component of the single scattering $I_{ss,geo}$ is determined by the between-crown light penetration and the visibility of illuminated objects. This component is particularly relevant for discontinuous canopies. For example, forest reflectance is dominated by the contrast between the sunlit and shaded components, especially in the visible parts of the spectrum. One question that arises is to describe the

contribution of shaded and illuminated ground and crown, even when overlapping complicates the generalisation for denser canopies. Intercepted fluxes were formulated in terms of horizontal projection of the crown. Let denote by $P_0(\theta)$ the (between-crown) monodirectional gap fraction, which corresponds to the fraction of soil seen in the direction θ (Nilson, 1971). It is a biophysical variable of prime interest for remote sensing since it directly determines the single scattering process in the radiative transfer process (Weiss and Baret, 1999). LAI and fAPAR are strongly related to the monodirectional gap fraction. In fact, P_0 at particular directions provides an indirect way to estimate LAI and fAPAR (Weiss and Baret, 1999). For homogeneous Poisson distribution, the probability of observing the ground under the tree crowns in any given pixel approaches to (Jasinski and Eagleson, 1989):

$$P_0(\theta_s) = (1 - g_c)^{(\eta+1)} \quad (8)$$

where η is defined as the ratio of ground projected shadow to plant area. It absorbs all the geometric factors which relate canopy area to shadowing area into only one variable. Its analytical expression for the most common geometrical bodies is provided in Jasinski and Eagleson (1990). For example, for the case of square cylinders, we have $\eta = \tan \theta / b$, where b is the similarity parameter, defined as the ratio of the mean width D to the mean height H . The probability of having sunlit ground P_{ig} and viewed ground P_{vg} can be expressed as follows:

$$P_{vg} = P_0(\theta_v) \quad P_{ig} = P_0(\theta_s) \quad (9)$$

A functional relationship can be also found between subpixel shaded ground P_{sg} and fractional vegetation cover:

$$P_{sg} = 1 - g_c - (1 - g_c)^{(\eta_b+1)} \quad (10)$$

Logically, the vertical crown cover projections in the view and sun directions are given by:

$$P_{vc} = 1 - P_0(\theta_v) \quad P_{ic} = 1 - P_0(\theta_s) \quad (11)$$

The above equations are applicable at large sampling scales, when imaging stands resolutions greater than the size of the tree crowns. In order to confirm these mathematical relationships, different nadir images were simulated by means of a canopy reflectance model (García-Haro and Sommer, 2002). The spatial distribution of subcanopies, dimensions, density and sun geometry were systematically altered, allowing us to evaluate the conditions in which the proposed parameterisation is applicable. For each simulated image, the subpixel proportions of shaded ground, sunlit ground, shaded crown and sunlit crown were obtained. Figure 1a shows an example corresponding to a 200m pixel with Poisson plant distribution. Figure 1b shows the relationship found

between subpixel shaded ground and FVC. The figure reveals a close agreement between the values of P_{sg} derived using the simulation model (symbols) and the values obtained using Eq. (10) (dashed line). Similar simulations were undertaken varying plant distribution (regular, clumped). In general, the relationships derived from non-Poisson spatial distributions of plants differed from those predicted by Eq. (10).

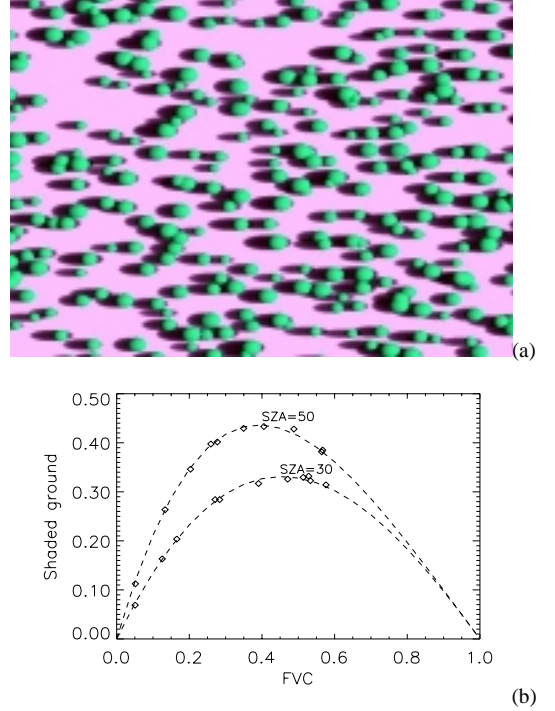


Figure 1. (a) Example of simulated nadir image. Input parameters are: $\theta_s=50^\circ$, Poisson plant distribution, FVC=0.30 and elongated plants ($b=2.5$). (b) Shaded ground P_{sg} vs FVC, for two different sun zenith angles.

The probability of observing sunlit crown when P_{ic} and P_{vc} are not correlated is simply the product of both probabilities $P_{ic}P_{vc}$, where P_{ic} controls the amount of light intercepted by crowns and P_{vc} controls the contribution of visible crowns to the scene radiance. However, hot spot kernels are necessary to account for the correlation between the two gap probabilities along sun and view directions. They should be unity when the sun and view positions align (i.e. at the hot spot) and vanish when the shift ξ of the illumination angle relative to the view angle is large enough. Direct calculations for the joint probability are, however, very complicated and require the use of certain simplifications. For example, they usually assume known the distribution of gap size inside and between tree crowns (Chen and Leblanc, 1997) or use a simple prescribed representation of crown trees sizes, shapes

and distributions (Li and Strahler, 1992; Qin and Goel, 1995). The simulation of physical scenarios provides alternative methods to determine the between crown gap probability and the hot spot kernel for a wide range of biomes and spatial resolutions (García-Haro et al., 2002). GO models also allow us to address the clumping nature of vegetation at a patch scale, which is usually ignored. For example, for large pixels, the hot spot effect seems to be dominated by the radiation transmission between the gaps of macroscale elements forming the landscape such as groups of trees instead of microscale elements like needles (Lacaze et al., 2002).

We assumed that the hot spot has a minor influence on the multiple scattered interception at a crown level:

$$I_{ms,geo} = P_{ic} P_{vc} \quad (12)$$

A hot spot kernel $F_c(\xi)$ was used to modulate the dependence between the optical paths for the single scattered radiation:

$$I_{ss,geo} = P_{ic} P_{vc} + [P_{ic} - P_{ic} P_{vc}] F_c(\xi) \quad (13)$$

where $F_c(\xi)$ was obtained from the overlap function between viewing and illuminated shadows as projected on the background (Li and Strahler, 1992).

2.3 Soil component

The soil contribution R_s is expressed as the product of soil bidirectional reflectance γ_s and vegetation transmittance T :

$$R_s = T \gamma_s \quad (14)$$

The vegetation transmittance can be expressed as the sum of the probability that a solar ray beam will reach the ground without intercepting any crown T_{geo} plus the probability of intercepting a crown without hitting any foliage element, i.e.:

$$T = T_{geo} + (1 - T_{geo}) T_{vol} \quad (15)$$

The following expressions were considered for the transmissions:

$$T_{vol} = \exp(-\Delta LAI \Omega_E \gamma / g_c) \quad (16)$$

$$T_{geo} = P_{ig} P_{vg} + [P_{ig} - P_{ig} P_{vg}] F_G(\xi) \quad (17)$$

where F_G is a hot spot kernel, which tends to zero when the sun and view directions are far apart, i.e. when the viewer sees the sunlit ground through a gap different from that of illumination. In this study, it has been parameterized using a simple analytical expression. For one gap of size λ , the following hot spot function applies (Chen and Leblanc, 1997):

$$F_G(\xi) = 1 - \frac{\xi}{\tan^{-1}(\lambda/H)} \quad (18)$$

The typical size of the between-crowns gap size, λ_{ave} , was fixed, combining the dimensions of three crowns and FVC.

Model neglects side scattered diffuse radiation incident on ground surface after multiple scattering with leaves of neighboring plants. Field measurements and radiosity models all show that the side scattered light can be very significant (Roberts et al., 1990; Borel and Gerstl, 1994). The model is thus generally accurate for visible part of the solar spectrum, but less accurate at near-infrared wavelengths at which multiple scattering in plant canopies is the strongest within the solar spectrum. These non-linear effects exert a strong impact at shrub scale but they can be considered small at landscape scales when there is an horizontal mixing of vegetation types or materials (Asner et al., 1998; Qin and Gerstl, 2000).

2.4 Diffuse component

The above equations consider only the contribution of direct radiation to the reflectance. Considering also the presence of skylight irradiance, the reflectance can be expressed as a sum of the direct and isotropic diffuse components:

$$R = (1 - k_d) R_{direct} + k_d R_{diffuse} \quad (19)$$

where the component of diffuse reflectance was calculated as the average of the measurements in the principal plane. k_d denotes the fraction of diffuse irradiance, which was parameterised as follows (Lacaze and Roujean, 2001):

$$k_d = \frac{0.09}{0.09 + \mu_s} \quad (20)$$

In addition, the model allows us to derive other parameters like the entire BRDF distribution, albedo or absorptance, including the relative contribution of vegetation and soil. For example, the spectral absorptance within the canopy can be evaluated as

$$A_h = 1 - R_h - (1 - \gamma_{s,h}) T_h \quad (21)$$

where the subscript h stands for values integrated over the full view hemisphere. The fractional amount of incident photosynthetically active radiation absorbed by the vegetation canopy (fAPAR) can be evaluated by averaging the spectral canopy absorptance within the PAR region, i.e.:

$$fAPAR = \int_{400}^{700} E_o(\lambda) A_h(\lambda) d\lambda \quad (22)$$

where $E_{o,\lambda}$ is the normalised solar irradiance spectrum.

3. MODEL INVERSION

The inversions are achieved simultaneously for all spectral bands, i.e. by coupling the spectral and directional data available. The variables to be retrieved are LAI and g_c . Given BRDF values r_i ($i=1, \dots, N$), representing the conditions of observation (i.e. wavelengths and view and illumination geometries), the retrievals are performed by comparing observed and modeled y_i ($i=1, \dots, N$) BRDF's. The comparisons

are evaluated for a full set of prescribed canopy realisations (g_c , LAI) that cover a range of expected natural conditions. Those pairs for which the canopy model generates inputs comparable with measured data, within the limits of accuracy of data ϵ_i ($i=1,...,N$), i.e.:

$$(\mathbf{r}-\mathbf{y})^T \mathbf{W}^{-1}(\mathbf{r}-\mathbf{y}) \leq N \quad (23)$$

are considered as acceptable solutions, where \mathbf{W} is the covariance matrix of the measurements. The diagonal elements of \mathbf{W} are the variance ϵ^2 , which should account for both data uncertainty and unquantified errors associated with the simplifying assumptions of the theoretical model. The distribution of solutions define a domain for g_c and LAI around the “true” values. Mean values of g_c and LAI averaged over the set of acceptable solutions are taken as solutions. This procedure not only increases the numerical stability of the inversion but also enables us to derive the uncertainty and correlation of derived parameters.

In this study, secondary model parameters (LAD, b , λ_{ave}) were fixed based on the apriori expected values. The model requires the optical properties of the underlying soil γ_s as input. It was estimated either using soil BRFs observations in surrounding bare soil areas which were subsequently extrapolated to the POLDER observation geometries or modelled with the aid of BRDF models (Walthall et al., 1985; Jacquemod et al., 1992). In this study the extrapolation of measured BRFs provided better results. It was assumed for simplicity that reflectance and transmittance of leaves are similar. The leaf albedo ω was assessed previously by adjusting the model for each individual band. The procedure consisted in (1) setting spectral bounds that stand for the uncertainty limits of ω , and (2) adjusting them based on the best fit of the model to the directional signature, for a reduced set of canopy realisations.

Although the model has been validated against real data, a comparative analysis has also been undertaken on NADIM (Gobron et al., 1997), an invertible model of homogeneous canopies. NADIM simulates the radiation regime in the solar domain in the case of horizontally homogeneous canopies. Unlike the proposed model, which is very fast because of its analytical nature, NADIM is more expensive computationally since it explicitly solves the radiation transfer problem using a discrete representation of the canopy. The model simulates the relevant scattering processes as a function of the size (d_L) and orientation (LAD) of the leaves, as well as the total height of the canopy (H) and LAI. NADIM uses a turbid medium approach to represent the multiple scattering contribution.

NADIM has been inverted using a simple searching look-up table method, similar to the method

described above. However, $g_c=1$ is implied and, therefore, the only unknown parameter is LAI. Primary model parameters (LAD, H , d_L) were fixed based on a priori expected values. Optical parameters (ω , γ_s) were obtained using the procedure described above. Although in its original formulation NADIM assumed an isotropic soil background, soil BRFs observations were used to represent more accurately γ_s . This allowed us to remove modelling errors found in low vegetated canopies, mainly induced by a strong soil backscattering.

4. VALIDATION

4.1 Airborne POLDER data set

The model invertibility was evaluated using data acquired by the POLDER onboard an ARAT plane during the DAISEX campaign. The experiment site selected by ESA for the DAISEX campaigns is a 3 km by 3 km area centred at 39° 3' N, 2° 5' W, which is located 28 km from Albacete (Spain), (Camacho-de Coca et al., *this issue*). Its spectral filters are centered at 443, 500, 550, 590, 670, 700, 720, 800, and 864 nm wavelength. At a typical flight altitude of 3000 m, the spatial resolution was 20 m (Leroy et al., 2001). Four flights were undertaken during 3-5 June 1999. Each flight records around 140 spectral images, offering thus a wide range of view directions. The POLDER reflectance images were calibrated, geo-coded and corrected for atmospheric effects as it is specified in Leroy et al (2001). In this work the BRDF has been interpolated for the full range of view angles for every pixel. The BRDF was then retrieved considering uniform sites of 3x3 pixels (60x60 m²). The model has been inverted against a set of bidirectional reflectance factors taken along the principal plane, i.e. the region with the strongest anisotropy.

4.2 Results and discussion

Figures 2 and 3 show a few examples of measured BRFs along with the values predicted by both the proposed model and NADIM, respectively. The analysis includes five bands, two sun zenith angles and two different vegetation types. The figures reveal the potential of the information contained in the directional domain of BRDF, as it was demonstrated in a preliminary work (Camacho-de Coca et al. *this issue*). Vegetation *in-situ* measurements were taken during the campaign corresponding to major agricultural units (see LAI and height values in table 1). Wheat and senescent barley presented a vertical structure. Alfalfa and legumes were lower in height, with smaller leaf size and a high LAI. Sugar beet and corn were markedly row-distributed with large contribution of the bare soil.

We can observe as both models have potential to accurately explain the spectral and angular variations of the BRDF. They capture the essential BRDF features such as bowl shape, backscattering and broad hot spot. In general, a good agreement is found between measured and modelled signatures. In general, the agreement is slightly worse when the SZA is high, i.e. when the anisotropy is higher.

The proposed model works better in the visible regions, when the first order scattering effects predominate but in the NIR region (band 8) the discrepancies are higher. In this region directional effects are less apparent due to the reduction of contrast between canopy components and the prevalence of multiple scattering. NADIM works better for dense homogeneous canopies, like alfalfa and legumes. However, it seems to be more limited when the canopy cover is lower (e.g. sugar beet), i.e. when the medium is less uniform and the reflectance is dominated by geometric effects. One source of error for both models is attributable to unquantified influences of foliage clumping. In particular, the main problems are found in erectophile canopies like wheat, with vertical structure and well-developed spikes. It causes a very pronounced ‘bowl-shape’ signature, especially when SZA is high. This is mainly due to the gap effect or increase of illuminated upper canopy layers viewed from the sensor at large off-nadir angles (Camacho-de Coca et al., 2002b).

Estimated parameters are presented in table 1. The inversion of both models provides reasonably accurate estimates of LAI. Furthermore, the retrievals were quite consistent, e.g. rather insensitive respect to sun zenith angle and spectral subset. In addition, the proposed model allowed us to address the FVC, obtaining values that are coherent with the field information available.

Although the inversion algorithm is satisfactory, different difficulties still arise. The main problem derives from the determination of the spectral properties, in particular for the leaf albedo. The estimation of leaf-level properties is impaired by canopy-level variables like LAI. The interdependence between leaf-level and canopy-level affects the model inversion. For example, the underestimation of leaf albedo in the visible regions usually results in an underestimation of LAI and vice versa. This may be minimised by introducing the correlation between model variables. In addition, some knowledge of ecosystem characteristics can be used to constrain the solution domain, using a merit function weighted scheme (Privette et al., 1997). The merit function could be defined as a RMSE computed both on the radiometric measurements and on the canopy variables prior information (Combal et al., 2002). Another difficulty derives from the necessity to determine the

optical properties for each individual band. For further reduction of model parameters, the canopy model will be coupled with a leaf radiative transfer model like PROSPECT (Jacquemoud et al., 1996).

Table 1. Retrieved parameters for the dominant vegetation types (G=measured; NAD=estimated from NADIM; M=estimated from the proposed model).

Sample	H (m)	LAI _M	LAI _{NAD}	LAI _M	FVC _M	fAPAR _M
Alfalfa	0.5-0.6	2.6	3.0	2.3	0.97	0.90
Legumes	----	----	1.2	1.2	0.80	0.86
Wheat	0.7-0.85	1.6	1.4	1.9	0.91	0.82
Sugar beet	0.1-0.15	1.2	0.6	0.9	0.55	0.64
Corn	0.1-0.2	0.3	0.2	0.2	0.27	0.26
Dry	0.55-	2.9	1.2	2.3	0.73	0.43
Barley	0.65					

5. CONCLUSION AND PROSPECTS

This study aims to develop a simple, fast and operational approach to deconvolve the angular reflectance into single landcovers reflectances, attempting to solve the inconsistencies of 1-D models and linear mixture approaches. The result is a fast invertible canopy reflectance model of discontinuous canopies. The model relates the spectral and angular variation with the main optical and structural parameters of discontinuous canopies. A random spatial distribution of plants is assumed to simplify the gap probability computation, which may be applicable when imaging stands resolutions greater than the size of the tree crowns. Unlike BRDF models of homogeneous canopies, the model can be inverted to estimate both FVC and LAI. Moreover, the model may provide as a subproduct entire BRDF, albedo, and absorptance (including fAPAR) for the sampled scene, along with the relative contribution of vegetation and soil.

Although the model is less suited for homogeneous canopies, it can be also applicable to vegetation like grasslands and cereal crops, producing results similar to accurate BRDF models of homogeneous canopies like NADIM. The inversions revealed the model potential to combine spectral and directional information in order to increase the likely accuracy of the retrievals.

Future work will consist in coupling the model with a leaf-level radiative transfer model, which will moreover reduce the model parameters and provide a stronger connection between leaf optical properties and leaf biochemical and structural parameters. The model will be tested on existing BRDF datasets comprising different vegetation types (shrublands, forests). Intercomparisons will be also undertaken with other modelling approaches in the frame of DAISEX.

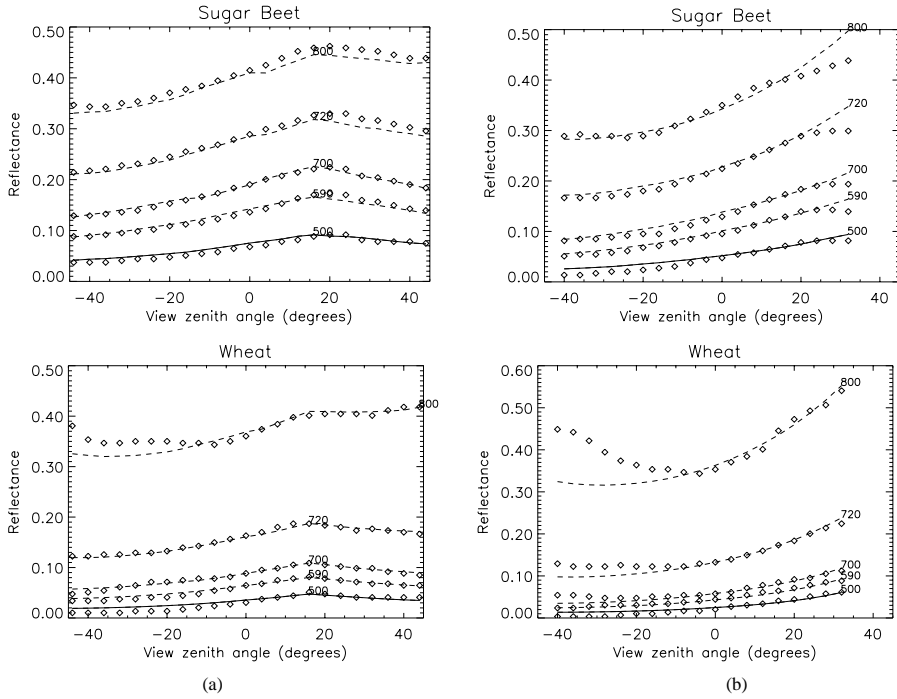


Figure 2. Comparison of directional signatures in the principal plane measured by POLDER (symbols) and simulated by the proposed model (dashed lines) at five different spectral bands (2, 4, 6, 7 and 8) over two different vegetation types. (a) Noon image ($\theta_v=17^\circ$) (b) 14:30 UT ($\theta_v=37^\circ$).

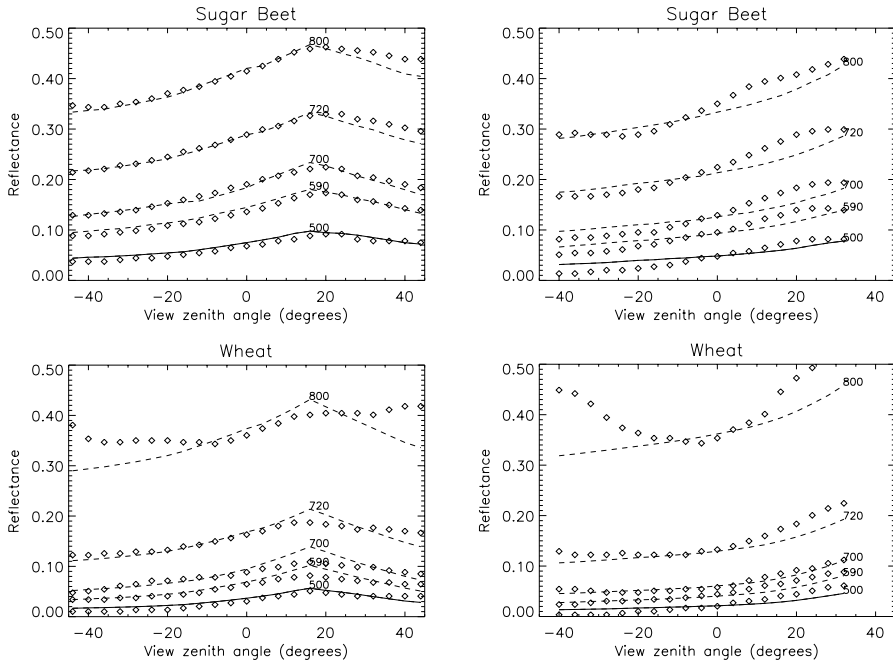


Figure 3. The same as in figure 2 but using NADIM.

ACKNOWLEDGEMENTS

This work was partially supported by the projects LSA SAF (EUMETSAT), DAISEX (ESA) and CICYT (CLI 99-0793). J. García-Haro has currently a research position (Ramon y Cajal) from MCyT, Spain. The authors want to thank N. Gobron (JRC, Ispra, Italy) for providing the NADIM model.

REFERENCES

- Asner, G.P., Wessman, C.A. and Privette, L., 1997, Unmixing the directional reflectances of AVHRR sub-pixel landcovers. *IEEE Trans. Geosci. Remote Sens.* 35: 868-878.
- Asner, G. P., Bateson, C. A., Privette, J. L., El Saleous, N., and Wessman, C. A., 1998, Estimating vegetation structural effects on carbon uptake using satellite data fusion and inverse modeling. *J. Geophys. Res.* 103:28,839-28,853.
- Bégué, A., 1993, Leaf area index, intercepted photosynthetically active radiation, and spectral vegetation indices: a sensitivity analysis for regular-clumped canopies, *Remote Sens. Environ.*, 45, 45-59.
- Borel, C. C., and Gerstl, S. A. W. 1994. Nonlinear spectral mixing models for vegetative and soil surfaces, *Remote Sens. Environ.* 47:403-416.
- Camacho-de Coca, F., García-Haro, F.J. and Meliá, J., 2002a, Quantitative analysis of cropland's BRDF anisotropy using airborne POLDER data, *Proc. 1st Int. symposium on Recent advances in quantitative remote sensing*, Torrent, in press.
- Camacho-de Coca, F., F.J. García-Haro, M.A. Gilabert and J. Meliá, 2002b, La anisotropía de la BRDF: Una nueva signatura de las cubiertas vegetales, *Revista de Teledetección*, in press.
- Combal, B., Baret, F., Weiss, M., Trubuil, A., Macé, A., Pragnère, A., Myneni, R., Knyazihin, Y. And Wang, L., 2002, Retrieval of biophysical variables from bidirectional reflectance using prior information to solve ill-posed inversion problems. *Remote Sens. Environ.*, in press.
- Chen, J.M. and Leblanc, S.G., 1997, A four-scale bidirectional reflectance model based on canopy architecture. *IEEE Trans. Geosci. Remote Sens.* 35:1316-1337.
- García-Haro, F. J and Sommer, S., 2002, A canopy reflectance model to simulate realistic remote sensing scenarios. *Remote Sens. Environ.* 81: 205-227.
- García-Haro, F.J., Camacho-de Coca, F. and Gilabert, M.A., 2002, Simulation of BRDF data to support biophysical parameters retrieval in the LSA SAF context, *Proceedings of the LSA SAF Training Workshop*, (Ed. EUMETSAT: Darmstadt), Lisbon, 8-10 July, in press.
- Gobron, N., B. Pinty, M. M. Verstraete, and Y. Govaerts, 1997, A semidiscrete model for the scattering of light by vegetation. *J. Geophys. Res.* 102(D8): 9431-9446.
- Hapke, B., 1981, Bidirectional reflectance spectroscopy: 1. Theory. *J. Geophys. Res.* 86: 3039-3054.
- Jacquemoud, S., Baret, F. and Hanocq, J.F., 1992, Modeling spectral and bi-directional soil reflectance. *Remote Sens. Environ.*, 41:123-132.
- Jacquemoud S., Ustin S.L., Verdebout J., Schmuck G., Andreoli G., Hosgood B., 1996, Estimating leaf biochemistry using the PROSPECT leaf optical properties model, *Remote Sens. Environ.*, 56:194-202
- Jasinski, M.F. and Eagleson, P.S., 1989, The structure of red-infrared scattergrams of semivegetated landscapes. *IEEE Trans. Geosci. Remote Sens.* 27: 441-451.
- Jasinski, M.F. and Eagleson, P.S., 1990, Estimation of subpixel vegetation cover using red-infrared scattergrams. *IEEE Trans. Geosci. Remote Sens.* 28: 253-267.
- Lacaze, R. and Roujean, J.L., 2001, G-function and Hot SpOT (GHOST) reflectance model. Application to multi-scale airborne POLDER measurements. *Remote Sens. Environ.*, 76:67-80.
- Lacaze, R., Chen, J.M., Roujean, J.L. and Leblanc, S.G., 2002, Retrieval of clumping index using the hot spot signatures measured by POLDER instrument. *Remote Sens. Environ.*, 79:84-95.
- Leroy, M, O. Hatecoeur, F. Ponchaut, L. Alonso-Chorda, and J. Moreno, 2001, The airborne POLDER data in the DAISEX'99 campaign, ESA SP-499, ESA Publication Division, ESTEC, The Netherlands, July 2001, 13-22.
- Li, X. and Strahler, R.A., 1992, Geometrical-optical modeling of the discrete-crown vegetation canopy: effect of crown shape and mutual shadowing. *IEEE Trans. Geosci. Remote Sens.* GE-30: 276-292.
- Nilson, T. 1971, A theoretical analysis of the frequency of gaps in plant stands. *Agric. Meteorol.* 8:25-38.
- Privette, J.L., Emery, W.J., and Schimel, D.S., 1996, Inversion of a vegetation reflectance model with NOAA AVHRR data, *Remote Sens. Environ.*, 58: 187-200.
- Qin, W. and N.S. Goel, 1995, An evaluation hotspot models for vegetation canopies, *Remote Sensing Reviews*, 13:121-159.
- Qin, W. and Gerstl, S.A.W., 2000, 3-D scene modeling of semidesert vegetation cover and its radiation regime, *Remote Sens. Environ.*, 71: 197-206.
- Roujean, J.L., M. Leroy, P.Y. Deschamps and A. Podaire, 1992, Evidence of surface reflectance bidirectional effects form a NOAA/AVHRR multitemporal data set. *Int. J. Remote Sens.*, 13:685-698.
- Roujean, J.L., 2000, A parametric hot spot model for optical remote sensing application, *Remote Sens. Environ.*, 71:197-206.
- Roberts, D. A., Adams, J. B., and Smith, M. O., 1990, Transmission and Scattering of Light by Leaves: the Effect on Spectral Mixtures, *Proc. 10th Annual IGARSS*, College Park, Md, May 20-24, pp. 1381-1384.
- Ross, J.K., 1981, The radiation regime and architecture of plants stands. *Norwell, MA: Dr. W. Junk*, 391 pp.
- Scarth, P. and Phinn, S., 2000, Determining forest structural attributes using an inverted geometric-optical model in mixed eucalypt forests, Southeast Queensland, Australia. *Remote Sens. Environ.*, 71:141-157.
- Van-Leeuwen, W.J.D. and Roujean, J.L., 2002, Land surface albedo from the synergistic use of polar (EPS) and geostationary (MSG) observing systems. An assessment of physical uncertainties, *Remote Sens. Environ.*, 81: 273-289.
- Walthall, C.L., J.M. Norman, J.M. Welles, G. Campbell, and B.L. Blad, 1985, Simple equation to approximate the bidirectional reflectance from vegetative canopies and bare soil surfaces, *Applied Optics*, 24: 383-387.
- Weiss, M. and Baret, F., 1999, Evaluation of canopy biophysical variable retrieval performances from the accumulation of large swath satellite data, *Remote Sens. Environ.*, 70: 293-306.

Directional effects in observations of land surface temperature with AVHRR over Africa

Pinheiro^{*#}, A.C., J.L. Privette[#], R. Mahoney[&], and C.J. Tucker[#]

^{*} *New University of Lisbon, Portugal*

[#] *NASA's GSFC, Code 923, Greenbelt, Maryland*

[&] *Global Sciences and Technology, Greenbelt, Maryland*

ana@fado.gsfc.nasa.gov

ABSTRACT *We characterize the directional variability in the thermal infrared signal retrieved by the NOAA Advanced Very High Resolution Radiometer (AVHRR). Our approach assumes that directional variability results mainly from the relative fractions of scene endmembers, including shadow, viewed by AVHRR as it samples. We developed continental maps of vegetation structure and computed the projected fractions of scene endmembers into the AVHRR view directions with a Geometric Optics (GO) model. Tests with ground measurements in a savanna (Skukuza, South Africa) suggest that the endmember approach accurately reproduces scene exitance over the diurnal cycle. We therefore processed day and night GAC data using the full swath width of the AVHRR/2. Application over the full continent revealed that the angular variability of AVHRR LST and our model are consistent, suggesting a bias may exist in uncorrected AVHRR LST due to vegetation structure and sun-view geometry. Upon further development, our approach may be able to reduce or eliminate the bias by normalizing LST values to the nadir observation direction.*

1 INTRODUCTION

The need for accuracy in the retrieval of land surface temperature (LST) is well recognized. The surface temperature describes the state of the surface and the partitioning of available energy into sensible and latent heat flux. Studies have shown that the uncertainty in the retrieval of LST can have significant impacts in the estimation of surface fluxes, with errors up to 100 W/m² (Kustas & Norman, 1996). Moreover, the timely prediction of vegetation hydric stress and water requirements for crop requires accurate retrieval of LST (Jackson *et al.*, 1981).

Remote sensing is one of the few means available to monitor, in a synoptic and regular basis, the temperature of the surface. The NOAA AVHRR instrument has measured the brightness temperature of the earth for over 20 years. However, the raw data set has limitations imposed on this by inherent characteristics of the satellite and sensor, which produce temporal and spatial uncertainties.

Some attention has been given to the drift of the orbit of the NOAA afternoon satellites and attempts have been made to correct for such effects (Gutman, 1999). The drift is of approximately one half hour per year through their three to five-year orbital life (Price, 1991). For NOAA-14 this causes the local solar observation time, at the equator, to drift from 1:30 PM to later than 4:00 PM. Given the diurnal character of surface temperature, such bias should be considered when looking at long term records.

The effect of the angular variability of the observation and illumination on the LST retrieval has received considerably less attention. This variability

results from two factors: (1) the angular and temporal variation across a single scan and (2) the nine-day periodicity of the ground track. With a sensor scan of $\pm 55^\circ$ from nadir (equivalent to a 68° on the earth's surface), the swath spans about two hours in local time of observation targets. These time differences grow larger with increasing latitude. The nine-day periodicity of NOAA platform means that the unique observation and illumination geometry for a given pixel is only repeated every 9 days.

For a flat and homogeneous surface, the time of observation would be the major cause of variability for the retrieved radiance by the sensor. However, for a non-homogeneous and structured surface, the illumination and observation geometries impact the relative amounts of each surface components observed and therefore the composite temperature, or ensemble temperature, of the scene.

Theoretical and empirical studies of the angular effects, at local scale, have been given significant attention over the last 20 years (Kimes *et al.*, 1983). The effects at regional scales were addressed after the launch of the Along Track Scanning Radiometer (ASTR) in 1991. The dual angle observations of the ATSR have been used to improve the retrieval of LST and Sea Surface Temperature (SST) (Sobrino *et al.*, 1996).

We address angular variability at the continental scale and attempt to characterize the effects of varying observation and illumination geometry on AVHRR measurements with a spatial resolution in the order of several kilometers. We focus in particular on the LST retrieved from NOAA-14 AVHRR channels 4 and 5 over the African continent. We assume here that the

angular variability of the LST varies as a function of local vegetation structure and the temperatures of the endmembers, including shadows.

First, we briefly describe the theory and methods that are the basis of our approach. We then test our methodology at the local scale by assessing the ability to reconstruct the thermal signal from the knowledge of the structure of the surface and the temperatures of endmembers of that surface. We proceed by describing the NOAA AVHRR LST data set used for testing the methodology at the continental scale, and the methods used to characterize the surface structure for continental Africa. We finally show the bias introduced in the thermal data set by geometry variation.

2 THEORY AND METHODS

The radiance reaching the sensor in the thermal infrared bands, at height h , is the sum of two main components: the radiance emitted and reflected by the surface multiplied by the spectral transmittance of the atmosphere, and the upwelling radiance from the atmosphere integrated over the depth of the atmosphere. This can be formulated as:

with $L(\lambda, T_{at}(z))$ being the upwelling hemispherical longwave radiance emitted by the atmosphere at

$$L(\lambda, \theta, \phi, h) = L(\lambda, \theta, \phi, 0) + \int_0^h L(\lambda, T_{at}(z)) \frac{\partial \tau_\lambda(\phi, \theta, z)}{\partial z} dz \quad (1)$$

height z , and $L(\lambda, \theta, \phi, 0)$ being the radiance emitted by the surface and observed with a zenith angle θ , and azimuth angle ϕ at wavelength λ such that,

$$L(\lambda, \theta, \phi, 0) = B(T_{sr}) = \epsilon_\lambda B(T_{sr}) + (1 - \epsilon_\lambda) (E_{at} / \pi) \quad (2)$$

$B(T_{sr})$, in units of $\text{W} \cdot \text{m}^{-2} \cdot \mu\text{m}^{-1} \cdot \text{sr}^{-1}$, is given by the Planck's function for a blackbody at temperature T_{sr} , ϵ_λ is the emissivity of the surface assuming thermal equilibrium and lambertian surface, and E_{at} is the total downwelling irradiance emitted by the atmosphere.

Let us consider a large area, with a spatial extent in the order of a satellite observation, composed of N homogeneous elements (endmembers), each of which is characterized by a temperature T_k , emissivity ϵ_k and fractional cover $X_{(k, \theta, \phi)}$ for the plane perpendicular to the vector of observation (hereafter referred as projected fractional cover), with the sum of all fractions equal to unity.

We will assume that the radiance emitted from that area is a linear contribution of the radiances emitted by each endmember weighted by their projected fractional cover. Moreover, we will assume that endmembers are isotropic reflectors and emitters and that any variation in the scene emitted radiance depends on the variation of the projected fractions

only. The general formulation of such relationship was described by Becker & Li (1995) and is shown in equation 3.

$$\langle L(\lambda, \theta, \phi, h) \rangle = \sum_{k=1}^N L(\lambda, \theta, \phi, h)_k X_{(k, \theta, \phi)} \quad (3)$$

with $\langle L(\lambda, \theta, \phi, h) \rangle$ being the ensemble radiance emitted for wavelength λ and $L(\lambda, \theta, \phi, h)_k$ the radiance emitted by endmember k . Assuming the hemispherical radiation emitted for the full spectrum, or a close approximation, we can define a radiative temperature (T_{sf}) for the scene, such that:

$$\langle T_{sf} \rangle = \left[\frac{1}{\langle \epsilon \rangle} \sum_{k=1}^N \epsilon_k T_{sk}^4 X_{(k, \theta, \phi)} \right]^{1/4} \quad (4)$$

with

$$\langle \epsilon \rangle = \sum_{k=1}^N \epsilon_k X_{(k, \theta, \phi)} \quad (5)$$

For the AVHRR bands in the interval from 10 to 12 μ , Becker & Li (1995) demonstrated that $\langle T_{sf} \rangle$ and $\langle T_{sr} \rangle$ are very similar. This formulation neglects the temperature vertical profile of the endmembers and the emissivity cavity effects, but it is adequate for a first order of approximation.

In this study we consider a scene with discontinuous canopies, as composed of four endmembers: sunlit crown, shaded crown, sunlit background, and shaded background. The fraction covers, X_k can be modeled as a function of the shape and size of the crowns, their count densities and illumination and viewing geometries.

To obtain the fractional cover for each of the endmembers we used the GORT (geometric optics bidirectional reflectance) model (Ni et al, 1999). The GORT model was developed to estimate the bidirectional reflectance distribution function (BRDF). For the purpose of this work we will use mainly the geometric optics (GO) component of the model. With a general description of the canopy structure the model calculates the gap probability for that scene. The gap probability is defined as the probability that a beam misses the overstory foliage and intersects the background. For discontinuous canopies two sets of gap probabilities are calculated: small canopy gaps within the crowns (or within-canopy gaps) and the larger canopy gaps between crowns (or between-canopy gaps).

3 SAVANNA AS A CASE STUDY

We will test the validity of this method by reconstructing the upwelling longwave radiation emitted by an area of a circle with radius of approximately 145 meters centered on the main tower of the Skukuza site and comparing it to the exitance

measured by a pyrgeometer placed on top of the referred tower. For an hemispherical scenario, the ensemble exitance, $\langle M(h) \rangle$, at height h , can be reconstructed using equation 6.

$$\langle M(h) \rangle = \frac{\sigma}{\pi} \int_{\theta=0}^{\frac{\pi}{2}} \int_{\phi=0}^{2\pi} \left(\sum_{k=1}^N \varepsilon_k T_{sk}^4 X_{(k,\theta,\phi)} \right) \sin\theta d\theta d\phi \tag{6}$$

For the purpose of this work we assumed that the scene is composed of two representative elements; crown and background. Moreover, we assumed for this comparison study that the endmembers behave as blackbodies and that the flux measured by the pyrgeometer is a close approximation to the full spectrum exitance.

3.1 Skukuza core site

The Skukuza site (latitude: 25.02, longitude: 35.10) is one of the core sites of the SAVE (Southern African Validation of EOS) and SAFARI 2000 projects, selected to represent a major biome of the southern African landscape, the acacia/combretum savanna woodland.

This site includes a 22 meter tower placed among a fairly homogeneous mixture of trees and interspersed grass. The main characteristics of the vegetation structure (Scholes *et al.*,2001), are shown in Table 1.

Table 1: Skukuza vegetation structural characteristics

Parameter	
Maximum height f crown center	8.20* meters
Minimum height of crown center	2.07** meters
Average canopy horizontal radius	2.65 meters
Average canopy vertical radius	3 meters
Woody percent cover (tree + shrub)	31 %
LAI(canopy) -peak	0.67
LAI(canopy) -June	0.15

Note: * 2/3 of maximum tree height, ** 2/3 of minimum tree heights

This validation site was equipped with instruments to measure incoming and outgoing radiation and a eddy flux system has been running since 2000. We installed additional precision infra-red thermocouple transducers from Apogee Instruments Inc. (Logan, UT), hereafter designated as thermal infrared radiometers or TIRs. These sensors monitor, on a continuous basis, the radiometric temperatures of the crown and the background.

3.2 Reconstruction of the exitance

We compared the hemispherical upward longwave radiation measured by a pyrgeometer located at 22 m height on the main tower with the composited exitance created following equation 6. The CG1 pyrgeometer by Sci-tec Instruments (Delft, Holland) is a sensor

designed to measure the far infrared (5 to roughly 25 micros) radiant flux on a plane surface and has an accuracy of $\pm 10\%$.

We approximated the full integration with the use of a Gaussian quadrature with n equal to 10 and assuming symmetry of emitted radiation about the principal plane.

Figure 1 shows a representative comparison between the estimated exitance calculated using the equation 6 and the measured flux. The comparison was made for every half-hour measurement taken from day of year (DOY) 84 to DOY 207 of 2000.

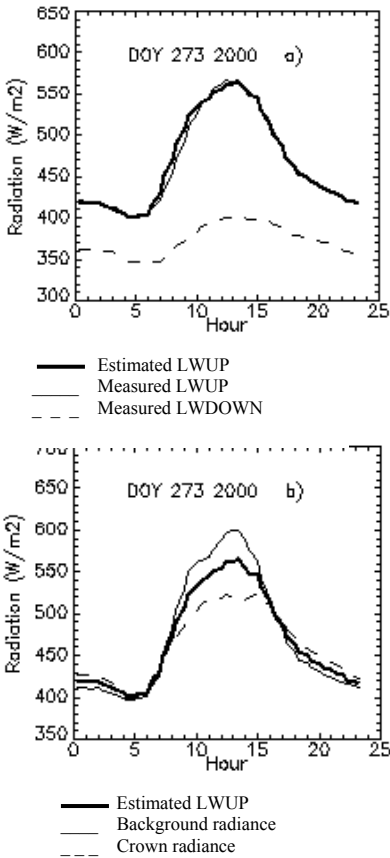


Figure 1: a) Measured and estimated upwelling longwave radiation (LWUP) and dowelling longwave radiation (LWDOWN). b) estimated LWUP and radiances from endmembers: crown and background.

The curves in Figure 1 show a good overall agreement between the two data sets. In most cases, our method reproduced closely the behavior of the measured diurnal. The lines tend to overlap better for days with a smaller diurnal range variation. For most of these days the two curves agree almost completely.

For days with higher variation of the diurnal range, the estimated value tends to overestimate the

exitance during the morning. This may be explained by the fact that the TIR sensor monitoring the background temperature is overlooking a sunlit area during most of the morning. This results in an overestimation of the signal since we are not accounting for shadowed surfaces viewed by the pyrgeometer. Similarly, in the late morning the background area monitored by the TIR is in the shadow (see Figure 1b around 10 AM) and therefore the estimated flux underestimates the overall exitance. Indeed, night comparisons reveal a good agreement between both datasets. At this time of day there are only two main contributions to the thermal signal: the background and the crown temperatures, with no distinction between shadowed and sunlit surfaces. Therefore, the two TIR sensors seem to account for all the thermal variability of the scene.

This study suggests that the linear composite approach, as expressed in equation 6, is able to reconstruct the exitance from a structured surface and that consideration should be given to the fractional cover and radiance for shadowed surfaces.

4 ANGULAR EFFECTS AT THE CONTINENTAL SCALE

In order to effectively study the angular variability of LST at the continental scale we created a new land surface temperature data set from the NOAA AVHRR brightness temperature. In addition, maps describing the surface structure were generated and allowed the parameterization of the GO model for each vegetated pixel of the African continent.

4.1 AVHRR LST data set

The data set used in this study was produced using a modified version of the GIMMS processing system (Tucker *et al.*, 1994).

Specifically, we developed a daily, day time and night time, LST data set for the lifetime of the NOAA-14 satellite (from 1995 to 2000). For that purpose, we used Global Area Coverage (GAC) data using the full swath width of the AVHRR/2. The NOAA Level1B data from the Satellite Active Archive was acquired and a subset was created for the African continent and processed to a primary level for top of the atmosphere (TOA) brightness temperature for channels 4 and 5 and collateral products (such as observational angles, illumination angles, and local solar time of overpass). The data was projected to Albers Equal area and aggregated to 8-km spatial resolution. The estimation of brightness temperature from the radiances, for channels 4 and 5, was accomplished using the sensor spectral sensitivity method.

We created an additional field of data with cloud classification based on the CLAVR-1 algorithm (Stowe *et al.*, 1999) for the day and night data sets. In

window channels where the AVHRR channels 4 and 5 are placed, the main atmospheric effect results from the water vapor absorption. To reduce those effects we used a split-window technique (Ulivi *et al.*, 1994) which takes advantage of the differential absorption of the thermal infrared signal in bands 4 and 5. Equation 7 presents the formulation used for such correction.

$$T = T_4 + 1.8(T_4 - T_5) + 48(1 - \varepsilon) - 75\Delta\varepsilon \quad (7)$$

where T_4 and T_5 are the brightness temperatures of channels 4 and 5, respectively, of AVHRR sensor, and:

$$\varepsilon = (\varepsilon_4 + \varepsilon_5)/2 \quad (8)$$

$$\Delta\varepsilon = \varepsilon_4 - \varepsilon_5 \quad (9)$$

To account for the spatial variability of the surface emissivity, we created spatial fields of emissivity for channels 4 and 5. We followed a similar method to Snyder *et al.* (1998) by creating the emissivity maps based on static landcover classification maps (Hansen *et al.*, 2000). In addition to the landcover maps we used continuous fields of woody, herbaceous and barren percent cover for the African continent (DeFries *et al.*, 2000) to generate fields of vegetation and soil fractional cover. These fields were created using the composite approach described in equation 5. We assumed that the homogeneous components of each pixel are Lambertian and that any directional effects observed are dominated by the structure (Snyder *et al.*, 1998). Emissivity values for the different endmembers were estimated based on the Salisbury and D'Aria (1992) spectral library using the spectral filter function for AVHRR/2 channels 4 and 5. The spatial variability for the barren soil was considered by using the FAO Soil Map of Africa (FAO-UNESCO, 1987).

To assess the general effectiveness of the split-window algorithm and the cloud detection algorithm we compared the AVHRR LST, for day time and night time overpasses, with the ensemble land surface temperature at the Skukuza site. For the time and geometry of each AVHRR overpass between DOY 87 and DOY 310 of 2000, we generated the fractional cover using the GO model. We then calculated the correspondent radiometric temperatures using equation 4. Because the 8 km scale of AVHRR observations is not commensurate with our 145 meters ground area, we expect some deviations. Moreover, we are in fact comparing kinetic and radiometric temperature. However, the results show that, for the period of study, the LST estimates follow closely the general trends of the ensemble surface temperature with a root mean square error (RMSE) for the non cloudy retrievals of 1.299 (with 94 clear days) and 2.356 (with 97 clear nights), for day and night retrievals respectively.

4.2 Vegetation structure and fractional cover fields

The structural maps required to run the GO model for Africa were generated based on the continuous fields and land cover classification maps described in section 4.1 in conjunction with vegetation structural information compiled by White (1983).

The original global 0.0625 by 0.0625 degrees map of for woody cover, herbaceous and barren percentage cover were subsetting for the African continent and re-binned for a 8-km by 8-km pixel size in Albers Equal Projection.

Using a decision tree approach, we assigned the attributes of vegetation described by White to each pixel. We used spatial linear interpolation for pixels with missing data.

Note that the continuous fields of woody cover contains no data for areas classified as open shrubland or closed shrubland due to constraints in their approach for pixels with woody cover less than 5 meters tall (DeFries *et al.*, 2000). This limits our approach to sub-Saharan Africa excluding barren parts of the southern Kalahari.

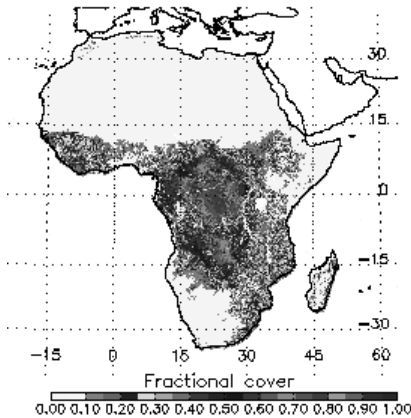


Figure 2: Sunlit crown fractional cover as viewed by the AVHRR NOAA-14, on DOY 71, 1998 (color version in appendix of proceedings).

Based on the vegetation structural maps we parameterized the GO model for each pixel of continental Africa and Madagascar and created fields of fractional cover for each observation geometry of the NOAA-14 AVHRR. Four types of fractional cover maps were created: sunlit crown, shadowed crown, sunlit background and shadowed background.

We focused our analysis of LST variability around the Equinox and Solstice periods for the different years, covering extreme cases in sun elevation for both northern and southern hemispheres.

As expected, we observed evidence of 9-day repeat cycle of NOAA-14 in the fractional cover maps. Figures 2 and 3 are examples of the sunlit crown cover

maps for two days, just 4-days apart. Within a single day, the effects produced by changes in scan angle are obvious with the more clear effects occurring on the edge of the scanning swath. In the mentioned figures below this effect is more easily noticeable over the Congo forest region (from approximately 5 degrees north of the equator to 7 degrees south of the equator). Between the two observation days, the fractional cover variability is also clear over Angola and Zambia where the sunlit crown fractional cover changes from more than 50 % to less than 40%.

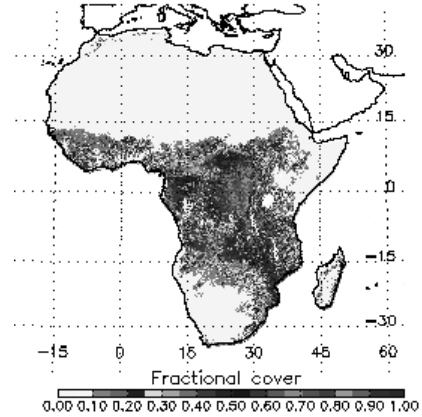


Figure 3: Sunlit crown fractional cover as viewed by the AVHRR NOAA-14, on DOY 75, 1998 (color version in appendix of proceedings).

4.3 Spatial and temporal variability of AVHRR LST as a function of fractional cover

To assess the impact of the variability of fractional cover in the temperature retrieved by AVHRR we assigned a fixed temperature to each of the four endmembers of the scenes: $T_{sc}=295$ K, $T_{shc}=T_{sc}-\Delta T_c$ K, $T_{sb}=305$ K, $T_{shb}=T_{sb}-\Delta T_b$ K, with $\Delta T_c=2$ and $\Delta T_b=13$. We then calculated the ensemble temperature based on the fractional cover maps for DAY 71 and DOY 75. To facilitate the comparison of simulated temperatures, we created a map of ΔT (Figure 4). As expected, the differences in temperature follow the pattern of the viewing geometry of the AVHRR. The smaller effects are observed over the Congo forest region where the crown density is high (approximately 80 %) and where the main contributors to the emittance are the sunlit crown and shadowed crown. We also observe that, for this time of year, the signal seems to be stronger north of the equator where observations are made closer to the principle plane.

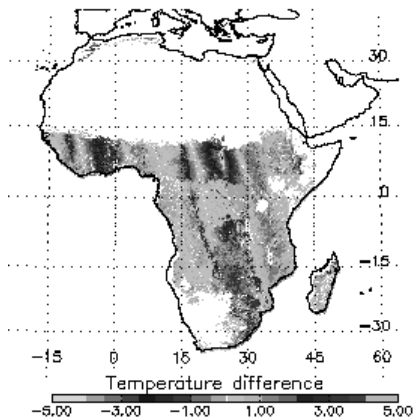


Figure 4: Differences in simulated temperature observed by NOAA-14 AVHRR between DOY 71 1998 and DOY 75 1998, due strictly to sun-target-sensor geometry (color version in appendix of proceedings).

If indeed the sun-target-sensor geometry impacts the retrieved LST, it may be possible to make the data set more uniform, in time and space, by normalizing it to nadir observation, and optimally to a fix time of observation. To evaluate the differences between the temperature observed with the AVHRR geometry observation and the nadir geometry observation we used the same temperatures as above. An example is shown in Figure 5, for DOY 75 1998. The spatial distribution of temperatures has the same general pattern observed in Figure 4, showing the longitudinal shift for successive orbits. The differences in temperature seen are again lowest for the densely vegetated forest. Moreover, we can identify the effects of forward and back emittance in the principle plane (relative to the solar incident direction). The arrows in Figure 5 show the AVHRR ground track for which the nadir zenith angles are zero.

To the right of the ground track we see a positive bias due to minimization of shadows observed (for AVHRR observations made close to the principle plane). Conversely, the results reveal a negative temperature bias for pixels to the left of the ground track due to increase in shadow visibility.

To assess if those effects actually impact the actual AVHRR LST we plotted the LST versus the view zenith angle (with positive angles for forward emittance) for a box of 30 by 30 pixels shown in Figure 5. We selected pixels with the same land cover type classification (woodland) and collected data for 16 days, or two cycles of the AVHRR, to make sure that we had a significant sample and that we cover all the possible geometries.

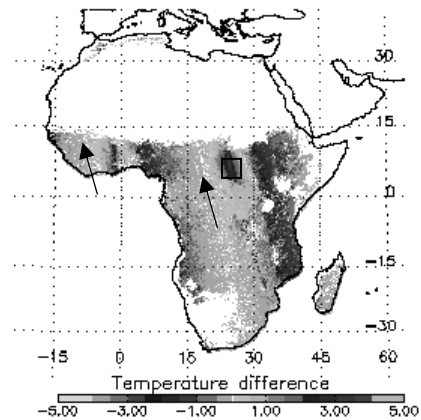


Figure 5: Differences in temperature between AVHRR NOAA-14 geometry and view nadir observation, for DOY 75 1998 (color version in appendix of proceedings).

The dependency of LST on view zenith angle is shown in Figure 6. For such a moderate tree cover (45%) we would expect to have the sunlit background dominate the signal, since this is probably the hottest endmember of the scene. The plots in Figure 7 show the fractional cover for that same box and for the same period of time. A visual analysis of the plots suggests that the LST follow the trend of the sunlit background percentage cover. A correlation of 0.64 was found between these two parameters. This means that 41% of the total variance of the LST can be explained, in this case, by the sunlit background fractional cover. Variability in the time of observation and in the surface thermodynamic characteristics for each of the 16 days observed will contribute to the noise in the relationship between LST and fractional cover.

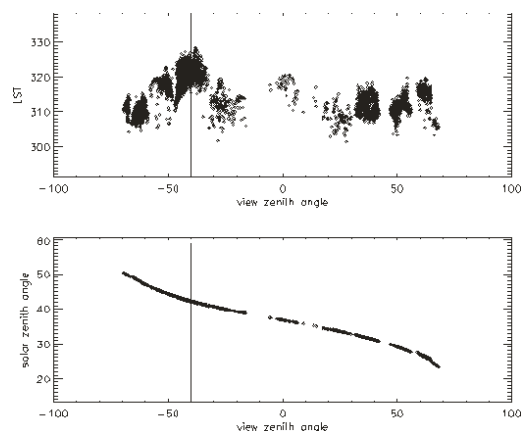


Figure 6: AVHRR LST versus view zenith angle and solar zenith angle versus observation geometry

As expected, we observe a hot spot around -40 degrees view zenith angle since the relative azimuth angles in the backward view are close to 0 degrees (not shown). The primary cause of the hotspot is the absence of shadows when the viewing direction coincides with the illumination direction (for solar zenith angle at 40 degrees).

Similar analysis for different land cover types have shown very different patterns. For very densely vegetated areas (over forests) our results suggest that the LST is mostly related with the amount of crown fraction cover (sunlit and shadowed). A more detailed and extensive analysis is however required before extrapolating the results found in this study.

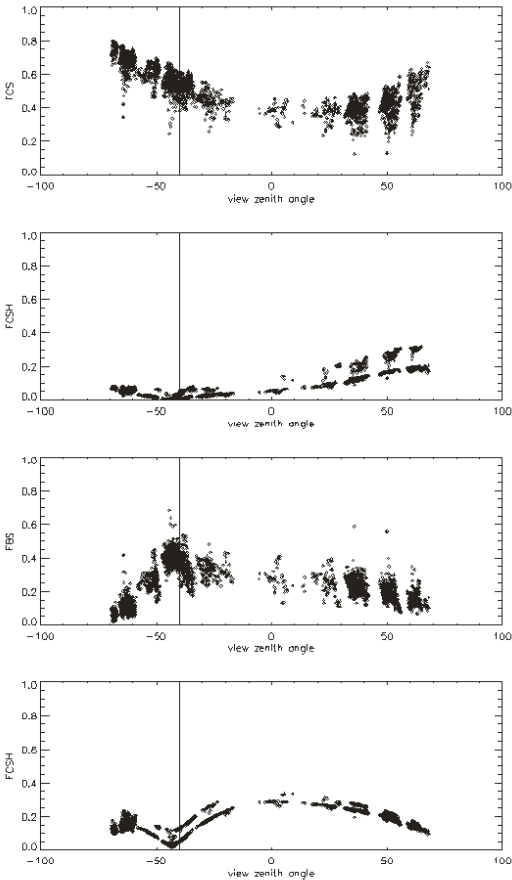


Figure 7: Fractional cover for each endmember as a function of view zenith angle.

5 CONCLUSIONS

We studied the angular variability of LST at the continental scale from the NOAA14 AVHRR sensor. We assumed that the radiation observed is a linear sum

of the radiation emitted by the N homogeneous endmembers of the scene, weighted by their fractional cover, as seen by the sensor. We tested this method at the local scale by comparing the hemispherically integrated ensemble temperature, generated based on the endmembers contribution, with the flux measured by a pyrgeometer located on a tower in Skukuza, South Africa. The fractional cover is generated using the optical geometric (GO) component of the GORT model parameterized with information about the structural characteristics of the area. The results suggest that the method provides reasonable estimates of the scene temperature. Moreover, the local scale study highlights the importance of accounting for shadowed fractional cover.

We generated a new day and night GAC AVHRR LST data set, over Africa, for the 6-year life-time period of the NOAA-14 using the full swath width. Pixels were aggregated to 8 km. Using woody, herbaceous and barren fractional cover data (DeFries *et al.*, 2000) and information compiled by White (1983), we generated structural maps for the vegetated areas. We used these maps to parameterize the GO model over continental Africa and Madagascar. We run the GO model for each pixel and for each sun-view geometry of the NOAA-14 AVHRR to determine the endmember fractions projected into the AVHRR observation direction. The projected fractional maps show a dependency of the fractional cover on the sun-target-sensor geometry. By assuming static temperatures for the endmembers, we simulated the spatial variation in temperature as a function of the projected fractional cover. For the areas where the model results show more significant effects on the land surface temperature, we studied the relationship between the actual AVHRR LST and the view zenith angle, and found evidence of such dependency. For sparsely vegetated areas (woodlands, savannas) the LST tends to follow the pattern of sunlit background fractional cover. For densely vegetated areas (forests) the LST is better correlated with the projected sunlit crown fractional cover. We are currently conducting a more detailed study in an attempt to generalize the results. Initial results suggest, for the day time observations, a bigger dependency of the LST on the viewing geometry during the early years of the lifetime of the NOAA-14. Measurements taken earlier in the afternoon will capture larger differences in temperatures between the endmembers, particularly for those with different thermal inertia properties. For the nighttime observations the effects will be reversed since the drift will place the overpass closer to dawn.

The main limitations in our approach result from the lack of detailed information on vegetation structure at the continental level. Moreover, due to a lack of information about the overstory effective LAI, the fractional cover maps generated for each geometry better reflect the conditions at maximum foliage. We

assessed the sensitivity of the GO model to errors in the structural information used and the results show that the main impact result from errors in the woody vegetation fractional cover, and to a lesser extent on the tree height.

This study does not address the angular impacts in areas classified as shrubland since no fractional cover information is available for those areas.

The effects observed in this study may be extended to other wide field of view sensors that observe the surface in the principle plane, where variations in shaded and sunlit areas are more pronounced.

ACKNOWLEDGEMENT

This project was financed by the PRAXIS Program (MCT, Portugal) and by the Calouste Gulbenkian Foundation (Portugal). This project is part of the Southern African Validation of EOS (SAVE) founded under the EOS Validation Program, and SAFARI 2000. We thank Dr. Niall Hanan for the data from the pyrgeometer.

REFERENCES

- Becker, F. and Li, Z-L., 1995, Surface temperature and emissivity at various scales: definition, measurement and related problems. *Remote Sensing Reviews*, **12**, 225-253.
- DeFries, R.S., Hassen, M.C., and Townshend, J. R.G., 2000, Global continuous fields of vegetation characteristics: a linear mixture model applied to multi-year 8 km AVHRR data. *International Journal of Remote Sensing*, **21** (6 & 7), 1389-1414.
- FAO-UNESCO, 1987, Soils of the World, Food and Agriculture Organization and United Nations Education and Cultural Organization, Elsevier Science Publishing Co. Inc., New York, NY.
- Gutman, G.G., 1999, On the monitoring of land surface temperature with the NOAA/AVHRR: removing the effect of satellite orbit drift. *International Journal of Remote Sensing*, **20** (17), 3407-3413.
- Hansen, M.C., DeFries, R.S., Townshend, J.R.G., and Sohlberg, R., 2000, Global land cover classification at 1 km spatial resolution using a classification tree approach. *International Journal of Remote Sensing*, **21** (6 & 7), 1331-1364.
- Jackson R.D., Idso, S.B., Reginato R.J. and Pinter Jr., P.J., 1981, Canopy temperature as a crop water stress indicator. *Water Resources Research*, **17** (4), 1133-1138.
- Kimes, D.S., Smith, J.A. and Link, L.E., 1981, Thermal IR exitance model of a plant canopy, *Applied Optics*, **20**, 623-632.
- Kustas, W.P., and Norman, J.M., 1996, Use of remote sensing for evapotranspiration monitoring over land surfaces. *Hydrological Sciences*, **41**(4), 495-515.
- Ni, W., Li, X., Woodcock, C.E., Caetano, M.R. and Strahler, A.H., 1999. An analytical hybrid GORT model for bidirectional reflectance over discontinuous canopies. *IEEE Transactions on Geoscience and Remote Sensing*, **37** (2), 987-999.
- Price, J.C., 1991, Timing of NOAA afternoon passes. *International Journal of Remote Sensing*, **12** (1), 193-198.
- Salisbury, J.W. and D'Aria, D.M., 1992. Emissivity of Terrestrial Materials in the 8-14 μ m atmospheric window. *Remote Sensing of the Environment*, **42**, 83-106.
- Scholes, R.J., Gureja, N., Gianecchini, M., Dovie, D., Wilson, B., Davidson, N., Piggott, K., McLoughlin, C., Van der Velde, K., Freeman, A., Bradley, S., Smart, R., and Ndala, S., 2001, The environment and vegetation of the flux measurement site near Skukuza, Kruger National Park. *Koedoe*, **44** (1), 73-83.
- Snyder, W.C., Wan, Z., Zhang, Y. and Feng, Y.-Z., 1998. Classification-based emissivity for land surface temperature measurement from space. *International Journal of Remote Sensing*, **19** (14), 2753-2774.
- Sobrino J.A., Li, Z-L., Stoll, M.P. and Becker, F., 1996. Multi-channel and multi-angle algorithms for estimating sea and land surface temperature with ATSR data. *International Journal of Remote Sensing*, **17** (11), 2089-2224.
- Stowe L.L., Davis, P.A, and McClain, E.P., 1998, Scientific Basis and Initial Evaluation of the CLAVR-1 Global Clear/Cloud Classification Algorithm for the Advanced Very High Resolution Radiometer. *Atmospheric and Oceanic Technology*, **16**, 656-681.
- Tucker, J.C., Newcomb, W.E., and Dregne, H.E., 1994, Improved data sets for determination of desert spatial extent. *International Journal of Remote Sensing*, **15**, 3519-3545.
- Ulivieri, C., Castronuovo, M.M., Francioni, R. and Cardillo, A., 1994, A split window algorithm for estimating land surface temperature from satellites. *Advances Space Research*, **14** (3): 59-65.
- White, F., 1983. The vegetation of Africa, a descriptive memoir to accompany the UNESCO/AETFAT/ UNSO vegetation map of Africa. UNESCO, *Natural Resources Research*, **20**, 1-356.

AUTHOR INDEX

A

Allard, D., 199
Alonso, L., 45
Andrieux, P., 167
Antolín-Tomás, C., 496
Ariza, F. J., 541, 550
Asrar, G., 1
Atenciano, S., 69, 309
Atzberger, C., 121, 129
Ayres, F. M., 93

B

Bach, H., 863
Bacour, C., 503
Badea, A., 921
Baghdadi, N., 724, 810
Baldasano, J. M., 261, 268
Bannari, A., 61, 77, 210, 216
Baret, F., 167, 184, 199, 503, 509, 874, 921
Barthelmie, R. J., 778
Bauer, P., 751
Beisl, U., 371
Belot, A., 431
Ben-Dor, E., 904
Berger, M., 363
Bodas-Salcedo, A., 496, 956
Boegh, E., 646
Boschetti, M., 885, 900
Bourgine, B., 810
Braud, I., 329, 442
Brisson, N., 329
Brivio, P. A., 900

C

Calera, A., 522, 530
Calle, A., 537
Calpe, J., 488
Calvet, J. C., 329, 363, 741
Camacho-de-Coca, F., 108, 303, 963
Campeaux, J. L., 246
Camps, A., 707, 761
Camps-Valls, G., 488
Cañas, I., 287, 927
Carreras, J., 348
Casanova, J. L., 537
Caselles, V., 557, 707
Castell-Balaguer, N., 496
Castronuovo, M. M., 631
Cavelier, S., 810
Cerovic, Z. G., 339, 509
Champagne, C.M., 77, 159
Chanzy, A., 839
Chehbouni, G., 177, 450, 458, 847
Chelle, M., 184
Chen, L., 609
Chen, L. F., 624
Chen, S., 624
Chevrier, M., 61
Chilès, J. P., 810
Christensen, J. H., 646
Clastre, P., 397
Cloude, S. R., 731
Coll, C., 707
Colombo, R., 885, 900
Combal, B., 184
Courault, D., 397, 450
Cuenca, J., 946, 952
Cuevas, J. M., 537

D

Dabrowska-Zielinska, K., 380
Dall'Olmo, G., 354
Daniels, P., 810
De Fraipont, P., 426
Deboissezon, H., 921
Dechambre, M., 724
Dedieu, G., 177, 880
Deguise, J.C., 61, 77, 210
Demarty, J., 329, 442
Doménech-García, C., 496
Duchemin, B., 177, 802, 880

E

Edwards, M. C., 656, 857
ElKharraz, J., 566, 935, 941, 952
España-Boquera, M. L., 874
Estellés, V., 100, 295
Evain, S., 509

F

Faid, A., 139, 146
Fan, W., 600, 605
Farias de Souza, A. L., 639
Favard, J. C., 921
Fedosejevs, G., 216
Fernandes, R. A., 152
Fernandes, R., 159
Fernández-Rebollo, P., 277
Fernández-Sarria, A., 514
Ferrando, M., 823
Ferrazzoli, P., 839
Ferrer, F., 496
Flores-Tovar, H., 261
Floricioiu, D., 116
Font, J., 707, 761
Fors, O., 228
Franchistéguy, L., 246
Frangi, J. P., 442
Frappart, F., 177
French, A., 474, 585, 913

Frison, P. L., 802
Furevik, B., 778

G

Gabarró, C., 761
Gao, F., 7
Gao, X., 21
García, J. C., 282
García, J. L., 550
García, R., 228
García-Ferrer, A., 69, 309
García-Haro, F. J., 108, 303, 963
Garcia-Meléndez, E., 371
García-Torres, L., 69, 309
Garrigues, S., 199, 246
Gascon, F., 431
Gastellu-Etchegorry, J. P., 108, 431
Gentine, P., 431
Gil, M. L., 287, 927
Gilabert, M. A., 303, 560
Gimeno-Ferrer, J. F., 496, 560, 956
Giráldez-Cervera, J. V., 277
Gómez, M., 566, 935, 941, 952
Gómez-Amo, J.L., 100, 295
Gómez-Chova, L., 488
González, A., 287, 927
González-Alonso, F., 537
González-Andújar, J. L., 309
González-Audicana, M., 228
González-Dugo, M. P., 277
González-Piqueras, J., 522
González-Rebollar, J. L., 348
Göttsche, F. M., 651
Goulas, Y., 339, 509
Guerrero-Ginel, J. E., 277
Guijarro, L. N., 847
Gruszczynska, M., 380

H

Haboudane, D., 45, 891
Hajnsek, I., 731

Hanocq, J. F., 874
Hasager, C., 450, 458, 466, 646, 778
Hausold, A., 371
Henry, J. B., 426
Herold, M., 770
Hiernaux, P., 802
Hoscilo, A., 380
Huete, A., 21

I

Inoue, Y., 329, 793
Ishikawa, H., 416

J

Jacob, F., 191, 397, 450, 458, 474, 585, 913
Jacquemoud, S., 503
Jarlan, L., 802
Jeanjean, H., 199
Jensen, N. O., 466, 646
Jia, L., 686
Jiang, X. G., 403
Jiménez-Muñoz, J. C., 482, 566, 935, 941, 952
Jin, G., 818
Jorge, J., 268
Jorba, O., 268
Jurado-Expósito, M., 69, 309

K

Karnieli, A., 354, 904
Kerr, Y. H., 847
Kerr, Y., 741
Kim, H.J., 21
King, C., 810
Kogan, F., 409
Koike, T., 416
Kowalik, W., 380
Kozu, T., 793
Kurosu, T., 793
Kustas, B., 474
Kuusk, A., 31

L

Labeled-Nachbrand, J., 566
Lacarrère, P., 397
Lacaze, R., 246
Lakshmi, V., 847
Laneve, G., 631
Lanjeri, S., 530
Lauvernet, C., 921
Lázar, C., 921
Le Dimet, F. X., 921
Le Hégarat-Masclé, S., 52
Leblanc, S. G., 152
Lecharpentier, P., 329, 397, 450
Legendre, P., 348
Leroy, M., 108
Li, X., 7,
Li, X. W., 664
Li, Z. L., 416, 575, 590, 616, 624, 679, 686
Liu, Q., 388, 609
Liu, Q. H., 609, 624
Liu, W. T., 93, 409
Llewellyn-Jones, D., 656, 857
Lobo, A., 348
López-Baeza, E., 363, 496, 956
López-Granados, F., 69, 309
Louis, J., 509
Lugasi, R., 904

M

Ma, Y. M., 416
Maeno, H., 793
Magnac, M., 177
Mahoney, R., 971
Maisongrande, P., 177, 880
Malaplate, A., 692
Marino, C. M., 885
Marloine, O., 397, 450
Marni, S., 199
Martín, D., 831
Martin, E., 431

Martín, F. J., 541
 Martín, J. D., 488
 Martínez-Lozano, J. A., 100, 295
 Massambani, O., 639
 Mauser, W., 85
 Mazzega, P., 802
 McNairn, H., 61, 77, 210
 Mediavilla, R., 371
 Meliá, J., 522, 530, 560, 963
 Menenti, M., 416, 686
 Meroni, M., 885, 900
 Mette, T., 731
 Miller, J.R., 45, 885, 891, 900
 Mito, C. O., 631
 Miura, T., 21
 Morales, L., 698
 Moreno, J., 45, 282, 488
 Mougenot, B., 177
 Mougin, E., 802
 Moya, I., 339, 509

N

Nadal, P., 261
 Nerry, F., 692
 Niclòs, R., 707
 Nielsen, N. W., 646
 Nilson, T., 31
 Ninot, J. M., 348
 Niu, Z., 388, 672
 Noland, T., 885
 Noyes, E. J., 656
 Nuñez, J., 228

O

Ogawa, K., 474, 585, 913
 Olensen, F. S., 651
 Oliso, A., 191, 329, 397, 442, 450, 458, 466
 Omari, K., 216
 Oppelt, N., 85
 Oriol-Pibernat, E., 871

Ortega-Farias, S., 329
 Otazu, X., 228
 Ottlé, C., 52, 329, 442
 Ounis, A., 339, 509
 Ourtirane, K., 139, 146

P

Pacheco, A., 210
 Packalen, M., 885
 Padovani, C., 93
 Panigada, C., 885, 900
 Paolini, L., 482
 Papathanassiou, K. P., 731
 Pardé, M., 741, 839
 Pardo-Pascual, J. E., 238
 Parra, J. C., 698
 Pattey, E., 891
 Pedrós, R., 100
 Pellarin, T., 363, 741
 Peña-Barragán, J.M., 69, 309
 Perrin, J., 810
 Pineda, N., 268
 Pinheiro, A. C., 971
 Pinilla, C., 541, 550
 Poiars-Baptista, J. P. V., 956
 Pokrovsky, O., 252
 Porres-de-la-Haza, M. J., 238
 Prata, A. J., 952
 Prévot, L., 397
 Privette, J. L., 971
 Pryor, S. C., 778

R

Rasmussen, M. S., 646
 Recio, J., 514
 Remedios, J.J., 656
 Rianza, A., 371
 Richard, D., 52
 Riedel, T., 783
 Riedl, C., 116
 Ritchie, J., 913

Rivas, R., 557
 Robbez-Masson, J. M., 167
 Rochdi, N., 184
 Romaguera, M., 935
 Romo, A., 537
 Rossini, M., 900
 Rott, E., 116
 Rott, H., 116
 Roujean, J. L., 246, 252
 Rubio, E., 707
 Ruiz, L. A., 514

S

Saleh, K., 363, 496
 Salles, A. T., 93
 Sánchez-Alandí, M. A., 496
 Sánchez-de-la-Orden, M., 69, 309
 Schlerf, M., 121
 Schmidl Søjbjerg, S., 741
 Schmugge, T., 474, 585, 913
 Schmullius, C.C., 770, 783
 Schoenauer, M., 802
 Schulz, J., 751
 Segarra, A., 295
 Segarra, D., 530
 Shi, J., 713, 770
 Shihao, T., 207
 Simmonds, L., 363
 Smith, D., 857
 Sobrino, J. A., 482, 566, 679, 698, 935, 941, 946, 952
 Soegaard, H., 646
 Soria, E., 488
 Sòria, G., 566, 935, 941, 946, 952
 Souza, A. L., 409
 Staenz, K., 61, 77, 159, 210
 Stankiewicz, K., 380
 Stoll, M. P., 692
 Strachan, I., 891
 Strahler, A., 7
 Su, H. B., 590, 616, 679
 Su, L., 7, 207

Su, Z. B., 319, 416
 Suarez, M., 371
 Sun, L., 159
 Sun, X., 590, 616, 679

T

Tang, L., 403
 Tang, X. Z., 590, 616, 679
 Tang, Y., 624
 Teillet, P.M., 216
 Tholey, N., 426
 Tian, G. L., 609
 Tracol, Y., 802
 Truffert, C., 810
 Tsukamoto, O., 416
 Tucker, C. J., 971

U

Uratsuka, S., 793
 Ustin, S.L., 39
 Utrillas, M. P., 100, 295

V

Vall-llosera, M., 761
 Valor, E., 557
 Van Der Werff, H., 371
 Velázquez-Blánquez, A., 496
 Vera, N., 261
 Verhoef, W., 11, 863
 Vidal-Pantaleoni, A., 823, 831
 Vintila, R., 921

W

Wan, Z., 575, 664
 Wang, C., 388, 403, 672
 Wang, C., 403
 Wang, J., 7, 207, 818
 Wang, P., 207
 Wang, P. X., 664
 Wassenaar, T., 167, 450, 458

Weiss, M., 199
White, H.P., 77, 159
Widen, N., 56
Wigner, J.P., 329, 363, 741, 839
Wu, M., 207

X

Xiang, Y., 207
Xiao, Q., 609
Xu, Q., 818
Xu, X., 600, 605

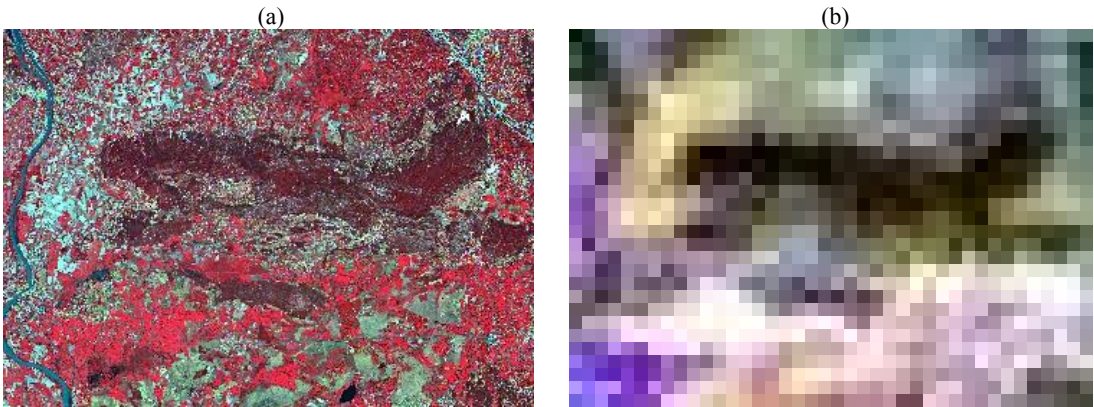
Y

Yan, C., 388
Yan, H., 672
Yoshioka, H., 21
Yunden, B., 904

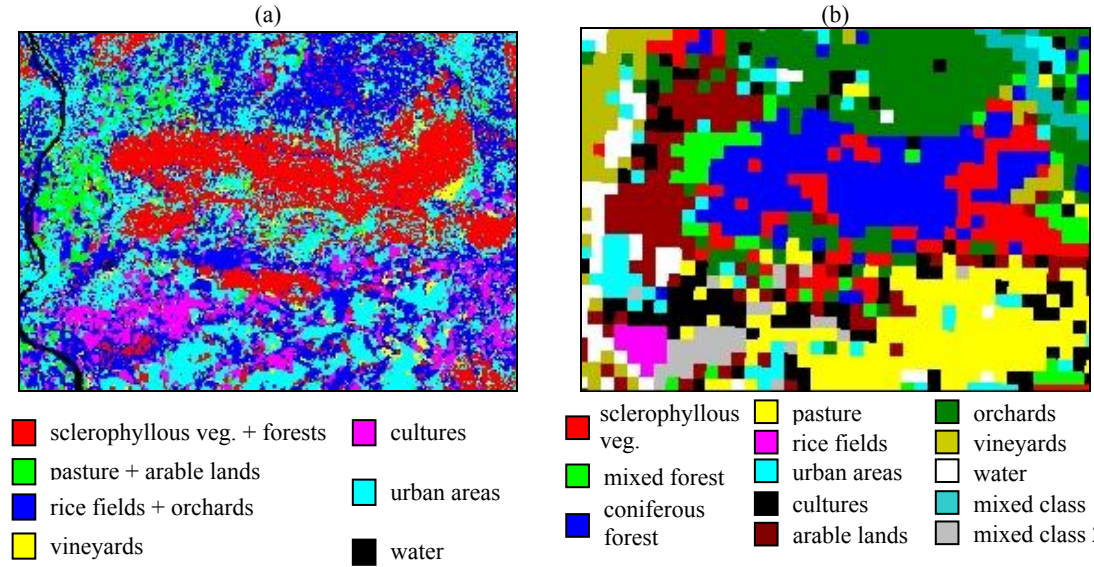
Z

Zarco-Tejada, P.J., 39, 45, 891
Zhang, Q., 575
Zhang, R. H., 590, 616, 679, 818
Zhang, Y., 575, 600, 605
Zhong, B., 624
Zhu, C., 590, 818
Zhu, Q., 207
Zhu, Z., 590, 616, 679
Zribi, M., 724

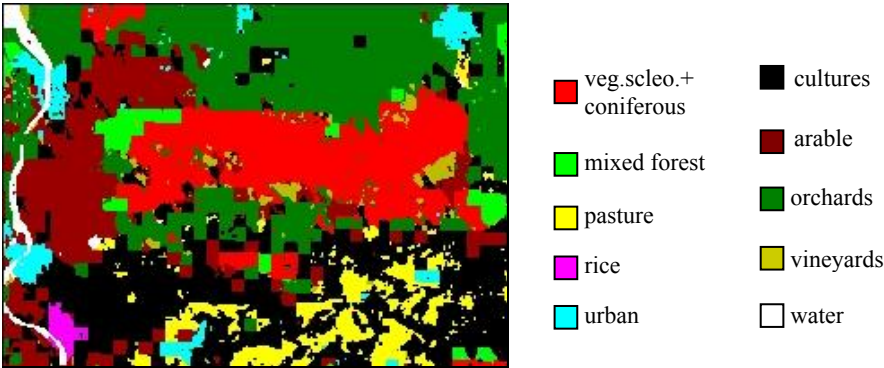
FIGURES IN COLOUR



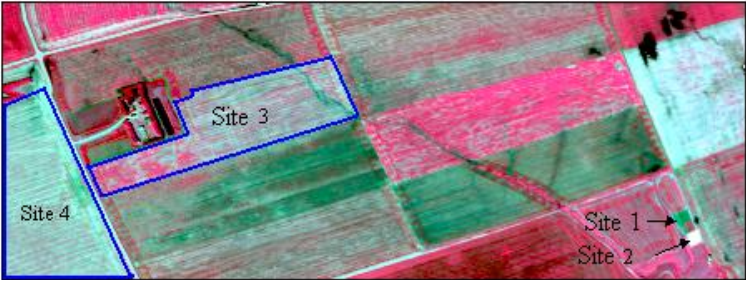
(page 53) **Figure 1.** Colored composition of (a) SPOT/HRV spectral bands, (b) NOAA/AVHRR NIR band respectively acquired on March 10, April 10, and September 9.



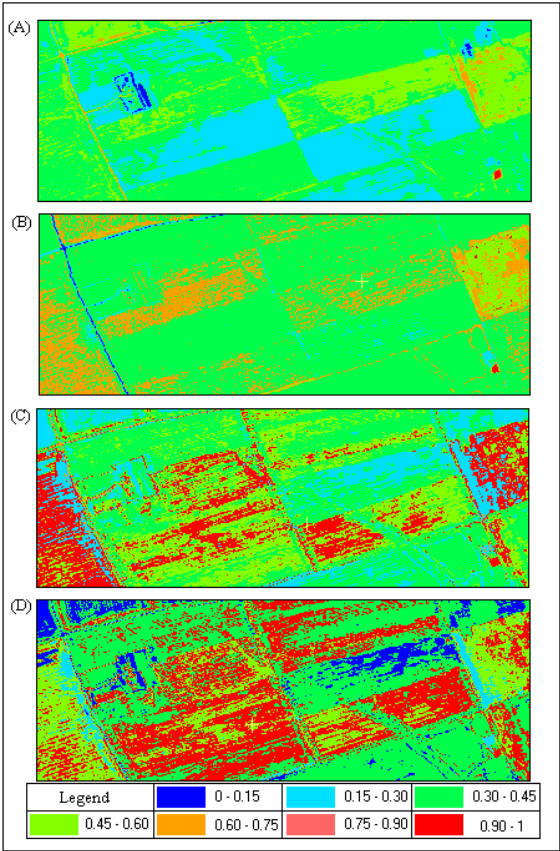
(page 54) **Figure 2.** Results of mono-source classifications: (a) SPOT/HRV, and (b) NOAA/AVHRR



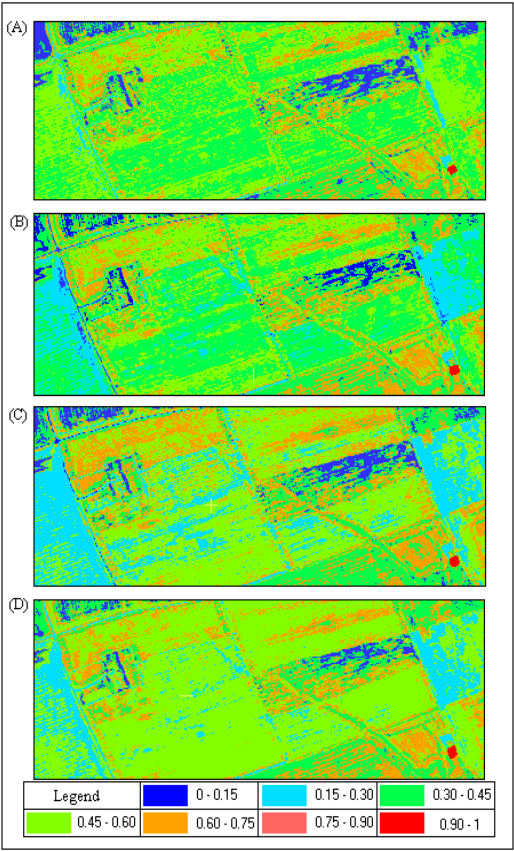
(page 54) **Figure 3.** Results of SPOT-AVHRR data fusion.



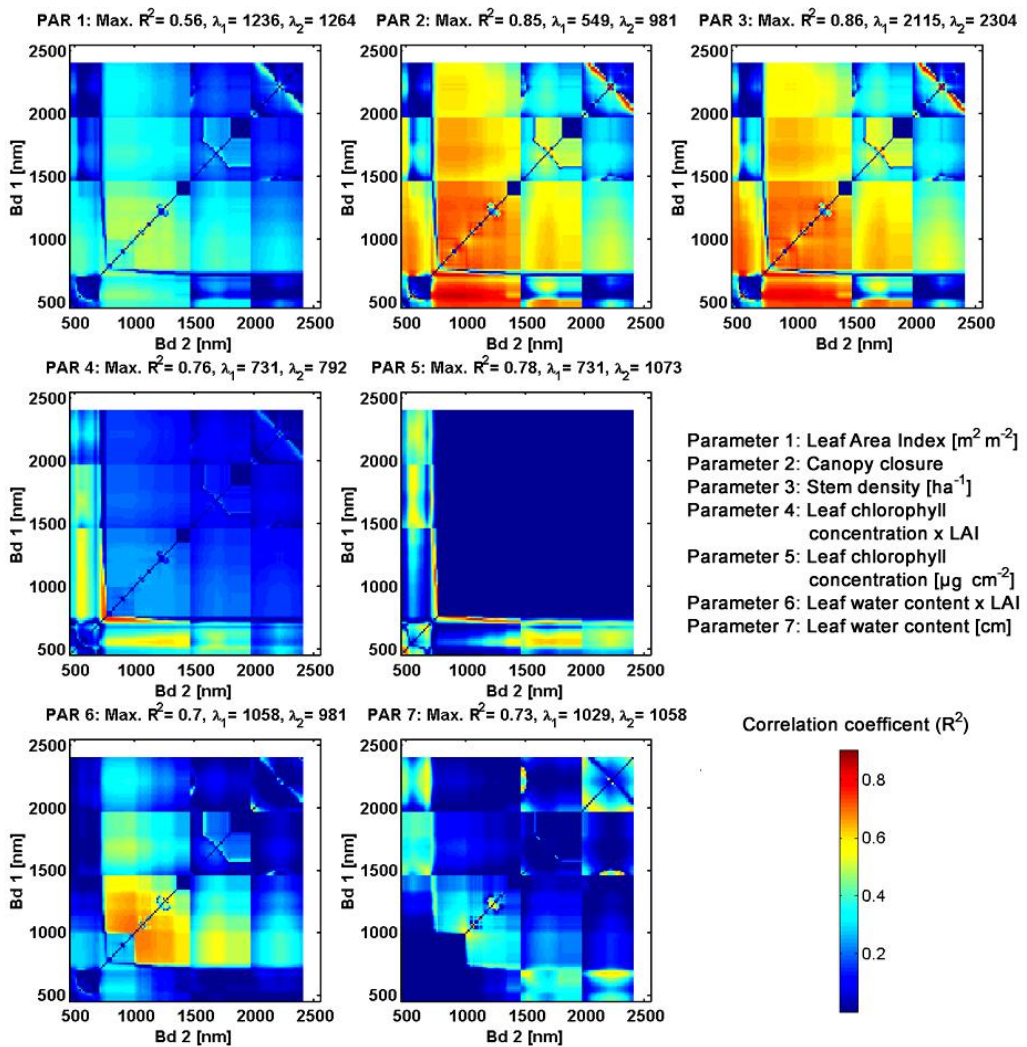
(page 65) **Figure 7.** Probe-1 image of the IHARF farm in Saskatchewan, Canada.



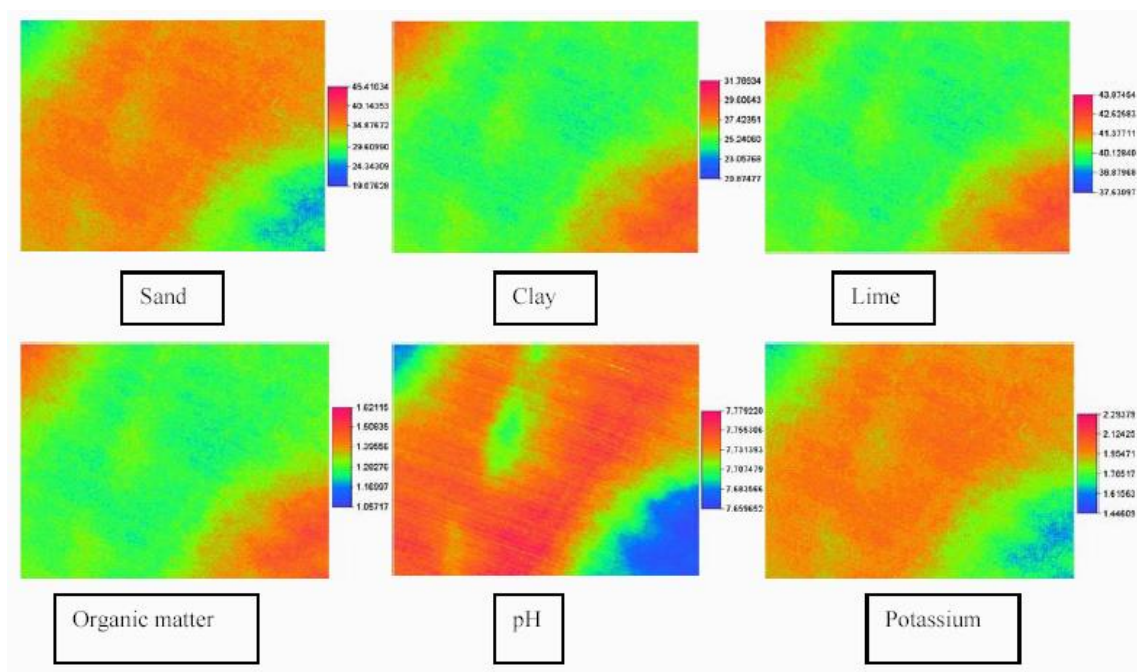
(page 66) **Figure 8.** BI (A), CAI (B), NDI-1 (C), and NDI-2 indices extracted from fields of the IHARF farm.



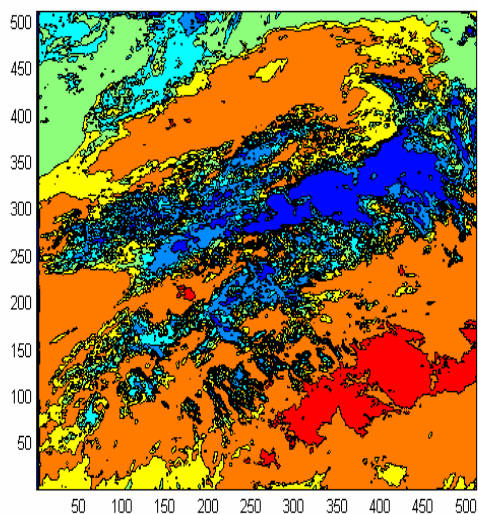
(page 66) **Figure 9.** SACRI-1 (A), SACRI-2 (B), MSACRI-1 (C), AND MSACRI-2 (D) indices extracted from field of the IHARF farm.



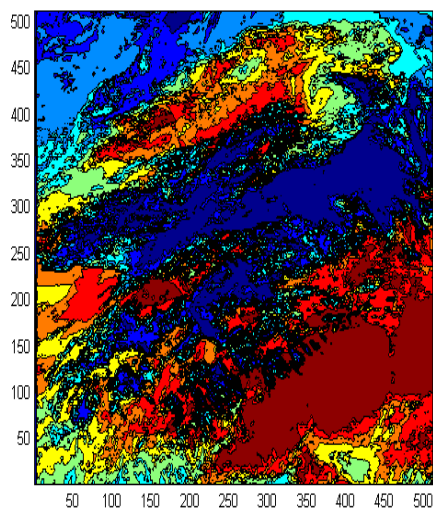
(page 125) **Figure 1.** Two-dimensional correlation matrices. Each matrix consists of 114*114 elements. Each element is the result of a correlation analysis of up to 20.000 data points (see text for details).



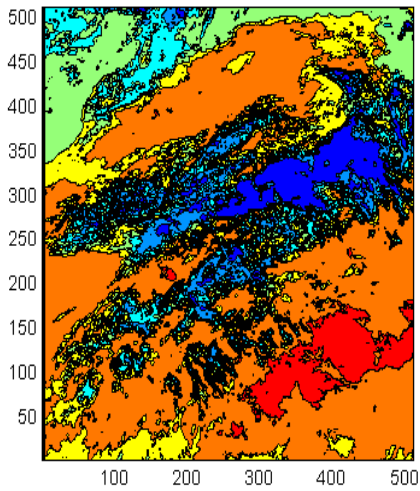
(page 76) **Figure 2.** Sand, clay, lime, organic-matter, pH and potassium maps obtained when applying the ordinary kriging plus regression.



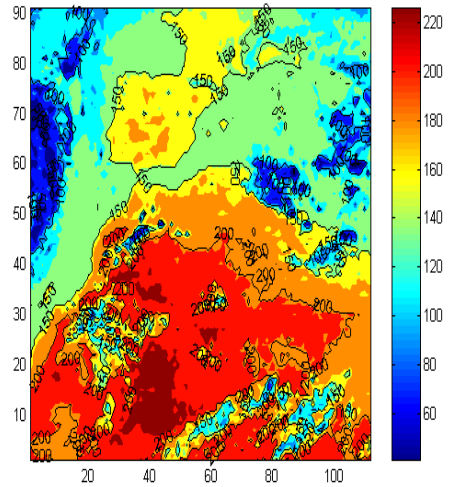
(page 141) **Figure 1.** Original image



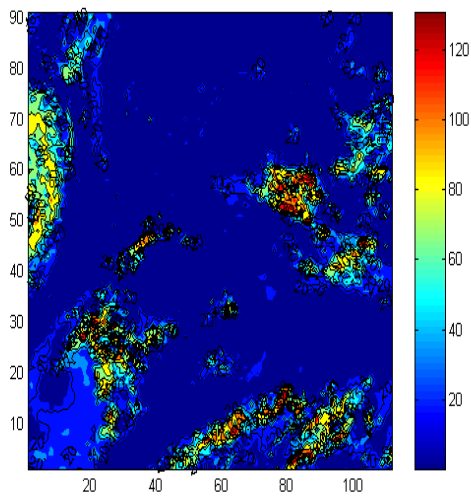
(page 141) **Figure 2.** Image obtained after histogram equalization



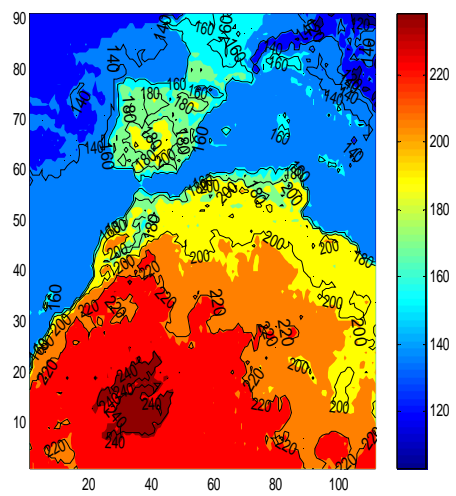
(page 142) Figure 5. Image obtained after Gaussian filtering.



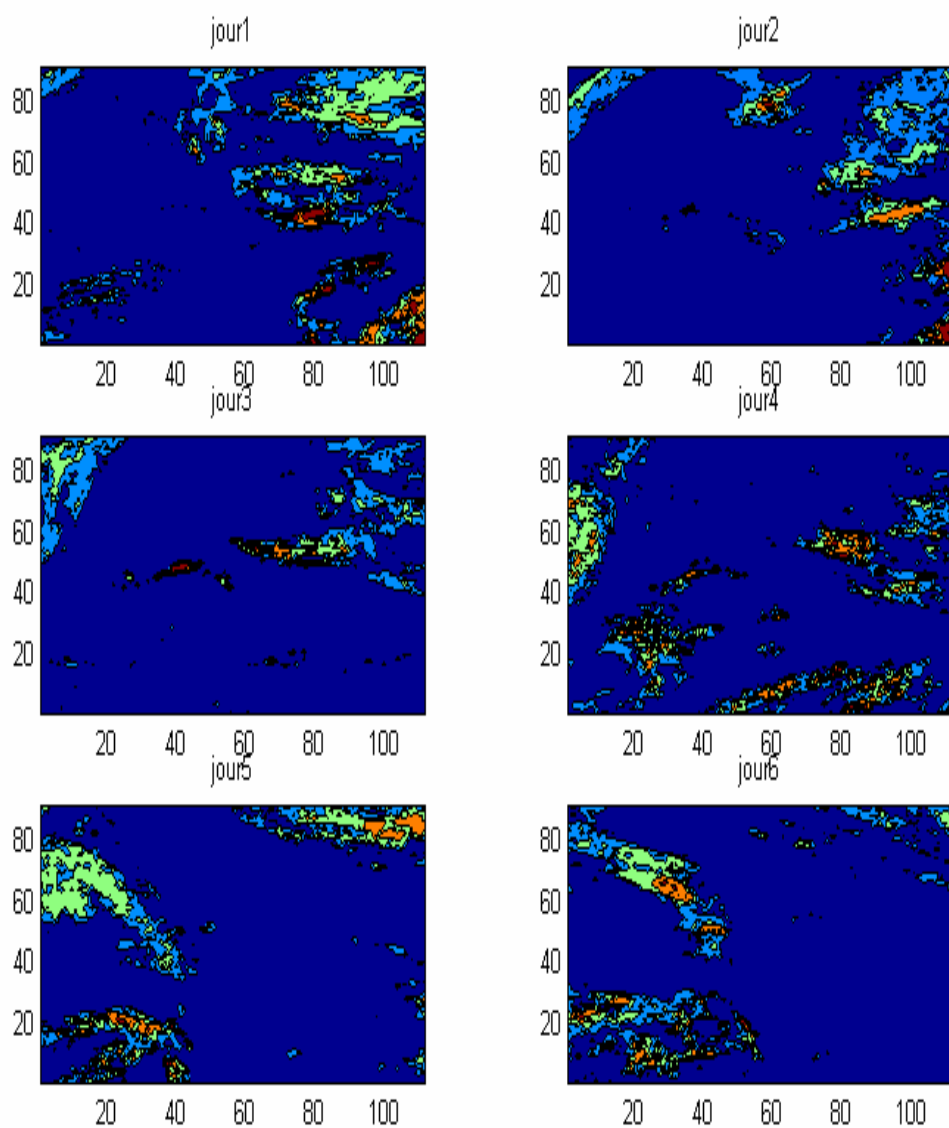
(page 142) Figure 6. Outline of original image.



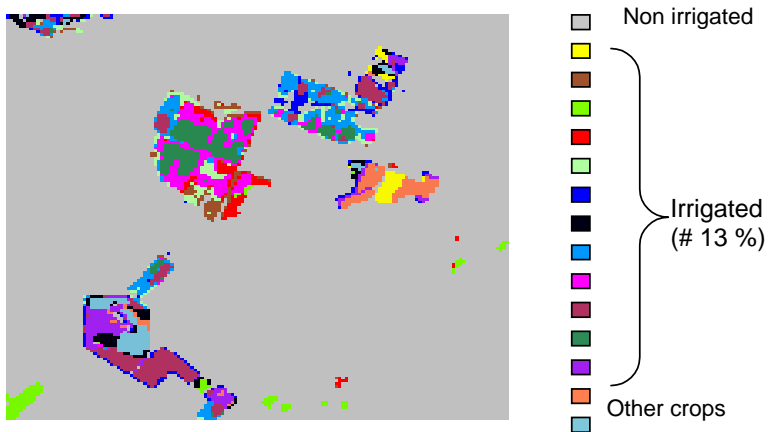
(page 142) Figure 7. Outline of reference image



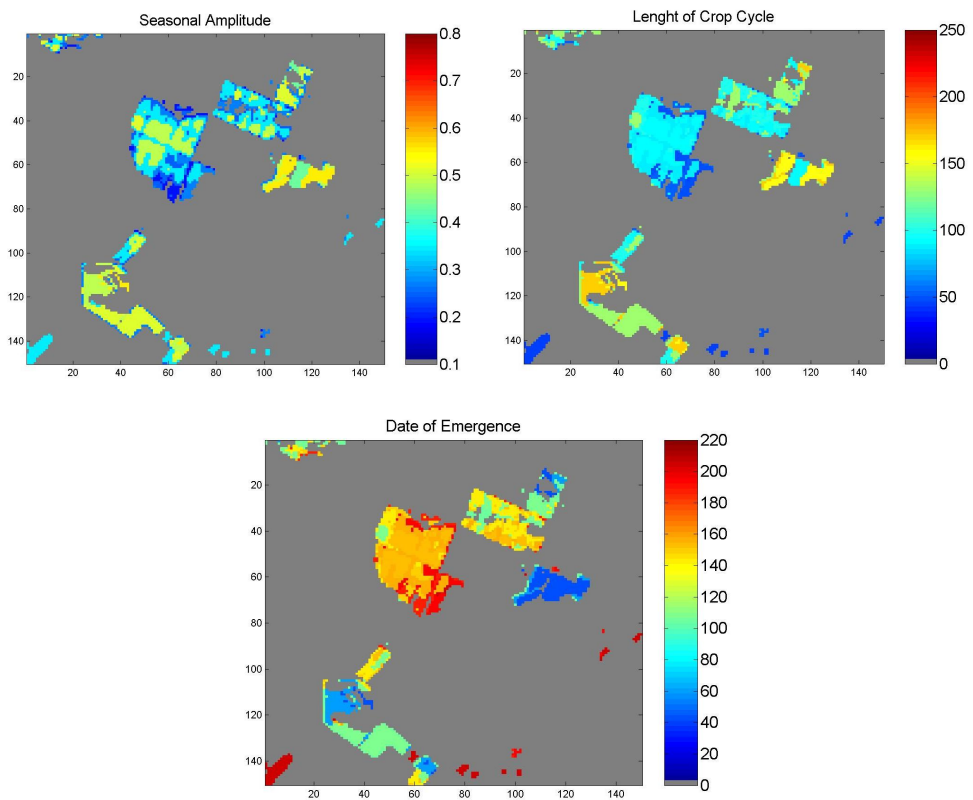
(page 142) Figure 8. Outline of image obtained after Differential filtering



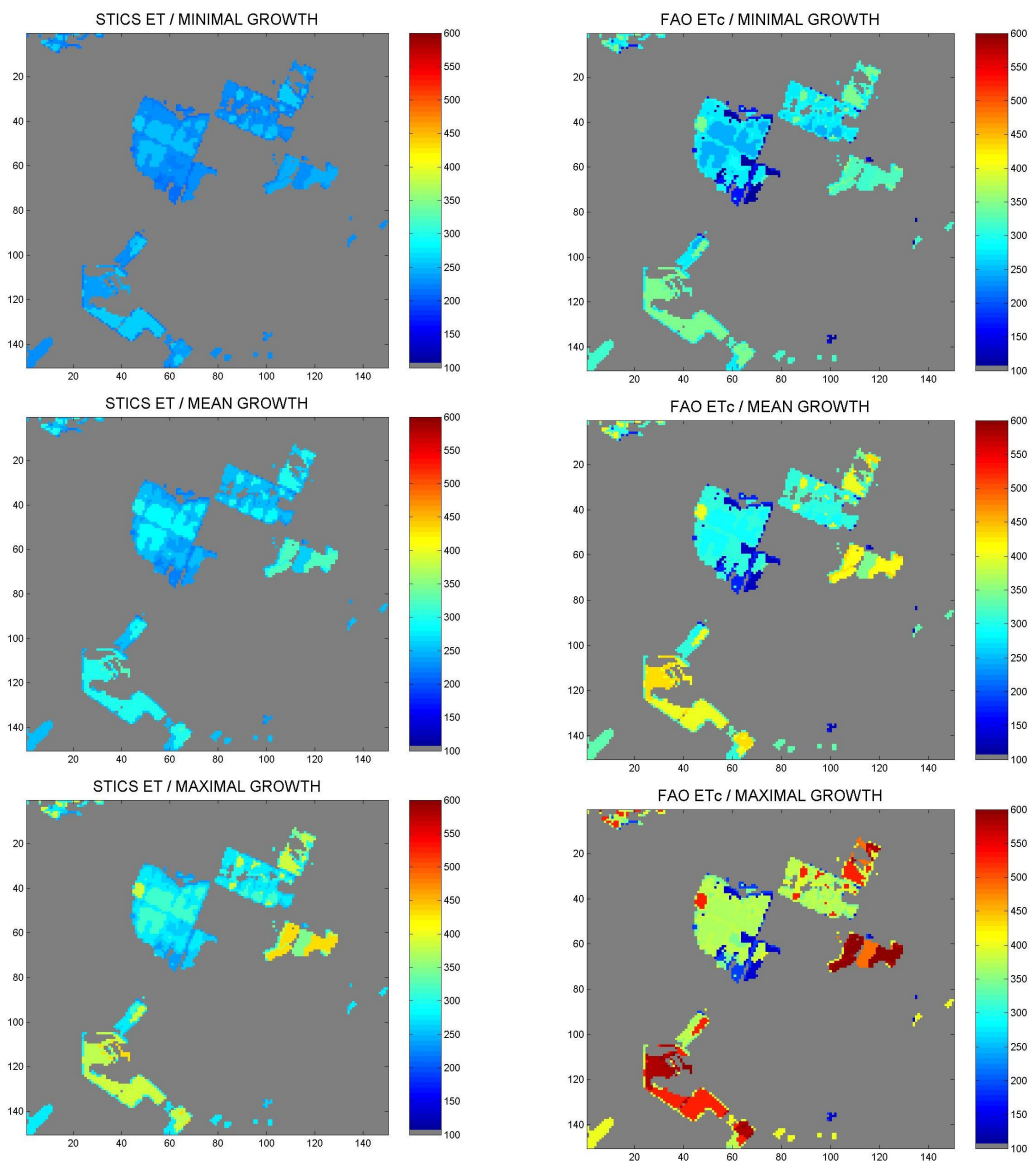
(page 143) **Figure 9.** Aerosol movement followed from the first day (jour 1) to the sixth day (jour 6)



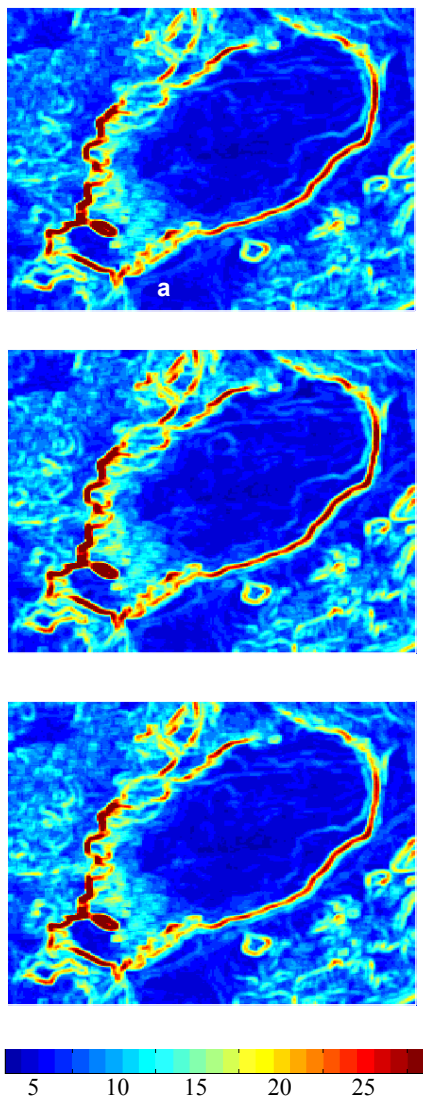
(page 178) **Figure 1.** Classification of the test site based on the NDVI time series derived from SPOT/HRVIR



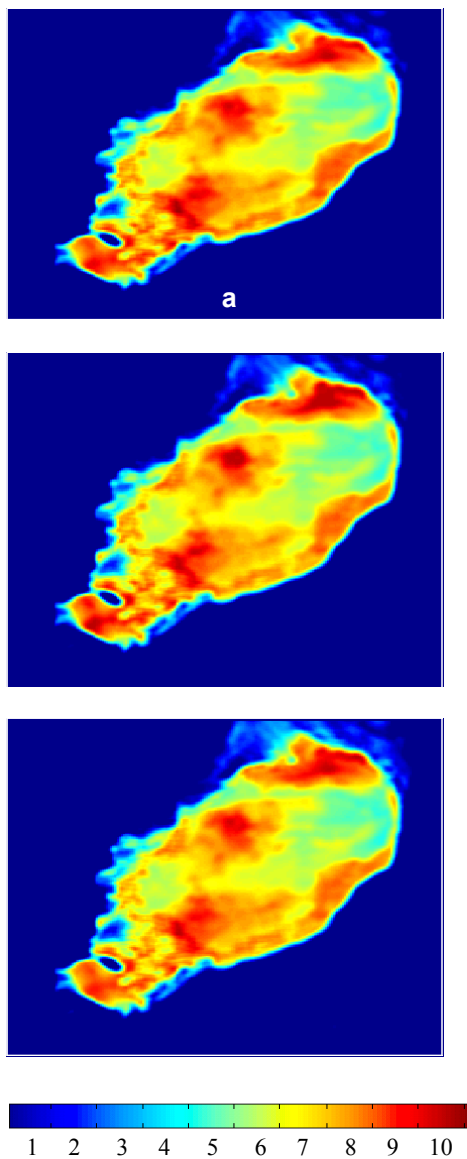
(page 179) **Figure 3.** Features of crop development pattern extracted from the sinusoidal curves fitted on NDVI time series : seasonal amplitude (up left, in NDVI units), length of crop cycle (up right, in days), date of plant emergence (bottom, in days).



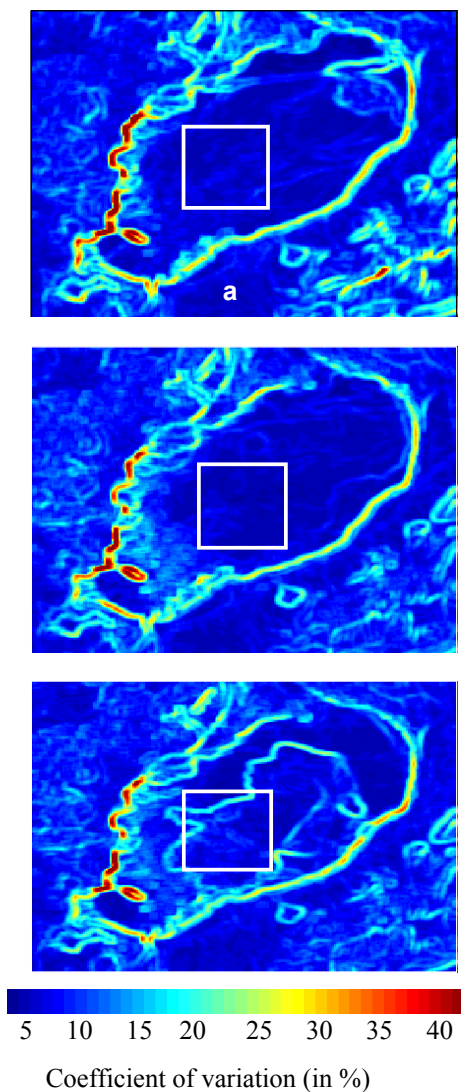
(page 181) **Figure 4.** Estimate of crop water requirement (mm) during the agricultural season for the minimum (up), the mean (middle) and the maximum (bottom) scenario of crop growth. These results are obtained by cumulating the daily values obtained with STICS-based (left) and FAO-based (right) approaches.



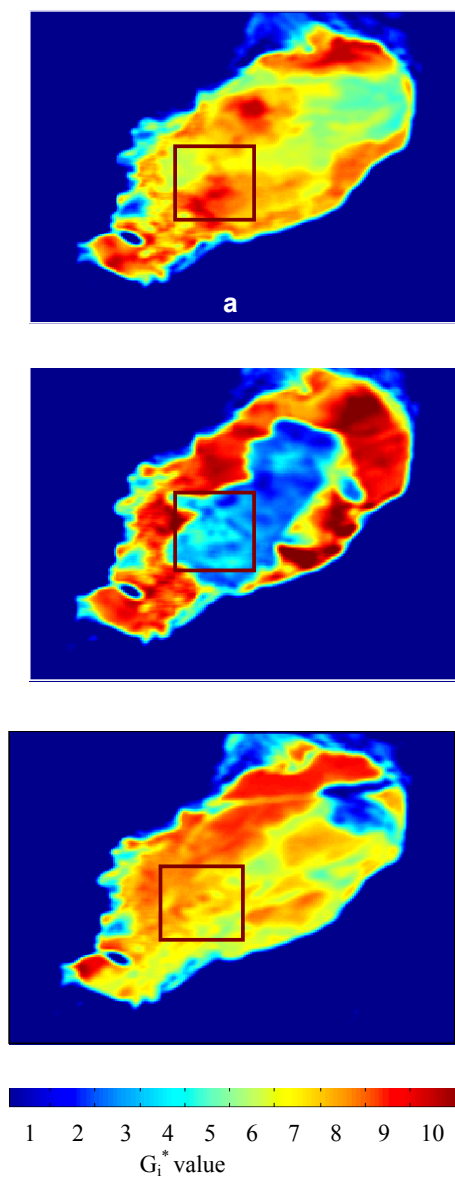
(page 221) **Figure 2.** Images of the coefficient of variation calculated using a 5x5 pixel window in the three bands (HRV1 (a), HRV2 (b) and HRV3 (c)) of a SPOT-HRV image acquired over Lunar Lake Playa in March 1997



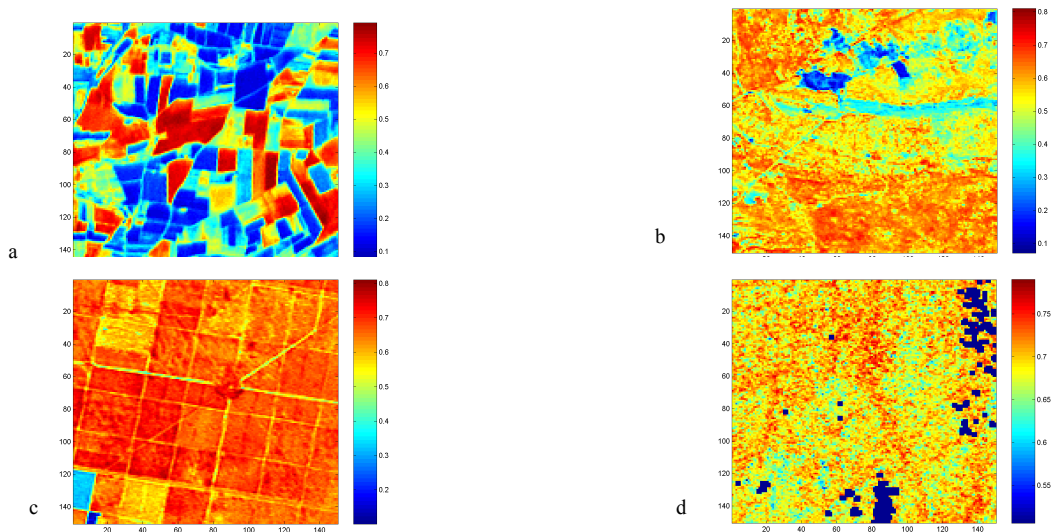
(page 222) **Figure 3.** Images of the Getis statistics calculated using a 5x5 pixel window in the three bands (HRV1: (a), HRV2: (b) and HRV2: (c)) of a SPOT-HRV image acquired over the Lunar Lake Playa in March 1997.



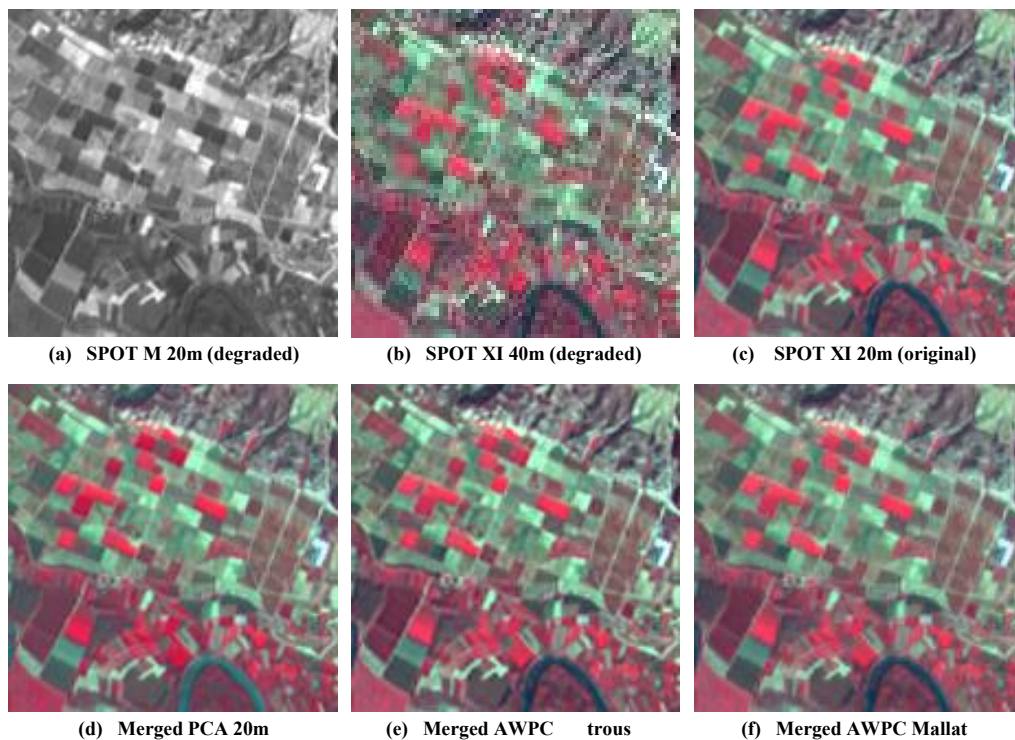
(page 224) Figure 6. Images of the coefficients of variation calculated using a 5x5 pixel window in the HRV red band HRV ((a) March 1997, (b) June 1997 and (c) June 1998).



(page 224) Figure 7. Images of the Getis statistics using a 5x5 pixel window in the HRV red band ((a) March 1997, (b) June 1997 and (c) June 1998).



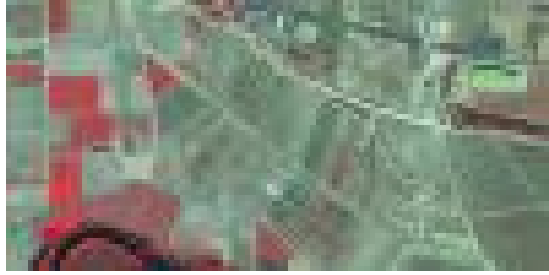
(page 201) **Figure 1.** NDVI images of the studied sites (3km*3km): a Alpilles, Crop Site (March), mean NDVI=0.41, std NDVI=0.19; b: Puechabon (France), Mediterranean Forest (June), mean=0.54, std=0.1; c: Nezer (France), Pine Forest (June), mean=0.65, std=0.06; d: Counami (French Guyana), Tropical Forest (October), mean=0.69, std=0.029.



(page 235) **Figure 3.** SPOT degraded, original and merged images.



IKONOS Pan 4m (degraded)



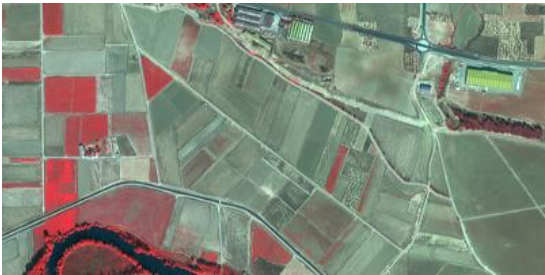
IKONOS MS 16m (degraded)



IKONOS MS 4m (original)



Merged IHS 4m (merged)

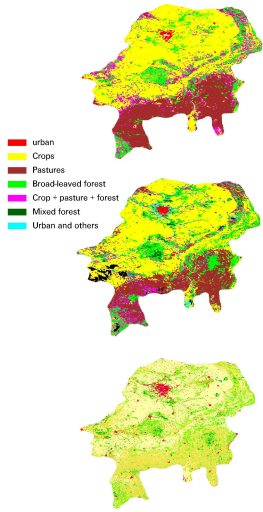


Merged AWL trous



Merged AWL Mallat

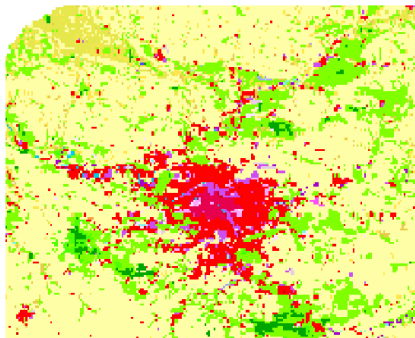
(page 236) Figure 4. SPOT degraded, original and merged images



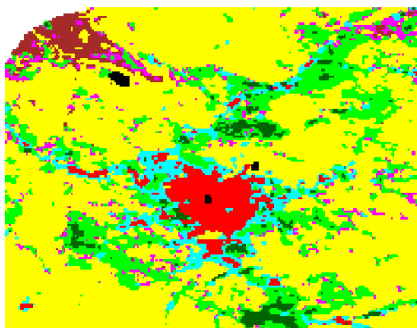
(page 248) Figure2.
VGT classification
using NDVI profiles

(page 248) Figure3.
VGT classification using
daily reflectances

(page 248) Figure1.
Corine classification



Corine Land Cover

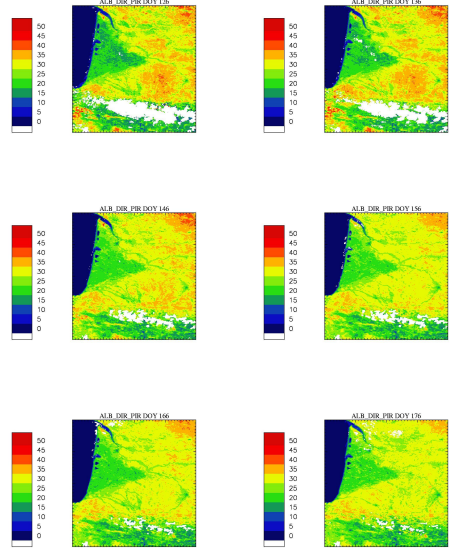


VGT classification

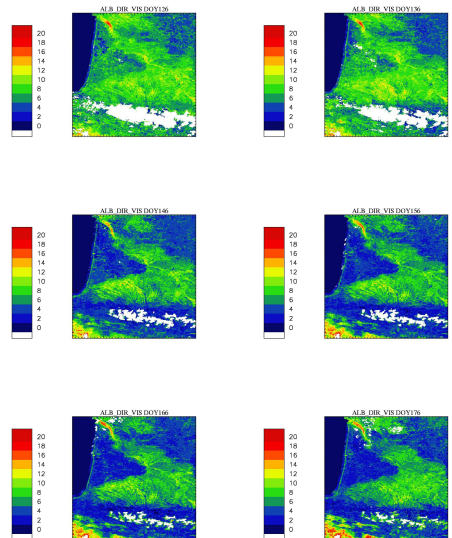
(page 248) Figure 4. Corine classification on Paris

(page 248) Figure 5. VGT classification on Paris

(page 249) Figure 7. NIR 10-days
surface albedos. 05/05-24/06/2000



(page 249) Figure 8: VIS 10-days
surface albedos. 05/05-24/06/2000



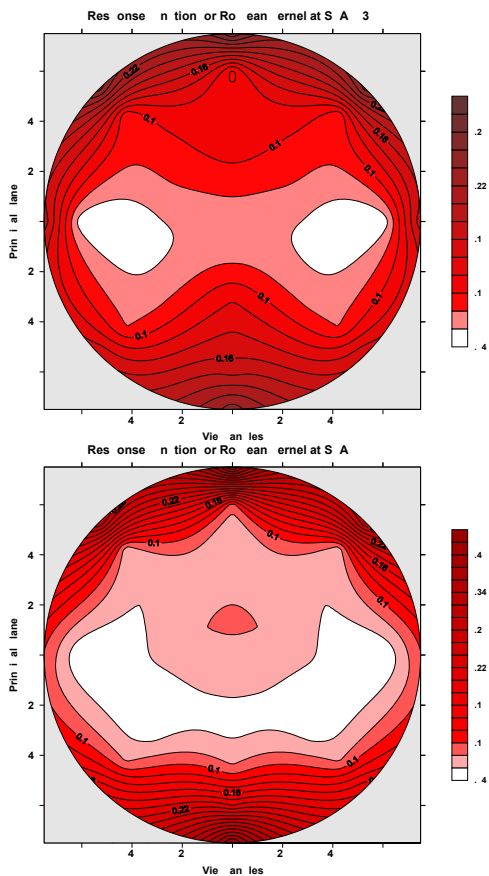


Fig.5. Response functions for Roujean kernel at SZA=30°(top), 60°(bottom).

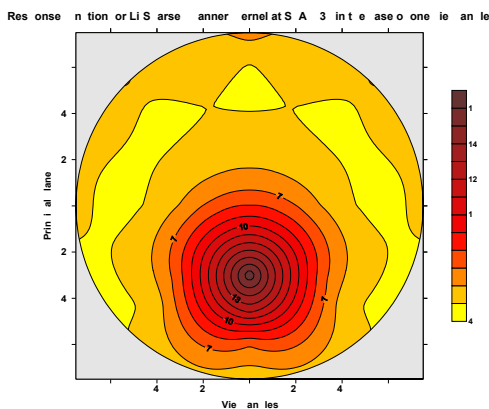
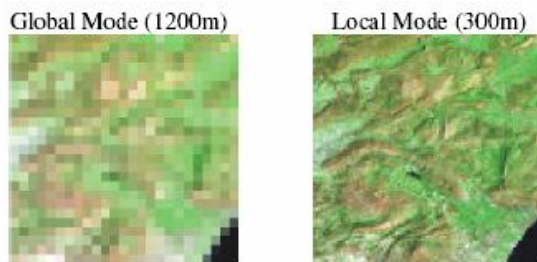
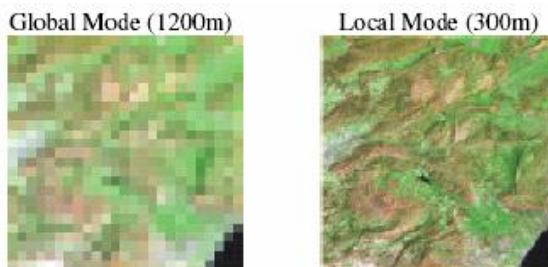


Fig. 6. Response functions for Li-Sparse model at SZA=30°.

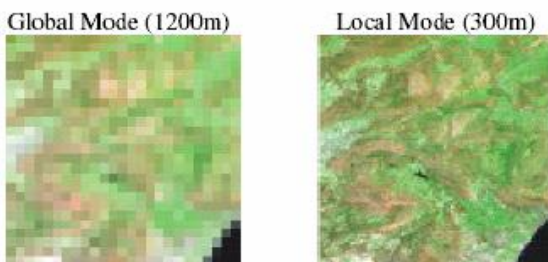
(page 258) Figure 5 and Figure 6



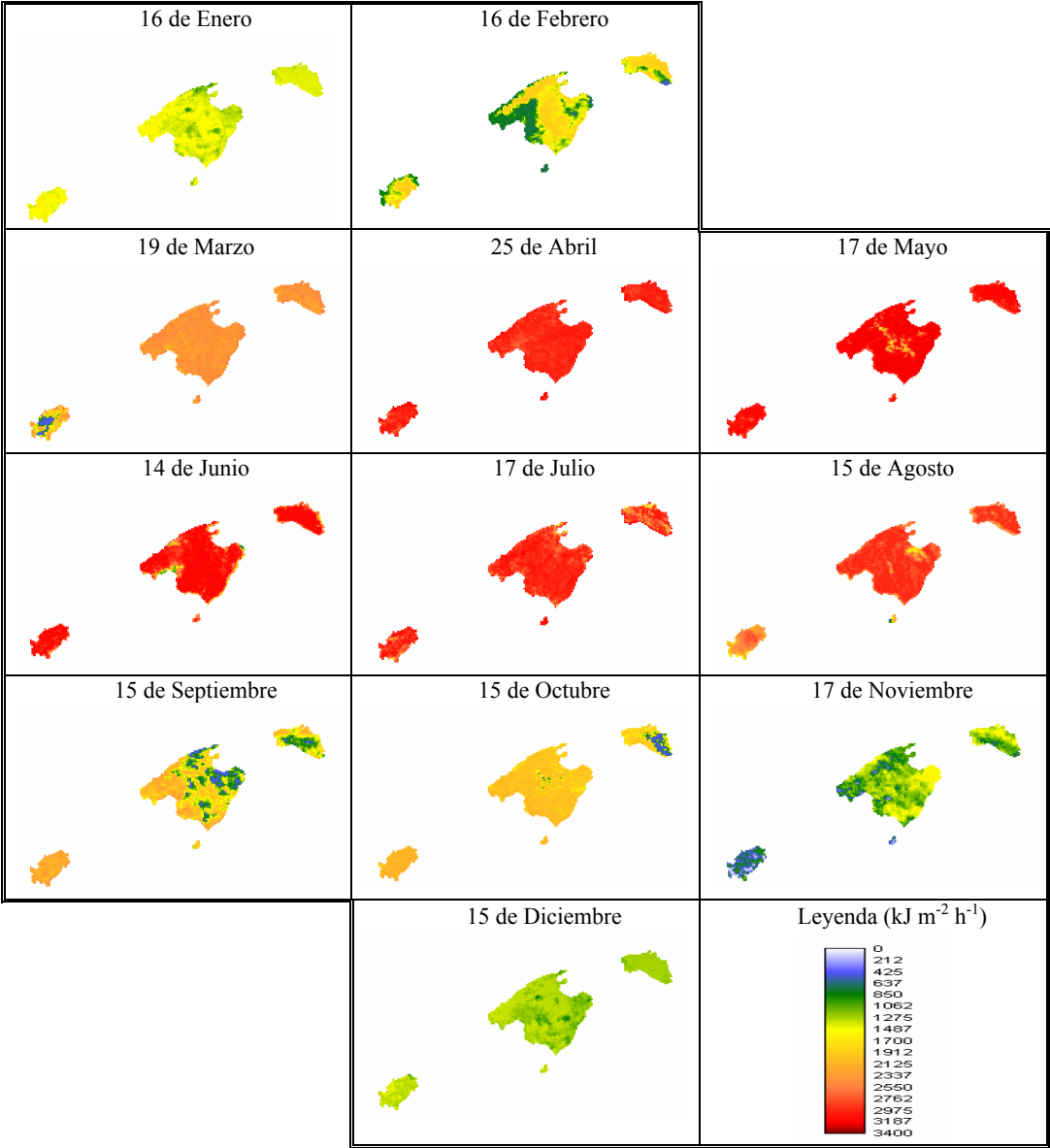
(page 285) Figures 12. Original Global and Local Mode images



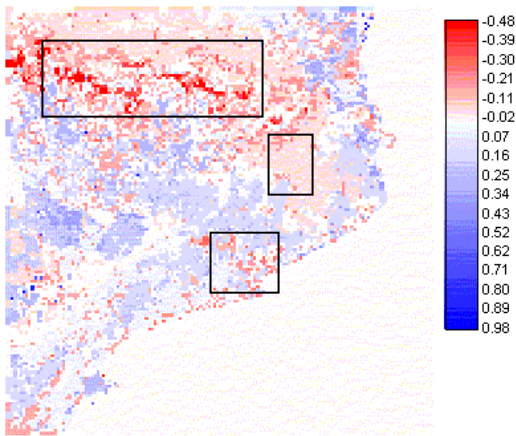
(page 285) Figures 13. Corrected images for the Global and Local Modes using the traditional method



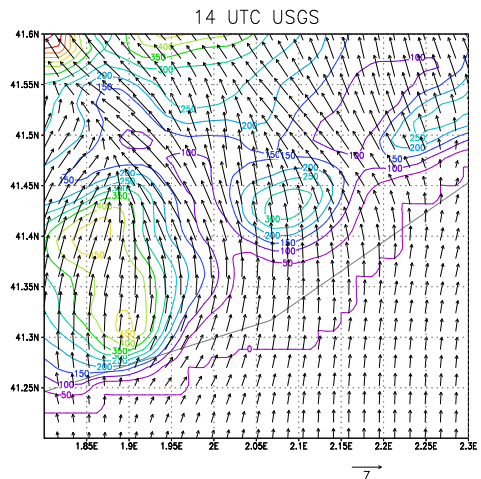
(page 285) Figures 14. Corrected images for the Global and Local Modes using the within pixel slope method



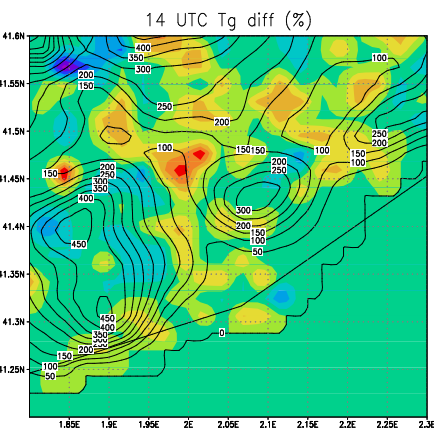
(page 264) **Figura 2.** Mapa de radiación solar global horaria de las Islas Baleares entre las 14:00 y 15:00 h (LST), para el año 1998.



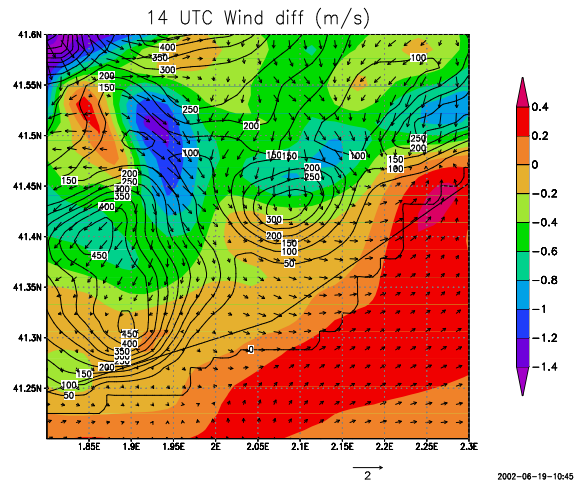
(page 272) **Figure 5.** Differences in moisture availability between the two MM5 simulations (CORINE - USGS).



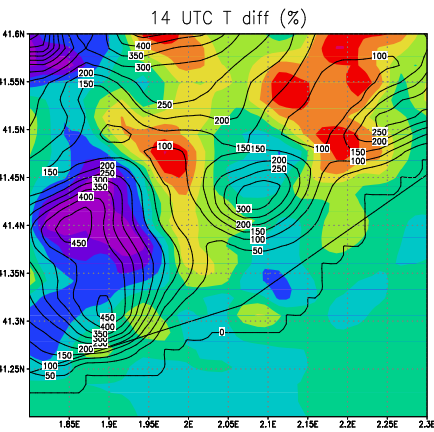
(a)



(a)

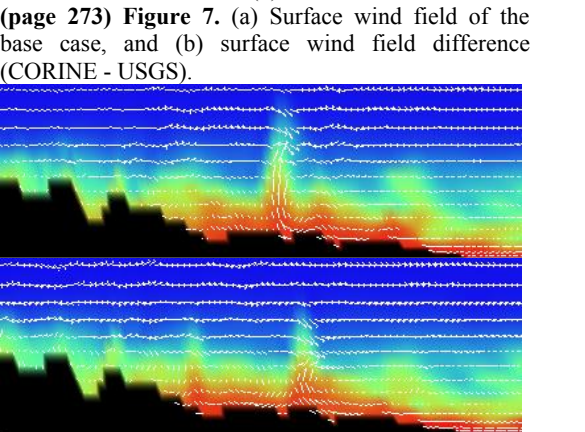


(b)

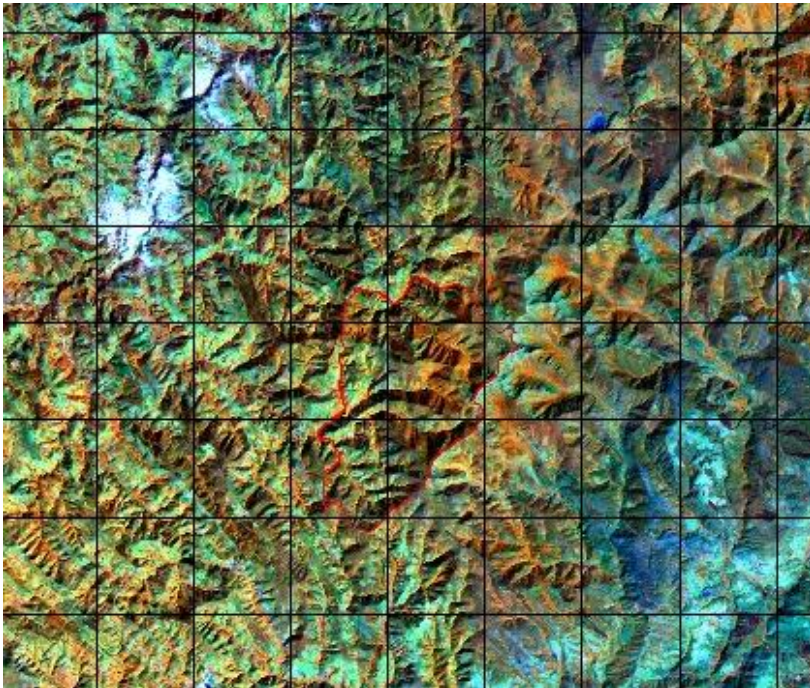


(b)

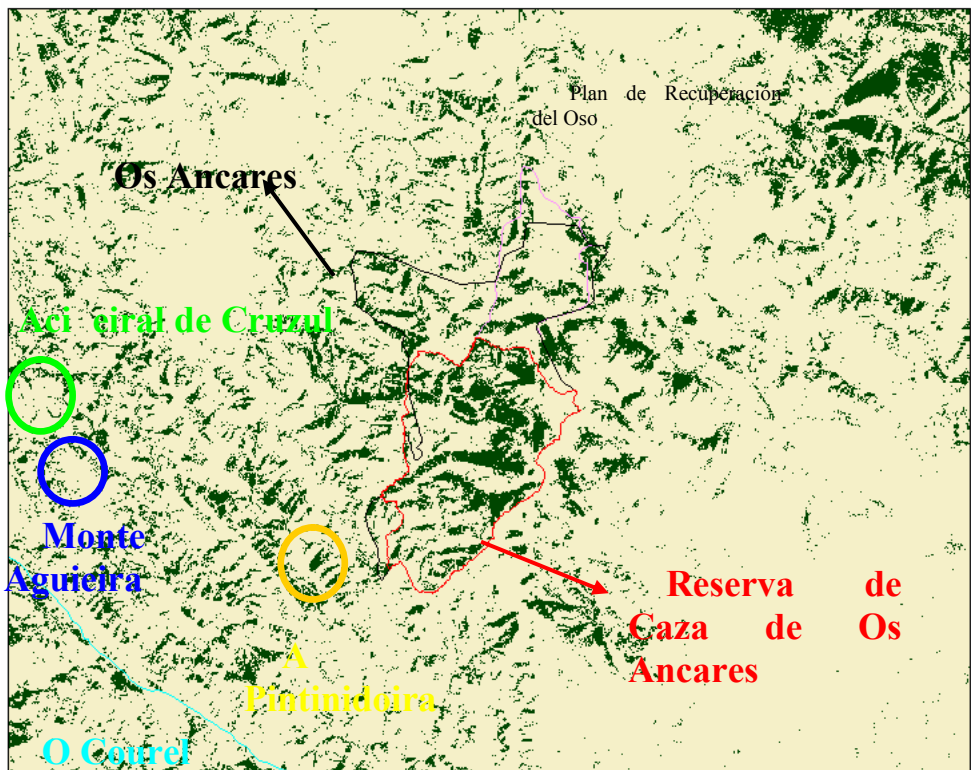
(page 272) **Figure 6.** Differences in (a) ground temperature (CORINE-USGS) and (b) first level temperature.



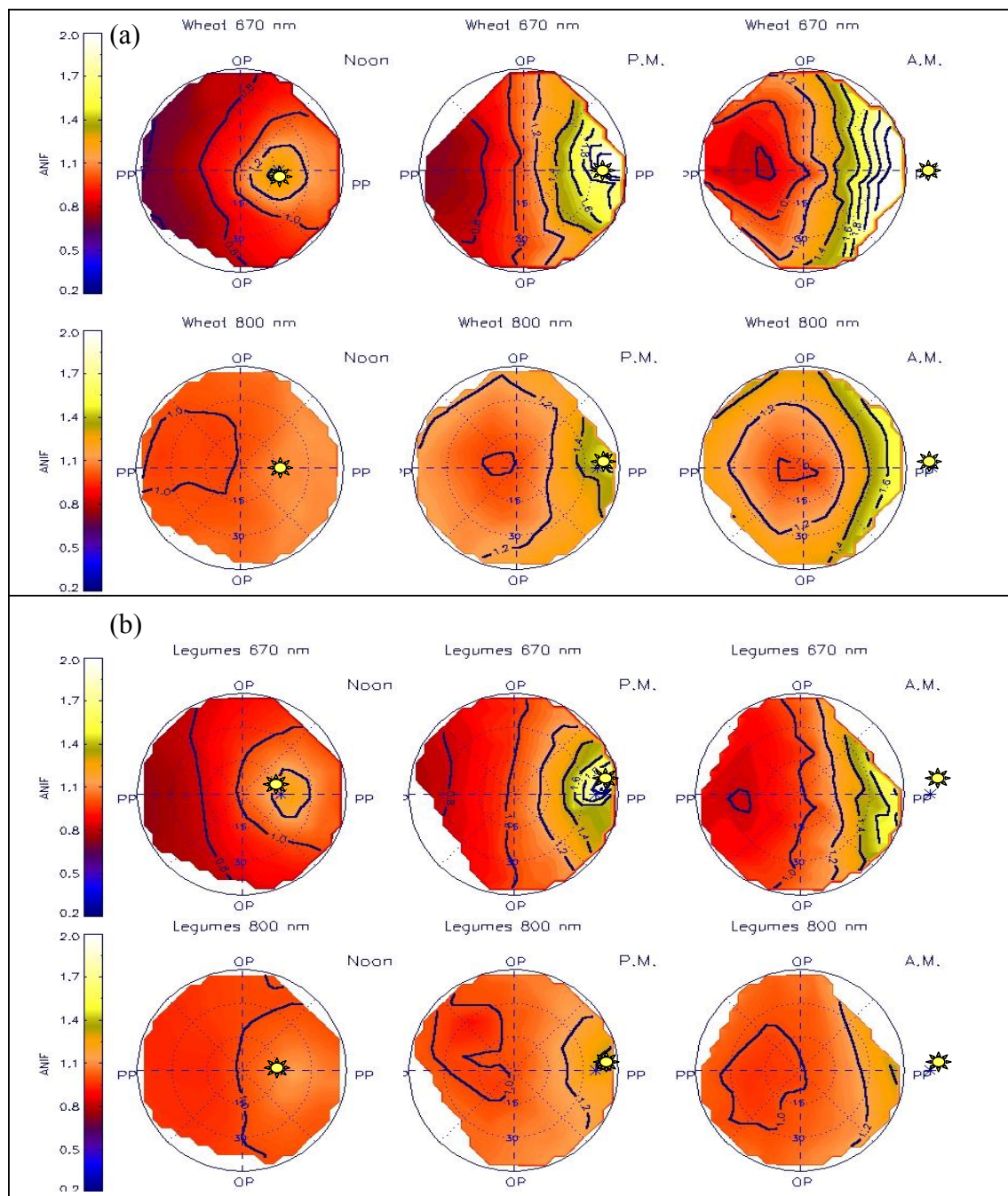
(page 274) **Figure 9.** Cross section of the wind field and the mixing ratio along 1.55°E (CORINE upper, USGS bottom panel).



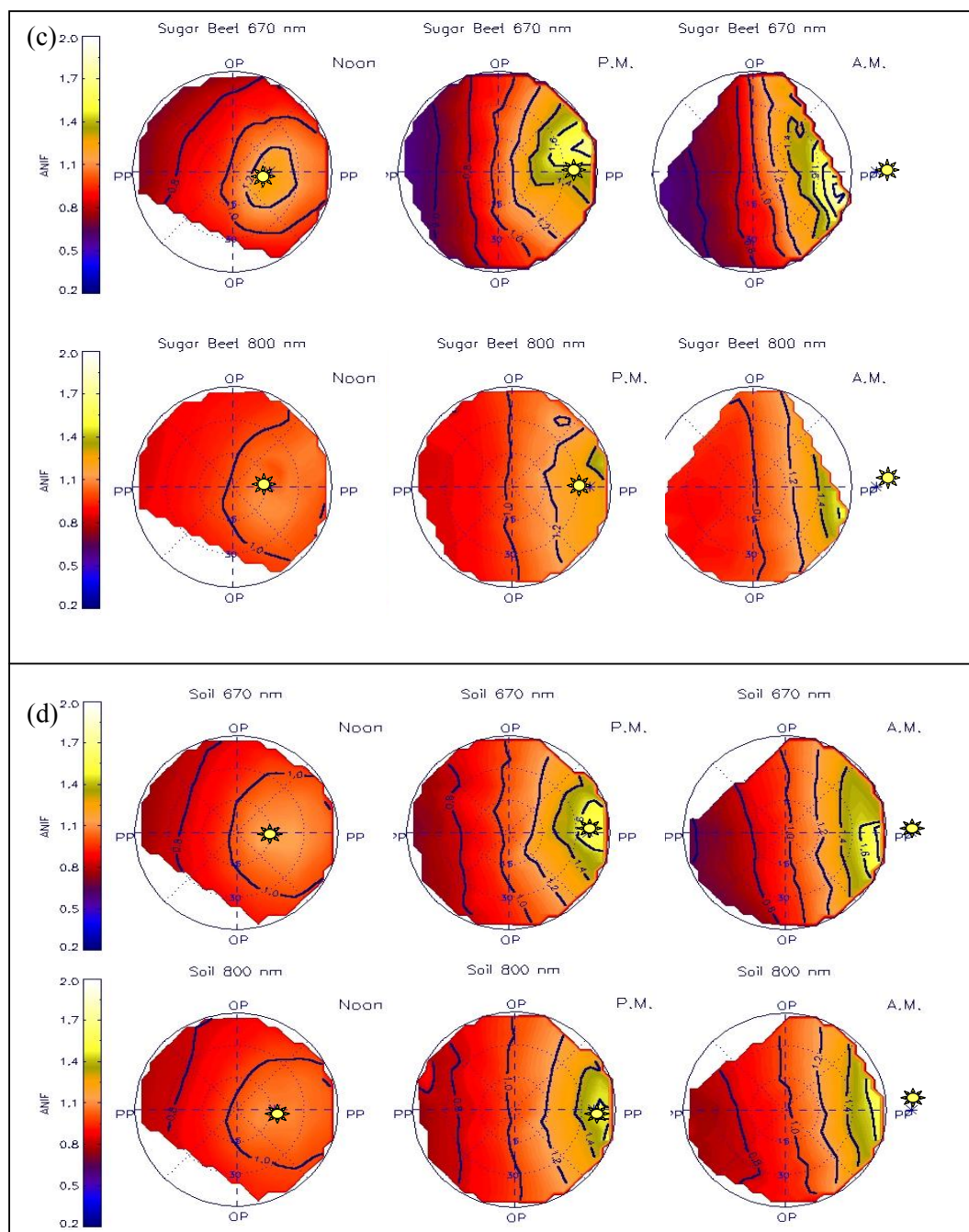
(page 292) Figure 2. Imagen resultante de la Sierra de los Ancares gallegos. Composición coloreada 4/5/3.



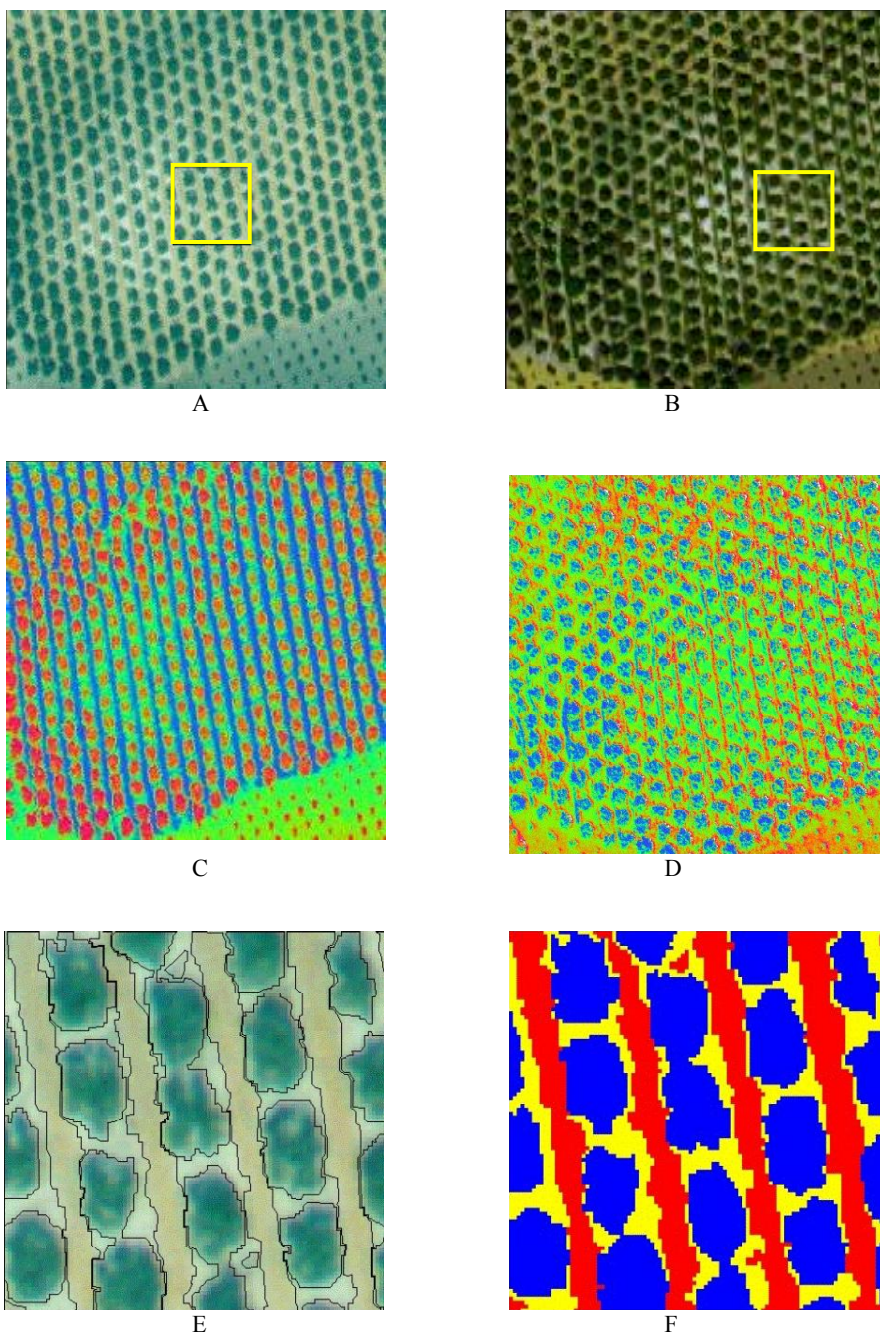
(page 293) Figure 3. Mapa de masas boscosas de la Sierra de Ancares



(page 306) **Figure 2.** Anisotropy Factors at 670 and 800 nm for three sun zenith angles (17°, 37°, 56°): (a) Wheat, (b) Legumes, (c) Sugar beet and (d) Bare soil.

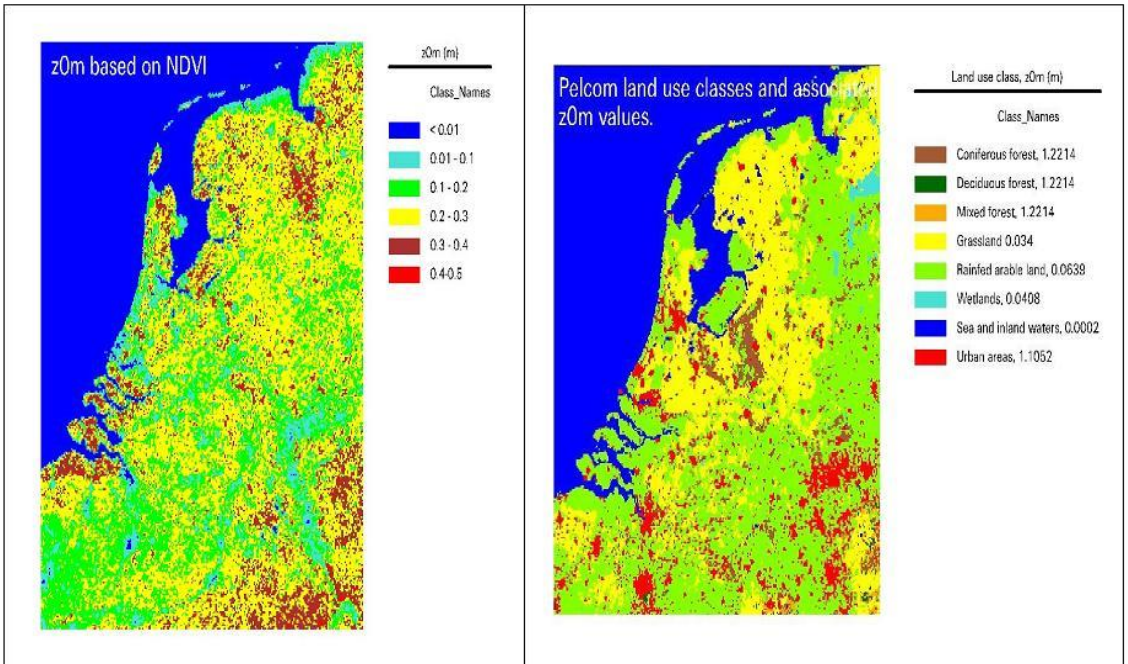


(page 306) **Figure 2.** Anisotropy Factors at 670 and 800 nm for three sun zenith angles (17°, 37°, 56°):(a) Wheat , (b) Legumes, (c) Sugar beet and (d) Bare soil.

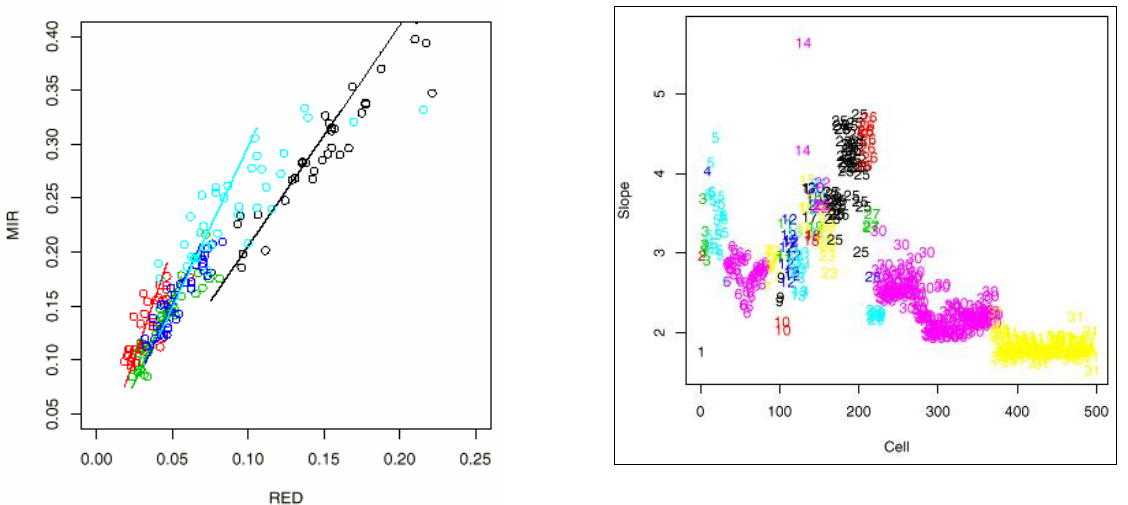


(page 312) Figure 2. (A) and (B) Views of training (TP, 500 x 500 pixels) and sub-training plots (SP, 100 x 100 pixels) at Cortijo del Rey farm in summer and spring 2000, respectively. (C) and (D) Visually acceptable and rejected soil uses discrimination by the vegetation indexes $B/(B+G+R)$ and B/R at Cortijo del Rey farm, in summer and spring 2000, respectively. (E) “Ground Truth Map” (GTM) TS manual vectorization of soil uses boundaries; and (F) Edition and rasterization of the GTM, where blue is olive tree, yellow is bare soil and red is cover crop.

Uncertainties in Input Parameters -Z0m

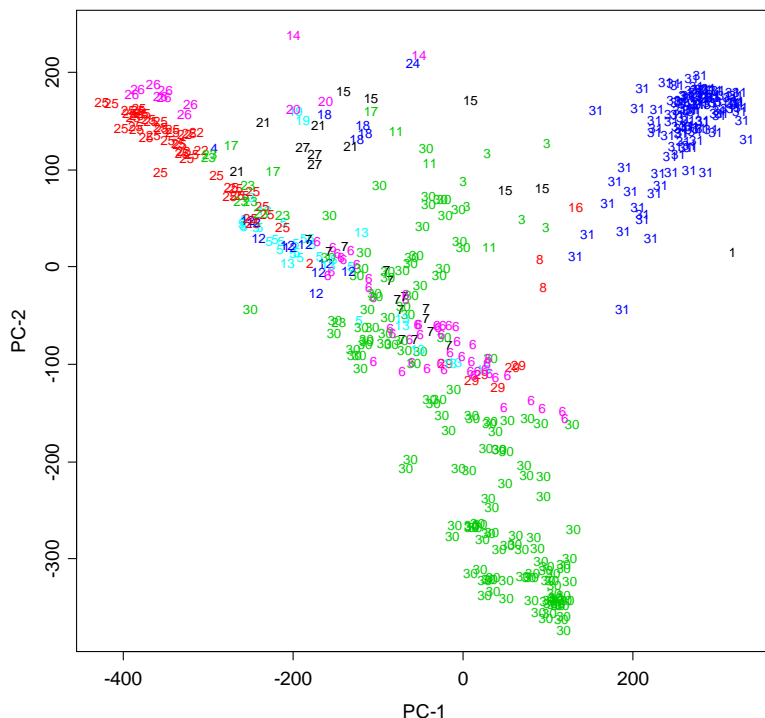


(page 324) **Figure 7.** Comparison of aerodynamic roughness height maps derived with two different methods



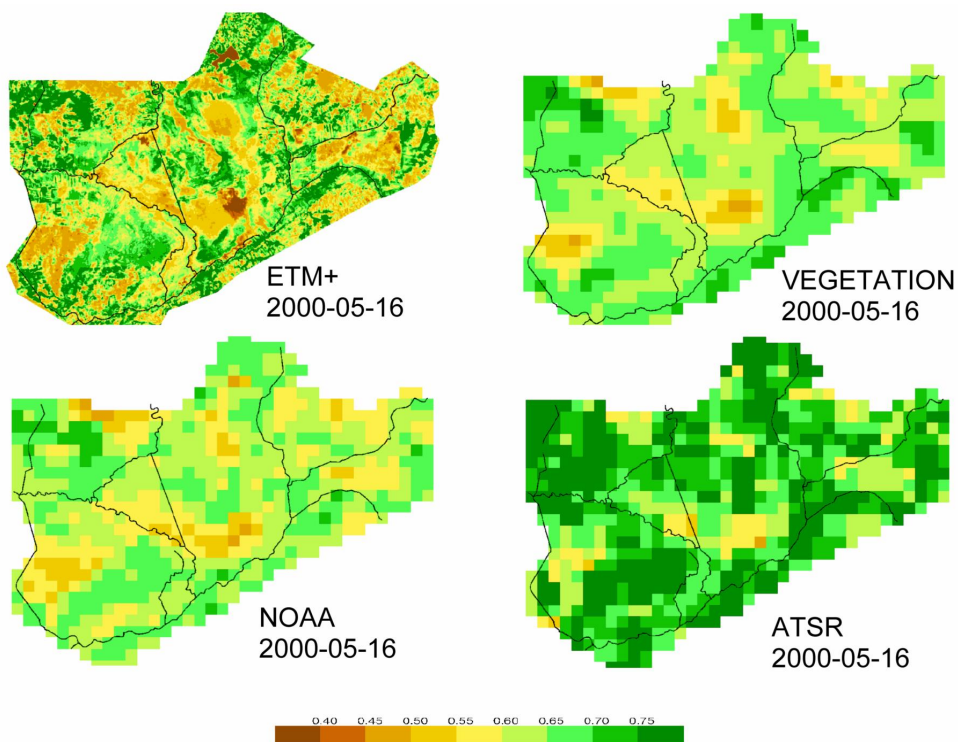
(page 350) **Figure 1.** Examples of four robust fits of a regression line to the mir vs. red reflectance values of four selected cells, constraining the intercept to a 0 value. Black symbols, a non-irrigated cereal crop (code 30); red, evergreen oak forest (code 25) Catalonia (NE Spain).

(page 352) **Figure 4.** Values of the slope of the MIR vs. RED regression line with 0 intercept. Cells coded, and ordered, by habitat.

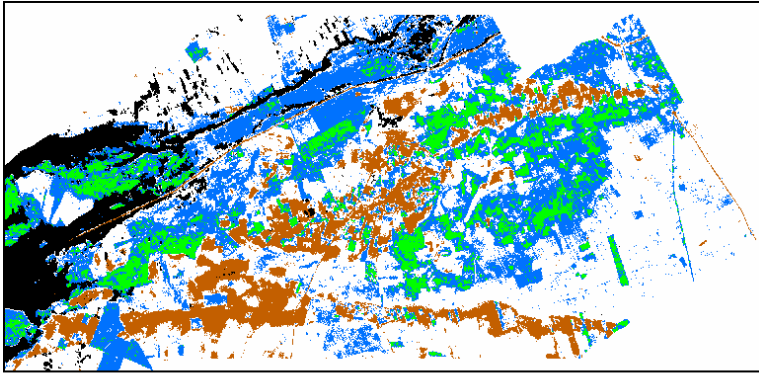


(page 351) Figure 2.

Projection of the selected cells (identified by their habitat codes) on the plane of the first two PCs. See Fig. 3 for time profiles of representative cells with habitats coded as 25 (forest of evergreen oak), 30 (not-irrigated cereal fields), 3 (montane fields of *Genista purgans*) and 31 (rice fields). Other relevant codes: 5 (bushland of *Cistus sp.* on siliceous soils), 6 (garrigues of *Rosmarinus officinalis*), 7 (garrigues of *Cistus clusii* and *Anthyllis cytisoides* on calcareous soils), 14 (forests of *Abies alba*), 15 (forests of *Pinus uncinata*).

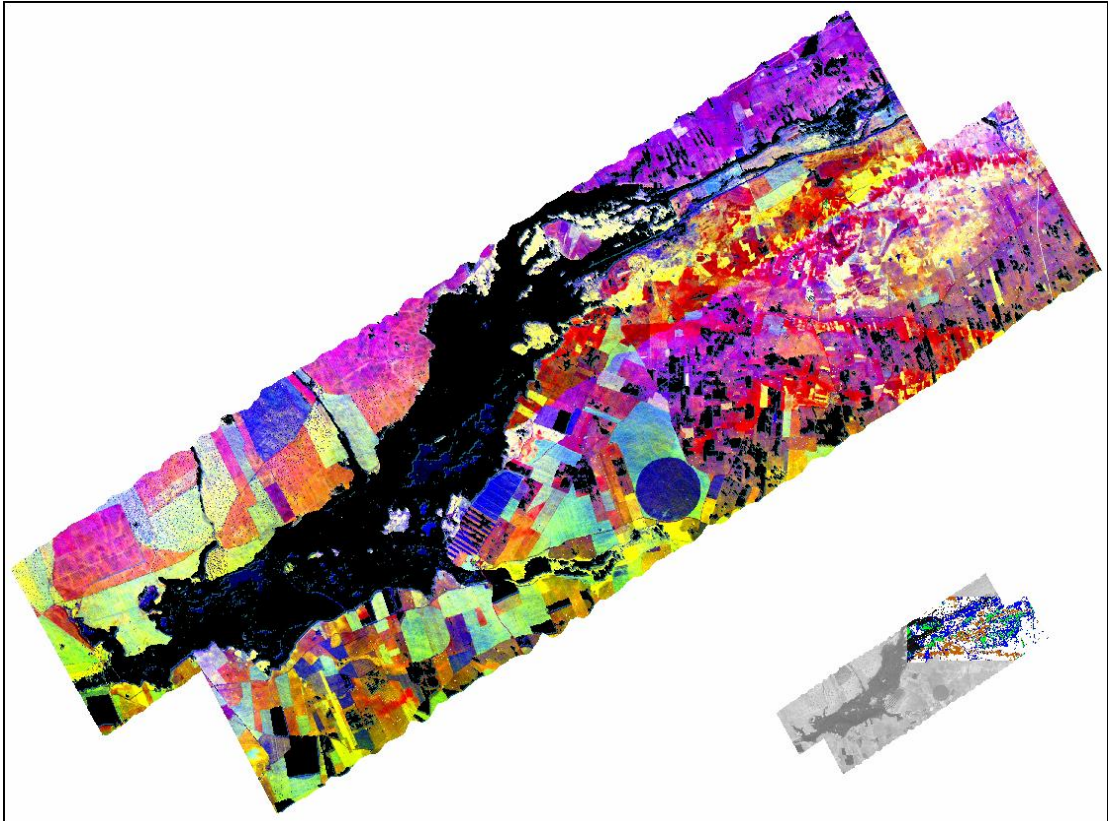


(page 385) Figure 5. Distribution of GEMI from different satellites in the Middle Biebrza Basin

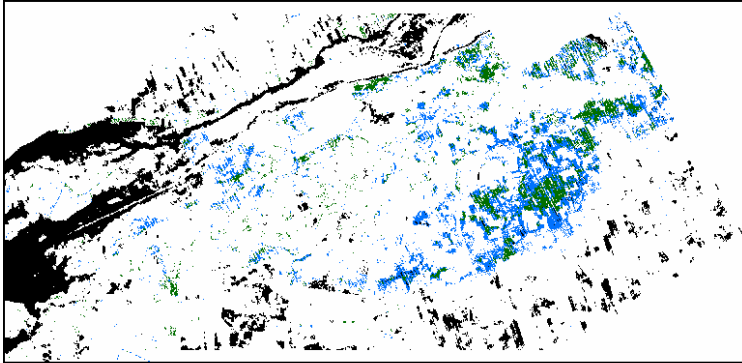


■ red emerged sands
■ red mudflat "playa" sands
■ peat

(page 373) **Figure 2.**
Geological map composed from DAIS images indicating the main sedimentary units.

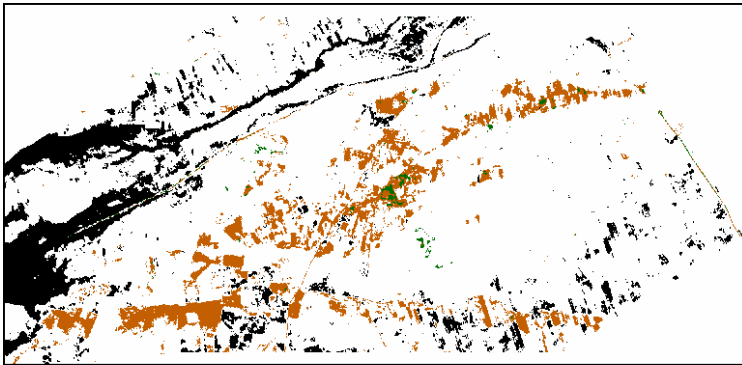


(page 373) **Figure 3.** False colour composite with Principal components 1 (red), 2 (green) and 3 (blue) computed from the six thermal infrared DAIS channels on the flight line mosaic after masking water and dense vegetation. Indication of the northeastern area selected for mapping.



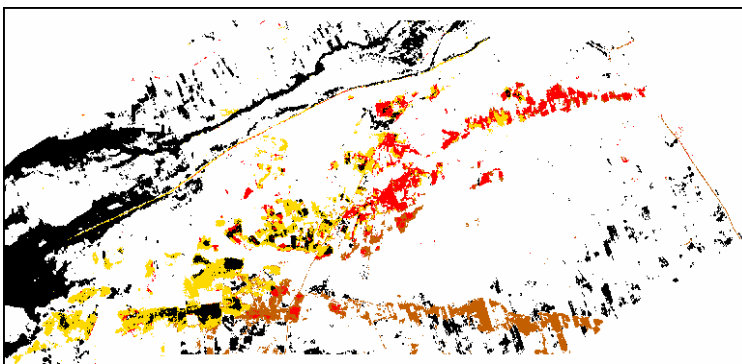
■ pool bottom rich in organic matter and carbonate
■ mudflat with saline soils

(page 374) **Figure 4.** Map built using Spectral Angle Mapper on the grey mudflat "playa" sands on the 72 VIS-NIR DAIS channels using six selected field spectra taken with a GER spectrometer (fig.6). The deeper areas of the paleopool richer on organic matter and carbonate are isolated from the flooded mudflats on a fluctuating shore developing saline soils.



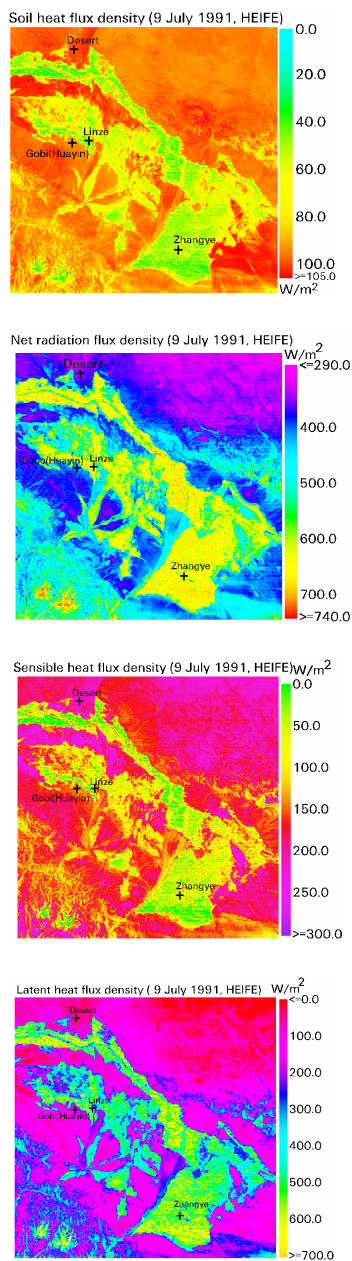
■ red emerged sands
■ channel connecting pools

(page 374) **Figure 5.** Map built using Spectral Angle Mapper on the red emerged sands on the 72 VIS-NIR DAIS channels using six selected field spectra taken with a GER spectrometer (fig.6). a channel connecting the two main paleopools is shown.

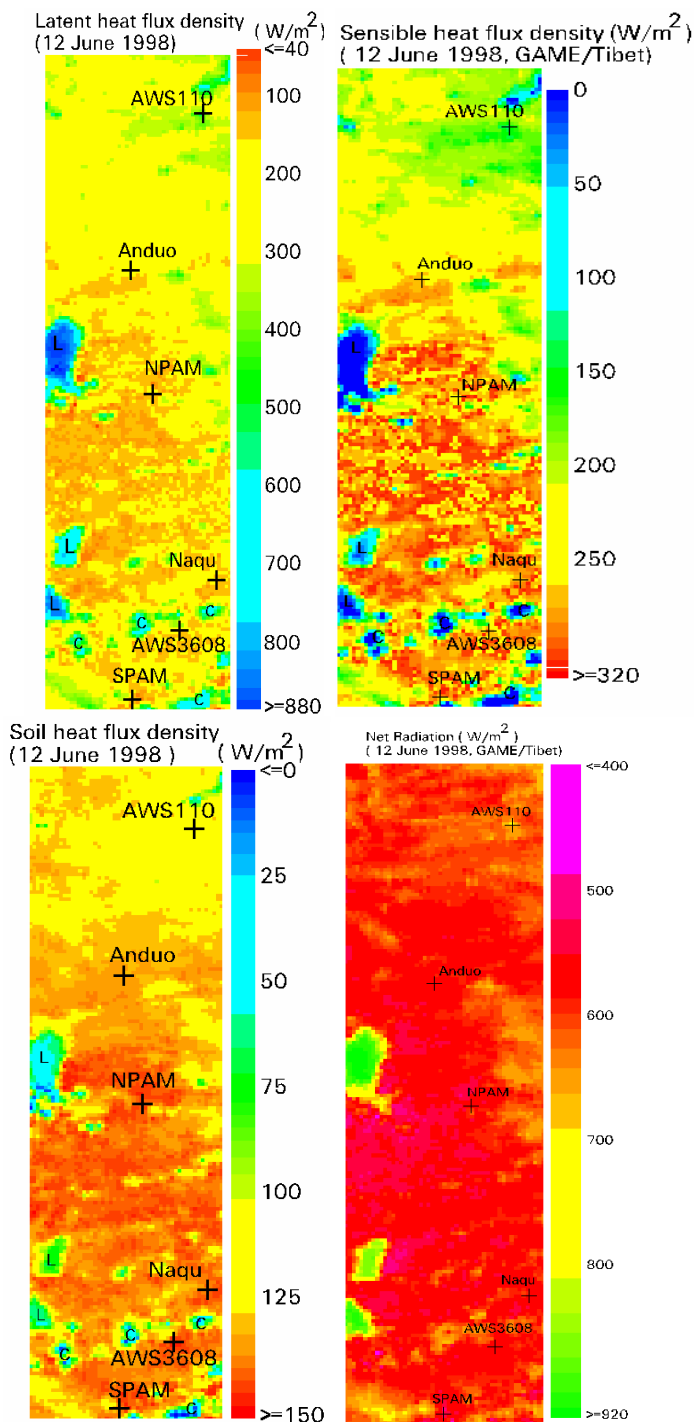


■ old red emerged sands
■ young red emerged sands
■ younger red emerged sands

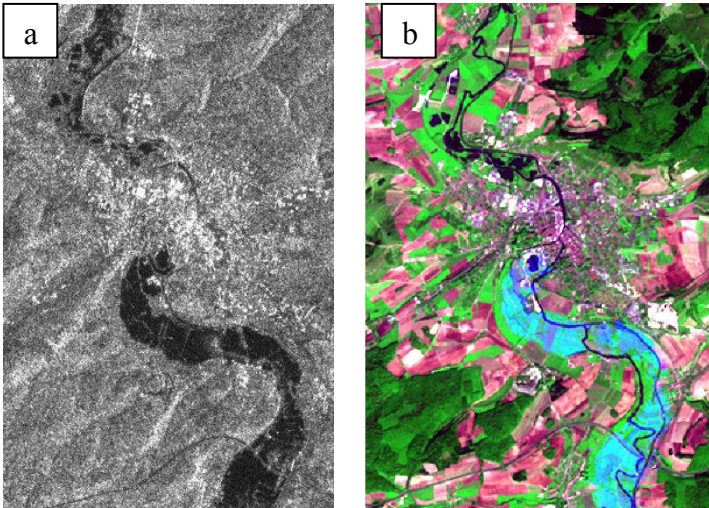
(page 376) **Figure 11.** Geological map on red emerged sands built from DAIS imagery associated to three main morphosedimentary surfaces.



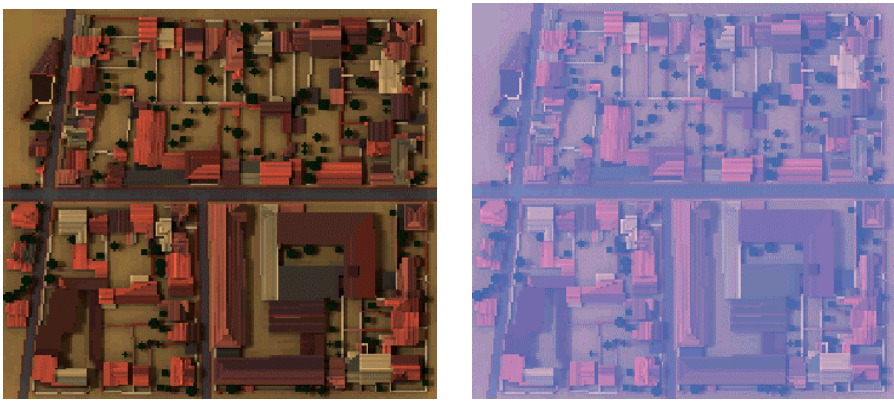
(page 421) **Figure 5.** Maps of land surface heat fluxes for the HEIFE area. 10:00(LT), July 9, 1991.



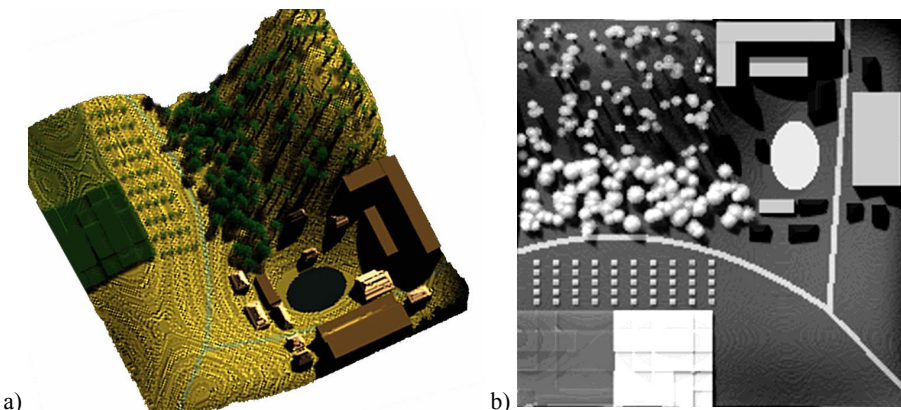
(page 421) **Figure 6.** The distribution maps of surface heat fluxes for GAME/Tibet area (June 12, 1998). C: cloud, L: lake



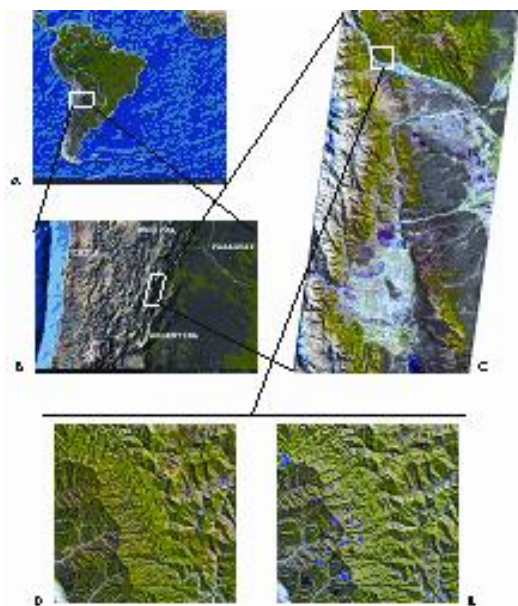
(page 428) **Figure 1.** Observed flood extent on ERS image (a) and fusion with a natural color image (b)



(page 435) **Figure 5.** Bottom (left) and top of the atmosphere (right) DART simulations of a Toulouse district.



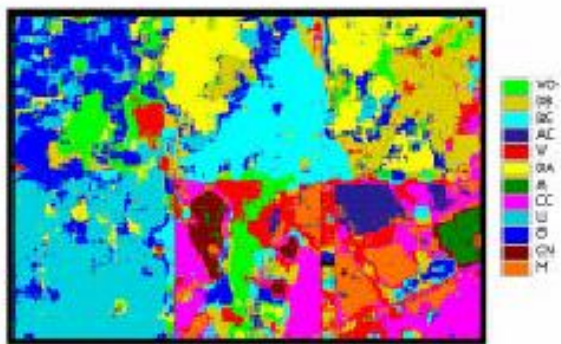
(page 435) **Figure 6.** DART simulation of a natural landscape (South west France). Colour composite (a). Thermal infrared (b).



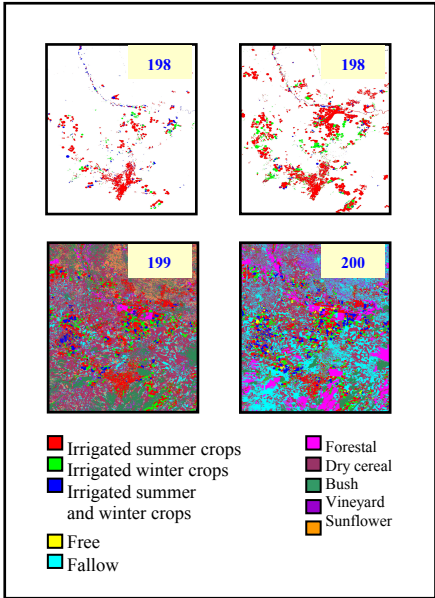
(page 485) **Figure 1.** Geographic location of the study area and analysis of landslides changes between 1986 and 2001. Argentina in Southamerica (A). Northwestern Argentina (B). Study area (C). Fresh landslides (in blue) in 1986 (D) and 2001.



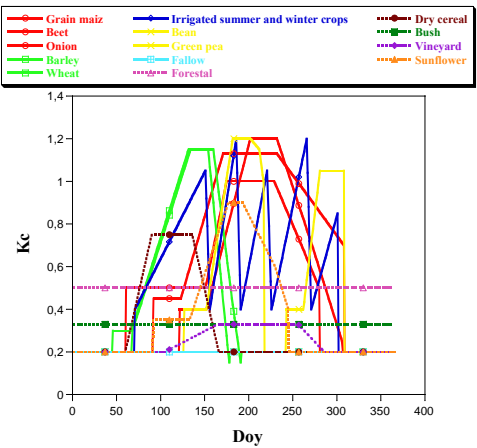
(page 512) **Figure 4.** Photograph of an irrigated maize canopy (left), and the same canopy under water stress (right).



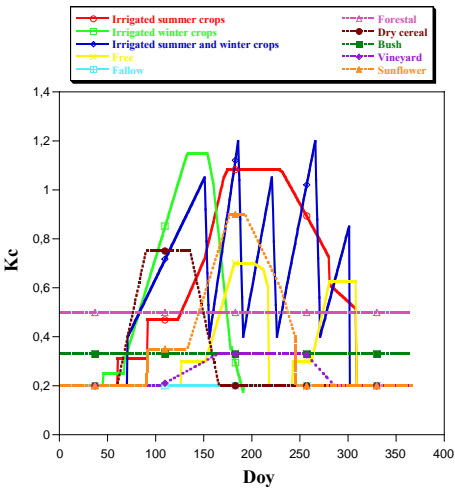
(page 520) **Figure 8.** Classification of the mosaic image on figure 1 in 12 agricultural classes using texture features



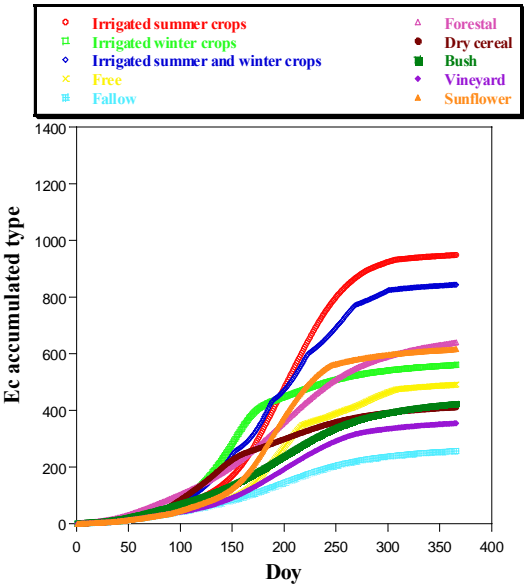
(page 531) **Figure 2.** Land cover maps of the Albacete zone for period 1982-2000, obtained using the Landsat MSS, TM and ETM+ imagery.



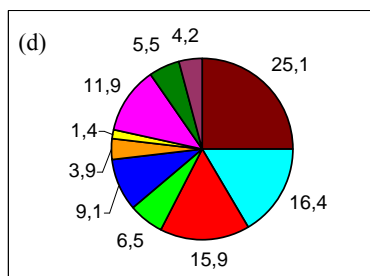
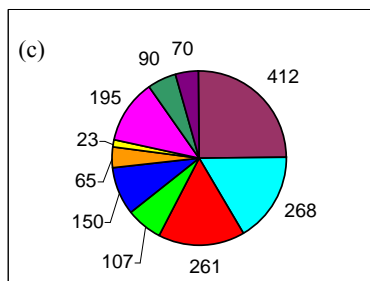
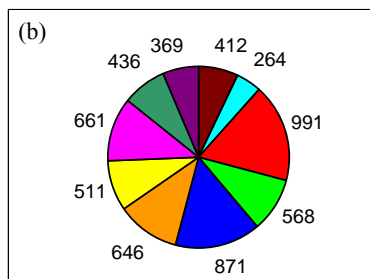
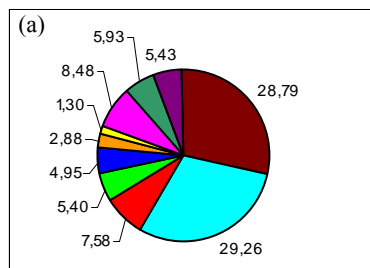
(page 532) **Figure 3.** Crop coefficient K_c curves for different vegetation land cover presented in the study area (ITAP).



(page 533) **Figure 4.** Crop coefficient K_c curves for the vegetation land cover presented in the study area for 2000.

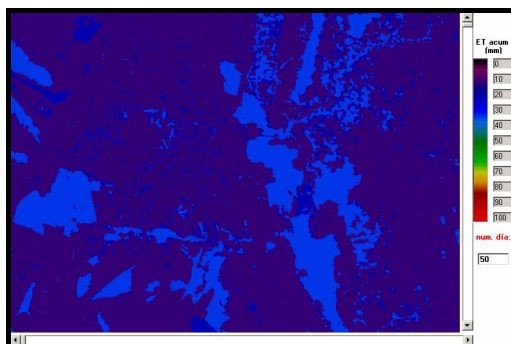


(page 534) **Figure 7.** Accumulated evapotranspiration vegetation cover curves type.

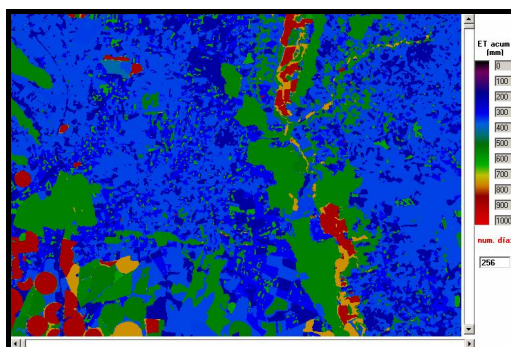


■ Irrigated summer crops
 ■ Irrigated winter crops
 ■ Irrigated summer and winter crops
 ■ Free
 ■ Fallow
 ■ Forestal
 ■ Dry cereal
 ■ Bush
 ■ Vineyard
 ■ Sunflower

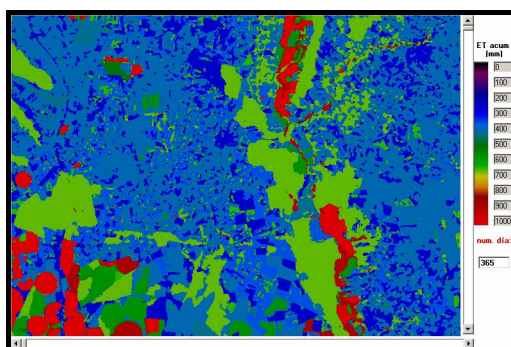
(page 534) **Figure 8** Analysis of the evapotranspiration data for 2000. The graphics (a) and (b) represent successively the surface area in % occupied by each vegetation cover in the study area in 2000 and the total land cover evapotranspiration (l/m²). While graphics (c) and (d) show the total water consumption by each land cover in hm³ and % successively.



(a) February 19th

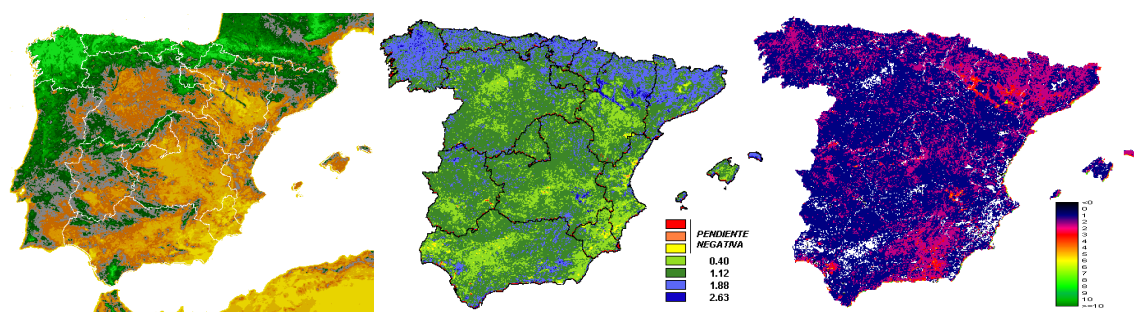


(b) September 12th

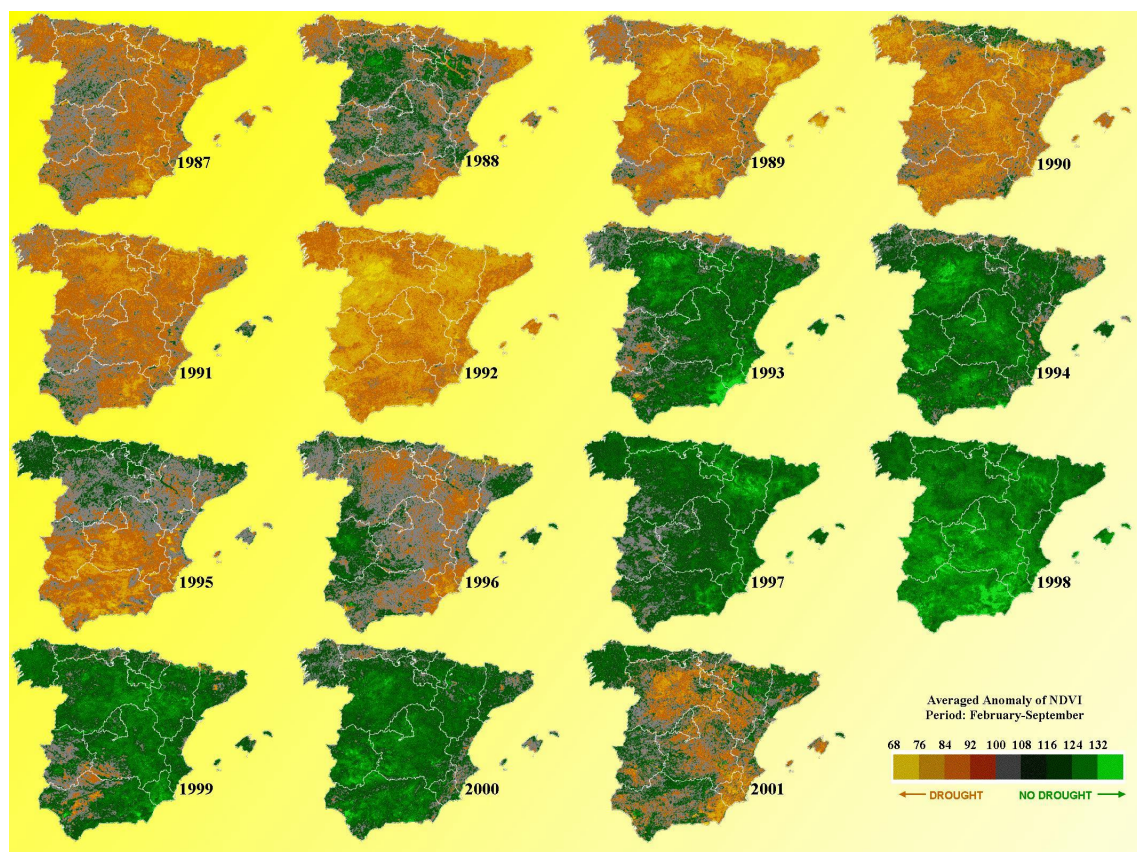


(c) December 30th

(page 535) **Figure 9.** Spatial distribution of the accumulated evapotranspiration crops at three dates of 2000, and which correspond to region of 10000 ha selected from the study area.



(page 539) **Figure 1.** a) Averaged NDVI values for 1987-2001 period; b) SLOPE image of NDVI values for 1987-2001 period; c) Yearly increase (%) of NDVI referred to 1987



(page 539) **Figure 2.** Serie of images of anomaly for Spain, on the period 1987-2001

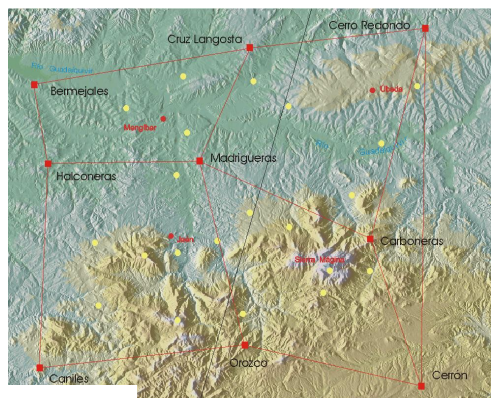


Figure 7

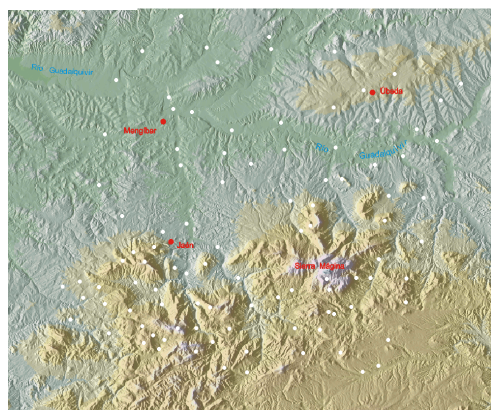


Figure 8

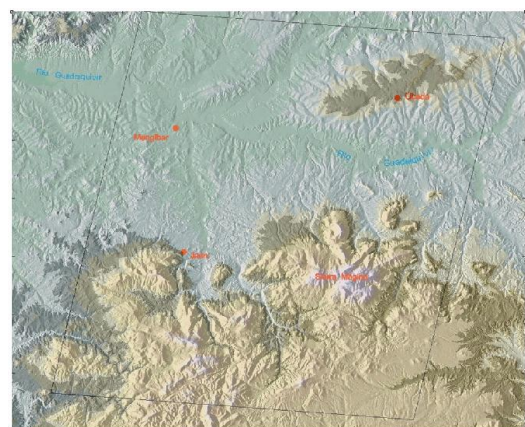


Figure 13

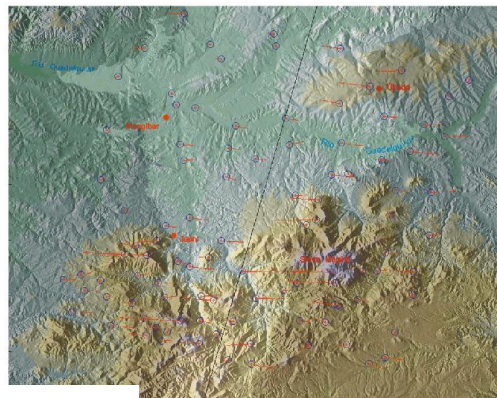


Figure 11

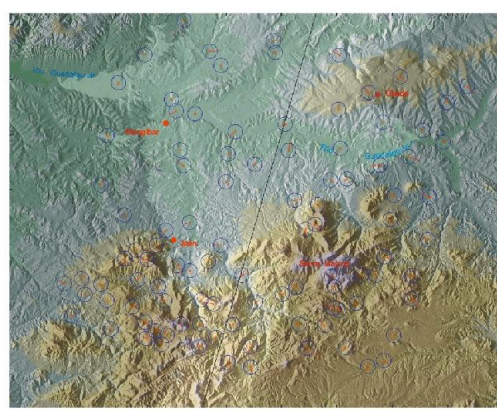


Figure 12

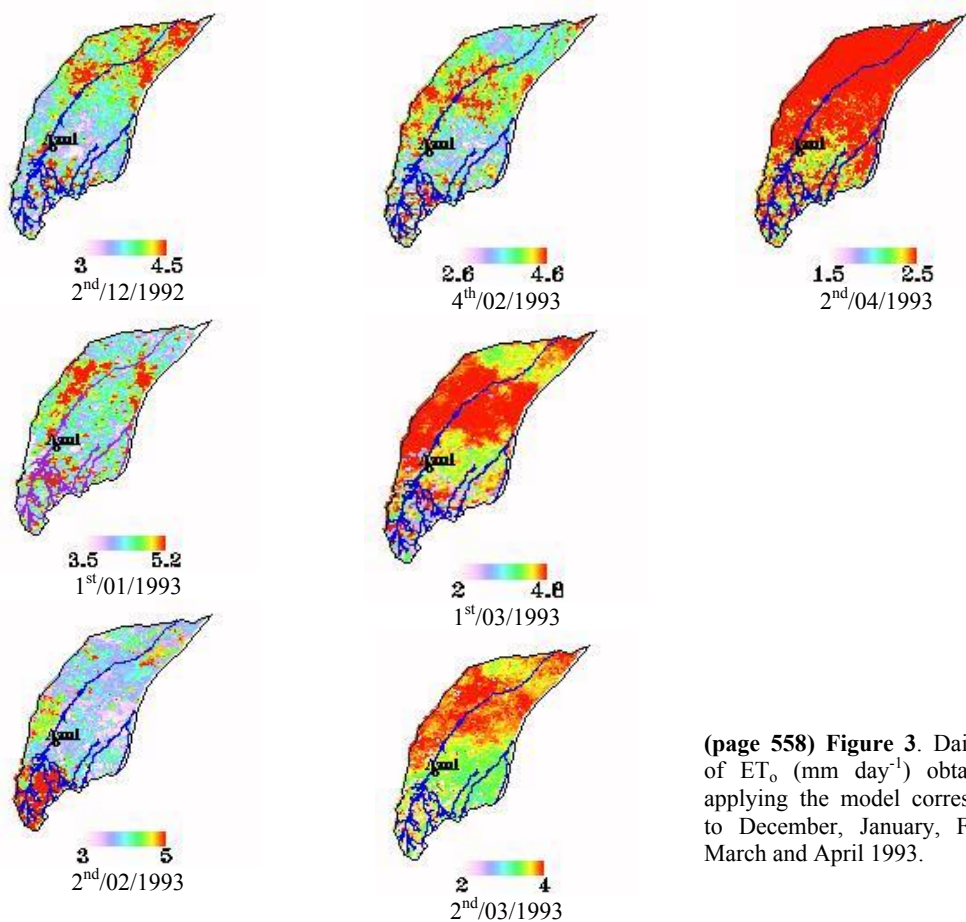
(page 544) **Figura 7.** Distribución en zona de estudio de 21 puntos CPs. (en amarillo) por sectores, para el cálculo de los parámetros de transformación, utilizando los vértices de la Red Regente.C.1.

(page 545) **Figura 8.** Elección de 100 GCPs, atendiendo a la morfología del terreno.

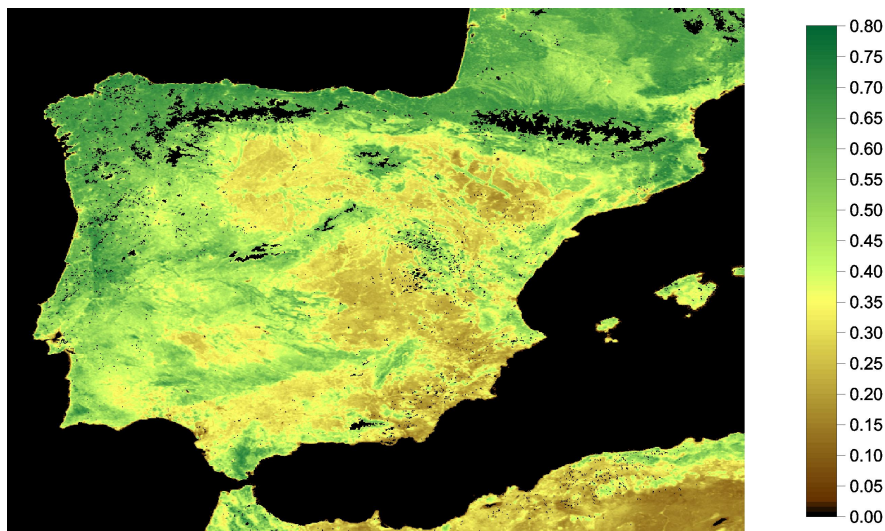
(page 547) **Figura 11.** Representación de residuo polinomio grado 1 junto a línea nadiral e imagen de desplazamiento debido al relieve.

(page 547) **Figura 12.** Representación gráfica de residuo polinomio Palà-Pons grado 1 junto a línea nadiral e imagen de desplazamiento debido al relieve.

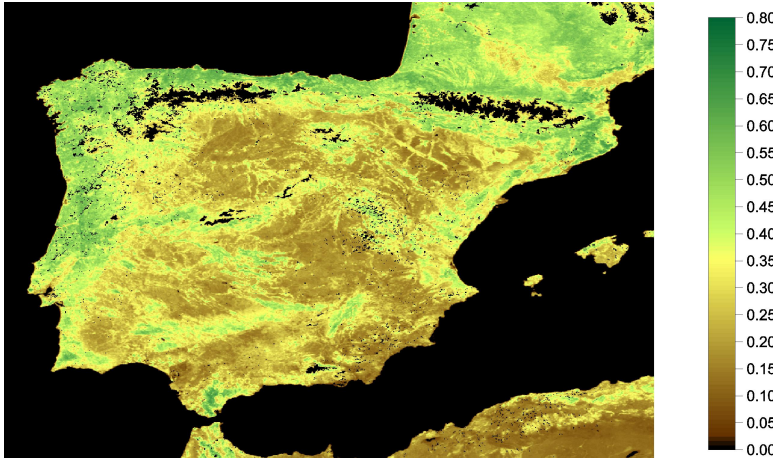
(page 548) **Figura 13.** Zonificación $\nabla V=1$ sombreado en negro. Polinomio grado 1.



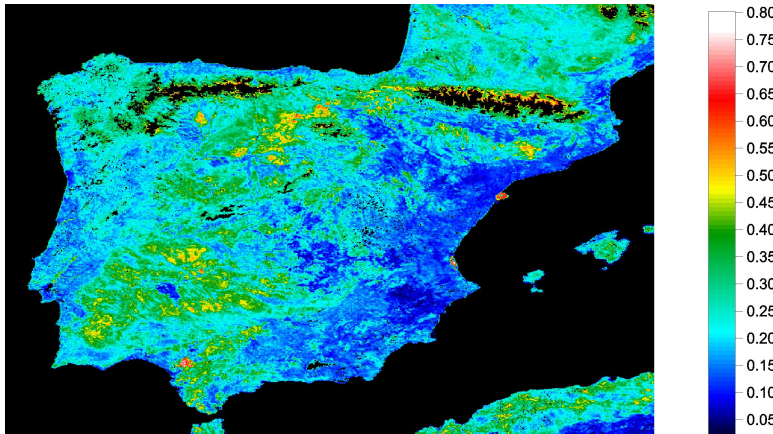
(page 558) **Figure 3.** Daily value of ET_0 (mm day⁻¹) obtained by applying the model corresponding to December, January, February, March and April 1993.



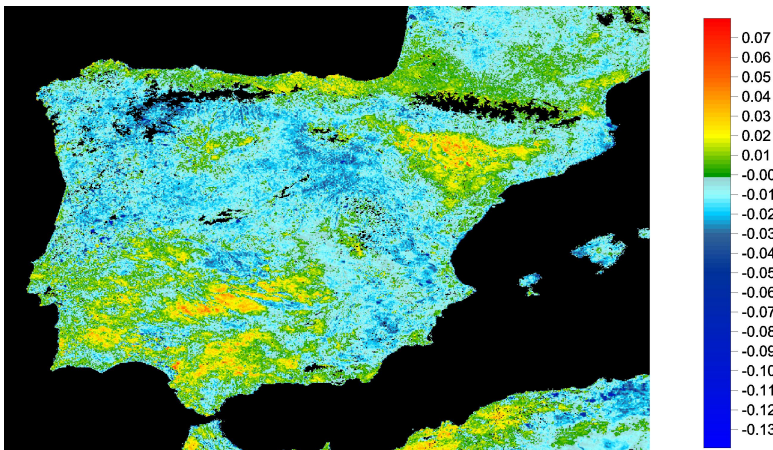
(page 563) **Figure 3.** Mean of the trend series extracted with wavelet analysis from the VEGETATION NDVI time series



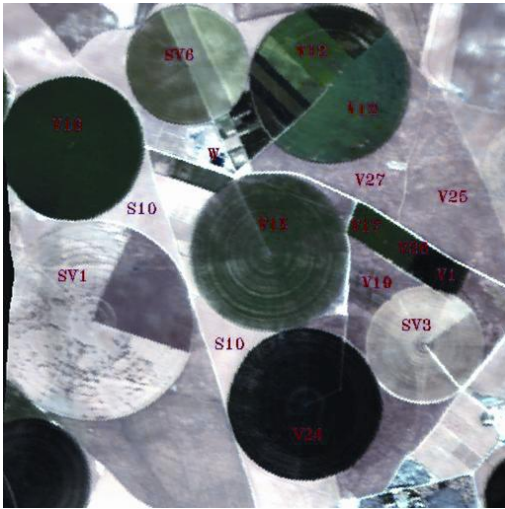
(page 563) **Figure 4.** Percentile 10% of the sum of the trend and variability series extracted with wavelet analysis from the VEGETATION NDVI series.



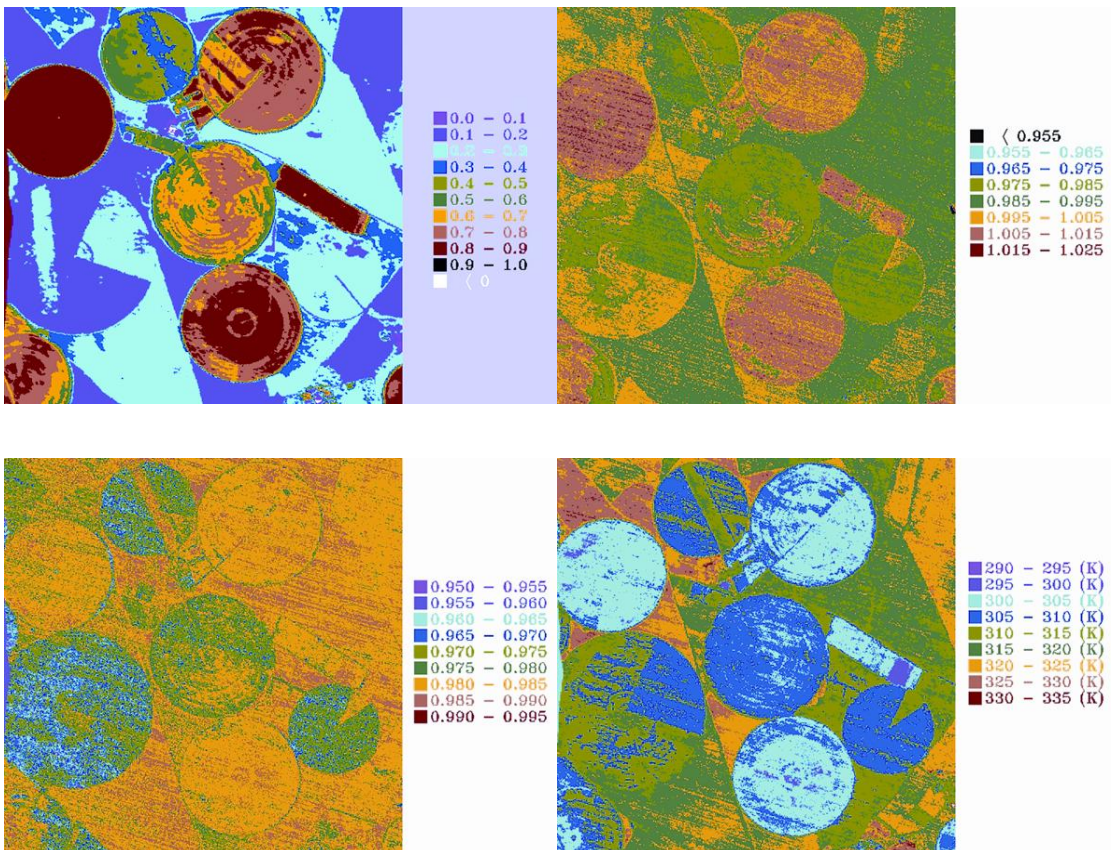
(page 564) **Figure 5.** Difference of the percentiles 90% and 10% of the variability series extracted with wavelet analysis from the VEGETATION NDVI time series



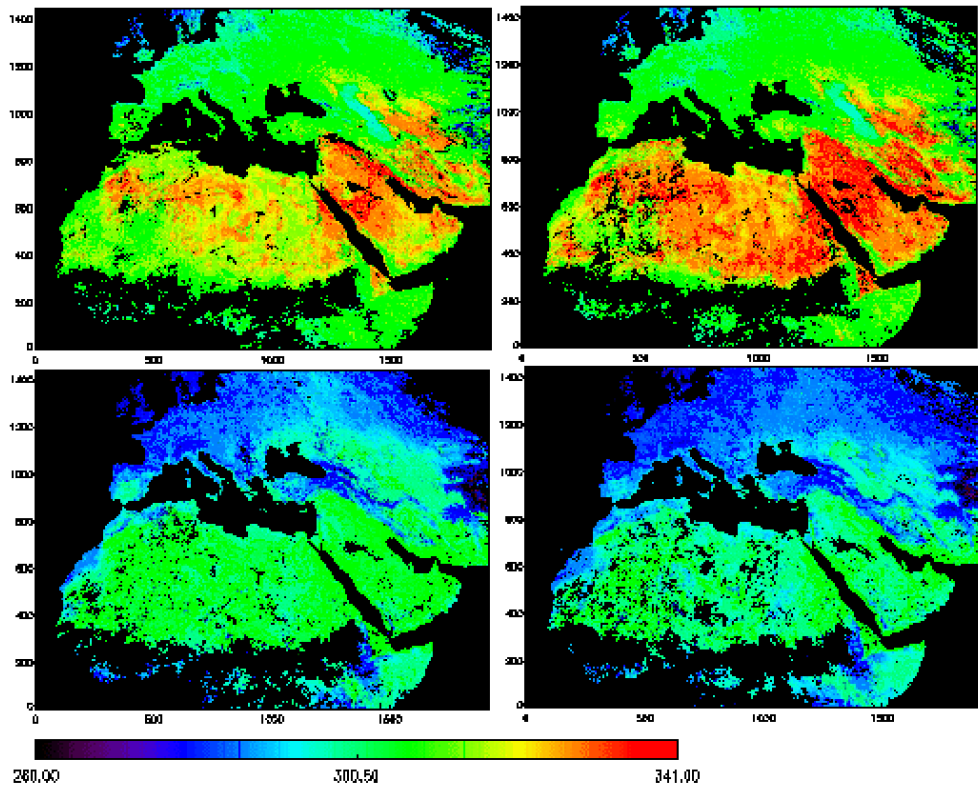
(page 564) **Figure 6.** Linear slope of the trend series extracted with wavelet analysis from the VEGETATION NDVI time series



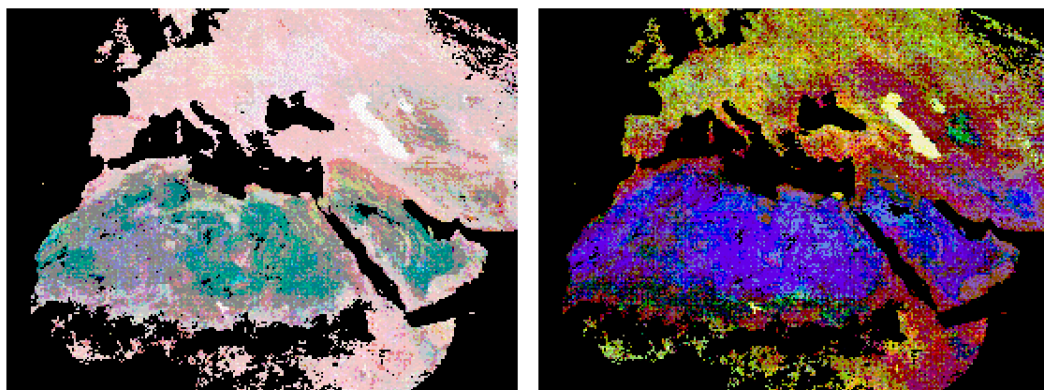
(page 571) **Figure 7.** The Barrax test site. False colour composite (RGB) using DAIS bands 10 (0.659 μ m), 4 (0.553 μ m) and 1 (0.498 μ m).



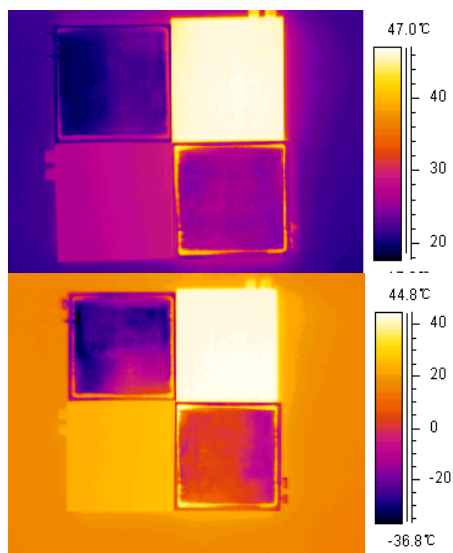
(page 571) **Figure 8.** Biophysical parameters maps from DAIS data: (a) NDVI map, (b) relative emissivity map applying the NOR method, (c) mean absolute emissivity map applying the NEM and (d) land surface temperature using a two-channel method and the emissivity image obtained with the NEM.



(page 582) **Figure 4.** Spatial distribution of the LST diurnal variation in the regions of Europe, North Africa and Mid East

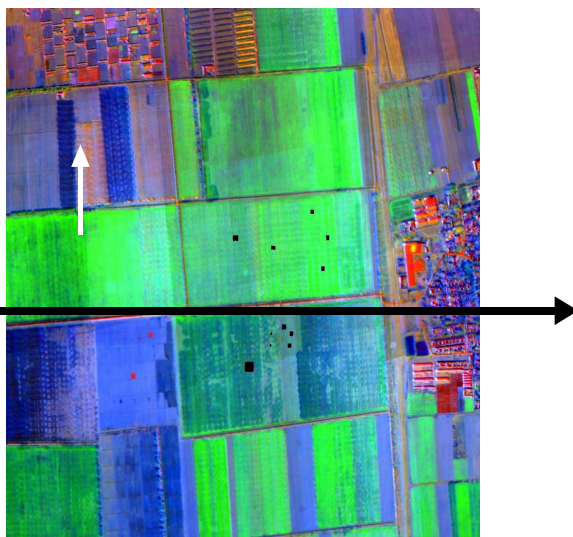


(page 582) **Figure 5.** Color composite image of the retrieved surface emissivities. (a) bands 29, 22 and 20 as RGB components, (b) bands 29, 31 and 32 enhanced by the equalization histogram method as RGB components.

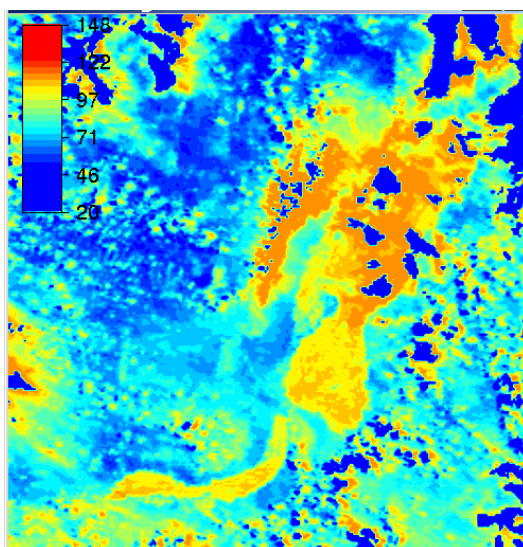


(page 592) **Figure 2.**

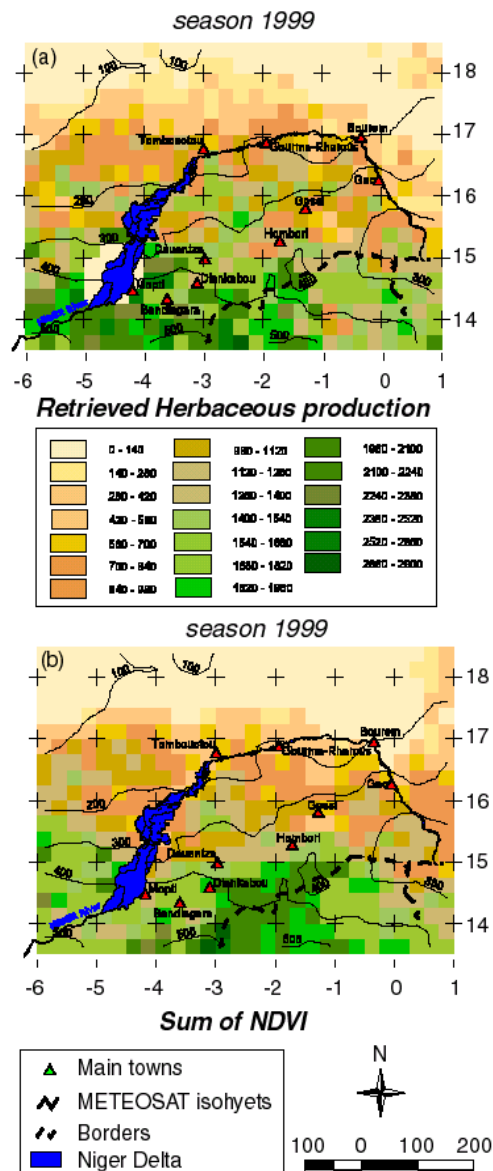
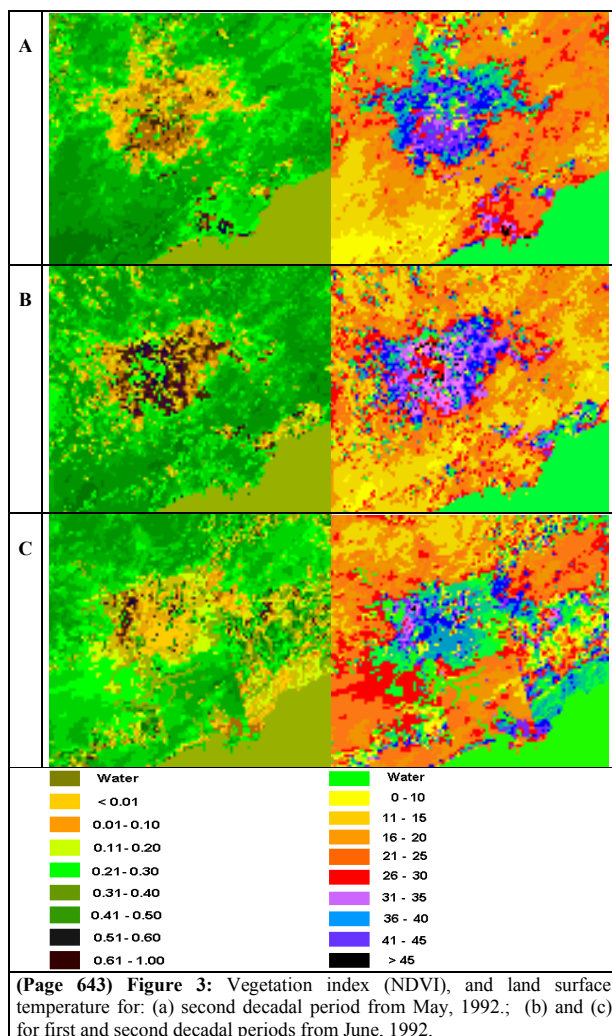
Radiometric temperatures of four sub-pixels
upper image: in tent, right image: out of tent.



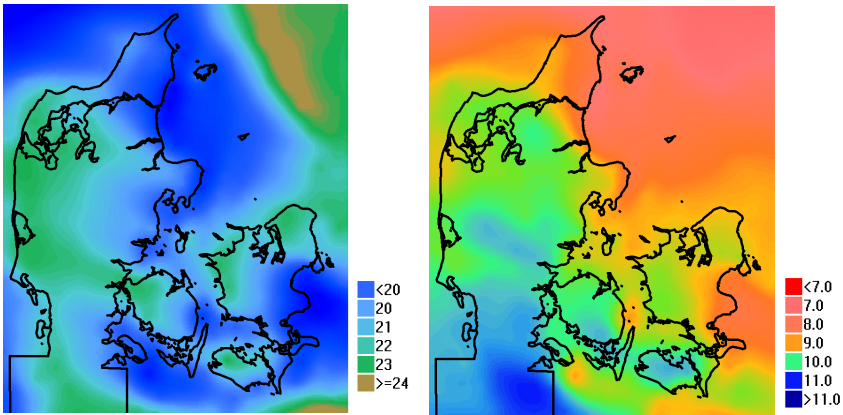
(page 603) **Figure 3.** Distribution of sample in the ground synchronism test area. (the black line is the flight course and the black boxes are the samples)



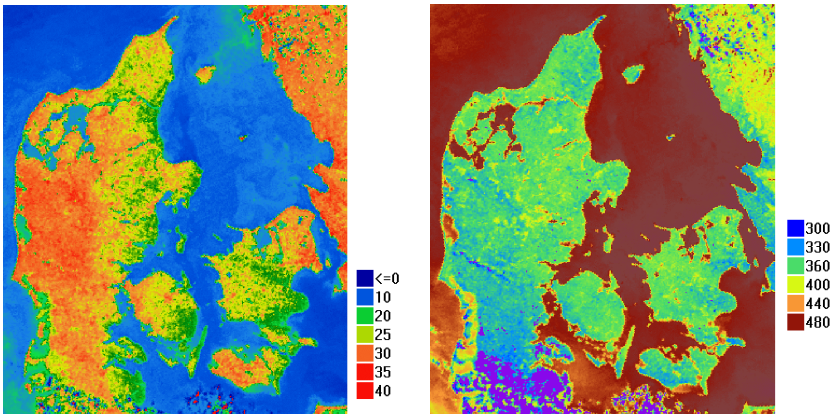
(page 622) **Figure 7.** Images of latent heat flux inverted by the model using differential thermal inertia parameter.



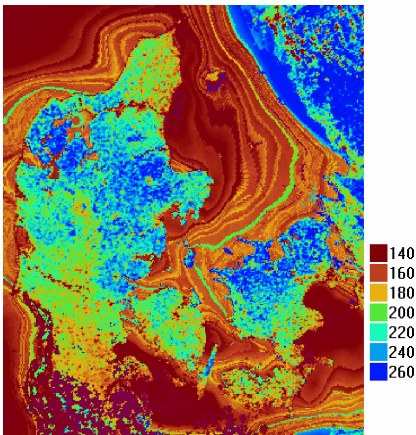
(Page 808) **Figure 5 :** Herbaceous production map estimated from the WSC data set during and the associated colorbar (a). NDVI sum acquired by the VEGETATION instrument on board SPOT4 (b). Isohyets computed from METEOSAT rainfall estimates and a mask delimiting the Niger river and delta have been added.



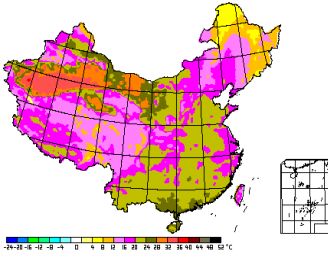
(Page 648) Fig. 1.
HIRLAM predicted air temperature in degrees Celsius (left) and air humidity in g m^{-3} (right). Denmark, 29th April 2000 at 12.00 GMT.



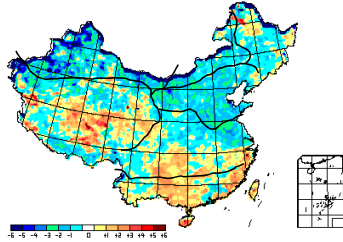
(Page 648) Fig. 2.
Surface temperature in degrees Celsius (left) and net radiation in W m^{-2} (right) calculated from NOAA-AVHRR. Denmark, 29th April 2000 at 14.00 GMT. The dark blue dots in the lower part of the surface temperature image (left) illustrates very low temperatures due to cloud coverage.



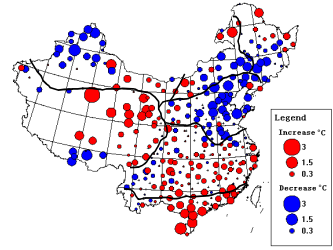
(Page 648) Fig. 3. Evapotranspiration rates in W m^{-2} calculated using HIRLAM weather predictions and NOAA-AVHRR observations. Denmark, 29th April 2000 at 14.00 GMT.



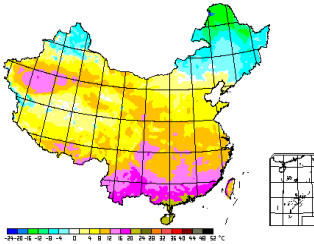
(Page 674) Figure 1 The map of annual LST



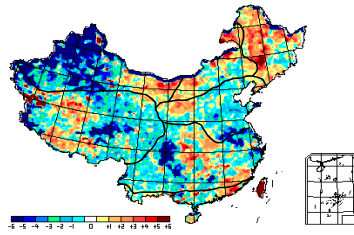
(Page 674) Figure 2 The annual change map of LST



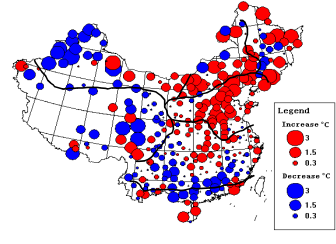
(Page 674) Figure3 The annual change map of 0cm surface temperature



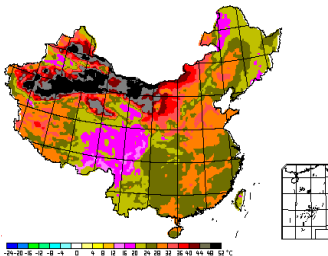
(Page 674) Figure 4 The map of average LST in January



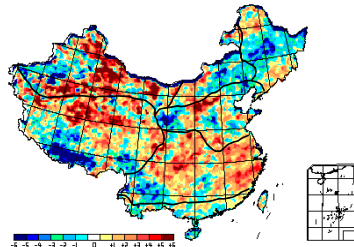
(Page 674) Figure 5 The change map of average LST in January



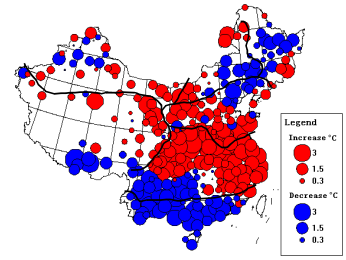
(Page 674) Figure 6 The change map of average 0cm surface temperature in January



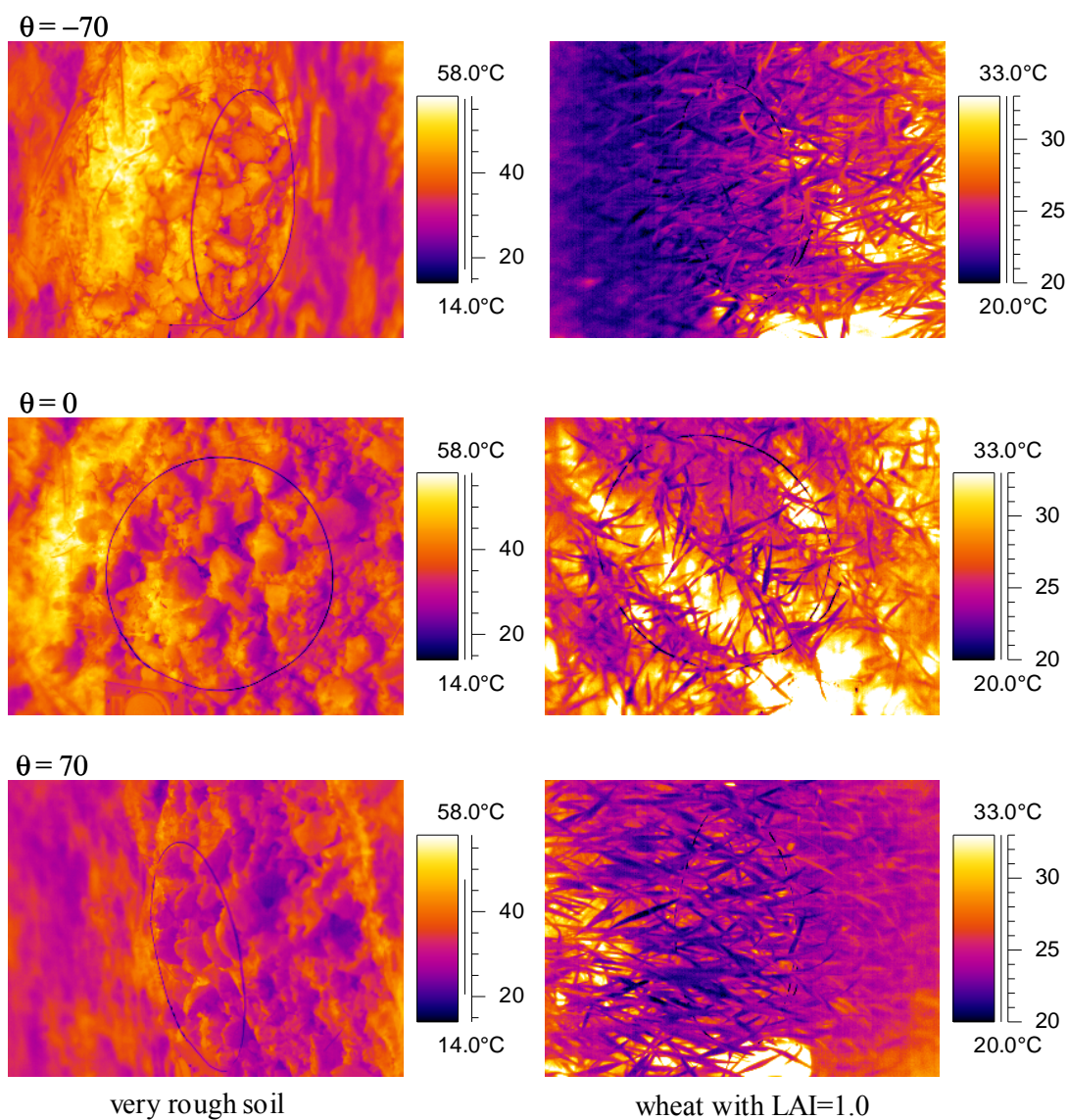
(Page 674) Figure 7 The map of average LST in July



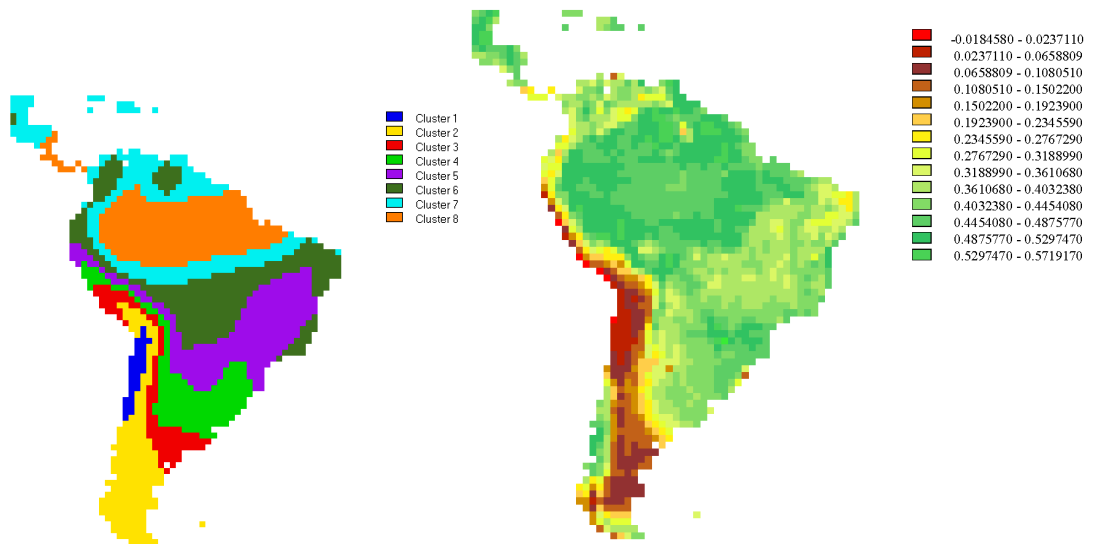
(Page 674) Figure 8 The change map of average LST in July



(Page 674) Figure 9 The change map of average 0cm surface temperature in July

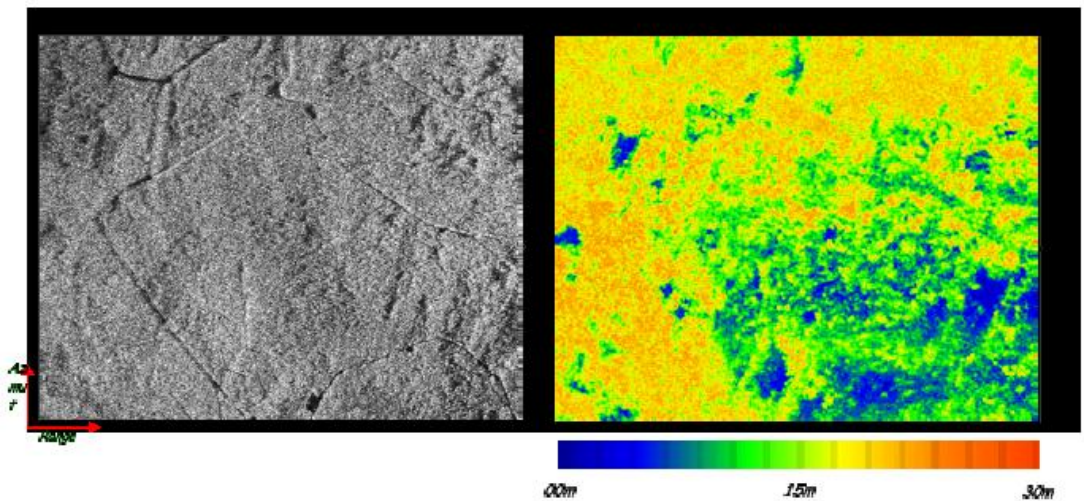


(page 682) **Figure 3.** Illustration of thermal images for different view angles with different surface types. The metal ring is recognizable and varies with view angle on the image.

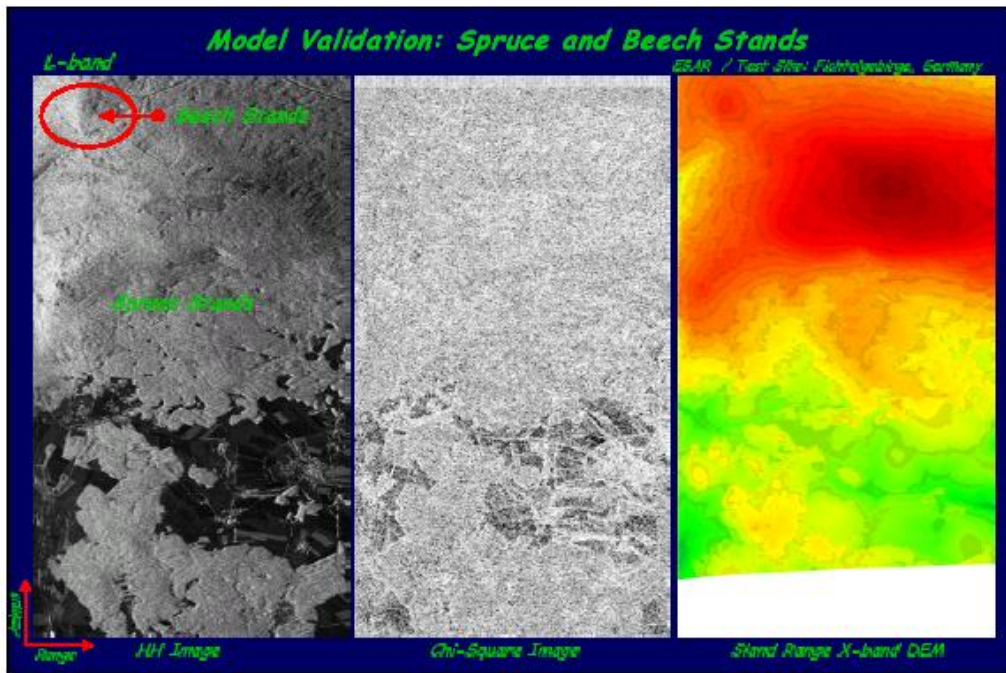


(Page 701) **Figura 2.-** Resultado del análisis de cluster sobre los valores medios mensuales de W utilizando la distancia euclidiana como medida de similitud

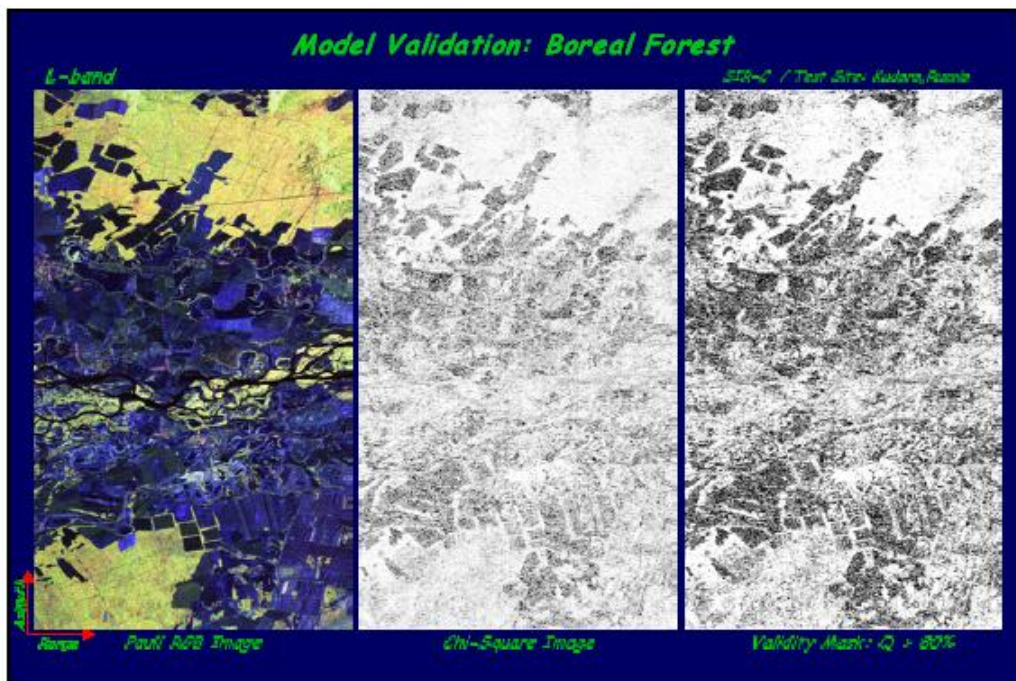
(Page 704) **Figura 3.-** Valores medios de NDVI para América del sur.



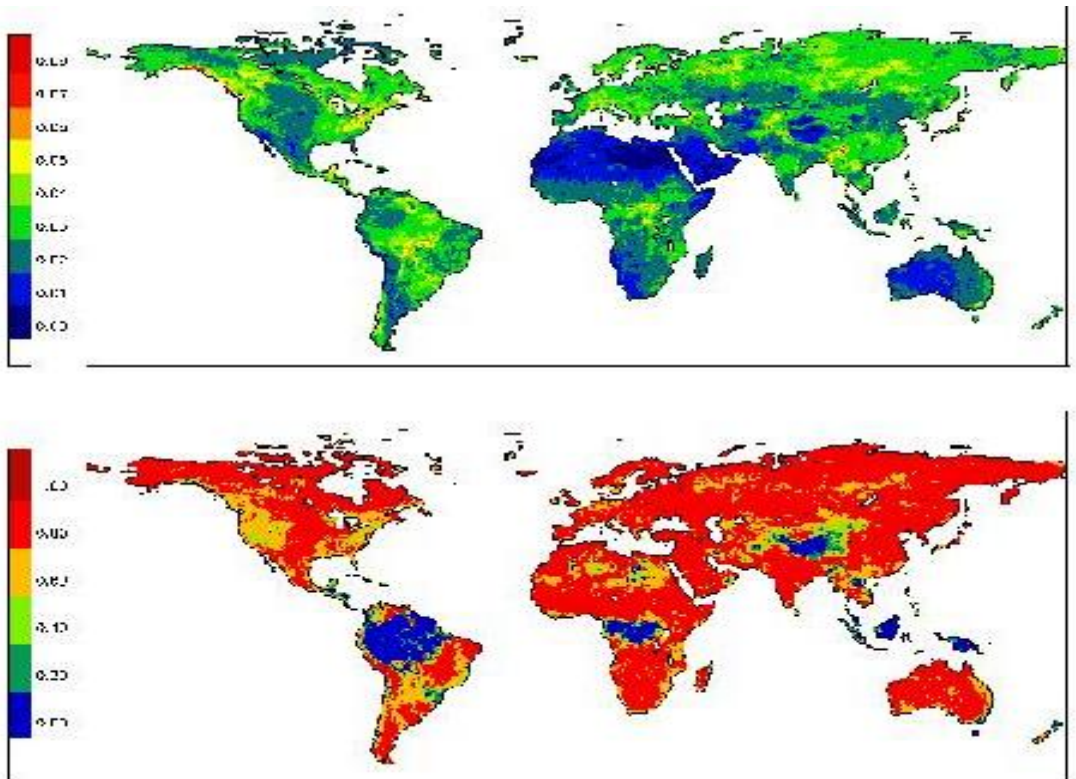
(Page 737) **Figure 2:** Left: L-band SAR Image. Right: Corresponding Forest Height Map



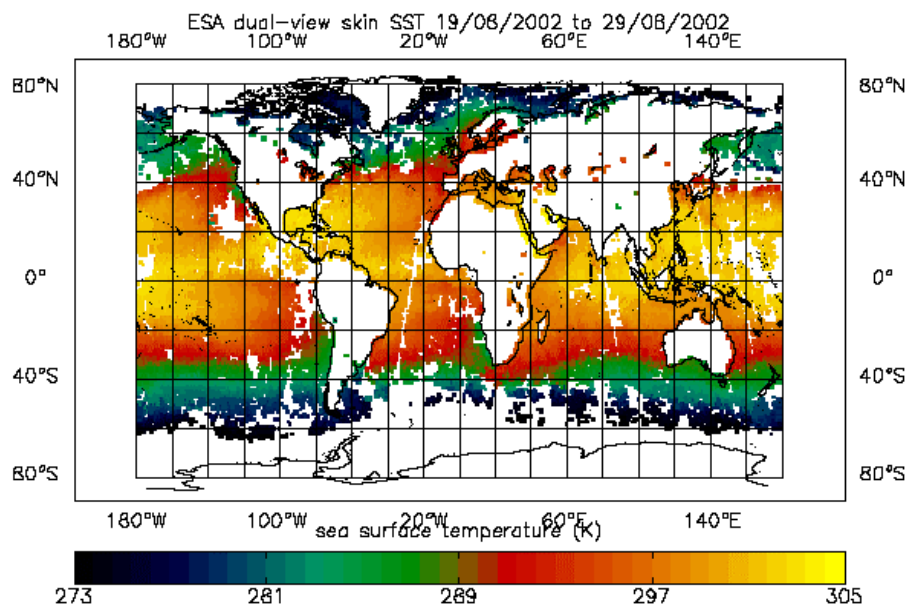
(Page 738) **Figure 4:** Left: SAR Image, Middle Q Map (White $Q=1$, black $Q=0$). Right: DEM of the Fichtelgebirge Test Site



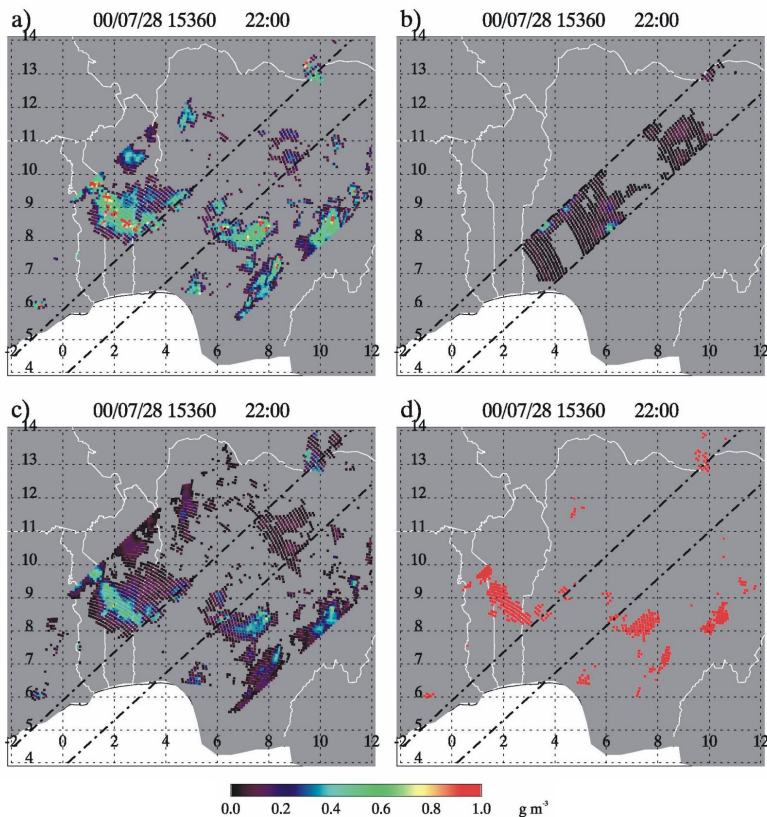
(Page 738) **Figure 5:** Left: SAR Image, Middle Q Map, Right Mask for $Q > 80\%$ for the Kudara Test Site



(Page 748) **Figure 1** Spatial distribution of the scores in soil moisture retrievals using LRM, for a 1 K noise level, in 1988: (top) RMS error, (bottom) efficiency. (Pellarin et al., 2002b).

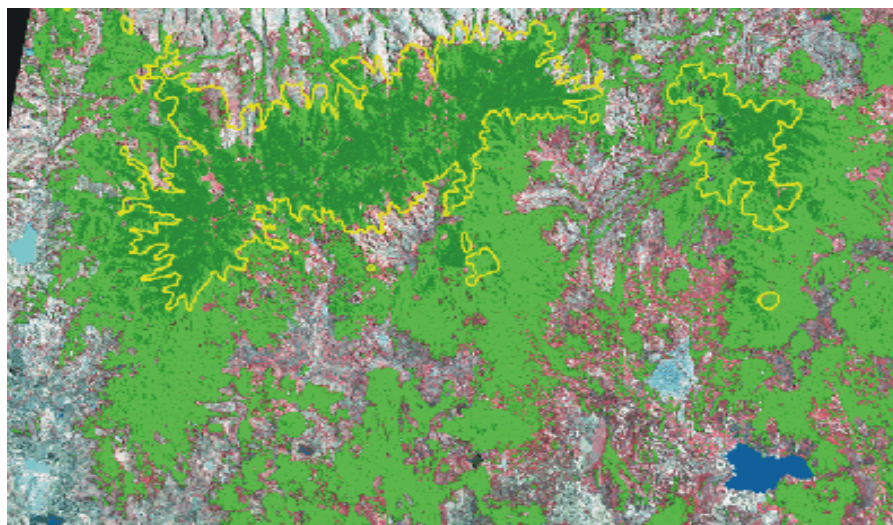


(Page 857) **Figure 1:** Spatially averaged, global SST data derived from AATSR data (Source: UK Met Office)

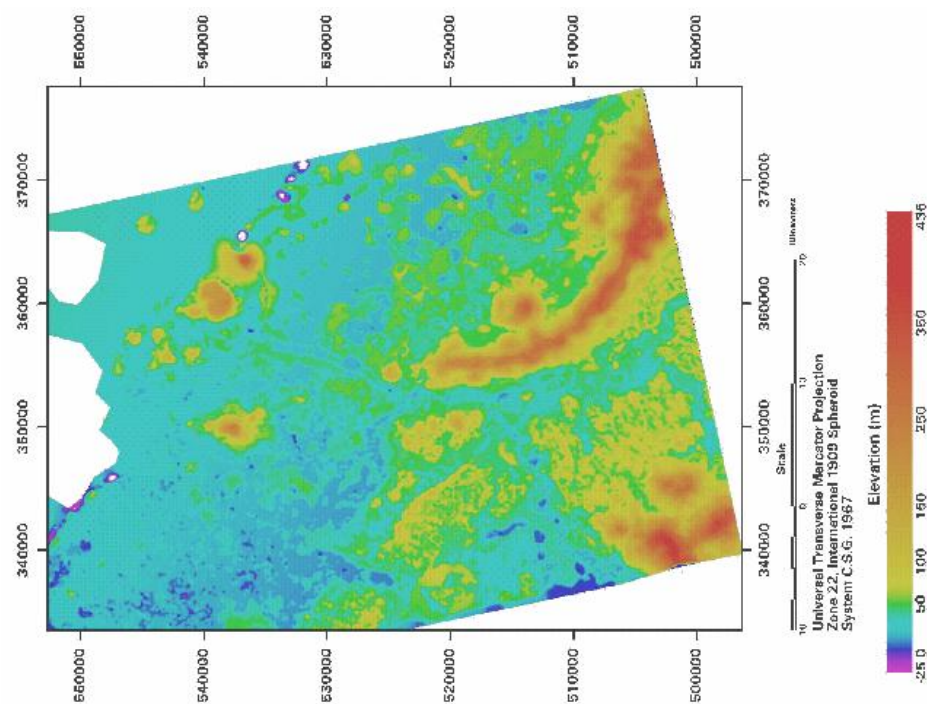


(Page 756) Fig. 4:
Distributions of retrieved rain water content for orbit 15360 on 28. July 2000 over Benin and Nigeria from (a) 2A12 V.5 algorithm, (b) PR estimates averaged to TMI reference resolution, (c) calibrated estimates from PI, and (d) pixels where the Ferraro et al. (1998) scattering index indicates rain.

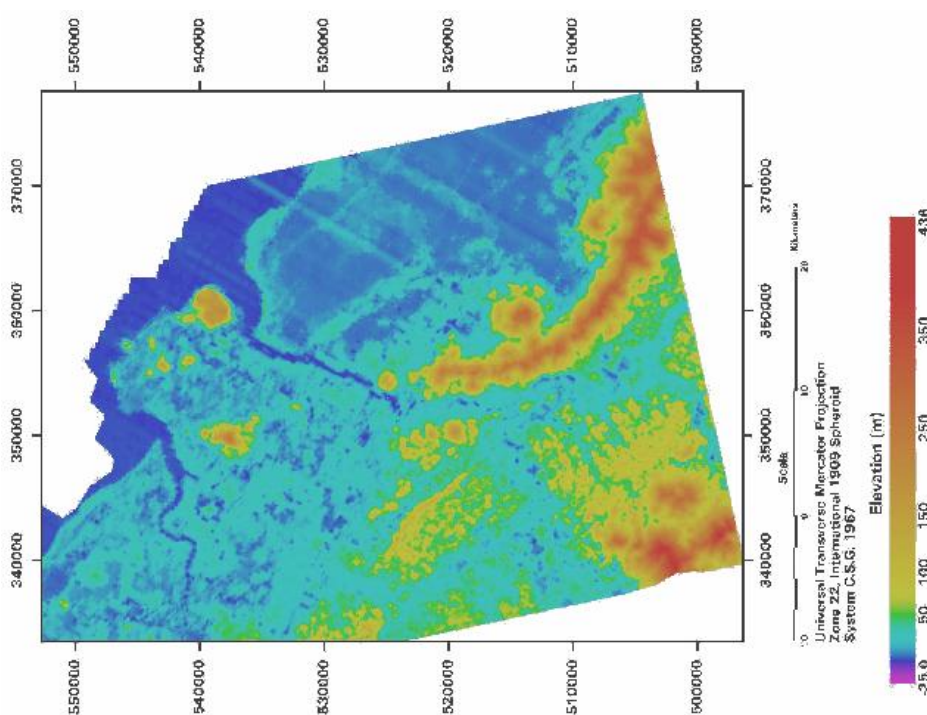
(Page 878) Figura 1: Imagen SPOT de la reserva de la mariposa monarca, del 18 de enero de 1999. En verde, superposición de la clasificación de la vegetación forestal: verde oscuro, bosque de oyamel; verde claro, otros tipos de bosque. En amarillo, superposición de la curva de nivel correspondiente a 3,000 metros de altitud.

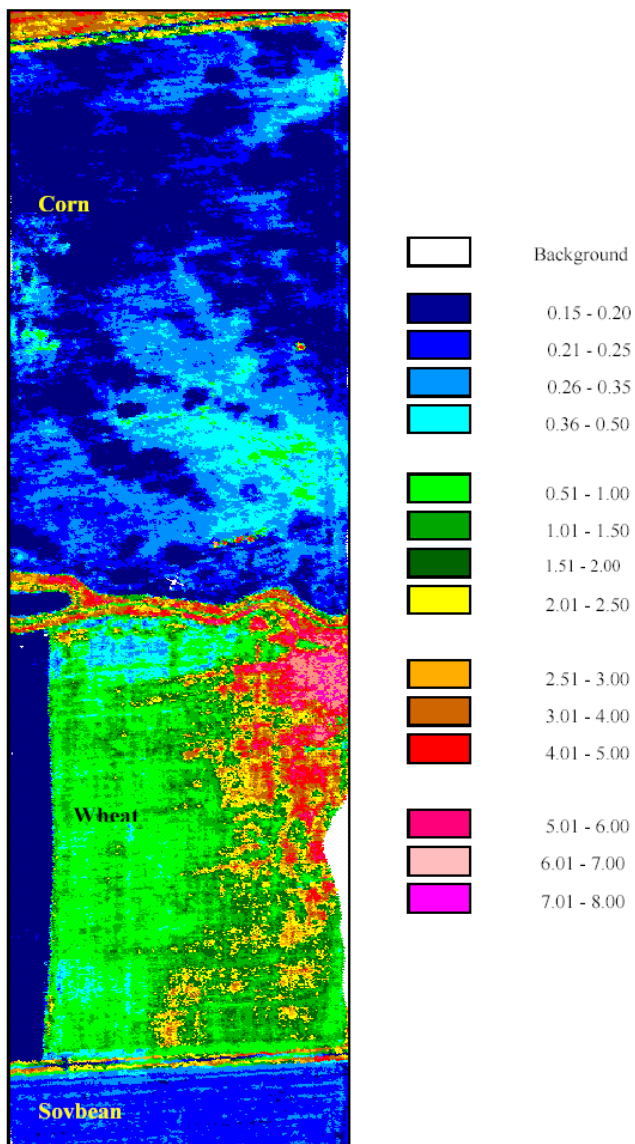


(Page 812) Figure 2 Corrected SAR DEM.



(Page 815) Figure 5 Final DEM obtained by merging a radargammmetric DEM and airborne laser data.





(Page 899) Figure 6: Map of green LAI determined with MCARI2-based algorithm from a CASI hyperspectral image.



(Page 929) Fig.1. Composición 4/3/2 RGB realzada mediante expansión lineal del contraste.



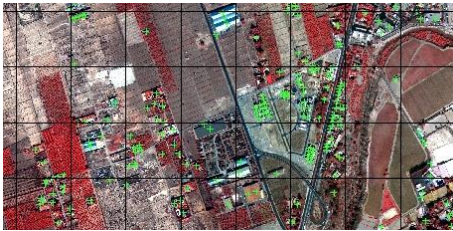
(Page 929) Fig. 2. Composición 2/4/1.



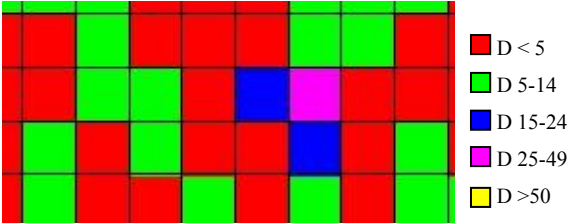
(Page 929) Fig. 3. Composición 4/3/2 RGB filtrada mediante filtro de realce de bordes 3x3 y realizada mediante expansión lineal del contraste.



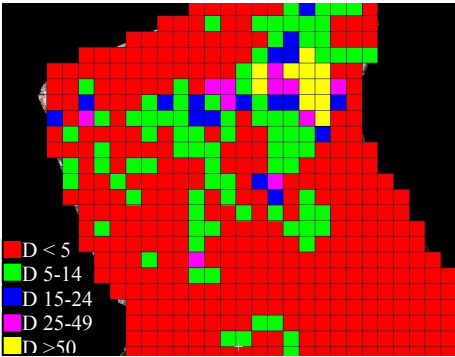
(Page 930) Fig. 4. Detalle de la composición 4/3/2 RGB de Ikonos realizada mediante expansión lineal del histograma.



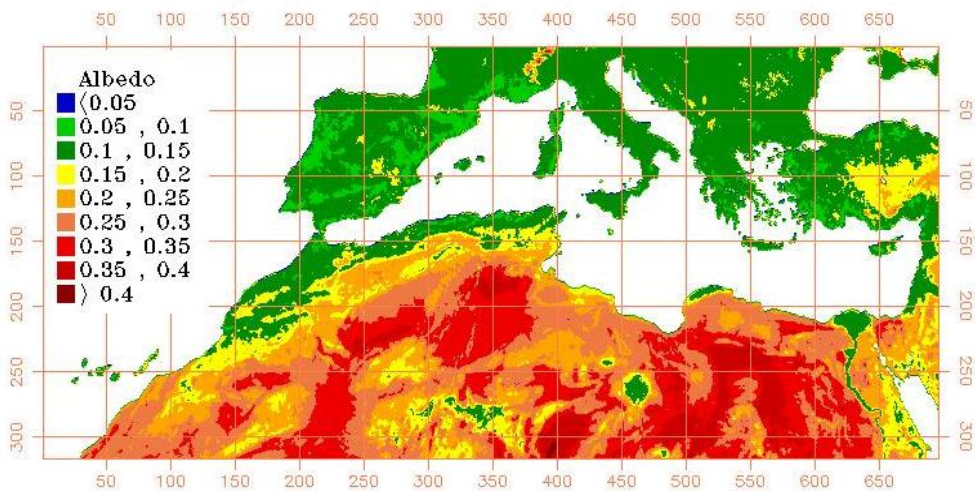
(Page 930) Fig. 5. Detalle del mapa de los edificios marcados sobre composición 4/3/2 RGB de Ikonos realizada mediante expansión lineal del histograma.



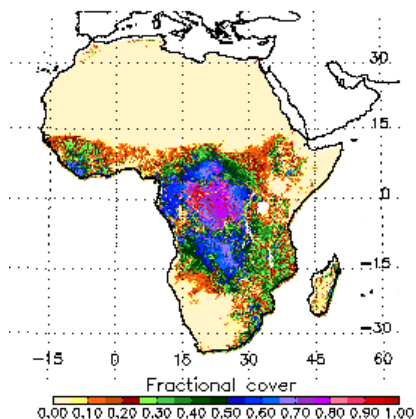
(Page 930) Fig. 6. Mapa de densidades por cuadrículas. A cada color lo corresponde una clase de densidad.



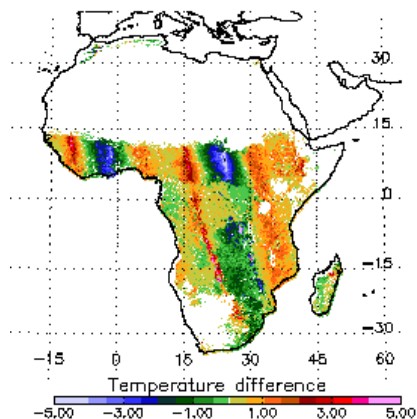
(Page 932) Fig. 8. Mapa de densidad de edificaciones para la pedanía de El Palmar (Murcia).



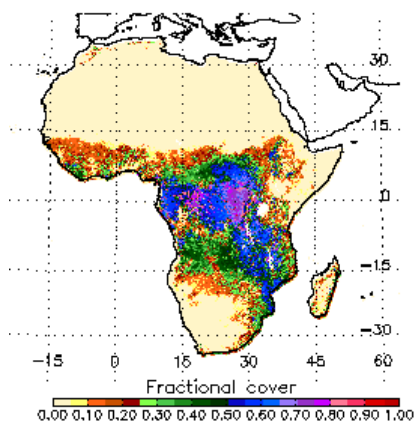
(Page 936) Figure 2.- Image of the Total Average of albedo.



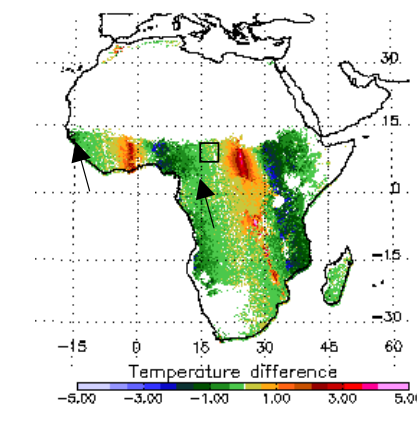
(Page 975) **Figure 2:** Sunlit crown fractional cover as viewed by the AVHRR NOAA-14, on DOY 71, 1998.



(Page 976) **Figure 4:** Differences in simulated temperature observed by NOAA-14 AVHRR between DOY 71 1998 and DOY 75 1998, due strictly to sun-target-sensor geometry.



(Page 975) **Figure 3:** Sunlit crown fractional cover as viewed by the AVHRR NOAA-14, on DOY 75, 1998.s



(Page 976) **Figure 5:** Differences in temperature between AVHRR NOAA-14 geometry and view nadir observation, for DOY 75 1998.